

# Encyclopedia of Nanoscience and Nanotechnology

Volume 6 Number 1 2004

- |                        |   |            |
|------------------------|---|------------|
| <a href="#">▶ view</a> | Nanoanalysis of Biomaterials<br><i>Matthias Mondon; Steffen Berger; Hartmut Stadler; Christiane Ziegler</i>           | <u>1</u>   |
| <a href="#">▶ view</a> | Nanoassembly for Polymer Electronics<br><i>Tianhong Cui; Yuri Lvov; Jingshi Shi; Feng Hua</i>                         | <u>23</u>  |
| <a href="#">▶ view</a> | Nanobiosensors<br><i>Tuan Vo-Dinh</i>   | <u>53</u>  |
| <a href="#">▶ view</a> | Nanocables and Nanojunctions<br><i>Yuegang Zhang; Weiqiang Han; Gang Gu</i>   | <u>61</u>  |
| <a href="#">▶ view</a> | Nanocapsules<br><i>Zhi-dong Zhang</i>   | <u>77</u>  |
| <a href="#">▶ view</a> | Nanocatalysis<br><i>S. Abbet; U. Heiz</i>   | <u>161</u> |
| <a href="#">▶ view</a> | Nanochemistry<br><i>Sebastian Polarz</i>  | <u>179</u> |
| <a href="#">▶ view</a> | Nanocluster Characterization by EXAFS Spectroscopy<br><i>Giuseppe Faraci</i>  | <u>197</u> |
| <a href="#">▶ view</a> | Nanoclusters and Nanofilaments in Porous Media<br><i>Parasuraman Selvam</i>   | <u>215</u> |
| <a href="#">▶ view</a> | Nanocomposites of Polymers and Inorganic Particles<br><i>Walter Caseri</i>  | <u>235</u> |
| <a href="#">▶ view</a> | Nanocomputers: Theoretical Models<br><i>Michael P. Frank</i>  | <u>249</u> |
| <a href="#">▶ view</a> | Nanocontainers<br><i>Samantha M. Benito; Marc Sauer; Wolfgang Meier</i>   | <u>301</u> |
| <a href="#">▶ view</a> | Nanocrystal Memories<br><i>E. Kapetanakis; P. Normand; K. Beltsios; D. Tsoukalas</i>                                  | <u>321</u> |
| <a href="#">▶ view</a> | Nanocrystalline Aluminum Alloys<br><i>Livio Battezzati; Simone Pozzovivo; Paola Rizzi</i>                             | <u>341</u> |
| <a href="#">▶ view</a> | Nanocrystalline and Amorphous Magnetic Microwires<br><i>A. Zhukov; J. González; M. Vázquez; V. Larin; A. Torcunov</i> | <u>365</u> |

<a href="#">▶ view</a>	Nanocrystalline Barium Titanate <i>Jian Yu; Junhao Chu</i>	<a href="#"><u>389</u></a>
<a href="#">▶ view</a>	Nanocrystalline Ceramics by Mechanical Activation <i>J. M. Xue; Z. H. Zhou; J. Wang</i>	<a href="#"><u>417</u></a>
<a href="#">▶ view</a>	Nanocrystalline Diamond <i>Narendra B. Dahotre; Padmakar D. Kichambare</i>	<a href="#"><u>435</u></a>
<a href="#">▶ view</a>	Nanocrystalline Phosphors <i>Guangshun Yi; Baoquan Sun; Depu Chen</i>	<a href="#"><u>465</u></a>
<a href="#">▶ view</a>	Nanocrystalline Silicon Superlattices <i>David J. Lockwood; Leonid Tsybeskov</i>	<a href="#"><u>477</u></a>
<a href="#">▶ view</a>	Nanocrystalline Silicon: Electron Spin Resonance <i>Takashi Ehara</i>	<a href="#"><u>495</u></a>
<a href="#">▶ view</a>	Nanocrystalline TiO <sub>2</sub> for Photocatalysis <i>Hubert Gnaser; Bernd Huber; Christiane Ziegler</i>	<a href="#"><u>505</u></a>
<a href="#">▶ view</a>	Nanocrystals Assembled from the Bottom Up <i>Edson Roberto Leite</i>	<a href="#"><u>537</u></a>
<a href="#">▶ view</a>	Nanocrystals from Solutions and Gels <i>Marc Henry</i>	<a href="#"><u>555</u></a>
<a href="#">▶ view</a>	Nanocrystals in Organic/Inorganic Materials <i>Peter Reiss; Adam Pron</i>	<a href="#"><u>587</u></a>
<a href="#">▶ view</a>	Nanodeposition of Soft Materials <i>Seunghun Hong; Ling Huang</i>	<a href="#"><u>605</u></a>
<a href="#">▶ view</a>	Nanodielectrophoresis: Electronic Nanotweezers <i>P. J. Burke</i>	<a href="#"><u>623</u></a>
<a href="#">▶ view</a>	Nanoelectromechanical Systems <i>Josep Samitier; Abdelhamid Errachid; Gabriel Gomila</i>	<a href="#"><u>643</u></a>
<a href="#">▶ view</a>	Nanoelectronics with Single Molecules <i>Karl Sohlberg; Nikita Matsunaga</i>	<a href="#"><u>665</u></a>
<a href="#">▶ view</a>	Nanoembossing Techniques <i>Yong Chen</i>	<a href="#"><u>683</u></a>
<a href="#">▶ view</a>	Nanofabrication by Glancing Angle Deposition <i>Brian Dick; Michael J. Brett</i>	<a href="#"><u>703</u></a>
<a href="#">▶ view</a>	Nanofibers <i>Jason Lyons; Frank K. Ko</i>	<a href="#"><u>727</u></a>



<a href="#">▶ view</a>	Nanofluidics <i>P. Mela; N. R. Tas; A. van den Berg; J. E. ten Elshof</i>	<u>739</u>
<a href="#">▶ view</a>	Nanofluids <i>Stephen U. S. Choi; Z. George Zhang; Pawel Koblinski</i>	<u>757</u>
<a href="#">▶ view</a>	Nanohelical/Spiral Materials <i>S. Motojima; X. Chen</i>	<u>775</u>
<a href="#">▶ view</a>	Nanoicosahedral Quasicrystal <i>J. Saida; A. Inoue</i>	<u>795</u>
<a href="#">▶ view</a>	Nanomagnetics for Biomedical Applications <i>Chong H. Ahn; Jin-Woo Choi; Hyoung J. Cho</i>	<u>815</u>
<a href="#">▶ view</a>	Nanomagnets for Biomedical Applications <i>Pedro Tartaj</i>	<u>823</u>
<a href="#">▶ view</a>	Nanomaterials by Severe Plastic Deformation <i>Yuntian T. Zhu; Darryl P. Butt</i>	<u>843</u>
<a href="#">▶ view</a>	Nanomaterials for Cell Engineering <i>Xiaoyue Zhu; Tommaso F. Bersano-Begey; Shuichi Takayama</i>	<u>857</u>
<a href="#">▶ view</a>	Nanomaterials from Discotic Liquid Crystals <i>Gregory P. Crawford; Robert H. Hurt</i>	<u>879</u>

---

Copyright © 2004 American Scientific Publishers

# Nanoanalysis of Biomaterials

Matthias Mondon, Steffen Berger,  
Hartmut Stadler, Christiane Ziegler

*University of Kaiserslautern, Kaiserslautern, Germany*

## CONTENTS

1. Introduction
  2. Biomaterials
  3. Nanoanalytical Tools
  4. Nanoanalysis of Biomaterials
  5. Conclusions
- Glossary  
References

## 1. INTRODUCTION

Nanotechnology has been a fast-developing field over the last decade. Features of dimensions below 100 nm are an interesting and important field of studies in a world of miniaturization in engineering but as well in the already small world of biology. New methods of analysis have to be developed along the way, as conventional light microscopy techniques are unable to resolve features of these dimensions.

In this chapter recent progress in nanoanalytics in biomaterial respectively biointerface research is reviewed, focusing on publications that are relevant for the characterization of the surfaces of biomaterials rather than the characterization of biofilms on biomaterials.

Scanning probe microscopy (SPM) methods, that is, scanning force microscopy (SFM), scanning tunneling microscopy (STM), and related techniques are unique to investigate on a molecular and even on an atomic level surfaces and molecules interacting with them. Morphology and roughness are important parameters that can be characterized with them. Further fields are the spatial arrangement of chemical functional groups and their interaction with the surrounding medium.

The techniques based on the electron-sample interaction like scanning electron microscopy (SEM) and transmission electron microscopy (TEM) are also able to achieve material- or morphology-dependent information with nanometer resolution and are therefore important tools in biological and materials science.

The issue of nanotechnology has become also part of the world of biomaterials for production as well as for analysis to investigate phenomena occurring on this scale. Biomaterials include a wide range of metals and alloys, glasses and ceramics, natural and synthetic polymers, biomimetics, composites, and natural materials, including combinations of synthetic and living tissue components. Materials in contact with biological systems are of great relevance not only in medicine but for many applications in engineering, food processing [1], marine environments [2], and biosensing [3]. The use of biomaterials is therefore part of the larger area of biological surface science (BioSS) that stretches as well into areas like tissue engineering, biosensors and biochips for diagnostics, artificial photosynthesis, bioelectronics, and biomimetic materials [4]. The market volume for medical biomaterials exceeds a billion Euro per year. In the United States alone the current value is over 700 million Euro [5]. More than 500,000 arthroplastic procedures and total joint replacements are performed annually in the United States [6]. Clinical implants like artificial tooth replica, knee and hip joints, blood vessels, heart valves, and intraocular lenses are in use for many years now and applied with hundreds of thousands of patients improving their quality of life. A lot of materials consist of metals and ceramics but the use of polymers for new medical products and materials has increased strongly over the last decades to keep improving current health care procedures.

These biomaterials must meet the demands of materials science on various length scales as well as clinical requirement. The mechanical specifications range from high loads in implantology for hip and knee replacements to high elasticity of artificial blood vessels. They have to be accompanied by others, for example, high transmittance in intraocular or contact lenses. In many cases blood compatibility with suppression of blood coagulation between the physiological environment and the biomaterial surface is necessary. A good understanding of the interaction with the biological environment, namely with biomolecules like proteins, cells and tissue, is crucial in order to be able to improve the functionality of biointerfaces. This interaction is essential for many applications like lubrication, adhesion, and recognition

in biological systems and for biocompatibility of the implant interface [7].

The interface is important for biomaterials, as it defines the interaction with the environment. The knowledge of the surface structure, the surrounding medium in direct contact (e.g., water structure [8]), and the chemical composition is essential to understand further reactions taking place at the biomaterial's surface. The interface structures are in dimensions of a few nanometers for proteins up to the micrometer range for cells in the field of biomaterials. In Figure 1 an overview of the interfaces on different scales is presented to show the parameters that can be of interest.

Macroscopically, the shape of an implant, the structure, and its mechanical stability are important. The microscopic level is determined by the morphology (i.e., the domain structure, the presence of ionic groups, and the chemical composition respectively modification), the topography (i.e., the surface roughness, planarity, and feature dimensions), and the hardness respectively elasticity (Young's modulus). These characteristics determine other features like wetting behavior and interaction forces (inter- and intramolecular) including cell-surface or cell-cell interactions. Various degrees of information about these properties can be

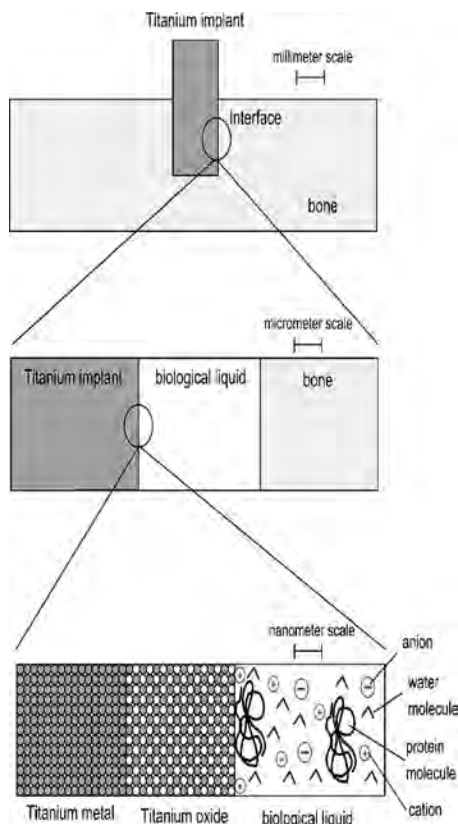


**Figure 1.** Different relevant length scales in biomaterials research demonstrated at hand of a bone implant. The biomaterial-tissue interaction is based on molecular events, which affect meso- and macroscopic material properties. On larger scales additional (e.g., cellular, mechanical) effects resulting from combining individual units (molecules, cells, crystallites) to a more extended ensemble arise.

obtained using different analysis methods including microscopic and spectroscopic methods.

The field of investigation is extending further as the material properties have to be characterized after manufacturing, sterilization, before and after clinical insertion, and before, after, and especially during the immersion in simulated natural environments. The resulting changes of the interaction, namely corrosion and the buildup of a biofilm, have to be characterized. The surface properties as well should be characterized thoroughly as it is essential for correlating any surface modifications with changes in biological performance.

In the following, techniques that are able to resolve features of materials on the nanometer scale (Section 3) as well as applications for biomaterial research (Section 4) are presented. The whole topic is introduced by a more general discussion of functionality, properties, and types of biomaterials (see Section 2). The focus in experimental work will be put on methods investigating materials on the nanometer scale, that apply to nanometer resolution in x-, y-, and z-direction. Methods leading to a resolution in the nanometer regime in only one or two dimensions will be described only shortly.

Investigations of the above introduced groups of biomaterials including metals, ceramics, polymers as well as biological specimens are presented. In the context of this review biomaterials are defined as materials used in medicine which are in contact with the tissue of the patient. Therefore special emphasis will be put on medical implant materials and the characterization with scanning probe techniques. Experiments dealing with hard tissues like teeth and bone and the influences of substrates on biofilm formation will be briefly mentioned.

## 2. BIOMATERIALS

Biomaterials can be classified with respect to their chemical composition and their use. Generally, the following criteria have to be fulfilled by biomaterials:

- **Functionality:** The biomaterial must replace at least in the important parts natural body functions. This means that, for example, for bone substitution a suitable mechanical stability has to be achieved.
- **Biocompatibility:** The biomaterial must not cause negative body reactions resulting, for example, in inflammation. Furthermore, a good integration into the body environment is favorable.
- **Aesthetical aspects:** Biomaterials used for external implants should not deface the patient. Preferably, they should look like the replaced tissue.

Surface properties influence strongly the mechanical function, the biochemical interaction, and the optical appearance of the biomaterial. Therefore the interface of the materials deserves special interest in investigation, control, and modification of properties to reach the criteria mentioned above.

Mechanical aspects are relevant for applications which require force transfer (e.g., bone substitution), which impose dynamic loads on, for example, artificial joints, and which, for example, in the case of substitutes for blood vessels, meet certain hydrodynamic respectively fluid-mechanical properties. The interaction of the biomaterial with the body

environment concerns the tissue contact (cell adhesion and fixation), the tissue organization (cell-to-cell linkage and communication), and the exchange of substances across the interface. Optical appearance is determined by light transmission (e.g., of contact lenses) or light reflection (e.g., of natural looking tooth replacements). Mechanical, biochemical, and optical properties depend mainly on the topography and the chemistry of the surface.

Topography may be defined as size, shape, distribution, and hierarchy of surface features. These features are either discrete (holes and peaks) or continuous (furrows and ridges) in random (statistical), fractal (self-similar on different length scales), or periodic distribution across the surface. Rough surfaces exhibit a larger surface area and more contact points for biological molecules and cells. The reason for larger entities like cells to adhere to the surface and how they arrange their layer growth is dependent on the size and distribution of the surface features: Cavities which are smaller than single cells cannot be colonized, while larger structures regulate the direction, connectivity, and differentiation of the growing cell layer. A hierarchical surface consists of structure elements with increasing complexity, for example, two-dimensional planes scrolled up to three-dimensional fibers which are organized in three-dimensional fiber composites. Examples of those materials were synthesized with carbon nanotubes with increased mechanical stability and electrical conductivity and decreased thickness compared to common wires [9–11]. In principle such materials are also interesting for biomaterials as on one hand they show a very large surface area and on the other hand they enable combinations of surface sections with different properties and therefore different cell types within a single superstructure.

The chemical properties of the interface between biomaterial and body environment determine the interaction of the surface with water molecules, ions, biological macromolecules, and cells. The surface reactivity depends on the chemical composition, the production process, and the pretreatment before use of the materials and is essential for fixation, growth, and proliferation of tissue and bone cells. Cell adherence via membrane receptors and adhesion proteins is influenced by active surface groups (generated, e.g., by oxidation of metals or coating of materials with specially designed polymer layers) which regulate the adsorption of the anchoring protein layer. The functionalization of the substrate additionally controls the wetting behavior where particularly hydrophilic surfaces show enhanced cell adhesion. The latter is due to the fact that systems like cells and hydrophilic surfaces reach a thermodynamically favorable state by combining their high-energy surfaces. In addition, even hydrophobic interfaces like gold can get more hydrophilic by protein adsorption [12] which may help to increase biocompatibility. Polarizability and charging of the interface affect electrostatic interactions between charged species and the surface. Charge screening and complexation by multivalent ions present in all types of body fluids allow attraction between molecular and surface groups of like charges and stabilize the biological layers. At conductive interfaces electrochemical reactions with charge transfer between the electrolyte solution and the substrate may occur, which interfere with the cellular metabolism and the

conformation of adsorbed adhesion proteins. This can set free toxic substances and cause allergic and inflammatory body reactions.

Topographical as well as chemical effects play a role for tribological properties of biomaterials. Tribology describes the behavior of interfaces in motion and gets important when implants are designed to support body movements. In this case friction, wear, and lubrication of implant and body respectively different moving implant elements influence function and longevity of the applied biomaterial. Interfacial friction depends on kind and strength of interaction forces, the clasping of surface uprisings and troughs, and force transfer properties of intermediate fluids. Hardness, cohesion, and adhesion of the individual surfaces in contact determine to what extent the materials are worn off by abrasion (e.g., scratch and particle formation), adhesion (e.g., welding processes), and surface fatigue (e.g., crack formation). Liquid films in the crevice between two hard surfaces can reduce friction and wear. The effect of such lubricants is influenced by surface chemistry and separation as well as by the viscoelastic and hence force transferring properties of the fluids themselves.

This comprehensive discussion of biomaterials in view of surface properties shows that the interplay between implant and body environment can be very complex and includes a large variety of parameters from materials science, biology, and medicine explained in more detail in [7]. The need of surface analysis with nanometer resolution arises on one hand from the importance of the interface between natural and artificial material and on the other hand from the high dependence of the macroscopic behavior on the microscopic appearance of the biomaterial.

In the following the main different chemical substance classes for biomaterials will be described shortly.

Biomaterials can be divided into native materials like teeth and bone, and artificial biomaterials which are in contact with biological systems like implants in medicine. Within these fields the materials in their actual state of occurrence and model surfaces like thin layers on supports are under investigation.

The three *metal* systems mainly utilized in implantology are stainless steel, cobalt-chromium alloys, and titanium. Such metals are mainly used in bone replacement and here titanium is the most important metal because of its good biocompatibility and nearly bonelike mechanical properties. That is why titanium and its alloys TiAl6V4 and TiAl6Nb7 are frequently applied as biomaterials for hard tissue replacement such as dental and orthopedic (e.g., hip and knee joint prosthesis) implants, in the audiological field, and for cardiovascular applications such as mechanical heart valves and as material for surgical instruments such as vascular clamps, needle holders, and forceps [13]. Titanium surfaces are covered by a 2- to 6-nm-thick oxide layer that is formed spontaneously in the presence of oxygen. This layer contributes to the biocompatibility of titanium by preventing corrosion and the release of ions from the metal surface [7]. The oxide layer thickness and surface morphology can be altered by according treatment or coatings applied to change the physicochemical properties and the biological response [13].

Stainless steel is also used for orthopedic implants. Its lower biocompatibility and its mechanical properties, which are less bonelike than titanium, reduce the use as human implant material, but it is cheaper than other metals and therefore is still used in animal medicine and for surgical instruments. Other applications of steel are cardiovascular stents.

Cobalt-chromium-molybdenum alloys are very hard and in combination with other smooth surfaces very abrasion-proof. They are therefore an ideal material for joint implants. In many patients Co-Cr-Mo, that is sintered from Co-Cr-Mo beads, is used as a femoral hip implant.

Gold as one of the oldest implant materials is used not only as dental restorative material but also as electrode material for implantable biosensors or to increase the contrast in electron microscopy. An overview on studies concerning metals as biomaterials is given in Section 4.1.

Bone, tooth enamel, and dentin have a composition which is very similar to that of special *ceramic materials* like hydroxyapatite, calcium phosphate, and calcium carbonate. These materials in their natural or manmade origin are used as coatings to increase the biocompatibility of implant materials. On the other hand they can replace parts of bones; for example, porous hydroxyapatite is a good basis for new bone growth. Biologically active glass or *bioglass* is similar to ceramics and assists actively new bone formation. It is therefore used in every place where bone has to be built up. This is necessary after tumor surgery or if natural bone is destroyed by an inflammation. Ceramic and glassy materials are further considered in Section 4.2.

Another kind of biomaterials are the *polymers*. They can be tailor-made for many different applications as their properties and their composition are variable in a large range. Polymers can be used as manufactured or treated with different techniques to yield special functional groups at the surface for specific interaction, increased surface energy, hydrophilicity respectively hydrophobicity, or chemical inertness. Furthermore, such surface layers may induce cross-linking to increase hardness, remove weak boundary layers or contaminants, modify the surface morphology (increase or decrease of surface crystallinity and roughness), or increase surface electrical conductivity or lubricity. A review of these modifications, examples, and characterization is given in [14]. Polymers like high molecular weight polyethylene (HMWPE) are used as counterpart for the titanium ball head in artificial hip joints. Poly(tetrafluoro ethylene) (PTFE) and other fluorinated polymers are used for blood vessel replacements and catheters, poly(methyl methacrylate) (PMMA) for intraocular lenses, silicone acrylate for contact lenses, polyurethane for pacemakers and left ventricular assist devices, cellulose for renal dialyzers, and silicone for catheters and breast implants [15]. Biodegradable polymers like poly(sebacic anhydride) (PSA) and poly(DL-lactic acid) (PLA) are naturally removed from the body after a definitive time span and can be used for controlled drug delivery [16]. Generally, carbon in different forms (e.g., diamond, graphite, or activated carbon) is an important biomaterial particularly because of its high blood compatibility. Glassy polymeric carbon (GPC) made from phenolic resins by pyrolyzation, is mostly used as coating, for example, in prosthetic heart valves and other prosthetic devices [17, 18]. Some selected studies on polymers are discussed in Section 4.3.

A newer group of materials used in implantology are composites, especially composites of inorganic material and polymers which combine the advantages of both. Examples can be found in Section 4.4.

### 3. NANOANALYTICAL TOOLS

A wide range of applications use the methods described in this section as nanoanalytical tools. This field is extending rapidly and new applications and methods are developed constantly. A short description will be given of the methods and the parameters investigated with them. The possible areas of application and examples are given in Section 4. Particularly, scanning force microscopy (SFM) is stressed which has proven to be a valuable and easy to handle method for studies on biomaterials. Additional advantages can be found in the nondestroying operation which is applicable under ambient conditions. Experimental setups revealing nanometer resolution in only one dimension are discussed at the end of this section.

#### 3.1. Scanning Probe Techniques

Scanning probe techniques have been a valuable tool since their invention in the 1980s [19, 20]. In these experimental methods distance-dependent interactions like tunneling current, force, or light transmission between a sharp needle (“tip” or “probe”) in close proximity to a surface (“sample”) are utilized to produce an image of the sample. Two principal measurement modes were implemented: (i) to maintain a constant vertical probe position while measuring the interaction change often due to surface topography (“constant distance mode”), and (ii) to maintain constant interaction while adjusting the distance with the feedback signal reflecting surface topography (“constant interaction mode”). Both modes offer the possibility to characterize surfaces down to the atomic scale in a great variety of environments from ultrahigh vacuum to aqueous solutions. It is as well possible to characterize time-dependent reactions like crystallization or corrosion processes, as it can be done continuously and hence on-line. To scan a probe over a surface in the desired way while reacting to the topography of the sample, positioning tools with spatial resolution in the 0.1-nm regime are necessary. The latter is fulfilled by piezoelectric actuators made of ceramics like PZT (lead zirconate titanate) or PMN (lead magnesium niobate), which in different directions can be extended by less than the size of one crystal unit cell. With a suitable detection unit to measure small interaction changes connected to a distance feedback circuit and digital data representation, an image of the surface can be portrayed. Experimental adaptations and extensions based on the interaction mechanisms originally used for imaging purposes lead the way to monitor more complex features than the topography as described below.

In scanning tunneling microscopy (STM) the current of electrons tunneling between a conductive wire (preferentially heavy metals like tungsten, platinum, or iridium) with an atomically sharp tip and a (semi-) conductive surface across vacuum is measured (Fig. 2). The tunneling current decays exponentially with increasing distance between tip

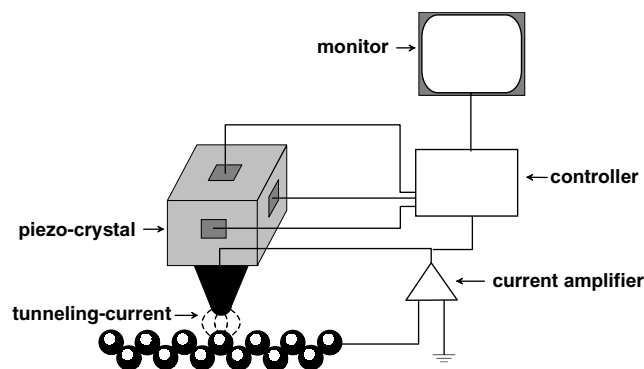


Figure 2. Schematic drawing of the STM principle.

and surface and additionally depends on the local densities of electronic states of the tunneling partners and the work function of the sample. Because of its strong distance behavior only the atom at the very end of the tip and the nearest surface atom are involved within the tunneling event. A slight change in distance according to progression along rows of surface atoms alters the tunneling current in a measurable manner so that true atomic resolution can be achieved.

Experimentally the onset of a tunneling current is obtained by approaching tip and surface to less than a few tenths of a nanometer under a constant bias voltage. The sign of the bias determines the direction of the tunneling current; this means unoccupied electronic surface states are probed with occupied electronic tip states or vice versa. Scanning the surface row by row either at constant height or constant current (see above) reveals the surface topography.

Additionally, STM can be applied to probe electronic structures. Modulating the tip-surface distance and measuring the change of the tunneling current at constant bias allows to extract the local work function of the sample. Modulating the bias and measuring the corresponding current changes at a constant tip-surface distance allows to extract the electronic states around the Fermi level of the sample (STS, scanning tunneling spectroscopy). This can lead to some chemical information about the surface, but for more detailed information electronic core levels have to be sensed, which is not possible with the STM (see [21] and especially references therein).

Scanning electrochemical microscopy (SECM) measures highly localized electrochemical currents associated with charge transfer reactions on metallic sample surfaces under liquid environment [22, 23]. In macroscopic measurements it can be compared with cyclic voltammetry. The reactions occur in a four-electrode electrochemical cell under bipotentiostatic control. There are two mechanisms respectively pathways of image production. Electron tunneling and electrochemical reactions via a water bridge occur according to the applied voltage. It can be used for the detection of localized electrochemical reactions at surfaces. It can also be used for microstructuring biomaterials like titanium [24]. In addition SECM is also capable of probing the kinetics of solution reactions and adsorption phenomena and monitoring heterogeneous electron transfer kinetics associated with processes on conducting surfaces [25].

The invention of the scanning force microscopy (SFM) was a breakthrough for these techniques as it is possible to image nonconducting substrates with a resolution of 0.2 nm laterally and 0.001 nm vertically. It does not require specimens to be metal coated or stained. Noninvasive imaging can be performed on surfaces in their native states and under near physiological conditions. It has been proven to be particularly successful for imaging biological samples, such as proteins, nucleic acids, and whole cells. By scanning, dynamic processes can be imaged, such as erosion, hydration, physicochemical changes, and adsorption at interfaces. Therefore the SFM is currently the SPM technique with the widest applicability for biomaterial research.

In SFM a small tip attached to a micro beam (cantilever) is scanned across the surface of the specimen and deflected by topographic features. The force of interaction may be repulsive or attractive, giving rise to different modes of operation. Moving the cantilever from the interaction free zone far above the surface, it snaps into contact (Fig. 3) due to the attractive force between the tip and the sample, which can be described in a simple way by the Lennard Jones potential. The piezo pushes the tip further towards the sample and the positive repulsive force reaches a maximum. As the piezo is retracted the repulsive force is reduced and the force changes sign. If the bending force of the cantilever gets larger than the attractive force towards the surface, the tip loses contact. The tip can be held in the repulsive regime of the Lennard Jones potential or oscillated in the attractive or repulsive regime, resulting in different interactions [26, 27]. These differences are important as biomolecules are deformed by applying a load of some nanonewtons as present in contact mode [28].

The deflection is usually monitored by a laser beam that is reflected and detected with a four split photodiode. This signal is used to maintain a constant force via a feedback loop and to monitor the height data. The SFM can be operated in a variety of modes that can provide different information about the sample. Usually the z-deflection is monitored and interpreted according to the parameters under investigation. An easy to read overview covering many scanning probe

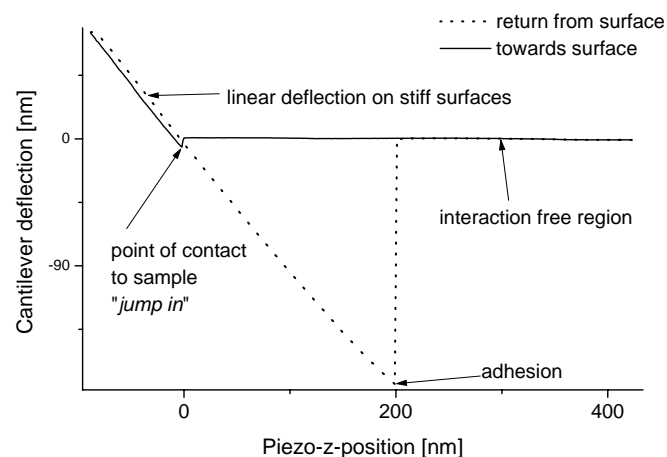


Figure 3. Cantilever deflection versus sample-z-position curve on a stiff surface monitored via SFM.

techniques is given in [29] while in [30] results obtained by SFM in the field of nanotribology are reviewed.

Sensing of the z-position is usually done via the monitoring of the z-piezo voltage. This can cause ambiguities as piezo crystals exhibit hysteresis. This is overcome by monitoring the distance separately via inductive or fiber-optical sensors [31].

For dynamic modes [32] the application of an additional oscillation to the cantilever by a piezo crystal has to be performed. Magnetically driven cantilevers are used as well for actuation [33].

The quality of SFM data is essentially determined by the cantilever and the tip, influencing the resolution of topography and force measurements. Micromechanical properties of the cantilever and the shape and chemical composition of the tip, which comes into direct contact with the sample, are essential. High aspect ratios and small tip radii are desirable for imaging steep slopes and deep crevices. Depending on the mode of operation, different parameters have to be optimized, which can be realized according to the methods described in the following.

Silicon and silicon nitride cantilever fabrication based on photolithographic techniques is well established. Metal-based (Ni) cantilevers [34] and cantilevers made of piezoelectric material (lead zirconate titanate) are produced as well for independent actuation and sensing [35]. Cantilevers of various shapes (e.g., rectangular or V-shaped) and dimensions (usually 100 to 200  $\mu\text{m}$  in length) are available. New approaches to a further miniaturization of the system have been made on microfabricated aluminum probes with length scales of 9  $\mu\text{m}$  [36–39].

Coatings (Cr-Au, Pt, Al, TiN,  $\text{W}_2\text{C}$ ,  $\text{TiO}_2$ , Co, Ni, Fe, Au with biological coating) can be applied to the cantilever to modify it against corrosion in the liquid phase or for different applications when conductive, magnetic, or biological properties are necessary.

The resonance frequency of the cantilever ranges between several kHz to several hundred kHz. Cantilevers with high resonance frequencies are used in dynamic modes as the tip oscillates with several hundred kHz above the surface.

The stiffness of the cantilever is defined by the force constant  $k$  and ranges between 0.01 and 100 N/m for the vertical deflection. The soft ( $k < 0.1$  N/m) cantilevers are used in contact modes to minimize the disturbance of the sample. Rigid cantilevers with a force constant larger than 1 N/m are used in noncontact or dynamic modes since they exhibit high resonant frequencies and small oscillation amplitudes of about several nanometers. The force constant for the lateral twisting can be determined for friction measurements [40] and the movement of the cantilever has been modeled accordingly with finite element analysis [41]. The mechanical behavior and the determination of the spring constant are well described in literature [42–49].

The tip itself can consist of different materials or is coated according to the application. For some applications a hard surface is necessary and a diamond-like coating (DLC) is applied [34]. The production of DLC coatings is described in [50]. Different functionalities [51–53] can be applied. Cantilever tips can be modified by chemical [54] and biochemical [55] functionalization. Via silanization [56, 57] or via thiols, self-assembled monolayers (SAMs) are produced for

further modification [53]. Proteins and bacteria [58] can be attached to the tip.

Additional materials which vary the shape of the tip can be deposited, such as polystyrene, borosilicate and silica spheres,  $\text{C}_{60}$  molecules [59], carbon-nanotubes in general [60–63], or single-wall nanotubes with diameters of  $< 3$  nm [64] or functionalized nanotubes [65]. The first are, for example, used to have a defined contact area. The latter are important because tips produced by lithographic methods are of pyramidal shape but do not present the necessary sharpness for high-resolution images. As the tip convolutes with the surface features [66], its shape determines accordingly the lateral resolution, and the width the possibility to enter small features. Electrochemical etching can produce sharper tips with an open angle near the apex of  $20^\circ$ . For sharper tips an extra tip is grown on the apex of the conventional pyramidal tip using electron beam deposition (EBD) [67], which leads to a curvature radius of 2 to 20 nm, or the above-mentioned nanotube-functionalized tips are used. The real tip shape can be calculated and, by deconvolution, hidden information extracted [68–71]. The resolution of steep slopes can additionally be improved by slow scanning and a repeated z positioning at each pixel [72].

Usually the typical scan range is up to 150  $\mu\text{m}$  but also larger scan areas can be reached with a scan area up to 25  $\text{mm}^2$  [72].

### 3.1.1. Contact Mode

Topography and roughness can be characterized by monitoring the vertical excursion of the cantilever in contact with the surface. Assigning a deflection signal in z-direction to each point while scanning leads to the image. Two typical examples, one of a biological and one of a biomaterial surface, are shown in Figure 4 respectively in Figure 5a. Roughness can be calculated from the acquired data.

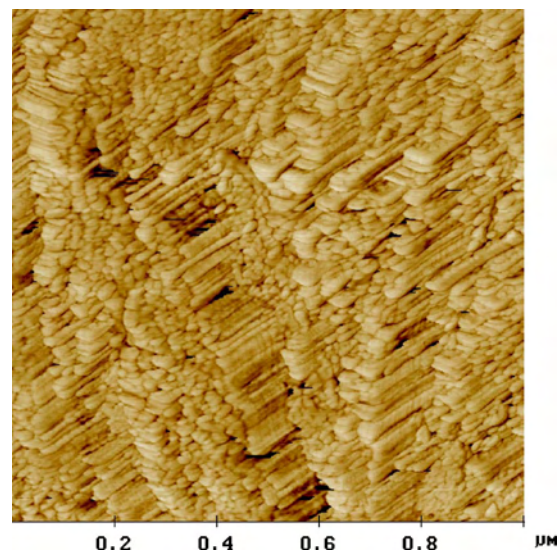


**Figure 4.** Typical contact mode SFM image of human enamel showing different crystals. Unpublished data with kind permission from M. Hannig, Clinic for Dentistry, Stomatology, and Oral Maxillo-Facial Surgery, Saarland University.



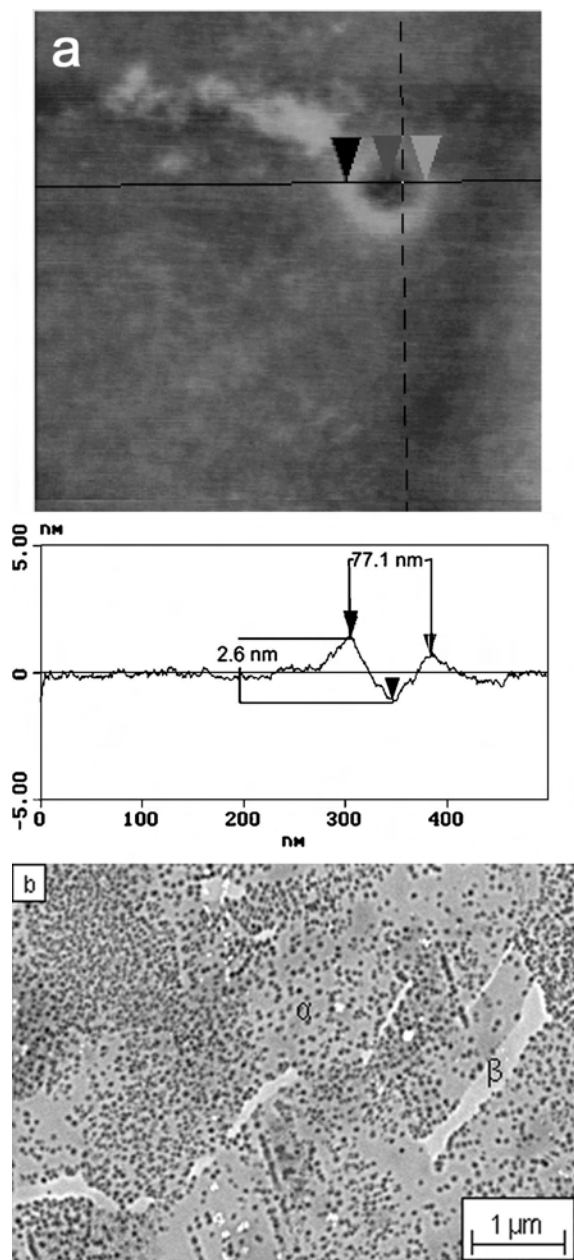


**Figure 5.** Comparison of (a) SFM and (b) SEM images of TiAl6Nb7 alloy treated with anodic oxidation under galvanostatic conditions in 1 M H<sub>2</sub>SO<sub>4</sub> at room temperature with a current density of 10 mA/cm<sup>2</sup> up to a final potential of 40 V. The SEM image shows the surface on a larger scale exhibiting the differences of the  $\alpha$  and  $\beta$  phase of the alloy. The small black dots that cannot be further identified with this technique are characterized further with SFM to yield topographical information of the structure. SEM image reprinted with permission from [245], C. Leinenbach et al., *Mater. Sci. Eng. Technol.* 8, 442 (2002). © 2002, Wiley-VCH.

Friction force microscopy is done by monitoring the twist of the cantilever while scanning over the surface [73]. With this nanomechanical measurement the shear strength can be determined. An overview on friction on the atomic scale is given in [74]. After chemical modification, the tip of the cantilever can be used to gain information about the chemical

properties, respectively forces between a biomolecule and a biomaterial surface. Images are produced that display predictable contrast and correspond to the spatial distribution of functional groups on the sample surface. Surfaces can be imaged in friction mode down to a resolution of about 0.5 nm [21]. An overview over several different chemical interactions of model surfaces with different chemical modifications is given in [75]. An image contrast is achieved between regions terminated by different functional groups [76] but can be influenced by topographical features. Hydrophobic and hydrophilic parts of the surface can be distinguished [77]. It is even possible to gain information about chirality [78], which in this case was done, on immobilized molecules by investigation of the friction and adhesion force. The load dependency is another important parameter. The atomic stick slip mechanism and interfacial friction, adhesion, and elastic properties measured by friction force microscopy are reviewed in [30].

In scanning spreading resistance microscopy (SSRM), different conductivity of the substrate surface is monitored by applying a voltage and measuring the resistance while scanning in contact mode with DLC-coated tips for better wear properties [79].

In force modulation mode (FM), the force between the cantilever and the sample surface is modulated by vibrating the sample respectively the tip in vertical direction while scanning in contact mode. The modulation frequency is in the range of 5 to 30 kHz with a cantilever resonance frequency of more than 200 kHz. The lateral distribution of the hardness can be obtained by monitoring the amplitude changes [80].

Imaging at the resonance frequency of the tip in contact with the surface is called contact resonance imaging (CRI) [81] and can be used for imaging soft and sticky surfaces like proteins on surfaces.

The modulation of the probe can also be carried out just above the resonance frequency of the cantilever to monitor viscoelastic and anelastic properties of submicron phases. This mode, which can also be done with temperature ramping, is called scanning local-acceleration microscopy (SLAM) [82].

A new technique called atomic force acoustic microscopy (AFAM) uses ultrasonic actuation of the cantilever while scanning in contact mode above its resonance frequency. It is possible to measure the contact stiffness and to distinguish between different orientations of a silicon wafer surface [83].

Besides the actuation of the sample in the normal direction, a high-frequency lateral vibration can be applied. By doing so, local measurements of shear strength and Young's modulus can be undertaken. The indentation of the tip into the surface is reduced and accordingly the possible damage. This method was introduced as harmonically modulated lateral force microscopy (HM-LFM) in [84, 85].

### 3.1.2. Dynamic Modes

In the dynamic modes [86–88] the cantilever is oscillated near its resonance frequency by an additional piezo crystal. The amplitude signal of the oscillating cantilever yields the information about the interaction.

A distinction between noncontact and the dynamic mode in the repulsive regime is often made. In real noncontact



mode attractive forces are measured while the tip is oscillated above the sample with an amplitude of about 10 nm, never touching the sample surface.

In the dynamic mode [89], the tip is oscillated with an amplitude of 20 to 100 nm and touches the surface at some point. The feedback loop works as in contact mode maintaining a constant amplitude. Topography and roughness information are obtained as described earlier. Additionally and simultaneously, a phase image can be recorded.

In phase imaging the phase lag between the excitation frequency and the cantilever response signal is monitored. If the cantilever is oscillating freely in air, the waveform signal detected by the photodiode should be in phase with the signal driving the piezo element. This signal is sensitive to the interaction force between the cantilever and the surface. The phase contrast arises from the different amount of energy dissipated by the tip while oscillating on surface areas with different elastic properties. A short overview of experiments and theoretical descriptions is given in [90]. The mechanical properties [91–93] as well as chemical differences can yield a phase lag, which has been correlated quantitatively to the chemical interactions on chemically microstructured surfaces [90, 94].

In pulsed force mode (PFM), force distance respectively indentation curves are recorded in z-direction continuously [95]. A sinusoidal modulation far below the resonance frequency of the cantilever is applied to the z-piezo. Typical parameters are for the amplitudes 10 to 500 nm and for the frequency values between 0.1 and 2 kHz. A complete force distance cycle from the interaction free distance to the direct contact with the probe respectively the indentation is carried out. By measuring the maximum adhesion force an adhesion image is obtained; the slope in the repulsive regime is correlated with the stiffness of the substrate and long-range forces like electrostatic forces caused by surface charges influence the baseline. Accordingly it is possible to gain information about adhesive, elastic, and electrostatic sample properties. By chemical modification of the tip it is also possible to image differences between chemically different areas on a sample surface. Typical PFM images are given in Figure 6.

Electrostatic contributions to the tip-sample interaction can be isolated to yield surface charge density information. A theoretical and analytical framework for determining relative charge densities from arrays of SFM force curves without the need for an absolute measurement of the tip-sample separation is presented in [96] labeling it D-D method.

Polar interactions probed with SFM using a charged tip can lead in the future to atomic resolution of polar surfaces [97].

Magnetic interactions can be measured with magnetically coated cantilevers [98] but are, in the further investigations of biomaterials, of lesser importance.

In addition SFM is also being used for applications in which no scanning is required, where the tip is used as a sensitive force sensor (force spectroscopy) [99–101]. Loads of 1 to 1000 nN can be applied with tips that have tip radii of up to 1  $\mu\text{m}$ , leading to an investigation of the first 0.1 to 10 nm [102]. Forces on a larger scale can also be measured by using the force apparatus by Israelachvili [103, 104]. This

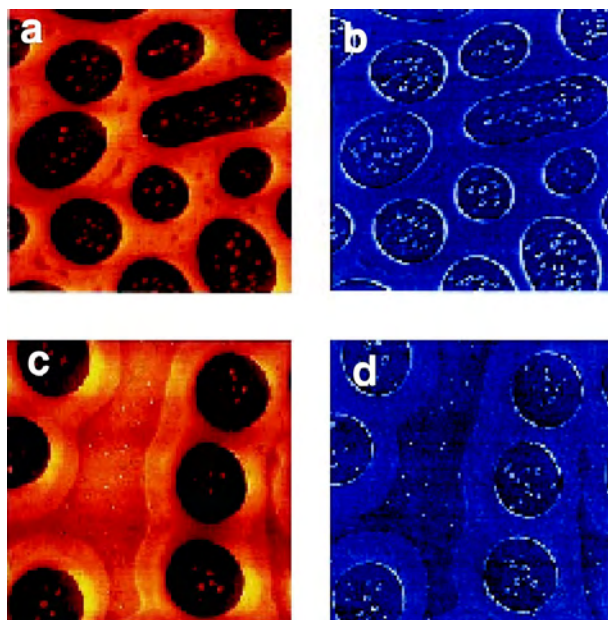


**Figure 6.** Pulsed force mode images of blends of PS/PMMA spin-coated on silicon substrate [95]: topography (a), (c) and adhesion (b), (d) images; lighter color corresponds to lower adhesive forces. The composition of PS/PMMA is 58/42 (a), (b); and 69/31 (c), (d), scan range: 10  $\mu\text{m}$ .

will cover larger areas and the limitation to mica or a modification of it is given. However, absolute force values can be determined with high accuracy because the interaction area is well known.

With the setup of an SFM, surface and adhesion forces [105] between two surfaces and the elasticity respectively hardness by indentation of the substrate can be obtained. The data are investigated by plotting the bending of the cantilever versus the load applied to the sample. By indenting the surface it is possible to gain information about the elasticity and Young's modulus [28, 106] as well as time-dependent processes happening on polymers [102]. By monitoring the forces between the tip and the surface, chemical patterns on a surface can be characterized [52].

To monitor hardness by nanoindentation usually blunter tips are used to be able to relate to macroscopical hardness testing. The Berkovich tip with nominal radius of 150 nm is used to monitor the hardness, which is defined as the ratio of the maximum load to the projected contact area [107].

By force mapping, two-dimensional arrays of force curves are recorded while scanning the tip across the sample. By this the elastic properties can be monitored over the whole scan area. From the force curves Young's modulus can be calculated according to Sneddon's modification of the Hertzian model for elastic indentation [108].

Viscoelastic properties can be also monitored on a micrometer and submicrometer scale by microrheological measurements done with magnetic beads [109]. The loads applied are in the range of 10 nN. Mainly it is applied to monitor viscoelastic properties of cells using the parameters of an effective elastic constant, a viscosity, and a relaxation time. Viscoelastic properties can also be monitored via laser-tracking microrheology by looking at the Brownian motion

of individual spherical particles embedded in the viscoelastic material by monitoring the forward scattered light [110]. As particles, polystyrene beads of 0.27  $\mu\text{m}$  diameter are used.

### 3.2. Electron Microscopies

A totally different approach to get information in the nanometer regime is based on the particle-wave dualism of the electron, which was proposed in 1924 by de Broglie [111]. This offers the possibility to use electrons as a probe in a similar way as light with a wavelength  $\lambda$  depending on the electron mass  $m$  and velocity  $v$ :

$$\lambda = \frac{h}{mv}$$

According to Abbe, the resolution  $A$  of an imaging system depends on the wavelength, the diffraction index of the area between sample and objective  $n$ , and the angle  $\alpha$  under which the light passes through the objective:

$$A = 0.61 \frac{\lambda}{n \cdot \sin \alpha}$$

The term  $n \cdot \sin \alpha$  is called numerical aperture. This could only be varied to a small extent, so the resolution of light microscopy with typical wavelengths around 500 nm is limited to 200 nm. The much lower wavelength, which electrons can reach, offers therefore a much better resolution. In electron microscopy the glass lenses have to be replaced by electrical and magnetical lenses, which deflect the electron beam in the same way as glass lenses do the light. Because of the aberration of these electromagnetic lenses, the resolution in electron microscopy is limited to 0.2 nm.

In the sample a variety of different interactions between the probe electrons and the sample atoms take place:

- transmission of primary electrons
- secondary electron emission
- Auger electron emission, a special type of secondary electron emission
- electron backscattering
- absorption of electrons
- characteristic X-ray emission
- emission of light

One big disadvantage of electrons as a probe is the charging of the sample during electron bombardment. In principle only conducting samples can be imaged. In a special case nonconducting samples can be imaged if the number of the absorbed electrons is equal to the number of secondary electrons leaving the sample. In all other cases the sample has to be coated by metal or a conducting replica has to be made. Both methods may give artifacts.

There are two approaches to using electron beams for microscopy. The first is the transmission electron microscope realized by Ernst Ruska in 1933 [112, 113]. The TEM can be compared with a transmitted-light microscope: the electrons pass through a thin sample [114] and can be detected at a fluorescence screen. Because of the strong absorption and scattering processes which take place if free electrons interact with matter, only very thin samples in the range of 10 nm to 100 nm thickness can be passed by electrons.

As in a light microscope, there are different mapping modes [111]:

1. *Bright-field Image*: The image is made of electrons which directly pass through the sample. The image plane of the objective is mapped by the projector lens. The contrast is given by the loss of electrons by scattering and absorption on their way through the sample. It depends on the density of the sample and the atomic number of the sample components. In Figure 7 two examples of this imaging technique are presented.
2. *Diffraction Image*: This uses also the electrons which directly pass through the sample. But in this mode the focal plane of the objective is imaged by the projector lens. By this one gets a diffraction image which yields information on the crystal structure of the sample in a similar way to an X-ray-Laue-diffraction image (Fig. 8).
3. *Dark-field Image*: The electrons which scattered inside the sample are imaged on the screen and the electrons which pass the sample in a direct way are filtered out.

The TEM should theoretically reach a resolution which is 1,000,000 times better than light microscopes. The lens aberration, especially the spherical and chromatical aberration, decreases this theoretical value to 1,000 times better resolution in practice. Therefore, points which are separated by 0.2 nm can be imaged.

Furthermore, energy-filtering transmission electron microscopy [115] or TEM with attached energy dispersive X-ray analysis (EDX) is used which gives the elemental composition.

There are three main disadvantages of the TEM:

1. Only very thin samples can be investigated.
2. The samples have to be stable under electron irradiation.
3. The whole TEM has to be held under high vacuum conditions or one has to build a special environmental cell for the sample which is differentially pumped against the other parts.

The second approach to use electrons as a probe for imaging is the scanning electron microscope (SEM) [116],

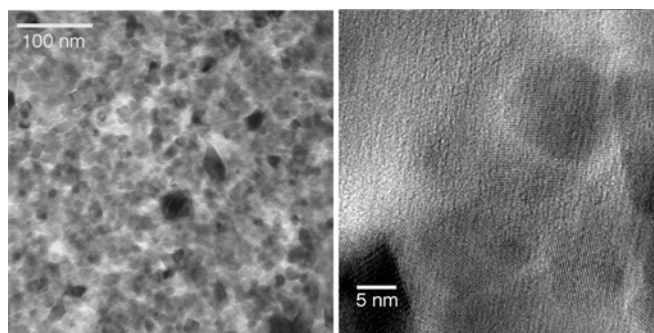


**Figure 7.** Two typical TEM images of  $\text{TiO}_2$  nanoparticles (particle diameter 16 nm, crystal modification anatase). Picture (a) is a low-resolution image where the distribution of the nanoparticles is visible, while the resolution in picture (b) is much higher with clearly visible crystal plates (line-shaped structures) inside the nanoparticles (round structures) [246].

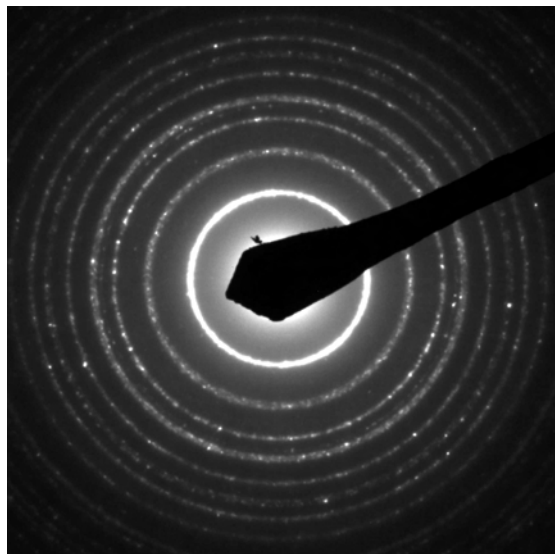


**Figure 8.** Diffraction pattern of the sample in Figure 7. The rings have their origin in the diffraction at different crystal planes. The radii of the rings are correlated with the Miller indices of their diffraction plane [246].

which was invented by Knoll and v. Ardenne [117] in the 1930s. The first realization to image a surface was described by Knoll and Thiele [118]. This microscope scans a very well-focused electron beam over the sample surface. The electrons which leave the sample surface are accelerated by a voltage to the detector, for example, an Everhart–Thornley detector [111], which transforms the electrons into an electrical signal. This is used to control the intensity in a cathode-ray oscillograph while the same signal that scans the electron beam in SEM is used as deflection signal in the oscillograph. So an image of the electrons leaving the sample is obtained.

The resolution in SEM is estimated by the area where the electrons leave the sample. The dimensions of this area depend on the spot radius of the electron beam on the sample surface and the scattering processes inside the sample.

In SEM there are several kinds of electrons which could be detected:

1. Secondary electrons which are produced by primary electrons near the surface with enough energy to pass through the surface barrier. These produce the highest resolution.
2. Secondary electrons which are produced by backscattered electrons. These produce the lowest resolution.
3. Secondary electrons which are produced from the backscattered electrons out of the pole shoes of the last lens.
4. Primary electrons which hit the aperture and produce there secondary electrons.

The last two cases increase only the noise without any further information on the sample.

The backscattered electrons themselves are too fast to reach the secondary electron detector. They can, however, be also used for imaging with a different detector. The backscattered electrons give a high material contrast because their number depends on the nuclear charge.

The resolution of the SEM depends on how well the electron beam is focused on the sample. This could give a resolution of 3–6 nm. The depth of focus can reach up to 1 mm, compared to only 100–1000 nm in a light microscope. An example of a SEM image is given in Figure 5b.

A review of spatially resolved spectroscopies in electron microscopy for the study of nanostructures of different metals, semiconductors, and biomaterials is given in [119].

### 3.3. Other Methods

One problem of the techniques presented so far is the lack of chemical information, except in TEM with additional EDX or energy filter characteristics. Because the surface chemistry is a very important parameter determining the properties of biomaterials, often additional methods are applied. They have usually a high surface sensitivity, but their lateral resolution is limited. These complementary methods are in particular:

- X-ray photoelectron spectroscopy (XPS) in which the kinetic energy of photoemitted core electrons gives information on the elemental composition and the binding state of these elements. Thus metals can be distinguished from their oxides because they present another oxidation state. The surface sensitivity is several tens of nanometers; the lateral resolution is poor (between 100  $\mu\text{m}$  and 5 mm). Quantification is possible within an accuracy of 5–10%.
- Auger electron spectroscopy (AES) in which also the kinetic energy of electrons is measured. These electrons are electrons which arise from a special intra-atomic relaxation process, the Auger process. After a core electron hole is produced in an atom (by X-rays, primary electrons, or ions), an electron with higher binding energy relaxes into the deep hole. This energy can then be transferred to an electron which has now enough energy to overcome the binding energy and leave the material. The energy of Auger electrons is also characteristic for the elemental composition, and the surface sensitivity is similar to XPS. There are two main differences: Because in the Auger process more electrons are involved, there is usually no easy interpretation of the chemical state of the electrons. However, because in Auger electron spectroscopy the primary hole-producing process can be by a focused electron beam, the lateral resolution can be in the tens of nanometers range.
- Secondary ion mass spectrometry (SIMS), the third important technique, in which, through ion bombardment, secondary ions are sputtered from the surface which are further analyzed in a mass spectrometer. Because there are also molecular ionic fragments, a huge amount of chemical information can be obtained. If a time-of-flight detector is used, also very large and heavy molecules, for example, biomolecules and polymers, can be detected. The surface sensitivity can be tuned by the ion bombardment and can be restricted to the first monolayer. By harsh bombardment also depth profiles can be measured. The lateral resolution is usually several hundred nanometers. However, the current limit is therefore well below 100 nm.

## 4. NANOANALYSIS OF BIOMATERIALS

### 4.1. Metals and Oxides

#### 4.1.1. Titanium and Titanium Alloys

Titanium is one of the most important materials in implantology. Therefore, many investigations with nanoanalytical tools are performed on titanium or titanium-containing implants.

**Single Crystalline Model Surfaces** To get insight into the basic material interactions, a defined surface has to be prepared. In the case of titanium and its natural surface oxide, these standards are TiO<sub>2</sub> single crystals.

An overview covering atomic resolution investigations with STM and SFM of different TiO<sub>2</sub> modifications is given in [120].

Intrinsic defects on single crystals of TiO<sub>2</sub> were characterized with STM [121–123]. In these investigations STM was also combined with other techniques like XPS and low-energy electron diffraction (LEED) to investigate the structure after argon sputtering and annealing in oxygen plasma and to detect calcium impurities. These are eliminated after the treatment, which improves the surface morphology of the TiO<sub>2</sub> (110) crystal [124].

TiO<sub>2</sub> as substrate and the structure of the adhering biofilm were monitored also via SFM [125].

**Surface Treated Titanium** The high biocompatibility of titanium has its origin in the natural oxide layer on the titanium surface. A further property that influences the ingrowths of titanium implants into bone is their surface roughness. So different surface treatments, for example, chemical, electrochemical, or mechanical techniques, are used to increase the biocompatibility of titanium.

The oxide layer at electropolished and anodically oxidized titanium was investigated in different ways, for example, by SEM, XPS, AES, SIMS [126]. This showed that the oxide formed is mainly TiO<sub>2</sub>, but the chemical composition can be modified by anion adsorption when H<sub>2</sub>SO<sub>4</sub> or H<sub>3</sub>PO<sub>4</sub> electrolytes are used. The hydrophilicity of TiO<sub>2</sub> films obtained by different techniques (radio frequency magnetron sputtering (RFMSD) and plasma enhanced chemical vapor deposition (PECVD)) and the influence of UV irradiation were monitored via SFM. The interaction caused by the capillary water bridge formed at the tip-sample interface was investigated [127]. The adhesive force shows a highly inhomogeneous surface for RFMSD films and an increase in adhesion force upon UV irradiation. For PECVD a more homogeneous surface was observed. Surface characterization of a titanium oxide layer, grown on commercial Ti substrates by metal organic chemical vapor deposition (MOCVD) technique, was monitored with STM and the chemical composition with XPS [128].

Another widely used surface modification method is sandblasting. This not only increases the surface roughness but also changes the chemical composition because some shot particles remain adhered on the metal. In [129] the percentage of surface area covered by the remaining shot particles was ascertained by SEM and a following digital image analysis.

Titanium surfaces used in oral implantology were submitted to various treatments such as mechanical polishing, acid attack in HCl/H<sub>2</sub>SO<sub>4</sub>, after mechanical polishing or sandblasting, and titanium plasma-spray. Polished titanium exhibits a peak-to-valley roughness of 81 nm; the acid-treated surfaces show an increased roughness in the micrometer range (2100 nm for polished and acid attacked; 3600 nm for sandblasted and acid attacked). The chemical composition has been measured by Auger electron spectroscopy. The treatments had no major influence on the surface chemical composition [130].

Titanium implants with different surface properties reached by various surface treatments (mechanically polished, mechanically ground, sandblasted with alumina and etched in HF/HNO<sub>3</sub>, sandblasted with alumina and etched in HCl/H<sub>2</sub>SO<sub>4</sub>, mechanically polished and etched in HCl/H<sub>2</sub>SO<sub>4</sub>, and plasma-sprayed) were investigated according to roughness and morphology and the subsequent biofilm formation [131]. The adsorption of human plasma fibrinogen (HPF) was tested but the SFM phase imaging technique could only detect HPF on the first two of the investigated seven samples due to resolution problems. Additionally, the chemical composition was examined by XPS and ToF-SIMS and some impurities used during sample production and treatment were detected.

A further item of investigation are titanium alloys and, in this field, the cell attachment to the implants [132]. As on Ti, there are different ways to prepare the alloy surface, for example, thermal oxidation, machining, or electrochemical polishing. TEM and STEM studies [133] show that the microstructure of the anodic oxide films is rather heterogeneous with areas of different porosity, which can be correlated with the grain structure of the bulk metals. These oxides on Ti alloys are more heterogeneous than that on pure Ti, due to the more complex microstructure of the bulk material. TiO<sub>x</sub> films deposited on TiAl6V4 by plasma immersion ion implantation (PIII) with different compositions and properties were fabricated as model for artificial heart valve implants. They were evaluated with SFM revealing a dense surface. Microhardness was tested and related to the oxygen pressure upon production. A maximum hardness of 17 GPa is obtained with an oxygen partial pressure of  $3 \times 10^{-2}$  Pa [134]. This is also correlated with a development of Ti<sub>3</sub>O<sub>5</sub> and TiO<sub>2</sub> phases as monitored with XPS.

The effect of sterilization with different techniques such as dry heat, steam autoclaving, ethylene oxide, peracetic acid, and plasma-based sterilization techniques on the surface properties of NiTi (Nitinol) was investigated with AES and SFM. Dry heated, steam autoclaved, and ethylene oxide treated surfaces present thicker oxide layers where the first two treatments yield a threefold increase in surface roughness. Plasma-based sterilization has a lesser effect on the oxide layer thickness, roughness, and morphology [135].

The influence of functionalization of titanium surfaces was monitored in [136]. No change in surface structure was observed upon coating with silanes.

The corrosion of titanium surfaces was monitored *in-situ* with electrochemical SFM by changing the applied voltage on the titanium. The growth of oxide domes could be observed [137]. Further STM experiments are presented

in [120]. Titanium surfaces exposed to conditions of corrosion in a biological environment were examined with STM *ex-situ* and nanoscale topographical changes could be determined [138].

**Structured Titanium Surfaces** Nanostructured Ti films were characterized with respect to interaction with proteins like F-actin via SFM. An influence of the structure height between 1 and 4 nm on the alignment and adsorption amount (scan ranges: 0.158, 6, and 17.8  $\mu\text{m}$ ) [24] could be determined. Using a photolithographic technique, the flanks of Ti-implant screws were patterned with round etched regions of 10  $\mu\text{m}$  diameter, and placed in a square matrix with a pitch of 20  $\mu\text{m}$  [139]. This surface morphology was investigated by SEM after implantation, but no statistically significant differences were seen in fixation, with respect to bone-to-implant contact, between the patterned and control implants. In another study 1-, 2-, 5-, and 10- $\mu\text{m}$ -wide Ti gratings were produced by microtechnology and plasma etching [140]. The biocompatibility was tested via incubation of rat dermal fibroblasts (RDFs) on the surfaces for 3 days. Observation by SEM, TEM, and confocal laser scanning microscopy showed that the RDFs as a whole and their stress fibers oriented strictly parallel to the surface pattern on the 1- and 2- $\mu\text{m}$  surface, while on the 5- and 10- $\mu\text{m}$  surfaces this orientation was not observed.

**Coated Titanium Surfaces** A further approach to increase the biocompatibility is to form a new surface consisting of more tissue-like material; especially phosphate (Ca-P) and hydroxyapatite (HA) deposited by different techniques are used to reach this [120, 136, 141–148].

One of these techniques is the ion-beam assisted sputter deposition (IBASD). Ca-P coatings yield columns of 40 to 80 nm on the flat surface as monitored with SFM. The quality of the coatings was monitored with XPS, AES, and FTIR studies [141]. IBASD was also used for the production of  $\text{TiO}_2$ ,  $\text{Al}_2\text{O}_3$ , and HA films. These were investigated concerning the roughness via SFM yielding a higher roughness of  $\text{TiO}_2$  surfaces [142].

Another deposition technique for Ca-P coatings was developed in [149]. This study showed proliferation of the osteoblast-like cells which was significantly higher on non-coated than on Ca-P-coated samples. On the other hand, more mineralized extracellular matrix (ECM) was formed on the coated surfaces. TEM confirmed that the cells on the coated substrates were surrounded by ECM.

Plasma-spray, sol-gel, and sputtering techniques were compared in [144] by SEM, XPS and X-ray diffraction (XRD). All coatings exhibited a rough morphology suitable for implant applications. The sputtered coatings were found to have a composition most similar to HA; the sol-gel deposits also showed a high concentration of hydroxyl ions. Plasma-spraying also results in a porous titanium coating in which  $\text{Ti}_3\text{O}_5$  was formed in the outermost surface due to oxidation [150]. The macropores in the outermost layer reached a diameter and even surpassed 150  $\mu\text{m}$ , which could be beneficial for tissue growth into the coating. Also plasma-sprayed coatings were investigated in [147] by TEM. Six months after insertion, an occasional lack of HA coating and phagocytosis of HA particles were noted. The implant was surrounded by well-mineralized bone investing the smallest

cavities of the plasma-sprayed layer. Plasma-sprayed hydroxy-apatite was also used to increase the biocompatibility of these materials. But there was no obvious difference in the *in vitro* and *in vivo* reactions of pure and coated Ti alloys [151].

In [145] different surface treatments were investigated by SEM. Here the HA coating on grid blasted Ti surfaces significantly improved fixation to the bone, while HA onto porous coating did not compared to pure Ti surfaces. Further SEM studies were performed on plasma sputtered HA thin coatings on Ti alloys [146]. For deposition temperatures as low as 67  $^\circ\text{C}$ , the crystalline phase of the HA coating is detectable and an underlying (TiAlV)N coating increases the crystallinity and thermostability of the HA coating before and after heat treatment. In a combined TEM, SEM, XRD, and FTIR study [148] it was shown that the morphology and composition of a plasma assisted electrophoretic deposited HA layer were significantly influenced by the solution pH values. SEM images out of this investigation are given in Figure 9. The electrophoretic method performed with ultrahigh surface area HA powder produces dense coatings when sintered at 875–1000  $^\circ\text{C}$ . SEM inspection of these layers showed that the use of dual coatings solves the problem of cracking HA layers during sintering [152]. Sol-gel derived hydroxyapatite coating morphology was also investigated with SFM and SEM in [143], revealing good homogeneity and a high surface roughness.

Other investigations on HA are presented in [120]. In [153] bioactive calcium phosphate invert glass-ceramic coatings on substrates such as pure titanium, conventional Ti-6Al-4V, or Ti-29Nb-13Ta-4.6Zr were analyzed to determine the optimum condition for preparation of fine joining. Cross-sectional SEM photographs and EDX measurements around the joining interface between substrate and coating show gradient zones of 3–4  $\mu\text{m}$  in thickness between substrate and ceramic layers. Ti concentrations in the zones decrease with decreasing distance from the glass-ceramic layers.

Another approach to increase the biocompatibility of Ti alloys is a laminin-5-coating which enhances cell attachment, spreading, and hemidesmosome assembly [154]. This may reflect better integration between epithelial cells and titanium alloy. TEM analysis of such a compound showed that cells formed significantly more hemidesmosomes on the surface of laminin-5 coated and passivated than on the surface of laminin-5 coated, unpassivated Ti alloys.

In some cases inert areas and areas of high biocompatibility are needed on the same substrate. Teflon (PTFE)

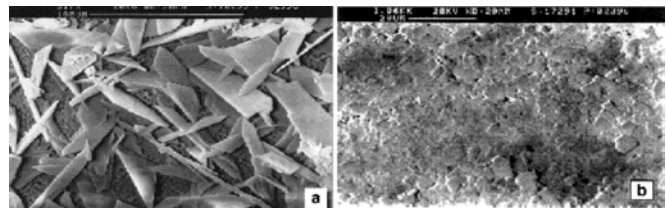


**Figure 9.** SEM micrographs of plasma-assisted electrophoretic deposited coatings [148]. (a) Calcium-phosphate coating, cathodic deposition by electrochemical reaction in a HA solution of pH 4–5. (b) HA coating anodic deposited at pH 10–11.

coatings on titanium substrates are an approach to build up an inert layer on a biocompatible titanium substrate. In Figures 10 and 11, SFM pictures of a Teflon layer on commercially pure titanium are shown [155]. In Figure 10 the Teflon is deposited by a dip coating technique. The structure of the underlying polished titanium surface is not visible. It is possible to compensate substrate roughness by this method. In Figure 11 an additional surface structure is caused by powder coating a Teflon layer, which increases the surface roughness.

**Implanted Materials** Implants can also be investigated after implantation.

SEM investigations showed that failed oral titanium implants [156] contained varying amounts of tissue residues while two control samples were essentially free from macroscopic contamination. The efficacy of cell adhesion on Ti, Ti-alloy, dental gold, and ceramic implants were also investigated by SEM [132]. By this investigation the better adhesion and spreading of the cells on metallic surfaces could be shown. One result of TEM is that the attachment zone between bone and implanted biomaterials consists of a mineralized collagen fiber matrix associated with an inorganic (hydroxyapatite) matrix [157, 158].

An important field of investigation is the drift of titanium far away from the dental implant into the surrounding bone tissue [159]. The same happened at metal-metal interfaces, for example, in hip implants, as was shown by TEM [160].

#### 4.1.2. Other Metals

Surface structure on the atomic level, the change of it by adsorption of ethane and other model molecules, and the techniques to monitor it are presented for Pt and Rh model surfaces in [161].

A copper (110) surface with homo- and heterochiral domains of adsorbed glycine could be distinguished with submolecular resolution via STM [162].

A Co-Cr-Mo (ASTM F-75) alloy and its corrosion were investigated by SECM in NaCl solutions. Corrosion took

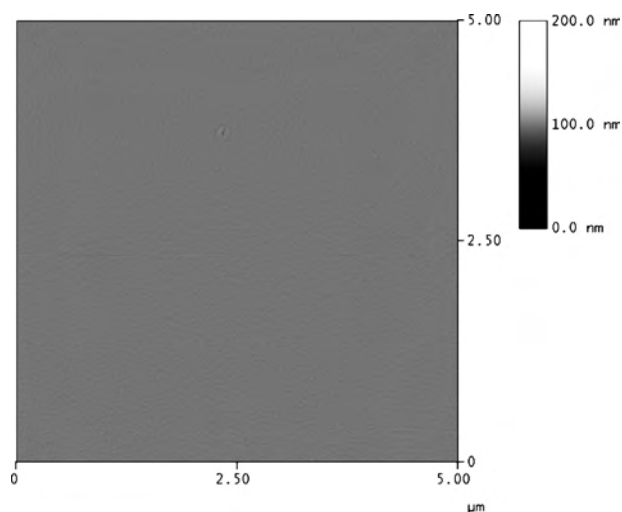


**Figure 10.** SFM image of a titanium substrate coated with Teflon (PTFE) by dip coating [155]. The underlying substrate surface is not visible. The coating flattens all the substrate roughness.

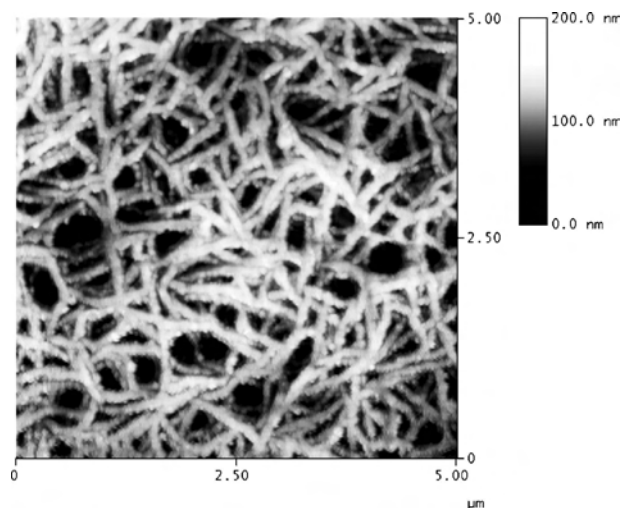


**Figure 11.** SFM image of a titanium substrate coated with Teflon (PTFE) by a powder method [155]. The Teflon layer forms a strongly structured surface.

place mainly at grain boundaries. Corroded material was additionally characterized by X-ray energy dispersive spectroscopy (EDX) analysis for chemical composition. Two types of corrosion products were seen as flakes on the surface, one with Co 3%, Cr 72%, Mo 24% and the other with Co 12%, Cr 88%, Mo 0%; on the tip abrasion flakes were determined as Co 11%, Cr 66%, Mo 24% [22].

Stainless steel, copper and alloys, and the corrosion processes induced by bacterial attachment including freshwater bacteria monitored with SFM are described in [163]. The electrostatic forces on the surfaces of stainless steel (316), gold, and an electropolished Nitinol surface were investigated via force curves with the SFM. Gold and stainless steel exhibit repulsive forces at pH 7, Nitinol a slight attractive force. Nitinol surfaces show a heterogeneity in the distribution of surface charges that is rendered more homogeneous upon oxidative treatment [164].

Although gold has been studied for a long time, it is still an actual field of investigation. Comparison of the cell adhesion properties with other materials is made, for example, by SEM examinations as mentioned earlier [132]. But Au is also useful in other applications. The protein adsorption on gold colloid particles, for example, is widely used in biotechnology for diagnostics and separations, for example, in combined fluorescent and gold immunoprobes for correlative light and electron microscopy [165]. To visualize the protein film on nanosized particles, a TEM approach was applied [166]. These proteins cause a significant scattering absorption contrast in TEM based on the materials' electron density. Thus the film thickness was directly measurable in planar projection and the shape of these films was visualized without negative staining methods.

Alkali- and heat-treated tantalum as implant material has been shown to bond to bone, for example, by SEM [167]. The treated implants showed weak bonding to bone after 8 weeks of implantation and exhibited significantly higher tensile failure loads compared with untreated Ta after 16 weeks. In contrast, the untreated TA implants had a intervening



fibrous tissue layer between the bone and the Ta and did not bond to bone after 8 and 16 weeks.

Techniques of SEM and light microscopy deal with retrieval analysis of different implanted biomaterials, for example, cobalt-chromium-molybdenum alloys [168]. Cases included both orthopedic and dental implants, as well as entire mandibles and portions of maxillae obtained at autopsy.

## 4.2. Ceramics and Glasses

Ceramics and their use as biomaterials is a hot topic of current research [132, 157, 169–176]. A review of the recent improvements in TEM to characterize microstructures in advanced ceramics is given in [173].

A disadvantage of ceramics is their sensitivity to microscopic cracks as investigated in [170]. The manufacturing process can introduce these cracks. This makes it critical to have analytical methods to detect such cracks. In an investigation light-optical microscopy, fluorescence microscopy, and SEM were compared. It was found that microscopic cracks of critical size could be detected using the fluorescent penetrant method, but not by light-optical microscopy and even not by SEM.

The results of an experimental process in which ceramic is formed without heating are investigated in [177]. Three calcium-deficient apatites (CDA: two powders and a fibrous compound) and a biphasic calcium phosphate (BCP) were examined. In this investigation the size of the single ceramic particles was studied by SEM showing that one powder CDA and the fibrous CDA had larger diameters (nearly  $24.65\ \mu\text{m}$ ) than the other powder CDA ( $13.2\ \mu\text{m}$ ) and the BCP ( $6.6\ \mu\text{m}$ ).

Precipitation of calcium phosphate in the presence of double-hydrophilic block copolymers leads to nontrivial superstructures of organized inorganic/organic hybrid material, as characterized in [178]. The polymer micelles act as interactive templates where the organic/inorganic superstructure can range between nested clusters of fine nanofibers to compact mesostructures in which nanoscaled calcium phosphate entities are interspersed with ordered polymers. TEM images of these structures are shown in Figure 12.

Ceramics used in dentistry, such as IPS-Empress 2<sup>TM</sup>, were characterized testing the influence of different immersion times in hydrofluoric acid. The increasing roughness was monitored after etching [179]. In [180] it was found that calcium complexation by albumin plays a key role in early mineralization kinetics of commercial hydroxyapatite and synthesized biphasic ceramics in a bufferless simulated inorganic plasma (HBSS). Mineralization is favored when albumin is preadsorbed and hindered when it is dissolved in HBSS. A review of the interaction between different mica glass-ceramics and bone was presented in [174].

Alumina (sapphire) fatigue was tested in the course of validation as a bioceramic. Corrosion morphologies and fracture surfaces were investigated via SEM and SFM. The fatigue limit was found to be decreased upon stress in isotonic solution with regard to the behavior in air [181].

The biocompatibility of ceramics could be influenced by a variety of parameters. By investigating the cell cytotoxicity and biomechanical strength of the ceramic diopside

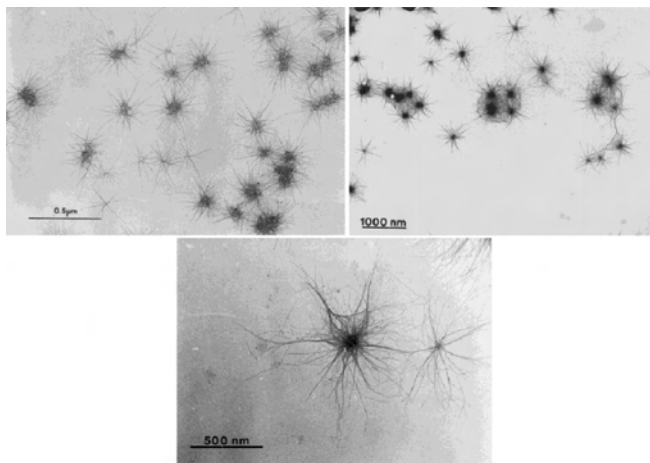


**Figure 12.** TEM images showing the growth of neuron-like calcium-phosphate/polymer mesostructures at pH 4.5 and 5.0 [178].

( $\text{CaOMgO}_2\text{SiO}_2$ ) [171], TEM photographs of osteogenic cells MC3T3-E1 on diopside after 14 days of incubation showed active secretion of crystals from osteoblast-like cells. The cells formed multiple cell layers similar to those on the control coverslips (Thermanox<sup>TM</sup> from NUNC Inc. Roskilde, Denmark). In so-called organoceramics the morphology and properties are significantly changed by the organic macromolecules [175]. In the absence of organics a flakelike morphology of the ceramic was obtained, while rosette-shaped composite particles were obtained in the presence of poly (vinyl alcohol). It is believed that the molecular manipulation of microstructure occurs through the role of polymer chains in nucleation of the inorganic layers.

Hydroxyapatite (HA) in its natural and synthetic origin is an interesting biomaterial not only as coating material as mentioned in Section 5.1 [140–147, 182]. Hydroxyapatite can be fabricated in a porous form. In [183] the authors presented a new method, which is based on the swelling ability of starch when it is heated to  $80\ ^\circ\text{C}$  in the presence of water. Different starch volume fractions and starch particle sizes were added on the HA slurries which were then heat-treated to promote consolidation by starch gelification. SEM pictures reveal the presence of interconnected pores with shape and sizes corresponding to the starch granules used. A degradation study in an acellular synthetic body fluid has shown that the prepared bodies keep their integrity under physiological conditions. The strength of interfacial attachment between bone and HA is related to the crystallinity, the grain size, the stability, and the morphology of the calcium phosphate coating. Post-heat treatment is an essential process of controlling the crystallinity and the grain size of HA coating [184]. The stability of hydroxyapatite was also tested in a saturated citric acid solution (pH1). Highly crystalline hydroxyapatite [185] was used which was produced in a novel pressurized hydrothermal post-plasma-spray process, that converts the amorphous components back to a 96% content of crystalline HA. These samples were compared to coatings with crystalline HA contents ranging from 37.5 to 82%. All coatings showed very similar steady-state dissolution rates except for highly amorphous coating, which was

significantly higher. A result of SEM analysis was that the amorphous coating was degraded substantially more than the other samples, resulting in partial coating exfoliation. The investigation suggests that the treated coating is significantly more resistant to degradation from aggressive detoxification procedures.

Because bioactive glasses (calcium phosphate ceramics) are one of the most biocompatible materials in relation to vertebrate tooth, enamel, dentin, and bone, they have gained a wide acceptance in dentistry and restorative orthopedics, for example, in middle ear reconstruction. Of special interest are the bonelike apatite layers that grow on such glass surface in biological environment [186–192], which is attributed to the catalytic effect of the Si-OH groups, which are formed on the surface of SiO<sub>2</sub>-based glasses [188]. TEM with attached energy dispersive X-ray spectrometer showed that the Ti-OH functional groups of TiO<sub>2</sub> induce apatite nucleation not directly, but through transformation of their calcium compounds and subsequent formation of amorphous calcium phosphate.

A content of recombinant mouse amelogenin (rM179) [186] and recombinant porcine amelogenin (rP172) [187] in a supersaturated calcification solution (SCS) was examined as to its effect on the growth of apatite crystals nucleated on Bioglass<sup>R</sup> 45S5; see also Figure 13. The purpose of this study was to gain a better understanding of the role of amelogenin protein in tooth enamel formation. Under SEM the rM179-containing solution leads to elongated, curve-shaped (500 nm long and 120 nm thick) crystals, while the immersion in blank and bovine serum albumin-containing solution results in smaller plate-shaped respectively needle-shaped crystals. TEM observations showed that the crystals generated by the rM179 immersion appeared to be composed of bundles of longish crystals (15–20 nm thick) orientated parallel to one other. During 0.5–4 h of rP172 solution immersion, the protein assemblies of rP172 remarkably induced the formation of orientated silica gel plates and subsequently of long and thin apatite needle crystals. In [169] bioactive glass discs were produced by forming thin polymeric sheets (100 μm thickness) loaded with jet-milled Bioglass<sup>R</sup> 45S5 particulate (1–10 μm). After heating the discs in air to remove the organic phase, they were sintered at 800, 900, or 1000 °C. The bioactivity was then assessed in Tris buffer. The discs sintered at 900 °C and 1000 °C formed crystalline HA layers after 24 h in Tris as indicated by FTIR, SEM, and EDX analysis. At a lower surface-area-to-volume ratio also on 800 °C sintered ceramic, the formation of HA could be observed. A comparison between ceramic and metal surfaces showed that epithelial cells adhere more on

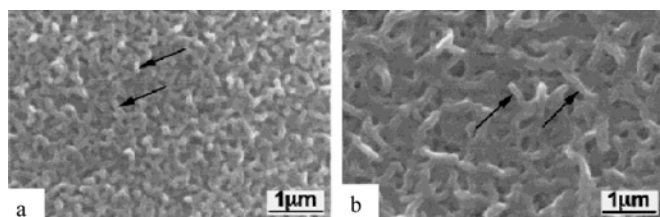


**Figure 13.** SEM micrographs of a bioglass surface [187] after (a) 2 and (b) 4 h of SCS immersion. Arrows point to apatite minerals.

metallic surfaces [132] (see also Section 4.1). A combined XRD, FTIR, EDX, and SEM examination of the *in vitro* reactivity of a sol-gel glass (80S20C) to simulated body fluid (SBF) was presented in [192]. Because of the partial dissolution of the glass in contact with SBF, there are remarkable variations in ionic concentration and pH of the solution. To avoid this behavior, a protocol for tests with continuous exchange was proposed. In a static control experiment a faster formation of the phosphate layer was detected only within the first 6 h. After 7 days large crystalline aggregates and apatite crystals were found on the freshly formed layer. Another form of bioactive glass is silica fibers, which provide alternatives for the design of novel products used in tissue guiding or bone repairs. In [190] the ability of such fibers to induce formation of bonelike calcium phosphate was investigated. The fibers were prepared by dry spinning. The structure of the fibers was varied using three different factors: (1) spinnable sols with different structures and sizes of polymers to establish varying viscosity levels; (2) aging of green-state fibers, and (3) heat treatment. The bioactivity tests were also done in SBF. Different fibers obtained clearly different properties. The fibers spun at about  $\eta > 3$  Pas had the best properties, especially when they were heat treated at 175 °C.

Controlled release glass (CRG) based on calcium and sodium phosphates differs substantially from commercial glass in that it dissolves completely in aqueous environment. The solution rate can be predetermined and adjusted by altering the chemical composition. A SEM study of the hemocompatibility [189] of such glass indicated that selected and controlled compositions of these materials might provide good blood-contacting surfaces.

### 4.3. Polymers

Many different ways to use polymers as biomaterial are reported. This field spreads from vascular implants [193–196] and bone replacement [197–200] to intraocular lenses [201].

#### 4.3.1. Structure and Mechanical Properties

High- and low-density polyethylene (HDPE and LDPE), isotactic and atactic polypropylene (iPP and aPP), and polymer blends were investigated regarding the friction coefficient and the elastic modulus via SFM. Structural changes and the mechanical property changes around the glass transition temperature have been monitored during temperature runs. The enhanced ordering of the backbone correlates to the increased surface modulus. Additionally, the elastic modulus, the time-dependent relaxation process, and the friction properties were measured as a function of pressure. Loads between 1 and 1000 nN were applied. At low pressure the deformation of the polymer is elastic. With increasing pressure there is a phase transition to a plastic behavior attributed to a polymer alignment effect. Friction properties were investigated concerning the contact pressure and contact area, revealing an increased elastic modulus with increased density and crystallinity and a linear increase with contact pressure. Stretching of LDPE was shown to lead to surface roughening and alteration of surface mechanical properties. These experiments show that a material subject



to complex mechanical stresses will change continuously its surface mechanical properties as the nature of the stress changes [102].

Polyethylene and the influence of low molecular weight additives that are added to prevent oxidation were investigated via friction versus load curves. For loads of 1000 nm, the lower friction of the polymer with additives gives way to friction properties of the different samples that are identical [102].

Polyurethane copolymers with hydrophobic and hydrophilic side chains were investigated regarding the mechanical properties changing with the hydrogen bonding between soft (SS) and hard segments (HS). The adhesion force showed a maximum at 57% HS correlated with the highest number of nonassociated urethane groups. The friction mechanisms were investigated as well, showing different mechanisms for the different compositions [102]. The surface structure of six different polycarbonate polyurethane copolymers was investigated with SFM in topography and phase modes. The stoichiometry of the reagents and the chemistry of the hard segment were changed, varying the contribution of diisocyanate, poly(hexyl, ethyl) carbonate, and butane diol. The 1,6-hexane diisocyanate showed a stronger phase separation and the highest values of mean square roughness (RMS) with 3.3 to 10.0 nm with regard to methylene bis(p-phenyl isocyanate) and methylene bis(p-cyclohexyl isocyanate) that have RMS values of 0.8 respectively 0.25 nm. These values have to be viewed with respect to the image processing of a third-order flatten. This is only obvious in this article as the image processing is usually not mentioned, and therefore the values of the other investigations must be examined closely as well. The polymers presented relatively stiff rodlike structures with dimensions of 12 nm in width and 170 nm in length [202].

Investigations on polyurethane and rubber were done with force indentation curves [28].

Differences between polystyrene (PS) and poly(methylmethacrylate) (PMMA) could be determined by measuring the adhesion differences of the different polymers by PFM [95]. Polymer blends of poly(styrene)-block-poly(ethene-co-but-1-ene)-block-poly(styrene) with isotactic and atactic polypropylenes were characterized observing the morphology according to different thermal treatments. It was possible to monitor microphase separations with tapping mode in the phase image [203]. Interfaces between PMMA and polystyrene (PS) could be identified with HM-LFM [84] as well as interfaces between poly(acrylonitrile-co-styrene) and polybutadiene respectively between polypropylene and poly(propylene-co-ethylene) [85].

Fractographic investigations looking at the surfaces after a fracture of dental composites consisting of silicon dioxide fillers in a matrix of dimethacrylate resins are presented in [107]. The pristine surfaces and the results of different preparation methods for poly(ethylene glycol) (PEGMA) grafted poly(tetrafluoro ethylene) (PTFE) surfaces were investigated with SFM. The PEGMA treated surfaces exhibited a larger RMS of 144 nm with regard to 129 nm RMS of the pristine PTFE [204]. Hexafluoroethane and tetrafluoroethylene films produced by glow discharge plasma deposition show with SFM a pinhole free and smooth surface

with a RMS roughness of 0.4 to 2 nm. Scanning in contact mode with moderate applied loads yields rippled films. At small scan sizes, and high velocities and load, the film disrupts. The surface modulus was estimated between 1.2 and 5.5 GPa [205]. Poly(vinylidene difluoride) (PVDF) and poly(vinylidene fluoride/hexafluoropropylene) [P(VDF-HFP)] polymers were radiation grafted with polystyrene (PS) yielding an increase in surface roughness upon irradiation and a smoothing of the valleys by further functionalization by chlorosulfonation and sulfonamidation [206].

#### 4.3.2. Response to Proteins

In the field of ultrafiltration of biological fluids such as blood, biofouling respectively membrane fouling is an important issue resulting in pore plugging, pore narrowing, and cake deposition. Hydrophobic polysulfone membrane interactions with hen egg lysozyme were investigated with the surface force apparatus and the topography with SFM [207]. Forces between cellulose acetate films and human serum albumin, HSA, respectively ribonuclease A, RNase, were investigated in the same way [208]. The comparison of forces between the proteins fibronectin, fibrinogen, and albumin and a hydrophilic cellulosic membrane, a hydrophilic glass surface, and a hydrophobic polystyrene surface showed that the forces on hydrophobic surfaces are an order of magnitude larger than the ones on hydrophilic surfaces. Additionally, the influence of surface structure on hydrophilic surfaces was described [209].

Collagen on native and oxidized poly(ethylene terephthalate) (PET) was investigated with the aid of X-ray photoelectron spectroscopy (XPS). Time-dependent differences were observed in stability at times between 5 s and 5 min with an easy-to-disturb surface structure (scan ranges from 2 to 5  $\mu\text{m}$ ) as monitored via SFM. The investigations were done in air, leaving the results ambiguous, as the topographical information can be altered by drying leading to different structures and orientations on the surface [210].

#### 4.3.3. Tissue Response

The tissue response to polymers is investigated in a variety of studies [200, 211–214].

There are different attributes, which complicate the use of polymer vascular implants. Especially for small-diameter vascular grafts the blocking is an important problem. For example, calcification decreases the vascular diameter. So calcification of subdermally implanted polyurethane is enhanced by calciphylaxis as shown by SEM [194]. Another aim is to decrease the thrombogenicity [195] of polymeric biomaterials. These “heparin-like” polymers have a specific affinity for antithrombin III and thus are able to catalyze the inhibition of thrombin. In this study sulfur, sodium, fluorine, and carbon are determined by SEM combined with energy dispersive X-ray analysis. The objective of another project [196] was to define a series of assays for the evaluation of hemocompatibility of cardiovascular devices. In [193] a polyamino-acid urethane copolymer coated vascular prosthesis (1.5 mm diameter) was developed to enhance endothelialization. SEM showed the homogeneous coating of clinically available synthetic PTFE grafts. Prosthetic heart valves made of isotropic pyrolytic carbon (LTIC) are

a successful biomaterial application which is investigated together with other difficult-to-image biomaterials in [17]. Low-voltage, high-resolution scanning electron microscopy shows that LTIC valve leaflets are significantly rougher than previously described, and that LTIC induces extensive platelet spreading *in vitro*, even in the presence of considerable albumin.

Calcification is also crucial in the use of intraocular lenses [201]. To assess this, intraocular lens optic materials were implanted intramuscularly and/or subcutaneously in rabbits for up to 90 days. SEM and energy dispersive X-ray spectroscopy (EDX) were used to detect discrete nodules containing both calcium and phosphate. Calcification only was noted on intramuscularly, subcutaneously, and intraocularly implanted experimental acrylic and intramuscularly implanted hydrogel material. In contrast, the intramuscularly or subcutaneously implanted silicon, PMMA, and acrylic optic materials showed no calcification.

Glassy polymeric carbon was treated by bombardment with energetic ions in different curing states. The roughness that leads to a better thromboresistance was monitored with SFM [18].

An approach to manage chronic osteomyelitis (inflammation of the periosteum) utilizes the implementation of antibiotic-impregnated PMMA beads for local delivery of antibiotics. The study of the getamycin sulphate release from a commercial acrylic bone cement was presented in [197].

A very interesting feature is the biodegradability of some polymers either natural or synthetic. The surface structure of blends with different composition of poly lactic acid (PLA) and poly sebaic acid (PSA) and their degradation properties were investigated. Single component PLA exhibits a smooth surface whereas PSA films possess spherulites at the surface. Blends of 70%, 50%, and 30% PLA exhibited granular respectively pitted surface structures but no fibrous structures visible in SFM. The monitoring of the erosion within 10 minutes showed that PLA is present in granules [16]. Phase imaging with the SFM yields phase shifts at different compositions ranging between 45° and 52°. The presence of PSA microdomains in blend of 50% PSA could be confirmed [215].

Screws, made of poly-L-lactic acid, were inserted axially into the right distal femur in 18 rabbits. The degradation and phagocytosis were assessed histologically and by TEM [198]. In the TEM specimens, polymeric particles of an average area of 2  $\mu\text{m}^2$  were seen to be located intercellularly with phagocytic cells. In 4.5-year specimens, the size of the polymeric particles, measured as area and perimeter, was significantly smaller than that of the 3-year specimens. The findings indicate that the ultimate degradation process of PLA is much longer than it was previously thought. Porous structured polymers to mimic natural extracellular matrix were investigated in [216] and in [217]. A biodegradable blend of starch with ethylene-vinyl alcohol copolymer (SEVA-C) with hydroxyapatite as filler was investigated, monitoring the degradation and the buildup of calcium phosphate crystals over a time span of up to 30 days in simulated body fluid. Only with the filler the buildup of the calcium phosphate layer could be observed. Within 8 hours

the roughness increased, after 24 hours calcium phosphate nuclei covered the surface, and after 126 hours a dense and uniform layer was present [218].

#### 4.4. Composites

Composites of different material systems can combine the advantages of both. Therefore a variety of composite materials have been developed. One distinguishes composites which work as bone cements [172, 219, 220] and those that include living cells and were used for tissue engineering [176, 221].

To quantify the bone-implant interface of high-strength HA/poly(L-lactide) (PLA) composite rods an affinity index was calculated, which was the length of bone directly joined to the rods, expressed as a percentage of the total length of the rod's surface [219]. Calcined and uncalcined HA particles which amount to 30 or 40% by weight of the composite were implanted in the distal femora of 50 rabbits and after 2, 4, 8, and 25 weeks they were examined by SEM, TEM, and light microscopy. In all composites new bone formation could be examined after 2 weeks. SEM showed direct bone contact with the composites without intervening fibrous tissue. The affinity indices of all the composite rods were significantly higher than those of unfilled control PLA rods. The maximum affinity index (41%) was attained at 4 weeks in 40% calcinated HA-containing rods.

Another approach to use composites is to increase the compressive strength of calcium phosphate cement (CPC) [220], which limits their use to non-load-bearing applications, by the means of water-soluble polymers. Composites formulated with the polycations poly(ethylenimine) and poly(allylamine hydrochloride) exhibited compressive strengths up to six times greater than that of pure CPC material. SEM results indicate a denser, more interdigitated microstructure. The increased strength was attributed to the polymer's capacity to bridge between multiple crystallites and to absorb energy through plastic flow. Glass-ceramic, as mentioned previously, is also used in composites with bisphenol-a-glycidyl dimethacrylate (Bis-GMA)-based resin. These were compared with composites containing HA or  $\beta$ -tricalcium phosphate (TCP) as the inorganic filler [172]. After 10 weeks of implantation into tibial metaphyses of rabbits, the ceramic-containing sample was in direct contact with bone and ceramic particles were partially adsorbed at the surface. The HA-containing cement was in contact with partially mineralized extracellular matrix. In 25-week specimens, ceramic particles were completely absorbed and replaced by new bone, and there was no intervening soft tissue. The tissue response of nano-hydroxyapatite/collagen composite was investigated in [176]. At the interface of the implant and marrow tissue, solution-mediated dissolution and giant-cell-mediated resorption led to the degradation of the composite. Interfacial bone formation by osteoblasts was also evident. The composite can be incorporated into bone metabolism instead of being a permanent implant. Nano-HA was also used in a porous collagen composite, to build up a three-dimensional osteogenic cell/nano-HA-collagen construct [221]. SEM and histological examination have demonstrated the development of the cell/material complex. Other biodegradable composites are

based on polyhydroxybutyrate-polyhydroxyvalerate (PHB-PHV) [222]. SEM showed that the intended compositions of composites were achieved and bioceramic particles were well distributed in the polymer.

#### 4.5. Biological Samples

In the dental field enamel and dentin are materials under investigation. Effects of demineralization, for example, by soft drinks on the natural tooth structure, and improvements of resin adhesion important in dental therapy were studied.

Topographical changes of human teeth in various liquids were characterized in [223]. The initially smooth and finely grained surfaces were changed to a rougher and more coarsely grained surface. Dissolution rates for soda pops with pH values between 4 and 5 were calculated to be 3 mm/year in contrast to water with a rate of 0.4 mm/year. The change in mechanical properties of tooth enamel induced by demineralization via soft drinks was investigated in [224]. The changes in hardness are the first step in the dissolution process. The influence of different drinks (orange juice, a black currant drink, and water) could be determined in hardness and topography, where orange juice showed the strongest demineralization. A small critical discussion about the applicability of the model of enamel erosion characterized via SFM topography measurements is given in [225].

The influence of sodium hypochloride on dentin and dentin collagen was characterized by checking on the topography and the hardness respectively the reduced elastic modulus via an SFM in contact mode respectively a nanoindenter [226]. Dentin was removed, leaving a remnant collagen matrix and resulting in a hardness of 75% of its original value. The enhanced roughness could provide a better bonding substrate because of the enhanced surface area. The mechanism of the bonding via the adhesive Gluma consisting of glutardialdehyde and hydroxyethylmethacrylate (HEMA) could be elucidated with SFM imaging of the interaction taking place upon introduction of the adhesive to the tooth hard tissue. It forms a solid layer covering the dentin tubules. The mechanism of the amide-induced polymerization of aqueous HEMA glutardialdehyde mixtures could be confirmed by SFM [227]. Other similar SFM investigations on dentin are published in [107] and a detailed review of characterization of dentin, enamel, and collagen covering as well macroscopical features is given in [120]. The ultrastructure and nanoleakage of dentin bonding by the use of a two-step, polyalkenoic acid-containing, self-priming dentin adhesive in human molars was observed by TEM [228] to also check the effect of a 5% sodium hypochlorite solution (NaOCl) treatment. The NaOCl should remove the collagen fibrils at demineralized dentin and so may facilitate the infiltration of adhesive resins into a dentin substrate. To get a comparison, dentin was also acid-etched by 35%  $H_3PO_4$ ; the leakage manifestations were similar for both treatments. So no additional advantage in using NaOCl with the used adhesives was found.

Some final features of surface investigations by nanoanalytical tools discussed in the remainder of this section show in which broad range of biologically modified surfaces scanning probe techniques can be used. These studies include molecular layers like lipids or proteins and extend to cellular

arrangements. They are only a small selection showing the principal ability of the technique.

The activity of a liposome layer with ganglioside G(M1) was tested with SFM [229]. Supported phospholipid bilayers (SPBs) as model substrates for cell membranes are imaged with SFM in [230]. The height, adhesion, and friction of mixed phospholipid layers is monitored in [231].

Microelastic mapping of living cells was done by SFM [28, 232].

A recent overview of the characterization of bacterial biofilms is given in [163].

Still a lot of experiments were done in ambient conditions and biological materials such as hexagonal packed intermediate (HPI) layers, DNA, tobacco mosaic virus, and collagen deposited on various substrates were imaged with noncontact dynamic force modes with little destruction but not in native states [233].

STM as well is usually used for investigations of biological films in air, leaving a change in structure. Pictures could be taken from C-phycocyanin (C-PC) which was isolated from the blue-green alga *Spirulina platensis* [234], and tobacco mosaic virus [235].

Nonhuman hard tissue like abalone nacre [236] was imaged and mineralization pathways revealed to form single crystals [237], and the elasticity of cow cartilage was tested [28].

The magnetic force from a magnetotactic bacterium [238] could be imaged with the magnetic force mode with SFM. Membrane deformation of living glial cells [239] or fibroblasts [240] were done via SFM. Other measurements are mentioned in [241] where local elastic properties respectively Young's modulus were mapped via force mapping.

The viscous properties of cells have been investigated on kidney epithelial cells with laser tracking microrheology. Comparisons with other authors are given, revealing cytoplasmic viscosities that range for different experiments within five orders of magnitude around  $2 \cdot 10^3$  Pa·s [110]. Also viscous properties of fibroblasts were measured with magnetic bead microrheometry [109].

An overview of renal cell characterization with the SFM is given in [242]. Immobilized antibodies have been characterized by SECM to monitor the active binding sites [243].

Microelastic properties of bone marrow (cow tibia) were measured via SFM in [244].

This demonstrates that nanoanalytical tools not only are useful for characterizing the pure biomaterial surface alone but are also helpful for investigating surfaces in contact with biological materials of all kinds.

## 5. CONCLUSIONS

This chapter illustrates the impact of new imaging techniques such as SPMs on biointerface analysis of biomaterials. SFM and STM investigations provide structural, rheological, and functional information about surfaces. Force distance curves contain complex information about interactions of biofilms with the substrate. Electron microscopy as a "classical" tool complements the techniques, in particular because imaging artifacts are much better known than in SPM.

There are two trends to be seen. First, new methods are being developed, such as scanning near-field optical microscopy, another member of the SPM family. This method will combine all possibilities of optical microscopies, in particular all labelling techniques, but without the diffraction limit of resolution. However, there are still technological hurdles, in particular to produce bright and narrow light sources routinely. As soon as these problems are overcome, this method will play an increasing role in biomaterial research.

The second trend goes to multifunctional analysis on the nanometer scale, which will allow the understanding of the basic mechanisms of interaction between biological and synthetic materials. This will further help to improve biointerfaces used for biomaterials. The challenge is now to develop multifunctional tools that are easily accessible and suitable for the analysis of biomaterials based on SPM techniques, as well as in combinations with methods characterizing macroscopic properties to bridge the gap between these two worlds.

Still, all these new methods are in their infancies in their use on biomaterials. However, in the near future they will become much more common and effective and will influence the field substantially.

## GLOSSARY

**Arene cavity** The cavity formed by the enclosure of the aromatic rings in a calixarene.

**Calix[n]arenes** A group of phenolic macrocyclic molecules resulted from the condensation of *para*-substituted phenol and formaldehyde. ('n' refers to the number of phenolic units.)

**Crystal structure** Three-dimensional arrangement of atoms derived from single crystal X-ray diffraction that provides information about the structure, conformation, and geometry of the molecule.

**Functionalization** Chemical modification on the lower or upper rim leading to the formation of derivatives containing appropriate functional groups.

**Lower rim** The rim containing the phenolic -OH groups in a *para*-substituted calixarene.

**Metalloenzymes** Those enzymes that exhibit their function as a result of the presence of a specific metal ion.

**Receptor** A molecule that possesses the ability to bind to neutral or ionic species through recognition.

**Upper rim** The rim containing the groups present at the *para*-position in a calixarene.

## REFERENCES

1. J. W. Arnold and G. W. Bailey, *Poultry Sci.* 78, 1839 (2000).
2. I. Chet and P. Asketh, *Appl. Microbiol.* 30, 1043 (1975).
3. L. Tiefenauer and R. Ros, *Colloids Surfaces B* 23, 95 (2002).
4. B. Kasemo, *Surf. Sci.* 500, 656 (2002).
5. E. Duncan, *Biomaterials Forum* 23, 3 (2001).
6. J. M. Gomez-Vega, E. Saiz, A. P. Tomsia, T. Oku, K. Sukanuma, G. W. Marshall, and S. J. Marshall, *Adv. Mater.* 12, 894 (2000).

7. E. Wintermantel and S.-W. Ha, "Biokompatible Werkstoffe und Bauweisen: Implantate für Medizin und Umwelt." Springer, Berlin, 1998.
8. E. A. Vogler, *Adv. Colloid Interface Sci.* 74, 69 (1998).
9. R. E. Smalley, "Proceedings of the Robert A. Welch Foundation Conference on Chemical Research—Regulation of Proteins by Ligands," 1992, Vol. 36, pp. 161–169.
10. B. Vigolo, A. Penicaud, C. Coulon, C. Sauder, R. Pailler, C. Journet, P. Bernier, and P. Poulin, *Science* 290, 1331 (2000).
11. P. Poulin, B. Vigolo, and P. Launois, *Carbon* 40, 1741 (2002).
12. H. Stadler, M. Mondon, and C. Ziegler, *Anal. Bioanal. Chem.* in print (2003).
13. D. M. Brunette, P. Tengvall, M. Textor, and P. Thomsen, "Titanium in Medicine: Material Science, Surface Science, Engineering, Biological Responses and Medical Applications." Springer, Berlin, 2001.
14. C. M. Chan, T. M. Ko, and H. Hiraoka, *Surf. Sci. Rep.* 24, 1 (1996).
15. D. G. Castner and B. D. Ratner, *Surf. Sci.* 500, 28 (2002).
16. M. C. Davies, K. M. Shakesheff, A. G. Shard, A. Domb, C. J. Roberts, S. J. B. Tendler, and P. M. Williams, *Macromolecules* 29, 2205 (1996).
17. S. L. Goodman, *Cells Mater.* 6, 303 (1996).
18. A. L. Evelyn, M. G. Rodrigues, D. Ila, R. L. Zimmerman, D. B. Poker, and D. K. Hensley, "Materials Research Society Symposium Proceedings," 2001, Vol. 629, FF9.6.1-FF9.6.6.
19. G. Binnig, H. Rohrer, C. Gerber, and E. Weibel, *Phys. Rev. Lett.* 49, 57 (1982).
20. G. Binnig, C. F. Quate, and C. Gerber, *Phys. Rev. Lett.* 56, 930 (1986).
21. R. M. Overney and E. Meyer, *Nature* 359, 133 (1992).
22. S. M. Smith and J. L. Gilbert, *Proc. Electrochem. Soc.* 94, 229 (1994).
23. H. G. Hansma, *Proc. Nat. Acad. Sci. USA* 96, 14678 (1999).
24. C. Galli, M. Collaud Coen, R. Hauert, V. L. Katanaev, M. P. Wymann, P. Gröning, and L. Schlapbach, *Surf. Sci.* 474, L180 (2001).
25. D. T. Pierce and P. R. Unwin, *Anal. Chem.* 64, 1795 (1992).
26. A. S. Paulo and R. García, *Surf. Sci.* 471, 71 (2001).
27. F. Dubourg and J. P. Aimé, *Surf. Sci.* 466, 137 (2000).
28. A. L. Weisenhorn, M. Khorsandi, S. Kasas, V. Gotzos, and H.-J. Butt, *Nanotechnology* 4, 106 (1993).
29. D. R. Luder and B. A. Parkinson, *Anal. Chem.* 297 (1995).
30. R. W. Carpick and M. Salmeron, *Chem. Rev.* 97, 1163 (1997).
31. M. Heyde, H. Sturm, and K. Rademann, *Surf. Interface Anal.* 27, 291 (1999).
32. M. Radmacher, W. T. R and E. G. H, *Biophys. J.* 64, 735 (1993).
33. W. Han, S. M. Lindsay, and T. Jing, *Appl. Phys. Lett.* 69, 4111 (1996).
34. T. Hantschel, S. Slesazeck, P. Niedermann, P. Eyben, and W. Vandervorst, *Microelectron. Eng.* 57–58, 749 (2001).
35. Y. Miyahara, T. Fujii, S. Watanabe, A. Tonoli, S. Carabelli, H. Yamada, and H. Bleuler, *Appl. Surf. Sci.* 140, 428 (1999).
36. T. E. Schäffer, M. Viani, D. A. Walters, B. Drake, E. K. Runge, J. P. Cleveland, M. A. Wendman, and P. K. Hansma, *SPIE* 3009, 48 (1997).
37. D. A. Walters, J. P. Cleveland, N. H. Thomson, P. K. Hansma, M. A. Wendman, G. Gurley, and V. Ellings, *Rev. Sci. Instruments* 67, 3583 (1996).
38. D. A. Walters, M. Viani, G. T. Paloczi, T. E. Schäffer, J. P. Cleveland, M. A. Wendman, G. Gurley, V. Ellings, and P. K. Hansma, *SPIE* 3009, 43 (1998).
39. M. B. Viani, T. E. Schäffer, G. T. Paloczi, L. I. Pietrasanta, B. L. Smith, J. B. Thompson, M. Richter, M. Rief, H. E. Gaub, K. W. Plaxco, A. N. Cleland, H. G. Hansma, and P. K. Hansma, *Rev. Sci. Instruments* 70, 4300 (1999).
40. A. Feiler, P. Attard, and I. Larson, *Rev. Sci. Instruments* 71, 2746 (2000).

41. J. L. Hazel and V. V. Tsukruk, *Thin Solid Films* 339, 249 (1999).
42. J. M. Neumeister and W. A. Ducker, *Rev. Sci. Instruments* 65, 2527 (1994).
43. J. L. Hutter and J. Bechhoefer, *Rev. Sci. Instruments* 64, 1868 (1993).
44. J. E. Sader and L. White, *J. Appl. Phys.* 74, 1 (1994).
45. J. E. Sader, *Rev. Sci. Instruments*, 66, 4583 (1995).
46. J. E. Sader, I. Larson, P. Mulvaney, and L. R. White, *Rev. Sci. Instruments* 66, 3789 (1995).
47. J. E. Sader, J. W. M. Chon, and P. Mulvaney, *Rev. Sci. Instruments* 70, 3967 (1999).
48. J. D. Holbery, V. L. Eden, M. Sarikaya, and R. M. Fisher, *Rev. Sci. Instruments* 71, 3769 (2000).
49. R. Lévy and M. Maaloum, *Nanotechnology* 13, 33 (2002).
50. P. Niedermann, W. Hänni, D. Morel, A. Perret, N. Skinner, P.-F. Indermühle, N.-F. d. Rooij, and P.-A. Buffat, *Appl. Phys. A Mater. Sci. Process.* 66, S31 (1998).
51. O. H. Willemsen, M. M. E. Snel, A. Cambi, J. Greve, B. G. D. Grooth, and C. G. Figdor, *Biophys. J.* 79, 3267 (2000).
52. T. Nakagawa, K. Ogawa, and T. Kurumizawa, *J. Vac. Sci. Technol. B* 12, 2215 (1994).
53. T. Han, J. M. Williams, and T. P. Beebe, Jr., *Anal. Chim. Acta* 307, 365 (1995).
54. T. Ito, M. Namba, P. Bühlmann, and Y. Umezawa, *Langmuir* 13, 4323 (1997).
55. X. Chen, M. C. Davies, C. J. Roberts, S. J. B. Tendler, and P. M. Williams, *Langmuir* 13, 4106 (1997).
56. J. Piehler, A. Brecht, K. E. Geckeler, and G. Gauglitz, *Biosensors Bioelectron.* 11, 579 (1996).
57. G. U. Lee, L. A. Chrisey, C. E. O'Ferrall, D. E. Pilloff, N. H. Turner, and R. J. Colton, *Isr. J. Chem.* 36, 81 (1996).
58. A. Razatos, Y.-L. Ong, M. M. Sharma, and G. Georgiou, *Proc. Natl. Acad. Sci. USA* 95, 11059 (1998).
59. S. Kim, S.-K. Park, C. Park, and I. C. Jeon, *J. Vac. Sci. Technol. B* 14, 1318 (1996).
60. R. M. D. Stevens, N. A. Frederick, B. L. Smith, D. I. E. Morse, G. D. Stucky, and P. K. Hansma, *Nanotechnology* 11, 1 (2000).
61. K. Moloni, M. R. Buss, and R. P. Andres, *Ultramicroscopy* 80, 237 (1999).
62. V. Barwich, M. Bammerlin, A. Baratoff, R. Bennewitz, M. Guggisberg, C. Loppacher, O. Pfeiffer, E. Meyer, H.-J. Güntherodt, J.-P. Salvetat, J.-M. Bonard, and L. Forró, *Appl. Surf. Sci.* 157, 269 (2000).
63. J. H. Hafner, C. L. Cheung, and C. M. Lieber, *Nature* 398, 761 (1999).
64. E. S. Snow, P. M. Campbell, and J. P. Novak, *J. Vac. Sci. Technol. B* 20, 822 (2002).
65. S. S. Wong, E. Joselevich, A. T. Wooley, C. L. Cheung, and C. M. Lieber, *Nature* 394, 52 (1998).
66. L. Montelius, J. O. Tegenfeldt, and P. v. Heeren, *J. Vac. Sci. Technol. B* 12, 2222 (1994).
67. F. Zenhausern, M. Adrian, B. ten Heggler-Bordier, F. Ardizzoni, and P. Descouts, *J. Appl. Phys.* 73, 7232 (1993).
68. J. S. Villarrubia, *Surf. Sci.* 321, 287 (1994).
69. J. S. Villarrubia, *J. Res. Nat. Inst. Stand. Technol.* 102, 425 (1997).
70. B. A. Todd and S. J. Eppell, *Surf. Sci.* 491, 473 (2001).
71. B. A. Todd, S. J. Eppell, and F. R. Zypman, *J. Appl. Phys.* 88, 7321 (2000).
72. S. Hosaka, T. Morimoto, K. Kuroda, H. Kunitomo, T. Hiroki, T. Kitsukawa, S. Miwa, H. Yanagimoto, and K. Murayama, *Microelectron. Eng.* 57–58, 651 (2001).
73. T. Göddenhenrich, S. Müller, and C. Heiden, *Rev. Sci. Instruments* 65, 2870 (1994).
74. J. Krim, *Surf. Sci.* 500, 741 (2002).
75. E. W. van der Vegte and G. Hadziioannou, *Langmuir* 13, 4357 (1997).
76. L. Frisbie, *Rozsnyai, Science* 265, 2071 (1994).
77. S. Akari, D. Horn, H. Keller, and W. Schrepp, *Adv. Mater.* 7, 549 (1995).
78. R. McKendry and M.-E. Theoclitou, *Nature* 391, 566 (1998).
79. T. Hantschel, P. Niedermann, T. Trenkler, and W. Vandervorst, *Appl. Phys. Lett.* 76, 1603 (2000).
80. F.-B. Li, G. E. Thompson, and R. C. Newman, *Appl. Surf. Sci.* 126, 21 (1998).
81. K. Wadu-Mesthrige, N. A. Amro, J. C. Garno, S. Cruchon-Dupeyrat, and G. Y. Liu, *Appl. Surf. Sci.* 175–176, 391 (2001).
82. F. Oulevey, G. Gremaud, A. Sémoroz, A. J. Kulik, N. A. Burnham, E. Dupas, and D. Gourdon, *Rev. Sci. Instruments* 69, 2085 (1998).
83. U. Rabe, S. Amelio, M. Kopycinska, S. Hirsekorn, M. Kempf, M. Göken, and W. Arnold, *Surf. Interface Anal.* 33, 65 (2002).
84. H. Sturm, *Macromol. Symp.* 147, 249 (1999).
85. H. Sturm, E. Schulz, and M. Munz, *Macromol. Symp.* 147, 259 (1999).
86. R. García and R. Pérez, *Surf. Sci. Rep.* 47, 197 (2002).
87. N. A. Burnham, O. P. Behrend, F. Oulevey, G. Gremaud, P.-J. Gallo, D. Gourdon, E. Dupas, A. J. Kulik, H. M. Pollock, and G. A. D. Briggs, *Nanotechnology* 8, 67 (1997).
88. G. Couturier, J. P. Aimé, J. Salardenne, R. Boisgard, A. Gourdon, and S. Gauthier, *Appl. Phys. A Mater. Sci. Process.* 71, S47 (2001).
89. C. A. J. Putman, K. O. Van der Werf, B. G. De Grooth, N. F. Van Hulst, and J. Greve, *Appl. Phys. Lett.* 64, 2454 (1994).
90. B. Basnar, G. Friedbacher, H. Brunner, T. Vallant, U. Mayer, and H. Hoffmann, *Appl. Surf. Sci.* 171, 213 (2001).
91. R. G. Winkler, J. P. Spatz, S. Sheiko, M. Möller, R. Reineker, and O. Marti, *Phys. Rev. B* 54, 8908 (1996).
92. J. Tamayo and R. García, *Langmuir* 12, 4430 (1996).
93. J. Tamayo and R. García, *Appl. Phys. Lett.* 71, 2394 (1997).
94. A. Noy, C. Sanders, D. Vezenov, S. Wong, and C. Lieber, *Langmuir* 14, 1508 (1998).
95. H.-U. Krotil, T. Stifter, H. Waschipky, K. Weishaupt, S. Hild, and O. Marti, *Surf. Interface Anal.* 27, 336 (1999).
96. W. F. Heinz and J. H. Hoh, *Biophys. J.* 76, 528 (1999).
97. J. Zhong, Q. Niu, and Z. Zhang, *Surf. Sci. Lett.* 516, L547 (2002).
98. H. Hosoi, M. Kimura, K. Hayakawa, K. Sueoka, and K. Mukasa, *Appl. Phys. A Mater. Sci. Process.* 72, S23 (2001).
99. N. A. Burnham, R. J. Colton, and H. M. Pollock, *Nanotechnology* 4, 64 (1993).
100. B. Cappella and G. Dietler, *Surf. Sci. Rep.* 34, 1 (1999).
101. B. Capella, P. Baschieri, C. Frediani, P. Miccoli, and C. Ascoli, *IEEE Eng. Medicine Biol.* 58 (1997).
102. A. Opdahl, S. Hoffer, B. Mailhot, and G. A. Somorjai, *Chem. Rec.* 1, 101 (2001).
103. J. N. Israelachvili and G. E. Adams, *J. Chem. Soc. Faraday Trans. I* 74, 975 (1978).
104. J. N. Israelachvili, "Intermolecular and Surface Forces," 2nd ed. Academic Press, San Diego, 1991.
105. N. A. Burnham and A. J. Kulik, in "Handbook of Micro/Nanotribology." CRC Press, Boca Raton, FL, 1997.
106. A. Vinckier and G. Semenza, *FEBS Lett.* 430, 12 (1998).
107. K. D. Jandt, *Surf. Sci.* 491, 303 (2001).
108. I. N. Sneddon, *Int. J. Eng. Sci.* 3, 47 (1965).
109. A. R. Bausch, F. Ziemann, A. A. Boulbitch, K. Jacobson, and E. Sackmann, *Biophys. J.* 75, 2038 (1998).
110. S. Yamada, D. Wirtz, and S. C. Kuo, *Biophys. J.* 78, 1736 (2000).
111. S. L. Flegler, J. W. Heckman, and K. L. Klomparens, "Elektronenmikroskopie." Spektrum Akademischer Verlag, Heidelberg, 1993.
112. E. Ruska, *Z. Phys.* 87, 580 (1934).
113. E. Ruska, *J. Ultrastructure Mole. Structure Res.* 95, 3 (1986).
114. D. Chescocoe and P. J. Goodhew, "Microscopy Handbooks 20: The Operation of Transmission and Scanning Electron Microscopes." Oxford Univ. Press, Oxford, 1990.
115. L. Reimer, "Optical Sciences 80: Energy-Filtering Transmission Electron Microscopy." Springer, Berlin, 1995.

116. H. Bethge and J. Heydenreich, "Elektronenmikroskopie in der Festkörperphysik." Springer, Berlin, 1982.
117. M. v. Ardenne, *Z. Phys.* 109, 553 (1938).
118. M. Knoll and R. Thiele, *Z. Phys.* 113, 260 (1939).
119. G. Valdre, "Fundamental Properties of Nanostructured Materials, National School of the Condensed Matter Group," 1994, 99–110.
120. F. H. Jones, *Surf. Sci. Rep.* 42, 75 (2001).
121. S. Fischer, K.-D. Schierbaum, and W. Göpel, *Vacuum* 48, 601 (1997).
122. S. Fischer, A. W. Munz, K.-D. Schierbaum, and W. Göpel, *Surf. Sci.* 337, 17 (1995).
123. S. Fischer, A. W. Munz, K.-D. Schierbaum, and W. Göpel, *J. Vac. Sci. Technol. B* 14, 961 (1996).
124. S. Gan and D. R. B. Y. Liang, *Surf. Sci.* 459, L498 (2000).
125. P. Cacciafesta, A. D. L. Humphris, K. D. Jandt, and M. J. Miles, *Langmuir* 16, 8167 (2000).
126. J. Lausmaa, B. Kasemo, H. Mattsson, and H. Odellius, *Appl. Surf. Sci.* 45, 189 (1990).
127. L. Sirghi, M. Nakamura, Y. Hatanaka, and O. Takai, *Langmuir* 17, 8199 (2001).
128. M. P. Casaletto, G. M. Ingo, S. Kaciulis, G. Mattogno, L. Pandolfi, and G. Scavia, *Appl. Surf. Sci.* 172, 167 (2001).
129. C. Aparicio, F. J. Gil, C. Fonseca, M. Barbosa, and J. A. Planell, *Biomaterials* 24, 263 (2003).
130. M. Taborelli, M. Jobin, P. Francois, P. Vaudaux, M. Tonetti, S. Szmukler-Moncler, J. P. Simpson, and P. Descouts, *Clin. Oral Implants Res.* 8, 208 (1997).
131. P. Cacciafesta, K. R. Hallam, A. C. Watkinson, G. C. Allen, M. J. Miles, and K. D. Jandt, *Surf. Sci.* 491, 405 (2001).
132. L. Raisanen, M. Kononen, J. Juhanaja, P. Varpavaara, J. Hautaniemi, J. Kivilahti, and M. Hormia, *J. Biomed. Mater. Res.* 49, 79 (2000).
133. J. Lausmaa, M. Ask, U. Rolander, and B. Kasemo, *Mater. Res. Soc. Symp. Proc.* 110, 647 (1988).
134. Y. X. Leng, J. Y. Chen, Z. M. Zeng, X. B. Tian, P. Yang, N. Huang, Z. R. Zhou, and P. K. Chu, *Thin Solid Films* 377–378, 573 (2000).
135. B. Thierry, M. Tabrizian, O. Savadogo, and L. H. Yahia, *J. Biomed. Mater. Res.* 49, 88 (2000).
136. A. Nanci, J. D. Wuest, L. Peru, P. Brunet, V. Sharma, S. Zalzal, and M. D. McKee, *J. Biomed. Mater. Res.* 40, 324 (1998).
137. J. P. Bearinger, C. A. Orme, and J. L. Gilbert, *Surf. Sci.* 491, 370 (2001).
138. A. A. Ejov, S. V. Savinov, I. V. Yaminsky, J. Pan, C. Leygraf, and D. Thierry, *J. Vac. Sci. Technol. B* 12, 1547 (1994).
139. C. Hallgren, H. Reimers, J. Gold, and A. Wennerberg, *J. Biomed. Mater. Res.* 57, 485 (2001).
140. E. T. den Braber, H. V. Jansen, M. J. de Boer, H. J. Croes, M. Elwenspoek, L. A. Ginsel, and J. A. Jansen, *J. Biomed. Mater. Res.* 40, 425 (1998).
141. J. L. Ong, L. C. Lucas, G. N. Raikar, J. J. Weimer, and J. C. Gregory, *Colloids Surf. A* 87, 151 (1994).
142. A. M. Ektessabi and H. Kimura, *Thin Solid Films* 270, 335 (1995).
143. A. Montenero, G. Gnappi, F. Ferrari, M. Cesari, E. Salvioli, L. Mattogno, S. Kaciulis, and M. Fini, *J. Mater. Sci.* 35, 2791 (2000).
144. C. Massaro, M. A. Baker, F. Cosentino, P. A. Ramires, S. Klose, and E. Milella, *J. Biomed. Mater. Res.* 58, 651 (2001).
145. M. Svehla, P. Morberg, B. Zicat, W. Bruce, D. Sonnabend, and W. R. Walsh, *J. Biomed. Mater. Res.* 51, 15 (2000).
146. W. J. Lo and D. M. Grant, *J. Biomed. Mater. Res.* 46, 408 (1999).
147. J. Hemmerle, A. Oncag, and S. Erturk, *J. Biomed. Mater. Res.* 36, 418 (1997).
148. X. Nie, A. Leyland, A. Matthews, J. C. Jiang, and E. I. Meletis, *J. Biomed. Mater. Res.* 57, 612 (2001).
149. J. E. Hulshoff, K. van Dijk, J. E. de Ruijter, F. J. Rietveld, L. A. Ginsel, and J. A. Jansen, *J. Biomed. Mater. Res.* 40, 464 (1998).
150. Y. Z. Yang, J. M. Tian, J. T. Tian, Z. Q. Chen, X. J. Deng, and D. H. Zhang, *J. Biomed. Mater. Res.* 52, 333 (2000).
151. I. C. Lavos-Valereto, S. Wolynec, M. C. Deboni, and B. Konig, Jr., *J. Biomed. Mater. Res.* 58, 727 (2001).
152. M. Wei, A. J. Ruys, M. V. Swain, S. H. Kim, B. K. Milthorpe, and C. C. Sorrell, *J. Mater. Sci. Mater. Med.* 10, 401 (1999).
153. T. Kasuga, M. Nogami, M. Niinomi, and T. Hattori, *Biomaterials* 24, 283 (2003).
154. A. El-Ghannam, L. Starr, and J. Jones, *J. Biomed. Mater. Res.* 41, 30 (1998).
155. M. Mondon, Untersuchungen zur Proteinadsorption auf medizinisch relevanten Oberflächen mit Rasterkraftmikroskopie und dynamischer Kontaktwinkelanalyse, Ph.D. Thesis, Department of Physics, University of Kaiserslautern, 2002.
156. M. Esposito, J. Lausmaa, J. M. Hirsch, and P. Thomsen, *J. Biomed. Mater. Res.* 48, 559 (1999).
157. D. E. Stefflik, R. S. Corpe, F. T. Lake, T. R. Young, A. L. Sisk, G. R. Parr, P. J. Hanes, and D. J. Berkery, *J. Biomed. Mater. Res.* 39, 611 (1998).
158. D. E. Stefflik, R. S. Corpe, T. R. Young, and K. Buttle, *Implant Dentistry* 7, 338 (1998).
159. N. Tanaka, S. Ichinose, Y. Kimijima, and M. Mimura, *Med. Electron Microsc.* 33, 96 (2000).
160. I. Catelas, J. D. Boby, J. J. Medley, D. J. Zukor, A. Petit, and O. L. Huk, *J. Biomed. Mater. Res.* 55, 330 (2001).
161. G. A. Somorjai and P. Chen, *Solid State Ionics* 141–142, 3 (2001).
162. Q. Chen, D. J. Frankel, and N. V. Richardson, *Surf. Sci.* 497, 37 (2002).
163. I. B. Beech, J. R. Smith, A. A. Steele, I. Penegar, and S. A. Campbell, *Colloids Surf. B* 23, 231 (2002).
164. E. A. Sprague, J. C. Palmaz, C. Simon, and A. Watson, *J. Long-Term Effects of Medical Implants* 10, 111 (2000).
165. R. D. Powell, C. M. Halsey, and J. F. Hainfeld, *Microscopy Res. Tech.* 42, 2 (1998).
166. L. Jurgens, A. Nichtl, and U. Werner, *Cytometry* 37, 87 (1999).
167. H. Kato, T. Nakamura, S. Nishiguchi, Y. Matsusue, M. Kobayashi, T. Miyazaki, H. M. Kim, and T. Kokubo, *J. Biomed. Mater. Res.* 53, 28 (2000).
168. D. E. Stefflik, R. S. Corpe, T. R. Young, G. R. Parr, M. Tucker, M. Sims, J. Tinley, A. Sisk, and M. McDaniel, *J. Oral Implantology* 27, 5 (2001).
169. D. C. Clupper, J. J. Mecholsky, Jr., G. P. LaTorre, and D. C. Greenspan, *J. Biomed. Mater. Res.* 57, 532 (2001).
170. H. Fischer, F. Karaca, and R. Marx, *J. Biomed. Mater. Res.* 61, 153 (2002).
171. T. Kobayashi, K. Okada, T. Kuroda, and K. Sato, *J. Biomed. Mater. Res.* 37, 100 (1997).
172. Y. Okada, M. Kobayashi, M. Neo, T. Kokubo, and T. Nakamura, *J. Biomed. Mater. Res.* 57, 101 (2001).
173. Y. Ikuhara, *J. Ceram. Soc. Jpn.* 110, 139 (2002).
174. W. Hoeland, W. Goetz, G. Carl, and W. Vogel, *Cells Mater.* 2, 105 (1992).
175. S. I. Stupp and P. V. Braun, *Science* 277, 1242 (1997).
176. C. Du, F. Z. Cui, Q. L. Feng, X. D. Zhu, and K. de Groot, *J. Biomed. Mater. Res.* 42, 540 (1998).
177. C. Nicolazo, H. Gautier, M.-J. Brandao, G. Daculsi, and C. Merle, *Biomaterials* 24, 255 (2003).
178. M. Antonietti, M. Breulmann, C. G. Goltner, H. Colfen, K. K. W. Wong, D. Walsh, and S. Mann, *Chemistry—A European Journal* 4, 2493 (1998).
179. X.-P. Luo, N. Silikas, M. Allaf, N. H. F. Wilson, and D. C. Watts, *Surf. Sci.* 491, 388 (2001).
180. P. A. A. P. Marques, A. P. Serro, B. J. Saramago, A. C. Fernandes, M. C. Magalhaes, and R. N. Correia, *Biomaterials* 24, 451 (2003).
181. Y. Kimura and S. Takubo, *Int. J. Fatigue* 22, 899 (2000).
182. H. Takadama, H. M. Kim, T. Kokubo, and T. Nakamura, *J. Biomed. Mater. Res.* 57, 441 (2001).

183. L. M. Rodriguez-Lorenzo, M. Vallet-Regi, and J. M. Ferreira, *J. Biomed. Mater. Res.* 60, 232 (2002).
184. Z. S. Luo, F. Z. Cui, and W. Z. Li, *J. Biomed. Mater. Res.* 46, 80 (1999).
185. B. J. Story, A. V. Burgess, D. La, and W. R. Wagner, *J. Biomed. Mater. Res.* 48, 841 (1999).
186. H. B. Wen, J. Moradian-Oldak, and A. G. Fincham, *Biomaterials* 20, 1717 (1999).
187. H. B. Wen, J. Moradian-Oldak, J. P. Zhong, D. C. Greenspan, and A. G. Fincham, *J. Biomed. Mater. Res.* 52, 762 (2000).
188. T. Kokubo, H. M. Kim, M. Kawashita, and T. Nakamura, *Z. Kardiol.* 90, iii/86 (2001).
189. S. H. Cartmell, P. J. Doherty, N. P. Rhodes, J. A. Hunt, D. M. Healy, and T. Gilchrist, *J. Mater. Sci. Mater. Med.* 9, 1 (1998).
190. T. Peltola, M. Jokinen, S. Veittola, J. Simola, and A. Yli-Urpo, *J. Biomed. Mater. Res.* 54, 579 (2000).
191. I. D. Xynos, M. V. Hukkanen, J. J. Batten, L. D. Buttery, L. L. Hench, and J. M. Polak, *Calcified Tissue Int.* 67, 321 (2000).
192. I. Izquierdo-Barba, A. J. Salinas, and I. M. Vallet-Reg, *J. Biomed. Mater. Res.* 51, 191 (2000).
193. C. Wang, Q. Zhang, S. Uchida, and M. Kodama, *J. Biomed. Mater. Res.* 62, 315 (2002).
194. R. R. Joshi, T. Underwood, J. R. Frautschi, R. E. Phillips, Jr., F. J. Schoen, and R. J. Levy, *J. Biomed. Mater. Res.* 31, 201 (1996).
195. M. C. Porte-Durrieu, C. Aymes-Chodur, N. Betz, and C. Baquey, *J. Biomed. Mater. Res.* 52, 119 (2000).
196. M. V. Sefton, A. Sawyer, M. Gorbet, J. P. Black, E. Cheng, C. Gemmell, and E. Pottinger-Cooper, *J. Biomed. Mater. Res.* 55, 447 (2001).
197. E. Diez-Pena, G. Frutos, P. Frutos, and J. M. Barrales-Rienda, *Chem. Pharmaceu. Bull.* 50, 1201 (2002).
198. O. Laitinen, H. Pihlajamaki, A. Sukura, and O. Bostman, *J. Biomed. Mater. Res.* 61, 33 (2002).
199. A. A. Amis and S. A. Kempson, *J. Biomed. Mater. Res.* 48, 534 (1999).
200. M. A. Attawia, K. E. Urich, E. Botchwey, R. Langer, and C. T. Laurencin, *J. Orthopaedic Res.* 14, 445 (1996).
201. S. Y. Buchen, C. M. Cunanan, A. Gwon, J. I. R. Weinschenk, L. Gruber, and P. M. Knight, *J. Cataract Refractive Surgery* 27, 1473 (2001).
202. I. Revenko, Y. Tang, and J. P. Santerre, *Surf. Sci.* 491, 346 (2001).
203. G. Bar, Y. Thomann, and M.-H. Whangbo, *Langmuir* 14, 1219 (1998).
204. P. Wang, K. L. Tan, and E. T. Kang, *J. Biomater. Sci. Polym. Ed.* 11, 169 (2000).
205. M. D. Garrison, R. Luginbuhl, R. M. Overney, and B. D. Ratner, *Thin Solid Films* 352, 13 (1999).
206. M. C. Porte-Durrieu, C. Aymes-Chodur, N. Betz, and C. Baquey, *J. Biomed. Mater. Res.* 52, 119 (2000).
207. J. A. Koehler, M. Ulbricht, and G. Belfort, *Langmuir* 13, 4162 (1997).
208. F. Pincet, E. Perez, and G. Belfort, *Langmuir* 11, 1229 (1995).
209. M. Conti, G. Donati, G. Cianciolo, S. Stefoni, and B. Samorý, *J. Biomed. Mater. Res.* 61, 370 (2002).
210. V. M. D. Cupere and P. G. Rouxhet, *Surf. Sci.* 491, 395 (2001).
211. I. Voronov, J. P. Santerre, A. Hinek, J. W. Callahan, J. Sandhu, and E. L. Boynton, *J. Biomed. Mater. Res.* 39, 40 (1998).
212. G. Ramage, K. Vande Walle, B. L. Wickes, and J. L. Lopez-Ribot, *J. Clin. Microbiol.* 39, 3234 (2001).
213. R. Filmon, M. F. Basle, H. Atmani, and D. Chappard, *Bone* 30, 152 (2002).
214. D. J. Heath, P. Christian, and M. Griffin, *Biomaterials* 23, 1519 (2002).
215. X. Chen, S. L. McGurk, M. C. Davies, C. J. Roberts, K. M. Shakesheff, S. J. B. Tendler, P. M. Williams, J. Davies, A. C. Dawkes, and A. Domb, *Macromolecules* 31, 2278 (1998).
216. P. X. Ma and R. Zhang, *J. Biomed. Mater. Res.* 46, 60 (1999).
217. B. Saad, G. Ciardelli, S. Matter, M. Welti, G. K. Uhlschmid, P. Neuenschwande, and U. W. Suter, *J. Biomed. Mater. Res.* 39, 594 (1998).
218. I. B. Leonor, A. Ito, K. Onuma, N. Kanzaki, and R. L. Reis, *Key Eng. Mater.* 218–220, 55 (2002).
219. T. Furukawa, Y. Matsusue, T. Yasunaga, Y. Nakagawa, Y. Okada, Y. Shikinami, M. Okuno, and T. Nakamura, *J. Biomed. Mater. Res.* 50, 410 (2000).
220. R. A. Mickiewicz, A. M. Mayes, and D. Knaack, *J. Biomed. Mater. Res.* 61, 581 (2002).
221. C. Du, F. Z. Cui, X. D. Zhu, and K. de Groot, *J. Biomed. Mater. Res.* 44, 407 (1999).
222. L. J. Chen and M. Wang, *Biomaterials* 23, 2631 (2002).
223. O. Sollböhmer, K.-P. May, and M. Anders, *Thin Solid Films* 264, 176 (1995).
224. M. Finke, J. A. Hughes, D. M. Parker, and K. D. Jandt, *Surf. Sci.* 491, 456 (2001).
225. K. D. Jandt, M. Finke, and P. Cacciafesta, *Colloids Surf. B* 19, 301 (2000).
226. G. W. Marshall, N. Yucel, M. Balooch, J. H. Kinney, S. Habelitz, and S. J. Marshall, *Surf. Sci.* 491, 444 (2001).
227. C. Cassinelli and M. Morra, *J. Biomed. Mater. Res.* 28, 1427 (1994).
228. R. Osorio, L. Ceballos, F. Tay, M. A. Cabrerizo-Vilchez, and M. Toledano, *J. Biomed. Mater. Res.* 60, 316 (2002).
229. P. A. Ohlsson, T. Tjarnhage, E. Herbai, S. Lofas, and G. Puu, *Bioelectrochem. Bioenerge.* 38, 137 (1995).
230. I. Reviakine and A. Brisson, *Langmuir* 16, 1806 (2000).
231. Y. F. Dufrêne, W. R. Barger, J.-B. D. Green, and G. U. Lee, *Langmuir* 13, 4779 (1997).
232. E. A-Hassan, W. F. Heinz, M. D. Antonik, N. P. D'Costa, S. Nageswaran, C.-A. Schoenenberger, and J. H. Hoh, *Biophys. J.* 78, 1564 (1998).
233. D. Anselmetti, M. Dreier, R. Lüthi, T. Richmond, E. Meyer, J. Frommer, and H.-J. Güntherodt, *J. Vac. Sci. Technol. B* 12, 1500 (1994).
234. Y. Zhang, Z. Ma, X. Chu, T. Hu, B. Zhou, S. Pang, and C. K. Tseng, *J. Vac. Sci. Technol. B* 12, 1497 (1994).
235. R. Guckenberger, F. T. Arce, A. Hillebrand, and T. Hartmann, *J. Vac. Sci. Technol. B* 12, 1504 (1994).
236. T. E. Schäffer, C. Ionescu-Zanetti, R. Proksch, M. Fritz, D. A. Walters, N. Almqvist, C. M. Zarella, A. M. Belcher, B. L. Smith, G. D. Stucky, D. E. Morse, and P. K. Hansma, *Chem. Mater.* 9, 1731 (1997).
237. H. G. Hansma and L. Pietrasanta, *Curr. Opinion Chem. Biol.* 2, 579 (1998).
238. R. B. Proksch, T. E. Schäffer, B. N. Moskowitz, E. D. Dahlberg, D. A. Bazylnski, and R. B. Frankel, *Appl. Phys. Lett.* 66, 2582 (1995).
239. P. G. Haydon, R. Lartius, V. Parpura, and S. P. Marchese-Ragona, *J. Microsc.* 182, 114 (1996).
240. D. Ricci and M. Grattarola, *J. Microsc.* 176, 254 (1994).
241. C. Rotsch and M. Radmacher, *Biophys. J.* 78, 520 (2000).
242. R. M. Henderson and H. Oberleithner, *American J. Physiol. Renal Physiol.* 278, 689 (2000).
243. G. Wittstock, K. Yu, H. B. Halsall, T. H. Ridgway, and W. R. Heineman, *Anal. Chem.* 67, 3578 (1995).
244. N. J. Tao, S. M. Lindsay, and S. Lees, *Biophys. J.* 63, 1165 (1992).
245. C. Leinenbach, C. Fleck, and D. Eifler, *Mater. Sci. Eng. Technol.* 8, 442 (2002).
246. B. Huber, H. Gnaser, and C. Ziegler, to be published.

# Nanoassembly for Polymer Electronics

Tianhong Cui

*University of Minnesota, Minneapolis, Minnesota, USA*

Yuri Lvov, Jingshi Shi, Feng Hua

*Louisiana Tech University, Ruston, Louisiana, USA*

## CONTENTS

1. Introduction
  2. Polycation/Polyanion Layer-by-Layer Assembly
  3. Nanoparticle/Polyion Multilayers
  4. Spin-Coating for Layer-by-Layer Assembly
  5. Soft Lithography to Pattern 2D Patterns on Polyion Multilayers
  6. Lithographic Approach to Pattern Layer-by-Layer Thin Films
  7. Nanofabrication for Nanoelectronics
  8. Polymer Microelectronics
  9. Potential Applications of Nano Self-Assembly
  10. Conclusions
- Glossary  
References

## 1. INTRODUCTION

The self-assembly (SA) of nanoparticles in an organized array has become increasingly important. The current methods used for the design of ultra-thin films include: spin-coating and solution-casting, thermal deposition, polyion layer-by-layer assembly, chemical self-assembly, the Langmuir-Blodgett technique, and free-standing films. The optimal combination of molecular order and stability of films determines the practical usefulness of these technologies [1–6].

The most ordered macromolecular films are free-standing liquid crystalline films, but they are very unstable. The Langmuir-Blodgett method allows to construct lipid multilayers with a thickness from 5 to 500 nm, but only flat substrates can be covered by this film and it has intrinsic defects at the lipid grain borders. Another method that can be

applied to surface modification is a monolayer self-assembly, based on thiol or silane compounds [1]. By this method, one can achieve self-assembly of 2–5 nm thick organic layers on silicon or gold surfaces, but there is no simple means for thicker film construction. Other widely used methods for the industrial manufacture of thin films are spin-coating and thermal deposition of macromolecules onto a substrate. Unfortunately, unlike the methods considered above, these methods do not allow one to control a film composition in the direction perpendicular to the surface.

Finally, there is a newer method for film self-assembly that makes use of the alternate adsorption of oppositely charged components (polymers, nanoparticles, and proteins) [2–9]. The assembly of alternating layers of oppositely charged linear or branched polyions and nanoparticles is simple and provides the means to form 5–500-nm thick films with monolayers of various substances growing in a preset sequence on any substrate at a growth step of about 1 nm. Mallouk [4] has called this technique “molecular beaker epitaxy,” meaning that with simple instruments (exploiting the materials’ self-assembly tendency), one can produce molecularly organized films similar to the ones obtained with sophisticated and expensive molecular beam epitaxy technology.

One can assemble on a standard silicon wafer, multilayers containing different nanoparticles and polymers and then apply lithography to manufacture microdevices with nanostructured elements. Such a combination of nano-assembly with traditional micromanufacturing is the topic of this review.

## 2. POLYCATION/POLYANION LAYER-BY-LAYER ASSEMBLY

### 2.1. General Procedure

A cleaned substrate of any shape and dimension is immersed into a dilute solution of a cationic polyelectrolyte, for a time optimized for the adsorption of a single monolayer



(ca 1 nm thick), and then it is rinsed and dried. The next step is the immersion of the polycation-covered substrate into a dilute dispersion of polyanions or negatively charged nanoparticles (or any other nanosize-charged species) also for a time optimized for the adsorption of a monolayer; then it is rinsed and dried. These operations complete the self-assembly of a polyelectrolyte monolayer and monoparticulate layer sandwich unit onto the substrate (Fig. 1). Subsequent sandwich units are self-assembled analogously. Different nanoparticles, enzymes, and polyions may be assembled in a preplanned order in a single film.

The forces between nanoparticles and binder layers govern the spontaneous layer-by-layer self-assembly of ultra-thin films. These forces are primarily electrostatic and covalent in nature, but they can also involve hydrogen bonding, hydrophobic, and other types of interactions. The properties of the self-assembled multilayers depend on the choice of building blocks used and their rational organization and integration along the axis perpendicular to the substrate.

The sequential adsorption of oppositely charged colloids was reported in a seminal paper in 1966 by Iler [2]. The electrostatic self-assembly was subsequently “rediscovered” in the mid-nineties and extended to the preparation of multilayers of polycations and phosphonate ions, as well as to the layering of linear polyions, proteins, and nanoparticles by Decher, Mallouk, Möhwal, Lvov, Rubner, Fendler, Hammond, Kunitake, Schlenoff, Kotov, and others. This self-assembly is now employed in the fabrication of ultra-thin films from charged polymers (polyions) [3–47], dyes [48–51], nanoparticles (metallic, semiconducting, magnetic, insulating) and clay nanoplates [52–75], proteins [76–96], and other supramolecular species [79]. The greatest advantage of this self-assembly is that any of these species can be absorbed layer-by-layer in any order. The oppositely charged species

are held together by strong ionic bonds and they form long-lasting, uniform, and stable films. Self-assembly is economical and readily amenable to scaling-up for the fabrication of large-area, defect-free devices on any kind and shape of surfaces.

The main idea of this method is the resaturation of polyion adsorption, which results in the alternation of the terminal charge after each layer is deposited. This idea is general and implies that there are no major restrictions in the choice of polyelectrolytes. It is possible to design composite polymeric films in the range of 5 to 1000 nm, with a definite knowledge of their composition. For the successful assembly of nanoparticle or protein multilayers, the alternation with linear polyion layers is important. Flexible linear polyions penetrate between nanoparticles and act as electrostatic glue. The concept of “electrostatic polyion glue,” which keeps together neighboring arrays of nanoparticles, is central to this approach [77, 79]. The self-assembled film contains amorphous polyion interlayers, and this organization “heals” defects that arise because of the introduction of foreign particles during the process of film formation (dust, microbes) [13, 79].

### 2.1.1. Standard Assembly Procedure

As a standard approach to film preparation, we employ the following steps:

1. Take aqueous solutions of polyion, nanoparticles, or protein at a concentration of 0.1–1 mg/mL and adjust the pH in such a way that the components are oppositely charged.
2. Take a substrate carrying a surface charge (e.g., plates or polymer films covered by a layer of cationic poly(ethylenimine) that may be readily attached to many surfaces).
3. Carry out alternate immersion of the substrate in the component’s solutions for 10 min with 1 min intermediate water rinsing. To rinse a sample, use a solution with pH that keeps the polyions ionized.
4. Dry the sample using a stream of nitrogen (*Note*: drying may hinder the assembly process and it is not necessary for the procedure).

Linear polyions predominately used in the assembly are as follows: polycations—poly(ethylenimine) (PEI), poly(dimethyldiallylammonium chloride) (PDDA), poly(allylamine) (PAH), polylysine, chitosan, polyanions—poly(styrenesulfonate) (PSS), poly(vinylsulfate), poly(acrylic acid), dextran sulfate, sodium alginate, heparin, and DNA. One can grow polymer nanocomposite films by means of the sequential adsorption of different material monolayers that employ hundreds of commercially available polyions. The only requirement is that there be a proper (positive/negative) alternation of the component charges.

## 2.2. Kinetics of Polyion Adsorption

For the time-dependent control of adsorption and monitoring of the assembly *in-situ*, the quartz crystal microbalance method is quite suitable [23, 46, 86]. The kinetics of

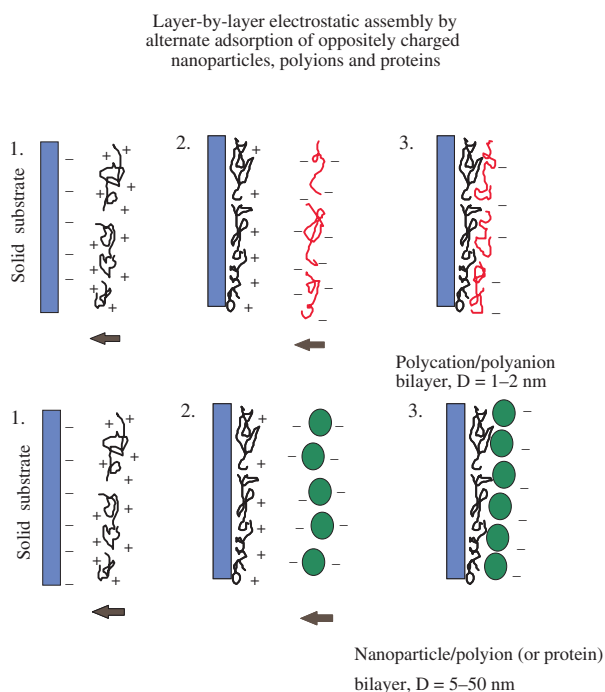


**Figure 1.** A scheme of the layer-by-layer assembly.

the adsorption process could be delineated by the QCM-technique, which is indispensable for establishing proper assembly conditions (e.g., a saturation adsorption time).

The multilayer assemblies are characterized by means of a quartz crystal microbalance technique in two ways:

1. After drying a sample in a nitrogen stream, we measured the resonance frequency shift and calculated an adsorbed mass by the Sauerbrey equation; or
2. By monitoring the resonator frequency during the adsorption process onto one side of the resonator, which was in permanent contact with polyion solutions. While performing experiments in permanent contact with the polyion solution, we touched the surface of solutions with one side of the resonator, while the upper electrode was kept open to air and the upper contact wire was insulated from the solution by a silicone paint covering.

The fitting of adsorption to an exponential law yields a first-order rate of adsorption for PSS  $\tau = 2.5 \pm 0.2$  min and for PAH  $\tau = 2.1 \pm 0.2$  min. This means that during the first 5 min ca 87% of the material is adsorbed onto the charged support and  $t = 8$  min ( $t = 3\tau$ ) gives 95% full coverage. Typically, in most publications on polyion assembly, adsorption times of 5 to 20 min are used. One does not need to maintain an adsorption time with great precision: a minute more or less does not influence the layer thickness if we are at the saturation region. For other species, PDDA, PEI, montmorillonite clay, myoglobin, lysozyme, and glucose oxidase, the first-order rate of adsorption onto an oppositely charged surface was found to be 2, 3, 1.8, 3, 4, and 5 min, respectively. Interestingly, 5–20 min is essentially greater than the diffusion-limited time (mass transport limitation), which is necessary for complete surface covering (for the used linear polyion concentrations it is a few seconds). Only for 45-nm silica/PDDA assembly do we have an example when 2 s time corresponds to the diffusion limited time for the SiO<sub>2</sub> monolayer adsorption.

One could suppose that linear polyion adsorption occurs in two stages: quick anchoring to a surface and slow relaxation. To reach a surface-charge reversion during linear polyion adsorption, one needs a concentration greater than  $10^{-5}$  M [23]. The dependence of polyion layer thickness on concentration is not great: thus, in the concentration range of 0.1–5 mg/mL PSS/PAH pair yielded a similar bilayer thickness. A further decrease in polyion concentration (using 0.01 mg/mL) decreases the layer thickness of the adsorbed polyion. An increase in the component concentrations to 20–30 mg/ml may result in the nonlinear (exponential) enlargement of the growth rate with adsorption steps, especially if an intermediate sample rinsing is not long enough [47].

### 2.3. First Layers and Precursor Film

At the very beginning of the alternate assembly process, one often sees nonlinear film growth [13, 23, 41]. At the first 2–3 layers, smaller amounts of polyion are adsorbed as compared with further assembly, when the film mass and thickness increase linearly with the number of adsorption cycles. Tsukruk et al. [41] explained this as an island-type

adsorption of the first polyion layer on a weakly charged solid support. In the following two-three adsorption cycles, these islands spread and cover the entire surface, and further multilayer growth occurs linearly. If a substrate is well charged, then a linear growth with repeatable steps begins earlier.

In studying the possibility of using new compound in approach [6, 13, 23]. On a substrate (silver electrode of quartz crystal microbalance (QCM) resonator or quartz slide), we deposited 2–3 layers of polyions, and on this “polyion blanket,” with a well-defined charge of the outermost layer, an assembly of proteins, nanoparticles, or other compounds was produced. In a typical procedure, precursor films were assembled by repeating two or three alternate adsorptions of PEI and PSS. The outermost layer became “negative,” or “positive,” respectively.

Quartz crystal microbalance monitoring of multilayer growth was often the first stage of the assembly procedure elaboration. Initially, we estimated the time needed for a component’s saturated adsorption in a kinetic experiment. Then we performed the assembly typically with 10 min alternate adsorption. After every other adsorption step, a layer was dried by a nitrogen stream and the QCM resonator frequency was registered. The frequency shift with adsorption cycles gave us the adsorbed mass at every assembly step. A linear film mass increase with the number of assembly steps indicated a successful procedure.

The following relationship is obtained between adsorbed mass  $M$  (g) and frequency shift  $\Delta F$  (Hz) by taking into account the characteristics of the 9 MHz quartz resonators used [23]:  $\Delta F = -1.83 \times 10^8 M/A$ , where  $A = 0.16 \pm 0.01$  cm<sup>2</sup> is the surface area of the resonator. One finds that a 1 Hz change in  $\Delta F$  corresponds to 0.9 ng, and the thickness of a film may be calculated from its mass. The adsorbed film thickness at both faces of the electrodes ( $d$ ) is obtainable from the density of the protein/polyion film (ca 1.3 g/cm<sup>3</sup>) and the real film area:  $d$  (nm) =  $-(0.016 \pm 0.02)\Delta F$  (Hz). The scanning electron microscopy data from a number of protein/polyion and linear polycation/polyanion film cross-sections permitted us to confirm the validity of this equation. Another powerful method for polyion film characterization was small-angle X-ray and neutron reflectivity.

### 2.4. Multilayer Structure

X-ray or neutron reflectivity measurements of polyion films show patterns with profound intensity oscillations, as demonstrated in Figure 2. They are so-called Kiessig fringes, due to the interference of radiation beams reflected from interfaces solid support/film and air/film. From the periodicity of these oscillations, one can calculate the film thickness (with the help of the Bragg-like equation and taking into account refraction phenomena that are essential at small angles). Growth steps for a bilayer of 1.1–2.0 nm are typical for alternate linear polyion assembly, and a thickness of one layer often equals to half of this value [6–14]. These values correspond to a polyion cross-section and show that in one cycle of excessive adsorption we have approximately one monolayer coverage of the substrate. The nanoparticle/polyion bilayer thickness is determined by the diameter of the particle. Model fitting of X-ray data gives

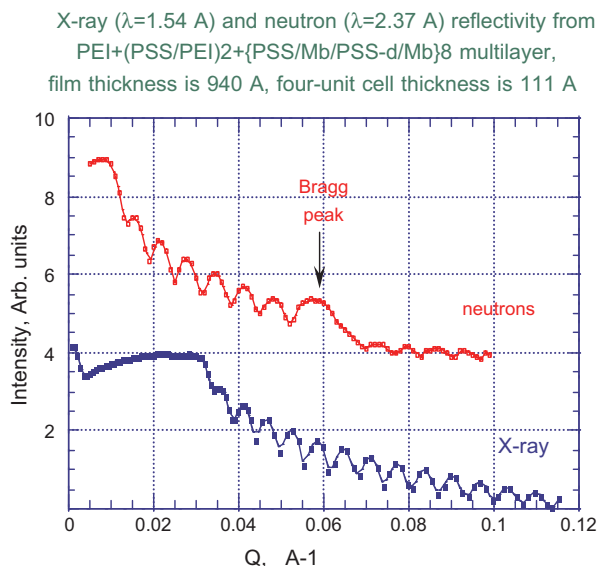


**Figure 2.** Small-angle X-ray and neutron reflectivity curves from (PSS/myoglobin/deuterated PSS/myoglobin)<sub>8</sub> multilayer.

a surface roughness of the polyion film on an order of 1 nm. Atomic force microscopy (AFM) and scanning electron microscopy (SEM) data revealed a surface roughness of 1–2 nm [42]. Polyion films are insoluble in water and in many organic solvents and are stable to 280 °C [38, 95].

Neutron reflectivity analysis of the films composed of alternate layers of deuterated PSS and hydrogen containing PAH has proved that polyanion/polycation films possess not only a high uniform thickness but a multilayer structure, too [19–22]. The interfaces between layers in polyion films are not sharp and partial interpenetration (30–40% of their thickness) between neighboring polymeric layers takes place [21–22]. A distinct spatial component separation may be reached between the first and the third or fourth neighboring polyion layers. In the neutron reflectivity experiments with the selectively deuterated component (usually d-PSS), it was possible to observe 1–3 Bragg reflections in addition to Kiessig fringes. This was not possible in the X-ray reflectivity experiments because of a small scattering contrast of neighboring polycations and polyanions, and because of their large interpenetration. X-ray Bragg reflections from the alternate gold nanoparticle/poly(allylamine) multilayers were observed by Schmitt et al. [55]. They demonstrated that in order to have good spatial separation between gold layers in the film, one needs to make a thicker polyion interlayer (of 3–4 PSS/PAH bilayers). In a similar approach, we formed the four-step unit cell multilayers of myoglobin, deuterated, and “usual” poly(styrenesulfonate): (myoglobin/deuterated-PSS/myoglobin/PSS)<sub>8</sub>. A Bragg reflection in the neutron reflectivity curve of this four-step unit cell multilayer was observed (Fig. 2). The film’s total thickness was calculated at 94.0 nm, and the four-unit cell thickness was 11.1 nm.

The polycation/polyanion bilayer thickness depends on the charge density of the polyions. It was shown that more than 10% of polyion side groups have to be ionized for a stable reproducible multilayer assembly via alternate electrostatic adsorption [34]. High ionization of polyions results

in a smaller step of film growth (1–2 nm) and lower ionization gives a larger growth step (3–6 nm). It can be reached either by adding salt to a polyion solution (as previously discussed for strong polyelectrolytes, such as PDDA and PSS), or by varying the pH for weak polyelectrolytes (e.g., polyacrylic acid (PAA) and PAH, as was analyzed by Yoo et al. [30]). Direct zeta-potential measurements confirmed a symmetric positive/negative alternation of the polycation/polyanion multilayer’s outermost charge with adsorption cycles [34].

## 2.5. Stoichiometry of the Components and Polyion Molecular Weight

A multilayer film has to be totally neutral, that is, a stoichiometry of charged groups in neighboring polycation and polyanion layers has to be 1:1. In many cases, we confirmed this (for PSS/PDDA, PSS/PEI, PSS/chitosan, DNA/PAH multilayers), but for PSS/PAH a deviation from 1:1 stoichiometry was found [34]. This is probably due to the incomplete dissociation of the polyions. It is difficult to control polyion dissociation because it depends on a concentration and on the presence of oppositely charged compounds in solution [97]. The complex stoichiometry did not depend on the ionic strength of polyion solutions, which indicates an absence of low molecular weight ions ( $K^+$ ,  $Na^+$ ,  $Cl^-$ ) in the films.

For deposition from water solutions, the PSS/PAH growth step was similar for PSS molecular weights varying from 40,000 to 1,000,000 [21]. The influence of the polymerization degree on the formation of stable interpolyelectrolyte bulk complexes was analyzed by Kabanov [97]. He found that such complexes were stable when a polyion contained more than 20 charged groups in the sequence. We used polyions, such as PSS, PVS, PDDA, PEI with molecular weights of 50,000–200,000. They contain hundreds of ionized groups in the pH range from 3 to 9. A cooperative electrostatic interaction between the polycations and polyanions used is strong and prevents the dissolution of the multilayers even in high ionic strength solvents.

## 2.6. Nonequilibrium Growth and Admixed Polyion Complexes

When the polyion assembly was performed at equilibrium conditions, a saturated adsorption was achieved at every deposition step and a careful intermediate sample washing removed all nonspecific polyion adsorption. Next, one has the permanent increment of the multilayer growth (i.e., the film mass and thickness increased linearly with the cycles of adsorption). In some cases, we encountered the situation when the film growth step exponentially increased with the number of adsorbed layers. We recognized such conditions as nonstable and usually reached a stable growth step by optimizing the solution pH or by decreasing the polyion concentration.

As we previously discussed, one can increase the speed of growth from 1–2 nm to 5–10 nm in 10 min by increasing the ionic strength of the polyion solutions. Another way to increase the assembly speed is by using preformed interpolyelectrolyte complexes (coacervates) [92]. The formation of

water-soluble polyelectrolyte complexes has been intensively studied by means of turbidity measurements [58]. Aqueous mixtures of oppositely charged polyelectrolytes are usually homogenous at the stoichiometry far from the neutralization point. First, such complexes permit an increase in the size of the assembly construction blocks. Second, they make it possible to immobilize with polyion, which were impossible to use in the assembly directly (poor charged nanoparticles, dyes, and proteins).

## 2.7. Polyion Films for Biocompatible Coverage

Multilayer assemblies of natural polyions, such as DNA, polynucleotides, polylysine, and polysaccharides (e.g., heparin, chondroitine, and chitosan) are interesting for biological and medical applications. DNA and polynucleotides (polyuridylic and polyadenylic acids) can be readily assembled in alternation with polycations (PEI, PAH, polylysine). The assembly of polysaccharides with oppositely charged polyions is possible as a means of biocompatible surface preparation. A chitosan and albumin/heparin multilayer assembly for such coatings has been developed [42–44].

## 2.8. Multipolar Dye and Liposome Assembly

The layer-by-layer assembly by alternate adsorption of oppositely charged molecules was applicable for multipolar dyes with symmetric charges possessing conjugated rings and other hydrophobic fragments [48–51]. Hydrophobic fragments probably enhance dye stacking. Interestingly, the dye/polyion bilayer has the same thickness in a wide range of dye concentrations. For Congo Red/PDDA films, the bilayer thickness was 1.5 nm for dye concentrations from 0.01 up to 10 mg/mL, that is, below and above the critical micelle concentration (CMC) of the dye.

The characteristic feature of the assembly of some dye multilayers was greater than the monolayer adsorption at the dye adsorption cycle followed by a depletion of the material during the following linear polyion adsorption step. In this process, we have substantial nonspecific adsorption at the dye adsorption step, and then the removal of nonspecific bond material by complexation with an oppositely charged polyion (at the next assembly step). The graph of the film mass against the number of adsorption steps, such as a growth mode, looks like “a large step up followed by a small step down” [46, 50]. A similar growth mode was observed for protein/polyion and nanoparticle/polyion assemblies, especially with a short intermediate sample washing time [58, 77].

## 3. NANOPARTICLE/POLYION MULTILAYERS

The construction of organic/inorganic nanostructured materials is an important goal of modern materials research. An alternate adsorption procedure was used for the following charged nanoparticles: clay and ceramic plates, nanotubes, 10, 20, 45, 75-nm silica spheres, 50, 150, 300-nm latex, 15-nm gold, 30-nm magnetic  $\text{Fe}_3\text{O}_4$ , 20–30 nm  $\text{CeO}_2$ ,  $\text{MnO}_2$ ,  $\text{ZrO}_2$ ,  $\text{SnO}_2$ ,  $\text{TiO}_2$  particles [23, 52–71], as well as

34-nm diameter spherical plant viruses [12]. Many oxide particles have a zero-charge point at pH 4–5. They are negatively charged at pH 7–8, and can be readily assembled by means of alternate adsorption with such polycations as PEI or PDDA. The number of particle monolayers in such “sandwich” multilayers is exactly known, and any profile across the film can be constructed with a resolution of 5–10 nm. Using a “soft” polymeric interlayer was important for the composite multilayers formation: flexible linear or branched polyions optimize electrostatic attraction. An organic component can change electrical properties of nanostructured material. Therefore, after the assembly is completed, organic interlayers can be removed by a 2-hour thermal treatment above 320 °C in air (calcination process), which results in direct contacts between the nanoparticles needed for improved electric or magnetic properties. Nanoparticles, such as gold, silver, and fullerenes may be “sandwiched” in multilayers with proteins providing electrically or optically induced electron donor-acceptor properties. Semiconductor nanoparticles, such as PbS, CdS, and CdSe, were used in this assembly [54, 67–69]. An assembly of core-shell nanoparticles, such as  $\text{Ag/TiO}_2$  or  $\text{Fe}_3\text{O}_4/\text{Au}$ , was also possible [71, 73].

## 3.1. Silica Multilayers

As an example of the nanoparticle architecture, let us analyze a 45-nm silica assembly by alternate adsorption with PDDA [58–59]. *In-situ* QCM monitoring of alternate PDDA and  $\text{SiO}_2$  adsorption gave the kinetics of the assembly process. In the first step, PDDA was adsorbed onto a Ag-electrode. The QCM frequency decreased during the first 60 s, after which a slower change was observed as adsorption saturation set in. Then the resonator was immersed in pure water for washing. Next, the film was immersed in  $\text{SiO}_2$  dispersion and silica adsorption saturation occurred within several seconds. After subsequent water rinsing, the film was immersed again in a PDDA solution, and so on. Each growth step was reproducible, and the adsorption process reached 90% saturation in 10 s for  $\text{SiO}_2$  and 30 s for PDDA. The film assembly was not possible simply by the multiple immersion of the substrate in the silica solution. An alternation with an oppositely charged polyion was necessary. At every assembly step, the component monolayers were formed, as was recorded by QCM, SEM (Fig. 3).

The average density of  $\text{SiO}_2$ /PDDA multilayers is  $\langle\rho\rangle = 1.43 \pm 0.05 \text{ g/cm}^3$ .  $\text{SiO}_2$ /PDDA film volume composition is: 60%  $\text{SiO}_2$  + 10% polycation + 30% air-filled pores. These pores are formed by closely packed 45-nm  $\text{SiO}_2$  and have a typical dimension of 20 nm. The films have controlled pores, which can be varied by the selection of the nanoparticle diameter. We estimated the diffusion limitation for surface coverage  $A(t)$  by adsorption from solution of particles with the diffusion coefficient  $D$  from  $A(t) = 2/\pi C\sqrt{Dt}$ . For  $t = 2 \text{ s}$ ,  $C = 10 \text{ mg/cm}^3$ , and assuming for 45-nm silica  $D = 1.1 \times 10^{-7} \text{ cm}^2/\text{s}$ ,  $A \approx 3 \times 10^{-6} \text{ g/cm}^2$  and the layer thickness:  $L = A(t)/\langle\rho\rangle \approx 21 \text{ nm}$ . This is reasonably close to the experimental silica monolayer thickness of 24.6 nm. Thus, 2 s corresponds roughly to the diffusion-limited time for the  $\text{SiO}_2$  monolayer adsorption; this time is the fastest nanoparticle monolayer formation rate that we have achieved.



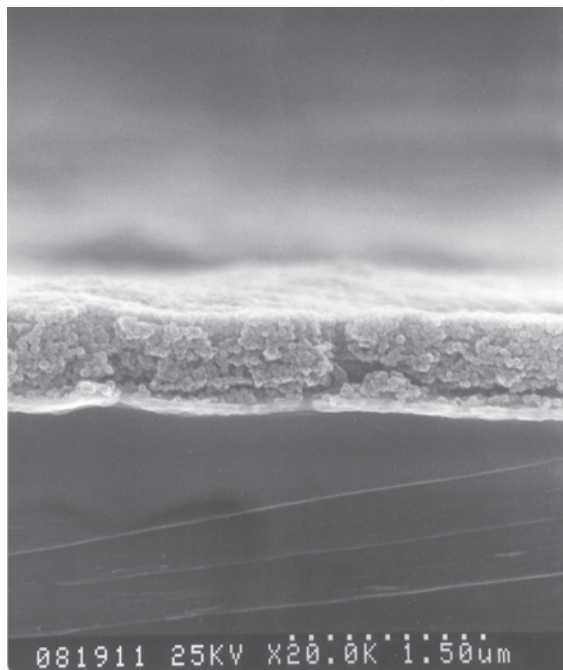


**Figure 3.** SEM image of multilayer containing 18 monolayers of 45-nm-diameter silica alternated with polycation PDDA.

### 3.2. Latex Assembly

Charged latex is a good building block for an electrostatic layer-by-layer assembly. Positively or negatively charged monodisperse lattices with diameters of 30, 40, 45, 50, or 75-nm and with different colors are commercially available, for example, from Seradyn Inc. or IDC-Ultraclean Uniform Latex Inc. For the first time, a multilayer assembly of negative latex spheres (carboxyl-modified or sulfate polystyrene) in alternation with positive latex (amidine-modified polystyrene) was reported by Bliznyuk and Tsukruk [57]. They have described a strong tethering of charged nanoparticles to the surface, which prevents surface diffusion and the rearrangement required for formation of perfect lateral ordering. This situation is different from the one with the formation of the ordered 3D-mesocrystals by slow crystallization of the monodispersed aqueous colloids [72]. In the nanoparticle/polyion multilayers, one loses the crystal-like ordering, but gains control of the process, preparing multilayers of close-packed nanoparticles with a precisely known number of monolayers. We demonstrated a regular layer-by-layer assembly of carboxylated 45-nm diameter Seradyn latex in alternation with PEI.

### 3.3. Compact Nanoparticle/ Poly(ethyleneimine) Multilayers

Figure 4 shows the assembly QCM monitoring and scanning electron micrographs of film cross-sections and a partial top view of a film with architecture PDDA/PSS/PDDA + (MnO<sub>2</sub>/PDDA)<sub>9</sub> and 190 nm thick SnO<sub>2</sub>/PDDA multilayer.

MnO<sub>2</sub>-film has a remarkably smooth surface and uniform thickness. The total frequency shift by QCM was 11,000 Hz and film thickness from SEM was 170 nm. Dividing the film

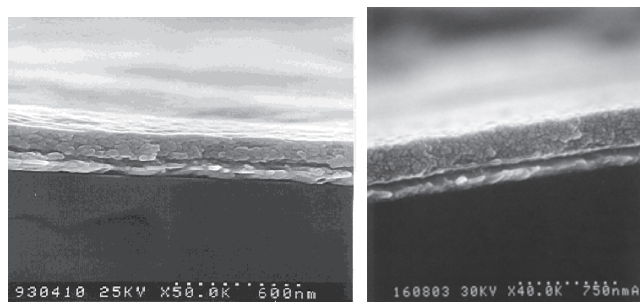


**Figure 4.** (a–b) SEM cross-sectional images of (MnO<sub>2</sub>/PDDA)<sub>9</sub> and, on right, (12-nm diameter SnO<sub>2</sub>/PDDA)<sub>18</sub> films. The films formed on a silver electrode.

thickness by the number of manganese oxide/PDDA bilayers, we obtain values slightly less than the 23-nm bilayer thickness found above from QCM because the first two layers of manganese oxide are thinner. We cannot detect separate layers in the film by SEM, but individual structures of about 20 nm dimensions are clearly visible and may be attached to nanoparticles.

We analyzed the chemical composition and the chemical state of Mn and N atoms on the surface of a film with architecture PDDA/PSS/PDDA + (MnO<sub>2</sub>/PDDA)<sub>9</sub> by XPS. Spectra revealed a surface rich in carbon and oxygen with manganese and nitrogen present in concentrations less than 7% and trace amounts of chlorine. The Mn (2p) region consists of a spin-orbit doublet with a Mn (2p<sub>1/2</sub>) binding energy of 653.30 eV and Mn (2p<sub>3/2</sub>) binding energy of 641.63 eV. This doublet can be assigned to a mixed valent manganese system, most likely Mn (4+) and Mn (3+) since the average oxidation state of Mn in the nanoparticles is 3.7. The N 1s region showed two peaks at 402.04 eV and 399.12 eV, indicating two different chemical environments for the nitrogen atoms. The difference in the chemical environment may reflect the formation of contact ion pairs and long-distance charge pairs between the MnO<sub>2</sub> particles and the polycation PDDA.

### 3.4. Open-Structured TiO<sub>2</sub>-Nanoparticle/ Poly(styrenesulfonate) Films

The assembly of 35-nm diameter TiO<sub>2</sub> (Degussa P25) was possible at pH 3.8 (when the particles were positive) in alternation with PSS. TiO<sub>2</sub> assembly with polycation PDDA at this pH was not possible. The saturation adsorption time for TiO<sub>2</sub> nanoparticles was 5 min. The growth step of the TiO<sub>2</sub>/PDDA multilayer was stable and linear, with the mass adsorption increment corresponding to the monolayer surface coverage. The SEM of the TiO<sub>2</sub>/PSS multilayer shows not a close-packed but an open structure of the film. It was possible to vary the porosity of the film by changing the ionic strength of nanoparticle dispersions. Such porous structures can be useful for catalytic applications.

### 3.5. Organized Gold/Polycation Multilayers

In [55–56], the self-assembly of 15-nm-diameter gold particles in alternation with polycation PAH was demonstrated. Gold alternation with the polycation was possible because

of negative nanoparticle charge (surface potential  $-35$  mV) due to the synthesis procedure. The saturation time needed for the formation of close-packed gold nanoparticle monolayer (full coverage) was 2 h because of the low particle concentration in solution [55]. An approach to a spatial separation of nanoparticle layers in such sandwich-like films was elaborated: three- to five polycation/polyanion interlayers were assembled between gold layers (e.g., Au/{PAH + (PSS/PAH)<sub>3-5</sub>}/Au). The gold surface (with a roughness of the order of the radius of nanoparticles) was covered and smoothed by the 6–10 nm polyion layer. Further “sandwiching” of gold nanoparticles with the thick polyion interlayers resulted in the ordered gold/polymer heterostructure. The low-angle, X-ray reflectivity of these samples gave 2–3 orders of Bragg reflections with the spacing corresponding to such a complex unit cell. We think that this is a general approach to creating ordered inorganic/organic heterostructure multilayers, and we have used it also for the formation of protein/polyion heterostructures [77, 79].

### 3.6. Layered Ceramics

Mica-type layered silicates can bear a natural negative charge because of the isomorphous substitution of silicon in octahedral sheets by aluminum or magnesium. The charge is generally balanced by potassium cations that reside in the galleries between layers. The intercalation of organic polymers between sheets of layered ceramics provides access to novel polymer-ceramic nanocomposites. These nanocomposites exhibit unique physical and mechanical properties attributable to the synergism of the individual components. The build-up of the multilayers in a stepwise manner rather than in the bulk “all-at-once” manner is of special interest. Kleinfeld and Ferguson [52] were first to apply the electrostatic layer-by-layer adsorption to produce multilayers of anionic synthetic silicate—hectorite and cationic PDDA. We used the polyion assembly to build up multilayers with alternating 1-nm-thick montmorillonite sheets and cationic PEI or PDDA [64–65]. The film thickness increase for the montmorillonite adsorption cycle was 1.1 nm and for PEI 2 nm. After 20 cycles, the resultant film had a permanent thickness of 63 nm.

### 3.7. Multilayer Reactors for Metallic and Semiconducting Particles. Microporous Films

This process was recently introduced by Joly et al. [75]. First, polyelectrolyte multilayers with controlled content of free nonionized carboxylic acid groups were fabricated with weak polyions (e.g., poly(acrylic acid) via suitable pH-adjustments of the processing solutions). These groups were then used to bind various inorganic ions that were subsequently converted into 2-nm diameter particles (e.g., Ag, Pb, or PbS). The spatial control over the growth of the nanoparticles was achieved by the use of multilayer heterostructures which also contain bilayer blocks that are not able to bind inorganic ions. These nonbonding bilayers were fabricated from strong polyions, such as poly(styrenesulfonate). A density

modulation with a few nanometer-resolution across the polymeric films is possible by selective synthesis of heavy atom nanoparticles.

A simple process to convert multilayers of weak polyelectrolytes (e.g., poly(acrylic acid) and poly(allylamine)) into uniform microporous films has been developed by Mendelsohn et al. [76]. These multilayers were immersed briefly into acidic solution (pH 2.4) to effect an irreversible transformation of the film morphology. The resulting microporous structure thickness is 2–3 times less than the thickness of the original films, and possesses reduced relative density of 1/2 to 1/3. The interconnected pores ranging in size from 100 to 500 nm. A refractive index of the porous PAA/PAH film was  $n = 1.18 \pm 0.01$ . It is much less than the origin  $n = 1.54$  for the untreated polyion multilayer. Correspondingly, a dielectric constant of the porous PAA/PAH film dropped to  $\epsilon' = 2$  from the initial  $\epsilon' = 5-7$ .

### 3.8. Protein Multilayers

In many cases, one can consider proteins as hard monodisperse nanoparticles with dimensions of 2–10 nm. Taking protein solution at pH well apart from its isoelectric point, one can provide 10–60 elemental charges for a protein globule due to ionization of its carboxyl or amine groups [77]. Multilayer films that contain ordered layers of protein species were assembled by means of alternate electrostatic adsorption mostly with positively charged PEI, PAH, PDDA, and chitosan or with negatively charged PSS, DNA, and heparin [77–96]. The pH of the protein solutions was set apart from the isoelectric point so that proteins were sufficiently charged under the experimental conditions. The assembly of 20 different proteins was successfully achieved (including cytochrome, carbonic anhydrase, myoglobin, hemoglobin, bacteriorhodopsin, pepsin, peroxidase, alcohol dehydrogenase, glucoamylase, glucose oxidase, immunoglobulin, catalase, and urease) (Fig. 5) [79]. The mass increment at each

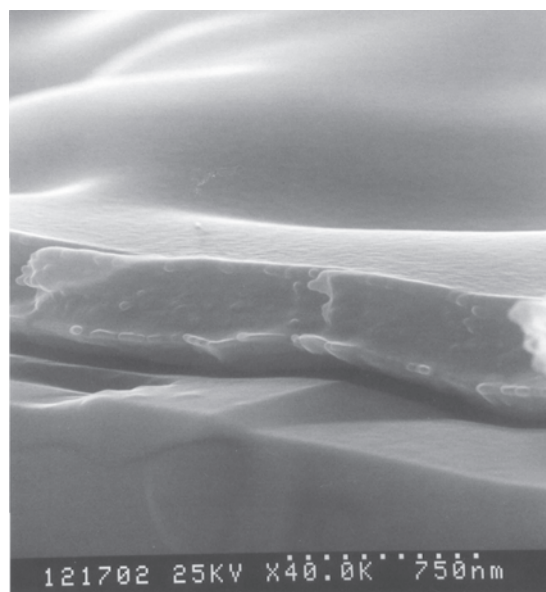


**Figure 5.** SEM image of cross-section of glucose oxidase/PEI multilayer (24 bilayers, thickness 270 nm) on quartz support.

step was quite reproducible. Proteins immobilized in multilayers with strong polyions such as PSS, PEI, and PDDA were insoluble in buffer for a pH range between 3 and 10. The assembled proteins are in most cases not denatured [77–78, 82, 87–88]. Moreover, the layer-by-layer immobilization with linear or branched polyions enhanced the enzymatic stability [95].

The enzymatic activity in multilayers increased linearly with the number of layers up to 10–15 protein layers, at which point the film bioactivity became saturated. This saturation was probably due to substrate diffusion limitations into the film, that is, accessibility to the protein requires a substrate transport through the multilayer [95]. For the antigen-antibody reaction in immunoglobulin (IgG)/PSS multilayers, the activity increased up to five immunoglobulin layers. Compactness or openness of protein multilayers may be regulated. Thus, glucose oxidase, myoglobin, and albumin multilayer films were compact, but immunoglobulin/PSS multilayers had an open structure with areas as large as 100-nm in diameter unfilled in the upper layers of the film [87].

Drying of polyion films exerts unclear influences on the structure. We do not need drying for the assembly process; samples were dried for control of the assembly. From the other hand, the importance of film drying (as a separate process) is still not fully understood. The assembly with a regular film, drying at every other adsorption step, gave polar multilayers with nonlinear optical properties [99]. A similarly prepared Photosynthetic Reaction Center/PDDA multilayer demonstrated second harmonic light generation [89]. Regular immunoglobulin/PSS assembly with the film drying at every adsorption cycle was possible at a pH close to the IgG isoelectric point, which again indicates an importance of hydrophobic interactions [87].

### 3.9. Different Proteins in Alternation with Polyions

An elaboration of the assembly technique for a variety of proteins makes it possible to construct multicomponent protein films (superlattices) [77, 79, 83]. We have described the formation of two types of superlattices:

1. The alternation of similarly charged proteins at identical pH conditions; both positively charged myoglobin and lysozyme in alternation with polyanion {myoglobin<sup>+</sup>/PSS/lysozyme<sup>+</sup>/PSS}; negatively charged glucose oxidase (GOx) and glucoamylase (GA) with polycation {glucose oxidase<sup>-</sup>/PDDA/glucoamylase<sup>-</sup>/PDDA}.
2. The combination of negative and positive proteins in the two-block film with the insertion of an additional polyion layer to change the assembly mode: {(lysozyme/PSS)<sub>3</sub> + PEI + (glucose oxidase/PEI)<sub>6</sub>}. The protein multicomponent films are extremely interesting as novel biologically active materials. One can arrange given protein layers according to a specific biological activity. Sequential enzymatic reactions and vectorial transfer of electrons and energy become feasible targets by the preparation of anisotropic protein layers with the precise control of the distances of active layers.

## 4. SPIN-COATING FOR LAYER-BY-LAYER ASSEMBLY

Spin coating, a technique used for casting chemical layers onto a rotating substrate, has been used extensively to prepare thin films for diverse industrial applications such as photolithography [100], light emission [101, 102], nuclear track detection [103], and gas sensing [104, 105]. Since the 1950s, monolayer film formation dynamics by spin-coating has been studied both experimentally and theoretically. Recently, ultra-thin multiplayer films have attracted much interest because of their wide applications as sensors, integrated optics, friction-reducing coatings, biological surfaces, light emitting devices (LEDs), or surface-orientation layers [106–110]. Most of these applications require preparation of stable and well-organized films with fast fabrication. The simplicity, time-efficiency, and cost-effectiveness of spin-coating have made it a practical method for the deposition of polymer thin films. Spin-assembly is a specialized application of spin-coating, in which a polyelectrolyte multilayered thin film is self-assembled onto a spinning substrate. The spin self-assembly method as an alternative for making well-organized multiplayer films in a very short process time has been described [111–113].

### 4.1. The Concentration and Spinning Rate Effect

Deposition of organic material by spin-coating has been done for almost a century [114]. Solution flow dynamics [115–117], film surface topography [118–120], and evaporate effects [121–123] has been explored both theoretically and experimentally. The two main parameters that control the amount of polyelectrolyte adsorbed onto the substrate are solute concentration and spin rate. These have been shown to directly influence the thickness of monolayer films [125, 126]. Dubas and Schlenoff have fabricated multiplayer polyelectrolyte films by immersing spinning substrate into polyelectrolyte solution. Peter and Malkiat investigated those variables in multiplayer polyelectrolyte films that are spin-assembled by dropping a solution onto a spinning substrate [113]. The materials used include the polyanion PAZO and polycation PEI. The thickness of a film of a single polyelectrolyte can be easily controlled by varying the concentration of polyelectrolyte and spin rates. Higher concentrations of PEI most likely lead to a greater amount of adsorbed PEI, and therefore lead to greater amounts of PAZO deposited on the film.

At faster spin rates, the films experience increased mechanical forces, which lead to shorter contact time between the polyelectrolyte [115]. The forces acting on a spinning film have been studied in detail [127, 128]. The effects of spin rate on both monolayer thickness [124, 125] and multiplayer thickness [113] have been studied.

### 4.2. Comparison of Spin SA Method and Dip SA Method

#### 4.2.1. The Adsorbed Amount Mechanism

The adsorbed amount between the dipping and the spinning methods is significantly different [113]. This is caused by different adsorption mechanisms. Fast elimination of water

in the spinning process significantly increased the molar concentration of the polyelectrolyte solution during the short deposition time [129] and this increases in the polyelectrolyte concentration yields of thick layers, despite the thin film formation typically provided by the centrifugal force and air shear force [130–132]. It also increases the electrostatic attraction between oppositely charged polymers because the presence of water molecules in the assemblies generally screens the electrostatic attraction. When water molecules are adsorbed onto the substrate, the preadsorbed water molecules may block polyelectrolyte adsorption onto the surface, and thus the surface coverage with polyelectrolyte chains may be incomplete. However, if polymer adsorption and water drainage are almost simultaneously realized in a short time, as in the case of the spin SA process, there would be more room for polyelectrolyte to adsorb onto the substrate.

#### 4.2.2. The Structure

The spin SA method has been found to have a significant effect on the surface roughness of prepared multiplayer films, presumably because of the air shear force caused by the spinning process [110]. It was proved that the internal structure of the spin SA films is highly ordered and the film prepared with the spin process contains rather distinct interfaces between respective layers in contrast to the film obtained by the dipping method. The distinct difference in the dip and spin SA multiplayer structure indicates that the spin SA method can easily provide the well-ordered internal structure, which cannot be achieved with the dip SA even containing a high ionic strength of the polyelectrolyte solution or multiple organic layers between inorganic particle layers [112].

#### 4.2.3. Single-Species Deposition

Another important advantage of spin assembly is that the film formation process is not solely dependent on electrostatics to induce deposition. The linear growth of a PAZO layer over 10 deposition cycles on top of a single positively charged PEI underlayer has been reported [113]. A thick PEI layer on a bare, negatively charged substrate using 10 deposition cycles of 10 Mm PEI was also built [111]. Whereas film formation in the case of ionic self-assembly is governed by electrostatics and entropy; the underlying mechanism for film formation in spin-assembly involves the mechanically induced entanglement between polyelectrolyte chains of different layers. Electrostatics, therefore, takes a supplementary role in spin-assembly, enhancing the deposition process when alternating charges are used. Single-species multiple deposition do not show linear growth when carried out using conventional dipping techniques [111].

In summary, a new ultra-thin film-forming process, spin-assembly, is an excellent method for controlling the amount and thickness of adsorbed polyelectrolyte in fabricating multiplayer thin film with highly ordered internal structure far superior to the structure obtained with the dip SA process. It also allows us to build multiplayer polyelectrolyte multilayered films without the absolute requirement of alternating charges.

## 5. SOFT LITHOGRAPHY TO PATTERN 2D PATTERNS ON POLYION MULTILAYERS

Soft lithography is an alternative, nonphotolithographic set of microfabrication methods [134–136]. All of its members share the common feature of using a patterned elastomer as the stamp, mold, or mask (rather than a rigid photomask) to generate micropatterns and microstructures. Such techniques include: microcontact printing ( $\mu$ CP) [137], replica molding (REM) [138], microtransfer molding ( $\mu$ TM) [139], micromolding in capillaries (MIMIC) [140], solvent-assisted micromolding (SAMIM) [141], phase-shift photolithography [142], cast molding [143, 144], embossing [145, 146], and injection molding [147–149]. These techniques have been explored and developed by The Whitesides Group and several other groups.

The key element of soft lithography is an elastomeric block with a patterned relief structure on its surface and poly(dimethylsiloxane) (PDMS) elastomers (or silicone rubbers) are used in most demonstrations. Poly(dimethylsiloxanes) have a unique combination of properties resulting from the presence of an inorganic siloxane backbone and organic methyl groups attached to silicon [150]. These liquid materials can be poured over a master having a relief structure on its surface, then easily converted into solid elastomer by curing and peeling off. Poly(dimethylsiloxane) has been widely used because they can make conformal contact with surfaces over relatively large areas and they can be released easily from rigid masters or from complex structures. The formulation, fabrication, and applications of PDMS elastomers have been extensively studied and are well-documented in the literature [150]. The master is, in turn, fabricated using microlithography techniques such as photolithography, micromachining, e-beam writing, or from available relief structures such as diffraction gratings [151], and relief structures etched in metals or Si [151, 152], or even by directly printing. Figure 6 illustrates the procedure for fabricating PDMS stamps.

Microcontact printing ( $\mu$ CP) is a flexible, nonphotolithographic method that routinely forms patterned SAMs containing regions terminated by different chemical functionalities with submicron lateral dimensions [153–158]. An elastomeric PDMS stamp is used to transfer molecules of the “ink” to the surface of the substrate by contact. After printing, a different SAM can be formed on the relief pattern on the surface of a PDMS stamp to form patterns. However, it differs from other printing methods [159] in the use of self-assembly (especially, the use of SAMS) to form micropatterns and microstructures of various materials.

Self-assembly is the spontaneous aggregation and organization of subunits (molecule or meso-scale objects) into a stable, well-defined structure via noncovalent interactions. The information that guides the assembly is coded in the properties (e.g., topologies, shapes, and surface functionalities) of the subunits; the individual subunits will reach the final structure simply by equilibrating to the lowest energy form.

Self-assembled monolayers are one of the most intensively studied examples of nonbiological self-assembling systems [161]. Self-assembled monolayers can be easily prepared by



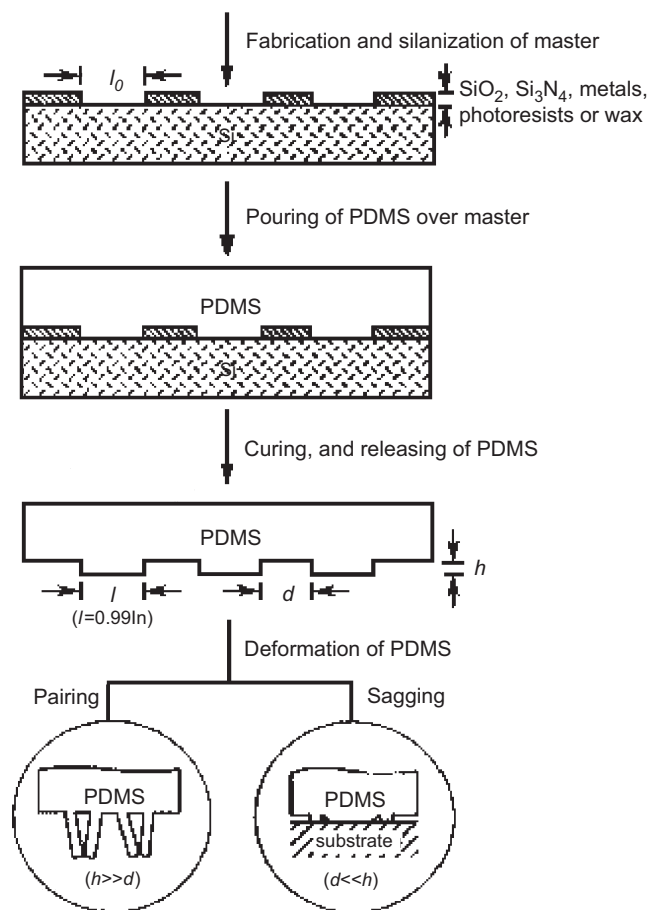


**Figure 6.** The procedures for fabricating PDMS stamps. Reprinted with permission from [160], Y. Xia, *Ann. Rev. Mater. Sci.* 28, 153 (1998). © 1998, Annual Reviews.

immersion of a substrate in the solution containing a ligand reactive toward the surface, or by exposure of the substrate to the vapor of a reactive species. The self-assembled multilayer can be formed by electrostatic layer-by-layer assembly process via the alternate adsorption of oppositely charged polyelectrolytes, as first demonstrated by Decher and Hong [162–165].

An important difference between traditional SAMs and the multilayer surfaces is that polyelectrolyte multilayers can be tuned during the layer-by-layer assembly process to vary surface charge density, density of functional groups at the surface, film thickness, and wetting properties [166–169].

The Hammond group at MIT has been investigating the use of this  $\mu$ CP technique on the self-assembly monolayer or multilayer for the formation of various patterns.

Their early studies were still on the Au substrate. The substrate was patterned by the chemically modified PDMS stamp. A polyelectrolyte multilayer film has been deposited on the chemically patterned surface via alternate adsorption of a polyanion and polycation. The polyelectrolyte used here include poly(diallyldimethylammonium chloride) (PDAC), a strong polycation and sulfonated polystyrene (SPS), a strong polyanion. Weak polyelectrolyte multilayers were formed from linear poly(ethylene imine) (LPEI), a weak polycation, and PAA, a weak polyanion. Five-and-one-half

polyelectrolyte pairs were deposited for each multilayer, such that each stack is terminated by the polycationic species. A net positive surface charge is thus presented to the microspheres. Solution pH and ionic strength were adjusted to achieve optimal selective deposition of the polyelectrolyte films. For the LPEI/PAA system, the optimum selectivity of polyelectrolyte adsorption onto the patterned SAM surface occurs at pH = 4.8 for the weak polyelectrolytes. For the PDAC/PSS system, the addition of NaCl electrolyte causes partial screening of charges for the strong polyelectrolyte, resulting in thick, loopy films and optimal selective adsorption onto the COOH regions.

The polyelectrolyte is subsequently immersed in an aqueous colloidal suspension of bare  $SiO_2$  microspheres or functionalized polystyrene latex particles. The colloids self-organized at the surface, are driven by the spatially varied electrostatic and secondary interactions between the colloid and the substrate. The polyelectrolyte multilayer platform provides a strong bond to the colloids and introduces the functionality into the underlying layers [170].

Three mechanisms have been demonstrated to control the adsorption—pH of the colloid suspension, ionic strength of the suspension, and concentration of added surfactant. By adjusting the pH of the colloidal slurry, it is possible to alter the strength of the electrostatic attraction between the colloid and the surface in weak polyelectrolyte systems. Adjusting the pH alters the equilibrium balance of the ionization reaction which occurs on the polyelectrolyte backbone. For the PDAC/SPS strong polyelectrolyte system, adjustment of electrolyte concentration in the colloid slurry results in varying strengths of the adsorption. When there is no electrolyte used, a strong electrostatic attraction exists between the polyelectrolyte surface and the  $SiO_2$  spheres, and results in the adsorption selectivity. When a small amount of NaCl is added, the counterions form a double layer that screen surface charges from the colloids. The double-layer screening also reduces interparticle repulsion, so that the spheres are more likely to form multiple layers. As the electrostatic repulsion between spheres decreases, the relatively neutral surface also becomes a more likely site for the deposition of particles on the basis of the secondary interaction. The net result is decreased selectivity. Further increasing the salt concentration will provide additional surface charge screening and then result in further reduced selectivity. However, the suspension aggregation limit will be approached upon increasing electrolyte. So manipulation of the pH appears to be a more effective way of controlling the selectivity and density of adsorption. The degree of ionization of the surface can be altered almost independently of  $SiO_2$  surface charge, and the stability of the colloidal suspension is maintained.

On the basis of  $\mu$ CP and LBL assembly techniques, a polymer on polymer stamping (POPS) process was developed to create the chemical pattern by direct stamping of functional polymers onto a surface containing complementary functional groups, which is illustrated in Figure 7. A polymer is transferred directly to the top surface of a polyelectrolyte multilayer thin film, based on covalent and/or noncovalent interactions. For example, a polyanion can be stamped directly onto a charged polycation top multilayer surface to create alternating regions of plus and minus

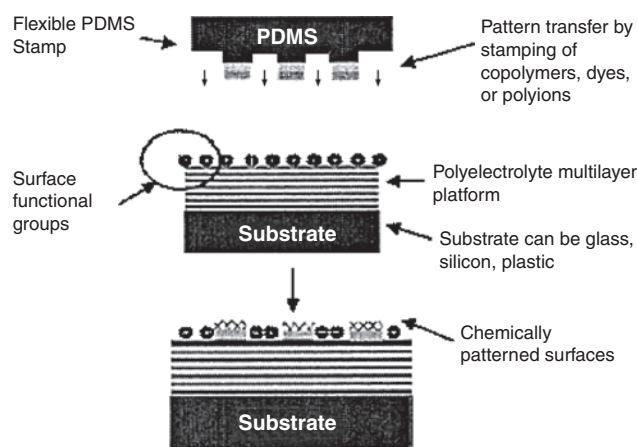


**Figure 7.** Schematic illustrating the transfer of a functional polymer to a surface with complementary functional using polymer-on-polymer stamping. Reprinted with permission from [172], X. Jiang et al., *Langmuir* 18, 2607 (2002). © 2002, American Chemical Society.

charge. On the other hand, blocks and graft copolymers can present both a reactive functional group for attachment to the surface and a second functional group to modify the surface. In either case, the goal is to create a stable functional surface, which is either charged or contains reactive functional groups. This approach can be applied to various functional polymer and substrate systems as well as different thin film deposition technique. The concept of polymer on polymer stamping was first illustrated by stamping a functional graft polymer onto a polyelectrolyte multilayer film [171], which utilized the polymers with anhydride groups that can react with the polymer surface.

Copolymers contain two different types of functional groups—one functional group that can attach itself to the polymer surface and a second functionality acting as the desired surface modifier onto polyelectrolyte multilayer surfaces. Such multifunctional molecules include a block and random copolymer, a graft copolymer, and some surfactants. The patterning of polyelectrolyte multilayer surfaces can be a stepping point to the creation of composite, multilevel structures [171].

To create templates for layer-by-layer adsorption, it is necessary to form surface regions that resist polyion adsorption. A random graft copolymer of oligoethylene oxide allylether and maleic anhydride (EO-MAL) was used as a multifunctional polymer. It is demonstrated that EO-MAL can be used to direct selective adsorption on various substrates, including plastic surfaces, and to create three-dimensional complex microstructures of multilayered polymer films. pH adjustment was used to control the effectiveness of EO-MAL templates.

Recently, this technique was further broadened to transfer surface chemistry to different regions of a substrate using a block copolymer and a common polyelectrolyte. A broad range of substrates, including the polymeric surfaces, has been explored and the complex multiple level heterostructures via stamping atop continuous or patterned polymer thin film was created. The use of functionalized polymer, polyions, and low molar mass substituents, which can be stamped directly onto other surfaces, particularly plastic

substrates and multilayer films, has been investigated [172–176]. And the ability to create multilevel microstructures with layer-by-layer self-assembly broadens the area by allowing the construction of devices such as transistors, diodes, sensors, and other optical and electrical components. The patterning of the top surfaces of the multilayer films also brings new opportunities to incorporate other materials onto multilayer films; the use of such patterns to direct material deposition can lead to the patterning of metal electrodes, the placement of colloidal particles, or the directed deposition of other polymer films atop layer-by-layer functional thin film. The Hammond's group created patterns on a polyelectrolyte surface. By this way, any surface that can be covered with at least one surface layer of polyion is able to be modified.

Many new functional surfaces can be achieved through the use of a block copolymer or a graft copolymer, because a number of existing polymers may be used for this technique. Examination of the effectiveness and stability of polymer-on-polymer requires an understanding of the interaction between the polymer to be transferred and the underlying surface. Conditions must be achieved that allow for effective contact of the desired functional group with the chemical functional group on the surface, and both the polymer “ink” and the surface functional groups must be in a form that encourages covalent, ionic, or hydrogen bonding. The influence of factors such as temperature and pH, as well as the stability of polymer-on-polymer-stamping on model and multilayer surfaces, were investigated by this group [172]. Another important aspect of this technique is the optimization of the underlying polymer surface to achieve a high density of desired functional groups. In Hammond's group, direct stamping of polystyrene-poly (acrylic acid) block copolymer (PSS-PAA) has been utilized to create the alternating hydrophobic/hydrophilic regions and polyelectrolytes to generate positively and negatively charged regions.

By stamping onto the top polyamine surface. When a patterned polyelectrolyte film is used as the base layer or substrate, a second pattern can be stamped atop the original pattern array. Subsequent selective adsorption of a polymer yields a second level of microstructures. In addition, a chemical pattern can be achieved by the direct stamping of functional polymers onto a surface containing complementary functional groups. The resulting pattern is then used as a template for the further deposition of the materials on the surface.

Two kinds of new patterns were generated using polyelectrolyte as inks and surface-treated PDMS stamps to create a patterned “plus/minus (+/–)” polyelectrolyte surface. Before using hydrophilic materials, such as charged polymers or proteins as ink, PDMS stamps are often treated with oxygen or air plasma [172, 175–178]. Air plasma is used to make the PDMS surface hydrophilic through the introduction of charged groups, making it wettable with aqueous solutions of charged polymers. It has been indicated that when the PDMS stamp is treated with air plasma for 20 s or more, the PDMS surface becomes completely wettable by aqueous solutions (a 0–5° contact angle with water) [172]. To transfer a negative image of the original PDMS stamp's pattern

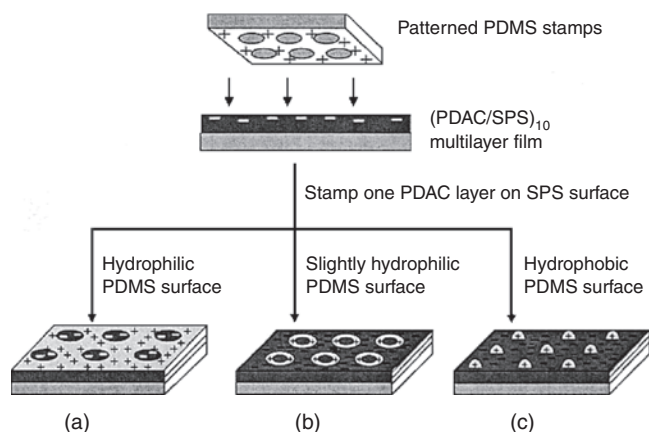


**Figure 8.** Schematic illustration of the procedure for creation of three kinds of transferred polyelectrolyte patterns in a POPS process. Reprinted with permission from [173], H. Zheng et al., *Langmuir* 18, 4505 (2002). © 2002, American Chemical Society.

(see Fig. 8a), the PDMS stamps were pretreated with air-plasma for 20 s to render them fully wettable to a 0.02 M PDAC aqueous solution with 0.1 M NaCl, which was used as ink [172].

By tuning surface properties of the PDMS stamp—the solvents of the polymer ink and controlled POPS conditions—two kinds of new patterns—ring patterns and small-dot patterns—were created from the same patterned PDMS stamps, as well as the uniform circle-grid patterns. When the PDMS stamps were plasma treated for 5–10 s and inked with 0.02 M PDAC/0.1 M NaCl aqueous solutions, PDAC ring patterns were transferred onto the SPS surface, as shown in Figure 8b. When the stamp is not plasma treated at all, and a mixed solvent polymer ink consisting of 0.01 M PDAC water/ethanol solution (50/50, v/v) is used, the transferred pattern consists of small periodic dots as shown in Figure 8c.

Two different particles on a defined array use two different approaches—ionic attractions coupled with hydrophobic and hydrogen bonding interactions, respectively. The first set of negatively charged particles were deposited on the multilayer surface primarily through electrostatic interactions, whereas the second set of colloidal particles adsorb onto a neutral SAM surface [174].

Two component colloidal arrays on a single-patterned PDAC/EG surface, were fabricated by adding surfactant, DTAB, to tune the selective deposition of the colloidal particles. When low concentrations of DTAB are added to the colloidal suspension ( $10^{-6}$ – $10^{-5}$  M), the PSS particles are deposited primarily on the multilayer surface with small changes in their packing density [179]. As more DTAB suspension ( $10^{-4}$ – $10^{-3}$  M) is added, the surfaces of the particles become increasingly hydrophobic as the negative charge density is reduced and alkyl chains are introduced. The selectivity of the particles for the PDAC surface decreases sharply at a given degree of surfactant shielding, resulting in little or no selectivity [179]. Finally, at a high degree of shielding, the selectivity is reversed, and the deposition occurs preferentially on the neutral surface.

## 6. LITHOGRAPHIC APPROACH TO PATTERN LAYER-BY-LAYER THIN FILMS

Nanoassembly of ultra-thin films through alternate adsorption of oppositely charged components (linear polyions, nanoparticles, and enzymes) allows the formation of layers with component location precision of a few nanometers in the direction perpendicular to the surface. Since its demonstration by Decher et al. [180, 181], applications have been found in electro-optical devices, biocompatible coverage, and in bioreactors [180–186]. The typical procedure of layer-by-layer self-assembly is as follows: A pretreated silicon substrate is immersed in a cationic solution for 10 min, forming a single layer of cationic polyelectrolytes on the substrate. The substrate is then rinsed. Next, it is immersed in a polyanion solution for 10 min to adsorb a layer of anionic polyelectrolyte. The process can be repeated indefinitely; the only condition is a proper alternation of positive and negative components. Linear polyions frequently used in the layer-by-layer (LbL) assembly are cationic poly(ethylenimine) (PEI), PDDA, PAH, polylysine, chitosan, and anionic sodium PSS, and poly(vinylsulfate), polyacrylic acid, and DNA. Enzymes and charged nanoparticles were also used in the LbL assembly [179]. To use LbL multilayers in devices, one has to provide film ordering not only in a vertical direction but also in the planar direction. This is critical for nanodevice production, such as nanoelectronic chips or nano electro mechanical systems (NEMS) [192–195].

There are works on applications of the layer-by-layer assembly on two-dimensional (2D) patterns [196–201]. They are based mostly on the microprinting of thiol compounds on gold and further assembly of the polyion multilayers on charged patterns, and they were developed by Hammond et al. [196–199]. This strategy is designed to produce patterns by stamping onto substrate chemicals with different functionalities, that is, polyion adhesive or resisting. The polyions were directed only to charge “attractive” regions and were repelled from the resistant regions. Whitesides et al. [200] crystallized latex particles in capillary channels produced by PDMS micromolding and made 3D ensembles of 450-nm spheres with a resolution of ca.1  $\mu\text{m}$ . In another approach [201], poly(pyrrole) and poly(styrenesulfonate) were LbL-assembled on the 2D charged micropattern produced on a fluoropolymer by plasma treatment. The three methods described were quite successful, but restricted in applications by substrate materials (gold, fluoropolymers) or by the necessity of special plastic stamps. We presented two approaches to realize 2D patterning of self-assembled multilayers by silicon-based lithographical technology, which is a well-established industrial process.

The first one is referred to as the metal mask approach. By using this method, we avoid the selective deposition, which demands strict control and consequently obtains extremely high reproducibility and a simplified process. Since layer-by-layer self-assembly and lithography techniques are mature processes, and lithography is widely applied to the modern semiconductor industry, a combinative technique will be economic and suitable for mass production. By just following the traditional process, the nanostructures comprised of nano-building bricks can be



realized. As it behaves in the semiconductor industry, the process results in such a high reproducibility that distinct patterns (in this experiment, 10  $\mu\text{m}$ ) can be created in almost all the dyes on the wafer. Commercial electronic and photonic devices, such as metal-oxide semiconductor FET (MOSFET) or solar cells with nanostructures, are expected to be fabricated by this method at a considerably lower cost and temperature. Layer-by-layer self-assembly was employed to deposit the nanoparticle-based thin film on a substrate while using a semiconductor process to pattern the thin film [202]. At first, a layer of nanoparticles is adsorbed onto a silicon wafer. Then a layer of aluminum and resist are deposited and coated on top of the nanoparticle layer. Patterns are made on resist by UV lithography and transferred to a aluminum layer by etching aluminum. As a result, nanoparticles previously covered under aluminum begin to be open to the air. Then, it is etched by oxygen plasma, and nanoparticles are removed in compliance with the designed patterns. During the etching process, metal acts as the mask over the nanoparticles. After the remaining aluminum and resist are dissolved, only the desired pattern is left on the substrate.

The second patterning approach is called a “lift-off” since lift-off acts as a critical step in the process. At the beginning, photoresist is spun on a silicon wafer and patterned. Then nanoparticles are deposited with layer-by-layer assembly on the whole wafer. Eventually, the wafer is put into acetone solution to dissolve resist and particles self-assembled on it are removed as well [202].

Both methods work well for the thin film patterning. As for the lift-off method, it can be applied to all types of nanoparticles. In the other experiments, the metal mask method succeeded in controlling the spatial position of organic polystyrene particle by oxygen plasma etching. As a matter of fact, it can also be applied to inorganic particles if the appropriate recipe is available. If not, the flexibility of the mature semiconductor process can provide a simple wet etching to deal with it as a substitute to the dry etching.

Both methods can be applied to 3D fabrication as well as functional devices. In the 3D case, some factors have to be seriously controlled such as height, surface or border roughness, and sidewall profile. Two methods can work out a 3D structure individually or both of them can be used if necessary. Table 1 shows the comparison of two methods.

In our experiment, the capacitor arrays were patterned by the “modified lift-off” as illustrated in Figure 9. These capacitors can be fabricated onto integrated circuit chips. Metal-oxide semiconductor (MOS) capacitors, with thermal  $\text{SiO}_2$  as the gate oxide, have become the prime structure to carry out digital functions in silicon-integrated circuits. However, the fabrication of a MOS capacitor, using the conventional silicon MOS technology, demands sophisticated facilities. High process temperature also needs to be balanced to avoid the damage to subsequent processes, and the growth rate of the thermal silicon dioxide is usually very low. Hereby, an approach to fabricate the basic MOS capacitor with a technique combining traditional lithographic technique and LbL self-assembly was developed because the dielectric layer consisting of silica and polyion can be self-assembled easily and rapidly. The insulating layer is made up of six layers of LbL, self-assembled silica nanoparticle thin

**Table 1.** Comparison of lift-off and metal mask methods.

	Metal mask	lift-off
Border sharpness		better
Surface roughness	better	
Defect in structure		more
Adhesion to substrate		better
contamination	more	
Channel cleanness		better
process		simple

Source: Reprinted with permission from [202], T. Cui et al., “Novel Lithography Based Approaches to Pattern Layer-by-Layer Self-Assembled Thin Films,” 2002. © 2002, ASME.

film. Capacitors are fabricated on 4-inch P-type and N-type silicon wafers. The measured CV curves are in compliance with typical MOS capacitors. Compared to the traditional process, this has the advantages of low temperature, low cost, and short processing time. The simplicity and reliability of this process to fabricate the simple MOS capacitor provides a new way to fabricate other microelectronic or optoelectronic devices by traditional lithography and LbL, self-assembled building blocks.

Figure 10(a) shows an SEM image of the  $(45\text{-nm silica/PDDA})_4$  multilayer cross-section. The film has a permanent thickness of 170 nm, leading to 43 nm for every bilayer close to the silica particle diameter. A film mass from QCM and a film thickness from SEM gives a density of the  $\text{SiO}_2/\text{PDDA}$  multilayers as  $\rho = 1.43 \pm 0.05 \text{ g/cm}^3$ . To calculate the silica-packing coefficient in the films, it is reasonable to assume that the dry film consists of  $\text{SiO}_2$ , PDDA, and air-filled pores. The mass ratio of PDDA to  $\text{PDDA}/\text{SiO}_2$  bilayer obtained from QCM measurements is 0.08. Taking

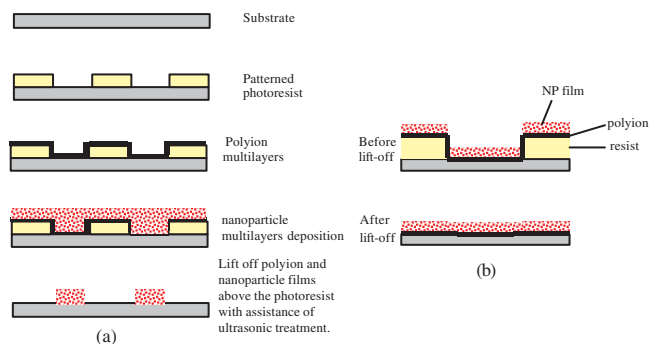


**Figure 9.** (a) Scheme of patterning nanoparticle thin films with ultrasonic treatment. (b) Scheme of patterning nanoparticle thin films without ultrasonic treatment. NP and polyion films cannot be lifted off because of the linkage between polyion molecules are not disconnected. Reprinted with permission from [203], F. Hua et al., *Nanotechnology* 14, 453 (2003). © 2003, Institute of Physics.

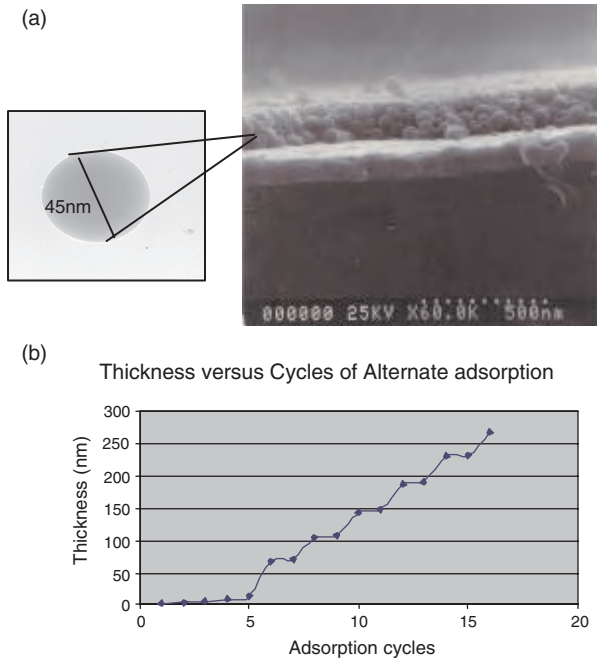


**Figure 10.** (a) SEM image of cross-section of (45-nm silica/PDDA)<sub>4</sub> multilayer on silver electrode (b) QCM-monitored, 45-nm silica growth. Reprinted with permission from [203], F. Hua et al., *Nanotechnology* 14, 453 (2003). © 2003, Institute of Physics.

into account component densities ( $\rho = 1.43$ ,  $\rho_{\text{SiO}_2} = 2.2$ , and  $\rho_{\text{PDDA}} = 1.1 \text{ g/cm}^3$ ), the volume ratio is obtained as  $V_{\text{PDDA}}/V_{\text{bilayer}} = 0.1$ . From the equation  $\rho_{\text{PDDA}}V_{\text{PDDA}} + \rho_{\text{SiO}_2}V_{\text{SiO}_2} + \rho_{\text{air}}V_{\text{air}} = \rho V$ , where the air-term is very small,  $V_{\text{SiO}_2}/V = 0.7$ . This is very close to the theoretical dense-packing coefficient for spheres (0.63), and corresponds to details in the SEM micrographs. SiO<sub>2</sub>/PDDA film volume composition is: 70% SiO<sub>2</sub> + 10% polycation + 20% air-filled pores. These pores are formed by closely packed 45-nm SiO<sub>2</sub> and have a typical dimension of 15 nm. Therefore, the dielectric constant of our silica/PDDA multilayer is different from silica due to about 30% of inclusions, such as air, polycation layers, etc. In the analysis of the MOS devices, it is found that the dielectric constant was slightly higher than the one for thermal silica. In our group, it is possible to produce ultra-thin multilayers of silica nanoparticles in the thickness ranging from 100 nm to hundreds of nm with a precision of about 10 nm. These films have a porous structure related to the close packing of silica spheres in the layer.

As shown in Figure 11, clear patterns of the capacitor arrays with sharp borders were created on a silicon wafer. The arrays consist of round and square capacitors with various sizes. All 45 nm SiO<sub>2</sub> spheres were closely packed to form a dense structure. The surface roughness of the capacitor was 6.5 nm measured by RST. The growth step can be easily estimated by measuring the frequency shift of the quartz crystal microbalance resonator, and the monolayer thickness can be calculated accordingly by the Sauerbrey equation. Figure 10(b) gives the QCM monitoring of alternate PDDA and SiO<sub>2</sub> adsorption, where the thickness was calculated from frequency shifts with formula 2. As recorded by QCM, at every assembly step, the component

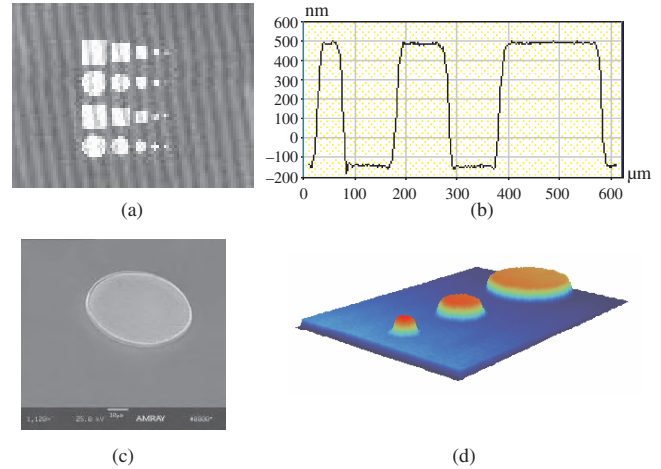


**Figure 11.** (a) Optical image of the capacitor arrays, the minimum diameter or size is 50 μm. (b) 2D profile (c) SEM image of layers of 45-nm silica particle thin film. (d) 3D plot of the capacitors. Reprinted with permission from [203], F. Hua et al., *Nanotechnology* 14, 453 (2003). © 2003, Institute of Physics.

monolayer was formed. It shows that at the sixth cycle, the thickness of the SiO<sub>2</sub> layers is 260 nm. When added to the 300 nm aluminum electrode, the height of the whole device is 567 nm, well in compliance with the 2D profile of Figure 11(b).

The fabricated device demonstrates the C-V curve of a typical MOS capacitor with distinct accumulation, depletion, and inversion regions, as shown in Figure 12. The MOS structure is basically a capacitor with the silica as the dielectric material. If the silicon were a perfect conductor, the parallel-plate capacitance would be determined by the oxide capacitance as it is in the accumulation region. However, it always deviates from the oxide capacitance due to the voltage dependence of the surface space-charge layer in silicon. The space-charge occurring at the interface of silicon and oxide acts as another capacitance in a series with the oxide capacitor, giving an overall capacitance that is smaller than the pure oxide capacitance. Since the inversion of a P-type MOS capacitor happens at a positive voltage and an N-type one at a negative voltage, the C-V curves move in opposite directions for P- and N-type MOS capacitors. If the layer of silicon dioxide was produced by conventional thermal oxidation, the dielectric constant would be 3.9. Given the size of each square device, 200 μm by 200 μm and 267 nm high, the oxide capacitance is calculated as 5.2 pF, reasonably close to the experimental data, 8 pF. The slightly larger value means a larger dielectric constant of the LbL, self-assembled insulator layer. The precursor and intermediate polyion multilayer is the root for the higher dielectric constant because the dielectric constant of the polyion film is normally 10 times higher than silica [204]. The experimental results also show that the capacitance of each device is strictly proportional to the area of the electrode, implying an extremely high reproducibility of the processes.

In our process, a conventional lithographic technique, such as lift-off, was used to pattern the capacitors on multilayer films. However, because the LbL-self-assembled nanoparticle films are unlike the conventional thin films in

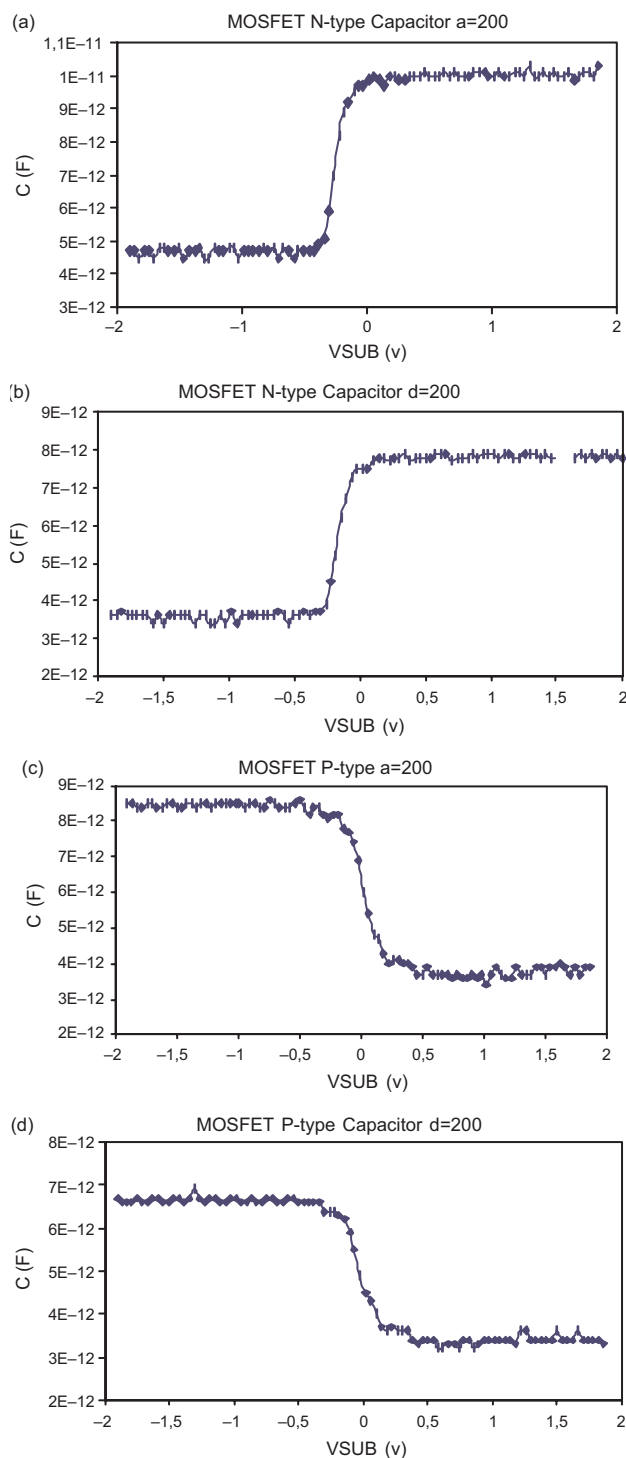


**Figure 12.** Capacitance versus voltage curves of MOS P- and N-type capacitors (a) N-type square capacitor with size of  $200 \mu\text{m}$ . (b) N-type round capacitor with diameter of  $200 \mu\text{m}$ . (c) P-type square capacitor with size of  $200 \mu\text{m}$ . (d) P-type round capacitor with diameter of  $200 \mu\text{m}$ . Reprinted with permission from [203], F. Hua et al., *Nanotechnology* 14, 453 (2003). © 2003, Institute of Physics.

many respects, modification and optimization of the traditional process is required.

During the lift-off, it was better to introduce ultrasonic treatment for 3 seconds when the wafer was soaked in

developer solution. Inside the structure of the nanoparticle film, polyion multilayers such as PDDA and PSS were sandwiched between the nanoparticle film and photoresist as a kind of “chemical glue.” The structure of the polyion is like a long thread that strongly links one to the other. It is hard to break them up during the lift-off, so at some areas the nanoparticle and polyion multilayer cannot be removed when the photoresist is dissolved. They just drop down and reattach to the film underneath, as shown in Figure 9(b). The ultrasonic treatment is introduced to disconnect the linkage between polyion branches and obtain a more distinct pattern with higher reproducibility.

Other dielectric materials, such as montmorillonite, has also been tested as the insulating layer. They did not perform as well as the silica nanoparticle, although the monolayer thickness can be more precisely controlled. There are many other nanoparticles suitable for LbL self-assembly that may function differently for various devices.

## 7. NANOFABRICATION FOR NANO-ELECTRONICS

The semiconductor industry has seen a remarkable miniaturization trend, driven by many scientific and technological innovations. However, if the trend is to continue and provide even faster and cheaper computers, the size of microelectronic circuit components will soon need to reach the scale of atoms or molecules [205].

Photolithography, the technology used to manufacture computer chips and virtually all other microelectronic systems, can be refined to make structures smaller than  $100$  nanometers, but doing so is very difficult, expensive, and inconvenient.

The electronics industry is deeply interested in developing new methods for nanofabrication so that it can continue its long-term trend of building even smaller, faster, and less expensive devices.

Despite enormous recent progress in the fabrication and demonstration of nanoelectronic devices, many challenges remain. For solid-state electronics, one of the most important challenges is to be able to produce reliable and uniformly in silicon the characteristic nanometer-scale features required for nanoelectronics: nanometer-scale islands, barriers, and “heterojunctions” between islands and barriers.

One leading contender is electron-beam lithography [206]. In this method, the circuitry pattern is written on a thin polymer with a beam of electrons. An electron beam does not diffract at atomic scales, so it does not cause blurring of the edges of features. Researchers have used this technique to write lines with widths of only a few nanometers in a layer of photoresist on a silicon substrate. The electron-beam instruments currently available, however, are very expensive and impractical for large-scale manufacturing.

Another contender is lithography using X-rays with wavelengths between  $0.1$  and  $10$  nanometers or extreme ultraviolet light with wavelengths between  $10$  and  $70$  nanometers. Because these forms of radiation have much shorter wavelengths than the ultraviolet light currently used in photolithography, they minimize the blurring caused by

diffraction [206]. But these technologies have their own problems: conventional lenses are not transparent to extreme ultraviolet light and do not focus X-rays.

For top-down lithography, they begin with a pattern generated on a larger scale and reduce its lateral dimensions. But no top-down method is ideal; none can conveniently, cheaply, and quickly make nanostructures of any materials. Thus researchers have shown a growing interest in bottom-up methods, which start with atoms, molecules, and nanoparticles to build up nanostructures with dimensions between 2 and 10 nanometers and do so inexpensively [207].

Bottom-up approaches to nanoelectronics [208], where the functional electronic structures are assembled from well-defined nanoscale building blocks, such as carbon nanotubes [203–208], molecules [215–217], and/or semiconductor nanowires [218–220], inorganic nanoparticles have the potential to go far beyond the limits of top-down manufacturing.

The formation of carbon nanotubes could be traced back to the discovery of the fullerene structure  $C_{60}$  (buckball) in 1985 [221]. The structure of the buckball, comprised of 60 carbon atoms arranged by 20 hexagonal and 12 pentagonal faces to form a sphere, is elongated to form a long and narrow tube with a diameter of approximately 1 nm, which is the basic form of a carbon nanotube [222]. Nanotubes have extraordinary mechanical, electrical, and thermal properties while providing strong, light, and high toughness characteristics. Since the discovery of nanotubes, extensive research in carbon, fullerene, nanosensor, nano-indentator, and nanomachine has blossomed in many different directions, and has attracted a great deal of attention to advanced composite society. It is well understood that carbon fibers or nanotubes could not be utilized alone without any supporting medium, such as a matrix to form structural components. Whereas, the investigation on the interfacial bonding properties between the nanotube and matrix system is of great interest, it ensures a good stress transfer between the nanotube and matrix of nanocomposite structures in the development of nanotube composites.

Carbon nanotubes exhibit several technologically important characteristics. Metallic(m) nanotubes can carry extremely large current densities [223, 224]. Semiconducting nanotubes can be electrically switched on and off as field-effect transistors (FETs) [225, 226]. The two types may be joined covalently [227, 228].

Carbon nanotubes [222, 229–234] are very attractive because they are capable of emitting high currents (up to 1 A/cm<sup>2</sup>) at low fields ( $\sim 5$  V/ $\mu$ m), and their potential as emitters in various devices have been amply demonstrated [235]. Furthermore, the controlled deposition of nanotubes on a substrate has become possible through the combined use of chemical vapor deposition (CVD) methods and catalyst patterning techniques.

The study of nanometer-sized semiconductor crystals has been advancing at a rapid pace. Much of the interest in these materials stems from the fact that their physical and chemical properties can be systematically tuned by variation of the size, according to increasingly well-established scaling laws. In the semiconductor quantum dot (QD), the electrons and holes are three dimensionally confined inside a nanometer scale “quantum box.” The confinement causes a discrete

atomic-like, energy-level structure for the carriers and a variety of new physical phenomenon are observed [236, 237]. Researchers have been exploring the possibility of combining quantum confinement with the introduction of extra carriers by means of doping and charging to obtain a new set of properties in these materials [238–244]. The impurity doping which is routine in bulk semiconductors is now extended to semiconductor nanocrystals. Many efforts that try to attack these problems have focused on doping II–VI semiconductor nanocrystals with metals such as Mn, 10, 11, or Cu<sup>12</sup> and rare-earth elements such as Tb.<sup>13</sup> These impurities do not affect the adsorption spectrum, but strongly modify the luminescence properties [245].

A PBG crystal (or photonic crystal) is a spatially periodic structure fabricated from materials having different dielectric material constants [246]. It can influence the propagation of electromagnetic waves in a similar way as a semiconductor does for electrons. The concept of this new class of material was first proposed independently by Yablonovich [247] and John [248] in 1987, and since then a wide variety of applications has been envisioned or demonstrated for this new class of materials. In silicon and other semiconductors, adjacent atoms are separated by about a quarter of a nanometer. Photonic bandgap materials involve similar structures but on a larger scale. A photonic crystal, for example, provides a convenient and powerful tool to confine, control, and manipulate photons in all three dimensions of space, for example, to block the propagation of photons irrespective of their polarization or direction; to localize photons to a specific area at restricted frequencies; to inhibit the spontaneous emission of an excited chromophore; to modulate or control simulated emission; and to serve as a lossless waveguide to direct the propagation of photons along a specific direction [249–254]. All of these photonic properties are technologically important because they can be exploited, in principle, to produce light-emitting diodes (LEDs) that display coherence properties, fabricate thresholdless semiconductor diode lasers, and significantly enhance the performance of many other types of optical, electro-optical, and quantum electronic devices. Patterning photonic crystal thin films into optical circuits would represent the ultimate limit of optoelectronic miniaturization.

Ultimately, it will be desirable to build ultra-dense, low-power nanoelectronics circuits made from purely nanometer-scale switching devices and wires. Molecules electronics, using individual covalently bonded molecules to act as wires and switching devices, is another longer-term alternative to build ultra-dense, low-power nanoelectronics circuits. Individual molecular switching devices could be as small as 1.5 nanometers across, with densities of approximately 10<sup>12</sup> devices per sq cm. A primary advantage of molecular electronics is that molecules are natural nanometer-scale structures that can be made absolutely identical in vast quantities. Also, synthetic organic chemistry (the chemistry of carbon-based compounds) offers more options for designing and fabricating these intrinsically nanometer-scale devices than the technology presently available for producing solid-state chips with nanometer-scale features. It has been shown that small organic molecules can conduct and control electricity [255–260] and large organic biomolecules are conductive [261].



There has been a great deal of interest in the use of both supermolecular assemblies and nanoparticle structures as components of electronic circuits [262, 263]. A machine based on molecules acting as components also requires a high level of complexity in the actual chemistry required. Switches are key components of any electronic device to be used for computational purposes, and for these uses, quantum states appear as the obvious choice to achieve this functionality. In order to construct useful switching structures based on individual molecules, the transfer function of a two-contact switching unit must involve a range of applied potentials in which the device exhibits a negative resistance.

Another approach in nanoscale electronics is based on the use of nanoparticles for the construction of electronic components of nanometer dimensions. Well-defined rules of how these materials can be organized have emerged. The vigorous recent efforts in synthesizing MPCs have resulted in the availability of functionalized nanomaterials that while retaining the properties of a metallic core can be handled like simple, stable chemical compounds. The question that needs to be addressed is would it be possible to synthesize chemically functionalized nanoscale objects that would spontaneously organize into superstructures with desirable functionalities?

Many ways have been developed for preparing nanostructures, ranging from single-atom manipulation to organic synthesis. The tremendous strength of the colloidal preparation routes is that they yield large amounts of monodisperse nanocrystals with easy size tuning. Furthermore, the presence of organic molecules on the surface of the nanocrystals enables extensive chemical manipulation after the synthesis.

The development of advanced materials from inorganic nanoparticles (NPs) is currently one of the most dynamic areas of science. Nanoparticles are attracting significantly fundamental and commercial interest, with a wide range of applications including the next generation of optics, electronics, and sensors [264]. In optical, electrical, and magnetic devices, NPs will be mostly used in the form of thin films. Currently, such films are typically made by spin-coating, spraying, or sometimes simple painting of nanoparticle-matrix mixtures.

There has recently been an intense effort to produce metal nanoparticles capped with a variety of functional groups [265]. The rapid development of this field is resulting in the availability of many different functionalized nanoparticles that can be used in much the same way as organic chemical reagents. The main synthetic strategies that have been developed are based on either the direct one-step, single-phase reduction (gas-phase synthesis) or on the two-phase reduction (sol-gel processing), and also on the use of place-exchange reactions with a target ligand. Sol-gel processing is a wet chemical synthesis approach that can be used to generate nanoparticles by gelation, precipitation, and hydrothermal treatment (Fig. 13). Size distribution of semiconductor, metal, and metal oxide nanoparticles can be manipulated by either dopant introduction or heat treatment. Better size and stability control of quantum-confined semiconductor nanoparticles can be achieved through the use of inverted micelles, polymer matrix architecture based on block copolymers or polymer blends, porous glasses,

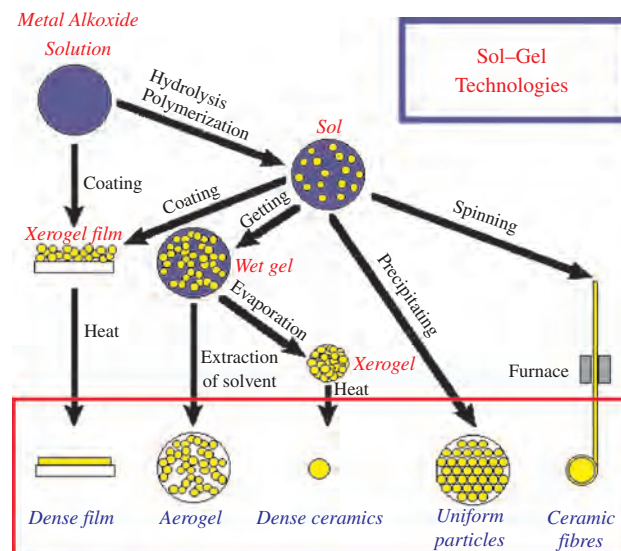


**Figure 13.** Sol-gel technology in nanoparticle synthesis. Reprinted with permission from [267], <http://www.chemat.com/html/solgel.html>. © Chemat Technology, Inc.

and *ex-situ* particle-capping techniques. Supercritical solvents represent convenient media for synthesis because their solvation properties can be easily controlled by varying the pressure. Supercritical fluids exhibit gas-like mass transfer properties and yet have liquid-like solvation capability. Carbon dioxide is one of the mostly widely used gases for supercritical fluid applications because of its moderate critical constants, nontoxic nature, low cost, and availability in pure form. Metal ions are insoluble in supercritical  $\text{CO}_2$  because of the charge neutralization requirements and the weak solute-solvent interactions. However, when metal ions are bound to organic ligands, they may become quite soluble in supercritical  $\text{CO}_2$  [266].

Microemulsions have been extensively employed for nanoparticle synthesis because the reaction can be confined in a well-defined environment. This approach has been successfully developed for the synthesis of Ag nanoparticles in supercritical carbon dioxide ( $\text{sc-CO}_2$ ) by the reduction of  $\text{Ag}^+$  incorporated in a water-in  $\text{CO}_2$  microemulsion. In addition, phase-extraction methods, in which the aqueous colloidal metal solution is extracted into an immiscible organic phase containing the capping reagent, have been employed. Microemulsion copolymerization is shown to be a very useful method to produce stable aqueous suspensions of ultra-fine, selective metal-complexing nanoparticles with controlled size and adjustable metal-binding capacity [268].

The ability to assemble nanoparticles into highly ordered 2D or 3D arrays is very important in fabricating novel devices utilizing quantum dots and inorganic (or organic) colloidal particles. Several techniques have been demonstrated for forming such arrays: for example, 2D arrays have been fabricated using methods based on chemical vapor deposition, Langmuir-Blodgett films, molecular beam epitaxy, pulsed electrochemical deposition, and microcontact printing [269–275]; 3D arrays have been realized through self-assembly approaches that usually involve electrostatic interaction [276–281], sedimentation [282–287], and solvent evaporation [288–289].



Layer-by-layer assembly is one of the new methods of thin-film deposition, often realized as a sequentially absorbed monolayer of oppositely charged polyelectrolytes [290]. Layer-by-layer assembly has also been successfully applied to thin films of NPs and nanocolloids, that is, dispersed species with only one or two spatial dimensions in the nanoscale regime. A large number of studies on the assembly of semiconductor, metallic, magnetic, insulating, composite, and other materials have been undertaken [291–299]. The main advantages are the simplicity, universality, and high quality of the resulting coating. Based on this, LBL assembly can be a convenient method for processing NPs into thin films, both for advanced materials research and industrial production.

Soft lithography generates micropatterns of SAMs [300–305] by contact printing, and also forms microstructures in materials by embossing (imprinting) [306–315] and replica molding [316–318]. The strength of soft lithography is in replicating rather than fabricating the master, but rapid prototyping and the ability to deform the elastomeric stamp or mold gives it unique capabilities even in fabricating master patterns. Soft lithography is not subject to the limitation set by optical diffraction and optical transparency and can be usually carried out in the laboratory environment.

Researchers have recognized the utility of DNA in nanofabrication [319–323]. DNA oligonucleotides contain hybridization information encoded in their sequences. In exploiting this phenomenon of DNA hybridization, interactions can be made specific by the DNA sequence, while interparticle distance can be controlled through the selection of the oligonucleotide length. Consequently, a nanostructure much more complex than that which is possible using SAMs might be achieved by using DNA as a “linker” of the nanoparticles.

Template-directed synthesis is a convenient and versatile method for generating porous material. It is also a cost-effective and high-throughput procedure that allows the complex topology present on the surface of a template to be duplicated in a single step. In this technique, the template simply serves as a scaffold around which other kinds of materials are synthesized. By templating against supermolecular assemblies self-organized from small molecules, surfactants, and block copolymers, it has been possible to prepare various types of porous materials with pore sizes in the range of 0.3–10 nm [324–328]. With the use of mesoscale objects such as templates, the dimension of these pores can be significantly extended to cover a wide range that spans from  $\sim 10$  nm to  $10 \mu\text{m}$  [329–332]. In particular, templating against opaline arrays of colloidal spheres offers a generic route to macroporous materials which exhibit precisely controlled pore size and highly ordered 3D porous materials [333–339]. The fidelity of this procedure is mainly determined by van der Waals interactions, the wetting of the template surface, a kinetic factor such as the filling of the void spaces in the template, and the volume shrinkage of precursors during the solidification. Templating against opaline arrays of colloidal spheres has been successfully applied to the fabrication of 3D microporous structures from a wide variety of materials, including organic polymers, ceramic materials, inorganic semiconductors, and metals [333–350].

Fabrication based on this approach is remarkable for its simplicity and its fidelity in transferring the structure from the template to the replica. The size of the pores and the periodicity of the porous structures can be precisely controlled and readily tuned by changing the size of the colloidal spheres.

Although this templating procedure may lack the characteristics required for high-volume production, it does provide a simple and effective route to 3D porous materials having tightly controlled pore sizes and well-defined periodic structures. These porous structures can serve as a unique model system to study many interesting subjects such as adsorption, condensation, transport (diffusion and flow), and separation of molecules in macroporous materials, as well as mechanical, thermal, and optical properties of 3D porous materials.

## 8. POLYMER MICROELECTRONICS

Polymer microelectronics/optoelectronics is an emerging field of research and development. Nanoassembly and other nanofabrication techniques can be applied to the fabrication of polymer microelectronics/optoelectronics to improve the fabrication efficiency and reduce the cost. Here we review the recent progress in materials, current fabrication technologies, devices designs, and applications related to polymer microelectronics, including transistors and integrated circuits.

Since the 1950s, inorganic silicon and gallium arsenide semiconductors, silicon dioxide, silicon nitride, and metals such as aluminum and copper have been the backbone of the semiconductor industry. However, since the late 1980s, there has been a growing interest in polymer or organic microelectronics based on the conjugated polymers, oligomers, or other molecules. By recent research efforts through novel synthesis and process techniques, the performance as well as the stability and ability to process these active materials has been greatly improved. Although polymer microelectronic devices cannot rival the traditional, mainstream inorganic microelectronic devices due to the relatively low mobilities of the organic semiconductive materials, they can be competitive for the applications requiring structural flexibility, low temperature processing, large-area coverage on materials such as plastic and paper, batch production, and especially low cost. The applications of the polymer microelectronics include the active-matrix flat-panel displays [351] based on the OLEDs, low-end smart cards, electronic identification tags, photovoltaic cells, high bandwidth photodetectors [352], high density memory chips, sensors and actuators, and some pervasive computing needs. The main fabrication technologies include ink-jet printing, photochemical lithography [363], spin-coating, vacuum evaporation, soft lithography (contact transfer) [353], RIE, and nano self-assembly.

### 8.1. Materials and Physics

Alan MacDiarmid, Alan Heeger, and Hideki Shirakawa won the 2000 Nobel Prize in Chemistry for the discovery and development of conductive polymers. Most polymers are insulators because their electrons are localized, that is, each of the electrons is attached to its own nucleus. However, the conducting or semiconducting polymers have conjugated

double bonds. The double bond consists of a  $\sigma$  bond and a  $\pi$  bond. Due to the conjugated structure, the electrons have gained the freedom to move along the entire chain. In metals and conventional semiconductors, charge-transport occurs in delocalized states. Such a model is no longer valid in low conductivity organic semiconductors, where a simple estimate shows that the mean-free path of carriers would become lower than the mean atomic distance. In these materials, carrier-transport occurs through hopping of charges between localized states. The modeling of organic field effect transistors (OFETs) is currently hampered for several reasons. First, the charge-transport in organic semiconductors is still not well understood. Second, there are great differences between the behaviors of OFETs made from different compounds. Furthermore, the fabrication method seems to strongly affect the device performance. Nevertheless, some attempts [354–356] have been made, such as the model based on a simple trap distribution applied on the dihexylquaterthiophene (DH4T).

The charge mobility increases with temperature in most organic materials. A useful model to describe the charge-transport in organic materials is that of the small polaron, developed by Holstein [357]. Localization in conjugated organic materials occurs via the formation of polarons resulting from the deformation of the conjugated chain under the action of the charges. This mechanism of self-trapping is often described through the creation of localized states in the gap between the valence and the conduction bands.

In a multiple trapping and release (MTR) model, a narrow delocalized band is associated with a high concentration of localized levels that act as traps. During their transition through the delocalized levels, the charge carriers interact with the localized levels via trapping and thermal release. The prominent feature of OFETs is that the field-effect mobility is gate bias dependent. A general feature of charge-transport in organic materials is that the mobility becomes field dependent at high electric field (namely, at fields in excess of  $\sim 10^5$  V/cm).

Figure 14 shows the structures of the several conducting or semiconducting polymers. The conductivity of the

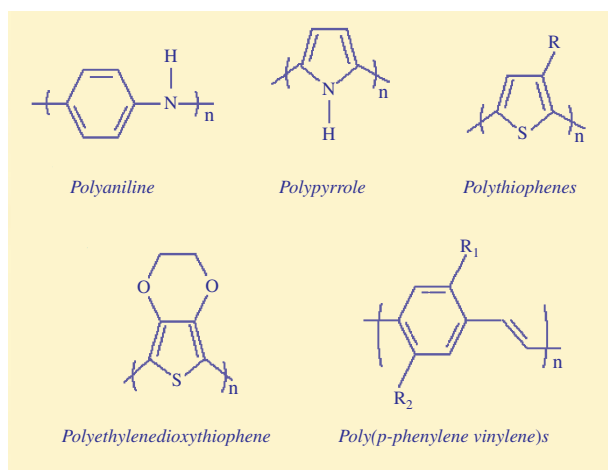


**Figure 14.** The chemical structures of polymers for devices. Reprinted with permission from [363], <http://www.conductivepolymers.com/#1>. © Advanced Polymer Courses.

polymer materials have been improved quickly in recent years. For example, Ormecon Chemie, Germany, which developed polyaniline, has developed grades of polyaniline with conductivity of 300 S/cm in 1998.

## 8.2. Polymer Transistors and Integrated Circuits

In 1930, Lilienfeld first proposed the principle of the field-effect transistor (FET) [358]. And in 1960, Kahng and Atalla [359] fabricated the first silicon-based MOSFET. Although first descriptions of the field effect in organic semiconductors can date back to 1970, organic FETs (OFETs) have only been identified as potential elements of electronic devices since the report by Koezuka et al., in 1987, on a structure based on electrochemically polymerized polythiophene [360]. But the first all-polymer transistor was fabricated by the team of Francis Garnier et al. after 24 years [361].

The performance of OFETs has been continuously improved since the 1980s, and some OFETs can now compete with amorphous silicon FETs. The performance of OFETs is primarily limited by the relatively low electron or hole mobility of the channel materials, either polymers or small molecules. Due to the molecular vibrations and large intermolecular distances (typically about 0.35 nm), conductivity in small molecule organic films depends on the rate of electron- or hole-hopping between the molecules. Polymers show even lower mobility than small molecules due to their less ordered structures. Figure 26 shows the highest field-effect mobilities ( $\mu$ ) reported for OTFTs fabricated from the most promising polymeric and oligomeric semiconductors versus year from 1986 to 2000 [362].

Organic FETs and integrated circuits recently reported by Philips [364], IBM, Lucent Technologies, and Pennsylvania State University [365, 366] indicate that great advances have been made.

Pentacene OTFTs have produced the highest performances with mobility as large as  $1.5 \text{ cm}^2 \text{ V}^{-1} \text{ S}^{-1}$  and an on/off ratio larger than  $10^8$  in 1997 [367, 313]. However, the operating voltage requiring such performance was too high (100 V). Using much higher dielectric constant metal oxide film, barium zirconate titanate (BZT) as a gate insulator, researchers at IBM reported a similar performance of pentacene TFT fabricated on transparent polycarbonate substrates and operated at a maximum voltage of only 4 V, with the mobility values of  $0.38 \text{ cm}^2 \text{ V}^{-1} \text{ S}^{-1}$  [362]. As most organic materials, pentacene is intolerant to exposure of various chemicals used in traditional lithography. Therefore, they are difficult to be patterned using lithography. Usually shadow masks are used during the deposition. To overcome this, researchers at Pennsylvania State University used a double-layer resist active-layer patterning technique that does not require the organic film to be exposed to process chemicals. This patterning technique also reduces the current leakage in the pentacene film outside the active device areas [365, 366]. By 2000, the maximum field-effect mobility was reported to be  $2.7 \text{ cm}^2/\text{VS}$  for holes in a pentacene single crystal by Schön et al. at Bell Laboratories [369].

Researchers at the Philips Company have also made impressive progress, developing the first all-polymer ICs

consisting of 326 transistors with a 2- $\mu\text{m}$  gate length and more than 300 vertical contacts in 1998 [364]. It involves reproducible fabrication of field-effect transistors in which the semiconducting, conducting, and insulating parts are all made of polymers. The interconnections between the transistors are also conducting polymers. The transistor structures are created by masking the polyaniline and irradiating it with UV radiation to reduce its conductivity by almost 10 orders of magnitude, from  $10^3$  Ohm/sq to more than  $10^{13}$  Ohm/sq. Philips developed a 15-bit programmable code generator with bit rates of 30 bits/sec. The circuits remain functional when the foils (substrate) are sharply bent. Recently, Philips is also working on polymer memory chips and displays.

Lucent Bell Laboratories reported the large scales of integration up to 864 transistors per circuit and operation speeds of  $\sim 1$  KHz in clocked sequential complementary circuits [370]. Bell Labs have been able to print functional circuits on flexible sheets of plastics using inexpensive screen-printing techniques in 1997 [371]. After that, Lucent Bell Laboratories and Opticom ASA have entered into an agreement to develop the plastic memory using polymer integrated circuits.

The disadvantage of using well-ordered pentacene as the active material in the TFT is that it needs the vacuum evaporator to deposit the crystalline film layer. The technologies that are believed to have the potential to produce the highest impact on polymer microelectronics are large-area stamping, ink-jet printing, screen-printing, and self-assembling using the soluble polymer semiconductors without the lithography process. Ink-jet printing deposition is a method in which the pattern can be directly printed onto the substrate, giving very high-resolution patterns and the ability to separate pixels of red, green, and blue-emitting polymers onto the substrate. Using this technology will not only lower the production cost but will also make it possible to fabricate flexible and large area devices. The University of Cambridge reported the all-polymer thin-film transistors fabricated by high-resolution ink-jet printing for the first time in 2000 [372, 373]. They realized a channel length of down to 5  $\mu\text{m}$  and fabricated the TFT with a high mobility of  $0.02 \text{ cm}^2 \text{ V}^{-1} \text{ S}^{-1}$  and an on/off ratio of more than  $10^5$  by aiding a self-aligning flow of solution.

In recent years, most studies on the solution-processable polymeric semiconductor focused on poly(3-hexylthiophene). With the treatment of  $\text{SiO}_2$  with hexamethyldisilazane (HMDS) or an alkyltrichlorosilane, the OTFTs from highly regioregular poly(3-hexylthiophene) with the mobilities of  $0.05$  to  $0.1 \text{ cm}^2 \text{ V}^{-1} \text{ S}^{-1}$  has been reported [374–376]. Other regioregular poly(3-alkylthiophene), such as poly(3-octylthiophene) and poly(3-dodecylthiophene) have also been used to fabricate the field-effect transistors [371].

More recently, mobilities in the range of  $10^{-2}$  to  $10^{-1} \text{ cm}^2 \text{ V}^{-1} \text{ s}^{-1}$  have been achieved using solution-processed, substituted oligothiophenes [377–379]. The mobility is found to strongly depend on film morphology, which can be controlled by the processing conditions. In one study,  $\alpha, \alpha'$ -dihexylhexathiophene (DH6T) and  $\alpha, \alpha'$ -dihexylquaterthiophene (DH4T) were dissolved in hot chlorobenzene or 1,2,4-trichlorobenzene, then solution-cast onto bottom-contact substrates. The solvent was evaporated

in a vacuum oven at temperatures between room temperature and  $100^\circ\text{C}$ . For DH6T films prepared in this way, the mobilities ranged from  $4 \times 10^{-3}$  to  $5 \times 10^{-2} \text{ cm}^2 \text{ V}^{-1} \text{ s}^{-1}$ , with the highest mobilities corresponding to trichlorobenzene and  $70^\circ\text{C}$  solvent evaporation. The mobilities of DH4T films ranged from  $1 \times 10^{-3}$  to  $7 \times 10^{-2} \text{ cm}^2 \text{ V}^{-1} \text{ s}^{-1}$ , slightly lower than those of DH6T films prepared under the same conditions [378]. In another study, additional solvents including 3-methylthiophene, anisole, and toluene were investigated. Chlorobenzene, 1,2,4-trichlorobenzene, and 3-methylthiophene all yielded smooth films and mobilities occasionally as high as  $0.1 \text{ cm}^2 \text{ V}^{-1} \text{ s}^{-1}$  and routinely  $0.03 \text{ cm}^2 \text{ V}^{-1} \text{ s}^{-1}$  when the DH6T concentration was less than 0.1%. From a film of  $\alpha, \alpha'$ -dihexylquinquethiophene (DH5T) cast from chlorobenzene onto a  $50^\circ\text{C}$  substrate, the mobility of  $0.03 \text{ cm}^2 \text{ V}^{-1} \text{ s}^{-1}$  was obtained [379]. But a subsequent study reported a mobility of  $0.1 \text{ cm}^2 \text{ V}^{-1} \text{ s}^{-1}$  from a DH5T film solution-cast from toluene [377].

Other soluble organic oligomers have also been investigated as semiconducting materials for OFETs. Anthradithiophene, a fused heterocycle compound similar to pentacene, is soluble in its dihexyl end-substituted form. Dihexylanthradithiophene (DHADT)-based transistors were fabricated by solution-casting from hot chlorobenzene, then evaporating the solvent in a vacuum oven at various temperatures. However, the electrical characteristics of the films were strongly dependent on the solvent evaporation temperature. The highest mobilities,  $0.01$  to  $0.02 \text{ cm}^2 \text{ V}^{-1} \text{ s}^{-1}$ , were obtained for a drying temperature of  $100^\circ\text{C}$  [379, 380]. In comparison, vacuum-evaporated films of DHADT gave mobilities as high as  $0.15 \text{ cm}^2 \text{ V}^{-1} \text{ s}^{-1}$  [380]. Organic FETs utilizing another thiophene-containing oligomer, trans-trans-2,5-bis-[2-{5-(2,2'-bithienyl)}ethenyl]thiophene (BTET), were fabricated by spin-coating from hot NMP. The mobility of such a device was  $1.4 \times 10^{-3} \text{ cm}^2 \text{ V}^{-1} \text{ s}^{-1}$  compared to  $0.012 \text{ cm}^2 \text{ V}^{-1} \text{ s}^{-1}$  for a vacuum-evaporated device [381].

Another approach to solution-processable oligomeric materials is to begin with a precursor molecule that is soluble but not semiconducting, and then convert it to its semiconducting, insoluble form. This approach has been realized for pentacene, with initial mobilities of  $0.01$  to  $0.03 \text{ cm}^2 \text{ V}^{-1} \text{ s}^{-1}$  reported [383–385]. The pentacene precursor is soluble in dichloromethane and forms continuous, amorphous films when spun onto transistor substrates. The conversion to pentacene is accomplished by heating the films to a temperature of  $140$ – $220^\circ\text{C}$  in a vacuum for several minutes to 2 hours. Tetrachlorobenzene is eliminated in the conversion process, and electron microscopy reveals microcrystallites in converted films. In a subsequent study, by treatment of the  $\text{SiO}_2$  substrate with HMDS prior to spin-coating the precursor and optimizing the conversion conditions, a mobility of  $0.2 \text{ cm}^2 \text{ V}^{-1} \text{ s}^{-1}$  was achieved [386].

The precursor approach can also be applied to polymers. In fact, one of the first reported polymer transistors with mobilities in the range of  $10^{-4}$  to  $10^{-5} \text{ cm}^2 \text{ V}^{-1} \text{ s}^{-1}$  used precursor-route polyacetylene as the semiconducting layer [387, 388]. Recently, another polymeric semiconductor that has been processed from a soluble precursor polymer is polythiophenevinylene (PTV). In the study, a PTV film was spun from dimethylformamide and then coated with a layer of precursor poly(p-phenylene vinylene) (PPV). Both the

PTV and PPV were converted at 100–300 °C in a N<sub>2</sub> atmosphere, with the PPV precursor supplying protons to catalyze the PTV conversion. A mobility of  $6 \times 10^{-4} \text{ cm}^2 \text{ V}^{-1} \text{ s}^{-1}$  was reported for a device prepared in this way [389]. Subsequent studies have spun the PTV precursor from chloroform and dichloromethane, and have converted the PTV at 140–160 °C in a N<sub>2</sub> atmosphere with a flow of HCl gas to catalyze the reaction [364, 383, 385]. Although the mobilities remain fairly low, one advantage of this processing approach is that organic solvents can be used in subsequent device-processing steps without disturbing the converted PTV [364].

Most polymer semiconductors, including the oligomers discussed above, are p-type semiconductors. As for the n-type semiconductor, the highest mobilities have been found with C<sub>60</sub>-based TFTs:  $0.08 \text{ cm}^2 \text{ V}^{-1} \text{ s}^{-1}$  for the neat material, and a factor of 3–4 higher for devices grown on substrates pretreated with tetrakis(dimethylamino)ethylene [382]. However, a naphthalenetetracarboxylic diimide derivative with fluorinated R groups has been reported as a solution-processable, n-type organic semiconductor [377]. This compound is soluble in hot  $\alpha, \alpha, \alpha$ -trifluorotoluene. Solution-casting of this material results in morphologically nonuniform films, with some regions of the films giving mobilities greater than  $0.01 \text{ cm}^2 \text{ V}^{-1} \text{ s}^{-1}$ .

Because the field-effect mobility for the polymer TFT is relatively low and because of the large horizontal geometry of the transistors, the operating frequency of the circuits is only around 200 Hz at the working voltage of 3 V. Compared to the inorganic microelectronics, the performance and the integration level are still poor. If we can successfully fabricate the OTFTs with vertical device architecture instead of that with horizontal structure, the circuit bandwidth around several hundred MHz at the low working voltage could be expected as well as the high integration level.

### 8.3. OLEDs and Polymer Displays

OLEDs have three main advantages over its silicon counterpart: high contrast, high brightness, and low power consumption. And in addition, the OLED has fewer restrictions in terms of size. Organic light-emitting diodes were invented by Tang and Van Slyke [390], who found that p-type and n-type organic semiconductors could be combined to form diodes. This breakthrough initiated great efforts in the development of new molecular materials and device structures. In 1990, the researchers at Cambridge University, under the direction of Richard Friend, reported a similar light-emitting effect in a semiconducting organic polymer film consisting of PPV [391].

In recent years, not only polymer transistors and ICs obtain fast progress, but also polymer OLEDs and displays have impressive development. Major electronic firms such as Philips, Pioneer, Lucent Technologies, IBM, Dupont, Xerox, Mitsubishi, and Hitachi, and smaller companies such as Cambridge Display Technology (CDT), Universal Display, the Franco-German group Aventis, and UniAx, are currently working on the OLEDs and organic full-color displays. CDT Company, which was founded when luminous polymers were discovered at the University of Cambridge, owns the patent to the first luminous polymer, PPV. Cambridge Display Technology is working on flexible displays

based on poly LED and has shown a first prototype of a polymer display developed in cooperation with Seiko-Epson in 1998. In 1999, the color polymer display by ink-jet printing of emitting layers such as PPV and poly-fluorene (F8) was reported [251]. Here, control of the thickness and shape of the droplet, which eventually sets into a high-resolution pixel, remains an as-yet-unsolved problem. As the light-emitting polymer films are very thin, it is quite difficult to use the conventional photolithography technique to pattern them. In 2001, the University of Cambridge has made an agreement with Seiko-Epson and a regional Cambridge operation called Plastic Logic to manufacture full-color display from sophisticated polymers using ink-jet printing [392].

Since the late 1990s, OLEDs have entered the stage of commercialization. In November 1997, Pioneer Company in Japan commercialized a monochrome  $256 \times 64$  dot matrix OLED display for automotive applications [393]. After that, Pioneer Electronics has launched production of a car-stereo system that has an organic multicolor graphic display, while Philips is currently setting up a production line for polymer displays [394]. Organic EL was originally released by Pioneer with three models in 1999 and is now taken to the next level with the ability to download images directly to the face of the radio. Its OEL displays working at very low voltage requirements (<5 volts) have three models, including DEH-P9300, DEH-P6300, and DEH-P7300 [395]. Multi-color organic EL provides a very wide viewing angle, eliminates the need for backlighting, without loss of visibility from sunlight or a bright environment.

In September 2001, Lucent Bell Laboratories and E-Ink, a Cambridge, MA, Company, have developed a flexible electronic display prototype that is the world's first electronic paper [396, 397]. This prototype electronic paper display, holds its image when its power is shut off, so it only requires electric current when the screen changes. The display is made up of a flexible electronic circuit printed on a sheet of mylar and electronic ink made up of tiny capsules that hold white particles suspended in black dye. An electrical current moves the particles to the top or bottom of the capsules, changing the display's image. The display represents a significant scientific advance over previous works in plastic electronics and paper-like displays. The prototypes consist of a 25-square-inch display area made up of several hundred pixels. The transistors in these circuits are made of plastic materials and are fabricated with a low-cost printing process that uses high-resolution rubber stamps.

Recent advances in boosting the efficiency of OLED have also been made. By using guest-host organic material systems, where the radiative guest fluorescent or phosphorescent dye molecule is doped at a low concentration between 0.5 and 5% into the conducting host molecule, the efficiency can be increased to 10% or higher for phosphorescence or up to about 3% for fluorescence. Currently, the best efficiency of OLED has exceeded that of incandescent light bulbs. Efficiencies of 20 lumens per watt have been reported for yellow-green emitting polymer devices, and 40 lm/W attained for phosphorescent molecular OLEDs, compared to less than 20 lm/W for a typical incandescent lightbulb [390]. According to the report by Yu et al., the luminance efficiency of 3.3 lumens per watt has been reached for the red-light emitting of double-layer organic EL devices by doping the

emitting layer with the *N,N'*-bis[4-(*N,N*-dimethylamino)-benzylidene]diaminomaleonitrile (BAM) [398].

Vladimir Bulovic and co-workers at Princeton University demonstrated transparent OLEDs (or TOLEDs), which could be used in either transparent head-up or high-contrast displays [391]. But, developing reliable organic devices remains a challenge. Charge conduction requires very high electrical fields (1–5 MV/cm), so it is only the extreme thinness of OLEDs that enables them to operate at relatively low voltages. That thinness can contribute to rapid device degradation through the generation and subsequent growth of dark spots. The problem is especially acute when the devices are exposed to the atmosphere. Organic displays work reliable only when their constituent organic materials are stable. One use means to extend the lifetime of the devices by using organic phosphors. The key point of this approach is to reduce the amount of time a light-emitting molecule remains in the excited state. Through use phosphor emitters, OLEDs have the potential to achieve operational lifetimes of many hundreds of thousands of hours, easily meeting the demands on display performance. The ultimate goal of using high-efficiency, phosphorescent, flexible OLED displays in the cell phones, personal digital assistants, laptop computers, and even for home video applications may be realized no more than in a few years. However, there are still some challenges to be met, such as achieving higher efficiencies, lower power consumption, and longer device lifetime.

Princeton University developed a micro-patterning technique of organic electronic devices by the process of cold-welding of metal cathodes followed by lift-off from the organic substrate [399]. They fabricated a  $17 \times 17$  passive matrix display, with a pixel size of  $440 \mu\text{m}$  by  $320 \mu\text{m}$ .

There have been tremendous advances in polymer microelectronics and optoelectronics during the last decade. Such achievement will have huge impacts on the future of polymer microelectronics in various applications like information technology. Some kinds of polymer-integrated circuits and field-effect transistors with high mobilities have already been fabricated. The performance can even compete with the amorphous silicon device in some cases. Polymer semiconductors, such as pentacene, deposited by vacuum sublimation, have the best performances because of their very well-ordered structures. However, great improvements made in solution-processable organic semiconductors, with their mobilities only one order of magnitude lower than those of vapor-deposited TFTs, result in even lower process technologies, such as the stamping, ink-jet printing, and self-assembling without the lithography and vacuum facilities. Using the organic LEDs with high efficiencies, full color displays may eventually replace LCDs for use in laptops, PDAs, and even home video displays. Although the chemistry and physics behind the polymer or plastics are not well understood, science is close to creating a next-generation chip that can help the digital revolution mature. More and more polymer microelectronic and optoelectronic devices may enter the stage of commercialization. However, there is still much to be done for the commercialization of polymer or organic electronic devices in the market. Higher operation frequency, a higher integrated level, higher device performance, a lower power consumption, a longer device lifetime, and performance stability are all challenges to us.

Nano self-assembly and other nanofabrication techniques could be approaches in resolving the above problem and can lead to the commercialization of polymer microelectronics/optoelectronics.

## 9. POTENTIAL APPLICATIONS OF NANO SELF-ASSEMBLY

### 9.1. Current Applications

- Biocompatible coverage of eye lenses and implants.
- Precise dye casting on optical elements (film thickness 50–200 nm,  $\pm 5$  nm).
- Increase of bioreactor efficiency by deposition of enzyme/polyion multilayers.
- Formation of polyion capsules for drug delivery.

### 9.2. Potential Applications

#### 9.2.1. Surface Modifications

- Surface wettability, hardness, magnetic properties, lubrication, biocompatibility can be modified by self-assembly of ultrathin nanostructured coating (e.g., plastic hardening by coating with  $\text{Al}_2\text{O}_3$  or  $\text{ZrO}_2$  nanoparticle multilayer; precise  $\lambda/4$  dye-coating of lenses and optical fibers, and other antireflection coating, paper processing). In biomaterials the assembly is applicable directly to tissue surfaces.
- The concept of a “smart” surface may be realized by including functional proteins in biocompatible films (e.g., lipases destroying harmful lipids in contact with biological liquids).
- Filter layer with calibrated nano-pores.
- Nanoparticle catalytic multilayers.

#### 9.2.2. Sensor Layers and Bioreactors

The protein films can be made very thin and contain precisely 1, 2, 3, 4, 5, or more monolayers, which is important for biosensor elements. The deposition of enzyme/polyion multilayers onto carriers of biological reactors permits an increase in their output proportionate to the number of immobilized enzyme layers. Sequential 2–3 step catalytic reactions can be realized in multiprotein films (cascade bioreactions). Enzymes in the polyion films are stabilized and could work with nonaqueous substrate solutions. Polyions, which keep together enzyme layers in the films, can be doped by vitamins (co-factors), specific dyes, or nanoparticles of metal catalysts to mediate reaction activity.

#### 9.2.3. Nanoreactors

Construction of tiny catalytic units containing ordered multilayer shells of enzymes, nanoparticles and polymers.

#### 9.2.4. Electronics

- Conductive thin films. Electrical conductivity of up to 200 S/cm in 50-nm thick polypyrrole/poly(styrenesulfonate) film was achieved.

- Light emitting diodes and display devices of large area and low operating voltage. Light emitting diodes based on multilayer heterostructure of alternate poly(phenylene vinylene) and sulfonated polyaniline were made.
- Electrodes for lithium storage batteries based on graphite nanoplate/polycation multilayers.
- Magnetic nanoparticle mono- and multilayers, including formation of magnetic/dielectric superlattices and soft/hard magnet nanocomposites.
- Optical second harmonic generation layers.

## 10. CONCLUSIONS

- (1) Nano self-assembly has been described as an approach to design organized films that contain different polymer, protein, dye, and nanoparticle monolayers in precise locations perpendicular to the surface. The films are amorphous in plane but organized in the third direction with a precision of a few nanometers. Surfaces, porous carriers, and fibers of any dimension, curvature, or complexity may be covered by the self-assembled films. A layer-by-layer assembly is an easy and general fabrication process. It does not demand a high purity of components. It can be automated and scaled-up for mass production.
- (2) Soft lithography and conventional lithography are two approaches to realize the patterning of self-assembled thin films for device fabrication. The combination of conventional lithography and nano self-assembly has higher precision and reproducibility than soft lithography. Since layer-by-layer self-assembly and lithography techniques are mature processes and lithography is widely applied to the modern semiconductor industry, a combinative technique will be economical and suitable for mass production. By just following the traditional process, the nanostructures comprised of nano building blocks can be realized. As it reacts in semiconductor industry, the process results in such a high reproducibility that distinct patterns can be created in almost all chips on the wafer.
- (3) Polymer microelectronics/optoelectronics is an emerging field of research and development with huge potential commercialization market. Nano self-assembly and other nanofabrication techniques will open new approaches to nanoelectronics. Nano self-assembly will be one of the dominant techniques in realizing commercial polymer microelectronics/optoelectronics with high efficiency and low cost. Thus, polymer microelectronics/optoelectronics could be the revolution of solid-state microelectronics in low-end applications.

## GLOSSARY

**Bottom-up** It starts with atoms, molecules and nanoparticle to build up nanostructures with dimensions between 2 and 10 nanometers- and do so inexpensively.

**Carbon nanotube** The structure of the buckball comprised of 60 carbon atoms arranged by 20 hexagonal and 12 pentagonal faces to form a sphere, when the buckyball is elongated

to form a long and narrow tube with a diameter of approximately 1 nm, which is the basic form of a carbon nanotube.

**Conjugated polymers** Conjugated polymers are polyunsaturated compounds in which all backbone atoms are sp- or sp<sup>2</sup>-hybridized. Conjugated polymers are -in their pristine, neutral state- either insulators or wide-gap semiconductors, and some of them turn into metallic type conductors only after a process called doping.

**Lift-off** This patterning approach is called by us “lift-off” since lift-off acts as a critical step in the process. At the beginning, photoresist is spun on silicon wafer and got patterned. Then nanoparticles are deposited with layer-by-layer assembly on the whole wafer. Eventually, the wafer is put into acetone solution to dissolve resist and particles self-assembled on it are removed, too.

**Metal mask method** This patterning approach is called “metal mask”. At first, a layer of nanoparticles are adsorbed onto silicon wafer. Then a layer of aluminum and resist are deposited and coated on top of nanoparticle layer. Patterns are made on resist by UV lithography and transferred to aluminum layer by etching aluminum. As a result, nanoparticles previously covered under aluminum begins to be open to the air. Then it is etched by oxygen plasma and nanoparticles are removed in compliance with the designed patterns. During the etching process, metal acts as the mask over the nanoparticles. After remained aluminum and resist are dissolved, only the desired pattern is left on the substrate.

**Microcontact printing ( $\mu$ CP)** Microcontact printing is a flexible, non-photolithographic method that routinely forms patterned SAMs containing regions terminated by different chemical functionalities with submicron lateral dimensions.

**Microemulsions** Microemulsions are thermodynamically stable systems (usually in the size range of 5–50 nm).

**Nano self-assembly** A layer-by-layer (LbL) assembly of alternating layers of oppositely charged polyelectrolytes and nanoparticles provides the formation of 5–500 nm thick films with monolayers of various substances growing in a preset sequence on any substrates at a growth step of about 1 nm. This technique was called “molecular beaker epitaxy” meaning by this that with simple instruments (exploiting the materials self-assembly tendency) one can get molecularly organized films similar to the ones obtained with highly sophisticated and expensive molecular beam epitaxy technology for metals and semiconductors.

**PBG crystal (or photonic crystal)** A PBG crystal (or photonic crystal) is a spatially periodic structure fabricated from materials having different dielectric material constants [246]. It can influence the propagation of electromagnetic waves in a similar way as a semiconductor does for electrons.

**Poly(dimethylsiloxane) (PDMS) elastomers (or silicone rubbers)** Used in most demonstrations. Poly(dimethylsiloxanes) have a unique combination of properties resulting from the presence of an inorganic siloxane backbone and organic methyl groups attached to silicon. These liquid materials can be poured over a master having a relief structure on its surface, then easily converted into solid elastomer by curing and peeling off PDM.

**Spin assembly** Spin-assembly is a specialized application of spin coating, in which a polyelectrolyte multilayered thin film is self-assembled onto a spinning substrate.

**Top-down** Top-down lithography, they begin with pattern generated on a larger scale and reduce its lateral dimensions.

## ACKNOWLEDGMENT

We are thankful for NSF-LEQSF 0092001 and NSF-0210298 grants supporting this work. Any opinions, findings, and conclusions or recommendations expressed in this material are those of the authors and do not necessarily reflect the view of the National Science Foundation.

## REFERENCES

1. A. Ulman, "An Introduction to Ultrathin Films, from Langmuir-Blodgett to Self-Assembly," pp. 1-440. Academic Press, Boston, 1991.
2. R. Iler, *J. Coll. Interface Sci.* 21, 569 (1966).
3. G. Decher, *Science* 227, 1232 (1997).
4. S. Keller, H.-N. Kim, and T. Mallouk, *J. Am. Chem. Soc.* 116, 8817 (1994).
5. G. Decher and J. Schlenoff, Eds., "Multilayer Thin Films: Sequential Assembly of Nanocomposite Materials," pp. 1-543. John Wiley, New York, Berlin, 2003.
6. P. Bertrand, A. Jonas, A. Laschevsky, and R. Legras, *Macromol. Rapid Commun.* 21, 319 (2000).
7. Y. Lvov, G. Decher, and H. Möhwald, *Langmuir* 9, 481 (1993).
8. Y. Lvov, F. Essler, and G. Decher, *J. Phys. Chem.* 97, 13773 (1993).
9. Y. Lvov, H. Haas, G. Decher, H. Möhwald, and A. Kalachev, *J. Phys. Chem.* 97, 12835 (1993).
10. G. Decher, F. Essler, J.-D. Hong, J. Schmitt, and Y. Lvov, *Polym. Prepr.* 34, 745 (1993).
11. G. Decher, Y. Lvov, and J. Schmitt, *Thin Solid Films* 244, 772 (1994).
12. Y. Lvov, H. Haas, G. Decher, H. Möhwald, A. Mikhailov, B. Mtchedlishvily, E. Morgunova, and B. Vainshtein, *Langmuir* 10, 4232 (1994).
13. Y. Lvov and G. Decher, *Cryst. Rep.* 39, 628 (1994).
14. G. Decher, J. Schmitt, and B. Struth, *Curr. Opin. Coll. Interface Sci.* 3, 32 (1998).
15. G. Mao, Y. Tsao, M. Tirrell, H. Davis, V. Hessel, and H. Ringsdorf, *Langmuir* 9, 3461 (1993).
16. G. Decher, B. Lehr, K. Lowack, Y. Lvov, and J. Schmitt, *Biosensors and Bioelectronics* 9, 677 (1994).
17. A. Tronin, Y. Lvov, and C. Nicolini, *Coll. Poly. Sci.* 272, 1317 (1994).
18. J.-D. Hong, K. Lowack, J. Schmitt, and G. Decher, *Progr. Colloid Poly. Sci.* 93, 98 (1993).
19. J. Schmitt, T. Grünwald, K. Krajer, P. Pershan, G. Decher, and M. Lösche, *Macromolecules* 26, 7058 (1993).
20. D. Korneev, Y. Lvov, G. Decher, J. Schmitt, and S. Yarodaikin, *Physica B* 214, 954 (1995).
21. M. Leasche, J. Schmitt, G. Decher, W. Bouwman, and K. Kjaer, *Macromolecules* 31, 8893 (1998).
22. M. Tarabia, H. Hong, D. Davidov, S. Kirshtein, R. Steitz, R. Neumann, and Y. Avny, *J. Appl. Phys.* 83, 725 (1999).
23. M. Sano, Y. Lvov, and T. Kunitake, *Ann. Rev. Mater. Sci.* 26, 153 (1996).
24. M. Onda, Y. Lvov, K. Ariga, and T. Kunitake, *Jpn. J. Appl. Phys.* 36, L1608 (1997).
25. J. Ramsden, Y. Lvov, and G. Decher, *Thin Solid Films* 254, 246 (1995).
26. G. Mao, Y. Tsao, M. Tirrell, H. Davis, V. Hessel, and H. Ringsdorf, *Langmuir* 11, 942 (1995).
27. J. Cheung, A. Fou, and M. Rubner, *Thin Solid Films* 244, 985 (1994).
28. M. Ferreira and M. Rubner, *Macromolecules* 28, 7107 (1995).
29. J. Cheung, W. Stockton, and M. Rubner, *Macromolecules* 30, 2712 (1997).
30. D. Yoo, S. Shiratori, and M. Rubner, *Macromolecules* 31, 4309 (1998).
31. P. Hammond and G. Whitesides, *Macromolecules* 28, 7569 (1995).
32. S. Clark, M. Montague, and P. Hammond, *Macromolecules* 30, 7237 (1997).
33. V. Tsukruk, V. Bliznyuk, D. Visser, A. Campbell, T. Bunnig, and W. Adams, *Macromolecules* 30, 6615 (1997).
34. N. Hoogveen, M. Cohen Stuart, and G. Fleer, *Langmuir* 12, 3675 (1996).
35. G. Sukhorukov, H. Möhwald, G. Decher, and Y. Lvov, *Thin Solid Films* 284, 220 (1996).
36. G. Sukhorukov, J. Schmitt, and G. Decher, *Ber. Bunsen. Ges. Phys. Chem.* 100, 948 (1996).
37. R. v. Klitzig and H. Möhwald, *Macromolecules* 29, 6901 (1996).
38. T. Farhat, G. Yassin, S. Dubas, and J. Schlenoff, *Langmuir* 15, 6621 (1999).
39. D. Laurent and J. Shlenoff, *Langmuir* 13, 1552 (1997).
40. J. Schlenoff, H. Ly, and M. Li, *J. Amer. Chem. Soc.* 120, 7626 (1998).
41. V. Tsukruk, F. Rinderspacher, and V. Bliznyuk, *Langmuir* 13, 2171 (1997).
42. Y. Lvov, M. Onda, K. Ariga, and T. Kunitake, *J. Biomater. Sci., Polym. Ed.* 9, 345 (1998).
43. T. Serizawa, S. Hashiguchi, and M. Akashi, *Langmuir* 15, 5363 (1999).
44. E. Brynda and M. Houska, *J. Coll. Interface Sci.* 183, 18 (1996).
45. I. Ichinose, K. Fujiyoshi, S. Mazurka, Y. Lvov, and T. Kunitake, *Chem. Lett.* 257 (1996).
46. Y. Lvov, K. Ariga, and T. Kunitake, *Coll. Surf. A* 146, 337 (1999).
47. D. Elbert, C. Herbert, and J. Hubbell, *Langmuir* 15, 5355 (1999).
48. D. Yoo, J. Lee, and M. Rubner, *Mat. Res. Symp. Proc.* 413, 395 (1996).
49. T. Cooper, A. Campbell, and R. Crane, *Langmuir* 11, 2713 (1995).
50. K. Ariga, Y. Lvov, and T. Kunitake, *J. Amer. Chem. Soc.* 119, 2224 (1997).
51. Y. Lvov, S. Yamada, and T. Kunitake, *Thin Solid Films* 300, 107 (1997).
52. E. Kleinfeld and G. Ferguson, *Science* 265, 370 (1994).
53. N. Kotov, I. Dekany, and J. Fendler, *J. Phys. Chem.* 99, 13065 (1995).
54. J. Fendler and F. Meldrum, *Adv. Mater.* 7, 607 (1995).
55. J. Schmitt, G. Decher, W. Dressik, R. Geer, R. Shashidhar, and J. Calvert, *Adv. Mater.* 9, 61 (1997).
56. J. Schmitt, P. Machtler, D. Eck, H. Möhwald, and A. Helm, *Langmuir* 15, 3256 (1999).
57. V. Bliznyuk and V. Tsukruk, *Poly. Prepr.* 38, 963 (1997).
58. Y. Lvov, K. Ariga, I. Ichinose, and T. Kunitake, *Langmuir* 13, 6195 (1997).
59. Y. Lvov, J. Rusling, D. Thomsen, F. Papadimitrakopoulos, T. Kawakami, and T. Kunitake, *Chem. Commun.* 1229 (1998).
60. Y. Lvov, B. Munge, I. Ichinose, S. Suib, and J. Rusling, *Langmuir* 16, 8376 (2000).
61. Y. Liu, A. Wang, and R. Claus, *Appl. Phys. Lett.* 71, 2265 (1997).
62. A. Rosidian, Y. Liu, and R. Claus, *Adv. Mater.* 10, 12087 (1998).
63. F. Caruso, H. Lichtenfeld, M. Giersig, and H. Möhwald, *J. Amer. Chem. Soc.* 120, 8523 (1998).
64. Y. Lvov, K. Ariga, and T. Kunitake, *Langmuir* 12, 3038 (1996).
65. Y. Lvov, R. Price, B. Gaber, and I. Ichinose, *Coll. Surf.* 198, 375 (2002).
66. I. Ichinose, H. Tagawa, Y. Lvov, and T. Kunitake, *Langmuir* 14, 187 (1998).
67. T. Cassagneau and J. Fendler, *Adv. Mater.* 10, 877 (1998).



68. T. Cassagneau, T. Mallouk, and J. Fendler, *J. Amer. Chem. Soc.* 120, 7848-50 (1998).
69. T. Cassagneau, J. Fendler, and T. Mallouk, *Langmuir* 16, 241 (2000).
70. M. Correa-Duarte, M. Giersig, N. Kotov, and L. Liz-Marzan, *Langmuir* 14, 6430 (1998).
71. I. Pastoriza-Santos, D. Koktysh, A. Mamedov, M. Giersig, N. Kotov, and L. Liz-Marzan, *Langmuir* 16, 2731 (2000).
72. F. Caruso, A. Susha, M. Giersig, and H. Möhwald, *Adv. Mater.* 11, 950 (1999).
- 73.
74. K. Ariga, Y. Lvov, M. Onda, I. Ichinose, and T. Kunitake, *J. Appl. Clay Sci.* (Special Issue "Nanocomposites") 15, 137 (1999).
75. S. Joly, R. Kane, L. Radzilovski, T. Wang, A. Wu, R. Cohen, E. Thomas, and M. Rubner, *Langmuir* 16, 1354 (2000).
76. J. Mendelsohn, C. Barrett, A. Pal, A. Mayes, and M. Rubner, *Langmuir* 16, 5017 (2000).
77. Y. Lvov, K. Ariga, I. Ichinose, and T. Kunitake, *J. Amer. Chem. Soc.* 117, 6117 (1995).
78. W. Kong, L. Wang, M. Gao, H. Zhou, X. Zhang, W. Li, and J. Shen, *J. Chem. Soc., Chem. Comm.* 1297 (1994).
79. Y. Lvov, "Protein Architecture: Interfacial Molecular Assembly and Immobilization Biotechnology" (Y. Lvov and H. Möhwald, Eds.), pp. 125-136. Marcel Dekker, New York, 2000.
80. Y. Lvov, K. Ariga, and T. Kunitake, *J. Chem. Soc., Chem. Commun.* 2313 (1995).
81. Y. Lvov, K. Ariga, I. Ichinose, and T. Kunitake, *Thin Solid Films* 284, 797 (1996).
82. M. Onda, Y. Lvov, K. Ariga, and T. Kunitake, *J. Ferment. Bioeng.* 82, 502 (1996).
83. X. Zhang, Y. Sun, and J. Shen, "Protein Architecture: Interfacial Molecular Assembly and Immobilization Biotechnology" (Y. Lvov and H. Möhwald, Eds.), pp. 229-251. Marcel Dekker, New York, 2000.
84. M. Houska and E. Brynda, *J. Coll. Interf. Sci.* 188, 243 (1997).
85. J. Hodak, R. Etchenique, E. Calvo, K. Singhal, and P. Bartlett, *Langmuir* 13, 2708 (1997).
86. F. Caruso, K. Niikura, N. Furlong, and Y. Okahata, *Langmuir* 13, 3427 (1997).
87. F. Caruso, N. Furlong, K. Ariga, I. Ichinose, and T. Kunitake, *Langmuir* 14, 4559 (1998).
88. Y. Lvov, Z. Lu, X. Zu, J. Schenkman, and J. Rusling, *J. Amer. Chem. Soc.* 120, 4073 (1998).
89. J.-A. He, L. Samuelson, L. Li, J. Kumar, and S. Tripathy, *Langmuir* 14, 1674 (1998).
90. J. Kong, Z. Lu, Y. Lvov, H. Frank, and J. Rusling, *J. Amer. Chem. Soc.* 120, 7371 (1998).
91. M. Onda, Y. Lvov, K. Ariga, and T. Kunitake, *Biotechnology and Bioeng.* 51, 163 (1996).
92. K. Ariga, M. Onda, Y. Lvov, and T. Kunitake, *Chem. Lett.* 25 (1997).
93. M. Houska and E. Brynda, *J. Coll. Interf. Sci.* 188, 243 (1997).
94. Y. Sun, X. Zhang, C. Sun, B. Wang, and J. Shen, *Macromol. Chem. Phys.* 197, 147 (1996).
95. M. Onda, K. Ariga, and T. Kunitake, *J. Ferment. Bioeng.* 87, 69 (1999).
96. K. Sirkar, A. Revzin, and M. Pishko, *Anal. Chem.* 72, 2930 (2000).
97. V. Kabanov, *Polymer Sci.* 36, 143 (1994).
98. D. Chang-Yen, Y. Lvov, M. McShane, and B. Gale, *Sensors and Actuators B* 87, 336 (2002).
99. M. Roberts, G. Lindsay, W. Herman, and K. Wynne, *J. Amer. Chem. Soc.* 120, 11202 (1998).
100. P. Murarka and M. C. Peckerar, "Electronic Materials Science and Technology," pp. 483-494. Academic Press, San Diego, CA, 1989.
101. A. Elschner, F. Bruder, H. W. Heuer, F. Jonas, A. Karbach, S. Kirchmeyer, S. Thern, and R. Wehrmann, *Synth. Met.* 139, 111 (2000).
102. Y. Shi, J. Liu, and Y. Yang, *J. Appl. Phys.* 87, 4254 (2000).
103. V. S. Nadkarni and S. D. Samant, *Radiat. Meas.* 27, 505 (1997).
104. H. Y. Bae and G. M. Choi, *Sens. Actuators B* 55, 47 (1999).
105. M. Nicolau, B. del Rey, T. Torres, C. Mingotaud, P. Delhaes, M. J. Cook, and S. C. Thorope, *Synth. Meth.* 102, 1462 (1999).
106. P. K. H. Ho, J.-S. Kim, J. H. Burroughes, H. Becker, S. E. Y. Li, T. M. Brown, F. Cacialli, and R. H. Friend, *Nature* 404, 481 (2000).
107. X. Zhang and J. Shen, *Adv. Mater.* 11, 1139 (1999).
108. J. D. Mendelson, C. J. Barrett, V. V. Chan, A. J. Pal, A. M. Mayes, and M. E. Ruber, *Langmuir* 16, 5017 (2000).
109. A. Lashewsky, E. Wischerhoff, M. Kauranen, and A. Persoons, *Macromolecules* 30, 8304 (1997).
110. Y. He, S. Gong, R. Hattori, and J. Kanicki, *Appl. Phys. Lett.* 74, 2265 (1999).
111. P. A. Chiarelli, M. S. Johal, D. J. Holmes, J. L. Casson, J. M. Robinson, and H. L. Wang, *Langmuir* 18, 168 (2002).
112. J. Cho, K. Char, J. D. Hong, and K. B. Lee, *Adv. Mater.* 14, 1076 (2001).
113. P. A. Chiarelli, M. S. Johal, D. J. Holmes, J. L. Casson, J. M. Robinson, J. B. Roberts, and H. L. Wang, *Adv. Mater.* 15, 1167 (2001).
114. P. H. Walker and J. G. Thompson, *Proc. Amer. Soc. Test. Mater.* 22, 464 (1992).
115. T. Obara, Y. Matsumoto, and H. Ohashi, *Phys. Fluids* 12, 1949 (1989).
116. A. G. Emslic, F. T. Bonner, and L. G. Peck, *J. Appl. Phys.* 29, 858 (1958).
117. A. V. Borkar, J. A. Tsamopoulos, S. A. Gupta, and R. K. Gupta, *Phys. Fluids* 6, 3539 (1994).
118. S. A. Gupta and R. K. Gupta, *Ind. Eng. Chem. Res.* 37, 2223 (1998).
119. P. Y. Wu, F. C. Chou, and S. C. Gong, *J. Appl. Phys.* 86, 4657 (1999).
120. L. L. Spangler, J. M. Torkelson, and J. S. Roy, *Polym. Eng. Sci.* 30, 644 (1990).
121. B. T. Chen, *Polym. Eng. Sci.* 23, 399 (1983).
122. S. Shimoji, *Jpn. J. Appl. Phys.* 26, L905 (1987).
123. D. P. Birnie III, B. J. J. Zelinski, and D. L. Perry, *Opt. Eng.* 34, 1782 (1995).
124. M. M. De Souza, K. D. Leaver, and M. H. Eskiyerli, *Comput. Mater. Sci.* 4, 233 (1995).
125. S. T. Dubas and J. B. Schlenoff, *Macromolecules* 32, 8153 (1999).
126. C. J. Lawrence, *Phys. Fluids* 31, 2786 (1988).
127. P. C. Sukhaek, *J. Imag. Technol.* 11, 184 (1985).
128. D. Meyerhofer, *J. Appl. Phys.* 49, 3993 (1978).
129. D. E. Bornside, *J. Electrochem. Soc.* 137, 2589 (1990).
130. S. Middleman, *J. Appl. Phys.* 62, 2530 (1987).
131. T. J. Rehg and B. G. Higgins, *Phys. Fluids* 31, 1360 (1988).
132. F. Ma and J. H. Hwang, *J. Appl. Phys.* 68, 1265 (1990).
133. F. C. Chou and P.-Y. Wu, *J. Electrochem. Soc.* 147, 699 (2000).
134. Y. Xia, "Soft Lithography: Micro and Nanofabrication Based on Microcontact Printing and Replica Molding," Ph.D. thesis, Harvard University, Cambridge, 1996.
135. X. M. Zhao, Y. Xia, and G. M. Whitesides, *J. Mater. Chem.* 7, 1069 (1997).
136. Y. Xia and G. M. Whitesides, *Angew. Chem. Int. Ed. Engl.* 1998, in press.
137. A. Kumar and G. M. Whitesides, *Appl. Phys. Lett.* 63, 2002 (1993).
138. Y. Xia, E. Kim, X. M. Zhao, J. A. Rogers, M. Prentiss, and G. M. Whitesides, *Science*, 273, 347 (1996).
139. X. M. Zhao, Y. Xia, and G. M. Whitesides, *Adv. Mater.* 8, 837 (1996).
140. E. Kim, Y. Xia, and G. M. Whitesides, *Nature* 376, 581 (1995).
141. E. Kim, Y. Xia, X. M. Zhao, and G. M. Whitesides, *Adv. Mater.* 9, 651 (1997).
142. J. A. Rogers, K. E. Paul, R. J. Jackman, and G. M. Whitesides, *Appl. Phys. Lett.* 70, 2658 (1997).

143. H. C. Haverkorn von Rijsewijk, P. E. J. Legierse, and G. E. Thomas, *Philips Tech. Rev.* 40, 287 (1982).
144. B. D. Terris, H. J. Mamin, M. E. Best, J. A. Logan, and D. Rugar, *Appl. Phys. Lett.* 69, 4262 (1996).
145. H. W. Lehmann, R. Widmer, M. Ebnoether, A. Wokaun, M. Meier, and S. K. Miller, *J. Vac. Sci. Technol. B* 1, 1207 (1983).
146. S. Y. Chou, P. R. Krauss, and P. J. Renstrom, *Appl. Phys. Lett.* 67, 3114 (1995).
147. H. Masuda and K. Fukuda, *Science* 268, 1446 (1995).
148. P. Hoyer, *Adv. Mater.* 8, 857 (1996).
149. T. E. Huber and L. Luo, *Appl. Phys. Lett.* 70, 2502 (1997).
150. S. J. Clarson and J. A. Semlyen, "Siloxane Polymers," Prentice Hall, Englewood Cliffs, NJ, 1993.
151. Y. Xia, J. Tien, D. Qin, and G. M. Whitesides, *Langmuir* 12, 4033 (1996).
152. J. L. Wilbur, E. Kim, Y. Xia, and G. M. Whitesides, *Adv. Mater.* 7, 649 (1995).
153. J. L. Wilbur, A. Kumar, E. Kim, and G. M. Whitesides, *Adv. Mater.* 6, 600 (1994).
154. A. Kumar, N. L. Abbott, E. Kim, H. A. Biebuyck, and G. M. Whitesides, *Acc. Chem. Res.* 28, 219 (1995).
155. G. M. Whitesides and C. B. Gorman, in "Handbook of Surface Imaging and Visualization" (A. T. Hubbard, Ed.), pp. 713–733. CRC Press, Boca Raton, FL, 1995.
156. J. L. Wilbur, A. Kumar, H. A. Biebuyck, E. Kim, and G. M. Whitesides, *Nanotechnology* 7, 452 (1996).
157. Y. Xia, X.-M. Zhao, and G. M. Whitesides, *Microelectron. Eng.* 32, 255 (1996).
158. H. A. Biebuyck, N. B. Larsen, E. Delamarche, and B. Michel, *IBM J. Res. Dev.* 41, 159 (1997).
159. A. Voet, "Ink and Paper in the Printing Process." Interscience, New York.
160. Y. Xia and G. M. Whiteside, *Ann. Rev. Mater. Sci.* 28, 153 (1998).
161. A. Ulman, "Introduction to Thin Organic Films: From Langmuir-Blodgett to Self-Assembly." Academic, Boston.
162. G. Decher and J. D. Hong, *Macromol. Chem., Macromol. Symp.* 46, 321 (1991).
163. G. Decher and J. D. Hong, *Ber. Bunsen-Ges. Phys. Chem.* 95, 1430 (1991).
164. G. Decher, J. D. Hong, and J. Schmitt, *Thin Solid Films* 210, 831 (1992).
165. G. Decher, *Science* 277, 1232 (1997).
166. D. Yoo, S. S. Shiratori, and M. F. Rubner, *Macromolecules* 3, (1998).
167. S. S. Shiratori and M. F. Rubner, *Macromolecules* 33, 4213 (2000).
168. G. Ladam, P. Schaad, J. C. Voegel, P. Schaaf, G. Decher, and F. Cuisinier, *Langmuir* 16, 1249 (2000).
169. J. B. Schlenoff, H. Ly, and M. Li, *J. Am. Chem. Soc.* 120, 7626 (1998).
170. I. Lee, H. Zheng, M. F. Rubner, and P. T. Hammond, *Adv. Mater.* 14, 572 (2002).
171. X. P. Jiang and P. T. Hammond, *Langmuir* 20, 8501 (2000).
172. X. Jiang, H. Zheng, S. Gourdin, and P. T. Hammond, *Langmuir* 18, 2607 (2002).
173. H. Zheng, M. F. Rubner, and P. T. Hammond, *Langmuir* 18, 4505 (2002).
174. H. Zheng, I. Lee, M. F. Rubner, and P. T. Hammond, *Adv. Mater.* 14, 569 (2002).
175. P. C. Hidber, W. Helbig, E. Kim, and G. M. Whitesides, *Langmuir* 12, 1375 (1996).
176. C. D. James, R. C. Davis, L. Kam, H. G. Craighead, M. Issacson, J. N. Turner, and W. Shain, *Langmuir* 14, 741 (1998).
177. T. Granlund, T. Nyberg, L. S. Roman, M. Svensson, and O. Inganas, *Adv. Mater.* 12, 269 (2000).
178. A. Bernard, J. P. Renault, B. Michel, H. R. Bosshard, and E. Delamarche, *Adv. Mater.* 12, 1067 (2000).
179. K. Chen, X. Jiang, L. C. Kimerling, and P. T. Hammond, *Langmuir* 16, 7825 (2000).
180. G. Decher, *Science* 227, 1232 (1997).
181. Y. Lvov, G. Decher, and H. Möhwald, *Langmuir* 9, 481 (1993).
182. Y. Lvov, K. Ariga, I. Ichinose, and T. Kunitake, *Langmuir* 13, 6195 (1997).
183. D. Yoo, S. Shiratori, and M. Rubner, *Macromolecules* 31, 4309 (1998).
184. Y. Lvov and H. Möhwald, Eds., "Protein Architecture: Interfacial Molecular Assembly and Immobilization Biotechnology," pp. 1–394. Marcel Dekker, New York, 2000.
185. Bezryadin and C. Dekker, *J. Vac. Sci. Technol. B* 15, 793 (1997).
186. C. Baur, A. Bugacov, and B. E. Koel, *Nanotechnology* 9, 360 (1998).
187. X. Lin, R. Parthasarathy, and H. Jaeger, *Appl. Phys. Lett.* 78, 1915 (2001).
188. G. Kenausis, I. Janos, and D. J. Elbert, *Phys. Chem. B* 104, 3298 (2000).
189. C. Bulthaupt, E. Wilhelm, and B. Hubert, *Appl. Phys. Lett.* 79, 1525 (2001).
190. G. Ozin and S. Yang, *Adv. Funct. Mat.* 2, 95 (2001).
191. L. Brott, R. Naik, and D. Pikas, *Nature* 413, 291 (2001).
192. T. Vossmeier, S. Jia, E. DeIonno, M. Diehl, and S. H. J. Kim, *Appl. Phys.* 84, 3664 (1998).
193. C. Haynes and V. R. Dwyne, *J. Phys. Chem. B* 105, 5599 (2001).
194. C. Hultheen and A. Treichel, *J. Phys. Chem. B* 103, 3854 (1999).
195. K. Chen, X. Jiang, L. Kimerling, and P. Hammond, *Langmuir* 16, 7825 (2000).
196. X. Jiang and P. Hammond, *Langmuir* 16, 8501 (2000).
197. X. Jiang, H. Zheng, S. Gourdin, and P. Hammond, *Langmuir* 18, 2607 (2002).
198. H. Zheng, I. Lee, M. Rubner, and P. Hammond, *Adv. Mat.* 14, 681 (2002).
199. E. Kim, Y. Xia, and G. Whitesides, *Adv. Mat.* 8, 245 (1996).
200. T. Vargo, J. Calvert, K. Wynne, K. Avlyanov, A. X MacDiarmid, and M. Rubner, *Supramol. Sci.* 2, 169 (1995).
201. T. Vargo, J. Calvert, K. Wynne, J. Avlyanov, A. MacDiarmid, and M. Rubner, *Supramol. Sci.* 2, 169 (1995).
202. T. Cui, Y. Lvov, F. Hua, and J. Shi, "Novel Lithography-Based Approaches to Pattern Layer-by-Layer Self-Assembled Thin Films," ASME International Mechanical Engineering Congress & Exposition, New Orleans, LA, November 17–22, 2002.
203. F. Hua, J. Shi, Y. Lvov, and T. Cui, *Nanotechnology* 14, 453 (2003).
204. Tedeschi, H. Mohwald, and S. Kirstein, *J. Am. Chem. Soc.* 123, 954 (2001).
205. C. Joachim, J. K. Gimzewski, and A. Aviram, *Nature* 408, 541 (2000).
206. G. M. Whitesides and J. C. Love, *Scientific American* 39–47 (2001).
207. [http://www.wtec.org/loyola/nano/02\\_01.htm](http://www.wtec.org/loyola/nano/02_01.htm).
208. S. J. Tans et al., *Nature* 386, 474 (1997).
209. M. Bockrath et al., *Science* 275, 1922 (1997).
210. Z. Yao, H. W. Ch. Postma, L. Balents, and C. Dekker, *Nature* 402, 273 (1999).
211. M. S. Fuhrer et al., *Science* 288, 494 (2000).
212. S. J. Tans, A. R. M. Verschueren, and C. Dekker, *Nature* 393, 49 (1998).
213. R. Martel, T. Schmidt, H. R. Shea, T. Hertel, and Ph. Avouris, *Appl. Phys. Lett.* 73, 2447 (1998).
214. H. W. Ch. Postma, T. Teepen, Z. Yao, M. Grifoni, and C. Dekker, *Science* 293, 76 (2001).
215. V. Derycke, R. Martel, J. Appenzeller, and Ph. Avouris, *Nano Lett.* 26 August 2001, online.
216. A. Bachtold et al., *Phys. Rev. Lett.* 84, 6082 (2000).
217. S. J. Tans and C. Dekker, *Nature* 404, 834 (2000).
218. T. W. Tombler, C. Zhou, J. Kong, and H. Dai, *Appl. Phys. Lett.* 76, 2412 (2000).

219. J. Lefebvre, J. F. Lynch, M. Llaguno, M. Radosavljevic, and A. T. Johnson, *Appl. Phys. Lett.* 75, 3014 (1999).
220. M. Krüger et al., *Appl. Phys. Lett.* 78, 1291 (2001).
221. M. S. Dresselhaus, G. Dresselhaus, and P. C. Eklund, Eds., "Science of Fullerenes and Carbon Nanotubes." Academic Press, London, 1996.
222. [http://www.chemistry.pomona.edu/Chemistry/periodic\\_table/Elements/Carbon/carbon.htm](http://www.chemistry.pomona.edu/Chemistry/periodic_table/Elements/Carbon/carbon.htm).
223. H. Dai, E. W. Wong, and C. M. Lieber, *Science* 272, 523 (1996).
224. J. E. Fischer et al., *Phys. Rev. B* 55, R4921 (1997).
225. S. J. Tans, A. R. M. Verschueren, and C. Dekker, *Nature* 393, 49 (1998).
226. R. Martel, T. Schmidt, H. R. Shea, T. Hertel, and Ph. Avouris, *Appl. Phys. Lett.* 73, 2447 (1998).
227. L. Chico, V. H. Crespi, L. X. Benedict, S. G. Louis, and M. L. Cohen, *Phys. Rev. Lett.* 76, 971 (1996).
228. R. Saito, G. Dresselhaus, and M. S. Dresselhaus, *Phys. Rev. B* 53, 2044 (1996).
229. T. W. Ebbesen, CRC Press, Boca Raton, 1997.
230. P. J. F. Harris, Cambridge University Press, Cambridge, 1999.
231. T. W. Ebbesen, *Phys. Today* 49, 26 (1996).
232. P. M. Ajayan and T. W. Ebbesen, *Rep. Prog. Phys.* 60, 1025 (1997).
233. C. Dekker, *Phys. Today* 52, 22 (1999).
234. C. N. R. Rao, *Phys. Chem.* 2, 78 (2001).
235. J. M. Bonard, H. Kind, T. Stöckli, and L. O. Nilsson, *Solid State Electron.* 45, 893 (2001).
236. M. A. Kastner, *Phys. Today* 46, 24 (1993).
237. R. C. Ashoori, *Nature* 379, 413 (1996).
238. M. Nirmal and L. E. Brus, *Acc. Chem. Res.* 32, 407 (1999).
239. A. P. Alivisatos, *Science* 271 (1996).
240. A. Eychmüller, *J. Phys. Chem. B* 104, 6514 (2000).
241. D. Bimberg, M. Grundmann, and N. N. Ledentsov, *MRS Bull.* 23, 31 (1998).
242. C. B. Murray, C. R. Kagan, and M. G. Bawendi, *J. Am. Chem. Soc.* 115, 8706 (1993).
243. C. B. Murray, C. R. Kagan, and M. G. Bawendi, *Ann. Rev. Mater. Sci.* 30, 545 (2000).
244. Yu. A. Vlasov, N. Yao, and D. J. Norris, *Adv. Mater.* 11, 165 (1999).
245. N. A. Kotov, *MRS Bull.*, December 2001.
246. J. D. Joannopoulos, R. D. Meade, and J. N. Winn, "Photonic Crystal," Princeton University Press, Princeton, NJ, 1995.
247. E. Yablonovitch, *Phys. Rev. Lett.* 58, 2059 (1987).
248. S. John, *Phys. Rev. Lett.* 58, 2486 (1987).
249. S. John, *Phys. Today* May, 32, 1991.
250. E. Yablonovitch, *J. Opt. Soc. Am. B* 10, 283 (1993).
251. J. D. Joannopoulos, P. R. Villeneuve, and S. Fan, *Nature* 386, 143 (1997).
252. C. M. Soukoulis, Ed., "Photonic Band Gap Materials," Kluwer, Boston, MA, 1996.
253. A. Scherer, T. Doll, E. Yablonovitch, H. O. Everitt, and J. A. Higgins, *J. Lightwave Technol.* 17, 1928 (1999), special issue.
254. <http://ab-initio.mit.edu/photons/>.
255. L. A. Bumm et al., *Science* 271, 1705 (1996).
256. C. Zhou et al., "Molecular Electronics," pp. 191–213. Blackwell Science Ltd., London, 1997.
257. C. Zhou et al., *Appl. Phys. Lett.* 71, 661 (1997).
258. J. Tour, "Chemical Synthesis of Molecular Electronic Devices," Presentation at the 1997 DARPA ULTRA Review Conference, Santa Fe, NM, October 1997.
259. M. Reed, "Self-Assembly-Based Approaches to Microelectronic Fabrication and Devices," Presentation at the 1997 DARPA ULTRA Review Conference, Santa Fe, NM, October 1997.
260. R. M. Metzger et al., *J. Am. Chem. Soc.* 15 October 1997.
261. E. K. Wilson, *Chemical and Engineering News* 17, 33 (1997).
262. J. R. Heath, *Pure Appl. Chem.* 72, 11 (2000).
263. A. R. Pease, J. O. Jeppesen, J. F. Stoddart, Y. Luo, C. P. Collier, and J. R. Heath, *Acc. Chem. Res.* 34, 433 (2001).
264. N. A. Kotov, *MRS Bull.* 12, 992 (2001).
265. D. J. Schiffrin, *MRS Bull.* 12, 1015 (2001).
266. C. M. Wai, H. Ohde, and J. Chin, *Inst. Chem. Engrs.* 32, 253 (2001).
267. <http://www.chemat.com/html/solgel.html>.
268. S. A. Gerbier, S. Desert, T. G. Kryswicki, and C. Larpent, *Macromolecules* 35, 1664 (2002).
269. D. C. Liu and C. P. Lee, *Appl. Phys. Lett.* 63, 3503 (1993).
270. X. K. Zhao and J. H. Fendler, *J. Phys. Chem.* 95, 3716 (1991).
271. R. Notzel, Z. Niu, M. Ramsteiner, H.-P. Schonherr, A. Tranpert, L. Dawertiz, and K. H. Ploog, *Nature* 392, 56 (1998).
272. J. R. Heath, R. S. Williams, J. J. Shiang, S. J. Wind, J. Chu, C. Dëmic, W. Chen, C. L. Stanis, and J. J. Bucchnano, *J. Phys. Chem.* 100, 3144 (1996).
273. G. S. Hsiao, M. G. Anderson, S. Gorer, D. Harris, and R. M. Penner, *J. Am. Chem. Soc.* 119, 1439 (1997).
274. A. Kumar, H. A. Biebuyck, and G. M. Whitesides, *Langmuir* 10, 1498 (1994).
275. S. Palacin, P. C. Hidlber, J.-P. Bourgoin, C. Miramond, C. Fermon, and G. M. Whiteside, *Chem. Mater.* 8, 1316 (1996).
276. N. Ise, *Angew. Chem. Int. Ed. Engl.* 25, 323 (1986).
277. H. B. Sunkara, J. M. Jethmalani, and W. T. Ford, *Chem. Mater.* 6, 362 (1994).
278. C. A. Murray and D. G. Grier, *Amer. Scientist* 83, 238 (1995).
279. A. van Blaaderen, R. Ruel, and P. Wiltzius, *Nature* 385, 321 (1997).
280. A. van Blaaderen, *MRS Bull.* 23, 39 (1998).
281. A. E. Lasen and D. G. Gier, *Nature* 385, 230 (1997).
282. S. R. Yeh, M. Seul, and B. I. Shraiman, *Nature* 386, 57 (1997).
283. M. Trau, D. A. Saville, and I. A. Aksay, *Science* 272, 706 (1996).
284. M. Trau, D. A. Saville, and I. A. Aksay, *Langmuir* 13, 6375 (1997).
285. M. Trau, S. Sankaran, D. A. Saville, and I. A. Aksay, *Nature* 374, 437 (1995).
286. M. Giersig and P. Mulvaney, *Langmuir* 9, 3408 (1993).
287. Y. Solomentsev, M. Böhmer, and J. L. Anderson, *Langmuir* 13, 6058 (1997).
288. N. D. Denkov, O. D. Velev, P. A. Kralchevsky, I. B. Ivanov, H. Yoshimura, and K. Nagayama, *Langmuir* 8, 3183–3190 (1996).
289. S. Raker, L. F. Chi, and H. Fuchs, *Langmuir* 13, 7121 (1997).
290. G. Decher, *Science* 277, 1232 (1997).
291. N. A. Kotov, I. Dekany, and J. H. Fendler, *J. Phys. Chem.* 99, 13065 (1995).
292. J. W. Ostrander, A. A. Mamedov, and N. A. Kotov, *J. Am. Chem. Soc.* 123, 1101 (2001).
293. F. Aliev, M. A. Correa-Duarte, A. Mamedov, J. W. Ostrander, M. Giersig, L. M. Liz-Marzán, and N. A. Kotov, *Adv. Mater.* 11, 1006 (1999).
294. K. Ariga, Y. Lvov, I. Ichinose, and T. Kunitake, *Appl. Clay Sci.* 15, 137 (1999).
295. F. Caruso, R. A. Caruso, and H. Möhwald, *Science* 282, 1111 (1998).
296. D. L. Feldheim, K. C. Grabar, M. J. Natan, and T. E. Mallouk, *J. Amer. Chem. Soc.* 118, 7640 (1996).
297. G. S. Ferguson and E. R. Kleinfeld, *Adv. Mater.* 7, 414 (1995).
298. T. Cassagneau, T. E. Mallouk, and J. H. Fendler, *J. Am. Chem. Soc.* 120, 7848 (1998).
299. C. A. Bruce, A. M. Homola, and M. R. Lorentz, U. S. Patent No. 4, 333, 961 (1982).
300. C. D. Bain and G. M. Whitesides, *Angew. Chem.* 101, 522 (1989).
301. *Angew. Chem. Int. Ed. Engl.* 28, 506 (1989).
302. G. M. Whitesides and P. E. Lanibinis, *Langmuir* 6, 87 (1990).
303. A. Ulman, "Introduction to Thin Organic Films: From Langmuir-Blodgett to Self-Assembly." Academic Press, Boston, 1991.
304. J. D. Swalen, *Ann. Rev. Mater. Sci.* 21, 373 (1991).
305. L. H. Dubois and R. G. Nuzzo, *Ann. Rev. Phys. Chem.* 43, 437 (1992).
306. J. S. Winslow, *IEEE Trans. Consumer Electron.* (Nov.), 318 (1976).
307. H. W. Lehmann, R. Widmer, M. Ebnoether, A. Wokaun, M. Meier, and S. K. Miller, *J. Vac. Sci. Technol. B* 1, 1207 (1983).

308. C. M. Rodia, *Proc. SPIE Int. Soc. Opt. Eng.* 529, 69 (1985).
309. K. H. Schlereth and H. Bötther, *J. Vac. Sci. Technol. B* 10, 114 (1992).
310. M. Emmelius, G. Pawlowski, and H. W. Vollmann, *Angew. Chem.* 101, 1475 (1989).
311. M. Emmelius, G. Pawlowski, and H. W. Vollmann, *Angew. Chem. Int. Ed. Engl.* 28, 1445 (1989).
312. F. P. Shvartsman, in "Diffractive and Miniaturized Optics" (S.-H. Lee, Ed.), pp. 165–186. SPIE Optical Engineering Press, Bellingham, WA, 1993.
313. Y. Chou, P. R. Krauss, and P. J. Renstrom, *Appl. Phys. Lett.* 67, 3114 (1995).
314. S. Y. Chou, P. R. Krauss, and P. J. Renstrom, *Science* 272, 85 (1996).
315. M. T. Gale in "Micro-Optics: Elements, Systems and Applications" (H. P. Herzig, Ed.), pp. 153–179. Taylor & Francis, London, 1997.
316. H. C. Haverkorn van Rijsewijk, P. E. J. Legierse, and G. E. Thomas, *Philips Tech. Rev.* 40, 287 (1983).
317. J. G. Kloosterboer, G. J. M. Lippits, and H. C. Meinders, *IBID.* 40, 198 (1982).
318. B. D. Terris, H. J. Mamin, M. E. Best, J. A. Logan, and D. Rugar, *Appl. Phys. Lett.* 69, 4262 (1996).
319. D. Bethell and D. J. Schiffrin, *Nature* 382, 581 (1996).
320. C. A. Mirkin, R. L. Letsinger, R. C. Mucic, and J. J. Storhoff, *Nature* 382, 607 (1996).
321. A. P. Alivisatos, K. P. Johnsson, X. Peng, T. E. Wilson, C. J. Loweth, M. P. Bruchez, and P. G. Schultz, *Nature* 382, 609 (1996).
322. R. Elghanian, J. J. Storhoff, R. C. Mucic, R. L. Letsinger, and C. A. Mirkin, *Science* 277, 1078 (1997).
323. J. J. Storhoff, R. Elghanian, R. C. Mucic, C. A. Mirkin, and R. L. Letsinger, *J. Am. Chem. Soc.* 120, 1959 (1998).
324. C. T. Kresge, M. E. Leonowicz, W. J. Roth, J. C. Vartuli, and J. S. Beck, *Nature* 359, 710 (1992).
325. D. D. Archibald and S. Mann, *Nature* 364, 430 (1993).
326. P. Behrens and G. D. Stucky, *Angew. Chem. Int. Ed. Engl.* 32, 696 (1993).
327. H. Yang, N. Coombs, and G. A. Ozin, *Nature* 386, 692 (1997).
328. M. Trau, N. Yao, E. Kim, Y. Xia, G. M. Whitesides, and I. A. Aksay, *Nature* 390, 674 (1997).
329. S. A. Davis, S. L. Burkett, N. H. Mendelson, and S. Mann, *Nature* 385, 420 (1997).
330. A. Imhof and D. J. Pine, *Nature* 389, 948 (1997).
331. M. Antonietti, B. Berton, C. Goltner, and H. P. Hentze, *Adv. Mater.* 10, 154 (1998).
332. A. Imhof and D. J. Pine, *Adv. Mater.* 10, 697 (1998).
333. O. D. Velev, T. A. Jede, R. F. Lobo, and A. M. Lenhoff, *Nature* 389, 447 (1997).
334. O. D. Velev, T. A. Jede, R. F. Lobo, and A. M. Lenhoff, *Chem. Mater.* 10, 3597 (1998).
335. S. H. Park and Y. Xia, *Chem. Mater.* 10, 1745 (1998).
336. S. H. Park and Y. Xia, *Adv. Mater.* 10, 1045 (1998).
337. B. Gates, Y. Yin, and Y. Xia, *Chem. Mater.* 11, 2827 (1999).
338. B. T. Holland, C. F. Blanford, and A. Stein, *Science* 281, 538 (1998).
339. B. T. Holland, C. F. Blanford, T. Do, and A. Stein, *Chem. Mater.* 11, 795 (1999).
340. S. A. Johnson, P. J. Ollivier, and T. E. Mallouk, *Science* 283, 963 (1999).
341. J. S. Yin and Z. L. Wang, *Adv. Mater.* 11, 469 (1999).
342. H. Yan, C. F. Blanford, B. T. Holland, M. Parent, W. H. Smyrl, and A. Stein, *Adv. Mater.* 11, 1003 (1999).
343. A. Vlasov, N. Yao, and D. J. Norris, *Adv. Mater.* 11, 165 (1999).
344. G. Subramanian, V. N. Manoharan, J. D. Thorne, and D. J. Pine, *Adv. Mater.* 11, 1261 (1999).
345. O. D. Velev, P. M. Tessier, A. M. Lenhoff, and E. W. Kaler, *Nature* 401, 548 (1999).
346. P. Jiang, J. Cizeron, J. F. Bertone, and V. L. Colvin, *J. Am. Chem. Soc.* 121, 7957 (1999).
347. P. V. Braun and P. Wiltzius, *Nature* 402, 603 (1999).
348. A. A. Zakhidov, R. H. Baughman, Z. Iqbal, C. Cui, I. Khayrullin, S. O. Dantas, J. Marti, and V. G. Ralchenko, *Science* 282, 897 (1998).
349. P. Yang, T. Deng, D. Zhao, P. Feng, D. Pine, B. F. Chmelka, G. M. Whitesides, and G. D. Stucky, *Science* 282, 2244 (1998).
350. K. P. de Jong and A. J. Koster, *CHEM PHYS CHEM* 3, 776 (2002).
351. T. Shimoda, R. H. Friend et al., *Tech. Digest, IEDM* 99, 107 (1999).
352. Peumans, V. Bulovic, and S. R. Forrest, *Appl. Phys. Lett.* 76, 3855 (2000).
353. Michel et al., *IBM J. Res. Dev.* 45, 697 (2001).
354. M. A. Alam, A. Dodabalapur, and M. R. Pinto, *IEEE Trans. Elect. Dev.* 44, 1332 (1997).
355. R. Bourguiga, F. Garnier, G. Horowitz, R. Hajlaoui, P. Delannoy, M. Hajlaoui, and H. Bouchriha, *Eur. Phys. J. AP* 14, 121 (2001).
356. Rita Tecklenburg et al., 8, 285 (1998).
357. T. Holstein, *Ann. Phys. (NY)* 8, 343 (1959).
358. J. E. Lilienfeld, U.S. Patent 1 745 175, 1930.
359. D. Kahng and M. M. Atalla, IRE Solid-State Devices Research Conference, Carnegie Institute of Technology, Pittsburgh, PA, 1960.
360. Koezuka, A. Tsumura, and T. Ando, *Synth. Met.* 18, 699 (1987).
361. F. Garnier, R. Hajlaoui, A. Yassar, and P. Srivastava, *Science* 265, 1684 (1994).
362. C. D. Dimitrakopoulos and D. J. Mascaró, *IBM J. Res. Dev.* 45, 11 (2001).
363. <http://www.conductivepolymers.com/#1>, Announcing the Xth International Seminar on the Technology of Inherently Conductive Polymers, Boston, MA, June 23–25, 2003.
364. C. J. Drury, C. M. J. Mutsaers, C. M. Hart, M. Matters, and D. M. de Leeuw, *Appl. Phys. Lett.* 73, 108 (1998).
365. H. Klauk, D. J. Gundlach, and T. N. Jackson, *IEEE Electron Device Lett.* 20, 289 (1999).
366. H. Klauk, D. J. Gundlach et al., *Solid State Technol.* 43, 63 (2000).
367. Y. Y. Lin, D. J. Gundlach, and T. N. Jackson, *IEEE Trans. Electron. Devices* 44, 1325 (1997).
368. Y. Lin, D. J. Gundlach, S. Nelson, and T. N. Jackson, *IEEE Electron. Device Lett.* 18, 606 (1997).
369. J. H. Schön, S. Berg, Ch. Kloc, and B. Batlogg, *Science* 287, 1022 (2000).
370. B. Crone, A. Dodabalapur et al., *Nature* 403, 521 (2000).
371. Z. Bao, Y. Feng, A. Dodabalapur, V. R. Raju, and A. J. Ovinger, *Chem. Mat.* 9, 1299 (1997).
372. H. Sirringhaus, T. Kawase, R. H. Friend, T. Shimoda, M. Inbasekaran, W. Wu, and E. P. Woo, *Science* 290, 2123 (2000).
373. T. Kawase, H. Sirringhaus, R. H. Friend, and T. Shimoda, *IEEE IEDM* 623 (2000).
374. H. Sirringhaus, N. Tessler, and R. H. Friend, *Science* 280, 1741 (1998).
375. H. Sirringhaus, P. J. Brown, R. H. Friend, M. M. Nielsen, K. Bechgaard, B. M. W. Langeveld-Voss, A. J. H. Spiering, R. A. J. Janssen, E. W. Meijer, P. T. Herwig, and D. M. de Leeuw, *Nature* 401, 685 (1999).
376. H. Sirringhaus, N. Tessler, and R. H. Friend, *Synth. Meth.* 102, 857 (1999).
377. H. E. Katz, A. J. Lovinger, J. Johnson, C. Kloc, T. Siergist, W. Li, Y.-Y. Lin, and A. Dodabalapur, *Nature* 404, 478 (2000).
378. H. E. Katz, J. G. Laquindanum, and A. J. Lovinger, *Chem. Mater.* 10, 633 (1998).
379. H. E. Katz, W. Li, A. J. Lovinger, and J. G. Laquindanum, *Synth. Meth.* 102, 897 (1999).
380. J. G. Laquindanum, H. E. Katz, and A. J. Lovinger, *J. Amer. Chem. Soc.* 120, 664 (1998).

381. C. D. Dimitrakopoulos, A. Afzali-Ardakani, B. Furman, J. Kymisis, and S. Purushothaman, *Synth. Meth.* 89, 193 (1997).
382. R. C. Haddon, A. S. Perel, R. C. Morris, T. T. M. Palstra, A. F. Hebard, and R. M. Fleming, *Appl. Phys. Lett.* 67, 121 (1995).
383. A. R. Brown, C. P. Jarrett, D. M. de Leeuw, and M. Matters, *Synth. Meth.* 88, 37 (1997).
384. A. R. Brown, A. Pomp, D. M. de Leeuw, D. B. M. Klaassen, E. E. Havinga, P. T. Herwig, and K. Müllen, *J. Appl. Phys.* 79, 2136 (1996).
385. A. R. Brown, A. Pomp, C. M. Hart, and D. M. de Leeuw, *Science* 270, 972 (1995).
386. P. T. Herwig and K. Müllen, *Adv. Mater.* 11, 480 (1999).
387. H. Burroughes, C. A. Jones, and R. H. Friend, *Nature* 335, 137 (1988).
388. J. H. Burroughes, R. H. Friend, and P. C. Allen, *J. Phys. D: Appl. Phys.* 22, 956 (1989).
389. A. Tsumura, H. Fuchigami, and H. Koezuka, *Synth. Meth.* 41, 1181 (1991).
390. C. W. Tang and S. A. Van Slyke, *Appl. Phys. Lett.* 51, 913 (1987).
391. S. Forrest, P. Burrows, and M. Thompson, *IEEE Spectrum* 37, n8 (2000).
392. [http://www.businessweekly.co.uk/news/view\\_article.asp?article\\_id=5301](http://www.businessweekly.co.uk/news/view_article.asp?article_id=5301)
393. W. Brütting et al., *Org. Electron.* 2, 1 (2001).
394. H. Klauk, *Phys. World* 13, 18 (2000).
395. <http://www.pioneer-racing.com/Pioneer/CDA/Common/ArticleDetails/0,1484,21370,00.html>
396. <http://www.lucent.com/pressroom/epaper.html>
397. <http://www.lucent.com/press/0901/010919.bla.html>
398. J. Yu et al., *Jpn. J. Appl. Phys.* 40, 3201 (2001).
399. C. Kim, P. E. Burrows, and S. R. Forrest, *Science* 288, 831 (2000).



# Nanobiosensors

Tuan Vo-Dinh

Oak Ridge National Laboratory, Oak Ridge, Tennessee, USA

## CONTENTS

1. Introduction
  2. Near-Field Optics and Nanofibers
  3. Biosensors
  4. Nanosensor Fabrication
  5. Experimental Protocol and Instrumental System
  6. Applications
  7. Conclusion
- Glossary  
References

## 1. INTRODUCTION

Biology has entered a new era with the recent advances in nanotechnology, which have recently led to the development of biosensor devices having nanoscale dimensions that are capable of probing the inner space of single living cells. Nanosensors provide new and powerful tools for monitoring *in vivo* processes within living cells, leading to new information on the inner workings of the entire cell. Such a systems biology approach could greatly improve our understanding of cellular function, thereby revolutionizing cell biology. Fiber-optic sensors provide useful tools for remote *in-situ* monitoring. Fiber-optic sensors can be fabricated to have extremely small sizes, which makes them suitable for sensing intracellular/intercellular physiological and biological parameters in microenvironments. A wide variety of fiber-optic chemical sensors and biosensors have been developed in our laboratory for environmental and biochemical monitoring [1–8]. Submicron fibers have been developed for use in near-field optics [9, 10]. Tapered fibers with submicron tip diameters have also been developed for near-field scanning optical microscopy (NSOM). NSOM was used to achieve subwavelength 100 nm spatial resolution in Raman detection [11–13]. Tan and co-workers developed and used chemical nanosensors to perform measurements of calcium and nitric oxide, among other physicochemicals in single cells [14, 15]. Vo-Dinh and co-workers

developed nanobiosensors with antibody probes to detect biochemical targets inside living single cells [16–23]. This chapter presents an overview of the principle, development, and applications of fiber-optic nanosensors.

## 2. NEAR-FIELD OPTICS AND NANOFIBERS

Nanoscale optical fibers were first developed for use in near-field optical microscopy, which is a relatively recent technique involving light sources or detectors that are smaller than the wavelength of light [9]. The first method developed for performing these experiments was to place a pinhole in front of the detector, thus effectively reducing the detector size. In a later variation to these pinholes, an excitation probe with dimensions smaller than the wavelength of the light was used for sample interrogation. Betzig and Chichester reported the development of one such probe capable of obtaining measurements with a spatial resolution of approximately 12 nm [10]. The probe was constructed by using a micropipet puller to pull a single-mode optical fiber to a tip diameter of 20 nm, and then coating the walls of the fiber with 100 nm of aluminum to confine the excitation radiation to the tip. With this nanoprobe, images of a pattern were reconstructed from a raster scan performed in the illumination mode, with the probe acting as a localized light source.

Due to its extremely high spatial resolution (subwavelength), near-field microscopy has received great interest, and has been used in many applications [9]. For example, a relatively new technique known as near-field surface-enhanced Raman spectroscopy (NF-SERS) has been used for the measurement of single-dye and dye-labeled DNA molecules with a resolution of 100 nm [11–13]. In this work, DNA strands labeled with the dye brilliant cresyl blue (BCB) were spotted onto a SERS-active substrate that was prepared by the evaporation of silver on a nanoparticle-coated substrate. The silver-coated nanostructured substrates are capable of inducing the SERS effect, which can enhance the Raman signal of the adsorbate molecules up to  $10^8$  times [24]. NF-SERS spectra were collected by illuminating the sample using the nanoprobe, and detecting the SERS signals



using a spectrometer equipped with a charge-coupled device (CCD). Raster scanning the fiber probe over the sample and normalizing for surface topography using Rayleigh-scattered light produced a two-dimensional SERS image of the DNA on the surface of the substrate with subwavelength spatial resolution. Near-field optical microscopy promises to be an area of growing research that could potentially provide an imaging tool for monitoring individual cells, and even biological molecules. Single-molecule detection and imaging schemes using nanofibers could open new possibilities in the investigation of the complex biochemical reactions and pathways in biological and cellular systems.

### 3. BIOSENSORS

#### 3.1. Biosensor Principle

A biosensor is generally defined as a measurement system that consists of a probe with a biological recognition element, often called a bioreceptor, and a transducer [3, 18, 22]. Two fundamental operating principles of a biosensor are: (1) “biological recognition,” and (2) “sensing.” Therefore, a biosensor can be generally defined as a device that consists of two basic components connected in series: (1) a biological recognition system, often called a bioreceptor, and (2) a transducer. The basic principle of a biosensor is to detect this molecular recognition, and to transform it into another type of signal using a transducer. The main purpose of the recognition system is to provide the sensor with a high degree of selectivity for the analyte to be measured. The interaction of the analyte with the bioreceptor is designed to produce an effect measured by the transducer, which converts the information into a measurable effect, such as an electrical signal.

Biosensors can be classified based on the transduction methods they employ. Transduction can be accomplished through a large variety of methods. Most forms of transduction can be categorized in one of three main classes: (1) optical detection methods, (2) electrochemical detection methods, and (3) mass-based detection methods. Other detection methods include voltaic and magnetic methods. New types of transducers are constantly being developed for use in biosensors. Each of these three main classes contains many different subclasses, creating a large number of possible transduction methods or combinations of methods. Special emphasis will be placed on the description of optical transducing principles, which is the focus of this chapter. Figure 1 illustrates the conceptual principle of the biosensing process using an antibody as the bioreceptor probe and fluorescence as the detection method.

#### 3.2. Bioreceptors

Bioreceptors are the key to specificity for biosensor technologies. They are responsible for binding the analyte of interest to the sensor for the measurement. These bioreceptors can take many forms, and the different bioreceptors that have been used are as numerous as the different analytes that have been monitored using biosensors. However, bioreceptors can generally be classified into five different major categories: (1) antibody/antigen, (2) enzymes, (3) nucleic

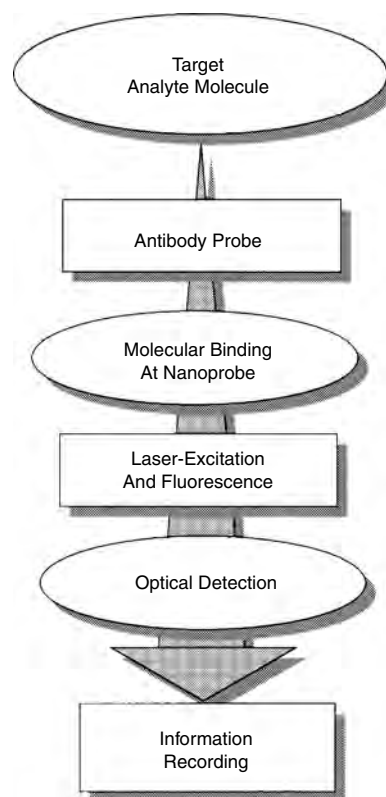


Figure 1. Operating principle of biosensor systems.

acids/DNA, (4) cellular structures/cells, and (5) biomimetic. This chapter deals with biosensor systems using antibody probes, often called immunosensors, with optical detection.

The antigen–antibody (Ag–Ab) binding reaction, which is a key mechanism by which the immune system detects and eliminates foreign matter, provides the basis for specificity of immunoassays. Antibodies are complex biomolecules, made up of hundreds of individual amino acids arranged in a highly ordered sequence. Antibodies are produced by immune system cells when such cells are exposed to substances or molecules, which are called antigens. The antibodies appearing following antigen exposure have recognition/binding sites for specific molecular structures (or substructures) of the antigen. The way in which an antigen and an antigen-specific antibody interact is analogous to a lock and key fit, in which specific configurations of a unique key enable it to open a lock. In the same way, an antigen-specific antibody fits its unique antigen in a highly specific manner, so that the three-dimensional structures of antigen and antibody molecules are complementary. Due to this three-dimensional shape fitting, and the diversity inherent in individual antibody make up, it is possible to find an antibody that can recognize and bind to any one of a large variety of molecular shapes. This unique property of antibodies is the key to their usefulness in immunosensors; this ability to recognize molecular structures allows one to develop antibodies that bind specifically to chemicals, biomolecules, microorganism components, and so on. One can then use such antibodies as specific probes to recognize and bind to an analyte of interest that is present, even in extremely small amounts, within a large number of other chemical substances.

In the 1980s, advances in spectrochemical instrumentation, laser miniaturization, biotechnology, and fiber-optics research provided opportunities for novel approaches to the development of sensors for the detection of chemicals and biological materials of environmental and biomedical interest. Since the first development of a remote fiber-optics immunosensor for *in-situ* detection of the chemical carcinogen benzo[a]pyrene [1], antibodies have become common bioreceptors used in biosensors today.

## 4. NANOSENSOR FABRICATION

### 4.1. Fabrication of Nanofiber Probes

This section discusses the protocols and instrumental systems involved in the fabrication of fiber-optic nanoprobes. Two methods are generally used for preparing the nanofiber tips. The so-called “heat-and-pull” method is the most commonly used. This method consists of local heating of a glass fiber using a laser or a filament, and subsequently pulling the fiber apart. The shape of the nanofiber tips obtained depends on controllable experimental parameters such as the temperature and the timing of the procedure. The second method, often referred to as “Turner’s method,” involves the chemical etching of glass fibers. In a variation of the standard etching scheme, the taper is formed inside the polymer cladding of the glass fibers. The description of these fabrication methods is given in the following section.

The fabrication of nanosensors requires techniques capable of making reproducible optical fibers with a submicron-size diameter core. Figure 2 illustrates the experimental procedures for the fabrication of nanofibers using the heat-and-pull procedure [21]. Since these nanoprobes are not commercially available, investigators have to fabricate them in their own laboratories. Our laboratory uses the heat-and-pull procedure, which consists of pulling a larger silica optical fiber to produce the tapered nanotip fiber using a special fiber-pulling device (Sutter Instruments P-2000). This method yields fibers with submicron diameters. One end of a 600  $\mu\text{m}$  silica/silica fiber is polished to a 0.3  $\mu\text{m}$  finish with an Ultratec fiber polisher. The other end of the optical fiber is then pulled to a submicron length using a fiber puller. A scanning electron microscopy (SEM) photograph of one of the

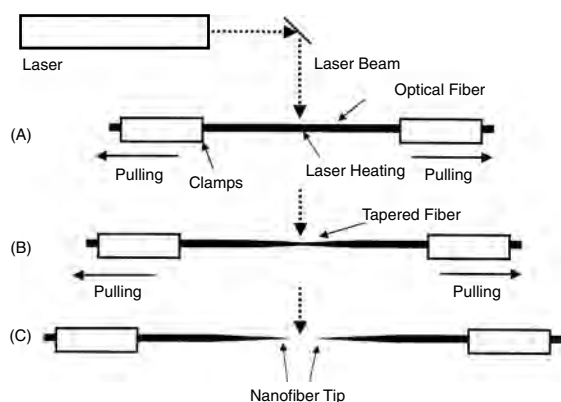


**Figure 2.** The “heat-and-pull” method for the fabrication of nanofibers.

fiber probes fabricated for studies is shown in Figure 3. The distal end of the nanofiber is approximately 30 nm.

To prevent light leakage of the excitation light on the tapered side of the fiber, the sidewall of the tapered end is then coated with a thin layer of metal, such as silver, aluminum, or gold (100 nm thickness) using a thermal evaporation metal coating device. The coating procedure is schematically illustrated in Figure 4 [21]. The metal coating is only for the sidewall, and leaves the distal end of the fiber free for subsequent binding with bioreceptors. The fiber probe is attached on a rotating plate inside a thermal evaporation chamber [3, 19, 21]. The fiber axis and the evaporation direction formed an angle of approximately 45°. While the probe is rotated, the metal is allowed to evaporate onto the tapered side of the fiber tip to form a thin coating. The tapered end is coated with 300–400 nm of silver in a Cooke Vacuum Evaporator system using a thermal source at  $10^{-6}$  torr. Since the fiber tip is pointed away from the metal source, it remains free from any metal coating. With the metal coating, the size of the probe tip is approximately 250–300 nm (Fig. 5).

Chemical etching using HF is the basis of the second method for fabricating optical nanofibers. There are two variations of the HF etching method: one method involving the use of a mixture of HF acid and organic solvent, known as Turner etching [25], and the second using only HF, known as tube etching [26–28]. In the Turner method, a fiber is placed in the meniscus between the HF and the organic overlayer, and over time, a small tip is formed, with a smooth, large-angled taper. This large taper angle provides much more light at the tip of the fiber, which in turn greatly increases the sensitivity of the nanosensors. The reproducibility of the Turner method is strongly affected by environmental parameters such as temperature and vibration because of the dual chemical nature of the etching process. To avoid this problem, a variation of the etching method was developed, which involves a tube-etching procedure. In this procedure, an optical fiber with a silica core and an organic cladding material is paced in an HF solution. The HF slowly dissolves the silica core, producing a fiber with a large taper angle and nanometer-sized tip. The HF begins first to dissolve the fiber’s silica core, while not affecting

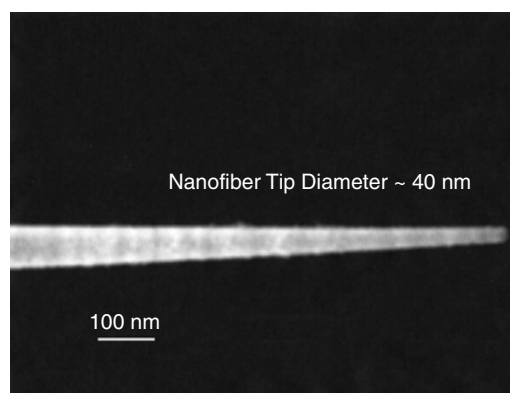


**Figure 3.** Scanning electron photograph of an uncoated nanofiber. The size of the fiber tip diameter is approximately 40 nm.

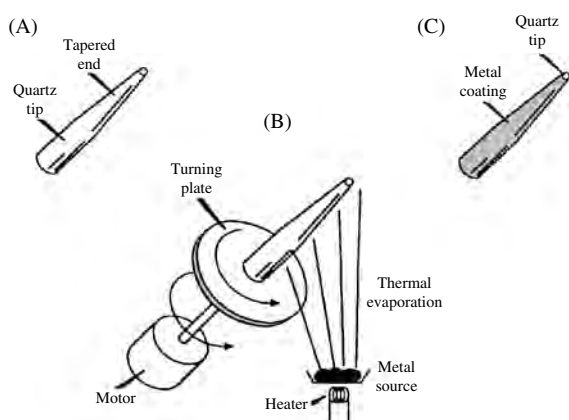


**Figure 4.** Procedure for coating a fiber with silver. (A) Uncoated fiber tip. (B) Fiber coating using metal evaporation over the rotating tip. (C) Coated fiber. Adapted from [21], T. Vo-Dinh et al., *Nature Biotechnol.* 18, 76 (2000). © 2000, Nature Publishing Group.

the organic cladding material. This unaffected cladding creates localized convective currents in the HF solution, which causes a tip to be formed. After some time, more of the silica core is dissolved, until it emerges above the surface of the HF solution. At this juncture, the HF is drawn up the cladding walls via capillary action, and runs down the silica core to produce a nanometer-sized tip. By varying the time of HF exposure and the depth to which the fiber is submerged in the HF solution, one can control the size of the fiber tip and the angle of the taper. Once the tip has been formed, the protruding cladding can be removed either with a suitable organic solvent or by simply burning it off. Nanotips fabricated using etching procedures, which can be designed to have sharp tips [13], have been used in NSOM studies to detect SERS-labeled DNA molecules on solid substrates at the subwavelength spatial resolution [11–13].

## 4.2. Antibody Immobilization

The next step in the preparation of the nanobiosensor probes involves the covalent immobilization of receptors onto the nanofiber tip. For antibody binding, several strategies can be used to retain the antibody at the sensing probe.

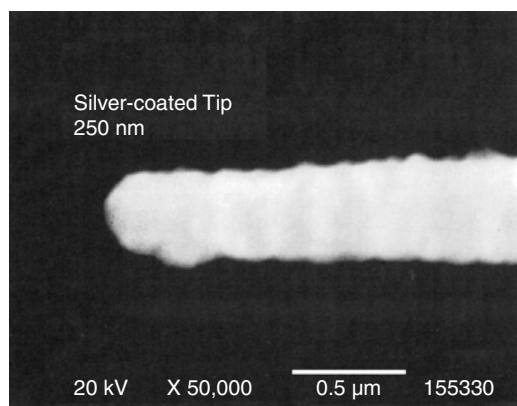


**Figure 5.** Scanning electron photograph of a nanofiber having the sidewall coated with silver.

Whatever procedure is involved, one requirement is that the antibody should retain its antigen-binding activity as much as possible. Perhaps the easiest procedure involves enclosure of the antibody in solution, within a semipermeable membrane cap, which fits over the end of the sensor [2]. However, this design is more complicated, and would increase the size of the tip of the nanosensor.

Antibodies can be immobilized onto the nanofiber probes by using a chemical immobilization method. The fiber is derivatized in 10% GOPS in H<sub>2</sub>O (v/v) at 90 °C for 3 h. The pH of the mixture is maintained below 3 with concentrated HCl (1 M). After derivatization, the fiber is washed in ethanol, and dried overnight in a vacuum oven at 105 °C. The fiber is then coated with silver as described previously. The derivatized fiber is activated in a solution of 100 mg/mL 1,1'-carbonyldiimidazole (CDI) in acetonitrile for 20 min, followed by rinsing with acetonitrile and then phosphate-buffered saline (PBS). The fiber tip is then incubated in a 1.2 mg/mL antibody solution (PBS solvent) for four days at 4 °C, and then stored overnight in PBS to hydrolyze any unreacted sites. The fibers are then stored at 4 °C, with the antibody-immobilized tips stored in PBS. This procedure has been shown to maintain over 95% antibody activity [21].

## 5. EXPERIMENTAL PROTOCOL AND INSTRUMENTAL SYSTEM

### 5.1. Experimental Procedure

An application that is truly unique to nanosensors involves monitoring living single cells *in vivo* [18–23]. Examples of this application in molecular biology will be discussed later. This section provides a description of the procedures for growing cell cultures for analysis using the nanosensors. Cell cultures were grown in a water-jacketed cell culture incubator at 37 °C in an atmosphere of 5% CO<sub>2</sub> in air. Clone 9 cells, a rat liver epithelial cell line, were grown in Ham's F-12 medium (Gibco), supplemented with 10% fetal bovine serum and an additional 1 mM glutamine (Gibco). In preparation for an experiment,  $1 \times 10^5$  cells in 5 mL of medium were seeded into standard dishes (Corning Costar Corporation). The growth of the cells was monitored daily by microscopic observation, and when the cells reached a state of confluence of 50–60%, the analyte solution was added and left in contact with the cells for 18 h (i.e., overnight). This procedure is designed to incubate the cells with the analyte molecules for subsequent monitoring using the nanosensors. The growth conditions were chosen so that the cells would be in log-phase growth during the chemical treatment, but would not be so close to confluence that a confluent monolayer would form by the termination of the chemical exposure. The analyte solution was prepared as a 1 mM stock solution in reagent grade methanol, and further diluted in reagent grade ethanol (95%) prior to addition to the cells. Following chemical treatment, the medium containing the analyte was aspirated and replaced with standard growth medium, prior to the nanoprobe procedure.

Monitoring target analyte molecules in single cells was then performed using antibody nanoprobe in the following way. A culture dish of cells was placed on the prewarmed microscope stage, and the nanoprobe, mounted on the

micropipette holder, was moved into position (i.e., in the same plane of the cells), using bright field microscopic illumination, so that the tip was outside the cell to be probed. The total magnification was usually 400 $\times$ . Under no room light and no microscope illumination, the laser shutter was opened to illuminate the optical fiber for excitation of the analyte molecules bound on the antibodies at the fiber tip. Usually, if the silver coating on the nanoprobe was appropriate, no light leaked out of the sidewall of the tapered fiber. Only a faint glow of laser excitation at the tip could be observed on the nanoprobe. A reading was first taken with the nanoprobe outside the cell and the laser shutter closed. The nanoprobe was then moved into the cell, inside the cell membrane, and extending into the cellular compartments of interest. The laser was again opened, and readings were then taken and recorded as a function of time during which the nanoprobe was inside the cell.

## 5.2. Instrumentation

The optical measurement system used for monitoring single cells using the nanosensors is schematically illustrated in Figure 6 [18–23]. Laser excitation light, either the 325 nm line of an HeCd laser (Omnichrome, 8 mW laser power) or the 488 nm line of an argon ion laser (Coherent, 10 mW), was focused onto a 600  $\mu\text{m}$  delivery fiber, which was connected to the nanofiber through an SMA connector. The nanofiber was secured to a micromanipulator on the microscope. The experimental setup used to probe single cells was adapted for this purpose from a standard micromanipulation/microinjection apparatus. A Nikon Diaphot 300 inverted microscope (Nikon, Inc.) with a Diaphot 300/Diaphot 200 Incubator, to maintain the cell cultures at  $\sim 37^\circ\text{C}$  on the microscope stage, was used for these experiments. The micromanipulation equipment used consisted of MN-2 (Narishige Company, Ltd.) Narishige three-dimensional manipulators for coarse adjustment, and Narishige MMW-23 three-dimensional hydraulic micromanipulators for final movements. The optical-fiber nanoprobe was mounted on a micropipette holder (World Precision Instruments, Inc.). The fluorescence emitted from the cells was collected by the microscope objective, and passed through an appropriate long-pass dichroic mirror to

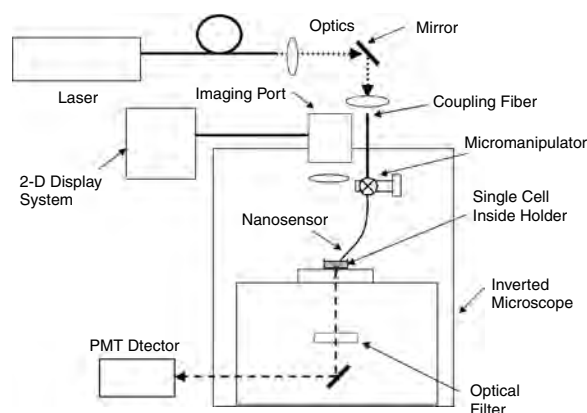


**Figure 6.** Instrumental system for fluorescence measurements of single cells using nanosensors.

eliminate the laser excitation scatter light. The fluorescence beam was then focused onto a photomultiplier tube (PMT) for detection. The output from the PMT was passed through a picoammeter, and recorded on a strip-chart recorder or a personal computer (PC) for further data treatment. To record the fluorescence of analyte molecules binding to antibodies at the fiber tip, a Hamamatsu PMT detector assembly (HC125-2) was mounted in the front port of the Diaphot 300 microscope, and fluorescence was collected via this optical path (80% of available light at the focal plane can be collected through the front port). A charge-coupled device mounted onto another port of the microscope could be used to record images of the nanosensor monitoring single cells.

## 6. APPLICATIONS

### 6.1. Nanofiber Probes for Intracellular Fluorescence Measurements

Optical nanofiber probes without antibody probes have been fabricated and used to monitor fluorescence emission from chemical species inside living single cells [17]. In this study, mouse epithelial cells were incubated with a fluorescent dye by incubating the cells in the dye solution and allowing membrane permeabilization to take place. Another procedure for loading cells with fluorophors involved the method called “scrape loading.” In the scrape loading procedure, a portion of the cell monolayer was removed by mechanical means, and cells along the boundary of this “scrape” were transiently permeabilized, allowing the dye to enter these cells. The dye was subsequently washed away, and only permeabilized cells retained the dye molecules, as they were not internalized by cells with intact membranes. Following incubation, the fluorescence signal of fluorescent dye molecules in single cells was detected using the optical nanofibers. A photograph of a nanosensor used to monitor clone 9 single cells is shown in Figure 7. Micromanipulators were used to move the optical fiber into contact with the cell membrane of a cell to be monitored. The fiber tip was then gently inserted just inside the cell membrane for fluorescence measurements. An argon-ion laser beam was transmitted through the optical nanofiber, and used for excitation. The dye molecules inside the cell were excited,

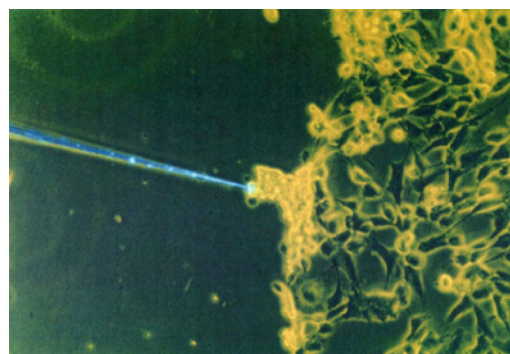


**Figure 7.** Photograph of single-cell sensing using a fiber-optic nanosensor.

and their fluorescence emission was collected and detected using the microscope instrumental system described previously. Background measurements were performed with cells that were not loaded with the fluorophores. Fluorescence signals were successfully detected inside the fluorophore-loaded cells, and not inside nonloaded cells. As another control, the optical-fiber probe was then moved to an area of the specimen where there were no cells, and the laser light was again passed down the fiber for excitation. No visible fluorescence (at the emission wavelength) was detected for this control measurement, thus demonstrating the successful detection of the fluorescent dye molecules inside single cells. These results demonstrated the capability of optical nanofibers for measurements of fluorophores in intracellular environments of single living cells.

## 6.2. Nanobiosensors for Monitoring Subcompartments of Single Cells

Nanosensors having antibody-based probes for use in measuring fluorescent targets inside a single cell have been demonstrated [18–23]. Since cells have very small sizes (1–10  $\mu\text{m}$ ), the success of intracellular investigations depends on several factors, including the sensitivity of the measurement system, the selectivity of the probe, and the small size of the nanofiber probes. The smallest cells to be nondestructively probed with a fiber-optic nanobiosensor were reported by Vo-Dinh and co-workers [21]. In that work, the antibody probe was targeted against benzopyrene tetrol (BPT), an important biological compound, which was used as a biomarker of human exposure to the carcinogen benzo[a]pyrene (BaP), a polycyclic aromatic hydrocarbon of great environmental and toxicological interest because of its mutagenic/carcinogenic properties and its ubiquitous presence in the environment. Benzo[a]pyrene has been identified as a chemical carcinogen in laboratory animal studies [29]. The small size of the probe allowed manipulation of the nanosensor at specific locations within the cells. The cells were first incubated with BPT prior to measurements using the experimental procedures described previously. Interrogation of single cells for the presence of BPT was then carried out using antibody nanoprobe for excitation and a photometric system for fluorescence signal detection.

Nanobiosensors for BPT were used for the measurement of intracellular concentrations of BPT in the cytoplasm of two different cell lines: (1) human mammary carcinoma cells, and (2) rat liver epithelial cells, following treatment of the culturing media with an excess of BPT. Figure 8 shows a digital image of the nanosensor actually being inserted into a single human mammary carcinoma cell. The measurements were performed on rat liver epithelial cells (Clone 9) used as the model cell system. The cells had been previously incubated with BPT molecules prior to measurements. The results demonstrated the possibility of *in-situ* measurements of BPT inside a single cell.

In this study, the nanosensors employed single-use bioprobes because the probes were used to obtain only one measurement at a specific time, and could not be reused due to the strong association constant of the antibody–antigen binding process. The antibody probes, however, could be regenerated using ultrasound methods. Our laboratory has

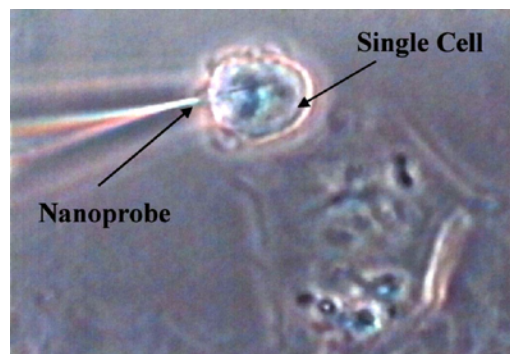


**Figure 8.** Digital image of a nanosensor inserted into a single human mammary carcinoma cell (the small size of the probe allowed manipulation of the nanoprobe at specific locations within a single cell).

successfully developed a method using ultrasound to non-invasively release antigen molecules from the antibodies, and therefore to regenerate antibody-based biosensors [30]. The results of the measurements with antibody against breast cancer antigen illustrate the effectiveness and potential of the regenerable immunosensor. A 65% removal of the antigens bound to the monoclonal antibodies immobilized on the fiber surface is attained after ultrasound regeneration. The ultrasound regeneration scheme is a non-destructive approach that has a great potential to be applied to nanosensors. The results demonstrate the effectiveness of this innovative ultrasound-based approach for biosensor regeneration, that is, releasing the antigen from the antibody probe.

Multiple (e.g., five) recordings of the fluorescence signals could be taken with each measurement using a specific nanoprobe. We have made a series of calibration measurements of solutions containing different BPT concentrations in order to obtain a quantitative estimation of the amount of BPT molecules detected. For these calibration measurements, the fibers were placed in petri dishes containing solutions of BPT with concentrations ranging from  $1.56 \times 10^{-10}$  to  $1.56 \times 10^{-8}$  M. By plotting the increase in fluorescence from one concentration to the next versus the concentration of BPT, and fitting these data with an exponential function in order to simulate a saturated condition, a concentration of  $(9.6 \pm 0.2) \times 10^{11}$  M was determined for BPT in the individual cell investigated [23].

Detection of BaP transport inside single cells is of great biomedical interest since it can serve as a means for monitoring BaP exposure, which can lead to DNA damage [29]. In another study, nanosensors were developed for *in-situ* measurements of the carcinogen BaP [31]. In order to perform these measurements, it was necessary to use antibodies targeted to BaP. The fluorescent BaP molecules were bound by interaction with the immobilized antibody receptor, forming a receptor–ligand complex. Following laser excitation of this complex, a fluorescence response from BaP provided a basis for the quantification of BaP concentration in the cell being monitored. The fluorescence signal generated allows for a high sensitivity of detection. The intracellular measurements of BaP depend on the reaction times involved. The reaction time established in this study for antibody–BaP complexing was 5 min. This was used as a standard



time to enable calibration from fiber to fiber. Additionally, the nanosensors were calibrated using standard analytical procedures using measurements of known concentration of reference solutions.

## 7. CONCLUSION

Dynamic information of signaling processes inside living cells is important to a fundamental biological understanding of cellular processes. Many traditional microscopy techniques involve incubation of cells with fluorescent dyes or nanoparticles, and examining the interaction of these dyes with compounds of interest. However, when a dye or nanoparticle is incubated into a cell, it is transported to certain intracellular sites that may or may not be where it is most likely to stay, and not to areas where the investigator would like to monitor. The fluorescence signals which are supposed to reflect the interaction of the dyes with chemicals of interest is generally directly related to the dye concentration as opposed to the analyte concentration. Only with optical nanosensors can excitation light be delivered to specific locations inside cells. An important feature of nanosensors is the minimal invasiveness of the monitoring process. A cell survival study was previously performed whereby an investigation was made to determine whether penetration of the cell by the nanosensor resulted in intracellular or membrane damage of such a nature as to compromise cellular viability. It was determined that the process of mitosis continued normally, and that nanosensor insertion and withdrawal did not affect the life cycle of the cell. Nanosensors are an important technology that can be used to measure biotargets in a living cell, and that does not significantly affect cell viability. Combined with the exquisite molecular recognition of antibody probes, nanosensors could serve as powerful tools capable of exploring biomolecular processes in subcompartments of living cells. They have a great potential to provide the necessary tools to investigate multiprotein molecular machines of complex living systems, and the complex network that controls the assembly and operation of these machines in a living cell. Future developments would lead to the development of nanosensors equipped with nanotool sets that enable tracking, assembly, and disassembly of multiprotein molecular machines and their individual components. These nanosensors would have multifunctional probes (antibody as well as DNA probes) that could measure the structure of biological components in single cells. Until now, scientists have been limited to investigating the workings of individual genes and proteins by breaking the cell apart and studying its individual components *in vitro*. The advent of nanosensors will hopefully permit research on entire networks of genes and proteins in an entire living cell *in vivo*.

## GLOSSARY

**Bioreceptor** A biological recognition element, such as antibody, DNA, enzyme, etc., used to bind selectively to a target analyte compound.

**Biosensor** A measurement system that consists of a probe with a bioreceptor, and a transducer.

**Nanobiosensor** Biosensor having nanoscale-dimension probe.

**Near-field scanning optical microscopy (NSOM)** Microscopy technique using scanning probe providing sub-wavelength spatial resolution.

**Surface-enhanced Raman scattering (SERS)** Enhanced Raman scattering of compounds adsorbed on nanostructures metallic materials.

## ACKNOWLEDGMENTS

The author acknowledges the contribution of G. D. Griffin, J. P. Alarie, B. M. Cullum, and P. Kasili. This research was sponsored by the LDRD Project (Advanced Nanosensors), and by the Office of Biological and Environmental Research and the National Nuclear Safeguard Agency (NN-20 Program), U.S. Department of Energy under Contract DE-AC05-00OR22725 managed by UT-Battelle, LLC.

## REFERENCES

1. T. Vo-Dinh, B. J. Tromberg, G. D. Griffin, K. R. Ambrose, M. J. Sepaniak, and E. M. Gardenshire, *Appl. Spectrosc.* 41, 735 (1987).
2. T. Vo-Dinh, G. D. Griffin, and M. J. Sepaniak, in "Chemical Sensors and Biosensors" (O. S. Wolfbeis, Ed.). CRC Press, Boca Raton, FL, 1991.
3. T. Vo-Dinh, M. J. Sepaniak, G. D. Griffin, and J. P. Alarie, *J. Immunomethods* 3, 85 (1993).
4. J. P. Alarie and T. Vo-Dinh, *Polycyclic Aromatic Compounds* 8, 45 (1996).
5. J. P. Alarie and T. Vo-Dinh, *Talanta* 38, 529 (1991).
6. J. P. Alarie, M. J. Sepaniak, and T. Vo-Dinh, *Anal. Chim. Acta* 229, 69 (1990).
7. B. J. Tromberg, M. J. Sepaniak, J. P. Alarie, T. Vo-Dinh, and S. M. Santella, *Anal. Chem.* 60, 1901 (1998).
8. J. P. Alarie, J. R. Bowyer, M. J. Sepaniak, A. M. Hoyt, and T. Vo-Dinh, *Anal. Chim. Acta* 236, 237 (1990).
9. D. W. Pohl, in "Advances in Optical and Electron Microscopy" (C. R. J. Sheppard, Ed.). Academic, London, 1984.
10. E. Betzig and R. J. Chichester, *Science* 262, 1422 (1993).
11. D. Zeisel, V. Deckert, R. Zenobi, and T. Vo-Dinh, *Chem. Phys. Lett.* 283, 38 (1998).
12. V. Deckert, D. Zeisel, R. Zenobi, and T. Vo-Dinh, *Anal. Chem.* 70, 2646 (1998).
13. V. Deckert, in "Biomedical Photonics Handbook" (T. Vo-Dinh, Ed.), Chap. 12. CRC Press, Boca Raton, FL, 2003.
14. W. Tan, Z. Y. Shi, and R. Kopelman, *Anal. Chem.* 64, 2985 (1992).
15. W. Tan, Z. Y. Shi, S. Smith, D. Birnbaum, and R. Kopelman, *Science* 258, 778 (1992).
16. B. M. Cullum, G. D. Griffin, G. H. Miller, and T. Vo-Dinh, *Anal. Biochem.* 277, 25 (2000).
17. T. Vo-Dinh, G. D. Griffin, J. P. Alarie, B. M. Cullum, B. Sumpter, and D. J. Noid, *J. Nanoparticle Res.* 2, 17 (2000).
18. T. Vo-Dinh and B. M. Cullum, *Fresenius J. Anal. Chem.* 366, 540 (2000).
19. B. M. Cullum and T. Vo-Dinh, *Trends Biotechnol.* 18, 388 (2000).
20. T. Vo-Dinh, B. M. Cullum, and D. L. Stokes, *Sensors Actuators B* 74, 2 (2001).
21. T. Vo-Dinh, J. P. Alarie, P. M. Cullum, and G. D. Griffin, *Nature Biotechnol.* 18, 76 (2000).



22. B. Cullum and T. Vo-Dinh, in "Biomedical Photonics Handbook" (T. Vo-Dinh, Ed.), Chap. 60. CRC Press, Boca Raton, FL, 2003.
23. T. Vo-Dinh, *J. Cell Biochem., Suppl.* 39, 154 (2002).
24. T. Vo-Dinh, *Trends Anal. Chem.* 17, 557 (1998).
25. D. R. Turner, U.S. Patent 4,469,554, 1984.
26. P. Hoffmann, B. Dutoit, and R. P. Salathe, *Ultramicroscopy* 61, 1 (1995).
27. P. Lambelet, A. Sayah, M. Pfeffer, C. Philipona, and F. Marquis-Weible, *Appl. Opt.* 37, 7289 (1998).
28. R. Stockle, C. Fokas, V. Deckert, R. Zenobi, B. Sick, B. Hecht, and U. P. Wild, *Appl. Phys. Lett.* 75, 160 (1999).
29. T. Vo-Dinh, Ed., "Chemical Analysis of Polycyclic Aromatic Compounds." Wiley, New York, 1989.
30. M. Moreno-Bondi, J. Mobley, and T. Vo-Dinh, *J. Biomed. Opt.* 5, 350 (2000).
31. P. M. Kasili, B. M. Cullum, G. D. Griffin, and T. Vo-Dinh, *J. Nanosci. Nanotechnol.* 6, 653 (2002).

# Nanocables and Nanojunctions

Yuegang Zhang

*Intel Corporation, Santa Clara, California, USA*

Weiqliang Han

*University of California, Berkeley, California, USA*

Gang Gu

*Molecular Nanosystems Inc., Palo Alto, California, USA*

## CONTENTS

1. Introduction
  2. Composite Nanotubes
  3. Nanocables
  4. Nanowire Superlattices
  5. Nanojunctions
- Glossary  
References

## 1. INTRODUCTION

Nanostructures have unique properties due to the quantum confinement effects arising from the reduced dimensions. One-dimensional nanostructures have received more and more attention in recent years following the discovery of carbon nanotubes [1, 2] and related nanowires [3]. Carbon nanotubes are structures made by rolling up graphite sheets into seamless cylinders with diameters in nanometer scale. The structural change from graphite sheets into carbon nanotubes introduces quantum confinement along the direction of the tube circumference. This confinement allows electron transport only along the direction of tube axis, which makes carbon nanotube a good one-dimensional electron system. It is interesting to note that the combination of the quantum confinement effect and the electronic structure of graphite can change the properties of carbon nanotubes more than other materials: A single carbon nanotube can be metallic or semiconductor depending on its diameter or its chirality—a notation on how the nanotube is rolled up [4]. This property gives us great hope to realize intramolecular devices by engineering the atomic structure of carbon

nanotubes and fusing them together into one molecule. Several theoretical and experimental investigations have shown the junction of a metallic tube and a semiconducting tube could work as a Schottky diode [5–7].

Although this kind of intramolecular junction is of great interest in molecular devices, it is difficult to find a practical method to fabricate the junctions in a controllable way. Comparing with carbon nanotubes, the properties of non-carbon nanotubes and nanowires are normally easier to control because they are primarily determined by their chemical composition instead of geometry. For example, BN is insulator independent of its chirality and diameter, and silicon nanowires are always semiconductors like their bulk counterpart. Similar quantum confinement effects, however, would exist for all these different one-dimensional structures. Construction of nanoscale heterostructures by combining these one-dimensional objects will provide great potential for future quantum devices. Although a rich variety of one-dimensional nanostructures has been discovered in recent years, a general technology to build the one-dimensional heterostructure has not been well established. Unlike the two-dimensional heterostructures such as thin-film semiconductor superlattices that can be precisely engineered by techniques such as molecular beam epitaxy (MBE), phase formation in one-dimensional nanostructures is not straightforward and is hard to control by simple physical deposition. Nevertheless, some very exciting progress has been made in synthesizing heterogeneous nanotubes, nanowires, and their junctions. And some have already show promises in real applications. For example, the method of making carbon nanotube and titanium carbide junction has been used to improve the contact in nanotube field-effect transistors [8, 9].

The heterogeneous one-dimensional nanostructures composed of nanotubes and nanowires can generally be divided

into two categories according to the direction of nanowire axes relative to the interfaces that separate different materials in the heterogeneous nanostructures. In the first category, the axes of the nanowires and nanotubes are parallel to the interface planes. The phase separation is in the radial direction. Most nanotubes or nanowires in this category have homogeneous phase distribution along the whole length. The nanostructures in this category are also called composite nanotubes or nanowires (different from nanotube or nanowire composite which normally refers to a material made by dispersing nanotubes or nanowires into a matrix material). A representative structure of this category is a “nanocable” that has a core nanowire sheathed by one or more layers of different materials [10]. Composite nanotubes and carbon nanotubes with a second material filled into their hollow cores also belong to this category. In the second category, the axes of the nanotubes and nanowires are normal to the heterointerfaces. This category includes heterojunctions connecting nanotubes and solid nanowires [8, 11] or nanowire superlattices that are composed of alternating semiconductor nanowire segments of different chemical composition [12–14]. Because of the small cross section of nanotubes and nanowires, the junctions formed from them are in nanometer scale. They are therefore called “nanojunctions.” The nanojunctions represent a new kind of structure that could have great potential applications in nanoscale electronics and optoelectronics. This chapter will give a review of the progress on fabrication and characterization of the heterogeneous one-dimensional nanostructures of both categories.

## 2. COMPOSITE NANOTUBES

A composite nanotube refers to a multiwalled nanotube (MWNT) that is composed of shells with more than one kind of chemical composition. There is a big difference between a composite nanotube and compound nanotubes. A composite nanotube has distinguishable phase separation between cylindrical shells that constitute the tube, while all the shells in a compound nanotube consist of a single compound phase. Examples of compound nanotubes are nanotubes of  $W_2S$  [15],  $Mo_2S$  [15, 16], BN [17–20]. Composite nanotubes synthesized today are normally a mixture of carbon shells and shells of compound materials such as BN. B-C-N nanotubes are widely studied because theoretical calculation predicts that their electrical properties are controlled by their chemical composition instead of the subtle geometrical parameters [21, 22]. Similar to their pure carbon and compound counterpart, composite nanotubes are normally produced by arc-discharge and laser ablation method.

The main tool used for characterizing composite nanotube is a high-resolution scanning transmission electron microscope (STEM) equipped with a parallel electron energy-loss spectrometer (PEELS) [23, 24]. The STEM-PEELS system has a spatial resolution in subnanometer scale which other analytical microscopes cannot compete with and thus can be used to map the spatial distribution of elements in nanostructures. A linear scan of focused electron beam across an object and measurement of the elemental concentration at each step during scanning is called

elemental profiling, which is a powerful technique to determine the structure of one-dimensional nanostructures.

Earlier arc-discharge experiments for synthesizing B-C-N nanotubes used anodes made of a mixture of B, N, and C [25–27]. The obtained products contained a majority of carbon and only a very low concentration of boron and nitrogen. Elemental analysis of the nanotubes in the products showed inhomogeneous distribution of B, N, and C in the radial direction with normally B and N rich at outer surface layer [25, 27]. The B:N ratio was close to 1:1. The very low concentration of B and N in the sample suggests these elements are doped into the lattice of carbon nanotubes. There are several possibilities for how these elements are distributed in the tubes. One is that they form homogeneous  $B_xC_yN_z$  compound shells that wrap the carbon nanotube cores. Another scheme is that BN exists in domains in the outer carbon shells. The weak signal of the B and N in STEM-PEELS, however, failed to give a conclusive evidence of intershell phase separation.

B-C-N nanotubes produced by laser ablation using a target made of a compressed mixture of BN and C powders gave a similar result as arc-discharge [24]. The results obtained by STEM-PEELS show all nanotubes are C rich although the BN and C ratio in the target is 1:1. A lot of BN crystallites were found in co-products. The tubes with a few walls are normally composed of pure carbon. Those with more walls are normally not uniform in diameter along their axis as well as the B and N distribution. The distribution of B and N is rich at the outer surface layers similar to the B-C-N nanotubes produced by earlier arc-discharge method [25, 27]. Again, it is unable to be determined whether the B and N are homogeneously doped into graphite lattice (true ternary  $B_xC_yN_z$  phase) or they are mixed binary phases such as BN or  $BC_x$  embedded in the graphite outer layers (subcomposite tubes).

The laser ablated B-C-N nanotubes not only have similar morphologies and element distribution as those in earlier arc-discharged products, they should also share a similar growth mechanism since both methods employ a local high-temperature process to vaporize graphite and BN. From the feature that all obtained composite nanotubes have carbon cores, a two-step growth model has been proposed and is shown in Figure 1 [24]. The first step is the nucleation and growth of pure multiwalled carbon nanotubes. This step occurs in the high-temperature plasma region where B and N can easily diffuse out of the graphite lattice and form more favorable BN crystallites of planar structure. Carbon nanotubes formed in the process are all multiwalled because the presence of B and N atoms in this step could introduce defects on the graphitic wall that are preferable nucleation

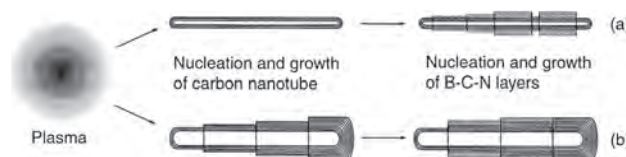


**Figure 1.** Growth model of heterogeneous B-N-C composite nanotubes. Reprinted with permission from [24], Y. Zhang et al., *Chem. Phys. Lett.* 279, 264 (1997). © 1997, Elsevier Science.

sites for additional layers and the foreign atoms could also serve as the bridging atoms in lip-lip growth model [28]. The second step is partial coating of B-C-N layers. The growth of additional walls could also initiate from the defects on the carbon nanotube wall. The B and N diffusion process is reduced by lower temperature when the nanotube moves out of the plasma center. The inert gas used in the arc-discharge and laser ablation processes provides an efficient heat exchange medium for cooling down the species and works as a barrier to confine the expansion of the plasma and sustain a high density of multielement vapor for doping BN in nanotubes.

The two-step model, however, is not adequate to explain the formation of all B-C-N nanotube structures. One exception is the sandwiched C-BN-C nanotubes, where carbon is rich both in core shells and in outer shells [23]. The growth mechanism for such sandwiched nanotubes is still not clear. One possible model is a simultaneous growth of multiphase shells through a lip-lip-interaction [28]. Another possibility is that the tube flies through three zones in the discharge chamber during its layer-by-layer growth, and the three zones have different concentrations of active elements and thus form sandwiched structure.

The sandwiched C-BN-C nanotubes were produced by arc-discharge in nitrogen atmosphere using a HfB anode and a carbon cathode [23]. The use of non-carbon anode increases the B and N concentration in the product because the carbon cathode is only slightly evaporated in the arc-discharge. The high concentration of B and N enables more precise determination of local chemical composition using a STEM-PEELS. Figure 2 shows a high-resolution electron

micrograph of such a B-C-N MWNT and its elemental profile measured by scanning electron beam across the tube [23]. The high-resolution image cannot give any information about phase separation because all possible phases in B-C-N system, BN,  $BC_2N$ ,  $BC_3$ , have very similar crystal structure with graphite, and thus give the same image in the transmission electron microscope. The elemental profile, however, can give detailed phase information of all shells assuming each shell is composed of a single phase. In a cross-section elemental profile of single-phase cylindrical structure, maximum only occurs at the position that corresponds to the inner edge parallel to the probing electron beam. This is because this position has the largest equivalent thickness through which electron beam transmits and loses its energy. The elemental profile of a multiwalled nanotube can be simulated by adding up the profiles of all the shells with each shell as a single-phase cylinder. For a single-phase MWNT, there should be only two maxima in the profile because the probe size of the STEM, 0.5–1 nm, cannot resolve adjacent individual shells in a MWNT. Figure 2B shows four maxima in the C profile and two maxima in the B and N profiles. The positions of the two maxima in the B and N profiles coincide with two minima of the C profile. The result can be interpreted as a C-BN-C three-layered tubular structure as modeled in Figure 2D. Simulated elemental profiles (Fig. 2C) from the model agree with the experimental results very well. The analysis of the C-BN-C nanotubes has provided the first clear evidence of intershell phase separation (with atomic-scale sharp interfaces) in composite nanotubes.

More recently, some other composite nanotubes have been reported. One example is the  $TiO_2$ - $SiO_2$  composite nanotubes synthesized by sol-gel template method presented in [29]. The coaxial structure is made by sequential formation of amorphous  $SiO_2$  nanotubes in the pores of anodic alumina and  $TiO_2$  nanotubes within the  $SiO_2$  nanotubes. The composite nanotubes have a relatively large diameter of 200–250 nm. Another type of novel composite nanotubes are produced by growth of  $NbS_2$  nanotubes on carbon nanotube templates. High-resolution transmission electron microscopy and energy dispersive X-ray analysis revealed that the uniform well-crystallized  $NbS_2$  is nucleated and grown from an intermediate phase of  $NbO_2$  which is unevenly wrapped on the carbon nanotube templates. A multipoint nuclei site growth mechanism has been proposed to account for nanotube formation [30].

### 3. NANOCABLES

A coaxial nanocable is generally defined as a multilayered structure with a core nanowire coaxially sheathed by one or more shells of different materials. Nanocables include filled nanotubes and core-shell nanowire heterostructures.

#### 3.1. Filling Carbon Nanotubes

The discovery of carbon nanotubes has stimulated scientists for a range of potential applications [1], including the filling of hollow carbon nanotubes with chosen materials. Three main approaches have been used for filling carbon nanotubes with both crystalline and noncrystalline

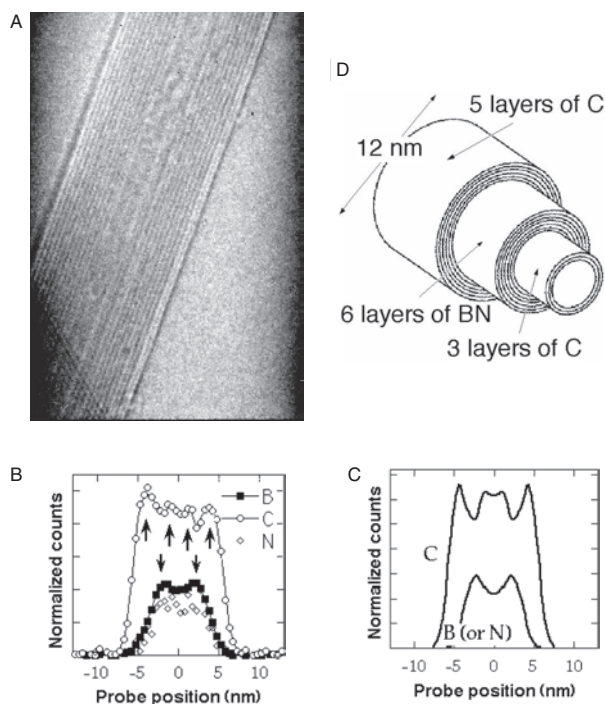


**Figure 2.** Phase separation in a C-BN-C composite nanotube. Reprinted with permission from [23], K. Suenaga et al., *Science* 278, 633 (1997). © 1997, American Association for the Advancement of Science.



materials. The first approach involves inserting the selected materials, either physically or chemically, into the opened carbon nanotubes [31, 32]. The as-produced carbon nanotubes, however, normally have closed caps at their ends. Filling of nanotubes, therefore, always relies on a method to open the ends of the nanotubes. Oxidation and acid treatment are two efficient routes for opening the tips of carbon nanotubes [33–35]. Open nanotubes can be filled via capillary action using either a low melting or low surface tension material (i.e., material with a surface tension lower than the threshold value of 100–200 millinewtons per meter) [36]. The first filling experiment reported by Ajayan et al. used an oxidation method to simultaneously open and fill multi-walled carbon nanotubes (MWCNTs) [31]. Metallic Pb was first deposited onto samples containing MWCNTs produced by arc-discharge method. The samples were then heated in air to about 400 °C which is above the melting point of Pb. High-resolution electron microscopy (HREM) images taken after the heat treatment show that MWCNTs are opened at their tips and filled with solid materials (Fig. 3). Using this approach, metal (Pd, Ag, Au, Bi), metal oxides (oxides of Mo, Sn, Ni, U, Co, Fe, Nd, Sm, Eu, La, Ce, Y, Cd), metal chlorides (AuCl, UCl<sub>4</sub>), FeBiO<sub>3</sub>, HReO<sub>4</sub>, MoO<sub>2</sub>, and SnO, have all been successfully filled into carbon nanotubes [33, 37–46]. This approach is also useful for filling single-walled carbon nanotubes (SWCNTs or SWNTs) with halides, oxides, carbides, and metals [47–63]. One good example is KI filled SWCNT prepared by heating KI with SWCNT inside an evacuated silica ampoule at the temperature of 954 K for 2 hr. Figure 4 shows a phase image reconstructed from a 20-member focal series of a 1.6-nm-diameter SWCNT containing a KI single crystal [49]. In cross section, the filled crystal can be regarded as a single KI unit cell viewed along the  $\langle 110 \rangle$  direction of the parent rock salt structure, with the  $\langle 001 \rangle$  direction parallel to the tube axis. The crystal is well resolved in regions 1 and 3 of the restoration, whereas in region 2, the crystal is rotated about

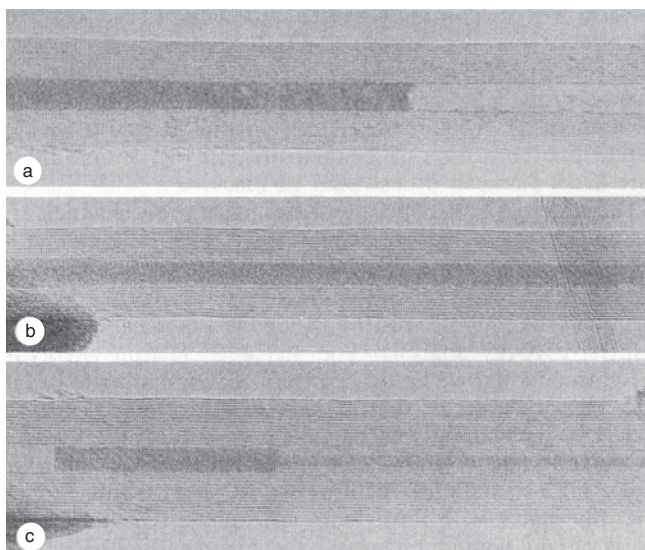


**Figure 3.** HREM images of MWCNTs filled with Pb compound (dark contrast). Reprinted with permission from [31], P. M. Ajayan and S. Iijima, *Nature* 361, 333 (1993). © 1993, Macmillan Magazines Ltd.

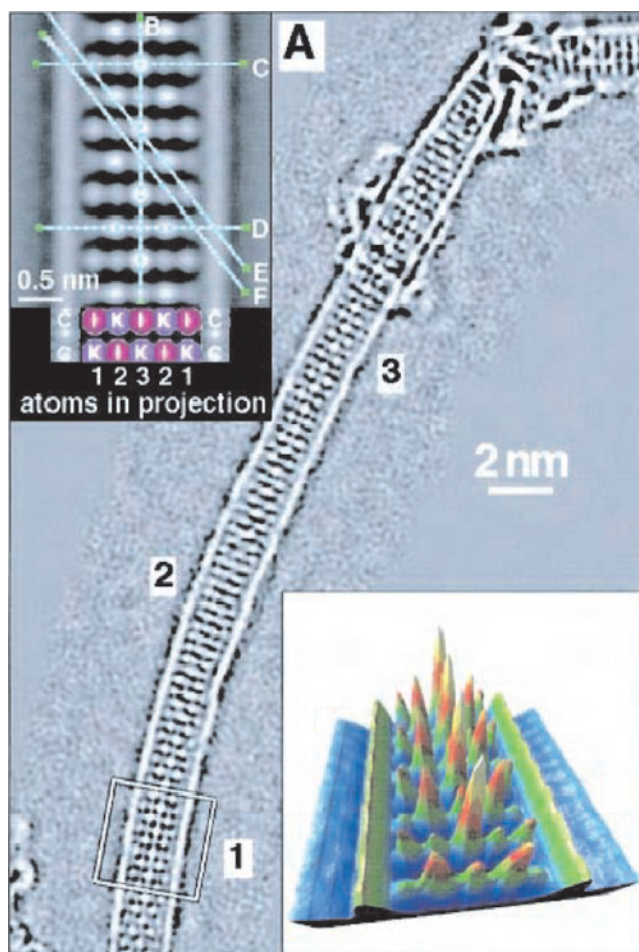


**Figure 4.** Phase image showing a  $\langle 110 \rangle$  projection of KI incorporated within a 1.6-nm-diameter SWCNT, reconstructed from a focal series of 20 images. The upper left inset shows an enlargement of region 1. The lower right inset shows the surface plot of the region 1. Reprinted with permission from [49], R. R. Meyer et al., *Science* 289, 1324 (2000). © 2000, American Association for the Advancement of Science.

its axis. In the  $\langle 110 \rangle$  projection, each white spot corresponds to a column of pure I or pure K that is exactly one, two, or three atoms in thickness, as can be seen in the enlargement of region 1 (upper left inset). The different phase shifts arising from different atomic columns are visible when region 1 is displayed as a surface plot (lower right inset) [49]. SWCNT filled with polystyrene and styrene-isoprene is also reported [64].

In 1998, a new type of self-assembled hybrid structures consisting of fullerene arrays inside SWCNTs, so-called “peapods,” were reported [65, 66]. Recent progress in the high yield synthesis opens up a huge possibility for the peapod research. Various types of fullerenes and endohedral metallofullerenes, such as C<sub>60</sub>, Gd@C<sub>82</sub>, Sm@C<sub>82</sub>, La@C<sub>82</sub>, La<sub>2</sub>@C<sub>82</sub>, La<sub>2</sub>@C<sub>80</sub>, Er<sub>x</sub>Sc<sub>3-x</sub>@C<sub>80</sub>, Dy@C<sub>82</sub>, can now be fully inserted inside SWCNTs [67–80]. Potential applications of peapods range from data storage to quantum cascade laser, quantum computing [81, 82], field-effect transistor [75], and hydrogen storage [83].

The second approach is to simultaneously encapsulate the materials during the formation of carbon nanotubes.

Such encapsulation has been observed in MWCNTs synthesized by arc-discharge [84–95], electrolysis [96–98], field-anode activation [99], laser ablation [100], chemical vapor deposition [101–103], and pyrolysis [104] with metals, oxides, carbide, nitrides, chlorides, and sulfides. Among these processes, arc-discharge produces the best-graphitized sheathing MWCNTs, which is also true in synthesizing hollow carbon nanotubes. Arc-discharge is also more versatile for encapsulation of different elements. In this process, a graphite anode is drilled and filled with a mixture of graphite and the chosen element powders. One then proceeds with the conventional Krätschmer–Huffman arc deposition technique. Encapsulation abilities of more than 41 elements have been systematically investigated [39, 85, 87, 89]. This approach is also useful for filling single-walled carbon nanotubes [105, 106].

The third approach is a two-step process. First, nanowires are synthesized and then used as templates to deposit graphite layers on their surface [107, 108]. Zhang et al. deposited thick graphitic layers on the surface of Si nanowires by using a hot filament chemical vapor deposition method. When the temperature was as high as 1000 °C, Si cores tended to transform into SiC cores [107]. Han et al. reported the synthesis of GaN nanorods coated with graphitic carbon layers (usually less than 5), including single carbon layers, on preproduced GaN nanorods using a conventional thermal chemical vapor deposition method. The graphitic carbon layers conform to the shape of the GaN nanorods [108].

### 3.2. Filling Inorganic Nanotubes

Analogous to filled carbon nanotubes, inorganic nanotubes, such as BN [17],  $B_xC_yN_z$  [25], and sulfide nanotubes [15], have also been filled with different materials. This category of nanocable is usually synthesized through a simultaneous phase separation process during the synthesis of nanotubes and nanowires.

The first sophisticated coaxial nanocable structure with insulated shells was produced via laser ablation of a composite target containing BN, graphite, and a small amount of SiO and  $Li_3N$  at high temperature [10]. Figure 5 shows the transmission electron microscope (TEM) images of the fabricated coaxial nanocables. They are normally a few tens of micrometers long and 10–100 nm in their diameters. The diameters are quite uniform throughout the whole length of the nanocable (Fig. 5A). High-resolution TEM images in Figure 5B and C indicate that the core of the nanowire has a crystalline phase whose electron diffraction pattern (left bottom inset of Fig. 5B) and lattice image (right bottom inset of Fig. 5C) fit well with that of cubic SiC. The intermediate layer shows an amorphous phase. The outermost layer consists of graphite multiwalls. A detailed elemental profile analysis across the nanocable by STEM-PEELS reveals the Si:C ratio in the core wire and Si:O ratio in the intermediate layer is 1:1 and 1:2, respectively. The outer layer of the nanocable is composed of C and BN with signature of intershell phase separation similar to that of composite nanotubes described in the previous section. The solid phases in the core and intermediate layer region have been

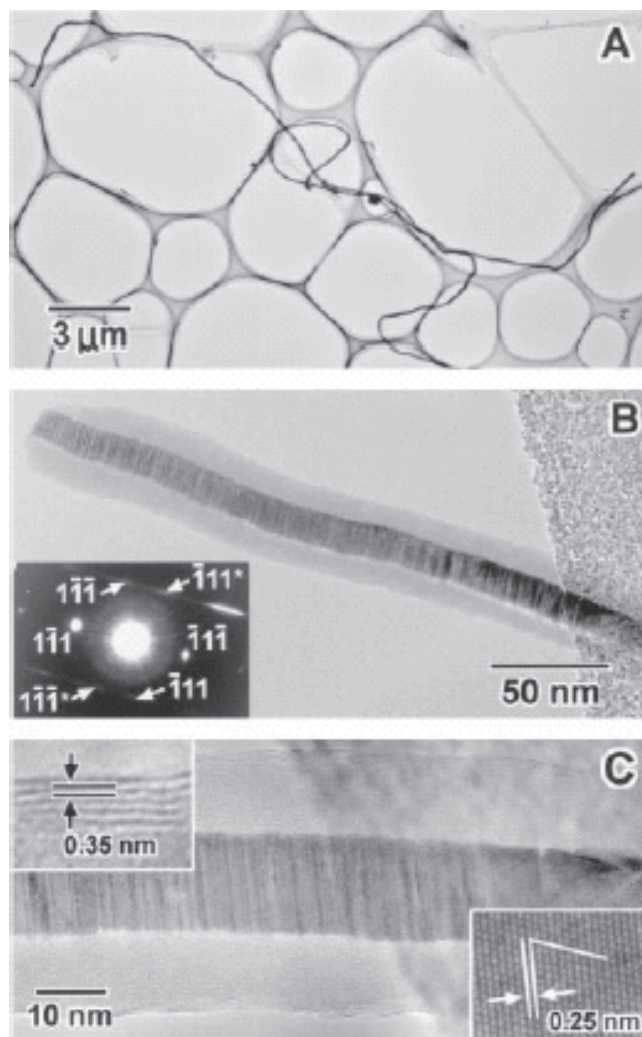


**Figure 5.** HREM images and selected-area electron diffraction pattern of  $SiC-SiO_2-(BN)_x C_y$  coaxial nanocables. Reprinted with permission from [10], Y. Zhang et al., *Science* 281, 973 (1998). © 1998, American Association for the Advancement of Science.

further confirmed by comparing the Si L-edge fine structure with those of SiC and  $SiO_2$  reference spectra (Fig. 6). The characterization therefore gives a well-defined composite nanowire structure with  $SiC-SiO_2-(BN)_x C_y$  multilayers forming a semiconductor-insulator-(semi)conductor coaxial nanocable.

BN nanotubes filled with SiC were synthesized by using multiwall carbon nanotubes as templates [109]. This method combines both carbon nanotubes (CNTs)-substitution reaction [110] and confined reaction [111, 112]. Through the CNT-substitution reaction, CNTs react with boron oxide vapor in the presence of nitrogen gas to form BN-NTs, whose diameters and lengths are similar to those of the starting CNTs. The formation of the SiC filling proceeds by the penetration of SiO vapor into the cavity of the nanotubes. The subsequent reaction of SiO vapor with the inner carbon layers or volatile carbon mono-oxide in the interior forms SiC nanowires. The entire length of the nanotubes can be filled. SiC filled  $(BN)_x C_y$  nanotubes, which are a metal(C)-insulator(BN)-semiconductor (SiC) (MIS)



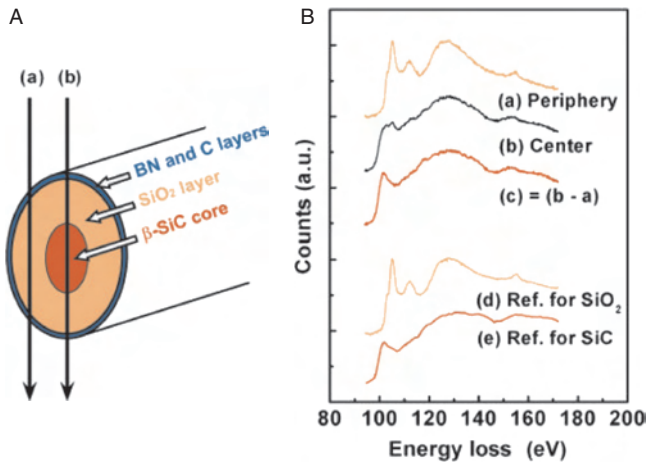


**Figure 6.** (A) A schematic illustration of a coaxial nanocable. (B) Si-L fine structure obtained from a nanocable with electron probe positions as indicated by arrows in (A). Spectrum c is obtained by subtracting a from b, representing a contribution from the core of the nanocable. Reference spectra from pure  $\text{SiO}_2$  and SiC phases are displayed for comparison. Reprinted with permission from [10], Y. Zhang et al., *Science* 281, 973 (1998). © 1998, American Association for the Advancement of Science.

structure, also form in the product. Using the same methods, BN and  $(\text{BN})_x\text{C}_y$  nanotubes filled with boron carbide [113] and  $(\text{BN})_x\text{C}_y$  nanotubes filled with iron boride [114] have been prepared. Other similar structures, such as Fe filled C-BN [115] and BN nanotubes [116], Fe-Ni alloy filled BN nanotubes [116], Mo filled BN nanotubes [117],  $\text{Al}_2\text{O}_3$  filled BN nanotubes [118], GaN filled BN nanotubes [119], BN nanotubes filled with SiC and SiN [120], and  $\text{ZrO}_2$  filled BN nanotubes [121] have also been reported.  $\text{C}_{60}$  filled BN nanotubes have been theoretically studied and experimentally achieved [122, 123].

Hofmann et al. found  $\text{Ni}_{17}\text{S}_{18}$  filled  $\text{MoS}_2$  nanotubes combined with sulfide nanowires when they checked nanostructures on processed, sulfur contaminated Mo grids. Carbon is found both in the outer walls and in the core of the wire [124].

### 3.3. Core-Shell Nanowire Heterostructures

One-dimensional core-shell nanowire heterostructures are another kind of nanocable with radial heterostructures. After high-temperature reaction processes, many semiconductors and metal nanowires are found to have a thin oxide shell, forming a core-shell nanowire. Such configurations are Si/ $\text{SiO}_x$  [125], SiC/ $\text{SiO}_x$  [126–128], Ge/ $\text{GeO}_2$  [129], GaN/ $\text{GaO}_x$  [130], and Zn/ $\text{ZnO}$  [131]. Other similar structures, such as  $\text{Si}_3\text{N}_4$ / $\text{Si}/\text{SiO}_2$  [132], B/ $\text{SiO}_2$  [133], Ge/ $\text{SiO}_2$  [134], Ag/ $\text{SiO}_x$  [135], CdS/ $\text{SiO}_2$  [136], Zr/ $\text{ZrO}_2$  [137],  $\text{La}(\text{OH})_3$ / $\text{Ni}(\text{OH})_2$  [138], NiFe/Cu [139], Au/Ag [140], and  $\text{Cu}_2\text{S}/\text{Au}$  [141], have also been synthesized using chemical vapor deposition, laser ablation, electrodeposition, and redox deposition techniques. In addition to the inorganic core-shell nanowires, semiconductor/polymer core-shell nanowires, such as CdSe/poly(vinyl acetate), have been produced using low-temperature solution methods [142].

Very recently, controlled growth of core-shell and multishell heterostructures of silicon-germanium systems has been approached using a chemical vapor deposition system [143]. This work is based upon control of radial versus axis growth (Fig. 7). Metal nanoparticles could act as a catalyst to direct axis growth by a vapor-liquid-solid growth process (Fig. 7a). Axial growth proceeds when reactant activation and addition occurs at the catalyst and not on the nanowire surface (Fig. 7b). By altering conditions to favor radial growth on the nanowire surface, it is possible to drive conformal shell growth (Fig. 7c). In this work, the radial growth is turned on by moving the growth substrate downstream to favor uncatalyzed surface growth. Subsequent introduction of different reactants and/or dopants produces multiple shell structures (Fig. 7d). By this method, core-shell structures such as intrinsic silicon (i-Si)/boron doped (p-type) silicon, i-Si/ $\text{SiO}_x$ /p-Si, i-Ge/p-Si, Si-Ge, Si-Ge-Si, and p-Si/i-Ge/ $\text{SiO}_x$ /p-Ge core-multishell nanowire structures have been synthesized [143]. TEM images and elemental mapping show the Si-Ge core-shell structure with a sharp interface (Fig. 8a). Figure 8b shows that the Ge shell is fully crystallized. Figure 8c shows a cross-section elemental mapping of a Si-Ge-Si core-double-shell nanowire. Another interesting experiment in this work is to measure the  $I$ - $V$  curve of p-Si/i-Ge/ $\text{SiO}_x$ /p-Ge core-multishell nanowires, which can be used as field-effect transistors. The source, drain, and gate contacts were made by selective etching and metal deposition onto the inner i-Ge shell and outer p-Ge shell, respectively.

Another controllable example is the growth of CdSe/CdS/ZnS core-shell nanorods [144]. Short CdSe nanorods (aspect ratios range from 2:1 to 10:1) were first grown by sol-gel processes [145] and then put into the precursor solution for the growth of CdS/ZnS graded shells at low temperature (160 °C) [144]. Interfacial segregation is used to

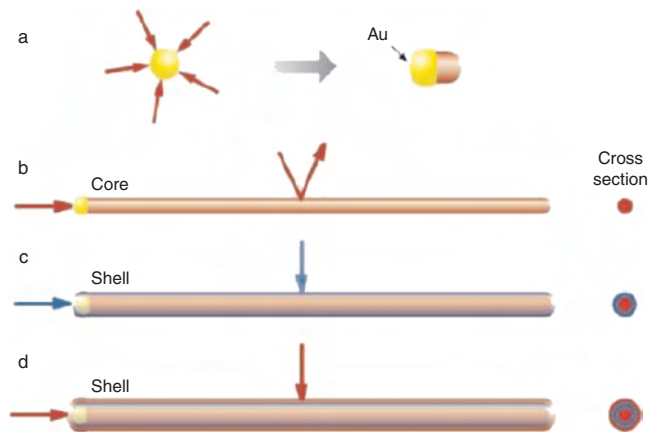


**Figure 7.** Synthesis of core-shell nanowires by chemical vapor deposition. (a) Gaseous reactants (red) catalytically decompose on the surface of Au nanocluster leading to nucleation and direct nanowire growth. (b) One-dimensional growth is maintained as reactant decomposition on the Au catalyst is strongly preferred. (c) Synthetic conditions are altered to induce homogeneous reactant decomposition on the nanowire surface, leading to a thin, uniform shell (blue). (d) Multishells are grown by repeated modulation of reactants. Reprinted with permission from [143], L. J. Lauhon et al., *Nature* 420, 57 (2002). © 2002, Macmillan Magazines Ltd.



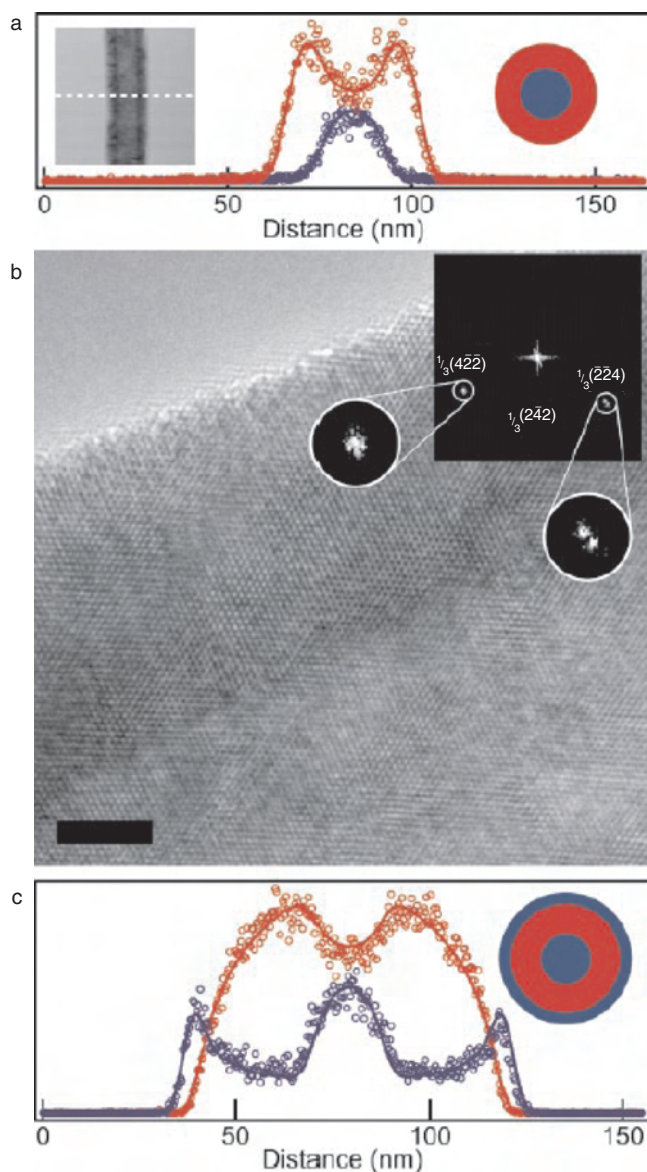


**Figure 8.** Si-Ge and Si-Ge-Si core-shell nanowires. (a) Cross-section elemental mapping indicating a 21-nm-diameter Si core (blue circles), 10-nm Ge core-shell (red circles), and  $<1\text{-nm}</math> interface. Inset, TEM image of the corresponding Si-Ge core-shell nanowire. (b) High-resolution TEM image of a representative crystalline nanowire core and shell from the same synthesis as the wire in (a). Scale bar is 5 nm. (c) Cross-section elemental mapping of a double-shell structure with an i-Si core (diameter, 20 nm), i-Ge shell (thickness 30 nm), and p-Si out-shell (4 nm). Si is blue circles and Ge is red circles. Reprinted with permission from [143], L. J. Lauhon et al., *Nature* 420, 57 (2002) © 2002, Macmillan Magazines Ltd.$

preferentially deposit CdS near the core since its lattice matches better to CdSe than ZnS does. This layer of CdS mediates the growth of the more highly strained ZnS. The shell growth is uniform and epitaxial, completely coating the CdSe core, although it may have defects present due to the lower growth temperature. After an irreversible photochemical annealing process, the core-shell nanorods have increased quantum efficiencies and are stable in air under visible or UV excitation [144].

#### 4. NANOWIRE SUPERLATTICES

Metallic nanoparticles have been demonstrated to play a key role for the synthesis of nanowires by a vapor-liquid-solid growth process [146, 147]. Moreover, a metallic nanoparticle could catalyze two different materials to grow nanowire heterojunctions, such as silicon/carbon nanotube nanowire heterojunctions [11]. Using the same tactic, several groups recently reported their work about the fabrication of semiconductor nanowires with segments of varying chemical- or dopant-composition superlattice nanowires. This greatly increases the versatility and power of these building blocks in the application of nanotechnology [12–14, 148–150]. All of this work focuses on semiconductors composed of modulated Group III-V [12, 14, 148], Group II-VI [149], and Group IV [13] elements. Gold nanoparticles have been used as catalysts in all this work.

In the synthesis of nanowire superlattices, a catalyst available to two or more different materials serves as the critical point for nucleation and directional growth of the nanowires. Meanwhile, the reactants are modulated during growth. Figure 9 is a schematic diagram of the process [14]. The nanoparticle catalyst (yellow) nucleates and directs the nanowire (blue) growth with the catalyst remaining at the terminus of the nanowire (Fig. 9a). To create a single junction within the nanowire, the addition of the first reactant is stopped during growth, and then a second reactant is introduced for the remainder of the synthesis (Fig. 9b). Repeated modulation of the reactants during growth produces nanowire superlattices (Fig. 9c).

Nanowire superlattices of gallium arsenide (GaAs)/gallium phosphide (GaP) were reported by Gudiksen et al. [14]. GaAs/GaP nanowire superlattices are an attractive system to explore for nanophotonic applications because GaAs is a direct-bandgap semiconductor, while GaP has an indirect gap. The GaAs/GaP nanowire superlattices were grown by laser-assisted catalytic growth using GaAs and GaP targets. Au nanoparticles were used as a catalyst to direct the growth. Solid targets of GaAs and GaP were ablated using either a pulsed ArF excimer or Nd:YAG lasers and growth was carried out at 700–850 °C in an argon flow. The number

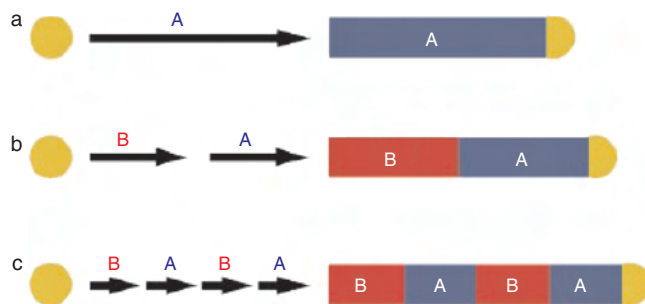


**Figure 9.** Synthesis of nanowire superlattices. (a) Nanocluster catalyst (gold) nucleates and directs one-dimensional semiconductor nanowire (blue) growth with the catalyst remaining at the terminus of the nanowires. (b) Upon completion of the first growth step, a different material (red) can be grown from the end of the nanowire. (c) Repetition of steps a and b leads to a compositional superlattice within a single nanowire. Reprinted with permission from [14], M. S. Gudiksen et al., *Nature* 415, 617 (2002). © 2002, Macmillan Magazines Ltd.

of periods and repeat spacing of the compositionally modulated nanowire superlattices can be readily varied during growth. High-resolution TEM images show that GaAs/GaP junction regions exhibit a crystalline nanowire core without obvious defects and can be abrupt. Photoluminescence, electrical transport, and electroluminescence measurements of single nanowire superlattices suggest potential applications ranging from nano-barcodes to polarized nanoscale LEDs [14].

Bjork et al. reported the growth of InAs/InP nanowire superlattices in an ultrahigh vacuum chamber designed for chemical beam epitaxy (CBE) [12, 148]. The rapid switching between InAs and InP is obtained via a sequence where growth is interrupted as the indium source (TMIn) is switched off, followed by a change of As or P source. Finally, the supersaturation conditions, as a prerequisite for reinitiation of growth, are reestablished as the indium source is again injected into the growth chamber. Significantly, their lattice-resolved TEM images show that the interfaces are atomically abrupt (Fig. 10). The periods of the modulated nanowire structures range from 100 to just several nanometers. Electrical measurements of thermionic emission across an 80-nm-wide INP heterobarrier, positioned inside InAs whiskers 40 nm in diameter, yield a barrier height of 0.6 eV.

Wu et al. reported a hybrid pulsed laser ablation/chemical vapor deposition process for the synthesis of Si/SiGe<sub>x</sub> nanowire superlattices [13]. Ge vapor is generated in pulsed ablation of a pure Ge target. A gas mixture of H<sub>2</sub> and SiCl<sub>4</sub> is continuously introduced into the reaction tube. Si precursors continuously deposit onto Au to induce the Si nanowire growth. During this growth process, if the laser is turned on, Ge vapor is generated and will react with Si precursors to grow SiGe<sub>x</sub>. By periodically turning the laser on and off, Si/SiGe<sub>x</sub> nanowire superlattices form. Solanki et al. focused on the growth of ZnSe/CdSe nanowire superlattices using an atomic layer deposition (ALD) technique [149]. ALD is a monolayer stepwise growth process that proceeds by exposing the substrate surface alternately to each precursor followed by an inert gas (N<sub>2</sub>) pulse to remove the excess species and by-products of the reaction [151]. The precursors for ZnSe and CdSe are elemental Zn, Se, and Cd.

Apart from the important contributions to materials science and nanostructure formation, these results could greatly increase the versatility and power of these building blocks in nanoscale electronic and photonic applications [150]. Potential applications include nano-barcodes, quantum cryptography and computing, “engineered” one-dimensional electron waveguides [14], heterostructures integrated in scanning probe- or field-emission, 1D-0D-1D resonant tunneling devices, one-dimensional superlattice arrays of intercoupled quantum dots [12, 148], nanoscale circuits, thermoelectrics [13], and light-emitting devices [13, 14, 149].

## 5. NANOJUNCTIONS

Nanoscale devices have great potential to replace traditional silicon-based devices because they can yield higher integration density, although many technical challenges exist.

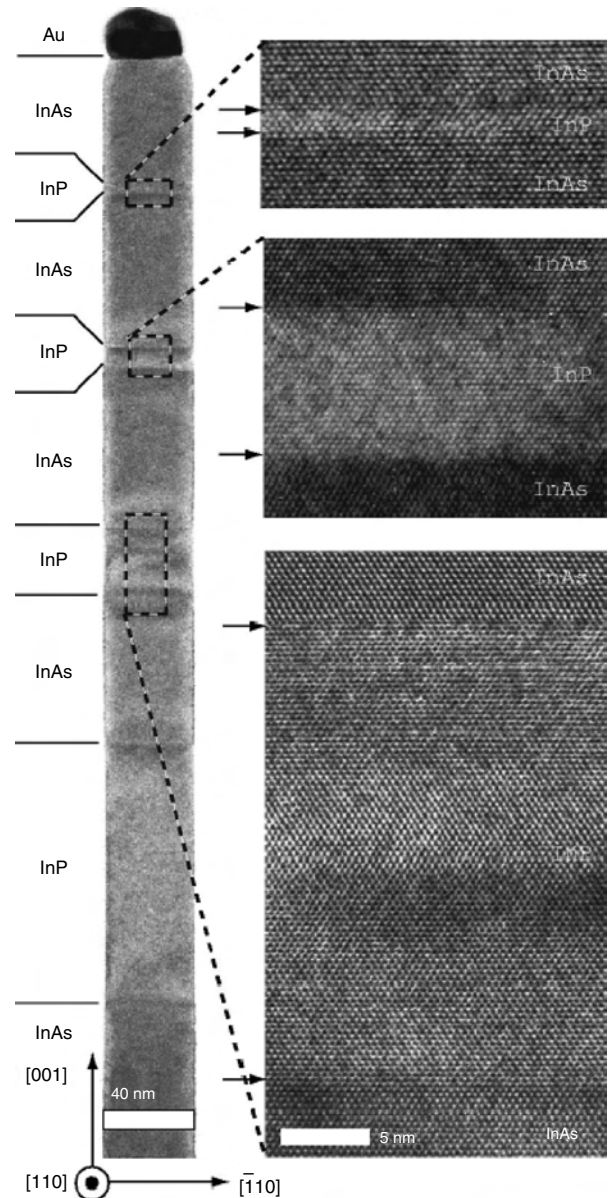


**Figure 10.** TEM image of an InAs whisker, 40 nm in diameter, containing four sequential InP barriers. The strain fields around each interface can be seen as elliptical, darker areas, having an extension of about 20 nm. In the thickest barrier the crystal is therefore completely relaxed. The magnified views prove that abruptness of the interfaces on the atomic scale is obtained. Reprinted with permission from [12], M. T. Bjork et al., *Appl. Phys. Lett.* 80, 1058 (2002). © 2002, American Institute of Physics.

Semiconductor-metal, semiconductor-semiconductor junctions are important building blocks which can be used for rectifiers, light-emitting diodes, and photodetectors. Recently, one-dimensional nanojunctions with different materials have been fabricated.

### 5.1. Silicon-Carbon Nanotube Junctions

Si nanowire-carbon nanotube junction was fabricated in Lieber's group [11] by two approaches as shown in Figure 11. The first approach is growth of silicon nanowires

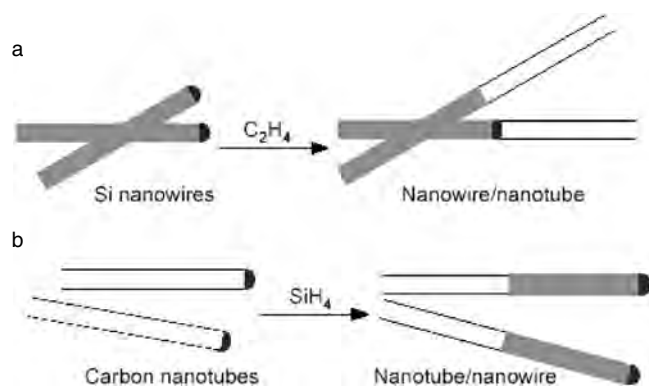


**Figure 11.** Synthetic approaches to nanotube-silicon nanowires junctions. (a) Growth of Si nanowires, afterwards growth of nanotube from the same catalytic particles. (b) Growth of nanotube and attachment of Au nanoparticles, then growing nanowires. Reprinted with permission from [11], J. T. Hu et al., *Nature* 399, 48 (1999). © 1999, Macmillan Magazines Ltd.

from iron nanoparticles. Afterwards, nanotubes were grown from the same particles by chemical vapor deposition method. The second approach: catalyst nanoparticles are deposited on nanotube ends and then used to direct the growth of Si nanowires. The key point for the first approach is that both growth processes share the same catalyst particle. The interface between nanowire and nanotube for the first approach might not be clean, while the second approach yields clean interface, considering that base growth model can be applied to carbon nanotube growth and that tip growth model can be applied to silicon nanowire growth. For base growth, the catalyst particles responsible for nucleation and growth remain pinned on the support surface, while tip growth involves a metal catalyst nanoparticle at a nanowire or nanotube end that is carried away as the nanowire or nanotube grows which is responsible for supply feedstock for the growth.

It is established that Fe and Fe/Au are efficient catalysts for the growth of silicon nanowires [3]. Meanwhile, it is found that Fe is a good catalyst for the growth of carbon nanotubes. Lieber's group used a laser to ablate a  $Fe_{0.9}Au_{0.1}$  target in 20-torr 10%/90% silane/He at 450 °C. After silicon nanowire growth, the nanotubes were grown from the same catalyst particles in 300-torr ethylene at 600 °C. A transmission electron microscope (TEM) image in Figure 12a shows that a silicon nanowire and multiwalled carbon nanotube junction were obtained. There is a common catalyst particle at the junction. Electron diffraction on silicon nanowires shows that the silicon nanowire maintains its crystalline structure after tube growth.

Lieber's group also used the second approach to fabricate nanojunctions. Gold cluster was deposited on the end of nanotubes by electrodeposition. Silicon nanowire was then grown from the attached gold cluster by using silane mixed with He for 15 min at 510 °C. A scanning electron microscope image of as-grown junction is shown in Figure 12b. The Au nanoparticle is sitting at the end of silicon nanowire. A clean interface was achieved.

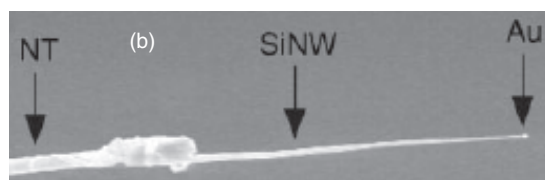
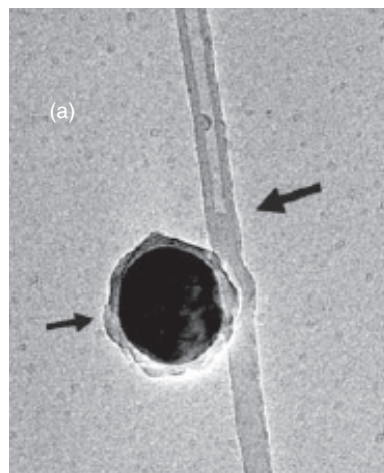


**Figure 12.** (a) TEM image of a nanotube-nanowire junction grown by approach a. The junction area was highlighted by a larger arrow. The small arrow indicates a metal catalyst particle. (b) SEM image of the nanotube/Si nanowire junction grown from a nanotube tip. Reprinted with permission from [11], J. T. Hu et al., *Nature* 399, 48 (1999). © 1999, Macmillan Magazines Ltd.

## 5.2. SiC-Carbon Nanotube and TiC-Carbon Nanotube Junctions

Zhang et al. [8] found an easy and simple approach to fabricate single-walled carbon nanotube-carbide junctions based on solid-solid reaction at a high temperature from 800 °C to 1000 °C. This method as shown in Figure 13 is based on a direct solid-solid reaction: C (carbon nanotube) + M (solid) = MC (solid), where M could be either silicon or a transition metal. The carbide initially forms at the C/M interface once a sufficient temperature is reached for the reaction to occur [152]. They found that the self-diffusion rate through bulk SiC or transition-metal carbide is extremely slow in the temperature range of 800 °C to 1000 °C, which guarantees a clean nanoscale interface between SiC and carbon nanotube.

In the experiments, the Si, Ti, and Nb substrates were thinned with perforations by means of conventional transmission electron microscopy sample preparation techniques.

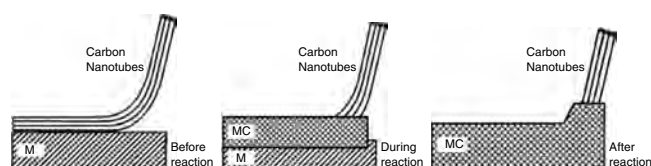


**Figure 13.** A schematic description of the method for fabricating nanotube/carbide heterostructures by a solid-solid reaction. Reprinted with permission from [8], Y. Zhang et al., *Science* 285, 1719 (1999). © 1999, American Association for the Advancement of Science.



Then single-walled carbon nanotubes were deposited on the substrates. The prepared substrates were heated in the ultrahigh-vacuum TEM column or in a side chamber either by an infrared heating lamp or by electrical current heating the substrate. They found that  $\beta$ -phase SiC was formed at the junction between silicon and single-walled carbon nanotube bundles according to high-resolution TEM as shown Figure 14. NaCl-structured TiC was obtained between Ti substrate and carbon nanotubes (Fig. 15). Improvement of the contact conductance between carbon nanotubes and Ti electrodes was demonstrated through the formation of TiC junctions (Fig. 15). This method has been used by other researchers to make ohmic contact between Ti electrode and semiconducting nanotubes by annealing devices above 700 °C in fabrication of nanotube transistors [153].

It was also found that carbon nanotube can react with Ti scanning tunneling microscope tip with solid-solid reaction after the nanotube was attached to the tip by using a nanomanipulator [8]. This kind of probe is supposed to be more robust than nanotube attached by glue or chemical vapor deposition growth [154, 155].

### 5.3. Boron Carbonitride-Carbon Nanotube Junction

Guo et al. [156] found a method to fabricate boron carbonitride nanojunctions by bias-assisted hot-filament chemical vapor deposition with a pause-reactivation two-stage process. They fabricated BCN nanotubes on polycrystalline nickel substrate by bias-assisted hot-filament chemical vapor deposition. A mixture of high-purity  $N_2$ ,  $H_2$ ,  $CH_4$ , and  $B_2H_6$  is utilized as the precursors. The composition of the BCN nanotubes is controlled simply by varying the flow rate of  $B_2H_6$ . This method results in a sharp interface structure and composition. A similar approach was used to synthesize  $CN_x$ /carbon nanotube junctions by using microwave chemical vapor deposition of  $N_2/CH_4$  and  $H_2/CH_4$  [157].

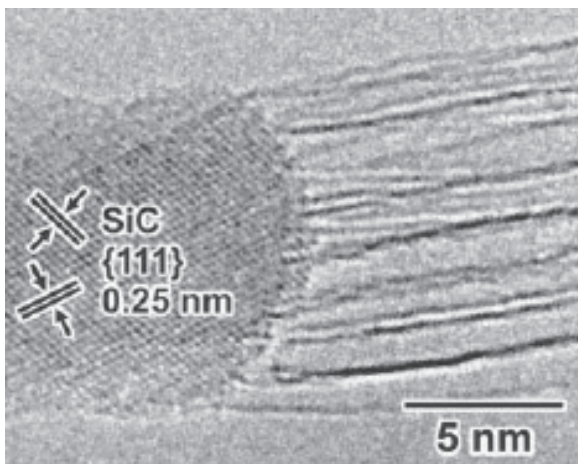


**Figure 14.** A TEM image showing a nanojunction between SiC nanorod and SWNT bundle. A clean interface was observed. Reprinted with permission from [8], Y. Zhang et al., *Science* 285, 1719 (1999). © 1999, American Association for the Advancement of Science.

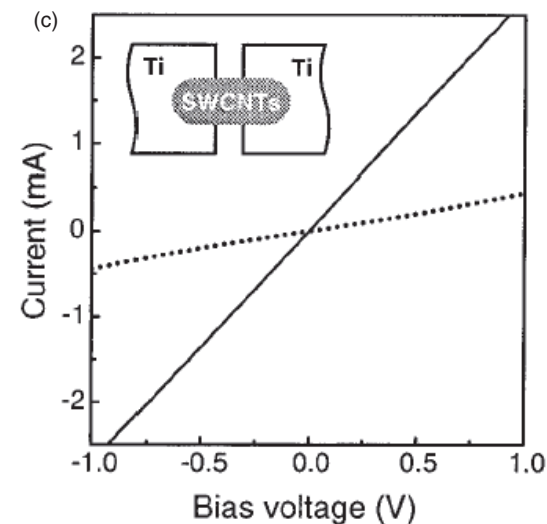
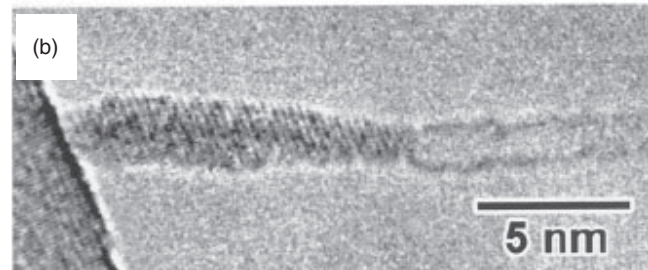
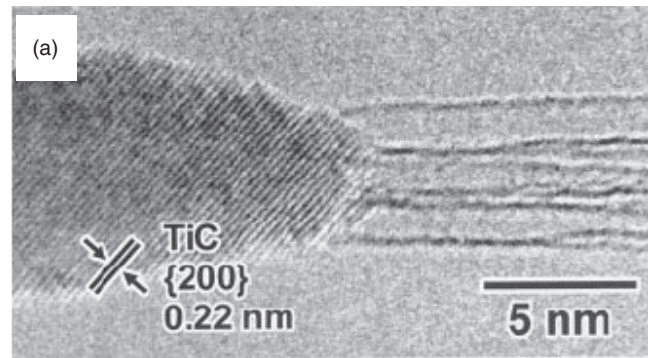


**Figure 15.** TEM images showing nanojunctions between TiC nanorod and SWNT bundle (a) and a single SWNT (b). (c) shows the  $I$ - $V$  curves of SWNTs crossing two Ti pads before (dotted line) and after (solid line) vacuum annealing. The improvement of the conductivity is attributed to the formation of Ti-TiC-SWNT junctions. Reprinted with permission from [8], Y. Zhang et al., *Science* 285, 1719 (1999). © 1999, American Association for the Advancement of Science.

### 5.4. Nanotube-Nanotube Junction

Nanotubes with different diameters can form junctions. Because bandgap of a nanotube is related with its diameter, semiconductor-semiconductor and semiconductor-metal junction can be formed between nanotubes. It can be defined as physical heterojunction.

Li et al. [158] used nanostructured alumina template channels to grow individual Y-junction carbon nanotube heterostructures by the pyrolysis of acetylene with cobalt catalysis. Multiwalled carbon nanotube Y-junctions were obtained

as shown in Figure 16. Ho et al. [159] applied high electric fields on multiwalled carbon nanotube arrays to create nanotube junctions. The high electric field as well as thermal effects result in carbon-carbon bond breaking and redeposition leading to nanojunction formation.

Satishkumar and colleagues [160] used a simple pyrolysis method to prepare multiwalled carbon nanotube Y-junctions. Organometallic precursor of nickelocene, together with thiophane, was decomposed at 1273 K. Two-temperature zone furnace was used for the synthesis; nickelocene was placed at the first zone with temperature of 623 K and thiophane was placed at the second zone with temperature of 1273 K. Argon and hydrogen are used as carrier gases. Y-junction structure was verified with HRTEM.

X- and Y-junctions of single-walled carbon nanotubes were fabricated by electron beam exposure at high temperatures [161]. The experiments were carried out in a high-voltage TEM with accelerating voltage of 1.25 MV. Carbon nanotubes were heated to 800 °C by using a Gatan heating stage in the TEM chamber. It was noted that high temperature is necessary to induce the formation of junctions because electron irradiation at room temperature would rapidly lead to heavy radiation damage of the tubes. The ready-formed X-junctions can be manipulated in order to create Y- and T-like molecular connections by using careful conditions of irradiation of electron beam. Single-walled carbon nanotube Y-junctions were also synthesized by chemical vapor deposition of methane and hydrogen on  $\text{Si}_3\text{N}_4$  membrane at 950 °C [162].

Chiu et al. [163] used a chemical approach to fabricate nanotube junctions. The single-walled carbon nanotubes were sonicated in  $\text{HNO}_3$  for 20 min to produce shortened and open-ended nanotubes, meanwhile to create defects on side walls. During the treatment, oxygen-containing groups are attached to opened ends of tube and side wall of tubes. Subsequently Chiu et al. converted these oxygen-containing groups to corresponding acid chloride by reacting with  $\text{SOCl}_2$  at room temperature for 24 hr. Then the solution was decanted and the deposit was rinsed with toluene followed by immersion in tripropyltetramine.

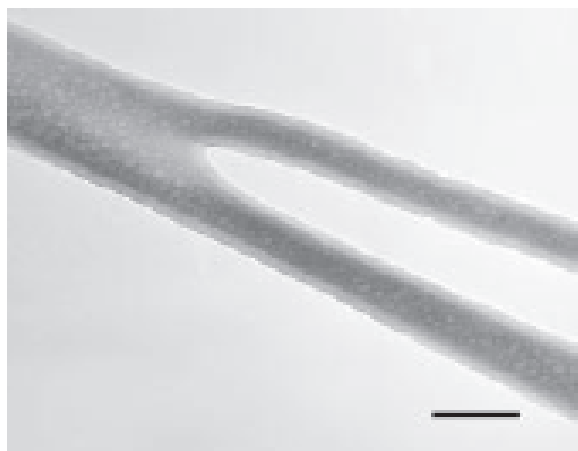


**Figure 16.** A TEM image of Y-junction nanotube with 50 nm scale bar. Reprinted with permission from [158], J. Li et al., *Nature* 402, 253 (1999). © 1999, Macmillan Magazines Ltd.

It was supposed that the bifunctionalized amine interconnects two nanotubes via formation of acidic amide bonding. Figure 17 shows the schematic representative junction structure. They found a lot of junctions with atomic force microscope after the chemical modifications.

Single-walled carbon nanotube p-n junctions were fabricated by Zhou et al. [164] by using modulated chemical doping method. A 340-nm-thick polymethylmethacrylate layer covers a half of the nanotube, leaving the other half exposed which was doped by potassium doping in vacuum by electrical heating of a potassium source. As-grown semiconducting tubes are p-type [165, 166]. After doping with potassium, the other half of tube becomes n-type; thus p-n junction formed within the same nanotube. One disadvantage of this method is that potassium-doped tube is unstable in air. Later the same group found a way to functionalize carbon nanotube with polyethyleneimine, which makes nanotube n-type and stable in air [167].

### 5.5. Nanojunction Fabrication Using Nanoporous Oxides as Templates

Besides nanotube Y-junction [158], different nanojunctions were fabricated by using nanoporous alumina as template.  $\text{Al}/\text{Al}_2\text{O}_3/\text{Ni}$  nanowire and  $\text{Al}/\text{Al}_2\text{O}_3/\text{carbon}$  nanotube arrays were prepared by using nanoporous  $\text{Al}_2\text{O}_3$  as templates [168–171]. A nanoporous alumina film prepared by electrochemical etching of an Al thin film has an array of nanosized diameter pores located like honeycomb. The nanopores have a straight-line shape perpendicular to Al substrate with a single tunnel barrier attached to each bottom. Ni nanowires were electrochemically deposited within the pores. Alternatively, multiwalled carbon nanotubes were grown within the pores with chemical vapor deposition of  $\text{C}_2\text{H}_2$  using a thin layer of Ni as catalyst. Coulomb blockade associated with weak localization in an array of single nano-tunnel junction/multiwalled carbon nanotubes was observed. Magnetoresistance jump in Ni-nanowire array was also found. The nanoporous templates can be extensively used to fabricate other nanowire junctions, such as silicon and germanium nanowire junctions.

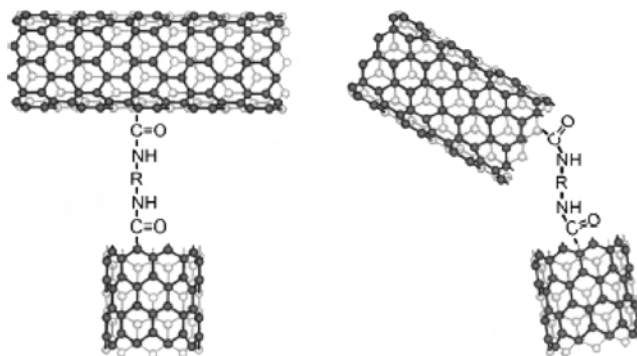


**Figure 17.** Schematic representation of nanotube junctions, where  $\text{R} = (\text{CH}_2)_3\text{NH}(\text{CH}_2)_3\text{NH}(\text{CH}_2)_3$ . Reprinted with permission from [163], P. W. Chiu et al., *Appl. Phys. Lett.* 80, 3811 (2002). © 2002, American Institute of Physics.

## 5.6. Nanojunction Fabrication by Scanning Probe Microscope

Due to their ultra-sharpness of scanning probe, scanning probe microscopes have been used to fabricate nanoscale p-n junction in silicon [172], and submicron bipolar transistors in CuInSe<sub>2</sub> [173, 174]. It was found that application of local, strong electric fields, at ambient temperatures, to originally electrically homogeneous crystals of doped Si and CuInSe<sub>2</sub> semiconductors induces nonequilibrium doping profiles in them. Conductive atomic force tips are used to induce a strong electric field between tip and semiconductor surface. Davidsson et al. [175] exposed thin resist layer with electrons by using atomic force microscope. Fifty nanometer long, 6-nm-thick Al lines were fabricated which can be used to define small tunnel junctions.

It is worth noting that another type of nanojunctions can be made by simply laying one nanowire or nanotube across another. Nanotube-V<sub>2</sub>O<sub>5</sub> nanofiber junction is an example [176]. Nanowire cross-junctions can be routinely obtained by microfluidic alignment method [177, 178]. However, in order to achieve high density and reliable nanojunction arrays, tremendous technical breakthroughs are necessary.

## 5.7. Electrical Properties of Nanojunctions

Use of nanojunctions for rectifiers, light-emitting diodes, and negative differential conductance have been demonstrated recently by different groups.

### 5.7.1. Negative Differential Conductance of Carbon Nanotube p-n Junctions

Negative differential conductance (NDC), discovered by Esaki in degenerately doped p-n junctions, has wide applications for high-frequency amplifiers and oscillators. Zhou et al. [164] observed negative differential conductance in single-walled carbon nanotube p-n junctions.

The method to prepare the p-n junction was introduced in Section 4.4. Device scheme with the SWNT contacted by two Ni/Au electrodes is shown in Figure 18a. A band diagram for the system is shown in Figure 18b by assuming that the tube is highly doped, therefore a p<sup>+</sup>/n<sup>+</sup> junction was formed. Zhou et al. controlled the doping level by changing gate voltage. By setting gate voltage at -9.5 V, NDC was observed at low temperatures as shown in Figure 19. Figure 19A shows negative differential conductance in an

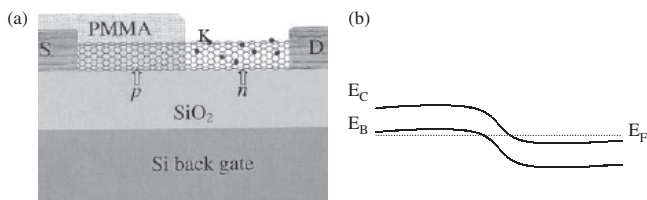


**Figure 18.** (a) Device scheme with the SWNT contacted by two Ni/Au electrodes. The tube was partially doped with potassium. (b) A band diagram for p<sup>+</sup>/n<sup>+</sup> junction, E<sub>c</sub>, E<sub>v</sub>, E<sub>f</sub> represent the conduction, valence band, and Fermi level, respectively. Reprinted with permission from [164], C. W. Zhou et al., *Science* 290, 1552 (2000). © 2000, American Association for the Advancement of Science.

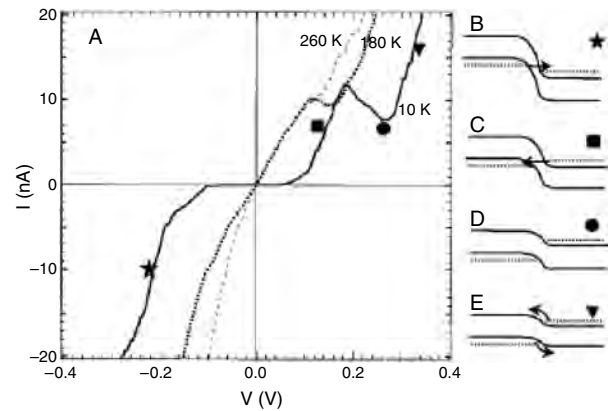


**Figure 19.** (A) Current versus bias voltage with -9.5 V gating. (B through E) Band diagrams show the transport mechanisms. The symbols in B to E match the ones in A with certain bias voltages. Reprinted with permission from [164], C. W. Zhou et al., *Science* 290, 1552 (2000). © 2000, American Association for the Advancement of Science.

intra-SWNT Esaki diode. Band diagrams of Figure 19B to E are shown at different bias voltage regions. NDC due to resonant tunneling was observed. At room temperature NDC is not obvious.

### 5.7.2. Nanojunction Rectifiers

The first nanowire-junction rectifier was demonstrated by Hu et al. [11]. Nanotube-silicon nanowire junction was synthesized by chemical vapor deposition and electrically connected to a Pt-Ir tip with silver paste at the nanotube end and to Ga-In liquid metal at the silicon nanowire end. *I-V* curves were measured with scanning tunneling microscope electronics.

The current-voltage measurements on NT/SiNW junctions with only the SiNW in contact with the Ga-In liquid exhibit reproducible rectifying behavior as shown in Figure 20. By doing several control experiments, Hu et al. concluded that the rectifying behavior is due to the metal-semiconductor Schottky barrier between NT and SiNW.

Electronic transport was also performed with Y-junction carbon nanotubes [179]. In order to make the measurement,

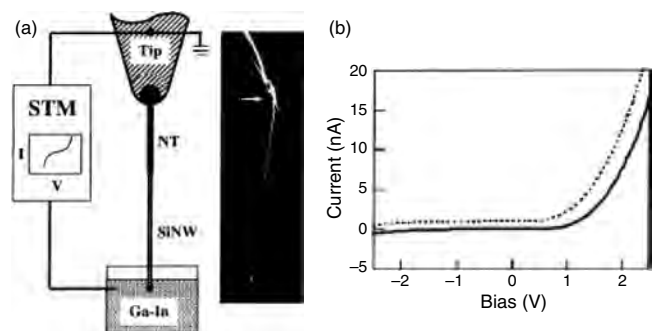


**Figure 20.** (a) Diagram of electrical measurement setup; a SEM image of NT/SiNW is shown. (b) *I-V* curve of two independent junctions. Reprinted with permission from [11], J. T. Hu et al., *Nature* 399, 48 (1999). © 1999, Macmillan Magazines Ltd.



individual Y-junctions were chemically removed from their growth template [158] and deposited on patterned electrodes. Electrical field enhanced diffusion of gold was applied to yield an ohmic contact between nanotube and electrodes.  $I$ - $V$  data display distinct asymmetric and rectifying behavior with current flowing more easily under negative bias. Li et al. modeled the Y-junction nanotube as a p-p isotype semiconductor heterojunction with different bandgaps using standard heterostructure semiconductor physics and explained the observed results. Rectifying behavior was also observed by Chiu et al. [163] using chemical functionalized nanotube junctions, by Kim et al. [176] using  $V_2O_5$  nanofiber-carbon nanotube junction, and by Zhou et al. [164] using carbon nanotube p-n junctions.

### 5.7.3. Nanojunction Light-Emitting Devices

In 1994, Katsuyama et al. [180] fabricated GaAs p-n nanowire junction based on reduced-pressure metal-organic vapor-phase epitaxy. Intense light emission was observed during carrier injection to the p-n junction formed in the GaAs whisker. The emitted light showed strong polarization anisotropy, which was explained by the quantum confinement effect. Recently, Gudiksen et al. [14] reported a method to synthesize p-n junctions. In order to create a single junction within a nanowire, the addition of the first reactant is stopped during growth, and then a second reactant is introduced for the remainder of the synthesis. Nanojunction with different elements or different major carrier types was obtained.

Using this method, InP nanowire p-n junction was fabricated. Besides this nanojunction showing rectifier behavior, light emitted from the p-n junction was observed as shown in Figure 21. The polarization direction is found to be along that of the nanowire. The light emission was found blue-shifted due to the one-dimensional structure and radial quantum confinement. The efficiency of their intranowire LEDs is around 0.1%, which can be improved by optimizing the devices. Recently, electrically driven lasing from single n-type CdS nanowire was achieved by Duan and his colleagues [181]. More exciting demonstrations on application of nanowire junctions can be expected and are appearing.

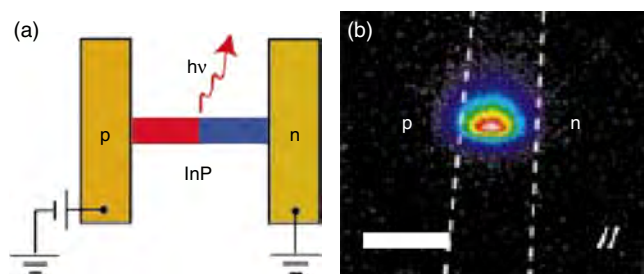


**Figure 21.** (a) Schematic of an InP nanowire LED. (b) Polarized emission from the LED along the nanowire growth direction. Dashed lines indicate the edge of the electrodes. Scale bar is 3  $\mu$ m. Reprinted with permission from [14], M. S. Gudiksen et al., *Nature* 415, 617 (2002). © 2002, Macmillan Magazines Ltd.

## GLOSSARY

**Carbon nanotube** A tubular structure made by rolling up graphite sheets into seamless cylinders with diameters on nanometer scale. Carbon is the only element in a carbon nanotube.

**Composite nanotube** A multiwalled nanotube composed of shells of more than one kind of chemical composition.

**Composite nanowire** A nanowire composed of two or more different materials or phases homogeneously distributed along its whole length.

**Compound nanotube** A nanotube composed of a single chemical compound. Almost all noncarbon nanotubes (inorganic nanotubes) are compound nanotubes.

**Nanocable** A composite nanowire (nanotube) that has a core nanowire (nanotube) sheathed by one or more layers of different materials or phases. Some nanocables resemble the structure of a coaxial cable.

**Nanojunction** An area formed by end-to-end connection of two types of nanowires (nanotubes), or one nanowire and one nanotube. Because of the small cross section of nanotubes and nanowires, the junctions formed from them are in nanometer scale.

**Nanowire** A wire with a thickness in nanometer scale.

**Nanowire superlattice** A nanowire composed of alternating semiconductor nanowire segments of different chemical compositions.

## REFERENCES

1. S. Iijima, *Nature* 354, 56 (1991).
2. S. Iijima and T. Ichihashi, *Nature* 363, 603 (1993).
3. A. M. Morales and C. M. Lieber, *Science* 279, 208 (1998).
4. M. S. Dresselhaus, G. Dresselhaus, and P. C. Eklund, "Science of Fullerenes and Carbon Nanotubes." Academic Press, San Diego, 1996.
5. P. Lambin and V. Meunier, "AIP Conference Proceedings," 1998.
6. Z. Yao, H. W. C. Postma, L. Balents, and C. Dekker, *Nature* 402, 273 (1999).
7. A. A. Odintsov, *Phys. Rev. Lett.* 85, 150 (2000).
8. Y. Zhang, T. Ichihashi, E. Landree, F. Nihey, and S. Iijima, *Science* 285, 1719 (1999).
9. R. Martel, H. P. Wong, K. Chan, and P. Avouris, "Proceedings IEDM," 2001, p. 159.
10. Y. Zhang, K. Suenaga, C. Colliex, and S. Iijima, *Science* 281, 973 (1998).
11. J. T. Hu, O. Y. Min, P. D. Yang, and C. M. Lieber, *Nature* 399, 48 (1999).
12. M. T. Bjork, B. J. Ohlsson, T. Sass, A. I. Persson, C. Thelander, M. H. Magnusson, K. Deppert, L. R. Wallenberg, and L. Samuelsson, *Appl. Phys. Lett.* 80, 1058 (2002).
13. Y. Y. Wu, R. Fan, and P. D. Yang, *Nano Lett.* 2, 83 (2002).
14. M. S. Gudiksen, L. J. Lauhon, J. Wang, D. C. Smith, and C. M. Lieber, *Nature* 415, 617 (2002).
15. R. Tenne, L. Margulis, M. Genut, and G. Hodes, *Nature* 360, 444 (1992).
16. Y. Feldman, E. Wasserman, D. J. Srolovitz, and R. Tenne, *Science* 267, 222 (1995).
17. N. G. Chopra, R. J. Luyken, K. Cherrey, V. H. Crespi, M. L. Cohen, S. G. Louie, and A. Zettl, *Science* 269, 966 (1995).
18. A. Loiseau, F. Willaime, N. Demoncey, G. Hug, and H. Pascard, *Phys. Rev. Lett.* 76, 4737 (1996).



19. M. Terrones, W. K. Hsu, H. Terrones, J. P. Zhang, S. Ramos, J. P. Hare, R. Castillo, K. Prassides, A. K. Cheetham, H. W. Kroto, and D. R. M. Walton, *Chem. Phys. Lett.* 259, 568 (1996).
20. D. Golberg, Y. Bando, M. Eremets, K. Takemura, K. Kurashima, and H. Yusa, *Appl. Phys. Lett.* 69, 2045 (1996).
21. A. Rubio, J. L. Corkill, and M. L. Cohen, *Phys. Rev. B* 49, 5081 (1994).
22. Y. Miyamoto, A. Rubio, M. L. Cohen, and S. G. Louie, *Phys. Rev. B* 50, 4976 (1994).
23. K. Suenaga, C. Colliex, N. Demoncy, A. Loiseau, H. Pascard, and F. Willaime, *Science* 278, 633 (1997).
24. Y. Zhang, H. Gu, K. Suenaga, and S. Iijima, *Chem. Phys. Lett.* 279, 264 (1997).
25. O. Stephan, P. M. Ajayan, C. Colliex, P. Redlich, J. M. Lambert, P. Bemier, and P. Lefin, *Science* 266, 1683 (1994).
26. Z. Weng-Sieh, K. Cherrey, N. G. Chopra, X. Blase, Y. Miyamoto, A. Rubio, M. L. Cohen, S. G. Louie, A. Zettl, and R. Gronsky, *Phys. Rev. B* 51, 11229 (1995).
27. P. Redlich, J. Loeffler, P. M. Ajayan, J. Bill, F. Aldinger, and M. Ruhle, *Chem. Phys. Lett.* 260, 465 (1996).
28. Y. K. Kwon, Y. H. Lee, S. G. Kim, P. Jund, D. Tomanek, and R. E. Smalley, *Phys. Rev. Lett.* 79, 2065 (1997).
29. M. Zhang, Y. Bando, and K. Wada, *J. Mater. Res.* 16, 1408 (2001).
30. Y. Q. Zhu, W. K. Hsu, H. W. Kroto, and D. R. M. Walton, *J. Phys. Chem. B* 106, 7623 (2002).
31. P. M. Ajayan and S. Iijima, *Nature* 361, 333 (1993).
32. S. C. Tsang, Y. K. Chen, P. J. F. Harris, and M. L. H. Green, *Nature* 372, 159 (1994).
33. P. M. Ajayan, T. W. Ebbesen, T. Ichihashi, S. Iijima, K. Tanigaki, and H. Hiura, *Nature* 362, 522 (1993).
34. S. C. Tsang, P. J. F. Harris, and M. L. H. Green, *Nature* 362, 520 (1993).
35. H. Hiura, T. W. Ebbesen, and K. Tanigaki, *Adv. Mater.* 7, 275 (1995).
36. P. M. Ajayan, O. Stephan, P. Redlich, and C. Colliex, *Nature* 375, 564 (1995).
37. E. Dujardin, T. W. Ebbesen, H. Hiura, and K. Tanigaki, *Science* 265, 1850 (1994).
38. S. Subramoney, R. S. Ruoff, D. C. Lorents, B. Chan, R. Malhotra, M. J. Dyer, and K. Parvin, *Carbon* 32, 507 (1994).
39. J. Sloan, J. Cook, M. L. H. Green, J. L. Hutchison, and R. Tenne, *J. Mater. Chem.* 7, 1089 (1997).
40. Y. K. Chen, M. L. H. Green, and S. C. Tsang, *Chem. Commun.* 2489 (1996).
41. D. Ugarte, A. Chatelain, and W. A. deHeer, *Science* 274, 1897 (1996).
42. Y. K. Chen, A. Chu, J. Cook, M. L. H. Green, P. J. F. Harris, R. Heesom, M. Humphries, J. Sloan, S. C. Tsang, and J. F. C. Turner, *J. Mater. Chem.* 7, 545 (1997).
43. J. Sloan, J. Cook, J. R. Heesom, M. L. H. Green, and J. L. Hutchison, *J. Cryst. Growth* 173, 81 (1997).
44. D. Ugarte, T. Stockli, J. M. Bonard, A. Chatelain, and W. A. de Heer, *Appl. Phys. A* 67, 101 (1998).
45. M. Terrones, N. Grobert, W. K. Hsu, Y. Q. Zhu, W. B. Hu, H. Terrones, J. P. Hare, H. W. Kroto, and D. R. M. Walton, *MRS Bull.* 24, 43 (1999).
46. J. Bao, Q. Zhou, J. Hong, and Z. Xu, *Appl. Phys. Lett.* 81, 4592 (2002).
47. J. Sloan, D. M. Wright, H. G. Woo, S. Bailey, G. Brown, A. P. E. York, K. S. Coleman, J. L. Hutchison, and M. L. H. Green, *Chem. Commun.* 699 (1999).
48. J. Sloan, M. C. Novotny, S. R. Bailey, G. Brown, C. Xu, V. C. Williams, S. Friedrichs, E. Flahaut, R. L. Callender, A. P. E. York, K. S. Coleman, M. L. H. Green, R. E. DuninBorkowski, and J. L. Hutchison, *Chem. Phys. Lett.* 329, 61 (2000).
49. R. R. Meyer, J. Sloan, R. E. DuninBorkowski, A. I. Kirkland, M. C. Novotny, S. R. Bailey, J. L. Hutchison, and M. L. H. Green, *Science* 289, 1324 (2000).
50. S. Friedrichs, J. Sloan, M. L. H. Green, J. L. Hutchison, R. R. Meyer, and A. I. Kirkland, *Phys. Rev. B* 64, 045406 (2001).
51. J. Sloan, M. Terrones, S. Nufer, S. Friedrichs, S. R. Bailey, H. G. Woo, M. Ruhle, J. L. Hutchison, and M. L. H. Green, *J. Am. Chem. Soc.* 124, 2116 (2002).
52. S. Seraphin, *J. Electrochem. Soc.* 142, 290 (1995).
53. J. Sloan, J. Hammer, M. ZwiefkaSibley, and M. L. H. Green, *Chem. Commun.* 347 (1998).
54. C. H. Kiang, J. S. Choi, T. T. Tran, and A. D. Bacher, *J. Phys. Chem. B* 103, 7449 (1999).
55. C. G. Xu, J. Sloan, G. Brown, S. Bailey, V. C. Williams, S. Friedrichs, K. S. Coleman, E. Flahaut, J. L. Hutchison, R. E. DuninBorkowski, and M. L. H. Green, *Chem. Commun.* 2427 (2000).
56. C. H. Kiang, *Carbon* 38, 1699 (2000).
57. Z. L. Zhang, B. Li, Z. J. Shi, Z. N. Gu, Z. Q. Xue, and L. M. Peng, *J. Mater. Res.* 15, 2658 (2000).
58. S. Friedrichs, R. R. Meyer, J. Sloan, A. I. Kirkland, J. L. Hutchison, and M. L. H. Green, *Chem. Commun.* 929 (2001).
59. J. Mittal, M. Monthieux, H. Allouche, and O. Stephan, *Chem. Phys. Lett.* 339, 311 (2001).
60. J. Sloan, S. Friedrichs, R. R. Meyer, A. I. Kirkland, J. L. Hutchison, and M. L. H. Green, *Inorg. Chim. Acta* 330, 1 (2002).
61. J. Sloan, A. I. Kirkland, J. Hutchison, and M. H. Green, *Acc. Chem. Res.* 35, 1054 (2002).
62. D. Danailov, P. Keblinski, S. Nayak, and P. Ajayan, *J. Nanosci. Nanotechnol.* 2, 503 (2002).
63. G.-H. Jeong, R. Hatakeyama, T. Hirata, K. Tohji, K. Motomiya, T. Yaguchi, and Y. Kawazoe, *Chem. Commun.* 152 (2003).
64. H. J. Barraza, F. Pompeo, E. A. O'Rear, and D. E. Resasco, *Nano Lett.* 2, 797 (2002).
65. B. W. Smith, M. Monthieux, and D. E. Luzzi, *Nature* 396, 323 (1998).
66. B. W. Smith, M. Monthieux, and D. E. Luzzi, *Chem. Phys. Lett.* 315, 31 (1999).
67. B. W. Smith and D. E. Luzzi, *Chem. Phys. Lett.* 321, 169 (2000).
68. D. E. Luzzi and B. W. Smith, *Carbon* 38, 1751 (2000).
69. J. Sloan, R. E. Dunin-Borkowski, J. L. Hutchison, K. S. Coleman, V. C. Williams, J. B. Claridge, A. P. E. York, X. Cigang, S. R. Bailey, G. Brown, S. Friedrichs, and M. L. H. Green, *Chem. Phys. Lett.* 316, 191 (2000).
70. K. Hirahara, K. Suenaga, S. Bandow, H. Kato, T. Okazaki, H. Shinohara, and S. Iijima, *Phys. Rev. Lett.* 85, 5384 (2000).
71. K. Suenaga, T. Tence, C. Mory, C. Colliex, H. Kato, T. Okazaki, H. Shinohara, K. Hirahara, S. Bandow, and S. Iijima, *Science* 290, 2280 (2000).
72. R. F. Service, *Science* 292, 45 (2001).
73. P. W. Chiu, G. Gu, G. T. Kim, G. Philipp, S. Roth, S. F. Yang, and S. Yang, *Appl. Phys. Lett.* 79, 3845 (2001).
74. D. J. Hornbaker, S. J. Kahng, S. Misra, B. W. Smith, A. T. Johnson, E. J. Mele, D. E. Luzzi, and A. Yazdani, *Science* 295, 828 (2002).
75. T. Shimada, T. Okazaki, R. Taniguchi, T. Sugai, H. Shinohara, K. Suenaga, Y. Ohno, S. Mizuno, S. Kishimoto, and T. Mizutani, *Appl. Phys. Lett.* 81, 4067 (2002).
76. S. Berber, Y. K. Kwon, and D. Tomanek, *Phys. Rev. Lett.* 88, 185502 (2002).
77. B. W. Smith, R. M. Russo, S. B. Chikkannanavar, and D. E. Luzzi, *J. Appl. Phys.* 91, 9333 (2002).
78. X. Liu, T. Pichler, A. Knupfer, M. S. Golden, J. Fink, H. Kataura, Y. Achiba, K. Hirahara, and S. Iijima, *Phys. Rev. B* 65, 045419 (2002).
79. M. Monthieux, *Carbon* 40, 1809 (2002).

80. Y. Maniwa, H. Kataura, M. Abe, A. Fujiwara, R. Fujiwara, H. Kira, H. Tou, S. Suzuki, Y. Achiba, E. Nishibori, M. Takata, M. Sakata, and H. Suematsu, *J. Phys. Soc. Jpn.* 72, 45 (2003).
81. Y. K. Kwon, D. Tomanek, and S. Iijima, *Phys. Rev. Lett.* 82, 1470 (1999).
82. J. Lee, H. Kim, S. J. Kahng, G. Kim, Y. W. Son, J. Ihm, H. Kato, Z. W. Wang, T. Okazaki, H. Shinohara, and Y. Kuk, *Nature* 415, 1005 (2002).
83. M. Shiraishi, T. Takenobu, A. Yamada, M. Ata, and H. Kataura, *Chem. Phys. Lett.* 358, 213 (2002).
84. P. M. Ajayan, C. Colliex, J. M. Lambert, P. Bernier, L. Barbedette, M. Tence, and O. Stephan, *Phys. Rev. Lett.* 72, 1722 (1994).
85. C. Guerret-Piecourt, Y. Le Bouar, A. Loiseau, and H. Pascard, *Nature* 372, 761 (1994).
86. M. Liu and J. M. Cowley, *Carbon* 33, 749 (1995).
87. A. Loiseau and H. Pascard, *Chem. Phys. Lett.* 256, 246 (1996).
88. W. Q. Han, P. Redlich, F. Ernst, and M. Ruhle, *Appl. Phys. Lett.* 76, 652 (2000).
89. A. Loiseau and F. Willaime, *Appl. Surf. Sci.* 164, 227 (2000).
90. Y. Murakami, T. Shibata, K. Okuyama, T. Arai, H. Suematsu, and Y. Yoshida, *J. Phys. Chem. Solids* 54, 1861 (1993).
91. Y. Yosida, *Appl. Phys. Lett.* 64, 3048 (1994).
92. Y. Saito, T. Masumoto, and K. Nishikubo, *Carbon* 35, 1757 (1997).
93. J. Y. Dai, J. M. Lauerhaas, A. A. Setlur, and R. P. H. Chang, *Chem. Phys. Lett.* 258, 547 (1996).
94. N. Demoncey, O. Stephan, N. Brun, C. Colliex, A. Loiseau, and H. Pascard, *Eur. Phys. J. B* 4, 147 (1998).
95. Y. L. Hsin, K. C. Hwang, F. R. Chen, and J. J. Kai, *Adv. Mater.* 13, 830 (2001).
96. W. K. Hsu, M. Terrones, J. P. Hare, H. Terrones, H. W. Kroto, and D. R. M. Walton, *Chem. Phys. Lett.* 262, 161 (1996).
97. W. K. Hsu, S. Trasobares, H. Terrones, M. Terrones, N. Grobert, Y. Q. Zhu, W. Z. Li, R. Escudero, J. P. Hare, H. W. Kroto, and D. R. M. Walton, *Chem. Mater.* 11, 1747 (1999).
98. M. Terrones, W. K. Hsu, A. Schilder, H. Terrones, N. Grobert, J. P. Hare, Y. Q. Zhu, M. Schwoerer, K. Prassides, H. W. Kroto, and D. R. M. Walton, *Appl. Phys. A* 66, 307 (1998).
99. F. Okuyama and I. Ogasawara, *Appl. Phys. Lett.* 71, 623 (1997).
100. W. S. Shi, H. Y. Peng, L. Xu, N. Wang, Y. H. Tang, and S. T. Lee, *Adv. Mater. Weinheim* 12, 1927 (2000).
101. Y. Gao, J. Liu, M. Shi, S. H. Elder, and J. W. Virden, *Appl. Phys. Lett.* 74, 3642 (1999).
102. C. H. Liang, G. W. Meng, L. D. Zhang, N. F. Shen, and X. Y. Zhang, *J. Cryst. Growth* 218, 136 (2000).
103. A. K. Sinha, D. W. Hwang, and L. P. Hwang, *Chem. Phys. Lett.* 332, 455 (2000).
104. C. N. R. Rao, R. Sen, B. C. Satishkumar, and A. Govindaraj, *Chem. Commun.* 1525 (1998).
105. K. Bladh, L. K. L. Falk, and F. Rohmund, *Appl. Phys. A* 70, 317 (2000).
106. M. Ata, A. J. Hudson, K. Yamaura, and K. Kurihara, *Japa. J. Appl. Phys. Part 1* 34, 4207 (1995).
107. Y. F. Zhang, Y. H. Tang, Y. Zhang, C. S. Lee, I. Bello, and S. T. Lee, *Chem. Phys. Lett.* 330, 48 (2000).
108. W. Han and A. Zettl, *Adv. Mater.* 14, 1560 (2002).
109. W. Q. Han, P. Redlich, F. Ernst, and M. Ruhle, *Appl. Phys. Lett.* 75, 1875 (1999).
110. W. Q. Han, Y. Bando, K. Kurashima, and T. Sato, *Appl. Phys. Lett.* 73, 3085 (1998).
111. H. Dai, E. W. Wong, Y. Z. Lu, F. Shoushan, and C. M. Lieber, *Nature* 375, 769 (1995).
112. W. Q. Han, S. S. Fan, Q. Q. Li, and Y. D. Hu, *Science* 277, 1287 (1997).
113. W. Q. Han, P. KohlerRedlich, F. Ernst, and M. Ruhle, *Chem. Mater.* 11, 3620 (1999).
114. W. Q. Han, P. KohlerRedlich, C. Scheu, F. Ernst, M. Ruhle, N. Grobert, M. Terrones, H. W. Kroto, and D. R. M. Walton, *Adv. Mater.* 12, 1356 (2000).
115. R. Z. Ma, Y. Bando, and T. Sato, *Chem. Phys. Lett.* 350, 1 (2001).
116. Y. Bando, K. Ogawa, and D. Golberg, *Chem. Phys. Lett.* 347, 349 (2001).
117. D. Golberg, Y. Bando, K. Kurashima, and T. Sato, *J. Nanosci. Nanotechnol.* 1, 49 (2001).
118. R. Z. Ma, Y. Bando, and T. Sato, *Adv. Mater.* 14, 366 (2002).
119. W. Han and A. Zettl, *Appl. Phys. Lett.* 81, 5051 (2002).
120. C. C. Tang, Y. Bando, T. Sato, and K. Kurashima, *J. Mater. Chem.* 12, 1910 (2002).
121. Z. Shen, L. He, E. Wu, Y. Fan, J. He, H. Cheng, D. Li, and H. Ye, *J. Mater. Res.* 17, 2761 (2002).
122. S. Okada, S. Saito, and A. Oshiyama, *Phys. Rev. B* 64, 201303 (2001).
123. A. Zettl, J. Cumings, W. Han, and W. Mickelson, *AIP Conf. Proc.* 591, 140 (2002).
124. S. Hofmann, C. Ducati, and J. Robertson, *Adv. Mater.* 14, 1821 (2002).
125. Y. F. Zhang, Y. H. Tang, N. Wang, C. S. Lee, I. Bello, and S. T. Lee, *J. Cryst. Growth* 197, 136 (1999).
126. G. W. Meng, L. D. Zhang, C. M. Mo, S. Y. Zhang, Y. Qin, S. P. Feng, and H. J. Li, *Solid State Commun.* 106, 215 (1998).
127. Y. J. Xing, Q. L. Hang, H. F. Yan, H. Y. Pan, J. Xu, D. P. Yu, Z. H. Xi, Z. Q. Xue, and S. Q. Feng, *Chem. Phys. Lett.* 345, 29 (2001).
128. H. F. Zhang, C. M. Wang, and L. S. Wang, *Nano Lett.* 2, 941 (2002).
129. Y. F. Zhang, Y. H. Tang, N. Wang, C. S. Lee, I. Bello, and S. T. Lee, *Phys. Rev. B* 61, 4518 (2000).
130. J. Zhu and S. Fan, *J. Mater. Res.* 14, 1175 (1999).
131. J. J. Wu, S. C. Liu, C. T. Wu, K. H. Chen, and L. C. Chen, *Appl. Phys. Lett.* 81, 1312 (2002).
132. X. C. Wu, W. H. Song, B. Zhao, W. D. Huang, M. H. Pu, Y. P. Sun, and J. J. Du, *Solid State Commun.* 115, 683 (2000).
133. K. Suenaga, Y. Zhang, and S. Iijima, *Appl. Phys. Lett.* 76, 1564 (2000).
134. J. Hu, X. Meng, Y. Jiang, C. Lee, and S. Lee, *Adv. Mater.* 15, 70 (2003).
135. Y. D. Yin, Y. Lu, Y. G. Sun, and Y. N. Xia, *Nano Lett.* 2, 427 (2002).
136. H. Kuang, Z. Deng, C. Li, X. Sun, J. Zhuang, and Y. Li, *Acta Phys. Chim. Sin.* 18, 477 (2002).
137. J. Hu, Q. Li, X. Meng, C. Lee, and S. Lee, *Chem. Mater.* 15, 305 (2003).
138. Y. Deng, J. Wu, J. Liu, G. Wei, and C. Nan, *J. Phys. Chem. Solids* 64, 607 (2003).
139. S. Dubois, C. Marchal, J. M. Beuken, L. Piraux, J. L. Duvail, A. Fert, J. M. George, and J. L. Maurice, *Appl. Phys. Lett.* 70, 396 (1997).
140. C. S. Ah, S. D. Hong, and D.-J. Jang, *J. Phys. Chem. B* 105, 7871 (2001).
141. X. G. Wen and S. H. Yang, *Nano Lett.* 2, 451 (2002).
142. Y. Xie, Z. Qiao, M. Chen, X. Liu, and Y. Qian, *Adv. Mater.* 11, 1512 (1999).
143. L. J. Lauhon, M. S. Gudiksen, C. L. Wang, and C. M. Lieber, *Nature* 420, 57 (2002).
144. L. Manna, E. C. Scher, L. Li, and A. P. Alivisatos, *J. Am. Chem. Soc.* 124, 7136 (2002).
145. X. Peng, L. Manna, W. Yang, J. Wickham, E. Scher, A. Kadavanch, and A. P. Alivisatos, *Nature* 404, 59 (2000).
146. R. S. Wagner and W. C. Ellis, *Appl. Phys. Lett.* 4, 89 (1964).
147. X. Duan and C. M. Lieber, *Adv. Mater.* 12, 298 (2000).

148. M. T. Bjork, B. J. Ohlsson, T. Sass, A. I. Persson, C. Thelander, M. H. Magnusson, K. Deppert, L. R. Wallenberg, and L. Samuelson, *Nano Lett.* 2, 87 (2002).
149. R. Solanki, J. Huo, J. L. Freeouf, and B. Miner, *Appl. Phys. Lett.* 81, 3864 (2002).
150. C. M. Lieber, *Nano Lett.* 2, 81 (2002).
151. R. Engelmann, J. Ferguson, and R. Solanki, *Appl. Phys. Lett.* 70, 411 (1997).
152. J. Graul and E. Wagner, *Appl. Phys. Lett.* 21, 67 (1972).
153. R. Martel, V. Derycke, C. Lavoie, J. Appenzeller, K. K. Chan, J. Tersoff, and P. Avouris, *Phys. Rev. Lett.* 87, 6805 (2001).
154. H. J. Dai, J. H. Hafner, A. G. Rinzler, D. T. Colbert, and R. E. Smalley, *Nature* 384, 147 (1996).
155. E. Yenilmez, Q. Wang, R. J. Chen, D. W. Wang, and H. J. Dai, *Appl. Phys. Lett.* 80, 2225 (2002).
156. J. D. Guo, C. Y. Zhi, X. D. Bai, and E. G. Wang, *Appl. Phys. Lett.* 80, 124 (2002).
157. X. C. Ma and E. G. Wang, *Appl. Phys. Lett.* 78, 978 (2001).
158. J. Li, C. Papadopoulos, and J. Xu, *Nature* 402, 253 (1999).
159. G. W. Ho, A. T. S. Wee, and J. Lin, *Appl. Phys. Lett.* 79, 260 (2001).
160. B. C. Satishkumar, P. J. Thomas, A. Govindaraj, and C. N. R. Rao, *Appl. Phys. Lett.* 77, 2530 (2000).
161. M. Terrones, F. Banhart, N. Grobert, J. C. Charlier, H. Terrones, and P. M. Ajayan, *Phys. Rev. Lett.* 89, 5505 (2002).
162. G. Gu, G. Philipp, X. C. Wu, M. Burghard, A. M. Bittner, and S. Roth, *Adv. Funct. Mater.* 11, 295 (2001).
163. P. W. Chiu, G. S. Duesberg, U. Dettlaff-Weglikowska, and S. Roth, *Appl. Phys. Lett.* 80, 3811 (2002).
164. C. W. Zhou, J. Kong, E. Yenilmez, and H. J. Dai, *Science* 290, 1552 (2000).
165. S. Tans, A. Verschueren, and C. Dekker, *Nature* 393, 49 (1998).
166. R. Martel, T. Schmidt, H. R. Shea, T. Hertel, and P. Avouris, *Appl. Phys. Lett.* 73, 2447 (1998).
167. M. Shim, A. Javey, N. W. S. Kam, and H. J. Dai, *J. Am. Chem. Soc.* 123, 11512 (2001).
168. A. A. Tager, D. Routkevitch, J. Haruyama, D. Almawlawi, M. Moskovits, and J. M. Xu, in "Future Trends in Microelectronics" (S. Luryi, J. M. Xu, and A. Zaslavsky, Eds.), p. 171. NATO ASI, 1996.
169. D. Routkevitch, A. A. Tager, J. Haruyama, D. Almawlawi, M. Moskovits, and J. M. Xu, *IEEE Trans. Electron. Devices* 43, 1646 (1996).
170. J. Haruyama, D. N. Davydov, D. Routkevitch, D. Ellis, B. W. Statt, M. Moskovits, and J. M. Xu, *Solid-State Electron.* 42, 1257 (1998).
171. J. Haruyama, I. Takesue, S. Kato, K. Takazawa, and Y. Sato, *Appl. Surf. Sci.* 175, 597 (2001).
172. L. Chernyak and A. M. Klimov, *Appl. Phys. Lett.* 78, 1613 (2001).
173. S. Richter, D. Cahen, S. R. Cohen, K. Gartsman, V. Lyakhovitskaya, and Y. Manassen, *Appl. Phys. Lett.* 73, 1868 (1998).
174. S. Richter, Y. Manassen, and D. Cahen, *Phys. Rev. B* 59, 10877 (1999).
175. P. Davidsson, A. Lindell, T. Makela, M. Paalanen, and J. Pekola, *Microelectron. Eng.* 15, 1 (1999).
176. G. T. Kim, U. Waizmann, and S. Roth, *Appl. Phys. Lett.* 79, 3497 (2001).
177. Y. Huang, X. F. Duan, Q. Q. Wei, and C. M. Lieber, *Science* 291, 630 (2001).
178. B. Messer, J. H. Song, and P. D. Yang, *J. Am. Chem. Soc.* 122, 10232 (2000).
179. C. Papadopoulos, A. Rakitin, J. Li, A. S. Vedenev, and J. M. Xu, *Phys. Rev. Lett.* 85, 3476 (2000).
180. T. Katsuyama, K. Hiruma, K. Ogawa, K. Haraguchik, and M. Yazawa, *Jap. J. Appl. Phys. Part 2* 34, 224 (1994).
181. X. Duan, Y. Huang, R. Agarwal, and C. M. Lieber, *Nature* 421, 241 (2003).

# Nanocapsules

Zhi-dong Zhang

*Shenyang National Laboratory for Materials Science, and  
International Centre for Materials Physics, and Chinese Academy of Sciences,  
Shenyang, China*

## CONTENTS

1. Introduction
  2. Theoretical Background
  3. Synthetic Methods
  4. Spectroscopic Characterization
  5. Physical Properties
  6. Biomedical Properties
  7. Concluding Remarks
- Glossary  
References

## 1. INTRODUCTION

Everyone can understand the meaning of the word “capsules,” when one takes medicine that is in the form of capsules. We are familiar with capsules where the medicine is inside, with a shell outside, which is used for prolonging or improving the absorption of the medicine. Nanocapsules are capsules of nanometer size (i.e.,  $10^{-9}$  m), which are normally composed of a core and a shell that are made of different materials. One can understand nanocapsules, when one imagines the reduction of hen eggs to nanometer scale. The shell has a number of names depending on the research field or industry, which can be referred to as a membrane, a wall, a covering, or a coating. The internal core material also goes by a number of terms such as payload, core, encapsulant, fill, active ingredient, internal phase (IP), or internal ingredient. For the purposes of this chapter we will refer to the terms shell and core.

The word “nanocapsules,” or “nanoencapsulations,” started to appear in the literature in the middle of 1970s, most of which was related to the topics of controlled release of drugs [1–5] and new drug carriers [6–13]. The word “nanocapsules” (or “nanoencapsulations”) emerged in the literature for carbon encapsulating materials at the beginning of 1990s [14–22], after the discovery of fullerenes

[23, 24]. Indeed, the discovery of  $C_{60}$  and successful preparation of the material in macroscopic quantities initiated extensive investigations of fullerenes [23, 24], carbon nanotubes [25, 26], carbon-coated nanocapsules [14–22], and a wide range of carbon-based materials [27, 28]. Recently, there has been extensive and increasing interest in the field of nanocapsules as well as nanoencapsulation.

Actually, nanoencapsulation is a more precise derivative of a well-developed process, called “microencapsulation,” which encloses very small-sized core materials, either solids or liquids, in the coating materials. This technique has played a significant role in a variety of industries for many years. These include medical, pharmaceutical, cosmetic, food, agricultural, plastic, paper, photographic printing, paint, adhesive, and computer industries. During nano/microencapsulation, very thin coatings of inert natural or synthetic (polymeric or others) materials are deposited around nano/microsized particles of solids or droplets of liquids. Products thus formed are known as nano/microcapsules, depending on their size scales. The unique feature of nanocapsules is the diminutive size of the coated particles. The particle size usually ranges from several nanometers to 1 micrometer. The coated particles between 1 and 1000 nanometers in diameter are referred to as the nanocapsules.

Various types of physical structure of the product of nanoencapsulation, such as mononuclear spheres, multinuclear spheres, and multinuclear irregular particles, can be obtained depending on the manufacturing process. The most common structure formed is the mononuclear sphere. The spherical surface is the smallest surface among all other shapes for the condensing/nanoencapsulation process, which is usually with a minimum free energy. Thus it is the common surface for most nanocapsules. However, other shapes are still possible, since the symmetry of the crystals could become dominant in a certain case.

The most applicable nanoencapsulation procedures include: physical techniques such as arc discharge, heat evaporation, laser/electron beam heating, sputtering, etc.; chemical techniques such as chemical vapor deposition, solid-state reactions, sol-gel, precipitation, hydrothermal

process, solvent process, latex process, oxidation process, polymerization, etc.; physicochemical techniques such as coacervation-phase separation, etc.; mechanical techniques such as air suspension, pan coating, spray-drying and congealing, and multiorifice centrifugation.

It is understandable that nanocapsules can possess the same (or similar) physical properties as those of nanoparticles. The activities in the field of the nanocapsules/nanoparticles could date back to the pioneering work of Japanese scientists Kubo [29], in theory, and Uyeda et al. [30–35], in experiments. Kubo [29] predicted in his theory that the thermal behavior at low temperatures of metal particles could be evidently different than that of bulk materials, because the average energy gap  $\delta$  close to the Fermi energy could be much larger than the thermal energy  $k_B T$  (where  $k_B$  is the Boltzmann constant and  $T$  is temperature) because of the discontinuity of the energy levels in the limited systems. Using a transmission electronic microscope (TEM), Uyeda et al. investigated systematically the crystallographic structures of various metal and nonmetal ultrafine particles (or nanoparticles) prepared by evaporation and condensation technology [30–53]. Because of their high surface activity, almost all nanoparticles possess the core/shell structure with a shell of oxides and thus belong to the nanocapsule category [30–53]. The exception is nanoparticles (like pure oxides, carbon) without the core/shell structure.

Nanocapsules are matters in intermediate states between bulk and atomic materials which offer an opportunity to investigate the dimensionally confined systems in basic research areas. Various abnormal phenomena, such as magic effects, quantum size effects, surface effects, hyperfine structure etc., in the nanocapsules, alter the physical behavior of the materials. The optical absorption, thermal resistance, melting points, and magnetic properties of the nanocapsules could be quite different than the bulk counterparts. Nanoscale magnetic capsules are expected to have potential applications in various areas such as magnetic recording, magnetic fluids, superconduction, and medicine. The study of the preparation, structure, and physical properties of the nanocapsules has become very important in the field of nanoscience and nanotechnology [54]. Furthermore, as the word “nanocapsules” originated from medicine, the medical and biomedical field is the most active one studying nanocapsules, driven by the motivation of discovering new drug carriers [1–13].

In this chapter, we give a comprehensive review of the advances in the area of the nanocapsules. We outline the theoretical background on this topic in Section 2, which describes energy levels, quantum effects, magic effects, surfaces/interfaces, and metastable phases in nanocapsules. In Section 3, we represent the most applicable nanoencapsulation procedures including physical, chemical, physicochemical, and mechanical techniques. In Section 4, we show the physical properties, including optical, electronic, magnetic, and dynamic properties, of nanocapsules. In Section 5, we concentrate on the biomedical properties, including artificial cell and red blood cell substitutes, drug delivery and controlled release, etc. of nanocapsules. Section 6 is for concluding remarks.

## 2. THEORETICAL BACKGROUND

### 2.1. Introduction

Nanocapsules have physical properties that differ from those of bulk materials. One of the main origins of such differences is the discreteness of the energy levels in the limited systems. According to the energy band theory, the energy levels of a bulk metal are in general continuum (or so-called quasi-continuum) because the number of electrons in the bulk is infinite. For limited systems, like clusters, nanoparticles, and nanocapsules, the limited number of electrons leads directly to the discreteness of the energy levels. When the energy gap is larger than the thermal, magnetostatic, electrostatic, photon, or condensation energy of the superconductivity, the quantum size effect would result correspondingly in different (thermal, magnetic, electronic, photon, or superconducting) behavior of the limited systems. In bulk materials, the cyclic condition and the translation symmetry in three dimensions lead to the plane wave character of electrons. When the size of limited systems is comparable to or even less than the optical wavelength, the de Broglie wavelength, the free path length of electrons, or the coherence length of the Cooper pair, the cyclic condition and the translation symmetry would be broken down, which also affects the physical properties of the systems. The quantum interference of electrons in the confined states could become more pronounced in the nanocapsule systems. The magic number effect is a character observed in the small systems, like clusters, nanoparticles, and nanocapsules. The lack of symmetry of the atoms located at the surfaces/interfaces affects the chemical and physical properties of nanocapsules. The typical core/shell structure could also contribute to the behavior of nanocapsules. Furthermore, the metastable phases could exist in nanocapsules, which could result in different properties of nanocapsules. In this section, we introduce several concepts and topics, such energy levels, quantum effects, magic effects, surfaces/interfaces, and metastable phases, which are particular for the nanoparticles/nanocapsules. Understanding these topics and their differences from those of bulk materials is extremely important for studying the properties of nanocapsules.

### 2.2. Energy Levels

The prediction of discontinuous energy levels was a breakthrough in the area of limited systems. The limited number of electrons results in different characters of electrons in the systems with a limited size. Two basic assumptions of Kubo’s theory are [29, 55–57]: (1) the Poisson distribution of the energy levels close the Fermi surface is held, while the Fermi statistics is invalid in the nanoparticles; (2) the electronic neutral is valid, because it is extremely difficult to take (or put) one electron out from (or in) a nanoparticle because it is necessary to overcome the extremely large Coulomb energy. Considering the effects of the discreteness of the energy levels on the physical properties of metal particles, Kubo and co-workers [29, 55–57] proposed a famous relation,

$$\delta = \frac{4E_F}{3N} \propto V^{-1} \quad (1)$$

for the gap between the nearest neighboring energy levels, where  $E_F$  is Fermi energy,  $N$  is the number of the conduction electrons in the particles, and  $V$  is the volume of the particles. If the particles were in the shape of balls, from Eq. (1), one would have a relation of  $\delta \propto d^{-3}$ . Therefore, the energy gap increases rapidly with decreasing particle size. Because the average energy gap  $\delta$  close to the Fermi energy could be much larger than the thermal energy  $k_B T$  at low temperatures, the discreteness of the energy levels would affect obviously the thermodynamic properties of the materials, and thus the specific heat; the susceptibility of the particles would differ evidently from those of bulk materials. It was found that the specific heat and the susceptibility of the particles depend on the parity (i.e., odd–even) of the number of the electrons in the systems. It is evident that this kind of the quantum size effect becomes much more pronounced only if the following condition is satisfied: the gap of the discreteness of the energy levels is larger than the thermal energy  $k_B T$ , the magnetostatic energy, the magnetoelectric energy, the photon energy, etc. It was estimated that the temperature for a metallic particle of 10 nm showing the quantum size effect is about 2 K; that for a particle of 2 nm could be room temperature. Several groups tried to modify Kubo's theory in order to detect the effects of different distributions of the energy levels and to reach a better agreement between the theoretical and experimental results [58–62]. For details of this topic, readers are referred to the review article by Halperin [63].

### 2.3. Quantum Effects

It is well known that besides the quantum size effect, other quantum effects could be very pronounced in limited systems, like thin films, chains, and particles, when at least one of the dimensions of the systems could be negligible compared to others. When the size of the nanoparticles as well as nanocapsules is reduced to be less than a certain critical value, the systems could be treated as zero (or quasi-zero) dimensional ones. In these cases, the quantum effects become dominant, which originate not only from the discreteness of the energy levels but also from the quantum interference as well as the quantum tunneling in the systems. The cyclic condition and the translation symmetry are lost, when the size of the systems is comparable to the optical wavelength, the de Broglie wavelength, the free path length of electrons, or the coherence length of a Cooper pair. Actually, the breaking down of the translation symmetry leads the wavevector of electrons to not be a “good” quantum number. In the limit case of large nanocapsules, one could treat the wavevector as a “pseudo-good” quantum number and deal with the problem approximately using bulk theory and perturbation theory. In the limiting case of small nanocapsules, such a concept and the corresponding approximation are not valid anymore [64]. The limited systems could be treated as quantum wells, in which the electrons feel the energy/potential difference between different materials when they move. The energy of electrons moving in a quantum well is quantized according to quantum mechanics. If the electrons move in two or more quantum wells separated by spacers, the quantum well interference

between the wells may be either neglected when the thickness of the spacers is thick enough or very pronounced when the wells are close enough. It is easy to find the solution of the quantization of the quantum well states in a single quantum well in any textbook on quantum mechanics [65–67]. Recently, the quantum interference in double quantum wells was studied systematically within the framework of the effective mass model [68]. It has been found that several types of quantum effects (e.g., macroscopic quantum tunnel effects, Coulomb blockade, and quantum tunnelling [69]) occur in the nanoparticles.

### 2.4. Magic Effects

The main feature of magic effects is the existence of magic numbers in elements, clusters, and nanoparticles. For elements, it was found that the protons and the neutrons each form particularly stable systems in an atomic nucleus when the number of either kind of nucleon is one of the so-called magic numbers 2, 8, 20, 50, 82, and 126, which relate to the stability of nuclei and the shell structure of atoms. Nuclei with these magic numbers of protons or neutrons exhibit certain properties which are analogous to closed shell properties in atoms, including anomalously low masses, high natural abundances, and high energy first excited states [70].

Analogically, the magic number has been observed in the systems of clusters and nanoparticles, with regard to their stability. It has been observed that the clusters of some size are much more abundant than others. These clusters containing certain a special number of atoms seem to be much more stable compared to others. These numbers are also referred to as magic numbers. It is understood that factors such as bonding energy, configuration, symmetry, geometry, surface, etc. could affect the magic effects, with respect to the minimum of the total free energy of the clusters or the nanoparticles. Only the more stable clusters/nanoparticles are found to be abundant. Thus, the magic numbers indicate the stability of certain clusters/nanoparticles [71, 72].

The magic numbers seen for rare-gas clusters like argon, krypton, and neon are well understood [71–73]. These magic numbers correspond to nicely close-packed structures that can be formed by packing spheres. The special stability of rare-gas clusters is due to the geometric close-packing of atoms in the clusters. Because spheres can be packed snugly together in certain configurations, one would expect the atoms of inert gases, such as helium, to cluster together in similar tightly packed groups. The numbers of spheres or atoms in these geometrically and energetically favored clusters are termed “magic.” One would expect, for example, the number 13 to be magic because this would be the number of spheres fitting tightly into a 20-sided solid. When clusters of helium atoms are “weighed” with a mass spectrometer, the number 13 is strongly favored; so are 19, 25, 55, 71, 87, and 147. Some of these experimentally derived magic numbers can be predicted theoretically, but some theoretical magic numbers did not turn out to be magic in reality, notably 7, 33, and 43 [74].

The clusters of various metals show the magic numbers which are very different from those of rare gases. The clusters of alkali metals, like lithium, sodium, potassium, and



other metals like aluminum, are stable when the total number of free electrons in the cluster is 8, 20, 34, 40, 58, ... [75, 76]. Notice that what is important here is the total number of free electrons, not the number of atoms in a cluster. This can be understood with the help of the so-called jellium model, in which one assumes that the outer electrons of the metal atoms are loosely bound so that when a cluster is formed, they can move around everywhere in the clusters and are not bound to a particular atom [75, 76]. The atoms without their outer electrons are positively charged ions. So the free electrons "see" a jellium of positive ions in the cluster and move around in the positive jellium. If one tries to theoretically solve the problem of free electrons in a positive jellium, one indeed observes that the clusters are energetically most stable when the total number of electrons in them is 8, 20, 34, 40, 58, etc. Another example of the magic effect is related to the members of the fullerene family, among which  $C_{36}$ ,  $C_{60}$ ,  $C_{72}$ , etc. are much more abundant than others fullerenes [23, 24]. Evidently, the magic effects become less pronounced when the size of the clusters or the particles becomes larger enough. A similar effect was found to be at work on surfaces, where vapor atoms can stick in clusters of specific sizes [77, 78].

## 2.5. Surfaces/Interfaces

The surface phenomenon is one of the most common ones in nature. Everyone can see in daily life the direct consequence of surface effects: water droplets automatically tend to be in the shape of balls. Surface effects originate basically from the surface energy, which is mainly ascribed to the crystallographic asymmetry of the surface atoms bearing the noncompensated forces from other atoms. Surface effects become much more important when one system is of nanocapsule/nanoparticle size [79]. The smaller the size of the particles, the higher the surface energy because of the larger specific surface area. The specific surface area is defined as the surface area  $A$  per the unit volume  $V$  of matter,

$$A_s = \frac{A}{V} \propto d^{-1} \quad (2)$$

where  $d$  is the diameter of a particle. When the diameter of the particle decreases, the specific surface area and the number of surface atoms increase evidently. For instance, when  $d = 10$  nm, 20% of the total  $3 \times 10^4$  atoms are located on the surface; when  $d = 4$  nm, 40% of the total  $4 \times 10^3$  atoms are the surface atoms. The large number of surface atoms, the high surface energy, and the lack of atomic coordination number lead to the high chemical activity of the surface atoms. Because the surface atoms possess less stabilized chemical bonds with neighboring atoms, they are very unstable and thus can combine easily with other atoms. The tendency to be stabilized results in the high chemical activity of the surfaces of the nanoparticles. It is very common for the metal nanoparticles spontaneously to burn in air. It is also a fact that the atoms at the surface of the inorganic particles could easily absorb the atoms/molecules, like gases, water, etc., in air. However, after the formation, the shells of some nanocapsules could prevent the particles from further oxidation.

The interfaces in the nanocapsules could be distinguished as: (1) the interface between different crystal grains of one phase, (2) the interface between different crystal grains of different phases, (3) the interface between the shell and the core, etc. For the small nanocapsules, it is possible that only a single phase exists in the core and the interface of the second type does not exist. In the limited case, the interface of the first type may not exist in the very small nanocapsules. In nanoparticles without the core/shell structure, the interface of the third type cannot be observed. However, in some cases, all interfaces of the three types may be observed in a nanocapsule with a large enough size.

The surfaces/interfaces play important roles in the physical properties of the nanocapsules, because the environments of the atoms at the surface/interface are totally different than those of the atoms inside the grains [80–83]. The physical behaviors of the atoms located inside the grains could be very close to those of atoms in bulk materials. The properties of the atoms at the surfaces/interfaces could differ from those of bulk materials, which are partially due to the lack of structural symmetry of these atoms, similar to what happens in thin films [80–83].

## 2.6. Metastable Phases

It is well known that the saturation evaporation pressure  $P'$  of a small liquid droplet with a radius  $r$  is larger than  $P$  of a liquid surface with an infinite radius, which is described by the famous Kelvin equation [79]

$$\ln \frac{P'}{P} = \frac{2\sigma M}{\rho R T r} \quad (3)$$

where  $\sigma$  is the surface tension,  $M$  is the molecular weight,  $\rho$  is the density of the liquid, and  $R$  is the Avogadro constant. A similar conclusion could be derived for the crystals. Namely, the saturation evaporation pressure of a small crystallite is larger than that of a bulk crystal. The saturation evaporation pressure affects the melting point and the solubility of the crystals. The smaller the crystallite, the lower the melting point and the higher the solubility. In saturated liquid, small crystallites can be spontaneously dissolved or melted, while large ones can spontaneously grow. On the contrary, it is easy to understand that the process of solidification or crystallization can be more difficult for the smaller crystallites. It is difficult to form a new phase out of a phase, which results in different kinds of supersaturation phenomena, like the supersaturation of a gas or a solution, the superheating or the supercooling of a liquid or a solid, etc. From the thermodynamic point of view, all types of supersaturated systems are in the nonequilibrium state. The matter formed during such procedures should be in the nonequilibrium state. Of course, the phases could remain in such a state for a long period, which could be defined as metastable. A metastable phase is a phase that does not exist in equilibrium conditions. It is not the thermodynamically most stable phase but rather a temporarily stable one in a certain condition. The metastable phase forms under conditions corresponding to a local minimum of the free energy. The large energy barrier between this local energy minimum and the lowest energy minimum hinders the formation of

the equilibrium phase in the sense of the dynamics. Nanoparticles as well as nanocapsules usually form in nonequilibrium conditions and consequently the phases formed can be metastable. It was found that in rare-earth transition-metal systems, the formation and phase transformation of rare-earth metastable phases depend sensitively on the structural symmetry of the metastable phases [84]. It is understandable that the structural symmetry of the metastable phases would be one of the most important factors that govern the formation and the phase transformation of the metastable phases in nanocapsules/nanoparticles.

### 3. SYNTHETIC METHODS

#### 3.1. Introduction

Nanocapsules are nanoparticles with a core/shell structure. Nanocapsules consist of two major parts. The inner part is the core material comprised of one or more active ingredients, which may be solids, liquids, or gases. The outer part is the coating material that is usually a high molecular weight polymer (or a combination of such polymers), carbon, or oxide. The polymer can be chosen from a wide variety of natural and synthetic polymers. Normally, the coating material must be nonreactive to the core material, preferably biodegradable, and nontoxic if used for medicine. Other components, such as plasticizers and surfactants, may also be added to the nanocapsules.

Nanocapsules can be prepared by various methods with different mechanisms, including physical, chemical, physicochemical, and mechanical ones. The structural, physical, and biomedical properties of nanocapsules depend sensitively on the processes used for sample preparation. For instance, the preparation procedure could control the size of the nanocapsules, the size distribution of the particles, the thickness of the shell, the size of the grains, the morphology of the nanocapsules, etc. Different nanocapsules may need to be synthesized by different types of preparation techniques. Some methods may be suitable for synthesis of only some typical nanocapsules.

In this section, we describe the most applicable nanocapsulation procedures, including physical methods such as heat evaporation, arc discharge, laser/electron beam heating, sputtering, etc.; chemical methods such as chemical vapor deposition, solid-state reactions, sol-gel, precipitation, hydrothermal process, solvent process, latex process, oxidation process, polymerization, etc.; physicochemical methods such as coacervation-phase separation, etc.; mechanical methods such as air suspension, pan coating, spray-drying and congealing, and multiorifice centrifugation. In this section, we concentrate mainly on the preparation procedures and leave the detailed description of the physical and biomedical properties to next two sections.

#### 3.2. Physical Methods

The physical methods for synthesizing the nanocapsules could be separated into two categories: breaking down and building up. The breaking-down process means to mill mechanically the bulk materials to be particles. In general, the breaking-down process could be employed to produce

particles of about 1  $\mu\text{m}$  in size and it is difficult to prepare nanoparticles and nanocapsules with sizes below 100 nm. We shall not discuss this type of the process in detail. The building-up process synthesizes nanoparticles and nanocapsules through the nucleation and growth processes of the elementary particles, like ions and atoms. The building-up process is one of the most effective processes for the formation of nanoparticles as well as nanocapsules, which satisfies the conditions requested for the preparing nanoparticles: (1) clean surfaces; (2) controllable sizes and narrow size distribution; (3) easy collections; (4) stability of the particles; (5) high efficiency for production; etc. The basic principles for the building-up process are at first heating metals in gas atmospheres of several hundred to thousands of Pa and then condensing. Depending on the heating procedures, the build-up process could be of several different kinds, such as evaporation, arc discharge/plasma, laser heating, electron beam heating, sputtering, etc. Depending on the gas atmospheres, the final production could be different kinds of nanoparticles/nanocapsules.

##### 3.2.1. Evaporation

Evaporation in gases is a method that evaporates metals, alloys, or ceramics so that the atoms bump each other and also atoms of inert gases, or they react with active gases. Condensation in the cold gases results in the formation of nanoparticles (or ultrafine particles as defined in some literature many years ago) and nanocapsules. Heating by a resistance heater or a high frequency induction furnace is the simplest method in laboratories for evaporating the metals [29–41]. The resistance heater can be made of graphite, tungsten wire, or other kinds of metal wires. In the earliest experiments, metals were put in a tungsten basket inside a vacuum chamber and then evaporated in argon atmosphere of 1–50 Torr [30]. The metal smoke deposited on the water-cooled inner wall of the chamber. Figure 1 shows iron and copper smoke [35]. The nanoparticles were collected by a TEM mesh grid for observation by a TEM. The crystallographic properties of various nanoparticles, such as Mg, Al, Cr, Mn, Fe, Co, Ni, Cu, Zn, Ag, Cd, Sn, Au, Pb, and Bi, were investigated systematically by TEM observations. It is a common fact that for all metals, the size of the particles is reduced with decreasing atmospheric pressure [30–35]. It is interesting to note that usually a shell of oxidations (commonly in amorphous) of several nanometers forms on the surface of the nanoparticles. The different metal nanoparticles have different crystallographic structures. For instance, Al, Bi, Sn, and Pb particles are balls, Mg particles are hexagons, and Cr particles are body-centered cubic (bcc) structures. Magnetic particles, like Fe and Co, can align as a necklace or a chain [30–35] due to the existence of stable magnetic moments and magnetostatic forces. Dipolar interaction plays an important role on such alignment of magnetic nanoparticles, which may become dominant compared to the van der Waals attraction and steric repulsion that usually lead to a close-packed arrangement [85, 86]. The magnetic domains in the particles were observed by means of Lorentz electron microscopy [87–90].

The character (i.e., the shapes and colors) of the metal smokes was found to depend on the gas pressure/density

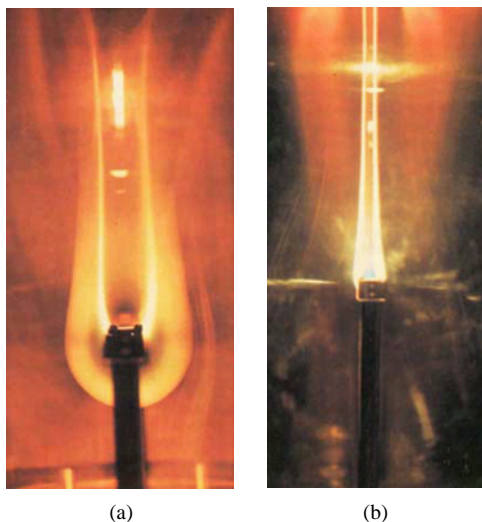


**Figure 1.** Iron and copper smokes. The smoke looks white for all metals and no color is observed. A beautiful color, however, characteristic of each metal, is seen in the neighborhood of the heater. (a) shows iron smoke in 50 Torr of helium, which has a typical candle-flame shape with inner, intermediate, and outer zones. The bright intermediate zone implies that the smoke is denser there than in the dark inner zone. In the case of iron, red light is emitted from the neighborhood of the heater. (b) shows copper smoke in 30 Torr of argon, which is thinner, because 30 Torr of argon is denser than 50 Torr of helium. The blue color is seen near the evaporation source. Adapted with permission from [35], R. Uyeda, in “Morphology of Crystals” (I. Sunagawa, Ed.), Ch. 6, p. 367. Terra Scientific, Tokyo, 1987. © 1987, Terra Scientific.

and the temperature/velocity of evaporation [35, 39, 42, 43]. The shape of the metal smoke can be candle-fire-, ring-, tulip-, and butterfly-like. The color of the smoke can be purple (for Al, Ag), green (for Au), red (for Be, Co, Fe, Ni), blue (for Cu, Nb, W), orange (for Ti), green plus orange (for Cr, Fe), yellow plus green (for Mo), etc. [35, 43, 46, 49, 50]. Granqvist and Buhrman obtained nanoparticles with an average size of about 10 nm by evaporating Al, Mg, Zn, Sn, Cr, Fe, Co, Ni, and Ca in argon atmosphere of 0.5–4 Torr by applying a facility with a graphite heater [91–96]. Increasing one of several factors (velocity of evaporation, temperature of the evaporating materials, evaporating pressure of the materials, press of inert gases) would increase the size of the nanoparticles/nanocapsules. Evaporation by a resistance heater is usually suitable for producing a small amount of the particles in laboratories, while heating by a high frequency induction furnace could be applied for producing a large amount of materials in the industrial scale. The advantages of the latter method are the stability of evaporation temperature, the homogenous melting alloys, the high energy power supply, etc. For details of the crystal habits and crystal structures of nanoparticles, the reader is referred to Uyeda’s book [35] and other original contributions [30, 36–53, 97–101].

### 3.2.2. Arc Discharge/Plasma

The formation mechanism of nanoparticles/nanocapsules in plasma is that matter clusters with high activity exist in the plasma, which could exchange rapidly the energy with the

reacted matter clusters, beneficial to the reaction between them. When the reacted matter clusters leave the high temperature in the flame tail region of the plasma, the rapid decrease of the temperature lets the clusters be in the saturation state in dynamic equilibrium; thus they are dissociated. The rapid cooling/quenching leads to the nucleation of crystallites and the formation of nanoparticles/nanocapsules. According to the method of production, the plasma can be of two kinds: direct current arc plasma and high frequency plasma. Direct current arc plasma uses the direct current arc in inert/active gases to ionize the gases, generate the high temperature plasma, and melt the materials. The cooling, reaction, and condensation of the evaporating matters lead to the formation of nanoparticles and nanocapsules. The high frequency plasma is produced by induction coils outside the quartz tube, which can generate the magnetic field with MHz frequency. The advantages of the high frequency plasma method are: less contamination because no cathode is used, the use of reaction gases, and enough space for plasma so that the reaction and heating are sufficient for the plasma matter. The direct current arc plasma and the high frequency plasma methods can be combined in equipment for industrial purposes.

There has been great interest in the incorporation of foreign materials into fullerene structures (C<sub>60</sub>, nanotubes, nanoparticles, onions), which has been driven by the potential applications of the filled fullerenes, which lie in diverse areas such as optics, electronics, magnetic recording materials, and nuclear medicine. In particular, the onion structures of extreme strength may offer excellent protection of their encapsulated nanomaterials for applications. The arc vaporization/discharge method has been widely used for the formation of fullerenes and related materials [102]. One of the remarkable properties of fullerenes and related materials is that they have hollow structures with a cavity of nanometer-scale diameter; outer cages are made up of single or concentric multilayers of graphene sheets. When foreign materials, such as metal atom(s) or nanocrystallites, are trapped in the inner cavity, unusual physical and chemical properties are brought about.

The structures of carbon polyhedral particles stuffed with YC<sub>2</sub>, synthesized by arc discharge of carbon rods containing yttrium, were studied with a TEM [103]. The YC<sub>2</sub> crystals with typical sizes of a few tens of nanometers were wrapped by multilayered graphitic sheets and were protected against hydrolysis. It was demonstrated that a finely focused electron beam opened the graphite cage. A growth model of the carbon nanocapsules stuffed with metal carbides was proposed. Then the encapsulation of metals in multilayered graphitic capsules was studied for all the rare-earth elements (Sc, Y, and R = La, Ce, . . . , Lu) excluding Pm by using electric arc discharge [104]. Most rare-earth metals (Sc, Y, La, Ce, Pr, Nd, Gd, Tb, Dy, Ho, Er, and Lu) were encapsulated in the form of carbides, but the others, Sm, Eu, and Yb, were not. The metals in the former group that were encapsulated had vapor pressures definitely lower than those in the latter group. In the case of thulium (Tm), whose vapor pressure was intermediate between the two groups, only a trace amount of encapsulated carbide was formed. The volatility of metal played an important role in the metal encapsulation process.

Crystallites of scandium carbides, nesting in multilayered polyhedral graphitic cages, were produced by evaporating a scandium–graphite composite rod in helium gas [105]. The encapsulated scandium carbide was identified as  $\text{Sc}_{15}\text{C}_{19}$ , instead of dicarbide  $\text{RC}_2$ , the form of carbide commonly found for other rare-earth-based nanocapsules. The size of the capsules ranged from about 10 to 100 nm. Morphological features of the outer graphitic carbon, multilayered and polyhedral, were quite similar to those for the capsules protecting  $\text{RC}_2$  ( $R = \text{Y}, \text{La}, \text{Ce}, \dots, \text{Lu}$ ) [104].

Experiments aimed at the encapsulation of foreign materials within hollow graphitic cages were carried for iron group metals (Fe, Co, Ni) [106–114]. For iron group metals, particles of both a carbide phase ( $\text{M}_3\text{C}$ ,  $M = \text{Fe}, \text{Co}, \text{Ni}$ ) and also a metallic phase [ $\alpha$ -Fe,  $\gamma$ -Fe, hexagonal close-packed (hcp) Co, face-centered cubic (fcc) Co, fcc Ni] were encapsulated in graphitic carbon [106, 107]. Sometimes, metallic nanocrystals of Fe, Co, and Ni were in the fcc phase, and no trace (or a trace amount) of the bulk equilibrium phases of bcc Fe and hcp Co was found [108, 109]. Especially for Ni, exotic carbon materials with hollow structures, bamboo-shaped tubes, and nanochains as well as single-layered nanotubes were discovered [110]. Figure 2 shows high resolution TEM (HRTEM) images of the shell/core structure of Ni(C) nanocapsules [109]. The particles were nominally spherical in shape and typically 10–100 nm in diameter. The core Co metal was protected against oxidation and coalescence.

Evaporation of Fe, Ni, or Co with graphite in a hydrogen atmosphere resulted in graphite encapsulated nanoparticles. Similar experiments in helium led to nanoparticles embedded in an amorphous carbon/fullerene matrix. Comparing the experimental results in helium and hydrogen, a mechanism for the formation of encapsulated nanoparticles was proposed [113, 114]. The hydrogen arc produced polycyclic aromatic hydrocarbon molecules, which can act as a precursor to the graphitic layers around the nanoparticles. Direct evidence for this mechanism was given by using methane ( $\text{CH}_4$ ) [113] or pyrene ( $\text{C}_{16}\text{H}_{10}$ ) [114], a polycyclic aromatic hydrocarbon molecule, as the only carbon source to form encapsulated nanoparticles. Pyrolysis of hydrocarbon

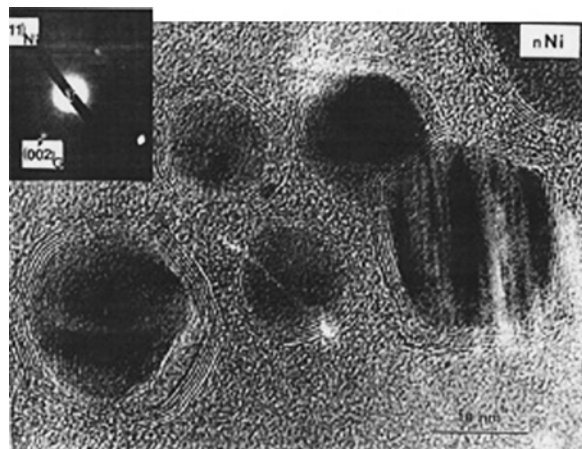


**Figure 2.** HRTEM images showing the shell/core structure of Ni(C) nanocapsules. After [109], V. P. Dravid et al., *Nature* 374, 602 (1995). © 1995, Macmillan Magazines Ltd.

compounds on evaporated metal-based catalysts was used to produce carbon shells, hollow fibers, and other hollow carbon forms [115]. A kinetic model for their formation and the mechanisms for obtaining different types of hollow carbons were proposed [115], in which two competing processes, the linear growth rate of the carbon and the catalyst outlet rate relative to the growing carbon, determined the type of hollow carbon.

A process of arc discharge was developed to fabricate carbon-encapsulated magnetic nanocapsules in methane ( $\text{CH}_4$ ) atmosphere, where a carbon rod was used as the cathode and a metal or alloy block was used as the anode [113].  $\gamma$ -Fe(C),  $\alpha$ -Fe(C) and  $\text{Fe}_3\text{C}$  [113, 116], Fe–Ni(C) [117, 118], and Fe–Co(C) [119–121] nanocapsules were synthesized successfully by arc discharge in methane. Figure 3 presents a HRTEM image showing the shell/core structure of Fe–Co(C) nanocapsules with a graphite shell of about 3.4 nm thickness and a crystalline Fe–Co core [121]. The shell is characterized by curved lattice fringes of interplanar spacing 0.34 nm corresponding to the (0002) lattice plane of graphite carbon [121]. This process was employed to produce nanocapsules with different types of shells and cores only by changing the atmosphere. Fe(B) and Co(B) nanocapsules sheathed with boron oxide were prepared in diborane ( $\text{B}_2\text{H}_6$ ) atmosphere [122–124]. Figure 4a shows a TEM photograph of Co(B) nanocapsules which arrange as a chain due to the magnetostatic energy, while Figure 4b gives a HRTEM image showing the shell/core structure of Co(B) nanocapsules with an amorphous boron oxide shell of about 4.0 nm thickness and a crystalline CoB core [124]. Amorphous boron nanoparticles and BN encapsulating boron nanocapsules were prepared by arc decomposing diborane and nitriding [125].

Twenty elements were co-deposited with carbon in an arc discharge between graphite electrodes [126]. The majority of them were evaporated from composite anodes that contained the elements or their oxides stuffed into central bores in the graphite rods. The deposits, found in the soot at the

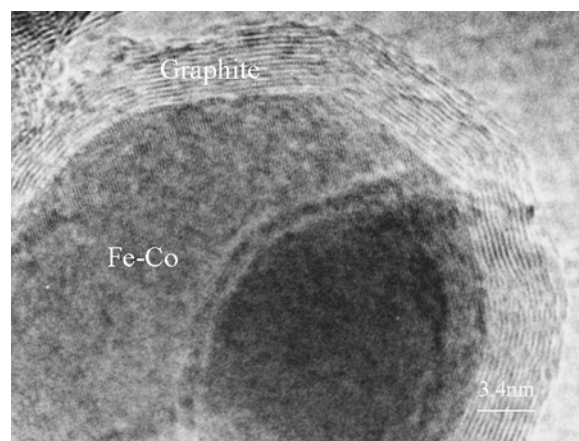


**Figure 3.** HRTEM image showing the shell/core structure of Fe–Co(C) nanocapsules with a graphite shell of about 3.4 nm thick and crystalline Fe–Co core. The shell is characterized by curved lattice fringes of interplanar spacing 0.34 nm corresponding to the (0002) lattice plane of graphite carbon. After [121], Z. D. Zhang et al., *J. Phys. Cond. Matter* 13, 1921 (2001). © 2001, IOP Publishing.

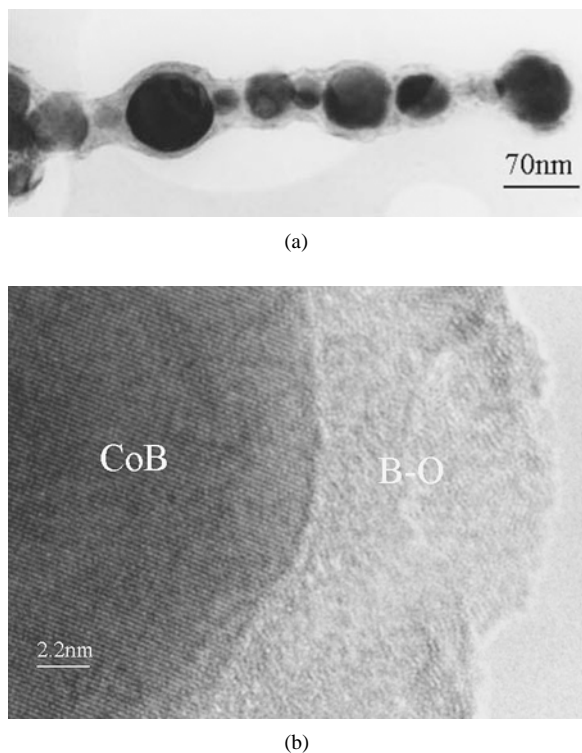


**Figure 4.** (a) TEM photographs of Co(B) nanocapsules which arrange as a chain due to the magnetostatic energy; (b) HRTEM image showing the shell/core structure of Co(B) nanocapsules with an amorphous boron oxide shell of about 4.0 nm thick and a crystalline CoB core with  $d = 0.219$  nm corresponding to the (111) lattice plane of CoB phase with  $a = 3.948$  Å,  $b = 5.243$  Å, and  $c = 3.037$  Å. After [124], I. Škorvánek et al., submitted for publication. Image courtesy of J. G. Zheng, Northwestern University, U.S.A.

reactor walls or as slag at the cathode, were characterized. The products fall into four categories: (1) elements that can be encapsulated in the form of their carbides (B, V, Cr, Mn, Y, Zr, Nb, Mo); (2) elements that are not encapsulated but tolerate the formation of graphitic carbon cages (Cu, Zn, Pd, Ag, Pt); (3) elements that form stable carbides, competing with and preempting the carbon supply for the graphitic cage formation (Al, Si, Ti, W); and (4) the iron-group metals (Fe, Co, Ni) that stimulate the formation of single-walled tubes and strings of nanobeads in the conventional arc discharge condition and produce nanometer-size carbon-coated ferromagnetic particles in a modified arc discharge in which metals are in molten form in graphite crucible anodes exposed to a helium jet stream. The criterion determining the formation was discussed, according to one of the four categories. It was apparent that the physical properties, such as vapor pressure, melting and boiling points, the completeness of the electronic shells of the elements, and the heat of carbide formation, were not sufficient to explain the selectivity of the encapsulation without exceptions. A hypothesis was advanced that emphasizes the existence of the carbide, interfacial compatibility with the graphitic network, as well as the transport and supply parameters in the reaction space.

Encapsulation of platinum-group metals (Ru, Ph, Pd, Os, Ir, Pt) within carbon nanocapsules and synthesis of single-layered carbon nanotubes by arc evaporation of metal/carbon

composites were studied [127]. All the platinum-group metals, forming small particles (10–200 nm in diameter), were encapsulated within multilayered graphitic cages. Particles trapped in the cages were single-domain crystallites in normal metallic phases. Ph, Pd, and Pt showed catalytic activity for growing single-layered carbon tubes, but the other metals did not.

Fine crystallites of titanium and hafnium carbides encapsulated within graphite cages were formed by arc discharge between a metal/carbon composite anode and a graphite cathode [128]. Encapsulated TiC crystallites ranging from 30 to 150 nm in size were found in carbonaceous materials formed around a cathode. Short, single-walled carbon nanotubes were also observed, extruding from carbon layers with complicated structures surrounding TiC crystallites. For hafnium whose vapor pressure was lower than that of carbon at high temperatures, the formation of HfC crystallites (20 to 80 nm in diameter) was limited within a slaglike deposit, which was also encapsulated in graphite cages.

Encapsulation of Cr, Mo, and W in multilayered graphitic cages by arc evaporation of metal/carbon composites under different pressures (100, 600, and 1500 Torr) of helium gas was studied [129]. The encapsulated crystallites were carbides, that is,  $\text{Cr}_7\text{C}_3$  and  $\text{Cr}_3\text{C}_2$  for Cr;  $\text{Mo}_2\text{C}$ ,  $\delta\text{-MoC}_{1-x}$  (NaCl-type), and  $\gamma'\text{-MoC}$  (AsTi-type) for Mo;  $\text{W}_2\text{C}$  and  $\beta\text{-WC}_{1-x}$  (NaCl-type) for W. The effect of helium gas pressure on the formation of the nanocapsules was found for tungsten: Encapsulated tungsten carbides were formed at the highest pressure, but not at the lower pressures.

A dc arc discharge was generated between graphite and molybdenum electrodes at 25 kPa of He gas ambient, in order to reveal the relation between nanotube growth and arc discharge phenomena [130]. Numerous multiwall carbon nanotubes and nanocapsules were observed at the cathode spot area of the C cathode. An explanation was presented for the growth of soft-core containing nanotubes and a hard shell in the usual arc with a C-cathode and C-anode electrode system.

A form of graphitic cage in nanometer scale, rectangular parallelepiped (or cube), was produced by arc evaporation of a carbon electrode containing calcium or strontium [131]. Both empty and filled rectangular nanocapsules averaging 20–100 nm in size were formed, though the empty ones were dominant. The rectangular cages were made up of multiwalled (5–20 layers) graphitic carbon. The encapsulated materials were  $\beta\text{-CaC}_2$  (tetragonal),  $\gamma\text{-CaC}_2$  (cubic), and  $\delta\text{-CaC}_2$  (monoclinic) for C/Ca evaporation, and  $\beta\text{-SrC}_2$  (tetragonal) and metallic Sr for C/S revaporation.

The growth phenomena of different metals encapsulated into carbon cages were studied in emphasizing the effect of carbon and metal supply on the size of particles [132, 133]. Postdeposition annealing was introduced as a process that induces structural rearrangements and thus enables changes in morphologies. Particles made under the same experimental conditions of the arc discharge process were of roughly the same size. The average diameter of the particles produced by using a larger diameter of the metal pool was bigger than those of the particles produced from the smaller metal pool. The annealing provided additional thermal energy making structural rearrangement possible long after the initial deposition process was terminated.

The effects of the carbon content, chamber pressure, arc current, and blowing gas velocity on the encapsulation of nickel in graphite layers were observed by systematically varying each of these variables in a tungsten-arc encapsulation setup [134]. The properties of the arc translated into changes in the encapsulated product. A larger and hotter arc resulted in more encapsulation in the final sample. These findings, along with evidence of graphite layers forming on precrystallized particles, indicated that the graphite layers might form by two sequential formation steps. The first step was the simple phase segregation of carbon from a cooling liquid particle, resulting in surface graphite. The second step was the growth of carbon on a crystallized nickel particle, regardless of the temperature at which this occurs.

Gold, iron oxide, and germanium nanocapsules encapsulated in the boron nitride sheets were produced by arc melting in a nitrogen gas atmosphere using a tungsten electrode and a boron-based mixture powder [135, 136]. Nanoscale materials created from boron nitride by arc discharge between  $ZrB_2$  electrodes in  $N_2$  atmosphere were investigated [137]. Boron nitride nanotubes were formed together with Zr-compound nanoparticles encapsulated in boron nitride cages. Concerning the helical structures of the boron nitride tubes, a variety of chiral angles, including the zigzag and the armchair types, were observed. Weak peaks of photoluminescence spectrum were observed from the nanocapsules with germanium nanoparticles [136].

The spatial distribution of the chemical species (B, C, N, and Hf) present in multielement nanoparticles and nanotubes, which were produced by arc discharging a hafnium diboride rod with a graphite rod in a nitrogen atmosphere [138], was investigated by means of electron energy loss spectroscopy (EELS). For the hafnium-boride metallic particles coated by C/BN envelopes, a model was proposed based on the solidification from the outside to the inside of isolated liquidlike droplets: the carbon phase solidifies first according to theoretical phase diagrams and forms the outer shells.

Various boron nitride and carbon nanocage fullerene materials (clusters, metallofullerenes, onion, nanotubes, and nanocapsules) were synthesized by arc melting, electron beam irradiation, chemical reaction, and self-organization [139–141]. Boron nitride nanotubes, nanocapsules, and nanocages were fabricated by arc melting  $LaB_6$  and boron/ $LaB_6$  powder compacts in a nitrogen/argon gas atmosphere [141]. A guideline for designing the boron nitride and carbon fullerene materials was summarized. B–C–N nanotubes prepared by a flush evaporation method using a dc arc plasma were characterized by TEM and EELS [140]. The nanotubes obtained were divided into three types, such as carbon, boron nitride, or carbon nanotubes surrounded with boron nitride nanotubes. These types of nanotubes were obtained only at temperatures higher than approximately 3000 K. On the other hand, nanocapsules were formed at all the temperature regions, but the nanocapsules obtained at lower temperatures were smaller. The addition of nickel produced a bundle of single-walled carbon nanotubes and boron nitride nanocapsules surrounding nickel particles.

Ge and SiC nanoparticles and nanowires encapsulated in carbon nanocapsules and nanotubes were produced by direct current and radio frequency hybrid arc discharge of

C, Ge, and Si elements [142, 143]. HRTEM images showed the formation of Ge and SiC nanoparticles and nanowires encapsulated in carbon nanocapsules and nanotubes. The growth direction of the Ge nanowires was found to be (111) of Ge, and a structure model for Ge/C interface was proposed. Silicon–fullerene compounds  $Si@C_n$  ( $n = 74, 86$ , etc.) and carbon nanocapsules filled with SiC were produced in a modified fullerene generator, where a direct current or radio frequency discharge was superimposed in the periphery region of an arc-discharge plasma [144].

HRTEM images of  $C_3N_{3.6-4.5}O_{1.1-1.2}H_{4.1-4.2}$  showed nanocage- and nanotube-like structures, which have cage and tube sizes in the range of 10–500 nm [145]. Electron diffraction of the cage structures indicated a disordered  $CN_x$  structure, and carbon and nitrogen were detected. Nanocrystalline grains encapsulated in  $CN_x$  nanotubes and nanocapsules were also observed, and carbon, oxygen, and a little nitrogen were detected.

### 3.2.3. Laser/Electron Beam Heating

Electron beam heating has been used widely in the fields of melting, welding, sputtering, and micromanufacturing. The electrons emit from the cathode of the electron gun where the temperature is very high due to the application of the high voltage that is necessary for the emission of electrons. Thus the high vacuum must be kept in the electron gun. Actually, the electron gun inside a TEM can be conveniently used for electron beam heating and irradiating of the materials. Another efficient method is laser heating, which has several advantages: the heating source is outside the evaporation system; any materials, including metals, compounds, ceramics, etc., can be evaporated; there is no contamination from/for the heating source. Both the laser and the electron beam heatings are efficient for evaporation of materials with high melting points.

A method was developed for formation of carbon nanotubes, carbon nanocapsules, and carbon nanoparticles in which polyyne-containing carbons were heated and irradiated by an electron beam in a TEM [146–149]. The technique was applied to carry out *in-situ* observation of those formation processes. Though carbon nanoparticles were formed accompanied by carbon nanotubes, carbon nanoparticles and nanocapsules were formed independently of the carbon nanotubes [146]. The carbon nanotubes were preferentially inside of the polyyne-containing carbon films, while the carbon nanoparticles/nanocapsules were outside of the films. The differences on the inside and the outside were discussed to understand the formation process of the carbon nanoparticles/nanocapsules. From *in-situ* observation, the existence of metal particles, the high surface energy, the high wettability, and the high viscosity of the polyyne-containing carbons were assumed to be relevant to the preferential formation of the carbon nanoparticles/nanocapsules to the carbon nanotubes.

Carbon onions were produced in a TEM by electron irradiation of amorphous carbon in the presence of Pd clusters [147]. HRTEM revealed the structural changes of the onion surface, and the atom clouds were observed at the pentagonal vertices. In some onions, Pd atoms were intercalated between the graphite onion sheets, and a structural model



for the intercalation was proposed. Electron beam irradiation of amorphous carbon in the presence of Pd clusters was shown to be an effective method for the formation of intercalated onions.

Metallic nanocrystals, such as cobalt or gold, were encapsulated by spherical graphitic shells under high-temperature electron irradiation [148]. The irradiation promoted a heavy contraction of carbon onions. The contraction forced the metal atoms to migrate outward through the shells, even without further irradiation. This led to a gradual but complete displacement of the encapsulated crystals. *In-situ* observation in a TEM allowed shrinkage of the encapsulated crystals and migration of the atoms through the shells to be monitored. The spherically curved graphene layers were permeable to metal atoms.

Copper substrates were implanted with carbon ions at temperatures ranging from 570 to 973 K [149]. Carbon onions and nanocapsules were observed together with amorphous carbon layers. Most of the nanocapsules were found to be hollow and rarely included copper nanoparticles. The encapsulating of Cu nanoparticles with graphene layers, the gradual shrinkage of the encapsulated clusters, and finally the disappearance of the clusters (leaving behind hollow nanocapsules) were observed under electron irradiation at 783 K. Statistics of cluster size as a function of ion fluence, implantation temperature, and substrate crystallinity gave insights into the nucleation processes of onions and nanocapsules. One process involved the formation of graphene layers on grain boundaries to encapsulate copper particles. Another process was the nucleation of graphene cages, probably fullerenes, due to a high concentration of carbon atoms and a high amount of radiation damage.

Nanocapsules of crystalline boron nitride with diameters ranging from 50 to 300 nm were synthesized by pulsed-laser vaporization of BN, where the laser plume was controlled by the modulated plasma jet flow field [150]. Their shapes varied from polyhedrons to cocoons and the interlayer spacings along the *c* axis were enlarged according to their size and shape (curvature). Without the synchronization of the laser pulses with the plasma modulation, sootlike BN was obtained.

Magnetic Fe<sub>3</sub>C and  $\alpha$ -Fe nanoparticles were prepared by laser-induced pyrolysis of Fe(CO)<sub>5</sub> and C<sub>2</sub>H<sub>4</sub> [151]. It was found that not only was oxygen content of the  $\alpha$ -Fe particles much higher than that of the Fe<sub>3</sub>C particles, but the oxygen was in different states for the two nanoparticles. The oxygen present on the Fe<sub>3</sub>C particles was primarily in absorbed form, compared to chemically combined oxygen as in the  $\alpha$ -Fe particles. Iron carbonitride nanoparticles (20–80 nm in size) were synthesized by laser-induced pyrolysis of a Fe(CO)<sub>5</sub>-NH<sub>3</sub>-C<sub>2</sub>H<sub>4</sub> mixture [152]. Surface morphology, structural characteristics, oxidation behavior, and magnetic properties of the iron carbonitride particles were reported. The unilateral lattice expansion of the iron carbonitride compound was interpreted in terms of the structural and chemical bonding features of the iron carbonitride compound.

$\alpha$ -Fe (bcc) and  $\gamma$ -Fe (fcc) nanoparticles were prepared by laser-induced pyrolysis [153]. The structures, morphologies, and magnetic properties of the oxide layers covering the iron

nanoparticles were investigated. The iron oxide layers consisted of very fine crystallites of 2–5 nm in diameter, and the layers were nonferromagnetic or superparamagnetic. The iron oxide layer formed on iron nanoparticles at room temperature was Fe<sub>3</sub>O<sub>4</sub>, rather than a mixture of Fe<sub>3</sub>O<sub>4</sub> and  $\gamma$ -Fe<sub>2</sub>O<sub>3</sub>.

$\gamma$ -Fe(N) nanoparticles (containing 5.9% N, atomic fraction) were prepared by laser induced pyrolysis [154]. The martensitic transformation temperature of the nanoparticles was much lower than that of the bulk materials with the same composition. The effect of particle size on the transformation temperature was discussed. It was suggested that the hydrostatic pressure resulting from surface tension of the nanoparticles was responsible for the decrease of the transformation temperature. In order to verify the plastic deformation induced martensitic transformation of the  $\gamma$ -Fe(N) nanoparticles, the effects of pressurization (0.5–4.0 GPa) on the martensitic transformation and microstructures of the particles were presented.

### 3.2.4. Sputtering

Sputtering is a convenient method for preparing films, by which different elementary materials are ionized or heated to form the plasma before depositing on substrates. Sputtering can be employed for preparing the nanoparticles embedded in the thin films, or so-called granular films. The mechanism of the sputtering is as follows: the direct current of hundreds of voltages applied between the cathode and the anode in atmosphere of inert and active gases leads to glow discharge. The ions during the process of discharge bump the target that serves as the cathode, so that the atoms of the target materials could evaporate from the surface. The cooling and the condensation in inert gases and/or the reaction in active gases of the evaporation atoms result in the formation of nanoparticles and nanocapsules, or thin films. The advantages of sputtering are as follows: no crucible is needed; particles of metals with a high melting point can be prepared; the evaporation surface can be large; particles of alloys can be synthesized using active gases; granular thin films can be prepared; the narrow size distribution of the particles can be controlled well; nanocomposite materials can be produced if several different materials are used as targets; etc. The voltage, current, gas pressure, and target are the most important factors which affect the formation of nanoparticles/nanocapsules.

A method was reported for fabricating thin films of carbon nanocapsules and onionlike graphitic particles [155], which consisted of cosputtering Ni and graphite and subsequent thermal annealing in vacuum. The films were composed of Ni-filled carbon nanocapsules with graphitic coatings several nanometers in thickness. Ni particles were removed by acid etching, resulting in the formation of thin films composed of onionlike graphitic particles. Electron field emission properties of the onionlike graphitic-particle films were studied.

C-Ag thin films were synthesized by cosputtering of a silver-graphite target [156]. The deposition temperature ranged from 77 to 773 K, while the silver concentration varied from 10 to 71 at%. The homogeneously distributed silver nanoparticles, having an elongated shape along the

direction of the thin film growth, formed within a more or less graphitized carbon matrix. A graphitization led to the encapsulation of the silver nanoparticles in graphite-like carbon when the depositions were performed at 773 K for lower silver concentrations without ion-beam assistance and below 573 K for upper silver concentrations with ion-beam assistance.

$(\text{Ni}_{66}\text{Fe}_{22}\text{Co}_{12})_x\text{C}_{1-x}$  nanocomposite films with  $x = 10\text{--}75$  at% were prepared by dc magnetron cosputtering [157]. Subsequent thermal annealing was performed in a vacuum ( $<2 \times 10^{-3}$  Pa) furnace for 1 h at various temperatures. The phase transition with increase of annealing temperature was closely dependent on the composition. Films with NiFeCo less than 20 at% showed an amorphous structure in the as-deposited samples and ones annealed up to 400 °C. After being annealed at 500 °C, a small amount of fcc crystalline NiFeCo precipitated while carbon remained amorphous. For the films with NiFeCo concentration of 30–55 at%, the as-deposited films consist of very small NiFeCo nanocrystals encapsulated in amorphous carbon. After being annealed, the crystal grain size of the alloys increased with increasing annealing temperature while carbon was graphitized. For the films with more than 62 at% NiFeCo, the as-deposited films went through a metastable stage at which a rhombohedral  $\text{Ni}_3\text{C}$  phase and fcc NiFeCo coexisted upon annealing to a temperature between approximately 300 and 400 °C (dependent on composition). Upon further annealing to a sufficiently high temperature between approximately 350 and 500 °C, the carbide phase decomposed and only the fcc NiFeCo nanocrystals encapsulated in graphite existed in the films.

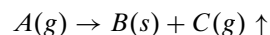
### 3.3. Chemical Methods

The chemical methods are useful fabrication methods for the mass production of the nanoparticles and the nanocapsules, compared to the physical methods. It is very typical that during the chemical methods, some chemical reactions occur, accompanying the formation of nanoparticles/nanocapsules. Chemical methods for preparation of nanoparticles and nanocapsules include chemical gas reaction [i.e., the chemical vapor deposition (CVD)], chemical vapor condensation (CVC), solid-state reaction, sol-gel, precipitation, hydrothermal process, solvent process, latex process, oxidation process, polymerization, etc. Different chemical methods have different procedures with different chemical reactions at various steps of the synthesis of nanoparticles/nanocapsules. Thus the abundance of chemical methods could be employed to synthesize many kinds of nanoparticles/nanocapsules with various shapes, morphologies, phases, structures, sizes, etc., for different kinds of materials, varying from metals, to oxides, ceramics, organics, etc. The advantages of these chemical methods are high purity, high uniformity, small particle size, narrow size distribution, good dispersal, good chemical homogeneity, high chemical reaction activity, and structural/composition uniformity. The chemical methods are also convenient, inexpensive, and effective for preparation of nanoparticles/nanocapsules in high yield.

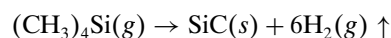
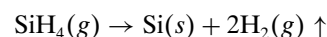
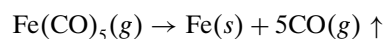
#### 3.3.1. Chemical Vapor Deposition

The CVD process is a method of chemical vapor reaction which utilizes the evaporation of volatile metal compounds and chemical reactions to form the compounds desired and the rapid cooling in gas atmospheres to result in the formation of nanoparticles/nanocapsules. The nanoparticles/nanocapsules produced by CVD have several advantages, like high purity, high uniformity, small particle size, narrow size distribution, good dispersal, and high chemical reaction activity. CVD is suitable for synthesizing not only nanoparticles/nanocapsules but also fibers/nanotubes of metals, metal compounds, for instance, nitrides, carbides, borides, etc. In accordance with the types of the reactions, CVD can be divided into two kinds of methods: vapor decomposition and vapor synthesis. According to the type of reaction precursor, the CVD can be classified to be the gas-gas reaction one, the gas-solid reaction one, and the gas-liquid reaction one. For the occurrence of the chemical reactions, it is used to utilize the heating and radiation activating the molecules in the reaction systems. The methods for the activation of the molecules include resistant heating, chemical flame heating, laser heating [158–160], plasma heating [161], X-ray radiation, etc.

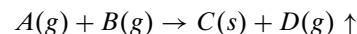
The vapor decomposition method is a so-called single compound heat decomposition method. The compound is heated to evaporate and decompose, as in the following reaction:



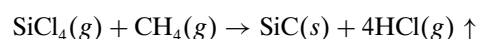
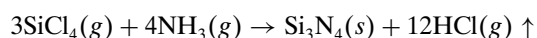
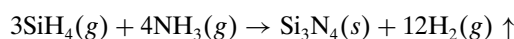
The materials used for the vapor decomposition method are usually the volatile metal compounds,  $\text{Fe}(\text{CO})_5$ ,  $\text{Si}(\text{NH})_2$ ,  $\text{SiH}_4$ ,  $\text{Si}(\text{OH})_4$ ,  $(\text{CH}_3)_4\text{Si}$ , etc., which have high evaporation pressure and high reaction activity. The reaction equations are as follows:

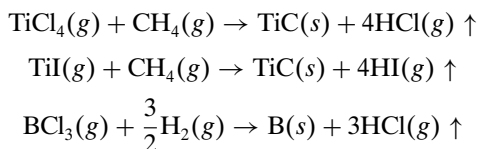


The vapor synthesis method usually utilizes the vapor reactions between two (or more than two) different materials to form the nanoparticles/nanocapsules of the new compounds. The common reaction equation is



The materials used for the vapor synthesis method can be  $\text{SiH}_4$ ,  $\text{CH}_3\text{SiCl}$ ,  $(\text{CH}_3)_4\text{Si}$ ,  $\text{SiCl}_4$ ,  $\text{BCl}_3$ ,  $\text{TiCl}$ ,  $\text{TiCl}_4$ ,  $\text{TiI}$ ,  $\text{TiI}_4$ ,  $\text{ZrCl}_4$ ,  $\text{MCl}_3$ ,  $\text{MoO}_3$ ,  $\text{WCl}_6$ ,  $\text{H}_2$ ,  $\text{NH}_3$ ,  $\text{CH}_4$ ,  $\text{C}_2\text{H}_4$ , etc. The vapor synthesis method is highly flexible because of the combination and the exchange of the different precursors. The following reactions are listed as examples:





The heating by a resistant furnace is a traditional procedure for chemical vapor reaction, which consists of precursor treatment, the parameter control of the reaction, nucleation and growth, cooling, and condensation. For both the vapor decomposition method and the vapor synthesis method, when the laser heating is used, one needs to choose the materials with high absorption ability of the laser beam as the reaction precursors [158–160]. The mechanism of laser induced chemical vapor reaction for synthesis of nanoparticles is that the gases strongly absorb the high energy of the laser beam so that the gas atoms/molecules are heated and activated instantly. The gases reach the high temperature needed for the chemical reactions and accomplish the reactions, nucleation, and growth in a very short time. The nanoparticles of metals Fe, Ni, Al, Ti, Cr, Zr, Mo, and Ta, their oxides, and nitrides have been synthesized [151–154, 158–160].

The different preparation methods of ultrafine powders of high melting point compounds (carbides, borides, nitrides, and oxides) were reviewed [161]. The consolidation behavior of these compounds in the nanocrystalline state was described in detail. Compaction by hot pressing, including high pressure and high temperature, sintering, and high-energy consolidation methods, was analyzed. The microstructure, recrystallization, and mechanical and physical properties of the nanocrystalline carbides, nitrides, and oxides were characterized [161].

Nanoparticles of uranium dicarbide encapsulated in carbon smaller than 100 nm were obtained by chemical reactions at high temperatures [162]. Two types of nanocapsules were identified and characterized. The majority of them had small diffuse kernel surfaces, with dimensions between 5 and 15 nm, surrounded by thick spherical carbon cover. Others, in minor quantity and ranging from 15 to 40 nm, were polyhedral and surrounded by several perfect graphite layers oriented parallel to their external surface. The nanocapsules are as chemically inert as graphite.

Pyrolysis of acetylene over quartz plates coated with various metal catalysts resulted in the formation of all-carbon nanostructures [163]. The nanotubes appear to grow as ultrathin tubes with a central hollow core and considerable thickening due to secondary pyrolytic deposition. In some cases, catalytic particles were entrapped within the tubes to form the nanocapsules. The efficiency of the catalysts was evaluated semiquantitatively.

Carbon nanocapsules with SiC and Au nanoparticles were produced by thermal decomposition of polyvinyl alcohol at about 500 °C in Ar gas atmosphere [164]. The formation mechanism of nanocapsules was discussed and a structural model for the nanocapsule/SiC interface was proposed. In addition, carbon clusters were formed at the surface of carbon nanocapsules, and carbon onions were produced by electron irradiation of amorphous carbon produced from polyvinyl alcohol. Silver nanoparticles encapsulated within boron nitride nanocages were produced from mixtures of

boric acid, urea, and silver nitrate upon reduction at 700 °C in hydrogen [165]. Multilayered polymer nanocapsules were fabricated via sequential adsorption of oppositely charged polyelectrolytes onto gold nanoparticles followed by dissolution of the gold core in cyanide solution [166]. A gold nanoparticle was coated with eight polyelectrolyte layers.

Preparation and layer-by-layer self-assembly of silver nanoparticles capped by graphite oxide nanosheets were carried out [167]. Sodium borohydride reduction of silver ions in aqueous dispersions of exfoliated graphite oxide (GO) resulted in the formation of remarkably monodisperse 10 nm diameter oblate Ag particles that are effectively protected by 0.5 nm thick GO sheets, Ag–GO. Ag–GO could be self-assembled onto poly(diallyldimethylammonium) chloride (PDDA) coated substrate, and subsequent layer-by-layer self-assembly of Ag–GO and PDDA led to well-ordered ultrathin films of S-(PDDA/Ag–GO)<sub>n</sub>.

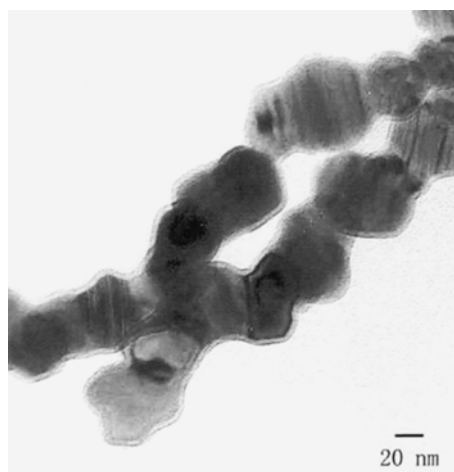
The specific features of the catalytic reduction of methylviologen by dihydrogen in water in the presence of platinum colloids synthesized by various methods were studied [168]. The colloids prepared by the radiation-chemical reduction of PtCl<sub>4</sub><sup>2-</sup> in the presence of polyacrylate or polyphosphate as stabilizers and those prepared by the reduction with dihydrogen efficiently catalyzed the reaction. The “citrate” colloids synthesized by the reduction of PtCl<sub>6</sub><sup>2-</sup> with citric acid were characterized by a prolonged induction period after which these colloids also gained catalytic activity.

A technique for the formation of carbon-encapsulated metal nanoparticles on silicon was developed [169]. Carbon encapsulated NiFe nanoparticles were prepared by high-temperature methane encapsulation of the bare bimetallic particles on alumina [170]. About 6-nm-thick carbon layers encapsulated 10–20 nm diameter NiFe nanoparticles. The NiFe nanoparticles were single crystalline and no carbide was found at the NiFe–C interface. Metallic Pd nanoparticles with a diameter of 1–2 nm were anchored on the carbon layers, which created a Pd/NiFeC&C type of catalyst that could be used for liquid phase reactions.

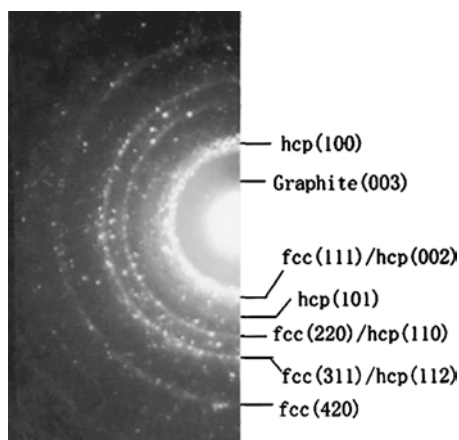
Carbon-encapsulated cobalt nanoparticles were prepared over a range of temperatures and partial pressures by CVD from cyclohexane on prepared substrates consisting of ground powders of SiO<sub>2</sub> impregnated with Co(NO<sub>3</sub>)<sub>2</sub> and (NH<sub>4</sub>)<sub>2</sub>Mo<sub>2</sub>O<sub>7</sub> [171]. The encapsulated cobalt nanoparticles were freed from the incorporated SiO<sub>2</sub> and molybdenum by treating the deposition product with aqueous hydrofluoric acid.

Carbon-coated cobalt nanocapsules were synthesized by CVD with cobalt carbonyl [Co<sub>2</sub>(CO)<sub>8</sub>] used as precursor and carbon monoxide (CO) as carrier gas [172]. The characterization and magnetic properties of carbon-coated cobalt nanocapsules were investigated systematically. Figure 5 shows a TEM image and a selected area diffraction (SAD) pattern of the Co(C) nanocapsules synthesized by the CVD process [172]. The decomposition of Co<sub>2</sub>(CO)<sub>8</sub> and CO gas can decrease efficiently the content of the oxygen in nanocapsules. The metal Co nanoparticles completely coated by carbon can resist the dilute acid erosion as well as the oxidation.

An *in-situ* process was developed to create a dispersed phase of lubricant MoS<sub>2</sub> nanoparticles in a matrix of a hard TiN coating [173]. The particle formation at different



(a)



(b)

**Figure 5.** (a) TEM image and (b) selected area diffraction (SAD) pattern of Co(C) nanocapsules with core-shell structure, which are synthesized by chemical vapor condensation process with the cobalt carbonyl ( $\text{Co}_2(\text{CO})_8$ ) used as precursor and the carbon monoxide (CO) as carrier gas. After [172], Z. H. Wang et al., *Carbon*, in press. © Elsevier Science.

total and partial pressures was investigated. High yields of particles with diameters of 30–50 nm were obtained thermally at temperatures  $> 300$  °C and pressures  $> 5$  hPa with  $\text{MoCl}_5/\text{H}_2\text{S}$  as precursors. In the low pressure range, particles were formed by a plasma CVD process using the reaction of elementary sulphur or  $\text{H}_2\text{S}$  with  $\text{MoCl}_5$ .

Plasma enhanced CVD was used to synthesize Fe nanoparticles in an amorphous boron carbide matrix [174]. The nanoparticles ranged in size from approximately 0.7 to 4.5 nm. The size of the nanoparticles was proportional to the density of the Fe precursor (ferrocene) in the vapor.

Anatase titania nanoparticles were prepared using pyrolysis of titanium tetrabutoxide in oxygen-free and oxygen containing atmospheres by metal organic chemical vapor deposition (MOCVD) [175]. Influence of oxygen on the properties of titania nanoparticles was investigated. With increasing oxygen flow rates, the average grain sizes of the nanoparticles decreased and the particle size distributions became uniform. Oxygen exerted great influence on the

nucleation rate of the nanoparticles and reaction kinetics occurred in the reactor. The formation of titania nanoparticles by MOCVD was not a growth controlled process but was a nucleation rate controlled process.

Cobalt nanoparticles encapsulated in carbon shells were synthesized by catalytic CVD in high yield by reducing with a  $\text{H}_2/\text{CH}_4$  gas mixture a  $\text{Mg}_{0.9}\text{Co}_{0.1}\text{O}$  solid solution impregnated MgO catalyst [176]. The carbon encapsulated Co nanoparticles had a narrow distribution of diameters within the range of 5–15 nm. They were made of fcc Co which is very stable to air oxidation and the magnetic properties confirmed that Co was present in the metallic state.

A modification of the conventional inert gas condensation apparatus was developed for making nanostructured powders, wherein an evaporative source was replaced by a chemical source [177]. CVC combines CVD together with cooling condensation in evaporation. This process was used to synthesize loosely agglomerated amorphous nanoparticles of  $\text{SiC}_x\text{N}_y\text{O}_z$ , starting from hexamethyldisilazane as precursor compound [177]. The density, surface area, particle size, and composition of as-synthesized nanoparticles of  $\text{SiC}_x\text{N}_y\text{O}_z$  were modified by changing the synthesis temperature and carrier gas. The phase and morphology of as-synthesized powders were modified by heat treatment.

A concept was introduced of synthesis of nonagglomerated nanoparticles by rapid condensation from the vapor phase in a reduced pressure environment [45]. The source of the material was an evaporative source, which is ideally suited for low vapor pressure and low melting point metals. A variation in this process was developed, in which the source of the nanophase material was a metalorganic precursor [178–180]. The process, called combustion flame chemical vapor condensation (CF-CVC), is a modification of the original CVC process which involves pyrolysis of chemical precursors in the gas phase. The key parameters are gas phase residence time, temperature of the hot-wall reactor, and precursor concentration in the carrier gas. Careful selection of flow parameters resulted in powders that were only loosely agglomerated, significantly enhancing their usefulness in commercial applications. The nanopowders had a narrow particle size distribution with a mean particle size controllable between 5 and 50 nm. The CVC processing unit is an effective nanoparticle generator that is suitable for many different types of materials, like SiC,  $\text{Si}_3\text{N}_4$ ,  $\text{Al}_2\text{O}_3$ ,  $\text{TiO}_2$ ,  $\text{ZrO}_2$ , and other refractory compounds. They extended the processing capabilities to include a flat flame combustor unit which is particularly suited to synthesis of oxide phases either as powders, films, coatings, or freestanding forms.

The ductile behavior of nanophase yttria doped zirconia ceramics was investigated during low-temperature deformation experiments [181]. Ceramics were produced by following a standard processing route of mechanical compaction of the dispersion mixed nanoparticles synthesized by inert gas condensation or CVC and pressureless sintering. The influence of initial grain size and porosity on strain and strain rate was a topic of interest as well as the microstructural evolution during deformation.

The effect of the ratio of  $\text{O}_2/\text{He}$  flow rate in the reactor on the characteristics of nanosized  $\text{TiO}_2$  powder synthesized

by CVC was investigated under fixed conditions of supersaturation ratio, collision rate, and residence time [182]. As the ratio of O<sub>2</sub>/He flow rate increased, the particle size of TiO<sub>2</sub> powder almost remained unchanged but the agglomeration of nanoparticles enlarged in which the degree of agglomeration was defined as the ratio of particle size to crystallite size.

A vapor phase synthesis process was developed, in which vapors of chemical precursors were pyrolyzed in a low pressure flat flame [183, 184]. By controlling the time-temperature history of the particles in the hot zone of the flame, high surface area nanopowders of oxides that have primary and secondary (aggregate) nanoscale particle sizes were produced. The synthesis process, scalability issues, powder properties, and areas of application were described.

Magnetic nanoparticles of Fe and Co were synthesized by CVC using the precursors of iron carbonyl [Fe(CO)<sub>5</sub>] and cobalt carbonyl as the sources under a flowing helium atmosphere [185–187]. Typical particle sizes were on the order of 5 to 13 nm with uniform dispersion. A correlation between the process parameters of CVC and the resulting microstructure of the nanoparticles was investigated. Average particle size increased with increasing the decomposition temperature of the precursor.

A series of iron-cobalt alloyed (Fe<sub>1-x</sub>Co<sub>x</sub>,  $x \leq 50$  wt%) nanoparticles with core/shell structure was prepared by CVC [188, 189]. The relation between the process parameters and the resulting characterization and microstructure and the crystalline structure after oxidation at different temperatures were studied. The particles had a mean size of 5–25 nm, which consisted of metallic cores and oxide shells. The nanoparticle size increased with increasing gas flow rate and decomposition temperature.

### 3.3.2. Solid-State Reactions

Solid-state reactions offer the possibility of generating nanoparticles by controlled phase transformations or reactions of solid materials. The advantage of this technology is its simple production route. The solid-state reaction technique is a convenient, inexpensive, and effective preparation method of monodisperse oxide nanoparticles/nanocapsules in high yield. Controlled growth of nanoparticles and their self-assembly into one-, two-, three-dimensional arrays by chemical methods are currently attracting considerable attention for potential applications in nanodevices.

An overview of the low-temperature heterogeneous and solid reactions was presented as a result of synthesis dispersed and nanophased powders of carbides based on molybdenum, tungsten, or titanium [190]. In known methods of synthesis of nanophased powders by physical and chemical vapor deposition, solution chemistry materials are assembled from atoms (or molecules) to nanoparticles in a bottom-up approach. Such methods have a long history of use in catalysis and colloid chemistry. Among known methods of low-temperature synthesis of nanophased powders, the catalytic reduction and following carbidization, activation of gas phase, and mechanical attrition were discussed. Primary attention was paid to the questions of dispersion and coalescence under topochemical reactions [190].

The different methods for encapsulating crystalline materials inside fullerene related structures were reviewed

[191]. The relationships between the mode of encapsulation and the crystallization behavior obtained in each case were described. The mechanisms of morphological and orientational control of crystallite growth inside carbon nanotubes and the comparative encapsulation behavior of materials encapsulated by physical and catalytic methods were discussed. The encapsulation of defect tungsten oxide structures within inorganic fullerene-like structures was described.

Preparation methods of zeolite molecular sieve membranes and films with and without support were reviewed [192]. Unsupported films were prepared by *in-situ* synthesis, casting of zeolite nanoparticles, and solid-state transformation, and supported films were obtained by *in-situ* synthesis, vapor-phase synthesis, secondary growth, casting of nanoparticles, and their combinations or modifications.

Core-shell nanoparticles of metal oxides ([Fe<sub>2</sub>O<sub>3</sub>]MgO, [Fe<sub>2</sub>O<sub>3</sub>]CaO, [V<sub>2</sub>O<sub>3</sub>]MgO, and the other first-row transition metal shell materials coated on nanoparticles of MgO or CaO) were studied as destructive adsorbents for CCl<sub>4</sub>, CHCl=CCl<sub>2</sub>, C<sub>5</sub>H<sub>4</sub>Cl<sub>2</sub>, CN<sub>3</sub>P(O)(OCH<sub>3</sub>)<sub>2</sub>, and SO<sub>2</sub> [193]. A catalytic effect due to the transition metal shell material was observed, where solid-state ion-ion exchange took place, thus allowing penetration into the MgO or CaO particles and thereby regenerating the transition metal oxide for additional catalytic action. Due to this catalytic effect, the destructive adsorption reaction became nearly stoichiometric, and therefore much higher capacities for destruction/immobilization of the adsorbate under study were realized. The catalytic effects were due to the intermediacy of transition metal chlorides, phosphates, or sulfites, which were mobile and sought out reactive sites on the MgO or CaO nanoparticles.

High yields of nanocrystals at ambient temperature were attained for several inorganic salts such as ZnS and CuO [194]. Edone-step, solid-state reactions between easily obtained starting materials such as CuCl<sub>2</sub> · 2H<sub>2</sub>O and NaOH were reported to give nanoparticles with narrow size distribution. The process was carried out in air and required no complex apparatus, reagents, or techniques and thus it showed potential for mass production of nanocrystals. All of the reactions involved hydrated salts, and the role of the water in the reaction mechanism was discussed.

Carbon-coated  $\alpha$ -iron particles were prepared through a simple heat treatment of mixtures of Fe<sub>3</sub>O<sub>4</sub> and polyvinylchloride at 1000 °C in an Ar flow [195]. Hollow carbon particles were obtained after HCl treatment of the particles to remove iron and iron compounds. According to thermogravimetric analysis of the Fe<sub>3</sub>O<sub>4</sub>-polyvinylchloride mixture, the formation of carbon-coated  $\alpha$ -iron particles proceeds in four steps with weight loss, the first two steps being due to the pyrolysis and carbonization of polyvinylchloride, and the last two to the reduction of Fe<sub>3</sub>O<sub>4</sub> to  $\alpha$ -Fe. Using the other transition metal oxides, NiO, CoO, and Cu<sub>2</sub>O, carbon-coated respective metal particles were also prepared using the same procedure.

Nano-oxides (SiO<sub>2</sub>, CeO<sub>2</sub>, SnO<sub>2</sub>) were successfully synthesized by solid-state reactions at ambient temperature [196–198]. For instance, tin oxide (SnO<sub>2</sub>) nanocrystals were synthesized by two-step solid-state reactions [198]. In the first step, the SnO fine particles were synthesized from the

reaction of  $\text{SnCl}_2 \cdot 2\text{H}_2\text{O}$  precursor with KOH in the size range of 500 nm. Then the fine particles were oxidized into nanosized  $\text{SnO}_2$  crystals with  $\text{O}_2$ . It is an environment friendly, convenient, inexpensive, and efficient preparation of  $\text{SnO}$  nanocrystals with grain size of 20 nm. Effects of calcination on the nanoparticles were studied. The mechanisms of the formation of nanomaterials by solid-state reactions at ambient temperature were primarily investigated. The shape and size control of nanoparticles with organic stabilizers were studied, which had one (or more) coordination group and long alkyl chain [199]. The organic stabilizers were used as the templates of nanoparticle self-assembly.

A simple one-step solid-state reaction in the presence of a suitable surfactant was developed for synthesizing PbS nanoparticles with diameters of 10–15 nm [200]. The surfactant  $\text{C}_{18}\text{H}_{37}\text{O}(\text{CH}_2\text{CH}_2\text{O})_{10}\text{H}$  in the formation of PbS nanoparticles was discussed, which played an important role in the preparation of PbS nanoparticles.

Barium hexaferrite particles between 1  $\mu\text{m}$  and 100 nm in diameter were prepared by solid-state reaction from different iron oxide precursors [201]. The characteristics of the iron oxide precursor in terms of particle size and its distribution were essential to prepare the hexaferrite at a significantly reduced temperature as well as to obtain particles with reduced size. When a goethite sample consisting of uniform particles of 200 nm length was used as iron oxide precursor, pure and uniform hexaferrite particles of around 100 nm diameter were obtained by heating up to 675 °C for 1 h the mixture of iron oxide and barium carbonate.

A form of fullerene-type carbon, named carbon nanoflask, was synthesized, using  $\text{CO}(\text{CO})_3\text{NO}$ , as a special precursor [202]. Upon its decomposition, the  $\text{CO}(\text{CO})_3\text{NO}$  was not only a source of carbon but also gave rise to fcc cobalt particles. After a careful purification process, the percentage of cobalt-filled carbon flasks was as high as 30%. The graphitic layers of the flask walls were over 100 nm thick, and much thicker than the flask cap. After an acid treatment of the sample, opened and empty carbon flasks were easily obtained.

Gold nanoparticles and nanowires encapsulated in carbon nanocapsules and nanotubes were spontaneously formed from one-dimensional self-organized gold nanoparticles on carbon thin films by annealing at 200–400 °C [203]. The one-dimensional arrangement of gold nanoparticles was strongly dependent on the adhesive force at the atomic step edges of amorphous carbon thin films. The gold crystals inside the nanotubes were distorted by the crystal growth of the nanowires. The result was expected as a fabrication technique for self-assembled ultra-large-scale-integration nanowires and cluster-protected quantum dots protected by nanocapsules and nanotubes at scales beyond the limits of current photolithography.

Stepwise adsorption of polyelectrolytes was used for the fabrication of micro- and nanocapsules with determined size, capsule wall composition, and thickness [204]. The capsule walls made of polyelectrolyte multilayers exclude high molecular weight compounds. Assembly of lipid layers onto these polyelectrolyte capsules prevented the permeation of small dyes. Encapsulation of magnetite nanoparticles and the features of these capsules were discussed.

Co-filled carbon nanocapsules, formed by a heat treatment of the mixture of Co and diamond nanoparticles, were studied [205]. The heat treatment reduced the surface native oxide ( $\text{Co}_3\text{O}_4$ ) of Co nanoparticles. The reduction was accompanied by graphitization of diamond nanoparticles, indicating that diamond nanoparticles in contact with the metallic Co were transformed into graphitic coating. *In-situ* TEM studies showed that the graphitic coating was formed in the heating process, not in the cooling process. Once the coating was completed, the number of the graphitic layers was almost constant on further heating and cooling. It was concluded that metallic Co particles simply acted as templates for graphitic coating.

Controlling the surface properties of nanoparticulate materials is necessary if they are exploited in applications such as colloidal crystals or biolabeling [206]. By tailoring the polymer flexibility and the electrostatic forces involved in polyelectrolyte adsorption onto highly curved gold surfaces, through variation of the total salt concentrations suspending the chains and spheres, the irreversible polyelectrolyte wrapping of gold nanoparticles can be affected. By consecutively exposing the nanoparticles to polyelectrolyte solutions of opposite charge, polyelectrolytes can be deposited in a layer-by-layer sequence, yielding gold nanoparticles coated with uniform polyelectrolyte multilayers. Self-supporting polyelectrolyte multilayered nanocapsules were formed after dissolution of the metallic core. The gold nanoparticle surface charge, created by the adsorption of anions, was insufficient to overcome the ionic and hydrophobic polyanion/polycation interactions, resulting in polymer desorption from the highly curved nanoparticle surface. One successful method to immobilize the charge on the gold nanoparticle surface was to covalently attach an anionic thiol before polyelectrolyte modification.

Formation of carbon nanocapsules with various clusters ( $\text{SiC}$ , Au, Fe, Co, Ge, and  $\text{GeO}_2$ ) by polymer pyrolysis was investigated [207], and nanocapsules with  $\text{SiC}$  and Au nanoparticles were produced by thermal decomposition of polyvinyl alcohol at around 500 °C in Ar gas atmosphere [164, 165, 207].

Preparation of polycyclodextrin hollow spheres by templating gold nanoparticles was reported [208]. Oxidation of gold nanoparticles protected by thiolated  $\beta$ -cyclodextrin molecules led to formation of water-soluble polycyclodextrin nanocapsules held together by S–S bonds.

$\beta$ - $\text{SiC}$  nanorods were synthesized by the reaction of  $\text{SiO}$  and carbon nanocapsules [209]. For the synthesis of  $\text{SiC}$  nanorods, the reaction temperature and the ratio of  $\text{SiO}$  to carbon nanocapsules were important and the most appropriate temperature and ratio were around 1380 °C and 5:2, respectively. Most of the  $\text{SiC}$  nanorods were straight and had diameters of 30–150 nm while the  $\text{SiC}$  tips of the  $\text{SiC}$  nanorods were 100–400 nm in size. Each  $\text{SiC}$  nanorod had one kind of preferential axis direction, which was either parallel or normal to the [111] direction. A possible growth mechanism of the  $\text{SiC}$  nanorods was proposed.

Dispersed  $\text{Eu}^{3+}$  cations in an aqueous  $\text{EuCl}_3$  solution easily incorporated in pores in a hydrogenated porous  $\text{AlO}(\text{OH}) \cdot \alpha\text{H}_2\text{O}$  boehmite powder [210].  $\text{H}_2$  gas in pores and  $\text{OH}^-$  anions from energized boehmite with pores converted  $\text{EuCl}_3$  into  $\text{Eu}_2\text{O}_3$  in pores as per the reaction 2



$\text{EuCl}_3 + 3/2\text{H}_2 + 3 \text{OH} \rightarrow \text{Eu}_2\text{O}_3 + 6 \text{HCl}$ , in a closed reactor at room temperature. The obtained  $\text{Eu}^{3+}:\text{Al}_2\text{O}_3$  product consisted of dispersed  $\text{Eu}_2\text{O}_3$  nanoparticles (crystallite size was about 30 nm) in an amorphous  $\text{Al}_2\text{O}_3$  in a mesoporous structure. On heating,  $\text{Eu}_2\text{O}_3$  nanoparticles dissolved in high surface energy pores and resulted in a complete amorphous structure of  $\text{Eu}^{3+}:\text{Al}_2\text{O}_3$  at about 700 K. A controlled reconstructive nucleation and growth into  $\gamma\text{-Al}_2\text{O}_3$  nanoparticles (crystallite size was about 6.5 nm) occurred from the amorphous state at about 1000 K.

### 3.3.3. Sol–Gel

The sol–gel method is a process, consisting of solution, sol, gel, solidification, and heat treatment of metal organic or inorganic compounds, which is applicable to preparation of metal oxides and other compounds [211, 212]. The processing parameters can be controlled well at the beginning step so that the uniformity can be achieved at the scale of micrometers, nanometers, and even at the level of molecules, and the micro/nanostructures of the materials can be controlled/designed. The advantages of the sol–gel method are high purity due to no need for mechanical mixing; good chemical homogeneity and structural/composition uniformity; small particle size and narrow size distribution; low process temperature; simple technology and equipment; etc. The mechanisms for the formation of the sol–gel are traditional colloid type, inorganic polymer type, and complex type. The sol–gel method can be used for producing nanoparticles, nanocapsules, thin films, fibres, nanocomposites, and bulk materials. The sol–gel procedure allows coating of templates with complex shapes on the micrometer to nanometer scale, which some commonly used coating procedures cannot achieve. In addition, sol–gel coating techniques can be applied to delicate systems without disruption of their structure or functionality, for example, the coating of bio-complexes or organic aggregates, such as organogelators. Three-dimensional structures with elaborate pore architectures, such as polymer membranes and gels, can also be infiltrated with sol–gel solutions to achieve nanocoatings.

Carbon nanocapsules and nanotubes were formed by one-dimensional self-organization of gold nanoparticles, caused by the adhesive force at the step edge of amorphous carbon thin films [213]. The technique used was expected to be promising for self-assembly of nanowires and cluster-protected quantum dots at scales beyond the limits of current photolithography.

Investigation of encapsulation and solvatochromism of fullerenes in binary solvent mixtures was reported [214]. Fullerenes, when dissolved in certain binary solvent mixtures, were found to exhibit strong solvatochromism and an unusual chemical inertness. From ultraviolet-visible (UV-vis) optical absorption measurements, dynamic light scattering size measurements, and chemical tests on  $\text{C}_{60}$ /pyridine/water mixtures, the origin of these unusual effects was the formation of monodisperse, spherical, and chemically inert  $\text{C}_{60}$  nanocapsules. Pyridine acted as a surfactant around fullerene molecules protecting them from chemical reagents. The hydrophobic surfactant interactions were thought to act in stabilizing the structures into chemically inert, uniformly sized particles.

Using vesicular polymerization, water-soluble polyelectrolyte nanocapsules were prepared which were able to undergo a reversible swelling transition upon changing the pH and/or salt concentration [215]. The solvation of Nafion oligomer in equimolar water–methanol solution was studied by means of molecular dynamics simulations [216]. Star-shaped patterns, which were composed of rodlike nanoparticles with diameters of 4–7 nm and lengths ranging from 150 to 200  $\mu\text{m}$ , were prepared by a convenient microemulsion technique at room temperature [217]. The hydrophobic carbon chain of surfactant played an important role in controlling the morphology of the product. This microemulsion method was relatively mild and of low toxicity, which provided a route to the production of other metal sulfide patterns at room temperature.

A type of supramolecular compound, molybdenum-oxide-based composite was formed, consisting of magnetic nanocapsules with encapsulated keggion electron reservoirs cross-linked to a two-dimensional network [218].

Ag colloid-containing coatings on soda lime glass and fused silica were prepared via the sol–gel process [219]. To incorporate  $\text{Ag}^+$  ions in the coatings homogeneously, they are stabilized by a functionalised silane (aminosilane) and then mixed with the basic sol prepared from 3-glycidoxypropyl trimethoxysilane and tetraethoxysilane. Crack-free and transparent coatings with thickness of 0.5 to 1.2  $\mu\text{m}$  were obtained by heat treatment between 120 and 600  $^\circ\text{C}$ . The Ag-colloid formation was monitored by UV-vis spectroscopy as a function of temperature. The substrate had a deciding influence on the Ag-colloid formation caused by alkali diffusion from the substrate into the coating. Polycrystalline  $\text{Ag}_x\text{O}_y$  nanoparticles formed during thermal densification in the coatings, which was accompanied by a vanishing of the yellow color of the coatings.

One-dimensional composite nanostructures (i.e., a  $\beta\text{-SiC}$  nanorod within a  $\text{SiO}_2$  nanorod) were synthesized by the combination of a carbothermal reduction at 1650  $^\circ\text{C}$  and a heating at 1800  $^\circ\text{C}$  of sol–gel derived silica xerogels containing carbon nanoparticles [220, 221]. The composite nanostructures were more than 20  $\mu\text{m}$  in length. The diameters of the center thinner  $\beta\text{-SiC}$  nanorods were typically in the range of 10–30 nm, while the outside diameters of the corresponding thicker amorphous  $\text{SiO}_2$  nanorods were between 20 and 70 nm. Large quantities of SiC rod nuclei and the nanometer-sized nucleus sites on carbon nanoparticles were both favorable to the formation of much thinner  $\beta\text{-SiC}$  nanorods. The formation of the outer coaxial thicker amorphous  $\text{SiO}_2$  nanorod was from the combination reaction of decomposed SiO vapor and  $\text{O}_2$  during cooling.

Two sol–gel fabrication processes were investigated to make silica spheres containing Ag nanoparticles: (1) a modified Stober method for silica spheres below 1  $\mu\text{m}$  size, and (2) a  $\text{SiO}_2$  film formation method on spheres of 3–7  $\mu\text{m}$  size [222]. The spheres were designed to incorporate silver nanoparticles in a spherical optical cavity structure for the resonance effect. For the incorporation, interaction between  $[\text{Ag}(\text{NH}_3)_2]^+$  ion and SiOH was important. In the Stober method, the size of the silica spheres was determined by a charge balance of plus and minus ions on the silica surface. In the film formation method, the capture of Ag complex ion on the silica surface depended on whether the surface

was covered with OH groups. After doping  $[\text{Ag}(\text{NH}_3)_2]^+$  into silica particles or  $\text{SiO}_2$  films on the spheres, these ions were reduced by  $\text{NaBH}_4$  to form silver nanoparticles. From plasma absorption at around 420 nm wavelength and TEM photographs of nanometer-sized silver particles, their formation inside the spherical cavity structures was confirmed.

Poly(*N*-vinyl 2-pyrrolidone)-protected gold clusters, incorporated into silica ( $\text{SiO}_2$ ) glass by a sol-gel process, were reported [223]. A sol-gel process was developed for fabricating inherently homogeneous nanocomposites involving precipitation of nanoparticles, coating the nanoparticles with a film of matrix phase, and powder formation and sintering [224].

Injectable and sprayable nanometer size hydrated silica particles encapsulating high molecular weight compounds such as [I-125]tyraminylinulin (mol wt 5 kD), fluorescein isothiocyanate-dextran (mol wt 19.6 kD), and horseradish peroxidase (mol wt 40 kD) were prepared [225]. The size of these particles was below 100 nm in diameter and the entrapment efficiency was found to be as high as 80%. Enzymes entrapped in these particles show Michaelis-Menten kinetics and the catalytic reaction took place only after the diffusion of substrate molecules into the particles through the pores of the silica matrix. Peroxidase entrapped into silica nanoparticles showed higher stability toward temperature and pH changes compared to free enzyme molecules.

A chemically bound  $\text{TiO}_2$  layer was created on silica using a grafting method of chemical surface coating [226].  $\text{TiCl}_4$  and  $\text{H}_2\text{O}$  were used as reagents in successive cycles. The  $\text{TiO}_x$  layer is constituted of nanoparticles of anatase homogeneously spread over the surface. Calcination of the  $\text{TiO}_2$ - $\text{SiO}_2$  materials led to a particle size increase. An extensive pore size analysis was undertaken to investigate the morphological changes as a function of the number of reaction cycles.

Nanosized Ce-doped silica particles (without and with Al addition) dispersed within pores of mesoporous silica host were synthesized by soaking and sol-gel techniques [227]. The dispersed phosphor particles were mainly located within the pores that were less than 4 nm in diameter. There existed two luminescence peaks at about 350 and 700 nm, respectively, for this phosphor in the dispersed or aggregated state. For the dispersed system, the luminescence intensities of both peaks are more than 14 times higher than those of the aggregated one, and the shoulders on the lower sides of the luminescence peaks disappear.

Ellipsoidal mesoscale “eggshells” were prepared by a template-directed synthesis using a sol-gel precursor [228].  $\text{TiO}_2$  shells of micrometer sizes would have great potential as containers in microencapsulation and their ellipsoidal shape would provide them with a range of interesting optical, mechanical, and hydrodynamic properties.

Nanohybrids containing nonstoichiometric zinc ferrite of spinel structure in an amorphous silica matrix exhibited a fundamentally different structure to that formed by stoichiometric zinc ferrite [229]. A unique cluster glass structure, where nanocrystallites of zinc ferrite existed in amorphous Fe-rich pockets, occurred at the significantly high Fe/Zn molar ratio of 10. The occurrence of zinc ferrite crystallites due to the  $\text{Zn}^{2+}$  deficiency, together with the confinement of

the silica matrix, suppressed the nucleation and crystallization of  $\alpha\text{-Fe}_2\text{O}_3$  to a temperature above 900 °C, preserving the cluster glass structure.

A route was described for the synthesis of nanometric Ni particles embedded in a mesoporous silica material with excellent potential for catalytic applications [230]. Mesoporous silica with a surface area in the range of 202–280  $\text{m}^2/\text{g}$  with narrow pore size distribution and Ni nanoparticles (particles in the range of 3–41 nm) were obtained in a direct process. A different approach was adopted to process such a nanocomposite, which was based on the formation of a polymer with the silicon oxianion and nickel cation chelated to the macromolecule structure and on the control of the pyrolysis step. The  $\text{CO}/\text{CO}_2$  atmosphere resulting from the pyrolysis of the organic material promoted the reduction of the Ni citrate.

The hybrid materials were investigated, consisting of nonagglomerated iron oxide particles hosted in silica aerogels [231]. The composite material can be produced as a monolith, in any shape, and with different dilutions of the iron oxide phase. Two sol-gel chemistry routes followed: a solution of  $\text{Fe}(\text{NO}_3)_3 \cdot 9\text{H}_2\text{O}$  was added either to the silica gel or to the initial sol, and the iron salt provided the water required for the gel polymerisation. To obtain monolithic aerogels, the gels were dried by hypercritical solvent evacuation. On the other hand, some gels were dried by slow and controlled evaporation of the solvent, resulting in xerogels. Several heat treatments were performed and the iron oxide particle phase, growth mechanism, and crystallinity were analyzed.

Mesoporous nanocrystalline titanium dioxide with narrow pore size distribution was prepared by a sol-gel technique, when butanediol mixed with tetrapropylthotitanate was used as precursor [232]. The aging time for the synthesis had an evident influence on the phase transition of  $\text{TiO}_2$  and the nucleation process. A very fine network texture made from uniform nanoparticles was revealed. The mesoporous structure of as-prepared titania was maintained after a heat treatment at 350 and 400 °C for 1 h, exhibiting a significant thermal stability. Four titania crystal phases (amorphous, anatase, anatase-rutile, rutile) were observed at different calcination temperatures.

$\gamma\text{-Fe}_2\text{O}_3/\text{SiO}_2$  nanocomposites were prepared using a sol-gel procedure, starting from iron nitrate and triethyl orthosilicate [233]. The addition of acids to the sols resulted in a way to increase particle size, keep iron concentrations low, and narrow the particle size distribution of  $\gamma\text{-Fe}_2\text{O}_3$  in the glass composite. The addition of 0.56 mmol HCl (approximate to 0.1 M) to a solution having an Fe/Si molar ratio of 18% led to an increase of  $\gamma\text{-Fe}_2\text{O}_3$  particle size from 6 to 13 nm together with a remarkable decrease in the polydispersity degree of the particle size from 66% to 15%. The iron oxide crystalline phase, the particle size and shape, and the homogeneity of the resulting nanocomposites were studied. The influence of acid addition on the size of the magnetic particles was found to depend on the matrix microstructure, the charge environment, and the presence of counteranions of the acids.

A study was reported of the formation of particles of Ni-Zn ferrites embedded in a xerogel  $\text{SiO}_2$  matrix [234]. Initial solutions were prepared mixing tetraethyl

orthosilicate, distilled water, ethanol, and three different nitrates: iron, nickel, and zinc. Formation of  $\text{Ni}_{0.5}\text{Zn}_{0.5}\text{Fe}_2\text{O}_4$  as well as structural modifications of the  $\text{SiO}_2$  matrix induced by these particles were discussed. The composites of  $\gamma\text{-Fe}_2\text{O}_3/\text{SiO}_2$  and  $\alpha\text{-Fe}_2\text{O}_3/\text{SiO}_2$  were reported, starting from three different iron precursors: iron nitrate, iron chloride, and nanometric Fe particles prepared by aqueous chemical reduction [235].

Nanocoating, the covering of materials with a layer on the nanometer scale or covering of a nanoscale entity, to form nanocomposites and structured materials using the sol-gel process was reviewed [236]. Templates from spherical nanoparticles to complex bicontinuous networks were discussed, where either the coated material or the structured inorganic hollow frame resulting after removal of the template were of interest in fields of application ranging from information storage to catalysis.

### 3.3.4. Precipitation

The precipitation method is a convenient and powerful technique for synthesizing nanoparticles and nanocapsules. Dissolvable salt solution consisting of one type or multitypes of ions could be hydrolyzed at a certain temperature when precipitator, like  $\text{OH}^-$ ,  $\text{C}_2\text{O}_4^{2-}$ ,  $\text{CO}_3^{2-}$ , etc., is added. The hydrates, hydrate oxides, or salt would form and separate out from solution. The oxide powders can be obtained by washing the anions in the solution and the solvent, and subsequently by pyrogenation or dehydration. When the precipitator is added in the solution consisting of multitypes of cations, the complete precipitation of all the ions is the so-called co-precipitation method. The co-precipitation method consists of single-phase co-precipitation and mixture co-precipitation. Only a single compound or solid solution is the sediment in the former process, whereas the mixture deposits in the latter one. If one of the sediments were grown on the surface of others and the powders were in nanoscale, nanocapsules would form by employing the co-precipitation method. The advantages of the precipitation method are: high purity, high uniformity, small particle size, narrow size distribution, and structural/composition uniformity. Precipitation is a promising method for the economical production of commercial amounts of nanoparticles/nanocapsules because it is fast and operable at ambient temperature.

ZnO nanoparticles in the size range from 2 to 7 nm were prepared by addition of LiOH to an ethanolic zinc acetate solution [237]. Nanoparticles of a model drug, viz. cholesteryl acetate, were prepared [238]. The cholesteryl acetate was dissolved in cyclohexane containing lecithin. The organic solution was emulsified in an aqueous solution containing a cosurfactant and a stable oil/water (o/w) emulsion resulted. The solvent was evaporated from the emulsion and cholesteryl acetate precipitated in the emulsion droplets. The size of the particles was almost unaffected by the concentration of cholesteryl acetate in cyclohexane.

A methodological description of heterogeneous polymerization processes, including suspension, emulsion, dispersion, and precipitation polymerization, was presented [239]. The discussion focused on the initial state of the polymerization mixture, the mechanism of particle formation, and

the shape and size of polymer particles produced in different heterogeneous polymerization systems. The dependence of particle size and morphology on manufacturing parameters such as emulsifier, stabilizer, reactor design, and stirring speed was discussed. Special topics, including emulsifier-free (soapless) emulsion polymerization, seeded polymerization, and the formation of core-shell particles were covered.

Nanoparticles of barium ferrite ( $\text{BaFe}_{12}\text{O}_{19}$ ) were synthesized using a method called microemulsion processing [240]. The aqueous cores (typically 5–25 nm in size) of water-cetyltrimethylammonium bromide-*n*-butanol-octane microemulsions were used as constrained microreactors for the co-precipitation of precursor carbonates (typically 5–15 nm in size). The carbonates formed were separated, dried, and calcined to form nanoparticles (less than 100 nm) of barium ferrite.

Cubic structured CdS, CdSe, and CdTe, II-VI semiconductor nanoparticles were synthesized using aqueous solution precipitation at room temperature [241]. Thermal annealing caused an increase in particle size, a structural transition from the cubic to the bulk hexagonal structure for CdS and CdSe, and no structural transition for CdTe.

Well defined spherical particles of  $\gamma\text{-Fe}_2\text{O}_3$  were synthesized in the pores of a polymer matrix in the form of beads by an ion exchange and precipitation reaction [242]. The particle size distribution was Gaussian with an average diameter of 8 nm. The particles were superparamagnetic with a blocking temperature  $T_b$  of about 55 K. The optical absorption edge of the mesoscopic system was redshifted with respect to single crystal films of  $\gamma\text{-Fe}_2\text{O}_3$  with an absorption tail extended deeply in the gap.

A kind of fullerene, a carbon nanoparticle encapsulating  $\beta\text{-SiC}$  grain, was precipitated during cooling  $\text{Al}_2\text{O}_3\text{-Y}_2\text{O}_3\text{-CaO}$  oxide melt containing SiC and C from 2023 K [243]. The SiC grains with a diameter of 5–20 nm were covered with 2–4 graphitic carbon layers with spacings of 0.34 nm.

Polyacrylamide-silver nanocomposites with silver nanoparticles well dispersed in polyacrylamide matrix were synthesized by  $\gamma$ -irradiation at ambient conditions in alcohol solvent [244]. The nanocomposites consisted of Mo phases, metallic silver, and polyacrylamide. The amount of silver present as metallic species in polyacrylamide matrix was measured by precipitation titration. The infrared (IR) spectrum confirmed the polymerization of acrylamide monomer and the formation of polyacrylamide in ethanol upon  $\gamma$ -irradiation.

The biocatalytic systems from nanocapsules containing  $\alpha$ -chymotrypsin in the inner aqueous cavities were prepared [245], which acted in both the organic solvent and the aqueous medium. For such encapsulation, the reversed hydrated micelles from *N,N*-diallyl-*N,N*-didodecyl ammonium bromide (DDAB) in cyclohexane ( $w_0 = 22$ ), including  $\alpha$ -chymotrypsin, were polymerized by UV initiation. After precipitation by acetone, these nanocapsules were moved into the aqueous medium with the aid of ionic or non-ionic surfactants. In this case, unilamellar liposomes were formed. They had the inner monolayer from the poly-DDAB network and the outer one predominantly from surfactant molecules. According to the light-scattering data, the average outer diameter of nanocapsules equals 20 nm. The

vesicular “coated”  $\alpha$ -chymotrypsin was used for study of enzymatic activity.

The lattice dynamics of nanoparticles of Co embedded in Ag, created by ion implantation and subsequent annealing, were investigated [246]. A type of material that was able to produce giant strain in a nonhomogeneous magnetic field was developed [247]. In these magnetic-field-sensitive gels (ferrogels) fine colloidal particles having superparamagnetic behavior were incorporated into a highly swollen elastic polymer network. Magnetic properties were interpreted on the basis of a core-shell model.

Mössbauer spectroscopy in combination with atomic scale modeling was used in order to gather a comprehensive understanding of the growth and the dynamics of cobalt nanoprecipitates in silver [248]. The modeling made use of classical molecular dynamics in the canonical ensemble by means of the Rahman-Parinello technique.

Organic nanoparticles of cholesterol, Rhovanil, and Rhodiarome were synthesized in different microemulsions [AOT/heptane/water; tritonidecanol/water; cetyltrimethylammonium bromide (CTABr)/hexanol/water] by direct precipitation of the active compound in aqueous core under continuous ultrasound treatment [249]. The size of the nanoparticles depended on different parameters such as the concentration of the organic molecules and the diameter of the water cores, which was related to the ratio  $R = [H_2O]/[surfactant]$ .

Polyvinyl alcohol coated magnetic particles (PVA ferrofluids) were synthesized by chemical co-precipitation of  $Fe^{2+}/Fe^{3+}$  salts in 1.5 mol/L  $NH_4OH$  solution at 70 °C in the presence of PVA [250]. The resultant colloidal particles had core-shell structures, in which the iron oxide crystallites formed the cores and PVA chains formed the shells. The hydrodynamic diameter of the colloidal particles was in the range of 108 to 155 nm, which increased with increasing PVA concentration from 5 to 20 wt%. The size of the magnetic cores was relatively independent of PVA concentration.

Nanoparticles of various compositions were fabricated by chemical processes [251], like sol-gel processes and precipitation processes, and surface modifiers acted as vehicles to tailor surface chemistry, to tailor the  $\zeta$  potential, and to avoid agglomeration.

A line was drawn from the controlled preparation and understanding of Langmuir monolayers to the fabrication of hollow capsules [252]. Polymeric ultrathin films were permeable to small molecules, which could be used to prepare capsules after coating depolymerizable colloids. The inside of the capsule was designed such that it was distinguished by inner walls and pH in the interior in order to perform a specific chemistry. As an application example, selective precipitation of a dye molecule as a model for drug loading was presented.

Precipitation in the nanostructured  $Cr_3C_2/NiCr$  coatings was investigated [253].  $Cr_2O_3$  particles with an average size of 8.3 nm were observed in the nanostructured  $Cr_3C_2/NiCr$  coatings exposed to elevated temperatures. In addition to the precipitation of oxide particles, the phase transformations in the original NiCr amorphous phase were always observed in the as-sprayed nanostructured  $Cr_3C_2/NiCr$  coatings. The increases in microhardness and scratch resistance

and decrease in coefficient of friction of the nanostructured coatings were attributed to a high density of oxide nanoparticles precipitating within the coating as the exposure temperature increased.

A composite film of titanium dioxide ( $TiO_2$ ) nanoparticles and hydrolyzed styrene-maleic anhydride alternating copolymer (HSMA) was obtained on a substrate when a  $TiCl_4$  solution was heated at 80 °C with a spin-cast thin HSMA film present in the solution [254]. The  $TiO_2$  nanoparticles discretely dispersed on the polymer layer, which were dominantly rutile phase, of a spherical shape and 18–20 nm in diameter. In contrast, mainly amorphous  $TiO_2$  powders were obtained from the identical  $TiCl_4$  solution by drying the solution with the absence of the HSMA film. The  $TiO_2$  nanoparticles deposited on the polymer layer were regarded to contain polymer chains, and a multilayered core-shell model was suggested for the formation of these composite nanoparticles.

Nanostructured coatings on metals, plastics, and textiles have numerous applications, for example, as antifogging and self-cleaning coatings as well as protective coatings against corrosion, heat, or wear. The preparation at low temperature of dense nanostructured tetragonal  $ZrO_2$  coatings via a modified emulsion precipitation method was presented [255]. The method, which involved the controlled preparation, crystallization, and densification of nonagglomerated  $ZrO_2$  nanoparticles, opened up the possibility of applying nanocoatings of high-melting oxides to steel or plastic, where low temperatures were required.

Spontaneous core-shell and shell-shell reactivities of thiolate-capped nanoparticles were exploited for assembling nanoparticle network thin films via an exchange-cross-linking-precipitation route [256]. Gold nanoparticles of two different core sizes (2 and 5 nm) capped with decanethiolates and alkylthiols of two different functionalities, 1,9-nonanedithiol (NDT) and 11-mercaptoundecanoic acids (MUA), were studied as the assembly components. The film formation and growth involved intercore covalent Au-thiolate bonding at both ends of NDT, or intershell non-covalent hydrogen bonding at carboxylic acid terminals of MUA shells.

Synthesis and coating of superparamagnetic monodispersed iron oxide nanoparticles were carried out by a chemical solution method [257]. A controlled coprecipitation technique was used to prevent undesirable critical oxidation of  $Fe^{2+}$ . The obtained  $Fe_3O_4$  nanoparticles were coated with sodium oleate.

Doped ZnS nanoparticles were synthesized using a chemical coprecipitation of  $Zn^{2+}$ ,  $Mn^{2+}$ ,  $Cu^{2+}$ , and  $Cd^{2+}$  with sulfur ions in aqueous solution [258]. The diameter of the particles was close to 2–3 nm. The unique luminescence properties, such as the strength (its intensity is about 12 times that of ZnS nanoparticles) and stability of the visible-light emission, were observed from ZnS nanoparticles codoped with  $Cu^{2+}$  and  $Mn^{2+}$ .

A method of preparing CdS nanoparticles inside MCM-41 was described [259]. This method made use of the unique interfacial properties of selectively functionalized ordered mesoporous materials to deliver cadmium ions inside the mesopores of MCM-41 via an ion-exchange reaction, thereby minimizing uncontrolled precipitation reactions of

cadmium ions outside the mesopores. The general methodology can also be used to prepare other sulfide, telluride, and oxide nanoparticles.

$\text{Co}_3(\text{BO}_3)_2$ /surfactant composites were prepared by the controlled precipitation of aqueous cobalt cations together with surfactant [260]. The composite showed a layered structure, in which the  $\text{Co}_3(\text{BO}_3)_2$  layers of about 6 Å in thickness were in alternation with surfactant bilayers. There was a freezing temperature at low temperature (<6 K) and the temperature was weakly frequency dependent. All the experimental observations suggested that the multilayers were spin glass in nature.

Thermoresponsive, core-shell poly-*N*-isopropylacrylamide (*p*-NIPAm) nanoparticles (microgels) were synthesized by seed and feed precipitation polymerization, and the influence of chemical differentiation between the core and shell polymers on the phase transition kinetics and thermodynamics was examined [261]. The core-shell architecture was a powerful one for the design of colloidal “smart gels” with tunable properties. The addition of small concentrations of a hydrophobic monomer (butyl methacrylate, BMA) into the particle shell produced large decreases in the rate of thermally induced particle collapse.

BN tassellike and treelike nanostructures were synthesized through a CVD method [262]. The tassellike morphology was made up of a BN bamboo-shaped nanotube and numerous polyhedral particles attached onto it. The tree consisted of a BN main stem and many BN nanotube branches growing outward from it. The attachments, either particles or nanotube branches, remained adhered to the primary stems even after 15 min sonication treatment, indicating the high stability of these nanostructures. The formation of these unusual structures was proposed to arise from a two-stage deposition process: First, primary BN stems were formed, followed by subsequent precipitation of amorphous clusters onto the rough outer surfaces. Second, polyhedral particles or BN nanotubes nucleated and grew on the outer surface as a result of further deposition from the vapor phase.

An approach to incorporate different polymers into micro- and nanocapsules fabricated by means of layer-by-layer adsorption of oppositely charged polyelectrolytes on colloidal particles was proposed [263]. This method comprised two stages. At first, the polymers, which were supposed to be incorporated, precipitated on the surface of colloidal particles. This can be done either by complexation of polyelectrolytes with multivalent ions or by adding miscible nonsolvents. Then stable layer-by-layer assembled polyelectrolyte shells were formed. After core decomposition, the inner polymer molecules were released from the wall but were captured by the outer shell and floated in the capsule interior. The possibilities to encapsulate a wide class of charged and noncharged polymers were demonstrated on such examples as sodium poly(styrene sulfonate) as a polyanion, poly(allylamine hydrochloride) as a polycation, and Dextrane as noncharged water soluble polymer.

A method for the preparation of composite nanoparticles  $\text{SiO}_2/\text{ZnO}$  by the controlled double-jet precipitation technique was described [264]. On the silica ( $\text{SiO}_2$ ) surface, the ZnO nanoparticles were coated as thin layers or nanoclusters, depending on the reaction conditions.

Various  $\text{Au}/\text{Fe}_2\text{O}_3$  catalysts were prepared by the coprecipitation method, and CO oxidation was studied at ambient temperature and in the presence of water vapor in the feed [265]. The precipitation method and the calcination temperatures had a significant effect on the catalytic performance of CO oxidation. The stability was related to the particle size of metallic gold and  $\alpha\text{-Fe}_2\text{O}_3$  and the oxidation state of gold and the iron crystalline phase. The sintering of the gold particles, the reduction of oxide gold to metallic gold, the accumulation of carbonate, and a decrease in the specific surface area were observed during the reaction.

The process control of precipitation, due to the rapidity of the involved processes of mixing, nucleation, growth and agglomeration, and the stabilization against agglomeration represented challenges to this method. Schwarzer et al. showed how these challenges can be successfully handled [266]. The focus was set on how to tailor the particle-size distribution in continuous precipitation [266]. Precipitation experiments with barium sulfate in a T-mixer were presented. It was found that the size of the precipitated primary particles was strongly dependent on the mixing intensity. On increasing the mixing intensity, it was possible to generate particles of approximately 50 nm in diameter. The second challenge, to stabilize the particles against agglomeration, was successfully met by adsorbing potential-determining ions on the particle surfaces (i.e., by increasing repulsive particle interactions). Thus, stable suspensions of barium sulfate nanoparticles were obtained.

Strontium ferrite nanoparticles were prepared by coprecipitation in a polyacrylic acid (PAA) aqueous solution [267]. The average diameter of the mixed hydroxide precipitates was 3.1 nm. The average diameters of the strontium ferrite nanoparticles calcined at 700 and 800 °C were 34 and 41 nm, respectively.

The effects of the interactions of metal ions with lipoic acid-capped Ag and Au nanoparticles were studied [268], which were dependent on the metal ion concentration. First, in the dilute regime, there was reversible chelation of the metal ions, causing a marked dampening of the plasmon resonance band of the nanoparticles, but there was no aggregation. The magnitude of plasmon dampening depended on the nature as well as the concentration of the metal ions. In the intermediate concentration regime, aggregation occurs, but in the high concentration regime, there was precipitation.

Nanoparticles of a series of magnetic ferrites ( $\text{MFe}_2\text{O}_4$ ,  $\text{M} = \text{Zn}, \text{Ni}, \text{Co}, \text{Cu}, \text{Mn}$ ) were fabricated by hydrothermal precipitation [269]. The results on the mechanochemical synthesis of  $\text{CaCO}_3$ ,  $\text{Cr}_2\text{O}_3$ , and  $\text{Nb}_2\text{O}_5$  nanopowders were reported [270]. The volume fraction of the matrix phase was crucial to the formation of separate, unagglomerated particles. With  $\text{Cr}_2\text{O}_3$  and  $\text{Nb}_2\text{O}_5$ , amorphous particles were formed by mechanochemical reaction and a low temperature heat treatment was required for crystallization.

A heterogeneous precipitation method was described for obtaining nanocomposite powders consisting of Ni nanoparticles homogeneously dispersed within  $\gamma\text{-Al}_2\text{O}_3$  [271]. The amorphous  $\text{Al}(\text{OH})_3$  was nucleated on the surfaces of NiO nanoparticles and crystallized to  $\gamma\text{-Al}_2\text{O}_3$  at 900 °C. The porosity of  $\gamma\text{-Al}_2\text{O}_3$  allowed the growth of NiO

nanoparticles during calcinations. After the calcined nanocomposite powders were selectively reduced at 700 °C in a hydrogen atmosphere, NiO nanoparticles were converted to Ni with the size of 25–35 nm, which were uniformly dispersed in the  $\gamma$ -Al<sub>2</sub>O<sub>3</sub> matrix.

Nanosized nickel aluminate spinel particles were synthesized with the aid of ultrasound radiation by a precursor approach [272]. Sonicating an aqueous solution of nickel nitrate, aluminum nitrate, and urea yielded a precursor that on heating at 950 °C for 14 h yielded nanosized NiAl<sub>2</sub>O<sub>4</sub> particles with a size of 13 nm and a surface area of about 108 m<sup>2</sup> g<sup>-1</sup>.

The precipitation and condensation of submicrometer organic particles were reviewed [273]. The importance of physical state effects was discussed, and the role of compartmentalization in controlling particle size was introduced. The thermodynamic driving forces for precipitation and phase transformation were briefly reviewed. The use of emulsification as a primary step in producing small particle dispersions was described with photographic and pharmaceutical applications. Precipitation driven by solvent shifting was illustrated and applications in preparing organic–inorganic composites and protein coacervation were described. Miscible solvent–nonsolvent induced precipitation was outlined and followed by related applications using supercritical fluid technology. The applications of organic particle precipitation in reverse microemulsion systems were described. The applicability of gas condensation methods and of precipitation in submicrometer hollow spheres and dye entrapment in submicrometer polymer gel networks were discussed.

### 3.3.5. Hydrothermal Methods

Hydrothermal methods include all chemical reactions in water in high temperatures and high pressures. The hydrothermal methods consist of hydrothermal oxidation, hydrothermal precipitation, precipitation synthesis, hydrothermal deoxidization, hydrothermal decomposition, hydrothermal crystallization, etc. The hydrothermal reactions can be used to prepare nanoparticles as well as nanocapsules. The typical chemical reactions are listed as follows:

- (1) the hydrothermal oxidation:  $mM + nH_2O \rightarrow M_mO_n + H_2$ , where M = Cr, Fe, and their alloys,
- (2) the hydrothermal precipitation:  $KF + MnCl_2 \rightarrow KMnF_2$ ,
- (3) the precipitation synthesis:  $FeTiO_3 + KOH \rightarrow K_2O \cdot nTiO_2$ ,
- (4) the hydrothermal deoxidization:  $Me_xO_y + yH_2 \rightarrow xMe + yH_2O$ , where Me = Cu, Ag, etc.,
- (5) the hydrothermal decomposition:  $ZrSiO_4 + NaOH \rightarrow ZrO_2 + Na_2SiO_3$ ,
- (6) the hydrothermal crystallite:  $Al(OH)_3 \rightarrow Al_2O_3 \cdot H_2O$ .

The hydrothermal methods are convenient, lower temperature, and environmentally friendly solution processing routes for synthesis of advanced ceramic materials with desired shapes, sizes, and form, compared with other ceramic materials processing methods such as solid-state reactions, CVD, MOCVD, and physical vapor deposition (PVD) involved using higher temperatures or toxic organometallic precursors, or complicated reaction and post-treatment systems.

Hydrothermal/solvothermal processing of advanced ceramic materials was reviewed [274]. The review focused on the development of the hydrothermal process, its integration with other activation methods such as electrochemistry, microwaves, and its counterpart the solvothermal process for fabrication of ceramic thin films, nanoparticles, and single crystals. The solvothermal process proved to play a significant role in synthesis of advanced nonoxide ceramic materials by using reactions in nonaqueous solutions, which will be an exciting and promising field for preparation of ceramic materials. Shapes, sizes, and phases of the synthesized ceramics can be well controlled by employing different solution processes, which will play a key role in tailoring the properties of ceramic materials.

A series of layered magnesium organosilicate nanocomposites containing covalently linked organic functionalities was prepared by a one-step, direct synthesis procedure [275]. The *in-situ* reactivity of organic moieties (e.g., phenyl, thiol) within the layered inorganic–organic nanocomposites, as well as the potential use of thiol-containing materials as host matrixes for the organized deposition of gold nanoparticles, was described.

Semiconductor nanoparticles assembled within a zeolite are an example to create a quantum confined system. Molecular sieves were prepared under hydrothermal conditions from Catapal alumina, aluminosilicate, silicate, and ethylsilicate gels, respectively, under carefully chosen conditions of pH, temperature, and crystallization time [276]. Coadded alkali metal cations, quaternary alkylammonium cation, and surfactant species functioned as charge balancing spacing-filling, and structure-directing agents to obtain an ultralarge pore molecular sieve.

Nanocrystalline titanium dioxide colloids were synthesized using a sol–gel technique followed by growth under hydrothermal conditions at temperatures between 190 and 270 °C [277]. Thin films were made from aqueous suspensions of these colloids. The rodlike particles self-organized into regular cubic arrays with the long axis of the rods aligned perpendicular to the film surface. This self-organization was dependent upon the base used in colloidal synthesis and also upon the dielectric constant of the medium used during film formation.

Colloidal solutions and redispersible powders of nanocrystalline, lanthanide-doped YVO<sub>4</sub> were prepared via a hydrothermal method at 200 °C [278]. The crystalline particles ranged in size from about 10 to 30 nm. The particles exhibit the tetragonal zircon structure known for bulk material.

A variety of synthetic methods of metal sulfide particles were reviewed [279]. Some research work via hydrothermal and solvothermal routes was summarized, concerning the synthesis of metal sulfide nanoparticles and the control of particle size, size distribution, as well as morphology. Nanocrystalline Co<sub>9</sub>S<sub>8</sub> was successfully prepared by a hydrothermal-reduction method at 120 °C [280]. The reducing agents were produced from disproportionation of white phosphorus in alkaline medium.

CeO<sub>2</sub> nanoparticles coated by sodium bis(2-ethylhexyl) sulfosuccinate were prepared by using the microemulsion method [281]. ZnGa<sub>2</sub>O<sub>4</sub> fine particles with a single phase of spinel were synthesized from a mixed solution of gallium



sulfate and zinc sulfate in the presence of aqueous ammonia under hydrothermal conditions above 180 °C [282]. The effects of treatment temperature and ZnO/Ga<sub>2</sub>O<sub>3</sub> molar ratio in the starting solution on the crystallite size, morphology, lattice parameter, and chemical composition of the ZnGa<sub>2</sub>O<sub>4</sub> spinel particles were examined. Spinel particles with different morphologies, cubic nanoparticles, and elongated rodlike particles were thought to be formed based on the structure of amorphous gallium hydroxide and needlelike GaO(OH) particles, respectively.

A hydrothermal CVD process was reported which produced self-assembled patterns of iron oxide nanoparticles [283]. By exposing a planar silica substrate to a prevaporized mixture of water, ferrocene [Fe(C<sub>5</sub>H<sub>5</sub>)<sub>2</sub>], and xylene (C<sub>8</sub>H<sub>10</sub>), at temperatures around 1000 °C, Fe<sub>2</sub>O<sub>3</sub> nanoparticles were deposited on the substrate surface, in regular circular patterns.

Nanosized TiO<sub>2</sub> particles coated with dodecylbenzenesulfonic acid (DBS) and stearic acid (St) were prepared using the hydrothermal procedure [284, 285]. The average size of the DBS/TiO<sub>2</sub> and St/TiO<sub>2</sub> particles was about 8 nm. Raman spectra from DBS/TiO<sub>2</sub> and St/TiO<sub>2</sub> were measured, and scattering signals from both TiO<sub>2</sub> and the coating were observed. In contrast to the redshift of Raman peaks in the nanoparticles with decreasing particle size, a blueshift, namely the Raman peak shift to the higher wavenumber side, in the coated particles was recorded. It was also found that different coatings show different extents of Raman shifts.

Organic monolayer-stabilized copper nanocrystals were synthesized in supercritical water [286]. When water was heated and pressurized above the critical point, it became a suitable solvent to employ organic capping ligands to control and stabilize the synthesis of nanocrystals. Without alkanethiol ligands, Cu(NO<sub>3</sub>)<sub>2</sub> hydrolyzed to form polydisperse Cu<sup>2+</sup> oxide particles with diameters from 10 to 35 nm. The use of a different precursor, Cu(CH<sub>3</sub>COO)<sub>2</sub>, led to particles with significantly different morphologies. A mechanism was proposed for sterically stabilized nanocrystal growth in supercritical water that described competing pathways of hydrolysis to large oxidized copper particles versus ligand exchange and arrested growth by thiols to produce small monodisperse Cu nanoparticles.

CdS and ZnO-capped CdS semiconductor nanoparticles were synthesized via a hydrothermal method by thermal decomposition of the cysteine-cadmium complex precursor [287]. Compared to CdS nanoparticles, the bandgap emission of CdS/ZnO was greatly improved, meaning that the shell of ZnO modified the surface of the CdS core and reduced the surface defect.

The increasing awareness of the need to create green and sustainable production processes in all fields of chemistry has stimulated materials scientists to search for innovative catalyst supports. These new catalytic supports should allow the heterogenization of most catalytic processes, increasing the efficiency and selectivity of the synthesis and reducing waste. A hexagonal material with large pore diameters and thick walls (4 nm), containing internal microporous silica nanocapsules, was developed [288]. These plugged hexagonal templated silicas had two types of micropores (originating from the walls and the nanocapsules respectively)

and a tunable amount of both open and encapsulated mesopores. The micropore volumes had a high value (up to 0.3 cm<sup>3</sup>/g) and the total pore volume exceeded 1 cm<sup>3</sup>/g. The obtained materials were much more stable than the conventional micellar templated structures and can easily withstand severe hydrothermal treatments and mechanical pressures.

The methods were investigated for preparation of Au/TiO<sub>2</sub> catalysts to obtain small gold metal particles (2–3 nm) and a higher Au loading [289]. The possible mechanisms of deposition of gold on the TiO<sub>2</sub> support by the different preparation methods were discussed.

In Mn<sub>1-x</sub>Zn<sub>x</sub>Fe<sub>2</sub>O<sub>4</sub> (x = 0 to 1) nanosize particles prepared through hydrothermal precipitation, a decrease in particle size was observed from 13 to 4 nm with increasing Zn concentration from 0 to 1 [290].

Hematite nanocrystals modified with surface layers of amorphous hydrous iron oxides (Fe<sub>2</sub>O<sub>3</sub>·1.64H<sub>2</sub>O) were prepared by hydrothermal conditions at 130 °C in the absence of alkali [291]. When the temperature was lower than 130 °C, no product was formed, while above this temperature, the amount of amorphous hydrous iron oxides at the surface of hematite nanocrystals was drastically decreased.

Rutile or anatase nanocrystals were prepared by a low temperature dissolution–reprecipitation process in HCl or H<sub>2</sub>SO<sub>4</sub> solutions around room temperature [292]. The reprecipitation temperature and organic solvent addition in the solution system greatly affected the phase composition of the final powders.

Semiconductor selenides of MSe (M = Cd, Hg) nanocrystalline powders were synthesized through the reactions between metal chlorides and sodium selenosulfate in the ammoniacal aqueous solution at room temperature for 6–10 h [293]. The average diameters of CdSe and HgSe nanocrystallites were 4 and 8 nm, respectively. The storage and an interesting phase transition under hydrothermal conditions were presented. The absorption spectrum of the as-prepared samples exhibited an obvious blueshift due to the size confinement.

Cerium oxide nanoparticles coated by cetyltrimethylammonium bromide were prepared using reverse micelles and the microemulsion method [294]. A chemical transformation from an amorphous Ce<sup>3+</sup> component to a crystalline Ce<sup>4+</sup> component was found in the temperature range of 200 to 400 °C. For the as-prepared nanoparticles without annealing (25 °C), a single shell (10 × 2.59 Å) was sufficient to describe its local structures, while two shells had to be used for the nanoparticles annealed at 200 and 350 °C. One shell corresponded to the Ce<sup>3+</sup> component. Another corresponded to the Ce<sup>4+</sup> component. A core–shell model was used to explain the structural parameters around cerium for the two samples annealed at 200 and 350 °C.

The covalent binding of yeast alcohol dehydrogenase to magnetic nanoparticles via carbodiimide activation was studied [295]. The magnetic nanoparticles Fe<sub>3</sub>O<sub>4</sub> were prepared by coprecipitating Fe<sup>2+</sup> and Fe<sup>3+</sup> ions in an ammonia solution and treating under hydrothermal conditions. The resultant magnetic nanoparticles were superparamagnetic characteristics, and their saturation magnetization was reduced only slightly after enzyme binding. The kinetic measurements indicated the bound yeast alcohol dehydrogenase

retained 62% of its original activity and exhibited a 10-fold improved stability than did the free enzyme.

Cerium oxide ( $\text{CeO}_2$ ) nanoparticles were prepared sonochemically, by using cerium nitrate and azodicarbonamide as starting materials, and ethylenediamine or tetraalkylammonium hydroxide as additives [296]. The additives had a strong effect on the particle size and particle size distribution.  $\text{CeO}_2$  nanoparticles with small particle size and narrow particle size distribution were obtained with the addition of additives, while highly agglomerated  $\text{CeO}_2$  nanoparticles were obtained in the absence of additives. Blueshifts of the absorption peak and the absorption edges of the products were observed in the UV-vis absorption spectra as a result of the quantum size effect.

Millerite NiS nanocrystals were prepared through the solvent (hydro)thermal method [297]. Using ethylenediamine and hydrazine hydrate as solvent resulted in the formation of rodlike nanocrystalline NiS, whereas spherical nanoparticles were obtained using aqueous ammonia as solvent.

The hydrolyze process consists of hydrolyzing compounds in water to form precipitates, which can be used to prepare nanoparticles/nanocapsules. Usually, the starting materials of the hydrolyze process are water and metal inorganic salts like chlorates, sulphates, nitrates, ammonium salts, etc. The metal organic salts, like metal alcoholic salts, which can be solved in organic solvents, can be used for the starting materials of the hydrolyze process. The products of the hydrolyze reactions are hydroxids and hydrates. The difference between the hydrolyze process and the hydrothermal process is that high temperature and pressure are not needed in the former. The following are several examples for the hydrolyze process. Pseudolatexes of the biodegradable polyesters poly(D,L-lactide) (PLA) and poly( $\epsilon$ -caprolactone) (PCL) were developed as potential aqueous coatings for sustained release [298]. The influence of the surfactant system, temperature, pH, and particle size on the chemical stability of the polymers as aqueous colloidal dispersions was investigated. The room-temperature reactions of the chemical warfare agents VX [*O*-ethyl S-2-(diisopropylamino) ethyl methylphosphonothioate], GD (3,3-dimethyl-2-butyl methylphosphonofluoridate, or Soman), and HD (2,2'-dichloroethyl sulfide, or mustard) with nanosize MgO were studied [299]. All three agents hydrolyzed on the surface of the very reactive MgO nanoparticles. Procedures for the preparation at low temperature (80 °C) of uniform colloids consisting of  $\text{Mn}_3\text{O}_4$  nanoparticles (about 20 nm) or elongated  $\alpha$ -MnOOH particles with length less than 2  $\mu\text{m}$  and width 0.4  $\mu\text{m}$  or less, based on the forced hydrolysis of aqueous  $\text{Mn}^{2+}$  acetate solutions in the absence ( $\text{Mn}_3\text{O}_4$ ) or the presence ( $\alpha$ -MnOOH) of HCl, were described [300]. The role that the acetate anions played in the precipitation of these solids was analyzed.

### 3.3.6. Solvent Process

The solvent process utilizes solvable salts or compounds that can be dissolved by acids as the raw materials; they are then mixed in water or other solvents to be uniform solutions. Then the solvents are evaporated by heating evaporation, spraying dryness, flaming dryness, or cooling dryness. Finally, the heat decomposition reactions result in the

nanoparticles/nanocapsules or nanocomposites. Besides the solvent evaporation method, the emulsion techniques, such as partial-microemulsion, double-microemulsion, pressure homogenization-emulsification, or modified spontaneous emulsification solvent diffusion methods, can be categorized as solvent methods. The solvents used vary from water, to organic solvents, like acetone, ethanol, chloroform, benzene, 2-propanol, 2-methoxyethanol, 1,2-dimethoxyethane, *N,N*-diethylaniline, *N,N'*-dimethylformamide, trihexylamine, ammonium carbonate, ammonia solution, etc. The polymers, like poly(D,L-lactic acid), poly(*N*-vinyl-2-pyrrolidone), poly(lactide-co-glycolide), poly- $\Sigma$ -caprolactone, poly( $\gamma$ -benzyl L-glutamate), poly(ethylene oxide), poly(ethylene glycol), etc., can be employed for this purpose, especially for coating the biomaterials. The solvent process has been used for encapsulation of not only metal nanoparticles, but also biomedical materials, such proteins, cyclosporin A, triptorelin, Rolipram, insulin, vitamin E, and so on. The solvent process is a simple and cheap method which is suitable for industrial production of uniform nanoparticles/nanocapsules in large batches.

Entirely biodegradable poly(D,L-lactic acid) nanoparticles coated with albumin were prepared by the solvent evaporation technique [301]. Their degradative properties were investigated in simulated gastric and intestinal fluids.

A synthetic route was developed for the preparation of clay intercalated palladium catalysts [302]. A toluene-rich bulk liquid phase was equilibrated with a swollen, ethanol-rich interlamellar phase having a volume of about 0.9  $\text{cm}^3/\text{g}$  organoclay. Introduction of  $\text{Pd}^{2+}$  acetate into the organoclay suspension led to the generation and deposition of a metallic palladium dispersion in the interlamellar space. This system behaved as a versatile nanophase reactor, wherein the ethanol functioned as both solvent and reducing agent. The mean diameter of monodispersed Pd nanoparticles could be controlled from 17 to 30 Å in a one-step reaction by changing the amount of protective polymer, poly(*N*-vinyl-2-pyrrolidone), and the kind and/or the concentration of alcohol in the solvent [303]. The Pd nanoparticles had fcc structures like that of bulk Pd, although the lattice constant increased with a decrease in the particle size.

The preparation and use of iron-based catalysts having performances very similar to those of NiMo/KB-based catalysts were described [304]. The iron-based catalysts were prepared by impregnating soluble iron salts onto KB.

The poly(lactide-co-glycolide) nanospheres were designed to deliver proteins for extended periods of time [305]. A water-in-oil-in-water (w/o/w) emulsion technique was modified. A study was performed to evaluate how the solvent elimination procedure, the copolymer type (different molecular weight and containing either free or esterified carboxyls), and the surfactant Poloxamer 188 affected the properties of the nanoparticles.

The long-term stability of cyclosporin A-loaded nanoparticle suspensions, stored at 8 and 25 °C, was evaluated [306]. The stability of freeze-dried samples was investigated. Nanoparticles of poly- $\Sigma$ -caprolactone, a biodegradable polymer, were obtained by a modified nanoprecipitation method. A central composite experimental design was used to investigate the simultaneous effect of technological factors (temperature of the aqueous phase and needle gauge) and

formulation variables (volume of acetone and the amount of polymer and surfactant). The effect of these variables on the stability of the 100–220 nm particles was evaluated.

Silica–copper composite powders with high surface areas of about 200–400 m<sup>2</sup>/g were synthesized by the controlled hydrolysis/polymerization of sodium metasilicate (Na<sub>2</sub>SiO<sub>3</sub>) and copper nitrate [Cu(NO<sub>3</sub>)<sub>2</sub> · 3H<sub>2</sub>O] via partial-microemulsion and double-microemulsion processes at 28 °C [307]. Each microemulsion system consisted of sodium 1,4-bis(2-ethylhexyl) sulfosuccinate and sodium dodecyl sulfate, cyclohexane, and an aqueous solution of sodium metasilicate or copper nitrate. The partial-microemulsion method produced silica–copper oxide composites consisting of nanoparticles ranging from 20 to 50 nm with a uniform elemental distribution.

The preparation and the characterization of poly(lactic acid) nanoparticles containing protein C, a plasma inhibitor, were reported. nanoparticles were prepared by the double-emulsion method (w/o/w), using methylene chloride as an organic solvent and polyvinyl alcohol or human serum albumin as a surfactant [308, 309]. The influence of experimental constraints such as sonication and organic solvent on protein C activity was evaluated.

Diblock copolymers composed of poly( $\gamma$ -benzyl L-glutamate) as the hydrophobic component and poly(ethylene oxide) as the hydrophilic component were obtained by the polymerization of  $\gamma$ -benzyl L-glutamate *N*-carboxyanhydride, initiated by the primary amino end group of the  $\alpha$ -methoxy-omega-amino poly(ethylene oxide) [310, 311]. Nanoparticles were formed from an organic solution of the block copolymers by the diafiltration method.

An oligonucleotide drug was encapsulated within poly(lactide) microparticles with high encapsulation efficiencies at high theoretical drug loadings by the solvent evaporation method [312]. With the conventional w/o/w method, the encapsulation efficiency decreased with increasing internal water content, increasing stirring time prior to filtration of the microparticles, and increasing drug loading. The encapsulation was improved by replacing methylene chloride with ethyl acetate, by using micronized drug powder instead of an internal aqueous phase or by adding electrolytes or non-electrolytes to the external phase.

The imaging of ultrafine Au, Pd, CdS, and ZnS particles prepared in reverse micelles was studied by atomic force microscopy [313]. Mica substrates, derivatized with a monolayer of amine or thiol-terminated silanes, were used to immobilize the particles. The incorporation of CdS nanoparticles, as prepared in reverse micellar systems, into silica matrices, via a sol–gel process, was investigated [314]. The silica colloids containing CdS nanoparticles were prepared via the surface modification of CdS nanoparticles using 3-mercaptopropyltrimethoxysilane in reverse micelles. The recovery and dispersion of the nanoparticles was performed in an appropriate organic solvent, followed by a sol–gel process, using tetramethyl orthosilicate or tetraethyl orthosilicate in MeOH or EtOH solution. The size and morphology of the resulting silica colloids containing CdS nanoparticles was controlled by changes in the silica source and the organic solvents.

An electrochemical procedure, based on the dissolution of a metallic anode in an aprotic solvent, was used to obtain

silver nanoparticles ranging from 2 to 7 nm [315]. The influence of the different electrochemical parameters on the final size of silver particles was studied by using different kinds of counterelectrodes. The effect of oxygen presence in the reaction medium and the type of particle stabilizer employed were investigated.

The first step toward hydrophobic, polymer-based nanospheres for gene delivery is to encapsulate and release plasmid DNA. However, encapsulating large hydrophilic molecules in very small nanospheres is difficult. For example, maximizing protein and peptide as well as small molecule encapsulation requires adjustments in pH or addition of excipients to charge neutralize, and make less hydrophilic, the compound to be encapsulated. A cationic lipid was used to load and release plasmid DNA from nanospheres made by the phase inversion/solvent diffusion method [316].

The structural and magnetic properties of two Fe<sub>2</sub>O<sub>3</sub>–SiO<sub>2</sub> nanocomposites, containing respectively 16.9 and 28.5 wt% Fe<sub>2</sub>O<sub>3</sub>, were investigated [317]. The nanocomposites were synthesized by a sol–gel method, using ethylene glycol as a solvent, and heating the gels gradually to 900 °C. The procedure allows one to obtain  $\gamma$ -Fe<sub>2</sub>O<sub>3</sub> nanoparticles homogeneously dispersed in the amorphous silica matrix.

Triptorelin is a decapeptide analog of luteinizing hormone releasing hormone, currently used for the treatment of sex-hormones-dependent diseases. The triptorelin-loaded nanospheres were prepared, which were useful for transdermal iontophoretic administration [318]. Nanospheres were prepared with the double-emulsion/solvent evaporation technique. The effect of three parameters on the encapsulation efficiency was determined: the role of the pH on the internal acid external aqueous phases.

The preparation of well-size-controlled colloidal gold nanoparticles in organic solvent was presented [319]. After the preparation of well-size-controlled aqueous colloidal gold particles, the solvent was changed to an organic one. This technique was required to enable a chemical reaction between gold particles and hydrophobic molecules, since a colloidal gold solution was typically prepared in water using a reduction process. The stability of the gold particle suspension was investigated, and it was found that the stability decreased in the sequence of water, ethanol, chloroform, and benzene solution.

Composite materials containing amorphous Cu nanoparticles and nanocrystalline Cu<sub>2</sub>O embedded in polyaniline matrices were prepared by a sonochemical method [320]. These composite materials were obtained from the sonication of Cu<sup>2+</sup> acetate when aniline or 1% v/v aniline–water was used as solvent. Mechanisms for the formation of these products were proposed. The physical and thermal properties of the as-prepared composite materials were presented.

The preparation of nanoparticles as a potential drug carrier and targeting system for the treatment of inflammatory bowel disease was investigated [321]. Rolipram was chosen as the model drug to be incorporated within nanoparticles. Pressure homogenization–emulsification with a microfluidizer or a modified spontaneous emulsification solvent diffusion method was used.

Di-*n*-hexadecyldithiophosphate (DDP)-coated ZnS nanoparticles and noncoated ZnS nanoparticles were chemically synthesized [322]. The antiwear ability of the DDP-coated ZnS nanoparticles and noncoated ZnS nanoparticles as additives in liquid paraffin were evaluated on a four-ball machine; the morphologies of the worn surfaces were examined.

Nanoparticles of tin disulfide were prepared by the solvent-thermal synthesis method using different precursors [323]. The products were of hexagonal SnS<sub>2</sub> phase, which were laminar particles with the average size of about 150 nm.

Pd Nanoparticles were synthesized by reduction of palladium acetate by ethanol in systems containing tetrahydrofuran (THF) as dispersion medium and tetradodecylammonium bromide (TDARr) surfactant as stabilizer [324]. The polar phase (ethanol) acted at the same time as the reducing agent. THF/TDABr/H<sub>2</sub>O inverse microemulsions containing micelles of various sizes were prepared, and the structure of complex liquids was studied by density measurements.

Nickel colloids were prepared by codeposition of the metal with several organic solvents: acetone, ethanol, 2-propanol, 2-methoxyethanol, and 1,2-dimethoxyethane at 77 K [325]. The stabilities of the colloids and fine powders were measured. The metallic films and active solids were obtained by evaporation under vacuum at room temperature.

A type of composite particle consisting of a zinc sulfide (ZnS) core and a silica (SiO<sub>2</sub>) shell or vice versa was reported [326]. Both kinds of morphologies were created using a seeded growth procedure using monodisperse seeds on which homogeneous layers with a well-defined thickness were grown.

Size-monodisperse metal nanoparticles were prepared via hydrogen-free spray pyrolysis [327]. Size-monodisperse pure copper particles are formed from metal salt precursors in a spray pyrolysis process using ethanol as cosolvent, thus avoiding the addition of hydrogen or other reducing gases.

Calix[4]resorcinarene-derived surfactants were highly effective at stabilizing metal nanoparticles of different sizes, creating opportunities to fabricate well-defined nanostructures with size-tunable materials properties [328]. The resorcinarenes had a critical role in the dispersion of nanoparticles under various solvent conditions and in the robustness of the protective surfactant layer. Magnetic cobalt particles stabilized by resorcinarenes self-assemble into nanostructured “bracelets” in toluene. Resorcinarene surfactants can promote the self-organization of gold nanoparticles as large as 170 nm into two-dimensional arrays.

The hybrid materials consisting of nonagglomerated iron oxide particles hosted in silica aerogels were investigated [329]. The composite material can be produced as a monolith, in any shape, and with different dilutions of the iron oxide phase. Two sol-gel chemistry routes were followed: a solution of Fe(NO<sub>3</sub>)<sub>3</sub>·9H<sub>2</sub>O was added either to the silica gel or to the initial sol; the iron salt provided the water required for the gel polymerization. To obtain monolithic aerogels, the gels were dried by hypercritical solvent evacuation.

Silver and gold nanocrystals, sterically stabilized with dodecanethiol ligands, were dispersed in supercritical ethane [330]. Nanocrystal dispersibility was measured as a function

of solvent density—with pressures and temperatures ranging from 138 to 414 bar and 25 to 65 °C, respectively. Dispersibility depended strongly on the nanocrystal size and solvent density.

Iron oxide aerogels were synthesized from tetraethoxysilicon(IV) or tetraethoxysilicon(IV) and iron nitrate using an acid-catalyzed solution sol-gel method combined with subsequent extraction of the alcoholic solvent with supercritical CO<sub>2</sub> [331]. The main parameters varied in the sol-gel synthesis were the type of *N*-base used as the gelation agent (*N*, *N*-diethylaniline, trihexylamine, ammonium carbonate, ammonia), the concentration of the iron precursor, and the water content. The silicon precursor was prehydrolyzed to improve its reactivity.

Insulin and insulin/poly(ethylene glycol)-loaded poly(L-lactide) nanoparticles were produced by gas antisolvent CO<sub>2</sub> precipitation starting from homogeneous polymer/protein organic solvent solutions [332]. Nanospheres with smooth surface and compact internal structure were observed by scanning electron microscopy. The nanospheres presented a mean particle diameter in the range 400–600 nm and narrow distribution profiles.

Biodegradable polymer nanocapsules containing the lipophilic sunscreen, Parsol MCX, as the oil core were prepared by solvent displacement [333]. The influence of polysorbate 85 (P-85) and poloxamer 188 (P-188) as stabilizing agents, the Parsol MCX loading capacity, and the photoprotective potential of the formulations were investigated. The formation of nanocapsules was due to an interfacial instability arising from rapid diffusion of the solvent across the interface.

In<sub>2</sub>S<sub>3</sub> nanoparticles, short nanowhiskers, nanorods, and finger-structure nanocrystals with stoichiometric composition and high quality were prepared by a solvent-reduction route [334]. The reagent concentrations, solvent, and reaction temperature played important roles in the shape control.

Polygonal (mainly triangular) silver nanoprisms were synthesized by boiling AgNO<sub>3</sub> in *N*, *N*-dimethyl formamide, in the presence of poly(vinylpyrrolidone) [335]. Although during the synthesis a mixture of nanoprisms and nanospheroids was formed, the latter can be removed through careful centrifugation. The UV-vis spectra of the nanoprisms displayed an intense in-plane dipolar plasmon resonance band, as well as weak bands for in-plane and out-of-plane quadrupolar resonances. The nanoprisms were also stable in other solvents, such as ethanol and water, and solvent exchange led to strong shifts of the in-plane dipole plasmon band.

An understanding of the mixing and characterization of nanosized powders was gained [336]. Three different nanosized material systems were selected based on their physical and chemical properties. Mixing experiments of the selected nanopowders were performed using a variety of environmentally friendly dry powder processing devices and the rapid expansion of supercritical CO<sub>2</sub> suspensions, compared with solvent-based methods coupled with ultrasonic agitation.

The formation of silver nanoparticles in the presence of various macrocyclic thiol compounds in *N*, *N*'-dimethylformamide solution was investigated *in-situ* through visible spectrophotometric and photon correlation spectroscopic measurements [337]. While temperature, solvent

nature, and concentration of thiol compounds were important parameters in the process of metal cluster and particle generation, the chemical structure of the thiol capping molecules also played a crucial role in determining the average particle size. The existence of a macrocyclic effect was reported on silver particle formation by using two types of thiol macrocyclic compounds, thiolated  $\beta$ -cyclodextrins and thiolated cavitands [337]. Perthiolated  $\beta$ -cyclodextrins were found to be more efficient as a capping ligand than monothiolated  $\beta$ -cyclodextrins.

Core-shell type nanoparticles of poly(L-lactide)/poly(ethylene glycol) diblock copolymer were prepared by a dialysis technique [338]. Their size was confirmed as 40–70 nm using photon correlation spectroscopy. The H-1-nuclear magnetic resonance (NMR) analysis confirmed the formation of core-shell type nanoparticles and drug loading. The particle size, drug loading, and drug release rate of the poly(ethylene glycol) nanoparticles were slightly changed by the initial solvents that were used.

A chemical reduction route at room temperature was described to synthesize nanocrystalline CdS, ZnS, and  $\text{Cd}_x\text{Zn}_{1-x}\text{S}$  [339]. Anhydrous  $\text{CdCl}_2$ , or  $\text{ZnCl}_2$ , S, and  $\text{KBH}_4$  powders reacted at room temperature in various organic solvents, and the effect of the solvent on the quality of the nanoparticle product was investigated. Among the solvents used, tetrahydrofuran was shown to produce the highest quality single-phase nanoparticles.

The D- $\alpha$ -tocopheryl polyethylene glycol 1000 succinate (vitamin E TPGS) was applied as surfactant stabilizer to fabricate paclitaxel-loaded poly(lactide-co-glycolide) nanospheres in the solvent evaporation/extraction technique [340]. Encapsulation efficiency and *in vitro* release were measured by the high-performance liquid chromatography.

The preparation of capped metal oxide nanoparticles through the hydrolysis of metal salts was made arduous by the difficulty of dissolving long organic chain capping agents in water. By performing the reaction in propylene glycol under reflux, instead of water, one can hydrolyze  $\text{FeCl}_3$  in the presence of *n*-octylamine to obtain (repeatedly) soluble, monodisperse (around 5 nm)  $\gamma\text{-Fe}_2\text{O}_3$  particles displaying a tendency to aggregate into superlattices [341].

A liquid-crystal system was used for the fabrication of a highly ordered composite material from genetically engineered  $M_{13}$  bacteriophage and ZnS nanocrystals [342]. The bacteriophage, which formed the basis of the self-ordering system, was selected to have a specific recognition moiety for ZnS crystal surfaces.

Surface interaction of gold nanoparticles with solvents and functionalized organic molecules was probed using the changes in the surface plasmon absorption band [343]. A redshift in the surface plasmon band was observed with an increase in solvent dielectric constant for solvents that do not complex with the metal surface. A plot of the square of the observed position of the surface plasmon bands of Au nanoparticles in these solvents as a function of medium dielectric function showed a linear dependence.

### 3.3.7. Latex Process

The latex process utilizes two different solvents that are not soluble each other to form a uniform and homogeneous microemulsion with the help of surfactants and dispersions.

Microemulsion is usually a transparent and isotropic thermodynamic system composed of surfactants, dispersions (polymers, alcoholic, etc.), oil (hydrocarbons), and water (or electrolytical water solutions). Polymer dispersions made of a variety of monomers, including styrene, butyl acrylate, and methyl methacrylate, surround the latex droplet. The solid phase could be from the emulsion, so that the processes of nucleation, growth, assembly, aggregation, etc. could be limited inside a micro/nanoemulsion droplet to form the micro/nanoparticles in the shape of spheres. The formation of micro/nanospheres avoids further aggregation of the nanoparticles. The key to this process is to form a system that every water solution droplet with precursors must be surrounded by a continuous oil phase and the precursors are not soluble in this oil phase. Namely, it is necessary to form a w/o-type latex so that the water phase cannot be formed, but instead a pseudo phase forms. In the latex, the latex beads serve as micro/nanoreactors, because each bead of several to hundreds of nanometers in size is separated by the layer of monomers. In some cases, the latex process using polymer dispersions can be combined with the polymerization process. The shape and the structure of the nanoparticles can be controlled by processes of layer-by-layer deposition, covering, coating, assembly, etc. The spherical latex can also serve as a template for the preparation of the nanomaterials, like porous materials, networks, etc. Thus the latex process can be used for synthesizing different types of nanomaterials, including nanoparticles, nanocapsules, nanoshells, etc. The creation of core-shell particles by the latex process has been attracting a great deal of interest because of the diverse applicability of these colloidal particles (e.g., as building blocks for photonic crystals, in magnetic storage, in multienzyme biocatalysis, and in drug delivery). The advantages of the latex process are narrow size distribution, easy control of size and shape, various synthesizable nanostructures, etc.

The processing, microstructure, and optical properties of CdS semiconductor nanoparticles sequestered in spin-coated polymer films were investigated [344]. A simple processing protocol was developed to form thin film structures consisting of CdS nanoparticles dispersed in the interstices created by a close-packed stacking of polystyrene spheres.

Poloxamer 407 and poloxamine 908 were used to modify the surface of both model latex and biodegradable nanospheres showing reduced protein adsorption *in vitro* and extended circulation times *in vivo* [345].

Model polymeric nanoparticles [aqueous colloidal polymer dispersions: Eudragit(R) RL 30D, L 30D, NE 30D, or Aquacoat(R)] with different physicochemical properties were incorporated into various solid dosage forms (granules, tablets, pellets, or films) [346]. The compatibility of the nanoparticles with commonly used tableting excipients and the redispersibility of the nanoparticles after contact of the solid dosage forms with aqueous media were investigated.

The core-shell latex morphology was used to produce three-dimensionally ordered arrays of fluorescent nanoparticles in polymer composite materials [347]. With their soft, inert shells, the particles were easily ordered into an array, after which heat treatment melted the soft shells to

give an array of nanoparticles in a transparent polymer matrix.

Colloidal particles with magnetic properties are attractive due to their tunable anisotropic interactions. A class of polystyrene-core magnetite-shell particles was produced by the sequential adsorption of nanoparticles and polyelectrolyte, a process that allowed the shell thickness and composition to be controlled with nanometer precision [348–350]. The nanocomposite particles were aligned in the presence of a magnetic field. Mesoscale hollow spheres of ceramic materials were prepared by templating an appropriate sol-gel precursor against a crystalline array of monodisperse polystyrene beads [351]. An array of TiO<sub>2</sub> hollow spheres of well-controlled, uniform size, and homogeneous wall thickness resulted.

Functional core-shell particles were prepared by assembling a composite multilayer shell of charged polyelectrolytes and luminescent CdTe(S) nanocrystals (cadmium telluride with a certain content of sulfide) via their consecutive electrostatic adsorption from solution onto micrometer-sized latex particles [352]. Variation of the size and surface chemistry of the semiconductor nanoparticles, the size and shape of the colloid templates, and the nature of the polyelectrolyte opened avenues for the production of a variety of core-shell materials.

Submicrometer core-shell polymer particles, with molecularly imprinted shells, were prepared by a two-stage polymerization process [353]. Particles, prepared with a cholesterol-imprinted ethyleneglycol dimethacrylate shell and in the absence of porogen, were found to be 76 nm in diameter with a surface area of 82 m<sup>2</sup> g<sup>-1</sup>. Imprinted shells were also prepared over superparamagnetic polymer cores and over magnetite ferrocolloid alone. The cholesterol binding to magnetic particles was very similar to that of equivalent nonmagnetic materials. Magnetic particles could be sedimented in as little as 30 s in a magnetic field.

Hierarchical assembly of zeolite nanoparticles into ordered macroporous monoliths was studied using core-shell building blocks [354]. Latex beads were used as a combined template and porogen in the fabrication of monolithic silica containing a hierarchy of pores. Prefabricated core/shell particles, prepared by the layer-by-layer assembly of zeolite (silicalite) nanoparticles onto spherical latex templates, were assembled into macroscopic close-packed structures. Calcination removed all organic components and caused densification of the inorganic structure producing a macroporous zeolite in which both the pore size and wall thickness can be varied.

Spherical polystyrene latex beads of about 2.0 μm diameter were coated with islands of silver or gold metal, about 5–200 nm in diameter, by reduction of aqueous silver or gold ions in the presence of sugar-coated polystyrene latex beads [355]. The metal islands were held on the bead surface by a polymeric sugar derivative, aminodextran, covalently bound to the polystyrene aldehyde/sulfate bead.

A review presented the state-of-the-art strategies for engineering particle surfaces, such as the layer-by-layer deposition process, which allows fine control over shell thickness and composition [356]. Nanocoating, the covering of materials with a layer on the nanometer scale, or covering of a nanoscale entity, to form nanocomposites and structured

materials using the sol-gel process was reviewed [357]. Templates from spherical nanoparticles to complex bicontinuous networks were discussed where either the coated material or the structured inorganic hollow frame resulting from removal of the template were of interest in fields of application ranging from information storage to catalysis.

The ultrasonic induced encapsulating emulsion polymerization technique was used to prepare polymer/inorganic nanoparticle composites [358]. The main factors affecting ultrasonic induced encapsulating emulsion polymerization were studied. The pH value, the type of monomers, the type, content, and surface properties of nanoparticles, and the type and concentration of surfactant had great influence on the ultrasonic induced encapsulating emulsion polymerization and the obtained latex stability. The mechanism of ultrasonic induced encapsulating emulsion polymerization and the composite latex stabilization were proposed.

Mesoscopic hollow spheres of ceramic materials with functionalized interior surfaces were synthesized [359]. Amphiphilic colloidal particles with hydrophobic cores and hydrophilic shells were prepared via a two-step method [360]. First, polystyrene cores were obtained through the concentrated emulsion polymerization. In the second step, the polystyrene particles were dispersed in water, after which acrylamide, *N*, *N*'-methylenebisacrylamide, and ferrous sulfate were added.

A procedure was developed to coat colloidal polystyrene spheres with a smooth and well-defined layer of amorphous titanium dioxide [361]. The thickness of the coating was easily varied from a few nanometers upward and increased further by seeded growth. The resulting composite particles were very monodisperse. The core-shell particles were turned into spherical hollow titania shells by dissolution of the polystyrene cores in suspension or by calcination of the dried particles in a furnace.

Polymer dispersions made of a variety of monomers, including styrene, butyl acrylate, and methyl methacrylate, were generated by the miniemulsion process in the presence of a coupling comonomer, a hydrophobe, and silica nanoparticles [362]. Depending on the reaction conditions and the surfactants employed, different hybrid morphologies were obtained, comprising a “hedgehog” structure where the silica surrounded the latex droplet and provided stabilization even without any low molecular weight surfactant.

The preparation of biocolloids with organized enzyme-containing multilayer shells for exploitation as colloidal enzymatic nanoreactors was described [363]. Urease multilayers were assembled onto submicrometer-sized polystyrene spheres by the sequential adsorption of urease and polyelectrolyte, in a predetermined order, utilizing electrostatic interactions for layer growth.

Fluorescently labeled core-shell latex particles composed mainly of the thermoresponsive polymer poly-*N*-isopropylacrylamide, were synthesized such that an energy transfer donor (phenanthrene) and an energy transfer acceptor (anthracene) were covalently localized in the core and shell, respectively [364]. Core-shell particles with different shell thicknesses displayed identical phase transition temperatures, with a clear increase in collapse temperature as the shell thickness was increased.



Encapsulation of silica nanoparticles was performed by dispersion polymerization of styrene, butyl acrylate, and butyl methacrylate in aqueous alcoholic media [365]. The silica beads were modified by reacting on their surface the 3-trimethoxysilyl propyl methacrylate coupling agent.

Core-shell composite materials, consisting of a silica core and a polystyrene shell, were prepared by colloidal assembly of polystyrene nanospheres onto silica microspheres [366]. The assembly process was controlled by specific chemical (amine-aldehyde) or biochemical (avidin-biotin) interactions between the nanospheres and microspheres. Colloidal assembly was performed using polymer nanoparticles and silica particles (3–10  $\mu\text{m}$  diameter). Heating the assembled materials to temperatures above the glass transition ( $T_g$ ) of the polymer nanoparticles allowed the polymer to flow over the microsphere surfaces, resulting in uniform core-shell materials. Nanosphere packing density on the microsphere surfaces influenced the uniformity of the resulting polymer shell.

A type of micrometer-sized entity containing silver was introduced [367]. Three different approaches were employed to modify the colloidal particles with silver. According to the first technique, the particles were first coated with layers of poly(styrenesulfonate) and silver ions followed by the reduction of silver by photoirradiation. The second technique involved coating the colloidal particles with a shell capable of reduction, and sequential addition of silver salt resulted in the reduction of metal in the shell matrix. The last approach utilized the reaction of a silver mirror to silver particles.

Acrylic/nanosilica composite latexes were prepared by blending via high shear stirring or ball milling and *in-situ* polymerization [368]. For comparison, composites filled with microsilica were also prepared. The mechanical and optical properties of the polymers formed by the composite latex filled with nano- or microsilica were investigated.

Raspberrylite hybrid organic-inorganic materials consisting of spherical silica beads supporting smaller polystyrene particles were prepared through a heterophase polymerization process [369]. In a first step, micrometer-sized silica particles were synthesized according to procedures inspired from the literature. In a second step, a poly(ethylene glycol) macromonomer was adsorbed on the surface of the silica beads. Finally, polymerization of styrene was achieved in water with a nonionic surfactant as an emulsifying agent and sodium persulfate as an initiator.

Nanoparticles of polystyrene ( $M_w = 1.0\text{--}3.0 \times 10^6$  g/mol) latexes were prepared from their respective dilute polystyrene (commercial) solutions in cyclohexane, toluene/methanol, or cyclohexane/toluene at each temperature [370]. The cationic surfactant cetyltrimethylammonium bromide was used to stabilize the formed PS latex particles. By varying different concentrations of cetyltrimethylammonium bromide and polystyrene solution of various  $M_w$ , stable bluish-transparent latex particles ranging from about 10 to 30 nm in diameter were produced.

Magnetically controllable photonic crystals were formed through the self-assembly of highly charged, monodisperse superparamagnetic colloidal spheres [371]. These superparamagnetic monodisperse charged polystyrene particles

containing nanoscale iron oxide nanoparticles were synthesized through emulsion polymerization.

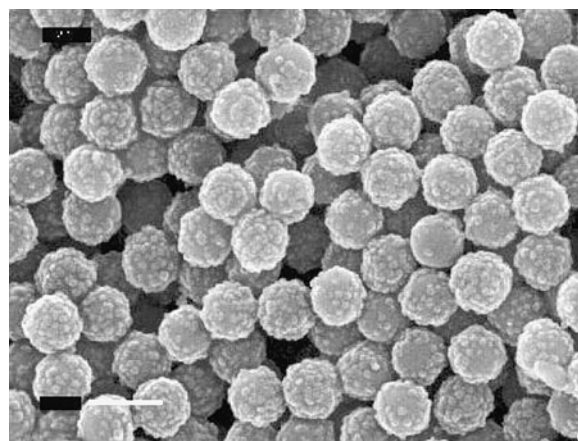
Polystyrene latex particles containing silanol groups were synthesized in emulsion polymerization using 3-(trimethoxysilyl)propyl methacrylate as a functional comonomer [372]. The surface properties of the functionalized polymer latexes were investigated using electrophoretic measurements and the soap titration method. This work illustrated the determining role of interfaces in the structuration of organic-inorganic colloids.

Figure 6 shows a scanning electron microscope (SEM) photograph of the conducting polymer deposited as an ultrathin overlayer onto preformed polystyrene latex particles [373]. A series of sterically stabilized polystyrene latex particles in the size range 0.1–5.0  $\mu\text{m}$  was coated with ultrathin (<50 nm) overlayers of either polypyrrole, polyaniline, or poly(3,4-ethylenedioxythiophene) [373]. In each case the conducting polymer overlayer allowed the latex particles to acquire surface charge and hence be accelerated up to hypervelocities ( $> 1 \text{ km s}^{-1}$ ) using a Van de Graaff accelerator. These coated latexes had two main advantages. First, a wider particle size range can be accessed. Second, the particle size distributions of the coated latexes are much narrower than those of the pure polypyrrole particles.

Polyaddition reactions in miniemulsions were performed by miniemulsification of mixtures of di-, tri-, and tetraepoxides with varying diamines, dithiols, or bisphenols and subsequent heating to 60  $^\circ\text{C}$  [374]. Figure 7 shows a TEM micrograph of polyaddition latex comprised of Epikote E828 and 4,4'-diaminobiphenyl. Depending on the chemical nature of the monomer, the amount of surfactant, and the pH of the reaction mixture, latex particles with diameters between 30 and 600 nm and narrow size distributions were obtained [374].

### 3.3.8. Oxidation Process

The oxidation process oxidizes and deoxidizes directly the raw materials in the liquid phase or quasi-liquid phase state. The oxidation process can be used to prepare the nanoparticles



**Figure 6.** Scanning electron microscopy (SEM) photographs of preformed polystyrene latex particles coated with the conducting polymer (poly(3,4-ethylenedioxythiophene)) as an ultrathin overlayer. After [373], M. J. Burchell et al., *J. Phys. D* 32, 1719 (1999). © 1999, IOP Publishing.

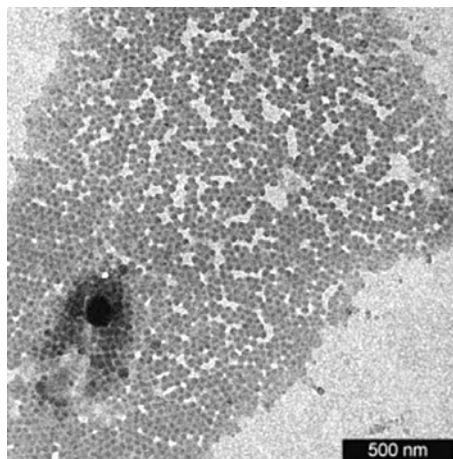


**Figure 7.** TEM micrograph of polyaddition latex comprised of Epikote E828 and 4,4'-Diaminobenzyl. After [374], K. Landfester et al., *Macromol. Chem. Phys.* 201, 1 (2000). © 2000, Wiley-VCH.

of metals, alloys, oxides, etc., in either water solutions or organic solutions. For water solutions, solutions of metal salts with different pH values can be deoxidized by the reducers in gases or liquids. Almost all the metal ions in the solutions can be deoxidized by H reduction to form nanoparticles. Usually, surfactants are needed in order to avoid aggregation of the nanoparticles. Nanoparticles can also be synthesized by thermal decomposition or reduction of the organic or metal organic solutions. On the other hand, the oxidation process can be employed for coating the cover layer of the nanoparticles to form the nanocapsules and for studying directly the oxidation behavior of the nanomaterials. The oxidation process is one of the most simple, cheap, and easily controlled processes for preparation of nanoparticles/nanocapsules.

A method was proposed for  $\text{Si}_3\text{N}_4$  ceramics by forming a nanocomposite grain-boundary phase of SiC nanoparticles in the weak grain-boundary phase [375]. The SiC nanoparticles were formed by *in-situ* reaction between an oxide phase on the surface of  $\text{Si}_3\text{N}_4$  powder and carbon, which was coated on  $\text{Si}_3\text{N}_4$  powder by thermal decomposition of methane ( $\text{CH}_4$ ) gas. The surface oxygen content increased by an oxidation process or decreased by a washing process. The precipitated SiC content depended on the coated carbon and surface oxygen content on the  $\text{Si}_3\text{N}_4$  powder surface. A surface oxidized  $\text{Si}_3\text{N}_4$  powder was regarded as an inferior powder and the oxidized powder was used to produce high quality  $\text{Si}_3\text{N}_4$  ceramics by applying the carbon coating method.

The oxidation behavior of silver (Ag) nanometer particles (about 3 nm in diameter) within pores of a silica host in ambient air (298 K) was investigated [376]. Exposure to air resulted in a blueshift of the absorption edge with time, which was attributed to the surface oxidation of Ag nanoparticles. In air at room temperature, oxidation occurred in surface layers of Ag particles in the form of a dense  $\text{Ag}_2\text{O}$  film. Once the dense film was formed, further oxidation was restrained.

$\text{TeO}_2/\text{ZnO}$  and  $\text{ZnS}/\text{ZnO}$  coated nanoparticles of a few nm in diameter were created using an oxidation process of ZnTe and ZnS particles produced by a gas evaporation technique [377]. In the case of  $\text{TeO}_2/\text{ZnO}$  production, the first phase formed on the ZnTe particle was a ZnO layer on the particle surface, and a part of the ZnTe particles was changed to Te. On further oxidation for a few hours in air at 300 °C, the Te region gradually changed to  $\text{TeO}_2$  with increasing ZnO layer. In the case of ZnS particles, the surface of the particles was gradually changed to ZnO by heat treatment above 700 °C.

Biferrocene-modified Au clusters, comprising a  $2.2 \pm 0.3$  nm diameter Au core covered with 20 biferrocene-terminated thiolates and 75 octyl thiolates on average, were synthesized by a substitution reaction of octanethiol-modified clusters with biferrocene-terminated alkanethiol,  $(\eta(5)\text{-C}_5\text{H}_5)\text{Fe}(\text{C}_{10}\text{H}_8)\text{Fe}(\eta(5)\text{-C}_5\text{H}_4\text{CO}(\text{CH}_2)_7\text{SH})$  [378]. The biferrocene-modified cluster underwent two-step oxidation reactions in  $\text{NBU}_4\text{ClO}_4 + \text{CH}_2\text{Cl}_2$  and the second oxidation process led to the formation of a uniform redox-active Au cluster film on electrode.

The electrocatalytic activities of two kinds of iridium oxide electrodes were studied for their ability to evolve hydrogen and oxygen in 1 M  $\text{H}_2\text{SO}_4$  at room temperature [379]. The first kind of electrode was made of anodic iridium oxide nanoparticles prepared by cycling well-defined iridium metal nanoparticles supported on carbon between  $\text{O}_2$  and  $\text{H}_2$  evolution potentials. The oxidation process was followed by cyclic voltammetry and CO oxidation experiments. The mechanism for the two evolution reactions and for the two different electrodes was discussed.

Anodes of SnO were charged reversibly with Li to capacities greater than 600 mAh/g. The anode materials were characterized by  $\text{Sn}^{119}$  Mossbauer spectrometry at 11 and 300 K [380]. Trends in the valence of Sn were as expected when the Sn oxides were reduced in the presence of Li. The oxidation process of Sn was very much the reverse of the Sn reduction during the Li insertion.

Weblike aggregates of coalesced Si nanocrystals were produced by a laser vaporization-controlled condensation technique, showing luminescence properties that were similar to those of porous Si [381]. The oxidized Si nanoparticles did not exhibit the red photoluminescence that was characteristic of the surface-oxidized Si nanocrystals. A significant blueshift in the red photoluminescence peak was observed as a result of the slow oxidation process. As the nanoparticles oxidize, the radius of the crystalline core decreased in size, which gave rise to a larger bandgap and consequently to the observed blueshift in the photoluminescence band.

The function of oxide film during the thermal oxidation process of Zn nanoparticles was reported [382]. A study was reported concerning oxidation of SiC and amorphous silicon ( $\alpha\text{-Si}$ ) nanoparticles obtained by plasma-enhanced CVD [383, 384]. The oxidation behavior of the as-grown powder was understood in view of its polymeric structure containing a large amount of hydrogen, allowing rapid diffusion of oxygen.

An X-ray photon spectroscopy method was used to investigate nanosize particles which worked as catalytical active surface probes for oxidation of benzene, toluene, and CO [385]. Active components in the process of benzene, toluene,

and CO oxidation were Co and B compounds with oxygen featuring dangling bonds at the surface of nanoparticles. The nanosize dimensions of the synthesized boride particles played a substantial role in the oxidation process.

SO easily reduced  $\text{Au}^{3+}$  ions (1 : 1 equiv.) to monovalent  $\text{Au}^+$  species [386]. A salt composed of oxidized dye/ $\text{Au}^+$  was isolated. This salt was further reduced by another SO (2 : 1 equiv.) leading to gold atoms that coalesce into gold powder.

Pure  $\gamma\text{-Fe}_2\text{O}_3$  particles were continuously prepared by a continuous wave  $\text{CO}_2$  laser-induced pyrolysis of iron pentacarbonyl vapor in an oxidizing atmosphere [387]. Two different oxidation procedures were investigated: (1) air-argon mixtures were employed to fill the apparatus; (2) air-ethylene mixtures were employed as carrier gas.

Electrooxidation of methanol in sulfuric acid solution was studied using Pt, Pt/Ni (1:1 and 3:1), Pt/Ru/Ni (5: 4:1 and 6:3.5:0.5), and Pt/Ru (1:1) alloy nanoparticle catalysts, in relation to methanol oxidation processes in the direct oxidation methanol fuel cell [388]. Pt/Ni and Pt/Ru/Ni alloys showed excellent catalytic activities compared to those of pure Pt and Pt/Ru. The role of Ni as a catalytically enhancing agent in the oxidation process was investigated. The presence of metallic Ni, NiO,  $\text{Ni}(\text{OH})_2$ , NiOOH, metallic Ru,  $\text{RuO}_2$ , and  $\text{RuO}_3$  was confirmed.

Supramolecular polymer structures were assembled using the layer-by-layer, polyionic deposition technique [389]. Depositing alternating layers of a polycation, poly(diallyldimethylammonium chloride), and a polyanion, poly(styrenesulfonate), formed the thin films. The nucleation of nickel hydroxide nanoparticles was achieved using a cyclical absorption-oxidation process in which nickel ions were absorbed into the polymer matrix (which bind to the sulfonate groups) and then oxidized in an alkali solution.

### 3.3.9. Polymerization

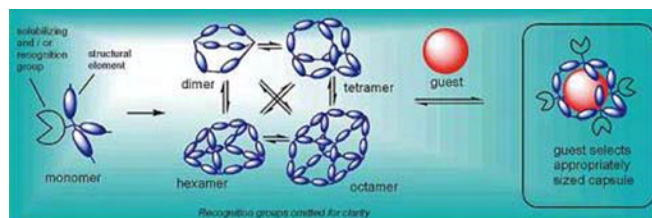
Polymerization is a very common method for preparation of nanomaterials. During polymerization, usually, the formation of microemulsion is a very important factor which has been the focus of extensive research worldwide due to its importance in a variety of technological applications. These applications include enhanced oil recovery, combustion, cosmetics, pharmaceuticals, agriculture, metal cutting, lubrication, food, enzymatic catalysis, organic and bio-organic reactions, chemical synthesis of nanoparticles and nanocapsules, etc. In particular, nanocapsules consisting of an inorganic core and a polymer shell offer interesting prospects in various applications. Miniemulsions are specially formulated heterophase systems where stable nanodroplets of one phase are dispersed in a second, continuous phase. It is delineated that miniemulsions rely on the appropriate combination of saturated high shear treatment, surfactants, and the presence of an osmotic pressure agent insoluble in the continuous phase. The droplet diameter is adjusted by the type and amount of surfactant, the volume fraction of disperse phase, and the general dispersion problem and lies between 30 and 500 nm. Since each of those droplets can be regarded as an individual batch reactor, a whole variety of polymerization reactions can be performed starting from miniemulsions, clearly extending the profile of classical emulsion polymerization. Actually, polymerization could be the only process or one of the multisteps

of a whole preparation procedure. The polymerization process varies, depending on the kinds of the polymers used and the reactions. There are different polymerization processes, such as polymerization, co-polymerization, tri-polymerization, etc., depending on how many kinds of polymers are used. The polymerization process could be enhanced or adjusted by ultrasonic, plasma, microwave, etc. methods. The polymerization could be used with combination of other synthesization processes. As shown previously, during the chemical vapor deposition, solid-state reaction, sol-gel, precipitation, hydrothermal, solvent, latex, or oxidation process, the polymers could be used as the starting materials, such as precursors, surfactants, dispersions, etc. The polymerization could occur in all these kinds of processes for synthesis of nanoparticles and nanocapsules. Furthermore, it is easy to control the preparation parameters during the polymerization so that lot of different nanomaterials, like nanoparticles, nanocapsules, nanoporous, hollow, nanowires, nanospheres, etc., can be synthesised. Figure 8 represents the design of water-soluble nanocapsules.

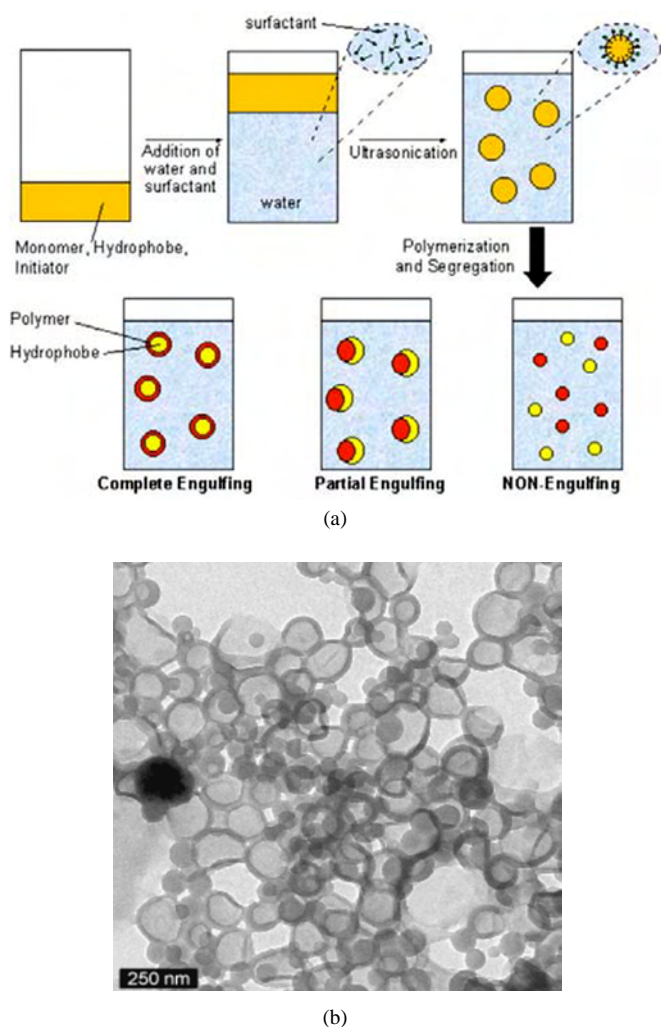
A review provided the features of microemulsions and their applications [390], which started with a brief introduction and focused on definition, structure, type, formation characteristics, stability, phase behavior, and the effect of additives, pressure, and temperature on the phase behavior of microemulsion. The physicochemical properties, state of water in the micropool, transport (electrical and hydrodynamic) behaviors, thermodynamics of formation, solubilization parameters, and uses and applications of microemulsions were presented.

Figure 9a represents the scheme of the formation of nanocapsules by miniemulsion polymerization and Figure 9b shows a TEM micrograph of nanocapsules of poly(styrene-co-acrylic acid) obtained by miniemulsion polymerization [391]. One major part of the work was concerned with the development of a convenient one-step synthesis of hollow polymer nanocapsules by the miniemulsion polymerization of different monomers in the presence of larger amounts of a hydrophobe. The idea was that hydrophobe and monomer formed a common miniemulsion, whereas the polymer was immiscible with the hydrophobe and demixed throughout polymerization to form a hollow structure surrounding the hydrophobe. It was found that the structure can be adjusted to cover the whole range from independent particles over partially engulfed structures to structurally integer nanocapsules of high uniformity [391].

An approach was presented for the identification of factors to permit the development of nanoparticle growth hormone



**Figure 8.** The design of water-soluble nanocapsules. Appropriately sized capsules are synthesised using dynamic combinatorial chemistry in an aim to develop efficient drug targeting systems. Image courtesy of S. Otto, Department of Chemistry, University of Cambridge, UK.



**Figure 9.** (a) Scheme of formation of nanocapsules by miniemulsion polymerization and (b) TEM micrograph of nanocapsules of poly(styrene-co-acrylic acid) obtained by miniemulsion polymerization. After [391], F. Tiarks et al., *Langmuir* 17, 908 (2001). © 2001, American Chemical Society.

releasing factor (GRF) formulation [392]. GRF can be associated with biodegradable poly(alkylcyanoacrylate) nanoparticles. Among other parameters, the moment at which GRF was incorporated in the polymerization medium was found to be a critical factor in avoiding the degradation of GRF and the covalent bonding of the peptide with the polymer.

Biodegradable colloids suitable for use as drug delivery systems can be formed by *in-situ* polymerization of isobutylcyanoacrylate monomers. The mechanisms of formation of colloidal systems of polyisobutylcyanoacrylate (PIBCA) obtained in the presence of oil and ethanol were studied [393]. A polymerization system, a Winsor I-like system, was used for polymerization of styrene at room temperature [394]. The system consisted of a microemulsion (lower) phase that was topped off with styrene. The factors affecting the polymerization were discussed.

Plasma polymer thin films with encapsulated dye molecules (rhodamine 6G) and silver nanoparticles were

deposited by alternating plasma polymerization, dye sublimation, and metal evaporation [395]. The interference between the optical absorption of the plasma polymer, the dye molecule absorption, and the plasma resonance absorption of the silver particles was measured in the UV-vis-near-infrared red spectral region. Fluorescence measurements demonstrated plasma polymer matrix effects on fluorescence of the dye molecules. Polymer thin films with embedded silver nanoparticles were deposited by simultaneous plasma polymerization and metal evaporation [396].

Silica (Aerosil A200 V) was functionalized by reaction with methacryloylpropyltrimethoxysilane (MPTMS) in toluene [397]. The grafting yield first increased with the ratio MPTMS/SiOH and then leveled off after full monolayer coverage, each molecule of MPTMS covering 7.1 nm. Silicone membranes with silica nanoparticles were prepared [398].

Inorganic  $\text{Fe}_2\text{O}_3$  nanoparticles of 3–5 nm diameter were assembled with polymer microspheres and then encapsulated in copolymer of St/BA/AA by a polymerization process [399].  $\text{Fe}_2\text{O}_3$  encapsulated microspheres were obtained through interaction between surface groups of the two component particles and by adjusting the pH value in the emulsion. Pretreatment of the composite particles using a certain amount of surfactant before polymerization gave a good encapsulation.

Enzyme superoxide dismutase incorporation parameters were evaluated after immobilization in polyisobutylcyanoacrylate nanoparticles [400]. After initialization of the anionic mechanism of polymerization, pH was increased and its effect on the characteristics of polyisobutylcyanoacrylate nanoparticles was analyzed. Optimization of enzyme activity during incorporation into nanoparticles and the influence on size distribution were studied.

Aiming at the preparation of nanometer-size polydiacetylene microcrystals, the crystallization process during the reprecipitation method was investigated. An amorphous nanoparticle was formed initially and subsequently crystallized [401].

AB diblock copolymers consisting of poly( $\gamma$ -benzyl-L-glutamate) (PBLG) as the hydrophobic part and poly(*N*-isopropylacrylamide) (PNIPAAm) as the hydrophilic one were prepared by polymerization of  $\gamma$ -benzyl-L-glutamate-*N*-carboxyanhydride (BLG-NCA) with semitelechelic PNIPAAm with amino end group as initiator [402]. The core-shell type nanoparticles of the block copolymers were obtained by the diafiltration method. The sizes of the nanoparticles were from about 73 to 359 nm and the shapes of them were spherical.

Low-water-content reverse micelles were formed in cyclohexane employing Triton X-100 or AOT (bis(2-ethylhexyl) sulfosuccinate sodium (salt) as the surfactant [403]. At low water content, reverse micelles cannot properly solubilize polar species but the surfactant molecules tended to reorganize themselves around the polar molecules forming structures depending on the nature of the surfactant and the charge. Solid and hollow, magnetic and nonmagnetic, organic-inorganic monodispersed hybrid microspheres were synthesized [404].

Amphiphilic block copolymers are important in interface and particle stabilization. Mesophases and micelles of block copolymers and the solubilization and adhesion of



amphiphilic block copolymers were considered [405]. AB-type amphiphilic copolymers composed of poly(L-leucine) as the A component and poly(ethylene oxide) as the B component were synthesized by the ring-opening polymerization of L-leucine *N*-carboxy-anhydride initiated by methoxy polyoxyethylene amine [406]. Core-shell type nanoparticles were prepared by the diafiltration method. Micelles were formed also by a polystyrene/poly(vinylpyridine) copolymer. Nanosized copper oxide particles dispersed in nylon 11 thin films were prepared by a thermal relaxation technique [407].

Conducting polymers and their processability problem were introduced, and the synthesis of an economically attractive and environmentally stable conducting polymer, viz., polyaniline in dispersion form, was discussed [408]. Nanoparticles of less than 20 nm in diameter were obtained from the particles in the dispersion by way of disintegrating them with the help of ultrasound. Nanoparticles produced inside of solutions of various matrix polymers underwent fractal aggregation.

An approach to prepare magnetic polymeric nanoparticles with narrow size distribution by synthesis of the magnetite core and polymeric shell in a single inverse microemulsion was reported [409]. The microemulsion seed copolymerization of methacrylic acid, hydroxyethyl methacrylate, and cross-linker resulted in a stable hydrophilic polymeric shell of the nanoparticles. The importance of three main parameters was emphasized in the nanostructured systems: the mechanical coupling between the two phases, the possible cross-linking of the macromolecules by the nanoparticles, and the connectivity between reinforcing particles [410].

Stable suspensions of superparamagnetic cobalt nanoparticles were prepared in poly(dimethylsiloxane) carrier fluids in the presence of poly[bis(dimethylsiloxane)-*b*-(3-cyanopropyl) methylsiloxane-*b*-dimethylsiloxane] triblock copolymers as steric stabilizers [411]. A series of polysiloxane triblock copolymers with systematically varied molecular weights were prepared via anionic polymerization using LiOH as an initiator. These copolymers formed micelles in toluene and served as "nanoreactors" for thermal decomposition of the  $\text{Co}_2(\text{CO})_8$  precursor.

Latexes with a poly(dimethyl siloxane) core and a poly(styrene-methyl methacrylate-acrylic acid) shell were prepared in two steps in order to generate particles that have a core with a very low glass transition temperature [412]. In the first step, poly(dimethyl siloxane) particles were obtained via the ring-opening emulsion polymerization of octamethyl tetracyclosiloxane (D-4). The polymerization was carried out using either an anionic or a cationic catalyst. Using a PD4 latex as seed, a seeded emulsion polymerization of poly(styrene-methyl methacrylate-acrylic acid) was conducted to obtain core-shell particles.

Core-shell particles consisting of a polystyrene latex colloidal core and  $\text{Fe}^{2+}$  metallosupramolecular polyelectrolyte/poly(styrenesulfonate) multilayer shells were fabricated by the consecutive assembly of these polymers on polystyrene particles [413]. Structurally well-defined metallosupramolecular polyelectrolyte-colloid assemblies were studied, which combined the functional units from supramolecular chemistry with the restricted dimensionality of colloids.

The encapsulation of seed polymer particles coated by anionic iron oxide nanoparticles was investigated using *N*-isopropylacrylamide as a main monomer, *N,N*-methylene bisacrylamide as a cross-linking agent, itaconic acid as a functional monomer, and potassium persulfate as an anionic initiator [414].

Dispersion copolymerization of styrene and a poly(*N*-isopropylacrylamide) macromonomer in ethanol water media was carried out in the presence of  $\text{AgNO}_3$  [415]. Nanoscopic silver particles were generated on their surfaces via *in-situ* reduction of  $\text{Ag}^+$  by radicals generated from the initiator, 2,2'-azobisisobutyronitrile. The particle sizes of both polystyrene microspheres and silver nanoparticles were affected by the initial 2,2'-azobisisobutyronitrile,  $\text{AgNO}_3$ , and macromonomer concentrations.

Monodisperse poly(4- and poly(2-vinylpyridine) nanoparticles in the 500 nm diameter range were prepared by emulsifier-free emulsion polymerization techniques under free radical initiation of the respective monomers with 4 wt% divinylbenzene as the cross-linking agent [416]. The size, integrity, and nature of the Pd-coated nanospheres were investigated.

The core-shell  $\text{Y}_2\text{O}_3\cdot\text{Eu}^{3+}$ /polystyrene particles were prepared by surface modification with citric acid and emulsion polymerization method with styrene [417]. The DTA curve of coated particles exhibits a small and wide exothermic peak of organic compound around 387 °C. The carbonyl stretching vibration band was shifted to low wavenumber in the Fourier transform IR (FTIR) spectrum and the binding energy of  $\text{Y}3d^{5/2}$  was shifted to the high-energy band in the X-ray photoelectron spectroscopy (XPS) spectrum.

Nanoporous carbons with extremely high mesopore volumes and surface areas were produced using silica nanoparticles as templates [418]. The polymerization of resorcinol and formaldehyde (RF) in the presence of silica sol particles generated RF gel-silica nanocomposites.

Uniform Ag nanowires were synthesized within nanoscale channels of mesoporous silica SBA-15 by a chemical approach, which involved  $\text{AgNO}_3$  impregnation followed by thermal decomposition [419].

The preparation, luminescent properties, and bioimaging applications of a novel zinc sulfide (core)-two-photon dye-silica (shell) multilayered heterostructure were reported [420]. The method utilized reverse micelle synthesis involving multistep reactions as a result of which composite nanoparticles having different sizes (typically 15–30 nm) and morphology were obtained. An increase in the luminescence intensity (similar to 70 times higher) and in fluorescence lifetime was observed for the dye encapsulated within the silica nanobubble.

Polymethyl methacrylate-based stealth and functional nanospheres, specifically designed for the reversible adsorption of oligonucleotides, were prepared by emulsion polymerization of methyl methacrylate in the presence of an ionic comonomer, namely a quaternary ammonium salt of 2-(dimethylamino)ethyl methacrylate, and a nonionic comonomer, namely a poly(ethylene glycol) methacrylate [421]. The nanosphere size was substantially affected by the amount of both the nonionic and ionic comonomers.

Silaferrocenophanes  $\text{fcSiMe}_2$  and  $\text{fcSi}(\text{CH}_2)_3$  [ $\text{fc} = \text{Fe}(\eta_5\text{-C}_5\text{H}_4)_2$ ] were incorporated into the well-ordered, hexagonal

channels of mesoporous silica (MCM-41) [422]. Characterization of the composite materials indicated the presence of ring-opened monomer, oligomer, and polymer. From the magnetization data, the two phases were best described as Fe nanoparticles with diameters of 5.0–6.4 nm coated with a thin (ca. 0.4–0.6 nm) oxide layer.

A tripodal alkythiolate ligand was assembled on gold nanoparticles, which upon metathesis polymerization and particle etching yielded cross-linked spherical hollow polymer capsules [423]. Silver nanoparticles coated with a uniform, thin shell of titanium dioxide were synthesized via a one-pot route, where the reduction of  $\text{Ag}^+$  to  $\text{Ag}^0$  and the controlled polymerization of  $\text{TiO}_2$  on the surface of silver crystallites took place simultaneously [424]. High quality ultrathin films of the core-shell clusters were prepared via layer-by-layer assembly. The nanoparticles were arranged in closely packed layers interlaced with polyelectrolyte producing a stratified core-shell hybrid material with unique structure and catalytic and electron-transport properties.

Two polymethylmethacrylate functional nanosphere series, specifically designed for the reversible adsorption of oligonucleotides, were prepared by emulsion polymerization in the presence of two structurally different ionic comonomers, namely two quaternary ammonium salts of 2-(dimethylamino)ethyl methacrylate [425]. The nanosphere size was substantially affected by the ionic comonomer structure and amount. The width of the size distribution tended to decrease with increasing comonomer amount in solution, and monosized nanosphere samples were obtained at a high comonomer amount.

Copolymers of  $\epsilon$ -caprolactone and L-lactide with different monomer ratios were synthesized by ring-opening polymerization, and drug-loaded nanoparticles of poly- $\epsilon$ -caprolactone, poly-L-lactide, and their copolymers were prepared by a precipitation method, respectively [426]. End-functionalized three-dimensional (3D) self-assembled monolayers on gold nanoparticles were used to initiate the living cationic ring-opening polymerization reaction directly on gold nanoparticle surfaces [427]. In this manner, dense polymer brushes were prepared in a “one-pot multistep” reaction.

Ultrasonic induced encapsulating emulsion polymerization was used to prepare the polymer/inorganic nanoparticle composites [428, 429]. The behaviors of several inorganic nanoparticles ( $\text{SiO}_2$ ,  $\text{Al}_2\text{O}_3$ ,  $\text{TiO}_2$ ) under ultrasonic irradiation, such as dispersion, crushing, and activation, were studied. The dispersion stability, morphology, and structure of the ultrasonic irradiated nanoparticles were characterized. The inorganic nanoparticles in the aqueous solution can redisperse more effectively by ultrasonic irradiation than by conventional stirring. The well-dispersed nanoparticles were encapsulated by the formed polymer with thickness in the range of 5–65 nm.

Core-shell CdS/ $\text{SiO}_2$  nanoparticles were prepared and modified with the atom transfer radical polymerization initiator 3-(2-bromopropionyloxy) propyl dimethylethoxysilane [430]. The initiator-modified nanoparticles were then used as macroinitiators for the polymerization of methyl methacrylate catalyzed by  $\text{NiBr}_2(\text{PPh}_3)_2$ .

The precipitation and condensation of submicrometer organic particles and the thermodynamic driving forces for

precipitation and phase transformation were reviewed [431]. The importance of physical state effects was discussed, and the role of compartmentalization in controlling particle size was introduced. The use of emulsification as a primary step in producing small particle dispersions was illustrated with photographic and pharmaceutical applications.

Static and dynamic magnetic experiments were conducted on polymer-coated Fe nanoparticles of 15–20 nm synthesized by a microwave plasma method [432]. The field-dependent magnetization data showed the presence of sharp switching at low fields (about 60 Oe) followed by a gradual approach to a saturation magnetization of about 80 emu/g.

The effect of composition on the dispersion of  $\text{Au}_x\text{Cu}_{1-x}$  bimetallic nanoparticles into nylon 11 matrix was investigated [433]. The changes in the composition of the bimetallic particles and in the depth distribution of the particles in the nylon 11 layer caused by heat treatment in  $\text{N}_2$  atmosphere were characterized. Islandlike bimetallic particles were found to be formed on the nylon 11 surface before heat treatment. By the heat treatment, the  $\text{Au}_x\text{Cu}_{1-x}$  bimetallic particles with  $x \leq 0.55$  were not dispersed into the nylon 11 layer while those with  $x \geq 0.70$  were homogeneously dispersed in the films.

The preparation of hybrid organic/inorganic nanocomposites comprised of well-defined polymers was reviewed [434]. Synthetic methods using controlled/“living” radical polymerization techniques, such as stable free radical/nitroxide-mediated polymerizations, atom transfer radical polymerization, and reversible addition-fragmentation chain-transfer polymerization, were described. The various approaches taken to prepare hybrid copolymers, nanoparticles, polymer brushes, dispersed silicate nanocomposites, and nanoporous materials were discussed.

Polymer dispersions made of a variety of monomers, including styrene, butyl acrylate, and methyl methacrylate, were generated by the miniemulsion process in the presence of a coupling comonomer, a hydrophobe, and silica nanoparticles [435]. Depending on the reaction conditions and the surfactants employed, different hybrid morphologies were obtained, comprising a “hedgehog” structure where the silica surrounds the latex droplet and provides stabilization even without any low molecular weight surfactant.

Thermoresponsive, core-shell poly-N-isopropylacrylamide nanoparticles (microgels) were synthesized by seed and feed precipitation polymerization, and the influence of chemical differentiation between the core and shell polymers on the phase transition kinetics and thermodynamics was examined [436]. The results suggested that the core-shell architecture is a powerful one for the design of colloidal “smart gels” with tunable properties. The addition of small concentrations of a hydrophobic monomer (butyl methacrylate) into the particle shell produced large decreases in the rate of thermoinduced particle collapse.

Silver nanoclusters in poly(methyl methacrylate) were prepared by bulk polymerization of methyl methacrylate with radical initiators (AIBN or BPO) in the presence of  $\text{Ag}^+$  trifluoroacetate, followed by a period of UV irradiation [437].

A versatile method for the generation of nanoparticulate metals, ceramics, and polymers based on synthesis in miniemulsions—highly stable small droplets in a continuous



phase—was presented [438]. In addition to nanoparticles, encapsulated materials, polymer capsules, and hollow particles can also be obtained by careful selection of the starting materials.

Melt mixing of nanoparticles with high performance polymers is not feasible due to severe shear heating and formation of particle aggregates. An alternative scheme was investigated involving the use of low molecular weight reactive solvents as processing aids and dispersion agents [439]. Dispersion of nanosize fumed silica particles in polyethersulphone matrix was studied with the aid of small amounts of low molecular weight epoxy. Viscosity and processing temperatures of polyethersulphone were significantly reduced and fumed silica particles were dispersed to nanoscales.

A method was developed for the controlled release of the hydrophobic polymer chains from the core of the shell of cross-linked nanoparticles by selective cleavage of labile C–ON bonds present at the core–shell interface [440]. This represented a methodology to probe the permeability of nanoscopic membranes and a means for applications in the controlled release of macromolecular species.

A water-in-oil microemulsion method was applied for the preparation of silica-coated iron oxide nanoparticles [441]. Three different nonionic surfactants (Triton X-100, Igepal CO-520, and Brij-97) and pure water were used for the preparation of microemulsions, and their effects on the particle size, crystallinity, and the magnetic properties were studied.

The incorporation of CdS nanoparticles, prepared in reverse micellar systems, into thiol-modified mesoporous silica, such as functionalized MCM-41 and MCM-48, was investigated [442]. The nanoparticles were immobilized in the mesopores via the incorporation of water droplets of the reverse micelles.

An irradiation grafting method was applied for the modification of nanoparticles so that the latter can be added to polymeric materials for improving their mechanical performance, using existing compounding techniques. The following items were discussed: (a) chemical interaction between the grafting monomers and the nanoparticles during irradiation; (b) properties including modulus, yield strength, impact strength, and fracture toughness of the resultant nanocomposites; and (c) possible morphological changes induced by the addition of nanoparticles [443].

The coating of different materials with conducting electroactive polymers (i.e. polyaniline, polypyrrole, polythiophene, and their derivatives), provided by means of chemical polymerization, was reviewed [444]. The topics covered included the deposition of conducting electroactive polymers (i) by bulk oxidative chemical polymerization, (ii) by surface-located polymerization, and (iii) by coating of micro- and nanoparticles. The coating of different materials like polymers, polymer particles, ion-exchange membranes, glass, fiber, textile, soluble matrices, and inorganic materials was reviewed.

Chitosan–poly(acrylic acid) complex nanoparticles, which were well dispersed and stable in aqueous solution, were prepared by template polymerization of acrylic acid in chitosan solution [445]. The molecular weight of poly(acrylic acid) in nanoparticles increased with increasing molecular weight of chitosan, indicating that the polymerization of

acrylic acid in the chitosan solution was a template polymerization. The prepared nanoparticles carried a positive charge and showed a size in the range from 50 to 400 nm. The surface structure and  $\zeta$  potential of nanoparticles were controlled by different preparation processes. The potential of chitosan as an emulsion stabilizer was combined with the miniemulsion technique to generate oil droplets, hollow capsules, and latex particles in the diameter range of 100–300 nm carrying a functional biopolymer surface [446]. Facile fabrication of hollow polystyrene nanocapsules was done by microemulsion polymerization [447].

Liquid nanodroplets within a size range of 50 to 500 nm were prepared by shearing a system containing oil, water, and a surfactant [448]. The growth of the nanodroplets can effectively be suppressed by using a strong hydrophobe as an additive to the oil and an effective surfactant. The hydrophobe acted as an osmotic agent which stabilized the system against Ostwald ripening. The growth of the droplets by collision was controlled by the density of the surfactant layer. Freshly prepared miniemulsions were “critically stabilized” and show a slow but pronounced growth, whereas a miniemulsion in “equilibrium” exhibited constant droplet size on longer time scales.

Surface-initiated living free radical polymerization was employed in a multistep procedure to prepare hollow polymeric nanocapsules [449]. Initially, trichlorosilyl-substituted alkoxyamine initiating groups were attached to the surface silanol groups of silica nanoparticles. This surface layer of initiating groups was then used to grow functionalized linear chains leading to a core–shell morphology. Under either chemical or thermal conditions, the reaction of these functionalities gave a cross-linked polymeric shell that was covalently attached to, and surrounded, the central silica core. Removal of the silica core then gave the hollow polymeric nanocapsules, which were stable under solvent dissolution and thermal treatment because of their cross-linked structure.

Electron affinities of methyl-2-cyanoacrylate and ethyl-2-cyanoacrylate were predicted using four different density functional or hybrid Hartree–Fock/density functional methods [450]. Equilibrium structures and harmonic vibrational frequencies were computed for the neutral and anionic species of each system.

The protective antioxidant role of idebenone both as free drug and drug-loaded Tween 80-coated polyethyl-2-cyanoacrylate nanocapsules was reported [451]. The relationship between oxidative damage and apoptotic or nonapoptotic cell death was evaluated *in vitro*.

A synthetic process for producing aromatic polycarbonate nanoparticles using supercritical CO<sub>2</sub> was developed [452]. High molecular weight polycarbonate nanoparticles were synthesized using transesterification between bisphenol-A and diphenyl carbonate in supercritical CO<sub>2</sub> which was an excellent plasticizing agent and a good solvent for phenol, a by-product of the reaction. Poly(propylene oxide)–poly(ethylene oxide)–poly(propylene oxide) tri-block copolymer with CO<sub>2</sub>-phobic anchor and CO<sub>2</sub>-philic tail group was used as a stabilizer for the preparation of stable dispersions of bisphenol-A–diphenyl carbonate mixture in a CO<sub>2</sub> continuous phase. The resulting polycarbonate particles with

a nanosize of 30–140 nm had a high molecular weight of  $3.1 \times 10^5$  (g/mol).

Functional arborescent graft polystyrenes prepared by a technique involving the iterative grafting of end functional polymer chains onto reactive polymer backbones were synthesized [453]. The zero-generation comb polymers and then the first generation hyperbranched structures were obtained by the coupling reaction of living (*x*-acetal polystyryllithium) onto linear or comb chains of poly(chloro ethyl vinyl ether) of controlled (DP) over bar (*n*) and structure.

A type of narrowly dispersed fluorescent cross-linked polystyrene nanoparticle (20–50 nm) was synthesized via a modified microemulsion copolymerization of styrene, cross-linker divinyl benzene, and a hydrophilic comonomer amino ethyl methacrylate hydrochloride, in the presence of pyrene [454]. Characterized by steady-state fluorescence spectra, these nanoparticles showed high luminescent intensity and the embedded pyrene had a negligible desorption from the nanoparticles.

Core-shell polymeric nanoparticles were prepared by self-assembly and step-growth polymerization [455]. An approach was presented for the controlled intramolecular collapse of linear polymer chains to give well-defined single-molecule nanoparticles whose structure was directly related to the original linear polymer [456]. By employing a combination of living free radical polymerization and benzocyclobutene chemistry, nanoparticles can be routinely prepared in multigram quantities with the size being accurately controlled by either the initial degree of polymerization of the linear chain or the level of incorporation of the benzocyclobutene coupling groups. The latter allowed the cross-link density of the final nanoparticles to be manipulated.

Stable colloidal solutions of gold nanoparticles surface-derivatized with a thiol monolayer were prepared using two-phase (water–nitrobenzene) reduction of  $\text{AuCl}_4^-$  by sodium borohydride in the presence of 2-mercapto-3-*n*-octylthiophene [457]. This kind of surface-functionalized gold nanoparticle was incorporated into the poly(3-octylthiophene) films on electrode in the process of electrochemical polymerization leading to poly(3-octyl thiophene)–gold nanoparticle composite films.

Polyphenylpyrrole coated silver nanoparticles at the liquid/liquid interface were produced [458]. In the electrochemical step of the reaction, *N*-phenylpyrrole facilitated the transfer of the silver ion from an aqueous to an organic phase. This step was followed by a slow homogeneous electron transfer reaction from the *N*-phenylpyrrole to the silver ion followed by polymerization and metal cluster growth.

Inorganic silica nanoparticles were encapsulated with an epoxy resin to give waterborne nanocomposite dispersions, using the phase-inversion emulsification technique [459]. Submicrometer-sized waterborne particles with narrow size distribution were prepared. All the silica nanoparticles were encapsulated within the composites and uniformly dispersed therein. Curing of the nanocomposite dispersions proceeded in a controlled manner.

A ternary microemulsion polymerization was used to prepare nanosized hollow polystyrene microlatexes with triblock copolymers of poly(oxyethylene)–poly(oxypropylene)–poly(oxyethylene)  $[(\text{EO})_x(\text{PO})_y(\text{EO})_x]$  [460]. Micelle formation

using triblock copolymers was a useful nanoreactor in order to make polymer nanoparticles in o/w microemulsions. Poly(methyl methacrylate)/cross-linked polystyrene core/shell nanospheres were fabricated by o/w microemulsion. Polystyrene hollow nanospheres were obtained using the polymer core etching technique. The size of the hollow nanoparticle was dependent on the surfactant concentration and the weight ratio of [surfactant]/[monomer].

Drug delivery systems had a great impetus to deliver a drug to diseased lesions. A suitable carrier was needed to deliver a suitable and sufficient amount of the drug to a targeted point; hence various kinds of formulations were developed. The state of the art was reviewed regarding the synthetic methods and characterization of nanoparticles, the suitability of polymeric systems for various drugs, drug loading, and drug release properties of various systems such as nanoparticles, hydrogels, microspheres, film and membranes, tablets, etc. [461].

An overview was given on the mechanisms of formation of polymerization in miniemulsions, the synthesis of new polymers, and dispersive hybrid systems from heterophase situations [462].

The *in-situ* formation of Au/Pt bimetallic nanoparticles on the surface of polystyrene microspheres was reported [463]. This was accomplished by dispersion copolymerization of styrene and a poly(*N*-isopropylacrylamide) macromonomer in ethanol–water media in the presence of  $\text{HAuCl}_4$  and  $\text{H}_2\text{PtCl}_6$ . The particle size and morphology of the polystyrene microspheres were changed by varying the molar ratio of Au/Pt. The propagation of oligomer radicals and nucleation of polystyrene microspheres were controlled by the Au/Pt molar ratio.

Nanometer-sized CoPt particles dispersed in a poly(methyl methacrylate) matrix were prepared, as a novel nanostructured magnetic plastic, through a soft chemical processing route [464]. CoPt nanoparticles were synthesized from a solution phase reduction system in the presence of capping ligands and stabilizing agents at high temperature. The CoPt nanoparticles were annealed at 400 °C for 3 h and were subsequently redispersed in methylmethacrylate (monomer).

To study interfacial particle-to-particle bonding mechanisms, an ultrathin film of pyrrole was deposited on alumina nanoparticles using a plasma polymerization treatment [465]. A thin film of the pyrrole layer (2 nm) was uniformly deposited on the surfaces of the nanoparticles. Particles of all sizes (10–150 nm) exhibited equally uniform ultrathin films indicating well-dispersed nanoparticles in the fluidized bed during the plasma treatment. The pyrrole-coated nanoparticles were consolidated at a temperature range (approximately 250 °C).

The synthesis and characterization of well-dispersed,  $\text{CoFe}_2\text{O}_4$  nanoparticles within a polymer matrix at room temperature were reported [466]. Comparable inorganic synthetic methods required heating at high temperatures in order to produce this particular mixed-metal oxide composition. The modification of templating schemes using block copolymers consisted of introducing a mixture of metal salts to a polymer solution before any microphase separation of the block copolymer constituents can occur, thus allowing fast diffusion of metals to the functional polymer

backbone. The diblock copolymer matrix was synthesized using ring-opening metathesis polymerization of norbornene derivatives.

The preparation and evaluation were reported of cyclophosphamide loaded-polyalkylcyanoacrylate nanospheres obtained by emulsion polymerization [467]. Nanoparticles of improved stability against long-term aggregation were prepared using poly(styrene)-*b*-poly(2-vinylpyridine) star-block copolymer architectures [468]. The star-block copolymers, physically resembling diblock copolymer micelles, were synthesized by anionic polymerization and coupling with ethylene glycol dimethacrylate.

Catalytic sites can be placed at the core, at interior positions, or at the periphery of a dendrimer. There are many examples of the use of peripherally functionalized dendrimers in catalysis. A review was concerned with dendrimer-based catalysis involving catalytic sites at the core of a dendrimer and within the interior voids [469]. Key features were positive and/or negative catalytic activity.

The synthesis and applications of organic-inorganic nanostructured colloids and colloidal-based materials were reviewed [470]. Emphasis was placed on the strategies and synthetic methods developed to organize organic-inorganic architectures. A description and a general hierarchical classification of different systems were given from inorganic particle synthesis and surface modification to more elaborate nanostructured colloids obtained through *in-situ* encapsulation and/or self-assembly techniques. Ordering of colloids into two- and three-dimensional arrays and their use as templates was considered. Some properties and applicability of organic-inorganic colloids in catalysis, medicine, and coating technologies were cited.

The photoinduced flocculation of a nonaqueous dispersion of core-shell nanoparticles (diameter = 50 nm) was described [471]. The particles consist of a tightly cross-linked core composed of poly(butyl methacrylate-co-ethylene glycol dimethacrylate) and a lightly cross-linked shell of poly(butyl methacrylate-co-ethylene glycol dimethacrylate-co-methacrylic acid). The process of particle aggregation kinetics was studied in the absence of long-range electrostatic interaction by using a combination of static and dynamic laser light scattering.

### 3.4. Physical-Chemical Methods

Physical-chemical methods are the processes that combine both the physical and chemical methods during the synthesis of the materials. As shown previously, there are many different methods based on the physical or chemical principles from which lot of the physical-chemical methods could be developed. For instance, it has been shown that, as a "bottom up" process, mechanochemical processing enables the build up of nanoparticles through solid-state chemical reaction in a microscopically uniform environment, leading to the formation of nanoparticles with narrow size distributions. The physical fields, like electric fields, magnetic fields, lights, etc., could be used to affect the chemical reactions and the processes. Coacervation-phase separation has been proved to be one powerful technique for preparation of the nanocapsules. In the following, we only introduce in detail the coacervation-phase separation and briefly other physical-chemical processes.

#### 3.4.1. Coacervation-Phase Separation

Coacervation-phase separation is a method to use a coacervation-inducing agent to reach the coacervation-phase separation during/after the solvent evaporation to form the microcapsules or the nanocapsules. The coating can be controlled by changing the parameters during the process, so that the drug content, particle size distribution, biomedical properties, etc. of the microcapsules/nanocapsules can be controlled. This procedure has been employed widely for preparation of microcapsules/nanocapsules for drug release.

Terbutaline sulphate microcapsules were prepared by coacervation-phase separation induced by the solvent evaporation technique [472–474]. The cellulose acetate phthalate was employed as coating material alone and in combination with ethyl cellulose. The prepared microcapsules were evaluated for their drug content, particle size distribution (microscopic method), flow properties, bulk density, and *in vitro* dissolution. Propranolol hydrochloride microcapsules were prepared by the coacervation-phase separation induced by the solvent evaporation technique [475].

Microcapsules of phenylpropanolamine HCl were prepared by three techniques, viz. coacervation-phase separation, air suspension, and pan coating, using different polymers and/or waxes as wall-forming materials [476].

Microcapsules were prepared from naproxen and ethylcellulose by coacervation phase separation, using polyisobutylene as a coacervation-inducing agent [477]. The micrometric properties of the microcapsules and dissolution behavior were examined. Using polyisobutylene at different concentrations, the release of naproxen during an *in vitro* dissolution test from 60 to 90% was regulated. The microcapsules were aggregates of individually coated naproxen crystals clustered together.

Using ethylcellulose and cellulose triacetate as co-wall materials, sustained release microcapsules of theophylline were prepared. The solid drug dispersed in the cellulose triacetate matrices was first prepared by solvent evaporation; then the matrices were microencapsulated by means of coacervation-phase separation of ethylcellulose from toluene solution on addition of petroleum ether [478].

Phenytoin sodium was microencapsulated with ethylcellulose by a coacervation-phase separation method from ethyl acetate solution to develop a prolonged release dosage form of phenytoin [479].

Microcapsules of phenylpropanolamine (PPA) hydrochloride with core:wall ratios of 1:1, 2:1, and 1:2 were prepared by the coacervation-phase separation method, using ethylcellulose as the coating material [480]. Two batches of PPA · HCl powder with different particle sizes were used as the core material. The different sizes of microcapsules were separated using a range of standard sieves. The effects of drug particle size, the media pH, and the core:wall ratio on the dissolution kinetics were evaluated kinetically.

The preparation of lipid vesicles using simple coacervation was described [481]. The optimal coacervation conditions for the formation of lipid vesicles by the triangular phase diagram of the lipid-alcohol-water system were examined. Four different alcohols (methanol, ethanol, *n*-propanol, and 2-propanol) were used as a lipid solvent, and deionized, distilled water was used as a poor solvent for the lipids. The lamellarity and size homogeneity of the resulting lipid vesicles were observed using a specific fixation

technique with malachite green. The majority of vesicles formed by methanol as a lipid solvent appeared to be large and unilamellar, ranging from 100 to 1000 nm in diameter.

Surfactant precipitation is one method of separating and concentrating surfactant for reuse from a subsurface surfactant-based remediation process. The dialkyldiphenylether disulfonates was shown to be very effective in this application as one class of surfactant [482]. The precipitation and coacervation phase boundaries for a surfactant mixture, which was primarily dicycldiphenylether disulfonate as a function of concentration of added NaCl and KCl, were reported [482].

Nicardipine hydrochloride (N.HCl) microcapsules were prepared by means of the coacervation phase separation technique using ethylcellulose as a coating material [483, 484]. Micromeritic investigations were carried out on nicardipine hydrochloride, ethylcellulose, and nicardipine hydrochloride microcapsules in order to standardize the microcapsule product and to optimize the pilot production of dosage forms prepared with these microcapsules.

Ketorolac tromethamine is a nonsteroidal drug with potent analgesic and anti-inflammatory activity and is absorbed rapidly [T-max (1.0 h) with an efficiency >87%] following oral and intramuscular administration. Microcapsules of the ketorolac tromethamine were prepared by means of the coacervation-phase separation technique induced by the addition of nonsolvent, and release rates from microcapsules were studied [485]. Eudragit S100 was used as the coating material.

Nitrofurantoin, a synthetic bactericidal drug, was encapsulated with Eudragit RS 100 polymer by a coacervation phase separation technique using variable proportions of polyisobutylene (0% to 3%) as a protective colloid [486]. The *in vitro* release experiments were carried out over the entire pH range of the gastrointestinal tract, the data obtained from the dissolution profiles were compared in light of different kinetic models, and the regression coefficients were compared. The *in vivo* studies were performed on female human volunteers.

Rhizobacteria-containing polymer microparticles were prepared using either a complex coacervation-phase separation method or a spray-drying technique [487]. The microparticles obtained were characterized with regard to their particle size distribution, morphology, and bacterial content. Long-term bacterial survival within the microparticles stored under controlled conditions (relative humidity and temperature) was investigated.

The aspirin-impregnated microspheres of chitosan/poly (acrylic acid) copolymer were produced in order to evaluate the release characteristics as a function of pH, simulating the fluids in the gastrointestinal tract [488]. Chitosan microspheres were obtained by the coacervation-phase separation method, induced by the addition of a nonsolvent (NaOH 2.0 M solution). The microspheres were cross-linked with glutaraldehyde, reduced with sodium cyanoborohydride, and grafted with poly(acrylic acid).

### 3.4.2. Other Methods

There are many other types of the physical-chemical methods for preparing the nanocapsules, among which emulsification evaporation, solvent displacement, salting

out, emulsification diffusion, pyrolysis of polymer materials, nitridation of nanoparticles, and various self-assembly and templating approaches are very convenient tools. Exposing the nanoparticles to polyelectrolyte solutions of opposite charge, the polyelectrolytes are deposited in a layer-by-layer sequence to form nanocapsules. The  $\gamma$  radiolysis method can be applied by optimizing various conditions like metal ion concentration, polymer or surfactant concentration, and pH. Some physical-chemical methods utilize the applied electric and magnetic fields and microwave plasma to affect the chemical process, like growth of colloid nanoparticles, etc. Photochemical generation, the electrochemical procedure, the pulsed laser vaporization-controlled condensation technique, controlled chemical passivation of extremely active particles, and the explosion method are all applicable for synthesizing nanomaterials such as clusters, onions, intercalations, nanopolyhedra, nanotubes and nanocapsules, etc.

The techniques available to prepare biodegradable nanoparticles, nanospheres, and nanocapsules from preformed polymers were reviewed [489]. Four techniques were discussed in terms of their technological advantages and drawbacks: emulsification evaporation, solvent displacement, salting-out, and emulsification diffusion. The mechanism of nanoparticle formation for each technique was proposed from a physicochemical perspective.

General aspects of nanocapsules used in drug delivery systems were reviewed from both a physicochemical and a therapeutic point of view [490]. The preparation methods and ways to characterize the size, surface, density, release, and stability of this o/w system were described, and the influence of encapsulation within nanocapsules on the biological activity of numerous drugs was discussed.

Carbon nanocapsules with SiC nanoparticles were produced by thermal decomposition of polyvinyl alcohol with SiC clusters at 500 °C in Ar gas atmosphere [491]. Carbon hollow structures such as nanoparticles, polyhedra, and clusters formed. The work indicated that the pyrolysis of polymer materials with clusters is a useful fabrication method for the mass production of carbon nanocapsules at low temperatures compared to the ordinary arc discharge method.

SiC nanorods were synthesized through carbothermal reduction of SiO by C nanocapsules or amorphous activated C [492]. The nanorods formed during a reaction between SiO and C nanocapsules were straight. The nanorods formed during reaction between SiO and amorphous activated C consisted of straight and curled parts or chains of SiC nanoparticles. A surface of the rod tip was covered with a thin amorphous layer of 3 nm thickness.

Encapsulation of cobalt oxide nanoparticles and Ar in boron nitride nanocapsules was reported [493]. A large quantity of boron nitride nanocapsules with cobalt nanoparticles was fabricated by nitridation of boron and cobalt nanoparticles with a H<sub>2</sub>/NH<sub>3</sub> gas mixture [494]. Cobalt nanoparticles were encapsulated by boron nitride layers with thickness of 5 nm. Ferromagnetism and luminescence at 3.8 eV were due to separation of Co nanoparticles by the BN layers. The nitridation of boron particles with catalytic metal is a useful fabrication method for mass production of BN nanocapsules at low temperatures.

Carbon and boron nitride fullerene materials (clusters, onions, intercalations, nanopolyhedra, nanotubes, and nanocapsules) were synthesized by polymer pyrolysis, chemical reaction, arc melting, and electron-beam irradiation [495]. Fullerene clusters and atomic clouds (atom hopping) were formed on the surface of the C and BN fullerene materials. They provided angular and spherical nanocage structures, consisting of four-, five-, six-, and seven-membered ring bondings. A guideline for designing the C and BN fullerene materials, which may have various atomic structures and properties, was summarized.

A selection of graphitic materials of both scientific as well as commercial importance was modified by deposition of various metals at very low coverages under overpotential or underpotential conditions [496].

A thermodynamic theory for the deliquescence behavior of soluble crystals in an atmosphere of solvent vapor was developed [497]. The free energy barriers that could impede deliquescence were studied [497]. The integral equation theory was applied to study the solvent-induced potential of mean force between two passivated nanoparticles in dilute solution [498]. This approach explicitly accounted for the molecular structure of the solvent and the anisotropy of its density profile induced by the pair of nanoparticles.

Controlling the surface properties of nanoparticulate materials is necessary if they are to be exploited in applications such as colloidal crystals or biolabeling. By tailoring the polymer flexibility and the electrostatic forces involved in polyelectrolyte adsorption onto highly curved gold surfaces, through variation of the total salt concentrations suspending the chains and spheres, irreversible polyelectrolyte wrapping of gold nanoparticles was affected [499]. By consecutively exposing the nanoparticles to polyelectrolyte solutions of opposite charge, polyelectrolytes were deposited in a layer-by-layer sequence, yielding gold nanoparticles coated with uniform polyelectrolyte multilayers. Self-supporting polyelectrolyte multilayered nanocapsules were formed after dissolution of the metallic core.

Polymer nanocapsules were reviewed [500]. Hollow polymer particles with dimensions in the submicrometer region possess great potential for encapsulation of large quantities of large sized guest molecules into their empty core domains. Various self-assembly and templating approaches were introduced.

Whiskers of iron carbide encased in carbon shells were prepared from  $\text{Fe}^{2+}$  phthalocyanine [501]. Solid FePc was oxygenated and then thermally treated under  $\text{H}_2$  flow. With proper control of conditions,  $\text{Fe}_3\text{C}$  free from metallic iron was synthesized. The iron carbide whiskers ranged in length from 300 to 500 nm, and their widths were approximately 100 nm. The carbon coating was uniform and about 2.7 nm wide.

The immobilization of nanometer-sized and cluster metal particles in polymeric matrices was systematized for both macroligands and the matrices formed *in-situ* [502]. Special attention was paid to the controlled chemical passivation (stabilisation) of extremely active particles of colloidal size using high-molecular-weight compounds. The routes of formation of polymer-immobilized nanoparticles directly in the polymer medium were analyzed. Studies in the field of

polymer-analogous transformations, which offered a promising approach to the binding of mono- and heterometallic clusters as a new direction in the physicochemistry of nanoparticles, were discussed.

Three different examples were presented of nanocrystals prepared by the pulsed laser vaporization-controlled condensation technique [503]. The photoluminescence properties of the Si nanocrystals were represented. A photoreduction of the white  $\text{WO}_3$  nanoparticles into the blue  $\text{W}_2\text{O}_5$  followed the irradiation of the particles with the second harmonic of the Nd:YAG laser at 532 nm.

Capped copper nanoclusters were synthesized by the  $\gamma$  radiolysis method by optimizing various conditions like metal ion concentration, polymer or surfactant concentration, and pH [504]. The increasing amount of capping agent was responsible for the decrease in size as small as 17 nm of the metal clusters.

An electrochemical procedure, based on the dissolution of a metallic anode in an aprotic solvent, was used to obtain silver nanoparticles ranging from 2 to 7 nm [505]. The influence of the different electrochemical parameters on the final size was studied by using different kinds of counterelectrodes.

Gold sol, photochemically prepared in aqueous Triton X-100 (TX-100) medium, was discolored by photoirradiation in the presence of  $\text{KBrO}_3$  and any one of the following bromine containing trihalomethanes, such as bromoform ( $\text{CHBr}_3$ ) chlorodibromomethane ( $\text{CHClBr}_2$ ), and bromodichloromethane ( $\text{CHCl}_2\text{Br}$ ) owing to the dissolution of colloidal gold nanoparticles [506]. Pt nanoparticles supported in nanoporous  $\text{Al}_2\text{O}_3$  catalyst were prepared by reduction of  $\text{K}_2\text{PtCl}_4$  solution using 112 solution in the presence of  $\text{Al}_2\text{O}_3$  and poly(acrylic acid) as capping material [507].

Effects of applied electric and magnetic fields on the 2D growth of colloid nanoparticles were studied. Two-dimensional photochemical generation of amorphous iron-containing magnetic nanoparticles was carried out via ultraviolet decomposition of a volatile organometallic compound, iron pentacarbonyl, in a mixed Langmuir monolayer at the gas/water interface with stearic acid as a surfactant matrix [508]. During the formation of nanoparticles, the monolayer was in the 2D gas phase state (at very low or no surface pressure). Controlling morphology of nanostructures by synthesis under applied fields could be a promising approach for nanophase engineering and nanotechnology.

The arc-discharge method was modified to produce nanoparticle Ni encapsulated in graphite shells [509, 510]. The carbon-encapsulated metal or metal carbide was prepared based on high-temperature ( $\sim 1800^\circ\text{C}$ ) treatment of microporous carbon materials impregnated with metal precursors. The microwave plasma enhanced CVD system was used to synthesize carbon-encapsulated metal nanoparticles on silicon wafer. An explosion method was developed to prepare the nanocapsules [513–515].

### 3.5. Mechanical Techniques

Mechanical techniques utilize mechanical forces and mechanical energies for preparation of nanomaterials, like nanoparticles and nanocapsules. Milling and vibrating are two typical methods using mechanical energies. Some

mechanical techniques could be categorized as physical methods.

Drug delivery systems improve the therapeutic efficacy and safety of drugs by delivering them at a controlled rate depending on the body requirements and the site of action. These systems aid in reducing the amount of drug required, the number of doses, side effects, and bioinactivation. Currently, delivery systems for drug targeting and controlled release are being developed using drug nanoparticles. Several techniques, such as air suspension, pan coating, spray drying, and milling have been used for the manufacture of drug nanoparticles. In this section, several mechanical techniques (i.e., air suspension, pan coating, spray-drying, and congealing) which are applicable for biomedicine and drug delivery are introduced briefly. For detailed biomedical properties of the nanocapsules, refer to Section 5.

### 3.5.1. Air Suspension

Air suspension is a common technique to utilize fluidized bed systems for selecting the particle materials, which can be developed for coating the nanoparticles to realizing the micro/nanoencapsulation of drug products and food particles. This technique has been used widely in the pharmaceutical/food industry for production of core material and for film coating.

A review examined advances in the commercial production of microencapsulated drug products [516]. Factors influencing drug selection were considered with particular reference to the design of controlled drug delivery systems. The formulation of both aqueous and nonaqueous coating materials was discussed with examples of common problems encountered in applied coatings. Methods of core production were considered with emphasis on spheronization procedures. Pan and air suspension techniques, together with modification, were discussed. Local average velocity of a particle cloud in an air suspension by cross-correlation of two attenuated laser beams was measured [517].

The characterization of microcapsules containing drugs was reviewed with particular emphasis on sustained-release products produced commercially by pan or air-suspension coating and intended for oral administration [518]. After considering aspects of the core and coating, various technologies used to assess microcapsules were discussed such as optical and spectroscopic evaluation, particle size analysis, filling into hard gelatin capsules, and disintegration, dispersion, and dissolution testing. The *in vivo* testing of microcapsules and correlation with *in vitro* data was considered.

Fluidized bed systems were used in the pharmaceutical industry for production of core material and for film coating [519]. Top spray coaters produced batches of fine, coated particles in excess of 500 kg. Wurster bottom spray equipment was used to manufacture pellets as well as to coat products ranging from powders to tablets.

Within the framework of the mechanics of heterogeneous media undergoing phase transformations, a mathematical model was proposed for describing a mixture of gas and liquid (solid) metal particles. The differences between the velocities and temperatures of the phases and the nonequilibrium nature of the phase transition were considered [520]. The problem of the structure of a shock wave in an air suspension of melting particles was solved.

A controlled release preparation of salbutamol may improve patient compliance, minimize side effects, and be valuable in the treatment of nocturnal asthma by extending drug action throughout the night. A controlled release pellet preparation of salbutamol via the air suspension technique was formulated [521].

The influence of spatial nonuniformity in the distribution of chemically inert particles in a screening layer on the process of interrupting the propagation of a heterogeneous-detonation wave was studied numerically within the framework of the equations of motion of a three-velocity, three-temperature, unipressure continuum [522]. The distribution of flame-quenching particles in the layer can affect significantly the extinguishing of combustion waves in a monofuel-air suspension.

Nonpareil cores were spray-coated with a chlorpheniramine maleate (an alkylamine antihistamine) layer and a Eudragit(R) NE30D overcoat in a Wurster air-suspension apparatus [523]. *In vitro* dissolution drug release was a function of polymer membrane thickness.

A varied description was presented of the fluid bed process for coating or air-suspension coating with emphasis on the most efficient batch fluid bed apparatus (the Wurster system) and the ideal continuous fluid bed [524]. Phenomena involved in the process of coating fluidized solid particles were studied. The problem of the application of this technology to coat food particles, in terms of feasibility and profitability, was discussed.

### 3.5.2. Pan Coating

Pan coating is a technique using a polymer or different mixtures of polymers as film coating agents. The method can be based on the simultaneous spraying of aqueous solutions of a film-forming polymer and an appropriate cross-linking agent. Cross-linking of the polymer is achieved *in-situ* in the film during coating of the pellets in a fluidized bed. The pan coating can be used for preparing the nanoparticle and the nanocapsules. The differences of the different types of pan coaters were discussed from the pharmaceutical and technological points of view [525]. Besides a classification by different criteria, aspects of automation, maintenance, scale-up, etc. were discussed.

Different series of Diltiazem pellets with slow release of the active substance were prepared, by the pan coating technique, using different mixtures of acrylic polymers (Eudragit E, L, RL, and RS) as film coating agents [526–530]. The thicknesses of the coatings were varied by different amounts of Eudragit. The propranolol-HCL sustained release coated beads were prepared [527] using Eudragit RS100 as release controlling materials [527, 529]. Granules containing indomethacin crystals were coated with Eudragit solutions of different RL/RS ratios [528]. Diclofenac sodium enteric-coated beads were prepared using Eudragit L-100 as a pH-dependent release-controlling polymer [530]. Overcoating of the beads with beeswax was investigated [526–530]. The beads were characterized for their particle size distribution, drug loading efficiency, and dissolution behavior in 0.1N HCl. The process was reproducible with regard to drug content and inexpensive, and the formed granules were directly compressed into tablets. *In vitro* release of



indomethacin from coated granules, tablets, and capsules was studied as a function of different ratios of Eudragit RL/RS in the coating solution. The coating level of the polymer, the particle size of the beads, and overcoating with beeswax played a major role in determining the release rate of the drug from the coated beads.

A technique for the manufacture of water-insoluble film coatings on drug-loaded saccharose pellets was described [531]. The method was based on the simultaneous spraying of aqueous solutions of a film-forming polymer and an appropriate cross-linking agent. Cross-linking of the polymer was achieved *in-situ* in the film during coating of the pellets in a fluidized bed. Uniform film coatings were formed without additives.

Aminophylline was formulated as small spherical cores for subsequent coating, to develop a competitor microencapsulated product to the commercially available sustained-release tablet Phyllocontin [532]. Optimum spherical crystallization conditions yielded cores of loosely adhering crystals of active, highly irregular surface morphology and poor mechanical strength during pan coating. Aqueous spheronization yielded satisfactory cores in high yield when microcrystalline cellulose and liquid paraffin were used.

The dissolution profile of various weight fractions of dipyrindamole:hydroxypropylmethylcellulose acetate succinate and dipyrindamole:hydroxypropylmethylcellulose phthalate coprecipitates lead to the choice of 1:2 dipyrindamole:hydroxypropylmethylcellulose acetate succinate as the controlled-release component [533]. It was deposited to form two-thirds of the total dose as an inner layer on inert sucrose cores by air suspension coating for release mainly in the small intestine.

The electrochemical deposition of copper was studied in polyaniline layers with different redox states before the onset of metal deposition [534].

### 3.5.3. Spray-Drying

Spray-drying is the process of spraying a solution into a warm drying medium to produce nearly spherical powder granules that are relatively homogeneous. There are four stages in the spray-drying: (1) rotary atomization of the liquid feed to generate a fine spray; (2) injection of the hot gas stream into the radially distributed spray; (3) rapid vaporization of the solvent to yield the powder product; (4) centrifugal separation of the spherical particles from the gas stream. Spray-drying is also suitable for synthesis of the nanoparticles and the nanocapsules.

Poly(L-lactic acid)-coated polyisobutylcyanoacrylate microcapsules containing protein molecules were prepared by a single-step procedure based on either a double-emulsion-solvent evaporation method or a spray-drying method [535]. First, an aqueous protein solution was emulsified in an organic phase of methylene chloride containing a wall-forming monomer (isobutylcyanoacrylate), various kinds of poly(L-lactic acid), and a surfactant. An immediate polymerization process of isobutylcyanoacrylate took place at the w/o interface upon contact with hydroxide ion in the aqueous phase, leading to the formation of a polyisobutylcyanoacrylate wall around the aqueous droplets. This w/o emulsion was reemulsified in an aqueous

solution to promote the solvent removal and, consequently, the precipitation of poly(L-lactic acid) onto polyisobutylcyanoacrylate microcapsules or was spray-dried to directly deposit the poly(L-lactic acid) on the wall. Three proteins, bovine serum albumin, horseradish peroxidase, and tetanus toxoid, were encapsulated in these poly(L-lactic acid)-coated polyisobutylcyanoacrylate microcapsules.

A synthesis method was developed for hydroxyapatite particles with different morphologies [536]. The process involved chemical precipitation and spray-drying, which produced spherical, agglomerated hydroxyapatite granules with controlled particle sizes and structures. These granules contained nanoparticles with an average crystalline size of about 10 nm. The morphologies of the granules were controlled by adjusting the spray-drying conditions, such as the volume fraction of feed slurry and the atomization pressure.

Fine powder of single and binary mixed oxides was produced by decomposition of the respective metal nitrates and polyvinyl alcohol or a mixture of polyvinyl alcohol and polyacrylic acids [537]. The nanoparticles of the oxide system studied are: spinels ( $MFe_2O_4$  where  $M = Ni^{2+}$ ,  $Co^{2+}$ ,  $Zn^{2+}$ ,  $Mg^{2+}$ ); orthoferrites ( $MFeO_3$  where  $M = Gd^{3+}$ ,  $Sm^{3+}$ );  $LaAlO_3$ ,  $NdGaO_3$ ,  $CaO/MgO/Y_2O_3$  stabilized zirconia ( $ZrO_2$ ); lead zirconate titanate, lanthanum modified lead zirconate titanate, and  $BaTiO_3$ .

Solid lipid nanoparticles possess a solid matrix composed of physiological lipids or lipoids with a mean diameter in the range of approximately 50 to 1000 nm. Solid lipid nanoparticles are an alternative particulate drug carrier to polymeric nanoparticles, emulsions, and liposomes [538–540]. They combine advantages of emulsions, liposomes, and polymeric particles. Similar to emulsions and liposomes, they are composed of physiological and well-tolerated substances and can be produced on an industrial scale [541–543]. The general features of solid lipid nanoparticles and their production techniques were presented [541]. The incorporation of lipophilic, hydrophilic and insoluble drugs was presented, and incorporation rates and loading capacity were discussed [542]. Long-term stability, lyophilization, spray-drying, and possible applications in cosmetics and pharmaceuticals were dealt with [543].

A sol-gel method was employed to produce a zinc oxide colloid consisting of ZnO nanocrystalline particles with an average diameter of around 3 nm and subsequently mixed with a silica colloid [544]. The mixture was spray-dried to form a powder nanocomposite. The green photoluminescence exhibited by the composite was very stable.

A technique was proposed to produce drug particles in the nanometer range as small as 125 nm with a narrow size distribution [545], which involved the use of a vibrating surface that atomizes the jet into microdroplets. The ultrasonic field generated by the vibrating surface enhanced mass transfer through increased mixings. Particle sizes were easily controlled using this technique by changing the vibrational intensity of the vibrating surface.

Porous titania granules (1–20  $\mu m$ ) were made by spray-drying titania solutions with and without peptization. An unpeptized titania slurry was prepared by hydrolyzing titanium tetraisopropoxide, while a peptized sol was prepared by adding nitric acid to the slurry [546]. The characteristics of the granules depended on the feed solution properties.

In particular, granules from the unpeptized slurry showed a bimodal pore size distribution, with a rough surface attributed to hard aggregates; granules from the peptized sol showed a monomodal bimodal pore size distribution, with a smooth surface of well-packed nanoparticles. The effect of dopants (alumina and zirconia) was investigated.

A spray-drying method was used to produce a silica powder that contained ordered mesopores [547, 548]. A colloidal mixture of silica nanoparticles and polystyrene latex nanoparticles was mixed and sprayed as droplets into a vertical reactor that contained two temperature zones. The solvent in the droplets was evaporated at the front part of the reactor to produce a powder composite consisting of silica and polystyrene nanoparticles. The polystyrene nanoparticles in the powder were evaporated in the back portion of the reactor to produce a silica powder consisting of mesopores.

### 3.5.4. Congealing

Rapidly cooled materials are often unstable as a result of changes in their physical properties due to imperfect crystallization. In the process of congealing, melted material is atomized into droplets that are very quickly solidified. This increases the possibility of the material crystallizing in different metastable forms. Congealing is applicable to formation of nanostructured materials, like nanoparticles and nanocapsules. Nanostructured materials have a relatively large proportion of their atoms associated with the grain boundary and the method used to develop the nanograins has a strong influence on the resulting grain boundary structure.

Isothermal microcalorimetry was used to observe the change in the thermodynamic state of spray-congealed carnauba wax during storage [549]. In order to accelerate the thermodynamic change in the spray-congealed wax, three annealing procedures were developed using isothermal microcalorimetry. By means of annealing, a spray-congealed product closer to a thermodynamically stable state was achieved.

Hard shell capsules containing four theophylline compounds of different solubilities (theophylline, etofylline, diprophylline, and proxiphylline) were prepared with saturated polyglycolized glycerides (Gelucires) [550]. A polyvalent formulation was obtained after granulation by melting and congealing and use of glyceryl behenate (Compritol) as a lubricant of the solidified suspensions.

Pseudoephedrine HCl–carnauba wax microparticles were prepared by a multiple emulsion–melt dispersion technique [551]. A heated aqueous drug solution was emulsified into the wax melt (w/o emulsion), followed by emulsification of this primary emulsion into a heated external aqueous phase (w/o/w emulsion). The drug-containing microparticles were formed after cooling and congealing of the wax phase. The encapsulation efficiencies were above 80% and actual drug loadings close to 50% were achieved.

An emulsion–congealing technique was used to prepare prolonged release lipid micropellets containing ketoprofen [552]. The lipid matrix consisted of cottonseed oil/beeswax mixture and was emulsified at 70 °C into 0.1 N HCl containing Tween 60 and gelatin.

The progress toward the development of a single dose tetanus vaccine is limited by the poor stability of the protein antigen, tetanus toroid, during its encapsulation in, and release from, biodegradable polymer microspheres. To investigate alternative microencapsulation approaches for improving the stability of the tetanus toroid under these conditions, a two-step microencapsulation method was devised to form microcapsules which consisted of forming microcores of the tetanus toroid in a hydrophilic support matrix by spray-congealing, followed by coating the microcores with poly(lactide-co-glycolide) by an oil-in-oil solvent extraction method [553]. Several protein stabilizers including gelatin (with or without poloxamer 188), dextran, sodium glutamate, and polyethylene glycol were examined as potential core materials.

The effects of operating conditions in the spray-congealing process on the release and the micromeritic properties of clarithromycin wax matrix were evaluated [554]. An atomizer that operates with ultrasonic energy was described which obtained microparticulate drug delivery systems through spray-congealing or spray-drying technologies [555]. The formulations under examination contained theophylline and fenbufen as model drugs and stearic acid, carnauba wax, Cutina HR, and Compritol 888 ATO as low melting excipients. Nonaggregate and spherical-shaped microparticles were obtained with all the materials tested.

The attrition milling iron powders and blends of iron powders produced micrometer-size particles composed of nanosize grains [556]. Mechanical cold-working powder resulted in dislocation generation, multiplication, and congealing that produced grain refinement. Mechanical alloying of substitutional aluminium atoms into iron powder resulted in the aluminium atoms substituting for iron atoms in the grain boundary cells. Attrition milling iron powder in nitrogen gas resulted in nitrogen atoms being adsorbed onto the particle surface.

Marking on a silicon wafer with a small dot matrix was performed using a diode-pumped second-harmonic generation laser of yttrium aluminum garnet, liquid-crystal-display mask, and projection optics [557].

As a novel alternative to the incorporation into hard gelatin capsules or tablets, extended-release (Aquacoat- or Eudragit RS-coated) or enteric (Eudragit L-coated) pellets were embedded into congealed tablet-shaped polyethylene glycol (PEG) plugs of different molecular weights, which rapidly released the pellets upon contact with aqueous fluids [558]. The lower-molecular-weight PEGs (600 and 1000) were not suitable carrier materials, since they dissolved the coatings or significantly increased their permeability. The release characteristics of the original pellets were maintained after embedding the pellets into the higher-molecular-weight PEG 4000 or 10,000.

The degree of bitterness of clarithromycin dry syrup was evaluated using several methods [559]. Using the inversion method, shaking method, and paddle method, a reasonable correlation between the bitter taste and the amount dissolved was not observed. A minicolumn packed with clarithromycin dry syrup was used for the release test.

The methods were used in ink application and combining ink-labeled biopsy specimens into fewer containers with the goal of maintaining information regarding location while

minimizing expense [560]. The ink adhered well to dry cores, but these cores exhibited dehydration artifacts. Placing the cores on a wet sponge avoided dehydration but caused ink spread. With protocol, all biopsy specimens were placed on separate moistened gauze sponges. Specimens from the right side of the prostate were marked with green ink, and those from the left side were marked with black ink using a cotton swab. After applying 1% acetic acid to each core, the left and right cores from each location were placed in a single container. This method curbed pathology expenses and maintained tumor location information.

The utilization of a spray-congealing technique using an ultrasonic atomizer to prepare enhanced-release, solvent-free microspheres of carbamazepine-Gelucire 50/13 in different drug-to-polymer ratios was considered [561]. The spherically shaped and nonaggregated microparticles were obtained and the microspheres had a good encapsulation efficiency (>90% in the prevalent size fraction).

## 4. SPECTROSCOPIC CHARACTERIZATION

### 4.1. Introduction

The structure and properties of the nanocapsules can be characterized by various spectroscopic techniques that we used to study the bulk materials. In this section, we shall introduce briefly the following techniques: X-ray diffraction and transmission electron microscope for characterizing the structures, Raman scattering spectroscopy for obtaining information on vibration and rotation of molecules, XPS for revealing binding energy of electrons, Mössbauer spectroscopy for detecting hyperfine fields, and vibrating sample magnetometer or superconducting quantum interference devices for measuring magnetic properties of the materials. We shall also give a brief description of several novel microscopies, including scanning tunneling microscopy, atomic force microscopy, and magnetic force microscopy, which has been used to solve processing and materials problems in a wide range of technologies affecting electronics, telecommunications, biological, chemical, automotive, aerospace, and energy industries. The materials being investigated by these microscopies include thin and thick film coatings, ceramics, composites, glasses, synthetic and biological membranes, metals, polymers, and semiconductors. It is evident that these novel techniques can be applicable for characterization of the nanocapsules. In this section, we shall describe the common use of each technique and then its characteristics for investigation of the nanocapsules.

### 4.2. X-Ray Diffraction

X-ray diffraction (XRD) is one of the most commonly used spectroscopic techniques which utilizes the diffraction of a light through the crystalline lattice serving as a diffraction grating. When X-ray radiation passes through matter, the radiation interacts with the electrons in the atoms, resulting in scattering of the radiation. If the atoms are organized in planes (i.e., the matter is crystalline) and the distances between the atoms are of the same magnitude as the wavelength of the X-rays, constructive and destructive interference will occur. This results in diffraction where X-rays are

emitted at characteristic angles based on the spaces between the atoms organized in crystalline structures called planes. Most crystals can have many sets of planes passed through their atoms. Each set of planes has a specific interplanar distance and gives rise to a characteristic angle of diffracted X-rays. The relationship between wavelength, atomic spacing  $d$ , and angle  $\theta$  is described geometrically by the Bragg equation as  $n\lambda = 2d \sin \theta$ . If the wavelength  $\lambda$  is known depending on the type of X-ray tube used and the angle  $\theta$  is measured with a camera or diffractometer, then the interplanar distance can be calculated from the Bragg equation.  $n$  is an integer and represents the order of reflection, as in the case of light diffracted from an optical grating. But whereas diffraction from an optical grating takes place essentially at a single plane, X-rays penetrate through many planes of atoms and diffraction takes within a certain volume of the crystal, which acts as a kind of three-dimensional diffraction grating. A set of  $d$ -spaces obtained from a single compound represents the set of planes that can be passed through the atoms and can be used for comparison with sets of  $d$ -spaces obtained from standard compounds.

There are many X-ray diffractometers made by different companies with different radiations, among which  $\text{CuK}\alpha$  or  $\text{CoK}\alpha$  radiation is the most common one. As an example, a Rigaku D/Max- $rA$  rotation target diffractometer is normally equipped with a graphite crystal monochromator for calibration. XRD can be used for analysis of the formation of the phases and their structures, not only for bulk materials but also for nanoparticles and nanocapsules. Since X-rays penetrate through many planes of atoms, XRD usually gives the information of a comparatively large (or macroscopic) amount of the materials, namely, that of the whole system. Detailed structural information, like space group, characteristic interplanar spacings, lattice parameters, atomic site coordinate, atomic occupation, etc., can be derived for the phases in the materials. It is easier to detect a bulk material with a single phase, or better a single crystal, for a quantitative characterization.

Due to advances in XRD technology, XRD data can be analyzed quantitatively for the relative amount of different phases in a bulk material, when the diffraction factors of each kind of atom or phase in the material are known. However, it is hard to derive the relative amount of different phases and to obtain detailed structural information on the nanocapsules from XRD observation. The difficulties are mainly due to the fact that too many XRD peaks of different phases mix each other and that the different mechanisms and/or factors for the contribution to the XRD peak strengths come from the nanoparticles, the bulk materials, and the interfaces/surfaces. The average grain sizes of the materials can be deduced from Scherrer's method of XRD, in which slow scans are performed around the properly selected reflections and each scan is corrected for  $K\alpha$  spectral and instrument broadening by a computer implementation of Stokes's procedure.

Fig. 10 shows the XRD spectrum of Fe(B) nanocapsules showing diffraction peaks associated with the existence of  $\alpha$ -Fe [ $\alpha$ -Fe(B) solid solution], FeB,  $\gamma$ -Fe, and  $\text{Fe}_3\text{B}$  phases in the cores [122]. There are some weak peaks corresponding to the  $\text{Fe}_3\text{O}_4$  [and/or  $\text{Fe}_3\text{O}_4(\text{B})$ ] phase. Almost all diffraction peaks in the XRD spectrum of the nanocapsules come

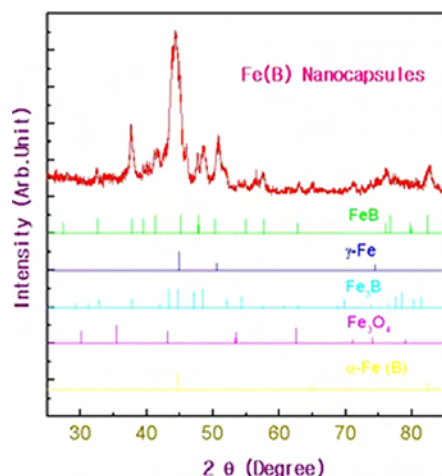


**Figure 10.** XRD spectrum of Fe(B) nanocapsules showing diffraction peaks associated with the existence of  $\alpha$ -Fe ( $\alpha$ -Fe(B) solid solution), FeB,  $\gamma$ -Fe and  $\text{Fe}_3\text{B}$  phases in the cores. There are some weak peaks corresponding to the  $\text{Fe}_3\text{O}_4$  (and/or  $\text{Fe}_3\text{O}_4(\text{B})$ ) phase. For comparison, the corresponding theoretical XRD patterns for the different phases are represented below the experimental data. After [122], Z. D. Zhang et al., *Phys. Rev. B* 64, 024404 (2001). © 2001, American Physical Society.

from the cores. It is understandable that, usually, there is no sharp peak corresponding to the shells in the XRD spectrum of the nanocapsules, because of the breakdown of the cyclic condition (the translation invariance) and the incompleteness of the crystal structure of the phases in the shells of the nanocapsules.

### 4.3. TEM

The basic mechanism of the transmission electron microscope is similar to that of XRD, but using the electron beams instead of the X-rays. The successful application of the TEM is beneficial to the discovery of the de Broglie (matter) wave. In this case, the crystalline lattice serves as a grating to lead to the diffraction of the electrons. With the TEM, essentially all incoming electrons are transmitted through a specimen that is suitably thin. Rather than being absorbed, electrons may be scattered (i.e., deflected in their path) by the atoms of the specimen. The fast electrons used in a TEM are capable of penetrating many atomic planes and so are diffracted by crystalline regions of material just like X-rays. Their wavelength ( $\sim 0.04$  nm for  $E_0 \sim 100$  keV) is much less than a typical atomic-plane spacing ( $\sim 0.3$  nm) so that, according to the Bragg equation of  $n\lambda = 2d \sin \theta$ , Bragg angles  $\theta$  are small. In addition, the integer  $n$  is usually taken as unity, since  $n$ 'th order diffraction from planes of spacing  $d$  can be regarded as first-order diffraction from planes of spacing  $d/n$ .

Diffraction represents elastic scattering of electrons (i.e., deflection by the Coulomb field of each atomic nucleus) in a crystal. The regularity of the spacing of these nuclei results in a redistribution of the angular distribution of scattered intensity. Instead of a continuous distribution over scattering angle, there are sharp peaks centered around certain scattering angles, each twice the corresponding Bragg angle  $\theta$ . In

the TEM, this angular distribution can be displayed by magnifying the diffraction pattern first formed at the back focal plane of the objective lens. Examination of the TEM image of a polycrystalline specimen shows that there is a variation of electron intensity within each crystallite. This diffraction contrast arises either from atomic defects (including point defects, dislocation, planar defects) within the crystal or from the crystalline nature of the material itself, combined with the wave nature of the transmitted electrons. In addition to diffraction (or amplitude) contrast, image contrast features can result from the phases of the electron waves after they have traversed the specimen. Although this phase cannot be detected directly, it can give rise to interference between electron waves that have passed through different regions of a specimen, and these electrons are brought together if the specimen image is defocused by changing the objective-lens current slightly. Phase contrast also occurs as a result of the regular spacing of atoms in a crystal, particularly if the specimen is oriented so that its atomic columns are parallel to the electron beam. The contrast seen in high magnification ( $>500,000$ ) images is of this type and allows the lattice of atoms to be seen directly (in projection). The atoms may appear as either bright or dark spots, depending on the amount of objective-lens defocus. A more complete interpretation of the atomic-scale structure may require recording of a through-focus series of images.

The nanoparticle/nanocapsule samples for TEM observation can be prepared in two steps: (a) the nanocapsules are first dispersed in ethyl alcohol by an ultrasonic field and (b) a drop of the suspension is then allowed to evaporate onto a carbon coated TEM mesh grid. At present, most commercial TEMs are Philips, Hitachi, JEOL, etc. A TEM can be used to obtain the detailed structural information, such as space group, characteristic interplanar spacings, lattice parameters, atomic site coordinate, atomic occupation, etc., for the phases in the materials. Figure 11 shows TEM photographs of Fe and Ni nanoparticles prepared by arc discharge. The size distribution of the nanoparticles can be seen and/or analyzed from the TEM image.

The resolution of the TEM could be improved by special arrangements of the magnetic fields serving as focuses

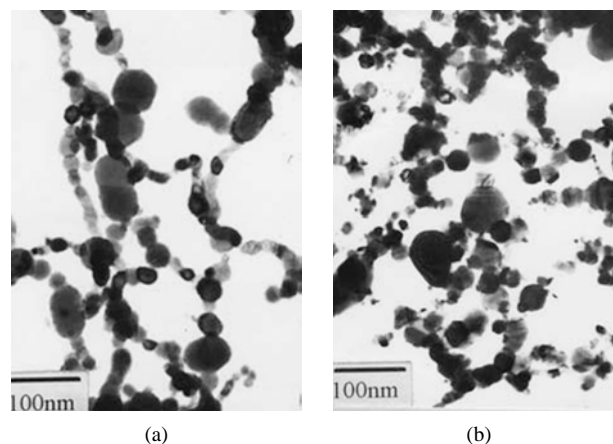


**Figure 11.** TEM photographs of (a) Fe and (b) Ni nanoparticles. After [604], X. L. Dong et al., *J. Mater. Res.* 14, 398 (1999). © 1999, Materials Research Society.

of the electron beams, by enhancing the energy of the electrons, and so on. The main advantages of the HRTEM are the direct observations of the detailed nanostructures, such as the core/shell structure, the interfaces, and the surfaces, the atomic defects (including point defects, dislocation, planar defects), the twin structures, etc. of the nanocapsules. Because the electron beam can be focused in a narrow range, the detailed structural information of the core and also the shell of the nanocapsules can be illustrated clearly. The most advanced HRTEMs can show the images of the arrangement of the atoms. Figure 12 represents a HRTEM image showing the shell/core structure of Fe(B) nanocapsules with an amorphous boron oxide shell of about 4.0 nm thick and a crystalline Fe core with  $d = 2.0268 \text{ \AA}$  [122]. Figure 13 shows a HRTEM image for the shell/core structure of Gd(C) nanocapsules with a graphite shell and crystalline Gd core. The shell is characterized by curved lattice fringes of interplanar spacing 0.34 nm corresponding to the (0002) lattice plane of graphite carbon. HRTEM observation can indicate whether different types of the core/shell structures form, whether the interface between the shell and the core is sharp, whether the intermediate phase exists between the shell and the core, and whether different phases coexist in the cores. Furthermore, energy dispersive X-ray (EDX) microanalysis and parallel electron energy-loss spectroscopy (PEELS) data equipped in a HRTEM can indicate the composition and its distribution in nanoscale of the phases in both the core and the shell of the nanocapsules. However, it is difficult to derive the relative amount of different phases in the nanocapsules from the HRTEM observation because only limited numbers of the particles can be observed.

#### 4.4. Raman

Raman scattering spectra are recorded for the inelastic scattering of a light on the materials. When light is scattered from a molecule, most photons are elastically scattered. The

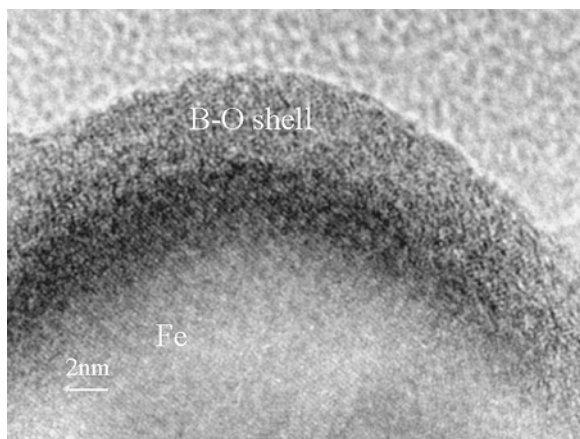


**Figure 12.** HRTEM image showing the shell/core structure of Fe(B) nanocapsules with an amorphous boron oxide shell of about 4.0 nm thick and a crystalline Fe core with  $d = 2.0268 \text{ \AA}$ . After [122], Z. D. Zhang et al., *Phys. Rev. B* 64, 024404 (2001). © 2001, American Physical Society. Image courtesy of J. G. Zheng, Northwestern University, USA.

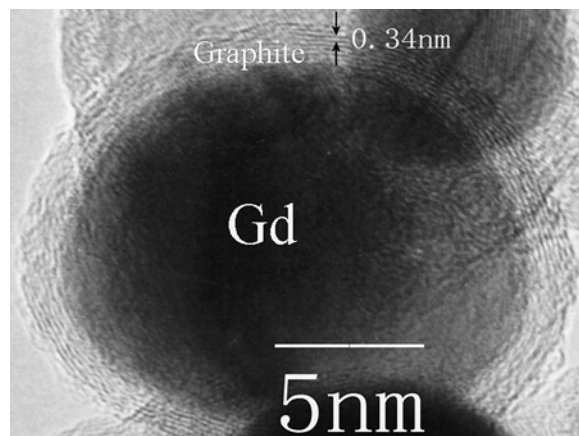


**Figure 13.** HRTEM image showing the shell/core structure of Gd(C) nanocapsules with a graphite shell and crystalline Gd core. The shell is characterized by curved lattice fringes of interplanar spacing 0.34 nm corresponding to the (0002) lattice plane of graphite carbon.

scattered photons have the same energy (frequency) and, therefore, wavelength, as the incident photons. However, a small fraction of light (approximately 1 in  $10^7$  photons) is scattered at optical frequencies different from, and usually lower than, the frequency of the incident photons. The process leading to this inelastic scatter is termed the Raman effect. Raman scattering can occur with a change in vibrational, rotational, or electronic energy of a molecule. The difference in energy between the incident photon and the Raman scattered photon is equal to the energy of a vibration or a rotation of the scattering molecule. A plot of intensity of scattered light versus the energy difference is a Raman spectrum.

The Raman effect arises when a photon is incident on a molecule and interacts with the electric dipole of the molecule. In classical terms, the interaction can be viewed as a perturbation of the molecule's electric field. In quantum mechanics, the scattering is described as an excitation to a virtual state lower in energy than a real electronic transition with nearly coincident deexcitation and a change in vibrational (or rotational) energy. The scattering event occurs in  $10^{-14}$  seconds or less. Numerically, the energy difference between the initial and final vibrational (or rotational) levels,  $\bar{\nu}$ , or Raman shift in wave numbers ( $\text{cm}^{-1}$ ), is calculated through

$$\bar{\nu} = \frac{1}{\lambda_{\text{incident}}} - \frac{1}{\lambda_{\text{scattered}}}$$

in which  $\lambda_{\text{incident}}$  and  $\lambda_{\text{scattered}}$  are the wavelengths (in cm) of the incident and Raman scattered photons, respectively.

At room temperature, the thermal population of vibrationally (or rotationally) excited states is low, although not zero. Therefore, the initial state is the ground state, and the scattered photon will have lower energy (longer wavelength) than the exciting photon. This Stokes shifted scatter is what is usually observed in Raman spectroscopy. A small fraction of the molecules are in vibrationally (or rotationally) excited states. Raman scattering from vibrationally (or rotationally) excited molecules leaves the molecule in the ground state. The scattered photon appears at higher energy. This

anti-Stokes-shifted Raman spectrum is always weaker than the Stokes-shifted spectrum, but at room temperature it is strong enough to be useful for frequencies less than about  $1500\text{ cm}^{-1}$ . The Stokes and anti-Stokes spectra contain the same frequency information. The ratio of anti-Stokes to Stokes intensity at any vibrational (or rotational) frequency is a measure of temperature. Anti-Stokes Raman scattering is used for contactless thermometry. The anti-Stokes spectrum is also used when the Stokes spectrum is not directly observable, for example because of poor detector response or spectrograph efficiency.

The frequency shifts in both the Stokes and the anti-Stokes spectra are characters for a bulk material. However, reducing the size of the material could change the frequency shifts in Raman scattering spectra. As discussed above, the limited systems could have different energy levels with those of the bulk materials. The energy levels for the vibrations and the rotations of the molecules can be different than those of the bulk materials. Thus the frequency shifts in Raman scattering spectra of the nanocapsules, which are responsible for the information of these energy levels, can be different with the bulk materials. Another reason for the change of the frequency shifts in Raman scattering spectra is the formation of the core/shell structures of the nanocapsules. The shape of the shell, the connection with the core materials, etc., could alter the vibration and the rotation of the molecules in the shell. Furthermore, usually, the peaks of the Raman scattering spectra become broad in the nanoparticles/nanocapsules. The broadening of the Raman peaks of the nanocapsules is ascribed to the decrease of the size of the material, the wide distribution of the size of the particles, the formation of the core/shell structure, etc. Figure 14 gives the Raman spectra of the B@BN nanocapsules [125].

#### 4.5. XPS

X-ray photoelectron spectroscopy is an electron spectroscopic method that uses X-rays to eject electrons from inner-shell orbitals. The kinetic energy,  $E_k$ , of these photoelectrons is determined by the energy of the X-ray radiation,  $h\nu$ , and the electron binding energy,  $E_b$ , as given by

$E_k = h\nu - E_b$ . The experimentally measured energies of the photoelectrons are given by  $E_k = h\nu - E_b - E_w$ , where  $E_w$  is the work function of the spectrometer. The electron binding energies are dependent on the chemical environment of the atom, making XPS useful to identify the oxidation state and ligands of an atom. XPS instruments consist of an X-ray source such as Al or Mg  $K_\alpha$ , an energy analyzer for the photoelectrons, and an electron detector. The analysis and detection of photoelectrons require that the sample be placed in a high-vacuum chamber. Since the photoelectron energy depends on X-ray energy, the excitation source must be monochromatic. The energy of the photoelectrons is analyzed by an electrostatic analyzer, and the photoelectrons are detected by an electron multiplier tube or a multichannel detector such as a microchannel plate. Surface spectroscopy serves to get information about the chemical nature of sample surfaces or surface near regions. XPS allows one to analyze the elemental surface composition quantitatively. Different binding states of the detected elements may be distinguished. Angle resolved XPS is a nondestructive method to investigate the distribution of elements or functional groups in the depth of the sample surface. The knowledge of the chemical surface composition and the kind of functional surface group is fundamental to evaluate surface reactivity and apply chemical and physico-chemical methods to modify the solid surface.

XPS is a very sensitive surface analysis technique providing elemental quantification and chemical information of the nanocapsules. The XPS detection therefore provides the information on the electrons and thus the materials the electrons belong to. Figure 15 shows XPS spectra of Fe(C) nanocapsules produced in methane at 13.3 kPa [113]. Figure 16 represents Fe $2p_{3/2}$ , Co $2p_{3/2}$ , and O $1s$  XPS spectra of as-prepared Fe-Co(C) nanocapsules and their surface cleaned samples [120]. XPS provides direct evidence for the existence of elements in the shells of the nanocapsules, and also for the formation of the core/shell structures. The binding energies of electrons can indicate well whether the atoms are free metal or oxides or ceramics, from which one can

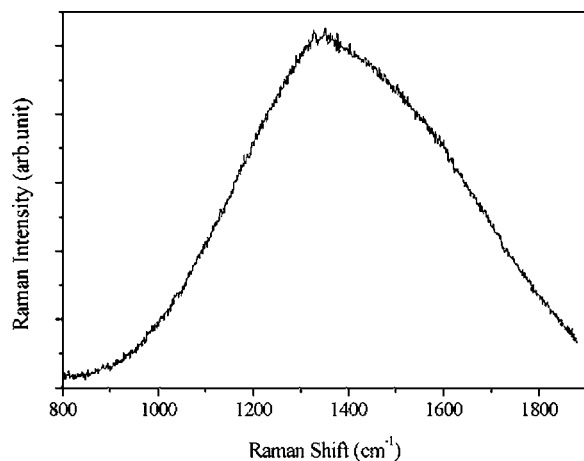


**Figure 14.** Raman spectra of the B@BN nanocapsules. After [125], P. Z. Si et al., *J. Mater. Sci.* 38, 689 (2003). © 2003, Kluwer Academic.

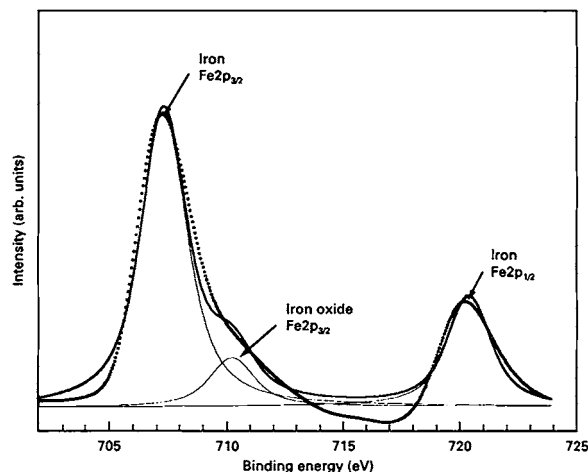


**Figure 15.** X-ray photoelectron (XPS) spectra of Fe(C) nanocapsules produced in methane at 13.3 kPa. Solid curves are fitted to experimental data (dots). After [113], X. L. Dong et al., *J. Mater. Sci.* 33, 1915 (1998). © 1998, Kluwer Academic.



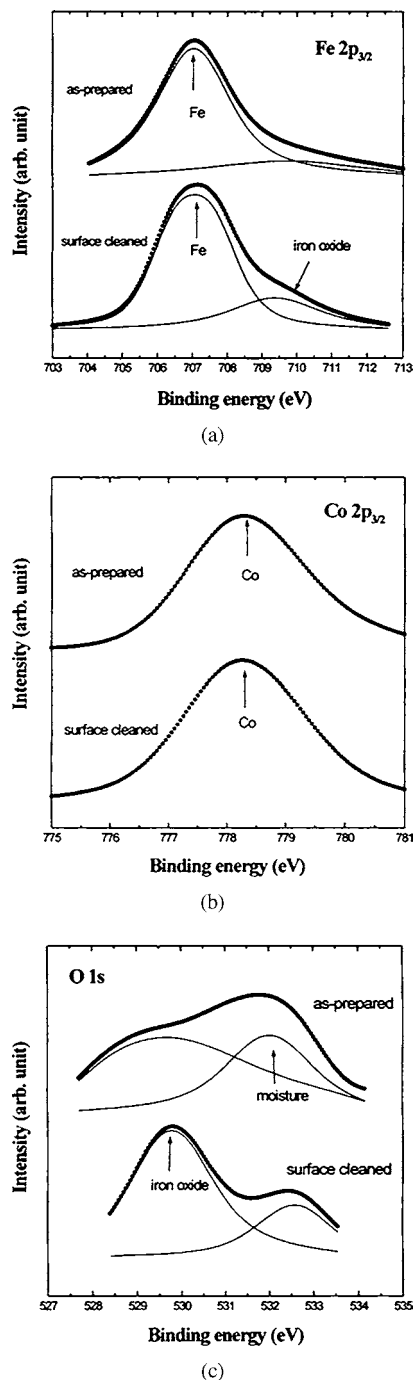


**Figure 16.** (a) Fe $2p_{3/2}$ , (b) Co $2p_{3/2}$  and (c) O 1s XPS spectra of as-prepared Fe-Co(C) nanocapsules and their surface cleaned samples. Solid curves are fitted to experimental data (dots). After [120], X. L. Dong et al., *J. Appl. Phys.* 86, 6701 (1999). © 1999, American Institute of Physics.

find whether the atoms in the core are oxidized, whether all particles are coated completely by the shells, and whether moisture absorbs on the surface of the nanocapsules.

#### 4.6. Mössbauer

The Mössbauer effect, a physical phenomenon discovered by Rudolf Mössbauer in 1957, refers to the resonant and recoil-free emission and absorption of  $\gamma$ -rays by atoms

bound in a solid. In general,  $\gamma$ -rays are a kind of electromagnetic wave with very short wavelengths less than  $10^{-8}$  cm, which are produced by nuclear transitions from an unstable high-energy state to a low-energy state. The energy of the emitted  $\gamma$ -ray corresponds to the energy of the nuclear transition minus an amount of energy that is lost as recoil to the emitting atom. If the lost recoil energy is small compared with the energy linewidth of the nuclear transition, then the  $\gamma$ -ray energy still corresponds to the energy of the nuclear transition and the  $\gamma$ -ray can be absorbed by another atom of the same type as the first. Such emission and subsequent absorption is called resonance. Additional recoil energy is also lost during absorption, so in order for resonance to occur the recoil energy must actually be less than half the linewidth for the corresponding nuclear transition. The amount of lost energy is described by the equation  $E_R = E_{\text{gamma}}^2/2Mc^2$ , where  $E_R$  is the energy lost as recoil,  $E_{\text{gamma}}$  is the energy of the  $\gamma$ -ray,  $M$  is the mass of the emitting or absorbing body, and  $c$  is the velocity of light. In the case of a gas the emitting and absorbing bodies are atoms, so the mass is quite small, resulting in a large recoil energy, which prevents resonance.

Due to the fundamental quantum nature of solids, atoms bound in solids are restricted to a specific set of vibrational energies called phonon energies. If the recoil energy is smaller than the phonon energy, there is insufficient energy to excite the lattice to the next vibrational state, and a fraction of the nuclear events, called the recoil-free fraction, occurs such that the entire crystal, rather than just the atom, acts as the recoiling body. Since the mass of the crystal is very large compared to that of a single atom, these events are essentially recoil-free. In these cases, since the recoil energy is negligible, the emitted  $\gamma$ -rays have the appropriate energy and resonance can occur. In general, the  $\gamma$ -rays have very narrow linewidths. This means they are very sensitive to small changes in the energies of nuclear transitions. In fact, the  $\gamma$ -rays can be used as a probe to observe the effects of interactions between a nucleus and its electrons and those of its neighbors. This is the basis for Mössbauer spectroscopy, which combines the Mössbauer effect with the Doppler effect to monitor such interactions.

Mössbauer spectroscopy is a spectroscopic technique based on the Mössbauer effect. In its most common form, Mössbauer absorption spectroscopy, a solid sample is exposed to a beam of  $\gamma$ -radiation, and a detector measures the intensity of the beam that is transmitted through the sample. The  $\gamma$ -ray energy is varied by accelerating the  $\gamma$ -ray source through a range of velocities with a linear motor. The relative motion between the source and sample results in an energy shift due to the Doppler effect. In the resulting spectra,  $\gamma$ -ray intensity is plotted as a function of the source velocity. At velocities corresponding to the resonant energy levels of the sample, some of the  $\gamma$ -rays are absorbed, resulting in a drop in the measured intensity and a corresponding dip in the spectrum. The number, positions, and intensities of the dips (also called peaks) provide information about the chemical environment of the absorbing nuclei and can be used to characterize the sample. In order for Mössbauer absorption of  $\gamma$ -rays to occur, the  $\gamma$ -ray must be of the appropriate energy for the nuclear transitions of the atoms being probed. Also,

the  $\gamma$ -ray energy should be relatively low; otherwise the system will have a low recoil-free fraction, resulting in a poor signal-to-noise ratio. Only a handful of elemental isotopes exist for which these criteria are met, so Mössbauer spectroscopy can only be applied to a relatively small group of atoms. The sources commonly used for the Mössbauer spectra are  $^{57}\text{Co}$ ,  $^{119\text{m}}\text{Sn}$ ,  $^{125}\text{Sb}$ ,  $^{133}\text{Ba}$ ,  $^{195}\text{Au}$ , and  $^{182}\text{Ta}$ . The most important source is  $^{57}\text{Co}$  and the Mössbauer leap of 14.4 keV of  $^{57}\text{Fe}$  is generated from the disintegration of  $^{57}\text{Co}$ . Thus  $^{57}\text{Fe}$  is by far the most common element studied using the technique.

The Mössbauer spectra provide the information of the inner magnetic fields in the nuclei and the hyperfine fields. The Mössbauer effects can be used to study the properties of nanoparticles/nanocapsules. Figure 17 gives the  $^{57}\text{Fe}$  Mössbauer spectrum at room temperature of the Fe(B) nanocapsules [122]. The relative amounts of different phases and the hyperfine fields in the phases can be obtained for the nanocapsules. The hyperfine fields of the phases in the nanocapsules may slightly differ with those in their bulk counterparts, due to the size effect. The disadvantage of the Mössbauer study is the limitation that it can detect information on the materials with elements the same as after disintegration of the source.

#### 4.7. Scanning Tunneling, Atomic Force, and Magnetic Force Microscopies

The scanning tunneling microscope (STM) is an analytical technique based on the quantum mechanical phenomenon called tunneling, by which a high potential barrier does not eliminate the possibility of finding a particle in a region of high potential or even beyond a region of high potential. A probe tip typically made out of tungsten is attached to a piezodriven system, which is a system of very sensitive piezocrystals that expand or contract in reaction to an applied voltage. By using the piezo to position the tip within a few angstroms

of the sample, the electron wavefunctions in the tip and the sample overlap, leading to a tunneling current flow when a bias voltage is applied between the tip and the sample. A computer in the STM measures the current flow between the metal tip and the sample, which are very close together. The tunneling current is amplified and fed into the computer while processing a negative feedback loop to keep the current constant. The potential barrier is a function of distance between the two surfaces and so is the current. If the current increases, the computer can move the tip farther away from the sample, thus increasing the potential barrier, decreasing the probability of an electron jumping from the tip to the sample, and thus decreasing the current. If the current is too low, the computer will do just the opposite, moving the tip closer to the sample. By keeping track of the movements of the tip, a realistic picture of the electron density of a surface can be created. The STM can resolve local electronic structure at an atomic scale on every kind of conducting solid surface. This electron density plot can then be interpreted as the general arrangement or positioning of atoms on a conductive surface. By tunneling current out of a single atom on the tip, the sensitivity of the instrument can be such that single atom layers on a surface can be measured. One major area of STM research currently is to study self-assembled monolayers, which is a single layer of molecules aggregating on a surface.

The atomic force microscope (AFM), also termed scanning force microscope (SFM), is a newly developed for observing nanoscale topography and other properties of a surface soon after the discovery of the STM. The principles on how the AFM works are very simple. An atomically sharp tip is scanned over a surface with feedback mechanisms that enable the piezoelectric scanners to maintain the tip at a constant force (to obtain height information) or height (to obtain force information) above the sample surface. Tips are typically made from  $\text{Si}_3\text{N}_4$  or Si and extended down from the end of a cantilever. The nanoscope AFM head employs an optical detection system in which the tip is attached to the underside of a reflective cantilever. A diode laser is focused onto the back of a reflective cantilever. As the tip scans the surface of the sample, moving up and down with the contour of the surface, the laser beam is deflected off the attached cantilever into a dual element photodiode. The photodetector measures the difference in light intensities between the upper and lower photodetectors and then converts to voltage. Feedback from the photodiode difference signal, through software control from the computer, enables the tip to maintain either a constant force or constant height above the sample. In the constant force mode, the piezoelectric transducer monitors real time height deviation. In the constant height mode, the deflection force on the sample is recorded. The latter mode of operation requires calibration parameters of the scanning tip to be inserted in the sensitivity of the AFM head during force calibration of the microscope. By using an AFM one can not only image the surface in atomic resolution but also measure the force at nano-Newton scale. The force between the tip and the sample surface is very small, usually less than  $10^{-9}$  N. The detection system does not measure force directly, which senses the deflection of the microcantilever. The detecting systems for monitoring the deflection fall into several categories, such as

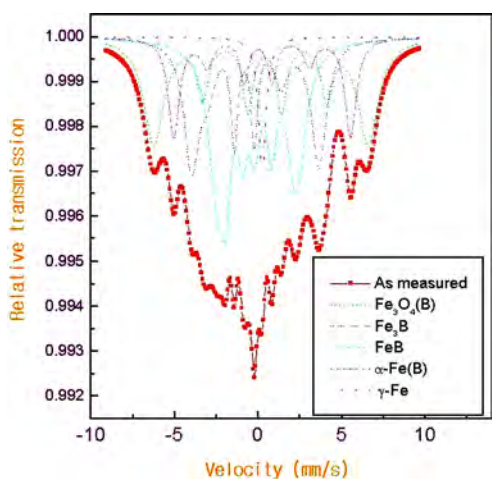


**Figure 17.**  $^{57}\text{Fe}$  Mössbauer spectrum at room temperature of the Fe(B) nanocapsules. The solid squares are the experimental data. The solid line is for the fitting results. The sub-spectra for  $\text{Fe}_3\text{O}_4(\text{B})$ ,  $\text{Fe}_3\text{B}$ ,  $\text{FeB}$ ,  $\alpha\text{-Fe}$  (and/or  $\alpha\text{-Fe}(\text{B})$  solid solution) and  $\gamma\text{-Fe}$  phases are represented as different lines, respectively. After [122], Z. D. Zhang et al., *Phys. Rev. B* 64, 024404 (2001). © 2001, American Physical Society.

the tunneling current, interferometer, beam bounce, diode laser, etc. According to the interaction of the tip and the sample surface, an AFM can be classified as repulsive contact mode and attractive noncontact mode. In its repulsive contact mode, the instrument lightly touches a tip at the end of a cantilever to the sample. As a raster scan drags the tip over the sample, some sort of detection apparatus measures the vertical deflection of the cantilever, which indicates the local sample height. Thus, in the contact mode the AFM measures hard-sphere repulsion forces between the tip and sample. In the noncontact mode, the AFM derives topographic images from measurements of attractive forces and the tip does not touch the sample. The AFM can achieve a resolution of 10 pm and can image samples in air and under liquids. The AFM is being applied to studies of phenomena such as abrasion, adhesion, cleaning, corrosion, etching, friction, lubrication, plating, and polishing. Figure 18 shows an AFM image of a layer-by-layer polyelectrolyte assembled capsule [562].

A magnetic force microscope (MFM) images the spatial variation of magnetic forces on a sample surface. The mechanism of the MFM is similar to that of the AFM, but for the MFM, the tip is coated with a ferromagnetic thin film. The alternating voltage on the probe tip of the AFM is replaced with an alternating magnetic field. The tip is used to probe the magnetic stray field above the sample surface, which is mounted on a small cantilever, translating the force into a deflection that can be measured. The system operates in noncontact mode, detecting changes in the resonant frequency of the cantilever induced by the magnetic field's dependence on tip-to-sample separation. The MFM can be used to image naturally occurring and deliberately written domain structures in magnetic materials. An image taken with a magnetic tip contains information about both the topography and the magnetic properties of a surface. Which effect dominates depends upon the distance of the tip from the surface, because the interatomic magnetic force

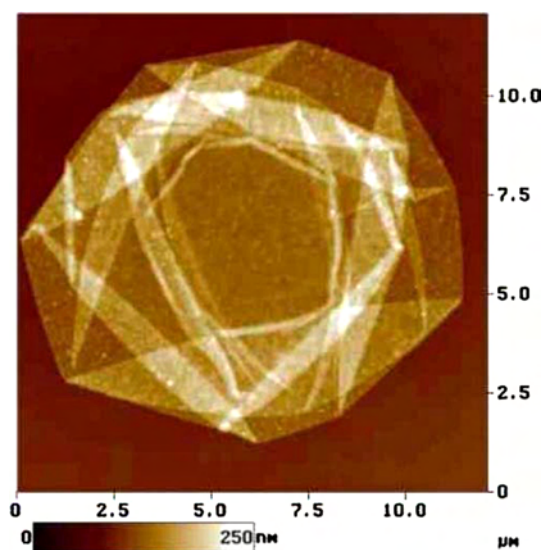


**Figure 18.** AFM image of a layer-by-layer polyelectrolyte assembled capsule. Reprinted with permission from [562], S. Loporatti et al., *Langmuir* 16, 4059 (2000). © 2000, American Chemical Society.

persists for greater tip-to-sample separations than the van der Waals force. If the tip is close to the surface, in the region where a standard noncontact AFM is operated, the image will be predominantly topographic. If the separation between the tip and the sample increases, magnetic effects become apparent. Collecting a series of images at different tip heights is one way to separate magnetic from topographic effects.

#### 4.8. Vibrating Sample Magnetometer/Superconducting Quantum Interference Device

Magnetic properties of a magnetic material could be measured by various types of facilities, among which a vibrating sample magnetometer (VSM) or a superconducting quantum interference device (SQUID) magnetometer is one of the most commonly used tools for purposes of the magnetic measurements. A VSM is a magnetometer based on the mechanism of the electromagnetic induction. A sample is vibrated in the vicinity of a set of pick-up coils. The flux change caused by the moving magnetic sample causes an induction voltage across the terminals of the pick-up coils that is proportional to the magnetization of the sample. The VSMs have a comparatively high sensitivity for measuring the magnetic moment, which can be up to  $5 \times 10^{-5}$ – $2 \times 10^{-9}$  Am<sup>2</sup>.

SQUID is a highly sensitive detector of the flux designed based on the concept of the flux quantization and the superconducting Josephson effect. The so-called Josephson junction is a junction at which a thin insulator is connected with two superconductors. When the magnetic field is applied to a superconducting ring with a Josephson junction, a stable current may pass the thin insulator between the two superconductors due to the tunneling. The sum of the flux due to the Josephson current density  $j_s$  and that of the external field, namely, the total flux of the superconducting ring, is the integer times the flux quanta  $\phi_0 = \hbar/2|e|$ . The Josephson current density  $j_s$  is the periodicity function of the external magnetic flux  $\phi$  as described as  $j_s = -j_c \sin(2\pi\phi/\phi_0)$ , where  $j_c$  is the critical current density. SQUID can measure not only the extremely weak magnetic fields with a resolution of  $10^{-19}$  Wb, but also susceptibilities, magnetic moments, magnetization curves, hysteresis loops, and their temperature dependences. SQUID can be used to measure very weak voltages and currents, to establish the voltage benchmark, and to measure directly the elementally physical constant  $|e|/\hbar$ , where  $e$  is electronic charge and  $\hbar$  is the Planck constant. SQUID is a powerful tool for validating in macroscopic range the basic principles of quantum mechanics. Figure 19 shows zero-field-cooled (ZFC) and field-cooled (FC) (in a field of 100 mT) magnetization curves of the Fe(B) nanocapsules [122].

## 5. PHYSICAL PROPERTIES

### 5.1. Introduction

The microworld is governed by atoms and molecules, while the macroworld consists of materials which contain a mind-boggling (or infinite) number of atoms or molecules. For

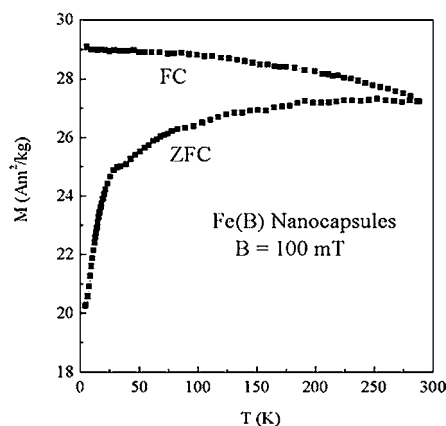


**Figure 19.** Zero-field-cooled (ZFC) and field-cooled (FC) (in a field of 100 mT) magnetization curves of the Fe(B) nanocapsules. After [122], Z. D. Zhang et al., *Phys. Rev. B* 64, 024404 (2001). © 2001, American Physical Society.

atoms and molecules, we face directly a world that can be described only by quantum mechanics, in which chemical bonds, reactivity of a molecule, electronic orbitals and spins, the energy band of the electrons, etc. are most important factors. In the macroworld, we see distinct phases of materials—liquid, solid, and gas—and talk of physical properties like magnetization, electrical resistance, thermal conductivity, internal energy, specific heat, stiffness, and so on. The bulk consists of atoms and molecules, so the properties of the atoms and molecules should decide the properties of the bulk materials. The physical properties of bulk materials can be described well either by quantum mechanics or by theories based on classical mechanics. According to the energy band theory, the energy levels of a bulk metal are in general continuum (or so-called quasi-continuum) because the number of electrons in the bulk is infinite. The cyclic condition and the translation symmetry in three dimensions of bulk materials lead to the plane wave character of electrons. The physical properties of bulk are the thermodynamical averages of the properties of an infinite number of electrons. Classical mechanics can be treated as an approximation of quantum mechanics in a continuous media or in a continuum limit for the macroworld.

One would like to see how things change as one goes from atoms and molecules to small assemblies of them, to large assemblies, to larger assemblies, and finally to the bulk. One would like to see how various atoms, which do not appear very different individually, work together to form bulk materials with abundance properties, like metals, insulators, and semiconductors. One would like to see whether the properties of the assemblies of atoms and molecules differ with those of bulk and how the assemblies of atoms and molecules behave. The world between atoms, molecules, and the bulk is so-called mesoworld. This is a challenging problem for scientists and only a little progress has been made in the area of the mesoscopic world.

It is clear that the physical properties of the mesoworld are quite different than those of the atoms, the molecules, and the bulk. The mesoworld is a bridge connecting with two ends: one is the microworld with the discreteness of the energy levels; another is the macroworld with the continuum

of the energy band. As a limited system, the discreteness of the energy levels is still held in the mesoworld because of the limited number of electrons. The small is different in an essential way when one (or more) of the physical dimensions of the material approaches a length-scale characteristic to a physical phenomenon (with different phenomena being characterized by different length scales), and similarly in the time domain. If the energy gap were larger than the thermal energy, the magnetostatic energy, the electrostatic energy, the photon energy, or the condensation energy of the superconductivity, the physical properties of the system would differ with those of bulk due to the quantum size effect. The cyclic condition and the translation symmetry would be broken down in the mesoworld, altering the physical properties of the systems. The quantum interference of electrons in the confined states could become more pronounced in the mesoscopic systems. The properties of the mesoscopic systems could be affected also by the magic number effect, the breakdown of the symmetry at the surfaces/interfaces, the formation of core/shell structure, the presence of metastable phases, etc. The classical mechanism can be used for description of the properties of the mesoscopic systems.

The properties of the mesoscopic systems depend sensitively on size, shape, structure, surface, etc. The sensitivity of sufficiently small materials aggregating to various shapes could change the properties of the materials. Most importantly, spontaneous shape selection occurs in the mesoscopic systems, originating from the ability of finite systems to adjust their shape and the structure in order to minimize the free energy of the systems. Small is beautiful not only since the limited systems could show the fascinating phenomena that do not exist in either the macroworld or the microworld, but also since the mesoscopic systems could be designed and constructed artificially, which could be so different from those formed naturally. For instance, the superlattices or multilayers could be grown artificially which show exchange coupling and the giant magnetoresistance effect that have been successfully applied in the reading head of the hard disk of a computer. The quantum dots could be designed to be applicable for high-density magnetic recording. Nanotubes and nanowires could be used as elementary parts of an apparatus like a quantum computer. Basic research of the structure and properties of the nanostructured materials and related issues underlies future technologies, from nanoscale machines, nanotribological systems, cellular injections, and nanocatalysis, to miniaturization of electronic circuitry and novel information storage and retrieval systems.

There is no doubt that nanocapsules are classified to the mesoscopic systems because nanocapsules are in nanoscales, having nanostructures. Indeed, nanocapsules are matter in intermediate states between bulk and atomic materials, which offer an opportunity to investigate dimensionally confined systems in basic research areas. Indeed, understanding the differences of the mesoworld to those of the bulk is extremely important for studying the properties of nanocapsules. The optical absorption, electric resistance, magnetic, and dynamic properties of nanocapsules are very different from the bulk counterparts, which would be applicable in various fields. For instance, nanocapsules could show strong band-edge photoluminescence shifting. Magnetic nanocapsules could show superparamagnetism or the

exchange bias. Graphite encapsulated nanocapsules have numerous possible applications due to their novel properties and their ability to survive rugged environments. In Sections 5.2–5.5 we shall represent the optical, electronic, magnetic, and dynamic properties of the nanocapsules (and also the nanoparticles for some materials), respectively. The biomedical properties of the nanocapsules will be introduced in the next section.

## 5.2. Optical Properties

Clusters of semiconducting materials are interesting considering their application as a photocathode. The silver chloride/silver cluster phase boundary plays a decisive role in the photocatalytic silver chloride electrode system. This system was studied by means of quantum chemical calculations [563]. The synthesis and properties of luminescent quantum-sized silver sulfide clusters in the cavities of zeolite A were reported. The color of the silver sulfide zeolite A composites ranged from colorless (low loading) to yellow–green (medium loading) to brown (high loading). A low silver sulfide content was characterized by a blue–green luminescence and distinct absorption bands, while samples with medium or high silver sulfide content showed an orange or red colored emission and a continuous absorption.

Linear (visible photoluminescence) and nonlinear (third-order susceptibility) optical properties were measured for laser-synthesized crystalline Si nanoparticles [564]. The observed luminescence was compared to that of nanocomposite aerogels prepared integrating the Si nanoparticles into a continuous silica phase by sol–gel processing. The incorporation of the Si nanoparticles into a silica matrix by sol–gel technology was not detrimental to the photoluminescence emission intensity.

Two methods for the preparation of semiconductor doped sol–gel films, for applications in nonlinear optics, were studied [565]. Porous films were spun from sols containing the cation precursor, reacted with H<sub>2</sub>S gas, and then the cation was adsorbed onto the pore surfaces of passive films from aqueous solution before the gas reaction. Preliminary results were reported for CdS doping and for other semiconductor species. The effects of heat treatment of doped films and the limitation of crystallite growth by pore size were described.

C nanoparticles embedded in  $x\text{Al}_2\text{O}_3 \cdot x\text{P}_2\text{O}_5 \cdot 100\text{SiO}_2$  ( $x = 0.25$  or  $0.5$ ) gel–glasses were prepared by a sol–gel process [566]. The gels synthesized through hydrolysis of  $\text{PO}(\text{OC}_2\text{H}_5)_3$ ,  $\text{Al}(\text{NO}_3)_3 \cdot 9\text{H}_2\text{O}$  and  $\text{Si}(\text{OC}_2\text{H}_5)_4$ , were heated at 600 °C for 10 h, in which  $-\text{OC}_2\text{H}_5$  was carbonized to precipitate nanosized C particles. Glasses doped with C nanoparticles showed a strong room-temperature photoluminescence with a peak at 630 nm under 532 nm Nd:YAG laser excitation. The photoluminescence spectra were caused by C nanoparticle embedded gel–glasses.

Structural, optical, electro-, and photoelectrochemical properties of amorphous and crystalline sol–gel Nb<sub>2</sub>O<sub>5</sub> coatings were determined [567]. The coatings were *n*-type semiconductor with indirect allowed transition and present an overall low quantum efficiency ( $\phi < 4\%$ ) for UV light to electric conversion. The photoconducting behavior of the coatings was discussed within the framework of the Gartner and Sodergren models. Improvement can be foreseen if Nb<sub>2</sub>O<sub>5</sub> coatings can be made of 10–20 nm size nanoparticles.

Nanocrystalline titanium and indium oxides and TiO<sub>2</sub>–In<sub>2</sub>O<sub>3</sub> composites were prepared by the sol–gel technique using concentrated hydrous titanium dioxide and indium hydroxide sols [568]. Structural, optical, and photoelectrochemical properties of the composites with different molar ratios of TiO<sub>2</sub> to In<sub>2</sub>O<sub>3</sub> were studied. Highly transparent TiO<sub>2</sub>–In<sub>2</sub>O<sub>3</sub> films fabricated by the spin-coating technique exhibited extreme dependencies of the various optical and photoelectrochemical properties on the film composition. The bandgap edge of the composite films was blueshifted, as compared with that of single-component films. The conductivity of TiO<sub>2</sub>–In<sub>2</sub>O<sub>3</sub> films changed by six orders of magnitude in the range of compositions near the calculated value for percolation threshold associated with the formation of 3D infinite clusters of interconnected In<sub>2</sub>O<sub>3</sub> nanoparticles.

A sol–gel method was employed to produce a zinc oxide colloid consisting of ZnO nanocrystalline particles with an average diameter of 3 nm subsequently mixed with a silica colloid [569]. The mixture was finally spray dried to form a powder nanocomposite. The green photoluminescence exhibited by the composite was very stable.

ZnS nanoparticles were prepared by chemical precipitation of Zn<sup>2+</sup> with sulfur ions in aqueous solution [570]. The ultraviolet-excited samples revealed detailed structure in the luminescence spectra. A doublet pattern observed in the long wavelength region was attributed to the coexistence of the two crystalline forms in ZnS particles.

Composite particles consisting of a zinc sulfide core and a silica shell or vice versa were reported [571]. These particles were optimized for photonic applications, because ZnS had a large refractive index and did not absorb light in the visible and both ZnS and SiO<sub>2</sub> can be easily doped with fluorophores. Both kinds of morphologies were created using a seeded growth procedure using monodisperse seeds on which homogeneous layers with a well-defined thickness were grown. The ZnS and SiO<sub>2</sub> cores could be completely dissolved leaving SiO<sub>2</sub> and ZnS shells, respectively, filled with solvent or air after drying.

Zinc sulphide nanoparticles were synthesized in silica matrix using a sol–gel method [572]. Silica could be loaded with zinc sulphide over a very wide range of concentration without changing the nanoparticle size. A strongly luminescent zinc sulphide–silica composite, thermally stable even up to around 700 °C, was obtained.

Synthesis and characterization of undoped and Mn<sup>2+</sup> doped ZnS nanocrystallites (radius 2–3 nm) embedded in a partially densified silica gel matrix were presented [573, 574]. Optical transmittance, photoluminescence, ellipsometric, and electron spin resonance measurements revealed manifestation of the quantum size effect [573]. A dramatic increase in cathodoluminescence emission was observed [574]. Photoluminescence spectra recorded at room temperature revealed a broad blue emission signal centered at around 420 nm and a Mn<sup>2+</sup> related yellow–orange band centered at around 590 nm, while electron spin resonance measurements indicated that Mn in ZnS was present as dispersed impurity rather than Mn clusters [573].

The influence of the particle size on the luminescence of nanocrystalline ZnS:Pb<sup>2+</sup> synthesised via a precipitation method was studied [575]. Depending on the excitation wavelength, nanocrystalline ZnS:Pb<sup>2+</sup> showed a very broad



white ( $\lambda_{\text{exc}} = 380 \text{ nm}$ ) or red emission ( $\lambda_{\text{exc}} = 480 \text{ nm}$ ). The decay kinetics of both emissions was typical for  $\text{Pb}^{2+}$ , independent of the particle size. The quenching of luminescence with increasing temperature was explained by photoionization. The lower quenching temperature for the luminescence of larger nanoparticles was explained by quantum size effects.

ZnS nanoparticles doped with  $\text{Ni}^{2+}$  [576],  $\text{Ti}^{3+}$  and  $\text{Ti}^{4+}$  [577],  $\text{Cu}^+$  and  $\text{Cu}^{2+}$  [578],  $\text{Co}^{2+}$  [579], and  $\text{Co}^{3+}$  [580], were obtained by chemical coprecipitation from homogeneous solutions of zinc and nickel (or titanium, copper, or cobalt) salt compounds, with  $\text{S}^{2-}$  as precipitating anion, formed by decomposition of thioacetamide. The average size of particles doped with different mole ratios, was about 2–3 nm [576–580]. The absorption spectra showed that the excitation spectra of Ni-doped ZnS nanocrystallites were almost the same as those of pure ZnS nanocrystallites ( $\lambda_{\text{exc}} = 308\text{--}310 \text{ nm}$ ) [576]. Because a  $\text{Ni}^{2+}$ ,  $\text{Ti}^{3+}$ , or  $\text{Co}^{2+}$  luminescent center was formed in ZnS nanocrystallites, the photoluminescence intensity increased with the amount of ZnS nanoparticles doped with these ions [576, 577, 579]. Stronger and stable green-light emission was observed from ZnS nanoparticles doped with  $\text{Ni}^{2+}$  [576],  $\text{Ti}^{3+}$  [577], and  $\text{Co}^{2+}$  [579]. The fluorescence intensity of the ZnS nanocrystallites doped with  $\text{Ti}^{4+}$  was almost the same as that of the undoped ZnS nanoparticles [577]. The fluorescence intensity of  $\text{Co}^{3+}$ -doped ZnS nanoparticles was much weaker than that of ZnS nanoparticles [580]. The emission spectrum of ZnS nanocrystallites doped with  $\text{Cu}^+$  and  $\text{Cu}^{2+}$  consisted of two emission peaks at 450 and 530 nm [578].

Monodispersed ZnS and  $\text{Eu}^{3+}$ -doped ZnS nanocrystals were prepared through the coprecipitation reaction of inorganic precursors  $\text{ZnCl}_2$ ,  $\text{EuCl}_3$ , and  $\text{Na}_2\text{S}$  in a water/methanol binary solution [581, 582]. The mean particle sizes were about 3–5 nm with cubic (zinc blende) structure [582]. Photoluminescence studies showed stable room temperature emission in the visible spectrum region, with a broadening in the emission band and, in particular, a partially overlapped twin peak in the  $\text{Eu}^{3+}$ -doped ZnS nanocrystals.

The processing, microstructure, and optical properties of CdS semiconductor nanoparticles sequestered in spin-coated polymer films were investigated [583]. A simple processing protocol was developed to form thin film structures consisting of CdS nanoparticles dispersed in the interstices created by a close-packed stacking of polystyrene spheres. Absorption, emission, and excitation spectra of CdS nanoparticles embedded in sol-gel silica glasses were reported [584]. The effects of temperature on emission behavior were investigated.

Spherical CdS particles similar to 100 nm were synthesized by a hydrothermal process [585]. The particle formation and growth depended on the rate of sulfide-ion generation and diffusion-controlled aggregation of nanoparticles. Photoluminescence studies on CdS particles showed two emission bands at room temperature. The red emission at 680 nm was due to sulfur vacancies, and an infrared red emission at 760 nm was attributed to self-activated centers. A redshift of the infrared red band with the decrease of temperature was explained with a configurational coordinate model.

Highly luminescent CdTe nanocrystals were synthesized by reacting dimethylcadmium with different tellurium

sources in mixtures of dodecylamine and trioctylphosphine as the coordinating and size-regulating solvent [586]. Colloids of crystalline CdTe nanoparticles with zinc blende lattice displaying mean particle sizes between 2.5 and 7 nm were prepared at temperatures from 150 to 220 °C. The particles showed strong band-edge photoluminescence shifting from green to red with increasing particle size. The photoluminescence quantum yield strongly depended on the tellurium source employed in the synthesis. The highest quantum yields were observed by using a suspension of tellurium powder in a mixture of dodecylamine and trioctylphosphine. These CdTe samples showed a photoluminescence quantum yield up to 65% at room temperature without covering the surface of the nanoparticles with a passivating inorganic shell.

A convenient and safe one-pot route was presented to capped 3 nm CdSe nanoparticles with a narrow size distribution making use of common starting materials and inexpensive, low-boiling solvents under solvothermal conditions [587].  $\text{H}_2\text{Se}$  required for the reaction is generated *in-situ* through the aromatization of tetralin by Se. Figure 20 represents the powder XRD pattern of CdSe and UV-vis absorption spectrum of the nanoparticles in toluene [587].

The synthesis, characterization, and purification of GaSe nanoparticles in the size range of 2–6 nm were described [588]. These particles had a two-dimensional single tetralayer type structure. The particles had absorption onsets in the 360 to 450 nm region, with the smallest particles absorbing furthest to the blue. The particles were emissive, with emission quantum yields of about 10%.

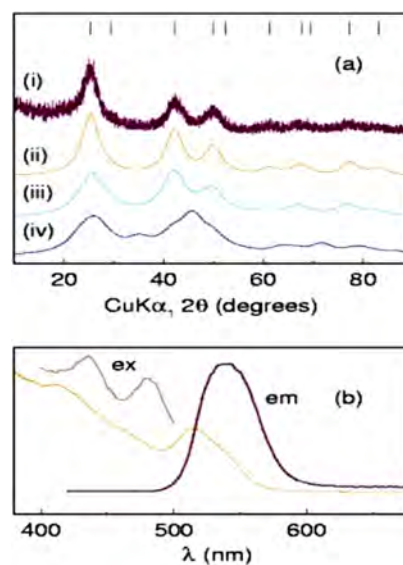


**Figure 20.** (a) (i) Powder XRD pattern of CdSe compared with (ii) the background-subtracted Rietveld fit, (iii) DIFFaX simulation of 3 nm cubic zinc blende stacking of CdSe, and (iv) DIFFaX simulation of a 3 nm hexagonal wurtzite stacking of CdSe. The vertical lines at the top are expected peak positions for the cubic zinc blende structure. (b) UV-Vis absorption spectrum of the nanoparticles in toluene. Luminescence spectra—emission (em) following excitation at 400 nm, and excitation (ex) following emission at 540 nm are also shown. After [587], U. K. Gautam et al., *Chem. Commun.* 7, 629 (2001). © 2001, Royal Society of Chemistry.



Uniformly dispersed transparent zinc ferrite nanoparticles were synthesized in a silica matrix with both the magnetic properties and optical transparency designed in the visible wavelength region [589]. The phases and morphologies of these zinc ferrite particles were examined. A much lower formation temperature of  $\text{ZnFe}_2\text{O}_4$  in nanocomposites was observed, compared to conventional ceramic processing. The particle size of zinc ferrite varied with the initial drying temperature, suggesting that a well-established silica network provided more confinement to the growth of  $\text{ZnFe}_2\text{O}_4$  particles. The optical properties of the nanocomposites were adjusted by varying the concentration of the zinc ferrite nanoparticles. The absorption edge at around 600 nm was blueshifted by 0.65 eV when the loading of  $\text{ZnFe}_2\text{O}_4$  particles was decreased from 30 to 5 wt%, while the absorption coefficient remained below  $400\text{ cm}^{-1}$  in the red visible region.

High-pressure optical absorption spectroscopic measurements of both erbium-doped and undoped Si nanoparticles were carried out in a diamond anvil cell up to pressures of 180 kbar [590]. The emphasis was with respect to the effect of particle size on the pressure dependence of the bandgap as well as the indirect examination of the structural impact of the erbium dopant on the pressure-induced phase transitions. In terms of electronic structure, these Er-doped Si nanocrystals acted very much like indirect gap silicon, with an observed bandgap pressure dependence of  $-1.4 \times 10^{-6}$  eV/bar. Measurements of the optical spectra in terms of integrated area as a function of pressure of these doped nanoparticles revealed that the first-order phase transition must lie above 180 kbar, substantially elevated from the bulk value of 120 kbar.

Two procedures were presented which allowed the homogeneous incorporation of silica-coated gold nanoparticles within transparent silica gels [591]. There was no aggregation of the metal particles during sol-gel transition. The optical properties of the gels were compared with those of the starting sols and interpreted on the basis of the porous structure of the gels and standard optical theories.

### 5.3. Electronic Properties

$\text{Co}_x\text{C}_{1-x}$  ( $x = 0.18, 0.25, 0.39$ ) nanogranular films were prepared by pulsed filtered vacuum arc deposition [592]. The as-deposited films with various Co concentrations were amorphous. Upon annealing, nanocrystalline Co grains were formed, while the carbon content remained amorphous. The electrical resistance of the films was measured as a function of temperature between 20 and 300 K. While the as-deposited films were metallic in the measured temperature range, annealed films showed complicated transport properties, depending on both the Co concentration and the annealing temperature. Experimental results were compared to the general predictions of theories of weak localization and/or electron-electron interaction on the metallic side of the metal-insulator transition and thermally assisted hopping or tunneling on the insulating side of the transition.

Composites of silica glass and metal nanoparticles of copper or nickel were synthesized by the hot compaction of sol-gel-derived glass-metal powders [593]. The metal particle sizes ranged from 5.1 to 7.2 nm. The electrical resistivity

of the composites was characterized by semiconductor-like behavior in the temperature range 235–340 K. This was believed to arise due to electron hopping between localized states within the bandgap of amorphous silica formed by the dispersed metal atoms.

Electrically conducting films of thickness approximately  $2\ \mu\text{m}$  were prepared on ordinary glass slides by growing nanoparticles of iron and copper, respectively, from a suitable precursor sol [594, 595]. The diameters of metal particles varied from 3 to 13 nm by controlling the heat-treatment schedule of the sol coating. The resistivity values in the range  $0.0001\text{--}0.0039\ \Omega/\text{cm}$  over the temperature range 80–300 K were obtained depending on the particle diameter and the type of metal used. The effective Debye temperature  $\theta_D$  for the different nanoparticle systems was estimated by fitting the experimental data to the Ziman equation.  $\theta_D$  varied from 346 to 408 K for iron with the particle size in the range 3.4–9.5 nm. The values obtained for copper are 243–307 K with particle diameters covering a range of 5.9–12.6 nm.

### 5.4. Magnetic Properties

The magnetic properties of carbon-coated iron and iron carbide nanocapsules, synthesized by arc discharge of carbon rods, were studied [596]. These nanocapsules consist of  $\alpha\text{-Fe}$ ,  $\gamma\text{-Fe}$ , and  $\text{Fe}_3\text{C}$ . Their coercive force was larger than that of bulk  $\alpha\text{-iron}$ , being ascribed to the small particle size.

Iron particles encaged in carbon nanocapsules were produced by the carbon arc-discharge method [597]. Soot, collarette, and cathode samples were characterized by Mössbauer spectroscopy and magnetic measurements in the temperature range 4.2–300 K. Different iron phases and iron-carbon solid solutions were detected. The Einstein model was used to evaluate the coupling constant between the particles and their environment, yielding values of the order 1–10 N/m. The superparamagnetism presented only if the particles presented a blocking temperature above 300 K.

Synthesis, crystal structures, and magnetic properties of Co particles encapsulated in carbon nanocapsules were studied [598]. Cobalt particles grown were in an fcc phase, with a trace amount of hcp Co. Thickness and structure of outer carbon layers could be controlled by varying the relative area of a Co-packed hole drilled in the graphite rod. Temperature dependence of the measured  $M_s$  was consistent with that for fcc Co. The highest value of  $M_s$  of  $160\ \text{Am}^2/\text{kg}$  at room temperature, nearly the same value for bulk fcc Co, was obtained for Co particles covered with thin carbon layers.

Magnetic properties of graphitically encapsulated nickel nanocrystals synthesized via a modified tungsten arc-discharge method were investigated [599]. By virtue of the protective graphitic coating, these nanocrystals were stable against environmental degradation, including extended exposure to strong acids. The magnetic properties of the encapsulated particles were characterized with regard to the nanoscale nature of the particles and the influence of the graphitic coating. The Curie temperature of graphitically encapsulated Ni nanocrystals was the same as that of microcrystalline Ni. The saturation magnetization, remanent magnetization, and coercivity of these particles were reduced, for a range of temperatures. The unique features were

compared with those of unencapsulated nanocrystalline and coarse microcrystalline nickel particles.

The structure and magnetic properties of carbon coated nickel and cobalt nanocrystals synthesized in a special low carbon to metal ratio arc chamber were reported [600, 601]. Magnetization measurements as a function of temperature in the range 20–900 °C gave a Curie temperature equal to that of bulk metal within experimental error. Upon heating and recooling of the particles, a large magnetization as high as 57% of bulk Co and 53% of bulk Ni was obtained. The dependence of room temperature saturation magnetization, remanent magnetization, and coercive field of the particles on annealing temperature was reported. These data were described by transition of particles from single domain to multidomain as a result of particle growth due to annealing. The particle size distribution measurements showed a log-normal behavior, indicating substantial particle size growth due to annealing.

Carbon-coated cobalt nanocrystals were prepared by a modified method of arc discharge under a He gas blow around a graphite rod cathode [602]. The magnetic properties of these particles after acid treatment were measured. Large shifts of Raman peaks were observed upon acid treatment, reflecting the structural change of the carbon shell induced by the acid treatment. The blocking temperature of the sample was estimated to be 373 °C.

Shell-core structures of Fe(C), Co(C), and Fe–Co(C) nanocapsules, prepared by an arc-discharge process in a mixture of methane and helium, were demonstrated by means of HRTEM [119–121, 123]. These nanoscale magnetic cores are protected by graphite shells. The ZFC magnetization of Fe–Co(C) nanocapsules, displaying different characteristics in three temperature ranges, can be well interpreted in terms of the unblocking of magnetization of small single-domain particles and the depinning of large multidomain particles. The saturation magnetization of these nanocapsules decreased monotonically, while the coercivity decreased significantly with increasing temperature. Figure 21 represents magnetization curves at room temperature of Fe–Co(C) nanocapsules [120]. Figure 22 shows ZFC and ( $B = 0.01$  T)

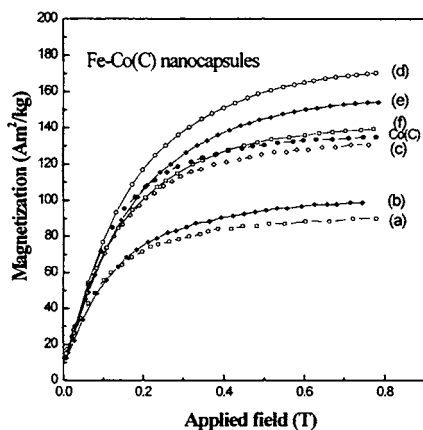


**Figure 21.** Magnetization curves at room temperature of Fe–Co(C) nanocapsules. Samples a–f correspond to 10 wt%, 20 wt%, 30 wt%, 45 wt%, 60 wt%, and 80 wt% Co content in master alloys, respectively. After [120], X. L. Dong et al., *J. Appl. Phys.* 86, 6701 (1999). © 1999, American Institute of Physics.

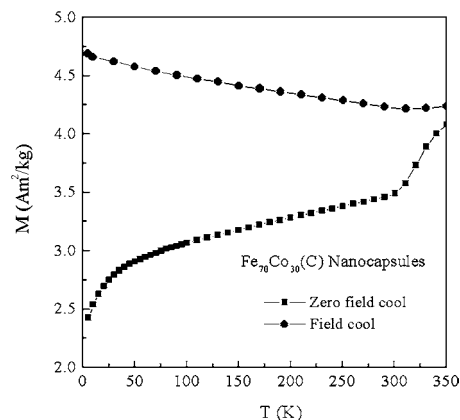


**Figure 22.** Zero-field-cooled (ZFC) and ( $B = 0.01$  T) field-cooled (FC) magnetization curves of Fe–Co(C) nanocapsules. After [121], Z. D. Zhang et al., *J. Phys. Cond. Matter* 13, 1921 (2001). © 2001, IOP Publishing.

FC magnetization curves of Fe–Co(C) nanocapsules [121]. The results could be used to compare with those of ultrafine Ni [603], Fe–Ni [604], and Fe–Co particles [605].

Carbon-encapsulated Ni nanoparticles were synthesized using a modified arc-discharge reactor under methane atmosphere [118, 606, 607]. The average particle size was revealed to be typically 10.5 nm with a spherical shape. Superparamagnetic property studies indicated that the blocking temperature ( $T_B$ ) was around 115 K at an applied field of 0.1 T. Below  $T_B$ , the temperature dependence of the coercivity was given by  $H_c = H_{ci}[1 - (T/T_B)^{1/2}]$ , with  $H_{ci}$  approximate to 500 Oe. Above  $T_B$ , the magnetization  $M(H, T)$  can be described by the classical Langevin function  $L$  using the relationship  $M/M_s(T = 0) = \coth(\mu H/k_B T) - k_B T/\mu H$ . The particle size can be inferred from the Langevin fit (particle moment  $\mu$ ) and the blocking temperature theory ( $T_B$ ), with values slightly larger than the HRTEM observations. It was suggested that these assemblies of carbon-encapsulated Ni nanoparticles had typical single-domain, field-dependent superparamagnetic relaxation properties.

The magnetic properties of boron-oxide-encapsulated magnetic nanocapsules fabricated by arc discharge in diborane ( $B_2H_6$ ) atmosphere were investigated in the temperature range from 4.2 to 300 K [122–124]. The saturation magnetizations of Fe(B) and Co(B) nanocapsules decreased monotonically with increasing temperature. The coercivities of the Fe(B) nanocapsules are almost two orders of magnitude higher than that of bulk Fe. The loop shift in the hysteresis loop the Fe(B) and Co(B) nanocapsules indicated the existence of the exchange bias between ferromagnetic and antiferromagnetic components. The  $Fe_3O_4$  or  $Co_3O_4$  phase in the shells contributed to the exchange bias as antiferromagnetic components. The very wide energy barrier distribution existed in these boron-oxide-encapsulated nanocapsules.

After passivation, the  $Fe_3C$  particles prepared by laser-induced pyrolysis of  $Fe(CO)_5$  and  $C_2H_4$  exhibited a high saturation magnetization of 132  $Am^2/kg$  compared to that of the  $\alpha$ -Fe particles, 95  $Am^2/kg$  [151]. Thin amorphous carbon layers, formed on the surfaces of the  $Fe_3C$  particles, inhibited oxidation of the  $Fe_3C$ , resulting in the high saturation

magnetization achieved by  $\text{Fe}_3\text{C}$  particles. The role the thin carbon layer formed on the iron carbonitride particle surface played in the oxidation behavior and in the enhancement of the magnetic properties was studied [152]. A carbon layer (1–2 nm) protected the particles effectively from reaction of the iron carbonitride with oxygen, and the iron carbonitride particles exhibited a high saturation magnetization of  $142 \text{ Am}^2/\text{kg}$ .

Ferromagnetic nanocrystallites of carbon- and  $\text{C}_x\text{N}$ -coated iron and its compounds were synthesized by a modified arc method in  $\text{N}_2$  buffer gas [608, 609]. The metal to carbon ratio of the particles, ranging from 73.5 to 80.5 wt%, was controlled by the pressure of the buffer gas charging from 0.06 to 0.01 MPa. Typical sizes of these particles were 10–30 nm. The magnetic properties of these particles were measured.

Glass–metal nanocomposite powders in the  $\text{Fe}/\text{SiO}_2$  and  $\text{Ni}/\text{SiO}_2$  systems were prepared by the sol–gel technique followed by reduction treatment [610]. Bulk nanocomposites were then fabricated by hot pressing these powders. The metal particle diameters ranged from 8.9 to 14.8 nm. The materials showed enhanced coercivities. The Mössbauer spectra of  $\text{Fe}/\text{SiO}_2$  samples were comprised of a ferromagnetic component superposed on a superparamagnetic doublet.

Nanocomposites of  $\gamma\text{-Fe}_2\text{O}_3$  in a silica matrix were prepared by the sol–gel method using tetramethylorthosilicate as a precursor of silica and introducing iron as  $\text{Fe}(\text{NO}_3)_3$  with  $\text{Fe}/\text{Si}$  ratios of 2, 5, 10, and 20% [611, 612]. Superparamagnetic  $\text{Fe}^{3+}$  oxide nanoparticles with a narrow size distribution, dispersed over the amorphous silica matrix, were present in  $\text{Fe}_2\text{O}_3\text{-SiO}_2$  nanocomposites (9–33 wt%  $\text{Fe}_2\text{O}_3$ ), prepared by a sol–gel method [613, 614]. Superparamagnetic magnetization curves were fitted by a Langevin function considering a log-normal particle size distribution. The specific Faraday rotation spectrum in a magnetic nanocomposite of  $\gamma\text{-Fe}_2\text{O}_3/\text{SiO}_2$  exhibited a narrow peak centered around 765 nm, reaching a value of 110 degrees/cm and an absorption coefficient of  $64 \text{ cm}^{-1}$  [612].

Iron particles having diameters around 8 nm and loosely packed with nanosized copper particles were prepared by a sol–gel route [615]. The samples exhibited coercivities in the range 200 to 500 Oe that were typical of single-domain iron grains. The Mössbauer spectrum was consistent with the presence of  $\alpha\text{-Fe}$  particles in the system. A finite value of the isomer shift was obtained, which was ascribed to possible electron transfer between the iron atoms and the surrounding copper matrix.

$\text{Mn}_{0.5}\text{Zn}_{0.5}\text{Fe}_2\text{O}_4$  ferrite nanoparticles (<100 nm) in  $\text{SiO}_2$  matrix were prepared by the sol–gel method [616]. The nanoparticles showed superparamagnetic behavior when the particle size was below 20 nm, which was confirmed by Mössbauer spectroscopy. The average particle size in the superparamagnetic state was also estimated from the low-field magnetization measurement by considering the samples as consisting of noninteracting single domain particles.

The phase formation of nanocrystalline  $\text{NiFe}_2\text{O}_4$  particles involved the nucleation of  $\text{Fe}_3\text{O}_4$  in amorphous silica at the initial stage of mechanical activation, followed by the growth of nickel ferrite by incorporation of  $\text{Ni}^{2+}$  cations into  $\text{Fe}_3\text{O}_4$  [617]. Their magnetic anisotropy, surface spin disorder, and

cation distribution were investigated by considering both the strain imposed by silica matrix and the buffer effect during mechanical activation.

The room temperature magnetic properties of Ir–Co and La–Zn substituted Ba-ferrite powders, prepared for the sol–gel method, were investigated [618]. Saturation magnetization increased with La–Zn substitution in contrast to Ir–Co substitution. La–Zn mixtures were the least effective in reducing coercivity, while Ir–Co led to a fast reduction at low levels of substitution.

$\text{Co}_{65}\text{C}_{35}$  nanocomposite film was prepared by pulsed filtered vacuum arc deposition [619]. The as-deposited film was found to be amorphous and ferromagnetically soft. No obvious magnetic domain structures can be observed in the MFM image, indicating the low anisotropy in the amorphous film. After annealing at a temperature between about 300 and 350 °C, the as-deposited amorphous films went through a metastable stage in which a cobalt carbide phase and hcp crystalline cobalt coexisted. Upon increasing the annealing temperature to 400 °C, the carbide phase decomposed into hcp crystalline cobalt nanograins and graphitelike carbon.

Polyelectrolyte multilayer capsules were introduced as versatile magnetic carrier systems [620]. Superparamagnetic magnetite was mounted to the multilayer shell itself or was a component of the capsule interior. The polyelectrolyte multilayer was formed at different (decomposable) colloidal templates (e.g., melamine formaldehyde resin, glutaraldehyde fixed red blood cells, emulsion oil droplets).

The catalytic synthesis of carbon nanotubes filled with long continuous cobalt nanowires by a simple chemical process and a following treatment with HCl were reported [621]. The average diameter of the multiwalled nanotubes was about 40 nm. The nanowires were a few micrometers long with a diameter of 20 nm. The cobalt nanowires, encapsulated in the carbon nanotubes, had a fcc structure. The filled nanotubes can be separated by using a permanent magnet.

The magnetic properties of boron nitride nanocapsules with iron oxide nanoparticles, fabricated by an arc-discharge method, were investigated [622]. The iron oxide nanoparticles of 20 nm size were encapsulated by boron nitride sheets of 4 nm width. Magnetization of the BN nanocapsules showed paramagnetism and the initial iron oxides showed ferromagnetism, suggesting the transformation into superparamagnetism by separating the iron oxide nanoparticles with BN sheets.

Efficient synthetic strategies were developed for single molecular magnets (i.e., the design of new magnetic polyoxometalate clusters) [623–637]. Polyoxometalate chemistry served as an inexhaustible source for molecular models for different reasons, especially due to their versatile redox chemistry. Referring to molecular magnets, paramagnetic centers can be embedded in a structure-determining diamagnetic polyoxometalate (linker) framework giving rise to properties which were intermediate between simple paramagnetism and bulk magnetism. For example, in  $\{\text{Mo}_5\text{M}_6\}$ -type cluster systems, it was even possible to place (or exchange) stepwise different (para)magnetic centers M like  $\text{Fe}^{2+/3+}$  and  $\text{V}^{4+}\text{O}^{2-}$  in the respective linker positions, thus allowing some control over the cluster's magnetic properties or even the tuning of these.

## 5.5. Dynamic Properties

Carbon nanocapsules containing nanometer-size particles of molybdenum carbide were irradiated by neutrons of flux  $10^{14} \text{ N cm}^{-2} \text{ s}^{-1}$  for 6 days [638]. The  $\gamma$ -ray spectrometry showed  $10^{10} \text{ Bqg}^{-1}$  of Mo-99 transformed from Mo-89 and decayed into Tc-99. The TEM investigation indicated that the nanocapsule was robust against the neutron irradiation and was used as a container for radioactive materials and tracer elements. The contents of the capsule in the nanometer scale were activated and transformed into other nuclei.

A reactor chamber was developed for the secure handling of radioactive materials [639]. Using the arc-discharge method for fullerene synthesis, the carbon encapsulation capability of uranium was tested. The uranium was encapsulated as a dicarbide with two types of carbon covers: graphene sheets parallel to the external surface and randomly oriented carbon crystallites. The covers with parallel sheets of graphite were present with two different interlayer spacings. One corresponded to polyhedral particles with an interior gap between the kernel and capsule. The other consisted of rounded-vertex particles with no gap and with interlayer spacing between that of graphite and that corresponding to polyhedral nanocapsules. Extensive studies were described for the resolution of carbon structures and a transformation mechanism was proposed for the interpretation of rounded-vertex onionlike structures. Closed carbon covers chemically protected the actinide kernel and provided safer handling and processing of toxic materials for medical and nuclear purposes.

*In-situ* and *ex-situ* TEM observation was performed in copper implanted with carbon ions at temperatures from 570 to 973 K [640]. Carbon onions (concentric graphitic spheres) and nanocapsules (concentric graphitic spheres with cavities) were observed together with amorphous carbon layers. Statistics of cluster size as a function of ion fluence, implantation temperature, and substrate crystallinity gave insights into the nucleation processes of onions and nanocapsules. One was the formation of graphitic layers on grain boundaries to encapsulate copper particles. The other was the nucleation of graphitic cages, probably fullerenes, due to both a high concentration of carbon atoms and a high amount of radiation damage. Simultaneous observation of microstructural evolution under implantation revealed that onions were formed inside the substrate, not the surface, and that they segregate at the surface due to radiation-enhanced evaporation.

A scanning tunneling microscopy study of carbon nanocapsules (onions) was reported [641]. Spherulitic graphite was shown to be purely crystalline graphite based on XRD and TEM studies. Carbon nanocapsules grown on pitch-based carbon fibers were investigated by HRTEM [642]. Two types of nanocapsules were formed during heating up to 2000 °C in 1 atm  $\text{N}_2$  gas: one was a capsule enclosing a CaS single crystal and the other was a cubic hollow capsule. The growth mechanism of these carbon nanocapsules was discussed by comparing the structures of particles formed at several temperatures.

## 6. BIOMEDICAL PROPERTIES

### 6.1. Introduction

Recently, much interest has been generated by colloidal drug delivery systems such as nanocapsules because of the possibilities for controlled release, increased drug efficacy, and reduced toxicity after parenteral administration. Nanocapsules can be formulated into a variety of useful dosage forms including oral liquid suspensions, lotions, creams, ointments, powders, capsules, tablets, and injections. Nanoencapsulation has been applied to solve problems in the development of pharmaceutical dosage forms as well as in cosmetics for several purposes. These include conversion of liquids to solids, separation of incompatible components in a dosage form, taste masking, reduction of gastrointestinal irritation, protection of the core materials against atmospheric deterioration, enhancement of stability, and controlled release of active ingredients.

Nanoparticles used in drug delivery are solid, colloidal particles consisting of macromolecular substances that vary in size from 10 to 1000 nm. The drug is dissolved, entrapped, adsorbed, attached, or encapsulated in the macromolecular materials. Nanoparticles, also called nanopellets or nanocapsules, can have a shell-like wall, called a nanosphere, or a polymer lattice. However, it is often difficult to determine whether nanoparticles have a shell-like wall or a continuous matrix. Nanocapsules present a liquid core surrounded by a polymeric shell, while so-called nanospheres consist of a dense polymeric matrix, in which the drug can be dispersed. Compared to other colloidal carriers, polymeric nanocapsules present a higher stability when in contact with biological fluids, and their polymeric nature allows one to obtain the desired controlled and sustained drug release. Nanocapsules represent drug delivery systems suitable for most of the administration routes, even if rapid recognition by the immune system limits their use as injectable carriers.

Different approaches to preparing biodegradable nanocapsules, consisting of biodegradable polymers, have been described, as well as the methods for preparing surface-modified sterically stabilized particles [643–654]. Nanocapsules can be prepared either from preformed polymers, such as polyesters (i.e., polylactic acid), or from a monomer during its polymerization, as in the case of alkylcyanoacrylates. Most of the methods based on the polymerization of monomers (i.e., alkylcyanoacrylates) consist of adding a monomer into the dispersed phase of an emulsion or an inverse microemulsion or dissolving it in a nonsolvent of the polymer. Starting from preformed polymers, nanoparticles are formed by the precipitation of synthetic polymers or by denaturation or gelification of natural macromolecules. Two main approaches have been proposed for the preparation of nanocapsules of synthetic polymers. The first one is based on the emulsification of the water-immiscible organic solution of the polymer by an aqueous phase containing the surfactant, followed by solvent evaporation. The second approach is based on the precipitation of a polymer after addition of a nonsolvent of the polymer. Concerning nanocapsules formed of natural macromolecules, the nanocapsules can be obtained by thermal denaturation of proteins (such as albumin) or by a gelification process, as in the case of alginates. The attachment of certain hydrophilic

polymers on the surface of the carriers reduces the uptake by the immune system, therefore prolonging the blood half-life of the nanospheres and thus allowing their intravenous administration. Characterization of sterically stabilized nanospheres allows the establishment of parameters that govern the *in vivo* behavior. In particular particle size and surface properties, such as chemical composition, charge, and hydrophobic, etc., are directly correlated with the nanoparticle fate. A drug or any biologically active compound can be dissolved, entrapped, or encapsulated into the nanocapsules or simply adsorbed onto its surface. It has been well known that polymeric particulate nanocarriers, able to deliver drugs or other compounds to specific sites of action for a prolonged time, represent a potential therapeutic approach for several diseases [643–654].

The pioneers in this field discovered that the nanocapsules could be used as new type of lysosomotropic carrier [6, 7], as new dosage forms [2, 655], or for controlled release of drugs [1]. Early work also focused on the preparation and characterization of hemolysate-loaded poly(N- $\alpha$ , N- $\epsilon$ -L-lysinediylterephthaloyl) [3], gelatin [4], and polyisobutyrylcyanoacrylate nanocapsules [8–10, 656]. It was found that the polyalkylcyanoacrylate nanocapsules increased the intestinal absorption of a lipophilic drug [5, 11]. Since the mid 1980s, many different active molecules, such as anti-inflammatory agents, anticancer drugs, immunostimulating compounds, anti-infectious agents, antiglaucomatous drugs, and even peptides have been encapsulated and as a result their pharmacological effect has been improved or their secondary effects reduced compared with free drugs after administration by oral, parenteral, or ocular routes. The nanocapsules have been found also to be suitable as a biodegradable drug carrier for the administration and controlled release of drugs, like insulin, indomethacin, calcitonin, doxorubicine, gangliosides, oligonucleotides, etc.

One of the major obstacles to the targeted delivery of colloidal carriers (nanocapsules) is the body's own defense mechanism in capturing foreign particles by the reticuloendothelial system. Following intravenous administration, practically all nanometer size particles are captured by the reticuloendothelial system (mainly the liver). The design of "macromolecular homing devices" seems to disguise nonparticles from the reticuloendothelial system, which is of potential interest for the targeted delivery of nanocapsular carriers [657]. The idea is based on a graft copolymer model embodying a link site for attachment (binding) to the carrier, a floating pad for maintaining the particles afloat in the bloodstream, an affinity ligand for site-specific delivery, and a structural tune for balancing the overall structure of the homing device.

Although the oral route is preferred route for drug delivery, numerous drugs remain poorly available when administered by the oral route. In order to circumvent this problem, some drugs are associated with colloidal polymeric particle systems. Orally administered nano and microparticles can follow at least three different pathways: (i) capture by gut-associated lymphoid tissue; (ii) mucoadhesion; and (iii) direct fecal elimination. Mucoadhesion of colloidal particulate systems in the gastrointestinal tract was emphasized [658]. On the one hand, *in vitro* adsorption and desorption

studies showed that particles could be captured to a considerable extent by the mucous gel layer lining the gastrointestinal tract through a mucoadhesion mechanism. On the other hand, the *in vivo* behavior of the particle in the intestinal lumen was accurately investigated by means of radiolabelled particles.

Recently a major breakthrough has been achieved in the formulation of polymeric artificial nanocapsules, which can be made in a reproducible manner having a specific size and shape and in reasonable quantities. This opens a new field of intelligent material with possible sophisticated applications. To achieve the goal to bring this research field from the level of basic science to possible application, the necessary techniques have been developed and expertise from different fields and laboratories has been combined [659–674]. The first step to allow specific applications is to functionalize the nanocapsules by coating the surface with active sites or to inserting them into the wall. One direction is to cover them with lipid membranes providing an artificial cell. These techniques have been combined with recent developments in molecular biology. The advantage of natural proteins already optimized by nature has been taken for specific tasks, which could be modified by genetic engineering to adopt them for purposes (e.g., such nanospheres can harvest specific substrates or release at a specific site encapsulated materials). A second aspect is that these nanocapsules provide a new class of surfaces which allows study of molecular interactions of surface attached proteins. These studies have permitted new types of measurements and thus provided new insights into protein–protein or protein–ligand interaction. Artificial cells for pharmaceutical and therapeutic applications have been expanded up to the higher range of macrocapsules and down to the nanometer range of nanocapsules and even to the macromolecular range of cross-linked hemoglobin as a blood substitute. Artificial cells have been being prepared by bioencapsulation in the laboratory for medical and biotechnological applications. Advances in molecular biology have resulted in the availability of non-pathogenic genetically engineered microorganisms that can effectively use uremic metabolites for cell growth. The three generations of blood substitutes have been developed based on an original idea of a completely artificial red blood cell.

In Section 6.2, we will focus on the advances in the area of artificial cell and red blood cell substitutes, most of which are based on Chang's concept [675–679]. In Section 6.3, various types of the drug delivery and controlled release are reviewed.

## 6.2. Artificial Cell and Red Blood Cell Substitutes

The artificial cell evolved from Chang's attempts to prepare artificial structures for possible replacement or supplement of deficient cell functions [675–679]. Artificial cells for pharmaceutical and therapeutic applications started as microencapsulation on the micrometer scale. This has expanded up to the higher range of macrocapsules and down to the nanometer range of nanocapsules and even to the macromolecular range of cross-linked hemoglobin as a blood

substitute. Artificial cells are now being prepared by bioencapsulation in the laboratory for medical and biotechnological applications [680–685]. Some exciting developments include research and clinical trials on modified hemoglobin for blood substitutes and the use of artificial cells for enzyme therapy, cell therapy, and gene therapy [686–691]. Like natural cells, biologically active materials inside the artificial cells are retained and prevented from coming into contact with external materials like leucocytes, antibodies, or tryptic enzymes. Molecules smaller than protein can equilibrate rapidly across the ultrathin membrane with a large surface to volume relationship. A number of potential medical applications using artificial cells have been proposed [692, 693]. One of these is hemoperfusion for uremia, intoxication, and hepatic failure [692], which has been developed successfully for routine clinical use [693]. Artificial cells containing enzymes have been used for inborn errors of metabolism and other conditions.

Semipermeable microcapsules containing catalase were implanted into acatalesemic mice, animals with a congenital deficiency in catalase [694], which replaced the deficient enzymes and prevented the animals from the damaging effects of oxidants. The artificial cells also protected the enclosed enzyme from immunological reactions [695]. The artificial cells containing asparaginase implanted into mice with lymphosarcoma delay the onset and growth of lymphosarcoma [11, 696]. The microencapsulated phenylalanine ammonia lyase given orally lowered the elevated phenylalanine levels in phenylketonuria rats [697], because of an extensive recycling of amino acids between the body and the intestine [698], which was developed for clinical trial in phenylketonuria [699].

A drop method was developed for the encapsulation of biological cells [677, 679] by using milder physical cross-linking [700], resulting in alginate–polylysine–alginate (APA) microcapsules containing cells. The preparative procedures and properties of microcapsule artificial kidneys were studied [701, 702]. Microencapsulated xanthine oxidase was used for experimental therapy in Lesch–Nyhan disease [703]. Microencapsulated islets were used as bioartificial endocrine pancreas [700]. The cell encapsulation was developed for cell therapy, including artificial cells containing endocrine tissues, hepatocytes, and other cells for cell therapy [686, 688, 704–707], for potential applications in amyotrophic lateral sclerosis, dwarfism, pain treatment, IgG<sub>1</sub> plasmacytosis, Hemophilia B, Parkinsonism, and axotomized septal cholinergic neurons. The effects on hyperbilirubinemia in Gunn rats were discussed for hepatocytes immobilized by microencapsulation in artificial cells [708]. Daka and Chang reported bilirubin removal by the pseudoperoxidase activity of free and immobilized hemoglobin and hemoglobin coimmobilized with glucose oxidase [709]. Preparation and characterization of xanthine oxidase immobilized by microencapsulation in artificial cells were reported for the removal of hypoxanthine [710]. Even for more immediate clinical applications [711], the ingenious use of capillary fiber to encapsulate cells allows one to implant cells followed by retrieval and reimplantation in clinical trials [711].

Advances in molecular biology have resulted in the availability of nonpathogenic genetically engineered

microorganisms that can effectively use uremic metabolites for cell growth. Prakash and Chang studied the oral use of microencapsulated genetically engineered nonpathogenic *E. coli* DH5 cells containing the Klebsiella aerogenes urease gene in renal failure rats [712–714]. *In vitro* removal of urea, ammonium, electrolytes, and other metabolites was studied [714–717]. Daily oral administration to partially nephrectomized rats including survival studies was investigated [712, 718–720]. Clinical potentials of oral encapsulated *E. coli* DH5 cells were studied [702, 721–723].

Polyhemoglobin has been used as a blood substitute. Native hemoglobin [tetramer] breaks down into half molecules [dimers] after infusion causing renal toxicity and other adverse effects. Chang extended his original approach of artificial cells containing hemoglobin and enzymes [675–677] to form polyhemoglobin—a molecular version of artificial cells which was based on the use of bifunctional agents like diacid [675–677] or glutaraldehyde [724, 725] to cross-link hemoglobin molecules into polyhemoglobin. This glutaraldehyde cross-linked polyhemoglobin approach has been extensively developed more recently [726–734].

Although polyhemoglobin is in the most advanced stages of clinical trial, there are other modified hemoglobins such as recombinant human hemoglobin [728, 735]. Unlike polyhemoglobin these are single tetrameric hemoglobin formed by intramolecular cross-linkage [736, 737] or recombinant human hemoglobin [738]. Clinical trials on these show vasoactivities and other effects of nitrate oxide removal [736–738]. A recombinant human tetrameric hemoglobin with markedly decreased affinity for nitric oxide was developed [739]. Rate of reaction with nitric oxide determines the hypertensive effect of cell-free hemoglobin. When infused into experimental animals, this did not cause vasoactivity.

There are other new generations of modified hemoglobin blood substitutes: Polyhemoglobin stays in the circulation with a half-time of only up to 27 hours. In order to increase this circulation time, Chang's original idea of a complete artificial red blood cell [675–677] is now being developed as a third generation blood substitute. Thus submicrometer lipid membrane microencapsulated hemoglobin [740] has been explored [728, 741, 742]. The surface properties were modified to result in a circulation half-time of about 50 hours [743]. A system was developed based on biodegradable polymer and nanotechnology resulting in polylactide membrane hemoglobin nanocapsules of about 150 nm diameter [744, 745]. This was smaller than the lipid vesicles and contained negligible amounts of lipids. The superoxide dismutase, catalase, and also multienzyme systems were used to prevent the accumulation of methemoglobin [746].

For detailed progress on artificial cell and red blood cell substitutes, refer to the literature [747–805].

### 6.3. Drug Delivery and Controlled Release

The great progress in drug delivery systems has recently been made in the treatment of a variety of diseases. Targeting delivery of drugs to the diseased lesions is one of the most important aspects of the drug delivery system. To convey a sufficient dose of drug to the lesion, suitable carriers of drugs are needed. Nano- and microparticle carriers



have important potential applications for the administration of therapeutic molecules. Nanocapsules, which are ultra-fine oily droplet-coated polymeric substances, are probably one of the most promising candidates for colloidal carriers. Surface engineering by the interfacial deposition method can provide a suitable size distribution and necessary surface characteristics to the nanocapsules. Microparticles and nanoparticles as colloidal drug carriers in the micrometer and submicrometer range have been developed to overcome solubility problems of poorly soluble drugs as well as for long acting injectable depot formulations and specific drug targeting options, and they have also been evaluated for ophthalmic drug delivery purposes. Figure 23 gives a diagrammatic representation of liposomes, nanospheres, and nanocapsules for drug targeting.

Drugs are loaded into the nanoparticles by several methods. One method is by producing the nanocapsules in the presence of the drug. Drugs may also be loaded into empty particles prepared ahead of time. The drug, the polymer, and the means of preparation all influence the type of interaction with the polymer, the attachment of the drug to the nanoparticles or nanocapsules, and the rate of their interaction. Encapsulating drug molecules inside host molecules has obvious benefits: (i) protection of the drug from degradation; (ii) control over the hydrophilic/lipophilic balance of the capsule by modification of the host molecule, and (iii) good potential for targeting of the drug by equipping the capsule with appropriate recognition groups.

Some important practices for which nanocapsules are used include the adsorbing and coating of organs and tissues, peroral administration of drugs, vaccinations, the delivery of anti-inflammatory drugs, and the delivery of drugs for diseases and tumors. Nanocapsules can be targeted to specific organs or tissues by coating their surface with different materials. Nanocapsules are useful in this application due to their stability. Liposomes, on the other hand, often disintegrate due to the surfactants that are present in this method. Nanocapsules are also often used for peroral administration. An example of this can be applied to the digestive system. In order to influence the mode of interaction of the intestinal fluids with the intestine, the properties of these fluids are monitored in different tissues in the gut. Liposomes are often depleted by the salts present in these intestinal fluids, whereas nanoparticles are stable in the presence of these substances. In vaccination methods, nanoparticles have an advantage due to their slow degradation. This slow process allows for a longer interaction of the antigen with the immunocompetent cells of the body. Nanocapsules, as well

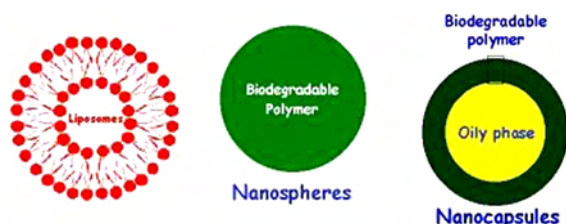


**Figure 23.** Diagrammatic representation of liposomes, nanospheres and nanocapsules for drug targeting. From homepage of E. Fattal, <http://efattal.free.fr/>.

as many other colloidal carriers, are enabling new methods for therapy in drug delivery.

The research in this area is being carried out all over the world at a great pace. Research areas cover novel properties that have been developed increased efficiency of drug delivery, improved release profiles and drug targeting. Many kinds of nanocapsules have been synthesized by a combination of different polymers and medicines as the shell and the core of the nanocapsules. The polymers, such as polyalkylcyanoacrylate, polyisobutylcyanoacrylate, poly(*N*- $\alpha$ , *N*- $\epsilon$ -L-lysinediylterephthaloyl), poly(D, L-lactide), poly(ethylcyanoacrylate), isohexylcyanoacrylate, poly- $\epsilon$ -caprolactone, poly(ethylene imine), poly(ethylene oxide-*b*-sebacic acid), polymethylidene, etc., and natural materials, like gelatin, melamine resin, etc., have been used to encapsulate various medicines, like insulin, peptides, indomethacin, cisplatin, calcitonin, doxorubicine, gangliosides, dodecanoate, oligonucleotides, etc. In the Sections 6.3.1–6.3.5, we collect literature with the same or similar topics concerning the materials used for the shell and the core of the nanocapsules. Ocular delivery and *in vitro/in vivo* studies will be represented separately in Sections 6.3.6 and 6.3.7. In the last Section, we will collect the review articles on the topic of drug delivery and controlled release.

### 6.3.1. Polyalkylcyanoacrylate/ Isobutylcyanoacrylate/Insulin/Peptides

Polyalkylcyanoacrylate or isobutylcyanoacrylate nanocapsules were used as a drug carrier also for oral administration [12, 13, 806–809] or enteral absorption [810] of insulin. The mechanism of formation of nanoparticles and nanocapsules of polyisobutyl-2-cyanoacrylate was studied [811]. The absorption of insulin was studied by measuring fasting glycemia in streptozotocin-induced diabetic rats after a single administration of encapsulated insulin (100 units  $\text{kg}^{-1}$ ) at various sites along the gastrointestinal tract [810]. The influence of sulfur dioxide and pH on the preparation and characterization of polyalkylcyanoacrylate nanoparticles was investigated [812]. Oral administration of insulin incorporated into the wall of isobutylcyanoacrylate nanocapsule to diabetic rats induces a long-lasting normalization of their fasting glycemia. The biological action of encapsulated insulin on DNA and glycogen syntheses in Chinese hamster ovary cells transfected with the human insulin receptor gene was examined [813].

Nonobese diabetic mice develop an autoimmune disease with a long prodromal period and constitute a model for investigating the prevention of human type-1 diabetes. Since prophylactic insulin injections reduced the incidence of diabetes in nonobese diabetic mice, a prophylactic strategy was tested to prevent diabetes in nonobese diabetic mice consisting of oral administration of insulin, protected in polyalkylcyanoacrylate nanocapsules from degradation in the gastrointestinal tract [814]. The early feeding with insulin nanocapsules reduced diabetes and insulinitis in the nonobese diabetic mouse model that mimics human type-1 diabetes.

Biological activity of insulin immobilized in a polymer hydrogel modified with a proteolytic enzymes inhibitor was examined in *in vitro* and *in vivo* studies. Immobilization of insulin did not affect its biological activity. Oral administration of the immobilized insulin led to a reliably reduced

concentration of glucose in the blood of test animals. The efficiency of the orally administered preparation amounted to 80% of the efficiency of hypodermally injected native insulin [815].

Physicochemical characterization of insulin-loaded polyisobutylcyanoacrylate nanocapsules obtained by interfacial polymerization was carried out [816]. The mechanism of insulin encapsulation and the type of interactions between the polymer forming the nanocapsule wall and the insulin were studied [817]. These nanocapsules showed unexpected biological activity after intragastric administration [816, 817]. The hypoglycemic effect was characterized by a period of 2 days and a prolonged effect over a period of 20 days. Insulin was found unmodified during the nanoencapsulation process, due to the large amount of ethanol used in the preparation of the nanocapsules that initiated the polymerization of isobutylcyanoacrylate preserving the peptide from a reaction with the monomer. Results of the  $\zeta$  potential measurements showed that insulin was located inside the core of the nanocapsules and not simply adsorbed onto their surface.

Cyclodextrins and their hydrophilic derivatives were used as solubilizers capable of enhancing the loading capacity of liposomes and microparticles. Two possibilities of using cyclodextrins in the design of colloidal carriers were presented [818]. The first possibility consists of increasing the loading capacity of polyisobutylcyanoacrylate nanospheres prepared by anionic polymerization, by employing hydroxypropyl cyclodextrins. The second possibility consists of the spontaneous formation of either nanocapsules or nanospheres by the nanoprecipitation of amphiphilic cyclodextrin diesters.

An improved method for the preparation of alkylcyanoacrylate nanocapsules was proposed that involved the intermediate synthesis of a well defined adduct of a single monomer unit to an ethanol molecule [819]. It led to thinner capsule walls and, generally, to a more reproducible capsule structure. The chemical composition of the intermediate organic phase was studied by nuclear magnetic resonance spectroscopy. The morphology and size of resulting structures was analyzed, applying analytical ultracentrifugation and light microscopic particle tracking. The sizes of capsules depended on the concentrations of the oil and the monomer components.

Alkylcyanoacrylates were polymerized anionically in water medium at different levels of pH. The effect of pH on the molecular weight and softening points of the polymers was studied [820]. Alkylcyanoacrylates were polymerized in suspension by using the combination of methanol-water, and also by using different catalysts such as triethylamine, diazabicyclooctane, and diazabicycloundecane. The polyacrylates were characterized by infrared and nuclear magnetic resonance spectroscopy. The molecular weight, molecular weight distribution, and the softening points of the polymers were determined.

The possibilities of sterilizing polybutylcyanoacrylate nanoparticle suspensions and lyophilized nanoparticle powders by autoclaving or formaldehyde treatment were evaluated [821]. The nanoparticles were fabricated with different stabilizers. In most conditions a significant increase in particle size was determined after autoclaving of the nanoparticle

suspensions and the nanoparticle powders were characterized by impaired resuspension characteristics.

Because poly(butyl  $\alpha$ -cyanoacrylate) was less toxic than poly(isobutyl  $\alpha$ -cyanoacrylate) and its nanocapsules could be orally absorbed via the intestine wall, polymeric nanocapsules as a drug delivery system of peptides were prepared by the interfacial polymerization of butyl  $\alpha$ -cyanoacrylate [822]. The aqueous phase contained a surfactant such as Tween 20 and polymeric stabilizer such as dextrin T-70, dextrin T-40, as well as Poloxamer 188. The organic phase was composed of monomer butyl  $\alpha$ -cyanoacrylate and a cosolvent such as glycerol trioleate or benzyl alcohol in bulky solvent ethanol or acetone.

A method for the determination of the cyclophosphamide content of polyalkylcyanoacrylate nanoparticles was developed [823]. The analyses were carried out by inductively coupled plasma/atomic emission spectrometry (ICP/AES) by measuring the phosphorus content in the drug. The results obtained were compared with those given by high performance liquid chromatography that permits the detection of the cyclophosphamide molecule, and its degradation products.

The ileal uptake of polyalkylcyanoacrylate nanocapsules (less than 300 nm in diameter) was investigated in the rat [824]. Iodized oil (Lipiodol) was used as the tracer for X-ray microprobe analysis in scanning electron microscopy. Polyalkylcyanoacrylate nanocapsules were able to pass through the ileal mucosa of the rat via a paracellular pathway in the nonfollicular epithelium and, most predominantly, via M cells and adjacent enterocytes in Peyer's patches.

The influence of several media (*in vitro* and *ex vivo*) present in the gastrointestinal tract on the stability of polyisobutylcyanoacrylate nanoparticles was investigated [825]. Polyisobutylcyanoacrylate nanoparticles were proven to be stable in a gastric environment and bioerodable in a simulated intestinal medium. Esterase caused a rapid degradation of the nanoparticles that was proportional to the amount of enzyme added to the medium.

The ability of polyisobutylcyanoacrylate nanocapsules was studied to protect insulin from degradation by proteolytic enzymes providing biologically active insulin by the oral route [826]. Insulin was labeled with Texas Red for release studies and microscopy observations. Turbidimetric measurements and electron microscopy observations confirmed that the nanocapsules were degraded in the reconstituted intestinal medium, whereas nanocapsule integrity was preserved in the reconstituted gastric medium.

Doxorubicin-loaded polybutylcyanoacrylate (PBCA) nanoparticles were prepared by an emulsifier-free emulsion polymerization technique [827]. The pH values of the polymerization medium and the weight ratios of doxorubicin to butylcyanoacrylate had a significant effect on the mean particle size. Drug loading and entrapment efficiency increased with increasing pH of the medium. Doxorubicin-loaded polybutylcyanoacrylate nanoparticles carried a positive charge, and the  $\zeta$  potential of drug-loaded nanoparticles increased with the increase of the polymerization pH. Figure 24 shows a TEM photograph of adriamycin-loaded polybutylcyanoacrylate nanoparticles [828].

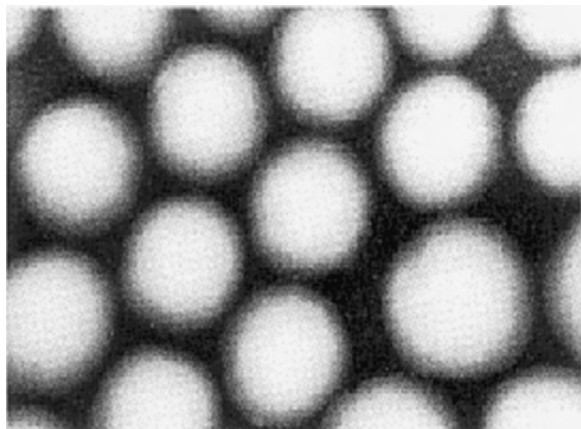


**Figure 24.** Transmission electron micrograph of adriamycin-loaded polybutylcyanoacrylate nanoparticles. After [828], J. H. Chen et al., *J. Fourth Military Med. Univ.* 21, 89 (2000) [in Chinese]. © 2000, Fourth Military Med. University, China.

The structure of gas-filled poly-*[n*-butyl-2-cyanoacrylate] (BCA) particles was demonstrated by negative staining with uranyl acetate, platinum-carbon shadowing of air-dried material, and thin sectioning of the aqueous suspension of BCA particles, embedded in water-soluble melamine resin [829]. The polymer shell of the hollow particles possessed a globular outer surface and a smoother inner surface.

A copolymeric nanoparticulate drug delivery system (i.e., copolymerized peptide particles) was developed as a carrier for the oral uptake of therapeutic peptides [830], based on the copolymerization of the active peptide derivative with *n*-butylcyanoacrylate (*n*-BCA), the resulting copolymer being formulated as nanoparticles. The peptide luteinizing hormone releasing hormone was used as a model drug to investigate the viability of the approach. The results demonstrated that chemical conjugation of a peptide within a protective particulate matrix was a viable approach for enhancing oral peptide delivery, presumably utilizing the gut-associated lymphoid tissue as a route of delivery [831]. The mechanism of uptake of biodegradable microparticles in Caco-2 cells was found to be microparticle diameter, concentration, and incubation time and temperature dependent [832]. The small diameter microparticles (0.1  $\mu\text{m}$ ) had significantly greater uptake compared to larger diameter microparticles.

The potency of surface coating liposomes with some materials was investigated for oral delivery of peptide drugs [833]. *In vitro* release of insulin, a model peptide, from liposomes in the bile salts solution was markedly reduced by coating the surface with the sugar chain portion of mucin or polyethyleneglycol. Encapsulation of insulin into mucin or polyethyleneglycol completely suppressed the degradation of insulin in the intestinal fluid, whereas uncoated liposomes suppressed it only partially. These results demonstrated that surface coating liposomes with polyethyleneglycol or mucin gained resistance against digestion by bile salts and increased the stability in the gastrointestinal tract.

Nanoparticles composed of new graft copolymers having a hydrophobic backbone and hydrophilic branches were prepared by the dispersion copolymerization of hydrophilic polyvinyl macromonomers with styrene in a polar solvent

[834]. The potential of these nanoparticles as carriers for oral peptide delivery was investigated using salmon calcitonin in rats. The rate of salmon calcitonin incorporated in nanoparticles was high and was affected by the macromonomer structure. Anionic nanoparticles having poly(methacrylic acid) macromonomer chains on their surfaces showed the highest incorporating activity.

Biodegradable polymer membrane nanocapsules containing hemoglobin were prepared with phase separation and polymer precipitation methods using different polymers including polylactic acid and polyisobutylcyanoacrylate [835]. Preliminary *in vivo* tests showed that surface modified nanocapsules containing hemoglobin can survive longer in the circulation.

W/o/w multiple emulsions composed of medium-chain triglycerides containing insulin with aprotinin, a protease inhibitor, and/or sodium taurocholate, an absorption enhancer, were prepared by a two-step emulsification method at 15 °C [836]. Whatever the nature of the substance introduced in the internal aqueous phase, all the emulsions obtained had very similar properties. The main release mechanism was a swelling-breakdown phenomenon after dilution of the emulsions under hypo-osmotic conditions. These emulsions were able to protect insulin against enzymatic degradation *in vitro*.

Poly(alkylcyanoacrylate) nanocapsules were used as biodegradable polymeric drug carriers for subcutaneous and peroral delivery of octreotide, a long-acting somatostatin analog. Their ability to reduce insulin secretion or prolactin secretion in response to oestrogens was studied in adult male rats [837].

In an *ex vivo* study, the absorption of cyclosporine A on bovine cornea after 24 h contact with various drug delivery systems containing 1% cyclosporine A was evaluated in comparison with an olive oil formulation as the reference vehicle for cyclosporine A [838]. The different formulations studied were poly(acrylic acid) polymeric gels in aqueous/nonaqueous solvents, polyisobutylcyanoacrylate nanocapsules, and a combination of both formulations.

### 6.3.2. Indomethacin/Cisplatin/Calcitonin/Doxorubicine

Indomethacin is an anti-inflammatory drug with serious side effects on the gastrointestinal tract. Encapsulation of the drug into nanocapsules allowed the therapeutic activity of the drug to be maintained while eliminating side effects [839]. Freeze-drying the suspension of indomethacin-loaded nanocapsules provided a dosage form that was stable over several years. The physical stability and inhibitory activity of the indomethacin nanocapsules on inflammation and platelet aggregation were evaluated [840]. The encapsulation of approximately 99% indomethacin within orally administered  $\beta\text{CD-C-6}$  nanocapsules with an average size of 194 nm protected against both gastric and intestinal ulceration was compared with an oral administration of an aqueous solution of Indocid (R) [841]. The relative bioavailability was increased by this encapsulation. PLA nanoparticles containing indomethacin were prepared by interfacial deposition of PLA following acetone displacement from a dichloromethane acetone solution toward an aqueous phase [842].

Indomethacin loaded poly(D, L-lactide) nanocapsules were investigated after intravenous and rectal administration to rabbits [843]. A rebound of indomethacin plasma concentrations attributed to enterohepatic circulation of indomethacin was observed with all preparations. Following i.v. infusions, results showed that the poly(D, L-lactide) nanocapsules altered the pharmacokinetics of indomethacin in ways that accelerated the extravascular distribution by enhancing the capture of the colloidal carrier by the liver and, at the same time, modifying the elimination rate of indomethacin. Bioavailability and tolerance of indomethacin as polymeric nanocapsules in humans were investigated [844].

The capacity for increasing the corneal penetration of drugs was investigated for three different colloidal carriers, namely, nanoparticles and nanocapsules made of poly- $\epsilon$ -caprolactone and submicrometer emulsions [845]. The three systems differed in their inner structure and composition, but with a similar size (200–250 nm) and a negative superficial charge (–16 to –42 mV). Release of the encapsulated indomethacin occurred very rapidly upon high dilution in a buffered medium and was independent of the composition of the system.

Influence of benzyl benzoate as oil core on the physicochemical properties of spray-dried powders from polymeric nanocapsules containing indomethacin was studied [846]. Intestinal toxicity exerted by indomethacin was compared to that induced by copper–indomethacinate, free or associated to zwitterionic phospholipids [847]. A single high dose of indomethacin (15 or 20 mg/kg), copper–indomethacinate (15 or 20 mg/kg), or copper–indomethacinate liposomes or nanocapsules (15 mg/kg) was orally administered. Anti-inflammatory activity of the drugs was investigated using the carrageenan-induced paw edema model. Indomethacin induced penetrating ulcerations of the intestine that were maximal at hour 24.

The loading of drugs into ultrafine host vesicles or colloidal capsules in the nanometer size range was an acknowledged technique for the optimization of controlled drug delivery [848, 849]. Two methods for the determination of cisplatin-loaded polyalkylcyanoacrylate nanoparticles were developed [850]. The analyses were carried out by high performance liquid chromatography (HPLC) with UV detection and results were checked with those obtained by inductively coupled plasma-optical emission spectrometry. A nanocapsule formulation with a hydrophilic core was applied to the oral administration of salmon calcitonin in rats [851].

The preparation from w/o microemulsion of polybutylcyanoacrylate nanocapsules incorporating doxorubicin was optimized applying a multivariate experimental design [852, 853]. Overcoming multidrug resistance with the aid of doxorubicin loaded onto the polyisobutylcyanoacrylate nanoparticles was associated with an increased intracellular drug content [854]. Multidrug-resistance bypass in cells exposed to doxorubicin-loaded nanosphere was studied in the absence of endocytosis [855]. The effect of isobutylcyanoacrylate nanoparticles, in the size range of 100–220 nm, on the disposition of doxorubicin was investigated [856].

### 6.3.3. Poly(D, L-Lactide)

A lipophilic derivative of muramyl dipeptide, muramyl tripeptide cholesterol, was incorporated into poly(D, L-lactide) nanocapsules and its immunomodulating properties were assessed *in vitro*. The nanocapsule form was more effective than the free drug in activating rat alveolar macrophages for a cytostatic effect toward syngeneic tumor cells [857, 858]. The lipophilic compound, a peptidomimetic inhibitor, CGP 57813, of human immunodeficiency virus type 1 (HIV-1) protease, was successfully entrapped into poly(D, L-lactic acid) and pH sensitive methacrylic acid copolymers nanoparticles [859]. The intravenous administration to mice of poly(D, L-lactic acid) nanoparticles loaded with CGP 57813 resulted in a two-fold increase of the area under the plasma concentration–time curve, compared to a control solution. The passage of intact poly(D, L-lactic acid) nanoparticles across the gastrointestinal mucosa appears to be very low. Induction of macrophage *no*-synthase by an immunomodulator entrapped within polymeric nanocapsules was studied [860]. Gastrointestinal tolerance following intravenous and oral administration of poly(D, L-Lactide) nanocapsules containing nonsteroidal anti-inflammatory drugs were investigated [861].

The nanocapsules prepared from poly(D, L-lactide) containing a nonsteroidal anti-inflammatory drug, diclofenac, were formulated and their stability during storage at room temperature was studied [862]. The influence of some factors that could affect stability, namely, the type of oily phase used or/and its concentration, the concentrations of drug and of surfactants, was investigated. The pH of the preparation, the particle size, and the quantity of drug remaining (encapsulated and total), and polymer molecular weight were determined at intervals for up to 8 months after nanocapsule preparation.

Atovaquone and rifabutin had potential therapeutic activity against toxoplasmosis but the low water solubility of these drugs reduced their bioavailability [863]. Their formulation as a colloidal suspension of poly(D, L-lactic acid) nanocapsules increased that effectiveness. The atovaquone formulation was more stable than the rifabutin one and was injected at 15 mg/kg per day by the intragastric route to mice infected with *Toxoplasma gondii*.

The mouse macrophage cell line RAW 264.7 was stimulated to produce nitric oxide by muramyltripeptide cholesterol included within biodegradable poly(D, L-lactide) nanocapsules [864]. The aim was to determine whether one or both of the cytokines transforming growth factor- $\beta$  (TGF- $\beta$ ) and interleukin -10 (IL-10) could be responsible for feedback, control seen at high concentrations.

Biodegradable C-14-poly-(D, L-lactic acid) [PLA(50)] nanoparticles coated either with a readily digestible protein albumin or with a nondigestible coating agent, polyvinyl alcohol (PVA), were prepared by the solvent evaporation technique [865]. The nanoparticles were administered perorally to guinea pigs to evaluate the gastrointestinal degradation of their PLA(50) matrix. In the case of PLA(50) nanoparticles coated with digestible albumin, substantial gastrointestinal degradation of the PLA(50) matrix occurred, leading to the passage of a considerable amount (greater than or equal to 45%) of water-soluble products across the gastrointestinal barrier.

The benzathine penicillin G nanoemulsion and nanocapsules were formulated, their physicochemical and stabilizing characteristics were evaluated, and their antimicrobial activity and penicillin *in vitro* release kinetics were determined [866]. Nanoemulsions were produced by the spontaneous emulsification approach and nanocapsules of poly(D, L-lactic acid-co-glycolic acid) (PLGA) polymer were prepared by the method of interfacial deposition of a preformed polymer.

Several formulations of poly( $\epsilon$ -caprolactone) (PCL), PLA, and PLGA nanocapsules containing phenylbutazone were prepared according to the interfacial deposition technique [867]. These formulations differed in the type of polymer used to form the shell of the nanocapsules. Analysis of particle size distribution and encapsulation efficiency of the nanocapsules revealed that the type and molecular weight of polyester used were the main factors influencing these properties. PLA had the highest encapsulation efficiency with the best reproducibility.

The loading capacity of pentamidine-loaded poly(D, L-lactide) nanoparticles, the factors influencing pentamidine release, and the cytotoxicity of nanoparticles prepared by nanoprecipitation method were reported [868]. Various concentrations of pentamidine base and polymer were tested. The influence of the dilution, temperature, and ionic strength was evaluated. A nonlinear increase in drug uptake per unit mass of polymer with the equilibrium pentamidine concentration was found.

The interactions of naked and surface-modified PLA nanocapsules, where PEG was adsorbed or covalently attached, were studied with a macrophage-like cell line [869]. The fluorescent oil marker, DID, was successfully encapsulated in nanocapsules in order to follow their interactions with cells. The cell-associated fluorescence obtained with PEG-PLA nanocapsules was about 3 to 13-fold lower than that obtained with naked-PLA nanocapsules.

The poly(D, L-lactide) nanocapsules containing bovine serum albumin were prepared by means of a modified w/o/w double-emulsion technology [870]. A mixture of glycerin and water was used instead of the traditional stabilizer system in the preparation of polymeric nanocapsules. The results showed that the high viscosity of the mixture and the hydroxyl group of the glycerin were helpful in the formation of the nanocapsules. The prepared nanocapsules had a similar spherical form.

Lectin poly(lactide) microsphere conjugates specifically designed for oral administration were prepared and their activity and specificity in the presence of mucus were characterized [871]. The presence of hydroxyl or amino groups suitable for covalent coupling of lectins by the glutaraldehyde method at the surface of the microspheres was ensured by preparing the particles in the presence of either PVA or bovine serum albumin (BSA).

Although the oral route for insulin delivery is the most convenient, directly administered oral insulin is degraded by proteolytic enzymes in the gastrointestinal (GI) tract. Poly(lactide) was prepared in order to microcapsulate the insulin to avoid the enzymes in the GI [872]. The poor selectivity of photosensitizers for tumor tissue remains a drawback in photodynamic therapy (PDT) and could be improved by adapted formulations. The cellular uptake,

localization, and phototoxicity of meta-tetra(hydroxyphenyl) chlorin (mTHPC) encapsulated in submicronic colloidal carriers were studied in macrophage-like J774 cells and EFT 29 human adenocarcinoma cells [873]. Nanocapsules with an external layer made of poly(D, L-lactic acid), PLA grafted with polyethylene glycol, PLA coated with poloxamer 188 (polox PLA NCs), and oil/water nanoemulsion were examined.

#### 6.3.4. Poly(ethylcyanoacrylate)/ Isohexylcyanoacrylate/ Dipeptide/ Gangliosides

Biocompatible and biodegradable colloidal drug delivery systems were obtained by means of *in-situ* polymerization of alkylcyanoacrylate [874]. In particular, nanocapsules of PECA were prepared by adding the monomer to an organic phase, consisting of Miglyol 812(R) and an organic solvent (ethanol, acetone, or acetonitrile), and subsequently mixing the organic phase with an aqueous phase containing Pluronic F68(R) at different concentrations. The mechanism of formation and the influence of preparation conditions on the quality of nanocapsule formulations were investigated by freeze-fracture electron microscopy and laser light scattering. The mechanism of drug release from PECA nanocapsules was mainly diffusion from the oil core through the intact polymer barrier. Figure 25a gives a diagrammatic representation of a microdelivery particle and Figure 25b shows PECA nanocapsules containing hydroquinone [875].

Macrophages can become cytotoxic toward tumor cells when activated by immunomodulators. Three different muramyl peptides were synthesized: one hydrolyzable lipophilic ester derivative (MTP-Chol) and two nonhydrolyzable lipophilic ether derivatives (MTP-octadecane and MTP-heptadecafluorooctadecane) [876]. Activation of the RAW 264.7 cell line was studied by measuring nitrite production as an indication of NO-synthase activity. The lipophilic ester derivative, incorporated within nanocapsules, was as active as a free muramyl dipeptide, whereas the lipophilic ether derivatives were unable to activate macrophages. The results indicated that lipophilic muramyl peptides needed to be hydrolyzed to yield a hydrosoluble metabolite in order to activate macrophages.

Poly(ethylcyanoacrylate) nanocapsules suitable for use as drug delivery systems were prepared by *in-situ* polymerization, addition of the monomer to an organic phase, and subsequent mixing of the latter to an aqueous phase containing a nonionic surfactant. Different preparation conditions were able to influence the final poly(ethylcyanoacrylate) nanocapsule colloidal suspension [877].

The drug-loaded polymeric nanospheres were prepared composed of the methoxy PEG (MePEG) and PCL that showed a narrow size distribution and average diameter of less than 200 nm [878]. The nanosphere having a relatively high drug-loading efficiency of about 42% was obtained when the feed weight ratio of indomethacin to polymer was 1:1.

The association with poly(alkylcyanoacrylate) nanospheres and nanocapsules of monosialoganglioside GM1 and other chemically modified gangliosides was investigated with the aim of developing a colloidal drug delivery system



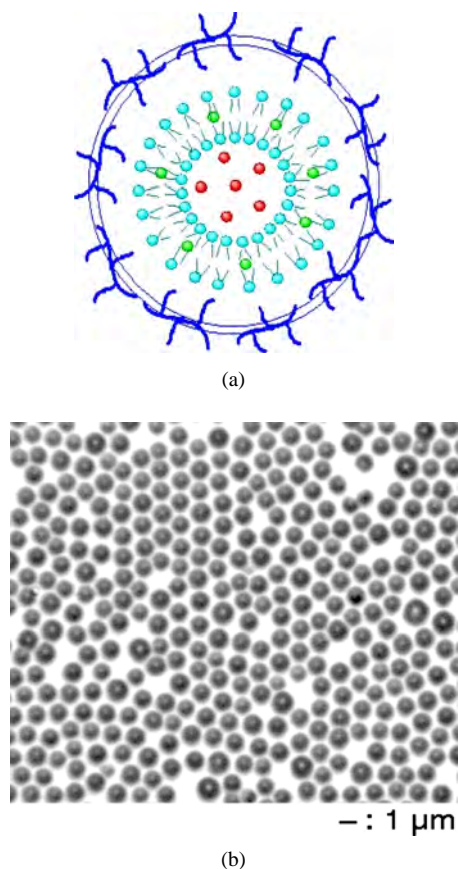


**Figure 25.** (a) Diagrammatic representation of a micro-delivery particle and (b) PECA nanoparticles containing hydroquinone. After [875], R. Arshady, in "Microspheres, Microcapsules and Liposomes," MML Series, Vols. 1 and 2. Citus Books, London, 1999. © 1999, Citus Books.

suitable for use by the oral route [879]. Gangliosides were successfully associated with a biodegradable cyanoacrylic carrier either in the form of nanospheres or as nanocapsules, avoiding any degradation of the ganglioside molecule during the polymerization process. The drug loading was found to be more efficient for nanocapsules.

Antihypertensive effects of a nanocapsular form of darodipine, a dihydropyridine calcium entry blocker, were studied [880]. Two problems were addressed, associated with the use of dihydropyridine calcium entry blockers in antihypertensive therapy, namely, potent vasodilation and short half-lives, by incorporating the representative blocker, darodipine, into a nanocapsular vehicle. The effect of various poloxamer coatings on *in vitro* adhesion of isohexylcyanoacrylate nanospheres to rat ileal segments under liquid flow was investigated [881]. Polyisohexylcyanoacrylate nanocapsules containing cyclosporin were prepared by mixing in a 1:2 ratio an oil/ethanol solution of monomer and drug with an aqueous phase [882, 883]. Drug nanoencapsulation rate was controlled by its partition coefficient between the inner (organic) and outer (aqueous) phases. The biodegradable polyisohexylcyanoacrylate nanoparticles were shown to be able to deliver the growth hormone releasing factor as a sustained-release system [884]. Nanocapsules were prepared by interfacial

polymerization of isohexylcyanoacrylate and coated with poloxamers to reduce the recognition and uptake by reticuloendothelial cells of the liver and spleen [885]. Several phthalocyanine derivatives were encapsulated into nanocapsules and their *in vitro* photocytotoxic activity against V-79 cells was compared to that of free drug. Nanoencapsulation did not reduce the activity of amphiphilic drugs while hydrophilic and lipophilic compounds were affected in diverse ways. Body distribution in mice of intravenously injected radiolabeled cyclosporine associated with polyisohexylcyanoacrylate nanocapsules or nanospheres was studied [886].

The nanoparticle uptake by the rat gastrointestinal mucosa, quantitation, and particle-size dependency were studied [887]. Polystyrene microspheres in the size range 50 nm to 3  $\mu\text{m}$  were fed by gavage to female Sprague Dawley rats daily for 10 days at a dose of 1.25 mg/kg. Histological evidence of the uptake of these particles and their absorption across the gastrointestinal tract and passage via the mesentery lymph supply and lymph nodes to the liver and spleen were confirmed by analysis of tissues for the presence of polystyrene by gel permeation chromatography. Measurement of radioactivity of tissues following administration of 100 nm and 1  $\mu\text{m}$  I-125-labelled polystyrene latex particles for 8 days was corroborative although less secure because of the potential lability of the labelled particles.

### 6.3.5. Poly- $\epsilon$ -caprolactone/Poly(ethylene imine)/Poly(ethylene oxide-*b*-sebacic acid) Polymethylidene/Dodecanoate/Oligonucleotides

Two dialkylmethylidenemalonate (DAMM) analogs, diallylmethylidenemalonate (AAMM) and cyclohexylethylmethylidenemalonate (CEMM), were synthesized and evaluated for their capacity to polymerize to stable nanoparticles and to adsorb primaquine diphosphate [888]. The interaction between polystyrene microspheres and the follicle-associated epithelium of rabbit Peyer's patches was examined [889].

In order to evaluate the concentration of a hydrophilic drug, phenobarbitone, in a suspension of poly- $\epsilon$ -caprolactone nanocapsules, a gas chromatographic-mass spectrometric procedure, performed after methylation of the drug, was developed and validated [890]. Treatment with muramyl dipeptide (MDP) or a lipophilic derivative (MTP-Chol) included in nanocapsules renders macrophages cytostatic toward tumor cells. At the same time, nitric oxide synthase (EC 1.14.23) activity was induced, as determined by measurement of the two end products of the reaction (nitrite and L-citrulline) [891].

In order to evaluate the concentration of a hydrophilic drug, phenobarbitone, in a suspension of poly- $\epsilon$ -caprolactone nanocapsules, a gas chromatographic-mass spectrometric procedure, performed after methylation of the drug, was developed and validated [892]. The preparation of primidone-loaded poly- $\epsilon$ -caprolactone nanocapsules according to the interfacial deposition technique was described [893]. The colloidal suspension obtained showed a monomodal size distribution with a mean diameter ranging from 308 to 352 nm. By adjusting the process parameters,



the encapsulation efficiency was about 74% with good reproducibility. Primidone release from the nanocapsules was found to be slower as compared to the oily control solution despite an important burst effect.

Amphiphilic diblock copolymers composed of MePEG and  $\epsilon$ -caprolactone ( $\epsilon$ -CL) were prepared for the formation of micelles [894]. The copolymer was formed by the ring-opening mechanism of  $\epsilon$ -CL in the presence of MePEG containing hydroxyl functional groups at one end of the chain. To estimate their feasibility as vehicles for drugs, MePEG/ $\epsilon$ -CL block copolymeric micelles were prepared by dialysis against water. Indomethacin was incorporated into the hydrophobic inner core of these micelles as a typical model drug for nonsteroidal anti-inflammatory drugs. From the dynamic light scattering measurements, the size of micelle formed was less than 200 nm, and their size increased with the amount of indomethacin encapsulated into the inner core of MePEG/ $\epsilon$ -CL block copolymers.

The influence of factors (pH, enzymes, etc.) chosen partially to mimic *in vivo* conditions on the release of a model drug, indium oxine, from PCL nanocapsules *in vitro* was determined [895]. A nanocapsule suspension, an emulsion (o/w), and a solution in olive oil were prepared in order to compare the release of a radioactive tracer, indium oxine, as a function of time by an *in vitro* dialysis method. Nanocapsules were prepared by interfacial deposition of PCL and characterized by particle size distribution (laser light scattering) and determination of the polymer molecular weight by gel permeation chromatography.

Nanocapsules of poly- $\epsilon$ -caprolactone and Eudragit S90(R) were prepared by using the spray-drying process using colloidal silicon dioxide as a technological carrier [896]. The morphological analysis of the surface at the powders showed that nanocapsules remained intact, and no change in particle size was detected after the spray-drying process.

Various methods were tested for sample preparation, in order to determine progesterone concentration in nanocapsules consisting of benzyl benzoate in a poly- $\epsilon$ -caprolactone shell [897]. The opening of nanocapsules by a dissolution-dilution in acetonitrile was validated.

The efficacy of colloidal particles as drug carriers is closely related to their interaction with proteins and enzymes in different body fluids [898]. A work analyzed the interaction phenomenon between lysozyme, a positively charged enzyme that was highly concentrated in mucosae, and two different drug carriers: nanocapsules made of an oily core coated by the polymer poly- $\epsilon$ -caprolactone (PECL) and nanoparticles made solely of poly- $\epsilon$ -caprolactone [898]. The interaction of lysozyme with these colloidal drug carriers was highly affected by their surface charge.

Polymethylidene malonate nanoparticles were prepared in phosphate buffer through emulsion polymerization of monomeric units; the kinetics of the reaction was monitored by spectrophotometry at 400 nm. Average nanoparticle sizes, molecular weights, and biodegradability of this potential drug carrier were determined under various conditions [899].

One of the major limiting steps for the absorption of peptide drugs from the intestine is proteolytic degradation. To slow this degradation, human calcitonin was trapped in polyacrylamide nanoparticles, and human calcitonin and

insulin were encapsulated with polyisobutylcyanoacrylate [900]. Human calcitonin trapped in polyacrylamide nanoparticles showed no delayed release characteristics and thus would not provide protection from proteases. Proteolytic degradation of human calcitonin and insulin in polyisobutylcyanoacrylate nanocapsules was slower than the free peptides in solution.

A rapid, sensitive, and selective HPLC assay was developed for the simultaneous determination of ethyl clofibrate and its major metabolite, clofibric acid, in plasma of humans and rats [901]. The assay involves extraction of the compounds into chloroform-isoamyl alcohol (99:1, v/v) from plasma acidified with sulfuric acid. The HPLC assay was used to monitor the plasma concentration-time profiles of ethyl clofibrate released from polylactic nanocapsules in both man and rat. Activity of  $\alpha$ -chymotrypsin immobilized in poly(*N,N*-diallyl-*N,N*-didodecylammonium) bromide nanocapsules was studied [902].

The synthesis and the characterization of a poly(2-methyloxazoline)-block-poly(dimethylsiloxane)-block-poly(2-methyloxazoline) triblock copolymer carrying polymerizable groups at both chain ends were described [903]. This copolymer forms vesicular structures in dilute aqueous solution, the size of which can be controlled in the range from 50 up to about 500 nm. The methacrylate end groups of the triblock copolymer can be polymerized in the vesicular aggregates using an UV-induced free radical polymerization.

A diblock copolymer, poly(ethylene oxide-*b*-sebacic acid), was prepared by polycondensation [904]. Its self-assembly in water via a microphase inversion resulted in narrowly distributed stable polymeric nanoparticles with a size around 70 nm. Such formed nanoparticles had a core-shell nanostructure, with the insoluble hydrophobic polysebacic acid blocks as the core and the soluble hydrophilic polyethylene oxide blocks as the protective shell. The core was degradable, and its degradation led to the disintegration of the nanoparticle. The degradation was a first-order reaction, and the degradation rate increased with the dispersion temperature.

ABA block copolymers of polylactide and poly(ethylene glycol) as amphiphilic bioabsorbable polymers were synthesized by the ring-opening polymerization of DL-lactide onto PEG 2000 or PEG 6000 and their structures were characterized on the basis of proton NMR. Biodegradable nanocapsules of an aqueous insulin solution were prepared from the block copolymers and polylactide by an improved interfacial coacervation technique [905]. The diameters of the nanocapsules were mainly dependent on the ratio of the two chains in the block polymers. The size of the nanocapsules decreased with an increase in the amount of surfactant used. More insulin solution resulted in an enlargement of the nanocapsules in diameter.

Poly(ethylene imine) was used for the complexation of dodecanoic acid resulting in a poly(ethylene imine) dodecanoate complex with a lamellar nanostructure and a repeat unit of 2.9 nm [906].

Antisense oligonucleotides are molecules that are able to inhibit gene expression being therefore potentially active for the treatment of viral infections or cancer. Antisense oligonucleotides with base sequences complementary to a

specific RNA can, after binding to intracellular mRNA, selectively modulate the expression of a gene. However, because of their poor stability in biological medium and their weak intracellular penetration, colloidal drugs carriers such as nanoparticles were developed for the delivery of oligonucleotides [907]. Oligonucleotides associated to nanoparticles were shown to be protected against degradation and to penetrate more easily into different types of cells. As a consequence, nanoparticles were shown to improve the efficiency of oligonucleotides for the inhibition of the proliferation of cells expressing the point mutated Ha-ras gene. Nanocapsules were prepared by interfacial polymerization of isobutylcyanoacrylate in a w/o emulsion [908]. A nanotechnology was said to be able to encapsulate oligonucleotides, rather than adsorbing them at the surface of a solid support, which had great potential for oligonucleotide delivery.

EWS Fli-1, a fusion gene resulting from a *t*(11;22) translocation, was found in 90% of both Ewing's sarcoma and primitive neuroectodermal tumor. The polyisobutylcyanoacrylate nanocapsules with an aqueous core were able to encapsulate efficiently high amounts of phosphorothioate oligonucleotides directed against EWS Fli-1 chimeric RNA [909].

### 6.3.6. Ocular

In order to reduce the lacrimal elimination and to increase the intraocular penetration of betaxolol after ocular administration, a drug carrier was prepared, polycaprolactone nanocapsules, containing betaxolol in the base form, which was applied in the medical treatment of glaucoma in rabbits [910–912]. Reduction of cardiovascular side effects associated with ocular administration of metipranolol by inclusion in polymeric nanocapsules was investigated [913]. Antimetastatic activity *in vivo* of MTP-Chol entrapped in polyisobutylcyanoacrylate nanocapsules was studied [914]. With the aim of exploring the potential of poly( $\epsilon$ -caprolactone) nanocapsules as drug carriers for ocular administration, the mechanism of interaction of these nanocapsules with the corneal and conjunctival epithelia was examined [915]. Ocular penetration of 1% cyclosporine A from nanocapsules and conventional formations in rabbit eyes was studied [916]. Topical application of nanocapsules of cyclosporine A on a penetrating keratoplasty rejection model was developed [917].

A research program was initiated to assess the ability of nanospheres to improve the biodelivery of active ingredients to plants [918]. The goal was to obtain stable poly( $\epsilon$ -caprolactone) nanospheres with the smallest size and the largest amount of encapsulated active ingredients, using a nanoprecipitation method.

Chitosan-coated and poly-L-lysine-coated poly( $\epsilon$ -caprolactone) nanocapsules were designed based on a strategy that combines the features of poly( $\epsilon$ -caprolactone) nanocapsules as ocular carriers with the advantages of a cationic mucoadhesive coating and their capacity for increasing the corneal penetration of drugs investigated [919]. The ability of different drug carriers to improve the ocular bioavailability of drugs was investigated in the rabbit eye [920]. The assayed drug carriers were suspensions of nanoparticles, nanocapsules, and microparticles made

of poly( $\epsilon$ -caprolactone) and a submicrometer emulsion. Polyester nanocapsules as new topical ocular delivery systems for cyclosporin A were developed [921–923]. The nanocapsules are an interesting alternative to the olive oil solution or ointments for the delivery of cyclosporin A to the eye [922].

Uptake of cyclosporine A loaded colloidal drug carriers by mouse peritoneal macrophages *in vitro* was studied [924]. The [H-3] cyclosporine A loaded colloidal particles, polylactic acid nanospheres, polylactic acid nanocapsules, and microemulsions, were prepared. The [H-3] cyclosporine A loaded colloidal particles were incubated with MPM for 30 min at 31 °C, then the cells were separated from the colloidal particles and the radioactivity was measured by a liquid scintillation counter.

Efficacy of topical cyclosporine A-loaded nanocapsules on keratoplasty rejection in the rat was evaluated [925]. Cyclosporine A formulated in migliol oil delayed corneal rejection onset, but blood levels were evident in this group. Cyclosporine A-loaded nanocapsules showed no effect on rejection and the drug was not detectable in blood.

Acyclovir-loaded polyethyl-2-cyanoacrylate (PECA) nanospheres were prepared by an emulsion polymerization process in the micellar phase and characterized [926]. The influence of the presence of nonionic surfactant as well as other substances [i.e., 2-hydroxypropyl- $\beta$ -cyclodextrin (HP- $\beta$ -CyD) and PEG] on formulation parameters and loading capacity was investigated. The presence of PEG resulted in an increase of mean size and size distribution. Ocular tolerability of PEG-coated PECA nanospheres was evaluated by the *in vivo* Draize test. The acyclovir-loaded PEG-coated PECA nanospheres showed a significant ( $p < 0.001$ ) increase of drug levels (25-fold) in aqueous humor compared with the free drug or the physical mixture.

The anatomical, physiological, and pharmacological properties of the eye explain the short precorneal residence time and the poor bioavailability of most eyedrop solutions [927]. Many approaches were proposed to increase ocular bioavailability of drugs. Most eyedrops included a viscosity agent in their formulation to significantly prolong residence time although the increased viscosity was limited due to patient discomfort. The developments included biodegradable inserts, eyedrops based on cyclodextrins, liposomes, or nanoparticles.

### 6.3.7. In Vitro/In Vivo Studies

The influence of three different enzymes (amylase, pepsin, and esterase) on the stability of polybutylcyanoacrylate nanoparticles was studied as an *in vitro* investigation using side-by-side diffusion cells [928]. *In vitro* resistance of tumor cells to doxorubicin was fully circumvented by using doxorubicin-loaded nanospheres, consisting of biodegradable polyisohexylcyanoacrylate polymers of 300 nm diameter and containing 2.83 mg of doxorubicin per 31.5 mg of polymer [929]. The *in vitro* release kinetic pattern of indomethacin from poly(D,L-lactide) nanocapsules was studied [930]. *In vivo* evaluation of polyisobutylcyanoacrylate microparticles containing fluorouracil was performed [931]. Effect on cerebral blood-flow, jejunal absorption,

and pharmacological activity and pharmacokinetic evaluation of orally administered indomethacin-loaded polyisobutylcyanoacrylate and poly(D,L-lactide) nanocapsules were investigated [932, 933]. The biliary clearance and enterohepatic circulation of indomethacin in the rabbit was examined [934]. Nanocapsules were used as carriers for oral peptide delivery [935].

Preparation methods of cyanoacrylic nanocapsules or nanoparticles containing phthalocyanines and naphthalocyanines were described [936]. Nanocapsules were obtained by interfacial polymerization in an oil-in-water emulsion. Drug encapsulation efficiency depended on drug concentration, ethanol concentration, and phthalocyanine sulfonation degree and reached 100% in some cases.

Poly(lactic acid) nanocapsules of clofibrate containing soybean oil or medium-chain triglycerides as the oil core were prepared [937]. The *in vitro* drug release kinetic profiles were determined and compared to those of a clofibrate sub-micron emulsion using two different kinetic techniques: the bulk equilibrium reverse dialysis sac technique and the centrifugal ultrafiltration technique.

The physical and chemical properties of tramcinolone acetonide nanocapsules, prepared by interfacial polymerization of isobutyl-2-cyanoacrylate at the oil/water interface, were studied [938]. The joint effect of monomer and oil in organic phase on the size and encapsulation efficiency was analyzed. Polymer coating around the oil droplets caused an important variation in droplet size and encapsulation efficiency. The release of drug from the nanocapsules was investigated *in vitro*.

A pharmaceutical form of atovaquone was developed and its activity against *Toxoplasma gondii* was studied *in vitro* and *in vivo* [939]. Nanocapsules were chosen as the oral dosage form of administration. The *in vitro* activity of atovaquone-loaded nanocapsules against tachyzoites of *T.gondii* (RH stain) was comparable to its suspension form. *In vivo* studies were carried out in murine models of acute and chronic toxoplasmosis. The sensibility of *T.gondii* to atovaquone was different according to the strains and the fact that the activity of atovaquone in the treatment of toxoplasmosis was enhanced when administered in nonparticulate form.

### 6.3.8. Reviews

The nanoparticles are colloidal polymeric drug carriers that hold promise for peroral drug delivery. The peroral administration of nanoparticles was reviewed [940]. Nanoparticles were retained in the gut of rats and mice in small quantities for substantial time periods (up to 6 days). They were taken up in particulate form in the intestine and appeared in the lymph nodes, blood, liver, spleen, and sites of inflammation in the body. Three possibilities in the mechanism of uptake were discussed: (1) intracellular uptake; (2) intercellular/paracellular uptake; and (3) uptake via the M-cells and Peyer's patches in the gut. The uptake was size-dependent; smaller particles were taken up to a higher degree than larger particles. Binding to nanoparticles enhanced the peroral bioavailability of a number of drugs, and a significantly enhanced and prolonged pharmacological activity by binding to nanoparticles was reported for insulin and hydrocortisone.

Nanoparticles and microparticles for the delivery of polypeptides and proteins [941, 942], and for ocular delivery [943] were reviewed. The main objective for these systems was to improve the classical aqueous eyedrop formulations that have major disadvantages like rapid elimination of drugs from the precorneal area. Consequently, colloidal carrier suspensions were designed to combine ophthalmic prolonged action with ease in application of liquid eyedrops. The review summarized the manufacturing methods and the materials used for these delivery systems with respect to ophthalmic purposes. The distribution and penetration pathways of the particulate delivery systems were described. The applications of drug-loaded particles were presented with focus on ophthalmic diseases like glaucoma, inflammations, or infections of the eye. Accordingly, particulate carriers, outlined in the review, included systems loaded with pilocarpine,  $\beta$ -blockers, hydrocortisone, amikacin, and miscellaneous drugs.

The applications of electron microscopic techniques to the characterization and evaluation of drug delivery systems were reviewed [944]. Various EM related techniques such as TEM, SEM, SEM with energy dispersive X-ray microanalysis, and freeze-fracture electron microscopy were extensively used for this purpose. Microcapsules, microspheres, nanocapsules, liposomes, polymeric carriers, and other drug delivery systems were characterized using EM related techniques for their surface topography, size and shape analysis, biodegradation, *in vitro-in vivo* evaluation, and drug excipient interactions and characterization. EM methods are very useful in understanding the mechanism of drug carrier formation, drug release in *in vitro-in vivo* situations, and drug carrier-body fluid interactions, and in studying ultrastructural disposition of drug carriers in body compartments.

A review focused on the gastrointestinal bioadhesion of micro- and nanoparticles [945]. Bioadhesion was obtained by the building of either nonspecific interactions with the mucosal surface, which were driven by the physicochemical properties of the particles and the surfaces, or specific interactions when a ligand attached to the particle was used for the recognition and attachment to a specific site at the mucosal surface. The relative merits of those systems were discussed. Their fate in the gastrointestinal tract, including three different pathways, (i) bioadhesion, (ii) translocation through the mucosa, and (iii) transit and direct fecal elimination, was presented.

The techniques available to prepare biodegradable nanoparticles (nanospheres and nanocapsules) from preformed polymers were reviewed [946]. Four techniques were discussed in terms of their technological advantages and drawbacks: emulsification evaporation, solvent displacement, salting-out, and emulsification diffusion. The proposed mechanism of nanoparticle formation for each technique was described from a physicochemical perspective. The effects of preparative variables on nanoparticle size and drug-entrapment efficiency were discussed.

Microparticulate delivery systems, potential drug/vaccine carriers for poorly bioavailable drugs and vaccines via mucosal (particularly oral) routes, were reviewed [947]. A variety of therapeutic moieties, including peptides and proteins, show enhanced oral uptake when entrapped within various types of microparticulate system constructs, and this

approach was used successfully for the oral, nasal, and rectal delivery of a variety of vaccines. As drug-delivery technology becomes more sophisticated and our understanding of the uptake and immunological mechanisms of mucosal sites becomes more defined, many further microparticulate constructs would emerge and demonstrate their potential.

The contribution of Francis Puisieux and his group to one of the greatest challenges in pharmaceutical science, namely, the development of an oral dosage form for insulin, was reviewed [948]. This review traced their work with liposomes, multiple emulsions, and nanoparticles as insulin vehicles for oral delivery.

Steroid receptors and immunophilin relationships in hormone-dependent cancers, use of long-circulation anti-steroid hormone and/or immunosuppressant carriers as a promising therapeutic approach, were reviewed [949]. General aspects of nanocapsules used in drug delivery systems were reviewed from both a physicochemical and a therapeutic point of view [950]. The preparation methods, ways to characterize this o/w system (size, surface, density, release, stability), and the influence of encapsulation within nanocapsules on the biological activity of numerous drugs were described. Among the indications for the therapeutic use nanocapsules, one can cite solubilization of poorly water-soluble drugs, protection of drugs from inactivation in the gastrointestinal tract, protection of mucosa from the toxicity of drugs, increased permeation of drugs through mucosal surfaces, and prolongation of the blood circulation of injected drugs.

The use of colloidal carriers made of hydrophilic polysaccharides (i.e. chitosan) arose as a promising alternative for improving the transport of such macromolecules across biological surfaces. The approaches aiming to associate macromolecules to chitosan in the form of colloidal structures were reviewed and the evidence of their efficacy in improving the transport of the associated molecule through mucosae and epithelia was analyzed [951]. Chitosan was shown to form colloidal particles and entrap macromolecules through a number of mechanisms, including ionic cross-linking, desolvation, or ionic complexation, though some of these systems were realized only in conjunction with DNA molecules. An alternative involving the chemical modification of chitosan was useful for the association of macromolecules to self-assemblies and vesicles. The *in vivo* efficacy of these chitosan-based colloidal carriers was reported for two different applications: while DNA-chitosan hybrid nanospheres were found to be acceptable transfection carriers, ionically cross-linked chitosan nanoparticles appeared to be efficient vehicles for the transport of peptides across the nasal mucosa.

The progress in the development of biodegradable nanoparticulate systems, including nanospheres, emulsions, and liposomes, was reviewed [952]. The major purpose of lymphatic targeting was to provide an effective anticancer chemotherapy to prevent the metastasis of tumor cells by accumulating the drug in the regional lymph node via subcutaneous administration. The objectives of lymph targeting involved the localization of diagnostic agents to the regional lymph node to visualize the lymphatic vessels before surgery, and the improvement of peroral bioavailability of macromolecular drugs, like polypeptides or proteins. The

*in vivo* study proved that polyisobutylcyanoacrylate nanocapsules showed enhanced accumulation of drug in the lymph node, compared with other carriers such as emulsions and liposomes.

Cyclosporin eyedrops allow local immunoregulation without systemic side effects and are an alternate to local steroids. Specific problems of product setup and clinical studies were reviewed [953]. The main problems in eyedrop preparation are sterility, pH, particles, and lipophilic properties. Numerous excipients were tested including oil solvents, alphacyclodextrin, collagen shields, liposomes, and polyester nanocapsules, but documentation on stability of the molecule was inadequate.

Acrylic nanoparticles for ocular drug delivery were developed [954]. The efficacy of ophthalmic drug delivery systems was governed by their ability to increase the ocular residence time. Several attempts were made to minimize the rapid and extensive precorneal loss of the administered drug. Besides the application of eyedrops with an enhanced viscosity, ocular inserts or soft contact lenses, and colloidal drug carriers, such as nanoparticles or nanocapsules as well as microspheres, were evaluated as ophthalmic delivery systems. In general, acrylic acid derivatives like polyalkyl cyanoacrylates and polyalkyl methacrylates were used for the preparation of drug carrier particles in the size range between 200 and 500 nm. That reviewed summarized the preparation methods of acrylic nanoparticles and their application in several *in vitro* and *in vivo* systems. The pharmacokinetic and pharmacodynamic effects after the application of drug-loaded nanoparticles to rabbit eyes were compared to conventional eyedrop preparations.

The nano/microparticles as drug delivery devices were reviewed [955]. The principal studies where peptide-loaded particles were administered by the oral route were reviewed [956]. The preparation methods and *in vitro* trials were presented and *in vivo* results were discussed with emphasis placed on the peptide blood levels reached or on the biological effects observed.

The advantages and disadvantages of the nanocapsules used in the drug delivery are as follows: There are many similarities between liposomes and nanoparticles. They are similar in size and thus are often used for similar purposes, and both have many advantages and disadvantages. Liposomes have the advantage of primarily consisting of lecithin and cholesterol, which are materials that occur naturally in the human body. Lecithin and cholesterol are also present in the body in large amounts and thus demand good bioacceptability. Nanoparticles or nanocapsules have the advantage of being more stable. Many types of drug targeting depend on good stability. A better penetration of the particles inside the body following administration, as well as longer shelf storage life, has several benefits of the good stability of nanoparticles. Artificial or natural polymers are the primary constituents of nanoparticles. Polymers are usually restricted by their bioacceptability. The bioacceptability is affected by the polymer and the supplementary components, as well as by particle size. A reduction in the particle size of the polymeric particles has many advantages: (1) Intravenous injection can be allowed if there is a decrease in the particle size. (2) Intramuscular and subcutaneous distribution require small particle size. (3) Irritant reactions at

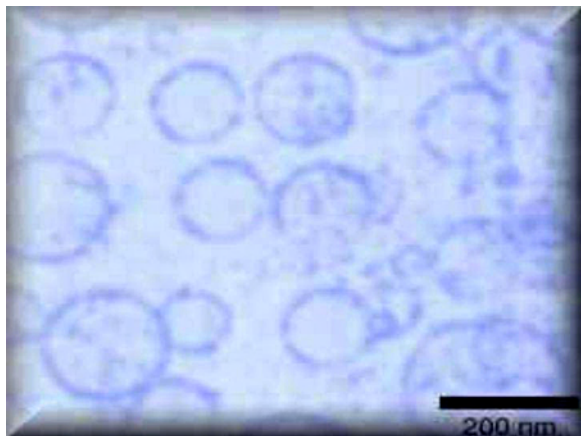


**Figure 26.** Water-soluble polyelectrolyte nanocapsules prepared by use of vesicular polymerisation, which undergo a reversible swelling process on changing pH and/or salt concentration, mimicking certain biological processes. After [1035], M. Sauer and W. Meier, *Chem. Commun.* 1, 55 (2001). © 2001, Royal Society of Chemistry.

the injection site are minimized by using small particle size. (4) Cancerogenic effects depend on particle size. Choosing the appropriate polymer, particle size, and method of production would depend on three major aspects: bioacceptability of the polymer, physicochemical properties of the drug, and the type of therapy the drug should have. Recent advances and many other studies on drug delivery and controlled release are found in the literature [957–1034]. Figure 26 shows water-soluble polyelectrolyte nanocapsules prepared by use of vesicular polymerization, which undergo a reversible swelling process on changing pH and/or salt concentration, mimicking certain biological processes [1035].

## 7. CONCLUDING REMARKS

A comprehensive review has been given of the advances in the area of nanocapsules. The outline of the theoretical background, including the energy levels, the quantum effects, the magic effects, the surfaces/interfaces, and the metastable phases in nanocapsules have been represented. The most applicable nanoencapsulation procedures, including physical, chemical, physicochemical, and mechanical techniques, have been introduced. The physical properties, including optical, electronic, magnetic, and dynamic properties, and the biomedical properties, including artificial cell and red blood cell substitutes, drug delivery, and controlled release, have been reviewed for nanocapsules.

Nanocapsules are the matter in intermediate states between bulk and atomic materials which offer a model system for investigation of the dimensionally confined systems in basic research areas. Nanocapsules have physical properties that differ distinctly from those of bulk materials. As a small limited system, three of the physical dimensions of nanocapsules could approach a length-scale characteristic of a physical phenomenon (with different phenomena being characterized by different length scales), and similarly in the time domain. The quantum size effects could contribute evidently to the properties, which originate mainly from the discreteness of the energy levels, and the breakdown of the

cyclic condition and the translation symmetry in the limited systems. The effects of the quantum interference, the magic number, the surfaces/interfaces, the core/shell structure, the metastable phases, etc. cannot be neglected in nanocapsules. Depending on the size, the shape, the core/shell structure, etc., the properties of nanocapsules could be very different individually, ranging from metals, insulators, and semiconductors, to optical absorption, magnetic hardening, etc.

Sufficiently small materials could aggregate sensitively to various shapes and nanostructures, which could change the properties of the materials. Spontaneous shape selection occurs in the mesoscopic systems, originating from the ability of finite systems to adjust their shape and structure in order to minimize the free energy of the systems. The small size is beautiful also due to the fact that mesoscopic systems could be designed and constructed artificially which would be so different with those formed naturally. It is clear that the properties of the nanocapsules depend sensitively on the procedures for sample preparation.

The different nanocapsules can be prepared by various methods with different mechanisms, which could control the size, the size distribution, the morphology, phases, and structure of the nanocapsules, the thickness of the shell, the size of the grains, etc. Some methods may be suitable for synthesis of only some typical nanocapsules. The most applicable nanoencapsulation procedures include: physical methods such as heat evaporation, arc discharge, laser/electron beam heating, sputtering, etc.; chemical methods such as chemical vapor deposition, solid-state reactions, sol-gel, precipitation, and hydrothermal, solvent, latex, oxidation, polymerization, processes etc.; physicochemical methods such as coacervation-phase separation, etc.; mechanical methods such as air suspension, pan coating, spray-drying and congealing, and multiorifice centrifugation.

Nanocapsules are designed to have a therapeutic action to release drugs in the right place or to have functionality to attack and reduce cancerous cells. Although many applications have not been investigated yet, current developments are becoming increasingly more useful in the field of medicine. Nanocapsules have been intensively studied not only because of the possibilities for controlled release, but also because of increased drug efficacy and reduced toxicity after parenteral administration. The nanocapsules have been formulated into a variety of useful dosage forms including oral liquid suspensions, lotions, creams, ointments, powders, capsules, tablets, and injections. Nanoencapsulation has been applied to solve problems in the development of pharmaceutical dosage forms as well as in cosmetics for several purposes including conversion of liquids to solids, separation of incompatible components in a dosage form, taste-masking, reduction of gastrointestinal irritation, protection of the core materials against atmospheric deterioration, enhancement of stability, and controlled release of active ingredients. Their pharmacological effect has been improved or their secondary effects reduced compared with free drugs after administration by oral, parenteral, or ocular routes. The nanocapsules have been found also to be suitable as biodegradable drug carriers for the administration and controlled release of drugs, like insulin, indomethacin, calcitonin, doxorubicine, gangliosides, oligonucleotides, etc.

Another major activity in the application of the nanocapsules has been focused on the topics of artificial cell and red blood cell substitutes. This is beneficial to the formulation of polymeric artificial nanocapsules, which can be made in a reproducible manner having a specific size and shape and in reasonable quantities. Artificial cells for pharmaceutical and therapeutic applications has been expanded up to the higher range of macrocapsules and down to the nanometer range of nanocapsules and even to the macromolecular range of cross-linked hemoglobin as blood substitutes. Artificial cells have been prepared by bioencapsulation in the laboratory for medical and biotechnological applications. The three generations of blood substitutes have been developed based on an original idea of a complete artificial red blood cell.

Basic research of the structure and properties of the nanocapsules and related issues (like nanotubes [1036–1046]) underlies future technologies, from nanoscale machines, nanotribological systems, cellular injections, and nanocatalysis, to miniaturization of electronic circuitry and novel information storage and retrieval systems. Furthermore, the nanoencapsulation process has been successfully applied to many industries as follows: as controlled-release systems of drugs and bioactive agents in pharmaceuticals; as creams, lotions, and fragrance in cosmetics; microgranules with protective colloids, fertilizers, insecticides, herbicides, microporous capsule walls for controlled release in agriculture; envelope manufacture using microencapsulated glues in adhesives; pigment presscakes, metal phosphate complex microcapsules, encapsulated aluminum flake pigments in pigments; encapsulation of heterogeneous catalysts, spherical alumina-containing particles, dual-walled hard microcapsules, hollow-ceramic-coated spheroid catalyst carriers in catalysts and catalyst carriers; photographic printing, light reflective dye-containing capsules for photographic film; food; paper; plastic; and others, such as microcapsulated liquid lubricants, chemiluminescent warning capsules, encapsulated thermonuclear fuel particles, encapsulated flame retardants, encapsulated liquid explosive compositions, and microcapsulated vulcanizing agents. Due to the length limit of this chapter, we could not have collected all the research work and applications in the fields above. Nevertheless, we are optimistic that nanocapsules as well as nanoencapsulations will be one of the most active fields in nanoscience and nanotechnology. Many novel nanocapsules will be synthesized by many novel procedures which will possess many novel properties that are helpful for a better understanding of the physical phenomena and natural rules in the mesosystems and are applicable in many novel fields and industries.

## GLOSSARY

**Coating** Process of forming the core/shell structures for nanocapsules, which may differ depending on different synthetic methods.

**Core/shell structures** Special structures of a nanocapsule, where the shell can be referred to as a membrane, a wall, a covering, or a coating, while the internal core can be defined as payload, core, encapsulant, fill, active ingredient, IP, or internal ingredient.

**Nanoencapsulations** Processes of encapsulating/coating nanoparticles to form nanocapsules.

**Nanocapsules** Capsules of nanometer size (i.e.,  $10^{-9}$  m), normally composed of a core and a shell that are made of different materials.

**Nanoparticles** Particles of nanometer size (i.e.,  $10^{-9}$  m), normally without a core/shell structure.

## ACKNOWLEDGMENTS

This work has been supported by the National Natural Science Foundation of China under grants 59725103 and 50171070 and the Science and Technology Commission of Shenyang.

## REFERENCES

1. P. Speiser, *Acta Pharm. Suec.* 13, 35 (1976).
2. J. Kreuter, *Pharm. Acta Helv.* 53, 33 (1978).
3. M. Arakawa and T. Kondo, *J. Pharm. Sci.* 70, 354 (1981).
4. H. J. Krause and P. Rohdewald, *Pharm. Res.* 5, 239 (1985).
5. C. Damge, M. Aprahamian, and G. Balboni, *Int. J. Pharm.* 36, 121 (1987).
6. P. Couvreur, P. Tulkens, M. Roland, A. Trouet, and P. Speiser, *FEBS Lett.* 84, 323 (1977).
7. P. Couvreur, B. Kante, M. Roland, P. Guiot, P. Bauduin, and P. Speiser, *J. Pharm. Pharmacol.* 31, 331 (1979).
8. N. A. Fallouh, L. Roblottreupel, and H. Fessi, *Int. J. Pharm.* 28, 125 (1986).
9. M. S. Elsamaligy, P. Rohdewald, and H. A. Mahmoud, *J. Pharm. Pharmacol.* 38, 216 (1986).
10. J. M. Rollot, P. Couvreur, L. Roblottreupel, and F. Puisieux, *J. Pharm. Sci.* 75, 361 (1986).
11. M. Aprahamian, C. Michel, W. Humbert, J. P. Devissaguet, and C. Damge, *Biol. Cell* 61, 69 (1987).
12. C. Damge, C. Michel, M. Aprahamian, and P. Couvreur, *Diabetes* 37, 246 (1988).
13. C. Damge, C. Michel, M. Aprahamian, and P. Couvreur, *Pharm. Weekblad.* 10, 53 (1988).
14. Y. Saito, T. Yoshikawa, M. Okuda, M. Ohkohchi, Y. Ando, A. Kasuya, and Y. Nishina, *Chem. Phys. Lett.* 209, 72 (1993).
15. T. Hihara, H. Onodera, K. Sumiyama, K. Suzuki, A. Kasuya, Y. Nishina, Y. Saito, T. Yoshikawa, and M. Okuda, *Jpn. J. Appl. Phys.* 2 33, L24 (1994).
16. Y. Saito, M. Okuda, T. Yoshikawa, S. Bandow, S. Yamamoto, K. Wakoh, K. Sumiyama, and K. Suzuki, *Jpn. J. Appl. Phys.* 2 33, L186 (1994).
17. Y. Saito, T. Yoshikawa, M. Okuda, N. Fujimoto, K. Sumiyama, K. Suzuki, A. Kasuya, and Y. Nishina, *J. Phys. Chem. Solids* 54, 1849 (1993).
18. Y. Saito, M. Okuda, T. Yoshikawa, A. Kasuya, and Y. Nishina, *J. Phys. Chem.* 98, 6696 (1994).
19. M. Kusunoki, Y. Ikuhara, and J. Kon, *Jpn. J. Appl. Phys.* 1 34, 1610 (1995).
20. N. S. Kopelev, V. Chechersky, A. Nath, Z. L. Wang, E. Kuzmann, and B. S. Zhang, *Chem. Mater.* 7, 1419 (1995).
21. Y. Saito, *Carbon* 33, 979 (1995).
22. Y. Saito and M. Masuda, *Jpn. J. Appl. Phys.* 1 34, 5594 (1995).
23. H. W. Kroto, J. R. Heath, S. C. O'Brien, R. F. Curl, and R. E. Smalley, *Nature* 318, 162 (1985).
24. W. Kräschmer, L. D. Lamb, K. Fostiropoulos, and D. R. Huffman, *Nature* 347, 354 (1990).
25. S. Iijima, *Nature* 354, 56 (1991).
26. S. Iijima and T. Ichihashi, *Nature* 363, 603 (1993).



27. D. S. Bethune, C. H. Kiang, M. S. de Vries, G. Gorman, R. Savoy, J. Vazquez, and R. Beyers, *Nature* 363, 605 (1993).
28. R. S. Ruoff, D. C. Lorents, B. Chan, R. Malhotra, and S. Subramoney, *Science* 259, 346 (1993).
29. R. Kubo, *J. Phys. Soc. Jpn.* 17, 975 (1962).
30. K. Kimoto, Y. Kamiya, M. Nonoyama, and R. Uyeda, *Jpn. J. Appl. Phys.* 2 702 (1963).
31. R. Uyeda, *J. Cryst. Growth* 24–25, 69 (1974).
32. R. Uyeda, *J. Cryst. Growth* 45, 485 (1978).
33. K. Kimoto, *J. Jpn. Assoc. Cryst. Growth* 6, 88 (1979).
34. R. Uyeda, *Progr. Mater. Sci.* 35, 1 (1991).
35. R. Uyeda, Crystallography of metal smoke particles, "Morphology of Crystals" (I. Sunagawa, Ed.), Ch. 6. p. 367. Terra Scientific, Tokyo, 1987.
36. K. Kimoto and I. Nishida, *Jpn. J. Appl. Phys.* 6, 1047 (1967).
37. K. Kimoto and I. Nishida, *J. Phys. Soc. Jpn.* 22, 744 (1967).
38. K. Kimoto and I. Nishida, *J. Phys. Soc. Jpn.* 22, 940 (1967).
39. N. Wada, *Jpn. J. Appl. Phys.* 6, 553 (1967).
40. N. Wada, *Jpn. J. Appl. Phys.* 7, 1287 (1968).
41. I. Nishida, *J. Phys. Soc. Jpn.* 26, 1225 (1969).
42. S. Yatsuya, S. Kasukabe, and R. Uyeda, *Jpn. J. Appl. Phys.* 12, 1675 (1973).
43. S. Kasukabe, S. Yatsuya, and R. Uyeda, *Jpn. J. Appl. Phys.* 13, 1714 (1974).
44. I. Nishida and K. Kimoto, *Thin Solid Films* 23, 179 (1974).
45. T. Ohno, S. Yatsuya, and R. Uyeda, *Jpn. J. Appl. Phys.* 15, 1213 (1976).
46. T. Hayashi, T. Ohno, S. Yatsuya, and R. Uyeda, *Jpn. J. Appl. Phys.* 16, 705 (1977).
47. K. Kimoto and I. Nishida, *Jpn. J. Appl. Phys.* 16, 941 (1977).
48. Y. Saito, S. Yatsuya, K. Mihama, and R. Uyeda, *Jpn. J. Appl. Phys.* 17, 291 (1978).
49. Y. Saito, K. Mihama, and R. Uyeda, *Jpn. J. Appl. Phys.* 19, 1603 (1980).
50. M. Kobeyashi, S. Yatsuya, and K. Mihama, *Jpn. J. Appl. Phys.* 20, 805 (1981).
51. Y. Fukano and K. Nakao, *Jpn. J. Appl. Phys.* 20, 477 (1981).
52. T. Ohno and K. Yamauchi, *Jpn. J. Appl. Phys.* 20, 1385 (1981).
53. Y. Ando, *J. Jpn. Assoc. Cryst. Growth* 8, 19 (1981).
54. H. Gleiter, *Progr. Mater. Sci.* 33, 223 (1989).
55. A. Kawabata and R. Kubo, *J. Phys. Soc. Jpn.* 21, 1765 (1966).
56. A. Kawabata, *J. Phys. (Paris) Colloq.* 38, 2 (1977).
57. R. Kubo, A. Kawabata, and S. Kobayashi, *Annu. Rev. Mater. Sci.* 14, 49 (1984).
58. L. P. Gor'kov and G. M. Eliashberg, *Zh. Eksp. Teor.* 48, 1407 (1965) [*Sov. Phys. JETP* 21, 940 (1965)].
59. R. Denton, B. Mühlischlegel, and D. J. Scalapino, *Phys. Rev. Lett.* 26, 707 (1971).
60. R. Denton, B. Mühlischlegel, and D. J. Scalapino, *Phys. Rev. B* 7, 3589 (1973).
61. J. Buttet, R. Car, and C. W. Myles, *Phys. Rev. B* 26, 2414 (1982).
62. R. E. Cavicchi and R. H. Silsbee, *Phys. Rev. Lett.* 52, 1453 (1984).
63. W. P. Halperin, *Rev. Mod. Phys.* 58, 532 (1986).
64. Z.-D. Zhang, in "Handbook of Thin Films Materials" (H. S. Nalwa, Ed.), Vol. 5, Ch. 4. Academic Press, San Diego, 2000.
65. D. Bohm, "Quantum Mechanics." Prentice-Hall, Englewood Cliffs, NJ, 1951. E. Merzbacher, "Quantum Mechanics." Wiley, New York, 1961.
66. C. Weisbuch and B. Vinter, "Quantum Semiconductor Structures, Fundamentals and Applications." Academic Press, San Diego, 1991.
67. L. D. Landau and E. M. Lifshitz, "Quantum Mechanics." Pergamon Press, Oxford, 1958. I. I. Goldman and V. D. Krivchenkov, "Problems in Quantum Mechanics." Pergamon Press, Oxford, 1961.
68. Z.-D. Zhang, in "Handbook of Thin Films Materials" (H. S. Nalwa, Ed.), Vol. 5, Ch. 5. Academic Press, San Diego, 2002.
69. D. L. Feldheim and C. D. Keating, *Chem. Soc. Rev.* 27, 1 (1998).
70. R. Kanungo, I. Tanihata, and A. Ozawa, *Phys. Lett.* 528, 58 (2002).
71. H. Haberland, "Clusters of Atoms and Molecules," Vols. 1 and 2, in Springer Series in Chemical Physics. Springer-Verlag, Berlin, 1994.
72. U. Kreibitz and M. Vollmer, "Optical Properties of Metal Clusters," in Springer Series in Materials Science. Springer-Verlag, Berlin, 1995.
73. O. Echt, K. Sattler, and E. Recknagel, *Phys. Rev. Lett.* 47, 1121 (1981).
74. *New Sci.* 92, 598 (1981).
75. W. D. Knight, K. Clemenger, W. A. de Heer, W. A. Saunders, M. Y. Chou, and M. L. Cohen, *Phys. Rev. Lett.* 52, 2141 (1984).
76. T. P. Martin, "Elemental and Molecular Clusters." Springer-Verlag, Berlin, 1988.
77. M. Y. Lai and Y. L. Wang, *Phys. Rev. B* 64, R241404 (2001).
78. J.-L. Li, J.-F. Jia, X.-J. Liang, X. Liu, J.-Z. Wang, Q.-K. Xue, Z.-Q. Li, J. S. Tse, Z. Zhang, and S. B. Zhang, *Phys. Rev. Lett.* 88, 066101 (2002).
79. P. C. Hiemenz, "Principles of Colloid and Surface Chemistry." Dekker, New York, 1977.
80. R. K. Kawakami, E. J. Escorcía-Aparicio, and Z. Q. Qiu, *Phys. Rev. Lett.* 77, 2570 (1996).
81. H. J. Choi, Z. Q. Qiu, J. Pearson, S. J. Jiang, D. Li, and S. D. Bader, *Phys. Rev. B* 57, R12713 (1998).
82. R. K. Kawakami, M. O. Bowen, H. J. Choi, E. J. Escorcía-Aparicio, and Z. Q. Qiu, *Phys. Rev. B* 58, R5924 (1998).
83. E. J. Escorcía-Aparicio, H. J. Choi, W. L. Ling, R. K. Kawakami, and Z. Q. Qiu, *Phys. Rev. Lett.* 81, 2144 (1998).
84. Z. D. Zhang, W. Liu, J. P. Liu, and D. J. Sellmyer, *J. Phys. D* 33, R217 (2000).
85. B. A. Korgel and D. Fitzmaurice, *Phys. Rev. B* 59, 14191 (1999).
86. P. N. Pusey, W. van Meegen, P. Bartlett, B. J. Ackerson, J. G. Rarity, and S. M. Underwood, *Phys. Rev. Lett.* 63, 2753 (1989).
87. M. S. Cohen, *J. Appl. Phys.* 36, 1602 (1965).
88. T. Aarii, S. Yatsuya, N. Wada, and K. Mihama, *Jpn. J. Appl. Phys.* 17, 259 (1978).
89. T. Aarii, K. Mihama, T. Matsuda, and A. Tonomura, *J. Electron Microsc.* 30, 121 (1981).
90. A. Tonomura, T. Matsuda, J. Endo, T. Aarii, and K. Mihama, *Phys. Rev. Lett.* 44, 1430 (1980).
91. K. Kimoto, Y. Kamiya, M. Nonoyama, and R. Uyeda, *Jpn. J. Appl. Phys.* 2 1047 (1963).
92. U. Fukano and K. Kimoto, *J. Phys. Soc. Jpn.* 23, 668 (1967).
93. T. Tanaka and N. Tamagawa, *Jpn. J. Appl. Phys.* 6, 1096 (1967).
94. A. Tasaki, S. Tomiyama, and S. Iida, *Jpn. J. Appl. Phys.* 4, 707 (1966).
95. C. G. Granqvist and R. A. Buhrman, *J. Appl. Phys.* 47, 2200 (1976).
96. N. Wada and M. Ichikawa, *Jpn. J. Appl. Phys.* 15, 775 (1976).
97. Y. Fukano, *Jpn. J. Appl. Phys.* 13, 1001 (1974).
98. I. Nishida and K. Kimoto, *Jpn. J. Appl. Phys.* 14, 1425 (1975).
99. Y. Saito, S. Yatsuya, K. Mihama, and R. Uyeda, *Jpn. J. Appl. Phys.* 17, 1149 (1978).
100. T. Okazaki, *J. Jpn. Assoc. Cryst. Growth* 9, 175 (1982).
101. T. Okazaki and R. Uyeda, *J. Jpn. Assoc. Cryst. Growth* 10, 157 (1983).
102. Y. Saito, *Surf. Rev. Lett.* 3, 819 (1996).
103. Y. Saito, T. Yoshikawa, M. Okuda, M. Ohkohchi, Y. Ando, A. Kasuya, and Y. Nishina, *Chem. Phys. Lett.* 209, 72 (1993).
104. Y. Saito, M. Okuda, T. Yoshikawa, A. Kasuya, and Y. Nishina, *J. Phys. Chem.* 98, 6696 (1994).
105. Y. Saito, M. Okuda, T. Yoshikawa, S. Bandow, S. Yamamuro, K. Wakoh, K. Sumiyama, and K. Suzuki, *Jpn. J. Appl. Phys.* 2 33, L186 (1994).

106. Y. Saito, T. Yoshikawa, M. Okuda, N. Fujimoto, K. Sumiyama, K. Suzuki, A. Kasuya, and Y. Nishina, *J. Phys. Chem. Solids* 54, 1849 (1993).
107. Y. Saito, *Carbon* 33, 979 (1995).
108. J. J. Host, M. H. Teng, B. R. Elliott, J. H. Hwang, T. O. Mason, D. L. Johnson, and V. P. Dravid, *J. Mater. Res.* 12, 1268 (1997).
109. V. P. Dravid, J. J. Host, M. H. Teng, B. Elliot, J. H. Hwang, D. L. Johnson, T. O. Mason, and J. R. Weertman, *Nature* 374, 602 (1995).
110. Y. Saito and M. Masuda, *Jpn. J. Appl. Phys.* 1 34, 5594 (1995).
111. S. C. Tsang, J. S. Qiu, P. J. F. Harris, Q. J. Fu, and N. Zhang, *Chem. Phys. Lett.* 322, 553 (2000).
112. P. E. Nolan, D. C. Lynch, and A. H. Cutler, *Carbon* 34, 817 (1996).
113. X. L. Dong, Z. D. Zhang, Q. F. Xiao, X. G. Zhao, Y. C. Chuang, S. R. Jin, W. M. Sun, Z. J. Li, Z. X. Zheng, and H. Yang, *J. Mater. Sci.* 33, 1915 (1998).
114. A. A. Setlur, J. Y. Dai, J. M. Lauerhaas, P. L. Washington, and R. P. H. Chang, *J. Mater. Res.* 13, 2139 (1998).
115. V. V. Kovalevski and A. N. Safronov, *Carbon* 36, 963 (1998).
116. X. L. Dong, Z. D. Zhang, X. G. Zhao, Y. C. Chao, S. R. Jin, and W. M. Sun, *J. Mater. Sci. Tech.* 14, 441 (1998).
117. X. L. Dong, Z. D. Zhang, X. G. Zhao, Y. C. Chuang, S. R. Jin, and W. M. Sun, *J. Mater. Res.* 14, 1782 (1999).
118. Z. J. Li, G. H. Wen, F. W. Wang, J. L. Yu, X. L. Dong, X. X. Zhang, and Z. D. Zhang, *J. Mater. Sci. Tech.* 18, 99 (2002).
119. X. L. Dong, Z. D. Zhang, Y. C. Chuang, and S. R. Jin, *Phys. Rev. B* 60, 3017 (1999).
120. X. L. Dong, Z. D. Zhang, S. R. Jin, and B. K. Kim, *J. Appl. Phys.* 86, 6701 (1999).
121. Z. D. Zhang, J. G. Zheng, I. Škorvánek, G. H. Wen, J. Kováč, F. W. Wang, J. L. Yu, Z. J. Li, X. L. Dong, S. R. Jin, W. Liu, and X. X. Zhang, *J. Phys. Cond. Matter* 13, 1921 (2001).
122. Z. D. Zhang, J. L. Yu, J. G. Zheng, I. Škorvánek, J. Kováč, X. L. Dong, Z. J. Li, S. R. Jin, H. C. Yang, Z. J. Guo, W. Liu, and X. G. Zhao, *Phys. Rev. B* 64, 024404 (2001).
123. Z. D. Zhang, J. G. Zheng, I. Škorvánek, J. Kováč, J. L. Yu, X. L. Dong, Z. J. Li, S. R. Jin, X. G. Zhao, and W. Liu, *J. Nanosci. Nanotech.* 1, 153 (2001).
124. I. Škorvánek, Z. D. Zhang, J. G. Zheng, J. Kováč, J. L. Yu, X. L. Dong, Z. J. Li, S. R. Jin, and X. G. Zhao, submitted for publication.
125. P. Z. Si, M. Zhang, C. Y. You, D. Y. Geng, J. H. Du, X. G. Zhao, X. L. Ma, and Z. D. Zhang, *J. Mater. Sci.* 38, 689 (2003).
126. S. Seraphin, D. Zhou, and J. Jiao, *J. Appl. Phys.* 80, 2097 (1996).
127. Y. Saito, K. Nishikubo, K. Kawabata, and T. Matsumoto, *J. Appl. Phys.* 80, 3062 (1996).
128. Y. Saito, T. Masumoto, and K. Nishikubo, *Carbon* 35, 1757 (1997).
129. Y. Saito, T. Matsumoto, and K. Nishikubo, *J. Crystal Growth* 172, 163 (1997).
130. H. Takikawa, O. Kusano, and T. Sakakibara, *J. Phys. D* 32, 2433 (1999).
131. Y. Saito and T. Matsumoto, *J. Crystal Growth* 187, 402 (1998).
132. J. Jiao and S. Seraphin, *J. Appl. Phys.* 83, 2442 (1998).
133. M. Masuda, K. Maeda, T. Kobayashi, S. Shiomi, Y. Fujiwara, and Y. Saito, *Jpn. J. Appl. Phys.* 39, L733 (2000).
134. J. J. Host, V. P. Dravid, and M. H. Teng, *J. Mater. Res.* 13, 2547 (1998).
135. T. Hirano, T. Oku, and K. Suganuma, *J. Mater. Chem.* 9, 855 (1999).
136. T. Hirano, T. Oku, M. Kawaguchi, and K. Suganuma, *Mol. Crystals Liq. Crystals* 340, 787 (2000).
137. Y. Saito, M. Maida, and T. Matsumoto, *Jpn. J. Appl. Phys.* 1 38, 159 (1999).
138. K. Suenaga, F. Willaime, A. Loiseau, and C. Colliex, *Appl. Phys. A* 68, 301 (1999).
139. T. Oku, M. Kuno, H. Kitahara, and I. Narita, *Inter. J. Inorganic Mater.* 3, 597 (2001).
140. Y. Moriyoshi, Y. Shimizu, and T. Watanabe, *Thin Solid Films* 390, 26 (2001).
141. M. Kuno, T. Oku, and K. Suganuma, *Diamond Related Mater.* 10, 1231 (2001).
142. T. Oku, T. Kusunose, T. Hirata, R. Hatakeyama, N. Sato, K. Niihara, and K. Suganuma, *Diamond Related Mater.* 9, 911 (2000).
143. T. Oku, T. Hirata, N. Motegi, R. Hatakeyama, N. Sato, T. Mieno, N. Y. Sato, H. Mase, M. Niwano, and N. Miyamoto, *J. Mater. Res.* 15, 2182 (2000).
144. T. Hirata, N. Motegi, R. Hatakeyama, T. Oku, T. Mieno, N. Sato, H. Mase, M. Niwano, N. Miyamoto, and N. Sato, *Jpn. J. Appl. Phys.* 2 39, L1130 (2000).
145. T. Oku and M. Kawaguchi, *Diamond Related Mater.* 9, 906 (2000).
146. A. Yasuda, N. Kawase, F. Banhart, W. Mizutani, T. Shimizu, and H. Tokumoto, *J. Phys. Chem. B* 106, 1247 (2002).
147. T. Oku, G. Schmid, and K. Suganuma, *J. Mater. Chem.* 8, 2113 (1998).
148. F. Banhart, P. Redlich, and P. M. Ajayan, *Chem. Phys. Lett.* 292, 554 (1998).
149. H. Abe, S. Yamamoto, A. Miyashita, and K. E. Sickafus, *J. Appl. Phys.* 90, 3353 (2001).
150. S. Komatsu, Y. Shimizu, Y. Moriyoshi, K. Okada, and M. Mitomo, *J. Appl. Phys.* 91, 6181 (2002).
151. X. Q. Zhao, Y. Liang, Z. Q. Hu, and B. X. Liu, *J. Appl. Phys.* 80, 5857 (1996).
152. X. Q. Zhao, Y. Liang, Z. Q. Hu, and B. X. Liu, *J. Appl. Phys.* 79, 7911 (1996).
153. X. Q. Zhao, Y. Liang, and Z. Q. Hu, *Acta Metal. Sinica* 37, 633 (2001).
154. X. Q. Zhao, Y. S. Li, Y. Liang, and Z. Q. Hu, *Acta Metal. Sinica* 38, 11 (2002).
155. O. Mamezaki, H. Adachi, S. Tomita, M. Fujii, and S. Hayashi, *Jpn. J. Appl. Phys.* 1 39, 6680 (2000).
156. D. Babonneau, T. Cabioc'h, A. Naudon, J. C. Girard, and M. F. Denant, *Surf. Sci.* 409, 358 (1998).
157. H. Wang, S. P. Wong, W. F. Lau, X. Yan, X. Lu, W. Y. Cheung, and N. Ke, *Thin Solid Films* 382, 133 (2001).
158. J. S. Haggerty and W. R. Cannon, in "Laser-Induced Chemical Process" (J. I. Steinfeld, Ed.), Ch. 3. Plenum Press, New York, 1981.
159. B. Lee, *Laser Appl.* 4, 28 (1983).
160. Y. Kizaki, T. Kandori, and Y. Fujitani, *Jpn. J. Appl. Phys.* 24, 800 (1985).
161. R. A. Andrievski, *J. Mater. Sci.* 29, 614 (1994).
162. E. Pasqualini, P. Adelfang, and M. N. Regueiro, *J. Nuclear Mater.* 231, 173 (1996).
163. T. E. Muller, D. G. Reid, W. K. Hsu, J. P. Hare, H. W. Kroto, and D. R. M. Walton, *Carbon* 35, 951 (1997).
164. T. Oku, T. Hirano, K. Suganuma, and S. Nakajima, *J. Mater. Res.* 14, 4266 (1999).
165. T. Oku, T. Kusunose, K. Niihara, and K. Suganuma, *J. Mater. Chem.* 10, 255 (2000).
166. D. I. Gittins and F. Caruso, *Adv. Mater.* 12, 1947 (2000).
167. T. Cassagneau and J. H. Fendler, *J. Phys. Chem. B* 103, 1789 (1999).
168. B. G. Ershov, *Russian Chem. Bull.* 50, 626 (2001).
169. S. H. Tsai, C. L. Lee, C. W. Chao, and H. C. Shih, *Carbon* 38, 781 (2000).
170. W. Teunissen, F. M. F. de Groot, J. Geus, O. Stephan, M. Tence, and C. Colliex, *J. Catal.* 204, 169 (2001).
171. Z. J. Liu, Z. Y. Yuan, W. Z. Zhou, Z. D. Xu, and L. M. Peng, *Chem. Vapor Deposition* 7, 248 (2001).
172. Z. H. Wang, C. J. Choi, B. K. Kim, M. S. Hur, and Z. D. Zhang, *Carbon*, in press.

173. H. Keune, W. Lacom, F. Rossi, E. Stoffels, W. W. Stoffels, and G. Wahl, *J. Phys. IV* 10, 19 (2000).
174. D. N. McIlroy, D. Zhang, M. G. Norton, W. L. O'Brien, M. M. Schwickert, and G. R. Harp, *J. Appl. Phys.* 87, 7213 (2000).
175. Y. J. Sun, A. Z. Li, M. Qi, L. Y. Zhang, and X. Yao, *J. Mater. Sci.* 37, 1343 (2002).
176. E. Flahaut, F. Agnoli, J. Sloan, C. O'Connor, and M. L. H. Green, *Chem. Mater.* 14, 2553 (2002).
177. W. Chang, G. Skandan, S. C. Danforth, M. Rose, A. G. Balogh, H. Hahn, and B. Kear, *Nanostructured Mater.* 6, 321 (1995).
178. Y. Chen, N. Glumac, B. H. Kear, and G. Skandan, *Nanostructured Mater.* 9, 101 (1997).
179. Y. J. Chen, N. G. Glumac, G. Skandan, and B. H. Kear, *Synthesis Charact. Adv. Mater.* 681, 158 (1998).
180. N. G. Glumac, G. Skandan, Y. J. Chen, and B. H. Kear, *Nanostructured Mater.* 12, 253 (1999).
181. U. Betz and H. Hahn, *Nanostructured Mater. B* 12, 911 (1999).
182. S. Y. Kim, J. H. Yu, and J. S. Lee, *Nanostructured Mater.* 12, 471 (1999).
183. A. Singhal and G. Skandon, *Int. J. Powder Metall.* 35, 45 (1999).
184. A. Singhal, G. Skandan, N. Glumac, and B. H. Kear, *Scripta Mater.* 44, 2203 (2001).
185. C. J. Choi, X. L. Dong, and B. K. Kim, *Scripta Mater.* 44, 2225 (2001).
186. C. J. Choi, X. L. Dong, and B. K. Kim, *Mater. Trans.* 42, 2046 (2001).
187. C. J. Choi, X. L. Dong, B. K. Kim, and J. H. Ahn, *Mater. Sci. Forum* 386, 485 (2002).
188. Z. H. Wang, M. S. Hur, C. J. Choi, B. K. Kim, O. V. Tolochko, and Z. D. Zhang, *Mater. Lett.* (2003).
189. Z. H. Wang, M. S. Hur, C. J. Choi, B. K. Kim, O. V. Tolochko, and Z. D. Zhang, in press.
190. I. Uvarova, *J. Mater. Proc. Manufact. Sci.* 6, 251 (1998).
191. J. Sloan, J. Cook, M. L. H. Green, J. L. Hutchison, and R. Tenne, *J. Mater. Chem.* 7, 1089 (1997).
192. F. Mizukami, *Porous Mater. Environ. Friendly Processes Stud. Surf. Sci. Catal.* 125, 1 (1999).
193. Y. Jiang, S. Decker, C. Mohs, and K. J. Klabunde, *J. Catal.* 180, 24 (1998).
194. X. R. Ye, D. Z. Jia, J. Q. Yu, X. Q. Xin, and Z. L. Xue, *Adv. Mater.* 11, 941 (1999).
195. M. Inagaki, Y. Okada, H. Miura, and H. Konno, *Carbon* 37, 329 (1999).
196. F. Li, X. H. Yu, H. J. Pan, M. L. Wang, and X. Q. Xin, *Solid State Sci.* 2, 767 (2000).
197. F. Li, H. G. Zheng, D. Z. Jia, X. Q. Xin, and Z. L. Xue, *Mater. Lett.* 53, 283 (2002).
198. F. Li, L. Y. Chen, Z. Q. Chen, J. Q. Xu, J. M. Zhu, and X. Q. Xin, *Mater. Chem. Phys.* 73, 335 (2002).
199. F. Li, Z. Hu, S. Jing, H. G. Zheng, and X. Q. Xin, *Chin. J. Inorganic Chem.* 17, 315 (2001).
200. W. Z. Wang, Y. K. Liu, Y. J. Zhan, C. L. Zheng, and G. H. Wang, *Mater. Res. Bull.* 36, 1977 (2001).
201. G. Benito, M. P. Morales, J. Requena, V. Raposo, M. Vazquez, and J. S. Moya, *J. Magn. Magn. Mater.* 234, 65 (2001).
202. S. W. Liu, S. Boeshore, A. Fernandez, M. J. Sayagues, J. E. Fischer, and A. Gedanken, *J. Phys. Chem. B* 105, 7606 (2001).
203. T. Oku and K. Suganuma, *Microelectron. Eng.* 51, 51 (2000).
204. G. B. Sukhorukov, E. Donath, S. Moya, A. S. Susha, A. Voigt, J. Hartmann, and H. Mohwald, *J. Microencapsulation* 17, 177 (2000).
205. S. Tomita, M. Hikita, M. Fujii, S. Hayashi, K. Akamatsu, S. Deki, and H. Yasuda, *J. Appl. Phys.* 88, 5452 (2000).
206. D. I. Gittins and F. Caruso, *J. Phys. Chem. B* 105, 6846 (2001).
207. T. Oku, T. Hirano, S. Nakajima, K. Suganuma, E. Aoyagi, and K. Hiraga, *Mol. Crystals Liq. Crystals* 340, 799 (2000).
208. L. Sun, R. M. Crooks, and V. Chechik, *Chem. Commun.* 4, 359 (2001).
209. Y. H. Gao, Y. Bando, K. Kurashima, and T. Sato, *J. Electron Microsc.* 49, 641 (2000).
210. P. Mohanty and S. Ram, *J. Euro. Ceramic Soc.* 22, 933 (2002).
211. C. J. Brinker, D. E. Clark, and D. R. Ulrich, "Better Ceramics through Chemistry." Elsevier Science, Amsterdam, 1994.
212. L. L. Hench and J. K. West, *Chem. Rev.* 90, 33 (1990).
213. T. Oku and K. Suganuma, *Chem. Commun.* 23, 2355 (1999).
214. A. Mrzel, A. Mertelj, A. Omerzu, M. Copic, and D. Mihailovic, *J. Phys. Chem. B* 103, 11256 (1999).
215. M. Sauer and W. Meier, *Chem. Commun.* 1, 55 (2001).
216. A. Vishnyakov and A. V. Neimark, *J. Phys. Chem. B* 105, 7830 (2001).
217. X. Mo, C. Y. Wang, L. Y. Hao, M. You, Y. R. Zhu, Z. Y. Chen, and Y. Hu, *Mater. Res. Bull.* 36, 1925 (2001).
218. A. Muller, S. K. Das, P. Kogerler, H. Bogge, M. Schmidtman, A. X. Trautwein, V. Schunemann, E. Krickemeyer, and W. Preetz, *Angew. Chem. Int. Ed.* 39, 3414 (2000).
219. M. Mennig, M. Schmitt, and H. Schmidt, *J. Sol-Gel Sci. Tech.* 8, 1035 (1997).
220. G. W. Meng, L. D. Zhang, C. M. Mo, S. Y. Zhang, Y. Qin, S. P. Feng, and H. J. Li, *Solid State Commun.* 106, 215 (1998).
221. G. W. Meng, L. D. Zhang, C. M. Mo, S. Y. Zhang, Y. Qin, S. P. Feng, and H. J. Li, *J. Mater. Res.* 13, 2533 (1998).
222. S. Shibata, K. Aoki, T. Yano, and M. Yamane, *J. Sol-Gel Sci. Tech.* 11, 279 (1998).
223. S. T. Selvan, Y. Ono, and M. Nogami, *Mater. Lett.* 37, 156 (1998).
224. A. J. Ruys and Y. W. Mai, *Mater. Sci. Eng. A* 265, 202 (1999).
225. T. K. Jain, I. Roy, T. K. De, and A. Maitra, *J. Amer. Chem. Soc.* 120, 11092 (1998).
226. K. Schrijnemakers, N. R. E. N. Impens, and E. F. Vansant, *Langmuir* 15, 5807 (1999).
227. W. P. Cai, Y. Zhang, and L. D. Zhang, *J. Mater. Res.* 14, 1922 (1999).
228. Y. Lu, Y. D. Yin, and Y. N. Xia, *Adv. Mater.* 13, 2771 (2001).
229. Z. H. Zhou, J. Wang, J. M. Xue, and H. S. O. Chan, *J. Mater. Chem.* 11, 3110 (2001).
230. E. R. Leite, N. L. V. Carreno, E. Longo, A. Valentini, and L. F. D. Probst, *J. Nanosci. Nanotech.* 2, 89 (2002).
231. L. I. Casas, A. Roig, E. Molins, J. M. Greneche, J. Asenjo, and J. Tejada, *Appl. Phys. A* 74, 591 (2002).
232. Y. H. Zhang, A. Weidenkaff, and A. Reller, *Mater. Lett.* 54, 375 (2002).
233. E. M. Moreno, M. Zayat, M. P. Morales, C. J. Serna, A. Roig, and D. Levy, *Langmuir* 18, 4972 (2002).
234. S. Ponce-Castaneda, J. R. Martinez, S. A. P. Sanchez, F. Ruiz, and J. A. Matutes-Aquino, *J. Sol-Gel Sci. Tech.* 25, 37 (2002).
235. S. Ponce-Castaneda, J. R. Martinez, F. Ruiz, S. Palomares-Sanchez, and O. Dominguez, *J. Sol-Gel Sci. Tech.* 25, 29 (2002).
236. R. A. Caruso and M. Antonietti, *Chem. Mater.* 13, 3272 (2001).
237. E. A. Meulenkamp, *J. Phys. Chem. B* 102, 5566 (1998).
238. B. Sjostrom and B. Bergenstahl, *Int. J. Pharm.* 84, 107 (1992).
239. Y. R. Arshad, *Colloid Polym. Sci.* 270, 717 (1992).
240. V. Pillai, P. Kumar, M. S. Multani, and D. O. Shah, *Colloids Surf. A* 80, 69 (1993).
241. R. J. Bandaranayake, G. W. Wen, J. Y. Lin, H. X. Jiang, and C. M. Sorensen, *Appl. Phys. Lett.* 67, 831 (1995).
242. J. K. Vassiliou, V. Mehrotra, J. W. Otto, and N. R. Dollahon, *Mater. Sci. Forum* 225, 725 (1996).
243. M. Mitomo, C. M. Wang, and H. Emoto, *J. Mater. Res.* 13, 2039 (1998).
244. Y. J. Zhu, Y. T. Qian, X. J. Li, and M. W. Zhang, *Nanostr. Mater.* 10, 673 (1998).
245. Y. E. Shapiro and E. G. Pykhteeva, *Appl. Biochem. Biotech.* 74, 67 (1998).

246. H. Pattyn, J. Verheyden, W. Deweerdt, G. E. J. Koops, G. L. Zhang, M. El Azzou, and M. Hou, *Hyperfine Inter.* 121, 291 (1999).
247. D. Szabo, I. Czako-Nagy, M. Zrinyi, and A. Vertes, *J. Colloid Interface Sci.* 221, 166 (2000).
248. M. Hou, M. El Azzou, H. Pattyn, J. Verheyden, G. Koops, and G. L. Zhang, *Phys. Rev. B* 62, 5117 (2000).
249. F. Debuigne, L. Jeuniau, M. Wiame, and J. B. Nagy, *Langmuir* 16, 7605 (2000).
250. X. P. Qiu and F. Winnik, *Chin. J. Poly. Sci.* 18, 535 (2000).
251. H. K. Schmidt, *Mol. Crystals Liq. Crystals* 353, 165 (2000).
252. H. Mohwald, *Colloid Surfaces A* 171, 25 (2000).
253. J. H. He and E. J. Lavernia, *Mater. Sci. Eng. A* 301, 69 (2001).
254. M. T. Wang and L. D. Zhang, *J. Mater. Res.* 16, 765 (2001).
255. F. C. M. Woudenberg, W. F. C. Sager, N. G. M. Sibelt, and H. Verweij, *Adv. Mater.* 13, 514 (2001).
256. L. Han, M. M. Maye, F. L. Leibowitz, N. K. Ly, and C. J. Zhong, *J. Mater. Chem.* 11, 1258 (2001).
257. D. K. Kim, Y. Zhang, W. Voit, K. V. Rao, and M. Muhammed, *J. Magn. Magn. Mater.* 225, 30 (2001).
258. P. Yang, M. Lu, D. Xu, D. Yuan, and G. Zhou, *Appl. Phys. A* 73, 455 (2001).
259. Z. T. Zhang, S. Dai, X. D. Fan, D. A. Blom, S. J. Pennycook, and Y. Wei, *J. Phys. Chem. B* 105, 6755 (2001).
260. X. X. Zhang, G. Gu, H. J. Huang, S. H. Yang, and Y. W. Du, *J. Phys. Cond. Matter* 13, 3913 (2001).
261. D. J. Gan and L. A. Lyon, *J. Amer. Chem. Soc.* 123, 7511 (2001).
262. R. Ma, Y. Bando, T. Sato, and L. Bourgeois, *Diamond Related Mater.* 11, 1397 (2002).
263. I. L. Radtchenko, G. B. Sukhorukov, and H. Mohwald, *Colloid Surfaces A* 202, 127 (2002).
264. H. L. Xia and F. Q. Tang, *Chin. J. Inorg. Chem.* 18, 769 (2002).
265. G. Y. Wang, H. L. Lian, W. X. Zhang, D. Z. Jiang, and T. H. Wu, *Kinetics Catalysis* 43, 433 (2002).
266. H. C. Schwarzer and W. Peukert, *Chem. Eng. Tech.* 25, 657 (2002).
267. D. H. Chen and Y. Y. Chen, *Mater. Res. Bull.* 37, 801 (2002).
268. S. Berchmans, P. J. Thomas, and C. N. R. Rao, *J. Phys. Chem. B* 106, 4647 (2002).
269. X. Chen, Z. X. Deng, Y. P. Li, and Y. D. Li, *Chin. J. Inorg. Chem.* 18, 460 (2002).
270. P. G. McCormick and T. Tsuzuki, *Mater. Sci. Forum* 386, 377 (2002).
271. G. J. Li, X. X. Huang, M. L. Ruan, and J. K. Guo, *Ceramics Int.* 28, 165 (2002).
272. P. Jeevanandam, Y. Kolytyn, and A. Gedanken, *Mater. Sci. Eng. A* 90, 125 (2002).
273. J. Texter, *J. Dispersion Sci. Tech.* 22, 499 (2001).
274. S. H. Yu, *J. Ceram. Soc. Jpn.* 109, S65 (2001).
275. S. L. Burkett, A. Press, and S. Mann, *Chem. Mater.* 9, 1071 (1997).
276. Y. X. Li, Z. Liu, C. R. Wu, and G. Li, *Ferroelectrics* 196, 377 (1997).
277. S. D. Burnside, V. Shklover, C. Barbe, P. Comte, F. Arendse, K. Brooks, and M. Gratzel, *Chem. Mater.* 10, 2419 (1998).
278. K. Riwozki and M. Haase, *J. Phys. Chem. B* 102, 10129 (1998).
279. L. Shu, S. H. Yu, and Y. T. Qian, *Chin. J. Inorg. Chem.* 15, 1 (1999).
280. C. Wang, X. M. Zhang, X. F. Qian, Y. Xie, and Y. T. Qian, *J. Phys. Chem. Solids* 60, 2005 (1999).
281. Z. H. Wu, L. Guo, H. J. Li, Q. L. Yang, Q. S. Li, and H. S. Zhu, *Mater. Sci. Eng. A* 286, 179 (2000).
282. M. Hirano, M. Imai, and M. Inagaki, *J. Amer. Ceram. Soc.* 83, 977 (2000).
283. Z. J. Zhang, B. Q. Wei, and P. M. Ajayan, *Appl. Phys. Lett.* 79, 4207 (2001).
284. C. Y. Xu and P. X. Zhang, and L. Yan, *J. Raman Spectrosc.* 32, 862 (2001).
285. C. Y. Xu and P. X. Zhang, *Spectrosc. Spectral Anal.* 21, 336 (2001).
286. K. J. Ziegler, R. C. Doty, K. P. Johnston, and B. A. Korgel, *J. Amer. Chem. Soc.* 123, 7797 (2001).
287. L. D. Sun, X. F. Fu, C. Qian, C. S. Liao, and C. H. Yan, *Chem. J. Chin. Univ.* 22, 879 (2001).
288. P. Van Der Voort, P. I. Ravikovitch, K. P. De Jong, M. Benjelloun, E. Van Bavel, A. H. Janssen, A. V. Neimark, B. M. Weckhuysen, and E. F. Vansant, *J. Phys. Chem. B* 106, 5873 (2002).
289. R. Zanella, S. Giorgio, C. R. Henry, and C. Louis, *J. Phys. Chem. B* 106, 7634 (2002).
290. C. Rath, S. Anand, R. P. Das, K. K. Sahu, S. D. Kulkarni, S. K. Date, and N. C. Mishra, *J. Appl. Phys.* 91, 2211 (2002).
291. G. S. Li, R. L. Smith, H. Inomata, and K. Arai, *Mater. Res. Bull.* 37, 949 (2002).
292. S. Yin, H. Hasegawa, and T. Sato, *Chem. Lett.* 6, 564 (2002).
293. Q. Yang, K. B. Tang, C. R. Wang, C. J. Zhang, and Y. T. Qian, *J. Mater. Res.* 17, 1147 (2002).
294. Z. H. Wu, J. Zhang, R. E. Benfield, Y. F. Ding, D. Grandjean, Z. L. Zhang, and X. Ju, *J. Phys. Chem. B* 106, 4569 (2002).
295. D. H. Chen and M. H. Liao, *J. Mol. Catal. B* 16, 283 (2002).
296. L. X. Yin, Y. Q. Wang, G. S. Pang, Y. Kolytyn, and A. Gedanken, *J. Colloid Interface Sci.* 246, 78 (2002).
297. N. Chen, W. Q. Zhang, W. C. Yu, and Y. T. Qian, *Mater. Lett.* 55, 230 (2002).
298. M. D. Coffin and J. W. McGinity, *Pharm. Res.* 9, 200 (1992).
299. G. W. Wagner, P. W. Bartram, O. Koper, and K. J. Klabunde, *J. Phys. Chem. B* 103, 3225 (1999).
300. M. Ocana, *Colloid Polymer Sci.* 278, 443 (2000).
301. F. B. Landry, D. V. Bazile, G. Spenlehauer, M. Veillard, and J. Kreuter, *Biomaterials* 17, 715 (1996).
302. Z. Kiraly, I. Dekany, A. Mastalir, and M. Bartok, *J. Catalysis* 161, 401 (1996).
303. T. Teranishi and M. Miyake, *Chem. Mater.* 10, 594 (1998).
304. K. Sakanishi, H. Taniguchi, H. Hasuo, and I. Mochida, *Ind. Eng. Chem. Res.* 36, 306 (1997).
305. M. D. Blanco and M. J. Alonso, *Euro. J. Pharm. Biopharm.* 43, 287 (1997).
306. J. Molpeceres, M. R. Aberturas, M. Chacon, L. Berges, and M. Guzman, *J. Microencapsulation* 14, 777 (1997).
307. K. Zhang, C. H. Chew, G. Q. Xu, J. Wang, and L. M. Gan, *Langmuir* 15, 3056 (1999).
308. M. F. Zambaux, F. Bonneaux, R. Gref, E. Dellacherie, and C. Vigneron, *J. Contr. Release* 60, 179 (1999).
309. D. Chognot, M. F. Zambaux, F. Bonneaux, P. Gaussem, J. L. Pittet, M. Aiach, and C. Vigneron, *J. Protein Chem.* 18, 779 (1999).
310. C. S. Cho, J. W. Nah, Y. I. Jeong, J. B. Cheon, S. Asayama, H. Ise, and T. Akaike, *Polymer* 40, 6769 (1999).
311. J. W. Nah, Y. I. Jeong, C. S. Cho, and S. I. Kim, *J. Appl. Polymer Sci.* 75, 1115 (2000).
312. T. Freytag, A. Dashevsky, L. Tillman, G. E. Hardee, and R. Bodmeier, *J. Contr. Release* 69, 197 (2000).
313. H. Sato, T. Ohtsu, and I. Komasa, *J. Colloid Interface Sci.* 230, 200 (2000).
314. T. Hirai, H. Okubo, and I. Komasa, *J. Mater. Chem.* 10, 2592 (2000).
315. L. Rodriguez-Sanchez, M. C. Blanco, and M. A. Lopez-Quintela, *J. Phys. Chem. B* 104, 9683 (2000).
316. S. Hirose, B. G. Muller, R. C. Mulligan, and R. Langer, *J. Contr. Release* 70, 231 (2001).
317. C. Cannas, G. Concas, D. Gatteschi, A. Falqui, A. Musinu, G. Piccaluga, C. Sangregorio, and G. Spano, *Phys. Chem. Chem. Phys.* 3, 832 (2001).
318. S. Nicoli, P. Santi, P. Couvreur, G. Couarraze, P. Colombo, and E. Fattal, *Int. J. Pharm.* 214, 31 (2001).
319. G. Tsutsui, S. J. Huang, H. Sakaue, S. Shingubara, and T. Takahagi, *Jpn. J. Appl. Phys.* 1 40, 346 (2001).

320. R. V. Kumar, Y. Mastai, Y. Diamant, and A. Gedanken, *J. Mater. Chem.* 11, 1209 (2001).
321. A. Lamprecht, N. Ubrich, H. Yamamoto, U. Schafer, H. Takeuchi, C. M. Lehr, P. Maincent, and Y. Kawashima, *J. Contr. Release* 71, 297 (2001).
322. S. Chen and W. M. Liu, *Mater. Res. Bull.* 36, 137 (2001).
323. B. Hai, K. B. Tang, C. R. Wang, C. H. An, Q. Yang, G. Z. Shen, and Y. T. Qian, *J. Crystal Growth* 225, 92 (2001).
324. S. Papp and I. Dekany, *Colloid Polymer Sci.* 279, 449 (2001).
325. G. Cardenas and J. Acuna, *Colloid Polymer Sci.* 279, 442 (2001).
326. K. P. Velikov and A. van Blaaderen, *Langmuir* 17, 4779 (2001).
327. J. H. Kim, T. A. Germer, G. W. Mulholland, and S. H. Ehrman, *Adv. Mater.* 14, 518 (2002).
328. A. Wei, B. Kim, S. V. Puszta, S. L. Tripp, and R. Balasubramanian, *J. Inclusion Phenomena Macrocyclic Chem.* 41, 83 (2001).
329. L. I. Casas, A. Roig, E. Molins, J. M. Greneche, J. Asenjo, and J. Tejada, *Appl. Phys. A* 74, 591 (2002).
330. P. S. Shah, J. D. Holmes, K. P. Johnston, and B. A. Korgel, *J. Phys. Chem.* 106, 2545 (2002).
331. P. Fabrizioli, T. Burgi, M. Burgener, S. van Doorslaer, and A. Baiker, *J. Mater. Chem.* 12, 619 (2002).
332. N. Elvassore, A. Bertuccio, and P. Caliceti, *J. Pharm. Sci.* 90, 1628 (2001).
333. R. Alvarez-Roman, G. Barre, R. H. Guy, and H. Fessi, *Euro. J. Pharm. Biopharm.* 52, 191 (2001).
334. Y. J. Xiong, Y. Xie, G. A. Du, and X. B. Tian, *J. Mater. Chem.* 12, 98 (2002).
335. I. Pastoriza-Santos and L. M. Liz-Marzan, *Nano Lett.* 2, 903 (2002).
336. D. G. Wei, R. Dave, and R. Pfeffer, *J. Nanopart. Res.* 4, 21 (2002).
337. J. Liu, W. Ong, A. E. Kaifer, and C. Peinador, *Langmuir* 18, 5981 (2002).
338. J. J. Yu, Y. I. Jeong, Y. H. Shim, and G. T. Lim, *J. Appl. Polymer Sci.* 85, 2625 (2002).
339. W. Z. Wang, I. Germanenko, and M. S. El-Shall, *Chem. Mater.* 14, 3028 (2002).
340. L. Mu and S. S. Feng, *J. Contr. Release* 80, 129 (2002).
341. M. Rajamathi, M. Ghosh, and R. Seshadri, *Chem. Commun.* 10, 1152 (2002).
342. S. W. Lee, C. B. Mao, C. E. Flynn, and A. M. Belcher, *Science* 296 (2002).
343. K. G. Thomas, J. Zajicek, and P. V. Kamat, *Langmuir* 18, 3722 (2002).
344. A. Chevreau, B. Phillips, B. G. Higgins, and S. H. Risbud, *J. Mater. Chem.* 6, 1643 (1996).
345. J. C. Neal, S. Stolnik, E. Schacht, E. R. Kenawy, M. C. Garnett, S. S. Davis, and L. Illum, *J. Pharm. Sci.* 87, 1242 (1998).
346. C. Schmidt and R. Bodmeier, *J. Contr. Release* 57, 115 (1999).
347. E. Kumacheva, O. Kalinina, and L. Lilge, *Adv. Mater.* 11, 231 (1999).
348. F. Caruso, A. S. Susha, M. Giersig, and H. Mohwald, *Adv. Mater.* 11, 950 (1999).
349. F. Caruso, C. Schuler, and D. G. Kurth, *Chem. Mater.* 11, 3394 (1999).
350. F. Caruso, R. A. Caruso, and H. Mohwald, *Chem. Mater.* 11, 3309 (1999).
351. Z. Y. Zhong, Y. D. Yin, B. Gates, and Y. N. Xia, *Adv. Mater.* 12, 206 (2000).
352. A. S. Susha, F. Caruso, A. L. Rogach, G. B. Sukhorukov, A. Kornowski, H. Mohwald, M. Giersig, A. Eychmuller, and H. Weller, *Colloids Surfaces A* 163, 39 (2000).
353. N. Perez, M. J. Whitcombe, and E. N. Vulfsen, *J. Appl. Polymer Sci.* 77, 1851 (2000).
354. K. H. Rhodes, S. A. Davis, F. Caruso, B. J. Zhang, and S. Mann, *Chem. Mater.* 12, 2832 (2000).
355. O. Siiman and A. Burshteyn, *J. Phys. Chem. B* 104, 9795 (2000).
356. F. Caruso, *Adv. Mater.* 13, 11 (2001).
357. R. A. Caruso and M. Antonietti, *Chem. Mater.* 13, 3272 (2001).
358. H. S. Xia, C. H. Zhang, and Q. Wang, *J. Appl. Polymer Sci.* 80, 1130 (2001).
359. Y. Yin, Y. Lu, B. Gates, and Y. Xia, *Chem. Mater.* 13, 1146 (2001).
360. Y. Yun, H. Q. Li, and E. Ruckenstein, *J. Colloid Interface Sci.* 238, 414 (2001).
361. A. Imhof, *Langmuir* 17, 3579 (2001).
362. F. Tiarks, K. Landfester, and M. Antonietti, *Langmuir* 17, 5775 (2001).
363. Y. Lvov and F. Caruso, *Anal. Chem.* 73, 4212 (2001).
364. D. J. Gan and L. A. Lyon, *J. Amer. Chem. Soc.* 123, 8203 (2001).
365. S. Chalaye, E. Bourgeat-Lami, J. L. Putaux, and J. Lang, *Macromol. Symp.* 169, 89 (2001).
366. M. S. Fleming, T. K. Mandal, and D. R. Walt, *Chem. Mater.* 13, 2210 (2001).
367. A. A. Antipov, G. B. Sukhorukov, Y. A. Fedutik, J. Hartmann, M. Giersig, and H. Mohwald, *Langmuir* 18, 6687 (2002).
368. M. N. Xiong, L. M. Wu, S. X. Zhou, and B. You, *Polymer Int.* 51, 693 (2002).
369. S. Reculusa, C. Poncet-Legrand, S. Ravaine, C. Mingotaud, E. Duguet, and E. Bourgeat-Lami, *Chem. Mater.* 14, 2354 (2002).
370. X. J. Xu, P. Y. Chow, and L. M. Gan, *J. Nanosci. Nanotech.* 2, 61 (2002).
371. X. L. Xu, G. Friedman, K. D. Humfeld, S. A. Majetich, and S. A. Asher, *Chem. Mater.* 14, 1249 (2002).
372. I. Tissot, J. P. Reymond, F. Lefebvre, and E. Bourgeat-Lami, *Chem. Mater.* 14, 1325 (2002).
373. M. J. Burchell, M. J. Cole, S. F. Lascelles, M. A. Khan, C. Barthelet, S. A. Wilson, D. B. Cairns, and S. P. Armes, *J. Phys. D* 32, 1719 (1999).
374. K. Landfester, F. Tiarks, H.-P. Hentze, and M. Antonietti, *Macromol. Chem. Phys.* 201, 1 (2000).
375. T. Yanai, Y. Kinemuchi, and K. Ishizaki, *J. Ceram. Soc. Jpn.* 103, 1177 (1995).
376. W. P. Cai, H. C. Zhong, and L. D. Zhang, *J. Appl. Phys.* 83, 1705 (1998).
377. N. Suzuki, S. Kimura, Y. Saito, and C. Kaito, *Phys. Low Dimen. Struct.* 3-4, 55 (1998).
378. T. Horikoshi, M. Itoh, M. Kurihara, K. Kubo, and H. Nishihara, *J. Electroanal. Chem.* 473, 113 (1999).
379. T. Pauporte, F. Andolfatto, and R. Durand, *Electrochim. Acta* 45, 431 (1999).
380. A. Hightower, P. Delcroix, G. Le Caer, C. K. Huang, B. V. Ratnakumar, C. C. Ahn, B. Fultz, and *J. Electrochem. Soc.* 147, 1 (2000).
381. I. N. Germanenko, M. Dongol, Y. B. Pithawalla, M. S. El-Shall, and J. A. Carlisle, *Pure Appl. Chem.* 72, 245 (2000).
382. R. Wu, C. S. Xie, J. H. Hu, H. Xia, and A. H. Wang, *Scripta Mater.* 43, 841 (2000).
383. D. Das, J. Farjas, P. Roura, G. Viera, and E. Bertran, *Diamond Related Mater.* 10, 1295 (2001).
384. D. Das, J. Farjas, P. Roura, G. Viera, and E. Bertran, *Appl. Phys. Lett.* 79, 3705 (2001).
385. D. R. Mehandjiev, I. D. Dragieva, V. Krastev, and G. Ivanov, *Oxidation Commun.* 24, 161 (2001).
386. P. Uznanski, C. Amiens, M. Bardaji, B. Donnadieu, Y. Coppel, B. Chaudret, and A. Laguna, *New J. Chem.* 25, 1495 (2001).
387. S. Veintemillas-Verdaguer, M. P. Morales, and C. J. Serna, *Appl. Organometallic Chem.* 15, 365 (2001).
388. K. W. Park, J. H. Choi, B. K. Kwon, S. A. Lee, Y. E. Sung, H. Y. Ha, S. A. Hong, H. Kim, and A. Wieckowski, *J. Phys. Chem. B* 106, 1869 (2002).
389. A. M. Fojas, E. Murphy, and P. Stroeve, *Ind. Eng. Chem. Res.* 41, 2662 (2002).
390. B. K. Paul and S. P. Moulik, *J. Dispersion Sci. Tech.* 18, 301 (1997).

391. F. Tiarks, K. Landfester, and M. Antonietti, *Langmuir* 17, 908 (2001).
392. J. L. Grangier, M. Puygrenier, J. C. Gautier, and P. Couvreur, *J. Contr. Release* 15, 3 (1991).
393. M. Gallardo, G. Couarraze, B. Denizot, L. Treupel, P. Couvreur, and F. Puisieux, *Int. J. Pharm.* 100, 55 (1993).
394. L. M. Gan, N. Lian, C. H. Chew, and G. Z. Li, *Langmuir* 10, 2197 (1994).
395. F. Homilius, A. Heilmann, and C. Vonborczyskowski, *Surface Coating Tech.* 74–75, 594 (1995).
396. A. Heilmann, J. Werner, D. Schwarzenberg, S. Henkel, P. Grosse, and W. Theiss, *Thin Solid Films* 270, 103 (1995).
397. E. Bourgeatlamy, P. Espiard, and A. Guyot, *Polymer* 36, 4385 (1995).
398. S. P. Nunes, J. Schultz, and K. V. Peinemann, *J. Mater. Sci. Lett.* 15, 1139 (1996).
399. H. Du, S. H. Kan, G. F. Zhang, F. Q. Liu, X. Y. Tang, and T. J. Li, *Chem. J. Chin. Univ.* 16, 33 (1995).
400. M. B. F. Martins, S. I. D. Simoes, M. E. M. Cruz, and R. Gaspar, *J. Mater. Sci.—Mater. Med.* 7, 413 (1996).
401. H. Katagi, H. Kasai, S. Okada, H. Oikawa, K. Komatsu, H. Matsuda, Z. F. Liu, and H. Nakanishi, *Jpn. J. Appl. Phys.* 35, L1364 (1996).
402. C. S. Cho, J. B. Cheon, Y. I. Jeong, I. S. Kim, S. H. Kim, and T. Akaïke, *Macromol. Rapid. Commun.* 18, 361 (1997).
403. E. Stathatos, P. Lianos, F. DelMonte, D. Levy, and D. Tsiourvas, *Langmuir* 13, 4295 (1997).
404. H. Bamnolker, B. Nitzan, S. Gura, and S. Margel, *J. Mater. Sci. Lett.* 16, 1412 (1997).
405. S. Forster and M. Antonietti, *Adv. Mater.* 10, 195 (1998).
406. H. J. Kim, Y. I. Jeong, S. H. Kim, Y. M. Lee, and C. S. Cho, *Arch. Pharm. Res.* 20, 324 (1997).
407. S. Deki, K. Akamatsu, T. Yano, M. Mizuhata, and A. Kajinami, *J. Mater. Chem.* 8, 1865 (1998).
408. B. M. Mandal, *J. Indian Chem. Soc.* 75, 121 (1998).
409. P. A. Dresco, V. S. Zaitsev, R. J. Gambino, and B. Chu, *Langmuir* 15, 1945 (1999).
410. E. Reynaud, C. Gauthier, and J. Perez, *Rev. Metall. D* 96, 169 (1999).
411. M. Rutnakornpituk, M. S. Thompson, L. A. Harris, K. E. Farmer, A. R. Esker, J. S. Riffle, J. Connolly, and T. G. St Pierre, *Polymer* 43, 2337 (2002).
412. X. Z. Kong and E. Ruckenstein, *J. Appl. Polym. Sci.* 73, 2235 (1999).
413. F. Caruso, C. Schuler, and D. G. Kurth, *Chem. Mater.* 11, 3394 (1999).
414. F. Sauzedde, A. Elaissari, and C. Pichot, *Colloid Polym. Sci.* 277, 1041 (1999).
415. C. W. Chen, T. Serizawa, and M. Akashi, *Langmuir* 15, 7998 (1999).
416. S. Pathak, M. T. Greci, R. C. Kwong, K. Mercado, G. K. S. Prakash, G. A. Olah, and M. E. Thompson, *Chem. Mater.* 12, 1985 (2000).
417. H. T. Cui and G. Y. Hong, *J. Rare Earths* 18, 104 (2000).
418. S. J. Han, K. Sohn, and T. Hyeon, *Chem. Mater.* 12, 3337 (2000).
419. M. H. Huang, A. Choudrey, and P. D. Yang, *Chem. Commun.* 12, 1063 (2000).
420. M. Lal, L. Levy, K. S. Kim, G. S. He, X. Wang, Y. H. Min, S. Pakatchi, and P. N. Prasad, *Chem. Mater.* 12, 2632 (2000).
421. K. Sparnacci, L. Tondelli, and M. Laus, *J. Polym. Sci. A* 38, 3347 (2000).
422. M. J. MacLachlan, M. Ginzburg, N. Coombs, N. P. Raju, J. E. Greedan, G. A. Ozin, and I. Manners, *J. Amer. Chem. Soc.* 122, 3878 (2000).
423. M. L. Wu, S. A. O'Neill, L. C. Brousseau, W. P. McConnell, D. A. Shultz, R. J. Linderman, and D. L. Feldheim, *Chem. Commun.* 9, 775 (2000).
424. I. Pastoriza-Santos, D. S. Koktysh, A. A. Mamedov, M. Giersig, N. A. Kotov, and L. M. Liz-Marzan, *Langmuir* 16, 2731 (2000).
425. M. Laus, K. Sparnacci, M. Lelli, R. Vannini, and L. Tondelli, *J. Polym. Sci. A* 38, 1110 (2000).
426. H. X. Ge, Y. Hu, S. C. Yang, X. Q. Jiang, and C. Z. Yang, *J. Appl. Polym. Sci.* 75, 874 (2000).
427. R. Jordan, N. West, A. Ulman, Y. M. Chou, and O. Nuyken, *Macromolecules* 34, 1606 (2001).
428. Q. Wang, H. S. Xia, and C. H. Zhang, *J. Appl. Polym. Sci.* 80, 1478 (2001).
429. H. S. Xia, C. H. Zhang, and Q. Wang, *J. Appl. Polym. Sci.* 80, 1130 (2001).
430. S. C. Farmer and T. E. Patten, *Chem. Mater.* 13, 3920 (2001).
431. J. Texter, *J. Dispersion Sci. Tech.* 22, 499 (2001).
432. H. Srikanth, R. Hajndl, C. Chirinos, J. Sanders, A. Sampath, and T. S. Sudarshan, *Appl. Phys. Lett.* 79, 3503 (2001).
433. K. Akamatsu, T. Kawamura, and S. Deki, *Euro. Phys. J. D* 16, 305 (2001).
434. J. Pyun and K. Matyjaszewski, *Chem. Mater.* 13, 3436 (2001).
435. F. Tiarks, K. Landfester, and M. Antonietti, *Langmuir* 17, 5775 (2001).
436. D. J. Gan and L. A. Lyon, *J. Amer. Chem. Soc.* 123, 7511 (2001).
437. N. Yanagihara, Y. Tanaka, and H. Okamoto, *Chem. Lett.* 8, 796 (2001).
438. K. Landfester, *Adv. Mater.* 13, 765 (2001).
439. S. C. Jana and S. Jain, *Polymer* 42, 6897 (2001).
440. K. S. Murthy, Q. G. Ma, C. G. Clark, E. E. Remsen, and K. L. Wooley, *Chem. Commun.* 8, 773 (2001).
442. Y. Yun, H. Q. Li, and E. Ruckenstein, *J. Colloid Interface Sci.* 238, 414 (2001).
441. S. Santra, R. Tapeç, N. Theodoropoulou, J. Dobson, A. Hebard, and W. H. Tan, *Langmuir* 17, 2900 (2001).
442. T. Hirai, H. Okubo, and I. Komasa, *J. Colloid Interface Sci.* 235, 358 (2001).
443. M. Z. Rong, M. Q. Zhang, Y. X. Zheng, H. M. Zeng, R. Walter, and K. Friedrich, *Polymer* 42, 167 (2001).
444. A. Malinauskas, *Polymer* 42, 3957 (2001).
445. Y. Hu, X. Q. Jiang, Y. Ding, H. X. Ge, Y. Y. Yuan, and C. Z. Yang, *Biomaterials* 23, 3193 (2002).
446. E. Marie, K. Landfester, and M. Antonietti, *Biomacromolecules* 3, 475 (2002).
447. J. Jang and K. Lee, *Chem. Commun.* 10, 1098 (2002).
448. K. Landfester, *J. Dispersion Sci. Tech.* 23, 167 (2002).
449. S. Blomberg, S. Ostberg, E. Harth, A. W. Bosman, B. Van Horn, and C. J. Hawker, *J. Polym. Sci. A* 40, 1309 (2002).
450. N. R. Brinkmann, H. F. Schaefer, C. T. Sanderson, and C. Kotal, *J. Phys. Chem. A* 106, 847 (2002).
451. M. Palumbo, A. Russo, V. Cardile, M. Renis, D. Paolino, G. Puglisi, and M. Fresta, *Pharm. Res.* 19, 71 (2002).
452. J. Y. Lee, C. H. Song, J. I. Kim, and J. H. Kim, *J. Nanoparticle Res.* 4, 53 (2002).
453. M. Schappacher, Z. Muchtar, J. Bernard, and A. Deffieux, *Macromolecular Symp.* 183, 23 (2002).
454. H. F. Gao, Y. Q. Zhao, S. K. Fu, B. Li, and M. Q. Li, *Colloid Polym. Sci.* 280, 653 (2002).
455. D. M. Knauss and S. L. Clark, *Abstracts Papers Amer. Chem. Soc.* 223, 266 (2002).
456. E. Harth, B. Van Horn, V. Y. Lee, D. S. Germack, C. P. Gonzales, R. D. Miller, and C. J. Hawker, *J. Amer. Chem. Soc.* 124, 8653 (2002).
457. Z. Q. Peng, E. K. Wang, and S. J. Dong, *Electrochem. Commun.* 4, 210 (2002).
458. C. Johans, J. Clohessy, S. Fantini, K. Kontturi, and V. J. Cunnane, *Electrochem. Commun.* 4, 277 (2002).
459. Z. Z. Yang, D. Qiu, and J. Li, *Macromol. Rapid Commun.* 23, 479 (2002).
460. J. Jang and H. Ha, *Langmuir* 18, 5613 (2002).



461. M. N. V. R. Kumar, N. Kumar, A. J. Domb, and M. Arora, *Adv. Polym. Sci.* 160, 45 (2002).
462. M. Antonietti and K. Landfester, *Progr. Polym. Sci.* 27, 689 (2002).
463. C. W. Chen, T. Serizawa, and M. Akashi, *Chem. Mater.* 14, 2232 (2002).
464. J. Y. Fang, L. D. Tung, K. L. Stokes, J. B. He, D. Caruntu, W. L. Zhou, and C. J. O'Connor, *J. Appl. Phys.* 91, 8816 (2002).
465. D. L. Shi, P. He, S. X. Wang, W. J. van Ooij, L. M. Wang, J. G. Zhao, and Z. Yu, *J. Mater. Res.* 17, 981 (2002).
466. S. R. Ahmed and P. Kofinas, *Macromolecules* 35, 3338 (2002).
467. A. Salgueiro, F. Gamisans, M. Espina, X. Alcober, M. L. Garcia, and M. A. Egea, *J. Microencapsulation* 19, 305 (2002).
468. J. H. Youk, M. K. Park, J. Locklin, R. Advincula, J. Yang, and J. Mays, *Langmuir* 18, 2455 (2002).
469. L. J. Twyman, A. S. H. King, and I. K. Martin, *Chem. Soc. Rev.* 31, 69 (2002).
470. E. Bourgeat-Lami, *J. Nanosci. Nanotech.* 2, 1 (2002).
471. C. L. Zhou, Y. Zhao, T. C. Jao, M. A. Winnik, and C. Wu, *J. Phys. Chem. B* 106, 1889 (2002).
472. N. C. Manekar, P. K. Puranik, and S. B. Joshi, *J. Microencapsulation* 8, 521 (1991).
473. N. B. Dharamadhikari, S. B. Joshi, and N. C. Manekar, *J. Microencapsulation* 8, 479 (1991).
474. N. C. Manekar, P. K. Puranik, and S. B. Joshi, *J. Microencapsulation* 8, 481 (1992).
475. N. C. Manekar, P. K. Puranik, and S. B. Joshi, *J. Microencapsulation* 9, 63 (1992).
476. H. H. Elshattawy, A. A. Kassem, A. T. Nouh, and M. A. Elrazzazma, *Drug Develop. Indust. Pharm.* 18, 55 (1992).
477. S. J. Sveinsson and T. Kristmundsdottir, *Int. J. Pharm.* 82, 129 (1992).
478. J. C. Wu, W. J. Jean, and H. Chen, *J. Chin. Chem. Soc.* 40, 23 (1993).
479. I. Karakasa, N. Yagi, M. Shibata, H. Kenmotsu, H. Sekikawa, and M. Takada, *Biol. Pharm. Bull.* 17, 432 (1994).
480. F. Sevgi, M. Ozyazici, and T. Guneri, *J. Microencapsulation* 11, 327 (1994).
481. F. Ishii, A. Takamura, and Y. Ishigami, *Langmuir* 11, 483 (1995).
482. Y. F. Yin, J. F. Scamehorn, and S. D. Christain, *Surfactant* 594, 231 (1995).
483. M. Ozyazici, F. Sevgi, and G. Ertan, *Int. J. Pharm.* 138, 25 (1996).
484. M. Ozyazici, F. Sevgi, and G. Ertan, *Drug Develop. Ind. Pharm.* 23, 761 (1997).
485. L. Genc, M. Demirel, E. Guler, and N. Hegazy, *J. Microencapsulation* 15, 45 (1998).
486. S. Bedi, S. Baidya, L. K. Ghosh, and B. K. Gupta, *Drug Develop. Ind. Pharm.* 25, 937 (1999).
487. C. Amiet-Charpentier, J. P. Benoit, D. Le Meurlay, P. Gadille, and J. Richard, *Macromol. Symp.* 151, 611 (2000).
488. A. Nascimento, M. C. M. Laranjeira, V. T. Favere, and A. Josue, *J. Microencapsulation* 18, 679 (2001).
489. D. Quintanar-Guerrero, E. Allemann, H. Fessi, and E. Doelker, *Drug Develop. Indust. Pharm.* 24, 1113 (1998).
490. P. Legrand, G. Barratt, V. Mosqueira, H. Fessi, and J. P. Devissaguet, *STP Pharm. Sci.* 9, 411 (1999).
491. T. Oku, K. Niihara, and K. Suganuma, *J. Mater. Chem.* 8, 1323 (1998).
492. Y. H. Gao, Y. Bando, K. Kurashima, and T. Sato, *Scripta Mater.* 44, 1941 (2001).
493. M. Kuno, T. Oku, and K. Suganuma, *Scripta Mater.* 44, 1583 (2001).
494. H. Kitahara, T. Oku, T. Hirano, and K. Suganuma, *Diamond Related Mater.* 10, 1210 (2001).
495. T. Oku, T. Hirano, M. Kuno, T. Kusunose, K. Niihara, and K. Suganuma, *Mater. Sci. Eng. B* 74, 206 (2000).
496. P. Mayer and R. Holze, *J. Solid State Electrochem.* 5, 402 (2001).
497. Y. S. Djikaev, R. Bowles, H. Reiss, K. Hameri, A. Laaksonen, and M. Vakeva, *J. Phys. Chem. B* 105, 7708 (2001).
498. E. Rabani and S. A. Egorov, *J. Chem. Phys.* 115, 3437 (2001).
499. D. I. Gittins and F. Caruso, *J. Phys. Chem. B* 105, 6846 (2001).
500. W. Meier, *Chem. Soc. Rev.* 29, 295 (2000).
501. N. S. Kopelev, V. Chechersky, A. Nath, Z. L. Wang, E. Kuzmann, B. S. Zhang, and G. H. Via, *Chem. Mater.* 7, 1419 (1995).
502. A. D. Pomogailo, *Uspekhi Khimii* 66, 750 (1997).
503. S. T. Li and M. S. El-Shall, *Appl. Surf. Sci.* 129, 330 (1998).
504. S. S. Joshi, S. F. Patil, V. Iyer, and S. Mahumuni, *Nanostructured Mater.* 10, 1135 (1998).
505. L. Rodriguez-Sanchez, M. C. Blanco, and M. A. Lopez-Quintela, *J. Phys. Chem.* 104, 9683 (2000).
506. A. Pal, *J. Photochem. Photobiol. A* 142, 59 (2001).
507. J. W. Yoo, D. Hathcock, and M. A. El-Sayed, *J. Phys. Chem.* 106, 2049 (2002).
508. G. B. Khomutov, S. P. Gubin, V. V. Khanin, A. Y. Koksharov, A. Y. Obydenov, V. V. Shorokhov, E. S. Soldatov, and A. S. Trifonov, *Colloids Surfaces A* 198, 593 (2002).
509. V. P. Dravid, J. J. Host, M. H. Teng, B. R. Eillott, J. H. Hwang, D. L. Johnson, T. O. Mason, and J. R. Weertman, *Nature* 374, 602 (1995).
510. M. H. Teng, J. J. Host, J. H. Hwang, B. R. Eillott, J. R. Weertman, T. O. Mason, V. P. Dravid, and D. L. Johnson, *J. Mater. Res.* 10, 233 (1995).
511. P. J. F. Harris and S. C. Tsang, *Carbon* 36, 1859 (1998).
512. S. H. Tsai, C. L. Lee, C. W. Chao, and H. C. Shih, *Carbon* 38, 781 (2000).
513. D. Tateishi, K. Esumi, and H. Honda, *Carbon* 29, 1296 (1991).
514. W. Z. Wu, Z. P. Zhu, and Z. Y. Liu, *Carbon* 41, 309 (2003).
515. W. Z. Wu, Z. P. Zhu, Z. Y. Liu, Y. N. Xie, J. Zhang, and T. D. Hu, *Carbon* 41, 317 (2003).
516. P. B. Deasy, *Crit. Rev. Therapeutic Drug Carrier Syst.* 8, 39 (1991).
517. C. Zhu, M. C. Slaughter, and S. L. Soo, *Rev. Sci. Instrum.* 62, 2036 (1991).
518. P. B. Deasy, *J. Microencapsulation* 11, 487 (1994).
519. D. Jones, *Drug Develop. Ind. Pharm.* 20, 3175 (1994).
520. A. V. Fedorov, *Combustion Explosion Shock Waves* 30, 492 (1994).
521. T. Govender and C. M. Dangor, *J. Microencapsulation* 14, 445 (1997).
522. A. G. Kutushev and O. N. Pichugin, *Combustion Explosion Shock Waves* 32, 449 (1996).
523. Z. M. Mathir, C. M. Dangor, T. Govender, and D. J. Chetty, *J. Microencapsulation* 14, 743 (1997).
524. E. Teunou and D. Poncelet, *J. Food Eng.* 53, 325 (2002).
525. R. Dietrich, *Pharm. Ind.* 54, 459 (1992).
526. K. Vasilevska, Z. Djuric, M. Jovenovic, and A. Simov, *Drug Develop. Ind. Pharm.* 18, 1649 (1992).
527. E. A. Hosny, G. M. Elmahrouk, and A. Alangary, *Drug Develop. Ind. Pharm.* 20, 1085 (1994).
528. A. G. Eshra, K. A. Elkhodairy, S. A. M. Mortada, and A. H. Nada, *J. Microencapsulation* 11, 271 (1994).
529. A. Bodea and S. E. Leucuta, *Int. J. Pharm.* 154, 49 (1997).
530. E. A. Hosny, G. M. El-Mahrouk, and M. W. Gouda, *Drug Develop. Ind. Pharm.* 24, 661 (1998).
531. C. B. Abletshauer, R. Schneider, and H. Rupprecht, *J. Contr. Release* 27, 149 (1993).
532. M. G. Boles, P. B. Deasy, and M. F. Donnellan, *J. Microencapsulation* 11, 55 (1994).
533. P. B. Deasy and P. W. Murtagh, *J. Microencapsulation* 13, 385 (1996).
534. V. Tsakova, D. Borissov, B. Ranguelov, C. Stromberg, and J. W. Schultze, *Electrochim. Acta* 46, 4213 (2001).
535. T. G. Park, M. J. Alonso, and R. Langer, *J. Appl. Polym. Sci.* 52, 1797 (1994).
536. P. Luo and T. G. Nieh, *Biomaterials* 17, 1959 (1996).
537. P. Pramanik, *Bull. Mater. Sci.* 19, 957 (1996).

538. R. H. Muller, W. Mehnert, J. S. Lucks, C. Schwarz, A. Zurmuhlen, H. Weyhers, C. Freitas, and D. Ruhl, *Euro. J. Pharm. Biopharm.* 41, 62 (1995).
539. C. Freitas and R. H. Muller, *Euro. J. Pharm. Biopharm.* 46, 145 (1998).
540. W. Mehnert and K. Mader, *Adv. Drug Delivery Rev.* 47, 165 (2001).
541. R. H. Muller, H. Weyhers, A. zurMuhlen, A. Dingler, and W. Mehnert, *Pharm. Ind.* 59, 423 (1997).
542. W. Mehnert, A. zurMuhlen, A. Dingler, and H. Weyhers, *Pharm. Ind.* 59, 511 (1997).
543. R. H. Muller, A. Dingler, H. Weyhers, A. zurMuhlen, and W. Mehnert, *Pharm. Ind.* 59, 614 (1997).
544. Mikrajuddin, F. Iskandar, K. Okuyama, and F. G. Shi, *J. Appl. Phys.* 89, 6431 (2001).
545. P. Chattopadhyay and R. B. Gupta, *Ind. Eng. Chem. Res.* 40, 3530 (2001).
546. J. Kim, O. Wilhelm, and S. E. Pratsinis, *J. Amer. Ceramic Soc.* 84, 2802 (2001).
547. F. Iskandar, Mikrajuddin, and K. Okuyama, *Nano Lett.* 1, 231 (2001).
548. F. Iskandar, Mikrajuddin, and K. Okuyama, *Nano Lett.* 2, 389 (2002).
549. M. Ermas and H. Nyqvist, *Int. J. Pharm.* 197, 117 (2000).
550. C. Brossard, V. Ratsimbazafy, and D. L. Desylouses, *Drug Develop. Ind. Pharm.* 17, 1267 (1991).
551. R. Bodmeier, J. Wang, and H. Bhagwatwar, *J. Microencapsulation* 9, 99 (1992).
552. E. E. Hassan, A. G. Eshra, and A. H. Nada, *Int. J. Pharm.* 121, 149 (1995).
553. S. P. Schwendeman, M. Tobio, M. Joworowicz, M. J. Alonso, and R. Langer, *J. Microencapsulation* 15, 299 (1998).
554. T. Yajima, N. Umeki, and S. Itai, *Chem. Pharm. Bull.* 47, 220 (1999).
555. L. Rodriguez, N. Passerini, C. Cavallari, M. Cini, P. Sancin, and A. Fini, *Int. J. Pharm.* 183, 133 (1999).
556. J. Rawers and D. Cook, *Nanostruct. Mater.* 11, 331 (1999).
557. T. Chiba, R. Komura, and A. Mori, *Jpn. J. Appl. Phys.* 1, 39, 4803 (2000).
558. C. Schmidt and R. Bodmeier, *Int. J. Pharm.* 216, 9 (2001).
559. T. Yajima, Y. Fukushima, S. Itai, and Y. Kawashima, *Chem. Pharm. Bull.* 50, 147 (2002).
560. M. K. Terris and J. E. McNeal, *Prostate* 50, 247 (2002).
561. N. Passerini, B. Perissutti, M. Moneghini, D. Voinovich, B. Albertini, C. Cavallari, and L. Rodriguez, *J. Pharm. Sci.* 91, 699 (2002).
562. S. Leporatti, A. Voigt, R. Mitlohner, G. Sukhorukov, E. Donath, and H. Mohwald, *Langmuir* 16, 4059 (2000).
563. G. Calzaferrri, D. Bruhwiler, S. Glaus, D. Schurch, A. Currao, and C. Leiggenger, *J. Imaging Sci. Tech.* 45, 331 (2001).
564. E. Borsella, M. Falconieri, S. Botti, S. Martelli, F. Bignoli, L. Costa, S. Grandi, L. Sangaletti, B. Allieri, and L. Depero, *Mater. Sci. Eng. B* 79, 55 (2001).
565. E. J. C. Dawnay, M. A. Fardad, M. Green, and E. M. Yeatman, *J. Mater. Res.* 12, 3115 (1997).
566. H. Q. Yang, Y. Y. Lin, M. Q. Wang, L. Y. Zhang, and X. Yao, *J. Inorganic Mater.* 15, 249 (2000).
567. D. D. Barros, P. P. Abreu, U. Werner, and M. A. Aegerter, *J. Sol-Gel Sci. Tech.* 8, 735 (1997).
568. S. K. Poznyak, D. V. Talapin, and A. I. Kulak, *J. Phys. Chem. B* 105, 4816 (2001).
569. Mikrajuddin, F. Iskandar, K. Okuyama, and F. G. Shi, *J. Appl. Phys.* 89, 6431 (2001).
570. D. Denzler, M. Olschewski, and K. Sattler, *J. Appl. Phys.* 84, 2841 (1998).
571. K. P. Velikov and A. van Blaaderen, *Langmuir* 17, 4779 (2001).
572. N. Hebalkar, A. Lobo, S. R. Sainkar, S. D. Pradhan, W. Vogel, J. Urban, and S. K. Kulkarni, *J. Mater. Sci.* 36, 4377 (2001).
573. B. Bhattacharjee, D. Ganguli, K. Iakoubovskii, A. Stesmans, and S. Chaudhuri, *Bull. Mater. Sci.* 25, 175 (2002).
574. A. D. Dinsmore, D. S. Hsu, S. B. Qadri, J. O. Cross, T. A. Kennedy, H. F. Gray, and B. R. Ratna, *J. Appl. Phys.* 88, 4985 (2000).
575. A. A. Bol and A. Meijerink, *Phys. Status Solidi B* 224, 173 (2001).
576. P. Yang, M. K. Lu, D. Xu, D. R. Yuan, J. Chang, G. J. Zhou, and M. Pan, *Appl. Phys. A* 74, 257 (2002).
577. P. Yang, M. Lu, D. Xu, D. Yuan, C. Song, and G. Zhou, *Appl. Phys. A* 74, 525 (2002).
578. P. Yang, C. F. Song, M. K. Lu, G. J. Zhou, Z. X. Yang, D. Xu, and D. R. Yuan, *J. Phys. Chem. Solids* 63, 639 (2002).
579. P. Yang, M. K. Lu, G. J. Zhou, D. R. Yuan, and D. Xu, *Inorg. Chem. Commun.* 4, 734 (2001).
580. P. Yang, M. Lu, D. Xu, D. Yuan, C. Song, and G. Zhou, *J. Phys. Chem. Solids* 62, 1181 (2001).
581. S. C. Qu, W. H. Zhou, F. Q. Liu, N. F. Chen, Z. G. Wang, H. Y. Pan, and D. P. Yu, *Appl. Phys. Lett.* 80, 3605 (2002).
582. A. A. Bol, R. van Beek, and A. Meijerink, *Chem. Mater.* 14, 1121 (2002).
583. A. Chevreau, B. Phillips, B. G. Higgins, and S. H. Risbud, *J. Mater. Chem.* 6, 1643 (1996).
584. W. Strek, K. Makuszewski, M. Jasierski, E. Lukowiak, L. Bryja, M. Ciorga, P. Sitarek, and J. Misiewicz, *Opt. Appl.* 29, 401 (1999).
585. G. Q. Xu, B. Liu, S. J. Xu, C. H. Chew, S. J. Chua, and L. M. Gana, *J. Phys. Chem. Solids* 61, 829 (2000).
586. D. V. Talapin, S. Haubold, A. L. Rogach, A. Kornowski, M. Haase, and H. Weller, *J. Phys. Chem. B* 105, 2260 (2001).
587. U. K. Gautam, M. Rajamathi, F. C. Meldrum, P. Morgan, and R. Seshadri, *Chem. Commun.* 7, 629 (2001).
588. V. Chikan and D. F. Kelley, *Nano Lett.* 2, 141 (2002).
589. Z. H. Zhou, J. M. Xue, H. S. O. Chan, and J. Wang, *J. Appl. Phys.* 90, 4169 (2001).
590. J. V. St John and J. L. Coffey, *J. Phys. Chem. B* 105, 7599 (2001).
591. Y. Kobayashi, M. A. Correa-Duarte, and L. M. Liz-Marzan, *Langmuir* 17, 6375 (2001).
592. H. Wang, S. P. Wong, W. Q. Li, M. F. Chiah, C. Y. Poon, W. Y. Cheung, and N. Ke, *Thin Solid Films* 405, 304 (2002).
593. S. Roy and D. Chakravorty, *J. Phys. Cond. Matter* 6, 8599 (1994).
594. A. Chatterjee and D. Chakravorty, *J. Mater. Sci.* 27, 4115 (1992).
595. S. Roy and D. Chakravorty, *Jpn. J. Appl. Phys.* 1 32, 3515 (1993).
596. T. Hihara, H. Onodera, K. Sumiyama, K. Suzuki, A. Kasuya, Y. Nishina, Y. Saito, T. Yoshikawa, and M. Okuda, *Jpn. J. Appl. Phys.* 2 Lett. 33, L24 (1994).
597. J. A. H. Coaquira, H. R. Rechenberg, C. Marquina, M. R. Ibarra, A. M. Benito, W. Maser, E. Munoz, and M. T. Martinez, *Hyperfine Inter.* 134, 103 (2001).
598. Y. Saito, J. Ma, J. Nakashima, and M. Masuda, *Z. Phys. D* 40, 170 (1997).
599. J. H. Hwang, V. P. Dravid, M. H. Teng, J. J. Host, B. R. Elliott, D. L. Johnson, and T. O. Mason, *J. Mater. Res.* 12, 1076 (1997).
600. J. J. Host, J. A. Block, K. Parvin, V. P. Dravid, J. L. Alpers, T. Sezen, and R. LaDuca, *J. Appl. Phys.* 83, 793 (1998).
601. J. A. Block, K. Parvin, J. L. Alpers, T. Sezen, R. LaDuca, J. J. Host, and V. P. Dravid, *IEEE Trans. Magn.* MAG-34, 982 (1998).
602. H. J. Huang, S. H. Yang, and G. Gu, *J. Phys. Chem. B* 102, 3420 (1998).
603. X. L. Dong, Z. D. Zhang, S. R. Jin, W. M. Sun, and Y. C. Chuang, *Nanostruct. Mater.* 10, 585 (1998).
604. X. L. Dong, Z. D. Zhang, X. G. Zhao, Y. C. Chuang, S. R. Jin, and W. M. Sun, *J. Mater. Res.* 14, 398 (1999).
605. X. L. Dong, Z. D. Zhang, S. R. Jin, and B. H. Kim, *J. Magn. Mater.* 210, 143 (2000).
606. X. C. Sun, A. Gutierrez, M. J. Yacaman, X. L. Dong, and S. R. Jin, *Mater. Sci. Eng. A* 286, 157 (2000).
607. X. C. Sun, X. L. Dong, and J. A. Toledo, *J. Nanosci. Nanotech.* 1, 291 (2001).

608. M. Jiang, X. G. Zhang, Y. Liu, and H. Mao, *J. Mater. Sci. Lett.* 21, 455 (2002).
609. M. Jiang, X. G. Zhang, Y. Liu, G. M. Hao, and H. Lin, *Mater. Sci. Eng. B* 87, 66 (2001).
610. S. Roy, D. Das, D. Chakravorty, and D. C. Agrawal, *J. Appl. Phys.* 74, 4746 (1993).
611. N. Viart, D. Niznansky, and J. L. Rehspringer, *J. Phys. IV* 7, 555 (1997).
612. H. Guerrero, G. Rosa, M. P. Morales, F. delMonte, E. M. Moreno, D. Levy, R. P. del Real, T. Belenguier, and C. J. Sema, *Appl. Phys. Lett.* 71, 2698 (1997).
613. C. Cannas, D. Gatteschi, A. Musinu, G. Piccaluga, and C. Sangregorio, *J. Phys. Chem. B* 102, 7721 (1998).
614. C. Cannas, G. Cancas, D. Gatteschi, A. Falqui, A. Musinu, G. Piccaluga, C. Sangregorio, and G. Spano, *Phys. Chem. Chem. Phys.* 3, 832 (2001).
615. A. Chatterjee, A. Datta, A. K. Giri, D. Das, and D. Chakravorty, *J. Appl. Phys.* 72, 3832 (1992).
616. K. Mandal, S. Chakraverty, S. Pan Mandal, P. Agudo, M. Pal, and D. Chakravorty, *J. Appl. Phys.* 92, 501 (2002).
617. Z. H. Zhou, J. M. Xue, J. Wang, H. S. O. Chan, T. Yu, and Z. X. Shen, *J. Appl. Phys.* 91, 6015 (2002).
618. J. C. Corral-Huacuz and G. Mendoza-Suarez, *J. Magn. Magn. Mater.* 242, 430 (2002).
619. H. Wang, S. P. Wong, W. Y. Cheung, N. Ke, W. F. Lau, M. F. Chiah, and X. X. Zhang, *Mater. Sci. Eng. C* 16, 147 (2001).
620. A. Voigt, N. Buske, G. B. Sukhorukov, A. A. Antipov, S. Leporatti, H. Lichtenfeld, H. Baumler, E. Donath, and H. Mohwald, *J. Magn. Magn. Mater.* 225, 59 (2001).
621. S. Liu and J. Zhu, *Appl. Phys. A* 70, 673 (2000).
622. T. Hirano, T. Oku, and K. Suganuma, *Diamond Related Mater.* 9, 476 (2000).
623. A. Müller, S. K. Das, H. Bögge, M. Schmidtman, P. Kögerler, A. X. Trautwein, V. Schünemann, E. Krickemeyer, and W. Preetz, *Angew. Chem. Int. Ed.* 39, 3413 (2000).
624. A. Müller, E. Krickemeyer, S. K. Das, S. Sarkar, H. Bögge, M. Schmidtman, P. Kögerler, and Sh. Sarker, *Angew. Chem.* 112, 1674 (2000).
625. A. Müller, P. Kögerler, and H. Bögge, *Springer Struct. Bonding* 96, 203 (2000).
626. L. Cronin, P. Kögerler, and A. Müller, *J. Solid State Chem.* 152, 57 (2000).
627. A. Müller, C. Beugholt, H. Bögge, and M. Schmidtman, *Inorg. Chem.* 39, 3112 (2000).
628. A. Müller, C. Beugholt, P. Kögerler, H. Bögge, S. Bud'ko, and M. Luban, *Inorg. Chem.* 39, 5176 (2000).
629. A. Müller, S. K. Das, H. Bögge, M. Schmidtman, and A. Botar, *Chem. Comm.* 657 (2001).
630. S. Tanase, M. Andruh, A. Müller, M. Schmidtman, C. Mathonière, and G. Rombaut, *Chem. Comm.* 1084 (2001).
631. M. T. Pope and A. Müller, in "Polyoxometalates: From Topology via Self-Assembly to Applications" (M. T. Pope and A. Müller, Eds.), p. 1. Kluwer, Dordrecht, 2001.
632. O. Delgado, A. Dress, and A. Müller, in "Polyoxometalates: From Topology via Self-Assembly to Applications" (M. T. Pope and A. Müller, Eds.), p. 69. Kluwer, Dordrecht, 2001.
633. D. Gatteschi, R. Sessoli, A. Müller, and P. Kögerler, in "Polyoxometalates: From Topology via Self-Assembly to Applications" (M. T. Pope and A. Müller, Eds.), p. 319. Kluwer, Dordrecht, 2001.
634. A. Müller, M. Luban, C. Schröder, R. Modler, P. Kögerler, M. Axenovich, J. Schnack, P. Canfield, S. Bud'ko, and N. Harrison, *Chem. Phys. Chem.* 2, 517 (2001).
635. I. Chiorescu, W. Wernsdorfer, A. Müller, H. Bögge, and B. Barbara, *Phys. Rev. Lett.* 84, 3454 (2000).
636. I. Chiorescu, W. Wernsdorfer, A. Müller, H. Bögge, and B. Barbara, *J. Magn. Magn. Mater.* 221, 103 (2000).
637. I. Chiorescu, W. Wernsdorfer, B. Barbara, A. Müller, and H. Bögge, *J. Appl. Phys.* 87, 5496 (2000).
638. A. Kasuya, H. Takahashi, Y. Saito, T. Mitsugashira, T. Shibayama, Y. Shiokawa, I. Satoh, M. Fukushima, and Y. Nishima, *Mater. Sci. Eng. A* 217, 50 (1996).
639. E. Pasqualini, *Carbon* 35, 783 (1997).
640. H. Abe, *Diamond Related Mater.* 10, 1201 (2001).
641. H. N. Aiyer, R. Seshadri, G. Raina, R. Sen, and C. N. R. Rao, *Fullerene Sci. Tech.* 3, 765 (1995).
642. M. Kusunoki, Y. Ikuhara, and J. Kon, *Jpn. J. Appl. Phys.* 1 34, 1610 (1995).
643. J. Kreuter, in "Colloidal Drug Delivery Systems" (J. Kreuter, Ed.), p. 219. Dekker, New York, 1994.
644. K. Petrak, in "Pharmaceutical Particulate Carriers" (A. Rofland, Ed.), p. 275. Dekker, New York, 1993.
645. M. Donbrow, "Microcapsules and Nanoparticles in Medicine and Pharmacy." CRC Press, Boca Raton, FL, 1992.
646. R. H. Mueller, "Colloidal Carriers for Controlled Drug Delivery and Targeting." CRC Press, Boca Raton, FL, 1991.
647. R. Gref, Y. Minan-iiitake, M. T. Peracchia, A. Domb, V. Trubetskoy, V. Torchilin, and R. Langer, in "Protein Delivery—Physical Systems" (L. M. Sanders and R. W. Hendren, Eds.), Plenum, New York, 1996.
648. R. Gref, Y. Minamitake, M. T. Peracchia, and R. Langer, in "Microspheres/Microparticles Characterization, and Pharmaceutical Application" (S. Cohen and H. Bemstein, Eds.). Dekker, New York, 1996.
649. E. Fattal, M. T. Peracchia, and P. Couvreur, in "Handbook of Biodegradable Polymers" (A. Domb, J. Kost, and D. Wiseman, Eds.). Harwood Academic, Chur, 1996.
650. P. Couvreur, C. Dubernet, and F. Puisieux, *Eur. J. Pharm. Biopharm.* 41, 2 (1995).
651. L. Brannon-Peppas, *Int. J. Pharm.* 116, 1 (1995).
652. C. Vauthier, S. Benabbou, G. Spenlehauer, M. Veillard, and P. Couvreur, *S.T.P. Pharma* 1, 109 (1991).
653. P. Couvreur, and C. Vauthier, *J. Controlled Release* 17, 187 (1991).
654. E. Allemann, R. Gummy, and E. Doelker, *Eur. J. Pharm. Biopharm.* 39, 173 (1993).
655. V. S. Lifshits and G. Y. Zaikov, *Khim.-Farm. Zh.* 25, 15 (1991).
656. F. Chouinard, F. W. K. Kan, C. Foucher, and V. Lenaerts, *Int. J. Pharm.* 72, 211 (1991).
657. R. Arshady, *J. Mol. Recognition* 9, 536 (1996).
658. G. Ponchel, M. J. Montisci, A. Dembri, C. Durrer, and D. Duchene, *Euro. J. Pharm. Biopharm.* 44, 25 (1997).
659. P. Van Gelder, F. Dumas, and M. Winterhalter, *Biophys. Chem.* 85, 153 (2000).
660. S. Bezrukov, M. Winterhalter, and M. Examining, *Phys. Rev. Lett.* 85, 202 (2000).
661. M. Winterhalter, *Curr. Opinion Colloids Interfaces* 5 (2000).
662. C. Nardin, S. Thoeni, J. Widmer, M. Winterhalter, and W. Meier, *Chem. Comm.* 1433 (2000).
663. F. Pincet, E. Perez, G. Bryant, L. Lebeau, and C. Mioskowski, *Phys. Rev. Lett.* 73, 2780 (1994).
664. F. Pincet, E. Perez, L. Lebeau, and C. Mioskowski, *Mod. Phys. Lett. B* 10, 81 (1996).
665. F. Pincet, W. Rawicz, E. Perez, L. Lebeau, C. Mioskowski, and E. Evans, *Phys. Rev. Lett.* 79, 1949 (1997).
666. E. Perez, F. Pincet, M. Goldmann, L. Lebeau, and C. Mioskowski, *Euro. Phys. J. B* 6, 1 (1998).
667. F. Pincet, S. Cribier, and E. Perez, *Euro. Phys. J. B* 11, 127 (1999).
668. U. B. Sleytr, P. Messner, D. Pum, and M. Sára, *Angew. Chem. Int. Ed.* 38, 1034 (1999).
669. B. Schuster, D. Pum, and U. B. Sleytr, *Biochim. Biophys. Acta Biomembranes* 1369, 51 (1998).
670. M. Weygand, B. Wetzler, P. D. Pum, U. B. Sleytr, K. Kjaer, P. B. Howes, and M. Lösche, *Biophys. J.* 76, 458 (1999).

671. M. Weygand, M. Schalke, P. B. Howes, K. Kjaer, J. Friedman, B. Wetzler, P. D. Pum, U. B. Sleytr, and M. Lösche, *J. Mater. Chem.* 1, 141 (2000).
672. S. Küpcü, M. Sára, and U. B. Sleytr, *Biochim. Biophys. Acta* 1235, 263 (1995).
673. C. Mader, S. Küpcü, M. Sára, and U. B. Sleytr, *Biochim. Biophys. Acta* 1418, 106 (1999).
674. C. Mader, S. Küpcü, U. B. Sleytr, and M. Sára, *Biochim. Biophys. Acta* 1463, 142 (2000).
675. T. M. S. Chang, Research Report for Honours Physiology, Medical Library, McGill University, 1957 [reprinted in *Biomater. Artif. Cells Artif. Organs* 16, 1 (1988)].
676. T. M. S. Chang, *Science* 146, 524 (1964).
677. T. M. S. Chang, F. C. MacIntosh, and S. G. Mason, *Can. J. Physiol. Pharmacol.* 44, 115 (1966).
678. T. M. S. Chang, *Trans. Am. Soc. Artif. Intern. Organs* 12, 13 (1966).
679. T. M. S. Chang, "Artificial Cells." Thomas Springfield, 1972.
680. T. M. S. Chang, *Biotechnol. Annu. Rev.* 4, 75 (1998).
681. T. M. S. Chang, *Ann. N. Y. Acad. Sci.* 831, 249 (1997).
682. T. M. S. Chang, *Ann. N. Y. Acad. Sci.* 875, 71, (1999).
683. T. M. S. Chang, *Biomater. Artificial Cells Immobilization Biotechnol.* 21, 291 (1993).
684. T. M. S. Chang, *Artificial Organs* 16, 8 (1992).
685. T. M. S. Chang, *Biomater. Artificial Cells Immobilization Biotechnol.* 20, 1121 (1992).
686. T. M. S. Chang, in "Encyclopedia of Human Biology" (R. Dulbecco, Ed.), p. 457. Academic Press, San Diego, 1997.
687. T. M. S. Chang, *Trends Biotechnol.* 17, 61 (1999).
688. T. M. S. Chang, *Biotechnol. Annu. Rev.* 1, 267 (1995).
689. T. M. S. Chang, *Bioprocess Technol.* 14, 305 (1991).
690. T. M. S. Chang, *Artif. Organs* 22, 958 (1998).
691. T. M. S. Chang, *Eur. J. Pharm. Biopharm.* 45, 3 (1998).
692. T. M. S. Chang, *Kidney Int.* 7, S387 (1975).
693. J. F. Winchester, Hemoperfusion, in "Replacement of Renal Function by Dialysis" (J. F. Maher, Ed.), p. 439. Kluwer Academic, Boston, 1988.
694. T. M. S. Chang and M. J. Poznansky, *Nature* 218, 242 (1968).
695. M. J. Poznansky and T. M. S. Chang, *Biochim. Biophys. Acta* 334, 103 (1974).
696. T. M. S. Chang, *Nature* 229, 117 (1971).
697. L. Bourget and T. M. S. Chang, *Biochim. Biophys. Acta* 883, 432 (1986).
698. T. M. S. Chang, L. Bourget, and C. Lister, *Artificial Cells Blood Substitutes Immobilization Biotechnol.* 23, 1 (1995).
699. C. N. Sarkissian, Z. Shao, F. Blain, R. Peevers, H. Su, R. Heft, and T. M. S. Chang, *Proc. Nat. Acad. Sci.* 96, 2339 (1999).
700. F. Lim and A. M. Sun, *Science* 210, 908 (1980).
701. T. M. S. Chang, *Kidney Int.* 10, S218 (1976).
702. E. A. Friedman, *Am. J. Kidney Dis.* 28, 521 (1996).
703. R. M. Palmour, P. Goodyer, T. Reade, and T. M. S. Chang, *Lancet* 2, 687 (1989).
704. W. M. Kulitreibez and P. P. Lauza, "Cell Encapsulation Technology and Therapy" (W. L. Cuicks, Ed.), Birkhauser, Boston, 1999.
705. D. Hunkeler, A. Prokop, A. D. Cherrington, R. Rajotte, and M. Sefton, *Ann. N. Y. Acad. Sci.* 875, 271 (1999).
706. K. E. Dionne, B. M. Cain, R. H. Li, W. J. Bell, E. J. Doherty, D. H. Rein, M. J. Lysaght, and F. T. Gentile, *Biomaterials* 17, 257 (1996).
707. T. M. S. Chang and S. Prakash, *Mol. Med. Today* 4, 221 (1998).
708. S. Bruni and T. M. S. Chang, *Biomater. Artificial Cells Artificial Organs* 17, 403 (1989).
709. J. N. Daka and T. M. S. Chang, *Biomater. Artificial Cells Artificial Organs* 17, 553 (1989).
710. T. M. S. Chang, *Biomater. Artificial Cells Artificial Organs* 17, 611 (1989).
711. P. Aebischer, M. Schluep, N. Deglon, J. M. Joseph, L. Hirt, B. Heyd, M. Goddard, J. P. Hammang, A. D. Zurn, A. C. Kato, F. Regli, and E. E. Baetge, *Nature Med.* 2, 696 (1996).
712. S. Prakash and T. M. S. Chang, *Nature Med.* 2, 883 (1996).
713. T. M. S. Chang and S. Prakash, in "Methods in Molecular Biology," Expression and Detection of Recombinant Gene Series, Ch. 23, p. 343. Humana, Clifton, NJ, 1996.
714. S. Prakash and T. M. S. Chang, *Biotechnol. Bioengi.* 46, 621 (1995).
715. S. Prakash and T. M. S. Chang, *Artificial Cells Blood Substitutes Immobilization Biotechnol.* 27, 291 (1999).
716. S. Prakash and T. M. S. Chang, *Artificial Cells Blood Substitutes Immobilization Biotechnol.* 27, 475 (1999).
717. C. Kjellstrand, H. Borges, C. Pru, D. Gardner, and D. Fink, *Trans. Am. Soc. Artif. Intern. Org.* 27, 24 (1981).
718. S. Prakash and T. M. S. Chang, *Artificial Cells Blood Substitutes Immobilization Biotechnol.* 28, 397 (2000).
719. S. Prakash and T. M. S. Chang, *Int. J. Artificial Organs* 23, 429 (2000).
720. S. Prakash and T. M. S. Chang, *Trans. Am. Soc. Art. Int. Org.* 45, 150 (2001).
721. T. M. S. Chang and E. Live, *Nature Med.* 3, 2 (1997).
722. K. Setala, H. Heinonen, and L. Schreck-Purla, *IRCS Med. Sci. Nephrol. Urol.* 73, 35 (1973).
723. O. M. Wrong, C. J. Edmonds, and V. S. Chadwick, "The Large Intestine." MTP, Lancaster, 1981.
724. T. M. S. Chang, *Biochem. Biophys. Res. Com.* 44, 1531 (1971).
725. T. M. S. Chang, *Transfusion Med. Rev.* 3, 213 (1989).
726. S. A. Gould, L. R. Sehgal, H. L. Sehgal, R. DeWoskin, and G. S. Moss, in "Blood Substitutes: Principles, Methods, Products and Clinical Trials" (T. M. S. Chang, Ed.), Vol. 2, p. 12. Karger, Basel, 1998.
727. R. Dudziak and K. Bonhard, *Anesthesist* 29, 181 (1980).
728. T. M. S. Chang, "Blood Substitutes: Principles, Methods, Products and Clinical Trials," Vol. 1. Karger, Basel, 1997.
729. L. B. Pearce and M. S. Gawryl, in "Blood Substitutes: Principles, Methods, Products and Clinical Trials" (T. M. S. Chang, Ed.), Vol. 2, p. 82. Karger, Basel, 1998.
730. T. M. S. Chang, "Blood Substitutes and Oxygen Carriers." Dekker, New York, 1992.
731. F. D'Agnillo and T. M. S. Chang, *Nature Biotechnol.* 16, 667 (1998).
732. F. D'Agnillo and T. M. S. Chang, *Free Radical Biol. Med.* 24, 906 (1998).
733. S. Razack, F. D'Agnillo, and T. M. S. Chang, *Artificial Cells Blood Substitutes Immobilization Biotechnol.* 25, 181 (1997).
734. T. M. S. Chang, *Artificial Cells Blood Substitutes Immobilization Biotechnol.* 25, 1 (1997).
735. R. M. Winslow, K. D. Vandegriff, and M. Intaglietta, "Blood Substitutes: Industrial Opportunities and Medical Challenges." Birkhauser, Boston, 1997.
736. H. F. Bunn and J. H. Jandl, *Trans. Assoc. Am. Physicians* 81, 147 (1968).
737. D. J. Nelson, in "Blood Substitutes: Principles, Methods, Products and Clinical Trials" (T. M. S. Chang, Ed.), Vol. 2, p. 39. Karger, Basel, 1998.
738. J. W. Freytag and D. Templeton, in "Red Cell Substitutes: Basic Principles and Clinical Application" (A. S. Rudolph, R. Rabinovici, and G. Z. Feuerstein, Eds.), p. 325. Dekker, New York, 1997.
739. D. H. Doherty, M. P. Doyle, S. R. Curry, R. J. Vali, T. J. Fattor, J. S. Olson, and D. D. Lemon, *Nature Biotechnol.* 16, 672 (1998).
740. L. Djordjevich and I. F. Miller, *Exp. Hematol.* 8, 584 (1980).
741. E. Tsuchida, "Blood Substitutes: Present and Future Perspectives." Elsevier, Amsterdam, 1998.
742. A. S. Rudolph, R. Rabinovici, and G. Z. Feuerstein, "Red Blood Cell Substitutes." Dekker, New York, 1997.

743. W. T. Philips, R. W. Klpper, V. D. Awasthi, A. S. Rudolph, R. Cliff, V. V. Kwasiborski, and B. A. Goins, *J. Pharm. Exp. Therapeutics* 288, 665 (1999).
744. T. M. S. Chang and W. P. Yu, *Artificial Cells Blood Substitutes Immobilization Biotechnol.* 24, 169 (1996).
745. T. M. S. Chang and W. P. Yu, "Blood Substitutes: Principles, Methods, Products and Clinical Trials" (T. M. S. Chang, Ed.), Vol. 2, p. 216. Karger, Basel, 1998.
746. T. M. S. Chang, *Best Practice Res. Clin. Haematol.* 13, 651 (2000).
747. J. Ning and T. M. S. Chang, *Biomater. Artificial Cells Artificial Organs* 18, 219 (1990).
748. J. Ning and T. M. S. Chang, *Biomater. Artificial Cells Artificial Organs* 18, 2037 (1990).
749. J. Ning and T. M. S. Chang, *Int. J. Artificial Organs* 13, 509 (1990).
750. S. V. Walter and T. M. S. Chang, *Biomater. Artificial Cells Artificial Organs* 18, 283 (1990).
751. K. F. Gu and T. M. S. Chang, *Appl. Biochem. Biotechnol.* 26, 115 (1990).
752. K. F. Gu and T. M. S. Chang, *Biotechnol. Appl. Biochem.* 12, 227 (1990).
753. R. Khanna and T. M. S. Chang, *Int. J. Artificial Organs* 13, 189 (1990).
754. V. Dixit and T. M. S. Chang, *ASAIO Trans.* 36, 21 (1990).
755. T. M. S. Chang and C. Lister, *Biomaterials, Artificial Cells Artificial Organs* 18, 693 (1990).
756. R. Sipehia, A. Garfinkle, W. B. Jackson, and T. M. S. Chang, *Biomater. Artificial Cells Artificial Organs* 18, 643 (1990).
757. T. M. S. Chang, *Ann. N. Y. Acad. Sci.* 613, 109 (1990).
758. H. Wong and T. M. S. Chang, *Biomater. Artificial Cells Immobilization Biotechnol.* 19, 675 (1991).
759. S. A. Kashani and T. M. S. Chang, *Biomater. Artificial Cells Immobilization Biotechnol.* 19, 579 (1991).
760. S. A. Kashani and T. M. S. Chang, *Biomater. Artificial Cells Immobilization Biotechnol.* 19, 565 (1991).
761. T. M. S. Chang and R. Dulbecco, Artificial cells, in "Encyclopedia of Human Biology," Vol. 1, p. 377. Academic Press, San Diego, 1991.
762. M. V. Cattaneo and T. M. S. Chang, *ASAIO Trans.* 37, 80 (1991).
763. H. Wong and T. M. S. Chang, *Biomater. Artificial Cells Immobilization Biotechnol.* 19, 687 (1991).
764. M. Mobed and T. M. S. Chang, *Biomater. Artificial Cells Immobilization Biotechnol.* 19, 731 (1991).
765. T. M. S. Chang and C. Lister, *Biomater. Artificial Cells Immobilization Biotechnol.* 20, 565 (1992).
766. M. Mobed and T. M. S. Chang, *Biomater. Artificial Cells Immobilization Biotechnol.* 20, 369 (1992).
767. M. Mobed, T. Nishiya, and T. M. S. Chang, *Biomater. Artificial Cells Immobilization Biotechnol.* 20, 365 (1992).
768. T. M. S. Chang and R. Varma, *Biomater. Artificial Cells Immobilization Biotechnol.* 20, 503 (1992).
769. Y. Ito and T. M. S. Chang, *Artificial Organs* 16, 422 (1992).
770. T. M. S. Chang, *ASAIO J.* 38, 128 (1992).
771. T. M. S. Chang, *Artificial Organs* 16, 71 (1992).
772. T. M. S. Chang, C. Lister, T. Nishiya, and R. Varma, *Biomater. Artificial Cells Immobilization Biotechnol.* 20, 611 (1992).
773. M. Mobed, T. Nishiya, and T. M. S. Chang, *Biomater. Artificial Cells Immobilization Biotechnol.* 20, 53 (1992).
774. T. M. S. Chang, *Biomater. Artificial Cells Immobilization Biotechnol.* 20, 159 (1992).
775. E. Ilan, P. G. Morton, and T. M. S. Chang, *Biomater. Artificial Cells Immobilization Biotechnol.* 20, 263 (1992).
776. I. Lloyd-George and T. M. S. Chang, *Biomater. Artificial Cells Immobilization Biotechnol.* 21, 323 (1993).
777. T. M. S. Chang, *Contributions Nephrol.* 103, 10 (1993).
778. T. M. S. Chang, *Hematol. Pathol.* 7, 49 (1993).
779. J. Koo and T. M. S. Chang, *Int. J. Artificial Organs* 16, 557 (1993).
780. E. Ilan, P. G. Morton, and T. M. S. Chang, *Biochim. Biophys. Acta* 1163, 257 (1993).
781. T. M. S. Chang and C. W. Lister, *Biomater. Artificial Cells Immobilization Biotechnol.* 21, 685 (1993).
782. F. D'Agnillo and T. M. S. Chang, *Biomater. Artificial Cells Immobilization Biotechnol.* 21, 609 (1993).
783. V. Coromili and T. M. S. Chang, *Biomater. Artificial Cells Immobilization Biotechnol.* 21, 427 (1993).
784. T. M. S. Chang and C. W. Lister, *Artificial Cells Blood Substitutes Immobilization Biotechnol.* 22, 171 (1994).
785. T. M. S. Chang and R. Varma, *Artificial Cells Blood Substitutes Immobilization Biotechnol.* 22, 159 (1994).
786. T. Nishiya and T. M. S. Chang, *Artificial Cells Blood Substitutes Immobilization Biotechnol.* 22, 883 (1994).
787. E. Ilan and T. M. S. Chang, *Artificial Cells Blood Substitutes Immobilization Biotechnol.* 22, 687 (1994).
788. E. A. Quebec and T. M. S. Chang, *Artificial Cells Blood Substitutes Immobilization Biotechnol.* 23, 693 (1995).
789. S. Safos and T. M. S. Chang, *Artificial Cells Blood Substitutes Immobilization Biotechnol.* 23, 681 (1995).
790. T. M. S. Chang, *Artificial Cells Blood Substitutes Immobilization Biotechnol.* 23, 257 (1995).
791. S. Prakash and T. M. S. Chang, *Artificial Cells Blood Substitutes Immobilization Biotechnol.* 26, 35 (1998).
792. S. Prakash and T. M. S. Chang, *Artificial Cells Blood Substitutes Immobilization Biotechnol.* 24, 201 (1996).
793. S. Prakash and T. M. S. Chang, *Biomater. Artificial Cells Immobilization Biotechnol.* 21, 629 (1993).
794. M. Mobed and T. M. S. Chang, *Artificial Cells Blood Substitutes Immobilization Biotechnol.* 25, 367 (1997).
795. M. Mobed, M. Eng, and T. M. S. Chang, *Artificial Cells Blood Substitutes Immobilization Biotechnol.* 24, 107 (1996).
796. F. D'Agnillo and T. M. S. Chang, *Artificial Cells Blood Substitutes Immobilization Biotechnol.* 25, 163 (1997).
797. W. P. Yu, J. P. Wong, and T. M. S. Chang, *Artificial Cells Blood Substitutes Immobilization Biotechnol.* 28, 39 (2000).
798. W. P. Yu, J. P. Wong, and T. M. S. Chang, *Artificial Cells Blood Substitutes Immobilization Biotechnol.* 27, 263 (1999).
799. W. P. Yu, J. P. Wong, and T. M. S. Chang, *J. Microencapsulation* 15, 515 (1998).
800. W. P. Yu and T. M. S. Chang, *Artificial Cells Blood Substitutes Immobilization Biotechnol.* 22, 889 (1994).
801. S. Bruni and T. M. S. Chang, *Artificial Cells Blood Substitutes Immobilization Biotechnol.* 27, 343 (1999).
802. S. Bruni and T. M. S. Chang, *Artificial Cells Blood Substitutes Immobilization Biotechnol.* 27, 357 (1999).
803. S. Bruni and T. M. S. Chang, *Int. J. Artificial Organs* 18, 332 (1995).
804. S. Bruni and T. M. S. Chang, *Artificial Organs* 19, 449 (1995).
805. S. Bruni and T. M. S. Chang, *Int. J. Artificial Organs* 14, 239 (1991).
806. M. Roques, C. Damge, C. Michel, C. Staedel, G. Cremel, and P. Hubert, *Diabetes* 41, 451 (1992).
807. D. Hillairebuys, R. Puech, A. Hoeltzel, M. Aprahamian, G. Ribes, and C. Damge, *Diabetologia* 35, A1 (1992).
808. C. Damge, D. Hillairebuys, R. Puech, A. Hoeltzel, C. Michel, and G. Ribes, *Diabetes Nutrition Metabolism* 8, 3 (1995).
809. C. Damge, H. Vranckx, P. Balschmidt, and P. Couvreur, *J. Pharm. Sci.* 86, 1403 (1997).
810. C. Michel, M. Aprahamian, L. Defontaine, P. Couvreur, and C. Damge, *J. Pharm. Pharmacol.* 43, 1 (1991).
811. M. Gallardo, G. Couarraze, B. Denizot, L. Treupel, P. Couvreur, and F. Puisieux, *Int. J. Pharm.* 100, 55 (1993).
812. F. Lescure, C. Zimmer, D. Roy, and P. Couvreur, *J. Colloid Interface Sci.* 154, 77 (1992).
813. M. Roques, G. Cremel, D. Aunis, and P. Hubert, *Diabetologia* 38, 180 (1995).

814. P. Sai, C. Damge, A. S. Rivereau, A. Hoeltzel, and E. Gouin, *J. Autoimmunity* 9, 713 (1996).
815. N. A. Plate, L. I. Valuev, L. K. Staroseltseva, T. A. Valueva, L. V. Vanchugova, M. V. Ulyanova, I. L. Valuev, G. A. Sytov, A. S. Ametov, and V. A. Knyazhev, *Vysokomolekulyarnye Soedineniya Ser. A Ser. B* 36, 1876 (1994).
816. M. Aboubakar, F. Puisieux, P. Couvreur, and C. Vauthier, *Int. J. Pharm.* 183, 63 (1999).
817. M. Aboubakar, F. Puisieux, P. Couvreur, M. Deyme, and C. Vauthier, *J. Biomed. Mater. Res.* 47, 568 (1999).
818. D. Duchene, G. Ponchel, and D. Wouessidjewe, *Adv. Drug Delivery Rev.* 36, 29 (1999).
819. M. Wohlgemuth, W. Machtle, and C. Mayer, *J. Microencapsulation* 17, 437 (2000).
820. D. Katti and N. Krishnamurti, *J. Appl. Polym. Sci.* 74, 336 (1999).
821. P. Sommerfeld, U. Schroeder, and B. A. Sabel, *Int. J. Pharm.* 164, 113 (1998).
822. P. Feng, J. B. Ma, Y. N. Wang, and B. L. He, *Acta Polym. Sinica* 5, 620 (2000).
823. A. Salgueiro, M. A. Egea, R. Valls, M. Espina, and M. L. Garcia, *J. Pharm. Biomed. Anal.* 21, 611 (1999).
824. C. Damge, M. A. A. Prahmanian, W. Humbert, and M. Pinget, *J. Pharm. Pharm.* 52, 1049 (2000).
825. A. Dembri, D. Duchene, and G. Ponchel, *STP Pharma Sci.* 11, 175 (2001).
826. M. Aboubakar, P. Couvreur, H. Pinto-Alphandary, B. Gouritin, B. Lacour, R. Farinotti, F. Puisieux, and C. Vauthier, *Drug Develop. Res.* 49, 109 (2000).
827. S. C. Yang, H. X. Ge, Y. Hu, X. Q. Jiang, and C. Z. Yang, *J. Appl. Polym. Sci.* 78, 517 (2000).
828. J. H. Chen, Z. M. Wang, D. C. Wu, S. D. Xu, H. W. Chen, and A. D. Wen, *J. Fourth Military Med. Univ.* 21, 89 (2000) [in Chinese].
829. J. R. Harris, F. Depoix, and K. Urich, *Micron* 26, 103 (1995).
830. A. M. Hillery, I. Toth, A. J. Shaw, and A. T. Florence, *J. Controlled Release* 41, 271 (1996).
831. A. M. Hillery, I. Toth, A. J. Shaw, and A. T. Florence, *J. Controlled Release* 42, 65 (1996).
832. M. P. Desai, V. Labhasetwar, E. Walter, R. J. Levy, and G. L. Amidon, *Pharm. Res.* 14, 1568 (1997).
833. K. Iwanaga, S. Ono, K. Narioka, K. Morimoto, M. Kakemi, S. Yamashita, M. Nango, and N. Oku, *Int. J. Pharm.* 157, 73 (1997).
834. S. Sakuma, N. Suzuki, H. Kikuchi, K. Hiwatari, K. Arikawa, A. Kishida, and M. Akashi, *Int. J. Pharm.* 149, 93 (1997).
835. W. P. Yu and T. M. S. Chang, *Artificial Cells Blood Substitutes Immobilization Biotechnol.* 24, 169 (1996).
836. A. SilvaCunha, J. L. Grossiord, F. Puisieux, and M. Seiller, *Int. J. Pharm.* 158, 79 (1997).
837. C. Damge, J. Vonderscher, P. Marbach, and M. Pinget, *J. Pharm. Pharm.* 49, 949 (1997).
838. C. A. LeBourlais, F. Chevanne, B. Turlin, L. Acar, H. Zia, P. A. Sado, T. E. Needham, and R. Leverage, *J. Microencapsulation* 14, 457 (1997).
839. S. Dechasteigner, H. Fessi, G. Cave, J. P. Devissaguet, and F. Puisieux, *STP Pharma Sci.* 5, 242 (1995).
840. A. Gursoy, L. Eroglu, and S. Ulutin, *Int. J. Pharm.* 52, 101 (1989).
841. M. Skiba, C. Morvan, D. Duchene, F. Puisieux, and D. Wouessidjewe, *Int. J. Pharm.* 126, 275 (1995).
842. P. Wehrle, B. Magenheimer, and S. Benita, *Euro. J. Pharm. Biopharm.* 41, 19 (1995).
843. F. Fawaz, F. Bonini, M. Guyot, A. M. Lagueny, H. Fessi, and J. P. Devissaguet, *Int. J. Pharm.* 133, 107 (1996).
844. C. W. Maboundou, G. Paintaud, Y. Ottignon, J. Magnette, Y. Bechtel, H. Fessi, F. Gouchet, P. Carayon, and P. Bechtel, *Therapie* 51, 88 (1996).
845. P. Calvo, J. L. VilaJato, and M. J. Alonso, *J. Pharm. Sci.* 85, 530 (1996).
846. S. S. Guterres, V. Weiss, L. D. Freitas, and A. R. Pohlmann, *Drug Delivery* 7, 195 (2000).
847. V. Bertrand, F. Guessous, A. L. Le Roy, B. Viossat, H. Fessi, A. El Abbouyi, J. P. Giroud, and M. Roch-Arveiller, *Digestive Disease Sci.* 44, 991 (1999).
848. P. P. Speiser, *Methods Findings Exp. Clin. Pharmacol.* 13, 337 (1991).
849. V. S. Livshits and G. E. Zaikov, *Int. J. Polym. Mater.* 16, 267 (1992).
850. M. A. Egea, J. Valero, M. V. Girona, and M. L. Garcia, *Analisis* 21, 373 (1993).
851. H. Vranckx, M. Demoustier, and M. Deleers, *Eur. J. Pharm. Biopharm.* 42, 345 (1996).
852. R. Carpignano, M. R. Gasco, and S. Morel, *Pharm. Acta Helveticae* 66, 28 (1991).
853. M. R. Gasco, S. Morel, M. Trotta, and I. Viano, *Pharm. Acta Helveticae* 66, 47 (1991).
854. A. C. Deverdiere, C. Dubernet, F. Nemati, M. F. Poupon, F. Puisieux, and P. Couvreur, *Cancer Chemotherapy Pharmacol.* 33, 504 (1994).
855. N. Henrytoulme, M. Grouselle, and C. Ramaseilles, *Biochem. Pharm.* 50, 1135 (1995).
856. N. Bapat and M. Boroujerdi, *Drug Develop. Ind. Pharm.* 19, 2667 (1993).
857. C. Morin, G. Barratt, H. Fessi, J. P. Devissaguet, and F. Puisieux, *Int. J. Immunopharmacol.* 16, 451 (1994).
858. G. Barratt, F. Puisieux, W. P. Yu, C. Foucher, H. Fessi, and J. P. Devissaguet, *Int. J. Immunopharmacol.* 16, 457 (1994).
859. J. C. Leroux, R. Cozens, J. L. Roesel, B. Galli, F. Kubel, E. Doelker, and R. Gurny, *J. Pharm. Sci.* 84, 1387 (1995).
860. I. Seyler, C. Morin, G. Barratt, M. Appel, J. P. Devissaguet, and F. Puisieux, *Eur. J. Pharm. Biopharm.* 41, 49 (1995).
861. S. S. Guterres, H. Fessi, G. Barratt, F. Puisieux, and J. P. Devissaguet, *Pharm. Res.* 12, 1545 (1995).
862. S. S. Guterres, H. Fessi, G. Barratt, J. P. Devissaguet, and F. Puisieux, *Int. J. Pharm.* 113, 57 (1995).
863. F. Dalencon, Y. Amjaud, C. Lafforgue, F. Derouin, and H. Fessi, *Int. J. Pharm.* 153, 127 (1997).
864. I. Seyler, M. Appel, J. P. Devissaguet, P. Legrand, and G. Barratt, *J. Leukocyte Biol.* 62, 374 (1997).
865. F. B. Landry, D. V. Bazile, G. Spenlehauer, M. Veillard, and J. Kreuter, *J. Drug Targeting* 6, 293 (1998).
866. N. S. Santos-Magalhaes, A. Pontes, V. M. W. Pereira, and M. N. P. Caetano, *Int. J. Pharm.* 208, 71 (2000).
867. H. Marchais, S. Benali, J. M. Irache, C. Tharasse-Bloch, O. Lafont, and A. M. Orecchioni, *Drug Develop. Ind. Pharm.* 24, 883 (1998).
868. M. Paul, A. Laatiris, H. Fessi, B. Dufeu, R. Durand, M. Deniau, and A. Astier, *Drug Develop. Res.* 43, 98 (1998).
869. V. C. F. Mosqueira, P. Legrand, R. Gref, B. Heurtault, M. Appel, and G. Barratt, *J. Drug Targeting* 7, 65 (1999).
870. Z. Lu, J. Z. Bei, and S. G. Wang, *J. Controlled Release* 61, 107 (1999).
871. M. J. Montisci, G. Giovannuci, D. Duchene, and G. Ponchel, *Int. J. Pharm.* 215, 153 (2001).
872. X. Y. Ma, G. M. Pan, Z. Lu, J. S. Hu, J. Z. Bei, J. H. Jia, and S. G. Wang, *Diabetes Obesity Metabolism* 2, 243 (2000).
873. O. Bourdon, V. Mosqueira, P. Legrand, and J. Blais, *J. Photochem. Photobiol. B* 55, 164 (2000).
874. M. Fresta, G. Cavallaro, G. Giammona, E. Wehrli, and G. Puglisi, *Biomaterials* 17, 751 (1996).
875. R. Arshady, in "Microspheres, Microcapsules and Liposomes," MML Ser., Vols. 1 and 2. Citus Books, London, 1999.
876. G. Merhi, A. W. Coleman, J. P. Devissaguet, and G. M. Barratt, *J. Med. Chem.* 39, 4483 (1996).



877. G. Puglisi, M. Fresta, G. Giammona, and C. A. Ventura, *Int. J. Pharm.* 125, 283 (1995).
878. S. Y. Kim, Y. M. Lee, H. J. Shin, and J. S. Kang, *Biomaterials* 22, 2049 (2001).
879. L. Polato, L. M. Benedetti, L. Callegaro, and P. Couvreur, *J. Drug Targeting* 2, 53 (1994).
880. B. Hubert, J. Atkinson, M. Guerret, M. Hoffman, J. P. Devissaguet, and P. Maincent, *Pharm. Res.* 8, 734 (1991).
881. C. Pimienta, F. Chouinard, A. Labib, and V. Lenaerts, *Int. J. Pharm.* 80, 1 (1992).
882. S. Bonduelle, C. Foucher, J. C. Leroux, F. Chouinard, C. Cadieux, and V. Lenaerts, *J. Microencapsulation* 9, 173 (1992).
883. F. Chouinard, S. Buczkowski, and V. Lenaerts, *Pharm. Res.* 11, 869 (1994).
884. J. C. Gautier, J. L. Grangier, A. Barbier, P. Dupont, D. Dussosoy, G. Pastor, and P. Couvreur, *J. Controlled Release* 20, 67 (1992).
885. V. Lenaerts, A. Labib, F. Chouinard, J. Rousseau, H. Ali, and J. Vanlier, *Eur. J. Pharm. Biopharm.* 41, 38 (1995).
886. S. Bonduelle, C. Pimienta, J. P. Benoit, and V. Lenaerts, *Eur. J. Pharm. Biopharm.* 41, 27 (1995).
887. P. Jani, G. W. Halbert, J. Langridge, and A. T. Florence, *J. Pharm. Pharmacol.* 42, 821 (1990).
888. T. K. M. Mbela, J. H. Poupaert, P. Dumont, and A. Haemers, *Int. J. Pharm.* 92, 71 (1993).
889. M. A. Jepson, N. L. Simmons, T. C. Savidge, P. S. James, and B. H. Hirst, *Cell Tissue Res.* 271, 399 (1993).
890. M. Berrabah, D. Andre, F. Prevot, A. M. Orecchioni, and O. Lafont, *J. Pharm. Biomed. Anal.* 12, 373 (1994).
891. C. Morin, H. Fessi, J. P. Devissaguet, F. Puisieux, and G. Barratt, *Biochim. Biophys. Acta—Mol. Cell Res.* 1224, 427 (1994).
892. M. Berrabah, D. Andre, F. Prevot, A. M. Orecchioni, and O. Lafont, *J. Pharm. Biomed. Anal.* 12, 373 (1994).
893. V. Ferranti, H. Marchais, C. Chabenat, A. M. Orecchioni, and O. Lafont, *Int. J. Pharm.* 193, 107 (1999).
894. I. L. G. Shin, S. Y. Kim, Y. M. Lee, C. S. Cho, and Y. K. Sung, *J. Controlled Release* 51, 1 (1998).
895. F. Kedzierewicz, P. Thouvenot, I. Monot, M. Hoffman, and P. Maincent, *J. Biomed. Mater. Res.* 39, 588 (1998).
896. C. R. Muller, V. L. Bassani, A. R. Pohlmann, C. B. Michalowski, P. R. Petrovick, and S. S. Guterres, *Drug Develop. Ind. Pharm.* 26, 343 (2000).
897. S. Benali, C. TharasseBloch, D. Andre, P. Verite, R. Duclos, and O. Lafont, *J. Liquid Chromatogr. Related Tech.* 20, 3233 (1997).
898. P. Calvo, J. L. VilaJato, and M. J. Alonso, *Biomaterials* 18, 1305 (1997).
899. F. Lescure, C. Seguin, P. Breton, P. Bourrinet, D. Roy, and P. Couvreur, *Pharm. Res.* 11, 1270 (1994).
900. P. J. Lowe, and C. S. Temple, *J. Pharm. Pharm.* 46, 547 (1994).
901. J. Barra, A. M. Taburet, A. Jardel, H. Fessi, and F. Puisieux, *J. Chromatogr. B* 661, 178 (1994).
902. Y. E. Shapiro, E. G. Pykhteeva, and G. V. Fedorova, *Bioorganicheskaya Khim.* 23, 174 (1997).
903. C. Nardin, T. Hirt, J. Leukel, and W. Meier, *Langmuir* 16, 1035 (2000).
904. C. Wu, J. Fu, and Y. Zhao, *Macromolecules* 33, 9040 (2000).
905. J. Ma, P. Feng, C. Ye, Y. Wang, and Y. Fan, *Colloid Polym. Sci.* 279, 387 (2001).
906. A. F. Thunemann and S. General, *J. Controlled Release* 75, 237 (2001).
907. G. Lambert, E. Fattal, and P. Couvreur, *Adv. Drug Delivery Rev.* 47, 99 (2001).
908. G. Lambert, E. Fattal, H. Pinto-Alphandary, A. Gulik, and P. Couvreur, *Int. J. Pharm.* 214, 13 (2001).
909. G. Lambert, J. R. Bertrand, E. Fattal, F. Subra, H. Pinto-Alphandary, C. Malvy, C. Auclair, and P. Couvreur, *Biochem. Biophys. Res. Commun.* 279, 401 (2000).
910. L. Marchalheussler, D. Sirbat, M. Hoffman, and P. Maincent, *J. Francais Ophthalmol.* 14, 371 (1991).
911. C. Losa, L. Marchalheussler, F. Orallo, J. L. V. Jato, and M. J. Alonso, *Pharm. Res.* 10, 80 (1993).
912. L. Marchalheussler, D. Sirbat, M. Hoffman, and P. Maincent, *Pharm. Res.* 10, 386 (1993).
913. C. Losa, M. J. Alonso, J. L. Vila, F. Orallo, J. Martinez, J. A. Saavedra, and J. C. Pastor, *J. Ocular Pharm.* 8, 191 (1992).
914. W. P. Yu, G. M. Barratt, J. P. Devissaguet, and F. Puisieux, *Int. J. Immunopharmacol.* 13, 167 (1991).
915. P. Calvo, C. Thomas, M. J. Alonso, J. L. Vilajato, and J. R. Robinson, *Int. J. Pharm.* 103, 283 (1994).
916. M. I. Lopez, J. Martinez, M. Calonge, J. R. Juberias, M. J. Alonso, P. Calvo, and J. C. Pastor, *Invest. Ophthalmol. Visual Sci.* 36, S539 (1995).
917. J. R. Juberias, M. Calonge, S. Gomez, M. I. Lopez, M. J. Alonso, P. Calvo, J. Martinez, I. Aizenman, J. M. Herreras, and J. C. Pastor, *Invest. Ophthalmol. Visual Sci.* 36, S1009 (1995).
918. A. L. L. Boehm, R. Zerrouk, and H. Fessi, *J. Microencapsulation* 17, 195 (2000).
919. P. Calvo, J. L. VilaJato, and M. J. Alonso, *Int. J. Pharm.* 153, 41 (1997).
920. P. Calvo, M. J. Alonso, J. L. VilaJato, and J. R. Robinson, *J. Pharm. Pharm.* 48, 1147 (1996).
921. P. Calvo, A. Sanchez, J. Martinez, M. I. Lopez, M. Calonge, J. C. Pastor, and M. J. Alonso, *Pharm. Res.* 13, 1423 (1996).
922. S. Bonduelle, M. Carrier, C. Pimienta, J. P. Benoit, and V. Lenaerts, *Eur. J. Pharm. Biopharm.* 42, 313 (1996).
923. P. Calvo, A. Sanchez, J. Martinez, M. I. Lopez, M. Calonge, J. C. Pastor, and M. J. Alonso, *Pharm. Res.* 13, 311 (1996).
924. J. Wang and Q. Zhang, *Acta Pharm. Sinica* 22, 57 (2001).
925. J. R. Juberias, M. Calonge, S. Gomez, M. I. Lopez, P. Calvo, J. M. Herreras, and M. J. Alonso, *Current Eye Res.* 17, 39 (1998).
926. M. Fresta, G. Fontana, C. Bucolo, G. Cavallaro, G. Giammona, and G. Puglisi, *J. Pharm. Sci.* 90, 288 (2001).
927. D. Sirbat, L. Marchal-Heussler, M. Hoffman, and P. Maincent, *J. Francais Ophthalmol.* 23, 505 (2000).
928. D. Scherer, J. R. Robinson, and J. Kreuter, *Int. J. Pharm.* 101, 165 (1994).
929. C. Cuvier, L. Roblottreupel, J. M. Millot, G. Lizard, S. Chevillard, M. Manfait, P. Couvreur, and M. F. Poupon, *Biochem. Pharmacol.* 44, 509 (1992).
930. N. Ammoury, H. Fessi, J. P. Devissaguet, F. Puisieux, and S. Benita, *J. Pharm. Sci.* 79, 763 (1990).
931. K. K. Sawant and R. S. R. Murthy, *Pharmazie* 48, 783 (1993).
932. N. Ammoury, H. Fessi, J. P. Devissaguet, M. Allix, M. Plotkine, and R. G. Boulu, *J. Pharm. Pharm.* 42, 558 (1990).
933. N. Ammoury, H. Fessi, J. P. Devissaguet, M. Dubrasquet, and S. Benita, *Pharm. Res.*, 8, 101 (1991).
934. F. Fawaz, F. Bonini, M. Guyot, A. M. Laguény, H. Fessi, and J. P. Devissaguet, *Pharm. Res.* 10, 750 (1993).
935. C. Damge, C. Michel, M. Aprahamian, P. Couvreur, and J. P. Devissaguet, *J. Controlled Release* 13, 233 (1990).
936. A. Labib, V. Lenaerts, F. Chouinard, J. C. Leroux, R. Ouellet, and J. E. Vanlier, *Pharm. Res.*, 8, 1027 (1991).
937. N. S. Magalhaes, H. Fessi, F. Puisieux, S. Benita, and M. Seiller, *J. Microencapsulation* 12, 195 (1995).
938. J. Valero, M. A. Egea, M. Espina, F. Gamisans, and M. L. Garcia, *Drug Develop. Ind. Pharm.* 22, 167 (1996).
939. F. Sordet, Y. Aumjaud, H. Fessi, and F. Derouin, *Parasite—J. Soc. Francaise Parasitol.* 5, 223 (1998).
940. J. Kreuter, *Adv. Drug Delivery Rev.* 7, 71 (1991).
941. P. Couvreur and F. Puisieux, *Adv. Drug Delivery Rev.* 10, 141 (1993).
942. V. Sailhan, L. Giral, C. Montginoul, and F. Schue, *Actualite Chim.* 6, 17 (1995).
943. A. Zimmer and J. Kreuter, *Adv. Drug Delivery Rev.* 16, 61 (1995).

944. Y. V. Pathak and V. D. Labhasetwar, *Cells Mater.* 3, 51 (1993).
945. G. Ponchel and J. M. Irache, *Adv. Drug Delivery Rev.* 34, 191 (1998).
946. D. Quintanar-Guerrero, E. Allemann, H. Fessi, and E. Doelker, *Drug Develop. Ind. Pharm.* 24, 1113 (1998).
947. A. M. Hillery, *Pharm. Sci. Tech. Today* 1, 69 (1998).
948. C. Vauthier, M. Seiller, C. Weingarten, and P. Couvreur, *STP Pharma Sci.* 9, 391 (1999).
949. V. Marsaud, C. Radanyi, and J. M. Renoir, *STP Pharm. Sci.* 9, 397 (1999).
950. P. Legrand, G. Barratt, V. Mosqueira, H. Fessi, and J. P. Devissaguet, *STP Pharm. Sci.* 9, 411 (1999).
951. K. A. Janes, P. Calvo, and M. J. Alonso, *Adv. Drug Delivery Rev.* 47, 83 (2001).
952. Y. Nishioka and H. Yoshino, *Adv. Drug Delivery Rev.* 47, 55 (2001).
953. P. Y. Robert, V. Leconte, C. Olive, V. Ratsimbazafy, M. Javerliat, and J. P. Adenis, *J. Francais Ophtalmol.* 24, 527 (2001).
954. K. Langer, A. Zimmer, and J. Kreuter, *STP Pharma Sci.* 7, 445 (1997).
955. M. N. V. R. Kumar, *J. Pharm. Pharm. Sci.* 3, 234 (2000).
956. E. Allemann, J. C. Leroux, and R. Gurny, *Adv. Drug Delivery Rev.* 34, 171 (1998).
957. L. Mu and S. S. Feng, *J. Controlled Release* 80, 129 (2002).
958. C. Ringard-Lefebvre, A. Bochot, E. Memisoglu, D. Charon, D. Duchene, and A. Baszkin, *Colloids Surfaces B* 25, 109 (2002).
959. T. Pitaksuteepong, N. M. Davies, I. G. Tucker, and T. Rades, *Eur. J. Pharm. Biopharm.* 53, 335 (2002).
960. E. Marie, K. Landfester, and M. Antonietti, *Biomacromolecules* 3, 475 (2002).
961. J. Jang and K. Lee, *Chem. Commun.* 10, 1098 (2002).
962. E. Memisoglu, A. Bochot, M. Sen, D. Charon, D. Duchene, and A. A. Hincal, *J. Pharm. Sci.* 91, 1214 (2002).
963. S. Watnasirichaikul, T. Rades, I. G. Tucker, and N. M. Davies, *Int. J. Pharm.* 235, 237 (2002).
964. Y. Y. Jiao, N. Ubrich, V. Hoffart, M. Marchand-Arvier, C. Vigneron, M. Hoffman, and P. Maincent, *J. Pharm. Sci.* 91, 760 (2002).
965. M. Matoga, F. Pehourcq, F. Lagrange, F. Fawaz, and B. Bannwarth, *J. Pharm. Biomed. Anal.* 27, 881 (2002).
966. J. Whelan, *Drug Discovery Today* 6, 1183 (2001).
967. N. R. Brinkmann, H. F. Schaefer, C. T. Sanderson, and C. Kotal, *J. Phys. Chem. A* 106, 847 (2002).
968. M. Palumbo, A. Russo, V. Cardile, M. Renis, D. Paolino, G. Puglisi, and M. Fresta, *Pharm. Res.* 19, 71 (2002).
969. J. Sinha, B. Raay, N. Das, S. Medda, S. Garai, S. B. Mahato, and M. K. Basu, *Drug Delivery* 9, 55 (2002).
970. I. Seyler, M. Appel, E. Mysiakine, J. P. Devissaguet, and G. Barratt, *STP Pharma Sci.* 11, 363 (2001).
971. M. R. Aberturas, J. Molpeceres, M. Guzman, and F. Garcia, *J. Microencapsulation* 19, 61 (2002).
972. A. P. Colombo, S. Briancon, J. Lieto, and H. Fessi, *Drug Develop. Ind. Pharm.* 27, 1063 (2001).
973. K. N. J. Burger, R. W. H. M. Staffhorst, H. C. de Vijlder, M. J. Velinova, P. H. Bomans, P. M. Frederik, and B. de Kruijff, *Mature Med.* 8, 81 (2002).
974. F. L. Lu and F. C. He, *Progr. Biochem. Biophys.* 28, 832 (2001).
975. M. A. Radwan, *Drug Develop. Ind. Pharm.* 27, 981 (2001).
976. C. R. Muller, S. R. Schaffazick, A. R. Pohlmann, L. D. Freitas, N. P. da Silveira, T. D. Costa, and S. S. Guterres, *Pharmazie* 56, 864 (2001).
977. V. C. F. Mosqueira, P. Legrand, J. L. Morgat, M. Vert, E. Mysiakine, R. Gref, J. P. Devissaguet, and G. Barratt, *Pharm. Res.* 18, 1411 (2001).
978. R. Alvarez-Roman, G. Barre, R. H. Guy, and H. Fessi, *Eur. J. Pharm. Biopharm.* 52, 191 (2001).
979. V. C. F. Mosqueira, P. Legrand, A. Gulik, O. Bourdon, R. Gref, D. Labarre, and G. Barratt, *Biomaterials* 22, 2967 (2001).
980. N. Hussain, V. Jaitley, and A. T. Florence, *Adv. Drug Delivery Rev.* 50, 107 (2001).
981. E. T. Baran, N. Ozer, and V. Hasirci, *J. Microencapsulation* 19, 363 (2002).
982. S. Watnasirichaikul, T. Rades, I. G. Tucker, and N. M. Davies, *J. Pharm. Pharm.* 54, 473 (2002).
983. M. A. Radwan, and H. Y. Aboul-Enein, *J. Microencapsulation* 19, 225 (2002).
984. Y. Y. Jiao, N. Ubrich, M. Marchand-Arvier, C. Vigneron, M. Hoffman, T. Lecompte, and P. Maincent, *Circulation* 105, 230 (2002).
985. M. Skiba, F. Nemat, F. Puisieux, D. Duchene, and D. Wouessidjewe, *Int. J. Pharm.* 145, 241 (1996).
986. I. Seyler, M. Appel, J. P. Devissaguet, P. Legrand, and G. Barratt, *Int. J. Immunopharm.* 18, 385 (1996).
987. M. P. Desai, V. Labhasetwar, G. L. Amidon, and R. J. Levy, *Pharm. Res.* 13, 1838 (1996).
988. J. Kreuter, *J. Anat.* 189, 503 (1996).
989. J. R. Juberias, M. Calonge, S. Gomez, M. I. Lopez, P. Calvo, J. M. Herreras, and M. J. Alonso, *Current Eye Res.* 17, 39 (1998).
990. J. Molpeceres, M. R. Aberturas, M. Chacon, L. Berges, and M. Guzman, *J. Microencapsulation* 14, 777 (1997).
991. A. J. Ferdous, S. D. Bennefield, and M. Singh, *J. Pharm. Biomed. Anal.* 15, 1775 (1997).
992. D. Roy, X. Guillon, F. Lescure, P. Couvreur, N. Bru, and P. Breton, *Int. J. Pharm.* 148, 165 (1997).
993. O. V. Kalyuzhin, A. E. Zemlyakov, and B. B. Fuchs, *Int. J. Immunopharmacol.* 18, 651 (1996).
994. O. Thioune, H. Fessi, J. P. Devissaguet, and F. Puisieux, *Int. J. Pharm.* 146, 233 (1997).
995. P. C. Schulz, M. S. Rodriguez, L. F. Del Blanco, M. Pistonesi, and E. Agullo, *Colloid Polym. Sci.* 276, 1159 (1998).
996. Y. E. Shapiro and E. G. Pykhteeva, *Appl. Biochem. Biotech.* 74, 67 (1998).
997. Y. E. Shapiro, E. G. Pykhteeva, and A. V. Levashov, *J. Colloid Interface Sci.* 206, 168 (1998).
998. D. Quintanar-Guerrero, E. Allemann, E. Doelker, and H. Fessi, *Pharm. Res.* 15, 1056 (1998).
999. A. Bargoni, R. Cavalli, O. Caputo, A. Fundaro, M. R. Gasco, and G. P. Zara, *Pharm. Res.* 15, 745 (1998).
1000. M. V. D. Silva, M. T. Rodriguez-Ares, M. Sanchez-Salorio, M. J. L. Diaz, J. C. Alvarez, J. L. V. Jato, and C. C. Tome, *Graefes Arch. Clin. Exp. Ophthalmol.* 237, 840 (1999).
1001. P. Caliceti and F. M. Veronese, *STP Pharma Sci.* 9, 107 (1999).
1002. L. Marchal-Heussler, P. Thouvenot, M. Hoffman, and P. Maincent, *J. Pharm. Sci.* 88, 450 (1999).
1003. J. M. Barichello, M. Morishita, K. Takayama, and T. Nagai, *Drug Develop. Ind. Pharm.* 25, 471 (1999).
1004. L. Araujo, M. Sheppard, R. Lobenberg, and J. Kreuter, *Int. J. Pharm.* 176, 209 (1999).
1005. K. Tsutsumiuchi, K. Aoi, and M. Okada, *Polym. J.* 31, 935 (1999).
1006. C. Durrer, J. M. Irache, D. Duchene, and G. Ponchel, *STP Pharma Sci.* 9, 437 (1999).
1007. A. Sunder, M. Kramer, R. Hanselmann, R. Mulhaupt, and H. Frey, *Angew. Chem. Int. Ed.* 38, 3552 (1999).
1008. A. M. De Campos, A. Sanchez, and M. J. Alonso, *Int. J. Pharm.* 224, 159 (2001).
1009. T. Govender, S. Stolnik, C. D. Xiong, S. Zhang, L. Illum, and S. S. Davis, *J. Controlled Release* 75, 249 (2001).
1010. Z. R. Cui and R. J. Mumper, *J. Controlled Release* 75, 409 (2001).
1011. B. Heurtault, P. Legrand, V. Mosqueira, J. P. Devissaguet, G. Barratt, and C. Bories, *Ann. Tropical Med. Parasitol.* 95, 529 (2001).
1012. S. S. Guterres, C. R. Muller, C. B. Michalowski, A. R. Pohlmann, and T. D. Costa, *STP Pharma Sci.* 11, 229 (2001).
1013. T. Hamaide, M. Pantiru, H. Fessi, and P. Boullanger, *Macromol. Rapid Commun.* 22, 659 (2001).

1014. W. Tiyaboonchai, J. Woiszwilllo, and C. R. Middaugh, *J. Pharm. Sci.* 90, 902 (2001).
1015. M. J. Montisci, A. Dembri, G. Giovannuci, H. Chacun, D. Duchene, and G. Ponchel, *Pharm. Res.* 18, 829 (2001).
1016. F. Gamisams, C. Solans, M. J. Garcia-Celma, N. Azemar, M. A. Egea, and M. L. Garcia, *J. Controlled Release* 72, 272 (2001).
1017. B. Heurtault, P. Legrand, V. Mosqueira, J. P. Devissaguet, G. Barratt, and C. Bories, *Ann. Tropical Med. Parasitol.* 95, 529 (2001).
1018. B. Z. Putlitz, K. Landfester, H. Fischer, and M. Antonietti, *Adv. Mater.* 13, 500 (2001).
1019. C. Nardin and W. G. Meier, *Chimia* 55, 142 (2001).
1020. S. S. Guterres, H. Fessi, G. Barratt, F. Puisieux, and J. P. Devissaguet, *J. Biomater. Sci. Polym. Ed.* 11, 1347 (2000).
1021. G. B. Sukhorukov, A. A. Antipov, A. Voigt, E. Donath, and H. Mohwald, *Macromol. Rapid Commun.* 22, 44 (2001).
1022. F. Tiarks, K. Landfester, and M. Antonietti, *Langmuir* 17, 908 (2001).
1023. S. D. Desai and J. Blanchard, *Drug Delivery* 7, 201 (2000).
1024. A. K. Gupta, S. Madan, D. K. Majumdar, and A. Maitra, *Int. J. Pharm.* 209, 1 (2000).
1025. S. Watnasirichaikul, N. M. Davies, T. Rades, and I. G. Tucker, *Pharm. Res.* 17, 684 (2000).
1026. G. Lambert, E. Fattal, H. Pinto-Alphandary, A. Gulik, and P. Couvreur, *Pharm. Res.* 17, 707 (2000).
1027. E. Lopes, A. R. Pohlmann, V. Bassani, and S. S. Guterres, *Pharmazie* 55, 527 (2000).
1028. A. R. Kulkarni, K. S. Soppimath, and T. M. Aminabhavi, *J. Microencapsulation* 17, 449 (2000).
1029. E. Cauchetier, M. Paul, D. Rivollet, H. Fessi, A. Astier, and M. Deniau, *Int. J. Pharm.* 30, 777 (2000).
1030. H. Mohwald, *Colloids Surf. A* 171, 25 (2000).
1031. V. C. F. Mosqueira, P. Legrand, H. Pinto-Alphandary, F. Puisieux, and G. Barratt, *J. Pharm. Sci.* 89, 614 (2000).
1032. T. M. S. Chang, F. D'Agnillo, W. P. Yu, and S. Razack, *Adv. Drug Delivery Rev.* 40, 213 (2000).
1033. T. M. S. Chang, *Best Practice Res. Clinical Haematol.* 13, 651 (2000).
1034. R. H. Baughman, A. A. Zakhidov, and W. A. de Heer, *Science* 297, 787 (2002).
1035. M. Sauer and W. Meier, *Chem Commun.* 1, 55 (2001).
1036. T. W. Ebbesen, *J. Phys. Chem. Solids* 58, 1979 (1997).
1037. S. Ahmad, *IETE Tech. Rev.* 16, 297 (1999).
1038. S. Subramoney, *Adv. Mater.* 10, 1157 (1998).
1039. M. S. Dresselhaus and P. C. Eklund, *Adv. Phys.* 49, 705 (2000).
1040. C. N. R. Rao, B. C. Satishkumar, A. Govindaraj, and M. Nath, *Chem. Phys. Chem.* 2, 78 (2001).
1041. P. Moriarty, *Rep. Progr. Phys.* 64, 297 (2001).
1042. J. C. Charlier and S. Iijima, *Topics Appl. Phys.* 80, 55 (2001).
1043. H. J. Dai, *Topics Appl. Phys.* 80, 29 (2001).
1044. S. B. Sinnott and R. Andrews, *Crit. Rev. Solid State Mater. Sci.* 26, 145 (2001).
1045. A. L. Ivanovskii, *Uspekhi Khimii* 71, 203 (2002).
1046. M. Monthieux, *Carbon* 40, 1809 (2002).
1047. Homepage of E. Fattal, <http://efattal.free.fr/>.

# Nanocatalysis

S. Abbet, U. Heiz

University of Ulm, Ulm, Germany

## CONTENTS

1. Introduction
  2. Chemical Reactions on Point Defects of Oxide Surfaces
  3. Chemical Reactions and Catalytic Processes on Free and Supported Clusters
  4. Chemical Reactions Induced by Confined Electrons
  5. Summary
- Glossary  
References

## 1. INTRODUCTION

In the Middle Ages, Jabir Ibn Haiyan, known by the name of the alchemist Geber, paved the way to modern catalysis, and in the beginning of the 19th century, Berzelius defined for the first time the term catalysis [1]. Fritz Haber introduced the important catalytic formation of ammonia at the end of the 19th century [2]. This process allowed the synthesis of fertilizer and explosives on a large scale, and accelerated industrialization in the western world. Today, the introduction of fertilizers still leaves traces in nature, as manifested in the sudden increase of annual rings in old trees. Most catalytically active materials are obtained by trial and error. Since 1960, however, a molecular understanding of catalytic processes has been emerging. The characterization of the active parts in a catalyst is mainly influenced by the resolution of the analytical instruments in use. Today, nanoprobe are capable of seeing single atoms, and thus, examples are emerging where very small clusters are responsible for the catalytic action. Nellist and Pennycook reported that clusters of two and three Pt atoms exist in industrial, naphtha-reforming catalysts [3]. Thus, catalysts in the nanoscale may have been present since the time of Geber, but could not have been detected with the analytical schemes of those days.

Here, we define nanocatalysis when two important conditions are fulfilled. First, the valence electrons of the active part of a nanocatalyst are highly confined, leading to physical and chemical properties nonscalable from bulk properties.

This condition is true for clusters/particles in the nanometer length scale or smaller. Second, nanocatalysts are designed in a controlled manner. The exploration of material properties in the nonscalable regime has profound consequences. Atomic clusters, for example, exhibit unique size-dependent electronic [4, 5], magnetic [6, 7], and chemical properties [8] that differ from those of bulk materials. In contrast to supported particles of larger size or extended solid surfaces, small clusters adsorbed at specific sites of a support material change their intrinsic properties to a large extent, in particular when charging of the cluster occurs. Nanocatalysts exhibit remarkable quantum size effects and structural fluxionality. This opens new avenues for the atom-by-atom design of nanocatalysts whose chemical activity, specificity, and selectivity can be tuned by controlling the cluster size, through the incorporation of impurity atoms, and via manipulation of the strength of the cluster-support interaction, the degree of charging of the cluster, and by changing their magnetic properties. In a completely different approach, catalytic reactions can be induced by nanodevices, where the energy of the localized electrons inducing the reaction can be tuned by changing the potential of the device. An example is the use of an STM tip in close contact with the reactants. In this review, we present some studies on model systems for nanocatalysts. With such systems, the complexity of working nanocatalysts can be reduced, and in many cases, simple reaction steps can be identified. It has to be pointed out that, in this review, we use the expression "catalysis" when a chemical reaction is catalyzed by a nanoscale system. We are aware, however, that none of the systems/methods presented here was tested to withstand the harsh conditions of real catalysis. We feel, though, that such studies are extremely important for developing guiding principles in nanocatalysis.

## 2. CHEMICAL REACTIONS ON POINT DEFECTS OF OXIDE SURFACES

In a recent review, Pacchioni presented a detailed classification of point defects on the surfaces of oxide materials [9]. He described at least four major kinds of irregularities: low-coordinated sites, divacancies, impurity atoms, and surface

vacancies. The last category includes cation vacancies, usually called V centers, as well as oxygen vacancies, which are called color centers or F centers (from the German word for “color”—“Farbe”). In a broader sense, an F center is defined as an electron trapped in an anion vacancy, and was first introduced to explain chemical- and radiation-induced coloration of alkali halides. In bivalent oxides, like MgO and CaO, two types of F centers exist. The vacancy containing two electrons is called the F center, and the one containing only one electron is labeled the  $F^+$  center. In both vacancies, the electrons are confined by the Madelung potential of the crystal. Thus, in a first approach, the  $F/F^+$  centers can be described as two/one electrons moving in a quantum box of nanometer length scale, that is,  $F/F^+$  centers are systems with highly confined electrons, and with our definition, they are examples of nanocatalysts.

The unique chemical activity of F centers has been demonstrated recently. In a combined theoretical and experimental study, it was shown that the heterolytic breaking of methanol on MgO thin films is catalyzed by surface oxygen vacancies [10]. In these films, the oxygen vacancies are generated by changing the preparation method [11], for example, the Mg evaporation rate and the oxygen background pressure. In this way, two kinds of films are prepared: defect-poor (Mg evaporation rate: 0.3–0.5 ML/min,  $O_2$  background:  $5 \cdot 10^{-7}$  torr) and defect-rich (Mg evaporation rate: 2–5 ML/min,  $O_2$  background:  $10^{-6}$  torr) films. Both films are annealed to 1200 and 840 K during 10 min, respectively. Auger electron spectroscopy (AES) measurements show a one-to-one stoichiometry for magnesium and oxygen and the absence of any impurity [12]. Typical thicknesses are about ten monolayers, as determined by AES peak intensities [12] and by X-ray photoemission (XPS), using the intensity attenuation of the Mo 3d core level with increasing film coverage [13]. Both films have also been studied by electron energy loss spectroscopy [13]. In contrast to defect-poor films, which are characterized by a loss at about 6 eV in the EEL spectra (Fig. 1a, in good agreement with previous studies on MgO(100) single crystals [14]), the EEL spectra of defect-rich films exhibit characteristic losses between 1 and 4 eV, lying within the MgO bandgap (Fig. 1a). Similar loss structures have been observed before [15], and according to first-principle calculations using large cluster models, they have been attributed to transitions, characteristic of neutral surface F centers in various coordinations on flat terraces, at steps, and at kinks [16]. The density of these oxygen vacancies is estimated to be larger than  $5 \times 10^{13}/\text{cm}^2$ .

The interaction of methanol with the defect-poor and defect-rich films was studied using thermal desorption spectroscopy (TDS) (Fig. 1c). For both films, the desorption of physisorbed methanol at around 180 K is most dominant. On the defect-poor films, small amounts of chemisorbed methanol desorb up to around 350 K. On defect-rich films, the desorption of chemisorbed methanol evolves in three distinct peaks at 200, 260, and 340 K. A small reproducible feature is observed at around 500 K. Most important,  $H_2$  desorbs at 580 K only on defect-rich films. The corresponding infrared spectra taken at 90 K (insets of Fig. 1c) confirm the presence of mainly physisorbed  $CH_3OH$  with the typical vibrational band for the OH group at  $3285\text{ cm}^{-1}$ , bands of the symmetric C–H stretch ( $2930\text{ cm}^{-1}/2828\text{ cm}^{-1}$ ) and

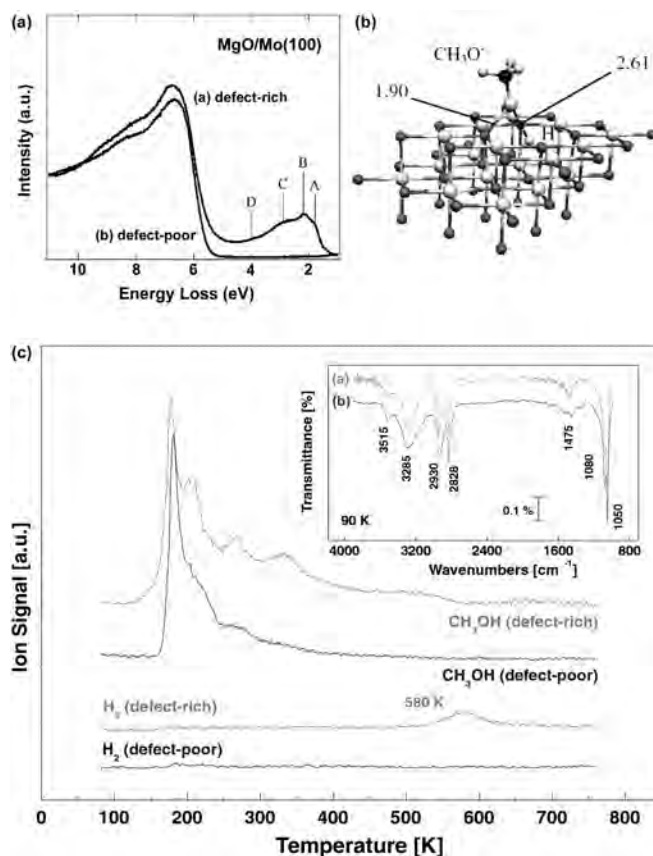


**Figure 1.** (a) EEL spectra of thin defect-poor and defect-rich MgO(100) films grown on Mo(100) at different experimental conditions (see text). A–D are losses, which are attributed theoretically to transitions characteristic of neutral F centers on MgO. (b) Model of an oxygen vacancy at a terrace of a MgO(100) surface with chemisorbed  $CH_3-OH$  ( $CH_3O^-H^+$ ). (c) Thermal desorption spectra of  $CH_3OH$  and  $H_2$  on defect-poor and defect-rich MgO(100) films. Note the desorption of  $H_2$  at 580 K for defect-rich films. The insets show FTIR spectra recorded at 90 K for adsorbed  $CH_3OH$  on both defect-poor and defect-rich films.

the C–H bending ( $1475\text{ cm}^{-1}$ ) modes of the  $CH_3$  group, as well as the C–O vibrational mode at  $1080\text{ cm}^{-1}/1050\text{ cm}^{-1}$ . For defect-poor films, most of the intensity of the vibrational bands disappears between 180 and 200 K, consistent with the desorption observed at 180 K in the TDS. Up to temperatures of about 400 K, small bands are observed for the  $CH_3$ - and C–O bands. Their intensity is decreasing with temperature. These bands are attributed to chemisorbed methanol. As for the defect-rich films, the evolution of the IR spectra with temperature is consistent with the corresponding TDS. Physisorbed methanol desorbs before 200 K (disappearance of the OH band), and the more intense vibrational features of chemisorbed methanol are unambiguously detected up to 360 K. At higher temperatures, a clear peak is observed at  $1070\text{--}1085\text{ cm}^{-1}$  [10]. It is interesting to note that the disappearance of this band correlates with the desorption of  $H_2$  from the surface at around 580 K, and therefore this peak is attributed, in accordance with theoretical studies, to a proton trapped in the cavity of an F center. The calculations show that F centers easily dissociate methanol, giving

a  $\text{CH}_3\text{O}$  group and an  $\text{H}^+$  ion adsorbed into the F center. This adsorbed proton is strongly bound as the dissociation of a neutral H atom,  $\text{F}_s/\text{H}^+ \rightarrow \text{F}_s^+ + \text{H}^\bullet$ , costs 4.1 eV. This represents a crude estimate of the barrier to overcome in order to observe  $\text{H}_2$  desorption from the surface. Once the H atom is detached from the  $\text{F}_s$  center, it will rapidly diffuse on the surface. In fact, the binding of an H atom to an  $\text{O}_{\text{sc}}$  ion on a terrace is about 0.5 eV. Diffusion will eventually lead to recombination with a second H to form  $\text{H}_2$ ;  $\text{H}_2$  is weakly bound to the MgO terrace sites, and at 580 K will immediately desorb. The adsorbed hydrogen gives rise to vibrations of strong intensity at 830–950  $\text{cm}^{-1}$  when isolated, and to an intense band at 1030  $\text{cm}^{-1}$  in the chemisorbed complex shown in Figure 1b. Therefore, the stable species is assigned to H atoms incorporated into oxygen vacancies.

In conclusion, this combined experimental and theoretical study of methanol adsorbed on MgO films with different defect density allows better identification of the surface sites responsible for the MgO reactivity. On the inert terrace sites, only physisorption is observed. Molecular chemisorption, activation, and heterolytic dissociation occur on irregular sites. The low-coordinated Mg–O pairs of ions located at edges and steps can lead to strongly activated, and even dissociated, methanol molecules. Adsorption of  $\text{CH}_3\text{O}$  and  $\text{H}^+$  fragments seems to be preferred over dissociation into  $\text{CH}_3^+$  and  $\text{OH}^-$  units. All of these species are stable on the surface for temperatures up to 350 K, and account for the TDS spectra of the defect-poor films. On defect-rich films (F centers), the O–H bond is selectively dissociated, resulting in the observed desorption of  $\text{H}_2$  at high temperature. Thus, these oxygen vacancy centers, called F centers, act as nanocatalysts.

### 3. CHEMICAL REACTIONS AND CATALYTIC PROCESSES ON FREE AND SUPPORTED CLUSTERS

#### 3.1. Catalytic Processes on Free Metal Clusters

Free clusters are ideal model systems to probe the influence of their intrinsic, size-dependent properties on the catalytic activity due to the lack of any support interactions. Free clusters are prepared by cluster sources [17], and only very low densities are obtained. They are highly unstable at normal conditions and, even under UHV conditions, exothermal catalytic reactions may lead to fragmentation without the presence of a buffer gas. Thus, free clusters may not become relevant for industrial applications. Nevertheless, they are important vehicles to gain a fundamental understanding of nanocatalysis.

The following principle is often used for producing free clusters. The material of interest is evaporated by means of intense laser pulses [18], electrical discharges [19], or highly energetic inert ions [20]. A buffer gas thermalizes the produced ultrahot plasma or supersaturated atomic gas. The mixture expands through a nozzle into the vacuum upon supersonic expansion. By this process, the formed clusters are cooled to cryogenic temperatures, and generate well-defined molecular beams of neutral and charged clusters.

The reactivity of the clusters can then be studied by various experimental techniques, including fast flow reactor kinetics in the postvaporization expansion region of a laser evaporation source [21, 22], ion flow tube reactor kinetics of ionic clusters [23, 24], ion cyclotron resonance [25, 26], guided-ion-beam [27], and ion-trap experiments [28–30]. Which of these techniques is applied depends on the charge state of reactants (neutral, cationic, anionic), on whether the clusters are size-selected before the reaction zone, on single or multiple collisions of the clusters with the reactants, on the pressure of a buffer gas if present, and on the temperature and collision energy of the reactant molecules.

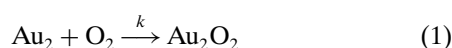
A representative experimental setup may be described in the following way [28]. The cluster anions are produced by a sputter source, and are extracted into a helium-filled quadrupole, where they are cooled down to room temperature and collimated to the axis of the ion optics. A second quadrupole selects a single cluster size. The cluster ions are then transferred with a quadrupole ion guide into an octopole ion trap, which can be continuously cooled from  $T_T = 350$  to 20 K. The potentials on the entrance and exit lenses can be switched in order to fill the trap, store the ions in the trap, and finally extract product ions for mass analysis. Through collisions with a buffer gas (helium or argon) in the trap, the clusters are already thermalized within a few milliseconds. Different reactants can be added to the ion trap under known partial pressures  $p_R$ . Typically, the number of reactant molecules is orders of magnitude higher than the number of clusters, and thus it can be taken as constant. After reaction time  $t_R$ , the charged products are extracted from the trap, and are analyzed by a quadrupole mass spectrometer as a function of  $t_R$ ,  $p_R$ , and  $T_T$ .

With such experimental techniques, the interaction of reactants, for example, CO and  $\text{O}_2$  molecules, or even complete catalytic cycles were observed on small  $\text{Au}_n^-$  anions [30, 31]. By varying the reaction temperatures and measuring the kinetics of the processes, the energetics of complete reaction mechanisms could be obtained and compared with *ab initio* simulations [29, 32]. The reactivity of  $\text{Au}_2^-$  toward  $\text{O}_2$  or CO, as well as the coadsorption of both molecules, revealed an interesting and unexpected selectivity.  $\text{O}_2$  only reacts with even- $n$   $\text{Au}_n^-$  clusters, while odd- $n$  clusters and  $\text{Au}_{16}^-$  are inert. In addition, the reactive clusters adsorb just one  $\text{O}_2$  molecule. The relative reactivities correlate well with measured electron affinities of neutral clusters, suggesting a mechanism involving the adsorption of  $\text{O}_2$  as a one-electron acceptor [33, 34]. The reactivity of gold cluster anions with CO also shows a distinct size selectivity, although less pronounced than the one with  $\text{O}_2$  [35]. In this reaction, the most reactive cluster sizes are  $\text{Au}_{11}$ ,  $\text{Au}_{15}$ , and  $\text{Au}_{19}$ . Most reactive cluster sizes readily adsorb several CO molecules in the saturation limit. Full geometric coverage, for example, one CO per surface gold atom, is, however, never reached. On real catalysts and single crystals, competitive adsorption is usually observed, meaning that, in many examples, CO poisons the active catalysts. This is not true for small  $\text{Au}_n^-$  clusters. On the contrary, for distinct cluster sizes, cooperative adsorption is observed, where the presence of preadsorbates enhances the adsorption probability of subsequent adsorbates. As examples, for  $\text{Au}_3^-$ , preadsorbed CO enables the

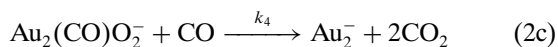
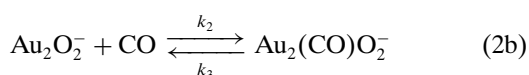
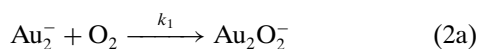


adsorption probability of  $O_2$ ;  $Au_2^-$  is inert for the adsorption of CO at around room temperature; the presence of preadsorbed  $O_2$ , however, makes the adsorption possible at this temperature [30]. A similar effect is observed for  $Au_{10}^-$ , where  $O_2$  enhances the adsorption of CO by more than a factor of 5. Finally,  $Au_6^-$  reveals even an enhanced cooperative adsorption with increasing numbers of adsorbate molecules [31].

Let us now turn our attention to  $Au_2^-$ , where a full catalytic cycle could unambiguously be observed by measuring the kinetics of the process at different temperatures [29]. At room temperature, oxygen reacts by a straightforward association reaction mechanism with the dimer anion, as determined from the measured product ion concentration as a function of the reaction time, and the negative dependence of the reaction rate with temperature:



As mentioned above, no adsorption of CO is observed at around room temperature. When both reactants  $O_2$  and CO are introduced into the ion trap, the reaction kinetics of  $Au_2^-$  changes drastically, as seen by the offset in the  $Au_2^-$  signal. This offset increases when the partial pressure of CO is augmented. In addition, at temperatures below 200 K, the intermediate with the stoichiometry  $Au_2(CO)O_2^-$  could be isolated (Fig. 2A and B). The ion stoichiometry clearly shows that CO and  $O_2$  are able to coadsorb onto an  $Au_2^-$  dimer. From the kinetics of all observable ions,  $Au_2^-$ ,  $Au_2O_2^-$ , and  $Au_2(CO)O_2^-$ , measured under a multitude of different reaction conditions, the catalytic conversion of CO to  $CO_2$  could unambiguously be detected. The reaction mechanism that fulfills all of the prerequisites and fits all kinetic data measured under all of the different reaction conditions could be described by the reaction equations below:



By studying these kinetics as a function of concentration and temperature (Fig. 2B), some important findings can be obtained.

1. Undoubtedly,  $O_2$  adsorption precedes CO adsorption in the catalytic reaction. This is further supported by the reaction kinetics of  $Au_2^-$  when solely  $O_2$  or CO are present in the trap: The adsorption of  $O_2$  is by at least a factor of 10 faster than the adsorption of CO molecules [36].
2. These experiments revealed that varying the oxygen partial pressure inside the trap mainly affects the rate constant  $k_1$  in such a way that  $k_1$  rises linearly with increasing  $p(O_2)$ , and to a smaller extent, the rate constant  $k_4$ , which was attributed to the higher abundance of  $Au_2(CO)O_2^-$ .

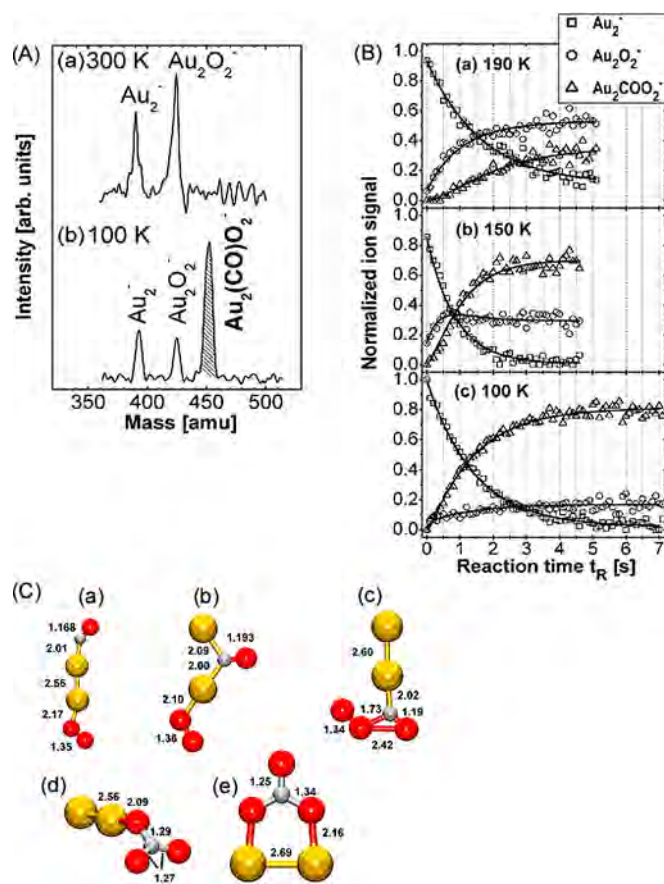


**Figure 2.** (A) Mass spectra of product ion distributions analyzed after trapping  $Au_2^-$  for 500 ms inside the octopole ion trap filled with 0.02 Pa  $O_2$ , 0.05 Pa CO, and 1.23 Pa He. (a) At a reaction temperature of 300 K, only  $Au_2^-$  and  $Au_2O_2^-$  are detected. No further ion signals are observed at temperatures above 200 K. Cooling further down reveals an additional ion signal appearing at the mass of  $Au_2(CO)O_2^-$ . Mass spectrum (b) shows the ion distribution at 100 K. (B) Product ion concentrations as a function of reaction time for three different reaction temperatures. (a)  $T_r = 190$  K;  $p(O_2) = 0.06$  Pa;  $p(CO) = 0.07$  Pa;  $p(He) = 1.0$  Pa. (b)  $T_r = 150$  K;  $p(O_2) = 0.04$  Pa;  $p(CO) = 0.04$  Pa;  $p(He) = 1.0$  Pa. (c)  $T_r = 100$  K;  $p(O_2) = 0.02$  Pa;  $p(CO) = 0.03$  Pa;  $p(He) = 1.0$  Pa. Open symbols represent the normalized experimental data. The solid lines are obtained by fitting the integrated rate equations of the catalytic reaction cycle (see text) to the experimental data. (C) Five optimized structures (a)–(e) of  $Au_2CO_3^-$ , with bond lengths in angstroms. The relative stability of these structures is shown in Table 1. (a), (b), (c), and (e) are planar, and the two carbonate species (d) and (e) have  $C_{2v}$  symmetry.

3. An increase in the carbon monoxide partial pressure results at room temperature in an increasing back reaction rate  $k_2$  in Eq. (2b), that is, the  $Au_2^-$  offset is increasing. Resolving the kinetics at lower temperatures at 190 K reveals a clearly positive dependence of  $k_4$  [in Eq. 2(c)] on  $p(CO)$ , also correlated to the  $Au_2^-$  offset.
4. Finally, with decreasing temperature, the final equilibrium concentration of  $Au_2(CO)O_2^-$  increases, whereas the  $Au_2O_2^-$  concentration decreases (Fig. 2B). This is consistent with the decreasing rate constants  $k_1$ ,  $k_2$ , and  $k_3$  with increasing temperature, and this negative temperature dependence is indicative of barrierless

reaction steps, explained in the framework of the Lindemann theory [36, 37]. Most importantly, however,  $k_4$  increases with increasing temperature. Hence, an activation barrier is involved in the corresponding reaction [Eq. 2(c)].

Further details of the reaction mechanism were obtained by complementary theoretical simulations [32], revealing that the bonding of  $O_2$  to  $Au_2^-$  is characterized by partial electron transfer ( $0.4e$ ) from the metal cluster to the anti-bonding  $\pi$ -orbital of the oxygen molecule, making the oxygen molecule a superoxo-like species. The binding energy is 1.39 eV. The molecular adsorption is energetically clearly favored over dissociative adsorption. In agreement with the experimental findings, the molecular binding is a nonactivated process, that is, a barrierless reaction channel exists for the approaching oxygen molecule, leading to the described configuration. The binding energy of CO to  $Au_2^-$  is 0.91 eV. The stronger binding of  $O_2$  to  $Au_2^-$  explains the observation that high CO partial pressures are required before CO adsorption can compete with  $O_2$  adsorption as the first reaction step.

Five structures corresponding to the mass of the complex  $Au_2(CO)O_2^-$  theoretically predicted, and the pertinent structural and energetic information are given in Figure 2C and Table 1. Structures (a) and (b) correspond to molecular coadsorption of CO and  $O_2$  to  $Au_2^-$ . From the two molecularly coadsorbed species, CO can readily (without barrier) bind to the end of the Au–Au axis [structure (a)], whereas a barrier of 0.2 eV was found for CO association from the gas phase to the Au–Au bridging site of structure (b). The barrier for forming (b) from (a) via diffusion of CO from the end of the complex to the Au–Au bridge is high, on the order of 0.9 eV. In both structures (a) and (b), the O–O bond is activated to a value typical to a superoxo-species (about 1.35 Å). Structure (c) is close to the stability of structure (a). It contains a reacted O–O–C–O group bound to the  $Au_2$  axis via the carbon atom. The O–O bond is activated to a superoxo state, and this species bears some resemblance to the gold–peroxyformate complex identified in the early experiments of gold atoms in cryogenic CO/ $O_2$  matrices [38]. The formation of this species was investigated via two routes: (1) a Langmuir–Hinshelwood (LH) mechanism that involves diffusion of CO from the bridging position in structure (b), and (2) an Eley–Rideal (ER) mechanism where CO(g) approaches the preformed  $Au_2O_2^-$ . The LH mechanism has a high activation barrier of 1.1 eV, and since the barrier is on the order of the activation energy for CO desorption from structure (b) (1 eV), formation of (c)

from (b) is unlikely. Interestingly, mechanism (2) does not involve an activation barrier.

By far the most stable structures corresponding to the mass of  $Au_2(CO)O_2^-$  are the two carbonate species (d) and (e). Structure (e) requires a preformed  $Au_2O_2^-$  where the molecular axes of  $Au_2$  and  $O_2$  lie parallel to each other. Since this structure of  $Au_2O_2^-$  is 1 eV less stable than the ground state discussed above (the binding energy of oxygen in this configuration is 0.39 eV versus the optimal binding energy of 1.39 eV), it is unlikely to be formed, and consequently, structure (e) does not play a relevant role in the catalytic cycle. On the other hand, formation of the most stable structure (d) by an ER mechanism with CO(g) inserted in the middle of the O–O bond in  $Au_2O_2^-$  requires a barrier of only 0.3 eV, which is easily overcome under the experimental conditions. The absence of the complex  $Au_2C_2O_4^-$  in the experimental mass spectrum, as well as the calculated high barriers for CO diffusion along the Au–Au axis, justify the considerations of only ER mechanisms for the final reaction step [Eq. 2(c)]. It is also worth noting that further intermediates such as  $Au_2O^-$  and  $Au_2CO_2^-$  are not observed experimentally. This leads to only two possible scenarios for the final reaction step 2c: ER reactions of CO(g) with structures (c) or (d), and the reaction proceeds to completion, releasing 2CO<sub>2</sub> molecules. The formation of CO<sub>2</sub> from the reaction between CO(g) and structure (c) (Fig. 2C) involves a low barrier of 0.3 eV, resulting in the formation of a metastable  $Au_2CO_2^-$  complex, where CO<sub>2</sub> is bound to  $Au_2$  via the carbon atom. However, the large heat of reaction (4.75 eV) from the formation of the first CO<sub>2</sub> molecule is much more than that needed to overcome the binding energy (0.52 eV) of the remaining CO<sub>2</sub> to  $Au_2^-$ , readily facilitating its desorption from the metal cluster. The second scenario involves two branches [32]. First, thermal dissociation of CO<sub>2</sub> from the carbonate (d) is endothermic by 1.12 eV, but produces highly reactive  $Au_2O^-$  which reacts without a barrier with CO(g) to produce CO<sub>2</sub>. Second, the ER reaction of CO(g) with (d) to produce CO<sub>2</sub> involves a modest barrier of 0.5 eV, but readily releases two CO<sub>2</sub> molecules since the remaining  $Au_2CO_2^-$  configuration, where CO<sub>2</sub> is bound to  $Au_2$  via one of the oxygen atoms, is unstable. This is the more likely branch to occur in the experiments (100–300 K) described above. Thus, these studies showed that both experimental and theoretical results prove the existence of the full catalytic cycle.

In another example [39, 40], it was demonstrated that gas-phase platinum cluster anions,  $Pt_n^-$  ( $n = 3-7$ ), efficiently catalyze the oxidation of CO to CO<sub>2</sub> in the presence of N<sub>2</sub>O or O<sub>2</sub> near room temperature in a full thermal catalytic reaction cycle. At the end of the process, the intact cluster is regenerated, and each step is exothermic, and occurs rapidly at thermal energies. In these experiments, the produced  $Pt_n^-$  clusters are first thermalized by collisions with a buffer gas. When either O<sub>2</sub> or N<sub>2</sub>O is introduced downstream in the flow tube,  $Pt_nO^-$  and  $Pt_nO_2^-$  ions are formed in rapid exothermic reactions [41]. With the introduction of CO into the gas cell, the  $Pt_n^-$  clusters reappear, as observed with mass spectrometry. From these experiments, it was concluded that neutral CO<sub>2</sub> is stoichiometrically formed on the clusters, and that negligible fragmentation of the metal cluster for  $n \geq 4$  occurs. Further experiments revealed that, at low energies,

**Table 1.** Relative stability, vertical electron detachment energy, binding energy of CO (with  $O_2$  preadsorbed) and binding energy of  $O_2$  (with CO preadsorbed), for the five structures (a)–(e) of  $Au_2CO_3^-$  shown in Figure 2C.

Structure	$\Delta E$ (eV)	VDE (eV)	BE(CO) (eV)	BE( $O_2$ ) (eV)
(a)	2.80	2.82	0.93	1.34
(b)	2.94	3.32	0.78	1.20
(c)	2.82	3.82	0.91	1.32
(d)	0	4.67	3.72	4.14
(e)	1.04	3.38	2.69	3.10

the cross section approaches the calculated collision limit, meaning that the reactions are quite efficient. When  $\text{Pt}_n\text{O}_2^-$  ions are selected initially, sequential loss of oxygen atoms is observed to form two  $\text{CO}_2$  products, as shown by CO pressure dependence studies. This observation implies that  $\text{O}_2$  is dissociatively adsorbed on the metal cluster as oxygen atoms, rather than chemisorbed or physisorbed as molecular  $\text{O}_2$ . Two other observations support this conclusion: (1)  $\text{Pt}_n\text{O}_2^-$  ions produced by reaction of the bare cluster with either  $\text{O}_2$  or  $\text{N}_2\text{O}$  show the same reactivity; and (2) collision-induced dissociation of  $\text{Pt}_n\text{O}_2^-$  shows a loss of oxygen atoms with no  $\text{O}_2$  loss. The regeneration of  $\text{Pt}_n^-$  ions at low energies proves that a full catalytic oxidation cycle can be completed at near room temperature, in either a single-step or a two-step process. Reaction efficiencies for the oxidation of the first CO molecule were measured for  $\text{Pt}_n\text{O}^-$  or  $\text{Pt}_n\text{O}_2^-$  ( $n = 3-6$ ). The reaction efficiencies for a single collision are greater than 40% for  $n \geq 4$ , so only a few collisions would be required for complete conversion. From this, it was concluded that, at near room temperatures, the gas-phase metal cluster anions are better catalysts than the supported catalysts used in current technology for automotive catalytic converters. These need to be heated to high temperatures, on platinum surfaces; temperatures of  $400 \pm 500$  K are typically required for the oxidation of CO [42].

Both examples revealed unique and size-dependent catalytic properties of very small metal clusters. As mentioned in the Introduction, gas-phase clusters will probably never be important in real catalysis; however, such small clusters can be stabilized on support materials, and they may become relevant for future applications.

## 3.2. Chemical Reactions and Catalytic Cycles on Supported Clusters

### 3.2.1. Single Atoms on Oxide Surfaces

F centers can act as nanocatalysts; however, few reactions are catalyzed by oxygen vacancies because only two confined electrons at the same energy level are present. In order to change these two parameters (number of confined electrons and energy levels) without modifying the size of the quantum box, the F center can be decorated with metal atoms to produce a third kind of nanocatalyst: supported atoms on oxide surfaces.

The metal atoms are produced by a recently developed high-frequency laser evaporation source [12]. The positively charged ions are guided by home-built ion optics through differentially pumped vacuum chambers, and are size-selected by a quadrupole mass spectrometer (Extrel Merlin System; mass limits: 1000, 4000, 9000 amu). In these experiments, it is important to deposit only 0.5–0.8% of a monolayer atom ( $1 \text{ ML} = 2 \times 10^{15}$  clusters/ $\text{cm}^2$ ) at 90 K with low kinetic energy in order to land them isolated on the surface and to prevent agglomeration on the defect-rich MgO films. The presence of isolated atoms is confirmed experimentally and theoretically. Experimentally, nickel atoms, dimers, and trimers are used as it is well known that they form stable metalcarbonyls. This carbonyl formation of small deposited  $\text{Ni}_n$  ( $n = 1-3$ ) was studied by exposing the deposited clusters to carbon monoxide. Mass

spectrometry experiments showed that the nuclearity of the formed  $\text{Ni}_n$  carbonyls ( $n = 1-3$ ) is not changed. The absence of, for example,  $\text{Ni}_2(\text{CO})_x$  and  $\text{Ni}_3(\text{CO})_x$  after deposition of Ni atoms directly excludes agglomeration, whereas the absence of  $\text{Ni}(\text{CO})_4$  after depositing  $\text{Ni}_2$  excludes fragmentation of the cluster, relevant for the experiments described in the next section [43]. Second, Monte Carlo simulations revealed that, under such experimental conditions, for example, cluster flux ( $\sim 10^9 \text{ cm}^{-1}$ ), cluster density ( $\sim 10^{13} \text{ cm}^{-1}$ ), and defect density ( $\sim 5 \cdot 10^{13} \text{ cm}^{-1}$ ) on the MgO(100) films, less than 10% of the atoms coalesce when migrating to the trapping centers [44].

To characterize the model catalysts in detail, it is, however, necessary to identify the adsorption sites of the clusters. One possibility is studying the adsorption of probe molecules on the deposited clusters by means of TDS and Fourier transform infrared (FTIR) spectroscopies. As an example [45], CO desorbs from the adsorbed Pd atoms at a temperature of about 250 K, which corresponds to a binding energy  $E_b$  of about  $0.7 \pm 0.1$  eV. FTIR spectra suggest that, at saturation, two different sites for CO adsorption exist on a single Pd atom. The vibrational frequency of the most stable, singly adsorbed CO molecule is  $2055 \text{ cm}^{-1}$ . Density functional cluster model calculations have been used to model possible defect sites at the MgO surface where the Pd atoms are likely to be adsorbed. CO/Pd complexes located at regular or low-coordinated O anions of the surface exhibit considerably stronger binding energies,  $E_b = 2-2.5$  eV, and larger vibrational shifts than were observed in the experiment. CO/Pd complexes located at oxygen vacancies (F or  $\text{F}^+$  centers) are characterized by much smaller binding energies,  $E_b = 0.5 \pm 0.2$  or  $0.7 \pm 0.2$  eV, which are in agreement with the experimental value. Such comparisons therefore identify adsorption sites of the clusters on the MgO surface; particularly in the examples shown below, these trapping centers are shown to be oxygen vacancies.

After characterizing this type of nanocatalyst consisting of metal atoms trapped on oxygen vacancies, simple reactions like acetylene polymerization or CO oxidation can be studied by means of temperature-programmed reaction studies and infrared spectroscopy.

For cyclotrimerization on Ag, Pd, and Rh atoms and CO oxidation on Pd atoms, the nanocatalysts were exposed at 90 K, using a calibrated molecular beam doser, to about 1 Langmuir (L) of acetylene or 1L of  $^{18}\text{O}_2$  and  $^{13}\text{CO}$ , respectively. In a temperature-programmed reaction (TPR) study, catalytically formed benzene ( $\text{C}_6\text{H}_6$ ), butadiene ( $\text{C}_4\text{H}_6$ ), and butene ( $\text{C}_4\text{H}_8$ ) or  $^{13}\text{C}^{18}\text{O}^{16}\text{O}$  molecules were detected by a mass spectrometer, and were monitored as a function of temperature. It is interesting to note that the reactants ( $^{13}\text{CO}$ ,  $^{18}\text{O}_2$ ,  $\text{C}_2\text{H}_2$ ) are only physisorbed on the MgO, and desorb at temperatures lower than 150 K in all three cases, for example, before the reaction takes place. In addition, the interaction of the product molecules with the model catalysts is weak, as described in [45, 46]. The thermal stabilities of the deposited Pd and Rh atoms were investigated by using Fourier transform infrared spectroscopy and the probe molecule CO. It was found that Pd starts to migrate at around 300 K [45], whereas Rh is stable up to 450 K [47].

Surprisingly, and in contrast to single-crystal studies [48], a single Pd atom already catalyzes the cyclotrimerization

reaction, and the benzene molecule ( $C_6H_6$ ) is desorbing at 300 K (Fig. 3a). No other product molecules of the polymerization reaction (e.g.,  $C_4H_6$ ,  $C_4H_8$ ) are observed. Thus, this model catalyst is highly selective for the polymerization reaction. We note that, on a clean MgO(100) surface,

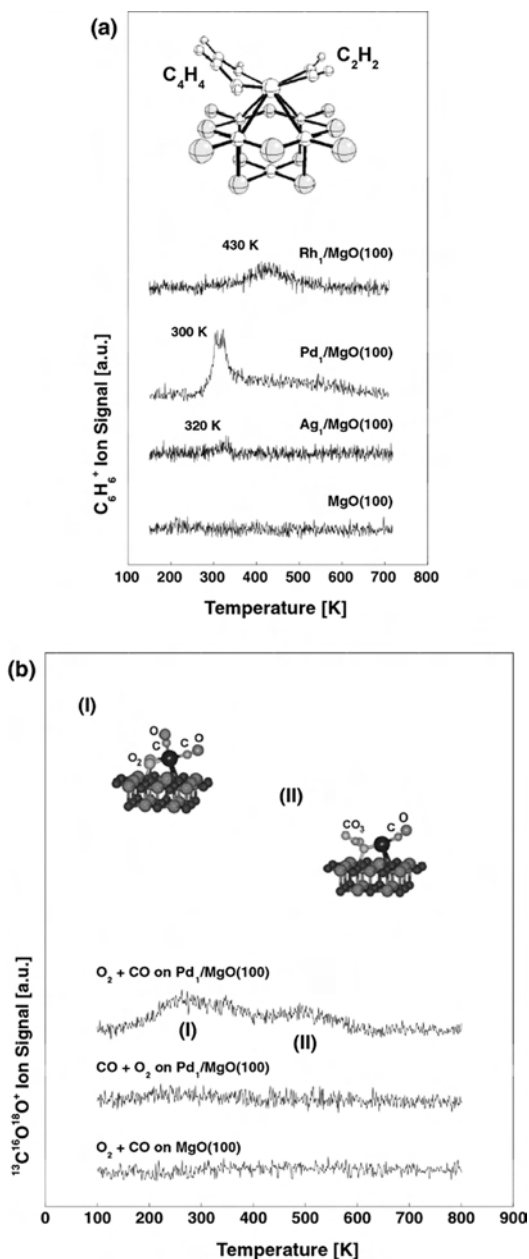


**Figure 3.** (a) Temperature-programmed reaction (TPR) spectra of  $C_6H_6$  formed on Ag, Pd, and Rh atoms deposited on defect-rich MgO thin films grown on Mo(100) surfaces. As a comparison, the same experiment was performed on a clean defect-rich MgO film. Also shown is the calculated  $(C_4H_4)(C_2H_2)/Pd_1/F_{5c}$  intermediate of the cyclotrimerization reaction on Pd atoms adsorbed on an F center of the MgO(100) surface. (b) TPR spectra of  $CO_2$  from a defect-rich MgO thin film and deposited Pd atoms after exposure to  $O_2$  and CO (lower and upper spectrum), as well as from deposited Pd atoms after exposure to CO and  $O_2$ . Calculated precursors of the two observed mechanisms (I) and (II) are also depicted.

none of the products is formed (Fig. 3a). This surprising result can be rationalized by theoretically studying a palladium atom adsorbed on different MgO sites represented by a cluster of ions embedded in an array of point charges [49]. First, a Pd atom was adsorbed on a five-coordinated oxygen ion on the MgO(001) terrace  $O_{5c}$ ; the binding energy is about 1 eV. It was found that, indeed, the  $Pd(C_4H_4)$  complex, is formed, but the third acetylene molecule is not bound to the complex, and therefore this configuration is catalytically inactive. Other bonding sites for the adsorption of Pd atoms are considered. On four-coordinated step or three-coordinated corner oxygen sites,  $O_{4c}$  and  $O_{3c}$ , respectively, the Pd atom binds slightly stronger, with an energy of 1.2–1.5 eV; in addition, the atom is more reactive. However, on both  $O_{3c}$  and  $O_{4c}$  sites, the third  $C_2H_2$  molecule is only weakly bound or even unbound to the  $Pd(C_4H_4)$  surface complex, with the binding energy smaller than the activation energy of the formation of  $C_6H_6$ . Thus, Pd atoms adsorbed on  $O_{nc}$  sites cannot explain the observed activity. This is consistent with the results of the study on the adsorption properties of CO on Pd<sub>1</sub>/MgO [45], as the experimental results have been rationalized in terms of Pd atoms, which are stabilized on oxygen vacancies (F centers) in neutral or charged states,  $F_s$  or  $F_s^+$ , respectively. The interaction of a Pd atom with the F center is much stronger, 3.4 eV, which makes these centers good candidates for Pd binding. On  $F_s^+$  centers, binding energies of about 2 eV have been computed [45]. The presence of trapped electrons at the defect site results in a more efficient activation of the supported Pd atom. In fact, the complex  $(C_4H_4)(C_2H_2)/Pd_1/F_{5c}$ , Figure 3a, shows a large distortion and a strong interaction of the third  $C_2H_2$  molecule. These results indicate that F and  $F^+$  centers can act as basic sites on the MgO surface, and turn the inactive Pd atom into an active catalyst. Notice that the supported Pd atoms on defect sites not only activate the cyclization reaction, but also favor benzene desorption, as shown by the very small  $(C_6H_6)/Pd_1/F_{5c}$  adsorption energy. The complete reaction path for this specific nanocatalyst has been calculated [49]. The first barrier of the reaction path is the one for the formation of the intermediate  $Pd(C_4H_4)$ , and it is 0.48 eV only. The formation of the  $C_4H_4$  intermediate is thermodynamically favorable by 0.82 eV. On  $(C_4H_4)/Pd_1/F_{5c}$ , the addition of the third acetylene molecule is exothermic by 1.17 eV, leading to a very stable  $(C_4H_4)(C_2H_2)/Pd_1/F_{5c}$  intermediate (Fig. 3a). To transform this intermediate into benzene, one has to overcome a barrier of 0.98 eV. The corresponding energy gain is very large, 3.99 eV, and mainly related to the aromaticity of the benzene ring. Once formed,  $C_6H_6$  is so weakly bound to the supported Pd atom that it immediately desorbs. Thus, the reaction on Pd/ $F_{5c}$  is rate-limited in the last step, the conversion of  $(C_4H_4)(C_2H_2)$  into  $C_6H_6$ . This is different from the Pd(111) surface where the rate-determining step for the reaction is benzene desorption. The calculations are consistent with the experimental data. In fact, on Pd<sub>1</sub>/ $F_{5c}$ , the computed barrier of 0.98 eV corresponds to a desorption temperature of about 300 K, as experimentally observed, Figure 3a. On Pd(111) surfaces, the bonding of benzene is estimated to be  $\approx 1.9$  eV. This binding is consistent with a desorption temperature of 500 K, as observed for a low coverage of  $C_6H_6$  on Pd(111) [50].

The electronic structure of palladium atoms,  $4d^{10}5s^0$ , is unique, and may be responsible for this specific catalytic property for acetylene cyclotrimerization. This raises the question of whether other transition metal atoms are also reactive for this reaction. Results are shown for deposited Rh ( $4d^85s^1$ ) and Ag ( $4d^{10}5s^1$ ) atoms. Ag atoms are almost unreactive (Fig. 3a); on supported Rh atoms, however, benzene is formed, and desorbs at around 430 K (Fig. 3a).

For CO oxidation, it was first verified that the clean MgO(100) thin films are inert; for example, no  $^{13}\text{C}^{16}\text{O}^{18}\text{O}$  was formed in a one-heating-cycle experiment after adsorbing  $^{18}\text{O}_2$  and  $^{13}\text{C}^{16}\text{O}$  (Fig. 3b) or vice versa [51]. When Pd atoms are trapped on the  $F_{5c}$ , preadsorption of oxygen and subsequent saturation of CO leads to the formation of carbon dioxide, with desorption peaks at 260 K and at around 500 K (Fig. 3b). The existence of two desorption peaks in the TPR spectrum (Fig. 3b) suggests the presence of two different reaction mechanisms. Note that preadsorption of  $^{13}\text{CO}$  suppresses the catalytic process as it poisons the nanocatalyst (Fig. 3b). *Ab initio* calculations showed that a single Pd atom strongly binds to the oxygen vacancy (binding energy of 3.31 eV), with a small amount of charge (0.15  $e$ ) transferred to the adsorbed atom. In comparison, the binding energy of Pd atoms to terrace oxygen sites is only 1.16 eV. The enhanced binding to the  $F_{5c}$  is also reflected in the corresponding bonding lengths of 1.65 and 2.17 Å for MgO( $F_{5c}$ )-Pd and MgO-Pd, respectively. Binding of two CO molecules saturates the MgO( $F_{5c}$ )-Pd system; occupying the MgO( $F_{5c}$ )-Pd system with three CO molecules leads to spontaneous (barrierless) desorption of one of the molecules. In the most stable configuration, the two CO molecules are not equivalent; one CO binds on top, and the second adsorbs on the side of the Pd atom (this top-side geometry is similar to that shown in Fig. 3bI, but without the  $\text{O}_2$ ), and the total binding energy of the two CO molecules is 1.62 eV. To study the oxidation mechanisms of CO on MgO( $F_{5c}$ )-Pd, the system was optimized first with coadsorbed  $\text{O}_2$  and two CO molecules. Two stable geometric arrangements were found, with the most stable one shown in Figure 3bI where the CO molecules bind in a top-side configuration, and the  $\text{O}_2$  is adsorbed parallel to the surface on the other side of the Pd atom. The adsorbed  $\text{O}_2$  molecular bond is stretched and activated (1.46 Å compared to the calculated gas-phase value of 1.25 Å). In addition, a stable carbonate complex Pd( $\text{CO}_3$ )(CO) was found (Fig. 3bII), whose binding energy is 4.08 eV larger than the aforementioned Pd( $\text{CO}$ ) $_2$ ( $\text{O}_2$ ) complex. These complexes were identified by comparison of calculated and spectroscopically measured CO vibrational frequencies [52]. Two reaction mechanisms are proposed corresponding to the two  $\text{CO}_2$  peaks observed experimentally (Fig. 3b). At low temperatures, the two relevant precursors are shown in Figure 3bI and 3bII. Corresponding to the  $\text{CO}_2$  desorption peak at 260 K, the following reaction mechanism is proposed. In a competitive process, CO desorbs or is oxidized upon heating. The theoretically estimated activation energies of the two processes are 0.89 eV for desorption and 0.84 for oxidation. The formation of  $\text{CO}_2$  at higher temperatures (corresponding to desorption at around 500 K, Fig. 3b) involves decomposition of the Pd( $\text{CO}_3$ )(CO) carbonate complex (Fig. 3bII).

This mechanism is observed in molecular dynamics simulations where the temperature is controlled to 500 K by Langevin dynamics.

### 3.2.2. Size-Selected Clusters on Oxide Surfaces

By decorating F centers with atoms, it is possible to increase the number of confined electrons, but modifying the size of the quantum box only slightly. By using size-selected clusters instead of atoms, the confinement of the valence electrons is subtler, and the examples presented below reveal the possibility of tuning the efficiency and selectivity of chemical reactions atom by atom by simply changing the cluster size or doping the cluster with impurity atoms. Furthermore, a comparison of the experimental results with first-principles theoretical simulations provides insights into the physical factors and microscopic mechanisms that govern nanocatalysis.

The metal clusters are produced by the same high-frequency laser evaporation source used to produce metal atoms. In this source, a cold He pulse (40 K) thermalizes the laser-produced plasma [12]. Subsequent supersonic expansion of the helium-metal vapor leads to cold clusters with a narrow kinetic energy distribution ( $E_{\text{kin}} \leq 0.2$  eV/atom). The positively charged clusters guided by ion optics through differentially pumped vacuum chambers and size-selected by a quadrupole mass spectrometer (Extrel Merlin System; mass limit: 1000, 4000, 9000 amu) are then deposited with low kinetic energy (<0.2 eV/atom) on MgO(100)/Mo(100) thin films; under these conditions, the clusters softland on the substrate. In fact, when exploring the chemical or catalytic properties of nanoassembled materials consisting of small monodispersed clusters on surfaces, the key challenge is to preserve the identity of the cluster upon deposition. Upon impact, a redistribution of the total energy of the cluster takes place. In the deposition process, this energy consists of the cluster's kinetic and internal energy, the binding energy between the cluster and substrate, and an eventual Coulomb energy between the cluster ion and an induced image charge (metal) or surface-charge density (dielectric) on the support. The amount of this energy is decisive for the degree of melting, disordering, fragmentation, implantation, or rebounding of the cluster. The cluster-surface and Coulomb interactions are intrinsically given by the chosen cluster and support materials, whereas the internal and kinetic energies can be changed, to a large extent, by the experimental conditions. Softlanding is defined as a collision outcome allowing for plastic deformation of the cluster, but not for fragmentation and implantation into the substrate [53]. Molecular dynamic studies [54–56] have shown that cluster implantation occurs at about 1 eV/atom kinetic energy of the cluster, regardless of the cluster-substrate system. Consequently, this value represents the upper kinetic energy limit for softlanding conditions. Softlanding of size-selected  $\text{Si}_{30}$  and  $\text{Si}_{39}$  clusters on Ag(111) was observed in recent low-temperature STM experiments performed at a kinetic energy well below the softlanding limit and without rare buffer layers, that is, under the same experimental conditions as the experiments shown below [57]. Finally, to prepare cluster-assembled nanocatalysts, less than 0.5% of an ML of size-selected clusters ( $1 \text{ ML} = 2 \times 10^{15}$  clusters/cm $^2$ ) are deposited at 90 K,



in order to land them isolated on the surface and to prevent agglomeration of the cluster on the surface. Under these experimental conditions, the landing and migration and trapping of the clusters on the surface were investigated with Monte Carlo simulations [44]. These simple calculations show that the preparation of samples with monodispersed clusters is possible only when a small number of clusters is deposited. In order to prepare clusters on identical adsorption sites, it is therefore essential to use support materials with low defect densities for systems with a strong cluster–support interaction or to use surfaces with high defect densities when the cluster–support interaction is weak. The deposition of the clusters on defects is additionally favored by the recently discovered “funnel” effect [7]; *ab initio* calculations revealed that clusters are attracted, for example, by F centers, well before landing on the surface.

### Changing Catalytic Efficiency Atom by Atom: Oxidation of Carbon Monoxide on Pure and Strontium-Doped Gold Nanocatalysts

In the first example, we focus on gold nanocatalysts, which led recently to the most remarkable and rather surprising findings. More specifically, low adsorption energies and high activation barriers for the dissociation of small molecules on extended gold surfaces are responsible for the nobleness of gold as bulk material [58]. Nanosize particles of gold, however, show high and rather unusual catalytic reactivity [59, 60]. While novel heterogeneous catalysis by nanosize gold aggregates supported on oxides is of great significance, the processes underlying the catalytic activity of gold in reduced dimensions and the reaction mechanisms are not yet understood, and still represent an enigma in catalysis. In the following, these issues are addressed theoretically and experimentally through investigations of the low-temperature combustion of CO on size-selected gold clusters,  $Au_n$  ( $n \leq 20$ ), and strontium-doped gold clusters,  $SrAu_n$  ( $n \leq 7$ ), supported on defect-poor and defect-rich MgO(100) films [11, 61].

Subsequent to verification that oxidation of CO does not occur on bare MgO substrate films (with and without defects), the catalyzed combustion of CO by nanosize gold and strontium-doped gold clusters adsorbed on the two different MgO films was studied by temperature-programmed reaction (TPR) experiments. Isotopically labeled  $^{18}O_2$  and  $^{13}CO$  were used to disentangle the  $CO_2$  production on the cluster from an eventual catalytic oxidation of CO involving oxygen atoms from the MgO substrate. Indeed, the  $^{13}CO$  molecule is exclusively oxidized by  $^{18}O_2$  since only the  $^{13}C^{16}O^{18}O$  isotopomer is detected. Furthermore, the experiments revealed that the pure gold clusters up to the heptamer are inert for the oxidation of CO, and that the low-temperature ( $T \sim 250$  K) combustion of CO is most effective for  $Au_8$ . By doping gold clusters with strontium, the number of gold atoms in the smallest catalytic active cluster size is reduced to just three. In addition, these results revealed that, for example,  $Au_8$ , the smallest active cluster size turns inert when depositing it on defect-poor films. This indicates that substrate defects are important when trying to understand the factors which govern the chemical properties of nanoscale, supported clusters (Fig. 4A).

Let us turn our intention first to the reaction mechanism and role of defect sites in the case of  $Au_8$ . When first

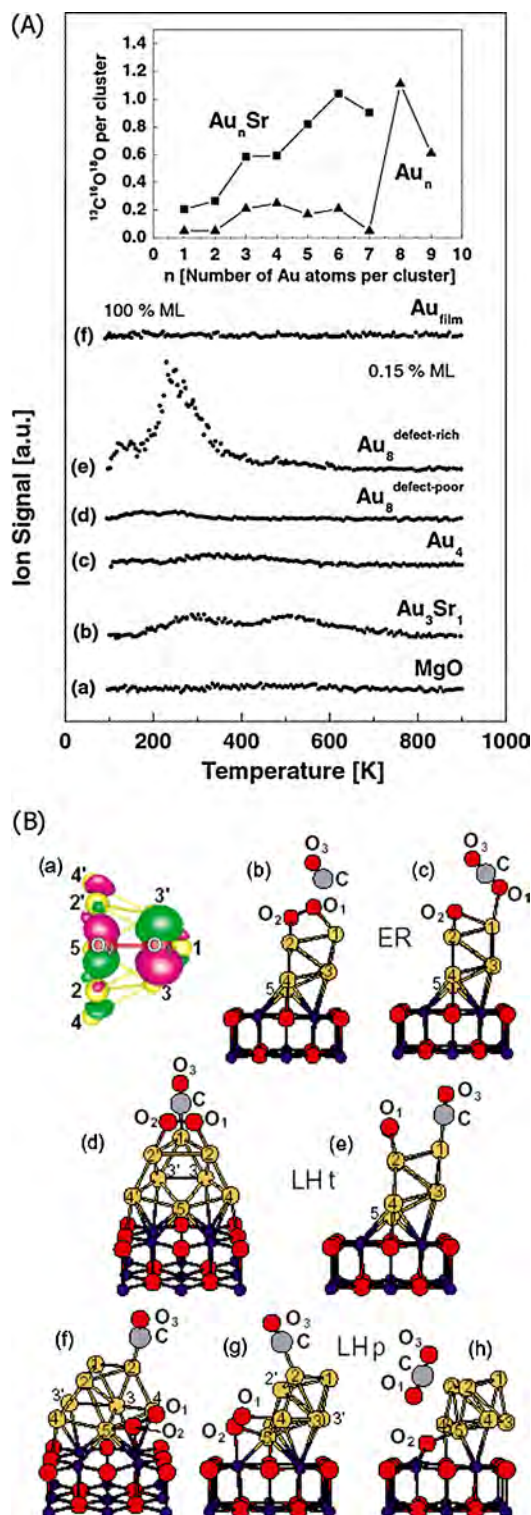


**Figure 4.** (A) TPR spectra of  $CO_2$  from a defect-rich MgO thin film (a), various pure and mixed  $Au_n$  and  $Au_nSr$  clusters (b)–(e), as well as from a thin Au-film grown on a defect-rich MgO thin film (f). The reactivity expressed as the number of formed  $CO_2$  molecules per cluster is shown for cluster sizes up to  $Au_9$ . (B) Calculated snapshots of three different reaction mechanisms (ER, LHt, LHp) for the oxidation of CO on  $Au_8$  adsorbed on an F center of an MgO(100) surface.



deposited on MgO(100) films with a vanishing number of F centers, the catalytic activity observed experimentally during one heating cycle reveals a very small combustion of CO at temperatures between 150 and 250 K (Fig. 4a–d). Surprisingly, the CO-combustion on Au<sub>8</sub> at 250 K dramatically increases when depositing the octamer on defect-rich MgO films (Fig. 4a–e). This particular behavior pertains even after several reaction cycles, up to temperatures of 350 K. It indicates that the model catalyst is thermally stable, and the reaction heat of the combustion of CO does not change the cluster's structure, an important issue when using Au<sub>8</sub> as a real catalyst. Evaluating the area of the TPR signal yields the production of about one CO<sub>2</sub> molecule per Au<sub>8</sub> cluster. To explore the energetics and reaction mechanisms underlying the above observations, extensive *ab-initio* simulations were performed [11, 62]. Figure 4B summarizes the energetics and atomic configurations of the initial, transition, and final states proposed for the combustion of CO at 140 and 250 K catalyzed by Au<sub>8</sub> clusters adsorbed on MgO(FC). Both O<sub>2</sub> and CO adsorb on the Au<sub>8</sub> cluster supported on the MgO(100) surface (with or without FC defects). However, the observed single sharply peaked stretch frequency of adsorbed CO with  $\nu_a = 2102 \text{ cm}^{-1}$  compared to  $\nu_a = 2143 \text{ cm}^{-1}$  for the free <sup>12</sup>C<sup>16</sup>O molecule implies a single adsorption site on the cluster, and a rather minor influence of adsorption on the internal structure and bonding of the molecule. Indeed, it is found that, in the optimal adsorption configuration, CO binds on top of an Au atom of the upper triangular facet of the adsorbed Au<sub>8</sub> cluster (see Fig. 4B(d), (f) initial state) with  $d(\text{CO}) = 1.14 \text{ \AA}$  (compared to 1.13 Å in the free molecule) and  $d(\text{AuC}) = 1.92 \text{ \AA}$ . On the other hand, an O<sub>2</sub> molecule may readily adsorb at several sites, both on the upper Au<sub>8</sub> facet (Fig. 4B(d)) and at the interface between the adsorbed gold cluster and the underlying magnesia surface (Fig. 4B(f)). In all cases, the adsorbed molecule is found to be activated to a peroxy O<sub>2</sub><sup>\*</sup> molecular state with a weakened highly stretched intramolecular bond length (1.41–1.46 Å) compared to that in the free molecule (1.24 Å). The activation of the adsorbed oxygen molecule involves occupation of the antibonding  $\pi^*$  molecular orbital (i.e., the molecular oxygen  $\pi_g^*$  orbital oriented parallel to the adsorbing surface), which hybridizes with the orbitals of neighboring gold atoms of the partially negatively charged adsorbed gold cluster.

The two reaction pathways, which may mainly contribute to the observed oxidation of CO, are of the Langmuir–Hinshelwood (LH) type. For the formation of CO<sub>2</sub> at 140 K, the two reactants are initially coadsorbed on the triangular top facet of the Au<sub>8</sub> cluster, with the distance between the carbon atom and one of the peroxy oxygens in this local minimum state equal to 3.11 Å ( $d(\text{CO}_1)$ ) (Fig. 4B(d); initial state); in the following, this LH top-facet reaction mechanism is labeled LHt. Through mapping of the potential energy surface along the C–O<sub>1</sub> reaction coordinate (via total relaxation of the system with the variable C–O<sub>1</sub> distance as a constraint), a rather low energy barrier  $\Delta E_b$  (LHt) = 0.1 eV occurring at  $d_b(\text{CO}_1) \approx 2.0 \text{ \AA}$  is determined for the LHt oxidation channel with the end product of a weakly adsorbed carbon dioxide molecule ( $\sim 0.2 \text{ eV}$ ). The total exothermicity of the reaction  $\text{MgO(FC)/Au}_8 + \text{O}_2(\text{g}) + \text{CO}(\text{g}) \rightarrow \text{MgO(FC)/Au}_8\text{O} + \text{CO}_2(\text{a})$  is  $\sim 4.8 \text{ eV}$ , and it is  $\sim 5 \text{ eV}$  when

the CO<sub>2</sub> product is desorbed; here, (g) and (a) denote gas-phase and adsorbed molecules, respectively. This LHt low-temperature oxidation mechanism was found by these studies (with similar energetics) for reactions on the gold cluster deposited on either a defect-free MgO(100) surface or on one containing an FC, and both are expected to be relatively insensitive to the Au<sub>n</sub> cluster size, correlating with the experimental results. As aforementioned, the higher temperature channel is strongly enhanced for Au<sub>8</sub> supported on a defect-rich MgO(100) support (compare the CO<sub>2</sub> signals at  $\sim 240 \text{ K}$  in Fig. 4A(d), (e)). This trend correlates with the simulations of an LH-periphery (LHp) reaction mechanism, starting with the CO adsorbed on the top facet of the Au<sub>8</sub> cluster and the peroxy O<sub>2</sub><sup>\*</sup> molecule bonded to the periphery of the interfacial layer of the cluster (Fig. 4B-f; initial state), where the distance between the C atom and the oxygen marked O<sub>1</sub> is  $d(\text{CO}_1) = 4.49 \text{ \AA}$ . Indeed, mapping of the potential energy surface along the C–O<sub>1</sub> reaction coordinate revealed for MgO(FC)/Au<sub>8</sub> a rather broad reaction barrier  $\Delta E_b(\text{LHp}) \sim 0.5 \text{ eV}$  at  $d_b(\text{CO}_1) \sim 2.0 \text{ \AA}$ , while for the defect-free substrate, a significantly higher barrier was found,  $\Delta E_b(\text{LHp}) \sim 0.8 \text{ eV}$ ; the reaction product is shown in Figure 4B-h for the MgO(FC)/Au<sub>8</sub> catalyst. Another reaction path was theoretically found, starting from the optimal configuration of O<sub>2</sub><sup>\*</sup> adsorbed on the MgO(FC)/Au<sub>8</sub> catalyst. A gas-phase CO molecule brought to the vicinity of the peroxy molecule reacts spontaneously (without an energy barrier), forming a carbon dioxide molecule weakly bound to the catalyst. This Eley–Rideal (ER)-type reaction mechanism corresponds to the low-temperature generation of (weakly adsorbed) CO<sub>2</sub> through direct reaction of gaseous CO with a preadsorbed peroxy O<sub>2</sub><sup>\*</sup> molecule. This reaction channel can occur even at 90 K, that is, during the initial dosing stage in the experiment.

The catalytic behavior can further be changed by cluster size and impurity doping. To understand the origin of this size-dependent and element-specific behavior, the atomic structure and the electronic spectra of these model catalysts were studied by extensive first-principles simulations, and the optimized structures of Au<sub>8</sub> (with two relevant isomers), Au<sub>4</sub>, and Au<sub>3</sub>Sr adsorbed on MgO(FC) are shown in Figure 5, before (a–d) and after (e–h) O<sub>2</sub> adsorption.

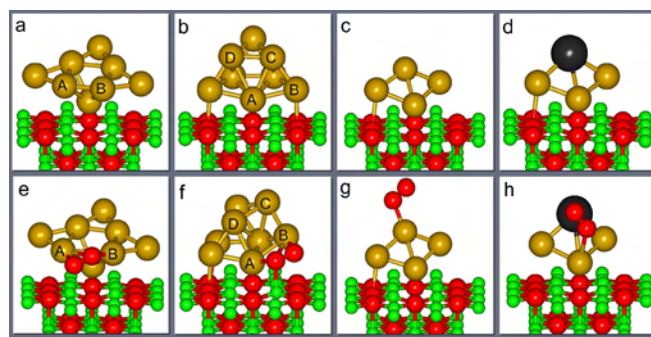


**Figure 5.** Optimized atomic structures of nanocatalysts comprised of Au<sub>8</sub> (a), (b), Au<sub>4</sub> (c), and Au<sub>3</sub>Sr (d) clusters adsorbed at an F center of an MgO(100). For Au<sub>8</sub>, two relevant isomers, separated by an energy difference of 0.29 eV, are shown. The optimal adsorption geometries of the O<sub>2</sub> molecule to these nanocatalysts are shown in panels (e)–(h).

As shown above, these clusters bind to the MgO(FC) surface quite strongly (calculated binding energy of 2.65–4.06 eV), and their binding is significantly enhanced (typically by about 2 eV) due to the F center defects. These high binding energies and the “anchoring” effect by the F centers correlate well with the observed thermal stability of the supported clusters in the TPR experiments. Another important finding pertains to the charge state of the adsorbed clusters—in particular, our calculations predict that the interaction with the surface is accompanied by a charge transfer [11] of  $0.5e$ ,  $0.3e$ , and  $0.3e$  to the adsorbed  $\text{Au}_8$ ,  $\text{Au}_4$ , and  $\text{Au}_3\text{Sr}$  clusters, respectively.

Binding and activation of molecular  $\text{O}_2$  by the model catalyst are necessary elementary steps in the CO oxidation process [63, 64], and thus, understanding the structural, dynamical, electronic, and compositional factors that govern these processes are key to elucidation of the observed size-dependent activity of the  $\text{Au}_n/\text{MgO}(\text{FC})$  model catalysts. Indeed, these first-principles simulations show that the binding energy of  $\text{O}_2$  to the supported  $\text{Au}_n$  clusters and the degree of O–O bond activation are strongly dependent on the cluster size. In contrast, the adsorption energy of CO to the supported clusters is relatively insensitive to the cluster size, and it is higher than that of oxygen (0.7–1.0 eV per CO molecule, depending on coverage). Consequently, in the following, the adsorption and activation of  $\text{O}_2$  by the supported gold nanoclusters is studied in more detail, to illustrate the aforementioned nanocatalytic factors that govern this key reaction step.

**Structural Dynamical Fluxionality** The capability of small clusters to exhibit several structural forms (isomers) of comparable energies, and to interconvert between such isomers at a finite temperature, is one of the hallmarks of cluster science. This unique structural variability may influence the chemical reactivity of nanocatalytic systems in two main ways. First, at a finite temperature, the model catalyst (and, in particular, the cluster component) will form an equilibrium ensemble of coexisting structural configurations, with various isomers exhibiting different chemical reactivities. This is illustrated here via the two structural isomers of the  $\text{Au}_8$  cluster with the two-layered one (Fig. 5b), which is thermodynamically less stable (by 0.29 eV) than the quasipolar isomer (Fig. 5a), showing a higher energy gain upon oxygen adsorption (0.47 eV compared to 0.28 eV for the latter isomer). Second, and most importantly, is the structural dynamic fluxionality of clusters in the course of reactions that expresses itself in the ability of a given structural isomer to dynamically adapt its structure such as to allow the reaction to evolve on the most favorable free-energy path. Such fluxional propensity is illustrated in Figure 5b and f, where the more reactive two-layered  $\text{Au}_8$  cluster is shown to undergo a large structural transformation upon adsorption of molecular oxygen at the “periphery site,” that is, the approximate bi-capped octahedral geometry (Fig. 5b) is transformed to a bi-capped trigonal prism (Fig. 5f). Note that the structural fluxionality is essential for the reaction to occur since it was found that constraining the cluster to maintain its original geometry (Fig. 5b) prevents the adsorption and activation of  $\text{O}_2$ .

**Electronic Size Effects** Understanding the size-dependent electronic structure of the  $\text{Au}_n/\text{MgO}(\text{FC})$  model catalysts, which is fundamental for elucidation of their atom-by-atom controlled reactivity, is facilitated by the analysis of the spectra of the local density of electronic states (LDOS) projected on the oxygen molecule and on the metal cluster; a similar analysis is often employed in the context of the interaction of adsorbates with extended surfaces [65]. The LDOS projected on the  $\text{O}_2$  molecule which is adsorbed at the periphery site (Fig. 5f) of the more reactive isomer of the  $\text{Au}_8/\text{MgO}(\text{FC})$  model catalyst was investigated. All of the prominent peaks of the LDOS spectrum can be unambiguously assigned to orbitals of (free) molecular oxygen origins. In addition, these states overlap with the entire  $d$  band of the  $\text{Au}_8$  cluster in the range of  $-7 \text{ eV} \leq E \leq E_F$ , where  $E_F$  is the Fermi energy. Bonding of the oxygen molecule to the gold octamer mainly involves hybridization of the  $5\sigma$ ,  $1\pi_{\parallel}$ , and  $1\pi_{\perp}$  oxygen states with the gold  $d$  band. Most importantly, the full spin manifold of the antibonding  $2\pi^*$  states of  $\text{O}_2$  is located below  $E_F$ , resulting in strong activation of the  $\text{O}_2$  molecule through occupation of the antibonding orbitals. This leads to weakening of the O–O bond that is reflected in a significant increase of its length (1.43 Å in Fig. 5f) compared to that of the free molecule (1.25 Å). Accompanying the activation process is a change in the spin state of the molecule from a triplet state in the gas phase to a peroxo-like adsorbed state with a zero net spin.

A drastically different scenario is found for the interaction of  $\text{O}_2$  with the smaller gold cluster,  $\text{Au}_4/\text{MgO}(\text{FC})$ , where molecular oxygen adsorbs in an “on-top” configuration, with one of the oxygen atoms binding to a single gold atom (Fig. 5g). This system exhibits rather weak binding of the molecule to the metal cluster (0.18 eV), an almost unperturbed O–O bond length (1.28 Å), and a spin splitting of the oxygen-projected LDOS spectrum. The weak binding is attributed to the narrower  $d$  band of the adsorbed  $\text{Au}_4$  cluster compared to that of  $\text{Au}_8$ , with a consequent lack of overlap between the states at the bottom of the  $d$  band of the gold cluster and the molecular oxygen states with energies  $E < -5 \text{ eV}$ . Moreover, the spin-down antibonding  $2\pi^*_{\perp}$  and  $2\pi^*_{\parallel}$  orbitals of the adsorbed oxygen molecule are now located above  $E_F$  (unlike the case of the larger cluster), which results in no activation of the molecule by the adsorbed  $\text{Au}_4$  cluster.

**Impurity-Doping Effects** Finally, we address the possibility of enhancing the catalytic activity of a nanocluster by designed incorporation (doping) of an impurity, demonstrated here by the catalyzed oxidation of CO on  $\text{Au}_3\text{Sr}/\text{MgO}(\text{FC})$ . The LDOS spectra projected onto the oxygen molecule, the Sr atom, and the  $\text{Au}_3$  part of the metal cluster were obtained. Doping by a single impurity atom significantly changes the bonding and activation of  $\text{O}_2$  compared to the pure gold tetramer,  $\text{Au}_4$ , case; the bonding of  $\text{O}_2$  is mainly to the strontium atom of the  $\text{Au}_3\text{Sr}$  cluster (Fig. 5h), and it is characterized by a substantially higher adsorption energy (1.94 eV compared to 0.18 eV for the configuration shown in Fig. 5g) and a significant activation of the O–O bond that is reflected in an increased bond length of 1.37 Å. This activation is due to occupation of the spin-down  $2\pi^*_{\perp}$  oxygen orbital, resulting in a superoxo-like state of the adsorbate. Bonding of the oxygen molecule

to  $\text{Au}_3\text{Sr}/\text{MgO}(\text{FC})$  occurs via resonances formed between the Sr states in the energy intervals 5–6 eV and 0–1 eV below  $E_F$ , with the spin-up  $1\pi_{\parallel}$  and  $2\pi_{\perp}^*$  states, as well as with the spin-down  $1\pi_{\perp}$  and  $2\pi_{\perp}^*$  orbitals, of the adsorbed activated  $\text{O}_2$ .

### Changing Catalytic Selectivity Atom by Atom: Polymerization of Acetylene on Palladium Nanocatalysts

Another important factor in catalysis is the selectivity of a catalytic reaction. So far, however, information on the atom-by-atom evolution of this astonishing catalytic selectivity is still lacking. In this example, we illustrate such a size-dependent selectivity with the polymerization of acetylene on palladium nanocatalysts [46]. This reaction over supported Pd particles reveals a direct correspondence between reactivities observed on model systems and the behavior of industrial catalysts under working conditions [66]. In ultra-high vacuum (UHV) [67] as well as under high pressure, large palladium particles of typically thousands of atoms show an increased selectivity for the formation of benzene with increasing particle size [66]. In contrast, small palladium particles of typically hundreds of atoms are less selective for the cyclotrimerization, and catalyze butadiene and butene as additional products [66].

The TPR spectra of the different products of the polymerization of acetylene on small, monodispersed palladium clusters supported on defect-rich MgO thin films are shown in Figure 6. Striking atom-by-atom size-dependent reactivities and selectivities are observed. Only the three reaction products  $\text{C}_6\text{H}_6$ ,  $\text{C}_4\text{H}_8$ , and  $\text{C}_4\text{H}_6$  are detected. Remarkably, no  $\text{C}_3\text{H}_n$ ,  $\text{C}_5\text{H}_n$ , and  $\text{C}_8\text{H}_n$  are formed, indicating the absence of C–C bond scission, as already observed on Pd single crystals [68] and Pd particles [66]. Up to  $\text{Pd}_3$ , only benzene is catalyzed, reflecting a high selectivity for the cyclotrimerization of acetylene.  $\text{Pd}_n$  ( $4 \leq n \leq 6$ ) clusters reveal a second reaction channel by catalyzing, in addition, the formation of  $\text{C}_4\text{H}_6$ , which desorbs at around 300 K. The third reaction product,  $\text{C}_4\text{H}_8$ , desorbing at a rather low temperature of 200 K, is clearly observed for  $\text{Pd}_8$ . For this cluster size, the abundance of the three reaction products is similar. For even larger clusters ( $13 \leq n \leq 30$ ), the formation of  $\text{C}_6\text{H}_6$  is increasing with cluster size, whereas the conversion of acetylene into  $\text{C}_4\text{H}_8$  reaches a maximum for  $\text{Pd}_{20}$ . Note that  $\text{Pd}_{30}$  selectively suppresses the formation of  $\text{C}_4\text{H}_6$ . (The peak in the TPR spectrum of  $\text{C}_4\text{H}_6$  at 200 K is part of the fragmentation pattern of  $\text{C}_4\text{H}_8$ .) For  $\text{Pd}_{20}$ , the experiments were repeated in the presence of  $\text{D}_2$  [46];  $\text{D}_2$  was exposed prior to and after  $\text{C}_2\text{H}_2$ . The results clearly indicate that no product containing deuterium is formed. Consequently,  $\text{D}_2$  is not involved in the polymerization reaction. However, the presence of  $\text{D}_2$  opens a new reaction channel, the hydrogenation of acetylene. In addition,  $\text{D}_2$  blocks the active sites on the palladium clusters for the polymerization, as the formation of the products is slightly reduced when exposing  $\text{D}_2$  prior to  $\text{C}_2\text{H}_2$ . On Pd(111), predosing with  $\text{H}_2$  completely suppresses the cyclotrimerization, but enhances the hydrogenation of acetylene to form ethylene [50].

The relative ion intensities of the products in the TPR spectra scale with the product formation by the model catalysts. By integrating the total area of the TPR spectra shown in Figure 6, the number of catalytically produced

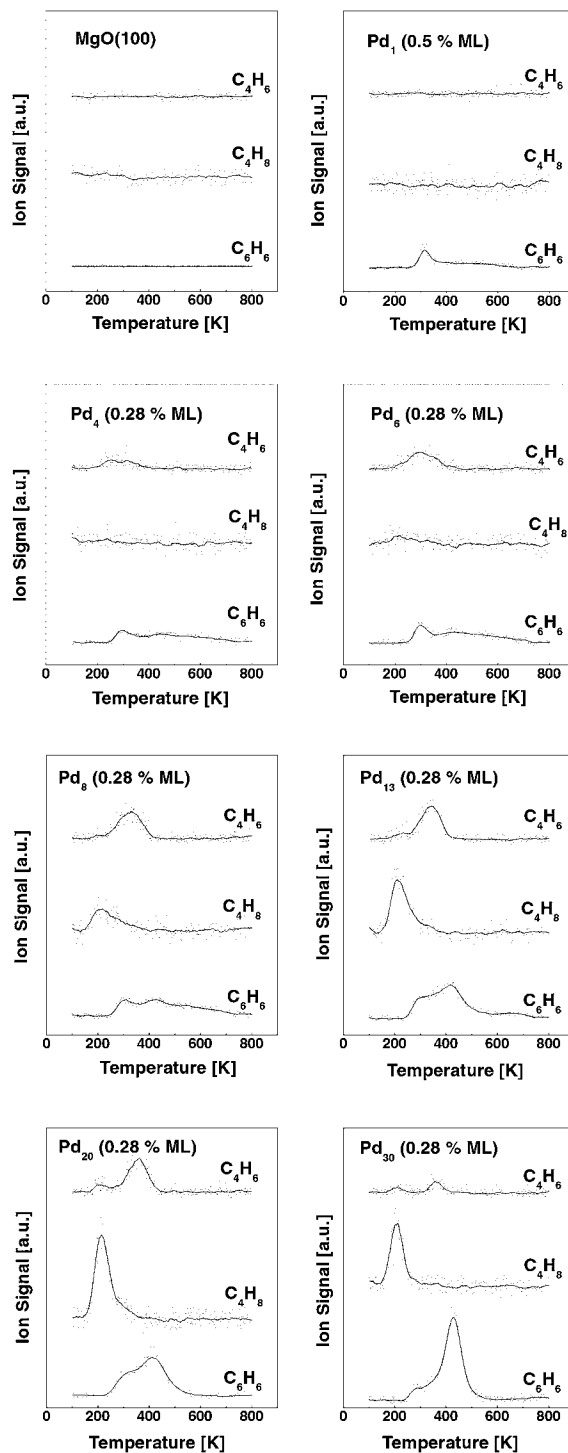


**Figure 6.** TPR spectra of the catalytic formation of  $\text{C}_6\text{H}_6$ ,  $\text{C}_4\text{H}_6$ , and  $\text{C}_4\text{H}_8$  for a defect-rich MgO thin film,  $\text{Pd}_1$ ,  $\text{Pd}_4$ ,  $\text{Pd}_6$ ,  $\text{Pd}_8$ ,  $\text{Pd}_{13}$ ,  $\text{Pd}_{20}$ , and  $\text{Pd}_{30}$ . The relative ion intensities are corrected with the relative detection efficiencies of the experiment, and scale with the number of formed product molecules per cluster.

benzene, butadiene, and butene molecules per cluster is obtained and illustrated in Figure 7a. Figure 7b shows the selectivities  $S$  for the formation of the products  $P_1(\text{C}_6\text{H}_6)$ ,  $P_2(\text{C}_4\text{H}_6)$ , and  $P_3(\text{C}_4\text{H}_8)$  for different cluster sizes calculated

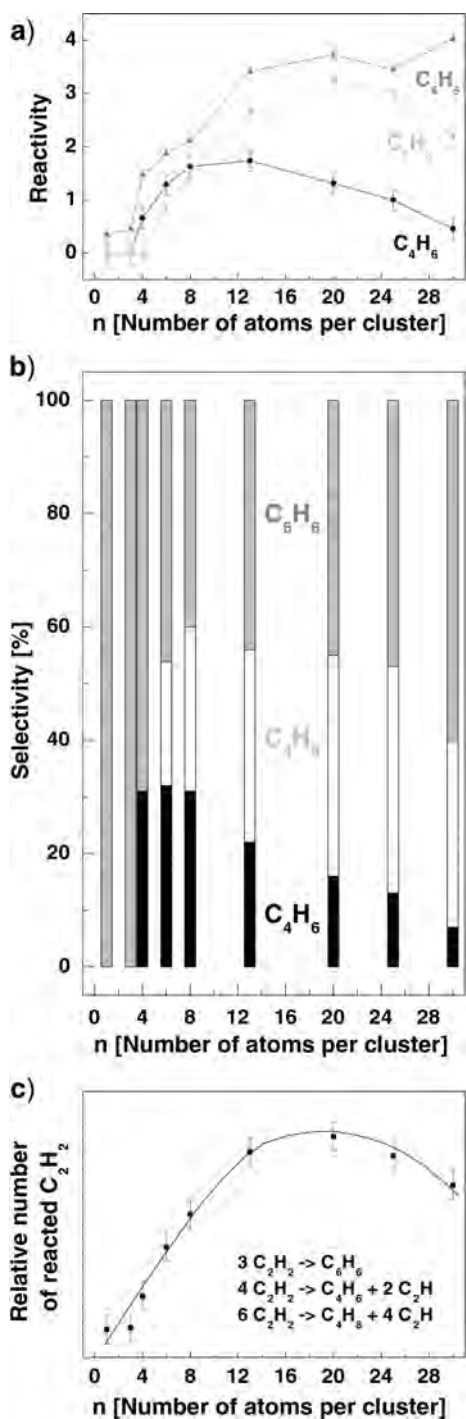


**Figure 7.** Reactivity (a) (expressed as the number of product molecules per cluster) and selectivity (b) (expressed as the relative amount in percent) of the polymerization of C<sub>2</sub>H<sub>2</sub> on size-selected Pd<sub>n</sub> (n = 1–30) deposited on defect-rich MgO thin films. Also shown is the relative number of reacted C<sub>2</sub>H<sub>2</sub> as a function of cluster size (c).

from, for example,

$$S(P_1) = \frac{\text{number of } P_1 \text{ per cluster}}{\text{number of } \sum P_n \text{ per cluster}} * 100 [\%]$$

The striking atom-by-atom size-dependent selectivity for the polymerization of acetylene is summarized as follows: C<sub>6</sub>H<sub>6</sub> is catalyzed with a selectivity of 100% on cluster sizes up to Pd<sub>3</sub>. The selectivity for C<sub>4</sub>H<sub>6</sub> reaches a maximum for Pd<sub>6</sub> (~30%), and the production of C<sub>4</sub>H<sub>8</sub> is most efficient (~40%) for Pd<sub>20–25</sub>. If one assumes stoichiometric reactions, as indicated in Figure 7c, and estimates the relative number of C<sub>2</sub>H<sub>2</sub> from Figure 7a, one observes a proportional increase of acetylene with the number of palladium atoms per cluster up to Pd<sub>13</sub>. Surprisingly, at this cluster size, the surface-to-bulk ratio, as well as the coordination number of Pd in the cluster, are changing, as at this size, one Pd atom sits completely in the cluster. In addition, according to the free stoichiometric chemical reactions, each reaction requires a minimum number of Pd atoms, which are three, four, and six. The experimental results are surprisingly consistent, that is, C<sub>4</sub>H<sub>6</sub> is formed for Pd<sub>n</sub> with n ≥ 4 and C<sub>4</sub>H<sub>8</sub> for cluster sizes with n ≥ 6.

Analyzing the products formed on small size-selected Pd<sub>n</sub> (1 ≤ n ≤ 30) clusters deposited on defect-rich MgO(100) thin films indicates that the surface intermediate C<sub>4</sub>H<sub>4</sub> is being produced efficiently on all cluster sizes. Thus, at least two acetylene molecules are adsorbed in a π-bonded configuration at the initial stage of the reaction [69]. The observed size-dependent selectivity may then be understood by regarding the influence of the cluster size to steer the reaction either toward the cyclotrimerization to form C<sub>6</sub>H<sub>6</sub> or toward a direct hydrogen transfer from adsorbed C<sub>2</sub>H<sub>2</sub> to the C<sub>4</sub>H<sub>4</sub> intermediate to catalyze the formation of C<sub>4</sub>H<sub>6</sub> or C<sub>4</sub>H<sub>8</sub>, respectively. Cyclotrimerization is generally observed when a third acetylene molecule is adsorbed in a π-bonded configuration, which results in a change from sp hybridization toward an sp<sup>2</sup> hybridization [70]. This bonding configuration leads to a weak activation of the C–H bond, in analogy to ethylene [71]. The hydrogenation of the Pd<sub>n</sub>(C<sub>4</sub>H<sub>4</sub>) metallocycle, on the other hand, is favored by the adsorption of di-σ/π bonded acetylene to three Pd atoms, effecting a more efficient activation of the C–H bond, in analogy to ethylene [71].

For Pd atoms adsorbed on defect sites, the Pd(C<sub>4</sub>H<sub>4</sub>) intermediate is formed with an energy gain of around 2 eV. A third adsorbed C<sub>2</sub>H<sub>2</sub> molecule is purely π-bonded (Fig. 3a), and the activated acetylene molecule reacts with the intermediate to form benzene with a total exothermicity of about 7 eV. The weakly bound C<sub>6</sub>H<sub>6</sub> (0.3 eV) then desorbs at low temperature from the nanocatalyst [69]. A second reaction channel, the formation of butadiene, C<sub>4</sub>H<sub>6</sub>, opens for Pd<sub>4</sub>. This channel reveals the highest selectivity for Pd<sub>6</sub>; in this case, a third C<sub>2</sub>H<sub>2</sub> molecule can bind in a di-σ/π bond configuration to three Pd atoms. The charge transfer from the substrate to the cluster further enhances the activation of the C–H bonds. For even larger cluster sizes, the adsorption of two di-σ/π-bonded C<sub>2</sub>H<sub>2</sub> molecules becomes possible, and opens up the third reaction path, the formation of C<sub>4</sub>H<sub>8</sub>. In our experiments, this is clearly observed for Pd<sub>8</sub>. Purely geometrical arguments (possible adsorption of two di-σ/π-bonded C<sub>2</sub>H<sub>2</sub> molecules close to the C<sub>4</sub>H<sub>4</sub> intermediate) suggest that this third channel is more pronounced for the larger clusters, and indeed our results show maximal C<sub>4</sub>H<sub>8</sub> formation for cluster sizes of 20–25 Pd atoms. For the largest clusters of the measured range, for example, Pd<sub>30</sub>,

the increased number of metal–metal bonds and the concomitant delocalization of the charge transferred from the substrate to the cluster results in less charge density available for the activation of the C–H bond [72]. Consequently, the cyclotrimerization again becomes more efficient than the hydrogenation of the  $C_4H_4$  intermediate. Going to even larger particles or to Pd(111) single crystals, the cyclotrimerization to benzene is selectively catalyzed.

#### 4. CHEMICAL REACTIONS INDUCED BY CONFINED ELECTRONS

In the examples described above, single chemical bonds of reactants and products are activated, dissociated, and formed by interacting with the electronic states of confined valence electrons of nanoscale systems, such as point defects, free or supported atoms, or clusters. In a completely different approach, single chemical bonds are manipulated by nanoscale devices. Such a device can be an STM (scanning tunneling microscope), where tunneling electrons resonate with single electronic states of molecules to induce chemistry by making and breaking bonds [73]. These two methods for doing chemistry in the nanoscale differ completely. In the first example, confinement is achieved by the system (point defects, atoms, clusters) itself, and in the best case, they may act as real nanocatalysts. The second method uses a nanoscale device, which can be applied to nonlocalized systems for inducing chemistry on the nanoscale.

The use of nanoscale devices for inducing chemical reactions was first introduced by the group of Somorjai in 1994, where a platinum–rhodium tip of an STM operating inside an atmospheric-pressure chemical reactor cell has been used to locally rehydrogenate carbonaceous fragments deposited on the (111) surface of platinum [74]. Recently, the groups of Rieder (FU-Berlin) [75] and Ho (Cornell) [76] used a tip of an STM as a local electron source to induce bond-selected chemistry with a spatial resolution of the atomic scale ( $\sim 1$  Å). With the same device, the induced changes can be imaged with similar spatial resolution. The sharp metal tip of an STM is held in close proximity to a conducting surface. The tip is then positioned above a selected bond of a reactant molecule, and by applying different bias voltages, the energy of the tunneling electrons is tuned to resonate with single bonds. At a tip–surface distance of about 6 Å, this process is dominant, and the overlap of the wavefunctions of the tip and the reactant molecule is negligible. In such a way, a chemically bound CO molecule on Cu(111) could, for example, be transferred to and from the tip in a reversible way [77], or in another example, tunneling-electron-stimulated desorption of H atoms from an Si(100)- $2 \times 1$  surface could be successfully used for nanopatterning [78]. They observed that, for localized and controlled reactions, the energies of the tunneling electrons ought to be below 1 eV (for bias voltages below 1 V). For example, the dissociation of a single  $O_2$  molecule on Pt(111) is confined to the molecule if the bias is less than 0.5 V [79]. However, when the bias is increased to 1.0 V, molecules as far as 100 Å away are also dissociated, even though the electrons are confined to atomic dimensions. The detailed mechanism for this nonlocal effect is not yet understood. In general, they conclude that, for bias voltages larger

than 2.5 V, nonlocal chemistry is dominant, whereas for voltages up to about 1–2 V, local, single-molecule chemistry takes place.

The Cornell group studied the local dissociation of a chemisorbed, single  $O_2$  molecule on Pt(111) in great detail. Obviously, this system is of relevance in catalysis. It is known that oxygen adsorbs molecularly on Pt(111) at temperatures below 100 K [80]. When the temperature is increased to about 150 K, some of the  $O_2$  molecules are desorbing, and the remaining molecules dissociate and recombine and desorb at about 600 K. The bonding configurations of molecular and atomic oxygen on Pt(111) could be detected by low-temperature STM (8–350 K) [79, 81]. The thermodynamically stable atomic O resides in face-centered cubic (fcc) three-fold hollow sites; O atoms on the hexagonal close-packed (hcp) sites are metastable, and can only be created nonthermally by irradiation with electrons or photons [81]. No molecules are observed at (100) steps. They then studied the dissociation of  $O_2$  induced by tunneling electrons on the bridge and three-fold hollow sites of Pt(111) [79]. The adjacent atoms of the underlying Pt atoms on the (111) surface are determined to be 2.77 Å; the observed separation of the two  $O_2$  molecules is 5.54 Å. The STM tip was then positioned about 6 Å above one of the molecules, and a voltage pulse of 0.3 V and 100 ms duration was applied. The sudden change in the tunneling current (12.5 nA) indicates the moment of dissociation. The image taken after the dissociation showed the two O products, one on the hcp site, and the other on the fcc site, as well as the other  $O_2$  molecule, which is not perturbed. The two O products are found to be within two lattice constants of the original molecule, and one–three lattice constants apart. Approximately 1.1 eV/O atom of energy is dissipated upon dissociation through substrate excitations. The rates of energy dissipation and scattering with the corrugated potential of the surface limit the range of motion of the products [82]. Ho and coworkers studied the mechanisms and dynamics of single-bond dissociation by measuring the dissociation rate as a function of bias voltage and tunneling current, and by theoretical modeling of the data [79]. The dissociation rate reveals a power-law dependence on the tunneling current. They proposed a mechanism based on inelastic vibrational excitations of an adsorbed molecule by the tunneling electrons [83–85]. In this process, tunneling electrons inelastically scatter from an adsorbed molecule, and transfer energy to the vibrational modes of the molecule. For the dissociation of  $O_2$ , an energy barrier of 0.35–0.38 eV needs to be overcome via one or multiple vibrational excitations in the ground electronic state. Such a vibrational ladder-climbing process requires one or multiple inelastic scatterings. For a 0.4 V bias used in the reported experiment, the  $O_2$  molecule can be dissociated with a single inelastic scattering event, leading a linear dependence of the dissociation rate with the current. However, at least two scatterings are required for 0.3 V bias, and the discrete nature of the vibrational levels requires three scatterings for 0.2 V bias. As the vibrational relaxation rate is greater than the excitation rate, the most probable path to dissociation is the one with the minimum relaxation probability, which is clearly the path with the fewest transitions. For 0.4 V bias, the bound-to-continuum transition corresponds to a single excitation to overcome



the dissociation barrier of 0.35–0.38 eV. Finally, it is interesting to calculate the electrical energy for this example to dissociate a single  $O_2$  molecule. At a voltage of 0.3 V, a current of 12 nA, and a pulse duration of 30 ms, an energy of  $1.1 \times 10^{-10}$  J is used. For the dissociation of 1 mol  $O_2$ , this corresponds to  $6.5 \times 10^{10}$  kJ/mol!

The dissociation of  $O_2$  is the rate-determining step in the catalytic oxidation of CO on metal surfaces; thus, Hahn and Ho showed in another experiment [86] that the bond-selected chemistry can even be used for inducing this catalytic reaction. After preparing oxygen atoms by dissociating single  $O_2$  molecules with tunneling electrons as described above, they exposed the surface at 13 K to a small amount of CO. The adsorbed reactants and products were then imaged by STM before, during, and after manipulation with the STM tip and reaction of a CO with one of the two O atoms. The CO was moved toward the O atoms by repeatedly applying sample bias pulses over the CO since the CO does not always move toward the O atoms. However, they succeeded in eventually forming the O–CO–O complex. With an additional sample bias pulse over the CO in the complex, they induced the formation of  $CO_2$ , and the product quickly desorbed, leaving the remaining O atom on the surface. From the spatial distribution of STM–IETS (inelastic electron tunneling spectroscopy [87]) intensity, they concluded that the CO in the complex is between the two Ag atoms along the [001] direction, and that the CO may be tilted by the repulsive interaction between the O atom of CO and adsorbed O atoms, as suggested for a transition state in CO oxidation on the Ru(0001) surface [88]. The Ho group illustrated another oxidation pathway by direct transfer of a CO molecule from

the tip to an adsorbed O atom. In this experiment [86], the CO-terminated tip was positioned over one of the O atoms. They applied a +470 mV pulse with the feedback turned off, and a rescanned of the same area showed the remaining O atom on the surface after  $CO_2$  formation.

In another example, the Rieder group induced all of the elementary steps of Ullmann synthesis [89], the formation of biphenyl out of iodobenzene on copper, on individual molecules with an STM in a controlled step-by-step manner, utilizing a variety of manipulation techniques [75]. Two reactant molecules are shown in Figure 8a. The first reaction step is the separation of iodine from iodobenzene by using tunneling electrons (Fig. 8b, c). After dissociation, iodine was moved to terrace sites of the copper surface by lateral manipulation (Fig. 8d). One chemisorbed phenyl reactant was then migrated close to another phenyl by soft lateral manipulation [90] (Fig. 8e). Finally the two phenyls were brought together by molecular excitation by inelastic tunneling (Fig. 8f). Successful chemical association was then verified by pulling the synthesized molecule by its front end with the STM tip.

## 5. SUMMARY

The term nanocatalysis was introduced by Somorjai in 1994, when he used confined electrons of an STM tip to induce an electrochemical process. Earlier experiments on free clusters pointed toward the possibility of using small clusters with intrinsically confined valence electrons as catalysts to tune the properties atom by atom. These two completely different pioneering ideas were further sophisticated during the last few years. It has become possible to use size-selected clusters on surfaces for catalyzing simple chemical reactions, and to tune the catalytic properties with size, as well as to use the tip of an STM to control every step of a chemical reaction on a local scale. With these examples, a deeper understanding of nanocatalytic factors is now emerging, and such studies will have a profound impact on the catalysis of systems at the ultimate size limit.

## GLOSSARY

**Acetylene cyclotrimerization** Formation of benzene from three acetylene molecules.

**Electronic size effects** Varying electronic structure as a function of cluster size.

**F center (FC)** Color center; defect sites (oxygen vacancies) existing on oxide surfaces.

**Impurity-doping effect** Incorporation of impurity atoms into atomic clusters.

**Metal cluster** Assembly of metal atoms exhibiting distinct quantum size effects.

**MgO(100) thin film** Magnesium oxide epitaxially grown on Mo(100) by evaporation of magnesium in an oxygen background.

**Nanodevices** Devices to manufacture materials, and to induce processes on the atomic scale.

**Structural dynamical fluxionality** Interconversion between different structural isomers at finite temperature.

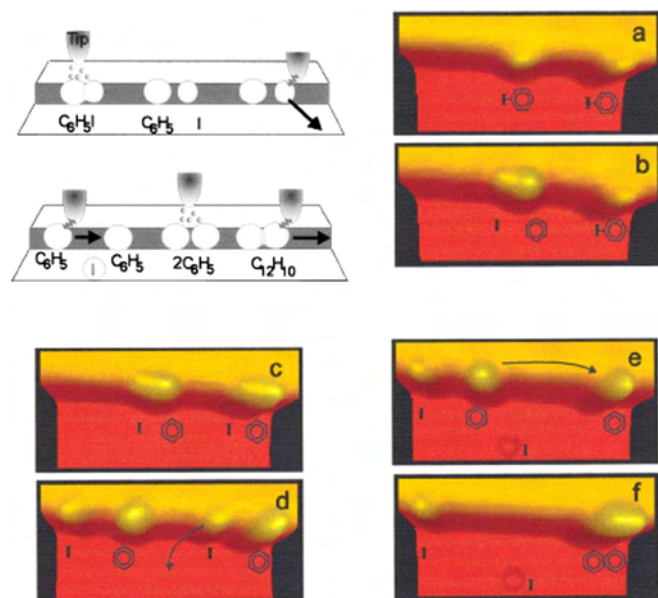


**Figure 8.** Schematic illustration and STM images of the STM tip-induced synthesis steps of biphenyl molecule from iodobenzene. (a) Two iodobenzene molecules adsorbed at a Cu(111) step edge. (b),(c) Iodine is abstracted from both molecules by applying a voltage pulse. (d) Iodine atoms and phenyl molecules are separated by lateral manipulation. (e) An iodine atom is removed onto the lower terrace. (f) The two phenyl molecules are moved together.



**Ullmann synthesis** Formation of biphenyl out of idobenzene.

## ACKNOWLEDGMENTS

This work was supported by the Deutsche Forschungsgemeinschaft (DFG), Alexander von Humboldt-Stiftung, and the Swiss National Science Foundation (SNSF). We are delighted to thank U. Landman, H. Häkkinen, G. Pacchioni, L. Wöste, and Th. Bernhardt for sharing their outstanding expertise with us. We also thank K. Judai, A. S. Wörz, J. Gong, F. Vanolli, A. Sanchez, L. D. Socaciu, J. Hagen, and L. Klinger for an excellent collaboration and stimulating discussions. It is a pleasure to acknowledge fruitful discussions with H.-J. Freund, C. Henry, W.-D. Schneider, R. J. Behm, and E. Schumacher.

## REFERENCES

- J. J. Berzelius, *Edinburgh New Philos. J.* XXI, 223 (1836).
- G. Morris, *Amer. Sci.* 401 (1947).
- P. D. Nellist and S. J. Pennycook, *Science* 274, 413 (1996).
- W. D. Knight, K. Clemenger, W. A. de Heer, W. A. Saunders, M. Y. Chou, and M. L. Cohen, *Phys. Rev. Lett.* 52, 2141 (1984).
- E. Schumacher, F. Blatter, M. Frey, U. Heiz, U. Roethlisberger, M. Schaer, A. Vayloyan, and C. Yerezian, *Chimia* 42, 357 (1988).
- I. M. L. Billas, A. Chatelain, and W. A. de Heer, *Science* 265, 1682 (1994).
- M. Moseler, H. Häkkinen, and U. Landman, *Phys. Rev. Lett.* 89, 176103 (2002).
- A. Kaldor, D. Cox, and M. R. Zakin, *Adv. Chem. Phys.* 70, 211 (1988).
- G. Pacchioni, *Surf. Rev. Lett.* 7, 277 (2000).
- C. Di Valentin, A. Del Vitto, G. Pacchioni, S. Abbet, A. S. Wörz, K. Judai, and U. Heiz, *J. Phys. Chem. B* 106, 11961 (2002).
- A. Sanchez, S. Abbet, U. Heiz, W.-D. Schneider, H. Häkkinen, R. N. Barnett, and U. Landman, *J. Phys. Chem. A* 103, 9573 (1999).
- U. Heiz, F. Vanolli, L. Trento, and W.-D. Schneider, *Rev. Sci. Instrum.* 68, 1986 (1997).
- U. Heiz and W.-D. Schneider, *J. Phys. D: Appl. Phys.* 33, R85 (2000).
- J.-W. He and P. L. Møller, *Chem. Phys. Lett.* 129, 13 (1986).
- D. Peterka, C. Tegenkamp, K. M. Schröder, W. Ernst, and H. Pfnür, *Surf. Sci.* 431, 146 (1999).
- F. Illas and G. Pacchioni, *J. Chem. Phys.* 108, 7835 (1998).
- W. A. de Heer, *Rev. Mod. Phys.* 65, 611 (1993).
- T. G. Dietz, M. A. Duncan, D. E. Powers, and R. E. Smalley, *J. Chem. Phys.* 74, 6511 (1981).
- H. R. Siekmann, C. Lüder, J. Fährmann, H. O. Lutz, and K. H. Meiwes-Broer, *Z. Phys. D—Atoms, Molecules and Clusters* 20, 417 (1990).
- R. Keller, F. Nöhmeier, P. Spädtke, and M. H. Schönenberg, *Vacuum* 34, 31 (1984).
- D. M. Cox, K. C. Reichmann, D. J. Trevor, and A. Kaldor, *J. Chem. Phys.* 88, 111 (1988).
- E. K. Parks, T. D. Klotz, and S. J. Riley, *J. Chem. Phys.* 92, 3813 (1990).
- X. Ren, P. A. Hintz, and K. M. Ervin, *J. Chem. Phys.* 99, 3575 (1993).
- R. E. Leuchtner, A. C. Harms, and A. W. Castelman, Jr., *J. Chem. Phys.* 92, 6527 (1990).
- C. Q. Jiao and B. S. Freiser, *J. Phys. Chem.* 99, 10723 (1995).
- J. M. Alford, F. D. Weiss, R. T. Laaksonen, and R. E. Smalley, *J. Phys. Chem.* 90, 4480 (1986).
- Y. Shi and K. M. Ervin, *J. Chem. Phys.* 108, 1757 (1998).
- L. D. Socaciu, J. Hagen, U. Heiz, T. M. Bernhardt, T. Leisner, and L. Wöste, *Chem. Phys. Lett.* 340, 282 (2001).
- L. D. Socaciu, J. Hagen, T. M. Bernhardt, L. Wöste, U. Heiz, H. Häkkinen, and U. Landman, *J. Am. Chem. Soc.* (submitted, 2002).
- J. Hagen, L. D. Socaciu, M. Eljazyfer, U. Heiz, T. M. Bernhardt, and L. Wöste, *Phys. Chem. Chem. Phys.* 4, 1707 (2002).
- W. T. Wallace and R. L. Whetten, *J. Am. Chem. Soc.* 124, 7499 (2002).
- H. Häkkinen and U. Landman, *J. Am. Chem. Soc.* 123 (2001).
- D. M. Cox, R. Brickman, K. Creegan, and A. Kaldor, *Z. Phys. D—Atoms, Molecules and Clusters* 19, 353 (1991).
- D. M. Cox, R. O. Brickman, K. Creegan, and A. Kaldor, *Mater. Res. Soc. Symp. Proc.* 206, 43 (1991).
- W. T. Wallace and R. L. Whetten, *J. Phys. Chem. B* 104, 10964 (2000).
- J. Hagen, L. D. Socaciu, M. Eljazyfer, U. Heiz, T. M. Bernhardt, and L. Wöste, (2002).
- J. I. Steinfeld, J. S. Francisco, and W. L. Hase, "Chemical Kinetics and Dynamics," 2nd ed. Upper Saddle River, NJ, Prentice Hall, 1999.
- H. Huber, D. McIntosh, and G. A. Ozin, *Inorg. Chem.* 16, 675 (1977).
- K. M. Ervin and A. Grushow, *J. Chem. Phys.* 106, 9580 (1997).
- K. M. Ervin, *Int. Rev. Phys. Chem.* 20, 127 (2001).
- P. A. Hintz and K. M. Ervin, *J. Chem. Phys.* 103, 7897 (1995).
- I. M. Campbell, "Catalysis at Surfaces." Chapman & Hall, London, 1988.
- U. Heiz, *Appl. Phys. A* 67, 621 (1998).
- S. Abbet, K. Judai, L. Klinger, and U. Heiz, *Pure Appl. Chem.* 74, 1527 (2002).
- S. Abbet, E. Riedo, H. Brune, U. Heiz, A. M. Ferrari, L. Giordano, and G. Pacchioni, *J. Am. Chem. Soc.* 123, 6172 (2001).
- S. Abbet, A. Sanchez, U. Heiz, and W.-D. Schneider, *J. Catal.* 198, 122 (2001).
- K. Judai, A. S. Wörz, S. Abbet, U. Heiz, L. Giordano, and G. Pacchioni (2003).
- R. M. Ormerod and R. M. Lambert, *J. Phys. Chem.* 96, 8111 (1992).
- A. M. Ferrari, L. Giordano, S. Abbet, U. Heiz, and G. Pacchioni, *J. Phys. Chem. B* 106, 3173 (2002).
- W. T. Tysoe, G. L. Nyberg, and R. M. Lambert, *J. Chem. Soc., Chem. Commun.* 623 (1983).
- U. Heiz, A. Sanchez, S. Abbet, and W.-D. Schneider, *Eur. J. Phys. D* 9, 35 (1999).
- S. Abbet, U. Heiz, H. Häkkinen, and U. Landman, *Phys. Rev. Lett.* 86, 5950 (2001).
- W. Harbich, in "Metal Clusters at Surfaces" (K.-H. Meiwes-Broer, Ed.), Springer Series in Cluster Physics, Berlin, 2000.
- C. L. Cleveland and U. Landman, *Science* 257, 355 (1992).
- H.-P. Cheng and U. Landman, *Science* 260, 1304 (1993).
- H.-P. Cheng and U. Landman, *J. Phys. Chem.* 98, 3527 (1994).
- S. Messerli, S. Schintke, K. Morgenstern, A. Sanchez, U. Heiz, and W.-D. Schneider, *Surf. Sci.* 465, 331 (2000).
- B. Hammer and J. K. Nørskov, *Nature* 376, 238 (1995).
- M. Haruta, *Catal. Today* 36, 153 (1997).
- M. Haruta, *Appl. Catal. A* 222, 427 (2001).
- H. Häkkinen, S. Abbet, A. Sanchez, U. Heiz, and U. Landman, *Angew. Chem. Int. Ed.* (in press).
- H. Häkkinen and U. Landman, *Phys. Rev. B* 62, R2287 (2000).
- K.-H. Allers, H. Pfnür, P. Feulner, and D. Menzel, *J. Chem. Phys.* 100, 3985 (1994).
- A. Eichler and J. Hafner, *Phys. Rev. B* 59, 5960 (1999).
- M. Scheffler and C. Stampfl, in "Electronic Structure" (K. Horn and M. Scheffler, Eds.), Vol. 2. Elsevier, Amsterdam, 1999.
- R. M. Ormerod and R. M. Lambert, *J. Chem. Soc., Chem. Commun.* 1421 (1990).

67. P. M. Holmblad, D. R. Rainer, and D. W. Goodman, *J. Phys. Chem. B* 101, 8883 (1997).
68. C. H. Patterson and R. M. Lambert, *J. Phys. Chem.* 92, 1266 (1988).
69. S. Abbet, A. Sanchez, U. Heiz, W.-D. Schneider, A. M. Ferrari, G. Pacchioni, and N. Rösch, *J. Am. Chem. Soc.* 122, 3453 (2000).
70. G. Pacchioni and R. M. Lambert, *Surf. Sci.* 304, 208 (1994).
71. A. Fahmi and R. A. van Santen, *J. Phys. Chem.* 100, 5676 (1996).
72. S. Burkart, N. Blessing, and G. Ganteför, *Phys. Rev. B* 60, 15639 (1999).
73. W. Ho, *Acc. Chem. Res.* 31, 567 (1998).
74. B. J. McIntyre, M. Salmeron, and G. A. Somorjai, *Science* 265, 1415 (1994).
75. S.-W. Hla, L. Bartels, G. Meyer, and K.-H. Rieder, *Phys. Rev. Lett.* 85, 2777 (2000).
76. H.-J. Lee and W. Ho, *Science* 286, 1719 (1999).
77. L. Bartels, G. Meyer, and K.-H. Rieder, *Appl. Phys. Lett.* 71, 213 (1997).
78. P. Avouris, *Acc. Chem. Res.* 28, 95 (1995).
79. B. C. Stipe, M. A. Rezaei, W. Ho, S. Gao, M. Persson, and B. I. Lundqvist, *Phys. Rev. Lett.* 78, 4410 (1997).
80. J. L. Gland, B. A. Sexton, and G. B. Fisher, *Surf. Sci.* 95, 587 (1980).
81. B. C. Stipe, M. A. Rezaei, and W. Ho, *J. Chem. Phys.* 107, 6443 (1997).
82. G. Wahnstrom, A. B. Lee, and J. Stromquist, *J. Chem. Phys.* 105, 326 (1996).
83. S. Gao, M. Persson, and B. I. Lundqvist, *Solid State Commun.* 84, 271 (1992).
84. S. Gao, M. Persson, and B. I. Lundqvist, *Phys. Rev. B* 55, 4825 (1997).
85. R. E. Walkup, D. M. Newns, and P. Avouris, *Phys. Rev. B* 48, 1859 (1993).
86. J. R. Hahn and W. Ho, *Phys. Rev. Lett.* 87, 166102 (2001).
87. B. C. Stipe, M. A. Rezaei, and W. Ho, *Science* 280, 1732 (1998).
88. C. Zhang, P. Hu, and A. Alavi, *J. Am. Chem. Soc.* 121, 7931 (1999).
89. F. Ullmann, G. M. Meyer, O. Loewenthal, and O. Gilli, *Justus Liebig's Annalen der Chemie* 331, 38 (1904).
90. G. Meyer, L. Bartels, S. Zöphel, E. Henze, and K.-H. Rieder, *Phys. Rev. Lett.* 78, 1512 (1997).



# Nanochemistry

Sebastian Polarz

*Ruhr-University Bochum, Bochum, Germany*

## CONTENTS

1. Nanochemistry: Definitions and Expectations
2. Nanochemically Designed Features in Nature
3. Nanochemical Strategies: Self-Assembly and the Nanoreactor Concept
4. Hard-Matter Chemical Confinements
5. Soft-Matter Chemical Confinements
6. Summary  
Glossary  
References

## 1. NANOCHEMISTRY: DEFINITIONS AND EXPECTATIONS

The term nanochemistry was originally invented by G. Ozin from Toronto back in 1992 [1]. In this article, Ozin described the state of the field at this point. Nanochemistry is highly related to the larger field of Nanotechnology [2–7], which promises to be a future focus for many sciences (chemistry, physics, engineering, etc.). One might say that nanotechnology contains the disciplines nanochemistry, nanophysics, nanoengineering, and many other disciplines. It might be questionable if such a differentiation makes much sense because as nanotechnology itself is highly interdisciplinary, a topic like nanochemistry cannot be reduced to one field as well. However, a definition as sharp as possible is required.

### 1.1. Definition of Nanochemistry and the Correlation to Nanotechnology

Obviously, the term nanochemistry is composed of the two words “nano” and chemistry. “Nano” is a description of the relevant lengthscales  $l$  or dimensions in this field, namely, the nanometer-sized dimension. Nowadays, this differentiation is not anymore absolutely correct because “nano” can mean everything above molecular dimensions ( $l > 1$  nm) and smaller than macroscopic sizes ( $< 1$   $\mu$ m) [8]. This might

have initiated Ozin to talk about “mesochemistry” rather than nanochemistry some time later [9].

For this chapter, chemistry (the second component of nanochemistry) stands for two sorts of events. Chemistry can mean the construction of larger units from smaller ones (synthetic point-of-view) also represented by the well-known expression “bottom-up approach,” or simple reactions between molecules without forming time-durable chemical bonds (physico-chemical point-of-view). The bottom-up approach stands in contrast to the “top-down approach” taken by nanophysics and nanoengineering. Therefore, nanochemistry is unique.

This new type of matter, created by nanochemistry, smaller than a macroscopic unit but significantly larger than a few pairs of atoms or molecules, should have unique and novel electronical, optical, magnetic, photochemical, electrochemical, catalytical, or mechanical properties (see Section 2.2 about quantum-size effects) and applications. In other words, nanochemistry describes how this special sort of matter can be created and organized by designing new experiments applying well-established chemical methods. Mainly, three strategies for this type of chemical syntheses can be mentioned [8]:

- Sequential formation of covalent bonds. This method allows the generation of structures of limited size but far away from the thermodynamic equilibrium.
- Covalent polymerization. High molecular mass macromolecules are produced. A control about a designed composition in these objects is difficult to achieve.
- Self-organizing synthesis. Smaller units are assembled by weak intermolecular forces (van der Waals, electrostatic) into organized structures. Examples are molecular crystals, liquid crystals, micelles, emulsions, phase-separated polymers, Langmuir–Blodgett films, and self-assembled monolayers. Several orders of magnitude can be addressed this way and the structures are in thermodynamic equilibrium.

On the other hand, the chemistry itself, the way molecules behave, might change when matter is confined to such small length scales as several nanometers. This is an extension of the original meaning of nanochemistry because chemical rules themselves may change.

In clear contrast to this stands nanophysics. Here, a top-down approach tries to scale down objects until they are in the nano-size regime [10]. For instance, one very important technique of nanophysics, is nanolithography [10, 11].

So, how does nanochemistry fit into the concept of nanotechnology and what is nanotechnology? Nanotechnology can be described as an engineering discipline in which the task is to prepare functional devices and structures that have every nanometer-sized subunit (molecules or atoms) in the proper place. Under these conditions, all units with their known properties act together and create new functions. This is just an extremely brief description and the further interested reader is referred to the literature [2–7, 12, 13]. Thus, nanochemistry covers strategies to prepare nanotechnologically relevant devices by a bottom-up approach.

## 1.2. Expectations

The structures that emerge from nanochemical experiments certainly have new and sometimes unexpected properties as will be mentioned later in this article. They are believed to be able to solve many problems (and already did), to overcome established materials, and to initiate completely new fields of applications [14]. Some points of interest are sensors [15–22], molecular recognition [23], controlling the mechanical strength of composites, drug release systems, clean up of environmental pollutants, electrochromic displays or paper, or separation and detection of biomolecules [9].

Two areas of materials derived by nanochemistry are of extraordinary importance. One is the so-called “smart-materials” area. These are materials that are able to dynamically respond to externally applied stimuli (chemical or physical ones) [24–27].

Second, nanostructures are expected to have a significant impact on computer technology via minimization of devices, increase of memory speed, and mesoscopic wires for nanosized electrical circuits [28–31].

Finally, the ultimate goal, which yet sounds like some type of science fiction, is to create nanomachines and finally a special nanomachine called “the assembler.” These types of systems have been defined nicely by G. M. Whitesides [32]:

“I choose to take a machine to be a device performing a task. Going further, a machine has a design; it is constructed following some process; it uses power; it operates according to information built into it when it is fabricated. . . why shouldn't a complex molecular system that performs a function also be considered a machine. . . So the issue is not whether nanoscale machines can exist—they already do—or whether they can be important. . . but rather where we should look for new ideas for design.”

And about the assembler he writes:

“It would be a new type of machine—a universal fabricator. It would make any structure, including itself. . .” The assembler essentially is a nanorobot able to put everything in a nano-device in the proper spot with atom precision.

In the future, it is believed that nearly everything will contain nanotechnology and, therefore, is connected to nanochemistry [6]. In the next section, it will be shown that nature already uses nanotechnology. Interestingly, nature exclusively applies nanochemistry and not nanophysics.

## 2. NANOCHEMICALLY DESIGNED FEATURES IN NATURE

Already Whitesides realized [32] that many prototypes with a nanochemical design can be found in nature driven to perfection by evolution. Some examples should elucidate this.

### 2.1. Examples

#### 2.1.1. Nature's Nanoarchitecture

Nanostructural features and their superior properties were discovered quite early due to the beauty connected to these features. Haeckel, who depicted the skeletal structure of diatoms and radiolariae [33], inspired many scientists and even architects. However, nature is not interested in beauty. Beauty is just an indirect, maybe logical consequence. Structures we find in living organisms, no matter if one considers diatoms, human bones, etc., exhibit maximum performance at minimum metabolic costs [34]. Unlike materials synthesis in the laboratory, living organisms are additionally restricted to prepare their materials at room temperature and neutral pH.

One ideal example for nanoarchitecture in natural systems is the abalone shell nacre. The material is composed of plates of calcium carbonate is used (interestingly, the thermodynamic unfavorable crystal modification aragonite is expressed) and interlayered biopolymer domains. It is assumed that the biopolymers guide the growth of the inorganic crystal phase by selectively binding to selective crystal sides. This model has been supported by Coelfen on the influence of double-hydrophilic polymers mimicking natural systems on the crystal growth of BaSO<sub>4</sub> [35–38]. It was reasonably demonstrated in these articles that the polymer recognizes specific crystal surfaces, adsorbs there, and blocks them for further growth. Crystal planes without polymer grow more and more, and this determines the crystals final shape. Other scientists argue that this model is too simple [39]. This shows that much more understanding about the “bottom-up” mechanisms nature uses is needed in order to be able to mimic such materials. Biomimetics is actually nanochemistry in most parts.

#### 2.1.2. Nature's Nanoparticle Factories

Much of the research attention in nanochemistry was and still is devoted to the production of nanoparticles of various compositions, selective sizes, and shapes, as will be seen later in this review article. Interestingly, there are also different cellular organisms creating and using nanoparticles. One can find Fe<sub>3</sub>O<sub>4</sub>, Fe<sub>3</sub>S<sub>4</sub>, CdS, La(NO<sub>3</sub>)<sub>2</sub>, H<sub>2</sub>UO<sub>2</sub>PO<sub>4</sub>, Ag, Te, Se, Au, and Tc nanoparticles in natural systems [40].

Presumably, the most amazing example is the creation and use of magnetite nanoparticles enabling the use of biomagnetism [41]. The Fe<sub>3</sub>O<sub>4</sub> crystals exhibit a magnetic moment and enable the organism to navigate within the magnetic field of the earth. Many birds possess magnetic senses [42], insects [43], fish [44] do, but interestingly there are also simple bacteria having magnetotactic properties [45]. These bacteria were discovered by Blakemore in 1975 [46]. Magnetotactic bacteria live in anaerobic environments and the magnetic sensor enables them to swim downwards, away

from the oxygen-rich water-air surface [47]. The magnetite particles themselves seem to be formed inside vesicles with a phospholipid/protein membrane, while different vesicles are aligned in chain-like structures. The particles are crystallographically oriented with the [111] crystal axis along the chain direction and the particle sizes range typically from 35–120 nm, which is the single-domain-size range for magnetite.

While magnetite is of real use for the mentioned organisms, it will be evolutionarily favorable especially for bacteria if they would be resistant against dissolved heavy-metal ions. Some microorganisms solve these problems by transforming heavy-metal poisoning into nanoparticle deposits inside the cell. Examples are the deposition of  $\text{Cd}^{2+}$  as CdS nanoparticles [48],  $\text{Ag}^+$  as Silver [49], or  $\text{Au}^{3+}$  as gold [50].

### 2.1.3. Nature's Anti-Freezing Systems

A completely different nanochemical task that nature has to cope with is to avoid crystallization. As temperatures can fall below  $0^\circ\text{C}$  in winter, it would be fatal for many organisms if the cell water starts to freeze and ice crystals grow. Nature's solution is to develop anti-freezing proteins. It seems that the protein possess functional groups in its backbone, which exhibits a geometrical motive fitting to the surface patterns of ice crystals [51]. Similarly to biomineralization, which was previously explained, these biopolymers block the growth of ice nuclei completely.

## 2.2. Quantum-Size Effects

The previous section demonstrated how nature is able to achieve desired mechanical, chemical, optical, magnetic, or electronically properties by making nano objects via nanochemistry ("bottom-up"). For the latter three target properties (electronically, magnetically, and optical) the internal electronic structure of the used nano objects is of particular importance. Indeed, the electronic properties of nanoparticles is somewhat special and, in general, is summarized under the expression quantum-size effects [52–54]. The properties of a semiconductor, for instance, can be related to its electronic structure, a bandgap between an electron-filled band and an electron-empty band (Fig. 1). Similarly, the properties of the atom is given by the energies and occupancies of the atomic orbitals. When the size of the particle is extended by a repetition of atoms in one, two, or three dimensions, a transition from molecular (or atomic) to solid state (or infinite) systems occurs. This transition is characterized by sometimes surprising properties of the nanoparticles and by a high size-dependence of these properties. One typical example is the size-dependence of the color (for instance, the UV/V is a spectrum of gold nanoparticles) [55].

## 2.3. Concluding Remarks

The previous section described just an infinitesimal fraction of nature's solution by nanochemical approaches. Confronted with this perfection, one might suspect that all optimum solutions already exist. Scientists would now just need to find these natural solutions for a particular application or problem and search for ways to translate nature's ideas into technologically realizable approaches. This route

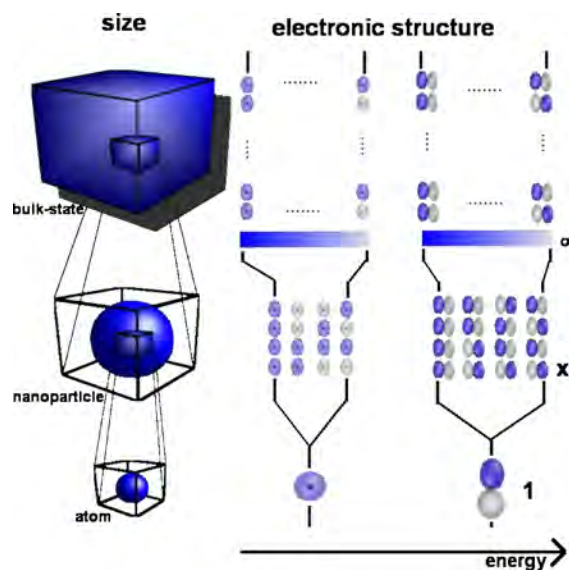


**Figure 1.** Schematic representation of quantum-size effects. The left side of the figure shows matter in decreasing size and the right side indicates the correlating electronic situation. On the atomic scale, one finds atomic orbitals (a s- and p-orbital are shown) separated by a certain energy. When atoms assemble to nanostructures or nanoparticles, respectively,  $x$  atomic orbitals of suitable symmetry lead to  $x$  combinations of orbitals. Every of these orbitals has a distinct energy, symmetry, and spin property. In this respect, the electronic situation of nanostructures is still somewhat similar to atoms. However, there is already delocalization of electrons in a certain volume leading to a decrease in the energy gap between the frontier orbitals. It should also be noticed that surface state (not indicated in the scheme) are of extreme importance for the electronic properties of nanostructures. Finally, when the number of interacting units exceeds a certain threshold, one obtains continuum behavior, the bulk state of matter, respectively. Bands separated by bandgaps have formed.

will be taken and is worth being taken by many groups (biomimetics). But the perfection seen in nature does not automatically mean that there are not better solutions or that there are problems not relevant or existing in nature [56].

One example that could elucidate this is photosynthesis. Photosynthesis transforms light into a different form of energy—chemical energy, respectively. For us, it is much more interesting to transform light into electrical energy, and it can be seen that even conventional solar cells show slightly higher efficiency performances than photosynthetical cells. Many more improvements are possible by nanochemical design as Graetzel et al. showed [57–59]. Nanocrystalline, nanoporous titania films sensitized with viologen dyes [60] are used to adsorb light and create charge carriers. The charges are then separated and collected at the counter electrode. This helps to avoid charge recombination and, therefore, enhances the efficiency, a true nanochemical solution.

Nature's solution can help but they are not the limit. However, it should be noted again that nature is restricted to ambient temperatures and predetermined concentrations of electrolytes. In order to synthesize nanocompounds, organisms cannot raise the cell-internal temperature and just by spending much energy are able to locally increase the



concentration of ions. This is a significant advantage for synthesis in the laboratory but also a challenge—to search for nanochemical routes avoiding extreme conditions.

### 3. NANO-CHEMICAL STRATEGIES: SELF-ASSEMBLY AND THE NANOREACTOR CONCEPT

The bottom-up approaches to prepare nanosized objects as introduced in section 1.1 are mainly covered by two strategies relevant for this review article. These are:

- self-assembly processes
- the nanoreactor concept

Methods, where larger structures are prepared by step-by-step covalent linkage and polymer chemistry, are not taken into consideration here and are not likely to be seen as nanochemical approaches, although the final products may be nanostructures.

Even self-assembly processes are, in principle, a separate topic. However, because self-assembly is of extreme importance for nanochemistry, it will be mentioned exemplarily for the aggregation of amphiphiles in aqueous media (Fig. 2) [61].

#### 3.1. Self-Assembly Processes

Figure 2 shows the principles of self-assembly and the emerging structures for amphiphile molecules in water. Figure 2(a) shows the pure water-air interface. Due to an anisotropic distribution of molecules at this interface, a resulting force pointing inwards to the solvent is present. When amphiphiles are added (Fig. 2(b)), they accumulate at this interface. The hydrophobic tail points towards the gas phase, while the hydrophobic part is located in the aqueous domain. The amphiphile is enriched at the interface until it is fully occupied. All further added molecules need to be dissolved in-phase or can macro-phase separately. However, dispersion of amphiphilic molecules in the continuous phase is possible when micelles are formed due to minimization of interface energy. In a micelle, the hydrophilic units point

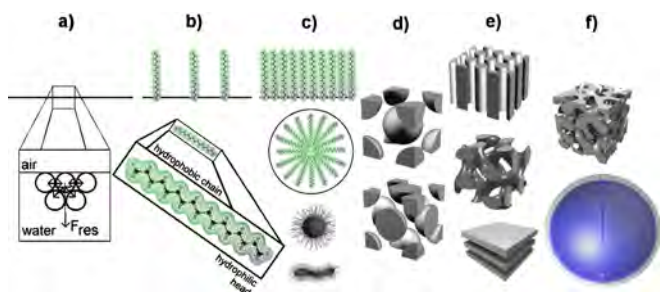


**Figure 2.** Schematic presentation of self-assembly processes of amphiphilic molecules. (a) shows the air-water interface and a force diagram; (b–c) shows the enrichment of amphiphiles at the air-water interface and the formation of micelles; (d–e) show higher order structures, dense micellar packings (hexagonal and cubic symmetry), and lyotropic phases (hexagonal, gyroid, and lamellar) obtained for higher amphiphile concentration. Even larger structures (f) are obtained when swelling agents or selective solvents are used—micro-emulsions and vesicles.

towards the solvent while the hydrophobic chains are separated from the water in a hydrophobic core (Fig. 2(c)). By the addition of more and more amphiphile, more and more micelles are formed. They can assemble to dense packings as fcc or bcc (Fig. 2(d)). Furthermore, at some point the micelles fuse and build more continuous structures, so-called lyotropic phases. First, two-dimensional phases as a hexagonal alignment of cylinders are built. Then, at higher concentrations even the cylinders fuse and build sheets of a lamellar lyotropic liquid crystal (Fig. 2(e)). Bicontinuous three-dimensional structures as the gyroid phase can emerge during the transition of hexagonal to lamellar phases. Micelles and lyotropic phases can be swollen by different solvents. The results are emulsions [61], for instance, microemulsions (Fig. 2(f)), or vesicles (Fig. 2(f)). Other self-assembly processes that occur in supramolecular chemistry are described elsewhere [23, 62]. This indicates that self-assembled structures are ideal helpers for nanochemistry due to the structural control over several length scales.

Although these structures themselves are already nanochemical structures, they are much more as will be described later. This builds the basis for the nanoreactor concept which is a most relevant idea for the concept of nanochemistry itself, which will be explained in the next section.

#### 3.2. The Nanoreactor Concept

A common theme of all the presented self-organizing structures is that they divide a macroscopic volume in small compartments. For instance, micelles create spherical compartments (the micellar cores) of just a few nanometer and hydrophobic conditions. Hydrophobic solvents can be introduced that lead to microemulsions (up to 50 nm in size). Inverted systems lead to other core properties (hydrophilic). For vesicles, the size of the compartment can be of the order of micrometers and is hydrophilic in nature.

Amphiphilic self-organized structures represent soft-matter spatial confinements and, therefore, are one prototype for nanoreactors. Chemistry can now be performed in these confinements (Fig. 3).

The requirements that can be identified for a good nanoreactor are quite similar to those present for the macroscopic reactors used in labs (for instance, glassware). The reactor volume should be accessible and the wall material should be able to exhibit variable properties independently from other parameters. The reactor should be controllable in size. This will enable control of the amount of matter (stoichiometry) and energy per nanoreactor.

Concerning these general requirements, hard-matter and soft-matter confinements can be very different as indicated in the following. It is the belief of this author that hard-matter structures, in other words porous materials, are more generally applicable as nanoreactors. However, for certain applications soft-matter nanoreactors can be more suitable. Soft- and hard-matter confinements are compared in Table 1, where + stands for favorable properties. It can be seen that these types of nanoreactors are quite different but often complementary.

As was previously mentioned, the prototype for a hard-matter nanoreactor (a) are porous materials, while the prototype for a soft-matter reactor (b) is an emulsion droplet.

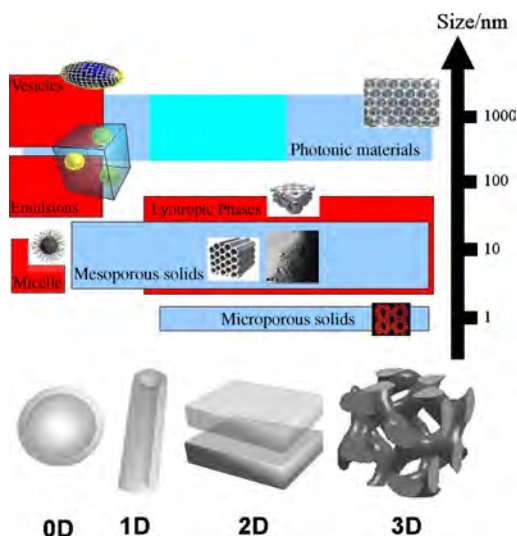


**Figure 3.** The variety of possible nanoreactors is shown and related to size and dimensionality. 0D systems are given for spherical reactors. Here, soft-matter reactors (color-coded red) are dominant (micelles → emulsion droplets → vesicles), although some hard-matter confinements can be found as well (see Section 3). 1D-confinements (cylinders) are mainly found for mesoporous materials (hard matter; blue). 2D-reactor systems (lamellar structures) are relevant for organic-inorganic hybrid materials and some pure inorganic compounds as clays. 3D reactors with a bicontinuous structure can be found in the field of porous materials (hard matter) but also in the case of micro-emulsions (soft-matter).

The nanoreactor volume can be accessed by the precursors equally well. For (a), it is diffusion into the porous system guided by capillary forces and for (b), the reaction educts can be dispersed from the beginning. Addition of chemicals might be more difficult for (a) once the pores are filled, and more easy for (b) because the reactor size is not so much restricted, and the droplets are in contact with a macro-reservoir that is the dispersion solvent. The single nanoreactor volume in a porous medium is neighbored by equal reactors separated by walls and is, therefore, not in direct contact with the macroscopic reservoir outside. The size of soft-matter structures can be easily varied, while it is a bit more difficult for hard-matter confinements to find appropriate templates to create a great diversity of sizes. The reactor volumes of porous materials are quite monodisperse and constant due to the rigid walls. This is often not

**Table 1.** Advantages (+) and disadvantages (–) of different nanochemical confinements.

Reactor requirements	Hard-matter confinement	Soft-matter confinement
Accessibility	+/-	+
Size variation	+/-	+
Monodispersity	+	–
Rigidity of size	+	–
Variation of walls	+	–
Control of stoichiometry	+	–
Control of energy	–	+
Ease of preparation	+	+/-
Processibility	+/-	+

the case for soft-matter structures (b); only in some cases these conditions are fulfilled and polydispersity is a major problem. The walls of soft-matter nanoreactors are always given by the flexible water-surfactant-solvent interface and, therefore, hard to vary systematically. For porous materials (a) on the other hand, modification techniques make nearly every wall composition possible [18, 63–88]. Because in a porous system all reactors are neighbored by equal ones and the reactor volume is constant at a given concentration, the stoichiometry can be easily controlled. For emulsion droplets, exchange processes through the continuous phase can have major effects and the polydispersity of volumes was previously mentioned. To reach energy equilibrium is more difficult for solid materials because one might create gradients from the material’s surface to the interior. It is much easier to reach energy equilibrium for independent particles like nanodroplets. The preparation of soft-matter structures is often very facile and sometimes requires special amphiphiles while the template concept [89] enables a simple way to porous materials. The soft-matter structures mentioned are dispersed in a liquid phase and, therefore, processibility is often advantageous for them in comparison to the solid-state confinements (a).

### 3.3. A General Concept of Nanochemistry

As was described in Section 1, a confinement leading to nanochemistry can have two different effects, namely, effects on molecular processes and effects on processes on a higher scale, which mainly describes the formation of special nanoparticles. Investigations in our group showed that these two areas of nanochemistry can be correlated to the nanoreactor dimensions itself (Fig. 4).

Figure 4 attempts to give a more general concept for nanochemistry. The nanoreactor possesses different structural features on different length scales. The smallest features are directly present at the nanoreactor surface, namely, the chemical surface-bound groups (alcohol, amino groups,

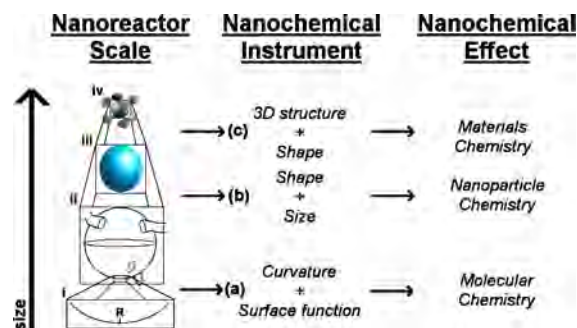


**Figure 4.** Schematic correlation between the nanoreactor features, the emerging nanochemical instruments, and the resulting nanochemical effects. A porous nanoreactor has different features being effective on different scales. On the lowest scale (below nanometer), one finds the functional groups (indicated R) determining the properties of the surface (i). Next, comes the pore sizes (above nm scale) which is also related to the curvature (ii). The next level of complexity is given by the pore shape (iii), and finally the pores are three-dimensionally aligned in space (iv). These different material features are combined at the intersections to three nanochemical instruments leading to three possible nanochemical effects.

etc.). These groups determine the functionality of the surface. Next, the nanoreactor has a certain size. It should also be noted that the radius of the reactor is related to the curvature  $H$  ( $H \propto r^{-2}$ ). On the third level, the nanoreactor has a specific shape. In the fields of nanoporous materials, this shape can range from spherical, cylindrical, worm-type to lamellar. Finally, the single nanoreactors are somehow distributed in three-dimensional space as, for instance, the hexagonal alignment of cylinders. These four structural features can be combined to result in three nanochemical instruments. The functional groups on the reactor surface determine if there is attraction or repulsion between the substrate in the pores and this surface. In case of attraction, molecules are located directly at the reactor's surface and experience the curvature. This combination of surface function and curvate gives the nanochemical instrument (Fig. 4(a)) and it confines molecules to a scale that effects molecular reaction (nanochemical effect). In case there is a slight repulsion, the substrates are located in the reactor volume and, therefore, the complete size of the reactor is relevant. Then the reactor size has to be combined with its shape to give a second nanochemical instrument (Fig. 4(b)). This nanochemical instrument (Fig. 4(b)) can be used to effect and control nanoparticle chemistry. The highest level of complexity is achieved when the shape (and size) is combined with the three-dimensional distribution of the nanoreactors, which results in the third nanochemical instrument (Fig. 4(c)). Now, nanoparticles can be forced into a distinct structural order as well and new materials emerge.

A worked-through example should elucidate this. As will be seen later, possible nanoreactors can be mesoporous silica materials. Silica  $\text{SiO}_2$  is normally derived by the sol-gel process [74, 90–94]. Depending on aging and post-treatment, the surface functionalities of the resulting materials can range from highly polar and protic Si-OH groups to relatively unpolar and unreactive Si-O-Si motives. Bronstein et al. prepared mesoporous silica differing only in pore-surface properties by liquid-liquid extraction and succeeding supercritical drying (silanol-rich material) and by high-temperature calcination (silanol-poor material) [95]. They further investigated the reduction of noble-metal precursors and  $[\text{PdCl}_4]^{2-}$  in such materials. A specific interaction between the  $[\text{PdCl}_4]^{2-}$  precursor and the pore surface, already evident by a change in coloration, is found (Fig. 5b) when the silanol-rich materials are infiltrated with the precursor solution. The palladium precursors are bound to the pore surface. This interaction by a square-planar Pd-complex and an Si-OH group would normally never occur because the Si-OH group is a weak ligand. However, under nanochemical conditions it does, the curvature of the mesopore presumably leads to a release of water from the pore surface when the complex is bound. This water release provides an entropic driving force for the formation of the unusual surface complex (molecular nanochemistry). When the  $[\text{PdCl}_4]^{2-}$  is reduced, this interaction prevents Ostwald-ripening after nucleation of  $\text{Pd}^0$  species to larger crystals. Therefore, no Pd-particles are visible in transmission electron microscopy (TEM) images (see Fig. 5b). It can be concluded that the nanochemical instrument was effective (see Fig. 4(a)). When on the other hand, the silanol-poor

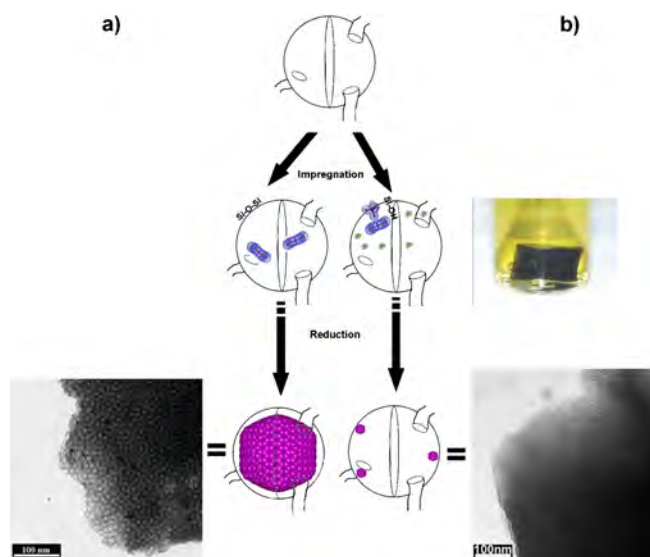


**Figure 5.** It is shown how the pore itself can be used to create new nanostructured matter as metal nanoparticles for instance. When the interaction between the pore walls and the precursors is tuned, it is possible to direct the growth of nanoparticles and obtain control about their size and properties of the hybrid materials (a). When the pore wall binds strongly to the metal precursors, Ostwald-ripening is kinetically suppressed and subnanometer nanoparticles cover the pore walls (b). For repulsive or nonbonding interactions, the size of the nanoparticles, their polydispersity, and their shape is dictated by the pore system.

material is used, this interaction is not present as can also be seen in the “normal color” of the infiltrated material (Fig. 5a). The  $[\text{PdCl}_4]^{2-}$  species that are located in the pore volume are free to move and, therefore, by Ostwald-ripening, larger particles are formed. However, the pore confines the growth of the nanoparticles until they match exactly the size and shape of the nanoreactor pores (see Fig. 5a). Obviously, now the nanochemical instrument (see Fig. 4(b)) is effective. If one would finally increase the loading of this material with more Pd, so that each pore is filled with metal, one would obtain a mutual ordering of the nanoparticles themselves. Via instrument (Fig. 4(c)), a new hybrid material is obtained.

## 4. HARD-MATTER CHEMICAL CONFINEMENTS

Up to this point, this chapter has discussed in a more general fashion, methods and strategies that are involved in nanochemistry. Following will be a highlight of specific achievements using these strategies and concepts.

### 4.1. Porous Materials

Porous materials are characterized by a solid network having voids throughout the material. According to the International Union of Pure and Applied Chemistry (IUPAC), porous materials are characterized by pore size categorized by sorption behavior [96–98]. There are microporous solids with pore sizes smaller than 2 nm, mesoporous materials with pores between 2 nm and 50 nm, and macroporous

materials with pores larger than 50 nm. Naturally, for performing nanochemistry, nanoporous materials are ideal target compounds. To describe nanoporous materials in detail here is beyond the scope of this article, but a comprehensive review can be found in literature of Polarz [2002, #2053].

#### 4.1.1. Zeolites and Catalysis

Zeolites are microporous materials, having very small pores ( $D_p > 2$  nm) that can be represented by the general formula  $M_2/nO \cdot Al_2O_3 \cdot SiO_2 \cdot yH_2O$  [99–101]. If one takes the general concepts about nanochemistry given in Section 3 into account, the substrates in microporous materials will be automatically forced to be at the pore wall. There is no other choice. Therefore, one has to expect effects of these kinds of materials mainly for molecular processes which was introduced as molecular nanochemistry.

This area of nanochemistry is extremely important because it contains zeolitic catalysis. Zeolites are amongst the most important modern catalyst materials [102, 103]. The realm of zeolite catalysis is vast, of course, and the interested reader is referred to the literature of Breck and Corma, respectively [99, 104]. Zeolites are known for their high catalytic activity and high selectivity [105]. In the sense of nanochemistry, zeolites already extend the classical meaning of catalysis, which is to accelerate chemical reactions. Zeolites, for instance in the case of the isomerization of olefins, selectively favor the formation of a particular product [106]. In other words, they alter chemical equilibria in comparison to the unconfined state. The activity of the zeolites is caused by active surface functions (for instance, acid sites) and the high electric fields present in zeolitic channels are summarized as coordination and coulombic effects [107]. Other typical nanochemical factors are the shape and size of zeolite pores favoring the formation of one product due to steric constraints. One product, for instance one isomer, may need slightly more space than the other isomers, so its production is repressed. Other factors are the differences in diffusion behavior and the lack of solvation of reactand molecules [101, 108–113]. It was further discussed by Zicovichwilson et al. that zeolites additionally modify the electronic structures of included guests and thus, increase the reactivity [107].

#### 4.1.2. Mesoporous Materials

As mesoporous materials are characterized by larger and a larger diversity of pore sizes (2–50 nm), these nanoreactor systems can be used to perform both molecular nanochemistry and nanoparticle chemistry.

In this section, we will begin to discuss phenomena where guests confined to the physical space of the ordered mesopore volume show some extraordinary characteristics not present in the bulk state.

One example for the unique feature occurring under confinements in the mesoporous range is the capillary condensation of gases during the sorption process. In comparison to the bulk, the temperature for the capillary critical temperature is far below the bulk critical temperature [114]. This confinement effect is very simple and has been recognized and studied for a long time. It is the basis for the Kelvin

equation (see Eq. 1) and all analytic techniques related to gas sorption.

$$r_p \left( \frac{p}{p_0} \right) = \frac{2\gamma V_L}{RT \ln \left( \frac{p}{p_0} \right)} + t \left( \frac{p}{p_0} \right) \quad (1)$$

$r_p \cong$  pore radius

$\gamma \cong$  surface tension

$t \cong$  thickness of the adsorbate film

$V_L \cong$  molecular volume of the condensate.

However, the development of ordered mesoporous materials allows one to perform much more systematic studies on sorption processes.

Also for water, one of the most common solvents, physical properties are influenced by geometrical confinements. The physical properties of water under confinement conditions are of particular interest due to the similarity to supercooled water in living biological cells. First indications for supercooled water in the pores of MCM-41 were found by Hansen et al. in 1995 [115, 116]. They applied  $^1H$ -NMR techniques to investigate water located in the mesopores and found two transition temperatures—one that was dependent on the pore size ( $T > 222$  K) and one that was independent at  $T = 209$  K. The latter transition point was attributed to water bound to the pore surface as a 5.4 Å thick interface layer. Baker et al. reported that the freezing point of water in MCM-41 is depressed to  $-21$  °C at a pore radius of  $\approx 3.4$  nm [117]. At extremely low temperatures, X-ray diffraction (XRD) data indicated a glassy state of ice (“frustrated nucleation”) while the cubic form of ice was also found [117]. This work was extended and it was seen that a pore system of 4.2 nm pores led to an abrupt crystallization of water to cubic ice at  $T = 232$  K, while the freezing process was very slow in 2.4 nm pores [118]. Quasi elastic neutron scattering revealed that the mobility of water is restricted under confinement [119]. Later, Smirnov et al. also investigates water in the fluid state [120]. With X-ray scattering methods, it was found that water exists in a distorted tetrahedral-like hydrogen-bonded network inside the porous environment.  $H_2O$ – $H_2O$  and  $H_2O$ – $SiO_2$  interactions were present simultaneously.

Other interesting guests are fullerene molecules as  $C_{60}$ . The first systematic study was presented by Rachdi et al. [83].  $C_{60}$  was deposited in MCM-41 with different pore sizes from the gas phase and the electron spin resonance (ESR) spectra were recorded. It could be seen that the confinement through the mesoporous host influenced the electronic band structure of the fullerenes. In contrast to the bulk state, an intense photoluminescence at 642 nm, as well as an emission at 484 nm, was created by inclusion of  $C_{60}$  to MCM-41 [121]. These features were attributed to strong interactions of the fullerene with the silica wall (“passivation of the surface”). Later, Chen et al. published a study with infrared (IR) spectroscopy and claimed that the fullerene reacts with hydroxyl groups on the wall surface (addition to the aromatic ring) during heat treatment [122].

A completely different idea was followed by Alvaro et al. [123]. They adsorbed the methyl viologen cation  $MV^{2+}$  in mobil composition of matter (MCM)-41 and created  $MV^+$  radicals by flash photolysis. The radicals were very time-stable and it was presumed that MCM could act as an



single electron donor. Acidic MCM-41 was loaded with thi-antrene and the corresponding radical cation was formed [124]. It is a very common feature that even very unstable species like radicals have a significant lifetime in ordered mesoporous hosts. The creation rate of radicals of *meso*-tetraphenylporphyrin was higher with increasing pore sizes of MCM-41 and the deactivation was also very slow for other radical cations like *N*-alkylphenothiazines [125–128]. Deactivation processes are also one limitation for photo-induced electron transfer reactions. By investigating the isomerization of *cis*-stilbene, it was shown that the stability and efficiency of the 2,4,6-triphenylpyrylium cation could be enhanced by immobilization in MCM-41 [129]. In particular, it was argued that the strong electrostatic field occurring in porous materials might be responsible for the stabilization of charged species.

Also macromolecules can be guests in porous silicas. They can be introduced via solution impregnation or they are created directly in the porous system as will be shown later.

A very interesting piece of research was presented by Tolbert et al. in 2000 [130, 131]. They could take advantage of some modern developments in the fields of mesoporous materials and polymer chemistry. As a mesoporous host, a MCM-related material that pore channels aligned parallel along one direction, was used. The alignment of the channels was achieved via treatment of the preparation sol under high magnetic fields during the sol–gel transition [130, 131]. This porous glass was then filled with the semiconducting polymer poly[2-methoxy-5-(2'-ethylhexyloxy)-1,4-phenylene vinylene]. The pore size of the silica was selected in a way that only one polymer molecule had sufficient room in the pore. This way, the polymer chains were isolated and aligned simultaneously. The composite material was excited and investigated with polarized femtosecond spectroscopy. It was seen that the excited states or the energy, respectively, moves from nonoriented polymer segments outside the silica to the oriented polymer confined to the mesopores. The polymers inside the material finally emit red-shifted light. As a consequence, this nanocomposite mimicks to a certain degree the antenna chromophores in photosynthesis.

In a similar fashion, mesoporous silica have shown their potential for creating new laser materials. Generally, an active laser dye is brought into a porous environment and its laser activity is studied. It was envisioned by Marlow et al. that a whole laser could be produced by using the self-assembly laws [132]. They could prepare a silica-surfactant laser dye (Rhodamine 6G) hybrid material, which had a fibrous morphology. The laser dye is located in the hydrophobic domains of the lyotropic template phase. The fiber was pumped perpendicular to the fiber direction and above a certain threshold, laser activity was detected. Wirnsberger and Stucky and Yang et al., respectively, extended their works [133, 134] and recently they prepared impressive waveguides by a combination of self-assembly and soft-lithography techniques [135]. Mesoporous silica (template removed) was deposited on silicon and as the third layer, they were the waveguides containing the dye-doped-ordered mesoporous silica [134]. The cylindrical channels were aligned throughout the whole waveguide and even the dye seemed to be oriented in the template phase.

As for most of the so-far mentioned examples, guests in the pore system have been quite static; it is an obvious extension to study chemical reactions inside pores.

Several researchers succeeded in the direct preparation of dye molecules in the channels of mesoporous silicas like MCM-41. The photosensitizer cation triphenylpyrylium TPP<sup>+</sup> [129], tris(4-methoxyphenyl)methylum, and malachite green [136] were prepared accordingly. These organic-inorganic hybrid materials can be used as a heterogeneous photosensitizer for the dimerization of cyclohexadienes [85, 137], electron transfer agents [129], and isomerization reaction of *cis*-stilbene [129].

A lot of research has been done in the field of polymerization in ordered mesoporous hosts. The polymer is directly created in the pore system of the silica and this method again organic-inorganic hybrid materials are obtained. It can be envisioned that future generations of these materials display electron and quantum confinement effects for the tailor-made provision of electronic, magnetic, and nonlinear optic effects.

Llewellyn et al. polymerized vinyl acetate, styrene, and methyl methacrylate (MMA) in MCM-41 [138]. It appeared that the termination rate could be decreased in comparison to the bulk polymerization. This leads to a molecular weight that can exceed the bulk situation by an order of magnitude [139]. Similarly, Moller et al. prepared poly(methyl methacrylate) (PMMA) in MCM-41 and MCM-48 [140]. They reported that the polymer dynamics changed dramatically. Cooperative polymer parameters like the glass transition was suppressed in their cases. Goeltner and Weißenberger used a bicontinuous mesoporous silica matrix as the template for the production of porous PMMA polymer monoliths [141]. Other polymer systems were introduced by Johnson et al. [142]. Phenol was adsorbed in MCM-41 and treated with formaldehyde vapor. The resulting phenolic resin was a structural imprint of the pores. After removal of the silica with HF the recovered polymer fibers were used to determine the length of the cylindrical pores in MCM-41 [142]. A two step “nanochemistry” was performed by MacLachlan et al. when he performed the ring-opening polymerization of a silaferrocenophane in MCM-41 and then transformed the polymer into nanoparticles of iron [143]. Polyesters were synthesized from lactones and alcohols in a living polymerization in Al-MCM-41. By using different lactones, block copolymer synthesis was accessible. Interestingly, no polymerization was found for pure SiO<sub>2</sub>-MCM-41 or microporous zeolites [144, 145]. Obviously, the mesopores, as well as the Lewis acidity, is necessary for this reaction. Also, mesoporous materials grafted with organo-metallic complexes have been used for polymerizations. A zirconocene containing silica was used to copolymerize ethylene and propylene [146–148]. It was seen that in the case of a chiral metallocene, selectivity towards isotactic and high molecular-weight polypropylene could be achieved. But a big breakthrough, and presumably the most ideal example of nanochemistry in ordered mesoporous silica materials, was provided by Kageyama et al. in 1999 [149]. They connected a titanocene catalyst covalently to the pore walls of MCM-41. When the polymerization of ethylene is performed the poly(ethylene) chain is hindered to bend backwards, so it has to grow along

the channel axes. This results in the situation where hexagonally aligned polymer fibers leave the MCM-41 “crystals.” Finally, bundles of several polymer fibers with diameters of 30–50 nm are formed. The obtained molecular weight is extremely high ( $M_n = 6.2 \cdot 10^7$ ).

Great attention has been devoted in the preparation of hybrids of a mesoporous silica hosting a conducting polymer [86]. Wu and Bein produced polyaniline in MCM-41 [150]. Aniline vapor was adsorbed by the silica which is then given to a solution of the oxidant to start the polymerization. The aniline filaments were several monomer units long and still had some conductivity [150, 151]. The polymers of Wu and Bein, when investigated, had lower molecular weights than in the corresponding bulk situation indicating diffusional constraints in the mesoporous host. The pore environment, therefore, seems to influence polymerization under confinement in two ways: (i) creating diffusional constraints, and (ii) an increase in the stability of transition states.

Polymer-silica hybrid materials can be further used to prepare carbon-silica hybrids. The preparation of elemental carbon is quite easy to achieve for several precursors. As shown by Wu and Bein, poly(acrylonitrile) confined to the pores of MCM-41 can be pyrolyzed to elemental carbon [152]. The authors argue that the growth of graphene layers is guided by the pores. At a pyrolysis temperature between 1070–1270 K, conductivity determined by microwave conductivity measurements emerged, which exceeded the conductivity of a carbon prepared under nonconfined conditions by one magnitude.

In the meantime carbon-silica nanocomposites with preservation of the mesoporous structure through the carbon have also been achieved by other methods (Fig. 6). One way is chemical vapor deposition of hydrocarbons and succeeding pyrolysis [153]. Other precursors like sucrose [154] are also successful and fascinating, three-dimensional-ordered carbon materials emerge [154–156]. This interesting area of producing ordered, porous carbon materials was reviewed elsewhere [156, 157]. The resulting carbon-silica hybrid materials can be transformed into pure nanostructured carbon materials by removal of the silica matrix via HF etching. The silica-carbon materials and the new carbon materials might become very important. As Mastai et al. showed, the hybrid materials can be applied as so-called selective solar absorbers [158].

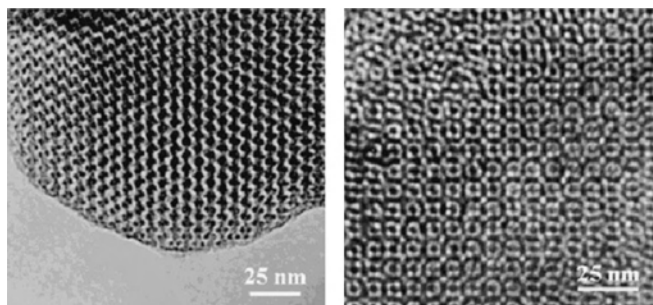


**Figure 6.** TEM images of two ordered mesoporous carbon materials CMK-1 and CMK-1 introduced by Ryoo et al. Reprinted with permission from [156], R. Ryoo, *Adv. Mater.* 13, 677 (2001). © 2001, Wiley-VCH.

As was previously described, the other important subfield of nanochemistry in ordered mesoporous materials is the creation of nanoparticles. Here in accordance with Figure 4, the size and shape of the nanoreactor becomes important. Due to the high interface energy once nucleated, nano-sized crystals tend to grow by Ostwald-ripening. This growth can be restricted by performing the crystallization inside the pore system of a mesoporous host. Often caused by quantum-size effects, interesting composite materials are created. Therefore, much of the work has been devoted to prepare semiconductor nanoparticles via this route. Examples are gallium nitride [159], cadmium selenide [160], cadmium sulfide [161], silicon [162, 163], titanium dioxide [164], Germanium [165], Galliumarsenide [166], zinc sulfide [167], and Indium phosphide [168]. Ordered mesoporous silica materials, especially of the MCM-41-type have also been used as matrices for the preparation of metal colloids. In this way, for example, metal nanowires have been produced with Pd [169, 170], Pt [171], or Ag [171, 172].

For all these materials, the relation between pore size and pore shape and the characteristics of the nanoparticles was obvious. A class of materials that is also quite important are derived, when ordered mesoporous silica materials are just supports. Due to the stability of amorphous silica, a huge number of compounds with ordered mesoporous materials as supports have been reported. The most common technique to prepare them is via liquid impregnation or via vapor deposition techniques.

It is known that the acidity of MCM-based materials is relatively low when the acidic centers are incorporated into the network. This is behind the scope of this review article and can be found in the literature of Corma [173]. A different strategy to introduce sufficient acidity for catalytic applications involves deposition of active species inside the pores. Ordered mesoporous  $\text{SiO}_2$  acts as a support or one could again say as a host. Quite often, polyoxometalate species were deposited on ordered mesoporous host systems. In 1994, heteropolyacids of the Keggin-type as, for instance,  $\text{H}_3\text{PW}_{12}\text{O}_{40}$  were taken [174–176]. Interestingly, high loadings up to 50 wt% were achieved without crystallization of the heteropolyacid. The new materials were acidic enough to catalyze even the alkylation of 4-*tert*-butylphenol with isobutene.

MCM-41 is very likely to act as a support for noble metal colloids. Junges et al. produced a MCM-41 with a high Pt loading [177] and catalytic activity for hydrogenation reactions of benzene, naphthalene, phenanthrene, and olefins were demonstrated [73, 178, 179]. For all of these strategies where the goal is to replicate the whole pore system with a different material, two points have to be considered in further detail:

1. if the used precursor solutions wets the pore wall,
2. if the reaction forming the new material is slow enough to avoid pore blocking.

Even more demanding is hydrogenation of aromatics in the presence of sulfur. Due to the shortage of nonregenerable energy sources, future diesel fuels will contain a significant amount of sulfur. To increase the cetane number of the fuel, a certain fraction needs to be hydrogenated by suitable catalysts. Corma et al. found out that Pt on a MCM-41



support was much more stable against sulfur determination than other supporting systems used like  $\text{Al}_2\text{O}_3$  [180].

Only few publications addressed the deposition of metal oxide particles in mesoporous oxides like MCM-41. Abe et al. [181] and, later, Froeba et al. [182] described the synthesis of iron oxide in the pore system of MCM-41. A simple impregnation technique was applied to obtain the final materials. Under similar conditions,  $\text{TiO}_2$  particles for purposes in photocatalysis [164, 183–186] and  $\text{VO}_x$  species in a tetrahedral coordination mode [70, 82, 187] were prepared. A Mo/MCM-41 with molybdenum in the oxidation state +VI are accessible via deposition of molybdocene dichloride as a precursor [188]. Depending on the concentrations of the precursor, discrete molybdate species or smaller polymolybdates were created as Mo K-edge X-ray absorption spectroscopy indicated. The resulting materials were used for the catalytic dehydrogenation of methanol to formaldehyde. A manganese-grafted MCM-41 was prepared via vapor deposition of  $\text{Mn}_2(\text{CO})_{10}$  [189–191]. This resulted in good oxidizing catalysts. Aronson et al. tried to obtain special structures of manganese oxide under confinement of the silica pores since they adapted a method for preparing layered compounds [192]. Unfortunately, this was not the case but the particles have been amorphous. Via deposition and decomposition of  $\text{Co}_2(\text{CO})_8$ , a Co/MCM-41 was created by Kim et al., which was then used to catalyze the Pauson–Khand reaction [193]. Schueth et al. deposited zirconia  $\text{ZrO}_2$ , iron oxide, and two rare metal oxides (europium oxide and yttrium oxide) in MCM-41 and SBA-15 [194]. The  $\text{Fe}_2\text{O}_3/\text{MCM-41}$  was catalytically tested towards the oxidation of  $\text{SO}_2$  to  $\text{SO}_3$ . Already in 1997, a very interesting article was presented by Shephard et al. [195]. They used a relatively complex bimetallic cluster as the precursor for a bimetallic Ru-Ag-O-species confined to MCM-41 pores. The introduction of two different species might be an interesting way to prepare new compounds in the future.

#### 4.1.3. Anodized Alumina: A Route Towards Nanowires

An alternative route towards porous nanoreactors is via the preparation of porous alumina. Porous alumina is prepared via the anodization of aluminum metal in an acidic solution. Further information about this process can be found in the literature by Despic and Parkhutik [196]. Porous alumina membranes have certain typical characteristics:

- They contain cylindrical pores of uniform diameter in a hexagonal array.
- The cylinder axes are strictly perpendicular to the membrane surface plane.

The pores can be produced with a great variety of pore sizes ranging from just 5 nm up to 200 nm [197, 198]. Pore densities on the membrane surface are of the order of  $10^{11}$  pores per  $\text{cm}^2$ . The membrane thickness is typically in the range of 10 to 100 nm.

Within the context of the concepts of nanochemistry described in Section 3.3, it is obvious that porous alumina membranes are ideal to illustrate the impact on particle preparation and materials chemistry. The size and shape of

nanoparticles will be predetermined by the shape and size of the pores. However, the shape and arrangement of new nanostructures is limited to hexagonally aligned cylinders. A nanorod of some material may be used as a nanowire as will be discussed later. Alternatively, hollow tubes, so-called nanofibrils, can be prepared.

Nanotubes and nanofibrils of conducting polymers [199–207], metals [197, 198, 208–216], semiconductors [217, 218], and carbon have been prepared [219].

The materials that one prefers to deposit inside the pores can be produced in several different ways:

- Electrochemical deposition: One face of the membrane is coated by a thin metal film acting as a cathode for the reduction of metals inside the pores. The more metal that is deposited, the longer the metal nanowires get. Also, some conductive polymers as polypyrrole or polyaniline can be deposited electrochemically.
- Chemical reduction.
- Chemical polymerization of organic monomers.
- Sol-gel processes: Sol-gel methods [74, 90–92, 220–222] are mainly used for the preparation of inorganic oxide-type nanostructures as  $\text{TiO}_2$ ,  $\text{ZnO}$ , or  $\text{WO}_3$ .
- Chemical vapor deposition (CVD).

Preparing nanowires by nanochemistry via porous alumina membranes has thus proved to be a very versatile tool. In further experiments, Mallouk et al. attempted to construct electrical circuits capable of performing simple calculations [223–228].

## 4.2. Other Hard Matter Nanoreactor Systems

### 4.2.1. Nanotubes

Recently, a new class of fascinating nanoreactors emerged through and through made from carbon. These are, in the meantime, famous carbon nanotubes and fullerenes [4, 229, 230]. However, fullerenes are not ideal nanoreactors because they are closed-shell objects. Therefore, carbon nanotubes are considered in much more detail here. Carbon nanotubes exhibit three different types of surfaces: the outer and inner surface as well as edges. Carbon nanotubes have been known since the ingenious discovery of Iijima in 1991 [231, 232]. The formation and chemistry of carbon nanotubes is reviewed in much more detail elsewhere [233, 234]. However, some of the nanochemical aspects in the area of carbon nanotubes should be highlighted. First of all, the formation of carbon nanotubes themselves can be seen as a nanochemical event. The thermodynamic stable form of carbon is graphite. When just a finite number of atoms are present to form a carbon allotrope, this situation changes because now the interface energy becomes much more important as the surface-to-volume ratio increases. Additionally, in a graphene layer of just a few nanometers extension, the amount of so-called dangling bonds at the edges of these surfaces becomes significant in determining the total energy of the structure. These dangling bonds become eliminated when the graphene layer folds and bonds to itself. To do so, exactly 12 carbon pentagons are needed—no more and no less. One alternative for stabilization are

the famous fullerenes, which are not described in further detail here [230]. Carbon nanotubes are highly related to fullerenes and can be understood as folded graphene sheets capped by half-fullerene caps. It was recognized very early that there is a tilting angle in the orientation of the graphene sheets leading to helicity [235–237]. This helicity is one of the most important features of carbon nanotubes. Two nanochemical applications of carbon nanotubes have been discussed in depth and often controversially. Much, even worldwide research attention, was focussed on the hydrogen storage properties of carbon nanotubes. The number of publications and groups are countless. Hydrogen uptakes from 0.4–68% hydrogen have been reported but lacked reproducibility [238]. The storage of hydrogen was explained by the small pores in carbon nanotubes and the related capillary pressure expressed by the Kelvin equation [239]. In the meantime, there are also indications that the high hydrogen storage capability is caused by metal impurities instead of the carbon nanotubes themselves [240].

A straightforward application of carbon nanotubes is to use the inner cavity as a nanotemplate for the creation of all kinds of nanowires. The first example for this was shown in 1993 [241] by Iijima himself when he was able to solidify a molten salt inside a carbon nanotube. Due to their good wetting properties, it is also possible to infiltrate the carbon nanotubes with dissolved species in organic solvents [242, 243]. Now the question arises how the solvents are able to penetrate into the internal cavity. Obviously, the carbon nanotubes have to be opened prior to their use as nano-reactors. This can be done by different methods of oxidation [244] and the secret is that the tips with their pentagonal defects are more reactive than the hexagonal sheets. Therefore, carbon nanotubes can be selectively opened at the tips. Interestingly, carbon nanotubes are more stable against oxidation than graphite. This is a result of the closed shell structure of the graphene sheets while graphite possesses exposed edges where oxidation starts.

Carbon nanotubes are representatives of a whole new class of compounds with varying compositions. The most related compounds are the isoelectronic boron-nitride (BN) nanotubes and, later, boron-carbide (BC) nanotubes [245–248].

Recently, some attention was devoted to the preparation of nanotubes with a more classic inorganic composition [240]. Interestingly, for some of these new nanotubes, carbon nanotubes have been used as templates. For instance,  $V_2O_5$  nanotubes have been prepared this way [249], but also strategies using amphiphiles as long-alkyle amines phases as templates are successful [250–252]. The interlayer distance in the latter system is determined by the length of the amines and can range from 1.7 nm to 3.8 nm. Vanadium pentoxide nanotubes are very interesting due to their high catalytic potential, as is  $TiO_2$ . The first examples of titania nanotubes were prepared by using polymer fibers as templates [253, 254]. Tenne et al. reported in 1992 about the preparation of the first chalkogenide nanotubes  $WS_2$  [255].

#### 4.2.2. Polyoxometalates

As was shown previously, complex structures emerge by self-assembly processes of amphiphilic molecules. Examples have been micelles or lyotropic phases.

A completely different system that nevertheless shows incredibly complex structures and a highly interesting nanochemistry are the so-called supramolecular polyoxometalates [256, 257]. It was Mueller et al. who showed in 1994 that solutions of the so-called “molybdenum-blue” contained molecular well-defined species possessing the structure of a giant molecular wheel (Fig. 7) [258]. This discovery is astonishing in two ways. First, molybdenum blue was known since 1783 [259] but its secrets were never unleashed completely until the investigations of Mueller et al. Second, one has to realize the simple way of preparing these compounds: An aqueous solution of a molybdate (for instance,  $Na_2MoO_4$ ) is acidified and a reducing agent is added in a certain amount. Within hours, the complex, highly-ordered giant polyoxometalates form. The first member of this new class of compounds contained 154 Mo atoms and its formula is  $(NH_4)_{28}[Mo_{154}(NO)_{14}O_{448}H_{14}(H_2O)_{70}] \cdot 350H_2O$ . Therefore, its molecular mass is similar to those of small proteins. Under certain conditions, even larger and more complex compounds can be obtained. Further larger giant wheels with the formulae  $[Mo_{176}O_{528}(H_2O)_{63}(CH_3OH)_{17}H_n]^{(32-n)-}$  and  $[H_{16}Mo_{248}O_{720}(H_2O)_{128}]^{16-}$  have been found [260, 261].

Concerning the emergence of these astonishing compounds, Mueller’s analyses [262–265]:

“According to our experiments, the following conditions favor the corresponding emergence of molecular complexity (in several successive reaction steps) at least in the system we are investigating: (1) Abundance of linkable units, that is, building blocks. (2) Possibility of generation of units with high free enthalpy to drive polymerization or growth processes, for example, by formation of  $H_2O$ . (3) Possibility of an easy structural change in the building blocks. (4) Possibility of including hetero elements in the fragments. (5) Possibility to form larger units which can be linked in different ways. (6) Bonding between fragments should neither be too strong nor too weak. (7) Possibility to control the structure-forming processes by templates. (8) Possibility to generate structural defects in reaction intermediates (leading to lacunary structures) by the presence of species which remove building units. (9) Presence of energetically low-lying unoccupied molecular orbitals in the fragments. (10) Possibility to localize and delocalize electrons in different ways in order to gain versatility. (11) Possibility to control and vary the charge (e.g. by protonation, electron transfer reactions, or substitution of building parts).”

Interestingly, under slightly different conditions, a new, closed-shell polyoxometalate with 132 Mo atoms and icosahedral symmetry is built (see Fig. 7b) [266].

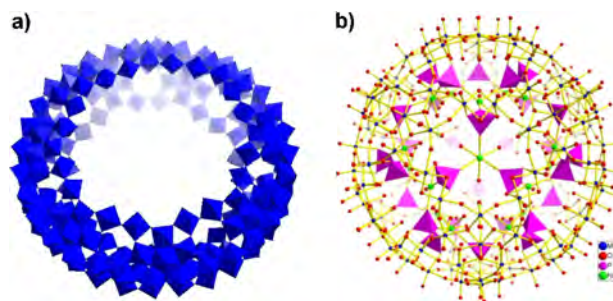


**Figure 7.** Two examples of giant polyoxometalate structures, (a) a giant wheel ( $Mo_{174}$ -cluster), and (b) a giant sphere ( $Mo_{132}$  cluster). (b) shows how the internal surface is covered by phosphate groups which have been introduced by the nanochemistry shown in Figure 7a.

Although the formation of these compounds can already be seen as a nanochemical event, the giant polyoxometalates are also promising nanoreactor candidates. These molecules possess well-defined inner cavities and have very high surface areas. From the huge possibilities for nanochemistry [262–265], just two should be selected in the following paragraph.

The spherical  $\text{Mo}_{132}$  cluster shows an astonishing nanochemistry in aqueous solution (Fig. 8a) [267]. A lid of this cluster opens and closes, and the ligands attached to the internal surface can be exchanged. This way, the internal surface of the molecular spheres can be varied from acetate, phosphate, sulfate, to adenosine-mono-phosphate or even phenylphosphonate ligand coverages. This allows the creation of any desired surface and the study of host-guest relations.

The second example (Fig. 8b) shows how the chemisorption of cationic surfactants on the molybdate cluster surface leads to new kinds of amphiphiles assembling to liquid-crystalline polyoxometalate-surfactant hybrid phases [268]. The surfactant selectively binds to the “equator region” of the giant wheel, resulting in a new supramolecular species being hard, hydrophilic, and inorganic in the core, and soft, hydrophobic, and organic in the shell. Therefore,

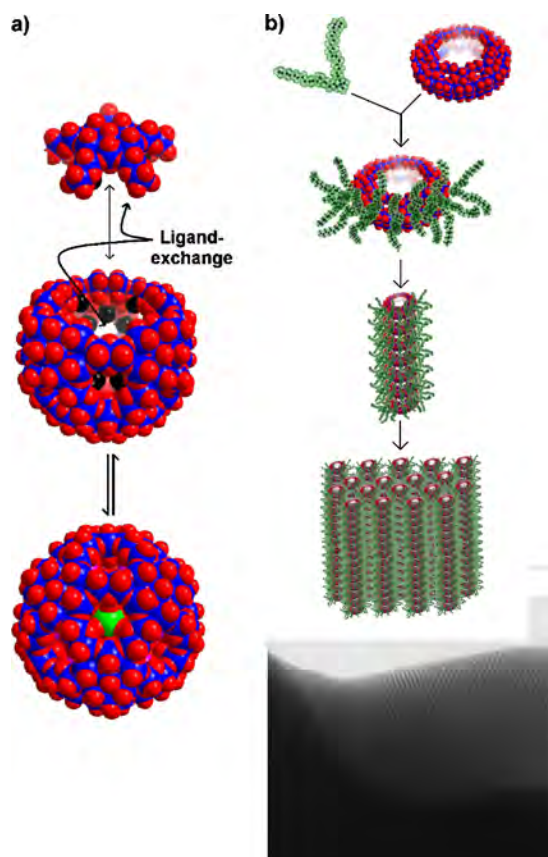


**Figure 8.** (a) shows the “open-and-shut” nanochemistry present in the  $\text{Mo}_{132}$  cluster system. In solution, the cluster opens and chemical compounds can get access to the internal cavity of the molecular hollow sphere. (b) shows the formation of quadrupolar surfactant-polyoxometalate hybrid amphiphiles and the resulting formation of hexagonally ordered lyotropic phases. A representative TEM micrograph of these liquid crystals is also shown.

these molecules are amphiphiles but with a quadrupolar distribution of different domains. It can be seen that these amphiphiles self-assemble into ordered hexagonal structures (Fig. 8b). Similar phenomena with other polyoxometalate clusters prove the generality of this approach [269–272].

## 5. SOFT-MATTER CHEMICAL CONFINEMENTS

In general, soft-matter chemical confinements are produced by self-assembly processes. The emergence of these structures were briefly explained in Section 2, but it should be pointed out that all nanoreactors themselves are the result of nanochemistry. However, the formations of the nanoreactors, as micelles, for instance, often belong to a completely different field. Therefore, the formation of the soft-matter nanostructures mentioned in this review is seen as a premise. The interested reader is referred to the literature of Antonietti and Goltner [273] concerning the nanochemical origins of the formation of complex soft-matter nanostructures.

### 5.1. Micelles

Simple micelles are formed by even relatively short chain surfactants and correspondingly formed micelles are small (2–4 nm). Additionally, micelles of this type undergo constant reconstruction on a timescale of  $10^{-5}$ – $10^{-9}$  s [274–276]. Therefore, micelles made from low molecular weight surfactant are of limited use as nanoreactors. Additionally, the “filling” of micelles often leads to the formation of emulsions that are discussed in the next section. The high exchange rates between micelles makes it even hard to control the polymerization of polymerizable surfactants although some interesting studies have been published [277–279]. Recently, a review article discussed the use of polymerizable surfactants to produce nanostructures [280].

Much more stable and larger micellar systems can be obtained when heavier amphiphilic block copolymers are used [281, 282]. The size of these micelles is ideal in determining the size of solids formed in the inner core [283–285]. The first step of this nanochemistry involves the loading of micelles with metal salts. Interestingly, this is less difficult than expected. The dispersion efficiency of the block copolymers is so huge that they even incorporate salt crystals into their micelles. The transformation of the precursors follows the loading step. Now kinetic considerations are extremely important. When the nucleation of the resulting material (e.g., the precipitation of sulfide nanoparticles in micelles) is slow, every nanoreactor will only contain one crystal that will grow to its maximum size. On the other hand, when the reaction is performed fast, each micelle will host several nuclei which will remain small [282, 285, 286]. Another ideal example is the production of PbS nanoclusters in block-copolymer micelles [287].

### 5.2. Emulsions, Micro-Emulsions, and Mini-Emulsions

Micelles and lyotropic phases also can be swollen by selective solvents. One possible solvent is a monomer for a succeeding polymerization reaction. The polymerization inside

the droplets leads to a huge variety of spherical nanostructures. This principle leads to the vast field of heterophase polymerization, which is also technologically highly relevant. In an ideal case, monodisperse nanostructures are obtained.

The most obvious choice for emulsion nanoreactors are micro-emulsions due to their thermodynamic stability and the correlating well-predictable properties [61]. The difficulty in using micro-emulsions as polymerization nanoreactors is to find a suitable surfactant system [288]. The approach of using micro-emulsions as nanoreactors enables micro-lattices with varying surface properties (aminated, hydroxylated, bipyridin, etc.) to be prepared [288, 289]. Of particular interest in this respect is also that biochemically relevant groups like enzymes can be incorporated into the surface of the micro-lattices [289–291]. Natural lipids are suitable surfactants for these micro-emulsions because they don't denaturalize the proteins [289–291]. Three-dimensional bicontinuous micro-emulsions can be used to produce interesting porous polymer-network materials [292–294]. One ideal example was presented by Chew et al. [295]. However, micro-emulsions can also be used to control the size of nucleating inorganic species such as  $\text{BaTiO}_3$ , for instance [296].

Another type of interesting nanoreactors are the so-called mini-emulsions [297]. Mini-emulsions are a special type of emulsion containing two immiscible liquids, a surfactant stabilizing the liquid-liquid interface, and an additive soluble in the dispersed phase [298, 299]. Mini-emulsions are kinetically stabilized in contrast to micro-emulsions. It has been shown that the lifetime of mini-emulsion droplets can be of the order of days to months [300], which makes them quite promising nanoreactor systems. One illustrative example for their final application is the preparation of asymmetric zirconyl chloride nanocrystals [301].

### 5.3. Lyotropic Phases

The next level of complexity is given when lyotropic phases (or bicontinuous micro-emulsions) act as hosts for nanochemistry educts as, for instance, the monomers which are then transformed into polymer rods, sponges, or sheets [302, 303]. It is evident in these experiments that due to their flexibility lyotropic phases are not able to effectively shape the formed polymers. The thermodynamic contribution of the forming polymer becomes more and more significant for the composite system in time [292]. The confinement of the polymer chains to the dimensions of the lyotropic phase is equivalent to a significant decrease in entropy. The polymer breaks free and destroys the order on a nanoscale. Although the produced materials are quite interesting [293, 304], lyotropic phases are of limited use to act as nanoreactors for polymerization reactions. For instance, Akagi et al. polymerized acetylene inside a thermotropic (nematic) chiral liquid crystal leading to helical fibers [305]. Although the final product is very interesting, it could not be predicted. The interested reader can find a more detailed review about polymerization in lyotropic phases in [306, 307].

### 5.4. Vesicles

Vesicles are practically a solvent droplet enclosed by a bi- or multi-layer made from surfactants. The size of vesicles is quite polydispersive and can exceed the nano-dimension

significantly. Therefore, vesicles are no favorable nanoreactors. However, there have been some reports in the literature that assign vesicles as nanoreactors. For example, Nardin et al. incorporated channel proteins into the walls of a vesicle containing polymerizable block copolymers amphiphiles [308], or Hubert et al. used vesicles to produce hollow silica spheres [309].

## 6. SUMMARY

We have seen that a nearly infinite number of single nanostructures (nanospheres, nanowires, etc.) with various compositions can be created by nanochemistry, where the key concept seems to be in step where the nanoreactor determines the accessible space for the chemical process. Definitely, this field will grow further and scientists will start to investigate the key properties of these new nanostructures.

However, if one comes back once again to the comparison to natural systems, it becomes obvious that working natural systems do not contain single nanostructures, although nature uses similar nanochemical methods. To obtain functional systems, the single nanostructures need to be implemented into a complex system [310] of nanostructures. These complex systems will eventually have two features: Every single nanostructures has to be exactly in the right place. The result of the interactions between the nanostructures might not be a linear one, but the superior functionality might result from synergistic effects and is, therefore, hard to predict or plan. These two problems need to be solved in the future in order to create functional nanodevices. It will not be enough to count on self-assembly processes. Additionally, still (and unlike to natural systems) the creation of particular nanostructures require unique nanochemical conditions. It follows that a necessary variety of nanostructures (let's imagine a device made from nanowires and semiconductor quantum dots) can only be currently produced step-by-step (first the nanowires and then the quantum dots). The next question that arises is how these independent nanostructures can be put in the right place (connected to each other). Currently, the only way to realize this is to use nanoengineering techniques that are yet limited.

Furthermore, current nanostructures and their already realized assemblies are static. Once they are formed, their phenotype and properties are fixed. This paradigm might be broken if one succeeds in connecting the mostly inorganic nanostructures to functional polymeric units with so-called smart properties [24–27]. Nanochemistry is the only possibility in obtaining these functional organic-inorganic nanocomposites.

As already indicated in the concept for nanochemistry described in more detail in Section 3.2, the current success in nanochemistry has been made in the field of nanoparticle chemistry. Single nanostructures have been obtained. The step to higher lengthscales seems to be quite easy to realize (creation of new materials by nanochemistry) as some examples have already demonstrated. The effect of spatial confinements on molecular chemical processes is much less explored.

## GLOSSARY

**Biom mineralization** A process used by nature to structure inorganic matter on the nanoscale using structure directing organic auxiliaries.

**Bottom-up** Describes one approach, mostly taken in chemistry, to derive nanostructured matter. Starting from atoms materials growth is initiated and stopped in the nano-regime when the objects reach a desired size.

**Hard-matter** Self-organized structures containing inorganic units.

**Lyotropic phases** Liquid crystals of an amphiphilic system in water.

**MCM-41** The first ordered mesoporous silica material. It possesses a hexagonal system of cylindrical 3 nm wide pores.

**Nanoreactor** A reaction vessel of a size of just few nanometers.

**Soft-matter** Self-organized structures containing organic units.

**Top-down** Describes one approach, mostly taken in physics, to derive nanostructured matter. Starting from bulk-materials matter is made smaller and smaller as much as possible.

## REFERENCES

- G. A. Ozin, *Adv. Mater.* 4, 612 (1992).
- J. Tersoff, *Nature* 412, 135 (2001).
- P. Ball, *Nature* 408, 904 (2000).
- L. Forro, *Science* 289, 560 (2000).
- C. A. Mirkin, *Science* 286, 2095 (1999).
- G. Whitesides, *Technol. Rev.* 101, 84 (1998).
- L. L. Sohn, *Nature* 394, 131 (1998).
- G. M. Whitesides, J. P. Mathias, and C. T. Seto, *Science* 254, 1312 (1991).
- G. A. Ozin, E. Chomski, D. Khushalani, and M. J. MacLachlan, *Curr. Op. Coll. Interf. Sci.* 3, 181 (1998).
- G. M. Whitesides and J. C. Love, *Sci. Am.* Sept., 33 (2001).
- G. M. Whitesides and Y. Xia, *Angew. Chem.* 110, 568 (1998).
- P. S. Weiss, *Nature* 413, 585 (2001).
- R. A. Vaia, T. B. Tolle, and G. F. Schmitt, *Sampe J* 37, 24 (2001).
- R. Dagani, *Chem. Eng. News* 69, 24 (1991).
- U. Narang, R. A. Dunbar, F. V. Bright, and P. N. Prasad, *Appl. Spectroscopy* 47, 1700 (1993).
- B. G. Maiya, *J. Porphy. Phthalocyanines* 4, 393 (2000).
- W. Gopel, *Microelectron. Eng.* 32, 75 (1996).
- W. Gopel, *Sens. Actuator B-Chem.* 4, 7 (1991).
- K. J. Kirk, *Contemp. Phys.* 41, 61 (2000).
- Y. Kostov, S. Tzonkov, L. Yotova, and M. Krysteva, *Anal. Chim. Acta* 280, 15 (1993).
- S. S. Iqbal, M. W. Mayo, J. G. Bruno, B. V. Bronk, C. A. Batt, and J. P. Chambers, *Biosens. Bioelectron.* 15, 549 (2000).
- L. M. Goldenberg, M. R. Bryce, and M. C. Petty, *J. Mater. Chem.* 9, 1957 (1999).
- J. M. Lehn, *Angew. Chem.-Int. Edit. Engl.* 29, 1304 (1990).
- C. M. Friend, *Interdiscip. Sci. Rev.* 21, 195 (1996).
- W. B. Spillman, J. S. Sirkis, and P. T. Gardiner, *Smart Mater. Struct.* 5, 247 (1996).
- I. Y. Galaev and B. Mattiasson, *Trends Biotechnol.* 17, 335 (1999).
- I. Y. Galaev, *Russ. Chem. Rev.* 65, 471 (1995).
- M. Reed and W. P. Kirk, "Nanostructures and Mesoscopic Systems." Academic Press, Boston, 1992.
- M. R. Bryce, *J. Mater. Chem.* Special Issue 7, 1069 (1997).
- Science*, Special Section 254, 1300 (1991).
- G. Ozin, *Sci. Am.* January, 7 (1998).
- G. M. Whitesides, *Sci. Am.* 285, 78 (2001).
- E. Haeckel, "Kunstformen der Natur." Dover Verlag, 1974.
- P. Ball, *Nature* 409, 413 (2001).
- L. Qi, H. Cölfen, and M. Antonietti, *Angew. Chem.* 112, 617 (2000).
- L. M. Qi, H. Cölfen, and M. Antonietti, *Angew. Chem.-Int. Edit.* 39, 604 (2000).
- M. Antonietti, M. Breulmann, C. G. Goltner, H. Colfen, K. K. W. Wong, D. Walsh, and S. Mann, *Chem.-Eur. J.* 4, 2493 (1998).
- H. Colfen and M. Antonietti, *Langmuir* 14, 582 (1998).
- A. M. Belcher, X. H. Wu, R. J. Christensen, P. K. Hansma, G. D. Stucky, and D. E. Morse, *Nature* 381, 56 (1996).
- M. Sarikaya, *Proc. Nat. Acad. Sci. USA* 96, 14183 (1999).
- C. E. Diebel, R. Proksch, C. R. Green, P. Neilson, and M. M. Walker, *Nature* 406, 299 (2000).
- R. Witschko and W. Witschko, "Magnetic Orientation in Animals." Springer, Berlin, Heidelberg, New York, 1995.
- B. A. Maher, *Proc. R. Soc. Lond. Biol.* 211, 1126 (1998).
- S. Mann, N. H. C. Sparks, M. M. Walker, and J. L. Kirschvinck, *J. Exp. Biol.* 140, 35 (1988).
- D. Schueler and R. B. Frankel, *Appl. Microbiol. Biotechnol.* 52, 464 (1999).
- R. P. Blakemore, *Science* 190, 377 (1975).
- R. B. Frankel and D. A. Bazylinski, *Hyperfine Interact* 90, 135 (1994).
- C. T. Dameron, R. N. Reese, R. K. Mehra, A. R. Kortan, P. J. Carroll, M. L. Steigerwald, L. E. Brus, and D. R. Winge, *Nature* 338, 596 (1989).
- T. Klaus, R. Joerger, E. Olsson, and C. G. Granqvist, *Proc. Nat. Acad. Sci. USA* 96, 13611 (1999).
- P. Mukherjee, A. Ahmad, D. Mandal, S. Senapati, S. R. Sainkar, M. I. Khan, R. Ramani, R. Parischa, P. V. Avajakumar, M. Alam, M. Sastry, and R. Kumar, *Angew. Chem. Int. Ed.* 40, 3585 (2001).
- S. P. Graether, M. J. Kuiper, S. M. Gagnés, V. K. Walker, Z. Jia, B. D. Sykes, and P. L. Davies, *Nature* 406, 325 (2000).
- U. Banin, C. J. Lee, A. A. Guzelian, A. V. Kadavanich, A. P. Alivisatos, W. Jaskolski, G. W. Bryant, A. L. Efros, and M. Rosen, *J. Chem. Phys.* 109, 2306 (1998).
- A. P. Alivisatos, *J. Phys. Chem.* 100, 13226 (1996).
- A. P. Alivisatos, *Science* 271, 933 (1996).
- M. Valden, X. Lai, and D. W. Goodman, *Science* 281, 1647 (1998).
- S. Vogel, "Cats' Paws and Catapults." Penguin, London, 1999.
- U. Bacht, D. Lupo, P. Comte, J. E. Moser, F. Weissortel, J. Salbeck, H. Spreitzer, and M. Gratzel, *Nature* 395, 583 (1998).
- B. Oregan and M. Gratzel, *Nature* 353, 737 (1991).
- M. Gratzel, *Curr. Opin. Colloid Interface Sci.* 4, 314 (1999).
- R. J. Mortimer, *Chem. Soc. Rev.* 26, 147 (1997).
- D. F. Evans and H. Wennerström, "The Colloidal Domain." Wiley-VCH, Weinheim, 1999.
- L. A. Cuccia, J. Lehn, J. Homo, and M. Schmutz, *Angew. Chem.* 112, 239 (2000).
- K. Moller and T. Bein, *Stud. Surf. Sci. Cat.* 117, 53 (1998).
- S. Spange, *Prog. Polym. Sci.* 25, 781 (2000).
- S. Furuta, H. Katsuki, and S. Komarneni, *J. Porous Mat.* 8, 43 (2001).
- [Anon], *Stud. Surf. Sci.* 93, 149 (1995).
- B. G. Belenkii, M. L. Davtyan, D. P. Dobyichin, A. N. Krasovskii, and P. P. Nefedov, *Vysokomolekulyarnye Soedineniya Seriya A* 17, 2811 (1975).
- S. O'Brien, J. Tudor, S. Barlow, M. J. Drewitt, S. J. Heyes, and D. Ohare, *Chem. Commun.* 641 (1997).
- C. S. Cundy, *Collect. Czech. Chem. Commun.* 63, 1699 (1998).
- P. Van Der Voort, M. Morey, G. D. Stucky, M. Mathieu, and E. F. Vansant, *J. Phys. Chem. B* 102, 585 (1998).
- X. S. Zhao and G. Q. Lu, *J. Phys. Chem. B* 102, 1556 (1998).



72. H. J. Shin, R. Ryoo, M. Kruk, and M. Jaroniec, *Chem. Commun.* 349 (2001).
73. T. Inui, J. B. Kim, and M. Seno, *Catal. Lett.* 29, 271 (1994).
74. J. Livage and C. Sanchez, *J. Non-Cryst. Solids* 145, 11 (1992).
75. P. M. Price, J. H. Clark, and D. J. Macquarrie, *J. Chem. Soc.-Dalton Trans.* 101 (2000).
76. V. M. Ogenko, *Adsorpt. Sci. Technol.* 14, 295 (1996).
77. P. Mezza, J. Phalippou, and R. Sempere, *J. Non-Cryst. Solids* 243, 75 (1999).
78. X. Feng, G. E. Fryxell, L. Q. Wang, A. Y. Kim, J. Liu, and K. M. Kemner, *Science* 276, 923 (1997).
79. J. H. Clark and D. J. Macquarrie, *Chem. Commun.* 853 (1998).
80. M. Rozwadowski, M. Lezanska, J. Wloch, K. Erdmann, R. Golembiewski, and J. Kornatowski, *Phys. Chem. Chem. Phys.* 2, 5510 (2000).
81. D. Brunel, *Microporous Mesoporous Mat.* 27, 329 (1999).
82. P. Van Der Voort, M. Mathieu, E. F. Vansant, S. N. R. Rao, and M. G. White, *J. Porous Mat.* 5, 305 (1998).
83. F. Rachdi, L. Hajji, C. Goze, D. J. Jones, P. Maireles-Torres, and J. Roziere, *Solid State Commun.* 100, 237 (1996).
84. P. Van Der Voort, M. Mathieu, M. Morey, G. D. Stucky, and E. F. Vansant, *Mesoporous Molecular Sieves 1998* 117, 333 (1998).
85. V. Fornes, H. Garcia, M. A. Miranda, F. Mojarrad, M. J. Sabater, and N. N. E. Suliman, *Tetrahedron* 52, 7755 (1996).
86. R. Gangopadhyay and A. De, *Chem. Mat.* 12, 608 (2000).
87. A. Stein, *Microporous Mesoporous Mat.* 44, 227 (2001).
88. N. Leventis and I. A. Elder, *Chem. Mater.* 11, 2837 (1999).
89. S. Polarz and M. Antonietti, *Chem. Comm. Advance Article* (2002).
90. R. A. Assink and B. D. Kay, *J. Non-Cryst. Solids* 99, 359 (1988).
91. J. Livage, C. Sanchez, M. Henry, and S. Doeuff, *Solid State Ionics* 32-3, 633 (1989).
92. L. L. Hench and J. K. West, *Chem. Rev.* 90, 33 (1990).
93. J. Livage, *Advanced Zeolite Science and Applications* 85, 1 (1994).
94. J. Livage, *Curr. Opin. Solid State Mat. Sci.* 2, 132 (1997).
95. L. M. Bronstein, S. Polarz, B. Smarsly, and M. Antonietti, *Advanced Materials* 13, 1333 (2001).
96. S. J. Gregg and K. S. W. Sing, "Adsorption, Surface Area, and Porosity." Academic Press, 1982.
97. K. S. W. Sing, D. H. Everett, R. A. W. Haul, L. Moscou, R. A. Pierotti, J. Rouqu rol, and T. Siemieniewska, *Pure Appl. Chem.* 57, 603 (1985).
98. J. Rouquerol, D. Avnir, C. W. Fairbridge, D. H. Everett, J. H. Haynes, N. Pernicone, J. D. Ramsay, K. S. W. Sing, and K. K. Unger, *Pure Appl. Chem.* 66, 1739 (1994).
99. D. W. Breck, "Zeolite Molecular Sieves: Structure, Chemistry, and Use." Wiley, London, 1974.
100. D. W. Breck, W. G. Eversole, R. M. Milton, T. B. Reed, and T. L. Thomas, *J. Am. Chem. Soc.* 78, 5963 (1956).
101. R. M. Barrer, "Zeolite and Clay Minerals as Sorbents and Molecular Sieves." Academic Press, London, 1978.
102. M. E. Davis, *Microp. Mesop. Mater.* 21, 173 (1998).
103. S. L. Suib, *Chem. Rev.* 93, 803 (1993).
104. A. Corma, in "Zeolites in Oil Refining and Petrochemistry," p. 373. Kluwer Academic, Netherlands, 1992.
105. C. B. Khouw and M. E. Davis, in "Selectivity in Catalysis" (M. E. Davis and S. L. Suib, Eds.). American Chemical Society, Washington D. C., 1994.
106. T. Baba, R. Koide, and Y. Ono, *Chem. Comm.* 691 (1991).
107. C. M. Zicovichwilson, A. Corma, and P. Viruela, *J. Phys. Chem.* 98, 10863 (1994).
108. E. Cohen de Lara and R. Kahn, *NATO ASI Series* 221, 169 (1990).
109. C. Mirodatos and D. Barthomeuf, *J. Catal.* 93, 246 (1985).
110. J. A. Rabo and G. J. Gajda, *NATO ASI Series* 221, 273 (1990).
111. L. Uytterhoeven, D. Dompas, and W. Mortier, *J. Chem. Soc., Faraday Trans.* 88, 2753 (1992).
112. E. H. Teunissen, R. A. van Santen, A. P. J. Jansen, and F. B. Van Duijneveldt, *J. Phys. Chem.* 97, 203 (1993).
113. E. G. Derouane, *J. Catal.* 100, 541 (1986).
114. K. Morishige, H. Fujii, M. Uga, and D. Kinukawa, *Langmuir* 13, 3494 (1997).
115. E. W. Hansen, M. Stocker, and R. Schmidt, *J. Phys. Chem.* 100, 2195 (1996).
116. E. W. Hansen, R. Schmidt, and M. Stocker, *Progress in Zeolite and Microporous Materials*, Pts. A-C 105, 543 (1997).
117. J. M. Baker, J. C. Dore, and P. Behrens, *J. Phys. Chem. B* 101, 6226 (1997).
118. K. Morishige and K. Nobuoka, *J. Chem. Phys.* 107, 6965 (1997).
119. S. Takahara, M. Nakano, S. Kittaka, Y. Kuroda, T. Mori, H. Hamano, and T. Yamaguchi, *J. Phys. Chem. B* 103, 5814 (1999).
120. P. Smirnov, T. Yamaguchi, S. Kittaka, T. S., and Y. Kuroda, *J. Phys. Chem. B* 104, 5498 (2000).
121. G. Gu, W. P. Ding, Y. W. Du, H. J. Huang, and S. H. Yang, *Appl. Phys. Lett.* 70, 2619 (1997).
122. J. S. Chen, Q. H. Li, H. Ding, W. Q. Pang, and R. R. Xu, *Langmuir* 13, 2050 (1997).
123. M. Alvaro, H. Garcia, S. Garcia, F. Marquez, and J. C. Scaiano, *J. Phys. Chem. B* 101, 3043 (1997).
124. A. Corma, V. Fornes, H. Garcia, V. Marti, and M. A. Miranda, *Chem. Mat.* 7, 2136 (1995).
125. S. Sinlapadech, R. M. Krishna, Z. H. Luan, and L. Kevan, *J. Phys. Chem. B* 105, 4350 (2001).
126. J. Y. Bae, K. T. Ranjit, Z. H. Luan, R. M. Krishna, and L. Kevan, *J. Phys. Chem. B* 104, 9661 (2000).
127. Z. H. Luan, J. Y. Bae, and L. Kevan, *Chem. Mat.* 12, 3202 (2000).
128. H. M. SungSuh, Z. H. Luan, and L. Kevan, *J. Phys. Chem. B* 101, 10455 (1997).
129. A. Corma, V. Fornes, H. Garcia, M. A. Miranda, and M. J. Sabater, *J. Am. Chem. Soc.* 116, 9767 (1994).
130. S. H. Tolbert, A. Firouzi, G. D. Stucky, and B. F. Chmelka, *Science* 278, 264 (1997).
131. A. Firouzi, D. J. Schaefer, S. H. Tolbert, G. D. Stucky, and B. F. Chmelka, *J. Am. Chem. Soc.* 119, 9466 (1997).
132. F. Marlow, M. D. McGehee, D. Y. Zhao, B. F. Chmelka, and G. D. Stucky, *Adv. Mater.* 11, 632 (1999).
133. G. Wirnsberger and G. D. Stucky, *Chem. Mat.* 12, 2525 (2000).
134. P. D. Yang, G. Wirnsberger, H. C. Huang, S. R. Cordero, M. D. McGehee, B. Scott, T. Deng, G. M. Whitesides, B. F. Chmelka, S. K. Buratto, and G. D. Stucky, *Science* 287, 465 (2000).
135. G. Wirnsberger, P. D. Yang, H. C. Huang, B. Scott, T. Deng, G. M. Whitesides, B. F. Chmelka, and G. D. Stucky, *J. Phys. Chem. B* 105, 6307 (2001).
136. J. Zhang, Z. Luz, and D. Goldfarb, *J. Phys. Chem.* 101, 7087 (1997).
137. M. L. Cano, A. Corma, V. Fornes, H. Garcia, M. A. Miranda, C. Baerlocher, and C. Lengauer, *J. Am. Chem. Soc.* 118, 11006 (1996).
138. P. L. Llewellyn, U. Ciesla, H. Decher, R. Stadler, F. Schuth, and K. K. Unger, *Zeolites and Related Microporous Materials: State of the Art 1994* 84, 2013 (1994).
139. S. M. Ng, S. Ogino, T. Aida, K. A. Koyano, and T. Tatsumi, *Macromol. Rapid Commun.* 18, 991 (1997).
140. K. Moller, T. Bein, and R. X. Fischer, *Chem. Mater.* 10, 1841 (1998).
141. C. G. Goltner and M. C. Wei benberger, *Acta Polym.* 49, 704 (1998).
142. S. A. Johnson, D. Khushalani, N. Coombs, T. E. Mallouk, and G. A. Ozin, *J. Mater. Chem.* 8, 13 (1998).
143. M. J. MacLachlan, P. Aroca, N. Coombs, I. Manners, and G. A. Ozin, *Adv. Mater.* 10, 144 (1998).
144. K. Kageyama, T. Tatsumi, and T. Aida, *Polym. J.* 31, 1005 (1999).
145. K. Kageyama, S. Ogino, T. Aida, and T. Tatsumi, *Macromolecules* 31, 4069 (1998).



146. L. K. Van Looveren, D. F. Geysen, K. A. Vercruyssen, B. H. Wouters, P. J. Grobet, and P. A. Jacobs, *Mesoporous Molecular Sieves* 1998 117, 477 (1998).
147. L. K. Van Looveren, D. F. Geysen, K. A. Vercruyssen, B. H. Wouters, P. J. Grobet, and P. A. Jacobs, *Angew. Chem.-Int. Edit.* 37, 517 (1998).
148. J. Tudor and D. O'Hare, *Chem. Comm.* 603 (1997).
149. K. Kageyama, J. Tamazawa, and T. Aida, *Science* 285, 2113 (1999).
150. C. G. Wu and T. Bein, *Science* 264, 1757 (1994).
151. C. G. Wu and T. Bein, *Chem. Mat.* 6, 1109 (1994).
152. C. Wu and T. Bein, *Science* 266, 1013 (1994).
153. S. S. Xie, W. Z. Li, C. Y. Wang, L. W. Xu, H. Zhang, Y. Zhang, and L. X. Qian, *Sci. China Ser. A-Math. Phys. Astron.* 40, 971 (1997).
154. R. Ryoo, S. H. Joo, and S. Jun, *J. Phys. Chem. B* 103, 7743 (1999).
155. S. Jun, S. H. Joo, R. Ryoo, M. Kruk, M. Jaroniec, Z. Liu, T. Ohsuna, and O. Terasaki, *J. Am. Chem. Soc.* 122, 10712 (2000).
156. R. Ryoo, S. H. Joo, M. Kruk, and M. Jaroniec, *Adv. Mater.* 13, 677 (2001).
157. T. Kyotani, *Carbon* 38, 269 (2000).
158. Y. Mastai, S. Polarz, and M. Antonietti, *Adv. Funct. Mater.* 12, 197 (2002).
159. H. Winkler, A. Birkner, V. Hagen, I. Wolf, R. Schmechel, H. v. Seggern, and R. A. Fischer, *Adv. Mater.* 11, 1444 (1999).
160. H. Parala, H. Winkler, M. Kolbe, A. Wohlfart, R. A. Fischer, R. Schmechel, and H. v. Seggern, *Adv. Mater.* 12, 1050 (2000).
161. T. Hirai, H. Okubo, and I. Komasa, *J. Phys. Chem. B* 103, 4228 (1999).
162. O. Dag, G. A. Ozin, H. Yang, C. Reber, and G. Bussiere, *Adv. Mater.* 11, 474 (1999).
163. E. Chomski, O. Dag, A. Kuperman, N. Coombs, and G. A. Ozin, *Chem. Vapor Depos.* 2, 8 (1996).
164. B. J. Aronson, C. F. Blanford, and A. Stein, *Chem. Mat.* 9, 2842 (1997).
165. R. Leon, D. Margolese, G. Stucky, and P. M. Petroff, *Phys. Rev. B* 52, R2285 (1995).
166. V. I. Srdanov, I. Alkneit, G. D. Stucky, C. M. Reaves, and S. P. DenBaars, *J. Phys. Chem. B* 102, 3341 (1998).
167. W.-H. Zhang, J.-L. Shi, H.-R. Chen, Z.-L. Hua, and D.-S. Yan, *Chem. Mater.* 13, 648 (2001).
168. J. R. Agger, M. W. Anderson, M. E. Pemble, O. Terasaki, and Y. Nozue, *J. Phys. Chem. B* 102, 3345 (1998).
169. H. Kang, Y. Jun, J. Park, K. Lee, and J. Cheon, *Chem. Mater.* 12, 3530 (2000).
170. K. B. Lee, S. M. Lee, and J. Cheon, *Adv. Mater.* 13, 517 (2001).
171. J. Han, J. M. Kim, and G. D. Stucky, *Chem. Mater.* 12, 2068 (2000).
172. M. H. Huang, A. Choudrey, and P. Yang, *Chem. Comm.* 1063 (2000).
173. A. Corma, *Chem. Rev.* 97, 2373 (1997).
174. C. T. Kresge, D. O. Marler, G. S. Rav, and B. H. Rose, U.S. Patent 5, 366, 945 (1994).
175. I. V. Kozhevnikov, K. R. Kloetstra, A. Sinnema, H. W. Zandbergen, and H. van Bekkum, *J. Mol. Catal. A-Chem.* 114, 287 (1996).
176. I. V. Kozhevnikov, A. Sinnema, R. J. J. Jansen, K. Pamin, and H. Vanbekkum, *Catal. Lett.* 30, 241 (1995).
177. U. Junges, W. Jacobs, I. Voigtmartin, B. Krutzsch, and F. Schueth, *J. Chem. Soc.-Chem. Commun.* 2283 (1995).
178. K. M. Reddy and C. S. Song, *Catal. Today* 31, 137 (1996).
179. J. N. Armor, *Appl. Catal. A-Gen.* 112, N21 (1994).
180. A. Corma, A. Martinez, and V. MartinezSoria, *J. Catal.* 169, 480 (1997).
181. T. Abe, Y. Tachibana, T. Uematsu, and M. Iwamoto, *J. Chem. Soc., Chem. Comm.* 1617 (1995).
182. M. Froeba, R. Kohn, G. Bouffaud, O. Richard, and G. van Tendeloo, *Chem. Mat.* 11, 2858 (1999).
183. T. Maschmeyer, F. Rey, G. Sankar, and J. M. Thomas, *Nature* 378, 159 (1995).
184. R. D. Oldroyd, G. Sankar, J. M. Thomas, and D. Ozkaya, *J. Phys. Chem. B* 102, 1849 (1998).
185. L. Marchese, E. Gianotti, V. Dellarocca, T. Maschmeyer, F. Rey, S. Coluccia, and J. M. Thomas, *Phys. Chem. Chem. Phys.* 1, 585 (1999).
186. Y. M. Xu and C. H. Langford, *J. Phys. Chem. B* 101, 3115 (1997).
187. M. Mathieu, P. Van Der Voort, B. M. Weckhuysen, R. R. Rao, G. Catana, R. A. Schoonheydt, and E. F. Vansant, *J. Phys. Chem. B* 105, 3393 (2001).
188. I. J. Shannon, T. Maschmeyer, R. D. Oldroyd, G. Sankar, J. M. Thomas, H. Pernot, J. P. Balikdjan, and M. Che, *J. Chem. Soc.-Faraday Trans.* 94, 1495 (1998).
189. D. Gleeson, R. Burch, N. A. Cruise, and S. C. Tsang, *Nanostruct. Mater.* 12, 1007 (1999).
190. R. Burch, N. A. Cruise, D. Gleeson, and S. C. Tsang, *J. Mater. Chem.* 8, 227 (1998).
191. R. Burch, N. Cruise, D. Gleeson, and S. C. Tsang, *Chem. Commun.* 951 (1996).
192. B. J. Aronson, C. F. Blanford, and A. Stein, *J. Phys. Chem. B* 104, 449 (2000).
193. S. W. Kim, S. U. Son, S. I. Lee, T. Hyeon, and Y. K. Chung, *J. Am. Chem. Soc.* 122, 1550 (2000).
194. F. Schuth, A. Wingen, and J. Sauer, *Microporous Mesoporous Mat.* 44, 465 (2001).
195. D. S. Shephard, T. Maschmeyer, B. F. G. Johnson, J. M. Thomas, G. Sankar, D. Ozkaya, W. Z. Zhou, R. D. Oldroyd, and R. G. Bell, *Angew. Chem.-Int. Edit. Engl.* 36, 2242 (1997).
196. A. Despic and V. P. Parkhutik, (J. O. Bockris, R. E. White, and B. E. Conway, Eds.), Chapter 6. Plenum Press, New York, 1989.
197. C. A. Foss, G. L. Hornyak, J. A. Stockert, and C. R. Martin, *J. Phys. Chem.* 96, 7497 (1992).
198. C. A. Foss, G. L. Hornyak, J. A. Stockert, and C. R. Martin, *J. Phys. Chem.* 98, 2963 (1994).
199. R. V. Parthasarathy and C. R. Martin, *J. Polym. Sci.* 62, 875 (1996).
200. C. R. Martin and R. V. Parthasarathy, *Adv. Mater.* 7, 487 (1995).
201. R. V. Parthasarathy and C. R. Martin, *Nature* 369, 298 (1994).
202. C. R. Martin, *Adv. Mater.* 3, 457 (1991).
203. C. R. Martin, R. V. Parthasarathy, and V. Menon, *Synth. Met.* 55-57, 1165 (1993).
204. Z. Cai, J. Lei, W. Liang, V. Menon, and C. R. Martin, *Chem. Mater.* 3, 960 (1991).
205. W. Liang and C. R. Martin, *J. Am. Chem. Soc.* 112, 9666 (1990).
206. L. S. Van Dyke and C. R. Martin, *Langmuir* 6, 1123 (1990).
207. R. M. Penner and C. R. Martin, *J. Electrochem. Soc.* 133, 2206 (1986).
208. J. C. Hulteen, V. Menon, and C. R. Martin, *J. Chem. Soc. Faraday Trans.* 92, 4029 (1996).
209. V. Menon and C. R. Martin, *Anal. Chem.* 67, 1920 (1995).
210. M. Nishizawa, V. Menon, and C. R. Martin, *Science* 268, 700 (1995).
211. C. J. Brumlik, V. Menon, and C. R. Martin, *J. Mater. Res.* 9, 1174 (1994).
212. C. A. Foss, G. L. Hornyak, J. A. Stockert, and C. R. Martin, *Adv. Mater.* 5, 135 (1993).
213. C. J. Brumlik, C. R. Martin, and K. Tokuda, *Anal. Chem.* 64, 1201 (1992).
214. C. J. Brumlik and C. R. Martin, *J. Am. Chem. Soc.* 113, 3174 (1991).
215. R. M. Penner and C. R. Martin, *Anal. Chem.* 59, 2625 (1987).
216. G. L. Hornyak and C. R. Martin, *J. Phys. Chem.* 101, 1548 (1997).
217. B. B. Lakshmi, P. K. Dorhout, and C. R. Martin, *Chem. Mater.* 9, 857 (1997).
218. J. D. Klein, R. D. I. Herrick, D. Palmer, M. J. Sailor, C. J. Brumlik, and C. R. Martin, *Chem. Mater.* 5, 902 (1993).
219. R. V. Parthasarathy, K. L. N. Phani, and C. R. Martin, *Adv. Mater.* 7, 896 (1995).

220. C. J. Brinker and G. W. Scherer, "Sol-Gel Science. The Physics and Chemistry of Sol-Gel Processing." Academic Press, London, 1990.
221. C. J. Brinker, A. J. Hurd, G. C. Frye, P. R. Schunk, and C. S. Ashley, *Nippon Seramikkusu Kyokai Gakujutsu Ronbunshi-Journal of the Ceramic Society of Japan* 99, 862 (1991).
222. C. J. Brinker, G. C. Frye, A. J. Hurd, and C. S. Ashley, *Thin Solid Films* 201, 97 (1991).
223. T. E. Mallouk, S. K. St. Angelo, and B. R. Martin, *Abstr. Pap. Am. Chem. Soc.* 224, 003 (2002).
224. Y. J. Glanville, D. G. Narehood, P. E. Sokol, A. Amma, and T. Mallouk, *J. Mater. Chem.* 12, 2433 (2002).
225. D. J. Pena, J. K. N. Mbindyo, A. J. Carado, T. E. Mallouk, C. D. Keating, B. Razavi, and T. S. Mayer, *J. Phys. Chem. B* 106, 7458 (2002).
226. J. K. N. Mbindyo, T. E. Mallouk, J. B. Mattzela, I. Kratochvilova, B. Razavi, T. N. Jackson, and T. S. Mayer, *J. Am. Chem. Soc.* 124, 4020 (2002).
227. J. K. N. Mbindyo, B. D. Reiss, B. R. Martin, C. D. Keating, M. J. Natan, and T. E. Mallouk, *Adv. Mater.* 13, 249 (2001).
228. T. E. Mallouk, *Science* 291, 443 (2001).
229. M. Prato, *Fullerenes and Related Structures* 199, 173 (1999).
230. M. S. Dresselhaus, G. Dresselhaus, and P. C. Eklund, *J. Mater. Res.* 8, 2054 (1993).
231. S. Iijima, *Nature* 354, 54 (1991).
232. S. Iijima and T. Ichihashi, *Nature* 363, 603 (1993).
233. P. M. Ajayan, *Chem. Rev.* 99, 1787 (1999).
234. P. M. Ajayan and O. Z. Zhou, *Top. Appl. Phys.* 80, 425 (2001).
235. M. Ge and K. Sattler, *Science* 260, 515 (1993).
236. J. W. C. Wiloer, L. C. Venema, A. G. Rinzler, R. E. Smalley, and C. Dekker, *Nature* 391, 59 (1998).
237. T. Odom, J. Huang, P. Kim, and C. Lieber, *Nature* 391, 62 (1998).
238. M. S. Dresselhaus, K. A. Williams, and P. C. Eklund, *MRS Bulletin* 24, 45 (1999).
239. M. Pederson and J. Broughton, *Phys. Rev. Lett.* 69, 2689 (1992).
240. G. R. Patzke, F. Krumreich, and R. Nesper, *Angew. Chem.* 114, 2554 (2002).
241. P. M. Ajayan and S. Iijima, *Nature* 333, 392 (1993).
242. S. C. Tsang, Y. K. Chen, P. J. F. Harris, and M. L. H. Green, *Nature* 372, 159 (1994).
243. E. Dujardin, T. W. Ebbesen, T. Hiura, and K. Tanigaki, *Science* 265, 1850 (1994).
244. P. M. Ajayan, T. W. Ebbesen, T. Ichihashi, S. Iijima, K. Tanigaki, and T. Hiura, *Nature* 362, 522 (1993).
245. W. Han, Y. Bando, K. Kurahima, and T. Sato, *Appl. Phys. Lett.* 73, 3085 (1998).
246. D. Goldberg, W. Han, Y. Bando, L. Bourgeois, K. Kurahima, and T. Sato, *J. Appl. Phys.* 86, 2364 (1999).
247. E. Bengu and L. D. Marks, *Phys. Rev. Lett.* 86, 2385 (2001).
248. B. C. Satishkumar, A. Govindaraj, K. R. Harikumar, J. P. Zhang, A. K. Cheetham, and C. N. R. Rao, *Chem. Phys. Lett.* 300, 473 (1999).
249. P. M. Ajayan, O. Stephan, P. Redlich, and C. Colliex, *Nature* 375, 564 (1995).
250. M. E. Spahr, P. Bitterli, R. Nesper, M. Mueller, F. Krumreich, and H. U. Nissen, *Angew. Chem. Int. Ed.* 37, 1263 (1998).
251. F. Krumreich, H. J. Muhr, M. Niederberger, F. Bieri, B. Schnyder, and R. Nesper, *J. Am. Chem. Soc.* 121, 8324 (1999).
252. H. J. Muhr, F. Krumreich, U. P. Schoenholzer, F. Bieri, M. Niederberger, L. J. Gauckler, and R. Nesper, *Adv. Mater.* 12, 231 (2000).
253. P. Hoyer, *Langmuir* 12, 1411 (1996).
254. R. A. Caruso, J. H. Schattka, and A. Greiner, *Adv. Mater.* 13, 1577 (2001).
255. R. Tenne, L. Margulis, M. Genut, and G. Hodes, *Nature* 360, 444 (1992).
256. M. T. Pope, "Heteropoly and Isopoly Oxometalates." Springer, 1983.
257. A. Müller and M. T. Pope, "Polyoxometalates: From Platonic Solids to Anti-Retroviral Activity; Topics in Molecular Organization and Engineering." Kluwer Academic Publishers, 1994.
258. A. Müller, E. Krickemeyer, J. Meyer, H. Bögge, F. Peters, W. Plass, E. Diemann, S. Dillinger, F. Nonnenbruch, M. Randerath, and C. Menke, *Angew. Chem.* 107, 2293 (1995).
259. C. W. Scheele, (D. S. F. Hermbstädt, Ed.). Martin Sändig oHG, Niederwallauf, 1971.
260. A. Müller, E. Krickemeyer, H. Bögge, M. Schmidtman, C. Beugholt, P. Kogerler, and C. Lu, *Angew. Chem.* 110, 1278 (1998).
261. A. Müller, S. Q. N. Shah, H. Bögge, and M. Schmidtman, *Nature* 397, 48 (1999).
262. A. Müller, D. Fenske, and P. Kogerler, *Curr. Opin. Solid State Mat. Sci.* 4, 141 (1999).
263. A. Müller, P. Kogerler, and H. Bögge, *Molecular Self-Assembly* 96, 203 (2000).
264. A. Müller and P. Kogerler, *Coordin. Chem. Rev.* 199, 335 (2000).
265. A. Müller, P. Kogerler, and A. W. M. Dress, *Coordin. Chem. Rev.* 222, 193 (2001).
266. A. Müller, E. Krickemeyer, H. Bögge, M. Schmidtman, and F. Peters, *Angew. Chem.* 110, 3567 (1998).
267. A. Müller, S. Polarz, S. K. Das, E. Krickemeyer, H. Bögge, M. Schmidtman, and B. Hauptfleisch, *Angew. Chem.* 111, 3439 (1999).
268. S. Polarz, B. Smarsly, and M. Antonietti, *Chem. Phys. Chem.* 2, 457 (2001).
269. D. G. Kurth, P. Lehmann, D. Volkmer, H. Cölfen, M. J. Koop, A. Müller, and A. D. Chesne, *Chem. Eur. J.* 6, 385 (2000).
270. F. Caruso, D. G. Kurth, D. Volkmer, M. J. Koop, and A. Müller, *Langmuir* 14, 3462 (1998).
271. D. G. Kurth, D. Volkmer, M. Ruttorf, B. Richter, and A. Müller, *Chem. Mater.* 12, 2829 (2000).
272. D. Volkmer, A. D. Chesne, D. G. Kurth, H. Schnablegger, P. Lehmann, M. J. Koop, and A. Müller, *J. Am. Chem. Soc.* 122, 1995 (2000).
273. M. Antonietti and C. Goltner, *Angew. Chem.-Int. Edit. Engl.* 36, 910 (1997).
274. S. M. Hamid and D. C. Sherrington, *J. Chem. Soc. Chem. Comm.* 936 (1986).
275. S. M. Hamid and D. C. Sherrington, *Polymer* 28, 332 (1987).
276. D. Cochlin, R. Zana, and F. Candau, *Macromolecules* 26, 5765 (1993).
277. C. E. Larrabee and E. D. Sprague, *J. Polym. Sci. Polym. Lett. Ed.* 17, 749 (1979).
278. K. Nagai, Y. Ohishi, H. Inaba, and S. Kudo, *J. Polym. Sci. Part A: Polym. Chem. Ed.* 23, 1221 (1985).
279. K. Ito, K. Tanaka, H. Tanaka, G. Imai, S. Kawaguchi, and S. Itsuno, *Macromolecules* 24, 2348 (1991).
280. S. A. Miller, J. H. Ding, and D. L. Gin, *Curr. Op. Coll. Interf. Sci.* 4, 338 (1999).
281. S. Förster, M. Zisenis, E. Wenz, and M. Antonietti, *J. Chem. Phys.* 104, 9956 (1996).
282. M. Antonietti, S. Heinz, M. Schmidt, and C. Rosenauer, *Macromolecules* 27, 3276 (1994).
283. M. Moffitt, H. Vali, and A. Einsenberg, *Chem. Mater.* 10, 1021 (1998).
284. H. Saito, S. Okamura, and K. Ishizu, *Polymer* 33, 1099 (1992).
285. M. Antonietti, E. Wenz, L. Bronstein, and M. Seregina, *Adv. Mater.* 7, 1000 (1995).
286. E. Wenz, A. Thuenemann, and M. Antonietti, *Colloid Polym. Sci.* 274, 795 (1996).
287. R. S. Kane, R. E. Cohen, and R. Silbey, *Chem. Mater.* 8, 1919 (1996).

288. M. Antonietti, S. Lohmann, and C. van Niel, *Macromolecules* 25, 1139 (1992).
289. M. Antonietti, S. Lohmann, C. D. Eisenbach, and U. S. Schubert, *Macrom. Chem. Rapid. Commun.* 16, 283 (1995).
290. E. Haltner, R. Basten, G. Borchard, M. Antonietti, and C. M. Lehr, *Proc. Int. Sym. Control. Rel. Bioact. Mater.* 22, 248 (1995).
291. M. Antonietti, R. Basten, and F. Groehn, *Langmuir* 10, 2498 (1994).
292. M. Antonietti and H. P. Hentze, *Colloid Polym. Sci.* 274, 696 (1996).
293. H. P. Hentze, C. G. Goltner, and M. Antonietti, *Ber. Bunsen-Ges. Phys. Chem. Chem. Phys.* 101, 1699 (1997).
294. H.-P. Hentze and M. Antonietti, *Curr. Op. Solid State Mater. Sci.* in press (2001).
295. C. H. Chew, T. D. Li, L. H. Gan, C. H. Quek, and G. L. M., *Langmuir* 14, 6068 (1998).
296. C. Beck, W. Haertl, and R. Hempelmann, *J. Mater. Res.* 13, 3174 (1998).
297. M. Antonietti, K. Landfester, and Y. Mastai, *Isr. J. Chem.* 41, 1 (2001).
298. J. Ugelstad, M. S. Elaasser, and J. W. Vanderho, *J. Polym. Sci. C* 11, 503 (1973).
299. J. Ugelstad, M. S. El-Aasser, and J. W. Vanderhoff, *Polym. Lett. Ed.* 11, 503 (1973).
300. M. Antonietti and K. Landfester, *Chem. Phys. Chem.* 2, 207 (2001).
301. N. Bechthold, F. Tiarks, M. Willert, K. Landfester, and M. Antonietti, "Miniemulsion Polymerization: Application and New Materials." Golm, 1999.
302. W. R. Palani, M. Sasthav, and H. M. Cheung, *Polymer* 34, 3305 (1993).
303. T. H. Cheing, L. M. Gan, C. H. Chew, S. Lee, S. C. Ng, K. L. Pey, and D. Grant, *Langmuir* 11, 3321 (1995).
304. M. Antonietti, C. Goltner, and H. P. Hentze, *Langmuir* 14, 2670 (1998).
305. K. Agaki, G. Piao, S. Kaneko, K. Sakamaki, H. Shirakawa, and M. Kyotani, *Science* 282, 1683 (1998).
306. H. P. Hentze and M. Antonietti, *Curr. Opin. Solid State Mat. Sci.* 5, 343 (2001).
307. K. Tajima and T. Aida, *Chem. Comm.* 2399 (2000).
308. C. Nardin, S. Thoeni, J. Widmer, M. Winterhalter, and W. Meier, *Chem. Comm.* 1433 (2000).
309. D. H. W. Hubert, M. Jung, and A. L. German, *Adv. Mater.* 12, 1291 (2000).
310. K. Mainzer, "Thinking in Complexity." Springer, 1996.

# Nanocluster Characterization by EXAFS Spectroscopy

Giuseppe Faraci

*Università di Catania;  
Istituto Nazionale di Fisica della Materia, Catania, Italy*

## CONTENTS

1. Introduction
2. EXAFS: General Considerations
3. EXAFS: Basic Principles
4. EXAFS Data Analysis
5. Phase and Amplitude Transferability
6. Characterization of Nanoclusters  
    Glossary  
    References

## 1. INTRODUCTION

An aggregate of atoms or molecules is commonly referred to as a cluster. The number of particles per cluster can be as small as two (dimer) up to several thousands. From the point of view of fundamental research, the physics of these agglomerates is of enormous interest. The possible realization of size-controlled clusters gives the promising opportunity of exploring the evolution of material properties step by step from the single atom to the bulk, following the modifications due to the addition of one or a few particles at a time. In addition, from a technological point of view, cluster and nanoscale physics are opening innovative frontiers in applied research and material science. In fact, quantum effects due to reduced dimensionality dramatically modify the geometrical, electronic, optical, and magnetic properties of materials, offering the unique opportunity of realizing innovative artificial materials that can be tailored toward a specific aim. This field is therefore very important, since the characteristics of any agglomerate can strongly depend not only on its size but also on its shape, as in on the specific spatial confinement. Since the pioneering work of Esaki and Tsu [1], the fabrication of layers with thickness of the order of nanometers is largely adopted for band gap “tailoring,” mainly in the fields of semiconductors and technological devices. A great impulse was certainly given by the advent of

sophisticated growth techniques such as molecular beam epitaxy or chemical vapor deposition, capable of controlling at the atomic level the interface between alternate films. Common nomenclature is by now widely accepted for nanosized structures: two-dimensional confined films are referred to as superlattices or quantum wells and one dimensional structures are named quantum wires, whereas zero-dimensional agglomerates are called quantum dots. For identifying an ensemble of atoms or molecules, we will adopt the term cluster since it does not contain any specific implication about the shape, which therefore can be of spherical or island-like configuration. The description of any cluster-related problem can also become dramatically complicated whenever the initial state properties, due to the cluster itself, are entangled with the so-called final state interactions, due to the presence of a substrate where the cluster usually is deposited, or a matrix containing embedded clusters. Of course, it would be greatly preferable to analyze an in-flight cluster if the intrinsic cluster characteristics should be investigated, avoiding therefore any influence of spurious contributions or interactions as those caused by a support. However, in several cases the presence of a matrix is absolutely necessary for the utilization of the clusters, for example, as catalysts or as luminescent centers; we mention, for example, the enormous interest found in microelectronics due to possible construction of predefined optical transitions by using size selected Si clusters and other semiconductor nanostructures [2–6]. Another interesting field is represented by the magnetic properties of low-dimension systems. Consider that in transition metals the average orbital magnetic moment is strongly dependent on the local coordination number; in fact, it is larger for open surfaces [7], with great implications on magneto-anisotropy of thin depositions. Superparamagnetic-ferromagnetic transitions, giant or colossal magneto-resistance etc., are other important examples in applications for magnetic recording, information transmission, sensors, and devices. Although the applied technological aspects have stimulated many studies, we also would like to point out the importance of clusters in

fundamental research. The investigation of phase transitions for rare gas clusters or films [8], “reentrant layering” [9], solid–liquid interface [8, 10, 11] are some important focuses of theoretical and experimental papers.

This paper presents an overview of investigation of small clusters by extended X-ray absorption fine structure (EXAFS) spectroscopy, which is a powerful tool for studying the structures of clusters. This article is organized as follows: first, we describe the spectroscopic technique in a plain style, avoiding complicated mathematical expressions, but referring the expert reader to a wide range of literature for details. In the sections following we give examples of metal, semiconductor, and rare gas clusters. Finally, molecular clusters will be briefly discussed.

## 2. EXAFS: GENERAL CONSIDERATIONS

The analysis of a cluster is not an easy task, considering the very small size of these structures. Cluster confinement is very often obtained with a size dispersion around an average value; this usually implies experimental information averaged over the size distribution. For the structural characterization of these aggregates, the X-ray diffraction is not a suitable technique since it requires a long range order to get the interference pattern typical of an ordered crystal. However, X-ray absorption offers a powerful tool for exploring the short range environment around a specific element as in the present case. In fact, if we look at the transmission spectrum of a thin metal foil (see Fig. 1), we observe a typical curve showing an absorption edge, corresponding to a core electron excitation from an internal shell, followed by a structured curve presenting some oscillations that can persist up to about 1000 eV after the threshold. These oscillations, absent in a gas, are caused by an interference effect of the photoelectron wave emitted by the absorbing

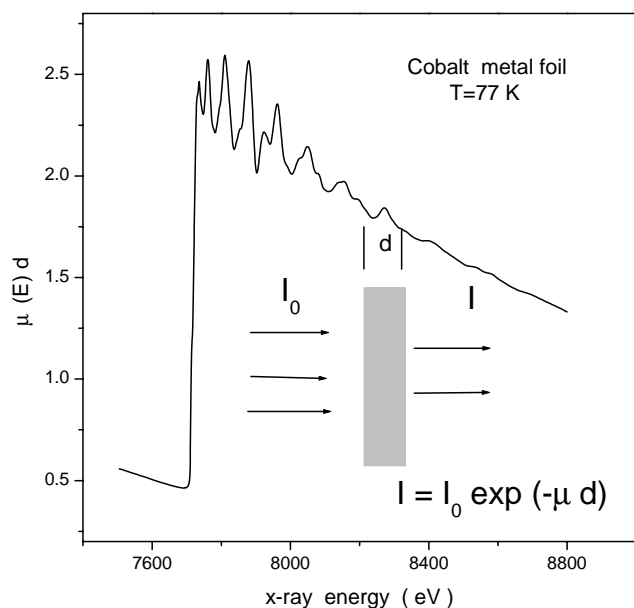


**Figure 1.** Transmission spectrum at the Co  $K$ -edge as a function of the photon energy;  $d$  is the thickness of the metal foil;  $\mu(E)$  is the absorption coefficient.

atom, with the surrounding atoms in the condensed state. This effect is called extended X-ray absorption fine structure (EXAFS), and, as explained in the following sections, gives very important information about the coordination shells around the absorbing atoms. For each coordination shell around the absorbers, we can obtain the radial distance, the coordination number, and the relative squared vibrational amplitude, due to the thermal disorder. For complicated situations, only the parameters of a single coordination shell can be extracted, but in simpler configurations even five or more shells can be disentangled, obtaining the corresponding parameters.

There is general agreement that the first experimental observation of the structured post-edge absorption curve should be attributed to Fricke [12] and Hertz [13] in 1920. In the same year Kossel [14] developed the first theory for explaining the near-edge structure. At that time, quantum mechanics was at its very beginning with contributions by Louis De Broglie, E. Schrödinger, P. Debye, A. Einstein, etc., and several efforts were made for explaining the observed effect [15, 16]. Also the modifications of the spectra as a function of the temperature [17] contributed toward the understanding of the experimental observations, as can be found in excellent historical reviews on EXAFS development [18, 19]. The initial theoretical attempts for a coherent interpretation of this effect, however, were based on a long range order theory, which we now know is incorrect to account for the effect. Therefore the technique was neither fully understood nor widely used until the development of a short range theory, reported for the first time by Sayers, Stern, and Lytle [20] on how to analyze the spectra using a Fourier transform algorithm. Since that time, a great proliferation of important contributions (see, e.g., recent reviews [21–23] and references therein) demonstrated the enormous relevance of this technique for investigating the short range environment around a specific absorber. Long range order is not necessary: Systems such as diluted solutions, biological molecules, disordered alloys, catalysts, atomic or molecular intercalated compounds, layered structures, and clusters can be investigated. In addition, for mixed compounds where two or more atomic species can be distinctly excited, independent EXAFS spectra can be collected around the corresponding edges, permitting a cross check of the information acquired at the single site, with high reliability of the specific structural details.

The great progress obtained in the analysis of smaller and smaller agglomerates should be attributed not only to the advent of the actual short range theory provided in 1971 [20], but also to the use of more brilliant X-ray sources such as modern synchrotrons. In fact, the EXAFS effect is a probabilistic interference effect implying a cross section, such as an overall interaction probability, which can be very small. If we consider, for example, that the case displayed in Figure 1 is referred to the cobalt  $K$  edge, we can give the following data: the  $K$  threshold is at 7709 eV corresponding to the excitation of a  $1s$  electron up to the Fermi level, with a total X-ray cross section of  $3360.6 \text{ cm}^{-1}$  immediately above threshold and smoothly decaying for higher energy. Similarly, as a further example, for indium the  $K$  threshold is at 27,940 eV with a total X-ray cross section of  $334 \text{ cm}^{-1}$  immediately above threshold; as shown in Figure 2, the  $L_I$  edge

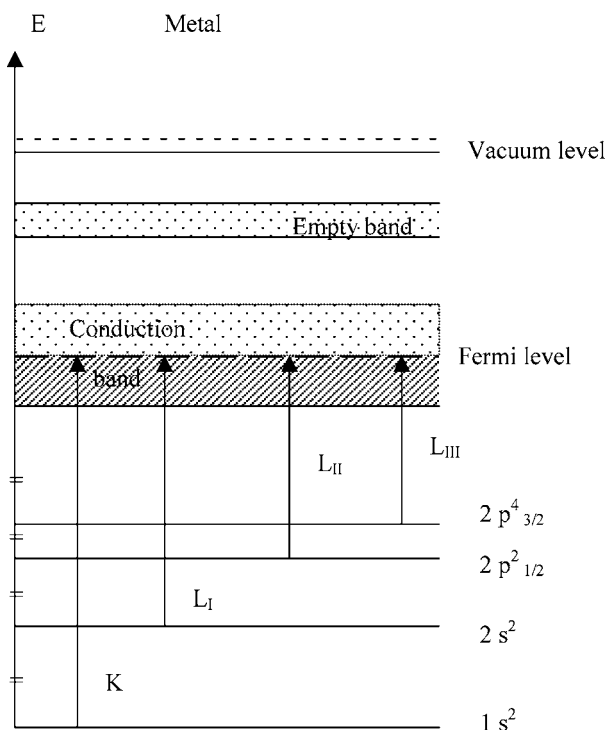


**Figure 2.** Energy scheme for a metal, showing the  $K$  and  $L$  absorption edges related to the excitation of an electron from the corresponding core level up to the Fermi level.

due to  $2s$  electron excitations is at 4238 eV,  $L_{II}$  edge, due to  $2p_{1/2}$  electrons at 3938 eV and  $L_{III}$  edge due to  $2p_{3/2}$  electrons at 3730 eV. The respective total cross sections are 9889, 12,024, and 13,889  $\text{cm}^{-1}$ .

The usual absorption law for a radiation beam of intensity  $I_0$ , partially transmitted through a layer of material is:  $I = I_0 \exp(-\mu d)$ , where  $\mu$  is the absorption coefficient and  $d$  the thickness of the material crossed by the X-ray beam; a suitable reduction of intensity of  $1/e$  can be obtained for a thickness of 3  $\mu\text{m}$  for the Co  $K$  edge, 33  $\mu\text{m}$ , for the In  $K$ -edge, 1  $\mu\text{m}$  for the In  $L_I$  edge and so on. Note that the photoelectric cross section with respect to the total at this energy is smaller than a few percent [24], or, the most important effect is the photoelectric one, but it varies as a function of the photon energy. As our effect is extracted from the structures of the  $\mu$  coefficient, energy dependent, it is obvious that an excellent statistical measurement should be performed of both  $I$  and  $I_0$ . The first, however, depends on the equivalent thickness of absorbers under the beam and therefore very diluted samples or small clusters embedded into a light matrix can be investigated when a high photon flux is available. Therefore, today synchrotrons are the most used sources; in fact, they provide a tunable energy through the use of monochromators, so that a long range of about 1000 eV can be explored past the threshold. Consider, for example, the European Synchrotron Radiation Facility (ESRF) where electrons in the storage ring reach an energy of 6 GeV, with a current higher than 200 mA in multibunch mode (see details at the Website [www.esrf.fr](http://www.esrf.fr)) and a lifetime longer than 30 hours. The brilliance of the photon beam obtained at 100 keV from an

undulator insertion device in multibunch mode can be as high as  $10^{19}$  phot/s/0.1 bw/mm<sup>2</sup>/mrad<sup>2</sup>. Even in the bending magnet beamlines, the flux at sample is larger than  $10^{11}$ – $10^{12}$  phot/s with a resolution  $\Delta E/E = 10^{-5}$ . Therefore, good EXAFS spectra can be collected in a reasonable time by scanning the energy of the photons in steps of 1–2 eV. Different detection methods can be used according to the experimental conditions of the sample to be investigated; we only mention the transmission, the fluorescence, and the total electron yield methods [25–27].

### 3. EXAFS: BASIC PRINCIPLES

As mentioned previously, since 1920 [12] the observations of X-ray absorption spectra realized that, at energies higher than typical thresholds, the absorption curve of condensed matter is not monotonic but contains some oscillations extending sometimes up to several hundreds of electronvolts beyond the threshold. This effect, called X-ray absorption fine structure (XAFS) [28] or extended XAFS (EXAFS) spectroscopy [18], is by now well understood, and a qualitative explanation will be given in the present section, whereas a more detailed treatment can be found in several excellent review articles [21–23, 25–27].

Let us consider, for the sake of clarity, a thin few- $\mu\text{m}$ -thick crystalline film made of a single element (e.g., Co as in Fig. 1). If the material is illuminated by an X-ray beam with energy  $E_p = h\nu$ , core electrons (let us suppose  $1s$  electrons, as in Fig. 1) can absorb the photon energy by photoelectric effect; if this energy is higher than the electron binding energy with respect to the vacuum, ejection of the electron occurs. This happens with a well known probability. The escaping electron, according to the Einstein theory, acquires a kinetic energy equal to the residual energy  $E = h\nu - E_0$  where  $\nu$  is the frequency of the X-ray and  $E_0$  the binding energy of the electron of the atomic element in consideration. In the wave description, the photoelectron has a wavelength  $\lambda = 2\pi/k = h/p = h/(2mE)^{1/2} = 1.23(E)^{-1/2}$  nm ( $E$  in eV units) where  $k$  is the electron wavelength,  $h$  the Planck's constant,  $p$  and  $m$  are the electron momentum and mass, respectively. Note that, in the following, for atomic distances the unit angstrom ( $\text{\AA}$ ) is often adopted because of its wide use in this field: 1 nm =  $10^{-9}$  m = 10  $\text{\AA}$ .

Therefore the electron possesses a wavelength  $\lambda$  and a velocity  $v$  depending on its residual energy (see Fig. 3). If this energy is, for example 100 eV, then  $\lambda = 0.12$  nm and  $v = 5.9 \times 10^{15}$  nm/s. If we consider that, as in modern synchrotrons, the X-ray beam energy can be tuned in a wide range, we can collect transmission spectra as a function of the X-ray energy, going, for example, from 200 eV before the threshold up to about 1000 eV beyond the threshold. From the simple formula  $I = I_0 \exp(-\mu(E)d)$  we can extract the absorption coefficient  $\mu(E) = \ln(I_0/I)/d$ , where  $d$  is the thickness of the metal film,  $I_0$  and  $I$  the intensity of the X-ray beam incident and transmitted from the metal layer, respectively. The coefficient  $\mu(E)$  is experimentally observed energy dependent, since the photoelectric cross section, involving electron transitions, does depend on the photon energy. However, it is without any structure in a gas-like sample, as in when the atoms of the material are very



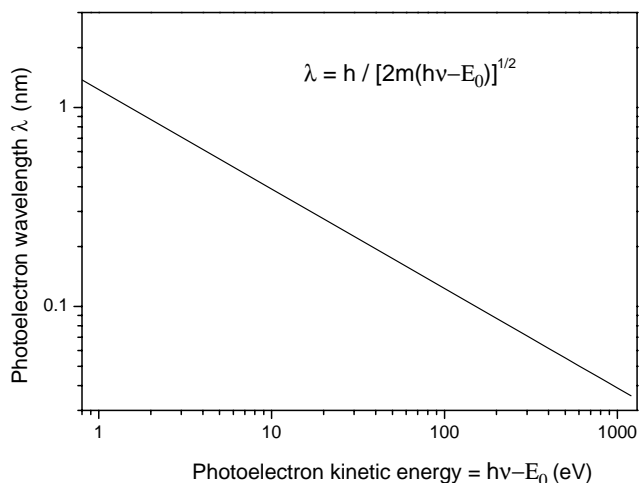


**Figure 3.** Photoelectron wavelength due to the extra-energy retained by the electron as kinetic energy after the absorption of the photon energy  $h\nu$ ;  $E_0$  is the electron binding energy.

far apart from each other; otherwise a structured oscillatory behavior (see Fig. 1) is observed. After the threshold, the EXAFS spectrum is conventionally indicated by:  $\chi(E) = \mu(E) - \mu_0(E) / \mu_{edge}$ , where  $\mu_0$  is the background absorption, or, the average continuous and structureless absorption that can be obtained just averaging over the oscillatory behavior;  $\mu_{edge}$  is a normalization factor that can be approximately obtained by the jump of the curve at the absorption edge.

A qualitative argument can show how to discriminate the two energy regions of the spectrum: the first between the threshold and about 30 eV above the edge, and the second at higher energy. In the first, the so-called XANES (X-ray absorption near edge structure), the electron wavelength is longer than the inter-atomic distance and the photoelectron “sees” many scatterers at a time; the interaction thus requires a many-body description. In the higher energy region of the spectrum, on the contrary, the photoelectron can be described by a short wavelength spherical wave; here, simple two-body interaction can be used and a simplified plane wave description of the photoelectron is quite adequate. In such a case, the EXAFS oscillations can be described as an interference effect between the outgoing photoelectron wave and the part of the same wave backscattered by the neighboring atoms; a simple schematic representation of the scattering process is shown in Figure 4; if the mutual interatomic distance is  $r_j$ , the phase difference between the two waves is of the order of  $2kr_j$ ,  $2r_j$  being the extra space traveled by the scattered wave with respect to the other in a time of the order of  $10^{-16}$  s. If the electron excitation is from a  $s$  state, averaging over the orientation of the sample, the oscillatory behavior of  $\chi$  as a function of the wave vector  $k$  is as follows [22, 29, 30]:

$$\begin{aligned} \chi(k) = & \sum_j \frac{S_0^2 N_j}{k r_j^2} F_j(k, \pi) \exp(-2\sigma_j^2 k^2) \\ & \times \exp(-2r_j/l_j) \exp[C_{4j}(k)] \\ & \times \sin[2kr_j + \theta_j(k) + 2\delta_{aj}(k) + C_{3j}(k)] \quad (1) \end{aligned}$$

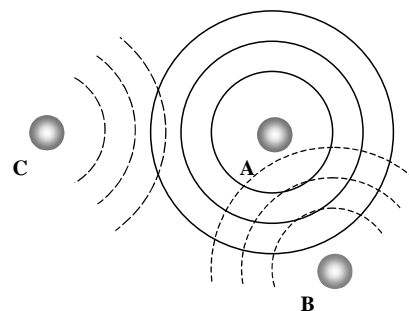


**Figure 4.** Schematic representation of the interference process. (A) represents the absorbing atom; (B) and (C) are two backscatterer atoms belonging to different coordination shells. The spherical photoelectron wave, emitted by the absorber (A), is represented by the circles (full line) and propagates toward the surrounding atoms; these backscatter the wave (dashed lines) towards the central atom. The EXAFS spectrum is originated by the interference between the outgoing wave from (A) and the backscattered wave from (B) and (C).

The  $\chi(k)$  curve extracted from the spectrum shown in Fig. 1 is reported in Figure 5.

Equation (1) describes the relative variation of the absorption coefficient  $\mu$  because of the modifications of the photoelectron wave function at the origin (i.e., at the center of the absorbing atom) caused by the scattering of the photoelectron wave.

This scattering can be provoked by an atom in the  $j$ -th coordination shell around the absorber; this shell has  $N_j$  atoms at  $r_j$  distance, with a backscattering amplitude  $F_j(k, \pi)$ .

Equation (1) takes into account the following effects:

1. The phase shift  $2kr_j$ ; this is due to the travel of the photoelectron toward the scatterer  $j$  and back to the absorber ( $2r_j$ ).

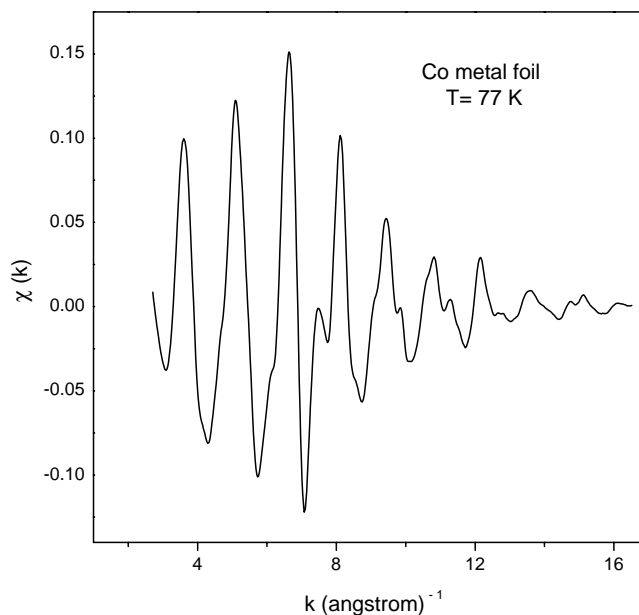


**Figure 5.** EXAFS curve  $\chi(k)$  as a function of the photoelectron wave vector  $k$ . Note that  $1 \text{ \AA} = 0.1 \text{ nm}$ ,  $1 \text{ \AA}^{-1} = 10 \text{ nm}^{-1}$ .

2. The phase shift  $\theta_j$  due to the scatterer.
3. The phase shift due to the absorber,  $2\delta_{aj}$ , counted two times because the photoelectron interacts with the absorber when it goes out and when comes back after being scattered. This shift takes also into account the core hole remaining in the center atom because of the electron ejection; actually this hole gives a unit positive extra charge seen by the escaping electron.
4. The relative thermal vibrational attenuation  $\exp(-2 \times \sigma_j^2 k^2)$ , called Debye–Waller (DW) factor, taking into account the static and dynamic disorder.
5. The cumulants  $C_{3j}(k)$  and  $C_{4j}(k)$ ; these are higher order corrections: the first enters the sine term, the second is another term entering the amplitude.
6. A damping factor  $\exp(-2r_j/l_j)$  taking into account how the wave is attenuated during the path  $2r_j$  because of the photoelectron mean free path  $l_j$ .
7. The  $S_0^2$  factor, an amplitude factor caused by shake-up or shake-off processes.

We now explain in more detail the various factors entering into Eq. (1), observing, first, that this equation can be considered as a sum of products of two factors, an amplitude factor  $A_j(k)$ , and a phase factor  $\sin[\Phi_j(k)]$ , over the  $j$  coordination shells:  $\chi(k) = \sum_j \chi_j(k) = \sum_j A_j(k) \sin[\Phi_j(k)]$ .

### 3.1. Amplitude Factor

The amplitude term  $A_j$  of the  $j$ -th coordination shell is determined by several weighting factors:

$$A_j(k) = \frac{S_0^2 N_j}{k r_j^2} F_j(k, \pi) \exp(-2\sigma_j^2 k^2) \times \exp(-2r_j/l_j) \exp[C_{4j}(k)] \quad (2)$$

First of all, it depends on  $F_j(k, \pi)$  the backscattering amplitude factor of the specific atom acting as a backscatterer of the photoelectron wave; here, the dependence of  $F$  on the wavevector  $k$  is explicitly indicated, together with the angle  $\pi$  due to the backscattering at  $180^\circ$ .

Each atom in the  $j$ -th coordination shell (formed by  $N_j$  identical atoms put at  $r_j$  distance from the central one) contributes by the factor  $F$  and, therefore, in the formula the factor  $N_j$  appears, whereas at the denominator  $k r_j^2$  is due to spherical wave factors [26]. The  $F$  factor can be calculated with high accuracy [31] using a plane wave approximation [32], valid as long as the dimensions of the atoms are small with respect to the curvature of the real spherical wave. Improved approximations were provided by successive contributions [33,34]; meanwhile curved wave treatments including multiple scattering effects, inelastic losses, and more accurate potentials were developed with better calculated amplitude and phase factors [35–38].

A damping factor in the amplitude is due to the thermal motion of the atoms, supposed of harmonic type  $\exp(-2\sigma_j^2 k^2)$ . This term appears in order to take into account the relative movement of the pair absorber-scatterer as a function of the temperature; it also includes the zero point energy, as in the static disorder of the absorber and of the scatterer, assuming that both are distributed according to a Gaussian function at a relative distance  $r_j$ :  $\sigma^2(T) = \sigma_0^2 + \sigma_{dyn}^2(T)$ .

Note that the static contribution  $\sigma_0^2$  can be deduced by measuring the DW factor as a function of the temperature, extrapolating the value for  $T = 0$  K.

A second damping factor  $\exp(-2r_j/l_j)$  is related to the finite mean free path of the electron, due to inelastic losses along the electron trajectory;  $l_j$  takes into account the mutual interaction with the medium, and it is a rather short length as in photoemission or Auger processes [39]. At the electron energy involved in EXAFS spectroscopy (30–1000 eV),  $l_j$  ranges between 0.5–1.5 nm for monoatomic crystals, somewhat higher for composite materials. The physical meaning of  $l_j$  can be regarded as the length over which coherence of the photoelectron wave for generating interference effect is still maintained; this length is therefore affected not only by inelastic losses but also by finite hole lifetime, by relaxation effects, etc. Details can be found in the literature [26]. In some cases [40], better approximations were obtained by subtracting an additional parameter from the path length  $r_j$  of the photoelectron, modifying the exponent of the damping factor as  $[-2(r_j - \beta)/l_j]$ . For the first shell of dichlorides and tetrahedral semiconductors [40], a value of the  $\beta$  parameter equal to the nearest neighbor distance was found. Determination of the electron mean free path  $l_j$ , as a function of the energy, with this algorithm can be found in Ref. [40] for some semiconductors such as Ge, GaAs, ZnSe, and CuBr.

$S_0^2$  factor is an amplitude reduction factor due to electron excitations from atomic low binding energy states. Some excess energy of the photoelectron escaping from the core level of the absorber can be transferred to valence electrons to produce transitions toward higher internal empty bands (shake-up processes) and/or toward the external continuum states (shake-off processes). This reduction factor was calculated by Carlson et al. [41] and was observed [27,42] with a  $k$  dependence up to  $80 \text{ nm}^{-1}$  roughly decreasing from 1.0 to 0.8. Often, however,  $S_0^2$  is considered as a constant ( $k$ -independent) factor and fitted in an ad hoc parameter. Values of  $S_0^2$  factor are reported in several papers in the range 0.7–0.8, but in some cases different values were obtained: for Au at the  $L_{III}$  edge, observed at 28 K, a value of  $S_0^2 = 1.1$  was adopted (see Ref. [43]); similarly,  $S_0^2$  was fixed at 1.09 for Ge, 1.11 for  $\text{GeCl}_4$ , and 1.08 for  $\text{Br}_2$  [37]; all these last measurements were done at the  $K$ -edge and at  $T = 300$  K.

### 3.2. Phase Factor

The sine term

$$\sin[2kr_j + \theta_j(k) + 2\delta_{aj}(k) + C_{3j}(k)] \quad (3)$$

is very important, as it gives the oscillating behavior as a function of  $k$  with a frequency  $2r_j$  somewhat modified by the phase shifts. The superposition of sinusoidal terms, weighted by different amplitudes, can in principle be disentangled by a Fourier transform (FT), which should provide a peak for each coordination shell containing structural information about that shell. Figure 6, for example, displays the FT of the EXAFS curve  $\chi(k)$ , shown in Figure 5 for a Co metal foil, weighted by  $k^3$ . This curve shows the peaks corresponding to the first, second, third, and fourth

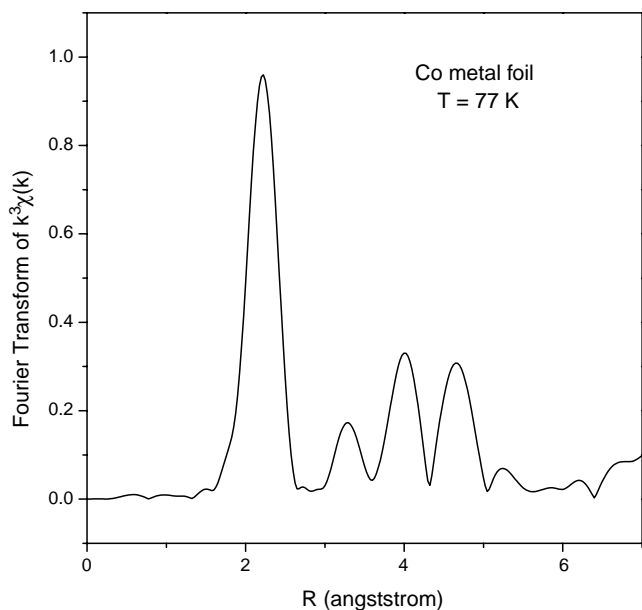


**Figure 6.** Fourier transform of the EXAFS curve  $\chi(k)$  weighted by  $k^3$ . The peaks correspond to the first, second, third, and fourth coordination shell for an hcp Co metal. In the first shell 12 Co atoms are located at 2.507 Å (the two subshells of the hcp lattice are not distinguishable since their distance differs by 0.01 Å), in the second 6 atoms at 3.54 Å, etc.

coordination shell of an hcp Co lattice, and can be used as a model compound, considering that the parameters of a Co crystal are well known. In fact, a direct comparison of the experimentally observed data for the unknown sample with reference spectra (provided that these are analyzed in the same conditions) provides the desired parameters.

An alternative equally feasible procedure can be a multi-parameter fitting of the  $\chi(k)$ , summing individual contributions with the proper structural parameters. Fortunately, this is not a prohibitive task because of the finite electron mean free path, appearing in the  $\chi(k)$  amplitude as the damping factor  $\exp[-2r_j/l_j(k)]$ . Only a few coordination shells actually remain in the sum, usually giving well separated peaks in the FT, with a reasonable number of parameters. Each peak of the Fourier transform is located at the interatomic distance  $r_j$  somewhat shifted by two phase shifts  $\delta_{aj}$  and  $\theta_j$ ; these enter the sine argument since the photoelectron is not a free particle but is influenced by the local potentials. The first  $\delta_a(k)$  is due [44] to the absorber, and it appears twice, as already mentioned, because the photoelectron is affected two times by the emitting atom, once at the emission and again on its way back;  $\delta_a(k)$  depends on the angular momentum quantum number and takes into account the potential of the central atom. The second  $\theta(k)$  is introduced by the scatterer and depends on the effective potential seen by the photoelectron during the scattering, which in turn depends on the photoelectron kinetic energy.

It is worth pointing out that the electron emission, leaving a hole in the core state, produces an atomic excited state, which tends to relax by some mechanism. The electron afterward can be restored in the hole. In any case, the perturbation introduced by the core hole involves all the atomic levels since they feel an internal charge augmented by  $+e$ . Therefore, several problems arise, concerning the core hole

width, the screening, the relaxation of the system, etc. On the other hand, the hole filling will be accomplished with a finite lifetime depending on the filling mechanism: For light elements the most probable is an Auger decay, for heavy elements a radiative (fluorescence) emission [45]. If we assume a core hole width  $W$  of about 2 eV [46], the Heisenberg principle gives a lifetime  $\Delta t = \hbar/W = 3.3 \times 10^{-16}$  s longer than the travel time of the photoelectron, calculated above. Therefore, it is assumed that the photoelectron and the outer electrons of the central atom see a  $Z + 1$  positive charge ( $Z$  is the atomic number), as in an electron charge missing from the negative cloud; actually, the relaxation time  $\tau_r$  of any atomic level is roughly proportional to the inverse of its binding energy  $E_b$ , and this implies  $\tau_r = \hbar/E_b$ . For binding energies higher than 20 eV, the corresponding relaxation time is shorter than  $3.3 \times 10^{-17}$  s. When comparing these values with the transit time of the photoelectron, which is of the order of  $10^{-16}$  s, care should be taken when assuming a time-dependent potential seen by the photoelectron. In practice, it is assumed that small perturbations can be accounted for by varying the phase shifts and by choosing ad hoc the threshold energy  $E_0$ , which is usually treated as a parameter adjustable within  $\pm 10$  eV around the edge.

### 3.3. Cumulants

As already mentioned, the short range pair distribution is probed by this technique through the Debye–Waller factor, accounting for the relative thermal vibrations. However, this conclusion is valid only for harmonic interactions and further corrections should be introduced when the nearest-neighbors distance distribution cannot be approximated by a Gaussian curve. In fact, EXAFS spectroscopy can also be quite valuable to detect anharmonic interactions through two (or more) refinement terms, which should be introduced into the  $\chi(k)$  formula. The first correction is the third cumulant  $C_3 = -(4/3)\sigma_j^{(3)}k^3$  (and eventually other higher-order odd terms) entering the phase of the sine term; the second is the fourth cumulant  $C_4 = (2/3)\sigma_j^{(4)}k^4$  (and eventually other higher-order even terms), which modifies the amplitude. A detailed analysis including the cumulants [29] was performed for a CuBr sample, investigated at different temperatures for the first shell contribution identified by Fourier filtering on both the Cu  $K$  edge and the Br  $K$  edge. The  $C_3$  and  $C_4$  cumulants were found not at all negligible even at about  $T = 210$  K; average values of  $\sigma^{(3)} = 0.23 \pm 0.04 \times 10^{-3} \text{ \AA}^3$  and  $\sigma^{(4)} = 0.32 \pm 0.12 \times 10^{-4} \text{ \AA}^4$  were obtained. Therefore, anharmonic behavior of single-particle Cu ions was deduced, although correlated motion was ignored. Small quantum effects [30] were also recently observed on the third cumulant at least for Ge, since a deviation from the classical  $T^2$  dependence was observed as a function of the temperature. Such effects were considered negligible for AgI and CdSe crystals.

## 4. EXAFS DATA ANALYSIS

As already mentioned, several methods have been developed for detecting an EXAFS spectrum; each one of these methods aims at optimizing the final spectrum characteristics (signal-to-noise ratio, resolution, etc.) for the specific

sample investigated. We mention only some of them here. The most frequently used is the transmission method, monitoring  $I$  and  $I_0$  (Fig. 1) and obtaining the absorption coefficient  $\mu$  as outlined in Section 2.

This method requires a uniform layer of material, illuminated by all the photons of the beam, a part of which (about 10%) should be absorbed. This method is therefore not adequate for a very low signal, due to a very low concentration or dilution in solid solutions, implanted materials, surface layers, impurities or clusters embedded into a matrix, etc. In these cases, different methods such as fluorescence or total electron yield should be used. These methods give a low signal proportional to the total absorption. For a detailed discussion of the best experimental conditions suggested by a panel of experts in this field, we recommend the report of an international workshop held in 1988 [47], where advantages and disadvantages of each experimental procedure can be found together with the evaluation of the experimental uncertainties. Of course, each detection scheme has its own peculiarity (e.g., electrons can escape only from a thin layer of the order of a few nm) and, therefore, should be used with great care, paying attention to all the probabilities or cross sections involved. Also of great importance are the correct choice of the proper concentration when using fluorescence detection [48] and the optimal thickness for absorption detection [49]. The procedure for the EXAFS data analysis can be found in many papers [25, 26]. Here, we give only a brief summary. In order to extract from a  $K$ -edge absorption spectrum a normalized  $\chi(k)$ , the first steps consist in:

1. Choice of the  $E_0$  threshold, often obtained by the maximum of the first derivative.
2. Fitting of the pre-edge region for background correction.
3. Fitting of the post edge curve by a continuous spline averaging the oscillations; this fit is subtracted for extracting the oscillation spectrum.
4. Evaluation of the jump at the threshold and consequent normalization.
5. Conversion from an energy scale to a wave vector scale so to obtain the  $\chi(k)$ .

The following step is represented by the FT of  $k^n\chi(k)$  where the weight  $k^n$  ( $n = 1, 2, 3$ ) can be inserted for the amplification of the oscillations of the  $\chi(k)$  curve, compensating for the attenuation of the experimental signal at high  $k$  values. In principle, the introduced weighting factor should not at all influence the information contained in the data; therefore, *a fortiori*, the FT of the weighted  $k^n\chi(k)$  should preserve the physical information since only the relative intensity of the various features can be modified. Of course, any comparison with a reference compound implies identical treatment of the compared data. A good check consists of verifying the previous point for different weighting factors. Each peak of the FT contains the physical information related to the distance, coordination number, and DW factor plus eventually the cumulants  $C_3$  and  $C_4$  for that shell. These parameters should be extracted. Two methods will be briefly presented in the next paragraph: the ratio method and the fitting method. Both imply phase and amplitude transferability.

## 5. PHASE AND AMPLITUDE TRANSFERABILITY

As mentioned in the previous sections, each term of Eq. (1) is a function of several parameters that should be determined. From the experimental data, after some manipulation sketched above, the total  $\chi(k)$  can be obtained, but this requires the conversion from an energy scale to a  $k$ -wavevector scale. This is possible if the "threshold"  $E_0$  is known, since  $k = \sqrt{2m(h\nu - E_0)/\hbar^2}$ . Unfortunately,  $E_0$  is not a well-defined energy in the absorption spectrum and several options can be adopted [26]. Note in fact that, as photoemission experiments have revealed [46, 50–52], chemical shifts can be caused by a different chemical environment. In order to overcome this difficulty, as outlined above, it is usual to treat the energy  $E_0$  as a free parameter in a range of about  $\pm 10$  eV around the jump of the absorption curve. This procedure assumes as negligible some effects due to valence or conduction bands, multiple scattering, core relaxation, etc., and applies the so-called phase transferability. This term resumes the concept that the phase function (at energy higher than 30 eV from the threshold) can be transferred from a known system to an unknown one, having however as absorber-scatterer the same pair of atoms. This is absolutely correct, such as when observing small modifications due only to the variation of temperature on the same crystalline sample, using, as a reference, the spectrum at a given temperature and looking only at the relative modifications. The use of an experimental reference is always preferable [53] and sometimes necessary whenever calculated phase shifts are not usable. In fact, if a careful Fourier transform is performed on the experimental  $\chi(k)$ , a new curve is obtained in the real space with several peaks related to the positions  $r_1, r_2, \dots, r_j$  of some coordination shells. Of course, the absolute distance  $r_j$  can be determined only if the proper phase shifts can be summed. Fortunately, very good theoretical calculations have provided accurate tables [31, 54] of such shifts. Today, more refined data can be obtained by computer programs (FEFF [33, 38, 55], GNXAS [56–58], etc.) which can also evaluate such shifts.

Similarly to the phase transferability, when the chemical environment between two different systems is reasonably quite similar and one of them is absolutely known, it is possible to assume amplitude transferability. Both phase and amplitude transferability imply independence of the chemical environment. Great care should be taken when assuming this concept of transferability, as in several cases where discrepancies were pointed out with respect to confirmed results [59].

We should point out that the transferability of the electron mean free path from a reference bulk sample to a small particle was questioned by Zhao and Montano [60]. These authors in fact emphasized that different contributions due to inelastic scattering should be ascribed to the surface of the cluster; they calculated the electron mean free path  $l$  as a function of the size for an Al particle. For a 1.0 nm Al cluster,  $l$  is about 60% of the value of the bulk. The use of a wrong  $l$  can cause an incorrect evaluation of the coordination number which can be therefore underestimated.

In general, careful use of the transferability concept is in any case very important since the comparison with a

reference compound is always necessary for the determination of the EXAFS parameters of unknown systems. To this purpose, for a long period the so-called ratio method was largely applied, whereas a fitting method is currently preferred.

### 5.1. Ratio Method

We recall that in the FT of the  $\chi(k)$ , a single peak in the real space can be worked out [25, 61] by means of a Fourier back-transform allowing one to extract a single oscillating contribution  $\chi_j(k)$  by separating amplitude and phase function. We can extract for each coordination shell its amplitude and phase by a two step algorithm: First, by Fourier transforming the entire  $\chi$  (multiplied by a window function [25, 26]) the various shells in real space are separately obtained; second, by a back FT of a single peak we can separate amplitude and phase of that peak from everything else.

If a reference compound can be experimentally processed in the same manner as the unknown sample under investigation, we can directly and separately compare the two phases and the two amplitudes.

For the phase concerned, if the phase of a single shell  $j$  is extracted as

$$\Phi = 2kr + \alpha \quad (4)$$

where  $\alpha$  is the total phase shift for that shell, we remark that a direct comparison can be performed with the phase of the reference obtained with the same procedure; in fact, dropping the index  $j$ , we can write the difference for the selected shell as

$$\Delta\Phi = \Phi - \Phi_{ref} = 2kr - 2k'r_{ref} + \alpha - \alpha_{ref} \quad (5)$$

If a plot of the phase shift (5) is performed as a function of  $k$ , we can obtain a linear plot passing through the origin:  $\Delta\Phi = 2k(r - r_{ref})$ , when the  $E_0$  value for the sample investigated can approximately make  $\alpha = \alpha_{ref}$  and  $k = k'$ ; from the slope of this straight line we can obtain the wanted value  $r$ .

In a similar procedure, writing the amplitude as

$$A(k) = \frac{N}{kr^2} F \exp[-2k^2\sigma^2] \exp(-2r/l) \quad (6)$$

where the cumulant contribution was neglected, we can compare with a known reference system, denoted by the index  $ref$ , and analyzed in the same way as the unknown:

$$\ln \frac{A(k)}{A_{ref}} = \ln \frac{Nr_{ref}^2}{r^2 N_{ref}} + 2k^2[\sigma_{ref}^2 - \sigma^2] + \left[ \frac{r_{ref}}{l_{ref}} - \frac{r}{l} \right] \quad (7)$$

Assuming the last term as negligible ( $l_{ref} \approx l$ , and the electron mean free path long enough with respect to the interatomic distance) [26], and knowing the reference parameters, we can plot as a function of  $k^2$  the curve  $\ln \frac{A(k)}{A_{ref}}$  evaluated experimentally. This curve should be a straight line having a slope equal to  $2[\sigma_{ref}^2 - \sigma^2]$  and an intercept for  $k = 0$  at the value  $\ln Nr_{ref}^2/r^2 N_{ref}$ . This procedure permits the determination of  $r$ ,  $N$ , and  $\sigma$  with good approximation.

The ratio method is instructive and was reported only for didactic purposes but presents several limitations [25–27]. In

fact the results obtained by the ratio method can be altered because of several approximations related to the choice of  $E_0$ , the data analysis, systematic errors, mean free path, etc.

### 5.2. Fitting Method

To date, a more sophisticated method is largely adopted combining theoretical calculations and multiparameter fitting. In fact, accurate theories were developed that take into account a curved wave description of the photoelectron, multiple scattering, relative vibrational behavior, electron mean free path, cumulants contributions for each shell, etc. All of these points are introduced into computer programs continuously updated such as FEFF [33, 38, 55] or GNXAS [56–58], which allow several tests on the experimental data: Typically the first check is done on the reference spectra collected in the same experimental conditions as the currently investigated sample. As the reference is well known by definition, its parameters, assumed correct, can be used for a double check, as in for a cross verification about the method and about the simulation. In fact, the first check is performed on the method itself, using the reference spectra, and verifying that the potentials adopted, the phase shifts calculated, the backscattering amplitude, etc. provide the correct environment and are consistent with the hypothesized structure. This permits the reproduction of the reference  $\chi(k)$  and its FT with self-consistent parameters.

Secondly, the simulation can be pursued searching, shell by shell, for the convenient parameters reproducing each shell of the FT, and afterward fitting the entire FT curve and the total  $\chi(k)$ . This implies not only that each oscillating contribution  $\chi_j(k)$  be correct, but also the multiscattering contributions (with three or more compatible paths) for that lattice and base be conveniently approximated.

Since the desired parameters are determined by accurately fitting one by one each shell in the FT (or all the shells together if the entire original  $\chi(k)$  is fitted), the fitting procedure should be accurately guided. Otherwise the mathematics can give any kind of results, especially when many shells are involved. Examples of fitting results can be found in the next section.

It is worth mentioning that a strong correlation exists between  $N$  and  $\sigma$ ; an analysis of this correlation [53] has shown a linear dependence of the relative uncertainties on the number of electrons  $Z$  of the backscattering atom. On the contrary,  $E_0$  and  $r$  for a given shell are not strongly correlated, as in the modification of  $E_0$  practically does not alter the correspondent shell distance since the change in  $E_0$  modifies mainly the low  $k$ -values of the  $\chi(k)$  whereas  $r$  is determined by the frequency of the oscillation. In fact, the fitting accuracy of the EXAFS technique in the evaluation of the interatomic distances can be better than 0.001 nm.

## 6. CHARACTERIZATION OF NANOCCLUSERS

We now describe the application of the EXAFS technique to a selected ensemble of clusters, showing how this tool has uniquely permitted a gain in structural characterization of nanodimensional systems. For a cluster population, the

knowledge of the interatomic distances and of the coordination numbers of a few shells around the absorbers allows us to determine the geometrical configuration averaged over the size distribution. Whenever the clusters are embedded in a different environment, this spectroscopy, sensitive to the specific atomic species in the couple absorber-backscatterer, can distinguish between internal and surface configuration. Also the thermodynamic parameters (Debye–Waller factor and/or Debye temperature), deduced by the vibrational behavior of  $\sigma^2$  as a function of the temperature, contribute toward this goal, by distinguishing the amplitude of the relative vibrations and therefore, their modifications, with respect to the bulk, can give valuable information related to the mutual binding forces.

### 6.1. Metal Clusters (Cu, Ag, Au)

Noble metal clusters were studied particularly for fundamental research, since they can address the morphology changes from the isolated atom to small clusters to bulk metal, mainly in relation to the study of the electronic and structural properties, catalysis, etc. As early as 1979 [62], copper clusters were studied by the EXAFS technique with particular emphasis to the determination of lattice contraction or expansion as a function of the cluster size. This is in fact an important question related to the reduced dimensionality and to the broken symmetry of the crystal.

Clusters of course should not interact with the substrate, or at least minimal interaction should be guaranteed. To this purpose, in this investigation, clusters were evaporated on a 500 nm polymer film, covered by a carbon overlayer 5–10 nm thick to avoid contamination; multiple layers were superimposed in order to obtain a reasonably good signal-to-noise ratio. Few coverages were explored: for Cu, from  $8 \times 10^{14}$  at/cm<sup>2</sup> up to  $8 \times 10^{16}$  at/cm<sup>2</sup>; samples were checked by transmission electron microscopy aimed at obtaining the size of the deposited clusters; at  $8 \times 10^{16}$  at/cm<sup>2</sup> the deposition corresponded to a continuous film, whereas the diameter of clusters obtained at  $8 \times 10^{15}$  was measured as 4–4.5 nm, about 1.3 nm at  $2.6 \times 10^{15}$  at/cm<sup>2</sup>, and 0.5 nm at  $8 \times 10^{14}$  at/cm<sup>2</sup>. The authors, analyzing the Fourier transforms of the EXAFS spectra, reported a Cu–Cu first distance of 0.256 nm for the thick film and a contraction of 9% for the smallest size ( $d = 0.5$  nm), about 3% for  $d = 1.7$  nm, and only 1% for  $d = 4$ –4.5 nm. Probably these values are somewhat overestimated. In fact, no detailed analysis was reported for the other parameters entering the EXAFS expression, such as the coordination numbers or the disorder as a function of the size. As a matter of fact, some doubts were raised by a Danish group [63] about the real contraction observed in small particles. In this paper, it is claimed that the average interatomic bond length should be independent of the particle size at least for diameters larger than 0.8 nm. In addition, it is shown that the anharmonic motion of atoms at the surface is strongly related to the anharmonicity of the radial distribution function  $g(r)$ . However, in EXAFS experiments, the FT of the data is usually performed by cutting the low  $k$  values of the  $\chi(k)$  curve dominated by multiple scattering, and assuming a  $g(r)$  of Gaussian form. This assumption can strongly modify the average values obtained by this spectroscopy, as the size

of the observed clusters (having a larger surface-to-volume ratio) becomes smaller.

With the contraction, for the lowest coverage a concomitant energy shift of the threshold was also observed toward higher binding energy of 0.7 eV. This is a well known effect in photoemission experiments [46, 50, 51] performed as a function of the size. A more refined investigation was reported in 1986 [64] by preparation of copper clusters ( $d = 0.7$ –1.5 nm) in an inert solid Ar matrix held at liquid helium temperature (4.2 K). This artifice prevents any interaction with the substrate. The EXAFS experiments were performed at Stanford Synchrotron Laboratory both in transmission and in fluorescence.

In Figure 7, some results from [64] are reproduced: The FT of  $k^3\chi(k)$  for a Cu foil and for Cu clusters 1 nm average diameter are shown. For this size, an average coordination number equal to 6, 3, and 5, respectively, for the first, second, and third shell was determined. For comparison, in the same figure the FT for Cu clusters was simulated with the following parameters: first, second, and third shell distance as for the bulk, coordination numbers 6, 3, and 5, respectively; Debye–Waller factors  $25, 29, \text{ and } 56 \times 10^{-4} \text{ \AA}^2$  respectively.

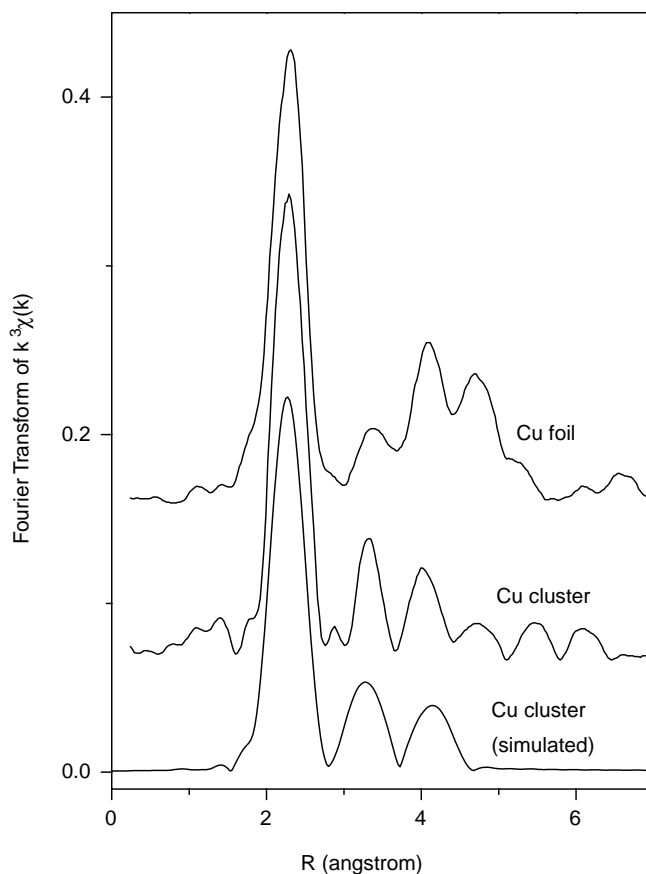


**Figure 7.** This figure shows the experimental data obtained by means of the FT of the  $\chi(k)$  weighted by  $k^3$ , for a Cu cluster of 10 Å (average diameter). For comparison the corresponding spectra for a Cu metal foil (experimental), and for a Cu cluster of the same size (calculated). Adapted from [64], P. Montano et al., *Phys. Rev. Lett.* 56, 2076 (1986). © 1986, American Physical Society.



Several interesting results were observed:

1. The first concerns, as above, a chemical shift of the edge of 1.4 eV towards higher binding energy.
2. The Xanes region for the clusters shows modifications related to the absence of fourth and higher shell atoms in the cluster, as visible in Figure 7.
3. Cu dimers were found with Cu-Cu distance of 0.223 nm; in fact, in Figure 3 of [64] the FT of the spectrum contains two peaks due to Cu-dimers (shorter distance) and to more distant Cu-Cu pairs in larger clusters ( $d = 0.6\text{--}0.7$  nm).
4. Contraction of the nearest-neighbors (nn) distance was found to be quite smaller than in earlier papers, and of the order of 1–1.5% for Cu clusters with  $d = 0.7\text{--}1.5$  nm.
5. As higher coordination shells are visible in the FT, a qualitative speculation can be done to calculate the number of surface atoms in specified clusters.

Whenever the clusters are deposited in or embedded into a noninert matrix (such as an oxide), as expected, the interaction of the surface of the cluster with the matrix atoms can modify the intrinsic properties of the clusters, their growth morphology, and the interface bonds [65]. However, it was demonstrated that the boundaries of nanocrystals should not be considered anomalous [66], as claimed by some authors [67] who hypothesized a completely disordered surface layer without any short range order.

Silver clusters also were investigated [68] for an average size of  $d = 2.5\text{--}13$  nm; the EXAFS data analyzed by the ratio method allowed only the determination of a nn contraction, which reached 0.004 nm, whereas the coordination numbers could not be accurately determined. Furthermore, in this case the near edge region around the  $K$  threshold did not show any significant modification with respect to the bulk. In contrast, the photoemission measurements on the core level Ag  $3d_{3/2}$  and  $3d_{5/2}$  have displayed a metal–nonmetal transition at about 100 atoms/cluster, with a shift of about 1.8 eV [51].

On gold clusters, a large debate was developed when conflicting results were reported [43, 69–73] about the structural and dynamical parameters for small size agglomerates. Actually, gold is an ideal element for studying size effects because of its great stability without any tendency to bind foreign impurities. Therefore, gold clusters prepared by different techniques were studied by EXAFS spectroscopy for a structural investigation; of course other complementary experiments were conducted, such as transmission electron microscopy (TEM) [43], core level and valence band photoemission spectroscopy [50], etc.

In EXAFS experiments performed on gold clusters since 1985, for more than a decade [43, 69–73], the data analysis was progressively more and more sophisticated with attention not only to the interatomic distance but also to the coordination number and to the DW factor. As gold is a heavy atom, EXAFS was collected on  $L_{III}$  edge, as it is legitimate [26], and also much more convenient as the cross section is higher at this energy by a factor 33 than at the  $K$  edge.

The disorder was also studied as a function of the temperature, also identifying the static contribution of the DW factor at a few degrees Kelvin. Recalling the Beni and Platzman

theory [74], we point out the several terms entering the DW factor of the EXAFS spectra and the difference with respect to the conventional X-ray diffraction. In X-ray diffraction, in fact, the Debye–Waller factor takes into account the total atomic mean square thermal displacement, whereas in EXAFS technique a pair of atoms is always involved and therefore the DW factor is a direct measurement of the mean square relative displacement of the pair absorber-backscatterer. For a monoatomic cubic crystal, using the Debye approximation for the density of states, Beni and Platzman gave the following expressions for the EXAFS DW factor of a pair at a distance  $r$  [71, 74]

$$\sigma^2 = \sigma_{diff}^2 - \sigma_{corr}^2$$

$$\sigma_{diff}^2(T) = \frac{3\hbar^2}{Mk_B\Theta_D} \left[ 0.25 + \frac{T^2}{\Theta_D^2} \right] G(T)$$

$$\sigma_{corr}^2(T) = \frac{3\hbar^2}{Mk_B\Theta_D} \left[ \frac{1 - \cos(rQ_D)}{\cos(rQ_D)} + \frac{T^2}{\Theta_D^2} H(T) \right]$$

$$G(T) = \int_0^{x_D} \frac{x dx}{\exp(x) - 1}$$

$$H(T) = \int_0^{x_D} \frac{\sin(\omega x) dx}{\omega[\exp(x) - 1]}$$

where  $\sigma_{diff}^2$  and  $\sigma_{corr}^2$  are the diffraction and correlated atomic root mean square displacement, respectively,  $\Theta_D$  and  $Q_D$  are the Debye temperature and the Debye wave vector,  $x_D = \frac{\Theta_D}{T}$  and  $\omega = \frac{rQ_D}{x_D}$ ,  $M$  is the atomic mass,  $k_B$  and  $\hbar$  are respectively the Boltzmann constant and the Planck constant divided by  $2\pi$ .

An extension of the previous formulae was developed for gold clusters [71], showing a decrease of the Debye temperature with respect to the bulk of the order of 10% for a diameter of the clusters of 3 nm. This decrease was explained by the contribution of the surface atoms having a higher mobility in the cluster, and applying the free-bounded sphere density of states in a Debye approximation.

In Figure 8, EXAFS spectra taken at different temperatures are displayed for bulk gold; these curves allow a precise determination of the dependence on the temperature of the DW factor for the bulk metal [71]. In Figure 9, in fact, the experimental  $\sigma^2$  for bulk gold gives a good agreement with the theory if a Debye temperature of 165 K is used. These authors, analyzing the cluster data with respect to the bulk, found a lower Debye temperature for clusters, accounting for surface mode contributions. The Debye temperature for a cluster of 1.5 nm diameter was reduced to 140 K, whereas for a 9.3 nm diameter was 150 K. Furthermore, small contraction was obtained for the nearest-neighbors first shell distance up to 0.005 nm.

In contrast with these data, another experiment was reported in 1990 for a  $\text{Au}_{55}$  single size cluster [72]. In principle an experimental investigation of clusters with a well defined size constitutes an excellent opportunity for obtaining very clear results, which should not be averaged over a size distribution. However, these  $\text{Au}_{55}$  clusters were chemically produced using a  $\text{ClAuP}(\text{C}_6\text{H}_5)_3$  compound in benzene reduced by diborane. This implied the presence of ligands, which were taken into account by monitoring the Au-Cl

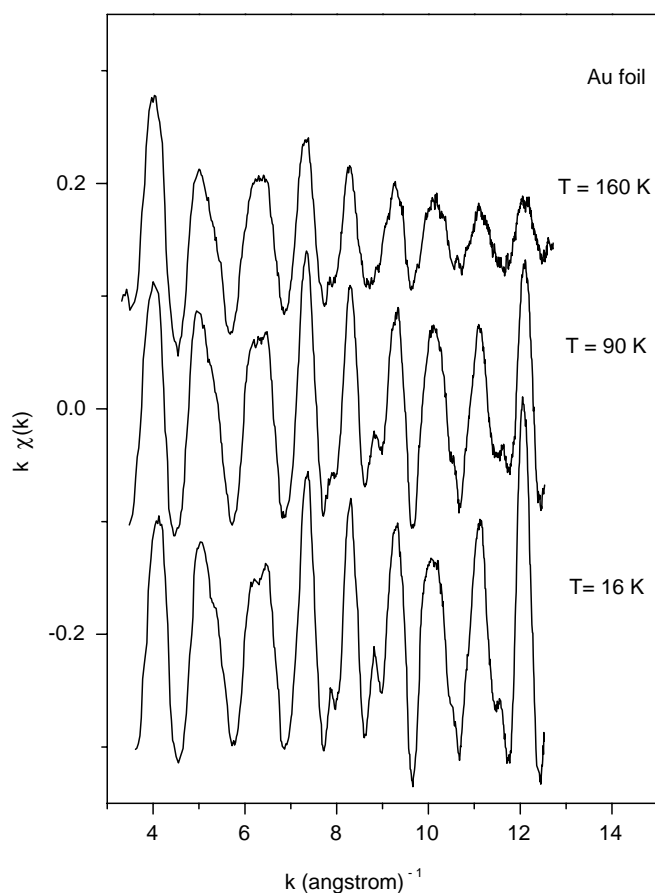


**Figure 8.** This figure shows the  $\chi(k)$  spectrum weighted by  $k$ , for a Au foil at three different temperatures. Note the attenuation of the oscillation for high  $k$ , at higher temperature. Adapted from [71], A. Balerna and S. Mobilio, *Phys. Rev. B* 34, 2293 (1986). © 1986, American Physical Society.

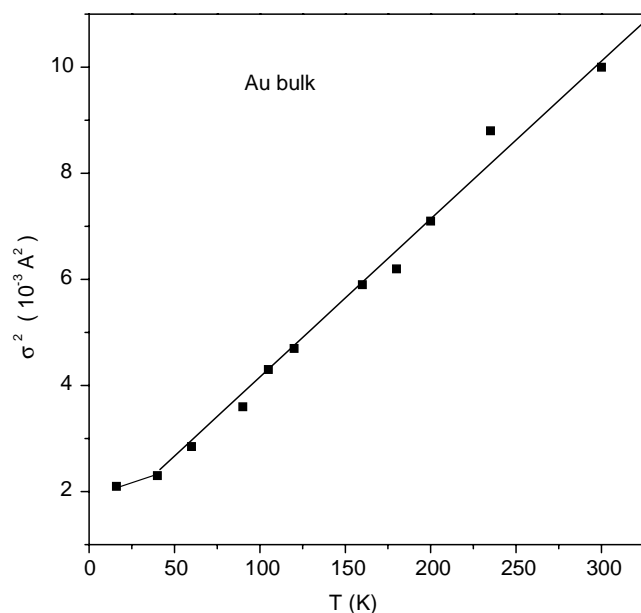


**Figure 9.** Debye–Waller factor for the first shell of bulk gold as a function of the temperature; Adapted from [71], A. Balerna and S. Mobilio, *Phys. Rev. B* 34, 2293 (1986). © 1986, American Physical Society.

signal from sodium chloroaurate. Here, Au–Au distance is found to be 0.231 nm with a total coordination number of 7.8, so that clusters were assumed of cubooctahedron shape with 12 triphenylphosphine and 6 Cl ligands. The analysis of the mean squared relative displacement lead to the conclusion that the clusters vibrate about 40% less than the bulk gold. Can the ligands be responsible for these different conclusions?

In this context, a more recent paper was published in 1995 [43]. In this paper, gold was evaporated at a very low rate on a thin mylar substrate, and afterward a few monolayers of mylar were deposited on the gold clusters so as to prevent any size modification. This process repeated many times produced a number of mylar layers containing gold clusters inside. Transmission electron micrographs confirmed a distribution of spherical clusters whose peak was at about 1.6 nm with a half width at half height of about 0.8 nm. EXAFS spectra were taken at the  $L_{III}$  edge at  $T = 28$  K.

As visible in the Fourier transform of figure 3 of Ref. [43], whereas the reference bulk gold shows first and higher shells peaks, the cluster ensemble presents only the nearest neighbors (nn) peak without higher features. These are missing not only because of the low signal-to-noise ratio but very likely also because of possible incoherent contributions due to a spread of distances; this last effect can cause, for higher shells, an attenuation of the amplitude further reduced when the surface layer is taken into account. A detailed fitting procedure is here performed with or without additional parameters (cumulants); as mentioned above, great care should be paid since i) the correlated parameters  $N$  and/or  $\sigma$  can be easily overestimated; ii) the use of cumulants can improve the fit, but somewhat modifies the peak position. These points stress that a speculative intelligent physics should always prevail over a crude mathematics. In fact, as reported in Table 1, an increase of  $N$  implies also the increase of  $\sigma$  for a best fit of the data; however, a detailed comparison with theoretical structures using the calculated parameters gives several possible scenarios. The most reliable was found for a mixture of three preferential sizes (38, 201, and 309 atoms/cluster) having truncated cubo-octahedral structures, composing the clusters with percentages respectively of 85%, 10%, and 5%. These results indicate a quite low nn contraction, an average coordination number of 8.7, and a DW factor  $\sigma^2 = 5.8 \times 10^{-3} \text{ \AA}^2$ ; furthermore, no evidence of  $C_3$

**Table 1.** Size  $d$ , nearest-neighbor distance  $r$ , coordination number  $N$ , and Debye–Waller factor  $\sigma^2$  for some gold cluster structures compared with the experimental fitting data for a cluster and for a bulk Au crystal.

Structure	$d$ (Å)	$r$ (Å)	$N$	$\sigma^2$ ( $\times 10^{-4} \text{ \AA}^2$ )
38 truncated octahedral	11.6	2.78	7.6	60.0
55 cubo-octahedral	13.8	2.78	7.9	46.0
55 icosahedral	13.6	2.81	8.5	80.0
201 truncated octahedral	20.5	2.83	9.4	45.0
309 cubo-octahedral	25.2	2.83	9.6	42.0
309 icosahedral	25.4	2.85	10.0	76.0
561 cubo-octahedral	30.8	2.84	10.0	38.0
561 icosahedral	30.1	2.85	10.0	70.0
exp. fit (bulk)		2.86	12.0	26.0
exp. fit (cluster)		2.81	8.0	56.0

Source: Some data are from [43].

and  $C_4$  cumulants was detected, showing that the harmonic approximation gives an adequate description of the vibrational behavior of these nanocrystals. The significantly lower value of the mean squared relative displacement detected for these cluster samples with respect to the value obtained for  $Au_{55}$  clusters [73] was ascribed to the higher temperature and to the presence of ligands in these monosized agglomerates.

Bimetallic clusters also were studied by this technique. We mention Ag-Cu and Au-Cu clusters [75] supported by a silica matrix. Owing to the slight miscibility, a higher segregation of copper in the interior of the cluster was found for Ag-Cu agglomerates, whereas gold rich region was preferentially detected on the surface.

Furthermore, it is worth mentioning the studies on metal catalysts [76] and the novel method for supporting Pt nanoparticles [77] using porous carbon nanotubes.

## 6.2. Clusters of Magnetic Elements (Fe, Co, Ni)

Magnetic materials exhibit very interesting properties for several fundamental and applied aspects. The confinement in small clusters, nanostructures, or superlattices has opened a great and growing number of exciting research studies [78–89]. We refer the reader to the wide literature, mentioning only a few topics particularly studied at present: the magnetic anisotropies of ultrafine Co agglomerates, the saturation ferromagnetism of  $Ni_{13}$  and  $Co_{13}$ , the important effects due to the matrix hosting the clusters [82–84], etc. In addition Fe, Co, and Ni are of particular interest because of possible structural transitions, size and temperature dependent. In Fe, for example, a transition from ferromagnetic bcc  $\alpha$  phase to fcc  $\gamma$  antiferromagnetic phase is observed at about 1183 K. Instead, cobalt metal structure is hexagonal close packed up to 725 K, whereas at higher temperatures a phase transition to fcc occurs. Co clusters seem to exhibit fcc structure, but other possible forms such as truncated octahedra [87], icosahedra [88], or chainlike agglomerates [89] can be obtained. On the other hand, Co films were grown in a bcc metastable phase [90] using epitaxial deposition on GaAs(110), with a lattice constant of 2.827 Å. In a silver matrix, a low concentration of Co shows an initial stage of Co in substitutional and dimer form with subsequent segregation and precipitation [85].

This topic then teems with challenging perspectives in particular related to the geometrical configuration of the clusters [88] and to the dynamical behavior under thermal treatment.

EXAFS and XANES spectroscopy therefore appear quite valuable for this investigation, involving the cluster confinement into a defined matrix, such as Co in Ag [78, 79], permitting one to distinguish whether Co faces another cobalt or an interface silver atom. In such a case, in order to obtain a very low cluster size, several methods were employed including ion implantation and molecular beam epitaxy, so as to have a homogeneous Co depth profile over about 800 nm, ranging from 0.1 at. % up to 6.0 at. %.

Experiments were performed at the GILDA beamline of the ESRF, Grenoble, France, around the Co K edge (7709 eV), in the range 7500–8700 eV, and in fluorescence

mode using 6 ultrapure Ge detectors cooled at 77 K. In these investigations, the samples were investigated at different temperatures, from 77 K up to 225 K.

The FT plots of the  $k\chi(k)$  spectra for some Co/Ag samples and their best fits (see Figs. 10 and 11) showed very interesting features [78, 79]:

First, the first, second, and third shell peaks are now split into two components corresponding to Co and Ag atoms around the Co absorber. This was attributed by the authors to evident clustering, since on the average a Co atom “sees” around itself partially atoms of the same species and partially atoms of the matrix; the relative weights depend on the size of the cluster and thus on the surface to volume ratio.

Second, in the most diluted (0.1%) sample, Co dimers were obtained, whereas clusters of different sizes (8 and 20 atoms/cluster) grew in the as prepared materials at 6% (co-evaporated sample) and 1.9% (implanted sample). After

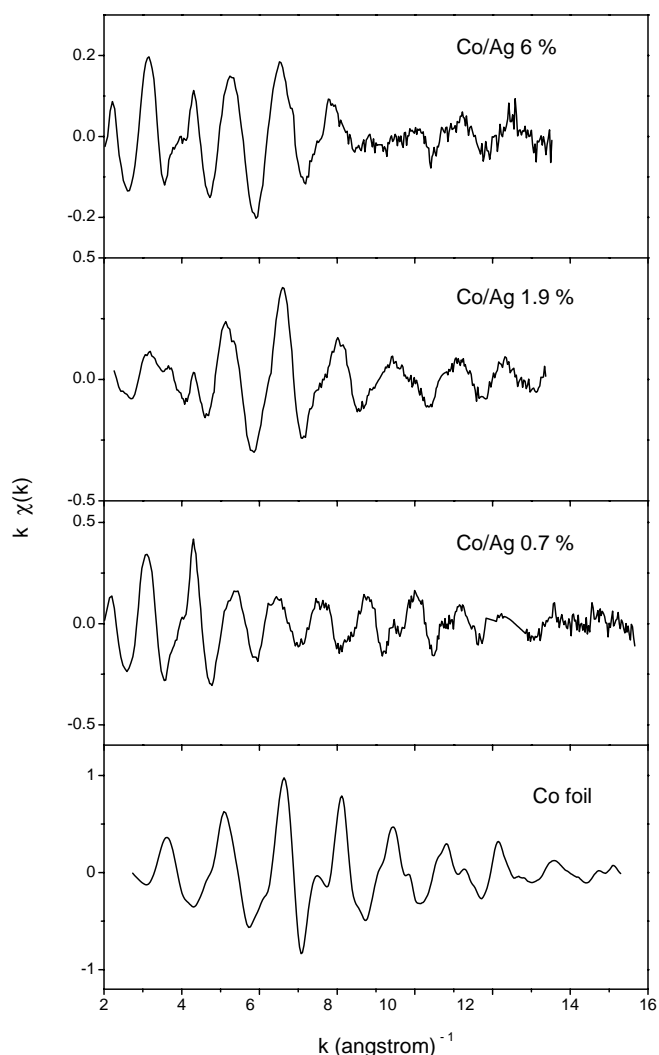


**Figure 10.** This figure shows the  $\chi(k)$  spectrum weighted by  $k$ , for some dilutions of cobalt in a silver matrix; for comparison, also the corresponding curve of a Co foil is displayed. Note the modifications of the curves with respect to one other. Adapted from [79], G. Faraci et al., “Physics of Low Dimensional Systems” (J. L. Moran-Lopez, Ed.), 2001. © 2001, Kluwer Academic-Plenum.

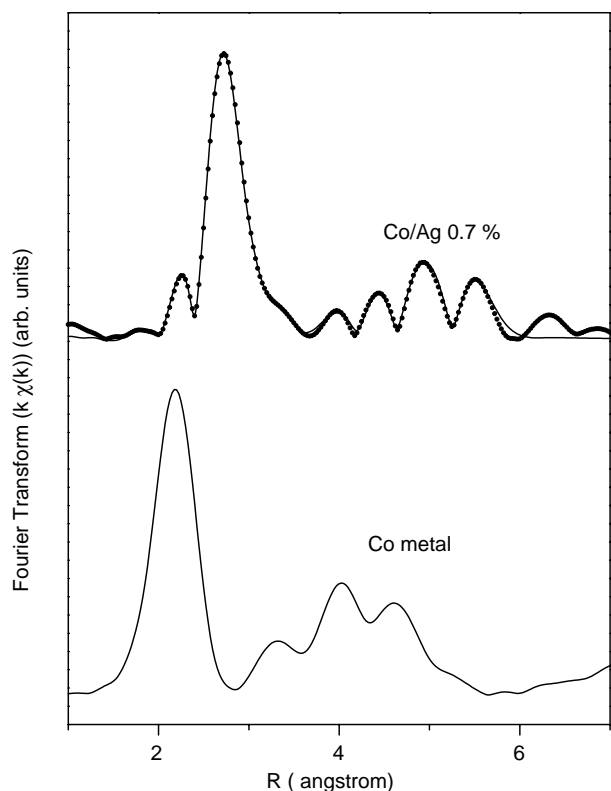


**Figure 11.** This figure shows the FT of two EXAFS  $\chi(k)$  curves weighted by  $k$ ; in the upper curves, the data for a diluted Co sample (dotted) are shown together with the fitting curve obtained using the FEFFIT code [33, 37, 38, 55]; for comparison, in the lower part of this figure, the corresponding curve for a Co metal foil is reported. Note that in the diluted sample, the Co-Co features are mixed up with the Co-Ag peaks. Adapted from [78], G. Faraci et al., *Phys. Rev. Lett.* 86, 3566 (2001a). © 2001, American Physical Society.

annealing at 350 °C, the cluster size increased up to 80 and 136 atoms/cluster, respectively, with a strong dependence on the preparation details; in fact, implantation at lower concentration caused larger clustering than molecular beam epitaxial evaporation. As already pointed out, for each sample the FT of the EXAFS spectra showed remarkable peaks corresponding to first, second, third, and even fourth coordination shells. Also, these features were analyzed and found to be split into two components, and the respective parameters corroborated the indications of the first shell.

The conclusion of a preferential arrangement of small Co clusters (dimers or chain of dimers) was advanced for 0.1 at. % Co in Ag supported by Mössbauer investigation of the primary stages of Co precipitation in Ag [91].

For discriminating between a dimer and other possible small clusters, some models were developed to compare the average first, second, and third coordination numbers; a multiple dimer configuration is displayed in Figure 12 with the dimers disposed along the fcc square faces of the Ag lattice in orthogonal direction to each other. This corresponded to a first, second, and third average coordination respectively calculated equal to 1, 0.83, 1.67, very close to the experimental ones.

Some complementary information was reported from the XANES spectra, shown in Figure 13; for the dimer

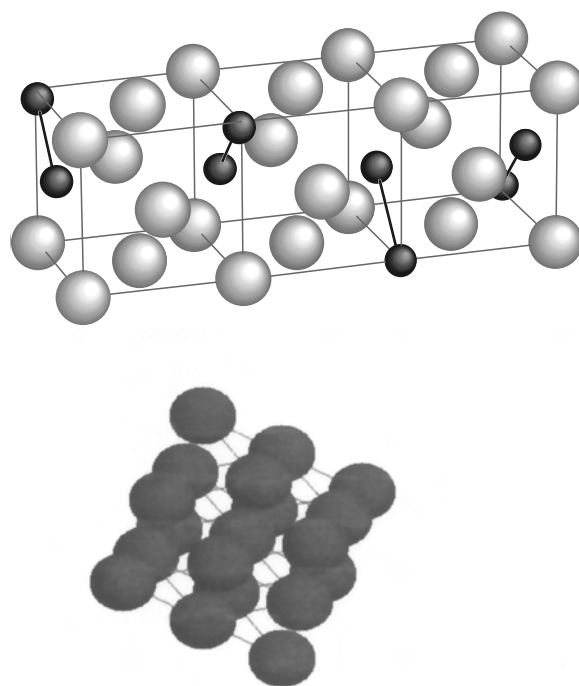


**Figure 12.** The top part of the figure displays the silver lattice (fcc) with 4 Co dimers put in quasi-substitutional position, at orthogonal angle to each other, and along opposite square faces of the lattice; the lower part, a Co cluster of 19 atoms is shown, with a first (12 atoms) and a second (6 atoms) shell around the central atom, in fcc configuration.

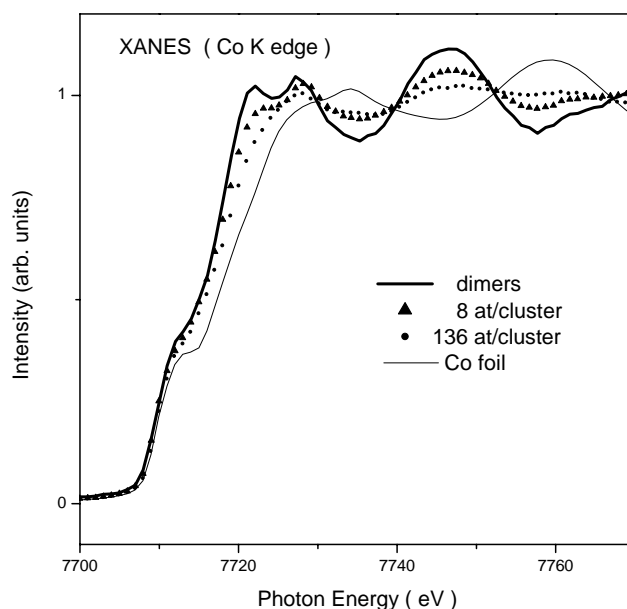


**Figure 13.** This figure shows the near edge structure of Co/Ag samples, where Co dimers, 8-atom clusters, and 136-atom clusters in a silver matrix are present. For reference the corresponding curve of a Co foil is reported in order to show the evolution of the curves: it is evident a hcp-fcc phase transition. Adapted from [79], G. Faraci et al., "Physics of Low Dimensional Systems" (J. L. Moran-Lopez, Ed.), 2001. © 2001, Kluwer Academic-Plenum.

ensemble, a chemical environment similar to that of an Ag matrix seems progressively modified towards that of the bulk cobalt as the size of the Co clusters increases.

The reported DW factors permitted evaluation of the corresponding Debye temperature  $\Theta_D$  for the different situations presently described. Values of  $\Theta_D = 418$  K at  $T = 77$  K (with a calculated  $\sigma^2 = 27 \times 10^{-4} \text{ \AA}^2$ ) obtained for bulk Co compares with  $\Theta_D = 285$  K for Co-Co at the dilution 1.9 at. % and  $\Theta_D = 260$  K at 6 at. % with a marked reduction with respect to the Co bulk value. This was attributed to a less rigid environment due to the soft Ag host lattice, through the large fraction of Co-Ag interface bonds; these bonds vibrate with a  $\Theta_D = 200$  K close to that of bulk silver.

Another study deals with a Co/Pt multilayer, prepared by electron beam deposition alternating Pt 1.8 nm films and Co 0.2 nm single layer. Polarized EXAFS spectra [92] at the Co *K*-edge were performed by orientation of the polarized electric field of the synchrotron radiation almost perpendicular or parallel to the film surface. The direct comparison of the corresponding EXAFS spectra and of their FT showed a strong anisotropy: In fact, data with in-plane polarization indicated intermixing at the Co/Pt interface whereas those measured with out-of-plane polarization showed an abrupt interface structure between Co and Pt clusters.

### 6.3. Clusters of Rare Gases: Ar, Kr, Xe

Rare gases are a class of very important elements for fundamental physics, since their electronic configurations with completely filled  $s^2$  (He) or  $s^2p^6$  shells (Ne, Ar, Kr, Xe, Ra) can give crystals with a very low binding energy of van der Waals type. Crystals of inert gases are transparent insulators, with low cohesive energy and low melting point (24 K for Ne, 84 K for Ar, 117 K for Kr, 161 K for Xe). Therefore, when introduced into a solid matrix, these inert gases tend to form clusters or bubbles. Ion implantation represents the most common and simple method for obtaining a uniform ensemble of rare gas agglomerates into a host layer a few hundred nm thick, using the proper ion beam, ion fluence, and implantation energy.

However, a semiconductor substrate can be amorphized by this method because of the large energy exchanged during the implantation process. As a consequence, it is necessary to anneal the sample for obtaining a crystalline substrate reconstruction; an alternative method can be the implantation at high temperature. Although noble gas inclusions in a solid matrix were obtained in the past as gaseous bubbles, in 1984 it was noted that small clusters of a rare gas could be confined in solid phase at room temperature, using the large pressure exerted by the host lattice against the foreign atoms, pushed into nanocavities within the matrix. These existed already in the as-prepared samples or as a consequence of an annealing process. Due to the very different nature of the substrate, thermal treatment, preparation process (fluence, implantation energy, ion penetration depth and profile, induced damage, etc.), and implanted rare gas, a large amount of data was collected by several experimental techniques. In 1984, overpressurized bubbles containing liquid Ne and solid clusters of Ar and Xe were observed [93] in Al at room temperature by transmission electron microscopy (TEM) and electron energy loss spectroscopy. Similar results

were obtained [94] for Ar, Kr, and Xe in Al with an epitaxial alignment of the solid noble gas with the matrix.

On this subject an excellent review can be found in the *Proceedings of the NATO Advanced Research Workshop* held in 1990 [95], and in a more recent article [96], both treating this matter with many details. We limit ourselves to mention the most relevant results and some controversial points. Of course the possibility of obtaining solid noble gases at room temperature, without resorting to more complicated apparatus such as the diamond anvil cells for getting high pressure, stimulated many studies for fundamental and applied reasons.

In implanted metals, Ar, Kr, and Xe form 1–2 nm radius solid clusters already at concentration 3–5 at. % with fcc lattice as observed by TEM [97], XRD [98], and EXAFS [99]. The nanocrystal inclusions at RT should be pressurized by the host matrix with a large pressure of the order of 1 GPa as confirmed by the pressure-volume curves [100–103].

In implanted Si, a more complicated scenario is determined by the amorphization of the matrix implanted at RT. In fact, while Ar was clearly detected in as-implanted samples [99] as crystalline agglomerates, Kr and Xe were not observed in the early agglomeration stage after simple implantation at high fluence; in the annealed samples, on the contrary, the rare gas was detected in compressed solid or fluid phase [104, 105].

Typical spectra for Xe/Si are shown in Figure 14, for several temperatures. We point out here that for fluid bubbles, the atoms of the clusters are in quite disordered configuration similar to liquid or amorphous systems. For such cases [23], the use of standard EXAFS expressions including the third and fourth cumulants are not adequate, since the absorber-backscatterer pair can be at a relative distance with asymmetric non-Gaussian distribution and/or anharmonic vibrational behavior.

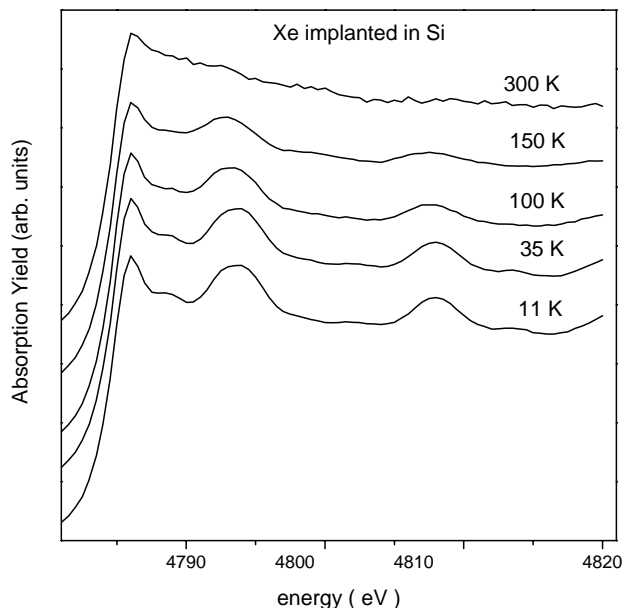


**Figure 14.** Fluorescence spectra of Xe implanted in a Si layer. Solid Xe clusters are evident at low temperature for the presence of high EXAFS oscillations damped at room temperature.

A correct average of the EXAFS formula over the effective pair distribution function  $g(r)$  can present many difficulties both because of the low- $k$  cut-off used in EXAFS analysis and the dramatic reduction of the signal-to-noise ratio. This can give an apparent bond length contraction and an incorrect evaluation of the coordination number. For these reasons, whenever fluid clusters are involved, a more accurate analysis ascertaining the consistency of the parameters should be performed. We suggest a cross check between EXAFS and XRD techniques.

In the literature, EXAFS characterization of fcc Ar clusters in Al and Si [99] at 300 K gave, in as implanted samples, a nearest-neighbors contraction of  $0.31 \pm 0.05$  Å for Ar/Al, whereas a higher value of  $0.42 \pm 0.05$  Å was deduced for Ar/Si. The overpressure obtained by this contraction was evaluated in 2.5 and 4.4 GPa, respectively. From the corresponding Debye–Waller factors, the authors calculated the increase of the Debye temperature  $\Theta_D$  due to the overpressure: Crystalline bulk Ar at low temperature has a  $\Theta_D = 93$  K, whereas the compressed nanocrystals reach a harder value of 212 K in Al and 300 K in Si, in agreement with values obtained by the thermodynamical equations [102] using the Grüneisen parameter  $\gamma_G$  and the isothermal compressibility  $\beta$ :  $-\gamma_G = \partial \ln \Theta_D / \partial \ln V$ ,  $-\beta = \partial \ln V / \partial P$ .

According to the authors, the very low value of the coordination numbers should be attributed to the quite small percentage of Ar in crystalline configuration with a large amount in disordered fluid or gas-like phase, contributing to the background. Similar results were reported for Xe in annealed Si [104], where a fraction of Xe atoms is found condensed in solid fcc clusters contracted by  $0.41 \pm 0.06$  Å at room temperature and by  $0.12 \pm 0.06$  Å at 70 K well below the Xe melting point (161 K). The value of the Debye temperature was obtained from the nearest-neighbor contraction and, independently, from the Debye–Waller factor with a nice agreement. These determinations, however, did not take into account any cumulant correction, so that some overestimation of the parameters could occur at temperature higher than the melting point where some clusters could be in a size range for which fluid or disordered configurations can be mixed up with reduced size clusters in crystal phase.

Actually, a recent XRD contribution for as-implanted Xe in Si [105] found, at room temperature, compressed fluid bubbles with 1 nm radius and a first coordination number of only 6 Xe, with a mutual distance of 4.22 Å reduced with respect to the value 4.37 Å of liquid Xe.

The reduction of the coordination, as far as the temperature increases beyond the transition temperature between the solid and the liquid phase, could be explained by a possible configuration of rare gas clusters with a solid small nucleus surrounded by a wide shell in liquid or amorphous phase. This last scenario has not been explored yet.

#### 6.4. Clusters of Binary and Ternary Compounds

It is worth mentioning some other experiments performed on molecular clusters [106], nanocrystals of semiconducting oxides [107], quantum dots [108], intercalated compounds [109–112], alloy clusters [113, 114], etc. Among the above

topics, recent accurate measurements concern the characterization of quantum dots (QD) of reduced size confined in a glass matrix ( $B_2O_3$ ) by a simple melting process. The objects of these studies were luminescent  $InBO_3$  [107] or semiconducting oxide  $SnO_2$  [108], since their confinement in the nanometer range can modify the absorption and the emission radiative transitions. For these clusters the EXAFS technique also can give accurate information about the average size of the QD, through the determination of the coordination numbers of several coordination shells; these can be compared with calculations performed for each shell, for example, in ternary compounds [107]; here, as shown in Figure 15, first In-O, second In-B, third In-O, and fourth In-In shell have been separately fitted and the corresponding parameters evaluated. The fitting procedure followed the FEFF code [33, 38, 55], shell by shell, using the corresponding parameters as best fit variables.

In Figure 16, we report the calculations related to the  $InBO_3$  and  $SnO_2$  structure, respectively, rhombohedral and distorted octahedral, as a function of the size; the simulation is very simple; it is enough to determine the geometric position of each atom in the corresponding structure; supposing a spherical atomic distribution of fixed size, it is now possible

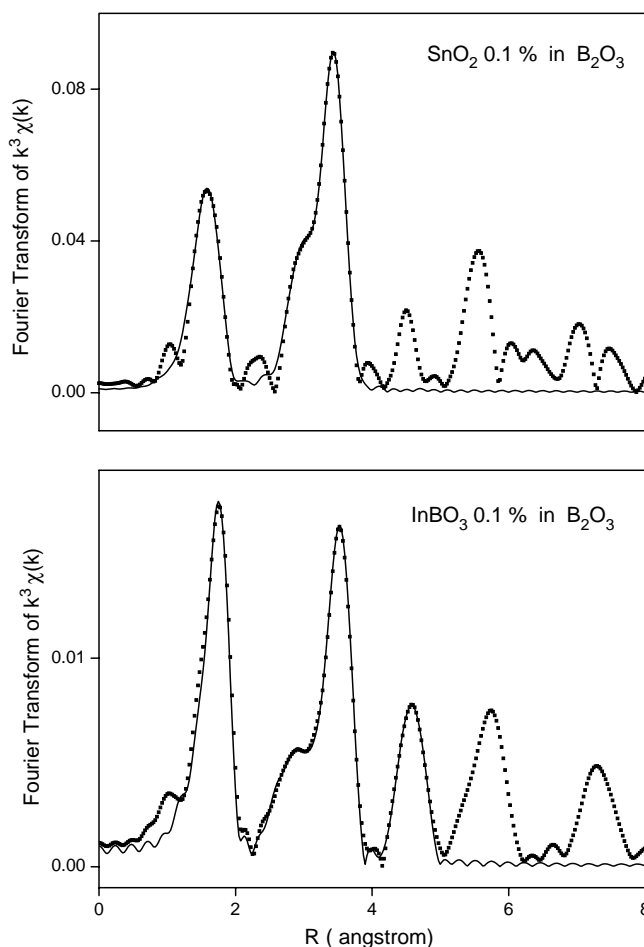


**Figure 15.** The figure displays the FT curves for 0.1% diluted solution of indium borate and tin dioxide in a glass matrix, at 77 K. Also shown is the corresponding fit. Note the different relative heights of the features present in the spectra, due to the coordination number of the peak.



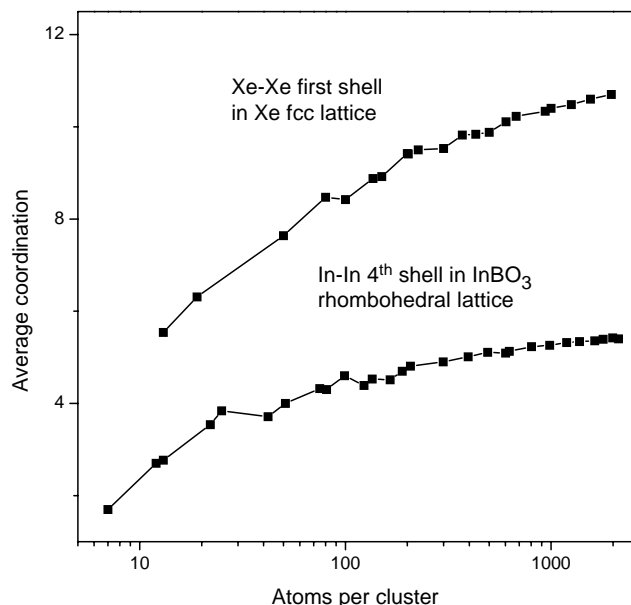


**Figure 16.** Typical average coordination numbers as a function of the total atoms in the cluster. In the upper data, the first shell average coordination is shown for a Xe solid cluster with fcc lattice; the bulk crystal value is 12. In the lower data, it is reported the fourth shell average coordination for an indium borate cluster with rhombohedral lattice; the bulk value is 6. The lines are a guide to the eye. Adapted from [107], © 2002, American Physical Society.

to count the number of atoms around each absorber inside the sphere and afterward to average the obtained data.

From the previous analysis, we can deduce the very important result related to the comparison between the experimental coordination number of each shell with the corresponding value calculated as a function of the radius  $r$  for a spherical nanocrystal of the material under study. For a spherical distribution of atoms with definite lattice configuration, or fcc, it is easy to evaluate the coordination number around each atom, calculating the average between all the atoms in the cluster. Surface atoms of course contribute much less than the internal ones, so that the average depends on the relative contribution of the surface-to-volume, as in on the ratio  $4\pi r^2 \rho_s / (4/3)\pi r^3 \rho_v = 3\rho_s / r\rho_v$ , where  $\rho_s$  and  $\rho_v$  are the surface and volume atom densities, respectively.

In these experiments, a glass matrix of boron oxide was used, and a simple melting procedure was adopted for synthesized quantum dots. For  $\text{InBO}_3$  clusters, a large range of dilution between 0.3% and 2.0% gave the same QD size of about 3 nm radius. For  $\text{SnO}_2$  it was instead possible to modify the QD size just by changing the concentration of the solute in the matrix: in fact, the QD radius obtained in this last case was 0.5, 1.0, and 1.4 nm for 0.1, 0.2, and 0.3% dilution of the semiconductor in the glass, respectively.

Another interesting study [115] concerns the growth of clusters with the “inverted hut” structure found for SiGe alloy in Si/Ge superlattices. These nanocrystals, observed by EXAFS, were determined as confined in the Si/Ge superlattice beneath the Ge wetting layer and grown into the Si deposition. Ge hut clusters, investigated by scanning tunneling microscopy and X-ray diffraction, were detected almost

fully strained with a minor misfit at the Ge/Si interface [116]; their density dramatically increases by capping the Ge layer with 6 Å of silicon [117], although the silicon-germanium intermixing in Ge/Si(100) islands varies as a function of the deposition temperature [118, 119]. Note, however, that the shape of Ge clusters on a Si(100) surface can be dependent on the hydrogen termination of the Si surface; in fact, when the Si surface is exposed to atomic hydrogen, large dome-shaped Ge clusters were observed; otherwise hut-shaped clusters grow with smaller size [120].

## GLOSSARY

**Cumulant** Correction factor in Exafs equation; the third cumulant enters the sine term, the fourth cumulant affects the amplitude. Generally they are  $k$  dependent.

**Fermi level** For a metal, it indicates the highest occupied electron state, at  $T = 0$  K, in the conduction energy band; for a semiconductor, it indicates usually the chemical potential, an energy level (commonly not an occupied state) in the prohibited energy gap between the valence and the conduction band, controlling the number of electron and hole occupied states in the mentioned bands.

**Phase shift** Shift of the photoelectron wave phase, that can be caused in the photoelectron emission from the absorber, or in the photoelectron scattering process.

**Shake-off** Electron transition from the valence band toward the external continuum states.

**Shake-up** Electron transition from the valence band toward a higher state of an internal empty band.

## ACKNOWLEDGMENTS

The author is grateful to Prof. Moog Gan Chow for a critical reading of the manuscript and to Prof. Agata R. Pennisi for helpful suggestions.

## REFERENCES

1. L. Esaki and R. Tsu, *IBM J. Res. Devel.* 14, 61 (1970).
2. G. Belomoin, J. Therrien, and M. Nayfeh, *Appl. Phys. Lett.* 77, 779 (2000).
3. F. Huisken, H. Hofmeister, B. Kohn, M. A. Laguna, and V. Paillard, *Appl. Surf. Sci.* 154, 305 (2000).
4. H. Rinnert, M. Vergnat, and A. Burneau, *J. Appl. Phys.* 89, 237 (2001).
5. H. Hiura, T. Miyazaki, and T. Kanayama, *Phys. Rev. Lett.* 86, 1733 (2001).
6. G. Ledoux, O. Guillois, D. Porterat, C. Reynaud, F. Huisken, B. Kohn, and V. Paillard, *Phys. Rev. B* 62, 15942 (2000).
7. J. Dorantes-Davila, R. A. Guirado-Lopez, and G. M. Pastor, “Physics of Low Dimensional Systems.” Kluwer Academic-Plenum Publishers, New York, 2001.
8. F. Celestini, D. Passerone, F. Ercolessi, and E. Tosatti, *Phys. Rev. Lett.* 84, 2203 (2000).
9. F. Baletto, C. Mottet, and R. Ferrando, *Phys. Rev. Lett.* 84, 5544 (2000).
10. A. Mascaraque, J. Avila, J. Alvarez, M. C. Asencio, S. Ferrer, and E. G. Michel, *Phys. Rev. Lett.* 82, 2524 (1999).
11. O. Gülseren, F. Ercolessi, and E. Tosatti, *Phys. Rev. Lett.* 80, 3775 (1998).

12. H. Fricke, *Phys. Rev.* 16, 202 (1920).
13. G. Hertz, *Z. Phys.* 3, 19 (1920).
14. W. Kossel, *Z. Phys.* 1, 119 (1920).
15. R. Kronig, *Z. Phys.* 70, 317 (1931).
16. T. Hayasi, *Sci. Rep. Tohoku Univ.* 33, 123 (1949).
17. J. Hanawalt, *Z. Phys.* 70, 293 (1931).
18. F. W. Lytle, *J. Synchr. Rad.* 6, 123 (1999).
19. R. S. von Bordewehr, *Ann. Phys. Fr.* 14, 377 (1989).
20. D. Sayers, E. Stern, and F. W. Lytle, *Phys. Rev. Lett.* 27, 1204 (1971).
21. A. Filipponi and A. D. Cicco, *Phys. Rev. B* 51, 12322 (1995).
22. J. Rehr and R. Albers, *Rev. Mod. Phys.* 72, 621 (2000).
23. A. Filipponi, *J. Phys.: Condens. Matter* 13, R23 (2001).
24. W. McMaster, N. K. D. Grande, J. H. Mallet, and J. Hubel, "Compilation of X-Ray Cross Sections." Lawrence Radiation Laboratory, 1969.
25. P. Lee, P. Citrin, P. Eisenberger, and B. Kincaid, *Rev. Mod. Phys.* 53, 769 (1981).
26. B. K. Teo, "EXAFS: Basic Principles and Data Analysis." Springer Verlag, Berlin, 1986.
27. E. A. Stern and S. M. Heald, "Handbook on Synchrotron Radiation." (E. E. Koch Ed.), Vol. 1, North Holland Publ., Amsterdam, 1983.
28. J. Rehr, R. Albers, C. Natoli, and E. Stern, *Phys. Rev. B* 34, 4350 (1986).
29. J. Tranquada and R. Ingalls, *Phys. Rev. B* 28, 3520 (1983).
30. G. Dalba, P. Fornasini, R. Grisenti, and J. Purans, *Phys. Rev. Lett.* 82, 4240 (1999).
31. B. K. Teo and P. Lee, *J. Am. Chem. Soc.* 101, 2815 (1979).
32. P. Lee and J. B. Pendry, *Phys. Rev. B* 11, 2795 (1975).
33. J. Rehr, J. M. de Leon, S. I. Zabinsky, and R. Albers, *J. Am. Chem. Soc.* 113, 5135 (1991).
34. A. McKale, G. Knapp, and S.-K. Chan, *Phys. Rev. B* 33, 841 (1986).
35. J. Rehr and R. Albers, *Phys. Rev. B* 41, 8139 (1990).
36. J. M. de Leon, Y. Yacobi, E. A. Stern, and J. J. Rehr, *Phys. Rev. B* 42, 10843 (1990).
37. J. M. de Leon, J. Rehr, S. I. Zabinsky, and R. Albers, *Phys. Rev. B* 44, 4146 (1991).
38. J. Rehr, R. Albers, and S. I. Zabinsky, *Phys. Rev. Lett.* 69, 3397 (1992).
39. D. A. Shirley, in "Photoemission in Solids," Vol. I. Springer-Verlag, Berlin, 1978.
40. E. A. Stern, B. A. Bunker, and S. M. Heald, *Phys. Rev. B* 21, 5521 (1980).
41. T. A. Carlson, C. W. Nestor, T. C. Tucker, and F. B. Malik, *Phys. Rev.* 169, 27 (1968).
42. E. A. Stern, S. M. Heald, and B. A. Bunker, *Phys. Rev. Lett.* 42, 1372 (1979).
43. A. Pinto, A. R. Pennisi, G. Faraci, G. D'Agostino, S. Mobilio, and F. Boscherini, *Phys. Rev. B* 51, 5315 (1995).
44. P. Lee and G. Beni, *Phys. Rev. B* 15, 2862 (1977).
45. B. Agarwal, "X-Ray Spectroscopy." Springer-Verlag, Heidelberg, 1979.
46. M. Cardona and L. Ley, in "Photoemission in Solids," Vol. I. Springer-Verlag, Berlin, 1978.
47. F. W. Lytle, D. Sayers, and E. A. Stern, *Report of the International Workshop on Standards and Criteria in X-ray Absorption Spectroscopy—Physica B*, 158 (1989).
48. Z. Tan, J. Budnick, and S. M. Heald, *Rev. Sci. Instrum.* 60, 1021 (1989).
49. E. A. Stern and K. Kim, *Phys. Rev. B* 23, 3781 (1981).
50. E. Costanzo, G. Faraci, A. R. Pennisi, S. Ravesi, and A. Terrasi, *Solid State Commun.* 81, 155 (1992).
51. G. Faraci, E. Costanzo, A. R. Pennisi, Y. Hwu, and G. Margaritondo, *Z. Phys. D: At., Mol. Clusters* 23, 263 (1992).
52. G. Faraci, S. L. Rosa, A. R. Pennisi, and G. Margaritondo, *Phys. Rev. B* 49, 2943 (1994).
53. G. G. Li, F. Bridges, and C. H. Booth, *Phys. Rev. B* 52, 6332 (1995).
54. A. McKale, B. Veal, A. P. Paulikas, S.-K. Chan, and G. Knapp, *J. Am. Chem. Soc.* 110, 3763 (1988).
55. S. I. Zabinsky, J. Rehr, A. Ankudinov, and R. Albers, *Phys. Rev. B* 52, 2995 (1995).
56. A. Filipponi, A. D. Cicco, T. A. Tyson, and C. R. Natoli, *Solid State Commun.* 78, 265 (1991).
57. A. D. Cicco, *Physica B* 208, 125 (1995).
58. A. Filipponi and A. D. Cicco, *Phys. Rev. B* 52, 15135 (1995).
59. P. Eisenberger and B. Lengeler, *Phys. Rev. B* 22, 3551 (1980).
60. J. Zhao and P. Montano, *Phys. Rev. B* 40, 3401 (1989).
61. E. Stern, D. Sayers, and F. W. Lytle, *Phys. Rev. B* 11, 4836 (1975).
62. G. Apai, J. F. Hamilton, J. Stohr, and A. Thompson, *Phys. Rev. Lett.* 43, 165 (1979).
63. L. B. Hansen, P. Stoltze, J. K. Nørskov, B. S. Clausen, and W. Niemann, *Phys. Rev. Lett.* 64, 3115 (1990).
64. P. Montano, G. K. Shenoy, E. Alp, W. Schulze, and J. Urban, *Phys. Rev. Lett.* 56, 2076 (1986).
65. S. Gota, M. Gautier, L. Douillard, N. Thromat, J. Duraud, and P. L. Fèvre, *Surf. Sci.* 323, 163 (1995).
66. E. A. Stern, R. W. Siegel, M. Newville, P. G. Sanders, and D. Haskel, *Phys. Rev. Lett.* 75, 3874 (1995).
67. T. Haubold, R. Birringer, B. Lengeler, and H. Gleiter, *Phys. Lett. A* 135, 461 (1989).
68. P. Montano, W. Schulze, B. Tesche, G. K. Shenoy, and T. I. Morrison, *Phys. Rev. B* 30, 672 (1984).
69. A. Balerna, E. Bernieri, P. Picozzi, A. Reale, S. Santucci, E. Burattini, and S. Mobilio, *Surf. Sci.* 156, 206 (1985).
70. A. Balerna, E. Bernieri, P. Picozzi, A. Reale, S. Santucci, E. Burattini, and S. Mobilio, *Phys. Rev. B* 21, 5058 (1985).
71. A. Balerna and S. Mobilio, *Phys. Rev. B* 34, 2293 (1986).
72. M. A. Marcus, M. P. Andrews, J. Zegenhagen, A. S. Bommannavar, and P. Montano, *Phys. Rev. B* 42, 3312 (1990).
73. M. C. Fairbanks, R. Benfield, R. J. Newport, and G. Schmid, *Solid State Commun.* 73, 431 (1990).
74. G. Beni and P. M. Platzman, *Phys. Rev. B* 14, 1514 (1976).
75. G. Meitzner, G. Via, F. W. Lytle, and J. H. Sinfelt, *J. Chem. Phys.* 83, 4793 (1985).
76. G. H. Via, J. H. Sinfelt, and F. W. Lytle, *J. Chem. Phys.* 71, 690 (1979).
77. S. H. Joo, S. J. Choi, I. Oh, J. Kwak, Z. Liu, O. Terasaki, and R. Ryoo, *Nature* 412, 169 (2001).
78. G. Faraci, A. R. Pennisi, A. Balerna, H. Pattyn, G. E. Koops, and G. Zhang, *Phys. Rev. Lett.* 86, 3566 (2001a).
79. G. Faraci, A. R. Pennisi, A. Balerna, H. Pattyn, G. Koops, and G. Zhang, "Physics of Low Dimensional Systems" (J. L. Moran-Lopez, Ed.). Kluwer Academic-Plenum Publishers, New York, 2001.
80. J. B. Kortright, D. Awschalom, J. Stöhr, S. Bader, Y. Idzerda, S. S. P. Parkin, I. K. Schuller, and H. C. Siegmann, *J. Magn. Magn. Mater.* 207, 7 (1999).
81. M. Respaud, J. M. Broto, H. Rakoto, A. R. Fert, L. Thomas, B. Barbara, M. Verelst, E. Snoeck, P. Lecante, A. Mosset, J. Osuna, T. Ould Ely, C. Amiens, and B. Chaudret, *Phys. Rev. B* 57, 2925 (1998).
82. H. A. Dürr, S. S. Dhesi, E. Dudzik, D. Knabben, G. van der Laan, J. B. Goedkoop, and F. U. Hillebrecht, *Phys. Rev. B* 75, R701 (1999).
83. J. Guevara, A. M. Lois, and M. Weissmann, *Phys. Rev. Lett.* 81, 5306 (1998).
84. X. Chuanyun, Y. Jinlong, D. Kaiming, and W. Kelin, *Phys. Rev. B* 55, 3677 (1997).
85. G. L. Zhang, J. Verheyden, W. Deweerdt, G. Koops, and H. Pattyn, *Phys. Rev. B* 58, 3026 (1998).
86. H. Yoshida, A. Terasaki, K. Kobayashi, M. Tsukada, and T. Kondow, *J. Chem. Phys.* 102, 5960 (1995).

87. B. C. Guo, K. P. Kerns, and A. W. Castleman Jr., *J. Chem. Phys.* 96, 8177 (1992).
88. V. Dupuis, J. Tuillon, B. Prevel, A. Perez, P. Melinon, G. Guiraud, F. Parent, L. B. Steren, R. Morel, A. Barthelemy, A. Fert, S. Mangin, L. Thomas, W. Wernsdor, and B. Barbara, *J. Magn. Magn. Mater.* 165, 42 (1997).
89. B. Schleicher, S. Künzel, and H. Burtscher, *J. Appl. Phys.* 78, 4416 (1995).
90. G. Prinz, *Phys. Rev. Lett.* 54, 1051 (1985).
91. J. Verheyden, G. Zhang, J. Dekoster, A. Vantomme, W. Deweerdt, K. Milants, T. Barancira, and H. Pattyn, *J. Phys. D: Appl. Phys.* 29, 1316 (1996).
92. I. B. Chung, Y. M. Koo, and J. M. Lee, *J. Appl. Phys.* 87, 4205 (2000).
93. A. V. Felde, J. Fink, T. Mueller-Heinzerling, J. Pflueger, B. Scheerer, G. Linker, and D. Kaletta, *Phys. Rev. Lett.* 53, 922 (1984).
94. C. Templier, H. Garem, and J. P. Riviere, *Philos. Mag. A* 53, 667 (1986).
95. S. Donnelly and J. H. Evans, in "Fundamental Aspects of Inert Gases in Solids." Plenum Press, New York, 1991.
96. E. L. Fleischer and M. G. Norton, *Heter. Chem. Rev.* 3, 171 (1996).
97. C. Templier, in "Fundamental Aspects of Inert Gases in Solids." Plenum Press, New York, 1991.
98. H. Andersen, J. Bohr, A. Johansen, E. Johnson, L. Sarholt-Kristensen, and V. Sarganov, *Phys. Rev. Lett.* 59, 1589 (1987).
99. G. Faraci, S. L. Rosa, A. R. Pennisi, S. Mobilio, and G. Tourillon, *Phys. Rev. B* 43, 9962 (1991).
100. J. Barker, *J. Chem. Phys.* 86, 1509 (1987).
101. M. Ross, H. Mao, P. M. Bell, and J. Xu, *J. Chem. Phys.* 85, 1028 (1986).
102. L. W. Finger, R. Hazen, G. Zou, H. K. Mao, and P. M. Bell, *Appl. Phys. Lett.* 39, 892 (1981).
103. K. Asami, *Phys. Rev. B* 29, 7026 (1984).
104. G. Faraci, A. R. Pennisi, A. Terrasi, and S. Mobilio, *Phys. Rev. B* 38, 13468 (1988).
105. F. Zontone, F. D'Acapito, G. Faraci, and A. R. Pennisi, *Eur. Phys. J. B* 19, 501 (2001).
106. P. Decoster, B. Swinnen, K. Milants, M. Rots, S. L. Rosa, A. R. Pennisi, and G. Faraci, *Phys. Rev. B* 50, 9752 (1994).
107. G. Faraci, A. R. Pennisi, R. Puglisi, A. Balerna, and I. Pollini, *Phys. Rev. B* 65, 24101 (2002).
108. G. Faraci, A. R. Pennisi, and A. Balerna, submitted to *Eur. Phys. J. B* 30, 393 (2002).
109. G. Faraci, S. L. Rosa, A. R. Pennisi, S. Mobilio, and I. Pollini, *Phys. Rev. B* 43, 1913 (1991).
110. G. Faraci, S. L. Rosa, A. R. Pennisi, S. Mobilio, and I. Pollini, *Phys. Rev. B* 45, 9357 (1992).
111. S. M. Heald and E. A. Stern, *Phys. Rev. B* 16, 5549 (1977).
112. S. M. Heald and E. A. Stern, *Phys. Rev. B* 17, 4069 (1978).
113. J. R. Regnard, J. Juanhuix, C. Brizard, B. Diény, and B. Mevel, *Solid State Commun.* 97, 419 (1996).
114. F. D'Acapito, G. Battaglin, E. Cattaruzza, F. Gonella, C. Maurizio, P. Mazzoldi, S. Mobilio, and F. Zontone, *Eur. Phys. J. D* 10, 123 (2000).
115. Y. L. Soo, G. Kioseoglou, S. Huang, S. Kim, and Y. Kao, *Appl. Phys. Lett.* 78, 3684 (2001).
116. A. J. Steinfors, P. Scholte, A. Ettema, F. Tuinstra, M. Nielsen, E. Landemark, D.-M. Smilgies, F. Feidenhans, G. Falkenberg, L. Seehofer, and R. L. Johnson, *Phys. Rev. Lett.* 77, 2009 (1996).
117. N. Usami, M. Miura, Y. Ito, Y. Araki, and Y. Shiraki, *Appl. Phys. Lett.* 77, 217 (2000).
118. G. Capellini, M. D. Seta, and F. Evangelisti, *Appl. Phys. Lett.* 78, 303 (2001).
119. S. A. Chaparro, J. Drucker, Y. Zhang, D. Chandrasekhar, M. R. McCartney, and D. J. Smith, *Phys. Rev. Lett.* 83, 1199 (1999).
120. T. Tezuka and N. Sugiyama, *J. Appl. Phys.* 83, 5239 (1998).

# Nanoclusters and Nanofilaments in Porous Media

Parasuraman Selvam

*Indian Institute of Technology—Bombay, Powai, Mumbai, India*

## CONTENTS

1. Introduction
  2. Nanomaterials in Confined Environment
  3. Molecular Sieve Host
  4. Microporous Molecular Sieves
  5. Mesoporous Molecular Sieves
  6. Nanoclusters/Nanofilaments  
In Mesoporous Bulk Materials
  7. Nanoparticles/Nanowires  
in Mesoporous Films
- References

## 1. INTRODUCTION

There is a tremendous worldwide interest in the area of nanotechnology, which encompasses the synthesis, organization, and application of materials on a nanoscale. The field of nanotechnology is highly interdisciplinary, and involves concepts from chemistry, physics, biology, and engineering with applications in electronic and photonic devices, computing and information technologies, health care, biotechnology, and clean-energy production. Further, the nanoscale materials are of great fundamental interest due to their exceptional optical, electrical, and magnetic properties, which are markedly different from those of the bulk. These properties are strongly dependent on the size and shape of the particle owing to their very small dimension and fundamental change in the coordination, symmetry, and confinement [1, 2]. Thus, the unique size-dependent electronic, optical, and chemical properties of nanoparticles have triggered considerable research activities, and have attracted significant attention in developing new-generation engineered materials, biological and photosensors, as well as advanced devices such as information storage processes, lasers, switches, transistors, light-emitting diodes, nonlinear

optics, photocatalysts, solar cells, and so on [3–8]. Moreover, the nanocrystals also exhibit remarkable physical phenomena such as enhanced local field effects for metals, quantum confinement for semiconductors, and superparamagnetism for magnetic materials. Hence, research and developmental activities on nanoscale magnetic metallic clusters/particles/crystals such as Fe, Co, and Ni have been intensively studied because of their fundamental characteristics, as well as several diverse applications in high-density magnetic recording media, magnetic (ferro) fluids, color imaging, magnetic refrigeration, and so on [7, 8]. In fact, the intrinsic magnetic properties are strongly influenced by the particle size; nanoscale magnetic particles usually display specific features such as superparamagnetism and quantum tunneling of magnetization [9–11]. Another well-known cluster-related concept is the so-called quantum size effect, which arises as a result of the (blue) shift in the optical absorption edge of nanoparticles [12]. On the other hand, nanowires/nanofilaments/nanofibers/nanorods have also attracted great interest because of the outstanding physicochemical properties and novel physics that they exhibit, as well as their potential applications as interconnects or functional components in future mesoscopic and optoelectronic devices [13, 14].

## 2. NANOMATERIALS IN CONFINED ENVIRONMENT

Traditionally, colloidal solutions [15], porous glasses [16], and certain polymers [17] have been used as hosts for the preparation of nanosized materials. In addition, several other approaches have also been considered for the synthesis of nanoparticles in aqueous as well as nonaqueous media by adopting chemical, sonolytic, radiolytic, and photolytic reactions [6]. Nanosized metal, metalloid, and semiconductor nanofilaments have been prepared using various methods such as templating [18, 19], photochemistry [20], seeding [21, 22], and electrochemistry [23, 24]. However, all of these methods are neither efficient in generating clusters of uniform size nor chemically inert toward

the guest molecules. Therefore, the self-assembly of nanoparticles into ordered morphologies is one of the promising alternatives, and hence forms the topic of current interest. Further, they are also expected to create nanostructured materials with unique physicochemical properties. Therefore, it has been realized that the preparation of nano-sized materials in periodic zeolitic pores is a viable option, and hence they have been considered as ideal systems for the growth of nanostructures [12, 25–28]. Indeed, the well-defined, regular nanoporous structure of zeolite (microporous) molecular sieves offers several advantages, including a unique microenvironment for the controlled assembling of nanostructured materials [27–42], and that the encapsulated metal/metal-oxide nanoclusters formed in these ordered porous materials can potentially be used in a variety of applications, including optics, electronics, sensors, and catalysis [33, 35]. Further, they also provide a simple way of coupling the reactivity of the metal complexes with the robustness and stereochemistry of the host matrix. Nevertheless, from the viewpoint of nanoclusters in a confined environment, only little effort has been directed. At this juncture, it is important to mention here that, according to the IUPAC nomenclature, the porous materials are classified into three types according to their pore diameters [43]: microporous (<2 nm), mesoporous (2–50 nm), and macroporous (>50 nm). The exceptionally large pore structure, for example, of mesoporous materials allows controlling the particle size, as well as the organization of nanoparticles in an orderly manner.

Thus, the confinement of nanoclusters/nanofilaments in the cavities/voids/pores of nanoporous inorganic matrices is attracting much more attention as a way to stabilize highly dispersed metals, metalloids, semiconductors, and so on, in the form of atoms, clusters, filaments, or colloids, and to prevent their coalescence into larger, ill-defined aggregates [44–56]. These new materials, however, are significantly different from the recently extensively reported glass–metal colloidal composites and organic–inorganic hybrid nanocomposites [57, 58]. Thus, the encapsulation or loading of mono- and bimetallic species, metalloids, mono- and mixed-metal oxides, polymers, and so on, in the form of clusters or filaments in so-called periodic porous molecular sieve materials possessing well-ordered and controllable nanopores with a narrow pore size distribution, has stimulated great interest owing to their novel properties and exotic applications [44, 45, 48, 59–66]. For example, Ag-loaded porous silica displays an optical switching effect and surface oxidation behavior [46], while the encapsulation or entrapment of metal complexes provides a convenient route for the heterogenization of homogeneous catalytic processes as these hybrid catalysts offer the advantage of site isolation, shape selectivity, and enhanced activity in several organic transformations with easy product separation and catalyst recovery [29].

### 3. MOLECULAR SIEVE HOST

The development of open-framework inorganic materials, for example, silica and carbon, of well-defined geometry with a precise and easily controllable pore shape and size, is of great importance in many areas of modern science and

technology. They attract much attention as catalysts, catalytic supports, and selective adsorbents, as well as templates for making new materials.

## 4. MICROPOROUS MOLECULAR SIEVES

Periodic microporous materials, for example, zeolites and zeolite-type materials, can exclusively be used for a variety of applications, including sorbents, ion exchangers, shape-selective catalysts, and molecular hosts [37–42]. The well-defined and uniform pore systems act as a suitable reaction chamber/support for the controlled assembling of nanocrystals, as well as for the encapsulation of organic/inorganic molecules within the voids of a zeolite host [28].

### 4.1. Nanoclusters/Nanoparticles in Microporous Materials

One of the fascinating examples of encapsulated species in zeolitic pores is the so-called “ship-in-bottle” metal complexes such as metallophthalocyanines and metal carbonyls in zeolites, which have been proposed as enzyme mimics [29, 67–80]. For steric reasons, these complexes have to be assembled *in-situ* by allowing the building blocks to diffuse through the windows of the zeolite cages and condense around a metal ion previously introduced into the voids by ion exchange. As shown in Figure 1, for example, several metal ions, including Co, Ru, Rh, Ir, Pd, and Pt, have been impregnated in the zeolite-Y matrix, followed by carbonylation, leading to the selective formation of triangular prismatic metal carbonyl clusters of the type  $[M_3(CO)_6]_n^{2-}$  ( $M = Co, Ru, Rh, \text{ and } Pt; n = 2-6$ ). Decarbonylation of the resulting metal carbonyl clusters in the void space yields metal

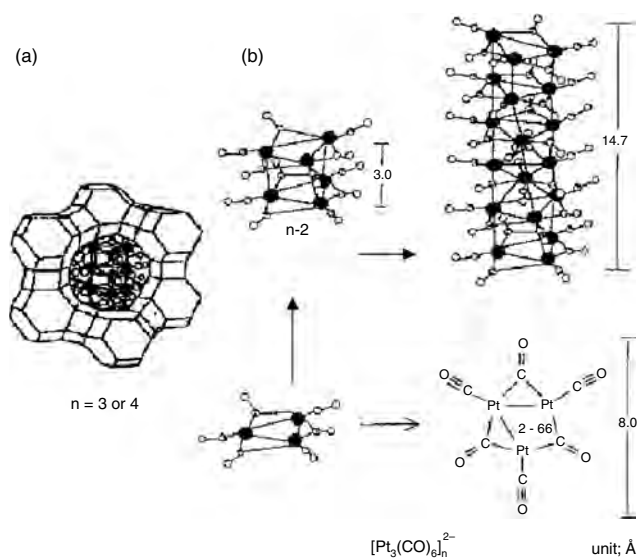


**Figure 1.** (a) Ship-in-bottle synthesis of Pt carbonyl clusters  $[Pt_3 \cdot (CO)_6]_n^{2-}$  ( $n = 3$  or  $4$ ) in zeolite-Y. Adapted with permission from [79], A. Fukuoka et al., *Catal. Today* 66, 21 (2001). © 2001, Elsevier Science. (b) Structure of Pt carbonyl anion clusters  $[Pt_3(CO)_6]_n^{2-}$  ( $n = 1, 2, \text{ and } 6$ ). Adapted with permission from [76], M. Sasaki et al., *J. Mol. Catal. A* 141, 223 (1999). © 1999, Elsevier Science.

nanoclusters. However, it is to be noted here that these complexes are forced to adopt a distorted geometry owing to the encapsulation of such larger complexes into the constrained environment. For example, the incorporation of a planar Co (II) phthalocyanine molecule in the super cage of zeolite-Y is considerably distorted [80] since the end-to-end diagonal distance (15 Å) of the neat complex is larger than the pore size of zeolite-Y (12.7 Å). This is clearly reflected in the magnetic measurements, where an increase in the magnetic moment of the entrapped complex is noticed (Fig. 2). However, when this moiety is encapsulated in much larger voids of the mesovoids of the so-called MCM-41 phase (for a detailed account, see Section 5), where it retains the square planar geometry, the magnetic moment values are similar to the free or neat complex.

On the other hand, luminescent Si nanoclusters have been encapsulated in the supercages of zeolite-Y [49] by adsorbing and anchoring disilane, followed by gentle thermolysis (Fig. 3). Further, the steric restriction imposed by the host ensures that disilane molecules are exclusively entrapped in the  $\alpha$  cages, and that the resulting Si clusters show atypical bandgap energy (2.2 eV). Likewise, unusual structure and stability have also been observed in the case of the  $\text{FeO}_x$  nanoclusters in ZSM-5 [81]. Also, CdS and PbS nanoparticles have been prepared from the respective metal ion-exchanged zeolites by reaction with  $\text{H}_2\text{S}$  [25]. In the same way, the loading of CdS and GaP nanoclusters in zeolite-Y and ultrastable zeolite-Y has also been reported [28]. More recently, the inclusion of solvatochromic dye Nile red in the pores of zeolites such as zeolite-Y, ZSM-5, and LTA (Fig. 4) has been reported, and the highly siliceous form of these zeolites can act as optical sensors [82]. Although the microporous (zeolite and zeolite-type) materials provide excellent hosts as a result of their crystalline network, well-defined pore size, and pore size distribution, their applications are, however, limited by the relatively small internal pore sizes and pore openings. On the other hand, the invention of ordered mesoporous materials [83, 84] in the early 1990s

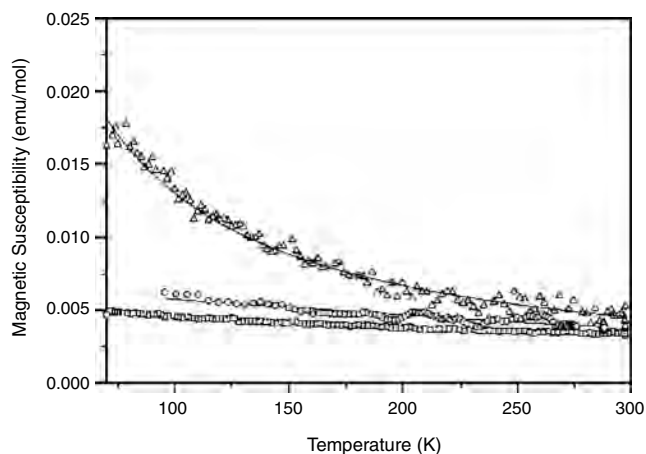


**Figure 2.** Temperature variation of magnetic susceptibilities of Co(II) phthalocyanine (free) complex ( $\Delta$ ), Co(II) phthalocyanine encapsulated in zeolite-Y ( $\square$ ), and Co(II) phthalocyanine encapsulated in MCM-41 ( $\circ$ ). Adapted with permission from [80], S. Ray and S. Vasudevan, *Inorg. Chem.* 42, 1711 (2003). © 2003, American Chemical Society.

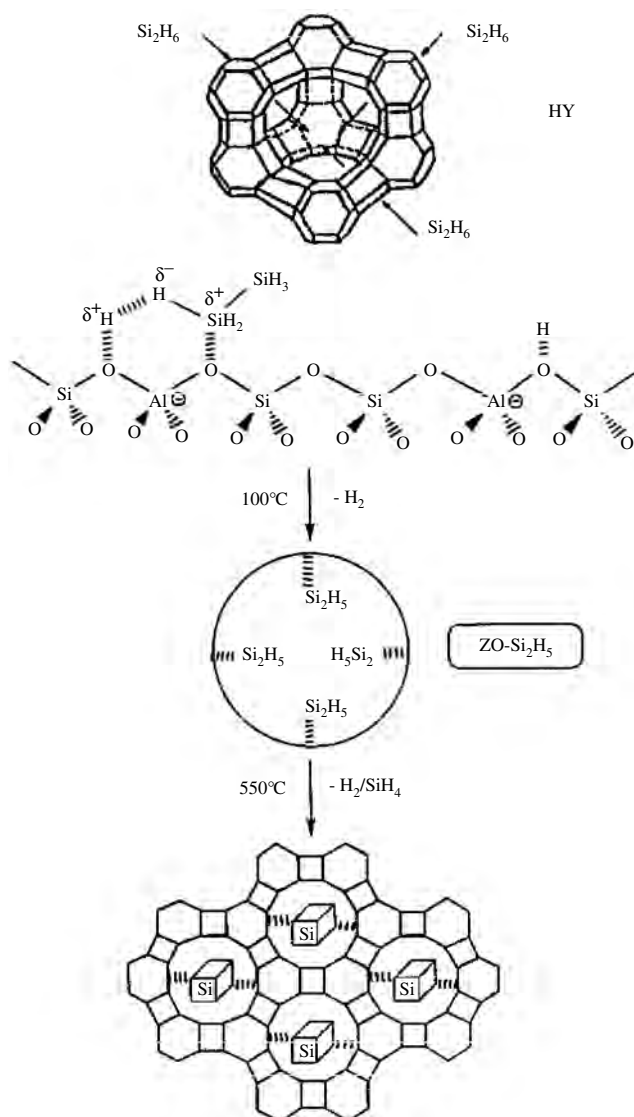


**Figure 3.** Schematic illustration of the encapsulation process of Si clusters in the  $\alpha$  cages of zeolite Y via CVD of  $\text{Si}_2\text{H}_6$ . Adapted with permission from [49], J. He et al., *J. Am. Chem. Soc.* 120, 10697 (1998). © 1998, American Chemical Society.

has opened a wide range of opportunities in porous solids, and has created new opportunities, not only in catalysis, but also has opened up new avenues in the areas of advanced materials, ion exchange, and environmental pollution control strategies [44, 45, 48, 59–66].

## 5. MESOPOROUS MOLECULAR SIEVES

The discovery of the so-called M41S family of periodic mesoporous materials [83, 84] has broadened the scope of applications in several areas [59–66], as well as opening new opportunities in the development of nanomaterials [44, 45, 48]. As illustrated in Figure 5, the mesostructures have been grouped into four main categories. Two of them have been identified as the thermally stable structures, viz. MCM-41 having a hexagonal structure with unidirectional



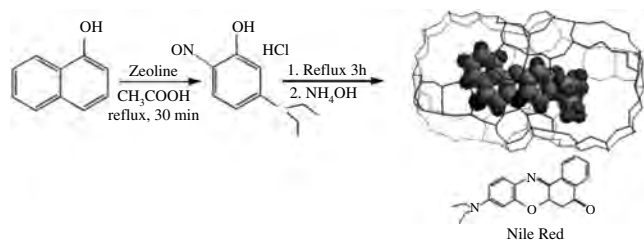


**Figure 4.** Schematic representation of the encapsulation of Nile Red in faujasite. Adapted with permission from [82], J. L. Meinershagen and T. Bein, *J. Am. Chem. Soc.* 121, 448 (1999). © 1999, American Chemical Society.

(both ordered and disordered) pore structure, and MCM-48 displaying a cubic structure with a three-dimensional pore system. Two other phases, viz. lamellar MCM-50 and molecular organic octamer, a surfactant-silica composite species ( $\text{surf}, \text{SiO}_{2.5}$ )<sub>8</sub>, are unstable. Thus, two of the stable members, that is, MCM-41 and MCM-48, can comfortably trap the guest molecules in the mesopores, and hence form perfect candidates for the loading and encapsulation of metal/semiconductor nanoclusters and nanofilaments with controlled size and shape. Owing to some of these unique and excellent characteristics such as the flexibility in terms of synthetic conditions, pore size tuning (2–20 nm), high surface area (1000–1600  $\text{m}^2 \cdot \text{g}^{-1}$ ), large internal hydroxyl groups (40–60%), framework substitution, and so on (for recent reviews, see [64] and [65]), in recent years, the scientific community has witnessed a great deal of work and rapid expansion of the activities in mesoporous materials (Fig. 6).

The well-defined regular pore size and shape, very large pore volume, huge surface area, tunable pore opening, narrow pore size distribution, and structural diversity of these materials are widely exploited for the selective adsorption of a variety of gases, liquids, and solids, and they also provide

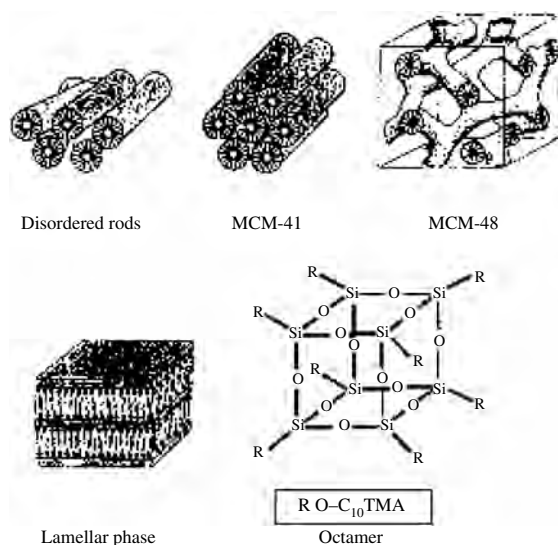


**Figure 5.** Formation of various mesophases. Adapted with permission from [64], P. Selvam et al., *Ind. Eng. Chem. Res.* 40, 3237 (2001). © 2001, American Chemical Society.

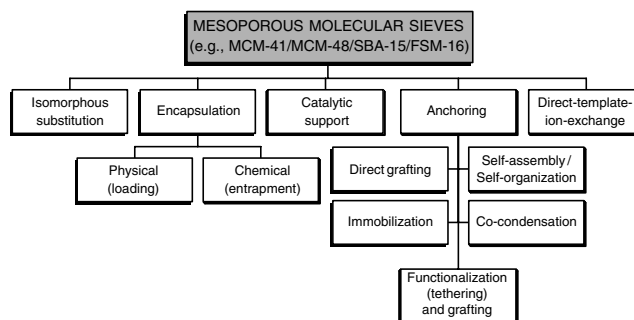


**Figure 6.** Schematic representation of the various possible modifications of the mesoporous materials.

a suitable matrix for the control growth of nanostructured materials [44, 45, 48, 59–66]. The mesoporous materials have been synthesized via the polymerization of inorganic species such as silica, alumina, and so on, around a periodic bulky organic template, for example, surfactant micelles or polyethylene oxide or copolymers (Table 1) [64]. After the thermal treatment (calcination) of the synthesized materials, for example, MCM-41 (see Fig. 5), a hollow cylindrical porous matrix is obtained whose cavities are the perfect replicas of the organic species (Fig. 7). Numerous silica-based mesostructured materials such as MCM-41 [83, 84], MCM-48 [83, 84], FSM-16 [85, 86], HMS [87, 88], and SBA-15 [89, 90] with different pore sizes, shapes, and periodicities have been prepared by varying the synthesis conditions and the surfactant molecules (Table 2) [64]. In addition, the literature provides many nonsilica mesostructured materials of mono- and mixed-metal oxides, for example, aluminophosphates [91], transition metal oxides [92–95], and so on. These materials, including a new (organic-inorganic) hybrid HMM-1 [96], are frequently used as templates to synthesize various metal nanoclusters and nanowires by photo- and hydrogen reduction and different composite/ceramic nanoparticles by impregnation and calcination.

## 6. NANOCCLUSERS/NANOFILAMENTS IN MESOPOROUS BULK MATERIALS

As described in the previous section, the mesoporous materials have many favorable properties in conjunction with high thermal, hydrothermal, chemical, and mechanical stability. Therefore, they are highly conducive for a number of important applications, thus providing real opportunities in the area of separation technology, heterogeneous catalysis, and sensors, and in the synthesis of novel nanostructured materials such as metals, metalloids, oxides, chalcogenides, and so on [44, 45, 48, 56, 59–66, 97–108]. Other guest molecules encapsulated within the mesopore channels include several organic and inorganic polymers, complex ions, photocatalysts, chemically active colloids, semiconducting particles, luminescent silicon clusters, conducting polymer and carbon filaments, fullerenes, long-chain alkythiolates, enzymes, and a wide variety of organic, inorganic, and organometallic compounds [44, 45, 48, 109–118].

**Table 1.** Physical properties of various mesoporous silica materials.

Mesophase terminology	Dimensionality and crystal system and space group	Unit cell dimension (nm)	Mean pore size (nm)
MCM-41	2D, hexagonal, P6mm	$a = 4.04$	3.25
MCM-48	Cubic, Ia3d	$a = 8.08$	3.50
FSM-16	2D, hexagonal, P6mm	$a = 4.38$	3.52
SBA-1	Cubic, Pm3n	$a = 7.92$	3.05
SBA-2	3D, hexagonal, P6 <sub>3</sub> /mmc	$a = 5.40$ ; $c = 8.70$	3.41
SBA-3	2D, hexagonal, P6mm	$a = 4.75$	3.48
SBA-8	2D, rectangular, cmm	$a = 7.57$ ; $b = 4.92$	2.98
SBA-11	Cubic, Pm3m	$a = 10.64$	3.60
SBA-12	3D, hexagonal, P6 <sub>3</sub> /mmc	$a = 5.40$ ; $c = 8.70$	4.09
SBA-14	Cubic, Pm3n	$a = 4.47$	3.46
SBA-15	2D, hexagonal, p6mm	$a = 11.6$	8.73
SBA-16	Cubic, Im3m	$a = 17.6$	8.35
HMM <sup>d</sup>	2D, hexagonal, P6mm	$a = 5.70$	3.85
	3D, hexagonal, P6 <sub>3</sub> /mmc	$a = 8.86$ ; $c = 5.54$	3.58
MSU-1	Hexagonal (disordered)	$a = 4.73$	3.60
MSU-2	Hexagonal (disordered)	$a = 7.16$	3.50
MSU-3	Hexagonal (disordered)	$a = 7.04$	5.80
MSU-4	Hexagonal (disordered)	$a = 6.01$	3.63
MSU-V	Lamellar <sup>e</sup>	$a = 3.87$	— <sup>i</sup>
MSU-G	Lamellar <sup>e</sup>	$a = 6.54$	3.61
HMS	Hexagonal (disordered)	$a = 4.55$	3.85
KIT-1	Hexagonal (disordered)	$a = 4.80$	3.89
CMK-1 <sup>a</sup>	Cubic, I4 <sub>1</sub> 32	$a = 8.33$	3.84
APO <sup>b</sup>	2D, hexagonal, P6mm	$a = 4.27$	3.35
MLMS <sup>c</sup>	2D, hexagonal, P6mm	$a = 13.05$	8.51
HMP <sup>f</sup>	2D, hexagonal, P6mm	$a = 4.40$	3.19
MSM <sup>g</sup>	2D, hexagonal, P6mm	$a = 4.55$	3.35
MMS <sup>h</sup>	2D, hexagonal, P6mm	$a = 4.70$	3.00 <sup>i</sup>

<sup>a</sup>Mesoporous carbon molecular sieve.<sup>b</sup>Mesoporous aluminophosphate.<sup>c</sup>Thermally stable mesophase.<sup>d</sup>Hybrid mesoporous material.<sup>e</sup>Monolithic mesoporous silica.<sup>f</sup>Hexagonal mesophase.<sup>g</sup>Mesoporous silica material.<sup>h</sup>Mesoporous molecular sieves.<sup>i</sup>Data not available.

Source: Adapted with permission from [64], P. Selvam et al., *Ind. Eng. Chem. Res.* 40, 3237 (2001). © 2001, American Chemical Society.

## 6.1. Nanomono- and Nanobimetallic Clusters and Nanofilaments

Recently, the ship-in-bottle synthesis methodology (Fig. 8) has been adopted for the encapsulation of larger complexes into mesopore channels [55, 73, 76, 79, 11, 119–121], and they can be transformed into nanometal clusters (1.5 nm size) by the controlled removal of CO (partial decarbonylation). In a similar manner, Pt nanoparticles and Pt nanowires of 2–4 nm diameter and 50–500 nm length have been prepared in the channels of FSM-16 by the reduction of H<sub>2</sub>PtCl<sub>6</sub> followed by the exposure to <sup>60</sup>Co  $\gamma$ -ray or UV light ( $\lambda_{\max} = 254$  nm) in the presence of 2-propanol and water at 300 K. In contrast, H<sub>2</sub> reduction of H<sub>2</sub>PtCl<sub>6</sub>/FSM-16 at 673 K resulted in the formation of Pt nanoparticles (Fig. 9). It is also interesting to note that the Pt wires consist of a single-crystal phase of Pt (110) having a lattice

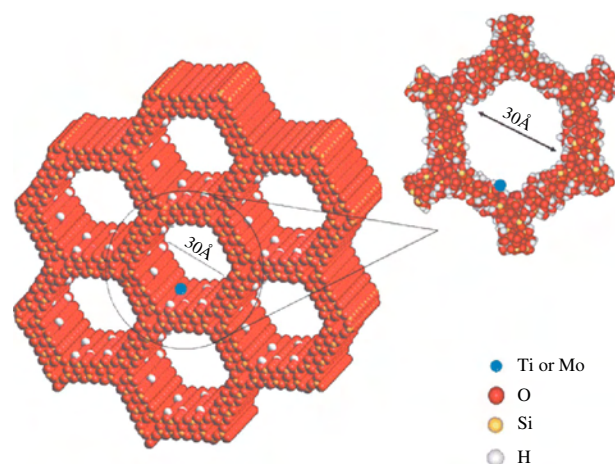


**Figure 7.** Catalytically active sites (e.g., Ti or Mo) on the interior surfaces of MCM-41. The inset shows the disordered walls of the mesopores structure. Adapted with permission from [66], J. M. Thomas et al., *Chem. Commun.* 2921 (2002). © 2002, Royal Society of Chemistry.

fringe of 2.27 Å. However, the Pt nanofilaments are scattered and rather uniformly formed in alignment with the ordered channels of FSM-16 (Fig. 10).

At this juncture, it is also interesting to note that the Pt nanowires and Pt nanoparticles in FSM-16 display a unique IR spectrum for CO adsorption (Fig. 11), and that the latter yields a linear CO band at 2060 cm<sup>-1</sup> with an intensity over an order of magnitude higher than the former. In fact, the chemisorption measurements of CO and H<sub>2</sub> on Pt nanowire in FSM-16 showed that the adsorbed amounts are much smaller (about an order of magnitude) than those on Pt nanoparticles in FSM-16 [76]. In a similar way, Rh nanoparticles have also been prepared in FSM-16 by calcination of RhCl<sub>3</sub>/FSM-16 at 673 K and subsequent reduction with H<sub>2</sub>. Pt–Rh nanowires of 2.5 nm diameter and 10–50 nm length have been prepared in FSM-16 by the photoreduction of FSM-16 coimpregnated with H<sub>2</sub>PtCl<sub>6</sub> and RhCl<sub>3</sub> [120]. Mono- (Pt and Rh) and bimetallic (Pt–Rh and Pt–Pd) nanowires in hybrid (organic–inorganic) mesoporous materials (HMM-1) have also been synthesized by photoreduction of H<sub>2</sub>PtCl<sub>6</sub>·6H<sub>2</sub>O and/or RhCl<sub>3</sub>·3H<sub>2</sub>O and/or H<sub>2</sub>PdCl<sub>4</sub> [55]. Accordingly, the HMM-1 host was impregnated with an aqueous solution of the respective salts, and the sample was irradiated, in the presence of water and methanol, with a high-pressure mercury lamp (100 W, 250–600 nm) at room temperature (Fig. 12). Interestingly, the Pt–Pd/HMM-1 system shows a huge increase in the magnetic susceptibility below 90 K (Fig. 13), which is two–three orders of magnitude higher than the sum of the values of bulk Pt and Pd. The unusual enhancement of the magnetization may be attributed to the low dimensionality of the bimetallic wires.

On the other hand, Au nanoparticles have been prepared in the mesopore channels of monolithic porous silica [122] and FSM-16 [119] by soaking chloroauric acid (HAuCl<sub>4</sub>), followed by thermal reduction in hydrogen atmosphere. Uniform Ag nanowires have also been synthesized inside the channels of SBA-15 by wet impregnation of AgNO<sub>3</sub>, followed by thermal decomposition [52]. Likewise, impregnation of MCM-41 with an organic solution of a well-defined low-oxidation-state heterometallic organometallic cluster of

**Table 2.** Various mesoporous silicas based on 2D hexagonal (P6mm) MCM-41 structure.

Mesophase terminology	Silica sources	Surfactant/templates	Reaction conditions
MCM-41	Sodium silicate	Alkyltrimethyl-ammonium halides	Hydrothermal synthesis at 373 K for 144 h
FSM-16	Sodium kanemite	Cetyltrimethyl-ammonium chloride	Silica/surfactant/water mixture heated at 343 K under stirring. After 3 h, pH adjusted to 8.5, and again heated at 343 K for 3 h
FSM-16	Sodium kanemite	Cetyltrimethyl-ammonium chloride	Silica: surfactant ratio = 1:20 (w/w); final pH = 11.3 (without adjustment); stirred at 353 K for 3 h
SBA-3	Tetraalkyl orthosilicate	Cetyltrimethyl-ammonium bromide + HBr	Silica/surfactant/acid/water mixture stirred at room temperature (RT) for $\geq 30$ min
SBA-15	Tetraalkyl orthosilicate	Poly(ethylene oxide) oligomers— $C_{16}EO_{10}^c$ Triblock copolymer $EO_{20}PO_{70}EO_{20}^c$	Silica/surfactant/water mixture heated at 373 K for 24 h
MLMS <sup>a</sup>	Tetraalkyl orthosilicate	Triblock copolymers— $EO_{106}PO_{70}EO_{106}$	Silica/surfactant/water mixture heated at 313 K for 24 h
HMP <sup>b</sup>	Tetramethyl orthosilicate	$C_{12}EO_8$ (octaethylene glycol monododecyl ether)	Silica/surfactant/water mixture was aged for 18 h at room temperature; the ratio of surfactant to water was 50 wt%
	Cab-O-Sil	Glycosilicate surfactant <sup>f</sup>	Nonaqueous synthesis: the mixture is aged at 353 K for 3 days
MSM <sup>c</sup>	$(NH_4)_2SiF_6$	Cetyltrimethyl-ammonium bromide	Silica/surfactant/water mixture (pH = 8) stirred at RT for 1 h
MMS <sup>d</sup>	$H_2SiF_6$	Cetyltrimethylammonium bromide	Silica/surfactant/water mixture (pH = 7–8) aged at 343 K for 5 h

<sup>a</sup>Monolithic mesoporous silica.

<sup>b</sup>Hexagonal mesophase.

<sup>c</sup>Mesoporous silica material.

<sup>d</sup>Mesoporous molecular sieves.

<sup>e</sup>Commercial surfactants: EO—poly(ethylene oxide); PO—poly(propylene oxide).

<sup>f</sup>Solubilization of silica with sodium hydroxide in ethylene glycol in presence of CTACl.

Source: Adapted with permission from [64], P. Selvam et al., *Ind. Eng. Chem. Res.* 40, 3237 (2001). © 2001, American Chemical Society.

the type  $[NEt_4]-[Co_3Ru(CO)_{12}]$  into pores followed by thermal treatment (523–773 K) under inert atmosphere leads to highly dispersed magnetic nanoparticles at temperatures as low as 523 K [53]. The magnetic measurements at room temperature show no open (hysteresis) loop for the doped MCM-41 treated below 623 K, which is consistent with the particle sizes. On the other hand, the xerogels display a ferromagnetic behavior when treated at or above 523 K (Fig. 14). Nanostructured Pt wires have been synthesized in MCM-41, MCM-48, or SBA-15 by the impregnation method using an aqueous solution of  $Pt(NH_3)_4(NO_3)_2$ , followed by reduction in hydrogen at 573 K [54, 123, 124]. Nanoparticles of Ag, Pd, and Pt have also been prepared in AlMCM-41 by loading of the metal ions, followed by reduction in hydrogen [125]. The conduction electron paramagnetic resonance line width studies of these nanoclusters incorporated in the aluminosilicate matrix indicate that the line widths are independent of metal ion loading, which suggests that the metal particles are located inside the mesopore channels, and the size of the particle is constrained by the channel diameter. In the same way, nano-sized Ni metal particles (1–2 nm) also have been prepared in an AlMCM-41 host by ion exchange in an aqueous solution, followed by reduction with sodium borohydride [126]. The resulting nanoparticles showed superparamagnetic behavior with a blocking temperature of 5 K.

Recently, template syntheses of Au nanowires and nanoparticles onto FSM-16 have been reported by the chemical vapor deposition (CVD) or wet impregnation methods with subsequent reduction [121]; see Figure 15. In the case

of the former method, initially, an organogold (III) complex ( $AuMe_2(HFA)$ ; HFA = hexafluoroacetylacetoato) was adsorbed on the mesoporous matrix, followed by irradiation using UV light, leading to the formation of Au nanowires (diameter, 2.5 nm; mean length, 17.1 nm). On the other hand, in the case of the latter, the sample was impregnated using  $HAuCl_4$  at pH 5, followed by reduction in  $H_2$  at 673 K, giving a mixture of Au nanowires and nanoparticles. In contrast,  $H_2$  reduction of the impregnated sample prepared at pH 10 produces a homogeneously dispersed Au nanoparticle in FSM-16 with a mean diameter 1.7 nm. A novel supercritical fluid solution phase technique has also been utilized to fill the channels of a hexagonal mesoporous silica matrix with quantum-confined Si nanowires [127] as well as Pt nanoclusters [128]. The Si nanowires were formed within the mesopores by degrading diphenylsilane in a high-pressure reaction cell at 773 K and 375 bar [127]. The high diffusivity of the supercritical fluid phase, on the order of  $10^{-3}$ – $10^{-4}$   $cm^2 \cdot s^{-1}$ , enables rapid diffusion of the reactant precursor into the pores of the silica matrix, where swift nucleation and growth of the particles occur, resulting in a reaction rate much faster (several orders of magnitude) that is obtainable using traditional vapor-phase or liquid-phase deposition methods [48, 106, 129]. In the same way, size-controlled Pt nanoparticles were prepared using supercritical solvents. Accordingly,  $Pt(acac)_2$  ( $acac$  = acetylacetonate) dissolved in supercritical  $CO_2$  with acetone was loaded into FSM-16, followed by reduction in flowing  $H_2$  [128]. On the other hand, Ge was deposited using vapor-phase epitaxy, where the mesophase walls acted as anchor points to

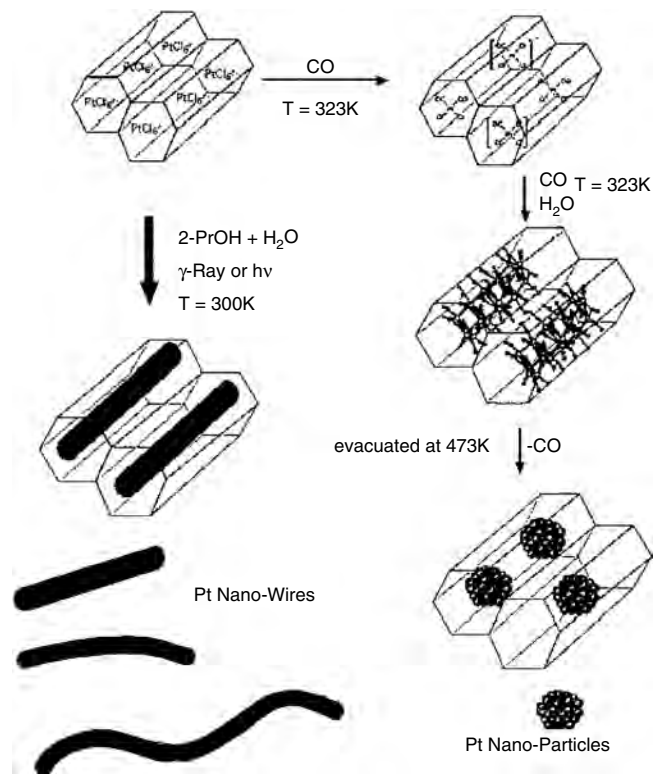


**Figure 8.** Templating fabrication of Pt nanoparticles derived from Pt cluster anions  $[Pt_3(CO)_6]_n^{2-}$  ( $n = 5$  or  $6$ ) in the mesoporous channels of FSM-16 by the controlled removal of CO, and Pt nanowires by the exposure of  $H_2PtCl_6/FSM-16$  with 2-propanol and water to  $\gamma$ -ray or UV-light irradiation. Adapted with permission from [76], M. Sasaki et al., *J. Mol. Catal. A* 141, 223 (1999). © 1999, Elsevier Science.

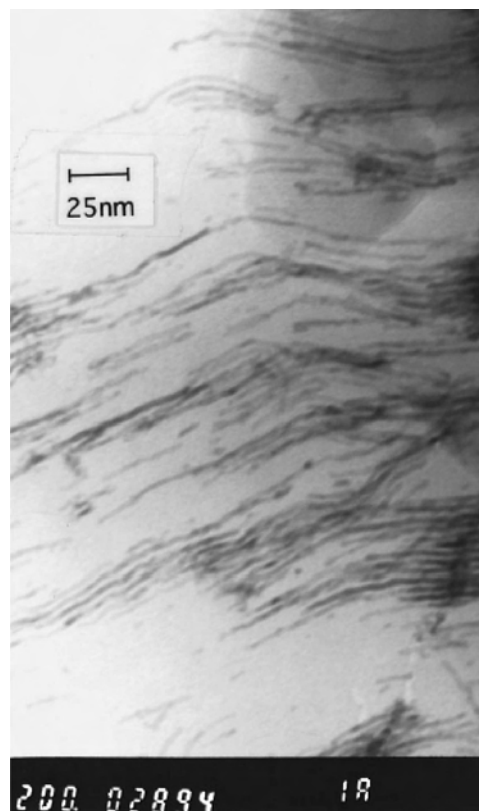


**Figure 10.** Transmission electron micrograph of Pt nanowire in FSM-16. Adapted with permission from [79], A. Fukuoka et al., *Catal. Today* 66, 21 (2001). © 2001, Elsevier Science.

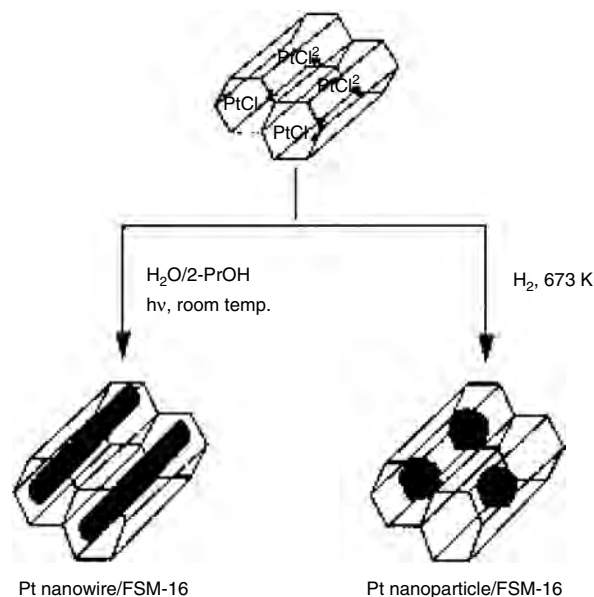


**Figure 9.** Schematic representation of the preparation of Pt nanowires and nanoparticles in FSM-16. Adapted with permission from [79], A. Fukuoka et al., *Catal. Today* 66, 21 (2001). © 2001, Elsevier Science.

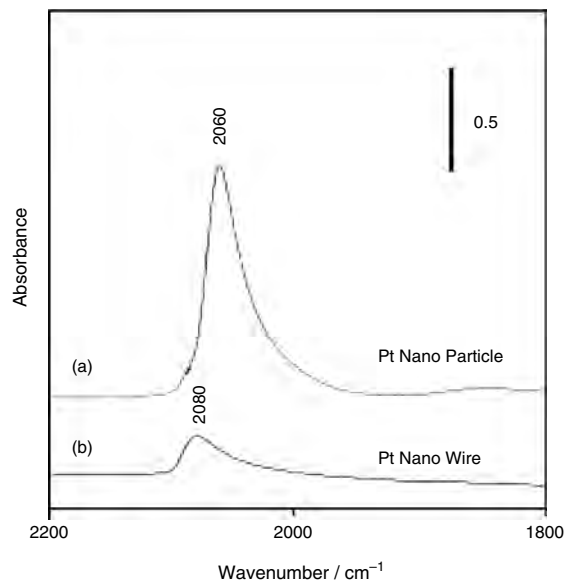


**Figure 11.** IR spectra for CO chemisorption on Pt nanoparticles and Pt nanowires in FSM-16. Adapted with permission from [79], A. Fukuoka et al., *Catal. Today* 66, 21 (2001). © 2001, Elsevier Science.

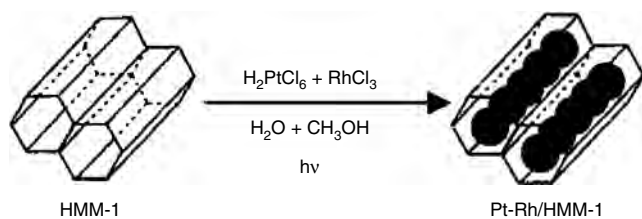


**Figure 12.** Template synthesis of novel necklace-shaped bimetallic nanowires in hybrid organic-inorganic mesoporous HMM-1 molecular sieve material. Adapted with permission from [55], A. Fukuoka et al., *J. Am. Chem. Soc.* 123, 3373 (2001). © 2001, American Chemical Society.

seed the nucleation of semiconductor clusters in the channels [106].

## 6.2. Metal-Oxide Nanoclusters

The dispersion of nanosized metal-oxide particles has been carried out within the pores of mesoporous silica by soaking (loading) the corresponding metal salts in the host matrix, followed by thermal decomposition (Fig. 16). In other words, the nanocrystals are prepared via the adsorption/impregnation of the metallic precursor, or by the chemical modification of the mesopores, followed by thermal treatment [44, 45, 48, 56, 118]. Figure 17 illustrates a representative example of a direct imaging of the filling of the mesopores of MCM-41 by metal/semiconductor clusters. Several metal-oxide particles, including  $\text{TiO}_2$ ,  $\text{Fe}_2\text{O}_3$ ,  $\text{ZnO}$ , and  $\text{PbO}$ , have been dispersed within the pores of mesoporous MCM-41 and MCM-48 by soaking the corresponding metal salts via adsorption or wet impregnation of the metallic precursors or by chemical modification of the mesophases, followed by thermal decomposition [56, 97, 99, 101, 104, 105, 130–133]. Transmission electron microscopy studies demonstrated that the particle size of the incorporated  $\text{Fe}_2\text{O}_3$  in the mesopores of MCM-48 and  $\text{ZnO}$  nanoclusters in MCM-41 is smaller than the pore diameter [99, 134]. Further, it is interesting to note that the entrapped

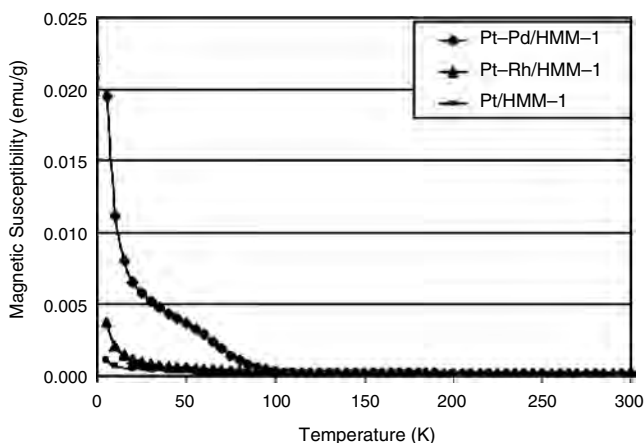


**Figure 13.** Temperature dependence of magnetic susceptibility for Pt-Pd/HMM-1, Pt-Rh/HMM-1, and Pt/HMM-1. Adapted with permission from [55], A. Fukuoka et al., *J. Am. Chem. Soc.* 123, 3373 (2001). © 2001, American Chemical Society.

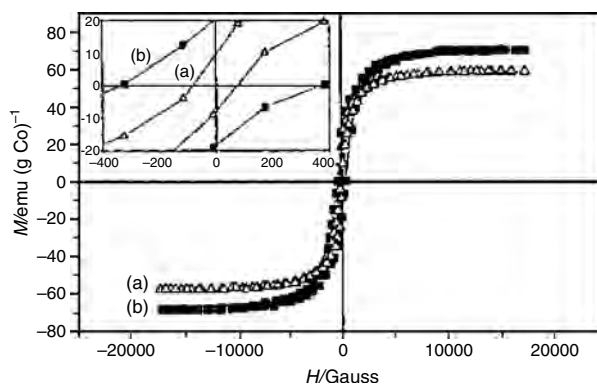


**Figure 14.** Isothermal magnetic measurements at room temperature of MCM-41 (a) and silica xerogels (b) impregnated with a saturated THF solution of  $[\text{NET}_4][\text{Co}_3\text{Ru}(\text{CO})_{12}]$ , after 1 h treatment under Ar at 773 K. Inset: expansion near zero shows an increase of the coercivity for the monoliths. Adapted with permission from [53], F. Schwyer et al., *Chem. Commun.* 1271 (2000). © 2000, Royal Society of Chemistry.

$\text{Fe}_2\text{O}_3$  shows an unusual bandgap energy of  $>4.0$  eV as compared to 2.14 eV for the bulk oxide [104]. Similarly, highly dispersed monometal oxides such as  $\text{Fe}_2\text{O}_3$ ,  $\text{Fe}_3\text{O}_4$ ,  $\text{Co}_2\text{O}_3$ , and  $\text{Co}_3\text{O}_4$ , as well as bimetallic (or mixed-metal) oxides, for example,  $\text{CoFe}_2\text{O}_4$ , have also been synthesized within the mesopore channels of MCM-48 by multiple impregnation/drying/calcination cycles [24, 99]. In a similar way, uniform nanosized crystallites of  $\text{U}_3\text{O}_8$  have been dispersed in mesopores of MCM-41 and MCM-48 by direct exchange of the template cations with the uranyl ( $\text{UO}_2^{2+}$ ) ions, followed by calcination in air at 823 K [118]; see Figure 18. This method makes use of the unique interfacial properties of selectively functionalized mesoporous materials to deliver uranyl ions inside the channels via an ion-exchange reaction, thereby minimizing the uncontrolled precipitation reaction of uranyl ions outside the mesopores. The dispersed nanoparticles of  $\text{U}_3\text{O}_8$  are found to exhibit higher catalytic activity for the decomposition of methanol as compared to bulk  $\text{U}_3\text{O}_8$  or MCM-48 [107, 108]. Alternatively, the preparation of size-controllable  $\text{Fe}_3\text{O}_4$  nanoparticles has been reported by the alkaline oxidation of a ferrous ion adsorbed in sulfonated mesoporous styrene-divinylbenzene copolymer [135]. On the other hand, rhodium oxide ( $\text{RhO}_x$ ) nanoparticles, with different coordination spheres of Rh ions, in an MCM-41 host have been prepared by the hydrothermal

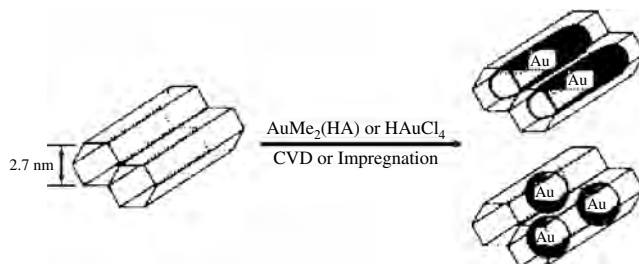


**Figure 15.** Template synthesis of gold nanowire and nanoparticle onto mesoporous FSM-16. Adapted with permission from [121], H. Araki et al., *J. Mol. Catal. A* 199, 95 (2003). © 2003, Elsevier Science.

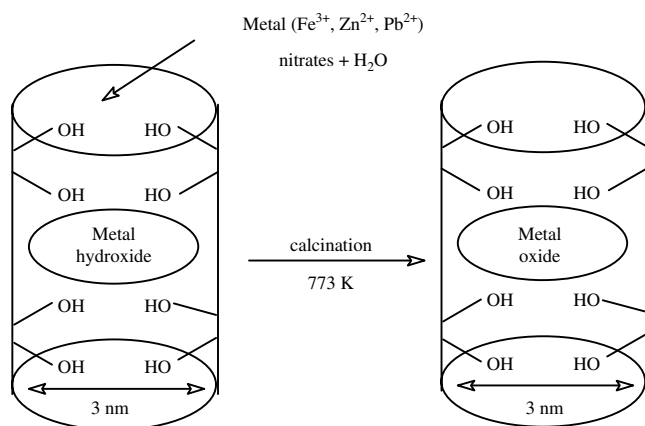


**Figure 16.** Schematic representation of the encapsulation of nanosized metal oxides inside the mesoporous channels of MCM-41 and MCM-48 silicates molecular sieves. Adapted with permission from [56], S. E. Dapurkar et al., *Catal. Today* 68, 63 (2001). © 2001, Elsevier Science.

synthesis of Rh–MCM-41, followed by calcination in air at 823 K [136].

### 6.2.1. Iron-Oxide Nanoparticles in MCM-41/MCM-48

Although many studies report the encapsulation of metal-oxide nanoparticles in mesoporous materials, the interpretation of experimental data, however, requires careful

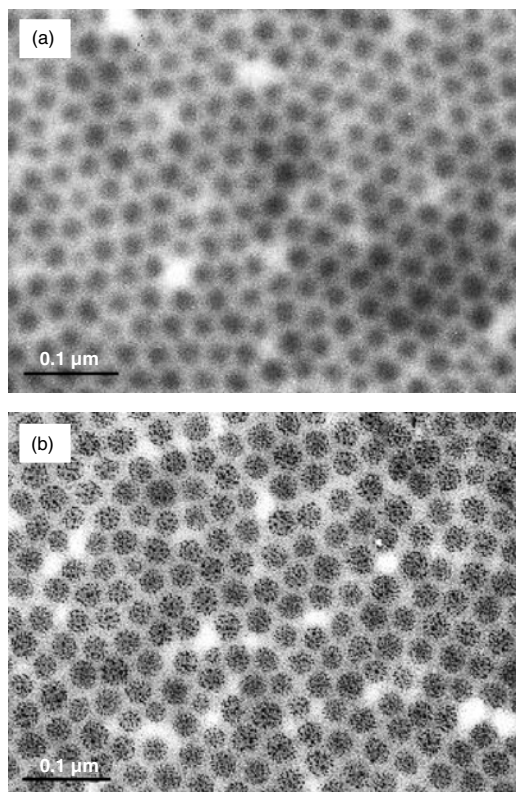


**Figure 17.** (a) TEM micrograph of block copolymer micelles containing an inorganic precursor. (b) TEM micrograph of block copolymer micelles containing inorganic nanoparticles.

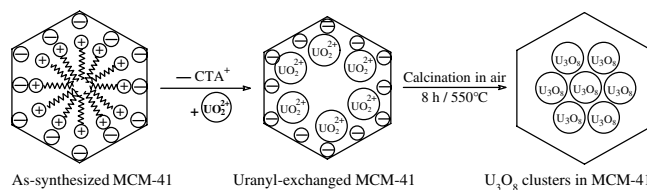


**Figure 18.** Schematic representation of direct ion-exchange process in MCM-41 and MCM-48.

analysis owing to the complication involved in the loading of these clusters into the host matrix. The host materials possess various kinds of sites, for the accommodation of guest atoms, molecules, and ions, viz. framework and extra framework, in addition to the pores (nonframework site). In fact, the guests can also react with both the framework and extra-framework sites, even at ambient condition, rather than simply occupying/residing the pores. For example, under the standard loading/impregnation conditions, metal ions such as  $\text{Al}^{3+}$  and  $\text{Fe}^{3+}$  substitute isomorphously in the silicate framework of MCM-41 and MCM-48, resulting in the formation of AIMCM-41 [137], AIMCM-48 [138], FeMCM-41 [101, 105, 139], and FeHMS [140]. Thus, the loading of  $\text{Fe}^{3+}$ , for example, in MCM-41 and MCM-48, not only results in the formation of  $\text{Fe}_2\text{O}_3$  (or  $\text{FeO}_x$ ) nanoclusters in the mesovoids, but also substitutes (isomorphously) in the silicate matrix [105, 141]. The resulting nonframework ( $\text{Fe}_2\text{O}_3$  nanoclusters) and framework trivalent iron (FeMCM-41/FeMCM-48) exhibit superparamagnetic and paramagnetic properties, respectively. In this regard, if the loaded nanoparticles reside exclusively inside the mesopores of MCM-41 and MCM-48, then no significant change is expected in the X-ray diffraction data. On the other hand, it is interesting to note that the  $d_{100}$ -spacing values of the  $\text{Fe}_2\text{O}_3$ -loaded MCM-41 ( $d_{100} = 38.71 \text{ \AA}$ ) are significantly higher as compared to the unloaded MCM-41 ( $d_{100} = 36.18 \text{ \AA}$ ); see also Figure 19. A similar observation

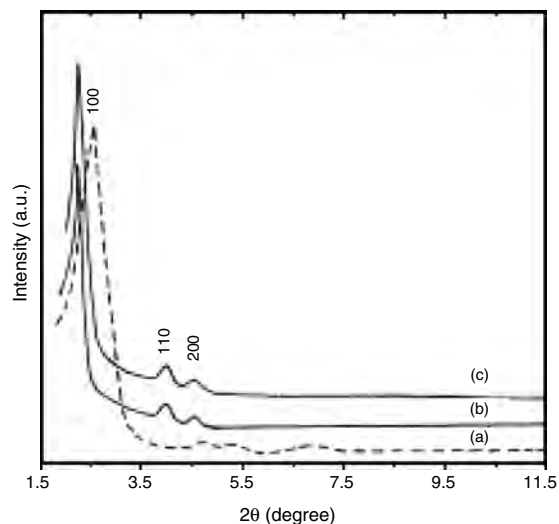


**Figure 19.** XRD patterns of: (a) calcined MCM-41, (b) FeO(OH)/MCM-41, (c)  $\text{Fe}_2\text{O}_3$ /MCM-41. Adapted with permission from [56], S. E. Dapurkar et al., *Catal. Today* 68, 63 (2001). © 2001, Elsevier Science.



was also noted for  $\text{Fe}_2\text{O}_3/\text{MCM-48}$  ( $d_{211} = 37.80 \text{ \AA}$ ) and  $\text{MCM-48}$  ( $d_{211} = 36.40 \text{ \AA}$ ) [140]. Such an expansion in the interplanar distances is in line with the isomorphous substitution of  $\text{Fe}^{3+}$  for the  $\text{Si}^{4+}$  in the silicate framework of MCM-41 [142, 143]. A comparable expansion in lattice parameter has also been observed for  $\text{Fe}^{2+}$ -exchanged MCM-41 [144]. In contrast, a decrease in  $d_{100}$  spacing was also reported for the  $\text{Fe}_2\text{O}_3$ -encapsulated MCM-41 [104].

Figure 20 depicts the DRUV-Vis spectra of various iron-containing MCM-41 and MCM-48, including bulk  $\text{Fe}_2\text{O}_3$  [105, 140]. As expected, the bulk  $\text{Fe}_2\text{O}_3$  [Fig. 20(f)] shows a broad band with a strong maximum at 560 nm arising from all possible  $d-d$  transitions. On the other hand, the loaded samples show absorption bands at 250 nm [Fig. 20(b)–(4e)]. The significant shift in the absorption bands is attributed to the encapsulation of  $\text{Fe}_2\text{O}_3$  nanoparticles inside the mesopores [97, 104, 145]. In fact, such a large (blue) shift in the absorption maxima of bulk or colloidal  $\text{Fe}_2\text{O}_3$  is associated with the transition in the particle size from bulk to the molecular order, viz. the quantum size effect [97, 104, 145–149]. At this juncture, it is interesting to note that no bulk  $\text{Fe}_2\text{O}_3$  particles exist on the outer surface (no absorption in the region 350–550 nm) of MCM-41 and MCM-48 unless the metal ion concentration exceeds 0.01M [Fig. 20(c) and (d)]. It is, however, interesting to note that the absorption band [Fig. 20(e)] for the isomorphously substituted metal ions in the mesoporous framework, for example,  $\text{FeMCM-41}$  [142, 143] and  $\text{FeMCM-48}$  [140], also appears nearly in the same region as that of the incorporated nanoparticles, viz.  $\text{Fe}_2\text{O}_3/\text{MCM-41}$ , and  $\text{Fe}_2\text{O}_3/\text{MCM-48}$ , thus complicating the spectral analysis. Figure 21 presents the EPR spectra of  $\text{Fe}_2\text{O}_3$ -loaded MCM-41 and MCM-48, as well as  $\text{FeMCM-48}$

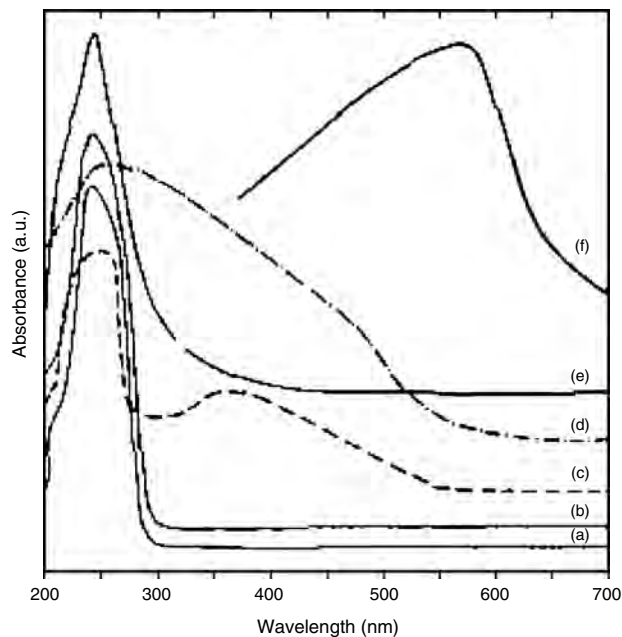


**Figure 20.** DRUV-Vis spectra of: (a)  $\text{Fe}_2\text{O}_3/\text{MCM-41}$ , (b)  $\text{Fe}_2\text{O}_3/\text{MCM-48}$ , (c)  $\text{Fe}_2\text{O}_3/\text{MCM-41}$  (0.01 M), (d)  $\text{Fe}_2\text{O}_3/\text{MCM-41}$  (0.1 M), (e)  $\text{FeMCM-48}$ , (f) bulk  $\text{Fe}_2\text{O}_3$ . Adapted with permission from [141], S. E. Dapurkar and P. Selvam, *Mater. Phys. Mech.* 4, 13 (2001). © 2001, Advanced Study Center Company Ltd.

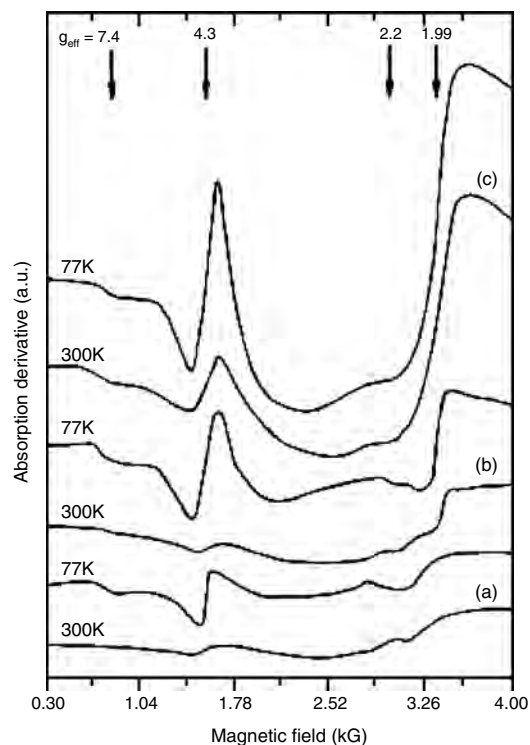


**Figure 21.** EPR spectra (300 and 77 K) of: (a)  $\text{Fe}_2\text{O}_3/\text{MCM-41}$ , (b)  $\text{Fe}_2\text{O}_3/\text{MCM-48}$ , (c)  $\text{FeMCM-48}$ . Adapted with permission from [141], S. E. Dapurkar and P. Selvam, *Mater. Phys. Mech.* 4, 13 (2001). © 2001, Advanced Study Center Company Ltd.

[105, 140]. As can be seen from this figure, four different signals appeared at various  $g_{\text{eff}}$  values: 7.4, 4.3, 2.2, and 1.99. On the basis of signal assignment, the transitions at 7.4, 4.3, and 1.99 are attributed to (paramagnetic)  $\text{Fe}^{3+}$  in distorted and symmetrical tetrahedral framework sites, while the weak signal at 2.2, which is prominent at 77 K, is assigned to nano-sized (superparamagnetic) clusters within the mesopores, which is in agreement with the literature [150].

Figure 22 shows the Mössbauer spectra of  $\text{Fe}_2\text{O}_3/\text{MCM-41}$  recorded at different temperatures [105]. The room-temperature (295 K) spectrum is composed of quadrupole doublets corresponding to (framework) paramagnetic and (nonframework) superparamagnetic species, which is indicative of high-spin (paramagnetic)  $\text{Fe}^{3+}$  in the tetrahedral framework. A similar observation has also been reported in certain microporous ferrisilicate [36, 151, 152] and  $\text{FeMCM-41}$  [101]; see Figure 23. However, upon cooling to 23 K ( $\text{Fe}_2\text{O}_3/\text{MCM-41}$ ) or 15 K ( $\text{FeMCM-41}$ ), a strong quadrupole doublet (due to high-spin  $\text{Fe}^{3+}$ ) along with a weak six-line pattern are also noticed. The latter is typical characteristic of superparamagnetic particles at low temperatures, which disappears as the temperature increases, ca. 77 K [153, 154]. Further, this observation is well supported by the temperature dependence of the susceptibility measurements for  $\text{FeMCM-41}$  [101]. Figure 24 shows the temperature dependence of the normal ( $\chi'$ ) and reciprocal ( $-1/\chi'$ ) susceptibilities of  $\text{FeMCM-41}$ . The low temperature (<150 K) part of the Curie-Weiss fit, a straight line passing through the origin, shows the paramagnetic

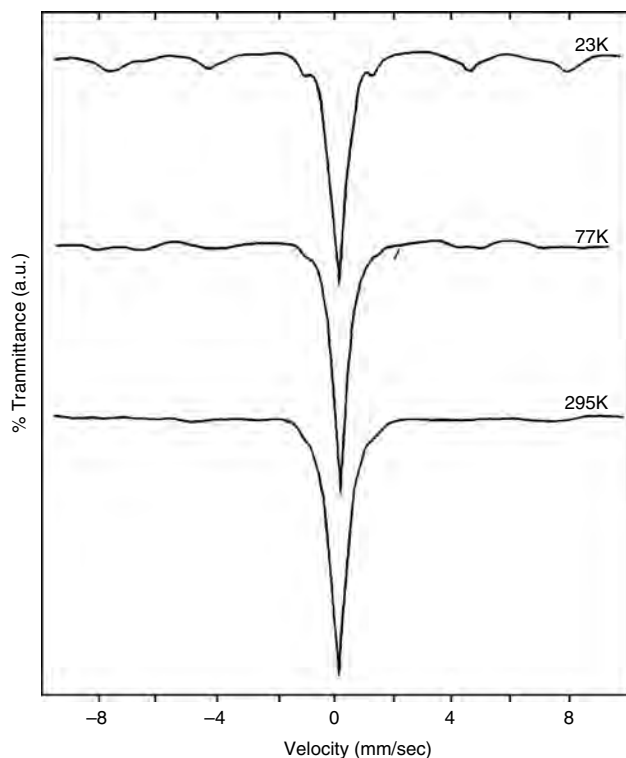


**Figure 22.** Mössbauer spectra of: (a)  $\text{Fe}_2\text{O}_3/\text{MCM-41}$ . Adapted with permission from [105], P. Selvam et al., *Catal. Today* 68, 69 (2001). © 2001, Elsevier Science.

behavior due to the isolated  $\text{Fe}^{3+}$  in the framework structure of MCM-41. On the other hand, the upward bending of the curve at higher temperatures ( $>150$  K) is attributed to the dependence of spontaneous magnetization on temperature. That is, the magnetic characteristics depart from the paramagnetic behavior due to the interaction between the constituent ions of the small clusters [155] that may be present in the system, viz. the superparamagnetic particles. Thus, the above findings clearly support the hypothesis of the coexistence of both paramagnetic and superparamagnetic species in the loaded samples which, however, cannot be distinguished by DRUV-Vis studies.

### 6.3. Metal Chalcogenide Nanoclusters and Nanofilaments

Metal sulfide nanoparticles, for example, CdS, have been synthesized within the mesopores of MCM-41 by the functionalization with 3-mercaptopropyltrimethoxysilane [156]. It was also noticed that the particle size decreases with an increasing number of thiol groups, while the increase of temperature resulted in an increase in the particle size. Alternatively, controlled synthesis of CdS nanoparticles inside MCM-41 has been described using an ion-exchange reaction, in a similar way as that described for the preparation of  $\text{U}_3\text{O}_8$  nanoparticles (see Fig. 18), followed by sulphidation with  $\text{H}_2\text{S}$  [157]. In order to have complete control of the nanoparticles inside the pore channels, the external surface is selectively functionalized with inert hydrophobic

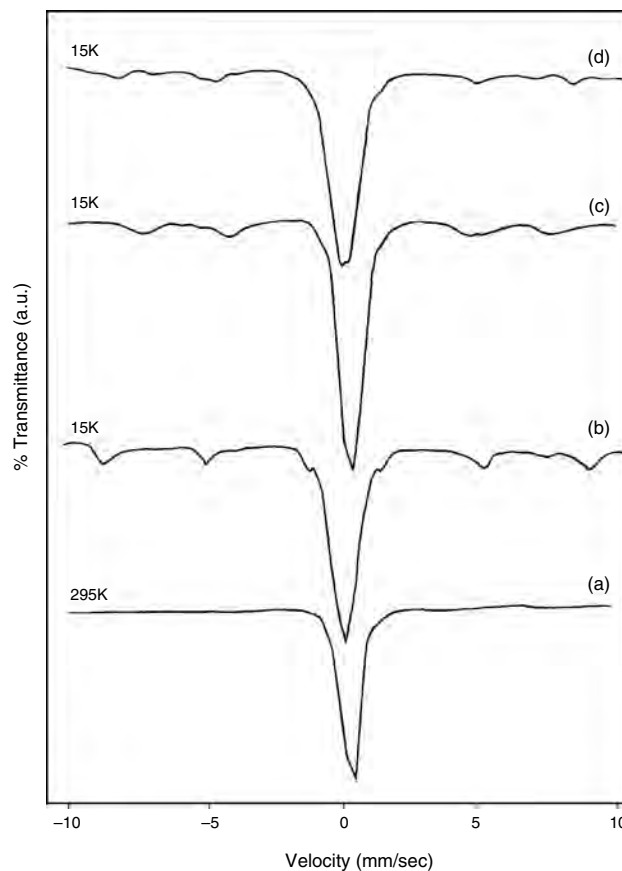


**Figure 23.** Mössbauer spectra of FeMCM-41(50): (a) 300 K and (b) 15 K, (c) FeMCM-41(100), (d) FeMCM-41(200). Adapted with permission from [101], P. Selvam et al., in "Recent Trends in Catalysis" (V. Murugesan, B. Arabindoo, and M. Palanichamy, Eds.), p. 556. 1999. © 1999, Narosa Publishing House, New Delhi.

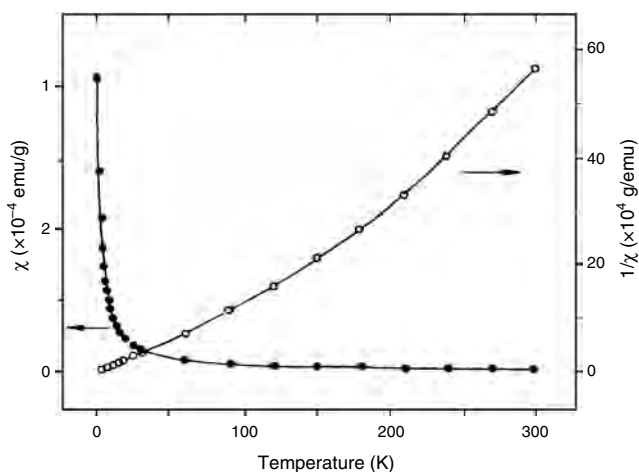


**Figure 24.** Temperature dependence of susceptibility of FeMCM-41. Adapted with permission from [101], P. Selvam et al., in "Recent Trends in Catalysis" (V. Murugesan, B. Arabindoo, and M. Palanichamy, Eds.), 1999. © 1999, Narosa Publishing House, New Delhi.

phenyl groups (Fig. 25), which eliminates the possibility of adsorption of hydrophilic metal ions on the external surfaces during the ion-exchange reaction, thereby directing charged hydrophilic species selectively into the mesopore channels. Crystalline CdS nanoarrays have also been prepared through a single precursor decomposition route at a low temperature, employing mesoporous SBA-15 as a template [158]. In this case, SBA-15 is first impregnated with an aqueous solution of cadmium thioglycolate, followed by drying and thermal treatment at 433 K, resulting in a CdS–SBA-15 composite. The template-free CdS, having a surface area as high as  $101 \text{ m}^2 \cdot \text{g}^{-1}$ , was then obtained by the dissolution of the silica matrix with NaOH. On the other hand, the nanoparticles/nanofilaments may also be isolated from the porous matrix by treating them with HF [28, 54]. On the contrary, the CdS nanoparticles formed in reverse micelles have also been incorporated into thiol-modified mesoporous materials [50, 112], where a particle-sieving effect was observed, that is, the amount of incorporated nanoparticles decreases with an increase of the particle size or a decrease of the pore size.

High-quality nanocrystalline CoP clusters have been obtained by grafting diphosphine-substituted molecular Co clusters ( $\text{Co}_4(\text{CO})_{10}(\mu\text{-dppa})$ ;  $\mu\text{-dppa} = (\text{Ph}_2\text{P})_2\text{NH}$ ) onto an alkoxy-silyl-substituted short-bite diphosphine,  $(\text{Ph}_2\text{P})_2 \cdot \text{N}(\text{CH}_2)_3\text{Si}(\text{OMe})_3$ , functionalized SBA-15, followed by thermal treatment under inert atmosphere [159]. At this juncture, it is quite fascinating to note that inorganic nanowires of certain metal sulfides can be produced inside a liquid-crystal template; see Figure 26 [160]. Accordingly, at first, an inverted Hexagonal liquid crystal from oligo (ethylene oxide) oleyl ether amphiphiles was produced, followed by the impregnation of  $\text{Zn}(\text{NO}_3)_2$  using  $\text{CS}_2$  or thiourea. The doped crystals were then irradiated with  $\gamma$  rays to produce ZnS *in-situ* through a radical process. The ZnS thus precipitated takes the shape of the tube-like pores in the liquid-crystal templates, resulting in  $\sim 5 \text{ nm}$  diameter nanofibers. More importantly, several close-packed nanowires tend to aggregate into bundles of 10–30 nm diameter, duplicating the hexagonal structure of the inverted micelles formed by amphiphiles.

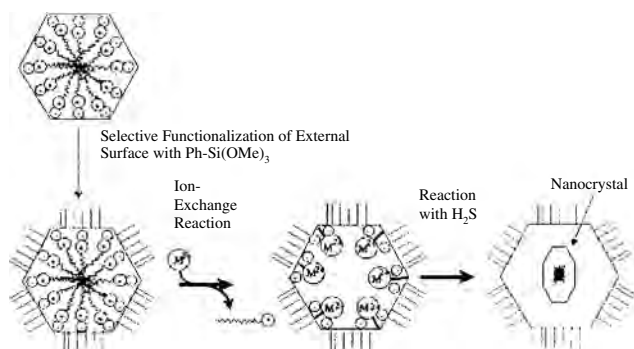


**Figure 25.** Schematic diagram of transportation of metal ions into a mesopore and space-confined growth of metal sulfide nanocrystals. Adapted with permission from [157], Z. Zhang et al., *J. Phys. Chem. B* 105, 6755 (2001). © 2001, American Chemical Society.

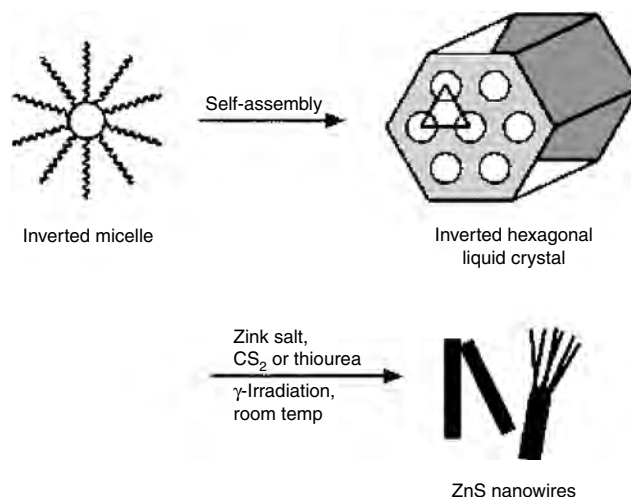


**Figure 26.** Schematic representation of the encapsulation of ZnS nanowires inside a liquid-crystal template. Adapted with permission from [160], X. Jiang et al., *Chem. Mater.* 13, 1213 (2001), © 2001, American Chemical Society.

#### 6.4. Nanometal-Supported Nanometal-Oxide Clusters

The ship-in-bottle synthesis strategy described earlier (see Fig. 8) has also been adopted successfully for the preparation of novel Pt-supported titania ( $\text{TiO}_2$ ) or zirconia ( $\text{ZrO}_2$ ) in the mesoporous channels of FSM-16 molecular sieves by the modification of the pores with  $\text{TiO}_2$  or  $\text{ZrO}_2$  by impregnation and hydrolysis of the respective alkoxides followed by thermal decomposition [119, 161]. Accordingly, Pt carbonyl clusters of the type  $[\text{Pt}_3(\text{CO})_6]_n^{2-}$  ( $n = 4\text{--}6$ ) were deposited on the preadsorbed  $\text{TiO}_2$  or  $\text{ZrO}_2$  in the mesoporous matrix by the reaction of  $\text{H}_2\text{PtCl}_6$  with CO and  $\text{H}_2\text{O}$  at 323 K (Fig. 27). In a similar way, the preparation of Pt-supported  $\text{Fe}_2\text{O}_3$  nanoclusters has also been demonstrated by the photodeposition technique [104]. In other words, the presence of iron-oxide nanoparticles in the pores of MCM-41 has also been confirmed by platinum loading on iron-oxide particles [97, 104].

#### 6.5. Metal Complexes, Metalloenzymes, and Molecular Materials

The modification of the mesoporous silica surface with covalently bonded organic species, especially functional organosilanes [159, 162, 163], has attracted much attention in order to design hybrid materials for advanced applications, for example, in catalysis, selective adsorption of organics and metals, and so on. Functionalization of MCM-41 has been achieved by silanation (Fig. 28) of the surface using 3-amino and 3-halogeno-propyl alkoxy-silane. The grafted halogeno organic moieties [Fig. 28(a)] have been further modified by halogen substitution of other functions such as primary, secondary, and tertiary amines, diamines ammonium hydroxide, and guanidines [Fig. 28(b)]. It was found that the mesoporous silica-bound primary and tertiary amine functions [Fig. 28(c)] have been effective catalysts for Knoevenagel condensation and selective monoglyceride synthesis.

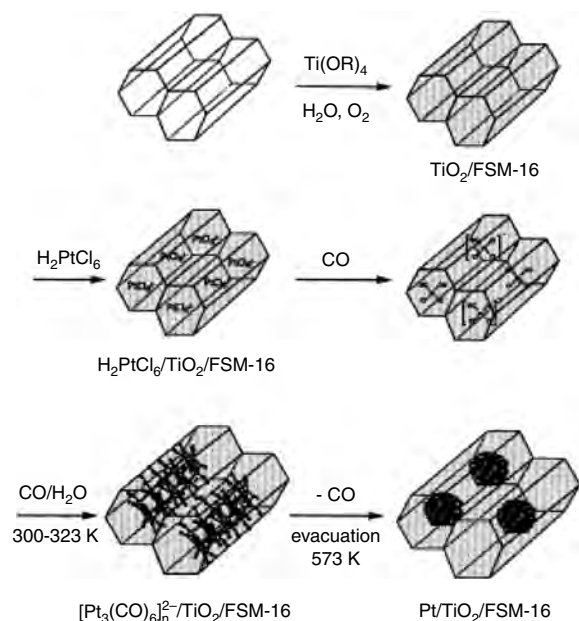


**Figure 27.** Schematic representation of the preparation and transformation of the Pt/TiO<sub>2</sub> cluster in FSM-16. Adapted with permission from [104], M. Iwamoto et al., *J. Mol. Catal. A* 155, 143 (2000). © 2000, Elsevier Science.

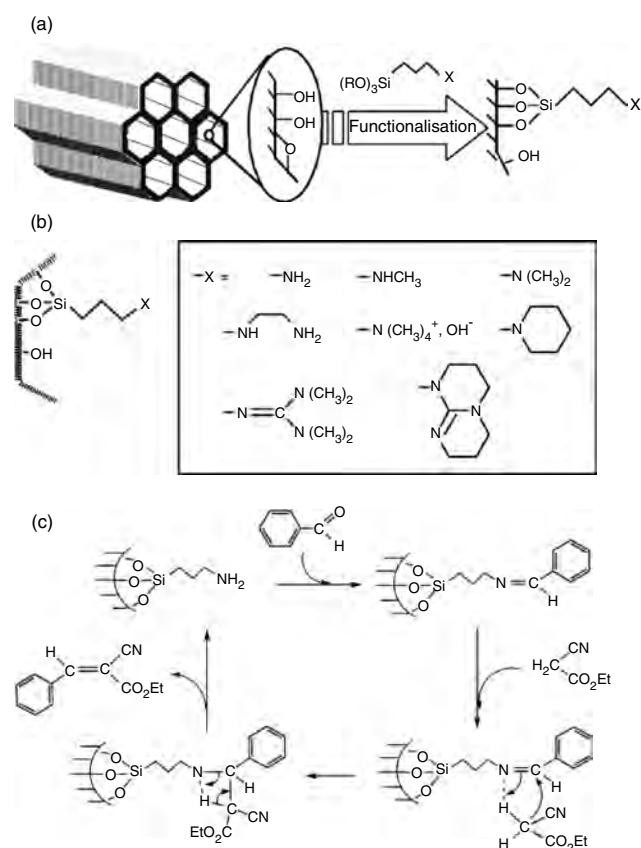


**Figure 28.** (a) Functionalization of MCM-41 surface. (b) Organic bases anchored on the functionalized surface. (c) Catalytic cycle during Knoevenagel condensation using MCM-41-grafted primary amine form. Adapted with permission from [163], D. Brunel et al., *Catal. Today* 73, 139 (2002). © 2002, Elsevier Science.

On the other hand, ship-in-bottle synthesis methodology has also been adopted for the grafting of larger complexes into mesopore channels of FSM-16 and MCM-41, for example, hybrid composites of metalloporphyrins and fullerenes [164], fullerenes (C<sub>60</sub> and C<sub>70</sub>; Fig. 29) [165, 166], trinuclear oxomolybdenum complex [Mo<sub>3</sub>O(CCH<sub>3</sub>)(OAc)<sub>6</sub>(MeOH)<sub>3</sub>] [167], polynuclear molybdenum complexes [168], ruthenium complexes having bipyridine and chloride ligands [169], Cu (II) phthalocyanine [170], and so on. For example, the Cu (II) phthalocyanine was formed within the mesopores of previously ion-exchanged Cu-MCM-41 by CVD of 1,2-dicyanobenzene; see Figure 30. Unlike the Cu phthalocyanine complex entrapped in zeolite-Y, the complex encapsulated in the MCM-41 showed (Fig. 2) nearly the same magnetic moment value [80], which is similar to the free or neat complex, suggesting that the planar geometry of the complex is retained in the mesopores. On the other hand, Pt cluster anions such as [Pt<sub>3</sub>(CO)<sub>6</sub>]<sub>5</sub><sup>2-</sup> and [Pt<sub>3</sub>(CO)<sub>6</sub>]<sub>6</sub><sup>2-</sup> have been respectively prepared in the mesoporous channels of FSM-16 via [Pt(CO)Cl<sub>3</sub>]<sup>-</sup> and *cis*-Pt(CO)<sub>2</sub>Cl<sub>2</sub> by the reductive carbonylation of H<sub>2</sub>PtCl<sub>6</sub>·6H<sub>2</sub>O at 323 K [76, 171]. They exhibit markedly higher catalytic activities for <sup>13</sup>CO exchange and water-gas shift reactions at ambient temperatures as compared with [Pt<sub>3</sub>(CO)<sub>6</sub>]<sub>5</sub><sup>2-</sup> and [Pt<sub>3</sub>(CO)<sub>6</sub>]<sub>4</sub><sup>2-</sup> clusters encapsulated in zeolite-Y.

Since the immobilization of enzymes in a confined environment improves the stability, enzymes such as horseradish peroxidase (HRP) and subtilisin have been immobilized in FSM-16 and MCM-41 (Fig. 31), prepared with a cationic surfactant, whose pore sizes were just over the molecular diameters (~43 Å) of the enzymes [172, 173]. It is also interesting to note here that the immobilized HRP on FSM-16 and MCM-41 with a pore diameter of 50 Å showed the highest enzymatic activity [Fig. 31(b)]. The immobilized enzymes on the other mesoporous materials including large [90 Å; Fig. 31(c)] or small [30 Å; Fig. 31(a)] pore-sized FSM-16 showed lower enzymatic activity and thermal stability. Thus, both surface character and size matching between pore sizes and the molecular diameters of HRP

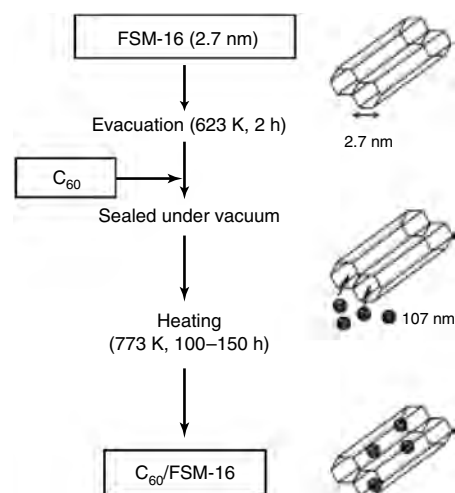


**Figure 29.** Preparation of fullerene-grafted mesoporous FSM-16. Adapted with permission from [165], A. Fukuoka et al., *Catal. Lett.* 68, 241 (2000). © 2000, Plenum Publishing Corporation.

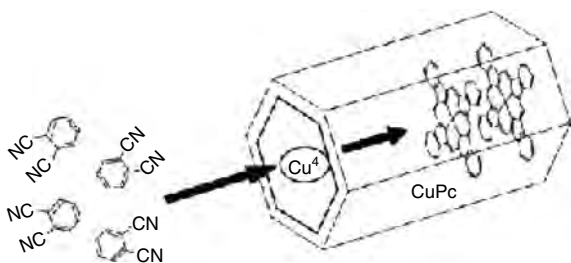
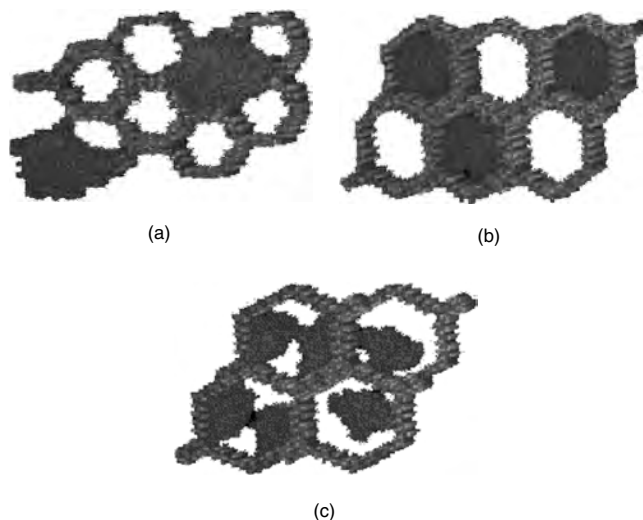


**Figure 30.** Ship-in-bottle synthesis of Cu (II) phthalocyanine complex in MCM-41.

were important in achieving high enzymatic activity and high thermal stability. However, no appreciable adsorption of the enzymes was noted for SBA-15 prepared with a nonionic surfactant [172, 173].

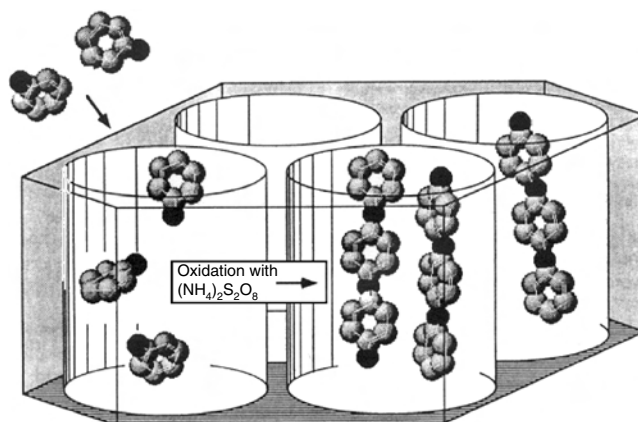
### 6.6. Conducting Polymeric Filaments

In the recent past, nanometer electronic materials have been created by the chemical/electrochemical polymerization of monomers inside the porous structures. The molecular wires thus produced inside the pore system are several hundred molecules long, and show significant conductivity while encapsulated. They possess a blend of interesting electronic, optical, and mechanical properties [174], which makes it possible to use them in situations where inorganic materials are unsuitable. Furthermore, the conducting polymer films have attracted wide attention due to their unique properties, such as easy synthesis by chemical methods, reversible and adjustable conductivity, and so on. In addition, enhanced electronic conductivities are obtained if polymers with enhanced molecular and supramolecular order, that is, a polymer containing fewer conjugation-interrupting defect sites, can be prepared. In this regard, template synthesis of such materials provides a route for enhancing the order, and therefore the conductivity [175].

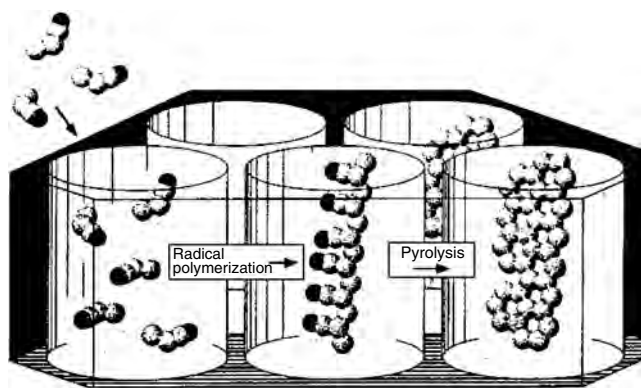


**Figure 31.** Schematic models of immobilized HRP in FSM-16 with various pore sizes: (a) 30 Å, (b) 50 Å, and (c) 90 Å. Adapted with permission from [173], H. Takahashi et al., *Micropor. Mesopor. Mater.* 44–45, 755 (2001). © 2001, Elsevier Science.

Conducting polymeric materials can also be grown electrochemically within the host material [176, 177] or chemically with oxidizing agents [178]. Previous studies [45, 175, 179] have shown the formation of intrazeolite polyaniline by chemical oxidation. However, these filaments do not show any significant conductivity [45, 178]. This may be due to the small pore dimension of the zeolites used for the preparation, which may possibly restrict the oxidant/counter ion to enter inside the pore, and may result in an incomplete polymerization/oxidation. On the other hand, conducting polyaniline filaments (Fig. 32) have been produced inside the mesopore channels of AlMCM-41 by chemical oxidation [44]. Accordingly, the adsorption of aniline into the dehydrated host, followed by reaction with peroxydisulfate ( $(\text{NH}_4)_2\text{S}_2\text{O}_8$ ), leads to encapsulated polyaniline filaments, which show significant conductivity. Likewise, the entrapment of graphite-type carbon wires in mesoporous MCM-41 (Fig. 33) has also been demonstrated [45]. First, acrylonitrile monomers are introduced through vapor or solution transfer in the channels, and are subsequently polymerized with radical initiators such as  $\text{K}_2\text{S}_2\text{O}_8$  or  $\text{NaHSO}_3$ . Pyrolysis of the resulting polyacrylonitrile produces filaments whose microwave conductivity is higher by an order of magnitude than that of bulk carbonized polyacrylonitrile. Likewise, 3-methacryloxypropyl species grafted onto the surface of mesoporous materials act as seeds for the polymerization of these monomers, leading to the formation of polymethacrylate fibres [180]. On the other hand, radical polymerization of methyl methacrylate in the presence of initiators such as 2,2'-azobisisobutyronitrile or benzoyl peroxide has been carried out within the channels of a MCM-41 [181]. Linear nanofibers of polyethylene with ultrahigh molecular weight (6,200,000) and a diameter of 30–50 nm have been produced through an “extrusion polymerization” mechanism, as illustrated in Figure 34 [182], in which a new class of mesoporous silica fibers is used as a support for ethylene polymerization with titanocene in conjunction with methylalumoxane (MAO) as a cocatalyst. Similarly, polymerization of cyclohexyl vinyl ether within MCM-41 channels yields hybrid materials [183].

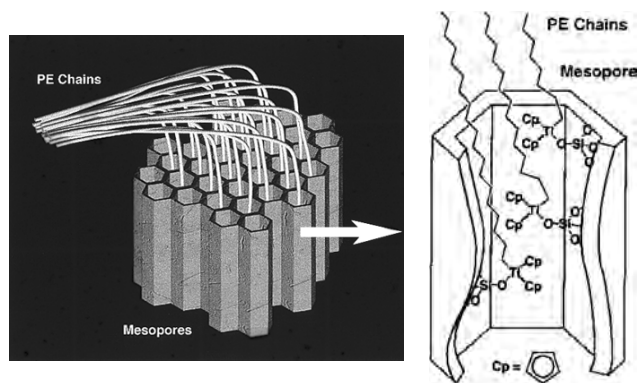


**Figure 32.** Schematic representation of the growth of polyaniline filaments in the channels of mesoporous AlMCM-41. Adapted with permission from [44], C.-G. Wu and T. Bein, *Science* 264, 1757 (1994). © 1994, American Association for the Advancement of Science.

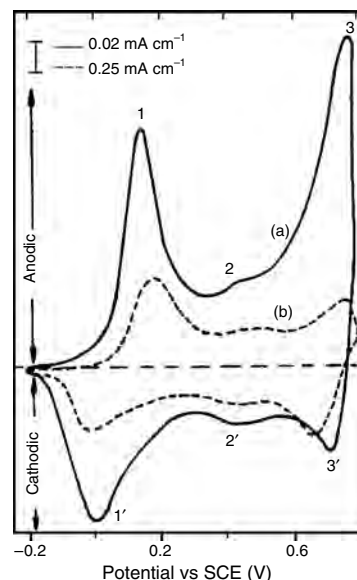


**Figure 33.** Schematic representation of the growth of carbon wires in the channels of mesoporous MCM-41. Adapted with permission from [45], C.-G. Wu and T. Bein, *Science* 266, 1013 (1994). © 1994, American Association for the Advancement of Science.

On the other hand, electrochemical polymerization of aniline to polyaniline was carried out inside the mesoporous channels of an MCM-41 molecular sieve host [102]. The distinct color (peacock blue) change at higher potentials, not seen in the case of conventional electrochemically polymerized films, could be an indication of intrazeolite polymerization. *In-situ* UV-Vis and resistance/conductance studies confirm the formation of intrazeolite polyaniline chains. The electrochemical behavior of polyaniline films was examined by cyclic voltammetry in aqueous 0.5 M  $\text{H}_2\text{SO}_4$ . Interesting changes in the redox behavior of polyaniline have been observed on using different forms of siliceous MCM-41 (condition A: time taken for bridging = 45 min;  $R_{\text{max}}/R_{\text{min}} = 126$ ) and AlMCM-41 (condition B: time taken for bridging = 45 min;  $R_{\text{max}}/R_{\text{min}} = 1585$ ). The cyclic voltammograms (Figs. 35 and 36) give three rapid and reversible redox systems, which are typical of polyaniline. They are referred to as (1,1'), (2,2'), and (3,3') systems. The second one (2,2') becomes more prominent after the oxidation of aniline at higher potential. It has generally been attributed to a quinone-hydroquinone type of redox process. The peaks (1,1') are associated with a



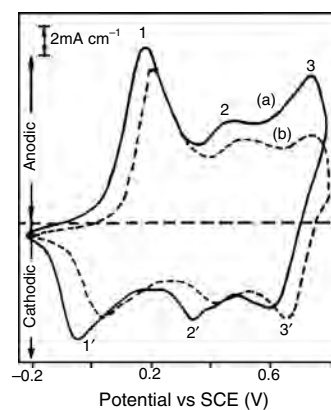
**Figure 34.** Schematic representation of the growth of polyethylene filaments in the channels of mesoporous silica fibers. Adapted with permission from [182], K. Kageyama, J. I. Tamazawa, and T. Aida, *Science* 285, 2113 (1999). © 1999, American Association for the Advancement of Science.



**Figure 35.** CV of MCM-41/PANI on Pt twin wire electrode. (a) Monomer solution. (b) 0.5 M  $\text{H}_2\text{SO}_4$ . The polymer was grown under condition A. Adapted with permission from [102], P. Selvam et al., in “Recent Trends in Catalysis” (V. Murugesan, B. Arabindoo, and M. Palanichamy, Eds.), p. 550. 1999. © 1999, Narosa Publishing House, New Delhi.

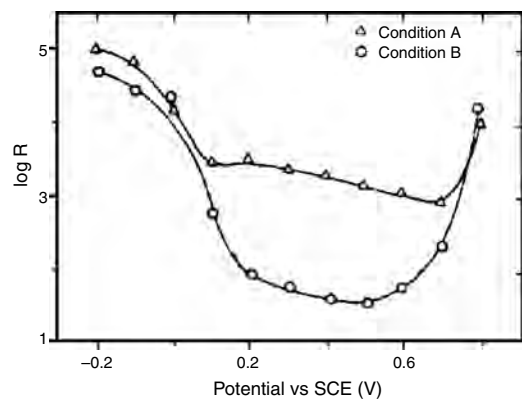
deprotonation-protonation reaction, and are strongly pH dependent, with  $\partial E_p/\partial \text{pH} \cong 59 \text{ mV}$ .

Figure 37 depicts the measured resistance of polyaniline films. In all of the cases, the polymer is highly resistive at  $-0.2 \text{ V}$ , and the anodic polarization results in a decrease of the resistance. The minimum in the resistance is observed between 0.1 and 0.7 V, with a sharp increase in resistance on further anodic polarization. The results of *in-situ* UV-Vis studies are presented in Figure 38. The absorbance at 320 and 420 nm is shown as a function of potential for polyaniline grown on an ATO glass [184], ITO + MCM-41, and ITO + AlMCM-41 [102]. Again, one can see that the



**Figure 36.** CV of AlMCM-41/PANI on Pt twin wire electrode. (a) Monomer solution. (b) 0.5 M  $\text{H}_2\text{SO}_4$ . The polymer was grown under condition B. Adapted with permission from [102], P. Selvam et al., in “Recent Trends in Catalysis” (V. Murugesan, B. Arabindoo, and M. Palanichamy, Eds.), p. 550. 1999. © 1999, Narosa Publishing House, New Delhi.





**Figure 37.** Change in resistance with potential for polyaniline grown under different conditions. Adapted with permission from [102], P. Selvam et al., in "Recent Trends in Catalysis" (V. Murugesan, B. Arabindoo, and M. Palanichamy Eds.), p. 550. 1999. © 1999, Narosa Publishing House, New Delhi.

behavior of the polymer films is distinctly different. There is a small change in the shape of these two bands for each sample. These two bands have generally been found to be complementary. The change in shape and the differences in potential dependence must be attributed to the different environments in which the polymer is grown and studied. This supports our visual observation of the intrazeolite polymerized samples as compared to samples polymerized on an open surface. These are the first definitive results relating the conductivity to the electrochemical potential

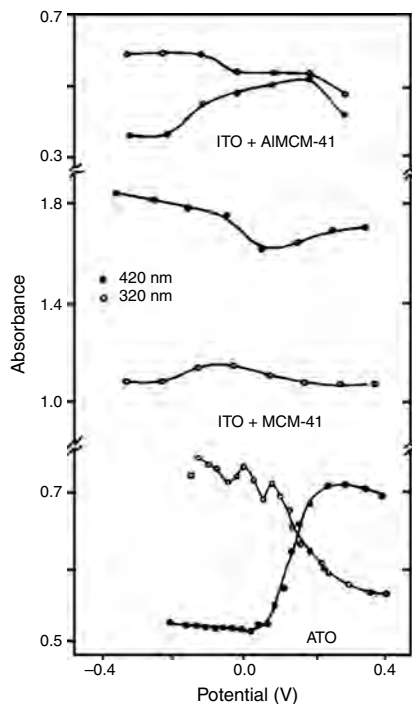


**Figure 38.** Absorbance versus potential for polyaniline grown on different substrates. Adapted with permission from [102], P. Selvam et al., in "Recent Trends in Catalysis" (V. Murugesan, B. Arabindoo, and M. Palanichamy, Eds.), p. 550. 1999. © 1999, Narosa Publishing House, New Delhi.

for intrazeolite polymerized polyaniline. It was found that the UV-Vis data also show a shift from interfacial polymerization data. The conductivity of template-synthesized polyaniline changes with the change in the extent of acidic sites in the host. Therefore, the fabrication of these types of stabilized conducting systems will be important for the understanding of charge transport at the nanometer scale, and for the development of nanosized electronic devices. Similar experiments have been performed with acetonitrile, *p*-nitroniline, and pyrrole; however, it is difficult to control the properties of the composite material.

## 7. NANOPARTICLES/NANOWIRES IN MESOPOROUS FILMS

Up to now enormous amount of studies have concerned the growth of nanoparticles inside the pores of bulk (powder) materials. However, for several optical applications, it would be better to dispose of coatings filled with nanoparticle arrays instead of powders. The direct growth of semiconductor nanostructures, for example, has the distinct advantage of no process-induced damage or defects, as frequently observed in the nanofabricated wires and dots. Several groups have reported the synthesis of nanoparticle-loaded mesoporous films using different methodologies [128, 185–189]. A new route [185] describes the preparation of high-density nanometer-scale SiGe quantum dots on ordered mesoporous silica-coated Si substrate. On the other hand, Si nanoclusters were grown on mesoporous film by CVD [128] during the formation of Ag nanoparticles within a mesoporous template-structured silica film, which includes ion exchange with  $\text{Ag}(\text{NH}_3)_2^+$  followed by reduction [186]. Likewise, the synthesis of CdS quantum dots inside 3D hexagonal mesoporous silica films has been reported by a chemical route employing wet impregnation of Cd ions, followed by precipitation using  $\text{H}_2\text{S}$ . These two steps were also repeated until the film saturation was obtained [187]. Uniform nanoparticles of Au and Pt with ordered structures were deposited on mesoporous silica films, and the unsupported Au nanoparticle, isolated by the dissolution of silica film in dilute HF and 1-dodecanethiol solution [188]. Recently, novel mesostructured titania in the form of monolith and film samples have shown to function as nanovessels for trapping metal complexes of the type  $\text{Ag}^+$ ,  $\text{AuCl}_4^-$ , and  $\text{PtCl}_6^{2-}$  which, upon thermal treatment, transformed to the respective metal clusters [189].

## ACKNOWLEDGMENTS

The author thanks all of the co-workers listed in the References for the significant contribution toward the progress and understanding of nanomaterials in a confined environment.

## REFERENCES

1. J. A. Creighton and D. G. Eadon, *J. Chem. Soc., Faraday Trans.* 87, 3881 (1991).
2. Y. W. Cao, R. Jin, and C. A. Mirkin, *J. Am. Chem. Soc.* 123, 7961 (2001).

3. A. P. Alivisatos, *J. Phys. Chem.* 100, 13226 (1996).
4. A. Henglein, *J. Phys. Chem.* 97, 5457 (1993); *Ber. Bunsen-Ges. Phys. Chem.* 99, 903 (1995); *Langmuir*, 14, 6738 (1998).
5. Y. Wang and N. Herron, *Science* 273, 632 (1996).
6. For a recent review, see: P. V. Kamat, *J. Phys. Chem.* 106, 7729 (2002).
7. J. L. Dorman and D. Fiorani, "Magnetic Properties of Fine Particles." North-Holland, Amsterdam, 1992.
8. D. D. Awschalom and D. P. DiVincenzo, *Phys. Today* 4, 43 (1995).
9. X. X. Zhang, J. Tejata, J. M. Hernandez, and R. F. Ziolo, *Nanostruct. Mater.* 9, 301 (1997).
10. Q. Chen and Z. J. Zhang, *Appl. Phys. Lett.* 73, 3156 (1998).
11. X. Zhang, S. A. Jenekhe, and H. Perlstein, *J. Chem. Mater.* 8, 1571 (1996).
12. C. P. Bean and T. D. Livingston, *J. Appl. Phys.* 30, 120 (1959).
13. J. Hu, T. W. Odom, and C. M. Lieber, *Acc. Chem. Res.* 32, 435 (1999).
14. C. Dekker, *Phys. Today* 52, 22 (1999).
15. R. Rossetti, R. Hall, J. M. Gibson, and L. E. Brus, *J. Chem. Phys.* 83, 1406 (1985).
16. A. I. Ekimov, Al. L. Efros, and A. A. Onushchenko, *Solid State Commun.* 56, 921 (1985).
17. E. Dalas, J. Kallitsis, S. Sakkopoulos, E. Vitoratos, and P. G. Koutsoukos, *J. Colloid Interface Sci.* 141, 137 (1991).
18. M. R. Böhmer, L. G. J. Fokkink, C. Schönenberger, and B. M. I. van der Zande, *J. Phys. Chem. B* 101, 852 (1997).
19. S. R. Nicewarner-Pena, R. G. Freeman, B. D. Reiss, L. He, D. J. Pena, I. D. Walton, R. Cromer, C. D. Keating, and M. J. Natan, *Science* 294, 137 (2001).
20. F. Kim, J. H. Song, and P. Yang, *J. Am. Chem. Soc.* 124, 14316 (2002).
21. C. J. Murphy and N. R. Jana, *Adv. Mater.* 14, 80 (2002).
22. Y. G. Sun and Y. N. Xia, *Adv. Mater.* 14, 833 (2002).
23. Y. Y. Yu, S. S. Chang, C. L. Lee, and C. R. C. Wang, *J. Phys. Chem. B* 101, 6661 (1997).
24. S. S. Chang, C. W. Shih, C. D. Chen, W. C. Lai, and C. R. C. Wang, *Langmuir* 15, 701 (1999).
25. M. Wark, G. Schulz-Ekloff, and N. I. Jaeger, *Catal. Today* 8, 467 (1991).
26. G. Telbiz, A. Shwets, V. Gunko, J. Stoch, G. Tamulajtis, and N. Kukhtarev, *Stud. Surf. Sci. Catal.* 84, 1099 (1994).
27. Y. Wang and N. Herron, *J. Phys. Chem.* 91, 257 (1987).
28. N. Herron, Y. Wang, M. E. Eddy, G. D. Stucky, D. E. Cox, K. Moller, and T. Bein, *J. Am. Chem. Soc.* 111, 530 (1989).
29. G. A. Ozin and C. Gil, *Chem. Rev.* 89, 1749 (1989).
30. C. R. Martin, *Acc. Chem. Res.* 3, 457 (1991).
31. P. Behrens and G. D. Stucky, *Angew. Chem., Int. Ed. Engl.* 32, 696 (1992).
32. Y. Nozue, "Optical Properties of Low-Dimensional Materials" (T. Ogawa and K. Kanemitsu, Eds.), p. 387. World Scientific, Singapore, 1995.
33. J. H. Fendler, *Chem. Mater.* 8, 1616 (1996).
34. J. L. Garcia, A. Loper, F. T. Lazaro, C. Martinez, and A. Corma, *J. Magn. Magn. Mater.* 157/158, 272 (1996).
35. X. Zhang, S. A. Jenekhe, and J. Perlstein, *Chem. Mater.* 8, 1571 (1996).
36. A. Loper, F. J. Lazaro, J. L. Garcia-Palacios, A. Larrea, Q. A. Pankhurst, C. Martiner, and A. Corma, *J. Mater. Res.* 12, 1519 (1997).
37. D. W. Breck, "Zeolite Molecular Sieve." Wiley, New York, 1974.
38. A. Dyer, "An Introduction to Zeolite Molecular Sieves." Wiley, New York, 1988.
39. R. Szostak, "Molecular Sieves: Principles of Synthesis and Identification." van Nostrand Reinhold, New York, 1989.
40. G. O. Ozin, A. Kuperman, and A. Stein, *Angew. Chem., Int. Ed.* 101, 373 (1989).
41. M. E. Davis, *Ind. Eng. Chem. Res.* 30, 1675 (1991).
42. H. Weitkamp and L. Puppe, Eds., "Catalysis and Zeolites: Fundamentals and Applications." Springer-Verlag, Berlin, 1999.
43. K. S. W. Sing, D. H. Everett, R. H. W. Hall, L. Moscou, R. A. Pierotti, J. Rouquerol, and T. Siemieniowska, *J. Pure Appl. Chem.* 57, 603 (1985).
44. C.-G. Wu and T. Bein, *Science* 264, 1757 (1994).
45. C.-G. Wu and T. Bein, *Science* 266, 1013 (1994).
46. W. Cai, M. Tan, G. Wang, and L. Zhang, *Appl. Phys. Lett.* 69, 2980 (1996).
47. C. Weiping and Z. Lide, *J. Phys.: Cond. Matter* 9, 7257 (1997).
48. K. Moller and T. Bein, *Chem. Mater.* 10, 2950 (1998).
49. J. He, Y. Ba, C. I. Ratcliffe, J. A. Ripmeester, D. D. Klug, J. S. Tse, and K. F. Preston, *J. Am. Chem. Soc.* 120, 10697 (1998).
50. T. Hirai, H. Okubo, and I. Komasa, *J. Phys. Chem. B* 103, 4228 (1999).
51. H. Zhou, W. Cai, and L. Zhang, *Mater. Res. Bull.* 34, 845 (1999).
52. M. H. Huang, A. Choudrey, and P. Yang, *Chem. Commun.* 1063 (2000).
53. F. Schweyer, P. Braunstein, C. Estournès, J. Guille, H. Kessler, J.-L. Paillaud, and J. Rosé, *Chem. Commun.* 1271 (2000).
54. Z. Liu, Y. Sakamoto, T. Ohsuna, K. Hiraga, O. Terasaki, C. H. Ko, H. J. Shin, and R. Ryoo, *Angew. Chem., Int. Ed. Engl.* 39, 3107 (2000).
55. A. Fukuoka, H. Araki, Y. Sakamoto, S. Guan, S. Inagaki, N. Sugimoto, Y. Fukushima, K. Hirahara, S. Iijima, and M. Ichikawa, *J. Am. Chem. Soc.* 123, 3373 (2001).
56. S. E. Dapurkar, S. K. Badamali, and P. Selvam, *Catal. Today* 68, 63 (2001).
57. P. Judeinstein and H. Schmidt, *J. Sol-Gel Sci. Technol.* 3, 189 (1994).
58. K. Kundu and D. Chakravorty, *Appl. Phys. Lett.* 66, 3576 (1995).
59. X. S. Zhao, G. Q. Lu, and G. J. Millar, *Ind. Eng. Chem. Res.* 35, 2075 (1996).
60. A. Sayari, *Chem. Mater.* 8, 1840 (1996).
61. A. Corma, *Chem. Rev.* 95, 559 (1995); *Chem. Rev.* 97, 2373 (1997).
62. J. V. Smith, *Chem. Rev.* 88, 149 (1988).
63. J. Y. Ying, C. P. Mehnert, and M. S. Wong, *Angew. Chem., Int. Ed.* 38, 56 (1999).
64. P. Selvam, S. K. Bhatia, and C. Sonwane, *Ind. Eng. Chem. Res.* 40, 3237 (2001).
65. D. T. On, D. Desplandier-Giscard, C. Danumah, and S. Kaliaguine, *Appl. Catal. A* 222, 299 (2001).
66. J. M. Thomas, C. R. A. Catlow, and G. Sankar, *Chem. Commun.* 2921 (2002).
67. N. Herron, G. D. Stucky, and C. A. Tolman, *J. Chem. Soc., Chem. Commun.* 1521 (1986).
68. F. Bedioui, E. De Boysson, J. Devynch, and K. J. Balkus, Jr., *J. Chem. Soc., Faraday Trans.* 87, 3831 (1991).
69. E. Paez-Mozo, N. Gabriunas, R. Maggi, D. Acosta, R. Ruiz, and Delmon, *J. Mol. Catal.* 91, 251 (1994).
70. B. M. Weckhuysen, A. A. Verberckmoes, I. P. Vannijvel, J. A. Pelgrims, P. L. Buskens, P. A. Jacobs, and R. A. Schoonheydt, *Angew. Chem., Int. Ed. Engl.* 34, 2652 (1995).
71. M. Ledney and P. K. Dutta, *J. Am. Chem. Soc.* 117, 7687 (1995).
72. R. F. Parton, I. F. J. Vankelecom, D. Tas, K. B. M. Janssen, P.-P. Knops-Gerrits, and P. A. Jacobs, *J. Mol. Catal. A* 113, 283 (1996).
73. M. Ichikawa, W. Pan, Y. Imada, M. Yamaguchi, T. Shido, and K. Isobe, *J. Mol. Catal. A* 107, 23 (1996).
74. G. Schulz-Ekloff and S. Ernst, in "Handbook of Heterogeneous Catalysis" (G. Ertl and H. Knözinger, Eds.), p. 374 VCH, Weinheim, 1997.
75. R. Raja and R. Ratnasamy, *Appl. Catal. A* 158, L7 (1997); *J. Catal.* 170, 244 (1997); *Catal. Lett.* 48, 1 (1997).
76. M. Sasaki, M. Osada, N. Higashimoto, T. Yamamoto, A. Fukuoka, and M. Ichikawa, *J. Mol. Catal. A* 141, 223 (1999).
77. S. Seelan, A. K. Sinha, D. Srinivas, and S. Sivasanker, *J. Mol. Catal. A* 157, 163 (2000).

78. R. Grommen, P. Manikandan, Y. Gao, T. Shane, J. J. Shane, R. A. Schoonheydt, B. M. Weckhuysen, and D. Goldfarb, *J. Am. Chem. Soc.* 122, 11488 (2000).
79. A. Fukuoka, N. Higashimoto, Y. Sakamoto, M. Sasaki, N. Sugimoto, S. Inagaki, Y. Fukushima, and M. Ichikawa, *Catal. Today* 66, 21 (2001).
80. S. Ray and S. Vasudevan, *Inorg. Chem.* 42, 1711 (2003).
81. R. W. Joyner and M. Stockenhuber, *Catal. Lett.* 45, 15 (1997).
82. J. L. Meinershagen and T. Bein, *J. Am. Chem. Soc.* 121, 448 (1999).
83. C. T. Kresge, M. E. Leonowicz, W. T. Roth, J. C. Vartuli, and J. S. Beck, *Nature* 359, 710 (1992).
84. J. S. Beck, J. C. Vartuli, W. J. Roth, M. E. Leonowicz, C. T. Kresge, K. D. Schmitt, C. T. W. Chu, D. H. Olson, E. W. Sheppard, S. B. McCullen, J. B. Higgins, and J. L. Schelinker, *J. Am. Chem. Soc.* 114, 10834 (1992).
85. S. Inagaki, Y. Fukushima, and K. Kuroda, *J. Chem. Soc., Chem. Commun.* 680 (1993).
86. S. Inagaki, A. Koiwai, N. Suzuki, Y. Fukushima, and K. Kuroda, *Bull. Chem. Soc. Jpn.* 69, 1449 (1996).
87. P. T. Tanev, M. Chibwe, and T. J. Pinnavaia, *Nature* 368, 321 (1994).
88. P. T. Tanev and T. J. Pinnavaia, *Science* 167, 865 (1995).
89. D. Zhao, J. Feng, Q. Huo, N. Melosh, G. H. Fredrickson, B. F. Chmelka, and G. D. Stucky, *Science* 279, 548 (1998).
90. D. Zhao, Q. Huo, J. Feng, B. F. Chmelka, and G. D. Stucky, *J. Am. Chem. Soc.* 120, 6024 (1998).
91. T. Kimura, Y. Sugahara, and K. Kuroda, *Chem. Lett.* 983 (1997); *Chem. Commun.* 559 (1998); *Micropor. Mesopor. Mater.* 22, 115 (1998); *Chem. Mater.* 11, 508 (1999).
92. Q. Huo, D. I. Margolese, U. Ciesla, D. G. Demuth, P. Feng, T. E. Gier, P. Sieger, A. Firouzi, B. F. Chmelka, F. Schüth, and G. D. Stucky, *Chem. Mater.* 6, 1176 (1994).
93. Q. Huo, D. I. Margolese, U. Ciesla, P. Feng, T. E. Gier, P. Sieger, R. Leon, P. M. Petroff, F. Schüth, and G. D. Stucky, *Nature* 368, 317 (1994).
94. D. M. Antonelli and J. Y. Ying, *Chem. Mater.* 8, 874 (1996); *Angew. Chem., Int. Ed. Engl.* 35, 426 (1996).
95. D. Khushalani, G. A. Ozin, and A. Kuperman, *J. Mater. Chem.* 9, 1491 (1999).
96. S. Inagaki, S. Guan, Y. Fukushima, T. Ohsuna, and O. Terasaki, *J. Am. Chem. Soc.* 121, 9611 (1999).
97. T. Abe, Y. Tachibana, T. Uemastu, and M. Iwamoto, *J. Chem. Soc., Chem. Commun.* 1617 (1995).
98. E. S. Brighan, C. S. Weibecker, W. E. Rudzinski, and T. E. Malouk, *Chem. Mater.* 8, 467, 2121 (1996).
99. M. Fröba, R. Köhn, and G. Bouffaud, *Chem. Mater.* 11, 2858 (1999).
100. S. K. Badamali, R. Vinodhkumar, U. Sundararajan, and P. Selvam, in "Recent Trends in Catalysis" (V. Murugesan, B. Arabindoo, and M. Palanichamy, Eds.), p. 545. Narosa, New Delhi, 1999.
101. P. Selvam, S. K. Badamali, M. Murugasen, and H. Kuwano, in "Recent Trends in Catalysis" (V. Murugesan, B. Arabindoo, and M. Palanichamy, Eds.), p. 556. Narosa, New Delhi, 1999.
102. P. Selvam, D. Singh, R. Tyagi, S. K. Badamali, V. Raghini, and A. Q. Contractor, in "Recent Trends in Catalysis" (V. Murugesan, B. Arabindoo, and M. Palanichamy, Eds.), p. 550. Narosa, New Delhi, 1999.
103. J. Wu, A. F. Gross, and S. H. Tolbert, *J. Phys. Chem. B* 103, 2374 (1999).
104. M. Iwamoto, T. Abe, and Y. Tachibana, *J. Mol. Catal. A* 155, 143 (2000).
105. P. Selvam, S. E. Dapurkar, S. K. Badamali, M. Murugasen, and H. Kuwano, *Catal. Today* 68, 69 (2001).
106. R. Leon, D. Margolese, G. Stucky, and P. M. Petroff, *Phys. Rev. B* 52, R2285 (1995).
107. K. Vidya, S. E. Dapurkar, P. Selvam, S. K. Badamali, D. Kumar, and N. M. Gupta, *J. Mol. Catal. A* 181, 91 (2002); *J. Mol. Catal. A* 191, 149 (2003).
108. D. Kumar, V. Krishna, P. Selvam, G. K. Dey, and N. M. Gupta, in "Advances in Nanoscience and Nanotechnology." NISCOM (CSIR), 2003.
109. J. F. Diaz and K. J. Balkus, Jr., *J. Mol. Catal. B* 2, 115 (1996).
110. Z. R. Tian, W. Tong, J. Y. Wang, N. G. Duan, V. V. Krishnan, and S. Suib, *Science* 276, 926 (1997).
111. M. Linden, S. Schacht, F. Schüth, A. Steel, and K. K. Unger, *J. Porous Mater.* 5, 177 (1998).
112. Y. Xu and C. H. Langford, *J. Phys. Chem. B* 101, 3115 (1997).
113. M. E. Gimón-Kinsel, V. L. Jimenez, L. Washmon, and K. J. Balkus, *Stud. Surf. Sci. Catal.* 117, 373 (1998).
114. M. Eswaramoorthy, S. Neeraj, and C. N. R. Rao, *Chem. Commun.* 615 (1998).
115. N. Suzuki, H. Asami, T. Nakamura, T. Huhn, A. Fukuoka, M. Ichikawa, M. Saburi, and Y. Wakatsuki, *Chem. Lett.* 341 (1999).
116. T. Hirai, H. Okubo, and I. Komasa, *J. Colloid Interface Sci.* 235, 358 (2001).
117. R. Ganesan and B. Viswanathan, *J. Mol. Catal. A* 181, 99 (2002).
118. K. Vidya, S. E. Dapurkar, P. Selvam, S. K. Badamali, and N. M. Gupta, *Micropor. Mesopor. Mater.* 50, 173 (2001).
119. M. Sasaki, M. Osada, N. Sugimoto, S. Inagaki, Y. Fukushima, A. Fukuoka, and M. Ichikawa, *Micropor. Mesopor. Mater.* 21, 597 (1998).
120. A. Fukuoka, N. Higashimoto, Y. Sakamoto, S. Inagaki, Y. Fukushima, and M. Ichikawa, *Micropor. Mesopor. Mater.* 48, 171 (2001).
121. H. Araki, A. Fukuoka, Y. Sakamoto, S. Inagaki, N. Sugimoto, Y. Fukushima, and M. Ichikawa, *J. Mol. Catal. A* 199, 95 (2003).
122. H. Shi, L. Zhang, and W. Cai, *Mater. Res. Bull.* 35, 1689 (2000).
123. Y.-J. Han, J. M. Kim, and G. D. Stucky, *Chem. Mater.* 12, 2068 (2000).
124. H. J. Shin, R. Ryoo, Z. Liu, and O. Terasaki, *J. Am. Chem. Soc.* 123, 1246 (2001).
125. J. Michalik, D. Brown, J.-S. Yu, M. Danilczuk, J. Y. Kim, and L. Kevan, *Phys. Chem. Chem. Phys.* 3, 1705 (2001).
126. J.-S. Jung, W.-S. Chae, R. A. McIntyre, C. T. Seip, J. B. Wiley, and C. J. O'Connor, *Mater. Res. Bull.* 34, 1353 (1999).
127. N. R. B. Coleman, M. A. Morris, T. R. Spalding, and J. D. Holmes, *J. Am. Chem. Soc.* 123, 187 (2001).
128. Ö. Dag, G. A. Ozin, H. Yang, C. Reber, and G. Bussiere, *Adv. Mater.* 11, 474 (1999).
129. H. Wakayama, N. Setoyama, and Y. Fukushima, *Adv. Mater.* 15, 742 (2003).
130. T. Maschmeyer, F. Rey, G. Sankar, and J. M. Thomas, *Nature* 378, 159 (1995).
131. B. J. Aronson, C. F. Blanford, and A. Stein, *Chem. Mater.* 9, 2842 (1997).
132. S. G. Zhang, Y. Fujii, H. Yamashita, K. Koyano, T. Tatsumi, and M. Anpo, *Chem. Lett.* 659 (1997).
133. Y. Xu and C. H. Langford, *J. Phys. Chem. B* 101, 3115 (1997).
134. W.-H. Zhang, J.-L. Shi, L.-Z. Wang, and D.-S. Yan, *Chem. Mater.* 12, 1408 (2000).
135. D. Rabelo, E. C. D. Lima, A. C. Reis, W. C. Nunes, M. A. Novak, V. K. Garg, A. C. Oliverira, and P. C. Morais, *Nano Lett.* 1, 105 (2001).
136. R. S. Mulukutla, K. Asakura, S. Namba, and Y. Iwasawa, *Chem. Commun.* 1425 (1998).
137. H. Hamdan, S. Endud, H. He, M. N. N. Muhid, and J. Klinowski, *J. Chem. Soc., Faraday Trans.* 92, 2311 (2003).
138. K. Schumacher, M. Grun, and K. K. Unger, *Micropor. Mesopor. Mater.* 27, 201 (1999).
139. N. Y. He, J. M. Cao, S. L. Bao, and Q. H. Xu, *Mater. Lett.* 31, 133 (1997).
140. A. Tuel, I. Arcon, and J. M. M. Millet, *J. Chem. Soc., Faraday Trans.* 94, 3501 (1998).
141. S. E. Dapurkar and P. Selvam, *Mater. Phys. Mech.* 4, 13 (2001).

142. S. K. Badamali and P. Selvam, *Stud. Surf. Sci. Catal.* 113, 749 (1998).
143. S. K. Badamali, A. Sakthivel, and P. Selvam, *Catal. Lett.* 65, 153 (2000).
144. A. B. Bourlinos, M. A. Karakassides, and D. Petridis, *J. Phys. Chem.* 104, 4375 (2000).
145. J. Kiwi and M. Gratzel, *J. Chem. Soc., Faraday Trans.* 83, 1101 (1987).
146. L. Brus, *J. Phys. Chem.* 90, 2555 (1986).
147. A. P. Alivisatos, *Science* 271, 933 (1996).
148. J. Z. Zhang, *Acc. Chem. Res.* 30, 423 (1997).
149. H. Miyoshi and H. Yoneyama, *J. Chem. Soc., Faraday Trans.* 85, 1873 (1989).
150. E. G. Derouane, M. Mestdagh, and L. Vielvoye, *J. Catal.* 33, 169 (1974).
151. D. H. Lin, G. Coudurier, and J. C. Viedrine, *Stud. Surf. Sci. Catal.* 49, 1431 (1989).
152. S. Schubert, H. M. Zithen, A. X. Trautwein, F. Schmidt, H.-X. Li, J. A. Martens, and P. A. Jacobs, *Stud. Surf. Sci. Catal.* 46, 735 (1989).
153. W. Kündig, H. Bommel, G. Constabaris, and R. H. Lindquist, *Phys. Rev.* 142, 327 (1966).
154. A. Vértes, K. Lazar, K. Kelemen, and Bogucér, *Radiochem. Radioanal. Lett.* 4, 375 (1970).
155. I. S. Smart, in "Magnetism" (G. T. Rado and H. Suhl, Eds.), Vol. III. Academic, 1963.
156. H. Wellmann, J. Rathousky, M. Wark, A. Zukal, and G. Schulz-Ekloff, *Micropor. Mesopor. Mater.* 44–45, 419 (2001).
157. Z. Zhang, S. Dai, X. Fan, D. A. Blom, S. J. Pennycook, and Y. Wei, *J. Phys. Chem. B* 105, 6755 (2001).
158. F. Gao, Q. Lu, and D. Zhao, *Adv. Mater.* 15, 739 (2003).
159. F. Schweyer-Tihay, P. Braunstein, C. Estournès, J. Guille, B. Lebeau, J.-L. Paillaud, M. Richard-Plouet, and J. Rosé, *Chem. Mater.* 15, 57 (2003).
160. X. Jiang, Y. Xie, J. Lu, L. Zhu, W. He, and Y. Qian, *Chem. Mater.* 13, 1213 (2001).
161. A. Fukuoka, M. Osada, T. Shido, S. Inagaki, Y. Fukushima, and M. Ichikawa, *Inorg. Chim. Acta* 294, 281 (1999).
162. D. Brunel, *Micropor. Mesopor. Mater.* 27, 329 (1999).
163. D. Brunel, A. C. Blanc, A. Galarneau, and F. Fajula, *Catal. Today* 73, 139 (2002).
164. J. Tachibana, M. Chiba, M. Ichikawa, T. Imamura, and Y. Sasaki, *Supramol. Sci.* 5, 281 (1998).
165. A. Fukuoka, K. Fujishima, M. Chiba, J. Tachibana, and M. Ichikawa, *Catal. Lett.* 68, 241 (2000).
166. F. Rachdi, *Solid State Commun.* 100, 237 (1996).
167. K. Zama, A. Fukuoka, Y. Sasaki, S. Inagaki, Y. Fukushima, and M. Ichikawa, *Catal. Lett.* 66, 251 (2000).
168. K. Zama, Y. Imada, A. Fukuoka, and M. Ichikawa, *Appl. Catal. A* 194–195, 285 (2000).
169. K. Fujishima, A. Fukuoka, A. Yamagishi, S. Inagaki, Y. Fukushima, and M. Ichikawa, *J. Mol. Catal. A* 166, 211 (2001).
170. Y. Tanamura, T. Uchida, N. Teramae, M. Kikuchi, K. Kusaba, and Y. Onodera, *Nano Lett.* 1, 387 (2001).
171. T. Yamamoto, T. Shido, S. Inagaki, Y. Fukushima, and M. Ichikawa, *J. Am. Chem. Soc.* 118, 5810 (1996).
172. H. Takahashi, B. Li, T. Sasaki, C. Miyazaki, T. Kajino, and S. Inagaki, *Chem. Mater.* 12, 3301 (2000).
173. H. Takahashi, B. Li, T. Sasaki, C. Miyazaki, T. Kajino, and S. Inagaki, *Micropor. Mesopor. Mater.* 44–45, 755 (2001).
174. M. J. Bowden and S. R. Turner, Eds., "Advances in Chemistry Series," Vol. 218, p. 26. 1988.
175. C. R. Martin, *Acc. Chem. Res.* 3, 457 (1991).
176. R. M. Penner and C. R. Martin, *J. Electrochem. Soc.* 133, 2206 (1986).
177. S. Sukeerthi and A. Q. Contractor, 10, 2412 (1998); *Anal. Chem.* 71, 2231 (1999).
178. R. Parthasarathy and C. R. Martin, *Nature* 369, 298 (1994).
179. P. Zuppiroli, F. Beuneu, J. P. Mory, P. Enzel, and T. Bein, *Syn. Met.* 55–57, 15081 (1993).
180. K. Moller, T. Bein, and R. X. Fischer, *Chem. Mater.* 11, 665 (1999).
181. S. M. Ng, S.-I. Ogino, T. Aida, K. A. Koyano, and T. Tatsumi, *Macromol. Rapid Commun.* 18, 991 (1997).
182. K. Kageyama, J. I. Tamazawa, and T. Aida, *Science* 285, 2113 (1999).
183. S. Spange, A. Graeser, P. Rehak, C. Jager, and M. Schulz, *Macromol. Rapid Commun.* 21, 146 (2000).
184. M. Gholamian, T. N. Sureshkumar, and A. Q. Contractor, *Proc. Indian Acad. Chem. Sci.* 97, 457 (1986).
185. Y. S. Tang, S. J. Cai, G. L. Jin, K. L. Wang, H. M. Soyey, and B. S. Dunn, *Thin Solid Films* 321, 76 (1998).
186. Y. Plyuto, J.-M. Berquier, C. Jacquiod, and C. Ricolleau, *Chem. Commun.* 1653 (1999).
187. S. Besson, T. Gacoin, C. Ricolleau, C. Jacquiod, and J.-P. Boilot, *Nano Lett.* 2, 409 (2002).
188. A. Fukuoka, H. Araki, Y. Sakamoto, N. Sugimoto, H. Tsukada, Y. Kumai, Y. Amimoto, and M. Ichikawa, *Nano Lett.* 2, 793 (2002).
189. Ö. Dag, I. Soten, Ö. Celik, S. Polarz, N. Coombs, and G. A. Ozin, *Adv. Funct. Mater.* 13, 30 (2003).



# Nanocomposites of Polymers and Inorganic Particles

Walter Caseri

ETH Zentrum, Zürich, Switzerland

## CONTENTS

1. Introduction
  2. Early Investigations
  3. Preparation of Nanocomposites
  4. Properties of Nanocomposites
- Glossary  
References

## 1. INTRODUCTION

This chapter deals with composites comprised of polymers and inorganic nanoparticles of rather uniform shape. Such composites are attributed to the class of nanocomposites because of the small size of the embedded particles, while the polymer phase is continuous. The attribution of particles to the class of nanoparticles is somewhat arbitrary; often particles of dimensions up to 50–100 nm are assigned to this notion, and expressions such as nanosized particles, colloids, or, occasionally, ultrafine particles are also used to designate particles as nanoparticles. The small size of the incorporated particles can induce materials properties which differ from those of related composites containing larger particles, for example, as a result of an extremely large interface area, which can readily amount to  $10^7$ – $10^9$  m<sup>2</sup> in a cube meter of nanocomposite, or a markedly reduced scattering of visible light. The latter is important if transparent or translucent materials are required for optical applications. This intensity loss of transmitted light by scattering can be estimated with the equation [1]

$$\frac{I}{I_0} = e^{-\left[\frac{3\phi_p x r^3}{4\lambda^4} \left(\frac{n_p}{n_m} - 1\right)\right]}$$

which is valid for spheric particles with radius  $r$  and refractive index  $n_p$  dispersed in a matrix with refractive index  $n_m$ , with  $I$  the intensity of the transmitted and  $I_0$  of the incident light,  $\phi_p$  the volume fraction of the particles,  $\lambda$  the wavelength of the incident light, and  $x$  the optical path length. From the above equation, it is evident that composites with

thicknesses in the millimeter range can be virtually transparent if the particle diameter is below ca. 50 nm even for high volume contents of inorganic particles or large refractive index differences between polymer and particles, provided the particles are randomly dispersed in the polymer matrix. If, however, the particles are present as agglomerates, light scattering is significantly enhanced even if the size of the primary particles is far below the wavelength of the incident light. Note that composites of polymers and inorganic particles typically contain particles or particle aggregates with dimensions in the  $\mu\text{m}$  range [2, 3]; that is, they are opaque unless the refractive indices of the components are equal [4].

Many physical properties of metals and semiconductors are determined by correlated interactions of many atoms [5, 6]. The energy levels of the basic units split upon formation of clusters and particles into more and more components with increasing number of atoms until they attain the quasi-continuous band structure of the bulk solid [6]. As a consequence, optical and electronic characteristics of nanoparticles can differ from those of the bulk materials and in addition depend on the particle size [7–19]. The particle diameter at which optical changes become significant depends on the substance and amounts to ca. 2 nm for CdSe, 2.8 nm for GaAs, 20 nm for PbS, and 46 nm for PbSe [20]. The bandgap energy and the absorption threshold of CdS begins to differ significantly from the bulk values at particle diameters around 10 nm [21]. Ultraviolet/visible (UV/vis) absorption spectra of nanoparticles can depend on the size of the nanoparticles and differ markedly from those of larger particles or the bulk solids. The UV/vis absorption spectrum of CdS particles of ca. 4 nm diameter with a narrow size distribution showed a well pronounced maximum at 368 nm and no essential absorption above 420 nm [22] while the spectrum of bulk CdS was characterized by a continuous decrease in absorbance in the wavelength range of 300–550 nm [23]. CdSe particles of 3.9 nm diameter exhibited an absorption edge of 558 nm and a bandgap of 2.22 eV compared to more than 700 nm and 1.74 eV, respectively, for bulk CdSe [24]. As a consequence of the variations of the spectra in the visible range on the particle size, the color of related nanocomposites can depend on the particle size.



For example, poly(vinyl alcohol) containing gold particles [25–27] of average size 9.5, 43, and 79 nm displayed in transmission the red, purple, and blue color of the corresponding nanoparticles [28, 29].

Finally, it should be noted that the sizes of the inorganic particles in nanocomposites always vary to some extent although “monodisperse” particles are occasionally mentioned in the literature. However, these particles usually show some polydispersity when the size distribution is carefully analyzed, and accordingly the expression “particles with narrow size distribution” better represents the status. The particle sizes in the literature as well as in this chapter typically refer to number average particle diameters  $d_n$

$$d_n = \frac{\sum_i n_i d_i}{\sum_i n_i}$$

with  $n_i$  the number of particles of diameter  $d_i$ . Since physical properties (e.g., the refractive index of nanocomposites) are related rather with the volume fraction of the particles, the volume-weighted average diameter  $d_v$  may also be of interest, where

$$d_v = \sqrt[3]{\frac{\sum_i n_i d_i^3}{\sum_i n_i}}$$

The number-weighted and the volume-weighted average diameters of the particles differ often by 20–30%, which is, fortunately, usually of little importance for the conclusions from the respective experiments.

## 2. EARLY INVESTIGATIONS

### 2.1. Colloids

Gold belongs to the substances which have been the focus of numerous studies from the beginning of chemistry. In the course of the experiments with this metal in ancient times, gold nanoparticles have obviously been prepared centuries ago. For example, such particles were synthesized *in-situ* in water by Paracelsus around 1570 [30, 31]. He used the resulting gold-containing liquid, called *aurum potabile* (potable gold), for medical purposes. The *aurum potabile* could also be gained as a viscous substance [31], probably due to the presence of organic compounds which adsorbed at the surface of the gold particles. Other matter described centuries ago most likely also contained nanoparticles of gold [32] or silver (*luna potabile*) [33]. In particular, glass was colored with metal nanoparticles for at least the middle of the 16th century (so-called gold ruby glasses) [34]. In a recipe from Neri published in 1662, a transparent ruby glass was prepared starting from bulk gold which was treated several times with *aqua regia* [35]. The resulting gold salts were calcined for many days until a red powder arose which was mixed slowly with glass. Purple, violet, brown, or almost black colloidal gold powders were manufactured in 1765 as paints for enamel [36]. These materials were fabricated by dissolution of gold in *aqua regia*, and the nanoparticles were subsequently precipitated as powders by reduction of the *in-situ* prepared gold(III) ions with tin.

Since the color of gold nanoparticles differs from that of bulk gold, as indicated in the Introduction, there was some confusion about the nature of the nanoparticles for a long time, although, for instance, Macquer believed already in 1774 that the *aurum potabile* indeed contained extremely small gold particles [37]. Nobel prize winner Ostwald, a pioneer in colloid chemistry, attributed the first experimental evidence for the elemental nature of gold colloids to Richter [38]. Richter described among many other experiments that fine gold powders with a golden appearance could be transformed into violet powders and vice versa by mechanical treatments [39]. Further, the chemical behavior of violet gold powders agreed with typical characteristics of bulk gold: the powders did not dissolve in hydrochloric acid but in *aqua regia*, and the powders formed an amalgam with mercury. In addition, bulk gold could be converted by certain chemical treatments into violet powder without a significant difference in mass. Richter also perceived that the color of some gold powders depended on the observation angle, and he suggested that the color of very small gold particles was determined by refraction of light. Further evidence for the elemental nature of gold nanoparticles was found around 1860 by Fischer [40] and Faraday [41, 42]. Faraday suggested that the color of colloidal gold in its elemental state depends on the particle size. Based on the observation that it was possible to prepare blue from red gold dispersions but not reverse and that blue particles precipitated much faster than red ones, Faraday assumed that the blue particles were larger in size than the red ones [41, 42]. The purification of colloids from reaction side products by dialysis was described by Graham in 1862 [43]. For instance, silver [44] or red aqueous gold dispersions [45] did not penetrate dialysis membranes, even under application of an electric field, which clearly indicated that colloids indeed consisted of particles. Besides gold and silver, colloids of other substances were also synthesized 100–150 years ago. For example, reduction of  $\text{PtCl}_4$  with hydrazine in aqueous solution yielded colloidal platinum [44], colloidal  $\text{SiO}_2$  was obtained by hydrolysis of tetramethoxysilane [46], colloidal aluminum oxides by hydrolysis of aluminum chloride [43], colloidal iron oxides by hydrolysis of iron chloride [43], and colloidal  $\text{TiO}_2$  by treatment of a gellike titanate with a small amount of hydrochloric acid followed by dialysis [47].

Already before electron microscopes were available, the dimensions of nanoparticles were determined with ultramicroscopes [48, 49] which had been invented by Siedentopf and Zsigmondy in 1903 [48]. These instruments allowed the visualization of colloids by light scattering which enabled the detection of particles in dilute systems below the resolution limit of optical microscopes. The particle size was finally estimated as the edge length of a cube with volume  $V = A/(\rho \cdot n)$ , where  $A$  denotes the total mass of the particles in a volume unit,  $\rho$  denotes the density of the particles, and  $n$  denotes the number of particles in a volume unit, whereby the number of particles was counted with the help of the ultramicroscope [49]. In the first report on an ultramicroscope [48], various glass-gold nanocomposites were investigated, and average gold particle diameters were found down to the resolution limit which amounts to ca. 6 nm for gold [50] and which depends not only on the particle size but also

on the optical constants of particles and matrix [49]. Generally, the resolution limit of metal particles is particularly low [49], while typical values for metal oxides and organic colloids lie in the range of 30–40 nm [50]. Diameters of gold particles obtained with ultramicroscopy were confirmed by Scherrer in 1918 from analysis of the linewidth in X-ray diffraction patterns [51]. Scherrer also showed then for the first time that the gold lattice in colloidal and bulk gold is identical [51].

In 1904, Kirchner and Zsigmondy suggested that the color of metal particles can depend not only on the size of the primary particles but also on the distance between the particles [52, 53]. Their conclusion is based on the observation that nanocomposites of colloidal silver or gold and gelatin reversibly changed color from blue to red upon swelling with water or acetic acid, and in addition they found a bathochromic shift of the absorption maximum in the UV/vis spectra upon drying of the materials. The influence of the particle size and the distance between particles on the colors of gold was described theoretically by Maxwell Garnett around 1905 [54, 55]. A little later, Mie and his Ph.D. student Steubing measured quantitatively the scattered and the absorbed light intensity of illuminated dispersions of gold nanoparticles [8–11]. They found that the intensity loss of the transmitted light in dispersions of gold particles with diameter below 50 nm originated preferentially from absorption [8–11], but scattering became more pronounced for larger particles [56] (in fact, it has since been reported that light scattering in colloidal gold solutions manifests visually only for particle diameters above 50 nm) [57], and they fortified their observations with a theoretical fundament.

## 2.2. Polymer–Inorganic Nanocomposites

Nanocomposites of polymers and inorganic colloids were prepared in 1833 [58]. The first step in nanocomposite manufacture was the dissolution of gold in *aqua regia*. A part of the volatile contents of the resulting solution was evaporated at elevated temperature until a solid skin formed at the surface of the solution. Thereafter, the solution was allowed to cool to room temperature whereupon the solution transformed completely to a solid, hygroscopic matter containing gold salts. The solids were rapidly dissolved in water. This solution was mixed with a solution containing dissolved  $\text{SnCl}_2$  and gum arabic, whereupon red gold colloids arose by reduction of the gold salts with tin(II) ions. Upon addition of ethanol, a gold–gum arabic nanocomposite was obtained by coprecipitation. A few decades later, nanocomposites of gum and silver were also described [59]. Similarly to the gold–gum arabic nanocomposites, those with silver were gained by coprecipitation upon addition of ethanol to an aqueous phase containing gum and *in-situ* prepared silver colloids.

Very remarkably, polymer nanocomposites with uniaxially oriented assemblies of inorganic particles were prepared around 1900 [60, 61]. An uniaxial orientation of particle assemblies was indicated by the dichroic behavior of the respective samples (i.e., their colors changed under observation in linear polarized light upon rotation of the polarizer). As an example, plant and animal fibrils, such as linen, cotton, spruce, or chitin, were first treated with solutions of

silver nitrate, silver acetate, or gold chloride [60]. The metal ions, which were incorporated in the fibrils, were reduced to elemental metal particles by exposure to light. The color of such samples was different for parallel and perpendicular orientation of the polarization direction of the light with respect to the fiber axis, for example red and blue green for gold in spruce wood fibers. Further, dichroic nanocomposite films were produced with gelatin as the matrix polymer [61]. The gelatin was impregnated with gold chloride solution, subsequently drawn, dried, and finally irradiated with light, whereupon elemental gold formed. Dichroic samples were also obtained when gelatin was mixed with colloidal gold or silver before drying and drawing [61]. Up to 1930, dichroic fibers were prepared with a number of metals other than gold or silver, such as rhodium, osmium, palladium, platinum, or copper, but also with nonmetals (e.g., phosphorous, sulfur, or iodine) [62–66]. Based on Scherrer's equation, the particle diameters of silver and gold crystallites in dichroic samples were determined in fibers of ramie, hemp, bamboo, silk, wool, viscose, and cellulose acetate, and values between 5 and 14 nm were found [67]. The ringlike interference patterns of the metal crystallites in oriented ramie fibers revealed that the individual primary crystallites themselves were not oriented [66, 68], indicating that the dichroism was indeed the result of a cooperative effect involving many particles.

## 3. PREPARATION OF NANOCOMPOSITES

### 3.1. Inorganic Colloids

Typical specific surface free energies of inorganic solids amount to 500–2000  $\text{mJ/m}^2$  [69, 70] compared to 20–50  $\text{mJ/m}^2$  for polymers [71]. As a result of the high values of the inorganic compounds, nanocomposites can be far from equilibrium [72] if the interfacial energy in the system is not compensated by interactions between the polymer and the inorganic particles. As a consequence, agglomeration of inorganic colloids can in fact be a problem in the synthesis of nanocomposites [73, 74]. Once the nanocomposites are formed, however, the activation energy needed for reaching the equilibrium state is too high to allow one to establish the equilibrium in a perceptible period. For example, in nanocomposites comprising an ethylene–methacrylic acid copolymer and ca. 3% v/v PbS, the agglomeration of PbS was estimated to require periods of  $10^5$  years at 25 °C [17], and nanocomposites of gold colloids in amine-terminated poly(ethyleneoxide) were found to be essentially unchanged for more than a year [75]. In powders consisting of bare, isolated nanoparticles, however, the high specific surface energies of inorganic materials cause the primary particles typically to agglomerate to secondary particles. In this case, the common methods of technical composite fabrication, which are based on the mixing of polymer and isolated powders, are usually not successful for the preparation of nanocomposites with randomly dispersed primary particles because the aggregates commonly do not break into their primary particles during the procedures applied for the nanocomposite manufacture. Therefore, agglomeration makes the use of grinded particles difficult for the preparation of nanocomposites with randomly dispersed particles.

In addition, the energy transferred to the particles by the grinding process can induce changes in the constitution of the surface region [76–81]. Therefore, grinded nanoparticles have quite rarely been used for nanocomposite fabrication but examples still exist. Silicon particles of 20–40 nm diameter were prepared with high energy milling of powders which were subsequently subjected in ethanolic suspension to ultrasound [82, 83]. After sedimentation of the coarse fractions, dispersions of silicon nanoparticles were obtained which were suited for the incorporation in polymers.

Agglomeration of nanoparticles is frequently avoided by *in-situ* synthesis (i.e., the particles are not isolated but used in the as-prepared dispersions for the incorporation in polymers). This method was used for, for example, the preparation of nanocomposites with PbS which can easily be synthesized in aqueous solution by combination of water-soluble lead(II) salts [e.g., lead(II) acetate or lead(II) nitrate] and H<sub>2</sub>S, alkaline metal sulfides, or organic sulfides such as thioacetamide [84–86]. Hydrolysis is often a suited reaction for *in-situ* nanoparticle fabrication, which was used, for example, for the synthesis of silica particles from tetraethoxysilane [87–89]. While many inorganic salts which are suited as starting materials for the synthesis of nanoparticles are better soluble in water than in organic solvents, there also exist numerous inorganic compounds which are soluble in organic solvents, thus allowing the *in-situ* preparation of nanoparticles also in such media. For instance, CdS or Cu<sub>2</sub>S colloids were prepared in *N*-methylpyrrolidone by addition of Li<sub>2</sub>S to a solution of Cd(CF<sub>3</sub>SO<sub>3</sub>)<sub>2</sub> or [Cu(CH<sub>3</sub>CN)<sub>4</sub>](CF<sub>3</sub>SO<sub>3</sub>)<sub>3</sub>, respectively [90], or colloids of elemental platinum in styrene were produced from tris(styrene)platinum(0) dissolved in styrene [91]. The tris(styrene)platinum(0) decomposed under formation of nanoparticles simply upon evaporation of a part of the styrene at reduced pressure and ambient temperature.

As an alternative to the *in-situ* preparation of the inorganic particles, colloids with a strongly bound surface layer of organic molecules may be used if they can be isolated and if the primary particles can be redispersed. Here, agglomeration is suppressed by the surface layer which markedly diminishes the specific surface free energy and, therefore, tends to decrease the attraction between the particles. Surface-modified colloids may be present as viscous substances or solids. In the last decade, a number of well defined surface-modified colloids have been isolated, for example, gold or silver nanoparticles with phosphines or thiols attached to their surfaces [92–102], CdS covered with aromatic or aliphatic thiols [23, 103–107], CdSe coated with tri-*n*-octylphosphine oxide [108] or pyridine [109], thioglycerol-capped CdTe nanoparticles [110], or stearic acid-modified CaCO<sub>3</sub> [111]. Dispersible colloidal silver covered with a citrate layer could have been prepared already more than 100 years ago [112, 113].

### 3.2. Incorporation of Nanoparticles in Polymers

Nanoparticles are frequently incorporated in polymers using dispersions of *in-situ* synthesized nanoparticles or surface-modified colloids in presence of a polymer which is dissolved in the dispersions. If the polymer destabilizes the colloidal

dispersion, the particles can precipitate together with the polymer (coprecipitation), which was described for example for the fabrication of poly(ethylene oxide)–PbS nanocomposites [84]. On the other hand, polymers stabilize colloidal dispersions in many systems. In such cases, coprecipitation can often be induced by addition of a nonsolvent for the polymer. Upon precipitation of the polymer, the nanoparticles then precipitate as well. This principle was applied for instance for the preparation of nanocomposites comprising poly(aniline) and CdS or Cu<sub>2</sub>S which coprecipitated after addition of ethanol to a mixture of the nanoparticles and the polymer in *N*-methylpyrrolidone [90]. The coprecipitation methods typically yield powders while for many applications or physical investigations films are required. Films can readily be obtained by evaporation of the solvent in a system containing both dispersed particles and dissolved polymer, which was applied, for example, in the case of dispersed dodecanethiol-modified gold particles and dissolved poly(ethylene) in *p*-xylene [102]. Another method for the preparation of nanocomposite films is the spin coating process which was applied, for example, at a dispersion of dodecanethiol-coated gold particles dispersed in a poly(phenylmethylsilane) solution in toluene [100]. If the particles have been prepared *in-situ*, attention has to be paid to the reaction by-products stemming from the particle synthesis since those by-products could be incorporated in nanocomposites in particular when they are prepared by solvent evaporation or spin coating. In this respect, the formation of volatile by-products is advantageous, as for example in nanocomposites produced by solvent evaporation or spin coating from aqueous gelatin–PbS systems where acetic acid resulted as the by-product of the reaction of lead(II) acetate and hydrogen sulfide [85]. Ultrathin nanocomposite films were prepared with the Langmuir–Blodgett (LB) technique [114, 115]. For example, *in-situ* synthesized Fe<sub>3</sub>O<sub>4</sub> colloids were codeposited with a poly(maleic acid ester) as LB films on glass substrates [114]. Nanoparticles were also produced *in-situ* in LB layers. When Langmuir–Blodgett films of poly(aniline) or poly(3-octylthiophene) were deposited together with cadmium arachidate on quartz or ZnSe substrates, CdS nanoparticles formed upon exposure to gaseous H<sub>2</sub>S [115].

When surface-modified colloids are available, nanocomposites may be obtained by addition of the nanoparticles to a polymer melt as in the example of dodecanethiol-coated silver colloids which were mixed in an extruder at 180 °C for 10 min with poly(ethylene) and further homogenized by compression molding at 180 °C [101]. Polymer melts were also employed for the synthesis of metal colloids prepared *in-situ* from a dissolved precursor [116]. Upon dropping solutions with the precursors to polymer melts at 200–260 °C, elemental metals formed under concomitant evaporation of the solvent and mixing of the solid components. For example, Cu(HCOO)<sub>2</sub>, Ti(C<sub>6</sub>H<sub>5</sub>CH<sub>2</sub>)<sub>4</sub>, or Fe(CO)<sub>5</sub> decomposed into the respective metal colloids under release of volatile reaction by-products [116]. This method was found to be suited also for the preparation of large amounts of nanocomposites (i.e., in the kilogram range) [116].

While polymers have been frequently employed in their final states for nanocomposite preparation, they have

also been synthesized *in-situ* in presence of dispersed nanoparticles which become trapped in the matrix after polymerization. This method can be particularly suited for polymers which are, in the final state, widely insoluble in common solvents. As an example for nanocomposite fabrication starting with monomers, surface-modified CdS particles were dispersed in a diisocyanate and a diol or dithiol, respectively, and poly(urethanes) or poly(thiourethanes), respectively, were subsequently obtained by polyaddition [104, 105]. Polymerization can also proceed in microemulsions (e.g., in systems consisting of an aqueous phase with *in-situ* prepared PbS colloids and an organic phase containing vinyl monomers) [86]. The latter were polymerized *in-situ* with the help of the UV initiator 2,2-dimethoxy-2-phenylacetophenone. Nanocomposite films have also been fabricated by coevaporation of an inorganic species and a monomer. While the monomer undergoes *in-situ* polymerization upon deposition on a substrate, the inorganic vapors grow to nanoparticles in the matrix. As an example, paracyclophane was evaporated and heated in the evaporation zone to 650–700 °C which caused a conversion to *p*-xylylene [117]. These vapors were codeposited with palladium, tin, or copper vapors on quartz slides which were cooled to –196 °C. Upon warming to room temperature, the *p*-xylylene polymerized to poly(*p*-xylylene) which is otherwise difficult to process.

The final step in nanocomposite preparation can also proceed in the solid polymer matrix, in particular by reaction of a precursor which has been previously incorporated in the matrix. Also in this case, the by-products from the reaction only leave the matrix if they are sufficiently volatile. In the simplest case, the particles are synthesized by thermal decomposition of the precursor. For example, copper formate embedded in poly(2-vinylpyridine) was reduced to elemental copper nanoparticles under formation of H<sub>2</sub> and CO<sub>2</sub> after heating to temperatures above 125 °C [118], and decomposition of silver heptafluorobutyrate or sodium tetrachloroaurate(III) in poly(vinyl butyral) to elemental metal colloids proceeded at 150 °C [119]. Another possibility is conversion of an incorporated precursor with a gaseous reagent, such as the synthesis of PbS colloids in an ethylene–methacrylic acid copolymer by reaction of Pb(CH<sub>3</sub>COO)<sub>2</sub> with gaseous H<sub>2</sub>S [14, 15, 17, 120], or with a dissolved reagent, such as the synthesis of PbS nanoparticles in poly(aniline) (PANI) by contact of Pb(NO<sub>3</sub>)<sub>2</sub>–PANI films with a Na<sub>2</sub>S solution [121]. Rarely, nanocomposites were produced by diffusion of dispersed nanoparticles into a polymer matrix. In the ideal case, the polymer swells but does not dissolve in the dispersing agent thus creating space for the diffusing particles. As an example, CdTe–poly(aniline) nanocomposites were prepared by exposure of a PANI film to an aqueous dispersion of thioglycerol-capped CdTe particles [121].

## 4. PROPERTIES OF NANOCOMPOSITES

### 4.1. Absorption of Visible Light

Nanocomposites containing colored colloids can act as color filters. Such materials were obtained, for instance, with poly(vinyl alcohol) and gold [28]. The sizes of the gold parti-

cles were varied by reduction of tetrachloroaurate(III) with various amounts of citrate [26, 27]. Aqueous suspensions with *in-situ* generated gold particles were mixed with aqueous poly(vinyl alcohol) solutions and nanocomposites were produced by casting followed by evaporation of the water [28]. According to the color of the gold colloids [26, 57], the nanocomposites appeared in transmission pink at 16 nm, purple at 43 nm, and blue at 79 nm diameter of the gold particles [28]. The color of the materials with the particles of 16 and 43 nm diameter did not vary with the observation angle but the samples with 79 nm particle diameter changed their color under oblique observation where they looked brown due to the Tyndall effect [26]. Similar observations were reported for gold dispersed in liquids [26, 57].

Color filters comprising poly(*N*-vinylpyrrolidone) and silver particles were prepared starting from a solution of Ag(NO<sub>3</sub>)<sub>2</sub> and the polymer in ethylene glycol which also acted as the reducing agent for the silver salt [122, 123]. Nanocomposites containing 2–8% w/w silver were coprecipitated with acetone and reprecipitated from ethanol with acetone [122, 123]. Depending on the reaction conditions, translucent yellow or red color filters were obtained [122, 123] with particle diameters between 6 and 12 nm [123]. The smallest particles resulted when the reaction solutions were mixed fast under sonication or strong stirring [123]. It was proposed that the use of polymers other than poly(*N*-vinylpyrrolidone), for example, poly(vinyl alcohol) or poly(methylvinylether), could change the color of the particles and, correspondingly, of the nanocomposites since the Fermi level depends not only on the particle size but also on the interaction of the particles with the surrounding molecules, according to the formula [123]

$$\Delta\varepsilon_F = \frac{2}{3}\varepsilon_F \frac{n_s}{N} x \delta_e$$

with  $\Delta\varepsilon_F$  the difference in the Fermi level  $\varepsilon_F$ ,  $n_s$  the number of atoms at the surface of a particle,  $N$  the total number of atoms in a particle,  $x$  the fraction of the surface atoms chemically interacting with functional groups of the surroundings, and  $\delta_e$  the fractional charge associated with each chemically interacting moiety.

Irradiation of colorless photochromic nanocomposites can also lead to color filters. Transparent aqueous solutions of a commercially available polynuclear phosphotungstic acid and poly(acrylamide) were used for the preparation of films of 2.1 μm thickness by evaporation of the water [124]. The resulting nanocomposites contained 9% or 38% w/w phosphotungstic acid particles with diameters of 45–55 and 55–65 nm, respectively, for the two phosphotungstic acid contents. Before UV irradiation, optical absorption spectra of the films did not show bands between 400 and 1000 nm. However, phosphotungstic acid readily undergoes redox processes under irradiation which results in colored species. Accordingly, upon irradiation of the nanocomposites with a mercury lamp, the samples with 9% w/w phosphotungstic acid became blue exhibiting in UV/vis spectra a shoulder at 490 nm and a very broad absorption maximum at

620 nm while the samples with 38% w/w phosphotungstic acid turned to brown with a very broad absorption maximum at 540 nm in UV/vis spectra.

## 4.2. Absorption of UV Radiation

Polymers often undergo unwanted reactions under the action of ultraviolet light. As a consequence, mechanical or optical properties can be affected by UV irradiation. The organic stabilizers which are commonly added to avoid such undesired effects are, however, consumed over long periods of time, in particular upon exposure to intense light. Further, attention has to be paid to migration of organic UV stabilizers. Inorganic particles which absorb UV light close to the visible wavelength range in which they are transparent are interesting alternatives for the UV protection of polymers. Numerous inorganic particles are UV-stable and, in addition, do not migrate in polymers.

In order to prepare a visually transparent material which absorbs UV light, nanocomposites of ZnO and a statistical copolymer of ethylene and vinyl acetate (EVA) were produced starting from immersion of EVA in a diethyl zinc solution [125]. The zinc compound diffused rapidly into the polymer. When the films were removed from the solution, the diethyl zinc trapped in the polymer hydrolyzed after contact with the ambient humidity, leading to the formation of ZnO colloids with diameters around 10 nm. After immersion of an EVA sheet of 194  $\mu\text{m}$  thickness at  $-15^\circ\text{C}$  for 40 min in the diethyl zinc solution, the resulting ZnO particles were concentrated in a region of 1–2  $\mu\text{m}$  thickness to the surface because of the limited diffusion rate of the diethyl zinc. Hence, the bulk mechanical properties of the polymer were not affected by the presence of the ZnO. The nanocomposites absorbed UV light up to 370–380 nm while light loss by scattering was virtually absent in the visible wavelength range.

Visually transparent nanocomposites of ZnO and poly(propylene) (PP) or poly(ethylene) (PE) were also described [126]. Unfortunately, the ZnO source is not evident and there is some uncertainty in the diameter of the ZnO particles which seems to be 20 nm in a figure caption but was denoted with 180 nm in the experimental section; the latter diameter appears to be too large to be suited for visually transparent nanocomposites. Nonetheless, the UV-protective effect of the ZnO colloids was clearly demonstrated. Upon exposure to UV radiation, discoloration of PP or carbonyl formation in PE was substantially reduced by the presence of 1–2% w/w ZnO. It also appeared that ZnO colloids reduced the thermally induced cross-linking of poly(propylene) [127].

Nanoparticles of rutile, a crystal modification of  $\text{TiO}_2$ , of ca. 2 nm diameter and a surface coating of dodecylbenzenesulfonic acid (DBSA) were isolated and dispersed in solutions of polymers in dichloromethane [128]. Nanocomposites were produced from those dispersions by casting followed by solvent evaporation at ambient conditions. Thus, films of ca. 100  $\mu\text{m}$  thickness and 4% w/w DBSA-coated rutile were prepared with poly(styrene) or a poly(carbonate) based on bisphenol A. The nanocomposites appeared transparent to the eye but absorbed UV light to a high extent up to ca. 300 nm.

## 4.3. Iridescence

Nanocomposites with particles forming a regular lattice in a polymer matrix have been prepared with silica particles synthesized *in-situ* by hydrolysis of tetraethoxysilane in a mixture of water, ethanol, and ammonia [87, 88]. The particles were of a diameter around 150 nm, if not otherwise indicated, and very uniform in size [87, 88]. The surfaces of the particles were modified by conversion of the surface hydroxyl groups with 3-(trimethoxysilyl)propyl methacrylate [87, 88]. The solvents in the silica dispersions were exchanged first with methanol and then with methyl methacrylate (MMA) [88] or methyl acrylate (MA) [87] by dialysis. Thus, dispersions of 35–40% w/w (19.5–22.7% v/v) silica in MMA or 35–45% w/w in MA were produced in liquid cells of 1 mm thickness in the case of MMA and 264  $\mu\text{m}$  thickness in the case of MA. After periods ranging from minutes to days, depending on the system, the cloudy dispersions became iridescent, indicating the formation of a lattice [88] which induced diffraction of light according to Bragg's equation [87],

$$\lambda = 2nd \sin \theta$$

with  $\lambda$  the wavelength of diffracted light,  $d$  the interplanar spacing,  $n$  the refractive index of the dispersion, and  $\theta$  the Bragg angle. The iridescence also manifested in UV/vis spectra of silica samples in MMA which were investigated with the incident beam perpendicular to the face of the liquid cell. After 7 d storage of the dispersions, a sharp band appeared at 554 nm at a silica volume fraction  $\phi$  of 0.195 [88]. This band must originate in diffraction of light at the lattice formed by the particles because neither silica itself nor methyl acrylate absorbs in the visible wavelength range. Application of Bragg's equation results in an interplanar spacing  $d$  of 176 nm ( $n = 1.4210$ ) in those specimens.

For the production of nanocomposites, MMA was polymerized in the dispersions by irradiation at ambient temperature with a mercury lamp in presence of a photoinitiator, 2,2-dimethoxy-2-phenylacetophenone [88]. It has been suggested, but not proven, that methacrylate groups bound to the silica surfaces reacted with the growing poly(methyl methacrylate) chains. Due to the shrinking of the volume of the organic phase upon polymerization,  $\phi$  increased from 0.195 to 0.235 and accordingly the absorption maximum in UV/vis spectra of the nanocomposites shifted from 554 nm in the MMA dispersion to 490 nm in the polymer. The absorption band corresponded to an interplanar spacing of 190 nm according to Bragg's equation ( $n = 1.4819$ ) and was still relatively sharp [full width at half maximum (FWHM) 13.6 nm] although somewhat broader than before polymerization (FWHM 4.0 nm). Scanning electron microscopy images revealed a hexagonal pattern of the spheric silica particles with a distance between two adjacent centers of 234 nm and to a large spacing between two adjacent surfaces of 82 nm. Therefore, the order in the dispersions seems to be rather due to long-range interactions than to close packing of the spheres.

Dispersions with MA were investigated with silica particles of diameter 142, 153, and 330 nm [87]. The weight fraction  $f$  of silica in these dispersions amounted typically

to 0.40 but in the case of the particles with 153 nm diameter dispersions with  $f$  of 0.35 and 0.45 were also prepared. In all samples, distinct absorption maxima arose in UV/vis spectra, with a FWHM of 4–6 nm at the samples with particle diameters 142 and 153 nm. At the samples with particle diameter 330 nm, the lines were considerably broader (FWHM of 35–50 nm) which may indicate a less pronounced order of the particles in those dispersions. At  $f$  of 0.40, the maximum absorption wavelength  $\lambda_{\max}$  decreased from 600 nm for a particle diameter  $l = 330$  nm to  $\lambda_{\max}$  of 490 nm for  $l = 142$  nm, corresponding to a decrease in the distance between the lattice planes from 211 to 173 nm (calculated with Bragg's equation). Further,  $\lambda_{\max}$  decreased in dispersions with particles of  $l = 153$  nm with increasing silica content from 582 nm at  $f = 0.35$  to 528 nm at  $f = 0.45$ .

Nanocomposites were also prepared by photopolymerization of MA analogous to the samples with MMA described above [87]. SEM images of thin sections of those materials showed hexagonally ordered arrays of silica particles. A blueshift of  $\lambda_{\max}$  around 30 nm and an increase in the full width at half maximum from ca. 5 to 15 nm was observed upon polymerization. The absorption maximum in UV/vis spectra and the distances of the lattice planes decreased with increasing silica content (particle diameter 153 nm). For  $f = 0.35$  and 0.45, respectively,  $\lambda_{\max}$  decreased from 502 to 466 nm and the lattice plane distance from 171 to 159 nm. The absorption bands were still quite narrow after polymerization (FWHM around 15 nm). When a film containing 40% w/w silica of particle diameter 153 nm was stretched up to 35%,  $\lambda_{\max}$  decreased linearly with increasing stretching ratio from 486 to 440 nm. After the stress was released, the films adopted their original lengths within 2–4 h and reached the initial  $\lambda_{\max}$  within 2–4 nm. Upon tilting the films away from perpendicular incidence of the incoming light to an incidence angle of 68°,  $\lambda_{\max}$  shifted from 490 to 472 nm, in agreement with Bragg's law.

#### 4.4. Dichroism

As mentioned in the historical outline above, dichroic nanocomposites on the basis of natural polymers were described already 100 years ago. It was supposed that the dichroism resulted from the formation of uniaxially oriented particle assemblies [63, 67, 129]. More recently, dichroic nanocomposites have been prepared with synthetic polymers, in particular poly(vinyl alcohol) (PVAL) and PE [28, 29, 101, 102, 130–132]. Dichroism was induced by drawing of the respective isotropic nanocomposites. In the PVAL systems, colloids of elemental gold were synthesized *in-situ* by reduction of  $[\text{AuCl}_4]^-$  with citrate in aqueous solution. After mixing the as-prepared gold dispersions with aqueous PVAL solutions, nanocomposites were obtained after solvent evaporation [28, 29]. These materials, which contained 5% w/w gold and reaction by-products stemming from the reduction of tetrachloroaurate(III) with sodium citrate, were drawn at 120 °C up to maximum draw ratios of 5. Transmission electron microscopy revealed linear particle assemblies which were oriented in the drawing direction and which caused a dichroic behavior. In polarized light, the color of the

drawn nanocomposites depended on the angle  $\varphi$  between the polarization direction of the incident light and the drawing direction of the films. Nanocomposites with gold particles of a diameter of 16 nm appeared blue at  $\varphi = 0^\circ$  and red at  $\varphi = 90^\circ$ , and accordingly the absorption maximum shifted from 772 nm ( $\varphi = 0^\circ$ ) to 528 nm ( $\varphi = 90^\circ$ ).

For the preparation of nanocomposites with PE as the matrix polymer, gold and silver nanoparticles coated with a self-assembled monolayer of dodecanethiol were used [28, 29, 101, 102, 130–132]. The colloid diameters were around 2–3 nm in the case of gold and around 4–5 nm of silver. In PE–silver samples, the particle size increased from approximately 4 to 10 nm upon annealing at 180 °C for 15 h which caused a shift of the absorption maximum of the particles from 435 to 463 nm. In order to obtain nanocomposites, the surface-modified particles were either dispersed in *p*-xylene–PE solutions at 130 °C followed by solvent evaporation, or the particles were mixed with PE in the molten state. The resulting isotropic materials, which contained usually 2 or 4% w/w colloid, were oriented by drawing on a hot stage at 120 °C to typical draw ratios around 15. In order to obtain highly dichroic nanocomposites with dodecanethiol-modified gold, the colloids were kept in a PE–*p*-xylene solution at 130 °C for 300 min [102, 132]. During this period, the color of the dispersion and the resulting nanocomposites changed from brown to blue. It seems that the heating caused a partial desorption of the dodecanethiol layer which favored an agglomeration of the particles; agglomerates in TEM images were indeed found in samples which had been preannealed for 300 min. In the case of silver, aggregates were obviously present already in the xylene dispersion prior to film manufacturing, as evident from TEM images [101, 130]. Upon drawing of the nanocomposites, arrays of nanoparticles formed along the drawing direction (as evident from TEM images) [101, 102, 130, 132], probably as a consequence of the tensile deformation in the drawing process [101].

In polarized light, the UV-vis spectra of the drawn gold–PE or silver–PE nanocomposites strongly depended on  $\varphi$ . At  $\varphi = 0^\circ$  the absorption maximum,  $\lambda_{\max}(0)$ , appeared at higher wavelengths than at  $\varphi = 90^\circ$ ,  $\lambda_{\max}(90)$ , and the spectra were further characterized by isosbestic points [101, 102, 130, 131]. For example, a PE–silver nanocomposite showed a  $\lambda_{\max}(0)$  at 489 nm,  $\lambda_{\max}(90)$  at 398 nm, and an isosbestic point at 425 nm, and a PE–gold nanocomposite a  $\lambda_{\max}(0)$  at 669 nm, a  $\lambda_{\max}(90)$  at 545 nm, and isosbestic points at 483 and 541 nm. The difference between  $\lambda_{\max}(0)$  and  $\lambda_{\max}(90)$  was essentially independent of the fabrication method (solution casting or melt processing) of the silver–PE nanocomposites [101]. When the gold content in PE was varied between 0.9 and 7.4% w/w, most pronounced differences in the absorption maxima at  $\varphi = 0^\circ$  and  $\varphi = 90^\circ$  were observed at particle contents of 2–4% w/w [102]. The optical behavior of the dichroic nanocomposites resembled that of systems with wire-type metal nanoparticles [133–138] or oriented metal strips [139] which also showed isosbestic points and a variation of the absorption maxima on  $\varphi$ . According to the dependence of  $\lambda_{\max}$  on  $\varphi$ , the color of the drawn nanocomposites changed with variation of  $\varphi$ . PE–silver films appeared red and yellow at  $\varphi$  of 0° and 90°, respectively,



annealed PE–silver films appeared purple and amber, and PE–gold films appeared blue and red. Such materials are potentially useful in liquid crystal display applications. When the top polarizer in a twisted-nematic electro-optical cell was replaced by dichroic nanocomposites, the display appeared bicolored [102, 109].

## 4.5. Nonlinear Optical Properties

Materials with nonlinear optical (NLO) properties are of interest for optical switching and wavelength manipulation [20]. Nanocomposites which exhibit NLO effects have been described thoroughly in two recent reviews [20, 21]. For example, in nanocomposites comprised of surface-modified CdSe particles and poly(methyl methacrylate), third-order nonlinear susceptibilities ( $\chi^3$ ) ranging from  $6.5 \times 10^{-8}$  to  $2.9 \times 10^{-7}$  esu were found [20]. Silver or gold nanoparticles prepared by reduction of respective metal salts at 150 °C in poly(vinyl butyral) films yielded materials with  $\chi^3$  of  $2 \times 10^{-9}$  and  $1 \times 10^{-8}$  esu and  $\chi^3/\alpha$  (where  $\alpha$  denotes the absorption coefficient) of  $1 \times 10^{-12}$  and  $2 \times 10^{-12}$  esu/cm, respectively (i.e.,  $\chi^3/\alpha$  was on the same order for both metals while  $\chi^3$  of the gold nanocomposites strongly exceeded the value of the films containing silver) [119]. This observation was attributed to the different local field enhancements inside the metal particles. The local field factor  $f_1$  is 2.2 for gold and 7.1 for silver, and  $\chi^3$  is proportional to the fourth power of this factor. Nanocomposites with nonlinear optical properties were also prepared with gold particles coated with a dodecanethiol monolayer [100]. The materials were obtained by dispersion of the particles in methylmethacrylate which was subsequently polymerized with a radical initiator or by spin coating of gold dispersed in a poly(phenylmethylsilane) solution. The highest  $\chi^3$  values observed with the two polymer matrices were around  $10^{-12}$  esu.

More recently, a nonlinear refractive index of  $-6.8 \times 10^{-12}$  cm<sup>2</sup>/W was found for nanocomposites comprising cubic PbS nanocrystals of ca. 5 nm edge length and a polymer prepared *in-situ* from a mixture of monomers and oligomers [86]. This nonlinear refractive index of the nanocomposite was clearly above that of bulk PbS measured under the same conditions ( $1.71 \times 10^{-14}$  cm<sup>2</sup>/W). This was explained as follows: As the particle size decreases, the ratio between surface and volume increases and consequently recombination of induced charge carriers at the surface becomes more important [86]. In semiconductor nanocrystals, a large percentage of defects are located at the surface which can act as traps for electron and hole annihilation unless these defects are passivated [108]. Hence, the trapping of charge carriers at the surface is influenced by the interaction of the surface atoms with the matrix [86]. It was assumed that coordination of carboxylic acid groups from the polymer to lead atoms reduced the trapping probability of electrons at the surface while the holes were rather localized at the surface and that, as a consequence, the surface-induced separation of charge between delocalized electrons and localized holes was the origin of the large nonlinear optical response in the PbS nanoparticles [86].

## 4.6. Extreme Refractive Index

### 4.6.1. General Remarks

The refractive index is a key feature in optical applications. The refractive indices of most organic polymers are located in the relatively narrow range of 1.3 and 1.7 [140]. Isotropic refractive indices around 2.1, found, for example, for poly(thiophene) or aromatic poly(imides) [141–143], are extraordinarily high for polymers. The theoretical lower limit of the refractive index of organic polymers has been estimated to be close to 1.29 [144]. It appears that an isotropic refractive index above 2.5 or below 1.25 has not been reported so far for a pure organic polymer. Inorganic materials cover a more extended range of refractive indices. For example, the refractive indices of silicon, germanium, and GaAs are above 3.5 at wavelengths of 413, 620, and 827 nm, whereas the refractive index of silver is below 0.2 at those wavelengths [145]. As a consequence, the incorporation of inorganic nanoparticles with extreme refractive indices in organic polymers can result in composite materials with refractive indices outside of the typical range of organic polymers.

### 4.6.2. High Refractive Index

The high refractive index of PbS over a broad wavelength range (4.0–4.6 between ca. 420 nm and 11  $\mu$ m [145]) and the straightforward synthesis of colloidal PbS renders PbS attractive for model experiments on the refractive index modification of polymer nanocomposites. Nanocomposites with PbS contents above 20% v/v were prepared with different methods [84, 85]. As the polymer matrix, poly(vinyl alcohol), poly(acrylamide), poly(acrylic acid), poly(ethylene oxide), and gelatin were employed. In particular, ultrahigh refractive index materials were described with poly(ethylene oxide) (PEO) [84]. These materials were readily obtained by addition of a H<sub>2</sub>S solution to a PEO-Pb(CH<sub>3</sub>COO)<sub>2</sub> solution, whereupon nanocomposites with a PbS content of 88% w/w (ca. 50% v/v) and particle size of 19 nm precipitated immediately. In numerous PEO–PbS samples, refractive indices between 2.9 and 3.4 were measured at wavelengths of 632.8 and 1295 nm.

Dissolution of gelatin in a solution of Pb(CH<sub>3</sub>COO)<sub>2</sub> at 50–60 °C followed by cooling to room temperature and addition of an aqueous H<sub>2</sub>S solution resulted in a stable gelatin–PbS dispersion with acetic acid as reaction by-product [85]. This dispersion was suited for the preparation of films with thicknesses in the range of 40 nm–1  $\mu$ m by spin coating. The films, which contained crystalline particles of diameters below 15–20 nm, stayed homogeneous up to PbS contents of 86.4% w/w. Refractive indices of samples with 30–86% w/w (17–53% v/v) PbS were determined at 632.8 nm [85]. The highest refractive indices, 2.4–2.5, were measured at PbS contents between 82 and 86% w/w (45–53% v/v). Within the experimental precision, the refractive indices increased linearly with increasing volume content of PbS by 0.0193 per % v/v of PbS. The regression analysis resulted in an extrapolated refractive index of  $1.49 \pm 0.05$  at 0% v/v PbS and  $3.4 \pm 0.1$  at 100% v/v PbS. While the former value agreed with the refractive index of pristine gelatin ( $1.537 \pm 0.008$ ), the latter was clearly below the refractive index of bulk PbS (ca. 4.3 at

633 nm [145]). This difference between the refractive index of the colloidal and the bulk PbS is supposed to be predominantly due to a refractive index dependence on the particle size, as shown in the next paragraph. Linear dependencies of refractive indices of nanocomposites on the volume fraction of the particles have also been found for other systems [83, 146–148]. Theoretical considerations are in agreement with a linear or a nonlinear relation between the refractive index of composites and the volume content of the incorporated particles, depending on the model [83, 140, 149, 150]. In the systems described experimentally, some deviation from the linear relationship might be consistent with the experiments especially at high particle loadings because of the precision of the experiments.

The size of PbS particles in nanocomposites with PEO varied by the presence of various amounts of acetic acid or sodium dodecylsulfate (SDS), respectively, during the *in-situ* synthesis of PbS from  $\text{Pb}(\text{CH}_3\text{COO})_2$  and  $\text{H}_2\text{S}$  [151]. Acetic acid caused an increase and SDS caused a decrease in the size of the PbS colloids, and after coprecipitation, nanocomposites containing particles with average sizes between 4 and 80 nm were obtained. The materials containing particles above ca. 20–25 nm diameter showed refractive indices of 3.5–3.8 at 632.8 nm and 3.3–3.7 at 1295 nm whereas the refractive indices of the samples with particles below ca. 20 nm decreased continuously at both wavelengths down to 1.7–1.8 for 4 nm diameter. The refractive indices of the PbS particles were estimated by linear extrapolation of the PbS volume content to 100% as mentioned above for the example of PbS–gelatin nanocomposites. At 632.8 and 1300 nm, refractive indices of ca. 4.0–4.3 were thus calculated for PbS particles with sizes above ca. 20 nm. These values are in the range of those reported for bulk PbS (4.3 at 619.9 and 1300 nm [145]). However, the extrapolated refractive indices of PbS decreased at 632.8 and 1300 nm at average diameters below 15–20 nm, as supported by theoretical analyses [16, 152]. For diameters of 4 nm, the extrapolated refractive indices for the PbS colloids were as low as 2.3 at 632.8 nm and 2.0 at 1300 nm.

Silicon is also an attractive inorganic component for nanocomposites with high refractive index. The refractive index of silicon amounts to 5.57 at 400 nm and 3.91 at 620 nm [83]. Compared to PbS, the absorption coefficient of silicon (0.34 at 400 nm, 0.022 at 620 nm) [83] is by far lower (2.02 at 400 nm and 1.77 at 620 nm for PbS [145]). Hence, nanocomposites with silicon should exhibit lower absorbance at the visible wavelengths than materials with PbS at the same volume fraction of inorganic particles [83]. Silicon nanoparticles, which are difficult to synthesize by chemical procedures in solution, were prepared by high-energy milling of coarser particles. After dispersion of the grinded silicon powders in ethanol and centrifugation, the supernatant liquid contained particles with average diameters of 20–40 nm. Finally the ethanol dispersion was added to a gelatin solution, and films were produced by spin coating. The films contained 50% w/w (ca. 64% v/v) silicon. X-ray diffraction proved that the silicon particles contained at least a crystalline core, which might be surrounded by a layer of amorphous silica since it was obvious from infrared spectra that the surface of the particles was covered by an oxide layer. The refractive index of the nanocomposites was measured

between 400 and 1000 nm. It gradually decreased from 3.3 at 400 nm to 2.5 at 1000 nm, in agreement with the assumption that the refractive index of the nanocomposites was proportional to the volume fractions and the refractive indices of the components, as mentioned above for the PbS–gelatin system.

High refractive index nanocomposites of poly(ethylene oxide) and various iron sulfides were prepared by *in-situ* synthesis starting from iron(II) and iron(III) salts, such as  $\text{FeCl}_2$ ,  $\text{FeSO}_4$ ,  $(\text{NH}_4)_2\text{Fe}(\text{SO}_4)_2 \cdot 6\text{H}_2\text{O}$  (Mohr's salt), or  $\text{FeCl}_3$  [153]. These compounds were converted in an aqueous poly(ethylene oxide) solution with  $\text{H}_2\text{S}$ , NaHS,  $\text{Na}_2\text{S}$ , or a sodium oligosulfide at different pH values, temperatures, and reaction times. Nanocomposites coprecipitated upon formation of the iron sulfides. The highest refractive indices were found to be 2.6–2.8 at 632.8 and 1295 nm. In those samples, greigite ( $\text{Fe}_3\text{S}_4$ ) and mackinawite ( $\text{FeS}_{1-x}$ ) were identified as the iron sulfides by X-ray analysis. The iron sulfide particles were very small and could essentially not be visualized clearly in TEM images.

#### 4.6.3. Low Refractive Index

The refractive index of gold is below 0.5 between wavelengths of 540 and 1450 nm [145]. The incorporation of gold in polymers should therefore result in nanocomposites with very low refractive indices. The synthesis of gold nanoparticles is well established as evident from the above historic outline. For the production of low refractive index nanocomposites, gelatin and  $\text{H}[\text{AuCl}_4]$  were dissolved in a water–acetone mixture [146]. Upon addition of hydrazine hydrate, colloidal gold formed rapidly. Nanocomposite films were obtained from the gelatin–gold dispersions by spin coating. Scanning electron microscopy disclosed that reaction by-products crystallized at the surface of these films. Fortunately, those by-products could easily be removed by a brief dipping of the films in cold water. The nanocomposites contained 9.5–92.9% w/w (0.7–48% v/v) gold and showed the typical colors of colloidal gold [57, 154] (i.e., the nanocomposites appeared blue at high and purple–reddish at low gold contents). The particle diameters increased from 6.7 nm in a nanocomposite containing 9.5% w/w gold to ca. 50 nm at the highest gold contents. The lowest refractive indices, 0.96 at 632.8 nm and 1.04 at 1295 nm, were observed for a film containing 92.9% w/w gold (note that the refractive index of bulk gold is ca. 0.2 lower at 632.8 nm than at 1295 nm [145]). Since the nanocomposite surfaces were not ideally flat and the refractive indices were determined by ellipsometry, the incident laser light was scattered more pronouncedly at 632.8 nm than at 1295 nm. As a result, a number of samples were better suited for refractive index determinations at the higher wavelength at which a linear dependency of the refractive index on the volume content of gold was observed. Due to the low refractive index of gold, the refractive index of the nanocomposites decreased by 0.00994 per % v/v of gold. Extrapolation of the refractive index to 0% v/v gold resulted in a value of  $1.53 \pm 0.04$ , that is, close to the value of pristine gelatin ( $1.491 \pm 0.011$  at 1295 nm), and extrapolation to 100% v/v gold yielded a refractive index of  $0.51 \pm 0.07$  which is in the range of that of bulk gold (0.403 at 1291 nm [145]).

#### 4.7. Photoconductivity

Upon irradiation of light, semiconductors can induce charges in polymers. A semiconducting polymer matrix is able to transport the charge carriers (electrons or holes) which have been generated in the nanoparticles upon irradiation of light and which subsequently move to the surface [155]. Thus, photoconducting composites can be created, for example, by combination of a *p*-type semiconducting polymer matrix such as PANI and *n*-type semiconducting particles such as CdS or PbS. In nanocomposites, the large internal interface area enables an efficient separation of photoinduced charges and the number of carrier traps caused by the so-called grain boundaries between particles and matrix is reduced [155, 156]. The amount of nanoparticles required for photoconductivity is typically a few weight percent [155]. Hence, the respective particle fractions are well below the percolation threshold of ca. 15% v/v [155] (note that the density of inorganic materials is usually above that of polymers).

Photoconducting nanocomposites were prepared with PANI as matrix polymer. In a dispersion of TiO<sub>2</sub> particles (30% rutile and 70% anatase) in aqueous aniline, the latter was polymerized *in-situ* with peroxydisulfate [157]. After coprecipitation of the PANI and the TiO<sub>2</sub> with methanol, nanocomposites with 11–61% w/w TiO<sub>2</sub> of a diameter of 21 nm were obtained. Under the applied experimental conditions, poly(aniline) itself showed only little photoconductivity, if at all, but in presence of TiO<sub>2</sub> a photocurrent was observed with the highest values at irradiation at the absorption maximum of the TiO<sub>2</sub> particles of 337 nm. This indicates an improved efficiency in exciton dissociation in the presence of TiO<sub>2</sub>. Upon irradiation, electrons appear to be transferred from PANI to TiO<sub>2</sub> and the charges move subsequently to the respective electrodes. At a TiO<sub>2</sub> content of 33% w/w and irradiation with monochromatic light of a wavelength of 344 nm at an intensity of 19.5 μW/cm<sup>2</sup>, a short-circuit current density of 3 μA/cm<sup>2</sup> and an open-circuit voltage of 790 mV were measured. As another example, nanocomposites comprising PANI and PbS of a diameter of 2.6 nm, prepared by exposure of a PANI film containing lead(II) nitrate to an aqueous solution of sodium sulfide, showed photoconductivity in the entire visible spectrum with quantum yields on the order of 10<sup>-4</sup> [121].

Nanocomposites of poly(*N*-vinylcarbazole) (PVK), a hole-transporting polymer, and CdS also showed photoconductivity [106, 107, 158]. Materials containing CdS particles of 1–2 nm diameter were produced by spin coating from thioglycerol-capped CdS dispersed in a PVK solution in pyridine [107]. Films of 3–5 μm thickness were obtained. The photoconductivity  $\sigma$  at an applied field of 54 V/μm and an irradiation wavelength of 514.5 nm increased linearly with increasing intensity *I* of the incident light. At *I* = 3 W/cm<sup>2</sup>, a  $\sigma$  around  $8 \times 10^{-11}$  S/cm was measured. This indicates an absence of a bimolecular recombination mechanism which would lead to a dependency of  $\sigma$  on *I*<sup>2</sup>. Because the CdS content (ca. 1% w/w) lay clearly below the percolation threshold, it was assumed that the photoconductivity mechanism was initiated by absorption of a photon by a CdS particle whereas PVK acted as the charge transporting medium. It is not evident how the charges were transported through the bound surface layer to the polymer matrix.

Probably, a part of the organic layer bound to the surface was removed during nanocomposite fabrication. Other PVK–CdS nanocomposites were prepared by exposure of a spin-coated PVK–[Cd<sub>10</sub>S<sub>4</sub>(C<sub>6</sub>H<sub>5</sub>S)<sub>12</sub>] film to gaseous H<sub>2</sub>S [106]. The resulting materials contained ca. 1% v/v CdS of average diameter 1.6 nm. These nanocomposites showed a low dark conductivity but irradiation at 340 nm induced photoconductivity with a charge generation efficiency of 0.16.

Photoconductivity was also observed for nanocomposites of PVK and HgS colloids of ca. 10 nm diameter or PbS particles of ca. 50 nm diameter [159]. The mercury-containing materials were produced from polymer films which contained Hg(CH<sub>3</sub>COO)<sub>2</sub> and, in addition, a plasticizer and a chromophore. The films were exposed to H<sub>2</sub>S whereupon HgS formed. The volatile by-product acetic acid was removed under vacuum. For the manufacture of the composites with PbS, particles modified with *p*-thiocresol at their surfaces were dispersed in an organic solvent and casted together with PVK. The photocharge generation quantum efficiency increased with increasing electric field (*E*<sub>0</sub>) to ca. 0.12 at *E*<sub>0</sub> = 20 V/μm in the PVK–PbS and to ca. 0.002 at *E*<sub>0</sub> = 80 V/μm in the PVK–HgS nanocomposites.

#### 4.8. Catalytic Activity

The high specific surface area of the colloids in nanocomposites can render such materials suited for heterogeneous catalysis because of the large contact area between the particles and the reacting agents. As an example, catalytic active nanocomposites composed of silica and 10–13% w/w Nafion<sup>®</sup>, a perfluorinated resin with sulfonic acid groups, were prepared via two different routes [160]. In one method, colloidal silica (specific surface area 500 m<sup>2</sup>/g) was suspended in a 2-propanol–water mixture in the presence of Nafion<sup>®</sup>. After stirring for 2 h, the volatile components were removed by evaporation. In the other method, which probably yielded nanocomposites with less agglomerated particles, the silica was synthesized *in-situ* by hydrolysis of Si(OC<sub>2</sub>H<sub>5</sub>)<sub>4</sub>. The nanocomposites catalyzed the reaction of toluene with 1-bromoadamantane at 111 °C, the conversion of allyl phenyl ether to *o*-allyl phenol in benzene at 80 °C, and the transformation of phenyl acetate to phenol in nitrobenzene at 220 °C. In all those catalytic processes, the composites with the *in-situ* synthesized silica were clearly more effective than the materials prepared with the preformed colloids, the differences in the initial rate amounting to a factor of ca. 5–20,000, depending on the reaction. The catalysts with the preformed particles, however, often showed better selectivity in the catalytic reactions. For example, the transformation of phenyl acetate to phenol proceeded with an initial rate of 95 mmol/(min g<sub>catalyst</sub>) with the *in-situ* prepared and 0.0055 mmol/(min g<sub>catalyst</sub>) with the preformed silica but the latter produced phenol as the only detectable product while the fraction of phenol in the former was around 45% since other products such as 4-hydroxyacetophenone also arose. Remarkably, when phenol was added, 4-hydroxyacetophenone emerged exclusively with the nanocomposite containing the *in-situ* prepared silica.

Photocatalytic processes may be particularly favored by nanoparticles since the diffusion of electrons and holes

in nanoparticles is probably more efficient than in large particles [104]. Photoconductive nanocomposites were produced by dispersion of surface-modified CdS nanoparticles in toluene containing hexamethylene diisocyanate and an aromatic dithiol [104]. The diisocyanate and the dithiol were polymerized *in-situ* yielding a poly(thiourethane) with a Cd content of 1–2 mol/kg. While related composites containing bulk CdS did not exhibit a significant photocatalytic activity for the production of hydrogen from a 2-propanol/water mixture, the nanocomposites caused evolution of hydrogen. After a delay period of a few hours, hydrogen evolved linearly at a rate of ca. 0.04  $\mu\text{mol}/(\mu\text{mol Cd/h})$  for benzylthiol-modified (CdS-BT) and ca. 0.025  $\mu\text{mol}/(\mu\text{mol Cd/h})$  for phenylthiol-modified particles (CdS-PT) [104]. This difference could arise as a consequence of a higher agglomeration tendency of CdS-PT compared to CdS-BT (i.e., a reduced contact area of the CdS particles and the reacting agents in the case of CdS-PT) or as a consequence of a hampered transfer of the photogenerated electrons in CdS-PT to the reactive species [104]. Similarly, poly(urethanes) containing 0.07–0.14 mol CdS/kg composite were prepared with surface-modified CdS particles [105]. The polymer was prepared *in-situ* in a dispersion of CdS in dimethylsulfoxide containing dissolved ethylene glycol and toluenediyl-2,4-diisocyanate. Upon irradiation of the resulting materials with a xenon lamp, 2-propanol decomposed catalytically under release of hydrogen. The reaction was characterized by a delay period of ca. 1.5 h, thereafter hydrogen evolved proportionally to the irradiation time. After 18 h, 0.4–0.6  $\mu\text{mol H}_2/\mu\text{mol Cd}$  were produced.

Other photocatalytically active nanocomposites were produced by *in-situ* synthesis of CdS or ZnS in a reverse micellar system in water and isooctane [161]. Upon addition of hexamethyl diisocyanate, a polyurea formed under the effect of the water present in the system. The resulting materials contained 1.71 mmol/kg CdS of 4.7 nm diameter or 1.56 mmol/kg ZnS of 4.4 nm diameter, respectively. In aqueous suspensions containing 10% v/v 2-propanol, irradiation with a xenon lamp induced the generation of  $\text{H}_2$ . After 18 h, 2.6 mmol  $\text{H}_2$  per kg CdS–polyurea and 8.6 mmol  $\text{H}_2$  per kg ZnS–polyurea composite evolved.

## GLOSSARY

**Aurum potable** Dispersion of gold nanoparticles prepared in medieval times, mainly for medical purposes.

**Coprecipitation** Simultaneous precipitation of different species, for example, of nanoparticles and polymer.

**Dichroism** Difference in colors when an oriented material is viewed in linearly polarized light with the orientation axis parallel and perpendicular, respectively, to the polarization plane.

**Gold ruby glass** Ruby nanocomposite comprising gold colloids in a glass matrix, fabricated in medieval times where it was used in particular as colored church windows.

**Photochromism** Color change under the action of visible or ultraviolet light.

**Spin coating** Technique for the preparation of thin films, based on the placement of a dissolved substance on a rotating substrate whereupon the liquid is distributed uniformly

over the substrate and the solvent evaporates leaving a thin film of the substance on the substrate.

**Ultramicroscope** Apparatus for the determination of particle diameters below the wavelength of visual light, based on the visualization of the particles by light scattering.

## REFERENCES

1. B. M. Novak, *Adv. Mater.* 5, 422 (1993).
2. "International Encyclopedia of Composites" (S. M. Lee, Ed.), Vol. 2. VCH, New York, 1990.
3. "Encyclopedia of Polymer Science and Engineering" (H. F. Mark, N. M. Bikales, C. G. Overberger, G. Menges, and J. I. Kroschwitz, Eds.), Vol. 7. Wiley, New York, 1987.
4. P. N. Dunlap and S. E. Howe, *Polym. Compos.* 12, 39 (1991).
5. J. Israelachvili, "Intermolecular and Surface Forces." Academic Press, London, 1992.
6. U. Kreibitz and M. Vollmer, "Optical Properties of Metal Clusters." Springer, Berlin, 1995.
7. T. Trindade, P. O'Brien, and N. L. Pickett, *Chem. Mater.* 13, 3843 (2001).
8. G. Mie, *Ber. Deutsch. Phys. Ges.* 492 (1907).
9. G. Mie, *Phys. Z.* 8, 769 (1907).
10. G. Mie, *Z. Chem. Ind. Kolloide* 2, 129 (1907).
11. W. Steubing, *Ann. Phys., vierte Folge (Drude's Ann.)* 26, 329 (1908).
12. S. Gallardo, M. Gutiérrez, A. Henglein, and E. Janata, *Ber. Bunsenges. Phys. Chem.* 93, 1080 (1989).
13. R. Rossetti, R. Hull, J. M. Gibson, and L. E. Brus, *J. Chem. Phys.* 83, 1406 (1985).
14. Y. Wang, A. Suna, and W. Mahler, *Mater. Res. Soc. Symp. Proc.* 109, 187 (1988).
15. Y. Wang, A. Suna, W. Mahler, and R. Kasowski, *J. Chem. Phys.* 87, 7315 (1987).
16. Y. Wang and N. Herron, *J. Phys. Chem.* 95, 525 (1991).
17. W. Mahler, *Inorg. Chem.* 27, 435 (1988).
18. Y. Nosaka, K. Yamaguchi, H. Miyama, and H. Hayashi, *Chem. Lett.* 605 (1988).
19. M. T. Nenadović, M. I. Čomor, V. Vasić, and O. I. Mičić, *J. Phys. Chem.* 94, 6390 (1990).
20. L. L. Beecroft and C. K. Ober, *Chem. Mater.* 9, 1302 (1997).
21. D. Yu. Godovski, *Adv. Polym. Sci.* 119, 81 (1995).
22. A. Chevreau, B. Phillips, B. G. Higgins, and S. H. Risbud, *J. Mater. Chem.* 6, 1643 (1996).
23. N. Herron, Y. Wang, and H. Eckert, *J. Am. Chem. Soc.* 112, 1322 (1990).
24. X.-D. Ma, X.-F. Qian, J. Yin, H.-A. Xi, and Z.-K. Zhu, *J. Colloid Interface Sci.* 252, 77 (2002).
25. J. Turkevich, P. C. Stevenson, and J. Hillier, *Trans. Faraday Soc. Discuss.* 11, 55 (1951).
26. G. Frens, *Nat. Phys. Sci.* 241, 20 (1973).
27. S. L. Goodman, S. L. Hodges, L. K. Trejdosiewicz, and D. C. Livingston, *J. Microsc.* 123, 201 (1981).
28. W. Heffels, J. Friedrich, C. Darribère, J. Teisen, K. Interewicz, C. Bastiaansen, W. Caseri, and P. Smith, *Recent Res. Devel. Macromol. Res.* 2, 143 (1997).
29. C. Bastiaansen, W. Caseri, C. Darribère, S. Dellsperger, W. Heffels, A. Montali, C. Sarwa, P. Smith, and C. Weder, *Chimia* 52, 591 (1998).
30. A. T. Paracelsus, "Item zwen tractat von läme sampt gründtlicher gewisser irer cur." Adam von Bodenstein, Basel, 1563. Reprinted as "Theophrast von Hohenheim, gen. Paracelsus, Sämtliche Werke, 1. Abteilung, Medizinische, naturwissenschaftliche und philosophische Schriften," (K. Sudhoff, Ed.), Vol. 2. R. Oldenbourg, München, 1930.
31. T. von Hohenheim, "Drey herrliche Schrifften Herrn Doctors/Theophrasti/von Hohenheim: Das erst/vom geist des lebens und

- seiner krafft/Das ander von krafft innerlicher/geistlicher und leiblicher glider/Das dritt/von krafft eusserlicher glider/unnd sterckung der inneren." Adam von Bodenstein, Basel, 1572. Reprinted as "Theophrast von Hohenheim, gen. Paracelsus, Sämtliche Werke, 1. Abteilung, Medizinische, naturwissenschaftliche und philosophische Schriften" (K. Sudhoff, Ed.), Vol. 3. R. Oldenbourg, München, 1930.
32. H. Lösner, *Z. Chem. Ind. Kolloide* 6, 1 (1910).
  33. B. Valentinus, "Fr. Basilii Valentini Benedictiner Ordens Chymische Schriften alle/so viel derer verhanden/anitzo Zum Ersten mahl zusammen gedruckt/auss vielen so wol geschriebenen als gedruckten Exemplaren vermehret und verbessert und in Zwey Theile verfasst," part 2 (Ander Theil, Das Vierdte Buch). Johann Naumann und Georg Wolff, Hamburg, 1677. Facsimile editon by Verlag Dr. H. A. Gerstenberg, Hildesheim, 1976.
  34. A. Cornejo, *Z. Chem. Ind. Kolloide* 12, 1 (1913).
  35. A. Neri, "The Art of Glass, WHEREIN Are shown the wayes to make and colour Glass, Pastes, Enamels, Lakes, and other Curiosities." English translation from the Italian original text, printed by A. W., London, 1662. Facsimile reproduction by UMI Books on Demand, Ann Arbor, 2002.
  36. D'Arclais de Montamy, "Traité des Couleurs pour la Peinture en Émail et sur la Porcelaine; Précédé de l'Art de Peindre sur l'Email, Et suivi de plusieurs Mémoires sur différents sujets intéressants, tels que le travail de la Porcelaine, l'Art du Stuccateur, la maniere d'exécuter les Camées & les autres Pierres figurées, le moyen de perfectionner la composition du verre blanc & le travail des Glaces, &c." G. Cavelier, Paris, 1765. Facsimile edition by Georg Olms Verlag, Hildesheim, 1981.
  37. Macquer, "Dictionnaire de Chymie." Paris, 1774; cited by T. Svedberg, "Colloid Chemistry." The Chemical Catalog Company, New York, 1924; cf. also R. G. Neville and W. A. Smeaton, *Ann. Sci.* 38, 613 (1981).
  38. W. Ostwald, *Z. Chem. Ind. Kolloide* 4, 5 (1909).
  39. D. J. B. Richter, "Ueber die neueren Gegenstände der Chymie. Eilftes Stück. Vorzüglich über die Glucine, Agust-Erde und einige besondere Eigenschaften des Goldes." Johann Friedrich Korn der Ältere, Breslau, 1802, word by word citation of selected paragraphs by [38].
  40. J. C. Fischer, *Dingl. Polytech. J.* 182, 129 (1866).
  41. M. Faraday, *Philos. Trans. Roy. Soc. London* 147, 145 (1857).
  42. M. Faraday, "Experimental Researches in Chemistry and Physics." Taylor and Francis, London, 1859.
  43. T. Graham, *Ann. Chem. Pharm. (Liebig's Ann.)* 121, 1 (1862).
  44. A. Gutbier, *Z. anorg. Chem.* 32, 347 (1902).
  45. R. Zsigmondy, *Ann. Chem.* 301, 29 (1898).
  46. E. Grimaux, *Compt. Rend. Acad. Sci.* 98, 1434 (1884).
  47. T. Graham, *Ann. Chem. Pharm. (Liebig's Ann.)* 135, 65 (1865).
  48. H. Siedentopf and R. Zsigmondy, *Ann. Phys., vierte Folge (Drude's Ann.)* 10, 1 (1903).
  49. R. Zsigmondy, "Kolloidchemie, 1. Allgemeiner Teil." Otto Spamer, Leipzig, 1925.
  50. R. Zsigmondy, *Ann. Chem. (Liebig's Ann.)* 301, 46 (1898).
  51. P. Scherrer, *Nachr. Königl. Ges. Wiss. Göttingen, Math.-phys. Klasse* 98 (1918).
  52. F. Kirchner and R. Zsigmondy, *Ann. Phys., vierte Folge (Drude's Ann.)* 15, 573 (1904).
  53. F. Kirchner, *Ber. Königl. Sächs. Ges. Wiss., Math.-Phys. Klasse* 54, 261 (1902).
  54. J. C. Maxwell Garnett, *Philos. Trans. Roy. Soc. London Ser. A* 205, 237 (1906).
  55. J. C. Maxwell Garnett, *Philos. Trans. Royal Soc. London Ser. A* 203, 385 (1904).
  56. G. Mie, *Ann. Phys., vierte Folge (Drude's Ann.)* 25, 377 (1908).
  57. J. Turkevich, G. Garton, and P. C. Stevenson, *J. Colloid Sci. Suppl.* 1 9, 26 (1954).
  58. Mr. Lüdersdorff, *Verh. Verein. Beförderung Gewerbeleiss. Preussen* 12, 224 (1833).
  59. K. Stoeckl and L. Vanino, *Z. Phys. Chem. Stöchiom. Verwandtschaftslehre* 30, 98 (1899).
  60. H. Ambronn, *Königl. Sächs. Ges. Wiss.* 8, 613 (1896).
  61. H. Ambronn and R. Zsigmondy, *Ber. Sächs. Ges. Wiss.* 51, 13 (1899).
  62. F. Braun, *Ann. Phys., vierte Folge (Drude's Ann.)* 16, 238 (1905).
  63. A. Frey, *Jahrbuch wiss. Bot.* 67, 597 (1927).
  64. A. Frey, *Z. wiss. Mikrosk.* 42, 421 (1925).
  65. A. Frey, *Naturwiss.* 13, 403 (1925).
  66. F. Bion, *Helv. Phys. Acta* 1, 165 (1928).
  67. A. Frey-Wyssling, *Protoplasma* 27, 372 (1937).
  68. S. Berkman, J. Böhm, and H. Zocher, *Z. Phys. Chem.* 124, 83 (1926).
  69. A. J. Kinloch, "Adhesion and Adhesives." Chapman and Hall, London, 1987.
  70. H. Salmang and H. Scholze, "Keramik," part 1. Springer, Berlin, 1982.
  71. A. Carre and J. Vial, in "Preprints EURADH '92" (J. Schultz and W. Brockmann, Eds.), p. 90. DECHEMA, Frankfurt am Main, 1992.
  72. R. Roy, in "Ceramic Microstructures '86" (J. A. Pask and A. G. Evans, Eds.), p. 25. Plenum Press, New York, 1987.
  73. P. D. Calvert and R. A. Broad, "Contemporary Topics in Polymer Science," Vol. 6. Plenum Press, New York, 1989.
  74. G. Carotenuto, Y.-S. Her, and E. Matijevic, *Ind. Eng. Chem. Res.* 35, 2929 (1996).
  75. S. Deki, K. Sayo, T. Fujita, A. Yamada, and S. Hayashi, *J. Mater. Chem.* 9, 943 (1999).
  76. P. B. Dempster and P. D. Ritchie, *Nature* 169, 538 (1952).
  77. P. B. Dempster and P. D. Ritchie, *J. Appl. Chem.* 3, 182 (1953).
  78. P. A. Rehbindler and G. S. Chodakow, *Silikatechnik* 13, 200 (1962).
  79. R. Schrader and W. Dusdorf, *Krist. Tech.* 1, 59 (1966).
  80. U. Steinike, I. Ebert, J. Jedanzik, U. Kretzschmar, and H.-P. Hennig, *Krist. Tech.* 13, 1229 (1978).
  81. U. Voland, R. Schrader, and H. Schneider, *Z. anorg. allg. Chem.* 368, 317 (1969).
  82. T. Phely-Bobin, D. Chattopadhyay, and F. Papadimitrakopoulos, *Chem. Mater.* 14, 1030 (2002).
  83. F. Papadimitrakopoulos, P. Wisniecki, and D. E. Bhagwagar, *Chem. Mater.* 9, 2928 (1997).
  84. M. Weibel, W. Caseri, U. W. Suter, H. Kiess, and E. Wehrli, *Polym. Adv. Technol.* 2, 75 (1991).
  85. L. Zimmermann, M. Weibel, W. Caseri, and U. W. Suter, *J. Mater. Res.* 8, 1742 (1993).
  86. B. Liu, H. Li, C. H. Chew, W. Que, Y. L. Lam, C. H. Kam, L. M. Gan, and G. Q. Xu, *Mater. Lett.* 51, 461 (2001).
  87. J. M. Jethmalani and W. T. Ford, *Chem. Mater.* 8, 2138 (1996).
  88. H. B. Sunkara, J. M. Jethmalani, and W. T. Ford, *Chem. Mater.* 6, 362 (1994).
  89. J. Liu, Y. Gao, F. Wang, D. Li, and J. Xu, *J. Mater. Sci.* 37, 3085 (2002).
  90. D. Yu. Godovsky, A. E. Varfolomeev, D. F. Zaretsky, R. L. N. Chandranthi, A. Kündig, C. Weder, and W. Caseri, *J. Mater. Chem.* 11, 2465 (2001).
  91. M. Gianini, W. R. Caseri, and U. W. Suter, *J. Phys. Chem. B* 105, 7399 (2001).
  92. G. Schmid, *Chem. Rev.* 92, 1709 (1992).
  93. G. Schmid, S. Peschel, and T. Sawitowski, *Z. anorg. allg. Chem.* 623, 719 (1997).
  94. A. C. Templeton, M. J. Hostetler, C. T. Kraft, and R. W. Murray, *J. Am. Chem. Soc.* 120, 1906 (1998).
  95. M. J. Hostetler, J. E. Wingate, C.-J. Zhong, J. E. Harris, R. W. Vachet, M. R. Clark, J. D. Londono, S. J. Green, J. J. Stokes, G. D. Wignall, G. L. Glish, M. D. Porter, N. D. Evans, and R. W. Murray, *Langmuir* 14, 17 (1998).

96. J. R. Heath, C. M. Knobler, and D. V. Leff, *J. Phys. Chem. B* 101, 187 (1997).
97. M. G. Samant, C. A. Brown, and J. G. Gordon II, *Surf. Sci.* 365, 729 (1996).
98. M. Brust, M. Walker, D. Bethell, D. J. Schiffrin, and R. Whyman, *J. Chem. Soc., Chem. Commun.* 801 (1994).
99. B. A. Korgel and D. Fitzmaurice, *Adv. Mater.* 10, 661 (1998).
100. K. E. Gonsalves, G. Carlson, J. Kumar, F. Aranda, and M. Jose-Yacamán, *ACS Symp. Ser.* 622, 151 (1996).
101. Y. Dirix, C. Bastiaansen, W. Caseri, and P. Smith, *J. Mater. Sci.* 34, 3859 (1999).
102. Y. Dirix, C. Darribère, W. Heffels, C. Bastiaansen, W. Caseri, and P. Smith, *Appl. Opt.* 38, 6581 (1999).
103. K. Murakoshi, H. Hosokawa, M. Saito, Y. Wada, and S. Yanagida, *J. Colloid Interface Sci.* 203, 225 (1998).
104. T. Hirai, M. Miyamoto, T. Watanabe, S. Shiojiri, and I. Komasaawa, *J. Chem. Eng. Japan* 31, 1003 (1998).
105. T. Hirai, M. Miyamoto, and I. Komasaawa, *J. Mater. Chem.* 9, 1217 (1999).
106. Y. Wang and N. Herron, *Chem. Phys. Lett.* 200, 71 (1992).
107. J. G. Winiarz, L. Zhang, M. Lal, C. S. Friend, and P. N. Prasad, *J. Am. Chem. Soc.* 121, 5287 (1999).
108. T. Trindade, M. C. Neves, and A. M. V. Barros, *Scripta Mater.* 43, 567 (2000).
109. M. M. Erwin, A. V. Kadavanich, J. McBride, T. Kippeny, S. Penneycook, and S. J. Rosenthal, *Eur. Phys. J. D* 16, 275 (2001).
110. N. P. Gaponik, D. V. Talapin, and A. L. Rogach, *Phys. Chem. Chem. Phys.* 1, 1787 (1999).
111. M. L. di Lorenzo, M. E. Errico, and M. Avella, *J. Mater. Sci.* 37, 2351 (2002).
112. C. Lea, *Am. J. Sci.* 37, 476 (1889).
113. E. A. Schneider, *Ber. deutsch. chem. Ges.* 25, 1281 (1892).
114. D. K. Lee, Y. S. Kang, C. S. Lee, and P. Stroeve, *J. Phys. Chem. B* 106, 7267 (2002).
115. V. Vidya, N. P. Kumar, S. N. Narang, S. Major, S. Vitta, S. S. Talwar, P. Dubcek, H. Amenitsch, and S. Bernstorff, *Colloids Surf. A* 198–200, 67 (2002).
116. S. P. Gubin, *Colloids Surf. A* 202, 155 (2002).
117. S. A. Zavyalov, A. M. Pivkina, and J. Schooman, *Solid State Ionics* 147, 415 (2002).
118. A. M. Lyons, S. Nakahara, M. A. Marcus, E. M. Pearce, and J. V. Waszczak, *J. Phys. Chem.* 95, 1098 (1991).
119. S. Ogawa, Y. Hayashi, N. Kobayashi, T. Tokizaki, and A. Nakamura, *Jpn. J. Appl. Phys.* 33, L 331 (1994).
120. K. Moller, T. Bein, N. Herron, W. Mahler, and Y. Wang, *Inorg. Chem.* 28, 2914 (1989).
121. N. P. Gaponik and D. V. Sviridov, *Ber. Bunsenges. Phys. Chem.* 101, 1657 (1997).
122. G. Carotenuto, G. P. Pepe, and L. Nicolais, *Eur. Phys. J. B* 16, 11 (2000).
123. G. Carotenuto, *Appl. Organomet. Chem.* 15, 344 (2001).
124. W. Feng, T. R. Zhang, Y. Liu, R. Lu, Y. Y. Zhao, and J. N. Yao, *J. Mater. Sci. Lett.* 21, 497 (2002).
125. T. Kyprianidou-Leodidou, P. Margraf, W. Caseri, U. W. Suter, and P. Walther, *Polym. Adv. Technol.* 8, 505 (1997).
126. A. Ammala, A. J. Hill, P. Meakin, S. J. Pas, and T. W. Turney, *J. Nanoparticle Res.* 4, 167 (2002).
127. J. I. Hong, K. S. Cho, C. I. Chung, L. S. Schadler, and R. W. Siegel, *J. Mater. Res.* 17, 940 (2002).
128. R. Nussbaumer, W. Caseri, and P. Smith, *J. Nanoparticle Res.*, 4, 319 (2002).
129. H. Ambronn, *Z. wiss. Mikrosk.* 22, 349 (1905).
130. Y. Dirix, C. Bastiaansen, W. Caseri, and P. Smith, *Adv. Mater.* 11, 223 (1999).
131. Y. Dirix, C. Bastiaansen, W. Caseri, and P. Smith, *Mater. Res. Soc. Symp. Proc.* 559, 147 (1999).
132. W. Heffels, C. Bastiaansen, W. Caseri, and P. Smith, *Mol. Cryst. Liq. Cryst.* 353, 191 (2000).
133. G. Chumanov, K. Sokolov, and T. M. Cotton, *J. Phys. Chem.* 100, 5166 (1996).
134. W. Gotschy, K. Vonmentz, A. Leitner, and F. R. Aussenegg, *Opt. Lett.* 21, 1099 (1996).
135. M. Takakuwa, K. Baba, and M. Miyagi, *Opt. Lett.* 21, 1195 (1996).
136. K. Baba, J. Katsu, and M. Miyagi, *Opt. Lett.* 17, 622 (1992).
137. K. Baba and M. Miyagi, *Opt. Lett.* 16, 964 (1991).
138. A. H. Lu, G. H. Lu, A. M. Kessinger, and C. A. Foss, Jr., *J. Phys. Chem. B* 101, 9139 (1997).
139. A. G. de León, Y. Dirix, Y. Staedler, K. Feldman, G. Hähner, W. R. Caseri, and P. Smith, *Appl. Opt.* 39, 4847 (2000).
140. "Polymer Handbook" (J. Brandrup and E. H. Immergut, Eds). Wiley, New York, 1989.
141. T. Sugiyama, T. Wada, and H. Sasabe, *Synthet. Met.* 28, C323 (1989).
142. R. A. Gaudiana and R. A. Minns, *J. Macromol. Sci. A* 28, 831 (1991).
143. H. G. Rogers, R. A. Gaudiana, W. C. Hollinsed, P. S. Kalyanaraman, J. S. Manello, C. McGowan, R. A. Minns, and R. Sahatjian, *Macromolecules* 18, 1058 (1985).
144. W. Groh and A. Zimmermann, *Macromolecules* 24, 6660 (1991).
145. "Handbook of Optical Constants of Solids" (E. D. Palik, Ed.). Academic Press, Orlando, 1985.
146. L. Zimmermann, M. Weibel, W. Caseri, U. W. Suter, and P. Walther, *Polym. Adv. Technol.* 4, 1 (1993).
147. E. J. A. Pope, M. Asami, and J. D. Mackenzie, *Mater. Res. Soc. Symp. Proc.* 132, 105 (1989).
148. E. J. A. Pope, M. Asami, and J. D. Mackenzie, *J. Mater. Res.* 4, 1016 (1989).
149. J. C. Seferis and R. J. Samuels, *Polym. Eng. Sci.* 19, 975 (1979).
150. A. R. Wedgewood and J. C. Seferis, *Polym. Eng. Sci.* 24, 328 (1984).
151. T. Kyprianidou-Leodidou, W. Caseri, and U. W. Suter, *J. Phys. Chem.* 98, 8992 (1994).
152. S. Schmitt-Rink, D. A. B. Miller, and D. S. Chemla, *Phys. Rev. B* 35, 8113 (1987).
153. T. Kyprianidou-Leodidou, H.-J. Althaus, Y. Wyser, D. Vetter, M. Büchler, W. Caseri, and U. W. Suter, *J. Mater. Res.* 12, 2198 (1997).
154. K. Miura and B. Tamamushi, *J. Electron Microsc.* 1, 36 (1953).
155. Y. Wang, *Stud. Surf. Sci. Catal.* 103, 277 (1996).
156. Y. Wang and N. Herron, *J. Lumin.* 70, 48 (1996).
157. W. Feng, E. Sun, A. Fujii, H. Wu, K. Niihara, and K. Yoshino, *Bull. Chem. Soc. Jpn.* 73, 2627 (2000).
158. C. L. Yang, J. N. Wang, W. K. Ge, S. H. Wang, J. X. Cheng, X. Y. Li, Y. J. Yan, and S. H. Yang, *Appl. Phys. Lett.* 78, 760 (2001).
159. J. G. Winiarz, L. Zhang, J. Park, and P. N. Prasad, *J. Phys. Chem. B* 106, 967 (2002).
160. B. Török, I. Kiricsi, Á. Molnár, and G. A. Olah, *J. Catal.* 193, 132 (2000).
161. S. Shiojiri, T. Hirai, and I. Komasaawa, *Chem. Commun.* 1439 (1998).





# Nanocomputers: Theoretical Models

Michael P. Frank

University of Florida, Gainesville, Florida, USA

## CONTENTS

1. Introduction
  2. Fundamental Physics of Computing
  3. Traditional Models of Computation
  4. New Models of Nanocomputers
  5. Generic Realistic Model of Nanocomputers
  6. Specific Nanocomputing Technology Proposals
  7. Conclusion
- Glossary  
References

## 1. INTRODUCTION

In this chapter, we survey a variety of aspects of theoretical models of computation, with an emphasis on those modeling issues that are particularly important for the engineering of efficient nanoscale computers.

Most traditional models of computing (such as those treated in Savage's textbook [1]) ignore a number of important fundamental physical effects that can dramatically impact computational performance at the nanoscale, such as the basic thermodynamic limits on information processing [2], and the possibility of utilizing quantum physical superpositions (essentially, weighted combinations) of logic states [3]. New, alternative models of computing that allow *reversible computing* [4], while respecting the laws of thermodynamics may (gradually, over the next ~50 years) achieve a level of performance and cost efficiency on all types of computational tasks that is literally *thousands* of times greater than the best that is physically possible using conventional *irreversible* models [5]. Also, those models that are not only reversible but also allow coherent *quantum computing*, based on self-interference of entangled superpositions of states, furthermore permit expressing algorithms (for at least some special-purpose problems) that require *exponentially* fewer steps in these models than the best known algorithms in the older models that do not [3].

Because of such discrepancies, the scope and precision of our models of computation *must* be revised and extended in

order to take these new considerations into account, if we wish our models to continue to be an accurate and powerful guide to the engineering design of computer architectures and to the performance of algorithms, even as technology approaches the nanoscale. We describe some ways in which this has already been done, by the author and others, show some example results of this modeling effort (such as the quantitative performance advantages of reversible and quantum computing quoted previously), describe a variety of proposed nanocomputing technologies, and identify which technologies have the potential to implement these most powerful models. We conclude with a discussion of future work that is needed to further develop and flesh out these models to the point where future nanocomputer engineers and programmers will find them maximally useful.

### 1.1. Definition of “Nanocomputer”

For purposes of this chapter, a *nanocomputer* is simply any computer whose *characteristic length scale*—the average spacing between the centers of neighboring primitive functional components, such as transistors or other switching elements—falls within the three-orders-of-magnitude-wide range that is centered on 1 nanometer (that is, ~0.032 to ~32 nanometers). (Anything in the next larger range might be better called a *microcomputer* and anything in the next smaller range, if that were possible, a *picocomputer*.)

Under this definition, note that even traditional semiconductor-based computers are expected to qualify as nanocomputers in only about 13 more years—to wit, the semiconductor industry's goals [6] specify that the *pitch* between neighboring wires should fall only slightly above this range, specifically at a level of 44 nanometers, by 2016. Furthermore, the semiconductor industry's stated milestones such as this have historically proven conservative, and indeed, Intel [7], IBM [8], and AMD [9] have already demonstrated ~10-nm gate-length field-effect transistors in the lab which, if aggressively packed together, might allow a pitch below the 30-nm *nanoscale* mark within 10 years, which historically is the approximate lag time between laboratory demonstrations of transistors and their availability in commercial processors. (Of course, if some alternative,

non-transistor-based nanotechnology development proceeds especially rapidly, this scale might be reached even sooner.)

Note that by focusing on the *pitch* rather than *diameter* of the primitive elements, we insist that computers based on narrow-diameter components, such as the carbon nanotube [10] or semiconductor nanowire [11] logic gates that have already been demonstrated, would not count as viable nanocomputers *unless* the average *spacing*, as well as the size, of these devices across a large and economically manufacturable array is made sufficiently small, which has not yet been accomplished, but which may be in the future.

## 1.2. Theoretical Models of Computing—Key Model Components

Now, what do we mean by a theoretical model of computing? In general, a theoretical model of any size computer (whether “nano” or not) can involve a number of different aspects that are relevant to computer engineering, any of which may be more or less abstract (or even left completely unspecified) in any particular model. These modeling areas include:

1. A *device model* specifies the physical and/or information-processing characteristics of the individual, lowest level information-processing functional elements (*devices*, which we will sometimes call *bit devices* when they are based on binary information encodings, to distinguish them from larger machines) within the computer.
2. A *technology scaling model* specifies how device characteristics change as the physical dimensions of the devices are scaled to smaller sizes, when this is possible.
3. An *interconnection model* specifies how information is communicated between devices. When wires are considered to be one of these types of devices, the interconnect model can be considered part of the device model. But wires and other types of permanent physical structures are not the only possible way for devices to communicate; various types of interconnects involving physical entities moving through free space are also conceivable. The precise nature of the interconnection model has greater implications than one might at first expect.
4. A *timing model* specifies how the activities of different devices are to be synchronized with each other. The timing model also has more of an impact than might at first be realized.
5. A *processing architecture model*, or just *architecture*, specifies how devices are *functionally* connected to form a larger unit called a *processor*, which is complex enough to be programmed to carry out any desired type of computation, or at least, to carry out a specific type of computation on different input information.
6. A (*capacity*) *scaling model* is a more general sort of architecture (sometimes called an *architecture family* [12]) that allows the capacity of the processor (in bits of storage, and/or ops-per-cycle of performance) to be scaled up, via some specified regular transformation, to ever-larger sizes. This stands in contrast to nonscalable architectures where the processor is specified to have a fixed, constant number of bits of state, and ops-per-cycle of performance. The most common type of scaling model is a *multiprocessor* scaling model, which defines larger processors as simply being assemblages of smaller processors that are interconnected together, using some processor-level interconnect model, which might be different from the interconnect model that is used at the device level.
7. An *energy transfer model* specifies how “clean” power is to be supplied, and “dirty” power (waste heat) removed, from all parts of a scaled processor. The energy system can also be viewed from an informational perspective as supplying known information in a standard state (in the stable power signal) and removing unknown information (entropy, in the waste heat). As such, it is subject to the fundamental limits on information processing to be discussed.
8. A *programming model* specifies how the computer can be configured to carry out different types of computations (as opposed to just performing the same computation on different input information). A programming model that happens to be based on traditional types of computer machine-language instructions is called an *instruction set architecture*, but other, radically different types of programming models also exist, such as those that are used today to program field-programmable gate arrays (which are general-purpose reconfigurable logic circuits) and dataflow-style machines, as well as earlier, more abstract models such as Turing machines and cellular automata. A high-level programming language is a very abstract sort of programming model that is relatively far removed from the architecture of any specific machine and that is usually translated into a more architecture-specific programming model such as machine language, before execution by the hardware.
9. An *error handling model* sets forth a scheme for dealing with hardware errors, whether they be *defects* (persistent errors due to malformation or degradation of device structures during manufacturing or operation) or *faults* (dynamically arising temporary errors, due to, example, thermal noise, cosmic rays, energy leakage, or quantum tunneling). Techniques such as error correction codes, J. Baylis, *Error-Correcting Codes*, Chapman-Hall, London, 1998, and defect-tolerant architectures, J. Heath, P. Kuekes, G. Snider, S. Williams, “A defect-Tolerant Computer Architecture: Opportunities for Nanotechnology,” *Science* 280, 1716 (1998), can dynamically detect such errors and correct them (in the case of faults) or work around them (in the case of defects). Note that each new error occurrence generates some entropy which must eventually be removed from the machine by the energy transfer system, if it is not to accumulate to the point of total degradation of the machine’s structure.
10. A *performance model* can be used to determine quantitatively (to some degree of accuracy) how quickly any specific algorithm implemented in the programming model will execute on the specific architecture.

Performance can be considered a special case of *cost efficiency*, in which cost is considered to be directly proportional to time (which is appropriate in many circumstances).

11. A *cost model* quantifies the *cost*, according to one or more measures, of manufacturing a computer of given capacity, and/or of executing a specified computation on it. Note that a performance model can actually be considered to be a special case of a cost model in which there is a single cost measure, namely *execution time*; performance (or “quickness”) is just the reciprocal of this. As we will discuss, it is also useful to consider other physically reasonable cost measures such as energy costs, spacetime-proportional costs, and total dollar cost of both energy and spacetime. Whatever the cost measure, *cost efficiency* (or just *efficiency*) in general is the ratio between the minimum possible cost to perform a computation and the actual cost. Even if the minimum possible cost of a computation is unknown, we know that to maximize the cost efficiency of a given task, we must minimize its actual cost.

### 1.3. Desiderata for Models of Computing

What do we want our models of computing to be like? Well, here are some properties that we might desire a computer model to have:

- *Ease of programming*: The programming model (when specified) should be intuitive and easy for programmers to understand and work with.
- *Ease of implementation*: It should be possible and straightforward to design and build actual physical implementations of the given architecture.
- *Physical realism*: The predictions of the cost/performance model should be, at least approximately, physically realizable in feasible implementations. This feature, though it is very important for real-world engineering purposes, is unfortunately neglected by many of the theoretical models that have been studied in some of the more pure-mathematics-oriented branches of computer science (more on this issue later).
- *Efficiency*: The cost efficiency achievable by programs running on top of direct physical implementations of the model should be as high as possible, ideally close to 100% (best possible), but in practice at least lower bounded by some constant minimum level of efficiency that holds independently of parameters of the application (more on this later).
- *Technology independence*: If possible, the model should be applicable to a wide range of different possible technologies for its physical implementation, rather than being tied to a very specific technology. Later we will give an example of a technology-independent model. However, technology-specific models do also play an important role, for example, for accurately assessing the efficiency characteristics of that particular technology.

### 1.4. Physical Realism

A theoretical model of computation (at whatever level of abstraction) that includes at least a programming model, an architecture, and a performance or cost model will be called *physically realistic* (abbreviated *PR*) if it does not significantly overstate the performance or (understate the cost) for executing any algorithm on top of physically possible implementations of that architecture. Physical realism is also (somewhat cryptically) termed *congruence* in some of the parallel computing literature (cf. [83]).

As we will survey, not all of the theoretical models of computation that have traditionally been studied by computer scientists are actually physically realistic, according to our best-available present-day understanding of physical law; some even overstate performance (or more generally, cost efficiency) by multiplicative factors that become unboundedly large as one increases the capacity of the machine. These factors can be anywhere from polynomially large in the machine capacity [*e.g.*, for irreversible three-dimensional (3D) mesh models, which ignore the laws of thermodynamics] to exponentially large or even larger (*e.g.*, seemingly so for nondeterministic models, and also for unrealistically profligate interconnect models that ignore the speed-of-light limit). This lack of realism may be acceptable from the perspective of studying the pure mathematical structure of various models in the abstract, but, as engineers, we prefer for our models to correspond well to reality. So we must be careful in our modeling not to overstate what physics can do, or we may mislead ourselves into wasting time designing, building, and programming machines that cannot possibly live up to the unrealistic performance expectations that we may have for them if we are fooled and believe some of the traditional models.

### 1.5. Scalability of Efficiency

Similarly, computer modeling will also not well serve us if it significantly *understates* what physics can do, that is, if the architecture and programming model do not allow one to express algorithms that are as cost efficient as is physically possible. Of course, no specific mechanism (other than raw physics itself) can be expected to be exactly maximally cost efficient for *all* computations, but we will argue that it is possible to devise physically realistic models that understate the best physically possible cost efficiency of computations by only, at most, a reasonably small (that is, not astronomically large) constant factor, and one that furthermore does not increase as the machine is scaled to larger capacities. We call such models *universally maximally scalable* (*UMS*). Models possessing this UMS property (in addition to physical realism) would be the ideal architectural templates for the detailed design and engineering of future general-purpose nanocomputers, since they would pose no barrier to an application algorithm designer’s choosing and programming the most cost-efficient, physically possible algorithm for any given computational task.

As we will survey, out of the various physically realistic traditional models of computation that have been proposed to date, absolutely *none* so far have qualified as UMS models. We describe some new candidates for UMS models that

we have recently proposed, and we mention the possible remaining flaws in these models that may still prevent them from being *completely* accurate across all regimes of physically possible computations in the very long term.

## 2. FUNDAMENTAL PHYSICS OF COMPUTING

Let us begin by briefly reviewing how the capabilities and limitations of computers are impacted by very general considerations within the well-established consensus model of fundamental physics, known as the Standard Model of particle physics.

The Standard Model is not yet complete, in that it does not yet incorporate all aspects of Einstein’s General Theory of Relativity (another well-established model), and so various new models that attempt to merge the two theories are currently in development, such as String Theory [13], M-Theory [13], and Loop Quantum Gravity [14]. Whichever extension of the Standard Model (if any) turns out to be correct will doubtless have some implications for the ultimate limits of computing; however, any modifications that these extensions might make to the current models are only expected to become relevant at an energy density scale that is so high that we do not expect these modifications to be technologically relevant any time soon (in this century, say). It seems that the Standard Model suffices for characterizing the ultimate limits of all more near-term technologies.

Tables 1 and 2 summarize the major limiting factors imposed by the laws of physics as we know them, as well the opportunities for increased computational power afforded by those laws. More detailed accounts of these limits can be found in [4, 15, 16].

### 2.1. Concepts of Physical Information Processing

In this section, we give a brief overview of a number of basic concepts that are needed for a correct physical understanding of information processing. This can also be viewed as an explanation of basic physical concepts *themselves* in terms of information processing. Reference [24] develops some of these ideas in more detail. Some of the following identities and definitions may be considered approximate and even a bit speculative, given that we do not yet have a complete computational model of physics, but they can all be argued to be roughly correct, at least to first order.

#### 2.1.1. States

A *state* or *configuration* of a system can be understood as a complete description of that system that is valid, in principle, at some point in time. Quantum mechanics, or specifically, Heisenberg’s *uncertainty principle*, teaches us that not all of the mathematically different states that a physical system may be in are actually *operationally distinguishable* from each other by *any* physically possible attempt to discriminate them

**Table 1.** Summary of all known ways in which fundamental physical principles limit information processing.

Physical considerations	Limits on computational capabilities
1. Principle of locality; speed-of-light limit on velocity of propagation of information through space.	1a. Lower bound on communications latency across systems of given diameter [12, 17].
2. Wave aspect of quantum mechanics; uncertainty principle.	2a. Upper bound on information capacity for systems of given diameter and energy [15, 16].
3. Considerations 1 and 2, taken together.	3a. Upper bound on rate of bits communicated per unit area, with given power [4, 15].
4. Fundamental quantum relationship between frequency and energy.	3b. Lower bound for average random access time for a memory of given size and energy density.
5. Reversibility of quantum mechanics; thermodynamic relationships between information and energy.	4a. Upper bound on rate of useful bit operations per second in systems containing a given amount of free energy [16, 18].
6. Considerations 3 and 5, taken together.	5a. Lower bound on energy wasted per irreversible bit operation, given external temperature [19].
7. Second law of thermodynamics; rate of entropy increase is $>0$ in all nonequilibrium systems.	5b. Upper bound on rate of irreversible bit operations performed per watt of power consumption, given external temperature [4].
8. Adiabatic theorem of quantum mechanics.	6a. Upper bound on sustainable rate of irreversible bit operations within an enclosure of given area and external temperature [20].
9. Considerations 6 and 8 taken together.	7a. $>0$ rate of energy waste per bit stored.
10. Gravity, as per Einstein’s theory of general relativity.	7b. Upper bound on number of bits stably stored, given rate of heat removal and rate of entropy generation per bit [21].
	8a. Energy waste proportional to speed in reversible bit-operations [22].
	9a. Upper bound on rate of reversible operations given system diameter, device quality, heat flux or power limits, and external temperature [21].
	10a. Upper bounds on internal energy of computers of given diameter, in turn limiting their speed and capacity [4].

*Note:* Many older models of computation fail to respect all of these limits and therefore are physically unrealistic, except in restricted regimes in which these constraints are far away. Constraint 1 already affects communication delays and computer performance today. Constraints 2–9 are still far from being reached today, but they are all expected to become important limiting factors over the course of the next 50 years. Larger scale analogs to these fundamental considerations are also important today. In contrast, constraint 10 requires extremely high energy densities (near black hole density) in order to become relevant and therefore is not expected to be a concern any time in the near future (the next 100 years, for example).

**Table 2.** Summary of ways in which physics offers opportunities for more cost-efficient computing than would have been thought possible using earlier, physically realistic (but overly conservative) models of computation that ignored those opportunities.

Physical observations	Opportunities for computing
1. Events can occur in different places at the same time.	Parallel computation; a machine can perform different operations in different devices simultaneously [23].
2. Our universe has three (and only three) usable spatial dimensions.	The number of bit locations accessible within a given time delay can scale up as quickly as (at most) the third power of the delay; this fact can help performance of some parallel algorithms, compared to the 2D or 1D cases [17, 23].
3. Some types of physical transformations can occur in a way that generates an amount of entropy approaching zero.	Such nearly <i>reversible</i> transformations can perform computations with less loss of free energy, and as a result less total cost in many situations, compared to irreversible methods. This is called <i>reversible computing</i> [4].
4. Quantum mechanics allows a system to be in a superposition (weighted sum) of many distinct states simultaneously.	Carefully controlled systems that use superposition states can take shortcuts to arrive at solutions to some problems in many fewer steps than is known to be possible using other methods. This is called <i>quantum computing</i> [3].

*Note:* Parallelism is already heavily used at many levels, from logic circuits to wide-area distributed computing, as are architectural configurations that take some advantage of all three dimensions of space, though to a limited extent (constraint 6 in Table 1 is an important limit on three-dimensional computing today). Reversible computing and quantum computing, in contrast, are still very much in the research stage today, but they are both expected to become increasingly important for competitive computing as device sizes approach the nanoscale. Reversible computing is important because it directly alleviates constraints 5 and 6 from Table 1 (which are already relevant, in a scaled-up way, today), and quantum computing offers a totally new class of algorithms that will be important in and of themselves for certain problems, regardless of whether quantum computing turns out to be useful for general-purpose algorithms, or whether general-purpose nanocomputing itself even becomes feasible.

[25]. Fundamentally, this is because not all pairs of quantum states are totally mutually exclusive with each other. Rather, states can *overlap*, in a certain mathematically well-defined way, which results in the phenomenon that a system that is prepared in a certain state has a necessarily diffuse sort of *presence*, so to speak, a presence that extends to partly include other, sufficiently nearby states as well.

### 2.1.2. State Space

The *state space* of a system is the set of all of its possible states. In quantum theory, a state space has the mathematical structure of a Hilbert space (a complex vector space having an inner product operation).

### 2.1.3. Dimensionality

The *dimensionality* of a system's state space is simply the number of states in a maximum-sized set of states that are all mutually exclusive (mutually orthogonal vectors). For example, the spin orientation of a single spin one-half subatomic particle has two distinguishable states and thus has a state space of dimensionality 2. Two such particles together have four distinct states, and a four-dimensional state space.

### 2.1.4. Amount of Information

The total *amount of information* contained in a system is just the logarithm of the dimensionality of its state space, that is, the logarithm of its maximum number of mutually distinguishable states [26]. The base of the logarithm is arbitrary and yields a corresponding unit of information. Taking the log base 2 measures the information in units of bits (binary digits). Using the natural logarithm (base  $e \approx 2.717, \dots$ ), the corresponding information unit is called the *nat*. The physical quantities that are traditionally known as Boltzmann's constant  $k_B$  and the ideal gas constant  $R$  are simply different names for 1 nat of information, but they are usually

expressed in different (though still compatible) units, such as Joules per Kelvin, or kilocalories per mole per Kelvin, and are usually also reserved specifically for discussing information that happens to be entropy.

Note that the total amount of information contained in any system is constant over time, so long as its maximum number of states is also. This is the case for any system with constant total energy and volume.

### 2.1.5. Information

The *specific* information that is in a system (as opposed to the *amount* of information) is the particular *choice* of state, itself. We can say that the actual state of a system *is* the information in the system.

### 2.1.6. Entropy

Entropy  $S$  was originally just an unnamed, abstract quantity (the ratio between heat and temperature) of unknown physical significance when its usefulness in thermodynamic calculations was first recognized by Rudolph Clausius in 1850. But entropy is now understood to simply represent that portion of the information in a system that is not redundant (correlated) with the information in other parts; that is, it cannot be derived from the other information. As such, the distinction between which pieces of physical information are effectively entropy, and which are not, depends, to some extent, on the information-processing capabilities of the entity that might be doing the deriving. A specific body of information may appear at first to be haphazard and random, but with sufficient processing, we may eventually notice an underlying order to it.

Right now, the amount of information that is under explicit control within our computers is just a tiny fraction of the total physical information in the world around us,



and so we do not notice the effect that information processing capabilities can have on entropy. But, as computation approaches the nanoscale, an increasingly large fraction of the information inherent in the physical material making up our computer circuits will be explicitly manipulated for computational purposes, and as a result, the ultimate computational nature of entropy will start to become more and more apparent. As we will see, it turns out that the amount of entropy that a nanocomputer produces actually depends heavily on whether its design recognizes that all of the information that it deterministically computes is actually *not* entropy, since it was derived from other information in the machine and therefore is redundant with it. Current machine designs ignore this fact and simply discard intermediate results after they are no longer needed, irreversibly committing them to the great entropy dump in the sky. (Literally: the discarded information flows out of the machine and eventually out into space.)

So, to sum up, entropy is defined as simply any and all information whose identity (as opposed to amount) happens to be unknown by a given entity of interest, an entity whose interactions with the system we are concerned with describing. (This entity in question can itself be any kind of system, from a human to a logic gate.) The state of *knowing* can itself be defined in terms of the presence of accessible correlations between the state of the knower and the state of the system in question, but we will not get into that here.

### 2.1.7. Subsystems

Consider a maximal set of distinguishable states of a system. If this set is partitioned into  $N$  equal-sized subsets, then the selection of one subset from the partition can be considered a *part* of the state of the whole system. It corresponds to a *subsystem* of the original system. The amount of information in the subsystem is  $\log N$ . This much of the whole system's information can be considered to be located *in* the subsystem. Two subsystems are *independent* if they partition the state space along independent (orthogonal) directions, so to speak. (This concept can be made more precise but we will not do so here.) A set of mutually independent subsystems is *complete* if specifying the state of each subsystem is enough to specify the state of the whole system exactly. A minimal-sized subsystem (one that cannot be further broken down into independent subsystems) is sometimes also called a *degree of freedom*.

### 2.1.8. Bit Systems

A *bit system* or just *bit* is any degree of freedom that contains only 1 bit of information, that is, a bit is a partition of the state set into two equal sized parts. Note the dual usage of the word *bit* to refer to both a unit for an amount of information and to a system containing an amount of information that is equal to that unit. These uses should not be confused. Systems of sizes other than 1 bit can also be defined, for example bytes, words, *etc.*

### 2.1.9. Transformations

A *transformation* is an operation on the state space, mapping each state to the corresponding state resulting from the transformation. It is a fundamental fact of quantum

mechanics (and all Hamiltonian mechanical theories, more generally) that the transformations corresponding to the passage of time are reversible (that is, one-to-one, invertible, bijective). The *size* of a given transformation can be described in terms of the average distance between old states and new states, by some appropriate metric.

### 2.1.10. Operations

A *primitive orthogonalizing operation* (or just *operation* for short) is a transformation that maps *at least one* state to some new state that is distinguishable from the original state, and that cannot be composed of smaller operations. An operation is *on* a particular subsystem if it does not change the state of any independent subsystem. An operation on a bit system is called a *bit operation* (and similarly for other sizes of systems). Two operations *commute* if performing them in either order has the same net effect. Operations on independent systems always commute.

### 2.1.11. Transformation Trajectory

A transformation trajectory is a transformation expressed as a sequence of (primitive orthogonalizing) operations, or pieces of such operations, operating on individual degrees of freedom (*e.g.*, a quantum logic network Nielsen and Chuang [3]).

### 2.1.12. Number of Operations

The total *number of operations* that take place along a given transformation trajectory can be defined. *Planck's constant*  $h$  (or  $\hbar \stackrel{\text{def}}{=} h/2$ ) can be viewed as a unit for expressing a number of operations. The unreduced Planck's constant  $h$  represents two primitive operations (for example, a complete rotation of a particle spin through an angle of  $360^\circ$ ), while the reduced constant  $\hbar$  represents a fraction  $1/\pi$  of a primitive operation, for example, a rotation of a spin through an angle of only 1 radian.

### 2.1.13. Steps

A *complete parallel update step* or just *step* is a transformation of a system that can be described by composing operations on each subsystem in some maximal, complete set of subsystems, such that the total number of operations in bits is equal to the amount of information in bits. In other words, it is a complete overhaul of *all* of the state information in the system, whereas an *operation* on the system only potentially changes some *part* of the state.

### 2.1.14. Dynamics

The *dynamics* of a system specifies a transformation trajectory that is followed as the system evolves in time.

### 2.1.15. Amount of Time

Given the dynamics, the amount of time itself can be defined in terms of the number of steps taken by some fixed reference subsystem, during a given trajectory taken by the

system. Note that if the system and the reference subsystem are both taken to be just the whole universe, then time just represents the total “amount of change” in the universe, in terms of number of parallel update steps performed. (Such concepts harken back to the relativist philosophies of Leibniz and Mach which helped inspire Einstein’s general relativity [27].)

### 2.1.16. Energy

Now, the *energy* in a subsystem is the rate at which primitive operations are taking place in that subsystem, according to its dynamics. In other words, energy is *activity*; it is *computing* itself. This can be proven from basic quantum theory [16, 18, 28].

As a simple way to see this, consider any quantum system with any subsystem whose physical Hamiltonian induces any two energy eigenstates of distinct energies; call these states  $|0\rangle$  and  $|2E\rangle$  arbitrarily. Now, if the subsystem happens to be in the state  $|0\rangle + |2E\rangle$ , which has (expected) energy  $E$ , then the quantum time evolution given by the system’s Hamiltonian takes it to the orthogonal state  $|0\rangle - |2E\rangle$  in time  $(\hbar/4)/E$ . Margolus and Levitin [18] show that a system with energy  $E$  can never change to an orthogonal state any faster than this, no matter what its initial state. Therefore, we can say that any  $E$ -sized chunk of energy is, every  $\hbar/4E$  time, “performing” the operation “If I am in this subsystem and its state is  $|0\rangle + |2E\rangle$ , make its state  $|0\rangle - |2E\rangle$ , otherwise . . . .” This transformation counts as an operation, by our definition, because it does orthogonalize *some* states. However, this particular operation is somewhat limited in its power, because the subsystem in question subsequently immediately cycles right back to its original state. We call this special case an *inverting op* (*iop*); its magnitude in terms of Planck’s constant is  $(\hbar/4)$ . Margolus and Levitin show that an op that instead takes a system to the next state in a repeating cycle of  $N$  states requires more iops worth of time, in fact,  $2(N-1)/N$  times more ops, or  $[(N-1)/2N]\hbar$ .

In the limit as the cycle length  $N$  approaches infinity (as it does in any complex system), the time per orthogonal transition approaches 2 iops worth, or  $(\hbar/2)$ , so we define this as the magnitude of a generic “op” as previously.

Incidentally, when applying the Margolus–Levitin relation to the example of a simple freely rotating system,  $N$  can be argued to be equal to the system’s total angular momentum quantum number  $l$  plus 1, and with a few more steps, it turns out that the relation can be used to independently confirm the usual angular momentum quantization formula  $(L/\hbar)^2 = l(l+1)$ , much more easily than by the usual derivation found in quantum physics textbooks.

### 2.1.17. Heat

Heat is just the energy in those subsystems whose state information is entirely unknown (entropy).

### 2.1.18. Temperature

The *temperature* of a subsystem is the average rate at which complete update steps are taking place in that subsystem (*i.e.*, the average rate of operations per bit) [28]. Note that energy divided by temperature gives the amount of information in the subsystem. This is, historically, how physical

information (in the form of entropy) was first noticed as an important thermodynamic quantity (by Rudolph Clausius, in 1850), even before the fact that it was really just information was understood.

Note that the *reciprocal* of temperature is just the time required for a complete step that, on average, updates all parts of the state information, once each.

This definition of temperature, in contrast to traditional ones, is general enough that it applies not just to systems in a maximum-entropy equilibrium state (all of whose information is entropy), but more generally to any system, even systems in a completely known state with no entropy, which according to traditional definitions of temperature would always be at absolute zero. However, for any system we can also identify a *thermal temperature* which is the average temperature of any of its subsystems whose state information is entropy, and then consistently define that the thermal temperature of a system having *no* entropy is zero. Thermal temperature is, then, just the traditional thermodynamic concept of temperature. But our more general temperature concept is somewhat more flexible.

Note also that energy spontaneously flows from “hot” subsystems to “cold” ones, rather than vice versa, simply because the fast-changing pieces of energy in the hot system more frequently traverse the trajectories through state space that cross over the boundary between the two systems.

These are enough definitions to support our later discussions in this chapter. A more complete discussion of the relationships between physics and information processing can be found in [24] (in progress).

Discussions of *quantum information* and how it extends the classical concepts of information can be found in [3].

## 3. TRADITIONAL MODELS OF COMPUTATION

In this section, we systematically survey a wide variety of early models of computing and identify exactly which of the limits or opportunities listed in the previous section each one fails to account for, which result in the model’s lacking one or the other of the properties of PR or UMS. Furthermore, we consider what types of costs are respected in the model.

In the next section, we will present the newer models which may actually come close to being both PR and UMS for all practical purposes in the foreseeable future.

Here are some contributions to real-world costs that an economically thorough cost model ought to take into account:

1. Manufacturing cost to build a machine that can perform a given computation. We may expect this to be roughly proportional to its total information capacity. However, if the machine can be reused for more than one computation, then the cost model should account for this properly (cf. item 3a below).
2. Costs that may be considered to scale roughly proportionally to the execution time of programs, but not to the machine’s manufacturing cost, such as, for example, the inconvenience cost to the user of waiting to receive a desired result.

3. Costs that can be expected to scale proportionally to both execution time *and* manufacturing cost, such as:
  - a. Hardware *rental* cost, or essentially manufacturing cost amortized per unit time, given some fixed expected lifetime for the machine.
  - b. Maintenance and operation costs for the machine per unit time, including cost of energy used by components that are operating at constant power levels.
  - c. Opportunity cost foregone by not applying the machine’s capacity toward some alternative useful purpose.
4. Total cost of energy spent for the computation. We list this separately from item 3b because later we will see that there are significant components of energy that are *not* necessarily proportional to spacetime usage.

Traditional computational complexity theory (cf. [29]) considers purely time-proportional costs like item 2, simplified to just the total number of discrete time-steps (clock ticks) performed (*i.e.*, assuming a fixed rate of steps per unit time), and dubbed *time complexity*. It also considers a rough measure of manufacturing cost, in the form of the total number of bits of storage required to perform the computation and calls this *space complexity*. However, most work in complexity theory does not combine the two in the natural way suggested by items 2b–2e, which is that real costs are usually proportional to *both* space and time, or in other words to the *spacetime* utilized, that is to say, the cost to *rent* the required amount of hardware for the amount of time needed to perform the computation, and to other costs that can be assumed to scale proportionally to this quantity, such as maintenance cost, opportunity cost, and energy used (typically).

Some cost models in complexity theory count the number of fixed-size computational *operations* that are performed, rather than the number of parallel steps. This comes closer

to spacetime cost but still does not quite hit the mark, since there are real costs even associated with those bits that are just sitting statically and not being operated on at all (hardware rental cost, maintenance cost, opportunity cost).

Newer models such as VLSI theory (very large scale integrated circuits cf. [30]) address these problems somewhat by considering the *hardware efficiency* of algorithms, which is essentially the reciprocal of their spacetime usage. However, these models still do not usually integrate the cost of energy into the analysis in a way that treats it as somewhat independent from spacetime cost, which it is, as we will see.

Table 3 summarizes how a variety of existing theoretical models of computation fare with respect to the fundamental limits and opportunities discussed in Section 2, and the costs discussed previously. A discussion follows.

### 3.1. Turing Machines

The *Turing machine* [31] was the first universal, physically evocative (as opposed to totally abstract and formal) model of computation. It has a single fixed-size processor (the *head*) and a memory laid out in one dimension that is accessed in serial fashion (the *tape*). The Turing machine model does not violate any of the fundamental physical limits on information processing, and therefore it is physically realistic.

However, since a Turing machine has only a single, fixed-size “processor” (the tape head), it does not leverage the possibility of parallelism. Multitape and multihead Turing machines provide limited parallelism, but true parallelism in the model requires that the number of processors must be scaled up in proportion to the information capacity of the machine. Turing machine models usually do not try to do this, but later we will see other models that do.

It is possible to analyze space and time costs in a Turing machine model, but the joint spacetime cost is not usually a concern, since the model has such understated efficiency in any case. Due to its drastic suboptimality, the Turing

**Table 3.** We can compare various models of computation as to which fundamental physical limits they violate (see Table 1), which opportunities for more efficient computing they leverage (Table 2), and which aspects of cost they take into account.

Model	Fundamental limits violated										Opportunities leveraged				Costs considered			
	1	2	3	4	5	6	7	8	9	10	1	2	3	4	1	2	3	4
Turing machine [31]												1			✓	✓	1/2	
RAM machine [32]			× (b)									∞			✓	✓	1/2	
PRAMs, <i>etc.</i>			× (b)								✓	∞			✓	✓	1/2	
1D cellular automata [33]											✓	1			✓	✓	✓	
2D cellular automata [33]											✓	2			✓	✓	✓	
3D cellular automata [33]						×				×	✓	3			✓	✓	✓	
Reversible logic networks [34]			× (b)				×	×			✓	∞	✓		✓	✓	✓	✓
Quantum logic networks [35]			× (b)								✓	∞	✓	✓	✓	✓	✓	✓
Reversible 3D mesh [4]										×	✓	2–3	✓		✓	✓	✓	✓
Quantum R3M [4]										×	✓	2–3	✓	✓	✓	✓	✓	✓

*Note:* Opportunity #2 gives the number of dimensions explicitly or implicitly assumed by the model; three or more is unrealistic, two or less is underambitious. Cost measure #3 (spacetime) is denoted “half-way considered” if spacetime cost *could* be easily measured in the model but is typically ignored instead. Note that the quantum reversible 3D mesh model described in Section 6 (first introduced in [4]) strictly dominates all earlier models in realism and comprehensiveness, so long as gravity (limit #10) is not a concern, which we can expect to remain true for very long time. (This limit would only become relevant if/when we come to build computer systems of near black-hole density, *e.g.*, by building them out of several suns’ worth of matter, or alternatively by somehow achieving an average device-pitch scale nearly as small as the Planck length scale of fundamental particles. Both of these possibilities seem *extremely* distant at present, to say the least.)

machine and related models are primarily only suitable for the following purposes:

- Determining whether a desired class of computations is possible to do at all, even given unlimited resources (its *computability*).
- Proving that other models of computation are universal, by showing that they are capable of simulating a Turing machine.
- Determining the time required to perform a computation to a very rough degree of accuracy, that is, to within a polynomial factor (a factor growing as  $\sim n^k$  where  $n$  is the size of the input data set and  $k$  is any constant). The *strong Church's thesis* [36] is the hypothesis that Turing machines are satisfactory for this purpose. However, results in quantum computing suggest strongly that ordinary nonquantum Turing machines may actually *overstate* the physically required minimum time to solve some problems by *exponentially large* factors (that is, factors growing roughly like  $e^n$ ) [3], in which case the strong Church's thesis would be false.
- Determining the space (measured as number of bits) required to perform a computation within a constant factor.

These concerns are generic ones in computing and are not tied to nanocomputing specifically but can be used in that context as well. However, if one wishes a more precise model of costs to perform a desired computation than can be provided by Turing machines, one must turn to other models.

### 3.2. RAM Machine

One limitation of the Turing machine was that since the memory tape was laid out serially in only one dimension, merely traversing it to arrive at a desired item consumed a large portion of the machine's time. For early electronic memories, in contrast, the time required for a signal to traverse the distance through the machine was negligible in comparison to the time taken to perform logic operations. Therefore, it was useful to model memory access as requiring only a single step, regardless of the physical distance to the desired memory location. This fast memory access model is the defining characteristic of the RAM or random-access machine model of computation [32]. The RAM model is occasionally called the von Neumann machine model, after the inventor of architectures having a central processing unit (CPU) with a separate random-access memory for storing programs and data. The RAM model is also sometimes extended to a parallel model called the PRAM.

Today, however, individual transistors have become so fast that the speed-of-light travel time across an ordinary-sized machine is becoming a significant limiting factor on the time required to access memory, especially for computations requiring large-scale supercomputers having large numbers of processors. For example, at the 3 GHz processor clock speeds that are now routinely available in commercial off-the-shelf microprocessors, light can only travel 10 cm in one clock cycle, so the memory accessible within a round-trip latency of one cycle is limited to, at most, the amount that will fit within a 5-cm radius sphere centered on the processor. (In practice, at present, the situation is even

worse than this, because the time to access today's commercial memory technologies is much greater than the speed-of-light travel time.) And, when considering a wide-area distributed computation, communication halfway around the Earth (*i.e.*,  $\sim 20,000$  km) requires at least 200 million clock cycles! Delays like these can be worked around somewhat by using architectural *latency hiding* techniques in processor architectures and parallel algorithms, but only to a very limited extent [12, 37]. Furthermore, these problems are only going to get worse as clock speeds continue to increase. Communication time is no longer insignificant, except for the restricted class of parallel computations that require only very infrequent communication between processors, or for serial computations that require only small amounts of memory. For more general purposes, the RAM-type model is no longer tenable.

Slightly more realistic than the RAM are models that explicitly take communication time into account, to some extent, by describing a network of processing nodes or logic gates that pass information to each other along explicit communication links. However, depending on the topology of the interconnection network, these models may not be physically realistic either. *Binary trees*, *fat trees*, *hypercubes*, and *butterfly* or *omega* networks are all examples of interconnection patterns in which the number of locations accessible within  $n$  hops grows much faster than  $n^3$ , and therefore, these networks are impossible to implement with unit-time hops above a certain scale within ordinary 3D space. The *only* scalable networks in 3D space are the locally connected or *mesh*-type networks, and subgraphs of these [12, 17].

### 3.3. Cellular Automata

Cellular automaton (CA) models, also originally due to von Neumann [33], improve upon the RAM-type or abstract-network model in that they explicitly recognize the constraints imposed by communication delays through ordinary Euclidean space. CAs are essentially equivalent to mesh-interconnected networks of fixed-capacity processors. The one-dimensional and two-dimensional CA variations are entirely physically realistic, and the 2D CA can be used as a starting point for developing a more detailed theoretical or engineering model of today's planar circuits, such as, for example, the VLSI theory of Leiserson [30].

However, ordinary CAs break down physically when one tries to extend them to three dimensions, because the entropy that is inevitably produced by irreversible operations within a 3D volume cannot escape quickly enough through the 2D surface. To circumvent this constraint while still making some use of the third dimension requires avoiding entropy production using *reversible* models, such as we will discuss in Section 4.1. These models can be shown to have better cost-efficiency scaling than *any* physically possible nonreversible models, even when taking the overheads associated with reversibility into account [4].

Finally, all of these models, in their *traditional* form, miss the opportunity afforded by quantum mechanics of allowing machine states that are *superpositions* (weighted combinations) of many possible states, within a single piece of hardware, which apparently opens up drastic shortcuts to the solution of at least certain specialized types of problems. We will discuss quantum models further in Section 4.2.

## 4. NEW MODELS OF NANOCOMPUTERS

Computer technology already is forced to contend with the limits to communication delays imposed by the speed-of-light limit. Over the next 20–50 years, we can expect the limits that thermodynamics and quantum mechanics place on bit energies, sizes, and bit-device speeds to become plainly manifest as well. Other fundamental constraints, such as the one that gravity imposes on machine size (namely, that any sufficiently large 3D computer with a fixed energy density will collapse under its own gravity to form a black hole) are still very far away (probably many centuries) from being relevant.

So what we want is to have a model of computation that is physically realistic, at least with respect to the relatively near-term constraints, and that also provides a cost efficiency that scales as well as possible with increasing computation size, for all classes of computations. We can argue that there is an existence proof that such a model must be possible, for the laws of physics *themselves* comprise such a model, when looked at from a computational perspective. However, raw physics does not provide a very convenient programming model, so our task is to develop a higher level programming model that scales as well as possible, while also providing a relatively easy-to-understand, comprehensible framework for programming.

In Sections 4.1 and 4.2 we survey a couple of new classes of models which attempt to make progress toward this goal, namely the reversible and quantum models.

### 4.1. Reversible Computing

The fundamental insight of reversible computing is that there is absolutely nothing about fundamental physics that in any way requires that the free energy that goes into bit manipulations must be discarded after each operation, in the form of waste heat. This is because bits that have been computed are not (yet) entropy, because they are derived from, and thus correlated with, other bits that are present in the machine. Present-day computers constantly discard temporary results that are no longer needed, in order to free up storage space for newer information. This act of wanton erasure causes the old information and energy associated with those bits to be relegated to the degraded status of effectively becoming entropy and heat, respectively. Once this is done, it cannot be undone, since the second law of thermodynamics tells us that entropy can never be destroyed. Information erasure is irreversible [19].

However, we can *avoid* this act of “trashification” of bits by instead *recycling* bits that are no longer needed, by taking advantage of their redundancy with other bits present in the machine to restore the unneeded bits to a standard state (say “0” for an empty memory cell), while leaving the bit’s associated energy (or most of it, anyway) in the machine, in the form of free energy which can go on to perform another useful computational operation [38].

#### 4.1.1. Adiabatic Principle

Of course, no machine is perfect, so even in a reversible machine, some of the kinetic energy associated with the performance of each operation goes astray. Such events are

called *adiabatic losses*. The detailed accounting of adiabatic losses can be proven from basic quantum theory as in the *adiabatic* theorem [39], which tells us that as a system proceeds along a given trajectory under the influence of slowly changing externally applied forces, the total energy dissipation is proportional to the speed with which the external forces change; however, rather than getting into the technical mathematical details of this theorem here, we discuss some more intuitive ways to understand it.

First, the amount of adiabatic loss is roughly proportional to the number of elementary quantum operations performed, and thus to the energy involved in carrying out transition times the time over which it is performed, divided by a technology-dependent constant that specifies the quantum *quality factor* of the system, that is, how many quantum operations can be performed on average without an error (decoherence event).

As the speed of carrying out a given transformation is decreased, the kinetic energy associated with the system’s motion along the desired trajectory through configuration space decreases quadratically (in proportion to the square of the speed, since as we all know, kinetic energy is  $\frac{1}{2}mv^2$ ), and so the total adiabatic losses over the entire motion decrease in inverse proportion to the time taken for the transformation.

However, when the kinetic energy involved in carrying out transformations decreases to a level that is close to the static bit energies themselves, further decreases in speed do not help, because entropy generation from degradation of the static bits comes to dominate the total dissipation. That is, some of the energy whose job it is to maintain the very structure of the machine, and/or the state of its stored information, also leaks out, in a continual slow departure from the desired configuration (this is called *decay*), which must be periodically repaired using correction mechanisms if the computation is to continue indefinitely. For example, all of the following phenomena can be considered as simply different examples of decay processes:

- Charge leakage from DRAM (dynamic RAM) cells, requiring periodic refreshing.
- Bit errors due to thermal noise, cosmic ray impacts, *etc.*, requiring the use of error-correction algorithms.
- Decoherence of quantum bits from various unwanted modes of interaction with a noisy, uncontrolled environment, requiring quantum error correction.
- Gradual diffusion of the atoms of the devices into each other (*e.g.*, from electromigration), leading to eventual failure requiring remanufacture and replacement of all or part of the machine.

All of these kinds of decay processes incur a cost in terms of free energy (to periodically correct errors, or to repair or replace the machine) that is proportional to the *space-time* usage, or space to hold bits, times time occupied, of the computation. This spacetime usage cannot be adequately reduced to time alone, space alone, or even to the number of logical operations alone, since, depending on the computation to be performed, not all bits may be actively manipulated on every time step, and so the spacetime usage may not be simply proportional to the number of operations.

Adiabatic (or kinetic) losses, on the other hand, do effectively count the number of operations performed, but these are *quantum* operations, whose number is not necessarily directly proportional to the number of classical bit operations, even when the algorithm being carried out is a classical one. This is because the number of quantum operations involved in carrying out a given classical bit operation increases in proportion to the speed with which the desired trajectory through state space is followed.

There are two ways to see this. First, the de Broglie wavelength  $\lambda$  of the “particle” wave packet representing the system’s state in configuration space is inversely proportional to its momentum, according to the formula  $\lambda = h/p$ . Momentum is proportional to velocity, so following a given trajectory will involve a larger number of distinct transitions of the system’s wave packet (*i.e.*, translations through about a wavelength) the faster it is done; each of these can be considered a orthogonalizing quantum operation.

Second, recall that kinetic energy increases with the square of velocity, whereas the frequency or quickness with which a fixed-length classical trajectory is followed increases only linearly with velocity. Therefore, the interpretation of energy as the rate of quantum operations requires that the number of operations on a given trajectory must increase with the speed at which that trajectory is followed.

With this interpretation, the technology-dependent coefficients (such as frictional coefficients, *etc.*) that express the energy dissipation per unit quickness for an adiabatic process can be seen as simply giving the decoherence times for those qubits whose transitioning corresponds to kinetic energy. The decoherence of qubits carrying energy causes the dissipation of that energy. The adiabatic principle (which states that the total energy dissipation of an adiabatic process is proportional to its speed) can be derived from the postulate that a fixed fraction of kinetic energy is dissipated each time unit [22]. Adiabatic coefficients are therefore lower bounded by the decoherence rates that can be achieved for qubits whose transitions carry us from one logical machine state to another.

The adiabatic principle also tells us that whenever logical transitions are carried out by a process that uses multiple quantum operations (in place of a single one), we are doing extra unnecessary work, and thus generating more entropy (and energy dissipation) than necessary. This happens whenever we try to do a process faster than strictly necessary.

As a simple example, consider a hollow cylinder of radius  $r$  and mass  $m$ , rotating with rim velocity  $v$ . Let us consider a rotation of this wheel to carry out a “cycle” in our computer, a complete transition from one logical state to another. A simple calculation shows that the number of quantum orthogonal transitions (angle  $\pi/2$  rotations of the state vector in Hilbert space) that occur during one complete rotation is given by  $4L/\hbar$ , where  $L = mvr$  is the wheel’s angular momentum about its axis, and  $\hbar$  is Planck’s (reduced) constant,  $h/2$ . Total angular momentum for any system is quantized, and the minimum possible rotation speed occurs when  $L = \hbar$ . At this speed, the kinetic energy is just enough to carry out one quantum logic operation (an iop, for example, a bit toggle) per quarter-cycle. At this rate, the rotation of the wheel through a quarter-turn *is*, from a quantum mechanical

perspective, a bit flip. The decoherence rate of this spin qubit determines the rate at which the wheel’s energy dissipates.

In contrast, if the wheel were spun faster ( $L$  were higher), there would be proportionally more distinct rotational positions around 1 complete rotation, and the total energy is quadratically higher, so the average energy per location (or the generalized temperature) is proportional to  $L$ . With order  $L$  more locations, each carrying order  $L$  more energy, a fixed decoherence rate per location yields a quadratically higher total rate of energy dissipation, and thus a linearly higher amount of entropy generation per complete cycle. This is an example of why the dissipation of an adiabatic process is proportional to the speed at which it is carried out.

Simply put, a faster process has quadratically greater kinetic energy and so, given a fixed mean-free time or decoherence time for that energy, energy dissipates to heat at a quadratically faster rate, for linearly more energy dissipation during the time of the operation.

The minimum energy dissipation of an adiabatic process occurs when the speed of the transition is slow enough that the dissipation of kinetic energy is not much greater than the dissipation of static (potential) energy. If the decoherence rates are comparable for the two types of energy, then the kinetic energy for bit change should be of the same order as the static energy in the bits themselves, as in our previous wheel example.

This makes sense, since if energy *is* computing, we want as much as possible of our available energy to be actively engaged in carrying out transitions at all times. Having a kinetic energy that is much larger than bit energy would mean that there was a lot of extra energy in the system that was not directly occupied in carrying out bit transitions. In such cases, a more direct and economical design would be preferable. This is what a good optimized adiabatic design attempts to accomplish.

#### 4.1.2. Device Implementation Technologies

Reversible, adiabatic logical mechanisms can be implemented in a wide variety of physical systems; indeed, nearly every type of bit-device technology that has been proposed (whether electrical, mechanical, or chemical) admits some sort of reversible variant. Virtually all of these technologies can be usefully characterized in terms of the bistable potential-well paradigm introduced by Landauer [19]. In this framework, a bit is encoded by a physical system having two distinct meta-stable states. The relative energies of these states, and the height of a potential barrier between them, is adjustable by interactions with nearby bits. Figure 1 illustrates this model.

Irreversible erasure of a bit in this model corresponds to lowering a potential-energy barrier (*e.g.*, by turning on a transistor between two circuit nodes) regardless of the state of the bit under consideration (say, the voltage on one of the nodes). Due to the energy difference between biased states, this in general leads to large, nonadiabatic losses (thick red arrows in the diagram), which reversible logic must avoid. Even the lowering of a barrier between two states of equal energy still creates at least 1 bit’s worth of entropy, even when done infinitesimally slowly, if the state of the bit was not already entropy (medium red arrows).



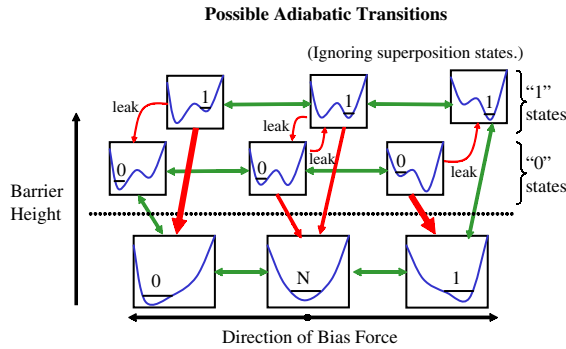


**Figure 1.** Possible adiabatic (green) and nonadiabatic (red) transitions between states of any device technology that provides a generic bistable potential well. Each box indicates a different abstract configuration of the system. Within each box, the  $x$  axis is some continuous state variable in the system (such as the position of a mechanical component or a charge packet), and the  $y$  axis is potential energy for the given value of the state variable. Small black horizontal lines show the energy level occupied (or the surface of a set of occupied levels). The  $x$  position of the occupied state encodes the value of the bit. Device configurations encoding logical values of 0, 1, and an in-between neutral level “N” are shown. Thick arrows between configurations indicate nonadiabatic active transitions, while thin arrows indicate possible leakage pathways (activated thermally or by tunneling). Note the lower three boxes show the potential barrier lowered, while the upper three show it raised. The left–right position of the box in the diagram corresponds roughly to the direction of an external force (e.g., from a neighboring device) that is applied to the system.

Of course, even in reversible logic systems, we must still contend with the smaller losses due to thermally excited transitions or tunneling of the bit system’s state over the potential energy barriers (thin red arrows labeled “leak”)

Now, a number of different reversible logical and storage mechanisms are possible within this single framework. We can categorize these as follows:

1. *Input-bias, clocked-barrier latching logic (type I):* In this method, the device barriers are initially lowered, and input data to the device apply a bias, pulling the device toward a specific bit value. Optionally in this stage, forces applied by several input bits can be combined together to carry out majority logic (or switch gates can be used to do logic, as in [40]). Next, a timing signal raises the barrier between the two states. This step can also serve to amplify and restore the input signal. After the barrier is raised, the input data can be removed, and the computed state of the device remains stored. Later, the stored data can be reversibly *unlatched*, if desired, by the reverse sequence of steps.

Specific physical examples of the type I technique include the adiabatic quantum dot cellular automaton of Lent and Tougaw [41], the complementary metal-oxide semiconductor (CMOS) transmission-gate latch of Younis and Knight [42], the reversible rod logic latch of Drexler [43], the reversible superconducting Parametric Quantron logic of Likharev [44], the mechanical buckled logic of Merkle [45], and the electronic helical logic of Merkle and Drexler [40].

2. *Input-barrier, clocked-bias retractile logic (type II):* In this technique, the input data, rather than applying a bias force, conditionally raise or lower the potential energy

barrier. Arbitrary AND/OR logic can be done in this stage, by using series/parallel combinations of several barriers along the path between bit states. Then, a timing signal unconditionally applies the bias force, which either pushes the system to a new state, or not (depending on whether the barrier between states was raised). Since the output state is not inherently latched by this timing signal, the input signal cannot then be removed (if this would lower the barriers) until other “downstream” devices have either latched a copy of the output or have finished using it. So these gates cannot by themselves perform sequential logic (e.g., memory, networks with feedback, or pipelined logic), although they can be used in combination with latching gates to do so.

Examples of the type II technique are Hall’s retractile electronic logic [46], the nonlatching portions of Younis and Knight’s CMOS SCRL gates [42], and Drexler’s rod logic interlocks [47].

3. *Input-barrier, clocked-bias latching logic (type III):* Finally, from Figure 1, one can immediately see that there is a third possibility, one that has not previously been considered. It is more efficient than either (1) or (2), in the sense that it combines AND/OR logic with latching in a single operation. In this scheme, as with the previous one, the input signal sets the barrier height, doing logic in series/parallel networks, and then a timing signal applies an unconditional bias force. But we note that the input signal can now be immediately removed, *if* in doing so we restore the barriers to a null state that consists of *barriers unconditionally raised*. Then, when the bias timing signal is removed, the output bit remains latched in to its new state. The bit can be unlatched using the reverse sequence along the same path, or a different one.

This general method for doing reversible logic apparently has not been previously described in the literature, but we have developed a straightforward technique for implementing this model in standard CMOS technology. It is significantly more efficient than previous truly adiabatic logic families, by several different metrics.

The bistable potential-well model is basically one in which we model one subsystem (the output bit) as being subject to a time-varying Hamiltonian (essentially, a matrix representing the forces on the system) that is provided by the device’s interaction with some other subsystems (the input and clock bits). However, one must stay aware that there is really just a *single* system that evolves according to an actual *underlying* Hamiltonian which is time-*independent*, being itself just an expression of the unchanging laws of physics. So, in general, one cannot ignore the back-reaction of the controlled system (the output bit) on the system that is doing the controlling (the input bit), especially if we want to be accurate about the total energy consumption in the entire system, including the controlling system, which in practice is just some other logic element within the computer. For example, it is easy to design adiabatic gates using transistors that dissipate almost no energy internally, whose transitions are

controlled by some large external signal generator. But it is much harder to integrate the signal generator and design a complete, self-timed system that is nevertheless almost reversible. For this reason, some authors have unjustly criticized the concept of adiabatic circuits in general, solely on the basis of the poor quality of the particular signal generators that were assumed to be used in the author's particular analysis. But the failure of a single short-sighted designer to imagine an efficient resonator does not mean that such a thing is impossible, or that alternative designs that avoid these timing-system inefficiencies are impossible to build.

For example, Bennett [2] illustrated a proof-of-concept mechanical model of a self-contained reversible computer by doing away with directed kinetic energy entirely, and instead letting the system take a random walk, forward or backward, along its nonbranching path through configuration space. Unfortunately, doing away with kinetic energy entirely is not such a good thing, because random walks are very slow; they take expected time that increases quadratically with the distance traveled. (Chemical computing techniques in which communication relies primarily on molecular diffusion in solution also have performance problems, for the same reason.) Thus, we would prefer to stick with designs in which the system *does* have a substantial net kinetic energy and momentum along the "forward" direction of its motion through configuration space, while yet dissipating  $\ll kT$  energy per logic operation performed, due to a high quality factor for the individual logic interactions. We call such trajectories *ballistic*.

I emphasize that we still know of absolutely *no* fundamental reasons why ballistic reversible computation cannot be done, and with arbitrarily high quality factors. A series of increasingly realistic models have been proposed that illustrate steps along the path toward actually doing this. Fredkin and Toffoli [34] described a ballistic "billiard ball model" (BBM) of reversible computation based on collisions between idealized elastic spheres. Their original model contained chaotic instabilities, although these can be easily fixed by confining the balls to travel along valleys in configuration space, and by keeping them time-synchronized through a few additional mechanical interactions. A concrete example of an electronic model similar to the BBM that avoids these instability problems entirely is described in [40]. Pure-mechanical equivalents of the same synchronization mechanism are also straightforward to design.

Now, the BBM was primarily just a classical model. Richard Feynman and Norm Margolus made some initial theoretical progress in devising a totally quantum-mechanical model of ballistic reversible computation, Feynman with a serial model [48], and Margolus with a self-synchronized parallel model [49]. However, Margolus' model was restricted to allowing parallelism in only one dimension, that is, with only a linear chain of active processors at any time. As of this writing, we do not yet have an explicit, fully detailed, quantum physical model of totally three-dimensional parallel reversible computing. But we *know* that it must be possible, because we can straightforwardly design simple classical-mechanical models that already do the job (essentially, reversible "clockwork") and that do not suffer from any instability or timing-system inefficiency problems. Since these models are *manifestly* physically realizable (obviously

buildable, once you have conceived them), and since all real mechanical systems are, at root, quantum mechanical, a detailed quantum-mechanical fleshing out of these classical-mechanical models, if mapped to the nanoscale, would fit the bill. But significant work is still needed to actually do this translation.

Finally, in general, we should not assume that the best reversible designs in the long run necessarily must be based on the adiabatic bistable-potential-well-type model, which may be unnecessarily restrictive. A more general sort of model of reversible computing consists simply of a dynamic quantum state of the machine's "moving parts" (which may be just spinning electrons) that evolves autonomously according to its own built-in physical interactions between its various subparts. As long as the evolution is highly coherent (almost unitary), and we can accurately keep track of how the quantum state evolves over time, the dissipation will be kept small. The devil is in figuring out the details of how to build a quantum system whose built-in, internal physical interactions and natural evolution will automatically carry out the desired functions of logic, communication, and synchronization, without needing a full irreversible reset of the state upon each operation. But as I stated earlier, we *can* be confident that this is possible, because we can devise simple mechanical models that already do the job. Our goal is just to translate these models to smaller sized and higher frequency physical implementations.

#### 4.1.3. Algorithmic Issues

For now, we take it as given that we *will* eventually be able to build bit devices that *can* operate with a high degree of thermodynamic reversibility (*i.e.*, very small entropy generation per operation), and that the details of ballistic signal propagation and timing synchronization can also be worked out. What, then, can we do with these devices?

One key constraint is that physically reversible devices are necessarily also logically reversible; that is, they perform invertible (one-to-one, bijective) transformations of the (local) logical machine state.

**Debunking Some Misunderstandings** First, the preceding statement (physical reversibility requires logical reversibility) has occasionally been questioned by various authors, due to some misunderstanding either of physics, or of the meaning of the statement, but it is not really open to question! *It is absolutely as certain as our most certain knowledge about physical law.* The reversibility of physics (which follows from the unitarity of quantum mechanics, or from the mathematical form of all Hamiltonian dynamical systems in general) *guarantees* that physics is reverse-deterministic, that is, that a given (pure, quantum) state of a closed system can only have been arrived at along a specific, unique trajectory. Given this fact, any time we have a mechanism that unconditionally erases a bit (*i.e.*, maps both of two distinct initial logical states onto a single final logical state), without regard to any other knowledge that may be correlated to that bit's state, there *must* be a compensatory splitting of some *other* adjoining system from one state into two distinct states, to carry off the "erased" information, so that *no* merging of possible state trajectories happens in the system overall. If the state distinction happens to become lost

somewhere, then it is, by definition, entropy. If the erased bit was itself not already entropy before the erasure, then this entropy is furthermore newly generated entropy, and the mechanism is then by definition not physically reversible. In contrast, if the state information remains explicitly present in the logical state that is transformed in the operation, then the mechanism is by definition logically reversible.

If you think that you have found a way to unconditionally erase known logical bits without generating new entropy (without having also disproved quantum mechanics in the process), then check your work again, a lot more carefully! Such a device would be exactly equivalent to the long-debunked perpetual motion machine [50]. I will personally stake my reputation on your having made a mistake somewhere. For example, did you analyze the “erasure” of a logical bit that was uncorrelated with any other bits and thus was *already* entropy? No new entropy need be generated in that case. Or did you just reversibly decrement a long counter until it was zero, but you forgot that an exactly equal amount of timing information about *when* you finished counting, relative to other subsystems, is still present and still must be got rid of in order to interact with outside systems? Or did you rely on an exponential number of high-energy states all “decaying” to a single slightly lower energy state, while forgetting that the exponentially larger *number* of higher energy states and slow decay rate will mean that there is an exactly equal chance to go the other way and make a transition to occupy the high-energy state instead, excited by thermal noise? These issues are rather subtle, and it is easy to make mistakes when proposing a complicated new mechanism. In contrast, the impossibility proof from basic, uncontroversial axioms of physics is straightforward and easily verified to be correct. If you want to erase logical bits without generating entropy, you will first have to go back and show why most of the basic physics that has been learned in the last 150 years (such as statistical mechanics and quantum mechanics) must be totally wrong, despite agreeing perfectly with all our myriad experiments!

**Algorithmic Overheads** Now, those misconceptions aside, let us take a clear look at the algorithmic issues that result from the need for logical reversibility. (These issues apply equally whether the logic of the particular computation is implemented in hardware or in software.) Apparently, the requirement of logical reversibility imposes a nontrivial constraint on the types of algorithms we can carry out. Fortunately, it turns out that any desired computation *can* be emulated by a reversible one [38], although apparently with some algorithmic overheads, that is, with some increases in the number of bits or ops required to carry out a given computation.

First, some history: Rolf Landauer of IBM realized, as early as 1961 [19], that information-“destroying” operations such as bit erasure, destructive (in-place) AND, and so forth can be replaced by analogous reversible operations that just move the “erased” information somewhere else rather than really erasing it. This idea is now known as a *Landauer embedding* of an irreversible computation into a reversible one. But, at the time, Landauer thought this approach would pointlessly lead to an accumulation of unwanted information in storage that would still have to be irreversibly erased

eventually. In 1963, Yves Lecerf [51], working independently on a related group theory problem, reinvented the Landauer embedding and furthermore noted that the intermediate results could also be reversibly *uncomputed* by undoing the original computation. We call this idea *Lecerf reversal*. In 1973, Charles Bennett independently rediscovered Lecerf reversal [38], along with the observation that desired results could be reversibly copied (known as a *Bennett copy*) before undoing the computation. Simple as it was, this was the final key insight showing that computation did not necessarily require entropy generation, as it revealed that a given area of working storage could indeed be reversibly reused for multiple computations that produce useful results. All of these ideas were independently rediscovered in a Boolean logic circuit context by Ed Fredkin and Tom Toffoli during their work on *information mechanics* at MIT in the late 1970s [34].

Unfortunately, although the extra storage taken up by the Landauer embedding can be reused, it does still at least *temporarily* take up space in the computation and thus contributes to economic spacetime costs. Even this temporary usage was shown not to be technically necessary by Lange et al. [52], who showed how to compute reversibly in general using virtually *no* extra space, essentially by iterating through all possible machine histories. (The technique is very similar to earlier complexity theory proofs showing that deterministic machines can simulate nondeterministic machines in-place, using the same space [53].) But unfortunately, the Lange et al. technique is not at all close to being practical, as it generally requires taking an exponentially longer time to do the computation.

Today, we know of a continuous spectrum of possible trade-offs between algorithmic space and time overheads for doing reversible computation. In 1989, Bennett described a space of trade-offs between his original technique and a somewhat more space-efficient one [54], and later work by Williams [55] and Burhman et al. [56] showed some ways to extrapolate between the Bennett-89 approach and the Lange et al. one. However, these latter approaches are apparently not significantly more efficient in terms of overall *spacetime* cost than the older Bennett-89 one. It is, however, possible to reduce the spacetime cost of the Bennett-89 algorithm by simply increasing its degree of parallelization (activity factor, hardware efficiency) so that less time is spent waiting for various subcomputations. But this apparently gives only a small improvement also.

At present, we do not know how to reversibly emulate arbitrary computations on reversible machines without, at least, a small polynomial amount of spacetime overhead. It has been conjectured that we cannot do better than this in general, but attempts (such as [57]) at a rigorous proof of this conjecture have so far been inconclusive. So, as far as we know right now, it is conceivable that better algorithms may yet be discovered. Certainly, we know that much more efficient algorithms do exist for many specific computations, sometimes with no overhead at all for reversible operation [4]. But Bennett’s algorithm and its variations are the best we can do currently for *arbitrary* computations.

Given the apparent algorithmic inefficiencies of reversible computing at some problems, as well as the limited quality factor of reversible devices even for ideal problems, it does not presently make sense to do all computations in a *totally*

reversible fashion. Instead, the computation should be broken into pieces that are internally done reversibly, but with occasional irreversible logical operations in between them. The size of the reversible pieces should be chosen so as to maximize the overall cost efficiency, taking into account both the algorithmic overheads and the energy savings, while optimizing the parameters of the emulation algorithms used. Examples of how to do this via analytical and numerical methods are illustrated in [5, 21, 58]. That work shows that reversible computing remains advantageous for overall cost efficiency, despite its algorithmic overheads, even for worst-case types of computations, for which we do not know of any better reversible algorithm than Bennett's.

In cases where the reversible devices have a high quantum quality  $q$ , it turns out to make sense to do a substantial amount of reversible computing in between irreversible operations. Since the most efficient use of these reversible computing resources may, in some cases, call for a hand-optimized reversible algorithm, the architecture and programming model should best include directives that directly expose the underlying reversibility of the hardware to the programmer, so that the programmer (as algorithm designer) can perform such optimizations [4]. In other words, the algorithm designer should be able to write code that the architecture *guarantees* will be run reversibly, with *no* unnecessary overheads. Some examples of architectures and programming languages that allow for this can be found in [4, 59, 60].

Can the machine's potential reversibility be totally hidden from the programmer while still preserving asymptotic efficiency? Apparently not. This is because the best reversible algorithm for a given problem may in general have a very different form than the best irreversible algorithm [4]. So we cannot count on the compiler to automatically map irreversible code to the best reversible code, at least, given any compiler technology short of a very smart general-purpose artificial intelligence which we could rely on to invent optimal reversible algorithms for us.

How hard is it to program in reversible languages? At first it seems a little bit strange, but I can attest from my own experience that one can very quickly become used to it. It turns out that most traditional programming concepts can be mapped straightforwardly to corresponding reversible language constructs, with little modification. I have little doubt that shortly after reversibility begins to confer significant benefits to the cost efficiency of general-purpose computation, large numbers of programmers, compiler writers, *etc.* will rush to acquire the new skills that will be needed to harness this new domain, of computing at the edge of physics.

However, even reversible computing does not yet harness all of the potential computational power offered by physics. For that, we must turn our sights a bit further beyond the reversible paradigm, toward *quantum computing*.

## 4.2. Quantum Computing

### 4.2.1. Generalizing Classical Computing Concepts to Match Quantum Reality

The core fact of quantum mechanics is that not all of the conceivable states of a physical system are actually operationally distinguishable from each other. However, in the

past, computer scientists artificially constrained our notion of what a computation fundamentally *is*, by insisting that a computation be a trajectory made up of primitive operations, each of which takes *any* given legal state of the machine and changes it (if at all) to a state that is *required* to be operationally distinguishable from the original state (at least, with very high probability). For example, a traditional Boolean NOT gate, or logical *inverter*, is designed to either leave its output node unchanged (if its input remains the same), or to change its output to a new state that is clearly distinct from what it was previously.

But really this distinguishability restriction on operations was an *extra* restriction that was, in a sense, arbitrarily imposed by early computer designers, because this type of operation is *not* the only type that exists in quantum mechanics. For example, when a subatomic particle's spin is rotated  $180^\circ$  around its  $x$  axis, if the spin vector was originally pointing up ( $+z$ ), it will afterward be pointing down ( $-z$ ), and this state is completely distinct from the up state. But if the spin was originally pointing at an angle *halfway between* the  $x$  and  $z$  axes, then this operation will rotate it to an angle that is only  $90^\circ$  away from its original angle (namely, halfway between the  $x$  and  $z$  axes). This spin state is *not* reliably distinguishable from the original. Although it is at right angles to the original state in 3D space, its *state vector* is *not* orthogonal to the original state in the *Hilbert space* of possible quantum state vectors. Orthogonality in Hilbert space is the technical quantum-mechanical requirement for distinguishability of states. Thus, the operation "rotate a spin by  $180^\circ$  around a given axis" does not change *all* states by orthogonalizing amounts, only *some* of them.

What if we allow a computation to be composed of operations that do *not* necessarily change all legal states by an orthogonalizing amount? Then the new state after the operation, although possibly different from the original state, will not necessarily be reliably observationally distinguishable from it. However, if we do not try to observe the state but instead just let it continue to be processed by subsequent operations in the machine, then this lack of distinguishability is not necessarily a concern. It can simply be the situation that is intended. In essence, by loosening our requirement that every state of the computation be distinguishable from the previous one, we open up the possibility of performing new types of operations, and thus traversing new kinds of trajectories through state space, ones that were not previously considered to be legal computations.

Does this new possibility confer additional computational power on the model? We cannot prove that it does, but it is currently strongly believed to. Why? Because specific, well-defined algorithms have been found that use these new types of trajectories to perform certain kinds of computational tasks using exponentially fewer operations than with the best classical algorithms that we know of [3]. In other words, opening up this larger space of operations reveals drastic "shortcuts" through state space; that is, transformation trajectories that get us to where we want to go using exponentially fewer steps than the shortest classical paths that we know of.

The two most important examples of these apparent exponential shortcuts that have been found so far are the

following: (1) Shor's quantum factoring algorithm [61] and (2) simulations of quantum systems [62].

Shor's factoring algorithm can factor  $n$ -digit numbers using a number of quantum operations that increases only quadratically with the number of digits  $n$ , whereas the best known classical algorithms require time that increases exponentially in the number of digits. The primary application of Shor's algorithm would be to break the public-key cryptosystems such as RSA [63] that are popularly used today for encryption and authentication of data for e-commerce and other purposes over the internet. For example, someone armed with a good-sized quantum computer and eavesdropping on your internet connection could steal your account information whenever you do home banking or credit-card purchases over a supposedly secure `https`: or secure socket layer connection that uses RSA for security. In other words, that little padlock icon in your web browser gives you no protection against a quantum computer!

However, perhaps a more widely useful application for quantum computers is to simulate quantum physics. This was the original motivation for quantum computers that was proposed by Feynman [64]. We now know that the statistical behavior of any quantum-mechanical system can be accurately simulated in polynomial time on a quantum computer [62], even though quantum systems in general seem to require *exponential* time to simulate accurately on *classical* (nonquantum) computers.

Another quantum algorithm that is useful, but that provides a less-than-exponential speedup, is Grover's quantum "database search" algorithm that can locate a specified item, out of  $n$  items, in  $\Theta(n^{1/2})$  lookup steps [65].

However, Grover's algorithm is, unfortunately, misnamed, since it is not really useful at all for real database searches, in the usual sense of the term "database," meaning an explicit table of arbitrary data. First, such a table, in general, requires just as much space to store in a quantum system as in a classical one (see "Myth #1"). Also, real commercial databases always include the capability to index the table by the most commonly used types of search keys, in which case a lookup, even on a classical computer, already requires only  $\Theta(1)$  lookup step. More precisely, the time required scales like  $\Theta(n^{1/3})$  or  $\Theta(n^{1/2})$ , if the speed-of-light travel time to the desired search item in 3D space or on a 2D surface is taken into account. But this is still less than in Grover's algorithm.

Also, even if the database is *not* indexed by the desired type of search key, if the data are stored in a processing-in-memory architecture, in which each area of storage of some constant size has an associated processor, then lookup can be done in parallel, achieving the same light-limited  $\Theta(n^{1/3})$  time, or at least  $\Theta(n^{1/2})$  time, if the machine must be laid out in two dimensions, rather than three. Anyway, in random-data-lookup applications where the speed-of-light travel time to the data is the limiting factor, Grover's algorithm cannot help us.

However, Grover's algorithm is still useful, not for database search, but rather for a different kind of application called *unstructured search of computed (not tabulated) search spaces*. This is because a search space can be much larger than the physical size of the machine if the "data values" (really, function values) are computed as a *function*

of the data's index, rather than being explicitly stored. In cases where no more efficient algorithm is known for "inverting" the function (that is, finding an index that maps to a given value), Grover's algorithm can still be used to obtain a speedup, although not one that is so large as is traditionally claimed. A simple classical parallel search can still outperform the *serial* Grover's algorithm in terms of time alone; for example, if  $\Theta(n^{3/4})$  processors simultaneously each search a different  $\Theta(n^{1/4})$ -size piece of the search space, the search can be completed in  $\Theta(n^{1/4})$  time classically in 3D space. However, given Grover's algorithm, we can use a smaller number  $\Theta(n^{3/5})$  of processors, each searching  $\Theta(n^{2/5})$  items in  $\Theta(n^{1/5})$  time. But note that the speedup is now only  $\Theta(n^{1/4})/\Theta(n^{1/5}) = \Theta(n^{1/20})!$  However, the benefit in terms of *spacetime* cost can be still as great as  $\Theta(n^{1/2})$ , since a single quantum processor searching for  $\Theta(n^{1/2})$  time consumes only  $\Theta(n^{1/2})$  spacetime, whereas the best classical unstructured search through  $n$  items requires  $\Theta(n)$  spacetime.

#### 4.2.2. Dispelling Some Myths

In addition to the misconceptions arising from the inappropriate association of Grover's algorithm with database search, there are a few other popular myths about quantum computers that, although widely repeated, are entirely false, and we would like to dispense with them here and now.

**Myth #1** "Quantum computers with a given number of bits can store exponentially more information than classical computers having the same number of bits."

This is patently false, because the maximum amount of information that can be stored in any physical system is just the logarithm of its number of *distinguishable* states. Although an  $n$ -bit quantum computer can be put into an infinite number of different quantum states, only  $2^n$  of these states can be reliably differentiated from each other by *any physical means whatsoever*, no matter how cleverly you try to design your measurement apparatus. In other words, the presence of all those extra, "in-between" superposition states can have *zero* causal impact on the total amount of information you can reliably extract from the system. This basic feature (or "bug" if you prefer) of all physical systems was demonstrated convincingly by Heisenberg long ago [25].

**Myth #2** "Quantum computers can perform operations at an exponentially faster rate than classical computers."

This is also false, because the Margolus–Levitin bound on processing speed [18] applies to quantum computers as well as classical ones. Operations (if defined as transformations that orthogonally transform some states) can only be performed, at best, at the rate  $4E/h$ , or  $2E/h$  for nontrivial ops, for a system of average energy  $E$  above its ground state. Small *pieces* of operations (small transformations that do not orthogonally transform any states) may be done more often [66], but these pieces arguably also perform correspondingly less computational work than do complete operations.

Why? Note that a *small piece* of a (primitive orthogonalizing) operation (which transforms *every* state into a new state that is almost completely indistinguishable from the original) can be omitted *entirely* from a computation, and the end result of the computation will necessarily be almost completely indistinguishable from the case where

that small “operation piece” was included. (This is because the property of the near-indistinguishability of the two states *must* be preserved by *any* subsequent operations on the system—otherwise, the states would not be indistinguishable! Mathematically, this is ensured by the linearity of quantum evolution.) So it is fair to count the computational work performed by a transformation by counting the number of *complete* operations, as we have defined them (transformations that at least orthogonalize *some* states). Whether or not a given operation orthogonalizes the actual computational state that is presented to it as its input in a specific situation is another question altogether. It need not do so in order for the operation to be considered useful. For example, an ordinary “AND” gate, upon receiving new inputs, is considered to be doing useful work even when its output does not change. Namely, it is doing the work of determining *that* its output should not change.<sup>1</sup> Similarly, a quantum operation that does not orthogonalize its actual initial state, but that might orthogonalize others, is, at least, doing the work of determining *that* that specific input is not one of the ones that was supposed to have been orthogonalized.

Therefore, the Margolus–Levitin bound does indeed give a valid limit on the rate of useful operations that can be performed in *any* computer (classical or quantum).

The correct interpretation of why a quantum computer provides exponentially faster algorithms for some problems (such as factoring, and simulating quantum physics) is *not* that the quantum computer is carrying out operations at an exponentially more frequent rate, but *rather* that the new *types* of operations that can be performed by the quantum computer make use of the fact that there actually exist exponentially shorter paths (requiring exponentially fewer total operations to traverse) leading from the input state to the desired final state than was previously recognized.

As an analogy: Suppose you have a computer with integer registers, but the only arithmetic operation provided is “decrement/increment,” which subtracts 1 from one register, while adding 1 to another register. With this operation, you could still add two registers together, by repeatedly performing this operation on the two registers, until the first one equals zero. But this would generally take exponential time in the length of the registers. Now, suppose we introduce a new operation, which is the standard direct bitwise ripple-carry add of one register into the other. Then, the add only takes time proportional to the length of the registers. Thus we have gained an “exponential speedup” for the add operation, but not by doing increment/decrement operations exponentially more frequently, but rather by choosing a type of operation that allows us to do an exponentially smaller number of steps in order to get to the result that we want.

The key insight of quantum computing was that nature provides for us a type of operation (namely, operations that might incompletely orthogonalize some input states) that was not previously recognized in any of our early computing models and that, moreover, adding this kind of operation allows some problems to be solved using exponentially fewer total operations than was previously realized. Therefore, omitting the capability of performing quantum operations from our future computer designs is, in a sense,

just as foolish as omitting the capability for bitwise addition (as opposed to just decrement/increment) from the design of our arithmetic units!

One caveat is that, at present, only a few kinds of problems (such as those mentioned previously) have been found so far for which quantum operations provide a drastic speedup. However, since a low decoherence rate will eventually be needed anyway, in order to allow for high-speed reversible operations that avoid excessive dissipation, it makes sense for us to aim toward a full quantum computing technology in the long run. Also, quantum computing is still only in its infancy, and many useful new quantum algorithms may yet be discovered.

**Myth #3** “Quantum computers are known to be able to solve nondeterministic polynomial (NP)-complete problems in polynomial time.”

If this were true, it would be wonderful, because all problems whose solutions can be *checked* in polynomial time (this is the definition of the NP problems) could then also be *solved* in polynomial time using a quantum computer. Among other applications, this would revolutionize the way we do mathematics, because very complex proofs of difficult mathematical theorems could be found very quickly by computer, that is, in time only polynomial in the length of the proof. Unfortunately, no one has shown a way to use quantum computers to solve NP-hard problems efficiently, and furthermore, a result due to Bennett et al. [67] provides some mild theoretical evidence suggesting that it is not possible. The factoring problem and other problems that apparently do have exponential shortcuts from using quantum computing have never been proven to be NP-complete, so they do not constitute examples of NP-complete problems that can be efficiently solved on a quantum computer. However, more research on this question is needed.

**Myth #4** “Quantum computers have been proven to be far more powerful than classical computers.”

First, we know that a quantum computer can be perfectly simulated by a classical computer, though most likely this requires exponential slowdown. So any problem solvable on a quantum computer can be *eventually* solved on a classical computer, given unbounded resources. So quantum computers are not *any* more powerful in terms of the *kinds* of problems that they can solve *at all* in principle; rather, at best, they are just exponentially *more efficient* at solving some problems. But even the exponential efficiency advantage has never *really* been proven. For all we know *for sure* today, there could still exist a (not yet discovered) polynomial-time classical algorithm for simulating all quantum computers, in which case every efficient quantum algorithm could be translated to a similarly efficient classical one. Other than in various artificial oracle scenarios, we still have no rock-solid proof that quantum computers confer *any* extra computational power, although most researchers expect that they do. Moreover, for practical purposes today, they *would effectively* confer that exponential extra power, because of the existing problems for which the best quantum algorithm we know is far more efficient than the best classical algorithm we know. But this situation could change someday, if equally efficient classical algorithms were eventually to be discovered, which has not (yet) been proven to be impossible.

<sup>1</sup> Seth Lloyd pointed out this analogy to me in personal discussions.



**Myth #5** “Quantum computers require exponential space to simulate on a classical computer.”

This myth is often quoted as the “reason” simulating a quantum computer on a classical one must also take exponential time. But the myth is simply not true; it has been recognized since at least 1992 [68] that a polynomial-space simulation of quantum computers on classical ones is easy. The technique used is pretty obvious to anyone who is familiar with Feynman’s path-integral formulation of quantum mechanics, which has been around much longer. It tells us that the amplitude of a given final basis state can be computed via a sum over trajectories (here, sequences of basis states) that terminate at that final state. A given sequence requires only polynomial space to store, and we can just iterate serially through all possible sequences, accumulating the final state’s net amplitude. This is all that is needed to compute the statistical behavior of the quantum system (*e.g.*, quantum computer) being simulated.

**Myth #6** “Large-scale quantum computers are fundamentally impossible to build, due to the phenomenon of decoherence.”

Our best models to date tell us that this is not so. We only require a quantum device technology that has a quality factor  $q$  that is above a certain finite threshold (currently estimated to be around  $10^3$ – $10^4$ ) [69] that allows known robust, fault-tolerant quantum error-correction algorithms to be applied, thereby allowing the scale of the achievable computations to be scaled up *arbitrarily*, just as classical error correction techniques allow classical computations to be scaled up arbitrarily, despite the small but not perfectly zero error rates in current-day bit devices. A high quality factor like this will be required anyway, if we wish to ever perform computation at rates well beyond those planned in the present semiconductor roadmap, which would imply computational temperatures that would quickly melt the computer’s structure, if the computational degrees of freedom were not extraordinarily well isolated from interactions with structural ones. So quantum computing is, in a sense, no harder than any technology that aims at capabilities well beyond the present semiconductor roadmap. Of course, many important engineering details remain to be worked out.

However, for a densely packed, 3D parallel quantum computer to be able to handle a noticeable rate of decoherence using fault-tolerant error correction techniques may require hardware implementation of the error correction algorithms, internally to the processor’s architecture, rather than just in software. Because of this, a quantum computer requires a somewhat different and more elaborate hardware architecture, as compared with a simple reversible computer, which would not need to maintain superposition states and so could make do with simple classical approaches to error correction, such as encoding computational bits redundantly in numerous physical bits, whose values can be “replenished” to stay locked with their nominal value by more trivial mechanisms (*e.g.*, by connecting a voltage-coded circuit node statically to a reference power supply, as is done in ordinary static CMOS logic circuits today).

### 4.2.3. Implementation Technologies

Many potential implementation technologies for quantum computers have been proposed and are being experimented on. These include nuclear spin systems [70], electron spin systems [71], superconducting current states of various sorts [72], and even mechanical vibrational systems [73]. To date, all of these approaches rely on an externally supplied signal for control and timing of operations. (As Lloyd says, “Almost anything becomes a quantum computer if you shine the right kind of light on it.”) But really, there seems to be no fundamental reason why the generator of the programmed control signal could not eventually be integrated with the actual devices, in a more tightly coupled fashion. For scalability to large arrays of self-timed processors, synchronization becomes a concern but can presumably be handled in much the same ways as we discussed for the case of reversible processors earlier.

### 4.2.4. Architectures and Programming Models

A self-contained quantum computer architecture looks very similar to a classical reversible architecture, but with some added instructions that can perform quantum operations that might not orthogonalize the input state. In principle, it suffices to include a single quantum instruction operating on a one-bit register, while keeping all other instructions simply coherent classical reversible [74], but a larger variety of quantum operations would probably also be useful. A self-contained, stored-program quantum architecture should probably have built-in support for fault-tolerant error correction algorithms, to avoid the overheads of implementing these in software. However, it is important to note that the entire architecture need not be coherent at all times, only the parts that are directly storing and manipulating the quantum data of interest. It may be beneficial to design each processor as a classical reversible processor (kept reversible and mildly coherent for speed and energy efficiency) paired with a relatively small quantum subprocessor whose state is kept highly coherent through the use of quantum error correction. The quantum component might be kept at a relatively low temperature to help avoid decoherence, since its speedups come from the use of superpositions in quantum algorithms, not from a fast operation rate (high computational temperature). Meanwhile, the classical part of the processor can perform in software, at relatively much higher frequencies, the meta-computation needed to determine which quantum operation should be performed next on the quantum subprocessor.

However, if a much wider range of useful quantum algorithms is eventually discovered, we may eventually find ourselves wishing to do quantum operations more pervasively throughout a wider range of applications, and also at higher frequencies, in which case the quantum functions might be integrated more thoroughly into the primary reversible processor. Without the availability of a classical processor running at higher speed, more of the low-level quantum algorithms such as error correction would need to be done “in hardware,” incorporated directly into the design, arrangement, and interactions of the individual quantum devices. The technique of using decoherence-free subspaces [75] provides one example of how to cope with errors

directly in the hardware design. Other methods may eventually be discovered.

Now, given our recognition of the need to incorporate the possibility of reversibility and quantum computing into our nanocomputer models, while respecting fundamental physical constraints as well, what will the resulting nanocomputer models look like? Let us take a look.

## 5. GENERIC REALISTIC MODEL OF NANOCOMPUTERS

In this section, we give a detailed example of what we consider to be a reasonably simple, realistic, and efficient model of computing which remains valid at the nanoscale. It is realistic in that it respects all of the important fundamental constraints on information processing except for gravity, which, unlike the other constraints, is not expected to become relevant yet within the coming half-century of technological development. The model is efficient in that it is not expected to be asymptotically less cost efficient (by more than a constant factor) than any other model that respects all of the same fundamental physical constraints. To achieve this, it must recognize the possibility of reversible and quantum computing.

The focus of this particular model is on enabling the analysis of the complete cost-efficiency optimization of parallel computer systems, when simultaneously taking into account thermodynamic constraints, communications delays, and the algorithmic overheads of reversible computing.

### 5.1. Device Model

A machine instance can be subdivided into logical *devices*. The total number of devices in the machine can be scaled up with the memory requirement of the given application.

Each device has a *logical state*, which is an encoded, desired classical or quantum state (possibly entangled with the state of other devices) for purposes of carrying out a classical or quantum computation. The logical state is encoded by a *coding physical state*, which is the portion of the device's physical state that encodes (possibly redundantly) the desired logical state. The device will probably also have a *noncoding physical state*, which is the rest of the device's physical state, which is not used for encoding computational information. The noncoding state can be further subdivided into a *structural state*, which is the part of the state that is required to remain constant in order for the device to work properly (if it is changed, the device becomes defective), and the *thermal state*, which is the unknown part of the device's physical state that is free to change because it is independent of the logical and structural state and so is not required to remain constant in order to maintain proper operation.

The device mechanism can be characterized by the following important parameters. In any given technology, the value of each of these parameters is assumed to be designed or required to fall within some limited range, for all devices in the machine.

- **Amount of logical information**,  $I_{\text{log}}$ , that is, information in the logical subsystem.

- **Amount of coding information**,  $I_{\text{cod}}$ , that is, information in the coding subsystem (in which the logical subsystem is represented).
- **Amount of thermal information**,  $I_{\text{therm}}$ , that is, information in the thermal subsystem, given the device's allowed range of thermal temperatures.
- **Computational temperature**  $T_{\text{cod}}$  of the coding state. This is the rate at which minimal desired changes to the entire coding state (*steps*) take place, that is, transitions which change all parts of the coding state in a desired way. Its reciprocal  $t_{\text{cod}} = 1/T_{\text{cod}}$  is the time for a step of updating the coding state to take place.
- **Decoherence temperature**  $T_{\text{dec}}$ . The rate at which undesired coding-state steps take place due to unwanted, parasitic interactions between the coding state and the thermal/structural state of the device or its environment. Its reciprocal  $t_{\text{dec}} = 1/T_{\text{dec}}$  is the decoherence time, the characteristic time for coding state information to be randomized.

Of course, it is desirable to select the coding subsystem in a way that minimizes the decoherence rate; one way to do this is to choose a subsystem whose state space is a *decoherence-free subspace* [75], or one that is based on *pointer states*, which are those states that are unaffected by the dominant modes of interaction with the environment [76]. The stable, "classical" states that we encounter in everyday life are examples of pointer states. Of course, even in nominal pointer states, some residual rate of unwanted interactions with the environment always still occurs; that is, entropy always increases, however slowly.

- **Thermal temperature**  $T_{\text{therm}}$ . The rate at which the entire thermal state of the device transforms. This is what we normally think of as the ordinary thermodynamic operating temperature of the device.
- **Decay temperature**  $T_{\text{struc}}$ . The rate at which decay of the device's structural state information takes place. It depends on the thermal temperature and on how well the structural subsystem's design isolates its state from that of the thermal degrees of freedom in the device. Its reciprocal  $t_{\text{struc}}$  is the expected time for the device structure to break down.
- **Device pitch**  $l_p$ . For simplicity, we can assume, if we wish, that the pitch is the same in orthogonal directions, so the device occupies a cube-shaped volume  $V_d = l_p^3$ . (This assumption can be made without loss of generality, since devices of other shapes can always be approximated by a conglomeration of smaller cubes. However, allowing alternative device shapes may give a simpler model overall in some cases.)

We are also assuming here that the region of space occupied by distinct devices is, at least, nonoverlapping, as opposed to (for example) different devices just corresponding to different degrees of freedom (*e.g.*, photonic vs electronic vs vibrational modes) within the same region. Again, this is not really a restriction, since such overlapping phenomena could be declared to be just internal implementation details of a single device whose operation comprises all of them simultaneously. However, we can loosen this no-overlap restriction if we wish. But if we do so, care should be taken not to

thereby violate any of the fundamental physical limits on entropy density, *etc.*

- **Information flux density**  $I_{\text{At}}$  (rate of information per unit area) through the sides of the device. This includes all physical information such as thermal entropy (flux  $S_{\text{At}}$ ) or redundant physical coding information (flux  $I_{\text{At,cod}}$ ) of logical bits (flux  $I_{\text{At,log}}$ ). Note that since the motion of information across the device boundary constitutes a *complete update step* for the location of that information, we know that  $I_{\text{At}} \ell_p^2 \leq IT$  where  $I$  is the information of a given type within the device, and  $T$  is the temperature (rate of updating) of the location information for that type of information.

Additionally, one of course also needs to define the specifics of the internal functionality of the device. Namely, what intentional transformation does the device perform on the incoming and internal coding information, to update the device's internal coding information and produce outgoing coding information? To support reversible and quantum computing, at least some devices must reversibly transform the coding information, and at least some of these devices must perform nonorthogonalizing transformations of some input states.

The device definition may also provide a means to (irreversibly) transfer the content of some or all of its coding information directly to the thermal subsystem, causing that information to become entropy.

For example, a node in static or dynamic CMOS circuit effectively does this whenever we dump its old voltage state information by connecting it to a new fixed-voltage power supply. However, a metal-oxide-semiconductor field effect transistor's (MOSFET) built-in dynamics can also be used to transform coding states *adiabatically*, thereby avoiding transformation of all of the coding information to entropy.

Most generally, the device's operation is defined by some reversible, unitary transformation of its entire state (coding, thermal, and structural), or, if the transform is not completely known, a statistical mixture of such. The actual transformation that occurs is, ultimately, predetermined solely by the laws of quantum mechanics and the state of the device and its immediate surroundings. So device design, fundamentally, is just an exercise of "programming" the "machine" that is our universe, by configuring a piece of it into a specific initial state (the device structure) whose built-in evolution over time automatically carries out a manipulation of coding information in such a way that it corresponds to a desired classical or quantum operation on the encoded logical information.

As we will see, this notion of a device is general enough that not only logic devices but also interconnects, timing sources, and power supply/cooling systems can be defined in terms of it.

## 5.2. Technology Scaling Model

The technology scaling model tells us how functional characteristics of devices change as the underlying technology improves. Just from basic physical knowledge, we already know some things about the technological characteristics of

our device model:

First,  $I_{\text{log}} \leq I_{\text{cod}}$ . That is, the amount of logical information represented cannot be greater than the amount of physical information used to do so. We can thus define the *redundancy factor*  $N_r \stackrel{\text{def}}{=} I_{\text{cod}}/I_{\text{log}} \geq 1$ .

Next, note that for devices that are *occupied* by information of interest (that is, actively maintaining a desired logical state), the rate  $S_{\text{dt}}$  of standby entropy generation is at least  $I_{\text{cod}} T_{\text{dec}}$  as coding information decays. The coding state of devices that are not occupied (not currently allocated for holding information) can be allowed to sit at equilibrium with their thermal environment, so their rate of standby entropy generation can be zero (or more precisely, some extremely low rate determined by the rate of structural decay  $T_{\text{struc}}$ ).

Next, if we assume that changing a logical bit is going to in general require changing all  $N_r$  of the physical bits used to redundantly encode it, we can immediately derive that logical bits, as well as physical bits, change at most at the rate  $T_{\text{cod}}$  [77]. If the computational temperature were only room temperature (300 K), then, expressed in terms of ops ( $h/2$ ) per bit ( $k_B \ln 2$ ), this temperature would allow a maximum rate of only one bit-op per 0.115 ps, that is, a bit-device operating frequency of at most 10 THz.

Note that this operating frequency is only about a factor of 3000 times faster than the actual  $\sim 3$  GHz working clock speeds in the fastest microprocessors that are currently commercially available, and furthermore it is only about a factor of 10 faster than the fastest present-day NMOS switches (which already have minimum transition times of  $\sim 1$  ps [6]) are theoretically capable of. By 2016, minimum transition times are planned to be almost as small as 0.1 ps, according to the semiconductor industry's roadmap [6]. So, in other words, taking device speeds significantly beyond the end of the present semiconductor roadmap will *require* temperatures in the computational degrees of freedom that are significantly *above* room temperature. This does not conflict with having *structural* temperatures that are relatively close to room temperature (to prevent the computer from melting), insofar as the computational degrees of freedom can be well isolated from interactions with the thermal and structural ones. But such isolation is desired anyway, in order to reduce decoherence rates for quantum computations and entropy generation rates for reversible classical computations.

Looking at the situation another way, given that increasing operating frequency significantly beyond the end of the semiconductor roadmap would require computational temperatures at significant multiples of room temperature, and given that solid structures melt at only moderate multiples of room temperature, the computational degrees of freedom *must* become increasingly well isolated from interactions with the rest of the system. This high-quality isolation, in turn, in principle enables reversible and quantum computation techniques to be applied. In other words, going well beyond the semiconductor roadmap requires entering the regime where these alternative techniques should become viable.

Let us look more carefully now at entropy generation rates. Since a step's worth of desired computation is carried out each  $t_{\text{cod}} = 1/T_{\text{cod}}$  time, whereas a step of unwanted

state modifications occurs each  $t_{\text{dec}} = 1/T_{\text{dec}}$  time, a key measure of the quality of the device technology is given by  $q = t_{\text{dec}}/t_{\text{cod}} = T_{\text{cod}}/T_{\text{dec}}$ , the ratio between decoherence time and state-update time, or in other words between state update rate and rate of state decay. Since the unwanted decay of a bit effectively transforms that bit into entropy, the entropy generated per desired logical bit operation must be at least  $N_r/q \geq 1/q$  bits, even for logically reversible operations. Note that our  $q$  is, effectively, just another equivalent definition for the quality ratio  $Q$  (the fraction of energy transferred that is dissipated by a process) that is already commonly used in electronics. We use lower case here to indicate our alternative definition in terms of quantum decoherence rates.

Now, for specific types of devices, we can derive even more stringent lower bounds on entropy generation in terms of  $q$ . For example, in [77], we show that for field-effect based switches such as MOSFETs, the entropy generated must be at least  $\sim q^{0.9}$ , with the optimal redundancy factor  $N_r$  to achieve this minimum growing logarithmically, being  $\sim 1.12 \lg q$ . However, it is reassuring that in this more specific device model, entropy generation can still go down *almost* as quickly as  $1/q$ . It may be the case that all reversible device models will have similar scaling. The key assumption made in that analysis is just that the amount of energy transfer required to change the height of a potential energy barrier between two states is of the same magnitude as the effected amount of change in height of the barrier. If this is true in all classes of reversible logic devices, and not just in field-effect-based devices, then the results of [77] hold more generally. See Figures 2 and 3.

However, in contrast to the reversible case, *irreversible* erasure of a bit of logical information by direct means (*e.g.*, grounding a voltage node) in general requires discarding *all*  $N_r$  of the redundant bits of physical information that are associated with that bit, and thus generating  $N_r$  bits of physical entropy which must be removed from the machine. At best, at least 1 bit of physical entropy must be generated for each logical bit that is irreversibly erased (see discussion in Section 5.2.5). Thus, when the device quality factor  $q$  is large (as must become the case when computational rates far exceed room temperature), the reversible mode of operation is strongly favored.

### 5.3. Interconnection Model

For simplicity, we can adopt an interconnection model in which interconnects are just another type of device, or are considered to be a part of the logic devices, and so are subject to the same types of characterization parameters as in our general device model. The machine need not be perfectly homogeneous in terms of its device contents, so interconnects could have different parameter settings than other types of devices. Indeed, they could be physically very different types of structures. However, it is critical that the interconnection model, however it is described, should at least accurately reflect the actual delay for a signal to traverse the interconnect. To save space we will not develop the interconnection model in detail here.

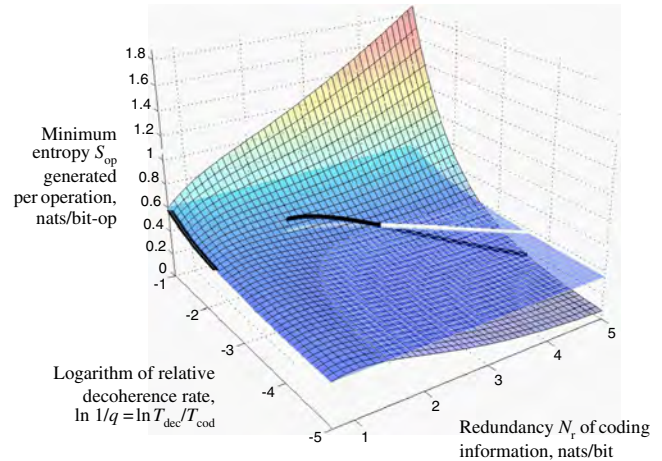


**Figure 2.** Minimum entropy generation per bit-op in field-effect devices, as a function of quality factor  $q$  and redundancy  $N_r$  of physical encoding of logical information. When  $q \leq e^2$ , the function is monotonically nondecreasing in  $N_r$ , but for larger  $q$ , it has a local minimum which first appears at  $N_r = 2$  nats per bit. The black line curving horizontally across the figure traces this local minimum from its first appearance as  $q$  increases. This local minimum becomes the absolute minimum when  $(1/q) \leq 0.0862651, \dots$  (numerically calculated), when the black line dips below the surface that we have visualized by sweeping the left edge of the figure (where  $N_r = 2$  nats/bit, its minimum) through the  $x$  direction. (The white line is there only to help visualize how far above or below that surface the black line lies at a given  $q$ .) The other black line, along the left edge of the figure, marks the approximate range of  $q$  values for which  $N_r = \ln 2$  nats/bit is indeed the optimal choice. Note that as  $q$  increases, ever-lower entropy generation per bit-op becomes possible, but only by increasing the redundancy of the encoding (which raises energy barriers and improves the achievable on/off power transfer ratios).

### 5.4. Timing System Model

Again, for simplicity, we can assume that timing synchronization functions are just carried out in special devices designated for this purpose or are integrated into the logical devices. Timing synchronization (correction of errors in timing information) can be carried out in an entirely local fashion. This is illustrated by the extensive literature on clockless (self-timed, or asynchronous) logic circuits. Reversible circuits cannot be allowed to operate in a completely *asynchronous* mode, in which substantial-size timing errors are constantly appearing and being corrected, since each synchronization operation would be irreversible and thus lossy, but they *can* be maintained in a closely synchronized state via local interactions only. Margolus showed explicitly how to do this in a simple 1D quantum model in [49]. But it is also clear that locally synchronized reversible operation can be generalized to three dimensions, just by considering simple mechanical models in which arrays of high-quality mechanical oscillators (*e.g.*, springs or wheels) are mechanically coupled to their neighbors (*e.g.*, via rigid interconnecting rods like those between the wheels on an old steam locomotive). An interesting research problem is to develop analogous reversible local-synchronization mechanisms that are entirely electronic rather than mechanical or, if this is impossible, prove it.

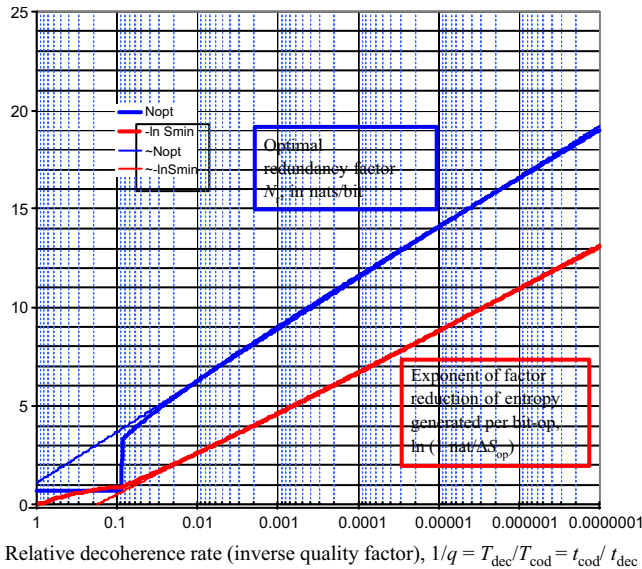


**Figure 3.** Scaling of optimal redundancy factor and maximum entropy reduction with decreasing relative decoherence rate. In the graph, the horizontal axis sweeps across different  $q$  factors (decreasing values of  $1/q$ ), and we show the corresponding optimal choice of  $N_r$  (found via a numerical optimization) and the natural logarithm of the maximum entropy reduction factor (factor of entropy reduction below the reference  $1 k_B = 1$  nat) that may be obtained using this choice. The thin, straight trend lines show that for large  $q$  (small  $1/q$ ), the optimal  $N_b$  (for minimizing  $\Delta S$ ) scales as roughly  $1.1248(\ln q)$ , while the minimum  $\Delta S$  itself scales as about  $q^{0.9039}$ .

### 5.5. Processor Architecture Model

For purposes of analyzing fundamental trade-offs, this need not be particularly restrictive. A processor should contain some memory, with a low standby rate of entropy generation for bits that are occupied but are not being actively manipulated, and zero standby rate of entropy generation in unallocated, powered-down bits (after they equilibrate with their environment). The processor should contain some logic that can actively process information in some way that can be programmed universally (any desired program can be written, given sufficiently many processors). It should be able to perform fully logically reversible operations which are carried out via reversible transformations of the coding state. Some examples of reversible architectures can be found in [4, 59, 60, 78, 79]. For convenience, the architecture should also permit irreversible operations which treat the information in the coding state as entropy and transfer it to a noncoding subsystem that is basically just a heat flow carrying entropy out of the machine. (There is no point in keeping unwanted information in a coded state and wasting error correction resources on it.) However, the reversible operations provided by the architecture should also allow an alternative, of *uncomputing* the undesired information, so as to return the coding state to a standard state that can be reused for other computations, without needing to ever treat the coding information as if it were entropy. The architecture should be able to be programmed to efficiently carry out any reversible algorithm.

Ideally, the architecture should also support performing nonorthogonalizing quantum operations (that is, operations

that create quantum superpositions of logical basis states), so that, in combination with classical coherent reversible operations, arbitrary quantum computations can be programmed. If quantum computation is to be supported, simply using classical pointer basis states in the device is no longer sufficient for representing the logical state, and full quantum superpositions of logical basis states (spanning some relatively decoherence-free subspace) should be permitted.

The key criteria are that the architecture should be both physically realistic and universally maximally scalable. These goals, together with ease of programmability, imply that it should look something like we described previously.

### 5.6. Capacity Scaling Model

An ordinary multiprocessor model can be adopted, scaling up total machine capacity (both memory and performance) by just increasing the number of processors. However, we must be careful to be realistic in specifying the interconnection network between the processors. It has been shown that no physically realizable interconnection model can perform significantly better than a 3D mesh model, in which all interconnections are local (*i.e.*, between processors that are physically close to each other) [17]. Moreover, although the planar width of the whole machine can be unlimited, the effective thickness or depth of the machine along the third dimension is inevitably limited by heat removal constraints [4]. However, insofar as reversible operation can be used to reduce the total entropy generated per useful logical operation, it can also increase the *effective* thickness of the machine, that is, the rate of useful processing per unit of planar area [20]. This, in turn, can improve the performance of parallel computations per unit machine cost, since a thicker machine configuration with a given number of processors has a lower average distance between processors, which reduces communication delays in parallel algorithms [4, 58].

### 5.7. Energy Transfer Model

The flow of energy through the model should, ideally, be explicitly represented in the model, to ensure that thermodynamic constraints such as conservation of energy are not somewhere implicitly violated. A piece of energy  $E$  that is changing state at average rate (temperature)  $T$  contains  $I = E/T$  amount of information, by our definitions of energy and temperature. Likewise, for  $I$  amount of information to be transitioning at rate  $T$  requires that energy  $E = IT$  be invested in holding that information. Entropy  $S$  is just information whose content happens to be unknown, so ejecting it into an external atmosphere where it will transition at room temperature, or  $\sim 300$  K, always requires that an accompanying  $S(300 \text{ K})$  energy (heat) also be ejected into the atmosphere. (Or, if the cosmic microwave background is used as a waste heat reservoir, an ambient temperature of  $2.73$  K applies instead.) The same relation between energy, information, and temperature of course applies throughout the system: Whenever an amount of information  $I$  is added to any subsystem that is maintained at a specific, uniform temperature  $T$ , an amount  $E = IT$  of energy must also be added to that subsystem.



Thus, the continual removal of unwanted entropy from all parts of the machine by an outward flow of energy (heat) requires that this lost energy be replenished by an inward-flowing energy supply going to all parts of the machine, complementing the outward heat flow. This inward-flowing supply also has a generalized temperature  $T_{\text{sup}}$  and carries information, which must be known information in a standard state, or at least contain less entropy than the outward flow (otherwise we could not impress any newly generated entropy onto the energy flow).

The total rate of energy flow to the machine's innards and back might be greater than the minimum rate needed for the entropy internally generated to be emitted, if the heat is being moved actively (e.g. by a directed flow of some coolant material). This may be required to keep the thermal temperature of internal components low enough to maintain their structure. If the coolant is flowing at such a speed that the effective temperature of its motion is greater than the desired internal structural temperature, then we must isolate this flow from direct thermal contact with the structure, in order to avoid its *raising* the structural temperature rather than lowering it. Nevertheless, a well-isolated coolant flow can still be used to remove heat, if the unwanted heat is sent to join the coolant stream by a directed motion.

Note that the extra, directed energy flow in an active cooling system (its moving matter and kinetic energy) can be *recycled* (unlike the heat) and directed back into the machine (after being cooled externally) to carry out additional rounds of heat removal. So all the energy contained in the inward coolant flow does not necessarily represent a permanent loss of free energy.

To minimize the total rate of free-energy loss needed to achieve a given internal processing rate, we should minimize the rate at which entropy is produced internally, the inefficiencies (extra entropy generation) introduced by the cooling system, and the temperature of the external thermal reservoir (for example, by placing the computer in primary thermal contact with outer space, if possible).

One way to approach the energy transfer model treats the energy flow pathways as just yet another type of information-processing device, subject to the same type of characterization as we discussed earlier in Section 6.1. The only difference is that there need be no coding information present or error correction taking place in a device whose only purpose is to carry waste entropy out of the machine to be externally dissipated.

## 5.8. Programming Model

For purposes of this discussion, we do not particularly care about the details of the specific programming model, so long as it meets the following goals:

- **Power.** Harnesses the full power of the underlying hardware (*i.e.*, does not impose any asymptotic inefficiencies). In the long run, this implies further that it supports doing the following types of operations, if/when desired and requested by the programmer:
  - Parallel operations.
  - Reversible classical operations (implemented with as little entropy generation as the underlying device quality permits in the given technology).

- Quantum coherent operations (with as little decoherence as the device quality permits).

- **Flexibility.** The efficiency of the machine will be further improved if it provides several alternative programming models, so that whichever one that is most efficient for a particular application can be used. For example, each processor might provide both a CPU running a fairly conventional style of instruction set architecture (although augmented by reversible and quantum instructions) which efficiently maps the most common operations (such as integer and floating-point calculations) to device hardware, as well as a section of reconfigurable logic (also offering reversible and quantum operation), so that specialized, custom application kernels can be programmed at a level that is closer to the hardware than if we could only express them using traditional software methods.
- **Usability.** The programming model should be as straightforward and intuitive to use by the programmer (and/or compiler writer) as can be arranged, while remaining subject to the previous criteria, which are more important for overall efficiency in the long run. At present, programmer productivity is arguably more immediately important than program execution efficiency for many kinds of applications (for example, in coding business logic for e-commerce applications), but in the long run, we can expect this situation to reverse itself, as fundamental physical limits are more closely approached, and it becomes more difficult to extract better performance from hardware improvements alone. When this happens, the efficiency of our programming models will become much more critical.

Also, there may be a period where our choice of programming models is constrained somewhat by the type of hardware that we can build cost-effectively. For example, processors might be forced to be extremely fine-grained, if it is initially infeasible to build very complex (coarse-grained) structures at the nanoscale. Papers on NanoFabrics [80] and the Cell Matrix [81] describe examples of fine-grained parallel models based on very simple processing elements. In the case of [80], the processing elements are ones that can be built by making heavy use of certain chemical self-assembly techniques that are deemed more feasible by the authors than other fabrication methods.

However, my own opinion is that the need for such fine-grained architectures, if there ever is one, will only be a short-term phenomenon, needed at most only until manufacturing capabilities improve further. In the longer run, we will want direct hardware support (*i.e.*, closer to the physics) for very common operations such as arithmetic, and so eventually our nanoarchitectures will also contain prefabricated coarse-grained elements similar to the integer and floating-point ALUs (arithmetic-logic units) which are common today, which will be naturally programmed using instruction sets that are, in large measure, similar to those of today's processors.

To see why, consider this: The cost efficiency of a very fine-grained architecture, such as the Cell Matrix, on any application is reduced by at most a factor of 2 if we take



half of the area that is devoted to these fine-grained reconfigurable cells and use it to build fixed 128-bit ALUs (say) directly in hardware instead, even in the worst case where those ALUs are never used. But those general applications that *can* use the ALUs (which is probably most of them) will run hundreds of times more cost-efficiently if the ALUs are directly available in hardware than if they have to be emulated by a much larger assemblage of simple reconfigurable cells.

However, including *some* amount of reconfigurable circuitry is probably also desirable, since there are some specialized applications that will probably run more cost-efficiently on top of that circuitry than in a traditional instruction set.

The most basic law of computer architecture, Amdahl's law (in its generalized form [82] which applies to all engineering fields, and to any measure of cost efficiency), can be used to show that so long as the costs spent on both reconfigurable circuitry and traditional hardwired ALUs are comparable in a given design, and both are useful for a large number of applications, there will be little cost-performance benefit to be gained from eliminating either one of them entirely. Furthermore, it seems likely that the business advantages of having a single processor design that can be marketed for use for either kind of application (ALU-oriented vs more special-purpose) will probably outweigh the small constant-factor cost efficiency advantage that might be gained on one class of application by killing the cost efficiency of the other class.

Since arithmetic-intensive computing drives most of the market for computers and will probably continue to do so, I personally think it most likely that we will follow a evolutionary (not revolutionary) manufacturing pathway that continues to make smaller and smaller ALUs, which continue to be programmed with fairly traditional (CISC/RISC/DSP) instruction-set styles, and that gradually evolves toward the point where these ALUs are composed of truly nanoscale devices. The alternative scenario promoted by these authors, that the majority of computing will suddenly change over to using some radically different alternative architecture which lacks efficient low-level hardware support for such application-critical operations as "add," does not seem very plausible.

Now, of course, above the instruction-set level, higher level programming models (languages) may take a variety of forms. For example, Skillicorn [83] discusses issues in the design of high-level parallel models that map efficiently to hardware.

Some discussion of reversible programming languages can be found in [4, 84, 85], and some examples of quantum programming languages are [86–91].

## 5.9. Error Handling Model

Typically, the physical coding state will be chosen in such a way that any errors that appear in the coding state can be detected and corrected, before enough of them accumulate to cause the logical state information to be lost.

Ordinary static CMOS logic provides a simple example of this. The coding state is the analog voltage on a circuit node. A fairly wide range of possible voltages (thus, a relatively large amount of coding state information) is taken

to effectively represent a given logical value (0 or 1). The *ideal* coding state is some power-supply reference voltage, GND or  $V_{dd}$ . If, through leakage, a node voltage should drift away from the ideal level, in a static CMOS circuit, the level will be immediately replenished through a connection with the appropriate power supply. A simple static CMOS storage cell, for example, may include two *inverter* logic gates that continuously sense and correct each other's state. This can be viewed as a simple hardware-level form of error correction.

In dynamic digital circuits, such as a standard DRAM chip, a similar process of error detection and correction of logic signals takes place, although periodically (during refresh cycles) rather than continuously.

Of course, many other coding schemes other than voltage-level coding are possible. Electron spin states [71], current direction states [72], AC current phase states [92], electron position states [41], and atomic position states are just some of the examples. Whatever the coding scheme used, a similar concept applies, of redundantly representing each logical bit with many physical bits, so that errors in physical bits can be detected and corrected before enough of them change to change the logical bit. This idea applies equally well to quantum computing [93].

If the architecture does support quantum computing and is self-contained, then, for efficiency, fault-tolerant quantum error correction algorithms [69] should probably eventually be implemented at the architectural level in the long term, rather than just (as currently) in software.

Note that to correct an error is by definition to remove the "syndrome" information that characterizes the error. Insofar as we do not know precisely how the error was caused, and thus how or whether it might be correlated with any other accessible information, this syndrome information is effectively entropy, and so we can do nothing sensible with it except expel it from the machine. Unless the error rate is negligibly small, the resources required for removal of this error information must be explicitly included in any realistic model of computing that takes energy costs or heat-flux constraints into account.

## 5.10. Performance Model

Given the care we have taken to recognize fundamental physical constraints in our model components, a correct performance model will fall out automatically, as the architectural details are filled in. As we compose a large machine out of individual devices characterized as described, our device model forces us to pay attention to how energy and information flow through the machine. An algorithm, specified by an initial coding state of all of the devices, runs at a rate that is determined by the device dynamics, while respecting the time required for signals to propagate along interconnects throughout the machine, and for generated entropy to flow out along cooling pathways.

## 5.11. Cost Model

As we described earlier, a good cost model should include both spacetime-proportional costs (which include manufacturing cost, amortized over device lifetime), and energy-proportional costs. The energy costs can easily be dominant,

if the machine is to be operated for a long lifetime, or in an environment where energy is hard to come by and thereof expensive (or, complementarily, where heat is hard to get rid of).

As a pragmatic example, suppose a battery in a 30-W laptop lasts 5 hours, thus supplying 0.15 kW-hrs of energy. Assuming the recharge process can be done very efficiently, the raw cost of energy for a recharge, at typical current U.S. electric utility rates, is therefore less than one cent (US\$0.01). However, the inconvenience to a business traveler of having to charge and carry extra batteries in order to make it through a long international flight could well be worth tens of dollars, or more, to him or her. Also, having a particularly hot laptop sitting on one's lap can be a significant discomfort that users may be willing to pay a significant amount of money to reduce. The effective cost of energy can thus be many orders of magnitude higher than usual in these scenarios.

As additional examples, think of the cost to supply fresh fuel for energy to soldiers in the field, or to wireless transponders that may be mounted on autonomous sensors, or on goods during warehousing and shipping, for electronic inventory and tracking systems. Or, think of the cost to supply extra energy to an interstellar probe in deep space. Moreover, space vehicles also can have difficulty getting rid of waste heat, due to the absence of convective or conductive modes of heat transport.

These examples serve to illustrate the general point that circumstances in particular application scenarios can inflate the effective cost of energy by a large factor, perhaps hundreds or thousands of times over what it would be normally.

Even at normal wall-outlet electricity rates, a 200-W high-performance multiprocessor desktop workstation that remained in continuous service would use up  $\sim$ US\$1,700 worth of electricity over 10 years, which may be comparable to the cost of the machine itself. (However, for as long as Moore's law continues, the computer would probably be replaced about every 3 years anyway, due to obsolescence.)

Also, the cost of energy could increase further if and when the rate of fossil fuel extraction peaks before energy demand does, if more cost-effective energy technologies do not become available sooner than this. However, such variations in the cost of energy may not affect the trade-off between manufacturing cost and energy cost much, because manufacturing costs are, probably, ultimately also dominated by the cost of energy, either directly or indirectly through the manufacturing tool supply chain. Also, offsetting the fossil fuel situation, nanotechnology itself may eventually provide us new and much cheaper energy technologies, in which case the cost of energy might never be significantly higher than it is at present.

However, even if the cost of energy always remains low, or even goes much lower than at present, the discomfort to a human user of holding or wearing a computer that is dissipating much more than  $\sim$ 100 W will always remain an important concern for as long as there remain biological humans who want to carry their computers around with them, and who comprise a significant part of the market for computing.

## 5.12. Some Implications of the Model

In some previous work that did a complete system-level analysis based on a model highly similar to the one just described [21], we demonstrated (based on some straightforward technology scaling assumptions) that the cost-efficiency advantages of reversible computing, compared to irreversible computing, for general-purpose applications in a 100 W, US\$1,000 machine could rise to a factor of  $\sim$ 1000 by the middle of this century, even if no more efficient algorithms for general-purpose reversible computing are found than those (specifically, [54]) that are already known. In the best case, for special-purpose applications, or if ideal general purpose reversibilization algorithms are discovered, the cost-efficiency benefits from reversibility could rise to a level  $\sim$ 100,000  $\times$  beyond irreversible technology. See Figure 4.

However, that particular analysis assumed that a very high  $q$  value of  $\sim 10^{12}$  could be achieved at that time and, further, that it could be maintained as manufacturing costs per device continued to decrease. If this does not happen, then the gains from reversibility will not be so great. Unfortunately, the exponentially increasing rate at which electrons tunnel out of structures as distances shrink [94] makes it seem that very high  $q$ 's—corresponding to very strongly confined electron states—will be very hard to achieve in any technology at the deep nanoscale ( $< \sim 1$  nm device pitch). The resulting fast decay rate of any meta-stable electronic states is a problem even for irreversible technologies. It essentially means that the performance density (ops per second per unit area) and even memory density (bits per unit area) of deep-nanoscale electronic computers would inevitably be *strongly* limited by high leakage power dissipation of individual devices.

Generally, electron tunneling becomes significant compared to desired electron motions wherever interdevice distances become on the order of the Fermi wavelength of electrons in the conductive material in question, which

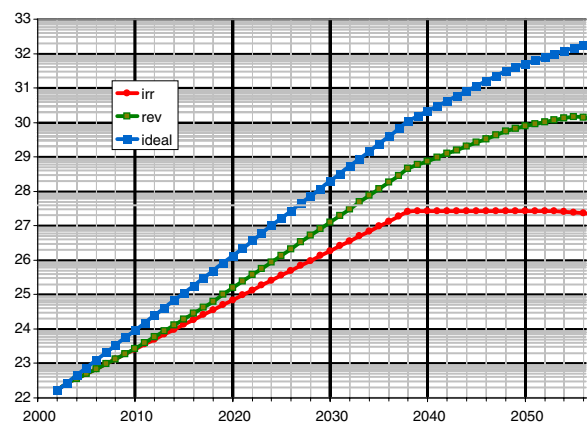


**Figure 4.** Base-10 logarithm of cost efficiency, in effective logic operations per dollar, for irreversible (lower line), general reversible (middle line), and best-case reversible (upper line) computations, as a function of year, for a \$1,000/100 W “desktop” computing scenario, using a model similar to the one described in this chapter and assuming that a high  $q$  value for devices can be maintained. Reprinted with permission from [5], M. P. Frank, Nanocomputer systems engineering, in “Technical Proceedings of the 2003 Nanotechnology Conference and Trade Show.” © 2003, Nano Science and Technology Institute.

ranges from on the order of  $\sim 0.5$  nm for highly conductive metals to on the order of  $\sim 20$  nm for semiconductors.

But because of the substantial energy savings to be gained, it may, in fact, turn out to be better for overall performance *not* to make device pitch quite so small as may become physically possible to manufacture, and instead keep devices spread far enough apart from each other so that tunneling currents remain negligible. Even with this restriction, average interdevice interconnect lengths in complex circuits can still become far shorter than they are at present, especially if circuit buildout begins to use the third dimension significantly, which is in turn enabled by the exponential reduction in tunnel-current power that is made possible by keeping device pitch relatively large, and by the resulting large savings in total power that can be obtained by using reversible computing, if high-quality, self-contained coupled logic/oscillator systems can be built.

## 6. SPECIFIC NANOCOMPUTING TECHNOLOGY PROPOSALS

So far, most of our nanocomputing discussions have been fairly general and technology-independent. In this section, we proceed to review and summarize a variety of more specific nanocomputer technologies (that is, potential physical implementations of nanocomputer models and architectures) that have been proposed to date.

### 6.1. Taxonomy of Nanocomputing Hardware Technologies

In this list, we attempt to subdivide and categorize a sampling from the already vast spectrum of radically differing technologies that have been proposed to date for the physical implementation of future nanocomputers. Further discussion of some of these categories follows in subsequent subsections.

- Solid state
  - Pure electronic (only electrons moving)
    - Using inorganic (non-carbon-based) materials
      - Using semiconducting materials
        - Scaled field-effect transistors
          - Alternative device geometries
            - Double-gate, FinFET, *etc.*
          - Semiconductor nanowires
        - Single-electron transistors
          - Coulomb blockade effect devices
        - Resonant tunneling diodes/transistors
        - Quantum dot based
          - Quantum dot cellular automata
        - Spintronics (using electron spins)
      - Using conducting materials
        - Helical logic (Merkle and Drexler)
      - Using superconducting materials
        - Josephson-junction circuits
    - Organic (carbon-based) molecular electronics
      - Carbon nanotube electronics (can be conducting, semiconducting, or superconducting)
      - Surface-based organic-molecular electronics

- Mechanical (whole atoms moving)
  - Rod logic (Drexler)
  - Buckled logic (Merkle)
  - Brownian clockwork (Bennett)
- Electromechanical
  - Micro/nanoelectromechanical systems (MEMS/NEMS) technologies
    - Electrostatic relays, dry-switched
    - MEMS-resonator-powered adiabatics
  - Configuration-based molecular electronics
- All-optical (only photons moving)
- Opto-electronic (photons and electrons)
- Fluid state
  - Molecular chemical approaches (*in vitro*)
    - Biomolecular chemical computing
      - DNA computing
        - DNA tile self-assembly
  - Biocomputing (*in vivo*)
    - Genetic regulatory network computing
  - Fluidic (fluid flows confined by solid barriers)
  - High-level fluidity (solid-state devices suspended in fluid)
    - Hall's utility fog
    - Amorphous computing over ad hoc networks of mobile devices
  - Gas state
    - Gas-phase chemical computing
- Plasma state (speculative)
  - Smith-Lloyd quantum-field computer
- Black-hole state (speculative)
  - Beckenstein-bound black hole computer

### 6.2. Nanoelectronic Logic Technologies

By far, the most well-researched category of nanocomputer technologies at this time is the solid-state, purely electronic technologies. Pure electronic computing technologies are ones those in which the entities whose motions are involved in carrying out a computation are electrons only, not atoms or photons (aside from the virtual photons that implement the quantum-electrodynamic interactions between the charge carriers).

At around the 10 nm scale, the ordinary bulk materials models currently used in electronics, and the standard field-effect based semiconductor device operation mechanisms that rely on those models, begin to break down. At this technological *mesoscale*, surface effects and quantization effects become important, or even dominant. Some of the new effects that need to be considered include:

- Quantization of the number of atoms in a given structure. This is a problem for the low-density implanted dopants used today in semiconductor devices, as the statistical nature of the present dopant implantation processes means that there is a high variance in the dopant concentration in a sufficiently small structure, which leads to unpredictable variation in MOSFET threshold voltages, and possibly a low device yield. In principle, this problem can be dealt with if nanomanufacturing techniques allow the number and location of dopant atoms in a given structure to be chosen

- precisely, or by using alternative dopant-free device designs.
- Quantization of charge (number of electrons). This is realized today in a number of single-electron devices that have been demonstrated in the lab. It is also the basis for the *Coulomb blockade* phenomenon, which is the basis for some proposed device mechanisms.
  - Quantum tunneling of electrons through any very narrow, very low potential energy barriers. This is already a concern today that is preventing significant further thinning of MOSFET gate oxides, and ultimately this may be the key factor limiting shrinkage of overall device pitch. The problem is that electrons will tend to migrate easily between adjacent nanostructures, unless the potential energy barriers preventing this tunneling are extremely large, which may be difficult to arrange. This presents a problem for dense information storage using electrons. The densest possible forms of stable storage may therefore turn out to consist of states (position or spin states) of entire atoms or nuclei, rather than electrons.
  - Quantization of electron energies when confined to small spaces. That is, energy “bands” can no longer be treated as if they were continuous. Similarly, electron *momentum* does not vary continuously along any specific direction in which the electron is highly confined.
  - If the quantum quality factor of devices is low, so that there is a large interaction between the coding state and the surrounding thermal state, then thermal noise also becomes significant, since the redundancy of the coding information is necessarily reduced in small devices. Due to the lack of redundancy, the expected time for a coding state to change to an error state due to thermal interactions corresponds to a relatively small number of computational steps of the device, so there is less opportunity for computational error correction techniques to apply.

These small-scale effects can be considered to be obstacles, but we should also recognize that knowing how these effects work may also enable the development of entirely new operating principles upon which logic mechanisms can be based.

In the taxonomy in Section 7.1, we broke down the solid-state electronic technologies according to the conductivity properties of the material used for electron transfer (semiconductor, conductor, superconductor). But an alternative way to categorize them would be according to the primary physical principle that is harnessed in order to perform logical operations. We can do this as follows:

- Coulombic (electrostatic) attraction/repulsion effects:
  - Field effect devices:
    - Scaled bulk field-effect transistors
    - Carbon nanotube FETs
    - FETs made of crossed semiconductor nanowires
  - Charge quantization/Coulomb blockade effect
    - Single-electron transistors
  - Helical logic
- Energy quantization/resonant tunneling effects
  - Resonant tunneling diodes
  - Resonant tunneling transistors

- Quantum wells/wires/dots
  - Quantum dot cellular automata
- Atomic-configuration-dependent electronic properties
  - MEMS/NEMS electromagnetic switches/relays
  - Configuration-dependent conductivity of carbon nanotubes
  - Configuration-based molecular switches
- Superconductivity effects
  - Josephson effect
- Electron spin effects (in spintronics)
  - Spin-based transistors
  - Single-electron-spin-based quantum computing

### 6.2.1. Nanoscale Field-Effect Transistors

The *field effect* used in today’s MOSFETs is essentially just a result of the Coulombic attraction or repulsion between the static electric charge that is present on a *gate* electrode, and the charge carriers in a nearby semiconducting pathway (the *channel*). Depending on the applied gate voltage and the channel semiconductor characteristics, the concentration of mobile charge carriers in the channel may be either enhanced far above or depleted far below the default level that it would have if the gate were not present. Also, the types of the dominant charge carriers that are present in the channel (electrons versus holes) may even be inverted. The carrier concentration (and type) in turn affects the density of current flow through the channel when there is a voltage difference between the two ends (“source” and “drain”) of the channel wire, giving the transistor a larger or smaller effective resistance.

For fundamental reasons, the effective resistance of a minimum-size turned-on field-effect transistor, in any given technology, is roughly (within, say, a factor of 10, depending on the details of the device geometry) of the same magnitude as the quantum unit of resistance  $h/2e^2 \approx 12.9 \text{ k}\Omega$ , which is the built-in resistance of a single ideal quantum channel. But the effective resistance of a turned-off field-effect device can be much larger. For relatively large devices (above the nanoscale) in which electron tunneling across the channel is not significant, the off-resistance is limited only by the decrease in concentration that can be attained for whichever type of current carrier is available within the source and drain electrodes. By the equipartition theorem of statistical mechanics, the reduction in the channel concentration of these carriers scales with  $\exp(-E/kT)$ , where  $E$  gives the potential energy gained by a charge carrier that is in the channel, and  $kT$  is the thermal energy per nat at thermal temperature  $T$ . To increase the potential energy for a single charge carrier to be in the channel by an amount  $E$ , at least a corresponding amount  $E$  of electrostatic energy needs to be moved onto the gate electrode, even in the best case where the gate electrode was somehow occupying the same space as the channel (while somehow being prevented from exchanging charge with it). Actually, in real devices, the gate electrode will usually be only located next to (or at best, wrapped around) the channel, in which case some, but not all, of the energy of its electrostatic field will be contained inside the channel itself. Together with other nonidealities, this leads to an actual scaling of current with the exponential of only some *fraction*  $1/(1 + \alpha)$  of the ratio

between gate voltage and thermal energy. Empirically measured values of  $\alpha$  today are around 1.0 (*i.e.*, only about half of the gate's electrostatic energy is visible inside the channel) [95]. The results described in Section 6.12 assume that further device or materials improvements can reduce  $\alpha$  to be close to 0, so that field-effect devices are thus operated in a regime where their on/off ratios are close to  $e^{E/kT}$ . (If not, then those results need to be revised accordingly.)

The basic principles of operation of field-effect devices have been shown to remain valid at least in the near-nanoscale (1–32 nm) regime. As early as 2001, Intel reported field-effect operation of MOSFETs in the lab having channel lengths as small as  $\sim 20$  nm [96], and IBM just announced a working 6-nm channel-length MOSFET (called XFET) at the December 2002 International Electron Devices Meeting [97]. Furthermore, academic groups such as Lieber's at Harvard [98] have successfully demonstrated field-effect transistors and logic gates using chemically synthesized (rather than lithographically etched) inorganic semiconducting wires having similar diameters and channel lengths. Also, carbon molecular nanotubes in certain configurations can act as semiconductors and have been demonstrated to be usable as channels of field-effect transistors [99]. Finally, some theoretical studies have indicated that even a one-atom-wide "wire" of silicon atoms adsorbed on a crystal surface, with exactly periodic interspersed dopant atoms, can behave as a material having a semiconductor band structure [100], and thus serve as a transistor channel.

However, for scaling of channel length below about the 10 nm range, tunneling of charge carriers through the channel barrier may begin to become a limiting concern in semiconductors. This is because at that scale, the Fermi wavelength of the conduction-band electrons (that is, the de Broglie wavelength of those electrons traveling at the *Fermi velocity*, the characteristic velocity of the mobile electrons at the surface of the "Fermi sea" of conduction band states) begins to become significant.

In contrast, metals usually have relatively low Fermi wavelengths, under 1 nanometer, because they have a high level of degeneracy, meaning that their low-energy states are packed full, so these low-momentum states are unavailable for charge transport, and so all of their activated (mobile) electrons must travel relatively fast (at the *Fermi velocity*). For example, among pure elemental metals, cesium has one of the lowest Fermi energies, 1.59 eV, while beryllium has one of the highest, 14.3 eV. Taking these as kinetic energies of free electrons with mass  $m_e$ , the Fermi velocities  $v_F$  are 748 km/s for Ce and 2240 km/s for Be. The Fermi wavelength  $\lambda_F = h/m_e v_F$  scales as the inverse square root of the Fermi energy and comes out to be 0.97 nm for Ce and 0.32 nm for Be.

However, in semiconductors, the Fermi wavelength is typically much larger than this, because the activated electrons can occupy even the lowest energy of the conduction band states, since those states are not normally occupied. Typical kinetic energies of mobile electrons in semiconductors can thus be as low as on the order of the thermal energy  $kT$ , which is 0.026 eV at room temperature, corresponding to an electron velocity of only 95 km/s. The corresponding de Broglie wavelength for electrons moving in vacuum at room temperature speeds would be 7.6 nm. Furthermore, in

practice, Fermi wavelengths in semiconductors turn out to be even several times larger than this, typically in the range 20–60 nm, due in part to the reduced effective mass of the electron, as a result of its interactions with the surrounding crystal lattice structure.

Due to these relatively large wavelengths, mobile electrons in semiconductors will tend to spread out over regions of about the same size, unless confined by sufficiently high energy barriers. A turned-off transistor gate can provide such a barrier against electrons moving through the channel region. However, the effective confinement length of an energy barrier against electron tunneling is only on the order of the corresponding wavelength  $h(2mE)^{-1/2}$ , where  $m$  is the effective electron mass in the barrier region and  $E$  is the height of the barrier. Figure 5 graphs this relation, for electrons of effective mass  $m_e$  (in vacuum) or  $0.2 m_e$  (in some semiconductors). Notice that as the height of the energy barrier shrinks toward small multiples of the room-temperature thermal energy, the minimum width of the barrier increases, toward sizes on the order of 5–10 nm. The trend toward shorter channel lengths thus directly conflicts with the trend toward decreasing voltages in MOSFETs. For this reason, it seems that aggressively voltage-scaled field-effect devices are not likely to ever get much below  $\sim 10$  nm in channel length.

What about using higher barrier heights? From Figure 5, we can see that barriers narrower than even 1 nm may

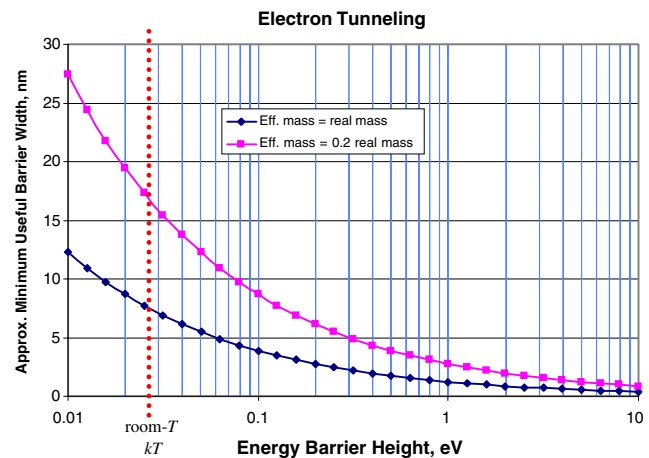


**Figure 5.** Approximate lower limit of the width of an energy barrier of given height needed to prevent electron tunneling across the barrier from becoming significant, for both free electrons (lower curve) and electrons in a fairly typical semiconductor in which the effective electron mass is only  $m \approx 0.2 m_e$  (upper curve). The minimum width is estimated as being roughly equal to the de Broglie wavelength  $= h(2mE)^{-1/2}$  of electrons having kinetic energy equal to the barrier height. A more accurate calculation (specifically, based on Eq. 6-54 on p. 207 of [101]) would multiply this figure by  $\ln(1/p)/4\pi$  to give the width of a barrier that has probability  $p \ll 1$  of being tunneled through by an electron having an initial kinetic energy  $E$  less than the barrier height. Our graph here then corresponds to the case where the tunneling probability  $p = 3.5 \times 10^6$ , and where  $E$  represents the barrier height relative to the Fermi energy of the region on either side of the barrier. The dotted red line indicates the room-temperature (300 K) value of  $kT = 26$  mV; the energy barrier must be at least about this high anyway, in order to prevent thermally activated leakage from dominating.

still prevent tunneling, so long as the barrier has a height of several electron volts. Actual energy barriers of such heights, due to high molecular electron affinities, are exactly what prevent many everyday materials, such as plastics, from being good conductors, despite the sub-nm distances between adjoining molecules in these molecular solids. However, using such high voltages in the gates of nanoscale field-effect devices may backfire, by causing high gate-to-channel tunneling. Frank [94] looks carefully at all of these tunneling considerations and concludes that irreversible CMOS technology cannot scale effectively to less than  $\sim 10$  nm, given realistic power constraints. Alternative field-effect structures such as nanotubes [99] and nanowires [98], despite their very narrow linewidths, remain subject to identical kinds of source-to-drain and gate-to-channel tunneling considerations and so cannot really be expected to fare much better, in terms of the scaling of their overall device pitch.

How might we do significantly better than this? Arguably, this will require (eventually) abandoning the field-effect operating principle entirely. Field-effect devices are based on a controllable potential energy barrier, whose height is adjusted simply by moving a corresponding amount of static electrical energy onto or off of a nearby gate electrode. But the problem is that this mobile gate charge is subject to parasitic tunneling into the very system, the transistor channel, that it is supposed to be controlling. Decreasing the gate voltage reduces this tunneling but also increases leakage across the channel. Keeping the gate relatively far away from the channel is another way to reduce gate-to-channel tunneling, but it also reduces the gate's effect on the channel, due to decreased gate-channel capacitance and thus indirectly increases leakage. The use of high-dielectric-constant materials such as silicon nitride between the gate and channel can help keep to keep the capacitance high and the gate leakage low, but only to a limited extent. An extreme example would be if ultrapure water could be used as a gate dielectric, since its dielectric constant is  $\sim 80$  times vacuum, or 20 times higher than the usual  $\text{SiO}_2$  glass, while its resistivity is still  $> 10^{14} \Omega \cdot \text{nm}$ . However, even this would not permit gate voltage swings greater than about 1.23 V, since at that level, even pure water conducts, via electrolysis. And even a 1.23 V barrier in the channel would still not allow channel lengths less than roughly 2–3 nm (depending on the particular semiconductor's effective electron mass) without significant tunneling occurring between the source and drain electrodes.

But if we widen our perspective a bit, we can note that there are other ways to control a potential-energy barrier between two electron-position states, besides just the field effect, which, at root, is only a simple application of ordinary Coulombic repulsion, together with the carrier-depletion phenomenon in semiconductors. For example, one could mechanically widen or narrow the separation between two conductive regions—this is the principle used in old electromechanical relays. Or a piece of conductive material could be inserted and removed from the space between the source and drain—ordinary toggle switches work this way. One can easily imagine performing the same general types of electromechanical interactions at the molecular level, and thereby perhaps obtaining device sizes closer to 1 nm. Vacuum gaps between conductors constitute fairly high energy

barriers, due to the multi-eV electron affinities (work functions) of most conductive materials, and therefore such gaps can be made significantly smaller than semiconductor channel lengths, while still avoiding the electron tunneling problem.

So, ironically, electromechanical devices, which today we think of as being terribly antiquated, might, in the nanomolecular realm, turn out to scale to higher device densities than can our vaunted field-effect devices of today. However, whether this potentially higher device density may be enough to compensate for the relatively sluggish inertia of entire atoms, compared to electrons, when switching a gate, is still dubious. Nevertheless, one fortunate coincidence is that the relative slowness of the mechanical motions seems to be exactly what is needed anyway for efficient adiabatic operation in the electronics, which is necessary to maintain high performance in the face of heat flow constraints.

So my tentative (and ironic) nomination for the “most likely contender” to be the dominant nanocomputing technology a few decades hence is nanoscale electrostatic relays using a dry-switching discipline. “Dry-switching” is an old term from electromechanical relay technology, meaning “do not open (resp. close) a switch when there is a significant current through (resp. voltage across) it.” Historically, this was done to prevent corrosion of the relay contacts due to air-sparking. But this is also exactly the key rule for adiabatic operation of any switch-based circuitry. The thought of using electromechanical relays sounds slow at first, until you consider that, at the nanoscale, their characteristic speeds will be on the order of the rates at which chemical reactions occur between neighboring molecules—since both processes will consist of essentially the same kinds of operations, namely molecule-sized objects bumping up against each other, and interacting both electrostatically via conformational changes and via actual exchange of electrons. The molecule-size gate, moved into place by an impinging electrostatic signal, can be thought of as the “catalyst” whose presence enables a source–drain electron-exchange “reaction.” In other words, this technology could be thought of as a sort of “controlled chemistry,” in which the “chemical” interactions happen at predetermined places at predetermined times, and information flows not randomly, via a slow diffusive random walk through solution, but instead at near-lightspeed along hard-wired electrically conductive paths to specific destinations where it is needed. This NEMS vision of computing does not yet specifically include quantum computing capabilities, but it might be modified to do so by including some spintronic device elements [102].

We briefly discuss some of the other alternative switching principles that have been considered. See also [103] for an excellent review of most of these.

### 6.2.2. Coulomb-Blockade Effect Single-Electron Transistors

These devices are based on the quantum principle of charge quantization. They typically consist of a conductive island (although semiconductors may also be used) surrounded by insulator and accessed via some fairly narrow (typically 5–10 nm) tunnel junctions. The Coulomb blockade effect is



the observation that the presence of a single extra electron on these small, low-capacitance structures may have a significant effect on their voltage, which, if greater than thermal voltage, thereby suppresses additional electrons from simultaneously occupying the structure. The Coulomb blockade effect may be significant even in cases where the number of electron energy levels is not itself noticeably quantized. In these devices, a voltage applied to a nearby gate allows one to choose the number of electrons (in excess of the neutral state) that occupy the island to a precision of just a single electron out of the millions of conduction electrons that may be present in, say, a 20 nm cube of material. The Coulomb blockade effect has also been demonstrated on a molecular and even atomic [104] scale, at which even room-temperature manifestation of the effect is permitted.

### 6.2.3. Quantum Wells/Wires/Dots

These are typically made of semiconductor materials. They are based on confinement of electron position in one, two, or three dimensions, respectively. Increased confinement of electron position in a particular direction has the effect of increasing the separation between the quantized momentum states that are oriented along that direction. When all three components of electron momentum are thus highly quantized, its total energy is also; this leads to the quantum dot, which has discrete energy levels. In quantum dots, the total number of activated conduction electrons may be as small as 1! Based on a thorough understanding of the quantum behavior of electrons, some researchers have developed alternative, non-transistor-like quantum-dot logics. A notable example is the paradigm of quantum dot cellular automata (QDCA) introduced by the group at Notre Dame [105]. The name QCA is also sometimes used for these structures, but I dislike that abbreviation, because it can be confused with quantum cellular automata, which is a more general and technology-independent class of abstract models of computation, whereas the QDCA, on the other hand, comprise just one very specific choice of device and circuit architecture, based on quantum dots, of the many possible physical implementations of the more general QCA concept.

Also worth mentioning are the quantum computing technologies that are based on externally controlling the interaction of single-electron spins between neighboring quantum dots [71].

### 6.2.4. Resonant Tunneling Diodes/Transistors

These structures are usually based on quantum wells or wires, and therefore may still have 2 or 1 (resp.) effectively “classical” degrees of freedom. In these structures, a narrow-bandgap (conductive) island is sandwiched between two wide-bandgap (insulating) layers separating the island from neighboring source and drain terminals. When the quantized momentum state directed across the device is aligned in energy with the (occupied) conduction band of the source terminal, electrons tunnel from the source onto the island, and then to unoccupied above-band states in the drain terminal. But a small bias applied to the device can cause the quantized momentum state in the island to no

longer be aligned in energy with the source terminal’s conduction band, in which case tunneling across that barrier is suppressed, and less current flows. Since multiple harmonics of the lowest momentum state also appear in the spectrum of the device, these devices typically have a periodic dependence of current on bias voltage.

Resonant tunneling transistors are just like resonant tunneling diodes, except that there is an additional gate terminal near the island that provides an additional means for adjusting the energy levels in the island.

### 6.2.5. Electromechanical Devices

Several kinds of nanoscale devices have been proposed which use mechanical changes (movements of atoms or assemblages of atoms) to control electrons, or vice versa. The molecular switches of [106] fall in this category, as would NEMS switches and relays based on nanoscale solid-state structures. Electromechanical structures offer somewhat of a design advantage in that the mechanism of their operation is relatively easy to visualize, due to the explicit change in their structural configuration.

But the primary disadvantage of electromechanical operation is that atoms are many thousands of times as massive as electrons and therefore accelerate many thousands of times more gradually in response to a given force. As a result, the characteristic frequencies for oscillation of mechanical components tend to be many thousands of times less than those of similar-sized electrical ones.

However, this disadvantage might conceivably be offset if it turns out that we can design NEMS devices that have much higher quality factors than we manage to obtain using electronics alone. This is suggested by the very high  $Q$ ’s (in the billions) for a perfect diamond crystal vibrating in vacuum, and by the practical  $Q$ ’s in the tens of thousands that are achievable today for MEMS mechanical resonators (essentially, springs) in vacuum. In contrast, the  $Q$ ’s that have been obtained in simple microelectronic circuits such as  $LC$  oscillators tend to be much lower, usually in the tens or at most hundreds. We (or more precisely, I) do not (yet) know any *fundamental* reasons why a high- $Q$  all-electronic nanoscale oscillator cannot be built, but it is not yet clear how to do so.

In the meantime, hybrid electromechanical approaches might take up some of the slack. Resistive elements such as transistors naturally have high  $Q$  when they are operated at relatively slow speeds (*i.e.*, adiabatically). If these are coupled to high- $Q$  electromechanical oscillators, a high overall  $Q$  might be obtained for the complete self-contained system, thereby enabling  $\ll kT$  energy dissipation per bit operation. For example, if a mechanical oscillator with  $Q = 10,000$  is coupled to an adiabatic electronic FET which has a similarly high  $Q$  at the low frequency of the oscillator, so that the overall  $Q$  of the system is still 10,000, and if tunneling currents are kept negligible, then if we use a redundancy factor in the logic encoding of  $\sim 11.5$  nats/bit (*i.e.*, on the order of 0.3 eV switching energy per minimum-sized transistor gate at room temperature), then one could theoretically achieve an on/off ratio of order  $e^{11.5} \approx 100,000$  and a best-case minimum entropy generation per bit-op on the order of  $e^7$  nat  $\approx 0.001 k_B$  (refer to Fig. 3). This could be advantageous in

that it would permit a  $\sim 700 \times$  higher total rate of computation per watt of power consumption (and per unit area, given heat-flux constraints) than in *any* physically possible *fully irreversible* technology (even if all-electronic), in which the entropy generated per bit-op must be at least  $\sim 0.7k_B$ .

Another potential advantage of electromechanical operation is that mechanically actuated switches for electricity may be able to change electron currents by relatively large factors while using a relatively small amount of energy transfer. This is because a mechanical change may significantly widen a tunneling barrier for electrons, which has an exponential effect on electron tunneling rates. Therefore, it is not clear that an electromechanical system must be subject to the same kind of lower bound on entropy generation for given quality index as we discussed in Section 6.12. Thus, an electromechanical system with a  $Q$  of 10,000 might be able to achieve an even lower rate of entropy generation than we described in the previous paragraph, perhaps of the order of 1/10,000th of a bit of entropy generated per bit-op.

An interesting corollary to this electromechanical line of thought is this: If the operating frequency of the logic is going to be set at the relatively low frequency of nanomechanical oscillators anyway, in order to achieve low power consumption, then is there any remaining benefit to having the actual logic be carried out by electrons? Why not just do the logic, as well as the oscillation, mechanically? This leads back to the idea of using all-mechanical logic at the nanoscale, an idea that was first promoted by Drexler [47]. We will discuss this possibility further in Section 7.3.

However, there is still one clear advantage to be gained by using electrons for logic signals, and that is simply that the propagation speed of electronic signals can easily be made close to the speed of light, while mechanical signals are limited to about the speed of sound in the given material, which is much lower. Thus, communication delays over relatively long distances would be expected to be much lower in electromechanical nanocomputers than in all-mechanical ones. This is an important consideration for the performance of communication-dominated parallel algorithms.

### 6.2.6. Superconductive Devices

Complex integrated circuits using high-speed ( $\sim 100$  GHz) digital logic based on superconductive wires and Josephson junctions have already existed for many years [107], although they are unpopular commercially due to the requirement to maintain deep cryogenic (liquid helium) temperatures. Another problem for these technologies is that their speed cannot be further increased by a very large factor unless much higher temperature superconducting material can be effectively integrated. This is because flipping bits at a rate of 100 GHz already implies an effective coding-state temperature of at least 3.5 K; thus increasing speed by another factor of 100, to 10 THz, would require room-temperature superconductors, which have not yet been discovered.

Superconductive devices therefore might never have an opportunity to become competitive for general-purpose computing, since traditional semiconductor devices are expected to reach  $\sim 100$  GHz frequencies in only about another 15 years.

Also, it appears that it may be difficult to scale superconducting technology to the nanoscale, because ordinary

superconductivity is based on Cooper pairs of electrons, which have a relatively large spacing (order of 1 micrometer) in the usual superconducting materials [108]. However, this may turn out not really be a problem, since even carbon nanotubes have already been found to superconduct under the right conditions [109].

Even if superconductive technologies turn out not to achieve extremely high densities, they may still be useful at relatively low densities, for those particular applications that happen to require the special-purpose features of quantum computing. Superconductor-based devices for quantum computing are currently being aggressively explored [72], and this may turn out to be a viable technology for creating large scale integrated quantum computer circuits. But if the technology is not also simultaneously dense, low power, and high frequency, then it will likely be relegated to a “quantum coprocessor,” while the main CPU of the computer (used for more general-purpose applications) remains nonsuperconducting.

### 6.2.7. Spintronic Devices

Spintronics [102] is based on the encoding of information into the spin orientation states of electrons, rather than the usual approach of using energy (voltage) states. Spin information typically persists for nanoseconds in conduction electrons, compared with the typical  $\sim 10$  fs lifetime for decay of momentum information (except in superconductors). Spintronics requires various technologies for spin control, propagation of spins along wires, selection of electrons based on their spin, and detection of electrons. Some examples of spintronic devices are the Datta–Das [110] and Johnson [111] spin-based transistors. Electron spins are also a potential medium for quantum computation, as is illustrated by the spin-based quantum dot quantum computers being explored by Friesen et al. [71]. Nuclear spins have already been used for quantum computing experiments for some time [70]. It is currently still unclear whether spintronic nanoelectronic technologies might eventually outperform nanoelectronics based on other properties.

## 6.3. Nanomechanical Logic Technologies

Way back in the late 1980s and early 1990s, Drexler and Merkle proposed a number of all-mechanical technologies for doing logic at the nanoscale [43, 45, 47]. There is an argument why technologies like these might actually be viable in the long run, despite the slow speed of mechanical (atomic) signals. That is, if all-mechanical nanotechnologies turn out (for some reason) to be able to be engineered with much higher  $Q$ 's than electronic or electromechanical nanotechnologies can be, then the all-mechanical technologies would be able to operate with greater parallel performance per unit power consumed, or per unit surface area available for cooling. Presently, it is not yet clear whether this is the case. One approach called “buckled logic” [45] was specifically designed by Merkle to have very high  $Q$ , because it completely eliminates sliding interfaces, rotary bearings, stiction-prone contacts, moving charges, *etc.* and instead consists of an electrically neutral one-piece mesh of rods that simply flexes internally in a pattern of vibrational motions that is designed to be isomorphic to a desired

(reversible) computation. If the computational vibrational modes can all be well insulated from other, noncomputational ones, then in principle, the  $Q$ 's obtainable by such structures, suspended in vacuum, might even approach that of pure crystal vibrations, that is, on the order of billions. This may enable a level of entropy generation per bit-op that is so low (maybe billionths of a nat per bit-op) that a vastly higher overall rate of bit-ops might be packed into a given volume than by using any of the feasible alternatives. However, until many more of the engineering details of these interesting alternatives have been worked out, the all-mechanical approach remains, for now, as speculative as the others.

#### 6.4. Optical and Optoelectronic Technologies

For purposes of high-performance, general-purpose parallel nanocomputing, all purely optical (photonic) logic and storage technologies are apparently doomed to failure, for the simple reason that photons, being massless, at reasonable temperatures have wavelengths that are a thousand times too large, that is, on the order of 1 micrometer, rather than 1 nanometer. Therefore, the information density achievable with normal-temperature (infrared, optical) photons in 3D space is roughly  $1000^3$  or a *billion* times lower than what could be achieved using electronic or atomic states, which can be confined to spaces on the order of  $1 \text{ nm}^3$ . Light with comparable 1 nm wavelengths has a generalized temperature on the order of  $1000 \times$  room temperature, or hundreds of thousands of Kelvins! These 1-nm photons would have to be extremely stringently confined while remaining somehow isolated from interaction with the computer's material structure, in order to keep the computer from immediately exploding into vapor, unless a solid structure could somehow still be maintained despite these temperatures by (for example) applying extremely high pressures.

The only exception to this problem might be if mutually entangled photons can be used, as these behave like a single, more massive object and thus have a lower effective wavelength at a given temperature. This wavelength reduction effect has recently been directly observed experimentally [112]. However, we presently have no idea how to produce a conglomeration of 1000 mutually entangled photons, let alone store it in a box or perform useful logic with it.

Even if this problem were solved, photons by themselves cannot perform universal computation, since under normal conditions they are noninteracting, and thus only linearly superpose with each other (they cannot, for example, carry out nonlinear operations such as logical AND). However, photons may interact with each other indirectly through an intermediary of a material, as in the nonlinear photonic materials currently used in fiber optics [113]. Also, *extremely* high-energy photons (MeV scale or larger, *i.e.*, picometer wavelength or smaller) may interact nonlinearly even in vacuum, without any intermediary material, due to exchange of virtual electrons [15], but the temperatures at which this happens seem so high as to be completely unreasonable.

To deal with the problem of low information density and photon noninteraction, hybrid optoelectronic technologies have been proposed, in which electron states are used to

store information and do logic, while photons are used only for communication purposes. However, even in this case, we have the problem that the bit flux that is achievable with photons at reasonable temperatures is still apparently far lower than with electrons or atoms [114]. Therefore, it seems that light is not suitable for communication between densely packed nanoscale devices at bit rates commensurate with the operating speeds of those devices. This is again due to the limit on the information density of cool, nonentangled light. Communicating with (unentangled) photons therefore only makes sense for communications that are needed only relatively rarely, or between larger scale or widely separated components, for example, between the processors in a loosely coupled distributed multiprocessor.

#### 6.5. Fluid (Chemical, Fluidic, Biological) Technologies

##### 6.5.1. Chemical Computing

Not all proposed nanotechnologies rely primarily on solid-state materials. Computing can also be done in molecular liquids, via chemical interactions. Much work has been done on chemical computing, especially using DNA molecules as the information-carrying component, since it is naturally designed by evolution for the purpose of information storage. Universal computing in DNA appears to be possible; for example, see [115]. Unfortunately, it seems that chemical techniques in a uniform vat of solution can never really be viable for large-scale, general-purpose parallel nanocomputing, for the simple reason that the interconnects are much too slow. Information is propagated in 3D space only by molecular diffusion, which is inherently slow, since it is based on a random walk of relatively slow, massive entities (molecules). Information transmission is thus many orders of magnitude slower than could be achieved in, say, a solid-state nanoelectronic technology in which signals travel straight down predetermined pathways at near the speed of light. Chemical methods also tend to be difficult to control and prone to errors, due to the generally large numbers of possible unwanted side-reactions.

##### 6.5.2. Fluidics

However, the situation may be improved slightly in fluidic systems, in which the chemicals in question are actively moved around through microchannels. Desired materials may be moved in a consistent speed and direction and brought together and combined at just the desired time. This more direct method gives a much finer degree of control and improves the interconnect problem a bit, although transmission speeds are still limited by fluid viscosity in the channel.

One can also dispense with the chemical interactions and just use pressure signals in fluidic pipes to transmit information. Pressure-controlled valves can serve as switches. This technique is highly analogous to ordinary voltage-state, transistor-based electronics, with pressure in place of voltage, and fluid flow in place of electric current. Fluidic control and computation systems are actually used today in some military applications, for example, those that cannot use electronics because of its vulnerability to the electromagnetic pulse that would result from a nearby nuclear blast.

However, insofar as all fluid-based techniques require the motion of entire atoms or molecules for the transmission of information, one does not anticipate that any of these techniques will ever offer higher computational densities than the solid-state all-mechanical technologies, in which state changes are much more well controlled, or than the electromechanical or pure-electronic technologies in which signals travel at much faster speeds.

### 6.5.3. Biological Computing

Computing based on chemical interactions is, at best, likely to only be useful in contexts where a chemical type of input/output (I/O) interface to the computer is needed anyway, such as inside a living cell, and where the performance requirements are not extremely high. Indeed, a biological organism itself can be viewed as a complex fluidic chemical computer. In fact, it is one that can be programmed. For example, Knight and Sussman at MIT are currently experimenting with reengineering the genetic regulatory networks of simple bacteria to carry out desired logic operations [116].

Notice, however, that even in biology, the need for quick transmission and very fast, complex processing of information in fact fostered the evolution of a nervous system that was based on transmission of signals that were partly electrical, and not purely chemical, in nature. And today, our existing electronic computers are far faster than any biological system at carrying out complex yet very precisely controlled algorithms. For less precisely controlled algorithms that nevertheless seem to perform well at a wide variety of tasks (vision, natural language processing, *etc.*), the brain is still superior, even quantitatively in terms of its raw information processing rate. But by the time we have nanocomputers, the raw information-processing capacity of even a \$1,000 desktop computer is expected to exceed the estimated raw information-processing capacity of the human brain [117].

One attempt at a generous overestimate of the raw information-processing capacity of the brain is as follows. There are at most  $\sim 100$  billion neurons, with at most  $\sim 10,000$  synapses/neuron on average, each of which can transmit at most  $\sim 1000$  pulses per second. If each pulse can be viewed as a useful computational “operation,” this gives a rough maximum of  $\sim 10^{18}$  operations per second.

Conservatively, today’s largest microprocessors have on the order of  $\sim 100$  million transistors (Intel’s Itanium 2 processor actually has 220 million) and operate on the order of  $\sim 1$  GHz (although 3 GHz processors now can be bought off-the-shelf, in early 2003). Such densities and clock speeds permit  $\sim 10^{15}$  transistor switching operations to be performed every second. This is only a  $1000 \times$  slower raw rate than the human brain, assuming that the transistor “ops” are roughly comparable to synaptic pulses, in terms of the amount of computational work that is performed as a result. The historical Moore’s law trend has raw performance nearly doubling about every 1.5–2 years, so we would expect a factor of 1000 speedup to only take around 15–20 years.

So the nanocomputer that will be sitting on your desk in the year 2020 or so (just a little way beyond the end of today’s roadmap for traditional semiconductor technology) may well have as much *raw* computational power as

the human brain. Of course, it is another matter entirely whether software people will have figured out by then how to effectively harness this power to provide (for example) an automated office assistant that is anywhere close to being as generally useful as a good human assistant, although this seems rather doubtful, given our present relative lack of understanding of the organization and function of the brain, and of human cognition in general.

### 6.6. Very Long-Term Considerations

What are the ultimate limits of computing? As we have seen, to maximize rates of computation, both high computational temperatures and very precise control and isolation of the computation from the environment are simultaneously required. However, as computational temperatures increase, it becomes increasingly difficult to isolate these fast-changing, thus “hot,” computational degrees of freedom from the relatively cool degrees of freedom inherent in ordinary matter having stable structure (*e.g.*, solids, molecules, atoms, nuclei). At some point, it may be best not to try to keep these structures stable anymore, but rather to let them dissolve away into fluids, and just harness their internal fluid transitions as an intentional part of the computation. In other words, it may eventually be necessary to take some of the energy that is normally tied up in the binding energy of particles, and thus is not doing useful computational work (other than continually computing that a given structure should remain in its current state), and release that energy to actively perform more useful computations.

Smith [15] and later Lloyd [16] explored this hypothetical concept of a plasma-state computer and quantitatively analyzed the limits on its performance and memory capacity, which are determined by fundamental considerations from quantum field theory. As expected, performance is dependent on temperature. If material having the mass density of water is converted entirely to energy with no change in volume, it forms a plasma of fundamental particles (mostly photons) with a temperature on the order of  $10^9$  kelvins, hotter than the highest temperatures reached at the core of an exploding thermonuclear (hydrogen fusion) bomb.

How can such a violent, high-temperature state possibly be configured in such a way as to perform a desired computation? Of course, this is totally impractical at present. However, in principle, if one prepares a system of particles in a known initial quantum state and thoroughly isolates the system from external interactions, then the unitary quantum evolution of the system is, at least, deterministic and can be considered to be carrying out a quantum computation of sorts. In theory, this fact applies to hot plasmas, as well as to the relatively cool computers we have today.

However, even if the required exquisite precision of state preparation and isolation can someday be achieved, the question of how and whether any desired program can be actually “compiled” into a corresponding initial state of a plasma has not yet even begun to be explored. For the remainder of this section, we will pretend that all these issues have been solved, but alternatively, it may well be the case that we are never able to organize stable computation, without relying on an underlying infrastructure made of normal solid (or at least atomic) matter.

Lloyd [16] points out that at normal mass-energy densities (such as that of water), a plasma computer would be highly communication-limited, that is, heavily limited by the speed-of-light limit, rather than by the speed of processing. But in principle the communication delays could be reduced by compressing the computer's material beyond normal densities. As the energy density increases, the entropy density increases also, though more slowly (specifically, as energy density to the  $\frac{3}{4}$  power), and so energy per unit entropy is increased; that is, the temperature goes up.

The logical (if extreme) conclusion of this process, for a given-size body of matter, is reached when the ratio of the system's mass-energy to its diameter exceeds the critical value  $c^2/4G$ , at which point the system comprises a black hole, disappearing into an event horizon, and the effects of any further compression cannot be observed. For a 1-kg-mass computer, the critical size is extremely small, about  $10^{-27}$  m, or roughly a trillionth of the diameter of an atomic nucleus. (Needless to say, this degree of compression would be very difficult to achieve.)

Due to gravitational time dilation (redshifting), although the compressed matter would be very hot in its own frame of reference, it appears somewhat cooler than this to the outside world. In other words, the system's output bandwidth is decreased by gravitational effects. This is because, simply stated, the outgoing information tends to be pulled back by gravity.

Classically, in general relativity, the temperature of a black hole as measured from outside would by definition always be zero (no information can leave the hole), but, as shown in the now-famous work by Stephen Hawking [118], the temperature of a black hole is actually *not* zero when quantum uncertainty is taken into account. Effectively, particles can tunnel out of black holes ("Hawking radiation"), and the smaller the black hole, the quicker this rate of tunneling becomes. So smaller black holes have higher output temperatures and thus effectively make faster "computers," at least from an I/O bandwidth point of view. A 1-kg-mass black hole would have a temperature of about  $10^{23}$  K, and a presumed minimum-mass (Planck mass) black hole would have a temperature of  $\sim 10^{32}$  K.

This last temperature, the *Planck temperature*, may be a fundamental maximum temperature. It corresponds to a maximum rate of operation of  $\sim 10^{43}$  parallel update steps per second, or 1 step per Planck time. This may be considered the fastest possible "clock speed" or maximum rate of operation for *serial* computation. It is interesting to note that if processor frequencies continue doubling every 2 years, as per the historical trend, then this ultimate quantum-gravitational limit on clock frequency would be reached in only about 200 more years. At this point, the only possible improvements in performance would be through increased parallelism. Moreover, the parallel machine would have to be very loosely coupled, since Planck-mass black holes could not be packed together very densely without merging into a larger black hole, whose temperature, and output communication bandwidth, would be proportionately lower. The problem is that a black hole outputs information in only a single quantum channel, with bandwidth proportional to its

temperature [119]. However, its internal rate of operations can be considered to still be given by its total mass-energy. It is interesting to note that within a black-hole computer, the interconnection problem becomes a nonissue, since the time to communicate across the hole is comparable to the time to flip a bit [16].

Of course, all of these considerations remain extremely speculative, because we do not yet have a complete theory of quantum gravity that might be able to tell us exactly what happens inside a black hole, in particular, near the presumably Planck-scale sized "singularity" at its center. Conceivably, at the center is a busy froth of very hot fundamental particles, perhaps near the Planck temperature, which occasionally tunnel (although greatly gravitationally redshifted) out beyond the horizon. But we do not know for certain.

Regardless of the precise situation with black holes, another speculative long-term consideration is the potential computational capacity of the entire universe, in bits and in ops. Lloyd has estimated upper bounds on these quantities, over the history of the universe so far [28]. Other papers by Dyson [120], and more recently by Krauss and Starkman [121], attempt to characterize the total amount of future computation that an intelligent civilization such as ours might eventually harness toward desired purposes. Significantly, it is still a matter for debate whether the total number of future ops that we may be able to perform over all future time is finite or infinite. Krauss and Starkman present arguments that it is finite, but they do not seem to take *all* possible considerations into account. For example, it may be the case that, by engineering reversible computational systems having ever-higher quality factors as time goes on, an infinite *number* of operations might be performed even if only a finite total supply of energy can be gathered, a possibility which they do not consider. Memory capacity is not necessarily limited either, since as the universe expands and cools, our energy stores might be allowed to expand and cool along with it, thereby increasing without bound the amount of information that may be represented within them. In any event, whether the total number of future ops that we may perform is infinite or not, it is undoubtedly very large, which bodes well for the future of computing.

## 7. CONCLUSION

To conclude, we already have an arguably valid, if still rather rough, idea of what the most cost-effective general-purpose future nanocomputer architectures over the coming century should look like. Most concretely, high-performance nanocomputers will generally be flattened slabs of densely packed computing "material" (of limited thickness), consisting of 3D locally connected meshes of processors that include local memory and *both* traditional hardwired arithmetic-logic units *and* reconfigurable logic blocks, built from nanoscale, probably solid-state, electronic, or electromechanical devices. The device technology and architecture must also support *both* mostly reversible classical operation *and* fault-tolerant quantum algorithms, if it aspires to be universally maximally scalable.

Devices must be well insulated from their environment, that is, designed to have a very high quantum *quality* factor (*i.e.*, low relative decoherence rate) which allows their internal coding state to transition reversibly and coherently at a fast rate (thus, a high effective temperature) relative to the rate of undesired interactions between the coding state and the (probably cooler) thermal state of the machine's physical structure. Even when an application does not need to use quantum superposition states, well-isolated, high- $Q$  reversible operation remains particularly critical for general-purpose parallel computation, in order to maximize the effective computation rate and number of active processors per unit area enclosed, and thereby to minimize the communication delays in communication-limited parallel algorithms.

In these parallel architectures, the processors will be kept synchronized with each other via local interactions. Meanwhile, free energy will be supplied, and waste heat removed, by active flows of energy and/or coolant material which pass perpendicularly through the computing slab, and which are recirculated back through the machine to be reused, after their entropy and the accompanying waste heat are deposited in some external reservoir.

This vision, although it places a number of constraints on what nanocomputing will look like, still provides a lot of flexibility for device physicists to do creative engineering design and optimization of the specific device mechanisms to be used for logic, memory, interconnect, timing, energy transfer, and cooling, and it leaves a lot of room for computer engineers and computer scientists to come up with more efficient new processor organizations and programming models that recognize the need to support reversible and quantum, as well as parallel, modes of operation and that respect fundamental physical constraints.

Finally, if we are successful in converging on a nanocomputing technology that indeed approaches the quantum limits discussed in Section 2, and if our civilization's demand for computational power continues to increase beyond that point, then we can expect that the fraction of the available material (mass-energy) that is devoted toward nanocomputing will increase as well. If our civilization continues to thrive and grow, then eventually, in the extremely long term (perhaps hundreds or thousands of years hence), we may find ourselves wanting to build nanocomputers that are *so* massive (using many planets' or stars' worth of raw material) that their self-gravitation becomes a significant concern. This will bring a new fundamental physical concern into play, namely general relativity, which this chapter has not yet thoroughly considered. At that distant future time, the form of our computer models may need to change yet again, as we figure out how best to maximize cost-efficiency of computing in the face of this new, gravitational constraint. But in the meantime, until that happens, the simpler type of nanocomputer model that we discussed in Section 6 is expected to last us for a very long time. The primary goal for the current generation of nanocomputer engineers is, then, to flesh out and optimize the technological and architectural details of the general class of models that we have outlined, guided by our rapidly improving understanding of the basic principles of nanoscale science and technology, as documented throughout this encyclopedia.

## GLOSSARY

**Å** Standard abbreviation for *Ångstrom*.

**Adiabatic** A process is *adiabatic* to the extent that it can take place with arbitrarily little generation of entropy. Originally in thermodynamics, "adiabatic" literally meant "without flow of heat" and applied to any physical process in which there was no (or negligibly little) heat flow. However, today in applied physics, "adiabatic" means "asymptotically isentropic," that is, approaching zero total entropy generation, in the limit of performing the process more slowly, and/or with diminished parasitic interactions with its environment. The old and new definitions are not equivalent.

**Adiabatic losses** Energy that is dissipated to heat due to the imperfections present in a nominally adiabatic process, as opposed to energy that is necessarily dissipated due to logical irreversibility.

**Adiabatic principle** The total adiabatic losses of a given process scale down in proportion to quickness as the process is carried out more slowly.

**Adiabatic theorem** A theorem of basic quantum theory that says that so long as the forces on a system (expressed in its Hamiltonian) are changed sufficiently slowly, and some additional technical conditions on the spectrum of energy eigenstates are met, a system that is initially in a pure state will remain in an almost pure state, that is, with a total generation of entropy that is inversely proportional to the quickness of the transition. The theorem is very general; adiabatic processes are therefore nearly ubiquitously available, that is, in almost any reasonable nanodevice technology.

**Adjoint** A term from matrix algebra. The adjoint of a matrix is its conjugate transpose.

**Algorithm** A precise description of a particular type of computation, abstracted away from the specific inputs, and often also abstracted away from the machine architecture and the details of the programming model.

**Amplitude** Complex number giving the value of a quantum wavefunction at a given state. It can be broken into phase and magnitude components. The squared magnitude of the amplitude corresponds to the probability density at the given state.

**Amu** Unified atomic mass unit, equal to  $1.6605402 \times 10^{-24}$  g. About the mass of a proton or neutron. Originally defined as 1/12 the mass of a carbon-12 atom. In computational units, equal to 450 zettapops per second.

**Ångstrom** A unit of length equal to  $10^{-10}$  meters, or 0.1 nm. One Ångstrom is the approximate radius of a hydrogen atom.

**Angular momentum** In computational terms, this is the ratio between the number of quantum operations required to rotate an object by a given angle around a point, and the magnitude of the angle. It is quantized, so that a rotation by  $180^\circ$  or  $\pi$  radians always involves an integer number of  $\pi$ -ops (ops of magnitude size  $\hbar/2$ ), and a rotation by 1 radian involves an integer number of  $\pi$ -ops (ops of magnitude  $\hbar$ ).

**Architecture** An activity, namely, the functional and structural design of any complex artifact, such as a skyscraper or a computer. Within the field of computer architecture, a specific *architecture* refers to a particular computer design, which may include any levels of design from the logic circuits



up through the interconnection networks of a multiprocessor computer.

**Architecture family** A class of architectures of unbounded capacity (a specific architecture may have only constant capacity). That is, a recipe for creating architectures of any desired capacity. I also frequently use the phrase *capacity scaling model* rather than *architecture family*, since it is more descriptive.

**ASCII** American Standard Code for Information Exchange; a widely used standard for representing Latin alphabet characters, digits, and simple punctuation marks using 8-bit numbers.

**Ballistic** An adiabatic process that also has a nonzero net “forward” momentum along the desired trajectory through configuration space. This is opposed to adiabatic processes that have zero net momentum and progress only via a random walk (Brownian motion).

**Bandgap** In condensed matter theory, the bandgap in a semiconducting or insulating material is the magnitude of separation in energy level between the top of the valence band and the bottom of the conduction band. Insulators have a large bandgap; semiconductors have a relatively small one. In metals the bandgap is negative (meaning the bands overlap).

**Bandwidth** In computer science, a rate of information transfer (e.g., in bits per second). This meaning is closely related to the original, literal meaning, which was the width (in Hertz) of a frequency band used for wave-based communications. In communications theory, a single classical wave-based communication channel with a given frequency bandwidth can be shown to have a proportional maximum rate of information transfer.

**Basis** A term from linear algebra. A complete set of (often orthogonal, but at least linearly independent) vectors, sufficient to define a given vector space. In quantum theory, a complete set of distinguishable states forms a basis.

**Basis state** Any single state that is aligned along one of the axes of a given basis.

**Bennett’s algorithm** A reversibilization algorithm discovered by Bennett. The 1973 version of the algorithm (which takes linear time but polynomial space) is a special case of a more general version of the algorithm described in 1989.

**Bennett copy** To rescue desired information from being uncomputed during Lecerf reversal by reversibly copying it before performing the reversal.

**Binary number** A number represented in base-2 notation, using a series of bit systems.

**Binary tree** An interconnection network structure in which each node is connected to 1 “parent” node and 2 “child” nodes. Binary trees are not physically realistic with unit-time hops.

**Bistable** Having two stable states.

**Bit** Shorthand for *binary digit*, this is the log-base-2 unit of information or entropy. (The abbreviation *bit* for this concept was coined by John Tukey in 1946.) An *amount* of information can be counted by a *number* of bits. In addition, the word bit can also be used to mean a *bit system*; in this usage, a bit denotes not only a measure of amount of information, but also a specific *piece* of information.

**Bit device** Any device that is designed for storing and/or processing a single logical bit, or a small constant-size collection of logical bits, at any given time. For example, a transistor or a logic gate could be considered to be a bit device, but an *n*-bit adder is larger than that. (We sometimes use the term *bit device* when we wish to be clear that we are referring to individual logic devices, rather than to more complex “devices” such as CPUs or laptop computers.)

**Bit operation** An operation that manipulates only 1 or at most a small constant number of (physical or logical) bits.

**Bit system** A system or subsystem containing exactly 1 bit of physical information. That is, a specific instance of a type of system or subsystem having exactly two distinguishable states (see *qubit*) or with a particular pair of distinguishable states for the subsystem (i.e., a particular partition of a set of distinguishable states for the entire system into two equal sized parts).

**Bitwise ripple-carry add** In computer arithmetic, a hardware or software algorithm for adding two binary numbers using the base-2 equivalent of the traditional grade-school algorithm, with a carry from each place to the next.

**Black box** Name applied to a device, function, process, or transformation when one is allowed to use the entity to produce outputs from inputs but is not allowed to “open the box,” to directly determine anything about its internal structure.

**Black hole** An object whose escape velocity (due to its gravity) exceeds the speed of light.

**Boltzmann’s constant** See *nat*.

**Butterfly network** An interconnection network similar to a sort of unfolded hypercube. Butterfly networks are not physically realistic (see PR) given unit-time hops.

**Byte** Usually, 8 bits. Sufficient to denote 1 Latin character, number, or punctuation symbol in the ASCII character set.  
*c* See *speed of light*.

**CA (cellular automaton)** The cellular automaton is a model of computation, first envisioned by von Neumann [33], consisting of a regular mesh of finite-capacity processing elements operating in parallel. Two-dimensional cellular automata have the maximum scalability among fully irreversible models of computing. Three-dimensional reversible cellular automata are conjectured to be a universally maximally scalable model of computation, up to the gravitational limit.

**Calorie** Unit of energy originally defined as the heat required to increase the temperature of 1 g of water by 1 degree Kelvin. Equal to 4.1868 J.

**CAM (cellular automata machine)** A type of parallel computer architecture in which the programming model is based upon the cellular automaton model of computation. A number of CAMs were designed and built by the information mechanics group at MIT in the 1980s and 1990s. (See [122].)

**Capacity** The *computational capacity* or just *capacity* of a computer is measured by two parameters: (1) How many bits of logical information can it store? (2) How many bit operations per second can it perform?

**Carbon nanotube** Sometimes called *buckytubes* (for Buckminster Fuller), these are nanometer-scale (in diameter)

hollow tubes made out of pure carbon, consisting essentially of a graphene (graphite-like) sheet rolled into a cylinder. They have a higher strength-to-weight ratio than steel, conduct electricity better than copper, and have a high thermal conductivity, making them a promising component for future nanomechanical and nanoelectronic applications.

**Cellular automaton, cellular automata** See *CA*.

**Channel** The region of a transistor through which current flows (between source and drain) when the transistor is turned on.

**Characteristic length scale** For any engineered system, its characteristic length scale is defined as the average distance between neighboring instances of the smallest custom-designed functional components of the system (for example, the average distance between neighboring transistors in a densely packed electronic circuit). The characteristic length scale of a traditional semiconductor-based computer is determined by the minimum wire *pitch* (distance between center lines of neighboring wires) in integrated circuits, which in early 2003 is roughly 0.2 micrometers.

**Church's thesis** Also known as the Church–Turing thesis. This physical postulate claims that any reasonable (physically realizable) model of computation yields the same set of computable functions as does recursive function theory (Church's original model of computing) or (equivalently) the Turing machine model. See also the *strong Church's thesis* and the *tight Church's thesis*.

**Circuit node** In lumped models of electronic circuits, a node is a region of the circuit that is modeled as being at a uniform voltage level.

**Classical computing** Computing in which the only coding states used are pointer states.

**Classical information** Information that is sufficient to pick out a single basis state from a given basis, but that does not itself specify the basis.

**CMOS** Complementary metal–oxide–semiconductor, the dominant process/device technology for digital electronic computing today, involving PFET and NFET field-effect transistors, which complement each other (the PFETs conduct the high-voltage signals, and the NFETs conduct the low-voltage ones).

**Coding state** Also *coding physical state*. This is the state of the *coding subsystem* of a given system, that is, the physical information that represents (perhaps very redundantly) the logical information that is intended to be encoded.

**Coherent** Term for a quantum system that can remain in a superposition of pointer states for long periods, which requires a very low decoherence rate. Because of the low decoherence rate, a coherent system undergoing a definite evolution produces no entropy and evolves adiabatically, even ballistically. (In contrast, noncoherent adiabatic evolution occurs when the evolution is restricted to a trajectory consisting of only pointer states; superpositions of these must be avoided in order to achieve adiabatic operation if the system is decoherent.)

**Combinational logic** Digital logic in which outputs are produced by a combination of Boolean operators applied

to inputs, as soon as inputs are available, as fast as possible. Less general than sequential logic, because intermediate results cannot feed back into the inputs to be reused, and data cannot be stored.

**Communication** The movement of information from one physical system to another.

**Commute** Mathematical term. Two operators *commute* with each other if performing them in either order always gives the same result. Measurements in quantum theory are represented by observables, that is, Hermitian operators, which leave the eigenstates unchanged, except for scaling by the measured value. Two observables commute if one can measure them in either order and always obtain the same result. If this is not the case, then we can say that one measurement has disturbed the value that would have been obtained for the other, and vice versa. This fact is the origin of Heisenberg's uncertainty principle.

**Complete (parallel) update step** See *step*.

**Complex number** When the theory of the real numbers is extended by closing it under exponentiation, the result is a unique theory in which numbers correspond to real vectors (called *complex numbers*) in a 2D vector space over the reals, and the vectors corresponding to reals themselves all lie along a given axis. The other orthogonal axis is called the *imaginary* axis. The imaginary unit vector  $i$  is defined as  $i = (-1)^{1/2}$ . In complex vector spaces, complex numbers themselves are considered as being just scalar coefficients of vectors, rather than as vectors themselves.

**Complexity** In *computational complexity theory*, a major branch of theoretical computer science, “complexity” is simply a fancy name for *cost* by some measure. There are other definitions of complexity, such as the *algorithmic* or Kolmogorov complexity of objects, often defined as the length of the shortest program that can generate the given object. However, we do not make use of these concepts in this chapter.

**Compute** To *compute* some information is to transform some existing information that is in a known, standard state (e.g., empty memory cells), in a deterministic or partially randomized fashion, based on some existing information, in such a way that the “new” information is at least *somewhat* correlated with the preexisting information, so that from a context that includes the old information, the new information is not entirely entropy. See also *uncompute*.

**Computable** A function is considered *computable* if it can be computed in principle given unlimited resources.

**Computation** The act of computing. When we refer to computation in general, it is synonymous with computing, but when we reify it (talk about it as a thing, as in “a computation”), we are referring to a particular episode or session of information processing.

**Computational temperature** Also *coding temperature*. The temperature (update rate) of the coding state in a machine.

**Computing** Information processing. The manipulation and/or transformation of *information*.

**Computer** Any entity that processes (manipulates, transforms) *information*.

**Conductance** The ratio between the current flowing between two nodes and the voltage between them. A single

quantum channel has a fundamental quantum unit of conductance,  $2e^2/h$ , where  $e$  is the electron charge and  $h$  is Planck's constant.

**Conduction band** In condensed matter theory, the conduction band is the range of energies available to electrons that are free to move throughout the material.

**Conductor** An electrical *conductor* is a material in which the valence and conduction bands overlap, so that a significant fraction of electrons in the material occupy unbound states with wavefunctions that spread throughout the material. The electrons in the highest energy of these states can very easily move to other states to conduct charge. However, they have a minimum velocity called the *Fermi velocity*.

**Conjugate** The *conjugate* of a complex number is found by inverting the sign of its imaginary part. The conjugate of a matrix is found by conjugating each element.

**Cost** Amount of resources consumed. To the extent that multiple types of resources can be interconverted to each other (e.g., by trade, or by indifference in decision-making behavior), cost for all types of resources can be expressed in common units (e.g., some currency, or utility scale). This should be done when possible, because it greatly simplifies analysis.

**Cost measure** A way of quantifying cost of a process based on one or more simpler characteristics of the process (e.g., time or spacetime used).

**Cost efficiency** The cost efficiency of any way of performing a task is the ratio between the minimum possible cost of resources that could have been consumed to perform that task using the best (least costly) alternative method, and the cost of resources consumed by the method actually used. It is inversely proportional to actual cost.

**COTS** Commercial off-the-shelf; a currently commercially available, noncustom component.

**Coulomb blockade effect** The phenomenon, due to charge quantization, whereby the voltage on a sufficiently low-capacitance node can change dramatically from the addition or removal of just a single electron. This effect can be utilized to obtain nonlinear, transistorlike characteristics in nanoscale electronic devices.

**Coulombic attraction/repulsion** The electrostatic force, via which like charges repel and unlike charges attract, first carefully characterized by Coulomb.

**CPU** Central processing unit. The processor of a computer, as opposed to its peripheral devices, enclosure, *etc.* Today's popular CPUs (such as Intel's Pentium 4) reside on single semiconductor chips. However, the future trend is toward having increasing numbers of parallel CPUs residing on a single chip.

**Current** In electronics, the *current* is a rate of flow of charge; it is measured in units of charge per unit of time. The SI unit of current is the Ampere.

**Database** In the real world, a database means an explicit table listing arbitrary data (perhaps in a constrained format), or a collection of such tables. With this standard definition, quantum "database search" is misnamed; it is *not* actually beneficial for searching such databases. (See Section 5.2.)

**de Broglie wavelength** In quantum mechanics, a fundamental particle (or entangled collection of fundamental

particles) having total momentum  $p$  is described by a quantum wavefunction over position states having an associated wavelength  $\lambda = h/p$ , with the wave vector oriented in the same direction of the momentum vector. The wavelength is called the de Broglie wavelength of the particle.

**Decay temperature** The rate of decay of structural information.

**Decoherence** A quantum system *decoheres* (increasing the entropy of its density matrix) when it undergoes either an unknown unitary transformation, or a known interaction with an environment whose state is itself unknown. Maximum decoherence occurs when the state has become a Boltzmann maximum-entropy state (uniform distribution). Continuous decoherence can be factored into a superposition of discrete quantum decoherence *events*, each of which changes the sign or value of an individual qubit.

**Decoherence-free subspace** Some quantum systems that as a whole are highly decoherent may include natural subsystems (perhaps internally redundant ones) that are highly coherent, due to cancellation or interference effects that naturally suppress the subsystem's interactions with the environment. Quantum error correction is the algorithmic construction and maintenance of a decoherence-free subspace, achieved through explicit coding schemes.

**Decoherent** Having a high decoherence rate.

**Decoherence rate** A measure of the rate at which the off-diagonal elements of the density matrix approach zero, meaning that the quantum state is approaching a plain statistical mixture of pointer states. Can be characterized in terms of number of discrete quantum decoherence events per unit time.

**Decoherence temperature** The temperature (step rate) of decoherence interactions. Same thing as (one measure of) decoherence rate. The reciprocal of decoherence time.

**Density matrix** A representation of mixed states, generated by right-multiplying the state vector by its adjoint.

**Device** In general, this means any physical mechanism; however, in the context of computer architecture, it usually refers to the lowest level functional components of the design, such as (in electrical circuits) transistors, capacitors, resistors, and diodes, although sometimes even interconnecting wires are also explicitly considered as devices (since they do have physical characteristics that affect their functionality). In this chapter, I use the phrase *bit device* instead of just *device* when I wish to emphasize the primitive components of digital systems.

**Device pitch** The pitch between devices. See *device, pitch*.

**Dimensionality** A term from linear algebra. The maximum number of mutually orthogonal vectors in a given vector space.

**Distinguishable states** Two quantum states are considered to be entirely distinguishable from each other if and only if their state vectors are orthogonal (perpendicular to each other).

**Dopants** Impurities (sparse atoms) that are added to a semiconductor to adjust its equilibrium concentration of mobile charge carriers, and their dominant type (electrons vs holes).

**Dynamics** The *dynamics* of a system specifies a transformation trajectory that applies to the system over time.

**Effective mass** In condensed matter theory, it is found that an electron of given velocity has a longer wavelength than the de Broglie wavelength of a free electron with the same velocity. This phenomenon is concisely handled by ascribing an effective mass to the electron in matter that is smaller than the actual rest mass of the particle.

**Eigenstate** A state of a quantum system that remains unchanged by a given measurement, interaction, or time evolution. An eigenvector of the measurement observable, interaction Hamiltonian, or the unitary time-evolution matrix.

**Eigenvalue** A term from linear algebra. An eigenvalue of an eigenvector of a particular linear transformation is the scalar value that the vector gets multiplied by under that specific transformation. The eigenvalue of a measurement observable is the numerical value of the measured quantity.

**Eigenvector** A term from linear algebra. An eigenvector of a particular linear transformation is any vector that remains unchanged by the transformation apart from multiplication by a scalar (the corresponding *eigenvalue*).

**Electromigration** When the motion of a current through a solid material causes gradual rearrangement of the atoms of the material. A problem in today's microcircuitry. If a wire happens to be narrower than intended at some point, electromigration can accelerate the wire's degradation until it breaks. Note: adiabatic operation can help prevent this.

**Emulate** Simulate exactly (with complete digital precision).

**Energy** Energy (of all kinds) can be interpreted, at a fundamental level, as just the *performing of physical computation* at a certain rate in terms of quantum bit operations per second, according to the formula  $E = \frac{1}{4}hR$ , where  $h$  is Planck's (unreduced) constant and  $R$  is the rate of complete bit operations [16, 18]. For most forms of energy, we do not notice the computation that is associated with it, because that computation is only performing such familiar, everyday sorts of information processing as shifting a physical object through space (kinetic energy) or exchanging force particles between two objects (binding energy, a.k.a. potential energy). Also, depending on the state, much of the energy may have a null effect. Only a miniscule part of the energy in most computers is actually directed toward performing information transformations that are of interest for carrying out the logic of the application. As technology advances, we learn to harness an increasing fraction of systems' energy content for computational purposes. The *first law of thermodynamics* expresses the observation that total energy is conserved (*i.e.*, that the total physical computation taking place within a closed system proceeds at a constant rate), which we know from *Noether's theorem* is equivalent to the postulate that the laws of physics (as embodied in the global Hamiltonian) are unchanging in time.

**Energy eigenstate** An eigenstate of the energy observable.

**Energy transfer model** In a model of computation, the model of the flow of energy and information (including entropy) through the machine.

**Entangle** Two quantum systems are *entangled* if their joint state cannot be expressed as the tensor product (essentially,

a concatenation) of simple pure or mixed states of the two systems considered separately. This is really nothing more than a straightforward generalization to quantum systems of the simple classical idea of a *correlation*. For example, if I flip a coin and then, without looking at it or turning it over, chop it in half, then I may know nothing about the state of either half by itself, but I *do* know that the two halves will show the same face when I look at them.

**Entropy** Information that is unknown to some particular entity (unknown in the sense that the *amount* of information in the system can be known, but the specific *content* of the information is not).

**Equilibrium** A given system is considered to be at *equilibrium* if all of its physical information is entropy, that is, if it has maximum entropy given the constraints implicit in the system's definition. Due to the second law of thermodynamics, the equilibrium state (a mixed state) is the only truly stable state; all other states are at best *meta-stable*.

**Error correction** Through decay/decoherence interactions, the logical or coding state of an information-processing system may gradually accumulate unwanted departures away from the desired state. The information in these unwanted variations represents a form of entropy. Error correction is the removal of this entropy and recovery of the original, desired logical and coding state. Being an entropy removal process, it is just a special case of refrigeration. Error correction can be implemented physically (*e.g.*, by connecting a circuit node to a high-capacitance power supply reference node with a stable voltage), or algorithmically, by using redundant error correction codes and explicitly detecting and correcting bit errors one by one. Error correction techniques exist for quantum superposition states, as well as for classical state spaces.

**Euclidean space** A space in which the metric is *flat*, and classical flat-plane geometry like Euclid's remains valid. Measurements show that the physical spacetime that we live in is very nearly Euclidean.

**Far nanoscale** The range of pitch values between 0.032 and 1 nm. Contrast *near nanoscale*.

**Fat tree** Another interconnection network structure similar to a binary tree, except that each node is connected to several parent nodes for additional communication bandwidth and redundancy. Fat trees are not physically realistic with unit-time hops.

**Fermi level** The average energy of electrons at the "surface" of the Fermi sea.

**Fermi velocity** The average velocity of electrons having sufficient energy to be at the Fermi level.

**Fermi wavelength** The de Broglie wavelength of electrons moving at the Fermi velocity, that is, having enough kinetic energy to put them at the Fermi level (the surface of the Fermi sea of electrons).

**Fermi sea** Electrons, being Fermions, obey the Pauli exclusion principle (no two can occupy the same state at the same time), and therefore, given a set of available states, electrons will "fill up" the available states, from lowest to highest energy. This is called the "Fermi sea." The surface of the Fermi sea may be called the "Fermi surface"; it is at the Fermi level of energy. All the action (transitions of electrons

and holes to new states) happens near the Fermi surface, because the deeper electrons have no available states nearby to transition to.

**FET** Field-effect transistor; a transistor (voltage controlled current switch) whose operation is based on the field effect.

**Field effect** An effect seen in semiconductors where an applied electrostatic field significantly changes the mobile charge-carrier concentration in a material, as a result of moving the Fermi level farther toward or into the valence band or the conduction band.

**Flux** In general, for our purposes, a rate of transfer of some conserved substance or material per unit area of some surface it is passing through. Sometimes called *flux density* or *flux rate*. In nanocomputer systems engineering, we consider key quantities such as information flux (bandwidth density), entropy flux, energy flux, and heat flux. The former two are fundamentally limited as a function of the latter two.

**FPGA (field-programmable gate array)** A type of processor consisting of a regular array of low-level functional units or logic gates, which is programmed by configuring the function and interconnection of the individual elements. Commonly used today in embedded applications; major commercial manufacturers in 2003 include Xilinx and Altera. Many future general-purpose processors will likely include an FPGA-like module that can be reconfigured for efficient special-purpose processing.

**Free energy** For our purposes, the free energy in a system is its total energy minus the spent energy, that is, the amount of energy  $ST$  that would be needed to move all of the system's entropy  $S$  to the lowest temperature available thermal reservoir, at temperature  $T$ . Compare to *Gibbs free energy* and *Helmholtz free energy*.

**Frequency** The quickness of a process that continually repeats itself. In other words, periods or cycles per time unit. Typical unit: the Hertz (inverse second).

**G** Newton's gravitational constant,  $6.67259 \times 10^{11} \text{ Nm}^2/\text{kg}^2$ . Still used in Einstein's general relativity, the modern theory of gravity.

**g** Abbreviation for gram (the mass unit).

**Gate** There are two meanings used in this document. The gate of a transistor is the circuit node that controls its conductance. A *logic gate* is a bit device that carries out a specified Boolean logic operation. A logic gate today consists of several transistors and may contain several transistor gates.

**General-purpose processor** A processor that can be programmed to carry out any algorithm (up to the limit set by its storage capacity).

**General Theory of Relativity** Also just general relativity (GR), Einstein's theory of gravity, based on the principle that gravity is equivalent to an accelerated reference frame. GR predicts a number of surprising phenomena, such as curved spacetime, black holes, and gravity waves, all of which have been (at least indirectly) confirmed by experiment. Eventually GR needs to be unified with the Standard Model. GR provides the only fundamental physical limit to computer scaling that is not already incorporated into the model described in this chapter.

**Gibbs free energy** The Helmholtz free energy, plus the energy of interaction with a surrounding medium at pressure

$p$  given by  $pV$  where  $V$  is the volume of the system. See *free energy* for an even more comprehensive concept that includes all energies that are not clearly spent energy.

**Gram** SI mass unit originally defined as the mass of 1 cubic centimeter of water at a certain standard temperature and pressure.

**Ground state** The lowest energy state of a given system of variable energy. That is, the energy eigenstate having the lowest (most negative) possible energy eigenvalue.

**Grover's algorithm** A quantum algorithm originally characterized as a database search algorithm that is (more usefully) really an algorithm for the *unstructured search* problem.

**Hamiltonian** This is a term from classical mechanics that remains valid in quantum mechanics. The Hamiltonian is a function that gives a system's energy as a function of its state variables. The Hamiltonian incorporates all of the interactions between the subsystems of a given system. All of the dynamical laws of mechanics can be expressed in terms of the system's Hamiltonian. In quantum mechanics, this remains true; the dynamics is given by Schrödinger's equation. The Hamiltonian is an observable, an Hermitian transformation of state vectors. In quantum field theory, the Hamiltonian can be expressed as a sum of local interactions, which makes it consistent with special relativity.

**Hardware efficiency** The reciprocal of the spacetime cost of a computation. A figure of merit used in VLSI theory that is appropriate for some nanocomputer system optimizations, in limited contexts. However, in general, it is incomplete, because it ignores energy costs, as well as costs that are proportional to time alone (such as inconvenience to the user).

**Heat** Heat is simply that part of a system's total energy that resides in subsystems whose physical information is entirely unknown (entropy).

**Heisenberg's uncertainty principle** The most general form of this principle is that two quantum states that are not orthogonal to each other are not operationally distinguishable, by any physical possible means whatsoever. It manifests itself frequently in statements that two observables that do not commute with each other (*e.g.*, position and momentum of a particle) cannot both be precisely measured for the same system.

**Helical logic** A reversible logic scheme proposed by Merkle and Drexler in which a rotating electromagnetic field adiabatically shuttles charge packets around a network of wires in which they steer each other via Coulombic interaction.

**Helmholtz free energy** The free energy (see our definition) of a system, minus that portion that is not considered to be internal energy. To the extent that internal energy is less well defined than is total energy (for instance, how much of the rest mass-energy does it include?), Helmholtz free energy is less well defined than is our free energy.

**Hermitian operator** An operator on quantum states that is equal to its adjoint (conjugate transpose). Hermitian operators have real-valued eigenvalues. In quantum mechanics, Hermitian operators represent both measurements of observable characteristics and interactions (Hamiltonians)

between systems (which makes sense, since a measurement is just a type of interaction).

**Hilbert space** This is a term from linear algebra. A Hilbert space is simply a complex vector space that supports an inner product (dot product) operation between vectors. In quantum mechanics, the set of possible quantum states of a system is described mathematically as a Hilbert space. Not all states in the Hilbert space are operationally distinguishable from each other. Two states are distinguishable if and only if their state vectors are orthogonal.

**Hole** The absence of an electron in a state below the Fermi surface. (Think of it as a bubble in the Fermi sea.)

**Hop** The propagation of information from one node in an interconnection network to another node to which it is directly connected.

**Https** Hyper text transfer protocol, secure: a protocol for secure communication of web pages and form data based on the transport layer security (TLS) protocol, which may use RSA internally (thus being vulnerable to cracking by a quantum computer).

**Hypercube** An  $d$ -dimensional interconnection network formed by connecting corresponding nodes of a  $(d - 1)$ -dimensional hypercube. Hypercubes are not physically realistic with unit-time hops.

**Ideal gas constant** See *nat*.

**Information** That which distinguishes one thing from another, in particular, different (distinguishable) states of a physical system. We say that a system in a particular state *contains* the information specifying its state. An *amount* of information can be quantified in terms of the *number* of (equally probable) distinct states that it suffices to distinguish. The natural convention is that the information corresponds to the *logarithm* of the number of distinguishable states; this measure has the advantage of being additive whenever multiple independent systems are considered together as one system. Any real number  $r > 1$ , when used as the base of the logarithm, yields a corresponding unit of information. The unit of information corresponding to the choice  $r = 2$  is called the *bit*, whereas the unit corresponding to  $r = e$  (the base of the natural logarithms) is called the *nat*. (Boltzmann's constant  $k_B$  and the ideal gas constant  $R$  turn out to be simply alternative names for 1 nat.)

**Instruction set architecture (ISA)** A traditional type of programming model in which serial computations are expressed by a sequence of low-level instructions which tell the computer to do a simple arithmetic or logical operation (such as adding two numbers), or to transfer control to a different point in the instruction sequence. Other, very different types of programming models are also possible, such as models used in FPGAs and cellular automata machines.

**Insulator** An *insulator* is a material in which the bandgap between the valence band and the conduction band is so large that there is negligible charge-carrier concentration and therefore negligible conductivity. (Compare *semiconductor*.)

**Integrated circuit** A complex circuit manufactured as a single solid-state component.

**Interference** In any wave-based process, waves *interfere* when they add linearly in superposition; this interference can be either *constructive* with two waves have the same sign or *destructive* when they have opposite sign. Since everything is a wave in quantum mechanics, two different trajectories in a quantum computer can interfere destructively if they arrive at a given state out of phase with each other. Such interference between trajectories is necessary to get added power from quantum algorithms.

**Interconnect** A pathway for communication.

**Internal energy** Energy in a system other than the kinetic energy of its overall motion and energies of interaction with other external systems. Sometimes in the traditional thermodynamics definitions of this concept, rest mass-energy is also omitted from the definition, although this is an arbitrary and artificial step, since internal potential energy (which is usually included in internal energy) is technically (in relativity) an *indistinguishable* concept from rest mass-energy, which necessarily includes the binding energies (which *are* internal potential energies) of, for example, atoms, protons, and neutrons.

**Internal ops** Operations that are concerned with updating the internal state of an object, as opposed to propagating the object through space translationally or rotationally. The rate of internal ops is the rest mass-energy or internal energy of an object. The total number of internal steps taken, relative to that of a comoving reference object (clock), is the *proper time* experienced by the system.

**Invertible** A mathematical term. A function is invertible if its inverse relation is also a function, that is, if the original function is one-to-one.

**Iop** Short for "*inverting op*," a unit of computational work equal to one-half of a pop.

**Irreversible computing** The traditional computing paradigm, in which every computational operation erases some amount of known information and therefore necessarily generates a corresponding amount of new physical entropy.

**Isentropic** Literally, "at the same entropy." A process is *isentropic* if it takes place with no new generation of physical entropy.

**J** Abbreviation for Joule (the energy unit).

**Josephson effect, Josephson junction** A superconducting current can even pass through a sufficiently narrow tunnel barrier (Josephson junction) without resistance, up to some critical current at which the junction abruptly switches off (Josephson effect). This phenomenon is the basis for some superconducting logic technologies, such as the fairly successful rapid single-flux quantum technology developed by Konstantin Likharev's group at SUNY.

**Joule** A unit of energy defined as 1 N · m. In computational units, a Joule is equal to a potential computing rate of  $6.036 \times 10^{33}$  primitive operations (pops) per second.

**k** In Roman font, k, an abbreviation for kilo-. In italic font *k*, often used to represent Boltzmann's constant.

**kT** Called the *thermal energy*, this product of Boltzmann's constant  $k$  and the thermal temperature  $T$  is the average energy (or rate or operations) per nat's worth of state information in a thermal system. However, it also applies just as well to nonthermal systems at generalized temperature  $T$ .



**Kelvin** SI unit of absolute temperature, defined originally as 1/100th the absolute temperature difference between the freezing and boiling points of water at atmospheric pressure. In computational units, 1 Kelvin is equal to an average rate of state change of 28.9 billion steps (pops per bit) per second, that is, an update frequency of 28.9 GHz.

**Kilo** SI unit prefix meaning 1000.

**Kinetic energy** Energy associated with the overall motion of a system as a whole.

**Known** A given piece of information is *known* by a given entity (which can be any kind of entity, a human, organization, computer, or logic gate) to the extent that it is correlated with other information that is accessible by that entity, in a such a way that the entity can make use of this correlation in a well-defined way.

**Landauer embedding** The technique of embedding a desired logically irreversible computation into a logically reversible computation by simply keeping a copy of all information that would otherwise be thrown away.

**Latch** To store a copy of an input signal so that it remains available when the signal is removed. Conceptually, the information is “latched into place,” like a mechanical part can be.

**Latency** In computer architecture, the amount of time that passes while waiting for something.

**Latency hiding** A computer architecture trick of “hiding” delays to high-latency operations (*e.g.*, communicating with memory or distant processors) by finding other useful work to do in the meantime. Unfortunately, there are limits to the extent to which the technique can improve the overall cost efficiency of a computation.

**LC oscillator** A simple electrical circuit in which an inductance ( $L$ ) is connected to a capacitance ( $C$ ). In this circuit, energy oscillates between the magnetic field of the inductor and the electric field of the capacitor. Unfortunately, the  $Q$ 's obtainable in nanoelectronic inductors are quite limited.

**Lithography** Literally, “stone writing,” this refers generically to any technique for forming a patterned structure on a solid surface. *Photolithography* is a photochemical technique for etching specific patterns using projected light; it is the most widely used technique today. However, it is limited by the wavelengths of easily manipulated light. Other emerging lithography techniques such as electron-beam lithography, deep reactive ion etching (DRIE), and direct-imprint lithography are helping extend minimum feature sizes to the nanometer realm.

**Logical basis** The particular basis of a qubit's state space, chosen by convention, in which the two orthogonal basis vectors are taken represent a pure logic 0 and 1 respectively. If the qubit system contains natural pointer states, these may conveniently be selected as the basis (especially if the system is not highly coherent). Sometimes, it may be more convenient to use an alternative description of quantum architectures in which the logical basis is considered to change over time.

**Logical bit** Also *coded bit*, *computational bit*. This is a bit that the logical or coding state of a bit device is intended to represent. Note: Every logical bit that we can actually manipulate is also a physical bit!

**Lecerf reversal** To reversibly clear temporary storage used up by a reversible computation by running the steps of the computation in reverse. Used in Bennett's algorithm and in retractile cascade circuits.

**Logically reversible** A computational process is logically reversible if every logic operation performs an invertible transformation of the logical state.

**Logical state** The part of a bit device's state that corresponds to the intended digital information to be stored. May be determined redundantly by a large amount of physical coding-state information.

**Logic gate** A *bit device* that operates on logical bits of interest in a computation.

**Logic operation** A transformation that takes a logical state to a distinguishable logical state. May be implemented by a collection (in series or in parallel) of operations carried out on coding state information.

**Loop Quantum Gravity** The leading competitor to String Theory as a potential path toward the unification of the Standard Model and general relativity. Interestingly, in Loop Quantum Gravity, spatial area and volume are quantized, and the exact maximum number of quantum states (and thus the exact maximum information content) of any region of space can be counted and matches the limit found earlier by Bekenstein and Mayo [119]. In this limit, the maximum information capacity within a given surface is given by the surface area in Planck units. This suggests that a limiting model of computing in the high-density regime may be only two-dimensional. But it is still too early to tell.

**m** Abbreviation for meter (the length unit).

**Machine language** The language in which algorithms are expressed when they can be directly processed by a given machine. The *instruction set architecture* of a conventional machine specifies the rules of its machine language.

**Magnitude** The complex number  $c$  has *magnitude*  $m \geq 0$  if and only if  $c = me^{i\theta}$  for some real number. An equivalent definition: If  $c = a + bi$  for real numbers  $a, b$ , then  $m = (a^2 + b^2)^{1/2}$ .

**Majority logic** A type of logic operation in which the value of an output bit is set to the majority value of an odd number of input bits.

**Mass** Relativistic mass is total energy, converted to mass units (by dividing by  $c^2$ ). See also *rest mass*.

**MEMS** Microelectromechanical systems. Denotes a lithography-based technology for fabrication of mechanical or electromechanical structures and systems on surfaces. MEMS technologies are available today.

**Mesh** An interconnection network based on local (bounded-length) connections between nodes located in a space having (if realistic) three or fewer dimensions.

**Mesoscale** Literally, “middle scale,” an intermediate scale between the nanoscale and the microscale at which surface effects and quantum effects begin to become important but do not yet entirely dominate the physics of materials and devices.

**Meta-stable** A state is called meta-stable if it has a relatively slow rate of decay toward an equilibrium (maximum-entropy) state.

**Meter** Unit of length originally defined as ten-millionth of the distance from the Earth's equator to its north pole.

**Metric** A function that gives the distance, according to some method of measurement, between any two given points.

**Microcomputer** For our purposes, a computer whose *characteristic length scale* is anywhere between  $10^{-4.5}$  and  $10^{-7.5}$  meters (*i.e.*, between 32 and 0.032 m; *i.e.*, closer to 1 micrometer than to 1 millimeter or 1 nanometer on a logarithmic scale).

**Micrometer** A unit of length equal to  $10^{-6}$  meters. Typical length of a bacterial cell.

**Micron** Shorthand name for *micrometer*.

**Mixed state** A statistical mixture of (pure) quantum states, which may be represented by a *density matrix*, which can always be diagonalized or transformed to an alternative basis in which it consists of a mixture of orthogonal states. Therefore a mixed state can be understood as nothing more than a classical statistical mixture of pure quantum states.

**Mole** Quantity of molecules (or other objects) such that the collection's mass in grams is equal to the individual object's mass in atomic mass units (amu). Number of amus per gram. Equal to Avagadro's number,  $6.0221367 \times 10^{23}$ .

**Momentum** In computational terms, the physical momentum  $p$  is the total number of operations per distance required to translating a system spatially in a given direction. Such a transformation is orthogonal to any internal transformations, whose rate is given by the system's rest mass, so the total rate of operations  $E$  for a system of rest mass  $m_0$  with momentum  $p$  is given by the Pythagorean theorem as  $E^2 = m_0^2 + p^2$ , the correct relativistic formula.

**MOSFET** Metal-oxide-semiconductor field-effect transistor. A field-effect transistor structure constructed by sandwiching a layer of insulating material (usually silicon dioxide or another oxide) in between a metallic (or actually, often polysilicon) gate electrode and a semiconducting substrate.

**M-theory** A generalization and unification of several leading string theories in which  $d$ -dimensional membranes, rather than one-dimensional strings, are the fundamental entities. Like the individual string theories themselves, M-theory has made no confirmed predictions and therefore remains fairly speculative. Even if true, I do not expect it to radically change our understanding of the physical limits of computing.

**$\mu\text{m}$**  Standard abbreviation for *micrometer*.

**N** Abbreviation for Newton (the force unit).

**Nano-** SI unit prefix, denoting multiplication of the unit by  $10^{-9}$ . Abbreviated n.

**Nanocomputer** A computer whose characteristic length scale is between  $10^{-7.5}$  and  $10^{-10.5}$  meters (*i.e.*, between  $\sim 32$  and  $\sim 0.32$  nm, *i.e.*, closer to 1 nanometer than to 1 micrometer or 1 picometer on a logarithmic scale).

**Nanocomputing** Computing using nanocomputers.

**Nanometer** A unit of length equal to  $10^{-9}$  meters, or  $10 \text{ \AA}$ . A typical length for a small molecule, such as an amino acid. About five carbon-carbon bond lengths. About the radius of the smallest carbon nanotubes.

**Nanoscale** Although definitions vary, for purposes of this chapter, we define *nanoscale* as meaning a characteristic length scale that falls anywhere in the three-order-of-magnitude range between  $\sim 30$  and  $\sim 0.03$  nm. That is, the logarithm of the characteristic length scale is closer to 1 nm than to either  $1 \mu\text{m}$  or  $1 \text{ pm}$ .

**Nanowire** A wire (made of conductive or semiconductive material) that has a nanoscale diameter.

**Nat** The natural-log unit of information or entropy. Also known as *Boltzmann's constant*  $k_B$  or the *ideal gas constant*  $R$ .

**Near nanoscale** The range of pitch values between 1 and 32 nanometers. Contrast *far nanoscale*.

**NEMS** Nanoelectromechanical systems. Basically, just MEMS technology scaled down to the nanoscale. More generically, NEMS could be used to refer to any nanoscale technology for building integrated electromechanical systems.

**Newton** A unit of force equal to  $1 \text{ kg m/s}^2$ .

**NFET** A field-effect transistor in which the dominant charge carriers are negative (electrons).

**nm** Standard abbreviation for *nanometer*.

**NMR** Nuclear magnetic resonance, a technology used in chemical NMR spectrometers and modern medical (magnetic resonance imaging) scanning machines. In the mid 1990s, NMR technology was used to implement simple spin-based quantum computing (massively redundantly encoded) using nuclear spins of selected atoms of a molecular compound in solution.

**Noncoding physical state** The part of the physical state of a computing system or device that is uncorrelated with its logical state, for example the detailed state of unconstrained thermal degrees of freedom (see *thermal state*). However, another part of the noncoding state (the *structural state*) is correlated with the system's ability to *have* a well-defined logical state. For example, if a transistor gate is in a state of being shorted out then its nodes may no longer be able to maintain a valid logic level.

**Nondeterministic models of computing** The adjective "nondeterministic" is used misleadingly in computer science theory as jargon for models of computation in which not only is the computer's operation at each step nondeterministic, in the sense of not being determined directly by the machine's current state, but furthermore it is assumed to be *magically* selected to take the machine directly to the desired solution, if it exists (or equivalently, all solutions are magically tried in parallel, and the correct one is then selected). Computer scientists really ought to rename "nondeterministic" models as magical models of computing, to emphasize their total lack of realism. Probably this was not done historically for fear of scaring off potential funding agencies. In any case, the name seems intentionally misleading.

**NP** *Nondeterministic polynomial-time*, the set of problem classes in which a proposed solution can be checked or verified within an amount of time that is polynomial in the length  $n$  of the problem description in bits, that is, in which the time to check the solution grows as  $(n^k)$  for some constant  $k$ .

**NP-hard** The set of problems such that any problem in NP can be reduced (in polynomial time) to an instance of that problem. If any NP-hard problem can be solved in polynomial time, then all of them can.

**NP-complete** The set of problems that are both in *NP* and in *NP-hard*.

**Number of operations** A characteristic of a transformation trajectory that counts the total number of primitive orthogonalizing operations that occur along that trajectory. The number of operations can be counted in units of Planck's constant or pops.

**Observable** In quantum theory, an observable is just any Hermitian operator on states. The eigenstates of an observable are orthogonal (distinguishable), and its eigenvalues are real-valued (zero imaginary component). The eigenstates of the observable have a definite value of the measured quantity, and its numerical value is given by the eigenvalue.

**Omega network** Similar to a butterfly network. Omega networks are not physically realistic for unit-time hops.

**Op** Short for *operation*, or pop. We also sometimes use ops to refer to operation units of other sizes besides pops, such as rops and iops.

**Operation** In this document, shorthand for *primitive orthogonalizing operation*. Also used sometimes to mean the special case of *logic operation*, a primitive orthogonalizing operation, or series of such, that effects a single change in the logical state.

**Operational** In the scientific method, a defined characteristic of a system is called *operational* in nature if there exists a reliable, physically realizable procedure for measuring or confirming that characteristic. For example, two states are operationally distinguishable if there exists a definite experiment that can reliably distinguish them from each other.

**Operator** In mathematics, a function that operates on a sequence of a prespecified number of members of a given set and returns a member of that same set. Functions that operate on sequences of length 1 are called *unary* operators or *transformations*.

**Opportunity cost** In economics, the implicit cost of consumption of resources that results from foregoing the best alternative use of those same resources.

**Orthogonal** A term from vector mathematics. Two vectors are orthogonal if and only if, considered as lines, they are perpendicular, or (equivalently) if their inner product (dot product) is zero. Orthogonality is the requirement for two quantum state vectors to be operationally distinguishable from each other.

**Orthogonalize** To transform a vector (such as a quantum state vector) to another vector that is orthogonal to the original one.

**Parallel** Two processes are *parallel* if they take place simultaneously.

**p**— Short for *pico*, SI unit prefix meaning  $10^{12}$ .

**Performance** Performance is a figure of merit for computing. It is equal to the *quickness* of a reference computation.

**PFET** A field-effect transistor in which the dominant charge carriers are positive (holes).

**Phase** The complex number  $c$  has *phase*  $0 \leq \theta < 2\pi$  if and only if  $c = m \cdot e^{i\theta}$  for some real number  $m$ .

**Physical bit** Any bit of physical information.

**Physical entropy** Physical information that is entropy (unknown to a particular observer).

**Physical information** Information contained in a physical system, defining that system's state. Of course, all the information that we can access and manipulate is, ultimately, physical information.

**Physically reversible** Synonym for *adiabatic*, *isentropic*, and *thermodynamically reversible*.

**Physical realism** In this chapter, a property had by a model of computation when it does not significantly (by unboundedly large factors) overstate the performance or understate the cost for executing any algorithm on top of physically possible implementations of the architecture. WARNING: Many models of computing that are studied by computer scientists lack this important property and therefore can be very misleading as guides for computer engineering and algorithm design.

**Physical system** In essence this is an undefined term, based on intuition. But we can distinguish between abstract *types* of physical systems, constrained by their descriptions, and specific *instances* of physical systems embedded within our actual universe. For a specific instance of a system, we may in general have incomplete knowledge about its actual state. We should emphasize that a particular system might be defined to consist of only specified state variables within a particular region of space, as opposed to the entirety of the physical information within that region.

**Pico**— SI unit prefix, denoting multiplication of the unit by  $10^{-12}$ . Abbreviated p.

**Picometer** A unit of length equal to  $10^{-12}$  meters, or 0.01 Å. Roughly 1/100 the radius of a hydrogen atom, or 100 times the diameter of an atomic nucleus.

**Pipelined logic** A deep combinational network can be broken into a series of shorter stages which can be used simultaneously to process different sequential inputs, resulting in a higher overall hardware and cost efficiency for most irreversible computations. However, pipelined reversible logic is *not* always more cost efficient than is nonpipelined reversible logic.

**Pitch** The distance between the center lines of neighboring wires in a circuit.

**Planck energy** The fundamental constants  $h, G, c$  can be combined to give an energy unit,  $E_p = (\hbar c^5/G)^{-1/2} \simeq 1.956$  GJ. This energy, or something close to it, is believed to be a fundamental maximum energy for a fundamental particle in whatever turns out to be the current unified theory of quantum gravity. It is the energy of a particle when traveling at a velocity so high that that its de Broglie wavelength is equal to the Planck length.

**Planck length** The fundamental constants  $h, G, c$  can be combined to give a length unit,  $\ell_p = (\hbar G/c^3)^{-1/2} \simeq 1.616 \times 10^{-35}$  m. This length, or something close to it, is believed to be a fundamental minimum length scale in whatever turns out to be the correct unified theory of quantum gravity. For example, it is already known that the maximum information

in any region, in nats, is given by the area of the smallest enclosing surface around that region, in units of  $(2\ell_p)^2$ .

**Planck mass** The fundamental constants  $h, G, c$  can be combined to give a mass unit,  $m_p = (\hbar c/G)^{-1/2} \approx 2.177 \times 10^{-8}$  kg. This mass, or something close to it, is believed to likely be a maximum mass for a fundamental particle, and perhaps the minimum mass of a black hole, in whatever turns out to be the current unified theory of quantum gravity. It is the mass of a particle when traveling at a velocity so high that that its de Broglie wavelength is equal to the Planck length.

**Planck's constant** Expresses the fundamental quantum relationship between frequency and energy. Comes in two common forms, Planck's unreduced constant,  $h = 6.6260755 \times 10^{34}$  Js, and Planck's reduced constant,  $\hbar = h/2\pi$ . In computational terms, Planck's constant is a fundamental unit of computational work;  $h$  can be viewed as equal to two primitive orthogonalizing operations.

**Planck temperature** Dividing the Planck energy by Boltzmann's constant  $k$ , we get a temperature  $T_p \simeq 1.417 \times 10^{32}$  K. This temperature, or something close to it, is believed to be a fundamental maximum temperature in whatever turns out to be the correct unified theory of quantum gravity. It is the temperature of a Planck-mass (minimum-sized) black hole, or a single photon of Planck energy. In computational terms it corresponds to 1 radian-op per Planck time, or 1 pop per  $\pi$  Planck times, which gives a maximum possible frequency of complete state update steps in a computational process of  $\sim 5.9 \times 10^{42}$  steps per second.

**Planck time** The fundamental constants  $h, G, c$  can be combined to give a time unit,  $t_p = (G\hbar/c^5)^{-1/2} \simeq 5.391 \times 10^{-43}$  s. This time, or something close to it, is believed to be a fundamental minimum time unit in whatever turns out to be the correct unified theory of quantum gravity. It is the time for light to travel 1 Planck length and is the reciprocal of the angular phase velocity of a quantum wavefunction of a Planck-mass particle, or in other words the minimum time per rop. The minimum time for a primitive orthogonalizing operation is  $t_p \simeq 1.69 \times 10^{-42}$  s.

**pm** Standard abbreviation for *picometer*.

**Polynomial time** In computational complexity theory, having a time complexity that grows as  $\Theta(n^k)$  in input length  $n$  for some constant  $k$ .

**Pop** Abbreviation for *primitive orthogonalizing operation*  $\pi$ -op.

**Pointer state** A state of a quantum system that remains stable under the most frequent modes of interaction with the environment, that is, an eigenstate of the observable that characterizes the interaction. The states chosen to represent logical bits in a classical (nonquantum) computer are usually pointer states. Quantum computers, however, are not restricted to using only pointer states. This is what gives them additional power. However, it requires a high degree of isolation from unwanted interactions with the environment, which will destroy (decohere) nonpointer states.

**Polysilicon** Sometimes abbreviated just *poly*, this is polycrystalline silicon, a quasi-amorphous state of solid silicon, made of numerous nanoscale crystal grains. Often used for

local interconnect layers, in contrast with the single-crystal silicon forming the chip substrate.

**Power** Rate of energy transfer, often measured in Watts.

**PR** See *physical realism*.

**PRAM** Parallel variant of the RAM machine model of computation. There are several varieties of PRAM model. One simply has  $n$  RAMs accessing the same shared memory in parallel. PRAM models are not physically realistic, in the sense used in this chapter.

**Primitive orthogonalizing operation** Also pop,  $\pi$ -op. In this chapter, a unitary transformation that takes some quantum states to new states that are orthogonal to the original state. A  $\pi$ -op is equal to  $\pi$  rops or to  $\pi\hbar = h/2$ .

**Principle of locality** Casual effects can only happen through local interactions in space. This is a consequence of special relativity, and it is obeyed by modern quantum field theory, in which the global Hamiltonian is composed from local interaction terms only. Einstein thought that quantum mechanics was nonlocal, but it turned out he was wrong.

**Processor** Short for *information processor*, this refers either to a computer or to a part of a computer (e.g., a CPU) that is large and complex enough to be programmed to perform different types of computations.

**Program** Information specifying in complete detail an algorithm that a computer will perform. Relates to a specific *programming language* or to a computer's specific *programming model*.

**Programming model** Specifies how a given architecture can be *programmed* to carry out whatever computation is desired. Most computers today have a specific type of programming model called an *instruction set architecture*. Other kinds of programming models exist, such as those used in FPGAs, CAMs, and dataflow machines.

**Programming language** A standard language, usually textual (although graphical languages are also possible) for representing algorithms. A *compiler* translates a program from an easily human-readable programming language into a form that can be utilized by a given machine's programming model.

**Proper time** In relativity, this is the amount of time (number of reference-system update steps) to pass, as experienced in a reference frame moving along with a given object, rather than in some other arbitrarily chosen reference frame.

**Public-key cryptography** An approach to cryptography and authentication based on a complementary pair of keys, a public key and a private key, each of which decrypts the code that the other encrypts. The most popular known public-key cryptography algorithms are vulnerable to being broken by quantum computing.

**Pure state** See *quantum state*.

**Q3M** Quantum 3D mesh, a model of computing consisting of a three-dimensional mesh-connected network of fixed-size, arbitrarily reversible, and quantum-coherent processing elements. The Q3M is postulated by the author to be a UMS model. See *tight Church's thesis*.

**Quality** In this chapter, the *quality* or  $q$  factor of a device or process is defined as the ratio of energy transferred to energy dissipated, or (quantum) bit operations

performed to entropy generated, or quantum bit operations performed to decoherence events. It is also the ratio between the coding-state temperature and the temperature of the decoherence interaction, or the ratio between the coherence time and the operation time.

**Quantum algorithms** Algorithms for a quantum computer, which use superpositions of states and interference effects in an essential way. Quantum algorithms must be reversible to avoid decoherence.

**Quantum computer** A computer that uses superpositions of pointer states as intended intermediate states in a computation. Ordinary classical computers are restricted to only using pointer states. The less-constrained state space available in a quantum computer opens up exponentially shorter trajectories toward the solution of certain problems, such as the factoring problem. The more constrained state space available to a classical computer appears to require exponentially more steps to arrive at solutions to this problem.

**Quantum dot** A mesoscale or nanoscale structure in which conduction-electron energies are quantized.

**Quantum dot cellular automaton** Abbreviated QDCA or just QCA, this is a particular logic scheme using quantum dots which was invented at Notre Dame. Involves “cells” (made of four dots) which interact with each other locally; in this respect, it roughly resembles the cellular automaton model of computing. QDCA also includes adiabatic variants.

**Quantum electrodynamics** Abbreviated QED, this is the quantum field theory that deals with charged particles, photons, and the electromagnetic field. Now subsumed by the Standard Model of particle physics.

**Quantum field theory** When quantum mechanics is unified with special relativity, the result is a field theory. The Standard Model of particle physics is the modern working quantum field theory. Other, simplified models, which omit some details of the Standard Model, including quantum electrodynamics, the quantum field theory of electric charge and electromagnetism, and quantum chromodynamics, the quantum field theory of “color” charge (carried by quarks and gluons) and the strong nuclear force.

**Quantum information** The specific quantum information contained in a system can be identified with the actual quantum state of the system, itself. The total *amount* of quantum information is the same as the amount of classical information—namely, the logarithm of the number of orthogonal states—except it is measured in qubits rather than bits. The quantum information can be thought of as a choice of basis, together with the classical information inherent in the selection of one of the basis states. The classical information is only the selection of basis state, with the basis itself being fixed.

**Quantum mechanics** Modern theory of mechanics, initiated by Planck’s discovery of the fundamental relationship between frequency and energy, namely that a system performing transitions between distinguishable states at a given rate or frequency must contain a corresponding minimum amount of energy. (This fact was first discovered by Planck in the context of blackbody radiation.)

**Quantum state** Also called a pure state, the state of a quantum system is identified with a vector (normalized to

unit length) in the system’s many-dimensional *Hilbert space*. Two states are distinguishable if and only if their state vectors are orthogonal (perpendicular to each other).

**Qubit** A unit of quantum information, as well as a name for any particular instance of a physical system or subsystem that contains this amount of quantum information. A system that contains one qubit of information has only two distinguishable states. A qubit may be in a state that is superposition of pointer states, and this state may be entangled (correlated) with the states of other systems.

**Quickness** The *quickness* of any process is the reciprocal of the total real time from the beginning of that process to the end of the process. Quickness is measured in units of Hertz (inverse seconds).

**R3M** Reversible 3D mesh, a model of computing consisting of a three-dimensionally connected mesh network of fixed-size, arbitrarily reversible processors. The R3M is postulated to be a UMS model for nonquantum computations. See also Q3M.

**RAM** Random access memory, a memory in which any random element can be accessed (read or written) equally easily, by supplying its numeric address. Also stands for random access machine, an early non-PR, non-UMS model of computation in which any random element of an unboundedly large memory can be accessed within a small constant amount of time.

**Radian-op** See *rop*.

**Random access** To access (read or write) a bit of memory selected at random (*i.e.*, arbitrarily).

**Resonant tunneling diodes/transistors** Structures in which the rate of tunneling between source and drain electrodes is controlled by the resonant alignment of electron energy levels in an intervening island with the Fermi energies of free conduction electrons in the source terminal.

**Rest mass** Computationally, the rate of ops in a system that are concerned with the internal updating of the system’s state, rather than with net translation of the system in a particular direction (*i.e.*, that portion of a system’s total energy that is not kinetic energy).

**Retractile cascade logic** Or just retractile logic. A reversible combinational logic style in which inputs are presented and intermediate results computed and then (after use) are uncomputed by “retracting” the operations that produced the results, in reverse order.

**Reversibility** A process or dynamical law is reversible if the function mapping initial state to final state is one-to-one (that is, its inverse is a function). Reversible is synonymous with reverse-deterministic (deterministic looking backwards in time). It is *not* synonymous with *time-reversal symmetric*. A dynamical law is time-reversal symmetric if it has the identical form under negation of the time component. Modern particle physics actually has a slightly changed form under time reversal (namely, charges and handedness must also be changed), but it is still reverse-deterministic, thus still reversible.

**Reversible algorithms** Algorithms composed of reversible operations.

**Reversible operations** An operation is reversible if it transforms initial states to final states according to a one-to-one (bijective) transformation.

**Reversible computing** A paradigm for computing in which most logical operations perform a logically reversible (bijective) transformation of the local logical state; this transformation can then be carried out adiabatically (nearly thermodynamically reversibly).

**Reversibilize** To translate a computation described as an irreversible algorithm to an equivalent but reversible form, often by reversibly emulating the steps of the irreversible algorithm.

**Rop** Short for *radian-op*, a unit of computational work equal to Planck's reduced constant  $\hbar$ . Equal to  $1/\pi$  of a  $\pi$ -op (pop). An example would be the rotation of a quantum spin by an angle of 1 radian.

**RSA** Rivest, Shamir, Adleman, the abbreviation for a popular public-key cryptography algorithm whose security depends on the assumed hardness of factoring large numbers. The advent of large-scale quantum computing would falsify this assumption and permit RSA codes to be broken.

**RTD** See *resonant tunneling diode*.

**s** Abbreviation for second (the time unit).

**SI** Standard abbreviation for *Système Internationale d'Unites*, the International System of Units, adopted by the 11th General Conference on Weights and Measures (1960).

**Second law of thermodynamics** The law that entropy always increases in closed systems. The law can be proven trivially from the unitarity of quantum theory, together with von Neumann's definition of entropy for a mixed quantum state, by analyzing the effect when a quantum system evolves according to a Hamiltonian that is not precisely known or interacts with an environment whose state is not precisely known.

**Semiconductor** A semiconductor is a material in which there is (small but positive) gap (called the *bandgap*) between the highest energy levels of valence electrons that are bound to specific atoms, and the lowest energy levels of conduction electrons, electrons that are freely moving through the material. Due to the bandgap, only a small number of electrons will be free to move, and the material will not conduct electricity well. However, addition of dopants, applied fields, *etc.*, can significantly change the concentration of charge carriers in the material. The ease of manipulation of carrier concentration is what makes a semiconductor a useful material for controlling conductance in transistors. Contrast *conductor* and *insulator*.

**Sequential logic** Digital logic with feedback loops and storage capability, in which new results are produced sequentially, one at a time in definite steps, and in which a given piece of hardware is reused, in sequence, for calculating results of subsequent steps. Compare *combinational logic*.

**Shannon entropy** The appropriate definition of entropy for a situation in which not all possible states are considered equally probable. The Shannon entropy is the expected amount of information gain from learning the actual state.

**Single-electron transistor** A transistor whose conductance changes significantly upon the addition or removal of a single electron to/from its gate electrode. Can be built today.

**Space complexity** In traditional computational complexity theory, this is the machine capacity (in bits) required to perform a computation. In physical computing theory, this is seen as an inaccurate measure of the true economic cost of a computation; spacetime cost is a more accurate substitute.

**Spacetime** A volume of physical spacetime is measured as the physical volume of a region of space, integrated over an interval of time. Computational spacetime reflects the same idea, for the region of space actually utilized to perform computations or store intermediate results during a computation. It may be approximated in restricted contexts by just integrating the number of bits in use over the number of parallel update steps performed.

**Special relativity** Einstein's theory based on the principle that the speed of light is independent of the observer's velocity. It revolutionized mechanics with the discovery that space and time are interwoven with each other, and that moving objects slow down, shorten, and become more massive, and that mass itself is nothing but a bound form of energy. It predicts that nothing can go faster than light. Its predictions have been exhaustively confirmed to high accuracy by myriad experiments. It was later generalized to incorporate gravity and accelerated motion in the General Theory of Relativity.

**Speed of light** Denoted by  $c \simeq 3 \times 10^8$  m/s, the speed of light is the maximum propagation velocity of information and energy through space, as was discovered by Einstein in his theory of relativity. Computationally speaking, the speed of light is that speed at which *all* of the quantum operations taking place in a system are spatial-translation ops, which makes it clear why this speed cannot be exceeded and why nonzero rest-mass systems (which have a nonzero rate of internal ops) cannot achieve it. We should emphasize that modern quantum field theory, being entirely local, definitely and explicitly obeys the constraint that information (both classical and quantum information) can travel at most at the speed of light.

**Spent energy** The spent energy in a system is defined as the system's entropy  $S$  times the temperature  $T$  of the coolest available thermal reservoir of effectively unlimited capacity. At least  $ST$  energy must be permanently dedicated in order to remove the entropy to the reservoir (unless a cooler reservoir later becomes available). Spent energy is total energy minus free energy.

**Spin** Fundamental particles in quantum field theory have a *spin*, an inherent angular momentum whose absolute numerical value is always an integer multiple of  $\hbar/2$ . (This prediction arose from the unification of quantum theory and special relativity and was subsequently confirmed.) Spin states have an orientation; oppositely oriented spins are distinguishable, but other pairs of orientations are not. A spin can hold only 1 qubit of quantum information, and only 1 bit of classical information.

**Spintronics** Electronic technology in which electron and/or nuclear spin states (instead of or in addition to the position and momentum states of electric charges) are used to store, transmit, or process information. Magnetic storage



technology can be considered an early example of spintronics. NMR quantum computing is a more recent example. Spintronic diodes and switches are also being developed.

**Standard Model of particle physics** This is the consensus bedrock of modern physics. It treats electromagnetism and the strong and weak nuclear forces together in a single quantum field-theoretic framework. It encompasses all known fundamental particles, and all forces except for gravity. Its predictions have been verified to many decimal places. Aside from an eventual unification with general relativity, which would modify the theory's predictions only at extremely high-energy scales, there is no indication that any future developments in physics would change the Standard Model's ramifications for nanoscale engineering. In other words, the Standard Model seems to be a totally complete model so far as nanotechnology is concerned. This allows us to make confident predictions about the fundamental limits of computing based on the Standard Model.

**State** An exact configuration of a given type of physical system. States of quantum systems are identified with mathematical vectors. (See *quantum state*.)

**State space** The set of all possible states of a system.

**Statistical mechanics** Branch of mechanics dealing with the statistical behavior of large numbers of simple systems. The foundation of thermodynamics. Modern statistical mechanics is based on quantum-mechanical counting of distinguishable states and is sometimes called *quantum statistical mechanics*.

**Statistical mixture** An ensemble of systems, characterized by a probability distribution, that is, a function from states to their probability.

**Step** A *complete parallel update step* or just *step* of a quantum system or subsystem is a transformation that can be expressed as a trajectory (sequence) of quantum bit operations totaling an average amount of computational work performed of 1 pop per bit of physical information contained in the system. Physical temperature is just a measure of the rate at which steps are performed.

**Stored-program computer** A computer in which the program to be executed can be stored in the computer's memory along with the data to be manipulated.

**String Theory** A hypothetical extension of the Standard Model of particle physics in which fundamental particles of different masses are explained as different modes of vibration of tiny strings and closed loops. String Theory is not yet a complete theory that yields testable predictions, and so it has not yet been experimentally confirmed. It does, however, predict a number of surprising things such as the existence of extra "hidden" spatial dimensions. However, these are not expected to have a major bearing on the physical limits of computing beyond what we already know based on the Standard Model and general relativity.

**Strong Church's thesis** This early expectation of computer science theory claimed that any physically realizable model of computation has a time cost for all problems that is within at most a polynomially growing factor above or below the minimum time to solve the same problem on a Turing machine. However, if quantum computers can be built on arbitrarily large scales, and if no polynomial-time classical

algorithm exists for emulating them to arbitrary precision, then the strong Church's thesis is false. See also *Church's thesis*, *tight Church's thesis*.

**Structural state** The part of the noncoding physical state of a computer/device that is required to remain unchanged in order for the machine to even continue functioning as intended. For example, for a given circuit to function as intended, its wires must remain unbroken, although in practice they may actually break occasionally, due to electromigration effects, an example of state decay.

**Superposition of states** A superposition of states in a quantum system is a linear combination (with complex-valued coefficients) of those states, considered as vectors. The coefficients are normalized so that their squared magnitudes sum to 1. A superposition of states is therefore another vector and therefore is a quantum state, just as much as the states being superposed. However, a superposition of pointer states will not generally be a pointer state and thus may be subject to decay (decoherence) to a statistical mixture of pointer states upon interaction with the environment.

**Subsystem** Informally, a piece of a larger (physical) system. Often (but not always) identified with a particular region of space. May include some degrees of freedom but not others.

**Superconductor** In a superconducting material, pure electron momentum states occupy a decoherence-free subspace and therefore constitute pointer states that are immune from decoherence via ordinary modes of interaction with the environment. A current in a superconductor is therefore maintained indefinitely (with zero resistance). In the more well-understood superconductors, this occurs as a result of a pairing-up of electrons (into *Cooper pairs*) due to indirect mutually attractive interactions intermediated by phonon exchange through the material's crystal lattice.

**Syndrome** In error correction, when an error occurs, the syndrome is the information contained in the exact identity of the error (when/where/what/how it occurred). This information is entropy from the perspective of the designer of the error-correction mechanism and so must be removed from the device in question in order to free up space for desired computational purposes.

**Technology** For purposes of this chapter, a *technology* refers to a device-level technology, for example a specific fabrication process for circuits of electronic or electromechanical devices, or to another low-level physical mechanism used for communication, cooling, *etc.* Higher level design elements such as processor architecture or software algorithms also represent technology, in the broader sense of the word, but we will reserve the word for lower level technology in this chapter (the parts that are not traditionally the domain of the computer scientist).

**Technology scaling model** A part of a model of computing that describes how key characteristics of devices and systems change as the parameters of the underlying manufacturing process technology are varied, for example by scaling devices to smaller sizes, or by scaling cooling technology to effect higher or lower operating temperatures.

**Temperature** The physical temperature of any system can be interpreted as the average rate of quantum operations

per bit of physical information, that is, the average rate at which the system's quantum information is (potentially) completely updated. Usually in thermodynamics we are only interested in the temperature of an *entropic* subsystem (that is, a subsystem whose state information is all unknown); however, the temperature of the *known* information in a system (that is, of the subsystems whose state information is known) is related and also important. If the known information is transitioning at a much faster rate than is the entropy, then an increasing degree of thermal insulation of the known information from the entropy is necessary in order to prevent the entropic subsystem from becoming too hot (and causing the computer to melt).

**Tensor product** A term from vector algebra. The tensor product of two vectors of dimensionality  $d_1$  and  $d_2$  is a new vector of dimensionality  $d_1 d_2$  whose components in a given basis are obtained by pairwise multiplying components of  $d_1$  and  $d_2$ .

**Thermal energy** See  $kT$ .

**Thermal state** That part of the state of a physical system that is entirely entropy, and whose exact state under normal circumstances and intended operating temperatures is expected to fluctuate constantly and unpredictably. For example, a circuit node may be at a fairly definite average voltage level, and so its logic state (high or low) may have low entropy, but at the same time, the detailed occupancy numbers of all of the electron states within a few  $kT$ 's of the Fermi surface will be rapidly and unpredictably fluctuating, and so will constitute another, high-entropy part of the state.

**Thermal temperature** The temperature of those subsystems whose physical information happens to be entropy (*i.e.*, whose energy is heat). Thermal temperature is the traditional thermodynamic concept of temperature, but it is subsumed by the more general, modern definition of temperature given previously.

**Thermodynamically reversible** Synonym for *adiabatic* or *isentropic*. A process is thermodynamically reversible to the extent that it does not produce any new entropy, that is, to the extent that the modeler does not become increasingly uncertain about the identity of the actual state. Even though quantum physics itself is reversible, a quantum process can still be *thermodynamically* irreversible, to the extent that the state of known parts of the system become mixed up with and affected by the state of unknown parts.

**Theta**  $\Theta(f)$  is a mathematical *order-of-growth* notation denoting any function that is constrained to be within a constant factor of the given function  $f$ , for all sufficiently large inputs.

**Tight Church's thesis** This thesis (by the author) postulates that a reversible, quantum 3D mesh (Q3M) is a UMS model of computing, that is, that the minimum time cost to solve any problem in any physically realizable machine lies within a *constant* factor of the time cost in the Q3M model. See also *Church's thesis*, *strong Church's thesis*.

**Time** A quantity of physical time itself (specifically, relativistic proper time) can be defined computationally, in terms of the number of (parallel complete update) steps taken by a fixed reference subsystem (perhaps, a Planck-mass photon) over the course of a particular transformation

trajectory that is undergone by an entire system as it follows its dynamics.

**Time complexity** In traditional computational complexity theory, this is the number of update steps of the logical state of a computation. In physical computing theory, this quantity is seen as an insufficient basis for a correct engineering optimization, and we prefer to use the actual physical time cost, together with other components of true economic cost, instead. In an optimized family of adiabatic architectures, it turns out that time and number of logical steps are *not* always proportional to each other, since the optimum frequency varies with the machine capacity as well as the algorithm to be performed.

**Total energy** The total energy of all kinds in a system can be measured by weighing the mass of the system in a gravitational field and converting to energy units using  $E = mc^2$ . This includes rest mass-energy as well as thermodynamic internal energy.

**Transformation** A unary operator on a state space (or any other set), mapping states to states. The transformation corresponding to time evolution in quantum mechanics is unitary.

**Transformation trajectory** A transformation expressed as a sequence of simpler, irreducible local transformations (*e.g.*, bit operations). A *quantum logic network* is a description of transformation trajectories in a particular graphical language.

**Transistor** An electronic device that is a voltage-controlled current switch. That is, the conductance between two nodes is determined by the level of voltage (relative to some threshold) on a third *gate* node.

**Transmission gate** A circuit element buildable from parallel NFET and PFET transistors that conducts at any voltage level between logic high and low levels when turned on.

**Tunneling** Quantum mechanical phenomenon in which an electron of given energy can penetrate a potential energy barrier that would be too high for it to penetrate classically. This occurs because the inherent indistinguishability of nearby quantum states means that if a barrier is narrow enough, the electron wavefunction can have significant amplitude even on the other side of the barrier.

**Turing machine** A simple early mathematical model of computing due to Alan Turing, in which a fixed-size processor serially traverses an unbounded, one-dimensional memory. The Turing machine is a physically realistic model, but it is not universally maximally scalable.

**UMS** See *universal maximum scalability*.

**Uncompute** To *uncompute* some information that is correlated with other information is to remove the correlation, by undoing (performing in reverse) a transformation that could have computed the information to begin with. *Uncomputing* and related operations provide the *only* physically and logically reversible way to remove known information so as to return a memory cell to a standard state that can be reused for later computations. The ability to uncompute is a key capability for reversible algorithms. (However, uncomputing an old result and computing a new one can sometimes be combined in a single operation, so uncomputing *by itself* is not always strictly necessary for reversible operation.)

**Unitary transformation** A term from linear algebra. An invertible, length-preserving linear transformation of a vector space. All quantum systems evolve over time via a unitary transformation  $U = \exp(iHt/\hbar)$  of their state vector in each unit of time  $t$ , where  $i^2 = -1$ ,  $H$  is the system's Hamiltonian, and  $\hbar$  is Planck's reduced constant.

**Universal** A model of computation is called *universal* if it can emulate any Turing machine, given sufficient resources.

**Universal maximal scalability (UMS)** A model of computation has this property if there is no physically realizable algorithm that is asymptotically more cost efficient (by unboundedly large factors) than all algorithms possible in a physical realization of the given model. None of the models of computation that have been traditionally studied by computer scientists in the past have this property. Nevertheless, it is a desirable property to have, from a computer engineering and algorithm-design standpoint. A reversible 3D mesh that supports quantum operations is conjectured to be a physically realistic, UMS model.

**Unstructured search** A class of problems characterized by the following general description: Given a black-box function  $f$  over some domain, and a target element  $y$ , find a value  $x$  in the domain such that  $f(x) = y$ .

**Valence band** In condensed matter theory, the valence band is the range of energies accessible to electrons that are bound to specific atoms and therefore not free to move throughout the material.

**Velocity** Computationally speaking, velocity is a dimensionless quantity whose square gives the fraction of ops taking place in a system that are devoted to the spatial translation of the system in a particular direction. There is therefore a maximum velocity for all systems of 1, which is equal to the speed of light. Only systems with zero rest mass can actually attain this speed. Of course, we all know that velocity also expresses the distance traversed per unit time.

**Virtual particles** In quantum field theories, fundamental forces are transmitted via the exchange of "virtual" particles (called such because they are not directly observed). For example, the electromagnetic force is transmitted via the exchange of virtual photons.

**VLSI** Very large scale integrated circuits. That is, monolithic chips fabricated with tens of thousands to millions of devices.

**VLSI theory** A model of computation, invented by Charles Leiserson of MIT, that is appropriate for a wide variety of VLSI design applications that focuses on concerns with circuit area and hardware efficiency. It is more suitable for engineering purposes than is traditional computational complexity theory. However, VLSI theory is still not the most comprehensive possible model, because it does not take energy costs and heat-dissipation considerations into account and also does not always account adequately for communications delays. The example model presented in this chapter removes these limitations.

**Voltage** The *voltage* between two circuit nodes or points is the electrostatic potential energy difference between those points per unit charge, for an imaginary infinitesimal test charge located at either point.

**Voltage coding** A simple physical logic coding scheme (the one used today in digital electronics) that considers all voltage states above a certain threshold to represent a logic 1, and all voltage states below a certain threshold to represent a logic 0. However, many other coding schemes are possible (e.g., using superconducting current states, or electron spin states).

**von Neumann entropy** The appropriate definition of entropy for an uncertain quantum state, or mixed state. It is equal to the Shannon entropy of the mixed state when expressed in the diagonalized basis, as a statistical mixture of orthogonal pure states.

**von Neumann machine** A simple computer architecture often attributed to von Neumann, consisting of a single fixed-capacity serial processor that accesses an external memory of arbitrary capacity. Closely related to the RAM machine model of computation.

**Watt** A unit of power (rate of energy transfer) equal to 1 Joule per second.

**Wavefunction** A particular quantum state can be identified with a function that maps all state vectors to the corresponding complex number that arises when the given state vector is combined by a dot product with the state vector of the particular state in question. This function is called the state's *wavefunction*. The wave has nonzero amplitude for most states (all except the ones that are orthogonal to the particular state). It is a consequence of this wave aspect of quantum mechanics that states can never be totally localized with infinite precision; any system of finite size and energy can have only a certain finite number of distinguishable states, corresponding to different normal modes of vibration of the given wave [15, 16] up to the maximum energy.

**Wave packet** A wavefunction whose magnitude approaches zero for all position states outside of a given region of space. A system whose position is localized is in a wave packet state.

**Zetta** SI unit prefix meaning  $10^{21}$ .

## REFERENCES

1. J. E. Savage, "Models of Computation: Exploring the Power of Computing." Addison-Wesley, Reading, MA, 1998.
2. C. H. Bennett, *Int. J. Theoret. Phys.* 21, 905 (1982).
3. M. A. Nielsen and I. L. Chuang, "Quantum Computation and Quantum Information." Cambridge Univ. Press, Cambridge, UK, 2000.
4. M. P. Frank, Reversibility for Efficient Computing, manuscript based on Ph.D. thesis, MIT, 1999.
5. M. P. Frank, Nanocomputer systems Engineering, in "Technical Proceedings of the 2003 Nanotechnology Conference and Trade Show," 2003.
6. Semiconductor Industry Association, "International Technology Roadmap for Semiconductors," 2002 Update.
7. B. Doyle et al., *Intel Technol. J.* 6, 42 (2002).
8. B. Doris et al., Extreme scaling with ultra-thin silicon channel MOSFET's (XFET), in "2002 IEEE International Electron Devices Meeting," San Francisco, 9–11 December 2002.
9. B. Yu et al., FinFET scaling to 10nm gate length, in "2002 IEEE International Electron Devices Meeting," San Francisco, 9–11 December 2002.
10. V. Derycke et al., *Nano Lett.* 1, 453 (2001).

11. Yu Huang et al., *Science* 294, 1313 (2001).
12. F. Preparata and G. Bilardi, in "25th Anniversary of INRIA 1992," pp. 155–174.
13. B. Greene, "The Elegant Universe: Superstrings, Hidden Dimensions, and the Quest for the Ultimate Theory." Norton, New York, 1999.
14. L. Smolin, "Three Roads to Quantum Gravity," Basic Books, New York, 2002. For a more recent and more technical introduction, also see L. Smolin, Quantum gravity with a positive cosmological constant, ArXiv.org preprint hep-th/0209079, 2002.
15. W. Smith, Fundamental Physical Limits on Computation, NECI Technical Report, May 1995.
16. S. Lloyd, *Nature* 406, 1047 (2000).
17. P. Vitányi, *SIAM J. Comput.* 17, 659 (1988).
18. N. Margolus and L. Levitin, *Physica D* 120, 188 (1998).
19. R. Landauer, *IBM J. Res. Devel.* 5, 183 (1961).
20. M. Frank and T. Knight, *Nanotechnology* 9, 162 (1998).
21. M. Frank, Realistic Cost-Efficiency Advantages for Reversible Computing in Coming Decades, UF Reversible Computing Project Memo #M16, <http://www.cise.ufl.edu/research/revcomp/memos/Memo16-three-d.doc>, 2002.
22. M. Frank, The Adiabatic Principle: A Generalized Derivation, UF Reversible Computing Project Memo #M14, [http://www.cise.ufl.edu/research/revcomp/memos/M14\\_adiaprinc.ps](http://www.cise.ufl.edu/research/revcomp/memos/M14_adiaprinc.ps), 2001.
23. F. Thomson Leighton, "Introduction to Parallel Algorithms and Architectures: Arrays · Trees · Hypercubes." Morgan Kaufmann, San Mateo, CA, 1992.
24. M. P. Frank, *Nanocomputer Systems Engineering*, CRC Press, 2004 (in preparation). <http://www.cise.ufl.edu/research/revcomp/memos/Memo17-PhysComp.doc>, 2002.
25. W. Heisenberg, "The Physical Principles of the Quantum Theory." Dover, New York, 1949.
26. L. Boltzmann, *Wiener Berichte* 2, 373 (1877).
27. J. Barbour, "The End of Time: The Next Revolution in Physics." Oxford Univ. Press, London, 1999.
28. S. Lloyd, *Phys. Rev. Lett.* 88, 237901 (2002).
29. C. H. Papadimitriou, "Computational Complexity." Addison-Wesley, Reading, MA, 1994.
30. C. Leiserson, "Area-Efficient VLSI Computation." MIT Press, Cambridge, MA, 1983.
31. A. M. Turing, *Proc. London Math. Soc. Ser. 2* 42, 230/43, 544 (1936/1937).
32. J. C. Shepherdson and H. E. Sturgis, *J. ACM* 10, 217 (1963).
33. J. von Neumann, "Theory of Self-Reproducing Automata." Univ. of Illinois Press, Champaign, 1966. [This is a posthumous collection of earlier work.]
34. E. F. Fredkin and T. Toffoli, *Int. J. Theoret. Phys.* 21, 219 (1982).
35. D. Deutsch, *Proc. Roy. Soc. London Ser. A* 425, 73 (1989).
36. P. van Emde Boas, in "Handbook of Theoretical Computer Science" (J. van Leeuwen, Ed.), pp. 1–66. Elsevier, Amsterdam, 1990.
37. J. Hennessy and D. Patterson, "Computer Architecture: A Quantitative Approach," 3rd ed. Morgan Kaufmann, San Mateo, CA, 2002.
38. C. H. Bennett, *IBM J. Res. Devel.* 17, 525 (1973).
39. J. E. Avron and A. Elgart, *Commun. Math. Phys.* 203, 445 (1999).
40. R. C. Merkle and K. E. Drexler, *Nanotechnology* 7, 325 (1996).
41. C. S. Lent and P. D. Tougaw, *Proc. IEEE* 85, 541 (1997).
42. S. G. Younis and T. F. Knight, Jr., in "International Workshop on Low Power Design", pp. 177–182 (1994).
43. K. E. Drexler, "Nanosystems." Wiley, New York, 1992.
44. K. K. Likharev, *Int. J. Theoret. Phys.* 21, 311 (1982).
45. R. C. Merkle, *Nanotechnology* 4, 114 (1993).
46. J. Storrs Hall, An electroid switching model for reversible computer architectures, in "PhysComp '92: Proceedings of the Workshop on Physics and Computation," 2–4 October 1992, Dallas, TX. IEEE Computer Society Press, Los Alamitos, CA, 1992. Also in "Proceedings ICCI '92, 4th International Conference on Computing and Information," 1992.
47. K. E. Drexler, in "Molecular Electronic Devices" (F. L. Carter et al., Eds.), pp. 39–56. Elsevier, New York, 1988.
48. R. Feynman, *Opt. News* 11 (1985). Also in *Foundations Phys.* 16, 507 (1986).
49. N. H. Margolus, Parallel quantum computation, in "Complexity, Entropy, and the Physics of Information" (W. Zurek, Ed.). 1990.
50. "Maxwell's Demon: Entropy, Information, Computing" (H. S. Leff and A. F. Rex, Eds.). American Int. Distribution, 1990.
51. Y. Lecerf, *C. R. Acad. Sci.* 257, 2597 (1963).
52. K.-J. Lange, P. McKenzie, and A. Tapp, in "Proceedings of the 12th Annual IEEE Conference on Computational Complexity (CCC '97)," pp. 45–50, 1997.
53. M. Sipser, *Theoret. Comput. Sci.* 10, 335 (1980).
54. C. H. Bennett, *SIAM J. Comput.* 18, 766 (1989).
55. Ryan Williams, Space-Efficient Reversible Simulations, CMU, [http://www.cs.cmu.edu/~ryanw/spacesim9\\_22.pdf](http://www.cs.cmu.edu/~ryanw/spacesim9_22.pdf), 2000.
56. H. Buhrman, J. Tromp, and P. Vitányi, Time and space bounds for reversible simulation, in "Proceedings of the International Conference on Automata, Languages, and Programming," 2001.
57. M. P. Frank and M. J. Ammer, Relativized Separation of Reversible and Irreversible Space-Time Complexity Classes, UF Reversible Computing Project Memo M6, [http://www.cise.ufl.edu/~mpf/rc/memos/M06\\_oracle.html](http://www.cise.ufl.edu/~mpf/rc/memos/M06_oracle.html), 1997.
58. M. P. Frank, Cost-Efficiency of Adiabatic Computing with Leakage and Algorithmic Overheads, UF Reversible Computing Project Memo M15, <http://www.cise.ufl.edu/research/revcomp/memos/Memo15-newalg.ps>, 2002.
59. M. P. Frank et al., in "Unconventional Models of Computation," (Calude, Casti, and Dineen, Eds.) pp. 183–200. Springer, New York, 1998.
60. C. J. Vieri, Reversible Computer Engineering and Architecture, Ph.D. thesis, MIT, 1999.
61. P. W. Shor, Algorithms for quantum computation: Discrete log and factoring, in "Proc. of the 35th Annual Symposium on Foundations of Computer Science," pp. 124–134. IEEE Computer Society Press, New York, 1994.
62. S. Lloyd, *Science*, 273, 1073 (1996).
63. R. L. Rivest, A. Shamir, and L. A. Adleman, *Commun. ACM* 21, 120 (1978).
64. R. Feynman, *Int. J. Theoret. Phys.* 21, 467 (1982).
65. L. Grover, in "Proceedings of the 28th Annual ACM Symposium on the Theory of Computing (STOC)," pp. 212–219, 1996.
66. V. Giovannetti et al., Quantum Limits to Dynamical Evolution, ArXiv.org preprint quant-ph/0210197, 2002.
67. C. H. Bennett et al., *SIAM J. Comput.* 26, 1510 (1997).
68. E. Bernstein and U. V. Vazirani, in "25th ACM Symposium on the Theory of Computing," pp. 11–20, 1993.
69. A. M. Steane, Overhead and Noise Threshold of Fault-Tolerant Quantum Error Correction, ArXiv.org preprint quant-ph/0207119, 2002.
70. D. Cory et al., *Proc. Nat. Acad. Sci.* 94, 1634 (1997).
71. M. Friesen et al., Practical Design and Simulation of Silicon-Based Quantum Dot Qubits, ArXiv.org preprint cond-mat/0208021, 2002.
72. J. E. Mooij et al., *Science* 285, 1036 (1999).
73. J. I. Cirac and P. Zoller, *Phys. Rev. Lett.* 74, 4091 (1995).
74. A. Barenco et al., *Phys. Rev. A* 52, 3457 (1995).
75. P. Zanardi and M. Rasetti, *Phys. Rev. Lett.* 79, 3306 (1998).
76. W. H. Zurek, Decoherence, Einselection, and the Quantum Origins of the Classical, ArXiv.org preprint quant-ph/0105127, 2002.
77. M. P. Frank, Scaling of Energy Efficiency with Decoherence Rate in Closed, Self-Timed Reversible Computing, UF Reversible Computing Project Memo M18, <http://www.cise.ufl.edu/research/revcomp/memos/Memo18-Timing.doc>, 2002.

78. A. Ressler, The Design of a Conservative Logic Computer and a Graphical Editor Simulator, MIT Master's Thesis, 1981.
79. J. Storrs Hall, in "PhysComp '94: Proceedings of the Workshop on Physics and Computation," 17–20 November 1994, Dallas, TX, pp. 128–134. IEEE Computer Society Press, Los Alamitos, CA, 1994.
80. S. Goldstein and M. Budiú, NanoFabrics: Spatial computing using molecular electronics, in "28th Annual International Symposium on Computer Architecture (ISCA'01)," June 2001.
81. L. Durbeck and N. Macias, *Nanotechnology* 12, 217 (2001).
82. M. P. Frank, Computer Architecture Principles, course lecture slides, <http://www.cise.ufl.edu/class/cda5155fa02/>, 2002.
83. D. B. Skillicorn, Parallelism and the Bird–Meertens Formalism, Dept. of Computing and Information Science, Queen's University, Kingston, Canada, <http://citeseer.nj.nec.com/skillicorn92parallelism.html>, 1992.
84. C. Lutz and H. Derby, Janus: A Time-Reversible Language, CalTech class project, <http://www.cise.ufl.edu/~mpf/rc/janus.html>, 1982.
85. H. Baker, NREVERSAL of fortune—the thermodynamics of garbage collection, in "Proceedings of the International Workshop on Memory Management," St. Malo, France, 1992. Also in Lecture Notes in Computer Science, Vol. 637, New York, Springer, 1992.
86. S. Bettelli et al., Toward an Architecture for Quantum Programming, IRST technical report 0103-010, 2001.
87. B. Ömer, A Procedural Formalism for Quantum Computing, Master's Thesis, Dept. of Theoretical Physics, Technical University of Vienna, 1998.
88. B. Ömer, QCL—A Programming Language for Quantum Computers, Master's Thesis, Institute of Information Systems, Technical University of Vienna, 2000.
89. J. W. Sanders and P. Zuliani, Quantum Programming, TR-5-99, Programming Research Group, OUCL, Oxford, 1999.
90. P. Selinger, Towards a Quantum Programming Language, Dept. of Mathematics, University of Ottawa, 2002.
91. G. Baker, "Qgol": A System for Simulating Quantum Computations: Theory, Implementation and Insights, Honors Thesis, Macquarie University, 1996.
92. R. L. Wieginton, *Proc. IRE* 47, 516 (1961).
93. P. Shor, *Phys. Rev. A* 52, 2493 (1995).
94. D. Frank, *IBM J. Res. Dev.* 46, 235 (2002).
95. J. M. Rabaey, "Digital Integrated Circuits: A Design Perspective." Prentice Hall, New York, 1995.
96. R. Chau, 30nm and 20nm physical gate length CMOS transistors, in "Silicon Nanoelectronics Workshop," 2001.
97. B. Doris et al., Extreme scaling with ultra-thin silicon channel MOSFET's (XFET), in "2003 International Electron Devices Meeting (IEDM)," San Francisco, 9–11 December 2002.
98. Y. Huang et al., *Science* 294, 9 (2001).
99. V. Derycke et al., *Nano Lett.* 1, 9 (2001); A. Bachtold et al., *Science* 294, 9 (2001).
100. T. Yamada, Doping scheme of semiconducting atomic chain, in "Fifth Foresight Conference on Molecular Nanotechnology," Palo Alto, CA, 5–8 November 1997.
101. R. Eisberg and R. Resnick, "Quantum Physics of Atoms, Molecules, Solids, Nuclei, and Particles," 2nd ed. Wiley, New York, 1985.
102. S. Das Sarma, *Am. Sci. Nov.–Dec.* (2001).
103. D. Goldhaber-Gordon et al., *Proc. IEEE* (1997).
104. J. Park et al., *Nature* 417, 6890 (2002).
105. G. L. Snider et al., *J. Appl. Phys.* 85, 4283 (1999).
106. C. P. Collier et al., *Science* 285, 391 (1999).
107. K. K. Likharev, Rapid Single-Flux-Quantum Logic, Dept. of Physics, State University of New York, <http://pavel.physics.sunysb.edu/RSFQ/Research/WhatIs/rsfqre2m.html>, 1992
108. T. van Duzer and C. W. Turner, "Principles of Superconductive Devices and Circuits," 2nd ed. Prentice Hall, New York, 1999.
109. Z. K. Tang et al., *Science* 292, 2462 (2001).
110. S. Datta and B. Das, *Appl. Phys. Lett.* 56, 665 (1990).
111. M. Johnson, *IEEE Spectrum* 31, 47 (1994).
112. M. D'Angelo et al., *Phys. Rev. Lett.* 87, (2001).
113. G. He and S. Liu, "Physics of Nonlinear Optics." World Scientific, Singapore, 2000.
114. M. Frank, *Comput. Sci. Eng.* 4, 16 (2002).
115. M. Frank, Cyclic Mixture Mutagenesis for DNA-Based Computing, Ph.D. Thesis proposal, MIT, <http://www.cise.ufl.edu/~mpf/DNAprop/phd-proposal.html>, 1995.
116. T. F. Knight, Jr. and G. J. Sussman, Cellular Gate Technology, MIT AI Lab, <http://www.ai.mit.edu/people/tk/ce/cellgates.ps>, 1997.
117. R. Kurzweil, "The Age of Spiritual Machines: When Computers Exceed Human Intelligence." Penguin, Baltimore, 2000.
118. S. W. Hawking, *Commun. Math. Phys.* 43, 199 (1975).
119. J. D. Bekenstein and A. Mayo, *Gen. Rel. Grav.* 33, 2095 (2001).
120. F. J. Dyson, *Rev. Modern Phys.* 51, 447 (1979).
121. L. M. Krauss and G. D. Starkman, *Astrophys. J.* 531, 22 (2000).
122. T. Toffoli and N. Margolus, "Cellular Automata Machines: A New Environment for Modeling." MIT Press, Cambridge, MA, 1987.

# Nanocontainers

Samantha M. Benito, Marc Sauer

*Universität Basel, Klingelbergstrasse, Basel, Switzerland*

Wolfgang Meier

*Universität Basel, Klingelbergstrasse, Basel, Switzerland, and  
International University of Bremen, Bremen, Germany*

## CONTENTS

1. Introduction
  2. Natural Nanocontainers
  3. Nanocontainers Formed by Self-Assembly
  4. Template-Directed Preparation of Nanocontainers
  5. Nanocontainers Prepared by Emulsion/Suspension Polymerization
  6. Dendrimer Nanocontainers
- Glossary  
References

## 1. INTRODUCTION

Design and synthesis of materials with micrometer (microscopic) and nanometer dimensions (mesoscopic) with well-defined structures in the sub-micrometer region have attracted increasing interest recently. The idea in this context is to tailor the composition, structure, and function of materials with control at the nanometer level, which may lead to new properties for well-known standard materials and hence to new applications. In addition, increasing progress has been attained in the last decade in nanostructured materials using block copolymers.

The amount of research on this area is at constant growth, which makes a comprehensive or exhaustive review almost impossible; therefore, we intend here to give mainly the outlines of the field and some interesting illustrative examples.

In the following we will focus on nanometer-sized hollow spheres, or so-called nanocontainers. Such particles produce great interest due to their potential for encapsulation of large quantities of guest molecules or large-sized guests within their empty core domain. They can be useful for applications in areas such as biological chemistry, synthesis, or catalysis. In this context monodispersity of the capsule's

size, stability of the particle, and permeability of the shell are key parameters in order to obtain materials with enhanced performance.

Nature itself uses similar and very effective nanocontainers like micelles, vesicles, and viruses in biological systems, for example, for transport and delivery of sensitive compounds such as hormones or DNA [1]. However, these highly functionalized assemblies of proteins, nucleic acids, and other (macro)molecules perform very complicated tasks that are still too complex to be completely understood. Although the particles are perfectly designed to fulfill their tasks in biological environment after millions of years of evolution, their direct use in many technical applications is often not feasible. In many cases this is due to the non-covalent interactions responsible for their formation and hence their limited stability. This leads, for example, to a rapid clearance of conventional lipid vesicles (liposomes) from the blood after their intravasal administration [2]. Many applications require, however, more stable particles. Therefore, a great effort has been devoted within the last years to prepare size- and shape-persistent nanocontainers and up to now a huge variety of different techniques has been described, each of them having its special advantages and of course also disadvantages. This chapter is divided into different subsections according to the different approaches that are commonly used to attain the desired particle morphology. This division is somewhat arbitrary, especially since a certain overlap between the different methods exists. However, the first part of the chapter gives a short introduction to natural nanocontainers, which, besides their limited technical applicability, are of major importance for the understanding of natural processes. Although they are naturally occurring substances, the use of lipids and liposomes will be considered together with polymer amphiphiles since both share analogous characteristics such as self-organization. The following three sections describe approaches in which mainly non-covalent interactions (i.e., van der Waals, electrostatic, or hydrophobic interactions) are used to imprint the characteristic shape



onto the resulting particles. Once obtained, though, these self-assembled superstructures based on the aforementioned non-covalent interactions can be further stabilized by cross linking, thus obtaining shape-persistent particles. The last section deals with single polymers that have, by design of their architecture, intrinsic hollow-sphere morphology in the nanometer range.

## 2. NATURAL NANOCONTAINERS

Although many naturally available nanocontainers are not suited for technical applications, much interesting research work has been published within the last years that describes the use of various natural systems in nanomaterial science [3].

Especially in the field of biomineralization a significant progress has been made with so-called bio-nanoreactors [4–7]. Among the different types of possible mineralization vessels, ferritin is probably the most intensively studied and best understood [8]. Nature uses ferritin as a storage device for iron, where it is encapsulated as hydrated iron (III) oxide within a multisubunit protein shell. After the iron has been removed from inside the protein shell, the remaining cavity has been successfully used to generate various nanometer-sized inorganic particles, such as, for example, manganese oxide or uranyl oxyhydroxide crystals [9].

Virus particles are another type of biological structures that can be applied as a template for biomineralization processes, like the tobacco mosaic virus (TMV) or the cowpea chlorotic mottle virus (CCMV). As indicated in Figure 1, several routes were explored for the synthesis of nanotubes composites that use TMV templates [10].

The spherical protein cage of the CCMV shows a completely reversible pH-induced swelling transition of approximately 10%, in case it is incubated in media of a pH value above 6.5 (Fig. 2) [11]. During this swelling, gated pores are opened along the viral shell that allow a free molecular exchange between the viruses interior and the surrounding bulk medium. In contrast, no exchange of larger molecules occurs at pH values lower than 6.5. This property has successfully been used for controlled host-guest encapsulation

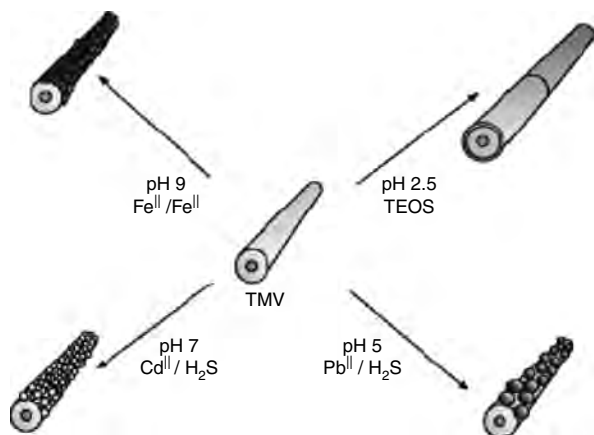


**Figure 1.** Synthesis of nanotubes composites by using TMV templates. (TEOS = tetraethoxysilane.) Reprinted with permission from [10], W. Shenton et al., *Adv. Mater.* 11, 253 (1999). © 1999, Wiley-VCH.

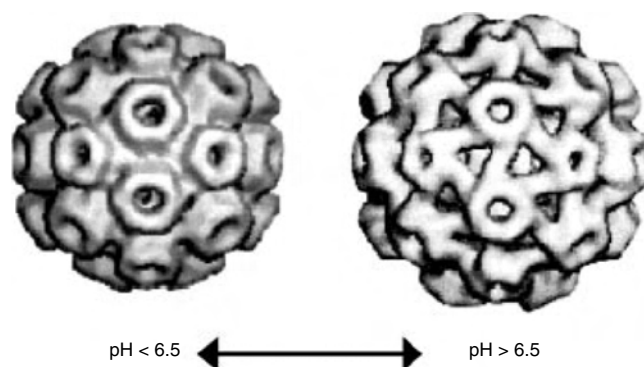


**Figure 2.** Cryoelectron microscopy and image reconstitution of the Cowpea chlorotic mottle virus (CCMV). Contracted structure at low pH values (left) and swollen structure at high pH values (right). Swelling results in the formation of 60 pores with a diameter of 2 nm. Reprinted with permission from [11], T. Douglas and M. Young, *Nature* 393, 152 (1998). © 1998, Macmillan Magazines Ltd.

and crystal growth of inorganic and organic materials within such virus [12].

These examples demonstrate clearly that biological nanocontainers are well suited for the formation of new materials. However, in addition to their low mechanical stability, it seems that their major drawbacks are the isolation and handling of larger quantities of such bioreactors.

## 3. NANOCONTAINERS FORMED BY SELF-ASSEMBLY

### 3.1. Lipids

Due to their amphiphilic nature and molecular geometry, lipid molecules can aggregate in dilute aqueous solution into different morphologies, depending on many factors such as the molecular shape of the lipid, concentration, and temperature. Particularly spherical morphologies, micelles and vesicles, have attracted considerable interest in the scientific community. Micelles consist of aggregates in which the nonpolar chains of the lipid form a core surrounded by their polar heads [2]. In case of micellar structures in aqueous solutions, the inner core represents a hydrophobic domain capable of solubilizing hydrophobic substances. This solubilization of sparingly soluble substances is widely used, for example, in drug delivery [13, 14]. However, we will not discuss this here in detail.

Spherically closed lipid bilayer structures enclosing an aqueous compartment are called vesicles or liposomes [2]. Here we reserve the term vesicle for polymer vesicular structures, while vesicles constituted from lipids are preferably referred to as liposomes. Owing to their similarity to the cell membrane, liposomes are widely employed as models and mimetic systems for biological membranes [15]. The aqueous volume entrapped within the liposome can serve as a reservoir for sensitive water-soluble compounds, protecting them from hostile environments. Enzymes, for instance, have been long protected by this procedure [16]. To make use of the catalytic activity, either the enzyme has to be released from the protecting vessel in order to enter into

contact with the substrates in the surrounding milieu, or the substrates have to permeate the membranes to be able to undergo the reactions catalyzed by such enzymes in the interior of the vesicular structure. Since the membrane acts as a diffusion barrier for the substrates, this usually decreases the turnover of the enzyme.

A great deal of research has been devoted to the use of liposomes as drug carriers; it is not the intention to cover this area here in detail. The interested reader may consult some recent reviews [17–20]. The main disadvantage of liposomes is their inherent instability to both mechanical and environmental changes [19, 20]. One strategy to overcome this is to polymerize the constituent lipids within the membrane, thus producing robust entities. However, stabilizing the structure usually renders a decrease in its permeability, which is also a crucial parameter in the context of drug delivery [19]. Thus ways have to be found to overcome this.

Lipid vesicles can be regarded as spherical capsules comprising a shell of the lipid bilayer and an aqueous core. Hence, it is straightforward to use them as precursors for the preparation of size- and shape-persistent nanocontainers. This can be achieved using different concepts. Figure 3 gives an overview of various methods. For example, lipids that are functionalized with polymerizable groups can be polymerized within such vesicular structures. As a result of the polymerization reaction, the individual lipid molecules are interconnected via covalent bonds, which stabilizes considerably the liposome membrane [21, 22]. In some sense the polymerized lipids can be regarded to mimic the role of the cytoskeleton or of the murein network (i.e., the polymer structures which Nature uses to stabilize biological cell membranes) [23]. In contrast to these natural polymer scaffolds that are simply attached to the lipid membrane via

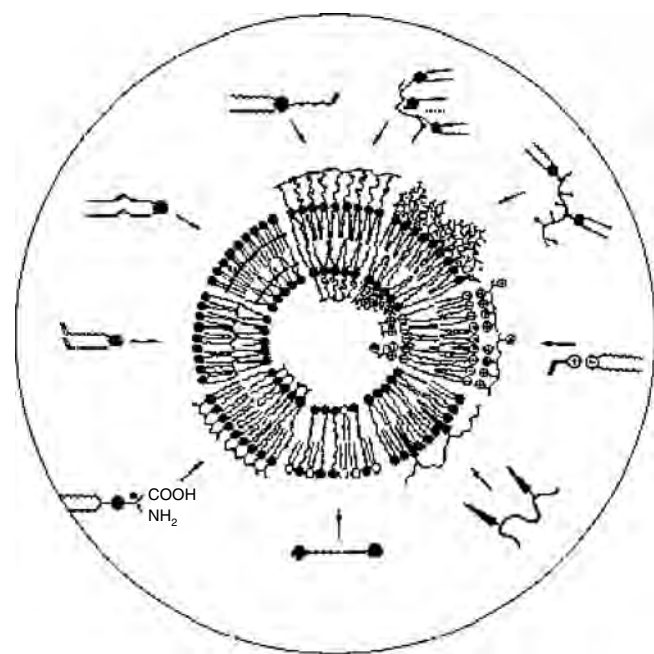


**Figure 3.** Schematic representation of the different possibilities for stabilizing lipid vesicles. Reprinted with permission from [21], H. Ringsdorf et al., *Angew. Chemie* 100, 117 (1988). © 1988, Wiley-VCH.

hydrophobic interactions, the polymerized lipids are, however, all covalently connected to each other. Cross-linking converts the structures held together solely by van der Waals forces into covalently bonded macromolecules. As a result of this procedure, a considerable obstruction of the lipid lateral mobility within the membrane is observed, leading to a reduced permeability of encapsulated substances [22].

Interestingly, the polymerization of reactive lipids in bilayers formed from mixtures of different lipids may induce phase separation phenomena within the membranes. This can be exploited to produce labile domains in a controlled manner in the shell of the polymerized vesicles. These domains can be plugged or unplugged using external stimuli, which renders such particles suitable for applications in the area of controlled or triggered release. Since the pioneering studies on polymerized vesicles derived in the late 1970s and early 1980s, this area has developed into a broad and active field of research. A detailed discussion of all its different aspects would lead too far here, all the more since several recommendable reviews and books have already appeared on this topic, to which the interested reader may refer [21, 22, 24, 25].

Even though liposomes are biocompatible and biodegradable materials and structurally and chemically closely related to cell membranes, they are recognized as foreign bodies in living systems. This recognition by the reticuloendothelial system (RES) accounts for their low circulation times after parenteral administration [2].

One important milestone in the development of liposome and liposome-related structures was the discovery of so-called stealth liposomes [26, 27]. These particles are ignored by the reticuloendothelial system and, hence, they show prolonged circulation times [28, 29]. Additionally, they are more stable towards oxidation, enzyme degradation, and reaction with plasma lipoproteins [2]. The stealth liposomes comprise “pegylated” lipids, that is, lipids covalently attached to poly(ethylene glycol) (PEG) chains [30]. This external brush of hydrophilic polymer chains at the surface of the lipid bilayer shields them from the recognition by opsonins and plasma lipoproteins. Additionally, the hydrophilic coating of the surface of the liposomes produces a steric repulsion towards adhesion to other surfaces (e.g., opsonins). In contrast to adsorbed polymers on liposomes, which also yield certain steric stabilization, the sterically stabilized liposomes are covalently bonded, thus increasing, for instance, the stability towards dilution. By the conjugation of lipids with polymers one obtains not only a more stable structure but also a very versatile system, that can easily be modified at its outer surface; that is, the system can be decorated with antibodies, receptors, and ligands, by using heterobifunctional PEG [26, 27]. A comprehensive collection of papers dealing with the theory and applications of liposome steric stabilization can be found in [26].

Recently an interesting application-relevant approach has been presented to release encapsulated material from liposomes under controlled conditions. Using a synthetic triple-chain amphiphile to produce stable vesicles, pH-influenced release of encapsulated substrates was achieved. The artificial lipid used carried carboxylic end-groups. Interestingly, less than 10% of the encapsulated water-soluble probe was

released at pH 7.5 over a year of storage. However, by lowering the pH to 3.5, the vesicles were disrupted, thus expelling their content into the surrounding medium [31].

Functional materials with enhanced properties can be obtained by properly combining different starting materials. Composite materials are a good example of this approach. For example, by inserting Prussian blue, a well-known ferromagnet at low temperatures, into a bilayer of photoresponsive azobenzene containing vesicles, a very interesting kind of composite is obtained. The magnetic properties of such composites can be triggered by photoillumination. Upon irradiation the azobenzene-containing vesicles undergo a cis-trans photoisomerization. This in turn has an effect on the electrostatic interactions between the incorporated Prussian blue and the lipid membrane, thus providing a tunable system [32].

### 3.2. Nanocontainers from Amphiphilic Block Copolymers

Similarly to lipids, also synthetic amphiphilic block copolymers may form superstructures, like vesicles, in aqueous media [33–43].

The most simple block copolymer architecture consists of a sequence of repetitive units of the homopolymer A tethered to a sequence of repetitive units of homopolymer B. However, also more sophisticated polymer architectures are accessible, such as, for instance, triblock, multiblock, graft, and star copolymers, and combinations thereof.

The characteristic molecular design of amphiphilic block copolymers consists of a minimum of two blocks of different chemical composition connected one to the other through a covalent bond. A good review of the synthetic pathways for the production of amphiphilic block copolymers can be found in [44, 45].

Block copolymers consisting of blocks with different solubility, that is, amphiphilic block copolymers, exhibit self-assembly behavior in solution. Within the self-assembled superstructures, the insoluble blocks are shielded as far as possible by the soluble ones from the surrounding solvent. Depending on block length ratio, the hydrophilic-to-lipophilic balance (HLB), concentration, temperature, preparation method, etc., different morphologies can be observed in solution.

Generally, the morphology of their self-assembled superstructures can be regarded as core-shell micellar structures in which the core and the shell consist of the insoluble block and the soluble one, respectively. It has been observed [34, 40] that in aqueous solutions, decreasing the relative length of the hydrophilic block leads to a transition from spherical (micelles) to cylindrical (rods) and later to lamellar (vesicular) structures.

Generally, the self-assembly of amphiphilic block copolymers follows the same principles as that of low-molecular-weight amphiphiles. However, block copolymer aggregates and particularly vesicles may be significantly more stable than those formed from conventional lipids due to the larger size and the slower dynamics of the underlying polymer molecules [46].

In contrast to lipid bilayers, the longer underlying polymeric chains with higher conformational freedom of

polymeric membranes gives the latter not only increased toughness, elasticity, and mechanical stability but also a considerably rather low permeability [46].

An excellent and very recent review on the field of polymeric vesicles can be found in [47].

Nanocontainers based on block copolymer vesicles possess great potential in a broad area of applications, such as controlled release systems [48–54], confined nanometer-sized reaction vessels, or templates for the design of new materials. In this context it is particularly interesting that the physical properties of their polymer shells can be controlled to a large extent by the block length ratio or the chemical constitution of the underlying polymer molecules [34, 45]. Furthermore, synthetic polymers provide a wide spectrum of alternatives to design materials with responsive behavior towards external stimuli.

Similarly to conventional lipid self-assembled morphologies, block copolymer vesicles are held together solely by non-covalent interactions. Hence they can disintegrate under certain conditions (e.g., dilution or presence of detergent) and dissolve as individual block copolymer molecules. It is obvious that, analogous to the reactive lipids, also block copolymer molecules could be modified with polymerizable groups. A subsequent polymerization of the resulting “macromonomers” interconnects them via covalent bonds, which stabilizes the whole particle.

Up to now, however, only a few papers dealing with such particles have appeared. In one reported case, using a diblock copolymer consisting of poly(1,2-butadiene)-*b*-poly(ethylene oxide), vesicular structures were locked in by  $\gamma$ -irradiation in aqueous solutions. The resulting cross-linked vesicles could be dispersed in solvents that are good for both blocks, without losing the fixed vesicular structure [39].

In another paper, the formation of vesicles from a poly(isoprene)-*b*-poly(2-cinnamoyl methacrylate) (PI-PCEMA) diblock copolymer in hexane-tetrahydrofuran mixtures has been exploited as a starting point [55]. Converting these vesicles into stable, water-soluble polymer nanocapsules requires, however, a rather costly procedure. The PCEMA blocks were photocross-linked and then, in a second step, the PI blocks had to be hydroxylated to make these hollow nanospheres water-soluble. The radii of the nanocapsules were about 50 to 60 nm and changed only very slightly during these conversions. After loading the nanocontainers with Rhodamine B, the dye could be quantitatively released in water and water-ethanol mixtures in a way that the release rate could be tuned by the composition of the water-ethanol mixtures. Ethanol seems to be a good solvent for the underlying block copolymers. Hence higher ethanol content in the solvent mixture increases the solvent quality and the cross-linked shell of the cross-linked particles swells increasingly. As a result, the shell permeability increases and release of the dye becomes faster. This feature makes such systems attractive for applications, since prefabricated particles can be loaded effectively in an organic solvent and subsequently the encapsulated material slowly released in water.

In a similar approach, a rather simple one-step procedure has been used to prepare vesicular structures from

poly(2-methyloxazoline)-*b*-poly(dimethylsiloxane)-*b*-poly(2-methyl-oxazoline) (PMOXA-PDMS-PMOXA) triblock copolymers directly in aqueous solution. One remarkable characteristic of this type of triblock copolymers, in contrast to diblock copolymers, is that the resulting vesicles are composed of a single layer of polymer instead of a bilayer. The size of the resulting vesicles could be controlled from 50 nm to 100  $\mu\text{m}$  [33]. The underlying triblock copolymers were modified with polymerizable methacrylate end-groups without changing their aggregation behavior in water. These “macromonomers” were polymerized within the vesicles using a UV-induced free-radical polymerization, which did not lead to any measurable changes in size, size distribution, or even molecular weight of the particles [33]. Obviously the polymer chain reaction occurs mainly intravesicularly. Intervesicle reactions such as exchange of individual triblock copolymer molecules or a chain propagation reaction involving more than one vesicular aggregate play only a minor role on the time scale of the experiment.

The covalently cross-linked polymer network structures result in particles that possess solid-state properties such as shape persistence. Therefore they are able to preserve their hollow-sphere morphology even after their isolation from the aqueous solution and redispersion in an organic solvent, such as chloroform, tetrahydrofuran, or ethanol. This is documented in Figure 4, which shows a transmission electron micrograph of polymerized triblock copolymer vesicles isolated from water and redispersed in ethanol. Ethanol is a good solvent for the whole underlying block copolymer molecule. Hence, nonpolymerized vesicles would immediately disintegrate under such conditions into singly dissolved polymer molecules. In contrast to their fluid-like, nonpolymerized precursors, a shear deformation of the polymerized vesicles may lead to cracks characteristic for solid materials [56]. This is directly demonstrated in the reflection intensity contrast micrographs of Figure 5 that show a giant polymerized triblock copolymer vesicle before and after shear-induced rupture. This shape-persistence allows the use of such vesicles as a delivery system since they can be loaded with guest molecules in an organic solvent. After isolation of the loaded polymer shells and redispersion in aqueous media, the encapsulated material can be subsequently released.

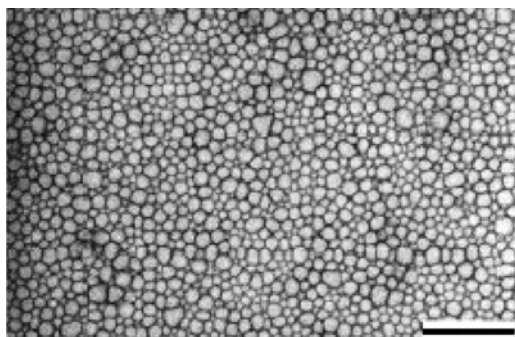


**Figure 4.** Transmission electron micrograph of polymerized ABA-triblock copolymer vesicles. The length of the bar corresponds to 1  $\mu\text{m}$ . Reprinted with permission from [33], C. Nardin et al., *Langmuir* 16, 1035 (2000). © 2000, American Chemical Society.

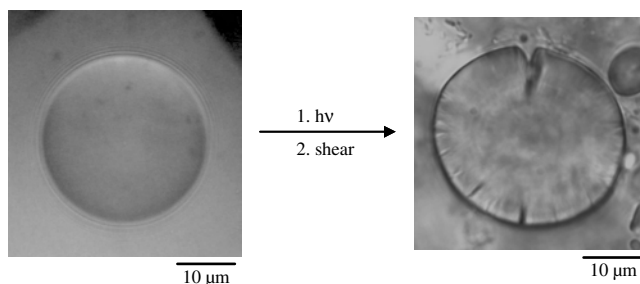


**Figure 5.** Reflection intensity contrast micrograph of a giant, polymerized PMOXA-PDMS-PMOXA triblock copolymer vesicle before (left) shear-induced rupture and after (right) shear-induced rupture.

A more specific uptake and release of substances could be achieved by reconstitution of membrane proteins in the completely artificial surrounding of the block copolymer membrane [57–59]. It has been shown that the functionality of the incorporated proteins is fully preserved even after polymerization of the vesicular membrane. With regard to the wide range of membrane proteins Nature provides, such copolymer-protein hybrid materials possess a great potential in many areas of application, such as, for example, gene therapy [60] or biomineralization [61].

By encapsulating an enzyme ( $\beta$ -lactamase) in the aqueous core domain of the nanocapsule and reconstituting a membrane protein (OmpF) in the polymer shell, a novel kind of nanoreactor could be designed (see Fig. 6) [58]. Furthermore, the channels of this protein close reversibly above a critical transmembrane potential. By simply adding a large enough polyelectrolyte to the external solution, that cannot pass the protein channels, a Donnan potential is created across the vesicular membrane. If this potential exceeds

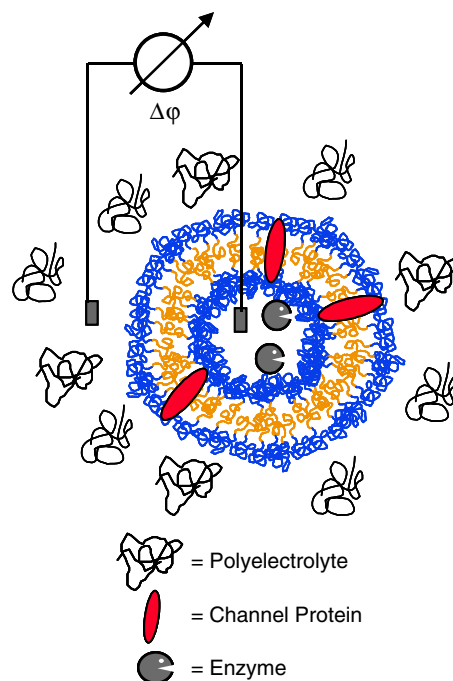


**Figure 6.** Schematic view of a PMOXA-PDMS-PMOXA nanoreactor with encapsulated  $\beta$ -lactamase and of the Donnan potential induced by polyelectrolyte present in the external solution.

the critical voltage necessary for closure of the protein, also small substrates can no longer enter the vesicular interior and the reactor is deactivated. Decreasing the potential below the critical voltage (e.g., by dilution) reactivates the reactor. The possibility to trigger the activation (or deactivation) of such systems is highly interesting for applications since it allows local and temporal control on the uptake and release of substrate.

Very recently the use of polypeptide-based diblock copolymers, poly(butadiene)-*b*-poly(L-glutamate) (PB-PGA) for the preparation of vesicular structures has been described [62, 63], Figure 7. Particularly interesting here is that the solvating chains are polypeptides and form vesicles, or so-called "peptosomes," composed of modified protein units. A subsequent polymerization of the poly(butadiene) block leads to shape-persistent nanocontainers that possess, due to their polypeptide block, a certain pH- and ionic strength-sensitivity [63]. By changing these parameters, the particles dimension changes reversibly as a result of the polypeptide block transition from a compact helical secondary structure at low pH values to a more extended random-coil conformation in basic media.

### 3.3. Nanocontainers Derived from Lipid Vesicles

Alternatively to the stabilization of lipid vesicles via intrapolymerization of cross-linkable lipids [21, 22], also known as polymerization of vesicles [64], another strategy makes use of the vesicular morphology simply as a template to imprint its hollow structure to other materials. Here two main approaches can be differentiated.

One concept uses just the geometry of the vesicular aggregates as a template [64–72]. In this case the amphiphilic molecules themselves are not polymerized to freeze in

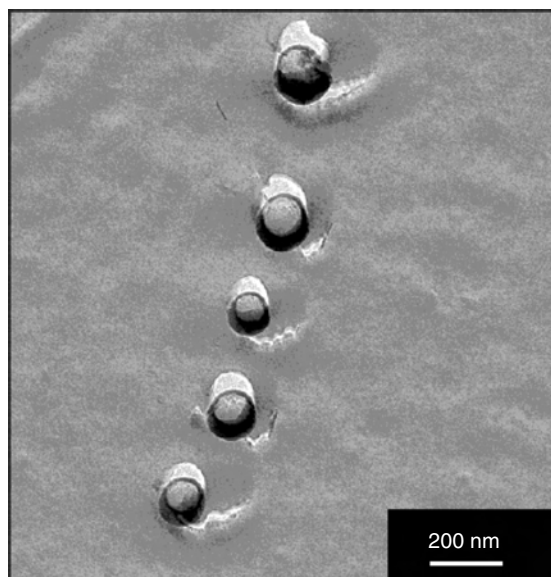


**Figure 7.** Freeze-fracture electron micrograph of a vesicular solution of poly(butadiene)<sub>85</sub>-*b*-poly(glutamate)<sub>55</sub> in pure water (pH ~ 6.0). Reprinted with permission from [62], H. Kukula et al., *J. Am. Chem. Soc.* 124, 1658 (2002). © 2002, American Chemical Society.

the whole superstructure of the supramolecular aggregate; they just provide a geometrically restricted environment for dissolving and polymerizing conventional monomers. This approach is also known as polymerization in vesicles or morphosynthesis [64–73]. In a second approach, vesicular templates are used solely to impart a surface onto which materials are grown from. This is known as transcriptive synthesis, since the structure of the vesicle is transcribed onto the new material, or sometimes called vesicle directed growth [73].

It is well known that vesicles or liposomes are able to solubilize hydrophobic substances to a certain degree. Such compounds are usually dissolved in the hydrophobic part of the lipid bilayer. If such substances also carry polymerizable groups, their subsequent polymerization should lead to the formation of polymer chains entrapped in the interior of the membrane. In contrast to polymerizable lipids, the polymer chains are now simply dissolved within the alkane part of the bilayer forming lipids. Hence, they are of minor influence on the overall physical properties of the membranes.

One special feature of vesicular polymerization of conventional hydrophilic or hydrophobic monomers is that the different compartments provided by the self-assembly of the lipid molecules generally serve only as a template, which determines size and shape of the resulting polymers. Thus, it is possible to use nearly every natural or synthetic lipid, without any modification. Although in most reported studies on vesicular polymerization of conventional monomers, synthetic lipids like dioctadecyl diammonium bromide (DODAB), chloride (DODAC), sodium di-2-ethylhexyl phosphate (SEHP), or even spontaneously formed vesicles prepared from mixtures of cationic and anionic surfactants have usually been used, any natural lipid would provide a suitable matrix. Moreover, a combination of polymerizable lipids and conventional monomers could be incorporated in templating vesicles to yield hybrids with interesting new polymer structures [64, 74, 75]. Of course, the incorporation of hydrophobic substances into lipid bilayers should not exceed certain saturation concentration [76]. Above this concentration the monomer is no longer homogeneously distributed within the bilayers. This has been shown for toluene in phospholipid vesicles at concentrations above the saturation level. Moreover, exceeding this saturation concentration may also disrupt the whole bilayer structure, thus converting the system into a conventional emulsion or even leading to the formation of a separate monomer phase in the presence of intact vesicles.

It is obvious that the overall thickness of the lipid membranes has to increase upon the solubilization of hydrophobic substances. The maximum swelling of the membrane leads typically to an increase from about 3 to 5 nm [77]. This is, however, a negligible effect compared to the overall diameter of typical small unilamellar vesicles, which is about 100 nm. Therefore no dimensional changes of the underlying vesicles can usually be detected upon swelling the lipid bilayers of the vesicles, as long as the monomer concentration stays below the saturation value in the membranes.

It has been shown that the hydrophobic portion of lipid bilayers can be selectively swollen by a variety of hydrophobic monomers, such as styrene [65, 66, 68, 69], alkyl(meth)acrylates [67, 70, 71], or even lipofullerenes

carrying polymerizable octadecadiene side chains [72]. A cross-linking polymerization of such monomers leads to the formation of two-dimensional polymer networks in the interior of the membranes. Such networks can act as a polymeric scaffold that increases the mechanical stability of lipid membranes considerably without impeding the mobility of the lipid molecules within the aggregates.

The free-radical polymerization of the hydrophobic monomers incorporated into the lipid membranes of vesicles can be initiated, similarly to the polymerization of reactive lipids, by UV irradiation, thermal, or redox chemical radical generation. The polymerization process itself seems, however, to be rather sensitive towards the composition of the system, that is, the chemical constitution of the monomer and the lipid and the concentration of the monomers in the bilayer, which, of course, limits its possible applications. While polymerization of alkyl (meth)acrylates in dioctadecyl-ammonium chloride vesicles [70, 71], the reaction of lipofullerenes in dipalmitoyl-phosphatidylcholine vesicles [72], or styrene/divinyl benzene mixtures in equilibrium vesicles formed by CTAT/SDBI or CTAB/SOS mixtures [79] clearly lead to the formation of polymer hollow spheres, in case of styrene/divinylbenzene in dioctadecyl-ammonium bromide vesicles, an intravesicular phase separation occurs during polymerization, thus leading to the formation of so-called parachute-like structures [69, 78].

An interesting aspect of the formation of cross-linked polymer particles in vesicular dispersions arises from the fact that, in contrast to linear polymers, they should be able to retain their structure even after their isolation from the lipid matrix [70, 79]. Although the particles contract considerably after their isolation from the lipid membrane, they preserve their spherical shape. Their dimensions always remain, however, directly proportional to those of the underlying vesicles. This is not too surprising since the polymer chains are expected to be forced into a nearly two-dimensional conformation in the interior of the lipid membrane. After their liberation from the membrane, the polymer chains can gain entropy by adopting a three-dimensional conformation. To do this, such spherically closed polymer shells have to shrink and the thickness of their shells increases.

The extent of the observed contraction of the particles depends sensitively on the cross-linking density of the polymer network structure. The contraction increases with increasing cross-linking density, thereby showing the same scaling behavior as branched polymers upon variation of their number of branches. For the highest cross-linking densities, the particles contract to about 1/10 of the original size of the templating vesicles.

In context with possible applications, it would be of great interest to have detailed information about the permeability of these polymer hollow spheres. It has to be expected that, besides the chemical constitution of the polymer backbone, the mesh size, that is, the cross-linking density of the polymer network structure, also plays an important role. Only molecules that are smaller than this mesh size should be able to diffuse across the polymer shell. Molecules which are larger cannot pass the polymer membrane for geometrical reasons.

Whereas the templating vesicles directly determine the size and shape of the resulting polymer particles, the

polymer scaffold can be modified rather easily using conventional chemical reactions. This allows, for example, sulfonation of poly(styrene) containers [79] or the conversion of poly(*tert*-butyl acrylate) hollow spheres into poly(acrylic acid) hollow spheres. The resulting polyelectrolyte nanocapsules can swell as a response to changes in the pH of their environment [80]. This pH-dependent transition influences considerably the permeability of such polyelectrolyte shells and can be used to selectively entrap and release specific substances.

Although such a vesicular polymerization represents a rather elegant approach to produce polymeric nanocontainers, their possible technical application is expected to be rather limited. The reason for this lies in the low economical efficiency of this method. Apart from the often energy-consuming vesicle preparation procedure, the synthesis of one gram of pure polymer nanocapsules already requires approximately 1.5–2 times their weight of lipid, a reaction volume of about 300–400 milliliters of water, and additionally several liters of organic solvents (for purification).

### 3.4. Nanocontainers Derived from Polymer Micelles

Since block copolymers are very versatile materials, they are broadly used as scaffold structures to construct sophisticated and complex materials with new properties. The richness of the block copolymer field relies on the fact that by choosing different repeating units to form each of the blocks, a great variety of starting materials is at hand. Additionally, synthetic polymers provide a wide spectrum of alternatives to design materials with responsive behavior towards external stimuli; this combined with their supramolecular aggregation makes polymers very interesting raw materials.

Not only vesicular structures but also micelles can be used for the controlled formation of nanocontainers. It is, for example, well known that block copolymers may assemble into polymeric micelles with diameters in the 10- to 100-nm range. An important issue in making these self-assembled systems useful for specific applications is again their capability to respond to external stimuli, that is, to interact with their surrounding environment. Very recently the formation of three-layer micelles in water from polystyrene-*b*-poly(2-vinylpyridine)-*b*-poly(ethylene oxide) (PS-*b*-P2VP-*b*-PEO) triblock copolymers was reported [81]. It was demonstrated that the pH sensitivity of the P2VP shell can be used to tune the micelle size from a hydrodynamic diameter ( $D_h$ ) of 75 nm at pH > 5 to 135 nm at pH < 5. This effect is based on the electrostatic repulsion between the charged P2VP blocks and is not completely reversible because of the formation of salt with each pH cycle. Although this feature makes this system useful for encapsulation and release of active species and has already been used for the synthesis of well-defined gold nanoparticles, its long-term stability is still questionable.

One major aspect of block copolymers is that they can be modified so that either the interior or the exterior blocks within the micelles contain polymerizable groups. For example, poly(isoprene)-*b*-poly(acrylic acid) (PI-PAA) diblock copolymers form micelles in aqueous solution with a PI core and a PAA shell. It has been shown that the PAA



shell can be cross-linked with  $\alpha,\omega$ -diamino-poly(ethylene glycol), giving shell-cross-linked nanoparticles also known as shell-cross-linked knedels (SCK) [82, 83]. Similarly, a poly(isoprene)-*b*-poly(2-cinnamoyl ethyl methacrylate)-*b*-poly(*tert*-butyl acrylate)(PI-PCEMA-PTBA) triblock copolymer forms micelles with a PTBA corona, PCEMA shell, and a PI core in THF-methanol mixtures [84]. In this case the micellar structure could be locked in by UV-cross-linking of the PCEMA within the micelles. Subsequently the PI cores of both the cross-linked PI-PAA and the PI-PCEMA-PTBA micelles could be degraded by ozonolysis into small fragments that could diffuse into solution and leave nanospheres with a central cavity. A schematic representation of the whole process is given in Figure 8. The potential of such systems for encapsulation of small molecules has been demonstrated by loading the cross-linked PCEMA-PTBA capsules with Rhodamine B [84]. The incorporation of the dye into the central cavity of the particles could readily be visualized by transmission electron microscopy (TEM).

The degradation of the shell-cross-linked PI-PAA micelles leads to water-soluble cross-linked poly(acrylamide) hollow spheres which considerably increase the  $D_h$  of their shells after removal of the core [83]. The increase of  $D_h$  from 27 to 133 nm has been explained by the fact that the cross-linked poly(acrylamide) shells can be regarded as a hydrogel that swells when the core domain fills with water after the PI core has been removed. The diameter of the hollow-sphere products depends sensitively on both the degree of polymerization of the block copolymers originally used to form the micelle and the nature of the cross-linking diamine used to prepare the shell-cross-linked micelles.

By the same approach, poly( $\epsilon$ -caprolactone)-*b*-poly(acrylic acid)-co-poly(acrylamide) SCKs with a biodegradable core were prepared [85]. The synthetic approach included initially the hydrolysis of poly( $\epsilon$ -caprolactone)-*b*-poly(*tert* butyl acrylate) to give poly( $\epsilon$ -caprolactone)-*b*-poly(acrylic acid), followed by micellization. Cross-linking

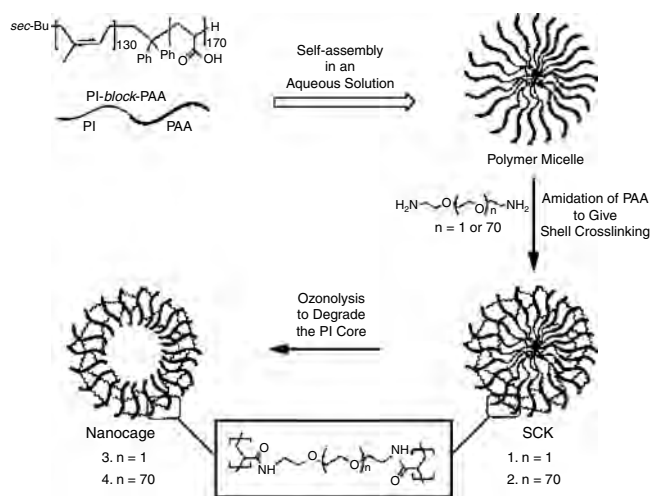


**Figure 8.** Procedure for the preparation of nanocages from amphiphilic diblock copolymers. The shell of the final nanocages consists of cross-linked poly(acrylamide). Reprinted with permission from [83], H. Huang et al., *J. Am. Chem. Soc.* 121, 3805 (1999). © 1999, American Chemical Society.

of the carboxylic groups present in their corona was performed with 2,2'-(ethylenedioxy)bis(ethylamine) to render finally the poly( $\epsilon$ -caprolactone)-*b*-poly(acrylic acid)-co-poly(acrylamide) SCK, while hydrolysis of the core was achieved by either acidic- or basic-promoted degradation of the ester linkages to produce the hollow capsules. Such mild core removal is of particular interest in biological applications, especially since the monomers released are biocompatible [85]. Moreover, these shell-cross-linked particles were surface functionalized to promote cell binding [86] via conjugation with a peptide sequence.

Using also the SCK technique as above but without removal of the core, such shell-cross-linked particles have been modified in order to respond to environmental stimuli [87]. Interestingly, here the hydrophobic core consisting of poly(methyl acrylate) is hydrolyzed to give hydrophilic poly(acrylate) chains. The nanoparticles thus obtained, although not completely hollow, have a nanocage-like structure, due to the fact that the shell swells considerably after the hydrolysis of the core chains. Additionally, the nanocage-like particles undergo a pH-controllable swelling, due to electrostatic repulsive forces acting among the ionized core chains [87]. The extent of swelling depends on the percentage of cross-linking of the shell. In contrast with the initial core-shell particles, the particles with modified core are capable of encapsulating hydrophilic guest molecules.

One can produce hollow capsules not only by degradation of the core to monomer or oligomers, but also by selectively detaching both core- and shell-forming block copolymer chains. Obviously, the particles have to be previously stabilized in some way, to prevent disruption of the whole self-assembled superstructure. For example, this concept has been used to prepare SCK in which the core was cleaved by thermolysis of the bond connecting it to the shell. Surprisingly, the polymeric chains are able to permeate the cross-linked shell membrane, and this permeability is found to be inversely dependent on the degree of cross-linking of the shell. Nevertheless, the removal of the core by this approach is not complete, since less than 30% of the total poly(styrene) chains were released even for the lower cross-linking densities [88].

One “block-copolymer free strategy” to prepare micelles solely by hydrophobic interactions between the core and the shell of the structures instead of using covalent attachment, has been described by Liu et al. [89]. They report the preparation of hollow capsules via self-directed assembly of a homopolymer (poly( $\epsilon$ -caprolactone)) and a random graft copolymer comprising a hydrophilic backbone of poly(methylmethacrylate) and poly(methylacrylic acid) and hydrophobic branches of poly( $\epsilon$ -caprolactone). Upon addition of water to a DMF solution of the above mentioned polymers, micelles form in which the poly( $\epsilon$ -caprolactone) constitutes the core and the graft copolymer arranges as the shell. The structure is achieved only by the anchoring of the branches of the graft copolymer into the poly( $\epsilon$ -caprolactone) core; thus, no covalent or hydrogen bonding is needed. Although they report a block-copolymer free approach with no need of covalent bonding between the core and the shell, they use a further stabilization of the system by (covalent) cross-linking the carboxylic and amino groups present in the shell, via a carbodiimide derivative.

The structures thus obtained resemble the shell-cross-linked micelles described by Wooley and co-workers [82]. Removal of the core to give the hollow counterparts was achieved by enzymatic degradation of the poly( $\epsilon$ -caprolactone) with a lipase [89].

Another approach used self-assembled superstructures as templates for the production of inorganic  $\text{MoO}_3$  nanospheres. A micelle forming triblock-copolymer, comprising poly(oxyethylene)-*b*-poly(oxybutylene)-*b*-poly(oxyethylene), served as the templating matrix for the formation of thin-layered hollow nanospheres. The latter were obtained with  $\text{MoO}_2(\text{OH})-(\text{OOH})$  which upon decomposition affords  $\text{MoO}_3$  and  $\text{O}_2$ , a precipitation crystallization process taking at least two weeks for completion. The template forming triblock-copolymer was removed by solubilization in excess water. Apparently and against expectation, the crystallization of  $\text{MoO}_3$  occurs at the interface between the core and the shell of the micellar scaffolds. This follows from the observation of smaller radii for the inorganic cages obtained in comparison with the external radius of the micellar templates used [90].

#### 4. TEMPLATE-DIRECTED PREPARATION OF NANOCONTAINERS

Another possibility for generating polymer nanocapsules is to form a polymer shell around a preformed template particle that can subsequently be removed, thus leaving an empty polymer shell. There are several methods of conducting such a template synthesis of hollow polymer particles. Different templates have been used so far, including silica micro and nanoparticles (usually prepared by Stober synthesis) [91], colloidal or latex particles, gold nanoparticles, etc.

##### 4.1. LbL Deposition

A convenient way to produce nanocapsules is to exploit the well-known polyelectrolyte self-assembly at charged surfaces. This chemistry uses a series of layer-by-layer (LbL) deposition steps of oppositely charged polyelectrolytes [92]. The driving force behind the LbL method at each step of the assembly is the electrostatic attraction between the added polymer and the surface. One starts with colloidal particles carrying surface charges, for example, a negative surface charge. Polyelectrolyte molecules having the opposite charge (e.g., polycations) are readily adsorbed due to electrostatic interactions with the surface. Not all of the ionic groups of the adsorbed polyelectrolyte are consumed by the electrostatic interactions with the surface. As a result, the original surface charge is usually overcompensated by the adsorbed polymer. Hence, the surface charge of the coated particle changes its sign and is now available for the adsorption of a polyelectrolyte of again opposite charge (i.e., a polyanion). As sketched in Figure 9, such sequential deposition produces ordered polyelectrolyte multilayers.

The size and shape of the resulting core-shell particles is determined by the template colloidal particle, where the formation of particles with diameters ranging from 0.2 to 10  $\mu\text{m}$  has been reported. The thickness of the layered shell is determined by the number of polyelectrolyte layers and can be adjusted in the nanometer range.

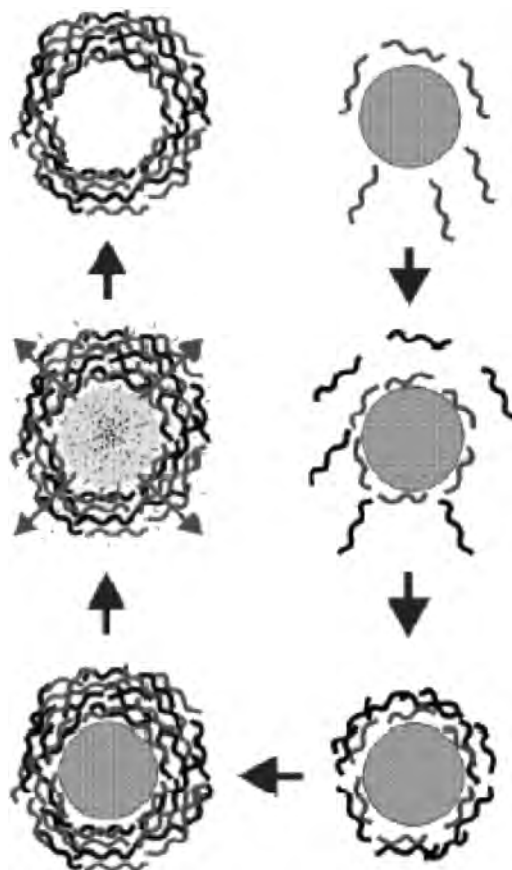


**Figure 9.** Illustration of the procedure for preparing hollow spheres using layer-by-layer deposition of oppositely charged polyelectrolytes on colloidal particles. Reprinted with permission from [92], E. Donath et al., *Angew. Chem. Int. Ed.* 37, 2201 (1998). © 1998, Wiley-VCH.

Up to now, a variety of charged substances, such as synthetic polyelectrolytes, biopolymers, lipids, and inorganic particles have been incorporated as layer constituents to build the multilayer shell on colloidal particles [93–95]. As templates for this approach, mainly colloids consisting of polystyrene latexes or melamine formaldehyde particles [96] have been used, but also gold [97] and proteins [98] have been tested.

To avoid, however, a polyelectrolyte-induced particle flocculation, one has to work at rather low particle concentrations and excess polyelectrolyte not adsorbed to the surface has to be removed carefully after each step by washing, which makes this technique rather tedious.

After completed deposition of a predefined number of layers, the colloidal core can be dissolved and removed. If one uses human erythrocytes as colloidal templates, they can be oxidatively decomposed in an aqueous solution of sodium hypochlorite. When using weakly cross-linked melamine-formaldehyde particles, the core is dissolved upon exposure to an acidic solution of  $\text{pH} < 1.6$ . Products of both decomposition methods are expelled through the shell wall and removed by several centrifugation and washing cycles. Although the core removal takes place under harsh conditions, neither the acid treatment nor the oxidative decomposition affects the polyelectrolyte layer shells, as can be seen in Figure 10 [92]. They clearly preserve their hollow-sphere

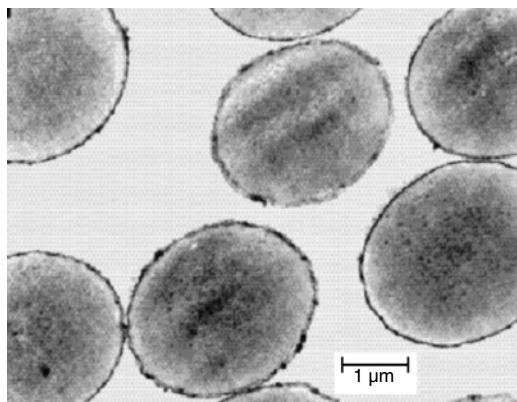


**Figure 10.** Transmission electron micrograph of polyelectrolyte hollow spheres. The shell of the particle consists of 9 layers ((poly(styrene sulfonate)poly(allylamine hydrochloride))<sub>4</sub>/poly(styrene sulfonate)). Reprinted with permission from [92], E. Donath et al., *Angew. Chem. Int. Ed.* 37, 2201 (1998). © 1998, Wiley-VCH.

morphology and are shape-persistent. It has been shown that small dye molecules can readily permeate such layered polyelectrolyte shells while larger-sized polymers with molecular weights larger than 4000 Da obviously do not [99–101].

Nevertheless, it has to be expected that their long-term stability will depend sensitively on the surrounding environment of the particles. Especially in biological fluids (e.g., blood plasma), or in media of high ionic strength, which may screen the ionic interactions responsible for maintaining their integrity, the long-term stability of such polyelectrolyte shells may be rather limited.

However, this sensitivity towards the physico-chemical conditions of the surrounding medium, in particular to pH and ionic strength changes, was successfully used to get control over the permeability of multilayer shells consisting of poly(styrene sulfonate) and poly(allylamine) hydrochloride [103, 104]. By this control it is possible to release from these capsules in a controlled manner prior encapsulated biomacromolecules or fluorescent probes, even with molecular weights of 70,000 Da, or to use them as templates for the selective crystallization of various dyes [102, 103, 105]. Even loading and releasing of substances was accomplished by pH-induced or salt-triggered permeability of the mentioned polyelectrolyte capsules.

Another interesting point is that the capsules could be filled with oils by sequential exchange of the solvent. These oil-filled capsules could be dispersed in water due to their amphiphilic nature, thus leading to a stable, surfactant-free oil-in-water emulsion [106, 107]. Additionally, applying this concept of polyelectrolyte layering onto substrates, a protein aggregate has been encapsulated in a process similar to that already described for other templates such as latex particles. Although the hybrid aggregates obtained were amorphous and removal of the core-forming template was not attempted, this shows the potential of the LbL approach, where, for instance, the encapsulating substrate and templating material can be the same and one [98, 102].

Functionalized polystyrene latex particles carrying surface charges are also suitable substrates for the polyelectrolyte self-assembly technique. In one case, inorganic particles

were incorporated into the adsorbed shells by a sequential adsorption of nanometer-sized SiO<sub>2</sub> particles with negative surface charge and cationic poly(diallyldimethyl-ammonium chloride) (PDAD-MAC) [96, 108]. Layers with a thickness ranging from tens to hundreds of nanometers could be prepared by this procedure. Removing the polystyrene core, either with acid solutions or with solvents such as THF or DMSO, leaves SiO<sub>2</sub>/PDAD-MAC hybrid nanocomposite shells and after calcination even pure SiO<sub>2</sub> hollow spheres. Both the inorganic-organic composite and the pure inorganic capsules can be expected to show interesting physical properties such as enhanced mechanical stability or exceptional permeability behavior. By exactly the same strategy but using melamine formaldehyde as templates, micrometer-size hollow hybrid organic-inorganic capsules and hollow silica spheres were also obtained [96].

With a similar approach, void spheres of titania, iron oxide (magnetic hollow nanocapsules), zeolite, clay, and their respective composites were also prepared [109–112]. Using the LbL technique, gold nanoparticles were used as templates for the production of polymer multilayer shells [97]. In the first reported case of metal particles as templates using the LbL method, the particles had to be surface modified to allow good deposition of the polyelectrolyte. Such functionalization of the gold particles was achieved by covalent bonding of alkanethiols, which also possessed ionic moieties that promoted the adsorption of the layers of polyelectrolytes. In this context, core dissolution via etching with cyanide produced the desired hollow polymeric nanoparticles, with reported diameters ranging from 15 to 50 nm.

Not only stabilization due to electrostatic interactions of the polyelectrolyte forming shells may be used but also their stability can be enhanced by a subsequent cross-linking procedure. For example, by using diazoresins and alternating its deposition with poly(styrenesulfonate) or poly(acrylic acid) onto a sacrificial core, followed by UV irradiation to covalently cross-link the shells, and subsequent removal of the core, hollow polymeric capsules with enhanced stability were obtained [113]. Comparison of ionically cross-linked and covalently cross-linked capsules upon exposure to organic solvents and high-ionic-strength solutions shows a considerable increase of the stability of the latter ones, which is attributed to the covalent attachment. Although the capsules seem to retain to some extent their permeability, since removal of the core could be done either prior to the cross-linking step or after it, their permeability appears to be lower than in other polyelectrolyte capsules. Moreover, in contrast to poly(allylamine hydrochloride)-poly(styrenesulfonate) containers, osmotic pressure resulted in almost no deformation for both polymerized and nonpolymerized diazoresin-poly(styrenesulfonate) capsules [113].

As already mentioned, one of the main interests in this field is to control the permeability and encapsulation of substrates. One way to achieve this is to modify the capsules' shells, particularly their internal walls. With this aim in view, polymerization of monomers was carried out in the void volume of such polyelectrolyte capsules. While polymers cannot, monomers easily permeate the shell [99–101]. If monomers are introduced in the empty volume of the containers, followed by a polymerization reaction, the resulting macromolecules are entrapped inside the capsules.

By using this approach to encapsulate a polyelectrolyte macromolecule, it was possible to obtain a pH of about 2 in the interior of the spheres. This is of interest, for example, in the context of nanoreactors, to carry out acid catalyzed reactions within the capsules. Interestingly, swelling and shrinking of the shells could be tuned by changing the osmotic pressure. Moreover, it was observed that the polymerization of encapsulated monomers took place mainly within the walls of the capsules which gave, for poly(styrenesulfonate), the possibility to modify the ionic selectivity of the shells. Thus, fluorescent anions could not translocate the functionalized walls, while cationic probes did. Surprisingly, the adsorption of oppositely charged ions on the walls resulted in an increase of the permeability of the shell, through the formation of pores which finally released the encapsulated macromolecules into the bulk of the solution. Therefore a tunable control of the permeability is achieved [114].

#### 4.2. *In-Situ* Polymerization

Similarly, poly(N-vinylpyrrolidone)-stabilized polystyrene latex particles were coated with thin overlayers of poly(aniline) to produce electrically conductive core-shell particles [115]. In contrast to the LbL deposition method where preformed polymers are adsorbed to a surface, here the polymer is formed *in-situ* by oxidative coupling of monomers at the particle surface. The poly(aniline) layers had, however, a rather nonuniform and inhomogeneous morphology. Therefore extraction of the polystyrene core left poly(aniline) shells that displayed a so-called “broken egg-shell morphology”; that is, they were largely disrupted. Also gold nanoparticles have successfully been used as templates for nucleation and growth of surrounding poly(pyrrole) and poly(N-methylpyrrole) shells [116, 117]. Etching the gold leaves structurally intact hollow polymer particles with a shell thickness governed by the polymerization time. This formation of polymer-coated colloids involves trapping and aligning the particles in the pores of membranes by vacuum filtration and a subsequent polymerization of a conducting polymer inside the pores (Fig. 11).

In a first step, the gold nanoparticles are being filtered into a porous  $\text{Al}_2\text{O}_3$  support membrane with a pore size of 200 nm. After an initiator ( $\text{Fe}(\text{ClO}_4)_3$ ) has been poured into the top of the membrane, monomer (pyrrole or N-methylpyrrole) is placed underneath the membrane. Upon diffusion of the monomer vapor into the membrane, it contacts the initiator to form polymer, preferentially at the surface at the gold particles. The resulting polymer-encapsulated nanoparticles can be isolated by dissolution of the membrane in basic media. The shell thickness depends on the polymerization time and can be controlled in a range from 5 to 100 nm. In order to obtain hollow particles, the gold was etched, for example, with a  $\text{KCN-K}_3[\text{Fe}(\text{CN})_6]$  solution, prior to dissolution of the membrane material. Thus hollow cores with a diameter of 30 nm were seen by TEM, where the 30-nm Au particle was previously located, indicating that almost no reorganization, collapse, or shrinkage takes place when the empty shells are dried. Indeed, the diameter of the hollow core could be tuned by choosing an appropriate Au particle of different size. In this context it was shown that the gold particles are not only

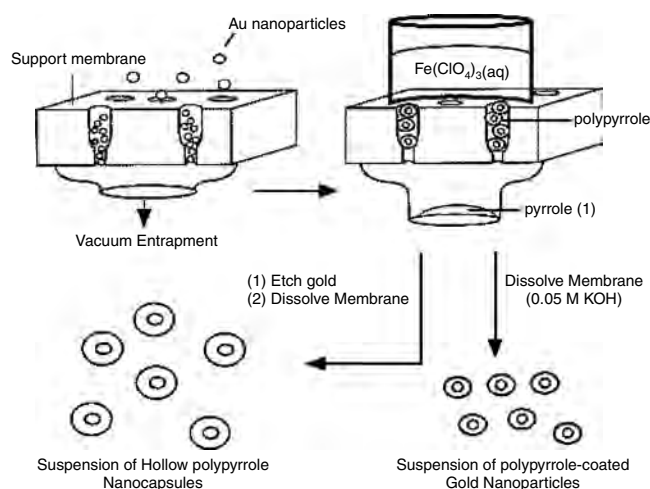


**Figure 11.** Schematic diagram of the membrane-based method for synthesizing gold-core/polymer-shell nanoparticles. The particles are first trapped and aligned in the membrane pores by vacuum filtration and subsequently coated with poly(pyrrole), which occurs via polymerization of the monomer vapor when it diffuses into the membrane and interacts with the initiator ( $\text{Fe}(\text{ClO}_4)_3$ ). The membrane is then dissolved, leaving behind nanoparticle composites. The gold can also be etched first and the membrane then dissolved, resulting in hollow poly(pyrrole) nanocapsules. Reprinted with permission from [116], M. Marinakos et al., *J. Am. Chem. Soc.* 121, 8518 (1999). © 1999, American Chemical Society.

useful as a template material but can also be used to deliver guest molecules into the capsule core. For example, ligands attached to the gold surface, via alkanethiol-Au bonds or simply by physisorption, prior to polymerization remained trapped inside the hollow particles after gold etching, which demonstrates their potential as protective shells for sensitive compounds like enzymes. Indeed, the ability of the capsule to protect an encapsulated enzyme was studied [118].

Obviously the ions of the gold etchant were able to diffuse across the polymer shell, the permeability of which could even be tuned by the oxidation state of the polymer or the counter ion present during polymerization of the pyrroles. However, even rather small organic guest molecules like Rhodamine B [116] or anthraquinone-terminated hexanediol [118] were not released again from the interior of the particles, even over periods of up to three weeks. That means that there is only very restricted access to enclosed substances in the interior of the shells. In addition, the particle type appears to be limited to those that fit into the membrane supports used, which also restricts its applications. Nevertheless, it shows promise for coating of various templates like metals and biomacromolecules. One advantage in the use of conductive polymers, from the triggering or stimuli-response point of view, is that they could be interchanged from their cationic, anionic, and neutral forms, either chemically or electrochemically. Interestingly, quasi-1D arrays of the Au-polymer composite and the hollow polymeric particles fabricated by this method could be obtained [117], which could be of advantage in the production of sensors, for example.

### 4.3. Surface Initiated Living Polymerization

In another approach, hollow cross-linked polymeric nanoparticles are obtained by a template-assisted surface initiated living free-radical polymerization [119]. In this procedure, the surface silanol groups of silica nanoparticles, used as templates, are initially reacted with trichlorosilyl-substituted alkoxyamines as radical initiator groups. Subsequently, this layer of surface initiator groups is used to start linear polymer chains of poly(styrene) or poly(styrene-co-maleic anhydride) by free-radical polymerization, thus leading to a hybrid core-shell morphology. In a following step, the shell is cross-linked and still covalently attached to the silica core; then removal of the core by HF treatment gives hollow polymeric particles, whereas the non-cross-linked particles after etching of the core gave linear polymers with loss of the capsular structure. Two different approaches were used to cross-link the shells; one involved thermal reaction of polystyrene with 4-vinylbenzocyclobutene, the other a two-step reaction in which a poly(styrene-co-maleic anhydride) is cross-linked with a diamine. This last cross-linking procedure resembles the one used by Wooley [82]. The obtained nanocapsules are stable against solvent dissolution and thermal treatment due to their cross-linked structure, although some disruption of the particles was observed and the solvent treatment followed by drying led to collapse of the spheres [119].

A similar approach was carried out [120] by using initiating sites for atom transfer radical polymerization (ATRP) [121] at the surface of silica microparticles, with a subsequent dissolution of the silica core to render hollow polymeric nanocapsules. Silica microspheres (3  $\mu\text{m}$  diameter) were used as templates to achieve hollow polymeric microspheres via surface initiated living radical polymerization of benzyl methacrylate followed by core dissolution. In a first step, living atom transfer radical polymerization was conducted via initiators attached to the surface of the template, leading thus to hybrid core-shell particles in which the template and the shell were covalently attached. In a following step, the sacrificial cores were dissolved, giving then hollow polymeric microcapsules. In this case control over the shell thickness was achieved by variation of the reaction time [120]. In both approaches the attained polymer chains are well defined in terms of polydispersity due to the living nature of the polymerization process [119, 120], thus leading to highly uniform shell thickness. Again cross-linking of the shells provides extra stabilization of the structures which otherwise would disintegrate upon dilution or during the subsequent manipulations necessary to obtain the hollow particles.

### 4.4. Nanocontainers from Inorganic Templates

Taking into account the usually low permeability of nanocapsules and the difficulties encountered to load or to release molecules from them in a controlled way, some strategies have been proposed to overcome these disadvantages. For instance, Zha et al. [122] have used the well-known thermoresponsive poly(N-isopropylacrylamide) to obtain stimuli-responsive containers. Poly(N-isopropylacrylamide), which has a rather low (32° C) lower

critical solution temperature (LCST), undergoes a conformational change from coil to globule at its LCST [123]. The strategy used for obtaining the capsules was a colloid templated polymerization with a posterior removal of the core. As templates, silica particles (obtained by Stober synthesis [91]) with diameters from 10 to 100 nm were utilized, the surface of which was modified by 3-(trimethoxysilyl)propyl methacrylate, thus rendering a surface decorated with double bonds. In a seed precipitation polymerization, using the functionalized particles as seeds, N-isopropylacrylamide was polymerized in the presence of N,N'-methylene bisacrylamide as cross-linker, in order to obtain hybrid particles, with a silica core and a cross-linked poly(N-isopropylacrylamide) shell structure. Hollow polymeric capsules were achieved by an etching step using HF. The hollow particles could maintain their shape after the dissolution of the core since they were cross-linked. While the size and shape obtained was found to be related to the templating particle, the shell thickness depended on different variables such as the amount of poly(N-isopropylacrylamide) and the size and concentration of the template particles. Also the degree of cross-linking influenced the morphology of the structures achieved. In this context, discs and dented structures, both due to collapsed capsules and intact spheres were observed. Most interestingly, the temperature dependence of the nanocapsules was investigated. In general, for all cross-linking densities, the capsules shrank as the temperature increased and their volume phase transition was 32 °C. Additionally, the degree of shrinkage was found to be a function of the cross-linking density. Important is the fact that the swelling and shrinking cycles were repeatable and reproducible. Although it would be very interesting for applications like drug delivery, since the LCST of the polymer is close to biologically related applications, no attempt of encapsulation was reported [122].

Silica hollow spheres were synthesized by seeded polymerization of tetraethoxysilane on the surface of polystyrene particles followed by calcination [124]. Also microcapsules with magnetic interiors have been reported. By deposition of iron salts, coating of a crystalline shell of  $\text{Fe}_3\text{O}_4$  on polystyrene template particles was achieved. Following a posterior calcination of the core, hollow magnetic capsules were obtained. The stability of the spheres produced was low; nevertheless, this could be improved by additionally coating the spheres with a shell of silica nanoparticles via seeded polymerization of tetraethoxysilane according to the Stober technique [91]. Interestingly, these capsules are hydrophilic and thus can be dispersed in water, whereas heating to 100 °C produces hydrophobic capsules by silica conversion to siloxane [124]. A similar approach to obtain submicron-sized hollow inorganic microcapsules consisting of yttrium was described by Kawahashi and Matijevic [125]. In this particular case, coating polystyrene latex with basic yttrium carbonate layers and subsequently calcining at elevated temperatures in air, resulted in the desired inorganic hollow particles.

A self-aggregating polymer can be also used as a template for the formation of inorganic hollow spheres. Poly(L-lysine) in conjugation with hydrophobic amines was found to form

aggregates in solution, and this was used to imprint their structure into silica [126].

Additionally, poly(L-lysine) is a well-known biocompatible polymer, which has the interesting property of showing strong pH-dependent behavior. In acidic solutions it adopts a random coil conformation, while at higher pH it undergoes a transition to  $\alpha$ -helix or  $\beta$ -sheet conformations [127–129]. When tetraethyl ortosilicate was added to an aqueous solution of poly(L-lysine) in the presence of benzylamine, at pH 11.6, hybrid polymer core–silica shell capsules were formed with diameters from 100 nm to 1.5  $\mu\text{m}$ . The high polydispersity is a direct consequence of the broad size distribution of the template aggregates used, as confirmed by light-scattering techniques. Elimination of the core was achieved by subsequent calcination of the hybrid structures. Apparently both the poly(L-lysine) and the benzylamine are necessary to obtain the hollow silica structures, since attempts to use the individual components separately or other amines led only to the formation of silica particles or mixtures of particles and capsules. The advantages of this preparation method are the use of commercially available reactants, a biocompatible and biodegradable polymer, and a simple procedure in comparison with more established strategies like LbL in which many steps are required [126].

The advantages of inorganic hollow nanocapsules are their higher mechanical and thermal stabilities compared to the organic counterparts. However, encapsulation of molecules in their interior is quite challenging due to their rather impermeable shells.

Zeolites have the advantage of imprinting micro pores on the shells of the nanospheres rendering readily permeable structures, and great research has been done in this area. We do not intend to cover this vast research field in detail. Nevertheless, it should be mentioned that very recently a new approach for the production of hollow zeolite microcapsules has been presented. Dong et al. [130] report the preparation of novel zeolite nanocapsules that comprise functionalized interiors. This is achieved by pre-encapsulating a specific substrate, followed by a vapor phase treatment (VPT). Mesoporous silica spheres (3–6  $\mu\text{m}$ ) were coated with nano zeolite particle seeds (60 nm) and then these particles were treated with amine vapor in an autoclave (VPT). In this process the surface of the particle grows at expense of the silica core and finally once the silica is consumed, a hollow crystalline zeolite shell with a thickness on the order of 200 nm is obtained. Guest molecules, inorganic species like iron oxide ( $\text{Fe}_2\text{O}_3$ ), were encapsulated into the pores of the templating mesoporous silica, prior to the vapor phase treatment, thus rendering hollow capsules with an interior decorated by clusters of iron oxide [130].

Similarly, also porous carbon containers were prepared [131]. Using silica particles with solid core and mesoporous shell as templates, phenol resin or poly(divinylbenzene) was polymerized on their surface, thus giving a polymer-silica composite with the polymers being located inside the pores of the silica particles. A posterior carbonization of the polymer leads to carbon aluminosilicate nanocomposites. In a following step, hollow carbon capsules of 220 to 500 nm diameter and shell thickness of 55 to 90 nm were obtained by dissolution of the silica core with HF or NaOH when using phenol formaldehyde or poly(divinylbenzene), respectively.

Additionally, the diameter of the sphere and thickness of the capsule wall could be adjusted by careful choice of the silica templates. Interestingly, these carbon nanocapsules contain pores with size on the order of 2.8 to 4 nm, and constitute an inverse replica of the silica templates used [131].

One interesting approach using gold particles as templates has been reported by Sun et al. [132]. Hollow monolayer-thick organic spheres were obtained by attaching thiolated  $\beta$ -cyclodextrines to gold particle templates. The Au particles are synthesized *in-situ* by reduction of Au (III) in the presence of thiolated  $\beta$ -cyclodextrines; this gives in turn particles coated with the thiolated substrate. Subsequent oxidation of the Au particles with iodine leads to dissolution of the gold and formation of disulfide bonds between the thiolated substrates. A key strategy in this approach is the use of molecules with many thiol groups to provide good cross-linking since, after dissolution of the Au core, the structure is held together solely by S—S bonds. Confirmation of the hollow structures was done by solubility experiments; while the  $\beta$ -cyclodextrines are insoluble in water, the hollow shells are soluble since they expose only their hydrophilic portions towards the bulk of the solution. The internal wall of the shells is hydrophobic, due to the disulfide bonds present, and to prove this, encapsulation of ferrocene was studied. As a result of disproportionation of the disulfide bonds, long storage in aqueous solution led to a precipitate of an insoluble disulfide polymer. This in turn could be used as a way of controlling the release of molecules encapsulated in such nanocontainers [132].

## 5. NANOCONTAINERS PREPARED BY EMULSION/SUSPENSION POLYMERIZATION

In this section the formation of nanocontainers which can be achieved by several suspension and emulsion polymerization techniques is described. Although in most cases these methods have been shown to lead to particles with diameters of several micrometers, recent developments demonstrate that nanometer-sized polymer hollow spheres are also accessible.

One example was described by Okubo et al. [133, 134] where the penetration and release behavior of various solvents from or into the interior of monodisperse cross-linked poly(styrene)/poly(divinylbenzene) composite particles could be investigated. The hollow structure of the particles is in this case achieved by a seeded polymerization utilizing the so-called dynamic swelling method. For example, the polymerization of divinylbenzene in toluene/divinylbenzene swollen polystyrene latex particles or in poly(styrene) containing toluene droplets leads to the formation of hollow poly(divinylbenzene) (PDVB) particles. This is a result of a micro phase separation due to the limited compatibility of the chemically different polymers in solution, which leads to the formation of a PDVB shell around a toluene-polystyrene core. After evaporation of the toluene, a cavity remains in the center of such particles.

Another rather convenient method leading to hollow polymer particles proceeds via emulsion polymerization. Usually a two-stage process via seeded latex particles with physical or time separation between the two steps is applied.



In a first step, the core particles are synthesized by a conventional emulsion polymerization. Then in a second step, a different monomer or monomer mixture is added and a cross-linked shell is polymerized around the previously formed core particle. Although the preparation of such core-shell particles seems to be quite simple in theory, it is rather difficult in practice. This holds particularly if one is interested in well-defined and homogeneous particle morphologies, which is a basic requirement for the preparation of hollow polymer particles. It has been demonstrated that in this context both thermodynamic and kinetic factors are of crucial importance [135, 136]. The direct influence of many process parameters controlling the particle morphology, such as surface polarity, mode of monomer addition, role of surfactant and chain transfer agent, effect of polymer cross-linking and initiator, has already been demonstrated [137–143]. Additionally, to end up with a hollow polymer sphere one has finally to remove the core-forming material. Since core and shell are, however, frequently chemically rather similar, this is another critical step of the preparation procedure. Usually rather aggressive reaction conditions, like a prolonged alkali and acid treatment at high temperatures, are required to degrade the particle core [144, 145]. Although by using these methods clearly hollow particles can be formed, the question remains to what extent the polymer shells survive intact under these conditions.

A rather elegant approach to remove the core under very mild conditions has recently been demonstrated. The authors report the synthesis and characterization of nanometer-sized hollow organosilicon particles [146]. The synthesis of these particles followed a two-step procedure similar to that described above. The core of the particles was formed by a rather low-molecular-weight poly(dimethylsiloxane) (PDMS) around which a cross-linked organosilicon shell was formed in a second step. The PDMS core-forming material from the interior of the particles could be removed quantitatively by ultrafiltration. The remaining organosilicon nanoboxes possess typical diameters of 50 nm and a shell thickness of about 6 nm (Fig. 12).

Interestingly, they could be refilled with PDMS chains with a molecular weight of about 6000 Da, that is, rather large molecules, which reflects an obviously high porosity of the polymer shells. Hence, typical low-molecular-weight substances are expected to be released very quickly from such particles. Nevertheless, these organosilicon capsules represent a very promising system for applications in various areas.

The formation of nanocontainers with a stimuli-sensitive permeability could be achieved in a slight variation of this approach. Here, a poly(ethyl-hexylmethacrylate) (PEtHMA) core was covered by a cross-linked poly(tertiary butylacrylate) shell. Due to their low molecular weight, that is, below 10,000 g/mol, the single PEtHMA chains are able to diffuse across the particles shell and can be removed by ultrafiltration. The isolated poly(tertiary butyl)acrylate spheres could successfully be used for encapsulation of dye molecules (Fig. 13) and converted into stimuli-responsive polyelectrolyte nanocapsules by selective saponification of the tertiary butyl ester groups [147].

The preparation of nanometer-sized hollow polymer particles as a one-step emulsion process was recently

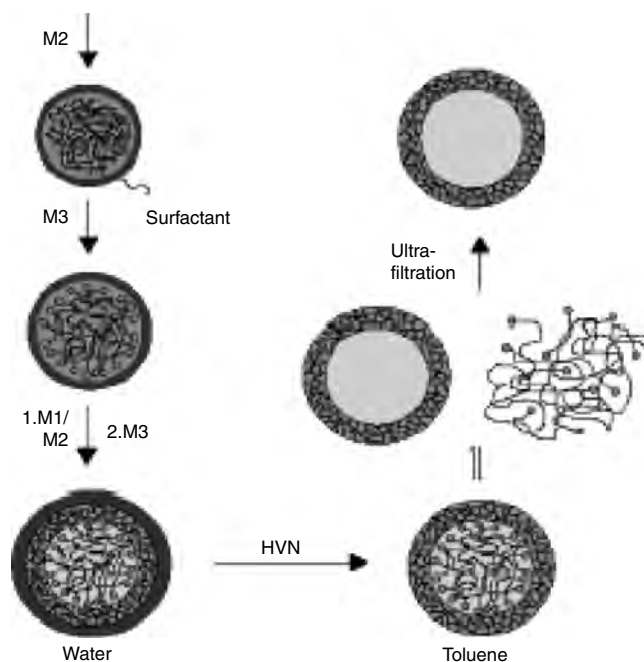


**Figure 12.** Preparation of organosilicon nanocapsules. M1:  $\text{MeSi}(\text{OMe})_3$ , M2:  $\text{Me}_2\text{Si}(\text{OMe})_2$ , M3:  $\text{Me}_3\text{SiOMe}$ , HMN: hexamethyldisilazane. Reprinted with permission from [146], O. Emmerich et al., *Adv. Mater.* 11, 1299 (1999). © 1999, Wiley-VCH.

described by applying a miniemulsion technique [148]. Such miniemulsions are typically formed by subjecting an oil/water/surfactant/co surfactant system to a high shear field created by devices such as an ultrasonifier and a microfluidizer. The thereby-formed droplets generally range in size from 50 to 500 nm, in contrast to the thermodynamically stable microemulsions where the droplet sizes vary usually from 10 to 100 nm. When monomer is used as the oil phase, free-radical polymerization can be carried out after the phase has been broken by high shear into droplets. If one uses for the synthesis an oil and a monomer in such a way that the two components are miscible in the monomeric state, but immiscible as soon as polymerization takes place, phase separation occurs and results in an oily core surrounded by a polymer shell. Figure 14 shows an image of nanocontainers that encapsulated a liquid during their formation [149].

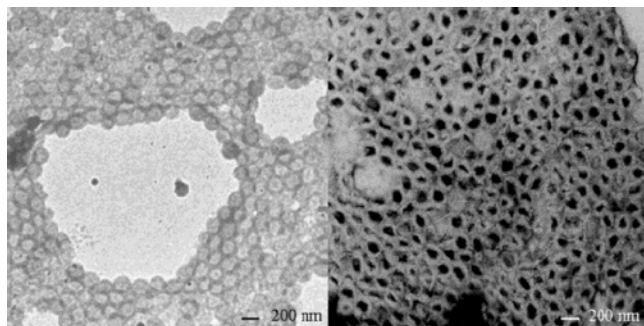


**Figure 13.** Transmission electron micrograph of nanocapsules before (left) and after (right) loading with pyrene. Reprinted with permission from [147], M. Sauer et al., *Adv. Mater.* 13, 1649 (2001). © 2001, Wiley-VCH.

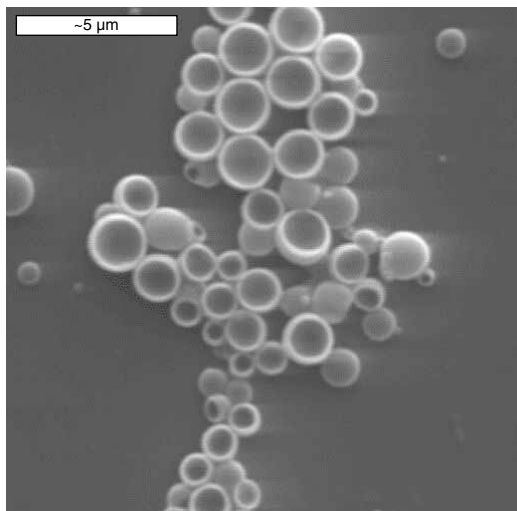


**Figure 14.** Encapsulation of liquid materials by the miniemulsion process to form nanocapsules. Reprinted with permission from [149], K. Landfester, *Adv. Mater.* 13, 765 (2001). © 2001, Wiley-VCH.

As already mentioned, one crucial step in emulsion polymerization is to obtain a reproducible formation of the particles structure and homogeneity. In conventional emulsion polymerization, this is mainly controlled by the concentration of surfactant and initiator. Although it was expected that in miniemulsions the particle formation would be independent of these parameters, this has been proven not to be the case [150]. However, the use of miniemulsions is of increasing interest and shows a great potential for the design of new materials, since it is not restricted to a single (radical) polymerization procedure and allows a low-cost reaction process (e.g., compared to microemulsions, considerably lower amounts of surfactant have to be employed).

## 6. DENDRIMER NANOCONTAINERS

Dendrimers are highly branched cascade molecules that emanate from a central core through a stepwise repetitive reaction sequence [151–156]. Dendritic macromolecules are also termed starburst dendrimers, denoting their characteristic radial symmetry. The question of the existence of a central cavity within dendrimers, that would make them a true nanocapsule, has been debated frequently. Indeed, molecules have been encapsulated within dendrimers, but this does not mean that dendrimers have a permanent and rigid cavity. However, by design such a molecule consists of three topologically different regions: first, a small initiator core of low density; second, the multiple repetitive branching units, whose density increases with increasing separation from the core, thus eventually leading to the third region, a rather densely packed shell constituted by the terminal functional groups. Characteristic of dendrimers are their well-defined structure, a three-dimensional globular shape, and a high density of terminal groups. In the context of dendrimer synthesis the term generation is used to describe each of the following stepwise reactions that give rise to the concentric growth of the macromolecule. Thus each of the subsequent layers of branched monomer units is termed a generation.

From their topology it follows that at some stage in the synthesis of a dendrimer, the space available for formation of the next generation is not sufficient to accommodate all of the atoms required for complete conversion. That means, dendrimers that have internal cavities with a dense outer shell may be synthesized by controlling the chemistry of the last step. This has been demonstrated by the preparation of the fifth-generation poly(propylene imine) dendrimer [157] shown in Figure 15.

Due to their dense outer shell, these molecules can be regarded as dendritic boxes [158] that are capable of retaining guest molecules trapped during synthesis. Subsequent guest diffusion out of the box was slow, since the dendrimer shell is close packed due to the bulky H-bonded surface groups. Guest molecules could diffuse out of the boxes if the tertiary butyl groups were removed, but only if the molecules were sufficiently small. Thus Rose Bengal remained in the containers while *p*-nitrobenzoic acid leaked out [157].

By synthetic design, dendrimers with tailored structures can be obtained. While the repeat units in the interior determine the solubilization characteristic of the dendrimer, that is, the capability to solubilize a molecule in the internal cavity, the outer units and functional terminal groups influence the solubility of the dendrimer itself in a given solvent. Thus by designing amphiphilic dendrimers, in which the interior is composed of hydrophobic moieties and the external groups consist of hydrophilic units, one can envision

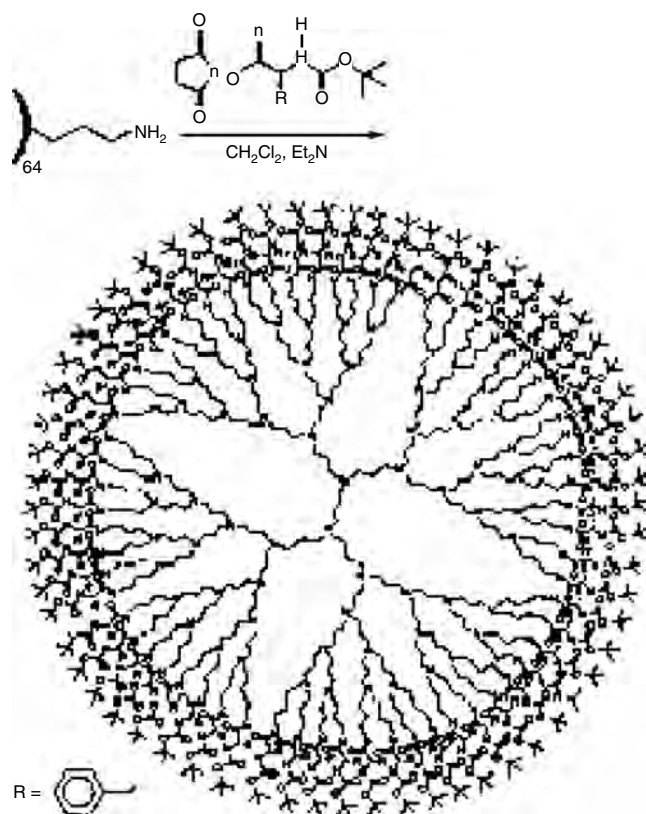


**Figure 15.** A dendritic box capable of encapsulating small guest molecules during construction. Reprinted with permission from [157], J. F. G. A. Jansen et al., *J. Am. Chem. Soc.* 117, 4417 (1995). © 1995, American Chemical Society.

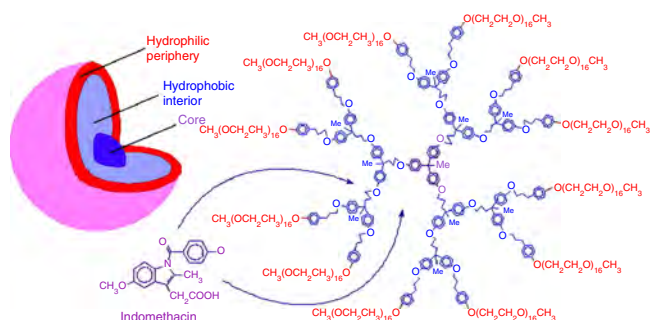


**Figure 16.** Dendritic “unimolecular micelle” used for the slow release of indomethacin. Reprinted with permission from [166], J. M. Fréchet, *Proc. Nat. Acad. Sci. USA* 99, 4782 (2002). © 2002, National Academy of Science.

potential encapsulation devices resembling micellar structures. It is straightforward that an inverted polarity construction of such dendrimers can be also possible.

Closely related to the already described dendritic boxes are amphiphilic dendrimers or hyperbranched molecules consisting of a hydrophobic (hydrophilic) core and a hydrophilic (hydrophobic) shell, so called unimolecular micelles [159–165]. In contrast to classical micelles that are aggregates of amphiphilic molecules and therefore dynamic assemblies of small molecules, these unimolecular micelles are static and retain their cohesion regardless of concentration. Due to their amphiphilic nature, these systems are able to solubilize selectively guest molecules within their core domain. For example, dendritic molecules with a hydrophobic interior and an oligoethylene glycol periphery have been used to entrap hydrophobic drugs, such as indomethacin (Fig. 16) [166]. For an overview of dendrimer application in diagnostics and therapy see [167].

A different type of encapsulation involving the formation of metal nanoparticles within dendrimers has been used to prepare inorganic-organic composite structures that are useful in catalytic applications. The formation of Cu-nanoparticles could be achieved by the use of poly(amidoamine) starburst dendrimers as a kind of nano-reactor. Due to the permeability of the outer shell for small molecules and ions,  $\text{Cu}^{2+}$  ions could diffuse into the interior of the dendritic boxes, where they were converted into Cu-nanoparticles upon reduction. Because of their rather large dimension, compared to single ions, with diameters of ca. 2 nm, the Cu-nanoparticles were too bulky to leak out of the dendritic cavity [168].

A different dendritic nanoreactor, a reverse micellar dendrimer, consists of a nonpolar aliphatic periphery and a polar inner functionality that has been used to catalyze the  $\text{E}_1$  elimination of a solution of tertiary alkyl halides in a nonpolar solvent. The alkyl halide has some polarity and becomes concentrated within the polar dendrimer, where it is converted into an alkene. As a result of its low polarity and the existence of a gradient of polarity between the dendrimer interior and the surrounding medium, the alkene product is readily expelled from the dendrimer back into the nonpolar solvent [169].

Recently also dendrimers with stimuli-response characteristics have been reported. Functionalization of the groups

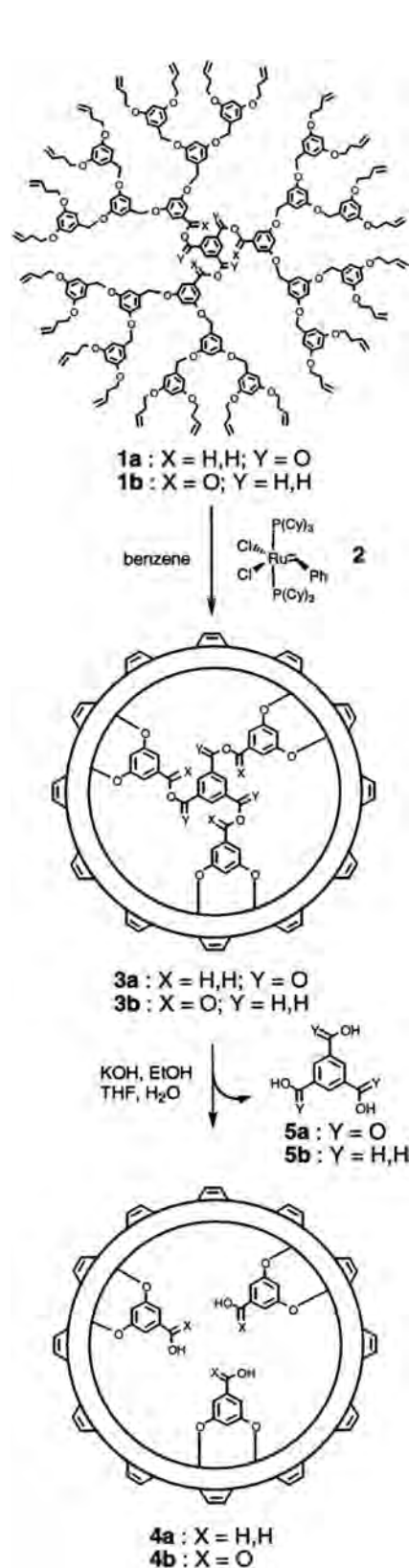


**Figure 17.** Preparation of a cored dendrimer. Reprinted with permission from [171], M. S. Wendland and S. C. Zimmermann, *J. Am. Chem. Soc.* 121, 1389 (1999). © 1999, American Chemical Society.

of amphiphilic dendrimers renders thus dendritic boxes with switchable permeabilities. The introduction of quaternary ammonium groups led to increased solubility in aqueous solutions and, due to the bulkiness of the added groups and their pH dependence, the desired release control of encapsulated molecules was achieved [170].

Although dendrimers show interesting and unique properties, they are, however, generally not real hollow particles, due to the fact that their core is covalently linked to the dendritic wedges of the molecule. It is obvious that this core is of crucial importance for the integrity of the whole molecule. Hence, removing the core requires another connection between the outer zones of the dendrimer. Indeed, applying similar concepts as shown in the approaches of Wooley [83] and Liu [84], it is also possible to produce real hollow structures from dendrimers. This has been recently demonstrated using a polyether dendrimer with a trimesic acid ester core. This polymer contains three cleavable ester bonds at its core and robust ether bonds throughout the rest of the molecule. As shown schematically in Figure 17 [171], the hollow particles were formed by selective cross-linking of homoallyl ether groups at their periphery and subsequent degradation of the core region by hydrolysis. An interesting possibility offered by this method is that the remaining functional groups in the interior of the container system could serve as endo-receptors available for molecular recognition. This approach allows a high control over the size and geometry of the formed nanocapsules. However, the preparation of the particles requires a rather costly and tedious procedure, which clearly presents a limiting factor for possible applications. Nevertheless, the quest for practical applications for dendrimers is becoming increasingly intense, but is still limited to highly specific areas.

## GLOSSARY

**Amphiphilic** Molecules consisting of two moieties, one hydrophobic (water-hating), the other hydrophilic (water-loving). Amphiphilic molecules show surfactant behavior.

**Block copolymer** A polymer in which at least two different constituting repeating units are joint in a block fashion; that is, a sequence of monomer A linked together to give a block of homopolymer A is followed by a sequence of linked monomer B (homopolymer B).

**Copolymer** A polymer in which the constituting units are two or more different ones.

**Critical micelle concentration (CMC)** Lowest concentration above which micellization can occur.

**Dendrimer** From dendro- branched and -mer part, a perfectly radial branched polymer molecule.

**Diblock copolymer** A (usually) linear block copolymer with only two types of repeating units.

**Generation** Each of the iterative reaction steps that give rise to a new layer of branched points in a dendrimer molecule.

**Graft copolymers** One special kind of comblike branched polymer, consisting of a linear chain of homopolymer A (backbone) from which shorter side chains of a different type of repeating unit (homopolymer B) emanate.

**Liposome** A vesicle-like structure composed of one or more concentric phospholipid bilayers.

**Micelle** Spherical or elongated aggregates of amphiphilic molecules, showing a core-shell structure. The hydrophobic inner core is shielded from the surrounding water media by the shell or corona formed by the hydrophilic part of the molecules that constitute the micelle.

**Polymer** From poly- many and -mer part, that is, consisting of many parts. A macromolecule consisting of individual repeating units, monomers, covalently linked together.

**Vesicle** Hollow aggregate consisting of a shell of one or more amphiphilic bilayers. Vesicles which have only one bilayer are termed unilamellar vesicles; if they show more bilayers, then they are called multilayered vesicles.

## REFERENCES

1. M. Rosoff, "Vesicles." Marcel Dekker, New York, 1996.
2. D. D. Lasic, "Liposomes from Physics to Applications." Elsevier, Amsterdam, 1993.
3. C. Niemeyer, *Angew. Chem. Int. Ed.* 40, 4128 (2001).
4. S. Mann, "Biomimetic Materials Chemistry." VCH, New York, 1996.
5. S. Hyde, "The Language of Shape." Elsevier, Amsterdam, 1997.
6. S. Mann, J. Webb, and R. J. P. Williams, "Biomaterialization: Chemical and Biological Perspectives." VCH, Weinheim, 1989.
7. S. Mann, *Angew. Chem.* 112, 3532 (2000).
8. N. D. Chasteen and P. M. Harrison, *J. Struct. Biol.* 126, 182 (1999).
9. F. C. Meldrum, V. J. Wade, D. L. Nimmo, B. R. Heywood, and S. Mann, *Nature* 349, 684 (1991).
10. W. Shenton, T. Douglas, M. Young, G. Stubbs, and S. Mann, *Adv. Mater.* 11, 253 (1999).
11. T. Douglas and M. Young, *Nature* 393, 152 (1998).
12. T. Douglas and M. Young, *Adv. Mater.* 11, 679 (1999).
13. D. D. Lasic, *Nature* 355, 279 (1992).
14. D. W. Yesair, "Proceedings of the 5th International Colloquium on Lecithin," 1990, p. 83.
15. F. M. Menger and M. I. Angelova, *Acc. Chem. Res.* 31, 789 (1998).
16. P. Walde and S. Ichikawa, *Biomolecular Eng.* 18, 143 (2001).
17. A. Chonn and P. R. Cullis, *Curr. Opin. Biotechnology* 6, 698 (1995).
18. M. Langer and T. E. Kral, *Polish J. Pharmacol.* 51, 211 (1999).
19. Y. Barenholz, *Curr. Opin. Colloid Interface Sci.* 6, 66 (2001).
20. A. Sharma and U. S. Sharma, *Int. J. Pharmaceutics* 154, 123 (1997).
21. H. Ringsdorf, B. Schlarb, and J. Venzmer, *Angew. Chemie* 100, 117 (1988).
22. D. F. O'Brien, B. Armitage, A. Benedicto, D. E. Bennett, H. G. Lamparski, Y. S. Lee, W. Srisri, and T. H. Sisson, *Acc. Chem. Res.* 31, 861 (1998).
23. B. Alberts, D. Bray, J. Lewis, M. Raff, K. Roberts, and J. D. Watson, "Molecular Biology of the Cell." Garland, New York, 1983.
24. D. D. Lasic, *Chimica Oggi* 18, 48 (2000).
25. D. D. Lasic, *Chimica Oggi* 19, 45 (2001).
26. D. D. Lasic and F. J. Martin, "Stealth Liposomes." CRC Press, Boca Raton, FL, 1995.
27. D. D. Lasic and D. Needham, *Chem. Rev.* 95, 2601 (1995).
28. A. L. Klibanov, K. Maruyama, V. P. Torchilin, and L. Huang, *FEBS Lett.* 268, 235 (1990).
29. M. C. Woodle, C. M. Engbergs, and S. Zalipsky, *Bioconjugate Chem.* 5, 493 (1994).
30. S. Zalipsky, *Bioconjugate Chem.* 4, 296 (1993).
31. Y. Sumida, A. Masuyama, M. Takasu, T. Kida, Y. Nakatsuji, I. Ikeda, and M. Nojima, *Langmuir* 17, 609 (2001).
32. Y. Einaga, O. Sato, T. Iyoda, A. Fujishima, and K. Hashimoto, *J. Am. Chem. Soc.* 121, 3745 (1999).

33. C. Nardin, T. Hirt, J. Leukel, and W. Meier, *Langmuir* 16, 1035 (2000).
34. L. Zhang and A. Eisenberg, *Science* 268, 1728 (1995).
35. K. Yu and A. Eisenberg, *Macromolecules* 31, 3509 (1998).
36. M. Regenbrecht, S. Akari, S. Förster, and H. Möhwald, *J. Phys. Chem. B* 103, 6669 (1999).
37. M. Moffit, K. Khougaz, and A. Eisenberg, *Acc. Chem. Res.* 29, 95 (1996).
38. H. Shen and A. Eisenberg, *J. Phys. Chem. B* 103, 9473 (1999).
39. M. Maskos and J. R. Harris, *Macromol. Rapid Commun.* 22, 271 (2001).
40. Y. Yu, L. Zhang, and A. Eisenberg, *Macromolecules* 31, 1144 (1998).
41. S. Burke, H. Shen, and A. Eisenberg, *Macromol. Symp.* 175, 273 (2001).
42. P. Alexandridis, *Curr. Opin. Colloid Interface Sci.* 1, 490 (1996).
43. B. M. Discher, D. A. Hammer, F. S. Bates, and D. E. Discher, *Curr. Opin. Colloid Interface Sci.* 5, 125 (2000).
44. S. Förster and M. Antonietti, *Adv. Mater.* 10, 195 (1998).
45. N. Hadjichristidis, "Block Copolymers: Synthetic Strategies, Physical Properties, Applications." Wiley, New York, 2002.
46. B. M. Discher, Y. Y. Won, D. S. Ege, J. C. M. Lee, F. S. Bates, D. E. Discher, and D. A. Hammer, *Science* 284, 1143 (1999).
47. D. E. Discher and A. Eisenberg, *Science* 297, 967 (2002).
48. D. D. Lasic, *Polymer News* 23, 367 (1998).
49. V. P. Torchilin, *J. Controlled Release* 73, 137 (2001).
50. A. V. Kabanov and V. Y. Alakhov, *Amphiphilic Block Copolymers* 347 (2000).
51. M. K. Pratten, J. B. Lloyd, G. Hörpel, and H. Ringsdorf, *Makromol. Chem.* 186, 725 (1985).
52. L. W. Seymour, K. Kataoka, and A. V. Kabanov, "Self-Assembling Complexes for Gene Delivery: From Laboratory to Clinical Trial." John Wiley, Chichester, 1998.
53. P. Lemieux, S. V. Vinogradov, S. L. Gebhard, N. Guerin, G. Paradis, H. K. Nguyen, B. Ochietti, Y. G. Suzdaltseva, E. V. Bartakova, T. K. Bronich, Y. St-Pierre, V. Y. Alakhov, and A. V. Kabanov, *J. Drug Target* 8, 91 (2000).
54. A. V. Kabanov and V. A. Kabanov, *Adv. Drug Delivery Rev.* 30, 49 (1998).
55. J. Ding and G. Liu, *J. Phys. Chem. B* 102, 6107 (1998).
56. C. Nardin and W. Meier, *Chimia* 55, 142 (2001).
57. W. Meier, C. Nardin, and M. Winterhalter, *Angew. Chem. Int. Ed.* 39, 4599 (2000).
58. C. Nardin, J. Widmer, M. Winterhalter, and W. Meier, *Eur. Phys. J. E* 4, 403 (2001).
59. C. Nardin, S. Thoeni, J. Widmer, M. Winterhalter, and W. Meier, *Chem. Comm.* 1433 (2000).
60. A. Graff, M. Sauer, P. Van Gelder, and W. Meier, *PNAS* 99, 5064 (2002).
61. M. Sauer, T. Haeefe, A. Graff, C. Nardin, and W. Meier, *Chem. Commun.* 2452 (2001).
62. H. Kukulka, H. Schlaad, M. Antonietti, and S. Förster, *J. Am. Chem. Soc.* 124, 1658 (2002).
63. F. Checot, S. Lecommandoux, Y. Gnanou, and H. A. Klok, *Angew. Chem. Int. Ed.* 41, 1339 (2002).
64. M. Jung, I. den Ouden, A. Montoya-Goñi, D. H. W. Hubert, P. M. Frederik, A. M. van Herk, and A. L. German, *Langmuir* 16, 4185 (2000).
65. J. Murtagh and J. K. Thomas, *Faraday Discuss. Chem. Soc.* 81, 127 (1986).
66. J. Kurja, R. J. M. Nolte, I. A. Maxwell, and A. L. German, *Polymer* 34, 2045 (1993).
67. N. Poulain, E. Nakache, A. Pina, and G. Levesque, *J. Polym. Sci. A: Polym. Chem.* 34, 729 (1996).
68. J. D. Morgan, C. A. Johnson, and E. W. Kaler, *Langmuir* 13, 6447 (1997).
69. M. Jung, D. Hubert, P. H. H. Bomans, P. M. Frederik, J. Meuldijk, A. van Herk, H. Fischer, and A. L. German, *Langmuir* 13, 6877 (1997).
70. J. Hotz and W. Meier, *Langmuir* 14, 1031 (1998).
71. J. Hotz and W. Meier, *Adv. Mater.* 10, 1387 (1998).
72. M. Hetzer, H. Clausen-Schaumann, S. Bayerl, T. M. Bayerl, X. Camps, O. Vostrowsky, and A. Hirsch, *Angew. Chem. Int. Ed.* 38, 1962 (1999).
73. D. H. W. Hubert, M. Jung, and A. L. German, *Adv. Mater.* 12, 1291 (2000).
74. S. Friberg, B. Yu, and G. A. Campbell, *J. Polym. Sci. A: Polym. Chem.* 28, 3575 (1990).
75. S. E. Friberg, B. Yu, A. U. Ahmed, and G. A. Campbell, *Colloids Surf.* 69, 239 (1993).
76. E. Brückner and H. Rehage, *Prog. Colloid Polym. Sci.* 109, 21 (1988).
77. T. J. McIntosh, S. A. Simon, and R. C. MacDonald, *Biochim. Biophys. Acta* 597, 445 (1980).
78. M. Jung, D. H. W. Hubert, P. H. H. Bomans, P. M. Frederik, A. van Herk, and A. L. German, *Adv. Mater.* 12, 210 (2000).
79. C. A. McKelvey, E. W. Kaler, J. A. Zasadzinski, B. Coldren, and H. T. Jung, *Langmuir* 16, 8285 (2000).
80. M. Sauer and W. Meier, *Chem. Commun.* 55 (2001).
81. J. F. Gohy, N. Willet, S. Varshney, J. X. Zhang, and R. Jerome, *Angew. Chem. Int. Ed.* 40, 3214 (2001).
82. K. B. Thurmond, T. Kowalewski, and K. L. Wooley, *J. Am. Chem. Soc.* 119, 6656 (1997).
83. H. Huang, E. E. Remsen, T. Kowalewski, and K. L. Wooley, *J. Am. Chem. Soc.* 121, 3805 (1999).
84. S. Stewart and G. J. Liu, *Chem. Mater.* 11, 1048 (1999).
85. Q. Zhang, E. E. Remsen, and K. L. Wooley, *J. Am. Chem. Soc.* 122, 3642 (2000).
86. J. Liu, Q. Zhang, E. E. Remsen, and K. L. Wooley, *Biomacromolecules* 2, 362 (2001).
87. Q. Ma, E. E. Remsen, T. Kowalewski, J. Shaefer, and K. L. Wooley, *Nanoletters* 1, 651 (2001).
88. K. S. Murthy, Q. Ma, C. G. Clark, E. E. Remsen, and K. L. Wooley, *Chem. Commun.* 773 (2001).
89. X. Liu, M. Jiang, S. Yang, M. Chen, D. Chen, C. Yang, and K. Wu, *Angew. Chem. Int. Ed.* 41, 2950 (2002).
90. T. Liu, Y. Xie, and B. Chu, *Langmuir* 16, 9015 (2000).
91. W. Stober and A. Fink, *J. Colloid Interface Sci.* 26, 62 (1968).
92. E. Donath, G. B. Sukhorukov, F. Caruso, S. A. Davis, and H. Möhwald, *Angew. Chem. Int. Ed.* 37, 2201 (1998).
93. G. Decher, *Science* 227, 1232 (1997).
94. P. Bertrand, A. Jonas, A. Laschewsky, and R. Legras, *Macromol. Rapid Commun.* 21, 319 (2000).
95. F. Caruso, *Adv. Mater.* 13, 11 (2001).
96. F. Caruso, R. A. Caruso, and H. Möhwald, *Chem. Mater.* 3309 (1999).
97. D. I. Gittings and F. Caruso, *Adv. Mater.* 12, 1947 (2000).
98. N. G. Balabushevitch, G. B. Sukhorukov, N. A. Moroz, D. V. Volodkin, N. L. Larionova, E. Donath, and H. Möhwald, *Biotechnol. Bioeng.* 76, 207 (2001).
99. P. Rilling, T. Walter, R. Pommersheim, and W. Vogt, *J. Membr. Sci.* 129, 283 (1997).
100. G. B. Sukhorukov, M. Brumen, E. Donath, and H. Möhwald, *J. Phys. Chem.* 103, 6434 (1999).
101. G. B. Sukhorukov, E. Donath, S. Moya, A. S. Susa, A. Voigt, J. Hartmann, and H. Möhwald, *J. Microencapsulation* 17, 177 (2000).
102. F. Caruso, D. Trau, H. Möhwald, and R. Renneberg, *Langmuir* 16, 1485 (2000).
103. G. B. Sukhorukov, A. A. Antipov, A. Voigt, E. Donath, and H. Möhwald, *Macromol. Rapid Commun.* 22, 44 (2001).
104. G. Ibarz, L. Dähne, E. Donath, and H. Möhwald, *Adv. Mater.* 13, 1324 (2001).

105. G. B. Sukhorukov, L. Dähne, J. Hartmann, E. Donath, and H. Möhwald, *Adv. Mater.* 12, 112 (2000).
106. E. Donath, G. B. Sukhorukov, and H. Möhwald, *Nachr. Chem. Tech. Lab.* 47, 400 (1999).
107. S. Moya, G. B. Sukhorukov, M. Auch, E. Donath, and H. Möhwald, *J. Colloid Interface Sci.* 216, 297 (1999).
108. F. Caruso, R. A. Caruso, and H. Möhwald, *Science* 282, 1111 (1998).
109. F. Caruso, X. Shi, R. A. Caruso, and A. Susha, *Adv. Mater.* 13, 740 (2001).
110. F. Caruso, M. Spasova, A. Susha, M. Giersig, and R. A. Caruso, *Chem. Mater.* 13, 109 (2001).
111. R. A. Caruso, A. Susha, and F. Caruso, *Chem. Mater.* 13, 400 (2001).
112. K. H. Rhodes, S. A. Davis, F. Caruso, B. Zhang, and S. Mann, *Chem. Mater.* 12, 2832 (2000).
113. I. Pastoriza-Santos, B. Schöler, and F. Caruso, *Advanced Functional Materials* 11, 122 (2001).
114. L. Dähne, S. Leporatti, E. Donath, and H. Möhwald, *J. Am. Chem. Soc.* 123, 5431 (2001).
115. C. Barthelet, S. P. Armes, S. F. Lascelle, S. Y. Luk, and H. M. E. Stanley, *Langmuir* 14, 2032 (1988).
116. M. Marinakos, J. P. Novak, L. C. Brouseau III, A. B. House, E. M. Edeki, J. C. Feldhaus, and D. L. Feldheim, *J. Am. Chem. Soc.* 121, 8518 (1999).
117. S. M. Marinakos, D. A. Schultz, and D. L. Feldheim, *Adv. Mater.* 11, 34 (1999).
118. S. M. Marinakos, M. F. Anderson, J. A. Ryan, L. A. Martin, and D. L. Feldheim, *J. Phys. Chem. B* 105, 8872 (2001).
119. S. Bloomberg, S. Ostberg, E. Harth, A. W. Bossman, B. van Horn, and C. J. Hawker, *J. Polym. Sci. A: Polym. Chem.* 40, 1309 (2002).
120. T. K. Mandal, M. S. Fleming, and D. R. Walt, *Chem. Mater.* 12, 3481 (2000).
121. D. Bontempo, N. Tirelli, K. Feldman, G. Masci, V. Crescenzi, and J. A. Hubbell, *Adv. Mater.* 14, 1239 (2002).
122. L. Zha, Y. Zhang, W. Yang, and S. Fu, *Adv. Mater.* 14, 1090 (2002).
123. S. Fujishige, K. Kubota, and I. Ando, *J. Phys. Chem.* 93, 3311 (1989).
124. H. Bamnolker, B. Nitzan, S. Gura, and S. Margel, *J. Mater. Sci. Lett.* 16, 1412 (1997).
125. N. Kawahashi and E. Matijevic, *J. Colloid Interface Sci.* 143, 103 (1991).
126. K. J. C. van Brommel, J. H. Jung, and S. Shinkai, *Adv. Mater.* 13, 1472 (2001).
127. J. L. Koenig and P. L. Sutton, *Biopolymers* 9, 1229 (1970).
128. B. Davidson and G. D. Fasman, *Biochemistry* 6, 1616 (1967).
129. T. J. Yu, J. L. Lippert, and W. L. Peticolas, *Biopolymers* 12, 2161 (1973).
130. A. Dong, Y. Wang, Y. Tang, N. Ren, Y. Zhang, and Z. Gao, *Chemistry of Materials* 14, 3217 (2002).
131. S. B. Yoon, K. Sohn, J. Y. Kim, C. H. Shin, J. S. Yu, and T. Hyeon, *Adv. Mater.* 14, 19 (2002).
132. L. Sun, R. M. Crooks, and V. Chechik, *Chem. Commun.* 359 (2000).
133. M. Okubo, Y. Konishi, and H. Minami, *Colloid Polym. Sci.* 276, 638 (1988).
134. M. Okubo and H. Minami, *Colloid Polym. Sci.* 274, 433 (1996).
135. D. Sundberg, A. P. Cassasa, J. Pantazopoulos, and M. R. Muscato, *J. Appl. Polym. Sci.* 41, 1429 (1990).
136. Y. C. Chen, V. N. Dimonie, and M. S. El-Aaser, *Macromolecules* 24, 3779 (1991).
137. V. L. Dimonie, M. S. El-Aaser, and J. W. Vanderhoff, *Polym. Mater. Sci. Eng.* 58, 821 (1988).
138. I. Cho and K. W. J. Lee, *J. Appl. Polym. Sci.* 30, 1903 (1985).
139. M. Okubo, A. Yamada, and T. Matsumoto, *J. Polym. Sci. A: Polym. Chem.* 18, 3219 (1980).
140. S. Lee and A. Rudin, in "Polymer Latexes," ACS Symposium Series 492, p. 234. American Chemical Society, Washington, DC, 1992.
141. M. P. Merkel, V. L. Dimonie, M. S. El-Aaser, and J. W. Vanderhoff, *J. Polym. Sci. A: Polym. Chem.* 25, 1755 (1987).
142. J. E. Jönsson, H. Hassander, L. H. Jansson, and B. Törnel, *Macromolecules* 27, 1932 (1994).
143. D. C. Sundberg, A. P. Cassasa, J. Pantazopoulos, M. R. Muscato, B. Kronberg, and J. Berg, *J. Appl. Polym. Sci.* 41, 1425 (1990).
144. X. Z. Kong, C. Y. Kan, H. H. Li, D. Q. Yu, and Q. Juan, *Polym. Adv. Technol.* 8, 627 (1997).
145. T. Dobashi, F. Yeh, Q. Ying, K. Ichikawa, and B. Chu, *Langmuir* 11, 4278 (1995).
146. O. Emmerich, N. Hugenberg, M. Schmidt, S. S. Sheikov, F. Baumann, B. Deubzer, J. Weiss, and J. Ebenhoch, *Adv. Mater.* 11, 1299 (1999).
147. M. Sauer, D. Streich, and W. Meier, *Adv. Mater.* 13, 1649 (2001).
148. F. Tiarks, K. Landfester, and M. Antonietti, *Langmuir* 17, 908 (2001).
149. K. Landfester, *Adv. Mater.* 13, 765 (2001).
150. P. A. Lovell and M. S. El-Aasser, "Emulsion Polymerization and Emulsion Polymers." Wiley, New York, 1997.
151. D. A. Tomalia, H. Baker, J. Dewald, J. M. Hall, G. Kallos, R. Martin, and J. Ryder, *Polym. J.* 17, 117 (1985).
152. G. R. Newkome, Z. Yao, G. R. Baker, and V. K. Gupta, *J. Org. Chem.* 50, 2003 (1985).
153. G. R. Newkome, C. N. Moorefield, and F. Vögtle, "Dendritic Molecules: Concepts, Synthesis, Perspectives." VCH, Weinheim, 1996.
154. J. M. Fréchet and D. A. Tomalia, "Dendrimers and other Dendritic Molecules." Wiley, Winchester, 2001.
155. C. J. Hawker and J. M. J. Fréchet, *J. Am. Chem. Soc.* 112, 7638 (1990).
156. K. L. Wooley, C. J. Hawker, and J. M. J. Fréchet, *J. Am. Chem. Soc.* 113, 4252 (1991).
157. J. F. G. A. Jansen, D. A. F. J. van Bortel, E. M. M. de Brabander-van den Berg, and E. W. Meijer, *J. Am. Chem. Soc.* 117, 4417 (1995).
158. J. F. G. A. Jansen, E. M. M. de Brabander-van den Berg, and E. W. Meijer, *Science* 266, 1226 (1994).
159. A. Sunder, M. Krämer, R. Hasselmann, R. Mülhaupt, and H. Frey, *Angew. Chemie* 111, 3758 (1999).
160. C. J. Hawker, K. L. Wooley, and J. M. J. Fréchet, *J. Chem. Soc. Perkin. Trans.* 1, 1287 (1993).
161. G. R. Newkome, N. Moorefield, G. R. Baker, M. J. Saunders, and S. H. Grossmann, *Angew. Chem. Int. Ed. Engl.* 30, 1178 (1991).
162. S. Mattei, P. Seiler, F. Diederich, and V. Gramlich, *Helv. Chim. Acta* 78, 1904 (1995).
163. S. Stevelmanns, J. C. M. van Hest, J. F. G. A. Jansen, D. A. F. J. van Bortel, E. M. M. de Brabander-van den Berg, and E. W. Meijer, *J. Am. Chem. Soc.* 118, 7398 (1996).
164. M. Liu, K. Kono, and J. M. J. Fréchet, *J. Controlled Release* 65, 121 (2000).
165. M. Liu, K. Kono, and J. M. J. Fréchet, *J. Polym. Sci. A: Polym. Chem.* 37, 3492 (1999).
166. J. M. Fréchet, *Proc. Nat. Acad. Sci. USA* 99, 4782 (2002).
167. S. E. Striba, H. Frey, and R. Haag, *Angew. Chem. Int. Ed.* 41, 1329 (2002).
168. M. Zhao, L. Sun, and R. M. Crooks, *J. Am. Chem. Soc.* 120, 4877 (1998).
169. M. E. Piotti, F. Rivera, R. Bond, C. J. Baker, and J. M. J. Fréchet, *J. Am. Chem. Soc.* 121, 9471 (1999).
170. Z. Sideratou, D. Tsiourvas, and C. M. Paleos, *Langmuir* 16, 1766 (2000).
171. M. S. Wendland and S. C. Zimmermann, *J. Am. Chem. Soc.* 121, 1389 (1999).





# Nanocrystal Memories

E. Kapetanakis, P. Normand

*Institute of Microelectronics, NCSR "Demokritos," Aghia Paraskevi, Greece*

K. Beltsios

*University of Ioannina, Greece*

D. Tsoukalas

*NTUA, Athens, Greece*

## CONTENTS

1. Introduction
  2. Nanocrystal Memory Approach
  3. Nanocrystal Floating-Gate Technology
  4. Nanocrystal Memory: Experimental Results
  5. Conclusions
- Glossary  
References

## 1. INTRODUCTION

The technologies that have been developed over the years in realizing data storage can be divided into semiconductor types (MOS, bipolar, and charge-coupled devices) and moving media types (magnetic disk, optical disk) which require mechanical equipment operation. Compared to disk devices, semiconductor memories exhibit superior characteristics in terms of cost and performance [1]. Furthermore, due to the advantages of MOS technology in device manufacturability and miniaturization, most ultralarge-scale integration (ULSI  $\geq 10^7$  transistors on a chip) memory circuits are made at the present time using MOS memories. The most important device for MOS memory technology today is the metal-oxide semiconductor (MOS) field-effect transistor (FET) [2, 3]. A simplified cross section of an *n*-channel MOS transistor is shown in Figure 1. It consists of a *p* ("positive")-type silicon substrate with a surplus of holes and a top gate electrode made of conducting material, between which an insulating dielectric (usually, a thermally grown silicon dioxide film) is formed. Two junctions, the source and the drain, that have an abundance of electrons are fabricated with a small overlap to the gate by *n* ("negative")-doped ionized

regions. When a positive voltage is applied to the gate, an electric field is set up that penetrates through the insulator, attracting electrons toward the surface of the substrate. An inversion layer designated as the channel is formed, allowing current to flow between the source and the drain regions.

Ideal memory devices ought to be low cost, nonvolatile, able to retain data without external power, have random access that features read-write access to any individual data location, high speed, high density, low power consumption, be easy to test, highly reliable, and compatible with established industrial manufacturing routes. Unfortunately a single type of memory device having all of these characteristics remains unfeasible to this day. Instead, the MOS memory devices that are used as the best alternatives in today's electronics systems can be classified in terms of their volatility and access speed as volatile random-access memories (RAMs) and nonvolatile non-RAMs. Volatile RAMs permit data to be stored and retrieved at comparable speeds. They include the two most common memory types: dynamic RAM (DRAM) and static RAM (SRAM). DRAM has a small cell size and a reasonably short access (read) time ( $<20$  ns), but the stored information in each cell must be refreshed more than once per second. The refreshing operation is what makes the difference between a dynamic and a static RAM. SRAM has the fastest access time ( $<5$  ns) and does not require refreshing, but has a larger cell size than DRAM. On the other hand, a nonvolatile non-RAM memory, more commonly called nonvolatile memory (NVM), is a device that can program (write) data electrically, and does not require any power for the maintenance of the data ("retention"), but for which the access operation is restricted in some sense. At present, the dominant technology for NVM implementation is based on the floating-gate (FG) concept [4]. All of the FG NVM memory cells have the same generic cell structure, and are roughly classified following their erasing

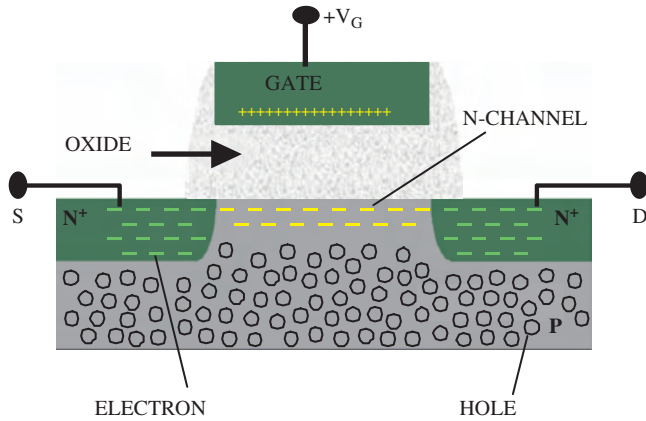


**Figure 1.** Schematic cross-section representation of an *n*-channel MOS transistor structure.

mode, to ultraviolet light UV-erasable EPROM (electrically programmable read-only memory) and EEPROM (electrically erasable PROM), including the most recent and important version of Flash EEPROM where the complete memory array is erased very quickly. Today, the name Flash EEPROM is used for all EEPROMs in which the erase operation is done not for every single cell, but for a whole memory array, or for a memory block (sector). The Flash memory has a small size, and does not require refresh, but has slow access time and even slower write/erase times ( $\sim 80$  ns access and  $\sim 1 \mu\text{s}/>10$  ms write/erase times for the case of NOR Flash). The slow write speed and the limited number of write/erase operations ( $10^5$ – $10^6$  write/erase cycles) preclude the usage of Flash memory as a RAM memory.

### 1.1. Dynamic RAM

The DRAM memories are commonly used as a main memory for personal computers because of their low cost and high-density capability. The modern one transistor/one capacitor (1T-1C) DRAM memory cell that emerged in the 1970s [5] consists of one MOS transistor (access or pass transistor) in series with one MOS storage capacitor [Fig. 2(a)]. Binary data are stored on the capacitor in the form of charge  $Q_s$ . By assuming that the capacitor's common node is biased at  $V_{CC}/2$ , a logic "0" in the cell requires a capacitor with a voltage of  $-V_{CC}/2$  across it, while a logic "1" in the cell requires a capacitor with a voltage of  $+V_{CC}/2$ . Therefore, the charge stored in the capacitor is  $Q_s = (-V_{CC}/2)C_s$  for logic "0" and  $Q_s = (V_{CC}/2)C_s$  for the case of logic "1," where  $C_s$  is the capacitance of the storage capacitor. In the memory-array configuration, shown in Figure 2(b), each capacitor is accessed through a transistor connected to an array of word lines and bit lines. A circuit called a sense amplifier is used to distinguish whether the memory cell is storing "0" or "1" information (read operation). During reading, the stored information is lost, and thus a write cycle must always follow. Even during normal operation, the stored charge can be slowly depleted due to several leakage mechanisms inevitably present, such as *p-n* junction leakage, subthreshold conduction in the pass transistor, leakage through the capacitor dielectric, or through high-energy-particle events (alpha particles, neutrons). Thus, essential

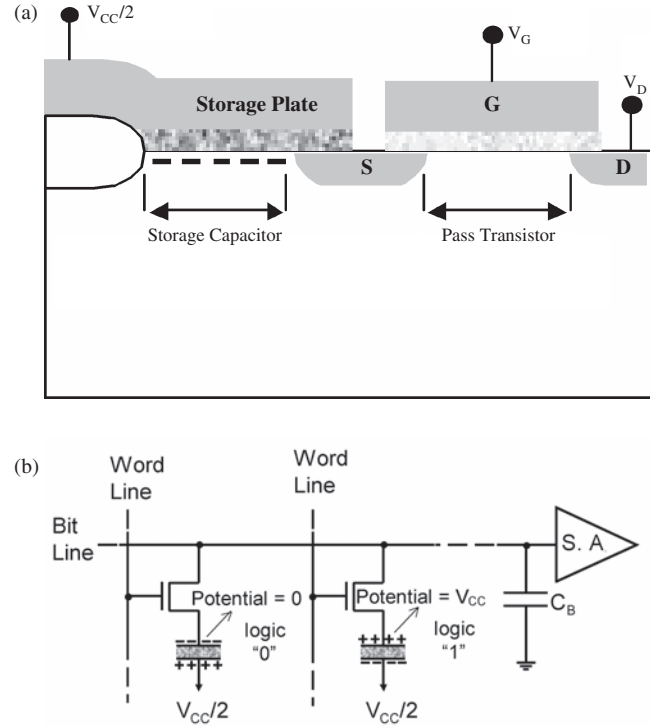


**Figure 2.** Schematic of (a) conventional planar one-transistor one-capacitor DRAM cell, and (b) DRAM circuit in a memory-array configuration (two memory cells are shown).

to the proper operation of a DRAM is the refresh operation. During refresh, the cell content is read, and the data bit is rewritten, thus restoring the capacitor voltage to its proper value. The refreshing operation increases the device power consumption, and also imposes a serious limitation in transistor scaling. In order to reach a long refresh time, the leakage of the access transistor must be low, thus requiring relatively high threshold voltages ( $>0.5$  V). This is the reason why DRAM transistors have not scaled as fast as logic transistors, and generally have longer channel lengths, thicker gate oxides, and higher operating voltages. An additional constraint in DRAM cell scaling is imposed by the scaling of the storage capacitor. Because the voltage available to the sense amplifier for signal detection is proportional to the  $C_s/C_b$  ratio, the storage capacitance  $C_s$  needs to be as large as possible in order to create a large enough signal ( $\sim 100$  mV) on the bit line.  $C_b$  is an unavoidable parasitic bit line capacitance coming from the transistor junction capacitance and bit-line wire capacitance.  $C_s$  also must substantially remain large enough to minimize the sensitivity of the cell to soft errors that originate from high-energy-particle events. Typical  $C_s$  values are in the range of 25–30 fF, and these values have remained constant over many generations of DRAM technology. According to the equation for the memory cell capacitance,  $C_s = \epsilon\epsilon_0 A/d$ , where  $\epsilon$  is the relative dielectric constant of the capacitor film material,  $\epsilon_0$  is the dielectric constant of free space,  $A$  is the capacitor area, and  $d$  is the thickness of the capacitor film, the approaches that have been used in order to maintain a constant  $C_s$  are as follows. First, in the simple planar cell [Fig. 2(a)], the pure oxide capacitor film with a dielectric

constant of 4 is replaced by a multilayer oxide/nitride/oxide (ONO) or nitride/oxide (NO) film with a dielectric constant of 7, followed by capacitor film thickness  $d$  scaling. Then, three-dimensional (3D) capacitor structures (stack or trench) in place of the conventional planar cell are developed to increase the capacitance per unit area. It is expected that future DRAM capacitors will need dielectric materials having high  $\epsilon$  values such as  $\text{Ta}_2\text{O}_5$  (tantalum pentoxide  $\epsilon = 25$ ) and, eventually, materials with even higher  $\epsilon$  values such as BST (barium strontium titanate,  $\epsilon = 500$ ) [6]. Although these exotic materials would significantly increase the capacitance per unit area, and thus the device integration density, they are not at this time compatible with the existing DRAM manufacturing process. All in all, it is unclear whether the DRAM memory cell will scale at gigabit densities due to the inherent constraints of low-leakage access transistors and the need for large storage capacitance.

## 1.2. Static RAM

The SRAM memory cell is a bistable circuit utilizing a pair of inverters connected back to back, and is mostly used as on-chip cache memory on microprocessors because of its faster speed compared to the DRAM cell. The most common version of the SRAM memory cell is the full complementary MOS (CMOS) with PMOS loads illustrated in Figure 3. It is a six-transistor (6T) memory cell consisting of two cross-coupled inverters and two access transistors connected to complementary bit lines. Since the inverters are cross coupled, the SRAM memory cell is a two-state circuit with excellent stability; either the “1” or “0” state will be maintained indefinitely by a continuous small dissipation of power in the cell unless changed by another write operation. The access transistors are turned on when the word line is selected, and they connect the inverters to the bit lines, allowing the read and write operations to be performed. One important parameter for the stability of the SRAM cell and a serious concern in SRAM scaling is that the two cross-coupled inverters must have well-matched transistor characteristics. Random variations of the transistor properties, mainly fluctuations of the transistor threshold voltages ( $V_{\text{TH}}$ ), result in an increased bit-fail rate of the memory

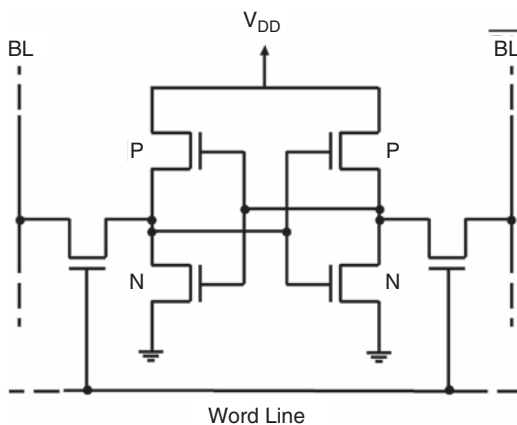


**Figure 3.** Circuit schematic of a six-transistor SRAM cell in a memory array configuration (one memory cell is shown).

cell [7]. Such fluctuations of  $V_{\text{TH}}$  MOSFETs are unavoidably caused by discrete dopant atoms or by the finite ability to control the fabrication process, and ultimately limit the number of devices which can be integrated on one chip. In addition, similar to the DRAM case, cosmic rays, mostly neutrons, can cause soft errors (temporary random errors) in SRAM cell operation, and thus impose another constraint in future cell scaling as the soft error rate increases as feature size and operating voltage decreases.

## 1.3. Flash EEPROM

The Flash memory appeared in 1984 [8], and was designed to be the solution to the scaling problem of EEPROMs by trading off memory size with functionality. It has already become the largest market in nonvolatile technology due to a high competitive tradeoff between functionality and cost/bit, and it is expected to be the optimum choice for mass storage in personal mobile systems. The generic Flash memory cell is a single stacked-gate MOS transistor, as illustrated in Figure 4. The conductive polysilicon layer between the externally accessible gate (called a control gate) and the substrate is denoted as the floating gate. The dielectrics between the FG and the substrate (usually a thermal silicon oxide) and between the FG and the control gate are usually referred to as the tunneling and the interpoly or control dielectrics, respectively. The idea of using an FG device to obtain a nonvolatile memory device was suggested for the first time in 1967 by Kahng and Sze [9]. The basic operation principle of the FG device is the storage of charge in the FG [Fig. 5(a)]. During programming (writing), electrons (for the case of an  $n$ -channel device) from the silicon conduction band are injected through the tunneling oxide, and subsequently stored on the floating gate. The stored electrons in the FG screen the mobile charge in the underlying channel, thus inducing a change in the conductivity of the channel, allowing the transistor threshold voltage to be electrically altered between a low and a high value, conventionally defined as the “1” or erased state and the “0” or written state [Fig. 5(a)]. The threshold voltage shift  $\Delta V_{\text{TH}}$  caused by the storage of the charge  $Q_{\text{FG}}$  is given by  $\Delta V_{\text{TH}} = -Q_{\text{FG}}/C_{\text{CG}}$ .  $C_{\text{CG}}$  is the capacitance between the control and the floating gates, and is given by  $C_{\text{CG}} = \epsilon A/t$ ,

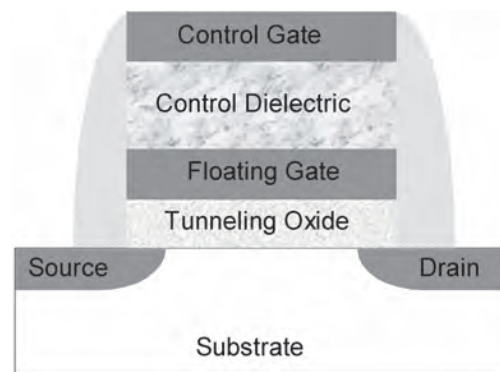


**Figure 4.** Generic stacked-gate MOS transistor Flash memory cell cross section.

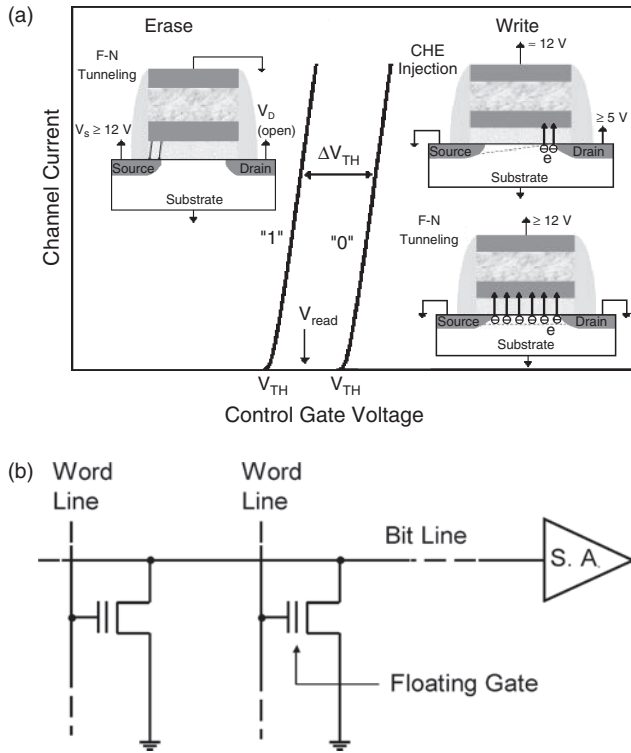


**Figure 5.** (a) Read and write/erase operation principles of a Flash memory. The schematic of the memory transistor illustrates the bias conditions that are employed for the case of CHE injection or F–N substrate electron injection write modes, and for the case of source-side electron extraction erase mode. (b) Circuit schematic of a one-transistor Flash memory cell in a memory array configuration (two memory cells are shown).

where  $A$  is the capacitor area, and  $\epsilon$  and  $t$  are the dielectric constant and thickness of the control dielectric, respectively. The information content of the cell is read by sensing the current through the bit line, while accessing the cell is achieved by applying a read voltage  $V_{\text{read}}$  at the gate or word line with a value between the two possible threshold voltages. In one state, the transistor is ON (“1”) (conducting current), while in the other, the transistor is OFF (“0”). An erase operation involves removing electrons from the FG, hence returning the device  $V_{\text{TH}}$  to a low state. The Flash memory cell can be erased electrically, but not selectively. The content of the whole memory chip is always cleared (Flash erase) in one step, and this design allows a single-transistor memory cell to be constructed [Fig. 5(b)]. In order to allow byte-selective write and erase, a select transistor, is added to the memory transistor, leading to the so-called two-transistor EEPROM memory cell. Therefore, Flash memories abandon the feature of single-cell erasability in favor of lower cost large-scale integration memory circuits. Once programmed, the cell is guaranteed to retain information for at least ten years (the industrial standard for nonvolatile memories), either under operation or with power turned off. Information can be lost if electron leak occurs, mainly through the tunneling dielectric. To maintain nonvolatility, relatively thick (about 10 nm) tunneling oxides are required, a feature that causes difficulty in charging the

FG as a very large amount of energy is needed for electrons to move into or from the FG. The physical mechanisms that are commonly used for this charge transfer are the field-induced (Fowler–Nordheim, F–N) tunneling [10] or channel hot-electron injection (CHE) [11] for the write operation and F–N tunneling for the erase operation. During CHE injection, a large drain  $V_D$  bias causes the generation of highly energetic electrons at the drain side in the channel, while a large control gate  $V_G$  bias, with  $V_G > V_D$ , generates an oxide field that favors the injection of the heated electrons over the Si–SiO<sub>2</sub> energy barrier [Fig. 5(a)]. F–N tunneling is the flow of electrons through the energy barrier of the tunneling oxide that has been modified by a high electric field for effective narrowing of the oxide barrier width. During F–N programming, a high voltage applied to the top control gate causes electrons from the source, drain, or substrate (depending on the voltages at that terminals) to be injected into the FG. A schematic description of write by F–N tunneling for the case of electron injection from the whole channel region is shown in Figure 5(a). The erase process can be accomplished by applying a high voltage to the source, drain, or to the substrate of the well with the control gate grounded. It can also be accomplished by applying a negative voltage to the control gate with the other terminals connected at different positive voltages. Depending on the programming mechanism, Flash memory arrays have two different configurations: NAND and NOR. NAND cells use F–N tunneling to program the FG, while NOR cells use CHE injection for write operation. Both NOR and NAND cells utilize F–N tunneling to erase the cell. The generation of highly energetic carriers during both programming operations introduces permanent damage, referred to as degradation, due to charge trapping in the tunneling oxide. As a result, the Flash memory can withstand a limited number, typically  $10^5$ , of write/erase cycles (called its endurance). Additionally, due to the small currents flowing through the tunneling oxide during both the CHE injection and F–N tunneling processes, the charging times are slow, resulting in typical write times in the microsecond and millisecond ranges, respectively. Although Flash memories have been designed as a solution to the scaling problem of conventional EEPROM devices, aggressive scaling of the transistor dimensions and the dramatic increase in the memory array size demand a lower voltage memory cell design for the future. As the technology for the CHE injection or F–N tunneling process has to support relatively high voltages (e.g., 8–9 V minimum and  $>12$  V for CHE and F–N tunneling programming, respectively), Flash memory cell scaling presents severe limitations. Constraints in vertical scaling of the memory cell, and therefore in scaling of the applied operating voltages, are imposed by the extreme requirements of incredibly low dielectric leakage (less than  $\sim 10^{-14}$  A/cm<sup>2</sup>) to ensure a ten-year data retention time. In the case of the control dielectric, an ONO composite dielectric is typically used, and allows for thinner control layers compared to silicon oxide layers, with much lower leakage currents. In the case of the tunneling oxide, the requirements are even more stringent as it must be thin enough to allow a fast write/erase speed at reasonable voltage levels with negligible degradation after  $10^5$  programming cycles, and thick enough to avoid charge loss during read or normal

operations. Thus, all scaling issues pertinent to Flash memories are ultimately related to the reliability of the tunneling oxide. Theoretically, in order to ensure ten-year data retention time, the tunneling oxide could be scaled until electron flow through the full oxide thickness becomes significant (i.e., down to ca. 5 nm). However, stress-induced leakage current (SILC) [12, 13] imposes a more stringent limitation on the tunneling oxide thickness as a single point of high leakage in the oxide can discharge the conducting polysilicon FG layer. This is the reason why the tunneling oxide of Flash memories was set as thin as about 10 nm from the beginning, and has scarcely been thinned over five successive generations to limit its thickness to 7–8 nm at the present state of nonvolatile memory technology. As a result, the dimensions of the FG transistor have been scaled much more slowly than those of the logic transistor, and therefore, the Flash memory performance in terms of access time, write/erase speeds, and operating voltages has not been substantially improved with device scaling. The increase in Flash memory capacity (thus, the decrease in the cost/Mbit) has been mainly achieved through different array architectures such as the NAND structure [14], which reduces the cell size by connecting the cells in series between a bit line and a source line. Another option for higher bit storage density without the need for aggressive technology scaling is the multilevel charge storage (MLCS) approach, where more than one bit is stored inside a single memory transistor [15].

## 2. NANOCRYSTAL MEMORY APPROACH

In order to overcome the technological constraints imposed as the device size approach dimensions below the 100 nm range, new memory concepts are needed for ultrahigh-density, low-voltage, low-power, and fast write/erase data storage. For this reason, various memory alternatives are actively investigated. The ferroelectric RAM (FRAM) [16] that replaces the DRAM capacitor's dielectric with ferroelectric material, and the one-transistor magnetic RAM (MRAM) [17] that replaces the capacitor with a magnetoresistor structure are two potential solutions. For such devices, the compatibility of the ferroelectric and magnetic materials with standard CMOS processes is an important technological issue that remains a subject of debate. Another promising alternative for low-cost ultradense data storage lies in the use of modified Flash memory structures. Nanocrystal memories are one particular implementation of this approach. In the subsections that follow, the operation principle and challenges of this new memory concept are reviewed, as well as the electrical characteristics of nanocrystal memory devices obtained through the use of various fabrication techniques of synthesizing nanocrystalline floating-gate layers.

### 2.1. Charge Storage in Spatially Isolated Trap Sites

Two different approaches for improving the performance of “scaled-Flash” memory have been proposed. The first includes the nonvolatile RAM (referred to as NOVORAM) suggested by Likharev [18], and the phase-state low-electron-number drive random (PLEDM) proposed by

Hitachi and the University of Cambridge [19]. NOVORAM uses a “crested” tunnel barrier that replaces the usual uniform oxide barrier (often called a “rectangular” barrier) with a stack of dielectric materials in order to create a special barrier shape for an effective F–N tunneling into/out of the floating gate. Thus, enhanced barrier height suppression is present during write/erase operations, while a higher barrier is present during the retention and read modes. In the PLEDM device, electrons are injected into the memory node through stacked multiple tunnel junctions. A second polysilicon gate that surrounds the memory cell is used to modulate the current flow through the tunnel junctions. For both devices, simulations have indicated write times potentially faster than DRAM and ~ten-year retention time. NOVORAM and PLEDM devices are currently in the concept stage since no memory operation has been experimentally demonstrated.

The second approach for overcoming scaling limitations of conventional Flash memory cells is based on the storage of charges in isolated charge-trapping sites in place of the conventional FG layer. Excellent immunity to oxide defects is thus ensured since, even if a pinhole exists in the tunneling oxide, leakage will only cause a few storage nodes to lose their charge. This allows the implementation of memory devices with thinner tunneling oxides, operating at lower voltages and/or faster programming speeds. In addition, compared to conventional FG memory devices, the single-transistor charge-trapping structure exhibits other important advantages such as: (1) the memory array requires only one level of polysilicon that simplifies the fabrication process and lowers the cost, (2) the memory cell permits further scaling (the cell size can be  $2F^2$ , where  $F$  is the minimum feature size), and (3) the absence of drain-to-FG coupling allows the use of higher drain reading voltages for faster memory access times, and also reduces the bit-line disturb as only storage nodes directly over the drain overlap region will be affected.

Historically, the first charge-trapping device was introduced in 1967 by Wegener et al. [20], almost simultaneously with the FG memory cell, and was the metal–nitride–oxide–silicon (MNOS) cell, where the discrete charge-storage elements are traps distributed in the nitride layer. Today, two types of charge-trapping memory devices are actively investigated: the polysilicon-blocking oxide–nitride–tunneling oxide–silicon (SONOS) device, including the most recent version of nitride read-only memory (NROM) and the nanocrystal memory. The SONOS [21] and NROM [22] storage transistors utilize an oxide–nitride–oxide trapping material instead of the normal gate dielectric of a conventional  $n$ -channel MOSFET. The difference between the two devices lies in the physical mechanisms involved during programming operations that are related to the thickness of the bottom tunneling oxide. For SONOS devices, charge injection (removal) into (from) the dielectric storage layer is performed by direct tunneling through thin tunneling oxide (~2–3 nm in thickness), while for NROM devices with tunneling oxide greater than 5 nm, program (erase) operation takes place by localized charge trapping (removal) of channel hot-electron injection (tunnel-enhanced hot-hole injection) in the dielectric storage layer.



The nanocrystal memory cell, proposed in the early 1990s by Tiwari's team at IBM [23, 24], consists of a single MOS transistor with an array of laterally uncoupled crystalline silicon or germanium nanoparticles embedded in the gate oxide in close proximity to the channel. A schematic cross section of the memory cell is shown in Figure 6. A thin tunneling dielectric, usually thermal oxide ( $\leq 5$  nm in thickness), separates the channel of an otherwise conventional MOSFET from a distributed charge-trapping layer that covers the entire transistor channel area. A thicker control oxide layer is used to electrically isolate the nanocrystal storage nodes from the control gate.

## 2.2. Operation Considerations and Challenges

The storage of charges in a layer made of mutually isolated nanocrystals (in analogy to a conventional floating-gate device) is the basic operating principle of a nanocrystal memory. Stored charge changes the conductivity of the transistor by shifting the threshold voltage  $V_{TH}$  of the device, for the case of negative stored charge, to more positive values. This single-transistor memory device has been introduced as an alternative structure to conventional DRAM for high-storage density and low-power operation, as well as to nonvolatile memories such as Flash EEPROMs for faster write/erase speed, lower write/erase bias, and better endurance [23]. There are, however, key issues to be solved before the practical implementation of this kind of memory. Of importance are: data retention, memory window, and device characteristic deviations. Here, we will briefly discuss the role of some of the main features that affect the operation of the device and its performance, as well as the progress in the area of nanocrystal memories.

### 2.2.1. Programming Mechanism

Figure 7 shows schematic energy band diagrams for Si nanocrystal memories during: (a) write (electron injection), and (b) erase (electron removal). During write (erase) operation, electrons are injected (removed) to (from) the nanocrystals by applying a positive (negative) voltage bias to the gate with respect to source and drain electrodes. The thickness of the control oxide must be relatively thin for reasonable low voltage operation, but not so thin as to cause the charge to eventually leak to the control gate. These constraints make an optimum control oxide thickness on the order of 5–15 nm [25]. For the case of thin tunneling oxides with

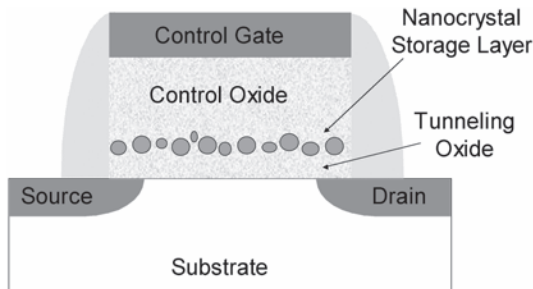


**Figure 6.** Schematic cross-section representation of a one-transistor nanocrystal floating-gate memory cell.

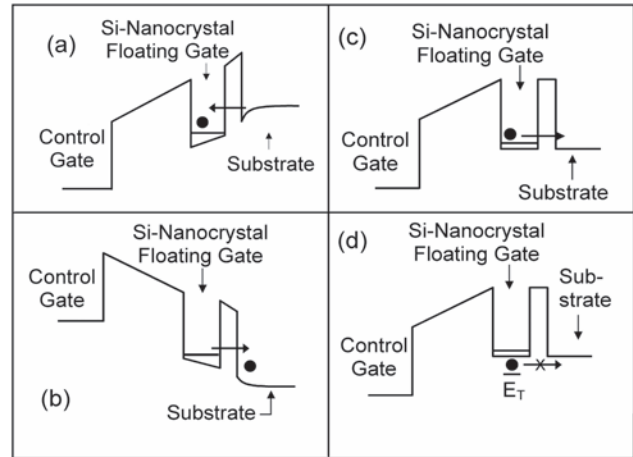


**Figure 7.** Potential diagrams of the conduction bands for an Si nanocrystal memory device during: (a) write (nanocrystal electron injection) mode, (b) erase (nanocrystal electron extraction) mode, (c), (d) charge-retention mode (at a reading gate voltage) for the case of (c) electron storage in a quantized nanocrystal energy level, (d) electron storage in deep energy level located in the nanocrystal or/and at the nanocrystal/SiO<sub>2</sub> interface.

thicknesses less than 3 nm, charge transfer takes place via direct tunneling (electron flow through the full oxide thickness, as illustrated in Fig. 7) instead of F–N tunneling. Since a large amount of current can pass through these thin oxides at low electric fields ( $< 3$  MV/cm) [26–27], superior performance characteristics compared to Flash memories can be achieved in terms of operation voltages and/or write/erase speeds. The generation of lower energetic carriers during programming operations (much less than 3 eV, that is, the threshold for several of the major hot carrier degradation mechanisms) reduces the oxide degradation encountered in F–N injection, resulting in better endurance and charge-to-breakdown characteristics [28].

### 2.2.2. Coulomb Blockade and Quantum Confinement

In addition to the direct tunneling programming mechanism, charge storage in nanocrystals offers several attractive characteristics that are absent in the conventional floating-gate structure. Charging the dots with an extra electron requires a charging energy  $E_C = e^2/2C + \Delta E_n$  [29, 30]. The first term is the classical electrostatic charging energy associated with placing a charge particle onto a small dot capacitance  $C$ , and varies inversely with dot dimension. The second term,  $\Delta E_n$ , due to quantum confinement, is the characteristic energy spacing between two adjacent energy levels of the dot. For metal dots where the density of states is enormous, confinement does not impose severe restrictions. In contrast, few “free-electron” systems, such as semiconductors, exhibit strong size-dependent quantization effects. When the characteristic length of an electron (or hole) wavefunction is on the order of the particle diameter, discrete energy levels appear near the conduction (valence) band edge (as shown in Fig. 7), with an approximate magnitude varying as the inverse square of the dot dimension, thus causing an increase of the energy bandgap. Resonant tunneling through oxide barriers involving discrete quantum states in Si nanocrystal and

the effect of quantized charge accumulation in ground-state energies of “few-electron” silicon dots have been experimentally demonstrated and discussed in [31–33].

The consequence of the Coulomb blockade and quantum confinement effects in a nanocrystal memory device is a reduction of the number of charged carriers used in the operation of the device that improves power and speed performance. To allow “few-electron” device operation, the charging energy must be greater than the thermal energy  $k_B T$  (where  $k_B$  is Boltzmann’s constant and  $T$  is the operation temperature). Room-temperature ( $k_B T$  ca. 26 meV) “few-electron” operation can be accomplished if the semiconductor nanocrystals have dimensions below ca. 10 nm. However, for the programming voltage and write time of interest, a minimum dot size is required. Neglecting band bending of the substrate in the inversion region, the write voltage  $V_{\text{write}}$  needed for a channel electron to tunnel into a dot state is approximately given by  $(E_C/e)(1 + t_{\text{ctrl}}/t_{\text{tun}}) + V_{\text{TH}}$ , where  $t_{\text{ctrl}}$ ,  $t_{\text{tun}}$  are the control and tunneling oxide thickness respectively, and  $V_{\text{TH}}$  is the threshold voltage. The large increase of the charging energy  $E_C$  (through the increase of the eigenenergies and the electrostatic charging energy) with dot size reduction increases the amount of gate voltage needed for charging. In addition, the reduced density of states restricts the states available for electrons to tunnel at a given voltage, resulting in lower programming speed. Thus, for an efficient operation at write voltages of  $\sim 3$  V, an optimum nanocrystal size in between 3–10 nm is estimated (for reasonable control-to-tunneling-oxide-thickness ratio on the order of 3–5) [25].

### 2.2.3. Memory Window

The resulting memory window  $\Delta V_{\text{TH}}$  due to single-electron storage in each nanocrystal is given by  $\Delta V_{\text{TH}} = eN_{\text{dot}}/C_{\text{gd}}$ , where  $e$  is the electron charge and  $N_{\text{dot}}$  is the aerial density of the nanocrystals (number of nanocrystals per  $\text{cm}^2$ ).  $C_{\text{gd}}$  is the capacitance per  $\text{cm}^2$  between the control gate and the nanocrystal, and is approximately given by [34]  $C_{\text{gd}} = \epsilon_{\text{ox}}/[t_{\text{ctrl}} + (\epsilon_{\text{ox}}/2\epsilon_{\text{dot}})t_{\text{dot}}]$ , where  $\epsilon_{\text{ox}}$  ( $\epsilon_{\text{dot}}$ ) are the oxide (nanocrystal) dielectric constants, and  $t_{\text{dot}}$  is the linear dimension of the nanocrystal. For spherical Si nanocrystals with 5 nm diameter, located at a distance of 7 nm from the control gate, the threshold voltage shift for one electron per nanocrystal is estimated to be  $\Delta V_{\text{TH}} \sim 0.36(N_{\text{dot}}/10^{12})$  V. The nanocrystal aerial density must be high enough in order to provide a large threshold voltage window, as well as to minimize low-resistance percolation paths in the channel underneath for an effective channel current modulation, but not so large as to cause lateral conduction between the dots. The maximum aerial density can be estimated from the nanocrystal size by setting optimum internanocrystal spacing (for negligible direct-tunneling probability between dots) on the order of 4–5 nm (i.e., for the case of dots of 5 nm in size, 5 nm apart, an optimum nanocrystal density of  $1 \times 10^{12} \text{ cm}^{-2}$  is estimated).

### 2.2.4. Channel Area

By shrinking the entire floating-gate transistor to nanoscale dimensions, the quantum dot or single-electron memory cell (SEMC) is obtained. It consists of a single floating quantum

dot located very close to the transistor nanoscale channel. Due to the ultrascale dimensions of the storage node, once an electron enters and becomes trapped in the quantum dot, quantum confinement and Coulomb blockade effects inhibit the tunneling of another electron. The addition of a single electron can change the transistor current considerably, resulting in an ultimate memory device that stores one bit of information by one electron. The precise control of the number of electrons on the storage node can be achieved by varying the voltage on the control gate electrode. The stored electrons on the floating dot electrostatically screen the entire channel from the potential on the control gate, which in turn changes the flow of electrons in the channel, resulting in a discrete shift in the device threshold voltage (see Fig. 8). The first SEMC based on GaAs was demonstrated at very low temperatures ( $\sim 4.2$  K) [35]. Room-temperature operation of SEMC based on Si was first demonstrated in MOSFETs with a nanometer-sized granular Si channel [36].

A more reliable technique to obtain room-temperature operation of Si-based SEMC uses electron-beam lithography and a self-aligned process to define narrow Si channels and quantum dots on silicon-on-insulator (SOI) material [34, 37–38]. A schematic cross section of this structure is illustrated in Figure 8. Despite these exciting experimental results and disregarding the reliability of the device fabrication process, the use of charge quantization effects in ULSI circuits remains uncertain in view of background charge (e.g., surface states on the nanocrystal), dopant fluctuations in the channel depletion region, and intrinsic statistical charge variations due to the Poisson nature of electron injection. These effects can lead to substantial variation of the threshold voltage from device to device. New architectures have been proposed to circumvent this problem [29, 39–40], but no devices have been demonstrated yet. In order to ensure reliable memory operation, the threshold voltage shift due to stored electrons must be significantly higher than that due to the other fluctuations. Calculations and experimental results indicate that “few” stored electrons (on the order of five–ten electrons, depending on dot and size dimensions) instead of a single electron are required for each memory state [25, 41–42]. As a result, the voltage of storing a single bit is increased, and it becomes even higher for multiple bit storage operation. In addition, because the electric field across the tunneling oxide increases with the number of stored electrons on the dot, a relatively thick tunneling oxide (i.e.,  $>5$  nm) must be used

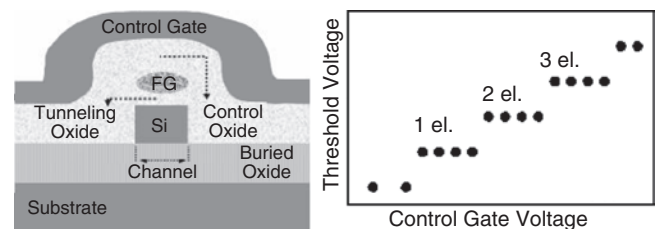


**Figure 8.** Schematic cross section of a self-aligned quantum-dot memory transistor, together with an illustration representing the discrete shifts in the device threshold voltage caused by the different number of electrons stored in the dot.

in order to ensure a long data-retention time. Since high voltages are required for multiple-level memory storage, the tradeoff is between integration density and operation power. Note that, for the case of a multiple-dot device, the presence of a sufficient number of nanocrystals in the memory operation suppresses cell-to-cell variation. This is an important advantage of multiple-dot structures as it allows effective operation at a lower number of stored electrons per nanocrystal compared to quantum dot memory. However, although single-electron charging effects have been demonstrated in large-area channel multiple-dot memories [43], even at room temperature [44–45], there are important technological issues to be resolved, such as high dot density and extremely high uniformity in dot size and dot position from the channel, before the practical exploitation of single-electron phenomena in nanocrystal memories.

### 2.2.5. Charge Storage

A major challenge of nanocrystal memory using thin tunneling oxides lies in the realization of long charge-retention times. Because of the sharp increase of the direct tunneling current at arbitrarily low voltages, a tradeoff exists between the write/erase time and retention time. By making the injection oxide thicker for a long retention time, the advantages of high-speed write/erase at reasonable voltage levels and of high endurance are lost rapidly. For the case of Si nanocrystals, an additional constraint for long-term charge retention is introduced by quantum confinement. This can be understood by reference to Figure 7(c), which illustrates an energy band diagram of Si nanocrystal memory under charge storage condition. After write operation [Fig. 7(a)], injected electrons that may initially tunnel into higher nanocrystal energy levels eventually will fall into lower energy states. Due to energy quantization, the lowest energy level at flat-band condition is above the conduction band edge in the channel region. Thus, a finite probability exists for an electron to tunnel back into the channel, affecting the retention characteristics of the device. It should be noted that most experimental results to date have shown significantly longer erase times than write times, reflecting relatively longer retention times than what was theoretically expected if both the write and erase process are due to direct tunneling. Several works attempting to explain the charging/discharging phenomena involved in Si nanocrystal memories have been carried out. Theoretical approaches, based upon [46] a master equation including quantum confinement and Coulomb blockade effects in Si dots [46], or on a semiclassical current continuity model [47, 48], have been proposed to describe the observed time-dependent charging/discharging behavior. Other work has shown that the influence of channel-depletion effects on carrier charging characteristics is very important for long charge retention in Si dot memory [49]. The presence of traps inside the nanocrystal or/and at the nanocrystal/SiO<sub>2</sub> interface [that causes electrons to be relaxed to lower trap states in the bandgap after injection, as illustrated in Fig. 7(d)] has been suggested to explain the observed relatively long-time charge-retention behavior [50]. However, the role of interface states on the charging/discharging phenomena in nanocrystal memories is still not entirely understood, and is possibly dependent

on the process conditions of nanocrystal formation. Experimental results related to the storage and erase process in these structures indicate two distinct time constants, which could be interpreted as fast nanocrystal-related emission followed by a slower interface state-related emission [51]. Another work has shown a small temperature dependence on the dynamic charging, at room/low temperatures, suggesting that Si-dot/SiO<sub>2</sub> interface states do not dominate the charge exchange between the Si dot and the channel [48]. Similar results, but for the case of a single Si nanocrystal, supporting the nanocrystal-related emission process were obtained in another work [52]. Recently, simulation results concerning the charging time response in silicon nanocrystal memory (obtained from the self-consistent solutions of the three-dimensional Kohn–Sham and Poisson equations) have shown write, erase, and retention time characteristics that are very sensitive to the shape of the Si nanocrystal storage nodes [53].

### 2.2.6. Storage Dot Engineering

In order to improve the performance of Si nanocrystal memory for high-speed nonvolatile applications, two different alternatives are actively investigated: a material and a structural engineering. Material engineering replaces the Si nanocrystal with a storage node composed of a material that allows long charge retention, while keeping the operation speed at acceptable levels. For example, this can be achieved if we use a storage node composed of a material having a conduction band edge (for the case of semiconductor material) or Fermi energy (for the case of metal) at least 26 meV (the room-temperature thermal energy) below the conduction band edge of the channel region [Fig. 9 (a)]. The energy band-edge difference creates an asymmetrical barrier

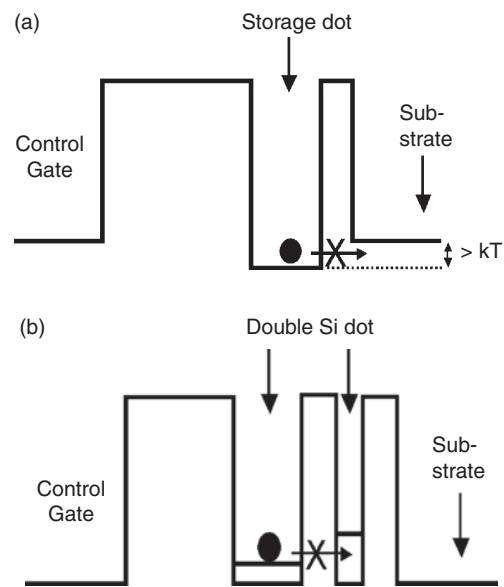


**Figure 9.** Potential diagrams of the conduction bands of a nanocrystal memory device during the charge-retention mode for the case of: (a) nanocrystalline material having a conduction band edge at least 26 meV below the conduction band edge of the channel region, and (b) double-stacked layer consisting of perfectly self-aligned (but different in size) Si nanocrystals.

between the channel and the storage node that combines the high transparency necessary for fast write/erase times with the low transparency necessary for long retention times at low voltages. This can be achieved if the storage nodes are composed of a material that has a larger electron affinity than the silicon substrate (i.e., metal, semiconductor-like Ge nanocrystals, or semiconductor heterostructures such as Ge/Si nanocrystals). Operation of Au, Ag, and Pt nanocrystal memories working in the F–N tunneling regime (as in the case of relatively thick tunneling oxides) has been demonstrated [54–55]. However, metal contamination (especially for the case of thin tunneling oxides) and CMOS process integration compatibility are important technological issues for such structures. For the case of Ge nanocrystals, charge-storage advantages over the corresponding Si case are not clear, as similar results have been obtained for Ge and Si nanocrystal-based memory structures [56]. Up to now, only simulated charge-retention data exist for the case of Ge/Si storage nodes [57].

Another particular implementation of material engineering is a memory structure with silicon nitride ( $\text{Si}_3\text{N}_4$ ) storage dots proposed in 2001 [58]. Charge storage in  $\text{Si}_3\text{N}_4$  dot memory takes place, as in the case of a SONOS device, at nitride traps distributed in the  $\text{Si}_3\text{N}_4$  dot. However, due to restricted dot dimensions, a finite number of traps is expected (e.g., two or three traps for the case of a 10 nm diameter dot), allowing (as for the case of Si dot memory) small and controllable numbers of electrons to be involved in the memory operation. Moreover, the absence of Coulomb blockade and confinement effects in an  $\text{Si}_3\text{N}_4$  dot allows charging with more than one electron at a low write voltage, resulting in a larger memory window compared to the Si dot device [58]. The exact number of traps involved and a fabrication route of forming well-controlled, in terms of size and position,  $\text{Si}_3\text{N}_4$  dots are key issues for practical use of this new memory concept.

Structural engineering replaces the single storage layer with a double-stacked layer consisting of perfectly self-aligned Si nanocrystals. The fabrication process and the memory characteristics of this structure are discussed in [59, 60]. For the case of a smaller dot at the lower stack with ultrathin tunneling oxides below and between the two stacks, fast write/erase speeds with a much better charge retention compared to single-dot memory have been demonstrated. Coulomb blockade and quantum confinement in lower dots [Fig. 9(b)] inhibit electrons in the upper dots to tunnel back into the channel. The smaller the size of the lower dots, the larger the improvement in data retention. An important point of this doubly stacked floating-dot memory device is its self-aligned structure. In addition, this concept is also applicable in the case of  $\text{Si}_3\text{N}_4$  dot memory for further improvement of data retention [58].

### 3. NANOCRYSTAL FLOATING-GATE TECHNOLOGY

The atom-like behavior of semiconductor nanocrystals embedded in  $\text{SiO}_2$  matrices is expected to lead to interesting optical and electronic properties. As a result, many applications and synthesis techniques are being explored.

The possibility of using Si or Ge as a light source in optoelectronic devices is very attractive because of the compatibility of these materials with existing Si-based MOS technologies [61–62]. Luminescent  $\text{SiO}_2$  films consisting of Si or Ge nanocrystals have been fabricated through the use of various deposition techniques [63–68] or, more recently, through Si or Ge ion implantation [69–75]. Implanted impurities have been used to shift the emission wavelength of Si nanocrystals (i.e., absorption of the nanocrystal emission, 0.81  $\mu\text{m}$  luminescence peak, from implanted Er causes strong excitations of  $\text{Er}^{3+}$  at 1.54  $\mu\text{m}$  [76]), indicating the potential of Si nanocrystals as sensitizers for use in Er-doped waveguide amplifiers or lasers [77]. A major effort has been directed toward the understanding of the origin of luminescence and electroluminescence spectra obtained from these materials. The sources of visible-range luminescence are still not entirely clear, and continue to be a subject of debate. The recombination of quantum-confined excitons in nanocrystals, defects in the surrounding matrix, electronic states at the nanocrystal surface, and foreign compounds have been named as sources. The origin of optical emission in the nanocrystals should be well understood, and a fabrication route of forming well-controlled depth and size distributions of nanocrystals should be established in order to optimize and control the optical properties for device applications.

Besides the attractive light-emitting property, semiconductor nanocrystals embedded in  $\text{SiO}_2$  matrices have regained interest due to their potential in future electronic devices. Resonant tunneling diodes [33, 78] and memory devices [23–24, 34–38] exploring quantum confinement and single-charge effects in Si nanocrystals have been demonstrated. For such applications, the nanocrystal characteristics have to satisfy certain specifications in order to provide reliable device operation. In particular, for multiple-dot memory applications, a fabrication route of forming high-density two-dimensional arrays of small, uniform size, noninteracting nanocrystals, and with well-controlled location without introducing defects at the  $\text{SiO}_2/\text{Si}$  interface or into the channel region, are important technological points. In addition, the synthesis technique should be as simple as possible (for low cost per bit) and compatible with existing CMOS processes. Because the optimum mean size of the storage dots is below the current lithography resolution, an attractive approach to fabricate a nanocrystal floating gate is through a self-assembling process [79]. This method also takes advantage of the whole-wafer nature of dot formation suitable for practical device implementation. Self-assembled semiconductor nanocrystal floating gates have been fabricated through various techniques, including Si-dot formation by low-pressure chemical vapor deposition (LPCVD) [24, 43], nanocrystal formation by a precipitation process during the annealing of a semiconductor-rich oxide layer (formed either by Si (Ge) ion implantation [56], or by deposition techniques such as LPCVD [80] or cosputtering of Si (Ge) and  $\text{SiO}_2$  [81–82]), rapid thermal oxidation either of a thin deposited amorphous Si [83] film or of amorphous silicon films deposited by ion-beam-assisted electron-beam deposition [84], molecular beam epitaxy combined with rapid thermal processing [85], aerosol deposition [86], and thermal oxidation of  $\text{Si}_{1-x}\text{Ge}_x$  [87]. Nanocrystal memory transistors

have been realized using these various self-assembling processes in combination with conventional MOS transistor fabrication steps. In the paragraphs below, nanocrystal synthesis through direct deposition techniques such as direct seeding on dielectric layers, or using a silicon-rich oxide layer, or through ion implantation techniques are briefly reviewed because of their advantages in terms of integration. In particular, we examine the case of the ion beam synthesis approach, as it is a simple and well-established technique within the semiconductor industry.

### 3.1. Direct Deposition Technique

#### 3.1.1. Direct Nanocrystal Seeding on Dielectric Substrates

Low-pressure chemical vapor deposition by pyrolysis of silane ( $\text{SiH}_4$ ) is a well-established technique within the microelectronic industry, and is commonly used for the fabrication of polycrystalline Si gates in MOS transistors and of thin-film transistors (TFTs). By controlling the early stages of Si film growth, a single layer of isolated Si nanocrystals a few nanometers in diameter can be formed on various dielectric substrates [88]. The size and density of the nanocrystals depend on the deposition parameters (pressure, temperature, and time) [77, 88, 89], as well as on the chemical treatments or on the chemical nature of the surface [77, 89–92]. Deposition on pure oxide substrates exhibits relatively low nanocrystal aerial density, while higher values have been observed for the case of deposition on nitride surfaces [89, 44]. The highest dot density, of  $10^{12} \text{ cm}^{-2}$  for optimized deposition conditions, has been obtained for the case of a pure  $\text{Si}_3\text{N}_4$  substrate [89] or, more recently, for an  $\text{Al}_2\text{O}_3$  surface [91]. A thermal oxidizing step after deposition is shown to improve dot size uniformity. A control oxide, formed by a second deposition step of  $\text{SiO}_2$ , covers the nanocrystals. The in-plane dot formation allows for excellent control of the tunneling oxide thickness without affecting the integrity of the oxide or of the oxide/channel interface. For these reasons, the LPCVD technique is an attractive option for nanocrystal memory device implementation. However, optimization of the deposition process (especially on  $\text{SiO}_2$  surfaces) and of the ultrathin tunneling dielectric formation step (especially for the case of  $\text{SiO}_2/\text{Si}_3\text{N}_4$  or  $\text{SiO}_2/\text{Al}_2\text{O}_3$  dielectric stacks) is still required in order to achieve high nanocrystal aerial density onto highly reliable dielectrics.

#### 3.1.2. Deposition and Precipitation of SRO

Silicon-rich oxide (SRO) or nonstoichiometric oxide is considered a solid solution of  $\text{SiO}_2$  and Si supersaturated in Si ( $\text{SiO}_x$ ,  $x < 2$ ). SRO films are usually prepared through chemical vapor deposition (either LPCVD or plasma-enhanced CVD) using a mixture of silane and  $\text{N}_2\text{O}$  or  $\text{SiH}_4$  and  $\text{O}_2$ . Changing the gas flow ratio controls the excess Si content in the SRO film. Thermal annealing during preparation processing or during an additional annealing step causes excess Si to precipitate in the form of amorphous or crystalline Si nanoclusters, depending on the annealing conditions (time, temperature) and the amount of excess Si [93, 94]. The diffusion of Si atoms in the nonstoichiometric oxide matrix has been found to control the precipitation of

Si clusters [94]. SRO layers have been proposed as interpoly dielectrics for enhanced electron injection [95–98], or as ultrathin tunneling oxide alternatives [99] in conventional nonvolatile memory devices for low-voltage operation. In addition, the electron trapping characteristics of SRO make it useful as a charge-storage material for memory applications. The charge-storage properties and charge transport through these films have been related to the Si quantum dots of the SRO film [93, 100]. For memory applications, a thin SRO layer ( $< 10 \text{ nm}$ ) is formed on top of oxidized Si substrates. In order to decrease the deposition growth rate for better control of the deposited SRO thickness, a dichrosilane gas instead of silane has been used [101]. By changing the gas ratio, a control oxide can also be deposited during the same furnace step. Because of the distributed nature of small Si grains in the film, charge storage takes place through the whole film volume. For better control over the tunneling oxide thickness, the in-plane growth of the charge-storage elements is required. This can be achieved if ultrathin SRO layers are used. However, certain limitations are imposed on making such ultrathin SRO layers reproducible with currently used CVD systems.

### 3.2. Ion Beam Synthesis

Ion implantation is a widely used technique in the semiconductor industry, and is commonly employed for doping silicon wafers. Because of the versatility and flexibility of this technique, ion beam synthesis (IBS) has recently become a popular method for synthesizing various types of nanocomposite materials (for a review, see [102]). In this technique, a given number of selected ions are introduced into a given dielectric layer. High-dose implantation can create a solid-state supersaturation of the implanted ions, and the subsequent thermal annealing can induce the implanted material to precipitate in the form of nanoparticles dispersed within the dielectric layer. Well-controlled depth and size distributions of nanocrystals can be achieved by adjusting the ion implantation conditions (dose, dose rate, and energy) and postimplantation annealing processing (temperature, time, and annealing environment). Moreover, a variety of embedded nanocrystal systems can be realized by changing the implanted ion element and the host material. In particular, regarding approaches targeting MOS memory devices, ion implantation of group IV semiconductor elements (e.g., Si or Ge) in an  $\text{SiO}_2$  matrix is fully compatible with Si microelectronic technology. In addition, from a device fabrication point of view, IBS is a quite simpler technique compared to the sophisticated multistep deposition ones, offering superior process controllability (i.e., the implanted ion concentration can be easily controlled through beam current adjustments), and thus better reproducibility of the resulting memory device characteristics. However, key points such as the in-plane size uniformity and arrangement of the nanocrystals, the precise adjustment of the control and tunneling oxide, and the implantation-related oxide and  $\text{SiO}_2/\text{Si}$  interface damage remain to be solved in order to implement practical memory devices through IBS technique. For this purpose, a substantial amount of experimental work on the charge-storage behavior of MOSFETs with Si- or Ge-implanted and annealed



gate oxides has been carried out over the past few years. A brief overview of the various implantation conditions and gate oxide thicknesses that have been explored follows in the paragraphs below.

### 3.2.1. MOSFETs with Si- or Ge-Implanted Gate Oxides

Following early investigations on the memory properties of SRO films [96], Kalnitsky et al. studied the electrical behavior of MOS structures with Si-implanted and annealed thin gate oxides (20–35 nm in thickness, implanted at energy ranging from 10 to 25 keV) [103]. Similar to the case of SRO films, this system was found to exhibit hysteresis in current–voltage ( $I$ – $V$ ) and capacitance–voltage ( $C$ – $V$ ) characteristics; however, no Si precipitates were observed for the Si-implanted oxides. Charge trapping and transport in this material were attributed to the trap-like behavior of excess Si atoms [104, 105]. The implanted Si atom was considered to serve as a neutral trap (a single trap capable of storing both positive and negative charge) that electrically communicates with both the conduction and valence bands of the Si substrate and the polysilicon gate via direct tunneling. This trap-assisted direct-tunneling model was used to describe most of the conduction effects experimentally observed in this material, such as a deviation of the slope of  $I$ – $V$  curves from the Fowler–Nordheim tunneling characteristics and a negative dynamic resistance effect [104]. From the fit of the experimental  $I$ – $V$  characteristics to the theoretical model, the energy level of the trap was estimated about 3 eV below the SiO<sub>2</sub> conduction band. The effect of Si implant-induced interface states on MOSFET characteristics was also discussed in [105]. Further investigations on such gate oxides (20–50 nm in thickness) implanted under various Si implantation conditions (10–50 keV/0.1–3 × 10<sup>16</sup> Si<sup>+</sup> cm<sup>-2</sup>) have revealed electrical characteristics (in terms of reliability, endurance, retention, programming window, and speed) potentially usable for MOS memory applications. Depending on the Si dose and the distance of the Si-implanted region from the Si/SiO<sub>2</sub> interface, the Si-implanted gate oxides have been introduced as gate dielectrics for realizing nonstacked gate, Flash EEPROM [106–109], analog-storage EEPROM [110], or nonvolatile RAM [111] devices. The origin of parasitic currents observed after large positive write voltages in these Si-implanted devices was also analyzed for practical memory device applications [112]. Note that the trap-like behavior of the implanted Si atoms that do not form Si islands was the major difference between these earlier charge-trapping studies on silicon-implanted oxides and those concerning deposited Si-rich oxides.

Hanafi et al. [56, 113] first interpreted the nonvolatile memory characteristics of MOSFETs with Si<sup>+</sup>- or Ge<sup>+</sup>-implanted gate oxides, in terms of electron charge storage in isolated nanoclusters formed by precipitation of the implanted material during postimplantation annealing treatment. Since that time, many studies have been performed in order to correlate the device electrical characteristics with the microstructure of the Si<sup>+</sup>- [114–119, 45] or Ge<sup>+</sup>- [120–123] implanted and annealed oxide layers. The charge-storage mechanism has been found to vary with the degree of precipitation of the implanted material and

the structural features of the nanoclusters (size, density, crystallinity), which in turn depend on the implantation and annealing conditions. By using an atomic-force microscope (AFM) [119] to locally inject and detect charge in annealed, Si-implanted SiO<sub>2</sub> films containing Si nanocrystals (2–6 nm in size), charge trapping due to the presence of Si nanocrystals has been inferred. In addition, a discrete build up of charge in the implanted oxide with gate bias has been recently observed for the case of well-crystallized and densely arranged Si grains with an average linear dimension of about 8 nm (the case of heavy Si implantation in SiO<sub>2</sub>), an indication of a nanocrystal-related charge-trapping process [117, 45]. On the other hand, the formation of Ge or Si/SiO<sub>2</sub> nonseparated glass [114, 120, 122] or of a Si or Ge band composed of amorphous and/or ill-crystalline grains [115–118, 121] has been shown to exhibit a continuous charge-storage process with gate bias indicative of a defect-related charge-trapping mechanism. However, the atomic structure of such defects and their exact location within the implanted oxide layer are not entirely clear. Si implant-related defect microstructures were recently studied experimentally and theoretically in [124]. Four possible molecular defect structures associated with excess Si in thermal oxides have been examined with ground and excited states within the bandgap of the amorphous SiO<sub>2</sub> structure. In addition, the observation of memory window narrowing after postmetallization annealing treatment in forming gas (N<sub>2</sub>/H<sub>2</sub> gas mixture) is an indication of hydrogen-related saturation of the defects acting as charge traps [115, 118]. Such defects could be associated with the nanocluster formation process, that is, Si dangling orbitals at the Si cluster/SiO<sub>2</sub> interface. The latter is further supported by the significant concentration of  $P_b$ -like centers that have been experimentally inferred from electron paramagnetic resonance studies ( $g \cong 2.005$  resonance) of Si-implanted SiO<sub>2</sub> films [125]. Despite these studies, further effort is needed in order to correlate the charge-trapping behavior of the implanted layers with the spatial state and structural arrangement of the implanted material after annealing, for the control and optimization of the memory characteristics of the resulting memory devices through adjustment of the IBS conditions.

### 3.2.2. Very-Low-Energy IBS Approach

For practical nanocrystal memory devices, the formation of an extremely narrow band of nanocrystals within thin SiO<sub>2</sub> layers is needed. In addition, the controllability of the location of such nanocrystalline bands from the SiO<sub>2</sub>/Si interface, as well as the elimination of implantation-related oxide and SiO<sub>2</sub>/Si interface damage, are necessary for the optimization of device performance. A promising approach to achieve this goal is to apply very-low-energy Si ion implants in thin SiO<sub>2</sub> films. Because the ion strangling decreases with implantation energy, the use of energies less than 2 keV is very attractive for making well-controlled depth and size distributions of nanocrystals with precise control of the tunnel oxide thickness [126–127]. The potential of this approach was first explored in experiments by our team at the Institute of Microelectronics of NCSR “Demokritos” in close collaboration with the University of Salford, in which well-localized layers of 2D arrays of Si nanocrystals are successfully formed both in thin (8–11 nm) and thick (35 nm) oxide



layers by 1 keV Si<sup>+</sup> implants at doses ranging from  $5 \times 10^{15}$  to  $5 \times 10^{16}$  cm<sup>-2</sup> and subsequent thermal annealing [128–130]. A short summary of the major characteristics of the resulting microstructures follows in the paragraph below.

For the case of implanted samples with an initial SiO<sub>2</sub> layer of 8 nm in thickness, an ultrathin layer of Si clusters (3–4 nm in thickness) located at a tunneling distance (ca. 2 nm) from both the oxide surface and the SiO<sub>2</sub>/Si substrate interface has been observed after postimplantation annealing at temperatures ranging from 900 to 1000 °C. Cross-sectional TEM observations for the case of a  $5 \times 10^{16}$  cm<sup>-2</sup> dose (Fig. 10) suggest that the presence of a protective polysilicon-capping layer during annealing does not significantly affect the evolution of the Si-nanocrystalline structures. In addition, related TEM work on very-low-energy Si-implanted and annealed thick oxide layers (Fig. 11) reveals Si nanocrystals with characteristics (size, density, and location) similar to those found for very thin oxides, indicating that the growth of the nanocrystals does not depend on the location of the SiO<sub>2</sub>/Si interface. The resulting microstructures have been found to exhibit a broad semiconductor domain-size distribution that depends upon the implanted dose and anneal temperature. Examples are shown in Figure 12. The amount of crystallized Si (proportional to the sum of white domains) appears to increase with the dose and temperature. Comparison of the (b), (f) and (d), (h) [or (c)/(g)] micrograph pairs shows clearly that, upon raising the annealing temperature, the extent of Si crystallization is enhanced much more for the former pair, that is, for the lower dose. Furthermore, although planar-view TEM micrographs in Figure 12(a) and (e) show no distinct structure, electron diffraction patterns [see inset

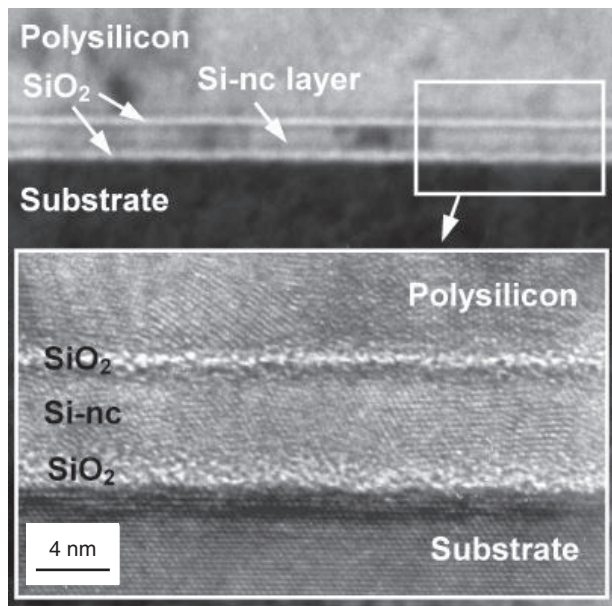


**Figure 10.** Cross-sectional TEM and HRTEM micrographs of 8 nm thick oxide implanted with  $5 \times 10^{16}$  Si<sup>+</sup> cm<sup>-2</sup> at 1 keV, capped with polysilicon, and subsequently annealed at 1000 °C for 30 min showing a 4 nm thick nanocrystal layer. Reprinted with permission from [130], P. Normand et al., *Nucl. Instrum. Meth., Phys. Res. B* 178, 74 (2001). © 2001, Elsevier Science.

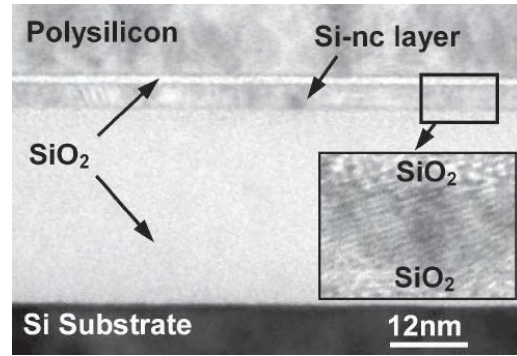


**Figure 11.** Cross-section TEM micrograph of 35 nm thick oxide implanted with  $5 \times 10^{16}$  Si<sup>+</sup> cm<sup>-2</sup> (1 keV), annealed at 1000 °C for 30 min, and subsequently capped with polysilicon. The presence of a 4 nm nanocrystal layer is shown in the inset. Reprinted with permission from [130], P. Normand et al., *Nucl. Instrum. Meth., Phys. Res. B* 178, 74 (2001). © 2001, Elsevier Science.

of Fig. 12(a)] hint at the presence of Si domains. Moreover, a strong correlation between the shape and size of the nanocrystals has been observed. Arrows in (g) shows Si nanocrystals of 12–14 nm diameter (compared to a 3.5 nm thickness of the Si-rich layer observed in cross-sectional TEM analysis), which suggests that, with increasing size, the nanocrystals change from quasispheres to platelet like. Details about the observed lateral crystallite growth (coarsening) are given in [129]. Note that, because of the dense arrangement, the large nanocrystals are almost in touch with each other [Fig. 12(d) and (h)], causing the narrow nanocrystal band to appear as a quasicontinuous polycrystalline layer (Fig. 10).

The potential of the very-low-energy IBS approach as a technique for implementing nanocrystal memories was explored in [115]. This work gave attractive results, but also revealed the need for further effort in order to optimize and control the performance of the resulting memory devices for practical applications. Because the electrical

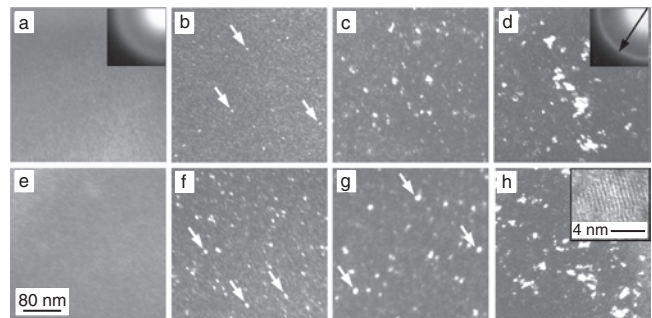


**Figure 12.** TEM micrographs from samples with 8 nm thick SiO<sub>2</sub> layer implanted with  $5 \times 10^{15}$  (a), (e),  $1 \times 10^{16}$  (b), (f),  $2 \times 10^{16}$  (c), (g) and  $5 \times 10^{16}$  (d), (h) Si<sup>+</sup> cm<sup>-2</sup> at 1 keV after thermal annealing at 900 °C for 60 min (a)–(d) and at 1000 °C for 30 min (e)–(h). Electron diffraction patterns of (a) and (d) are shown in insets (arrow indicates (111) Si ring). A silicon nanocrystal is shown in the inset of (h). Arrows in (b), (f), and (g) denote Si grains of 4–5, 8–9, and 12–14 nm diameter, respectively. Reprinted with permission from [130], P. Normand et al., *Nucl. Instrum. Meth., Phys. Res. B* 178, 74 (2001). © 2001, Elsevier Science.

characteristics of such devices are closely related to the microstructural features of the implanted gate oxides after annealing, an in-depth understanding of the structural evolution of the implanted Si material upon different implantation conditions and annealing treatments is necessary. For this purpose, theoretical works attempting to explain the mechanisms involved in the progress of phase transformations accompanying annealing have been carried out recently. The effect of the glass transition temperature ( $T_g$ ) of the as-implanted structure on the phase separation and crystallization of the implanted material was qualitatively discussed in [130, 131]. Process simulation based upon a combination of binary collision code [132] (for the study of the  $\text{Si}^+$  implantation process) and a kinetic lattice Monte Carlo code (for the study of phase separation process of Si from  $\text{SiO}_2$ ) [133] has revealed two regimes of Si nanocrystal formation for the case of 1 keV  $\text{Si}^+$ -implanted and annealed thin oxide layers. For a low implantation dose (below  $2 \times 10^{15} \text{ cm}^{-2}$ ), Si nanocrystals form by nucleation and growth, while at higher doses, spinodal decomposition occurs. It is interesting to note that the simulation results show the formation of Si nanocrystals at much lower Si concentrations than those observed in the previous experimental works. This is because annealing causes loss of the implanted Si material, resulting in a reduction of the implanted Si concentration. During annealing, part of the Si content of the initially single-phase Si– $\text{SiO}_2$  nanolayer (formed by very-low-energy Si implantation) can be lost either because it escapes from the top oxide surface or because it becomes captured by the Si/ $\text{SiO}_2$  substrate interface. In addition, part of the Si content can be lost by oxidation during annealing due to traces of moisture in the as-implanted sample or due to residual oxidizing species in the furnace. The later loss mechanism of implanted Si material can also explain the significant oxide swelling that has been reported [129, 134], and discussed in [134, 136], for the case of very-low-energy Si-implanted oxide layers.

Besides the thorough comprehension of the mechanisms involved during nanocrystal formation through the very-low-energy IBS technique, another important issue to be resolved before the practical application of this method is related to the damage induced by implantation. Such damage strongly affects the integrity of the implanted gate oxide, a fact that limits the operation of the memory device at relatively high voltages, as an additional deposited control oxide is unavoidable for proper operation. In addition, this oxide deposition step complicates the device fabrication process. In order to overcome this drawback of the IBS technique, an annealing step under an oxidizing environment ( $\text{N}_2/\text{O}_2$  gas mixture) was recently proposed [135]. MOS structures with very-low-energy ( $\leq 2$  keV)  $\text{Si}^+$ -implanted thin gate oxides ( $\leq 10$  nm in thickness) subjected to such an annealing treatment exhibit lower leakage currents and a large memory window at low gate voltages. The observed effective charge storage without the need for an additional deposited oxide indicates that postimplantation annealing in a diluted oxygen environment significantly restores the gate oxide integrity. In addition, TEM work for a high  $\text{Si}^+$ -implanted dose ( $1 \text{ keV}/2 \times 10^{16} \text{ cm}^{-2}$ ) reveals that the aforementioned annealing treatment increases the top control oxide thickness and narrows the size distribution of the

synthesized Si nanocrystals [136]. These promising results suggest that a combination of very-low-energy Si implants and annealing in diluted oxygen may lead to very-low-energy Si nanocrystal memory versions of substantial practical interest.

In contrast to the optimistic prospect of the Si-nanocrystal IBS technique, the possibility of forming a Ge nanocrystalline floating-gate layer by IBS remains questionable from a process reliability point of view. Several investigations indicate that the microstructure of Ge-implanted and annealed  $\text{SiO}_2$  oxide layers strongly depends on the processing parameters [120–122, 130–131, 137–140]. A narrow band composed either of crystalline or amorphous Ge clusters located very close to the Si/ $\text{SiO}_2$  interface has been reported for the case of  $\text{Ge}^+$ -implanted (at energies  $\geq 20$  keV) and annealed thick ( $\geq 30$  nm) oxide layers. However, this Ge nanocluster band is found to be metastable; it is only observable under specific implantation and annealing conditions. An interpretation regarding the existence and evolution of such a near interface nanocluster band is given in [137–139]. Note that, in some cases, implantation with various ions (e.g.,  $\text{Ag}^+$  [102],  $\text{Sn}^+$  [141], or  $\text{Sb}^+$  [142]) and subsequent annealing of the oxide layers result in localized precipitation of nanoparticles close to the Si/ $\text{SiO}_2$  interface, regardless of the implanted oxide thickness, indicating that migration of the implanted ions towards the interface during thermal processing is independent of the implanted species. On the other hand, initial attempts using very-low-energy (3 keV)  $\text{Ge}^+$  implantation in thin  $\text{SiO}_2$  films and subsequent annealing have produced an amorphous and single-phase Ge– $\text{SiO}_2$  nanolayer instead of the desired Ge nanocrystalline layer [120, 122, 130]. However, phase separation for this case can be induced under intense electron irradiation. Details of the structural evolution of the Ge– $\text{SiO}_2$  glass band upon TEM observation are presented in [131, 140]. All in all, the experiments up to now show that forming a technologically practical narrow Ge nanocrystalline band in  $\text{SiO}_2$  layers by the IBS technique remains a challenge.

#### 4. NANOCRYSTAL MEMORY: EXPERIMENTAL RESULTS

During the last few years, a large amount of experimental results on MOS capacitor and single-MOS transistor memory devices, with nanocrystal charge-storage nodes embedded in the gate oxide (and fabricated by various techniques), have been published. The reported memory characteristics (e.g., retention, endurance, programming voltage, and speed) have been found to vary significantly, depending on the oxide quality and thickness (mainly of the tunneling oxide), as well as on the structural characteristics of the nanocrystal charge-storage sites, parameters that in turn are closely related to the memory device fabrication process. Depending on these parameters, memory operation ranging from quasivolatile to long-refresh-time dynamic functions has been demonstrated. In addition, discrete threshold voltage shifts with programming voltage have been observed, a behavior that may allow a more reliable multibit-per-cell storage compared to the Flash multilevel storage approach.

In this section, we will discuss some of the main experimental results that reveal the key attributes of the nanocrystal memory in order to understand the potential gains and tradeoffs associated with this type of memory device. Selected experimental results of nanocrystal memory devices obtained by various techniques are listed in Table 1. For comparison, the tunneling and control oxide thicknesses of the structures and the characteristics of state-of-art Flash and DRAM memory devices are also included.

### 4.1. Quasinonvolatile Behavior—From NVRAM to Flash-Like Functions

Tiwary and his co-workers studied the memory properties of *n*-channel MOSFETs with self-assembled Si nanocrystals onto ultrathin thermally grown gate oxide films with different thicknesses and approximately comparable density [23, 24, 43, 56]. A control oxide exceeding 7 nm in thickness covers the nanocrystals. Memory operation with a programming window in the range of 0.5 V or higher at direct tunneling programming voltages ( $\leq 4$  V) is demonstrated with

write speeds dependent on the tunneling oxide thickness. By using ultrathin tunneling oxides ( $< 2$  nm in thickness), write times of 200 ns or faster and excellent endurance behavior (e.g., no observable memory window closure after more than  $10^9$  write/erase cycles at low programming voltages) are realized. In addition, for this case, a quasinonvolatile charge retention of days is measured at room temperature, demonstrating the advantage of the distributed nanocrystal charge-storage devices over the continuous polysilicon floating-gate EEPROM ones of comparable tunneling oxide thickness [56]. Similar fast write time ( $\sim 300$  ns) operation with limited nonvolatile data retention of hours at low programming voltage (4 V) also has been shown (by the same research group) for the case of MOSFETs with Si- or Ge-implanted and annealed gate oxides [56]. In contrast to the fast write operation, the erase speeds of the deposited and implanted devices are found to be relatively low (in the range of microseconds to seconds, depending on the gate erase voltage). By increasing the tunneling oxide thickness, programming in the microsecond (or millisecond) range at still lower voltages compared to Flash devices and limited endurance

**Table 1.** Selected experimental results of nanocrystal memory devices obtained by various techniques, including the tunneling and control oxide thicknesses of the structures. For comparison, state-of-the-art NOR Flash and DRAM memory attributes are listed.

Nanocrystal Float. Gate Technology	Tunnel Oxide	Control Oxide	Write Time	Erase Time/Voltage	Refresh Time (Room Tem.)	Endurance cycles	Write Voltage	$\Delta V_{TH}$
LPCVD [24, 56, 43]	1.6 nm	$> 7$ nm	$\sim 200$ ns	$\mu$ s to s range/ ( $-3$ V, $-5$ V)	$> 1$ week	$10^9$ s	3 V	$\sim 0.65$ V
	2.1 nm		$\sim 400$ ns				3 V	$\sim 0.48$ V
	3.0 nm		$\sim 1$ $\mu$ s				3 V	$\sim 0.55$ V
	3.6 nm		$\sim 5$ $\mu$ s		Large	4 V	$\sim 0.5$ V	
Ion Implantation (10 Ke V Ge implants) [56]	12 nm		300 ns	$\sim 10$ ms/ $-3$ V	$> 1$ day	$10^9$	4 V	$\sim 0.3$ V
	$\sim 2$ nm							
Aerosol Deposition Technique [86]	5.5–6 nm	8 nm	$\sim 50$ $\mu$ s	$\sim 100$ ms/ $-8$ V and $V_{sub} = 8$ V	$> 1$ day	$> 10^5$	8 V and $V_{sub} = -5$ V	$\sim 2.3$ V
Thermal Oxidation of Si-Ge [87]	1.5 nm	3 nm	$\sim 100$ ns	$\sim 100$ ns/ $-4$ V	$> 1$ day	$10^9$	4 V	$\sim 0.4$ V
SRO [101]	1.5 nm	5 nm	$\sim 100$ ns	$\sim 100$ ns/ $-5$ V	$\sim 1000$ s	$10^8$	5 V	$\sim 0.5$ V
Conventional Memory Technology								
DRAM			$< 20$ ns	$< 20$ ns	$< 1$ s	$> 10^{13}$	3 V	
NOR Flash	$\sim 7$ –8 nm	$\sim 15$ nm	$\sim 1$ $\mu$ s	F-N erase $> 10$ ms/ $> -12$ V	No refresh is needed	$> 10^5$	CHE write $V_G \sim 12$ V $V_D \sim 8$ –9 V	3–4 V

can be achieved to compete with Flash memory performance. For the case of tunneling oxide thicknesses comparable to, but still thinner than conventional Flash devices (e.g., ca. 6 nm), encouraging results in terms of disturb behavior and stress-induced leakage current have been obtained for aerosol deposition nanocrystal memory devices operating in the F–N tunneling regime [86]. In addition, the feasibility of hole-programming operation has been demonstrated for the case of *p*-channel deposited nanocrystal memory devices with 4 and 20 nm tunneling and control oxide thickness [92, 143]. Depending on the tunneling oxide thickness, nanocrystal memory devices have been introduced (similar to the case of scaled SONOS device [144]) as promising low-power operation candidates in applications ranging from Flash-like functions (slow programming in the millisecond range with long nonvolatile retention of years) to nonvolatile RAM (NVRAM)-like functions (fast programming in the microsecond range with limited nonvolatile retention). In addition, since the write/erase voltage pulses (for injection/extraction of charge into/from the nanocrystals) is not applied between the source or the drain of the memory cell, a reduced “punchthrough” effect can be achieved, allowing a shorter channel length and a smaller cell area than is possible in conventional floating-gate-type structures. Single-transistor nanocrystal arrays (organized in word lines, bit lines, and source lines, each connected to control gates, drains, and sources, respectively) with byte-addressable write/erase operations (or block-erase schemes for the case of very slow erase times) have been proposed for the incorporation of these structures into large-scale integration memory circuitry [56, 145]. However, the very stringent requirement for long-term charge retention (in particular, for the case of Flash functions) imposes serious constraints on the practical application of these structures in nonvolatile memory functions. Although promising charge-retention data have been published (e.g., retention times of hours have been measured at 200 °C [146]), the ultimate goal of true nonvolatility (e.g., data retention > ten years) at low voltage and at acceptable write/erase speeds still remains an important issue to be verified for nanocrystal memory devices. Due to the inherent constraint of back tunneling charges through thin tunneling oxides, it is unclear whether nanocrystal memories will ever meet the industrial data-retention standard, and further effort and process optimization are necessary in order to demonstrate the feasibility of this target.

#### 4.2. Volatile Behavior Long-Refresh-Time DRAM-Like Functions

Besides the potential in nonvolatile functions, another application of nanocrystal memory device is for a dynamic RAM concept of lower power dissipation (long refresh time), simpler operation, smaller cell area, and lower cost fabrication process than the conventional DRAM structures. Since the information, or charge, is stored into the gate oxide of a single transistor, no additional storage capacitor is needed, thus minimizing the cell size for higher packing densities. For applications targeting DRAM-like functions, fast write and erase speeds (in the nanosecond range) at low voltages

and endurance cycles exceeding  $10^{13}$  are important. In addition, for the case of the long (compared to conventional 1T-1C DRAM memory cell) refresh time requirement, data retention can be shortened to minutes or seconds; thus, quasinonvolatile retention is desired for DRAM functions, in contrast to the long-term retention of Flash and NVRAM functions. Hu and his co-workers at the University of Berkeley experimentally demonstrated the possibility of implementing DRAM functions by using single charge-trapping memory transistor structures with ultrathin tunneling oxides [101, 147]. For the case of SONOS devices with 1.2 nm tunneling oxide (the case of charge storage at traps distributed in the nitride layer), data-retention times as long as 1000 s are measured at 80 °C after a  $10^{11}$  cycle endurance test with 7 V/–7 V, 500 ns write/erase pulses [147]. For the case of nanocrystal-type memory with thin tunneling oxide (of ca. 1.5 nm) and a deposited SRO film as a charge-trapping layer, a fast write/erase speed that reaches 100 ns at 5 V write/erase voltage with a 0.5 V threshold voltage shift is reported [101]. In addition, a long refresh time of 1000 s is observed at room temperature after  $10^8$  write/erase cycles. Superior electrical characteristics in terms of write/erase speed/voltage and retention time (properties that also suggest the possibility of nanosecond programming range quasinonvolatile applications) have been recently reported for Ge nanocrystal memory devices obtained by thermal oxidation of  $S_{1-x}Ge_x$  [87]. For this case, data retention longer than one day at room temperature and about 1 h at 85 °C after a  $10^9$  cycle endurance test with 4 V/–4 V, 100 ns write/erase pulses are measured. Encouraging results suggest that DRAM-like functions also have been obtained for the simple and CMOS-compatible nanocrystal processing case of a very-low-energy Si nanocrystal memory device [148]. Fast write/erase characteristics at low electric fields with a large threshold voltage window under dynamic operation (using a gate-bias sine wave or pulsed signal) are measured in MOSFETs with embedded 2D arrays of Si nanocrystals at a distance ca. 3 nm from the channel obtained by 1 keV  $Si^+$  IBS in initially 8 nm thick gate oxides, and subsequently covered by 30 nm thick deposited control oxide. Endurance and retention-time characteristics of this memory cell using 15 V/–5 V, 100 ns write/erase pulses are shown in Figures 13 and 14. No degradation, even after a  $10^{10}$  cycle endurance test (Fig. 13) and less than 5% (20%) reduction in the memory window (Fig. 14) after 1 s (10 s), is observed at room temperature. Further process optimization (e.g., adjustments of the deposited control oxide thickness and improvements of the implanted oxide quality) is expected to reduce operation voltage and to increase the refresh-time characteristics of such devices [135, 136].

#### 4.3. Single-Electron Charging Effects

Similar to the case of single-dot device structures, single-electron charging phenomena also have been reported, and for the case of multiple-dot structures, consistent with the self-limiting charging process in nanocrystal storage nodes. However, in contrast to the former case, where a single dot is involved for screening the transistor channel, in the latter case (as discussed in Section 2), the uniformity of the size and depth distribution of the nanocrystals, as well as their density are critical parameters for



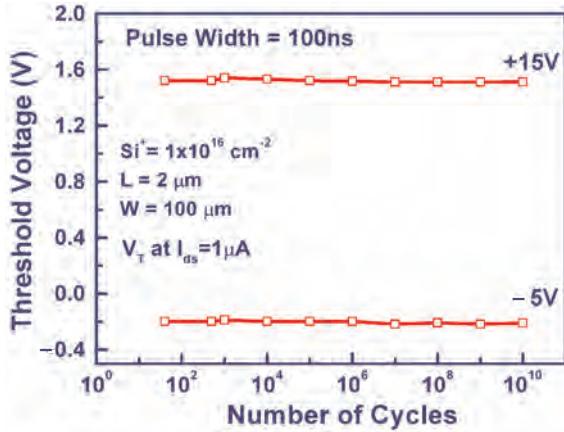


**Figure 13.** Endurance characteristic of a nanocrystal memory device obtained by implantation of 1 keV Si ions at a dose of  $1 \times 10^{16} \text{ cm}^{-2}$  into 8 nm thick oxide and subsequent annealing at 950 °C. A 30 nm thick oxide layer was deposited before annealing.

the observation of such discrete charging effects. Furthermore, concerning the magnitude of the threshold voltage shift caused by one stored electron in each nanocrystal, besides the nanocrystal size and the control oxide thickness (as in the single-dot case), the nanocrystal density is also very important for the case of a multidot memory device. Plateaus in the pulsed threshold voltage with static gate voltage characteristics have been observed at temperatures below 120 K in MOSFET structures with Si nanocrystals embedded in the gate oxide by deposition onto 1.9 nm thin tunneling oxide, and covered by a control oxide of ca. 9 nm in thickness [43]. The observation of threshold voltage plateaus in equidistant steps (of ca. 0.3 V) is found consistent with single-electron storage in the nanocrystals for the case of nanocrystal density of ca.  $6 \times 10^{11} \text{ cm}^{-2}$ , a value within the error margins of that estimated by structural observations. In addition, the temperature range wherein this phenomenon becomes pronounced is in agreement with the relatively large observable nanocrystal size (>10 nm). Room-temperature discrete threshold voltage

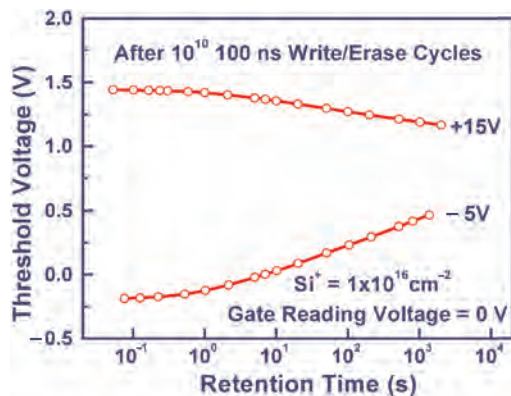


**Figure 14.** Charge-retention time characteristics after  $10^{10}$  cycle endurance test with +15 V/−5 V, 100 ns write/erase pulses of a nanocrystal memory device obtained by implantation of 1 keV Si ions at a dose of  $1 \times 10^{16} \text{ cm}^{-2}$  into 8 nm thick oxide and subsequent annealing at 950 °C. A 30 nm thick oxide layer was deposited before annealing.

shifts of 0.48 V have been observed for Si nanocrystal memories formed by LPCVD onto 2 nm in thickness oxide–nitride tunneling dielectric and covered by a 20 nm thick control oxide [44, 149–150]. The room-temperature single-electron charging phenomena in these structures have been attributed to the extremely small size (ca. 4.5 nm in diameter), the good size uniformity, and the aerial density of  $5 \times 10^{11} \text{ cm}^{-2}$  of the Si dots. Recently, Si-nanocrystal memory devices obtained by a high-dose ( $2 \times 10^{16} \text{ Si}^+/\text{cm}^2$ ) very-low-energy (1 keV) IBS technique have been found to exhibit step-like source–drain current versus time ( $I_{DS}$ – $t$ ) and periodic staircase plateau source–drain current versus gate voltage ( $I_{DS}$ – $V_G$ ) characteristics, both in support of the notion of room-temperature discrete electron storage in Si nanocrystals [45]. Structural study for this case reveals the formation of well-crystallized Si grains of about 7–8 nm average linear dimensions in a dense arrangement. The observation of discrete threshold voltage shifts of ca. 2 V in the  $I_{DS}$ – $V_G$  curves obtained during slow forward (Fig. 15)/fast backward (inset of Fig. 15) gate voltage sweeps is found to be consistent with successive single-electron injection/ejection into/from each nanocrystal for the case of nanocrystal density of ca.  $1 \times 10^{12} \text{ cm}^{-2}$ .

In spite of the inherent difficulties of controlling single-electron storage phenomena at a realistic level of integration, the experimental evidence of such effects at room temperature supports the pursuit of technologically practical large-channel devices operating on the basis of the Coulomb blockade principle. Successful exploitation of the discrete threshold voltage changes in multiple-dot structures may lead to the development of memory cells with a multi-level storage capability and current drive much higher than nanoscale Si channel FET devices with single (or few) nanocrystal storage nodes.

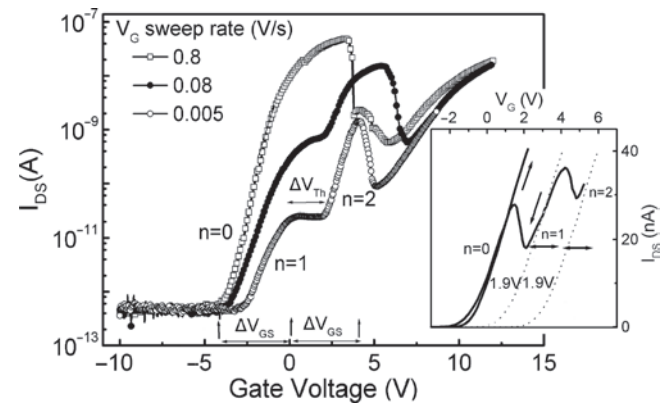


**Figure 15.** Room-temperature transfer characteristics for the very-low-energy Si nanocrystal memory devices (case of 1 keV/ $2 \times 10^{16} \text{ cm}^{-2}$   $\text{Si}^+$  implants). With decreasing sweep rate, the  $I_{DS}$ – $V_G$  curves show a clear staircase structure. The arrows indicate voltage regions  $\Delta V_{GS}$  with one and two stored electrons per nanocrystal ( $n = 1, 2$ ), while the initial part of the fast swept  $I_{DS}$ – $V_G$  curve corresponds to  $n = 0$ .  $\Delta V_{TH}$  is the threshold voltage shift caused by the storage of a single electron per nanocrystal. Inset:  $V_G$  is swept forward and backward after discharging at a rate of 0.8 V/s. The dot lines show  $I_{DS}$ – $V_G$  curves with  $n = 1$  and  $n = 2$  stored electrons per nanocrystal and are obtained by shifting the forward swept curve ( $n = 0$  stored electrons per nanocrystal) by 1.9 V and 3.8 V respectively.

## 5. CONCLUSIONS

Fundamental limits in (a) gate oxide thickness due to tunneling currents, (b) transistor channel length due to subthreshold leakage constraints, and (c) storage capacitor due to the need for large capacitance values, will become an important concern in the future scaling of conventional volatile and nonvolatile memory devices. Aggressive exploration of an alternate device architecture offers the best hope for continuing the current performance scaling trends seen in the last 20 years. A nanocrystal memory structure is one of the new promising memory concepts for overcoming the fast-approaching scaling limits of Flash and DRAM memories.

In this short chapter, the current status and challenges of this approach for memory applications have been presented. The self-limiting charging process in laterally uncoupled nanocrystal storage nodes (due to the Coulomb blockade effect), together with the distributed nature of the storage nodes (in contrast to the conventional continuous poly-Si floating-gate layer) promise the implementation of memory devices with thinner tunneling oxides for ultrahigh-density, low-voltage, low-power, and fast write/erase data storage. The progress in the area of practical nanocrystal floating-gate technology has been reviewed, and the potential of the very-low-energy ion beam synthesis approach has particularly been discussed. Encouraging electrical results of prototype nanocrystal single-transistor memory structures have been presented, indicating an optimistic prospect for applications ranging from Flash to DRAM-like functions, with the exotic possibility of multilevel storage capability.

However, the experimental memory characteristics up to now (e.g., data retention time, endurance, write/erase speed, programming voltages) span a very wide range of values, and definite conclusions concerning the scalability advantages of this type of memory device over the conventional DRAM or Flash ones cannot be fully evaluated at present. More extensive study and fabrication process optimization are required in order to realize the applicability of the nanocrystal memory concept. Important issues such as reliable low-voltage operation with long-term charge retention or fast write/erase speeds at low programming voltages with high endurance remain to be verified beyond doubt before the practical implementation of this device in nonvolatile or volatile memory circuitry, respectively. That is, it has yet to be clarified whether or not nanocrystal memories will be used for information data storage in place of the conventional memory devices.

## GLOSSARY

**Charge-trapping devices** Memory technology that stores binary information in the form of electric charge in discrete traps distributed in the gate insulator of a MOS transistor

**Coulomb blockade** Phenomenon in which the flow of current through a metallic quantum dot is inhibited until the electrostatic energy needed to move an electron onto the dot is overcome through an applied bias. For the case of a semiconductor quantum dot (a system with much lower electron densities, and larger electron wavelengths at the Fermi energy), the kinetic energy of the added electron (due to

quantum confinement) also must be supplied for overcoming current suppression.

**Dynamic random access memory (DRAM)** Memory technology that stores binary information in the form of presence and absence of electric charge on capacitors. The DRAM cell consists of a single capacitor and a single transistor to access the capacitor. This technology is considered dynamic because the stored charge degrades over time due to leakage mechanisms. Therefore, the cell data must be read and rewritten periodically (*refresh operation*), even when the memory cell is not accessed to replace the lost charge.

**Floating gate (FG)** Conductive polysilicon layer, completely embedded inside the gate oxide of a MOS transistor. As it is not externally connected to any other part of the device (rather, it is left floating), it is appropriately called a floating gate.

**Ion beam synthesis (IBS)** Method for synthesizing various types of quantum dots. In this technique, an appropriate number of selected ions are introduced into a given dielectric layer, and a subsequent thermal annealing can induce the implanted material to precipitate in the form of small particles dispersed within the host layer.

**Metal oxide semiconductor (MOS)** Sandwich structure consisting of three layers: the metal *gate electrode* (usually made of polysilicon), the insulating oxide ( $\text{SiO}_2$ ) layer, and the bulk semiconductor (*p*- or *n*-type Si), called the *substrate*, that make up the MOS capacitors and MOS transistors.

**MOS field-effect transistor (MOSFET) (or briefly, MOS transistor)** Synonym for insulated-gate FET. A four-terminal MOS device with the terminals designated as *gate*, *source*, *drain*, and *substrate* or *body* electrodes. Usually, the substrate terminal is connected to the source terminal. As a field-effect device, the electric field established by the voltage applied to the gate terminal controls the current flow in the transistor *channel* (the region between the source and drain electrodes).

**Nonvolatile memory (NVM)** Type of memory device in which the stored data are not lost when the power supply is off, and refresh operation is not required. Nonvolatile memories are classified into two main categories: FG NVMs and charge-trapping devices.

**Quantum confinement (or briefly, confinement)** Quantization of the kinetic energy of charge carriers, when their motion in a particular spatial dimension is confined to a region comparable to the de Broglie wavelength of the carriers.

**Quantum dot (or briefly, dot)** Synonym for island. An electrically insulated object, for example, a metal or semiconductor nanocrystal, in which charge can be transferred only through a tunneling mechanism. The confinement in all three spatial directions completely confines the motion of charge carriers, giving rise to a discrete energy spectrum much like an isolated atom or molecule. This is, in particular, the case of very small dots with a size close to or less than the electron wavelength on the Fermi surface  $F$ . In semiconductors,  $F \sim 50$  nm, and in metals,  $F \sim 1$  nm.



**Static random access memory (SRAM)** Memory technology that utilizes the bistable characteristics of a two cross-coupled inverter circuit (a circuit with two stable operating points) to store binary information. The most popular SRAM cell consists of two cross-coupled CMOS inverters and two access transistors. The memory cell is considered static because the cell data are kept as long as the power is turned on and refresh operation is not required.

**Tunneling** Quantum mechanical charge-transport process in which electrons are able to penetrate through a narrow potential energy barrier, when their energies happen to be smaller than the height of the potential energy barrier.

**Volatile memory** Type of a memory device in which the stored data are lost when the power supply voltage is turned off. Volatile memories are classified into two main categories: DRAMs and SRAMs.

## REFERENCES

1. B. Prince, "Semiconductor Memories," 2nd ed. Wiley, New York, 1991.
2. S. M. Sze, "Physics of Semiconductor Devices," 2nd ed. Wiley, New York, 1981.
3. Y. Tsididis, "The MOS Transistor: Operation and Modeling," 2nd ed. McGraw-Hill, New York, 1999.
4. G. Groeseneken, H. E. Maes, J. Van Houdt, and J. S. Witters, in "Basics of Nonvolatile Semiconductor Memory Devices" (W. D. Brown and J. E. Brewer, Eds.), pp. 1–88. IEEE Press, New York, 1998.
5. R. H. Dennard, *IEEE Trans. Electron Devices* ED-31, 1549 (1984).
6. C. Y. Chang and S. M. Sze, "ULSI Devices." Wiley, New York, 2000.
7. D. Burnett and S. W. Sun, *Proc. SPIE* 2636, 83 (1995).
8. F. Masuoka, M. Assano, H. Iwahashi, T. Komuro, and S. Tanaka, "IEEE IEDM Technical Digest," 1984, p. 464.
9. D. Kahng and S. M. Sze, *Bell Syst. Tech. J.* 46, 1288 (1967).
10. M. Lenzlinger and E. H. Snow, *J. Appl. Phys.* 40, 278 (1969).
11. B. Eitan and D. Frohman-Bentchkowsky, *IEEE Trans. Electron Devices* ED-28, 328 (1981).
12. R. Moazzami and C. Hu, "IEEE IEDM Technical Digest," 1992, p. 139.
13. D. J. DiMaria and E. Cartier, *J. Appl. Phys.* 78, 3883 (1992).
14. F. Masuoka, M. Momodomi, Y. Iwata, and R. Shirola, "IEEE IEDM Technical Digest," 1987, p. 552.
15. B. Eitan, R. Kazerounian, A. Roy, G. Crisenza, P. Cappelletti, and A. Modelli, "IEEE IEDM Technical Digest," 1996, p. 169.
16. J. Evans and R. Womack, *IEEE J. Solid-State Circuits* 23, 1171 (1998).
17. K. Inomata, *IEICE Trans. Electron.* E84-C, p. 740 (2001).
18. K. K. Likharev, *Appl. Phys. Lett.* 73, 2137 (1998).
19. K. Nakazato, K. Itoh, H. Mizuta, and H. Ahmed, *Electro. Lett.* 35, 848 (1999).
20. H. A. R. Wegener, A. J. Lincoln, H. C. Pao, M. R. O'Connell, and R. E. Oleksiak, "IEEE IEDM Technical Digest," 1967.
21. M. H. White, D. A. Adams, and J. Bu, *IEEE Circuits Devices*, 22 (July 2000).
22. Eitan, P. Pavan, I. Bloom, E. Aloni, A. Frommer, and D. Finzi, *IEEE Electron Device Lett.* 21, 543 (2000).
23. S. Tiwari, F. Rana, K. Chan, H. Hanafi, W. Chan, and D. Buchanan, "IEEE IEDM Technical Digest," 1995, p. 521.
24. S. Tiwari, F. Rana, H. Hanafi, A. Hartstein, and E. F. Crabbé, *Appl. Phys. Lett.* 68, 1377 (1996).
25. S. Tiwari, J. A. Wahl, H. Silva, F. Rana, and J. J. Welser, *Appl. Phys. A* 71, 403 (2000).
26. S.-H. Lo, D. Buchanan, Y. Taur, and W. Wang, *IEEE Electron Device Lett.* 18, 209 (1997).
27. F. Rana, S. Tiwari, and D. Buchanan, *Appl. Phys. Lett.* 69, 1104 (1996).
28. K. R. Farmer, M. O. Anderson, and O. Engstrom, *Appl. Phys. Lett.* 60, 730 (1992).
29. K. K. Likharev, *Proc. IEEE* 87, 606 (1999).
30. M. Tinkham, *Am. J. Phys.* 64, 343 (1996).
31. Q. Ye, R. Tsu, and E. H. Nicollian, *Phys. Rev. B* 44, 1806 (1991).
32. D. Babic, R. Tsu, and R. F. Greene, *Phys. Rev. B* 45, 14150 (1992).
33. E. H. Nicollian and R. Tsu, *J. Appl. Phys.* 74, 4020 (1993).
34. J. J. Welser, S. Tiwari, S. Rishton, K. Y. Lee, and Y. Lee, *IEEE Electron Device Lett.* 18, 278 (1997).
35. K. Nakazato, R. J. Blaikie, and H. Ahmed, *J. Appl. Phys.* 75, 5123 (1994).
36. K. Yano, T. Ishii, T. Hashimoto, T. Kobayashi, F. Murai, and K. Seki, *IEEE Trans. Electron Devices* 41, 1628 (1994).
37. L. Guo, E. Leobandung, and S. Y. Chou, *Science* 175, 649 (1997).
38. A. Nakajima, T. Futatsugi, K. Kosemura, T. Fukano, and N. Yokoyama, *Appl. Phys. Lett.* 70, 1742 (1997).
39. C. Wasshuber, H. Kosina, and S. Selberherr, *IEEE Trans. Electron Devices* 45, 2365 (1998).
40. A. K. Korotkov, *J. Appl. Phys.* 92, 7291 (2002).
41. K. Yano, T. Ishii, T. Sano, T. Mine, F. Murai, T. Hashimoto, T. Kobayashi, T. Kure, and K. Seki, *Proc. IEEE* 87, 633 (1999).
42. T. Usuki, T. Futatsugi, and A. Nakajima, *Jpn. J. Appl. Phys.* 37, L709 (1998).
43. S. Tiwari, F. Rana, K. Chan, L. Shi, and H. Hanafi, *Appl. Phys. Lett.* 69, 1232 (1996).
44. I. Kim, S. Han, H. Kim, J. Lee, B. Choi, S. Hwang, D. Ahn, and H. Shin, "IEEE IEDM Technical Digest," 1998, p. 111.
45. E. Kapetanakis, P. Normand, D. Tsoukalas, and K. Beltsios, *Appl. Phys. Lett.* 80, 2794 (2002).
46. F. Rana, S. Tiwari, and J. J. Welser, *Superlattices Microstruct.* 23, 757 (1998).
47. B. De Salvo, G. Ghibaudo, G. Pananakakis, B. Guillaumot, and T. Baron, *Superlattices Microstruct.* 28, 339 (2000).
48. B. De Salvo, G. Ghibaudo, G. Pananakakis, P. Masson, T. Baron, N. Buffet, A. Fernandes, and B. Guillaumot, *IEEE Trans. Electron Devices* 48, 1789 (2001).
49. R. Ohba, N. Sugiyama, J. Koga, K. Uchida, and A. Toriumi, *Jpn. J. Appl. Phys.* 39, 989 (2000).
50. Y. Shi, K. Saito, H. Ishikuro, and T. Hiramoto, *J. Appl. Phys.* 84, 2358 (1998).
51. J. A. Wahl, H. Silva, A. Gokirmak, A. Kumar, J. J. Welser, and S. Tiwari, "IEEE IEDM Technical Digest," 1999, p. 375.
52. B. J. Hinds, T. Yamanaka, and S. Oda, *J. Appl. Phys.* 90, 6402 (2001).
53. J. S. De Sousa, A. V. Thean, J. P. Leburton, and V. N. Freire, *J. Appl. Phys.* 92, 6182 (2002).
54. Z. Liu, C. Lee, V. Narayanan, G. Pei, and E. C. Kan, *IEEE Trans. Electron Devices* 49, 1606 (2002).
55. Z. Liu, C. Lee, V. Narayanan, G. Pei, and E. C. Kan, *IEEE Trans. Electron Devices* 49, 1614 (2002).
56. H. I. Hanafi, S. Tiwari, and I. Khan, *IEEE Trans. Electron Devices* 43, 1553 (1996).
57. H. G. Yang, Y. Shi, H. M. Bu, J. Wu, B. Zhao, X. L. Yuan, B. Shen, P. Han, R. Zhang, and Y. D. Zheng, *Solid-State Electron.* 45, 767 (2001).
58. J. Kora, R. Ohba, K. Uchida, and A. Toriumi, "IEEE IEDM Technical Digest," 2001, p. 143.
59. R. Ohba, N. Sugiyama, K. Uchida, J. Kora, and A. Toriumi, "IEEE IEDM Technical Digest," 2000, p. 313.
60. R. Ohba, N. Sugiyama, K. Uchida, J. Kora, and A. Toriumi, *IEEE Trans. Electron Devices* 49, 1392 (2002).
61. V. L. Colvin, M. C. Schlamp, and A. P. Alivisatos, *Nature* 370, 354 (1994).

62. L. Pavesi, L. Dal Negro, C. Mazzoleni, G. Franzo, and F. Priolo, *Nature* 408, 440 (2000).
63. Y. Maeda, N. Tsukamoto, Y. Yazawa, Y. Kanemitsu, and Y. Masumoto, *Appl. Phys. Lett.* 59, 3168 (1991).
64. D. J. DiMaria, J. R. Kirtley, E. J. Pakulis, D. W. Dong, T. S. Kuan, F. L. Pasavento, T. N. Theis, J. A. Cutro, and S. D. Brorson, *J. Appl. Phys.* 56, 401 (1984).
65. Q. Zhang, S. C. Bayliss, and D. A. Hutt, *Appl. Phys. Lett.* 59, 1977 (1995).
66. P. Photopoulos and A. G. Nassiopoulou, *Appl. Phys. Lett.* 77, 1816 (2000).
67. M. Fujii, M. Wada, S. Hayashi, and K. Yamamoto, *Phys. Rev. B* 46, 15930 (1992).
68. Y. Wakayama, T. Tagami, and S. Tanaka, *Thin Solid Films* 350, 300 (1999).
69. T.-S. Iwayama, Y. Terao, A. Kamiya, M. Takeda, S. Nakao, and K. Saitoh, *Nucl. Instrum. Meth., Phys. Res. B* 112, 214 (1996).
70. P. Mutti, G. Ghislotti, S. Bertoni, L. Bonoldi, G. F. Cerofolini, L. Meda, E. Grilli, and M. Guzzi, *Appl. Phys. Lett.* 66, 851 (1995).
71. G. Ghislotti, B. Nielsen, P.-A. Kumar, K. G. Lynn, L. F. Di Mauro, C. E. Bottani, F. Corni, R. Tonini, and G. P. Ottaviani, *J. Electrochem. Soc.* 144, 2196 (1997).
72. J. G. Zhu, C. W. White, J. D. Budai, S. P. Withrow, and Y. Chen, *J. Appl. Phys.* 78, 4386 (1995).
73. T. Komoda, J. Kelly, F. Cristiano, A. Nejm, P. L. F. Hemment, K. P. Homewood, R. Gwilliam, J. E. Mynard, and B. J. Sealy, *Nucl. Instrum. Meth., Phys. Res. B* 96, 387 (1995).
74. K. V. Shcheglov, C. M. Yang, K. J. Vahala, and H. A. Atwater, *Appl. Phys. Lett.* 66, 745 (1995).
75. J.-Y. Zhang, X.-L. Wu, and X.-M. Bao, *Appl. Phys. Lett.* 71, 2505 (1997).
76. M. Fujii, M. Yoshida, Y. Kanzawa, S. Hayashi, and K. Yamamoto, *Appl. Phys. Lett.* 71, 1198 (1997).
77. P. G. Kik and A. Polman, *J. Appl. Phys.* 88, 1992 (2000).
78. M. Fukuda, K. Nakagawa, S. Miyazaki, and M. Hirose, *Appl. Phys. Lett.* 70, 1291 (1997).
79. E. C. Kan and Z. Liu, *Superlattices Microstruct.* 27, 473 (2000).
80. D. J. DiMaria, R. Ghez, and D. W. Dong, *J. Appl. Phys.* 51, 4830 (1980).
81. S. Hayashi, T. Nagareda, Y. Kanzawa, and K. Yamamoto, *Jpn. J. Appl. Phys.* 32, 3840 (1993).
82. W. K. Choi, W. K. Chim, C. L. Heng, L. W. Teo, V. Ho, V. Ng, D. A. Antoniadis, and E. A. Fitzgerald, *Appl. Phys. Lett.* 80, 2014 (2002).
83. T. Maeda, E. Suzuki, I. Sakata, M. Yamanaka, and K. Ishii, *Nanotechnol.* 10, 127 (1999).
84. Y. Kim, K. H. Park, T. H. Chung, H. J. Bark, J.-Y. Yi, W. C. Choi, E. K. Kim, J. W. Lee, and J. Y. Lee, *Appl. Phys. Lett.* 78, 934 (2001).
85. A. Kanjilal, J. L. Hansen, P. Gaiduk, A. N. Larsen, N. Cherkashin, A. Claverie, P. Normand, E. Kapetanakis, D. Skarlatos, and D. Tsoukalas, *Appl. Phys. Lett.* 82, 1212 (2003).
86. M. L. Ostraat, J. W. De Blauwe, M. L. Green, L. D. Bell, M. L. Brongersma, J. Casperson, R. C. Flagan, and H. A. Atwater, *Appl. Phys. Lett.* 79, 433 (2001).
87. Y.-C. King, T.-J. King, and C. Hu, *IEEE Trans. Electron Devices* 48, 696 (2001).
88. A. Nakajima, Y. Sugita, K. Kawamura, H. Tomita, and N. Yokoyama, *Jpn. J. Appl. Phys.* 35, L189 (1996).
89. T. Baron, F. Martin, P. Mur, C. Wyon, M. Dupuy, C. Buseret, A. Soufi, and G. Guillot, *Appl. Surface Sci.* 164, 29 (2000).
90. S. Miyazaki, Y. Hamamoto, E. Yoshida, M. Ikeda, and M. Hirose, *Thin Solid Films* 369, 55 (2000).
91. A. Fernandes, B. DeSalvo, T. Baron, J. F. Damlencourt, A. M. Papon, D. Lafond, D. Mariolle, B. Guillaumot, P. Besson, P. Masson, G. Ghibaud, G. Pananakakis, F. Martin, and S. Haukka, "IEEE IEDM Technical Digest," 2001, p. 155.
92. K. Han, I. Kim, and H. Shin, *IEEE Trans. Electron Devices* 48, 874 (2001).
93. D. J. DiMaria, D. W. Dong, C. Falcony, T. N. Theis, J. R. Kirtley, J. C. Tsang, D. R. Young, F. L. Pasavento, and S. D. Brorson, *J. Appl. Phys.* 54, 5801 (1983).
94. L. A. Nesbit, *Appl. Phys. Lett.* 46, 38 (1985).
95. D. J. DiMaria and D. W. Dong, *J. Appl. Phys.* 51, 2722 (1980).
96. D. J. DiMaria, K. M. DeMeyer, and D. W. Dong, *IEEE Electron Device Lett.* 1, 179 (1980).
97. D. J. DiMaria, D. W. Dong, F. L. Pasavento, C. Lam, and S. D. Brorson, *J. Appl. Phys.* 55, 3000 (1984).
98. L. Dori, A. Acovic, D. J. DiMaria, and C.-H. Hsu, *IEEE Electron Device Lett.* 14, 283 (1993).
99. B. Maiti and J. C. Lee, *IEEE Electron Device Lett.* 13, 624 (1992).
100. A. Ron and D. J. DiMaria, *Phys. Rev. B* 30, 807 (1984).
101. Y.-C. King, T.-J. King, and C. Hu, *IEEE Electron Device Lett.* 20, 409 (1999).
102. A. Meldrum, R. F. Haglund, Jr., Lynn, Jr., L. A. Boatner, and C. W. White, *Adv. Mater.* 13, 1431 (2001).
103. A. Kalnitsky, M. I. H. King, A. R. Boothroyd, J. P. Ellul, and R. A. Hadaway, *IEEE Trans. Electron Devices* ED-34, 2372 (1987).
104. A. Kalnitsky, A. R. Boothroyd, J. P. Ellul, E. H. Poindexter, and P. J. Caplan, *Solid-State Electron.* 33, 523 (1990).
105. A. Kalnitsky, A. R. Boothroyd, and J. P. Ellul, *Solid-State Electron.* 33, 893 (1990).
106. M. Hao, H. Hwang, and J. C. Lee, *Appl. Phys. Lett.* 62, 1530 (1993).
107. T. Hori, T. Ohzone, Y. Odaka, and J. Hirase, "IEEE IEDM Technical Digest," 1992, p. 469.
108. T. Ohzone and T. Hori, *IEICE Trans. Electron.* E77-C, 952 (1994).
109. T. Matsuda, T. Ohzone, and T. Hori, *Solid-State Electron.* 39, 1427 (1996).
110. T. Ohzone, T. Matsuda, and T. Hori, *IEEE Trans. Electron Devices* 43, 1374 (1996).
111. T. Ohzone and T. Hori, *Solid-State Electron.* 37, 1771 (1994).
112. T. Ohzone, A. Michii, and T. Hori, *Solid-State Electron.* 38, 1165 (1995).
113. H. Hanafi and S. Tiwari, "Proceedings of the ESSDERC Technical Digest," 1995, p. 209.
114. E. Kameda, T. Matsuda, Y. Emura, and T. Ohzone, *Solid-State Electron.* 43, 555 (1999).
115. E. Kapetanakis, P. Normand, D. Tsoukalas, K. Beltsios, J. Stoemenos, S. Zhang, and J. van den Berg, *Appl. Phys. Lett.* 77, 3450 (2000).
116. P. Normand, E. Kapetanakis, D. Tsoukalas, G. Kamoulakos, K. Beltsios, J. van den Berg, and S. Zhang, *Mater. Sci. Eng. C* 15, 145 (2001).
117. E. Kapetanakis, P. Normand, D. Tsoukalas, and K. Beltsios, *Microelectron. Eng.* 61–62, 505 (2002).
118. J. v. Borany, T. Gebel, K.-H. Stegemann, H.-J. Thees, and M. Wittmaack, *Solid-State Electron.* 46, 1729 (2002).
119. E. A. Boer, M. L. Brongersma, and H. A. Atwater, *Appl. Phys. Lett.* 79, 791 (2001).
120. E. Kapetanakis, P. Normand, D. Tsoukalas, K. Beltsios, T. Travlos, J. Gautier, L. Palun, and F. Jourdan, "Proceedings of the ESSDERC Technical Digest," 1999, p. 432.
121. H.-J. Thees, M. Wittmaack, K.-H. Stegemann, J. V. Borany, K.-H. Heinig, and T. Gebel, *Microelectron. Rel.* 40, 867 (2000).
122. K. Beltsios, P. Normand, E. Kapetanakis, D. Tsoukalas, A. Travlos, J. Gautier, F. Jourdan, and P. Holliger, "Proceedings of the MMN," 2000, p. 69.
123. J. Zhao, L. Rebohle, T. Gebel, J. v. Borany, and W. Skorupa, *Solid-State Electron.* 46, 661 (2002).
124. C. J. Nicklaw, M. P. Pagey, S. T. Pantelides, D. M. Fleetwood, R. D. Schimpf, K. F. Galloway, J. E. Wittig, B. M. Howard, E. Taw,

- W. H. McNeil, and J. F. Conley, Jr., *IEEE Trans. Nucl. Sci.* 47, 2269 (2000).
125. A. Kalnitsky, J. P. Ellul, E. H. Poindexter, P. J. Caplan, R. A. Lux, and A. R. Boothroyd, *J. Appl. Phys.* 67, 7359 (1990).
  126. G. B. Assayag, C. Bonafos, M. Carrada, A. Claverie, P. Normand, and D. Tsoukalas, *Appl. Phys. Lett.* 82, 200 (2003).
  127. P. Dimitrakis, E. Kapetanakis, P. Normand, D. Skarlatos, D. Tsoukalas, K. Beltsios, A. Claverie, G. Benassyag, C. Bonafos, D. Chassaing, and V. Soncini, *Mater. Sci. Eng. B* (in press).
  128. P. Normand, D. Tsoukalas, E. Kapetanakis, J. A. van den Berg, D. G. Armour, and J. Stoemenos, *Microelectron. Eng.* 36, 79 (1997).
  129. P. Normand, D. Tsoukalas, E. Kapetanakis, J. A. van den Berg, D. G. Armour, J. Stoemenos, and C. Vieu, *Electrochem. Solid State Lett.* 1, 88 (1998).
  130. P. Normand, K. Beltsios, E. Kapetanakis, D. Tsoukalas, T. Travlos, J. Stoemenos, J. van den Berg, S. Zhang, C. Vieu, H. Launois, J. Gautier, F. Jourdan, and L. Palun, *Nucl. Instrum. Meth., Phys. Res. B* 178, 74 (2001).
  131. K. Beltsios, P. Normand, E. Kapetanakis, D. Tsoukalas, and A. Travlos, *Microelectron. Eng.* 61–62, 631 (2002).
  132. W. Möller, *Nucl. Instrum. Meth., Phys. Res. B* 15, 688 (1986).
  133. T. Müller, K.-H. Heinig, and W. Möller, *Appl. Phys. Lett.* 81, 3049 (2002).
  134. M. Carrada, N. Cherkashin, C. Bonafos, G. Ben Assayag, D. Chassaing, P. Normand, D. Tsoukalas, V. Soncini, and A. Claverie, *Mater. Sci. Eng. B* (in press).
  135. P. Normand, E. Kapetanakis, P. Dimitrakis, D. Skarlatos, D. Tsoukalas, K. Beltsios, A. Claverie, G. Benassyag, C. Bonafos, M. Carrada, N. Cherkashin, V. Soncini, A. Agarwal, Ch. Sohl, and M. Ameen, *Microelectron. Eng.* (in press).
  136. P. Normand, E. Kapetanakis, P. Dimitrakis, D. Skarlatos, D. Tsoukalas, K. Beltsios, A. Claverie, G. Benassyag, and C. Bonafos, *Appl. Phys. Lett.* (submitted).
  137. J. v. Borany, K.-H. Heinig, R. Grötzschel, M. Klimenkov, M. Strobel, K.-H. Stegemann, and H.-J. Thees, *Microelectron. Eng.* 48, 231 (1999).
  138. J. v. Borany, R. Grötzschel, K.-H. Heinig, A. Markwitz, B. Schmidt, W. Skorupa, and H.-J. Thees, *Solid-State Electron.* 43, 1159 (1999).
  139. J. v. Borany, R. Grötzschel, K.-H. Heinig, A. Markwitz, W. Matz, B. Schmidt, and W. Skorupa, *Appl. Phys. Lett.* 71, 3215 (1997).
  140. M. Klimenkov, W. Matz, and J. v. Borany, *Nucl. Instrum. Meth., Phys. Res. B* 168, 367 (2000).
  141. A. Nakajima, T. Futatsugi, H. Nakao, T. Usuki, N. Horiguchi, and N. Yokoyama, *J. Appl. Phys.* 84, 1316 (1998).
  142. A. Nakajima, H. Nakao, H. Ueno, T. Futatsugi, and N. Yokoyama, *Appl. Phys. Lett.* 73, 1071 (1998).
  143. K. Han, I. Kim, and H. Shin, *IEEE Electron Device Lett.* 21, 313 (2000).
  144. F. R. Libsch and M. H. White, in “Basics of Nonvolatile Semiconductor Memory Devices” (W. D. Brown and J. E. Brewer, Eds.), pp. 309–357. IEEE Press, New York, 1998.
  145. W. Chen, T. P. Smith, and S. Tiwari, U.S. Patent 5, 937, 295, Aug. 10, 1999.
  146. G. Ammendola, M. Vulpio, M. Bileci, N. Nastasi, C. Gerardi, G. Renna, I. Crupi, G. Nicotra, and S. Lombardo, *J. Vac. Sci. Technol. B* 20, 2075 (2002).
  147. H. C. Wann and C. Hu, *IEEE Electron Device Lett.* 16, 491 (1995).
  148. E. Kapetanakis, P. Normand, D. Tsoukalas, G. Kamoulakos, D. Kouvatso, J. Stoemenos, S. Zhang, J. van den Berg, and D. G. Armour, “Proceedings of the ESSDERC Technical Digest,” 2000, p. 476.
  149. Kim, S. Han, K. Han, J. Lee, and H. Shin, *IEEE Electron Device Lett.* 20, 630 (1999).
  150. Kim, S. Han, K. Han, J. Lee, and H. Shin, *Jpn. J. Appl. Phys.* 40, 447 (2001).

# Nanocrystalline Aluminum Alloys

Livio Battezzati, Simone Pozzovivo, Paola Rizzi

*Università di Torino, Torino, Italy*

## CONTENTS

1. Synthesis of Nanocrystalline Materials
2. Nanocrystalline Aluminum
3. Devitrification of Al Glasses
4. Al–TM–RE Alloys: Description and Properties
5. Ball Milling of Alloys
6. Nanoquasicrystalline Alloys
7. Nanocrystallization Induced by Deformation
8. Conclusions
- Glossary
- References

## 1. SYNTHESIS OF NANOCRYSTALLINE MATERIALS

### 1.1. Introduction

In order for a material to be defined nanocrystalline the size of its grains must be of the order of less than 100 nm. Such materials can be constituted by one or more phases distributed in one, two, or three dimensions. Examples are nanowires, layers either deposited on top of a substrate as coatings or stacked in suitable sequences, and bulk objects. If the material is fully made of nanograins the number density of crystals scales with their size (e.g., it can range from  $10^{25}$  to  $10^{21}$  m<sup>-3</sup> for sizes of 5 and 100 nm respectively). Correspondingly, a high density of grain boundaries (usually  $6 \times 10^{19}$  cm<sup>-3</sup>) is implied so a large quantity of the atoms constituting the material can be situated on interfaces (simple calculations provide estimates of 50% for grains of 5 nm; 30% for grains of 10 nm; 3% for grains of 100 nm) [1]. As a consequence, nanocrystalline systems can be looked at as if they contained two types of atoms: those resident on a crystal lattice and those belonging to interfaces. Analogous densities of crystals can be obtained in two-phase materials where the fine particles are dispersed in a matrix either crystalline or glassy. Here the interface and its properties have relevance in determining the rate of nucleation and of attachment kinetics during growth.

In classical physical metallurgy there are several examples of materials developed over several decades and owing their properties to the existence of extremely fine grains. Two obvious cases are those of Al alloys hardened by pre-precipitates or metastable precipitates and high strength–low alloy steels where nitrides and carbonitrides act as grain refiners. Conventionally, these are not listed among nanomaterials and their science and technology are dealt with in well-established treatises. Other metallic materials have recently been discovered following the same leading idea of nanocrystal research (i.e., of producing very fine particles to improve properties). This chapter deals with a new class based on aluminum.

### 1.2. Techniques for the Production of Nanocrystalline Materials

Nanocrystalline metals and alloys can be obtained essentially by means of four different techniques:

- (a) introducing a high number of defects (i.e., dislocations and grain boundaries) in initially perfect crystals by severe plastic deformation which is achieved by ball milling, extensive rolling, extrusion, and equichannel angular pressing;
- (b) condensation of clusters or deposition of atoms on a substrate by chemical or physical vapor deposition;
- (c) crystallization of metastable systems such as glassy metals or undercooled liquids or precipitation from supersaturated solid solutions;
- (d) two-step production routes in which nanocrystalline powders are consolidated in order to obtain a bulk material.

In the following the essential features of each technique are described. Electro- and electroless deposition can be employed for some metals and alloys, but they will not be dealt with here since they are not appropriate for Al.

#### 1.2.1. Production of Powders and Compaction

Amorphous or nanocrystalline powders can be produced by ball milling. The technique has been considered as a tool for refining minerals for a long time. It gained more widespread application when it was realized that the mechanical action

can drive phase transformations (amorphization, disordering, etc.) and chemical reactions. The initial stage of ball milling invariably implies the introduction of disorder and defects in the material leading to the formation of crystals with size of the order of nanometers [2]. During the first stage of the process the deformation is localized in deformation bands of about 1  $\mu\text{m}$  thickness and grains of low dimension nucleate into these bands. For long treatment times grains of tens of nanometers are obtained in pure metals, without preferred orientation and with high-angle grain boundaries. The grain size approximately scales with the inverse of the melting point. In alloys and intermetallic compounds the grain refinement can be a precursor of phase transformations. Bulk materials can be obtained if the ball-milled powders are compacted by any powder metallurgy technique. Since these mostly imply hot pressing, the nanograins must resist growth enough to avoid coarsening to a large extent.

Pure Al has been obtained in nanocrystalline form with an average size of 25.5 nm by cryogenic milling using liquid nitrogen as cooling agent. The powders were found to resist grain growth up to temperatures close to 0.78  $T_m$  ( $T_m$  is the melting temperature) because of impurity pinning of grain boundaries [3].

Another technique for subjecting a sample to a very intense plastic deformation is equichannel angular pressing in which the material is forced to flow through an L-shaped die. A large amount of shear stress is experienced by the material with consequent grain refinement [4].

Inert gas condensation also results in Al particles of the order of 30 nm which were shown to remain fine sized up to the melting temperature if passivated with a small amount of oxygen [5].

### 1.2.2. Crystallization of Glassy Precursors

The metastable systems used for the production of nanocrystalline materials are amorphous metals prepared by rapid solidification by means of melt spinning in order to obtain ribbons about 30–40  $\mu\text{m}$  thick. Powders of the same size can be produced by atomization. A careful control of the heat treatment and, as a consequence, of the crystallization kinetics allows either the complete crystallization of the amorphous precursors into a nanocrystalline structure, or a partial crystallization with nanocrystals dispersed in the remaining amorphous matrix [6].

Nanocrystalline materials obtained by crystallization of amorphous precursors have the advantage with respect to the other production techniques that the preparation procedure is simple, can be easily controlled, and allows one to obtain materials constituted by grains of different size, from a few nanometers to tens of microns, simply varying the heat treatment conditions. A large part of this chapter will deal with such alloys.

## 2. NANOCRYSTALLINE ALUMINUM

This chapter is devoted to the description of constitution, structure, and properties of nanocrystalline Al alloys. Most of them have been obtained by rapid solidification as amorphous solids and then heat treated. The two processing steps

may appear to be ruled by very different alloy properties or even to be apparently contradictory. The requirements for amorphizing an alloy are: composition suited for high undercooling, high liquid viscosity, and relatively low tendency to crystal nucleation of both stable and metastable phases. For nanocrystallization the nucleation rate is expected to be high and atomic mobility low. All of these aspects will be treated in detail in the following with the aim of showing how each material parameter influences the processing steps and how the alloy composition can be chosen in order to reconcile possible discrepant tendencies.

### 2.1. The Reasons for Amorphization: Alloy Constitution and Size Effect

It is well known that the presence of deep eutectics in the alloy phase diagram is indicative of the tendency to amorphization for the compositions around the eutectic point. The liquid of eutectic composition is relatively stable with respect to crystal phases and often displays strong resistance to crystallization. It, therefore, can be undercooled to the glass transition where it transforms to a glassy solid. A parameter useful for the evaluation of the glass forming ability is the reduced glass transition temperature,  $T_{gr} = T_g/T_l$  ( $T_g$  = glass transition temperature;  $T_l$  = liquidus temperature). Values of  $T_{gr}$  exceeding 0.5 are typical for metallic alloys. Values in excess of 0.6 are associated with good glass forming compositions and with formation of bulk metallic glasses. Since  $T_g$  does not present large variations as a function of composition, the most relevant parameter for evaluating the tendency to amorphize is  $T_l$ .

The number of elements in the alloy is also relevant. In fact, in an alloy made of a high number of elements there is the possibility of crystallizing several phases. The short range order in the liquid may not correspond to that of any crystal phase implying that it is difficult for the system “to choose” a crystalline structure (the confusion principle). Therefore the tendency to give an amorphous structure will be increased.

The atomic size effect on glass forming tendency was studied by Egami et al. [7] for binary alloys. The mismatch between the atomic radii of the constituent elements of the alloy,  $\Delta r$ , shows an inverse proportionality to the minimum solute concentration ( $C_B^{\text{min}}$ ),

$$\left| \frac{\Delta r}{r_A} \right| = \frac{|\lambda_0|}{C_B^{\text{min}}} \quad (1)$$

$$\frac{\Delta r}{r_A} = \frac{r_B - r_A}{r_A} = \left( \frac{r_B}{r_A} \right)^3 - 1 \quad (2)$$

where  $A$  and  $B$  are the solvent element and the solute element respectively. The minimum value of the parameter  $\lambda_0$  necessary to obtain amorphous phases in binary alloys was empirically determined to be about 0.1.

### 2.2. Thermodynamic Aspects

Alloys that are able to form amorphous phases by rapid solidification show a substantial degree of chemical order in the liquid state. Macroscopic evidence for preferential

interaction between unlike elements is given by the strongly negative enthalpy of mixing which is a common characteristic of glass-forming liquid alloys [8].

Another peculiar feature of glass-forming metallic liquids is that their thermodynamic properties are temperature dependent: the degree of order increases with decreasing temperature. So the excess enthalpy and entropy of mixing become more negative as the temperature is lowered and the undercooling regime is entered. This gives rise to an excess heat capacity in the liquid state, the existence of which has been demonstrated for both metal–metal and metal–metalloid systems.

The existing data show that the excess heat capacity can be substantial for some alloys and has often a maximum at compositions corresponding to a compound in the solid state. It is nil for pure components, which have liquid heat capacities very close to those of the crystal phases at the melting point. As crystalline alloys usually obey the additive Neumann–Kopp rule, the excess liquid specific heat for alloys may be approximated by the specific heat difference  $\Delta C_p$  between liquid and crystal phases. This quantity is measured easily at the melting point and more rarely on undercooling near the glass transition temperature.  $\Delta C_p$  is substantial in the temperature range from the melting point to the glass transition with values of the order of the entropy of fusion of the alloy.  $\Delta C_p$  for pure elements has been determined in the undercooled regime for a limited number of cases; in all of them it is close to zero. Therefore, it is reasonable to attribute the largest part of the specific heat difference between liquid and crystal phases in glass-forming alloys to topological and chemical effects produced on alloying and to use  $\Delta C_p$  as an appropriate approximation for the actual excess specific heat.

A high value of the liquid specific heat with respect to the crystal lets the entropy of the liquid phase approach that of the solid quickly on decreasing the temperature according to

$$\Delta S = \Delta S_f - \int_T^{T_f} \Delta C_p d(\ln T) \quad (3)$$

where  $\Delta S_f$  is the entropy of fusion.

$\Delta C_p$  is approximated either by a fraction of the entropy of fusion (on average  $0.8 \Delta S_f$ ) or by its value at the melting point. With this position, all the thermodynamic quantities can be calculated in the undercooled regime (Fig. 1). In particular the difference between the free energy of the liquid and crystal phases may be evaluated with some confidence and used in calculations of the nucleation frequency and growth rate of the crystals from the melt.

For a liquid pure metal at the melting point the specific heat is close to that of the crystal, whereas it attains slightly higher values on undercooling. This means that pure metals lose little entropy on undercooling, so their reduced glass transition temperature will be low with respect to glass-forming alloys. The isoentropic temperature for Al (i.e., the temperature at which the entropy of the undercooled liquid would equal that of the crystal) has been computed by Fecht and Johnson with Eq. (3) as  $0.24 T_f$  and may be considered an ideal glass transition.

This analysis has been pursued further to obtain trends for  $T_g$  as a function of composition.

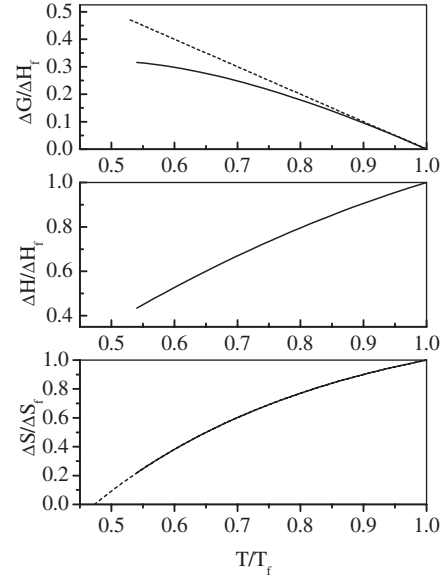


**Figure 1.** Schematic trend of the extensive thermodynamic functions for an undercooled metallic glass-forming liquid. Reduced coordinates are used. The reference state is the equilibrium crystal. The enthalpy and free energy are plotted from the melting point to the glass transition temperature. The entropy curve is extended (dashed line) to the hypothetical ideal glass transition,  $T_k$ . The enthalpy and entropy differences between liquid and crystals decrease on undercooling due to a positive  $\Delta C_p$ . Should  $\Delta C_p$  be zero, the free energy difference would follow the dashed line. The actual trend for a glass-former implies relative stabilization of the liquid, (i.e., a lower driving force for crystallization).

In a binary system an entropy balance can be established at every isoentropic temperature  $T_k$ .

Since the entropy of fusion at  $T_k$  is nil, an entropy cycle is written

$$\Delta S_{\text{for}} - x_A \Delta S_{f,A} - x_B \Delta S_{f,B} - \Delta S_{\text{mix}} = 0 \quad (4)$$

where  $\Delta S_{f,i}$  is the entropy of fusion of the constituents at  $T_k$ .  $\Delta S_{\text{mix}}$  is the entropy of mixing in the liquid state and  $\Delta S_{\text{for}}$  is the entropy of formation of the crystalline solid at the same temperature.  $\Delta S_{\text{for}}$  and  $\Delta S_{\text{mix}}$  may be inserted either as experimental data or by derivation from suitable models. If  $\Delta S_{f,A}$  and  $\Delta S_{f,B}$  are expressed through Eq. (3), using an effective value for  $\Delta C_p$  of pure elements, the temperature  $T_k$  which satisfies Eq. (4) may be calculated for every alloy composition. The result will be a trend of  $T_k$ , which can approximate that of  $T_g$  across the phase diagram. An example is shown in Figure 2 for a simple eutectic system displaying regular miscibility in the liquid state and assuming  $\Delta S_{\text{mix}} = 0$  in the solid state. Among glass-formers, the analysis was applied to the Al–Ce system [9] showing agreement with  $T_g$  values obtained both from experiments and extrapolation of data collected in ternary alloys.

### 2.3. Kinetic Aspects: Viscosity of Melts and Glass Transition

The glass transition is the phenomenon in which a viscous liquid passes continuously into the amorphous solid state during cooling [10]. In fact, when a liquid is cooled below its



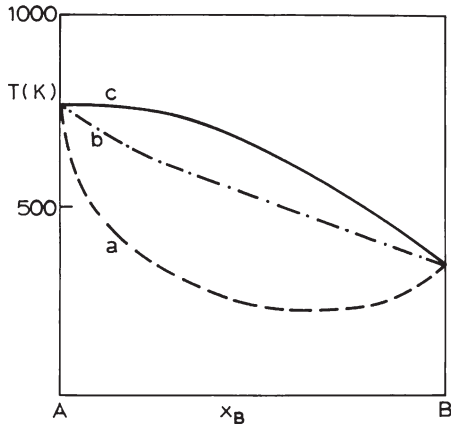


**Figure 2.** Hypothetical glass transition trends for a simple eutectic system. The lines refer to different positions for the entropy of mixing in the liquid state to be used in Eq. (4) where the entropy of formation of the crystal phases is taken as nil: (a)  $\Delta S_{\text{mix}}$  ideal, (b)  $\Delta S_{\text{mix}} = 0$ , (c)  $\Delta S_{\text{mix}}$  negative. The actual trend for metallic glasses is reproduced by curve (c) which is computed with an amount of entropy implying that the liquid is ordered at short range. Reprinted with permission from [8], L. Battezzati, *Phil. Mag. B* 61, 511 (1990). © 1990, Taylor & Francis.

melting point, if nucleation and growth of crystalline phases are avoided, the viscosity increases until the liquid is frozen in a structurally still, glassy state. Therefore, liquid viscosity is a central parameter for glass formation.

At the melting point the viscosity ( $\eta$ ) is of the order of  $10^{-2}$ – $10^{-1}$  Pa s for glass-forming metals, whereas it is  $10^{-3}$  Pa s for normal liquids. In general, viscosities of metallic liquids at the equilibrium melting point fit the Andrade formula:

$$\eta_{T_m} = A_C \frac{\sqrt{mT_m}}{V^{2/3}} \quad (5)$$

where  $m$  is the molecular mass,  $T_m$  is the eutectic melting temperature, and  $V$  is the molar volume. The empirical quantity  $A_C$  takes different values for metallic elements, intermetallic compounds, and normal eutectics  $\{1.8 \times 10^{-7} (\text{JK}^{-1} \text{mol}^{1/3})^{1/2}\}$  with respect to glass-forming eutectics  $\{6.5 \times 10^{-7} (\text{JK}^{-1} \text{mol}^{1/3})^{1/2}\}$  [11].

Conventionally, the viscosity at the glass transition is taken as  $10^{12}$  Pa s for extremely slow cooling [12]. The viscosity behavior in the undercooling regime can differ markedly for various substances: for silica the viscosity during cooling increases continuously according to the Arrhenius equation, whereas for other substances (e.g., molecular, polymeric, ionic, and metallic materials) it shows deviations from the Arrhenius rate law. In all these cases the activation energy for viscosity is a temperature-dependent parameter.

Since viscosity increases several orders of magnitude from the melting point to the glass transition, the more gradual the increase (i.e., that described as an Arrhenius behavior), the better the glass-forming ability of the liquid. Typical examples are silicate glasses. Marginal glass-formers present a rapid rise in viscosity during cooling when approaching the glass transition. Most metallic melts, including those based on Al, belong to this category.

The temperature dependence of viscosity for glass-forming liquids is given by the empirical Vogel–Fulcher–Tammann relation,

$$\eta = \eta_0 \exp\left(\frac{D \cdot T_0}{T - T_0}\right) \quad (6)$$

where  $D$  is the fragility parameter,  $T_0$  is the Vogel–Fulcher–Tammann temperature, and  $\eta_0$  is the high temperature limit of viscosity, determined according to the relationship

$$\eta_0 = \frac{h}{V_A} \quad (7)$$

where  $h$  is Planck’s constant and  $V_a$  is the atomic volume of the liquid. The fragility parameter is useful to classify “strong” and “fragile” liquids according to Angell [10]. The former follow silica behavior while the latter show deviations from the Arrhenius equation. For silica, the fragility parameter is 100, to be compared with 2 for the most fragile liquids [13]. The fragility parameter is also a good indicator of the glass-forming ability: the larger the fragility parameter, the better the glass-forming ability of the liquid. In fact glasses with large fragility parameter have slow kinetics in the undercooled liquid regime, inhibiting crystallization of the liquid.

The change in viscosity implies the change of thermodynamic properties as well: heat capacity and the expansion coefficient may decrease more than a factor of two with respect to their normal liquid state values.

Thermodynamic and kinetic parameters are combined in the Adam–Gibbs theory, based on entropy. This theory uses the idea of a cooperatively rearranging region, that is, the smallest group of atoms that must move in concert to change configuration. The sizes of these cooperatively rearranging regions grow with decreasing temperature, decreasing the configurational entropy of the system. With this theory, the viscosity is expressed as

$$\eta = \eta_0 \exp\left(\frac{C}{T \cdot S_c(T)}\right) \quad (8)$$

where  $\eta_0$  is the high temperature limit of viscosity,  $C$  is a constant related to the enthalpy barrier for a cooperative rearrangement,  $T$  is temperature, and  $S_c$  is the configurational entropy of the liquid.

The Adam–Gibbs theory is in agreement with Angell’s fragility classification. In fact strong liquids, with a tendency to short range order, have configurational entropy that is not strongly dependent on temperature, instead of fragile liquids that show non-Arrhenius behavior.

Viscosity is usually linked to atomic diffusivity,  $D$ , through the Stokes–Einstein equation:

$$\eta = \frac{kT}{6\pi rD} \quad (9)$$

This relationship is useful in estimating the diffusion coefficient in the undercooled liquid state where any experimental measurement would be almost impossible. However, it has been recently verified for molecular liquids and confirmed for metallic melts and glasses that it breaks down at temperatures in the range  $1.2$ – $1.3 T_g$  [14–16]. Below

such temperatures it is suggested that the product  $\eta \cdot D^2$  is constant at each temperature. The diffusion coefficient in the temperature range relevant for the formation of nanocrystals should be computed accordingly especially for Al alloys where no data are available for both viscosity and diffusivity in the liquid and glassy state. Below  $T_g$  the diffusivity can usually be described by the Arrhenius equation. For metallic alloys the temperature range of  $T_g$  is most often close to that where crystallization occurs and the two processes may overlap.

### 3. DEVITRIFICATION OF AI GLASSES

#### 3.1. Thermodynamics of Phase Transformations

Rapidly solidified materials contain usually metastable phases and/or microstructures which transform via nucleation and growth. The driving force is the difference between the free energy of the metastable and stable equilibrium states. A schematic free energy diagram is drawn in Figure 3 for devitrification. It is shown that a gain in free energy may involve three main types of transformations: primary, polymorphic, and eutectic transformation.

A *polymorphic transformation* is defined as partitionless formation of a phase with different structure but the same composition as the matrix.

During a *eutectic transformation* two crystalline phases grow cooperatively with a discontinuous reaction. There is no difference in the overall concentration across the reaction front, but diffusion takes place parallel to the reaction front and the two components must separate into two phases.

A *primary crystallization* causes the formation of a phase with composition different from the original matrix which still remains as a major constituent of the material. During this reaction, a concentration gradient may be formed ahead of the particle interface with the matrix becoming enriched in a solute until a metastable equilibrium is reached.

The driving forces can be computed with some confidence by means of approximate formulae which are available for the different transformations [16].

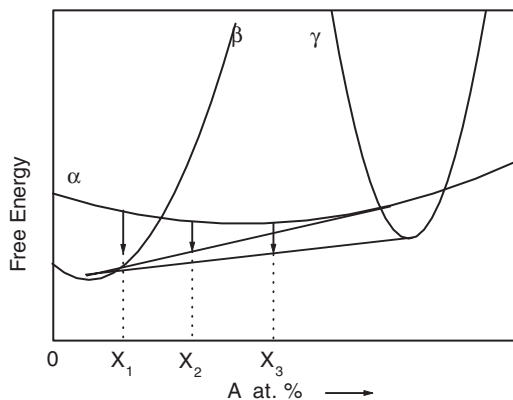


**Figure 3.** Schematic Gibbs free energy curves for  $\alpha$ , the undercooled phase, and  $\beta$  and  $\gamma$  equilibrium phases. The arrows marks the extent of driving force for transformations: at  $x_1$  for polymorphic, at  $x_2$  for primary, and at  $x_3$  for eutectic.

Figure 4 represents a free energy versus composition scheme for primary crystallization. At the liquidus temperature a common tangent to the liquid and crystal free energy determines the composition of the nucleating phase. On undercooling, however, it is demonstrated that the maximum driving force for nucleation is determined by drawing a line parallel to the tangent originating from the crystal free energy curve. The free energy available for subsequent growth is determined by the line joining the free energy of the crystal of nucleating composition to that of the liquid of interfacial composition.

The first approximated formula proposed to compute  $\Delta G_v$  for the most stable nucleus is

$$\Delta G_v = (T_l - T)(\Delta S_{A,f} - R \log x_{A,l}) \quad (10)$$

where  $T_l$  is the equilibrium liquidus temperature,  $\Delta S_{A,f}$  is the entropy of fusion of the pure nucleating component, and  $x_{A,l}$  is the  $A$  concentration at the liquidus temperature. It was derived under the assumption of regular solution behavior of the liquid phase and no miscibility in the crystalline phase. The former position does not hold for glass-forming melts which are characterized by a dependence of the thermodynamic functions on temperature through a positive value of the liquid excess specific heat,  $\Delta C_p^{\text{ex}}$ . Could the excess free energy of the liquid phase be expressed by means of the subregular model? If the excess free energy of the liquid phase is expressed by means of the subregular model and there is no miscibility in the crystalline state,  $\Delta G_v$  would become

$$\Delta G_v = (T_l - T)[\Delta S_{A,f} - R \log x_{A,l} + x_{B,l}^2(4qx_{A,l} - p - q)] \quad (11)$$

where  $p$  and  $q$  are parameters expressing the temperature dependence of the excess free energy of the liquid phase.

A more general approach, however, is to describe the thermodynamics of metastable and stable phases by means

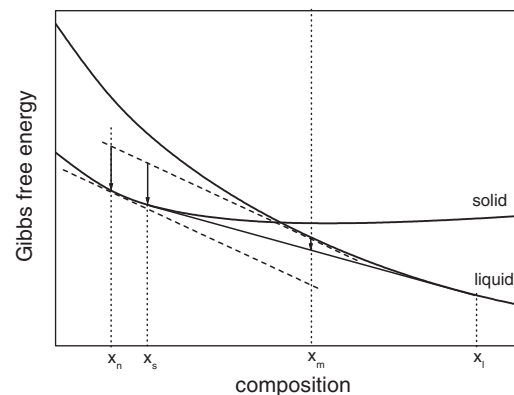


**Figure 4.** Schematic Gibbs free energy curves for liquid and crystal phases at a temperature where the liquid of composition  $x_m$  is in the undercooling regime. The line tangent to the liquid curve gives the chemical potential of the components. The arrows at  $x_s$  and  $x_n$  give the amount of variation in chemical potential of the components when a nucleus of these compositions is formed. The most probable nucleus has composition  $x_n$  since  $\Delta G(x_n) > \Delta G(x_s)$ .

of the optimization programs used to compute phase diagrams. This has been attempted in the case of the Al–Nd system for which the temperature- and composition-dependent driving forces for nucleation ( $\Delta G_v$ ) have been calculated after constructing free energy curves by means of the CALPHAD software [17].

In Figure 5 free energy curves are reported as a function of Nd content for the Al rich composition range at 700 K, a temperature in the undercooling regime. Note that the free energies of the metastable liquid and crystalline equilibrium phases are rather close due to the negative heat of mixing in the liquid being only slightly higher than the heat of formation of the stable intermetallic compound. After primary crystallization of Al the metastable equilibrium given by the dashed line will be established for compositions richer in Al than the tangent point to the liquid free energy. Since nucleation does not change significantly the composition of the matrix, the driving force for nucleation of primary Al, can be defined as the difference between the chemical potential of Al in the liquid and in the crystal phase, as shown by arrow a in Figure 5, for the  $\text{Al}_{97}\text{Nd}_3$  eutectic composition. Similarly, the driving force for primary nucleation of  $\text{Al}_{11}\text{Nd}_3$  is shown by arrow b. The driving force for the nucleation of Al is about twice as large as that for the nucleation of the  $\text{Al}_{11}\text{Nd}_3$  compound. Primary nucleation of face-centered-cubic (fcc)Al. Al will cause the rejection of Nd in the surroundings of primary precipitates reducing the driving forces for fcc-Al and enhancing that for  $\text{Al}_{11}\text{Nd}_3$ . So the intermetallic compound can nucleate beside fcc-Al leading to a eutectic crystallization. Once this has occurred growth is driven by the free energy difference indicated in Figure 5 by arrow c.

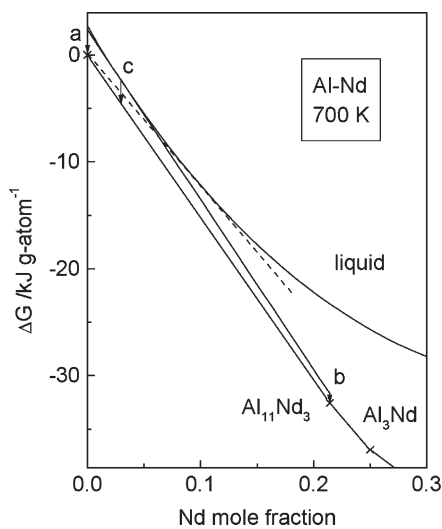


**Figure 5.** Gibbs energy versus composition for Al–Nd. The chemical driving force for crystallization are indicated: (a) primary Al, (b) primary  $\text{Al}_{11}\text{Nd}_3$ , (c) eutectic Al +  $\text{Al}_{11}\text{Nd}_3$ . Reference states are fcc-Al and hcp-Nd. Reprinted with permission from [17], M. Baricco et al., *Mater. Sci. Forum*, 269-272 553 (1998). © 1998, Trans Tech Publications.

## 3.2. Kinetics of Primary Crystallization

During primary crystallization, nanocrystals embedded in an amorphous matrix are formed. In rather wide temperature ranges their size increases quickly to a few nanometers and does not change significantly on further annealing. The usual requirements for obtaining this microstructure are high nucleation and growth rates in the very early stages of crystals formation and then both quantities must drop to negligible values. The two processes will now be described with reference to classical theories.

### 3.2.1. Nucleation

Nucleation can be homogeneous or heterogeneous. It is homogeneous if each point in the volume has the same probability of generating the new crystal. It is heterogeneous if it starts at sites either predictable or recognized *a posteriori*. They may be unevenly distributed in the matrix, but the process remains stochastic in each of them. In heterogeneous nucleation the term site not only has the meaning of place where the new phase originates, but it also conveys the idea of catalyzing the transformation.

In real systems there are interfaces, inclusions, or defects, so heterogeneous nucleation is extremely frequent. However, at times it is invoked also when the sites are unavoidable components (either known or unknown) of the matrix. If an impurity solute promotes the formation of a new phase, the nucleation may well be termed homogeneous since impurities are constituents of the material although being undesired. Analogously, point defects, such as vacancies, are intrinsic in solids and may occur in thermal equilibrium. Therefore, it would be preferable to consider them as components of the material instead of heterogeneities. A similar argument can apply to the free volume in liquids or glasses. On the other hand, excess vacancies, excess free volume, line defects, and interfaces introduce excess energy in the material and, as a consequence, are best considered as heterogeneities. Due to the excess energy associated with them, they can act as catalytic sites for transformations.

The steady-state nucleation rate in a condensed system,  $I_v^s$ , can be expressed as

$$I_v^s = \frac{24DN}{\lambda^2 n_c^{1/3}} \left( \frac{\Delta G^*}{3\pi k_B T} \right)^{1/2} \exp\left(-\frac{\Delta G^*}{k_B T}\right) \quad (12)$$

where  $D$  is a diffusion coefficient for atomic species crossing the interface between the matrix and the new embryo,  $N$  is the number of atoms per unit volume,  $\lambda$  is a diffusion distance,  $n_c$  is the number of elemental particles in the nucleus of critical size,  $\Delta G^*$  is the activation energy for the formation of a nucleus of critical size, and  $k_B$  is the Boltzmann constant. The above equation contains the product of two exponential terms (the one containing  $\Delta G^*$  is explicitly written; the other is  $D$ ). On increasing undercooling  $\Delta G^*$  decreases, favoring nucleation. If very low temperatures are reached, the nucleation rate decreases because the atomic mobility,  $D$ , is lower. The pre-exponential terms do not affect much the value of  $I_v$  when the temperature is changed.

Two thermodynamic parameters are relevant for  $\Delta G^*$ : the free energy difference between liquid (or glass) and crystals

and the interfacial free energy,  $\gamma$ , between the same phases. In fact,  $\Delta G^*$  for a spherical nucleus is defined as

$$\Delta G^* = \frac{16\pi}{3} \frac{\gamma^3}{(\Delta G_v)^2} \quad (13)$$

Expressions for the driving energy  $\Delta G$  have been discussed in the previous section. It is difficult to evaluate  $\gamma$ . It is taken to a first approximation as a fraction of the enthalpy of fusion or as an adjustable parameter. Recent theories are based on the concept of the interface not being a geometrical dividing surface but a diffuse layer. A discussion can be found in [16]. The practical outcome is an expression of  $\gamma$  as a function of temperature which apparently fits a number of experimental data on homogeneous nucleation rate. The formula is

$$\gamma(T)/\gamma(T_f) = \left[ 0.48 + 0.52 \cdot \frac{T}{T_f} \right] \quad (14)$$

where  $\gamma(T_f)$  is the interfacial free energy at the melting point.

In most transformations the time scale is such that the time necessary to reach the steady-state condition, the transient period,  $\tau$ , is negligible with respect to the overall transformation time. On the contrary, the time needed for quenching in rapid solidification experiments may become comparable to  $\tau$ . Actually it has been suggested that vitrification of some compositions occurs because the process is shorter than the transient time. The nucleation frequency during the transient period is given by the Kashchiev expression [18]

$$I(t) = I_{st} \left[ 1 + 2 \sum (-1)^n \exp\left(\frac{-n^2 t}{\tau}\right) \right] \quad (15)$$

During the quenching of a metallic alloy to a glass the transient period can be estimated using the expression [19]

$$\tau = \frac{r_c^2}{\pi^2 D} \quad (16)$$

where  $r_c$  is the radius of the nucleus of critical size.

Heterogeneous nucleation is so frequent because most substrates can act as catalysts by reducing the activation barrier due to interfacial energy provided that the new phase wets the substrate.

Information on the nucleation mechanism can be obtained by analyzing the distribution of dimensions of crystals in partially crystallized samples [20]. The model is based on the partition of the annealing time during an isothermal transformation in intervals,  $\Delta t$ . The number of crystals per unit volume ( $\Delta N_i$ ) formed in the time  $\Delta t$  depends on the nucleation mechanism. This approach provides a straightforward identification of the nucleation mechanism especially when applied to the initial stages of a polymorphic transformation and when the crystals are spherical and noninterfering. The expected distributions are described in the following.

**Quenched in Nuclei** Subcritical crystallike clusters are stochastically present in an undercooled melt. They are then frozen together with the matrix on rapid quenching [21]. Since the critical size decreases with decreasing temperature, a subcritical embryo may then become a nucleus and grow during an annealing treatment. Quenched-in nuclei are likely to have similar size, just above the critical one, and grow all at the same rate. Moreover there will be no other nucleus in the matrix since it will take time to induce further nucleation. Therefore it is expected that the crystal sizes are confined to a narrow range.

**Homogeneous Nucleation** If steady-state homogeneous nucleation is operative during a transformation the following equation will give  $\Delta N_i$ :

$$\Delta N_i = I(t)(1 - X_{i-1})\Delta t \quad i = 1, \dots, t/\Delta t \quad (17)$$

where  $X_{i-1}$  is the volume fraction transformed up to the  $(i-1)$ -th time interval and  $(1 - X_{i-1})$  accounts for the volume available for nucleation during the  $i$ th time interval. It is computed from

$$X_i = 4\pi/3u^3 \sum_{j=1}^i \Delta N_j [\Delta t(i+1-j)]^3 \quad (18)$$

where  $u_i$  is the crystal growth rate.

The resulting distribution has a decreasing number of crystals upon decreasing size because of the progressive reduction in the volume where nucleation is possible (Fig. 6a).

**Heterogeneous Nucleation** Heterogeneous nucleation is promoted by a limited number of active sites per unit volume,  $Z$ , so  $\Delta N_i$  can be calculated with the expression

$$\Delta N_i = I^*(t)(1 - X_{i-1}) \left( 1 - Z^{-1} \sum_{j=1}^{i-1} \Delta N_j \right) \Delta t \quad (19)$$

where  $(1 - Z^{-1} \sum \Delta N_j)$  gives the fraction of available sites at the  $i$ th time interval. Nuclei are formed when  $\sum \Delta N_j < Z$ ;  $\Delta N_j = 0$  when all sites are consumed. In Figure 6b the distribution of the crystals diameters is reported. There is a steady decrease in the number of crystals with decreasing size due to the reduction in both number of available sites and volume and a sudden drop to zero when no new nuclei can be formed.

**Homogeneous and Heterogeneous Nucleation with a Transient**

In the transient period an increasing number of nuclei form during each time interval before reaching the steady state. Then either a homogeneous process or a heterogeneous one sets in. As a consequence, the distribution has a similar shape as for either case (ii) (Fig. 6c) or (iii) (Fig. 6d) but decreases smoothly when reaching the higher values of the measured crystal sizes. These crystals are those formed in limited amounts during the early transient period and which had more time for growth.

For primary crystallization only a fraction of the alloy undergoes transformation so it is expected that a metastable equilibrium between crystals and amorphous matrix will be finally established and the amount of crystalline phase will

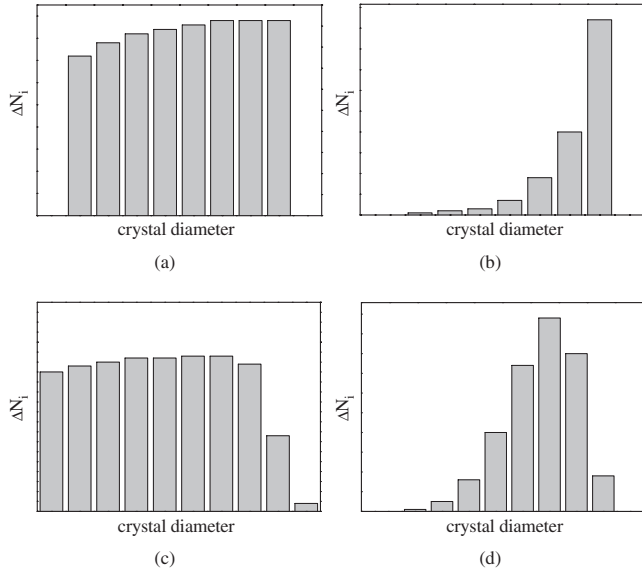


**Figure 6.** (a) The distribution of sizes of crystals grown after the occurrence of a homogeneous nucleation process. (b) The distribution of sizes of crystals grown after the occurrence of a heterogeneous nucleation process. (c) The distribution of sizes of crystals grown after the occurrence of a transient and a homogeneous nucleation process. (d) The distribution of sizes of crystals grown after the occurrence of a transient and a heterogeneous nucleation process. A similar distribution may be found in case of primary crystallization when only a fraction of the alloy transforms. In fact, the amount of crystals having small sizes would reduce quickly because of the reduction of volume available for transformation.

be determined by the lever rule. Therefore, the available volume for nucleation will be quickly reduced during the progress of transformation so there will be less crystals of small size. The size distribution of crystals could result in one similar to that expected for heterogeneous nucleation with a transient as shown in Figure 6d.

### 3.2.2. Growth

Considering a nucleus that starts to grow at the start of an isothermal anneal, different growth laws will be followed according to the transformation type (i.e., polymorphic, eutectic, or primary).

**Polymorphic Transformation** When crystals and matrix have the same composition, the growth process needs only the movement of atoms through the crystal–matrix interface. The growth rate ( $u_1$ ) is constant and has the temperature dependence

$$u_1 = u_0 \exp\left(\frac{-Q_s}{RT}\right) \cdot \left[1 - \exp\left(\frac{-\Delta G}{RT}\right)\right] \quad (20)$$

where  $Q_s$  is the growth activation energy and  $u_0$  is a pre-exponential factor. The term in square brackets contains the free energy difference between melt and crystal,  $\Delta G$ , and is nil at the melting point. It expresses the need for limiting the growth rate in proximity to the equilibrium transformation temperature when the rate of detachment of atoms from the crystal becomes sizeable. If the crystallization takes place in metallic glasses at temperatures well below the melting point

where  $\Delta G$  is substantial, then  $\exp(-\Delta G/RT)$  is negligible. Therefore at high undercoolings the growth rate follows an Arrhenius type equation:

$$u_1 = u_0 \exp\left(\frac{-Q_s}{RT}\right) \quad (21)$$

**Eutectic Transformation** When a eutectic transformation takes place the average composition of the transformed region equals the composition of the matrix before the occurrence of transformation. However, partition of species between the new phases is needed which takes place via long range diffusion. As a consequence, the growth rate depends on the interparticle spacing ( $\lambda$ ). In particular, if there is diffusion in the matrix ahead of the crystallization front, than  $u_e$  is proportional to  $\lambda^{-1}$ ; if there is diffusion at the interface between matrix and crystals then the growth rate is proportional to  $\lambda^{-2}$  [22]. Considering a high level of undercooling ( $\Delta G > RT$ ) the growth rate can be expressed as follows when diffusion occurs in the bulk volume:

$$u_e = \alpha_D \frac{4D}{\lambda} \quad (22)$$

where  $\alpha_D$  is the dimensionless supersaturation, a complex function of the elemental concentration in the matrix and the growing phase,  $D$  is a diffusion coefficient, and, when the diffusion occurs at the interface,

$$u_e = \alpha_D \frac{8 \cdot \delta \cdot D}{\lambda^2} \quad (23)$$

where  $\delta$  is the thickness of the crystallization front.

**Primary Crystallization** When a crystal poor in solute grows in a multicomponent matrix there is rejection of solute in the matrix. If the crystal grows richer in solute there is a depletion of solute in regions of the matrix near the particle. In both cases the growth of the new particle requires homogenization of the concentration gradient built up in the surrounding matrix, that is, a diffusion controlled process. So the growth rate is controlled by the diffusion rate.

If we assume that the diffusion coefficient is independent of concentration, the radius of a spherical particle during precipitation can be expressed as

$$r = \alpha \sqrt{Dt} \quad (24)$$

and the growth rate is

$$u_p = 1/2 \cdot \alpha \cdot D \cdot r^{-1} \quad (25)$$

where  $\alpha$  is a dimensionless parameter that depends on the composition of the material and on the composition of the crystal–amorphous interface.



### 3.3. Primary Nanocrystallization

#### 3.3.1. Nucleation and Growth During Nanocrystallization

At the very early stages of primary nanocrystallization high nucleation frequency and high growth rate occur on isothermal annealing at suitable temperatures. Soon after, both nucleation and growth slow down and in practical terms cease. During the formation of the Al nanocrystals a concentration gradient builds up in the amorphous phase at the crystal–matrix interface due to the rejection of solute from the crystal. The rare earth (RE) elements are slow diffusers in the alloy so their high content ahead of the interface reduces the rate of homogenization of the matrix and contributes to slowing of the growth rate of the Al crystals. In fact, when a high enough density of crystals is reached, impingement among their diffusional fields can become effective and change the growth law as described in the following section [23]. The ensemble of phenomena now described produce typical differential scanning calorimetry (DSC) results on continuous heating where the precipitation peak is rather sharp and then is followed by a long tail characteristic of the homogenization stage of the transformation.

#### 3.3.2. Soft Impingement

During the early stages of primary crystallization from an amorphous matrix, the growing crystals can be considered isolated because their diffusion fields do not interfere with each other. In this case the growth follows the parabolic behavior reported in Section 2.3. On the contrary, when the number of crystals becomes large (a good estimate is  $10^{14} \text{ m}^{-3}$ ) the growth rate slows down due to soft impingement. The situation of two growing grains is represented in Figure 7 at two different times,  $t_1$  and  $t_2$ . At  $t_1$  every particle is considered isolated and the concentration of the solute far from the particle is the initial solute concentration in the metastable phase ( $c^m$ ). At a later time  $t_2$  the two grains are in competition for the solute (i.e., their diffusion fields overlap and the solute concentration far from the particles changes from the initial  $c^m$ ). This implies that the quantity of solute available for growth is decreasing and the process is slowing down.

As early as 1950, Wert and Zener [24] first modelled soft impingement, considering spherical particles of a  $\beta$  phase

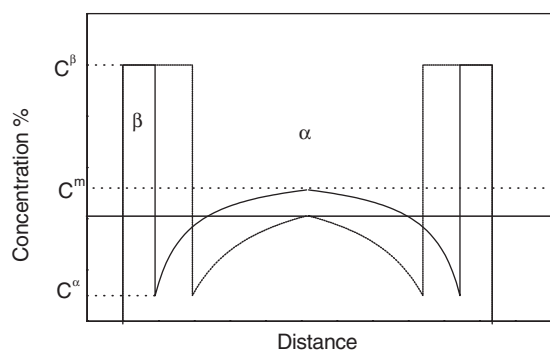


**Figure 7.** The solute concentration profiles in the  $\alpha$  matrix between two growing grains of  $\beta$  phase at two annealing times.

that grows with a parabolic law in an  $\alpha$  matrix and assuming that all the crystals are already nucleated when the transformation starts.

The volume fraction ( $X_i$ ) was defined as

$$X_i = \left( \frac{r^I}{r^f} \right)^3 \quad (26)$$

where  $r^I$  is the radius that identifies the position of the interface,  $r^f$  is the final radius of the transformed region, and

$$1 - X_i = \frac{c(t) - c^\alpha}{c^m - c^\alpha} \quad (27)$$

where  $c(t)$  is the time-dependent concentration of solute far from the growing crystal, and  $c^\alpha$  is the concentration of solute in the  $\alpha$  phase.

Zener and Wert derived the following equation for the increase in the transformed volume fraction:

$$\frac{dX_i}{dt} = \frac{3}{2} k^{2/3} D X_i^{1/3} (1 - X_i) \quad (28)$$

where  $k$  is

$$k^{2/3} = \frac{2(c^m - c^\alpha)}{(c^\beta - c^\alpha)(r^f)^2} \quad (29)$$

and  $c^\beta$  is the concentration of solute in the  $\beta$  phase. Equation (33) was solved numerically to obtain an expression for  $c(t)$  versus time and, as a consequence, of growth rate.

Another model was proposed by Ham in 1958 [25]. He considered spherical particles distributed on a regular cubic lattice, obtaining an equation identical to that presented by Zener and Wert for which he provided an analytical solution. The model was shown to explain rather nicely the rate of heat evolution in DSC when applied to the devitrification of  $\text{Al}_{88}\text{Y}_7\text{Fe}_5$  [26].

## 4. Al–TM–RE ALLOYS: DESCRIPTION AND PROPERTIES

This section reviews specific features of Al–TM–RE alloys with TM = transition metal and RE = rare earth element or Y which behaves similarly to RE in these materials. In the systems described below samples are all produced by melt spinning, using different wheel speeds that will be specified when possible. DSC, X-ray diffraction (XRD), and transmission electron microscopy (TEM) are the typical investigations adopted to study microstructural evolution during heat treatments.

### 4.1. Structural Aspects: Amorphous Structure

X-ray diffraction patterns of glass-forming Al–TM–RE alloys present a broad signal, called a prepeak, at angles much lower than the halos typical of the amorphous phase. Further, an unusual shoulder of the main halo of the diffraction pattern is found. The intensity of both signals depends on composition. These particular features of the XRD pattern are shown in Figure 8 in the case of  $\text{Al}_{87}\text{Ni}_7\text{Nd}_6$  amorphous ribbons [27].



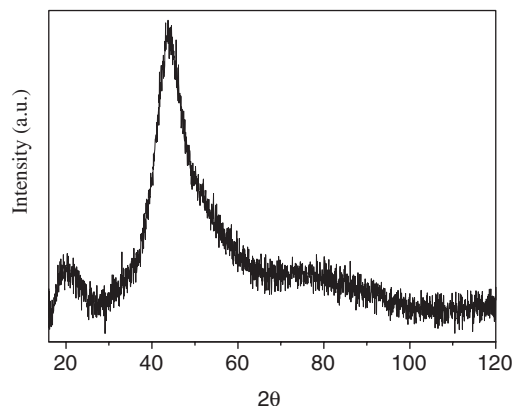


**Figure 8.** XRD pattern of the  $\text{Al}_{87}\text{Ni}_7\text{Nd}_6$  as-quenched alloy. It presents a prepeak at  $2\theta \sim 20^\circ$  and a composite halo. The maximum of the main halo is close also to the angular position of the (111) reflection of Al pattern and has a shoulder at high angles. There are no evident scattering contributions close to the angular position of the other reflections of Al. The explanation for the main composite halo is controversial. It was attributed to a contribution to the total diffracted intensity from very short Al-TM distance [28], at variance to the possibility of amorphous phase separation [56], or to the presence of quenched-in Al nuclei [29]. The appearance of a glass transition in the DSC trace of this alloy shows that it is mostly constituted by a homogeneous amorphous phase ruling out phase separation in the liquid. Therefore, the halo in the pattern should be attributed to the local environment of the elements in the amorphous alloy and to the contribution of small Al crystals present in the matrix. Reprinted with permission from [27], L. Battezzati et al., *Mater. Trans.*, 43, 2593 (2002). © 2002, The Japan Institute of Metals.

Amorphous ribbons of  $\text{Al}_{85}\text{Y}_x\text{Ni}_{15-x}$ , with  $2 < x < 12$ , show two different patterns: Y-rich glasses ( $x \geq 8$ ) have a single main halo; Y-poor glasses have a shoulder on the high-angle side of the main halo close to the (200) Bragg reflection of Al [28]. It was suggested that the shoulder is due to scattering from fine quenched-in Al nuclei. The main halo should mask the broad (111) Bragg peak. Since the intensity of the shoulder increases with decreasing Y content, it was concluded that the number of Al nuclei of critical size depends on RE content in the alloy.

The prepeak found at lower angles might suggest short range order due to Y–Y pairs. In fact, its intensity increases with Y content. This implies that the Y–Y distance is relevant for the prepeak and so most Y atoms must assume a definite configuration (Fig. 9), being all surrounded by Al atoms, so the Y–Y coordination number is zero. The prepeak shifts to higher angles as the Ni content is increased so this is attributed to the replacement of some of the Al atoms by the smaller Ni atoms.

In the case of  $\text{Al}_{90}\text{Fe}_x\text{Ce}_{10-x}$  ( $x = 5, 7$ ) [29] pulsed neutron diffraction indicates that the Al–Fe distances are anomalously short, while some Al–Al distances are anomalously long. The prepeak is present both in pulsed neutron and X-ray diffraction patterns. These results suggest a strong interaction between Al and Fe, leading to short range order. In neutron scattering experiments, the position of the prepeak shifts to higher  $Q$  on increasing Fe concentration. Analyzing the radial distribution functions, Ce atoms are basically randomly distributed in the glass. Fe atoms are

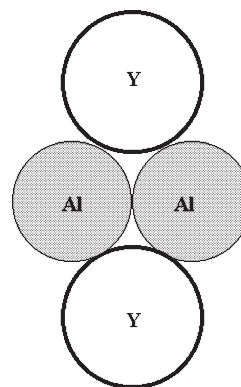


**Figure 9.** The most probable configuration of Al and Y atoms in an amorphous Al–Y–Ni alloy.

surrounded by about 10 Al atoms, with 6 of them in close contact with Fe, and the distance between Al–Fe in close contact is less than the sum of atomic radii, suggesting a strong interaction between Al and Fe more than Al and Ce with this alloy composition. This short range order, similar to the local order in quasicrystals, might explain the origin of the prepeak.

The atomic structure of  $\text{Al}_{87}\text{Y}_8\text{Ni}_5$  alloy was investigated by both ordinary and environmental radial distribution functions around Y and by anomalous X-ray scattering around the Ni  $K$ -edge [30]. From the distances between pairs of atoms and coordination numbers collected in these measurements it resulted that the number of Y–Y pairs is insignificant; about 16% of the atoms surrounding a Y atom are Ni and, therefore, the rest of the coordination shell is mostly occupied by Al. A strong interaction also between Y and Ni is inferred from the number of Ni–Y pairs, higher than that expected from the alloy composition. A locally ordered structure of the three elements is present in the amorphous phase, thus favoring glass formation in this alloy. These results seem apparently to be in contrast with those derived above with considerations of XRD patterns. It should, however, be noted that the composition is changed by a few atomic percent. This suggests that these materials are very sensitive to alloy formulation as both structure and transformation behavior are concerned. In the following detailed analysis of various binary and ternary systems this feature will clearly appear. Whenever possible the properties of the materials (mechanical, chemical) will be reported stressing the effect of refined microstructures.

#### 4.2. $\text{Al}_{100-x}\text{Sm}_x$ ( $8 < x < 12$ )

A varied transformation mechanism was found in this series of binary alloys which serve as model materials. In the case of  $\text{Al}_{92}\text{Sm}_8$ , primary crystallization occurs with the formation of Al nanocrystals with a grain size of about 15 nm. A polymorphic crystallization is found in  $\text{Al}_{90}\text{Sm}_{10}$ , with the formation of a metastable intermetallic phase. For  $\text{Al}_{88}\text{Sm}_{12}$  and  $\text{Al}_{86}\text{Sm}_{14}$  a eutectic crystallization gives a mixture of stable (Al and  $\text{Al}_{11}\text{Sm}_3$ ) and metastable phases.

### 4.2.1. $Al_{92}Sm_8$

Both partially and completely amorphous ribbons can be produced by melt spinning. In partially crystalline ribbons, Al and  $Al_{11}Sm_3$  crystallize during rapid solidification [31,32]. Even in the case of apparently amorphous ribbons, tiny fractions of  $\alpha$ -Al were detected by XRD and TEM on the air side. The stability of the amorphous phase was checked with DSC (Fig. 10) [33]. Continuous heating experiments evidenced the presence of two transformations, the first of which starts at 180 °C and the second at 266 °C (heating rate of 40 K min<sup>-1</sup>). XRD patterns of samples heated up to the end of the two transformations show the formation of Al nanograins of about 10 nm in size during the first transformation (Fig. 11) and, successively, the formation of Al and  $Al_{11}Sm_3$ . The kinetic of formation of the nanocrystals [34] was studied in isothermal conditions performing DSC measurements at various temperatures and annealing times. The evolution of the crystalline fraction of  $\alpha$ -Al (Fig. 12) versus time was determined for samples heated at 171 °C by comparing the amount of heat released after the isothermal treatments to the amount of heat evolved from a totally amorphous sample. A sigmoidal shape is expected for a single stage process; however, the crystalline fraction displays a more complex behavior as a function of time, suggesting a sum of different processes. The variation of the density of Al nanocrystals and their size versus time of annealing are reported in Figure 13 as obtained from TEM observations (Fig. 14). The transformation can be described with nucleation and growth of a high density of Al nanocrystals. The clustering of Al atoms to form crystalline grains implies rejection of Sm into the matrix and the establishment of a concentration gradient at the crystal–matrix interface. This concentration gradient is hardly recovered during isothermal annealing, because of the low diffusivity of Sm. An example of such nanocrystals is shown in the TEM image of Figure 15.

The size distribution of Al nanocrystals (a typical example is reported in Fig. 16) can be interpreted according to the classification described in Section 3.2.1. The frequency of crystal diameters has a tail at “high” values (>10 nm) indicating a transient effect. On decreasing size the number of crystals decreases with a shape which appears intermediate between Figure 6d and e. It may be due to homogeneous nucleation possibly occurring during quenching from

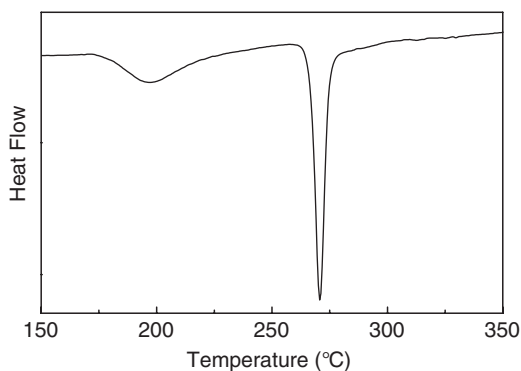


**Figure 10.** A DSC trace showing the exothermal signals due to crystallization of an amorphous  $Al_{92}Sm_8$ .

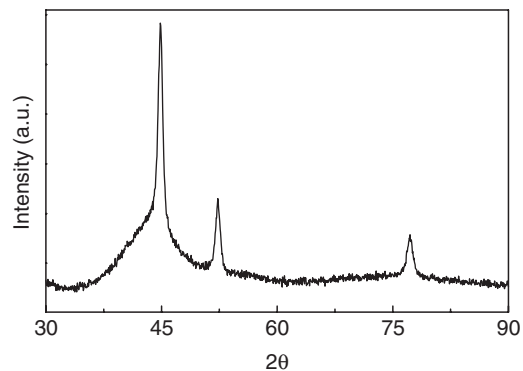


**Figure 11.** XRD pattern obtained with a  $Al_{92}Sm_8$  alloy after the first crystallization event shown in Figure 10.

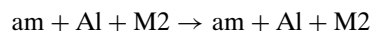
the melt and causing the formation of a distribution in the size of quenched-in nuclei which have grown during the anneal or to heterogeneous nucleation.

### 4.2.2. $Al_{90}Sm_{10}$ , $Al_{88}Sm_{12}$

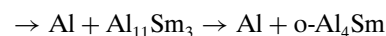
For  $Al_{90}Sm_{10}$  different phases were observed as a product of rapid solidification and, then, different transformation paths were found during heating [31,35]. If a full amorphization is obtained, it transforms polymorphically to a metastable cubic phase having large unit cell which then decomposes in two steps to the equilibrium phase mixture, as represented by



When crystalline phases are found in the as quenched ribbons then the transformation sequences are



(increase in crystalline fraction)



The structure of all metastable phases (MS1, M1, M2) has been determined [36]. M2 forms only during undercooling and does not nucleate from the glass. It simply grows if already present. Different phases are obtained on annealing the single phase glass. This reveals the existence of a hierarchy in stability of phases occurring in different temperature ranges.

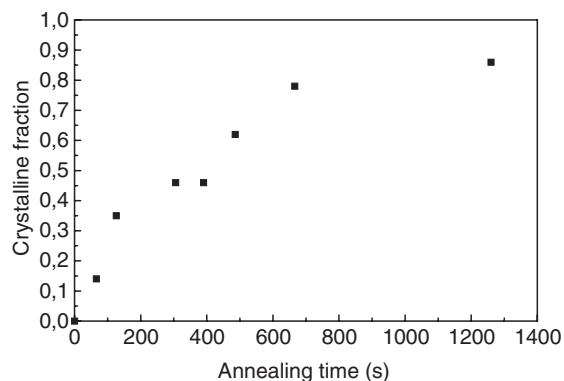


**Figure 12.** The evolution of the crystalline fraction of Al versus time for a  $Al_{92}Sm_8$  sample annealed at 171 °C.

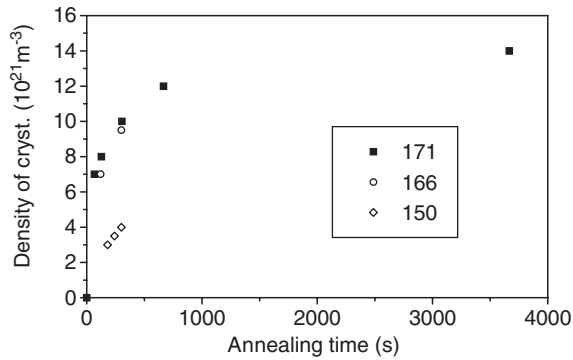


**Figure 13.** The number density of Al nanocrystals as a function of annealing time for the temperatures indicated in the insert for a  $\text{Al}_{0.2}\text{Sm}_8$  alloy.

Only partially crystallized samples were obtained for  $\text{Al}_{88}\text{Sm}_{12}$  alloy during rapid solidification. Al,  $\text{Al}_{11}\text{Sm}_3$ , and M1 compete with the formation of the amorphous phase and were found in the as quenched ribbons beside a little fraction of glassy phase.

#### 4.2.3. Al-RE (RE = Y, La, Ce, Pr, Nd, Sm, Gd, Tb, Dy, Ho, Er, or Yb) [37, 38]

In these binary alloys the glass-forming ability is probably due to a strong attractive interaction of the constituent elements. This should result in the diffusion of the constituent atoms becoming difficult and the viscosity high in the strongly supercooled liquid.

The composition range for the formation of the amorphous phase is 9–13% Y, 7–11% La or Ce, 10% Pr, 8–12% Nd or Gd, 8–16% Sm, 9–14% Tb, and 9–12% of Dy, Ho, Er, or Yb. Except for the Al-Nd system these ranges are situated between a shallow eutectic point and  $\text{Al}_{11}\text{R}_3$  (R=La,

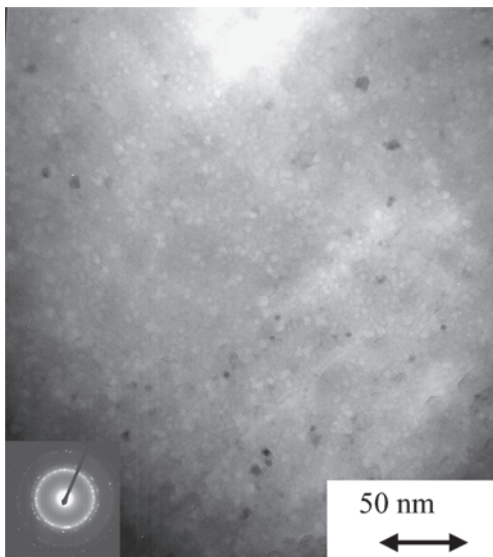


**Figure 14.** Bright field TEM image of nanosized Al crystals embedded in an amorphous matrix in  $\text{Al}_{0.2}\text{Sm}_8$  alloy annealed at 171 °C for 60 s. The corresponding diffraction pattern is also shown: there are crystalline reflections on top of amorphous halos.

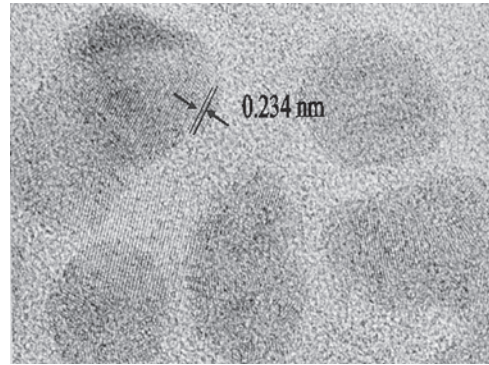


**Figure 15.** High resolution TEM image of isolated Al nanocrystals in an  $\text{Al}_{0.2}\text{Sm}_8$  rapidly quenched alloy annealed at 150 °C for 180 s. Lattice fringes correspond to the (111) lattice spacing of Al.

Ce, Pr, Nd, or Sm) or  $\text{Al}_3\text{R}$  (R=Y, Gd, Tb, Dy, Ho, Er, or Yb) compounds.

The onset temperature of the first DSC peak ( $T_x$ ) increases from 434 to 534 K with increasing RE content from 7 to 12 at%, but no further increase is seen in the concentration range 12–15 at%. Such a dependence is probably associated with different mechanisms of crystallization.

Actually, DSC curves for  $\text{Al}_{91}\text{Tb}_9$ ,  $\text{Al}_{90}\text{Tb}_{10}$ , and  $\text{Al}_{91}\text{Dy}_9$  show a first broad exothermic peak due to the precipitation of fine-grained fcc-Al and a second one due to a eutectic-like reaction involving Al, an unknown compound, and  $\text{Al}_3\text{Tb}$  or  $\text{Al}_3\text{Dy}$ . When the primary Al phase does not precipitate,  $T_x$  increases as seen in various Al-RE amorphous alloys with RE=Y, La, Ce, Nd, or Sm. So it is concluded that the strong compositional dependence of  $T_x$  is due to a change in crystallization process from  $\text{Am} \rightarrow \text{Am} + \text{Al} \rightarrow \text{Al} + \text{Al}_3\text{R}$  to  $\text{Am} \rightarrow \text{Al} + \text{X} + \text{Al}_3\text{R} \rightarrow \text{Al} + \text{Al}_3\text{R}$  or  $\text{Am} \rightarrow \text{Al} + \text{Al}_3\text{R}$ .

#### 4.3. Al-Ni-Ce

Ternary and multinary alloys will be discussed in the following. For some systems there has not been a systematic work as a function of composition so each alloy will be reviewed separately.

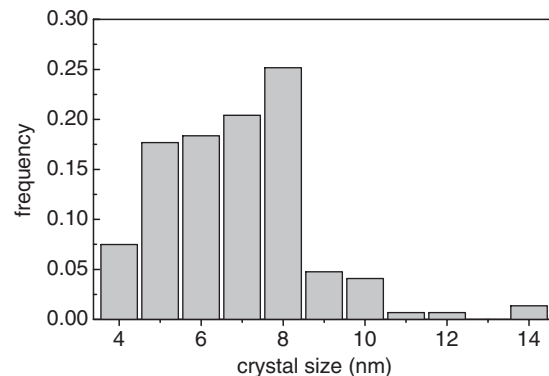


**Figure 16.** The distribution of the crystal sizes of Al in a  $\text{Al}_{0.2}\text{Sm}_8$  sample annealed at 171 °C for 4 minutes. The shape of the histogram is intermediate between those shown in Figure 6c and d (see text).

### 4.3.1. $Al_{88}Ni_{10}Ce_2$ [39]

Rapidly solidified ribbons were found to be completely amorphous in XRD and TEM analysis. Two DSC exothermic signals were detected in the temperature ranges from 405 to 540 K and from 595 to 630 K (heating rate of 0.67 K s) and were assigned respectively to the precipitation of fcc-Al from the amorphous phase and to the transformation of the remaining amorphous matrix to  $Al_3Ni$  and  $Al_{11}Ce_3$ .

The temperature dependences of nominal yield strength ( $\sigma_y$ ), nominal ultimate tensile strength ( $\sigma_b$ ), and elongation ( $\varepsilon_f$ ) of the amorphous alloy were investigated, pointing out that  $\varepsilon_f$  increases from 1.8 to 45% at 465 K and then decreases rapidly. This behavior was attributed to the effect of elongation induced crystallization; in fact TEM observations of the sample subjected to tensile tests at 465 K showed fcc-Al nanoparticles (10–15 nm) dispersed homogeneously in the amorphous matrix. This phenomenon was attributed to the following processes: (a) preferential precipitation along the shear planes due to an increase in temperature resulting from deformation, (b) increase in the flow stress at the precipitation sites, and (c) propagation of the deformation to other regions along the tensile direction. This large elongation is very important for the processing of gas atomized amorphous powders to be consolidated in a bulk form, because it occurs in a temperature range well below the precipitation temperature of the compounds.

### 4.3.2. $Al_{84}Ni_{10}Ce_6$ [40]

This alloy shows an high glass-forming ability and fully amorphous powders are produced by high pressure gas atomization that can be compacted by a high pressure die casting process obtaining sheet and cylinder samples with thicknesses of 0.5 and 5 mm respectively. For sheet samples an amorphous surface layer of about 0.03–0.05 mm was obtained; for cylinder samples the layer was 0.18–0.20 mm thick. The hardness of the amorphous layer of the sheet samples was 370  $H_v$  and the crystallization temperature was determined as 556 K. The corrosion resistance against NaOH solution for the amorphous layer was found to be better than the highest corrosion resistance in conventional alloys.

### 4.3.3. $Al_{87}Ni_{10}Ce_3$ , $Al_{85}Ni_{10}Ce_5$ , $Al_{80}Ni_{10}Ce_{10}$ , $Al_{87}Ni_7Cu_3Ce_6$ [41–44]

In these systems Ce plays an important role for the increase in glass-forming ability. The critical content in Ce for the formation of an amorphous phase was evaluated to be 3 at% since both partially and completely amorphous ribbons were produced with the  $Al_{87}Ni_{10}Ce_3$  alloy.

The XRD diffraction patterns revealed a single symmetric halo for  $Al_{80}Ni_{10}Ce_{10}$ , whereas  $Al_{85}Ni_{10}Ce_5$  shows a halo with a shoulder as discussed in Section 4.1. Also the DSC trace for  $Al_{80}Ni_{10}Ce_{10}$  is different from the others; in fact it has only one exothermic peak. In the cases of  $Al_{87}Ni_{10}Ce_3$  and  $Al_{85}Ni_{10}Ce_5$  there are two exothermic peaks. The XRD patterns of samples annealed up to the first crystallization step show the reflections due to fcc-Al nanocrystals and an amorphous matrix in the case of  $Al_{87}Ni_{10}Ce_3$  and fcc-Al plus two compounds in  $Al_{85}Ni_{10}Ce_5$ .

For  $Al_{87}Ni_{10}Ce_3$  amorphous ribbons, an atom probe analysis carried out to obtain a concentration depth profile (Fig. 17) provided the composition of the two phases of the alloy after heating up to the first crystallization peak. The  $\alpha$ -Al phase contains more than 95 at% Al and the remaining amorphous matrix has 25% Ni and 3% Ce. The  $\alpha$ -Al nanocrystals are evaluated to be about 15 nm in size by TEM. An enrichment in Ce content is found at the crystal–amorphous interfaces which is more evident when plotting the number of detected solute atoms versus the total number of detected atoms (Fig. 18a). The slope of the plot represents the local concentration of the alloy. Ni and Ce atoms are rejected from the growing Al crystals and an enrichment in Ce concentration is evident at the interface at a distance of about 3 nm. On the contrary, a similar enrichment is not observed for Ni atoms that display homogeneous concentration in the matrix. The concentration profile derived is schematically described in Figure 18b. It is concluded that faster homogenization is achieved for Ni than for Ce.

This family of Al-based alloys shows good mechanical properties; for example yield strength up to 800 MPa can be reached in the amorphous state, which can increase up to 1500 MPa after partial crystallization (i.e., when nanocrystals are embedded in the amorphous matrix).

Replacing Ni with Cu ( $Al_{87}Ni_7Cu_3Ce_6$ ) results in the increase in density of nanocrystalline particles formed during primary crystallization with the grain size becoming smaller (about 8 nm). Moreover Cu enriched clusters are present in the remaining amorphous phase, similar to Guinier–Preston zones in conventional crystalline alloys for precipitation hardening. These clusters may form in the early stage of annealing or even during cooling from the melt. They introduce a higher degree of heterogeneity in the local alloy composition and increase the density of nuclei during crystallization. The decrease in particle size of the Al phase causes an increase in tensile fracture strength with respect

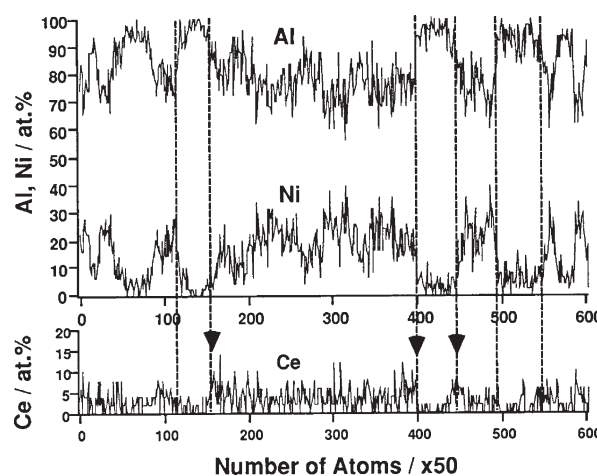


**Figure 17.** Chemical analysis of a  $Al_{87}Ni_{10}Ce_3$  amorphous alloy heated up to the first crystallization DSC peak obtained with spatial resolution by means of the atom probe-field ion emission technique. The arrows mark the position of interfaces between Al nanocrystal and amorphous matrix. There is enrichment in Ce ahead of the interface. Reprinted with permission from [41], K. Hono et al., *Scripta Metall. Mater.* 32, 191 (1995). © 1995, Elsevier Science.



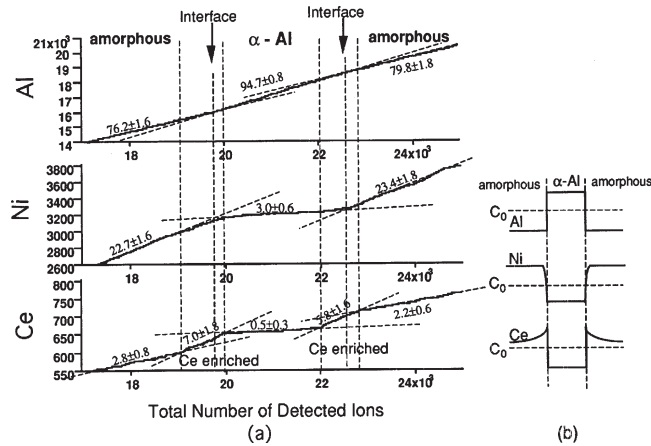


**Figure 18.** Total number of detected ions along a spatial direction in of a  $\text{Al}_{87}\text{Ni}_{10}\text{Ce}_3$  amorphous alloy heated up to the first crystallization DSC peak (a). The percentage of each element in the phases is reported. The slopes of the experimental traces suggest the concentration profile shown in (b). Reprinted with permission from [41], K. Hono et al., *Scripta Metall. Mater.* 32, 191 (1995). © 1995, Elsevier Science.

to the ternary alloy (from 1050 to 1250 MPa) and in hardness. Such an effect on mechanical properties was attributed by the authors to higher hardness of Al nanocrystals with respect to the amorphous phase. This statement was later questioned by others (see Section 4.4.2 below).

#### 4.3.4. $\text{Al}_{87}\text{Ni}_{10}\text{Ce}_3$ [45, 46]

This composition was confirmed to be a marginal glass-former by rapid solidification since partially amorphous ribbons were obtained. It is interesting to remark that they contained nanosized Al crystals dispersed in an amorphous matrix so a two-phase microstructure was produced directly by quenching. It was also found that the devitrification behavior is very sensitive to changes in composition. In fact one of two samples, apparently identical in XRD analyzes, was found to contain less than 1% Si as a contaminant. The silicon contamination produces a change in devitrification behavior evidenced by DSC (Fig. 19a) in which three transformation steps are present instead of the two observed in the uncontaminated  $\text{Al}_{87}\text{Ni}_{10}\text{Ce}_3$  sample (Fig. 19b).

### 4.4. Al–Ni–Y

#### 4.4.1. $\text{Al}_{88}\text{Ni}_{10}\text{Y}_2$ , $\text{Al}_{88}\text{Ni}_8\text{Y}_4$ [47]

Ribbons of these alloys were produced by melt spinning, using different wheel speeds (20, 30, 40, 55, and 63  $\text{ms}^{-1}$ ). A two-phase microstructure, composed by Al nanocrystals homogeneously dispersed in the amorphous matrix, was obtained using wheel speeds greater than 30  $\text{ms}^{-1}$  for  $\text{Al}_{88}\text{Ni}_{10}\text{Y}_2$  and 20  $\text{ms}^{-1}$  for  $\text{Al}_{88}\text{Ni}_8\text{Y}_4$ . The crystallite size and volume fraction of fcc-Al increases with decreasing wheel speed.  $\text{Al}_{88}\text{Ni}_{10}\text{Y}_2$  shows a higher tendency to form a nanocrystalline structure, confirmed by X-ray diffraction analysis. Moreover, increasing Y content in place of Ni, the crystallite size decreases and the volume fraction of fcc-Al increases.

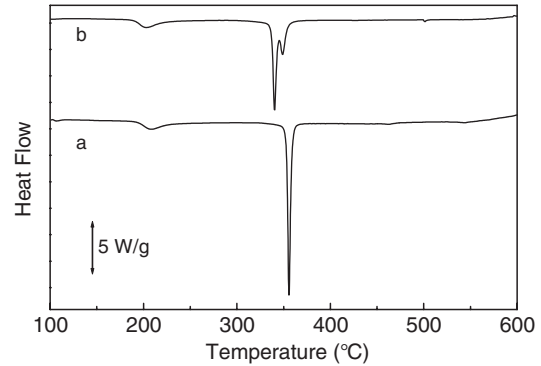


**Figure 19.** DSC traces for two ribbons of nominal composition  $\text{Al}_{87}\text{Ni}_{10}\text{Ce}_3$ . The ribbon which provided curve (b) was later found contaminated with 1% Si. There is a clear effect of the contaminant on temperatures and mechanism of transformations. Reprinted with permission from [46], L. Battezzati, et al., in *Proceedings of the 22nd Risø International Symposium on Material Science: Science of Metastable and Nanocrystalline Alloys, Structure, Properties and Modeling, 2001*, (A. R. Dinesen, M. Eldrup, D. Juul Jensen, S. Linderroth, T. B. Petersen, N. H. Pryds, A. Schröder Pedersen, and J. A. Wert, Eds.) Risø National Laboratory, Roskilde, Denmark, p. 211, 2001. © 2001, Risø National Laboratory.

TEM observations show that in  $\text{Al}_{88}\text{Ni}_{10}\text{Y}_2$  ribbons, produced with a wheel speed less than 30  $\text{ms}^{-1}$ , some intermetallic compounds (i.e.,  $\text{Al}_3\text{Y}$ ) are present beside fcc-Al. The ribbons structure is fully crystalline when using a wheel speed of 20  $\text{ms}^{-1}$ . On the contrary,  $\text{Al}_{88}\text{Ni}_8\text{Y}_4$  ribbons maintain a microstructure consisting of amorphous matrix and fcc-Al even at a wheel speed of 20  $\text{ms}^{-1}$ . For both alloys the diameter of fcc-Al crystallites ranges from 10 to 90 nm, when wheel speed is decreased.

DSC curves for  $\text{Al}_{88}\text{Ni}_{10}\text{Y}_2$  ribbons present three exothermic peaks in the temperature ranges from 437 to 446 K, from 600 to 603 K, and from 698 to 715 K, respectively (heating rate of 40  $\text{K min}^{-1}$ ). They are associated with (a) the precipitation of fcc-Al, (b) the transformation of the remaining amorphous matrix to fcc-Al plus an intermetallic compound ( $\text{Al}_3\text{Y}$ ), and (c) the transformation of phases induced by crystallization. The area of the first peak decreases with decreasing wheel speed, but that of the second peak remains unchanged. This means that the volume fraction of the fcc-Al phase increases on decreasing cooling rate and so it is possible to control the amount of the fcc-Al phase by changing the wheel speed. On the contrary, with increasing wheel speed, the crystallization temperature tends to increase indicating a higher stability of the remaining amorphous phase.

The microhardness of these alloys does not change linearly with wheel speed; its highest value is reached for a particle size of 10 nm and for volume fraction,  $V_f$ , of about 10%.

#### 4.4.2. $\text{Al}_{88}\text{Ni}_{10}\text{Y}_2$ , $\text{Al}_{86}\text{Ni}_{11.67}\text{Y}_{2.33}$ , $\text{Al}_{84}\text{Ni}_{13.33}\text{Y}_{2.67}$ , $\text{Al}_{82}\text{Ni}_{15}\text{Y}_3$ [48]

Different wheel speeds were used to produce ribbons by melt spinning. Samples with different compositions produced at 60  $\text{ms}^{-1}$  are compared to obtain information on their respective glass forming ability. A fully amorphous

material was obtained for  $\text{Al}_{86}\text{Ni}_{11.67}\text{Y}_{2.33}$  and  $\text{Al}_{84}\text{Ni}_{13.33}\text{Y}_{2.67}$  alloys, while only partially crystalline ribbons are produced in the case of  $\text{Al}_{88}\text{Ni}_{10}\text{Y}_2$  and  $\text{Al}_{82}\text{Ni}_{15}\text{Y}_3$  systems.

Analyzing XRD diffraction patterns of ribbons melt spun at different wheel speeds, it is concluded that for  $\text{Al}_{88}\text{Ni}_{10}\text{Y}_2$  there is a wide range of solidification rates in which a microstructure constituted by fcc-Al dispersed in the amorphous matrix is obtained. Using a wheel speed of  $20 \text{ ms}^{-1}$  a fully crystalline microstructure is evident. The same microstructural transitions were detected for  $\text{Al}_{86}\text{Ni}_{11.67}\text{Y}_{2.33}$ , but they occur at lower wheel speeds. In fact, a fully amorphous structure was obtained using a wheel speed of  $60 \text{ ms}^{-1}$ . In the case of  $\text{Al}_{84}\text{Ni}_{13.33}\text{Y}_{2.67}$  alloy, a limited range of wheel speeds can be used to obtain a nanocrystalline structure in which the presence of intermetallic compounds is evident. The results are similar for the  $\text{Al}_{82}\text{Ni}_{15}\text{Y}_3$  alloy, even if the glass-forming ability is lower than the previous case; in fact, fully amorphous ribbons are not obtained even using the highest wheel speed. When Al nanocrystals were obtained their dimensions, determined by Scherrer analysis, were about 10 nm; the result was confirmed by TEM observations.

The as-quenched ribbons were also studied by DSC, using the area of the first devitrification peak to determine the volume fraction crystallized to fcc-Al. These measurements indicate that glass formation is easiest at around 15 at% total solute content, corresponding to the composition for which nanoscale fcc-Al particles are obtained at the lowest quenching rate. Furthermore, at this solute content and below, there is a wide range of quenching conditions for the direct synthesis of a two-phase microstructure (fcc-Al plus amorphous matrix). At higher solute content, the glass-forming ability decreases and the two-phase structure is not obtained.

Microhardness measurements have been made for the ribbons of all compositions and a linear increase in microhardness with solute content was detected. The trend in mechanical properties of Al-Ni-Y alloys indicates that the main cause of increase in hardness is the solute content in the amorphous matrix and not the amount of nanocrystalline Al.

#### 4.4.3. $\text{Al}_y(\text{Ni}_{7/15}\text{Y}_{8/15})_{(100-y)}$ [28, 49]

These alloys can be divided into two distinct groups, based on their crystallization behavior.

Compositions with  $y < 85$  exhibit an endothermic glass transition just before the first exothermic peak.  $T_g$  ranges from 548 K ( $y = 84$ ) to 660 K ( $y = 75$ ). Similarly, the enthalpy of the first crystallization event increases from 44.8 to  $73.2 \text{ J g}^{-1}$ . On the contrary, for the alloys with  $y > 85$  no glass transition is visible; the first exothermic peak has an enthalpy of about  $24 \text{ J g}^{-1}$ . The activation energy,  $E_a$ , for the first peak, computed by means of the Kissinger method, increases from  $1.6 \pm 0.1 \text{ eV}$  ( $y = 81$ ) to  $2.1 \pm 0.3 \text{ eV}$  ( $y = 86$ ).

As for the mechanical properties, the Young modulus decreases from about 82 ( $y = 75$ ) to about 52 GPa ( $y = 88$ ).

#### 4.4.4. $\text{Al}_{85}\text{Ni}_{15-x}\text{Y}_x$ ( $3 < x < 12$ ) [49]

$\text{Al}_{85}\text{Ni}_{15-x}\text{Y}_x$  ( $3 < x < 12$ ) alloys can also be divided in two groups. For  $Y \geq 8$ , DSC curves show a well-defined glass transition and XRD patterns show a single main halo. But if

Y content is less than 8 at%, DSC curves do not show a glass transition and in the XRD pattern the halo has a shoulder.  $T_g$  increases from 526 K for  $x = 8$  to 538 K for  $x = 11$  and the enthalpy for the first peak increases from 43.1 to  $68.7 \text{ J g}^{-1}$  respectively. The first crystallization temperature,  $T_x$ , is about 560 K for alloys with Y content less or equal to 8 at% and is about 520 K for Y-poor ( $x < 8$ ) alloys, for which the enthalpy of the first crystallization increases from 22.4 to  $26.6 \text{ J g}^{-1}$ .

The activation energy for the first peak increases from  $2.8 \pm 0.2 \text{ eV}$  ( $x = 5$ ) to  $3.8 \pm 0.5 \text{ eV}$  ( $x = 10$ ). For these alloys, the Young modulus decreases from 58 GPa ( $x = 3$ ) to 48 GPa ( $x = 10$ ). The highest tensile strength found is 930 MPa and corresponds to  $x = 4$ .

## 4.5. Al-Ni-Sm

### 4.5.1. $\text{Al}_{85}\text{Ni}_{12-x}\text{Sm}_x$ ( $2 < x < 10$ ) [50]

Only fully crystallized ribbons were obtained in the case of  $\text{Al}_{88}\text{Ni}_{10}\text{Sm}_2$ . On the contrary,  $\text{Al}_{88}\text{Ni}_4\text{Sm}_8$  ribbons were obtained fully amorphous and their DSC curves show four exothermic peaks: the first transformation starts at  $250 \text{ }^\circ\text{C}$  and is due to the precipitation of  $\alpha$ -Al from the amorphous matrix. The other transformations are due to the formation of several intermetallic compounds. Isothermal treatments were performed at  $225 \text{ }^\circ\text{C}$  for different times and the crystalline fraction of  $\alpha$ -Al nanocrystals was determined: it reaches about 70% after 120 minutes of annealing. Microhardness also changes as a function of annealing time and, as a consequence, of the fraction of Al nanocrystals: it increases rapidly from  $280 H_v$  for as-quenched alloy to  $370 H_v$  after 120 minutes of annealing, when it reaches a plateau. Wear measurements show a relevant increase in resistance for alloys annealed from 30 to 120 minutes.

### 4.5.2. $\text{Al}_{88}\text{Ni}_4\text{Sm}_8$ [51]

The structural evolution of this alloy during devitrification was studied using TEM and atom probe field-ion microscopy.

TEM dark-field micrographs, together with the corresponding selected-area electron diffraction, of  $\text{Al}_{88}\text{Ni}_4\text{Sm}_8$  annealed at  $200 \text{ }^\circ\text{C}$  for 30 min show fine  $\alpha$ -Al nanoparticles embedded in an amorphous matrix. The average particle size is 20–25 nm and increases up to 30–35 nm in samples annealed at  $225 \text{ }^\circ\text{C}$  for 120 min. An increase in density of nanocrystals is also found for the latter heat treatment. High resolution TEM (HRTEM) observations show  $\alpha$ -Al nanoparticles composed of interconnected arms; such a shape suggests dendritic growth. The presence of an intermetallic compound in the partially crystallized alloy is evidenced by field-ion microscopy and TEM.

Three-dimensional elemental maps are represented in Figure 20. The distribution of Sm atoms in the as-quenched alloy is random (Fig. 20a), confirming its fully amorphous state. Then, after an annealing treatment at  $225 \text{ }^\circ\text{C}$  for 15 min (Fig. 20b), some regions appear to contain a lower density of Sm atoms. Figure 20c shows an isoconcentration surface of 100 at% Al, which corresponds to  $\alpha$ -Al nanoparticles in dendritic shape. This is a further confirmation of



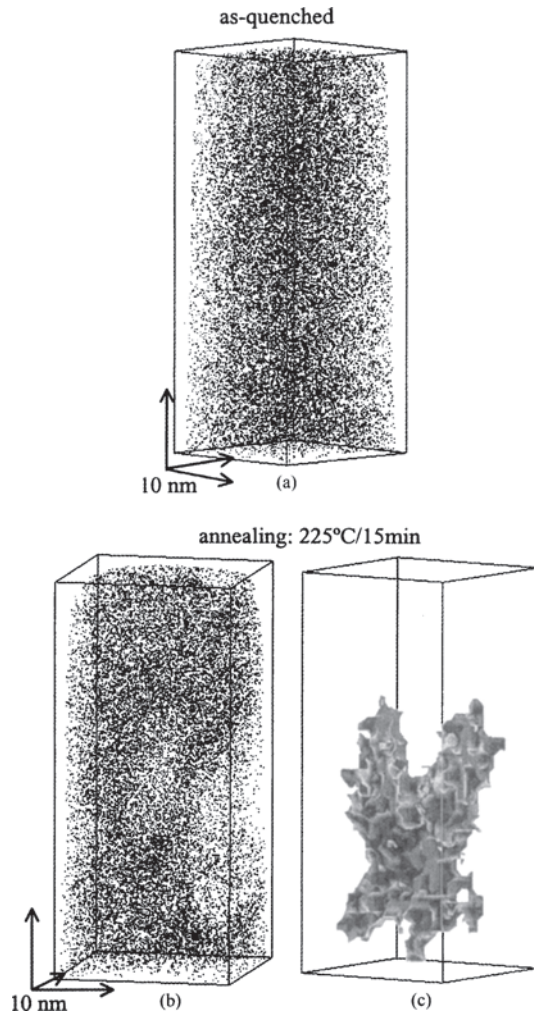


**Figure 20.** Three-dimensional map of the element concentrations in  $\text{Al}_{88}\text{Ni}_4\text{Sm}_8$  obtained by elaboration of atom probe data: (a) Sm in the amorphous alloy, (b) Sm in the partially crystalline ribbon, (c) Al in the partially crystalline ribbon. Reprinted with permission from [51], T. Gloriant et al., *Mater. Sci. Eng. A* 304–306, 315 (2001). © 2001, Elsevier Science.

the total rejection of the solutes from the crystallites during the nanocrystallization process.

Analyzing an integrated concentration depth profile of Sm and Ni obtained from an Al-amorphous interface it is deduced that there is no enrichment in solute at the interface. It is interesting to note the difference with respect to  $\text{Al}_{87}\text{Ni}_{10}\text{Ce}_3$  alloy described above; in fact the diffusion-field impingement occurs later during the reaction and does not limit crystal growth so that the nanoparticles can grow in dendritic shape.

The volume fraction of Al nanoparticles increases up to 35 ( $\pm 5$ )% in the material annealed for 225 °C for 30 min and, as a consequence, the Al content in the amorphous matrix passes from 88% in the as-quenched ribbon to 83.5%, the Ni content reduces to 3.5%, and the Sm content rises up to 13%.

## 4.6. Al–Ni–Nd

### 4.6.1. $\text{Al}_{96-x}\text{Ni}_x\text{Nd}_4$ ( $x = 2, 4, 6, 12$ ) [52]

The XRD results for these alloys indicate a change from crystalline to fully amorphous ribbons on increasing the Ni content. DSC curves show that in the case of compositions with  $x = 2$  and  $x = 4$  two exothermic peaks are present, corresponding to the precipitation of Al and intermetallic compounds. When the Ni content is higher than 6 at%, the first broad peak disappears and a sharp exothermic reaction takes place, due to the eutectic formation of Al and intermetallic compounds.

A change in mechanical properties is detected on increasing the Ni content. In fact  $\sigma_f$  rises from 400 MPa ( $x = 0$ ) to 1000 MPa ( $x = 2, 4$ ), when there is a coexistence of amorphous phase and nanocrystalline Al. It decreases to 850 MPa ( $x = 8$ ) because of the presence of only amorphous phase and then rises again up to about 1000 MPa when the Ni content is raised further.

### 4.6.2. $\text{Al}_{88}\text{Ni}_{10}\text{Nd}_2$ [53]

Two crystallization stages are again detected by DSC. The volume fraction of Al nanocrystals,  $V_f$ , increases from 0% for the as-quenched ribbons to 32% for ribbons heated up to 525 K.

Samples heated after the first crystallization peak show extraordinary values of tensile fracture strength ( $\sigma_f$ ), up to 1980 MPa, for alloys heated up to 430 K; this value is attributed to the microstructure constituted by Al nanoparticles dispersed in the amorphous matrix. In fact, in this annealing state  $V_f$  reaches 18% and correspondingly the maximum value of fracture elongation,  $\sigma_f$ , of about 3% is obtained.

The microhardness increases linearly from 220 to 400  $H_v$ , when samples are annealed at 525 K.

The size of Al particles in the two-phase state is about 8–10 nm.

## 4.7. Al–Ni–Gd

### 4.7.1. $\text{Al}_{100-x}\text{Ni}_x\text{Gd}_y$ ( $5 < x < 11$ $12 < x + y < 18$ ) [54]

In this study  $\text{Al}_{100-x}\text{Ni}_x\text{Gd}_y$  alloys with a fixed concentration of 7 at% of Ni or Gd were studied and a composition area near  $\text{Al}_{87}\text{Ni}_7\text{Gd}_6$  was identified for the best glass-forming tendency. Here good intermediates for developing a two-phase microstructure via thermal treatment should be found.

DSC patterns show always three exothermic peaks. On increasing the Ni content, the first crystallization peak becomes sharper and shifts to higher temperature, from 488 K for  $\text{Al}_{88}\text{Ni}_5\text{Gd}_7$  to 577 K for  $\text{Al}_{82}\text{Ni}_{11}\text{Gd}_7$ . Similarly, on increasing the Gd content, the first crystallization peak shifts from 451 K for  $\text{Al}_{88}\text{Ni}_7\text{Gd}_5$  to 601 K for  $\text{Al}_{82}\text{Ni}_7\text{Gd}_{11}$ . The activation energy (calculated by means of the Kissinger method) increases monotonically when the content of either Ni or Gd is increased with the Gd being more effective. A higher activation energy for crystallization (or a higher crystallization temperature) means higher thermal stability; so for this ternary system it is concluded that Gd is more effective than Ni in increasing the glass-forming ability. This

was attributed to sluggish mobility of Gd with respect to Ni atoms.

## 4.8. Al–Fe–Nd

### 4.8.1. $Al_{86}Fe_5Nd_9$ , $Al_{86}Fe_9Nd_5$ , $Al_{88}Fe_9Nd_3$ [55]

$Al_{86}Fe_5Nd_9$  melt spun ribbons were found to be fully crystalline by XRD and TEM analysis.

Their DSC curve has a principal exothermic peak and then two exothermic small signals. The first peak is due to the crystallization of fcc-Al and a metastable phase that transforms to the stable crystalline phases at higher temperatures. The equilibrium phases are Al,  $Al_3Fe$ , and a phase indicated as  $\Phi$ , which may be defined as  $Al_{10}Fe_2Nd$ .

The  $Al_{86}Fe_9Nd_5$  alloy has a fraction of fcc-Al nanocrystals besides the amorphous phase after melt quenching. Its DSC trace has three exothermic peaks; the first one corresponds to the transformation of the amorphous matrix to fcc-Al and the same metastable phase as  $Al_{86}Fe_5Nd_9$ . The equilibrium phases are again reproduced as in  $Al_{86}Fe_5Nd_9$ .

### 4.8.2. $Al_{88}Fe_9Nd_3$ [46]

This composition is a good example to show the quenching sensitivity of this class of alloys. In fact various microstructures were observed after rapid solidification, depending on the solidification rates (Fig. 21): predominance of amorphous phase + Al, predominance of Al + amorphous phase, fully crystalline state made of Al +  $Al_3Fe$  +  $\beta-Al_{11}Nd_3$ .

Different transformation paths were found on heating these ribbons (Fig. 22) but the same crystalline products

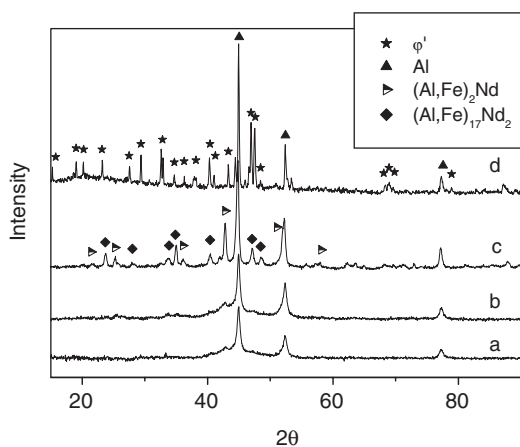


**Figure 21.** XRD patterns obtained with  $Al_{88}Fe_9Nd_3$  ribbons of increasing thickness from (a) to (d) (i.e., quenched at decreasing rate). In (a) the material is almost fully constituted by Al and amorphous phase. In (b) and (c) the metastable crystalline compounds  $(Al, Fe)_2Nd$  and  $(Al, Fe)_{17}Nd_2$  also appear. In (d) the pattern of the equilibrium phases was obtained. Reprinted with permission from [46], L. Battezzati, et al., in *Proceedings of the 22nd Risø International Symposium on Material Science: Science of Metastable and Nanocrystalline Alloys, Structure, Properties and Modeling*, 2001, (A. R. Dinesen, M. Eldrup, D. Juul Jensen, S. Linderroth, T. B. Petersen, N. H. Pryds, A. Schrøder Pedersen, and J. A. Wert, Eds.) Risø National Laboratory, Roskilde, Denmark, p. 211, 2001. © 2001, Risø National Laboratory.

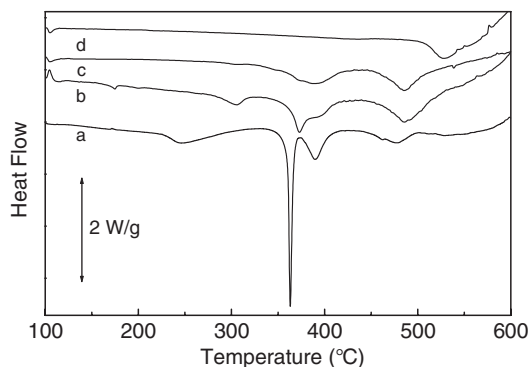


**Figure 22.** DSC traces obtained with the  $Al_{88}Fe_9Nd_3$  ribbons, the structure of which is shown in Figure 20. The differences in the exothermic signals show that various transformation paths are followed. Reprinted with permission from [46], L. Battezzati, E. Ambrosio, P. Rizzi, A. Garcia Escorial and K. R. Cardoso, in *Proceedings of the 22nd Risø International Symposium on Material Science: Science of Metastable and Nanocrystalline Alloys, Structure, Properties and Modeling*, 2001, (A. R. Dinesen, M. Eldrup, D. Juul Jensen, S. Linderroth, T. B. Petersen, N. H. Pryds, A. Schrøder Pedersen, and J. A. Wert, Eds.) Risø National Laboratory, Roskilde, Denmark, p. 211, 2001. © 2001, Risø National Laboratory.

were always recovered at 600 °C. The transformation paths of the partially crystalline materials are

amorphous phase + Al  $\rightarrow$  Al + amorphous phase

$\rightarrow$  Al +  $(Al, Fe)_{17}Nd_2$  +  $(Al, Fe)_2Nd$

$\rightarrow$  Al +  $Al_3Fe$  +  $\Phi$

Al + amorphous phase

$\rightarrow$  Al + unidentified metastable ternary phase

$\rightarrow$  Al +  $Al_3Fe$  +  $\Phi$

It is apparent that several intermetallic phases can form in a limited range of compositions. The local metastable equilibria and concentration profiles dictate the phase selection on annealing.

## 4.9. Al–Fe–Y

### 4.9.1. $Al_{90}Fe_5Y_5$ , $Al_{85}Fe_{7.5}Y_{7.5}$ , $Al_{80}Fe_{10}Y_{10}$ [56]

The XRD diffraction pattern of these ternary alloys shows a broad peak that indicates an amorphous material (result confirmed by TEM) and a prepeak due to local ordering of the Y–Y pair. The glass transition is evident in DSC curves followed by three exothermic peaks in all three alloys.

There is no primary crystallization of  $\alpha$ -Al phase. In fact, on annealing the samples after the first DSC peak, partial crystallization of an intermetallic compound,  $Al_9(Fe, Y)_2$ , takes place that then transforms into  $\alpha$ -Al and  $Al_{70}Fe_{16}Y_{14}$ .

### 4.9.2. $Al_{88}Fe_5Y_7$ [26]

TEM analysis of the  $Al_{88}Fe_5Y_7$  melt spun ribbons reveals an amorphous structure with a random distribution of micrometer size intermetallic crystals.

The DSC thermogram shows three peaks. The first one corresponds to Al nanocrystal precipitation, with dimension of about 20–30 nm; the second one and the last one are partially overlapped and are due to the precipitation of intermetallic compounds.

#### 4.9.3. $Al_{85}Y_{10}(Fe,Co,Ni,Cu)_5$ [57]

Completely amorphous ribbons were produced by melt spinning as confirmed by XRD and TEM analysis.

A change in transition metal produces a corresponding change in the devitrification behavior of the material, evidenced by DSC studies: the alloy with Cu shows two exothermic peaks, the alloys with Fe and Co show three peaks, and the alloy with Ni presents five signals. Furthermore, the transition metals have different effects on the stability of the amorphous phase. Specifically, a decrease in crystallization temperature is observed in the following order: Fe > Co > Ni > Cu. The same scaling is found for the melting temperature,  $T_m$ , of the Al rich compounds. Ni addition is the most effective in improving the glass-formation ability.

After heating samples through the first peak of crystallization, XRD patterns show a mixture of crystalline phases, consisting of a fcc solid solution possibly of Y and Ni, Cu, Fe, Co in Al. The other phases have not been identified. After heating through the second DSC peak fcc solid solutions and  $Al_3Y$  orthorhombic appear in all the ternary alloys.  $Al_3Co_2$  and  $Al_3Ni$  were identified in the respective alloys.

#### 4.9.4. $Al_{90}Fe_7Nb_3$ , $Al_{87}Fe_{10}Nb_3$ [58]

The rapidly solidified ribbons were found to be fully amorphous. DSC traces show two transformations; the first one corresponds to the precipitation of  $\alpha$ -Al nanocrystals with a size of 25–40 nm for  $Al_{87}Fe_{10}Nb_3$  and a size of about 200 nm for  $Al_{90}Fe_7Nb_3$ . The second peak is due to the precipitation of the equilibrium phases,  $Al_3Fe$  and  $Al_3Nb$ .

An increase in Fe content implies higher temperatures of transformation and smaller size of  $\alpha$ -Al nanocrystals.

### 4.10. Al–Ni–Fe–Nd

#### 4.10.1. $Al_{88}Ni_7Fe_3Nd_2$ , $Al_{88}Ni_5Fe_5Nd_2$ , $Al_{88}Ni_{10}Nd_2$ [59]

The melt-spun ribbons analyzed by TEM and XRD show only a single amorphous phase. Their DSC curves present two exothermic peaks. The first one is broad and corresponds to the precipitation of  $\alpha$ -Al nanocrystals. The second one is due to the precipitation of intermetallic compounds. The quaternary alloys present a shift to higher temperature of the transformations, due to a higher stability of the amorphous phase. The temperature increase is dependent on the Fe content.

A complex behavior as a function of testing temperature was found for tensile strength ( $\sigma_b$ ), yield strength ( $\sigma_y$ ), and fracture elongation ( $\epsilon_f$ ). All three alloys have  $\sigma_b$  higher than 800 MPa in the temperature range from room temperature to 580 K. This value is about 3 to 4 times higher than conventional heat resistant Al alloys. This is probably due to the Al nanoparticle dispersion and to the increase in thermal stability with solute enrichment of the amorphous matrix.

The elongation of  $Al_{88}Ni_{10}Nd_2$ ,  $Al_{88}Ni_7Fe_3Nd_2$ , and  $Al_{88}Ni_5Fe_5Nd_2$  at room temperature is 2–3% and reaches values of 42, 29, and 22% respectively at the first peak and 54, 48, and 39% at the second one.

### 4.11. Al–Ni–Fe–Gd [60, 61]

Twenty-four compositions were studied, containing 83, 85, and 87 at% Al.

The best glass-forming ability was found for 85 at% Al, followed by 87 at% Al. In the latter series the compositions with the best glass-forming ability are  $Al_{87}Ni_6Fe_1Gd_6$  and  $Al_{87}Ni_5Fe_1Gd_7$ .

Measurements gave the surprising result that the density of  $Al_{85}Ni_5Fe_2Gd_8$  exceeds the weighted average of its elemental densities by more than 5%, instead of less than 1% for  $Al_{85}Ni_6Fe_3Gd_6$  or  $Al_{87}Ni_6Fe_1Gd_6$ . This was attributed to a more closely packed atomic structure in the amorphous state and to stronger interactions between transition metal and rare-earth elements affecting glass-forming ability.

DSC traces of  $Al_{85}Ni_5Fe_2Gd_8$  show a  $T_g$  signal and then four exothermic peaks; a glass transition is not observed for  $Al_{85}Ni_6Fe_3Gd_6$  that shows five transformations steps from the amorphous phase to stable crystalline phases.

As for mechanical properties, tensile strength reaches values of 1280 and 1210 MPa for amorphous  $Al_{85}Ni_6Fe_3Gd_6$  and  $Al_{85}Ni_5Fe_2Gd_8$ , respectively, and Young's modulus values are 72.7 and 75.3 GPa.

### 4.12. Al–Ni–Zr, Al–Ni–Hf [62]

Melt-spun ribbons were completely amorphous as confirmed by TEM and XRD.

In Al–Ni–Zr alloys with Zr > 5 at%, DSC curves show two exothermic peaks; the first one is due to the precipitation of a fcc-Al phase. The precipitation temperature increases with increasing Zr content. The second peak corresponds to the crystallization of the remaining amorphous matrix. The same behavior was observed in Al–Ni–Hf alloys. Probably the atomic radius of the solute elements plays an important role in determining the formation of the amorphous phase and the mechanism of crystallization. In fact, comparing the minimum solute concentration in the  $Al_{90-x}Ni_{10}M_x$  systems for the single precipitation of fcc-Al particles, a critical concentration value was found of 5 at% for M = Ce and 7 at% for M = Zr.

The minimum solute concentration necessary to form amorphous phases is 2 at% for Ce, 3 at% for Zr, and 4 at% for Ti. For these elements, the atomic radius is quite different: 1.83 Å for Ce, 1.62 Å for Zr, and 1.47 Å for Ti. This values are also relevant to determine the grain size of the Al nanoparticles. TEM analysis reveals a larger crystal size when using Zr: 20 nm for the partially crystallized  $Al_{87}Ni_{10}Zr_3$  and 15 nm for the same composition with Ce.

### 4.13. $Al_{90}Fe_5Gd_5$ [63]

The as-quenched ribbons are fully amorphous to XRD and HRTEM. After an isothermal anneal up to 445 K (i.e., just below the crystallization temperature), the material becomes partially crystallized. Alloys with a slightly higher aluminium

content,  $\text{Al}_{90.5}\text{Fe}_{4.75}\text{Gd}_{4.75}$ , are obtained partially crystallized directly after quenching. For both of them the volume fraction of fcc-Al is about 28%. The size of crystalline particles is about 8 nm.

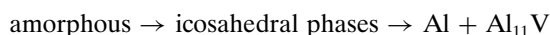
Tensile strength is shown to present a maximum for the annealed samples (1010 MPa), whereas Young's modulus is higher for the fully amorphous material.

The deformed materials were analyzed with scanning electron microscopy (SEM), which shown fracture surfaces typical of metallic glass materials, with vein patterns. Moreover the observations revealed that the distribution of macroscopic plastic deformation is extremely inhomogeneous.

#### 4.14. Al–V–M (M=Fe, Co, or Ni) [64]

The melt-spun ribbons present a nonequilibrium structure consisting of nanoscale amorphous particles surrounded by fcc-Al as revealed by XRD patterns and TEM images. The compositions which promote this structure are  $\text{Al}_{94}\text{V}_4\text{Fe}_2$ ,  $\text{Al}_{94}\text{V}_4\text{Co}_2$ , and  $\text{Al}_{93}\text{V}_5\text{Ni}_2$ . The sizes of the coexistent amorphous and Al phases are about 10 to 25 nm and 7 to 20 nm, respectively. The as-quenched structure is composed of the Al and amorphous phases for the alloys containing Fe and Co and by the Al and icosahedral phases for the alloy containing Ni.

Phase transitions take place through two stages, shown as exothermic signals in DSC traces. For  $\text{Al}_{94}\text{V}_4\text{Fe}_2$  the crystallization process may be described as



The mechanical properties are good. Measurements of tensile fracture stress,  $\sigma_f$ , and microhardness,  $H_v$ , yielded high values in the series  $\text{Al}_{98-x}\text{V}_x\text{M}_2$  at 4% V. In fact, for the as-quenched structure values of 1350 MPa and 470  $H_v$ , respectively, are obtained for the alloy with Fe, 1230 MPa and 460  $H_v$  for that with Co, and 1090 MPa and 430  $H_v$  for that with Ni. These values decrease after the first transition to icosahedral phase.

#### 4.15. Concluding Remarks

Although a large amount of information on Al–TM–RE alloys has been collected, there is some scatter in the data and there is still a lack of systematic representation of the results. For the ease of consultation the most relevant data discussed above are summarized in Table 1. For each alloy two temperatures are listed, as reported by the various authors, at the given heating rates: the onset of primary crystallization and that of the subsequent full devitrification of the matrix. Care should be taken in comparing the values since the microstructure of the rapidly solidified materials may differ from sample to sample. This information is provided in the Notes column detailing also the technique(s) used to study the sample structure, together with the value of the glass transition temperature when existing. The central column summarizes the most relevant mechanical properties of the ribbons either in the as-quenched state and/or after annealing.

In Figures 23 and 24 data extracted from Table 1 are plotted to display the most prominent chemical effects on

the first transformation temperature. Figure 23 is about  $\text{Al}_{88}\text{TM}_{12-x}\text{RE}_x$  alloys. When TM = Ni a clear increase in temperatures is found. The two alloys containing 88 at% Al and TM = Fe have much higher transformation temperatures. They are, however, less easily quenched to a glassy state. In Figure 24 the onset temperature is reported as a function of rare-earth element in alloys of  $\text{Al}_{88}\text{Ni}_7\text{RE}_6$  composition [27, 65]. It is apparent that the temperature decreases on increasing atomic number of rare-earth elements.

## 5. BALL MILLING OF ALLOYS

In the following systems the effect of the ball milling on the amorphization tendency and on devitrification behavior was studied.

### 5.1. Al–Ni–Co–Ti/Zr [66]

Mechanical grinding of Al-based alloys with Al > 80 at% containing late transition metals such as Ni (6–9 at%) and Co (3–5 at%) with an atomic ratio Ni/Co equal to 2 leads to the formation of nanostructured materials made of fcc-Al solid solution and  $\text{Al}_9(\text{Co,Ni})_2$  compound. Upon adding a few atomic percent of Zr or Ti there appear differences in the amorphization reactions. In fact, with  $(\text{Al}_{0.88}\text{Ni}_{0.08}\text{Co}_{0.04})_{100-x}(\text{Zr/Ti})_x$  for  $x = 1$  to 5%, partial to complete amorphization occurs via the following sequence: fcc-Al +  $\text{Al}_9(\text{Co,Ni})_2$  +  $\text{Al}_3\text{Zr}$  / or  $\text{Al}_3\text{Ti}$  → fcc-Al + amorphous I → amorphous II.

The experimental procedure consists of preparing by arc melting a mixture of pure elements under purified argon atmosphere, and then crashing them into fine powders. XRD patterns show complete amorphization after 100–120 h of milling.

### 5.2. $\text{Al}_{95}\text{Cu}_5\text{Zr}_5$ [67]

Atomized powder of 100–200  $\mu\text{m}$  diameter were milled up to 140 h. The microhardness of the as-milled material is higher than that of the as-cast powders indicating that a degree of metastability has been introduced in the material during ball milling. It approaches that of the as-spun ribbons of the same composition.

XRD patterns show only the presence of  $\alpha$ -Al, but SEM examinations also reveal other precipitates. After annealing at 500 °C, XRD patterns indicate the presence of  $\text{Al}_3\text{Zr}$  +  $\text{Al}_2\text{Cu}$  and the milled material still retains a considerable hardness. It is suggested that extrusion of ball-milled powders may be performed to obtain bulk materials.

### 5.3. $\text{Al}_{80}\text{Ni}_8\text{Fe}_4\text{Gd}_8$ [68]

Amorphous powders of this alloy were produced using the ball-milling technique after a treatment for 80 hours. The composition range for easy amorphization is different for rapid quenching and mechanical alloying. It was necessary to reduce the Al content for mechanical alloying with respect to that presenting good glass-forming ability in the melt-spinning process.

**Table 1.** A list of Al–TM–RE alloys produced by rapid solidification in the structural state given in the Notes column. The temperatures significant for phase transformations are provided at the given heating rate (glass transition temperature,  $T_g$ , onset of primary Al crystallization,  $T_1$ , onset of the second crystallization event,  $T_2$ ). The most relevant mechanical properties are collected (tensile strength,  $\sigma_b$ , Vickers hardness,  $H_v$ ).

Alloy	$T_1$ (K)	$T_2$ (K)	Rate (K min) <sup>-1</sup>	Mechanical Properties	Notes	Ref.
Al <sub>88</sub> Ni <sub>10</sub> Nd <sub>2</sub>	403	586	20	$\sigma_b = 1220$ MPa	Amorphous to XRD and TEM	[53]
Al <sub>88</sub> Ni <sub>7</sub> Fe <sub>3</sub> Nd <sub>2</sub>	413	615	20	$\sigma_b \sim 1250$ MPa	Amorphous to XRD and TEM	[59]
Al <sub>88</sub> Ni <sub>5</sub> Fe <sub>3</sub> Nd <sub>2</sub>	431	619	20	$\sigma_b \sim 1300$ MPa	Amorphous to XRD and TEM	[59]
Al <sub>90</sub> Ni <sub>8</sub> Nd <sub>2</sub>	366	590	40	$\sigma_f = 1330$ MPa; $H_v \sim 350$	Amorphous to XRD and TEM	[52]
				annealed up to 408 K for 60 s		
Al <sub>90</sub> Ni <sub>6</sub> Nd <sub>4</sub>	394	607	40	$\sigma_f = 1270$ MPa; $H_v \sim 330$	Amorphous to XRD and TEM	[52]
				annealed up to 438 K for 60 s		
Al <sub>90</sub> Ni <sub>4</sub> Nd <sub>6</sub>	438	605	40	$\sigma_f = 1010$ MPa; $H_v \sim 250$	Amorphous to XRD and TEM	[52]
				annealed up to 448 K for 60 s		
Al <sub>85</sub> Ni <sub>6</sub> Fe <sub>3</sub> Gd <sub>6</sub>	529	$\sim 615$	20	$\sigma_f = 1280$ MPa; $E = 72.7$ GPa	Amorphous	[60,61]
Al <sub>85</sub> Ni <sub>5</sub> Fe <sub>2</sub> Gd <sub>8</sub>	579.5	$\sim 615$	20	$\sigma_f = 1210$ MPa; $E = 75.3$ GPa	Amorphous $T_g = 570$ K	[60,61]
Al <sub>80</sub> Ni <sub>8</sub> Fe <sub>4</sub> Gd <sub>8</sub>	633	—	20		Amorphous Ball-milled powders	[60,61]
Al <sub>87</sub> Ni <sub>10</sub> Ce <sub>3</sub>	480	625	40		A.q. ribbons contain Al nanocrystals	[41–44]
Al <sub>88</sub> Ni <sub>10</sub> Ce <sub>2</sub>	405	595	40	$\sigma = 1100$	Amorphous to XRD and TEM	[39]
Al <sub>88</sub> Ni <sub>10</sub> Y <sub>2</sub>	437	600	40	$H_v \sim 3.25$ – $5.25$ GPa	A.q. ribbons contain Al nanocrystals	[47]
Al <sub>y</sub> (Y <sub>8/15</sub> Ni <sub>7/15</sub> ) <sub>100-y</sub>	552–660	560–675	40		Amorphous	[28,49]
Al <sub>85</sub> Y <sub>3</sub> Ni <sub>12</sub>	523	597	40		Amorphous to XRD	[49]
Al <sub>85</sub> Y <sub>4</sub> Ni <sub>11</sub>	520	614	40		Amorphous to XRD	[49]
Al <sub>85</sub> Y <sub>5</sub> Ni <sub>10</sub>	505	611	40		Amorphous to XRD	[49]
Al <sub>85</sub> Y <sub>6</sub> Ni <sub>9</sub>	525	610	40		Amorphous to XRD	[49]
Al <sub>85</sub> Y <sub>7</sub> Ni <sub>8</sub>	520	609	40		Amorphous to XRD	[49]
Al <sub>85</sub> Y <sub>9</sub> Ni <sub>6</sub>	557	—	40		Amorphous to XRD $T_g = 546$ K	[49]
Al <sub>85</sub> Y <sub>10</sub> Ni <sub>5</sub>	560	—	40		Amorphous to XRD $T_g = 551$ K	[49]
Al <sub>88</sub> Ni <sub>4</sub> Sm <sub>8</sub>	$\sim 525$	$\sim 595$	40		Amorphous to XRD and TEM	[51]
Al <sub>82</sub> Ni <sub>11</sub> Gd <sub>7</sub>	577	$\sim 625$	40		Amorphous to XRD $T_g \sim 550$	[54]
Al <sub>83</sub> Ni <sub>10</sub> Gd <sub>7</sub>	$\sim 565$	$\sim 580$	40		Amorphous to XRD $T_g \sim 540$	[54]
Al <sub>84</sub> Ni <sub>9</sub> Gd <sub>7</sub>	$\sim 550$	$\sim 580$	40		Amorphous to XRD $T_g \sim 530$	[54]
Al <sub>85</sub> Ni <sub>8</sub> Gd <sub>7</sub>	542	$\sim 580$	40		Amorphous to XRD $T_g \sim 520$	[54]
Al <sub>86</sub> Ni <sub>7</sub> Gd <sub>7</sub>	$\sim 515$	$\sim 580$	40		Amorphous to XRD $T_g \sim 510$	[54]
Al <sub>87</sub> Ni <sub>6</sub> Gd <sub>7</sub>	507	$\sim 580$	40		Amorphous to XRD	[54]
Al <sub>88</sub> Ni <sub>5</sub> Gd <sub>7</sub>	$\sim 475$	$\sim 580$	40		Amorphous to XRD	[54]
Al <sub>82</sub> Ni <sub>7</sub> Gd <sub>11</sub>	601	$\sim 615$	40		Amorphous to XRD	[54]
Al <sub>83</sub> Ni <sub>7</sub> Gd <sub>10</sub>	$\sim 590$	$\sim 615$	40		Amorphous to XRD $T_g \sim 580$	[54]
Al <sub>84</sub> Ni <sub>7</sub> Gd <sub>9</sub>	$\sim 565$	$\sim 585$	40		Amorphous to XRD $T_g \sim 555$	[54]
Al <sub>85</sub> Ni <sub>7</sub> Gd <sub>8</sub>	550	$\sim 585$	40		Amorphous to XRD $T_g \sim 530$	[54]
Al <sub>86</sub> Ni <sub>7</sub> Gd <sub>7</sub>	$\sim 520$	$\sim 585$	40		Amorphous to XRD $T_g \sim 505$	[54]
Al <sub>87</sub> Ni <sub>7</sub> Gd <sub>6</sub>	$\sim 470$	$\sim 585$	40		Amorphous to XRD	[54]
Al <sub>88</sub> Ni <sub>7</sub> Gd <sub>5</sub>	$\sim 430$	$\sim 585$	40		Amorphous to XRD	[54]
Al <sub>90</sub> Fe <sub>3</sub> Gd <sub>5</sub>	$\sim 445$		5	$\sigma = 735$ MPa a.q.; $E = 50.7$ GPa	Amorphous to XRD and TEM	[63]
				$\sigma = 1010$ MPa at 445 K, 20 min;		
				$E = 48.6$ GPa		
Al <sub>90.5</sub> Fe <sub>4.75</sub> Gd <sub>4.75</sub>				$\sigma = 938$ MPa	A.q. ribbons contain Al nanocrystals	[63]
				$E = 44.7$ GPa		
Al <sub>88</sub> Fe <sub>3</sub> Y <sub>7</sub>	553	649			Amorphous + intermetallic (<1%)	
Al <sub>88</sub> Fe <sub>9</sub> Nd <sub>3</sub>	500	618	40		A.q. ribbons contain Al nanocrystals	[46]
Al <sub>94</sub> Fe <sub>2</sub> V <sub>4</sub>	579	$\sim 680$	40	$\sigma_f = 1350$ MPa	A.q. ribbons contain Al nanocrystals	[64]
				$H_v = 470$		
Al <sub>90</sub> Fe <sub>7</sub> Nb <sub>3</sub>	533	693	40		Amorphous	[58]
Al <sub>87</sub> Fe <sub>10</sub> Nb <sub>3</sub>	623	729	40		Amorphous	[58]
Al <sub>87</sub> Ni <sub>7</sub> La <sub>6</sub>	525	605	40		A.q. ribbons contain Al nanocrystals;	[65]
					$T_g = 513$	
Al <sub>87</sub> Ni <sub>7</sub> Ce <sub>6</sub>	529	606	40		A.q. ribbons contain Al nanocrystals;	[27]
					$T_g = 515$	
Al <sub>87</sub> Ni <sub>7</sub> Nd <sub>6</sub>	517	608	40		A.q. ribbons contain Al nanocrystals;	[27]
					$T_g = 495$	
Al <sub>87</sub> Ni <sub>7</sub> Sm <sub>6</sub>	500	608	40		A.q. ribbons contain Al nanocrystals;	[65]
					$T_g = 501$ at 150 K min	



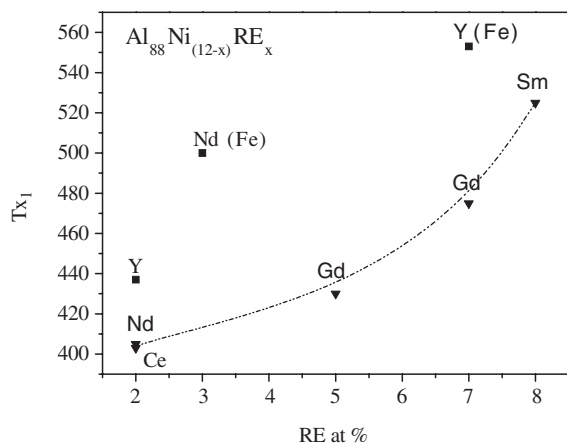


**Figure 23.** The onset temperature of primary Al crystallization as a function of rare-earth content in  $Al_{88}TM_{12-x}RE_x$  amorphous alloys. The rare symbol is accompanied by (Fe) when  $TM = Fe$ ; otherwise  $TM = Ni$ .

The DSC trace shows a sharp exothermic signal at a temperature 60 K higher than for 85 at% Al melt-spun ribbons.

Microhardness tests (performed with a load of 200 g) on powder consolidated into buttons present values of 625–650  $H_v$ . Measuring the length of cracks produced by indentation, fracture toughness is calculated to be 1–5  $MPa m^{1/2}$ . This value can be improved at the expense of hardness for example after a milling treatment of 20 h.

## 6. NANOQUASICRYSTALLINE ALLOYS

Quasicrystals have been one of the major discoveries in solid state research during the 1980s. Their structure is quasi-periodic and can be approximated by stacking of McKay polyhedral clusters. They were discovered as metastable phases in rapidly solidified Al–Mn alloys [69], but properties have been determined in single quasicrystals which are equilibrium phases in some ternary systems such as Al–Cu–Fe [70]. From the point of view of applications, quasicrystals contain dislocations which can hardly move in the quasiperiodic structure without destroying it. Although brit-

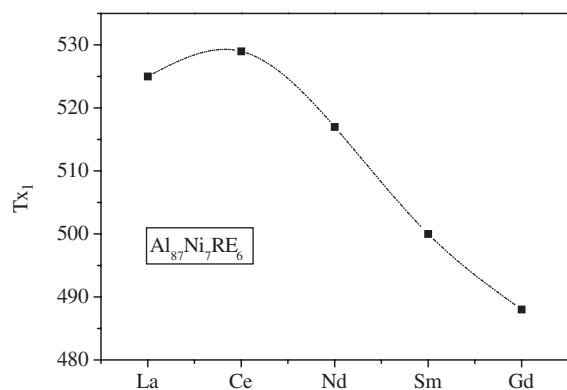


**Figure 24.** The onset temperature of primary Al crystallization as a function of rare-earth content in  $Al_{87}Ni_7RE_6$  amorphous alloys.

tle, it is expected that a dispersion of icosahedral particles can harden a ductile matrix [6].

The binary Al–Mn icosahedral phase occurs as a primary phase on solidification forming large dendritic quasicrystals. It was earlier shown that, due to the similarity of the structure of the liquid and the I-phase, the corresponding interfacial energy is much lower than that between liquid and crystalline intermetallic compounds. This explains their ease of nucleation at temperatures where the growth rate is high enough to cause the formation of particles of micrometer size in the time duration of the quench in a melt-spinning apparatus (of the order of milliseconds) [71].

Inoue adopted the strategy of alloying Al–Mn and Al–Cr with lanthanide elements with the aim of producing materials consisting of quasicrystals in an Al matrix. The addition of lanthanides which are usually amorphizing elements in Al would help in decreasing the nucleation and growth rates of the primary phase. The optimum microstructure was formed in ribbons of  $Al_{94.5}Cr_3Ce_1Co_{1.5}$  composition (Fig. 25) which were used to determine the relevant properties of the material. The tensile stress is 1340 MPa and hardness is of the order of 330  $H_v$ . There is a decrease in tensile strength from the value of as-prepared to those of cold rolled ribbons which is attributed to work softening caused by increase of the volume fraction of interfaces between Al and I-phase with increasing amount of deformation. The interfaces may act as sinks for dislocations produced in the ductile Al.

An analogous microstructure to that observed in ribbons was produced in atomized powders. The powders were extruded to obtain bulk specimens exhibiting tensile strength



**Figure 25.** High resolution TEM micrograph and selected area diffraction pattern of a rapidly solidified  $Al_{94.5}Cr_3Ce_1Co_{1.5}$  alloy. The area imaged has a disordered structure at short range since there are no lattice fringes visible, but an icosahedral configuration at long range is testified by the fivefold symmetry of the diffraction pattern superimposed to halo rings. Reprinted with permission from [64], A. Inoue et al., *Mater. Trans. JIM* 36, 6 (1995). © 1995, The Japan Institute of Metals.



above 500 MPa with elongation around 20% at room temperature and of 200 MPa at 573 K. Comparison with conventional Al alloys shows that these properties are by far superior [72].

In the development of the research, the same group discovered nanoquasicrystalline microstructures in the  $\text{Al}_{98-x}\text{V}_x\text{Fe}_2$  system with  $x = 3$  or 5 at% [64]. The striking finding is, however, that a nanogranular amorphous-crystalline microstructure occurred at the  $\text{Al}_{94}\text{V}_4\text{Fe}_2$  composition. The alloy apparently consists of a primary nanostructured amorphous phase surrounded by Al crystals. The cause for achieving such a microstructure was attributed to the high cooling rate which inhibited the formation of the I-phase but it is not fully clear yet. If the amorphous phase supplants the I-phase for kinetic reasons it has to be admitted that a liquid-liquid phase separation should occur prior to solidification. Although phase separation in glass-forming melts has been found in Zr based alloys, it has not been demonstrated in Al liquid alloys to date. There has been a report of phase separation at low temperature in a quaternary  $\text{Al}_{88}\text{Gd}_6\text{La}_2\text{Ni}_4$  [73] alloy which has not been confirmed yet. The other remarkable points are that well prepared ribbons show tensile strength close to 1400 MPa and hardness above 450  $H_v$ , and that the tensile strength is as high as 620 MPa at 680 K.

Further research on this type of alloy led to quaternary compositions such as  $\text{Al}_{93}\text{Fe}_3\text{Cr}_2\text{Ti}_2$  and  $\text{Al}_{92}\text{Fe}_3\text{Cr}_3\text{Ti}_2$  consisting again of a mixed Al-quasicrystal structure. They were produced as bulk cylinders by extruding atomized powders. The extrudates displayed ultimate tensile strength of 660 and 580 MPa with 5.8% and 3.5% elongation, respectively, and kept good strength at high temperature. In the above formulation Mn can substitute for Fe and Cu for Ti with still rather good properties. The amount of open information on these material is limited to date and it is expected that advancement will occur in producing high strength Al alloys [6, 74].

## 7. NANOCRYSTALLIZATION INDUCED BY DEFORMATION

Plastic deformation in metallic glasses is inhomogeneous in that it takes place in highly localized shear bands. They propagate in the material with negligible deformation hardening usually at 45° with respect to the tensile or compressive axis. Therefore, metallic glasses represent a class of perfectly elastic-plastic solids. Shear bands are observed in all deformation processes such as bending and rolling.

It was demonstrated by careful analysis of the microstructure of bent ribbons of amorphous  $\text{Al}_{90}\text{Fe}_5\text{Gd}_5$ ,  $\text{Al}_{90}\text{Fe}_5\text{Ce}_5$ , and  $\text{Al}_{87}\text{Fe}_{8.7}\text{Y}_{4.3}$  that Al nanocrystals formed within the shear bands and not in other portions of the alloys [75]. More recently, the phenomenon has been observed in other alloys either submitted to bending or tensile testing, having Al content of at least 87 at%. Usually alloys with Al content below this value do not present nanocrystal formation in shear bands [76].

The reason for partial crystallization is still not fully understood. It has been suggested that adiabatic heating within the shear bands may cause growth of crystal nuclei

quenched in the alloy during rapid solidification and that the local large plastic strain could promote short range rearrangement of atoms. It should be noted, however, that neither XRD patterns nor DSC traces are changed when employing heavily deformed samples with respect to as-quenched ones as shown by the analysis of heavily rolled  $\text{Al}_{87}\text{Ni}_7\text{Nd}_6$  ribbons [77]. More work should be done to elucidate the cause and the extent of precipitation induced by deformation. It is worth mentioning that amorphous Al-Sm phases could be produced by co-rolling foils of the two elements [78]. The process has some common features to that of ball milling mixtures of powders. However, the finding that deformation induces amorphization may appear in contrast to the effect of cold work for partial crystallization and shows that the whole topic is not yet fully understood.

## 8. CONCLUSIONS

In this chapter Al-TM-RE systems were described, focusing attention on the effects caused by atomic composition, rare-earth and transition metal type, and the addition of a fourth element on glass formation, their stability, and the transformation due to devitrification.

Nanocrystalline Al alloys can be obtained also by direct quenching from the liquid state for marginal glass-forming compositions. However, the two-stage process, quench plus annealing, provides means for a better control of microstructure.

The alloy compositions do not correspond to regions near deep eutectics as for most glass formers but to zones of the phase diagrams where intermetallic compounds exist having a high melting point. Nevertheless, there are zones of the multinary systems where glass formation is relatively easy because of the sluggish tendency of these compounds to nucleation in the highly undercooled melt. It is actually more likely that fcc-Al and/or metastable compounds form during the quench. The metastable phases are more frequently encountered in ternary Al-TM-RE alloys where TM = Fe which also possess a higher melting point. Therefore, quenching will be more effective when TM = Ni. Some alloys display a manifest glass transition before crystallization: the temperature interval in between the two transitions should be suited for processing the materials (e.g., compaction of rapidly solidified powders, flakes, or ribbons). However this interval is limited to a few tens of degrees even in the most favorable cases because of the inherent fragility of the melt where mobility soon becomes high above  $T_g$ .

The nucleation of Al is very frequent upon annealing on either pre-existing or new embryos. Growth and coalescence of crystals is hampered by the matrix surrounding the fine particles, the reason being that a compositional gradient for RE elements is established which are slow diffusers in these materials. This is shown also by the fact that the rare earths are more effective than the transition metals in raising the thermal stability.

The nanocrystalline Al alloys have promising mechanical properties. Their hardness and tensile or compressive strength are in the range of those of steels. Some of them also display good wear resistance. These properties deserve further research to optimize the alloy compositions and improve their thermal stability in view of selected applications.

## GLOSSARY

**CALPHAD** A computer technique for calculating phase diagram.

**Equichannel angular pressing** Technique for heavy deformation of materials in which the material is forced to flow along a L-shaped die.

**Eutectic transformation** A transformation of a phase which demixes into two phases of different structure and composition.

**Isoentropic temperature** The temperature at which the entropy of an undercooled melt would equal that of the corresponding crystal.

**Liquid fragility** Liquids are defined as fragile when their viscosity decreases rapidly above the glass transition temperature. Their viscosity is well represented by the Vogel-Fulcher-Tammann equation.

**Polymorphic transformation** A transformation of a phase into another phase having different structure.

**Primary transformation** The formation of a phase from a matrix having different structure and composition.

**Quasicrystals** Crystals with a quasi-periodic structure that can be approximated by stacking of McKay polyhedral clusters.

**Soft impingement** The impingement of the diffusion fields around growing crystals, acting during the primary crystallization, and causing growth rate to slow down.

## ACKNOWLEDGMENTS

The work on the topic of nanocrystalline Al alloys is performed within the Research Training Network of the European Commission “Nano Al” HPRN-CT-2000-00038. Studies on thermophysical properties of alloys are supported by ESA-ESTEC Contract 14306/01/NL/SH-MAP, Project AO-99-022 “Thermolab,” and ASI Contract. I/R/073/01.

## REFERENCES

1. C. Suryanarayana and F. H. Froes, *Nanostruct. Mater.* 3, 147 (1993).
2. H. Bakker, G. F. Zhou, and H. Yang, *Progr. Mater. Sci.* 39, 159 (1995).
3. F. Zhou, J. Lee, S. Dallek, and E. J. Lavernia, *J. Mater. Res.* 16, 3451 (2001).
4. R. Z. Valiev, N. A. Krasilnikov, and N. K. Tsenev, *Mater. Sci. Eng. A* 137, 35 (1991).
5. J. C. Sánchez-López, A. Fernández, C. F. Conde, A. Conde, C. Morant, and J. M. Sanz, *Nanostruct. Mater.* 7, 813 (1996).
6. A. Inoue, *Progr. Mater. Sci.* 43, 365 (1998).
7. T. Egami and Y. Waseda, *J. Non-Cryst. Solids* 64, 133 (1984).
8. L. Battezzati, *Philos. Mag. B* 61, 511 (1990).
9. H. M. Fernandez, M. Baricco, L. Battezzati, and L. J. Gallego, *J. Alloys Compounds* 184, 139 (1992).
10. C. A. Angell, *J. Phys. Chem. Solids* 49, 863 (1988).
11. L. Battezzati and A. L. Greer, *Acta Metall.* 37, 1791 (1989).
12. A. L. Greer, in “Rapidly Solidified Alloys” (H. H. Liebermann, Ed.), p. 287. M. Dekker, New York, 1993.
13. S. C. Glade and W. L. Johnson, *J. Appl. Phys.* 87, 7249 (2000).
14. I. Chang and H. Sillescu, *J. Phys. Chem. B* 101, 8794 (1997).
15. P. G. Debenedetti and F. H. Stillinger, *Nature* 410, 259 (2001).
16. L. Battezzati and A. Castellero, “Nucleation and the Properties of Undercooled Melts” (M. Magini and F. H. Wohlbiel, Eds.), Materials Science Foundations, Vol. 15, pp. 1–80. Trans Tech, Uetikon/Zurich, Switzerland, 2002.
17. M. Baricco, F. Gaertner, G. Cacciamani, P. Rizzi, L. Battezzati, and A. L. Greer, *Mater. Sci. Forum* 269–272, 553 (1998).
18. D. Kashchiev, *Surf. Sci.* 14, 209 (1969).
19. K. F. Kelton, A. L. Greer, and C. V. Thompson, *J. Chem. Phys.* 79, 6261 (1983).
20. U. Köster and U. Herold, in “Glassy Metals I” (H. J. Güntherodt and H. Beck, Eds.), p. 225. Springer-Verlag, New York, 1981.
21. M. Calin and U. Köster, *Mater. Sci. Forum* 269–272, 749 (1998).
22. E. Hornbogen, *Metall. Trans.* 10A, 947 (1979).
23. T. Pradell, D. Crespo, N. Clavaguera, J. Zhu, and M. T. Clavaguera, *Nanostruct. Mater.* 8, 345 (1997).
24. C. Wert and C. Zener, *J. Appl. Phys.* 21, 5 (1950).
25. F. S. Ham, *J. Phys. Chem. Solids* 6, 335 (1958).
26. J. C. Foley, D. R. Allen, and J. H. Perepezko, *Scripta Mater.* 35, 655 (1996).
27. L. Battezzati, S. Pozzovivo, and P. Rizzi, *Mater. Trans.*, 43, 2593 (2002).
28. R. Sabet-Sharghi, Z. Altounian, and W. B. Muir, *J. Appl. Phys.* 75, 4438 (1994).
29. H. Y. Hsieh, B. H. Toby, T. Egami, Y. He, S. J. Poon, and G. J. Shiflet, *J. Mater. Res.* 5, 2807 (1990).
30. E. Matsubara, Y. Waseda, A. Inoue, T. Ohtera, and K. Masumoto, *Z. Naturforsch.* 44a, 814 (1989).
31. P. Rizzi, C. Antonione, M. Baricco, L. Battezzati, L. Armelao, E. Tondello, M. Fabrizio, and S. Daolio, *Nanostruct. Mater.* 10, 767 (1998).
32. P. Rizzi, M. Baricco, S. Borace, and L. Battezzati, *Mater. Sci. and Eng. A* 304/306, 574 (2001).
33. P. Rizzi, M. Baricco, L. Battezzati, P. Schumacher, and A. L. Greer, *Mater. Sci. Forum* 195, 111 (1995).
34. P. Rizzi, M. Baricco, L. Battezzati, P. Schumacher, and A. L. Greer, *Mater. Sci. Forum* 235–238, 409 (1997).
35. L. Battezzati, M. Baricco, P. Schumacher, W. C. Shih, and A. L. Greer, *Mater. Sci. Eng. A* 179/180, 600 (1994).
36. J. Q. Guo, K. Ohtera, K. Kita, J. Nagahora, N. S. Kazama, A. Inoue, and T. Masumoto, “The 4th International Conference on Aluminium Alloys,” Atlanta, GA, 1993 (T. H. Sanders, Jr. and E. A. Starke, Jr., Eds.), Vol. 2, p. 753.
37. A. Inoue, K. Ohtera, and T. Masumoto, *Jpn. J. Appl. Phys.* 27, L736 (1988).
38. A. Inoue, T. Zhang, K. Kita, and T. Masumoto, *Mater. Trans. JIM* 30, 870 (1989).
39. A. Inoue, Y. H. Kim, and T. Masumoto, *Mater. Trans. JIM* 33, 487 (1992).
40. A. Inoue, K. Ohtera, and T. Masumoto, *Mater. Trans. JIM* 35, 808 (1994).
41. K. Hono, Y. Zhang, A. P. Tsai, A. Inoue, and T. Sakurai, *Scripta Metall. Mater.* 32, 191 (1995).
42. K. Hono, Y. Zhang, A. Inoue, and T. Sakurai, *Mater. Trans. JIM* 38, 909 (1995).
43. K. Hono, Y. Zhang, A. Inoue, and T. Sakurai, *Mater. Sci. Eng.* 226–228, 498 (1997).
44. A. P. Tsai, T. Kamiyama, Y. Kawamura, A. Inoue, and T. Masumoto, *Acta Mater.* 45, 1477 (1997).
45. P. Rizzi, S. Rolih, E. Ambrosio, and L. Battezzati, in “Proceedings of EUROMAT 2001 7th European Conference on Advanced Materials and Processes, AIM,” Milan, 2001.
46. L. Battezzati, E. Ambrosio, P. Rizzi, A. Garcia Escorial, and K. R. Cardoso, in “Proceedings of the 22nd Risø International Symposium on Material Science: Science of Metastable and Nanocrystalline Alloys, Structure, Properties and Modeling, 2001” (A. R. Dinesen, M. Eldrup, D. Juul Jensen, S. Linderroth, T. B. Petersen, N. H. Pryds, A. Schrøder Pedersen, and J. A. Wert, Eds.), p. 211. Risø National Laboratory, Roskilde, Denmark, 2001.
47. Z. C. Zhong and A. L. Greer, *J. Mater. Sci. Technol.* 12, 1 (1996).

48. Z. C. Zhong, X. J. Jiang, and A. L. Greer, *Philos. Mag. B* 4, 505 (1997).
49. J. M. Freitag, R. G. Koknaev, R. Sabet-Sharghi, M. Koknaeva, and Z. Altounian, *J. Appl. Phys.* 79, 3967 (1996).
50. T. Gloriant and A. L. Greer, *Nanostruct. Mater.* 10, 389 (1998).
51. T. Gloriant, D. H. Ping, K. Hono, A. L. Greer, and M. D. Baró, *Mater. Sci. Eng. A* 304–306, 315 (2001).
52. A. Inoue, T. Ochiai, Y. Hono, and T. Masumoto, *Mater. Sci. Eng. A* 179/180, 649 (1994).
53. G. S. Choi, Y. H. Kim, H. K. Cho, A. Inoue, and T. Masumoto, *Scripta Metall. Mater.* 33, 1301 (1995).
54. F. Guo, S. J. Poon, and G. Shiflet, *Mater. Sci. Forum* 331–337, 31 (2000).
55. L. Battezzati, M. Baricco, and C. Antonione, *J. Alloy Compounds* 209, 341 (1994).
56. Q. Li, E. Johnson, A. Johansen, and L. Sarholt-Kristensen, *J. Mater. Res.* 7, 2756 (1992).
57. J. Latuch and W. Dmowski, *Key Eng. Mater.* 81–83, 129 (1993).
58. F. Audebert, H. Sirkin, and A. Garcia Escorial, *Scripta Mater.* 36, 405 (1997).
59. Y. H. Kim, G. S. Choi, I. G. Kim, and A. Inoue, *Mater. Trans. JIM* 37, 1471 (1996).
60. G. M. Dougherty, Y. He, G. J. Shiflet, and S. J. Poon, *Scripta Metall. Mater.* 30, 101 (1994).
61. Y. He, G. J. Shiflet, and S. J. Poon, *J. Alloy Compounds* 207–208, 349 (1994).
62. A. P. Tsai, T. Kamiyama, Y. Kawamura, A. Inoue, and T. Masumoto, *Acta Metall.* 4, 1477.
63. H. Chen, Y. He, G. J. Shiflet, and S. J. Poon, *Scripta Metall. Mater.* 25, 1421 (1991).
64. A. Inoue, H. Kimura, K. Sasamori, and T. Masumoto, *Mater. Trans. JIM* 36, 6 (1995).
65. L. Battezzati, P. Rizzi, and V. Rontó, in “11th Intern. Conference on Rapidly Quenched and Metastable Materials RQ11,” Oxford, U.K., August 2002.
66. T. Benameur and A. Inoue, *Mater. Sci. Forum* 269–272, 163 (1998).
67. A. Garcia Escorial, M. Torralba, G. Caruana, and K. R. Cardoso, *Mater. Sci. Forum* 269–272, 169 (1998).
68. G. M. Dougherty, G. J. Shiflet, and S. J. Poon, *Acta Metall. Mater.* 42, 2275 (1994).
69. D. Schechtman, L. A. Blech, D. Gratias, and J. W. Cahn, *Phys. Rev. Lett.* 53, 1951 (1984).
70. A. P. Tsai, A. Inoue, and T. Masumoto, *J. Appl. Phys.* 26, L1505 (1987).
71. L. Battezzati, C. Antonione, and F. Marino, *J. Mater. Sci.* 24, 2324 (1989).
72. A. Inoue, H. M. Kimura, M. Watanabe, and A. Kawabata, *Mater. Trans. JIM* 38, 756 (1997).
73. A. K. Gangopadhyay, T. K. Croat, and K. Kelton, *Acta Mater.* 48, 4035 (2000).
74. A. Inoue and H. M. Kimura, *J. Light Metals* 1, 31 (2001).
75. H. Chen, Y. He, G. J. Shiflet, and S. J. Poon, *Nature* 367, 541 (1994).
76. M. C. Gao, R. E. Hackenberg, and G. J. Shiflet, *Mater. Trans.* 42, 1741 (2001).
77. P. Rizzi, R. Doglione, and L. Battezzati, in “11th Intern. Conference on Rapidly Quenched and Metastable Materials RQ11,” Oxford, U.K., August 2002.
78. G. Wilde, H. Sieber, and J. H. Perepezko, *J. Non-Cryst. Solids* 250–252, 621 (1999).

# Nanocrystalline and Amorphous Magnetic Microwires

A. Zhukov

*UPV/EHU, San Sebastián, Spain and TAMag Ibérica S.L., San Sebastián, Spain*

J. González

*UPV/EHU, San Sebastián, Spain*

M. Vázquez

*CSIC, Madrid, Spain*

V. Larin, A. Torcunov

*TAMag Ibérica S.L., San Sebastián, Spain*

## CONTENTS

1. Introduction
  2. Casting Method
  3. Magnetic Behavior
  4. Mechanical Properties
  5. Applications
  6. Conclusions
- Glossary  
References

## 1. INTRODUCTION

The development of soft magnetic wire-shaped materials with amorphous, nanocrystalline, and granular character has been demonstrated to improve the characteristics of different electromagnetic and electronic devices. Such magnetic wires with diameter ranging from 1 to 125  $\mu\text{m}$  can be obtained by different methods such as the in-rotating-water technique or the drawing glass-metallic quenching (Taylor-Ulitovsky) technique. The magnetic and transport properties of ferromagnetic amorphous wires obtained by in-rotating-water quenching technique with a typical diameter of around 120  $\mu\text{m}$  have become an interesting subject for applied and basic research studies owing to their outstanding magnetic properties. Peculiar magnetic phenomena associated with

the magnetization reversal process and the appearance of a large Barkhausen jump (denominated as magnetic bistability) and the giant magnetoimpedance (GMI) effect have been observed and intensively studied along the last decade [1, 2].

Recently the Taylor-Ulitovsky method, which has been known since the 1950s [3], has been employed to produce a long and thin ferromagnetic microwire with a tiny metallic nucleus (1–20  $\mu\text{m}$  in diameter) coated by an insulating sheath (1–10  $\mu\text{m}$  in thickness) [4]. Figure 1 shows a micrograph of a typical microwire where its composite character can be clearly seen. As will be presented in the next section, their amorphous or metastable crystalline (nanocrystalline or granular) character is achieved due to the high-quenching rate by the introduction of the molten alloy into a water jet during the drawing of the microwire. A number of outstanding magnetic properties, such as magnetic bistability, enhanced magnetic softness, and GMI effect (up to 600%), have been found recently in such microwires [4–8]. These properties are correlated with the shape and magnetoelastic anisotropies depending on the dimensions, microstructure, composition and strong internal stresses originating from the difference of the thermal expansion coefficients of the metal and the glass. Consequently, the magnetic properties could be modified by either heat treatment or chemical etching of the glass coating or by the selection of adequate chemical composition of the metallic nucleus.

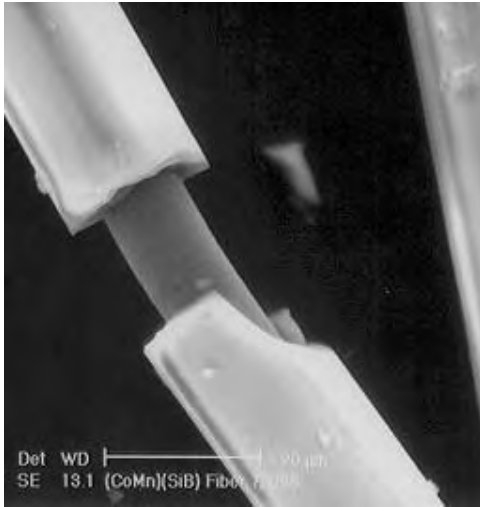


Figure 1. Micrograph of a glass-coated microwire.

It is well known that the two-phase system consisting of nanocrystallites randomly distributed in a soft magnetic amorphous phase is an important group of soft magnetic materials. Yoshizawa and co-workers [9, 10] revealed that the presence of small additions of Cu and Nb to some FeSiB-based alloys can allow the creation of a two-phase material by partial devitrification of the conventional amorphous alloy. These materials are obtained by annealing the amorphous precursor in the range of 500–600 °C, 1 hour (i.e., at temperatures between partial and full crystallization processes). In this way, materials with different microstructures and magnetic properties can be obtained depending on the annealing parameters as well as on the chemical composition. It must be mentioned that most results have been reported mainly on ribbon shaped materials. After partial devitrification, the sample consists of small (around 10 nm grain size) nanocrystals embedded in the residual amorphous matrix. In addition, the devitrification process of these amorphous alloys (most typical composition  $\text{Fe}_{73.5}\text{Cu}_1\text{Nb}_3\text{Si}_{13.5}\text{B}_9$  with trademark *finemet*) leads to the possibility of obtaining rather different microstructures depending on the annealing parameters as well as on the chemical composition. Its outstanding magnetic softness has been explained by Herzer [10, 11] and is related to the ratio of the exchange correlation length or domain-wall thickness,  $L$ , to the orientation fluctuation length of randomly distributed local easy axes, which can be approximated as the average crystalline size  $D$ . For  $L \gg D$ , the macroscopic magnetic anisotropy averages out and the domain wall can move without being pinned. For some particular compositions, and for a critical crystallized volume fraction when the average magnetostriction vanishes, the magnetoelastic contribution to the macroscopic anisotropy also becomes negligible.

Few attempts have been done to fabricate glass-coated amorphous microwires of *finemet*-type [4–6, 13–15]. Particularly a decrease of coercivity,  $H_c$ , has been generally observed at annealing temperature,  $T_{\text{ann}}$ , below 600 °C. Such decrease of  $H_c$  has been ascribed to the structural relaxation of the material within its amorphous charac-

ter in a similar way as for metallic glass alloys in the shape of a ribbon [10–12]. A considerable hardening is then observed in  $\text{Fe}_{73.4}\text{Cu}_1\text{Nb}_{3.1}\text{Si}_x\text{B}_{22.5-x}$  ( $x = 11.5, 13.5,$  and  $16.5$ ) microwires after treating at  $T_{\text{ann}}$  above 650 °C [13, 14]. This magnetic hardening irrespective of the amorphous nature of the alloy can be very useful for different technological applications such as information storage. Unfortunately, such magnetic hardening observed in conventional *finemet* compositions during the second recrystallization process is accompanied by a strong deterioration of mechanical properties [10–14]. But recently similar magnetic hardening has been observed at lower annealing temperature during the first recrystallization process [7, 15] allowing one in this way to avoid such brittleness.

On the other hand, granular systems based on immiscible (Co,Fe,Ni)–(Cu,Pt,Au,Ag) elements have been intensively studied in the last few years due to their potential technological applications. Such immiscible alloys exhibit peculiar magnetic transport properties as the giant magnetoresistance (GMR) effect and relative magnetic hardening which can be useful for various applications in magnetic recording and sensors [16–19]. These systems have been recently obtained by different routes such as sputtering, mechanical alloying, rapid solidification, etc. The samples obtained by these techniques have different shapes and geometry: thin films, powders, multilayers, and ribbons. The GMR effect and enhanced magnetic hardness have been observed for these materials consisting of ferromagnetic nanoparticles, usually of Co or Fe, embedded in a nonmagnetic metallic matrix (typically Cu, Au, or Ag). The high quenching rate characteristic of the melt spinning method has been used for fabrication of metastable crystalline materials where the crystalline phases, stable at high temperatures, can be quenched-in at room temperature. In this case, the GMR effect and enhanced coercivity were obtained after recrystallization of the metastable phases [20, 21]. At zero field, when magnetic moments of the particles are not aligned (e.g., oriented randomly), the resistivity of the material is high. When an external magnetic field aligns these moments, the resistivity decreases, as in the previously discovered multilayered GMR materials [18]. This effect is large and almost independent on the magnetic field direction [17, 19, 22]. (The maximum GMR amplitude of around 60% at ambient conditions was obtained in sputtered polycrystalline Co/Cu multilayers with (1, 1, 1) texture [23].)

It is noticeable that in the last few years the quenching and drawing technique has been developed to produce ferromagnetic microwire alloys of immiscible elements with magnetic and granular nature. Attempts have been done to fabricate and characterize the structure and the magnetic properties of glass-coated microwires produced from immiscible elements such as [(Co–Fe–Ni)–(Cu,Ag,Au,Pt)], which can be obtained from the decomposition of metastable and unstable phases of the so-called granular solids. The high quenching rate of the Taylor–Ulitsvski technique is useful for fabrication of metastable crystalline materials when the crystalline phases, stable at high temperature, can be quenched-in at room temperature [21, 24, 25].

The aim of this chapter is to present, first, the most relevant aspects concerning the fabrication process following by a section devoted to present significant results

on the remagnetization process, compositional dependence, and processing of glass-coated microwires with amorphous, nanocrystalline, and granular character in order to design their magnetic properties. The other section is devoted to the mechanical properties of glass-coated microwires.

## 2. CASTING METHOD

Microwires are manufactured by means of a modified Taylor–Ulitovsky process [3, 26–34] based on direct casting from the melt, as schematically depicted in Figure 2. In the laboratory process, a few grams of the master alloy with the desired composition is put into a glass (Pyrex, Nonex, etc.) tube and placed within a high frequency inductor heater. The alloy is heated up to its melting point, forming a droplet. While the metal melts, the portion of the glass tube adjacent to the melting metal softens, enveloping the metal droplet. A glass capillary is then drawn from the softened glass portion and wound on a rotating coil. At suitable drawing conditions, the molten metal fills the glass capillary and a microwire is thus formed where the metal core is completely coated by a glass shell. The amount of glass used in the process is balanced by the continuous feeding of the glass tube through the inductor zone, whereas the formation of the metallic core is restricted by the initial quantity of the master alloy droplet. The microstructure of a microwire (and hence its properties) depends mainly on the cooling rate, which can be controlled by a cooling mechanism when the metal-filled capillary enters into a stream of cooling liquid (water or oil) on its way to the receiving coil.

The main advantages of this method of microwire fabrication are:

- (i) repeatability of microwire properties in mass production;
- (ii) wide range of geometrical parameters and physical properties;
- (iii) fabrication of continuous, long pieces of microwire up to around 10,000 m;

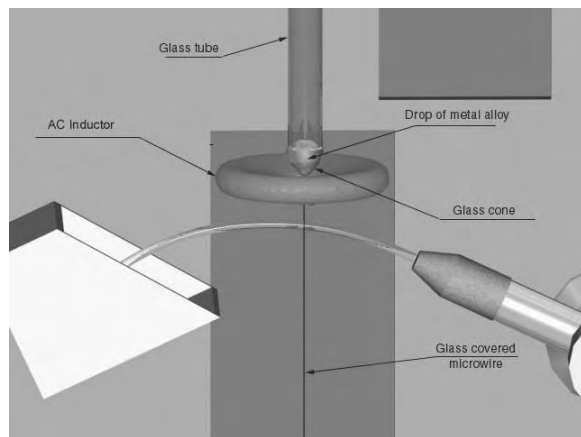


**Figure 2.** Schematic drawing of microwire fabrication process by the Taylor–Ulitovsky method. Reprinted with permission from [34], V. S. Larin et al., *J. Magn. Magn. Mater.* 249 39 (2002). © 2002, Elsevier Science.

- (iv) control and adjustment of geometrical parameters (inner metallic nucleus diameter and glass thickness) during the fabrication process

The casting process is carried out at a temperature that melts the alloy and softens the glass tube.

### 2.1. Fabrication Process and its Limitations

#### 2.1.1. Casting Rate

There are several factors affecting the casting rate. This rate is limited, first, by the ability of metal to follow the moving glass. Its actual limit can be calculated by assuming that it is necessary to accelerate the initially still molten metal and glass up to the operating rates [31, 32]. A force,  $F$ , must then be imposed to the metal to fill the capillary. Assuming a conical shape at the end of the glass capillary, the casting rate,  $V_c$  (which corresponds to the average speed of the accelerated metal  $\langle dz/dt \rangle$ ), is found from the balance between the work done by this force and the kinetic energy of metal filling the capillary,

$$(v\rho)V_c^2/2 = Fz \quad (1)$$

where  $v = \pi z(R^2 + r^2 + Rr)/3$  is the volume of the conical portion in Figure 3 (geometrical parameters are given there), and  $d_m$  is the density of metal. The value of  $r$  is determined by the final size of the metal core. The limit of the casting rate,  $V_c^*$ , can be obtained from (1), where  $F$  coincides with the adhesion force  $F_a$  for metal/glass interface:

$$V_c^* = \sqrt{\frac{6F_a}{\pi d_m (R^2 + r^2 + Rr)}} \quad (2)$$

Thus, the limiting rate of casting grows with an increase in the adhesion for a given metal/glass pair and drops with an increase in the core radius.

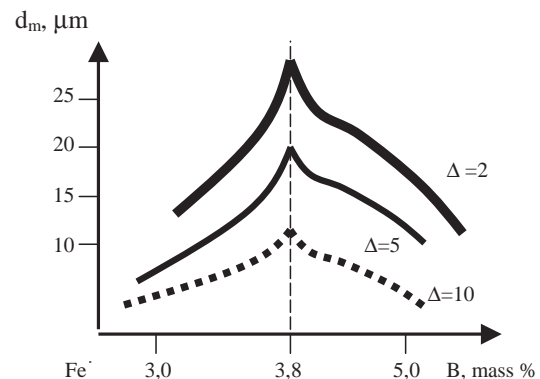


**Figure 3.** Maximum value of the diameters of the metallic nucleus to obtain microwire (FeSi system) with amorphous microstructure for a range of glass-coating thickness. Reprinted with permission from [34], V. S. Larin et al., *J. Magn. Magn. Mater.* 249, 39 (2002) © 2002, Elsevier Science.



The limiting casting rate associated with the dynamical viscosity of the glass (which is a function of temperature) and the acceleration of moving glass can be represented as

$$F = F_\eta(T) + F_a \quad (3)$$

$$F_\eta(T) = k(T)\eta(T)V_c S_{gl}/h \quad (4)$$

where  $F_\eta(T)$  is the tensile force acting on the microwire, which is related to the dynamical adhesion of glass at casting temperature,  $F$  is the total force,  $k(T)$  is the coefficient of resistance to fluidity,  $\eta(T)$  is the dynamical viscosity,  $S_{gl}$  is the cross-section of the glass coating,  $h$  is the length of the stretching path, and  $F_a$  is the force related to the acceleration of the glass portion. Thus, taking into account Eqs. (3) and (4), the limiting rate  $V_c^*$  is

$$V_c^* = 1/(k(T)\eta(T)S_{gl} + F_a)^{1/2} \quad (5)$$

### 2.1.2. Diameter of a Microwire

Typical limits for the metallic core diameter are between 0.8 and 30  $\mu\text{m}$ , while the thickness of the coating ranges between 2 and 15  $\mu\text{m}$ . It should be noted that even during the stationary casting process, there is some variation (although not large) in diameter of the metallic nucleus and in the glass coating thickness along the wire length. The experimental evaluation of this variation in terms of the diameter of metallic nucleus and the total diameter as a function of the sample length is shown in Figure 4 for the case of Fe–Si–B/Pyrex microwire.

The geometrical characteristics of the microwire depend on the physical properties of the glass and metal, the diameter of the initial glass tube, and the parameters of the heating inductor. It has been proved that the strongest effect on the geometry of a microwire comes from the glass properties. Therefore, the radius of the metal core is estimated to be [31–34]

$$r_m = 0,9 \left( \frac{\eta^5}{\sigma^2 v_\lambda} \right)^{\frac{1}{3}} \frac{1}{d} \frac{\eta^5}{\sigma^2 v_\lambda} f(v, \eta, \sigma, d_l) \quad (6)$$

with  $\eta$  as

$$\eta = 6\sqrt{6\rho} \left( \frac{\omega^2}{N_0} \right)^{\frac{1}{3}} M^{-5/6} d^{4/3} T^{1/2} \left( \cosh \frac{2\lambda_i^0}{\gamma R T} - 1 \right) \quad (7)$$

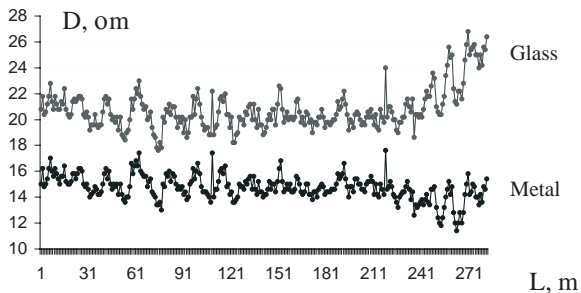


**Figure 4.** Variation of the diameter of the metallic nucleus (marked as Metal) and of the total diameter (marked as Glass) with the sample length in the case of Fe–Si–B–Pyrex microwire. Reprinted with permission from [34], V. S. Larin et al., *J. Magn. Magn. Mater.* 249, 39 (2002). © 2002, Elsevier Science.

where  $R$  is the universal gas constant,  $\omega$  is the internal volume of molecules in liquid per gram-molecule,  $N_0$  is the Avogadro constant,  $\lambda_i^0$  is the internal hidden evaporation heat per gram-molecule,  $\gamma$  is the coordination number,  $M$  is the molecular weight,  $\sigma$  is the surface tension,  $\rho$  is the curvature radius of the surface in the transition area between the liquid drop and microwire,  $d_l$  is the density of liquid,  $f(v, \eta, \sigma, d)$  is a factor which can be experimentally evaluated (it depends weakly on the casting rate), and

$$v_\lambda = \frac{2\nu r_w^2}{\sqrt{3}\rho^3} \pm \sqrt{\left( \frac{2\nu r_w^2}{\sqrt{3}\rho^3} \right)^2 - \frac{2\sigma}{r_w d_l}} \quad (8)$$

where  $\nu = \eta/d_l$  is the kinematical density and  $r_w$  is the total microwire radius. Taking Eqs. (1) to (8), it can be concluded that there exists a limiting casting rate for fabricating a microwire with the smallest possible diameter.

The limit for the upper diameter limit can be obtained at low casting rates, since the contribution of  $v_\lambda^2/2$  is neglected, yielding

$$r_{m,\max} = \left( \frac{\sqrt{3}\sigma}{2\nu d_l} \right)^{1/3} \frac{\rho}{v_\lambda^{1/3}} \quad (9)$$

Thus, the diameter of a microwire produced by the Taylor–Ulitovsky method has both upper and lower limits depending on the rate of casting.

### 2.1.3. Composition of the Metal Core

The present method allows preparation of pure metals such as Ag, Au, Cu, Ni, Sn, Pb, and Pt. Semiconductors such as Ge, Si, or Bi can also be cast. The alloys of these metals can be also processed, but not over the whole range of compositions. For example, the content of Cr in Ni and Co based alloys can be up to 20%; the content of Mo, W, V in Ni, Co, and Fe based alloys can be up to 8–10 at%. Some limitations relate to the melting temperature, which must not be too high. On the other hand, rare earth metals and metals which react with the glass and atmosphere (Ti, Cr, Mo, W, Nb, Al, Na, La, Nd) are not suitable for this technology.

Of principal interest is the fabrication of magnetic microwires with soft magnetic characteristics for which Fe, Ni, and Co are the main elements of the alloy. In the case of amorphous microwire, elements such as Si, B, C, and Al are added to enable the amorphicity of the alloys.

Metastable supersaturated solid solutions can be obtained for immiscible metal systems in a solid and even liquid state, such as Cu–Co, Cu–Co–Ni, Ag–Fe, Ag–Co. As-cast microwire can exhibit a structure of a supersaturated solid solution of transition metals in Cu or Ag. After suitable thermal treatments small single domain particles of Co or Fe can precipitate.

An overview of the metallic alloy compositions is presented in Table 1.

## 2.2. Microstructure of Cast Microwires

The properties of microwires are related to a great extent to the microstructure, geometry, and chemical composition of the metallic nucleus. The analyzed method of casting

**Table 1.** Glass coated microwires.

Material	Diameter of core ( $\mu\text{m}$ )	Total diameter ( $\mu\text{m}$ )	Characteristics
Silver (Ag)	2–30	12–36	$\rho = 0.020 \text{ Ohm/mm}^2\text{m}$ TRC = 3000 1/grad $10^6$
Gold (Au)	2–25	12–32	$\rho = 0.035 \text{ Ohm/mm}^2\text{m}$ TRC = 3200 1/grad $10^6$
Copper (Cu)	1–30	10–36	$\rho = 0.022 \text{ Ohm/mm}^2\text{m}$ TRC = 3000 1/grad $10^6$
Platinum (Pt)	4–20	8–30	$\rho = 0.127 \text{ Ohm/mm}^2\text{m}$ TRC = 3300 1/grad $10^6$
Nickel (Ni)	4–16	14–20	$\rho = 0.090 \text{ Ohm/mm}^2\text{m}$ TRC = 5000 1/grad $10^6$
Alloys with rectangular hysteresis loop Fe–B–Si	3–20	12–26	$H_s = 0.5\text{--}100 \text{ Oe}$
Soft magnetic alloys Co–Fe–B–Si, Co–Mn–B–Si	5–35	14–40	$\mu_i \approx 20,000\text{Gs/Oe}$
Alloys with GMI effect Co–Fe–Ni–B–Si	5–40	12–45	$\Delta Z/Z = 200\text{--}620\%$
Resistance alloys Cu–Ni–Si–Mn; Ni–Cr–Si–Mn	1.5–20	12–28	$R \approx 5\text{--}1000 \text{ kOhm/m}$ TCR = $2 \times 10^{-6}$
Metastable supersaturated solid solutions from immiscible metal systems Cu–Co, Cu–Co–Ni, Ag–Fe, Ag–Co.	2–20	12–40	$H_c = 10\text{--}800 \text{ Oe}$ , GMR up to 10%

Note: TRC—thermal resistance coefficient, TEMF—thermal electromotive force,  $\mu_i$ —initial magnetic permeability,  $H_s$ —switching field,  $\Delta Z/Z$ —GMI ratio, GMR—Giant magnetoresistance.

Source: "TAMAG Iberica S.L." web page, www.tamagiberica.com.

offers the possibility of rapid cooling and solidification of liquid metal in a nonequilibrium process, allowing the formation and existence of metastable metallic phases. The microstructure of rapidly cooled metal depends on its chemical composition, the melting temperature of metal, and the cooling rate. Depending on the critical cooling rates, different metastable phases can be formed (i.e., supersaturated solid solution, microcrystalline, nanocrystalline, granular and amorphous phases). In certain cases, a mixed microstructure consisting of nano- or microcrystals embedded in the amorphous matrix can be formed as well.

### 2.2.1. Cooling Rate of the Metallic Nucleus

The cooling rate  $V_t$  depends both on the geometry of the microwire (i.e., diameter  $d$  of the metallic nucleus and thickness  $t$  of the glass coating) and on the parameters of the technological process related to thermal conductivity [31],

$$V_t = \alpha(T_2 - T_k)(d + t)/[(\rho_m d^2 C_m + \rho_g C_g)(dt + t^2)] \quad (10)$$

where  $\rho_m$ ,  $\rho_g$ ,  $C_m$ ,  $C_g$  are the density and specific heat of metal and glass, respectively,  $T_k$  is the temperature of the cooling liquid,  $\alpha$  is thermoconductivity parameter at the boundary microwire/cooling medium, and  $T_2$  is the temperature of the metal when entering the cooling zone. The value of  $T_2$  can be deduced from

$$T_2 = \alpha^* T_1 \exp[1/Vl(T_1 - T_a)]/h \quad (11)$$

where  $T_1$  is the temperature at the base of the droplet,  $T_a$  is the air temperature,  $V$  is the casting rate, and  $\alpha^*$  is a

heat transmission parameter at the movement of a cylinder in the gaseous medium. The characteristic cooling rates of the metallic nucleus in the gaseous medium ranges from  $10^2$  to  $10^4 \text{ K}^{-1}$ , whereas in a stream of liquid it ranges between  $10^5$  and  $10^7 \text{ K}^{-1}$ .

### 2.2.2. Metastable Phases in Cast Microwire

Various types of metallic alloys of metastable systems can be prepared by increasing the cooling rate (the so-called quenching rate). In principle, phase diagram of metal–metaloid, metal–metal eutectic type, and alloys with a limited solidification range in a solid state have a significant role.

The "critical quenching rate,"  $V_{cr}$ , is

$$V_{cr}^* = (T_l - T_g)/t \quad (12)$$

where  $T_l$  and  $T_g$  are the liquids and devitrification temperatures respectively, and  $t$  is the maximum time at which any part of the material quenches from  $T_l$  to  $T_g$ . A "critical quenching rate" can be defined as the minimum quenching rate necessary to obtain any metastable structure at a given thermal exchange coefficient. The critical quenching rate can be characterized by the maximum metallic nucleus diameter (at a given glass-coating thickness and thermal exchange coefficient,  $\alpha$ ) at which any of the metastable phases can be obtained.

As an example, Figure 4 illustrates the maximum diameters of the metallic nucleus necessary to obtain a microwire in order for the FeB system to exhibit an amorphous

microstructure. Microwires with diameters below the corresponding curves are obtained in an amorphous state.

### 3. MAGNETIC BEHAVIOR

#### 3.1. Amorphous Glass-Coated Microwires

In fact studies of magnetic properties of amorphous glass coated microwires started even in the 1970s [35], but recently these tiny glass-coated ferromagnetic wires have been rediscovered mainly due to a number of unusual magnetic properties and their potential applications [4–7].

Hysteresis loops of three main families of amorphous microwires—Fe-rich (positive magnetostriction constant,  $\lambda_s$ ), Co-rich (negative  $\lambda_s$ ), and Co–Mn (nearly zero  $\lambda_s$ )—are shown in Figure 5 a–c, respectively. As can be observed, the shape of the hysteresis loops as well as the magnetic properties (coercivity,  $H_c$ , magnetic anisotropy field, magnetic permeability) depend drastically on the composition of the sample.

Mainly attention has been paid to the studies of samples with positive magnetostriction constant (Fe-rich compositions) exhibiting perfectly rectangular hysteresis loops (so-called magnetic bistability) and to nearly-zero magnetostriction compositions with good magnetic softness (Co-rich compositions). It must be noted that such magnetic behavior is drastically determined by the strong and complex internal stresses acting on the metallic nucleus due to the glass coating. In fact, investigations on the progressive elimination of the glass insulating coating by chemical etching on magnetic properties [36, 37] showed considerable change of the soft magnetic behavior as the thickness of glass coating has been diminished.

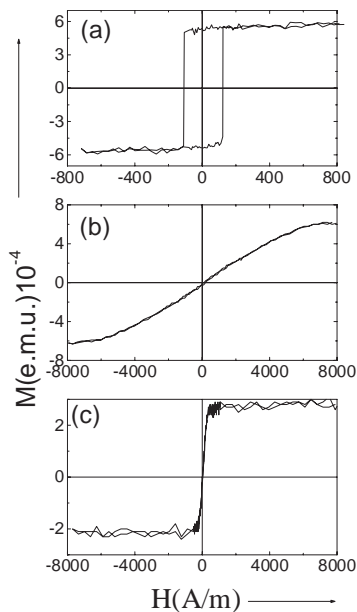


**Figure 5.** Hysteresis loops of  $\text{Fe}_{70}\text{B}_{15}\text{Si}_{10}\text{C}_5$  ( $\lambda_s > 0$ ),  $\text{Co}_{75}\text{Si}_{10}\text{B}_{15}$  ( $\lambda_s < 0$ ), and  $\text{Co}_{68}\text{Mn}_7\text{Si}_{10}\text{B}_{15}$  ( $\lambda_s \approx 0$ ) microwires. Reprinted with permission from [6], A. Zhukov et al., *J. Mater. Res.* 15, 2107 (2000). © 2000, Materials Research Society.

#### 3.1.1. Magnetic Bistability

As can be observed in Figure 6, the switching field,  $H_s$ , that is, the magnetic field required to reverse magnetization (so observing a rectangular hysteresis loop), increases and the remanent magnetization decreases for the same metallic nucleus composition ( $\text{Fe}_{65}\text{B}_{15}\text{Si}_{15}\text{C}_5$ ) with decreasing of the geometric ratio  $\rho (=r/R)$  (where  $r$  is metallic core radius and  $R$  is total radius). Such an increase of the switching field has been attributed to the increasing strength of internal stresses as well as increasing glass coating thickness. The switching field,  $H_s$ , should be proportional to the energy required to form the domain wall  $\gamma$  involved in the bistable process. The wall energy is related to the magnetoelastic anisotropy and, therefore, to the applied tensile stress as given by [38]

$$H_s \approx \gamma \propto [3A\lambda_s(\sigma_a + \sigma_r)]^{1/2} / \cos \alpha \quad (13)$$

where  $\alpha$  is the angle between magnetization and axial direction,  $A$  is the exchange energy constant,  $\lambda_s$  is the saturation magnetostriction constant, and  $\sigma_r$  is the residual tensile stress. Consequently,  $H_s$  must be proportional to  $(\sigma_a + \sigma_r)^{1/2}$  for  $\cos \alpha \approx 1$ . On the other hand, it was shown [39, 40] that the strength of the internal stresses increases as decreasing the ratio  $\rho$ .

From the rectangular shape of the hysteresis loop it should be suggested that the remagnetization process of such microwires is controlled by the nucleation or depinning and consequent fast domain wall propagation inside the single domain inner core of the metallic nucleus.

Temperature and field dependencies of the domain wall propagation velocity,  $v$ , have been measured in  $\text{Fe}_{65}\text{B}_{15}\text{Si}_{15}\text{C}_5$  amorphous microwire exhibiting rectangular hysteresis loops ( $H_s = 110 \text{ A/m}$ ) with diameter of the metallic nucleus around  $14 \mu\text{m}$  and length  $120 \text{ mm}$  (see Fig. 7) [41]. The measured values of  $v$  were found to be between 35 and 65 m/s. A slight increase of the domain wall velocity is observed as the measuring temperature increases from 5 to 300 K. Observed domain wall velocity was found to be much higher than in Ni single crystals ( $0.0001 \leq v \leq 10 \text{ m/s}$ )

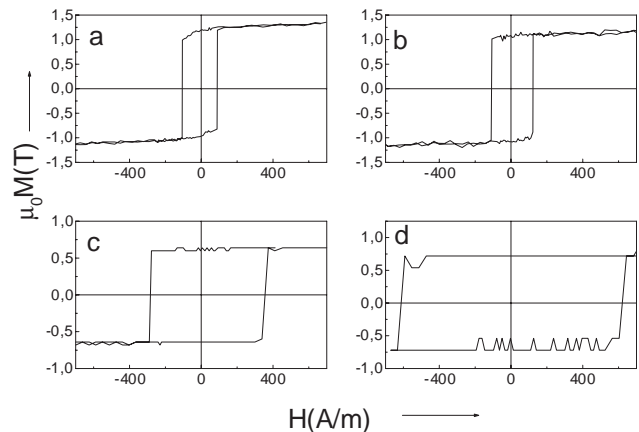


**Figure 6.** Effect of ratio  $\rho$  on hysteresis loop of  $\text{Fe}_{70}\text{B}_{15}\text{Si}_{10}\text{C}_5$  ( $\lambda_s > 0$ ) microwire. (a)  $\rho = 0.63$ ; (b)  $\rho = 0.62$ ; (c)  $\rho = 0.48$ ; (d)  $\rho = 0.26$ ; (e)  $\rho = 0.16$ . Reprinted with permission from [4] M. Vázquez and A. Zhukov, *J. Magn. Magn. Mater.* 160, 223 (1996). © 1996, Elsevier Science.

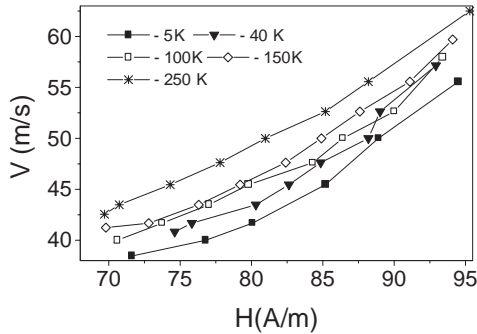


**Figure 7.** Effect of temperature and magnetic field on velocity of domain wall propagation of  $\text{Fe}_{65}\text{B}_{15}\text{Si}_{15}\text{C}_5$  microwire. Reprinted with permission from [40], A. Zhukov, *Appl. Phys. Lett.* 78, 3106 (2001). © 2001, American Institute of Physics.

[42] but lower than in FeSiB amorphous wires prepared by quenching into water ( $150 \leq v \leq 500$  m/s) [43]. Like in the case of Ni single crystals, significant deviations from the linear field dependencies  $v(H)$  have been observed.

The values of the magnetic field given on the horizontal axis in the Figure 7 are lower than the switching field. This means that after overcoming this first highest energy barrier corresponding to the domain wall nucleation, the domain wall propagates even in a field lower than the switching field (i.e., that the nucleation field is higher than the propagation field). The critical magnetic field,  $H_{cr}$ , actually can be obtained by the extrapolation of the curves that will be presented in Figure 9 at  $v = 0$ . This extrapolation gives values of  $H_{cr}$  around 5–10 A/m, which are one order of magnitude lower than the switching field.  $H_{cr}$  can be interpreted as the intrinsic coercivity of the material and characterizes the efficiency of the obstacles for the domain wall propagation. On the other hand, it was shown that the reversed domains already exist at the wire ends [44] due to the effect of the demagnetizing fields [45]. Therefore, one can assume that the appearance of the large Barkhausen jump should be related to the depinning of domain walls of such closure domains (i.e., to the critical size achieved by one of the reversed domains under the effect of the applied magnetic field).

### 3.1.2. Effect of Thermal Treatments (Tailoring of the Magnetic Properties)

In the vicinity of the zero magnetostriction alloy composition the hysteretic magnetic properties depend strongly on the metallic alloy composition, such as shown in Figure 8. The shape of the hysteresis loop of the sample with  $x = 0.08$  (Fig. 8a) suggests the presence of a transverse magnetic anisotropy. The initial magnetic permeability,  $\mu_{15}$ , estimated from the hysteresis loop is around 60 and the coercivity  $H_c \approx 5$  A/m. The sample with  $x = 0.09$  (Fig. 8b) exhibits a rather good combination of relatively low values of coercivity ( $H_c \approx 5$  A/m) and relatively high initial magnetic permeability ( $\mu_{15} \approx 2000$ ). The sample with  $x = 0.10$  (Fig. 8c) has a rectangular hysteresis loop (labeled as magnetic bistable behavior). This sample has  $H_c \approx 25$  A/m and relatively low magnetic permeability at magnetic field below coercivity ( $\mu_{15} \approx 1-10$ ).

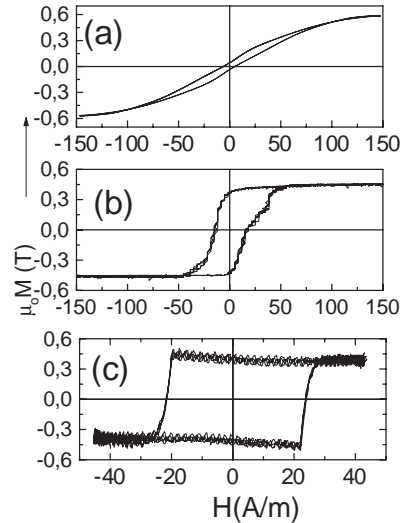


**Figure 8.** Effect of composition on hysteresis loop of  $(\text{Co}_{1-x}\text{Mn}_x)_{75}\text{Si}_{10}\text{B}_{15}$  ( $x = 0.08-0.11$ ) microwires. Reprinted with permission from [7], A. Zhukov, *J. Magn. Magn. Mater.* 242–245, 216 (2002). © 2002, Elsevier Science.

It is worth mentioning that as in the case of amorphous ribbons heat treatment especially in the presence of the external magnetic field and/or applied stress significantly affects the magnetic behavior of amorphous magnetic materials [46, 47]. Therefore similar studies have been performed in glass coated microwires.

Series of different treatments up to 473 K, such as conventional annealing (CA) and magnetic field annealing (FA), have been performed in the samples with  $x = 0.08$  [37]. Figure 9a shows as an example the hysteresis loops obtained for the sample  $x = 0.08$  after heat treatments at 373, 423, and 473 K. The conventional low-temperature thermal treatments (CA) (in the range of 373–473 K, 1 hour) produce small changes in the coercive field, which can be ascribed to the relaxation of internal stresses within the amorphous state. Nevertheless, when the thermal treatment was carried out under the presence of an axial magnetic field (FA), significant changes of the hysteresis loop were detected (see Fig. 9b). This change produces an increase of the initial permeability,  $\mu_i$ , coercivity,  $H_c$ , and remanent magnetization,  $\mu_0 M_r$ , and a decrease of the anisotropy field,  $H_K$  (see Fig. 10a). The changes of the shape of the hysteresis loop with FA should be connected to the induction of magnetic anisotropy with easy axis along the longitudinal direction of the microwire. This anisotropy is developed by the combined effect of the high internal stress and the magnetic field applied during the treatment [37, 46, 47].

Similarly to conventional furnace annealing, current annealing could be used for the tailoring of the magnetic properties of amorphous microwires [48, 49]. Dependencies of coercivity on the annealing time,  $t_{ann}$ , for CA and FA with current density 227 A/mm<sup>2</sup> for three microwires are shown in Figure 11. In the case of the  $\text{Fe}_{70}\text{B}_{15}\text{Si}_{10}\text{C}_5$  microwire, both treatments (CA, FA) at 30 mA ( $j = 227$  A/mm<sup>2</sup>) caused a decrease of  $H_c$  with  $t_{ann}$ . In the case of FA, such a decrease of coercivity is more significant. In contrast, in the case of  $\text{Co}_{56.5}\text{Fe}_{6.5}\text{Ni}_{10}\text{B}_{16}\text{Si}_{11}$  samples, both treatments result in

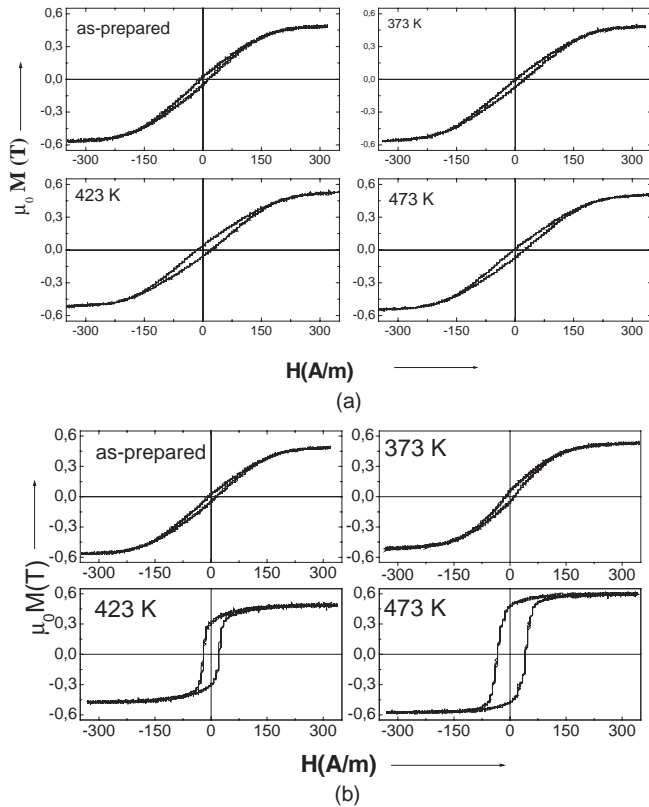


**Figure 9.** Effect of conventional (a) and magnetic field annealing (b) on hysteresis loops of  $(\text{Co}_{0.92}\text{Mn}_{0.8})_{75}\text{Si}_{10}\text{B}_{15}$  microwire at different annealing temperatures. Reprinted with permission from [36], A. Zhukov et al., *J. Appl Phys.* 87, 1402 (2000). © 2000, American Institute of Physics.

opposite effects [48]. CA treatment gives rise to a roughly monotonic decrease of the coercivity, while FA results in an increase of  $H_c$ , with a broad maximum at  $t_{\text{ann}} \approx 10$  min. Similarly to  $\text{Fe}_{70}\text{B}_{15}\text{Si}_{10}\text{C}_5$  samples, a monotonic decrease of  $H_c$  has been observed for the  $\text{Co}_{68}\text{Mn}_7\text{Si}_{10}\text{B}_{15}$  sample after both CA and FA treatments. Besides, as in the case of the  $\text{Co}_{56.5}\text{Fe}_{6.5}\text{Ni}_{10}\text{B}_{16}\text{Si}_{11}$  sample, the FA current annealing treatment results in higher  $H_c$ , as compared to the CA treatment.

The observed difference between the CA and FA should be attributed to the effect of the stress+longitudinal field induced magnetic anisotropy in the last case, where the strong internal stresses contribute as the reinforcing factor. This feature implies that the application of the longitudinal magnetic field during annealing favors the formation of the internal axially magnetized core with longitudinal magnetic anisotropy. In the mean time, the CA results only in internal stress relaxation.

### 3.1.3. Soft Magnetic Behavior and GMI Effect

Transformation of a rectangular hysteresis loop into a flat and almost unhysteretic loop is observed in nearly zero magnetostrictive compositions (Fig. 8) in the series of  $(\text{Co}_{1-x}\text{Mn}_x)_{75}\text{Si}_{10}\text{B}_{15}$  ( $x = 0.08, 0.09$ , and  $0.10$ ) microwire compositions (Fig. 8 a–c) with  $x$  increasing from 0.08 to 0.10. Careful selection of the metallic alloy composition permits

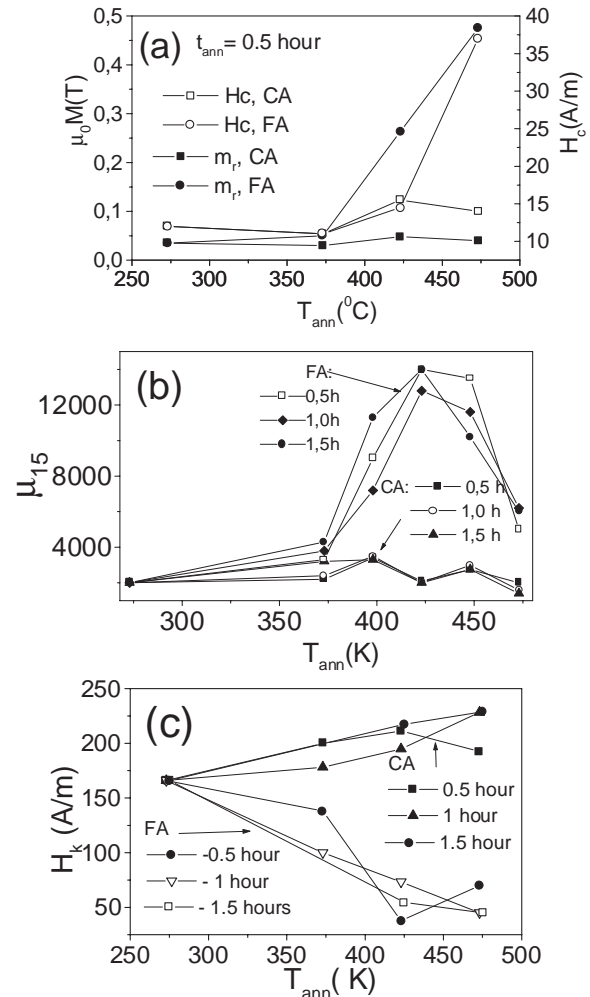


**Figure 10.** Effect of magnetic field annealing on some magnetic properties of  $\text{Co}_{69}\text{Mn}_6\text{Si}_{10}\text{B}_{15}$  microwires: initial magnetic permeability,  $\mu_{15}$  (a), anisotropy field,  $H_k$  (b), and coercivity and remanent magnetization (c). Reprinted with permission from [36], A. Zhukov et al., *J. Appl Phys.* 87, 1402 (2000). © 2000, American Institute of Physics.

one to obtain the sample with enhanced magnetic softness and small magnetic anisotropy (the sample with  $x = 0.09$  is an example).

The very soft magnetic behavior of CoMnSiB microwires makes them very interesting to investigate the magnetoimpedance effect. A high GMI has been observed in  $\text{Co}_{68.5}\text{Mn}_{6.5}\text{Si}_{10}\text{B}_{15}$  microwire annealed at  $100^\circ\text{C}$  for 1 hour (see Fig. 12a). A maximum GMI ratio,  $(\Delta Z/Z)_m$ , as well as a field of maximum,  $H_m$ , increases with the frequency of the driving current,  $f$  (see Fig. 12a) [50]. This GMI effect is extremely sensitive to the application of external tensile stresses: magnetic field,  $H_m$ , corresponding to the maximum of  $(\Delta Z/Z)$  shows a roughly linear increase with  $\sigma$  (Fig. 12b). The origin of this dependence should be related to the change of the domain structure inside the outer shell with circular orientation. As is well known, applied stress introduces a magnetoelastic anisotropy contribution which plays a very important role in the magnetization process of the metallic nucleus, even in this microwire



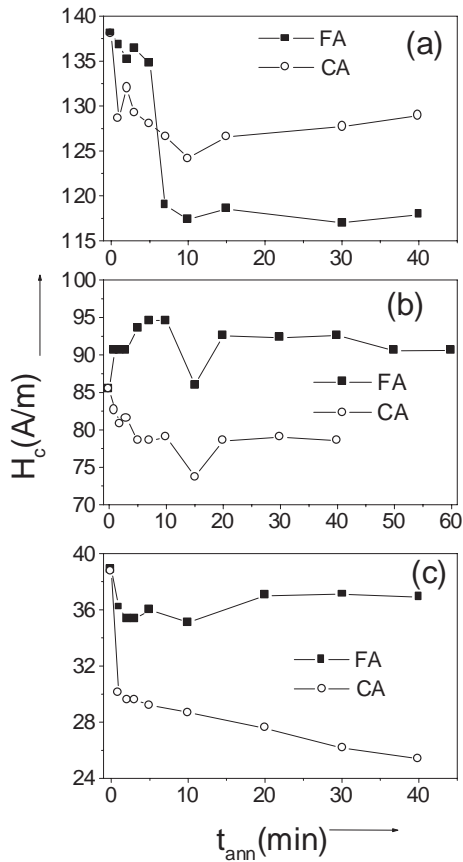


**Figure 11.** Comparative evolution of  $H_c$  with annealing time for CA and FA of  $Fe_{70}B_{15}Si_{10}C_5$  (a),  $Co_{56.5}Fe_{6.5}Ni_{10}B_{16}Si_{11}$  (b), and  $Co_{68}Mn_7Si_{10}B_{15}$  (c) microwires annealed at  $j \approx 227$  A/mm<sup>2</sup> with the annealing time,  $t_{ann}$ , as a parameter. Reprinted with permission from [47], V. Zhukova et al., *J. Non-Cryst. Solids* 287, 31 (2001). © 2001, Elsevier Science.

exhibiting an extremely low magnetostriction constant (of around  $-3 \times 10^{-7}$ ) [51–53].

It is remarkable to mention that according to [54, 55], the value of the dc axial field that corresponds to the maximum GMI ratio,  $H_m$ , should be attributed to the static circular anisotropy field,  $H_k$ . This argument allows us to estimate the magnetostriction constant using the dependence  $H_m(\sigma)$  presented in Figure 12c and the well-known expression for the stress dependence of anisotropy field [56]:

$$\lambda_s = (\mu_0 M_s/3)(dH_k/d\sigma) \quad (14)$$

The  $H_m(\sigma)$  dependence (see Fig. 12c) is roughly linear with a slope of around 0.7 A/(m×MPa), which allows an estimation of the unstressed value of the saturation magnetostriction constant,  $\lambda_{s,0}$ . We have found that  $\lambda_{s,0} \approx -2 \times 10^{-7}$ , which is rather reasonable in comparison with the recently reported values measured from the stress dependence of initial magnetic susceptibility ( $\lambda_{s,0} \approx -3 \times 10^{-7}$  for such composition) [51, 53].

Both hysteresis loop and GMI effect also depend on the internal stresses induced by the glass coating. The strength of such internal stresses depends on the glass-coating thickness, increasing with an increase of the relative volume of

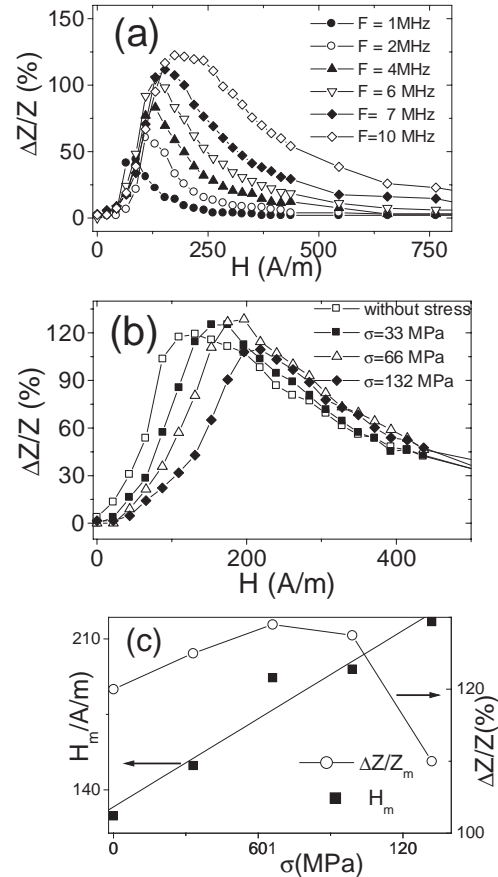


**Figure 12.** Effect of the frequency  $f$  (a) and applied stresses (b) on  $\Delta Z/Z$  ratio of  $Co_{68.5}Mn_{6.5}Si_{10}B_{15}$  amorphous microwire and dependence of  $H_m$  and  $\Delta Z/Z$  on applied stresses (c). Reprinted with permission from [7], A. Zhukov, *J. Magn. Magn. Mater.* 242–245, 216 (2002). © 2002, Elsevier Science.

the glass. Bulk hysteresis loops of three magnetically soft glass-coated  $Co_{67}Fe_{3.85}Ni_{1.45}B_{11.5}Si_{14.5}Mo_{1.7}$  microwires with different geometric ratios  $0.78 \leq \rho \leq 0.98$  are shown in Figure 13a. As can be observed in this figure, the magnetic anisotropy field,  $H_k$ , increases with decreasing ratio  $\rho$  (i.e., with the increase of the glass-coating thickness).

The  $(\Delta Z/Z)(H)$  dependencies measured at  $f = 10$  MHz and  $I = 0.75$  mA for the samples with ratios  $\rho = 0.98, 0.816,$  and  $0.789$  are presented in Figure 13b. A maximum relative change in the GMI ratio,  $\Delta Z/Z$ , up to around 615% is observed at  $f = 10$  MHz and  $I = 0.75$  mA in the sample with  $\rho \approx 0.98$  (see Fig. 13b) [7, 57].

As may be seen from Figure 13, the field corresponding to the maximum of the GMI ratio,  $H_m$ , increases and  $(\Delta Z/Z)_m$  decreases with  $\rho$ . Such  $H_m(\rho)$  dependence should be attributed to the effect of the above-mentioned internal stresses,  $\sigma$ , on the magnetic anisotropy field. Indeed, the value of the dc axial field corresponding to the maximum of the GMI ratio,  $H_m$ , should be attributed to the static circular anisotropy field,  $H_k$  [56]. The estimated values of the internal stresses in these amorphous microwires are of the order of 1000 MPa, depending strongly on the thickness of glass coating and metallic nucleus radius [5, 40]. Such elevated internal stresses give rise to a drastic change of the magnetoelastic energy,  $K_{me} \approx 3/2\lambda_s\sigma_i$ , even for



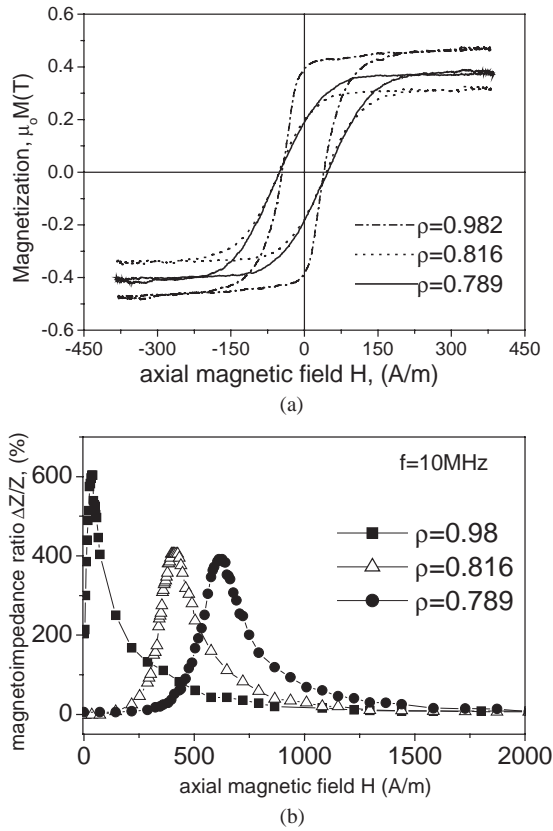


**Figure 13.** Effect of the geometrical parameter  $\rho$  on hysteresis loop (a) and  $\Delta Z/Z(H)$  dependencies (b) of  $\text{Co}_{67,05}\text{Fe}_{3,85}\text{Ni}_{1,4}\text{B}_{11,55}\text{Si}_{14,5}\text{Mo}_{1,65}$  microwires. Reprinted with permission from [57], V. Zhukova et al., *IEEE Trans Magn.* 38, 3090 (2002). © 2002. IEEE.

small changes of the glass-coating thickness at fixed metallic nucleus diameter. Consequently, such change of the ratio  $\rho$  should be related to the change of the magnetostriction constant according to Eq. (14).

**3.1.4. Magnetoelastic Properties**

The behavior of coercivity and remanence with applied tensile stress depends strongly on the microwire composition and geometrical characteristics exhibiting a quite different character for Fe- and Co-rich compositions (Fig. 14). Generally, a proportionality of the switching field,  $H_s$ , to the square root of the applied stresses has been observed in Fe-rich compositions, as predicted by Eq. (20) (Fig. 14a).  $H_s(\sigma)$  dependence in Co-rich  $(\text{Co}_{1-x}\text{Mn}_x)_{75}\text{Si}_{10}\text{B}_{15}$  ( $x = 0.08-0.11$ ) microwires with small positive magnetostriction constant is quite different from Fe-rich microwires [7]. Besides, the evolution of  $H_s(\sigma)$  depends also on the composition.

In fact, some increase of the coercivity  $H_c$  with  $\sigma$  after initial roughly independent behavior has been observed for  $x = 0.11$  (Fig. 14b). The sample  $(\text{Co}_{0,9}\text{Mn}_{0,1})_{75}\text{Si}_{10}\text{B}_{15}$  with an initially rectangular hysteresis loop shows a decrease of the coercivity and the remanent magnetization with  $\sigma$  and, finally, loses the magnetic bistability after application of certain  $\sigma$  (Fig. 14c).

The estimations of the magnetostriction constant were based on the variation of the initial magnetic permeability

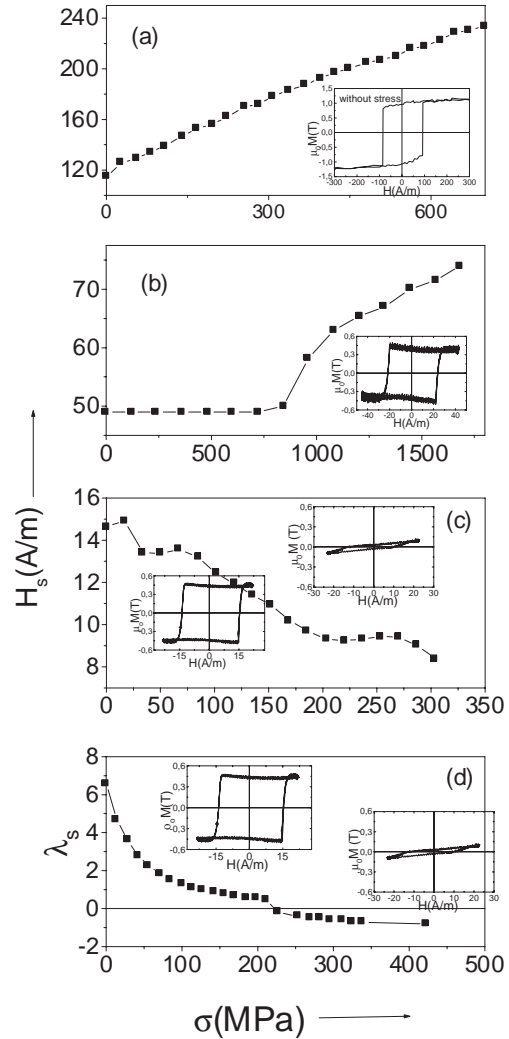


**Figure 14.** Effect of microwire composition on stress dependence of coercivity:  $\text{Fe}_{65}\text{B}_{15}\text{Si}_{15}\text{C}_5$  (a);  $(\text{Co}_{1-x}\text{Mn}_x)_{75}\text{Si}_{10}\text{B}_{15}$  with  $x = 0.11$  (b);  $x = 0.09$  (c); and stress dependence of the magnetostriction constant for  $x = 0.09$  (d). Reprinted with permission from [7], A. Zhukov, *J. Magn. Mater.* 242–245, 216 (2002). © 2002, Elsevier Science.

with tension in such microwires [56]. According to this method, the magnetostriction constant,  $\lambda_s$ , can be evaluated from the relation

$$\lambda_s = -(\mu_0 M_s^2/3)d(\chi_i^{-1})/d\sigma \quad (15)$$

where  $M_s$  is the saturation magnetization,  $\chi_i$  is the initial magnetic susceptibility, and  $\sigma$  is the applied tensile stress.

The dependence of  $\lambda_s(\sigma)$  for the samples with 0.09 is shown in Figure 14d. It should be noted that the observed evolutions have mostly an illustrative character, since the level of the magnetic response from a single microwire is quite small. The sample with  $x = 0.09$  exhibiting a positive magnetostriction constant shows also a decrease of the  $\lambda_s$  with  $\sigma$  and even changes its sign at certain  $\sigma$  (around 200 MPa).

The stress dependence of the magnetostriction constant,  $\lambda_s$  (Fig. 14d), allows one to ascribe positive values of the

order of  $10^{-7}$  for the magnetostriction constant in the sample with  $x \geq 0.09$ . Such as was found in other amorphous materials, the application of tensile stresses results in a decrease of the  $\lambda_s$  in the case of positive magnetostriction constant which even can change the sign of  $\lambda_s$  in the sample with  $x = 0.09$  when  $\sigma$  reaches some certain value (see Fig. 14d). In fact it was experimentally found in nearly zero magnetostrictive amorphous ribbons [58] that

$$\lambda(\sigma) = \lambda(0) - B\sigma \quad (16)$$

where  $\lambda(0)$  is the saturation magnetostriction constant without applied stresses and  $B$  is a positive coefficient of the order of  $10^{-10}$  (MPa) $^{-1}$ . For magnetostriction  $\lambda(0)$  of about  $1 \times 10^{-7}$  a stress of around  $10^3$  MPa needs to be applied to reach compensation of magnetostriction [56, 58, 59]. In fact, internal stresses induced during the preparation can reach values which indicate that high quenched-in internal stresses seem to be able to change effectively the value of the magnetostriction constant [60].

The small angle magnetization rotation method [61] also has been successfully applied to estimate the magnetostriction constant of Co-rich amorphous microwires exhibiting inclined hysteresis loops (i.e., with the magnetization rotation mechanism of the magnetization reversal) [60].

The microwires were submitted to current annealing at different annealing times,  $t_{\text{ann}}$ . The evolution of  $\lambda_s$  with the annealing time (the current,  $i$ , as parameter) for selected glass-coated amorphous microwires is presented in Figure 15a–d. As can be observed, all samples exhibit negative  $\lambda_s$  ranging between  $-0.9 \times 10^{-6}$  and  $-0.3 \times 10^{-6}$ . Under the effect of Joule heating, increasing both  $t_{\text{ann}}$  or  $i$ ,  $\lambda_s$  tends to increase approaching zero (see Fig. 15a–d). The general tendency of increasing of  $\lambda_s$  with  $t_{\text{ann}}$  and  $i$  should be attributed to the relaxation of the internal stresses during the annealing and consequently [see Eq. (22)] with the stress dependence of the  $\lambda_s$ . As has been mentioned, strong internal stresses have been predicted in glass-coated microwires due to a significant difference between the thermal expansion coefficients of the metallic nucleus and the glass coating [7]. Therefore one can expect an increase of the magnetostriction constant after annealing.

Similarly to the magnetostrictive behavior widely reported [58, 59] for amorphous ribbons and conventional wires of similar compositions, rather low magnetostriction values exhibited by annealed microwire samples could be explained assuming the existence of two kind of short ordering, namely: an ordered highly anisotropic phase centered at Fe atoms with uniaxial shape and magnetic anisotropy and with positive magnetostriction, mainly due to anisotropic exchange mechanism, and a disordered phase at Co-rich atoms with negative magnetostriction. If we also assume that the positive magnetostriction phase (Fe atoms) undergoes a first order transformation from the uniaxial structural units (low temperature phase) toward a more symmetric and less anisotropic structural unit (high temperature phase), this allows us to explain the general behavior of macroscopic average magnetostriction,  $\lambda_s^{\text{av}}$ , of such Co-rich alloys. In fact, for pure Co the magnetostriction at room temperature is  $-4 \times 10^{-6}$  and evolves with the temperature as expected from the single ion model. Therefore, the changes

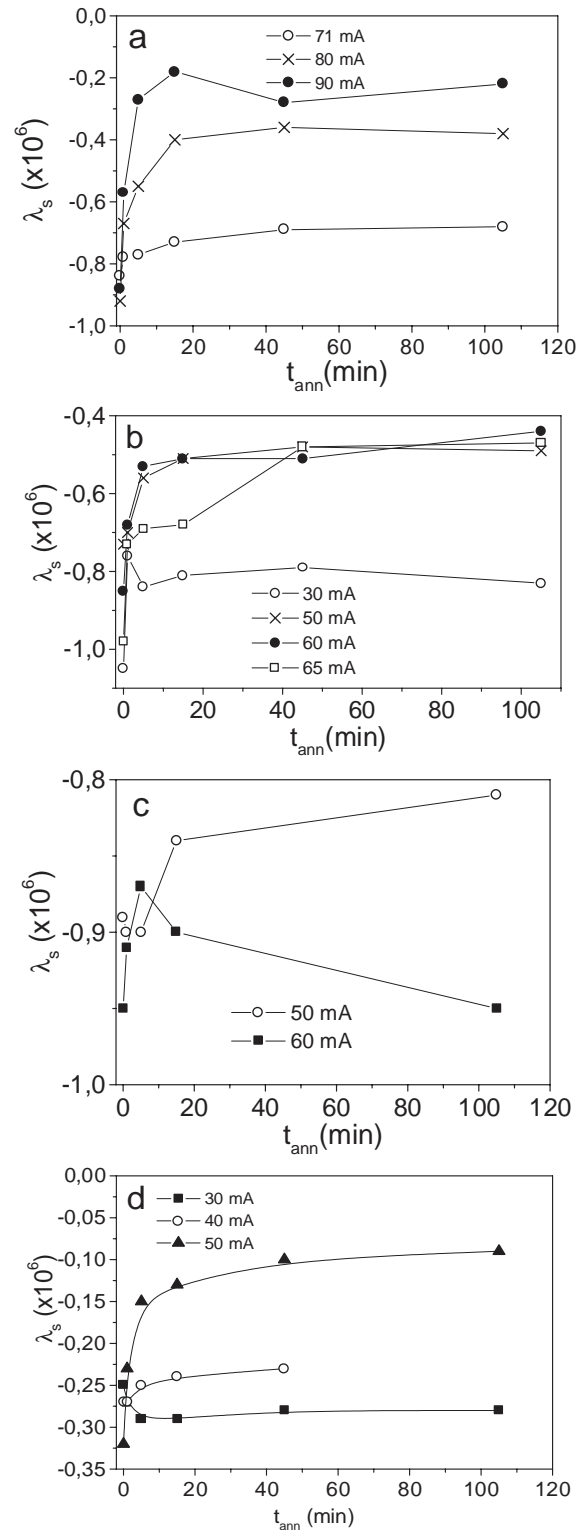


**Figure 15.**  $\lambda_s(t_{\text{ann}})$  dependences for glass-coated amorphous  $\text{Co}_{57}\text{Fe}_{6.1}\text{-Ni}_{10}\text{B}_{15.9}\text{Si}_{11}$  (a),  $\text{Co}_{67.5}\text{Fe}_4\text{Ni}_{1.5}\text{B}_{14}\text{Si}_{12}\text{Mo}_1$  (b),  $\text{Co}_{69.1}\text{Fe}_{3.2}\text{Ni}_{14.8}\text{Si}_{9.9}$  (c), and  $\text{Co}_{69.5}\text{Fe}_{3.9}\text{Ni}_{12.8}\text{Si}_{10.8}\text{Mo}_2$  (d) microwires. Reprinted with permission from [60], V. Zhukova et al., *J. Phys.* 34, L113 (2002). © 2002.

of  $\lambda_s^{av}$  with the current annealing treatment repeated in this work on glass-coated amorphous microwires are assumed to be a consequence of the atomic rearrangements of topological character associated with both structural and stress relaxation processes. These processes would produce relative changes of the two mentioned volume fractions, so affecting the  $\lambda_s^{av}$ . In this way some peculiarities observed in Figure 15b–d can be roughly understood. It is worth mentioning that the high value of the internal stresses of these glass-coated microwires allows the thermal treatments to be considered as a stress annealing and, consequently, they could develop an uniaxial magnetic anisotropy [37, 53], which should play an important role on the magnetostrictive behavior. Particularly, the induction of a strong magnetic anisotropy at low annealing temperature has been observed in CoMnSiB microwires under the effect of applied axial magnetic field. Such peculiar behavior was interpreted as a reinforcing effect of the mentioned high internal stresses during field annealing of Co-rich microwires [37].

As reported previously, the magnetostriction constant can be also estimated from the stress dependence of GMI (see Fig. 12 and its description in Section 3.1.3).

## 3.2. Nanocrystalline Microwires

### 3.2.1. Soft Nanocrystalline Microwires

Properties of as-prepared microwires of “finemet”-type compositions  $\text{Fe}_{73.4}\text{Cu}_1\text{Nb}_{3.1}\text{Si}_x\text{B}_{22.5-x}$  ( $x = 11.5, 13.5, \text{ and } 16.5$ ) significantly depend on their geometry [13, 62]. Hysteresis loops, of typically rectangular shape, have been observed in the as-prepared state. The coercivity of the sample  $\text{Fe}_{72.3}\text{Cu}_1\text{Nb}_{3.1}\text{Si}_{14.5}\text{B}_{9.1}$  strongly increases as the ratio  $\rho$  decreases. These results of  $H_c$  versus  $(d/D)$  could be understood taking into account that the strength of internal stresses acting in the metallic nucleus increases with  $\rho$  [39, 40, 63].

The typical dependence of the coercive field,  $H_c$ , of  $\text{Fe}_{71.8}\text{Cu}_{1.0}\text{Nb}_{3.1}\text{Si}_{15.0}\text{B}_{9.1}$  alloy on annealing temperature with the ratio  $\rho$  as parameter is presented in Figure 16 [13]. Generally, a decrease of  $H_c$  has been observed at  $T_{\text{ann}}$  below 400 °C. A weak local minimum of  $H_c$  has been observed at about 400–450 °C with the temperature of that minimum depending on both alloy composition and geometry. Such a decrease of  $H_c$  could be ascribed to the structural relaxation of the material remaining the amorphous character such as has been widely reported in metallic glass alloys. A small relative hardening (increase of coercivity) can be observed after annealing around 450–500 °C, which could be ascribed to the very beginning of the first stage of devitrification [9–13]. It is interesting to note that the sample’s geometry affects the value and the position of the local extremes on the  $H_c(T_{\text{ann}})$  dependence (see Fig. 16). A deeper softening (optimum softness) with a rather low value of  $H_c$  is obtained in samples treated at  $T_{\text{ann}} = 500\text{--}600$  °C. Such magnetic softening is related to the nanocrystallization, related to precipitation of fine grains (10–15 nm) of  $\alpha\text{-Fe}(\text{Si})$  phase within the amorphous matrix. Such interpretation has been confirmed by the X-ray diffraction studies of as-prepared and annealed at different temperatures samples [13, 14].

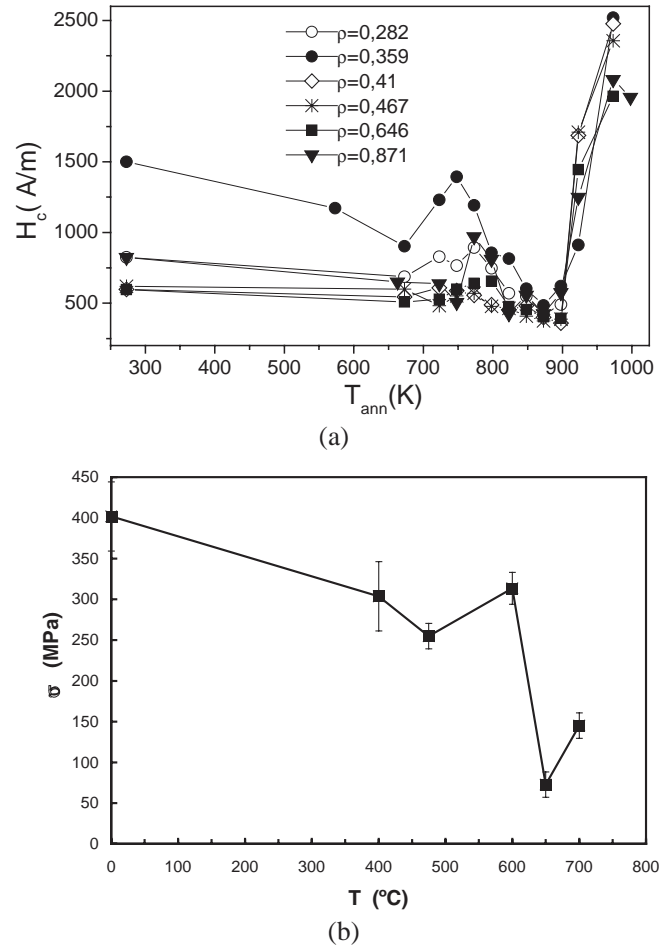


**Figure 16.** (a) Dependence of coercivity on the annealing temperature,  $T_{\text{ann}}$ , for  $\text{Fe}_{71.8}\text{Cu}_1\text{Nb}_{3.1}\text{Si}_{15}\text{B}_{9.1}$  with the ratio  $d/D$  ranging from 0.282 to 0.646. Reprinted with permission from [7], A. Zhukov *J. Magn. Magn. Mater.* 242–245, 216 (2002). © 2002, Elsevier Science. (b) Dependence of tensile yield on the annealing temperature in  $\text{Fe}_{71.8}\text{Cu}_1\text{Nb}_{3.1}\text{Si}_{15}\text{B}_{9.1}$  microwire. Reprinted with permission from [81], V. Zhukova et al., *J. Magn. Magn. Mater.* 249, 79 (2002). © 2002, Elsevier Science.

Excellent magnetic softness (coercivity of about 15 A/m) has been realized in  $\text{Fe}_{73.5}\text{Cu}_1\text{Nb}_3\text{Si}_x\text{B}_{22.5-x}$  microwires with  $x = 13.5$  [13, 14] at appropriate annealing conditions.

### 3.2.2. Semihard Magnetic Nanocrystalline Microwires

An abrupt increase of  $H_c$  is shown by the samples treated at  $T_{\text{ann}}$  above 600 °C, indicating the beginning of the precipitation of second crystalline phase—iron borides (with grain size larger than 50 nm). Such beginning of the increase of  $H_c$  varies depending mainly on sample composition as well as geometry. It must be noted that for the thickest glass coating the increase of  $H_c$  appears at lower temperature, which could be related to the fact that the internal stresses induce some ordering to hinder the crystallization. It is important that the hysteresis loop in certain microwire compositions remains roughly rectangular in the whole range of annealing temperatures for certain compositions (Fig. 17) [14]. Such

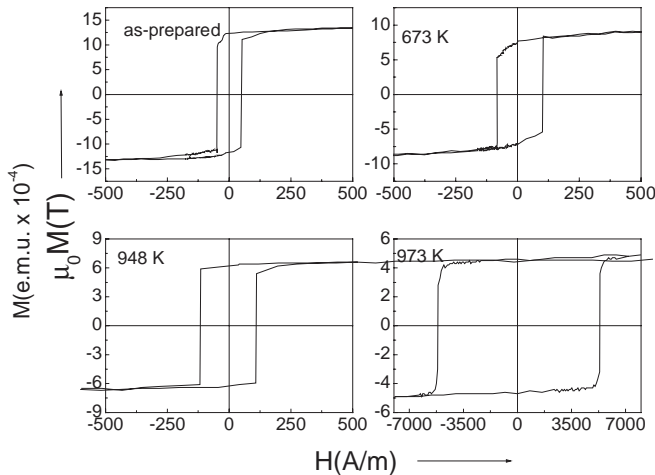


**Figure 17.** Hysteresis loop of  $\text{Fe}_{71.8}\text{Cu}_1\text{Nb}_{3.1}\text{Si}_{15}\text{B}_{9.1}$  in as-prepared and annealed at different temperature microwires (b). Reprinted with permission from [7], A. Zhukov, *J. Magn. Magn. Mater.* 242–245, 216 (2002). © 2002, Elsevier Science.

temperature dependence of the hysteresis loops permits one to tailor the coercivity of microwires with rectangular hysteresis loops in a wide range of coercivities. This fact is very important for some particular applications of glass-coated microwires (see Section 5).

The effect of annealing temperature on the coercivity,  $H_c$ , of the alloy  $\text{Fe}_{72.3}\text{Cu}_1\text{Nb}_{3.1}\text{Si}_{14.5}\text{B}_{9.1}$  with ratio  $\rho$  as parameter is shown in Figure 18. A sharp magnetic hardening (increase of coercivity) can be observed after annealing around 500–550 °C. It should be indicated that such maximum takes place at the same range of the annealing temperature as the first small increase of  $H_c$  in  $\text{Fe}_{73.4}\text{Cu}_1\text{Nb}_{3.1}\text{Si}_x\text{B}_{22.5-x}$  ( $x = 11.5$  and  $13.5$ ) related to the first recrystallization process (compare with Fig. 16a) [3, 11, 12, 62, 64].

This strong magnetic hardening is followed by new magnetic softening with an increase of  $T_{\text{ann}}$  above 550 °C and consequent new magnetic hardening at  $T_{\text{ann}} > 650$  °C which is accompanied by deterioration of mechanical properties.

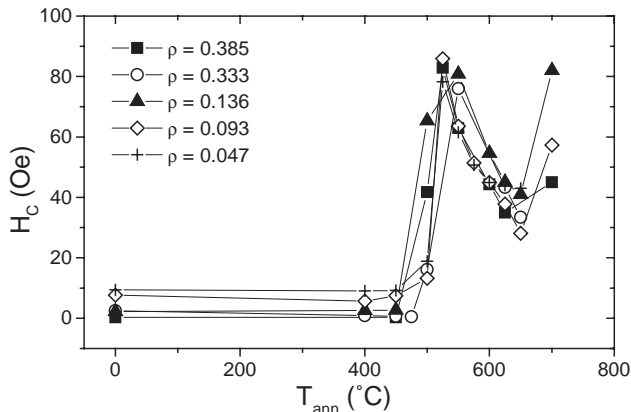


**Figure 18.** Coercivity dependence with the annealing temperature of  $\text{Fe}_{72.3}\text{Cu}_1\text{Nb}_{3.1}\text{Si}_{14.5}\text{B}_{9.1}$  microwire. Reprinted with permission from [62], J. González et al., *IEEE Trans. Magn.* 36, 3015 (2000). © 2000, IEEE.

In the case of  $\text{Fe}_{73.4}\text{Cu}_1\text{Nb}_{3.1}\text{Si}_{13.4}\text{B}_{9.1}$  samples such strong magnetic hardening is not observed (see Fig. 16).

X-ray analysis of  $\text{Fe}_{72.3}\text{Cu}_1\text{Nb}_{3.1}\text{Si}_{14.5}\text{B}_{9.1}$  does not detect a presence of crystalline phases in as-prepared state as well as after annealing at 550 °C. On the other hand, transmission electron microscopy (TEM) diagrams of the sample annealed at 550 °C permit one to detect a small amount of fine grains of  $\alpha$ -Fe,  $\gamma$ -Fe, and  $\alpha$ -Fe(Si) [62]. The TEM image presented in Figure 19 shows that the average grain size of such crystallites is around 20–70 nm in annealed sample at 550 °C.

Observed structural features permit one to correlate observed magnetic hardening with precipitation of fine crystallites. Such a difference in magnetic behavior with conventional *finemet*-type microwires can be attributed to different alloy compositions as well as to high internal stresses. It is well known that the best magnetic softness is achieved when the nanocrystalline structure consisting of small  $\alpha$ -Fe(Si) grains and amorphous matrix has a vanishing magnetostriction constant. It is possible that even a small change of the alloy composition does not permit one to achieve such a vanishing magnetostriction constant.

On the other hand, strong internal stresses due to glass coating can result in a change of structure of the precipitating fine grains. Thus, strong internal stresses (about  $10^3$  MPa or even more) are mainly induced by the difference in the thermal expansion coefficients of the glass and the metallic nucleus. It is well known that internal strains of different nature can be the origin of martensite-type transformation in alloys of Fe. Probably, the strong internal stresses induce a precipitation of the  $\gamma$ -Fe fine grains instead or apart from  $\alpha$ -Fe(Si) grains during the first stage of the crystallization process. Particularly, the presence of crystalline  $\gamma$ -Fe could be the reason for the observed magnetic hardening [62]. As a consequence, the origin of such strong magnetic hardening at low annealing temperatures without deterioration of mechanical properties could be ascribed to some peculiarities of the first recrystallization process under the effect of strong internal stresses induced by glass coating and differences in the alloy composition.

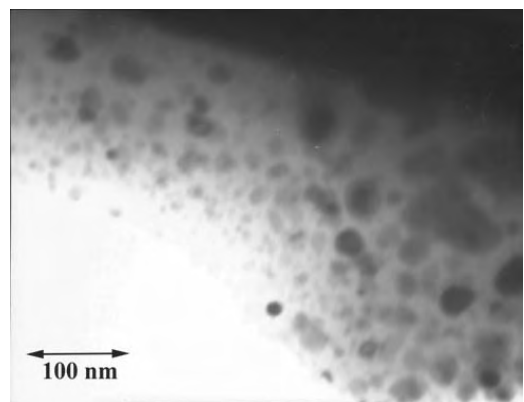


**Figure 19.** TEM diagram of  $\text{Fe}_{72.3}\text{Cu}_1\text{Nb}_{3.1}\text{Si}_{14.5}\text{B}_{9.1}$  microwire annealed at 550 °C. Reprinted with permission from [62], J. González, *IEEE Trans. Magn.* 36, 3015 (2000). © 2000, IEEE.



### 3.3. Granular Glass-Coated Microwires

#### 3.3.1. Structure and Phase Composition

Granular systems formed by immiscible elements (Co, Fe, Ni)–(Cu, Pt, Au, Ag) have been recently introduced [21, 65–67]. Such immiscible alloys exhibit unusual magnetic properties such as the GMR effect related to mixed ferromagnetic–paramagnetic microstructure and scattering of the electrons on grain boundaries between these two phases. A rapid quenching technique such as melt spinning has been employed recently for fabrication of Co–Cu ribbons [68]. The high quenching rate characteristic of the melt spinning method has been used for fabrication of metastable crystalline materials when the crystalline phases, stable at high temperature, can be quenched-in at room temperature. In this case the GMR and enhanced coercivity were obtained generally after recrystallization of such metastable phases.

Recently, the Taylor–Ulitsky technique has also been employed to obtain granular glass-coated microwires (km long) [21, 69] from immiscible elements. Such granular structure has been achieved mainly by decomposition of metastable crystalline phases. A high quenching rate is also useful for fabrication of metastable crystalline materials when the crystalline phases, stable at high temperature, can be quenched-in at room temperature.

Figure 20 shows the X-ray diffraction (XRD) analyses for the as-prepared  $\text{Co}_x\text{Cu}_{100-x}$  microwires, which confirms the presence of a single phase for  $x = 10$  with a lattice parameter  $a = 0.36$  nm, while in the other compositions, with  $x > 10\%$ , two phases were detected. It should be mentioned that  $\text{Co}_x\text{Cu}_{100-x}$  alloy ribbons obtained by rapid solidification were characterized by X-ray diffraction by various authors [67, 70, 71]. It was found by the XRD method that, in the as-quenched  $\text{Co}_x\text{Cu}_{100-x}$  ribbons, single phase face-centered cubic (fcc) peaks appear for  $x < 20\%$  [67] (sometimes only for  $< 10\%$  [72]) and  $x > 35\%$ . Since the lattice parameter was larger than for pure Co ( $a = 0.35447$  nm) and smaller than that of pure Cu ( $a = 0.3615$  nm), the same dissolution of Co atoms in the Cu matrix has been proposed. In any case, fcc Co particles were also reported in [72].

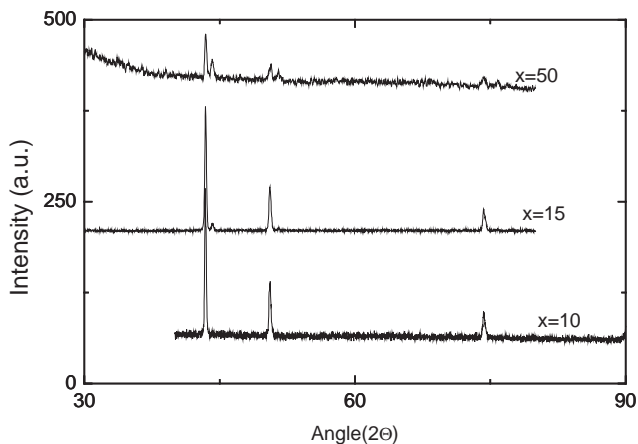


**Figure 20.** X-ray diffraction pattern of  $\text{Co}_x\text{Cu}_{100-x}$  microwires with  $x = 10, 15,$  and  $50\%$ . Reprinted with permission from [21], A. Zhukov et al., *J. Appl Phys.* 85, 4482 (1999). © 1999, American Institute of Physics.

The experimental data on X-ray diffraction of microwires from immiscible elements are generally in agreement with those previously reported for ribbons with small Co concentrations, when single phase peaks have been observed at  $x < 10\%$ . Indeed, the presence of two phases can be deduced from careful analysis of the maxima for  $x > 10\%$ , with interatomic spacings of 0.209 nm (Cu) and 0.206 nm (Co). Nevertheless, it is important to mention that the coexistence of two phases is found even for  $x > 35\%$ .

Like in  $\text{Co}_x\text{Cu}_{100-x}$  microwires with  $x > 10\%$ , the XRD analyses for the as-prepared Cu–Fe microwires showed two maxima in the diffraction peak with the lowest diffraction angle corresponding to the Cu and the body-centered cubic  $\alpha$ -Fe phases.

In some cases this granular structure is metastable at room temperature and the consequent heat treatment results in the recrystallization of this structure with the formation of stable phases. At certain conditions of such heat treatment this new granular structure can exhibit interesting magnetic and transport properties.

As an example, Figure 21a–c shows the X-ray diffraction patterns for the  $\text{Co}_{29}\text{Ni}_{25}\text{Cu}_{45}\text{Mn}_1$  sample, in its as-prepared state and after thermal treatment at two different temperatures  $T_{\text{ann}}$ . In the as-prepared microwire, quenched from a high temperature, only a single phase, with a lattice parameter  $a = 0.3573$  nm, was found (Fig. 21a). When the sample was heated at high temperatures, this metastable phase started to decompose. This can be seen in the sample treated at 973 K, where the segregation mechanism is

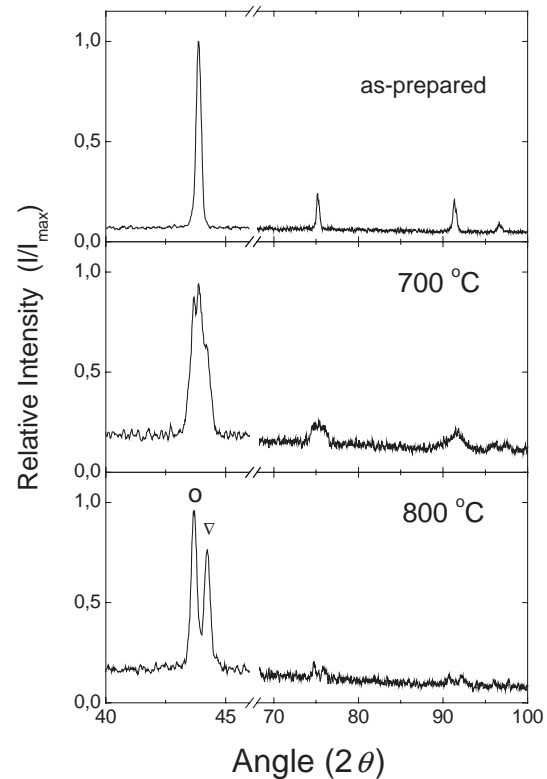


**Figure 21.** X-ray scan of as-prepared and annealed  $\text{Co}_{29}\text{Ni}_{25}\text{Cu}_{45}\text{Mn}_1$  microwires. Reprinted with permission from [21], A. Zhukov et al., *J. Appl Phys.* 85, 4482 (1999). © 1999, American Institute of Physics.

not yet complete (Fig. 21b). After annealing at 1073 K the sample shows the equilibrium phases, consisting of a copper-rich matrix ( $a = 0.3591$  nm) with Co-rich particles ( $a = 0.3545$  nm) (Fig. 21c) [68, 69]. Annealing at higher temperature results in a very marked embrittlement of the glass coating. For alloys in the Co–Ni–Cu system containing more than 20% Ni a continuous series of (fcc) solid solutions is found to be stable at high temperatures [73]. When the alloy is quenched from the melt during the production of the microwire, a metastable cubic phase is found at room temperature. On heat treating this material, the segregation takes place and the metastable phase starts to decompose into a paramagnetic Cu-rich phase with a larger lattice parameter than the precursor phase, and a fine grained Co-rich phase with a smaller lattice parameter.

It is well known that the presence of the glass coating introduces strong internal stresses inside the metallic nucleus due to the difference in the thermal expansion coefficients of metallic nucleus and glass coating [5, 38, 39]. The strength of such internal stresses depends on the metallic nucleus diameter as well as on the glass-coating thickness [38, 39]. Therefore, it is expected that the geometry affects the structural and magnetic features of glass-coated microwires.

X-ray diffraction patterns for the as-prepared  $\text{Co}_{20}\text{Cu}_{80}$  microwires with different values of the  $\rho$  show peaks corresponding to two crystalline phases. Figure 22 shows these XRD patterns for the three microwires in this system with different values of  $\rho$ . The diffraction peak with the lowest diffraction angle corresponds to the Cu matrix with an interatomic spacing,  $d$ , of 0.209 nm. A detailed examination of

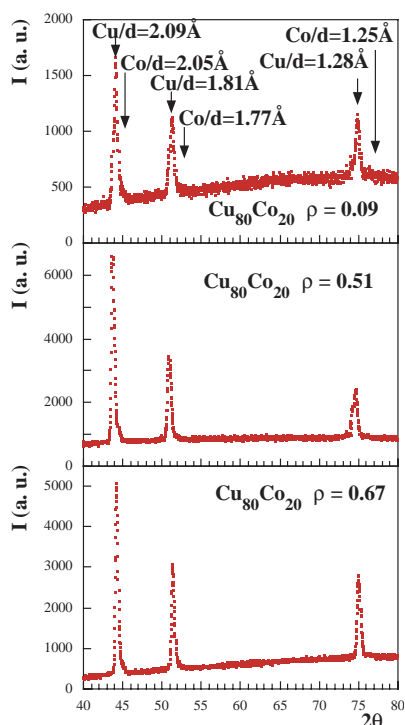


**Figure 22.** X-ray scan of  $\text{Co}_{20}\text{Cu}_{80}$  microwires with different ratios  $\rho$ . Reprinted with permission from [72], J. González et al. *J. Magn. Magn. Mater.* 221, 196 (2000). © 2000, Elsevier Science.

this peak allows the detection of a second small and broad maximum near this first peak which could be attributed to Co crystallites embedded in the Cu matrix. It can be observed that the higher the value of  $\rho$ , the more intense this second peak. The observed second crystallization peak corresponds to fcc metastable Co, as has been previously observed in ribbons [67, 70, 71].

Similar behavior in the XRD patterns was observed for microwires of composition  $\text{Co}_{19}\text{Cu}_{80}\text{Ni}_1$  with different  $\rho$  values (see Fig. 23). Inside the diffraction peak with the lowest diffraction angle two maxima were detected: the first one can be attributed to an overlapping of two peaks corresponding to interatomic spacings of 0.209 nm (Cu) and 0.208 nm ( $\text{Cu}_{3.8}\text{Ni}$ ) (the technique can hardly resolve these differences) and the second one corresponding to an interatomic spacing of 0.205 nm (Co) [74]. Figure 23 shows this first peak for the three values of the  $\rho$  parameter, which indicates its sensitivity to the geometry. This peak,

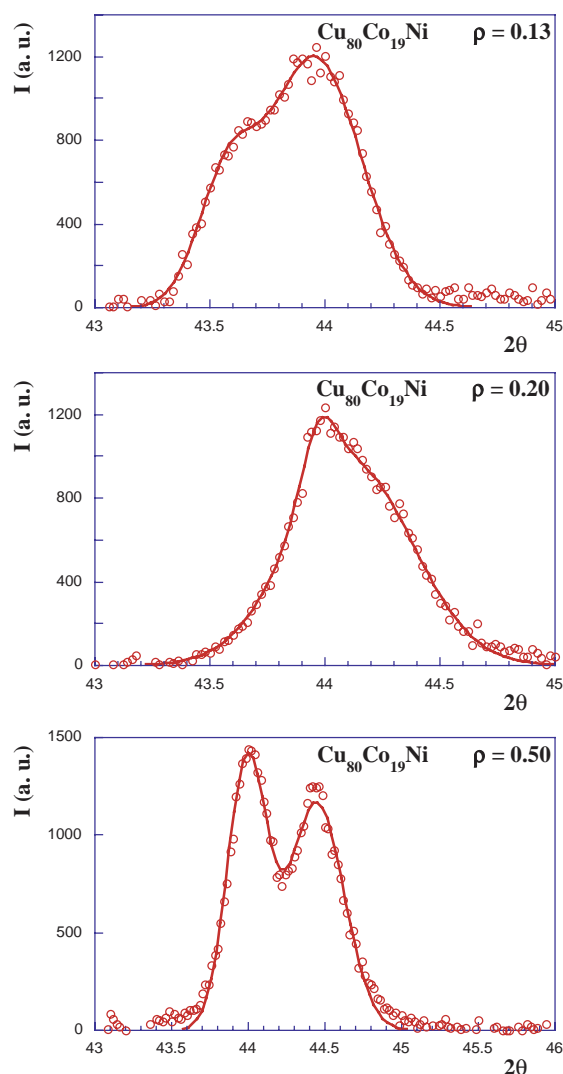


**Figure 23.** First crystalline peak and the corresponding fittings to a sum of two Gaussian functions for  $\text{Co}_{19}\text{Ni}_1\text{Cu}_{80}$  microwires with different ratios  $\rho$ . Reprinted with permission from [72], J. González et al. *J. Magn. Magn. Mater.* 221, 196 (2000). © 2000, Elsevier Science.



corresponding to the  $\text{Cu}_{3.8}\text{Ni}$  new phase in these samples, is accompanied by the presence of new peaks juxtaposed to the 0.181 and 0.128 nm (it is very clear in this last case) Cu spacings appearing in Figure 22 for the  $\text{Co}_{20}\text{Cu}_{80}$  system.

The proportions of each phase were calculated, for each sample, from the relative area under all the peaks measured over all the  $2\theta$  region of measurement. When relative peaks overlapped (which occurred in most cases), the experimental signal was fitted to the addition of two Gaussian functions in order to obtain the characterizing values of the position of the maximum and the width of the peak. Thus, the Co or Fe phase content in each sample was calculated as

$$\%_{\text{Co, Fe}} = \frac{\int_{40}^{80} I_{\text{corr Co, Fe}} d(2\theta)}{\int_{40}^{80} I_{\text{corr}} d(2\theta)} \quad (17)$$

where  $I_{\text{corr}}$  denotes the total measured diffracted intensity corrected for background and  $I_{\text{corr Co, Fe}}$  is the diffracted intensity corrected for background, corresponding to the peaks associated with Co or Fe phases.

The dependence of the Co particle content (in percentage) on the  $\rho$  parameter for  $\text{Co}_{19}\text{Cu}_{80}\text{Ni}_1$  and  $\text{Co}_{20}\text{Cu}_{80}$  microwires is shown in Figure 24. An increase of the Co-phase content with  $\rho$  can be observed in the  $\text{Co}_{20}\text{Cu}_{80}$  microwires, particularly at high values of  $\rho$ . This effect should be related to the strength and complexity of the internal stresses in the metallic core, arising from the insulating glass coating. It is reasonable to assume that these internal stresses increase as the  $\rho$  parameter decreases [38, 39] and, consequently, they could hinder the segregation of the magnetic Co phase. Surprisingly the  $\text{Co}_{19}\text{Cu}_{80}\text{Ni}_1$  alloy does not show such continuous behavior and the Co content is much higher than in CuCo microwires: this is evident in the raw diffraction patterns where the peak corresponding to the Co phase is much more intense.

Figure 25 shows the variations in the mean diameter  $\Delta$  of Cu and Co particles or grains as a function of the parameter  $\rho$  for  $\text{Co}_{20}\text{Cu}_{80}$  and  $\text{Co}_{19}\text{Cu}_{80}\text{Ni}_1$  alloys. From these results the dependence of the grain size seems to be quite insensitive to  $\rho$  in both alloys, although the presence of Ni increases significantly the size of such Co and Cu particles. The last two cases show that the presence of small amounts

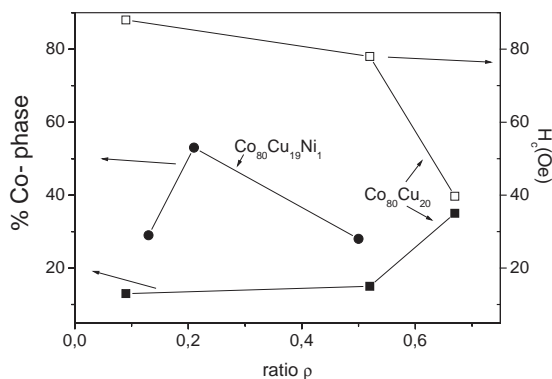


**Figure 24.** Effect of geometry on Co-phase content and coercivity in  $\text{Co}_{20}\text{Cu}_{80}$  and  $\text{Co}_{19}\text{Ni}_1\text{Cu}_{80}$  microwires. Reprinted with permission from [72], J. González et al., *J. Magn. Magn. Mater.* 221, 196 (2000). © 2000, Elsevier Science.

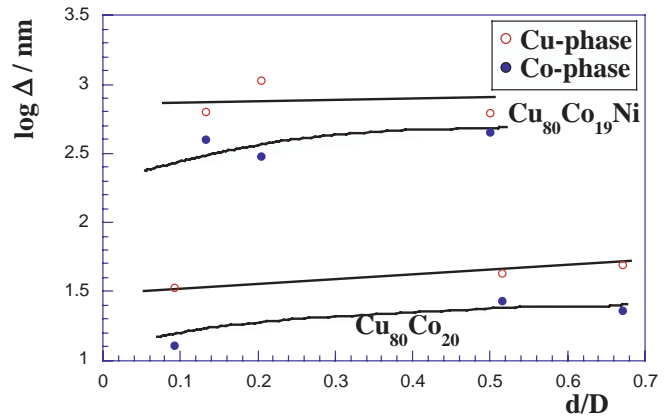


**Figure 25.** Effect of geometry on average grain size of  $\text{Co}_{20}\text{Cu}_{80}$  and  $\text{Co}_{19}\text{Ni}_1\text{Cu}_{80}$  microwires. Reprinted with permission from [72], J. González et al., *J. Magn. Magn. Mater.* 221, 196 (2000). © 2000, Elsevier Science.

of Ni atoms drastically changes the structural characteristics of these alloys.

The overview of Figures 20–25 indicates the sensitivity of the structure either to the composition (substitution of one atom of Co by Ni) or to the geometry (parameter  $\rho$ ) or both.

It must be pointed out here that the results for the  $\rho$  dependence of the Cu and Fe grain sizes and for the amount of Fe phase for the two different CuFe compositions is consistent with the fact that the different compositions show the same variations.

### 3.3.2. Effect of Composition and Geometry on Magnetic Behavior

The hysteresis loops, at room temperature, for three different compositions in the series  $\text{Co}_x\text{Cu}_{100-x}$  are presented in Figure 26. As can be observed, in as-prepared samples the saturation magnetization decreases and both the magnetic anisotropy field and the coercive field increase, as the Co content increases. As can be expected, the high saturation magnetic field of the samples with small Co content could be explained considering that Co precipitates behave as small superparamagnetic particles or as isolated spherical ferromagnetic particles. In the second case the magnetic

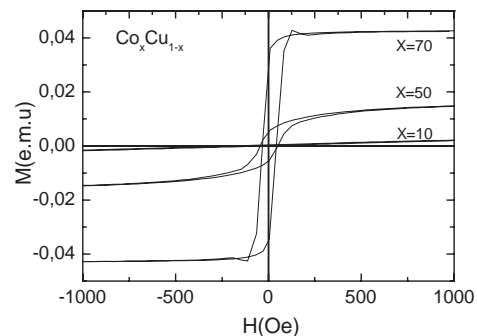


**Figure 26.** Hysteresis loops of  $\text{Co}_x\text{Cu}_{100-x}$  microwires. Reprinted with permission from [21], A. Zhukov et al., *J. Appl. Phys.* 85, 4482 (1999). © 1999, American Institute of Physics.

anisotropy field can be related to the demagnetizing factor of such particles, being in good accordance with experimental data for  $\text{Co}_{20}\text{Cu}_{80}$  particles ( $H_k = \mu_o M_s/3$ ). It should be also noted that the magnetization behavior of ribbons of similar composition is still a topic of discussion and sometimes it is interpreted as being superparamagnetic [67] and sometimes not [65].

It may be argued that the sample with  $x = 50$  is not entirely superparamagnetic since its coercivity as well as the remanence shows nonzero values being, however, relatively small. The variations of the magnetization with the Co content can be explained on the basis of two contributions, namely: one coming from the superparamagnetic particles and other from the ferromagnetic contribution which originates from large Co grains or agglomerates of smaller Co particles [65–69]. The first contribution is negligible for a large Co content (that is, the  $x = 70$  sample). Besides the large ferromagnetic grains, a source of the coercivity can also be, in the case of  $x = 10$ , the interactions between superparamagnetic particles.

The shape of the hysteresis loop seems to be rather insensitive to the  $\rho$  parameter: the magnetic anisotropy field remains almost unmodified by changes of the  $\rho$  parameter. In contrast, considerable changes in the coercive field have been detected when the  $\rho$  parameter changes. These changes are shown in Figure 24, together with changes of average grain size with  $\rho$ . Certain correlations, such as decrease of coercivity with increase of Co phase (Fig. 24) content and grain size (see Fig. 25), can be outlined.

The hysteresis loops of as-prepared  $\text{Fe}_{30}\text{Cu}_{70}$  samples for two different  $\rho$  values can be seen in Figure 27. The reduction of the  $\rho$  parameter leads to important changes in the hysteresis behavior. In fact, for the lower value of  $\rho = 0.3$  the hysteresis loop may indicate the presence of two magnetic phases with two different values of anisotropy field, one high and one low (see Fig. 27). On the other, hand, a single magnetic phase with enhanced anisotropy field can be deduced from the magnetization curve of the sample with the larger value of  $\rho = 0.6$  [72]. The coercive field is smaller in the sample with the lower  $\rho$ . As in Co–Cu microwires, an effect of internal stresses on the crystallization process can be deduced.

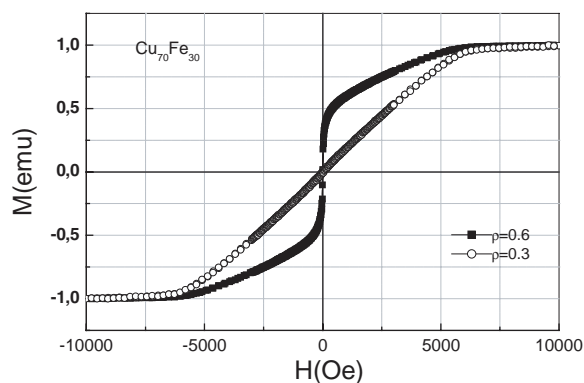


**Figure 27.** Hysteresis loop of  $\text{Fe}_{30}\text{Cu}_{70}$  microwires with different ratios. Reprinted with permission from [72], J. González et al., *J. Magn. Magn. Mater.* 221, 196 (2000). © 2000, Elsevier Science.

Comparison with structural analysis indicates that for  $\text{Fe}_{30}\text{Cu}_{70}$  microwires,  $\rho = 0.3$ , where the coexistence of two magnetic phases is suggested, corresponds to a maximum in the observed content of the Fe phase [74].

### 3.3.3. Effect of the Thermal Treatment on Magnetic Properties

In order to achieve higher coercivity, the different families of microwires were submitted to thermal treatments (up to 800 °C, for 1 hour). After the treatments, the magnetic properties of some samples underwent significant changes. Comparative results on the effects of annealing temperature,  $T_{\text{ann}}$ , on coercivity of all studied microwires are shown in Figure 28. The annealing temperature dependence of the coercivity can be explained qualitatively, by taking into account the structure of the as-prepared samples. It is evident that for the samples having a two-phase structure in the as-prepared state, no significant changes of the magnetic properties were observed. But for single phase as-cast microwires ( $\text{Co}_{10}\text{Cu}_{90}$  and  $\text{Co}_{29}\text{Ni}_{25}\text{Cu}_{45}\text{Mn}_1$ ) a substantial increase of the coercivity is observed after annealing above 500 °C [21]. Therefore, a precipitation of Co or Ni crystallites from the metastable Cu-rich solid solution can be responsible for the enhancement of the coercivity upon annealing [67]. The solubility of Co and Ni in Cu decreases as the temperature decreases and, at room temperature, it is quite small (less than 0.1% for Co). Consequently, these elements are almost immiscible at room temperature. Therefore, a single phase solid solution is unstable at room temperature and the annealing results in its decomposition.

A magnetic hardening (up to 200 Oe) is observed for the  $\text{Cu}_{90}\text{Co}_{10}$  microwires after annealing temperatures of around 500 °C. Most significant magnetic hardening was observed for the  $\text{Co}_{29}\text{Ni}_{25}\text{Cu}_{45}\text{Mn}_1$  microwire. The room temperature hysteresis loop of Co–Ni–Cu–Mn microwires is presented, as an example, in Figure 29a, after annealing for one hour at various temperatures. The variation of the coercivity with the annealing temperature for the different microwires was obtained from such curves. The as-prepared  $\text{Co}_{29}\text{Ni}_{25}\text{Cu}_{45}\text{Mn}_1$  sample shows a relatively low coercivity (50–100 Oe). When raising the annealing temperature to 700 °C, a strong increase in  $H_c$  is obtained, reaching

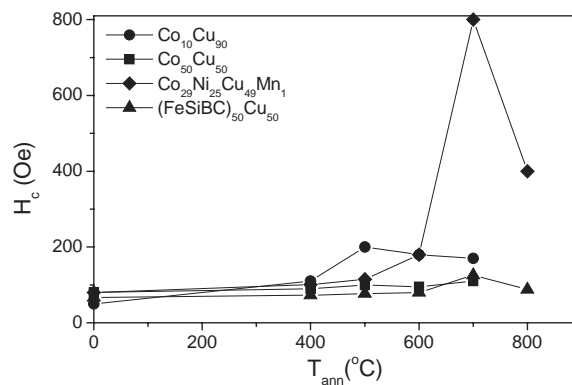


**Figure 28.** Effect of annealing temperature on coercivity of different microwires. Reprinted with permission from [21], A. Zhukov et al., *J. Appl. Phys.* 85, 4482 (1999). © 1999, American Institute of Physics.

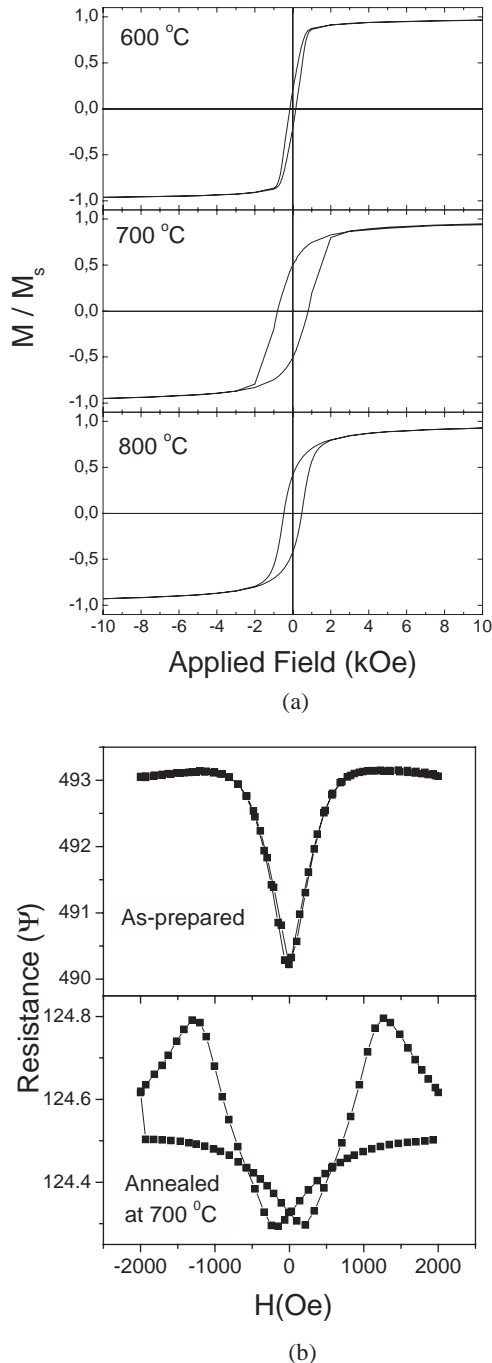


**Figure 29.** Hysteresis loops of  $\text{Co}_{29}\text{Ni}_{25}\text{Mn}_1\text{Cu}_{45}$  microwires measured at different annealing temperatures (a) and magnetoresistance (b) measured at 100 K in as-prepared and annealed at 700 °C microwires. Reprinted with permission from [72], J. González, et al., *J. Magn. Magn. Mater.* 221, 196 (2000). © 2000, Elsevier Science.

the maximum value of 700 Oe for the  $\text{Co}_{29}\text{Ni}_{25}\text{Cu}_{45}\text{Mn}_1$  microwire. A further increase of the annealing temperature results in a decrease of the coercivity. The largest reduced remanence ratio  $M_r/M_s = 0.5$  is also found after annealing at 700 °C and the estimated saturation magnetization for this sample is about 3.6 kG. As has been mentioned previously, the structure of these annealed samples consists

of a paramagnetic Cu-rich phase and a fine grained ferromagnetic Co phase; in this stage the coercivity increases quickly. Increasing the annealing temperature further, the equilibrium of phases is reached more rapidly, the grains start to grow, and the coercivity decreases. These results are in agreement with the magnetic hardening in bulk Co–Ni–Cu permanent magnet alloys, and the maximum value of the coercivity obtained after the annealing at 700 °C for one hour agrees with that previously reported [73].

Magnetoresistance (MR), up to about 8% has been recently found in granular Fe, Ni, Co-rich microwires [75, 76]. This MR correlates quite well with the structure and the magnetization curves. Thus, the micro-X-ray absorption near edge structure (micro-XANES) spectroscopy reflects that the MR is related to fcc small grains of Fe–Ni ( $\gamma_1$  phase) embedded in fcc Cu ( $\gamma_2$  phase). By the micro-XANES method it was shown that Fe atoms remain in the fcc  $\gamma_1$  phase even after the annealing. These data are consistent with the phase diagram of Fe–Ni–Cu alloys and with the similar results on the fcc small grain Co in Co–Cu and/or Co–Ni–Cu microwires.

In the case of Co–Ni–Cu–Mn microwires field dependence of MR is quite different for the as-prepared and heat treated samples, reflecting also the difference of their structure and magnetization curves (see Figs. 21, 29a). Only small hysteresis correlated with low coercivity has been observed in as-prepared sample, while significant hysteresis with the MR maximum at around  $\pm 1200$  Oe is observed in the sample annealed at 700 °C. The relative change of the resistance under magnetic field in Co–Ni–Cu–Mn microwires is around 4% (Fig. 29b).

#### 4. MECHANICAL PROPERTIES

Most early reports on glass-coated microwires were devoted to their mechanical properties [77–80]. Thus, the effect of annealing and crystallization on tensile strength and Young modulus was studied in amorphous Fe-rich and stainless steel microwires produced by the Taylor–Ulitsky technique [78, 79]. High tensile strength (around 250 kg/mm<sup>2</sup>) was observed in amorphous  $\text{Fe}_{80}\text{P}_{16}\text{C}_3\text{B}_1$  microwires as compared with the crystalline microwires (around 130 kg/mm<sup>2</sup>). Such tensile strength is found to decrease, increasing the metallic nucleus diameter. This tendency has been attributed to the higher cooling rate with decreasing metallic nucleus diameter. On the other hand, the Young modulus of amorphous samples (8000 kg/mm<sup>2</sup>) is found to be much lower than that of crystalline (13,000 kg/mm<sup>2</sup>) samples of the same composition. Fracture surfaces of the amorphous microwires consist of a smooth region produced by shearing and a vein pattern [79]. It was observed later that additions of Si, Co, or Cr result in increasing averaged tensile strength [80].

Recently interest in studies of mechanical properties has been renewed mostly due to the promising technological applications of glass-coated microwires. In this way, tensile strength and fracture character have been recently studied in CoMnSiB microwires [53]. A wide number of samples of the CoMnSiB series have been studied and the average load for fracture has been found to range between  $20 \pm 3$  g, with a maximum of 30 g and a minimum of 15 g. The tensile strength is then  $624 \pm 94$  MPa, with maximum and minimum

values of 936 and 468 MPa, respectively. The tensile strength in the amorphous state seems to be due to the metallic nucleus of the microwire. The glass coating does not seem to contribute significantly in resistance to fracture. The glass around the point of fracture breaks, probably because of the sound wave produced by the rupture or the metallic nucleus, which is then visible.

Moreover, samples with higher tensile strength seem to break in a slightly different mode than the ones breaking under lower stress. Thus sometimes the fracture plane is basically perpendicular to the axis of the microwire. On the other hand, another group of samples broken under stresses over the average show a more complex situation. These samples show some structure in the surface of the metallic nucleus of the microwire that could have improved the adhesion of the metallic nucleus to the coating and increased strength slightly.

An interesting correlation of mechanical and magnetic properties has been observed in *finemet*-type microwires during the devitrification [81]. As mentioned previously, annealing of initially amorphous  $\text{Fe}_{73.4}\text{Cu}_1\text{Nb}_{3.1}\text{Si}_{13.4}\text{B}_{9.1}$  microwires results in the two-step crystallization process. First fine  $\alpha$ -Fe(Si) nanocrystals of grain size around 10 nm have been precipitated at temperatures around 550–600 °C. At temperatures above 600 °C, the beginning of the precipitation of iron borides (with grain size larger than 50 nm) has been found [81].

Such as described in Section 3.2 typically a decrease of coercivity has been observed at annealing temperatures below 650 °C with two minimums of coercivity,  $H_c$ , at about 400–450 and at 550–650 °C. Such soft magnetic behavior has been ascribed to the first crystallization process leading to the precipitation of fine nanocrystals  $\alpha$ -Fe(Si) of grain size around 10 nm with 70–80% of relative volume, as has been widely reported for *finemet* ribbons (see for example [9–12, 14]). An abrupt increase of the coercivity is shown by the samples treated at temperature above 600 °C. The beginning of such an increase should be connected to the precipitation of iron borides (with grain size larger than 50 nm) which implies a magnetic hardening character.

Tensile yield,  $\sigma_y$ , has been measured for samples annealed at different temperatures. These results are presented in Figure 16b. Maximum  $\sigma_y$  was found for the as-fabricated sample (402 MPa). Then, a certain correlation can be outlined with respect to the dependence of coercivity on annealing temperature. Like in the case of coercivity, tensile yield,  $\sigma_y$ , decreases with  $T_{\text{ann}}$  with a small local minimum around  $T_{\text{ann}} = 450$  °C. Some increase of  $\sigma_y$  has been observed at  $T_{\text{ann}} = 575$  °C. Finally strong deterioration of the tensile yield has been observed at  $T_{\text{ann}} > 650$  °C and a small increase at  $T_{\text{ann}} = 700$  °C. The samples annealed at the two highest temperatures were extremely brittle. The  $\sigma_y$  results in Figure 16b for these types of microwires correspond only to the maximum measurable value. In most opportunities, samples would fracture even under very careful handling.

The character of the sample fracture has also been studied for the samples annealed at a few annealing temperatures by means of scanning electron microscopy. The annealing does not deteriorate significantly the glass coating as well as the metallic nucleus. The fracture character is complex.

The metallic nucleus seems to be responsible for the tensile yield, with the possible contribution of plasticity. It is possible that the thermal treatment deteriorates the glass-coating interface due to the difference in thermal expansion coefficients, having a slight effect on the tensile yield.

For the annealing temperatures higher than 600 °C, the character of the fracture is different. If the metal core is now brittle, the glass coating can be responsible for the sample fracture and the sample breaks immediately after the coating itself.

The correlation of the mechanical properties with magnetic behavior is to be related to structural changes introduced by the annealing. The precipitation of the second crystalline phase leads to a completely crystalline structure, introducing strong internal stresses and change in the character of the chemical bonding. This crystallization process makes the sample brittle [9–12].

## 5. APPLICATIONS

The latest advances in magnetic materials are based on the miniaturization of modern magnetic materials. In this sense tiny metallic wires (of the order of 3 to 30  $\mu\text{m}$  in diameter) covered by an insulating glass coating are quite suitable for the sensor applications. Such wires possess a number of excellent magnetic properties such as magnetic bistability with the extended range of the switching fields, enhanced magnetic permeability, GMI effect, and high stress sensitivity of the magnetic parameters (switching field, GMI effect, magnetic permeability, etc.), which can be tailored by varying the metallic alloy composition, sample geometry (metallic nucleus diameter and glass coating thickness), and conditions of heat treatment. Several examples of applications of tiny glass-coated microwires will be reviewed.

A magnetoelastic sensor of the level of liquid can be designed using the very sensible stress dependence of the hysteresis loop and particularly of the coercivity in nearly zero magnetostriction  $\text{CoMnSiB}$  microwires (see Fig. 14c). Such a sensor essentially consists of a piece of  $(\text{Co}_{0.9}\text{Mn}_{0.1})_{75}\text{Si}_{10}\text{B}_{15}$  microwire surrounded by primary and secondary coils [7, 82]. The sample is loaded with approximately 10 g and therefore exhibits a flat hysteresis loop. The weight is attached to the bottom of the sample. When a liquid arrives to cover the weight, the actual stress, affecting the sample, decreases giving rise to the appearance of the rectangular hysteresis loop. The principle of the work is based on the change of the voltage of the secondary coil, which increases drastically when the hysteresis loop of the sample C became rectangular after essential decrease of the stress. A simple circuit including the amplification of the signal and alarm set was used to detect changes of voltage in the secondary coil under the change of the tensile stresses due the floating effect of the weight on the liquid.

The other example is based on the wide range of coercivity which can be obtained in microwires due to its strong dependence on the geometric dimensions and heat treatment. It was realized in the method of magnetic codification using magnetic tags [7, 83]. The tag contains several microwires with well-defined coercivities, all of them characterized by a rectangular hysteresis loop. Once the magnetic tag is submitted to the ac magnetic field, each particular

microwire remagnetizes at a different magnetic field giving rise to an electrical signal on a detecting system (see Fig. 30). The extended range of switching fields obtained in Fe-rich microwires gives the possibility to use a large number of combinations for magnetic codification.

The high sensitivity of the GMI ratio to quite small values of mechanical load makes this stress sensitive GMI effect very interesting for practical purposes. Figure 30 shows a magnetoelastic sensor of air flux based on GMI exhibited by nearly zero magnetostrictive  $\text{Co}_{68.5}\text{Mn}_{6.5}\text{Si}_{10}\text{B}_{15}$  microwire. The principle of work of this sensor device is briefly described [7, 84]. The microwire has a rather high dc electrical resistance per length owing to its tiny dimensions. Therefore, large changes (about 130%) of the magnetoimpedance could induce rather large changes of the ac voltage under mechanical loading. Indeed, under the effect of tensile stresses, the GMI ratio at fixed applied field,  $H$ , decreases giving rise to a significant change of the ac voltage between the sample's ends. A dc magnetic field corresponding to the maximum ratio  $(\Delta Z/Z)_m$  without stresses has been applied by means of a small solenoid 7 cm in length and 1 cm in diameter. In the case of a driving current with frequency 10 MHz and amplitude 1.5 mA supplied by an ac current generator, the change of ac voltage (peak to peak) between the ends of the sample is around 3.5 V for small mechanical loads attached at the bottom of the microwire (see calibration curve in Fig. 31b). This huge change presented at the output permits one to use this kind of sensor in different technological applications related to the detection of small mechanical stress.

The observed magnetic response on the external variable stresses can be used in many applications to detect different temporal changes of stresses, vibrations, etc. As an example we introduce a "magnetoelastic pen" which can be used for identification of signatures [7, 85]. It is well known that the signature of each person can be represented by typical series of the stresses. The sequence and strength of those stresses are characteristic features of any personal signature. So temporal changes of the stresses while signing can be used for the identification of signature itself. We have used this behavior and designed a setup consisting of a ferromagnetic bistable amorphous wire with positive magnetostriction, a miniaturized secondary coil, and a simple mechanical system inside the pen containing a spring, which transfers the applied stresses to the ferromagnetic wire (see Fig. 32).

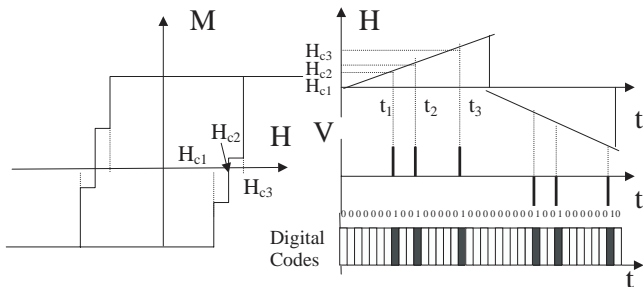


**Figure 30.** Schematic representation of the encoding system based on magnetic bistability of the microwires. Reprinted with permission from [6], A. Zhukov et al., *J. Mater. Res.* 15, 2107 (2000). © 2000, Materials Research Society.

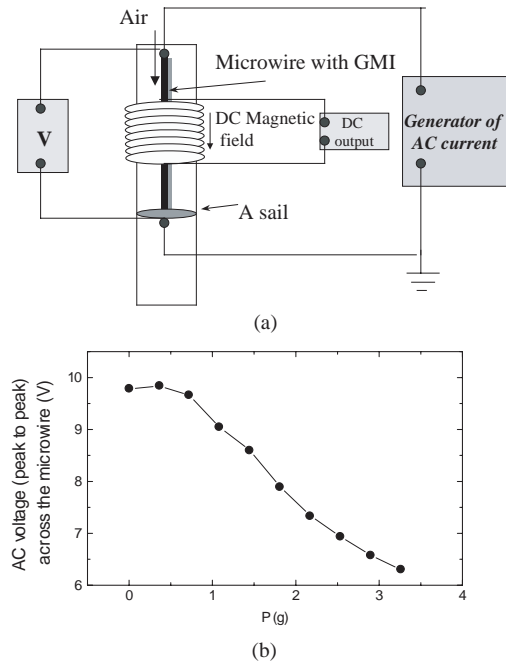


**Figure 31.** Schematic representation of the magnetoelastic sensor based on stress dependence of GMI effect (a) and its calibration curve (b). Reprinted with permission from [7], A. Zhukov et al., *J. Magn. Magn. Mater.* 242–245, 216 (2002). © 2002, Elsevier Science.

The resulting temporal dependence of the stresses, corresponding to a signature, is reproducible for each individual person. The main characteristics of this dependence are time of signature, sign, and sequence of the detected peaks.

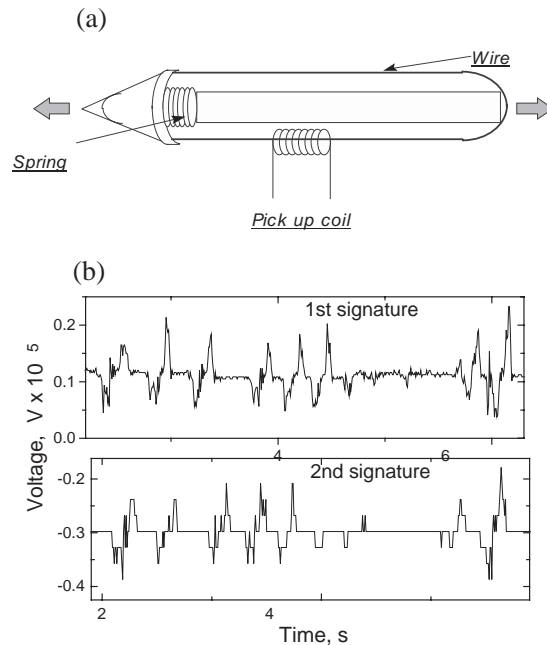


**Figure 32.** Schematic representation of the magnetoelastic pen (a) and two magnetoelastic signatures (b). Reprinted with permission from [7], A. Zhukov et al., *J. Magn. Magn. Mater.* 242–245, 216 (2002). © 2002, Elsevier Science.



Examples of two magnetoelastic signatures corresponding to the same person are shown in Figure 32b.

## 6. CONCLUSIONS

The following conclusions can be summarized:

The Taylor–Ulitsky technique can be fruitfully employed to fabricate technologically attractive ferromagnetic tiny amorphous, nanocrystalline, and granular system metallic wires covered by an insulating glass coating.

A single and large Barkhausen jump is observed for soft magnetic microwires with positive magnetostriction. Negative magnetostriction microwires exhibit almost unhysteretic behavior. The origin of such magnetic bistability is explained in terms and nucleation and domain wall propagation mechanism. In this way the appearance of a single and large Barkhausen jump is related to the fact that the nucleation magnetic field is higher than the propagation field.

The domain wall velocity measured at temperatures 5–300 K in the range of applied magnetic field of 65–100 A/m in amorphous Fe-rich microwire is found to be much higher than in Ni single crystals but slightly lower than in conventional amorphous wires due to the strong internal stresses. An increase of the domain wall velocity has been found with increasing temperature and magnetic field.

The internal stresses frozen-in during the fabrication process are much stronger than for “in-rotating-water quenching.” As a result, the coercivity decreases with the ratio  $\rho = d/D$ . Significant changes of the soft magnetic properties have been observed in Fe- and Co-rich microwires after different treatments (conventional and current annealing with or without axial magnetic field). Upon heat treatment, FeSiBCuNb initially amorphous microwires devitrificate into nanocrystalline structure. Such devitrification permits one to obtain enhanced magnetic softness in microwires of certain compositions. On the other hand at certain conditions the magnetic bistability has been observed even after the second crystallization process, allowing one to increase the switching field by more than two orders of magnitude up to 5.5 kA/m.

The experimental results on the soft magnetic properties obtained in Fe- and Co-rich microwires (submitted to conventional and current annealing with or without field) can be explained as a consequence of the induced magnetic anisotropy. This anisotropy is arising from the counterbalance between internal quenched-in stresses owing to the difference in thermal expansion coefficients of the metal and the glass. This induced anisotropy should be understood as originating from the simultaneous action of the large internal stresses and the axial applied magnetic field. A stress dependent GMI effect has been found under adequate treatment. Enhanced magnetic softness (initial permeability,  $\mu_1$ , up to 14,000) and GMI effect (up to 600%) were observed in amorphous Co-based microwires with nearly zero magnetostriction after adequate annealing. Large sensitivity of GMI and magnetic characteristics on the external tensile stresses have been observed.

The correlations between their structures and magnetic properties and the geometry (ratio  $\rho$ ) and compositions of Co–Cu, Fe–Cu, and Co–Ni–Cu microwires have been studied. The microstructural properties (interatomic distance,

lattice parameters, grain size, segregation, and relative percentage of phases) are strongly dependent on the geometrical parameters, that is, the relation rate of the diameter of the metallic core relative to the total diameter of the microwire. This effect should be attributed to the internal stresses within the metallic core arising from the different thermal expansion coefficients of the glass coating and the core.

On the other hand high quenching rate permits one to obtain microwires from immiscible elements in a metastable state. These microwires can exhibit hard magnetic behavior and magnetoresistance. The coercivity depends both on the composition of the metallic nucleus and on the thermal treatment. It is worthy to note that elevated coercivity (up to 800 Oe) and GMR have been obtained by annealing  $\text{Co}_{29}\text{Ni}_{25}\text{Cu}_{45}\text{Mn}_1$  samples with a metastable single phase structure in the as-prepared state after the decomposition of this metastable phase.

## GLOSSARY

**Coercivity** The value of reverse driving field required to drive the magnetization to zero after being saturated.

**Giant magneto-impedance effect** Large change of the electric impedance of a magnetic conductor when is subjected to an external dc magnetic field.

**Magnetic bistability** Magnetic flux reversal a single and large Barkhausen jump between two stable remanent states. This results in a macroscopic squared hysteresis loop.

**Magnetoresistance** Change of the electric resistance of a magnetic sample when is subjected to an external dc magnetic field.

**Saturation magnetostriction constant** The fractional change in length as the magnetization increases from zero to its saturation value.

## REFERENCES

1. K. Mohri, F. B. Humphrey, K. Kawashima, K. Kimura, and M. Muzutani, *IEEE Trans. Magn.* MAG-26, 1789 (1990).
2. K. Mohri, T. Uchiyama, L. P. Shen, C. M. Cai, and L. V. Panina, *Sensors Actuators A* 91, 85 (2001).
3. A. V. Ulitski, Method of continuous fabrication of microwires coated by glass, USSR Patent 128427, 1950.
4. M. Vázquez and A. P. Zhukov, *J. Magn. Magn. Mater.* 160, 223 (1996).
5. H. Chiriac and T. A. Ovari, *Progr. Mater. Sci.* 40, 333 (1997).
6. A. Zhukov, J. González, J. M. Blanco, M. Vázquez, and V. Larin, *J. Mater. Res.* 15, 2107 (2000).
7. A. Zhukov, *J. Magn. Magn. Mater.* 242–245, 216 (2002).
8. K. R. Pirota, L. Kraus, H. Chiriac, and M. Knobel, *J. Magn. Magn. Mater.* 221, L243 (2000).
9. Y. Yoshizawa, S. Oguma, and K. Yamauchi, *J. Appl. Phys.* 64, 6044 (1988).
10. Y. Yoshizawa and K. Ogumauchi, *Mater. Trans. JIM* 31, 307 (1990).
11. G. Herzer, *IEEE Trans. Magn.* 26, 1397 (1990).
12. G. Herzer, *Mater. Sci. Eng. A* 133, 1 (1991).
13. V. Zhukova, A. F. Cobeño, A. Zhukov, J. M. Blanco, V. Larin, and J. González, *Nanostruct. Mater.* 11, 1319 (1999).
14. J. Arcas, C. Gómez-Polo, A. Zhukov, M. Vázquez, V. Larin, and A. Hernando, *Nanostruct. Mater.* 7, 823 (1996).



15. P. Vojtanik, R. Varga, R. Andrejco, and P. Agudo, *J. Magn. Magn. Mater.* 249, 136 (2002).
16. A. E. Berkowitz, J. R. Mitchell, M. J. Carey, A. P. Young, S. Zhang, F. E. Spada, F. T. Parker, A. Hutten, and G. Thomas, *Phys. Rev. Lett.* 68, 3745 (1992).
17. J. Q. Xiao, J. S. Jiang, and C. L. Chien, *Phys. Rev. Lett.* 68, 3749 (1992).
18. M. N. Baibich, J. M. Broto, A. Fert, F. Nguyen Van Dau, F. Petron, P. Etienne, G. Creuzer, A. Friederich, and J. Chazelas, *Phys. Rev. Lett.* 61, 2472 (1988).
19. J. Q. Xiao, J. S. Jiang, and C. L. Chien, *Phys. Rev. B* 46, 9266 (1992).
20. R. H. Yu, X. X. Zhang, J. Tejada, J. Zhu, and M. Knobel, *J. Appl. Phys.* 79, 1979 (1996).
21. A. Zhukov, E. Sinnecker, D. Paramo, F. Guerrero, V. Larin, J. González, and M. Vázquez, *J. Appl. Phys.* 85, 4482 (1999).
22. C. L. Chien, J. Q. Xiao, and J. S. Jiang, *J. Appl. Phys.* 73, 5309 (1993).
23. S. S. P. Parkin, R. Bhadra, and K. P. Roche, *Phys. Rev. Lett.* 66, 2152 (1991).
24. K.-Y. Wang, J. Arcas, V. Larin, J. L. Muñoz, A. P. Zhukov, D.-X. Chen, M. Vázquez, and A. Hernando, *Phys. Status Solidi* 162, R5 (1997).
25. J. Tang, K.-Y. Wang, L. Spinu, H. Srikanth, P. J. Schilling, and N. Moelders, *J. Magn. Magn. Mater.* 249, 73 (2002).
26. G. F. Taylor, *Phys. Rev.* 23, 655 (1924).
27. G. F. Taylor, Process and apparatus for making filaments, U.S. Patent 1,793,529, 1931.
28. A. V. Ulitovsky, in "Micro-technology in Design of Electric Devices," Leningrad, 1951, No. 7, p. 6.
29. A. V. Ulitovsky and N. M. Avernin, Method of fabrication of metallic microwire, USSR Patent 161325, 1964; Bulletin 7, p. 14.
30. A. V. Ulitovsky, I. M. Maianski, and A. I. Avramenco, Method of continuous casting of glass coated microwire, USSR Patent 128427, 1960; Bulletin 10, p. 14.
31. Z. V. Balyuk, Modelling, Study of Mechanism of High Velocity Crystallization on Crystalline and Glass-like Substrates and Peculiarities of Phase and Structure Formation of Cast Microwire, Ph.D. Thesis, Dnepropetrovsk, 1997.
32. Z. I. Zelikovski, S. K. Zotov, and I. A. Nesterovski, *Cartia Moldavenske* 3 (1971).
33. S. K. Zotov, K. S. Kabisov, and I. G. Silkes, *Cartia Moldavenske* 3 (1974).
34. V. S. Larin, A. V. Torcunov, A. Zhukov, J. González, M. Vázquez, and L. Panina, *J. Magn. Mater.* 249, 39 (2002).
35. L. Kraus, J. Schneider, and H. Wiesner, *Czech. J. Phys. B* 26, 601 (1976).
36. C. F. Catalan, V. M. Prida, J. Alonso, M. Vázquez, A. Zhukov, B. Hernando, and J. Velázquez, *Mater. Sci. Eng. A Suppl.* 438 (1997).
37. A. Zhukov, J. González, J. M. Blanco, M. J. Prieto, E. Pina, and M. Vázquez, *J. Appl. Phys.* 87, 1402 (2000).
38. M. Vázquez and A. Hernando, *J. Phys. D* 29, 939 (1996).
39. H. Chiriac, T. A. Ovari, and Gh. Pop, *Phys. Rev. B* 52, 10104 (1995).
40. J. Velázquez, M. Vázquez, and A. Zhukov, *J. Mater. Res.* 11, 2399 (1996).
41. A. Zhukov, *Appl. Phys. Lett.* 78, 3106 (2001).
42. D.-X. Chen, N. M. Dempsey, M. Vázquez, and A. Hernando, *IEEE Trans. Magn.* 31, 781 (1995).
43. W. Riehemann and E. Nembach, *J. Appl. Phys.* 55, 1081 (1984).
44. T. Reininger, H. Kronmuller, C. Gomez-Polo, and M. Vázquez, *J. Appl. Phys.* 73, 5357 (1993).
45. A. P. Zhukov, M. Vázquez, J. Velázquez, H. Chiriac, and V. Larin, *J. Magn. Magn. Mater.* 151, 132 (1995).
46. M. Vázquez, J. González, and A. Hernando, *J. Magn. Magn. Mater.* 53, 323 (1986).
47. J. González, M. Vázquez, J. M. Barandiarán, V. Madurga, and A. Hernando, *J. Magn. Magn. Mater.* 68, 151 (1987).
48. V. Zhukova, A. F. Cobeño, A. Zhukov, J. M. Blanco, S. Puerta, J. González, and M. Vázquez, *J. Non-Cryst. Solids* 287, 31 (2001).
49. H. Chiriac, M. Knobel, and T. Ovari, *Mater. Sci. Forum* 302–303, 239 (1999).
50. A. F. Cobeño, A. Zhukov, J. M. Blanco, and J. González, *J. Magn. Magn. Mater.* 234, L359 (2001).
51. A. Zhukov, V. Zhukova, J. M. Blanco, A. F. Cobeño, M. Vázquez, and J. Gonzalez, *J. Magn. Magn. Mater.* 258–259, 151 (2003).
52. V. Zhukova, J. M. Blanco, A. Zhukov, and J. Gonzalez, *J. Phys. D* 34, L113 (2001).
53. A. F. Cobeño, A. Zhukov, A. R. de Arellano-López, F. Elías, J. M. Blanco, V. Larin, and J. González, *J. Mater. Res.* 14, 3775 (1999).
54. L. V. Panina and K. Mohri, *Appl. Phys. Lett.* 65, 1189 (1994).
55. M. Knobel, C. Gómez-Polo, and M. Vázquez, *J. Magn. Magn. Mater.* 160, 243 (1996).
56. J. González, A. P. Zhukov, J. M. Blanco, A. F. Cobeño, M. Vázquez, and K. Kulakowski, *J. Appl. Phys.* 87, 5950 (2000).
57. V. Zhukova, A. Chizhik, A. Zhukov, A. Torcunov, V. Larin, and J. Gonzalez, *IEEE Trans. Magn.* 38, 3090 (2002).
58. J. M. Blanco, P. Aragonese, J. González, A. Hernando, M. Vázquez, C. Gómez-Polo, P. T. Squire, and M. R. J. Gibbs, in "Magnetoelastic Effects and Applications" (L. Lanotte, Ed.), p. 253. Elsevier, New York, 1993.
59. J. M. Barandiarán, A. Hernando, V. Madurga, O. V. Nielsen, M. Vázquez, and M. Vázquez-López, *Phys. Rev. B* 35, 5066 (1987).
60. V. Zhukova, J. M. Blanco, A. Zhukov, and J. González, *J. Phys. D* 34, L113 (2001).
61. K. Narita, J. Yamasaki, and H. Fukunaga, *IEEE Trans. Magn.* MAG-16, 435 (1980).
62. J. González, A. Zhukov, V. Zhukova, A. F. Cobeño, J. M. Blanco, A. R. de Arellano-Lopez, S. Lopez-Pombero, J. Martínez-Fernández, V. Larin, and A. Torcunov, *IEEE Trans. Magn.* 36, 3015 (2000).
63. A. S. Antonov, V. T. Borisov, O. V. Borisov, A. F. Prokoshin, and N. A. Usov, *J. Phys. D* 33, 1161 (2000).
64. M. Vázquez, P. Marin, J. Arcas, A. Hernando, A. P. Zhukov, and J. González, *Textures Microstruct.* 32, 245 (1999).
65. M. N. Baibich, J. M. Broto, A. Fert, F. Nguyen Van Dau, F. Petroff, P. Etienne, G. Creucet, A. Friederich, and J. Chazelas, *Phys. Rev. Lett.* 61, 2472 (1988).
66. A. E. Berkowitz, J. R. Mitchell, M. J. Carey, A. P. Young, S. Zhang, F. E. Spada, F. T. Parker, A. Hutten, and G. Thomas, *Phys. Rev. Lett.* 68, 3745 (1992).
67. C. L. Chien, J. Q. Xiao, and J. S. Jiang, *J. Appl. Phys.* 73, 5309 (1993).
68. R. H. Yu, X. X. Zhang, J. Tejada, M. Knobel, P. Tiberto, and P. Allia, *J. Appl. Phys.* 78, 392 (1995).
69. E. H. C. P. Sinnecker, D. Páramo, V. Larin, A. Zhukov, M. Vázquez, A. Hernando, and J. González, *J. Magn. Magn. Mater.* 203, 54 (1999).
70. B. Busch, F. Gärtner, C. Borchers, P. Haasen, and R. Bormann, *Acta Metall. Mater.* 43, 3467 (1995).
71. V. Madurga, R. J. Ortega, V. N. Korenivski, H. Medelius, and K. V. Rao, *J. Magn. Magn. Mater.* 140–144, 465 (1995).
72. A. D. C. Viegas, J. Geshev, L. S. Domeles, J. E. Schmidt, and M. Knobel, *J. Appl. Phys.* 82, 3047 (1997).
73. R. M. Bozorth in "Ferromagnetism," p. 402. Van Nostrand, New York, 1951.
74. J. González, V. Zhukova, A. P. Zhukov, J. J. Del Val, J. M. Blanco, E. Pina, and M. Vázquez, *J. Magn. Magn. Mater.* 221, 196 (2000).
75. J. Tang, K.-W. Wang, L. Spinu, H. Srikanath, P. J. Schilling, and N. Moelders, *J. Magn. Magn. Mater.* 249, 73 (2002).
76. A. Zhukov, M. Vázquez, and J. L. Martinez, *J. Magn. Magn. Mat.* (accepted).
77. J. Nixdorf, *Draht-Welt* 53, 696 (1967).
78. T. Goto, M. Nagano, and N. Wehara, *Trans. JIM* 18, 759 (1977).

79. T. Goto, *Trans. JIM* 19, 60 (1978).
80. T. Goto, *Trans. JIM* 21, 219 (1980).
81. V. Zhukova, A. F. Cobeño, A. Zhukov, A. R. de Arellano Lopez, S. López-Pombero, J. M. Blanco, V. Larin, and J. Gonzalez, *J. Magn. Mater.* 249, 79 (2002).
82. A. Zhukov, J. González, J. M. Blanco, P. Aragoneses, and L. Domínguez, *Sensors Actuators A* 81, 129 (2000).
83. V. Larin, A. Torcunov, S. Baranov, M. Vázquez, A. Zhukov, and A. Hernando, Method of magnetic codification and marking of the objects, Spanish Patent 9601993, 1996.
84. A. F. Cobeño, A. Zhukov, J. M. Blanco, V. Larin, and J. Gonzalez, *Sensors Actuators A* 91, 95 (2001).
85. A. Zhukov, J. M. Garcia-Beneytez, and M. Vázquez, *J. Phys. IV* 8, 763 (1998).



# Nanocrystalline Barium Titanate

Jian Yu, Junhao Chu

Chinese Academy of Sciences, Shanghai 200083, China

## CONTENTS

1. Introduction
2. Syntheses of Nanocrystalline BaTiO<sub>3</sub>
3. Spectroscopic Characterization
4. Properties
5. Lattice Dynamics
6. Barium Strontium Titanate
7. Applications
8. Summary
- Glossary
- References

## 1. INTRODUCTION

A ferroelectric is a system that exhibits a spontaneous polarization below the Curie temperature,  $T_c$ , which can be reversed by the application of an electric field. Conventionally, a ferroelectric is called displacive when the elementary dipoles strictly vanish in the paraelectric phase, and order-disorder when they are nonvanishing but thermally average out to 0 in the paraelectric phase. More rigorously, one may distinguish the two types on the basis of the dynamics of their phase transition and the nature of the soft mode involved, whether the frequency shifts to 0 or the linewidth becomes broad [1, 2]. To date, barium titanate (BaTiO<sub>3</sub>) is well accepted as a displacive and order-disorder mixed type of ferroelectric [3–5].

Since the discovery of ferroelectricity in BaTiO<sub>3</sub> in the 1940s, it has been recognized as one of the most important functional materials and has been used in many practical applications in the form of single crystals and ceramics. At high temperature above  $T_c = 393$  K, BaTiO<sub>3</sub> is stabilized in a paraelectric cubic phase (space group  $O_h^1$ ). With decreasing temperature, it undergoes a sequence of structural phase transitions from the cubic to the ferroelectric tetragonal ( $C_{4v}^1$ ) at 393 K, orthorhombic ( $C_{2v}^{14}$ ) at 278 K, and rhombohedral ( $C_{3v}^5$ ) at 183 K, in which the spontaneous polarization,

$P_s$ , is along the prototype cube  $\langle 001 \rangle$ ,  $\langle 110 \rangle$ , and  $\langle 111 \rangle$  directions, respectively. Based on the temperature dependence of  $P_s$ , these three transitions are first-order transitions, the cubic-to-tetragonal phase transition being a first-order transition close to a second-order phase transition [1, 4–6]. In the three low-temperature ferroelectric phases, the existence of spontaneous polarization results in remarkable ferroelectric, dielectric, piezoelectric, pyroelectric, electrooptic, and nonlinear optical properties. As a result, the tetragonal and cubic phases are especially important for commercial technological applications. In ferroelectric BaTiO<sub>3</sub>, the spontaneous polarization, the ferroelectric distortion (tetragonality  $c/a$  ratio), and the tetragonal-cubic transition temperature can be altered by external field changes in the temperature, applied field, stress, or chemical composition. The temperature dependence of  $P_s$  is referred to as a pyroelectric property, the electric field dependence of  $P_s$  as a dielectric property, and the stress dependence of  $P_s$  as a piezoelectric property. They all possess anomalous peaks near the phase transition, particularly the ferroelectric tetragonal-paraelectric cubic phase transition. By varying the chemical composition of BaTiO<sub>3</sub> such as by the addition of strontium or calcium, the tetragonal-cubic phase transition temperature can be shifted downward so that the anomalous dielectric, piezoelectric, and pyroelectric properties can be used to build high-performance devices at ambient temperatures [1, 7].

For BaTiO<sub>3</sub> bulk materials, the room-temperature structural and physical properties are summarized in Table 1. In the ferroelectric tetragonal phase,  $P_s = 26 \mu\text{C}/\text{cm}^2$  with coercive field  $E_c = 1.5 \text{ kV}/\text{cm}$  at room temperature;  $P_s = 18 \mu\text{C}/\text{cm}^2$  at  $T_c$  and jumps to 0 above  $T_c$ . The dielectric constant is strongly anisotropic with  $\epsilon_c = 400$  along the  $c$  axis and  $\epsilon_a = 4000$  perpendicular to the  $c$  axis at room temperature. The piezoelectric coefficient is proportional to  $P_s$ , but the piezoelectric effect is 0 in the paraelectric phase above  $T$  [1, 2]. For conventional ceramics with a grain size of 20–50  $\mu\text{m}$ , the room-temperature dielectric constant is around 2000 at 1 kHz. Previous investigations revealed that the spontaneous polarization, tetragonality, Curie temperature, and various properties related to the spontaneous polarization of the final BaTiO<sub>3</sub> devices strongly depend on the

**Table 1.** Structural and physical constants of ferroelectric BaTiO<sub>3</sub> bulk materials and nanostructured materials in ambient environment except as noted.

Property	Bulk value	Ref.	Nano value	Ref.
Lattice parameter (Å)	$a = 3.996$ at 398 K $a = 3.992, c = 4.036, c/a = 1.011$	[1, 2]	$a$ anomalous expansion $c/a \rightarrow 1.000$ at $R_c$	[21, 22]
Curie temperature (°C)	120	[1]	$T_c = 128 - \frac{700}{R-110}$	[22]
Polarization ( $\mu\text{C}/\text{cm}^2$ )	$P_s = 26, P_r = 18$ (393 K)	[1, 2]	$P_r = 2.0\text{--}8.3$ (50 nm)	[23, 24]
Coercive field (kV/cm)	$E_c = 1.5$		$E_c = 27\text{--}50$	
Dielectric (1 kHz)	$\epsilon_c = 400, \epsilon_a = 4000$	[8–10]	120 (50 nm) (thin film)	[24]
	$\sim 2000$ (coarser ceramics)		430 (50 nm) (thick film)	[23]
	$\sim 5000$ (fine ceramics)		230–401 (25 nm)	[25, 26]
Piezoelectric (pC/N)	$d_{15} = 392, d_{31} = -34.5, d_{33} = 85.6$ (single crystal)	[11]		
	$d_{15} = 260, d_{31} = -78, d_{33} = 190$ (coarser ceramics)	[12]		
dc resistivity ( $\Omega$ cm)	$>10^{10}$ (pure ceramic)	[13, 14]	$2 \times 10^{11}$ (50 nm)	[24]
	$10^2\text{--}10^3$ (rare-earth-element doped)			
Mobility ( $\text{cm}^2/\text{V s}$ ) (single crystal)	$\mu_a = 0.5$ (cubic at 126 °C)	[15]		
	$\mu_a = 1.2 \pm 0.3, \mu_c = 0.13 \pm 0.03$ ( $e$ )			
	$\mu_a/\mu_c = 9.2 \pm 5.1$ ( $e$ )	[16]		
	$\mu_a/\mu_c = 19.6 \pm 0.6$ ( $h$ )			
Seebeck coefficient ( $\mu\text{V}/^\circ\text{C}$ ) ( $6.0 \times 10^{18} \text{ cm}^{-3}$ free $e$ concentration)	$S_a = -600, S_c = -660$	[15]		
Thermal expansion co-efficient ( $10^{-6}/^\circ\text{C}$ )	$\alpha_a = 15.7, \alpha_c = 6.2$	[17]		
Optical bandgap (eV)	3.2	[18]	3.68 (8 nm)	[18]
			3.53 (35 nm)	
Electrooptic (pm/V)	$\gamma_{51} = 820$ (632.8 nm)	[19]	$\gamma_{\text{eff}} \sim 50 \pm 5$ (dc) (1.54 $\mu\text{m}$ ) $\gamma_{\text{eff}} \sim 18 \pm 2$ (5 MHz) (1.54 $\mu\text{m}$ )	[27]
Second-harmonic generation (pm/V) (1.064 $\mu\text{m}$ )	$d_{15} \approx 17.0, d_{31} \approx 15.7, d_{33} \approx 6.8$	[20]	$d_{\text{eff}} = 2.13$ $c$ -oriented nc-film	[20]
			$d_{\text{eff}} = 1.5$ $a$ -oriented nc-film	

particle size. For example, the maximum room-temperature dielectric constant  $\epsilon \sim 5000$  was observed in fine ceramics with a grain size of about 1  $\mu\text{m}$  [8–10]. To elucidate the physical mechanism of the ferroelectric properties in reduced dimensions and to determine the ultimate level to which a microelectronic device based on such systems can be miniaturized, the grain size effects in ferroelectrics are most striking [21, 28–33]. These works pointed to prior studies on BaTiO<sub>3</sub> nanostructured materials and also facilitated the application of ferroelectric nanoparticles in advanced technologies.

In condensed-matter physics, many fundamental properties of materials are characterized by their feature length. For example, one of the feature lengths in a semiconductor is the exciton Bohr radius. Heath even stated that, if a crystal is fabricated such that at least one of its dimensions is comparable with the feature length of some property, the property is confined and becomes dependent on the size and shape of what is now called a *quantum crystal* [34]. In semiconductor nanosystems, the quantum size confinement effect, which establishes the physical fundamentals necessary to generate properties different from their bulk counterparts, has led to dipole-forbidden interband transitions,

exciton level discretization, bandgap enhancement, and so on [34–36].

In perovskite-type ABO<sub>3</sub> ferroelectric oxides (BaTiO<sub>3</sub> and PbTiO<sub>3</sub>), the characterizations showed a fascinating dependence of the structural and dynamical behaviors on both details of the chemical composition and the delicate balance between the long-range Coulombic interaction and the short-range electric repulsive and covalent interactions [5, 37–40]. The long-range Coulombic interaction was found to play an important role in forming ferroelectric phases, of which the correlation length between polar units was estimated to be 10–50 nm parallel to the polar direction and 1–2 nm perpendicular to the polar direction [6, 21]. If the dimensionality of the ferroelectric nanomaterials were comparable to this correlation length, the long-range cooperative interaction would be reduced, leading to a phase transformation. Preliminary experimental investigations have revealed some major impact on the lattice vibration, phase transitions, and dielectric, ferroelectric, and optical properties. Some results are presented in Table 1. With decreasing ferroelectric nanocrystallite size below the submicrometer scale, there was a monotonic reduction in the tetragonal–cubic phase transition temperature, a decrease in tetragonality, and a grain size-induced

tetragonal to high-symmetry paraelectric phase transition at/below room temperature. The concept of a ferroelectric critical size, which is necessary to support the long-range cooperative ordering processes necessary for ferroelectricity, has been applied in ferroelectric BaTiO<sub>3</sub> and PbTiO<sub>3</sub> nanocrystals [21, 22, 32, 33, 41].

In this review, we summarize the wet chemical solution methods for producing crystalline BaTiO<sub>3</sub> nanoparticles (nc-BaTiO<sub>3</sub>) with narrow size distributions and size tunability, the vapor deposition methods in particular for growing single crystal ultrathin films, and fabrications of nanoceramics and nanocomposites in Section 2. BaTiO<sub>3</sub> nanoparticle and single-crystal thin films are also treated as building blocks to create nanostructured materials, one-dimensional (1D) and 3D superlattices. The spectroscopic characterizations of structural changes and defects are presented in Section 3. In this section, the surface, defect, and microscopic interaction models for understanding the mechanism of grain size-induced phase transformations are also discussed. The dielectric, ferroelectric, and optical properties of nanocrystalline BaTiO<sub>3</sub> are summarized in Section 4. The lattice dynamic theory in ferroelectric nanocrystals is summarized and the present results on ABO<sub>3</sub> ferroelectric nanoparticles are discussed in Section 5. In addition to BaTiO<sub>3</sub> nanostructured materials, barium strontium titanate (Ba<sub>1-x</sub>Sr<sub>x</sub>TiO<sub>3</sub>) nanostructured materials, including synthesis, dielectric, and nonlinear optical properties, are presented in Section 6. Some applications of BaTiO<sub>3</sub> nanostructured materials in the fields of optical modulators, transducers and actuators, and thermal and chemical sensors are given in Section 7. Finally, a short summary is presented.

## 2. SYNTHESSES OF NANOCRYSTALLINE BaTiO<sub>3</sub>

Synthesizing crystalline BaTiO<sub>3</sub> nanostructured materials (nanocrystalline particles, rods, films, and their superlattices) of high purity, stoichiometry, grain size with tunability, and narrow distribution is one of the basic requirements for BaTiO<sub>3</sub> nanoscience and nanotechnology. Various wet chemical solution methods and vapor phase deposition methods have been developed to prepare BaTiO<sub>3</sub> and related nanostructured materials. Using these nanocrystals as building blocks, attempts to fabricate complex superlattices, nanoceramics, and nanocomposites were also performed. In Section 2.1, wet chemical solution methods to prepare nanoparticles and fine microstructure thin films are reviewed, by which the grain size and grain shape have been separately controlled during growth. In Section 2.2, vapor phase deposition methods to grow epitaxial single-crystal thin films and superlattices are discussed. In addition to nanoparticles of 0D nanocrystals and nanorods of 1D nanocrystals, single-crystal thin films with thickness on the nanometer scale form 2D nanocrystals. In Section 2.3, BaTiO<sub>3</sub> nanoceramics fabricated with BaTiO<sub>3</sub> nanopowders as starting materials are discussed. In Section 2.4, BaTiO<sub>3</sub> nanoparticle dispersoids composites are discussed.

### 2.1. Chemical Solution Methods

To date, various wet chemical methods have been developed to synthesize BaTiO<sub>3</sub> nanostructured materials, including coprecipitation such as barium titanate oxalate tetrahydrate (BTOT) and barium titanate oxalate [42–44], freeze-dried nitrate method [45], alkoxide hydrolysis [46], stearic acid gel (SAG) [47, 48], sol-gel [21], hydrothermal methods [31, 49, 50], and solution phase decomposition [51]. The most important advantages of the wet chemical solution methods are easily controlling the chemical stoichiometry and producing particles of grain size on the nanometer scale with a relatively narrow distribution, coupled with low crystallization temperature owing to constituent mixing on the quasi-atomic level in solution state [42]. Using these wet chemical solution methods, various BaTiO<sub>3</sub> nanostructured materials have been successfully fabricated. For example, an ensemble of monodispersed BaTiO<sub>3</sub> nanoparticles with grain size as small as 8 nm and a self-organization of BaTiO<sub>3</sub> nanoparticles are illustrated in Figure 1. Owing to the wet chemical solution process, a dopant such as paramagnetic ions or rare-earth ions could be easily introduced during preparation of the precursor solution [52–54].

In the wet chemical solution processes for synthesizing nc-BaTiO<sub>3</sub>, difficulties arise from the different behaviors of titanium and barium ions versus hydrolysis. To avoid the development of a highly cross-linked Ti–O network in the final structure, various methods were proposed to control the formation of Ti–O–Ti bonds. One method was to use titanium precursors with bidentate ligands (chelates, oxalate, citrate) attached to Ti<sup>4+</sup> ions before reaction with Ba<sup>2+</sup> ions [42, 46]. A second method was to employ organic solvent without water as the dispersing agent to realize the

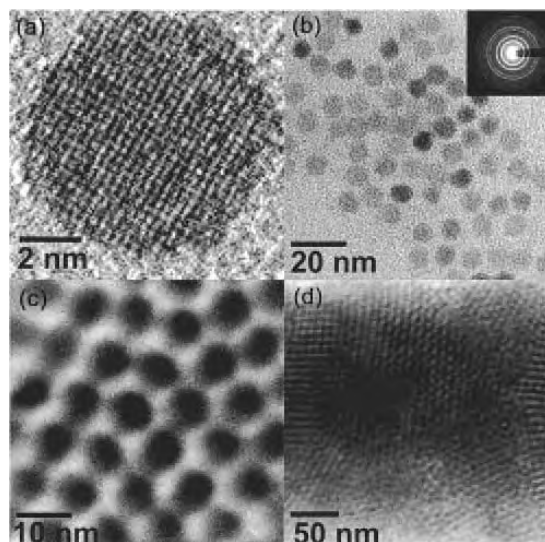


**Figure 1.** Transmission electron microscopy images of (a) a high-resolution lattice image of an individual 8-nm-diameter nanoparticle and (b) an ensemble of discrete BaTiO<sub>3</sub> 8-nm nanoparticles. Inset: Selected area electron diffraction pattern of (c) self-organization of BaTiO<sub>3</sub> nanoparticles and (d) superlattice of 8-nm-diameter BaTiO<sub>3</sub> nanoparticles. Reprinted with permission from [51], S. O'Brien et al., *J. Am. Chem. Soc.* 123, 12085 (2001). © 2001 American Chemical Society.



uniform distribution of barium and titanium metalorganics in the gels [47, 48, 55]. These methods involved several reaction steps to deposit the precursor and required calcination at higher temperature to generate crystalline BaTiO<sub>3</sub> nanopowders. Controlling the calcining temperature and time, BaTiO<sub>3</sub> nanopowders with various grain sizes were obtained. For instance, using the SAG technique, Wang et al. and Qiu et al. reported that the average grain size of BaTiO<sub>3</sub> nanopowders prepared at 600–950 °C ranged from 25 to 60 nm [47, 48]. In these methods, a key point was to obtain a homogeneous precursor with uniform distribution of the different components. If not, a number of defects could occur in the nanocrystals [56].

In contrast to those coprecipitation processes, by which the nanopowders obtained were usually aggregate, sol-gel methods with metal alkoxides allowed for fabrication of monodispersed nanoparticles of barium titanate with improved homogeneity and purity. The low-temperature hydrothermal methods (LTHMs) not only allowed fabrication of monodispersed nanoparticles but also reduced the crystallization temperature of BaTiO<sub>3</sub> to less than 100 °C. In the following, these two methods are discussed in detail for fabricating BaTiO<sub>3</sub> nanocrystals. Nanofabrication using mesoporous sieves and microemulsions are also reviewed. At the end of this section, the fabrication of nanocrystalline thin films using wet chemical solution methods is discussed.

### 2.1.1. Sol-Gel Method

The sol-gel method was widely used to produce nanocrystalline BaTiO<sub>3</sub> powders and films. This process involved dissolving the metal-containing compounds in the solvent, hydrolyzing to polymeric condensation, drying the resulting solution into various gels, and, finally, annealing the gels at high temperature to form BaTiO<sub>3</sub> nanocrystals [21, 25, 54, 57, 58]. In this process, the choice of starting materials, concentration, pH value, and heat treatment schedule had a strong influence on the properties of the BaTiO<sub>3</sub> nanoparticles. Barium acetate and titanium isopropoxide were often used as starting materials to generate BaTiO<sub>3</sub> nanopowders. However, the different rates in the hydrolysis and condensation of Ba and Ti precursors often led to chemical component segregation in the obtained gels. To avoid this problem, acetic acid or acetylaceton was used to modify the hydrolysis rate of the Ti precursor, because these complexing agents act as chelating agents to coordinate with Ti species [23, 25, 54].

Compared with the case of mixed Ba and Ti alkoxides, Gablenz et al. and Yang et al. demonstrated that using barium titanium double alkoxides as the raw materials allowed one to produce BaTiO<sub>3</sub> nanoparticles with a higher degree of homogeneity, a relatively narrow grain size distribution, and an exact [Ba/Ti] stoichiometry [59, 60]. In the case of double alkoxides, the absence of free barium alkoxide and titanium alkoxide led to relatively low hydrolysis and condensation rates, but the gelation time was remarkably increased, owing to the evolution of oligomeric structures. During the refluxing period, the oligomeric structures were found as a transition between noncrystalline and crystalline states. The shortest gelation time was observed near the crystalline state [60].

Furthermore, it was found that the pH value of the solvent had a great influence on colloid formation, gel structure, grain size distribution, and degree of aggregation [61, 62]. When the pH value was below 7, no gel formed and the obtained powder had a strong degree of aggregation. However, increasing the pH value above 8, the nanoparticles obtained at 600 °C were homogeneous with an average grain size of 13 nm and a high specific surface area of 33.27 m<sup>2</sup>/g. Luan and Gao analyzed the dependence of the zeta potential on the pH value and found that the hydrolysis was completed more rapidly than the polymerization as the hydrolysis speed was faster than that of polymerization under alkaline conditions. The hydroxide ions reacted with tetrabutyl titanate and water molecules to form the complexion [Ti(OH)<sub>6</sub>]<sup>2-</sup>, which neutralized with the Ba<sup>2+</sup> ion and then polymerized to Ba<sup>2+</sup>[Ti(OH)<sub>6</sub>]<sup>2-</sup>. At the same time, the high-repel potential energies among colloidal particles had reduced the degree of agglomeration, since the pH value was far away from the isoelectronic point (pH = 1.8). Therefore, the nanopowders obtained at high pH were homogeneous and ultrafine. In contrast, when the pH value was below 7, because the polymerization speed was much faster than the hydrolysis speed, polymerization had already started before the completion of hydrolysis. The product was hydrate TiO<sub>2</sub> instead of the Ti complexion. Because the pH value was near the isoelectronic point, the gel particles were much more highly agglomerated.

For the obtained gels, a high-temperature heat treatment above 600 °C was required to remove unreacted organics and to crystallize the films. The following steps represented the transformation from the precursor to the crystalline BaTiO<sub>3</sub>: transformation of the precursor to the amorphous barium titanate, three-dimensional nucleation of the crystalline barium titanate in the amorphous matrix, and crystal growth of BaTiO<sub>3</sub> by a solid-state reaction [63]. The choice of heat treatment schedule, including postannealing temperature and time, and the increased rate of temperature during heating affected the nucleation and crystal growth processes of BaTiO<sub>3</sub> and hence determined the nanocrystallite size and its distribution [62, 63]. The final annealing temperature played a dominant role in determining the grain size and its distribution in the obtained nanomaterials. Conventionally, the higher the annealing temperature or the longer the time, the larger the grain size obtained. In synthesizing ferroelectric Pb(Zr, Ti)O<sub>3</sub> nanoparticles [62], the slow heating rate was found to inhibit the interparticle sintering—nanoparticle aggregation. Moreover, the annealing atmosphere also affected the quality of the nanoparticles; the inert atmosphere reduced the interparticle sintering in comparison with air or oxygen atmosphere. However, these heat treatment techniques were not reported for synthesizing BaTiO<sub>3</sub> nanocrystalline particles and thin films. Because BaTiO<sub>3</sub> is similar to Pb(Zr, Ti)O<sub>3</sub> in its chemical qualities, these heat treatment techniques should be beneficial for synthesizing monodispersed freestanding BaTiO<sub>3</sub> nanocrystalline particles and thin films.

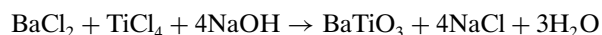
With these techniques, monodispersed BaTiO<sub>3</sub> nanoparticles and related nanostructured materials have been successfully fabricated. The grain size was adjusted from a few nanometers up to micrometer size by combining solid-state polymerization and heat treatment [21, 53, 59–61, 63].

### 2.1.2. Low-Temperature Hydrothermal Method

In contrast to sol-gel processing, the low-temperature (below 100 °C) hydrothermal method with inorganic precursors offers a promising cost-effective approach to producing crystalline BaTiO<sub>3</sub> nanoparticles and relevant nanomaterials. Thermodynamic calculations of the Ti-Ba-CO<sub>2</sub>-H<sub>2</sub>O system indicated that BaTiO<sub>3</sub> is the thermodynamically favored phase at pH greater than 12 and high concentrations (2 M) of Ba<sup>2+</sup> [64, 65]. Based on this prediction, BaTiO<sub>3</sub> nanocrystals were produced by rapid hydrolysis of compounds such as TiCl<sub>4</sub>, Ti alkoxides, or BaTi double alkoxides in an aqueous medium under strong alkaline conditions, and the grain size was tuned by controlling the reaction conditions such as concentration, pH, and temperature [31, 49, 52, 64–67].

Conventionally, the low-temperature hydrothermal synthesis of BaTiO<sub>3</sub> nanoparticles was carried out in a batch-type reactor below 100 °C under atmospheric pressure. There were two effective routes using synthesized titania gel or titania nanoparticles to produce BaTiO<sub>3</sub> nanoparticles.

For the case of titania gels, the raw materials were either inorganic such as barium chloride, titanium chloride, and sodium hydroxide base or organic salts such as barium acetate, titanium isopropoxide, and the organic base, tetramethylammonium hydroxide. A typical chemical reaction from inorganic salts can be written as



where the ionic species react in an aqueous solution with a temperature of 80–95 °C to form monodispersed crystalline nanoparticles with a grain size of 30–220 nm [31, 33, 52]. In a typical case, 164 mL NaOH solution of concentration 3.0 mol/L was preheated to 85 °C in a beaker, and 96 mL BaCl<sub>2</sub>-TiCl<sub>4</sub> solution of 1 mol/L was then added under stirring. The entire system was kept at 85 °C for 10 min. The nanoparticles obtained were determined to have an average grain size of approximately 80 nm and a specific surface area of 25 m<sup>2</sup>/g. In this route, the stoichiometry in nc-BaTiO<sub>3</sub> was achieved when the Ba/Ti molar ratio was 1.07 in the starting solution, and the aging time for full crystallization was as short as 4 min [31, 68]. Furthermore, Her et al. developed a controlled double-jet precipitation technique and realized continuous precipitation of monodispersed colloidal barium titanate nanopowders, for example, in a moderate-sized experimental reactor with about 50 pounds per day [31, 69]. The nanoparticle agglomeration could be avoided by controlling the flow rate and the volume of reactants. As known, one important source of contamination of nc-BaTiO<sub>3</sub> is the formation of BaCO<sub>3</sub>, through the reaction of Ba<sup>2+</sup> with CO<sub>3</sub><sup>2-</sup> ions coming from air or dissolved in alkaline solutions. To reduce the final amount of this secondary phase, special care was taken in avoiding contact of NaOH solution with the atmosphere.

Moreover, the crystalline BaTiO<sub>3</sub> nanoparticles were directly formed by hydrolyzing the barium titanium double alkoxides at 60 °C under a pH of 13 without any further calcination [60]. With barium titanium double alkoxides as the raw materials, a semicontinuous hydrothermal process was also designed to produce BaTiO<sub>3</sub> nanopowders [70]. The grain size of the nanoparticles obtained by

hydrolyzing double alkoxides was around 10 nm. MacLaren and Ponton investigated the formation mechanisms of low-temperature hydrothermal conversion of BaTiO<sub>3</sub> nanoparticles from an amorphous hydrous TiO<sub>2</sub> gel, which was derived from hydrolysis of titanium isopropoxide, in a solution of barium acetate and strong tetramethylammonium hydroxide base. On the basis of the fast reaction rate for the formation of nc-BaTiO<sub>3</sub>, it was proposed that the BaTiO<sub>3</sub> nanoparticles were formed by an *in-situ* transformation of amorphous TiO<sub>2</sub> gel [67].

The second route was low-temperature hydrothermal conversion of titania nanoparticles in barium hydroxide solutions [65, 71, 72]. This route coupled two low-temperature hydrothermal steps: synthesis of monodispersed titania nanoparticles and hydrothermal conversion of the prepared titania nanoparticles to nanocrystalline BaTiO<sub>3</sub>. At first, the morphology observations seemed to support a *dissolution-precipitation* mechanism—involving dissolution of TiO<sub>2</sub> into Ti(OH)<sub>x</sub><sup>4-x</sup> species, precipitative BaTiO<sub>3</sub> nucleation by reaction with barium ions/complexes in solution, and recrystallization/growth—for the hydrothermal conversion of titania nanoparticles into nc-BaTiO<sub>3</sub> [65, 71]. However, recent measurements indicated that the particle size and morphology of the BaTiO<sub>3</sub> nanoparticles remained the same as the precursor titania nanoparticles. A shrinking-core *in-situ* transformation diffusion-reaction mechanism was proposed for this TiO<sub>2</sub>-to-BaTiO<sub>3</sub> conversion process [72]. In principle, the grain size of the BaTiO<sub>3</sub> nanoparticles can be tuned by varying the size of the titania nanoparticles. In the development of nanocrystalline titania, TiO<sub>2</sub> nanoparticles with a grain size as small as approximately 3 nm were successfully prepared [73]. Thus, monodispersed BaTiO<sub>3</sub> nanoparticles with a grain size less than 10 nm can be prepared from titania nanoparticles by this low-temperature hydrothermal process.

As discussed above, the low-temperature hydrothermal process provides an alternative to postannealing to control the phase structure of ferroelectric nanocrystals. Combining these two crystallization methods, two-phase coexisting barium titanate nanoparticles were synthesized with TiCl<sub>4</sub> and BaCl<sub>2</sub> as the raw materials, of which the second-phase clusters of the BaTiO<sub>3</sub> hexagonal phase or BaTi<sub>2</sub>O<sub>5</sub> were embedded within the BaTiO<sub>3</sub> nanoparticles [49, 74, 75].

To date, the low-temperature hydrothermal method has enjoyed considerable success for the production of monodispersed barium titanate spheric nanoparticles with a grain size ranging from 5 nm to the submicrometer, with a narrow distribution, and with a high purity. It has promise not only as a suitable laboratorial process but also as a suitable industrial process to produce barium titanate nanoparticles, starting from cheaper inorganic precursors (titanium oxide or chloride; barium hydroxide or chloride) [69, 70].

### 2.1.3. Nanofabrication

Among the important characteristics of nanoparticle systems are facile manipulation and reversible assembly that allow for the possibility of incorporating nanoparticles into nanoscale electric, electronic, optical, and mechanical devices. Such bottom-up or self-assembly approaches have also been attempted in BaTiO<sub>3</sub> nanofabrications.

The mesoporous silicate molecular sieve has uniform columnar periodic hexagonal mesopores ranging from 15 to 100 Å and separated by 8- to 9-Å walls, and is an important nanoreactor. BaTiO<sub>3</sub> nanoparticles were embedded in the uniform mesopores by soaking a mesoporous silicate molecular sieve into a BaTiO<sub>3</sub> precursor solution and with calcination at 700 °C to crystallize BaTiO<sub>3</sub> nanoparticles [76, 77]. Using sol-gel-type hydrolysis [46, 60], the crystalline BaTiO<sub>3</sub> nanoparticles embedded in mesoporous sieves can also be directly fabricated without any calcination.

Water-in-oil microemulsions are another important kind of nanoreactor, which are also used to synthesize BaTiO<sub>3</sub> nanoparticles. The water droplet size in microemulsions can be tuned between 8 and 55 nm by varying the length of the hydrophilic part of the surfactant molecules, and, consequently, the size of the resulting BaTiO<sub>3</sub> nanoparticles can be determined [78]. In these microemulsions, the crystalline BaTiO<sub>3</sub> and SrTiO<sub>3</sub> nanoparticles were directly prepared by a sol-gel-type hydrolysis reaction without calcination [78, 79].

In the synthesis of nanostructured materials, a general approach based on solution phase decomposition in a structured inverse micelle medium has been developed to separately control the shape and size of colloidal inorganic nanocrystals. The anisotropic growth is controlled by using a mixture of surfactants, where the different surfactants are used to selectively control the growth rates of different faces [80]. Of interest, this technique was successfully extended to synthesize BaTiO<sub>3</sub> nanoparticles and nanorods. First, O'Brien et al. synthesized monodispersed perfect cubic BaTiO<sub>3</sub> nanoparticles with diameters ranging from 6 to 12 nm. At the same time, the propensity of these BaTiO<sub>3</sub> nanoparticles to self-assemble into superstructures was also demonstrated, as illustrated in Figure 1 [51]. In their typical synthesis, 1 mmol barium titanium ethyl hexanoisopropoxide was injected into a mixture of 50 mL diphenyl ether and 3 mmol stabilizing agent oleic acid at 140 °C under argon or nitrogen. Excess 2-propanol was removed under vacuum. The mixture was cooled to 100 °C and 30 wt% hydrogen peroxide solution (0.9 mL) was injected through the septum. The solution was maintained in a closed system and stirred at 100 °C (under a mild reflux with the remaining water content) over 48 h to promote further hydrolysis and crystallization of the product in an inverse micelle condition.

Recently, Urban et al. synthesized perfect single-crystalline cubic BaTiO<sub>3</sub> and SrTiO<sub>3</sub> nanorods with diameters ranging from 5 to 60 nm and lengths in excess of 10 μm [81, 82]. In their typical reaction, a 10-fold molar excess of 30% H<sub>2</sub>O<sub>2</sub> was added at 100 °C to 10 mL heptadecane solution containing 10 mmol barium titanium isopropoxide alkoxide precursor and 1 mmol oleic acid. The reaction mixture was subsequently heated to 280 °C for 6 h, and a white precipitate composed of nanorod aggregates was obtained. Anisotropic nanorod growth was due to precursor decomposition and crystallization in a structured inverse micelle medium formed by the precursor and oleic acid under these reaction conditions.

This developing nanotechnology will provide more complex nanostructured systems for fundamental investigations on nanoscale ferroelectricity, piezoelectricity, and paraelectricity.

### 2.1.4. Nanocrystalline Film Deposition

The microstructures of nanocrystalline BaTiO<sub>3</sub> thin films are mainly composed of ultrafine grains (random or highly oriented) and epitaxial single crystals. The epitaxial single-crystal thin films with thickness on the nanometer scale will be discussed in the next section. For ultrafine microstructured films, the sol-gel method is a good candidate for coating substrates with a large area or complex shape. Using the same precursors as in the preparation of nanoparticles, thin films were prepared by spin-coating, dip-coating, or spray-coating techniques [24]. For instance, BaTiO<sub>3</sub> nanocrystalline films of thickness 200 nm–3 μm were successfully produced on a Si single crystal or on platinum-coated Si single-crystal substrates, in which the average grain size was about 25 nm annealed at 750 °C [25, 54, 83]. Studies of the film deposition mechanism revealed that the nanocrystalline granular microstructure was formed due to homogeneous nucleation in a layer-by-layer film process. When one limits the trend of homogeneous nucleation but enhances the heterogeneous nucleation at the substrate via some tricks such as lowering the thickness of each coating layer, a nanocrystalline columnar microstructure was obtained [24, 84, 85].

The conventional sol-gel process required heat treatment at temperatures above 600 °C in order to crystallize the BaTiO<sub>3</sub> films. This limited the practical application of ferroelectric thin films in integrated semiconductor circuits owing to severe interface diffusion at high crystallization temperature. To reduce the processing temperature, an alternative was to combine the merits of the sol-gel and low-temperature hydrothermal methods. In this so-called sol-gel-hydrothermal process, the as-dried BaTiO<sub>3</sub> gel films were used as the precursor films for post hydrothermal treatment. Using this process, BaTiO<sub>3</sub> nanocrystalline thin films have been obtained at temperatures below 100 °C [86–88].

Alternatively, BaTiO<sub>3</sub> nanocrystalline thin films were also fabricated *in-situ* by low-temperature hydrothermal-electrochemical methods [64, 89–91]. One method was to use titanium metal electrode contributing the Ti source within BaTiO<sub>3</sub> thin films by anodic oxidation of Ti reacting with Ba<sup>2+</sup> and OH<sup>-</sup> ions [64, 90]. Another method was to electrophoretically deposit BaTiO<sub>3</sub> nuclei within solution on the substrates [89, 91]. With the latter technique, Tamaki et al. successfully obtained epitaxial nc-BaTiO<sub>3</sub> thin films with a grain size less than 10 nm on La<sub>0.7</sub>Sr<sub>0.3</sub>MnO<sub>3</sub>-coated SrTiO<sub>3</sub> single-crystal substrate [91]. It should be noted that these films were usually characterized by partial substrate coverage or high surface roughness.

## 2.2. Vapor Phase Methods

Besides wet chemical solution methods, BaTiO<sub>3</sub> nanostructured materials were also prepared by vapor deposition methods, in which vapor and/or plasma were generated by electrical, optical, or chemical methods [18, 92–97]. Among those various physical vapor deposition processes such as thermal evaporation, magnetron sputtering, and laser ablation, the main difference is the interaction process used to generate a vapor and/or plasma by the removal of the target material. The type, density, energy, and excitation of atoms, molecules, clusters, and micro- and macroparticles

within the generated vapor (plasma) resulted in different microstructures of nanocrystalline particles and thin films. Compared with the wet chemical solution methods, the unique advantage of the vapor deposition methods was to grow epitaxial single-crystal thin films. At present, BaTiO<sub>3</sub> epitaxial thin films have been achieved in an atomic scale layer-by-layer growth mode using metalorganic chemical vapor deposition (MOCVD) and laser molecular beam epitaxy (laser MBE) techniques [94–97]. In this section, the laser MBE technique for growing BaTiO<sub>3</sub> epitaxial single-crystal thin films and related superlattices is discussed in detail.

### 2.2.1. Epitaxial Thin Film

Pulsed laser deposition performed in an ultrahigh vacuum, that is, laser MBE, has been verified as a suitable method for growing single-crystal thin films and artificial superlattices in an atomic scale two-dimensional layer-by-layer growth mode. It combines the merits of pulsed laser deposition and conventional MBE for growing epitaxial thin films, especially suitable for high-melting-point perovskite oxide ceramics such as BaTiO<sub>3</sub> and multicomponent solids such as (Ba, Sr)TiO<sub>3</sub> controlled in atomic scale [96–99]. The details of the laser MBE apparatus and processes are described in the literature [97, 98].

Using the laser MBE technique, Lu et al. and Yoneda et al. fabricated *c*-axis-oriented BaTiO<sub>3</sub> ultrathin films of 1- to 50-unit-cell layers on SrTiO<sub>3</sub> (001) and MgO (001) substrates [96, 97]. The epitaxial relationship of BaTiO<sub>3</sub> films on both SrTiO<sub>3</sub> and MgO substrates was determined to be [100] film||[100] substrate (in the growth plane) and (001) film||(001) substrate (along the growth direction). For the BaTiO<sub>3</sub> single crystal, the thermal expansion coefficient is  $\alpha = 15.7 \times 10^{-6}/^{\circ}\text{C}$  along the *a* axis at room temperature [17]. In contrast, for the SrTiO<sub>3</sub> substrate, the cubic lattice parameter is  $a = 3.905 \text{ \AA}$  and  $\alpha = 11.7 \times 10^{-6}/^{\circ}\text{C}$  at 300 K, and for the cubic MgO substrate,  $a = 4.213 \text{ \AA}$  and  $\alpha = 14.8 \times 10^{-6}/^{\circ}\text{C}$  at 300 K [100]. From the viewpoint of lattice mismatch, the magnitude of mismatch between the MgO substrate and the bulk BaTiO<sub>3</sub> *c* axis is smaller than that between the MgO substrate and the bulk BaTiO<sub>3</sub> *a* axis. If the epitaxial relationship depends only on the lattice-matched condition, the *a* axis of the BaTiO<sub>3</sub> films on the MgO substrates should be oriented in the growth direction and the *c* axis in the growth plane. However, the BaTiO<sub>3</sub> films obtained on MgO substrates were *c*-oriented. Therefore, the lattice mismatch strain is not the only factor that determines the orientation of the BaTiO<sub>3</sub> films. Studying BaTiO<sub>3</sub> epitaxial films on various substrates, it was found that, owing to lattice and thermal expansion coefficients between the thin film and the substrate, the net elastic strain in the film growth dictated the orientation of the epitaxial BaTiO<sub>3</sub> thin films [100–102]. On the other hand, the magnitude of mismatch between the bulk BaTiO<sub>3</sub> *a* axis and the SrTiO<sub>3</sub> (+2.3%) was smaller than that between BaTiO<sub>3</sub> and MgO (−5.2%). Owing to this different epitaxial strain, the BaTiO<sub>3</sub> thin films had different crystal quality and tetragonality, for example,  $c/a = 1.003$  and  $1.018$  for the 200-nm-thick epitaxial film, respectively, on the SrTiO<sub>3</sub> and MgO substrates [96]. For BaTiO<sub>3</sub> epitaxial thin films on a MgO

substrate, the lattice parameter perpendicular to the surface was found to be nearly independent of the film thickness and close to the *c*-axis bulk value, while the in-plane lattice parameter was intermediate between the bulk *a*- and *c*-axis values and approached the bulk *a*-axis value with increasing film thickness to 2000 nm [102, 103]. In summary, the lattice strain in BaTiO<sub>3</sub> epitaxial thin films could be tuned by choosing the substrate and controlling the film thickness. To eliminate the substrate clamping effect, preparing freestanding BaTiO<sub>3</sub> single-crystal thin films is the next object.

On the SrTiO<sub>3</sub> substrates with various orientations, the surface morphology of BaTiO<sub>3</sub> epitaxial films exhibited different roughness. For the typical perovskite oxides with formula ABO<sub>3</sub>, there are two possible terminating atomic layers, AO (A-site plane) and BO<sub>2</sub> (B-site plane), on the (100) surface. In the 10-nm-thick BaTiO<sub>3</sub> (001) epitaxial thin film on a SrTiO<sub>3</sub> (001) substrate, the *in-situ* reflection high-energy electron diffraction intensity oscillation indicated the BaTiO<sub>3</sub> thin film to be in a unit-cell layer-by-layer growth. Angle-resolved X-ray photoelectron spectroscopy analysis revealed that the topmost surface atomic plane for this BaTiO<sub>3</sub> ultrathin film was the TiO<sub>2</sub> layer. Thus, the BaTiO<sub>3</sub> film growth sequence was determined as TiO<sub>2</sub> (substrate)/BaO/TiO<sub>2</sub>/.../BaO/TiO<sub>2</sub>. The root mean square surface roughness was 0.2 nm observed by atomic force microscopy [104]. In contrast, the topmost surface of BaTiO<sub>3</sub> (001) epitaxial films with a thickness greater than 80 nm was determined as the BaO plane, even though the SrTiO<sub>3</sub> (001) substrate had the dominant topmost surface of TiO<sub>2</sub> [96, 99]. These facts also suggested that the film growth did not simply depend on the lattice-matched condition between the BaTiO<sub>3</sub> films and the substrates [96, 105]. It should be noted that the substrate surface treatment was very important for the growth of high-quality epitaxial films in the layer-by-layer mode, especially for the ultrathin films of unit-cell layers [97, 99].

To date, epitaxial BaTiO<sub>3</sub> single-crystal thin films have been successfully deposited on various single-crystal substrates such as SrTiO<sub>3</sub>, LaAlO<sub>3</sub>, SrRuO<sub>3</sub>, MgO, MgAl<sub>2</sub>O<sub>4</sub>, and sapphire [94, 97–99, 103]. These epitaxial films may provide a wide range of applications in microelectronics, integrated optics, and microsystem technology, such as sensors, microactuators, memories, and optical waveguide devices. Of interest, BaTiO<sub>3</sub> is also a good candidate for the insulating layer in high-*T<sub>c</sub>* oxide devices due to its similar perovskite structure and small lattice mismatch with the high-*T<sub>c</sub>* oxide superconductors. The heteroepitaxial growth of BaTiO<sub>3</sub> ultrathin films using the laser MBE technique creates a new way to fabricate superconductor–insulator–superconductor tunnel junction devices [97, 99].

In semiconductor nanotechnology, the MBE technique was widely used to fabricate ordered nanostructures through the self-organized growth mode. For Ce:BaTiO<sub>3</sub> oxide, the strain-driven self-organized growth of nanoscale islands was also exploited using the laser MBE technique on MgO (100) substrates. The distributed coherent Ce:BaTiO<sub>3</sub> square base pyramidal nanoislands were fabricated on top of a thicker wetting layer [106].

### 2.2.2. Strained Superlattice

Synthetic superlattices are an essential approach to artificially controlling the crystal structures and ferroelectric properties. By changing the constituent layer thickness and stacking periodicity of the superlattice, the lattice strain stored in epitaxial thin films can be tuned [107]. With this approach, the dielectric constant, remanent polarization, Curie temperature, and/or lattice dynamics properties of BaTiO<sub>3</sub> have been remarkably tuned [99, 108–110].

In addition to BaTiO<sub>3</sub>, heteroepitaxial thin films of SrTiO<sub>3</sub>, CaTiO<sub>3</sub>, and BaZrO<sub>3</sub> perovskite oxides were also achieved in the layer-by-layer growth mode using laser MBE. Thus, atoms of Ba and Ti in BaTiO<sub>3</sub> can be replaced site selectively with atomic accuracy and lattice strain introduced by a combination of different layers. For instance, BaTiO<sub>3</sub>/SrTiO<sub>3</sub> artificial superlattices with periodicity of the BaTiO<sub>3</sub>/SrTiO<sub>3</sub> layers varying from 1 unit cell to 125 unit cells were obtained [98, 109]. In the BaTiO<sub>3</sub>/SrTiO<sub>3</sub> (BaTiO<sub>3</sub>/CaTiO<sub>3</sub>) superlattices, there is a relatively large mismatch of 2.5% (5.5%) between the in-plane lattice parameters. When the film thickness reaches a critical thickness, misfit dislocations will form, which relax lattice mismatch strain and deteriorate the surface roughness [111]. The critical thickness for the strained superlattice has been experimentally determined as 220 Å for the BaTiO<sub>3</sub>/SrTiO<sub>3</sub> superlattice and 55 Å for the BaTiO<sub>3</sub>/CaTiO<sub>3</sub> superlattice [107, 112].

### 2.3. Nanoceramics

For BaTiO<sub>3</sub> ceramics, not only their dielectric properties but also their mechanical properties were found to depend strongly on the microstructures, such as grain size, grain geometry, and relative density. Using BaTiO<sub>3</sub> nanoparticles as starting powders significantly lowers the sintering temperatures and enhances the mechanical and electrical properties of the final ceramics, due to improved homogeneity, purity, controlled grain size, and its distribution, and thus creates opportunity to develop better performing nanoceramic devices [79, 113–115].

With monodispersed BaTiO<sub>3</sub> nanoparticles as the starting material, Her et al. obtained BaTiO<sub>3</sub> fine ceramics using conventional ceramic processing. In a typical case, the polyvinyl alcohol was first added to BaTiO<sub>3</sub> nanopowders approximately 100 nm in size as a binder to prepare green pellets. Second, the polyvinyl alcohol-containing BaTiO<sub>3</sub> nanopowders were cold-pressed to form a pellet under 340 MPa. Then the pellet was sintered in air at a high temperature at a heating rate of 2°/min from room temperature to 600 °C and then at a heating rate of 8°/min from 600 °C to sintering temperature. Fine ceramics with a high density of 5.90 g/cm<sup>3</sup> (98.2% of the theoretical density of 6.01 g/cm<sup>3</sup>) and 6.00 g/cm<sup>3</sup> (99.8% of the theoretical density) were produced by sintering at temperature as low as 1200 °C and 1250 °C, respectively, in which the average grain size was over 1–2 μm. The dielectric constant for the ceramics sintered at 1200 °C was 9700 at 120 °C and 5000 (with a dissipation factor of 2.0%) at room temperature [31]. Intensive investigations indicated that the maximum room-temperature dielectric constant of BaTiO<sub>3</sub>

ceramics was obtained with density near the theoretical density and optimal grain size near 1 μm [10, 31, 113, 116, 117]. Moreover, using BaTiO<sub>3</sub> nanoparticles allows thinner layers of ceramic in multilayer capacitors without loss of dielectric properties.

BaTiO<sub>3</sub> nanoceramics were also fabricated by using BaTiO<sub>3</sub> nanoparticles with even smaller grain size and/or controlling the sintering schedule. Using nanopowders with a grain size of about 10 nm as the starting materials, Luan et al. fabricated BaTiO<sub>3</sub> nanoceramics under hot pressing at uniaxial pressures in vacuum. It was found that both the density and the grain size increase quickly with increasing sintering temperature. The average grain size and relative density changed from 280 to 1800 nm and from 93.2 to 98.8%, respectively, when the sintering temperature increased from 1050 to 1150 °C [118]. At 1250 °C under atmospheric pressure, Bocquet et al. obtained BaTiO<sub>3</sub> nanoceramics with a grain size of 200–800 nm and a relative density of 98%. The dielectric constant was measured as  $\epsilon_{RT} = 2780$  at room temperature and  $\epsilon_{max} = 10,520$  at  $T_c = 115$  °C [70].

Ragulya developed a rate-controlled sintering process, which controlled the densification rate instead of controlling the linear heating rate during sintering. Using this technique, he obtained BaTiO<sub>3</sub> nanoceramics with a relative density up to 99.9% and the average grain size ranged from 100 to 300 nm for BaTiO<sub>3</sub> nanopowders with a grain size of 20–25 nm. Two optimal rate-controlled temperature–time paths for preparing BaTiO<sub>3</sub> nanoceramics were also reported [119]. In comparison with conventional temperature-controlled sintering, the rate-controlled sintering allowed one to obtain nanoceramics of smaller grain size and narrower distribution.

Spark plasma sintering is a process that makes use of a microscopic electrical discharge between particles under mild pressure (30–50 MPa). This process enables a compact powder to be sintered to high density at relatively lower temperatures and in much shorter sintering times, typically a few minutes, compared with the conventional sintering process of cold isostatic pressing. Using the spark plasma sintering method, starting from BaTiO<sub>3</sub> nanopowders with a grain size of 60 nm, Takeuchi et al. produced dense BaTiO<sub>3</sub> nanoceramics with a relative density greater than 95% and an average grain size less than 500 nm under 1100 °C for 5 min. The temperature increased from room temperature to sintering temperature at a heating rate of approximately 160 °C/min, which was controlled by the applied current. It was found that the grain size of the initial nanopowders significantly affected the grain size of the resulting ceramics. For BaTiO<sub>3</sub> nanoceramics with an average grain size of 300 nm, the room-temperature dielectric constant, spontaneous polarization, and remanent polarization were measured as 3000 at 100 kHz, 15 μC/cm<sup>2</sup>, and 2 μC/cm<sup>2</sup>, respectively [10].

In addition to suppressing exaggerated grain growth, the lower sintering temperature and/or shorter sintering time allow use of less expensive electrode materials in fabricating ceramic multilayer capacitors [10, 45, 120].

## 2.4. Nanocomposites

### 2.4.1. Ceramic Matrix Composites

Since ceramic nanocomposites, materials reinforced by secondary dispersoids of a few tens to a few hundreds of nanometers in size (nanoparticles), were proposed in the field of engineering ceramics, significant improvements have been reported in their mechanical properties, such as fracture strength, hardness, and fracture toughness. From the viewpoint of mechanical properties, ferroelectricity or piezoelectricity shows an interesting property. By utilizing the electromotive force of the ferroelectric material, one is able to detect crack propagation. When the ferroelectric materials are subjected to an electric field, additional internal stresses are induced; since the internal stresses are anisotropic, they can increase or decrease fracture toughness, depending on the poling direction [121]. In this regard, ferroelectric nanoparticle-dispersed ceramic nanocomposites are expected to exhibit such intelligent functions as predicting fracture, controlling crack propagation, and so on.

As one of the most important ceramic nanocomposites, BaTiO<sub>3</sub> ferroelectric nanoparticle-dispersed MgO ceramic composites were developed through hot pressing or pulse electric current sintering (PECS) [122, 123]. Using nc-BaTiO<sub>3</sub> with an average grain size of 100 nm as the starting material, Hwang et al. obtained highly densified nc-BaTiO<sub>3</sub>/MgO ceramic nanocomposites and showed that these nc-BaTiO<sub>3</sub>/MgO ceramic nanocomposites introduced ferroelectricity/piezoelectricity into the nanocomposites and still retained their mechanical properties. They also demonstrated that the PECS technique took advantage of shorter time and lower temperature to sinter ceramic nanocomposites in comparison with the hot-pressing technique, which increased the tetragonality of the BaTiO<sub>3</sub> dispersoids because Mg<sup>2+</sup> was not substituted for Ti<sup>4+</sup> in the hot-pressed samples [123]. Compared with these two sintering methods, the PECS is a reasonably better sintering technique for fabricating various ceramic nanocomposites containing BaTiO<sub>3</sub> nanoparticles with even smaller grain size.

### 2.4.2. Polymer Matrix Composites

For ferroelectric nanoparticle dispersive nanocomposites, polymer is another kind of important matrix. The ferroelectricity impacted on polymeric nanocomposites could provide various applications in pyrosensors and piezosensors. In the 1990s, the considerable progress in nanotechnology rendered possible the fabrication of ferroelectric nanoparticle/polymeric nanocomposites. The basic process for fabricating polymer-based nanocomposites is to mix monodispersed ferroelectric nanoparticles into the polymer with the aid of suitable solvents [124–126].

The pyroelectric vinylidene fluoride/trifluoroethylene [P(VDF-TrFE)] copolymer is a useful matrix to form nanocomposites. P(VDF-TrFE) 70/30 mol% copolymer has a Curie temperature of 102 °C upon heating and a melting temperature of 150 °C. To prepare BaTiO<sub>3</sub> nanoparticles/copolymer nanocomposites, the copolymer was first dissolved in methyl-ethyl-ketone solvent and ferroelectric BaTiO<sub>3</sub> nanopowder was then blended into the solution to form a mixture. The powder in the mixture was dispersed

in an ultrasonic bath to produce a homogeneous suspension. The experiments revealed that the qualities of the BaTiO<sub>3</sub> nanoparticles such as agglomeration and grain size limited the volume fraction of nanoparticles in the composite. Using small uniform monodispersed BaTiO<sub>3</sub> nanoparticles can increase the volume fraction of nanoparticles in the composites. Thin films of ferroelectric nanoparticles/copolymer nanocomposites were also fabricated using the spin-coating technique. Finally, heat treatment at 120 °C was performed to remove the solvent. Experimental measurements indicated that all three figures of merit (current, voltage, and detectivity) increased with increasing volume fractions of nanoparticles in the composite [124, 125].

Using this mixing technique, Yamamoto et al. prepared 40 vol% nc-BaTiO<sub>3</sub>/chloroprene polymer composites and investigated the grain size effect on the piezoelectric properties of BaTiO<sub>3</sub>/polymer nanocomposites. It was revealed that the piezoelectric constant was closely related to the crystallographic phase of nc-BaTiO<sub>3</sub>. With BaTiO<sub>3</sub> nanoparticles in the cubic phase, the piezoelectric coefficient  $d_{33}$  of BaTiO<sub>3</sub>/polymer nanocomposites was very small (about 2 pC/N), but when the grain size was increased above the critical size, the  $d_{33}$  tetragonal nc-BaTiO<sub>3</sub> dispersoids increased rapidly to 23 pC/N [126].

At the conventional crystallization temperature of BaTiO<sub>3</sub> nanoparticles (>600 °C), the polymer matrix was severely destroyed. As discussed in Section 2.1, low-temperature hydrothermal processing can reduce the crystallization temperature of BaTiO<sub>3</sub> nanoparticles below 100 °C. Taking advantage of this property, Collins and Slamovich extended it to directly prepare nc-BaTiO<sub>3</sub>/polymer nanocomposite thin films. Thin-film composites of BaTiO<sub>3</sub> nanoparticles in polymeric matrix were processed by hydrothermally treating a film of titanium alkoxide mixed within polybutadiene-polystyrene triblock copolymer in an aqueous solution of 1.0 M Ba(OH)<sub>2</sub> at a temperature ranging from 60 to 90 °C. The subsurface growth of BaTiO<sub>3</sub> proceeded through the percolating network of hydrolyzed titanium alkoxide, which enabled the reaction solution to permeate throughout the thin films. In their BaTiO<sub>3</sub>/polymer nanocomposite thin films, the grain size of the subsurface BaTiO<sub>3</sub> nanoparticles was approximately 5–10 nm, independent of the processing temperature, but the grain size of the surface nanoparticles was over 60–180 nm, depending on the processing temperature. The room-temperature dielectric constant of the 90 wt% BaTiO<sub>3</sub>/polymer nanocomposite films was 10–15 at a frequency of 10 kHz. These ferroelectric nanoparticle/polymeric nanocomposite thin films could be used for applications ranging from nonlinear optics to abrasion-resistant coatings [127].

## 3. SPECTROSCOPIC CHARACTERIZATION

### 3.1. Structural Changes

In the BaTiO<sub>3</sub> nanocrystals, the structural and physical properties were strongly dependent on the grain size. With decreasing grain size of the nanoparticles, the anomalous lattice expansion, tetragonality decrease, and tetragonal-cubic phase transition were experimentally observed at room temperature [21, 22, 33, 44, 49, 128]. Figure 2 presents one



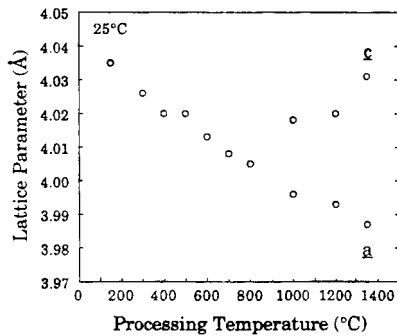


**Figure 2.** Lattice parameters determined from the (200) XRD data and representing the room-temperature cubic-to-tetragonal structural transition with increasing processing temperature. Reprinted with permission from [21], M. H. Frey and D. A. Payne, *Phys. Rev. B* 54, 3158 (1996). © 1996, American Physical Society.

example of lattice constant variation in the sol-gel-derived BaTiO<sub>3</sub> nanocrystalline particles as a function of heat treatment temperature, that is, nanoparticle grain size. It was clearly demonstrated that, with decreasing grain size, the lattice constant, *a*, of BaTiO<sub>3</sub> nanoparticles increased anomalously in both the tetragonal and the cubic phases, while the lattice constant, *c*, decreased, which resulted in a decrease in tetragonality and tetragonal-to-cubic phase transition [21]. In the monodispersed BaTiO<sub>3</sub> nanoparticles derived by the alkoxide method, the elongation of the lattice constant of *a* was measured to be greater than 2.5% in a 15-nm nanocrystallite using the electron diffraction technique [129]. In Figure 3, the room-temperature tetragonality as a function of grain size, which was determined using specific surface area data, is presented for hydrothermally derived BaTiO<sub>3</sub> nanoparticles. Below 300 nm, the tetragonality decreased exponentially, and the tetragonality of nc-BaTiO<sub>3</sub> became 1 at a critical size of approximately 120 nm, while a size-induced ferroelectric tetragonal-paraelectric cubic phase transition took place [22]. It should be noted that the reported critical size for the grain size-induced BaTiO<sub>3</sub> tetragonal-cubic phase was closely correlated with the particular processing and the grain size determination methods. Some experimentally obtained critical sizes are listed in Table 2. It can be seen that they are on the order of 50 nm as

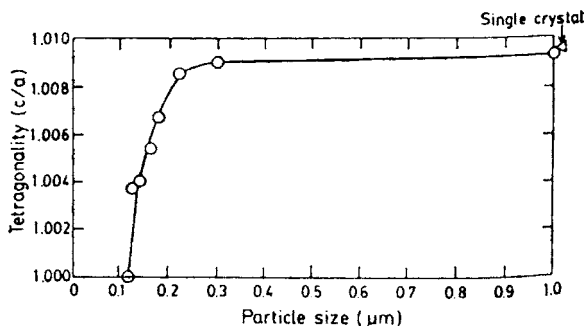


**Figure 3.** Change in tetragonality *c/a* with particle size at room temperature. Reprinted with permission from [22], K. Uchino et al., *J. Am. Ceram. Soc.* 72, 1555 (1989). © 1989, American Ceramic Society.

**Table 2.** Critical size of the tetragonal-cubic phase transition at room temperature for BaTiO<sub>3</sub> nanoparticles.

Synthesis method	Critical size	Measurement method	Ref.
sol-gel	50 nm	XRD SEM	[21, 58]
Hydrothermal	90 nm	XRD	[22]
BTOT	~30 nm	XRD TEM	[43, 44]
Alkoxide method	80 nm	TEM	[129]
LTHM	49 nm	XRD	[49]

determined by the X-ray diffraction (XRD) technique [21, 22, 25, 44, 49, 58, 128, 130].

Thermal measurements on BaTiO<sub>3</sub> polycrystals with a grain size ranging from 10 μm to 35 nm were performed using differential scanning calorimetry (DSC) [21, 128]. The DSC data are presented in Figure 4. As illustrated in Figure 4, endothermic features near 125 and 5 °C for larger grain specimens featured the first-order cubic-tetragonal and tetragonal-orthorhombic phase transformations, respectively. With decreasing grain size, the cubic-tetragonal and tetragonal-orthorhombic transformations shifted to lower and higher temperatures, respectively. For 35-nm nanocrystals, there was only a single very broad and weak endothermic peak, which featured BaTiO<sub>3</sub> nanocrystals in a locally acentric distorted cubic phase. In contrast to the 211 J/mol of cubic-tetragonal transformation enthalpy for a single crystal, the transformation enthalpy was reduced to 183 J/mol for the 10-μm grains and 78 J/mol for the 100-nm grains [21]. The thermal features observed in BaTiO<sub>3</sub> with finite grain size revealed the suppressed phase transformation characteristics.

Dielectric measurements of BaTiO<sub>3</sub> fine ceramics and nanocrystalline thin films showed also that the phase transitions were strongly dependent on the grain size [8–10, 23, 25]. Some experimental results are shown in Figure 5. It is obvious that, with decreasing grain size, the maximum value of the cubic-tetragonal phase transition decreased, and the dielectric peak became broader while the dielectric constant as a function of temperature deviated from the Curie-Weiss behavior above the ferroelectric phase transition and that the ferroelectric phase transformation at last disappeared over temperatures between -85 °C and 200 °C, as illustrated

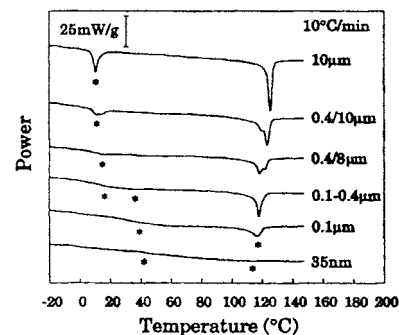


**Figure 4.** DSC data for BaTiO<sub>3</sub> polycrystals, illustrating the dependence of phase transition thermal characteristics on grain size. Reprinted with permission from [21], M. H. Frey and D. A. Payne, *Phys. Rev. B* 54, 3158 (1996). © 1996, American Physical Society.

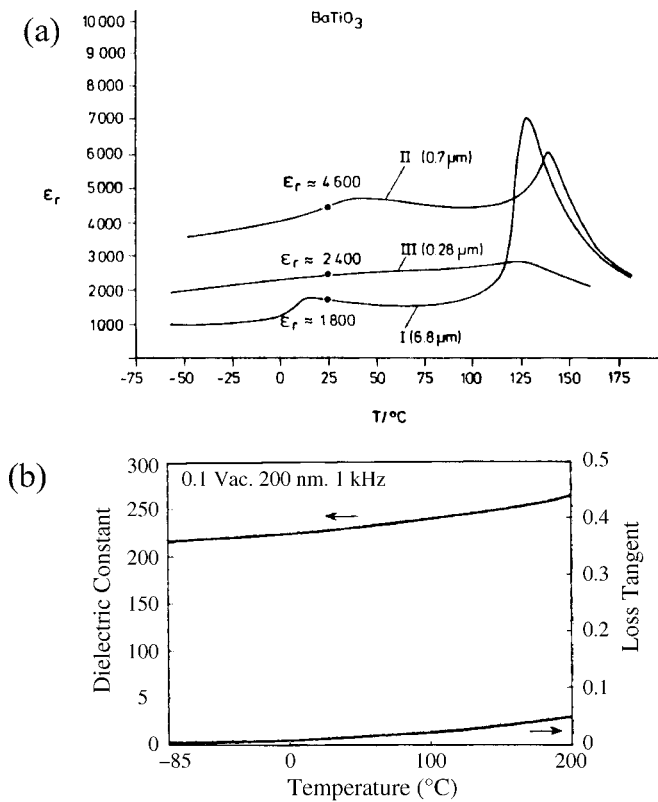


**Figure 5.** (a) Dielectric constant vs. temperature of BaTiO<sub>3</sub> fine ceramics with various grain sizes at 1 kHz. (b) Temperature dependence of dielectric constant and loss tangent for BaTiO<sub>3</sub> thin films with an average grain size of 25 nm. (a) reprinted with permission from [9], G. Arlt et al., *J. Appl. Phys.* 58, 1619 (1985). (b) reprinted with permission from [25], M. H. Frey and D. A. Payne, *Appl. Phys. Lett.* 63, 2753 (1993). © 1993, American Institute of Physics.

in BaTiO<sub>3</sub> nanocrystalline thin films with an average grain size of 25 nm. In most of the literature, the ferroelectric phase transition temperature  $T_c$  was observed to decrease with decreasing grain size [10, 22, 130]. It should be noted that, in Figure 5a, the cubic–tetragonal phase transition temperature for a 0.7- $\mu\text{m}$  ceramic was slightly higher than that for a 6.8  $\mu\text{m}$  ceramic, which was attributed to the strong elastic constraint being correlated with the grain size effect in this sample [9].

In BaTiO<sub>3</sub> fine ceramics and nanocrystalline thin films, the broadening of the ferroelectric–paraelectric phase transition as a function of grain size was even explained by an intrinsic grain size–induced diffuse phase transition model [131–133]. For the diffuse phase transition in ferroelectric perovskite solutions, the experimental data of dielectric constants above the phase transition were described by the empirical relationship:

$$\frac{1}{\epsilon} - \frac{1}{\epsilon_{\max}} = \frac{1}{\Lambda}(T - T_c)^\gamma \quad (3.1)$$

where  $\epsilon_{\max}$  is the maximum dielectric constant at the apparent transition temperature  $T_c$ ,  $\Lambda$  is a constant, and  $1 \leq \gamma \leq 2$ .  $\gamma = 1$  is the a normal phase transition and  $\gamma = 2$  is the a pure diffuse phase transition [134, 135]. For BaTiO<sub>3</sub> nanoceramics with various grain sizes, the experimental dielectric data

above the ferroelectric–paraelectric phase transition were successfully fitted with this relationship; the diffusivity, which was described by the critical exponent  $\gamma$ , was observed to increase with decreasing grain size [131, 132].

On the other hand, the room-temperature dielectric constant was strongly dependent on the grain size, which exhibited a maximum value for ceramics with a grain size around 1  $\mu\text{m}$ , but decreased dramatically with further decreasing grain size. The room-temperature dielectric constant was 230 for the sample with a grain size of 25 nm, which was one order of magnitude smaller than the maximum value of 5000 for fine ceramics with a grain size of 1  $\mu\text{m}$  [23, 25].

Of interest is to compare BaTiO<sub>3</sub> with another important ferroelectric PbTiO<sub>3</sub> system. A PbTiO<sub>3</sub> single crystal has a tetragonal structure ( $a = 3.899 \text{ \AA}$ ,  $c = 4.153 \text{ \AA}$ ,  $c/a = 1.065$ ) at room temperature and is transformed to a cubic paraelectric phase ( $a = 3.96 \text{ \AA}$ ) above  $T_c = 763 \text{ K}$ . At present, the experimental results on PbTiO<sub>3</sub> nanoparticles indicated that the lattice constant, tetragonality, Curie temperature, and phase transition latent heat changed similarly to nc-BaTiO<sub>3</sub> with varying nanocrystallite size. When the grain size was below approximately 150 nm, the lattice parameter  $a$  increased and  $c$  decreased with decreasing grain size. The resulting tetragonal distortion decreases exponentially below 60 nm and becomes 1 at a grain size extrapolated to be between 7 and 12.6. The Curie temperature of the tetragonal–cubic phase transition in nc-PbTiO<sub>3</sub> was also observed to decrease with decreasing grain size [32, 41, 136–139].

In the cases of BaTiO<sub>3</sub> and PbTiO<sub>3</sub> nanoparticles, the dielectric, thermal, and structural data indicated that the ferroelectric tetragonal–paraelectric cubic transition temperature,  $T_c$ , decreases monotonically and the transition peak becomes broad with decreasing grain size. The relationship between  $T_c$  and the nanocrystallite size,  $R$ , can be written as

$$T_c = T_c(\infty) - D/(R - R_c) \quad (3.2)$$

where  $T_c(\infty)$  denotes the value of the bulk crystals,  $R_c$  is the critical size, and  $D$  is a constant [22, 138, 139]. For BaTiO<sub>3</sub>,  $T_c(\infty) = 128 \text{ }^\circ\text{C}$ ,  $D = 700$ , and  $R_c = 110 \text{ nm}$  [22]. The broad tetragonal–cubic phase transition due to a reduction of grain size in nc-PbTiO<sub>3</sub> was also explained in terms of a diffuse phase transition model [32, 134].

### 3.2. Hydroxyl Defects

There were usually a lot of residual hydroxyl OH<sup>−</sup> defects within the BaTiO<sub>3</sub> nanoparticles derived from wet chemical solution methods. In the BaTiO<sub>3</sub> nanopowders prepared by the hydrothermal method, an absorption band near 3500  $\text{cm}^{-1}$  was observed. In contrast, the band was measured near 3510  $\text{cm}^{-1}$  in the sol–gel-derived nanopowders [21, 128]. This difference was attributed to different hydroxyl defect occupations within the nanoparticle matrix, since the hydrogen defects are very mobile in BaTiO<sub>3</sub> perovskite and able to possess several configurations [140]. With increasing annealing temperature, this absorption intensity decreased and became 0 above 600  $^\circ\text{C}$ , which demonstrated that the hydroxyl defects could be eliminated with heat treatment at high temperature and were totally removed

above 600 °C [21, 128, 141]. On one hand, the release of hydroxyl induced the lattice distance contraction with increasing annealing temperature. However, in most cases where the crystalline nanoparticles were prepared with heat treatment above 600 °C, the lattice contraction observed in nc-BaTiO<sub>3</sub> was mainly caused by the variation in grain size [43, 44, 129].

In Raman measurements, it was found that these residual hydroxyl defects affected the behavior of the optical modes of nc-BaTiO<sub>3</sub>, particularly the 257- and 308-cm<sup>-1</sup> modes, which caused a mode shift in the frequency of the Raman mode of 257 cm<sup>-1</sup> toward 297 cm<sup>-1</sup> and inhibited the 308-cm<sup>-1</sup> mode in the as-prepared samples. With a decrease in the concentration of residual hydroxyl defects, the peak position shifted from 297 cm<sup>-1</sup> toward 257 cm<sup>-1</sup> with increasing annealing temperature to 600 °C [21, 33, 58]. In contrast, the 308-cm<sup>-1</sup> mode was unambiguously observed in two-phase coexisting barium titanate nanopowders, even in the LTHM as-prepared samples with a large concentration of hydroxyl defects [33, 49]. This different behavior of the 308-cm<sup>-1</sup> mode in the single phase and in two-phase coexisting barium titanate nanoparticles also contributed to the different hydroxyl configurations within the nanocrystal lattice. Moreover, a new Raman mode at 806 cm<sup>-1</sup> was observed owing to the hydroxyl absorbed on the nanoparticle boundary [21, 33].

Figure 6 presents typical Raman spectra for single-phase BaTiO<sub>3</sub> nanoparticles derived by the low-temperature hydrothermal method. It can be seen that the peak position of the 257-cm<sup>-1</sup> mode shifted upward to 297 cm<sup>-1</sup> in the as-prepared sample and shifted downward with a reduction in hydroxyl concentration in the BaTiO<sub>3</sub> nanoparticles. In the samples annealed above 600 °C, the 308-cm<sup>-1</sup> mode started to be clearly distinguished and the 806-cm<sup>-1</sup> peak disappeared, in agreement with infrared measurements on the hydroxyl defects. In the pure cubic BaTiO<sub>3</sub> nanoparticles, which were obtained with heat treatment above 600 °C, five modes centered at 184, 257, 308, 518, and 716 cm<sup>-1</sup> were recorded. In the tetragonal nc-BaTiO<sub>3</sub>, the intensity of the 184-cm<sup>-1</sup> mode decreased with increasing tetragonality and

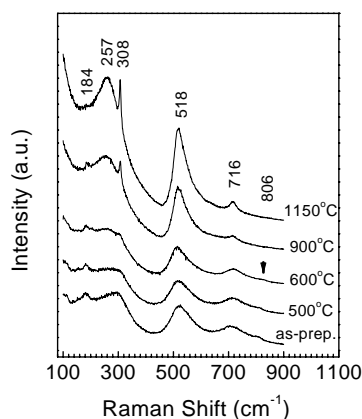


**Figure 6.** Raman spectra of BaTiO<sub>3</sub> nanoparticles derived by low-temperature hydrothermal method and annealed at various temperatures. Reprinted with permission from [33], J. Yu et al., *Mater. Res. Soc. Symp. Proc.* 718, 177 (2002). © 2002, Materials Research Society.

became negative when the tetragonality reached the value of the bulk materials. Therefore, the intensity of the 184-cm<sup>-1</sup> mode was an effective probe to check the structural changes induced by grain size variation in nc-BaTiO<sub>3</sub> [10, 21, 33].

### 3.3. Complex Defects

In Section 2.1, it was pointed out that a homogeneous precursor played an important role in the chemical solution methods to obtain defect-free BaTiO<sub>3</sub> nanocrystals. Using high-resolution transmission electron microscopy (HRTEM) Jiang et al. found many internal defect textures, including (111) nanoscale multiple twinning and complicated (111) intergrowth defects, in some barium titanate nanoparticles derived by the SAG and sol-gel methods [56]. As an illustration, Figure 7 presents an example of an SAG-derived BaTiO<sub>3</sub> nanocrystal with a grain size of 10 nm, which contained a complex arrangement of defects on the (111) planes indicated by the arrow. At the same time, image processing showed a high density of small defects within the nanocrystal matrix. The density of small defects was estimated to be on the order of 10<sup>27</sup>/m<sup>3</sup> in the SAG BaTiO<sub>3</sub> nanoparticles prepared at 600 °C and decreased as the annealing temperature (i.e., particle size) increased. After annealing at high temperature (>1200 °C), no hexagonal intergrowth structure and (111) multiple twinning defects were observed, but the small defect density was still high. In the sol-gel-derived BaTiO<sub>3</sub> nanoparticles, the defect density was much lower than in the SAG-derived samples, but some still contained many internal defects, including the (111) multiple twinning. Based on the HRTEM results, the authors speculated that these defects of high density were the reason that the SAG BaTiO<sub>3</sub> nanoparticles remained in the cubic phase even with grain size up to 3500 nm.

In those cubic nc-BaTiO<sub>3</sub> including (111) twinning planar and intergrowth defects, Raman scattering measurements recorded three novel peaks at 153, 640, and 1059 cm<sup>-1</sup> besides the five modes of 184, 257, 308, 518, and 716 cm<sup>-1</sup>

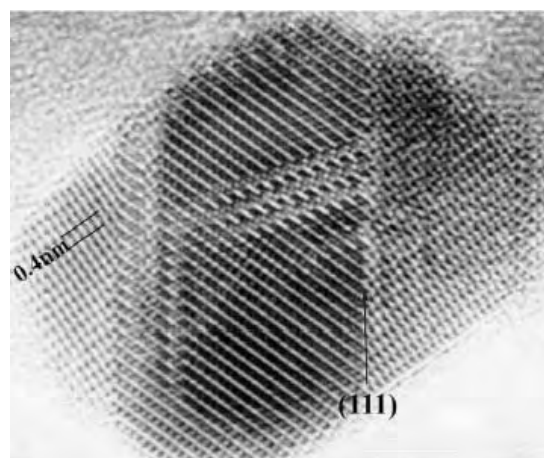


**Figure 7.** High-resolution transmission electron microscopy image of a 10-nm SAG BaTiO<sub>3</sub> nanocrystal with complex set of twins on (111) planes (prepared at 650 °C). Reprinted with permission from [56], B. Jiang et al., *Physica B* 291, 203 (2000). © 2000, Elsevier Science.

characteristic of cubic nc-BaTiO<sub>3</sub>. Although the 153- and 640-cm<sup>-1</sup> modes were attributed to the nc-BaTiO<sub>3</sub> hexagonal phase [142], the HRTEM measurements did not detect any hexagonal nanoparticles. The 153- and 1059-cm<sup>-1</sup> modes were from BaCO<sub>3</sub> contamination. These (111) twinning and intergrowth defects existing in SAG nc-BaTiO<sub>3</sub> prepared below 950 °C were attributed to the existence of the low oxidation state of Ti<sup>3+</sup> [56, 63].

### 3.4. Phase Transformation Mechanism

To understand the structural changes, in particular, the grain size-induced tetragonal-cubic phase transition in nc-BaTiO<sub>3</sub>, three models were proposed.

#### 3.4.1. Surface Model

In nanoparticles, there are two significant factors affecting their physical properties: One is a macroscopic effect related to the surface tension of the nanoparticle, and the other concerns the grain size effect on microscopic interactions which induce ferroelectricity instability in perovskite oxides [5, 128, 143]. First, Zhong et al. developed a Landau phenomenological theory to treat the case of ferroelectric nanomaterials, in which a surface layer with degraded polarization was held responsible for the ferroelectric-paraelectric phase transition [144]. Numerical calculations showed that the spontaneous polarization decreased with decreasing particle size and eventually disappeared; that is, a size-driven phase transition took place. The ferroelectric critical size was defined as the size at which the ferroelectric tetragonal-paraelectric cubic phase transition takes place at  $T_c \rightarrow 0$  K. For BaTiO<sub>3</sub> nanoparticles, the ferroelectric critical size was predicted to be 44 nm, and for nc-PbTiO<sub>3</sub> to be 4.2 nm, which were on the same order as the experimental values. The size dependence of  $T_c$  was found to be inversely proportional to the grain size  $R$ :  $T_c \propto 1/R$ . Second, Uchino et al. analyzed the surface tension effect on the Curie temperature and obtained the same inverse-proportion relationship between  $T_c$  and  $R$ , whereas the experimental relationship of (3.2) obtained in BaTiO<sub>3</sub> and PbTiO<sub>3</sub> nanoparticles included the critical size,  $R_c$  [22, 139]. On the other hand, for covalent crystals, surface tension-like forces would always lead to lattice contraction in small particles [136]. Obviously, this prediction was contrary to the experimental results in nc-BaTiO<sub>3</sub>. So far, it can be seen that the surface model is insufficient to understand the Curie temperature change and lattice expansion in BaTiO<sub>3</sub> ferroelectric nanoparticles. The grain size effect on the microscopic cooperative phenomenon must be taken into consideration [22].

The core-shell model was proposed to explain the anomalous dielectric behavior and the structural phase transition in fine BaTiO<sub>3</sub> ceramics, in which each crystallite consisted of a regular ferroelectric core with a tetragonality gradient toward the outer surface range, surrounded by a cubic surface layer with low permittivity. The cubic surface layer was estimated to be approximately 5–15 nm thick [53, 117]. However, HRTEM measurements of lattice images of BaTiO<sub>3</sub> and PbTiO<sub>3</sub> nanoparticles did not reveal the existence of a cubic surface layer [56, 126].

#### 3.4.2. Defect Model

In the hydrothermal-derived BaTiO<sub>3</sub> nanoparticles, it was found that the synthesized BaTiO<sub>3</sub> nanoparticles were stabilized in the cubic phase by numerous residual hydroxyl defects, independent of grain size [126, 141, 145]. This stabilization was interpreted with the model of lattice defects, in which the dipoles were introduced by hydroxyl defects within the nanoparticles; the correlation size of the dipoles decreased greatly with increasing concentration of hydroxyl defects and, consequently, stabilized the cubic phase in the nc-BaTiO<sub>3</sub>. Nevertheless, the hydroxyl defects derived from wet chemical solution methods could be totally eliminated from the nc-BaTiO<sub>3</sub> matrix, while the cubic phase remained stable in nc-BaTiO<sub>3</sub> with grain size below the ferroelectric critical size [21, 128]. Furthermore, the hydrothermal method was demonstrated to directly produce about 100-nm large tetragonal BaTiO<sub>3</sub> nanocrystals, of which the hydroxyl concentration exceeded that in hydrothermal cubic BaTiO<sub>3</sub> nanopowders [50, 128]. These facts indicated that the hydroxyl defect model is not responsible for the stabilization of the cubic nanophase.

#### 3.4.3. Microscopic Interaction Model

Before discussing the microscopic interaction model, let us recall the main results on the origin of ferroelectricity and the nature of the ferroelectric-paraelectric phase transition of ferroelectric titanates. The first-principle theoretical investigations revealed that the long-range Coulombic interactions favor the ferroelectric distortion, but the short-range electric repulsions favor the nonpolar cubic structure, and those ferroelectric phases result from softening of the short-range electric repulsions by Ti 3d–O 2p hybridization [5, 6, 37, 38, 146–148]. Most recently, Kuroiwa et al. measured the charge density distributions of the tetragonal and cubic phases of BaTiO<sub>3</sub> and PbTiO<sub>3</sub> by the maximum entropy method/Rietveld analysis using synchrotron-radiation powder diffraction, and verified the hybridization between the Ti 3d states and O 2p states in the ferroelectric tetragonal phase. At the same time, a charge transfer was found between the Pb 6s states and O 2p states through the cubic-to-tetragonal phase transition but the Ba–O bond was always ionic, which suggested that PbTiO<sub>3</sub> has a larger ferroelectricity than BaTiO<sub>3</sub> [39].

In ferroelectric nanomaterials, when the grain size of the nanoparticles was comparable to the correlation length describing the long-range Coulombic interaction, the long-range interaction remarkably decreased with a decrease in grain size. In creating balance, both the Ti–O hybridization and the short-range electric repulsion were correspondingly reduced [32, 33]. For the partially covalent-ionic crystals, the reduction in hybridization meant a loss in the directional character of the interionic bonds and the crystal tended to assume a structure with comparatively higher symmetry [136]. In the cubic nc-BaTiO<sub>3</sub>, the reduction in Ti–O hybridization has been proved using X-ray photoelectron spectroscopy and *ab initio* simulation [129, 149]. In nc-BaTiO<sub>3</sub>, the binding energy of the Ba 3d<sub>5/2</sub> electron was measured as 779.3 eV, independent of nanocrystallite size, but the binding energy of the Ti 2p<sub>3/2</sub> electron slightly decreased with decreasing grain size below the critical size and was the same as that in the bulk crystal, 458.5 eV,

above the critical size. This decrease reflected the character change of Ti–O bonds from covalent to ionic below the critical size [129]. In particular, for the covalent–ionic BaTiO<sub>3</sub> nanoparticles, the reduction in Ti–O hybridization induced the lattice distance expanded and the ferroelectric tetragonal phase became unstable, then transformed to high-symmetrical cubic at some critical grain size. So far, it is seen that those structural changes caused by grain size in nc-BaTiO<sub>3</sub> are well prescribed using the model of grain size effect on long-range interaction and its cooperative phenomena. In tetragonal PbTiO<sub>3</sub>, owing to the additional Pb–O hybridization [39], the stronger covalent bonding resulted in a smaller ferroelectric critical size for the size-induced tetragonal–cubic phase transition than that for BaTiO<sub>3</sub>. This further demonstrates that the hybridization change plays a dominant role in structural changes of ferroelectric nanomaterials.

The first-principle calculations indicated that the tetragonal *c/a* lattice strain is quite significant for ferroelectric tetragonal distortion, which enhances the hybridization between the Ti 3d states and the O 2p states and helps stabilize the tetragonal phase. The ferroelectric–paraelectric phase transition in BaTiO<sub>3</sub> arises from a complicated coupling of a displacive soft-mode, order–disorder hopping between wells and lattice strain. Under high pressure, the volume dependence of soft-mode potential surfaces is consistent with the loss of ferroelectricity in titanate. Under compression, the multiple-well structure disappears, and a continuous transition at zero temperature occurs at the pressure where the well depths vanish [5, 6, 37]. As indicated by (5.2), theoretical and experimental studies both revealed that the tetragonal strain scales with the spontaneous polarization (ferroelectricity) in BaTiO<sub>3</sub> [150]. In the case of ferroelectric nanocrystals, the reduced tetragonality (as illustrated in Figs. 2 and 3) with decreasing grain size thus weakens the ferroelectricity in the tetragonal nanophase and reduces the hybridization, thereby driving the structure change to paraelectric cubic below the ferroelectric critical size.

In nanomaterials of GaN [151] and a large majority of partially covalent oxides [32, 136, 152], which includes technologically important systems such as ferroelectrics, ferromagnets, superconductors, and structural ceramics, a structural change from low symmetry to high symmetry and lattice expansion were also observed with decreasing nanoparticle size. Similar to the case of nc-BaTiO<sub>3</sub>, these results could also be well prescribed by the model of grain size effect on long-range interaction and its cooperative phenomena [33]. That is to say, the model of grain size effect on long-range interaction and its cooperative phenomena has universality for covalent–ionic nanomaterials. The reduction in electronic covalency intrinsically involved in this model may cause nanomaterials to possess some different properties from their corresponding bulk, such as superparaelectricity, quantum ferroelectricity (discussed below), superparamagnetism [153], and so on.

## 4. PROPERTIES

Since the long-range Coulomb interaction is strongly reduced in BaTiO<sub>3</sub> ferroelectric nanocrystals, it is quite natural that ferroelectric nanostructured materials exhibit

different electrical and optical properties from those of bulk crystals. In this section, the present results of the electrical and optical properties on BaTiO<sub>3</sub> nanostructured materials are summarized in Sections 4.1 and 4.2, respectively.

### 4.1. Electrical Properties

The grain size effect on the phase transitions and physical properties of ferroelectrics has been known since the 1950s. The properties of Curie temperature ( $T_c$ ), spontaneous polarization, coercive field, switching speed, dielectric constant, and so forth, were found to depend on the grain size [28, 144, 154]. As illustrated in Figure 5, the dielectric constant of BaTiO<sub>3</sub> ceramics increased with decreasing grain size, and a maximum value of  $\epsilon_r \sim 5000$  was observed with a grain size around 1  $\mu\text{m}$ . With further decreasing grain size into the nanometer scale,  $\epsilon_r$  remarkably decreased [9, 10, 25, 31, 116, 117, 130]. For nanoceramics with an average grain size of 400 nm, the room-temperature dielectric constant was measured as 3500 at 100 kHz, but for a grain size of 300 nm,  $\epsilon_r = 3000$  [10]. For sol–gel-derived 50-nm BaTiO<sub>3</sub> nanocrystalline film on platinized silicon substrates with a thickness of 1.5  $\mu\text{m}$ , the dielectric constant and loss tangent were measured as 430 and 0.015, respectively, at 10 kHz under ambient conditions.  $\epsilon$  increased from 430 to 470, but  $\tan \delta$  remained unchanged as the measurement atmosphere was changed from air to vacuum [23]. In sol–gel-derived BaTiO<sub>3</sub> nanocrystalline thick films with an average grain size in the range of 15–25 nm, the films with larger grain size exhibited stronger frequency dependence of the dielectric constant. For a film with a grain size of 25 nm, the room-temperature dielectric constant decreased from 401 to 349 as the frequency was increased from 1 kHz to 10 MHz. When the grain size was increased from 15 to 25 nm, the relative dielectric constant increased from 207 to 401 at 1 kHz [26]. For sol–gel-derived BaTiO<sub>3</sub> nanocrystalline thin films with a grain size of 25 nm, the dielectric constant and loss tangent were 230 and 0.02 at room temperature, respectively. The temperature coefficient of capacitance was  $625 \times 10^{-6}/^\circ\text{C}$  between  $-55^\circ\text{C}$  and  $125^\circ\text{C}$  at 1 kHz, which exhibited a better temperature capacitance stability [25].

As discussed in the model of grain size effect on long-range Coulomb interactions and its cooperative phenomena, the reduced grain size in ferroelectric nanomaterials suppressed the long-range cooperative order process so that the temperature dependence of the dielectric properties exhibited different behaviors from their bulk counterparts. This grain size effect on the dielectric properties of nanostructured BaTiO<sub>3</sub> was referred as to the superparaelectric effect [130].

For BaTiO<sub>3</sub> nanoceramics with an average grain size of 400 nm, spontaneous polarization  $P_s = 17 \mu\text{C}/\text{cm}^2$  and remanent polarization  $P_r = 4 \mu\text{C}/\text{cm}^2$  were obtained from the polarization–electric field hysteresis loop at room temperature. For nanoceramics with a grain size of 300 nm,  $P_s = 15 \mu\text{C}/\text{cm}^2$  and  $P_r = 2 \mu\text{C}/\text{cm}^2$ . In contrast, BaTiO<sub>3</sub> fine ceramics with a grain size of 1.2  $\mu\text{m}$  exhibited  $P_s = 19 \mu\text{C}/\text{cm}^2$  and  $P_r = 6 \mu\text{C}/\text{cm}^2$ . The coercive field was  $E_c \sim 200 \text{ kV}/\text{cm}$  for these nano- and fine ceramics [10]. For sol–gel-derived BaTiO<sub>3</sub> nanocrystalline film on platinized silicon

substrates with a grain size of 50 nm and a thickness of 1.5  $\mu\text{m}$ , the observation of good capacitance–voltage butterfly curve and hysteresis loop indicated ferroelectricity behavior, while  $P_r = \sim 2.0 \mu\text{C}/\text{cm}^2$  with  $E_c = \sim 27 \text{ kV}/\text{cm}$  were obtained at room temperature. With increasing temperature, the dielectric constant increases and goes through a broad maximum around 125  $^\circ\text{C}$  and then decreases with a further increase in temperature. This broad phase transition in the nc-BaTiO<sub>3</sub> with a grain size of 50 nm was characterized by a diffuse phase transition feature. Regarding the low-temperature dielectric property, there was a lack of any anomalies at the phase transition temperatures corresponding to tetragonal–orthorhombic and orthorhombic–rhombohedral phase transitions, except for a change in the slope of the temperature dependence of the dielectric constant below about 50 K [23]. For 50-nm BaTiO<sub>3</sub> nanocrystalline thin film on metallic LaNiO<sub>3</sub>-coated LaAlO<sub>3</sub> (100) single-crystal substrates, a good hysteresis loop with  $P_r = 8.3 \mu\text{C}/\text{cm}^2$  and  $E_c = 50 \text{ kV}/\text{cm}$  was observed. The dielectric constant slowly decreased from 127 to 117 and the loss tangent changed from 0.02 to 0.05 when the frequency was increased from 100 Hz to 1 MHz. The leakage current density for 400-nm-thick film was found to be less than  $5 \times 10^{-7} \text{ A}/\text{cm}^2$  at an electrical field of 100 kV/cm [24]. In contrast, bulk single-crystal BaTiO<sub>3</sub> has  $P_s = 26 \mu\text{C}/\text{cm}^2$  and  $E_c = 1.5 \text{ kV}/\text{cm}$ . Therefore, there occurred suppressed dielectric and ferroelectric behaviors but increased  $E_c$  in BaTiO<sub>3</sub> nanostructured materials.

In cubic BaTiO<sub>3</sub> nanoparticles, the present electrical measurements indicated a lack of polarization–voltage hysteresis loops. It was found that this paraelectric cubic nanophase remained stable over a relatively large temperature range, preliminarily determined to be 80 up to 1000 K [25, 72, 128]. Surprisingly, using electrostatic force microscopy, a local polarization was induced and reversed repeatedly on cubic BaTiO<sub>3</sub> nanorods as small as 10 nm in diameter. The retention time for induced polarization exceeded 5 days in an ultrahigh vacuum environment, which demonstrated the potential of nanorods for fabricating nonvolatile memory nanodevices [82]. Nevertheless, it should be noted that these electrical measurements on cubic BaTiO<sub>3</sub> nanocrystals are just preliminary.

The suppressed dielectric and ferroelectric behaviors but increased  $E_c$  in BaTiO<sub>3</sub> nanostructured materials were attributed to the finite grain size effect and clamping of the film to the substrate. In the past, the finite grain size effect was widely investigated and has been determined to be an intrinsic resource for ferroelectric nanocrystals. Both theoretical and experimental studies revealed the structural changes of a multidomain–single-domain transformation, a decrease in tetragonal distortion, and a size-induced ferroelectric tetragonal–paraelectric cubic phase transition with decreasing grain size [9, 10, 22, 32]. Shaikh et al. measured the dielectric constant and spontaneous polarization of fine BaTiO<sub>3</sub> ceramics with various grain size and estimated the critical size for the multidomain–single-domain transformation to be about 400 nm [116]. Using the thermodynamical free-energy method, Hsiang and Yen calculated this critical grain size to be about 80 nm, but their experimental measurements indicated it was larger than 100 nm [43].

The dielectric constant increment in fine BaTiO<sub>3</sub> ceramics was attributed to the domain structure change from the multidomain to the single domain with decreasing grain size. In PbTiO<sub>3</sub>, another important ferroelectric nanomaterial, transmission electron microscopy (TEM) measurements indicated it changed from the multidomain to the single domain when the grain size was less than 20 nm [137].

In perovskite-type oxide ferroelectrics, the tetragonal strain scales with the spontaneous polarization. Owing to the smaller strain of 1% in BaTiO<sub>3</sub> bulk crystal compared to 6% in PbTiO<sub>3</sub>, BaTiO<sub>3</sub> has a weaker ferroelectricity than PbTiO<sub>3</sub> [37]. In nc-BaTiO<sub>3</sub>, the tetragonality changed from  $c/a = 1.01$  to 1.00 with decreasing particle size, as illustrated in Figure 3. Compared with the bulk crystal, a reduction in the  $c/a$  ratio in nc-BaTiO<sub>3</sub> implies a smaller strain and leads to a weakening of the ferroelectric tetragonal [33, 74]. These grain size–induced structural changes in the ferroelectricity and paraelectric cubic phase were the cause of the dielectric constant reduction observed in BaTiO<sub>3</sub> nanocrystals. For BaTiO<sub>3</sub> nanoceramics with a grain size of 300–400 nm, both XRD and Raman data indicated that the reduced electric properties were due to the reduced tetragonality; for example, the  $c/a$  ratio was measured as 1.008 in nanoceramics with a grain size of 400 nm [10]. In dense nanoceramics and films, the nanoparticles are elastically constrained by the surrounding environment, which makes the structural analysis complex. To understand the precise nature of ferroelectricity at the nanoscale, it is necessary to prepare freestanding BaTiO<sub>3</sub> nanocrystalline particles and films [62].

In the BaTiO<sub>3</sub>/SrTiO<sub>3</sub> superlattices, Kim et al. observed an increase in both the dielectric constant and its nonlinearity (voltage tunability) with decreasing stacking periodicity within the critical thickness. A maximum zero-field dielectric constant of 1600 at 1 MHz and a large voltage tunability of 94% were observed at the periodicity of the (BaTiO<sub>3</sub>)<sub>2-unit-cell</sub>/(SrTiO<sub>3</sub>)<sub>2-unit-cell</sub> superlattice, in comparison with 74% in Ba<sub>x</sub>Sr<sub>1-x</sub>TiO<sub>3</sub> thin film [112]. The high dielectric constant and large voltage tunability make BaTiO<sub>3</sub>/SrTiO<sub>3</sub> strained superlattices very attractive for electrically tunable microwave devices. With varying layer thickness of the constituents, Tsurumi et al. found the [(BaTiO<sub>3</sub>)<sub>10-unit-cell</sub>]/[(SrTiO<sub>3</sub>)<sub>10-unit-cell</sub>]<sub>4</sub> and [(BaTiO<sub>3</sub>)<sub>10-unit-cell</sub>]/[(BaZrO<sub>3</sub>)<sub>10-unit-cell</sub>]<sub>4</sub> superlattices having much higher dielectric permittivities and refractive indices than other superlattices [98]. In contrast to symmetric superlattices, Shimuta et al. studied epitaxial asymmetric BaTiO<sub>3</sub>/SrTiO<sub>3</sub> strained superlattices that had unequal BaTiO<sub>3</sub> and SrTiO<sub>3</sub> layer thickness and found that the superlattice with a stacking periodicity of 15 unit cells BaTiO<sub>3</sub>/3 unit cells SrTiO<sub>3</sub> showed the largest remanent polarization  $2P_r$  of 46  $\mu\text{C}/\text{cm}^2$  but the dielectric constant was 240 at 1 MHz [109]. These experiments demonstrated that the strained superlattice is an effective approach to enhance the properties of the constituents by controlling the stacking periodicity, the thickness of the alternative layers, and their thickness ratio. Playing the role of the pressure effect, the lattice strain in the superlattices affected not only the ionic polarization but also the electronic structure or chemical bonding nature of the superlattices [98, 107, 112].



## 4.2. Optical Properties

In this section, second-harmonic generation, light emission, and up-conversion optical properties of BaTiO<sub>3</sub> nanostructured materials are summarized.

### 4.2.1. Second-Harmonic Generation

Owing to spontaneous polarization, pure or rare-earth-doped BaTiO<sub>3</sub> single crystals have strong electrooptic, nonlinear optical, and photorefractive effects. In bulk barium titanate, the nonlinear coefficients for second-harmonic generation (SHG) were  $d_{15} \approx 17.0$  pm/V,  $d_{31} \approx 15.7$  pm/V, and  $d_{33} \approx 6.8$  pm/V. Theoretical calculations revealed that the nonlinear electronic polarizabilities are very sensitive to changes in electron covalency and electron correlation in the transition metal oxides [40]. Compared with BaTiO<sub>3</sub> bulk crystals, the reduction in hybridization must decrease the optical nonlinear coefficients of BaTiO<sub>3</sub> nanocrystalline particles and thin films. For epitaxial BaTiO<sub>3</sub> nanocrystalline thin films with a grain size of 10–80 nm on MgO substrates, the SHG was investigated at an incident wavelength of 1.064  $\mu$ m. The effective  $d$  coefficient was measured as 2.13 pm/V for the  $c$ -oriented films and 1.5 pm/V for the  $a$ -oriented films [20]. Compared with the values of the bulk crystal, these values were much lower, in agreement with the theoretical prediction. Frey and Payne investigated the nanocrystallite grain size effect on SHG of BaTiO<sub>3</sub>. In the cubic BaTiO<sub>3</sub> nanoparticles, a measurable SHG signal was detected, but it was a factor of 10<sup>3</sup> weaker than that in the coarser grain of 10  $\mu$ m. When the nanocrystallite size increased above 50 nm, the SHG signal rose significantly. XRD and Raman scattering measurements indicated that the tetragonality increases with increasing grain size above 50 nm but only a local acentric lattice distortion occurs in the cubic nanoparticles [21]. From these facts, it was concluded that the SHG processes would be enhanced by large tetragonal distortion in BaTiO<sub>3</sub> nanocrystals. As discussed in Section 2.2, the tetragonal distortion in epitaxial single-crystal thin films can be tuned over a large range. Therefore, the strained epitaxial thin films are expected to exhibit better SHG performance with tunability.

### 4.2.2. Light Emission

Spontaneous light emission is one of the basic properties of nanocrystals due to the quantum size confinement effect, and it is a powerful tool to probe the electronic structure and impurity. In bulk ferroelectric BaTiO<sub>3</sub>, a complex broad luminescence band around 500 nm was observed under valence band-to-conduction band excitation. With increasing temperature, the photoluminescent intensity decreased and was quenched above the tetragonal-to-cubic phase transition temperature [155]. The self-trapped exciton mechanism was proposed to understand this light emission band in ferroelectric phases.

In nanocrystallites, the quantum size confinement effect would cause an increase in bandgap with decreasing grain size [18, 77]. Optical measurements indicated that the optical band edge blueshifted toward 3.68 eV for nc-BaTiO<sub>3</sub> with a grain size of 8 nm, and 3.53 eV with a grain size of 35 nm, compared to the value of 3.2 eV for bulk single

crystal [18]. There are no reports in the literature on the light emission properties of BaTiO<sub>3</sub> nanocrystals under excitation from the valence band to the conduction band. Under excitation by an Ar<sup>+</sup> laser, a weak yellow luminescence around 570 nm was first observed in sol-gel-derived BaTiO<sub>3</sub> nanoparticles [156]. Later, three photoluminescence bands centered at 543 nm (green), 574 nm (yellow), and 694 nm (red), respectively, were observed in the LTHM-processed slightly Ti-rich barium titanate nanoparticles with heat treatment at various temperatures; the results are reproduced in Figure 8 [49, 74, 75]. Yu et al. found that a hexagonal phase and BaTi<sub>2</sub>O<sub>5</sub> clusters embedded within BaTiO<sub>3</sub> nanoparticles played the role of color centers for the 543- and 694-nm emission bands, respectively, but the Ti defects contributed to the yellow emission band. Under various annealing temperatures, the peak position of each luminescence band did not shift, despite the luminescent intensity. This phenomenon was understood by combining quantum size confinement and dielectric confinement effects, which had the opposite effect on the energy level of the color centers as a function of nanoparticle size and thus kept them unchanged within the band gap. In the experiments with excitation of various powers, all three light emission bands were found, characteristic of the self-trapped exciton emission mechanism [49]. The mechanism of self-trapped exciton light emissions in the cubic BaTiO<sub>3</sub> nanophase can be understood by the embedded-molecular-cluster model [157], in which the local rhombohedral distortion and lattice expansion in cubic nc-BaTiO<sub>3</sub> fulfill the requirements to make excitons self-trapped on second-phase clusters or defects. In particular, when the annealing temperature was increased to more than 900 °C, the spectrum shape of the red band changed and could be fitted from one Gaussian distribution to two Lorentzian ones. This change was closely associated with the crystalline field change in the nc-BaTiO<sub>3</sub> cubic-tetragonal phase transformation induced by the grain size [158].

In Er-doped BaTiO<sub>3</sub> nanostructured materials with an average grain size of 25 nm, a typical erbium spontaneous luminescence, corresponding to the intra-4*f* transition from <sup>4</sup>I<sub>13/2</sub> to <sup>4</sup>I<sub>15/2</sub>, was observed at 1.54  $\mu$ m with a fine width

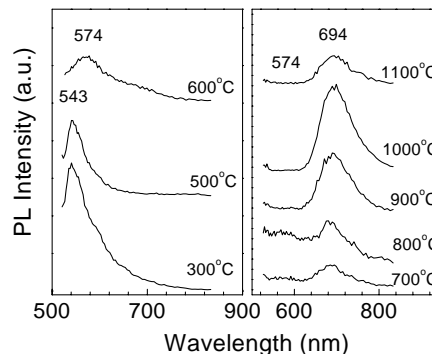


**Figure 8.** Room-temperature photoluminescence spectra for nc-BaTiO<sub>3</sub> annealed at various temperatures for 1 h. The photoexcitation line was 488.0 nm of Ar<sup>+</sup> laser with an output power of 200 mW at header. Reprinted with permission from [49], J. Yu et al., *Appl. Phys. Lett.* 77, 2807 (2000). © 2000, American Institute of Physics.

at half-maximum of approximately 45 nm under excitation of both 514- and 980-nm lasers [159]. The luminescent intensity and the  $1/e$  lifetime were closely dependent on the concentration of Er ions in the nanostructured materials. For the 3.0-mol% Er-doped BaTiO<sub>3</sub> nanomaterials, the 1.54- $\mu$ m emission decayed in a single exponential way with a  $1/e$  lifetime of approximately 5 ms. When the concentration was more than 3.0 mol%, the 1.54- $\mu$ m light emission was quenched. The quenching mechanism was explained by energy transfer and cross-relaxation processes between closely sited Er<sup>3+</sup> ions within the BaTiO<sub>3</sub> lattice, which are related to the up-conversion process discussed below.

### 4.2.3. Up-Conversion

Up-conversion to the visible spectrum from the near-infrared has been developing as an important approach for the generation of visible luminescence and short-wavelength lasing in some rare-earth-doped materials upon near-infrared excitation. Up-conversion is a nonlinear process, whereby two or more low-energy excitation photons are converted into one or two high-energy photons. It can find application in such as all-solid compact blue-green lasers pumped with near-infrared semiconductor laser diodes and infrared radiation detection by converting the invisible light into the visible range where conventional detectors are effective. In particular, Er<sup>3+</sup> has a favorable energy level structure with two transitions of  $^4I_{15/2} \rightarrow ^4I_{11/2}$  (at 980 nm) and  $^4I_{15/2} \rightarrow ^4I_{9/2}$  (at 810 nm), which can be efficiently pumped with high-power near-infrared semiconductor lasers to yield blue, green, and red up-conversion emissions. Compared with glasses and fluoride crystals, in which blue and red up-conversion emission and lasing have been realized, BaTiO<sub>3</sub> permits a high solid solubility of at least 10 at% at the Ti site of Er<sup>3+</sup> ions [14]. In addition, Er<sup>3+</sup> ions are homogeneously distributed throughout the depth of BaTiO<sub>3</sub> films. Thus, much higher overlap between Er<sup>3+</sup> distribution and optical field profile could be expected in the Er<sup>3+</sup>:BaTiO<sub>3</sub> film waveguides [54, 160].

In sol-gel-derived Er<sup>3+</sup>:BaTiO<sub>3</sub> nanocrystalline particles and thin films with an average grain size of 15–25 nm, three up-conversion emissions at 526 nm ( $^2H_{11/2} \rightarrow ^4I_{15/2}$ ), at 549 nm ( $^4S_{3/2} \rightarrow ^4I_{15/2}$ ), and at 670 nm ( $^4F_{9/2} \rightarrow ^4I_{15/2}$ ) were observed under excitation at 980 and 810 nm from both laser diodes and a xenon lamp, among which the transition  $^4S_{3/2} \rightarrow ^4I_{15/2}$  is spin-allowed so that the 549-nm emission was bright even to the naked eye [54, 159–161]. The absorption measurements in the ranges from 805 to 825 nm ( $^4I_{15/2} \rightarrow ^4I_{9/2}$ ) and from 960 to 1000 nm ( $^4I_{15/2} \rightarrow ^4I_{11/2}$ ) indicated that the laser diodes operating at 810 and 980 nm are efficient pump sources for the 549-nm up-conversion emission. Upon excitation at 980 and 810 nm, the predominant 549-nm emission had a different intensity and lifetime. The lifetime of the 549-nm emission increased sixfold with 980-nm excitation compared to that with 810-nm excitation, which resulted from the different population mechanisms. With the 980-nm excitation, both the excited state absorption (ESA) of individual Er<sup>3+</sup> ions and the cooperative energy transfer (CET) between two near Er<sup>3+</sup> ions

contributed to the 549-nm up-conversion emission. In contrast, the up-conversion emission under the 810 nm excitation was just through an ESA process. Therefore, the excitation around 980 nm was more effective for the 549-nm up-conversion emission from the Er:BaTiO<sub>3</sub> nanostructured materials [54, 160, 161]. For up-conversion lasing from Er:BaTiO<sub>3</sub> nanostructured materials, research is currently underway.

## 5. LATTICE DYNAMICS

### 5.1. Raman-Active Optical Modes

In the bulk BaTiO<sub>3</sub> paraelectric cubic phase, the space group  $O_h^1$  transforms as  $3T_{1u} + T_{2u}$  optical modes at the center of the Brillouin zone, which are triply degenerate. The long-range electrostatic forces split each of the optical modes into a doubly degenerate transverse optical (TO) mode and a singly degenerate longitudinal optical (LO) mode. The optical  $T_{1u}$  modes are infrared active, but the  $T_{2u}$  mode is neither infrared active nor Raman active [150, 162]. Nevertheless, two broad Raman modes centered around 250 and 515 cm<sup>-1</sup> were recorded in bulk BaTiO<sub>3</sub> single crystals and ceramics above  $T$  [95, 163, 164]. In the ferroelectric tetragonal phase, each cubic  $T_{1u}$  mode transforms as the  $A_1 + E$  irreducible representation and  $T_{2u}$  as  $B_1 + E$  of  $C_{4v}^1$ . The distinct Raman-active optical vibrations,  $3A_1(\text{TO}) + 3A_1(\text{LO}) + 3E(\text{TO}) + 3E(\text{LO}) + 1E(\text{LO} + \text{TO}) + 1B_1$ , were obtained for tetragonal BaTiO<sub>3</sub>. In single crystals, the first-order Raman modes at 36, 180, 305, 463, 470, 486, 518, 715, and 727 cm<sup>-1</sup> and two broad modes around 270 and 520 cm<sup>-1</sup> were obtained, while four modes at 270, 305, 516, and 719 cm<sup>-1</sup> and a negative intensity mode at 180 cm<sup>-1</sup> were obtained in ceramics [95, 162–164].

As illustrated in Figure 6, the depolarized Raman scattering measurements recorded five modes centered at 184, 257, 308, 518, and 716 cm<sup>-1</sup> in the single-phase cubic BaTiO<sub>3</sub> nanoparticles [21, 33, 58, 63, 95, 126]. In the cubic nanocrystal, of major importance was that the three first-order modes at 184, 308, and 716 cm<sup>-1</sup> were Raman active, even though these three modes typically conform to Raman selection rules in the bulk materials. These different lattice vibration properties indicated that the local structure of cubic nanocrystals was acentrically distorted, which relaxed the Raman selection rules. The second-harmonic generation and electron paramagnetic resonance spectroscopy measurements also revealed the occurrence of locally acentric distortion in the XRD-measured cubic nanoparticles [21, 53, 58]. Recent measurements showed that the change in the Ti–O bonding character of BaTiO<sub>3</sub> nanoparticles leads to elongation of both the Ba–Ti and the Ba–O bond lengths from 3.47 Å and 2.83 Å to 3.60 Å and 2.94 Å, respectively, while the Ti–O bond length remains nearly constant ( $\sim 2.0$  Å) [129]. Based on these bond lengths, the unit cell in cubic nc-BaTiO<sub>3</sub> has local rhombohedral distortion, but not the tetragonal or orthorhombic distortion assigned by other authors [21, 33, 63]. In the quantum phase transformations, the zero-point fluctuation energy is closely associated with the property of lattice dynamics. The first-order phonons being Raman active would have a strong influence on the

zero-point energy of the BaTiO<sub>3</sub> nanosystems and consequently, would shift the critical condition of phase transformation from classic to quantum [33, 158].

## 5.2. Soft-Mode Theory

In 1960, Cochran and Anderson independently pointed out that the ferroelectric–paraelectric structural phase transition in ABO<sub>3</sub> perovskite oxides was closely related to the dynamical behavior of the lowest frequency TO phonon mode, that is, the soft mode. Since then, the soft-mode theory has achieved great success in explaining ferroelectric phase transitions.

In the lattice dynamic model of displacive ferroelectric structural phase transitions, the dynamical behavior of ferroelectricity is closely associated with the softening of the lowest frequency TO mode at the center of the Brillouin zone, and its freezing corresponds to paraelectric–ferroelectric phase transition. As each transition temperature is approached, the frequency of the soft mode generally decreases and is described by the following relationship:

$$\omega_{\text{TO}}^2 = A(T - T_c)^{\gamma'} \quad (5.1)$$

where  $A$  is a constant: positive at  $T > T_c$  and negative at  $T < T_c$ . In cubic BaTiO<sub>3</sub>, the soft mode is the lowest frequency  $T_{1u}(\text{TO})$  mode, whose freezing induces the generation of ferroelectricity, but in the tetragonal phase, the lowest frequencies  $E(1\text{TO})$  and  $A_1(1\text{TO})$  are the soft modes, whose freezing induces the disappearance of ferroelectricity [1, 150]. The temperature dependence of the ferroelectric soft mode in ABO<sub>3</sub> reflects the variation of the anharmonic interactions due to the hybridization between transition metal d states and oxygen p states [165]. In the classical mean field region, the critical exponent  $\gamma' = 1$ , but when the quantum zero-point fluctuation prevails at low-temperature,  $\gamma'$  approaches 2, close to the quantum limit, and becomes 0 at  $T \rightarrow 0$  K [165, 166].

In addition to explaining the sequence of phase transitions, the soft-mode theory has been successful in other ways. In the ferroelectric phase of ABO<sub>3</sub> oxides, the spontaneous polarization  $P_s$  and spontaneous strain described by the tetragonality  $c/a$  are two important order parameters. In tetragonal BaTiO<sub>3</sub> and PbTiO<sub>3</sub> bulk materials, the connections between the temperature dependence of the soft-mode frequency  $\omega(A_1(1\text{TO}))$  and the spontaneous polarization and spontaneous strain were established [2, 150]:

$$\omega(A_1(1\text{TO})) \propto P_s \propto ((c/a) - 1)^{1/2} \quad (5.2)$$

The Curie–Weiss law characterizes the dielectric properties in the paraelectric phase of ferroelectric materials, and its general formulation is

$$\epsilon(T) = C(T - T_0)^{-\gamma_T} \quad (5.3)$$

where  $C$  is the Curie–Weiss constant and  $T_0$  is the Curie–Weiss temperature. In the classical regime, the critical exponent  $\gamma_T = 1$  was found for the static dielectric constant, but at relatively low-temperatures where zero-point quantum fluctuations prevented long-range order phase,

$\gamma_T$  approached 2, close to the quantum limit. With  $T \rightarrow 0$  K, the saturation of the low-frequency dielectric constant corresponded to  $\gamma_T = 0$ . These predictions have been experimentally demonstrated in incipient ferroelectrics such as SrTiO<sub>3</sub>, KNbO<sub>3</sub>, and KTaO<sub>3</sub> and normal ferroelectrics such as BaTiO<sub>3</sub> and PbTiO<sub>3</sub> [1, 2, 7, 166, 167]. Through the Lyddane–Sachs–Teller (LST) relationship, the Curie–Weiss law intrinsically reduces to the soft-mode theory [7, 166].

In ionic crystals, the LST relationship is

$$\frac{\epsilon(0)}{\epsilon(\infty)} = \frac{\omega_{\text{LO}}^2}{\omega_{\text{TO}}^2} \quad (5.4)$$

which relates the static dielectric constant,  $\epsilon(0)$ , and the high-frequency dielectric constant,  $\epsilon(\infty)$ , to the eigenfrequencies,  $\omega_{\text{LO}}$  and  $\omega_{\text{TO}}$ , of LO and TO phonons [1, 2]. The LST relationship has been proven quantitatively in the ferroelectric and paraelectric phases of ferroelectrics such as SrTiO<sub>3</sub>, PbTiO<sub>3</sub>, KNbO<sub>3</sub>, and KTaO<sub>3</sub>, and the dramatic change in the static dielectric constant is directly related to the soft-mode behavior [4, 150, 165, 166]. For example, in the case of tetragonal PbTiO<sub>3</sub>, the dielectric constant along the ferroelectric axis  $\epsilon_c$  is determined primarily by the lowest frequency  $A_1(1\text{TO})$  mode, and  $\epsilon_a$  perpendicular to the  $c$  axis by the lowest  $E(1\text{TO})$  mode at all temperatures upto  $T_c$  [150].

To date, it is accepted that BaTiO<sub>3</sub> is not a typical displacive ferroelectric [3, 4, 150]. In the tetragonal phase, the  $E(1\text{TO})$  soft mode was found to be highly overdamped, but the  $A_1(1\text{TO})$  soft mode was underdamped, both mixed with a certain amount of disorder character. Because of the large damping factor of the soft mode, it was very difficult to detect the soft modes by the conventional Raman spectroscopic method. At that time, the calculated  $\epsilon_{\text{LST}}$  from the soft mode was only about 25% of the experimentally determined  $\epsilon_c$  [150, 162]. In the 1990s, the femtosecond time-domain light-scattering spectroscopy technique was developed, which took advantage of determining the soft-mode frequency more accurately than conventional frequency-domain spectroscopy. Nevertheless, the static dielectric constant calculated via the LST relationship for BaTiO<sub>3</sub> bulk crystals still did not quantitatively agree with the present experimental value [4]. Dougherty et al. suggested reperforming dielectric measurements of BaTiO<sub>3</sub> to test the LST relationship, but the data are still lacking.

## 5.3. Finite-Size Effect

In the microscopic theory of displacive ABO<sub>3</sub> ferroelectrics, the dynamical behavior of the soft mode depends on the compensation of the long-range Coulomb force by the short-range electric repulsive and covalent forces. The hybridization between transition metal B ion d states and oxygen p states softens the ferroelectric soft mode and thus ferroelectric displacement can take place [5, 165, 168]. In ferroelectric nanocrystalline particles and thin films, the finite-size effect on the behavior of the soft modes also plays a central role in these changes in the structural and physical properties. When the grain size is comparable to the correlation length, both the long-range Coulomb forces and the short-range electric repulsive and covalent forces decrease with

decreasing nanocrystallite size, but the short-range forces decrease faster than the long-range Coulomb forces, and thus cause the  $A_1(1TO)$  and  $E(1TO)$  soft-mode frequencies to gradually decrease with decreasing grain size and finally to freeze out below a critical size. In accordance with (5.2), the reduction in soft-mode frequencies is accompanied by a weakening of the ferroelectricity and a decrease in tetragonality, and the soft mode freezing corresponds to the grain size-induced tetragonal–cubic phase transition [138, 139].

In  $PbTiO_3$ -based ferroelectric nanoparticles, with decreasing grain size, the room-temperature frequencies of the  $E(1TO)$  and  $A_1(1TO)$  soft modes were experimentally observed to decrease, but the linewidth increased, compared with those of the bulk materials [138, 169–171]. For example, in nc- $PbTiO_3$ , the  $E(1TO)$  soft mode shifted from  $83\text{ cm}^{-1}$  to  $72\text{ cm}^{-1}$  in frequency and increased from  $12\text{ cm}^{-1}$  to  $31\text{ cm}^{-1}$  in linewidth with decreasing grain size from  $50.5\text{ nm}$  to  $20\text{ nm}$  [170]. For nc- $PbTiO_3$ , with a grain size of  $50.5\text{ nm}$ , the squared frequency of the  $E(1TO)$  soft mode deviated from the straight-line dependence of pressure above  $4\text{ GPa}$ , which suggested that the  $PbTiO_3$  nanomaterials have a different phase transition from that of the bulk materials, where the  $E(1TO)$  soft-mode frequency decreased toward 0 as the pressure increased and all of the modes disappeared above  $11.63\text{ GPa}$  [170]. Varying the temperature and/or pressure, the partial softening and superlinear broadening of the  $E(1TO)$  soft mode implied that nanocrystalline  $PbTiO_3$  is no longer an ideal displacive ferroelectric, but mixed with an order–disorder feature [172].

For each grain size of  $PbTiO_3$  ferroelectric nanoparticles, taking (3.2) into (5.1), the temperature dependence of the  $A_1(1TO)$  soft-mode frequency was determined by the equation:

$$\omega^2 = A(T - T_c(\infty) + D/(R - R_c)) \quad (5.5)$$

On the other hand, the frequency of the soft mode decreased with decreasing nanocrystallite size, although they had the same dynamical behavior as described by (5.5) [138, 170]. This fact implies that the parameter  $A$  is a function of grain size, which decreases with decreasing grain size. Recently, the room-temperature spontaneous strain in nc- $PbTiO_3$  as a function of nanoparticle size was experimentally obtained:

$$c/a - 1 = E(1 - \exp(E(R_c - R))) \quad (5.6)$$

where the constant  $E = 0.065$  [32]. Under the first approximation ( $1 - e^{-x} \approx 1/x$ ), (5.6) can be simplified as

$$c/a - 1 \approx 1/(R - R_c) \quad (5.7)$$

Comparing (5.5) with (5.7), the relationship  $\omega^2(A_1(1TO)) \propto (c/a) - 1$  does not exist in the case of nc- $PbTiO_3$ . The reduced tetragonality ( $c/a$ ) in ferroelectric nanoparticles only provides partial contributions to the reductions in the soft-mode-frequency, dielectric, and ferroelectric properties. So far, it is concluded that the reduced tetragonal distortion is partially responsible for the suppressed ferroelectricity and related properties in ferroelectric nanoparticles, and the intrinsic grain size effect on the electronic structure plays a dominant role, especially in the variation of parameter  $A$ .

In quantum paraelectric  $SrTiO_3$  nanocrystals, the reduced long-range Coulomb forces would cause the frequency of the  $T_{1u}$  soft mode to increase with decreasing grain size, that is, soft-mode hardening. Raman and infrared spectroscopic measurements indicated that the zone center cubic  $T_{1u}$  soft-mode frequencies of the small nanoparticles were higher than those of the larger ones at low temperature [166, 173, 174]. The dielectric constant was measured as 770 with a grain size of  $44\text{ nm}$  but 350 with a grain size of  $12\text{ nm}$  at  $12\text{ K}$  and  $100\text{ kHz}$ . Compared with  $SrTiO_3$  bulk crystal, of which the static dielectric constant was about 20,000 below  $4\text{ K}$ , the quantum paraelectricity was strongly suppressed in  $SrTiO_3$  nanocrystals by the finite grain size. Through the LST relationship of (5.4), the soft-mode hardening observed in nanocrystals agreed with the dramatic reduction in the dielectric constant [173, 174]. For thick  $SrTiO_3$  films, the reduction in the dielectric constant was almost the consequence of the soft-mode hardening. But for thinner  $SrTiO_3$  films, the interfacial dead layer effect played a significant role in the reduction in the dielectric constant, in addition to the finite-size effect [166]. Moreover, the deviation from the classical Curie–Weiss law started at a higher temperature for smaller nanocrystallite size.

In ferroelectric  $BaTiO_3$  nanocrystals, the reduction in the p–d hybridization induced by the finite-size effect would no doubt influence the behavior of the soft mode [168]. Similar to  $PbTiO_3$  and  $SrTiO_3$ , the softening of the  $A_1(1TO)$  and  $E(1TO)$  soft modes in the tetragonal nanophase or the hardening of the  $T_{1u}$  soft mode in the cubic nanophase is also responsible for the reduction in the electrical properties of  $BaTiO_3$  nanocrystals. At present, there is a lack of experimental data on both the soft mode and the static dielectric constant with varying grain size for  $BaTiO_3$  nanocrystals.

#### 5.4. Quantum Ferroelectricity

For the displacive structural phase transitions in ferroelectrics such as  $BaTiO_3$ , the phase transition caused by variation of the parameters in a lattice dynamical system were investigated within the framework of both classical and quantum statistical mechanics [143]. For the ferroelectric–paraelectric transition Curie temperature  $T_c$ , it was found as a function of the interaction parameter  $S$ :

$$T_c(S) \propto (S_c - S)^{1/\phi} \quad (5.8)$$

where  $S$  is an interaction parameter—an external parameter such as pressure or chemical composition—that controls the interaction, and  $S_c$  is its value at  $T_c = 0$ . In the classical regime, the phase transitions were driven by thermal fluctuations, but when the  $T_c \rightarrow 0\text{ K}$ , quantum zero-point fluctuations, instead of thermal fluctuations, played a dominant role. The theoretical treatment predicted that  $T_c$  varied with the critical exponent  $\phi \equiv 2$ , close to the quantum limit, and  $\phi \equiv 1$ , close to the classical limit. The relationship  $T_c = A(S_c - S)^{1/2}$  is typical of quantum ferroelectricity,  $T_c = 0$  at  $S = S_c$  being the quantum limit. Conventionally,  $BaTiO_3$  was a normal ferroelectric with a critical exponent  $\phi = 1$  under low hydrostatic pressure or with a large concentration of strontium content. However, for  $BaTiO_3$  under a hydrostatic pressure of  $4\text{--}8\text{ GPa}$  and  $Ba_{1-x}Sr_xTiO_3$  with  $0.8 < x < 0.965$ ,

the critical exponent  $\phi$  changed to 2 [7, 167, 175]. That is to say, under these conditions, BaTiO<sub>3</sub> became a quantum ferroelectric and the nature of ferroelectric–paraelectric phase transition was controlled by quantum mechanics.

For BaTiO<sub>3</sub>, both theoretical and experimental results indicated the ferroelectric–paraelectric phase transformations change in nature from being controlled by classical mechanics to being controlled by quantum mechanics under high pressure (hydrostatic or chemical). In these pressure experiments, the interatomic distance played a crucial role in the pressure-established quantum ferroelectricity and paraelectricity. In the BaTiO<sub>3</sub> nanocrystals, as shown by Figures 2 and 3, the lattice parameter was a function of grain size and the ferroelectricity decreased with decreasing grain size. As indicated by (3.2), with decreasing grain size,  $T_c$  was shifted downward through room temperature, eventually tending toward 0 K at some critical grain size [22]. According to the scaling theory of phase transitions, the properties of ferroelectrics and the nature of the phase transition would be controlled by quantum mechanics under the condition of the polar order parameter being comparable with zero-point fluctuation [143]. Similar to the pressure effect, the grain size effect in ferroelectric nanomaterials could induce the spontaneous polarization to be reduced to 0, in accordance with (5.2) and (5.5), so that it might shift the critical conditions of classical-to-quantum ferroelectric and paraelectric phase variations. From the viewpoint of microscopic interaction, the predominant change in these phase transformations was found to be the reduction in the Ti–O hybridization, despite different birthrights—hydrostatic pressure, chemical pressure, grain size effect in nanomaterials. Based on these facts, nc-BaTiO<sub>3</sub> is expected in an analogous way to be quantum ferroelectric and paraelectric over some range of grain size [33, 158]. Equation (5.8) should also be suitable for nc-BaTiO<sub>3</sub>, where the grain size  $R$  can be used as the interaction parameter. In addition, preliminary measurements showed that the grain size effect in nc-BaTiO<sub>3</sub> plays an equivalent role of the pressure effect, spanning across the entire range of quantum ferroelectricity and paraelectricity of BaTiO<sub>3</sub> [7, 128]. Compared with the pressure effect, the grain size effect in nc-BaTiO<sub>3</sub> provides a method for stabilizing and utilizing those metastable phases in ambient environments. Of interest, in the experiments of pressure-induced phase transformation in CeO<sub>2</sub> nanoparticles, the critical pressure was reduced 28.1% and there was a larger volume change of 9.4% in the phase transformation than that for the bulk CeO<sub>2</sub> [176]. These facts supported in an experimental way the grain size effect in nanomaterials playing an equivalent role of the pressure effect.

The prediction of quantum behavior in nc-BaTiO<sub>3</sub> is significantly of interest for fundamental understanding of ferroelectric nanocrystals and technological applications, especially using its dielectric properties in such as infrared detection and electronic and photonic devices. However, in BaTiO<sub>3</sub> and PbTiO<sub>3</sub> nanoparticles with grain size above the critical size, the preliminary measurements revealed that the dependence of the Curie temperature on the grain size had a critical exponent  $\phi = -1$  [22, 139]. Taking  $R^{-1}$ , rather than  $R$ , as the interaction parameter, this sign discrepancy in the critical exponent may disappear. In the near future the nanocrystallite size–temperature phase diagram and the

temperature dependence of dielectric properties with various nanocrystallite size will be required.

In SrTiO<sub>3</sub> nanocrystals, electrical and Raman spectroscopic measurements revealed that the finite-size effect suppressed the zero-point quantum fluctuations and shifted the classical-to-quantum crossover towards higher temperature [174]. Since the finite-size effect plays the role of suppressing quantum fluctuation, the chemical pressure necessary for quantum ferroelectricity in Ba<sub>1-x</sub>Sr<sub>x</sub>TiO<sub>3</sub> nanocrystals would be smaller than in the bulk case; that is, the critical composition  $x_c$  increases with decreasing grain size.

## 6. BARIUM STRONTIUM TITANATE

SrTiO<sub>3</sub> is a well known quantum paraelectric or incipient ferroelectric. It is in the cubic phase (space group  $Pm3m$ ) at room temperature and undergoes an antiferrodistortive structural phase transition to the tetragonal phase (space group  $I4/mcm$ ) at 105 K. This transition results from the freezing of one of the triply degenerate  $R_{25}$  modes at the Brillouin zone boundary. With decreasing temperature, the dielectric constant increases but becomes saturate at  $\epsilon(0) \approx 20,000$  below 4 K. Above 40 K, a zone center TO mode exhibits a softening behavior, which agrees with the temperature dependence of the static dielectric constant via the LST relationship. Below 40 K, zero-point quantum fluctuations preclude the freezing of this soft mode, and SrTiO<sub>3</sub> remains in the tetragonal paraelectric phase even to absolute 0 K, which is known as the quantum paraelectric phase [166, 177]. Moreover, it is possible to suppress the quantum fluctuations and induce polar ordering in SrTiO<sub>3</sub> by chemical substitutions of Ba, Ca, Pb, and <sup>18</sup>O, application of an electric field, or application of mechanical stress [167].

In Ba<sub>1-x</sub>Sr<sub>x</sub>TiO<sub>3</sub> solid solutions, three phase transition temperatures of BaTiO<sub>3</sub> linearly decrease with increasing SrTiO<sub>3</sub> concentration up to  $x = 0.8$ . For the tetragonal–cubic phase transition, the Curie temperature obeys  $T_c(\text{K}) = 410 - 360x$ . When  $0.8 < x < 0.965$ , there is only one paraelectric–ferroelectric phase transition with  $T_c = 300(0.965 - x)^{1/2}$  (K). When  $x > 0.965$ , the ferroelectric phase transition is precluded by zero-point quantum fluctuations while barium strontium titanate exhibits a glasslike behavior [167]. For quantum ferroelectric Ba<sub>1-x</sub>Sr<sub>x</sub>TiO<sub>3</sub> ( $0.8 < x < 0.965$ ) bulk crystals, the critical exponent  $\gamma_T$  of the Curie–Weiss law at  $x$  near 0.8 is equal to 1 and then grows to about 1.5 when  $x$  increases. Lattice contraction as a function of Sr concentration obeys Vegard’s law,  $a = 3.905x + 3.992(1 - x)$ . So the chemical pressure effect could be compared with the hydrostatic pressure effect, which has a similar pressure–temperature phase diagram [7, 167].

For Ba<sub>1-x</sub>Sr<sub>x</sub>TiO<sub>3</sub> solid solutions, of technological interest is the room-temperature ferroelectric–paraelectric boundary around  $x = 0.3$ . They exhibit high room-temperature dielectric constant, high pyroelectric coefficient, and low dielectric loss, which have attracted considerable attention for applications such as dynamic random access memory (DRAM), microwave, and pyroelectric devices [167, 178].

In the remaining part of this section, the syntheses of Ba<sub>1-x</sub>Sr<sub>x</sub>TiO<sub>3</sub> nanocrystalline thin film are reviewed. Then the dielectric and nonlinear properties are summarized.

Those factors affecting the film performance, including small grain size, film thickness, crystallographic orientation, lattice strain, and acceptor doping, are also discussed.

## 6.1. Syntheses

In principle, all the synthesis methods for BaTiO<sub>3</sub> nanostructured materials could be used without difficulty to prepare Ba<sub>1-x</sub>Sr<sub>x</sub>TiO<sub>3</sub> nanostructured materials. Owing to the strong application background of Ba<sub>1-x</sub>Sr<sub>x</sub>TiO<sub>3</sub> and the facility of the synthesis methods, the sol-gel [55, 178, 179], pulse laser deposition [180–184], and magnetron sputtering [185] methods were widely utilized to fabricate barium strontium titanate nanocrystalline thin films. In this section, the sol-gel methods are discussed and an alkoxide method proposed to prepare Ba<sub>1-x</sub>Sr<sub>x</sub>TiO<sub>3</sub> nanoparticles.

Ba<sub>1-x</sub>Sr<sub>x</sub>TiO<sub>3</sub> nanocrystalline particles and thin films were widely synthesized using the same sol-gel method used for synthesizing nc-BaTiO<sub>3</sub>, in which the desired stoichiometry was controlled by the ratio of strontium acetate to barium acetate. In a typical process, barium acetate and strontium acetate were mixed and then dissolved in acetic acid above 90° under stirring. 2-Methoxyethanol was utilized to adjust the viscosity of the solution. Titanium isopropoxide was then added to the solution. For films, the gel precursor was spin-coated onto the substrates before heat treatment. Finally, the dried and solidified gel was heat-treated to obtain crystalline nanoparticles and thin films. The crystallization temperature for perovskite Ba<sub>1-x</sub>Sr<sub>x</sub>TiO<sub>3</sub> was 650 °C. With this technique, nanocrystalline barium strontium titanate thin films with an average grain size of 50 nm were obtained [55, 178, 179].

BaTiO<sub>3</sub> and SrTiO<sub>3</sub> nanoparticles were successfully produced using bimetallic alkoxide as the starting material [60, 174, 186]. Because Sr(OCH<sub>2</sub>OC<sub>2</sub>H<sub>4</sub>)<sub>2</sub> has a similar chemical behavior as Ba(OCH<sub>2</sub>OC<sub>2</sub>H<sub>4</sub>)<sub>2</sub>, the alkoxide method could be extended to synthesize (Ba, Sr)TiO<sub>3</sub> nanoparticles. Using Ti(*i*-OC<sub>3</sub>H<sub>7</sub>)<sub>4</sub>, Sr(OCH<sub>2</sub>OC<sub>2</sub>H<sub>4</sub>)<sub>2</sub>, and Ba(OCH<sub>2</sub>OC<sub>2</sub>H<sub>4</sub>)<sub>2</sub> as the starting materials and 2-methoxyethanol as the solvent, their stoichiometric mixture is refluxed to form a trimetallic alkoxide homogeneous precursor solution. Then hydrolysis is carried out by adding a mixture of deionized water and 2-methoxyethanol to the obtained precursor solution. Finally, the gelled precursor is pyrolyzed and calcined at high temperatures to obtain crystalline barium strontium titanate nanoparticles. On the other hand, similar to the case of nc-BaTiO<sub>3</sub>, crystalline barium strontium titanate nanoparticles may also be obtained by low temperature hydrolyzing of (Ba, Sr, Ti)-trimetallic alkoxides under highly alkaline condition [60, 186].

## 6.2. Low-Frequency Dielectric Properties

Ba<sub>0.7</sub>Sr<sub>0.3</sub>TiO<sub>3</sub> bulk material has a dielectric constant of approximately 5000 at 300 K. Parker et al. investigated the temperature and film thickness dependence of the dielectric constant of Ba<sub>0.7</sub>Sr<sub>0.3</sub>TiO<sub>3</sub> films on the platinized silicon substrate with a thickness ranging from 15 to 580 nm; the results are given in Figure 9. As the film thickness decreased, the maximum dielectric constant decreased from 660 to 110 at 4 kHz, which was more than one order of magnitude less

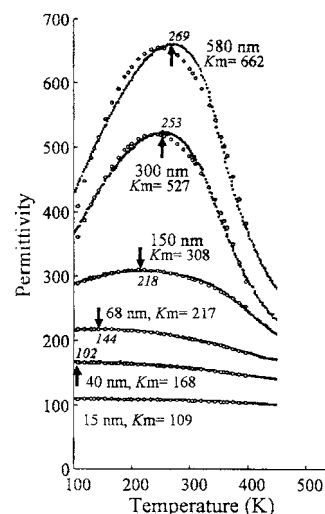


**Figure 9.** Permittivity as a function of temperature for six film thicknesses. The data are denoted by closed circles; the diffuse phase transition feature fit by open circles. The arrows denote the maximum value of permittivity. Tabulated with the arrow was the film thickness, the maximum permittivity, and the temperature at which the maximum permittivity occurred. Reprinted with permission from [187], C. B. Parker et al., *Appl. Phys. Lett.* 81, 340 (2002). © 2002, American Institute of Physics.

than the bulk value. The temperature at which the maximum dielectric constant occurred decreased from room temperature to 269 K for the 580-nm-thick film and to 102 K for the 40-nm-thick film. With decreasing film thickness, the temperature dependence of the dielectric constant anomalous peak became more broad. The film thickness dependence of the dielectric properties was explained in terms of a diffuse phase transition, in which the diffusivity increased with decreasing film thickness [187]. In Ba<sub>0.8</sub>Sr<sub>0.2</sub>TiO<sub>3</sub> nanocrystalline thin films on Pt/Ti/SiO<sub>2</sub>/Si substrates with an average grain size of 100 nm and a thickness of 400 nm, a broad tetragonal-to-cubic phase transition was observed around 35 °C, which was less than  $T_c = 80$  °C for the bulk material. Electrical measurements at room temperature showed a dielectric constant of 860 at 100 kHz,  $P_r = 6.5$   $\mu\text{C}/\text{cm}^2$ ,  $E_c = 41$  kV/cm, and a leakage current density of  $3.3 \times 10^{-7}$  A/cm<sup>2</sup> at 3 V [188]. In Ba<sub>0.8</sub>Sr<sub>0.2</sub>TiO<sub>3</sub> thin films, the tetragonal-to-cubic phase transition temperature was also observed to decrease with decreasing grain size [85, 188]. Similar to the case of BaTiO<sub>3</sub> nanostructured materials, the tetragonal-cubic phase transition temperature and dielectric constants of (Ba, Sr)TiO<sub>3</sub> nanocrystals were strongly suppressed by the reduced dimensionality, and an intrinsic finite-size effect and lattice strains introduced during film growth were proposed to understand these reductions in electrical properties [187, 189].

Owing to the strong anisotropy in ferroelectrics, the crystallographic orientation must influence the effective parameter normal to the film, as often reported in the literature. As an example, random and (100) oriented Ba<sub>1-x</sub>Sr<sub>x</sub>TiO<sub>3</sub> films with  $x = 0.33, 0.5, 0.67,$  and  $1.0$  were fabricated on base-metal (100) nickel tapes using a chemical solution deposition method. For randomly oriented films, zero-field room-temperature dielectric constants ranged from 250 to



420 at 100 kHz. But the films with enhanced (100) orientation exhibited zero-field dielectric constants of 980 to 1500, three times higher than the random films. The dielectric loss tangent was between 0.003 and 0.015 [190].

Taking advantage of the high dielectric constant, dynamic random access memories using barium strontium titanate thin film as the functional element were prepared for commercial use at the end of the 1990s.

### 6.3. Microwave Dielectric Properties

In heteroepitaxial  $\text{Ba}_{1-x}\text{Sr}_x\text{TiO}_3$  thin films, lattice strain was introduced during growth owing to lattice and thermal expansion mismatch between these films and the substrates, and the dielectric properties were able to be tuned by controlling the internal lattice strain [180, 181]. In the case of  $\text{Ba}_{0.5}\text{Sr}_{0.5}\text{TiO}_3$ , the bulk cubic lattice parameter is  $a = 3.95 \text{ \AA}$  and the thermal expansion coefficient  $\alpha = 10.5 \times 10^{-6}/^\circ\text{C}$  at 300 K. On the (001) MgO substrate, the in-plane tensile stresses of heteroepitaxial  $\text{Ba}_{0.5}\text{Sr}_{0.5}\text{TiO}_3$  thin films were found to decrease with increasing film thickness from 14 to 130 nm and were fully relaxed above thickness 130 nm. The microwave dielectric constant dropped from 2350 for highly stressed thin films to 1700 for relaxed thicker films at 1 MHz [180]. For the pseudocubic  $\text{LaAlO}_3$  substrate,  $a = 3.79 \text{ \AA}$  and  $\alpha = 10 \times 10^{-6}/^\circ\text{C}$  at 300 K. Because of the different lattice match conditions between the MgO and  $\text{LaAlO}_3$  substrates, different lattice strains occurred in the epitaxial  $\text{Ba}_{0.5}\text{Sr}_{0.5}\text{TiO}_3$  thin films. In these epitaxial films, either a large dielectric tuning (75%) or a high dielectric  $Q = 1/\tan \delta$  (100–250) but not both at the same time were typically observed [182].

To tune the lattice strain, various thin buffer layers were developed for epitaxially growing barium strontium titanate thin films. Using a thin ( $\sim 5 \text{ nm}$ ) amorphous  $\text{Ba}_{0.5}\text{Sr}_{0.5}\text{TiO}_3$  buffer layer, the strains in the crystalline films were relieved, and the films exhibited both high dielectric tunability and enhanced dielectric  $Q$  [182]. Alternatively, by inserting a very thin  $\text{Ba}_{1-x}\text{Sr}_x\text{TiO}_3$  ( $x = 0.1\text{--}0.7$ ) layer between the  $\text{Ba}_{0.6}\text{Sr}_{0.4}\text{TiO}_3$  thin film and the MgO (001) substrate, the lattice strain (described by the in-plane lattice constant/out-of-plane lattice constant ratio) in 400-nm-thick  $\text{Ba}_{0.6}\text{Sr}_{0.4}\text{TiO}_3$  epitaxial thin films was tuned from 0.9972 to 1.0051 by varying the interlayer composition. The dielectric constant varied between 512 and 1180 at a frequency of 1 MHz. On the  $\text{Ba}_{0.7}\text{Sr}_{0.3}\text{TiO}_3$  interlayer,  $\text{Ba}_{0.6}\text{Sr}_{0.4}\text{TiO}_3$  film showed a larger dielectric constant of 1180 and a tunability of 61% at a surface electric field of 80 kV/cm [181].

Silicon is a very technologically important substrate. Using a very thin yttria-stabilized zirconia buffer layer, epitaxial  $\text{Ba}_{0.5}\text{Sr}_{0.5}\text{TiO}_3$  thin films were successfully grown on the Si substrate using pulse laser deposition. The dielectric constant was as high as 1300 at 1 MHz when the lattice distortion of the in-plane lattice constant/out-of-plane lattice constant ratio was 1.007 [183].

For integrated film device applications, the better insulating (low leakage current density) quality is significantly attractive. In the metalorganic solution deposited  $\text{Ba}_{0.6}\text{Sr}_{0.4}\text{TiO}_3$  nanocrystalline thin films on a platinized silicon substrate, a typical resistivity was  $\rho = 0.04 \times 10^{13} \text{ \Omega cm}$

at an electric field of 100 kV/cm. However, the small concentration of acceptor dopants could dramatically modify the properties of the ferroelectrics. For instance, the 1-mol% La-doped  $\text{Ba}_{0.6}\text{Sr}_{0.4}\text{TiO}_3$  film (average grain size 50 nm and film thickness 150 nm) exhibited an enhanced resistivity of  $\rho = 31.4 \times 10^{13} \text{ \Omega cm}$  at 100 kV/cm. The dielectric constant, loss tangent, and tunability of the 1-mol% La-doped  $\text{Ba}_{0.6}\text{Sr}_{0.4}\text{TiO}_3$  films were 283 at 100 kHz, 0.019, and 21% at 200 kV/cm, respectively. The improved dielectric properties, low leakage current, and good dielectric tunability of the acceptor-doped barium strontium titanate thin films suggest their use in fabricating high-performance tunable microwave devices [55].

Owing to their large dielectric tunability and low dielectric loss, barium strontium titanate nanocrystalline thin films were widely used to fabricate electrically tunable microwave devices, such as phase shifters and harmonic generators. As an example, using sol-gel-derived highly oriented  $\text{Ba}_{0.6}\text{Sr}_{0.4}\text{TiO}_3$  thin films on a  $\text{LaAlO}_3$  (100) substrate, eight element coupled microstrip phase shifters were fabricated. An insertion loss of 8.435 dB, phase shift on the order of  $320^\circ$  ( $2.6\text{--}14.5 \text{ V}/\mu\text{m}$ ), and factor (phase shift/decibel of loss) of about  $38.0^\circ/\text{dB}$  were demonstrated [191].

### 6.4. Nonlinear Optical Properties

Similar to the dielectric properties, the nonlinear optical properties of  $\text{Ba}_{1-x}\text{Sr}_x\text{TiO}_3$  thin films were also dependent on the strontium composition and the lattice strain.

For  $a$ -oriented  $\text{Ba}_{1-x}\text{Sr}_x\text{TiO}_3$  thin films of thickness 200 nm on a (100)  $\text{LaAlO}_3$  substrate, Li et al. investigated the composition dependence of electrooptic properties at  $\lambda = 632.8 \text{ nm}$  of a He-Ne laser [184]. It was found that the linear electrooptic coefficient  $\gamma$  had maximum at  $x = 0.35\text{--}0.4$ . The quadratic electrooptic coefficient  $s$  initially decreased as  $x$  increased and reached a small plateau around  $x = 0.5$ . Both  $\gamma$  and  $s$  dropped to 0 when  $x > 0.7$ . For  $\text{Ba}_{0.7}\text{Sr}_{0.3}\text{TiO}_3$  film,  $\gamma$  was determined as 110 pm/V in the case of increasing electric field and 230 pm/V in the case of decreasing electric field;  $s = 0.55 \times 10^{-16} \text{ m}^2/\text{V}^2$ . For  $\text{Ba}_{0.5}\text{Sr}_{0.5}\text{TiO}_3$  film,  $\gamma$  was 70 pm/V in the case of increasing electric field and 115 pm/V in the case of decreasing electric field;  $s = 1.3 \times 10^{-16} \text{ m}^2/\text{V}^2$ . Compared with  $\text{BaTiO}_3$ , the large electrooptic coefficients of  $\text{Ba}_{1-x}\text{Sr}_x\text{TiO}_3$  ( $x = 0.3\text{--}0.5$ ) films make them well suited to integrated optoelectronic devices [27, 184].

For cubic  $\text{Ba}_{1-x}\text{Sr}_x\text{TiO}_3$ , second-harmonic generation is unexpected since the crystal structure is centrosymmetric under ambient conditions. However, due to large lattice and thermal expansion mismatches between the  $\text{Ba}_{1-x}\text{Sr}_x\text{TiO}_3$  film and the MgO substrate, the introduced lattice strains destroyed the inversion symmetry and induced second-harmonic generation. In a 30-nm-thick  $\text{Ba}_{0.48}\text{Sr}_{0.52}\text{TiO}_3$  epitaxial film grown on (001) MgO substrate, a tetragonal distortion induced by film strain was determined to be  $c/a = 1.015$ , and second-order nonlinear susceptibility was measured as  $d_{33} = 11.0 \text{ pm/V}$ ,  $d_{31} = 4.7 \text{ pm/V}$ , and  $d_{15} = 2.2 \text{ pm/V}$  at a fundamental wavelength of  $1.064 \text{ \mu m}$  [185]. As the strain decreased from 2.7% to 0.7%, corresponding to a decrease in the film thickness from 30 nm to 165 nm, the

second-harmonic signal decreased by a factor of 10. Therefore, the strain was the dominant factor controlling second-harmonic generation in  $\text{Ba}_{1-x}\text{Sr}_x\text{TiO}_3$  epitaxial thin films. Compared with  $\text{BaTiO}_3$  thin films [20], barium strontium titanate thin films have a large effective  $d$  coefficient, better chemical stability, and a higher dielectric constant as well.

## 7. APPLICATIONS

As discussed above, the grain size effect plays an important role in controlling the structural phases and properties of  $\text{BaTiO}_3$  nanostructured materials. Due to the grain size-induced tetragonal-cubic phase transition, the nanocrystalline  $\text{BaTiO}_3$  thin films with various grain sizes could find possible applications in integrated high-density memories ranging from dynamic random access memory using high dielectric constant to nonvolatile memory with spontaneous polarization being reversed between two opposite directions, surface acoustic wave devices, microactuators, and various electrooptic devices [29, 154]. Nanocrystalline  $\text{BaTiO}_3$  thick films of thickness up to several micrometers have potential applications in pyroelectric infrared microsensors and ultrasonic high-frequency transducers [26]. In the following,  $\text{BaTiO}_3$  nanostructured material applications in the fields of optical modulators, transducers and actuators, and thermal, humidity, and  $\text{CO}_2$  sensors are discussed in detail.

### 7.1. Optical Modulators

$\text{BaTiO}_3$  crystals have the highest known electrooptic coefficient  $\gamma_{51} = 820 \text{ pm/V}$  at 632.8 nm [19]. In epitaxial  $\text{BaTiO}_3$  thin-film waveguides on a  $\text{MgO}$  (001) substrate, a large effective dc electrooptic coefficient of  $\gamma_{\text{eff}} \sim 50 \pm 5 \text{ pm/V}$  and an electrooptic coefficient of  $\gamma_{\text{eff}} \sim 18 \pm 2 \text{ pm/V}$  at 5 MHz for  $\lambda = 1.54 \text{ }\mu\text{m}$  light were reported. The propagation loss in a 300-nm-thick planarized waveguide is typically 5 dB/cm for 1.5- $\mu\text{m}$  light [27]. Compared with barium titanate epitaxial thin films, the barium strontium titanate ( $x = 0.3\text{--}0.5$ ) epitaxial thin films exhibited a higher effective electrooptic coefficient, as discussed in Section 6.4. These experiments demonstrated the potential of  $\text{BaTiO}_3$  and  $(\text{Ba}, \text{Sr})\text{TiO}_3$  epitaxial thin films for low-voltage, highly confining, guided-wave electrooptic modulator structures. Moreover, thin-film devices offer unique characteristics superior to diffused waveguides fabricated on bulk ferroelectric crystals. The large index difference between the film and the substrate enables a high confinement effect in the waveguides, which creates the potential for high-speed, low-voltage electrooptic switching and for high energy density to be produced at moderate incidence power [159].

In sol-gel  $\text{Er}:\text{BaTiO}_3$  nanocrystalline thin films, optical waveguide double modes were observed with effective refractive indices of 2.122 and 1.868, respectively, at 632.8 nm of He-Ne laser [159]. These results were encouraging for the investigation of planar  $\text{Er}:\text{BaTiO}_3$  film waveguides and devices for optical amplifiers and laser applications. In most cases, the sol-gel-derived films were high loss and random oriented in nature, which resulted in a smaller electrooptic response compared with oriented films. Compared with the sol-gel methods, the MOCVD and laser

MBE techniques have more potential to fabricate high-quality optical waveguides with loss less than 1 dB/cm [54, 94, 192]. Epitaxial  $\text{BaTiO}_3$  optical waveguides and electrooptic modulators were fabricated with the MOCVD technique. Excellent modulation efficiency, frequency response, and losses as low as 3–4 dB/cm at 1.54  $\mu\text{m}$  were demonstrated [27, 94, 102, 192]. In the  $c$ -axis-oriented  $\text{BaTiO}_3$  epitaxial thin films on a  $\text{MgO}$  (001) substrate, the refractive index was  $2.378 \pm 0.002$  at 632.8 nm, and the waveguide loss was 2.9 dB/cm [103].

Nevertheless, future integrated optical circuits will require  $\text{BaTiO}_3$  thin films to be integrated with silicon or III–V compounds. To date, it is still difficult to prepare epitaxial  $\text{BaTiO}_3$  films directly on bare silicon substrates due to large lattice mismatch and severe interface diffusion. To obtain high-quality epitaxial ferroelectric thin films on those substrates, the approach using yttria-stabilized zirconia (YSZ) and  $\text{MgO}$  buffer layers was developed, and then epitaxial  $\text{BaTiO}_3$  and  $(\text{Ba}, \text{Sr})\text{TiO}_3$  thin films were obtained [183, 193, 194].

### 7.2. Transducers and Actuators

Piezoelectricity is the property of acquiring electric polarization under external mechanical stresses, or the *converse* property of changing dimension when subjected to external electric fields. The large piezoelectric coefficient, especially near the phase transition temperature, makes ferroelectrics attractive for transducers, which convert mechanical changes to electrical changes or vice versa. In some cases, the purpose of the transducer is to convert ac fields, or sudden change of field, into corresponding mechanical motions, as in ultrasonic generators, actuators, loudspeakers, or pulse generators. In other cases, a transducer uses piezoelectric effects to convert small motions into electric changes, as in ultrasonic detectors, strain-gauge, microphones, and devices to measure vibrations [2]. As illustrated in Table 1, ferroelectric  $\text{BaTiO}_3$  exhibits high piezoelectric coefficient potential for transducer and actuator applications.

According to (5.2), the spontaneous strain, which plays a dominant role in piezoelectricity, in ferroelectric  $\text{BaTiO}_3$  is proportional to the squared spontaneous polarization. Thus, the piezoelectric coefficient  $d_{31}$  in ferroelectrics is proportional to  $P$  [2, 150]. When the ferroelectrics are in the paraelectric cubic phase,  $P_s = 0$ , they have no piezoelectric effect. Therefore, cubic  $\text{BaTiO}_3$  nanostructured materials are precluded from application in transducers. The critical size of ferroelectricity is also the ultimate miniaturization level of piezoelectric  $\text{BaTiO}_3$ .

In  $\text{BaTiO}_3$  nanoceramics with an average grain size of 300 nm, the spontaneous polarization  $P_s = 15 \text{ }\mu\text{C}/\text{cm}^2$  at room temperature [10]. Although it was less than the  $P_s$  for single crystals and ceramics with a grain size of 1.2  $\mu\text{m}$ , in accordance with (5.2), nanoceramics still possess sufficient piezoelectric coefficient. In comparison with conventional ceramics, dense nanoceramics, nanocomposites, and thick films, which make use of nanoparticles as starting materials, facilitated versatile shapes. For various transducers, the chosen shape depends on the utilization field and required frequency. For example, a complex shape is required for

actuators, but a simple slab is required for ultrasonic frequency [2]. On the other hand, the high-dielectric-constant BaTiO<sub>3</sub> nanoceramics have a large electromechanical coupling factor—a measure of the proportion of electrical energy that can be stored elastically. Therefore, BaTiO<sub>3</sub> nanoceramics with versatile shapes could be applied for transducers and actuators with controlled oscillator frequencies and bands.

### 7.3. Thermal Sensors

The temperature dependence of spontaneous polarization, dielectric constant, or resistivity in ferroelectric BaTiO<sub>3</sub> and (Ba,Sr)TiO<sub>3</sub> was applied to fabricate bolometers for infrared detection, infrared imaging detection, and thermometers.

For pyroelectric bolometers, based on (5.1) and (5.2), the temperature dependence of spontaneous polarization in the ferroelectric nanoparticles can be written as

$$P_s \propto (|A|(T_c - T))^{\gamma/2} \quad (7.1)$$

where under  $\gamma = 1$  ambient conditions. By differentiating (7.1) with respect to temperature and substituting (3.2) into it, the pyroelectric coefficient of ferroelectric nanoparticles is obtained:

$$p = dP_s/dT \propto |A|^{1/2}(T_c(\infty) - D/(R - R_c) - T)^{-1/2} \quad (7.2)$$

From (7.2), it can be seen that the pyroelectric coefficient  $p$  could be enhanced by decreasing the ferroelectric nanoparticle size, owing to decreasing tetragonal–cubic phase transition temperature. But the parameter  $|A|$  was reduced greatly by decreasing grain size [138, 169–171]. Therefore, the resulting pyroelectric coefficient  $p$  was decreased in BaTiO<sub>3</sub> ferroelectric nanocrystals. For dielectric bolometers, the bulk dielectric constant changes anomalously near the ferroelectric–paraelectric phase transition, which obeys the Curie–Weiss law. However, in ferroelectric nanocrystals, this anomalous dielectric peak was suppressed to become flat, and even disappeared below a critical size, as illustrated in Figure 5. The preliminary measurements have demonstrated that the figure of merits, which is proportional to  $p$  and inversely proportional to  $\epsilon$ , in ferroelectric nanocrystalline BaTiO<sub>3</sub> and (Ba,Sr)TiO<sub>3</sub> was much lower than the value of bulk materials [85, 158, 187]. So the finite-grain-size effect precluded the small-grain-sized (Ba,Sr)TiO<sub>3</sub> nanocrystalline thin-film application for uncooled monolithic integrated ferroelectric thin-film infrared focal plane arrays [195]. To avoid this limit of small-grain-size effect on pyroelectric properties, (Ba,Sr)TiO<sub>3</sub> thin films with large grain size and columnar microstructure were prepared; they exhibited enhanced pyroelectric properties as expected [85, 188].

The vinylidene fluoride/trifluoroethylene [P(VDF-TrFE)] copolymers are useful pyroelectric organic materials without stretching and, thus, good candidates as solid-state imaging sensors. They have low thermal conductivity and can be fabricated into large-area thin films. Mixing ferroelectric nanoparticles and copolymer materials to form nanocomposites, improved pyroelectric performance was obtained [124, 125]. Because the piezoelectric coefficients

( $d_{33}$  as well as  $d_{31}$ ) of the ferroelectric and polymer phases have opposite signs, while the pyroelectric coefficients have the same sign, the piezoelectric contributions in composites from the two phases are partially cancelled, but the pyroelectric contributions are reinforced. Therefore, the ferroelectric nanoparticle/copolymer composite exhibits high pyroelectric activity but no spurious electrical signal due to mechanical strain or vibration owing to the minimized piezoelectric microphone effect, and is a promising candidate in the application field of integrated pyroelectric sensor arrays on silicon-based readout integrated electronic circuits. Based on the relationship between pyroelectric property and ferroelectric nanocrystallite size, it is necessary to choose large BaTiO<sub>3</sub> or (Ba,Sr)TiO<sub>3</sub> nanoparticles with good pyroelectric property and with grain size significantly smaller than the thickness of the nanocomposite films for pyroelectric sensor applications.

Usually, the pure BaTiO<sub>3</sub> ceramics were highly resistive at room temperature. Some donor-doped BaTiO<sub>3</sub> ceramics exhibited positive temperature coefficient of resistivity (PTCR) characteristics, which were used for infrared detection and temperature control [196, 197]. To optimize the sensor performance, the Ba or Ti elements were often substituted to tune the tetragonal–cubic phase transition temperature of BaTiO<sub>3</sub> ceramics over a large temperature range, for example, between  $-30$  °C and  $400$  °C [197]. With nanotechnology, the grain size in the nanometer scale can cause the tetragonal–cubic phase transition temperature of BaTiO<sub>3</sub> to decrease toward room temperature. On the other hand, the PTCR and anomalous dielectric properties were closely associated with the quality of grain boundaries [198, 199]. With low-temperature hydrothermal methods, the grain boundaries of BaTiO<sub>3</sub> nanoparticles could be easily modified [75]. Therefore, BaTiO<sub>3</sub> nanoceramics may find applications with the PTCR effect.

### 7.4. Humidity Sensor

The electrical conductance and capacitance of BaTiO<sub>3</sub> ceramics usually change in a humid environment due to water vapor chemisorption and physisorption and capillary condensation in the pores of the sensor element. Compared with conventional ceramics, BaTiO<sub>3</sub> nanoceramics have better humidity-sensing properties, such as lower resistance and higher sensitivity. Qiu et al. observed the resistance of nc-BaTiO<sub>3</sub> increasing with increasing grain size, for example, from 23 to 53 nm, while the linearity and slope in the high-humidity range were improved [48]. From the application point of view, the resistance for the resistive humidity sensor is better, ranging over  $10^6$ – $10^3$   $\Omega$ , for minimizing humidity hysteresis and increasing sensitivity and repeatability. To further improve the performance of nc-BaTiO<sub>3</sub> humidity sensors, Wang et al. proposed two methods of doping a certain amount of impurities into nc-BaTiO<sub>3</sub> and mixing some polymer humidity sensing materials with nc-BaTiO<sub>3</sub> to fabricate nanocomposite humidity sensors [47, 200, 201].

First, the experiments showed that doping Na<sub>2</sub>CO<sub>3</sub>, K<sub>2</sub>CO<sub>3</sub>, and sodium citrate modified the resistance of the nc-BaTiO<sub>3</sub> humidity sensor from  $10^6$  to  $10^3$   $\Omega$ , among which NaH<sub>2</sub>PO<sub>4</sub> was the best dopant for minimizing the humidity hysteresis of the BaTiO<sub>3</sub> sensor. The maximum humidity hysteresis of the sensor was 3% relative humidity (RH)

in the region of 30–90% RH [200]. Second, some polymer materials also show good humidity sensitivities such as long-term stability, repeatability, precision, and so forth. However, the polymer materials do not behave as well as ceramic and nanocrystal materials in complex environments, for example, in air with organic gas. Combining inorganic (ceramic or nanocrystal) materials with organic polymers may be expected to obtain better humidity-sensing materials. One example was to use polymer material of quaternary acrylic resin  $[(R)_nM^+X^-]$  mixed with nc-BaTiO<sub>3</sub> to form a nanocomposite. These nanocomposite materials exhibited much better sensing properties: The sensitivity was higher than that of pure nc-BaTiO<sub>3</sub>, and the maximum humidity hysteresis was about 3% RH in the range of 33–98% RH [47, 201].

### 7.5. CO<sub>2</sub> Sensors

In the fields of agricultural and biotechnological processes as well as air-conditioning systems and monitoring of exhaust gases, there is an increasing demand for CO<sub>2</sub> sensors. In addition to optical and electrochemical sensors, a new generation of low-cost solid-state CO<sub>2</sub> gas sensors based on nc-BaTiO<sub>3</sub> thick films is being developed. Nanocrystalline BaTiO<sub>3</sub> was used to fabricate CO<sub>2</sub> sensors owing to the semiconducting character that the conductance or capacitance changes due to adsorbed CO<sub>2</sub>. These sensors have the potential to further reduce production cost, increase sensor design versatility, and simplify integration with other gas sensors on the same substrate [202, 203].

Keller et al. systematically investigated the mechanical stability, sensitivity, reproducibility, detection limit, long-term stability, operating temperature, cross-sensitivity by interfering gases, and power consumption of nanocrystalline BaTiO<sub>3</sub>-based sensors [202]. It was found that nanocrystalline BaTiO<sub>3</sub>-based sensors had higher sensitivity to 0.01% CO<sub>2</sub> concentration, lower detection limit, minor influence of interfering gases, and reduced power consumption than microcrystalline sensors. The nanocrystalline BaTiO<sub>3</sub> thick films could also be applied as less power consuming CO<sub>2</sub> solid-state sensor devices for mobile CO<sub>2</sub> detection. In studying the CO<sub>2</sub>-sensing mechanism, the sensitivity was found to be closely related to lattice defects in the sensing layers—defect structures rather than the concentration of lattice vacancies [203]. Nevertheless, before entering the market, major drawbacks of semiconducting solid-state layers such as small long-term stability and signal drift must be overcome.

## 8. SUMMARY

In summary, perfect BaTiO<sub>3</sub> nanocrystalline materials ranging from 0D nanoparticles to 2D single-crystal films have been successfully fabricated. With the benefit of generalized solution-phase decomposition nanotechnology [51, 80, 81], fabrications of complex BaTiO<sub>3</sub> nanostructured systems (colloidal crystals) were also attempted, which would extend studying the properties and applications of nanostructured BaTiO<sub>3</sub>. Using BaTiO<sub>3</sub> nanocrystals as building block, strained superlattices, nanoceramics, and nanocomposites were also fabricated for technological applications.

The dielectric, ferroelectric, optical, and lattice dynamical properties of BaTiO<sub>3</sub> nanostructured materials could be tuned or enhanced by controlling the grain size and lattice strains. The finite-size effect on structural and physical properties was well understood with the model of grain size effect on long-range interaction and its cooperative phenomena. The finite-grain-size effect not only extended the application fields BaTiO<sub>3</sub> but also created some new fields such as optical modulators, transducers and actuators, and thermal and chemical sensors. Nevertheless, research is still needed to deepen our understanding of the grain size effect on those enhanced (novel) properties in BaTiO<sub>3</sub> nanostructured materials, such as low-temperature quantum ferroelectricity and paraelectricity, electronic structure changes, and soft-mode behavior with varying nanocrystallite size.

## GLOSSARY

**Ferroelectric critical grain size** The minimum grain size, below which the ferroelectricity disappears.

**Ferroelectric phase transition** A special class of structural phase transition where the transition from the high to the low symmetry phase is accompanied by the appearance of spontaneous polarization. They could be driven by external field applications of temperature, of pressure, of electric field, of composition substitution, and/or of grain size.

**Finite grain size effect** When the dimension of crystal is comparable with the feature length of some property, this property becomes dependent on the grain size and shape, which is named as finite grain size effect.

**Perovskite oxide** A family name of oxide materials having a chemical formula of ABO<sub>3</sub>. In the prototype cubic structure, the ionic A is at the corner, B at the bulk center, and O at the face center.

**Quantum ferroelectric phase transition** Instead of by thermal fluctuation, the ferroelectric phase transition from the paraelectric phase is driven by quantum fluctuation, of which the Curie temperature obeys the relation of  $T_c \propto (S - S_c)^{1/2}$ , changed from the classical law  $T_c \propto (S - S_c)$ .  $S$  is external parameter controlling interaction, and  $S = S_c$  at  $T_c$ .

**Soft mode** One of the lowest frequency transverse optical modes, of which the frequency is temperature dependent and reduces to zero as the transition temperature is approached, and at Curie temperature, the condensation of soft mode displacement determines the structure of the low temperature phase.

**Spontaneous polarization** The existence of electrical momentum in the noncentrosymmetric phases, which can be reversed or reoriented by application of external electrical field.

## ACKNOWLEDGMENTS

This work was partially supported by National Climbing Project, National Natural Science Fund of China, and Shanghai Natural Science Fund (Grant 02ZE14113).

## REFERENCES

1. B. A. Strukov and A. P. Levanyuk, "Ferroelectric Phenomena in Crystals: Physical Foundations," Springer-Verlag, Berlin/New York, 1998.
2. J. C. Burfoot, "Ferroelectrics: An Introduction to the Physical Principles," Van Nostrand, London, 1962.
3. A. Garcia and D. Vanderbilt, in "First-Principles Calculations for Ferroelectrics" (R. E. Cohen, Ed.), CP 436, p. 53. American Institute of Physics, New York, 1998.
4. T. P. Dougherty, G. P. Wiederrecht, K. A. Nelson, M. H. Garrett, H. P. Jensen, and C. Warde, *Science* 258, 770 (1992).
5. R. E. Cohen and H. Krakauer, *Phys. Rev. B* 42, 6416 (1990).
6. W. Zhong, D. Vanderbilt, and K. M. Rabe, *Phys. Rev. Lett.* 73, 1861 (1994).
7. T. Ishidate, S. Abe, H. Takahashi, and N. Mori, *Phys. Rev. Lett.* 78, 2397 (1997).
8. K. Kinoshita and A. Yamaji, *J. Appl. Phys.* 47, 371 (1976).
9. G. Arlt, D. Hennings, and G. de With, *J. Appl. Phys.* 58, 1619 (1985).
10. T. Takeuchi, C. Capiglia, N. Balakrishnan, Y. Takeda, and H. Kageyama, *J. Mater. Res.* 17, 575 (2002).
11. D. Burlincourt and H. Jaffe, *Phys. Rev.* 111, 143 (1958).
12. J. M. Ballantyne, MIT Lab. Insul. Res. Technical Report 188, 1964.
13. F. D. Morrison, D. C. Sinclair, and A. R. West, *J. Am. Ceram. Soc.* 84, 474 (2001).
14. M. T. Buscaglia, M. Viviani, V. Buscaglia, and C. Bottino, *J. Am. Ceram. Soc.* 85, 1569 (2002).
15. C. N. Berglund and W. S. Bear, *Phys. Rev.* 157, 358 (1967).
16. P. Bernasconi, I. Biaggio, M. Zgonik, and P. Gunter, *Phys. Rev. Lett.* 78, 106 (1997).
17. R. G. Rhodes, *Acta Cryst.* 4, 105 (1951).
18. J. S. Zhu, X. M. Lu, W. Jiang, W. Tian, M. Zhu, M. S. Zhang, X. B. Chen, X. Liu, and Y. N. Wang, *J. Appl. Phys.* 81, 1392 (1997).
19. A. M. Glass, *Science* 235, 1003 (1987).
20. B. Bihari, J. Kumar, G. T. Stauf, P. C. Van Buskirk, and C. S. Hwang, *J. Appl. Phys.* 76, 1169 (1994).
21. M. H. Frey and D. A. Payne, *Phys. Rev. B* 54, 3158 (1996).
22. K. Uchino, E. Sadanaga, and T. Hirose, *J. Am. Ceram. Soc.* 72, 1555 (1989).
23. R. Thomas, V. K. Varadan, S. Komarneni, and D. C. Dube, *J. Appl. Phys.* 90, 1480 (2001).
24. A. D. Li, C. Z. Ge, P. Lu, D. Wu, S. B. Xiong, and N. B. Ming, *Appl. Phys. Lett.* 70, 1616 (1997).
25. M. H. Frey and D. A. Payne, *Appl. Phys. Lett.* 63, 2753 (1993).
26. M. C. Cheung, H. L. W. Chan, Q. F. Zhou, and C. L. Choy, *Nanostruct. Mater.* 11, 837 (1999).
27. D. M. Gill, C. W. Conrad, G. Ford, B. W. Wessels, and S. T. Ho, *Appl. Phys. Lett.* 71, 1783 (1997).
28. J. F. Scott and C. A. Paz de Aranjó, *Science* 246, 1400 (1989).
29. E. W. Kreutz, J. Gottmann, M. Mergens, T. Klotzbucher, and B. Vosseler, *Surf. Coat. Technol.* 116–119, 1219 (1999).
30. T. T. Fang, H. L. Hsieh, and F. S. Shiau, *J. Am. Ceram. Soc.* 76, 1205 (1993).
31. Y. S. Her, E. Matijevic, and M. C. Chon, *J. Mater. Res.* 10, 3106 (1995).
32. S. Chattopadhyay, P. Ayyub, V. R. Palkar, and M. Multani, *Phys. Rev. B* 52, 13177 (1995).
33. J. Yu, X. J. Meng, J. L. Sun, G. S. Wang, and J. H. Chu, *Mater. Res. Soc. Symp. Proc.* 718, 177 (2002).
34. J. R. Heath, *Science* 270, 1315 (1995).
35. C. B. Murray, C. R. Kagan, and M. G. Bawendi, *Science* 270, 1335 (1995).
36. G. Allan, Y. M. Niquet, and C. Delerue, *Appl. Phys. Lett.* 77, 639 (2000).
37. R. E. Cohen, *Nature* 358, 136 (1992).
38. S. Saha, T. P. Sinha, and A. Mookerjee, *Phys. Rev. B* 62, 8828 (2000).
39. Y. Kuroiwa, S. Aoyagi, A. Sawada, J. Harada, E. Nishibori, M. Takata, and M. Sakata, *Phys. Rev. Lett.* 87, e217601 (2001).
40. S. Ishihara, M. Tachiki, and T. Egami, *Phys. Rev. B* 49, 16123 (1994).
41. P. Ayyub, S. Chattopadhyay, K. Sheshadri, and R. Lahiri, *Nanostruct. Mater.* 12, 713 (1999).
42. A. V. Prasadarao, M. Suresh, and S. Komarneni, *Mater. Lett.* 39, 359 (1999).
43. H. I. Hsiang and F. S. Yen, *J. Am. Ceram. Soc.* 79, 1053 (1996).
44. F. S. Yen, H. I. Hsiang, and Y. H. Chang, *Jpn. J. Appl. Phys.* 34, 6149 (1995).
45. J. M. McHale, P. C. McIntyre, K. E. Sickafus, and N. V. Coppa, *J. Mater. Res.* 11, 1199 (1996).
46. K. Kiss, J. Magder, M. S. Vukasovich, and R. J. Lockhart, *J. Am. Ceram. Soc.* 49, 291 (1966).
47. J. Wang, W. P. Yan, J. C. Zhang, F. B. Qiu, T. Zhang, G. F. Liu, and B. K. Xu, *Mater. Chem. Phys.* 69, 288 (2001).
48. F. B. Qiu, X. Li, K. Guo, B. Zou, M. Y. Zhao, D. O. Henderson, and R. X. Mu, *Mater. Chem. Phys.* 56, 140 (1998).
49. J. Yu, J. L. Sun, J. H. Chu, and D. Y. Tang, *Appl. Phys. Lett.* 77, 2807 (2000).
50. H. R. Xu, L. Gao, and J. K. Guo, *J. Am. Ceram. Soc.* 85, 727 (2002).
51. S. O'Brien, L. Brus, and C. B. Murray, *J. Am. Chem. Soc.* 123, 12085 (2001).
52. M. Leoni, M. Viviani, P. Nanni, and V. Buscaglia, *J. Mater. Sci. Lett.* 15, 1302 (1996).
53. R. Bottcher, C. Klimm, D. Michel, H.-C. Semmelhack, G. Volkel, H.-J. Glasel, and E. Hartmann, *Phys. Rev. B* 62, 2085 (2000).
54. H. X. Zhang, C. H. Kam, Y. Zhou, X. Q. Han, S. Buddhudu, Q. Xiang, Y. L. Lam, and Y. C. Chan, *Appl. Phys. Lett.* 77, 609 (2000).
55. M. W. Cole, P. C. Joshi, and M. H. Ervin, *J. Appl. Phys.* 89, 6336 (2001).
56. B. Jiang, J. L. Peng, L. A. Bursill, T. L. Ren, P. L. Zhang, and W. L. Zhong, *Physica B* 291, 203 (2000).
57. F. F. Lange, *Science* 273, 903 (1996).
58. S. Schlag and H.-F. Eicke, *Solid State Commun.* 91, 883 (1994).
59. S. Gablenz, H.-P. Abicht, E. Pippel, O. Lichtenberger, and J. Woltersdorf, *J. Eur. Ceram. Soc.* 20, 1053 (2000).
60. J. Yang, J. M. F. Ferreira, W. J. Weng, and Y. Tang, *Mater. Lett.* 42, 257 (2000).
61. W. L. Luan and L. Gao, *Ceram. Int.* 27, 645 (2001).
62. C. Liu, B. S. Zou, A. J. Rondinone, and Z. J. Zhang, *J. Am. Chem. Soc.* 123, 4344 (2001).
63. W. S. Cho, *J. Phys. Chem. Solids* 59, 659 (1998).
64. P. Bendale, S. Venigalla, J. R. Ambrose, E. D. Verink, Jr., and J. H. Adair, *J. Am. Ceram. Soc.* 76, 2619 (1993).
65. A. T. Chien, L. S. Speck, F. F. Lange, A. C. Daykin, and C. G. Levi, *J. Mater. Res.* 10, 1784 (1995).
66. M. Viviani, J. Lemaitre, M. T. Buscaglia, and P. Nanni, *J. Eur. Ceram. Soc.* 20, 315 (2000).
67. I. MacLaren and C. B. Ponton, *J. Eur. Ceram. Soc.* 20, 1267 (2000).
68. Y. S. Her, E. Matijevic, and M. C. Chon, *J. Mater. Res.* 11, 3121 (1996).
69. Y. S. Her, S. H. Lee, and E. Matijevic, *J. Mater. Res.* 11, 156 (1996).
70. J. F. Bocquet, K. Chhor, and C. Pommier, *Mater. Chem. Phys.* 57, 273 (1999).
71. J. O. Eckert, Jr., C. C. Hung-Houston, B. L. Gersten, M. M. Lericka, and R. E. Riman, *J. Am. Ceram. Soc.* 79, 2929 (1996).
72. M. Z. C. Hu, V. Kurian, E. A. Payzant, C. J. Rawn, and R. D. Hunt, *Powder Technol.* 110, 2 (2000).
73. C. Kormann, D. W. Bahnemann, and M. R. Hoffmann, *J. Phys. Chem.* 92, 5196 (1988).
74. M. S. Zhang, J. Yu, W. C. Chen, and Z. Yin, *Prog. Cryst. Growth Charact. Mater.* 40, 33 (2000).
75. J. Yu, J. Chu, and M. Zhang, *Appl. Phys. A* 74, 645 (2002).

76. K. Yamada and S. Kohiki, *Physica E* 4, 228 (1999).
77. S. Kohiki, S. Takada, A. Shimizu, K. Yamada, H. Higashijima, and M. Mitome, *J. Appl. Phys.* 87, 474 (2000).
78. C. Beck, W. Hartl, and R. Hempelmann, *J. Mater. Res.* 13, 3174 (1998).
79. H. Herrig and R. Hempelmann, *Nanostruct. Mater.* 9, 241 (1997).
80. V. F. Puentes, K. M. Krishnan, and A. P. Alivisatos, *Science* 291, 2115 (2001).
81. J. J. Urban, W. S. Yun, Q. Gu, and H. K. Park, *J. Am. Chem. Soc.* 124, 1186 (2002).
82. W. S. Yun, J. J. Urban, Q. Gu, and H. K. Park, *Nano. Lett.* 2, 447 (2002).
83. H. Kumazawa and K. Masuda, *Thin Solid Films* 353, 144 (1999).
84. C. L. Jia, K. Urban, S. Hoffmann, and R. Waser, *J. Mater. Res.* 13, 2206 (1998).
85. J. G. Cheng, X. J. Meng, J. Tang, S. L. Guo, and J. H. Chu, *J. Am. Ceram. Soc.* 83, 2616 (2000).
86. H. Shimooka and M. Kuwabara, *J. Am. Ceram. Soc.* 78, 2849 (1995).
87. H. Matsuda, N. Kobayashi, T. Kobayashi, K. Miyazawa, and M. Kuwabara, *J. Non-Cryst. Solids* 271, 162 (2000).
88. J. M. Zeng, C. L. Lin, J. H. Li, and K. Li, *Mater. Lett.* 38, 112 (1999).
89. Y. Matsumoto, T. Morikawa, H. Adachi, and J. Hombo, *Mater. Res. Bull.* 27, 1310 (1992).
90. R. R. Basca, G. Rutsch, and J. P. Dougherty, *J. Mater. Res.* 11, 194 (1996).
91. J. Tamaki, G. K. L. Goh, and F. F. Lange, *J. Mater. Res.* 15, 2583 (2000).
92. E. W. Kreutz, M. Alunovic, T. Klotzbucher, M. Mertin, D. A. Wesner, and W. Pfleging, *Surf. Coat. Technol.* 74, 1012 (1995).
93. D. Y. Kim, S. G. Lee, Y. K. Park, and S. J. Park, *Mater. Lett.* 40, 146 (1999).
94. B. W. Wessels, *J. Cryst. Growth* 195, 706 (1998).
95. L. H. Robins, D. L. Kaiser, L. D. Rotter, P. K. Schenck, G. T. Stauf, and D. Rytz, *J. Appl. Phys.* 76, 7487 (1994).
96. Y. Yoneda, T. Okabe, K. Sakaue, and H. Terauchi, *Surf. Sci.* 410, 62 (1998).
97. H. B. Lu, N. Wang, W. Z. Chen, F. Chen, T. Zhao, H. Y. Peng, S. T. Lee, and G. Z. Yang, *J. Cryst. Growth* 212, 173 (2000).
98. T. Tsurumi, T. Ichikawa, T. Harigai, H. Kakemoto, and S. Wada, *J. Appl. Phys.* 91, 2284 (2002).
99. G. H. Lee, M. Yoshimoto, T. Ohnishi, K. Sasaki, and H. Koinuma, *Mater. Sci. Eng., B* 56, 213 (1998).
100. K. S. Lee, J. H. Choi, J. Y. Lee, and S. Baik, *J. Appl. Phys.* 90, 4095 (2001).
101. V. Srikant, E. J. Tarsa, D. R. Clarke, and J. S. Speck, *J. Appl. Phys.* 77, 1517 (1995).
102. C. Buchal, L. Beckers, A. Eckau, J. Schubert, and W. Zander, *Mater. Sci. Eng., B* 56, 234 (1998).
103. L. Beckers, J. Schubert, W. Zander, J. Ziesmann, A. Eckau, P. Leinenbach, and C. Buchal, *J. Appl. Phys.* 83, 3305 (1998).
104. D. F. Cui, Z. H. Chen, T. Zhao, F. Chen, H. B. Lu, Y. L. Zhou, G. Z. Yang, H. Z. Huang, and H. X. Zhang, *Microelectron. Eng.* 51–52, 601 (2000).
105. T. Ohnishi, K. Takashashi, M. Nakamura, M. Kawasaki, M. Yoshimoto, and H. Koimura, *Appl. Phys. Lett.* 74, 2531 (1999).
106. W. S. Shi, Z. H. Chen, N. N. Liu, Y. L. Zhou, and S. H. Pan, *J. Cryst. Growth* 197, 905 (1999).
107. H. Tabata, K. Ueda, and T. Kawai, *Mater. Sci. Eng., B* 56, 140 (1998).
108. N. A. Pertsev, A. G. Zembilgotov, and A. K. Tagantsev, *Phys. Rev. Lett.* 80, 1988 (1998).
109. T. Shimuta, O. Nakagawara, T. Makino, S. Arai, H. Tabata, and T. Kawai, *J. Appl. Phys.* 91, 2290 (2002).
110. F. Le Marrec, R. Farhi, M. E. Marssi, J. L. Dellis, M. G. Karkut, and D. Ariosa, *Phys. Rev. B* 61, R6447 (2000).
111. Y. Kohama, *Appl. Phys. Lett.* 52, 380 (1988).
112. J. H. Kim, Y. N. Kim, Y. S. Kim, J. C. Lee, L. J. Kim, and D. G. Jung, *Appl. Phys. Lett.* 80, 3581 (2002).
113. W. J. Dawson, J. C. Preston, and S. L. Schwartz, *Ceram. Trans.* 22, 27 (1991).
114. A. C. Caballero, J. F. Fernandez, C. Moure, P. Duran, and J. L. G. Fierro, *J. Eur. Ceram. Soc.* 17, 1223 (1997).
115. W. H. Tuan and S. K. Lin, *Ceram. Int.* 25, 35 (1999).
116. A. S. Shaikh, R. W. Vest, and G. M. Vest, *IEEE Trans. Ultrasonics, Ferroelectrics, Frequency Control* 36, 407 (1989).
117. T. Takeuchi, K. Ado, T. Asai, H. Kageyama, Y. Saito, C. Masquelier, and O. Nakamura, *J. Am. Ceram. Soc.* 77, 1665 (1994).
118. W. L. Luan, L. Gao, and J. K. Guo, *Ceram. Int.* 25, 727 (1999).
119. A. V. Ragulya, *Nanostruct. Mater.* 10, 349 (1998).
120. S. P. Li, J. A. Eastman, and L. J. Thompson, *Appl. Phys. Lett.* 70, 2244 (1997).
121. K. Okazaki, *Ceram. Soc. Bull.* 63, 1150 (1984).
122. T. Nagai, H. J. Hwang, M. Yasuoka, M. Sando, and K. Niihara, *J. Am. Ceram. Soc.* 81, 425 (1998).
123. H. J. Hwang, T. Nagai, M. Sando, M. Toriyama, and K. Niihara, *J. Eur. Ceram. Soc.* 19, 993 (1999).
124. C. E. Murphy, T. Richardson, and G. G. Roberts, *Ferroelectrics* 134, 189 (1992).
125. Y. Chen, H. L. W. Chan, and C. L. Choy, *Thin Solid Films* 323, 270 (1998); *J. Am. Ceram. Soc.* 81, 1231 (1998).
126. T. Yamamoto, K. Urabe, and H. Banno, *Jpn. J. Appl. Phys.* 32, 4272 (1993).
127. D. E. Collins and E. B. Slamovich, *J. Mater. Res.* 15, 1834 (2000).
128. B. D. Begg, E. R. Vance, and J. Nowotny, *J. Am. Ceram. Soc.* 77, 3186 (1994).
129. S. Tsunekawa, S. Ito, T. Mori, K. Ishikawa, Z. Q. Li, and Y. Kawazoe, *Phys. Rev. B* 62, 3065 (2000).
130. T. Kanata, T. Yoshikawa, and K. Kubota, *Solid State Commun.* 62, 1987 (1987).
131. H. Diamond, *J. Appl. Phys.* 32, 909 (1961).
132. R. P. S. M. Lobo, N. D. S. Mohallem, and R. L. Moreira, *J. Am. Ceram. Soc.* 78, 1343 (1995).
133. D. McCauley, R. E. Newnham, and C. A. Randall, *J. Am. Ceram. Soc.* 81, 979 (1998).
134. Y. Park, K. M. Knowles, and K. Cho, *J. Appl. Phys.* 83, 5702 (1998).
135. R. Clarke and J. C. Burfoot, *Ferroelectrics* 8, 505 (1974).
136. P. Ayyub, V. R. Palkar, S. Chattopadhyay, and M. Multani, *Phys. Rev. B* 51, 6135 (1995).
137. B. Jiang, J. L. Peng, L. A. Bursill, and W. L. Zhong, *J. Appl. Phys.* 87, 3462 (2000).
138. K. Ishikawa, K. Yoshikawa, and N. Okada, *Phys. Rev. B* 37, 5852 (1988).
139. W. L. Zhong, B. Jiang, P. L. Zhang, J. M. Ma, H. M. Cheng, Z. H. Yang, and L. X. Li, *J. Phys.: Condens. Matter* 5, 2619 (1994).
140. G. H. Yi, B. A. Block, and B. W. Wessels, *Appl. Phys. Lett.* 71, 327 (1997).
141. S. Wada, T. Suzuki, and T. Noma, *Jpn. J. Appl. Phys.* 34, 5368 (1995).
142. N. G. Eror, T. M. Loehr, and B. C. Cornilsen, *Ferroelectrics* 28, 321 (1980).
143. R. Morf, T. Schneider, and E. Stoll, *Phys. Rev. B* 16, 462 (1977).
144. W. L. Zhong, Y. G. Wang, P. L. Zhang, and B. D. Qu, *Phys. Rev. B* 50, 698 (1994).
145. C. Herard, A. Faivre, and J. Lemaitre, *J. Eur. Ceram. Soc.* 15, 145 (1995).
146. A. Filippetti and N. A. Hill, *Phys. Rev. B* 65, 195120 (2002).
147. A. Bussmann, H. Bilz, R. Roenspiess, and K. Schwartz, *Ferroelectrics* 25, 343 (1980).
148. A. Khalal, D. Khatib, and B. Jannot, *Physica B* 271, 343 (1999).
149. S. Tsunekawa, K. Ishikawa, Z.-Q. Li, Y. Kawazoe, and A. Kasuya, *Phys. Rev. Lett.* 85, 3440 (2000).



150. G. Burns and B. A. Scott, *Phys. Rev. B* 7, 3088 (1973).
151. Y. Xie, Y. T. Qian, W. Z. Wang, S. Y. Zhang, and Y. H. Zhang, *Science* 272, 1926 (1996).
152. J. M. McHale, A. Auroux, A. J. Perrotta, and A. Navrotsky, *Science* 277, 788 (1997).
153. D. D. Awschalom and D. P. DiVincenzo, *Phys. Today* 48, 43 (1995).
154. J. F. Scott, *Ferroelectric Rev.* 1, 1 (1998).
155. M. Aguilar, C. Gonzalo, and G. Godefroy, *Ferroelectrics* 25, 467 (1980).
156. J. Meng, Y. Huang, W. Zhang, Z. Du, Z. Zhu, and G. Zou, *Phys. Lett. A* 205, 72 (1995).
157. A. Shluger and N. Itoh, *J. Phys.: Condens. Matter* 2, 4119 (1990).
158. J. Yu, Ph.D. Thesis, Shanghai Institute of Technical Physics, Chinese Academy of Sciences, 2001.
159. H. X. Zhang, C. H. Kam, Y. Zhou, X. Q. Han, Q. Xiang, S. Buddhudu, Y. L. Lam, and Y. C. Chan, *J. Alloys Compd.* 308, 134 (2000).
160. H. X. Zhang, C. H. Kam, Y. Zhou, S. L. Ng, Y. L. Lam, and S. Buddhudu, *Spectrochim. Acta, Part A* 56, 2231 (2000).
161. H. X. Zhang, C. H. Kam, Y. Zhou, X. Q. Han, S. Buddhudu, and Y. L. Lam, *Opt. Mater.* 15, 47 (2000).
162. M. DiDomenico, Jr., S. H. Wemple, and S. P. S. Porto, *Phys. Rev.* 174, 522 (1968).
163. C. H. Perry and D. B. Hall, *Phys. Rev. Lett.* 15, 700 (1965).
164. P. S. Dabal, A. Dixit, R. S. Katiyar, Z. Yu, R. Guo, and A. S. Bhalla, *J. Appl. Phys.* 89, 8085 (2001).
165. H. Bilz, G. Benedek, and A. Bussmann-Holder, *Phys. Rev. B* 35, 4840 (1987).
166. A. A. Sirenko, C. Bernhard, A. Golnik, A. M. Clark, J. H. Hao, W. D. Si, and X. X. Xi, *Nature* 404, 373 (2000).
167. V. V. Lemanov, E. P. Smirnova, P. P. Syrnikov, and E. A. Tarakanov, *Phys. Rev. B* 54, 3151 (1996).
168. R. Migoni, H. Bilz, and D. Bauerle, *Phys. Rev. Lett.* 37, 1155 (1976).
169. Q. F. Zhou, H. L. W. Chan, Q. Q. Zhang, and C. L. Choy, *J. Appl. Phys.* 89, 8121 (2001).
170. J. F. Meng, G. T. Zou, Q. L. Cui, Y. N. Zhao, and Z. Q. Zhu, *J. Phys.: Condens. Matter* 6, 6543 (1994).
171. J. F. Meng, G. T. Zou, J. P. Li, Q. L. Cui, X. H. Wang, Z. C. Wang, and M. Y. Zhao, *Solid State Commun.* 90, 643 (1994).
172. M. S. Zhang, *Prog. Nat. Sci.* 1, 497 (1991).
173. T. K. Song, J. Kim, and S. I. Kwun, *Solid State Commun.* 97, 143 (1996).
174. S. I. Kwun and T. K. Song, *Ferroelectrics* 197, 125 (1997).
175. J. G. Bednorz and K. A. Muller, *Phys. Rev. Lett.* 52, 2289 (1984).
176. Z. W. Wang, S. K. Saxena, V. Pischedda, H. P. Liermann, and C. S. Zha, *Phys. Rev. B* 64, e012102 (2001).
177. S. K. Mishra, R. Ranjan, D. Pandey, and B. J. Kennedy, *J. Appl. Phys.* 91, 4447 (2002).
178. S. Y. Kuo, W. Y. Liao, and W. F. Hsieh, *Phys. Rev. B* 64, 224103 (2001).
179. F. Wang, A. Uusimaki, S. Leppavuori, S. F. Karmanenko, A. I. Dedyk, V. I. Sakharov, and I. T. Serenkov, *J. Mater. Res.* 13, 1243 (1998).
180. H. Li, A. L. Roytburd, S. P. Alpay, T. D. Tran, L. Salamanca-Riba, and R. Ramesh, *Appl. Phys. Lett.* 78, 2354 (2001).
181. B. H. Park, E. J. Peterson, Q. X. Jia, J. Lee, X. Zeng, W. Si, and X. X. Xi, *Appl. Phys. Lett.* 78, 533 (2001).
182. W. T. Chang, C. M. Gilmore, W. J. Kim, J. M. Pond, S. W. Kirchoefer, S. B. Qadri, D. B. Chirsey, and J. S. Horwitz, *J. Appl. Phys.* 87, 3044 (2000).
183. S. J. Jun, Y. S. Kim, J. C. Lee, and Y. W. Kim, *Appl. Phys. Lett.* 78, 2542 (2001).
184. J. W. Li, F. Duewer, C. Gao, H. Chang, X. D. Xiang, and Y. L. Lu, *Appl. Phys. Lett.* 76, 769 (2000).
185. U. C. Oh, J. Ma, G. K. L. Wong, J. B. Ketterson, and J. H. Je, *Appl. Phys. Lett.* 76, 1461 (2000).
186. J. Okayama, I. Takaya, K. Nashimoto, and Y. Sugahara, *J. Am. Ceram. Soc.* 85, 2195 (2002).
187. C. B. Parker, J. P. Maria, and A. I. Kingon, *Appl. Phys. Lett.* 81, 340 (2002).
188. F. M. Pontes, E. R. Leite, D. S. L. Pontes, E. Longo, E. M. S. Santos, S. Mergulhao, P. S. Pizani, F. Lanciotti, Jr., T. M. Boschi, and J. A. Varela, *J. Appl. Phys.* 91, 5972 (2002).
189. K. Binder, *Ferroelectrics* 35, 99 (1981).
190. J. T. Dawley and P. G. Clem, *Appl. Phys. Lett.* 81, 3028 (2002).
191. S. B. Majumder, M. Jain, A. Martinez, R. S. Katiyar, F. W. Van Keuls, and F. A. Miranda, *J. Appl. Phys.* 90, 896 (2001).
192. D. M. Gill, B. A. Block, C. W. Conrad, B. W. Wessels, and S. T. Ho, *Appl. Phys. Lett.* 69, 2968 (1996).
193. C. H. Lei, C. L. Jia, M. Siegert, J. Schubert, C. Buchal, and K. Urban, *J. Cryst. Growth* 204, 137 (1999).
194. K. Nashimoto, D. K. Fork, and T. H. Geballe, *Appl. Phys. Lett.* 60, 1199 (1992).
195. C. M. Hanson, H. R. Beratan, J. F. Belcher, K. R. Udayakumar, and K. L. Soch, *Proc. SPIE* 3379, 59 (1998).
196. M. E. V. Costa and P. Q. Mantas, *J. Eur. Ceram. Soc.* 19, 1077 (1999).
197. B. Huybrechts, K. Ishizaki, and M. Takata, *J. Mater. Sci.* 30, 2463 (1995).
198. R. Moos, M. Fandel, and W. Schafer, *J. Eur. Ceram. Soc.* 19, 759 (1999).
199. S. Urek and M. Drogenik, *J. Eur. Ceram. Soc.* 19, 913 (1999).
200. J. Wang, B. K. Xu, G. F. Liu, J. C. Zhang, and T. Zhang, *Sens. Actuators, B* 66, 159 (2000).
201. J. Wang, B. K. Xu, J. C. Zhang, G. F. Liu, T. Zhang, F. B. Qiu, and M. Y. Zhao, *J. Mater. Sci. Lett.* 17, 857 (1998).
202. P. Keller, H. Ferkel, K. Zwiackner, J. Naser, J. U. Meyer, and W. Riehemann, *Sens. Actuators, B* 57, 39 (1999).
203. M. S. Lee and J.-U. Meyer, *Sens. Actuators, B* 68, 293 (2000).

# Nanocrystalline Ceramics by Mechanical Activation

J. M. Xue, Z. H. Zhou, J. Wang

*National University of Singapore, Singapore*

## CONTENTS

1. Introduction
  2. Mechanically Activated Processes
  3. Mechanical Activation Devices
  4. Nanocrystalline Ceramic Materials
  5. Nanocrystalline Ceramics  
by Mechanical Activation
  6. Mechanical Crystallization and  
Precursor to Ceramic Conversions
  7. Summary
- Glossary  
References

## 1. INTRODUCTION

Ceramic materials are traditionally synthesized by solid-state reactions of the starting constituents (such as oxides, nonoxides, carbonates, and precursors) at elevated temperatures. It is, however, difficult to realize a nanocrystalline feature by the conventional ceramic process, as a high temperature calcination always leads to coarsening and aggregation of fine ceramic particles. Similarly, most of the wet-chemistry-based processing routes for ceramic materials have failed to deliver a true nanocrystalline structure, again due to the unwanted particle and crystallite coarsening and aggregation at the calcination temperature, which is unavoidably required for chemistry-derived ceramic precursors. In a fundamentally different approach, phase formation in mechanical activation is realized at room temperature, via one or more of the mechanically triggered chemical reactions, nucleation and growth from an amorphous state, decompositions, and phase transformations, depending on the specific ceramic material concerned. Little progress was made in synthesizing ceramic materials by mechanical activation until about 10 years ago when the potential of this novel

synthesis technique was demonstrated, although mechanical alloying for metals and intermetallics was devised more than 30 years ago. Over the past 5 years, there has been a surge in effort to employ mechanical activation for synthesis of a wide range of nanocrystalline ceramic materials including ceramic oxides, oxides of complex perovskite, spinel and layer structures, nonoxides, magnetic ceramics, electroceramics, and ceramic nanocomposites. While research focus on mechanical activation, on the one hand, is directed at synthesis of nanocrystalline ceramic materials, many of the underlying physical phenomena in association with mechanical activation have yet to be properly studied and made understood. On the other hand, mechanical activation promises a significant technological implication, whereby the currently employed multiple steps of phase-forming calcination/annealing at high temperatures for ceramic materials can be skipped, when the required nanocrystalline ceramic phases are realized at room temperature in an enclosed mechanical activation chamber. In this chapter, recent progress in mechanical activation for synthesis of nanocrystalline ceramic materials is reviewed and a number of new and unique phenomena brought about by mechanical activation in functional ceramics are discussed, together with a short discussion on the possible future development of this novel technique.

## 2. MECHANICALLY ACTIVATED PROCESSES

Mechanically activated processes are among the earliest phenomena created by humankind and the use of flint to trigger fires is perhaps one of the best known examples [1]. Mechanochemical reactions were documented and date back as early as several hundred B.C., when a number of chemical reactions were noted under the influence of one or more types of mechanical actions. However, mechanochemistry was not developed in a systematic manner until late 19th century, along with solid state chemistry, when the

effects of high pressure, mechanical impact, and combination of high pressure and temperature on the rates of solid state chemical reactions and phase transitions were studied [2]. Following the steady establishment of physical metallurgy in the first half of 20th century and then materials science, the potential of mechanically activated processes for materials synthesis was first demonstrated by Benjamin [3], who devised “mechanically alloying” for oxide-dispersed nickel- and iron-based super alloys. This marked a new era of successfully employing mechanically activated process in materials synthesis, and it was followed by the extension and application of this novel technique to a wide range of structural and functional materials, including intermetallics and metal matrix composites in the early stage of development, and then magnetic materials, semiconductors, and more recently nanocrystalline ceramic materials and ceramic matrix composites.

In the recent development history of mechanically activated processes, there existed a number of terminologies, each of which was adopted by the inventor of a specific fabrication technique [4]. In several cases, there is no clear boundary between two or more such terminologies. Mechanical alloying is used to describe a process where the powder mixture of different metals, alloys, or compounds is ultimately mixed together and the formation of a new alloy phase involves mass transfer. In comparison, mechanical milling refers to a milling process of homogenized compositions where mass transfer is not required. Therefore, it is often associated with milling of a pure metal or compound that is already in a state of thermodynamic equilibrium. Similarly, mechanical grinding refers to a milling process where mechanical milling is dominated by abrasion or shear stresses and chip formation. Mechanical disordering is specifically phrased for the milling process that is designed for destruction of the long-range order in intermetallics and production of either a disordered intermetallic or an amorphous phase. Mechanical crystallization describes the nucleation and crystallite growth triggered by a mechanical process from either an amorphous state or an amorphous precursor.

Mechanochemical synthesis/process is the general phrase that has been widely given to any high energy milling process of powdered materials involving one or more chemical reactions occurring during milling [5, 6]. Most of the mechanically activated processes for synthesis of nanocrystalline ceramic materials fall into this category. In mechanochemical synthesis, mechanical activation is employed to trigger the chemical reaction, structural change, and nucleation and growth of nanocrystallites from an amorphous state, leading to a product phase, with or without the need of a further thermal treatment at elevated temperatures. In combination with mechanical alloying, mechanochemical synthesis has been used to describe majority of the mechanically activated processes that have been devised and utilized in materials synthesis, while several other terms, such as reactive milling [7], rod milling [8], and mechanically activated self-propagating high temperature synthesis [9], can easily be categorized into either of these two general categories. Reaction milling, for example, pertains to the mechanical alloying process that is accompanied by one or more solid state reactions. Rod milling is a specific technique that was

developed in Japan to trigger the mechanochemical reaction by a predominant shear process, in order to reduce the level of contamination. Mechanically activated self-propagating high temperature synthesis refers to any mechanically activated reaction that is self-propagating in nature once triggered [10], which again can be categorized into the general terminology of mechanochemical synthesis. It must be pointed out that phase formation of several nanocrystalline ceramic materials, such as those via nucleation and subsequent crystallite growth from an amorphous state, is not a result of any chemical reactions that are described in the traditional mechanochemical process. Therefore, the terminology of mechanical activation is adopted in this chapter, which is aimed at covering most of the mechanically activated processes for synthesis of nanocrystalline ceramic materials.

### 3. MECHANICAL ACTIVATION DEVICES

Although syntheses of ceramic materials and many other types of materials have been successfully realized by various mechanically activated processes, there has been little specification and standardization with the types of mechanical activation devices and setups [4]. Conventional ball milling, which is commonly employed for mixing and blending of raw materials and refinement in particle and agglomerate sizes in ceramic industry, is generally unsuitable for mechanochemical synthesis, although certain phase transformations (such as those in PbO) and a number of chemical reactions can occur in conventional ball milling. Generally speaking, mechanical activation devices are those of high energy milling and modifications of high energy milling, which were originally designed for mechanical alloying. SPEX shaker mills and planetary ball mills are among the very few choices of commercially available high energy mills. SPEX Shaker mills are designed for a relatively small capacity of up to 20 grams and are therefore popularly adopted for laboratory investigation. They typically consist of one vial, containing the sample composition and activation media (typically of one or more high density balls made of ceramics or stainless steel), secured in clamps and swung energetically back and forth up to several thousand times per minute. The back and forth shaking motion of the vial is also combined with lateral movements. By simple calculation, ball velocity in SPEX Shaker mills is up to the order of 5 m/s, generating an unusually high impact force at a very high frequency.

Planetary mills, which are designed for relatively large quantities in the range up to a few hundred grams of powder per batch, are manufactured by Fritsch GmbH in Germany. Vials of planetary mills are arranged on a rotating support disk by a specifically designed drive mechanism to cause them to rotate around their own axes. There is a strong centrifugal force produced by the rotating vials around their own axes, together with that generated by the rotating support disk; both act on the vial contents and the activation balls. Because the vials and the supporting disk rotate in opposite directions, the centrifugal forces alternately act in like and opposite directions. This enables the activation balls to run against the internal walls of the vial, generating a friction effect, and at the same time the activation balls lift off and travel freely through the inner chamber of the vial and

collide against the opposing inside wall generating a strong impact effect.

An attrition mill, which is a modification of the conventional ball mill, consists of a vertically aligned drum with several impellers being set progressively at right angles to each other. The impellers energize the medium charge, causing impacts between activation media, between the medium and the drum wall, and between the medium, agitator shaft, and impeller. Attrition mills are capable of larger batch quantity (up to tens of kilos) than both planetary mills and shaker mills, although they are generally regarded as being of low energy type and unsuitable for successful mechanical activation syntheses in many cases.

There have been several new designs of mechanical activation devices, including rod mills, vibrating mills, and those shaker and planetary mills in combination with the application of an electrical discharge, magnetic field, temperature, and hydrothermal conditions, in an effort to combine mechanical activation with other processing controls [11–14]. Typical processing parameters that can be controlled in mechanical activation include the activation (or mill) speed, activation time, choices, size and combination of vial and milling media, media to powder weight ratio, activation media and atmosphere, activation temperature, and pressure.

#### 4. NANOCRYSTALLINE CERAMIC MATERIALS

Performance and functional properties of ceramic materials are critically dependent on a number of compositional and structural parameters in atomic, nanometer, and microstructural scales. Over the past four decades starting from the 1960s following the wide application of electron microscopes in materials characterization, there has been a steady accumulation of knowledge and understanding on the microstructure and microstructure–property relationships in ceramic materials. At the same time, in particular over the past two decades, research focus on ceramic processing has been shifting from the traditional solid state reactions to wet-chemistry-based syntheses, in order to refine the microstructure into nanometer scales. There are two major driving forces behind the current surge in pursuit of a nanocrystalline structure for ceramic materials: (i) the unique physical and functional properties arising from a nanostructure and (ii) a much lowered processing temperature for ceramic materials.

As a result of the significant refinement in particle size (for powdered ceramics) and grain size (for sintered bulk ceramics) into the nanometer range, surfaces, interfaces, and grain boundaries play a critically important role in determining the physical and functional behaviors of nanocrystalline and nanostructured ceramic materials, which can be considerably different from those of their counterparts with structural features in the micrometer scales. For example, a flexural strength of >2000 MPa and excellent superplasticity, which were traditionally considered as being impossible for brittle ceramic materials, have been demonstrated with both oxide ceramics (alumina and zirconia) and ceramic nanocomposites (e.g., alumina–SiC and  $\text{Si}_3\text{N}_4$ –SiC) [15–17].

Ultrafine ceramic powders consisting of well dispersed nanocrystalline particles of <100 nm in size have received considerable attention for technologically demanding application in micro- and nanoelectronics, materials processing and manufacturing, medicine and biotechnology, catalysts, new energy sources, and environmental protections. As a result of the much enlarged surface to volume ratio and one or more quantum and confinement effects, nanocrystalline ceramic particles exhibit many unique properties that can be fundamentally different from those of their coarse counterparts. Nanocrystalline ferrites of spinel structure are among many such well established examples. For example, zinc ferrite ( $\text{ZnFe}_2\text{O}_4$ ) in bulk ceramic form possesses a normal spinel structure with the tetrahedral A sites exclusively being occupied by  $\text{Zn}^{2+}$  ions. As such, the predominant magnetic interaction in  $\text{ZnFe}_2\text{O}_4$  is the weak B–B interaction (i.e., the negative superexchange interaction among  $\text{Fe}^{3+}$  ions in the octahedral sites) [18, 19].  $\text{ZnFe}_2\text{O}_4$  is therefore traditionally regarded as an antiferromagnetic with Néel temperature of about 10 K, above which it becomes paramagnetic. Several unusual magnetic phenomena have been observed in nanosized zinc ferrite particles synthesized via a number of different processing routes, including mechanical activation [20–24]. They exhibit unusually high magnetizations and higher Néel temperatures than those of bulk  $\text{ZnFe}_2\text{O}_4$ . Recent investigation has confirmed that this is related to a partially inverted spinel structure in the nanocrystalline  $\text{ZnFe}_2\text{O}_4$  particles, in which a small number of  $\text{Fe}^{3+}$  ions occupy the tetrahedral A sites, causing formation of magnetic clusters by the A–B interactions [25]. A similar structure disorder has been observed in nanocrystalline  $\text{NiFe}_2\text{O}_4$  derived from mechanical activation [26].

Employment of nanocrystalline ceramic powders as the starting materials can dramatically lower the sintering temperature of ceramic materials. While many ceramic materials are indispensable for functioning of almost all electronic, microelectronic, and data storage devices, integration of ceramic materials into wafer-based technology inevitably requires a processing temperature for ceramic materials be compatible to those for silicon and wafer technology. There is therefore a significant technological implication in lowering the sintering temperature of these ceramic materials. For example, use of an electroceramic material in co-fired multilayer devices requires the electroceramic composition be sinterable at a temperature below 1000 °C. A low enough firing temperature will apparently alleviate, if not completely eliminate, the detrimental interactions between alternative layers of ceramic and metal electrode at the co-firing temperature. For multilayer ceramic capacitors, for example, a large enough reduction in sintering temperature will lead to substitution of the very expensive electrodes of platinum and palladium, by much cheaper ones, such as those made of silver, nickel, copper, and their alloys [27].

To prepare nanocrystalline ceramic particles, many chemistry-based processing routes have been attempted, including for example, sol–gel [28], hydrolysis [29], hydrothermal reaction [30], and coprecipitation [31]. Chemistry-based processing techniques inevitably use high-purity inorganic, organic, and metallorganic chemicals as the starting materials, and they are associated with high production cost and low production yield. Furthermore, almost all the chemistry-derived

precursors require a calcination step at elevated temperatures, which unfortunately ruins almost all the advantages offered by chemistry-based novel processing techniques, including a very high specific surface area, ultrafine particle size, and narrow particle size distribution. Any thermal annealing and calcination inevitably causes crystallite coarsening and particle aggregation in the resulting ceramic powders. The occurrence of hard particle aggregates adversely affects subsequent compaction and sintering behaviors and leads to a low density and the occurrence of microstructural defects in sintered ceramic bodies. In the ceramic industry, one or more postcalcination conventional ball milling steps are often carried out, in order to modify the particle characteristics (e.g., particle and aggregate sizes, particle morphology) before subsequent shaping and then sintering at high temperatures. However, hard enough particle aggregates cannot be effectively eliminated by a conventional ball mill.

In a fundamentally different approach from the conventional ceramic processing and most chemistry-based synthesis techniques for ceramic materials, mechanical activation offers the following distinctions and advantages:

- (i) In mechanical activation, phase formation is realized by an input of mechanical activation, instead of the thermal activation (i.e., calcination and annealing at high temperatures) that is employed in the conventional ceramic processing and most chemistry-based synthesis routes.
- (ii) Mechanical activation is conducted at a much lower temperature, often at room temperature, than required in either conventional ceramic processing or wet-chemistry-based synthesis routes.
- (iii) Ceramic phases derived from mechanical activation exhibit a nanocrystallinity and particle sizes in the nanometer range, together with a minimized degree of particle agglomeration.
- (iv) Being conducted in an enclosed chamber and by skipping the thermal activation at elevated temperatures for phase formation, mechanical activation exercises a strict control on chemical and compositional stoichiometry, which is critically important for functional and electroceramic materials where volatile components are often lost at the solid state reaction or calcination temperatures.
- (v) Mechanical activation employs commonly available ceramic raw materials, such as oxides and nonoxides as the starting materials, and at the same time skips the phase-formation calcination and postcalcination comminution, leading to a much lower production cost than that of either conventional ceramic processing or a chemistry-based synthesis route.
- (vi) Nanocrystalline ceramic materials derived from mechanical activation demonstrate a number of unique structural and physical behaviors, such as structural metastability, cation inversion in spinel structure, and order-disorder transition in complex perovskites, which are not shown by the materials synthesized via either conventional ceramic processing or chemistry-based synthesis routes.
- (vii) As a result of the fundamentally different phase-forming mechanisms from those of conventional solid

state reactions in the conventional ceramic processing, mechanical activation can skip transitional and impurity phases, which are largely concerned with functional and electroceramic materials with complex perovskite, spinel, and layered perovskite structures.

- (viii) Mechanical activation can be employed to synthesize several nanocrystalline ceramic materials that cannot possibly be synthesized via either conventional ceramic or chemistry-based processing routes.
- (ix) As a result of the nanocrystallinity and ultrafine particle sizes, ceramic materials derived from mechanical activation exhibit a much lowered sintering temperature. For example,  $\text{PbZr}_{1-x}\text{Ti}_x\text{O}_3$  (PZT) derived from mechanical activation can be sintered at a temperature as low as 1000 °C [32].
- (x) There are a number of unique phenomena that have been observed in association with mechanical activation, including extension of solubility [33], formation of metastable structures [34], amorphization of a crystalline phase [35], phase transition [36, 37] order-disorder transformation [38], cation inversions [26], and crystallization from amorphous states and amorphous precursors [39–41].

## 5. NANOCRYSTALLINE CERAMICS BY MECHANICAL ACTIVATION

In syntheses of nanocrystalline ceramic materials by mechanical activation, one or more chemical reactions, phase transformations, decompositions, and nucleation and subsequent crystallite growth are associated with mixing, deformation, fracture, refinement, and amorphization of the starting materials, leading to formation of a product phase, with or without the need for further thermal activation at elevated temperatures. In comparison with the solid-state reaction in conventional ceramic processing at high temperatures, a distinct feature of mechanical activation is the realization of particle and crystallite sizes in the nanometer ranges. Nanocrystalline ceramic particles of as fine as 4 nm in size and varying particle morphologies (rounded, rod-like, and platelike) can be synthesized [42]. Several types of chemical reactions can be triggered by mechanical activation, including displacement reaction [43], oxidation [44], reduction [45], decomposition [46], and incipient reaction [47]. Depending on the nature of the starting material and experimental parameters chosen for mechanical activation, phase-formation mechanisms during mechanical activation can be fundamentally different from those in thermal activation.

Several very different phase formation mechanisms have been suggested for ceramic materials triggered by mechanical activation, including various mechanochemical reactions at the interface in microsecond or nanosecond duration of shock, impact, and collision in a highly activated state [37], local temperature-facilitated solid state reactions [39], nucleation at interface [40], and nucleation from the highly activated matrix and subsequent growth of crystallites [48]. It is commonly believed that mechanical activation can significantly increase the reactivity of a solid system, as a result of the refinement in particle and crystallite sizes and creation

of various structural and surface defects, and therefore diffusion and reaction kinetics are enhanced. This is supported by the much lowered reaction and phase formation temperatures that are brought about by mechanical activation. Mechanical activation can lead to a significant departure from the equilibrium state. In some cases, the free energy level raised by mechanical activation is above that of an amorphous state. The much refined particle and crystallite sizes, with or without presence of structure defects, enable chemical reactions which otherwise require high temperatures to occur. Thermodynamically, this is accounted for by the energy accumulation process during mechanical activation. A further contribution to the enhanced reactivity is the alleviation, if not elimination, of the diffusion barrier generated by the product phase that separates the reactants.

High temperature and pressure at the collision points can give rise to a new and product phase, although the overall temperature of the mechanical activation chamber normally does not exceed 100 °C in most cases. However, it is questionable whether the short interval of *in-situ* temperature at the collision points, which may be high enough to trigger many types of solid state reaction, will be sufficient for formation of a product phase of several nanometers in dimensions. In discussing the mechanisms of incipient reaction at solid–solid boundary under mechanical stresses, Senna [49] outlined the importance of coordination states, symmetry disturbance, and change in electronic states. Similarly, Boldyrev and Tkacova [2] considered the increase in solid density under a hydrostatic loading, which can cause a decrease in the width of forbidden band and conduction states. The process can be further facilitated by an appropriate combination of hydrostatic stress and shear component, which apparently occur in certain mechanical activation processes. One of the common features in all mechanical activation processes is the involvement of strain, which manifests itself by the shift of atoms from their equilibrium positions and the change in bond lengths and angles. Therefore, structural defects, amorphization and metastable states often occur prior to formation of the product phase with increasing degree of mechanical activation.

There is no doubt that the significant refinement in particle and crystallite sizes during the initial stage of mechanical activation creates newly formed, clean surfaces, which can quickly absorb and react with species that are in direct contact. In the presence of moisture or a liquid phase, hydrothermal processes can occur at the collision points, which can also lead to formation of a product phase [50]. This belief has encouraged the attempt to combine mechanical activation and hydrothermal reaction. In recent studies of mechanical activation for synthesis of electroceramic materials of complex perovskite structure [48], where multiple oxides are involved as the starting materials, a completely different phase formation process has been observed. Nucleation of nanocrystallites of perovskite structure occurs in a highly activated oxide matrix, where a significant refinement in particle and crystallite sizes together with a degree of amorphization have taken place. Subsequent growth of the nanocrystallites with further mechanical activation is a consequence of the equilibrium between the activation-driven buildup and destruction involving the entire masses of nanocrystallites. Constant collisions and rearrangement

of nanocrystallites provided by mechanical activation create opportunities for two or more of them to meet at favorable positions leading to growth in the crystallite size. At the same time, there is also a probability that the nanocrystallites are distorted and fragmented by mechanical activation.

While the phase-formation mechanisms and physical phenomena in many systems have yet to be properly understood, numerous nanocrystalline ceramic materials have been successfully synthesized by mechanical activation. They include simple oxides, such as  $\text{Al}_2\text{O}_3$ ,  $\text{ZrO}_2$ ,  $\text{Fe}_2\text{O}_3$ ,  $\text{ZnO}$ , and  $\text{CeO}_2$ , complex oxides of perovskite structure, spinel structure, aurivillius type compound and layered perovskite structure and their solid solutions, nonoxide ceramics such as nitrides, carbides, oxynitrides, sulphides, and ceramic nanocomposites. Table 1 lists examples of the typical nanocrystalline ceramic materials synthesized by mechanical activation. In the following, a brief review is given to each of these major types of nanocrystalline ceramic materials synthesized by mechanical activation.

### 5.1. Simple Ceramic Oxides

A large number of simple oxides, examples of which include  $\text{Al}_2\text{O}_3$  [51],  $\text{ZrO}_2$  [52–54],  $\text{Fe}_2\text{O}_3$  [55],  $\text{Gd}_2\text{O}_3$  [56],  $\text{CeO}_2$  [57],  $\text{SnO}_2$  [58],  $\text{ZnO}$  [59],  $\text{Cr}_2\text{O}_3$  [60],  $\text{Nb}_2\text{O}_5$  [60], and  $\text{TiO}_2$  [61], have been synthesized by mechanical activation. Starting with an inorganic salt, such as chloride, an oxide can be realized by a simple replacement reaction during mechanical activation, followed by a calcination/annealing at temperatures in the range of 150 to 600 °C. To synthesize nanocrystalline  $\text{Al}_2\text{O}_3$ , for example [51], an appropriate powder mixture of  $\text{AlCl}_3$  and  $\text{CaO}$  is mechanically activated, followed by calcination at progressively rising temperatures, leading to formation of  $\gamma\text{-Al}_2\text{O}_3$  within  $\text{CaCl}_2$  matrix at 350 °C and then  $\alpha\text{-Al}_2\text{O}_3$ . Nanocrystalline  $\text{Al}_2\text{O}_3$  particles are then recovered by washing off  $\text{CaCl}_2$ . Similarly, nanocrystalline  $\text{ZrO}_2$  [52] particles are produced by mechanical activation of  $\text{ZrCl}_4$  together with  $\text{CaO}$  ( $\text{NaOH}$  and  $\text{LiOH}$  can also be used) and the subsequent thermal annealing at 300 °C, leading to formation of zirconia particles of 5 to 10 nm in size and of metastable cubic structure. Other examples of simple oxides that have been successfully synthesized by the replacement reaction triggered by mechanical activation include  $\text{Fe}_2\text{O}_3$ ,  $\text{Gd}_2\text{O}_3$ ,  $\text{CeO}_2$ ,  $\text{SnO}_2$ , and  $\text{ZnO}$ , where the starting chemicals are corresponding chlorides in combination with an alkaline or oxide of an alkaline earth. Transitional and metastable phases may well be involved in some cases. For example [55],  $\text{FeOOH}$  can occur prior to formation of  $\alpha\text{-Fe}_2\text{O}_3$  during mechanical activation of  $\text{FeCl}_3$  together with  $\text{Ca}(\text{OH})_2$  and subsequent thermal annealing with rising temperature. To further modify the particle size and degree of particle aggregation of nanocrystalline oxides derived from mechanical activation, dispersion/dilution agents, such as  $\text{NaCl}$  and  $\text{CaCl}_2$ , have been proven effective.

In an analog to formation of simple oxides by thermal decomposition of corresponding hydroxides, decomposition of several hydroxides is obtainable by mechanical activation, leading to formation of nanocrystalline particles. For example, mechanical activation of  $\text{Zr}$ -hydroxides [62] results in formation of nanocrystalline zirconia particles of 4 to 10 nm



**Table 1.** Examples of typical nanocrystalline ceramic materials synthesized by mechanical activation.

Nanocrystalline ceramics	Size range	Ref.
$\alpha$ -Al <sub>2</sub> O <sub>3</sub>	~15 nm	[67]
	~100 nm	[68]
$\alpha$ -Al <sub>2</sub> O <sub>3</sub> , TiAl <sub>3</sub> , Fe <sub>4</sub> Al <sub>13</sub>	5–15 $\mu$ m	[72]
$\alpha$ -Al <sub>2</sub> O <sub>3</sub> /TiN	<10 nm	[148]
$\gamma$ -Al <sub>2</sub> O <sub>3</sub>	10–20 nm	[51]
Al <sub>2</sub> TiO <sub>5</sub>	~50 nm	[97]
BaFe <sub>12</sub> O <sub>19</sub>	~50 nm	[126, 127]
BaTiO <sub>3</sub>	10–15 nm (crystallite size)	[74]
	16–20 nm	[75]
CaBi <sub>4</sub> Ti <sub>4</sub> O <sub>15</sub>	30 nm	[64]
CaTiO <sub>3</sub>	20 nm	[105]
CdS	4–8 nm	[157]
CeO <sub>2</sub>	8–50 nm	[42]
	>10 nm	[57]
	10 nm	[59]
CoFe <sub>2</sub> O <sub>4</sub>	10–40 nm	[127]
CoO, Co <sub>3</sub> O <sub>4</sub> , NiO	<20 nm	[44]
Cu <sub>2</sub> O	15–30 nm	[45]
Fe $\alpha$ -Al <sub>2</sub> O <sub>3</sub> and Fe-Ti/ $\alpha$ -Al <sub>2</sub> O <sub>3</sub>	10 nm (crystallite size)	[6]
$\alpha$ -Fe <sub>2</sub> O <sub>3</sub>	10–50 nm	[55]
	~10 nm	[64]
	10–50 nm	[116]
$\gamma$ -Fe <sub>2</sub> O <sub>3</sub>	10–12 nm	[118]
Fe <sub>3</sub> O <sub>4</sub>	10–15 nm	[117]
	10–20 nm (crystallite size)	[128]
Gd <sub>2</sub> O <sub>3</sub>	20 nm	[56]
LaFeO <sub>3</sub>	~100 nm	[100]
MgFe <sub>2</sub> O <sub>4</sub>	15 nm	[135]
MgTiO <sub>3</sub>	11–12 nm	[76]
MnFe <sub>2</sub> O <sub>4</sub>	9.5–40 nm	[132]
	~82 nm	[134]
$\alpha$ -MoSi <sub>2</sub>	88 nm	[10]
NiFe <sub>2</sub> O <sub>4</sub>	8.05 nm	[26]
	6 nm (crystallite size)	[121]
	10 nm	[127]
	15 nm	[135]
Pb(Sc <sub>1/2</sub> Ta <sub>1/2</sub> )O <sub>3</sub>	7–10 nm (crystallite size)	[161]
Pb(Zr <sub>0.52</sub> Ti <sub>0.48</sub> )O <sub>3</sub>	20–40 nm	[32]
	30–50 nm	[159]
PbNb <sub>2</sub> O <sub>6</sub>	10–15 nm (crystallite size)	[160]
PbTiO <sub>3</sub>	16.5 nm	[78]
PMN	~15 nm (crystallite size)	[81]
0.4PMN-0.6PMW	7–12 nm	[38]
PMN-PZN-PT	5–10 nm (crystallite size)	[89]
PZN	10–15 nm (crystallite size)	[90]
SiC	20–30 nm	[13]
SnO <sub>2</sub>	20–30 nm (crystallite size)	[58]
	40 nm	[59]
SrBi <sub>4</sub> Ti <sub>4</sub> O <sub>15</sub>	~50 nm	[63]
TiN	9 nm	[7]
TiN/TiB <sub>2</sub>	5–10 nm	[145]
WC/MgO	4–20 nm	[147]
ZnFe <sub>2</sub> O <sub>4</sub>	20 nm	[21]
	15–20 nm	[22]
	11 nm	[119]
	8–10 nm	[120]
	40 nm	[133]
ZnO	20 nm	[63]
	28 nm	[59]
ZnS	~16 nm	[156]

continued

**Table 1.** Continued

Nanocrystalline ceramics	Size range	Ref.
ZrN	14 nm	[7]
ZrO <sub>2</sub>	6 nm	[42]
	5–10 nm	[52]
	9–13 nm	[53]
	49 nm (dry activation)	[54]
	14 nm (wet activation)	
	15–42 nm	[62]
	0.1–1.5 $\mu$ m	[65]
ZrSi	45 nm (crystallite size)	[158]
ZrSi <sub>2</sub>	23 nm (crystallite size)	[158]

in sizes and of metastable tetragonal structure, in contrast to the monoclinic structure for ZrO<sub>2</sub> particles derived from thermal annealing of the hydroxide precursor. This is apparently related to the much refined crystallite size derived from mechanical activation, where the crystallite coarsening and particle aggregation that are always observed at a calcination temperature as low as 500 °C are avoided. Other successful examples of mechanical activation in decomposing ceramic precursors include ZnO [63] and Fe<sub>2</sub>O<sub>3</sub> [64]. For example, zinc oxide particles of 10 to 20 nm in size were successfully obtained, when zinc nitrate hydroxide hydrate precursor, (Zn<sub>5</sub>(NO<sub>3</sub>)<sub>2</sub>(OH)<sub>8</sub>·2H<sub>2</sub>O), was mechanically activated in NaCl for 15 hours, where NaCl was used as a drying and dispersion agent [63]. Several decomposition steps were triggered by mechanical activation prior to nucleation and subsequent growth of ZnO particles with increasing degree of mechanical activation. The nanocrystalline ZnO particles thus synthesized exhibited a well-established hexagonal morphology and are almost agglomeration-free, which were compared favorably with those derived from conventional calcination of the same precursor at 400 °C.

Extraction of zirconia from zircon, which is the principal mineral source for zirconia, is traditionally carried out at very high temperatures. When mechanically activated with calcium and magnesium [65], zircon undergoes decomposition to form zirconia and Ca- or Mg-silicates. Similarly, zirconia can be produced by mechanical activation of zircon together with oxides of alkaline earth metals [65]. Unlike the zirconia phase derived from high temperature calcination, nanocrystalline zirconia particles thus produced exhibit a metastable tetragonal structure, which undergoes phase transformation into monoclinic upon heating up to 1200 °C. The occurrence of metastable tetragonal structure is apparently related to the fine nanocrystallites derived from mechanical activation.

Alumina (Al<sub>2</sub>O<sub>3</sub>), which is one of the most studied ceramic materials and is widely employed in numerous structural and functional applications, is traditionally derived from bauxite, for example by the Bayer process [66] involving digestion and calcination at high temperatures. There exist several transitional phases of aluminum hydroxides/hydrates and oxides, which normally occur prior to formation of thermodynamically stable  $\alpha$ -Al<sub>2</sub>O<sub>3</sub> at a high enough calcination temperature. On the one hand, as a result of the enhanced reactivity of bauxite brought about by mechanical activation, the extraction rate of aluminum hydroxides from bauxite is significantly improved in

the Bayer process. On the other hand, in the search for alternative routes for the aluminum hydroxide/hydrate to alumina conversion, which is traditionally realized by calcination at high temperatures, mechanical activation has been attempted by several investigators. To date, the experimental observations reported by different research groups are rather sketchy. For example, an identical sequence of phase transitions to those commonly observed in calcination of gibbsite was reported by Tonejc et al. [67], who employed high energy ball milling for mechanical activation, while others observed a rather different sequence of phase transitions between mechanical activation and thermal activation. These differences are accountable for by the differences in experimental setup and experimental parameters employed by different investigators. In a recent study conducted by Yong and Wang on gibbsite [68], it was observed that mechanical activation of monoclinic gibbsite  $[\text{Al}(\text{OH})_3]$  in nitrogen led to formation of nanocrystalline boehmite ( $\text{AlOOH}$ ) of orthorhombic structure, which cannot be converted into alumina by prolonging the mechanical activation process. Nanocrystalline boehmite phase started to appear at merely 3 hours of mechanical activation followed by a steady development in both phase purity and crystallite size with increasing mechanical activation time. Forty hours of mechanical activation produced in an essentially single-phase boehmite, together with nanocrystallites of  $\alpha\text{-Al}_2\text{O}_3$  of 2 to 3 nm in sizes dispersed in the boehmite matrix. Upon subsequent thermal annealing, mechanically activated boehmite transformed to  $\gamma\text{-Al}_2\text{O}_3$  at 520 °C and then to  $\alpha\text{-Al}_2\text{O}_3$  at around 1100 °C. The fine  $\alpha\text{-Al}_2\text{O}_3$  particles thus produced are 100 to 200 nm in size and exhibit a rounded particle morphology. This is in contrast to the calcination temperature of 1400 °C required for gibbsite that was not subjected to any mechanical activation, which undergoes transition at above 220 °C to boehmite and then to transitional phases of  $\delta\text{-Al}_2\text{O}_3$  and  $\theta\text{-Al}_2\text{O}_3$ , prior to formation of  $\alpha\text{-Al}_2\text{O}_3$ .

There are a number of other types of reaction that can be triggered by mechanical activation and lead to formation of simple oxides of nanocrystallinity. For example, CoO and NiO nanoparticles [44] can be formed by mechanical activation of corresponding metal elements in a highly oxidizing environment, where the oxidation is speeded up by mechanical activation. Mechanical activation of  $\text{Fe}_3\text{O}_4$  together with Al [69] leads to formation of a mixture of  $\alpha\text{-Al}_2\text{O}_3$ ,  $\text{FeAl}_2\text{O}_4$ , and  $\alpha\text{-Fe}$ . Reduction reaction of  $\text{FeTiO}_3$  by Si is obtainable at room temperature by mechanical activation [70, 71], leading to formation of nanocrystalline  $\text{TiO}_2$  in an amorphous  $\text{SiO}_x$ , together with intermetallic compounds and  $\alpha\text{-Fe}$ , depending on Si content in the starting mixture. These mechanical activation-driven processes consist of an initiation stage and subsequent reaction stage, where the length of initiation stage and subsequent reaction rate are largely controlled by the mechanical activation intensity. A similar mechanochemical reaction [72] has been reported for between  $\text{FeTiO}_3$  and Al during mechanical activation, producing nanocrystalline  $\text{Al}_2\text{O}_3$  together with intermetallic phases of  $\text{TiAl}_3$  and  $\text{Fe}_4\text{Al}_{13}$ .

## 5.2. Complex Ceramic Oxides

A number of complex oxides of nanocrystallinity, including those of perovskite structure, complex perovskite structure, aurivillius type and layered perovskite structure, and spinel structure and their solid solutions, have been successfully synthesized by mechanical activation of either constituent oxides or ceramic precursors, such as hydroxides and oxalates, or a mixture of these. Depending on the nature of the starting materials and the experimental setup for mechanical activation, there can be considerable differences in the types of mechanochemical reaction involved and the phase-formation steps during mechanical activation. In several cases, complex oxides of nanocrystallinity are formed as a result of one single step of mechanical activation, while in others a subsequent thermal annealing step is required before designed nanocrystalline ceramic phases are realized. As a consequence of the enhanced reactivity brought about by mechanical activation, phase-formation temperature for complex oxides can be significantly lowered.

Among the complex oxides of nanocrystallinity that have been successfully synthesized by mechanical activation, alkaline earth titanates, such as  $\text{BaTiO}_3$  and  $\text{SrTiO}_3$ , exhibit a perovskite structure.  $\text{BaTiO}_3$ , which is one of the most widely used electroceramic materials for numerous applications in electronics and microelectronics, is traditionally synthesized by the solid-state reaction between  $\text{TiO}_2$  and  $\text{BaCO}_3$  at temperatures above 1000 °C [73]. The conventional solid-state reaction between  $\text{TiO}_2$  and  $\text{BaCO}_3$  at high temperatures is associated with several fatal disadvantages. For example, the interfacial reaction between  $\text{TiO}_2$  and  $\text{BaCO}_3$  is accompanied by several intermediate phases, which often occur as unwanted impurity phases together with the product phase of  $\text{BaTiO}_3$ . The high calcination temperature that is required by phase formation in the solid state reaction always results in unwanted particle coarsening and aggregation, the presence of which adversely affects subsequent sintering and densification of  $\text{BaTiO}_3$ . It is therefore both scientifically interesting and technologically demanding to search for alternative synthesis routes for  $\text{BaTiO}_3$ . In an attempt to synthesize nanocrystalline  $\text{BaTiO}_3$  of perovskite structure, Xue et al. [74] carried out mechanical activation of  $\text{TiO}_2$  and BaO in a nitrogen atmosphere, leading to steady formation of  $\text{BaTiO}_3$  of 10 to 15 nm in crystallite sizes. Employment of the nitrogen atmosphere is to stop BaO from reaction with  $\text{CO}_2$  in air. In addition to BaO as the source material for Ba in  $\text{BaTiO}_3$ ,  $\text{Ba}(\text{OH})_2 \cdot 8\text{H}_2\text{O}$  was also used [75]. When mechanically activated together with  $\text{TiO}_2$  in acetone, nanocrystallites of  $\text{BaTiO}_3$  steadily resulted. The crystallinity of thus derived  $\text{BaTiO}_3$  was further enhanced by subsequent thermal annealing. There are several other examples of nanocrystalline titanates that have been synthesized by mechanical activation, including  $\text{MgTiO}_3$  [76, 77] and  $\text{PbTiO}_3$  [78–80]. For example, mechanical activation of PbO and  $\text{TiO}_2$  at room temperature led to formation of  $\text{PbTiO}_3$  (PT) of perovskite structure and nanocrystallinity. Figure 1 is a transmission electron microscopy (TEM) micrograph showing the nanoparticles of PT derived from mechanical activation of the constituent oxides at room temperature. They are 5 to 10 nm in size and spherical in particle morphology. While  $\text{PbTiO}_3$  was nucleated in the

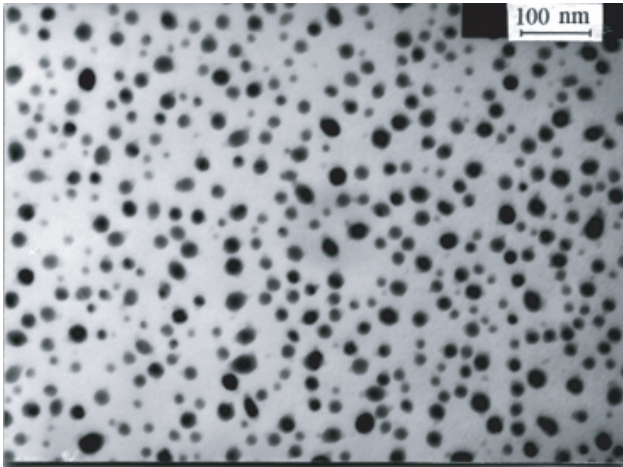


**Figure 1.** A bright field TEM micrograph showing the nanoparticles of lead titanate ( $\text{PbTiO}_3$ ) synthesized by mechanical activation of  $\text{PbO}$  and  $\text{TiO}_2$  at room temperature.

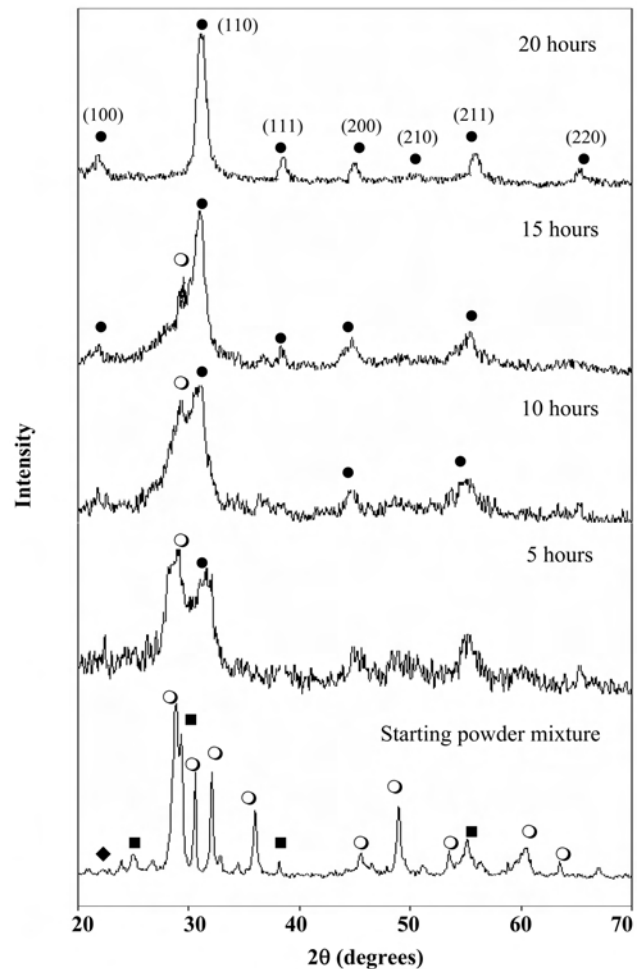
highly activated matrix of oxides, strong deviation from compositional stoichiometry, vacancy generation, and occupation of B-sites by  $\text{Pb}^{2+}$  in the perovskite structure may well occur during mechanical activation.

Lead zirconate titanate (PZT), which is the classical piezoelectric, has recently been synthesized by mechanical activation of constituent oxides of  $\text{PbO}$ ,  $\text{ZrO}_2$ , and  $\text{TiO}_2$  at room temperature [32]. Unlike in the solid state reaction of these oxides at high temperatures, transitional  $\text{PbZrO}_3$  (PZ) and PT phases were not observed during mechanical activation of these oxides. This represents a significant step forward in synthesizing this technologically demanding material for a number of applications in sensors, transducers, and actuator devices using the low-cost oxides as starting materials. As will be discussed later, the phase-formation process of complex perovskites during mechanical activation is fundamentally different from that in the conventional solid-state reaction, where the process is controlled by one or more interfacial diffusions and reactions. In contrast, mechanical activation triggered the nucleation and subsequent crystallite growth of complex perovskites in a highly activated matrix of oxide composition. Owing to the unique nanocrystalline structures of PZT derived from mechanical activation, they can be sintered to a >99% theoretical density at a temperatures as low as 1000 °C, which is about 200 °C lower than what is normally required for this classical piezoelectric.

Another most remarkable example of mechanical activation in synthesizing nanocrystalline electroceramic materials of complex perovskite structure is  $\text{PbO}$ -based relaxor ferroelectrics [81].  $\text{Pb}(\text{Mg}_{1/3}\text{Nb}_{2/3})\text{O}_3$  (PMN), for example, is a relaxor-type ferroelectric of perovskite structure exhibiting some of the most desirable dielectric and electrostrictive properties for a number of applications in sensors and actuators [82]. Behind PMN, there is a big family of  $\text{Pb}$ -based relaxor ferroelectrics, typical examples of which are  $\text{Pb}(\text{Mg}_{1/3}\text{Nb}_{2/3})\text{O}_3$ – $\text{Pb}(\text{Zn}_{1/3}\text{Nb}_{2/3})\text{O}_3$  (PMN–PZN) and  $\text{Pb}(\text{Mg}_{1/3}\text{Nb}_{2/3})\text{O}_3$ – $\text{Pb}(\text{Zn}_{1/3}\text{Nb}_{2/3})\text{O}_3$ – $\text{PbTiO}_3$  (PMN–PZN–PT). Constituent oxides are undoubtedly the starting materials of lowest cost for these relaxor ferroelectrics. It is,

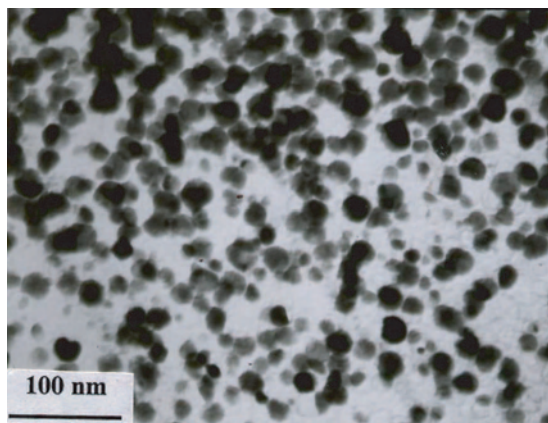
however, impossible to synthesize a single phase PMN and PMN-based relaxor ferroelectrics of perovskite structure from their constituent oxides by one-step solid-state reaction at high temperatures [83]. Calcination of a powder mixture of  $\text{PbO}$ ,  $\text{MgO}$ , and  $\text{Nb}_2\text{O}_5$ , for example, always produces one or more transitional pyrochlore phases (notably  $\text{Pb}_3\text{Nb}_4\text{O}_{13}$  and  $\text{Pb}_2\text{Nb}_2\text{O}_7$ ), prior to formation of perovskite PMN phase. On the one hand, this is related to the difference in reactivity among the three oxides over a wide range of temperatures. On the other hand, there apparently exists a much larger interfacial area between any two of these three oxides than the common contact area where all three oxides are present, creating opportunities for the preferred interfacial reaction between  $\text{PbO}$  and  $\text{Nb}_2\text{O}_5$  to take place [84]. To overcome the much unwanted pyrochlore phases in PMN and PMN-based relaxors, multiple steps of calcination and postcalcination comminution are necessary in the well known Columbite method [83].

Figure 2 shows the X-ray diffraction (XRD) traces of mixed oxides of  $\text{PbO}$ ,  $\text{MgO}$ , and  $\text{Nb}_2\text{O}_5$  upon mechanical



**Figure 2.** XRD patterns of mixed oxides of  $\text{PbO}$ ,  $\text{MgO}$ , and  $\text{Nb}_2\text{O}_5$  mechanically activated for various time periods from 0 to 20 hours. O:  $\text{PbO}$ , ■:  $\text{Nb}_2\text{O}_5$ , ◆:  $\text{MgO}$ , ●: PMN. Reprinted with permission from [85], J. Wang et al., *Solid State Ionics* 124, 271 (1999). © 1999, Elsevier Science.

activation for various time periods up to 20 hours [85]. Sharp peaks of crystalline PbO, MgO, and Nb<sub>2</sub>O<sub>5</sub> are observed for the starting oxide mixture, indicating that little or no reaction took place during the conventional ball milling, which was employed for mixing of the constituent oxides. A few broadened peaks were observed when the oxide mixture was mechanically activated for 5 hours. The strongest one at a  $2\theta$  angle of  $\sim 29.1^\circ$  corresponds to the PbO (111) peak, which was seen as a sharp one before mechanical activation. This implies that the initial 5 hours of mechanical activation led to a significant refinement in particle and crystallite sizes, together with a degree of amorphization of constituent oxides. This is supported by a rise in the specific surface area from 1.20 m<sup>2</sup>/g for the oxide mixture that was not subjected to mechanical activation to 9.52 m<sup>2</sup>/g for the powder composition subjected to 5 hours of mechanical activation. The second strongest broadened peak at a  $2\theta$  angle of  $\sim 31.2^\circ$  and those at  $2\theta$  angles of 44.7 and 55.5° are newly formed. They are assigned to perovskite PMN (110), (200), and (211) peaks, respectively, suggesting that nanocrystallites of perovskite PMN phase had been formed as a result of the initial 5 hours of mechanical activation. The intensity of the perovskite PMN (110) peak increases with increasing mechanochemical treatment time, at the expense of the PbO (111) peak. In the composition mechanically activated for 20 hours, nanocrystalline PMN is the only XRD-detectable phase, as confirmed by the well defined peaks at  $2\theta$  angles of 21.9, 31.2, 38.5, 44.7, 50.2, 55.5, and 65.0°, respectively. There is also an apparent sharpening in PMN (110), (111), (200), (210), and (211) peaks when the mechanical activation time is extended to 20 hours, demonstrating that there is an increase in the crystallinity of perovskite PMN phase. Calculation using the Scherrer equation [86] on the basis of peak broadening of the perovskite (110) peak showed that the PMN nanocrystallites exhibited an average crystallite size of  $\sim 15$  nm upon 20 hours of mechanical activation, in comparison to  $\sim 9$  nm for the powder composition that was mechanically activated for 5 hours. Figure 3 is a bright field TEM micrograph showing the PMN nanoparticles that were synthesized by mechanical activation at room temperature of constituent oxides. Pyrochlore phases,



**Figure 3.** A bright field TEM micrograph showing the nanoparticles of lead magnesium niobate that were synthesized by mechanical activation of constituent oxides at room temperature.

such as Pb<sub>3</sub>Nb<sub>4</sub>O<sub>13</sub> and Pb<sub>2</sub>Nb<sub>2</sub>O<sub>7</sub> that are always observed as transitional phases in the temperature-driven solid-state reaction, are apparently not involved prior to formation of perovskite phase, while the perovskite nanocrystallites of lead magnesium niobate underwent a steady growth with increasing degree of mechanical activation.

It has been established that phase formation of PbO-based relaxor ferroelectrics from constituent oxides triggered by mechanical activation is not a result of one or more interfacial reactions as stated by the Roller model [87]. Instead, they occur via a nucleation process involving all three oxides in a highly activated oxide matrix, where a significant refinement in particle and crystallite sizes together with a degree of amorphization had taken place. There is a much smaller amount of common contact areas involving all oxides than the interfacial contact areas between any two of them (e.g., between PbO and Nb<sub>2</sub>O<sub>5</sub> particles). On the one hand, this, together with the high reactivity between PbO and Nb<sub>2</sub>O<sub>5</sub>, accounts for the occurrence of transitional pyrochlore phases in the conventional solid-state reaction when mixed oxides of PbO, MgO, and Nb<sub>2</sub>O<sub>5</sub> are calcined at elevated temperatures. On the other hand, it is very unlikely that the formation of nanocrystallites of perovskite PMN phase triggered by mechanical activation is a result of the interfacial reactions involving all three oxides without first going through any of the transitional pyrochlore phases. The subsequent steady growth of PMN nanocrystallites of perovskite structure with increasing mechanical activation time is a consequence of the equilibrium between activation-driven buildup and destruction involving the entire masses of perovskite nuclei [88]. Constant collisions and rearrangement of perovskite nuclei provided by mechanical activation create opportunities for two or more of these nuclei to meet at favorable positions leading to growth in crystallite size. At the same time, there is also a probability that the perovskite nanocrystallites are distorted and fragmented by mechanical activation.

Nucleation and subsequent growth of perovskite nanocrystallites triggered by mechanical activation of constituent oxides have also been observed in a number of PMN-based relaxor ferroelectrics. For example, mechanical activation of mixed oxides of PbO, MgO, ZnO, TiO<sub>2</sub>, and Nb<sub>2</sub>O<sub>5</sub> equivalent to stoichiometric composition of 0.9·[0.4Pb(Mg<sub>1/3</sub>Nb<sub>2/3</sub>)O<sub>3</sub>–0.6Pb(Zn<sub>1/3</sub>Nb<sub>2/3</sub>)O<sub>3</sub>]–0.1PbTiO<sub>3</sub> led to formation of perovskite nanocrystallites [89]. The multiple oxide composition would maximize the involvement of several transitional phases prior to formation of perovskite PMN–PZN–PT nanocrystallites, if phase formation triggered by mechanical activation proceeded via one or more interfacial reactions. In other words, it would be almost impossible not to go through one or more transitional phases if the phase formation of activation-triggered perovskite nanocrystallites is controlled by one or more interfacial reactions, while the chance to involve all five oxides at an interfacial location is minimum. Phase analyses at various stages of mechanical activation, however, demonstrated that no intermediate phases occurred prior to nanocrystalline PMN–PZN–PT phase with increasing mechanical activation time. A single perovskite phase was obtained at 20 hours of mechanical activation. Figure 4 is a high resolution TEM (HRTEM) micrograph together with the selected



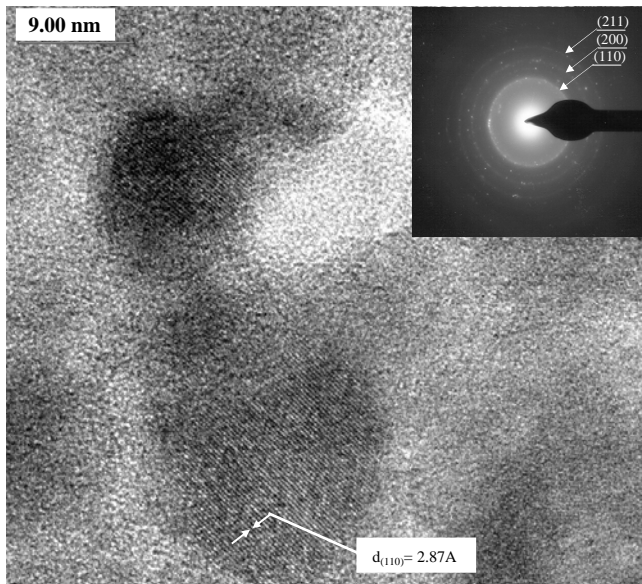


**Figure 4.** A HRTEM micrograph together with the selected area diffraction patterns showing the nanocrystallites of perovskite PMN-PZN-PT in an amorphous matrix triggered by 10 hours of mechanical activation. Reprinted with permission from [48], J. Wang et al., *J. Solid State Chem.* 154, 321 (2000). © 2000, Elsevier Science.

area diffraction patterns showing the nanocrystallites of perovskite PMN-PZN-PT in an amorphous matrix triggered by 10 hours of mechanical activation [48]. They are well established perovskite crystallites of 5 to 10 nm in dimension dispersed in an amorphous oxide matrix. Measurement of lattice spacing (e.g.,  $d_{110} = 2.87 \text{ \AA}$ ) confirmed that these nanocrystallites were perovskite PMN-PZN-PT.

Mechanical activation is successful in synthesizing complex perovskites of nanocrystallinity that cannot possibly be synthesized by any other processing techniques. For example,  $\text{Pb}(\text{Zn}_{1/3}\text{Nb}_{2/3})\text{O}_3$  is a relaxor ferroelectric exhibiting a partially disordered perovskite structure and showing many of the most desirable dielectric and piezoelectric properties for a number of applications in sensors and actuators. However, the pursuit to synthesize a  $\text{Pb}(\text{Zn}_{1/3}\text{Nb}_{2/3})\text{O}_3$  (PZN) of perovskite structure via both traditional ceramic and chemistry-based novel processing routes over the last three decades has failed. The difficult-to-synthesize nanocrystallites of PZN have, however, been successfully synthesized by mechanical activation of either constituent oxides of  $\text{PbO}$ ,  $\text{ZnO}$ , and  $\text{Nb}_2\text{O}_5$  or a mixture of  $\text{PbO}$  and prereacted  $\text{ZnNb}_2\text{O}_6$  from  $\text{ZnO}$  and  $\text{Nb}_2\text{O}_5$  [90]. The activation-derived PZN exhibits a well established perovskite structure and a crystallite size in the range of 10 to 15 nm.

Bismuth titanate ( $\text{Bi}_4\text{Ti}_3\text{O}_{12}$  or BIT) and bismuth titanate-based electroceramics are examples of layered perovskites that have been successfully synthesized by mechanical activation. These electroceramic materials, which exhibit a high Curie temperature ( $\sim 675 \text{ }^\circ\text{C}$  for BIT) and excellent piezoelectric and dielectric properties, are promising candidates for high temperature piezoelectric and ferroelectric applications [91]. They are traditionally prepared by solid-state reaction among the constituent oxides at elevated temperatures. However, due to the high volatility of  $\text{Bi}_2\text{O}_3$  at

elevated temperatures, it is rather difficult to synthesize a bismuth-based ceramic of stoichiometry by the conventional solid-state reaction. Several bismuth titanate-based functional ceramics, including  $\text{Bi}_4\text{Ti}_3\text{O}_{12}$  [92],  $\text{SrBi}_4\text{Ti}_4\text{O}_{15}$  [93], and  $\text{CaBi}_4\text{Ti}_4\text{O}_{15}$  [94], have been synthesized by mechanical activation of mixed oxides at room temperature. Figure 5 shows the XRD traces of starting oxide mixture of  $\text{SrO}$ ,  $\text{Bi}_2\text{O}_3$ , and  $\text{TiO}_2$  together with those mechanically activated for 5, 10, 15, and 20 hours, respectively [93]. Sharp peaks of crystalline  $\text{Bi}_2\text{O}_3$  and  $\text{TiO}_2$  are observed with the starting oxide mixture, while  $\text{SrO}$  is not detected by XRD due to the relatively small amount involved. Upon 5 hours of mechanical activation, XRD peaks of these oxides are broadened. The small peak at a  $2\theta$  angle of  $30.5^\circ$  is newly formed, which is assigned to the  $\text{SrBi}_4\text{Ti}_4\text{O}_{15}$  (SBIT) (119) plane, indicating the formation of nanocrystalline SBIT by mechanical activation for 5 hours. Almost all the sharp peaks of oxides have vanished in the composition mechanically activated for 10 hours, and they are replaced by a few broadened ones. The  $\text{Bi}_2\text{O}_3$  (120) peak, which is seen as a sharp one in the powder mechanically activated for 5 hours, has broadened considerably. The disappearance of sharp peaks for oxides and subsequent formation of broadened peaks, with increasing mechanical activation time, suggest that a significant

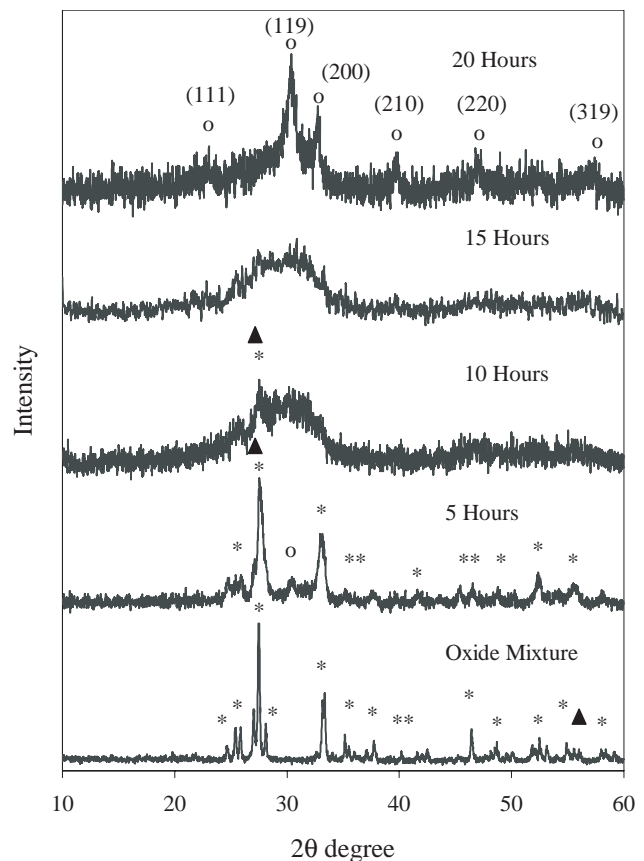


**Figure 5.** XRD patterns of the mixed oxides of  $\text{Bi}_2\text{O}_3$ ,  $\text{TiO}_2$ , and  $\text{SrO}$  equivalent to SBIT subjected to mechanical activation for various time periods ranging from 0 to 20 hours. \*:  $\text{Bi}_2\text{O}_3$ , ▲:  $\text{TiO}_2$ , o: SBIT. Reprinted with permission from [93], S. H. Ng et al., *Mater. Chem. Phys.* 75, 131 (2002). © 2002, Elsevier Science.

refinement in particle and crystallite sizes, together with a degree of amorphization of mixed oxides, took place at the initial stage of mechanical activation. This is followed by nucleation and subsequent growth of SBIT nanocrystallites. As shown in Figure 5, diffraction peaks at  $2\theta$  angles of 23.1, 30.5, 39.8, 47.2, and 57.2° are established for the composition mechanically activated for 20 hours. They correspond to SBIT (111), (119), (0210), (220), and (319) planes, respectively, of the layered perovskite phase.

There are a number of other complex oxides of nanocrystallinity that have been successfully synthesized by mechanical activation of either constituent oxides or chemical precursors or a mixture of the two. They include  $\text{La}_{0.7}\text{Sr}_{0.4}\text{MnO}_3$  from constituent oxides of  $\text{La}_2\text{O}_3$ ,  $\text{SrO}$ , and  $\text{MnO}_2$  [95],  $\text{LaMnO}_3$  from  $\text{La}_2\text{O}_3$  and  $\text{Mn}_2\text{O}_3$  [96],  $\text{Al}_2\text{TiO}_5$  from  $\text{Al}_2\text{O}_3$  and  $\text{TiO}_2$  [97],  $\text{Sn}_{0.5}\text{Ti}_{0.5}\text{O}_2$  from  $\text{TiO}_2$  and  $\text{SnO}$  [98],  $\text{Bi}_3\text{NbTiO}_9$  from  $\text{Bi}_2\text{O}_3$ ,  $\text{Nb}_2\text{O}_5$ , and  $\text{TiO}_2$  [99],  $\text{LaFeO}_3$  from  $\text{La}_2\text{O}_3$  and  $\text{Fe}_2\text{O}_3$  [100],  $\text{LiCoO}_2$  from  $\text{LiOH}\cdot\text{H}_2\text{O}$  and  $\text{Co(OH)}_2$  [101],  $\text{ZrTiO}_4$  from  $\text{ZrO}_2$  and  $\text{TiO}_2$  gels [102],  $\text{LiMn}_2\text{O}_4$  from  $\text{MnO}_2$  with  $\text{LiOH}$  [103],  $\text{MgAl}_2\text{O}_4$  from  $\text{Mg(OH)}_2$  and  $\text{Al(OH)}_3$  [104],  $\text{CaTiO}_3$  from  $\text{CaO}$  and  $\text{TiO}_2$  [105],  $\text{Sr}_3\text{Ti}_2\text{O}_7$  from  $\text{SrO}$  or  $\text{SrCO}_3$  or  $\text{Sr(OH)}_2\cdot 8\text{H}_2\text{O}$  and  $\text{TiO}_2$  [106],  $\text{LaCrO}_3$  from amorphous  $\text{Cr}_2\text{O}_3\cdot n\text{H}_2\text{O}$  and  $\text{La}_2\text{O}_3$  [107], aurivillius type compounds from constituent oxides and precursors [108, 109], and fluorite type phases in the system  $\text{Bi}_2\text{O}_3\text{--Nb}_2\text{O}_5\text{--Ta}_2\text{O}_5$  [110]. Mechanochemical reactions responsible for formation of these oxides are dependent on the nature of starting materials and processing parameters chosen for mechanical activation. For example, mechanical activation of  $\text{TiO}_2$  together with  $\text{Mg(OH)}_2$  triggered an incipient reaction between them in association with dehydration of the hydroxide [111]. Use of hydroxide precursors or hydrated oxides as the starting materials can generate local hydrothermal environments responsible for formation of a product phase.

Silicates constitute a big family in the complex oxides, which are traditionally synthesized by conventional solid-state reaction at high temperatures. Mechanical activation has been applied to synthesis of several technologically demanding silicates, which otherwise require a very high calcination temperature. For example, mullite is a compound formed between alumina and silica at temperatures well above 1000 °C. Mechanical activation of constituent oxides and hydroxides (for example, gibbsite and silica gel) significantly lowers the crystallization of mullite [112], which often occurs via one or more transitional spinel phases in the conventional solid-state reaction. Mechanical activation of  $\text{MgO}$  and  $\text{SiO}_2$  produces a magnesium silicate of low crystallinity similar to what is formed under certain hydrothermal reaction conditions [113]. Magnesium silicate of well established crystallinity is obtained by subsequent thermal annealing. Hydrated calcium silicates can also be synthesized mechanochemically at room temperature where the presence of water and moisture employed play a significant role [114]. Mechanochemical reactions between kaolinite and several oxides (such as  $\text{ZnO}$  and  $\text{CaO}$ ) and nonoxides have been studied by several investigators. For example, cesium aluminum silicate and intercalation complexes occur as a result of mechanical activation of kaolinite together with  $\text{CsF}$  [115].

### 5.3. Nanocrystalline Oxide Ferrites

Nanocrystalline ferrites, magnetite ( $\text{Fe}_3\text{O}_4$ ), and maghemite ( $\gamma\text{-Fe}_2\text{O}_3$ ) were among the ceramic materials synthesized by mechanical activation in the early development stage of this novel technique. They were synthesized from corresponding oxides, hydroxides, precursors, and chemicals (such as chlorides) or a mixture of these. The types of mechanochemical reaction leading to formation of nanocrystalline ferrite phases include replacement reaction [116], decomposition [66], oxidation/reduction [117], and mechanical activation-induced nucleation and crystallite growth [118]. Very different magnetic behaviors are observed with these nanocrystalline ferrites derived from mechanical activation, as compared to those of their coarse/bulk counterparts and those materials derived from either conventional ceramic processing or wet-chemistry routes. For example,  $\text{ZnFe}_2\text{O}_4$  and  $\text{NiFe}_2\text{O}_4$  derived from mechanical activation demonstrate a much enhanced magnetization, as a result of the partially inverted spinel structure [26, 119].

Mechanical activation triggers a steady occurrence of nanocrystalline  $\text{ZnFe}_2\text{O}_4$  [120],  $\text{NiFe}_2\text{O}_4$  [121],  $\text{MnFe}_2\text{O}_4$  [122], and  $\text{Ni-Zn}$  ferrite [123] of particle size in the range of 5 to 20 nm from corresponding oxide mixtures, for example,  $\alpha\text{-Fe}_2\text{O}_3$  and  $\text{ZnO}$  for  $\text{ZnFe}_2\text{O}_4$ . Subsequent annealing at a temperature in the range of 600 to 800 °C enhances their crystallinity and magnetic properties in association with superparamagnetic to ferromagnetic transition. They can also be synthesized by mechanical activation of corresponding hydroxides, with or without involvement of certain transitional phases such as  $\text{Fe}_3\text{O}_4$  and  $\gamma\text{-Fe}_2\text{O}_3$ , depending on the selection of mechanical activation conditions [124]. A replacement reaction is apparently involved in mechanical activation of chlorides, such as  $\text{ZnCl}_2$  and  $\text{FeCl}_3$ , with  $\text{NaOH}$  for synthesis of  $\text{ZnFe}_2\text{O}_4$ , the crystallinity and magnetic behavior of which are largely controlled by the post-activation thermal annealing [22].

Several different combinations of starting materials have been experimented for synthesis of nanocrystalline  $\text{BaFe}_{12}\text{O}_{19}$  by mechanical activation, including  $\text{Fe}_2\text{O}_3$  and  $\text{Ba(OH)}_2$  [125],  $\text{BaCl}$  and  $\text{FeCl}$  [126], and co-precipitation-derived hydroxide precursors [127]. Formation of  $\text{BaFe}_{12}\text{O}_{19}$  of high crystallinity and hexagonal platelike morphology requires a postactivation annealing at a temperature in the range of 600 to 800 °C. Transitional phases, such as  $\alpha\text{-Fe}_2\text{O}_3$ ,  $\gamma\text{-Fe}_2\text{O}_3$ , and  $\text{Fe}_3\text{O}_4$ , can occur, prior to  $\text{BaFe}_{12}\text{O}_{19}$ , during mechanical activation and subsequent thermal annealing, depending on the nature of starting materials and processing conditions of mechanical activation. For example, when a co-precipitated hydroxide precursor is mechanically activated together with sodium chloride as a dispersion agent, nanocrystallites of  $\alpha\text{-Fe}_2\text{O}_3$  and spinel  $\gamma\text{-Fe}_2\text{O}_3$  of <10 nm in size occurred together with  $\text{BaFe}_{12}\text{O}_{19}$ . A single phase  $\text{BaFe}_{12}\text{O}_{19}$  of 50–100 nm in size and of platelike morphology is developed upon subsequent calcination at 800 °C [127]. Using  $\text{BaCl}$  and  $\text{FeCl}$  as the starting materials, mechanical activation in  $\text{NaOH}$  led to formation of a mixture of Fe oxides and hydroxides together with  $\text{NaCl}$  as a by-product [126]. Nanocrystalline  $\text{BaFe}_{12}\text{O}_{19}$  resulted upon subsequent calcination at 800 °C. Crystallite size and degree of agglomeration of thus derived  $\text{BaFe}_{12}\text{O}_{19}$  can be further tailored by employing  $\text{NaCl}$  as an effective dispersion agent.



Phase transformations among  $\alpha$ - $\text{Fe}_2\text{O}_3$ ,  $\gamma$ - $\text{Fe}_2\text{O}_3$ , and  $\text{Fe}_3\text{O}_4$  can be triggered by mechanical activation and are critically dependent on the oxygen partial pressure [128–131]. For example, mechanical activation of  $\alpha$ - $\text{Fe}_2\text{O}_3$  in vacuum can lead to complete transformation to  $\text{Fe}_3\text{O}_4$ , involving a significant refinement in crystallite size at the initial stage of mechanical activation prior to nucleation and growth of  $\text{Fe}_3\text{O}_4$  [128]. Mechanical activation of  $\gamma$ - $\text{Fe}_2\text{O}_3$  and  $\text{Fe}_3\text{O}_4$  in air gives rise to formation of  $\alpha$ - $\text{Fe}_2\text{O}_3$  [132].

Nanocrystalline ferrites derived from mechanical activation demonstrate very different structural and magnetic behaviors. For example,  $\text{MnFe}_2\text{O}_4$  derived from mechanical activation of  $\text{FeCl}$  together with  $\text{MnO}$  exhibits a unique core-shell structure, which consists of a ferrimagnetic core surrounded by a spin-glass shell, and therefore there occur a coupling and exchange between the spin in the core and that in the shell [132]. The most remarkable structural feature brought about by mechanical activation in nanocrystalline ferrites is the cation inversion. In bulk ceramic forms, spinel ferrites consist of close-packed face-centered cubic arrays of O anions, with the tetrahedral (A) and octahedral (B) sites partially occupied by metal cations. Due to the specific electronic configurations of cations and types of superexchange interactions among them, their magnetic properties are strongly dependent on the occupancy and exchange of cations in the two sites and among them. Unusual cation distribution has been observed in  $\text{ZnFe}_2\text{O}_4$ ,  $\text{MnFe}_2\text{O}_4$ , and  $\text{NiFe}_2\text{O}_4$  nanoparticles derived from mechanical activation [133–135]. This gives rise to a significant enhancement in magnetization and several other anomalous behaviors, although the exact reasons behind the inversion are yet properly established. Figure 6 [26] is a magnetization hysteresis loop measured at 5 K for  $\text{NiFe}_2\text{O}_4$  particles formed in silica matrix by mechanical activation of a gel precursor, where nanocrystallites of  $\text{Fe}_3\text{O}_4$  were first nucleated followed by incorporation of  $\text{Ni}^{2+}$  into  $\text{Fe}_3\text{O}_4$  leading to formation of  $\text{NiFe}_2\text{O}_4$  nanoparticles of  $\sim 8$  nm in size. Although magnetization is not saturated at a magnetic field of 9 T due to the surface strain arising from silica matrix,

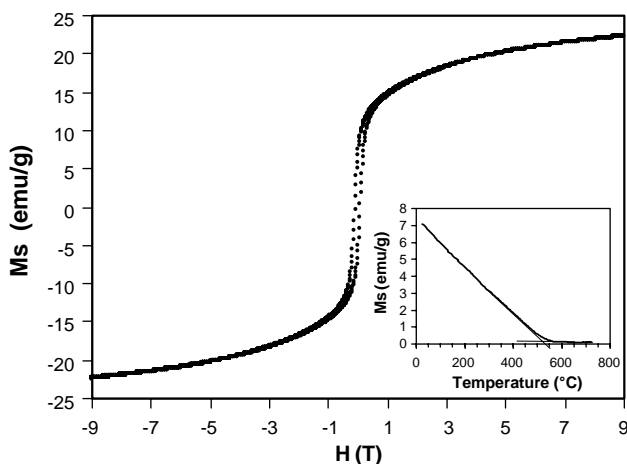


**Figure 6.** Magnetization hysteresis loop, measured at 5 K, for gel composition of  $\text{NiFe}_2\text{O}_4$  mechanically activated for 30 hours. Inset shows the magnetization as a function of measuring temperature.

these  $\text{NiFe}_2\text{O}_4$  nanoparticles demonstrate an unusually high magnetization of 74.3 emu/g at 9 T.

In the inverse spinel structure of  $\text{NiFe}_2\text{O}_4$ , equal numbers of  $\text{Fe}^{3+}$  cations in tetrahedral (A) and octahedral (B) sites are coupled in an antiparallel arrangement. The net magnetic moment is therefore originated from the octahedrally coordinated  $\text{Ni}^{2+}$  cations. Displacement of an A-site  $\text{Fe}^{3+}$  ion with moment of  $5 \mu_B$  by a  $\text{Ni}^{2+}$  ion with moment of  $2.3 \mu_B$  gives rise to an increase in the net moment. The enhancement of magnetization shown in Figure 6 for  $\text{NiFe}_2\text{O}_4$  nanoparticles derived from mechanical activation arises from occupation of  $\text{Ni}^{2+}$  cations in the tetrahedral sites, which have been confirmed by Raman, Fourier transform infrared, and Mössbauer studies [26, 135]. The cation inversion also explains the shift in Curie temperature from 585 °C for bulk  $\text{NiFe}_2\text{O}_4$  to 530 °C for the nanocrystalline  $\text{NiFe}_2\text{O}_4$  particles. Since the  $\text{Fe}^{3+}$ (A)–O– $\text{Fe}^{3+}$ (B) interaction is the strongest one among those in nickel ferrite [136], any displacement of A site  $\text{Fe}^{3+}$  will reduce the overall superexchange interaction and hence decrease the Curie temperature. Furthermore, upon displacement of A site  $\text{Fe}^{3+}$  ions by  $\text{Ni}^{2+}$  ions,  $\text{O}^{2-}$  anions in the A sites are forced to shift in the direction to give space to  $\text{Ni}^{2+}$  ions of larger ionic radii. This leads to reduction in the cation(A)–O–cation(B) bond angles and hence weakens the superexchange interaction.

The observed disorder of cations for nanocrystalline  $\text{NiFe}_2\text{O}_4$  particles formed *in-situ* in silica matrix by mechanical activation occurs in conjunction with the phase formation process. As discussed, initial mechanical activation led to nucleation of  $\text{Fe}_3\text{O}_4$  nanocrystallites, which was followed by the incorporation of  $\text{Ni}^{2+}$ . Site occupancy of cations are affected by a combination of a number of parameters. Although  $\text{Ni}^{2+}$  possesses a high octahedral site preference energy, the electrostatic energy favors a normal spinel arrangement, as  $\text{NiFe}_2\text{O}_4$  has a deformation parameter  $\mu$  of 0.3823. The normal spinel configuration is more stable when  $\mu > 0.379$  [136]. Very often, however, the difference in total energy between the normal and inverse spinel distributions is very small. Therefore, when  $\text{Ni}^{2+}$  approaches an octahedral site that has already been occupied by  $\text{Fe}^{2+}$ , which also possesses a high octahedral site preference energy, it will be forced to occupy one of the nearest tetrahedral sites. This is particularly so when the incorporation of  $\text{Ni}^{2+}$  was triggered by mechanical activation, which can only promote short-range diffusion [137].  $\text{Ni}^{2+}$  then displaces the  $\text{Fe}^{3+}$  cations if the nearest tetrahedral sites are preoccupied by  $\text{Fe}^{3+}$  cations, which have zero octahedral site preference energy.

#### 5.4. Carbides, Nitrides, Nonoxides, and Nanocomposites

In parallel to the success of synthesizing ceramic oxides and complex oxide ceramics of nanocrystallinity, mechanical activation has been successfully applied to synthesis of several nonoxide ceramics, including carbides, nitrides, borides, and ceramic nanocomposites [12, 13, 138–144]. In several cases, mechanical activation of metallic elements together with carbon (graphite) and boron in a nitrogen environment produce corresponding carbides, borides, and nitrides. For example,

TiC [141] and TiB<sub>2</sub> [142] can be synthesized by mechanical activation of powder mixtures of elemental Ti and C and Ti and B, respectively, in a planetary ball mill using tungsten carbide balls as the activation media. The phase formation steps during mechanical activation consisted of diffusion of carbon or boron into titanium in the initial stage, whereby a small amount of TiC and TiB<sub>2</sub> was formed, followed by the mechanically triggered self-propagating reaction. Titanium nitride is produced by mechanical activation of titanium in nitrogen gas, where the reaction proceeded via a surface reaction between titanium particles and nitrogen and then diffusion of nitrogen into titanium under mechanical activation [143]. Nitridation of silicon at high temperatures (e.g., 1250 °C) is accelerated by factors of 9 and 23 by mechanical activation of silicon in either N<sub>2</sub> or NH<sub>3</sub>. This has been attributed to the enhanced reactivity of Si and the entrapment of N<sub>2</sub> by mechanical activation [144].

Nanocomposite compositions consisting of titanium nitride and titanium diboride of particle sizes in the range of 5 to 10 nm were obtained by mechanical activation of Ti together with BN [145]. Similarly, AlN–TiB<sub>2</sub> nanocomposites can be fabricated by mechanical activation of Ti and Al together with BN, followed by sintering or hot pressing in order to densify the nanocomposites [146]. A nanocrystalline mixture of WC and intermediate tungsten carbide phases was generated by mechanical activation of WO<sub>3</sub> together with Mg and graphite, where the mechanochemical reaction took place in two steps [147], namely, formation of  $\alpha$ -W as a result of explosive reduction of WO<sub>3</sub> by Mg and then the diffusion reaction between  $\alpha$ -W and C. The product therefore consists of WC nanoparticles of 4 to 20 nm in size dispersed in MgO matrix, which can be washed off using HCl solution. Prolonged mechanical activation of rutile (TiO<sub>2</sub>) together with aluminum in nitrogen produced a composite consisting of nanocrystalline alumina and titanium nitride, which undergo growth in crystallite and particle sizes upon subsequent annealing at 1200 °C [148].

In addition to carbides, nitrides, borides, and nanocomposites consisting of one or more carbide, nitride, and boride phases, other nonoxide ceramics and their nanocomposites that have been synthesized by mechanical activation include sulphides, silicides, and phosphates [149–158]. For example, mechanical activation of Ni together with P, and Al together with P, can lead to formation of nanocrystalline Ni- and Al-phosphides [154]. Bi<sub>2</sub>Se<sub>3</sub> and BiSe were synthesized by mechanical activation of Bi + Se mixtures in the molar ratio of 2:3 and 1:1, respectively [155]. Formation of ZnS is realized by mechanical activation of ZnCl<sub>2</sub> and CdS in CaCl<sub>2</sub>, which acts as a dispersion agent in refining the particle and agglomerate sizes [156]. Similarly, nanocrystalline cadmium sulphide (quantum dots) can be obtained by the displacement reaction between CdCl<sub>2</sub> and Na<sub>2</sub>S triggered by mechanical activation, giving rise to CdS and NaCl [157]. Zirconium silicides can be synthesized by a mechanically induced self-propagating reaction, which is analogous to the thermally ignited self-propagating syntheses, where the explosive formation of zirconium silicides is attributed to the relatively large heat of formation involved [158].

## 6. MECHANICAL CRYSTALLIZATION AND PRECURSOR TO CERAMIC CONVERSIONS

High sintered density and uniform microstructure/nanostructure are among the most desirable features for almost all ceramic materials, as far as most of the functional and structural applications are concerned. Synthesis of a fine and sinterable ceramic powder is the first and perhaps the most important step in realization of a high sintered density and desirable microstructure/nanostructure at lowered sintering temperatures. Phase formation by a conventional ceramic fabrication technique (i.e., solid-state reaction of constituent oxides/nonoxides at elevated temperatures) is unable to deliver a fine and sinter-reactive ceramic powder, due to the unavoidable particle coarsening and aggregation at the calcination temperature, in combination with several other apparent detrimental effects such as nonstoichiometry and occurrence of impurity phases. This explains why for the past two decades considerable research efforts have been directed towards synthesis of nanocrystalline ceramic powders via a number of chemistry-based routes. Unfortunately, as mentioned earlier, almost all ceramic precursors derived from wet-chemistry routes have to be calcined at a temperature in the range of 500 to 1000 °C, in order to materialize the precursor to ceramic convention. Calcination of a ceramic precursor at an intermediate temperature ruins almost all the advantages offered by chemistry-based novel synthesis techniques, as a consequence of the particle coarsening and aggregation in the calcined ceramic powders. In this context, there is no fundamental difference between conventional ceramic and chemistry-based processing routes, where the problems are caused by the unavoidable calcination at high temperatures. Therefore, realization of the precursor to ceramic convention via an alternative, low temperature route represents a major advance in ceramic processing.

Mechanical crystallization in Fe-based amorphous alloys at room temperature was extensively studied following the pioneering work of Trudeau and Schulz [39], who demonstrated that nanocrystalline metallic phases of crystallite size in the range of 2 to 5 nm were triggered to form in certain amorphous alloy compositions by an input of mechanical energy [40]. The feasibility of mechanical crystallization in ceramic composition and the precursor to ceramic conversion by mechanical activation have been successfully demonstrated with an amorphous hydroxide precursor of PZT prepared via a co-precipitation route [159]. Figure 7 shows the XRD traces of the co-precipitated hydroxide precursor upon mechanical activation for 5, 15, and 35 hours, respectively, together with that of the amorphous precursor that was not subjected to any mechanical activation. Only one strong and broadened peak is observed over the  $2\theta$  angle of 28 to 35° for the starting hydroxide precursor, indicating its amorphous nature. Five hours of mechanical activation apparently led to a steady formation of PZT nanocrystallites in an essentially amorphous PZT precursor, while the transitional PT and PZ phases were not observed prior to formation of perovskite PZT phase. The intensity and sharpness of perovskite PZT (110), (100), (111), (200), (210), (211), and

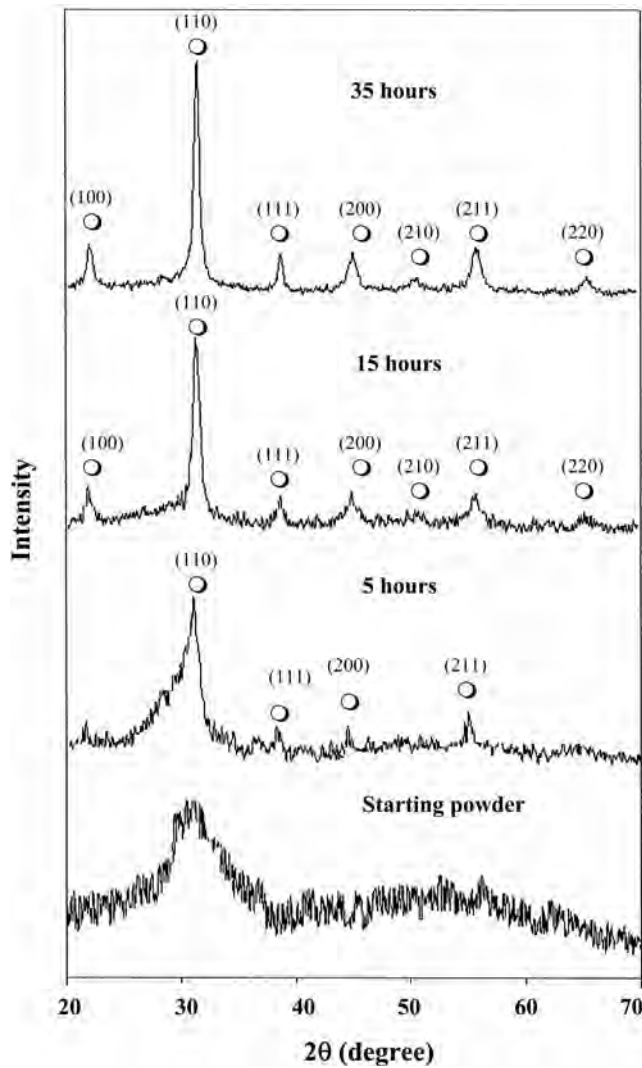


**Figure 7.** XRD traces of PZT precursor derived from co-precipitation when mechanically activated for various times ranging from 0 to 35 hours (O: PZT). Reprinted with permission from [159], J. M. Xue et al., *J. Amer. Ceram. Soc.* 82, 1641 (1999). © 1999, American Ceramic Society.

(220) peaks were further established when the mechanical activation was extended to 15 and then 35 hours.

Mechanical activation has also been successfully applied to the precursor to ceramic transition in several other oxide ceramic systems, including  $\alpha$ - $\text{Fe}_2\text{O}_3$ , ZnO,  $\text{CeO}_2$ ,  $\text{Al}_2\text{O}_3$ , and oxides ferrites. In general, oxide particles of nanocrystallinity and a minimized degree of particle aggregation are obtained, although the phase-forming mechanisms involved varied considerably from one material system to another. For example, formation of  $\gamma$ - $\text{Fe}_2\text{O}_3$  nanocrystallites triggered by mechanical activation, in an amorphous silica matrix from a sol-gel-derived precursor at room temperature, occurred by involving  $\text{Fe}_3\text{O}_4$  as a transitional phase. Prolonged mechanical activation led to a steady phase transformation from  $\text{Fe}_3\text{O}_4$  to  $\gamma$ - $\text{Fe}_2\text{O}_3$ , as confirmed by phase identification and measurement in magnetic behavior [118].

Mechanical crystallization in oxide glass has recently been demonstrated by Xue and Wang [160], who employed

two slightly different  $\text{PbNb}_2\text{O}_6$  glass samples, which were quenched from 1300 and 1350 °C, respectively, for experimentation. As a result of the much higher glass-forming ability of the oxide glass than that of a metallic glass, it is much more difficult to induce crystallization in the former than that in the latter. Nevertheless, mechanical crystallization was observed in the glass quenched from 1300 °C, where a density of  $\text{PbNb}_2\text{O}_6$  nuclei existed prior to mechanical activation. Mechanical activation promoted a steady growth in nanocrystallites of  $\text{PbNb}_2\text{O}_6$ , up to 15 nm in size. Due to the lack of  $\text{PbNb}_2\text{O}_6$  nuclei in the glass quenched from 1350 °C, mechanical crystallization was not initiated by mechanical activation. This has led the investigators to believe that the mechanical crystallization in  $\text{PbNb}_2\text{O}_6$  glass is nucleation-controlled. Although nucleation is thermodynamically favored at a low temperature, the inability of mechanical activation in triggering nucleation in the highly amorphous oxide glass is apparently due to its higher structural stability, as compared to that of Fe-Si-B based metallic glass.

## 7. SUMMARY

As a newly developed synthesis technique for nanocrystalline ceramic materials, mechanical activation can deliver the designed ceramic phase(s) and structure(s) by a single step of mechanical activation conducted in an enclosed activation chamber at room temperature. By employing the widely available oxides and nonoxides as the starting materials and skipping the multiple steps of phase formation at elevated temperatures that are always required in conventional solid state reaction, mechanical activation offers a lower manufacturing cost and a higher production yield, when compared to wet-chemistry-based synthesis techniques for ceramic materials. More importantly, mechanical activation delivers the much wanted nanocrystalline structures that cannot possibly be realized by either conventional ceramic processing or wet-chemistry-based synthesis techniques. In addition, a number of nanocrystalline ceramic materials derived from mechanical activation demonstrate unique structural metastability, extended solid solubility, and surface and structural defects (such as cation inversion in the spinel structures and order-disorder transitions in complex perovskites), which give rise to a number of unique electrical, electronic, magnetic, and functional properties.

On the one hand, phase formation processes triggered by mechanical activation are fundamentally different from those in the conventional solid-state reaction in many ceramic systems studied to date; mechanical activation can be used to synthesize ceramic materials that cannot possibly be synthesized by either conventional ceramic processing or wet-chemistry-based techniques. Nanocrystalline PZN of complex perovskite structure is one such good example [89, 90]. On the other hand, a number of solid-state phenomena that are traditionally triggered by thermal activation can be made to take place by mechanical activation, including phase transition, order-disorder transformation in complex perovskite structure, and precursor to ceramic phase conversions,

which are traditionally realized by calcination at elevated temperatures.

Mechanical activation has been successfully utilized to synthesize a wide range of nanocrystalline ceramic materials, including ceramic oxides, oxides of complex perovskite, spinel and layered perovskite structures, ceramic ferrites, nonoxide ceramics, and their nanocomposites. While phase formation triggered by mechanical activation is different from that in the conventional solid-state reaction, understanding the exact phase formation mechanisms in some of these nanocrystalline ceramic materials will apparently be one of the future developments in the study of mechanical activation. There are several unique phenomena that have been observed in association with mechanical activation, including the occurrence of metastable structures, order-disorder transformation in complex perovskites, and cation inversion in spinel structures. Both short-range and long-range structural disordering can be induced in certain Pb-based complex perovskites, for example in  $\text{Pb}(\text{Sc}_{1/2}\text{Ta}_{1/2})\text{O}_3$ ,  $\text{Pb}(\text{Mg}_{1/3}\text{Nb}_{2/3})\text{-Pb}(\text{Mg}_{1/2}\text{W}_{1/2})\text{O}_3$ , by mechanical activation [38, 161]. There exists an equilibrium between mechanical activation and thermal activation in leading to the order-disorder transition in these perovskite structures, where mechanical activation induces disorder while thermal activation tends to recover the structural ordering. It will be considerably interesting to understand the exact physical principles behind these unique phenomena, as triggered by mechanical activation.

In order to further tailor the characteristics of nanocrystalline ceramic materials, mechanical activation can be combined with one or more other types of processing control. For example, mechanical activation can be assisted by an electrical discharge, magnetic field, hydrothermal conditions, and an effective integration of mechanical and thermal activations [11, 13, 14]. There is no doubt that this will also be one of the interesting areas for further development of mechanical activation.

Success of mechanical activation in synthesis of nanocrystalline ceramic material promises a significant technological implication, whereby the currently employed multiple steps of phase-forming calcination/annealing at high temperatures for ceramic materials can be skipped, when designed ceramic phases and chemical stoichiometry are realized at room temperature in an enclosed mechanical activation chamber. The scale-up of this novel synthesis technique to industrially useful batches will be technologically demanding and also a challenge in the future development of mechanical activation.

## GLOSSARY

**Complex ceramic oxide** Those oxides containing more than one type of cation in structure, including those of perovskite structure, complex perovskite structure, aurivillius type compound and layered perovskite structure, spinel structure, and their solid solutions.

**Mechanical activation** A mechanical process, typically involving one or more processes of mechanical impact, shear, straining, deformation, mixing, and fracture at room temperature, above or below room temperature, that can

activate the phenomena such as phase transformation, order-disorder transformation, structure change, surface modification, and in particular, formation of a new material phase as a result of the nucleation and crystallization triggered by such mechanical process. High energy mills are widely employed for mechanical activation.

**Mechanical amorphization/crystallization** Amorphization/crystallization triggered by a mechanical activation process.

**Mechanochemical synthesis** Materials synthesis involves one or more types of chemical processes/reactions triggered by a mechanical process, with or without the need for subsequent thermal annealing at elevated temperatures, in order to form the designed material phase/structure.

**Nanocrystalline ceramics** Those ceramic materials with microstructural feature in the nanometer scales, typically in the range of 1.0 to 100 nm.

**Simple ceramic oxide** Those oxides containing one predominant cation in structure, regardless of the structure types, with or without the involvement of other cations at a tracing level added as dopants. Typical examples of simple ceramic oxides are  $\text{ZrO}_2$ ,  $\text{CeO}_2$ ,  $\text{ZnO}$  and  $\text{Al}_2\text{O}_3$ .

## ACKNOWLEDGMENTS

The authors acknowledge the input of and discussions with Wan Dongmei, Ng Wei Beng, Ang Seok Khim, Ng Sze Hwee, Gan Xingsen, Lim Hua Wei, and Liu Xiangyuan. Financial support by the National University of Singapore, the Institute of Materials Research and Engineering (IMRE, Singapore), and A\*Star (Singapore) are acknowledged.

## REFERENCES

1. P. G. McCormick and F. H. Froes, *JOM* 11, 61 (1998).
2. V. V. Boldyrev and K. Tkacova, *J. Mater. Synth. Process.* 8, 121 (2000).
3. J. S. Benjamin, *Sci. Amer.* 234, 40 (1976).
4. C. Suryanarayana, *Progr. Mater. Sci.* 46, 1 (2001).
5. E. Gaffet and O. Tillement, *Ann. Chim. Sci. Mater.* 22, 417 (1997).
6. E. Gaffet, F. Bernard, J. C. Niepce, F. Charlot, C. H. Gras, G. Le Caer, J. L. Guichard, P. Delcroix, A. Mocellin, and O. Tillement, *J. Mater. Chem.* 9, 305 (1999).
7. A. Calka, *Appl. Phys. Lett.* 59, 1568 (1991).
8. M. S. El-Eskandarany, K. Aoki, and K. Suzuki, *J. Less-Common Metals* 167, 113 (1990).
9. V. Gauthier, C. Josse, F. Bernard, E. Gaffet, and J. P. Larpin, *Mater. Sci. Eng. A* 265, 117 (1999).
10. C. H. Gras, F. Charlot, E. Gaffet, F. Bernard, and J. C. Niepce, *Acta Mater.* 47, 2113 (1999).
11. L. L. Shaw, *Mater. Manuf. Process.* 16, 405 (2001).
12. L. L. Shaw, *Adv. Eng. Mater.* 2, 721 (2000).
13. R. M. Ren, Z. G. Yang, and L. L. Shaw, *J. Amer. Ceram. Soc.* 85, 819 (2002).
14. A. Calka and D. Wexler, *Nature* 419, 147 (2002).
15. K. Niihara and A. Nakahira, *Ann. Chim. Sci. Mater.* 16, 479 (1991).
16. B. N. Kim, K. Hiraga, K. Morita, and Y. Sakka, *Nature* 413, 288 (2001).
17. F. Wakai, N. Kondo, and Y. Shinoda, *Current Opinion Solid State Mater. Sci.* 4, 461 (1999).
18. E. J. W. Verwey and E. L. Hailmann, *J. Chem. Phys.* 15, 174 (1947).
19. W. D. Kingery, H. K. Bowen, and D. R. Uhlmann, in "Introduction to Ceramics," p. 991. Wiley, New York (1976).

20. K. Tanaka, M. Makita, Y. Shimizugawa, K. Hirao, and N. Soga, *J. Phys. Chem. Solids* 59, 1611 (1998).
21. G. F. Goya and H. R. Rechenberg, *J. Magn. Magn. Mater.* 196–197, 191 (1999).
22. T. M. Clark and B. J. Evans, *IEEE Trans. Magn.* 33, 3745 (1997).
23. J. F. Hochepped, P. Bonville, and M. P. Pileni, *J. Phys. Chem. B* 104, 905 (2000).
24. T. Sato, K. Haneda, T. Iijima, and M. Seki, in “Proceedings of the Sixth International Conference on Ferrites (ICF6),” Tokyo and Kyoto, Japan, p. 984, 1992.
25. T. Kamiyama, K. Haneda, T. Sato, S. Ikeda, and H. Asano, *Solid State Comm.* 81, 563 (1992).
26. Z. H. Zhou, J. M. Xue, J. Wang, H. S. O. Chan, T. Yu, and Z. X. Shen, *J. Appl. Phys.* 91, 6015 (2002).
27. O. Furukawa, M. Harata, Y. Yamashita, K. Inagaki, and S. Mukaeda, *Jpn. J. Appl. Phys.* 26, 34 (1987).
28. L. F. Francis, Y. J. Oh, and D. A. Payne, *J. Mater. Sci.* 25, 5007 (1990).
29. K. S. Mazdiyasn and L. M. Brown, *J. Amer. Ceram. Soc.* 55, 633 (1972).
30. T. R. N. Kutty and R. Balachandran, *Mater. Res. Bull.* 19, 1497 (1984).
31. J. H. Choy, Y. S. Han, and J. T. Kim, *J. Mater. Chem.* 5, 65 (1995).
32. J. M. Xue, D. M. Wan, S. E. Lee, and J. Wang, *J. Amer. Ceram. Soc.* 82, 1687 (1999).
33. B. L. Huang, R. J. Perez, E. J. Lavernia, and M. J. Luton, *Nanostruct. Mater.* 7, 67 (1996).
34. K. Chattopadhyay, X. M. Wang, K. Aoki, and T. Masumoto, *J. Alloys Compds.* 232, 224 (1996).
35. H. J. Fecht, *Nature* 356, 133 (1992).
36. B. Bokhonov, I. Konstantchuk, E. Ivanov, and V. Boldyrev, *J. Alloys Compds.* 187, 207 (1992).
37. B. Bokhonov, I. Konstantchuk, and V. Boldyrev, *J. Non-Cryst. Solids* 153–154, 606 (1993).
38. X. S. Gao, J. M. Xue, T. Yu, Z. X. Shen, and J. Wang, *J. Amer. Ceram. Soc.* 85, 833 (2002).
39. M. L. Trudeau and R. Schulz, *Phys. Rev. Lett.* 64, 99 (1990).
40. H. Chen, Y. He, G. J. Shiflet, and S. J. Poon, *Nature* 367, 541 (1994).
41. J. J. Gilman, *Science* 274, 65 (1996).
42. P. G. McCormick, T. Tsuzuki, J. S. Robinson, and J. Ding, *Adv. Mater.* 13, 1008 (2001).
43. J. Ding, T. Tsuzuki, P. G. McCormick, and R. Street, *J. Alloys Compds.* 234, L1 (1996).
44. G. Garcia-Pacheco, J. G. Cabanas-Moreno, F. Cruz-Gandarilla, H. Yee-Madeira, and M. Umemoto, *Mater. Sci. Forum* 386, 281 (2002).
45. H. Yang, G. Nguyeb, and P. G. McCormick, *Scripta Metall. Mater.* 32, 681 (1995).
46. V. V. Blaskov, D. D. Radev, D. Klissurski, and N. D. Yordanov, *J. Alloys Compds.* 206, 267 (1994).
47. T. Watanabe, T. Isobe, and M. Senna, *J. Solid State Chem.* 122, 74 (1996).
48. J. Wang, J. M. Xue, D. M. Wan, and B. K. Gan, *J. Solid State Chem.* 154, 321 (2000).
49. M. Senna, *Int. J. Inor. Mater.* 3, 509 (2001).
50. V. V. Boldyrev, *Powder Tech.* 122, 247 (2002).
51. J. Ding, T. Tsuzuki, and P. G. McCormick, *J. Amer. Ceram. Soc.* 79, 2956 (1996).
52. J. Ding, T. Tsuzuki, and P. G. McCormick, *Nanostruct. Mater.* 8, 75 (1997).
53. A. C. Dodd and P. G. McCormick, *J. Euro. Ceram. Soc.* 22, 1823 (2002).
54. P. N. Kuznetsov, L. I. Kuznetsova, A. M. Zhyzhaev, G. L. Pashkov, and V. V. Boldyrev, *Appl. Catal. A* 227, 229 (2002).
55. J. Ding, T. Tsuzuki, and P. G. McCormick, *Nanostruct. Mater.* 8, 739 (1997).
56. T. Tsuzuki, E. Pirault, and P. G. McCormick, *Nanostruct. Mater.* 11, 125 (1999).
57. T. Tsuzuki and P. G. McCormick, *J. Amer. Ceram. Soc.* 84, 1453 (2001).
58. U. Kerson, *Appl. Phys. A* 75, 559 (2002).
59. T. Tsuzuki and P. G. McCormick, *Mater. Sci. Forum* 343, 383 (2000).
60. P. G. McCormick and T. Tsuzuki, *Mater. Sci. Forum* 386, 377 (2002).
61. Y. Chen and J. S. Williams, *Mater. Sci. Forum* 235, 985 (1997).
62. P. N. Kutnesov, L. I. Kuznetsova, A. M. Zhizhaev, S. M. Kolesnikova, G. L. Pashkov, and V. V. Boldyrev, *Russ. J. Inor. Chem.* 47, 393 (2002).
63. P. F. Chong, J. M. Xue, and J. Wang, *J. Amer. Ceram. Soc.* 85, 273 (2002).
64. J. Subrt, V. Balek, J. M. Criado, L. A. Perez-Maqueda, and E. Vecernikova, *J. Therm. Anal. Calorim.* 53, 509 (1998).
65. T. Puclin, W. A. Kaczmarek, and B. W. Ninham, *Mater. Chem. Phys.* 40, 73 (1995).
66. K. A. Evans, *Key Eng. Mater.* 122, 489 (1996).
67. A. Tonejc, A. M. Tonejc, D. Bagovic, and C. Kosanovic, *Mater. Sci. Eng. A* 182, 1227 (1994).
68. C. C. Yong and J. Wang, *J. Amer. Ceram. Soc.* 84, 1225 (2001).
69. P. M. Botta, P. G. Beroff, E. F. Ahlietti, H. R. Bertorello, and J. M. P. Lopez, *J. Mater. Sci.* 37, 2563 (2002).
70. Y. Chen and J. S. Williams, *J. Mater. Res.* 13, 3499 (1998).
71. N. J. Welham, *J. Alloys Compds.* 274, 303 (1998).
72. N. J. Welham, *J. Alloys Compds.* 270, 228 (1998).
73. P. P. Pradeep and H. R. Subhash, *J. Mater. Sci.* 25, 1169 (1990).
74. J. M. Xue, J. Wang, and D. M. Wan, *J. Amer. Ceram. Soc.* 83, 232 (2000).
75. O. Abe and Y. Suzuki, *Mater. Sci. Forum* 225, 563 (1996).
76. N. J. Welham, *J. Mater. Res.* 13, 1607 (1998).
77. J. G. Baek, T. Isobe, and M. Senna, *Solid State Ionics* 90, 269 (1996).
78. D. Durovic, E. Kostic, S. J. Kiss, and S. Zec, *J. Alloys Compds.* 279, L1 (1998).
79. V. V. Zyryanov, *Inor. Mater.* 35, 935 (1999).
80. K. Hamada and M. Senna, *J. Mater. Sci.* 31, 1725 (1996).
81. J. M. Xue, D. M. Wan, and J. Wang, *Solid State Ionics* 151, 403 (2002).
82. S. L. Swartz, T. R. Shrout, W. A. Schulze, and L. E. Cross, *J. Amer. Ceram. Soc.* 67, 311 (1984).
83. S. L. Swartz and T. R. Shrout, *Mater. Res. Bull.* 17, 1245 (1982).
84. T. R. Shrout and A. Halliyal, *Amer. Ceram. Soc. Bull.* 66, 704 (1987).
85. J. Wang, J. M. Xue, D. M. Wan, and W. B. Ng, *Solid State Ionics* 124, 271 (1999).
86. H. P. Klug and L. E. Alexander, “X-ray Diffraction Procedures for Polycrystalline and Amorphous Materials,” pp. 491–538. Wiley, New York, 1954.
87. A. N. Dremin and O. N. Breusov, *Russ. Chem. Rev.* 37, 392 (1968).
88. N. N. Thadhani, *J. Appl. Phys.* 76, 2129 (1994).
89. D. M. Wan, J. M. Xue, and J. Wang, *J. Amer. Ceram. Soc.* 83, 53 (2000).
90. J. Wang, D. M. Wan, J. M. Xue, and W. B. Ng, *J. Amer. Ceram. Soc.* 82, 477 (1999).
91. Y. Noguchi, I. Miwa, Y. Goshima, and M. Miyayama, *Jpn. J. Appl. Phys.* 39, L1259 (2000).
92. J. G. Lisoni, P. Millan, E. Vila, J. L. M. de Vidales, T. Hoffmann, and A. Castro, *Chem. Mater.* 13, 2084 (2001).
93. S. H. Ng, J. M. Xue, and J. Wang, *Mater. Chem. Phys.* 75, 131 (2002).
94. M. H. Sim, J. M. Xue, and J. Wang, submitted for publication.
95. Q. W. Zhang, T. Nakagawa, and F. Saito, *J. Alloys Compds.* 308, 121 (2000).
96. Q. W. Zhang and T. Saito, *J. Alloys Compds.* 297, 99 (2000).

97. R. Uribe, C. Baudi, L. Mazerolles, and D. Michel, *J. Mater. Sci.* 36, 5105 (2001).
98. L. B. Kong, J. Ma, and H. Huang, *J. Alloys Compds.* 336, 315 (2002).
99. A. Castro, P. Millan, L. Pardo, and B. Jimenez, *J. Mater. Chem.* 9, 1313 (1999).
100. Q. W. Zhang, and F. Saito, *J. Mater. Sci.* 36, 2287 (2001).
101. W. T. Jeong and K. S. Lee, *J. Power Sources* 104, 195 (2002).
102. Y. Okamoto, T. Isobe, and M. Senna, *J. Non-Cryst. Solids* 180, 171 (1995).
103. N. V. Kosova, E. T. Devyatkina, and S. G. Kozlova, *J. Power Sources* 97, 406 (2001).
104. K. J. D. Mackenzie, J. Temuujin, T. Jadambaa, M. E. Smith, and P. Angerer, *J. Mater. Sci.* 35, 5529 (2000).
105. G. M. Mi, Y. Murakami, D. Shindo, and F. Saito, *Powder Tech.* 105, 162 (1999).
106. T. Hungria, J. G. Lisoni, and A. Castro, *Chem. Mater.* 14, 1747 (2002).
107. Q. W. Zhang, J. F. Lu, and F. Saito, *Powder Tech.* 122, 145 (2002).
108. L. Pardo, A. Castro, P. Millan, C. Alemany, R. Jimenez, and B. Jimenez, *Acta Mater.* 48, 2421 (2000).
109. J. Ricote, L. Pardo, A. Castro, and P. Millan, *J. Solid State Chem.* 160, 54 (2001).
110. A. Castro and D. Palem, *J. Mater. Chem.* 12, 2774 (2002).
111. J. F. Liao and M. Senna, *Mater. Res. Bull.* 30, 385 (1995).
112. J. Temuujin, K. Okada, and K. J. D. MacKenzie, *J. Euro. Ceram. Soc.* 18, 831 (1998).
113. J. Temuujin, K. Okada, and K. J. D. MacKenzie, *J. Solid State Chem.* 138, 169 (1998).
114. F. Saito, G. M. Mi, and M. Hanada, *Solid State Ionics* 101, 37 (1997).
115. I. Lapidés, S. Yariv, N. Lahav, and I. Brodsky, *Colloid Polymer Sci.* 276, 601 (1998).
116. J. Ding, T. Tsuzuki, and P. G. McCormick, *Nanostruct. Mater.* 8, 739 (1997).
117. M. Zdujic, C. Jovalekic, L. Karanovic, M. Mitric, D. Poleti, and D. Skala, *Mater. Sci. Eng. A* 245, 109 (1998).
118. J. M. Xue, Z. H. Zhou, and J. Wang, *J. Amer. Ceram. Soc.* 85, 807 (2002).
119. C. N. Chinnasamy, A. Narayanasamy, N. Ponpandian, K. Chattopadhyay, H. Guerault, and J. M. Greneche, *J. Phys. Condens. Mater.* 12, 7795 (2000).
120. J. S. Jiang, X. L. Yang, L. Gao, J. K. Guo, and J. Z. Jiang, *Nanostruct. Mater.* 12, 143 (1999).
121. C. Jovalekic, M. Zdujic, A. Radakovic, and M. Mitric, *Mater. Lett.* 24, 365 (1995).
122. D. J. Fatemi, V. G. Harris, V. M. Browning, and J. P. Kirkland, *J. Appl. Phys.* 83, 6867 (1998).
123. J. S. Jiang, L. Gao, J. K. Guo, and X. L. Yang, *J. Inor. Mater.* 13, 415 (1998).
124. D. Arcos, N. Rangavittal, M. Vazquez, and M. Vallet-Regi, *Mater. Sci. Forum* 269, 87 (1998).
125. O. Abe and M. Narita, *Solid State Ionics* 101, 103 (1997).
126. J. Ding, T. Tsuzuki, and P. G. McCormick, *J. Magn. Magn. Mater.* 177, 931 (1998).
127. J. Ding, X. Y. Liu, J. Wang, and S. Yu, *Mater. Lett.* 44, 19 (2000).
128. M. Zdujic, C. Jovalekic, L. Karanovic, and M. Mitric, *Mater. Sci. Eng. A* 262, 204 (1999).
129. S. J. Campbell, W. A. Kaczmarek, and G. M. Wang, *Nanostruct. Mater.* 6, 735 (1995).
130. M. Hofmann, S. J. Campbell, and W. A. Kaczmarek, *Mater. Sci. Forum* 228, 607 (1996).
131. I. Mitov, Cherkezova, Z. Zheleva, and V. Mitrov, *Physica Status Solidi A* 161, 475 (1997).
132. M. Muroi, R. Street, P. G. McCormick, and J. Amighian, *Phys. Rev. B* 63, 184414 (2001).
133. H. H. Hamdeh, J. C. Ho, S. A. Oliver, R. J. Willey, G. Oliveri, and G. Busca, *J. Appl. Phys.* 81, 1851 (1997).
134. M. H. Mahmoud, H. H. Hamdeh, A. I. Abdel-Mageed, A. M. Abdallah, and M. K. Fayek, *Physica B* 291, 49 (2000).
135. V. Sepelak, A. Buchal, K. Tkacova, and K. D. Becker, *Mater. Sci. Forum* 278–281, 862 (1998).
136. V. Raul, "Magnetic Ceramics." Cambridge Univ. Press, Cambridge, UK, 1994.
137. B. Yao, S. E. Liu, L. Liu, L. Si, W. H. Su, and Y. Li, *J. Appl. Phys.* 90, 1650 (2001).
138. Y. HiBi and Y. Enomoto, *J. Mater. Sci. Lett.* 16, 316 (1997).
139. S. Horiuchi, J. Y. Huang, L. L. He, J. F. Mao, and T. Taniguchi, *Philos. Mag.* 78, 1065 (1998).
140. K. Kudaka, K. Iizumi, and T. Sasaki, *J. Ceram. Soc. Jpn.* 107, 1019 (1999).
141. A. A. Popovich, *Steel Transl.* 23, 56 (1993).
142. D. D. Radev and D. Klisurski, *J. Alloys Compds.* 206, 39 (1994).
143. F. J. Gotor, M. D. Alcalá, C. Real, and J. M. Criado, *J. Mater. Res.* 17, 1655 (2002).
144. L. L. Shaw, Z. G. Yang, and R. M. Ren, *J. Amer. Ceram. Soc.* 81, 760 (1998).
145. J. L. Li, K. Hu, and Y. Zhong, *J. Mater. Sci. Tech.* 17, S101 (2001).
146. H. J. Kim, H. J. Choi, and J. G. Lee, *J. Amer. Ceram. Soc.* 85, 1022 (2002).
147. G. L. Tan and X. J. Wu, *Powder Metall.* 41, 300 (1998).
148. N. J. Welham, T. Kerr, and P. E. Willis, *J. Amer. Ceram. Soc.* 82, 2332 (1999).
149. G. V. Golubkova, E. Y. Belyaev, and O. I. Lomovsky, *J. Alloys Compds.* 270, 224 (1998).
150. J. H. Shim, J. S. Byun, and Y. W. Cho, *Scripta Mater.* 47, 493 (2002).
151. D. I. Kochubey, E. B. Burgina, R. Roy, and D. K. Agrawal, *J. Mater. Synth. Process.* 8, 279 (2000).
152. P. Balaz, L. Takacs, T. Ohtani, D. E. Mack, E. Boldizarova, V. Soika, and M. Achimovicova, *J. Alloys Compds.* 337, 76 (2002).
153. K. Kudaka, K. Iizumi, T. Sasaki, and H. Izumi, *J. Amer. Ceram. Soc.* 83, 2887 (2000).
154. L. Takacs and S. K. Mandal, *Mater. Sci. Eng. A* 304, 429 (2001).
155. E. Klose and R. Blachnik, *Thermochim. Acta* 375, 147 (2001).
156. T. Tsuzuki, J. Ding, and P. G. McCormick, *Physica B* 239, 378 (1997).
157. T. Tsuzuki and P. G. McCormick, *Appl. Phys. A* 65, 607 (1997).
158. B. K. Yen, *J. Alloys Compds.* 268, 266 (1998).
159. J. M. Xue, D. M. Wan, S. E. Lee, and J. Wang, *J. Amer. Ceram. Soc.* 82, 1641 (1999).
160. J. M. Xue and J. Wang, *J. Amer. Ceram. Soc.* 84, 2691 (2001).
161. X. S. Gao, J. Lim, J. M. Xue, J. S. Wang, and J. Wang, *J. Phys. Condens. Mater.* 14, 8639 (2002).





# Nanocrystalline Diamond

Narendra B. Dahotre

*The University of Tennessee, Knoxville, Tennessee, USA*

Padmakar D. Kichambare

*The University of Kentucky, Lexington, Kentucky, USA*

## CONTENTS

1. Introduction
  2. Methods of Preparation
  3. Nucleation and Growth Kinetics
  4. Spectroscopic Characterization
  5. Physical Properties
  6. Applications
  7. Summary
- Glossary  
References

## 1. INTRODUCTION

Polycrystalline diamond (PCD) film has excellent mechanical and tribological properties such as extreme hardness, chemical inertness, and high electric resistance [1–3]. Hence there is considerable interest in the synthesis of diamond film by various chemical vapor deposition techniques for wide range of applications from hard coating to electron emitting surfaces for flat panel display devices. However, the surface of these films is often very rough due to the polycrystalline nature with crystallite sizes of the order of micrometers. Such a rough surface causes excessive light scattering, reducing the optical transparency, causing high friction and wear losses on mating surface, and thereby limiting its use for various applications. Hence attempts were made to develop effective chemical etching and mechanical polishing techniques to get smooth diamond films. Because of chemical inertness and extreme hardness of diamond films, these techniques are not efficient and cost effective. Since one can change neither the microstructure nor the composition of diamond, the best way to get these desired properties will be to control the microstructure of diamond films [4].

Recently the nanocrystalline diamond (NCD) films have been recognized as an important class of structure in the family of diamond materials [4, 5]. It has been investigated that the microstructure of diamond films could be controlled so that crystallite size ranges from micrometer to nanometer. The size can be controlled continuously over this range by changing the gas phase chemistry of the plasma enhanced chemical vapor deposition technique. The enhancement in mechanical, electrical, and optical properties of NCD films over the PCD film has been achieved. This is due to the reduction in crystallite size of diamond particles. The decrease in crystallite size increases vastly the number of grain boundaries and the entire film becomes electrically conducting. Second, the reduction in crystallite size increases the smoothness of the NCD films. Such ultra-smooth films not only provide an opportunity for tribological applications but also their wide bandgap makes them suitable to act as ideal transparent film for optical components. The lower friction coefficient and higher hardness makes NCD a better material for coating mechanical tools. Thus controlling the microstructure of diamond films could bring many remarkable properties for various industrial applications [4].

There are a few articles related to the preparation of NCD films and several reporting the unique properties of NCD. A number of different deposition techniques and conditions have been used to get smooth films that are summarized below.

Gruen and co-workers reported the nucleation and growth of NCD film on silicon from hydrogen-poor argon plasma using fullerene as growth precursors [6, 7]. Deposition of NCD film was performed by introducing  $C_{60}$  into an argon microwave discharge in contact with a silicon wafer at 750 °C. The growth of NCD film was carried out on the substrates that were previously mechanically scratched with 0.1  $\mu\text{m}$  diamond powder. The deposition of NCD films was carried out with total argon pressure of 98 Torr,  $C_{60}$  partial pressure of  $10^{-2}$  Torr, flow rate of 100 sccm, and

microwave power of 800 W. It is difficult to get stable argon plasma in absence of  $\sim 1\%$  added hydrogen. The presence of 1 to 3% hydrogen in the carbon containing argon plasma does not appreciably affect the properties of the diamond films. The phase pure diamond films have been grown from  $C_{60}/Ar$  microwave plasmas and these films have nanocrystalline microstructure.

Zhou and co-workers prepared NCD films in an  $Ar-CH_4$  microwave discharge without addition of molecular hydrogen [8]. *N*-type single crystal silicon wafers with (100) orientation were used as the substrate, and mechanical polishing with fine diamond powder ( $0.1 \mu m$ ) was employed to enhance the nucleation density. The NCD films consist of a pure NCD phase with grain sizes ranging from 3 to 20 nm. The films have very smooth surfaces, which do not depend on the thickness of the film at least in the range of 1–5  $\mu m$ .

Erz et al. grew 800 nm thick NCD films with up to 10%  $CH_4$  in  $H_2$  [9]. Characterization was done with X-ray diffraction (XRD), Raman, and visible infrared spectroscopy. Incorporated diamondlike carbon (DLC) degrades the transmissivity, which in some samples reaches 93%. Meanwhile Konov et al. and Nistor et al. deposited 0.2–1  $\mu m$  thick films from  $CH_4/H_2/Ar$  mixtures that were characterized with XRD, high-resolution transmission electron microscopy (HRTEM), and Raman spectroscopy [10–13]. The percentage of Ar in the mixtures was always kept at 50%, while the  $CH_4/(CH_4 + H_2)$  ratio was varied. Grain sizes were found to be in the range 30–50 nm. TEM did not reveal amorphous carbon in significant quantities, but disordered  $sp^3$  and  $sp^2$  bonded amorphous carbon was detected, presumably located at grain boundaries. The diamond crystallites are highly defected with many twins and other planar defects.

Gu and Jiang prepared NCD films by continuous  $H^+$  ion bombardment of different energies induced by applying a negative substrate bias voltage in microwave plasma assisted chemical vapor deposition (CVD) [14]. The growth of NCD films was carried out on mirror polished *n*-type Si (001) wafers with a diameter of 50 mm and thickness of 300  $\mu m$ . They used a three-step process. In the first step, the Si wafer was etched *in-situ* in hydrogen plasma for 40 min at 860 °C. The second step involves bias pretreatment for the film nucleation at 845 °C in 5% methane in hydrogen plasma at 20 mbar and 840 W power, while the negative bias voltage was kept at  $-150$  V relative to the vacuum chamber, which was electrically grounded. In the last step,  $H^+$  ion bombardment assisted growth of diamond films was performed at different negative dc bias voltages (0–140 V), substrate temperatures (730–900 °C), and total pressures of 15–50 mbar. The nucleation density was about  $10^{10} \text{ cm}^{-2}$  after 17 min.

A series of NCD films was grown with grain size ranging from 4 nm to a few hundreds of nanometers using a microwave plasma enhanced chemical vapor deposition (MPCVD) technique by Chen et al. [5]. The deposition of NCD films was carried out on ultrasonically polished quartz substrates in a 5 kW microwave reactor. A mixture of semiconductor grade  $CH_4$ ,  $H_2$ , and  $O_2$  was used as source gas, wherein the fraction of methane was varied between 4 and 42%, while  $O_2$  was always kept constant at 0.1%. The total flow rate was 200 sccm, the chamber pressure was 22 Torr,

the microwave power was 1 kW, and the substrate temperature was maintained at 590–600 °C. Effects of the substrate pretreatment and the methane fraction in the source gas on the microstructure, surface roughness, and optical transmittance of the NCD films were studied. Specifically, comparison was made between two different sizes, 4 nm and 0.1  $\mu m$ , of the diamond powder used for substrate pretreatment. Interestingly, the films grown on substrates scratched with coarser powder (0.1  $\mu m$ ) are smoother and more transparent than those on substrates scratched with finer powder (4 nm) despite the similarity in the grain size of these two types of films prepared at high methane fractions. It is also observed that the major factor that controls the optical transparency is the surface roughness irrespective of the grain size as long as the  $sp^2$ -bonded carbon in the film is avoided.

Sharda et al. have grown the NCD films by biased enhanced growth in a MPCVD system on mirror polished Si (100) [15, 16]. No diamond powder or any other *ex-situ* treatment was performed prior to the depositions. A mixture of 5%  $CH_4$  in  $H_2$  was used at a pressure of 30 Torr with a microwave power of 1000 W for deposition of NCD films. The whole growth was performed for 1 hour in a single stage while applying a negative dc bias voltage of 260 V to the Si substrates with respect to the chamber that was grounded.

Hong et al. prepared NCD films on Si substrate from  $CH_4$ ,  $H_2$ , and  $O_2$  gas mixture by microwave plasma enhanced CVD and performed real time spectroscopic ellipsometry to understand the growth process of NCD films [17]. This study emphasizes the broad utility of the ellipsometric measurements to obtain accurate substrate surface temperature and characterization of the initial substrate damage that occurs upon seeding, the annealing of the substrate damage that occurs upon heating to the growth temperature, and the structure of the diamond film during the nucleation and bulk film growth regimes.

The effect of methane pressure on the film growth was studied by Fedoseev et al. [18]. The films deposited by Zarrabian et al. from an electron cyclotron resonance (ECR) plasma were found to consist of 4–30 nm crystallites embedded in DLC [19]. Magnetron sputtering of vitreous carbon leads to the nanocrystallites of 55 to 75 nm in size that were embedded in an amorphous carbon matrix. The sputtering was carried in Ar with 0–10% added  $H_2$ . Amaratunga et al. reported mixed phases using films containing 10–200 nm diamond crystallites embedded in a nondiamond carbon matrix [20]. In another report, ultrananocrystalline diamond films with up to 0.2% total nitrogen content were deposited by a MPCVD method using a  $CH_4(1\%)/Ar$  gas mixture and 1–20% nitrogen gas added. An enhancement in electrical conductivity of nitrogen doped NCD by five orders of magnitude was observed.

The surface morphologies of as grown NCD films have been studied by atomic force microscopy (AFM) [21]. Three-dimensional AFM images of the films with different thicknesses of 1 and 5  $\mu m$  illustrate that the NCD films produced from the  $Ar-CH_4$  plasma have very smooth surfaces. The surface roughnesses measured over an area of 5  $\mu m^2$  for these two films are 36.5 and 38.6 nm, respectively, suggesting thereby that the surface roughness of NCD films is largely insensitive to the film thickness, which is in

contrast to the conventional CVD PCD films prepared by an atomic hydrogen-rich microwave plasma. It is observed that the NCD film hardness depends on the methane content used for diamond deposition. The hardness of these films falls in the narrow range from 73 to 85 GPa that is lower by  $\sim 20\%$  than the value reported for the hardest direction (100) in natural diamond stones. A combination of high hardness and low surface roughness of the NCD films suggests the films to be perspective coatings for tribological applications. The transparency of NCD film is strongly dependent not only on the methane fraction but also on the pretreatment of the substrate. Optical transparency over 60% in the spectral range of 0.6–2.0  $\mu\text{m}$  is considered sufficiently high for most of optical applications. The NCD films also exhibit remarkable electron emission behavior. A high current density of  $4 \times 10^{-4}$  amps/cm<sup>2</sup> with turn-on field of  $\sim 1$  V/ $\mu\text{m}$  was reported for NCD films grown from C<sub>60</sub>(80%)–Ar(20%)–H<sub>2</sub> microwave plasmas. Similarly these NCD films were successfully deposited on sharp Si microtip emitters in order to enhance the electron emission properties of bare Si microtips. The Si tip emitter coated with 0.1  $\mu\text{m}$  thick NCD demonstrates a substantial reduction in the threshold field and an increase in the maximum emission current in comparison to the uncoated Si tip. The NCD films produced from C<sub>60</sub>–Ar plasma have several interesting electrochemical properties. These films have a wide working potential window, a low voltametric background current, and a high degree of electrochemical activity for several inorganic redox systems.

## 2. METHODS OF PREPARATION

In the conventional diamond films grown by CVD, the gas mixture of hydrocarbon–hydrogen is used. Typically NCD deposition requires a gas mixture of 1% CH<sub>4</sub> in 99% H<sub>2</sub>. It has been thought that atomic hydrogen is an absolutely essential ingredient of vapor from which the diamond films are grown. Atomic hydrogen is also generated by thermal decomposition or by collision processes in the plasma. There are various methods of preparation of NCD films among which plasma CVD and magnetoactive CVD are worth mentioning and most attractive. Various hydrocarbon precursors are available for the CVD processes of diamond films, among which the precursor having methyl group is favored for the preparation of diamond films. Methane (CH<sub>4</sub>), which dissociates into CH<sub>3</sub> in plasma and was preferred over other precursors such as CH<sub>4</sub> with hydrogen, produced diamond easily compared to other hydrocarbon precursors.

### 2.1. From Fullerene-Argon Microwave Plasma

The production in large quantities of the fullerenes [22] provides an opportunity to deposit diamond films from noble gas plasmas with very low hydrogen contents using C<sub>60</sub> as a precursor. The fragmentation mechanism of C<sub>60</sub> and kinetics of the process have been studied in detail [23] and it is observed that fragmentation of C<sub>60</sub> by photon, collisions with surfaces, or gas-phase collisions occurs primarily by the elimination of carbon dimer, C<sub>2</sub>. This is a highly reactive chemical species and is one of the carbon species resulting from

the sublimation of graphite. It is produced in microwave plasmas under nonequilibrium conditions from hydrocarbon molecules, resulting in supersaturated carbon vapor. With CH<sub>4</sub> as the precursor, the C<sub>2</sub> stationary concentration in argon microwave plasmas is higher than that of saturated carbon vapor by many orders of magnitude at the neutral Ar gas temperature 1600 K. At this temperature, CH<sub>4</sub> thermally decomposes to C<sub>2</sub>H<sub>2</sub>. The fraction of C<sub>2</sub>H<sub>2</sub> is then converted into C<sub>2</sub> during plasma processes by nonequilibrium processes. The dimer, C<sub>2</sub>, has a gas kinetic pseudo-first-order rate reaction with both CH<sub>4</sub> and C<sub>2</sub>H<sub>2</sub> and leads to likely formation of methylacetylene [24] and cyclobutene, respectively, as product. This high probability of formation of these products of reaction and successively larger hydrocarbon molecules is regarded as a process of homogeneous nucleation. As a result, there is a deposition of graphitic carbon. On the other hand, if the goal of the experiment is to deposit the diamond, that could be achieved by suppressing a gas-phase reaction of the sort described for heterogeneous nucleation on the diamond nuclei initially placed on the substrate *ex-situ*. Hence, there is a low probability of reactions by C<sub>2</sub> to form higher carbon clusters. Under these conditions, diamond could nucleate and grow using carbon dimer.

The growth of NCD films consisted of introducing C<sub>60</sub> into an argon microwave plasma at 750 °C on Si substrates [6, 7]. The Si substrates were mechanically treated with 0.1  $\mu\text{m}$  diamond powder. The deposition was performed for several hours with total argon pressure of 98 Torr, C<sub>60</sub> partial pressure of 10<sup>-3</sup> Torr, flow rate of 100 sccm, and microwave power of 800 W. It is difficult to operate and get the stable microwave plasma in the absence of 1% added hydrogen. The presence of 1–3% hydrogen in the carbon containing film does not appreciably affect the properties of diamond films, which are different from conventionally grown film with 1% CH<sub>4</sub> and 99% H<sub>2</sub>.

### 2.2. MPCVD

NCD films have been deposited on the quartz substrates by the MPCVD method [5]. A schematic diagram of the system employed during the work is shown in Figure 1 and consists

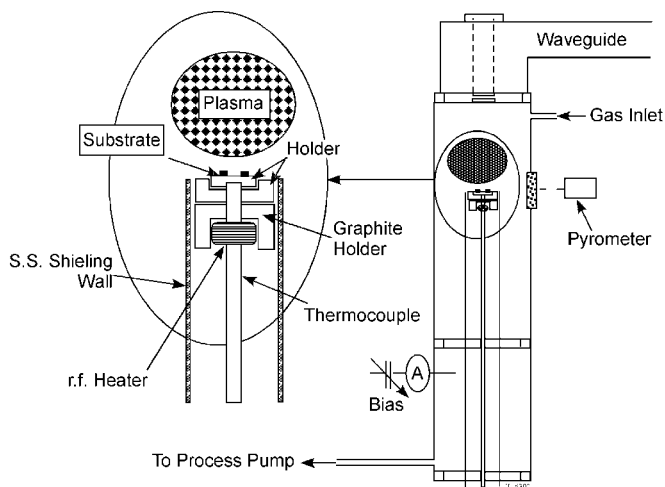


**Figure 1.** Schematic diagram of microwave plasma enhanced chemical vapor deposition chamber.

of a stainless steel four-way deposition vacuum chamber, a graphite holder that is attached to an induction heater, 5 kW microwave power supply, various gas lines connected to a vacuum chamber, and a vacuum pumping system. A mixture of semiconductor grade  $\text{CH}_4$ ,  $\text{H}_2$ , and  $\text{O}_2$  was used as a source gas, wherein the fraction of  $\text{CH}_4$  was varied between 4% and 42% and  $\text{O}_2$  was always kept constant at 0.1%. The total flow rate was 200 sccm, the chamber pressure was 22 Torr, the microwave power was 1 kW, and the substrate temperature was maintained at 600 °C during deposition. An independent radio-frequency (rf) heater was used to control the substrate temperature. During deposition, a single-color optical pyrometer was used to record the temperature from the front surface of the substrate.

The smooth films were deposited on the pretreated quartz substrates. The substrate pretreatment could be carried by first chemically cleaning the quartz plates with acetone and doubly distilled water and then these plates could be used for the ultrasonic polishing with diamond powder having grain sizes 4 nm and 0.1  $\mu\text{m}$ . The ultrasonic polishing of the quartz substrates is simple. This involves the preparation of suspension of diamond powder in acetone, placing the substrates in this suspension, and subjecting the beaker to ultrasonic vibration for at least 8 h.

### 2.3. Biased Enhanced MPCVD

The growth of diamond is considered to be taking place via surface processes of addition and subtraction of radicals from the gas phase [25, 26]. During the growth of diamond, ions enhance lattice disorders and also promote graphitic content in the deposit. On the other hand, in the growth of carbon films by hyperthermal species, ions with energy in the range 40–200 eV produce a high concentration of  $sp^3$  carbon in the film [27–30]. In this case, the growth is controlled by a subplantation mechanism, which relies on the shallow subsurface implantation of the carbon ions. Both of these routes of growth of carbon films are totally different. In the bias enhanced route the NCD films are deposited in a CVD diamond environment while continuously biasing the substrate to take advantage of both the processes in the growth. The CVD diamond conditions result in high etching rates of the nondiamond carbon from the surface processes while continuous biasing takes advantage of subsurface phenomena. This route is simply an extension of bias enhanced nucleation of CVD diamond and results in the growth of hard and smooth NCD films.

The NCD films could be grown in a MPCVD reactor on mirror polished silicon substrate placed on an Mo holder [15]. No diamond powder or any other *ex-situ* treatment is required prior to the deposition. The substrate is then immersed in methane and hydrogen plasma. A mixture of 5%  $\text{CH}_4$  in  $\text{H}_2$  should be used at a pressure of 30 Torr, with a microwave power of 1 kW for all the films. A negative dc bias voltage of 260 V should be applied to the substrate with respect to the chamber that is grounded. The whole growth of NCD film could be achieved in a single stage and requires a 1 hour duration without breaking the bias to the substrate. While holding the bias voltage constant throughout the deposition, bias current could be varied with time in the same fashion as commonly observed in biased

enhanced nucleation in the growth of CVD diamond; the current increases after some incubation period followed by saturation at longer deposition time. It is observed that there is an increase in the current attributed to enhancement in electron emission from the surface as highly emissive diamond is deposited on silicon.

### 2.4. Ar- $\text{CH}_4$ MPCVD

Atomic hydrogen plays a crucial role in the growth of PCD films by CVD using hydrocarbon as a carbon source [31, 32]. It is well known that atomic hydrogen from a hydrogen-rich reactant gas can terminate the carbon dangling bonds with a tetrahedral  $sp^3$  configuration and etch out nondiamond materials at the growth surface of diamond. The reduction in concentration of atomic hydrogen causes the growth of nondiamond phase or no diamond film deposition. Hence, argon has been used in place of hydrogen. A mixture of Ar (99 sccm) and  $\text{CH}_4$  (1 sccm) was used as the reactant gas for growth of NCD film. *N*-type single crystal silicon (100) wafers were used as substrates. These substrates were polished mechanically with 0.1  $\mu\text{m}$  diamond powder. During the entire film growth, the substrate temperature and input microwave power were 800 °C and 800 W, respectively. The films prepared in this work were 1 or 5  $\mu\text{m}$  thick. As grown films prepared from the Ar- $\text{CH}_4$  plasma, they consist of phase-pure crystalline diamond grains ranging from 3 to 20 nm in size independent of the NCD film thickness [21].

### 2.5. Hot Filament CVD

It has been shown that the addition of Ar into the  $\text{CH}_4$ - $\text{H}_2$  or  $\text{C}_{60}$  MPCVD can provide a route for controlling the microstructure of the diamond film, leading to thick and smooth NCD films at an Ar concentration of 90% [33, 34]. Due to the very high concentration of  $\text{C}_2$  species at higher percentage of Ar, it has been concluded that  $\text{C}_2$  dimer may be the growth precursor for NCD films in the MPCVD system. While most of studies on growth of NCD are focused on using MPCVD, there are only few reports on the use of the hot-filament CVD (HFCVD) system for the growth of NCD films. An interesting question is whether the chemistry observed in the MPCVD system for the growth of NCD films can be extended to HFCVD as the mechanism for gas activation is different in both these methods. Similarly the fraction of argon ions and electron density is significantly lower in the HFCVD system than the MPCVD system.

Lin et al. employed a conventional HFCVD system using curved tantalum wire arrays for the growth of NCD films [35]. A  $\text{CH}_4/\text{H}_2$  gas feed ratio that can yield the growth of high quality, well-faceted diamond film was used. Ar was then introduced in increasing concentration to the system in order to investigate the changes in microcrystallinity of the film as a function of Ar: $\text{H}_2$  ratio. The  $\text{H}_2$  and  $\text{CH}_4$  flow rates were fixed at 0.05 and 0.0013 l/min, respectively. The Ar/ $\text{H}_2$  ratio was adjusted by increasing the Ar flow rate from 0 to 0.43 l/min. In order to get a higher Ar: $\text{H}_2$  ratio, the  $\text{H}_2$  flow rate was reduced. The total pressure was kept at 60 Torr. The substrate temperature was held at 950 °C for Ar concentration below 92%. When higher Ar concentration was used, the substrate temperature was reduced to 870 °C to

avoid the deposition of graphite. The Si (100) wafer used in this work was supersonically scratched with diamond powder prior to the deposition of diamond films. The range of Ar concentration in the Ar-CH<sub>4</sub>-H<sub>2</sub> mixture that permits well-faceted diamond growth is up to 90%. At a concentration of 95.5%, there is a marked transition into NCD phase without graphitic phases. Such compositional mapping is one of the effective routes to prepare thick and smooth NCD films.

## 2.6. CVD of Camphor

It is well established that the methyl radical along with atomic hydrogen is key to growing the diamond films. A wide variety of precursor materials are available for the CVD processes of diamond films. Although any carbon containing precursor material may be used in the CVD technique, the preparation of diamond film is favored by the presence of a methyl group [36, 37]. Hence, methane, which dissociates into CH<sub>3</sub> in plasma, has been preferred over other precursor materials because CH<sub>4</sub> with hydrogen produced the diamond easily. Similarly the organic compounds, which can easily generate methyl radicals, may also be suitable for the growth of diamond films. Camphor (C<sub>10</sub>H<sub>16</sub>O) as the precursor material has been mentioned for the growth of NCD films. In camphor, there are three carbon atoms attached to three methyl groups while the remaining seven carbon atoms are associated with a ring structure.

NCD films were deposited by CVD of camphor and hydrogen (~75%) [38]. Camphor is a natural source which sublimates at room temperature and is soluble in alcohol, ether, acetone, and benzene. Figure 2 [38] depicts the schematic diagram of the apparatus used for CVD of camphor. The camphor vapor was passed through a heated stainless steel tube into a cylindrical deposition vacuum chamber. The heating tape was used over the stainless steel tube in order to prevent condensation of camphor vapor

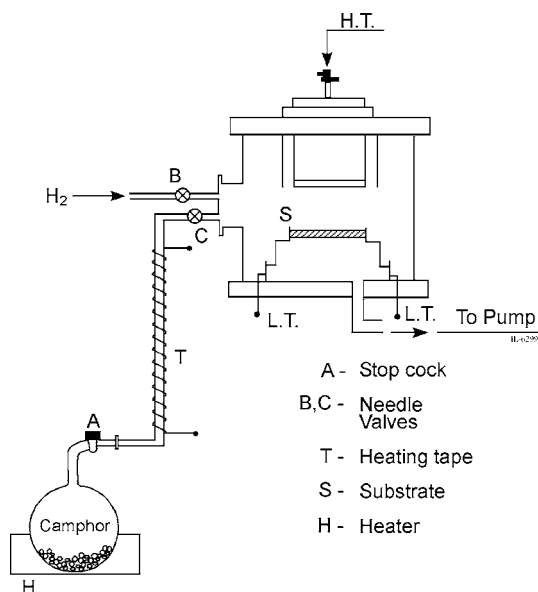


**Figure 2.** Schematic diagram of the deposition system. Reprinted with permission from [38], K. Chakrabarti et al., *Diamond Relat. Mater.* 7, 845 (1998). © 1998, Elsevier Science.

before entering the deposition chamber. NCD films were deposited at 1.5 kV with 75 mA current at a chamber pressure of ~0.3 mbar on glass, quartz, and silicon substrates. The substrate temperature was varied within 573–713 K depending on the substrate material. The value of  $T_s$  for glass substrate was within 573–623 K, while for quartz it was within 573–713 K. The substrates could be heated to the desired temperature inside the substrate holder with proper insulation.

## 3. NUCLEATION AND GROWTH KINETICS

The preparation of pure and compact diamond thin films by MPCVD from CH<sub>4</sub>, H<sub>2</sub>, and O<sub>2</sub> gas mixture on non-diamond surfaces has a great potential for various commercial applications [39–41]. Such thin films can endow solid surfaces with one or more of the superlative properties of diamond, including resistance to wear and chemical attack, optical as well as infrared transparency, and high thermal conductivity. The limitations in achieving these prospective properties include: (a) the high substrate temperatures required for diamond nucleation with reasonable growth rates, (b) the surface pretreatments like abrasion with diamond powder for high nucleation density, and (c) the defective nature of the resulting nano- and/or PCD film. Diamond film deposited on nondiamond substrates exhibits a variety of difficulties related to their nano/polycrystalline structure, mostly in the appearance of a second phase of  $sp^2$  bonded C atoms. The transmission electron microscopy and Raman spectroscopy studies performed on the underside of a 20  $\mu\text{m}$  diamond film removed from its substrates revealed that diamond clusters are surrounded by  $sp^2$ -bonded C phase in the form of graphite crystals [42], while the growth side of these films exhibited the pure diamond phase. The formation of a defective region near the substrate interface has been attributed to heteroepitaxy [42] or to impurities that arise from the interaction of the plasma with the substrate during the nucleation stage [43]. Previous studies have revealed a 0.7 to 0.8 eV optical gap for the graphitic component of thin (0.2  $\mu\text{m}$ ) diamond films [44] consistent with the existence of  $sp^2$  bonded C atoms in clustered units sufficiently small so that a gap has developed [45]. A dominant graphite phase has also been detected in the grain boundary regions for 30–40  $\mu\text{m}$  thick diamond films prepared with excess CH<sub>4</sub> in the CH<sub>4</sub>/H<sub>2</sub> mixture. On the other hand, in the films prepared with an optimum CH<sub>4</sub>/H<sub>2</sub> mixture, this phase is no longer dominant and contains dilute  $sp^2$  C atoms within the diamond grains [46].

These pioneering studies of diamond thin films demonstrate that the atom fraction, physical location (intragrain or grain boundary), and nature (clustered versus dilute) of the dominant  $sp^2$  bonded C are sensitive parameters for the evolutionary stage of the film and the preparation conditions. The characteristics of the  $sp^2$  C phase and the void network are of greatest interest because such bonding and structural defects lead to degradation in the mechanical, optical, and electrical properties of diamond thin films deposited on non-diamond substrates. In view of this, real time monitoring of the deposition process becomes increasingly important in



order to quantify these characteristics as a function of film thickness and to exert greater control over the growth process for improved near-interface and bulk properties. Optical probes are beneficial in this role as they are passive and require no instrumentation internal to the reactor [47–50] because of the adverse environment of diamond deposition, highly reactive gases, high gas pressures, and high temperatures.

### 3.1. Real Time Spectroscopic Ellipsometry

Spectroscopic ellipsometry (SE) and optical emission spectroscopy (OES) are powerful, real time optical probes for characterizing film growth. Ellipsometry has an advantage over other optical techniques for characterizing the evolution of diamond thin films because it can provide the volume fractions of diamond,  $sp^2$  C, and void with good sensitivity in the films as thin as 40 Å [51, 52]. Hong et al. have applied real time SE to characterize the preparation of ~2000 Å thick NCD film on Si substrate by MPCVD [53]. Si wafers were seeded and placed on a graphite substrate platform. The platform is rf heated to a temperature that can be controlled independently of microwave power over a relatively wide range. In order to achieve a stable plasma configuration, a pure H<sub>2</sub> plasma was ignited with the substrate platform about 2 cm above the optical plane. The substrate platform was adjusted until optical alignment was achieved. CH<sub>4</sub> and O<sub>2</sub> were introduced, defining time zero in the data collections. The spectroscopic ellipsometer employs a polarizer rotating at 15.6 Hz that modulates the polarization state of an incident, collimated, white light beam generated by an Xe source. A fixed analyzer and a photodiode array based detection system should be used for the analysis of the polarization state change induced by the growing film over a range of photon energies [54, 55]. The resulting spectra consist of ~110 pairs of ellipsometry angles ( $\Psi$ ,  $\Delta$ ) from 1.5 to 4.5 eV and were obtained as an average of 40 rotations in an acquisition time of 2.6 s. In this time, ~1 Å accumulates at the maximum bulk layer deposition rate of 0.4 Å/s. The repetition time for the collection of successive spectra is adjusted to achieve sufficient thickness resolution for the growth rate measurements. The ( $\Psi$ ,  $\Delta$ ) spectra were analyzed by least-squares regression [56].

The nuclei studied in the first 5 Å of mass thickness  $d_m$  are simulated using a simplified single layer model consisting of a composite of diamond and  $sp^2$  carbon with void. The optical properties of this layer are calculated with the Bruggeman effective medium approximation (EMA) using a fixed nuclei composition established after  $d_m \sim 50$  Å. The outcome of the analysis in the first 5 Å is the physical thickness  $d$ , from which  $d_m = f_d d$  can be determined, where  $f_d$  is the diamond volume fraction. The continuous film is simulated as a two layer, roughness/bulk combination, where the surface roughness is modeled with the EMA as a 0.5/0.5 mixture of diamond/void, and the bulk layer is modeled as a composite of diamond,  $sp^2$  C, and void. The output of the analysis includes the bulk and roughness layer thickness,  $d_b$  and  $d_s$ , and the bulk composition, from which  $d_m = f_{ab} d_b + 0.5 d_s$ , where  $f_{ab}$  is the volume fraction of diamond in the bulk. The  $d_m$  versus time in the first 5 Å of the nucleation regime and in the bulk film growth regime

shows a linear fit that yields the deposition rates in terms of mass thickness. The mass thickness deposition rates are then plotted vs  $T^{-1}$  from 390 to 840 °C in Figure 3 [57]. A well-defined activation energy of  $8 \pm 0.5$  kcal/mol has been noted for diamond growth for  $390 \text{ °C} \leq T \leq 800 \text{ °C}$  in the bulk regime. Above 800 °C, a deviation from activated behavior could be observed, characterized by a maximum in the rate near 800 °C followed by a decrease with increasing  $T$ , and is attributed to a reduction in the incorporation probability. It should be noted that the 8 kcal/mol activation energy deduced in the bulk growth regime is close to the values obtained for diamond homoepitaxy on (100) and (111) surfaces [57]. This activation energy is attributed to  $sp^3$  C atom incorporation in specific atomic sites on these surfaces. Figure 3 shows larger scatter for individual depositions in the nucleation regime due to substrate seeding variation. During nucleation, the rates are  $10\text{--}10^2$  times lower than in the bulk regime with an apparent activation energy of  $17 \pm 2$  kcal/mol. The lower rates arise from growth at discrete nucleation centers, in which case only C-containing precursors that arrive within ~100 Å of a center can be incorporated. The higher activation energy is attributed to a decrease in the capture area as the nucleation density and precursor surface diffusion length decrease with decreasing  $T$ .

Figure 3 gives a clear understanding of the limitation of diamond film growth at low temperature. Lee et al. [57] suggested that the apparent activation energy of ~17 kcal/mol in the nucleation regime is a characteristic of the seeding process. Higher activation energies are expected with less effective seeding, and this explains values as high as ~30 kcal/mol [58, 59]. Figure 3 also demonstrates that the nuclei growth rate at  $T = 400$  °C is ~ $10^3$  times lower than the bulk rate at 800 °C. Of this factor of  $10^3$ , one order is attributed to the decrease in the average incorporation

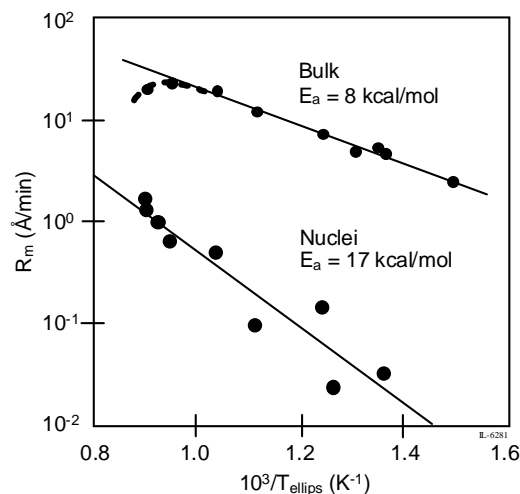


**Figure 3.** Diamond growth rates in terms of mass thickness vs inverse temperature. The lines are the best linear fits for  $T > 800$  °C in the bulk growth regime, and to the full data set in the nucleation regime. The slopes of these lines yield the activation energies as shown. The broken line indicates a reproducible deviation from activated behavior. Reprinted with permission from [17], B. Hong et al., *Diamond Relat. Mater.* 6, 55 (1997). ©1997, Elsevier Science.

probability from 800 to 400 °C, another order is due to the fraction of the substrate area from which initial nuclei can collect impinging flux, and factors of 4 and 2 are due to the reduction in the nucleus capture radius and nucleation density, respectively. Thus considerable gains can be achieved in preparing diamond at reasonable rates on nondiamond substrates at low  $T$  by enhancing the density and area of the nucleation centers and retaining these characteristics as  $T$  is reduced. It is most probable that disordered  $sp^2$  or  $sp^3$  C embedded within the silicon during seeding is converted to NCD nuclei by H exposure in the initial stages of nucleation and that this process becomes more effective as  $T$  increases. Although gains in diamond film can be made at low  $T$  by increasing the precursor flux, a primary limitation is the low capture cross-sectional area of nuclei at low density on the substrate.

### 3.2. Optical Emission Spectroscopy

The diamond films were deposited on pretreated quartz substrates by the MPCVD technique as described in detail elsewhere [5]. In order to obtain information on plasma chemistry, OES was employed to monitor the  $H_2$ - $CH_4$  plasma. A monochromator with a focal length of 500 mm and grating of 1200/mm, which gives a resolution of 0.05 nm and a precision of about  $\pm 0.2$  nm/500 nm, was used for the OES measurements. Figure 4 [5] presents some typical optical emission spectra of the  $H_2$ - $CH_4$  plasma used for the NCD film deposition. The  $H_2$  spectrum consists mainly of emission from atomic H Balmer lines ( $H_\alpha$  and  $H_\beta$  lines at 656.3 and 486.1 nm, respectively) and excited  $H_2$  lines at around 460 and 590 nm. When methane was introduced into the system,  $C_3$  emission lines at around 400 nm,  $CH^+$  emission at 417 nm, CH lines at around 431 nm, and the  $C_2$  Swan bands around 469 and 515 nm appeared in the emission spectrum. Using the  $H_2$  line at 580.6 nm as reference, the relative intensities of emissions from the latter four species as a function of the methane fractions in the source gas are plotted in Figure 5 [5]. All emissions except that of  $C_2$

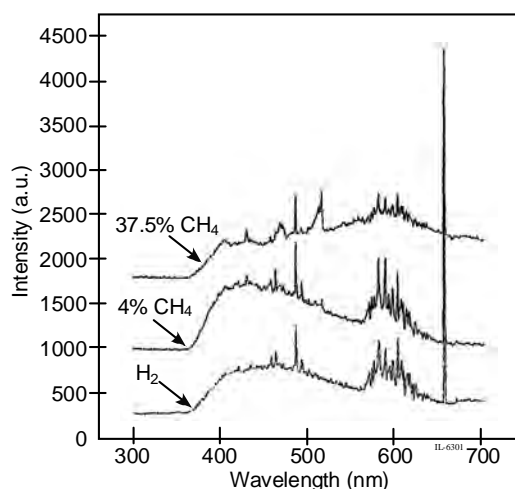


**Figure 4.** Some typical optical emission spectra of the  $H_2/CH_4$  plasma. Reprinted with permission from [5], L. C. Chen et al., *J. Appl. Phys.* 89, 753 (2001). © 2001, American Institute of Physics.

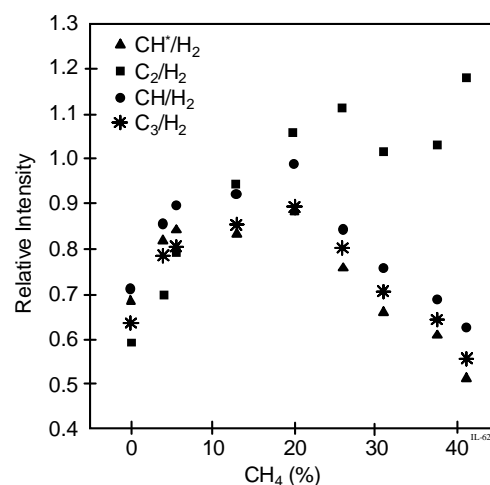


**Figure 5.** The relative intensity of the  $CH^+$  (▲),  $C_2$  (■),  $CH$  (●), and  $C_3$  (\*) emissions with respect to that of  $H_2$  as a function of the methane fraction in the source gas. Reprinted with permission from [5], L. C. Chen et al., *J. Appl. Phys.* 89, 753 (2001). © 2001, American Institute of Physics.

dimer increased with increasing methane content, reached a maximum at around 20%, and decreased at higher methane content. Emission from  $C_2$  dimer, however, showed a continuing increase above 20% methane content. It can be seen from Figure 4 that the 515 nm  $C_2$  emission line was very pronounced at high methane content. Due to the fact that the emission intensity is a function of many factors including Frank–Condon factor, the density of states, various quenching effects, etc., a quantitative description of the observation is very complicated and is beyond the scope of this chapter. The gas-phase analysis by OES or any other single technique is far from complete since it is not possible to detect some important growth species such as  $CH_3$  by this technique. It is observed from these studies that the gas phase experienced substantial change when the methane fraction went from below to above 20%, with which the optical transmittance and surface roughness data [5] also exhibited similar crossover behavior.

Shown in Figure 6 [5] is the intensity ratio of two atomic hydrogen lines at 486.1 nm ( $H_\beta$ ) and 656.3 nm ( $H_\alpha$ ) as a function of the methane fraction in the source gas. It is quite clear from the graph that the intensity ratio of  $H_\beta/H_\alpha$ , which is related to the electronic temperature in the plasma, showed a maximum value at a methane fraction of 20% and declined rapidly with variation in methane content on either side. Once again, the electronic temperature exhibited a methane-fraction dependence similar to that of most emissions (except  $C_2$ ) as shown in Figure 5. From Figures 5 and 6, it is speculated that a change in major growth species might have occurred around a methane fraction of 20%. Most of the conventional PCD films were grown in low methane fraction. The major growth species  $C_2$  has been identified for the growth of NCD films using  $C_{60}$  as precursor under hydrogen-free or hydrogen-deficient environments [60]. For the conditions during this work [5], growth involving  $CH_3$  was expected since all depositions were carried out

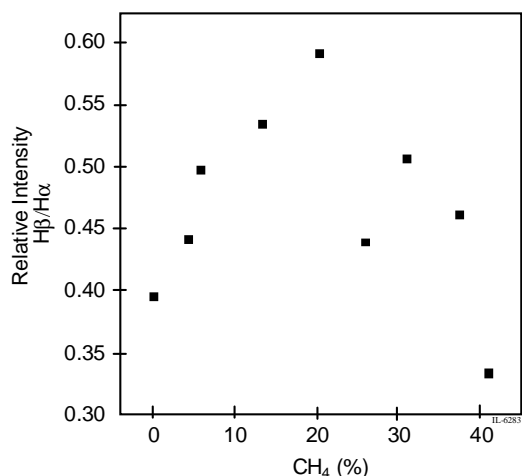


**Figure 6.** The relative intensity of  $H_{\beta}/H_{\alpha}$  as a function of the methane fraction in the source gas. Reprinted with permission from [5], L. C. Chen et al., *J. Appl. Phys.* 89, 753 (2001). © 2001, American Institute of Physics.

in  $H_2$ - $CH_4$  plasma. However, it is clear from OES studies that  $C_2$  dimer becomes the predominant growth species at methane fractions far above 20%.

### 3.3. Vacuum Ultraviolet Absorption Spectroscopy

The deposition of NCD film by using a low-pressure inductively coupled plasma (ICP) was employed by Teii et al. [61]. NCD films were grown at a pressure of 80 mTorr using  $CO/CH_4/H_2$  and  $O_2/CH_4/H_2$  gas mixtures. The densities of C atoms in ground state are measured by vacuum ultraviolet absorption spectroscopy (VUVAS).  $CO$  is employed as one of the simple gases that yield C atoms, through the primary reaction:  $CO + e^- \rightarrow C + O + e^-$ .

The emissive species observed in the  $CO/CH_4/H_2$  plasmas in the wavelength range of 300–800 nm were OH, CH, H,  $C_2$ , and Ar. In addition to these species, pronounced emissions from O were observed in the  $O_2/CH_4/H_2$  plasmas. The normalized emission intensity of OH, CH,  $H_{\alpha}$ ,  $C_2$ , and O [62, 63] and the normalized absorption of C atoms as a function of  $X_{CO}$  and  $X_{O_2}$  for a fixed  $X_{CH_4}$  of 5% are depicted in Figure 7 [61], respectively. It was very difficult to obtain sufficient absorption by C atoms when an emission line at 296.7 nm was initially used in (UVAS). It therefore follows from this that the absolute C atom density was lower than  $1 \times 10^{12} \text{ cm}^{-3}$ , the lower detection limit in this UVAS system [64]. The trend of the C atom density as determined by VUVAS was consistent with that by OES under experimental conditions, indicating thereby that the influence of collisional excitation processes was small. In Figure 7a, the  $H_{\alpha}$  and CH intensity ratios remain constant independent of  $X_{CO}$ , while the C atom absorption and OH and  $C_2$  intensity ratios increase in proportion to  $X_{CO}$ . To ensure that an increase in C and  $C_2$  was not due to an overall increase in the total carbon concentration in the feeding gas, a comparative experiment was performed by varying  $X_{CO}$  with the sum of  $X_{CO} + X_{CH_4}$  kept constant at 5%. This experiment gave similar results except for a slight decrease in the CH

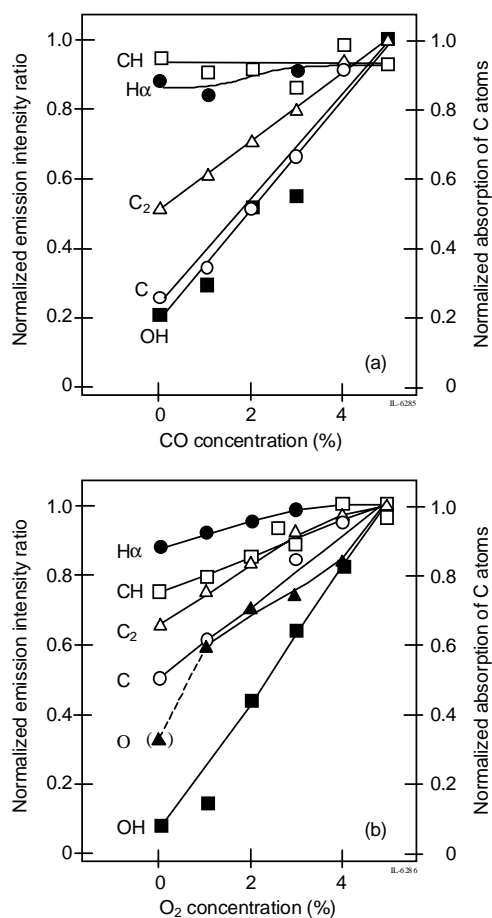


**Figure 7.** Variations of the normalized emission intensity ratios of OH, CH,  $H_{\alpha}$ ,  $C_2$ , O, and the normalized absorption of C atoms (a) as a function of  $X_{CO}$  for a  $X_{CH_4}$  of 5%, and (b) as a function of  $X_{O_2}$  for a  $X_{CH_4}$  of 5%. Reprinted with permission from [61], K. Teii et al., *J. Appl. Phys.* 87, 4572 (2000). © 2000, American Institute of Physics.

intensity ratio probably due to a decrease in parent  $CH_4$ , informing thereby that the major origin of C and  $C_2$  is  $CO$ . In Figure 7b, the intensity ratios of OH, CH, H,  $C_2$ , and O as well as the C atom absorption increase with increasing  $X_{O_2}$ . Emissions from O for  $X_{O_2} = 0\%$ , arising from the impurity from quartz windows, were as low as the noise level. An increase in C atom absorption is ascribed to the result of sequential reactions induced by O atoms.

For the transition from upper state  $j$  to lower state  $i$ , the relationship between the emission line intensities  $I_{ji}$  and excitation temperature  $T_{ex}$  is given in detail elsewhere [65]. The relative excitational population of H atoms in the Balmer series as a function of excitation level for the three gas mixtures is shown in Figure 8 [61]. The emission line of  $H_{\epsilon}$  was not available because of its low signal-to-noise ratio. The distribution equilibrium of excitation levels of the  $H_{\alpha}$  atom Balmer series is not satisfied because the three sets of plots do not produce straight lines, in accordance with the previous study in the same pressure range [66]. The energy distribution is almost equivalent in any gas mixture, suggesting a common excitation process of H atoms. Furthermore, the overall emission intensities are equivalent in any gas mixture, indicating that the H atom density was

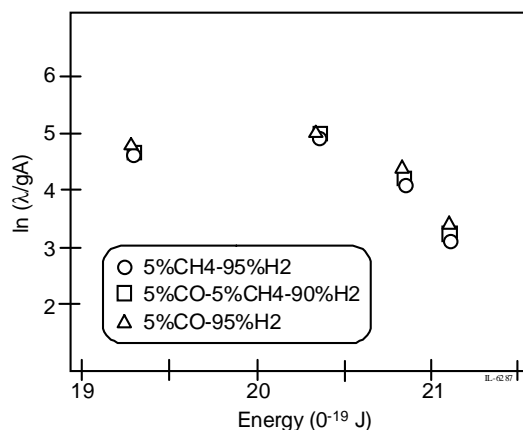


**Figure 8.** Energy distribution of the H atom Balmer series as a function of excitation level for the three sets of data in the 5%CH<sub>4</sub>-95%H<sub>2</sub>, 5%CO-5%CH<sub>4</sub>-90%H<sub>2</sub>, and 5%CO-95%H<sub>2</sub> plasmas. Reprinted with permission from [61], K. Teii et al., *J. Appl. Phys.* 87, 4572 (2000). © 2000, American Institute of Physics.

almost equivalent and the H atoms were produced mainly by dissociation of hydrogen molecules. These similarities for H atoms regardless of the gas mixtures imply that the H atoms were not responsible for the difference in the grown phases. Thus VUVAS analysis suggests that the C atoms resulting mainly from CO by electron impact dissociation increased the precursors to nondiamond phase by promoting gas-phase polymerization, while the OH radicals resulting predominantly by loss reactions of O atoms with H<sub>2</sub> and CH<sub>4</sub> were responsible for the enhancement of diamond growth. An excess amount of O atoms resulting from O<sub>2</sub> interrupt the formation of nuclei at the initial stage of the growth. Besides, the production path of C atoms induced by O atoms is also possible.

#### 4. SPECTROSCOPIC CHARACTERIZATION

NCD films are materials of a great potential use in various fields such as tools, optical windows, microelectromechanical systems (MEMS), etc., due to their remarkable properties. In recent years, attempts have been made to develop NCD films with a smooth surface and special attention has been paid to NCD films with characteristics of a small crystallite size. In order to understand and improve the properties of NCD films, it is desirable to relate the remarkable properties of NCD with their microstructure. The various techniques used for characterization of NCD are discussed next.

##### 4.1. Transmission Electron Microscopy

Transmission electron microscopy has been the most powerful technique for characterizing the microstructure of NCD and is widely used to obtain bonding information. Figure 9 [5] depicts a typical TEM bright-field image of a diamond film deposited on a nanometer-scratched substrate with a methane fraction of 4% [5]. A typical selective-area diffraction pattern (not shown here) of a nanometer-scratched sample prepared with a methane fraction of 41% indicates

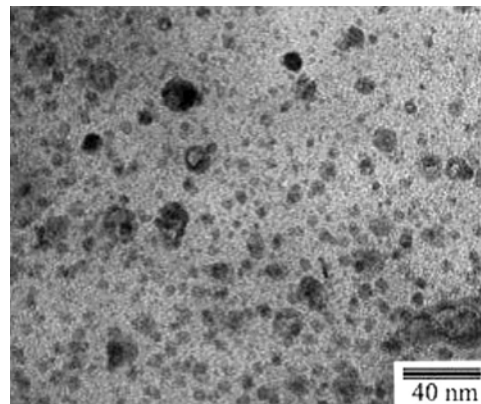


**Figure 9.** Bright-field TEM image of a NCD film grown on nanometer-scratched quartz substrate with a methane fraction of 4%. Reprinted with permission from [5], L. C. Chen et al., *J. Appl. Phys.* 89, 753 (2001). © 2001, American Institute of Physics.

high degree of diamond phase. All the sharp diffraction rings can be indexed to the diamond structure. It is observed that diamond films consist of randomly oriented grains and that the substrate pretreatment has a strong effect on the average grain size of the resulting films. With a methane fraction of 4%, the average grain size of the micrometer-scratched sample was about 200 nm, whereas the corresponding value of the nanometer-scratched sample was only about 4 nm. As the methane fraction was increased from 4% to 41%, the grains of the micrometer-scratched samples became coarser and coarser. In fact, it is noted that the average grain size of the nanometer-scratched sample prepared at a methane fraction of 41% is quite similar to that of its micrometer-scratched counterpart.

High-resolution transmission electron microscopy has been utilized to understand the initial stages of diamond film growth [12, 67–69]. The detailed electron microscopic study [70] of NCD films grown from C<sub>60</sub> fullerene precursors showed that various planar defects such as twinning boundaries and stacking faults were observed in large crystallites found in the films. Similarly, measurements of the diamond crystallite size distribution using diffraction contrast TEM followed a gamma distribution with an average grain size of 15 nm [71]. Since the resolution of the TEM technique is limited by the small objective aperture, HRTEM has a great edge for reliable grain size measurements [72]. In addition, the TEM imaging techniques give additional information that can be used to determine the phase purity of NCD films. The selected-area electron diffraction is a powerful method to examine the phase composition of these films as short-range order in either sp<sup>2</sup>-bonded glassy carbon or predominantly sp<sup>3</sup>-bonded diamondlike amorphous carbon as they provide different diffraction intensities.

Gruen et al. have grown NCD films on (100) surfaces of n-doped silicon wafers using electrical biasing of the silicon substrate to initiate nucleation [4]. Growth was carried out at a rate of about 0.5–1 μm/h. Although NCD films have uniform morphology, two additional factors mandate the use of the HRTEM technique. When the packing density is high, the diffraction contrast due to orientational differences of the diffracting crystallites appears weak for

bright-field images. Also, the resolution of the diffraction-contrast method is quite low, and, therefore, it is difficult to resolve nanosized crystallite boundaries. For all the reasons mentioned above, reliable information on grain size could be determined from lattice images of nanodiamond crystallites. Mostly the (111) lattice planes are resolvable in the microscopes. Hence, the lattice images from those crystallites are oriented such that at least one set of their (111) lattice planes is parallel to the incident imaging electron beam. The crystallite size with high accuracy can be measured because of the low contrast from surrounding structures is close to random white noise. Although lattice images reveal individual crystallites at atomic resolution, the presence of amorphous carbons cannot be determined. When the crystallite size is reduced to the nanometer scale, the percentage of atoms located at the grain boundaries increases drastically with decrease of grain size. It is estimated that for NCD films, the fraction of atoms residing at grain boundaries can be as high as 10% when the average crystallite size becomes 3 to 5 nm. On the other hand, electron microscopy observations show that there is no graphitic phase between the grain boundaries. The presence of  $sp^2$  bonds suggests that carbons are  $\pi$ -bonded across sharply delineated grain boundaries limited to widths of 0.2–0.5 nm [73].

## 4.2. Electron Energy Loss Spectroscopy

Shown in Figure 10 [74] are high-resolution electron energy loss spectroscopy (EELS) spectra of the plasmon for  $C_{60}$  fullerene, amorphous, nanocrystalline, and polycrystalline diamond [74].  $C_{60}$  fullerene shows peaks around 6.5 eV which are  $\pi$ -plasmons due to the  $\pi$ - $\pi^*$  band transition

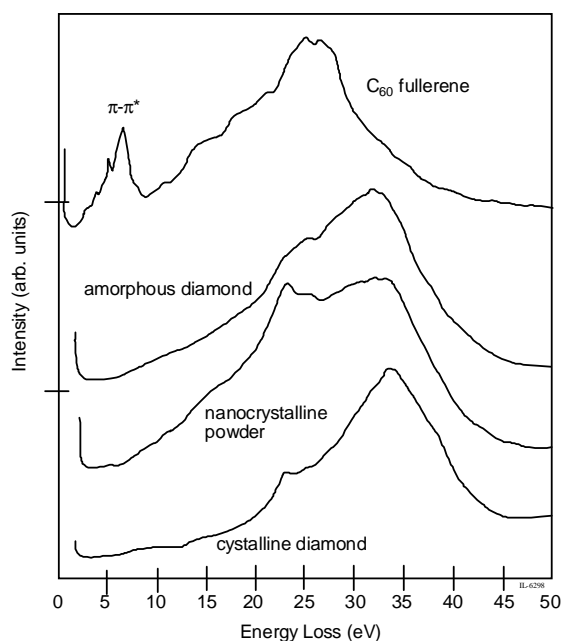


**Figure 10.** High-resolution EELS plasmon spectra for  $C_{60}$  fullerene, amorphous diamond, nanocrystalline powder, and crystalline diamond. Reprinted with permission from [74], H. Hirai et al., *Diamond Relat. Mater.* 8, 1703 (1999). © 1999, Elsevier Science.

[75, 76]; such peaks are not observed in the amorphous diamond, indicating thereby the absence of  $\pi$ -plasmons. Among the three diamond materials,  $\sigma$ -plasmon peaks that appear around 30–34 eV [77] are different in peak position and shape. Plasmon excitation of valence band electrons of EELS spectra is related to the dielectric function by an equation [78]. Applying the Kramers–Kronig equation, the real and imaginary parts of the dielectric function,  $\epsilon_1$  and  $\epsilon_2$ , can be estimated from the plasmon of EELS. The calculated  $\epsilon_2$  for the diamond materials is shown in Figure 11 [74]. The rise-up position of  $\epsilon_2$  corresponds to the bandgap.

For the natural crystalline diamond, the rise-up position is 5.5 eV, indicating excellent agreement with the established bandgap of diamond (5.5 eV). Two peaks appear at 8.2 and 12.7 eV, and the former is assigned to direct excitation of an electron at the  $\Gamma$  point, the latter being assigned to X and L positions, respectively [79]. For the amorphous diamond, the rise in peak is gradual and the rise-up position changes with the sample from 3.5 to 4.5 eV. In any case, the magnitude of the bandgap is smaller than that of crystalline diamond. A large peak at 7.2 eV, corresponding to point  $\Gamma$ , is observed. For the nanocrystalline powder, the rise-up position is at 3.0 eV and occurs very gradually. This implies that the present method of estimating  $\epsilon_2$  from the EELS plasmon is reliable. For the amorphous diamond, the magnitude of the bandgap is 3.5 to 4.5 eV, smaller than that of diamond. The variation in magnitude of the bandgap may be caused by the temperature distribution during the synthesis. In addition, the amorphous diamond exhibited the characteristic distribution in  $\epsilon_2$  and only  $\Gamma$  excitation at the point

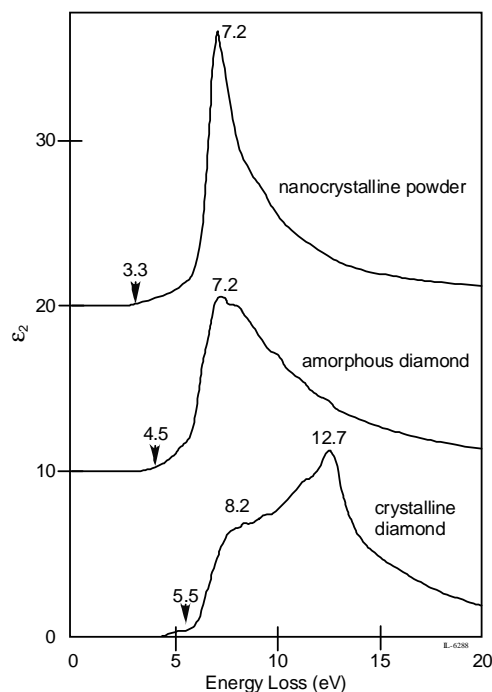


**Figure 11.** Imaginary part of the dielectric function obtained from EELS spectra for diamond materials, showing different rise-up manners. Reprinted with permission from [74], H. Hirai et al., *Diamond Relat. Mater.* 8, 1703 (1999). © 1999, Elsevier Science.

appeared, while excitations at X and L points were not noticed or considerably weakened. X and L points, where the wave number vector has a certain value, are defined when the direction and periodicity exit in the material, whereas the  $\Gamma$  point is independent of direction and periodicity. The observed characteristics might have originated from the short-range structure of the amorphous diamond.

For the nanocrystalline powder the small bandgap of 3.3 eV and the gradual increase in  $\epsilon_2$  are probably generated from the disordered carbon layer surrounding individual nanometer-sized crystallites observed under high resolution TEM. It is quite likely to tailor the bandgap of diamond films by controlling the synthesis parameters.

### 4.3. X-Ray Photoelectron Spectroscopy

The NCD films with a thickness of 800 nm were grown by MPCVD and these films were implanted with nitrogen ions at energy of 110 keV [80]. During the implantation process, the temperature of the samples was controlled below 80 °C using a water-cooling device. X-ray photoelectron spectroscopy (XPS) was used to analyze the changes in surface structure and chemical state of the films before and after implantation.

Figure 12 [80] presents the XPS spectra for C 1s and O 1s states of the as-deposited film. The C 1s envelope has been deconvoluted into three components (Fig. 12a). The main peak at 284.5 eV can be attributed to contribution from C–C and C–H bonds [81]. The peak signals at 285.8 and 286.9 eV are indications of the presence of C–O

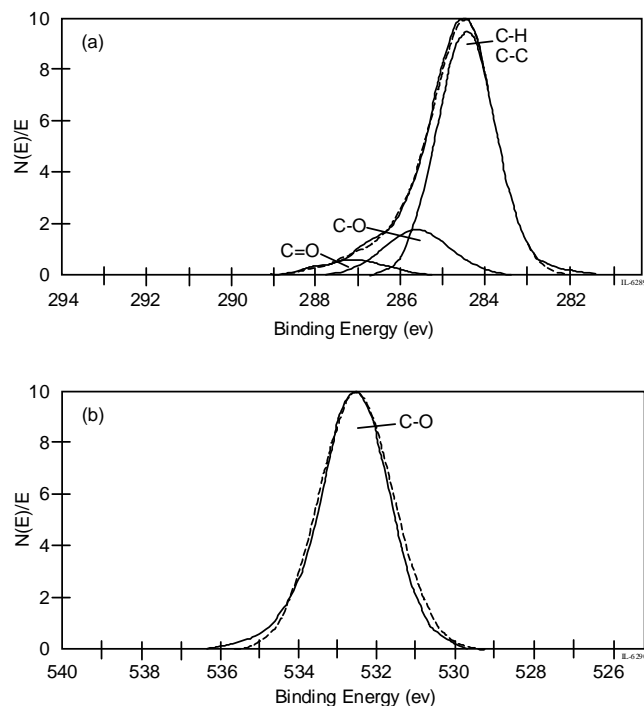


**Figure 12.** XPS spectra for: (a) C 1s and (b) O 1s states for the as-deposited film. Reprinted with permission from [80], T. Xu et al., *Diamond Relat. Mater.* 10, 1441 (2001). © 2001, Elsevier Science.

and C=O [82], respectively. Figure 12b is the O 1s spectra of the as-deposited film. A single-peak signal centered at 532.8 eV is evident, which may be assigned to the C–O bond [83]. The surfaces of as-grown CVD diamond films are typically terminated with hydrogen atoms [84]. However, the film grown as previously stated indicates that the O concentration on the surface reaches 9.83%, which implies that the terminals of dangling bonds of  $sp^3$  C–C atoms on the surface are occupied not only by hydrogen atoms but also by some oxygen atoms and absorption of hydrogen and oxygen may also exit on the surface [85]. Shown in Figure 13 [80] are the XPS spectra for C 1s and O 1s states of the film implanted with  $1 \times 10^{17}$  ions  $\text{cm}^{-2}$ . As compared with the unimplanted sample, distinct changes in the C 1s and O 1s spectra are observed. The C 1s core-level spectrum shifts to a higher binding energy, and the intensity of peaks for C–O and C=O shows an obvious increase (Fig. 13a). The O 1s lines are asymmetric, and more than one binding state is presented. Absorbed oxygen (529.6 eV), C=O (531.5 eV), C–O (532.8 eV), and absorbed  $\text{H}_2\text{O}$  (534.9 eV) [86] are shown in the O 1s spectrum of Figure 13b.

These studies show that nitrogen-ion implantation changes the surface chemical state of the NCD film. The C–H and C–O bonds on the surface of as-deposited films were broken by highly energetic nitrogen ions. Hydrogen and oxygen desorb from the diamond surface and yield unoccupied surface states, which cause the change in the surface state of the as-deposited film. These chemically unsaturated surface carbon atoms have free valences that may be saturated by chemisorption of foreign elements or may react with foreign elements to form bonded surface functional groups [87]. When the implanted samples are exposed in ambient atmosphere, the dangling bonds can be quickly

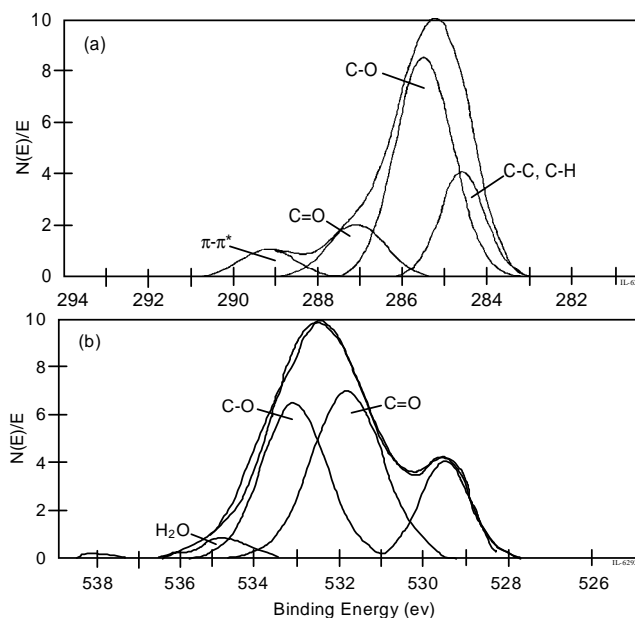


**Figure 13.** XPS spectra for (a) C 1s and (b) O 1s states for the film implanted with  $1 \times 10^{17}$  ions  $\text{cm}^{-2}$ . Reprinted with permission from [80], T. Xu et al., *Diamond Relat. Mater.* 10, 1441 (2001). © 2001, Elsevier Science.



occupied by OH, CO<sub>2</sub>, or H<sub>2</sub>O molecules and ions in air. In this way the surfaces of NCD films are covered by a layer of oxygen-containing groups after high fluence implantation, thereby resulting into the change in chemical state of oxygen on the surface.

#### 4.4. Raman Spectroscopy

It is well known that Raman spectra, that are sensitive to changes in translational symmetry, are very powerful for the study of disorder and crystalline formation in thin carbon films [88]. In Raman spectroscopy, a visible laser is used for excitation, and a sharp peak at 1333 cm<sup>-1</sup> appears in the spectrum. For NCD films, with decreasing the grain size, the grain surface area and grain boundary that mainly consist of amorphous sp<sup>2</sup> C phases increase. In the Raman spectrum, a broad D peak (disorder-induced mode) at 1350 cm<sup>-1</sup> will appear and possibly overlap the diamond peak at 1333 cm<sup>-1</sup> with increasing sp<sup>2</sup> C bonding. The high frequency stretch modes of sp<sup>2</sup> C atoms are overemphasized due to the π-π\* transition resonance effects [89], and the sp<sup>2</sup> C network exhibits resonance enhancement in the Raman cross-section since the local sp<sup>2</sup> C energy gap of approximately 2 eV is comparable to the energy of the incident photons. The sp<sup>3</sup> C atoms do not exhibit such a resonance effect because of the higher local gap of approximately 5.5 eV. Hence the Raman spectra obtained with visible excitation are completely dominated by the sp<sup>2</sup> C atoms [90]. Raman scattering in the UV region is promising for vibrational studies of sp<sup>3</sup> bonded C phase [91]. Advantages of using UV over visible photons include the suppression of the dominant resonance Raman scattering from sp<sup>2</sup> C atoms and increase in the intensity from sp<sup>3</sup> C bonding [92].

Figure 14 [93] is the Raman spectra of NCD films grown by the MPCVD technique at different temperatures [93]. The Raman spectrum of the NCD films mainly exhibits three features near 1150, 1350, and 1580 cm<sup>-1</sup>. The bands in the Raman spectra of these films near 1350 and 1580 cm<sup>-1</sup>, popularly known as D and G bands, are related to graphitic

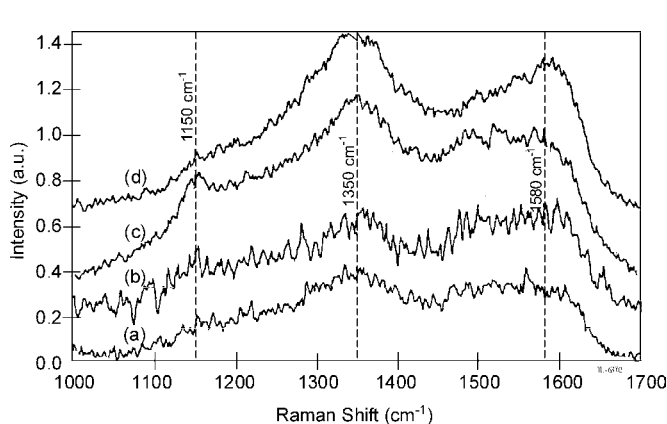


**Figure 14.** Raman spectra of the films deposited at different temperatures: (a) 400 °C, (b) 500 °C, (c) 600 °C and (d) 700 °C. The samples were excited by a 488-nm Ar<sup>+</sup> laser. The three positions 1150, 1350 and 1580 cm<sup>-1</sup> correspond to nanocrystalline diamond, graphitic D and G bands, respectively. Reprinted with permission from [93], T. Sharda et al., *Diamond Relat. Mater.* 10, 1592 (2001). © 2001, Elsevier Science.

islands [90]. The D band appears due to small domain size in graphite. The band near 1150 cm<sup>-1</sup> is shown to be related to the calculated photon density of states of diamond and has been assigned to the presence of a nanocrystalline phase of diamond [94, 95]. It is observed from Figure 14 that the NCD feature is almost missing in the film grown at 400 °C, and this feature increases with temperature in the film grown at 500 °C and becomes quite pronounced in the films grown at 600 °C followed by a drastic decrease in its intensity at higher temperature. It has also been observed as a weak band in the microcrystalline diamond films along with a sharp peak near 1332 cm<sup>-1</sup> giving thereby the signature of crystalline cubic diamond [21, 96]. It is interesting to note that though the film grown at 600 °C shows an intense band related to NCD, it does not show any peak near 1332 cm<sup>-1</sup>. This is mostly due to uniformly distributed short-range sp<sup>3</sup> crystallites in the films [96, 97]. However, the higher intensities of the graphitic bands in the films grown at 600 °C, as compared to the intensity of NCD features, do not represent high amounts of sp<sup>2</sup> carbon in the film. This is because the cross-section of Raman scattering is 50–60 times higher for sp<sup>2</sup>-bonded carbon in comparison to sp<sup>3</sup>-bonded carbon [98]. This small amount of graphitic carbon in the film may exit between the nanodiamond grains [99]. The variation in the intensity of NCD peak can be taken as a qualitative measure of concentration of NCD grain in the film. It appears that the growth of NCD starts at 500 °C, becomes a maximum at 600 °C, and decreases at higher temperatures.

#### 4.5. Infrared

NCD films deposited by CVD of camphor on Si substrate were analyzed by infrared (IR) spectroscopy [38]. Figure 15 [38] shows the variation of transmittance with wave number of thermal CVD of diamond (curve a) and by rf + dc plasma CVD of CH<sub>4</sub> and hydrogen (curve b). It is observed from these figures that over the IR region, the transmittance of NCD is comparable to that of PCD film [100]. The transmittance of bulk diamond (curve c) is also shown

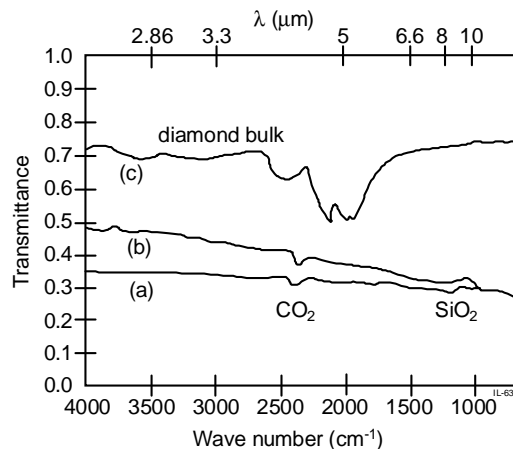


**Figure 15.** IR spectra of two representative films deposited on Si substrates: (a) deposited by CVD of camphor and hydrogen, (b) deposited by rf + dc plasma CVD of CH<sub>4</sub> + H<sub>2</sub>, (c) the spectrum of bulk diamond for comparison. Reprinted with permission from [38], K. Chakrabarti et al., *Diamond Relat. Mater.* 7, 845 (1998). © 1998, Elsevier Science.

in Figure 15. Clearly, the transmittance of bulk diamond is higher than that of NCD and PCD film. The reduction in transmittance of the CVD diamond is related to the formation of the initial layer of silicon carbide on Si substrate, while for bulk diamond the transmittance is higher as no such substrate effect is observed in this case. In addition, the two-phonon absorption is prominent in bulk diamond. The IR spectrum of CVD film exhibits two small peaks at wave numbers  $\sim 2325$  and  $1050\text{ cm}^{-1}$  that are due to  $\text{CO}_2$  and  $\text{SiO}_2$  absorptions. The CVD diamond films deposited by CVD of camphor +  $\text{H}_2$  have much lower average grain size of  $0.1\text{ }\mu\text{m}$  and smoother surface whereas the films deposited by rf + dc plasma CVD have large polycrystals with average grain size of  $\sim 3.2\text{ }\mu\text{m}$ . No prominent C–H absorption peak around  $2900\text{ cm}^{-1}$  was noticed in IR spectra indicating thereby a good quality of NCD films. On the other hand, the IR spectra of diamond films grown on Si substrates by MPCVD exhibit predominant C–H bands [101]. In particular,  $sp^3\text{-CH}_2$  symmetric stretch at  $2850\text{ cm}^{-1}$  and  $sp^3\text{-CH}_2$  asymmetric stretch at  $2925\text{ cm}^{-1}$  were identified.

## 5. PHYSICAL PROPERTIES

Diamond has unique and remarkable properties, for instance high hardness, low friction coefficient [102], high thermal conductivity [103], high chemical stability, and low or negative electron affinity (NEA) [104]. NEA enables electrons at the conduction band minimum to escape from the diamond without an energy barrier at the surface. However, diamond is a good insulator and therefore it is difficult to deliver electrons to the surface. Similarly diamond is a potential material for wear-resistant applications due to its excellent physical and chemical properties. However, conventional CVD diamond coatings that are deposited at high temperatures possess rough surfaces. The high surface roughness is a major problem when these diamond films are used for machining and wear applications. The successful growth of thin films of NCD at low deposition pressures opens up their large scale uses in tribological applications and field emission display devices.

### 5.1. Mechanical Properties

#### 5.1.1. Surface Roughness

The surface of PCD films is often very rough and hinders their use for optical and tribological applications. The consensus is that efficient ways must be developed to produce smooth diamond films wherein high  $sp^3$  content can be maintained. The NCD films appear promising toward this goal. It is well known that the key parameter to obtain smooth NCD films is the primary nucleation density of diamond nuclei on the substrate. Nucleation densities exceeding  $10^{10}\text{ cm}^{-2}$  can be achieved by ultrasonically scratching the substrate surface with fine-grained diamond powder [9, 105, 106]. A direct relationship between the grain size of diamond powder and primary nucleation density on the substrates, and consequently the optical transparency, has been observed. Other parameters such as the methane fraction in the source gas and the substrate temperature can also affect the morphology and the size of the crystallites. However, previous studies

have only focused on the variations in grain size of the diamond powder, keeping the methane fraction in the source gas either constant or varying it over only a small range. The optimized value of the optical transparency at  $700\text{ nm}$  and beyond was about 60% and the surface roughness was about  $20\text{ nm}$  [9, 105, 106]. The effects of both the grain size of diamond powder and methane fraction in the source gas over a wide range on the microstructure and the optical transmittance of the films have been investigated by these researchers.

The substrate pretreatment involved ultrasonic polishing of the substrates with diamond powder of two different grain sizes,  $4\text{ nm}$  and  $0.1\text{ }\mu\text{m}$ , for  $8\text{ h}$ , followed by standard chemical cleaning with acetone and de-ionized water. For convenience, hereafter the substrates treated with  $4\text{ nm}$  diamond powder will be designated as nanometer-scratched and those treated with  $0.1\text{ }\mu\text{m}$  diamond powder as micrometer-scratched. Both types of substrates were placed together in the deposition chamber. Notably, for no ultrasonic polishing at all or polishing for less than  $8\text{ h}$  with either of the powders, the resulting films were not continuous, indicating that the substrates were not uniformly and entirely scratched for less than  $8\text{ h}$  of treatment. The substrates were also cleaned in pure hydrogen plasma at  $1.5\text{ kW}$  for  $30\text{ min}$  before the depositions. Typical deposition time was about  $3\text{--}4\text{ h}$  to give a film thickness of about  $0.5\text{ }\mu\text{m}$ .

Typical surface profiles of NCD films grown at two methane fractions on nanometer- and micrometer-scratched substrates are presented in Figure 16 [5]. At low methane fraction, the micrometer-scratched sample had a rough surface whereas the nanometer-scratched sample was smooth. Under this specific condition, the average surface roughness is comparable to the respective average grain size, which in turn is directly related with the powder size used for substrate pretreatment. Surprisingly, this correlation between the average grain size and the surface roughness was not observed in the samples prepared at high methane fraction. For films deposited at 31% methane fraction, despite the similarity in the grain size distribution and the average grain size ( $\sim 30\text{ nm}$ ), the nanometer-scratched sample has a much rougher surface [root mean square (rms) of roughness  $\sim 100\text{ nm}$ ] than its micrometer-scratched counterpart with rms of roughness  $\sim 8\text{ nm}$ . Shown in Figure 17 [5] are some typical transmission spectra of these NCD films. It is observed that the transparency of NCD film is strongly dependent not only on the methane fraction but also on the pretreatment of the substrate. The optical absorption edge for most of the NCD films was quite similar to that for type IIa diamond. However, detail tailing near the absorption edge varied from sample to sample, presumably due to the structural imperfections of the films, as well as the internal light scattering at the grain boundaries. Optical transparency over 60% in the spectral range of  $0.6\text{--}2.0\text{ }\mu\text{m}$  is considered sufficiently high for most practical applications [105].

For comparison, a variation in the transmittance at  $700\text{ nm}$  as a function of the methane content of the source gas is depicted in Figure 18 [5]. Since most of the optical transmittance spectrum showed the influence of interference of the light in the film, the value of a smooth curve that represented the average behavior has been used. At lower methane fractions, the films grown on nanometer-scratched

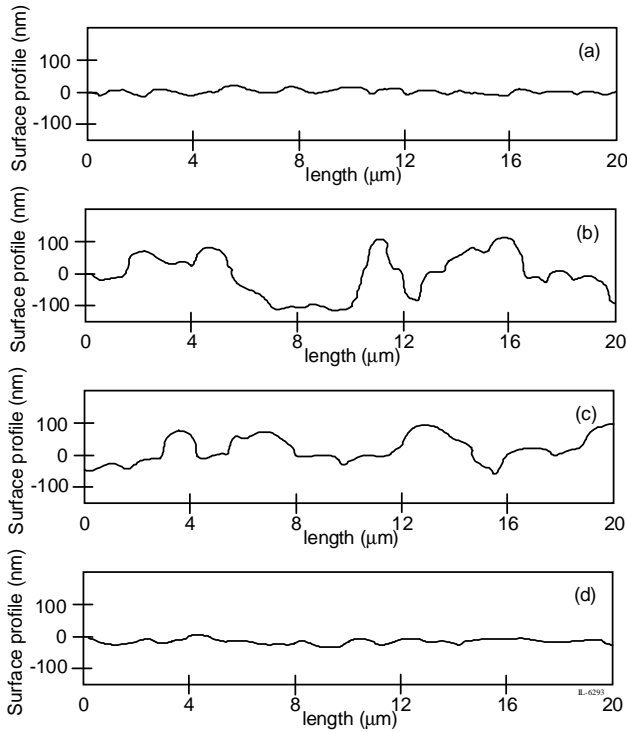


**Figure 16.** Surface profiles of NCD films grown at (a), (b) methane fraction of 4%, nanometer- and micrometer-scratched substrates, respectively; (c), (d) methane fraction of 31%, nanometer- and micrometer-scratched substrates, respectively. Both pairs of films have similar thickness of about  $0.55 (\pm 0.05) \mu\text{m}$ . Reprinted with permission from [5], L. C. Chen et al., *J. Appl. Phys.* 89, 753 (2001). © 2001, American Institute of Physics.

substrates were considerably more transparent than those on micrometer-scratched substrates. However, as the methane fraction increased, the difference between the transmittance of these two types of films diminished and actually reversed at a methane fraction of 20%, such that beyond this methane fraction, the films grown on micrometer-scratched substrates were more transparent than those on nanometer-scratched substrates. The films grown on micrometer-scratched substrates remained highly transparent until a methane fraction of 42%, while those on nanometer-scratched substrates became fairly opaque for methane fractions beyond 25%. Figure 19 [5] shows the plot between the optical transmittance at 700 nm and the inverse surface roughness and clearly reveals the existence of a region showing a linear relationship between the two parameters. In a second region, saturation of the optical transmittance of the films to 80% to 84% occurred despite continuing reduction in their surface roughness. Thus, the major factor that dictates the optical transmittance of NCD films is the surface roughness, instead of the grain size, provided that the contents of the  $sp^2$ -bonded carbon and the structural disorder were negligible.

### 5.1.2. Hardness

The indentation technique has been most widely used for the determination of hardness. This technique is suitable for films with higher thickness since the method requires

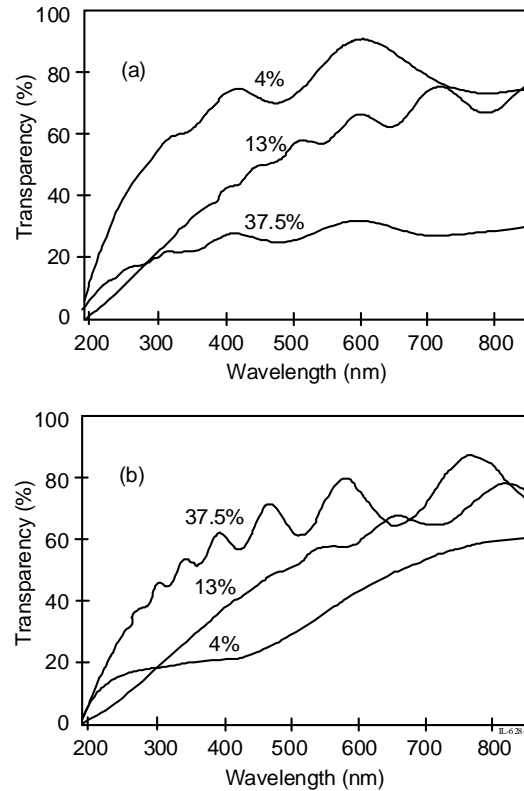


**Figure 17.** Optical transmittance spectra of the NCD films grown on (a) nanometer-scratched and (b) micrometer-scratched substrates at various methane fractions. Reprinted with permission from [5], L. C. Chen et al., *J. Appl. Phys.* 89, 753 (2001). © 2001, American Institute of Physics.

a penetration depth ( $h$ ) so that  $h < 0.1d$ , where  $d$  is the film thickness [107]. The stress/strain and hardness in thin films may be evaluated indirectly by measuring the physical properties that are influenced by the mechanical properties.

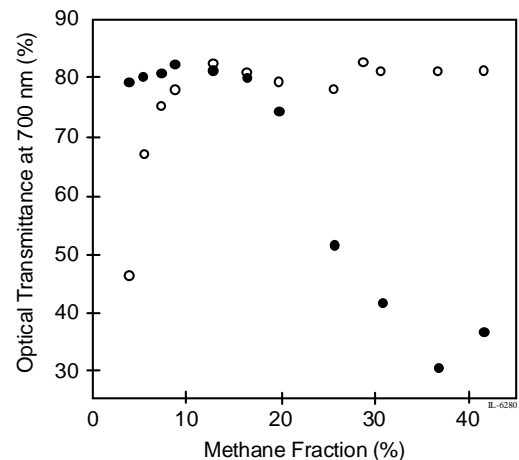


**Figure 18.** Variations in optical transmittance at 700 nm as a function of methane fraction for NCD films grown on nanometer-scratched (●) and micrometer-scratched (○) substrates. Reprinted with permission from [5], L. C. Chen et al., *J. Appl. Phys.* 89, 753 (2001). © 2001, American Institute of Physics.

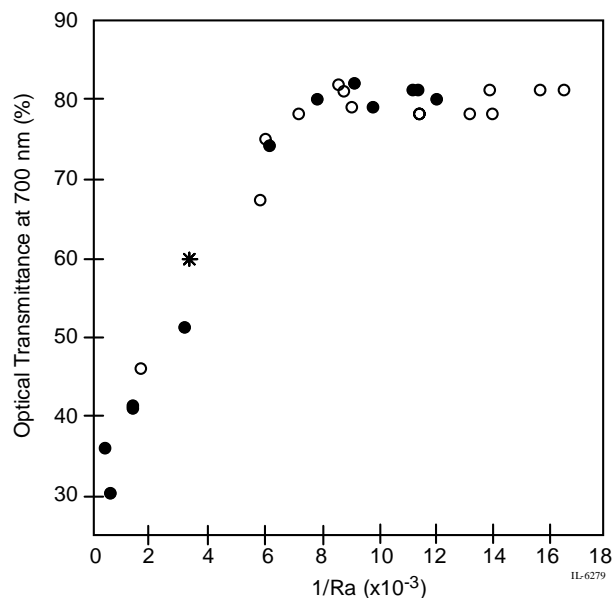


**Figure 19.** Correlation between optical transmittance at 700 nm and average surface roughness for NCD films grown on nanometer-scratched (●) and micron-scratched (○) substrates. The asterisk (\*) denotes the data from Reference 9. Reprinted with permission from [5], L. C. Chen et al., *J. Appl. Phys.* 89, 753 (2001). © 2001, American Institute of Physics.

Chakrabarti et al. [38] studied the effect of mechanical stress on the optical absorption band tail to determine the strain ( $\delta a/a$ ) from the theoretical curve-fitting method. This being a nondestructive technique is often very useful since the film may be utilized for other applications.

If  $\alpha$  and  $\alpha_0$  are the absorption coefficients at any wavelength ( $\lambda$ ) and at the band edge, respectively, then a plot of  $\alpha/\alpha_0$  vs  $(Eg - h\nu)$ , as shown in Figure 20 [38], may be used to obtain the strain ( $\delta a/a$ ) in the film by using the curve-fitting procedure [108]. The stresses ( $S$ ) in the films were obtained from the relation

$$S = Y(\delta a/a)/(1 - \gamma)$$

with Young's modulus  $Y = 600$  GPa and Poisson's ratio  $\gamma = 0.11$ . The hardness ( $Hv$ ) in the films were obtained from [109]

$$Hv = 2.9[Y/(1 - \gamma)](100.0/x)^{-nc}(\delta a/a)^{1-nc}$$

where  $nc$  is the strain-hardening coefficient and  $x$  is the indentational strain. The values of  $S$ , ( $\delta a/a$ ), and  $Hv$ , for NCD films grown from CVD of camphor at various temperatures, were obtained and are in the range 1.9–8.4 GPa,  $(2-12) \times 10^{-3}$ , and 47–62 GPa, respectively [38].

## 5.2. Thermal Properties

### 5.2.1. Thermal Stability

To investigate the thermal stability of NCD films grown on mirror-polished Si substrates by biased enhanced MPCVD, the NCD films were annealed in an ambient Ar atmosphere at 200, 400, 600, and 800 °C [110]. The structural and

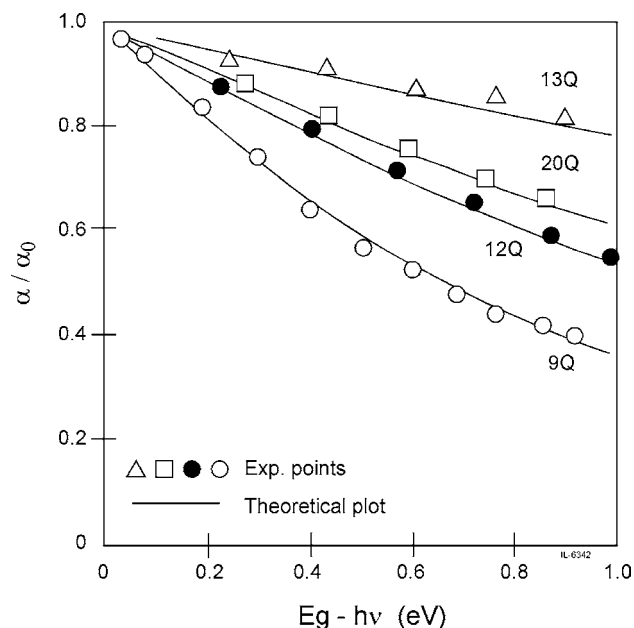


**Figure 20.** Plot of  $\alpha/\alpha_0$  vs  $(Eg - h\nu)$  for four representative films deposited on quartz substrates,  $\alpha_0$  being the absorption coefficient at the band edge  $Eg$ . Reprinted with permission from [38], K. Chakrabarti et al., *Diamond Relat. Mater.* 7, 845 (1998). © 1998, Elsevier Science.

mechanical properties of as-grown and annealed NCD films were evaluated. Shown in Figure 21 [110] are the Raman spectra of the as-grown and annealed samples of NCD films. The spectra consist of bands near 1150, 1350, 1500, and 1580  $\text{cm}^{-1}$ . The bands near 1350 and 1580  $\text{cm}^{-1}$  are D and G bands, respectively, and are related to graphitic islands. Another band near 1150  $\text{cm}^{-1}$  is assigned mainly to the presence of the nanocrystalline phase of diamond [15, 88, 90]. The band intensity near 1500  $\text{cm}^{-1}$  varies proportionally with

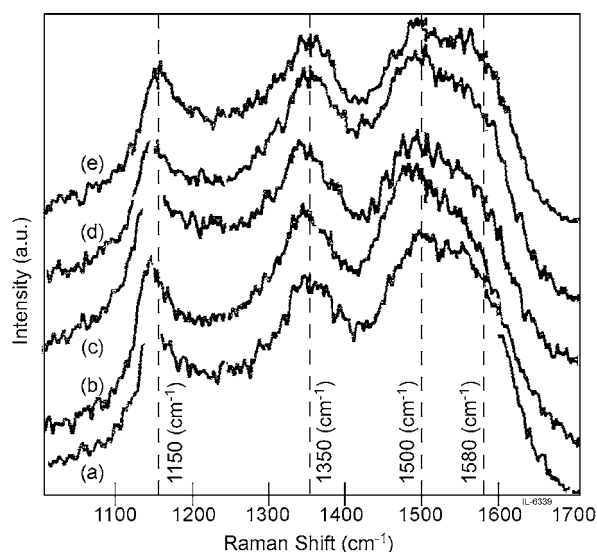


**Figure 21.** Raman spectra of the (a) as-grown and annealed samples at (b) 200 °C, (c) 400 °C, (d) 600 °C, and (e) 800 °C. Reprinted with permission from [110], T. Sharda et al., *J. Nanosci. Nanotech.* 1, 287 (2001). © 2001, American Scientific Publishers.

the band intensity near  $1150\text{ cm}^{-1}$  and is related to the disordered  $sp^3$  carbon in the films [12, 15]. The Raman results in this case indicate association of these Raman features closer to NCD. If these features were related to hydrogen, their intensity should have decreased with annealing temperature, because the hydrogen should have started to evolve from the samples after  $200\text{ }^\circ\text{C}$  [111]. On the other hand, if these features are related to  $sp^2$ -bonded carbon, their intensities should have increased with annealing temperature as the concentration of  $sp^2$  carbon increases with annealing temperature [111, 112]. Figure 22 [110] depicts the plot of the intensity ratio of the Raman features near  $1150\text{ cm}^{-1}$  to the graphitic G band as a function of annealing temperature. The ratio does not change significantly as a function of annealing temperature and shows an increasing trend up to  $400\text{ }^\circ\text{C}$  but saturates at higher temperatures to a lower value, which is identical to the value of the as-grown sample. Figure 23 [110] depicts the cubic crystalline diamond features in the XRD patterns of the NCD films, which also support to some extent the conjecture that the Raman feature near  $1150\text{ cm}^{-1}$  is related to NCD. In addition, the calculated interplanar spacings corresponding to the peaks at  $2\theta \sim 44.05^\circ$  and  $75.25^\circ \pm 0.20^\circ$  in XRD patterns of the films closely match the interplanar  $d$ -values of (111) and (220) planes of cubic diamond, respectively. The full width at half maximum of diamond peaks in the films is high as compared to the CVD grown microcrystalline films and these observations are well correlated with that of diamond nanocrystallites [21]. It should be noted that no XRD peaks associated with graphite or features related to amorphous carbon could be identified either in the as-grown films or in the annealed films. These results support the assignment of the Raman feature near  $1150\text{ cm}^{-1}$  to the presence of NCD. Similarly, the intensity ratio of the Raman NCD to the graphitic G band does not change much with annealing temperature, indicating thereby the structural stability of NCD films to temperatures as high as  $800\text{ }^\circ\text{C}$ .

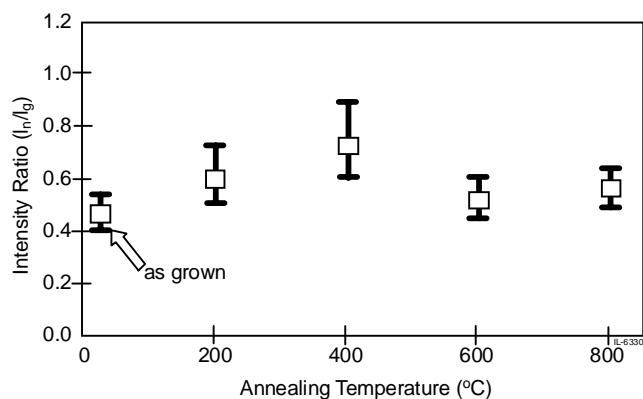


**Figure 22.** Plot of the Raman intensity ratio of NCD ( $I_n$ ) to the graphitic G band ( $I_g$ ) as a function of annealing temperature. The error bar is the standard error in fitting the individual Raman curves. Reprinted with permission from [110], T. Sharda et al., *J. Nanosci. Nanotech.* 1, 287 (2001). © 2001, American Scientific Publishers.

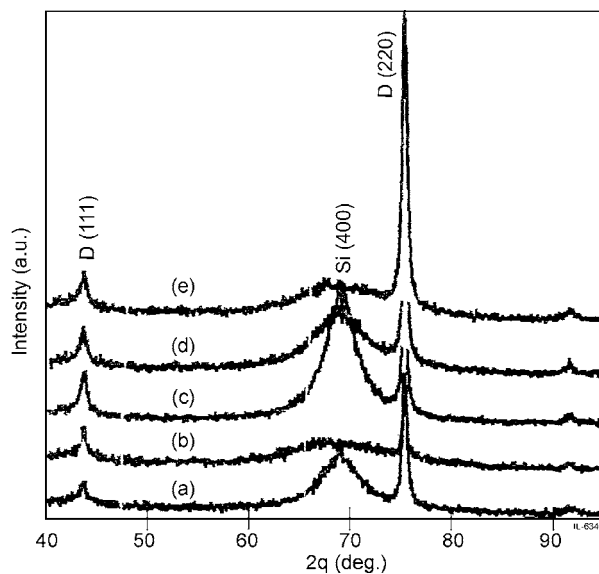


**Figure 23.** XRD patterns of the (a) as-grown and annealed samples at (b)  $200\text{ }^\circ\text{C}$ , (c)  $400\text{ }^\circ\text{C}$ , (d)  $600\text{ }^\circ\text{C}$ , and (e)  $800\text{ }^\circ\text{C}$ . Reprinted with permission from [110], T. Sharda et al., *J. Nanosci. Nanotech.* 1, 287 (2001). © 2001, American Scientific Publishers.

### 5.2.2. Specific Heat Capacity

The specific heat capacity bears important implications on various parameters like thermal conductivity, diffusivity, and thermal expansion. The independent measurement of this quantity is important to gain an understanding of the thermodynamic behavior of NCD. The specific heat capacity of NCD samples has been measured by differential scanning calorimetry [113]. Shown in Figure 24 [113] is the plot of the specific heat at constant pressure  $C_p$  for the type IIb diamond stone, coarse-grained diamond, NCD, amorphous carbon, and reference data (solid line [114]) vs temperature. The  $C_p$  values of the coarse-grained sample are found to be lower than the reference data by less than 10% but are consistent with the measured  $C_p$  of the diamond single

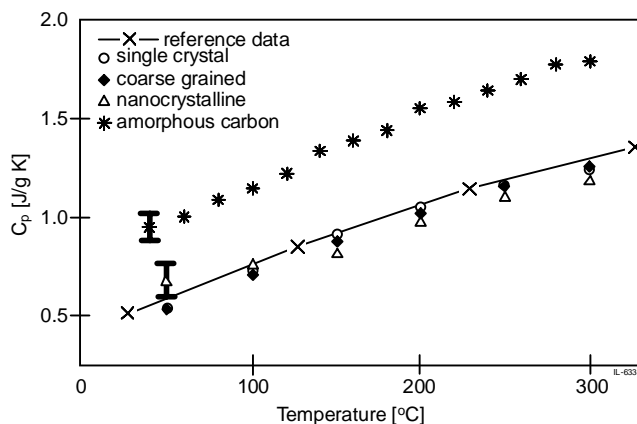


**Figure 24.** Specific heat  $C_p$  of poly- and nanocrystalline CVD diamond, amorphous carbon and single-crystalline diamond (solid line: [114]) versus temperature. Reprinted with permission from [113], C. Moelle et al., *Diamond Relat. Mater.* 7, 499 (1998). © 1998, Elsevier Science.

crystal. The NCD sample exhibits a higher  $C_p$  at 50 °C and slightly lower values for  $T > 100$  °C. The accuracy of the experimental values for the NCD and amorphous sample is limited by the very small sample amount and is estimated to be about 15% based on repeated test runs. The  $C_p$  values of the amorphous carbon films are found to be increased by  $0.5 \text{ J g}^{-1} \text{ K}^{-1}$  compared to the reference data and are due to the different atomic short-range order and the  $sp^2:sp^3$  bonding composition in the amorphous structure. Additionally, the large amount of hydrogen homogeneously incorporated in the amorphous structure contributes to the increase of  $C_p$ .

The  $C_p$  data of the coarse-grained diamond and NCD sample deviate from the reference data by a maximum of 15%. Since the microstructure and hydrogen concentration considerably differ between them, it can be concluded that these properties have a negligible impact on the specific heat. These results are in good agreement with those of large-grained thick CVD diamond films [115]. The impact of nondiamond phases on the specific heat appears to be small. A residual volume fraction of amorphous carbon in the nanocrystalline sample should make a small contribution to  $C_p$ , with  $C_p$  of the second amorphous phase being increased by a factor of about 2. The fact that the specific heat data of the CVD diamond samples fall within a 15% interval around the reference data up to 300 °C implies that the temperature dependence of the thermal expansion coefficient should be the same as that of single-crystalline diamond.

### 5.3. Optical Properties

Figure 25 [38] presents the optical transmittance ( $T_r$ ) versus wavelength ( $\lambda$ ) traces of three NCD films deposited at different substrate temperature ( $T_s$ ) on quartz. It may be observed that the transmittance ( $T_r$ ) had a high value ( $\sim 93\%$ ) for  $T_s > 673$  K. The direct and indirect bandgaps ( $E_{gd}$  and  $E_{gi}$ ), estimated from the corresponding plots of  $(\alpha h\nu)^2$  vs  $h\nu$  and  $(\alpha h\nu)^{1/2}$  vs  $h\nu$  is presented in Figure 26 [38], where  $E_{gd} = 4.84$  eV and  $E_{gi} = 2.18$  eV. It may be noted that both the direct and indirect bandgaps were high and their values increased with increasing  $T_s$ . The surfaces of the as-deposited films were generally  $sp^2$  rich. The  $sp^2$  phases from the surfaces of the films could be removed either by etching in oxygen plasma or by using a chemical process [116, 117]. After etching, the absorption edge of the optical spectra became sharper than that of the as-deposited film as presented in Figure 27 [38]. There was also a substantial increase in the direct bandgap ( $E_{gd}$ ) due to the removal of the  $sp^2$  phase from the film surface by etching, although the change of indirect bandgap ( $E_{gi}$ ) was insignificant. The variation of bandgap energy due to removal of the  $sp^2$  phase etching was similar to that reported earlier for NCD films deposited by high pressure sputtering of vitreous carbon target [118] and for diamond films deposited by CVD of freon-22 and hydrogen [119]. In fact, the etching characteristics of diamond films may provide the information of  $sp^2$  graphitic and  $sp^3$  diamond structure in the film because the trigonal  $sp^2$  phase can be more easily etched than the tetragonal  $sp^3$  [120, 121]. The etch rate will be higher in films

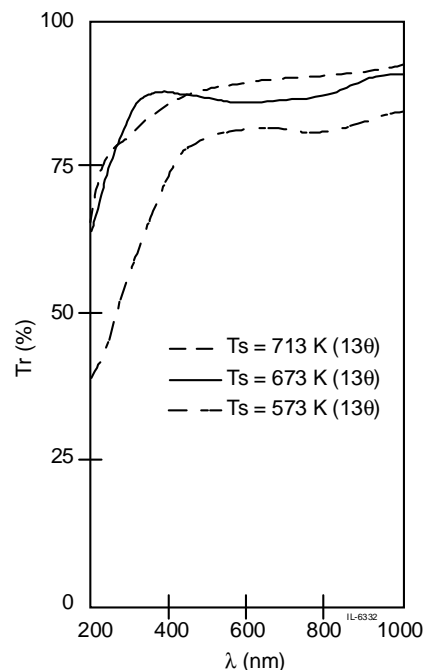


**Figure 25.** Transmittance ( $T_r$ ) vs wavelength ( $\lambda$ ) of three representative films deposited on fused silica at different substrate temperature ( $T_s$ ). Reprinted with permission from [38], K. Chakrabarti et al., *Diamond Relat. Mater.* 7, 845 (1998). © 1998, Elsevier Science.

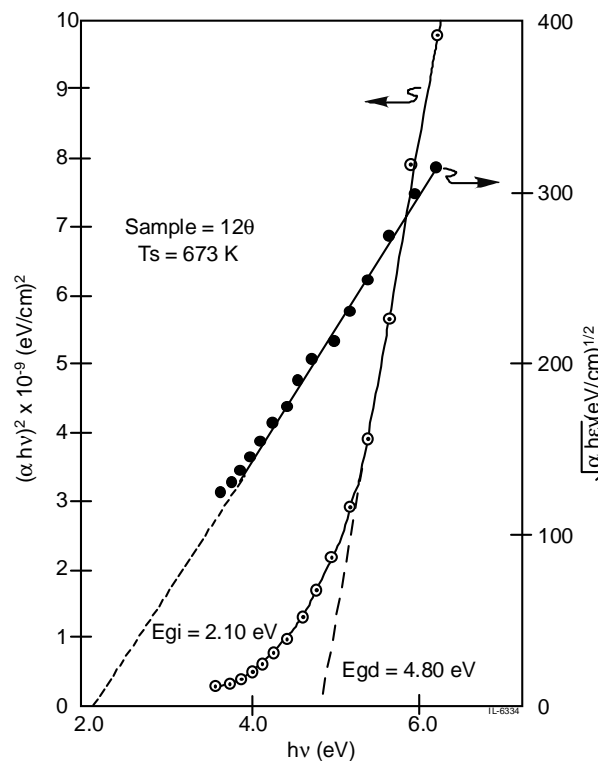


**Figure 26.** Plots of  $(\alpha h\nu)^2$  vs  $h\nu$  and  $(\alpha h\nu)^{1/2}$  vs  $h\nu$  for a representative film deposited on quartz. Reprinted with permission from [38], K. Chakrabarti et al., *Diamond Relat. Mater.* 7, 845 (1998). © 1998, Elsevier Science.



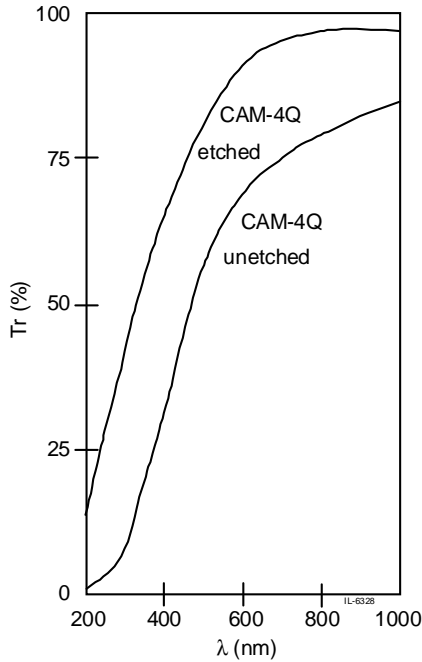


**Figure 27.** Variation of transmittance ( $T_r$ ) with wavelength ( $\lambda$ ) for a representative film before and after removal of  $sp^2$ -rich surface layer by chemical etching. Reprinted with permission from [38], K. Chakrabarti et al., *Diamond Relat. Mater.* 7, 845 (1998). © 1998, Elsevier Science.

having low  $sp^3/sp^2$  ratio and also the effect of the etching on the optical absorption edge will be higher in  $sp^2$ -rich film.

The refractive index ( $n$ ) of the films was estimated from the transmittance spectra.  $n$  varied within 1.3 to 1.5 in most of the as-deposited nanodiamond films showing practically no significant change with the variation of wavelength. The low value of  $n$  may be due to the presence of a significant amount of  $sp^2$  phases in the surface of the as-deposited film. Removal of  $sp^2$  by surface etching resulted in higher  $n$  values (i.e., within 1.8–2.2).

#### 5.4. Electrical Conductivity

Nitrogen doped ultrananocrystalline diamond (UNCD) films with 0.2% of total nitrogen content were synthesized by MPCVD, and temperature dependences of electrical conductivity of these films are reported [122]. These results are shown in Figure 28 [122]. In addition, Figure 28a shows secondary ion mass spectroscopy (SIMS) data for the total nitrogen content in the films as a function of the percentage of  $N_2$  gas added to the plasma. Along with these data is a plot of the room temperature conductivities for the same. The graph shows that the nitrogen content in the films initially increases but then saturates at  $\sim 2 \times 10^{20}$  atoms/cm<sup>3</sup> for 5%  $N_2$  in the plasma, which is  $\sim 0.2\%$  total nitrogen content. The increase in room temperature conductivity is dramatic and represents an increase by roughly five orders of magnitude over undoped UNCD films. The value of conductivity increases from  $0.016 \Omega^{-1} \text{cm}^{-1}$  for 1%  $N_2$  to  $143 \Omega^{-1} \text{cm}^{-1}$  for 20%  $N_2$ . The latter value is much higher than  $n$ -type diamond [123, 124] and is comparable to heavily boron-doped  $p$ -type diamond [125].

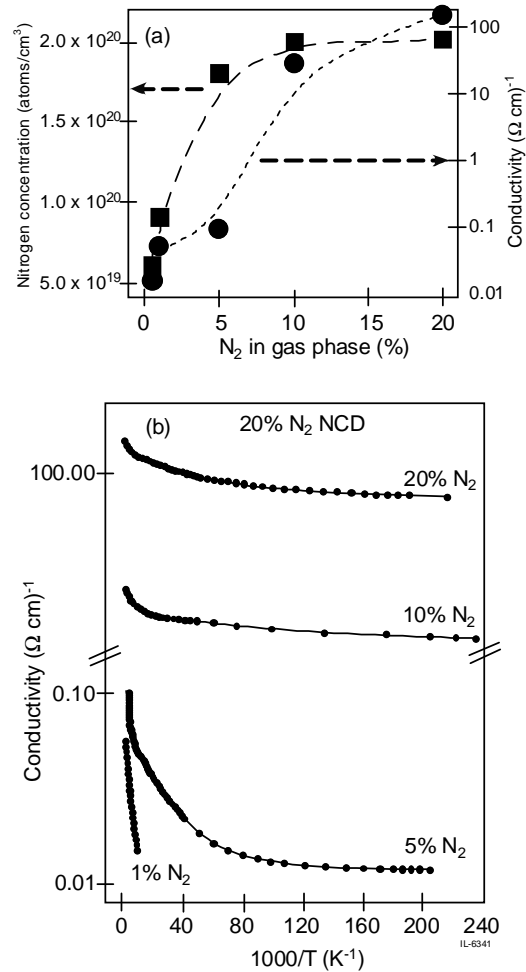


**Figure 28.** (a) Total nitrogen content (left axis) and room temperature conductivity (right axis) as a function of nitrogen in the plasma. (b) Arrhenius plot of conductivity data obtained in the temperature range 300–4.2 K for a series of films synthesized using different nitrogen concentrations in the plasma as shown. Reprinted with permission from [122], S. Bhattacharya et al., *Appl. Phys. Lett.* 79, 1441 (2001). © 2001, American Institute of Physics.

Figure 28b depicts the temperature dependent conductivity of nitrogen doped UNCD film over the temperature range of 300 to 4.2 K. This graph clearly exhibits finite conduction for temperatures even as low as 4.2 K. This behavior is also seen in heavily boron-doped diamond thin films. These graphs are indicative of multiple, thermally activated conduction mechanisms with different activation energies. Hall measurements have been carried on two samples. The carrier concentrations for the 10% and 20%  $N_2$  sample were found to be  $2.0 \times 10^{19}$  and  $1.5 \times 10^{20} \text{cm}^{-3}$ , respectively, and the carrier mobility of 5 and  $10 \text{cm}^2/\text{Vs}$  for 10% and 20%  $N_2$  samples, respectively. The negative value of the Hall coefficients indicates that electrons are the majority carriers in these films. It is proposed that conduction occurs via the grain boundaries. Nitrogen in microcrystalline diamond thin films usually forms a deep donor level with an activation energy of 1.7 eV [123]. It is therefore likely that the enhanced conductivity in UNCD is due to nitrogen doping

of the grains. The nitrogen in these films is present predominantly in the grain boundaries and not within the grains.

## 6. APPLICATIONS

The high optical transmittance, mechanical, and electrical properties of NCD films offer ample opportunities for applications in electron emitting cold cathodes, tribology, MEMS, electrochemical electrodes, surface acoustic wave (SAW) devices, and NCD coatings. A brief discussion of the results of research in these areas is provided.

### 6.1. Electron Emission

Field electron emission, which has important applications in the field of flat panel displays and high performance electron guns, has been a subject of extensive studies for many years. Early studies used sharp geometry [126] to attain the local field enhancement necessary to extract electron from materials with high work functions, such as Mo or W. This requires complex and expensive patterning and fabricating process. Another approach is to explore new materials with lower emission thresholds. In the past few years, diamond [125, 127] has attracted much attention. It is widely recognized that the property of NEA that can be displayed by diamond does not alone make this material ideal for low field electron emission applications. Few electrons exit in the conduction band of diamond, which is difficult to dope *n*-type, making transport of electrons from metallic contacts and emission of electrons from the diamond surface difficult. However, fine grain, highly defective diamond films have shown more promise, presumably due to the presence of a network of grain boundaries and a higher level of nondiamond carbon, which can increase the material's conductivity. These films, often called NCD films, are being investigated for field emission display devices [4].

The development of field emission flat panel displays (FEDs) has triggered very intense research especially in various kinds of carbon thin films because one of their properties is to emit electrons at relatively low applied electric field [127, 128]. A wide range of carbon films, such as amorphous and diamondlike carbon [129, 130], CVD diamond [125, 131], and single and multiwalled carbon nanotubes [132, 133], have shown field emission current in the mA range for applied fields below 10 V/ $\mu\text{m}$ . Cold cathode field emission has been demonstrated in CVD PCD films. In the undoped CVD diamond films, the space-charge-limited current limits the conductance of the bulk. As a result, grain boundaries, which are highly disordered and may contain codeposited graphitic impurities, have been suggested as the main conducting pathway. Because reduction in diamond grain size may increase the conducting pathways, it is possible to improve diamond field emission by depositing size controlled diamond films.

The field emission of CVD grown diamond films shows very analogous behavior to the emission of diamondlike carbon films. CVD diamond films of good quality characterized by a sharp and intense 1332  $\text{cm}^{-1}$  Raman peak seem to exhibit poor field emission properties. Zhu et al. [134] reported a relation between the quality of the diamond films measured by the full width at half maximum (FWHM) of

the Raman 1332  $\text{cm}^{-1}$  line and the field emission properties. By decreasing the crystalline quality and monitoring it by the FWHM of the 1332  $\text{cm}^{-1}$  Raman line, the threshold field to get an emission current of 1 nA decreases [134]. The NCD films show a very weak Raman line or even its absence and exhibit threshold field below 5 V/ $\mu\text{m}$ . Numerous models such as classical tip emission [135], emission from the conduction band due to a negative electron affinity [136], defect band emission [134], and field enhancement at conducting channels in an insulating matrix [137] have been suggested to explain the low field electron emission of CVD diamond films.

The current-voltage characteristics of NCD films were measured at a base pressure of  $10^{-8}$  Torr. The field emission measurements were performed using a Keithley 237 instrument with an incorporated high voltage. The emission current is collected by a graphite counter electrode placed 30  $\mu\text{m}$  above the anode. The experimental procedures for current density measurements were described in detail elsewhere [138]. Figure 29 [139] shows the typical electron emission characteristics of a NCD film deposited on nanometer-scratched (4 nm) substrate with methane of 20%. These films were grown for 4 h at 900  $^{\circ}\text{C}$  and demonstrate an emission current density of 15  $\text{mA}/\text{cm}^2$  at an applied field of 17 V/ $\mu\text{m}$  with turn-on field of 12 V/ $\mu\text{m}$ . Here the turn-on field expresses a value of field at emission current density of 0.01  $\text{mA}/\text{cm}^2$ . The field emission characteristics of the NCD films are further analyzed by the Fowler-Nordheim (FN) plot, a plot of  $\log I/V^2$  vs  $1/V$ , as depicted in Figure 30 [139]. The plot yields a straight line according to the FN equation [140],

$$J = \frac{A}{\phi} \left( \frac{\beta V}{d} \right)^2 \exp \left( \frac{-B\phi^{3/2}}{\beta V} \right)$$

where  $A$  and  $B$  are constants, current density  $J$  is in  $\text{A}/\text{m}^2$ , voltage  $V$  is in volts, anode-to-cathode distance  $d$  is in meters,  $\phi$  is the effective barrier height for electrons in eV, and  $\beta$  is the field enhancement factor that depends on the

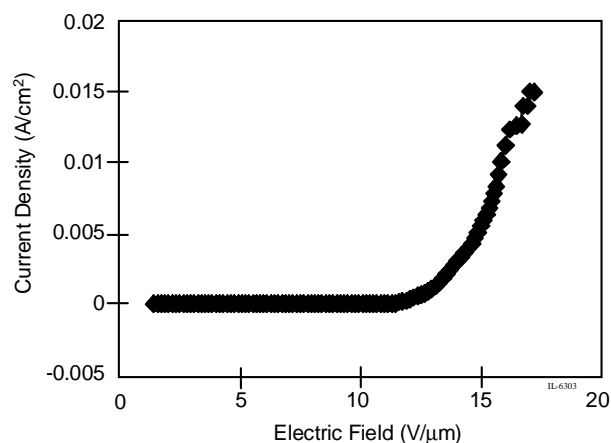


**Figure 29.** Electron emission characteristics of a NCD film deposited on nanometer-scratched substrate with methane of 20%. Reprinted with permission from [139], P. D. Kichambare, Center for Applied Energy Research, University of Kentucky, Lexington, KY, unpublished work, 2001.

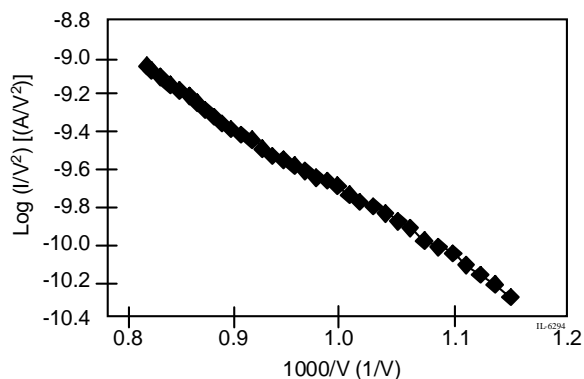


**Figure 30.** The Fowler-Nordheim plot depicting field emission characteristics of NCD film. Reprinted with permission from [139], P. D. Kichambare, Center for Applied Energy Research, University of Kentucky, Lexington, KY, unpublished work, 2001.

emitter geometry. Consequently, a plot of  $\log(J/V^2)$  vs  $1/V$  yields a straight line with slope  $B\phi^{3/2}d/\beta$  indicating that the field emission property can be explained by a tunneling mechanism. The slope of the FN plot can be used to determine the work function of the emitter. These studies indicate that the NCD films would be suitable for application in electron emission devices as these devices operate at  $10 \text{ mA/cm}^2$ .

The field emission properties of the NCD films [138] can be explained by a conducting-tunneling mechanism. A model based on the graphite/nanodiamond mix-phase structure reported earlier [141] is considered. The NCD films used for field emission measurements were grown on silicon substrates. In such a structure, graphite plays the role of conducting channels from the silicon substrate to the film surface. While on the surface, it is assumed that the nanodiamond has a relatively low or even NEA as that of bulk. Thus electron will first tunnel through the nearby diamond edges and then emit from the diamond surface [127, 142]. There are two main parameters deciding the field emission. The first is the diamond grain size and the other is graphite content in the film. As electrons from the diamond/graphite interface must tunnel through a barrier between them, the diamond grain size is a critical factor determining the tunneling probability. For large-size diamond grains, electrons can only be emitted from regions close to crystal edges, which are thin enough for electrons to tunnel through. In contrast, for small-size diamond grains, electrons can be effectively emitted from a larger surface area, or even the whole diamond surface, thus greatly increasing the emission site density. The graphite content is another critical factor as the emission starts from the diamond/graphite interface. There is an optimum graphite content for maximizing the graphite/diamond interface area on the film surface. The optimal value of the graphite content is just enough to fill the gaps between the densely agglomerated diamond grains. Above this value, a decrease in graphite content will increase the diamond/graphite interface area and thus enhance field emission. But when the graphite content is below this value, a decrease in graphite content will decrease the interface area at the surface, and the field emission properties will drop. Moreover, a further decrease of the graphite content

will make it insufficient to form conducting channels; thus the emission properties will be rapidly degraded. Recently, field emission from nitrogen-incorporated NCD films has also been reported [143]. All these studies indicate that NCD will be an excellent candidate for cold cathode materials for field emission devices.

## 6.2. Electrochemical Electrodes

The use of diamond in electrochemistry is a relatively new field of research that has begun to blossom in recent years [144, 145]. Conductive diamond possesses several properties that distinguish it from conventional  $sp^2$  carbon electrode, like glassy carbon, and makes it most promising for electroanalysis [146–148]. These distinguishing properties are (i) background current densities an order of magnitude lower than freshly polished glassy carbon, (ii) a working potential window of 3 to 4 V in aqueous media, (iii) an extremely stable surface structure resulting in better response precision and long-term response stability, (iv) a high degree of response activity for several aqueous-based analytes, and (v) weak adsorption of polar adsorbates such that the electrode material resists fouling and passivation. It has been demonstrated that untreated diamond outperforms freshly polished glassy carbon in terms of limit of quantitation, response precision, and response stability [146–148].

It is therefore necessary to understand the factors that influence electron transfer at conducting diamond thin film electrode. These electrode materials are challenging to investigate because these are typically polycrystalline with multiple crystallographic orientations, and because they contain extended and point defects, grain boundaries, and low levels of nondiamond carbon impurity. The multiple crystallites, defects, and possible nondiamond carbon phases could provide discrete sites for heterogeneous electron transfer. Within this context, NCD films are challenging as it is nearly pure diamond. Recently, the electrochemical properties of NCD thin films deposited from  $C_{60}/Ar$  and methane/nitrogen gas mixture were investigated [149].

Figure 31 [149] depicts the cyclic voltammetric  $i$ - $E$  curve for a nanocrystalline diamond film deposited from a  $C_{60}/Ar$  mixture and a boron-doped, microcrystalline diamond film deposited from a  $CH_4/H_2$  mixture. The voltammograms were obtained in  $1 \text{ M H}_2\text{SO}_4$  at  $50 \text{ mV/s}$ . The open circuit potential of the untreated nanocrystalline film was  $+174 \text{ mV}$  (vs saturated calomel electrode (SCE)). Figure 31a shows voltammograms for nanocrystalline and microcrystalline film between  $-0.5$  and  $1.0 \text{ V}$  (vs SCE). The curve for the nanocrystalline film is basically featureless within this potential range, and after the initial scan, the curves are reproducible in shape. The anodic current at  $0.1 \text{ V}$  is  $2.5 \mu\text{A/cm}^2$ , and this is significantly smaller than the cathodic current,  $20 \mu\text{A/cm}^2$  observed for polished glassy carbon. The open circuit potential for the untreated microcrystalline film was  $+205 \text{ mV}$  (vs SCE). The voltammogram for this film between  $-0.5$  and  $1.0 \text{ V}$  is not quite as featureless, as there are two small anodic and cathodic peaks at  $0.75$  and  $0 \text{ V}$ , respectively. These features are associated with a quasi-irreversible but as yet unknown surface redox process, probably at the nondiamond carbon impurities in the grain boundaries. The peak current ratio is near 1, so the

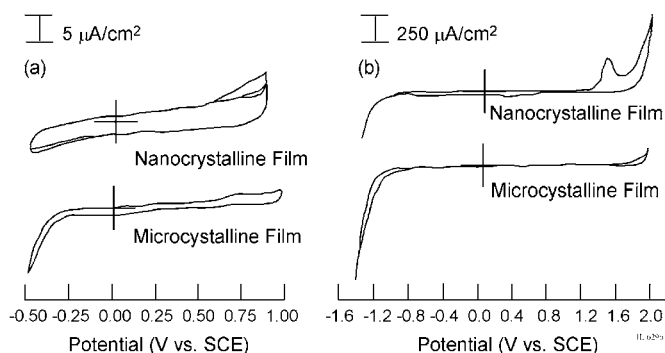


**Figure 31.** Cyclic voltammetric  $i$ - $E$  curves for a nanocrystalline diamond film deposited from a 1%  $C_{60}/Ar$  gas mixture and a boron-doped microcrystalline diamond film deposited from a 0.3%  $CH_4/H_2$  gas mixture over (a) a potential range from  $-0.5$  to  $1.0$  V (vs. SCE) and (b) a potential range from  $-1.6$  to  $2.0$  V (vs. SCE). The electrolyte was  $1$  M  $H_2SO_4$  and the potential sweep rate for (a) was  $50$  mV/s and for (b) was  $25$  mV/s. Reprinted with permission from [149], B. Faussett et al., *Electroanalysis* 12, 7 (2000). © 2000, Wiley-VCH.

surface sites that are being oxidized on the forward sweep are fully reduced on the reverse sweep. The anodic current at  $0.1$  V is  $0.7 \mu A/cm^2$ , which is a factor of 4 lower than the value observed for the NCD. It should be noted that the microcrystalline films show no evidence for any surface redox processes. The slightly higher background current for this particular nanocrystalline film has been mentioned due to the increased fraction of grain boundary carbon.

Figure 31b shows voltammograms for the nanocrystalline and microcrystalline films between  $-1.4$  and  $2.0$  V (vs SCE). The electrolyte was  $1$  M  $H_2SO_4$  and the potential sweep rate was  $25$  mV/s. The working potential window in this medium for the NCD film is ca.  $3$  V ( $\pm 250 \mu A/cm^2$ ) and is larger than the ca.  $2.5$  V window observed for freshly polished glassy carbon. The response shows a large anodic peak at  $1.5$  V and a smaller cathodic peak at  $0.4$  V. The anodic peak at  $1.5$  V is likely due to redox-active carbon in the grain boundaries. This indicates that some reduction of these surface carbon-oxygen functionalities must occur during the cathodic potential sweep in order to allow for their reoxidation on the subsequent forward sweep. The voltammogram for the boron-doped microcrystalline film, between  $-1.4$  and  $2.0$  V, reveals a working potential window of  $3.3$  V, which is slightly wider than observed for NCD films. The voltammogram shows an anodic peak at  $1.8$  V just prior to oxygen evolution; however, the peak charge is significantly less than that for the NCD films. This reflects the reduced coverage of redox-active grain boundary carbon on the microcrystalline films.

These studies indicate that NCD films prepared from  $C_{60}/Ar$  gas mixtures appear to have basic electrochemical properties similar to boron-doped microcrystalline diamond films with a wide working potential window and a low voltammetric background current. The potential application of NCD in electroanalysis seems to be due its nanocrystalline structure.

### 6.3. Tribology

The unique properties of diamond (i.e. the highest hardness, stiffness, and thermal conductivity as well as imper-

viousness to acidic and saline media) are exceptional and far exceed those of any other known material. The cleaved diamond surfaces exhibit one of the lowest friction coefficients of any known material. The combination of these qualities in a material is ideal for highly demanding tribological applications. The prospects for large-scale uses of diamond in tribology increased sharply when it was discovered that diamond can be grown as thin films at low deposition pressures by various methods [150–153]. High quality microcrystalline diamond films exhibit most of the desired properties of the natural diamonds. They are made up of large columnar grains that are highly faceted and generally rough. They tend to grow continuously rougher as the thickness of the deposited films increases. The generally rough surface finish of these films precludes their immediate uses for most machining and wear applications. When used in sliding-wear applications, such rough films cause high friction and very high wear losses on mating surfaces [154–156]. The rough surface can be polished by laser beams and fine diamond powders or by rubbing against a hot iron plate [157]. Despite the high interest in using diamond films for diverse tribological applications, their widespread utilization in the industrial world has not yet met expectations [158–160]. Recently, new methods have been developed for deposition of smooth NCD films [161] and the films afford ultralow friction and wear in sliding tribological applications.

As elaborated above, conventional diamond films are generally rough and consist of large grains. Depending on deposition conditions, these grains exhibit  $\langle 111 \rangle$  or  $\langle 100 \rangle$  crystallographic growth orientations. Figure 32 [162] depicts the friction coefficients of microcrystalline diamond films (surface roughness:  $0.35 \mu m$ , rms) and NCD (surface roughness:  $30$  nm, rms) films against  $Si_3N_4$  balls in open air and dry  $N_2$  [162]. After an initial run-in period during which friction is relatively high, the friction coefficient of the NCD film decreases rapidly to  $\sim 0.1$  in open air and to  $\sim 0.05$  in dry  $N_2$ , whereas the friction coefficient of the microcrystalline diamond film remains high and unsteady in both test environments.

Wear rates of  $Si_3N_4$  balls slid against the smooth NCD and rough microcrystalline diamond films in air and dry  $N_2$  are shown in Figure 33 [162] which clearly shows that the wear rates of balls slid against the NCD films are more than two orders of magnitude lower than the wear rates of balls slid against the rough microcrystalline diamond (MCD) films. The high friction coefficients of rough diamond films can be attributed to the abrasive cutting and plowing effects of sharp asperity tips on softer counterface pins, whereas the plowing effects created by smooth NCD films on counterface balls are minimal and thus exhibit lower friction. Previous studies also demonstrated a close correlation between higher surface roughness and greater frictional losses [155, 163, 164]. When the rough MCD films were polished and then used in sliding-contact experiments, very low friction coefficients were obtained [161, 163, 164].

Apart from physical roughness, surface chemistry and tribo-induced adhesive interactions can also occur and play a dominant role in the friction and wear performance of all diamond films [165]. The nature and extent of interactions may be controlled by the environmental species or by ambient temperature [166]. Mechanistically, the low-friction

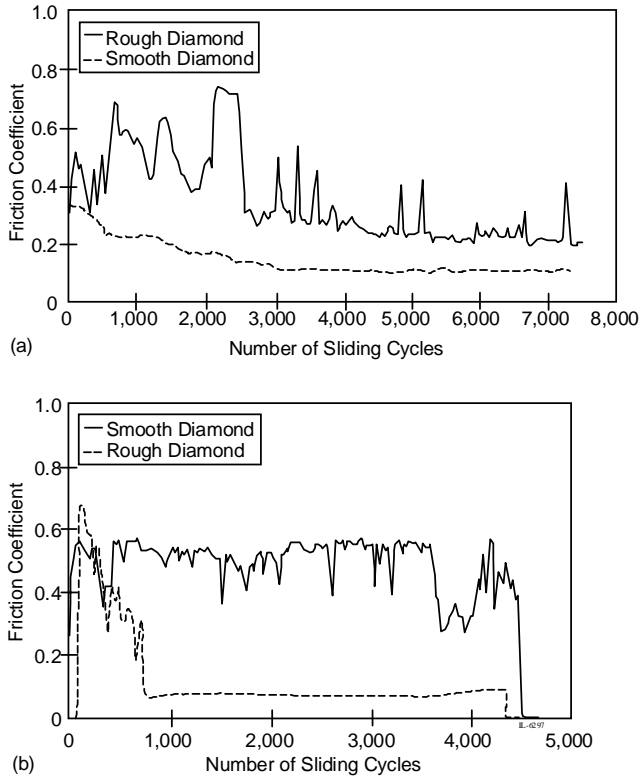


**Figure 32.** Friction coefficients for rough MCD and smooth NCD films against  $\text{Si}_3\text{N}_4$  balls in (a) open air and (b) in dry  $\text{N}_2$ . (Test conditions: load, 2 N; velocity,  $0.05 \text{ m s}^{-1}$ ; relative humidity, 37%, sliding distance, 40 m, ball diameter, 9.55 mm.) Reprinted with permission from [162], A. Erdemir et al., *Surf. Coat. Technol.* 120–121, 565 (1999). © 1999, Elsevier Science.

nature of smooth or cleaved diamond surfaces has long been attributed to the highly passive nature of their surfaces [167, 168]. Specifically, it has been postulated that gaseous adsorbates, such as hydrogen, oxygen, or water vapor, can effectively passivate the dangling surface bonds of diamond. When the dangling bonds become highly passive, the adhesion component of friction is diminished [162]. Thus, unlike most other engineering materials, NCD offers

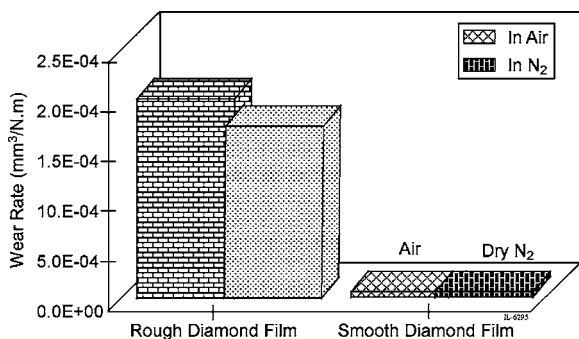


**Figure 33.** Wear rates of  $\text{Si}_3\text{N}_4$  balls slid against smooth NCD and rough MCD in air and dry  $\text{N}_2$  (test conditions: load, 2 N; velocity,  $0.05 \text{ m s}^{-1}$ ; relative humidity, 37%; sliding distance, 40 m; ball diameter, 9.55 mm). Reprinted with permission from [162], A. Erdemir et al., *Surf. Coat. Technol.* 120–121, 565 (1999). © 1999, Elsevier Science.

a combination of low friction and high wear resistance under a wide range of sliding-contact conditions. NCD coatings have been applied to seals using dc-biased substrates and an oxyacetylene torch [161, 169].

#### 6.4. Superhard Nanocrystalline Composites

Materials with Vickers hardness of  $\geq 40 \text{ GPa}$  are called superhard materials. The hardness of diamond depends on its quality and is typically in the range of 70 to 90 GPa. It is limited by dislocation sliding and crack propagation along the  $\langle 111 \rangle$  crystallographic direction [170, 171]. The theoretical strength of ideal single crystalline materials can be easily estimated from the critical stress, which is needed to cause shear sliding of lattice planes [172]. However, the practically achievable strength of single crystals and engineering materials is orders of magnitude smaller because plastic deformation and fracture occur due to inherent flaws, such as multiplication and propagation of dislocations and crack growth, which are present in the materials. The design of novel superhard materials is based on the formation of stable nanocomposite consisting of two or more phases, for example nanocrystals of hard transition metal nitride imbedded in an amorphous phase [173–175]. When such a nanostructure is formed by a thermodynamically driven segregation of transition metal nitride and silicon or boron nitride, it is fairly stable against recrystallization even at high temperatures of  $\geq 1000 \text{ }^\circ\text{C}$  [176, 177]. The resulting strong interface and compact grain boundaries avoid grain boundary sliding, which would otherwise limit the strength and hardness of nanocrystalline materials [178–181]. Beside the hardness, the nanocomposites also show a very high elastic recovery of 80% to 90% and toughness. The nanocrystalline diamond seems to be one of the promising superhard nanocomposite materials if the properties of NCD are properly tailored. The superhardness combined with a high elastic recovery and toughness will be very important for many practical applications.

Hardness of a material is a measure of its ability to resist deformation upon load. Hence, the meaning of hardness depends on the exact nature of that load resulting in various kinds of engineering scales of hardness, such as scratch, static contact indentation, or dynamic ones. The most universal measure of the hardness is the energy of the plastic or pseudoplastic deformation, which is calculated from the ratio of the applied load to the area of that deformation. Depending on the shape of the indenter used, various scales of the static hardness result. For the characterization of thin films the Vickers or alternatively Knoop hardness is most commonly used. During the measurement a diamond indenter of pyramidal shape with an angle between the opposite faces of  $136^\circ$  is pressed into a material with a given load  $L$  and after unloading, the area of the remaining plastic deformation  $A$  is measured. The hardness in GPa or  $\text{kg/mm}^2$  is then calculated from the equation  $H = \alpha L/A$ , where the constant  $\alpha$  depends on the type of the indenter which differs by the angles between the opposite faces of the diamond pyramid. Figure 34 [175] shows examples of indentation into a NCD and into ultrahard  $nc\text{-TiN}/a\text{-}$  and  $nc\text{-TiSi}_x$ ,  $x \approx 2$ . It should be noted that the measurements on super- and ultrahard materials including diamond show large scattering and, therefore,

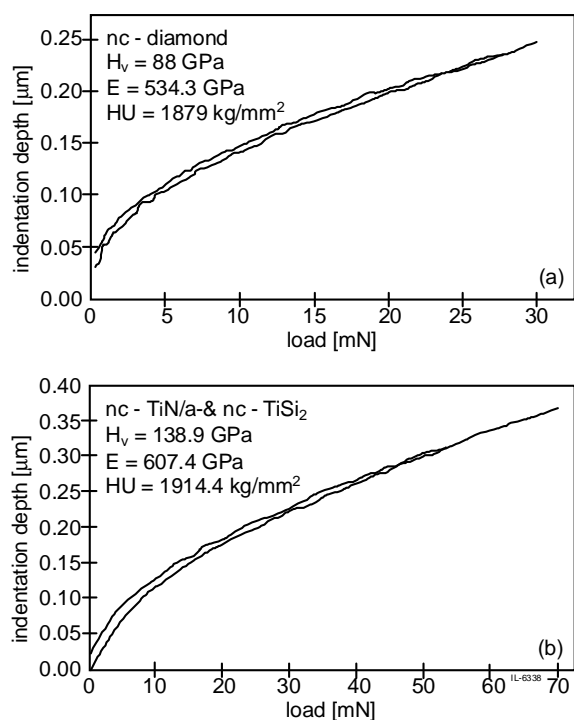


**Figure 34.** Example of indentation into (a) NCD and (b) nc-TiN/a- & nc-TiSi<sub>x</sub> ( $x \sim 2$ ) coatings. The area between the lower (loading) and upper (unloading) curve corresponds to the energy of pseudoplastic deformation, the area between the loading curve and the y-axis corresponds to the total energy of deformation. Reprinted with permission from [175], P. Nesladek and S. Veprek, *Phys. Status Solidi A* 177, 53 (2000). © 2000, Wiley-VCH.

the obtained values of hardness should be considered as relative ones. Therefore, one can conclude from Figure 34 that the microhardness of the nc-TiN/a- and nc-TiSi<sub>x</sub> films is at least equal to that of the hardest diamond.

## 6.5. Conformal Coatings

The excellent mechanical properties of diamond suggest that diamond is one of the best materials for MEMS applications. In addition, the chemical inertness of diamond makes it a suitable as a corrosion protection material. Recently, NCD film growth has been demonstrated on various substrates of engineering interest [182]. The substrate of choice in most diamond deposition studies has been silicon while for metals, the thermal expansion mismatch between the diamond film and substrate gives rise to thermal stress, which often results in delamination of the film. Thus, one of the major barriers in obtaining a diamond film that is resistant to delamination is the inherent difference between the coefficient of thermal expansion between the diamond film and a metal substrate.

The desirable mechanical properties with coating containing NCD and/or amorphous carbon have been reported [183]. The combination of nanocrystalline and amorphous carbon components can result in coatings with high toughness, high hardness, and low surface roughness [183, 184]. These films are believed to consist of NCD grains imbedded in a primarily amorphous carbon matrix, which itself

has some  $sp^3$ -bonded carbon content. These coatings have been produced with hardness up to 80% that of natural diamond and yet still exhibit appreciable toughness uncharacteristic of a pure ceramic material [182]. NCD coatings can be tailored in their coating structure and mechanical properties by appropriate changes in CVD feed gas chemistry [182]. The relative concentration of CH<sub>4</sub> and N<sub>2</sub> is shown to strongly influence coating structure, hardness, and adhesion. This can provide an opportunity to choose a balance between coating hardness and toughness as required for a particular application.

There is general agreement that diamond film growth occurs most readily on pure metal that supports the formation of a stable carbide layer. There has been controversy as to whether the formation of a surface carbide film was a prerequisite for diamond growth. Ramanathan et al. [185] have studied the transition metals and found that diamond growth is supported by those metals that tend to produce stabilized  $sp^3$  carbon structures. Diamond film adhesion is critically linked to the thermal expansion mismatch between diamond and metal. At higher deposition temperatures more stress may be induced in the film, providing a higher driving force for film buckling or delamination. Ager and Drory [186] measured a residual compressive stress of about 7 GPa for a diamond film on Ti-6Al-4V that was in excellent agreement with the stress predicted from calculation. With such large residual film stresses it would be advantageous to be able to deposit diamond at low substrate temperature. It has been well established that adding small quantities of oxygen can lower the temperature range for which diamond can grow [187, 188]. A small amount of CO and O<sub>2</sub> diluted in H<sub>2</sub> has also resulted in high quality diamond growth at substrate temperatures in the range of 411 to 750 °C [189]. However, in high H<sub>2</sub>-dilution conditions, the deposition rate decreases rapidly with temperature. This is because the precursor radical that is widely believed to be responsible for diamond growth under high H<sub>2</sub> dilution is thermally activated [190, 191].

An interlayer can be used as a barrier to the diffusion of carbon into the substrate, thus providing sufficient carbon concentrations at the surface to nucleate diamond. The interlayer may also be used in order to minimize interfacial stresses and to provide an intermediate layer for bonding. Diamond deposition onto WC-Co and steel substrates has been achieved using a multilayer structure of silver and refractory metals with a resulting improvement in adhesion [192]. Such coating is typical of that required for good WC-Co cutting tool properties. Figure 35 [182] shows a thick NCD film grown on WC-Co that was prepared with a chemical treatment prior to coating and it depicts an extremely smooth and flat surface. Similarly, results of conformal coatings of NCD are very encouraging and a good degree of coating conformality has been reported wherein a hexagonal shaped silicon needle  $\sim 5 \mu\text{m}$  in diameter was successfully coated with  $\sim 2000 \text{ \AA}$  NCD [4].

## 6.6. SAW Devices

SAW devices have found several key applications in radio frequency and microwave electronics [193]. They offer a high degree of frequency selectivity with low insertion loss,



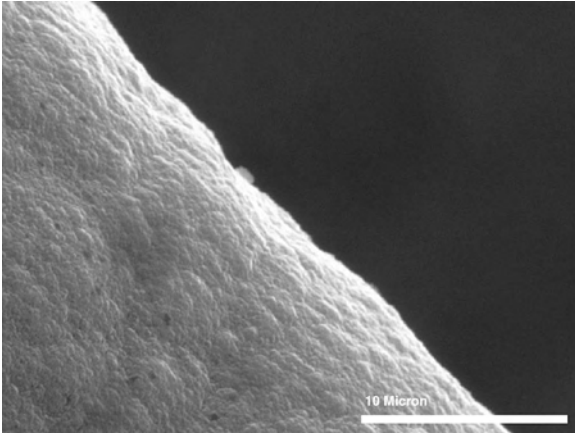


**Figure 35.** Thick NCD coating made on chemically treated surface of WC-Co cutting tool insert. Edge shown is a cutting edge of the tool. Reprinted with permission from [182], R. Thompson et al., in "Proceedings of the 1st ASM International Surface Engineering and the 13th IFHTSE Congress and Exposition" (O. Popoola et al., Eds.), 7–10 October 2002, Columbus, OH. © 2002, ASM International.

making them highly suitable for use as narrow band filters. SAW devices are particularly well adapted to microwave integrated circuits since they can provide a significant size reduction over purely electromagnetic devices. These devices are most typically implemented on piezoelectric substrates on which thin metal film interdigitated transducers (IDTs) are fabricated using photolithography. The use of diamond as a SAW substrate offers an attractive means for relaxing the lithographic criteria [194]. With a surface wave velocity  $\nu \sim 1 \times 10^{14} \text{ m s}^{-1}$ , diamond allows SAW device operation near 2.5 GHz with nominal  $1 \mu\text{m}$  linewidths. Since diamond is not piezoelectric, additional complexity is introduced by a requisite overlayer of a piezoelectric thin film, typically ZnO. Sound propagation in layered media may be highly dispersive and in general admits a multiplicity of allowed modes. Nevertheless, highly successful devices based on ZnO/polycrystalline diamond/Si layered structures have been reported [195–199].

NCD is a new form of diamond and differs from diamondlike carbon in that it contains relatively little hydrogen or  $sp^2$ -bonded carbon. The properties of NCD films like smooth surfaces and small crystallite size are most attractive and relevant for SAW applications, since standard PCD on Si is quite rough and must be smoothed by mechanical polishing before photolithographic processing can be attempted. Furthermore, one expects acoustic scattering at large angle grain boundaries in PCD, especially if lateral grain dimensions exist on length scales between acoustic wavelength and SAW device apertures and transducer separations. The use of NCD eliminates these concerns. SAW devices based on NCD have been fabricated [200] as shown schematically in Figure 36 [200]. This device was studied using a frequency and time domain method. Phase velocities were obtained from device resonant frequencies measured with a network analyzer. Figure 37 [200] presents a compilation of experimental results and calculations of the phase velocity  $\nu$  as a function of  $kh_{\text{ZnO}}$ . It is evident that several modes are allowed for a given value of  $kh_{\text{ZnO}}$ . The modes

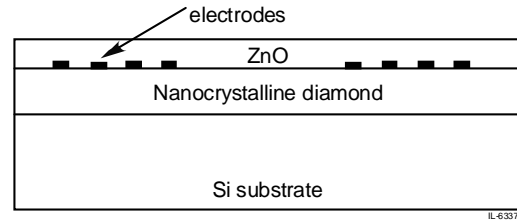


**Figure 36.** Schematic diagram of the surface acoustic wave device multilayer structure. Reprinted with permission from [200], B. Bi et al., *Diamond Relat. Mater.* 11, 677 (2002). © 2002, Elsevier Science.

are highly dispersive at small values of  $kh_{\text{ZnO}}$  (i.e., the phase velocity is strongly dependent on  $kh_{\text{ZnO}}$ ). As expected, the lowest order mode tends toward the phase velocity of the Rayleigh wave on (0001) ZnO at large  $kh_{\text{ZnO}}$  but approaches the diamond Rayleigh wave velocity as  $kh_{\text{ZnO}} \rightarrow 0$ . It should be noted that the large phase velocity suggests that carbon within the grain boundaries is strongly bonded. Since surface waves are dominated by elastic shear strains, the grain boundary carbon is highly resistant to bond-bending forces. This indicates that most of the carbon is highly coordinated.

## 6.7. MEMS Devices

Thin film ferroelectrics are important for MEMS because of their strong piezoelectric effect and high energy density originating from the very high dielectric constant of ferroelectric materials [201, 202]. Further, these MEMS devices are fabricated primarily in silicon because of the available surface machining technology. A major problem with Si-based

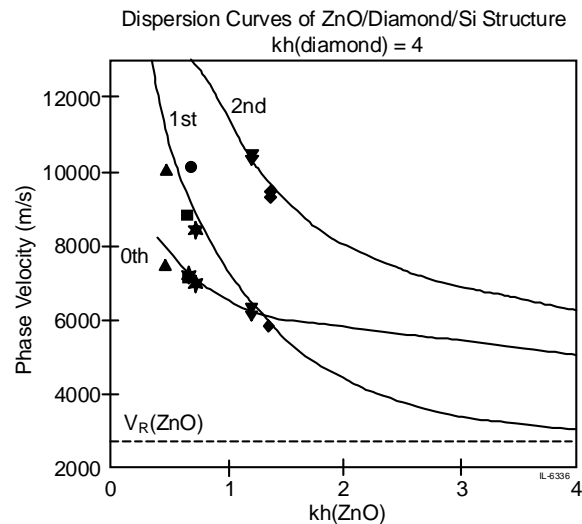


**Figure 37.** Phase velocities as measured for surface waves on NCD, diamond ( $\blacktriangle$  $\blacklozenge$  $\blackstar$ ) and on large-grain polycrystalline diamond ( $\blacksquare$  $\bullet$ ). The solid line represent calculations of phase velocities based on single crystal diamond material parameters. The label denotes the Rayleigh mode indices for the layered medium. The dashed line shows the Rayleigh wave velocity on ZnO. Reprinted with permission from [200], B. Bi et al., *Diamond Relat. Mater.* 11, 677 (2002). © 2002, Elsevier Science.

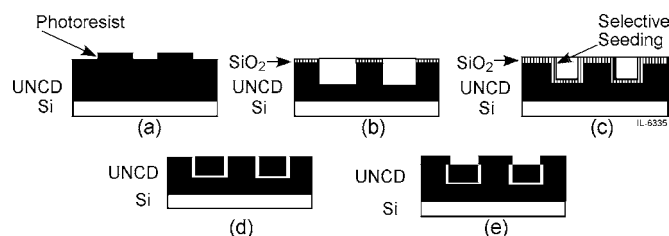


**Figure 38.** Combined lithographic patterning and selective deposition methods. Reprinted with permission from [207], A. R. Krauss et al., *Diamond Relat. Mater.* 10, 1952 (2001). © 2001, Elsevier Science.

MEMS technology is that Si has poor mechanical and tribological properties [203, 204]. On the other hand, diamond is an ultrahard material with high mechanical strength, exceptional chemical inertness, and outstanding thermal stability. The friction coefficient of diamond is exceptionally low and the projected wear life is 10,000 times greater than that of Si, making diamond an ideal tribomaterial for MEMS components [205, 206]. Lubrication poses a major limitation on the design of MEMS devices since the usual methods of delivering lubricant to the interface between contacting parts are very difficult to implement. There are a number of ways in which diamond components can be fabricated for MEMS applications using thin film deposition methods [207].

One of the methods of obtaining the tribological benefits of diamond while exploiting the availability of Si fabrication technology is to produce Si components to near-net shape and then to provide a thin, low wear, low friction diamond coating [208–213]. This approach only works if the diamond film can be produced as a thin, continuous, conformal coating with exceptional low roughness on the Si component. Conventional diamond CVD deposition methods result in discontinuous films with a low density of large grains and poor ability to form thin conformal coatings on Si microstructures [214]. Recently, Krauss et al. successfully developed a fabrication technique [207] for conformal UNCD coating that is comparable to the lithography, galvanofarming, Abformung (LIGA) method and permits fabrication of complex three-dimensional shapes as opposed to the two-dimensional structures produced by Si microfabrication methods. The selective deposition represents a second method that may be used for the production of UNCD microstructures but has no analog in Si microfabrication technology. All diamond films require a nucleation layer, usually achieved by exposing the substrate to a suspension

**Table 1.** Mechanical properties of diamond thin films.

Thin films	NCD	UNCD	PCD	Ref.
Grain size	50–100 nm	2–5 nm	0.5–10 $\mu\text{m}$	[113]
Specific heat ( $\text{J g k}^{-1}$ )	0.68	—	0.54	[113]
Friction coefficient	0.06	—	0.35	[168, 207]
Surface roughness	50–100 nm	20–40 nm	400 nm–1 $\mu\text{m}$	[207]
Young's modulus	600 GPa	—	1200 GPa	[38, 207]
Hardness	62 GPa	—	100 GPa	[10, 38]

**Table 2.** Electrical properties of diamond thin films.

Thin films	NCD	UNCD	PCD	Ref.
Direct bandgap	4.84 eV	—	5.45 eV	[38, 74]
Indirect bandgap	2.18 eV	—	—	[38]
Field emission threshold field	1 $\text{V}/\mu\text{m}$	3.2 $\text{V}/\mu\text{m}$	22 $\text{V}/\mu\text{m}$	[8, 140]
Electronic bonding	up to 50% $sp^2$	2–5% $sp^2$	$sp^3$	[207]
H content	<1%	<1%	<1%	[207]

of fine diamond particles. It is possible to seed a selected portion of the substrate by (a) using photoresist to prevent exposure of selected areas to the diamond powder, (b) using diamond-loaded photoresist to produce a patterned nucleation layer, or (c) seeding the substrate uniformly and then selectively etching portions of the surface to remove diamond seeded areas. Alternatively, it is possible to use  $\text{SiO}_2$  as a mask [215–217], since diamond films grown from  $\text{CH}_4\text{--H}_2$  plasmas are normally unable to form on  $\text{SiO}_2$  substrates. The feature resolution that can be achieved by this method is limited by the grain size [216]. The lithographic patterning is the third method to produce diamond multiplayer structures. In this method, it is necessary to deposit a thin diamond film on a sacrificial release layer such as  $\text{SiO}_2$ . Methods have been reported [216, 217] to force the growth of conventional CVD diamond on  $\text{SiO}_2$ , typically by damaging the  $\text{SiO}_2$  surface by ultrasonic abrasion in a diamond powder suspension. Continuous diamond films have been achieved using this method for film thickness in the range 15–20  $\mu\text{m}$  although there are gaps between the film and the substrate, and the films are extremely rough [217]. Diamond films grown from  $\text{CH}_4\text{--Ar}$  plasmas are able to form directly on  $\text{SiO}_2$  substrates without the need for damaging the  $\text{SiO}_2$  layer since the gas-phase carbon dimer growth species in the UNCD process forms an intermediate SiC nucleation layer. The use of  $\text{SiO}_2$  as a sacrificial substrate layer for fabrication of multiplayer UNCD devices has also been demonstrated [207].

Thus by combining selective deposition and lithographic etching of blanket UNCD films, Krauss et al. fabricated multilevel diamond devices [207] using methods that are not feasible or require a large number of steps in Si. A scheme for fabricating a captive rotor using combined methods is shown in Figure 38 [207]. A blanket UNCD film is deposited on a Si substrate, followed by deposition of photoresist to yield the structure shown in Figure 38a. A  $\text{SiO}_2$  layer is then deposited and used as a hard mask in combination with an oxygen plasma etch to produce the structure shown in Figure 38b. A conformal  $\text{SiO}_2$  layer is then deposited, and the trenches are selectively seeded as shown in Figure 38c using one of the methods described in the previous paragraph. The seeded trenches are filled with UNCD, and the  $\text{SiO}_2$  layer is then removed by HF etch, leaving the wheel free within the retaining trench of the stator as presented in Figure 38d. Further UNCD growth results in both an increase in height and a lateral spread of the stator components, which act to capture the rotor within the track as shown in Figure 38e.

## 7. SUMMARY

NCD has many remarkable properties for variety of applications and these films have been recognized as an important class of structures in the family of diamond materials. With the advent of low pressure and temperature CVD techniques, it is now possible to control the microstructure, surface roughness, and optical transmittance of the NCD films. The grain size of the NCD films can be varied from 4 nm to a few hundred of nanometers. The OES investigations indicate that the nucleation and growth mechanism depends on a methane fraction. It is observed that C<sub>2</sub> dimer is the predominant growth species and plays a major role in the growth of NCD films.

The optical transmittance of NCD films is a strong function of the surface roughness but not the grain size of the NCD films. Ultrasoother and highly transparent NCD films can be grown on either nanometer- or micrometer-scratched substrates with either low or high, respectively, methane fractions. These smooth diamond films can be used in mechanical-seal applications, for protection against wear, and as abrasion resistant coatings in several demanding tribological applications. The field emission studies of NCD films showed a substantial reduction in emission turn-on voltage indicating their tremendous promise as a cold cathode material. In addition, these NCD films possess unique electrochemical behavior and also exhibit a great potential for application in SAW and MEMS devices. Thus in view of many interesting properties of NCD films that have been summarized in Tables 1 and 2, they proved to be one of the important emerging nanostructured materials with many potential applications.

## GLOSSARY

**Chemical vapor deposition (CVD)** A method for depositing some of the layers which function as dielectric, conductor, or semiconductor. A vaporized chemical containing atoms of the materials to be deposited reacts with another, liberating the desired material, which deposits on the substrate while the by-products of reaction are removed from the reaction chamber.

**Electron emission** The liberation of electrons from an electrode into the surrounding space, usually under the influence of a high electric field, light, or heat.

**Electron energy loss spectroscopy (EELS)** A technique for studying atoms, molecules, or solids in which a substance is bombarded with monochromatic electrons, and the energies of scattered electrons are measured to determine the distribution of energy loss.

**Field emission display (FED)** This is an array of a million or more electron guns, each exciting a single phosphor pixel. The electron guns are typically triodes.

**Hardness** The measure of a material's resistance to deformation by surface indentation or by abrasion.

**Specific heat capacity** The heat capacity per unit mass of material.

**Surface roughness** The finer irregularities of the surface texture that usually result from the inherent action of the production process or material condition.

**Thermal conductivity** For steady-state heat flow, the proportionality constant between the heat flux and the temperature gradient. Also, a parameter characterizing the ability of a material to conduct heat.

**Transmission electron microscopy (TEM)** A microscope that produces an image by using electron beams to transmit (pass through) the specimen, making examination of internal features at high magnification possible.

**Tribology** The science and technology of two interacting surfaces in relative motion and of related subjects and practices. The popular equivalent is friction, wear, and lubrication in surfaces sliding against each other, as in gears and bearings.

## ACKNOWLEDGMENTS

P. D. K. is thankful to Professor L. C. Chen, National Taiwan University, Taipei, Taiwan, and Professor K. H. Chen, Institute of Atomic and Molecular Sciences, Taipei, Taiwan, for introducing him to the field of nanocrystalline diamond. In addition, he gratefully acknowledges a Post-Doctoral Fellowship from the National Science Council, Taiwan and National Science Foundation–Nanoscale Interdisciplinary Research Teams, USA.

## REFERENCES

1. R. C. DeVries, *Annu. Rev. Mater. Sci.* 17, 161 (1987).
2. J. C. Angus and C. C. Hayman, *Science* 241, 913 (1988).
3. K. E. Spear, *J. Am. Ceram. Soc.* 72, 171 (1989).
4. D. M. Gruen, *Annu. Rev. Mater. Sci.* 29, 211 (1999).
5. L. C. Chen, P. D. Kichambare, K. H. Chen, J.-J. Wu, J. R. Yang, and S. T. Lin, *J. Appl. Phys.* 89, 753 (2001).
6. D. M. Gruen, S. Liu, A. R. Krauss, J. Luo, and X. Pan, *Appl. Phys. Lett.* 64, 1502 (1994).
7. D. M. Gruen, S. Liu, A. R. Krauss, and X. Pan, *J. Appl. Phys.* 75, 1758 (1995).
8. D. Zhou, A. R. Krauss, L. C. Qin, T. G. McCauley, D. M. Gruen, T. D. Corrigan, R. P. H. Chang, and H. Gnaser, *J. Appl. Phys.* 82, 4546 (1997).
9. R. Erz, W. Dotter, D. Jung, and H. Ehrhardt, *Diamond Relat. Mater.* 2, 449 (1993).
10. V. I. Konov, A. A. Smolin, V. G. Ralchenko, S. M. Pimenov, E. D. Obratsova, E. N. Loubnin, S. M. Metev, and G. Sepold, *Diamond Relat. Mater.* 4, 1073 (1995).
11. V. I. Konov, E. D. Obratsova, S. M. Pimenov, V. G. Ralchenko, and A. A. Smolin, *Proc. SPIE* 2428, 612 (1995).
12. L. C. Nistor, J. Van Landuyt, V. G. Ralchenko, E. D. Obratsova, and A. A. Smolin, *Diamond Relat. Mater.* 6, 159 (1997).
13. L. C. Nistor, J. Van Landuyt, V. G. Ralchenko, E. D. Obratsova, K. G. Korotushenko, and A. A. Smolin, *Mater. Sci. Forum* 239–241, 115 (1997).
14. C. Z. Gu and X. Jiang, *J. Appl. Phys.* 88, 1788 (2000).
15. T. Sharda, M. Umeno, T. Soga, and T. Jimbo, *Appl. Phys. Lett.* 77, 4304 (2000).
16. T. Sharda, T. Soga, T. Jimbo, and M. Umeno, *Diamond Relat. Mater.* 9, 1331 (2000).
17. B. Hong, J. Lee, R. W. Collins, Y. Kuang, W. Drawl, R. Messier, T. T. Tsong, and Y. E. Strausser, *Diamond Relat. Mater.* 6, 55 (1997).
18. D. V. Fedoseev, V. L. Bukhovets, I. G. Varshavskaya, and Y. N. Tolmachev, *Russ. J. Phys. Chem.* 70, 1594 (1996).
19. M. Zarrabian, N. Fourches-Coulon, G. Turban, C. Marhic, and M. Lancin, *Appl. Phys. Lett.* 70, 2535 (1997).

20. G. Amaratunga, A. Putnis, K. Clay, and W. Milne, *Appl. Phys. Lett.* 55, 634 (1989).
21. D. Zhou, T. G. McCauley, L. C. Qin, A. R. Krauss, and D. M. Gruen, *J. Appl. Phys.* 83, 540 (1998).
22. W. Kratschmer, L. D. Lamb, K. Fostiropoulos, and D. R. Huffman, *Nature* 347, 354 (1990).
23. D. M. Gruen, *Nucl. Instrum. Methods Phys. Res.* 78, 118 (1993).
24. D. A. Horner, L. A. Curtiss, and D. M. Gruen, *Chem. Phys. Lett.* 233, 243 (1995).
25. W. Banholzer, *Surf. Coat. Technol.* 53, 1 (1992).
26. L. S. Pan and D. R. Kania, "Diamond: Electronic Properties and Application." Kluwer Academic, London, 1995.
27. D. R. McKenzie, D. A. Muller, and B. A. Paithorpe, *Phys. Rev. Lett.* 67, 773 (1991).
28. Y. Lifshitz, G. D. Lempert, and E. Grossman, *Phys. Rev. Lett.* 72, 2753 (1994).
29. P. J. Fallon, V. S. Veerasamy, C. A. Davis, J. Robertson, G. A. J. Amaratunga, W. I. Milne, and J. Koskinen, *Phys. Rev. B* 48, 4777 (1993).
30. M. Weiler, S. Sattel, K. Jung, H. Ehrhardt, V. S. Veerasamy, and J. Robertson, *Appl. Phys. Lett.* 64, 2797 (1994).
31. P. K. Bachman, D. Leers, and H. Lydtin, *Diamond Relat. Mater.* 1, 1 (1991).
32. S. Matsumoto, Y. Saito, M. Tsutsumi, and N. Setaka, *J. Mater. Sci.* 17, 3106 (1981).
33. A. Erdemir, G. R. Fenske, A. R. Krauss, D. M. Gruen, T. McCauley, and R. T. Csencsits, *Surf. Coat. Technol.* 120, 565 (1999).
34. A. Erdemir, C. Bindal, G. R. Fenske, C. Zurker, A. R. Krauss, and D. M. Gruen, *Diamond Relat. Mater.* 5, 923 (1999).
35. T. Lin, G. Y. Yu, A. T. S. Wee, Z. X. Shen, and K. P. Loh, *Appl. Phys. Lett.* 77, 2692 (2000).
36. M. Tsuda, M. Nakajima, and S. Oikawa, *J. Am. Chem. Soc.* 108, 5780 (1986).
37. R. Haubner and B. Lux, *Diamond Relat. Mater.* 2, 1277 (1993).
38. K. Chakrabarti, R. Chakrabarti, K. K. Chattopadhyay, S. Chaudhuri, and A. K. Pal, *Diamond Relat. Mater.* 7, 845 (1998).
39. M. W. Geis and M. A. Tamor, "Encyclopedia of Applied Physics," Vol. 5. VCH, New York, 1993.
40. W. A. Yarbrough and R. Messier, *Science* 247, 605 (1990).
41. W. Zhu, B. R. Stoner, B. E. Williams, and J. T. Glass, *Proc. IEEE* 79, 621 (1991).
42. W. Zhu, C. A. Randall, A. R. Badzian, and R. Messier, *J. Vac. Sci. Technol. A* 7, 2315 (1989).
43. B. E. Williams, J. T. Glass, R. F. Davis, K. Kobashi, and Y. Kawate, in "Materials Research Society Extended Abstracts," EA-15, (G. H. Johnson, A. R. Badzian, and M. W. Geis, Eds.). Materials Research Society, Pittsburgh, 1988.
44. Y. Cong, R. W. Collins, R. Messier, K. Vedam, G. F. Epps, and H. Windischmann, in "New Diamond Science and Technology" (R. Messier, J. Glass, J. Butler, and R. Roy, Eds.), p. 735. Materials Research Society, Pittsburgh, 1991.
45. J. Robertson and E. P. O'Reilly, *Phys. Rev. B* 35, 2946 (1987).
46. Y. Sato and M. Kamo, *Surf. Coat. Technol.* 39/40, 183 (1989).
47. Y. Cong, I. An, H. V. Nguyen, K. Vedam, R. Messier, and R. W. Collins, *Surf. Coat. Technol.* 49, 381 (1991).
48. K. A. Snail and C. M. Marks, *Appl. Phys. Lett.* 60, 3135 (1992).
49. L. Fayette, B. Marcus, M. Mermoux, L. Abello, and G. Lucazeau, *Diamond Relat. Mater.* 3, 438 (1994).
50. C. D. Zulkar, D. M. Gruen, and A. R. Krauss, *Mater. Res. Soc. Bull.* 20, 29 (1995).
51. B. Hong, M. Wakagi, R. W. Collins, I. An, N. C. Engdahl, W. Drawl, and R. Messier, *Diamond Relat. Mater.* 3, 431 (1994).
52. H. Windischmann, G. F. Epps, Y. Cong, and R. W. Collins, *J. Appl. Phys.* 69, 2231 (1991).
53. B. Hong, J. Lee, R. W. Collins, Y. Kuang, W. Drawl, R. Messier, T. T. Tsong, and Y. E. Strausser, *Diamond Relat. Mater.* 6, 55 (1997).
54. R. W. Collins and Y. T. Kim, *Anal. Chem.* 62, 887A (1990).
55. R. W. Collins, *Rev. Sci. Instrum.* 61, 2029 (1990).
56. B. Hong, M. Wakagi, W. Drawl, R. Messier, and R. W. Collins, *Phys. Rev. Lett.* 75, 1122 (1995).
57. J. Lee, B. Hong, R. Messier, and R. W. Collins, *Appl. Phys. Lett.* 69, 1716 (1996).
58. E. Kondoh, T. Ohta, T. Mitomo, and K. Ohtsuka, *Appl. Phys. Lett.* 59, 488 (1991).
59. W. Zhu, R. Messier, and A. R. Badzian, in "Proceeding of the First International Symposium on Diamond and Diamond-like Films" (J. P. Dismukes, Ed.), Electrochemical Society, Pennington, NJ, 1989.
60. C. Zuiker, A. R. Krauss, D. M. Gruen, X. Pan, J. C. Li, R. Scencsits, A. Erdemir, C. Bindal, and G. Fenske, *Thin Solid Films* 270, 154 (1995).
61. K. Teii, H. Ito, M. Hori, T. Takeo, and T. Goto, *J. Appl. Phys.* 87, 4572 (2000).
62. R. W. B. Pearse and A. G. Gaydon, "The Identification of Molecular Spectra," 4th ed. Wiley, New York, 1976.
63. W. L. Wiese, M. W. Smith, and B. M. Miles, "Atomic Transition Probabilities," Vols. I and II. National Standard Reference Data Series, Washington, DC, 1966.
64. H. Ito, M. Ikeda, M. Ito, M. Hori, T. Takeo, T. Kato, and T. Goto, *Jpn. J. Appl. Phys.* 2 36, L880 (1997).
65. D. Robinson and P. D. Lenn, *Appl. Opt.* 6, 983 (1967).
66. K. Teii, *J. Vac. Sci. Technol. A* 17, 138 (1999).
67. S. Iijima, Y. Aikawa, and K. Baba, *J. Mater. Res.* 6, 1491 (1991).
68. M. Avalos-Borja, G. A. Hiraata, O. Contreras, X. G. Ning, A. Duarte-Moller, and A. Barna, *Diamond Rel. Mater.* 5, 1249 (1996).
69. J. Singh, *J. Mater. Sci.* 29, 2761 (1994).
70. J. S. Luo, D. M. Gruen, A. R. Krauss, X. Z. Pan, and S. Z. Liu, in "Recent Advances in the Chemistry and Physics of Fullerenes and Related Materials" (R. S. Ruoff and K. M. Kadish, Eds.). SPIE, Bellingham, WA, 1995.
71. R. Csencsits, C. Zurker, D. M. Gruen, and A. R. Krauss, *Solid State Phenom.* 261, 51 (1996).
72. L. C. Qin and L. W. Hobbs, *Mater. Res. Soc. Symp. Proc.* 373, 341 (1995).
73. P. Keblinski, D. Wolf, S. R. Phillpot, and H. Gleiter, *J. Mater. Res.* 13, 2077 (1998).
74. H. Hirai, M. Terauchi, M. Tanaka, and K. Kondo, *Diamond Relat. Mater.* 8, 1703 (1999).
75. R. Kuzuo, M. Terauchi, M. Tanaka, Y. Saito, and H. Shinohara, *Jpn. J. Appl. Phys.* 30, 1817 (1991).
76. R. Kuzuo, M. Terauchi, and M. Tanaka, *Jpn. J. Appl. Phys.* 31, 1484 (1991).
77. R. F. Egerton and M. J. Whelan, *Philos. Mag.* 309, 739 (1974).
78. R. F. Egerton, "Electron Energy Loss Spectroscopy in the Electron Microscope." Plenum, New York, 1966.
79. R. A. Roberts and W. C. Walker, *Phys. Rev.* 161, 7730 (1967).
80. T. Xu, S. Yang, J. Lu, Q. Xue, J. Li, W. Guo, and Y. Sun, *Diamond Relat. Mater.* 10, 1441 (2001).
81. B. Fabre, F. Kanoufi, and J. Simonet, *J. Electroanal. Chem.* 434, 225 (1993).
82. F. Fusallba, N. El. Mehdi, L. Breau, and D. Belanger, *Chem. Mater.* 11, 2743 (1999).
83. S. C. Ng, P. Fu, W. L. Yu, H. S. O. Chan, and K. L. Tan, *Synth. Met.* 87, 119 (1997).
84. S. P. Lawrence and R. K. Don, "Diamond: Electronic Properties and Applications." Kluwer Academic, Boston, 1995.
85. S. E. Grillo and J. E. Field, *J. Phys. D* 33, 595 (2000).

86. G. Ilangovan and K. Chandrasekara Pillai, *Langmuir* 13, 566 (1997).
87. T. Jiang and K. Xu, *Carbon* 12, 1663 (1995).
88. S. Prawer, K. W. Nugent, D. N. Jamieson, J. O. Orwa, L. A. Bursill, and J. L. Peng, *Chem. Phys. Lett.* 332, 93 (2000).
89. J. Wagner, M. Ramsteiner, Ch. Wild, and P. Koidl, *Phys. Rev. B* 40, 1817 (1989).
90. R. J. Nemanich, J. T. Glass, G. Lucovsky, and R. E. Shroder, *J. Vac. Sci. Technol. A* 6, 1783 (1988).
91. V. I. Merkulov, J. S. Lannin, C. H. Munro, S. A. Asher, V. S. Veerasamy, and W. I. Milne, *Phys. Rev. Lett.* 78, 4869 (1997).
92. S. M. Leeds, T. J. Davis, P. W. May, C. D. O. Pickard, and M. N. R. Ashfold, *Diamond Relat. Mater.* 7, 233 (1998).
93. T. Sharda, T. Soga, T. Jimbo, and M. Umeno, *Diamond Relat. Mater.* 10, 1592 (2001).
94. V. Paillard, P. Melinon, V. Dupuis, J. P. Perez, and A. Perez, *Phys. Rev. Lett.* 71, 4170 (1993).
95. V. Paillard, P. Melinon, V. Dupuis, A. Perez, J. P. Perez, G. Guiraud, J. Fornazero, and G. Panczer, *Phys. Rev. B* 49, 11433 (1994).
96. J. Lee, R. W. Collins, R. Messier, and Y. E. Strausser, *Appl. Phys. Lett.* 70, 1527 (1997).
97. S. A. Catledge and Y. K. Vohra, *J. Appl. Phys.* 84, 6469 (1998).
98. N. Wada and S. A. Solin, *Physica B* 105, 353 (1981).
99. H. Windischmann, G. F. Epps, Y. Cong, and R. W. Collins, *J. Appl. Phys.* 69, 2231 (1991).
100. K. K. Chattopadhyay and S. Matsumoto, *Appl. Phys. Lett.* 67, 3972 (1995).
101. H. Yoshikawa, C. Morel, and Y. Koga, *Diamond Relat. Mater.* 10, 1588 (2001).
102. V. F. Dorfman, *Thin Solid Films* 212, 267 (1992).
103. D. M. Bhusari, J. R. Yang, T. Y. Wang, S. T. Lin, K. H. Chen, and L. C. Chen, *Solid State Commun.* 107, 301 (1998).
104. F. J. Himpsel, J. A. Knapp, J. A. VanVechten, and D. E. Eastman, *Phys. Rev. B* 20, 624 (1979).
105. T. P. Ong and R. P. H. Chang, *Appl. Phys. Lett.* 55, 2063 (1989).
106. R. L. C. Wu, A. K. Rai, A. Garscadden, P. Lee, H. D. Desai, and K. Miyoshi, *J. Appl. Phys.* 72, 110 (1992).
107. C. Friedrich, G. Berg, E. Broszeit, and C. Berger, *Thin Solid Films* 290–291, 216 (1996).
108. K. K. Chattopadhyay, J. Dutta, S. Chaudhuri, and A. K. Pal, *Diamond Relat. Mater.* 4, 122 (1995).
109. A. B. Maity, M. Basu, S. Chaudhuri, and A. K. Pak, *J. Phys. D* 28, 2547 (1995).
110. T. Sharda, T. Soga, T. Jimbo, and M. Umeno, *J. Nanosci. Nanotech.* 1, 287 (2001).
111. D. R. Tallant, J. E. Parmeter, M. P. Siegal, and R. L. Simpson, *Diamond Relat. Mater.* 4, 191 (1995).
112. T. A. Friedmann, K. F. McCarty, J. C. Barbour, M. P. Siegal, and D. C. Dibble, *Appl. Phys. Lett.* 68, 1643 (1996).
113. C. Moelle, M. Werner, F. Szucs, D. Wittorf, M. Sellschopp, J. von Borany, H. J. Fecht, and C. Johnston, *Diamond Relat. Mater.* 7, 499 (1998).
114. I. Bahrin, in "Thermochemical Data of Pure Substances," Part I. VCH, Weinheim, 1993.
115. C. Moelle, F. Szucs, H. J. Fecht, P. Rohrs, C. Johnston, P. R. Cholker, and M. Werner, in "Proc. of the Micromaterials Conference." Berlin, 1997.
116. P. K. Bachmann, D. Leers, and D. U. Wiechert, *Diamond Relat. Mater.* 2, 683 (1993).
117. Y. Muto, T. Sugino, K. Kobashi, and J. Shirafuji, *J. Appl. Phys.* 59, 843 (1991).
118. S. N. Kundu, M. Basu, A. B. Maity, S. Chaudhuri, and A. K. Pal, *Mater. Lett.* 31, 303 (1997).
119. R. Chakrabarti, K. Chakrabarti, A. B. Maity, S. Chaudhuri, and A. K. Pal, *Diamond Relat. Mater.* 6, 991 (1997).
120. J. Seth, R. Padiyath, S. V. Babu, and M. David, *Thin Solid Films* 212, 251 (1992).
121. E. G. Spencer, P. H. Schmidt, D. C. Joy, and F. J. Sansalane, *Appl. Phys. Lett.* 29, 118 (1976).
122. S. Bhattacharya, O. Auciello, J. A. Carlisle, L. A. Curtiss, A. N. Goyette, D. M. Gruen, A. R. Krauss, J. Schlueter, A. Sumant, and P. Zapol, *Appl. Phys. Lett.* 79, 1441 (2001).
123. J. Robertson and C. A. Davis, *Diamond Relat. Mater.* 4, 441 (1995).
124. T. Nishimori, K. Nakano, H. Sakamoto, Y. Takakuwa, and S. Kono, *Appl. Phys. Lett.* 71, 945 (1997).
125. K. Okano, S. Koizumi, S. R. P. Silva, and G. A. J. Amaratunga, *Nature (London)* 381, 140 (1996).
126. C. A. Spindt, I. Brodie, L. Humphrey, and E. R. Westerberg, *J. Appl. Phys.* 47, 5248 (1976).
127. N. S. Xu, R. V. Latham, and Y. Tzeng, *Electron Lett.* 29, 1596 (1993).
128. C. Wang, A. Garcia, D. C. Ingram, M. Lake, and M. E. Kordesch, *Electron Lett.* 27, 1459 (1991).
129. G. A. J. Amaratunga and S. R. P. Silva, *Appl. Phys. Lett.* 68, 2529 (1996).
130. O. Groning, O. M. Kuttel, P. Groning, and L. Schlapbach, *Appl. Surf. Sci.* 111, 135 (1997).
131. M. W. Geis, J. C. Twichell, J. Macaulay, and K. Okano, *Philos. Appl. Phys. Lett.* 67, 1328 (1995).
132. B. F. Coll, J. E. Jaskie, J. L. Markham, E. P. Menu, A. A. Talin, and P. Von Allmen, *Mater. Res. Soc. Symp. Proc.* 498, 185 (1998).
133. A. G. Rinzler, J. H. Hafner, P. Nikolaev, L. Lou, S. G. Kim, D. Tomanek, P. Nordlander, D. T. Colbert, and R. E. Smalley, *Science* 269, 1550 (1995).
134. W. Zhu, G. P. Kochanski, S. Jin, and L. Seibles, *J. Appl. Phys.* 78, 2707 (1995).
135. V. V. Zhirnov, E. I. Givargizov, and P. S. Plekhanov, *J. Vac. Sci. Technol. B* 13, 418 (1995).
136. R. Schlessler, M. T. McClure, B. L. McCarson, and Z. Sitar, *J. Appl. Phys.* 82, 5763 (1997).
137. F. Lacher, C. Wild, D. Behr, and P. Koidl, *Diamond Relat. Mater.* 6, 1111 (1997).
138. P. D. Kichambare, F. G. Tarntair, L. C. Chen, K. H. Chen, and H. C. Cheng, *J. Vac. Sci. Technol. B* 18, 2722 (2000).
139. P. D. Kichambare, Center for Applied Energy Research, The University of Kentucky, Lexington, KY 40511, unpublished work, 2001.
140. R. H. Fowler and L. W. Nordheim, *Proc. Roy. Soc. London Ser. A* 119, 173 (1928).
141. K. Wu, E. G. Wang, Z. X. Cao, Z. L. Wang, and X. Jiang, *J. Appl. Phys.* 88, 2967 (2000).
142. M. W. Geis, J. C. Twichell, and T. M. Lyszczarz, *J. Vac. Sci. Technol. B* 14, 2060 (1996).
143. K. Wu, E. G. Wang, J. Chen, and N. S. Xu, *J. Vac. Sci. Technol. B* 17, 1059 (1999).
144. Y. V. Pleskov, A. Y. Sakharova, M. D. Krotova, L. L. Bouilov, and B. V. Spitsyn, *J. Electroanal. Chem.* 228, 19 (1987).
145. M. Iwaki, S. Sato, K. Takahashi, and H. Sakairi, *Nucl. Instrum. Methods* 209/210, 1129 (1983).
146. J. Xu, M. C. Granger, Q. Chen, T. E. Lister, J. W. Strojek, and G. M. Swain, *Anal. Chem.* 69, 591A (1997).
147. R. Tenne and C. Levy-Clement, *Israel J. Chem.* 38, 57 (1998).
148. J. Xu and G. M. Swain, *Anal. Chem.* 71, 4603 (1999).
149. B. Fausett, M. C. Granger, M. L. Hupert, J. Wang, G. M. Swain, and D. M. Gruen, *Electroanalysis* 12, 7 (2000).
150. J. Angus, in "Synthetic Diamond: Emerging CVD Science and Technology" (K. E. Spear and J. P. Dismukes, Eds.). Wiley, New York, 1994.

151. "Status and Applications of Diamond and Diamond-like Materials: An Emerging Technology." National Materials Advisory Board, Washington, DC, 1990.
152. W. J. P. van Enckevort, *J. Hard Mater.* 1, 247 (1990).
153. S. J. Bull, *Diamond Relat. Mater.* 4, 827 (1995).
154. D. G. Bhat, D. G. Johnson, A. P. Malshe, H. Naseem, W. D. Brown, L. W. Schaper, and C. H. Shen, *Diamond Relat. Mater.* 4, 921 (1995).
155. I. P. Hayward, *Surf. Coat. Technol.* 49, 554 (1991).
156. A. K. Gangopadhyay and M. A. Tamor, *Wear* 169, 221 (1991).
157. S. K. Choi, D. Y. Jung, S. Y. Kweon, and S. K. Jung, *Thin Solid Films* 279, 110 (1996).
158. B. E. Williams and J. T. Glass, *J. Mater. Res.* 4, 373 (1989).
159. S. J. Bull and A. Mathews, *Diamond Relat. Mater.* 1, 1049 (1992).
160. K. V. Ravi, in "Synthetic Diamond: Emerging CVD Science and Technology," Electrochem. Soc. Monograph. Wiley, New York, 1994.
161. S. Hogmark, O. Hollman, A. Alahelisten, and P. Hedenqvist, *Wear* 200, 235 (1996).
162. A. Erdemir, G. R. Fenske, A. R. Krauss, D. M. Gruen, T. McCauley, and R. T. Csencsits, *Surf. Coat. Technol.* 120-121, 565 (1999).
163. A. Erdemir, M. Halter, G. R. Fenske, A. Krauss, D. M. Gruen, S. M. Pimenov, and V. I. Konov, *Surf. Coat. Technol.* 94-96, 537 (1997).
164. I. P. Hayward, I. L. Singer, and L. E. Seitzman, *Wear* 157, 215 (1992).
165. M. N. Gardos and K. V. Ravi, *Diamond Films Technol.* 4, 139 (1994).
166. M. N. Gardos and K. V. Ravi, *J. Mater. Res.* 5, 2599 (1990).
167. S. V. Pepper, *J. Vac. Sci. Technol.* 20, 643 (1982).
168. S. Chandrasekar and B. Bhushan, *Wear* 153, 79 (1992).
169. P. Hollman, O. Wanstrand, and S. Hogmark, *Diamond Rel. Mater.* 7, 1471 (1998).
170. S. Veprek, *J. Vac. Sci. Technol. A* 17, 2401 (1999).
171. A. Kelly and N. H. Macmillan, "Strong Solids," 3rd ed. Clarendon, Oxford, 1986.
172. R. W. Hertzberg, "Deformation and Fracture Mechanics of Engineering Materials," 3rd ed. Wiley, New York, 1989.
173. S. Veprek, S. Reiprich, and Li Shizhi, *Appl. Phys. Lett.* 66, 2640 (1995).
174. S. Veprek, *Thin Solid Films* 317, 449 (1998).
175. P. Nesladek and S. Veprek, *Phys. Status Solidi A* 177, 53 (2000).
176. S. Veprek, P. Nesladek, A. Niederhofer, H. Mannling, and M. Jilek, TMS Annu. Meeting, San Diego, 28 February-4 March, 1999, in "Surf. Eng. Science and Technology I" (A. Kumar, Y. W. Chung, J. J. Moore, and J. E. Smugeresky, Eds.) (1999).
177. A. Niederhofer, P. Nesladek, H. D. Mannling, K. Moto, S. Veprek, and M. Jilek, *Surf. Coat. Technol.* 120/121, 173 (1999).
178. J. E. Carsley, J. Ning, W. W. Milligan, S. A. Hackney, and E. C. Aifantis, *Nanostruct. Mater.* 5, 441 (1995).
179. R. W. Siegel and G. E. Fougere, *Nanostruct. Mater.* 6, 205 (1995).
180. E. Arzt, *Acta Mater.* 46, 5611 (1998).
181. J. Schiotz, F. D. Di Tolla, and K. W. Jacobsen, *Nature* 391, 561 (1998).
182. R. Thompson, Y. Vohra and M. Koopman, Surface engineering: Coatings and heat treatments in "Proc. of the 1st ASM International Surface Engineering and the 13th IFHTSE Congress and Exposition" (O. O. Popoola, N. B. Dahotre, S. J. Midea, and H. Kopech, Eds.), 7-10 October 2002. Columbus, OH, 2003.
183. N. Toprani, S. A. Catledge, Y. K. Vohra, and R. Thompson, *J. Mater. Res.* 15, 1052 (2000).
184. S. A. Catledge and Y. K. Vohra, *J. Appl. Phys.* 86, 698 (1999).
185. T. Ramanathan, K. Jagannadhan, K. Mallika, and R. Komanduri, *Philos. Mag. B* (1999).
186. J. W. Ager III and M. D. Drory, *Phys. Rev. B* 48, 2601 (1993).
187. Y. Muranaka, H. Yamashita, and H. Miyadera, *J. Vac. Sci. Technol. A* 9, 76 (1991).
188. Y. Liou, A. Inspektor, R. Weimer, D. Knight, and R. Messier, *J. Mater. Res.* 5, 2305 (1990).
189. Y. Muranaka, H. Yamashita, and H. Miyadera, *J. Appl. Phys.* 69, 8145 (1991).
190. C. E. Johnson, W. A. Weimer, and F. M. Cerio, *J. Mater. Res.* 7, 1427 (1992).
191. C. J. Chu, R. H. Hauge, J. L. Margrave, and M. P. D'Evelyn, *Appl. Phys. Lett.* 61, 1393 (1992).
192. C. Nesladek, J. Spinnewin, R. Lebout, and R. Lorent, *Diamond Relat. Mater.* 3, 912 (1994).
193. C. Campbell, "Surface Acoustic Wave Devices and their Signal Processing Applications." Academic Press, New York, 1989.
194. K. Yamanouchi, N. Sakumi, and T. Satoh, *Proc. IEEE* 351 (1989).
195. H. Nakahata, A. Hachigo, S. Shikata, and N. Fujimori, *Proc. IEEE* 361 (1995).
196. S. Fujii, Y. Seki, and K. Yoshida, *Proc. IEEE* 183 (1997).
197. K. L. Dreifus, J. J. Higgins, R. B. Henard, R. Almar, and L. P. Solie, *Proc. IEEE* 191 (1997).
198. H. Nakahata, H. Kitabayashi, and A. Hachigo, *Proc. IEEE* 319 (1998).
199. A. Hachigo, H. Nakahata, K. Itakura, S. Fujii, and S. Shikata, *Proc. IEEE* 325 (1995).
200. B. Bi, W. S. Huang, J. Asmussen, and B. Golding, *Diamond Relat. Mater.* 11, 677 (2002).
201. L. E. Cross and S. Trolier-McKinstry, *Encl. Appl. Phys.* 21, 429 (1997).
202. D. L. Polla and L. F. Francis, *Mater. Res. Soc. Bull.* 21, 59 (1996).
203. J. J. Sniegowski, in "Tribology Issues and Opportunities in MEMS" (B. Bhushan, Ed.), Kluwer Scientific, Dordrecht, 1998.
204. A. P. Lee, A. P. Pisano, and M. G. Lin, *Mater. Res. Soc. Symp. Proc.* 276, 67 (1992).
205. M. N. Gardos, in "Tribology Issues and Opportunities in MEMS" (B. Bushan, Ed.). Kluwer Scientific, Dordrecht, 1998.
206. M. N. Gardos, *Surf. Coat. Technol.* 113, 183 (1999).
207. A. R. Krauss, O. Auciello, D. M. Gruen, A. Jayatissa, A. Sumant, J. Tucek, D. C. Mancini, N. Moldovan, A. Erdemir, D. Ersoy, M. N. Gardos, H. G. Busmann, E. M. Meyer, and M. Q. Ding, *Diamond Relat. Mater.* 10, 1952 (2001).
208. J. L. Davidson, R. Ramesham, and C. Ellis, *J. Electrochem. Soc.* 137, 3206 (1990).
209. M. Aslam, G. S. Yang, and A. Masood, *Sensors Actuators A* 45, 131 (1994).
210. D. R. Wur, J. L. Davidson, W. P. Kang, and D. L. Kinser, *J. Micromech. Syst.* 4, 34 (1994).
211. O. Dorsch, K. Holzner, and M. Werner, *Diamond Relat. Mater.* 2, 1096 (1993).
212. G. Zaho, E. M. Charlson, and E. J. Charson, *J. Appl. Phys.* 73, 1832 (1993).
213. S. Moller, E. Obermeir, and J. Lin, *Sensors Actuators B* 25, 343 (1995).
214. E. I. Givargizov, V. V. Zhirnov, A. V. Kuznetsov, and P. S. Plekhanov, *Mater. Lett.* 18, 61 (1993).
215. P. K. Bachmann and H. J. Hagemann, *Diamond Relat. Mater.* 4, 820 (1995).
216. C. F. Chen, S. H. Chen, T. M. Hong, and M. H. Tsai, *J. Appl. Phys.* 77, 941 (1995).
217. M. D. Irwin, C. G. Pantano, P. Gluche, and E. Kohn, *Appl. Phys. Lett.* 71, 716 (1997).





# Nanocrystalline Phosphors

Guangshun Yi, Baoquan Sun, Depu Chen

*Tsinghua University, Beijing, China*

## CONTENTS

1. Introduction
  2. Semiconductor  
Nanocrystalline Phosphors
  3. Doped Nanocrystalline Phosphors
  4. Conclusion
- Glossary  
References

## 1. INTRODUCTION

Phosphors are defined as solid, inorganic, crystalline materials that show luminescence upon excitation [1]. According to the excitation source, phosphors can be divided into photoluminescence phosphors, cathode luminescence phosphors, X-ray luminescence phosphors, electroluminescence phosphors, etc. The excitation sources are, respectively, photons, electrons with a high kinetic energy, X-ray, and electrons with a low kinetic energy [2].

Phosphors have been studied for a long time, and have been widely used in such areas as fluorescent lamps (FLs), X-ray photography, cathode-ray tube (CRTs), electroluminescence display (ELDs), and so on. With the development of nanoscience and nanotechnology, many investigations have focused on nanocrystalline phosphors, including semiconductor nanocrystals and doped nanocrystals. It is interesting to know what the differences are between the bulk and nanoscale phosphors in terms of their properties. In addition, there is currently a great deal of interest in the production of novel types of bright, high-resolution, and high-contrast emissive displays, such as high-definition TVs, field-emission displays, plasma displays, and electroluminescent devices. In these applications, the required properties are high purity, compositional uniformity, high luminous efficiency, low-energy excitation source, and small and uniform particle-sized powders [3, 4]. Nanocrystalline (<50 nm) luminescent materials are potentially well suited for the applications [5]. The demand of these new technologies has stimulated a search for new materials and synthesis techniques to improve the performance of phosphors.

In the early stage, most of the studies in nanocrystalline phosphors focused on semiconductor phosphors. This is because, when semiconductor particles become smaller than the Bohr radius, the so-called quantum-size effect occurs. As a result, these semiconductor nanocrystals not only provide many unique opportunities for studying physics in low dimensions, but also exhibit novel optical properties which are potentially useful for technological applications. It is important in both basic and applied research.

Recently, the number of scientific publications on the optical properties of transition or rare-earth metal-doped nanocrystals has increased. Some new nano-related phenomena, such as luminous efficiency, lifetime, quenching concentration, and so on, have been reported. Many new methods for the preparation of nanocrystalline phosphors have also been developed.

This chapter reviews recent work on the synthesis, luminescent properties, and potential applications of nanocrystalline phosphors. In Section 2, we discuss semiconductor nanocrystalline phosphors, and in Section 3, we discuss doped nanocrystalline phosphors.

## 2. SEMICONDUCTOR NANOCRYSTALLINE PHOSPHORS

Semiconductor nanocrystals (also known as quantum dots or QDs) have attracted a great deal of interest from all disciplines, including chemistry, physics, materials, and even biology, due to their attractive properties such as size-tunable optical properties [6, 7]. Furthermore, many promising technical applications in the field of biomolecular labeling [8, 9], solar cell [10, 11], laser [12], and light-emitting diodes [13, 14] have attracted commercial interest. Over the last decade, rapid progress has been made in the preparation of nanocrystal semiconductors. They mainly include the II–IV compounds (ZnS, CdSe, CdS) [15], III–V compounds (InP, GaAs) [16], IV–VI compounds (which mostly refers to some kinds of chalcogenides [17]), and Si [18]. In the following, we discuss them respectively. Because the II–VI and III–IV semiconductor nanocrystals share almost the same synthesis procedure and optical properties as CdSe, these two parts are discussed together.

## 2.1. II–IV and III–V Compounds

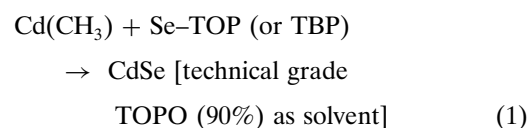
### 2.1.1. Synthesis

**Synthesis of CdSe Nanocrystals** In particular, II–IV and III–V compounds have attracted much attention because the preparation of nanocrystalline CdSe leads to an unprecedented degree of monodispersity and crystalline order [19]. Shape-controlled methods have been developed to prepare nanocrystals of different shapes [20, 21]. The investigation of the size-dependent optical absorption has been carried in detail [22]. In the following section, CdSe is used as an example for semiconductor nanocrystals. Its preparation, optical properties, and technical application are discussed. The synthesis of other II–IV and III–V semiconductor nanocrystalline phosphors is shown in Table 1.

There are two main synthetic methods for the preparation of nanosized CdSe. However, both need ligands to derivatize the surface to keep the nanocrystals stable in a solution. Stabilizing ligands must be present during growth to prevent aggregation and precipitation of the nanocrystals. The stabilizing molecules attach onto the nanocrystal surface as a monolayer through covalent, dative, or ionic bonds. Most of them use organic surface derivation in organic solution, and

others use organic or inorganic ones (such as cetyltrimethylammonium bromide, CTAB) in an aqueous solution, as shown in Figure 1.

The synthesis of colloid semiconductor nanocrystal CdSe is based on the pyrolysis of organometallic reagent (cadmium dimethyl,  $\text{Cd}(\text{CH}_3)_2$ ) with selenium (Se) powder by injection into a vigorously stirred flask containing a hot coordinating solvent (200–360 °C) [23]. The coordinating solvent can be amine, phosphonic acid, or phosphine oxide, which serves as a ligand/solvent for the synthesis of high-quality CdSe nanocrystals, as shown in Eq. (1):



Furthermore, fatty acids have also been developed as useful coordinating solvents. This method provides temporally discrete nucleation, and permits controlled growth of macroscopic quantities of nanocrystallites. Size-selective precipitation of crystallites from portions of the growth solution isolates samples with narrow size distributions

**Table 1.** Synthesis of other II–IV and III–V nanocrystals.

Semiconductor	Synthetic method	Size (nm)	Quantum efficiency	Ref.
CdSe	$\text{Cd}(\text{CH}_3)_2 + \text{Se-TOP}$ (in hot TOPO)	1.1–11.5		[40]
	$\text{CdCl}_2 + \text{Na}_2\text{Se}$ (CTAB as surfactant)	Nanorods		[41]
	$\text{Cd}^{2+} + \text{SeO}_3^{2-} + \text{N}_2\text{H}_4$ (hydrothermal method)	Nanorods and fractal		[42]
	$[\text{Cd}(\text{SePh})_2]$ thermolysis	3		[43]
	$\text{Cd}[\text{Se}_2\text{CNRR}']_2$ thermolysis	3–8		[44]
	$\text{CdO}$ [or $\text{Cd}(\text{C}_2\text{O}_4)$ ] + HPA (or TDPA, ODPA) + Se TOPO	Nanorods, tetrapods		[45]
CdS	$\text{CdC}_2\text{O}_4 + \text{Se}$	6–20 × 100–500 (nanorods)		[46]
	$\text{Li}_4[\text{Cd}_{10}\text{Se}(\text{Sph})_{16}]$ , pyrolysis	2–9		[47]
	$\text{S}$ (in THF) + $\text{CdCl}_2 + \text{KBH}_4$	4–8		[48]
	$\text{CdO} + \text{S} + \text{oleic acid} + \text{octadecene}$	1–6		[49]
	$\text{Cd}[\text{S}_2\text{CNRR}']_2$ , thermolysis	3–7		[50]
	$\text{Cd}(\text{NO}_3)_2 + \text{P}_2\text{S}_5$ in ethanol	Less than or equal to 6		[51]
ZnSe	$\text{Cd}(\text{CH})_3 + \text{S}(\text{TMS})_2$ in hot TOPO	2–3		[52]
	$\text{Li}_4[\text{Zn}_{10}\text{Se}(\text{Sph})_{16}]$ , pyrolysis	2–5		[53]
ZnS	$\text{Zn}(\text{CH}_3)_2 + \text{Se-TOP}$ (hexadecylamine/trioctylphosphine)	4.3–6	20–50%	[54]
	$\text{S}$ (in THF) + $\text{ZnCl}_2 + \text{KBH}_4$	4–8		
CdTe	$\text{Zn}[\text{S}_2\text{CN-Me}(\text{C}_6\text{H}_{13})_2]$ in hot TOPO			[55]
	$\text{H}_2\text{Te} + \text{Cd}(\text{ClO}_4)_2 + \text{RSH}$	2–5	40%	[56]
	$\text{Cd}(\text{CH}_3)_2 + \text{Te}$ (TOP + dodecylamine as solvents)	2.5–7	30–65%	[57]
ZnTe	$\text{Cd}^{2+} + \text{NaHTe} + \text{mercaptoacetic acid}$		18%	[58]
	$[\text{Zn}(\text{TePh})_2][\text{TMEDA}]$ with TOP in dodecylamine	4.2–5.4		[59]
InAs	$\text{InCl}_3 + \text{As}[\text{Si}(\text{CH}_3)_3]_3$ (TOP)	2.5–6		[60]
	$\text{In}(\text{Ac})_3 + \text{As}(\text{TMS})_3 + \text{octadecene}$			[61]
InP	$\text{In}(\text{PBut}_2)_3 + 4\text{-ethylpyridine}$	7.4		[62]
	$\text{InCl}_3 + \text{KBH}_4 + \text{P}$	11.3–20		[64]
	$\text{In}(\text{Ac})_3 + \text{P}(\text{TMS})_3 + \text{octadecene}$			[65]
	$[\text{R}_2\text{InP}(\text{TMS})_2]_2$ in hot TOPO and TOP	2–6.5		[66]
GaP	$\text{InX}_3$ ( $X = \text{Cl, Br, I}$ ) + $\text{P}(\text{SiMe}_3)_3$			[67]
	$\text{Na, P, and GaCl}_3$ in benzene	20–40 × 200–500 nanorod		[68]
	$(\text{Na/K})_3\text{P} + \text{GaCl}_3$ in 1,4-dioxane	11–21		[69]
GaAs	$[\text{R}_2\text{GaP}(\text{TMS})_2]_2$ in hot TOPO and TOP	2–6.5		[70]
	$(\text{Na/K})_3\text{As} + \text{GaCl}_3$ in 1,4-dioxane	6–36		[71]
	$\text{GaCl}_3 + \text{As}(\text{SiMe}_3)_3$ in quinoline	4.5		[72]

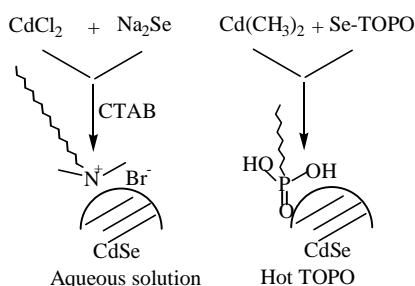


**Figure 1.** Two major surface modification schemes for the CdSe nanocrystals.

(<5% rms in diameter). Although numerous reports have been published in which CdSe was prepared using inorganic cadmium salts in an aqueous solution [24], the luminescence is much lower than organometallic synthesis. One possible reason is that the synthesis process operates at a much higher temperature, and may crystallize better than in an aqueous solution. It would be very helpful for the colloidal nanocrystals to have a good optical property [25].

It is well known that organometallic compounds are very unstable, apart from being toxic, expensive, and explosive. They are usually stored in the refrigerator inside a glove box. Fortunately, some alternative cadmium compounds have been developed via a different route. Simple inorganic and organic cadmium such as CdO [26] and  $\text{Cd}(\text{Ac})_2$  [27] can be candidates for the cadmium precursor. They are low-cost, safe, and easily controlled precursors. The resulting nanocrystal is nearly monodispersed without any exceptional size separation, and is reproducible. The reaction is simple and mild. Furthermore, the formation of nanocrystals with the concept of “user-friendly chemistry” was achieved by growing the nanocrystals in a mixture of octadecene (ODE) and oleic acid with CdO as the cadmium precursor [28].

Apart from spherical nanocrystals, the formation of nanocrystals of various shapes, including nanorods, -arrows, -teardrop, -tetrapod, and branched tetrapod-shaped nanocrystals, has also been achieved by adjusting the components of the coordinating solvent [21, 29]. The coordinating solvent is a mixture of pure trioctylphosphine oxide (TOPO) and hexylphosphonic acid (HPA). In general, experimental results show that the coordinating solvent TOPO must be technical grade if the semiconductor nanocrystal is synthesized using an organometallic precursor. In fact, TOPO and HPA are very similar. HPA can be called a ligand, which can be substituted by tetradecylphosphonic acid or octadecylphosphonic acid. The initial cadmium and selenium precursor ratio (Cd:Se ratio), the injection and growth temperature, and the concentration of the precursor all play key roles in determining the shape of the resulting nanocrystals and luminescent quantum efficiency. Usually, low temperature and a high precursor concentration lead to the formation of perfect nanorods.

In comparison with bulk semiconductors, there are more surface atoms for nanocrystals. Thus, the semiconductor nanocrystals are more likely to undergo epitaxial overgrowth than other inorganic compounds. Furthermore, there are many defective surface atoms unless they are passivated. To remove these defects, core/shell-type composite CdSe/ZnS

has been studied by several groups [30–32]. Overcoating the core of lower bandgap nanocrystals with a higher bandgap shell has improved the photoluminescence quantum yield by passivating surface nonradiative recombination sites. It has also been reported that the epitaxial growth graded CdS/ZnS shells on the colloidal CdSe nanorods [33]. The core/shell nanorods have increased the photoluminescence quantum yield and improved the photostability.

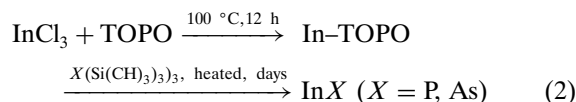
**Modification of CdSe** As mentioned earlier, nanocrystal CdSe is prepared in a coordinating solvent such as an amine, or a phosphine oxide with long alkyl tails. These organic reagents are usually called surfactants, a capping group, or ligands. They improve the stability of nanocrystals by adsorbing a monolayer on the surface. If nanocrystals lose the surface ligand, they will precipitate out, and the luminescence is totally lost. The ligands are usually hydrophobic. So the nanocrystal CdSe can easily be dispersed in many nonpolar solvents such as hexane, toluene, and pyridine.

Usually, it is necessary to modify the nanocrystals with a hydrophilic reagent if they are going to be dispersed in an aqueous solution. Some strategies have been pursued to develop hydrophilic nanocrystals [8, 34, 35]. The trick depends on supplying the nanocrystal surface with thiolated molecules having a free carboxyl group facing the solution that warrants water solubility. In general, the longer the alkyl chain is, the longer the modified nanocrystals remain dispersed in the aqueous solution. To improve the stability of thiol-coated nanocrystals in an aqueous solution, chelating agents were introduced for surface modification, instead of the commonly used monothiols [36]. In fact, all monothiol-coated CdSe nanocrystals have shown very profound photochemical instability in an aqueous solution [37]. The main reason is that the mercapto ligands on the surface can be oxidized photochemically to disulfides, which then leave the surface and expose the nanocrystal in air. The naked nanocrystals could also be photooxidized, and eventually precipitate out. So free thiols in a solution help to improve the stability of nanocrystals modified with hydrophilic thiols. According to the above mechanism of the photochemical instability of the thiol-coated nanocrystals, it is believed that a thick and densely packed ligand layer would be helpful in inhibiting the photooxidation. Organic dendritic ligands have been developed to stabilize nanocrystals [38]. They are hyperbranched organic molecules with thiol groups as the central focal point of the binding site for the cationic elements, and hyperbranched groups to inhibit oxygen diffusion to the surface of nanocrystals. The closely packed and tangled ligand shell provides sufficient stability to withstand the rigor of the coupling chemistry.

An alternative was reported in which CdSe nanocrystals were embedded in a polymerized silica shell [9, 39]. Mercapto silane was attached onto the surface, and a siloxane shell of 1–5 nm thickness was developed through pyrolysis of the silane reagent. The siloxane shell can be functionalized with thiols and/or amines on the surface. The silanized nanocrystal can be dispersed in buffer solutions in a wide pH range, even at a high salt concentration. The photoluminescence properties depend weakly on the pH of the solution due to the protection of the silicon shell. The silanized nanocrystals have quite a good quantum yield, and

are stable for months. They also have optical properties similar to that of thiol-coated nanocrystals. However, the thiol modification is much easier to carry out. The silanization process, although rather difficult to develop, results in better stability.

**Synthesis of Other II–IV and III–V Nanocrystals** The popular pyrolysis method with TOPO as the solvent medium has also been used by Alivisatos [8, 9] in the synthesis of InP (2–5 nm) or InAs nanocrystals (2.5–6 nm). The method was based on the reaction of  $\text{InCl}_3$  and  $X[\text{Si}(\text{CH}_3)_3]_3$  ( $X = \text{P}$  or As) in TOPO at elevated temperatures, as shown in Eq. 2:



The nanocrystals are highly crystalline, monodisperse, and soluble in various organic solvents. Improved size distributions have been obtained by size-selectively reprecipitating the nanocrystals. X-ray photoelectron spectroscopy (XPS) shows that the nanocrystals have a nearly stoichiometric ratio of indium to phosphorus, with the TOPO surface coverage ranging from 30 to 100%.

The synthesis of other II–IV and III–V nanocrystals is summarized in Table 1.

### 2.1.2. Optical Properties

**Optical Properties of CdSe** Due to the quantum-size effect, semiconductor nanocrystals exhibit many unique properties when their size is smaller than their Bohr radius (about 1–5 nm) [7, 73]. Semiconductor nanocrystals of different sizes show diverse properties. The optical absorption spectrum of semiconductor nanocrystals supplies accessible and straightforward information to evaluate the quantum-size confinement effect. An electron was excited from the valence band to the conduction band via absorbing a photon, which is associated with the bandgap energy ( $E_g$ ). The absorption of photons with energy similar to that of the bandgap,  $h\nu \geq E_g$ , leads to an optical transition producing an electron in the conduction band and a hole in the valence band.

CdSe semiconductor nanocrystals have a broad excitation range and a narrow emission range compared with temporal organic dyes. Their spectral width (full width at half maximum) usually spans 27–40 nm at room temperature, compared with 20 nm for a CdSe single crystal because of the inhomogeneous emission properties of the nanocrystals [74, 75]. Different from organic dyes, there is a

substantial Stokes shift in the luminescence of nanocrystals. The optimized excitation and emission filters for semiconductor nanocrystals can allow light passage for nearly the entire excitation and emission peaks, which permits detection of more fluorescence output than that of organic dyes. Semiconductor nanocrystals have a rather high cross section ( $\sim 10^5$  mol/cm), which means that they can efficiently absorb the light that is irradiated. And the photoluminescence quantum yield for the as-prepared nanocrystals increases by about 20% for bare dots, and by 30–50% for dots passivated with ZnS at wavelengths of 520 and 600 nm. Photoefficiency is lower at wavelengths below 520 nm or longer than 600 nm. [76]. It can be concluded that the semiconductor nanocrystals have a strong emission due to their large cross section and high quantum yield. The CdSe nanocrystals are rather stable against photobleaching. The emission wavelength of CdSe can be tuned from 450 (center) to 650 nm (center) by changing the particle size [77, 78]. It has been reported that light emission from single CdSe under continuous excitation turns on and off intermittently with a characteristic time scale of about 0.5 s [79–81]. The on/off time can change when a passivating, high-bandgap shell of ZnS encapsulates the nanocrystal.

### Optical Properties of Other II–IV and III–V Nanocrystals

The optical properties of other II–IV and III–V semiconductor nanocrystals are shown in Table 2.

## 2.2. IV–VI Compounds (Lead Chalcogenides)

Just as we reviewed earlier, II–IV and III–V semiconductor nanocrystals have been widely investigated. As for the IV–VI semiconductor nanocrystals, reports in this area mainly focus on lead chalcogenides, that is, PbS, PbSe, and PbTe. The growth of these semiconductor nanocrystals of uniform size distribution has been reported [89–92]. These nanocrystals are of interest because of their large Bohr radius (10 nm for PbS and 15 nm for PbSe), which permits quantum-size effects to be clearly visible, even for large particles or crystallites. These large Bohr exciton radii result in a strong confinement of the electron–hole pair. Nasu et al. [93] observed a significant bandgap shift from the IR region to the near-UV region, depending on the small size of the PbS crystallites. An enhanced photoluminescence was also reported [94] for PbS nanocrystals by Thielsch and co-workers. But reports on their optical properties remain scarce; studies in this area are preliminary; more work needs to be done.

**Table 2.** Optical properties of other II–IV and III–V semiconductor nanocrystals.

Semiconductor	Bandgap (bulk, eV)	Electron affinity (eV)	Bandgap (nanocrystals, eV)	Quantum efficiency (nanocrystals, %)
ZnSe	2.58	4.09		20–50 [82]
CdSe	1.74	4.95	1.88–3.62	20–85 [83]
CdTe	1.5	4.28	1.9–2.2	35–65 [84]
CdS	2.53	4.79	3.0–4.06 [85]	
InAs	0.36	4.9	1.05–1.55 [86]	8–20 [87]
InP	1.28	4.4	2.1–2.5 [88]	

### 2.3. Si

Since the strong room-temperature visible luminescence in porous silicon was discovered by Canham [95] in 1990, the study of the fabrication and light-emitting properties of various Si-based nanomaterials has received worldwide attention over the past few years. Si-based nanomaterials are some new photoelectronic and informational materials developed rapidly in recent years. These kinds of materials include nanoscale porous silicon, Si nanocrystalline-embedded SiO<sub>2</sub> matrices, Si nanoquantum dot, Si/SiO<sub>2</sub> superlattice, etc.

The synthesis of Si-based nanomaterials with high quality is very important in order to obtain efficient and stable luminescence. Thus far, various growth technologies have been developed, including chemical-vapor deposition [96, 97], Si-ion implantation [98], laser-ablation deposition [99], self-assembling growth [100], and so on.

When the Si nanocrystallite size is reduced, the bandgap will become large, and will create the quantum energy level in the conductor band and valence band. As a result, not only is the luminescent intensity increased, but also the peak energy is blue shifted [101]. Kanzawa et al. [102] measured the photoluminescence spectra of Si nanocrystals embedded in SiO<sub>2</sub> films as a function of size. They found that, as the average particle size decreased from 3.8 to 2.7 nm, the photoluminescence peak energy exhibited a blue shift from 1.42 to 1.54 eV, and its peak intensity increased progressively. This phenomenon was also observed by Takagi et al. [103]. They found that the luminescent intensity was inversely proportional to the square of the crystallite size from 2.8 to 5.6 nm.

## 2.4. Applications of Semiconductor Nanocrystals

Due to the attractive characteristics of colloid semiconductors, that is, variable emission colors, electron affinities, and ionization potentials, they have showed significant potential as luminescent chromophores ranging from biological luminescent tags, lasers, as well as light-emitting diodes to solar cells.

### 2.4.1. Biological Application

The fluorescent tag is a popular tool in biological detection. Organic dyes are most widely used in this area. Semiconductor nanocrystals have been applied as promising luminescent tags. Compared with the dyes, they have several potential advantages: a rather large Stokes shift, wide excitation and a relatively narrow emission peak (full width at half maximum, 20–30 nm), various emission wavelengths (400–2000 nm), a large extinction coefficient in the visible and ultraviolet range ( $\sim 10^5 \text{ M}^{-1} \cdot \text{cm}^{-1}$ ), high quantum yield (core-shell nanocrystals, >50%), a rather strong antiphotobleaching capability, and a relatively long luminescence lifetime ( $\sim 30$ –100 ns) at room temperature. Furthermore, semiconductor nanocrystals of different sizes may be excited with a single wavelength, resulting in many emission colors that may be detected simultaneously. The environment of semiconductor nanocrystals contributes little to their emission.

Consequently, semiconductor nanocrystals might be promising biological tags. There have been reports on immunoassay [104], immunohistochemical assay [105], live-cell detection [106], and multicolor detection [107].

### 2.4.2. Photovoltaic Device and Solar Cell

The semiconductor nanocrystals possess a relative large electron affinity and spectrally narrow luminescence compared to many traditional electroluminescent organic polymers. They show some desirable properties in that they can be spin coated, can be used on a large area. They are flexible, with potential thermal and electronic stability [108–109]. Consequently, the semiconductor nanocrystals have been made into bilayer light-emitting diodes with organic electroluminescent semiconducting polymers such as poly(p-phenylenevinylene). The device made from different sized semiconductor nanocrystals can emit from red to green with a relatively high conversion efficiency, a low operating voltage, and hundreds of hours of lifetime under constant current flow. As a class of electroluminescent materials, semiconductor nanocrystals offer many of the processibility advantages of polymers, along with potentially stable, long-lived operation. If the semiconductor nanorods are mixed with some conjugated polymers, they can be manipulated readily [110]. Tuning the length and diameter of the nanorods, the distance of electron transfer and the overlap between the absorption spectrum and the solar emission can be optimized. The power conversion efficiency of the reported device can be 1.7%.

### 2.4.3. Laser

Theoretically, semiconductor nanocrystals have some advantages as a gain medium, including temperature insensitivity, lower lasing threshold, and a gain profile concentrated into a much narrower luminescence spectrum. Such advantages have motivated the use of semiconductor nanocrystals as the medium of the laser. Semiconductor nanocrystal-based lasers with optical pumping have been successfully developed using nanocrystal-titania chemistry [111]. The output color of the laser can be selected by choosing appropriately sized nanocrystals, operating at room temperature or below. The experience with semiconductor nanocrystal thin-film systems has opened the possibility of UV and IR lasers using corresponding nanocrystals.

## 3. DOPED NANOCRYSTALLINE PHOSPHORS

In addition to semiconductor phosphors, there is another very important class of phosphors, called transition or rare-earth metal-doped phosphors. For the doped phosphors, transition or rare-earth metals act as luminescent centers. Since the wavelength of the characteristic luminescence of the doped metals hardly changes with size confinement, doped nanocrystals do not require the stringent control of size needed in semiconductor nanocrystalline phosphors. In fact, most of the phosphors employed in technological applications belong to doped phosphors. Such phosphors find



applications ranging from conventional fluorescent lighting to color TV picture tubes, X-ray photography, and so on. For example, the three components in trichromatic fluorescent lamps are  $\text{BaMgAl}_{10}\text{O}_7:\text{Eu}^{2+}$  (blue),  $\text{CeMgAl}_{10}\text{O}_{19}:\text{Tb}^{3+}$  (green), and  $\text{Y}_2\text{O}_3:\text{Eu}^{3+}$  (red) [112].

Nanoscale doped-phosphors are currently attracting a great deal of interest for both fundamental photophysics study, and important applications including display and sensor technologies [5, 113–115]. New synthetic techniques and effects of nanoscale confinement have motivated significant new interest in these materials [116, 117]. It is important and interesting to study the doped nanocrystalline phosphors.

So far, reports on doped nanocrystalline phosphors mainly focus on the following areas: (1) rare-earth metal-doped nanocrystals, such as  $\text{Y}_2\text{O}_3:\text{Eu}$ ,  $\text{Y}_2\text{O}_3:\text{Tb}$ ,  $\text{ZnS}:\text{Eu}$ ,  $\text{ZnS}:\text{Tb}$ ,  $\text{ZnS}:\text{Sm}$ ,  $\text{YVO}_4:\text{Ln}$ ,  $\text{LaPO}_4:\text{Ln}$ ,  $\text{ZnSiO}_4:\text{Ln}$  ( $\text{Ln} = \text{Eu}^{3+}$ ,  $\text{Tb}^{3+}$ ),  $\text{Y}_2\text{SiO}_5:\text{Eu}$ , and (2) transition metal-doped nanocrystals, such as  $\text{ZnS}:\text{Mn}$ ,  $\text{ZnS}:\text{Cu(I)}$ ,  $\text{ZnS}:\text{Cu(II)}$ ,  $\text{ZnS}:\text{Cu,In}$ , and  $\text{CdS}:\text{Mn}$ . In the following part, the preparation method, nanosize-related optical properties, and technical applications of doped nanocrystalline phosphor will be reviewed.

### 3.1. Rare-Earth Metal-Doped Nanocrystals

#### 3.1.1. Synthesis

The reported preparation methods include gas-phase condensation, flame-spray pyrolysis (FSP), coprecipitation, sol-gel, block copolymer, reverse microemulsion, combustion synthesis, colloidal chemistry, and hydrothermal method.

**Gas-Phase Condensation Method** Tissue and co-workers have prepared monoclinic nanocrystals by a gas-phase condensation method using  $\text{CO}_2$ -laser vaporization of  $\text{Y}_2\text{O}_3:\text{Eu}$  ceramic pellets, and condensing the nanocrystals from the gas phase [5, 118].  $\text{Y}_2\text{O}_3:\text{Eu}$  with an average diameter of 23 nm was obtained. The average production rate was 11 mg/h. The main problem of the method is, when the doped concentration of  $\text{Eu}^{3+}$  is above 0.7%,  $\text{Y}_2\text{O}_3:\text{Eu}$  and a secondary  $\text{Eu}_2\text{O}_3$  phase will occur due to a kinetic effect of the gas-phase condensation method.

**Flame-Spray Pyrolysis Method** There is also a well-established technology called flame-spray pyrolysis (FSP), which is used by the industry to produce nanocrystalline phosphors [119–121]. This process involves combusting aerosols of single-metal and mixed-metal metalloorganic alcohol solutions with oxygen or air in a reaction chamber at temperatures of 1200–2000 °C. By this method, rare-earth doped  $\text{Y}_2\text{O}_3$  nanocrystalline phosphors with a size of 60 nm have been prepared.

**Sol-Gel Method** For the sol-gel method, dilute solutions of metalloorganics or metal salts are reacted to form an irreversible gel, then dried and shrunk to an amorphous or weakly crystalline mass. This kind of method has been widely used to prepare different kinds of doped nanosized phosphors, including  $\text{Tb}^{3+}$  and  $\text{Eu}^{3+}$  doped  $\text{Zn}_2\text{SiO}_4$  [122],  $\text{Y}_2\text{SiO}_5:\text{Eu}$  [123],  $\text{Y}_2\text{O}_3:\text{Eu}$  [124],  $\text{SrAl}_2\text{O}_4:\text{Dy, Eu}$  [125], etc. Sharma et al. have synthesized nanocrystalline  $\text{Y}_2\text{O}_3:\text{Eu}$  by an improved sol-gel method in the presence of surface modifiers. The particle size gradually decreased from 6  $\mu\text{m}$

to 10 nm with an increase of the modifier from 0 to 10wt% with respect to  $\text{Eu}_2\text{O}_3/\text{Y}_2\text{O}_3$  [126].

The advantage of this method is that atomically mixed powders are obtained in the as-synthesized condition. However, these as-synthesized materials must also be heat treated to high temperatures to crystallize the desired phase. Also, the processing steps to prepare the precursor powders are complicated and time consuming.

**Homogeneous Coprecipitation Method** In this kind of method, urea or thioacetamide is used to produce  $\text{OH}^-$  or  $\text{S}^{2-}$ . Due to the characteristics of urea and thioacetamide,  $\text{OH}^-$  or  $\text{S}^{2-}$  may be increased very slowly and homogeneously throughout the whole solution. The gradual and uniform rise in  $\text{OH}^-$  or  $\text{S}^{2-}$  can result in the nucleation and growth of uniformly nanosized hydroxide or metal sulfide particles. Nanocrystalline  $\text{Y}_2\text{O}_3:\text{Eu}$  has been prepared by the homogeneous precipitation of  $\text{Y}^{3+}$  and  $\text{Eu}^{3+}$  with urea [127].

**Block Copolymer Method** This method uses copolymers as steric stabilizers. The copolymers form micelles, and serve as nanoreactors for the preparation of nanoparticles. For example, by utilizing polyacrylamide gel, nanosized  $\text{Y}_2\text{O}_3:\text{Eu}^{3+}$  [128] and  $\text{Y}_3\text{Al}_5\text{O}_{12}:\text{Ce}^{3+}$  (YAG) [129] have been prepared.  $\text{ZnS}:\text{Tb}$  nanocrystals [130] have also been synthesized in a similar way. This kind of synthesis scheme could be used with various combinations of metal salts to yield many different doped nanocrystalline phosphors. Also, the size of the nanoparticle can be controlled by adjusting the size of the micelle.

**Reverse Microemulsion Method** Reverse microemulsion is also called the reverse micelle method. In reverse microemulsion, the aqueous phase is dispersed as microdroplets, which are usually less than 100 nm. So the dispersed water droplets behave as nanoreactors for the synthesis of nanoparticles. By using this method, 10 nm  $\text{Y}_2\text{O}_3:\text{Eu}$  [131] nanoparticles with a narrow-size distribution have been prepared successfully.

**Combustion Synthesis Method (or Propellant Synthesis)** The combustion synthesis process involves the exothermic reaction of an oxidizer such as metal nitrate, ammonium nitrate, and ammonium perchlorate [132], and an organic fuel, typically urea, carbonylhydrazide, or glycine [3, 133]. During the process, the chemical energy released from the exothermic reaction between the metal nitrate and fuel can rapidly heat the system to high temperatures (>1600 °C) without an external heat source; at the same time, a large amount of gaseous product such as  $\text{N}_2$ ,  $\text{CO}_2$ ,  $\text{H}_2\text{O}$  is produced, which generates nanostructure phosphors with higher surface areas and high luminescence emission. Tao et al. have prepared nanoscale  $\text{Y}_2\text{O}_3:\text{Eu}$  phosphors by glycine-nitrate solution combustion synthesis [134]. An average particle size of 8, 40, 70, and 160 nm was obtained by adjusting the glycine-to-nitrate ratio.  $\text{Y}_3\text{Al}_5\text{O}_{12}:\text{Eu}$  (YAG:Eu) nanocrystalline phosphors are prepared by employing a combustion synthesis with urea as a fuel [135]. The size of the phosphor particles is in the range of 60–90 nm. The disadvantage of this method is that it can only be used to prepare oxide phosphors.

**Colloidal Chemical Methods** Colloidal chemical methods have often been utilized to prepare colloidal solutions of highly crystalline and well-separated nanoparticles. These methods have been widely used for the preparation of semiconductor nanocrystals, such as CdSe, as mentioned in Section 2. They have also been applied to the preparation of doped nanocrystals. Colloidal nanocrystals of  $\text{LaPO}_4\text{:Eu}$ ,  $\text{CePO}_4\text{:Tb}$  [136],  $\text{LaPO}_4\text{:Ce}$ , and  $\text{LaPO}_4\text{:Ce,Tb}$  [137] have been prepared by this method.

**Hydrothermal Method** Hydrothermal synthesis is a low-temperature and high-pressure decomposition technique that produces fine, well-crystallized powders.  $\text{YVO}_4\text{:Ln}$  (Ln = Eu, Sm, Dy) nanocrystals have been prepared via a hydrothermal method at 200 °C. Highly crystalline particles ranging in size from about 10 to 30 nm were obtained [138]. The authors have prepared  $\text{La}_2(\text{MoO}_4)_3\text{:Yb,Er}$  up-conversion nanocrystalline phosphors through the hydrothermal method [139].

For some time, a number of papers have reported on the preparation and luminescence of nanocrystalline rare-earth doped II–VI semiconductors, such as  $\text{ZnS:Tb}^{3+}$  [140],  $\text{ZnS:Eu}^{3+}$  [141], and  $\text{ZnS:Er}^{3+}$  [142]. Recently, Bol et al. repeated some of the experiments, and investigated the results systematically [143]. They concluded that it was not possible to incorporate rare-earth ions in the nanocrystalline semiconductors due to the large size, chemical differences, and the need for charge compensation for rare-earth ions. The observed rare-earth emission is really from the ions absorbed on the surface.

### 3.1.2. Optical Properties

**Emission Wavelength** Li et al. found that, when the size of nanocrystalline  $\text{Y}_2\text{O}_3\text{:Eu}$  [127] and  $\text{Y}_3\text{Al}_6\text{O}_{12}\text{:Ce}$  [144] became smaller, a blue shift was observed for the emission spectrum. For example, nanocrystalline  $\text{Y}_2\text{O}_3\text{:Eu}$  of different sizes with an average diameter of 43, 55, 68, 71 nm were prepared; the central emission wavelengths were, respectively, 610, 612, 614 and 614 nm.

**Luminous Efficiency** Bhargava reported [145] that the photoluminescence efficiency of nanocrystalline  $\text{Y}_2\text{O}_3\text{:Tb}^{3+}$  with a size between 2–4 nm was at least five times higher than that of bulk samples. He also proved that smaller nanocrystalline  $\text{Y}_2\text{O}_3\text{:Tb}^{3+}$  particles were far more efficient than larger ones or bulk-like samples. For the phosphor of  $\text{Y}_2\text{O}_3\text{:Eu}$ , Lee et al. [131] found that  $\text{Y}_2\text{O}_3\text{:Eu}$  nanoparticles produced by a reverse microemulsion method with an average size of 30 nm displayed a stronger photoluminescence intensity than the bulk samples. They attributed this fact to higher crystallinity and more densely packed crystal with few void spaces. Sharma et al. reported that the peak emission intensity of  $\text{Y}_2\text{O}_3\text{:Eu}^{3+}$  increased approximately five-fold as the average particle size decreased from 6  $\mu\text{m}$  to 10 nm [126]. Ihara and co-workers synthesized glass-coated  $\text{ZnS:Tb}$  and  $\text{ZnS:Eu}$  nanocrystals. They found that the photoluminescence intensities were about three times higher than those of bulk [146].

However, Li et al. [127] obtained a different result. Nanocrystalline  $\text{Y}_2\text{O}_3\text{:Eu}^{3+}$  has been prepared with a homogeneous precipitation method. The relative luminescent

intensity changed from 100 to 64% as the size decreased from 68 to 43 nm.

**Quenching Concentration** Nanosized phosphors doped with rare-earth elements have increased the quenching concentration. Tao et al. reported that the quenching concentration of  $\text{Y}_2\text{O}_3\text{:Eu}$  prepared by conventional synthesis is 6% mol europium, but for their nanoscale samples prepared by combustion synthesis, the quenching concentration was apparently 14% mol [134]. Li et al. found that the quenching concentration was 8% for nanocrystal  $\text{Y}_2\text{O}_3\text{:Eu}$  [147], as compared with 6% in bulk samples.

**Luminescent Lifetime** As for the lifetime of  $\text{Y}_2\text{O}_3\text{:Eu}$  nanocrystals, Tissue and co-workers have done much research. They observed that the fluorescent lifetime was obviously longer in the monoclinic  $\text{Y}_2\text{O}_3\text{:Eu}^{3+}$  nanocrystals than in the bulk material [5]. Li et al. also obtained the same result [148].

## 3.2. Transition Metal-Doped Nanocrystals

### 3.2.1. Synthesis

**Colloidal Chemical Method** For the synthesis of transition metal-doped nanocrystals, colloidal chemical methods have been widely used, and the most thoroughly investigated systems are manganese-doped zinc sulfide and cadmium sulfide. Liu et al. have prepared well-dispersed  $\text{CdS:Mn}$  nanocrystals in an aqueous solution by using mercapto acetate as a capping reagent [149], while our group has synthesized  $\text{ZnS:Mn}$  nanocrystals in a similar way by using histidine as a capping reagent [150]. In both methods, transparent colloidal solutions of  $\text{CdS:Mn}$  and  $\text{ZnS:Mn}$  nanocrystals were acquired. Bawandi and co-workers [151] synthesized TOPO-capped  $\text{CdSe:Mn}$  using two different manganese precursors. They found that almost all of the manganese resides near the surface in the doped sample obtained by using manganese salts as the manganese source, whereas by use of an organometallic complex  $[\text{Mn}_2(\mu\text{-SEMe})_2(\text{CO})_8]$ , manganese was incorporated in the lattice. Recently, TOPO-capped, nearly monodispersed  $\text{ZnS:Mn}$  and  $\text{CdS:Mn}$  nanocrystals were prepared by Malik et al. [152].

**Coprecipitation Method** Through this process, nanocrystalline  $\text{ZnS:Mn}$  was prepared by coprecipitation of zinc acetate and manganese acetate with sodium sulfide in methanolic media [153].  $\text{ZnS:Cu}^+$ ,  $\text{ZnS:Cu}^{2+}$  [154], and  $\text{ZnS:Cu,In}$  [155] nanocrystalline phosphors have been obtained by the chemical homogeneous precipitation of cation solutions, with  $\text{S}^{2-}$  as the precipitating anion, which was formed by the decomposition of thioacetamide.

**Reverse Microemulsion Method** By using this method,  $\text{ZnS:Mn}$  [156, 157],  $\text{ZnS:Cu}$  [157, 158], and  $\text{CdS:Mn}$  [159] nanoparticles with a narrow-size distribution have been prepared successfully.

### 3.2.2. Optical Properties

**Luminous Efficiency** In 1994, Bhargava et al. [160] first observed that nanocrystalline  $\text{ZnS:Mn}$  has a high luminous efficiency. The efficiency in these nanocrystals was measured to be 18%, as compared to 16% for the bulk.

**Table 3.** Nanocrystalline phosphors reported in the literature.

	Semiconductor	Size (nm)	Optical properties	Ref.
Semiconductor nanocrystalline phosphors	CdSe	1.1–11.5		[40]
		Nanorods		[41]
		Nanorods and fractal		[42]
		3		[43]
		3–8		[44]
		Nanorods, teprapods		[45]
	CdS	6–20 × 100–500 (nanorods)	Quantum efficiency 20–85%	[46]
		2–9		[83]
		4–8		[47]
		1–6		[48]
		3–7		[49]
		Less than or equal to 6		[50]
	ZnSe	2–3		[51]
		2–5	Quantum efficiency 20–50%	[52]
	ZnS	4.3–6	Quantum efficiency 20–50%	[53]
		4–8		[82]
	CdTe			[54]
		2–5	Quantum efficiency 40%	[55]
		2.5–7	Quantum efficiency 30–65%	[56]
	ZnTe		Quantum efficiency 18%	[57]
		4.2–5.4		[58]
	InAs	2.5–6		[59]
			Bandgap: 1.05–1.55	[60–61]
	InP	7.4		[86]
		11.3–20		[62]
			Bandgap: 2.1–2.5 eV	[64–65]
	GaP	2–6.5		[88]
20–40 × 200–500 nanorod			[66]	
11–21			[67]	
GaAs	2–6.5		[68]	
	6–36		[69]	
PbS	8–30	Spectral blue shift	[70]	
	Nanofilm	Bandgap blue shift from IR region to near-UV region	[71]	
PbSe		Enhanced photoluminescence	[89]	
		Quantum-size effect	[93]	
Si	Film	Enhanced photoluminescence	[94]	
	Porous silicon	Enhanced photoluminescence	[91]	
Doped nanocrystalline phosphors	Y <sub>2</sub> O <sub>3</sub> :Eu	3.8–2.7	Enhanced photoluminescence	[95]
		23	Longer fluorescent lifetime	[101]
		23		[5]
		60		[118]
		6 m, 10 nm	Enhanced photoluminescence (fivefold)	[119]
		43, 55, 68, 71	Emission blue shift decreased emission intensity	[126]
		10–30	Enhanced photoluminescence	[127]
		8, 40, 70, and 160	Quenching concentration increased to 14%	[131]
			Quenching concentration increased to 8%	[134]
			Long luminescent lifetime	[147]
			Enhanced photoluminescence (five times greater)	[148]
	Y <sub>2</sub> O <sub>3</sub> :Tb	2–4		[145]
	Zn <sub>2</sub> SiO <sub>4</sub> :Eu	40–100		[122]
	Zn <sub>2</sub> SiO <sub>4</sub> :Tb			
	Y <sub>2</sub> SiO <sub>5</sub> :Eu	50		[123]
Y <sub>3</sub> Al <sub>5</sub> O <sub>12</sub> :Eu	60–90		[135]	
LaPO <sub>4</sub> :Eu, CePO <sub>4</sub> :Tb	5		[136]	
YVO <sub>4</sub> :Ln (Ln = Eu, Sm, Dy)	10–30		[138]	
La <sub>2</sub> (MoO <sub>4</sub> ) <sub>3</sub> :Yb,Er	50	Enhanced up-conversion fluorescence	[139]	
Y <sub>3</sub> Al <sub>6</sub> O <sub>12</sub> :Ce		Emission blue shift	[144]	
ZnS:Tb and ZnS:Eu	2, 3	Enhanced photoluminescence (three times higher)	[146]	
ZnS:Mn	8.3		[150]	
	3.5–7.5	High luminous efficiency, short lifetime (4 ns)	[160]	

continued

Table 3. Continued

Semiconductor	Size (nm)	Optical properties	Ref.
	3–5	Normal lifetime of 1.9 ms	
	100	Low-voltage excitation	[169]
CdS:Mn	4		[149]
CdSe:Mn	5		[151]
ZnS:Cu	2–2.5		[154]
ZnS:Cu,In	2–3		[155]

**Luminescent Lifetime** Bhargava et al. also reported an ultrafast decay time for nanocrystal ZnS:Mn. The lifetime of the Mn emission was shortened from 1.8 ms in the bulk powder to 4 ns in the doped nanocrystalline phosphor, which is five orders of magnitude shorter than that of bulk ZnS:Mn [160].

However, it was later shown that lifetime shortening in nanocrystalline ZnS:Mn did not occur. The  $Mn^{2+}$  emission of nanocrystalline ZnS:Mn has a normal millisecond lifetime. To test the result, a systematic investigation was carried out by Bol and Meijerink [161]. From lifetime measurements and time-resolved spectroscopy, they concluded that the  ${}^4T_1-{}^6A_1$  transition of the  $Mn^{2+}$  had a normal decay time of about 1.9 ms. The short decay time reported by Bhargava was ascribed to a defect-related emission of ZnS, and was not from the decay of the  ${}^4T_1-{}^6A_1$  transition of the  $Mn^{2+}$  impurity. More recent work on ZnS:Mn [156, 162] and CdS:Mn nanocrystals [159, 163] confirmed this conclusion [156].

### 3.3. Application of Doped Nanocrystals

As we reviewed earlier, doped nanocrystalline phosphors have many new optical characteristics. Such a system offers numerous possibilities for the next-generation devices in the field of lighting, displays, sensors, bio tags, and lasers. In the following, we will discuss the application of display and bio tags in detail.

#### 3.3.1. Display Applications

The development of new types of flat-panel and projection displays has created a need for optical phosphors with new or enhanced properties [164]. For application in these areas, thermally stable, high-luminous-efficiency, radiation-resistant, fine particle size powders are required [3]. Nanophase and nanocrystalline materials, typically particles with diameters of 100 nm or less, offer new possibilities for advanced phosphor applications [165–167]. On the other hand, for display applications, multiple particle layers are required to achieve optimal light output [5]. Large particles require thicker layers, increasing the phosphor cost, and also producing more light scattering [168]. Small and uniform particles with high luminous efficiency are preferred for new flat-panel displays [3].

Dinsmore et al. [169] found that ZnS:Mn nanoparticles exhibit less current saturation than bulk phosphors, which is an important feature for use in field-emission displays. Furthermore, the nanoparticles were annealed at a temperature far below the processing temperatures of standard phosphors.

By using nanometer-sized rare-earth doped phosphors as layers, Chinese scientists have successfully manufactured a field-emission display recently. This display has the advantages of high definition, bright emission, sharp dynamic color image, large angle of view (nearly  $180^\circ$ ), and so on [170].

#### 3.3.2. Biological Application

Nowadays, most of the biological luminescent tags are organic dyes, such as rhodamine, FITC, Cy3, and Cy5. In comparison, the luminescence of doped phosphors is stronger, nonfading, not significantly influenced by pH or temperature, and has a longer lifetime [171]. Inorganic phosphors with a size of 100–300 nm, such as  $Zn_2SiO_4:Mn$ , As, ZnS:Ag, and  $Y_2O_3:Eu$ , have already been used for the detection of proteins and nucleic acids [171–173]. By using these kinds of labels, 10 fg protein and 300 fg nucleic acids have been detected. Nanosized phosphors with a narrow size distribution and high fluorescent efficiency are theoretically advantageous and favorable [172].

The uses of up-conversion phosphors as fluorescent labels for the sensitive detection of biomolecules have attracted even more interest recently [174, 175]. Phosphors that emit lower energy photons when excited by higher energy photons are down-conversion phosphors. For example, ZnS:Mn and  $Y_2O_3:Eu$  are well-known down-conversion phosphors. On the other hand, phosphors that emit higher energy photons after absorbing lower energy excitation photons are up-conversion phosphors. At least two low-energy photons are required to generate a higher energy photon. In comparison with organic dye labels, up-conversion phosphor fluorescent labels show very low background noise without photobleaching. By using up-conversion phosphor as labels, 1 ng/ $\mu$ L DNA could be detected, which is four times more sensitive than that labeled with cy5 [116].

## 4. CONCLUSION

Here, we have presented an overview of the synthesis and optical properties of nanocrystalline phosphors (see Table 3). The potential applications of these novel materials are also highlighted. For semiconductor nanocrystalline phosphors, a wide range of synthetic methods are now available. Particles with diameters in the range of 1–20 nm have been prepared, and quantum-size effects have been observed experimentally for many nanocrystalline semiconductors. However, most of the studies up to now have focused on II–IV and III–V compounds; there is still a major problem associated with the reproducible preparation of this kind of material that will be needed for technological applications, and the applications of semiconductor nanocrystals remain scarce, except for CdSe.

Studies of doped nanocrystalline phosphors, including synthesis, optical properties, and their applications, are discussed. Some new nano-related optical properties, such as high efficiency, high quenching concentration, and so on, have been reported. However, research in this area is preliminary; some results are quite confusing, and even contradicting. Most of the studies concentrated on a few of this kind of material, such as ZnS:Mn and Y<sub>2</sub>O<sub>3</sub>:Eu. There is still a lack of a guiding theory for the study of doped nanocrystalline phosphors. Systematic research needs to be done.

## GLOSSARY

**Down-conversion phosphor** Phosphor that emits lower energy photons when excited by higher energy photons.

**Emission spectrum** Wavelength distribution of the emission, measured at a single constant excitation wavelength.

**Excitation spectrum** Dependence of emission intensity, measured at a single emission wavelength, upon the excitation wavelength.

**Fluorescence** Emission of light by a substance immediately after the absorption of energy from light of usually shorter wavelength.

**Luminescent lifetime** Average fluorescence time between its excitation and its return to the ground state.

**Luminous efficiency** Also called quantum yields, is the number of emitted photons relative to the number of absorbed photons.

**Phosphors** Solid, inorganic, crystalline materials that show luminescence upon excitation.

**Up-conversion phosphor** Phosphor that emits higher energy photons after absorbing lower energy excitation photons. At least two low-energy photons are required to generate a higher energy photon.

## REFERENCES

1. K. H. Butler, "Fluorescent Lamp Phosphors." Pennsylvania State University Press, University Park and London, 1980.
2. C. R. Ronda, *J. Lumin.* 72-74, 49 (1997).
3. J. McKittrick, L. E. Shea, C. F. Bacalski, and E. J. Bosze, *Displays* 19, 169 (1999).
4. G. Wakefield, H. A. Keron, P. J. Dobson, and J. L. Hutchison, *J. Colloid Interface Sci.* 215, 179 (1999).
5. D. K. Williams, B. Bihari, B. M. Tissue, and J. M. McHale, *J. Phys. Chem. B* 102, 916 (1998).
6. A. P. Alivisatos, *J. Phys. Chem.* 100, 13226 (1996).
7. A. P. Alivisatos, *Science* 271, 933 (1996).
8. W. C. W. Chan and S. M. Nie, *Science* 281, 2016 (1998).
9. M. Bruchez, M. Moronne, P. Gin, S. Weiss, and A. P. Alivisatos, *Science* 281, 2013 (1998).
10. W. U. Huynh, J. J. Dittmer, and A. P. Alivisatos, *Science* 295, 2425 (2002).
11. W. U. Huynh, X. G. Peng, and A. P. Alivisatos, *Adv. Mater.* 11, 923 (1999).
12. H. J. Eisler, V. C. Sundar, M. G. Bawendi, M. Walsh, H. I. Smith, and V. Klimov, *Appl. Phys. Lett.* 80, 4614 (2002).
13. M. C. Schlamp, X. G. Peng, and A. P. Alivisatos, *J. Appl. Phys.* 82, 5837 (1997).
14. H. Mattoussi, L. H. Radzilowski, B. O. Dabbousi, E. L. Thomas, M. G. Bawendi, and M. F. Rubner, *J. Appl. Phys.* 83, 7965 (1998).
15. L. Brus, *Appl. Phys. A Solid* 53, 465 (1991).
16. S. S. Kher and R. L. Wells, *Chem. Mater.* 6, 2056 (1994).
17. H. Weller, *Adv. Mater.* 5, 88 (1993).
18. S. Schuppler, S. L. Friedman, M. A. Marcus, D. L. Adler, Y. H. Xie, F. M. Ross, T. D. Harris, W. L. Brown, Y. J. Chabal, L. E. Brus, and P. H. Citrin, *Phys. Rev. Lett.* 72, 2648 (1994).
19. X. G. Peng, J. Wickham, and A. P. Alivisatos, *J. Am. Chem. Soc.* 120, 5343 (1998).
20. Z. A. Peng and X. G. Peng, *J. Am. Chem. Soc.* 123, 1389 (2001).
21. X. G. Peng, L. Manna, W. D. Yang, J. Wickham, E. Scher, A. Kadavanich, and A. P. Alivisatos, *Nature* 404, 59 (2000).
22. D. J. Norris, A. Sacra, C. B. Murray, and M. G. Bawendi, *Phys. Rev. Lett.* 72, 2612 (1994).
23. C. B. Murray, D. J. Norris, and M. G. Bawendi, *J. Am. Chem. Soc.* 115, 8706 (1993).
24. J. P. Ge, Y. D. Li, and G. Q. Yang, *Chem. Commun.* 17, 1826 (2002).
25. X. G. Peng, *Chem.-Eur. J.* 8, 335 (2002).
26. Z. A. Peng and X. G. Peng, *J. Am. Chem. Soc.* 123, 183 (2001).
27. L. H. Qu, Z. A. Peng, and X. G. Peng, *Nano Lett.* 1, 333 (2001).
28. M. W. Yu and X. G. Peng, *Angew. Chem. Int. Ed.* 41, 2368 (2002).
29. L. Manna, E. C. Scher, and A. P. Alivisatos, *J. Am. Chem. Soc.* 122, 12700 (2000).
30. M. A. Hines and P. Guyot Sionnest, *J. Phys. Chem.—US* 100, 468 (1996).
31. B. O. Dabbousi, J. Rodriguez Viejo, F. V. Mikulec, J. R. Heine, H. Mattoussi, R. Ober, K. F. Jensen, and M. G. Bawendi, *J. Phys. Chem. B* 101, 9463 (1997).
32. X. G. Peng, M. C. Schlamp, A. V. Kadavanich, and A. P. Alivisatos, *J. Am. Chem. Soc.* 119, 7019 (1997).
33. L. Manna, E. C. Scher, L. S. Li, and A. P. Alivisatos, *J. Am. Chem. Soc.* 124, 7136 (2002).
34. G. P. Mitchell, C. A. Mirkin, and R. L. Letsinger, *J. Am. Chem. Soc.* 121, 8122 (1999).
35. C. C. Chen, C. P. Yet, H. N. Wang, and C. Y. Chao, *Langmuir* 15, 6845 (1999).
36. H. Mattoussi, J. M. Mauro, E. R. Goldman, G. P. Anderson, V. C. Sundar, F. V. Mikulec, and M. G. Bawendi, *J. Am. Chem. Soc.* 122, 12142 (2000).
37. J. Aldana, Y. A. Wang, and X. G. Peng, *J. Am. Chem. Soc.* 123, 8844 (2001).
38. Y. A. Wang, J. J. Li, H. Y. Chen, and X. G. Peng, *J. Am. Chem. Soc.* 124, 2293 (2002).
39. D. Gerion, F. Pinaud, S. C. Williams, W. J. Parak, D. Zanchet, S. Weiss, and A. P. Alivisatos, *J. Phys. Chem.* 105, 8861 (2001).
40. C. B. Murray, D. J. Norris, and M. G. Bawendi, *J. Am. Chem. Soc.* 115, 8706 (1993).
41. C. C. Chen, C. Y. Chao, and Z. H. Lang, *Chem. Mater.* 12, 1516 (2000).
42. Q. Peng, Y. J. Dong, Z. X. Deng, and Y. D. Li, *Inorg. Chem.* 41, 5249 (2002).
43. J. G. Brennan, T. Siegrist, P. J. Carroll, S. M. Stuczynski, L. E. Brus, and M. L. Steigerwald, *J. Am. Chem. Soc.* 111, 4141 (1989).
44. T. Trindade, P. O'Brien, and X. M. Zhang, *Chem. Mater.* 9, 523 (1997).
45. L. H. Qu, Z. A. Peng, and X. G. Peng, *Nano Lett.* 1, 333 (2001).
46. S. H. Yu, Y. S. Wu, J. Yang, Z. H. Han, Y. Xie, Y. T. Qian, and X. M. Liu, *Chem. Mater.* 10, 2309 (1998).
47. S. L. Cumberland, K. M. Hanif, A. Javier, G. A. Khitrov, G. F. Strouse, S. M. Woessner, and C. S. Yun, *Chem. Mater.* 14, 1576 (2002).
48. W. Z. Wang, I. Germanenko, and M. S. El-Shall, *Chem. Mater.* 14, 3028 (2002).
49. M. W. Yu and X. G. Peng, *Angew. Chem. Int. Ed.* 41, 2368 (2002).
50. T. Trindade, P. O'Brien, and X. M. Zhang, *Chem. Mater.* 9, 523 (1997).

51. M. Ohtaki, K. Oda, K. Eguchi, and H. Arai, *Chem. Commun.* 10, 1209 (1996).
52. C. B. Murray, D. J. Norris, and M. G. Bawendi, *J. Am. Chem. Soc.* 115, 8706 (1993).
53. S. L. Cumberland, K. M. Hanif, A. Javier, G. A. Khitrov, G. F. Strouse, S. M. Woessner, and C. S. Yun, *Chem. Mater.* 14, 1576 (2002).
54. M. A. Hines and P. Guyot-Sionnest, *J. Phys. Chem. B* 102, 3655 (1998).
55. W. Z. Wang, I. Germanenko, and M. S. El-Shall, *Chem. Mater.* 14, 3028 (2002).
56. B. Ludolph, M. A. Malik, P. O'Brien, and N. Revaprasadu, *Chem. Commun.* 1849 (1998).
57. N. Gaponik, D. V. Talapin, A. L. Rogach, K. Hoppe, E. V. Shevchenko, A. Kornowski, A. Eychmuller, and H. Weller, *J. Phys. Chem. B* 106, 7177 (2002).
58. D. V. Talapin, S. Haubold, A. L. Rogach, A. Kornowski, M. Haase, and H. Weller, *J. Phys. Chem. B* 105, 2260 (2001).
59. M. Y. Gao, S. Kirstein, H. Mohwald, A. L. Rogach, A. Kornowski, A. Eychmuller, and H. Weller, *J. Phys. Chem. B* 102, 8360 (1998).
60. P. Yan, Y. Xie, W. Z. Wang, F. Y. Liu, and Y. T. Qian, *J. Mater. Chem.* 9, 1831 (1999).
61. D. Battaglia and X. G. Peng, *Nano Lett.* 2, 1027 (2002).
62. M. Green and P. O'Brien, *Chem. Commun.* 2459 (1998).
63. P. Yan, Y. Xie, W. Z. Wang, F. Y. Liu, and Y. T. Qian, *J. Mater. Chem.* 9, 1831 (1999).
64. D. Battaglia and X. G. Peng, *Nano Lett.* 2, 1027 (2002).
65. O. I. Micic, J. R. Sprague, C. J. Curtis, K. M. Jones, J. L. Machol, A. J. Nozik, H. Giessen, B. Fluegel, G. Mohs, and N. Peyghambarian, *J. Phys. Chem.* 99, 7754 (1995).
66. R. L. Wells, S. R. Aubuchon, S. S. Kher, M. S. Lube, and P. S. White, *Chem. Mater.* 7, 793 (1995).
67. S. M. Gao, Y. Xie, J. Lu, G. A. Du, W. He, D. L. Cui, B. B. Huang, and M. H. Jiang, *Inorg. Chem.* 41, 1850 (2002).
68. S. S. Kher and R. L. Wells, *Chem. Mater.* 6, 2056 (1994).
69. O. I. Micic, J. R. Sprague, C. J. Curtis, K. M. Jones, J. L. Machol, A. J. Nozik, H. Giessen, B. Fluegel, G. Mohs, and N. Peyghambarian, *J. Phys. Chem.* 99, 7754 (1995).
70. S. S. Kher and R. L. Wells, *Chem. Mater.* 6, 2056 (1994).
71. M. A. Olshavsky, A. N. Goldstein, and A. P. Alivisatos, *J. Am. Chem. Soc.* 112, 9438 (1990).
72. L. Brus, *New J. Chem.* 11, 123 (1987).
73. J. Lee, V. C. Sundar, J. R. Heine, M. G. Bawendi, and K. F. Jensen, *Adv. Mater.* 12, 1102 (2000).
74. D. V. Talapin, A. L. Rogach, A. Kornowski, M. Haase, and H. Weller, *Nano Lett.* 1, 207 (2001).
75. L. H. Qu and X. G. Peng, *J. Am. Chem. Soc.* 124, 2049 (2002).
76. L. Brus, *Appl. Phys. A—Solid* 53, 465 (1991).
77. A. P. Alivisatos, A. L. Harris, N. J. Levinos, M. L. Steigerwald, and L. E. Brus, *J. Chem. Phys.* 89, 4001 (1988).
78. M. Nirmal, B. O. Dabbousi, M. G. Bawendi, J. J. Macklin, J. K. Trautman, T. D. Harris, and L. E. Brus, *Nature* 383, 802 (1996).
79. S. A. Blanton, M. A. Hines, and P. Guyot-Sionnest, *Appl. Phys. Lett.* 69, 3905 (1996).
80. S. A. Empedocles, D. J. Norris, and M. G. Bawendi, *Phys. Rev. Lett.* 77, 3873 (1996).
81. M. A. Hines and P. Guyot-Sionnest, *J. Phys. Chem. B* 102, 3655 (1998).
82. L. H. Qu and X. G. Peng, *J. Am. Chem. Soc.* 124, 2049 (2002).
83. D. V. Talapin, S. Haubold, A. L. Rogach, A. Kornowski, M. Haase, and H. Weller, *J. Phys. Chem. B* 105, 2260 (2001).
84. M. W. Yu and X. G. Peng, *Angew. Chem. Int. Ed.* 41, 2368 (2002).
85. A. A. Guzelian, U. Banin, A. V. Kadavanich, X. Peng, and A. P. Alivisatos, *Appl. Phys. Lett.* 69, 1432 (1996).
86. Y. M. Cao and U. Banin, *J. Am. Chem. Soc.* 122, 9692 (2000).
87. D. Battaglia and X. G. Peng, *Nano Lett.* 2, 1027 (2002).
88. N. F. Borrelli and D. W. Smith, *J. Non-Cryst. Solids* 180, 25 (1994).
89. D. E. Bliss, J. P. Wilcoxon, P. P. Newcomer, and G. A. Samara, *Mater. Res. Soc. Symp. Proc.* 358, 265 (1995).
90. S. Gorer, A. Albn-Yaron, and G. Hodes, *J. Phys. Chem.* 99, 16442 (1995).
91. Y. Jiang, Y. Wu, B. Xie, S.W. Yuan, X. M. Liu, and Y. T. Qian, *J. Cryst. Growth* 231, 248 (2001).
92. H. Nasu, H. Yamada, J. Matsuoka, and K. Kamiya, *J. Non-Cryst. Solids* 183, 290 (1995).
93. R. Thielsch, T. Bohme, R. Reiche, D. Schlafer, H. D. Bauer, and H. Bottcher, *Nanostruct. Mater.* 10, 131 (1998).
94. L. T. Canham, *Appl. Phys. Lett.* 57, 1046 (1990).
95. Y. C. Peng, Y. L. He, and M. Liu, *Chinese J. Vac. Sci. Technol.* 18, 283 (1999).
96. S. Tong, X. N. Liu, and T. Gao, *J. Non-Cryst. Solids* 227, 498 (1998).
97. T. S. Iwayama, K. Fujita, and S. Nakao, *J. Appl. Phys.* 75, 7779 (1994).
98. E. Werwa, A. A. Seraphin, L. A. Chiu, C. X. Zhou, and K. D. Kolenbrand, *Appl. Phys. Lett.* 64, 1821 (1994).
99. M. Fukuda, K. Nakagawa, S. Miyazaki, and M. Hirose, *Appl. Phys. Lett.* 70, 2291 (1997).
100. L. D. Zhang and J. M. Mu, "Nanomaterial and Nanostructure." Science Press, Beijing, 2001.
101. Y. Kanzawa, T. Kageyama, S. Takeoka, M. Fujii, S. Hayashi, and K. Yamamoto, *Solid State Commun.* 102, 533 (1997).
102. H. Takagi, H. Ogawa, and Y. Yamazaki, *Appl. Phys. Lett.* 56, 2379 (1990).
103. B. Q. Sun, W. Z. Xie, G. S. Yi, D. P. Chen, Y. X. Zhou, and J. Cheng, *J. Immunol. Meth.* 249, 85 (2001).
104. A. Sukhanova, L. Venteo, J. Devy, M. Artemyev, V. Oleinikov, M. Pluot, and I. Nabiev, *Lab Invest.* 82, 1259 (2002).
105. G. S. Harms, L. Cognet, P. H. M. Lommerse, G. A. Blab, and T. Schmidt, *Biophys. J.* 80, 2396 (2001).
106. T. D. Lacoste, X. Michalet, F. Pinaud, D. S. Chemla, A. P. Alivisatos, and S. Weiss, *Proc. Nat. Acad. Sci. U.S.A.* 97, 9461 (2000).
107. V. L. Colvin, M. C. Schlamp, and A. P. Alivisatos, *Nature* 370, 354 (1994).
108. M. C. Schlamp, X. G. Peng, and A. P. Alivisatos, *J. Appl. Phys.* 82, 5837 (1997).
109. W. U. Huynh, J. J. Dittmer, and A. P. Alivisatos, *Science* 295, 2425 (2002).
110. H. J. Eisler, V. C. Sundar, M. G. Bawendi, M. Walsh, H. I. Smith, and V. Klimov, *Appl. Phys. Lett.* 80, 4614 (2002).
111. L. D. Wang and Y. C. Yang, *Rare Metals* 20, 129 (1996).
112. D. J. Norris, N. Yao, F. Tcharnock, and T. A. Kennedy, *Nano Lett.* 1, 3 (2001).
113. F. Parsapour, D. F. Kelley, and R. S. Williams, *J. Phys. Chem. B* 102, 7971 (1998).
114. R. N. Bhargava, *J. Lumin.* 70, 85 (1996).
115. H. S. Yang, K. S. Hong, S. P. Feo. lov, B. M. Tissue, R. S. Meltzer, and W. M. Dennis, *J. Lumin.* 83–84, 139 (1999).
116. W. Chen, J. O. Malm, V. Zwiller, R. Wallenberg, and J. O. Bovin, *J. Appl. Phys.* 89, 2671 (2001).
117. B. Bihari, H. Eilers, and B. M. Tissue, *J. Lumin.* 75, 1 (1997).
118. <http://www.talmaterials.com>.
119. R. M. Laine, K. Waldner, C. Bickmore, and D. R. Treadwell, U.S. Patent 5, 958, 361, 1999.
120. R. M. Laine, S. C. Rand, T. Hinklin, and G. Williams, WO Patent 0038282 H01S20000629.
121. H. X. Zhang, S. Buddhudu, C. H. Kam, Y. Zhou, Y. L. Lam, K. S. Wong, B. S. Ooi, S. L. Ng, and W. X. Que, *Mater. Chem. Phys.* 68, 31 (2001).
122. M. Yin, W. Zhang, S. Xia, and J. C. Krupa, *J. Lumin.* 68, 335 (1996).

124. J. Y. Zhang, Z. L. Tang, Z. T. Zhang, W. Y. Fu, J. Wang, and Y. H. Lin, *Mater. Sci. Eng. A Struct. Mater.: Prop. Microstruct. Process.* 334, 246 (2002).
125. J. Y. Zhang, Z. L. Tang, Z. T. Zhang, F. D. Lin, and Y. H. Lin, *Key. Eng. Mater.* 224-2, 229 (2002).
126. P. K. Sharma, M. H. Jilavi, R. Nass, and H. Schmidt, *J. Lumin.* 82, 187 (1999).
127. Q. Li, L. Gao, and D. S. Yan, *J. Inorg. Mater.* 12, 237 (1997).
128. Q. Li, L. Gao, and D. S. Yan, *J. Inorg. Mater.* 14, 150 (1999).
129. Q. Li, L. Gao, and D. S. Yan, *Mater. Chem. Phys.* 64, 41 (2000).
130. R. S. Kane, R. E. Cohen, and R. Silbey, *Chem. Mater.* 11, 90 (1999).
131. M. H. Lee, S. G. Oh, and S. C. Yi, *J. Colloid Interface Sci.* 226, 65 (2000).
132. J. J. Kingsley and L. R. Pederson, *Mater. Res. Soc. Symp. Proc.* 296, 361 (1993).
133. S. Ekamparam and K. C. Patil, *Bull. Mater. Sci.* 18, 921 (1995).
134. Y. Tao, G. W. Zhao, W. P. Zhang, and S. D. Xia, *Mater. Res. Bull.* 32, 501 (1997).
135. S. K. Shi and J. Y. Wang, *J. Alloy. Comp.* 327, 82 (2001).
136. K. Riwotzki, H. Meyssamy, A. Kornowski, and M. Haase, *J. Phys. Chem. B* 104, 2824 (2000).
137. H. Meyssamy, K. Riwotzki, A. Kornowski, S. Naused, and M. Haase, *Adv. Mater.* 11, 840 (1999).
138. K. Riwotzki and M. Haase, *J. Phys. Chem. B* 102, 10129 (1998).
139. G. S. Yi, B. Q. Sun, F. Z. Yang, D. P. Chen, Y. X. Zhou, and J. Cheng, *Chem. Mater.* 14, 2910 (2002).
140. M. Ihara, T. Igarashi, T. Kusunoki, and K. Ohno, *J. Electrochem. Soc.* 147, 2355 (2000).
141. S. J. Xu, S. J. Chua, B. Liu, L. M. Gan, C. H. Chew, and Q. Q. Xu, *Appl. Phys. Lett.* 73, 478 (1998).
142. T. Schmidt, G. Muller, and L. Spanhel, *Chem. Mater.* 10, 65 (1998).
143. A. A. Bol, R. van Beek, and A. Meijerink, *Chem. Mater.* 14, 1121 (2002).
144. Q. Li, L. Gao, and D. S. Yan, *J. Inorg. Mater.* 12, 575 (1997).
145. R. N. Bhargava, *J. Cryst. Growth* 214, 926 (2000).
146. M. Ihara, T. Igarashi, T. Kusunoki, and K. Ohno, *J. Electrochem. Soc.* 149, H72 (2002).
147. Q. Li, L. Gao, and D. S. Yan, *J. Inorg. Mater.* 13, 899 (1998).
148. Q. Li, L. Gao, and D. S. Yan, *Adv. Ceram. Eng., Suppl.* 155 (1998).
149. S. M. Liu, F. Q. Liu, H. Q. Guo, Z. H. Zhang, and Z. G. Wang, *Solid State Commun.* 115, 615 (2000).
150. G. S. Yi, B. Q. Sun, F. Z. Yang, and D. P. Chen, *J. Mater. Chem.* 11, 2928 (2001).
151. F. V. Mikulec, M. Kanu, M. Bennati, D. A. Hall, R. G. Griffin, and M. G. Bawandi, *J. Am. Chem. Soc.* 122, 2532 (2000).
152. M. A. Malik, P. O'Brien, and N. Revaprasadu, *J. Mater. Chem.* 105, 4128 (2001).
153. I. Yu, T. Isobe, and M. Senna, *J. Phys. Chem. Solids* 57, 373 (1996).
154. P. Yang, C. F. Song, M. K. Lu, G. J. Zhou, Z. X. Yang, D. Xu, and D. R. Yuan, *J. Phys. Chem. Solids* 63, 639 (2002).
155. P. Yang, M. K. Lu, C. F. Song, D. Xu, D. R. Yuan, F. C. Xiu, and D. R. Yuan, *Opt. Mater.* 20, 141 (2002).
156. B. A. Smith and J. Z. Zhang, *Phys. Rev. B* 62, 2021 (2000).
157. S. J. Xu, S. J. Chua, B. Liu, L. M. Gan, C. H. Chew, and G. Q. Xu, *Appl. Phys. Lett.* 73, 478 (1998).
158. W. X. Que, Y. Zhou, Y. L. Lam, Y. C. Chan, C. H. Kam, B. Liu, L. M. Gan, C. H. Chew, G. Q. Xu, S. J. Chua, S. J. Xu, and F. V. C. Mendis, *Appl. Phys. Lett.* 73, 2727 (1998).
159. M. A. Chamarro, V. Voliotis, R. Grousson, P. Lavallard, T. Gacoin, G. Cournio, J. P. Boilot, and R. Cases, *J. Cryst. Growth* 159, 853 (1996).
160. R. N. Bhargava, D. Gallagher, X. Hong, and A. Nurmikko, *Phys. Rev. Lett.* 72, 416 (1994).
161. A. A. Bol and A. Meijerink, *Phys. Rev. B* 58, R15997 (1998).
162. J. H. Chung, C. S. Ah, and D. J. Jang, *J. Phys. Chem. B* 105, 4128 (2001).
163. Y. Kanemitsu, H. Matsubara, and C. W. White, *Appl. Phys. Lett.* 81, 535 (2002).
164. P. Maestro and D. Huguenin, *J. Alloy Comp.* 225, 520 (1995).
165. G. C. Hadjipanayis and R. W. Siegel, "Nanophase Materials: Synthesis Properties Applications, NATO ASI Series E 260." Kluwer, Dordrecht, 1993.
166. H. Gleiter, *Prog. Mater. Sci.* 33, 223 (1989).
167. M. Ihara, T. Igarashi, T. Kusunoki, and K. Ohno, *J. Electrochem. Soc.* 149, H72 (2002).
168. A. P. Burden, *Int. Mater. Rev.* 46, 213 (2001).
169. A. D. Dinsmore, D. S. Hsu, H. F. Gray, S. B. Qadri, Y. Tian, and B. R. Ratna, *Appl. Phys. Lett.* 75, 802 (1999).
170. <http://www.casnano.ac.cn/gb/xinwen/yaowen/yw192.html>.
171. H. B. Beverloo, A. van Schadewijk, H. J. M. A. A. Zijlmans, and H. J. Tanke, *Anal. Biochem.* 203, 326 (1992).
172. H. B. Beverloo, A. van Schadewijk, S. van Gelderen-Boele, and H. J. Tanke, *Cytometry* 11, 784 (1990).
173. H. B. Beverloo, A. van Schadewijk, J. Bonnet, R. Van der Geest, R. Runia, N. P. Verwoerd, J. Vrolijk, J. S. Ploem, and H. J. Tanke, *Cytometry* 13, 561 (1992).
174. F. V. D. Rijke, H. Zijlmans, S. Li, T. Vail, A. K. Raap, R. S. Niedbala, and H. J. Tanke, *Nat. Biotechnol.* 19, 273 (2001).
175. J. Hampl, M. Hall, N. A. Mufti, Y. M. Yao, D. B. Macqusee, W. H. Wright, and D. E. Cooper, *Anal. Biochem.* 288, 176 (2001).



# Nanocrystalline Silicon Superlattices

David J. Lockwood

*National Research Council, Ottawa, Canada*

Leonid Tsybeskov

*New Jersey Institute of Technology, Newark, New Jersey, USA*

## CONTENTS

1. Introduction
2. Superlattice Fabrication Techniques and Post-Treatment Procedures
3. Structural Characterization of Nanocrystalline Silicon–Silicon Dioxide Superlattices
4. Raman Spectroscopy of Nanocrystalline Silicon–Silicon Dioxide Superlattices
5. Photoluminescence Spectroscopy of Nanocrystalline Silicon–Silicon Dioxide Superlattices
6. Resonant Carrier Tunneling in Nanocrystalline Silicon–Silicon Dioxide Superlattices
7. Summary  
Glossary  
References

## 1. INTRODUCTION

This review chapter is focused on the fabrication and characterization of layered Si-based nanostructures, which have been termed nanocrystalline silicon (nc-Si)–silicon dioxide superlattices [1]. Among the many semiconducting materials, silicon is well studied and certainly the most important material for commercial microelectronics. During the past several decades, the exponential growth of electronic chip complexity and drastic decrease of transistor dimensions have highlighted requirements for new directions in electronic device evolution and the potential applicability of Si nanocrystals for nanoelectronics and integrated light-emitters. The latter was stimulated by the discovery of efficient light emission in different forms of Si nanostructures [2] and by the demonstration of a Si-based light-emitting device prototype integrated into conventional microelectronic circuitry [3]. Hence, the interest in reliable fabrication

of Si-based nanostructures with control over the nanocrystal size, shape, and crystallographic orientation has been growing continuously over the last decade. Recently, the application of Si nanocrystals in electronic devices was suggested and proved by the demonstration of a Si nanocrystal nonvolatile memory and other devices utilizing the Coulomb blockade effect [4, 5].

Despite the strong interest in different forms of nc-Si, the fabrication of Si nanocrystals with control over the nanocrystal size and shape has been significantly less successful compared to other semiconducting materials. The latest advances in semiconductor nanocrystal fabrication have been based on chemical synthesis in II-VI materials [6] and the successful application of the Stranski–Krastanow growth mode in molecular beam epitaxy (MBE) for III-V semiconductors. Neither of these techniques is applicable for Si/SiO<sub>2</sub> structures. In general, crystalline Si (c-Si) and amorphous SiO<sub>2</sub> are quite different materials with large mismatches between their local crystallographic order and thermal expansion. Therefore, crystalline Si does not wet the SiO<sub>2</sub> surface, and standard heteroepitaxy based on MBE, chemical vapor deposition (CVD), or magnetron sputtering, produces highly disordered polycrystalline Si on SiO<sub>2</sub>-covered substrates.

Several attempts to introduce layered Si/SiO<sub>2</sub> nanoscale structures were reported in the mid and late 1990s, aiming for deep carrier confinement in Si nanocrystals due to high Si/SiO<sub>2</sub> barriers. Two major approaches were focused on (1) high-quality amorphous Si (a-Si)/amorphous SiO<sub>2</sub> (a-SiO<sub>2</sub>) structures [7, 8] and (2) layers of Si nanocrystals sandwiched between tunnel transparent, nanometer-thin a-SiO<sub>2</sub> separating layers [1]. In the former case, involving a-Si layer thicknesses between 1 and 2 nm, the ultrathin Si layers could not be crystallized even after extended annealing at high temperatures owing to the strain at the Si/SiO<sub>2</sub> interface [9]. Nevertheless, clear optical evidence of carrier confinement in the Si layers was obtained [7, 8, 10]. The other approach utilizes a unique property of the c-Si/SiO<sub>2</sub> interface, the same property that made the MOSFET the unique generic

device for modern electronics. Since crystalline (or nanocrystalline) Si and amorphous SiO<sub>2</sub> belong to different thermodynamic classes of materials, they do not mix but rather segregate at high temperatures. Therefore, an atomically smooth interface and very homogeneous growth of SiO<sub>2</sub> on c-Si can be produced by a simple technological procedure: namely, Si thermal oxidation. In general, controlled crystallization of amorphous Si/SiO<sub>2</sub> superlattices follows the same rules with only one exception: the a-Si layer must be crystallized before interstitial oxygen diffuses into the Si layer. It was realized almost immediately that rapid thermal annealing, which currently is a standard fabrication procedure for many semiconductor processes, is able to provide very fast crystallization of nanometer-thick a-Si layers. At the same time, an a-SiO<sub>2</sub> layer remains amorphous, because annealing at temperatures close to 1200 °C merely improves its stoichiometry.

This technological process (full details are presented in Section 2) is able to produce layers of Si nanocrystals sandwiched between a-SiO<sub>2</sub> layers or nc-Si/a-SiO<sub>2</sub> superlattices. In view of considerable prior research, the physical properties of these structures could be expected to be similar to those of grainy polycrystalline Si and should be affected by nanocrystal (or nanograin) boundaries. However, it turns out that many interesting and unique properties of nc-Si/a-SiO<sub>2</sub> superlattices stem from their vertical periodicity and nearly defect-free, atomically flat, and chemically abrupt nc-Si/SiO<sub>2</sub> interfaces [11]. In addition, by combining a less than 5% variation in a-Si layer thickness with control over the Si nanocrystal shape and crystallographic orientation [11, 12], a system of nearly identical Si nanocrystals can be produced and studied.

The aim of this chapter is to review in detail the fabrication of nc-Si/a-SiO<sub>2</sub> superlattices and their structural and optical (mainly Raman scattering and photoluminescence) properties. Recently, a number of surprising results (such as resonant tunneling and quantum carrier transport [13]) were obtained from investigations of the electronic properties of these structures. Carrier transport in layered structures of Si nanocrystals is a complex subject, and by itself could provide material for another chapter. Therefore, we only briefly mention here the most interesting and significant results on the electronic properties of nc-Si/a-SiO<sub>2</sub> superlattices.

## 2. SUPERLATTICE FABRICATION TECHNIQUES AND POST-TREATMENT PROCEDURES

Amorphous layered structures or amorphous superlattices have distinct advantages when compared to crystalline materials: since long-range order is not preserved, virtually any two materials can be deposited in the form of a heteropair or layered structure. However, the observation of desired physical phenomena such as Brillouin zone folding, band structure modification, and quantum carrier transport requires minimization of charge carrier scattering, and potential sources of such scattering are structural defects. Another important issue is a leaky and/or rough barrier. To avoid this problem, chemically abrupt and defect-free interfaces must be preserved. Since the great majority of amorphous superlattices studied to date were fabricated using

plasma enhanced chemical vapor deposition (PE CVD) [14–16], the most significant problem affecting the quality of these structures (a-Si:H/a-SiN:H, a-Si/a-SiC:H, etc.) is their diffused interfaces. Realizing this fact, Lockwood et al. [10] proposed to use MBE growth of a-Si in combination with ozone oxidation to achieve a perfect control over the a-Si layer thickness and abrupt a-Si/a-SiO<sub>2</sub> interfaces.

In 1995, Lu et al. [7] reported visible light emission at room temperature from ultrathin-layer a-Si/a-SiO<sub>2</sub> superlattices grown by MBE that exhibited a clear quantum confinement shift with Si layer thickness, as shown in Figure 1. According to effective mass theory and assuming infinite potential barriers, which is a reasonable approximation since wide-gap (~9 eV) 1-nm-thick a-SiO<sub>2</sub> barriers are used, the energy gap  $E$  for one-dimensionally confined Si should vary as  $E = E_g + (\pi\hbar^2/2d^2)[1/m_e^* + 1/m_h^*]$ , where  $E_g$  is the bulk material bandgap,  $d$  is the a-Si well thickness, and  $m_e^*$  and  $m_h^*$  are the electron and hole effective masses [10]. This simple model is a reasonable first approximation to compare with experiment for quantum wells. The shift in photoluminescence (PL) peak energy with a-Si well thickness is well represented by this equation, as can be seen in Figure 1, with  $E$  (eV) = 1.60 + 0.72 $d^{-2}$ . The very thin layers of Si ( $1 < d < 3$  nm) have a disordered, but nearly crystalline, structure owing to the growth conditions and the huge strain at the a-Si/a-SiO<sub>2</sub> interfaces [9]. The fitted  $E_g$  of 1.60 eV is larger than that expected for c-Si (1.12 eV at 295 K), but is in excellent agreement with that of bulk a-Si (1.5–1.6 eV at 295 K). These strong indications of direct band-to-band recombination were confirmed by measurements via X-ray techniques of the conduction and valence band shifts with layer thickness [7]. The fitted confinement parameter of 0.72 eV/nm<sup>2</sup> indicates  $m_e^* \approx m_h^* \approx 1$ , comparable to the effective masses of c-Si at room temperature [10]. The integrated intensity at first rises sharply with decreasing Si thickness until  $d \approx 1.5$  nm and then decreases again, which is consistent with quantum well exciton emission. The PL intensity is enhanced by factors of up to 100 on annealing and is also selectively enhanced and bandwidth narrowed by incorporation into an optical microcavity [8]. In a high-quality cavity, a very sharp

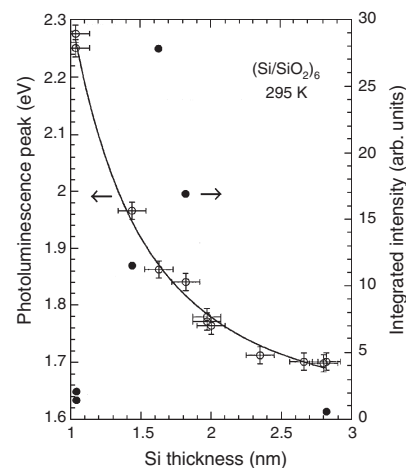


**Figure 1.** The PL peak energy (open circles) and integrated intensity (filled circles) at 295 K in (a-Si/a-SiO<sub>2</sub>)<sub>6</sub> superlattices as a function of the a-Si layer thickness. The solid line is a fit to the peak energy data using effective mass theory.

(17 meV full width at half maximum) PL peak has been observed [8]. Thus, in general, the wavelength of light emission in these structures can be controlled by the thickness of the a-Si layers and the design of the optical cavity within which they are contained.

The use of an a-Si layer as a quantum well is quite limited due to intrinsic structural defects. Silicon dangling bonds are the most well-known type of such defects [17], and they affect the quality of both the a-Si wells and a-Si/SiO<sub>2</sub> interfaces. Silicon dangling bonds in the a-Si matrix appear due to the absence of long-range order. The generally accepted model considers significant deviations in the Si bond angle and length and agrees with the fact that the a-Si density is typically 80% that of c-Si [18]. The model requires some critical thickness for the a-Si layer before the Si bonds are stretched enough to be broken. Therefore, the dangling bond density per unit volume is reduced in nanometer-thin a-Si layers compared to bulky, micron-thick layers of a-Si and the nanometer-thin a-Si layer density is 98% that of c-Si [9].

The fact that a-Si/a-SiO<sub>2</sub> superlattices are not defect-free structures stimulated a search for a post-treatment procedure that can reduce the defect density. Normally, structural defects that have been introduced by ion implantation or some other manufacturing steps can be eliminated using thermal annealing. Defect annealing utilizes the strong covalent nature of Si bonds and the ability of the crystal lattice to recover the initial, thermodynamically stable bond arrangement. Unfortunately, a-Si/a-SiO<sub>2</sub> superlattices cannot be treated the same way, because oxygen diffusion and the oxidation rate in a-Si is orders of magnitude faster at a given temperature compared to c-Si. Therefore, some intermixing of a-Si and a-SiO<sub>2</sub> may occur. Technically, an ideal solution is to have a stack of nanometer-thick layers of c-Si sandwiched between SiO<sub>2</sub> barriers. However, current technology is not able to provide the required dimensions and the interface quality for such structures and many approaches (e.g., SIMOX, smart-cut, and MBE growth of Si on dispersed SiO<sub>2</sub> layers) eventually failed to demonstrate the feasibility of reliable fabrication.

Several independent reports proposed thermal crystallization of nanometer-thick a-Si layers sandwiched between a-SiO<sub>2</sub> [19–21], and they indicated that the crystallization temperature (normally  $\leq 600$  °C for a micrometer-thick a-Si layer) increases significantly, and may reach 1000 °C or more for a-Si layers thinner than 2–3 nm. Detailed studies [22] supported the same conclusion, but they attributed such a strong increase in crystallization temperature to very strong strain within nanometer-thin a-Si layers sandwiched between layers of a-SiO<sub>2</sub>. A model has been developed [20, 23] that is able to describe the influence of strain at Si/SiO<sub>2</sub> interfaces, but it contains many empirical parameters. In fact, Figure 2, which compares the crystallization temperature for two series of samples having different SiO<sub>2</sub> thickness fabricated by magnetron sputtering, proves that a thicker SiO<sub>2</sub> layer actually introduces more strain into the layered Si/SiO<sub>2</sub> system. Therefore, the conclusion [22, 23] that the thickness of a partially disordered Si layer along such interfaces remains  $\sim 5$  Å even for completely crystallized structures may not be exactly correct. Most likely, as proved by several unsuccessful attempts to crystallize a-Si/SiO<sub>2</sub> superlattices

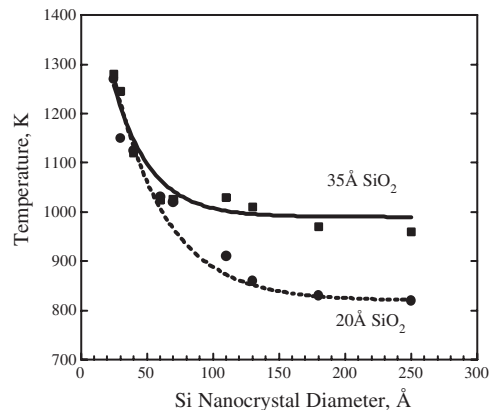


**Figure 2.** Crystallization temperature as a function of the Si nanocrystal vertical dimension in nc-Si superlattices with different thicknesses of a-SiO<sub>2</sub> separating layer.

fabricated by MBE and ozone oxidation [9], the values of the strain and crystallization parameters strongly depend on the local order of a-Si/SiO<sub>2</sub> structure, and such order may vary significantly for different fabrication techniques.

Compared to other a-Si/SiO<sub>2</sub> fabrication techniques, [e.g., radio-frequency (RF) sputtering and CVD], MBE in combination with ozone oxidation is the least desirable technique owing to its complexity. However, the alternatives to MBE fabrication are not able to produce abrupt a-Si/SiO<sub>2</sub> interfaces. Several experiments involving Auger microanalysis and transmission electron microscopy (TEM) showed the existence of a 20-Å-thick interface layer at a-Si/SiO<sub>2</sub> interfaces in samples prepared by RF sputtering [24]. Detailed studies have shown that such diffuse Si/SiO<sub>2</sub> interfaces may result in strong intermixing and the total destruction of the defined layered structures or superlattices after annealing (see Fig. 3).

In addition to these interdiffused a-Si/SiO<sub>2</sub> interfaces produced by CVD or sputtering growth methods, the quality of CVD or sputtered SiO<sub>2</sub> is known to be poor. Detailed analysis had shown that most of the SiO<sub>2</sub> structural defects originate from the formation of a columnar structure, which contains a large density of dangling Si bonds [25]. Such columns appear during growth due to the quasi-equilibrium (or low-rate) growth mode. To avoid the formation of the columnar structure, growth of amorphous materials (including a-Si and SiO<sub>2</sub>) should be done under highly non-equilibrium conditions. To achieve these conditions, CVD

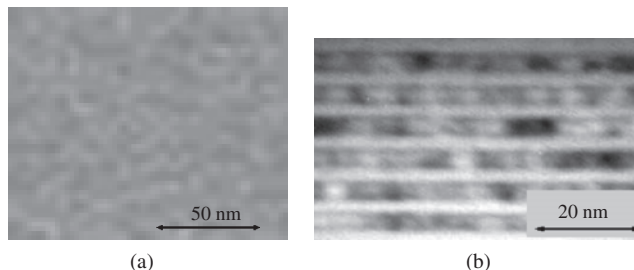


**Figure 3.** TEM micrograph showing the result of thermal crystallization in an amorphous Si/SiO<sub>2</sub> superlattice with (a) initially diffuse ( $>20$  Å) and (b) abrupt ( $<5$  Å) Si/SiO<sub>2</sub> interfaces.

requires a specific range of gas flow, reaction temperature, and other growth parameters. Considering RF or magnetron sputtering, an increase in RF power generates highly energetic ions, which result in the destruction of the columnar structure. Figure 4 compares two samples of a-SiO<sub>2</sub> fabricated by RF sputtering using different RF power, and lower RF power visibly results in the formation of the unwanted columns.

The most basic figure of merit for these three growth techniques in a-Si/SiO<sub>2</sub> fabrication is the ability to control the growth rate and thus provide layers of both materials with angstrom precision. This is important for Si, because of the relatively large value of the reduced electron effective mass ( $\sim 0.5$  of the electron mass,  $m_e$ ), and a simple calculation shows that a desirable thickness for tunnel devices utilizing carrier confinement is of the order of 50 Å or less. It is even more important for SiO<sub>2</sub> barriers, because the large barrier offset of several electron volts constrains the barrier thickness to be thinner than 20 Å. Compared to the complex chemistry of CVD, RF or magnetron sputtering has the clear advantage of a physical deposition process, that is, a linear dependence in the deposition rate as a function of time at a given RF power. Sputtering, as in any other plasma induced process, is a self-cleaning procedure, and it can be done in a moderate vacuum of  $\sim 10^{-7}$  Torr. The process allows the simple cleaning of a target and substrate as a pre-deposition step. A modern sputtering system also provides very good stabilization of the plasma and is able to bring the deposition rate down to 100 Å per minute or even less.

Thermal crystallization of a-Si/SiO<sub>2</sub> superlattices can be carried out in a conventional, hot-wall furnace with control over the ambient conditions to avoid unwanted oxidation. At moderate temperatures (200–400 °C) it was found that the interstitial oxygen may quickly diffuse into a-Si and initiate a-Si/SiO<sub>2</sub> intermixing [26]. It also was noticed that CVD or sputtered SiO<sub>2</sub> introduces less strain into layered a-Si/SiO<sub>2</sub> structures, and this is most likely due to the lower density of sputtered SiO<sub>2</sub> layers compared to SiO<sub>2</sub> fabricated by ozone or thermal oxidation. By considering these issues, it was suggested [27] that the best growth choice would be sputtered or CVD deposited a-Si/SiO<sub>2</sub> layers, but thermal crystallization must be performed using rapid thermal annealing (RTA). The RTA approach was found to provide very efficient crystallization of nanometer-thick a-Si layers with thickness down to  $\sim 2$  nm [27]. It was also found that

the combination of RTA with subsequent furnace annealing results in the segregation of crystallized Si and amorphous SiO<sub>2</sub> layers, together with pronounced improvement in the nc-Si/SiO<sub>2</sub> interface abruptness and flatness. At the same time, thermal annealing at a temperature  $\leq 1200$  °C improves the a-SiO<sub>2</sub> layer stoichiometry and density, and reduces the number of defects at the Si/SiO<sub>2</sub> interfaces.

To summarize this brief review of Si/SiO<sub>2</sub> layered structure fabrication, amorphous Si/SiO<sub>2</sub> superlattices can be prepared by several techniques, but only one post-treatment process can bring them to the level of device-quality structures. This process is a properly controlled thermal annealing, and it results in (1) crystallization of a-Si, (2) enhancement of the Si/SiO<sub>2</sub> interface abruptness, and (3) reduction in the interface and intrinsic defect density (mostly Si dangling bonds).

### 3. STRUCTURAL CHARACTERIZATION OF NANOCRYSTALLINE SILICON–SILICON DIOXIDE SUPERLATTICES

Ever since the first report on the successful fabrication of nanocrystalline Si superlattices [28], a wide variety of techniques have been proposed and employed to characterize these structures. The obvious initial focus was on transmission electron microscopy (TEM), which, despite its complexity, remains the most important technique to study nanocrystal geometry (size, shape, etc.) and crystallography. TEM is particularly difficult to perform in Si/SiO<sub>2</sub> structures, because of the relatively low contrast and significant probability of charging the SiO<sub>2</sub> layers. However, due to the considerable interest in Si-based nanostructures, considerable experience has been developed in the last decade, and a number of useful methods for sample preparation and image enhancement [29] finally allowed TEM to become a routine characterization method. In nc-Si/a-SiO<sub>2</sub> superlattices, TEM images have provided critical information and a number of important results will be presented below.

The TEM images in Figure 5 show a clear size-dependent trend in the Si nanocrystal shape: smaller Si nanocrystals with vertical sizes  $\leq 6$  nm are spherical or slightly elliptical but larger nanocrystals ( $\geq 10$  nm) clearly have a rectangular (or brick-like) shape. For the brick-shaped nanocrystals, the ratio between lateral and vertical dimensions is close to

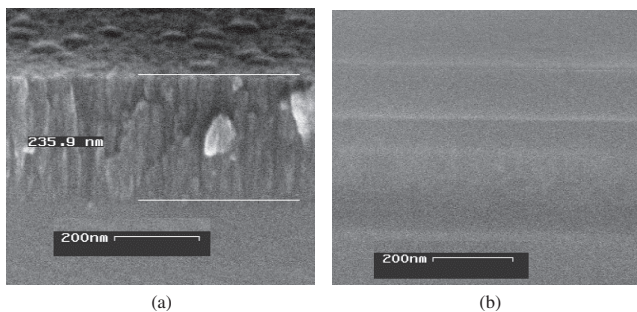


**Figure 4.** Two examples of sputtered a-SiO<sub>2</sub> layers (a) with and (b) without columnar microstructure. The sample with columnar microstructure was prepared using a low ( $< 50$  W) RF power.

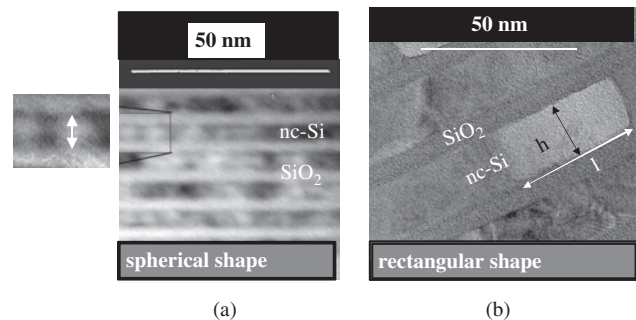


**Figure 5.** TEM micrograph showing examples of (a) spherical and (b) rectangular-shape Si nanocrystals termed “quantum dots” and “quantum bricks.”



2 : 1. A high-resolution TEM image of an individual, brick-shaped Si nanocrystal (Fig. 6) proves that the nc-Si/SiO<sub>2</sub> interfaces are flat and abrupt. This observation highlights at least two issues: (1) brick-shaped Si nanocrystals should have a better nc-Si/SiO<sub>2</sub> interface than spherically shaped nanocrystals; and (2) it is important to fabricate laterally extended Si nanocrystals with an even higher aspect ratio. Laterally extended Si nanocrystals can be considered and used as a Si quasi-well sandwiched between SiO<sub>2</sub> barriers. Figure 7 shows that by utilizing a series of annealing cycles in different ambient conditions (e.g., N<sub>2</sub> or diluted O<sub>2</sub> [12]), the aspect ratio in the Si nanocrystal lateral and vertical dimensions can be extended to  $\geq 3 : 1$ . Finally, nearly continuous Si layers with a thickness of  $\sim 25$  nm have been produced (Fig. 8), but some of them clearly show fluctuations in the brightness of the reflected electron beam indicating possible intrinsic defects.

TEM analysis shows that annealing in dry oxygen not only reduces the Si nanocrystal size but also changes the nanocrystal shape. Nanocrystals originally spherical in shape become more dome-like and larger in size; brick-shaped Si nanocrystals change very little. The modification in nanocrystal shape is extremely slow and requires hours of oxidation at a temperature  $\sim 1000$  °C confirming the strong resistance of Si nanocrystals to oxidation in dry oxygen. In contrast, wet oxidation is extremely aggressive and destroys Si nanocrystals very effectively. The precise mechanism of Si nanostructure oxidation is not understood, but most likely it is connected with different oxidation rates in different crystallographic directions. Figure 9 confirms this preliminary conclusion and shows that the originally brick-shaped Si nanocrystals after several minutes exposure to N<sub>2</sub>-diluted H<sub>2</sub>O vapor at 950 °C have been transformed into pyramids of different sizes but having the same angles.

Another interesting feature has been found in nc-Si/SiO<sub>2</sub> superlattices with a large number of periods ( $\gg 20$ ). In some parts of the initial layers of nanocrystals (closer to the Si substrate), large crystalline grains are observed (Fig. 10). These grains are seen as bright spots, which is due to a specific crystallographic orientation of these grains. These “broken” layers most likely appear due to strain forces. This strain is built in during crystallization, because of the significant difference in thermal expansion between Si and SiO<sub>2</sub>. Interestingly, this local distortion does not propagate throughout the nc-Si superlattices, and the rest of the structure is

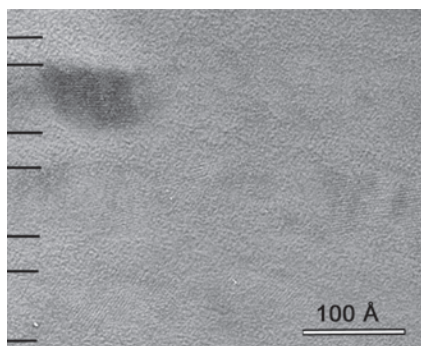


**Figure 6.** A lattice image of a rectangular Si nanocrystal (i.e., quantum brick) showing nearly atomically flat interfaces with a-SiO<sub>2</sub>.

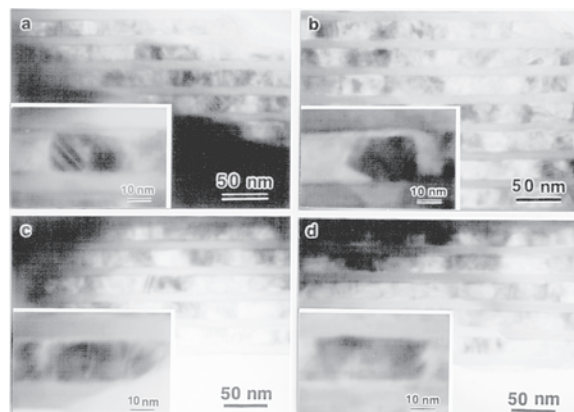


**Figure 7.** TEM images of a nc-Si/a-SiO<sub>2</sub> superlattice subjected to (a) initial two hours of annealing at 950 °C in dry nitrogen; (b) 15 min annealing at 750 °C in  $\sim 15\%$  nitrogen diluted water vapor followed by (a); (c) 30 min annealing at 750 °C in  $\sim 15\%$  nitrogen diluted water vapor followed by (a); (d) 45 min annealing at 750 °C in  $\sim 15\%$  nitrogen diluted water vapor followed by (a). From (a) to (d), the Si nanocrystal size slightly reduces in vertical dimension and significantly increases laterally.

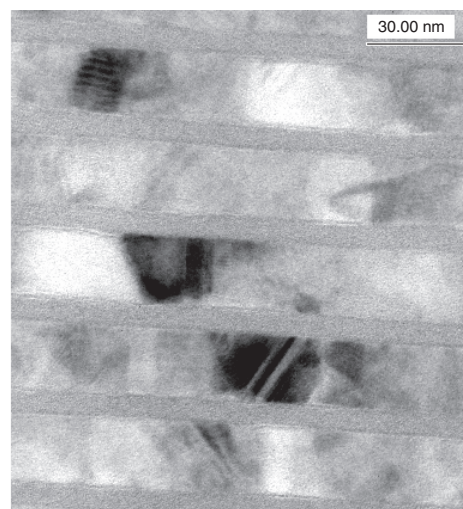


**Figure 8.** Nearly continuous, nanometer-thin nc-Si layer produced by RTA followed by 30 min wet oxidation at 800 °C and 2 h annealing in dry N<sub>2</sub> at 1100 °C.

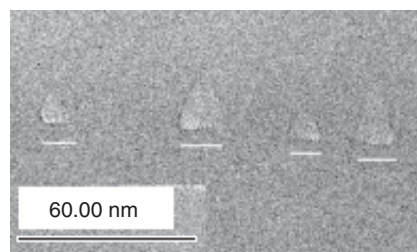


**Figure 9.** TEM micrograph showing pyramid-shape Si nanocrystals produced by 15 min wet oxidation at 950 °C in 15–20% diluted water vapor of initially brick-shape Si nanoclusters. The pyramid locations are indicated.

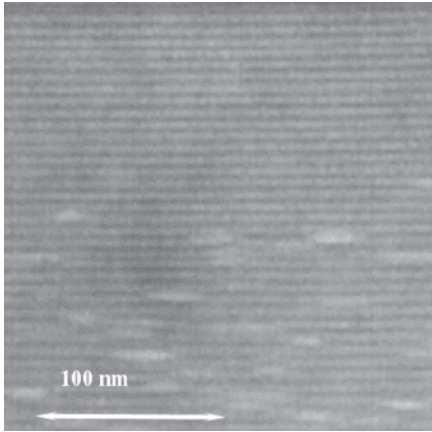


**Figure 10.** Multiperiod nc-Si/a-SiO<sub>2</sub> with areas of “broken” Si layers.

perfectly ordered. This observation proves that the ordered structure in nc-Si superlattices is robust and can survive during post-crystallization treatments and additional fabrication steps.

Among the many other characterization techniques, X-ray diffraction (XRD) shows reasonable agreement with TEM results (Fig. 11) using conventional analysis for the grain sizes [30, 31]. However, the quantitative application of XRD is limited to moderate sizes of Si nanocrystals (>2.5 nm). It is not clear if the reason for this limitation arises from a distortion of the lattice structure in small size Si nanocrystals, the presence of residual a-Si tissue, or something else.

#### 4. RAMAN SPECTROSCOPY OF NANOCRYSTALLINE SILICON–SILICON DIOXIDE SUPERLATTICES

Raman scattering in nanocrystals is a well-developed subject, starting with the work of [32] and [33] where a semiquantitative model considering a partial modification of the phonon selection rules was developed. Controlled crystallization is a fabrication method where Raman scattering can be a very informative characterization method, due to the easily observed difference between the spectra of amorphous

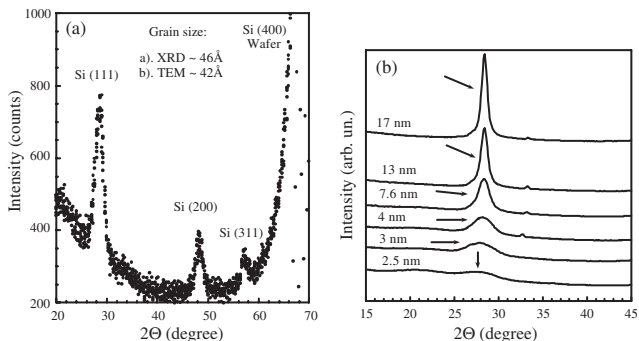


**Figure 11.** XRD data showing (a) peaks attributed to different crystallographic directions in Si nanocrystals and (b) the Si  $\langle 111 \rangle$  diffraction peak for Si nanocrystals of different sizes. (The X-ray measurements were kindly provided by (a) T. N. Blanton and (b) M. Zacharias.)

and nc-Si phases. Figure 12 compares the Raman spectra of several samples. In the as-prepared a-Si (11 nm)/a-SiO<sub>2</sub> superlattice, a strong Raman peak at  $\sim 470$  cm<sup>-1</sup> clearly indicates a purely amorphous phase. Rapid ( $\sim 30$  s) thermal annealing at 700 °C partially crystallizes the samples and a Raman contribution from both amorphous and nc-Si phases is shown by the two peaks at 485 and 520 cm<sup>-1</sup>, respectively. Rapid ( $\sim 30$  s) thermal annealing at 900 °C further reduces the contribution from the amorphous phase. Finally, furnace annealing for 30 min at 1050 °C completes the crystallization, and this can be verified from the Raman spectrum as a perfectly symmetric, slightly broader peak at 520 cm<sup>-1</sup>.

More detailed Raman measurements (Fig. 13) show that in smaller Si nanocrystals (from 14 down to 4 nm), several features associated with the disordered Si phase can be seen. The major feature related to small Si nanocrystals is a first-order, transverse-optical (TO) Raman peak at 520–500 cm<sup>-1</sup> (depending on the Si nanocrystal size) with a broad tail to the lower wavenumbers. Qualitatively similar broadening is observed for overtones related to combinations of acoustic and optical phonons at 150 and 300 cm<sup>-1</sup> as well as for the second-order Raman scattering at  $\sim 1000$  cm<sup>-1</sup>. The Raman data indicate not only the modification of phonon selection rules in small Si nanocrystals but also the presence of partial disorder, most likely due to the higher surface-to-volume ratio and stronger contribution from the nc-Si/SiO<sub>2</sub> interface. Following a semiquantitative analysis developed for a-Si [34, 35], we can consider that the degree of disorder is indicated by the intensity ratio between the major Raman peak at 520 cm<sup>-1</sup> and overtones ( $\sim 300$  cm<sup>-1</sup>) that are forbidden in perfect c-Si [36]. Figure 13 shows that this ratio between the Raman peaks at 300 and 520 cm<sup>-1</sup> increases as the Si nanocrystal size decreases.

The Campbell–Fauchet and other models that describe the changes in the phonon selection rules in nanometer-size Si nanocrystals have been criticized for being both a simplified theoretical approach and inconsistent with experiments [37–39]. However, it is not possible to combine all desirable considerations (nanocrystal size reduction, shape influence, strain, specific interface, etc.) in one model. It is also impossible to separate such effects as, for example, partial disorder due to a strained interface and phonon selection rule

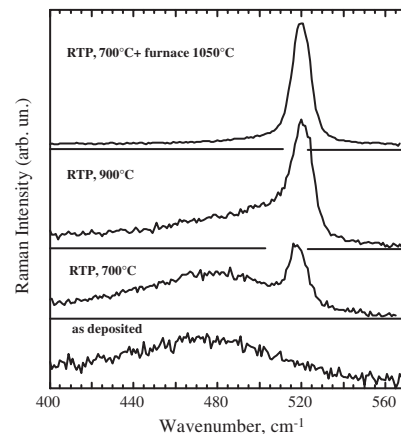


**Figure 12.** Raman scattering in several samples of a nc-Si/a-SiO<sub>2</sub> superlattice annealed under different conditions, as indicated.

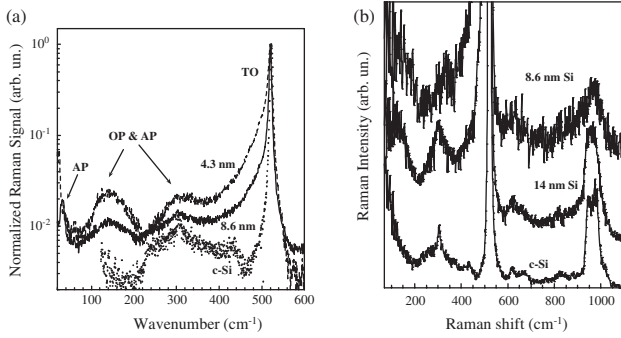


**Figure 13.** (a) Raman spectra and (b) details of second-order Raman scattering ( $\sim 1000 \text{ cm}^{-1}$ ) and overtones ( $\sim 300 \text{ cm}^{-1}$ ) for c-Si and Si nanocrystals of different sizes.

modification due to a nanocrystal size reduction. All these complications have made quantitative analysis of the optical phonon Raman spectra in Si nanocrystals difficult, if not impossible.

The fact that a nc-Si/a-SiO<sub>2</sub> superlattice is a layered, periodic structure with flat and abrupt interfaces stimulated interest in Raman measurements in the wavenumber range of acoustic phonons. We follow here the original Rytov model [40], which has been successfully applied to conventional MBE-grown superlattices [41]. In a more simplified picture, a superlattice made of alternating layers of nc-Si having thickness  $d_1$  and a-SiO<sub>2</sub> having thickness  $d_2$ , induces a new periodicity  $d = d_1 + d_2$  and leads to a reduction of the bulk crystal Brillouin zone in the superlattice growth direction. A new minizone is created with a maximum wavevector  $q_{mz} = \pi/d$ . Since the nc-Si/a-SiO<sub>2</sub> superlattice contains more than 10 atomic layers per period, it can be treated as an elastic medium and the elastic continuum model of acoustic vibrations can be used to calculate the superlattice phonon dispersion [40, 41]. According to this theory, the acoustic phonon dispersion in the superlattice is obtained by folding the acoustic phonon branches of the average compound into the superlattice minizone. For bulk acoustic phonons with frequencies less than  $100 \text{ cm}^{-1}$ , the dispersion is almost linear, and in the superlattice away from the Brillouin minizone center ( $q = 0$ ) and edge ( $q = q_{mz}$ ) it can be described by  $\omega = 2mv_{SL} \pi/d \pm qv_{SL}$ , where  $m = 0, 1, 2, \dots$  is the Brillouin zone folding index and  $q$  is the phonon wavevector. The superlattice sound velocity  $v_{SL}$  is given by

$$v_{SL} = d / [(d_1/v_1)^2 + (d_2/v_2)^2 + (\kappa + 1/\kappa) \cdot (d_1 d_2 / v_1 v_2)] \quad (1)$$

where  $\kappa = \rho_1 v_1 / \rho_2 v_2$ , and  $v_1$  and  $v_2$ ,  $\rho_1$  and  $\rho_2$  are the sound velocities and densities, respectively, in the nc-Si and a-SiO<sub>2</sub> layers. In the backscattering geometry, Raman scattering from phonons with wavevector  $q_p = 4\pi n_{SL} / \lambda$  is observed, where  $n_{SL}$  is the superlattice effective refractive index at the laser wavelength  $\lambda$ , defined as

$$n_{SL} = \xi n_1^2 + (1 - \xi) n_2^2 \quad (2)$$

where  $n_1$  and  $n_2$  are the corresponding refractive indices for the nc-Si and a-SiO<sub>2</sub> layers, respectively, and  $\xi = d_1/d$ . The case of  $m = 0$  corresponds to conventional Brillouin scattering from acoustic phonons ( $\omega_{Br} = q_p v_{SL}$ ). Each value

of the folding index  $m$  ( $m \neq 0$ ) gives rise to a doublet ( $\omega_{\pm m} = 2mv_{SL} \pi/d \pm \omega_{Br}$ ), which is the signature of the folded phonon modes in Raman scattering. In the exact continuum theory [42], small energy gaps appear in the phonon dispersion at the minizone center ( $q_p/q_{mz} = 0$ ) and edge ( $q_p/q_{mz} = 1$ ) due to a mismatch between the acoustic impedances  $\rho v$  of the nc-Si and a-SiO<sub>2</sub> layers. The gaps can be ignored when  $q_p/q_{mz}$  is not close to 0 or 1.

The a-Si/a-SiO<sub>2</sub> superlattices investigated by Raman spectroscopy were grown on a Si wafer by RF magnetron sputtering and plasma oxidation. The layer thicknesses for both a-Si and a-SiO<sub>2</sub> were kept constant throughout the superlattice. The a-Si layers were crystallized by RTA at  $900 \text{ }^\circ\text{C}$  for 60 s followed by quasi-equilibrium furnace annealing starting at  $750 \text{ }^\circ\text{C}$  with a  $10 \text{ }^\circ\text{C}/\text{min}$  temperature ramp-up to  $1100 \text{ }^\circ\text{C}$  (see [11, 12] for details). Rapid thermal and furnace annealing were performed in a nitrogen atmosphere. The layer thicknesses were determined using TEM.

Raman spectra were measured in a  $90^\circ$  scattering geometry with the sample surface inclined at an angle of  $12.3^\circ$  to the incident light, which is near to Brewster's angle in c-Si [41]. This configuration is close to exact backscattering inside the sample since the superlattice has a quite large refractive index ( $n_{SL} > 3$  as calculated below). The excitation source was an argon ion laser light giving wavelengths of 457.9, 476.5, 488.0, 496.5, and 514.5 nm. The scattered light was analyzed with low- and high-resolution double spectrometers. All measurements were carried out at room temperature in a helium atmosphere.

The Raman spectrum measured with a resolution of  $0.06 \text{ cm}^{-1}$  and 457.9 nm excitation is shown in Figure 14. Scattering from the longitudinal acoustic (LA) phonons with  $m = 0$  ( $\omega_{Br} = 3.4 \text{ cm}^{-1}$ ) and  $m = \pm 1$  ( $\omega_{-1} = 17.4 \text{ cm}^{-1}$  and  $\omega_{+1} = 24.3 \text{ cm}^{-1}$ ) can be easily identified. Brillouin scattering from LA and transverse acoustic (TA) phonons in the c-Si (100) substrate is also observed at 5.6 and  $3.9 \text{ cm}^{-1}$ , respectively. The observation of weak scattering from TA phonons is consistent with the small deviation from the exact backscattering geometry, for which Raman scattering from TA phonons in (100) Si is forbidden. The observation of

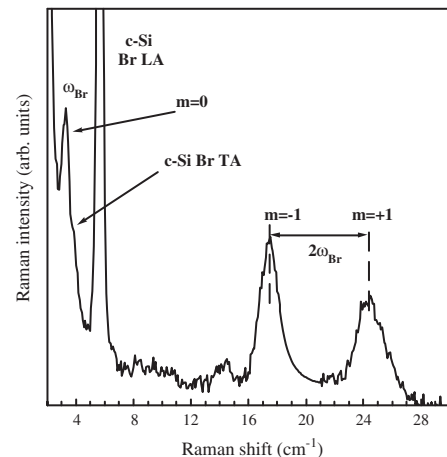


**Figure 14.** A high-resolution Raman spectrum in the vicinity of folded acoustic phonons (indices are shown) in a fully crystallized nc-Si/a-SiO<sub>2</sub> superlattice comprised of brick-shape Si nanocrystals.



Brillouin scattering is possible only in the case of a very low laser light-scattering background, proving that the sample had a very smooth surface and flat nc-Si/a-SiO<sub>2</sub> interfaces. The  $m = \pm 1$  doublet was also resolved in Raman spectra measured with a lower resolution of about 0.1 cm<sup>-1</sup> and excited by 457.9, 476.5, 488.0, 496.5, and 514.5 nm lines of the Ar<sup>+</sup> laser.

Using the experimentally determined  $d$  and  $\omega_{\pm 1}$ , it is possible to estimate the nc-Si/a-SiO<sub>2</sub> superlattice sound velocity. We found that  $v_{\text{SL}} = d(\omega_{+m} + \omega_{-m})/4\pi$ , averaged over the data obtained with different laser excitation lines, is  $7.5 \times 10^5$  cm/s. The reduced wavevectors of phonons participating in the scattering were calculated from  $q_p/q_{mz} = d(\omega_{+m} - \omega_{-m})/2\pi v_{\text{SL}}$ . Use of the different excitation wavelengths allows the observation of scattering from the LA phonons in the 0.26–0.31 reduced wavevector range of the Brillouin minizone. The assumption that the phonon dispersion is linear (i.e., the gaps can be ignored) is indeed justified by the above result: the light scattering involved phonons far from the minizone center or edge. Several measurements over the sample area of 2–3 cm<sup>2</sup> show very small deviation in the difference of the position of folded phonon peaks, and this difference indicates less than 5% variation in the superlattice thickness. Also, assuming that the sound velocity in the a-SiO<sub>2</sub> layers is identical to that in bulk a-SiO<sub>2</sub> ( $6.0 \times 10^5$  cm/s), the sound velocity in the Si nanocrystals is calculated as  $8.6 \times 10^5$  cm/s. This calculated sound velocity in nc-Si is close to the sound velocity in c-Si along the [100] direction ( $8.5 \times 10^5$  cm/s), compared with  $9.2 \times 10^5$  cm/s and  $9.4 \times 10^5$  cm/s along the [110] and [111] directions, respectively [43–45]. This result indicates that the Si nanocrystals might have some degree of preferential [100] orientation. This conclusion is not unreasonable, since under certain experimental conditions crystallized poly-Si films have [100] preferential orientation due to the fact that [100] is the fastest growing crystallographic direction [46]. The effective refractive index of the superlattice for different  $\lambda$  is calculated from  $n_{\text{SL}} = \lambda(\omega_{+m} - \omega_{-m})/8\pi v_{\text{SL}}$ . The refractive index in Si nanocrystals,  $n_1$ , then can be derived assuming that the refractive index of a-SiO<sub>2</sub>,  $n_2$ , is 1.46. The refractive index of nc-Si with an average nanocrystal size of 8.6 nm is noticeably lower than that of c-Si or a-Si.

Figure 15 shows moderate resolution ( $\sim 0.2$  cm<sup>-1</sup>) Raman spectra in the range of acoustic phonons for three samples of nc-Si/a-SiO<sub>2</sub> superlattices with different vertical sizes of the Si nanocrystals: 2.5, 4.2, and 8.5 nm. In agreement with the simplified theory of acoustic phonon dispersion in a layered structure, the Raman signal associated with folded acoustic phonons shifts to greater wavenumbers as the Si nanocrystal size decreases: from  $\sim 20$  cm<sup>-1</sup> for 8.5-nm Si nanocrystals to  $\sim 45$  cm<sup>-1</sup> for 2.5-nm Si nanocrystals. However, the structure of the observed Raman signal is then not clearly resolved, and that could be due to a decrease in quality of the nc-Si/a-SiO<sub>2</sub> interfaces. This decrease of the interface flatness is expected for the observed changes in Si nanocrystal shape: Si nanocrystals smaller than 7 nm are more spherical in shape compared to the brick-shape found in larger-size Si nanocrystals. In addition, these uncertainties in Si nanocrystal shape may be accompanied by some changes in other structural properties, for example, their crystallographic orientation.

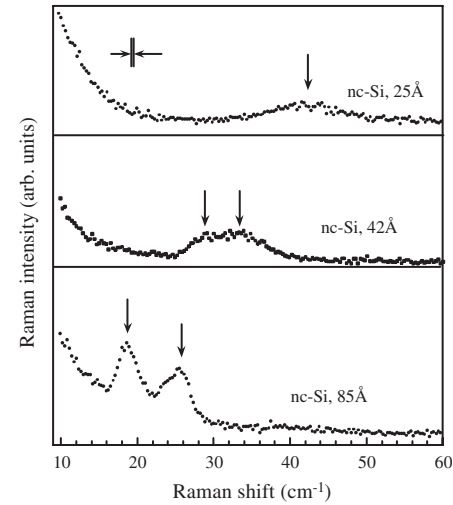


**Figure 15.** Moderate-resolution low-frequency Raman spectra for samples of nc-Si/a-SiO<sub>2</sub> superlattices with different sizes of Si nanocrystals.

For many applications, it is very important to know and control the crystallographic orientations of Si nanocrystals. In particular, many physical effects (e.g., energy quantization) can only be observed for nanocrystals with similar crystallographic orientations, because of the sixfold symmetry of the electron energy dispersion in Si. Among other non-destructive and relatively fast analytical techniques, polarized Raman spectroscopy can be used directly to determine the crystallographic orientations of a Si film. We briefly review the theoretical approach developed in [47, 48] for the Raman polarization analysis and apply it to characterize nc-Si films.

Raman scattering is a two-photon process and the scattering intensity is determined by second-rank Raman tensors ( $R_{ij}$ , with  $i, j = x, y, z$ ). As a result, the Raman intensity depends on the orientations of polarization vectors of the incident and scattered light relative to the crystallographic axes of the sample. This means that the crystallographic orientation of the sample can be determined by examining the anisotropy of the Raman scattering intensity. Crystalline Si belongs to the O<sub>h</sub> point group of the 32 crystal classes, and the Raman-active optical phonon has F<sub>2g</sub> symmetry, which is triply degenerate. Raman tensors for the F<sub>2g</sub> mode in a crystal axis coordinate system are represented by

$$R_{yz} = \begin{pmatrix} 0 & 0 & 0 \\ 0 & 0 & d \\ 0 & d & 0 \end{pmatrix}, \quad R_{zx} = \begin{pmatrix} 0 & 0 & d \\ 0 & 0 & 0 \\ d & 0 & 0 \end{pmatrix}, \quad R_{xy} = \begin{pmatrix} 0 & d & 0 \\ d & 0 & 0 \\ 0 & 0 & 0 \end{pmatrix} \quad (3)$$

Raman polarization experiments are performed in the exact backscattering geometry, where the wavevectors of the incident ( $k_i$ ) and scattered ( $k_s$ ) light are normal to the crystal surface. In this configuration, changing the incident polarization direction has no effect on the percentage of incident laser light being absorbed by the sample. The Raman scattering intensity is given by

$$S = \eta \sum_j (e_i R_{ij} e_s)^2 \quad (4)$$

where  $\eta$  is a constant of proportionality related to the standard Raman cross section and depends on the frequency of the scattered light and the intensity of the incident laser light,  $e_i$  and  $e_s$  are unit polarization vectors of the incident and scattered light, respectively, expressed in the crystal axis coordinate system using  $\theta$ ,  $\phi$ ,  $\psi_0$ ,  $\psi$ , and  $\psi'$ . Angles  $\theta$ ,  $\phi$ , and  $\psi_0$ , relate the laboratory coordinate system (fixed with respect to the sample) to the crystal axis coordinate system and must be known to identify the crystallographic orientation of the sample. By definition,  $\theta$  is the angle made by the  $\langle 001 \rangle$  axis and  $k_s$ ,  $\phi$  is the angle between the  $\langle 100 \rangle$  axis and the projection of  $k_s$  onto the  $(001)$  plane, and  $\psi_0$  is the angle between the  $x$  axis of the laboratory coordinate system and the projection of the  $\langle 001 \rangle$  axis onto the  $xy$  plane. In addition,  $\psi$  ( $\psi'$ ) is introduced as the angle between the  $x$  axis and  $e_i$  ( $e_s$ ). Equation (4) can be rewritten in terms of the angle  $\psi$  as

$$I(\theta, \phi, \psi_0; \psi, \psi') = S/\eta d^2 \\ = A(\theta, \phi, \psi_0; \psi') + B(\theta, \phi, \psi_0; \psi') \cos 2\psi \\ + C(\theta, \phi, \psi_0; \psi') \sin 2\psi \quad (5)$$

The determination of the crystallographic orientation of the sample requires the measurement of its Raman intensity as a function of the angle  $\psi$  for at least two linear polarization directions of the scattered light. Usually, these two directions are chosen to be orthogonal to each other. When the polarization vector of the scattered light is parallel to the  $x$  axis ( $\psi' = 0$ ) or  $y$  axis ( $\psi' = 90$ ) in the laboratory coordinate system, Eq. (5) becomes

$$I_0 = A_0(\theta, \phi, \psi_0) + B_0(\theta, \phi, \psi_0) \cos 2\psi \\ + C_0(\theta, \phi, \psi_0) \sin 2\psi \quad (5a)$$

$$I_{90} = A_{90}(\theta, \phi, \psi_0) + B_{90}(\theta, \phi, \psi_0) \cos 2\psi \\ + C_{90}(\theta, \phi, \psi_0) \sin 2\psi \quad (5b)$$

By combining coefficients  $A_0$ ,  $B_0$ ,  $C_0$ ,  $A_{90}$ ,  $B_{90}$ , and  $C_{90}$ , and eliminating  $\psi_0$ , we obtain quantities that are functions of only  $\theta$  and  $\phi$ :

$$G(\theta, \phi) \equiv (\beta_+^2 + \gamma_+^2)/\alpha_+^2 = (k_1^2 + k_2^2)/k_0^2 \quad (6)$$

and

$$H(\theta, \phi) \equiv [(2\beta_- - \alpha_+ + 1)^2 + 4\gamma_-^2]/\alpha_+^2 \\ = [(k_3 - k_4)^2 + 4k_5^2]/k_0^2 \quad (7)$$

where  $\alpha_+ = A_0 + A_{90}$ ,  $\beta_+ = B_0 + B_{90}$ ,  $\gamma_+ = C_0 + C_{90}$ ,  $\alpha_- = A_0 - A_{90}$ ,  $\beta_- = B_0 - B_{90}$ ,  $\gamma_- = C_0 - C_{90}$ ;

$$k_0 = [4x(1-x) + 2 + (x-1)^2y]/2$$

$$k_1 = [-4x + (x+1)y](x-1)/2$$

$$k_2 = (1-x)[xy(1-y)]^{1/2}$$

$$k_3 = [4x(1-x) - 2 + (x+1)^2y]/2$$

$$k_4 = 1 - 2xy$$

$$k_5 = (1+x)[xy(1-y)]^{1/2}$$

with  $x = \cos^2 \theta$ ,  $y = \sin^2 2\phi$ .

Angles  $\theta$  and  $\phi$  are found by solving simultaneously Eqs. (6) and (7). The angle  $\psi_0$  can be found by solving

$$\alpha_- = k_1 \cos 2\psi_0 - k_2 \sin 2\psi_0 \quad (8)$$

With the restrictions  $\theta \geq 0$  and  $\phi \leq 90^\circ$ , six sets of  $(\theta, \phi)$  satisfy Eqs. (6)–(8). Determination of the angle  $\psi_0$  reduces the six sets  $(\theta, \phi)$  into three equivalent orientations  $(\theta, \phi, \psi_0)$  that are obtained by the rotation of the surface normal by  $120^\circ$  about the  $\langle 111 \rangle$  axis. For the  $(001)$  and  $(111)$  surfaces the variation of Raman intensity is given by

$$I_{001} = \sin^2(\psi + \psi' + 2\psi_0) \quad (9)$$

$$I_{111} = [\cos^2(\psi - \psi') + 2]/3 \quad (10)$$

Any oblique incidence and scattering will have a negligible effect on the Raman polarization analysis of Si when one uses an objective lens with numerical aperture (NA) smaller than 0.5. This is because the refractive index of Si at 514.5 nm is 4.22 and the collection cone within the sample is only  $6.6^\circ$ .

The experimental setup for these measurements is quite standard. The 514.5-nm line of an Ar ion laser was focused on a sample surface by a lens of NA = 0.1. The scattered light was collected by an objective lens of NA = 0.5 and focused onto the entrance slit of a double spectrometer. The signal was detected by a photomultiplier with photon-counting electronics. A Glan–Thompson beam-splitting prism is used to produce linearly polarized light from the elliptically polarized light coming from the laser. A  $\lambda/2$  wave plate was used to rotate the polarization of the incident light. The sample was mounted on a movable X–Y stage and adjusted to be normal to the incident light. A sheet polarizer was used as an analyzer of the scattered light. A scrambler that compensates for the polarization-dependent transmission of the spectrometer was placed between the analyzer and the spectrometer entrance slit.

Raman polarization measurements were performed by varying the polarization of the incident light ( $\psi$ ) in  $10^\circ$  steps. The polarization of the scattered light is fixed at either perpendicular or parallel to the entrance slit of the spectrometer, that is, H (horizontal) or V (vertical) configurations, respectively. For each of the polarization configurations the spectrum in the 505–535  $\text{cm}^{-1}$  range was measured, the intensity of the background at 505  $\text{cm}^{-1}$  was subtracted, and the spectrum was numerically integrated. The spectral slit width of the spectrometer was  $\sim 1 \text{ cm}^{-1}$  and the Raman intensity was measured in 0.5- $\text{cm}^{-1}$  increments.

For Raman polarization measurements,  $(100)$  and  $(111)$  oriented single crystal Si wafers were used as test samples. Figure 16 shows their integrated Raman intensity in the radial direction as a function of the rotation angle of the polarizer ( $\psi$ ). Two sets of data (H and V) were collected for two orthogonal polarizations of the scattered light (along the  $x$  and  $y$  axes, respectively). The dots are experimental points fitted by Eqs. (9) and (10) (solid lines). The deviation between the calculated and nominal crystallographic orientations of Si  $(100)$  and  $(111)$  single crystals is found to be less than  $1^\circ$ .

For nc-Si/a-SiO<sub>2</sub> superlattices grown on c-Si substrates, a quantitative Raman polarization analysis is possible when

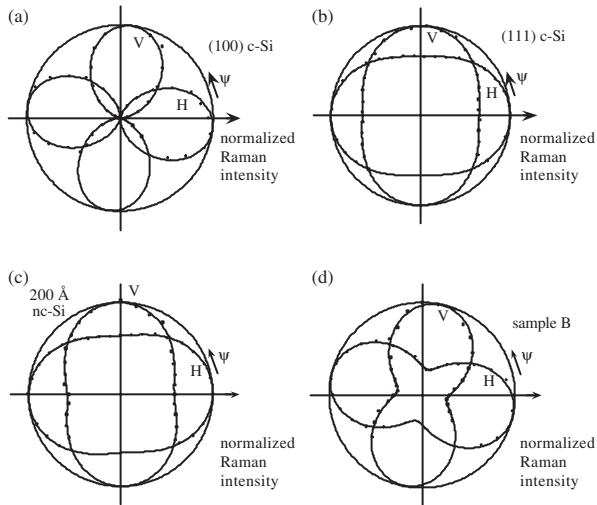


**Figure 16.** Polarization Raman diagram for (a)  $\langle 100 \rangle$  and (b)  $\langle 111 \rangle$  single crystal Si and (c) and (d) samples of crystallized nc-Si/a-SiO<sub>2</sub> superlattices.

the condition  $d_{\text{Si}} N \alpha(\lambda) \geq 1$  is satisfied ( $d_{\text{Si}}$  is a nc-Si layer thickness,  $N$  is a number of periods, and  $\alpha(\lambda)$  is the absorption coefficient of nc-Si). This condition ensures that the excitation light is completely absorbed within the nc-Si layers and no signal from the substrate will be detected: For a sample with 60 periods and a layer thickness of  $d_{\text{Si}} = 14$  nm,  $\alpha_{\lambda=514.5\text{nm}} = 1.465 \times 10^4 \text{ cm}^{-1}$ , where  $\alpha$  is the absorption coefficient of c-Si. Indeed, no difference in the shapes of normalized Raman spectra measured for orthogonal polarizations of the analyzer is observed. This proves that the Raman scattering is entirely determined by the nc-Si layers. Figure 16 shows the measured integrated Raman intensity as a function of a rotation angle of the polarizer (dots) for a sample having  $d_{\text{Si}} = 20$  nm. The solid lines are the curves obtained from a least-squares fit of the experimental data to Eq. (10). Using Eqs. (6)–(8) we find that  $\theta = 52^\circ$ ,  $\phi = 45^\circ$ ,  $\psi_0 = 13^\circ$ . This set of  $(\theta, \phi)$  angles is very close to the one defined by a  $\langle 111 \rangle$  surface:  $\theta = \arctan(\sqrt{2}) \approx 54.8^\circ$ ,  $\phi = \arctan(1) = 45^\circ$ . This result suggests that the majority of Si nanocrystals have their  $\langle 111 \rangle$  axis normal to the sample surface or, in other words, they have preferred  $\langle 111 \rangle$  crystallographic orientation.

The same Raman polarization analysis has been applied to samples with smaller Si nanocrystals ( $\sim 8.6$  nm in vertical dimension). Figure 16d shows the result, and our immediate impression (see Fig. 16) is that the Raman signal from the  $\langle 100 \rangle$  single crystal Si substrate is interfering with the signal from Si nanocrystals. The result of the numerical deconvolution of the Raman polarization signal is not accurate enough for any solid conclusions. However, a recent luminescence polarization analysis and additional structural measurements [49] indicate that Si nanocrystals smaller than 10 nm most likely have random crystallographic orientation. We will discuss the crystallographic orientation of smaller Si nanocrystals in a later paragraph on luminescence in nc-Si superlattices.

During studies of solid phase crystallization of a-Si films on amorphous substrates such as a-SiO<sub>2</sub>, it has been found that

crystallized a-Si films may exhibit a preferred crystallographic orientation only in cases when an orientation-dependent crystallization process (e.g., laminar crystallization along the a-Si/a-SiO<sub>2</sub> interfaces) takes place [50]. In c-Si, growth rates along  $\langle 113 \rangle$ ,  $\langle 110 \rangle$ ,  $\langle 112 \rangle$ , and  $\langle 111 \rangle$  crystallographic directions are 1, 1.5, 3, 5, and 24 times slower than the growth along the  $\langle 100 \rangle$  direction [51]. That difference is related to the number of Si atoms that are necessary to complete a crystal plane during the crystallization process. The crystallographic orientation of the crystallized a-Si film is strongly dependent on the density of nucleation centers, their location in the film, and the thickness of the film. Normally, crystallization of a-Si films on a-SiO<sub>2</sub> starts near the Si/SiO<sub>2</sub> interface where a large strain is present due to a difference in the thermal expansion coefficients of Si and SiO<sub>2</sub>. In the case of interface nucleation, crystallization of a-Si proceeds in columnar or laminar fashion, depending on the ratio between the film thickness  $h$  and the mean distance  $d$  between nuclei. When  $d \ll h$ , the crystallites grow in a three-dimensional way until they impinge on each other, then the growth continues in a one-dimensional way along a direction perpendicular to the Si/SiO<sub>2</sub> interface. In this case, the structure of the film is columnar and has a  $\langle 110 \rangle$  or  $\langle 112 \rangle$  crystallographic orientation, since the fastest growth occurs by the formation of twins along  $\langle 110 \rangle$  and  $\langle 112 \rangle$  axes. If  $d \gg h$ , crystallites grow in a three-dimensional way until they reach the surface and then the growth proceeds in a two-dimensional way. Nuclei with an orientation permitting a fast lateral rate of growth extend at the expense of other less favorably oriented nuclei. The resultant structure is laminar and has a  $\langle 111 \rangle$  orientation. When  $d \approx h$ , no preferred crystallographic orientation is expected because crystallites have the same chance to grow in any direction. It is quite possible that this particular scenario is realized in the case of Si nanocrystals smaller than 10 nm.

Our results show that the initial thickness of the a-Si film during crystallization controls not only the Si nanocrystal size but also the nanocrystal shape and crystallographic orientation. The shape of relatively large Si nanocrystals ( $> 10$ – $20$  nm) is rectangular and expanded laterally (i.e., bricks). In contrast, smaller Si nanocrystals ( $< 10$  nm) are nearly spherical. Also, our results have proved that brick-shape Si nanocrystals have preferred  $\langle 111 \rangle$  orientations while smaller, spherical nanocrystals are suspected to have random crystallographic orientation.

## 5. PHOTOLUMINESCENCE SPECTROSCOPY OF NANOCRYSTALLINE SILICON–SILICON DIOXIDE SUPERLATTICES

Intense interest in the optical properties of Si nanocrystals was stimulated by the initial report of a high-efficiency, room-temperature visible PL in porous Si [52], and by the subsequent discussions as to the origins of the PL [53–57]. This subject has already been covered extensively in many papers, reviews, and book chapters [2, 58, 59]. The aim of this review is to compare the PL properties of nc-Si/a-SiO<sub>2</sub> superlattices with similar data obtained in other materials containing Si nanocrystals (e.g., porous Si,

Si nanocrystals prepared by CVD, and ion implantation) and to examine the correlation between the Si nanocrystal structural (i.e., size, shape, and crystallographic orientation) and light-emitting properties. From the beginning of these studies it was obvious that one should start with relatively large-size ( $>20$  nm) Si nanocrystals of well-defined, brick-like shape and  $\langle 111 \rangle$  crystallographic orientation, and should continue toward much smaller, but less well controlled in shape, Si nanograins. Such a research strategy provided a unique opportunity to observe the transformation of phonon-assisted carrier recombination controlled by well-understood selection rules to a much less ordered process where phonons are still involved in carrier recombination but all selection rules are significantly relaxed. Figure 17 perfectly illustrates this statement where a set of narrow PL lines in a bulk Si sample where the dominant TO-phonon line practically does not move, but broadens and slightly changes the ratio between the TO-, TA-, and second TO-phonon lines in Si nanocrystals having sizes down to 8.6 nm in the vertical (growth) dimension. Continuing to decrease the Si nanocrystal size down to  $\sim 6$  nm, we observe a blue (toward higher photon energy) shift in the PL peak (which is at  $\sim 1.32$  eV) and significant broadening up to  $\sim 100$  meV in the PL full width at half maximum (FWHM). The phonon involvement can be recognized by the much less pronounced but still observable structure, with the main PL peak separated by  $\sim 60$  meV (TO-phonon) from a shoulder at lower photon energy (Fig. 17). A further decrease in Si nanocrystal size down to 4.2 nm results in a shift of the PL peak to 1.4 eV and an almost 200 meV FWHM. This PL looks quite different compared to PL from bulk Si and, at the same time, is similar to PL spectra observed in porous Si and Si nanocrystals prepared by ion implantation [58, 60]. The dependence of the PL peak position and FWHM as a function of Si nanocrystal size is summarized in Figure 18, showing a clear correlation between the PL broadening and PL peak blue shift. Note that the PL peak in smaller Si nanocrystals shifts to higher photon energy in a just slightly superlinear fashion, but the PL FWHM increases exponentially as the Si nanocrystal size decreases. To our surprise, we have found that the observed selection rule relaxation in PL

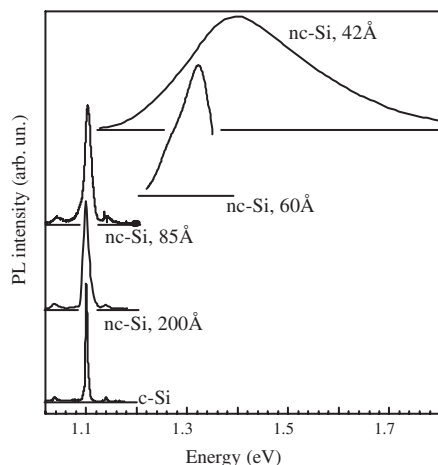


**Figure 17.** PL spectra from samples of nc-Si/a-SiO<sub>2</sub> superlattices with different sizes of Si nanocrystals, as indicated.

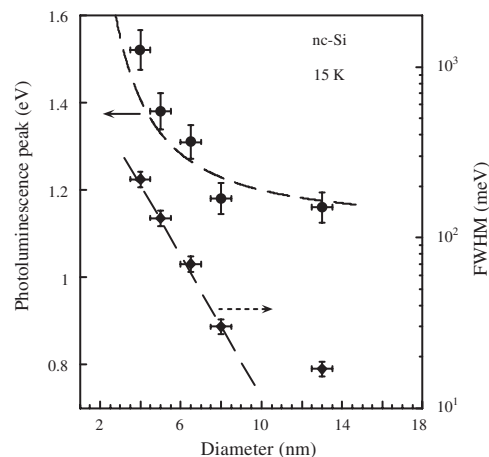


**Figure 18.** The PL peak energy and full width at half maximum (FWHM) as a function of Si nanocrystal size.

from small Si nanocrystals is very similar to the conclusions that we were able to draw from the Raman studies.

Considering the origin of this broad PL band, we concentrate on two major possibilities. After more than a decade of searching for a convincing experimental method of determining the origin of a broad and featureless PL in Si nanocrystals, the technique of resonant PL excitation has been widely recognized as the most useful one [58, 61]. The PL has been linked to carrier recombination in Si nanocrystals due to a clear indication of a phonon-assisted PL mechanism and the observation of structure in PL spectra where almost all of the characteristic Si phonons and their combinations are found [58]. Tuning the wavelength of optical excitation toward the PL band, the inhomogeneous PL broadening due to the Si nanocrystal size distribution is reduced [58]. In addition, resonant PL excitation may require phonon absorption due to the indirect nature of optical transitions in Si nanocrystals. These measurements have been described and performed in porous Si and other systems containing Si nanocrystals [58, 62]. In the case of nc-Si/a-SiO<sub>2</sub> superlattices, an additional contribution to the inhomogeneous broadening is, most likely, coming from the previously mentioned uncertainties in the shape and crystallographic orientation of small-size Si nanocrystals. This is particularly important for Si due to its indirect band structure and strong dispersion in the effective mass along different crystallographic directions.

From a technical point of view, the experiment requires a source of tunable excitation, which is usually a tunable laser (e.g., Ti:Al<sub>2</sub>O<sub>3</sub>), because the desired condition is to bring the excitation wavelength as close as possible to the PL line. This is demonstrated in Figure 19a, where a decrease of the excitation photon energy from 1.66 to 1.42 eV depicts a step-like structure more clearly. Figure 19b shows a higher-resolution PL spectrum under resonant excitation, and contributions from specific Si phonons and their combinations are indicated.

However, the fact that the PL lifetime has a strong temperature dependence (see Fig. 20) indicates that at least two competing mechanisms (most likely radiative and nonradiative) may contribute to the overall PL signal. Interestingly,

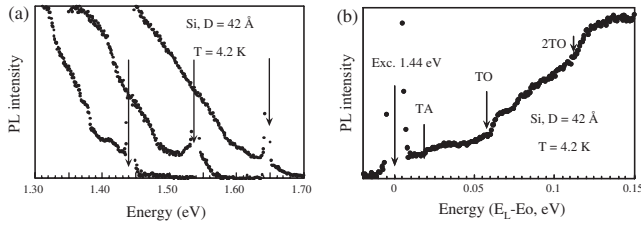


**Figure 19.** (a) An example of resonantly excited PL spectra in a nc-Si/a-SiO<sub>2</sub> superlattice with 42-Å-diameter Si nanocrystal showing better-resolved PL structure as the excitation photon energy decreases. (b) A high-resolution resonantly excited PL spectrum with energies of characteristic Si phonons indicated.

the PL kinetics appear single exponential compared to the more complex, usually stretched exponential behavior reported in Si nanocrystals prepared by other techniques [63]. Another indication that the PL may have a more complex rather than single origin comes from the data in Figure 21, where we compare PL spectra in a nc-Si superlattice with an average Si nanocrystal size of  $\sim 4.2$  nm. At low excitation power ( $0.05 \text{ W/cm}^2$ ), the PL peak is at  $\sim 1.4$  eV, but with the increase of the excitation up to  $10 \text{ W/cm}^2$ , the PL spectrum broadens and the PL peak shifts to  $>1.7$  eV. The observed broadening of the PL spectra has triggered a search for another technique that is able to separate different possible contributions to the luminescence in nc-Si superlattices.

To our surprise, the most interesting results with a very clear interpretation have been found in studies of the PL spectral response as a function of external magnetic and electric fields. Following the initial report that an external magnetic field increases the gap between singlet and triplet states in Si nanocrystals, the fact that the PL lifetime increases and intensity decreases in Si nanocrystals is quite well understood [64–66]. However, our studies show that in nc-Si superlattices this PL quenching is selective and

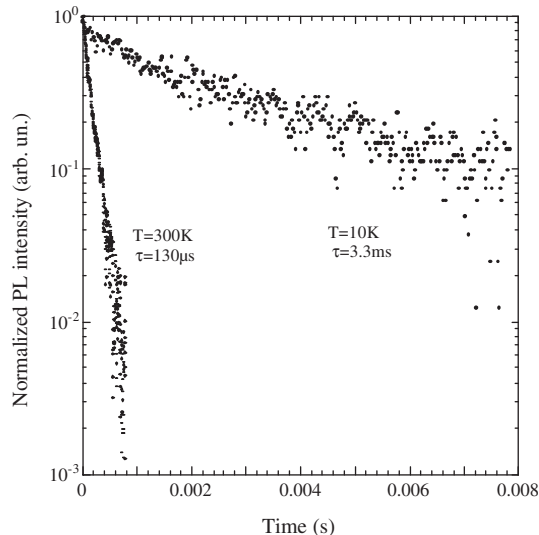


**Figure 20.** PL decay time in a fully crystallized nc-Si/a-SiO<sub>2</sub> superlattice with 42-Å-diameter Si nanocrystals showing a single exponential decay and a strong PL lifetime temperature dependence.

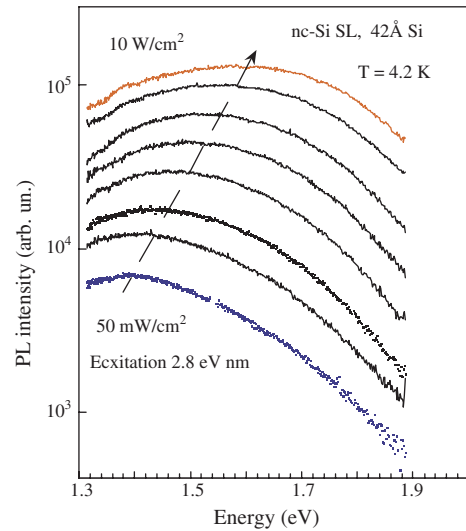


**Figure 21.** PL spectra in a nc-Si/a-SiO<sub>2</sub> superlattice with 42-Å-diameter Si nanocrystals under different excitation intensity.

affects only PL at wavelengths longer than  $\sim 750$  nm. The PL intensity at shorter wavelength does not show any quenching under an applied magnetic field as high as 9 T (Fig. 22). The observed selective quenching of PL in nc-Si superlattices proves that the PL origin is more complex than just a single mechanism based on the quantum confinement effect in Si nanocrystals.

The application of an external electric field is also an informative experiment due to quite different mechanisms of PL quenching, including direct exciton deformation and dissociation under an external electric field and exciton impact ionization. Different electric-field-induced PL quenching mechanisms have very different thresholds and field dependences. Therefore, we studied the PL dependence as a function of the applied electric field in nc-Si/a-SiO<sub>2</sub> superlattices. Our technique is based on the application of an AC

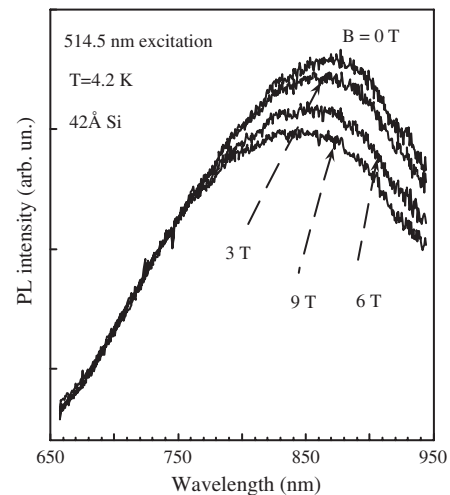


**Figure 22.** PL spectra in a nc-Si/a-SiO<sub>2</sub> superlattice with 42-Å-diameter Si nanocrystals in an applied magnetic field of different strengths. A selective quench of PL intensity is clearly shown.



electric field and detection of a modulated PL component using a lock-in amplifier. This technique is more sensitive compared to the standard technique where CW PL is influenced by an applied dc electric field. We have found that an electric-field-dependent PL spectral component is strongly correlated with magneto-PL measurements: the modulated PL component is red-shifted compared to CW PL at zero electric field, and the electric field modulates only the PL at wavelengths longer than 750 nm (Fig. 23). These data are in complete agreement with the magneto-PL measurements. Therefore, we can conclude that a portion of the PL in nc-Si superlattices at shorter wavelengths does not depend on the electric or magnetic field and most likely has a different origin than PL associated with confined excitons in Si nanocrystals. Additional support for this conclusion can be found in early work on porous Si showing that the PL peak follows the ratio between the numbers of Si-O and Si-H bonds in samples with different degrees of oxidation [67].

## 6. RESONANT CARRIER TUNNELING IN NANOCRYSTALLINE SILICON-SILICON DIOXIDE SUPERLATTICES

Amongst a wide variety of phenomena exhibited in semiconductor quantum transport, resonant carrier tunneling (RCT) and negative differential conductivity (NDC) due to a non-monotonic dependence of the carrier tunnel transmission through potential barriers has always been associated with nearly perfect semiconductor heterostructures and superlattices with a long carrier mean free path [68–70]. The question as to how RCT can be preserved in a structure with a partial disorder is important both for the physics of quantum structures and for practical quantum device applications [71–76]. A system with a controlled degree of disorder, combining for example a periodic potential in the  $z$  direction (i.e., the growth direction) with the presence of grain boundaries separating nanocrystals laterally in the  $xy$  plane, is a special case of general interest. A nc-Si superlattice fabricated by controlled crystallization of amorphous Si/SiO<sub>2</sub> layered structures forms a perfect example of such a system.

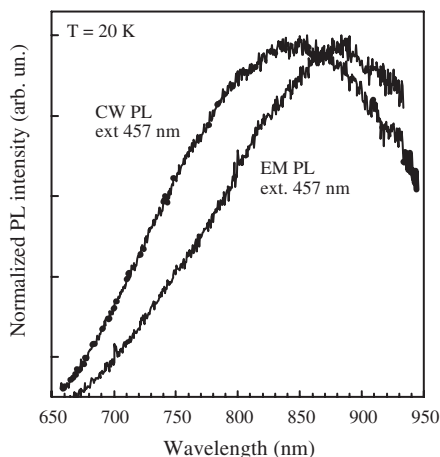


**Figure 23.** Strong red shift of the electric-field-modulated PL spectrum in a 20-period nc-Si/a-SiO<sub>2</sub> superlattice with 42-Å-diameter Si nanocrystals measured using a lock-in amplifier and an ac voltage of 15 V.

The flat and chemically abrupt SiO<sub>2</sub> layers of low defect density [77] separate the Si nanocrystals and provide vertical carrier confinement, which is a key condition for functional quantum devices. This structure has a well-defined order in the  $z$  direction, but is partially disordered laterally due to the nanograin boundaries and the limited degree of Si nanograin crystallographic orientation, as discussed earlier in this chapter. Using such a novel structure, the vertical carrier transport has been investigated and entirely unexpected effects such as narrow resonances in the conductivity, stable self-oscillations, and the strong influence of a low magnetic field applied in the  $z$  direction have been observed [13]. The surprising results show that even though there is significant carrier scattering, resonant tunneling and the formation of electron standing waves is still possible.

A typical sample for this work was prepared in the form of a 10-period nc-Si superlattice on an  $n$ -type, high-resistivity ( $\rho > 1$  k $\Omega$  cm) c-Si substrate, with a Si nanocrystal diameter of  $\sim 45$  Å and with  $\sim 15$ -Å-thick SiO<sub>2</sub> layers. The low-temperature (4.2 K) hole transport measurements were performed in the sandwich geometry. A He-Ne laser (632.8 nm) was used to generate electron-hole pairs, mostly within the depletion region of the positively biased Si substrate, and holes were extracted through the superlattice structure toward the negatively biased top Al contact. Standard direct current (dc) current-voltage (I-V) measurements were performed using a Keithley 595 electrometer. Measurements of alternating current (ac) differential conductivity were obtained using an HP 4192A impedance analyzer.

The experiments were carefully designed to avoid a nonuniform electric field, which may destroy the symmetry of barriers and reduce the effects of resonances. Using a superlattice-type structure confined in a  $p$ - $i$ - $n$  diode or Schottky barrier minimizes these effects. In addition, the use of light to generate carriers is a relatively nondestructive way to manipulate the carrier density without significant screening and distortion of the electric field uniformity. Finally, special attention was paid to transient conductivity characteristics. Resonant carrier tunneling in a structure with large (Si/SiO<sub>2</sub>) barriers is not an immediate phenomenon. In a practical device, resonant tunneling is time-dependent and needs a non-negligible time to become fully established. This process mainly requires the accumulation of tunneling carriers within the resonant well. Each electron localized within the well modifies the local potential, and a feedback mechanism, which often can be limited (at least in part) by the circuit resistance-capacitance time constant, increases the time of the resonant transition [78]. In the extreme case, this process may generate an oscillating current. Therefore, the dc current measurement should be accompanied by frequency- and phase-sensitive ac conductivity measurements.

Figure 24 shows a TEM micrograph of the investigated structure and a set of dc I-V characteristics measured under different levels of photoexcitation. The I-V curves clearly exhibit a step-like structure between 1 and 3 V of the applied reverse bias, with current steps shifted to slightly higher voltage as the excitation power increases (shown in the figure by the arrows). The observation of a step-like structure indicates the expected RCT in a multibarrier structure, which results from a non-monotonic dependence of the barrier tunnel transmission on the applied bias. However, in dc



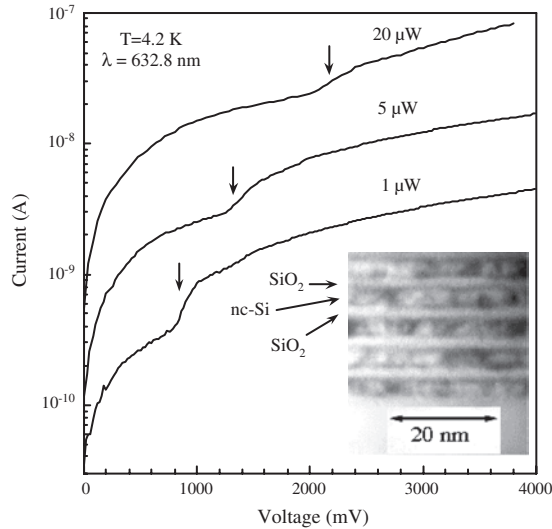


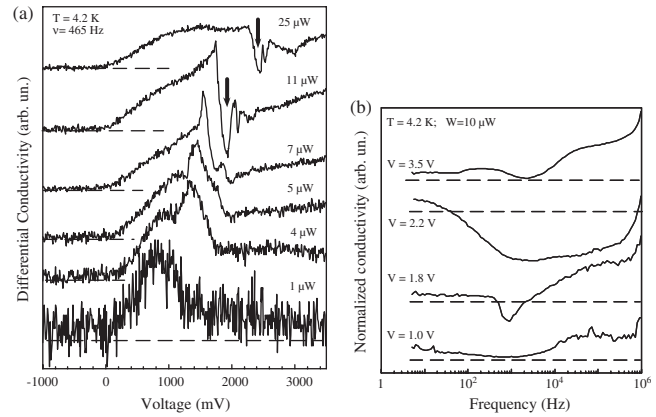
**Figure 24.** Step-like direct current (dc) current-voltage (I-V) characteristics in a Si (45 Å)/SiO<sub>2</sub> (15 Å) 10-period superlattice with different levels of photoexcitation. The inset shows a TEM of a fragment of the sample. Reprinted with permission from [13], L. Tsybeskov et al., *Europhys. Lett.* 55, 552 (2001). © 2001, EDP Sciences.

conductivity measurements no fine structure was observed, which can be used in the identification of particular resonant transitions. Also, no NDC was found in these experiments, showing that carrier scattering in the structures is not negligible.

The measurements of ac differential conductivity  $\sigma_{ac}(V)$  proved to be much more sensitive. Figure 25a shows several traces of  $\sigma_{ac}(V)$  with different levels of photoexcitation (corresponding to different levels of carrier concentration) recorded at a frequency of 465 Hz. At the lowest level of excitation we detect a broad peak at  $V \approx 850$  mV with a full width at half maximum of about 600 meV. On increasing the carrier concentration, the peak is split and another peak rises near 1.3–1.5 V, which quickly becomes dominant. With further increase of carrier concentration, a sharp ( $\leq 100$  mV) asymmetric peak, the NDC regime, and an oscillating behavior near 2 V applied bias are found. At an even higher level of photoexcitation, the sharp peak and NDC regime could disappear, leaving a remnant in the form of a broad feature near 1.6 V and a sharp minimum at 2 V. The rich structure becomes less pronounced for temperatures above 20 K and practically cannot be detected at temperatures much greater than 60 K.

The expected time dependence of carrier tunneling in a barrier structure is demonstrated by the frequency dependence of the ac differential conductivity under experimental conditions close to the resonance condition (see Fig. 25b). The NDC regime has not been found for biases lower than 1.0 V. On increasing the applied bias ( $V \geq 1.8$  V), NDC is observed localized near 1 kHz. When a larger bias is applied, the NDC regime may occupy a broad frequency range, anywhere from 10 Hz to 10<sup>6</sup> Hz. Finally, at a large bias ( $V \geq 3.5$  V) NDC is no longer observed, which indicates that the system is out of resonance.

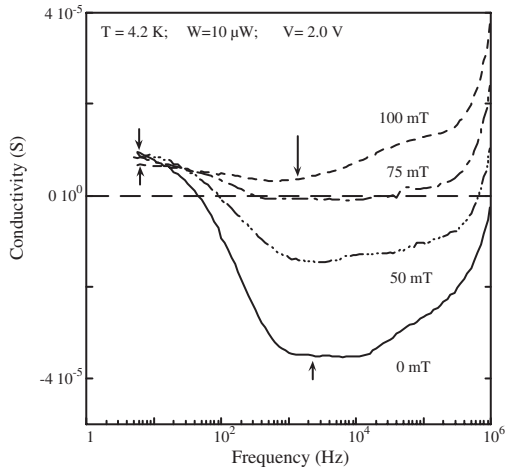
The observed step-like dc I-V characteristics, rich structure, and the NDC regime in the ac differential conductivity



**Figure 25.** (a) Differential alternating current (ac) conductivity as a function of the applied bias measured under different levels of photoexcitation. The NDC regime is shown by arrows. (b) Frequency dependence of the ac differential conductivity measured at the specified applied bias and light intensity. The traces are shifted for clarity and the zero level is indicated by dashed lines. Reprinted with permission from [13], L. Tsybeskov et al., *Europhys. Lett.* 55, 552 (2001). © 2001, EDP Sciences.

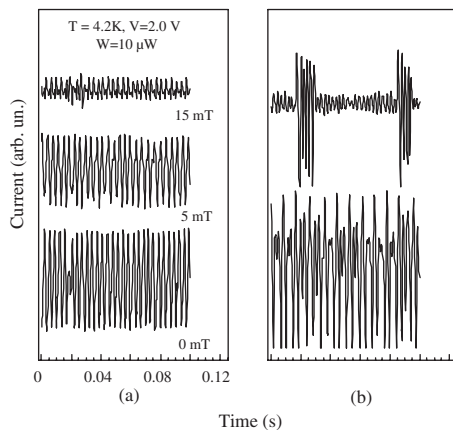
measurements convincingly show that the conductivity in nc-Si/SiO<sub>2</sub> samples exhibits a non-monotonic dependence as a function of the applied bias. However, the conductivity  $\sigma = e\mu n$ , where  $e$  is the electron charge, is a function of the carrier mobility  $\mu$  and carrier concentration  $n$ . It is well known that a non-monotonic carrier density dependence on the applied electric field also causes NDC, and an example of such a process is the electric field ionization of the Si/SiO<sub>2</sub> interface traps [79]. In general, the observation of NDC does not imply a resonant tunneling mechanism, and a test, independently probing tunnel transmission through the barriers, is necessary to prove the existence of RCT. This test can be performed using measurements of the longitudinal magnetoresistance for low applied magnetic fields.

Figure 26 shows that at nearly resonant conditions, the ac conductivity at low frequency ( $< 20$  Hz) displays a measurable magnetoresistance effect of the order of 10%. However, at higher frequency, where NDC takes place, the influence of the low magnetic field is much stronger, showing a complete destruction of NDC at a longitudinal magnetic field of less than 100 mT. The influence of a low magnetic field was investigated in a more sensitive fashion by employing an inductance-capacitance-resistance (LCR)-resonant circuit. Since the samples exhibit the NDC regime and  $N$ -shaped switching, a properly loaded LCR-resonant circuit allows stable self-oscillations, as can be seen in Figure 27. Any small changes in the circuit parameters affect the self-oscillations resonant conditions, and thus can be used to detect a weak magnetoresistance effect. Figure 27 shows that a very low ( $< 5$  mT) magnetic field applied in the  $z$  direction may strongly decrease the amplitude of the oscillations. Also, the applied magnetic field can generate beating effects, showing that self-oscillations with more than one frequency may coexist (see Fig. 27). This sensitive detection technique was applied to check the angular dependence of the magnetoresistance in the  $xz$  plane, but no significant angular dependence was found.



**Figure 26.** Frequency dependence of the ac differential conductivity measured at the specified longitudinal magnetic field. Arrows show the magnetoresistance effect at low frequency, which is similar to dc conductivity, and near the resonant frequencies. The zero level is shown by a dashed line. Reprinted with permission from [13], L. Tsybeskov et al., *Europhys. Lett.* 55, 552 (2001). © 2001, EDP Sciences.

Why does a low magnetic field applied parallel to the current direction drastically affect the sample conductivity? In general, under such conditions only the transverse magnetoresistance should be detectable. However, it has been noted previously that the interface roughness in superlattices creates an additional lateral component in the initially vertical carrier transport [80], and this lateral conductivity would be responsible for the observed changes in current as a function of the parallel magnetic field. It is reasonable to assume that nc-Si/SiO<sub>2</sub> interface roughness and a variation in the Si nanocrystal crystallographic orientation complicate the carrier trajectories. Therefore, no significant magnetoresistance angular dependence can be anticipated. In addition, the self-oscillations beating and thus coexistence of several oscillation frequencies clearly indicate that



**Figure 27.** The influence of a weak longitudinal magnetic field under the experimental conditions indicated on self-oscillations: (a) self-oscillations suppression and (b) creation of self-oscillations beating. Reprinted with permission from [13], L. Tsybeskov et al., *Europhys. Lett.* 55, 552 (2001). © 2001, EDP Sciences.

the sample conductivity may not be homogeneous over the entire sample area. In other words, instead of a single standing wave, carrier transport in the sample can be represented by a number of interfering modes. Performing dc conductivity measurements and averaging over all time-dependent processes, only a remnant of RCT with a step-like I-V response was observed. This consideration is fully consistent with the properties of RCT in conventional superlattices, where the peak-to-valley ratio in I-V measurements is strongly affected by scattering processes [69, 70]. The ac conductivity measurement, which by definition is a frequency- and phase-selective technique, allows one to focus on just a portion of the carrier transport that is associated with particular dwell time. This is why such a rich structure and the NDC regime could be found. The electron dwell time in 2D wells separated by a rectangular Si/SiO<sub>2</sub> barrier can be estimated using an approach outlined in [81] and [82] and a characteristic time of the order of  $\sim 10^{-3}$  s is obtained. In a more complex situation, such as where tunneling occurs between two Si quantum dots separated by a thin oxide layer, additional information about the electronic structure of the system is needed. This calculation has been performed taking into account the inter-dot interaction [83], and resulted in an electron dwell time of the order of  $\geq 10^{-3}$  s. These two dwell time numbers are close not only to each other but also to the experimental results (see Fig. 25). A broadening of the resonant frequency range (shown in Fig. 25b) evident under a larger applied bias most likely reflects several simultaneous processes such as a reduction of the Si/SiO<sub>2</sub> barrier effective height, which decreases the electron dwell time, and partial distortion of the symmetry of barriers with increasing contribution of phonon-assisted transitions, which increases the electron dwell time.

The low-magnetic-field ( $< 10$  mT) experiments indicate that carrier transport in nc-Si superlattices is, at least in part, phase coherent. The magnetic length for a wide ( $\sim 1$  mm) and short ( $\sim 600$  Å) sample can be estimated from  $l_m \sim (h/2\pi eB)^{0.5}$  [84, 85] as  $100 \text{ Å} \leq l_m \leq 1000 \text{ Å}$ . Phase coherence can be destroyed by the dynamic scattering that becomes significant at higher temperature due to the electron-phonon interaction and at higher carrier concentration due to the electron-electron interaction [86]. Assuming that the dynamic scattering at higher temperatures is due to the interaction between carriers and Si acoustic phonons, the temperature threshold for this process should be  $\sim 30$  K. Dynamic scattering due to carrier-carrier interaction should become noticeable when the carrier concentration becomes  $\geq 10^{14} \text{ cm}^{-3}$  (i.e., it becomes comparable with the Si nanocrystal volume density). Both of these general arguments are in good agreement with the experimental results.

Hole tunneling via Si nanocrystal quantized states is the major mechanism contributing to RCT in nc-Si/SiO<sub>2</sub> samples. This is verified from tight binding (TB) calculations [13] applied to various  $\langle 100 \rangle$  oriented Si nano-objects including (1) spherical Si nanocrystals with diameters of 33 Å and 40 Å; (2) a Si ellipsoid with 46 Å vertical and 65 Å lateral dimensions; and (3) a 42-Å Si quantum well sandwiched between tunnel transparent SiO<sub>2</sub> layers. To obtain accurately the hole states in  $\sim 40$ -Å nano-objects, the spin-orbit coupling was included in the calculation. An orthogonal  $sp^3$  TB model

with up to third nearest neighbor interactions and three-center integrals was used: the TB parameters given in [87] provide an accurate description of the bulk effective masses as well as the overall band structure. The eigenstates were calculated using an efficient conjugate gradient algorithm [87]. Results of these calculations are shown in Figure 28. To compare the calculations with experiment, the applied bias is divided equally between all 10 quasi-wells in the nc-Si/SiO<sub>2</sub> superlattice. Therefore, the voltage separating the two peaks ( $\sim 400$  mV) observed in the tunnel spectroscopy experiments corresponds to a  $\sim 40$ -meV energy separating the predominantly heavy and light hole states. According to these simulations of the experimental conditions, a part of the applied bias ( $\sim 30\%$ ) is dropped on the Si substrate, and thus the estimated energy separating heavy and light hole states is  $\sim 25$  meV. This result is very close to the energy calculated for a weakly isolated (laterally) Si  $\langle 100 \rangle$  ellipsoid with 46 Å and 65 Å vertical and lateral dimensions, respectively (see Fig. 28). Indeed, the TEM micrograph shown in the inset of Figure 24 confirms that the majority of Si nanocrystals possess a nearly elliptical shape.

The results presented in this section demonstrate that a great deal of information can be obtained from properly performed tunnel spectroscopy measurements based on ac conductivity. They have enabled the observation of discrete quantized energy levels in a Si nanocrystal. These energy levels have been suspected and discussed for a long time, but had never been experimentally observed before [88, 89]. Most importantly, this distinct observation of resonant tunneling in an imperfect Si/SiO<sub>2</sub>-based layered structure enables new efforts in the development of practical Si/SiO<sub>2</sub> quantum devices.

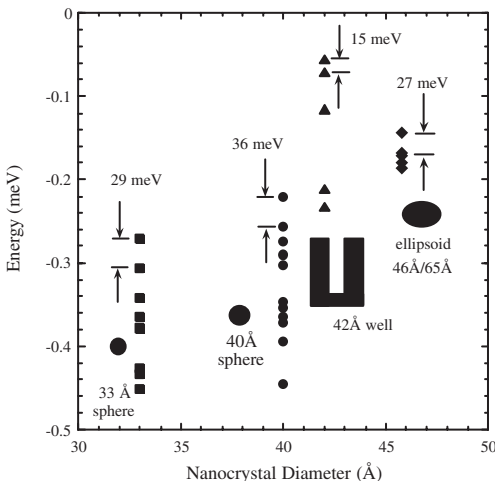


**Figure 28.** The electronic structure of the valence band in  $\langle 100 \rangle$  Si nano-objects obtained using TB calculations: Si ellipsoid with 46 Å vertical and 65 Å lateral sizes; 42 Å Si well sandwiched between tunnel transparent SiO<sub>2</sub> layers; and spherical Si nanocrystals with diameters of 33 Å and 40 Å. The first two hole energy levels are indicated for each nano-object. Reprinted with permission from [13], L. Tsybeskov et al., *Europhys. Lett.* 55, 552 (2001). © 2001, EDP Sciences.

## 7. SUMMARY

As has been mentioned earlier, the initial interest in structures based on Si nanocrystals was raised mostly due to their unusual optical properties, for example, visible PL with high quantum efficiency as reported first in 1990 [52]. The experimental fact that PL in Si nanocrystals as small as 2–3 nm remains slow and requires phonon assistance to conserve momentum, due to the indirect nature of their quasi-band structure, prevents their use in practical light-emitters utilizing intrinsic radiative transitions [90]. In contrast, recent work on complex or doped (e.g., Er<sup>+</sup> ions) Si nanocrystals and nc-Si superlattices is important due to the observation of an anti-correlation between the intrinsic PL and PL related to dopants [91]. However, at least two critical steps still need to be made: (1) a better understanding of the charge-transfer mechanism, and (2) a significant increase in the PL and EL quantum efficiency.

Following the first paper reporting the charging effect and possible applications of Si nanocrystals in memory devices [92], additional interest in their electronic properties has grown quickly. The fact that Si nanocrystals can be prepared in the form of a layered structure with precise control over their size, shape, and crystallography has also stimulated general interest in carrier transport in such systems. Despite such obvious imperfections as the grain boundaries that are separating laterally the Si nanocrystals, the periodic nature of the nc-Si/a-SiO<sub>2</sub> superlattices with tunnel transparent SiO<sub>2</sub> barriers controls carrier transport at low temperatures and many interesting and potentially important features such as sequential resonant tunneling, unusual magnetoresistance, and sustained oscillations can be observed [13]. In addition, it has been predicted that vertical quantum carrier transport can significantly be enhanced in structures where their nanocrystals display vertical self-alignment due to uniform strain propagation. So far, this work has been done primarily in epitaxial crystal growth (MBE, MOCVD, or CVD) of III-V and IV-IV semiconductors. The first successful attempt to achieve similar results in nc-Si/a-SiO<sub>2</sub> superlattices with a focus on the vertical self-alignment of Si nanocrystals is shown in Figure 29. Preliminary results indicate that quantum carrier transport in these structures is enhanced, and thus these structures can find applications

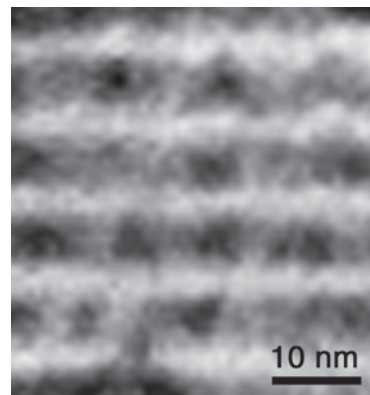


**Figure 29.** TEM micrograph showing vertical self-organization in a nc-Si/a-SiO<sub>2</sub> superlattice. Note the nearly pyramidal shape of the Si nanocrystals.

in practical electron devices. Therefore, it is quite possible that the most interesting results in the development of novel electron devices based on nc-Si superlattices are yet to come.

## GLOSSARY

**Absorption coefficient** A measure on an exponential scale of the degree of the attenuation of light propagating through a material.

**Brillouin scattering** As for Raman scattering, but very low energy excitations are involved, e.g., acoustic phonons.

**Epitaxy** Growth of materials atomic layer by atomic layer coherently on some single crystal planar substrate.

**Heterostructure** The joining of two dissimilar planar crystalline materials with a common in-plane lattice constant, usually produced by epitaxial growth.

**Minizone** A Brillouin zone of reduced size created within a superlattice along the growth direction.

**Nanocrystalline silicon** Single crystals of silicon of nanometer dimensions typically 110 nm in size.

**Photoluminescence** Light emitted by a material under illumination by light of usually shorter wavelength.

**Point group** A mathematical construct that describes the symmetry possessed by a crystal.

**Quantum well** A thin layer of a semiconductor in which charge carriers are confined by the higher band potential of the adjacent material.

**Raman spectroscopy** Inelastic scattering of light by vibrational or electronic excitations in a material.

**Resonant carrier tunneling** Quantum mechanical propagation of charge carriers through a potential barrier.

**Superlattice** Artificial lattice created in one direction by growing alternating layers of different materials on a planar substrate.

## ACKNOWLEDGMENTS

We would like to thank our many colleagues from the University of Rochester (P. M. Fauchet, L. Rothberg, and D. G. Hall), National Research Council of Canada (J. P. McCaffrey, J.-M. Baribeau, G. I. Sproule, and H. J. Labbé), the Technical University of Munich (F. Koch, M. Stutzmann, D. Kovalev, J. Diener, and V. Timoshenko), Motorola (B. E. White and S. Zollner), Kodak (T. N. Blanton), and other collaborators (M. Zacharias, G. Allan, C. Delerue, I. Aleiner, and B. Likhtman) for their help and diverse contributions. LT specifically thanks his former graduate student at the University of Rochester, Dr. G. F. Grom. He also thanks the German Academic Exchange Service (DAAD) for a 1999 summer research program in Germany and the National Science Foundation, Semiconductor Research Corporation, Motorola, Foundation at NJIT, and Army Research Office for financial support.

## REFERENCES

1. L. Tsybeskov, K. D. Hirschman, S. P. Duttagupta, M. Zacharias, P. M. Fauchet, J. P. McCaffrey, and D. J. Lockwood, *Appl. Phys. Lett.* 72, 43 (1998).
2. D. J. Lockwood, "Light Emission from Silicon: From Physics to Devices." Academic Press, San Diego, 1998.
3. K. D. Hirschman, L. Tsybeskov, S. P. Duttagupta, and P. M. Fauchet, *Nature* 384, 338 (1996).
4. T. Baron, P. Gentile, N. Magnea, and P. Mur, *Appl. Phys. Lett.* 79, 1175 (2001).
5. N. Takahashi, H. Ishikuro, and T. Hiramoto, *Appl. Phys. Lett.* 76, 209 (2000).
6. M. G. Bawendi, P. J. Carroll, William L. Wilson, and L. E. Brus, *J. Chem. Phys.* 96, 946 (1992).
7. Z. H. Lu, D. J. Lockwood, and J.-M. Baribeau, *Nature* 378, 258 (1995).
8. B. T. Sullivan, D. J. Lockwood, H. J. Labbé, and Z. H. Lu, *Appl. Phys. Lett.* 69, 3149 (1996); D. J. Lockwood, B. T. Sullivan, and H. J. Labbé, *J. Lumin.* 80, 75 (1999).
9. Z. H. Lu, D. J. Lockwood, and J.-M. Baribeau, *Solid State Electron.* 40, 197 (1996).
10. D. J. Lockwood, Z. H. Lu, and J.-M. Baribeau, *Phys. Rev. Lett.* 76, 539 (1996).
11. G. F. Grom, D. J. Lockwood, J. P. McCaffrey, H. J. Labbé, L. Tsybeskov, P. M. Fauchet, B. White, J. Diener, H. Heckler, D. Kovalev, and F. Koch, *Nature* 407, 358 (2000).
12. G. F. Grom, Ph.D. Thesis, University of Rochester, 2001, p. 134.
13. L. Tsybeskov, G. F. Grom, R. Krishnan, L. Montes, P. M. Fauchet, D. Kovalev, J. Diener, V. Timoshenko, F. Koch, J. P. McCaffrey, H. J. Labbé, G. I. Sproule, D. J. Lockwood, Y. M. Niquet, C. Delerue, and G. Allan, *Europhys. Lett.* 55, 552 (2001).
14. P. D. Persans, A. F. Ruppert, B. Abeles, and T. Tiedje, *Phys. Rev. B* 32, 5558 (1985).
15. P. V. Santos, M. Hundhausen, L. Ley, and C. Viczian, *J. Appl. Phys.* 69, 778 (1991).
16. J. Kakalios, H. Fritzsche, N. Ibaraki, and S. R. Ovshinsky, *J. Non-Cryst. Solids* 66, 339 (1984).
17. T. Sakurai and T. Sugano, *J. Appl. Phys.* 52, 2889 (1981).
18. W. Y. Ching, C. C. Lin, and L. Guttman, *Phys. Rev. B* 16, 5488 (1977).
19. A. F. Ruppert, P. D. Persans, G. J. Hughes, K. S. Liang, B. Abeles, and W. Lanford, *Phys. Rev. B* 44, 11381 (1991).
20. P. D. Persans, A. Ruppert, and B. Abeles, *J. Non-Cryst. Solids* 102, 130 (1988).
21. M. Zacharias and P. Streitenberger, *Phys. Rev. B* 62, 8391 (2000).
22. J. Gonzalez-Hernandez and R. Tsu, *Appl. Phys. Lett.* 42, 90 (1983).
23. M. Zacharias, J. Heitmann, M. Schmidt, and P. Streitenberger, *Physica E* 11, 245 (2001).
24. J. P. McCaffrey, private communication.
25. P. Wickboldt, D. Pang, W. Paul, J. H. Chen, F. Zhong, J. D. Cohen, D. L. Williamson, and Y. Chen, *J. Non Cryst. Solids* 198–200, 567 (1996).
26. L. Tsybeskov, unpublished.
27. L. Tsybeskov, K. D. Hirschman, S. P. Duttagupta, M. Zacharias, P. M. Fauchet, J. P. McCaffrey, and D. J. Lockwood, *Phys. Stat. Sol.* 165, 69 (1998).
28. L. L. Chang, L. Esaki, W. E. Howard, R. Ludeke, and G. Schul, *J. Vac. Sci. Technol.* 10, 655 (1973).
29. S. D. Walck and J. P. McCaffrey, *Thin Solid Films* 308–309, 399 (1997).
30. S. T. Ngiam, K. F. Jensen, and K. D. Kolenbrander, *J. Appl. Phys.* 76, 8201 (1994).
31. D. Reznik, C. H. Olk, D. A. Neumann, and J. R. D. Copley, *Phys. Rev. B* 52, 116 (1995).
32. H. Richter, Z. P. Wang, and L. Ley, *Solid State Commun.* 39, 626 (1981).
33. I. H. Campbell and P. M. Fauchet, *Solid State Commun.* 58, 739 (1986).
34. S. T. Kshirsagar and J. S. Lannin, *Phys. Rev. B* 25, 2916 (1982).
35. J. S. Lannin, L. J. Pilione, S. T. Kshirsagar, R. Messier, and R. C. Ross, *Phys. Rev. B* 26, 3506 (1982).

36. P. A. Temple and C. E. Hathway, *Phys. Rev. B* 7, 3685 (1973).
37. Y. Sasaki and M. Kitahara, *J. Appl. Phys.* 76, 4344 (1994).
38. G. Mariotto, F. Ziglio, and F. L. Freire, Jr., *J. Non-Cryst. Solids* 192–193, 253 (1995).
39. N. Brunetto and G. Amato, *Thin Solid Films* 297, 122 (1997).
40. S. M. Rytov, *Akust. Zh.* 2, 71 (1956).
41. D. J. Lockwood, M. W. C. Dharma-wardana, J.-M. Baribeau, and D. C. Houghton, *Phys. Rev. B* 35, 2243 (1987).
42. C. Colvard, R. Merlin, and M. V. Klein, *Phys. Rev. Lett.* 45, 298 (1980).
43. D. Royer and E. Dieulesaint, *J. Acoust. Soc. Am.* 76, 1438 (1984).
44. M. A. Tamor and J. P. Wolfe, *Phys. Rev. B* 26, 5743 (1982) and references therein.
45. I. R. Cox-Smith, H. C. Liang, and R. O. Dillon, *J. Vac. Sci. Technol. A* 3, 674 (1985).
46. G. D. Ivlev and E. I. Gatskevich, *Appl. Surf. Sci.* 143, 265 (1999).
47. J. B. Hopkins and L. A. Farrow, *J. Appl. Phys.* 59, 1103 (1986).
48. K. Mizoguchi and S.-I. Nakashima, *J. Appl. Phys.* 65, 2583 (1989).
49. L. Tsybeskov, unpublished.
50. R. A. Street, “Technology and Applications of Amorphous Silicon,” Springer Series in Materials Science, Vol. 37, pp. 94–146 and references therein. Springer, Berlin, 2000.
51. H. F. Wolf, “Silicon Semiconductor Data,” p. 648. Pergamon, New York, 1969.
52. L. T. Canham, *Appl. Phys. Lett.* 37, 1046 (1990).
53. A. G. Cullis and L. T. Canham, *Nature* 353, 335 (1991).
54. L. Tsybeskov, Ju. v. Vandyshev, and P. M. Fauchet, *Phys. Rev. B* 49, 7821 (1994).
55. M. S. Brandt, H. D. Fuchs, M. Stutzmann, J. Weber, and M. Cardona, *Solid State Commun.* 81, 307 (1992).
56. Y. Kanemitsu, *Phys. Rep.* 263, 1 (1995).
57. D. Kovalev, H. Heckler, B. Averboukh, M. Ben-Chorin, M. Schwartzkopff, and F. Koch, *Phys. Rev. B* 57, 3741 (1998).
58. A. G. Cullis, L. T. Canham, and P. D. J. Calcott, *J. Appl. Phys.* 82, 909 (1997).
59. R. T. Collins, P. M. Fauchet, and M. A. Tischler, *Phys. Today* 50, 83 (1997).
60. D. Kovalev, H. Heckler, G. Polisski, J. Diener, and F. Koch, *Opt. Mater.* 17, 35 (2001).
61. D. Kovalev, H. Heckler, M. Ben-Chorin, G. Polisski, M. Schwartzkopff, and F. Koch, *Phys. Rev. Lett.* 81, 2803 (1998).
62. M. Fujii, D. Kovalev, J. Diener, F. Koch, S. Takeoka, and S. Hayashi, *J. Appl. Phys.* 88, 5772 (2000).
63. L. Pavesi and M. Ceschini, *Phys. Rev. B* 48, 17625 (1993).
64. H. Heckler, D. Kovalev, G. Polisski, N. N. Zinov'ev, and F. Koch, *Phys. Rev. B* 60, 7718 (1999).
65. C. H. Perry, F. Lu, F. Namavar, N. M. Kalkhoran, and R. A. Soref, *Appl. Phys. Lett.* 60, 3117 (1992).
66. J. Diener, D. Kovalev, H. Heckler, G. Polisski, and F. Koch, *Phys. Rev. B* 63, 73302 (2001).
67. L. Tsybeskov and P. M. Fauchet, *Appl. Phys. Lett.* 64, 1983 (1994).
68. L. Esaki and R. Tsu, *IBM J. Res. Develop.* 14, 61 (1970).
69. F. Capasso, “Physics of Quantum Electron Devices,” p. 107. Springer-Verlag, Berlin, 1990.
70. H. Mizuta and T. Tanoue, “The Physics and Application of Resonant Tunneling Diodes,” p. 239. Cambridge University Press, Cambridge, 1995.
71. M. He and B.-Y. Gu, *Phys. Rev. B* 41, 2906 (1990).
72. Q.-Y. Ye, R. Tsu, and E. H. Nicollian, *Phys. Rev. B* 44, 1806 (1991).
73. C. Y. Fong, J. S. Nelson, L. A. Hemstreet, R. F. Gallup, L. L. Chang, and L. Esaki, *Phys. Rev. B* 46, 9538 (1992).
74. R. Tsu, *Nature* 364, 19 (1993).
75. B. Su, V. J. Goldman, and J. E. Cunningham, *Science* 255, 313 (1992).
76. N. Z. Zou and K. A. Chao, *Phys. Rev. Lett.* 69, 3224 (1992).
77. L. Tsybeskov, G. F. Grom, P. M. Fauchet, J. P. McCaffrey, J.-M. Baribeau, G. I. Sproule, and D. J. Lockwood, *Appl. Phys. Lett.* 75, 2265 (1999).
78. B. Ricco and M. Ya. Azbel, *Phys. Rev. B* 29, 1970 (1983).
79. D. M. Fleetwood, P. S. Winokur, L. C. Riewe, and R. A. Reber, Jr., *J. Appl. Phys.* 84, 6141 (1998).
80. D. L. Miller and B. Laikhtman, *Phys. Rev. B* 54, 10669 (1996).
81. T. Weil and B. Winter, *Appl. Phys. Lett.* 50, 1281 (1987).
82. M. Jonson and A. Grincwaig, *Appl. Phys. Lett.* 51, 1729 (1987).
83. C. Delerue, unpublished.
84. S. Washburn and R. A. Webb, *Adv. Phys.* 35, 375 (1986).
85. D. K. Ferry and S. M. Goodnick, “Transport in Nanostructures,” p. 512. Cambridge University Press, New York, 1997.
86. C. Bruder, R. Fazio, and H. Schoeller, *Phys. Rev. Lett.* 76, 114 (1996).
87. Y. M. Niquet, C. Delerue, G. Allan, and M. Lannoo, *Phys. Rev. B* 62, 5109 (2000).
88. R. T. Collins, P. M. Fauchet, and M. A. Tischler, *Phys. Today* 50, 24 (1997).
89. S. S. Iyer and Y. H. Xie, *Science* 260, 5104 (1993).
90. L. Tsybeskov, *Mat. Res. Soc. Bull.* 23, No. 4 (1998).
91. J. Heitmann, R. Scholz, and M. Zacharias, *J. Non-Cryst. Solids* 299–302, 678 (2002).
92. S. Tiwari, F. Rana, H. Hanafi, A. Hartstein, E. F. Crabbé, and K. Chan, *Appl. Phys. Lett.* 68, 1377 (1996).



# Nanocrystalline Silicon: Electron Spin Resonance

Takashi Ehara

*Ishinomaki Senshu University, Minamisakai, Ishinomaki, Miyagi, Japan*

## CONTENTS

1. Introduction
  2. Basics of Electron Spin Resonance
  3. n-Type Nanocrystalline Silicon
  4. p-Type Nanocrystalline Silicon
  5. Light-Induced Electron Spin Resonance
  6. Dangling Bond Defects
  7. Other Detection Method of Spin Resonance
  8. Summary
- Glossary  
References

## 1. INTRODUCTION

Since the report of deposition using chemical transport method by Veprek and Marecek [1], hydrogenated nanocrystalline silicon (nc-Si:H), usually called hydrogenated microcrystalline silicon ( $\mu$ c-Si:H), has gathered much interest. The primary preparation method of nc-Si:H is plasma-enhanced chemical vapor deposition (PECVD) using highly diluted  $\text{SiH}_4$  in  $\text{H}_2$  [2–5]. In this method, dangling bond (DB) defects are decreased due to termination by hydrogen atoms. In addition, impurity doping can be done using phosphine gas or diborane gas as phosphorus or boron source, as well as in the case of hydrogenated amorphous silicon (a-Si:H) [6]. Moreover, doping efficiency of nc-Si:H is higher than that in a-Si:H. Dark conductivity of  $10^{-1} \text{ cm}^{-1}$  has been achieved by doping [7–9]. Due to the properties shown here, nc-Si:H has been a promising thin-film material for some optical devices such as solar cells [10–15] or thin solid transistors. As highly diluted  $\text{SiH}_4$  gas has been used as a silicon source, the deposition rate of nc-Si:H was extremely low; however, high-rate deposition of nc-Si:H films at low temperature has been reported [16]. This kind of work is thought to enhance the use of nc-Si:H thin films for devices. Recently, as another kind of low-temperature deposition

method, hot-wire chemical vapor deposition (HWCVD) has been extensively studied. In the method, a thermal and catalytic reaction between deposition source gas and tungsten hot-wire catalyzer that causes the film deposition instead of plasma decomposition of  $\text{SiH}_4$  is used for deposition of films [17–19].

Although the growth mechanism of nc-Si:H by the CVD method is still under discussion [4, 20–22], the structure of nc-Si:H has been studied and reported. The nc-Si:H is a heterogeneous material consisting of small crystallites with size on the order of 5 to 30 nm which are embedded in columns structure that is parallel to the film growth axis with a diameter of 50 to 200 nm [23, 24]. In such mixed phase structure, electron spin resonance (ESR) spectroscopy is an important method to study a particular electronic state, because the techniques are sensitive to the microscopic environment of this state.

In this chapter, ESR studies of nc-Si:H are reviewed. After the section of basics of ESR, the signal of conduction electrons, conduction holes, light-induced ESR, and dangling bond defects signals will be reviewed.

## 2. BASICS OF ELECTRON SPIN RESONANCE

ESR spectroscopy is a very important method to study the characteristics of paramagnetic species. In the case of nc-Si:H, ESR has been used for the study of silicon DB defects and carriers, mainly conduction electron (CE) in n-type materials. In the study of nanocrystalline or related material such as a-Si:H, ESR spectroscopy has been used in a great deal of work to estimate spin densities by intensity of corresponding signals. However, the ESR spectroscopy can also be used for the research of paramagnetic characteristics of the paramagnetic species in the material. The important information of ESR spectroscopy to clarify the characteristics of paramagnetic species in nc-Si:H are  $g$ -value, spin-lattice relaxation time, and line width. In this section, basic theories of these important data are explained.



The  $g$ -value is the magnitude of the electron Zeeman factor for the paramagnetic species considered. The  $g$ -value can be determined by the equation

$$E = g\mu_B B$$

In it,  $E$  is energy of microwave,  $\mu_B$  is Bohr magnetron, and  $B$  is magnetic field.  $g$ -value becomes 2.0023 in the case of free electron. In the case of actual paramagnetic species, the value becomes different because of the effect of local magnetic field. In the case of DB defects in a-Si:H or nc-Si:H, the effect of spin-orbit coupling is important. The spin-orbit coupling is caused by local magnetic field due to movement of electrons in its orbit. Thus, the  $g$ -value determined by spin-orbit coupling depends on the structure of the orbit. The effect of spin-orbit coupling is anisotropic; thus, it also depends on axis determined by magnetic field. Here, we assume the spin-orbit coupling of DB with a state in silicon. If we take a DB orbital along the  $z$ -axis, the anisotropic  $g$ -values are given by

$$g_{\parallel} = g_z = g_e$$

$$g_{\perp} = g_x = g_y = g_e \left\{ \delta_{ij} - \lambda \sum_{n=x,y,z} \frac{\langle \phi_{\text{DB}} | L_i | \varphi_n \rangle \langle \varphi_n | L_j | \phi_{\text{DB}} \rangle}{E_n - E^{\text{DB}}} \right\}$$

where  $g_e$ ,  $\phi$ , and  $E^{\text{DB}}$  are the  $g$ -value of free electron, the wave function of DB, and the energy of the DB, respectively.  $\varphi_n$  and  $E_n$  stand for the wavefunction and the energy of a coupling state.  $\lambda$  is a coupling constant of the spin-orbit interaction, which is  $149 \text{ cm}^{-1}$  in the case of silicon. The  $g$ -value observed in the spectra is

$$g = \sqrt{g_x^2 + g_y^2 + g_z^2}$$

Spin-lattice relaxation time is also one of the important characteristics for paramagnetic species. When ESR happens, the spin system absorbs the microwave with appropriate energy. Hence, the spin system can be thought as with high energy compared with its surroundings. The actual spin system undergoes interactions with the surroundings until its energy eventually is restored to the same as that of the surroundings through contact with it. As with any sufficiently simple thermodynamic system that receives an extra energy  $\delta U_0$  at  $t = t_0$ , it loses this excess energy to its surroundings with an exponential decay, described as

$$\delta U = \delta U_0 \exp[-(t - t_0)/T_1]$$

where  $\delta U_0$  is the excess energy at time  $t = t_0$ , and  $T_1$  is the characteristic time called relaxation time that corresponds to the energy flow rate magnitude from the spin system to the surroundings. Relaxation time  $T_1$  reflects the degree to which the spin system is connected to its surroundings.

Finally, we mention the line width of ESR signals. The spectral lines are classified into those that are homogeneously broadened and those that are inhomogeneously broadened. Homogeneous line broadening for a set of spins occurs when all the spins are in the same magnetic condition and have the same spin Hamiltonian parameters. This means all the spins have the same line shape of the signal. The line shapes of homogeneous broadening have a

lorentzian line shape. The actual homogeneous linewidth  $\Gamma$  is determined by the equation

$$\Gamma = \frac{1}{2T_1} + \frac{(1 + \gamma_e^2 B_1^2 T_1 T_2)^{1/2}}{T_2}$$

In the equation,  $T_1$  and  $T_2$  are the relaxation time of spins,  $B_1$  is oscillating magnetic field, and  $\gamma_e$  corresponds to

$$\gamma_e = \frac{g_e \mu_B}{\hbar}$$

The line width of homogeneously broadened lines depends on the relaxation time of the spins.

The inhomogeneous broadening mechanism distributes the resonance magnetic field frequencies without line broadening due to individual equivalent spins. The observed signal is a superposition of a large number of individual spin packets, all of which have slightly different  $g$ -values from each other. Even if the outer magnetic field is homogeneous, the inhomogeneous broadening is caused by various factors. With an anisotropic interaction in a randomly oriented system in a solid, the distribution of local magnetic field resulting from the anisotropic  $g$ -tensor gives rise to the inhomogeneous broadening. This corresponds to asymmetrical line shape in many cases. The DBs in the silicon are included in this case. Another factor that induces the inhomogeneous line shape is the unresolved hyperfine structure. This occurs when the number of hyperfine components located near nuclei is so great that no clear hyperfine structure is observed. In the hydrogen in the nc-Si:H, the line broadening due to the hyperfine structure by the hydrogen atoms may cause this broadening.

### 3. n-TYPE NANOCRYSTALLINE SILICON

In this section, ESR studies of doped n-type nc-Si:H are described. In the beginning of ESR studies of nc-Si:H, most of the studies published were devoted to n-type materials. In the n-type materials, the spectra are dominated by CE signal at  $g = 1.997\text{--}1.999$  rather than silicon DB defects signals. The studies of the CE signal are described in this section.

Before the first report of ESR study of n-type nc-Si:H, many works of related material such as n-type a-Si:H, crystalline silicon, and polycrystalline-silicon (poly-Si) have been reported. The first report of CE ESR signals in crystalline silicon was done by Portis and co-workers [25]. They described a lorentzian line of CE that has dependence of line width and reciprocal paramagnetic susceptibility on temperature. The ESR study of CE in crystalline silicon has been followed by a great deal of work [26–30]. For example, Feher reported a  $g$ -value of the CE of 1.99865–1.99885. Kodera reported the CE signals at averaged  $g$ -value of 1.99869 and hyperfine splitting of 41.7 G due to doped phosphorus atoms. In the case of doped poly-Si, ESR study of CE has been reported by Hasegawa et al. in 1979 [32]. In their work, the DB signal observed for phosphorus-doped samples disappeared by annealing at above 700–750 °C, where the sample crystallized, and a new signal that has similar  $g$ -value as CE in crystalline silicon has been observed at  $g = 1.997\text{--}1.999$ . ESR spectra of phosphorus-doped a-Si:H have also been reported by various workers [33–36]. For example,

Dersch observed a new signal at  $g = 2.0043$  beside the DB signal at  $g = 2.0055$  in the case of highly phosphorus-doped sample. The result is different from that in crystalline silicon or poly-Si. The signal broadens with increasing phosphorus doping due to hyperfine interaction with the phosphorus nuclei. A new signal with  $g = 2.0043$  is suggested to be due to electrons in localized conduction band tail states.

As an early ESR work of nc-Si:H, Hasegawa et al. have also reported the ESR spectra of undoped and phosphorus-doped nc-Si:H [37]. They observed the signals due to DB with  $g$ -value of 2.0049 when the doping level, gas flow rate ratio of  $\text{SiH}_4$  and  $\text{PH}_3$ , is below  $10^{-4}$ . In Figure 1, ESR spectra of phosphorus-doped nc-Si:H with various doping levels are shown. The CE signal at  $g = 1.9970$  has been observed in the sample at the doping level of  $10^{-3}$ . Other signals were observed at  $g = 2.0043$  in more highly doped samples than a doping level of  $10^{-2}$  with the decrease of crystalline fraction volume ratio observed by Raman spectra. The  $g$ -value of the signal is similar to that in localized electron near the tail of the conduction band in the a-Si:H. The DB signals observed in undoped or slightly doped samples have not been observed in phosphorus-doped sample with doping level more than  $10^{-3}$ . In the work, Hasegawa et al. [37] described the dependence of the ESR signals with  $g = 2.0049$ , 2.0043, and 1.997 on the doping level and rf power for films preparation. The result indicates that spin density of the signal with  $g = 1.997$  due to CE does not increase appreciably with increasing doping ratio above  $10^{-3}$ . The result is different from that in phosphorus-doped poly-Si in which CE signal increases with doping level.

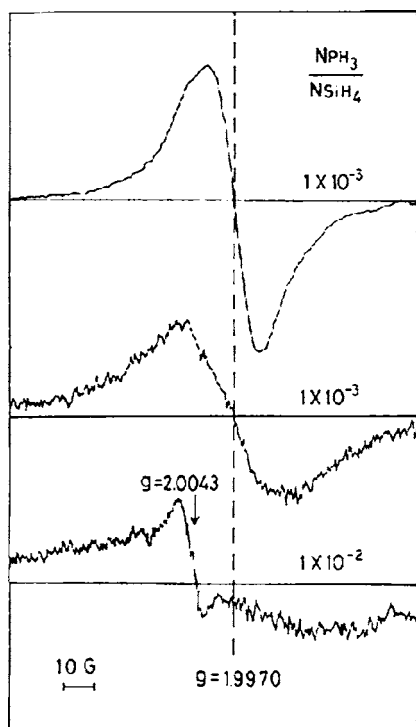


**Figure 1.** ESR spectra measured at 77 K for nc-Si:H films deposited at various doping levels. Reprinted with permission from [37], S. Hasegawa et al., *Phil. Mag. B* 48, 431 (1983). © 1983, Taylor & Francis Ltd.

Finger and co-workers have reported the temperature dependence of nc-Si:H ESR spectra [38]. In Figure 2, ESR spectra of undoped and phosphorus-doped nc-Si:H at various temperatures from 10 K to 300 K are shown. Both samples show a resonance of DB at  $g = 2.0049$ – $2.0055$  with spin density of  $1$ – $2 \times 10^{17}$ . As the temperature is decreased, resonance of CE appears at  $g = 1.9981$ – $1.9985$  with characteristic asymmetric Dysonian line shape [27]. The signal due to CE becomes stronger with respect to the DB signal with a decrease of measurement temperature. The signal intensity of the CE follows the Curie law, that the signal intensity is proportional to  $T^{-1}$ , down to 10 K at below 200 K. The CE peak is not detectable above 200 K because of a strong line broadening. Finger et al. reported details of their ESR work of nc-Si:H in 1998 [39]. They have reported measurement of ESR spectra of the samples prepared with different n- and p-type doping at 40 K. Over a wide range of conductivities, they observed the DB and CE simultaneously in n-type nc-Si:H. The intensity of the CE signal, calculated from a gaussian line shape, shows a clear correlation with conductivity of the samples. This correlation supports the attribution of the signal at 1.998 as a CE.

Müller and co-workers also have reported the ESR of doped nc-Si:H [40]. In highly doped n-type sample (doping level of 17 ppm) at 20 K with high microwave power of 25 mW where all signal beside CE are saturated, the signal of hyperfine interaction of  $^{31}\text{P}$  has been observed as a shoulder of CE signals. The hyperfine splitting is about 110 G and the intensity ratio of hyperfine signal with respect to total CE signal is about 10%. In the report, they studied the dependency of  $g$ -value and line width of the CE signals on doping level. At higher doping level, the CE signal intensity significantly increases, whereas the DB signals are almost independent of doping condition. Therefore, the resonance of the DB signals becomes less visible with increase of doping level. They also have investigated dependence of  $g$ -value on conductivity. For the doped samples, the  $g$ -value of the CE signals is around 1.9980 at doping levels below 33 ppm and decreases continuously for

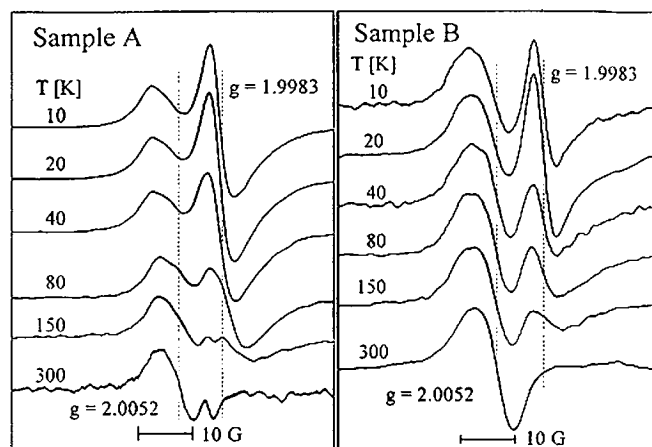


**Figure 2.** ESR signals of nc-Si:H at different temperatures. The spectra are normalized to similar peak-to-peak height. The  $g$ -value of the free electron ( $g = 1.9983$ ) and the dangling bond ( $g = 2.0052$ ) are indicated. Reprinted with permission from [38], F. Finger et al., *Phil. Mag. B* 70, 247 (1994). © 1994, Taylor & Francis Ltd.

higher doping level to 1.9972 at 133 ppm. The undoped samples have  $g$ -value of 1.9980–1.9985 with a large scatter due to the overlap with DB signals. The  $g$ -value also shows dependence on the measurement temperature. The  $g$ -value decreases with rising temperature between 4.5 and 300 K. The  $g$ -values observed in nc-Si:H are generally lower than what is reported for crystalline silicon ( $g = 1.9985$ – $1.9995$ ) [25–30] or poly-Si ( $g = 1.997$ – $1.999$ ) [32]. The peak-to-peak line width also shows dependence on the measurement temperature. Above 30 K, all samples with various doping levels from 1 to 133 ppm show a large increase in the CE line width with rising temperature. All samples exhibit line width of 9 G at 30 K and increased to 27–34 G at 300 K. They attributed the strong increase in line broadening with rising temperature for  $T > 60$  K to the corresponding decrease in spin-lattice relaxation time, because of their previous report of a steep decrease of  $T_1$  in nc-Si:H [41]. In their measurement, the minimum line width has not been observed at the lowest temperature but at 30 K. The line width increased again at the temperature lower than 30 K as well as in slightly doped crystalline Si [42–45]. In the case of crystalline silicon, Maekawa and Kinoshita explained the increase of line width by decrease of temperature by a change in the correlation frequency of the exchange interaction due to reduction of electron hopping rate between neighboring sites at lower temperature [42]. Maruyama and co-workers explained this phenomenon by condensation of the donor electrons into singlet ground states of donor cluster by coupling each other by antiferromagnetic exchange interaction [43].

Malten and Finger and co-workers have reported pulsed-ESR study of nc-Si:H [39, 41]. In the pulsed-ESR spectrum of n-type nc-Si:H, CE resonance dominates and DB signal is only visible as a shoulder. In addition, two hyperfine lines are observed as a shoulder with a hyperfine splitting of about 110 G. [They assigned as hyperfine] due to  $^{31}\text{P}$  nuclei, by comparison with phosphorus-doped a-Si:H and crystalline silicon samples. They also estimated spin-lattice relaxation time,  $T_1$ , by inversion recovery curves. The shape of recovery curve observed in nc-Si:H sample measurements is not simple single exponential form, because of overlapping with other resonance curves or distribution of relaxation time due to the structural disorder of the samples. They fit the recovery curve with stretched exponentials, which was reported by Durny and co-workers [46] and actually applied in the case of pulsed-ESR study of a-Si:H [47]. The fitting of the curve is in the form

$$I(t) = I_0 \left\{ \exp \left[ - \left( \frac{t}{T_1} \right)^\beta \right] - 1 \right\}$$

In this equation, the dispersion parameter  $\beta$  represents a distribution of relaxation time  $T_1$ . Obtained  $T_1$ , relaxation time of CE, is faster than that in DB by two or three orders at the temperature lower than 100 K.

Lips, Fuhs, and co-workers reported ESR study of band tail states and free electron in phosphorus-doped nc-Si:H in a study of metal-insulator transition (MIT) [48–50]. In the plot susceptibility of the CE line as a function of doping level, the susceptibility increases linearly with doping level below  $3 \times 10^{18} \text{ cm}^{-3}$ . In contrast, susceptibility increases sub-linearly above doping level of  $4 \times 10^{18} \text{ cm}^{-3}$ . At the MIT,

the paramagnetic susceptibility changes from Curie-type to Pauli-type [51]. This MIT occurs at a similar doping concentration as crystalline silicon, indicating that the donors are distributed homogeneously in the crystalline phase of the films. In degenerately doped films, they detect a Curie contribution to CE signal at spin density of  $4\text{--}8 \times 10^{18} \text{ cm}^{-3}$ . They assign this signal to tail states originating from disorder at the grain boundary.

In the case of a-Si:H, nitrogen-doping effect has been studied by Morimoto, Zhou, and co-workers [52, 53]. They found similarity between the nitrogen doping and that of phosphorus doping found in conductivity, and the photo-conductivity decay indicates that nitrogen can act as donor in a-Si:H. Although the nitrogen doping is also of substitutional type, the solid phase doping efficiency of nitrogen is estimated to be three orders of magnitude lower than that of phosphorus. In the case of nc-Si:H, nitrogen-doping effect has been studied by Ehara and co-workers [54–56]. In the nitrogen-doped nc-Si:H, conductivity was not increased, but rather decreased at higher doping level of  $10^{-1}$  because of structural change to amorphous. We also have studied ESR of nitrogen-doped nc-Si:H [55, 57]. Figure 3 shows the temperature dependence of the ESR spectra of undoped and nitrogen-doped nc-Si:H. As shown in Figure 3, both silicon DB and CE peaks have been observed at  $g = 2.005$ – $2.006$  and  $1.9975$ – $1.9985$ , respectively. In the undoped sample, signal intensity of the CE showed a maximum at 40 K and decreased at lower temperature. This may be interpreted as the interruption of the thermal excitation of electron. In the doped sample, the CE signal intensity exhibited a maximum at 20 K. The difference in the temperature dependence suggests that the doped samples have shallower donor levels. The result indicates that the nitrogen atoms work as an electron donor in the nc-Si:H, although the efficiency is far less than that of phosphorus as well as in the case of nitrogen-doped amorphous silicon.

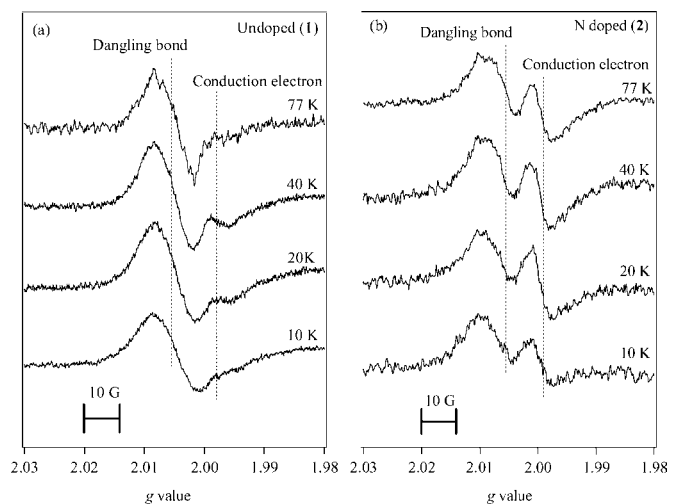


**Figure 3.** Temperature dependence of the ESR spectra of undoped and nitrogen-doped nc-Si:H. Reprinted with permission from [57], T. Ehara et al., *Jpn. J. Appl. Phys.* 39, 31 (2000). © 2000, Institute of Pure and Applied Physics.

The ESR signals of CE in another formed nanocrystalline silicon have also been reported. Young and co-workers have reported the ESR study of porous silicon (PS) at liquid helium temperature [58, 59]. They observed a new isotropic resonance center at  $g = 1.9995$  in both p-type and n-type PS. The paramagnetic center observed was identified due to the conduction band electrons in silicon nanocrystals by comparing its  $g$ -value with those of shallow donors in bulk silicon. Bardeleben and co-workers also reported  $n^{+}$ ,  $p^{+}$ , and p-type substrate supported and freestanding PS [60]. Signal of CE has been observed in  $n^{+}$ -type substrate supported PS as well as previous works at 40 K. However, the CE signal has not been observed in freestanding PS in spite of their careful search in the temperature range 4–300 K. In their possible explanation, they have considered that the strong hydrogen contamination range might have led to the passivation of the phosphorus donor.

#### 4. p-TYPE NANOCRYSTALLINE SILICON

ESR studies of p-type, boron-doped a-Si:H, as well as phosphorus-doped a-Si:H, have been reported by various workers [33–36]. Boron-doped a-Si:H shows a broad line at  $g = 2.01$  with line width of 20 G, beside the DB line. The signal attribution and line width have been assigned as holes in localized valence band tail states, and due to  $g$ -distribution, respectively. In contrast, ESR spectra of p-type, boron-doped nc-Si:H have not been well studied. Possible signals to be observed beside the DB are due to holes; however, it has been difficult in the p-type samples using continuous wave (CW) ESR measurement. Finger et al. reported absence of CE signal by CW-ESR spectrum of a boron-doped sample with doping level of 23 ppm [39]. This result is consistent with the doping effect. However, any peaks corresponding to holes have not been observed clearly.

The signals of holes induced by boron doping have been observed by pulsed ESR spectroscopy using an electron spin echo field sweep (ESE-FS) method [41, 61]. This measurement mode is preferable for measurement of broad signals, because it suppresses base line contributions. At lower temperature than 40 K, the spectra of p-type sample show a very broad line at around  $g = 2.1$  with peak-to-peak width of 500 G in addition to DB signal. In the case of a-Si:H, a possible origin of the peak, resonance of holes trapped in valence band tail states, shows different parameters ( $g = 2.01$  and width of 20 G). In crystalline silicon, the resonance of holes is only observed under external strain [62, 63] or extremely pure materials [64]. However, the observed signals under those conditions have some similarity with the broad peak of their work. Therefore, they tentatively attribute this broad resonance to hole states in the crystalline area of the material.

Another group also observed signal of holes by pulsed ESR spectroscopy in p-type nc-Si:H sample [65]. Kanschat et al. observed a broad structure of conduction holes (CH) at  $g = 2.08$  which they identify with holes trapped in valence band tail states. It is shown that the CH state behaves very similarly on illumination as the CE center.

#### 5. LIGHT-INDUCED ELECTRON SPIN RESONANCE

The light-induced ESR (LESR) is an effective method to study the transport mechanism or band structure of the material. In the case of a-Si:H, LESR signals of  $g = 2.004$  and  $g = 2.01$  are observed at low temperature beside the DB signal at  $g = 2.0055$  observed in dark. These signals have been tentatively attributed to conduction band tail electron ( $g = 2.004$ ) and valence band tail holes ( $g = 2.01$ ) based on the results of doping and photoluminescence experiments [33, 66–69].

The LESR spectrum of nc-Si:H was first reported in 1994 [38]. The light illumination by a 100-W halogen lamp enhances the free electron resonance at  $g = 1.9983$  in ESR of undoped nc-Si:H at 40 K. The signal of CE increased by a factor of about 3. Finger and co-workers reported details of LESR of nc-Si:H in [39]. In Figure 4, the LESR spectrum of an n-type nc-Si:H is shown with its dark ESR spectrum. In the figure, dark and LESR of a-Si:H are also shown for comparison. As shown in the figure, increase of both DB signal and CE signal is observed. The LESR-CE line is assigned to photoexcited CEs and increased DB signal can be due to newly appeared neutral DB changed from negatively charged DB by photoexcitation. The result observed in LESR of nc-Si:H is significantly different from the LESR of a-Si:H as shown in the figure.

Finger and co-workers also have studied the various kinds of LESR transient of nc-Si:H using white light and infrared light source. The LESR of nc-Si:H shows different transient characteristics from that in a-Si:H. After switching off of white light, decay of LESR signal has not been observed by infrared light illumination. The result is different from that in the case of a-Si:H. They have studied various transient characteristics of LESR intensity using sub-bandgap illumination. Lima and co-workers have also reported decay of LESR after illumination is discontinued [70]. In their case, the spin signal does not go to zero even after a few thousand seconds after the switch off of lamp, remaining around 20% of the original intensity. Although the time scales of the samples they measured are different from each other, the decay curve can be fitted using a model by Yan et al. [71] for

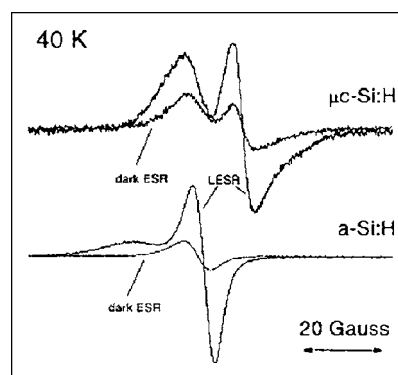


**Figure 4.** LESR together with dark ESR spectra of an n-type nc-Si:H sample, in comparison with a high-quality a-Si:H sample. Reprinted with permission from [39], F. Finger et al., *Phil. Mag. B.* 77, 805 (1998). © 1998, Taylor & Francis Ltd.

distant-pair recombination via tunneling between localized states.

Kondo and co-workers have reported light-induced phenomena in nc-Si:H [72]. They have measured excitation photon energy dependence of LESR response in nc-Si:H using lamp with monochromator at 5 K. The intensity of LESR decreases at 1.1 eV with decrease of the excitation energy, and this energy coincides with the crystalline silicon bandgap energy. They also reported details of temperature dependence of LESR signal intensity and concluded that the LESR signal does not arise from a mobile electron but from a localized electron trapped at a shallow level center close to the conduction band edge. They assigned the measured activation energy of 11 meV to the binding energy of the center. These shallow states that provide electrons probably originated from the conduction band tail caused by the structural disorder. They also have studied increase in the neutral DB density due to light exposure and suggested the defect formation correlates with the surface oxidation and surface band-bending model due to the oxidation.

The assignment of the peak at  $g = 1.998$  to shallow localized states close to the conduction band is also reported by Kanschä and co-workers [73]. They studied ESR, photoconductivity, and electrically detected magnetic resonance (EDMR) [74]. At low temperature, they have plotted increased density of CE centers by illumination and photoconductivity as a function of generation rate. If the CE resonance were due to free electrons, a linear relationship between increased CE spin density and photoconductivity would be expected. However, they observed almost the same dependence as that in a-Si:H [75]. Therefore, they assigned the CE states monitored at  $T = 30$  K to shallow localized states below the conduction band edge.

## 6. DANGLING BOND DEFECTS

Before the review of the ESR study of DB in nc-Si:H, ESR studies of DB in nc-Si:H related materials are reviewed for comparison. DB defects in crystalline silicon surface or Si/SiO<sub>2</sub> interface, P<sub>b</sub> center, which gives  $g$ -value of  $g_{\parallel} = 2.001$ – $2.002$ ,  $g_{\perp} = 2.008$ – $2.009$ , have been reported by some workers [76, 77]. ESR studies of DB in a-Si:H have also been reported. The asymmetric ESR signal of DB in a-Si:H is observed at  $g = 2.0055$  with peak-to-peak width of 5–7 G [66, 78]. Calculation of the  $g$ -value of a-Si:H DB using an interactive extended Hückel theory has been reported and the  $g$ -value of 2.0055 was explained by threefold-coordinated silicon atoms [79, 80]. Complicated ESR spectra of dislocations in crystalline silicon have been reported by a few groups [81, 82]. Hasegawa and co-workers have reported ESR spectra of poly-Si prepared by annealing of amorphous silicon films by low-pressure chemical vapor deposition (LPCVD) [83]. In the case of poly-Si,  $g$ -value of DB in the poly-Si depends on the annealing condition. The  $g$ -value observed depends on annealing time rather than temperature. The sample annealed for 24 h shows  $g$ -value of 2.0048 that is lower than the sample annealed for 2 h that has  $g$ -value of 2.0055–2.0057. The same group also reported ESR spectra of poly-Si prepared by PECVD [84]. The  $g$ -value and the stress strongly depended on the rf power and the thickness. In addition, the  $g$ -value of the DB

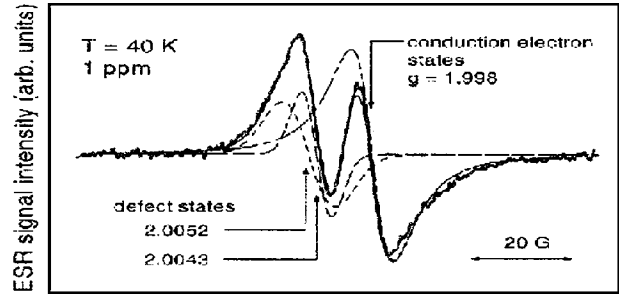


**Figure 5.** Dark CW ESR spectrum of nc-Si:H at 40 K. Included are numerical deconvolutions. Reprinted with permission from [40], J. Müller et al., *Phys. Rev. B* 60, 11666 (1999). © 1999, American Physical Society.

decreased from 2.0054 to 2.0042 with H<sub>2</sub> plasma annealing time [85]. These results are examined in terms of formation of different types of grain boundary that can be associated with a lattice deformation around the DB.

In the 1980s, a few groups reported ESR studies of nc-Si:H. Veprek and co-workers reported the ESR spectra of nc-Si:H sample prepared by the chemical transport method [86]. The spectra showed the peak of DB defect at  $g = 2.0055$ – $2.0059$  with the peak-to-peak width of 9 to 11 G. They analyzed that most of the samples have a line shape that could be approximated by a gaussian. However, line shape was not a simple gaussian or lorentzian function and appeared to be possibly a superposition of plural signals in some cases. The observed  $g$ -value of silicon DB is similar to that in a-Si:H ( $g = 2.0055$ ). However, the peak width was larger than that in a-Si:H (5–9 G). They determined the defects density in the films as between  $5 \times 10^{17}$  and  $2 \times 10^{18}$  by the spectra. However, they did not discuss the detail of the DB defect using the spectra. As far as the author knows, it is the first report of ESR study of DB in nc-Si:H.

Hasegawa and co-workers reported ESR of undoped nc-Si:H with a preferential orientation [87]. They prepared the undoped nc-Si:H sample at various substrate temperatures and rf powers. They reported that the increase in substrate temperature and decrease in rf power induce the change of orientation of nanocrystalline silicon from (111) to (220).  $g$ -value of ESR increased from 2.0048 to 2.0056 with increase in substrate temperature, and decreased from 2.0056 to 2.0049 by increase in rf power. This means change in orientation from (111) to (220) causes the increase in  $g$ -value. They explain the shift of  $g$ -value by change in morphology around the spin.

Finger et al. reported the temperature dependence of undoped and doped nc-Si:H [38, 39]. They observed asymmetric DB signal at  $g = 2.0049$ – $2.0055$  with spin density of  $10^{17}$ . They observed saturation effect in the DB signal at low temperature as a result of the increase in spin-lattice relaxation time. Later, they determined the spin-lattice relaxation time as  $10^{-4}$ – $10^{-2}$  s at the temperature of 20–100 K by measurement of pulsed ESR spectra. In the nitrogen-doped nc-Si:H, similar asymmetric signal of DB has been observed [55, 57]. Although the change in signal shape has been observed, it has been caused by structural change from nanocrystalline to amorphous, not by doped nitrogen.

In most of the ESR studies of nc-Si:H, the DB signals have been observed as an asymmetric line at around  $g = 2.005$ . Müller and co-workers reported the numerical fits for two-defect resonance of the asymmetric DB signal [40, 61]. The first center is supposed to be a silicon DB at  $g = 2.0052$ . The second center is signal at 2.0043. The origin of the second center was initially attributed to electron trapped in the conduction band tail, since  $g$ -value of this center is similar to that in n-type a-Si:H [33–36] and LESR of undoped a-Si:H [66–69]. However, this assignment is considered to be ambiguous, because the center is also observed in p-type nc-Si:H. Therefore, another explanation of the second center at  $g = 2.0043$  is needed. Müller suggested the attribution of the second center as the DB states in Si-rich Si-O layers as an attribution of the peak [88], because an increase of the signal at  $g = 2.0044$  in nc-Si:H samples was observed after exposure to air for several weeks [89]. Pulsed-ESR study of nc-Si:H, reported by Kanschat and co-workers, supported the existence of two centers [65]. They identified two DB-like structures at  $g = 2.0052$  and  $g = 2.0043$ . Whereas, the  $g = 2.0052$  signal is evenly distributed in the gap, the signal at  $g = 2.0043$  states is found to be localized in the lower part of the gap. Kondo and co-workers studied nc-Si:H DB to investigate its microscopic structure [90]. They have suggested DB at grain boundary with  $g$ -tensor of  $g_{\parallel} = 2.0022$  and  $g_{\perp} = 2.0078$  similar to the  $P_b$  center. They have simulated the DB signal in Q-band ESR spectra well by assuming randomly oriented grain boundary defects and DB in amorphous fraction. Lima and co-workers reported the simulation of asymmetric line shape of DB assuming a powder pattern of single center with  $g_{\parallel} = 2.0096$  and  $g_{\perp} = 2.0031$ , and a gaussian broadening of 3.2 G.

As another approach of ESR study of DB in nc-Si:H, our group studied X- and Q-band ESR spectra of various kinds of nanocrystalline silicon [91]. We have prepared unhydrogenated nanocrystalline silicon (nc-Si) [92, 93] and nanocrystalline silicon embedded in  $\text{SiO}_2$  (nc-Si in  $\text{SiO}_2$ ) [94–96] and compared their ESR spectra with that of nc-Si:H. ESR spectra of nc-Si at room temperature shows asymmetric DB signal at  $g = 2.0055$  with peak-to-peak width of 10–11 G. Although the peak width is larger, that  $g$ -value is similar to that in unhydrogenated amorphous silicon (a-Si) prepared by low-pressure Ar sputtering. However, in the Q-band ESR measurement, spectra of nc-Si show larger  $g$ -value ( $g = 2.006$ ) and significantly asymmetric signal compared with that in a-Si. In the case of the nc-Si in  $\text{SiO}_2$ , X-band ESR shows signal of DB at  $g = 2.005$ – $2.006$  with peak-to-peak width of 13 G. In Q-band ESR spectra, the signal of silicon DB has been observed at  $g = 2.006$ . In Figure 6, Q-band ESR spectra of silicon DB signal in nc-Si:H, nc-Si, nc-Si in  $\text{SiO}_2$ , and a-Si are shown. As shown in the figure, spectra of nc-Si:H and nc-Si have a similar shape beside the intensity of sharp signal of carbon contamination observed at  $g = 2.0026$ . We have simulated the broad DB signal in the Q-band ESR spectrum of nc-Si in  $\text{SiO}_2$ , using anisotropic distribution of  $g$ -tensor that  $g_{\perp}$  has larger distribution than  $g_{\parallel}$ , with  $g$ -value of  $g_{\parallel} = 2.0022$  and  $g_{\perp} = 2.0078$ . We suggested the DB structure corresponding to this simulation as distribution in  $C_{3V}$  symmetry.

Another kind of nanocrystalline silicon defect, DB in PS, has also been studied. Bhat and co-workers reported the

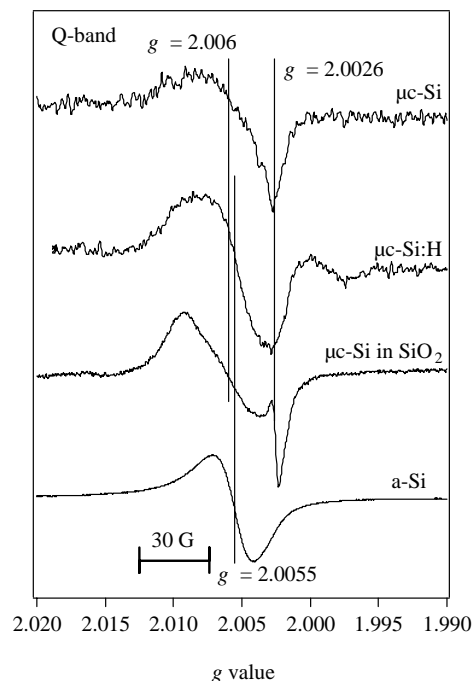


**Figure 6.** Q-band ESR spectra of unhydrogenated nanocrystalline silicon (nc-Si), hydrogenated nanocrystalline silicon (nc-Si:H), and nanocrystalline silicon embedded in  $\text{SiO}_2$  (nc-Si in  $\text{SiO}_2$  and a-Si).

ESR spectra of PS for various angles [97]. They observed the narrow signal of DB at 2.0052. Pokes and co-workers determined the DB density in the PS layer as roughly  $3 \times 10^{16} \text{ cm}^{-3}$  by measurement of ESR [98]. They observed anisotropic ESR spectra in the PS prepared using 0.1- $\Omega$  cm Si wafers. Rong and co-workers reported detail of  $g$ -value dependence on measurement axis and hyperfine by  $^{29}\text{Si}$  and attributed the defect in the PS as  $P_b$ -like centers [99]. Some groups reported the annealing effect of ESR spectra that induces the broadening of spectra by the increase in the strain of the back bonds. Meyer and co-workers reported the effect of rapid oxidation of PS to ESR spectra [100]. They observed two different types of defects after oxidation. One is isotropic and very similar to the DB in a-Si:H; the other is  $P_b$  center-like defects. Two signals show difference in the rotation pattern in the ESR signals. As a similar oxidation, heat treatment effect in air to ESR spectra has also been reported by Laiho et al. [101]. Plasma nitridation effect to ESR spectra of PS has also been reported by Yokomichi and co-workers [102]. They observed increase of  $P_b$  center density and decrease of PL intensity by plasma treatment.

## 7. OTHER DETECTION METHOD OF SPIN RESONANCE

Optically detected magnetic resonance (ODMR) study of nc-Si:H has been reported by Boulitrop and co-workers [103]. In their work, they have monitored the defect-related luminescence bands at 0.75 and 0.85 eV at 5 K. They detected quenching resonance at  $g = 2.0043$  and enhancing resonance at  $g = 1.9997$  and  $g = 2.016$ . The signals at  $g = 2.0043$  and  $g = 1.9997$  are similar to the DB signal and CE



signal observed by conventional ESR spectroscopy. The signal at  $g = 2.016$  has a very large line width of about 100 G.

As mentioned in Section 5, EDMR studies of nc-Si:H have been reported [49, 89]. Lips and co-workers have reported the bandtail states in phosphorus-doped nc-Si:H using ESR and EDMR [104]. They have shown that the CE states originate from both delocalized electrons in the impurity and conduction band as well as from trapped electron in bandtail states at grain boundary. Bronner and co-workers reported EDMR study of nc-Si:H before and after the electron irradiation [105]. Their measurement of EDMR spectra in the photocurrent mode shows an increased DB contribution and change in recombination path with sample irradiation. They find an EDMR signal attribute to recombination of CE in shallow traps and DB defects.

## 8. SUMMARY

In ESR spectra of nc-Si:H, signals of carrier (electrons or holes) and DB defect have been observed. Signals of the CE have been observed in undoped, phosphorus-doped, and nitrogen-doped samples at  $g = 1.997$ – $1.999$ . The CE signal is sharp and has a faster spin-lattice relaxation time than the DB signal. In the case of p-type nc-Si:H, it has been difficult to observe the signal of the conduction holes, because of the very broad line shape. However, the signals of holes can be observed at  $g = 2.01$  with line width of 500 G by pulsed-ESR spectroscopy. In the light-induced ESR spectra, enhancement of CE peak has been observed in undoped and phosphorus-doped samples. The ESR signals of DB defects have been observed at  $g = 2.005$ – $2.006$ . Several authors have attributed the asymmetric shape of the DB signal to the existence of two centers, silicon DB at  $g = 2.0052$  and oxygen-related center at  $g = 2.0043$ .

## GLOSSARY

**Hydrogenated amorphous silicon (a-Si:H)** The amorphous silicon in which some of the dangling bond defects are terminated by hydrogen atoms.

**Conduction electron (CE)** The electrons conduct in the Si.

**Dangling bond defect (DB)** The unpaired electrons of Si atoms that do not participate in the formation of Si-Si covalent bonds.

**Electron spin resonance (ESR)** One of the magnetic resonance techniques. ESR absorption corresponds to the energy difference of spin states in magnetic field.

**Light-induced electron spin resonance (LESR)** ESR under light illumination.

**Hydrogenated nanocrystalline silicon (nc-Si:H)** The material that contains nanocrystalline grain with the size of a few tens to a few hundred nanometers. In the material, some of the dangling bond defects are terminated by hydrogen atoms.

**Pulsed ESR** Electron spin resonance measurement using microwave pulse instead of continuous wave microwave.

## REFERENCES

1. S. Veprek and V. Marecek, *Solid State Electron.* 11, 683 (1968).
2. S. Usui and M. Kikuchi, *J. Non-Cryst. Solids* 34, 1 (1979).
3. A. Matsuda, S. Yamasaku, K. Nakagawa, H. Okushi, K. Tanaka, and S. Iijima, *Jpn. J. Appl. Phys.* 20, L305 (1980).
4. A. Matsuda, *J. Non-Cryst. Solids* 59–60, 767 (1983).
5. S. Oda, J. Noda, and M. Matsumura, *Jpn. J. Appl. Phys.* 29, 1889 (1990).
6. W. E. Spear and P. G. LeComber, *Solid State Commun.* 17, 1193 (1975).
7. G. Willeke, W. E. Spear, D. I. Jones, and P. G. LeComber, *Phil. Mag. B* 46, 177 (1982).
8. Y. Mishima, T. Hamasaki, H. Kurata, M. Hirose, and Y. Osaka, *Jpn. J. Appl. Phys.* 20, L183 (1981).
9. S. Hasegawa, S. Narikawa, and Y. Kurata, *Physica B* 117–118, 914 (1983).
10. H. Keppner, J. Meier, P. Torres, D. Fischer, and A. Shah, *Appl. Phys. A* 69, 196 (1999).
11. K. Yamamoto, M. Yoshima, Y. Tawada, Y. Okamoto, N. Nakajima, and S. Igari, *Appl. Phys. A* 69, 179 (1999).
12. O. Vetterl, F. Finger, R. Carius, P. Hpke, L. Houben, O. Kluth, A. Lambertz, A. Mück, B. Rech, and H. Wanger, *Solar Energy Mater. Solar Cells* 62, 97 (2000).
13. J. Meier, E. Vallat-Sauvain, S. Dubail, U. Knoll, J. Dubail, S. Golay, L. Feitknecht, P. Torres, S. Fay, D. Fische, and A. Shah, *Solar Energy Mater. Solar Cell* 66, 73 (2000).
14. M. Kondo, Y. Nasuno, H. Mase, T. Wada, and A. Matsuda, *J. Non-Cryst. Solids* 299–302, 108 (2002).
15. A. L. Baja Neto, A. Lambertz, R. Carius, and F. Finger, *J. Non-Cryst. Solids* 299–302, 274 (2002).
16. M. Kondo, M. Fukawa, L. Guo, and A. Matsuda, *J. Non-Cryst. Solids*, 266–269, 84 (2000).
17. H. Matsumura and H. Tachibana, *Appl. Phys. Lett.* 47, 833 (1985).
18. A. H. Mahan, J. Carapella, B. P. Nelson, R. C. Crandall, and I. Balberg, *J. Appl. Phys.* 69, 6728 (1991).
19. H. Matsumura, *Jpn. J. Appl. Phys.* 37, 3175 (1998).
20. C. C. Tsai, G. B. Anderson, R. Thompson, and B. Wacker, *J. Non-Cryst. Solids* 114, 151 (1989).
21. N. Shibata, K. Fukuda, H. Ohtoshi, J. Hannna, S. Oda, and I. Shimizu, *Mat. Res. Soc. Symp. Proc.* 95, 225 (1987).
22. Y. H. Yang, M. Katiyar, G. F. Fang, N. Maley, and K. R. Abelson, *Appl. Phys. Lett.* 65, 1789 (1994).
23. M. Luysberg, P. Hapke, R. Carius, and F. Finger, *Phil. Mag. A* 75, 31 (1997).
24. L. Houben, M. Luysberg, P. Hapke, R. Carius, F. Finger, and H. Wagner, *Phil. Mag. A* 77, 1447 (1998).
25. A. M. Portis, A. F. Kip, C. Kitteland, and W. H. Brattain, *Phys. Rev.* 90, 988 (1953).
26. G. Feher and A. F. Kip, *Phys. Rev.* 90, 337 (1955).
27. F. J. Dyson, *Phys. Rev.* 98, 349 (1955).
28. G. Feher and A. E. Gere, *Phys. Rev.* 114, 1247 (1959).
29. H. Kodera, *J. Phys. Soc. Jpn.* 19, 915 (1964).
30. S. Hasegawa, R. Konatani, and T. Shimizu, *J. Appl. Phys.* 10, 1641 (1971).
31. H. Noda, K. Oikawa, and H. Kamada, *Jpn. J. Appl. Phys.* 32, 1515 (1983).
32. S. Hasegawa, T. Kasajima, and T. Shimizu, *J. Appl. Phys.* 50, 7256 (1979).
33. J. C. Knight, D. K. Biegelsen, and I. Solomon, *Solid State Commun.* 22, 133 (1977).
34. S. Hasegawa, T. Kasajima, and T. Shimizu, *Solid State Commun.* 29, 13 (1979).
35. H. Dersch, J. Stuke, and J. Beichler, *Phys. Stat. Sol. B* 105, 265 (1981).
36. R. A. Street, D. K. Biegelsen, and J. C. Knight, *Phys. Rev. B* 24, 969 (1981).

37. S. Hasegawa, S. Narikawa, and Y. Kurata, *Phil. Mag. B* 48, 431 (1983).
38. F. Finger, C. Malten, P. Hapke, R. Carius, R. Flückiger, and H. Wagner, *Phil. Mag. B* 70, 247 (1994).
39. F. Finger, J. Müller, C. Malten, and H. Wagner, *Phil. Mag. B* 77, 805 (1998).
40. J. Müller, F. Finger, R. Carius, and H. Wagner, *Phys. Rev. B* 60, 11666 (1999).
41. C. Malten, J. Müller, and F. Finger, *Phys. Stat. Sol. B* 201, R15 (1997).
42. S. Maekawa and N. Kinoshita, *J. Phys. Soc. Jpn.* 20, 1447 (1965).
43. C. T. Maruyama, W. G. Clark, and J. Sanny, *Phys. Rev. B* 29, 6063 (1984).
44. A. Stesmans and G. De Vos, *Phys. Rev. B* 34, 6499 (1986).
45. J. D. Quirt, *Phys. Rev. B* 7, 3842 (1973).
46. R. Durny, S. Yamasaki, J. Isoya, A. Matsuda, and K. Tanaka, *J. Non-Cryst. Solids* 164–166, 233 (1993).
47. J.-H. Zhou, S. Yamasaki, J. Isoya, K. Ikuta, M. Kondo, A. Matsuda, and K. Tanaka, *Mat. Res. Soc. Symp. Proc.* 452, 821 (1996).
48. K. Lips, P. Kanschhat, S. Brehme, and W. Fuhs, *J. Non-Cryst. Solids* 299–302, 350 (2002).
49. K. Lips, P. Kanschhat, S. Brehme, and W. Fuhs, *Thin Solid Films* 403–404, 47 (2002).
50. S. Brehme, P. Kanschhat, K. Lips, I. Sieber, and W. Fuhs, *Mater. Sci. Eng. B* 69–70, 232 (2000).
51. H. Ue and S. Maekawa, *Phys. Rev. B* 3, 4232 (1971).
52. A. Morimoto, M. Matsumoto, M. Kumeda, and T. Shimizu, *Jpn. J. Appl. Phys.* 29, L1747 (1990).
53. J.-H. Zhou, K. Yamaguchi, Y. Yamamoto, and T. Shimizu, *J. Appl. Phys.* 74, 5086 (1993).
54. T. Ehara, *Thin Solid Films* 310, 322 (1997).
55. T. Ehara, *Appl. Surf. Sci.* 113–114, 126 (1997).
56. T. Ehara, *Thin Solid Films* 379, 292 (2000).
57. T. Ehara, T. Amino, H. Shinomiya, T. Ikoma, K. Akiyama, and S. Tero-Kubota, *Jpn. J. Appl. Phys.* 39, 31 (2000).
58. C. F. Young, E. H. Poindexter, G. J. Gerardi, W. L. Warren, and D. J. Keeble, *Phys. Rev.* 55, 16245 (1997).
59. C. F. Young, E. H. Poindexter, and G. J. Gerardi, *J. Appl. Phys.* 81, 7468 (1997).
60. H. J. von Bardeleben, C. Ortega, A. Grosman, V. Morazzani, J. Siejka, and D. Stievenard, *J. Lumin.* 57, 301 (1993).
61. J. Müller, F. Finger, C. Malten, and H. Wagner, *J. Non-Cryst. Solids* 227–230, 1026 (1998).
62. H. Neubrand, *Phys. Stat. Sol. B* 86, 269 (1978).
63. H. Neubrand, *Phys. Stat. Sol. B* 90, 301 (1978).
64. G. Feher, J. C. Hensel, and E. A. Gere, *Phys. Rev.* 5, 309 (1960).
65. P. Kanschhat, H. Mell, K. Lips, and W. Fuhs, *Mat. Res. Symp. Proc.* 609, A27.3.1 (2000).
66. R. A. Street and D. K. Biegelsen, *Solid State Commun.* 33, 1159 (1980).
67. R. A. Street and D. K. Biegelsen, *J. Non-Cryst. Solids* 35–36, 651 (1980).
68. S. Yamasaki, H. Okushi, A. Matsuda, and K. Tanaka, *Phys. Rev. Lett.* 65, 756 (1990).
69. T. Umeda, S. Yamasaki, J. Isoya, A. Matsuda, and K. Tanaka, *Phys. Rev. Lett.* 77, 4600 (1996).
70. M. M. de Lima, Jr., P. C. Taylor, S. Morrison, A. LeGeune, and F. C. Marques, 65, 235324 (2002).
71. B. Yan, N. A. Shultz, A. Z. Efros, and P. C. Taylor, *Phys. Rev. Lett.* 84, 4180 (2000).
72. M. Kondo, T. Nishimiya, K. Saito, and A. Matsuda, *J. Non-Cryst. Solids* 227–230, 1031 (1998).
73. P. Kanschhat, K. Lips, and W. Fuhs, *J. Non-Cryst. Solids* 266–269, 524 (2000).
74. K. Lips, C. Lerner, and W. Fuhs, *J. Non-Cryst. Solids* 198–200, 267 (1995).
75. H. Dersch, L. Schweitzer, and J. Stuke, *Phys. Rev. B* 28, 4678 (1983).
76. Y. Nishi, *Jpn. J. Appl. Phys.* 10, 52 (1971).
77. K. L. Brower, *Appl. Phys. Lett.* 43, 1111 (1986).
78. M. H. Brodsky and R. S. Title, *Phys. Rev. Lett.* 23, 581 (1969).
79. N. Ishii, M. Kumeda, and T. Shimizu, *Jpn. J. Appl. Phys.* 20, L673 (1981).
80. N. Ishii and T. Shimizu, *J. Non-Cryst. Solids* 227–230, 358 (1998).
81. V. A. Grazhults and Yu. A. Osip'yam, *Sov. Phys. JETP*, 33, 623 (1971).
82. E. Weber and H. Alexander, *J. Phys.* 40, C6-101 (1979).
83. S. Hasegawa, S. Watanabe, T. Inokuma, and Y. Kurata, *J. Appl. Phys.* 77, 1939 (1995).
84. S. Hasegawa, E. Fujimoto T. Inokuma, and Y. Kurata, *J. Appl. Phys.* 77, 357 (1995).
85. H. Shirai, D. Das, J. Hannna, and I. Shimizu, *Appl. Phys. Lett.* 29, 1096 (1991).
86. S. Veprek, Z. Iqbal, R. O. Kühne, P. Capezzuto, F.-A. Sarottand, and J. K. Gimzewski, *J. Phys. C: Solid State Phys.* 16, 6242 (1983).
87. S. Hasegawa, K. Kishi, and Y. Kurata, *Phil. Mag. B* 52, 199 (1985).
88. E. Holzenkämpfer, F.-W. Richter, J. Stuke, and U. Voget-Grote, *J. Non-Cryst. Solids* 32, 327 (1979).
89. K. Lips, P. Kanschhat, D. Will, C. Lerner, and W. Fuhs, *J. Non-Cryst. Solids* 227–330, 1021 (1998).
90. M. Kondo, S. Yamasaki, and A. Matsuda, *J. Non-Cryst. Solids* 266–269, 544 (2000).
91. T. Ehara, T. Ikoma, and S. Tero-Kubota, *J. Non-Cryst. Solids* 266–269, 540 (2000).
92. S. Okada, T. Iwaki, K. Yamamoto, H. Kasahara, and K. Abe, *Solid State Commun.* 48, 809 (1984).
93. T. Ehara, T. Ikoma, K. Akiyama, and S. Tero-Kubota, *J. Appl. Phys.* 88, 1698 (2000).
94. Y. Osaka, K. Tsunetomo, F. Toyomura, H. Myoren, and K. Kohno, *Jpn. J. Appl. Phys.* 31, L365 (1992).
95. S. Hayashi, T. Nagareda, Y. Kanzawa, and K. Yamamoto, *Jpn. J. Appl. Phys.* 32, 3840 (1993).
96. K. Toshikiyo, M. Tokunaga, S. Takeoka, M. Fujii, and S. Hayashi, *J. Appl. Phys.* 89, 4917 (2001).
97. S. V. Bhat, K. Jayaram, D. Victor, S. Muthu, and A. K. Sood, *Appl. Phys. Lett.* 60, 2116 (1992).
98. S. M. Pokes, W. E. Carlos, and V. Bermudez, *Appl. Phys. Lett.* 61, 1447 (1992).
99. F. C. Rong, J. F. Harvey, E. H. Poindexter, and G. J. Gerardi, *Appl. Phys. Lett.* 63, 920 (1993).
100. B. K. Meyer, V. Petrova-Koch, T. Muschik, H. Linke, P. Omling, and V. Lehmann, *Appl. Phys. Lett.* 63, 1930 (1993).
101. R. Laiho, L. S. Valsenko, M. M. Afanasiev, and M. P. Vlasenko, *J. Appl. Phys.* 76, 4290 (1994).
102. H. Yokomichi, A. Masuda, Y. Yonezawa, and T. Shimizu, 281–282, 568 (1996).
103. F. Boulitrop and A. Chenevas-Paule, *J. Phys. (Paris)* 43, C1 (1982).
104. K. Lips, P. Kanschhat, S. Brehme, and W. Fuhs, 299–302, 350 (2002).
105. W. Bronner and M. Mehring, *Phys. Rev.* 65, 165212 (2002).



# Nanocrystalline TiO<sub>2</sub> for Photocatalysis

Hubert Gnaser, Bernd Huber, Christiane Ziegler

*Universität Kaiserslautern, Kaiserslautern, Germany*

## CONTENTS

1. Introduction
  2. Electronic and Charge-Transfer Processes in Photocatalysis
  3. Preparation of Nanostructured Materials and Thin Films
  4. Structural Properties of Nanocrystalline TiO<sub>2</sub> Films
  5. Electrical Properties of Nanocrystalline TiO<sub>2</sub> Films
  6. Photocatalytic Properties of Nanocrystalline TiO<sub>2</sub>
  7. Photocatalytic Applications of Nanocrystalline TiO<sub>2</sub>
- Glossary  
References

## 1. INTRODUCTION

The development of novel materials and the assessment of their potential application constitutes a major fraction of today's scientific research efforts. In fact, there exist various major governmental research and development programs related to nanostructured materials. Furthermore, it is estimated that nanotechnology has grown into a multi-billion dollar industry and may become the most dominant single technology of the twenty-first century. To allow for this fact, this encyclopedia [1] encompasses a series of contributions devoted to a very prominent field of current materials research activities, namely, nanoscience and nanotechnology. The importance of these developments is reflected also in a number of recent books and articles reviewing this rapidly evolving field [2–10].

This article focuses on a specific class of such novel nano-scaled materials, nanocrystalline TiO<sub>2</sub>, and its photocatalytic properties. The title of this article encompasses three main terms (“(photo)catalysis,” “nanocrystalline,” and “TiO<sub>2</sub>”) which, individually, stand for very important areas of scientific research and of, perhaps even more important, technological applications. Their synergistic combination, as

indicated by the present theme, has stimulated great hopes in accomplishing thereby achievements with paramount benefits for human beings and the global environment. To outline the present state of that quest is the major goal of this article.

“Catalysis” is probably the most familiar of the three terms mentioned. A catalyst is incorporated in essentially everybody's automobile, with the goal of reducing or even eliminating the engine's toxic gaseous components by converting them into less harmful (albeit not necessarily benign) substances. As is the case in all catalytic reactions, the catalyst itself is not part of the reaction, but is expected to enhance its rate, that is, the velocity of the transformation from the original components (the “educts” in the chemist's terminology) into the final ones (the “products”). Hence, a catalyst is an entity that accelerates a chemical reaction without being consumed itself in the process. Without catalysts, various chemical reactions of great importance would proceed too slowly [11]. The economic significance of catalysis is enormous. In the U.S. alone, the annual value of products manufactured with the use of catalysts is roughly in the vicinity of one trillion dollars [12]. Indeed, more than 80% of the industrial chemical processes in use nowadays rely on one or more catalytic reactions [13]. A number of those, including oil refining, petrochemical processing, and the manufacturing of commodity chemicals (olefins, methanol, ethylene glycol, etc.), are already well established. But many others, as will be seen in this contribution, represent challenges requiring the development of entirely new approaches. But apart from their industrial importance, catalytic phenomena effect virtually all aspects of our lives. They are crucial in many processes occurring in living things, where enzymes are the catalysts. They are important in the processing of foods and the production of medicines. The reader may have noticed that we have as yet refrained from specifying the meaning of photocatalysis; which will be one of the major topics of this article. This term refers to a catalytic process that is triggered by illuminating the system by visible light or ultraviolet irradiation. Ideally, that light flux would be the sun's radiance.

Next we shall consider the meaning of “nanocrystalline.” First, it is noted that in today's science world rather inflationary used, the prefix “nano” refers to a fraction of

one part in one billion (10<sup>9</sup>) and, hence, its correct usage would require it being connected to some kind of unit (e.g., of length, time, energy, mass, etc.). In the present context (and in that of “nanotechnology”), “nano” most often relates to the dimension, that is, the size of an object. Therefore, nanocrystalline in the ensuing discussions will designate particles (of crystalline structure and, primarily, with the chemical composition of titanium dioxide) whose typical sizes are in the range of a few to several nanometers (nm), that is, of the order of the one billionth part of one meter. Obviously, these are extremely tiny objects and can be “seen” and studied only with the help of sophisticated analytical instruments like an electron microscope.

At first glance, it may appear that such tiny particles are a rather modern contrivance, but this is probably a premature conclusion. In fact, it is quite firmly established that nm-sized particles (mostly very refractory ones like corundum, diamond, or silicon carbide) are ubiquitous in the universe [14] and that they were already present at the time and the location of the formation of the solar system. This “stardust” originated from stellar outflows and supernova ejecta, which may have occurred eons before the gas and dust condensed into what is now the sun, the earth, and the planets. In fact, this dust has intrigued astronomers since the days of William Herschel who noted, in the 1780’s, the existence of small regions in the sky where there appeared to be a complete absence of stars [15]. These regions are most easily seen against the rich star-fields of the Milky Way. Evidence of the presolar origin of these nanocrystalline particles comes primarily from their isotopic abundance pattern [16], which deviates typically to such an extent from any other known matter that a terrestrial or solar origin is virtually impossible. (Most of these particles that have been investigated were extracted from primitive meteorites in which they were incorporated during the formation stage of the solar system; these did not experience any later modification and, hence, preserved the presolar dust particles unaltered [17].)

Only now, some billions of years later, mankind has initiated the manufacture and application of such nanocrystalline materials. Nanostructured materials with crystal sizes in the range of 5–50 nm of a variety of materials, including metals and ceramics, have been artificially synthesized by many different techniques in the past couple of years [2, 3, 5–7]. Such new ultrafine-grained materials have properties that are often significantly different and greatly enhanced as compared to coarser-grained or bulk substances. These favorable changes in properties result generally from their small grain sizes, the large percentage of atoms in grain boundaries and at surfaces, the large surface-to-bulk ratio, and the interaction between individual crystallites. Since these features can be tailored to a considerable extent, during synthesis and processing, such nanophase materials are thought to have great technological potential even beyond their current applications.

Let us finally turn to a brief discussion of the third term, “TiO<sub>2</sub>” (i.e., titanium dioxide). TiO<sub>2</sub> has three different crystal structures [18]: rutile, anatase, and brookite; only the former two of them are commonly used in photocatalysis. Like for many other metal oxides (also for titanium oxide) have the respective structural, optical, and electronic properties

been elucidated through several decades of intense scientific research (for a review see, e.g., [19]); some of them will be referred to in the course of the present overview. The feature probably most important in the present context is the fact that TiO<sub>2</sub> is a semiconductor with a bandgap of ~ 3.2 eV. On the other hand, TiO<sub>2</sub>, in its nanocrystalline form, constitutes an enormously important commercial product. In fact, the world production of titanium dioxide white pigments amounts to some 4.5 million tons per annum and the global consumption may be considered a distinct economic indicator. White pigments of TiO<sub>2</sub> have average particle sizes of around 200–300 nm, optimized for the scatter of white light, resulting, thereby, in a hiding power. Reducing the crystallite size (to ≤ 100 nm), the reflectance of visible light (vis) decreases and the material becomes more transparent; it is widely employed, for example, in paints, plastics, paper, or pharmaceuticals. Nanocrystalline TiO<sub>2</sub> exhibits, in addition, a pronounced absorption of ultraviolet (UV) radiation. Because of this high UV absorption and the concurrent high transparency for visible light, TiO<sub>2</sub> particles with a size of <100 nm have found widespread use in such diverse areas as sun cosmetics, packaging materials, or wood protection coatings. Hence, although perhaps not generally realized, TiO<sub>2</sub> is ubiquitous in our everyday life. Apart from this well-established range of usage, an increasing number of catalytic applications of nanocrystalline TiO<sub>2</sub> have emerged in recent years.

At this point, it appears appropriate to return to a more general view of the present topic. Nanostructured materials have generally the potential [3] for incorporating and taking advantage of a number of size-related effects in condensed matter ranging from electronic effects (so-called “quantum size effects”) caused by spatial confinement of delocalized valence electrons and altered cooperative (“many-body”) atom phenomena, like lattice vibrations or melting, to the suppression of such lattice-defect mechanisms as dislocation generation and migration in confined grain sizes. The possibilities to assemble size-selected atom clusters into new materials with unique or improved properties will likely create a revolution in our ability to engineer materials with controlled optical, electronic, magnetic, mechanical, and chemical properties for many pending future technological applications.

Among those nanocrystalline materials, semiconductors appear to play a pivotal role in such distinct fields as [20]:

- (i) heterogeneous photocatalysis;
- (ii) photoelectrochemistry, including electrochemical photovoltaic cells;
- (iii) photochemistry in zeolites, intercalated materials, thin films, and membranes (like self-assembled structures);
- (iv) supramolecular photochemistry.

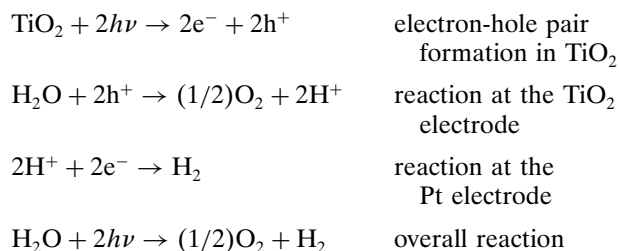
This diversity is thought to be largely due to the fact that heterogeneously dispersed semiconductor surfaces provide both a fixed environment to influence the chemical reactivity of a wide range of adsorbates and, in addition, a means to initiate light-induced redox reactivity in these weakly associated molecules [21]. Upon photoexcitation of semiconductor nanoparticles, either in solutions or fixed to a suitable substrate, simultaneous oxidation and reduction reactions may

occur; molecular oxygen is often assumed to serve as the oxidizing agent. Such semiconductor-mediated redox reactions are commonly grouped under the rubric of heterogeneous photocatalysis [21].

In a heterogeneous photocatalytic system, photo-induced molecular reactions take place at the surface of the catalyst. Depending on where the initial excitation occurs, photocatalysis can be generally divided into two classes of processes [22]: In the case that the initial photoexcitation occurs in the adsorbate molecule, which then interacts with the ground state catalyst substrate, the process is referred to as a catalyzed photoreaction. On the other hand, when the initial excitation takes place in the catalyst substrate and the excited catalyst transfers an electron or energy into a ground state molecule, this process is referred to as a sensitized photoreaction [22]. Apparently, a considerable degree of synergism may be crucial when, for example, a transition metal oxide photocatalysts is combined with supramolecular spectral sensitizing ligand complexes used to harvest light and vectorially transfer photo-generated electrons and holes along selected energetic pathways.

In 1972, Fujishima and Honda reported [23] the photocatalytic splitting (i.e., the simultaneous oxidizing and reducing) of water upon illumination of a TiO<sub>2</sub> single-crystal electrode; in analogy to natural photosynthesis, they demonstrated the photoelectrolysis of water making use of a photoexcited semiconductor in what was essentially a photochemical battery. In that system, an *n*-type TiO<sub>2</sub> semiconductor electrode, which was connected through an electrical load to a platinum counter electrode, was exposed to near-UV light (cf. Fig. 1). When the surface of the TiO<sub>2</sub> electrode was illuminated with light of wavelength shorter than ~415 nm, photocurrent was observed to flow [23, 24]. Furthermore, oxygen evolution (i.e., an oxidation reaction) on the TiO<sub>2</sub> and hydrogen evolution (a reduction) on the Pt electrode was observed. The photoexcitation of TiO<sub>2</sub> injects electrons from its valence band into its conduction band; the electrons flow through the external circuit to the Pt cathode where water molecules are reduced to hydrogen gas and the holes remain in the TiO<sub>2</sub> anode where water molecules are oxidized to oxygen. These observations indicate that water can be decomposed by means of UV-VIS light according to the

following scheme



It appears to be generally accepted that this discovery boosted extensive research efforts in the era of heterogeneous photocatalysis [21, 25–27]. These studies, often carried out in an interdisciplinary fashion with the participation of physicists, chemists, and chemical engineers, focused on issues that are of great relevance both economically as well as ecologically like energy renewal and storage [28–30], the decomposition of organic compounds in polluted air and wastewaters [31–33], chemical energy generation [34, 35], and photovoltaic devices [36, 37]. Most of these either already proven or envisaged applications are intimately linked to the extraordinary properties of nanocrystalline TiO<sub>2</sub>. In fact, nanocrystalline metal-oxide semiconductors such as TiO<sub>2</sub> have been applied successfully in modern technologies including solar energy conversion, gas sensors, catalysis, and photocatalysis [38–42].

Following the first examination in 1977, using TiO<sub>2</sub> to decompose cyanide in water [43, 44], a great deal of effort has been devoted in recent years to developing heterogeneous photocatalysts with high photocatalytic activities for their applications in solving environmental cleanup and pollution remediation problems [31, 32, 45, 46]. Photocatalytic reactions on TiO<sub>2</sub> surfaces are very important in such environmental processes, as the oxidation of organic materials and the reduction of heavy metal ions in industrial waste waters. Apart from the utilization for water and air purification, TiO<sub>2</sub> photocatalysis has been shown useful for the destruction of microorganisms such as bacteria [47] and viruses [48], for the inactivation of cancer cells [46, 49], the clean-up of oil spills [50, 51], and other applications [45]; a more detailed account will be given later in this article.

As mentioned, TiO<sub>2</sub> is a semiconductor with a bandgap of 3.2 eV; when excited by light of energy equal to or exceeding that value, electrons are promoted from the valence band to the conduction band leaving positive holes in the valence band. These electrons and holes are capable of, respectively, reducing and oxidizing compounds at the TiO<sub>2</sub> surface. If the electrons and holes do not recombine (and produce heat), they can follow various reaction pathways; it is commonly accepted that the hole is quickly converted to the hydroxyl radical ( $\cdot\text{OH}$ ) upon oxidation of surface-adsorbed water and that the hydroxyl radical is the major reactant responsible for the oxidation of organic compounds. Typical reductive and oxidative reactions could be

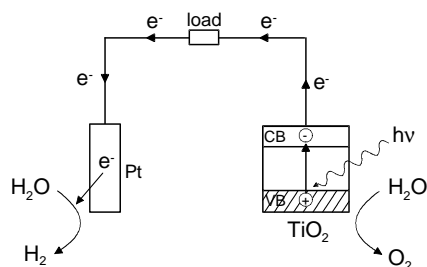
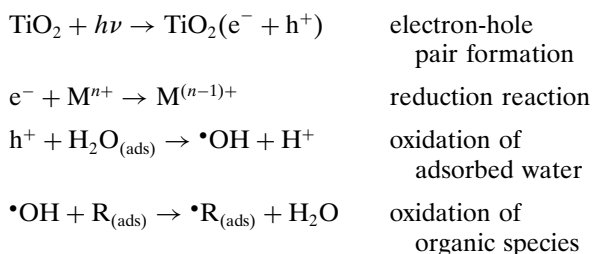


**Figure 1.** Schematic arrangement for the photosplitting of water in an electrochemical cell (in the actual setup, both electrodes are immersed in an aqueous solution and the chambers are separated by an ionically conducting porous material). When the TiO<sub>2</sub> photoanode is irradiated with light, O<sub>2</sub> evolves from it, whereas H<sub>2</sub> evolves from the Pt counter-electrode, while electrons will flow through an external load.



the following [25, 52–54]



where  $M^{n+}$  is the oxidized compound and  $\text{R}_{(\text{ads})}$  the adsorbed organic species. Because the production of the hydroxyl radical is considered the decisive step, the determination and optimization of the corresponding quantum yield in illuminated TiO<sub>2</sub> is an important task [55, 56].

According to those concepts, TiO<sub>2</sub> nanoparticles are expected to show a unique surface chemistry due to their larger surface area [57]. The origin of the distinct photocatalytic activities exhibited by nanoparticles of TiO<sub>2</sub> is crucial in understanding the reaction mechanisms, for example, if they are purely due to the increased surface area or if they have to be addressed to the presence of distorted sites on the surface or to the whole lattice of the particles. In order to commercialize these treatment techniques, it is of great importance to improve the preparative methods of titania, because the photocatalytic activity and phase transition behavior of TiO<sub>2</sub> are significantly influenced by the preparative conditions [58–63]. As previously mentioned, these catalytic processes constitute a major issue of this work and will be outlined in the following sections.

The photocatalytic activity of TiO<sub>2</sub> is very useful not only in environmental purification by decomposition of organic substances, but also in the materials industry such as mirrors and glasses due to its self-cleaning [64] and antifogging effects. The latter has been attributed to the photo-induced hydrophilic nature of the surface [65, 66]. A further enhancement of the photocatalytic activity could be effected by means of composite TiO<sub>2</sub> materials; examples would be metal doping, mixing with insulating substances like SiO<sub>2</sub> or Al<sub>2</sub>O<sub>3</sub> [67], and monolayer coverage by SiO<sub>2</sub> [68].

Another prominent future application of nanocrystalline semiconductors is thought [69–71] to lie in photovoltaics, that is, the conversion of sunlight into electrical power. The limited reserves of fossil fuels and the increasing concern of global warming due to the greenhouse effect caused by the combustion of those fuels has triggered, in the last decades, widespread efforts into the development of photovoltaic devices. With an energy supply from the sun to the earth of  $3 \times 10^{24}$  Joule per year (about 10,000 times the global annual energy consumption), this enterprise appears all but unreasonable. In such solar cells, photon incident on a semiconductor can create electron-hole pairs, basically a result of the photoelectric effect, discovered by Becquerel already in 1839 [72]. At a junction between two different materials, this may establish an electrical potential difference across this interface. Until now, the material of choice for manufacturing such junctions has been (doped) silicon (crystalline or amorphous), with compound semiconductors also being considered more recently. While this traditional

approach clearly has room for further improvements, it may ultimately face limitations in terms of cost efficiency (manufacturing costs per unit of energy produced). Novel materials and fabrication schemes are therefore explored. A promising approach consists of electrochemical photovoltaic cells utilizing nanoporous semiconducting electrodes fabricated by lightly sintering nanosized TiO<sub>2</sub> particulates, followed by spectral sensitization with an appropriate dye.

Metal oxide particles with diameters of some 10 nm can be prepared as paste and spread out over a surface of fluorine-doped SnO<sub>2</sub> conducting glass to form a three-dimensional network of interconnected nanoparticles. These nanostructured metal oxide layers, and in particular those constructed from anatase titanium dioxide (TiO<sub>2</sub>), have aroused great interest because of their unprecedented properties as electrodes. They find application in dye-sensitized solar cells, which nowadays show light-to-electricity conversion efficiencies of 10% [69, 73–77]. The nature of electron migration in these electrodes has been debated in past years as the experimental results and their interpretation does not converge to a generally accepted model. Instead, the exact role of electron trapping and the concomitant screening of the electric field remain unclear. It is reported that soon after electrons are injected into the conduction band of TiO<sub>2</sub> a large fraction of them get trapped in surface states. Migration of these electrons must then proceed with a hopping-type process in which the electrons remain most of the time in localized states [78–83]. On the other hand, it is also reported that the injection of electrons into the conduction band shows the so-called “free-electron” absorption, which extends over a wide spectral range from the visible to the infrared [84–88]. This suggests that not all injected electrons become trapped but that a substantial fraction of them remain in the conduction band.

This article is organized in the following way: Section 2 outlines the electronic and charge-transfer processes as relevant for photocatalysis, with a special emphasis towards nanocrystalline TiO<sub>2</sub>. Since in photocatalysis and related applications the respective nanostructured materials are employed either in colloidal solutions or attached to a suitable support (e.g., as electrodes or thin films), both of these preparation techniques are discussed (Section 3). Furthermore, various approaches for surface and thin-film modification are described, as well as novel deposition methods and structures. The structural and electronic properties of nanocrystalline TiO<sub>2</sub> films are examined in Sections 4 and 5, respectively. The photocatalytic properties of nanocrystalline TiO<sub>2</sub> constitute the central theme of Section 6, highlighting the dependence of the photocatalytic activity on different parameters like film structure and phase, surface morphology, electronic properties, and the effects induced by various surface modifications. Representative examples of photocatalytic applications utilizing nanocrystalline TiO<sub>2</sub> materials are presented in Section 7. Finally, an extensive set of references is provided that should be useful for further study: although the number is substantial, no attempt was made, however, to be comprehensive; any such attempt might be bound to fail due to the rapidity with which this field is evolving.

## 2. ELECTRONIC AND CHARGE-TRANSFER PROCESSES IN PHOTOCATALYSIS

### 2.1. Electronic Excitations and Charge-Carrier Trapping

A photocatalytic process is initiated by the absorption of photons by a molecule or the substrate to produce highly reactive electronically excited states. The efficiency is controlled by the system's light absorption properties. Three fundamental steps are of relevance: (1) the electronic excitation of a molecule upon photon absorption, (2) the band-gap excitation of the semiconductor substrate, and (3) the interfacial electron transfer. Since a detailed account of these processes has been given in a lucid treatise by Linsebigler et al. [22], we shall briefly summarize here only the more important points, referring thereby partly to that work. The probability of an electronic transition can be calculated from quantum mechanical perturbation theory and is proportional to the square of the amplitude of the radiation field and the square of the transition dipole moment [89, 90]. The latter may be computed via the molecular wave function which, in turn, depends on the product of the electronic spatial wave function, the electronic spin wave function, and the nuclear wave function. Further arguments [89] lead to some general selection rules in terms of which electronic transitions are allowed and which might be forbidden. Typically, the excitation of a weak transition will not effectively induce a photochemical reaction, because few of the incident photons will be absorbed (low cross-section); however, an overall high reaction rate may still be possible in the case of a high quantum yield, that is, if the probability of product molecule formation per absorbed photon is high. The photochemical efficiency will also be determined by which deexcitation channels are dominant. In particular, the pertinent lifetimes of the involved processes are to be considered. Whereas the absorption of a photon occurs very rapidly on the order of  $10^{-15}$  s, deexcitation events are much slower, favoring the decay channel which minimizes the lifetime of the excited state.

The initial process for heterogeneous photocatalysis of organic and inorganic compounds by semiconductors is the generation of electron-hole pairs in the semiconductor particles. Once excitation across the bandgap has occurred, the lifetime is sufficient (in the nanosecond regime [91]) for the created electron-hole pair to undergo charge transfer to adsorbed species on the semiconductor surface from solution or gas phase. Figure 2 exemplifies these processes. The enlarged section shows the excitation of an electron from the valence band to the conduction band initiated by light absorption with energy equal or greater than the bandgap of the semiconductor. The figure also illustrates several deexcitation pathways for the electrons and holes. The electron transfer to adsorbed species or to the solvent results from migration of electrons or holes to the surface. At the surface, the semiconductor can donate electrons to reduce an electron acceptor (often oxygen in an aerated solution), corresponding to pathway *c* in Figure 2; conversely, a hole can migrate to the surface where an electron from a donor species can combine with the surface hole

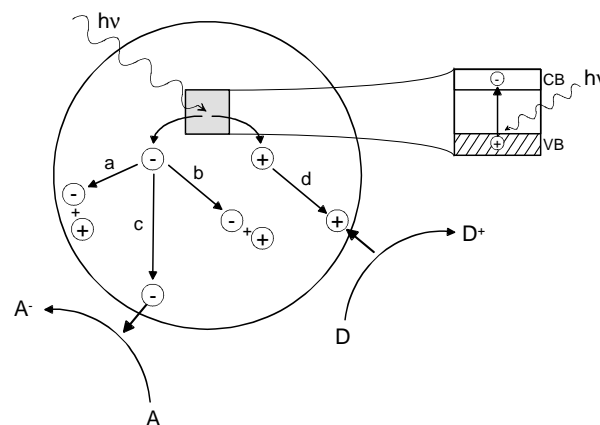


**Figure 2.** Schematic illustration of the photoexcitation in a semiconductor particle followed by deexcitation events. CB and VB designate the conduction and valence band, respectively. For further details see text.

oxidizing the donor (pathway *d*). Competing with charge transfer to adsorbed species is electron and hole recombination, occurring either in the volume (pathway *b*) or on the surface of the semiconductor (pathway *a*); in both cases heat will be released. Naturally, electron and hole recombination is detrimental to the efficiency of a semiconductor photocatalyst. Modifications to semiconductor surfaces, such as metal addition, dopants, or combination with materials, can be beneficial in decreasing the recombination and concurrently increasing the quantum yield of the process.

An efficient means to retard the recombination of photoexcited electron-hole pairs may proceed via the trapping of charge carriers. The occurrence of surface and bulk irregularities resulting from the preparation process is associated with surface electron states; these may serve as charge carrier traps and can suppress the recombination of electrons and holes. The charge carriers trapped in such states are localized to a specific site on the surface or in the bulk; their population is dependent on the energy difference between the trap and the bottom of the conduction band. Experimental observations of such trapped states in TiO<sub>2</sub> will be reported later.

On the basis of laser flash photolysis measurements [45, 92], the characteristic times for the individual steps occurring during heterogeneous photocatalysis on TiO<sub>2</sub> have been derived. Whereas the primary process of charge-carrier generation is extremely fast ( $\sim$ fs), charge-carrier recombination may occur on time scales of 10–100 ns. Charge-carrier trapping can be very fast (100 ps) for the (reversible) trapping of a conduction-band electron in a shallow trap, but moderately fast ( $\sim$ 10 ns) for a deep trap or for the surface trapping of a valence-band hole, resulting in a surface-bound hydroxyl radical. Finally, interfacial charge transfer can be slow ( $\sim$ 100 ns) for the oxidation of an electron donor or very slow ( $\sim$ ms) for the reduction of an electron acceptor. In general, the valence-band holes are powerful oxidants (+1.0 to +3.5 V versus NHE depending on the type of semiconductor and pH), while the conduction-band electrons are good reductants (+0.5 to  $-1.5$  V vs NHE) [93]; most organic photodegradation reactions utilize the oxidizing power of these photo-generated holes.

## 2.2. Band-Edge Position and Band Bending

The ability of a semiconductor to undergo photo-induced electron transfer to adsorbed species on its surface is governed by the band energy position of the semiconductor and the redox potentials of the adsorbate. The relevant potential of the acceptor must be below (more positive than) the conduction band potential of the semiconductor. By contrast, the potential of the donor needs to be above (more negative than) the valence-band position of the semiconductor in order to donate an electron to the vacant hole. The band-edge positions of several semiconductors are depicted in Figure 3; the internal energy scale is given both with respect to the vacuum level (left scale) and for comparison to normal hydrogen electrode (NHE) in a solution of an aqueous electrolyte at pH = 1.

When a semiconductor is brought into contact with another phase (e.g., liquid, gas, or metal), the transfer of mobile charges across this junction occurs until electronic equilibrium is reached. This redistribution of charges involves the formation of a space-charge layer, that is, the charge distribution on each side of the interface differs from the bulk material (cf. Fig. 4). Depending on whether the electrons accumulate or deplete at the semiconductor side, an accumulation or depletion layer is formed, causing concurrently a shift in the electrostatic potential and a downward (or upward) bending of the bands in the semiconductor. The depletion of electrons may reach such an extent that their concentration at the surface decreases below the intrinsic level. As a consequence, the Fermi level is closer to the valence than to the conduction band; this situation is called an inversion layer, as the semiconductor is *p*-type at the surface and *n*-type in the bulk. These features are well documented [94] and will not be further discussed here. Of some interest in the present context is the situation encountered

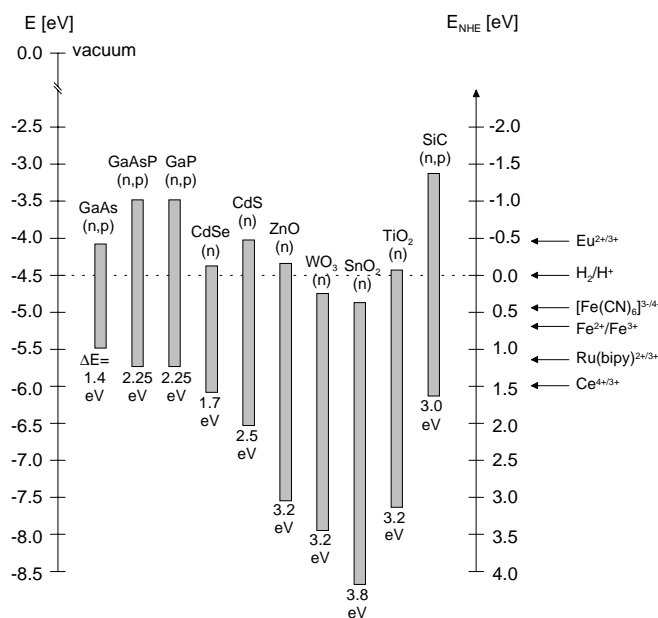


**Figure 3.** Bandgap energies of various semiconductors in an aqueous electrolyte at pH = 1.

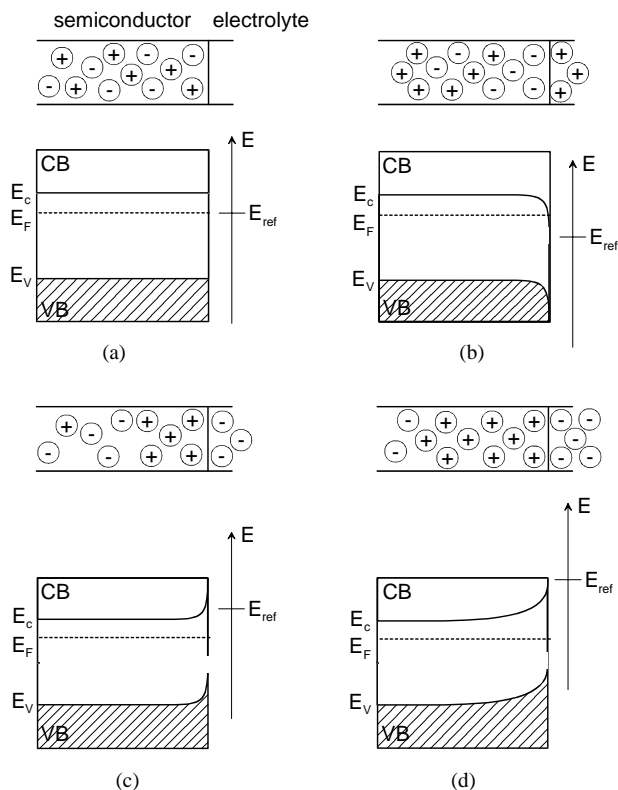


**Figure 4.** Space-charge layer of an *n*-type semiconductor in contact with another phase (e.g., an electrolyte or gas): (a) flat band situation, (b) accumulation layer, (c) depletion layer, and (d) inversion layer.

when an *n*-type semiconductor like TiO<sub>2</sub> is in contact with an electrolyte as in a photoelectrochemical cell [71]; such devices are thought to have great potential both in photovoltaics for producing electric current and as fuel cells for the generation of hydrogen via photo-cleavage of water. Because of these potential applications, the characteristics of the semiconductor-electrolyte interface have been investigated in great details [93, 95, 96].

In particular, the potential distribution within a spherical semiconductor particle could be derived [97] using a linearized Poisson–Boltzmann equation. As discussed in [69], two limiting cases are of special importance for light-induced electron transfer in semiconductor dispersions. For large particles, the total potential drop within the particle is

$$\Delta\Phi = \frac{kT}{2e} \left( \frac{w}{L_D} \right)^2 \quad (1)$$

where  $w$  is the width of the space charge layer and  $L_D = (\epsilon_0 \epsilon kT / e^2 N_d)^{0.5}$  is the Debye screening length [94], which depends on the dielectric constant,  $\epsilon$ , of the material and on the number density of ionized dopants,  $N_d$ . This potential variation is identical with that of a planar Schottky depletion layer [98]. For very small semiconductor particles (with radius  $R$ ) the potential drop within the particle becomes

$$\Delta\Phi = \frac{kT}{6e} \left( \frac{R}{L_D} \right)^2 \quad (2)$$

From the latter equation, it is found that the electrical field in nano-sized semiconductors will usually be small and that high dopant levels are required to produce a significant potential difference between the center and the surface. For example [69], in order to obtain a 50 meV potential drop in a nanocrystalline TiO<sub>2</sub> particle with  $R = 6$  nm, a concentration of  $5 \times 10^{19} \text{ cm}^{-3}$  of ionized donor impurities is necessary. Undoped TiO<sub>2</sub> nanocrystallites have a much lower carrier concentration and the band bending within the particles is therefore negligibly small.

### 2.3. Photo-Induced Charge-Transfer Processes on the Catalyst Surface

The principle of electron and hole transfer at the photoexcited semiconductor particle has already been alluded to previously in Fig. 2. Both free and trapped charge carriers participate in these interfacial redox reactions. Due to the quantization effects, by decreasing the particle's size, it is possible to shift the conduction band to more negative potentials and the valence band to more positive values. It was concluded [99] that the shift of the bandgap is proportional to  $1/R^2$ ,  $R$  being the particle size. Therefore, redox processes that cannot occur in bulk materials can be facilitated in quantized semiconductor particles. Figure 5 shows schematically such possible transfer reactions for an adsorbate at the surface of a semiconductor. When there are accessible energy levels in the substrate, an electron may be transferred from the donor (D) into a substrate level and then into the acceptor orbital as shown in Figure 5(a). This scheme operates in the photosensitization of semiconductor particles by dye molecules. An electron is injected from the excited state dye molecule into the semiconductor, which then reduces another adsorbate particle. Early experimental confirmation [100, 101] of these processes used the reduction of methyl viologen in colloidal semiconductor systems and the water splitting process. Later, such reductive processes have been investigated for many different systems (see, e.g., [102]); some illustrative examples will be presented in Section 6.

For an initial excitation on the semiconductor substrate (Fig. 5(b)), a positively charged hole is created at the band-edge of the valence band. An electron is transferred into

the empty acceptor orbital and, simultaneously, an electron is donated from the filled donor level to recombine with the original hole. This is a very general process for wide bandgap oxide semiconductors like TiO<sub>2</sub> and others. For example, the oxidation of many organic substances in colloidal suspensions has been investigated [102]. The energetics of the semiconductor valence band and the oxidation potential of the redox couple influence this photocatalytic oxidation. For example, the enhancement in the efficiency of halide oxidation at TiO<sub>2</sub> follows the sequence  $\text{Cl}^- < \text{Br}^- < \text{I}^-$ , correlating with the decrease in the oxidation potential. Again, some recent examples will be presented in Section 6.

The kinetic analysis [103] of electron transfer in colloidal semiconductor systems is often complex. Apart from the energetics of the conduction band of the semiconductor and the redox potential of the acceptor, factors such as the surface charges of the colloids, adsorption of the substrates, participation of surface states, and competition with charge recombination influence the rate of charge transfer at the semiconductor interface [102]. This fact is evident from the widely differing rates of experimentally observed charge transfer rates, with time scales ranging from picoseconds to milliseconds for different experimental conditions and various semiconductor systems.

### 2.4. Quantum-Size Effects

Size quantization effects in metals or semiconductors have attracted considerable attention in the past decade [104–107]. Semiconductor nanoparticles may experience a transition in terms of electronic properties from those typical for a solid to that of a molecule, in which a complete electron delocalization has not yet occurred. These quantum-size effects arise when the Bohr radius of the first exciton (an interacting electron-hole pair) and the semiconductor becomes comparable with or larger than that of the particle; the Bohr radius [94]

$$r_B = 4\pi\epsilon_0\epsilon\hbar^2/(e^2m^*) \quad (3)$$

depends on the dielectric constant  $\epsilon$  and the effective mass  $m^*$  of the charge carriers (electrons and holes). The latter is frequently radically different for holes and electrons and, in some cases,  $m^*$  is more than an order of magnitude smaller than the free-electron mass  $m_e$ . Hence, such quantum-size effects play a role for crystallites of approximately 1–10 nm in diameter. Under these conditions, the energy levels available for the electrons and holes in the conduction and valence bands become discrete and the effective bandgap of the semiconductor is increased. To a first approximation, the energy spacing between quantized levels is inversely proportional to the effective mass and the square of the particle diameter. A schematic energy diagram resulting from such confinement effects is shown in Figure 6.

Several attempts have been carried out to compute the electronic energy levels in such quantum dots [99, 108–110]. According to these concepts, the energy of the lowest excited state of a semiconductor particle with radius  $R$  is given approximately by

$$E(R) = E_g + \frac{\hbar^2\pi^2}{2R^2} \left[ \frac{1}{m_e^*} + \frac{1}{m_h^*} \right] - \frac{1.8e^2}{\epsilon R} \quad (4)$$

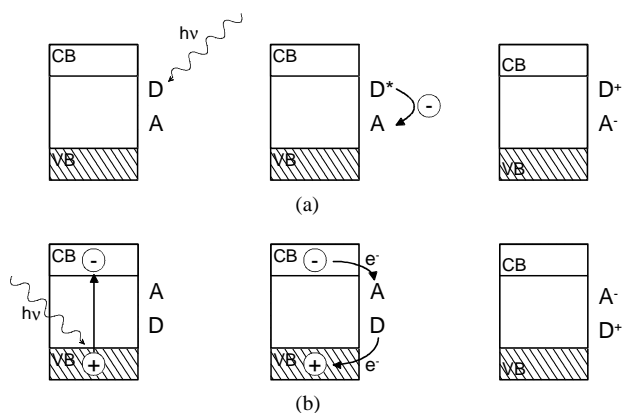


**Figure 5.** Sensitized photoreaction with (a) an initial excitation of the adsorbate, or (b) an initial excitation of the solid.

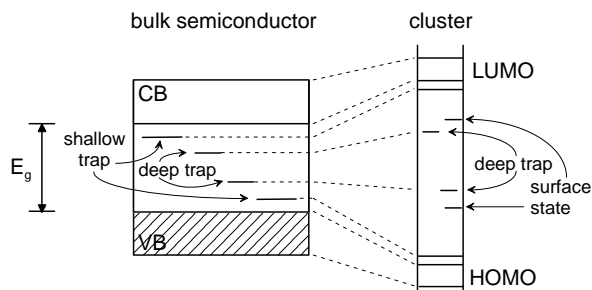


**Figure 6.** Schematic correlation diagram relating bulk-semiconductor electronic states to quantum crystalline states. Adapted from [110], M. G. Bawendi et al., *Annu. Rev. Phys. Chem.* 41, 477 (1990). © 1990, Annual Reviews.

Here  $E_g$  is the bandgap of the bulk semiconductor, the second term is the quantum energy of localization, increasing as  $R^{-2}$  for both electron and hole, and the third term is the Coulomb attraction [99]; whereas the Coulomb term shifts  $E(R)$  to smaller energy as  $R$ , the quantum confinement contribution increases  $E(R)$  as  $R^2$ . As a result, the apparent bandgap will always increase for small enough  $R$ . But while the shift can be appreciable ( $\sim 1$  eV) for small band gap materials like InSb, it might be considerably smaller ( $\sim 0.2$  eV) for semiconductors with a large bandgap like TiO<sub>2</sub> or ZnO [99]. Apart from a large effect on the optical properties (e.g., a change in color of the material due to the blue shift of the absorption), size quantization may also lead to major changes in the photocatalytic properties. While these effects have been studied in great detail for several compound semiconductor materials like CdS, ZnO, or PbS, related data for TiO<sub>2</sub> appear to be still rather limited.

## 2.5. Optical Properties

Semiconductors absorb light below a threshold wavelength  $\lambda_g$  which is related to the bandgap energy  $E_g$  by [93]

$$\lambda_g \text{ (nm)} = 1240/E_g \text{ (eV)} \quad (5)$$

Within the solid, the extinction of light follows an exponential law

$$I = I_0 \exp(-\alpha z) \quad (6)$$

where  $z$  is the penetration depth and  $\alpha$  is the reciprocal absorption length. For TiO<sub>2</sub>, for example,  $\alpha = 2.6 \times 10^4 \text{ cm}^{-1}$  at a wavelength of 320 nm; this implies that such light is extinguished to 90% after passing a distance of 390 nm in the semiconductor. Near threshold, the value of  $\alpha$  increases with increasing photon energy. Frequently, a proportionality of the type

$$\alpha h\nu = C(h\nu - E_g)^n \quad (7)$$

provides a satisfactory description of the absorption where  $h\nu$  is the photon energy.  $C$  is a constant scaling with the effective masses of the charge carriers, but is independent of the photon frequency. The exponent  $n$  has a value of 0.5 for a direct semiconductor and 2 for an indirect one [94]. Experimental data [111, 112] obtained on both anatase and rutile TiO<sub>2</sub> thin films indicated, however, that the actual situation might be more complex.

In colloidal solution, semiconductor particles reduce the light intensity of the incident beam both by scattering and absorption. In the absence of quantum-size effects the extinction spectrum is described by the Mie theory [113, 114]. This theoretical approach can be applied to an assembly of spherical particles if the interparticle distance is larger than the wavelength of the incident light (i.e., the particles scatter independently); if, furthermore, the particle size is much smaller than the wavelength, the energy-dependent absorption cross-section  $\sigma(\omega)$  for the irradiation of a solution containing the particles can be derived [115–117]:

$$\sigma(\omega) = 9V_p \frac{\omega}{c} \frac{\epsilon_s^{3/2} \epsilon_2}{(\epsilon_1 + 2\epsilon_s)^2 + \epsilon_2^2} \quad (8)$$

where  $\epsilon(\omega) = \epsilon_1 + i\epsilon_2$  is the complex, frequency-dependent dielectric constant of the semiconductor particle,  $\epsilon_s$  is the dielectric constant of the embedding medium (the solvent),  $V_p$  is the volume of a particle,  $\omega$  is the frequency of the incident light, and  $c$  is the velocity of light. For the case of a dilute system of particles with the number density  $n$ ,  $\sigma(\omega)$  can be related to the reciprocal absorption length  $\alpha(\omega)$ :  $\alpha(\omega) = n\sigma(\omega)$ . It follows that the imaginary part of the dielectric constant is a direct measure of the light absorption by the particles; it increases steeply near the absorption edge, that is, for  $\omega$  close to the threshold frequency. As noted in [69], Mie's theory has been widely employed to interpret the extinction spectra of colloidal systems [118]. For example, the brilliant ruby or yellow colors caused, respectively, by colloidal gold or silver particles are distinctly explained by this theory.

## 3. PREPARATION OF NANOSTRUCTURED MATERIALS AND THIN FILMS

Several distinct techniques have been utilized in recent years to synthesize nanocrystalline TiO<sub>2</sub> thin films by chemical, electrochemical, and organized assembly methods [69, 119–121]. A simple approach involves casting of the thin film directly from colloidal suspensions [122]. This method of preparation is relatively simple and inexpensive compared with other existing methods such as chemical vapor deposition or molecular beam epitaxy. Preparation of nanoclusters in polymer films and Langmuir–Blodgett films has also been considered. The sol–gel technique has been found to be useful in developing nanostructured semiconductor membranes with either a two-dimensional or three-dimensional configuration. Organic-template-mediated synthesis has been employed to develop nanoporous materials. The nanostructured materials are highly porous and can easily be surface modified with sensitizers, redox couples, and/or other nanostructured films.

### 3.1. Preparation from Colloidal Suspensions

Nanostructured semiconductor films of TiO<sub>2</sub> have been prepared frequently from colloidal suspensions [123–133]. By controlling the preparative conditions of the precursor colloids, it is possible to tailor the properties of these films.

Typically, these thin TiO<sub>2</sub> films exhibit interesting photochromic, electrochromic, photocatalytic, and photoelectrochemical properties that are inherited from the native colloids. The synthetic procedure involves the preparation of ultrasmall particles (diameter 2–10 nm) in aqueous or ethanolic solutions by controlled hydrolysis. The colloidal suspension is coated onto a conducting glass plate (an optically transparent electrode (OTE)) and dried; finally, the film is annealed at 200–400 °C in air for some 1–2 h. The conducting surface facilitates direct electrical contact of the nanostructured thin film. This simple approach of coating preformed colloids onto a surface and annealing generally produces an oxide film, which is robust and exhibits an excellent stability in both acidic and alkaline media, a feature very important in several potential applications. Generally, some optimization is required for thicker films and for higher colloidal concentrations in order to avoid cracking of the films upon drying. Further details of the methodology of preparation can be found in [134–136]. Transmission electron micrographs of nanostructured films prepared from colloidal suspensions show a three-dimensional network of oxide nanocrystals of particle diameter as small as a few nanometers. No significant aggregation or sintering effects are observed during the annealing process. X-ray diffraction analysis also confirms the crystallinity of these nanostructured films. Composite films, which in some cases may exhibit improved properties as compared to single-component films, can be manufactured by mixing two or more components prior to casting of the film.

Titania sol and gel prepared through the hydrolysis of tetrabutyl titanate in acid water solution are sensitive to ultraviolet (UV) irradiation and turn into blue color [137]. Electron spin-resonance measurement showed that the photochromism was ascribed to the presence of titanium (III) ions in the Ti-O-Ti network. The titanium (III) ions could be oxidized by the oxygen in the atmosphere, and then the sol and gel faded slowly. The absorption peaks in the optical absorption spectra of the titania gel were attributed to the transition of 3-dimensional electrons of a trivalent titanium in certain environments.

The morphology of TiO<sub>2</sub> particles affects their catalytic activity and electrical properties. In recent years, many methods for preparing TiO<sub>2</sub> nanoparticles and thin films have been studied [138]. TiO<sub>2</sub> nanocrystals prepared by the sol-gel method often have fully hydroxylated surfaces and these hydroxyl groups have a strong influence on the catalytic and photocatalytic properties such as electron-transfer rates and reducing properties [139]. In order to develop photocatalysts with high activities, it is very important to prepare porous anatase nanoparticles with a high specific surface area. Furthermore, the preparation method should be simple and should be a low temperature process. Mixtures of rutile and anatase precipitates could be obtained by the hydrothermal treatment of an alcohol solution of Ti alkoxide at 573 K [140], while anatase nanoparticles were prepared by heat treatment of a H<sub>2</sub>O-EtOH solution of TiOSO<sub>4</sub> at 373 K [141]. Thus, the anatase and rutile particles were usually formed in a solution by conventional soft chemical synthesis methods. The preparation of monodispersed oxide particles by the “sol-gel method” enables the manufacture of oxide particles through a gel state with a regulated

particle growth rate [142–144]. In a recent study [145], anatase nanoparticles were prepared in a Ti-peroxy gel without the collapse of the gel during the particle formation process. The gel was made from titanium tetraisopropoxide (Ti(O-iPr)<sub>4</sub>) and H<sub>2</sub>O<sub>2</sub>.

The crystallization rate of titania gels was found to be much higher in water than in methanol or *n*-hexane [146]; also, the crystallite size of anatase prepared in water was larger than those in organic solvents. Processing parameters very often control the crystallite size and phase. Nonagglomerated, ultrafine anatase particles have been generated by hydrothermally treating sol-gel-derived hydrous oxides [147]. The degree of crystallinity and purity of the synthesized materials may affect their structural evolution during any heat treatment.

TiO<sub>2</sub> thin films with different surface structures were prepared from alkoxide solutions containing polyethylene glycol (PEG) via the sol-gel method [148]. The larger the amount of PEG added to the precursor solution, the larger the size and number of pores produced in the resultant films. When PEG was added to the gel, the films decomposed completely during heat treatment. The adsorbed hydroxyl content of such porous thin films is found to increase with increasing amount of PEG. However, the transmittance of the films decreases due to the scattering of light by pores of larger size and a higher number in the films. Photocatalytic degradation experiments show that methyl orange is efficiently decolorized in the presence of the TiO<sub>2</sub> thin films by exposing its aqueous solution to ultraviolet light. However, in films deposited on soda-lime glass [149], diffusion of sodium and calcium ions from the glass into the nascent TiO<sub>2</sub> films was found to be detrimental to the photocatalytic activity of the resulting films. Sodium and calcium diffusion into nascent TiO<sub>2</sub> films was effectively retarded by a 0.3 μm SiO<sub>2</sub> interfacial layer formed on the soda-lime glass [149, 150].

TiO<sub>2</sub> thin film photocatalysts coated onto glass plates were prepared [151] by thermal decomposition of tetraisopropyl orthotitanate with a dip-coating process using alpha-terpineol as a highly viscous solvent. Two types of ligands—polyethylene glycol 600 and (ethoxyethoxy)ethanol—were added to the dip-coating solution as the stabilizer of titanium alkoxide and thin films were obtained after calcination at 450 °C for 1 h. The film thickness obtained with a single dipping was proportional to the viscosity of the dip-coating solutions. The thin films obtained were transparent with a thickness of 1 μm. The crystal form of the films was anatase alone. The thin films were formed with aggregated nanosized TiO<sub>2</sub> single crystals (7–15 nm), and the size of the TiO<sub>2</sub> crystals became smaller for the polymer-added systems.

Transparent anatase TiO<sub>2</sub>-based multilayered photocatalytic films synthesized via a sol-gel process on porous alumina and glass substrates showed a sponge-like microstructure and a mean crystallite dimension of ca. 8 nm [152]. Doping such films with iron(III) impeded the photocatalytic activity.

The effects of calcination on the microstructures of nanosized titanium dioxide powders prepared by vapor hydrolysis was investigated in detail [153–155]: Among the factors examined [153], large surface area and good dispersion of the powders in the reaction mixture are favorable to photoactivity. Conversely, prolonged calcination at high



temperatures is detrimental to photoactivity. Powders produced at higher temperatures are predominantly anatase and are generally more photoactive.

The formation, structure, and photophysical properties of functional mixed films of 5,10,15,20-tetra-4-(2-decanoic acid)phenyl porphyrin (TDPP) with TiO<sub>2</sub> nanoparticles formed from the two-dimensional sol-gel process of tetrabutoxytitanium (TBT) at the air/water interface was reported [156]. The composite multilayer films were assembled by transferring the mixed monolayer onto quartz plates. The sensitization of TDPP upon TiO<sub>2</sub> nanoparticles was confirmed by the spectral changes of UV-visible absorption and fluorescence of TDPP in the composite films. Furthermore the photosensitization greatly affected the photocatalytic activity of TiO<sub>2</sub> particles with respect to the degradation of methylene blue.

Crystalline titania thin films were obtained [157] on glass and various kinds of organic substrates at 40–70 °C by deposition from aqueous solutions of titanium tetrafluoride. Transparent films consisting of small anatase particles (~20 nm) exhibited excellent adhesion to relatively hydrophilic surfaces. Uniform coatings were successfully prepared on substrates with complex shapes such as cotton and felt fiber. Growth rate and particle size were controlled by both the deposition conditions and the addition of an organic surfactant. Organic dyes were incorporated into the anatase films using organic-dye dissolving solutions and a surfactant.

### 3.2. Chemical Precipitation

Rutile-phase nano-sized TiO<sub>2</sub> powders having a high specific surface area of 180 m<sup>2</sup>/g were prepared by homogeneous precipitation at ambient or very low temperatures (<100 °C) [158]. Ultrafine SnO<sub>2</sub>–TiO<sub>2</sub>-coupled particles could be synthesized [159] by homogeneous precipitation; they were employed for photocatalytic degradation of azo dye active red X-3B in aerated solution. The results show that a very rapid and complete decolorization of the azo dye can be achieved, and the photoactivity of the coupled particles is higher than that of pure ultrafine TiO<sub>2</sub>, and the optimum loading of SnO<sub>2</sub> on TiO<sub>2</sub> is 18.4%. The enhanced degradation rate of X-3B using coupled photocatalysts is attributed to increased charge separation in these systems.

### 3.3. Gas Condensation and Consolidation

Another method to synthesize nanostructured materials is by way of gas condensation followed by the *in-situ* consolidation under high-vacuum conditions [2]. This approach can produce ultrafine-grained materials which may exhibit size-related effects. The basic aspects of the generation of nanometer-sized materials via gas condensation are conceptually rather simple [2]: A precursor material, either an element or a compound, is evaporated in a gas maintained at a low pressure, usually well below one atmosphere. The evaporated atoms or molecules lose energy via collisions with the gas atoms and undergo a homogeneous condensation to form atomic or molecular clusters in the highly supersaturated vicinity of the precursor source. In order to maintain small cluster sizes, by minimizing further atom/molecule accretion and cluster-cluster coalescence, the clusters once

nucleated must be removed from the region of high supersaturation. Since the aggregates are already entrained in the condensing gas, this is readily accomplished by setting up conditions for moving this gas.

Typically, there are three fundamental rates that essentially control the formation of the clusters in the gas-condensation process [160]. These are

- (i) the rate of supply of atoms to the region of supersaturation where condensation occurs,
- (ii) the rate of energy removal from the hot atoms via the condensing medium, the gas,
- (iii) the rate of removal of the cluster upon nucleation from the supersaturated region.

The clusters that are collected via thermophoresis on the surface of a cold finger usually form very open, fractal structures. The clusters are held on the collector surface rather weakly, via Van-der-Waals forces, and are easily removed by means of a scraper. The material removed is consolidated in a compaction unit at typical pressures of 1–2 GPa; the scraping and consolidation are carried out under ultra-high-vacuum conditions *in-situ* after the removal of the gas from the chamber, in order to maximize the cleanliness of the particle surfaces and the interfaces that are formed.

### 3.4. Film Deposition by Sputtering and Vacuum-Based Techniques

Crystalline titanium dioxide films are often deposited by various techniques employing vacuum conditions, using, for example, RF magnetron [161–166], DC sputtering [167–171], chemical vapor deposition [172, 173], plasma spraying [174, 175], or related techniques [176, 177]. Rapid electroplating of photocatalytically highly active TiO<sub>2</sub>-Zn nanocomposite films on steel was achieved [178] and the gas-phase oxidation of CH<sub>3</sub>CHO was employed as an indicator of the photocatalytic activity. Not surprisingly, the film and surface morphologies and the crystallinity are strongly dependent on the total and the oxygen partial pressure, the deposition rate, and the phase composition; the resulting photocatalytic properties can be modified over a wide range by those parameters. Such films may show good uniformity of thickness over large areas, high optical transmittance (~80%) in the visible region, and considerable mechanical durability [169].

Transmission electron microscopy was used to study [179] the structure, morphology, and orientation of thin TiO<sub>2</sub> films prepared by reactive magnetron sputtering on glass slides at different substrate temperatures (100 to 400 °C). The microstructure and photocatalytic reactivity of TiO<sub>2</sub> films have been shown to be functions of deposition temperature. In the temperature range examined, all film samples have a porous nanostructure and the dimension of particles grew with increasing deposition temperature. Films are amorphous at temperatures of 100 °C and only the anatase phase forms at 200 °C and above. Films deposited between 200 to 300 °C show a preferred orientation, while films at 400 °C change into complete random orientation. Deposition at 250 °C yields high efficiency in photocatalytic degradation owing to the high degree of preferred orientation and nanocrystalline/nanoporous anatase phase.

Another frequently employed and convenient way for the preparation of TiO<sub>2</sub> thin films is pulsed laser deposition [180], although this technique does not produce nanocrystalline structures.

### 3.5. Surface and Film Modifications

The surface of as-deposited films has frequently been modified in the quest to enhance the catalytic activity. For example, Fe [181] or Sn [182] ions have been implanted into transparent and colorless TiO<sub>2</sub> thin films fabricated on microscope glass slides by DC magnetron reactive sputtering using Ar and O<sub>2</sub> as working gases. The efficiency of this procedure could not as yet be proven unambiguously. Apart from grain size, the presence of reactive species on the surface [183] may influence the photocatalytic activity. Implanted metal ions (V or Cr) were observed [184] located at the lattice positions of Ti<sup>4+</sup> in TiO<sub>2</sub> and were stabilized after calcination of the samples in an O<sub>2</sub> ambient at around 775 K. Spectroscopic studies showed that the presence of these substitutional metal ion species are, in fact, responsible for a large shift in the absorption spectra of these catalysts toward visible light regions. Porous anatase TiO<sub>2</sub> films were densified by Zn<sup>2+</sup> ion implantation up to the ion penetration depth [185]. After the subsequent annealing at 800 °C, the phase transformation from anatase to rutile accompanied with grain growth up to the film thickness was observed. In addition, the phase transformation was not induced by the annealing up to 800 °C with or without preceding Ar<sup>+</sup> ion implantation. Thus, the implanted impurity Zn assisted the phase transformation. Annealing in O<sub>2</sub> tends to reduce the rate of phase transformation and create ZnTiO<sub>3</sub>. Optical absorption above the photon energy of 2.9 eV was increased remarkably by the Zn<sup>2+</sup> or Zn<sup>+</sup> and O<sup>+</sup> ion implantation and subsequent annealing and is due to the phase transformation.

The presence of active species such as Ti<sup>3+</sup> and hydroxyl on the surface of ultrafine TiO<sub>2</sub> particles, prepared by a colloidal chemical approach and subjected to different heating treatments, was inferred [186] from optical absorption and photoelectron spectra; these species may enhance the photocatalytic activity of particles. Treating TiO<sub>2</sub> powder by a hydrogen plasma resulted in a reduction of the oxide particles and electrons trapped at the oxygen-defect sites were found [187]. Also laser ablation of TiO<sub>2</sub> photocatalysts aiming at the enhancement of the activity was reported [188].

Noble metal particles of Au, Pt, and Ir were deposited on nanostructured TiO<sub>2</sub> films using an electrophoretic approach [189]. The improved photoelectrochemical performance of the semiconductor-metal composite film was attributed to the shift in the quasi-Fermi level of the composite to more negative potentials. Continuous irradiation of the composite films over a long period causes the photocurrent to decrease as the semiconductor-metal interface undergoes chemical changes.

Doping of nanostructured TiO<sub>2</sub> both as particles and in thin films with a variety of metals has been reported, some common examples being Pt [190, 191], Pb [192], Au [193], or others [194]. A shift of the UV-vis absorption towards longer wavelengths was observed upon Pb doping, which indicates a decrease in the bandgap of TiO<sub>2</sub>. In TiO<sub>2</sub> films embedding Au nanoparticles [193], the specific resistance of

the films experienced a rising phase, followed by a dramatic drop with an increasing number of Au particles. Ultrafine Pt particles [191] were embedded into rutile TiO<sub>2</sub> particles by decomposing a colloidal organic-Pt complex, resulting in very narrow size distribution with a mean diameter of 3 nm. These nm-sized Pt particles were found to grow epitaxially on the TiO<sub>2</sub> crystallites with a well-defined crystallographic relationship.

Doping a nano-structured TiO<sub>2</sub> electrode sensitized with tetrasulfonated gallium phthalocyanine with tetrasulfonated zinc porphyrin (ZnTsPP) greatly enhances the photoelectric conversion at long wavelengths, with 20- and 60-fold improvement of the quantum efficiency at 680 and 700 nm [195].

Semiconductor/metal composite nanoparticles have been synthesized [196] by chemically reducing HAuCl<sub>4</sub> on the surface of preformed TiO<sub>2</sub> nanoparticles. These gold-capped TiO<sub>2</sub> particles (diameter 10–40 nm) were stable in acidic (pH 2–4) aqueous solutions. The role of the gold layer in promoting the photocatalytic charge transfer has been probed using thiocyanate oxidation at the semiconductor interface. More than 40% enhancement in the oxidation efficiency was found with TiO<sub>2</sub>/Au nanoparticles capped with low concentration of the noble metal.

Magnetic photocatalysts were synthesized by coating titanium dioxide particles onto colloidal magnetite and nanomagnetite particles [197]. The photoactivity of the prepared coated particles was lower than that of single-phase TiO<sub>2</sub> and was found to decrease with an increase in the heat treatment. These observations were explained in terms of an unfavorable heterojunction between the titanium dioxide and the iron oxide core, leading to an increase in electron-hole recombination.

TiO<sub>2</sub>-based powders, doped with a small amount of SiO<sub>2</sub>, were prepared by a sol-gel method and were subsequently heated to precipitate fine anatase crystals [198]. The obtained powders have large specific surface areas (~200 m<sup>2</sup>/g) and upon treating them chemically with aqueous NaOH, the photocatalytic property of the powders was extremely improved and the powders showed higher activity than the undoped TiO<sub>2</sub> powders.

In composite TiO<sub>2</sub>-SiO<sub>2</sub> thin films prepared by a sol-gel process, the refractive index and the photocatalytic activity decrease with increasing SiO<sub>2</sub> content in these films [199]. Alkoxide sol-gel processing has been investigated for the synthesis of stable SiO<sub>2</sub>-TiO<sub>2</sub> high-permeability catalytic membranes to be used in alkene isomerization [200]. Nanocrystalline TiO<sub>2</sub> was prepared on mesoporous silica both by sol-gel processes [201] and by an impregnation method with titanium complexes featuring different ligands [202].

Binary mixed oxide of Fe/Ti (1:1 composition) with homogeneous distribution of iron into the TiO<sub>2</sub> has been prepared by sol-gel impregnation using metal alkoxide precursors and firing at different temperatures (500, 700, and 900 °C) [203]. The mixed oxide exhibits excellent absorption in the visible spectral region (570–600 nm). The photocatalytic activity of the Fe/Ti oxide reduces to a large extent at a high sintering temperature of the sample due to the presence of a increasing amount of the inactive (Fe<sub>2</sub>/TiO<sub>3</sub>) pseudobrookite phase. Nanostructured TiO<sub>2</sub>/SnO<sub>2</sub> binary oxides were prepared by

combustion of stearic acid precursors [204], with metal precursors being dispersed in the stearic acid at the molecular level. It was found that preparative methods affected the crystalline structure of the powders and the anatase phase of TiO<sub>2</sub> was stabilized by the addition of SnO<sub>2</sub>.

Spray "painted" (spray deposited) titanium dioxide coatings were sensitized [205] with chemically deposited cadmium selenide thin films; the structural, optical, and photoelectrochemical characterization of these composite films indicate the importance of thermal treatments in improving the photocurrent quantum yields. Up to 400 °C, the effect of air annealing is to shift the onset of absorption to longer wavelengths and improve the photocurrent substantially.

Organic compounds may play a crucial role in chemical processes for ceramic coatings [206]. Organic compounds remained in a fixed position in the coating, which was prepared from the chemically modified titanium tetraisopropoxide solution and heated at temperatures as high as 673 K. It was not until the organic compounds decomposed to carbon dioxide and the gas phase was left from the coating that the nanostructure, consisting of nano-sized pores and anatase crystallites with preferred orientation, developed at 723 K.

Cobalt(II) 4,4',4'',4'''-tetrasulfophthalocyanine, covalently linked to the surface of titanium dioxide particles, TiO<sub>2</sub>-CoTSP, was shown [207] to be an effective photocatalyst for the oxidation of sulfur (IV) to sulfur (VI) in aqueous suspensions. Upon bandgap illumination of the semiconductor, conduction-band electrons and valence-band holes are separated; the electrons are channeled to the bound CoTSP complex resulting in the reduction of dioxygen, while the holes react with adsorbed S(IV) to produce S(VI) in the form of sulfate.

The photoactivity of the Pt/TiO<sub>2</sub> system in the visible region was improved [208] by the addition of the sensitizer ([Ru(dcbpy)<sub>2</sub>(dpq)]<sup>2+</sup>) [where dcbpy = 4,4'-dicarboxy 2,2'-bipyridine and dpq = 2,3-bis-(2'-pyridyl)-quinoxaline] leading to an efficient water reduction.

Photocatalytic properties for hydrogen production were investigated [209] on layered titanium compounds intercalating CdS in the interlayer, which were prepared by direct cation exchange reactions and sulfurization processes. The photocatalytic activity of the compounds intercalating CdS was superior to those of simple CdS and the physical mixture of CdS and metal oxides. The improvement might be attributed to the formation of microheterojunctions between the CdS nanoparticles and the layers of oxides.

### 3.6. Novel Deposition Methods and Structures

In recent years, there has been increased interest in studying and manufacturing nanoscaled TiO<sub>2</sub> materials as nanoparticles [210], nanowires [211], nanorods [212], whiskers [213], and nanotubes [214–217].

There are many synthetic routes for the creation of nanocrystals of oxides and the controlled hydrolysis of metal alkoxides is the most generalized solution-phase synthetic strategy [218]. Increased photocatalytic activity was reported recently for TiO<sub>2</sub> prepared by ultrasonic irradiation and glycothermal methods. This novel method [219] for preparing highly photoactive nanometer-sized TiO<sub>2</sub> photocatalysts

with anatase and brookite phases has been developed by hydrolysis of titanium tetraisopropoxide in pure water or a 1 + 1 EtOH–H<sub>2</sub>O solution under ultrasonic irradiation; the photocatalytic activity of TiO<sub>2</sub> particles prepared by this method exceeded that of Degussa P25 and was the first report that showed high photocatalytic activity of a photocatalyst containing an 80% anatase and 20% brookite phase.

A novel and convenient nonhydrolytic approach to the preparation of uniform, quantum confined TiO<sub>2</sub> nanocrystals, using an intramolecular adduct stabilized alkoxide precursor, was described recently [220]. In contrast to established aqueous sol–gel-techniques, the processing in hydrocarbon solvents at high temperatures allows access to very small free-standing crystallites, and opens up new possibilities for control over size distribution, surface chemistry, and particle agglomeration.

It has been reported that the columnar morphologies in sputtered TiO<sub>2</sub> films enhances the photocatalytic [221] and photovoltaic [222] efficiency. Following these studies, enhanced surface-reaction efficiency has been demonstrated in the photocatalysis of sculptured thin films of TiO<sub>2</sub> [223]. In obliquely deposited films with variously shaped columns such as zigzag, cylinder, and helix, the columnar thickness and spacing play an important role in the enhancement of the effective surface area, while the columnar shape is less important. The optimum morphology for a surface reaction has been obtained at the deposition angle of 70°, where the photocatalytic activity is 2.5 times larger than that at 0°. The morphology of these obliquely deposited thin films appears well suited for application as solar cells, electro- and photochromic devices, and photocatalysts.

The template method for synthesizing nanostructures involves the synthesis of the desired material within the pores of a nanoporous membrane or other solid. This approach has been used in several experiments [224–229] for the preparation of TiO<sub>2</sub> nanotubes and nanorods; typically, porous aluminum oxide (PAO) nano-templates were used.

Compact, continuous, and uniform anatase nanotubules with diameters in the range 50–70 nm were produced inside PAO nano-templates by pressure impregnating the PAO pores with titanium isopropoxide and then oxidatively decomposing the reagent at 500 °C [230]. Cleaning the surface of the template and repeating the process several times produced titania nanotubules with a wall thickness of ~3 nm per impregnation. The tube exteriors appeared to be faithful replicas of the pores in which they were formed.

Nano-TiO<sub>2</sub> whiskers were prepared by various techniques [213, 231]; using, for example, controlled hydrolysis of titanium butoxide [231] it was found that the nano-TiO<sub>2</sub> whiskers obtained were anatase and grew selectively in the [001] direction with a diameter of about 4 nm and a length of about 40 nm. Acetic acid played an important role in the oriented growth of nano-TiO<sub>2</sub> whiskers.

Highly ordered TiO<sub>2</sub> nanowire (TN) arrays were prepared [211] in anodic alumina membranes by a sol–gel method. The TNs are single crystalline anatase phase with uniform diameters around 60 nm. At room temperature, photoluminescence measurements of the TN arrays show a visible broadband with three peaks, which are located at about 425, 465, and 525 nm that are attributed to self-trapped excitons, *F*, and *F*<sup>+</sup> centers, respectively.

## 4. STRUCTURAL PROPERTIES OF NANOCRYSTALLINE TiO<sub>2</sub> FILMS

### 4.1. The Lattice Structure of Rutile and Anatase

Three different crystal structures of TiO<sub>2</sub> exist [18]: rutile, anatase, and brookite; only the former two of them are commonly used in photocatalysis, with anatase typically exhibiting the higher photocatalytic activity [232]. The structure of rutile and anatase can be described in terms of chains of TiO<sub>6</sub> octahedra. The two structures differ by the distortion of each octahedron and the actual pattern of the chains. Figure 7 depicts the unit cell structures of rutile and anatase crystals [233–235]. Each Ti<sup>4+</sup> ion is surrounded by an octahedron of six O<sup>2-</sup> ions. The octahedron in rutile shows a slightly orthorhombic distortion, whereas the respective octahedra in anatase are significantly distorted, resulting in a symmetry that is lower than orthorhombic. The Ti-Ti distances in anatase are greater (0.379 and 0.304 nm as compared to 0.357 and 0.296 nm in rutile) while the Ti-O distances are shorter than in rutile (0.1934 and 0.1980 nm in anatase versus 0.1949 and 0.1980 nm in rutile). In the rutile structure, each octahedron is in contact with 10 neighboring ones (two sharing edge oxygen pairs and eight sharing corner oxygen atoms), whereas in the anatase crystal each octahedron is in contact with eight neighbors (four sharing an edge and four sharing a corner). These differences in lattice structure result in different mass densities ( $\rho = 4.250 \text{ g/cm}^3$  for rutile and  $\rho = 3.894 \text{ g/cm}^3$  for anatase) and electronic band structures for the two forms of TiO<sub>2</sub>.

Synthetic titanium oxide crystallizes in two polymorphs: anatase and rutile. Anatase is metastable and transforms exothermally and irreversibly to rutile. Some properties of TiO<sub>2</sub> may strongly depend on its polymorphic phase. The anatase-rutile transformation is strongly influenced by the synthesis method, atmosphere, grain growth, and impurities. Some additives, such as ZrO<sub>2</sub> and Al<sub>2</sub>O<sub>3</sub>, retard the anatase-rutile transformation, whereas others, such as CoO and ZnO, accelerate such a process [236]. The anatase-to-rutile phase transformation of doped nanostructured titania was studied [237] using differential thermal analysis (DTA) and X-ray diffraction (XRD). The presence of Cu and Ni was found to enhance transformation as well as sintering.

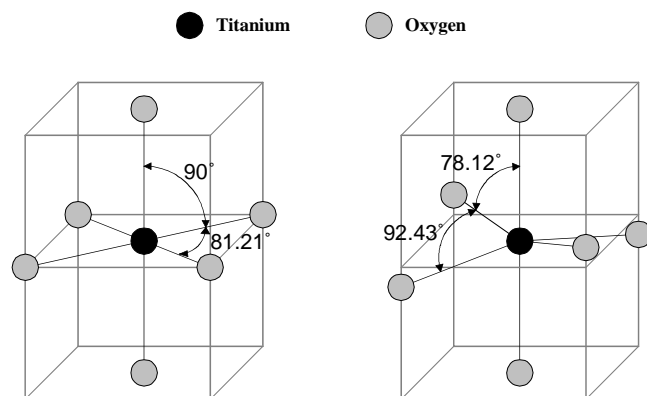


**Figure 7.** Crystal structures of rutile (left) and anatase (right) TiO<sub>2</sub>.

On the other hand, La retarded both transformation and densification.

Transmission electron microscopy (TEM) is typically used to investigate the crystal size distribution, grain-boundary disorder, and defect structure in nanocrystalline TiO<sub>2</sub> materials prepared by the various techniques outlined in the previous section. In a recent study of films with an average grain size of 15 nm prepared by reactive sputtering [238], evidence of both ordered and disordered grain-boundary regions was found and planar defects were observed in grain interiors identified as (011) deformation twins. Also, crystallographic shear defects can occur as a result of aggregation of oxygen vacancies in understoichiometric titanium oxide. Figure 8 shows results of TEM investigations [239] of nanocrystalline TiO<sub>2</sub> films prepared from colloidal suspensions; the TiO<sub>2</sub> crystallites were nominally pure anatase phase with a size of 16 nm.

### 4.2. Structure of Crystalline TiO<sub>2</sub> Surfaces

The geometric structure of crystalline surfaces of TiO<sub>2</sub> has been studied predominantly on (macroscopically) large single crystals; in particular, the (110) surface of rutile, being thermodynamically the most stable one [240], has been investigated extensively by a broad variety of surface science tools [241–243]. Among the different questions addressed therein, a prominent one was related to the possible types of oxygen defects at the surface; in fact, three distinct oxygen vacancy sites were tentatively identified: lattice, single-bridging, and double-bridging vacancies [244]. With the widespread use of scanning-tunneling microscopy (STM), atomically resolved investigations of TiO<sub>2</sub> surfaces became feasible and a more detailed picture of the rutile (110) surface structure emerged [245–248]. Consistently, these studies corroborate the longstanding notion about the prominent importance of surface defects as the active sites for various types of chemical reactions [249–251], for example, for

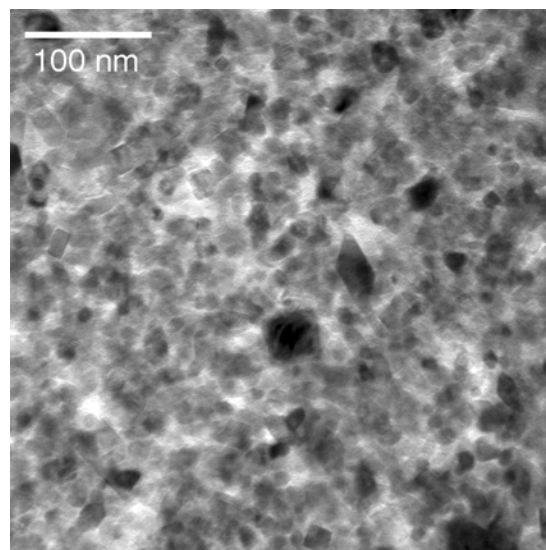


**Figure 8.** Cross-section transmission electron microscopy image of a nanocrystalline TiO<sub>2</sub> anatase film. The nominal crystallite size is 16 nm.

the dissociation of water [252, 253]. The number of studies on the structural properties of anatase single crystals is considerably smaller, which appears to be largely due to the difficulties encountered in preparing such surfaces in a defect-free state. Nevertheless, a rather distinct picture of the anatase TiO<sub>2</sub> surface structure [254–257] and its properties in terms of adsorption/desorption reactivity [258–260] has been achieved.

The structure and composition of a nanocrystalline surface may have a particular importance in terms of chemical and physical properties because of their small size. For instance, nanocrystal growth and manipulation relies heavily on surface chemistry [261]. The thermodynamic phase diagrams of nanocrystals are strongly modified from those of the bulk materials by the surface energies [262]. Moreover, the electronic structure of semiconductor nanocrystals is influenced by the surface states that lie within the bandgap but are thought to be affected by the surface reconstruction process [263]. Thus, a picture of the physical properties of nanocrystals is complete only when the structure of the surface is determined.

To understand and improve the applications of titanium-oxide nanoparticles, it is extremely important to perform a detailed investigation of the surface and the interior structural properties of nanocrystalline materials, such as rutile and anatase with diameter of a few nanometers. Detailed experiments using X-ray absorption near-edge structure spectroscopy (XANES) demonstrated [264] that the presence of both defects and surface states strongly influence the X-ray absorption spectra, even though the first nearest-neighbor geometrical arrangement around the central Ti atom in both rutile and anatase is quite similar: the differences in the XANES spectra arise from the outer-lying atomic shells, indicating that “medium” to “long-range” effects play an important role to the near-edge features. In another study of this kind [265], a shorter Ti-O distance for surface TiO<sub>2</sub>, resulting from Ti-OH bonding was observed together with a minor disorder of the lattice in smaller nanoparticles. Nevertheless, the Ti sites largely remain octahedral even in particles with diameters of 3 nm. Because the interfacial electron/hole transfer occurs via surface Ti or O atoms, the observed structural changes around the surface Ti atoms in small TiO<sub>2</sub> particles could be responsible [265] for the unique photocatalytic properties.

A qualitative analysis of opaque nanostructured glass-supported TiO<sub>2</sub> films was carried out [266] using scanning force microscopy (SFM), and surface parameters such as average grain diameter, roughness exponent, and fractal dimension [267] were determined. The TiO<sub>2</sub> surfaces exhibit distinct roughness due to the large aggregates formed by the interconnected TiO<sub>2</sub> particles. Fractal dimension was found to range between 2.10 and 2.45, depending on the scanned range and the preparation method. The surface morphology of nanocrystalline materials prepared by compacting nanometer-sized clusters was investigated by SFM [268]; these materials had a grain size of 5–15 nm and contained about 10<sup>19</sup> interfaces per cubic centimeter. Upon heat treatment, grains were found to fuse together forming bamboo-like structures and then lined up as tubular structures.

The influence of the iron concentration in mixed-oxide (TiO<sub>2</sub> and Fe<sub>2</sub>O<sub>3</sub>) thin films prepared by reactive

radio-frequency sputtering on the structural properties of the layers has been studied [269]. This characterization allowed the correlation of the inhibition of the grain growth of titania to the presence of iron oxide and its segregation at grain boundaries. This behavior could be ascribed to a superficial-tension phenomenon. As a possible application of these thin films, it was observed that they were able to sense CO down to the level requested for environmental monitoring.

A study [270] of the structure and morphology of a titanium dioxide photocatalyst (Degussa P25) reveals multiphase material consisting of an amorphous state, together with the crystalline phases anatase and rutile in the approximate proportions 80/20. Transmission electron microscopy provides evidence that some individual particles are a mixture of the amorphous state with either the anatase phase or the rutile phase, and that some particles, which are mostly anatase, are covered by a thin overlayer of rutile that manifests its presence by the appearance of Moiré fringes. The photocatalytic activity of this form of titanium dioxide is reported as being greater than the activities of either of the pure crystalline phases, and an interpretation of this observation has been given in terms of the enhancement in the magnitude of the space-charge potential, which is created by contact between the different phases present and by the presence of localized electronic states from the amorphous phase.

## 5. ELECTRICAL PROPERTIES OF NANOCRYSTALLINE TiO<sub>2</sub> FILMS

Most studies into the carrier transport in nanocrystalline TiO<sub>2</sub> were carried out with the films in contact with electrolytes, mostly due to their use in highly efficient electrochemical solar cells, often called “Grätzel cells” [38, 71]. In this application, the pore surface is covered with an ultrathin organic dye layer and contacted with an electrolytic solution that penetrates the pore structure. The experimental work indicates [271–274] that in this configuration the electrolyte screens any electric field within the porous structure and establishes diffusion conditions for the carrier propagation. On the other hand, investigations in which the nanopores are in contact with an insulating medium (a gas or vacuum) may allow one to obtain quantitative insight into the electronic properties of the material and the basic feature of carrier transport. In a series of measurements [275–277] on the electron transport in nanoporous TiO<sub>2</sub> films with gas-filled, insulating pores employing Pt/TiO<sub>2</sub>, Schottky barrier structures indicate a barrier height of 1.7 eV, compatible with an electron affinity of 3.9 eV for the TiO<sub>2</sub> films. Below ~300 K, tunneling transport through the barrier occurs, resulting in barrier lowering effects. Carrier drift mobilities, recombination lifetimes, and their dependence on injection level in TiO<sub>2</sub> are reported. It is found that the mobility-lifetime product is independent of injection level, while drift mobility and recombination lifetime change strongly with injection. A trap-filling model appears as the most plausible model compatible with the experimental findings [277]. Comparison with recent experiments on nanoporous films in contact with electrolytes indicate that the transport and recombination mechanism is qualitatively similar for the two cases.

Various observations indicate that electron transport in the nanocrystalline TiO<sub>2</sub> dominates the transient response of the system. Transient photocurrent measurements reveal a very slow (~millisecond), multiphasic response to both continuous wave [278, 279] and pulsed [280–282] illumination. The characteristic rise or decay time of the response is dependent upon the intensity of the light source [278, 281–283]. Comparison with the transient response without electrolyte indicates that it is the TiO<sub>2</sub>, and not the electrolyte, which is responsible for the very long tail [284, 275]. A slow and multiphasic time dependence has also been observed in the rereduction of oxidized dye molecules in a redox inactive environment [285]; the same work indicates that the rate of dye reduction is controlled by the concentration of electrons introduced into the TiO<sub>2</sub> by externally applied bias. The wide range of time scales is consistent with the assumption that electron transport within the TiO<sub>2</sub> is the rate limiting step.

The slow processes are attributed to the trapping of electrons by a high density of localized states in the TiO<sub>2</sub>. Since the TiO<sub>2</sub> grains are normally crystalline [286], the localized states are believed to be concentrated at the grain boundaries and on the very large surface. There is evidence for intraband-gap states in bias-dependent optical absorbance spectra [287] and surface photovoltage spectra. It would, therefore, be extremely useful to correlate the density and nature of those states with the electronic transport properties of the material.

Investigating electron migration in nanostructured anatase TiO<sub>2</sub> films with intensity-modulated photocurrent spectroscopy [288], it was found that, upon illumination, a fraction of the electrons accumulated in the nanostructured film is stored in deep surface states, whereas another fraction resides in the conduction band and is free to move. These data indicate that the average concentration of the excess conduction band electrons equals about one electron per nanoparticle, irrespective of the type of electrode, the film thickness, or the irradiation intensity.

The photocurrent in thin film TiO<sub>2</sub> electrodes prepared by sol-gel methods was studied in [289] as a function of film thickness. Films with thickness smaller than the space charge layer were found to show a larger photocurrent than films with thickness larger than the space charge layer. It was concluded that the increase in photocurrent is due to the effective electron-hole separation throughout the whole film thickness and the reduction of bulk recombination. The use of TiO<sub>2</sub> thin-film electrodes for photocatalytic devices might therefore be useful to gain high device performance.

In a series of papers, Dittrich et al. carried out extensive investigations of the electrical conductivity in nanoporous TiO<sub>2</sub> films [290–296]. Studying the temperature- and oxygen partial pressure-dependent conductivity  $\sigma$  of rutile and anatase, they noted [292] that  $\sigma$  is thermally activated with  $E_A = 0.85$  eV, independent of the absolute value of  $\sigma$  and depends on  $p(\text{O}_2)$  by a power law for  $p(\text{O}_2) < 1$ –10 mbar. The electrical properties of reduced nanoporous TiO<sub>2</sub> are determined by surface chemical reactions which lead to the formation of shallow donor and deep trap states. Furthermore, this group examined in detail the photovoltage in nanocrystalline TiO<sub>2</sub> [293, 295] and the injection currents in these porous specimens [294, 296].

Such a power dependence of  $\sigma$  on the oxygen partial pressure was noted also in recent work [297] investigating electrical and defect thermodynamic properties of nanocrystalline titanium oxide. At high O<sub>2</sub> pressures,  $p(\text{O}_2) > 1$  mbar, the conductivity is constant, whereas at values  $p(\text{O}_2) < 10^{-14}$  mbar a steep increase of  $\sigma$  with decreasing pressure was found, following a power dependence  $\sigma \propto [p(\text{O}_2)]^n$  with  $n = -1/2$  [297]. The plateau of conductivity at high oxygen pressures can be interpreted as being a domain of ionic conductivity, an unexpected behavior for titanium dioxide. In a coarse-grained material, dominant hole conductivity is observed in this partial pressure range. This difference may be due to the high density of grain boundaries in nanocrystalline ceramics, which can be preferred paths for diffusion at reduced temperatures. Furthermore, an increase in ionic conductivity is also expected due to enhanced defect formation in the space charge regions adjacent to grain boundaries [298]. At low oxygen partial pressure, nanocrystalline TiO<sub>2</sub> exhibits enhanced electronic conductivity as compared to coarse-grained TiO<sub>2</sub>. The power exponent  $n = -1/2$  can be explained under the assumption that doubly charged titanium interstitials are formed. The intrinsic disorder of titanium dioxide is reputedly of the cationic Frenkel-type [299–302], although alternative defect models based on Schottky disorder are also described in the literature [303, 304]. In the domain of ionic conductivity, the activation energy of conduction is  $\sim 1.0 \pm 0.1$  eV [297], a value typical of migration enthalpies for ionic defects. By contrast, the activation energy in the reduction-controlled regime was found to be  $\sim 3.9 \pm 0.2$  eV.

In titanium oxide thin films prepared by a d.c. sputtering technique onto glass substrates with average grain sizes of 100–200 nm, the surface structure and phase morphology of the films was found [305] to depend on the deposition conditions. The current-voltage characteristics of these films are ohmic for values of applied voltage lower than 0.5 V. For higher values, the mechanism of electrical conduction is determined by space-charge-limited currents [306]; then, a power-law dependence was observed with  $n \sim 2.3$ –2.9. In much thicker Ti oxide films (1.9–8  $\mu\text{m}$ ) deposited by sputtering [307], both the surface roughness and the internal surface area increased with film thickness; this resulted in an enhancement of the incident photon-to-current efficiency.

Electrical and optical spectroscopic studies of TiO<sub>2</sub> anatase thin films deposited by sputtering showed [308, 309] that the metastable phase anatase differs in electronic properties from the well-known, stable phase rutile. (From the broadening of the X-ray diffraction peaks, the average grain size of the films is estimated to be in the range of 30–40 nm [308].) Resistivity and Hall-effect measurements revealed an insulator-metal transition in a donor band in anatase thin films with high donor concentrations. Such a transition is not observed in rutile thin films with similar donor concentrations. This indicates a larger effective Bohr radius of donor electrons in anatase than in rutile, which in turn suggests a smaller electron effective mass in anatase. The smaller effective mass in anatase is consistent with the high-mobility, bandlike conduction observed in anatase crystals. It is also responsible for the very shallow donor energies in anatase. Luminescence of self-trapped excitons was



observed in anatase thin films, which implies a strong lattice relaxation and a small exciton bandwidth in anatase. Optical absorption and photoconductivity spectra show that anatase thin films have a wider optical absorption gap than rutile thin films. The extrapolated optical absorption gaps of anatase and rutile films were found to be 3.2 and 3.0 eV, respectively, at room temperature.

The observation of space charge limited currents (SCLC) in nanoscaled pure and chromium-doped titania was reported [310] and both the free-charge carrier density and the trapped-charge carrier density were given.

Photoconductivity was also studied in compound systems; for example, in a TiO<sub>2</sub>-C<sub>60</sub> bilayer system the conductivity increases significantly in the fullerene upon irradiation at wavelengths <300 nm [311].

Although being an efficient photocatalyst for the detoxification of organically charged waste water, titanium dioxide suffers from the drawback of poor absorption properties because of a bandgap of 3.2 eV. Thus, wavelengths shorter than 400 nm are needed for light-induced generation of electron-hole pairs. That is the reason why doping with transition metal ions is interesting for inducing a reduction of the bandgap. However, this doping changes other physical properties such as lifetime of electron-hole pairs and adsorption characteristics [312].

## 6. PHOTOCATALYTIC PROPERTIES OF NANOCRYSTALLINE TiO<sub>2</sub>

Most experimental investigations reported a higher photocatalytic efficiency in the anatase TiO<sub>2</sub> phase; as a possible reason it was suggested that the recombination of the electron-hole pairs produced by UV irradiation occurs more rapidly on the surface of the rutile phase, and the amount of reactants and hydroxides attached to this surface is smaller than on the surface of the anatase phase.

The study of the photocatalytic activity of nanocrystalline TiO<sub>2</sub> materials is a longstanding research effort [313–315]; in most lab-scale experiments it was evaluated by means of the degradation observed for typical substances (e.g., aqueous methyl orange, methylene blue, etc.) upon exposure of the specimen to UV irradiation. In such a way, the possible influence of light intensity, structural properties, surface morphology, phase and chemical composition, resulting from various deposition or preparation methods, could conveniently be explored [316–320]. Furthermore, any correlation with the optical or electrical properties of the nanocrystalline films could thereby be investigated. In addition, alternative approaches have come under scrutiny. A new simple method for characterizing photocatalytic activity by measuring photo-generated transient charge separation at the surface of semiconductor photocatalysts was proposed [321]. In this technique, the charge separation generated by a pulse dye laser is obtained as a function of the incident laser energy; thereby, the photocatalytic activity and the type of surface reaction (reduction or oxidation) in titanium dioxide films were rapidly determined. In the following sections some examples of such studies will be given.

### 6.1. Dependence of Photocatalytic Activity on Film Structure and Phase

The photoactivities of ultrafine TiO<sub>2</sub> nanoparticles in anatase, rutile, or mixed phases were tested in the photocatalytic degradation of phenol [322]. For TiO<sub>2</sub> nanoparticles, mainly in the anatase phase and mixed-phases, the photocatalytic activities increased significantly with the content of the amorphous part decreasing. The completely crystallized rutile nanoparticles exhibited size effects in this photocatalytic reaction and the photocatalytic activity of rutile-type TiO<sub>2</sub> nanoparticles with a size of 7.2 nm was much higher than that with 18.5 nm or 40.8 nm and was comparable to that of anatase nanoparticles.

A modified sol-gel process was used [323] to prepare nano-structured TiO<sub>2</sub> catalysts of controlled particle size (i.e., 6, 11, 16, and 20 nm). The effect of TiO<sub>2</sub> particle size on gas-phase photocatalytic oxidation of toluene was examined under dry and humid conditions. Main reaction products were CO<sub>2</sub> and water, although small amounts of benzaldehyde were also detected. The smaller particle size (i.e., 6 nm) led to higher conversion and complete mineralization of toluene into CO<sub>2</sub> and H<sub>2</sub>O. Electronic and structural effects (i.e., size and ensemble effects) were responsible for the excellent performance of a 6 nm TiO<sub>2</sub> catalyst for toluene photodegradation. The dependency of the photoactivity on the crystallite size of anatase titania for the decomposition of trichloroethylene (TCE) was investigated [324]. It was found that the photoactivity of all titania samples was linearly increased as the crystallite size of the anatase phase increased, regardless of the preparation method, as long as there was no significant rutile phase.

The enhancement of the photocatalytic activity of TiO<sub>2</sub> was investigated as a function of added amount of other oxides to promote desired oxidation or reduction reactions [325]. Mixed oxides of Nb<sub>2</sub>O<sub>5</sub> or Li<sub>2</sub>O with TiO<sub>2</sub> were prepared by the sol-gel process. The target material of dichloroacetic acid (DCA) was chosen for oxidation reactions and K<sub>2</sub>Cr<sub>2</sub>O<sub>7</sub> for reduction. While the Nb-oxide had a deleterious effect on the decomposition rate of DCA, the excess electrons due to the doping of Nb<sub>2</sub>O<sub>5</sub> into TiO<sub>2</sub> promoted the reduction process for Cr<sup>6+</sup>. Li<sub>2</sub>O (1 wt%) with TiO<sub>2</sub> was found to be the most efficient photocatalyst for DCA oxidation, resulting in photocatalytic activity of 50%.

A highly sensitive biochemical oxygen demand (BOD) sensor using a commercial TiO<sub>2</sub> semiconductor and photocatalytic pretreatment was developed to evaluate low BOD levels in river waters [326]. The photocatalytic oxidation was investigated as a function of irradiation times, TiO<sub>2</sub> concentrations, and pH. The optimal irradiation time was 4 min. The sensor response was increased with increasing pH and the responses obtained by photocatalysis to river samples were higher than those obtained without photocatalysis.

### 6.2. Influence of Surface Morphology and Defects

Photocatalytic reduction of CO<sub>2</sub> to organic compounds was carried out [327] in a semiconductor suspension system under simulated solar power using a TiO<sub>2</sub> catalyst. Experimental results show that the photocatalytic activity can be

improved by depositing Pd or Ru on the TiO<sub>2</sub> surface. Films of TiO<sub>2</sub> dispersed or coated with platinum were deposited on glass and Pt-buffered polyamide substrates, respectively, by magnetron sputtering [328]. The photocatalytic activity of the films was evaluated through the decomposition of acetic acid under UV irradiation. The Pt-dispersed TiO<sub>2</sub> film with approximately 1.5 wt% platinum shows a maximum activity due to the formation of anatase phase with a fine grain size. Platinum particles ~2 nm in thickness coated on anatase film greatly improves activity. The activity shows a step-like dependence of film thickness, where the critical thickness varies between 150 and 200 nm depending on the deposition temperatures. The correlation between defects and activity was verified by measuring either the temperature dependence of electric resistance or the shift of binding energy from X-ray photoelectron spectroscopy (XPS).

In crystalline TiO<sub>2</sub> films deposited by reactive RF magnetron sputtering on glass substrates without additional external heating, the photocatalytic activity was evaluated by the measurement of the decomposition of methylene blue under UV irradiation [162]. The results showed that crystalline anatase, anatase/rutile, or rutile films can be successfully deposited on unheated substrates. Anatase TiO<sub>2</sub> films with a more open surface, a higher surface roughness, and a larger surface area, formed at higher total pressures, exhibit the best photocatalytic activity. The photocatalytic activity of polycrystalline anatase TiO<sub>2</sub> films was found [329] to be affected by the crystalline orientation that depends on the deposition temperature; it was greater on the (112)-oriented than on the (001)-oriented film. The former film exhibited a columnar structure resulting in a larger surface area for photocatalytic reaction than the films with the (001)-preferred orientation. Furthermore, the introduction of structural defects associated with oxygen vacancies was found [169] to create some energy levels around the mid-gap, indicating that they could work as recombination centers of photo-induced holes and electrons, causing the decrease in photocatalytic activity. Therefore, the decrease in the structural defects associated with oxygen vacancies appears to be important for improving the photocatalytic activity of the films.

A marked difference of the photocatalytic activity between the TiO<sub>2</sub> films coated on quartz and glass substrates was confirmed [330], which would be interpreted in terms of the difference in the photocarrier's diffusion length induced by impurity Na<sup>+</sup> ions. These results lead to a conclusion that the crystallinity and defects of TiO<sub>2</sub> as well as the film thickness and surface area have a great influence on the photocatalytic activity. An enhanced photocatalytic activity of TiO<sub>2</sub> could be achieved also by deposition of the films on sulfonated glass substrates [331] or by using special support materials [332, 333].

Photo-oxidative self-cleaning and antifogging effects of transparent titanium dioxide films has attracted considerable attention for the past decade [334, 335]. In order to understand the photo-induced hydrophilic conversion on titanium dioxide coatings in details, it is inevitably necessary to understand the relationship between the photo reaction and the surface crystal structure; this can be done, for example, by an evaluation of the photo-induced hydrophilic conversion on the different crystal faces of rutile single crystals and also

polycrystalline anatase titanium dioxide [336]. Self-cleaning and antifogging effects of TiO<sub>2</sub> films prepared by magnetron sputtering were investigated [161, 163] in terms of the photocatalytic behavior by measuring the decomposition of methylene blue and the reduction of the contact angle between water and TiO<sub>2</sub> under ultraviolet irradiation. The phase conversion from the rutile to the anatase TiO<sub>2</sub> film leads to an enhancement of the activity; the anatase films with the best photocatalytic behavior are prepared at higher total pressures (>1.50 Pa) and characterized by a high decomposition efficiency, a contact angle about 10° after irradiation, and a good stability in darkness.

Titanium dioxide thin films prepared with various surface morphologies by metalorganic chemical vapor deposition were found to exhibit reversible wettability control by light irradiation [337]. These TiO<sub>2</sub> surfaces became highly hydrophilic by UV irradiation, and returned to the initial relatively hydrophobic state by visible-light (VIS) irradiation. The hydrophobic-hydrophilic conversion induced by UV light was ascribed to the increase in dissociated water adsorption on the film surface. By contrast, the conversion from hydrophilic to hydrophobic by VIS irradiation was caused by the elimination of water adsorbed on the surface due to the heat generated. Changes of the water contact angle between hydrophilic states and hydrophobic ones strongly depended on the roughness of the film surface.

The self-cleaning property of thin transparent TiO<sub>2</sub> coatings on glass under solar UV light was studied [338] for two compounds: palmitic (hexadecanoic) acid and fluoranthene, which are both present in the atmospheric solid particles. The removal rates of layers of these compounds sprayed on the self-cleaning glass were found to be sufficient for the expected application. The identified intermediates (about 40 for each compound) show the gradual splitting of the palmitic acid chain and the oxidative openings of the aromatic rings of fluoranthene. In the case of palmitic acid, the products give some indications about the photocatalytic mechanism. About 20% of the organic carbon contained in the initial compounds was transformed into volatile carbonyl products.

An extreme photo-induced hydrophilicity was achieved [339, 340] when TiO<sub>2</sub> films were covered by SiO<sub>2</sub> overlayers (with 10–20 nm in thickness). These multilayer films exhibited much more extreme hydrophilicity than a TiO<sub>2</sub> film without overlayer. The surface analyses revealed that the enhanced photo-induced hydrophilic surface of the multilayer films exhibited an improved photocatalytic activity towards decomposition of organic substances on their surfaces. An extreme light-induced superhydrophilicity was also reported [341] for mesoporous TiO<sub>2</sub> thin films (crystallite size ~15 nm, surface area ~50 m<sup>2</sup>/g, pore size ~3.6 nm). For such films, the water contact angle was found to be reduced essentially to zero upon UV-irradiation for a duration of about 60 min. In addition, the photocatalytic activity of those films could be enhanced by treating the substrate surfaces with an H<sub>2</sub>SO<sub>4</sub> solution [342].

In order to investigate the cathodic photoprotection of the steel from corrosion, stainless steel was coated with TiO<sub>2</sub> thin films, applied by a spray pyrolysis [343]. It was concluded that these coatings exhibit both a cathodic

photo-protection effect against corrosion and the frequently reported photocatalytic self-cleaning effect.

### 6.3. Influence of Electronic Properties

Detailed spectroscopic investigations of the processes occurring upon bandgap irradiation in colloidal aqueous TiO<sub>2</sub> suspensions in the absence of any hole scavengers showed [344] that while electrons are trapped instantaneously, that is, within the duration of the laser flash (20 ns), at least two different types of traps have to be considered for the remaining holes. Deeply trapped holes are rather long-lived and unreactive, that is, they are not transferred to the ions of model compounds for photocatalytic oxidation like dichloroacetate or thiocyanate. Shallowly trapped holes, on the other hand, are in a thermally activated equilibrium with free holes which exhibit a very high oxidation potential. The overall yield of trapped holes can be considerably increased when small platinum islands are present on the TiO<sub>2</sub> surface, which act as efficient electron scavengers competing with the undesired e<sup>-</sup>/h<sup>+</sup> recombination. While molecular oxygen, O<sub>2</sub>, reacts in a relatively slow process with trapped electrons, the adsorption of the model compounds on the TiO<sub>2</sub> surface prior to the bandgap excitation appears to be a prerequisite for an efficient hole scavenging.

### 6.4. Enhanced Photocatalytic Activity Via Surface Modifications

A driving force for research in heterogeneous photocatalysis using TiO<sub>2</sub> (and semiconductors in general) is the creation and application of systems capable of using natural sunlight to degrade a variety of organic and inorganic contaminants in wastewater or polluted air. As mentioned, the photocatalytic activity depends strongly, among other factors, on the wavelength range response. Since the bandgap of TiO<sub>2</sub> is ~3.2 eV, it is active only in the ultraviolet region which amounts to <10% of the overall solar intensity. Principally, there are several remedies to circumvent (at least partially) this limitation: (i) Deposition of metals on the semiconductor; (ii) using multicomponent semiconductors; (iii) surface modification with sensitizing dyes. The merits of these options will be outlined briefly in the following.

#### 6.4.1. Deposition of Metals on the Surface

The selectivity and efficiency of a photochemical reaction can be improved by modifying the surface with a noble metal. The deposition of metal particles on oxide surfaces has been the subject of several recent reviews [345–348] and therefore, there is, no need to duplicate it here. In terms of photocatalytic activity, a drastic enhancement has, for the first time, been observed for the photocatalytic conversion of water into hydrogen and oxygen upon a fractional coverage of the TiO<sub>2</sub> surface with platinum [349]. After excitation the electron migrates to the metal where it becomes trapped and electron-hole recombination is suppressed. The hole is then free to diffuse to the semiconductor surface where oxidation of organic species can occur. These processes are schematically depicted in Figure 9. The presence of the metal can be beneficial also because of its own catalytic

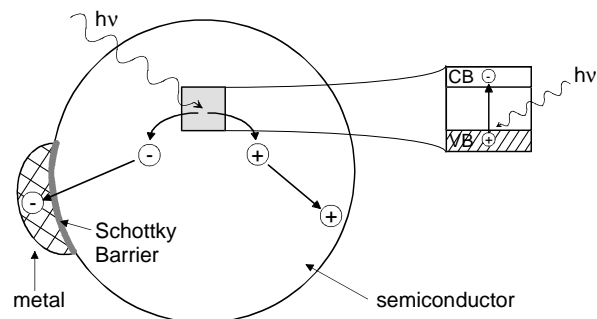


Figure 9. Metal-modified semiconductor photocatalyst particle.

activity. The Pt/TiO<sub>2</sub> system is probably the most frequently studied metal-semiconductor pair (see, e.g., [350, 351]); Figure 10 exemplifies the enhancement of the photocatalytic activity of nanocrystalline TiO<sub>2</sub> by platinumization [350]: three commercially available TiO<sub>2</sub>-catalysts, namely, Degussa P25, Sachtleben Hombikat UV100, and Millennium TiONA PC50, were platinumized by a photochemical impregnation method with two ratios of platinum deposits (0.5 and 1 wt%). The photocatalytic activities of these samples were determined using three different model compounds, EDTA, 4-chlorophenol (4-CP), and dichloroacetic acid (DCA). Platinumization resulted in all cases in an enhancement of the activity; Figure 10 shows the degradation of DCA as a function of illumination time (light intensity 23 W/m<sup>2</sup> at a wavelength of 320–400 nm) for pure TiO<sub>2</sub> and the two platinumized specimens. After 2 h of illumination, the initial concentration of 120 ppm total organic carbon (TOC) was reduced to 2.3 ppm at pH 3 employing the best photocatalyst, in this case, Hombikat UV100 with 0.5 wt% Pt. For this system, an initial photonic efficiency (i.e., number of degraded molecules per number of incident photons) of ~43% was obtained [350]. Apart from platinum, an enhanced photocatalytic activity has been also noted for other metals and semiconductors. Their influence on the photocatalytic activities has been studied in detail, for example, utilizing

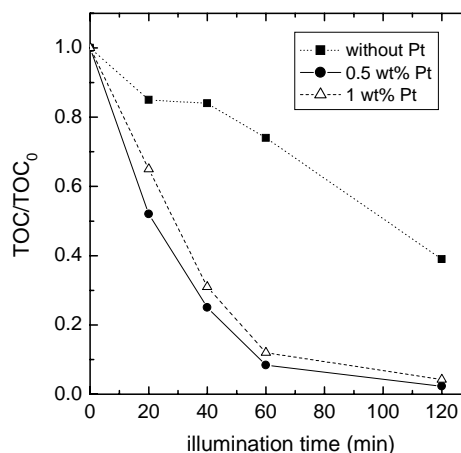


Figure 10. Degradation of dichloroacetic acid (expressed as the relative change of TOC) with platinumized TiO<sub>2</sub> in comparison to pure TiO<sub>2</sub> as a function of illumination at pH 3. Data from [350], D. Hufschmidt et al., *J. Photochem. Photobiol. A: Chem.* 148, 223 (2002).

the following systems: Au-modified TiO<sub>2</sub> [352, 353], silver-modified titanium particles [354], transition-metal doped TiO<sub>2</sub> photocatalysts [355–357], or rare-earth-doped TiO<sub>2</sub> nanoparticles [358].

It should be noted in this context that various analytical techniques like transmission electron microscopy or scanning force microscopy are often very useful in determining the size of the particles and their distribution in the bulk and at the surface of these nanocrystalline materials.

#### 6.4.2. Composite Semiconductors

The advantage of composite semiconductors is usually twofold: first, to extend the photo-response by coupling a large bandgap semiconductor with another featuring a smaller one and, second, to retard the recombination of photo-generated charge carriers by injecting electrons into the lower lying conduction band of the large bandgap material. Two types of geometries have been employed: capping the nanocrystallites of one semiconductor with those of the second or bringing the nanocrystalline particles of the two materials into intimate contact. The principle of charge exchange and separation for both arrangements is illustrated in Figure 11. Let us consider the case of coupling CdS with TiO<sub>2</sub>; the energy of the excitation light is too small to directly excite the TiO<sub>2</sub> particle, but it is large enough to excite an electron from the valence band across the bandgap of CdS ( $E_g = 2.5$  eV) to the conduction band. According to the energetics, the hole produced in the CdS valence band remains in the CdS particle, whereas the electron transfers to the conduction band of the TiO<sub>2</sub> particle; this increases the charge separation and efficiency of the photocatalytic process. The separated electrons and holes are then free to undergo electron transfer with adsorbates at the surface. While the mechanisms of charge separation in a capped system are similar, in a capped semiconductor only one of the charge carriers is accessible at the surface for catalytic reactions. Several semiconductors have been studied

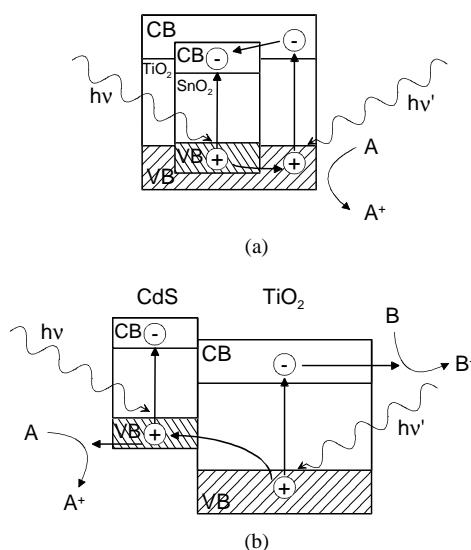


**Figure 11.** Photo-induced charge separation in composite semiconductor particles: (a) capped and (b) coupled semiconductor nanocrystallites. Photo-generated charge carriers move in opposite directions.

thoroughly in combination with TiO<sub>2</sub>: TiO<sub>2</sub>—CdS [359–361], TiO<sub>2</sub>—CdSe [362], TiO<sub>2</sub> coupled SnO<sub>2</sub> [363], TiO<sub>2</sub> capped SiO<sub>2</sub> [364], and some mixed-oxide systems like Fe<sub>2</sub>O<sub>3</sub>—TiO<sub>2</sub> [365] or ZrO<sub>2</sub>—TiO<sub>2</sub> [366].

#### 6.4.3. Surface Modification with Sensitizing Dyes

Surface sensitization of a wide bandgap semiconductor photocatalyst like TiO<sub>2</sub> via adsorbed dyes can increase the efficiency of the excitation step and, as a consequence, the activity. This process can also expand the wavelength range of excitation. Some common dyes that are used as sensitizers include erythrosin B, eosin, rhodamines, cresyl violet, thionine, porphyrins, [Ru(bpy)<sub>3</sub>]<sup>2+</sup> and its analogues, and many others (see, e.g., [102] for a more comprehensive list). The individual charge-transfer and excitation steps involved in the dye sensitizer surface process are exemplified in Figure 12. The primary excitation of an electron in the dye molecule occurs in either the singlet or triplet excited state of the molecule; if the oxidative energy level of the excited state of the dye molecule, with respect to the conduction band energy level of the semiconductor, is more negative, then the dye molecule can transfer the electron to the conduction band of the semiconductor. The surface accepts electrons from the dye molecules which, in turn, can be transferred to reduce an organic acceptor molecule adsorbed on the surface. The dye-sensitized semiconductor can also be used in oxidative degradation of the dye molecule itself after charge transfer; this appears to be an important process in view of the large quantities of dye substances in wastewater from the textile industries and others. In passing, it can be noted that the process of utilizing sub-bandgap excitation with dyes that absorb strongly in the visible for photosensitization is frequently employed in color photography and other imaging science applications. This approach of light-energy conversion is also similar to plant photosynthesis, in which chlorophyll molecules act as light harvesting antenna molecules.

Generally, the high porosity and strong bonding character of nanostructured TiO<sub>2</sub> (and other) semiconductor films facilitate the surface modification with organic dyes or organometallic complexes. For example, photoconversion efficiencies in the range 10–15% in diffused daylight have been reported [367] for nanostructured TiO<sub>2</sub> films modified with a ruthenium complex. The charge injection from a singlet excited sensitizer into the conduction band of a large bandgap semiconductor is thought to be an ultrafast process

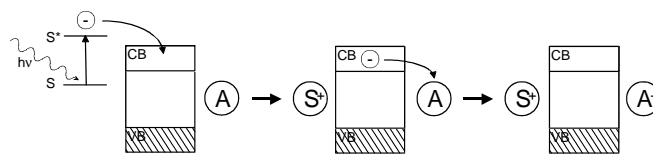


**Figure 12.** Sequence of excitation and charge-transfer steps using a dye-molecule sensitizer. In the first step, the sensitizer (S) is excited by an incident photon of energy  $h\nu$  and an electron is transferred into the conduction band of the semiconductor particle; the electron then can be transferred to reduce an organic acceptor molecule (A) adsorbed on the surface.

occurring at a picosecond time scale; in the case of different organic dyes, it has been shown [368, 369] that charge injection takes place within 20 ps. A similar fast electron transfer has also been noted for [Ru(H<sub>2</sub>O)<sub>2</sub>]<sup>2+</sup> on a TiO<sub>2</sub> surface at very low coverage [370]. Progress in femtosecond laser spectroscopy opened a venue for investigations on even much shorter time scales. In fact, in recent studies charge carrier injection times in the range of 20–200 fs were reported [371–375] for various dyes on nanocrystalline TiO<sub>2</sub> particles.

Significant enhancement effects of electron acceptors (additives) such as hydrogen peroxide, ammonium persulfate, potassium bromate, and potassium peroxymonosulfate (oxone) on the TiO<sub>2</sub> photocatalytic degradation of various organic pollutants were observed already in early investigations [376]. The results showed that these additives markedly improved the degradation rate of 2,4-dichlorophenol. The enhanced photocatalytic oxidation of sulfide ions on phthalocyanine modified titania was ascribed [377] to the additional formation of superoxide radicals.

Sensitization of wide bandgap semiconductor electrodes by dyes absorbing visible light are routinely used also in dye-sensitized photoelectrochemical cells, in order to achieve high photon-to-current conversion efficiencies [378, 379]. The preparation and dynamics of interfacial photosensitized charge separation in metal oxides such as TiO<sub>2</sub> films has been reviewed [70, 71, 380]. Principally, the photo-physical reactions occurring in those dye-sensitized injection solar cells, which are based on a dye adsorbed onto a porous TiO<sub>2</sub> layer, are very similar to those relevant to photocatalysis. Because of their importance as an energy source, Figure 13 presents a schematic drawing [69] of such

a dye-sensitized nanocrystalline TiO<sub>2</sub> solar cell, depicting the relevant energy levels and the pathway for the photo-excited electrons. In this specific example, a ruthenium complex [367] was adsorbed as a dye onto the TiO<sub>2</sub> and an I<sup>-</sup>/I<sub>3</sub><sup>-</sup> redox couple was used in the electrolyte. Contrary to conventional semiconductor devices, in the dye-sensitized cells the function of light absorption is separated from the charge-carrier transport. The Ru-complex has to absorb the incident sunlight and to effect, via this energy, the electron-transfer reaction (numbers ① and ② in Fig. 13). Apart from supporting the dye, the TiO<sub>2</sub> film acts as an electron acceptor and electronic conductor: the electrons injected into the TiO<sub>2</sub> conduction band drift across the nanocrystalline film to the conducting glass support which functions as current collector (③ in Fig. 13). At the counterelectrode, the electron is transferred to the redox couple in the electrolyte (④) which, in turn, serves to regenerate the dye (⑤). The cell voltage observed under illumination, Δ*V*, is determined by the difference between the Fermi-level of TiO<sub>2</sub> and the electrochemical potential of the electrolyte (cf. Fig. 13 [69]).

## 7. PHOTOCATALYTIC APPLICATIONS OF NANOCRYSTALLINE TiO<sub>2</sub>

While many examples of the photocatalytic activity of nanocrystalline TiO<sub>2</sub> have been presented already in the foregoing sections, the following discussions will focus on novel and important (and sometimes large-scale) applications. A very prominent area appears to be environmental catalysis [31, 32, 45] which, in recent years, has expanded considerably beyond the traditional fields like NO<sub>x</sub> removal from stationary and mobile sources, or the conversion of volatile organic compounds (VOC). According to [381], these potential new areas include:

- (i) catalytic technologies for liquid or solid waste reduction or purification;
- (ii) use of catalysts in energy-efficient catalytic technologies and processes;
- (iii) reduction of the environmental impact in the use or disposal of catalysts;
- (iv) new ecocompatible refinery, chemical or nonchemical catalytic processes;
- (v) catalysis for greenhouse gas control;
- (vi) use of catalysts for user-friendly technologies and reduction of indoor pollution;
- (vii) catalytic processes for sustainable chemistry;
- (viii) reduction of the environmental impact of transport.

Hence, (photo)catalysis in environmental applications can be instrumental in promoting the quality of life and environment, in promoting a more efficient use of resources, and in promoting sustainable processes and products.

Because of the tremendous importance of those environmentally related areas, the use of nanocrystalline TiO<sub>2</sub> for such photocatalytic applications is illustrated in this section by means of selected examples. Before doing so, it is stressed that there exists at least one other rather important issue in this context. In fact, hydrogen production from aqueous solutions using semiconductor particles such as, CdS, TiO<sub>2</sub>, WO<sub>3</sub> as photocatalysts is envisaged to become a potential

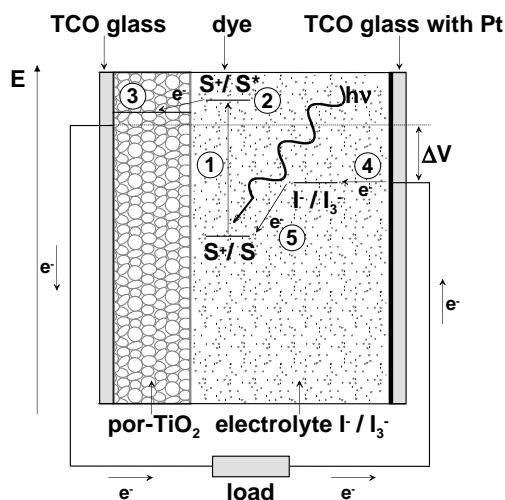


**Figure 13.** Schematic outline of a dye-sensitized photovoltaic cell, showing the electron energy levels in the different phases. The system consists of a semiconducting nanocrystalline TiO<sub>2</sub> film onto which a Ru-complex is adsorbed as a dye and a conductive counterelectrode, while the electrolyte contains an I<sup>-</sup>/I<sub>3</sub><sup>-</sup> redox couple. The cell voltage observed under illumination corresponds to the difference, Δ*V*, between the quasi-Fermi level of TiO<sub>2</sub> and the electrochemical potential of the electrolyte. S, S\*, and S<sup>+</sup> designate, respectively, the sensitizer, the electronically excited sensitizer, and the oxidized sensitizer. See text for details. Adapted from [69], A. Hagfeldt and M. Grätzel, *Chem Rev.* 95, 49 (1995). © 1995, American Chemical Society.

major application of these materials, and new concepts and approaches are developed continuously. For example, a new photocatalytic reaction that splits water into H<sub>2</sub> and O<sub>2</sub> was designed [382] by a two-step photo-excitation system composed of a IO<sub>3</sub><sup>-</sup>/I<sup>-</sup> shuttle redox mediator and two different TiO<sub>2</sub> photocatalysts, Pt-loaded TiO<sub>2</sub>-anatase for H<sub>2</sub> evolution and TiO<sub>2</sub>-rutile for O<sub>2</sub> evolution. Simultaneous gas evolution of H<sub>2</sub> (180 μmol/h) and O<sub>2</sub> (90 μmol/h) was observed from a basic (pH = 11) NaI aqueous suspension of two different TiO<sub>2</sub> photocatalysts under UV irradiation (λ > 300 nm, 400 W high-pressure Hg lamp). An extensive review [383] assesses photocatalytic efficiencies with reference to hydrogen production by means of light energy in the presence and absence of loaded metals, electron-donors/acceptors, and hole scavengers.

### 7.1. Reduction/Removal of Toxic Gases

The conversion of nitrogen oxides to less toxic compounds is important both because of their toxicity and the global atmospheric pollution. NO<sub>x</sub> can be converted to N<sub>2</sub> and other nitrogen compounds by reduction. TiO<sub>2</sub>-loaded zeolites and the vanadium silicate-1 were found [384] to decompose NO under irradiation, in particular, TiO<sub>2</sub> included in zeolite cavities results in complete decomposition into N<sub>2</sub> and O<sub>2</sub>. Titanium oxide catalysts prepared within the Y-zeolite cavities via an ion-exchange method exhibit [385] high and unique photocatalytic reactivities for the decomposition of NO into N<sub>2</sub> and O<sub>2</sub>, as well as the reduction of CO<sub>2</sub> with H<sub>2</sub>O showing a high selectivity for the formation of CH<sub>3</sub>OH. It was also found that the charge transfer excited state of the titanium oxide species, (T<sup>3+</sup>-O<sup>-</sup>)<sup>\*</sup>, plays a vital role in these unique photocatalytic reactions. In yet another approach, an efficient catalytic reduction of NO at low temperature by means of NH<sub>3</sub> could be achieved using Mn-, Cr-, or Cu-oxides on a nanocrystalline TiO<sub>2</sub> support [386].

The NO<sub>x</sub> removal process was studied experimentally in a pulsed corona discharge combined with the TiO<sub>2</sub> photocatalytic reaction [387]. NO<sub>2</sub> was found to adsorb easily on the photocatalyst surface, whereas NO was hardly adsorbed. Addition of water vapor enhanced the NO<sub>2</sub> adsorption. It was concluded that the main role of the plasma-chemical reaction in this system is the oxidation of NO into NO<sub>2</sub>. A considerable part of NO<sub>2</sub> is adsorbed on the photocatalyst surface, and is transformed to HNO<sub>3</sub> through photocatalytic reaction with OH.

The photocatalytic degradation of VOCs in the gas phase constitutes another very important example in this range of applications. Utilizing variously prepared TiO<sub>2</sub> photocatalysts (e.g., deposited on glass fiber cloth, as pellets or as thin films), the photo-induced reactions of trichloroethylene, acetone, methanol, and toluene were investigated [388–390]. The photocatalytic degradation rate was observed [388] to increase with increasing initial concentration of the VOCs, but remained almost constant beyond a certain concentration. It matched well with the Langmuir–Hinshelwood (L-H) kinetic model [11]. For the influence of water vapor in a gas-phase photocatalytic degradation rate, there was an optimum concentration of water vapor in the degradation of trichloroethylene and methanol. Furthermore, water vapor enhanced the photocatalytic degradation rate of toluene,

whereas it inhibited that of acetone. As for the effect of photon flux, it was found that photocatalytic degradation occurs in two regimes with respect to photon flux: for illumination levels distinctly below 1000–2000 μW/cm<sup>2</sup>, the photocatalytic degradation rate increased linearly with photon flux, whereas for power densities above that value, the rate was found to scale with the square root of the flux. Figure 14 shows some of those data [388], depicting in panel (a), the degradation of methanol as a function of UV illumination time for five different initial concentrations. (Using TiO<sub>2</sub> anatase nanocrystallites with 7 nm diameter in a solution, in this work photocatalytic TiO<sub>2</sub> films were deposited onto glass substrates by dip-coating.) The reaction kinetics were found to follow the L-H model, in which the reaction rate  $r$  varies proportionally with the surface coverage  $\theta$  according to

$$r = k\theta = \frac{kKc}{1 + Kc} \quad (9)$$

where  $c$  is the concentration of the VOC and  $k$  and  $K$  are, respectively, the reaction rate constant and the adsorption equilibrium constant. Figure 14(b) exemplifies this finding, showing the initial reaction rates  $r_0$  derived from data like those in Figure 14(a) as a function of the respective initial methanol concentrations  $c_0$ . The solid line in Figure 14(b) is a fit to the data according to Eq. (9).

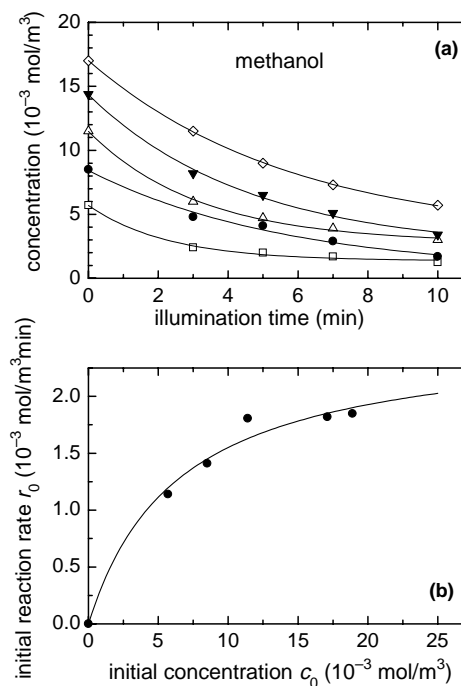


**Figure 14.** (a) Photocatalytic degradation of methanol with different initial concentrations as a function of UV illumination time (light intensity 2095 μW/cm<sup>2</sup> at a wavelength of 254 nm) at a H<sub>2</sub>O concentration of 0.38 mol/m<sup>3</sup> and a reaction temperature of 45 °C. (b) Initial reaction rates  $r_0$  as derived from the data in (a) versus the initial methanol concentrations; the solid line is a fit according Eq. (9). Data from [388], S. B. Kim and S. C. Hong, *Appl. Catal. B: Environ.* 35, 305 (2002).

## 7.2. Degradation of Organic Compounds

The degradation of organic compounds is probably the most widely used photocatalytic application of nanocrystalline TiO<sub>2</sub> and other semiconductor materials. In an aqueous environment, the holes created under UV irradiation are scavenged by surface hydroxyl groups to generate •OH radicals that then promote the oxidation of organics. This radical-mediated oxidation has been successfully employed in the mineralization of several hazardous chemical contaminants such as hydrocarbons, haloaromatics, phenols, halogenated biphenyls, surfactants, and textile and other dyes [102].

The possible photocatalytic decomposition of a broad range of organic compounds has been investigated using nanocrystalline TiO<sub>2</sub> particles. Detailed studies reported the oxidation of dissolved cyanide [391], the degradation of various kinds of acids [392–398], and of several herbicides [399–402], for the photocatalytic oxidation of toluene, benzene, cyclohexene, and benzhydrol [403–406] or for the 1,1'-dimethyl-4,4'-bipyridium dichloride decomposition [407]. In another application, a titanium oxide photocatalyst of ultra-high activity has been employed for the selective N-cyclization of an amino acid in aqueous suspensions [408]. Anatase crystallites of average diameter of ~15 nm were platinized by impregnation from aqueous chloroplatinic acid solution followed by hydrogen reduction. The catalyst was suspended in an aqueous L-lysine (Lys) solution and photoirradiated under argon at ambient temperature to obtain L-pipecolic acid.

The photocatalytic degradation and oxidation of phenol and phenol-based compounds has been examined quite frequently [409–414]. The decomposition of aqueous phenol solutions to carbon dioxide have been studied using natural sunlight in geometries simulating shallow ponds [415]. The photocatalyst was titanium dioxide freely suspended in the solution or immobilized on sand or silica gel. Photodegradation rates were approximately three times faster with the free suspension than with the immobilized catalyst under the same conditions, and were dependent on the time of year and the time of day. The seasonal variation correlated roughly with seasonal solar irradiance tabulations for the UV component of the spectrum. For 10 ppm of phenol, the maximum rate of solar degradation resulted in a decrease in concentration to 10 ppb in less than 80 min with total mineralization in 110 min.

An efficient degradation of aqueous phenol was achieved [416] by a new rotating-drum reactor coated with a TiO<sub>2</sub> photocatalyst, in which TiO<sub>2</sub> powders loaded with Pt are immobilized on the outer surface of a glass drum. The reactor can receive solar light and oxygen from the atmosphere effectively. It was shown experimentally that phenol can be decomposed rapidly by this reactor under solar light: with the used experimental conditions, phenol with an initial concentration of 22.0 mg/dm<sup>3</sup> was decomposed within 60 min and was completely mineralized through intermediate products within 100 min.

The photocatalytic degradation of various types of dyes appears to be another prominent and extensively explored application of nanocrystalline TiO<sub>2</sub> in environmental catalysis [417–423].

In a recent study [424], the photocatalytic degradation of five dyes in TiO<sub>2</sub> aqueous suspensions under UV irradiation has been investigated; it was attempted to determine the individual steps of such a degradation process by varying the aromatic structures, using either anthraquinonic (Alizarin S (AS)), or azoic (Crocein Orange G (OG), Methyl Red (MR), Congo Red (CR)) or heteropolyaromatic (Methylene Blue (MB)) dyes. Figure 15 exemplifies the photocatalytic degradation of three of these dyes (CR, OG, and MR) as a function of UV irradiation. The initial reaction rates were found to fall in the range from 1.9 μmol/l min (for CR) to 3.6 μmol/l min (for MR). In addition to a prompt removal of the colors, TiO<sub>2</sub>/UV-based photocatalysis was simultaneously able to fully oxidize the dyes, with a complete mineralization of carbon into CO<sub>2</sub>. Sulfur heteroatoms were converted into innocuous SO<sub>4</sub><sup>2-</sup> ions. The mineralization of nitrogen was more complex. Nitrogen atoms in the 3-oxidation state, such as in amino groups, remain at this reduction degree and produced NH<sub>4</sub><sup>+</sup> cations, subsequently and very slowly converted into NO<sub>3</sub><sup>-</sup> ions. For azo-dye (OG, MR, CR) degradation, the complete mass balance in nitrogen indicated that the central —N=N— azo group was converted into gaseous dinitrogen, which is the ideal issue for the elimination of nitrogen-containing pollutants. The aromatic rings were submitted to successive attacks by photogenerated •OH radicals leading to hydroxylated metabolites before the ring opening and the final evolution of CO<sub>2</sub> induced by repeated reactions with carboxylic intermediates.

The photocatalytic degradation of acid derived azo dyes in aqueous TiO<sub>2</sub> suspensions follows apparently first-order kinetics [425, 426]. The site near the azo bond (C—N=N-bond) is the attacked area in the photocatalytic degradation process, while the TiO<sub>2</sub> photocatalytic destruction of the C—N(=) bond and —N=N— bonds leads to fading of the dyes. The pH effect on the TiO<sub>2</sub> photocatalytic degradation of the acid-derived azo dyes varies with dye structure. Hydroxyl radicals play an essential role in the fission of the C—N=N— conjugated system in azo dyes in TiO<sub>2</sub> photocatalytic degradation. Metalized azo dyes were studied

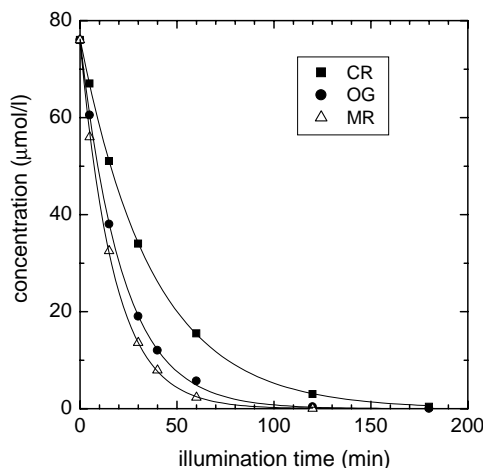


**Figure 15.** Photocatalytic degradation of three different dyes, Congo Red (CR), Crocein Orange (OG), and Methyl Red (MR), given in terms of the concentration versus the time of illumination. Data from [424], H. Lachheb et al., *Appl. Catal. B: Environ.* 39, 75 (2002).



[427] under TiO<sub>2</sub> photocatalytic and photosensitized conditions in aqueous buffering solutions. The size and strength of intramolecular conjugation determines apparently the light-fastness of the dyes; the more powerful OH radicals in TiO<sub>2</sub> photocatalytic process are highly reactive towards the azo dyes.

### 7.3. Wastewater and Soil Remediation

The major causes [428] of surface water and groundwater contamination are industrial discharges, excess use of pesticides, fertilizers (agrochemicals), and landfilling domestic wastes. Typically, the wastewater treatment is based upon various mechanical, biological, physical, and chemical processes. After filtration and elimination of particles in suspension, the biological treatment is the ideal process (natural decontamination). Unfortunately, organic pollutants are not always biodegradable; a promising approach then relies on the formation of highly reactive chemical species, which degraded the more recalcitrant molecules into biodegradable compounds. These are called the advanced oxidation processes (AOPs). Although there exist differences in their detailed reaction schemes, their common feature is the production of OH radicals ( $\cdot\text{OH}$ ); these radicals are extraordinarily reactive species (oxidation potential 2.8 V). They are also characterized by a low selectivity of attack, which is a useful attribute for an oxidant used in wastewater treatment and for solving pollution problems. These photocatalytic degradation of wastewater employing nanocrystalline TiO<sub>2</sub> has been examined in various set-ups [429] and pilot-plant scale solar photocatalytic experiments have been realized [428].

Several recent studies reported on the removal or reduction of metals or metal-containing contaminants in wastewater, based on the principles outlined in the foregoing paragraph. Those investigations examined, for example, the removal of cadmium and mercury from water using modified TiO<sub>2</sub> nanoparticles [430, 431], the radical, mediated photo-reduction of manganese ions in UV-irradiated titania suspensions [432], the simultaneous photocatalytic Cr(VI) reduction and dye oxidation in a TiO<sub>2</sub> slurry reactor [433], or the removal of iron(III) cyanocomplexes [434].

While the efficient use of a photocatalytic process in the presence of TiO<sub>2</sub> to degrade many different types of pollutants in wastewater has been confirmed repeatedly, the question of how to efficiently separate and reuse TiO<sub>2</sub> from treated wastewater became a notable problem in the application of a TiO<sub>2</sub> photo-oxidation process. A recent study [435] aimed to develop an advanced process for dyeing wastewater treatment, in which dyeing wastewater was initially treated by an intermittently decanted extended aeration (IDEA) reactor to initially remove biodegradable matters and further treated in a TiO<sub>2</sub> photocatalytic reactor for complete decolorization and high chemical oxygen demand (COD) removal. Suspended TiO<sub>2</sub> powder used in the photo-oxidation was separated from slurry by a membrane filter and recycled to the photo reactor continuously.

Photocatalytic destruction of chlorinated solvents in water with solar energy was investigated [436] using a near-commercial scale, single-axis tracking parabolic trough system with a glass pipe reactor mounted at its focus. In

the photocatalytic degradation of industrial residual waters, the use of peroxydisulfate ( $\text{S}_2\text{O}_8^{2-}$ ) as an additional oxidant (electron scavenger) was observed to have an outstanding effect, producing an important increase in the degradation rate [437]. The impact of pH and the presence of inorganic ions and organic acids commonly found in natural waters on rates of TiO<sub>2</sub> photocatalyzed trinitrotoluene (TNT) transformation and mineralization was examined [438]. Raising the pH slightly increased the rate of TNT transformation, primarily as a result of an increased rate of TNT photolysis, but significantly reduced rates of mineralization due to increased electrostatic repulsion between the catalyst surface and anionic TNT intermediates. The presence of inorganic anions did not substantially hinder TNT transformation at alkaline pH, but mineralization rates were diminished when the anion either adsorbed strongly to the photocatalyst or was an effective hydroxyl radical scavenger.

Immobilized TiO<sub>2</sub> photocatalysts were used to sterilize and reclaim the wastewater of bean sprout cultivation from a continuous hydrocirculation system [439]. The photocatalysts effectively killed bacteria and degraded organic pollutants in the wastewater. Stimulation of bean sprout growth and suppression of decaying pathogens were also induced by the TiO<sub>2</sub> photocatalytic activity.

Photocatalytic decomposition of seawater-soluble crude oil fractions using high surface area colloid nanoparticles of TiO<sub>2</sub> under UV irradiation was explored [440]; although no mineralization occurred due to photolysis, important chemical changes were observed in the presence of TiO<sub>2</sub>, with the degradation reaching 90% (measured as dissolved organic carbon, (DOC)) in waters containing 9–45 mg C/l of seawater-soluble crude oil compounds after 7 days of artificial light exposure. During light exposure, transient intermediates that showed higher toxicity than the initial compounds were observed, but were subsequently destroyed. Heterogeneous photocatalysis using TiO<sub>2</sub> was considered to be a promising process to minimize the impact of crude oil compounds on contaminated waters.

TiO<sub>2</sub>-photocatalytic degradation of a cellulose effluent was evaluated [441] using multivariate experimental design. The effluent was characterized by general parameters such as adsorbable organic halogens (AOX), TOC, COD, color, total phenols, acute toxicity, and by the analysis of chlorinated low molecular weight compounds using GC/MS. The optimal concentration of TiO<sub>2</sub> was found to be around 1 g/l. After 30 min of reaction more than 60% of the toxicity was removed and after 420 min of reaction, none of the initial chlorinated low molecular weight compounds were detected, suggesting an extensive mineralization.

Photocatalysts, based on titanium dioxide, were used for the purification of contaminated soil polluted by oil [442]. Commercially produced slurry of titanium dioxide was modified with barium, potassium, and calcium. The experiments were performed under natural conditions in summer months (July and August) applying direct solar-light irradiation. The most active photocatalyst for soil purification was titanium dioxide modified with calcium.

Two different photocatalysts, namely, Hombikat UV100 (Sachtleben Chemie) and P25 (Degussa) have been used in batch experiments [443] to compare their ability to degrade the toxic components of a biologically pretreated landfill

leachate. A strong adsorption of the pollutant molecules was observed for both TiO<sub>2</sub>-powders, with a maximum of almost 70% TOC reduction for Hombikat UV100.

#### 7.4. Purification of Drinking Water

Pathogens in drinking water supplies can be removed by sand filtration followed by chlorine or ozone disinfection. These processes reduce the possibility of any pathogens entering the drinking water distribution network. However, there is doubt about the ability of these methods to remove chlorine-resistant microorganisms including protozoan oocysts. Titanium dioxide (TiO<sub>2</sub>) photocatalysis is a possible alternative/complementary drinking water treatment method and several studies [444, 445] reported a strong and swift photocatalytic inactivation of bacteria and bacteriophages in aqueous solutions. For example, the rate of disinfection was explored using TiO<sub>2</sub> electrodes prepared by the electrophoretic immobilization of TiO<sub>2</sub> powders with different crystallinity. These electrodes were tested for their photocatalytic bactericidal efficiency with *E. coli* K12 as a model test organism [446]. Similar studies were reported for natural water from a river [447].

Cyanobacterial toxins produced and released by cyanobacteria in freshwater around the world pose a considerable threat to human health if present in drinking water sources. Therefore, various treatments have been applied to remove these toxins. The effectiveness of TiO<sub>2</sub> photocatalysis for the removal of microcystin-LR from water has been established [448]. Not only does the process rapidly remove the toxin but also the by-products appear to be nontoxic. The photocatalytic process has also significantly reduced the protein phosphatase 1 (PP1) inhibition. Protein phosphatase 1 inhibition is potentially one of the most serious harmful effects to humans who may consume water contaminated by microcystins. Figure 16 shows some of these data, namely, the reduction of the microcystin-LR concentration and the PP1 inhibition as a function of the illumination time. The results indicate that about 86% of

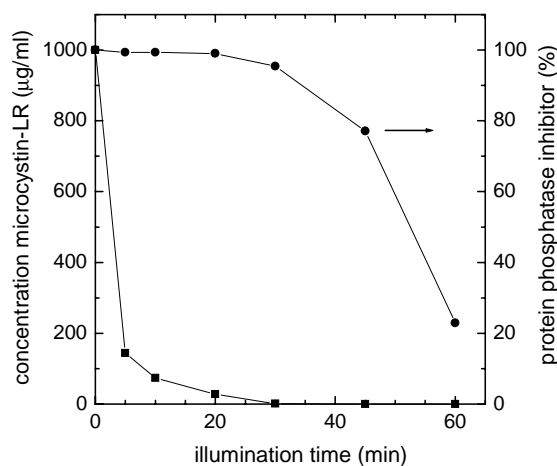


**Figure 16.** Destruction and protein phosphatase (PP1) inhibition of microcystin-LR via TiO<sub>2</sub> photocatalysis as a function of the duration of UV illumination (xenon lamp with 480 W at a wavelength of 330–450 nm). Data from [448], I. Liu et al., *J. Photochem. Photobiol. A: Chem.* 148, 349 (2002).

microcystin-LR was destroyed within the first 5 min of photocatalysis, with 97% of the toxin removed in 20 min. The addition of 0.1% H<sub>2</sub>O<sub>2</sub> to the photocatalytic system was found [448] to further enhance the degradation rate: 99.6% of microcystin-LR was destroyed within 5 min and no toxin was left after 10 min of photocatalysis.

Photocatalytic inactivation of different bacteria and bacteriophages in drinking water at different TiO<sub>2</sub> concentrations with or without concurrent exposure to O<sub>2</sub> was studied in [449] using UV irradiation (5.5 mW/cm<sup>2</sup> at 365 nm). For example, for this light intensity, the most effective inactivation of *Escherichia coli* CN13 was obtained at 1 g/l suspension of TiO<sub>2</sub>, resulting in a reduction by five orders of magnitude in 5 min. Under the same experimental conditions, MS2 bacteriophage was reduced by four orders of magnitude, also in 5 min. The addition of O<sub>2</sub> into the experimental environment increased the inactivation of *Deinococcus radiophilus* by four orders of magnitude in 60 min.

#### 7.5. Miscellaneous Photocatalytic Applications

It may have become apparent from the foregoing discussions and examples that the solution of environmental problems constitutes one of the (if not the) major driving forces in research and development in photocatalysis using nanometer-sized TiO<sub>2</sub> (and other semiconductor) particles. Another one, of course, is the production of hydrogen from water splitting. Apart from these main applications, there exist, on the other hand, many attempts to explore novel areas for the photocatalytic use of nanocrystalline TiO<sub>2</sub> materials. To give a flavor of the diversity of these efforts, some selected (and mostly recent) examples follow.

Nano-sized titanium oxide (TiO<sub>2</sub>) thin films have been explored for alcohol-sensing applications. TiO<sub>2</sub> thin films with different doping concentrations were prepared on alumina substrates [450] using the sol-gel process using the spin-coating technique for ethanol and methanol alcohol. Experimental results indicated that the sensor is able to monitor alcohols selectively at ppm levels; the films are stoichiometric with carbon as the dominant impurity on the surface. The morphologies and crystalline structures of the films were studied by scanning electron microscopy (SEM) and XRD. X-ray diffraction patterns showed that the films are pure anatase phase up to an annealing temperature of 600 °C. As the annealing temperature increased to 800 °C, a small amount of rutile phase formed along with the anatase phase.

Optical waveguides were prepared by depositing a sol-gel-derived titania film onto a silica substrate [451]. The titania film is mesoporous, with pore sizes ranging from 3 to 8 nm. Deposition of the titania does not change the critical angle of total internal reflection. Thus, the titania-coated waveguides propagate light in an attenuated total reflection mode, despite the relatively high refractive index ( $n = 1.8$  in air) of the titania film relative to the silica substrate ( $n = 0.5$ ).

The light output of electric lighting gradually decreases due to stain buildup on lamps and covers during operation. Roadway, and especially tunnel lighting, experiences a large amount of contamination due to dust, carbon particles found in vehicle engine exhausts and other airborne contaminants,

which results in the rapid deterioration of the light output. Photocatalytic reactions caused by TiO<sub>2</sub> are known to decompose such stains. This reaction is caused by the absorption of UV light ( $\lambda \leq 400$  nm, corresponding to the bandgap of  $\sim 3$  eV) irradiated from lamps or the sun, and followed by oxidation. Extensive field tests revealed [452] that a fine film coating of TiO<sub>2</sub> on lamps and luminaires can effectively decompose various organic compounds such as vehicle exhaust gases, oil, nicotine, etc. This leads to an improvement of the luminous performance of installed lighting systems and reduces the cost of maintenance by approximately one-half.

It has been recently found [453] that photocatalytic TiO<sub>2</sub> coated with polycarbonate (PC) releases a huge amount of exothermic energy in the temperature range between 200 and 400 °C (ca. 1.85 kJ/g). The strong interaction between oxygen-deficient sites in TiO<sub>2</sub> and carbonyl groups of PC mediated by a good PC solvent is found to be a prerequisite for a release of the enormous amount of exothermic energy. This finding suggests that PC-coated TiO<sub>2</sub> powders or related oxides work as a combustion-assisting agent in a relatively lower temperature range and can be utilized for incineration applications in order to suppress the formation of extremely toxic dioxins.

A somewhat unusual application reported [454] the photocatalytic deposition of a gold particle onto the top of a SiN cantilever tip, employing the photocatalytic effect of titanium dioxide. When the titanium dioxide immersed in a solution including gold ions is subject to optical exposure, the excited electrons in the conduction band reduce gold ions into gold metal. Illumination by an evanescent wave generated with a total reflection configuration limits the deposition region to the very tip. In the experiments, 100–300 nm gold particles on SiN cantilever tips for atomic force microscopes were obtained. In a related vein, photo-induced deposition of copper on nanocrystalline TiO<sub>2</sub> films was proposed [455].

Solar photocatalytic oxidation processes (PCO) for degradation of water and air pollutants have received increasing attention. In fact, some field-scale experiments have demonstrated the feasibility of using a semiconductor (TiO<sub>2</sub>) in solar collectors and concentrators to completely mineralize organic contaminants in water and air [456]. Although successful preindustrial solar tests have been carried out, there are still discrepancies and doubt concerning process fundamentals such as the roles of active components, appropriate modelling of reaction kinetics, or quantification of photo-efficiency. Challenges to development are catalyst deactivation, slow kinetics, low photo-efficiency and unpredictable mechanisms. The development of specific nonconcentrating collectors for detoxification and the use of additives such as peroxydisulfate have made competitive use of solar PCO possible.

## GLOSSARY

**Charge transfer** The transfer of a charge carrier (electron or hole) from an excited semiconductor to an adsorbed species on its surface. This transfer may initiate a reaction (oxidation or reduction) in the adsorbed molecule.

**Dye-sensitized semiconductor** Adsorbing a suitable dye on the surface of a wide band gap semiconductor (like TiO<sub>2</sub>) can

enhance the efficiency of the excitation step and, hence, the catalytic activity.

**Electron-hole pair** The absorption of a photon of sufficient energy may excite in a semiconductor an electron from the valence band to the conduction band, thereby creating a hole in the valence band.

**Nanocrystalline** A material composed of individual crystallites which have a size in the range of nanometer (nm); 1 nm = 10<sup>-9</sup> m.

**Photocatalysis** A catalytic reaction triggered or enhanced by illuminating the system with visible or ultraviolet irradiation. This reaction involves normally the electronic excitation of the catalyst via the absorption of photons and an interfacial charge transfer to an adsorbed species. Typically, the photocatalyst is not consumed in the reaction.

**Photocatalytic degradation** The removal or reduction of (usually unwanted) substances via a photocatalytic reaction.

**Quantum yield** The probability of product formation per adsorbed photon in a photocatalytic reaction.

**Titanium oxide** Titanium dioxide with the nominal composition TiO<sub>2</sub> is a semiconductor with a band gap of  $\sim 3.2$  eV; it exists in three different crystalline modifications, two of which (anatase and rutile) are commonly employed in photocatalysis.

## REFERENCES

1. H. S. Nalwa, Ed., "Encyclopedia of Nanoscience and Nanotechnology." American Scientific Publisher, Stevenson Ranch CA, 2003, in press.
2. J. H. Fendler, Ed., "Nanoparticles and Nanostructured Films." Wiley-VCH, Weinheim, 1998.
3. R. W. Siegel, in "Physics of New Materials" (E. Fujita, Ed.), p. 66. Springer, Berlin, 1998.
4. G. L. Timp, Ed., "Nanotechnology." Springer, New York, 1999.
5. V. A. Shchukin and D. Bimberg, *Rev. Mod. Phys.* 71, 1125 (1999).
6. H. S. Nalwa, Ed., "Handbook of Nanostructured Materials and Nanotechnology," Vols. 1–5. Academic, San Diego, 2000.
7. C. Binns, *Surf. Sci. Rep.* 44, 1 (2001).
8. J. Y. Ying, Ed., "Nanostructured Materials," Academic, San Diego, 2001.
9. M. Köhler, "Nanotechnologie." Wiley-VCH, Weinheim, 2001.
10. H. S. Nalwa, Ed., "Nanostructured Materials and Nanotechnology." Academic, San Diego, 2001.
11. J. M. Thomas and W. J. Thomas, "Principles and Practice of Heterogeneous Catalysis." VCH, Weinheim, 1997.
12. J. H. Sinfelt, *Surf. Sci.* 500, 923 (2002).
13. F. Zaera, *Surf. Sci.* 500, 947 (2002).
14. J. M. Greenberg, *Surf. Sci.* 500, 793 (2002).
15. D. A. Williams and E. Herbst, *Surf. Sci.* 500, 823 (2002).
16. E. Zinner, *Ann. Rev. Earth Planet. Sci.* 26, 147 (1998).
17. L. Grossman, *Geochim. Cosmochim. Acta* 36, 597 (1972).
18. B. Mason and L. G. Berry, "Elements of Mineralogy." Freeman, San Francisco, 1968.
19. V. E. Henrich and P. A. Cox, "The Surface Science of Metal Oxides." Cambridge University Press, Cambridge, 1996.
20. B. Levy, *J. Electroceram.* 1, 239 (1997).
21. M. A. Fox and M. T. Dulay, *Chem. Rev.* 93, 341 (1993).
22. A. L. Linsebigler, G. Q. Lu, and J. T. Yates, *Chem. Rev.* 95, 735 (1995).
23. A. Fujishima and K. Honda, *Nature* 238, 37 (1972).
24. A. Fujishima, K. Kobayakawa, and K. Honda, *J. Electrochem. Soc.* 122, 1487 (1975).
25. A. Mills and S. LeHunte, *J. Photochem. Photobiol. A: Chem.* 108, 1 (1997).

26. A. Fujishima and T. N. Rao, *Pure Appl. Chem.* 70, 2177 (1998).
27. A. Fujishima, K. Hashimoto, and T. Watanabe, "TiO<sub>2</sub> Photocatalysis: Fundamentals and Applications." BKC, Tokyo, 1999.
28. A. J. Bard, *J. Phys. Chem.* 86, 172 (1982).
29. M. Grätzel, Ed., "Energy Resources Through Photochemistry and Catalysis." Academic, New York, 1983.
30. E. Pelizzetti and M. Schiavello, Eds., "Photochemical Conversion and Storage of Solar Energy." Kluwer Academic Publishers, Dordrecht, 1991.
31. M. Schiavello, Ed., "Photocatalysis and Environment." Kluwer Academic Publishers, Dordrecht, 1988.
32. D. F. Ollis and H. Al-Ekabi, Eds., "Photocatalytic Purification and Treatment of Water and Air." Elsevier, Amsterdam, 1993.
33. J. Peral, X. Domènech, and D. F. Ollis, *J. Chem. Technol. Biotechnol.* 70, 117 (1997).
34. J. H. Fendler, *J. Phys. Chem.* 89, 2730 (1985).
35. M. Pessarakli, Ed., "Handbook of Photosynthesis." Marcel Dekker, New York, 1997.
36. K. Kalayanasundaram, M. Grätzel, and E. Pelizzetti, *Coord. Chem. Rev.* 69, 57 (1986).
37. B. A. Perkinson and M. T. Spitler, *Electrochem. Acta* 37, 943 (1992).
38. B. O'Regan and M. Grätzel, *Nature* 353, 737 (1991).
39. H. Weller, *Angew. Chem. Int. Ed. Engl.* 32, 41 (1993).
40. L. N. Lewis, *Chem. Rev.* 93, 2693 (1993).
41. A. Henglein, *J. Phys. Chem.* 97, 5457 (1993).
42. C. Bechinger, E. Wirth, and P. Leiderer, *Appl. Phys. Lett.* 68, 2843 (1996).
43. S. N. Frank and A. J. Bard, *J. Am. Chem. Soc.* 99, 303 (1977).
44. S. N. Frank and A. J. Bard, *J. Phys. Chem.* 81, 1484 (1977).
45. M. R. Hoffmann, S. T. Martin, W. Choi, and D. W. Bahnemann, *Chem. Rev.* 95, 69 (1995).
46. A. Fujishima, T. N. Rao, and D. A. Tryk, *J. Photochem. Photobiol. C: Photochem. Rev.* 1, 1 (2000).
47. J. C. Ireland, P. Klostermann, E. W. Rice, and R. M. Clark, *Appl. Environ. Microbiol.* 59, 1668 (1993).
48. J. C. Sjogren and R. A. Sierka, *Appl. Environ. Microbiol.* 60, 344 (1994).
49. R. X. Cai, Y. Kubota, T. Shuin, H. Sakai, K. Hashimoto, and A. Fujishima, *Cancer Res.* 52, 2346 (1992).
50. N. B. Jackson, C. M. Wang, Z. Luo, J. Schwitzgebel, J. G. Ekerdt, J. R. Brock, and A. Heller, *J. Electrochem. Soc.* 138, 3660 (1991).
51. H. Gerischer and A. Heller, *J. Electrochem. Soc.* 139, 113 (1992).
52. E. C. Butler and A. P. Davis, *J. Photochem. Photobiol. A: Chem.* 70, 273 (1993).
53. Y. Luo and D. F. Ollis, *J. Catal.* 163, 1 (1996).
54. L. R. Skubal, N. K. Meshkov, and M. C. Vogt, *J. Photochem. Photobiol. A: Chem.* 148, 103 (2002).
55. C. Wang, J. Rabani, D. W. Bahnemann, and J. K. Dohrmann, *J. Photochem. Photobiol. A: Chem.* 148, 169 (2002).
56. R. Gao, J. Stark, D. W. Bahnemann, and J. Rabani, *J. Photochem. Photobiol. A: Chem.* 148, 387 (2002).
57. K. J. Klabunde, J. Stark, O. Koper, C. Mohs, D. G. Park, S. Decker, Y. Jiang, I. Lagadic, and D. Zhang, *J. Phys. Chem.* 100, 12142 (1996).
58. K. N. P. Kumer, K. Keizer, A. J. Burggraaf, T. Okubo, H. Nagamoto, and S. Morooka, *Nature* 358, 48 (1992).
59. M. Gopal, W. J. Moberly Chan, and L. C. De Jonghe, *J. Mater. Sci.* 32, 6001 (1997).
60. S. Ito, S. Inoue, H. Kawada, M. Hara, M. Iwasaki, and H. Tada, *J. Colloid Interface Sci.* 216, 59 (1999).
61. K. Terabe, K. Kato, H. Miyazaki, S. Yamaguchi, A. Imai, and Y. Iguchi, *J. Mater. Sci.* 29, 1617 (1994).
62. K. S. Suslick, *Science* 247, 1439 (1990).
63. H. Tada, K. Teranishi, Y. Inubushi, and S. Ito, *Chem. Comm.* 2345 (1998).
64. S. Kambe, K. Murakoshi, T. Kitamura, Y. Wada, S. Yanagida, H. Kominami, and Y. Kera, *Solar Energy Mater. Solar Cells* 61, 427 (2000).
65. R. Wang, K. Hashimoto, A. Fujishima, M. Chikuni, E. Kojima, A. Kitamura, M. Shimohigoshi, and T. Watanabe, *Nature* 388, 431 (1997).
66. R. Wang, N. Sakai, A. Fujishima, T. Watanabe, and K. Hashimoto, *J. Phys. Chem. B* 103, 2188 (1999).
67. C. Anderson and J. A. Bard, *J. Phys. Chem.* 99, 9882 (1995); *ibid.* 101, 2611 (1997).
68. H. Tada, Y. Kubo, M. Akazawa, and S. Ito, *Langmuir* 14, 2936 (1998).
69. A. Hagfeldt and M. Grätzel, *Chem. Rev.* 95, 49 (1995).
70. T. Gerfin, M. Grätzel, and L. Walder, *Prog. Inorgan. Chem.* 44, 345 (1997).
71. M. Grätzel, *Nature* 414, 338 (2001).
72. E. Becquerel, *Compt. Rend.* 9, 145 (1839).
73. U. Bach, D. Lupo, P. Comte, J. E. Moser, F. Weissörtel, J. Salbeck, H. Spreitzer, and M. Grätzel, *Nature* 395, 583 (1998).
74. S. Södergren, A. Hagfeldt, J. Olsson, and S. E. Lindquist, *J. Phys. Chem.* 98, 5552 (1994).
75. G. K. Boschloo and A. Goossens, *J. Phys. Chem.* 100, 19489 (1996).
76. G. K. Boschloo, A. Goossens, and J. Schoonman, *J. Electroanal. Chem.* 428, 25 (1997).
77. D. Cahen, G. Hodes, M. Grätzel, J. F. Guillemoles, and I. Riess, *J. Phys. Chem. B* 104, 2053 (2000).
78. L. Kavan, K. Kratochvilová, and M. Grätzel, *J. Electroanal. Chem.* 394, 93 (1995).
79. P. E. de Jong and D. Vanmaekelbergh, *J. Phys. Chem. B* 101, 2716 (1997).
80. D. Vanmaekelbergh and P. E. de Jongh, *J. Phys. Chem. B* 103, 747 (1999).
81. G. Schlichthörl, S. Y. Huang, J. Sprague, and A. J. Frank, *J. Phys. Chem. B* 101, 8141 (1997).
82. S. Y. Huang, G. Schlichthörl, A. J. Nozik, M. Grätzel, and A. J. Frank, *J. Phys. Chem. B* 101, 2576 (1997).
83. G. Franco, J. Gehring, L. M. Peter, E. A. Ponomarev, and I. Uhlen-dorf, *J. Phys. Chem. B* 103, 692 (1999).
84. G. K. Boschloo and D. Fitzmaurice, *J. Phys. Chem. B* 103, 2228 (1999).
85. B. O'Regan, M. Grätzel, and D. Fitzmaurice, *Chem. Phys. Lett.* 183, 89 (1991).
86. A. Kay, R. Humphry-Baker, and M. Grätzel, *J. Phys. Chem.* 98, 952 (1994).
87. R. J. Ellingson, J. B. Asbury, S. Ferrere, H. N. Ghosh, J. R. Sprague, T. Lian, and A. J. Nozik, *J. Phys. Chem. B* 102, 6455 (1998).
88. J. B. Asbury, R. J. Ellingson, H. N. Ghosh, S. Ferrere, A. J. Nozik, and T. Lian, *J. Phys. Chem. B* 103, 3110 (1999).
89. W. S. Struve, "Fundamentals of Molecular Spectroscopy." Wiley, New York, 1989.
90. P. W. Atkins, "Molecular Quantum Mechanics," 2nd ed. Oxford University Press, Oxford, 1983.
91. Y. Nosaka and M. A. Fox, *J. Phys. Chem.* 92, 1893 (1988).
92. S. T. Martin, H. Herrmann, and M. R. Hoffmann, *Trans. Faraday Soc.* 90, 3315 and 3323 (1994).
93. M. Grätzel, "Heterogeneous Photochemical Electron Transfer." CRC Press, Boca Raton, FL, 1989.
94. P. Y. Yu and M. Cardona, "Fundamentals of Semiconductors." Springer, Berlin, 2001.
95. G. J. Kavarnos and N. J. Turro, *Chem. Rev.* 86, 401 (1986).
96. P. V. Kamat, *Chem. Rev.* 93, 267 (1993).
97. W. J. Albery and P. N. Bartlett, *J. Electrochem. Soc.* 131, 315 (1984).
98. H. Lüth, "Solid Surfaces, Interfaces and Thin Films." Springer, Berlin, 2001.
99. L. E. Brus, *J. Chem. Phys.* 80, 4403 (1984).
100. A. Henglein, *J. Phys. Chem.* 86, 2291 (1982).
101. D. Duonghong, J. Ramsden, and M. Grätzel, *J. Am. Chem. Soc.* 104, 2977 (1982).
102. P. V. Kamat, in "Handbook of Nanostructured Materials and Nanotechnology" (H. S. Nalwa, Ed.), Vol. 3, p. 291. Academic, San Diego, 2000.

103. N. S. Lewis, *Annu. Rev. Phys. Chem.* 42, 543 (1991).
104. A. Henglein, *Chem. Rev.* 89, 1861 (1989).
105. M. L. Steigenwald and L. E. Brus, *Acc. Chem. Res.* 23, 183 (1990).
106. L. Banyai and S. W. Koch, "Semiconductor Quantum Dots." World Scientific, Rivers Edge, NJ, 1993.
107. L. Jacak, P. Hawrylak, and A. Wójs, "Quantum Dots." Springer, Berlin, 1998.
108. L. E. Brus, *J. Chem. Phys.* 79, 5566 (1983).
109. H. M. Schmidt and H. Weller, *Chem. Phys. Lett.* 129, 615 (1986).
110. M. G. Bawendi, M. L. Steigenwald, and L. E. Brus, *Annu. Rev. Phys. Chem.* 41, 477 (1990).
111. H. Tang, H. Berger, P. E. Schmid, and F. Lévy, *Solid State Comm.* 92, 267 (1994).
112. H. Tang, F. Lévy, H. Berger, and P. E. Schmid, *Phys. Rev. B* 52, 7771 (1995).
113. G. Mie, *Ann. Phys.* 25, 377 (1908).
114. C. F. Bohren and D. R. Huffman, "Absorption and Scattering of Light by Small Particles." Wiley, New York, 1983.
115. U. Kreibitz and M. Vollmer, "Optical Properties of Metal Clusters." Springer, Berlin, 1995.
116. U. Kreibitz and C. v. Fragstein, *Z. Phys.* 224, 307 (1969).
117. M. M. Alvarez, J. T. Khoury, T. G. Schaaff, M. N. Shafiqullin, I. Vezmar, and R. L. Whetten, *J. Phys. Chem. B* 101, 3706 (1997).
118. G. C. Papavassiliou, *Prog. Sol. State Chem.* 12, 185 (1979).
119. P. V. Kamat, *Prog. Inorgan. Chem.* 44, 273 (1997).
120. G. Hodes, *Isr. J. Chem.* 33, 95 (1993).
121. G. J. Meyer and P. C. Searson, *Interface* 23–27 (1993).
122. P. V. Kamat, *Chemtech, June*, 22–28 (1995).
123. N. Uekawa, T. Suzuki, S. Ozeki, and K. Kaneko, *Langmuir* 8, 1 (1992).
124. D. V. Paranjape, M. Sastry, and P. Ganguly, *Appl. Phys. Lett.* 63, 18 (1993).
125. K. Vinodgopal, U. Stafford, K. A. Gray, and P. V. Kamat, *J. Phys. Chem.* 98, 6797 (1994).
126. A. Hagfeldt, S. E. Lindquist, and M. Grätzel, *Sol. Energy Mater. Sol. Cells* 32, 245 (1994).
127. N. A. Kotov, F. C. Meldrum, and J. H. Fendler, *J. Phys. Chem.* 98, 8827 (1994).
128. X.-Z. Ding, Z.-Z. Qi, and Y.-Z. He, *J. Mater. Sci. Lett.* 14, 21 (1995).
129. L. Su and Z. Lu, *Spectrochim. Acta* 53A, 1719 (1997).
130. X. Z. Ding and X. H. Liu, *Mater. Sci. Eng. A* 224, 210 (1997).
131. D. Robert and J. V. Weber, *J. Mater. Sci. Lett.* 18, 97 (1999).
132. H. Kozuka, Y. Takahashi, G. Zhao, and T. Yokoi, *Thin Solid Films* 358, 172 (2000).
133. L. Znaidi, R. Seraphimova, J. F. Bocquet, C. Colbeau-Justin, and C. Pommier, *Mater. Res. Bull.* 36, 811 (2001).
134. C. J. Brinker and G. W. Scherer, "Sol-Gel Science." Academic, San Diego, 1990.
135. L. C. Klein, Ed., "Sol-Gel Optics: Processing and Applications." Kluwer, Boston, 1994.
136. K. Vinodgopal, S. Hotchandani, and P. V. Kamat, *J. Phys. Chem.* 97, 9040 (1993).
137. M.-P. Zheng, M.-Y. Gu, Y.-P. Jin, and G.-L. Jin, *J. Mater. Sci. Lett.* 20, 485 (2001).
138. J. Livage, M. Henry, and C. Sanchez, *Prog. Solid State. Chem.* 18, 259 (1988).
139. J. Moser, S. Punchihewa, P. P. Infelta, and M. Grätzel, *Langmuir* 7, 3012 (1991).
140. H. Kominami, J. Kato, S. Murakami, Y. Kera, M. Inoue, T. Inui, and B. Ohtani, *J. Mol. Catal. A* 144, 165 (1999).
141. S. Ito, S. Inoue, H. Kawada, M. Hara, M. Iwasaki, and H. Tada, *J. Colloid Interface Sci.* 216, 59 (1999).
142. T. Sugimoto, H. Itoh, and T. Mochida, *J. Colloid Interf. Sci.* 205, 42 (1998).
143. T. Sugimoto, X. Zhou, and A. Muramatsu, *J. Colloid Interf. Sci.* 252, 339 (2002).
144. T. Sugimoto and X. Zhou, *J. Colloid Interf. Sci.* 252, 347 (2002).
145. N. Uekawa, J. Kajiwara, K. Kakegawa, and Y. Sasaki, *J. Colloid Interf. Sci.* 250, 285 (2002).
146. S. Yin, Y. Inoue, S. Uchida, Y. Fujishiro, and T. Sato, *J. Mater. Res.* 13, 844 (1998).
147. C.-C. Wang and J. Y. Ying, *Chem. Mater.* 11, 3113 (1999).
148. J. Yu, X. Zhao, and Q. Zhao, *Thin Solid Films* 379, 7 (2000).
149. J. Yu and X. Zhao, *Mater. Res. Bull.* 35, 1293 (2000).
150. N. Negishi, K. Takeuchi, T. Ibusuki, and A. K. Datye, *J. Mater. Sci. Lett.* 18, 515 (1999).
151. N. Negishi and K. Takeuchi, *Thin Solid Films* 392, 249 (2001).
152. P. Sawunyama, A. Yasumori, and K. Okada, *Mater. Res. Bull.* 33, 795 (1998).
153. C. K. Chan, J. F. Porter, Y.-G. Li, W. Guo, and C.-M. Chan, *J. Am. Ceram. Soc.* 82, 566 (1999).
154. A. V. Vorontsov, A. A. Altyinnikov, E. N. Savinov, and E. N. Kurkin, *J. Photochem. Photobiol., A: Chem.* 144, 193 (2001).
155. S. Yin, R. Li, Q. He, and T. Sato, *Mater. Chem. Phys.* 75, 76 (2002).
156. X.-S. Feng, S.-Z. Kang, H.-G. Liu, and J. Mu, *Thin Solid Films* 352, 223 (1999).
157. K. Shimizu, H. Imai, H. Hirashima, and K. Tsukuma, *Thin Solid Films* 351, 220 (1999).
158. S. J. Kim, S. D. Park, C. K. Rhee, W. W. Kim, and S. Park, *Scr. Mater.* 44, 1229 (2001).
159. L. Shi, C. Li, H. Gu, and D. Fang, *Mater. Chem. Phys.* 62, 62 (2000).
160. R. W. Siegel, in "Materials Science and Technology" (R. W. Cahn, Ed.), Vol. 15, p. 583. VCH, Weinheim, 1991.
161. K. Takagi, T. Makimoto, H. Hiraiwa, and T. Negishi, *J. Vac. Sci. Technol. A* 19, 2931 (1999).
162. P. Zeman and S. Takabayashi, *Surf. Coat. Technol.* 153, 93 (2002).
163. P. Zeman and S. Takabayashi, *J. Vac. Sci. Technol. A* 20, 388 (2002).
164. W. Zhang, Y. Li, and F. Wang, *J. Mater. Sci. Technol. (China)* 18, 101 (2002).
165. Y. Hou, D. Zhuang, D. Zhao, J. Zhang, and C. Wang, in "Advanced Photonic Sensors: Technology and Applications." Proc. SPIE, Vol. 4220, 2000, p. 34.
166. O. Banakh, P. E. Schmid, R. Sanjines, and F. Levy, *Surf. Coat. Technol.* 151–152, 272 (2002).
167. T. Wang, H. Wang, P. Xu, X. Zhao, Y. Liu, and S. Chao, *Thin Solid Films* 334, 103 (1998).
168. C.-C. Ting, S.-Y. Chen, and D.-M. Liu, *J. Appl. Phys.* 88, 4628 (2000).
169. S. Takeda, S. Suzuki, H. Odaka, and H. Hosono, *Thin Solid Films* 392, 338 (2001).
170. H. Ohsaki, Y. Tachibana, A. Mitsui, T. Kamiyama, and Y. Hayashi, *Thin Solid Films* 392, 169 (2001).
171. S. G. Springer, P. E. Schmid, R. Sanjines, and E. Levy, *Surf. Coat. Technol.* 151–152, 51 (2002).
172. J. A. Ayllon, A. Figueras, S. Garelik, L. Spirkova, J. Durand, and L. Cot, *J. Mater. Sci. Lett.* 18, 1319 (1999).
173. V. G. Bessergenev, I. V. Khmelinskii, R. J. F. Pereira, V. V. Krisuk, A. E. Turgambaeva, and I. K. Igumenov, *Vacuum* 64, 275 (2002).
174. Y. C. Zhu and C. X. Ding, *J. Eur. Ceram. Soc.* 20, 127 (2000).
175. Y. C. Zhu and C. X. Ding, *Nanostruct. Mater.* 11, 319 (1999).
176. A. Goossens and J. Schoonman, *Eur. J. Sol. State Inorgan. Chem.* 32, 779 (1995).
177. B. Major, R. Ebner, P. Zieba, and W. Wolzynski, *Appl. Phys. A* 69, 921 (1999).
178. T. Deguchi, K. Imai, H. Matsui, M. Iwasaki, H. Tada, and S. Ito, *J. Mater. Sci.* 36, 4723 (2001).
179. H. Wang, T. Wang, and P. Xu, *J. Mater. Sci., Mater. Electron.* 9, 327 (1998).
180. M. Terashima, N. Inoue, S. Kashiwabara, and R. Fujimoto, *Appl. Surf. Sci.* 169–170, 535 (2001).
181. S. K. Zheng, T. M. Wang, C. Wang, and G. Xiang, *Nucl. Instrum. Methods B* 187, 479 (2002).
182. S. K. Zheng, T. M. Wang, W. C. Hao, and R. Shen, *Vacuum* 65, 155 (2002).

183. X. Liu, C. Liang, H. Wang, X. Yang, L. Lu, and X. Wang, *Mater. Sci. Eng. A* 326, 235 (2002).
184. H. Yamashita, Y. Ichihashi, M. Takeuchi, S. Kishiguchi, and M. Anpo, *J. Synchrotron Radiat.* 6, 451 (1999).
185. K. Oyoshi, N. Sumi, I. Umez, R. Souda, A. Yamazaki, H. Haneda, and T. Mitsuhashi, *Nucl. Instrum. Methods B* 168, 221 (2000).
186. Z. Xu, J. Shang, C. Liu, C. Kang, H. Guo, and Y. Du, *Mater. Sci. Eng. B* 63, 211 (1999).
187. T. Ihara, M. Miyoshi, M. Ando, S. Sugihara, and Y. Iriyama, *J. Mater. Sci.* 36, 4201 (2001).
188. K. Furusawa, K. Takahashi, S.-H. Cho, H. Kumagai, K. Midorikawa, and M. Obara, *J. Appl. Phys.* 87, 1604 (2000).
189. V. Subramanian, E. Wolf, and P. V. Kamat, *J. Phys. Chem. B* 105, 11439 (2001).
190. T. Ohno, K. Fujihara, S. Saito, and M. Matsumura, *Sol. Energy Mater. Sol. Cells* 45, 169 (1997).
191. M. Tsujimoto, S. Moriguchi, S. Isoda, T. Kobayashi, and T. Komatsu, *J. Electron Microsc.* 48, 361 (1999).
192. J. Yu, J. C. Yu, B. Cheng, and X. Zhao, *J. Sol-Gel Sci. Technol.* 24, 39 (2002).
193. H. Wang, P. Xu, and T. Wang, *J. Vac. Sci. Technol. B* 19, 645 (2001).
194. Y. Wang, H. Cheng, Y. Hao, J. Ma, W. Li, and S. Cai, *Thin Solid Films* 349, 120 (1999).
195. H. Deng, Z. Lu, Y. Shen, H. Mao, and H. Xu, *Chem. Phys.* 231, 95 (1998).
196. A. Dawson and P. V. Kamat, *J. Phys. Chem. B* 105, 960 (2001).
197. D. Beydoun, R. Amal, G. K. C. Low, and S. McEvoy, *J. Phys. Chem. B* 104, 4387 (2000).
198. T. Kasuga, M. Hiramatsu, M. Hirano, A. Hoson, and K. Oyamada, *J. Mater. Res.* 12, 607 (1997).
199. S.-H. Hahn, D.-J. Kim, S.-H. Oh, E.-J. Kim, and S.-W. Kim, in "Proc. 5th Korea-Russia International Symp. on Science and Technology," p. 337. IEEE, Piscataway, 2001.
200. F. P. Getton, V. A. Self, J. M. Ferguson, J. G. Leadley, P. A. Sermon, and M. Montes, *Ceram. Trans.* 81, 355 (1998).
201. R. van Grieken, J. Aguado, M. J. López-Muñoz, and J. Marugán, *J. Photocem. Photobiol. A: Chem.* 148, 315 (2002).
202. T. Tanaka, K. Teramura, T. Yamamoto, S. Takenaka, S. Yoshida, and T. Funabiki, *J. Photocem. Photobiol. A: Chem.* 148, 277 (2002).
203. B. Pal, M. Sharon, and G. Nogami, *Mater. Chem. Phys.* 59, 254 (1999).
204. J. Yang, D. Li, X. Wang, X. Yang, and L. Lu, *J. Solid State Chem.* 165, 193 (2002).
205. M. E. Rincon, A. Jimenez, A. Orihuela, and G. Martinez, *Sol. Energy Mater. Sol. Cells* 70, 163 (2001).
206. K. Kato and K.-I. Niihara, *Thin Solid Films* 298, 76 (1997).
207. A. P. Hong, D. W. Bahnemann, and M. R. Hoffmann, *J. Phys. Chem.* 91, 6245 (1987).
208. K. B. Dhanalakshmi, S. Latha, S. Anandan, and P. Maruthamuthu, *Intern. J. Hydrogen Energy* 26, 669 (2001).
209. S. Wenfeng and A. Yoshida, *Sol. Energy Mater. Sol. Cells* 69, 189 (2001).
210. H. N. Ghosh and S. Adhikari, *Langmuir* 17, 4129 (2001).
211. Y. Lei, L. D. Zhang, G. W. Meng, G. H. Li, X. Y. Zhang, C. H. Liang, W. Chen, and S. X. Wang, *Appl. Phys. Lett.* 78, 1125 (2001).
212. T. Akita, K. Tanaka, K. Okuma, T. Koyanagi, and M. Haruta, *J. Electr. Microsc.* 50, 473 (2001).
213. G. L. Li, G. H. Wang, and J. M. Hong, *J. Mater. Res.* 14, 3346 (1999).
214. T. Kasuga, M. Hiramatsu, A. Hoson, T. Sekino, and K. Niihara, *Langmuir* 14, 3160 (1998).
215. H. Imai, Y. Takei, K. Shimizu, M. Matsuda, and H. Hirashima, *J. Mater. Chem.* 9, 2971 (1999).
216. T. Kasuga, M. Hiramatsu, A. Hoson, T. Sekino, and K. Niihara, *Adv. Mater.* 11, 1307 (1999).
217. G. H. Du, Q. Chen, R. C. Che, Z. Y. Yuan, and L. M. Peng, *Appl. Phys. Lett.* 79, 3702 (2001).
218. A. Chemseddine and T. Moritz, *Eur. J. Inorg. Chem.* 235 (1999).
219. J. C. Yu, J. Yu, W. Ho, and L. Zhang, *Chem. Comm.* 1942 (2001).
220. H. Parala, A. Devi, R. Bhakta, and R. A. Fischer, *J. Mater. Chem.* 12, 1625 (2002).
221. B. R. Weinberger and R. B. Garber, *Appl. Phys. Lett.* 66, 2409 (1995).
222. M. M. Gómez, J. Lu, E. Olsson, A. Hagfeldt, and C. G. Granqvist, *Sol. Energy Mater. Sol. Cells* 64, 385 (2000).
223. M. Suzuki, T. Ito, and Y. Taga, *Appl. Phys. Lett.* 78, 3968 (2001).
224. P. Hoyer, *Adv. Mater.* 8, 857 (1996).
225. P. Hoyer, *Langmuir* 12, 1411 (1996).
226. B. B. Lakshmi, C. J. Patrissi, and C. R. Martin, *Chem. Mater.* 9, 2544 (1997).
227. Y. J. Song and Z. L. Wang, *Adv. Mater.* 11, 469 (1999).
228. M. Adachi, Y. Murata, M. Harada, and S. Yoshikawa, *Chem. Lett.* 942 (2000).
229. M. Zhang, Y. Bando, and K. Wada, *J. Mater. Sci. Lett.* 20, 167 (2001).
230. A. Michailowski, D. AlMawlawi, G. Cheng, and M. Moskovits, *Chem. Phys. Lett.* 349, 1 (2001).
231. Y. C. Zhu and C. X. Ding, *Nanostruct. Mater.* 11, 427 (1999).
232. J. Augustynski, *J. Electrochim. Acta* 38, 43 (1993).
233. J. K. Burdett, *Inorgan. Chem.* 24, 2244 (1985).
234. J. K. Burdett, T. Hughbands, J. M. Gordon, J. W. Richardson, and J. V. Smith, *J. Am. Chem. Soc.* 109, 3639 (1987).
235. A. Fahmi, C. Minot, B. Silvi, and M. Causa, *Phys. Rev. B* 47, 11717 (1993).
236. X.-F. Yu, N.-Z. Wu, Y.-C. Xie, and Y.-Q. Tang, *J. Mater. Sci. Lett.* 20, 319 (2001).
237. J. Nair, P. Nair, F. Mizukami, Y. Oosawa, and T. Okubo, *Mater. Res. Bull.* 34, 1275 (1999).
238. D. G. Rickerby, *Philos. Mag. B* 76, 573 (1997).
239. B. Huber, H. Gnaser, and C. Ziegler, *Anal. Bioanal. Chem.* (2003).
240. P. A. Cox, F. W. H. Dean, and A. A. Williams, *Vacuum* 33, 839 (1983).
241. C. R. Henry, *Surf. Sci. Rep.* 31, 231 (1998).
242. H.-J. Freund, *Faraday Discuss.* 114, 1 (1999).
243. U. Diebold, in "The Chemical Physics of Solid Surfaces, Oxide Surfaces," Vol. 9. (D. P. Woodruff, Ed.), Elsevier, Amsterdam, 2001.
244. G. Lu, A. Linsebigler, and J. T. Yates, *J. Phys. Chem.* 98, 11733 (1994).
245. S. Fischer, A. W. Munz, K.-D. Schierbaum, and W. Göpel, *Surf. Sci.* 337, 17 (1995).
246. D. A. Bonnell, *Prog. Surf. Sci.* 57, 187 (1998).
247. U. Diebold, J. Lehman, T. Mahmoud, M. Kuhn, G. Leonardelli, W. Hebenstreit, M. Schmid, and P. Varga, *Surf. Sci.* 411, 137 (1998).
248. M. Li, W. Hebenstreit, U. Diebold, M. A. Henderson, and D. R. Jennison, *Faraday Discuss.* 114, 245 (1999).
249. R. A. Bennett, P. Stone, and M. Bowker, *Faraday Discuss.* 114, 267 (1999).
250. Y. Iwasawa, H. Onishi, K. Fukui, S. Suzuki, and T. Sasaki, *Faraday Discuss.* 114, 259 (1999).
251. T. Fujino, M. Katayama, K. Inudzuka, T. Okuno, and K. Oura, *Appl. Phys. Lett.* 79, 2716 (2001).
252. I. M. Brookes, C. A. Muryn, and G. Thornton, *Phys. Rev. Lett.* 87, 266103-1 (2001).
253. R. Schaub, P. Thostrup, N. Lopez, E. Lægsgaard, I. Stensgarrrd, J. K. Nørskov, and F. Besenbacher, *Phys. Rev. Lett.* 87, 266104-1 (2001).
254. G. S. Herman, M. R. Sievers, and Y. Gao, *Phys. Rev. Lett.* 84, 3354 (2000).
255. R. Hengerer, B. Bolliger, M. Erbudak, and M. Grätzel, *Surf. Sci.* 460, 162 (2000).
256. Y. Liang, S. Gan, and S. A. Chambers, *Phys. Rev. B* 63, 235402-1 (2001).
257. M. Lazzeri and A. Selloni, *Phys. Rev. Lett.* 87, 266105-1 (2001).
258. A. Vittadini, A. Selloni, F. P. Rotzinger, and M. Grätzel, *Phys. Rev. Lett.* 81, 2954 (1998).
259. R. E. Tanner, Y. Liang, and E. I. Altman, *Surf. Sci.* 506, 251 (2002).
260. A. El-Azab, S. Gan, and Y. Liang, *Surf. Sci.* 506, 93 (2002).
261. X. Peng, J. Wickham, and A. P. Alivisatos, *J. Am. Chem. Soc.* 120, 5343 (1998).
262. K. S. Hamad, R. Roth, J. Rockenberger, T. van Buuren, and A. P. Alivisatos, *Phys. Rev. Lett.* 83, 3474 (1999).

263. N. A. Hill and K. B. Whaley, *J. Chem. Phys.* 100, 2831 (1994).
264. Z. Y. Wu, J. Zhang, K. Ibrahim, D. C. Xian, G. Li, Y. Tao, T. D. Hu, S. Bellucci, A. Marcelli, Q. H. Zhang, L. Gao, and Z. Z. Chen, *Appl. Phys. Lett.* 80, 2973 (2002).
265. L. X. Chen, T. Rajh, Z. Y. Wang, and M. Thurnauer, *J. Phys. Chem. B* 101, 10688 (1997).
266. A. P. Xagas, E. Androulaki, A. Hiskia, and P. Falaras, *Thin Solid Films* 357, 173 (1999).
267. A. Provata, P. Falaras, and A. Xagas, *Chem. Phys. Lett.* 297, 484 (1998).
268. J. Y. Ying, L. F. Chi, H. Fuchs, and H. Gleiter, *Nanostruct. Mater.* 3, 273 (1993).
269. E. Comini, G. Sberveglieri, M. Ferroni, V. Guidi, C. Frigeri, and D. Boscarino, *J. Mater. Res.* 16, 1559 (2001).
270. R. I. Bickley, T. Gonzalez-Carreno, J. S. Lees, L. Palmisano, and R. J. D. Tilley, *J. Sol. State Chem.* 92, 178 (1991).
271. P. E. de Jongh and D. Vanmaekelbergh, *Phys. Rev. Lett.* 77, 3427 (1996).
272. A. Zaban, A. Meier, and B. A. Gregg, *J. Phys. Chem. B* 101, 7985 (1997).
273. A. Solbrand, H. Lindström, H. Rensmo, A. Hagfeldt, and S. Lindquist, *J. Phys. Chem. B* 101, 2514 (1997).
274. J. Nelson, *Phys. Rev. B* 59, 15 374 (1999).
275. R. Könenkamp, R. Henninger, and P. Hoyer, *J. Phys. Chem.* 97, 7328 (1993).
276. R. Könenkamp and R. Henninger, *Appl. Phys. A* 58, 87 (1994).
277. R. Könenkamp, *Phys. Rev. B* 61, 11057 (2000).
278. F. Cao, G. Oskam, G. J. Meyer, and P. C. Searson, *J. Phys. Chem.* 100, 17 021 (1996).
279. P. M. Sommeling, H. C. Rieffe, J. M. Kroon, J. A. M. van Roosmalen, A. Schonecker, and W. C. Sinke, in "Proceedings of the 14th EC Photovoltaic Solar Energy Conference" (H. Ossenbrink, P. Helm, and H. Ehmann, Eds.), pp. 1816–1819. H. S. Stephens and Associates, Bedford, 1997.
280. A. Solbrand, H. Lindstrom, H. Rensmo, A. Hagfeldt, S.-E. Lindquist, and S. Sodergren, *J. Phys. Chem. B* 101, 2514 (1997).
281. K. Schwarzburg and F. Willig, *Appl. Phys. Lett.* 58, 2520 (1991).
282. B. Levy, W. Liu, and S. E. Gilbert, *J. Phys. Chem. B* 101, 1810 (1997).
283. L. Dloczik, O. Ileperuma, I. Lauer mann, L. M. Peter, E. A. Ponomarev, G. Redmond, N. J. Shaw, and I. Uhlendorf, *J. Phys. Chem. B* 101, 10 281 (1997).
284. A. Hagfeldt, S.-E. Lindquist, and M. Grätzel, *Sol. Energy Mater. Sol. Cells* 32, 245 (1994).
285. S. A. Haque, Y. Tachibana, D. R. Klug, and J. R. Durrant, *J. Phys. Chem. B* 102, 1745 (1998).
286. C. J. Barbe, F. Arendse, P. Compte, M. Jirousek, F. Lenzmann, V. Shklover, and M. Grätzel, *J. Am. Ceram. Soc.* 80, 3157 (1997).
287. F. Cao, G. Oskam, P. C. Searson, J. M. Stipkala, T. A. Heimer, F. Farzad, and G. J. Meyer, *J. Phys. Chem.* 99, 11 974 (1995).
288. A. Goossens, B. van der Zanden, and J. Schooman, *Chem. Phys. Lett.* 331, 1 (2000).
289. M. Takahashi, K. Tsukigi, T. Uchino, and T. Yoko, *Thin Solid Films* 388, 231 (2001).
290. Th. Dittrich, E. A. Lebedev, and J. Weidmann, *Phys. Stat. Sol. (A)* 165, R5 (1998).
291. J. Weidmann, Th. Dittrich, E. Konstantinova, I. Lauer mann, I. Uhlendorf, and F. Koch, *Sol. Energy Mater. Sol. Cells* 56, 153 (1999).
292. T. Dittrich, J. Weidmann, F. Koch, I. Uhlendorf, and I. Lauer mann, *Appl. Phys. Lett.* 75, 3980 (1999).
293. V. Duzhko, V. Yu. Timoshenko, F. Koch, and Th. Dittrich, *Phys. Rev. B* 64, 075204 (2001).
294. V. Kytin and Th. Dittrich, *Phys. Stat. Sol. (A)* 185, 461 (2001).
295. V. Kytin, V. Duzhko, V. Yu. Timoshenko, J. Rappich, and Th. Dittrich, *Phys. Stat. Sol. (A)* 185, R1 (2001).
296. V. Kytin, Th. Dittrich, F. Koch, and E. Lebedev, *Appl. Phys. Lett.* 79, 108 (2001).
297. P. Knauth and H. L. Tuller, *J. Appl. Phys.* 85, 897 (1999).
298. J. Maier, *Prog. Solid State Chem.* 23, 171 (1995).
299. J. A. S. Ikeda and Y.-M. Chiang, *J. Am. Ceram. Soc.* 76, 2437 (1993).
300. J. F. Baumard and E. Tani, *J. Chem. Phys.* 67, 857 (1977).
301. D. M. Smyth, *Prog. Solid State Chem.* 15, 145 (1984).
302. K. Hoshino, N. L. Peterson, and C. L. Wiley, *J. Phys. Chem. Solids* 46, 1397 (1985).
303. F. Millot, M.-G. Blanchin, R. Tetot, J.-F. Marucco, B. Poumellec, C. Picard, and B. Touzelin, *Prog. Solid State Chem.* 17, 263 (1987).
304. A. Bernasik, M. Rekas, M. Sloma, and W. Weppner, *Solid State Ionics* 72, 12 (1994).
305. D. Mardare, M. Tasca, M. Delibas, and G. I. Rusu, *Appl. Surf. Sci.* 156, 200 (2000).
306. D. Mardare, C. Baban, R. Gavrilă, M. Modreanu, and G. I. Rusu, *Surf. Sci.* 507–510, 468 (2002).
307. M. Gómez, J. Rodríguez, S. Tingry, A. Hagfeldt, S.-E. Lindquist, and C. G. Granqvist, *Sol. Energy Mater. Sol. Cells* 59, 277 (1999).
308. H. Tang, K. Prasad, R. Sanjinès, P. E. Schmid, and F. Lévy, *J. Appl. Phys.* 75, 2042 (1994).
309. R. Sanjinès, H. Tang, H. Berger, F. Gozzo, G. Margaritondo, and F. Lévy, *J. Appl. Phys.* 75, 2945 (1994).
310. H. Wittmer, S. Holten, H. Kliem, and H. D. Breuer, *Phys. Stat. Sol. (A)* 181, 461 (2000).
311. V. I. Makarov, S. A. Kochubei, and I. Khmelinskii, *Chem. Phys. Lett.* 355, 504 (2002).
312. K. Wilke and H. D. Breuer, *Z. Phys. Chem.* 213, 135 (1999).
313. M. Anpo, *Sol. Energy Mater. Sol. Cells* 38, 221 (1995).
314. M. A. Fox, *Sol. Energy Mater. Sol. Cells* 38, 381 (1995).
315. V. Augugliaro, V. Loddo, L. Palmisano, and M. Schiavello, *Sol. Energy Mater. Sol. Cells* 38, 411 (1995).
316. D. Bahnmann, D. Bockelmann, and R. Goslich, *Sol. Energy Mater.* 24, 564 (1991).
317. D. M. Blake, J. Webb, C. Turchi, and K. Magrini, *Sol. Energy Mater.* 24, 584 (1991).
318. J. Yu, X. Zhao, and Q. Zhao, *J. Mater. Sci. Lett.* 19, 1015 (2000).
319. S. Ruan, F. Wu, T. Zhang, W. Gao, B. Xu, and M. Zhao, *Mater. Chem. Phys.* 69, 7 (2001).
320. K. Baba and R. Hatada, *Surf. Coat. Technol.* 136, 241 (2001).
321. T. Sumita, T. Yamaki, S. Yamamoto, and A. Miyashita, *Jpn. J. Appl. Phys., Part 1* 40, 4007 (2001).
322. L. Gao and Q. Zhang, *Scr. Mater.* 44, 1195 (2001).
323. A. J. Maira, K. L. Yeung, J. Soria, J. M. Coronado, C. Bolver, C. Y. Lee, and V. Augugliaro, *Appl. Catal. B: Environ.* 29, 327 (2001).
324. K. Y. Jung, S. B. Park, and S.-K. Ihm, *Appl. Catal. A: Gen.* 224, 229 (2002).
325. M. S. Jeon, T. K. Lee, D. H. Kim, H. Joo, and H. T. Kim, *Sol. Energy Mater. Sol. Cells* 57, 217 (1999).
326. G.-J. Chee, Y. Nomura, K. Ikebukuro, and I. Karube, *Sens. Actuators B* 80, 15 (2001).
327. Y. Xu, L. Jiang, X. Lu, J. Wang, and D. Zhou, *High Technol. Letters (China)* 6, 63 (2000).
328. J. Sheng, L. Shivalingappa, J. Karasawa, and T. Fukami, *J. Mater. Sci.* 34, 6201 (1999).
329. B. Kim, D. Byun, J. K. Lee, and D. Park, *Jpn. J. Appl. Phys., Part 1* 41, 222 (2002).
330. H. Tada and M. Tanaka, *Langmuir* 13, 360 (1997).
331. C.-G. Wu, L.-F. Tzeng, Y.-T. Kuo, and C. H. Shu, *Appl. Catal. A: Gen.* 226, 199 (2002).
332. A. Rachel, B. Lavedrine, M. Subrahmanyam, and P. Boule, *Catal. Comm.* 3, 165 (2002).
333. R. L. Pozzo, J. L. Giombi, M. A. Baltanás, and A. E. Cassano, *Appl. Catal. B: Environ.* 38, 61 (2002).
334. Y. Paz, Z. Luo, L. Rabenberg, and A. Heller, *J. Mater. Res.* 10, 2842 (1995).
335. M. Nakamura, L. Sirghi, T. Aoki, and Y. Hatanaka, *Surf. Sci.* 507–510, 778 (2002).
336. T. Watanabe, A. Nakajima, R. Wang, M. Minabe, S. Koizumi, A. Fujishima, and K. Hashimoto, *Thin Solid Films* 351, 260 (1999).



337. M. Miyauchi, N. Kieda, S. Hishita, T. Mitsushashi, A. Nakajima, T. Watanabe, and K. Hashimoto, *Surf. Sci.* 511, 401 (2002).
338. V. Romeas, P. Pichat, C. Guillard, T. Chopin, and C. Lehaut, *J. Phys. IV, Proc.* 9, PR3/247 (1999).
339. K. Miyashita, S. Kuroda, T. Ubukata, T. Ozawa, and H. Kubota, *J. Mater. Sci.* 36, 3877 (2001).
340. K. Miyashita, S. Kuroda, T. Sumita, and T. Ubukata, *J. Mater. Sci. Lett.* 20, 2137 (2001).
341. J. C. Yu, J. Yu, W. Ho, and J. Zhao, *J. Photochem. Photobiol. A: Chem.* 148, 331 (2002).
342. J. C. Yu, J. Yu, and J. Zhao, *Appl. Catal. B: Environ.* 36, 31 (2002).
343. Y. Ohko, S. Saitoh, T. Tatsuma, and A. Fujishima, *J. Electrochem. Soc.* 148, B24 (2001).
344. D. W. Bahnemann, M. Hilgendorff, and R. Memming, *J. Phys. Chem. B* 101, 4265 (1997).
345. D. W. Goodman, *Surf. Rev. Lett.* 2, 9 (1995).
346. C. T. Campbell, *Surf. Sci. Rep.* 27, 1 (1997).
347. M. Bäumer and H.-J. Freund, *Prog. Surf. Sci.* 61, 127 (1999).
348. H.-J. Freund, *Surf. Sci.* 500, 271 (2002).
349. S. Sato and J. M. White, *Chem. Phys. Lett.* 72, 83 (1980).
350. D. Hufschmidt, D. Bahnemann, J. J. Testa, C. A. Emilio, and M. I. Litter, *J. Photochem. Photobiol. A: Chem.* 148, 223 (2002).
351. U. Siemon, D. Bahnemann, J. J. Testa, D. Rodríguez, M. I. Litter, N. Bruno, *J. Photochem. Photobiol. A: Chem.* 148, 247 (2002).
352. F. B. Li and X. Z. Li, *Appl. Catal. A: Gen.* 228, 15 (2002).
353. M. Daté, Y. Ichihashi, T. Yamashita, A. Chiorino, F. Boccuzzi, and M. Haruta, *Catal. Today* 72, 89 (2002).
354. V. Vamathevan, R. Amal, D. Beydoun, G. Low, S. McEvoy, *J. Photochem. Photobiol. A: Chem.* 148, 233 (2002).
355. D. Dvoranová, V. Brezová, M. Mazúra, and M. A. Malati, *Appl. Catal. B: Environ.* 37, 91 (2002).
356. H. Yamashita, M. Harada, J. Misaka, M. Takeuchi, K. Ikeue, and M. Anpo, *J. Photochem. Photobiol. A: Chem.* 148, 257 (2002).
357. A. Di Paola, E. García-López, S. Ikeda, G. Marcì, B. Ohtani, and L. Palmisano, *Catal. Today* 75, 87 (2002).
358. A.-W. Xu, Y. Gao, and H.-Q. Liu, *J. Catal.* 207, 151 (2002).
359. R. Vogel, K. Pohl, and H. Weller, *Chem. Phys. Lett.* 174, 241 (1999).
360. S. Kohtani, A. Kudo, and T. Ssakata, *Chem. Phys. Lett.* 206, 166 (1993).
361. R. Vogel, P. Hoyer, and H. Weller, *J. Phys. Chem.* 98, 3183 (1994).
362. D. Liu and P. V. Kamat, *J. Phys. Chem.* 97, 10769 (1993).
363. K. Vinodgopal and P. V. Kamat, *Environ. Sci. Technol.* 29, 841 (1995).
364. I. Bedja and P. V. Kamat, *J. Phys. Chem.* 99, 9182 (1995).
365. R. Q. Long and R. T. Yang, *J. Catal.* 207, 158 (2002).
366. G. Colón, M. C. Hidalgo, and J. A. Navio, *Appl. Catal. A: Gen.* 231, 185 (2002).
367. M. K. Nazeeruddin, A. Kay, I. Rodicio, B. R. Humphry, E. Mueller, P. Liska, N. Vlachopoulos, and M. Grätzel, *J. Am. Chem. Soc.* 115, 6382 (1993).
368. F. Willig, R. Eichberger, N. S. Sundaresan, and B. A. Parkinson, *J. Am. Chem. Soc.* 112, 2702 (1990).
369. P. V. Kamat, S. Das, K. G. Thomas, and M. V. George, *Chem. Phys. Lett.* 178, 75 (1991).
370. R. Eichberger and F. Willig, *Chem. Phys.* 141, 159 (1990).
371. B. Burfeindt, T. Hannappel, W. Storck, and F. Willig, *J. Phys. Chem.* 100, 16463 (1996).
372. N. J. Cherepy, G. P. Smestad, M. Grätzel, and J. Z. Zhang, *J. Phys. Chem. B* 101, 9342 (1997).
373. T. Hannappel, B. Burfeindt, W. Storck, and F. Willig, *J. Phys. Chem. B* 101, 6799 (1997).
374. J. Randy, R. J. Ellingson, J. B. Asbury, S. Ferrere, H. N. Ghosh, J. R. Sprague, T. Lian, and A. J. Nozik, *J. Phys. Chem. B* 102, 6455 (1998).
375. A. Furube, T. Asahi, H. Masuhara, H. Yamashita, and M. Anpo, *J. Phys. Chem. B* 103, 3120 (1999).
376. H. Al-Ekabi, B. Butters, D. Delany, J. Ireland, N. Lewis, T. Powell, and J. Story, *Trace Met. Environ.* 3, 321 (1993).
377. V. Iliev and D. Tomova, *Catal. Comm.* 3, 287 (2002).
378. Q. Dai and J. Rabani, *J. Photochem. Photobiol. A: Chem.* 148, 17 (2002).
379. C. G. Garcia, C. J. Kleverlaan, C. A. Bignozzi, and N. Y. M. Iha, *J. Photochem. Photobiol. A: Chem.* 147, 143 (2002).
380. J. E. Moser, P. Bonhoefer, and M. Grätzel, *Coord. Chem. Rev.* 171, 245 (1998).
381. G. Centi, P. Ciambelli, S. Perathoner, and P. Russo, *Catal. Today* 75, 3 (2002).
382. R. Abe, K. Sayama, K. Domen, and H. Arakawa, *Chem. Phys. Lett.* 344, 339 (2001).
383. M. Ashokkumar, *Int. J. Hydrog. Energy* 23, 427 (1998).
384. M. Anpo, H. Yamashita, Y. Ichihashi, Y. Fujii, and M. Honda, *J. Phys. Chem. B* 101, 2632 (1997).
385. M. Anpo, *Nuovo Cimento* 19D, 1641 (1997).
386. P. G. Smirniotis, D. A. Peña, and B. S. Uphade, *Angew. Chem.* 113, 2537 (2001).
387. S. Daito, F. Tochikubo, and T. Watanabe, *Jpn. J. Appl. Phys., Part 1* 40, 2475 (2001).
388. S. B. Kim and S. C. Hong, *Appl. Catal. B: Environ.* 35, 305 (2002).
389. P. B. Amama, K. Itoh, and M. Murabayashi, *Appl. Catal. B: Environ.* 37, 321 (2002).
390. A. Bouzaza and A. Laplanche, *J. Photochem. Photobiol. A: Chem.* 150, 207 (2002).
391. B. Dąbrowski, A. Zaleska, M. Janczarek, J. Hupka, and J. D. Miller, *J. Photochem. Photobiol. A: Chem.* 151, 201 (2002).
392. J. Araña, O. González Díaz, M. Miranda Saracho, J. M. Doña Rodríguez, J. A. Herrera Melián, and J. Pérez Peña, *Appl. Catal. B: Environ.* 36, 113 (2002).
393. D. W. Bahnemann, S. N. Kholuisakaya, R. Dillert, A. I. Kulak, and A. I. Kokorin, *Appl. Catal. B: Environ.* 36, 161 (2002).
394. A. Rachel, M. Sarakha, M. Subrahmanyam, and P. Boule, *Appl. Catal. B: Environ.* 37, 293 (2002).
395. A. Rachel, M. Subrahmanyam, and P. Boule, *Appl. Catal. B: Environ.* 37, 301 (2002).
396. J. A. Byrne, A. Davidson, P. S. M. Dunlop, and B. R. Eggins, *J. Photochem. Photobiol. A: Chem.* 148, 365 (2002).
397. M. Bekbolet, A. S. Suphandag, and C. S. Uyguner, *J. Photochem. Photobiol. A: Chem.* 148, 121 (2002).
398. Y. Cho and W. Choi, *J. Photochem. Photobiol. A: Chem.* 148, 129 (2002).
399. S. Parra, J. Olivero, and C. Pulgarin, *Appl. Catal. B: Environ.* 36, 75 (2002).
400. M. Muneer and D. Bahnemann, *Appl. Catal. B: Environ.* 36, 95 (2002).
401. S. Parra, S. Malato, and C. Pulgarin, *Appl. Catal. B: Environ.* 36, 131 (2002).
402. E. Vulliet, C. Emmelin, J.-M. Chovelon, C. Guillard, and J.-M. Herrmann, *Appl. Catal. B: Environ.* 38, 127 (2002).
403. H. Einaga, S. Futamura, and T. Ibusuki, *Appl. Catal. B: Environ.* 38, 215 (2002).
404. M. C. Blount and J. L. Falconer, *Appl. Catal. B: Environ.* 39, 39 (2002).
405. K.-I. Shimizu, T. Kaneko, T. Fujishima, T. Kodama, H. Yoshida, and Y. Kitayama, *Appl. Catal. A: Gen.* 225, 185 (2002).
406. S. Vijaikumar, N. Somasundaram, C. Srinivasan, *Appl. Catal. A: Gen.* 225, 129 (2002).
407. M. Kang, *Appl. Catal. B: Environ.* 37, 187 (2002).
408. B. Ohtani, K. Iwai, H. Kominami, T. Matsuura, Y. Kera, and S. Nishimoto, *Chem. Phys. Lett.* 242, 315 (1995).
409. S. Horikoshi, N. Watanabe, H. Onishi, H. Hidaka, and N. Serpone, *Appl. Catal. B: Environ.* 37, 117 (2002).
410. N. San, A. Hatipoğlu, G. Koçtürk, and Z. Çýnar, *J. Photochem. Photobiol. A: Chem.* 146, 189 (2002).
411. V. Iliev, *J. Photochem. Photobiol. A: Chem.* 151, 195 (2002).
412. T. Nakashima, Y. Ohko, D. A. Tryk, A. Fujishima, *J. Photochem. Photobiol. A: Chem.* 151, 207 (2002).
413. G. Mele, G. Ciccarella, G. Vasapollo, E. García-López, L. Palmisano, and M. Schiavello, *Appl. Catal. B: Environ.* 38, 309 (2002).

414. V. Durgakumari, M. Subrahmanyam, K. V. Subba Rao, A. Ratnamala, M. Noorjahan, and K. Tanaka, *Appl. Catal. A: Gen.* 248, 155 (2002).
415. R. W. Matthews and S. R. McEvoy, *Sol. Energy* 49, 507 (1992).
416. L. Zhang, T. Kanki, N. Sano, and A. Toyoda, *Sol. Energy* 70, 331 (2001).
417. J. Grzechulska and A. W. Morawski, *Appl. Catal. B: Environ.* 36, 45 (2002).
418. J. Li, C. Chen, J. Zhao, H. Zhu, and J. Orthman, *Appl. Catal. B: Environ.* 37, 331 (2002).
419. Z. Sun, Y. Chen, Q. Ke, Y. Yang, and J. Yuan, *J. Photochem. Photobiol. A: Chem.* 149, 169 (2002).
420. M. Sökmen and A. Özkan, *J. Photochem. Photobiol. A: Chem.* 147, 77 (2002).
421. S. Sakthivel, M. V. Shankar, M. Palanichamy, B. Arabindoo, and V. Murugesan, *J. Photochem. Photobiol. A: Chem.* 148, 153 (2002).
422. S. Al-Qaradawi and S. R. Salman, *J. Photochem. Photobiol. A: Chem.* 148, 161 (2002).
423. T. Sauer, G. Cesconeto Neto, H. J. José, R. F. P. M. Moreira, *J. Photochem. Photobiol. A: Chem.* 149, 147 (2002).
424. H. Lachheb, E. Puzenat, A. Houas, M. Ksibi, E. Elaloui, C. Guillard, and J.-M. Herrmann, *Appl. Catal. B: Environ.* 39, 75 (2002).
425. H. Zhan and H. Tian, *Dyes Pigments* 37, 231 (1998).
426. H. Zhan, K. Chen, and H. Tian, *Dyes Pigments* 37, 241 (1998).
427. H. Zhan, H. Tian, K. Chen, and W. Zhu, *Toxicol. Environ. Chem.* 69, 531 (1999).
428. S. Malato, J. Blanco, A. Vidal, and C. Richter, *Appl. Catal. B: Environ.* 37, 1 (2002).
429. T. An, G. Li, Y. Xiong, X. Zhu, H. Xing, and G. Liu, *Mater. Phys. Mech.* 4, 101 (2001).
430. L. R. Skubal, N. K. Meshkov, T. Rajh, and M. Thurnauer, *J. Photochem. Photobiol. A: Chem.* 148, 393 (2002).
431. L. R. Skubal and N. K. Meshkov, *J. Photochem. Photobiol. A: Chem.* 148, 211 (2002).
432. Y. Ming, C. R. Chenthamarakshan, and K. Rajeshwar, *J. Photochem. Photobiol. A: Chem.* 147, 199 (2002).
433. S. G. Schrank, H. J. José, and R. F. P. M. Moreira, *J. Photochem. Photobiol. A: Chem.* 147, 71 (2002).
434. J. Aguado, R. van Grieken, M. J. López-Munoz, and J. Marugán, *Catal. Today* 75, 95 (2002).
435. X. Z. Li and Y. G. Zhao, *Water Sci. Technol.* 39, 249 (1999).
436. J. E. Pacheco, M. R. Prairie, and L. Yellowhorse, *Trans. ASME, J. Sol. Energy Engin.* 115, 123 (1993).
437. S. M. Rodriguez, C. Richter, J. B. Galvez, and M. Vincent, *Sol. Energy* 56, 401 (1996).
438. D. C. Schmelling, K. A. Gray, and P. V. Kamat, *Water Res.* 31, 1439 (1997).
439. J.-S. Hur and Y. Koh, *Biotechnol. Lett.* 24, 23 (2002).
440. R. L. Ziolli and W. F. Jardim, *J. Photochem. Photobiol. A: Chem.* 147, 205 (2002).
441. M. Perez, F. Torrades, J. Peral, C. Lizama, C. Bravo, S. Casas, J. Freer, and H. D. Mansilla, *Appl. Catal. B: Environ.* 33, 89 (2001).
442. M. Hamerski, J. Grzechulska, and A. W. Morawski, *Sol. Energy* 66, 395 (1999).
443. M. Bekbolet, M. Lindner, D. Weichgrebe, and D. W. Bahnemann, *Sol. Energy* 56, 455 (1996).
444. C. Wei, W. Lin, Z. Zainal, N. E. Williams, K. Zhu, A. P. Kruzic, R. L. Smith, K. Rajeshwar, *Environ. Sci. Technol.* 28, 934 (1994).
445. M. Bekbolet, *Water Sci. Technol.* 11–12, 95 (1997).
446. P. S. M. Dunlop, J. A. Byrne, N. Manga, and B. R. Eggins, *J. Photochem. Photobiol. A: Chem.* 148, 355 (2002).
447. J. Wist, J. Sanabria, C. Dierolf, W. Torres, and C. Pulgarin, *J. Photochem. Photobiol. A: Chem.* 147, 241 (2002).
448. I. Liu, L. A. Lawton, B. Cornish, and P. K. J. Robertson, *J. Photochem. Photobiol. A: Chem.* 148, 349 (2002).
449. R. Armon, N. Laot, N. Narkis, and I. Neeman, *J. Adv. Oxid. Technol.* 3, 145 (1998).
450. M. Z. Atashbar, in "Proceedings 1st IEEE Conference on Nanotechnology." p. 544. IEEE-NANO 2001, IEEE, Piscataway, NJ, 2001.
451. L. W. Miller, M. I. Tejedor, B. P. Nelson, and M. A. Anderson, *J. Phys. Chem. B* 103, 8490 (1999).
452. H. Honda, A. Ishizahi, R. Soma, K. Hashimoto, and A. Fujishima, *J. Illum. Eng. Soc. (USA)* 27, 42 (1998).
453. J. Mizuguchi, *J. Electrochem. Soc.* 148, J55 (2001).
454. T. Okamoto and I. Yamaguchi, *J. Microsc.* 202, 100 (2001).
455. Z. V. Saponjic, T. Rajh, J. M. Nedeljkovic, and M. C. Thurnauer, *Mater. Sci. Forum* 352, 91 (2000).
456. M. Romero, J. Blanco, B. Sanchez, A. Vidal, S. Malato, A. I. Carbona, and E. Garcia, *Sol. Energy* 66, 169 (1999).



# Nanocrystals Assembled from the Bottom Up

Edson Roberto Leite

*Federal University of São Carlos, Carlos, SP, Brazil*

## CONTENTS

1. Introduction
  2. Transition Metal Nanocrystals
  3. Metal Oxide Nanocrystals
  4. Nanocrystalline Composites
  5. Characterization of Nanocrystals
  6. Summary
- Glossary  
References

## 1. INTRODUCTION

The physical and chemical properties of materials on the nanoscale (usually defined in the 1–100 nm range) are of immense interest and increasing importance for future technological applications. Nanoparticles or nanocrystals (in this work the words nanoparticles and nanocrystals are synonymous) generally display properties that differ from those of bulk material. The literature provides several examples of properties, such as magnetic and optical properties, melting point, specific heat, and surface reactivity, which can be affected by particle size [1–5]. A material's properties are usually very substantially modified in the 1–10 nm sizes. These changes are known as quantum size effects and their origin is directly related to the type of chemical bond in the crystal [6]. The correlation between properties and particle size has been known since the 19th century, when Faraday demonstrated that the color of colloidal Au particles can be modified, changing the Au particle size [7]. However, despite the subject's long history, interest in nanoparticles has grown considerably over the last decade. The driving force for this increase in research activity is the ability to control a material's properties by controlling the size and shape of crystals and the arrangement of such particles. These developments can lead to new technologies, including energy conversion [8–12], catalysis and sensors [13, 14],

ultrahigh density data storage media [15–17], nanoparticle light-emitting diodes [18, 19], and special pigments [20].

The future of these new technologies is strictly dependent on the development of synthetic routes to process metal, metal oxides, and semiconductor nanoparticles, as well as processes that allow such nanoparticles to be manipulated and controlled. This chapter focuses precisely on these two topics (i.e., the synthesis and control of nanoparticles). Special attention is given to particle growth control during high temperature heat treatment.

This chapter is dedicated to presenting a concise description of different wet chemical processes to synthesize metal and metal oxide nanoparticles by “bottom-up” methods and of how to control the shape, size, and particle growth of such nanocrystals. This chapter will also analyze the synthesis of nanocomposites. Nanocomposite processing will be considered as a route to control the particle growth, surface oxidation, and agglomeration of nanoparticles. The fact that the combination of different phases may result in a material with superior performance will be considered a secondary, albeit no less important, effect. Indeed, these two factors, control and synergetic effect, must be considered during the selection of material for nanocomposite processing.

Neither the synthesis of metal and metal oxide nanoparticles by high energy mechanical milling (“top-down” methods) or vapor phase nor the synthesis of semiconductor nanoparticles, such as II–IV semiconductors crystals, is discussed in this chapter, since the literature contains excellent papers and reviews on these subjects [21–23].

## 2. TRANSITION METAL NANOCRYSTALS

The “bottom-up” methods of wet chemical nanocrystal synthesis are based on the chemical reduction of the salts, or the controlled decomposition of metastable organometallic compounds in an organic or water solution. These reactions are always carried out in the presence of a large variety of stabilizers, which are used basically to control the growth of the initial nanocluster and to avoid particle coagulation

or agglomeration. The mechanism of nanoparticle formation is generally based on a process of nucleation, growth, and coagulation. This process was proposed by Turkevich and is based on the synthesis of metal nanoparticles by salt reduction [24–26]. This model still is valid and has recently been refined. A recent review authored by Bönemann and Richards [27] contains a good discussion about the refined model and supplementary references on this subject are also available.

Since nanocrystals are unstable from the standpoint of agglomeration and bulk, coagulation and agglomeration are the paths that nanoparticles follow to decrease their high surface area, thus becoming more stable. In the absence of any extrinsic impediment, the unprotected particle coagulates, basically under the action of van der Waals forces. To prevent the coagulation process from occurring, the particle surface can be protected by electrostatic stabilization and/or steric stabilization [28].

Electrostatic stabilization is based on the Coulombic repulsion between particles, promoted by a double layer composed of ions adsorbed on the particle surface. The electrostatic stabilization process can be modified by several parameters, such as ionic strength of the dispersing media, ion concentration, and the presence of neutral adsorbate, which may replace the adsorbed ion on the particle surface.

Steric stabilization is based on the steric hindrance caused by organic molecules that are attached to the particle surface, forming a protective layer that prevents particle coagulation or agglomeration. This type of stabilizing system can be viewed as a nanocomposite material, since the organic layer forms a nanometric scale second phase [29, 30]. Several kinds of protective groups can be used as steric stabilization agents, among them polymers and block polymers, P, N, and S donors (phosphanes, amines, thioethers), surfactants, organometallic compounds, and solvents. A detailed description of the several types of steric stabilizers used during the synthesis of metal nanocrystals is given in Bradley's review [31].

The synthesis of transition metal nanocrystals can be divided basically into two major groups: salt reduction and decomposition method. Examples of these methods are described in the following section.

## 2.1. Synthetic Methods

The salt reduction method is a process by which a reduction agent reduces the metal salt, in solution, to metal. These reactions can be done in water or in an organic solution. In an organic solution, the solvent can also act as a reduction agent. Alcohols are generally useful reduction agents, particularly alcohols containing  $\alpha$ -hydrogen. In this process, the alcohol is oxidized to the corresponding carbonyl group. An example of this kind of synthesis is the processing of palladium nanoparticles through the reduction of palladium acetate by methanol [32]. Teranishi and Miyake [33] reported on the reduction of  $\text{H}_2\text{PdCl}_4$  by alcohols to synthesize Pd nanoparticles, demonstrating that the mean diameter of Pd nanocrystals can be controlled from 1.7 to 3.0 nm in a one-step process by changing the amount of protective polymer, poly(*N*-vinyl-2-pyrrolidone) (PVP) and the kind and/or concentration of alcohol in the solvent. The

solvent they used was water. They also showed that the reduction rate of  $[\text{PdCl}_4]^-$  ions is an important factor in the production of smaller Pd particles. The reduction rate was controlled using different kinds of alcohol.

The reduction of metal salts by the addition of a reducing agent in a nonreducing solvent is a well-established synthetic route for the preparation of aqueous suspensions of metal nanocrystals. Faraday, for instance, used phosphorous vapor to promote the reduction of  $[\text{AuCl}_4]^-$  in aqueous solution to synthesize gold nanoparticles [7]. Different kinds of reducing agents have been used to process gold nanocrystals, allowing for the processing of particles ranging from 1 to 100 nanometers in diameter. Turkevitch and co-workers [24, 26] established the first reproducible standard protocol for the synthesis of gold nanoparticles. Their processing of gold nanoparticles by the reduction of  $[\text{AuCl}_4]^-$  with sodium citrate, for example, became a standard for histological staining applications [34] and for undergraduate experiments in surface and nanomaterials chemistry [35].

Platinum nanoparticles can also be synthesized by the reduction of metal salts, using a reducing agent [36, 37]. Van Rheenen et al. [37] demonstrated that the morphology of platinum particles could be controlled by controlling the synthetic parameters, such as temperature, protective polymer, time, pH, reagent concentration, and the sequence of reagent additions. These authors used various reducing agents and chloroplatinic acid as platinum salt.

An interesting synthetic route was recently developed based on the reduction of organometallic compounds by dihydrogen at low pressure and temperature [38–42]. The organometallic compounds used were low-valent alkene or a poly-ene complex of the desired metal. Using this process, well-dispersed nanoparticles of Ru, Pt, Ni, and Co with a narrow size distribution were synthesized. The particles were stabilized by the presence of PVP. Based on a similar process, Ould Ely et al. [43] synthesized nanoscale bimetallic  $\text{Co}_x\text{Pt}_{1-x}$  particles, using  $\text{Co}(\eta^3\text{-C}_8\text{H}_{13})(\eta^4\text{-C}_8\text{H}_{12})$  and  $\text{Pt}_2(\text{dba})_3$  (dba = bis-dibenzylidene acetone) as organometallic compounds. They found that the alloy's composition was determined by the initial ratio of the two organometallic precursors.

Recently, the so-called "polyol process" [44] has been used successfully to process magnetic nanoparticles with a very narrow particle size distribution [44–46]. This process is based on the reduction of metallic salt in solution, at a high temperature ( $100 < T < 300$  °C), by the addition of a polyol (such as ethylene glycol), resulting in nanometric particles. In this process, surfactants such as oleic acid are used to control particle growth and stabilize the nanoparticles.

Park and Cheon [47] discussed an interesting synthetic route to process solid solution and core-shell type cobalt-platinum nanoparticles via a redox transmetallation reaction, reporting they had obtained nanoparticles of solid solution and core-shell structures smaller than 10 nm. These alloys were formed by redox transmetallation reactions between the reagents without the addition of reducing agents. The reaction between  $\text{Co}_2(\text{CO})_8$  and  $\text{Pt}(\text{hfac})_2$  (hfac = hexafluoroacetylacetonato) resulted in the formation of solid solution, while the reaction between Co nanoparticles and  $\text{Pt}(\text{hfac})_2$  in solution resulted in " $\text{Co}_{\text{core}}\text{-Pt}_{\text{shell}}$ "

type nanoparticles. Narrow particle size distributions were achieved in both processes.

The organometallic compounds of transition metals usually display low thermal stability, decomposing into their respective metals even under mild conditions. Owing to these properties, organometallic compounds can be considered good sources to process metal nanoparticles.

Metal carbonyl pyrolysis has been used for the synthesis of several metal nanoparticles, although a broad particle size distribution is usually obtained [48, 49]. Park et al. [50] reported on the synthesis of iron nanorods and spherical nanoparticles using the thermal decomposition of  $\text{Fe}(\text{CO})_5$ , in the presence of surfactant. They found that rodlike particles, with a higher aspect ratio, could be obtained by changing the concentration of didodecyldimethylammonium bromide during the reaction process.

Alivisatos et al. [51] recently reported on the control of the size and shape of Co nanocrystals. A synthetic route, based on the principles applied to the synthesis and control of CdSe nanocrystals, was used [52]. These authors discussed the synthesis of Co nanoparticles with high crystallinity, narrow particle size distribution, and a high degree of shape control. The nanocrystals are produced by injecting an organometallic precursor [ $\text{Co}_2(\text{CO})_8$ ] into a hot ( $T \sim 180^\circ\text{C}$ ) surfactant mixture [oleic acid and trioctylphosphine oxide (TOPO)] under an inert atmosphere.

An interesting approach to synthesize metal alloy nanocrystals is the use of simultaneous salt reduction and thermal decomposition processes. Sun et al. [53] reported on the synthesis of iron–platinum (FePt) nanoparticles through the reduction of platinum acetylacetonate by a diol, and decomposition of iron pentacarbonyl [ $\text{Fe}(\text{CO})_5$ ] in the presence of a surfactant mixture (oleic acid and oleyl amine). Based on a similar approach, Chen and Nikles [54] synthesized ternary alloy nanoparticles ( $\text{Fe}_x\text{Co}_y\text{Pt}_{100-x-y}$ ), using a simultaneous reduction of acetylacetonate and platinum acetylacetonate and thermal decomposition of  $\text{Fe}(\text{CO})_5$  and obtaining an average particle diameter of 3.5 nm and narrow particle size distribution.

The decomposition of the organometallic compounds can be promoted by different energy sources, such as acoustic waves (sonochemistry). Sonochemistry stems from acoustic cavitation—the formation, growth, and implosive collapse of bubbles in the liquid. These phenomena can generate high temperatures and high cooling rates [55, 56], creating a favorable environment to promote the decomposition of organometallic compounds and the synthesis of nanoparticles. Suslick et al. [57] used this approach to synthesize Fe nanocrystals. They used  $\text{Fe}(\text{CO})_5$  as the precursor, promoting sonochemical decomposition (by ultrasonic irradiation) in the presence of PVP as stabilizer and obtaining Fe nanoparticles with a mean particle size of 8 nm.

As previously described, the synthesis of metal nanocrystals is based on a colloidal process whereby a metallic salt or an organometallic compound, in solution, is reduced to a metal by a reducing agent (salt reduction method) or by thermal decomposition (thermal decomposition method). The reduction is developed in the presence of a stabilizer (electrostatic stabilization and or steric stabilization). These additives have two basic functions: to control particle growth and to prevent particle agglomeration.

These processes are based on nucleation, growth, and agglomeration, or coagulation. As illustrated in Figure 1, the general process of metal nanocrystal synthesis can be divided, for didactic purposes, into five steps. The first step (step I) consists of the reduction of the metallic precursor ( $\text{M}^+\text{X}^-$ ), which results in metal atoms ( $\text{M}^\circ$ ). These metallic atoms, ions, and metallic clusters will interact (step II), resulting in a metallic cluster growth process. Steps I and II are reversible. When the cluster grows to a critical size (step III), the process becomes irreversible (thermodynamic condition). Particle size can be controlled with the aid of stabilizers (step IV). The presence of only one stabilizer can result in a spherical particle. The origin of this morphology is thermodynamic. In fact, the cluster will grow in a geometrical arrangement in order to minimize the surface energy. The presence of two simultaneous stabilizers, on the other hand, may give rise to a preferential growth process caused by the preferential adsorption of one of the stabilizers. This process, which leads to the formation of anisotropic particles such as nanorods, occurs under a kinetic condition. Particle agglomeration, basically, is prevented by steric stabilization under the influence of the molecules attached to the particles' surface (step V). Step V is essential to control nanoparticle deposition. Thus, colloidal metal dispersion can be used as a building block to produce functional materials [58]. This nanocrystal-based self-assembly process is governed by particle–particle and particle–substrate interaction. The nanocrystal self-assembly process requires a monodispersion system (particle size deviating by less than 10% from the average size) [59] and can be achieved by solvent evaporation [53, 60] or polymer-mediated nanocrystal assembly [61].

Needless to say, the process described in Figure 1 is ideal. One of the major obstacles to achieving good control over metal colloidal synthesis is in separating the nucleation from the growth process. A positive advance in this direction is the synthesis of CdSe nanocrystals, in which nucleation is separated from the growth process by rapidly injecting the precursor in a solvent at high temperature [62, 63]. This approach has become the most suitable thermal decomposition method and has been applied successfully in the synthesis of Co nanocrystals [51], as discussed in Section 2.1.

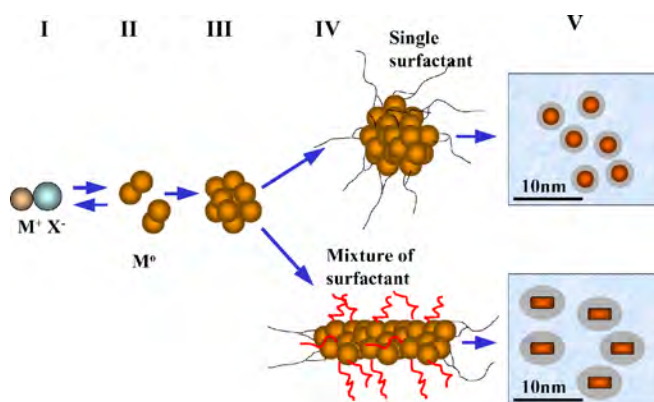


**Figure 1.** Schematic representation of the general process of metal nanocrystal synthesis.

## 2.2. Properties

When we talk about metal nanocrystal, two major application fields come to mind: catalysis and magnetic materials. In this section, we will present some examples of metal nanocrystal properties in these fields.

The magnetic properties of nanocrystals differ in several aspects from their bulk properties. These differences stem from the large fraction of atoms located on the surface or at the interface, leading to a local environment that differs greatly from that of the internal atoms. Hence, the intrinsic and extrinsic properties of nanostructured materials must be different. Besides these modifications, a second phenomenon must be considered as well. Unlike bulk ferromagnetic materials, which are composed of multiple ferromagnetic domains, a sufficiently small ferromagnetic particle consists of a single magnetic domain. These two effects can lead to new magnetic properties that can help the development of ultra-high-density magnetic recording, particularly on metal thin film media.

Metal thin film media are generally processed by physical deposition techniques, which usually require postdeposition annealing. This annealing treatment can result in loss of control over particle size and particle size distribution due to particle growth [64]. The use of nanoparticles as building blocks to fabricate magnetic thin films, via self-assembly, appears to be a good alternative to process metal thin film media [53, 61]. Sun and co-workers [53] showed that ferromagnetic FePt nanocrystal superlattices are chemically and mechanically robust and can support high-density magnetization reversal transitions.

The development of metal nanoparticles whose particle size, size distribution, and composition is strictly controllable can result in high performance catalysts. The preparation of metal nanoparticles prior to deposition on a support can provide fine control over the composition and microstructure [65]. Such control is difficult with the traditional impregnation/reduction catalyst preparation. Polymer-protected precious metal nanoparticles have been used with good results in the hydrogenation of unsaturated organic molecule catalysts [66–68].

Transition metal nanoparticles have recently become a fundamental component for the synthesis of carbon nanotubes. This synthesis can be done by noncatalytic and catalytic methods [69]. When the growth method of nanotubes by chemical vapor deposition (even of single-walled carbon nanotubes) is used, there is strong evidence that carbon nanotubes grow via the base-growth mode, with the catalytic nanoparticle acting as seed for the growth [70, 71]. In fact, the size of the nanoparticle determines the diameter of the nanotube [72]. In the catalyst method, Ni, Fe, and Co are the transition metals that can serve as catalysts for carbon nanotube growth [73]. The catalyst method produces large quantities of very long carbon nanotubes [74].

## 3. METAL OXIDE NANOCRYSTALS

Metal oxides represent an important class of materials with a variety of technological applications. Several reports in the literature describe the effects of size on the various properties of this class of materials. Nanocrystalline metal oxide

semiconductors such as TiO<sub>2</sub>, SnO<sub>2</sub>, and ZnO, for example, display a quantum confinement effect, with enlargement of the bandgap as the particle size decreases [75–77]. Colloidal nanocrystals with quantum size effects are promising building blocks for novel electrical and optoelectronic devices [2, 78]. The ferroelectric phenomena in complex ferroelectric oxides are suppressed when the particles are reduced to a critical size [79–81]. Ceramic materials with nanometric scale microstructures display superior mechanical properties and enhanced electronic conductivity [82, 83].

Based on the above analysis, the development of metal oxides of nanometric dimensions can result in devices and materials with superior performance. However, these developments are directly related to the development of synthesis methods that allow for controlled particle size, particle morphology, and deposition. Once again, the “bottom-up” methods of wet chemical nanocrystal synthesis are apparently the most viable approach to achieve such control. Compared to the control attained in the synthesis of metal and II–IV semiconductor nanocrystals, the control of metal oxide nanocrystals is still in its earliest stage, particularly insofar as the synthesis of complex metal oxide nanocrystals (oxides formed of more than one cation) is concerned.

The synthesis of metal oxide nanocrystals by wet chemical processes can be divided basically into two major groups: (a) chemical synthesis method based on the hydrolysis of metal alkoxides or metal halides; (b) chemical synthesis based on the nonhydrolytic method. Examples of these methods are described in the following section.

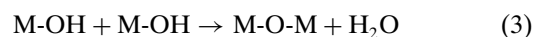
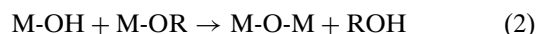
### 3.1. Synthetic Methods

The chemical synthesis of metal oxide nanocrystals based on hydrolysis falls into two major groups: hydrolysis of metal alkoxides and hydrolysis of metal halides and other inorganic salts. Following I give a description of these two groups.

Metal alkoxide compounds are defined as compounds that have metal–oxygen–carbon bonds. Si(OC<sub>2</sub>H<sub>5</sub>)<sub>4</sub>, for instance, which is known as tetraethyl orthosilicate (TEOS), is an alkoxide compound. This class of compound is highly reactive with water. Because the hydroxyl ion (OH<sup>−</sup>) becomes bonded to the metal of the organic precursor, this reaction is called hydrolysis. Reaction 1 shows a typical hydrolytic reaction of an alkoxide compound,



where M represents Si, Ti, Zr, Al, and other metals, R is a ligand such as an alkyl group, and ROH is an alcohol. Hydrolytic reactions are strongly dependent on water content and catalysts. Due to the high reactivity of alkoxide compounds with water, hydrolytic reactions must be carried out in an atmosphere devoid of water vapor and the solvents used must have a very low water content. A partially hydrolyzed metal alkoxide molecule can react with other partially hydrolyzed molecules by a polycondensation reaction, as described in the following equations.





This type of reaction leads to the formation of an inorganic polymer or a three-dimensional network formed of metal oxianions. The described process is called metal alkoxide-based sol-gel. The literature contains excellent reports providing in-depth analyses of this method [84, 85].

The sol-gel process allows for very good chemical homogeneity and offers the possibility of obtaining metastable phases, including the amorphous phase. This process normally promotes the formation of amorphous metal oxides, which require thermal or hydrothermal treatment to promote crystallization. Several factors affect the sol-gel process, including the kind of metal alkoxide, pH of the reaction solution, water:alkoxide ratio, temperature, nature of the solvent, and stabilizers [84]. By varying these parameters, particles can be synthesized with controlled size, morphology, and agglomeration. When the metal alkoxide's hydrolytic reaction rate is too fast, particle size and morphology are more difficult to control. A good alternative to overcome this problem is to use organic additives, which act as chelating ligands (carboxylic acids,  $\beta$ -diketones, and others) and decrease the precursor's reactivity [86].

The sol-gel process can generally be divided into three steps, as illustrated schematically in Figure 2: (1) precipitation of hydrous oxide particles; (2) control of hydrous oxide particle coagulation; and (3) crystallization of the hydrous oxide particle. Thus, the sol-gel process requires control of the particle size and morphology during the precipitation and coagulation steps and during the heat or hydrothermal treatment to promote crystallization. These three steps are now discussed in detail.

The precipitation of amorphous metal oxide (step 1) is controlled by a nucleation growth mechanism. The nucleation mechanism used in this step is well described by the LaMer and Dinegar theory [87]. Following this model, the supersaturation of hydrous oxides increases continuously (by a change in temperature or pH) until a critical concentration is reached. In this condition, nucleation occurs very rapidly and leads to precipitation. Precipitation decreases the supersaturation to levels below the critical concentration,

preventing further nucleation and precipitation. After nucleation occurs, the nuclei thus formed grow, reducing the concentration until an equilibrium concentration is achieved.

The solubility ( $S$ ) of the particle formed during nucleation is related to the particle's size ( $d$ ) by the Ostwald-Freundlich equation,

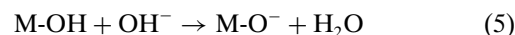
$$S = S_0 \exp(4\gamma_{SL}V_m/RTd) \quad (4)$$

where  $S_0$  is the solubility of the flat surface,  $\gamma_{SL}$  is the solid-liquid interfacial energy,  $V_m$  is the molar volume of the solid phase,  $R$  is the gas constant, and  $T$  is the temperature. This dependence controls the nucleation and the growth process. After the nucleation step, the smaller particles show a tendency to dissolve, increasing the supersaturation, which may cause reprecipitation of the larger particles. This mechanism, which controls particle growth, is known as Ostwald ripening.

Controlled hydrolysis is one of the most popular methods for processing silica spheres in the range of 10–1000 nm. The method was developed by Stöber et al. [88] and is based on the hydrolysis of TEOS in a basic solution of water and alcohol. Particle size depends on the reactant concentration, that is, the TEOS/alcohol ratio, water concentration, and pH ( $>7$ ). This method has been extended to other metal oxide systems with similar success, particularly for  $\text{TiO}_2$  synthesis [89, 90].

The hydrous oxide particles precipitated by the hydrolysis of an alkoxide compound have the same tendency to agglomerate as that described under item 2 for metal colloid systems. Different stabilizers can be used to stabilize these particles and prevent coagulation (step 2). These stabilizers control coagulation by electrostatic repulsion or by steric effects [28], similarly to the metal colloid systems.

There is not only a similarity but also a fundamental difference between the approach used to control coagulation in the sol-gel process and that used for metal nanocrystal systems. In the sol-gel process, the surface charge is controlled by the protonation or deprotonation of the hydrous oxide particle surfaces (M-OH). Thus, the charge-determining ions are  $\text{H}^+$  and  $\text{OH}^-$ . The ease with which protonation or deprotonation occurs depends on the metal atoms and can be controlled by the pH. The pH at which the particles are neutrally charged is called the isoelectric point. At the  $\text{pH} >$  isoelectric point, the particles are negatively charged [see Eq. (5)] while, at the  $\text{pH} <$  isoelectric point, the particles are positively charged [see Eq. (6)]:



Electrostatic stabilization is most commonly employed in the water solution system, while steric stabilization can be more effective in organic media [91, 92]. A steric stabilizer can be used to control the condensation reaction during the precipitation of hydrous oxides. In this case, the stabilizer is added during the hydrolysis step [93–96]. Peiró et al. [97] recently reported on the synthesis of  $\text{TiO}_2$  anatase phase with a nanorod morphology ( $9 \times 5$  nm size) using controlled hydrolysis of tetraisopropyl orthotitanate and tetrabutylammonium hydroxide as a steric stabilizer agent.

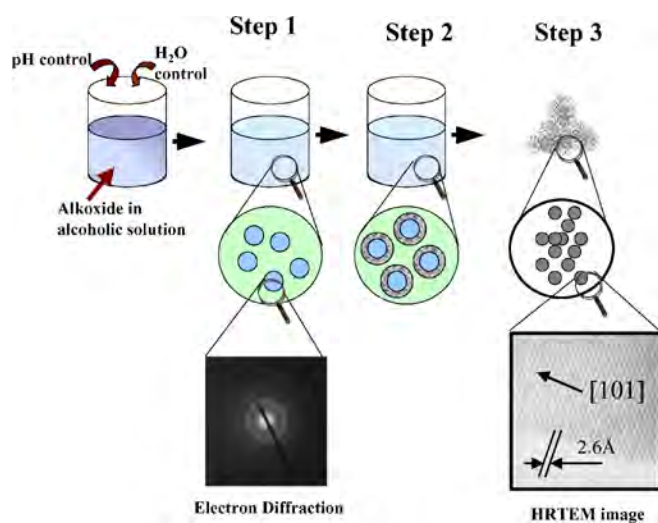


**Figure 2.** Schematic representation of the sol-gel process. For more details about each step, see Section 3.

The crystallization process (step 3) can be considered the critical step in the sol-gel process when a crystalline phase is desirable. If an amorphous phase is the final target, as in the case of SiO<sub>2</sub> nanoparticle processing, the synthesis ends with step 2. However, for crystalline materials, a heat or hydrothermal treatment is necessary to promote the crystallization of the amorphous hydrous oxide which is formed during hydrolysis. Such subsequent treatments can lead to particle growth and modify the particles' morphology.

In the case of crystallization by heat treatment, the hydrous oxide colloidal suspension must be dry before the treatment. During the heat treatment, normally done in an electric furnace, crystallization occurs by a nucleation growth process and can be described by the standard nucleation growth theory [84, 98].

Since the amorphous phase crystallizes via the nucleation-growth process, particle size and growth can be controlled based on the separation of the nucleation phenomena from the growth process. However, during crystallization, each hydrous metal oxide particle can generate several nuclei, rendering it very difficult to control particle morphology and shape. Figure 3 shows a high-resolution transmission microscopy (HRTEM) image of the nucleation of several PbTiO<sub>3</sub> nuclei in an amorphous inorganic nanoparticle. This figure shows the particle before and after crystallization induced by an electronic beam. The polynuclei process generates polycrystalline particles rather than freestanding ones. Controlling the generation of polynuclei in a single amorphous particle is the main challenge involved in obtaining crystalline metal oxide freestanding nanoparticles through the sol-gel process or by any other process that requires crystallization by heat treatment at high temperatures. The origin of the polynuclei process occurring during sol-gel amorphous precursor crystallization is assumed to be related to the preferential heterogeneous nucleation process (surface and interface nucleation) in detriment to homogeneous crystallization (bulk nucleation). The presence of hydroxyl groups and other defects on the particle surface can contribute to reduce the Gibbs free energy for crystallization, rendering the surface crystallization more favorable than the bulk crystallization. Since crystallization occurs in a scenario of high driving force (high temperature of heat treatment),

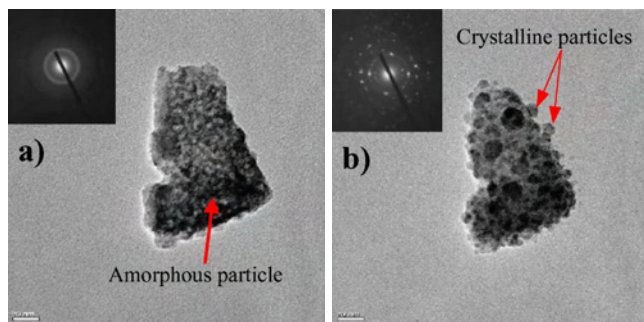


**Figure 3.** HRTEM image of the nucleation of several PbTiO<sub>3</sub> nuclei in an amorphous inorganic nanoparticle. (a) Amorphous particle before the crystallization (inset shows the electron diffraction pattern typical of amorphous materials) induced by the electron beam (300 kV); (b) the same particle after the crystallization process (inset shows the electron diffraction pattern of the crystalline materials).

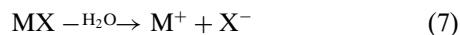
surface crystallization must occur first, followed by bulk crystallization, giving rise to a particle with several nuclei. A possible way to avoid this problem is to suppress surface crystallization by using an inhibitory surface layer. If crystallization occurs at a temperature that favors bulk crystallization, a single nucleus can be generated, resulting in a freestanding particle. This approach was used recently to process freestanding lead zirconate titanate (PZT) nanoparticles [99]. Liu and co-workers [99] used a sol-gel process based on controlled hydrolysis and a two-step heat treatment. They first applied a 12-h treatment in Ar atmosphere at 700 °C, which formed a surface layer rich in carbonaceous materials on the nanoparticles, inhibiting surface nucleation. A second treatment was carried out at 500–600 °C, in air, to burn out the carbon residue. Freestanding PZT nanoparticles with a mean particle size of 17 nm were reported.

Freestanding particles are desirable in a variety of fundamental studies and in some technologies, particularly for ferroelectric metal oxides such as PbTiO<sub>3</sub> (PT), Pb(Zr,Ti)O<sub>3</sub> (PZT), BaTiO<sub>3</sub> (BT), among others. Freestanding and single crystalline nanorods of BT and SrTiO<sub>3</sub> (ST) were recently obtained [100, 101]. The approach used in both these studies to obtain this type of material was the injection of a bimetallic alkoxide compound into a solvent at high temperature (100–280 °C), in which the hydrolysis took place (injection-hydrolysis method). Murray et al. [100] synthesized BT nanoparticles with diameters ranging from 6 to 12 nm based on this approach, controlling the particle size by the bimetallic alkoxide (BaTi(OR)<sub>6</sub>)/oleic acid ratio. Park and co-workers [101] reported on the synthesis of BT and ST single crystalline nanorods using a similar process. The origin of nanorod morphology is not yet well understood. Nonetheless, the above-described approach appears to promote and control crystallization with no extra heat treatment, allowing for good control of particle size and morphology.

Another alternative approach to avoid the heat treatment process is to promote crystallization under hydrothermal conditions, a process that is widely used in the synthesis of zeolites [102, 103]. Ying and Wang [104] used hydrothermal treatment to promote the crystallization of anatase and rutile phases, using an alkoxide sol-gel route and achieving the crystallization of anatase TiO<sub>2</sub> phase with a mean particle size of 10 nm at 180 °C, as well as the synthesis of ultrafine rutile TiO<sub>2</sub> phase obtained by hydrothermal treatment in an acidic medium.

The hydrolysis of metal halides and other inorganic salts is a method widely employed to process metal oxide nanoparticles, such as TiO<sub>2</sub> [105, 106], doped and undoped SnO<sub>2</sub> [107–111], ZnO [112, 113], ZrO<sub>2</sub> [114, 115], Y<sub>2</sub>O<sub>3</sub> [116], and others. This process is less sensitive to water content, requiring less control than the hydrolysis of metal alkoxide. In fact, the hydrolytic process normally occurs in a water solution. In solution, the metallic salt generates the anion (Cl<sup>-</sup>, F<sup>-</sup>, NO<sub>3</sub><sup>-</sup>, and others) and the cation (M<sup>n+</sup>). The cation is normally hydrolyzed by pH changing. Hydrolysis promotes the precipitation of an insoluble amorphous hydrous metal oxide. Thus, the steps illustrated in Figure 2 to describe the metal alkoxide hydrolysis-based sol-gel process can also be used to describe the sol-gel process based on inorganic salts. Equations (7) and (8) describe the reaction involved during

the hydrolysis of inorganic salt in water solution. Precipitation will occur by increasing the pH or the  $[\text{OH}^-]$  concentration



The synthesis based on this approach requires the same control described earlier for the sol-gel method related to the hydrolysis of metal alkoxide. However, control of the atmosphere and water content in the solvents is much less demanding.

Again, the major problem of the metal salt hydrolysis approach is the crystallization step, since a heat treatment or hydrothermal treatment is necessary to promote crystallization. The synthesis of metal oxides based on the hydrolysis of inorganic salts or metal alkoxides, with a high degree of crystallinity at room temperature, still represents a challenge.

The best route to obtain good crystallinity at low temperatures with minimum particle growth is the hydrothermal treatment. Nütz and Haase [107] synthesized well-crystallized Sb-doped  $\text{SnO}_2$  nanocrystals, with particles in the range of 4–9 nm, using a hydrothermal treatment of colloidal gel. The gel was treated in an autoclave at temperatures in excess of 250 °C. These researchers used a solution of  $\text{SnCl}_4$  and  $\text{SbCl}_3$  or  $\text{SbCl}_5$  in fuming  $\text{HCl}$  as precursors and promoted hydrolysis by increasing the pH (using aqueous ammonium). Goebbert et al. [110] also reported on the synthesis of well-crystallized Sb-doped  $\text{SnO}_2$  using the hydrothermal process. However, they used a solution of  $\text{SnCl}_4$  and  $\text{SbCl}_3$  or  $\text{SbCl}_5$  in ethanol, promoting hydrolysis by raising the pH (using aqueous ammonium). The hydrothermal treatment was carried out at 150 °C using 10 bar of pressure. This synthesis route produced nanocrystals in the range of 5 nm.

Leite [117] recently demonstrated that well-crystallized  $\text{SnO}_2$  nanocrystals could be produced at room temperature with no hydrothermal treatment. This process is based on the hydrolysis of  $\text{SnCl}_2$  in an ethanolic solution, followed by dialysis to remove the  $\text{Cl}^-$  ions. The result of this dialysis is a transparent colloidal suspension, as depicted in Figure 4a. Figure 4b shows an HRTEM image of typical  $\text{SnO}_2$  particles obtained by this process (particles in the range of 2–5 nm).

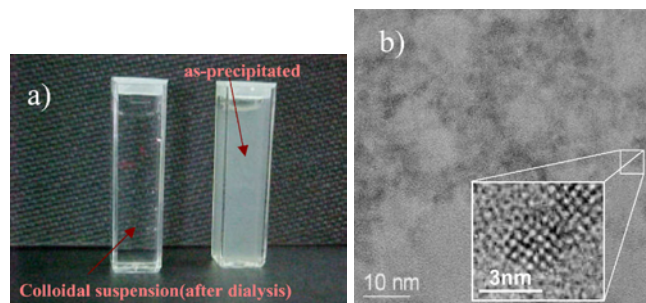


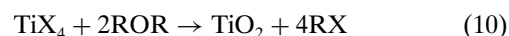
**Figure 4.** (a) Picture of the  $\text{SnO}_2$  colloidal suspension before and after the dialysis (transparent colloidal suspension); (b) HRTEM image of typical  $\text{SnO}_2$  particles obtained by the hydrolysis of  $\text{SnCl}_2$  in an ethanolic solution (particles in the range of 2–5 nm).

Zinc oxide ( $\text{ZnO}$ ) nanocrystals have also been synthesized at room temperature. The process, developed by Bahnmann et al. [118], consists of hydrolyzing zinc acetate dihydrate dissolved in 2-propanol by the addition of  $\text{NaOH}$  in a 2-propanol solution. A colloidal suspension of crystalline  $\text{ZnO}$  nanoparticles is obtained without hydrothermal treatment. Similar results were obtained by Spanhel and Anderson [119] and by Meulenkamp [112]; however, they dissolved the zinc acetate dihydrate ( $\text{Zn}(\text{Ac})_2 \cdot x\text{H}_2\text{O}$ ) in ethanol and used  $\text{LiOH}$  to promote the  $\text{Zn}^{+2}$  hydrolysis. Particles in the range of 3–6 nm were reportedly obtained by both of these processes.

Rusakova et al. [120] used an interesting approach to control the particle growth of hydrous metal oxide gels. They showed that the growth could be inhibited by replacing the surface hydroxyl group, before the crystallization step, with a functional group that does not condense and that can produce small secondary-phase particles which restrict boundary mobility at high temperatures. These authors reported that fully crystalline  $\text{SnO}_2$ ,  $\text{TiO}_2$ , and  $\text{ZrO}_2$  nanocrystals (ranging in size from 1.5 to 5 nm) can be obtained after heat treating the precipitate gel at 500 °C, by replacing the hydroxyl group with the methyl siloxyl group before firing.

The development of metal oxide nanocrystals by nonhydrolytic synthesis routes results in materials whose surfaces are free of  $\text{OH}^-$  groups and nanocrystals with different properties particularly suitable for catalytic and sensor applications. Several nonhydrolytic processes have been developed to process metal oxides, and the molecular chemistry of these various methods is discussed by Vioux [121].

Based on the strategy used to process II–IV semiconductor nanocrystals, using the rapid decomposition of molecular precursor in the presence of strong coordinating agents, Colvin and co-workers [122] proposed an interesting route to process  $\text{TiO}_2$  nanocrystals, based on the reactions



where X is a halide ion ( $\text{Cl}^-$ ,  $\text{F}^-$ ,  $\text{Br}^-$ ,  $\text{I}^-$ ) and R is an alkyl group. The synthetic route involved injecting the metal alkoxide  $[\text{Ti}(\text{OR})_4]$  into a titanium halide mixed with TOPO and a solvent at high temperature (300 °C). Nanoparticles with a mean particle size of 7.3 nm and anatase phase were obtained.

Alivisatos et al. [123] demonstrated that transition metal oxide nanocrystals ( $\gamma\text{-Fe}_2\text{O}_3$ ,  $\text{Mn}_3\text{O}_4$ ,  $\text{Cu}_2\text{O}$ ) could be prepared using a nonhydrolytic process based on the thermal decomposition of metal Cupferron complexes  $\text{M}_x\text{Cup}_x$  [ $\text{M}$  = metal ion,  $\text{Cup} = \text{C}_6\text{H}_5\text{N}(\text{NO})\text{O}^-$ ] in a hot solvent with surfactant. Their results suggest that a good level of control can be achieved when this approach is used to process metal oxide nanoparticles.

Camargo et al. [124–127] recently developed a new route to synthesize lead-based perovskite nanoparticles, such as PT [124], PZT [125],  $\text{PbZrO}_3$  (PZ) [126], and  $\text{PbHfO}_3$  (PH) [127]. This method, which apparently involves no hydrolytic reaction and is carbon- and halide-free, is called the oxidant-peroxo method (OPM) because it is based on the oxidation–reduction reaction between  $\text{Pb}(\text{II})$  ion and water-soluble



metal–peroxide complexes with high pH. This process results in an inorganic amorphous precursor that requires subsequent thermal treatment to promote crystallization of the desired phase. Figure 5 shows an HRTEM image of a PT nanoparticle obtained by this process. The low crystallization temperatures (400–450 °C for the PT phase) of the amorphous precursor suggest that the OPM method favors the formation of a homogeneous inorganic compound.

An important nonhydrolytic chemical process is the so-called Pechini process [128], or *in-situ* polymerizable complex (IPC) [129]. This process is based on the ability of polycarboxylic acids, particularly citric acid (CA), to form very stable water-soluble chelate complexes. Even cations with a high tendency to become hydrolyzed, such as  $\text{Ti}^{+4}$  and  $\text{Nb}^{+5}$ , can be chelated by CA in a water solution, preventing the hydrolysis and precipitation of hydrous metal oxide. The CA complex thus formed can be immobilized in a solid organic resin through a polyesterification reaction with ethylene glycol (EG). This process leads to the formation of a polymeric precursor with the cations of interest randomly distributed in a three-dimensional solid network, avoiding precipitation or phase segregation during the synthesis of the metal oxide compound [130]. Figure 6 schematically represents the IPC process used in the synthesis of very fine particles.

This method is widely used to process titanates [131–137], niobates [138–140], and other kinds of polycationic or single cationic metal oxides [141, 142]. In the last five years, this method has also proved suitable to process oxide thin films with superior performance [143–148]. Using this process,  $\text{PbTiO}_3$  thin film [148] and nanometric powder [149], for example, can be synthesized at temperatures as low as 450 °C, resulting in a metastable cubic  $\text{PbTiO}_3$  phase. Crystallization was observed at a temperature at which long-range diffusion had to be constrained, and the thermodynamic equilibrium configuration was kinetically suppressed [149]. The ability to form complex metal oxides at low crystallization temperatures and metastable phases is not yet well understood, but it is generally assumed to be associated with the tendency of a polycationic CA complex to develop during the chelation step in water solution [141], and/or the tendency to form an inorganic amorphous phase, with a local

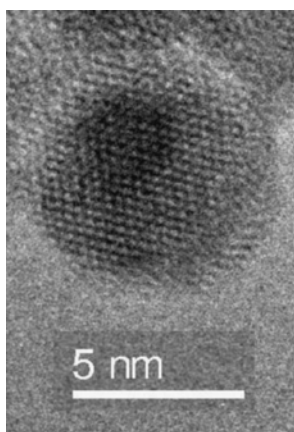


**Figure 5.** HRTEM image of a PT nanoparticle obtained by the OPM.

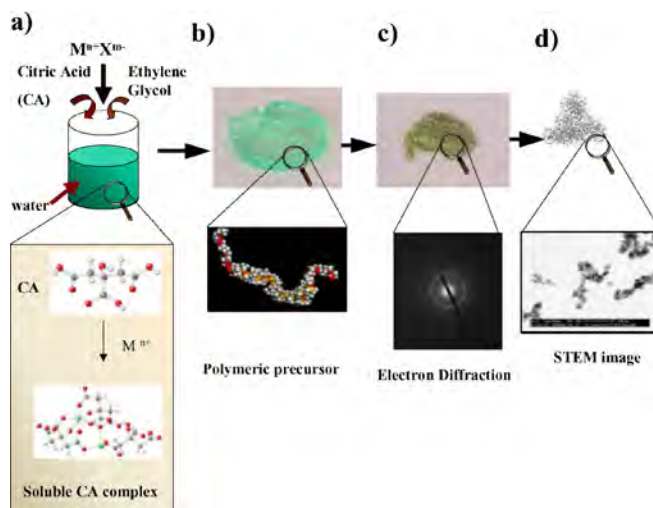


**Figure 6.** Schematic representation of the IPC process: (a) CA complex formation in water solution; (b) polymerization promoted through a polyesterification reaction between the CA complex and EG; (c) prepolymerization of the polymeric precursor. In this step an inorganic amorphous precursor is obtained (in detail electron diffraction pattern of an amorphous inorganic precursor); (d) crystallization process.

symmetry close to that of the crystalline phase, during the crystallization step [150].

The major problem with this process is maintaining control over the particle size and morphology. During the crystallization process, it is very difficult to keep the nucleation and growth processes separate, resulting in agglomerates made up of nanocrystals. The particle growth process, which was studied in the final stage of the crystallization of nanometric powder processed by the IPC method, showed that growth occurs in two different stages [151]. At heat treatment temperatures of <800 °C, the growth process was associated with the surface diffusion mechanism, with an activation energy in the range of 40–80 kJ/mol. At a temperature of >800 °C, particle growth is controlled by densification of the agglomerate formed by nanometric particles and by the neck-size-controlled growth mechanism [152].

Basically, two methodologies have been used to control the particle size of metal oxides processed by the IPC method. Quinelato et al. [142] demonstrated that the particle size and morphology of  $\text{CeO}_2$ -doped  $\text{ZrO}_2$  could be controlled by controlling the metal/CA ratio. A high concentration of CA leads to smaller particles with a soft agglomeration. Leite et al. [153, 154] showed that the particle size and morphology of  $\text{SnO}_2$  could be controlled by the addition of dopants such as  $\text{Nb}_2\text{O}_5$  and rare earths. The same authors [154] also showed that doped  $\text{SnO}_2$  nanocrystals are highly stable against particle growth, even at high temperatures. The technique used to achieve this high stability was to process supersaturated solid solution between the  $\text{SnO}_2$  and the dopant. Segregation of the dopant on the nanocrystal surface occurs during the heat treatment, decreasing the particle boundary mobility or the surface energy. This approach was originally developed to control the particle growth of metal nanocrystals [5, 155] and was used successfully to control the growth of metal oxide nanocrystals.

### 3.2. Properties

The development of metal oxide nanocrystals can lead to significant improvements of their properties, resulting in materials with superior chemical, electrical, and magnetic performance. An example of how metal oxide-based nanostructured materials can very substantially improve performance is in semiconductor gas sensors. The sensing characteristic of a semiconductor gas sensor using  $\text{SnO}_2$  can be improved by controlling basic parameters relating to the receptor and transducer functions. Stated simply, chemical sensors consist of two functions, that is, a receptor function, which recognizes a chemical substance, and a transducer function, which converts the chemical signal into an output signal.

The transducer function is associated directly with the grain size of the metal oxide and the depth of the surface-charge layer (Debye length) [14]. The semiconductor's sensitivity should improve dramatically when the grain size has the same order of magnitude as the Debye length ( $L_D$ ) (e.g., when the grain size is comparable to  $2L_D$ ). The  $L_D$  for  $\text{SnO}_2$  is  $\sim 3$  nm [156]. The sensitivity can therefore be improved by decreasing the grain size or modifying the  $L_D$  using impure-doped elements [14]. The sensor's response time can also be improved by controlling the particle size. Leite et al. [153, 157] demonstrated that the addition of  $\text{Nb}_2\text{O}_5$  resulted in a smaller  $\text{SnO}_2$  particle size and a shorter response time for the detection of methanol.

The receptor function can be modified by the introduction of dopants on the  $\text{SnO}_2$  surface. Yamazoe [14] showed that the addition of precious metal (Pd and Ag) on  $\text{SnO}_2$  can improve gas sensor performance. Carreño et al. [158] showed that the surface reactivity of doped  $\text{SnO}_2$  nanoparticles, in terms of methanol oxidation, can be modified by controlling the dopant's surface segregation.

Electrochemical devices based on the  $\text{Li}^+$  intercalation process, such as lithium batteries and electrochromic windows, constitute another area in which the development of nanostructured materials based on metal oxide semiconductors can result in high performance devices. Aurbach and co-workers [159] tested  $\text{SnO}$  nanoparticles processed by the sonochemical method for use as anodes in rechargeable Li batteries. The  $\text{SnO}$  nanocrystal was found to be an effective material for electrodes. These electrodes reached almost their theoretical capacity ( $\sim 790$  mAh/g) in electrochemical lithiation–delithiation processes as opposed to a Li counter-electrode in an aqueous Li salt solution.

Felde et al. [160] reported the remarkable electrochromic effect of layers of nanocrystalline  $\text{SnO}_2$  strongly doped with antimony (Sb). The layers were prepared by spin coating of  $\text{SnO}_2\text{:Sb}$  colloids onto conductive substrates. These researchers found that the rate of the color change promoted by the  $\text{Li}^+$  intercalation was determined mainly by the substrate's conductivity. Very fast coloration and decoloration were observed ( $< 10$  ms). Cummins et al. [161] built a dynamic color display based on an electrochromic cell, using two porous metal oxide thin films sandwiched between glass electrodes. The negative electrode was coated with a layer of  $\text{TiO}_2$  nanocrystals with viologen molecules anchored to the nanocrystal surface. Viologen molecules turn blue when injected with charge (e.g.,  $\text{Li}^+$ ). The positive electrode consists of a nanocrystalline  $\text{SnO}_2\text{:Sb}$  film, which is linked to

phenothiazine molecules that turn red when oxidized. The prototype built by Cummins and co-workers showed that the color in the display could be switched on and off in less than 250 milliseconds.

Even in ion-conducting polymer membranes used as electrolytes for lithium batteries, the nanocrystals can play an important role. Scrosati and co-workers [12] showed that ceramic nanoparticles can act as solid plasticizers for polyethylene oxide (PEO), an ion-conducting polymer membrane. They demonstrated  $\text{Li}^+$  ionic conductivities of around  $10^{-4}$   $\text{S cm}^{-1}$  at  $50^\circ\text{C}$  and  $10^{-5}$   $\text{S cm}^{-1}$  at  $30^\circ\text{C}$  in a PEO– $\text{LiClO}_4$  mixture containing  $\text{TiO}_2$  and  $\text{Al}_2\text{O}_3$  powders with 5.8–13 nm particle sizes. This may lead to the development of polymer electrolytes having a true solid-state configuration combined with high conductivity, a high lithium ion transference number, and high interfacial stability with the lithium metal electrode. In fact, the characteristics of the PEO–nanoparticle electrolyte render this material an ideal candidate for use in rechargeable lithium batteries.

In photovoltaic cells (i.e., devices that convert sunlight into electrical power), nanocrystals are responsible for a new and promising generation of devices [8, 162, 163]. The creation of these new devices is based on metal oxide nanocrystals, such as  $\text{TiO}_2$ ,  $\text{SnO}_2$ ,  $\text{ZnO}$ , and others, and on conducting polymers. Generally, the device is composed of a mesoporous oxide film and the pores are filled with a conducting medium (conducting polymers).

## 4. NANOCRYSTALLINE COMPOSITES

Several metal or metal oxide nanocrystal applications or processing steps require high temperature environments. A typical example is materials for heterogeneous catalysis processes, which usually require temperatures of over  $200^\circ\text{C}$  coupled with high pressure [164]. Under such conditions, most nanocrystals are unstable, resulting in particle growth and thus losing their nanoscale dimensions.

As discussed earlier, a good way to improve the thermal stability of nanocrystals and prevent particle growth is to use the supersaturated solid solution process. This process, however, has only been applied for tin oxide [154, 157, 165] and in some restricted metal systems [5, 155].

A satisfactory way of improving thermal stability against particle growth may be the development of nanocomposites (i.e., materials composed of two or more phases with nanometric scale sizes). These nanocomposites must display a special phase distribution, in which the dispersed active phase is isolated from the others, preventing particle growth by coagulation or coalescence at high temperature. This concept is based on the fact that the dispersed solid phase in a solid matrix grows preferentially by coalescence, since a growth process such as Ostwald ripening does not occur due to the low solubility of the dispersed phase in the solid matrix.

Based on this concept, two types of nanocomposite microstructures can be proposed to prevent particle growth: core–shell (CS) nanocomposites and embedded dispersed phase (EDP) nanocomposites. Figure 7 illustrates the two types of nanocomposites proposed. These two types of nanocomposite are now discussed in detail.

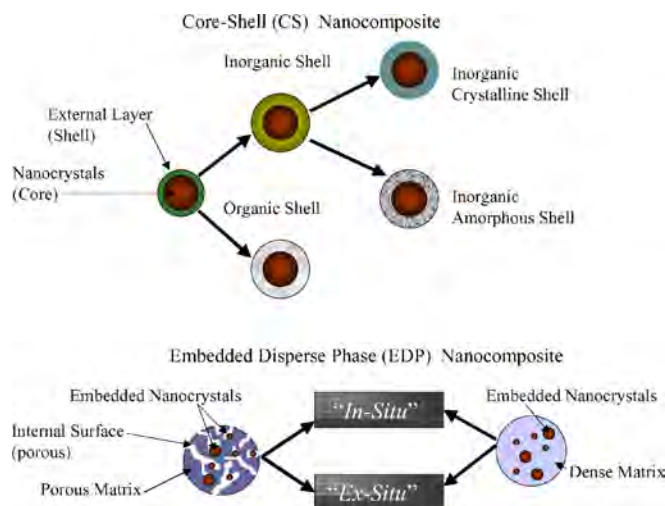


**Figure 7.** Nanocomposite microstructures proposed to prevent particle growth: CS nanocomposites and EDP nanocomposites.

#### 4.1. Synthetic Methods

CS nanocomposites composed of an organic shell are basically nanocrystals protected by a surfactant layer that controls particle growth during synthesis and particle coagulation by the steric effect [29, 30]. This process is useful to improve the stability of the nanocrystals in suspension; however, the organic layer is ineffective at high temperature due to its low thermal stability.

CS nanocomposites with inorganic shells can be divided in two subgroups (i.e., crystalline inorganic shells and amorphous inorganic shells). Good reviews about the CS nanocomposite with an inorganic layer are available in the literature [6, 166].

CS nanocomposites with amorphous inorganic shells are composed of metals or metal oxides nanocrystals (core) with an amorphous silica layer (shell) usually synthesized by the sol-gel process [6, 167, 168]. Silica shells have been used on gold nanoparticles to stabilize them and to modulate their optical properties. Liz-Marzán et al. [168] synthesized CS nanocomposites composed of gold nanoparticles and silica shell (these authors introduced the Au@SiO<sub>2</sub> nomenclature to signify gold core and silica shell), using gold nanocrystals prepared by citrate reduction of HAuCl<sub>4</sub>. The silica shell is prepared in two steps. First, the gold particles are coated with (3-aminopropyl)trimethoxysilane (primer layer). The organometallic compound becomes complexed to the gold surface (using the amine groups), replacing the adsorbed citrate ions. This primer layer prevents particle coagulation. The second step consists of adding sodium silicate to form a thin silica layer over the gold particle. The primer layer (formed in the first step) acts as an anchor upon which the silica layer is formed. Further growth of the silica layer can be achieved by transferring the gold-coated particles to an ethanol/water solution with a controlled amount of TEOS. Slow TEOS hydrolysis and a polycondensation reaction cause the silica layer to increase. This technique has been adapted successfully to process several CS nanocomposites such as CdS@SiO<sub>2</sub> [169] and Ag@SiO<sub>2</sub> [170]. Because the silica shell thickness can be controlled, these CS

nanocomposites can be used to process dense thin films with controlled intercore distances [171].

Lu et al. [167] used the sol-gel approach to coat iron oxide nanoparticles with a uniform shell of amorphous silica. The thickness of the silica layer was controlled within the range of 2–100 nm by changing the concentration of the sol-gel solution. In their study, TEOS was used as alkoxide precursor for the silica layer. A primer layer was not necessary to coat the iron oxide.

Oldfield et al. [172] also reported the formation of a tin oxide crystalline layer over gold nanoparticles (Au@SnO<sub>2</sub>) without a primer layer. The crystalline shell was produced through heat treatment and the gold nanocrystals were coated by adding Na<sub>2</sub>SnO<sub>3</sub>·3H<sub>2</sub>O (sodium stannate) to a gold sol with high pH (10.5). Bedja and Kamat [173] successfully prepared a TiO<sub>2</sub> layer on SnO<sub>2</sub> nanocrystals (TiO<sub>2</sub>@SnO<sub>2</sub>) using a sol-gel-like process. They reported on the improved photocatalytic efficiency of the TiO<sub>2</sub>@SnO<sub>2</sub> nanocomposite compared to pure SnO<sub>2</sub> nanocrystals.

As can be seen in Figure 7, the structure of EDP nanocomposites differs from that of CS nanocomposites. In this kind of nanocomposite, the dispersed phase (nanocrystals) is homogeneously distributed in a matrix. In fact, the nanocrystals are embedded in a matrix that can be either porous or dense. Basically, EDP nanocomposites can be divided into two classes: EDP nanocomposites formed by an *in-situ* process and EDP nanocomposites formed by an *ex-situ* process.

With the advent of mesoporous molecular sieves [174, 175], new possibilities for the development of EDP nanocomposites formed by *ex-situ* processing have arisen. These mesoporous sieves present a well-defined pore structure and large surface area, which makes them excellent matrixes for EDP nanocomposites. When these mesoporous materials are used as matrixes for EDP nanocomposites, a second processing step is needed to incorporate the dispersed phase (nanocrystals). This two-step process is called *ex-situ*. The dispersed phase is normally incorporated by liquid infiltration of metal salt solution with subsequent heat treatment in a hydrogen atmosphere, or by vapor phase [176]. The vacuum or electrophoretic method also can be used to fill the channels of mesoporous matrixes with colloidal suspension [177–179].

An alternative way to process EDP nanocomposites is through an *in-situ* process whereby the dispersed phase and the matrix are formed in a single step process. Rolison et al. [180–182] proposed an interesting synthetic route to process EDP nanocomposites by an *in-situ* process. They used silica sol (silica nanoparticles dispersed in a liquid) as a nanoscale glue to prepare composite aerogel by dispersing a nanometric solid together with the silica sol. With the condensation of the silica sol, the second phase was incorporated in a three-dimensional silica network. After gelation, the materials were dried by a supercritical process, keeping their three-dimensional structure and the dispersed phase (metal nanoparticles, carbon black, zeolites, or TiO<sub>2</sub>) embedded in a mesoporous matrix.

Leite et al. [183, 184] recently described a new *in-situ* route for the synthesis of EDP nanocomposites. A mesoporous silica matrix, with a surface area of more than 200 m<sup>2</sup>/g, a narrow pore size distribution, and transition

metal nanocrystals (Ni, Fe, Co, Ag) embedded in the matrix, was obtained in a direct process. Figure 8a shows a bright field (BF) transmission electron microscopy (TEM) image of Ni nanoparticles embedded in an amorphous mesoporous silica matrix processed by this method. A different approach was adopted to process such nanocomposites. This new approach is based on the formation of a hybrid polymer composed of Si, O, C, H, and metal cations arrested in the macromolecule chain and on the control of the pyrolysis step. The CO/CO<sub>2</sub> atmosphere resulting from the pyrolysis of the organic material leads to the reduction of the metallic salt. In this process, CA is used to chelate the Si, resulting in a Si-citric acid complex. EG and the metallic salt are then added to the citrate solution to promote a polyesterification reaction, resulting in a polymeric precursor. The polymeric precursor is then pyrolyzed in an N<sub>2</sub> atmosphere to promote the formation of the EDP nanocomposite. This process leads to the formation of nanocomposites with good catalytic [183, 185] and magnetic properties [186]. The same approach can also be used to process nanocomposites with matrixes other than silica, as illustrated in Figure 8b, which

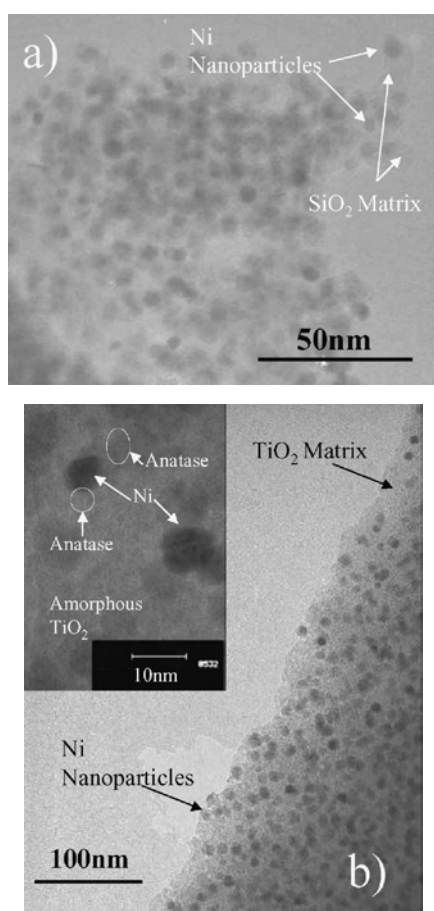


**Figure 8.** (a) BF TEM image of Ni nanoparticles (dark spots) embedded in an amorphous mesoporous silica matrix; (b) BF-TEM image of a nanocomposite composed of Ni nanocrystals (dark spots) with a mean particle size of 8.8 nm embedded in a matrix composed of amorphous and crystalline (anatase) TiO<sub>2</sub> phase (inset shows a HRTEM image of the nanocomposite, in which can be visualized the anatase, amorphous TiO<sub>2</sub>, and the Ni nanoparticles).

shows a BF-TEM image of a nanocomposite composed of Ni nanocrystals with a mean particle size of 8.8 nm (see inset of Fig. 8b) embedded in a matrix composed of amorphous and crystalline (anatase phase) TiO<sub>2</sub>. In this case, a polymeric precursor composed of Ti, O, C, and H was used.

Chiodini [77] and co-workers reported that they had synthesized SnO<sub>2</sub> nanocrystals embedded in a dense SiO<sub>2</sub> matrix. A modified sol-gel process was used to prepare the nanocomposite. The main step of this process consists of obtaining a starting low-density skeleton from the hydrolysis of organometallic precursors (TEOS as SiO<sub>2</sub> precursor and dibutyl tin diacetate as SnO<sub>2</sub> precursor). With controlled hydrolysis of the precursors and thermal treatment in a controlled atmosphere up to 1050 °C, an EDP nanocomposite is obtained, with SnO<sub>2</sub> nanocrystals (2–8 nm) dispersed in a dense SiO<sub>2</sub> matrix.

## 4.2. Properties

The properties of nanocomposites materials are directly related to the combination of different phases, which potentially result in a material with superior performance. This synergetic effect should, in fact, be considered in the selection of material for nanocomposite processing.

Mulvaney et al. [171] showed that the optical properties of Au nanoparticles can be modulated in a CS nanocomposite, whose shell consists of a silica layer. These authors found that the shell thickness controls the dipole coupling between particles and, hence, the color of the film composed of this CS nanocomposite [171]. The same group found [172] that CS nanocomposites composed of SnO<sub>2</sub> shells and Au cores have more advantageous capacitor properties than the uncoated gold particle. This superior performance derives from the considerable difference between the Fermi level of the core and the shell. This CS nanocomposite is potentially applicable for electron storage and electronic circuit components.

An interesting application for the SiO<sub>2</sub>@Fe<sub>2</sub>O<sub>3</sub> nanocomposite was proposed by Levy and co-authors [187], who used this nanocomposite for targeted diagnostics and therapy. The main purpose of their development was to use the CS material for enhanced contrast magnetic resonance imaging and magnetic-induced cancer therapy.

Nanocomposites also display excellent performance as catalytic material. Leite et al. [183] showed that EDP nanocomposites composed of Ni nanoparticles embedded in a mesoporous silica matrix possess good catalytic properties. This nanocomposite performed well in methanol decomposition and conversion to H<sub>2</sub> and CO. A high methanol conversion was observed (100%), as well as high selectivity for H<sub>2</sub> formation at a temperature of 263 °C, with 53 mg of catalyst mass, a total flow (Ar + CH<sub>3</sub>OH) of 30 cm<sup>2</sup>/min, and a weight hourly space velocity of 34,000 ml/hg. The same nanocomposite showed excellent catalytic performance for β-pinene hydrogenation. This catalytic material displayed high selectivity in relation to the β-pinene hydrogenation, with preferential formation of *cis*-pinane.

The same Ni-SiO<sub>2</sub> EDP nanocomposite showed interesting results as a catalyst for the conversion of methane into synthesis gas [185]. Carreño and co-workers reported that this catalyst presents singular properties to control



the carbon deposition and deactivation of active sites. A comparative study of EDP nanocomposites and conventional catalysts (prepared by impregnation) revealed that impregnated material showed preferential encapsulation and growth of carbon nanotubes on the metal surface. The impregnated catalyst displayed a higher tendency to form carbon nanotubes and whiskers. This tendency was not observed in the EDP nanocomposite.

Rolison et al. [182] have developed a highly active electrocatalytic EPD nanocomposite composed of Pt nanoparticles dispersed in a carbon–silica composite aerogel. They reported electrocatalytic activity for methanol oxidation four orders of magnitude per gram of Pt higher than native Pt-modified carbon powder.

EDP nanocomposites can also be used to process photonic materials for telecommunications. Chiodini et al. [77] developed an EDP nanocomposite with SnO<sub>2</sub> nanoparticles embedded in a dense SiO<sub>2</sub> matrix. The SnO<sub>2</sub> nanoparticles acted as wide-bandgap (>4 eV) quantum dots. In this system, unlike other semiconductor-doped glasses, both the glassy host and the nanophase are oxides of IV-group elements. Due to their thermochemical compatibility, the two phases give stable optical-grade glass ceramics with potential photonic applications.

## 5. CHARACTERIZATION OF NANOCRYSTALS

Because of the finite size of nanocrystals, their surface structure and composition are easily affected, resulting in materials with different chemical and physical properties. Thus the characterization of nanostructured materials is a key step in the development of nanocrystals. This characterization should, basically, answer the following questions: (a) What is the material's particle size and particle size distribution? (b) What is its composition? (c) What is its structure and how does its particle size affect this structure?

The answers to these questions therefore require the use of an arsenal of techniques that allow for characterizations of a morphological, chemical, and structural nature. However, the greatest challenge involves determining the superficial structure of nanocrystals and how the atoms located on their surface change their position (surface reconstruction) to accommodate high surface areas in finite sizes and the interaction of nanocrystals with additives such as surfactants. This section describes characterization techniques that provide answers to the above questions, particularly techniques that can provide information on the surface structure.

The first technique described here is TEM and scanning electron microscopy (SEM). These are quite straightforward techniques to determine the size and shape of nanostructured materials, as well as to obtain chemical and structural information.

TEM uses transmitted and diffracted electrons, which generate a two-dimensional projection of the sample. The principal contrast in this projection (or image) is provided by diffracted electrons. In the so-called bright-field images, the transmitted electrons generate bright regions while the diffracted electrons produce dark regions. In the so-called dark field image, the diffracted electrons preferentially form

the image. In this case, the bright areas in the dark field image represent the regions that produced the diffraction. This technique is useful to build the particle size distribution based on a sample composed of an amorphous phase and crystalline phases, as in EDP nanocomposites. Figure 9a shows a dark field TEM image of an EDP nanocomposite consisting of Ni nanoparticles embedded in an amorphous silica matrix. The bright points represent the Ni nanoparticles. The particle size distribution can be built from the TEM image, using an image analyzing software program that allows one to define the particle area of several particles [several particles (total number of particles >300) are normally necessary to obtain a good statistic] and to determine an equivalent particle size based on these areas. Figure 9b shows an example of particle size distribution of Ni nanoparticles in a Ni–SiO<sub>2</sub> EDP nanocomposite built from dark field TEM images.

In addition to morphological information, TEM provides crystallographic and chemical information. The crystallographic information can be obtained from the diffraction pattern of a selected area, using the so-called select area electron diffraction (SAED) technique. This technique allows for the indexing of crystallographic structures of small or even nanometric regions in the samples. Besides SAED, HRTEM can generate lattice images of the crystalline material, allowing for the direct characterization of a sample's atomic structure. Figures 4b and 5 contain examples of HRTEM images. HRTEM images are particularly sensitive to changes in a phase of the incoming parallel electron wave as it passes through the sample. The atomic structure can also be characterized by scanning transmission electron microscopy (STEM), using a high angle annular dark field detector (HAADF). In fact, the image generated by a HAADF detector, which is sensitive to the atomic number (*Z*), is also known as a *Z*-contrast image [188]. The high-resolution image generated by HAADF detector is sensitive to the chemical composition.

In TEM, the chemical information is provided by the X-rays generated through the interaction of the electronic

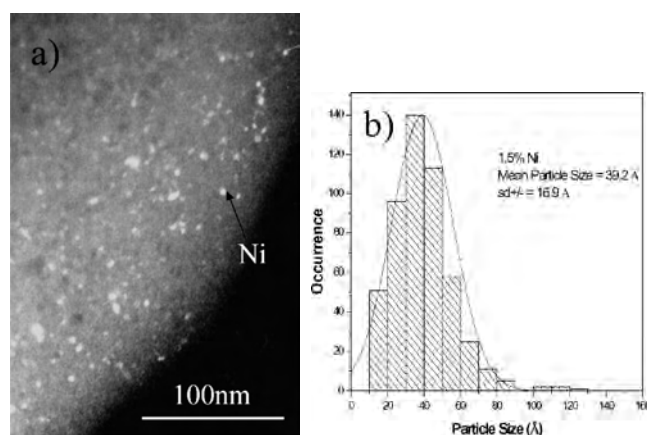


**Figure 9.** (a) Dark field TEM image of an EDP nanocomposite consisting of Ni nanoparticles embedded in an amorphous silica matrix. The bright points represent the Ni nanoparticles. (b) Particle size distribution of Ni nanoparticles in a Ni–SiO<sub>2</sub> EDP nanocomposite built from dark field TEM images.

beam with the sample. This technique, known as energy dispersive X-ray spectroscopy (EDS), allows regions as small as 2 nm in a TEM configuration or lower than 0.8 nm to be chemically characterized, using STEM equipment. In addition to EDS analyses, nanostructured materials can also be chemically characterized by electron energy loss spectroscopy (EELS), which allows for a better characterization of light elements, which usually pose a major problem in X-ray spectroscopy-based characterization. Another advantage of EELS spectroscopy is the fact that it is sensitive to the element's chemical environment, allowing information to be obtained on the local structure of the analyzed element. EDS analysis is insensitive to the chemical environment. Detailed information about TEM characterization is given in the book by William and Carter [189].

TEM characterization has been used more recently for *in-situ* studies of materials in the nanoscale range [190, 191]. Using *in-situ* TEM characterization to obtain atom-resolved images of copper nanocrystals on different supports, Hansen and co-workers [190] found that Cu nanocrystals undergo dynamic reversible shape changes in response to changes in the gaseous environment.

SEM is carried out by scanning an electron beam over the sample's surface and detecting the yield of low energy electrons (secondary electrons) and high-energy electrons (backscattered electrons) according to the position of the primary beam. The secondary electrons, which are responsible for the topologic contrast, provide mainly information about the surface morphology. The backscattered electrons, which are responsible for the atomic number contrast (*Z*-contrast), carry information on the sample's composition. Regarding this type of contrast, because the heavy elements (high *Z* value) have the ability to scatter the electrons more efficiently, an image composed of bright areas (consisting of high *Z* elements) and dark ones (consisting of low *Z* elements) is generated. A new generation of SEM has recently emerged as an important tool to characterize nanostructured materials. This state-of-the-art equipment, called a field emission gun (FEG)-SEM, has a FEG that provides the electron beam, and it uses in-lens or semi-in-lens secondary electron detectors to obtain images with a low acceleration voltage and a resolution as high as 1 nm. A STEM detector can be used in the FEG-SEM device, enabling one to obtain the transmitted dark and bright field images of thin specimens or nanoparticles, similar to images obtained with a dedicated STEM. Figure 10 shows images of SnO<sub>2</sub> nanoparticles, with rather good bright and dark field images, which were taken with a FEG-SEM instrument, using a STEM detector.

SEM can provide not only morphological but also chemical information about the sample; however, the spatial resolution is only about 1 μm<sup>3</sup>. This limitation has rendered the chemical characterization of nanostructured materials using SEM practically useless.

The second characterization technique to be analyzed is X-ray diffraction (XRD). XRD is the most popular technique for structural characterization, providing information about the phases present in the material, as well as refined crystallographic parameters and morphological information. XRD consists of the elastic scattering of X-ray photons by

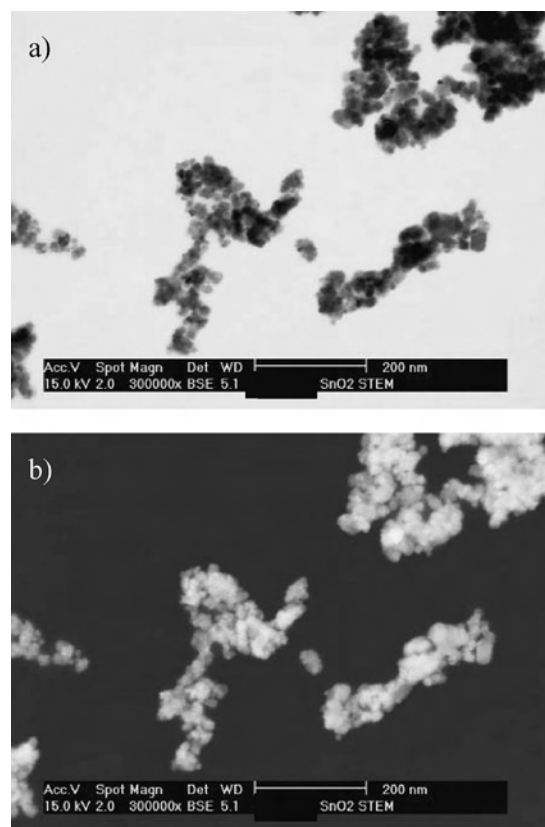


**Figure 10.** STEM images of SnO<sub>2</sub> nanoparticles, which were taken with a FEG-SEM instrument, using a STEM detector. (a) Bright field image; (b) dark field image.

atoms in a periodic lattice. The scattered X-rays (monochromatic) that are in phases provide constructive interference. The lattice space ( $d_{hkl}$ ), or the distance between two lattice planes in a crystal, is described by the Bragg relation

$$2 d_{hkl} \sin \theta = n \lambda \quad (11)$$

where  $\lambda$  is the X-ray wavelength,  $\theta$  is the diffracted angle, and  $n$  is the integer called order of the reflection. A  $d_{hkl}$  set is characteristic of a given compound.

Powder XRD has been used extensively to characterize nanoparticles; however, due to the small particle size, broadening of the diffraction lines occurs at the usual X-ray wavelengths, rendering analyses more complex. These analyses are more difficult if structural parameters are required. In such cases, special X-ray sources like synchrotron radiation and special fit analyses are required to achieve a good structural characterization [192].

X-ray line broadening analysis provides a fast and usually reliable estimate of the particle size [153, 154, 183, 184, 193]. The particle size or, more precisely, the crystallite size ( $\langle D_{hkl} \rangle$ ), can be calculated based on Scherer's equation,

$$\langle D_{hkl} \rangle = K \lambda / \beta \cos \theta \quad (12)$$

where  $K$  is a constant ( $0.9 \leq K \leq 1.0$ ), and  $\beta$  is the corrected full width at half maximum of the diffraction peak. This method of determining the crystallite size takes into account only the X-ray line broadening promoted by the

size effect. Other effects, such as the broadening induced by lattice strain, are not considered. However, considerable discrepancies can occur in metallic nanocrystalline systems [194], even in metal oxide nanoparticles [154]. In such situations, correction of the strain broadening is indispensable for a reliable characterization of the crystallite size. XRD refinement methods, such as the Rietveld method, can be used to correct the strain broadening [195].

Electron microscopy and XRD can provide good morphological, chemical, and structural characterization of nanocrystals; however, these techniques do not provide information about the disordered part of nanocrystals, such as their surfaces. An alternative technique to obtain information about structural disorder in nanocrystals, including surface information of nanocrystals, is X-ray absorption spectroscopy (XAS). This technique is based on the absorption of X-rays and the creation of photoelectrons that are scattered by nearby atoms in a structure. This technique provides information about local structures, such as distance and the number and type of neighbors of the absorbing atom, and can be used to characterize the bulk and surface of solid-state materials, including amorphous materials and catalysts [196, 197]. XAS techniques [X-ray absorption near-edge spectroscopy and extended X-ray absorption fine structure (EXAFS)] have been used to study the size dependence of structural disorder in semiconductors and metal oxide nanocrystals. The results of these techniques have demonstrated that this spectroscopic analysis is sensitive to the structure of the entire nanocrystal, including the surface [198, 199]. By EXAFS analyses of CdS nanoparticles (1.3–12 nm diameter), Rockenberger et al. [200] showed that the stabilization of nanoparticles influences the mean Cd–S distance. Thiol-capped nanoparticles display an expansion of their mean interatomic Cd–S distance, whereas polyphosphate-stabilized particles contract in terms of their CdS bulk. EXAFS has also proved to be highly sensitive in the identification of the surface segregation of foreign cations [201, 202].

Raman spectroscopy can also provide information about the overall nanocrystal structure. Raman spectroscopy is based on the inelastic scattering of photons, which lose energy by exciting vibration in the sample. This technique is very sensitive to the crystal's symmetry and any change can cause modifications in the spectrum, such as shift of the line position, broadening of the line, and new lines. The crystal symmetry of the nanocrystal surface must present differences in relation to the symmetry of the nanocrystal core. Hence, the Raman spectrum of a nanostructured material must be different from the Raman spectrum of the same material with bulk characteristics. In fact, several reports have described the influence of particle size on the Raman spectrum [203–206]. Figure 11a shows Raman spectra of a SnO<sub>2</sub> nanocrystal processed by the IPC process (particle size ~9 nm) compared with a spectrum of a SnO<sub>2</sub> single crystal (Fig. 11b). In addition to the classic modes of the rutile-like structure, the figure clearly shows bands associated with superficial disorder. A detailed discussion of the influence of particle size on the Raman spectrum of SnO<sub>2</sub> is given in the literature [205]. In that work, Dieguez and co-workers proposed a model in which the additional band is due to a

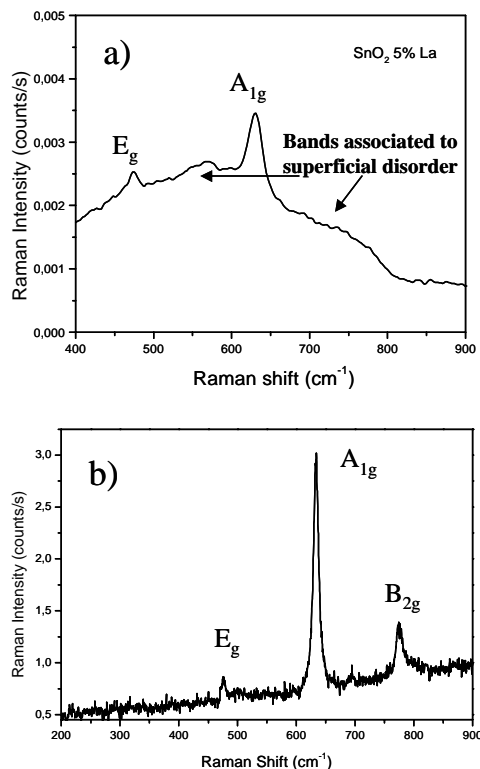


**Figure 11.** Raman spectra of a SnO<sub>2</sub>: (a) nanocrystal processed by the IPC process (particle size ~9 nm); (b) SnO<sub>2</sub> single crystal spectrum.

surface layer of SnO<sub>2</sub> with a dissimilar symmetry. The thickness of this layer was calculated at ~1.1 nm.

Analyses of the Raman line can provide important information about lattice disorder. Such analyses can be performed using the spatial correlation model described by Parayanthal and Pollak [207]. Basically, this model describes the crystal's quality by introducing a parameter called correlation length ( $L$ ), which can be interpreted as the average size of the region of homogeneous materials. According to this model, the Raman line intensity [ $I(\omega)$ ] can be written as

$$I(\omega) = \int_0^1 \exp(-q^2 L^2/4) d^3 q / \{[\omega - \omega(q)]^2 + (\Gamma_0/2)^2\} \quad (13)$$

where  $\omega$  is the frequency,  $q$  is the wave vector,  $\Gamma_0$  is the half-width of the Raman line, and  $\omega(q)$  is the Raman phonon dispersion.

Based on the spatial correlation model, Kosacki et al. [208] demonstrated that the Raman spectra of CeO<sub>2</sub> and Y-doped ZrO<sub>2</sub> thin film are influenced by defects attributed to grain size-controlled nonstoichiometry. Indeed, they proved that Raman spectroscopy could be an effective method to determine the concentration of oxygen vacancies in fluorite-structured oxides.

## 6. SUMMARY

An analysis of the various synthesis routes described above leads to the conclusion that the development of new synthesis routes or the improvement of routes currently under study are necessary to achieve greater control over

the synthesis of nanocrystals, particularly of metal oxide nanocrystals. The advances achieved over the last year in expanding our understanding of the synthesis and control of metal nanocrystals have led to the development of nanoparticles with strictly controlled particle size and particle size distribution, and good control of particle shape. Part of this progress can be attributed to the application of concepts used in the synthesis of semiconductor nanocrystals, such as the thermal decomposition of organometallic compounds and the use of surfactants for the control of particle growth and shape.

The same progress, however, has not been achieved in the synthesis of metal oxide nanocrystals, particularly of metal oxides composed of two or more cations. Part of the reason for this lack of progress is the fact that, during the process of hydrolysis and precipitation, a hydrated amorphous metal oxide phase is formed, requiring heat treatment or a hydrothermal process to promote crystallization of the desired phase. This crystallization step may lead to particle growth, particle shape modification, and particle agglomeration. The use of dopants and surface modifying agents during the synthesis of metal oxide nanoparticles may offer a good alternative to increase the thermal stability of nanocrystals, thus preventing particle growth.

The use of nanocomposites to prevent the growth of nanocrystals, particularly in the case of materials for use at high temperature, appears to be a good strategy. This approach can be combined with the synergism between phases to design nanocomposite materials with superior performance.

There is no doubt that considerable progress has been made in nanocrystal synthesis over the last few years. However, further studies are necessary to achieve improved control over particle size, particle shape, and particle size distribution, as well as to obtain nanoparticles with greater stability against particle growth at high temperatures.

## GLOSSARY

**Nanocomposite** Nanostructured material formed by two or more phases with nanometric scale (1–100 nm).

**Nanocrystal** Crystalline particle with size in the 1–100 nm range.

**Particle growth** Physical–chemical process promoted by the high superficial energy of the particles.

**Self-assembled** Controlled (ordered) particle deposition governed by particle–particle and particle–substrate interaction.

**Sol–gel** Chemical synthesis process in which a sol (often defined as a suspension of small particles or molecules in a liquid phase) undergoes a transition to a gel (a three-dimensional network structure spreading throughout the liquid medium).

## ACKNOWLEDGMENTS

The author thanks many colleagues for stimulating discussions and collaboration, especially Elson Longo, J. A. Varela, Carlos A. Paskocimas, Emersom R. Camargo, Fenelon M. Pontes, N. L. V. Carreño, and Adeilton

P. Maciel. The following Brazilian agencies have provided support for my work: FAPESP, CNPq, and CAPES.

## REFERENCES

1. L. V. Interrante and M. J. Hampden-Smith, "Chemistry of Advanced Materials." Wiley–VCH, New York, 1998.
2. A. P. Alivisatos, *J. Phys. Chem.* 100, 13226 (1996).
3. A. P. Alivisatos, *Science* 271, 933 (1996).
4. S. Morup, "Nanomagnetism" (A. Hernando, Ed.), p. 93. Kluwer Academic, Boston, 1993; K. O'Grady and R. W. Chantrell, "Magnetic Properties of Fine Particles," p. 93. Elsevier, Amsterdam, 1992.
5. H. Gleiter, *Acta Mater.* 48, 1 (2000).
6. P. Mulvaney, *Mater. Res. Soc. Bull.* 12, 1009 (2001).
7. M. Faraday, *Philos. Trans. Roy. Soc. London* 147, 145 (1857).
8. B. O'Regan and M. Grätzel, *Nature* 353, 737 (1991).
9. W. Li, H. Osora, L. Otero, D. C. Duncan, and M. A. Fox, *J. Phys. Chem. A* 102, 5333 (1998).
10. I. Bedja, P. V. Kamat, A. G. Lapin, and S. Hotchandani, *Langmuir* 13, 2398 (1997).
11. L. Kavan, K. Kratochvilova, and M. Grätzel, *J. Electroanal. Chem.* 394, 93 (1995).
12. F. Crou, G. B. Appetechi, L. Persi, and B. Scrosati, *Nature* 394, 456 (1998).
13. A. Hagfeldt and M. Grätzel, *Chem. Rev.* 95, 49 (1995).
14. N. Yamazoe, *Sensors Actuators B* 5, 7 (1991).
15. D. Weller and A. Moser, *IEEE Trans. Magn.* 35, 4423 (1999).
16. S. Sun and D. Weller, *J. Magn. Soc. Jpn.* 25, 1434 (2001).
17. J. Daí, J. Tang, S. T. Hsu, and W. Pan, *J. Nanosci. Nanotech.* 2, 281 (2002).
18. C. Wei, D. Grouquist, and J. Roark, *J. Nanosci. Nanotech.* 2, 47 (2002).
19. V. L. Colvin, M. C. Schlamp, and A. P. Alivisatos, *Nature* 370, 354 (1994).
20. C. Feldmann, *Adv. Mater.* 17, 1301 (2001).
21. H. Bakker, G. F. Zhou, and H. Yang, *Prog. Mater. Sci.* 39, 159 (1995).
22. E. R. Leite, L. P. S. Santos, N. L. V. Carreño, E. Longo, C. A. Paskocimas, J. A. Varela, F. Lanciotti, C. E. M. Campos, and P. S. Pizani, *Appl. Phys. Lett.* 78, 2148 (2001); T. Trindade, P. O'Brien, and N. L. Pickett, *Chem. Mater.* 13, 3843 (2001).
23. J. R. Blackborow and D. Young, "Metal Vapor Synthesis." Springer-Verlag, New York, 1979.
24. J. Turkevich, P. C. Stevenson, and J. Hillier, *Disc. Faraday Soc.* 11, 55 (1951).
25. J. Turkevich and G. Kim, *Science* 169, 873 (1970).
26. J. Turkevich, *Gold Bull.* 18, 86 (1985).
27. H. Bönemann and R. M. Richards, *Eur. J. Inorg. Chem.* 2455 (2001).
28. R. J. Pugh, in "Surface and Colloid Chemistry in Advanced Ceramics Processing" (R. J. Pugh and L. Bergström, Eds.). Dekker, New York, 1994.
29. E. Bourgeat-Lami, *J. Nanosci. Nanotech.* 1, 1 (2002).
30. C. Sanchez, G. J. de, A. A. Soller-Illia, F. Ribot, T. Lalot, C. R. Mayer, and V. Cabuil, *Chem. Mater.* 13, 3061 (2001).
31. J. S. Bradley, in "Clusters and Colloids" (G. Schmid, Ed.). VCH, Weinheim, 1994.
32. J. S. Bradley, J. M. Millar, and E. W. Hill, *J. Am. Chem. Soc.* 113, 4016 (1991).
33. T. Teranishi and M. Miyake, *Chem. Mater.* 10, 594 (1998).
34. M. A. Hayat, "Colloidal Gold: Methods and Applications." Academic, San Diego, 1989.
35. C. D. Keating, M. D. Musik, M. H. Keefe, and M. J. Natan, *J. Chem. Education* 76, 949 (1999).

36. D. N. Furlong, A. Launikonis, W. H. F. Sasse, and J. V. Saunders, *J. Chem. Soc., Faraday Trans.* 80, 571 (1988).
37. P. R. van Rheenen, M. J. Mckelvey, and W. S. Glaunsinger, *J. Solid State Chem.* 67, 151 (1987).
38. T. Ould Ely, C. Amiens, B. Chaudret, E. Snoeck, M. Verelst, M. Respaud, and J. M. Broto, *Chem. Mater.* 11, 526 (1999).
39. F. Dessenoy, K. Philippot, T. Ould Ely, C. Amiens, and B. Chaudret, *New J. Chem.* 22, 703 (1998).
40. J. Osuma, D. de Caro, C. Amiens, B. Chaudret, E. Snoeck, M. Respaud, J. M. Broto, and A. Fert, *J. Phys. Chem.* 100, 14571 (1996).
41. A. Rodriguez, C. Amiens, B. Chaudret, M. J. Casanove, P. Lecante, and J. S. Bradley, *Chem. Mater.* 8, 1978 (1996).
42. A. Duteil, R. Queau, B. Chaudret, R. Mazel, C. Roucau, and J. S. Bradley, *Chem. Mater.* 5, 341 (1993).
43. T. Ould Ely, C. Pan, C. Amiens, B. Chaudret, F. Dassenoy, P. Lecante, M. J. Casanove, A. Mosset, M. Respaud, and J. M. Broto, *J. Phys. Chem. B* 104, 695 (2000).
44. F. Fiévet, J. P. Lagier, and M. Figlarz, *Mater. Res. Soc. Bull.* 12, 29 (1989).
45. G. Viau, F. Ravel, O. Archer, F. Fiévet-Vicente, and F. Fiévet, *J. Magn. Magn. Mater.* 377, 140 (1995).
46. C. B. Murray, S. Sun, H. Doyle, and T. Betley, *Mater. Res. Soc. Bull.* 12, 985 (2001).
47. J.-I. Park and J. Cheon, *J. Am. Chem. Soc.* 123, 5743 (2001).
48. D. P. Dinega and M. G. Bawendi, *Angew. Chem. Int. Ed.* 38, 1788 (1999).
49. J. R. Thomas, *J. Appl. Phys.* 37, 2914 (1966).
50. S.-J. Park, S. Kim, S. Lee, Z. G. Khim, K. Char, and T. Hyeon, *J. Am. Chem. Soc.* 122, 8581 (2000).
51. V. F. Puentes, K. M. Krishnan, and A. P. Alivisatos, *Science* 291, 2115 (2001).
52. X. Peng, L. Manna, W. Yang, J. Wickham, E. Scher, A. Kadavanich, and A. P. Alivisatos, *Nature* 404, 665 (2000).
53. S. Sun, C. B. Murray, D. Weller, L. Folks, and A. Moser, *Science* 287, 1989 (2000).
54. M. Chen and D. E. Nikles, *Nano Lett.* 3, 211 (2002).
55. K. S. Suslick, *Science* 247, 1439 (1990).
56. E. B. Flint and K. S. Suslick, *Science* 253, 1397 (1991).
57. K. S. Suslik, M. Fang, and T. Hyeon, *J. Am. Chem. Soc.* 118, 11960 (1996).
58. S. R. Whaley, D. S. English, E. L. Hu, P. F. Barbara, and A. M. Belcher, *Nature* 405, 665 (2000).
59. L. O. Brown and J. E. Hutchison, *J. Phys. Chem. B* 105, 8911 (2001).
60. M. Chen and D. E. Nikles, *Nano Lett.* 3, 211 (2002).
61. S. Sun, S. Anders, H. F. Hamann, J.-U. Thiele, J. E. E. Baglin, T. Thomson, E. E. Fullerton, C. B. Murray, and B. D. Terris, *J. Am. Chem. Soc.* 124, 2884 (2002).
62. X. Peng, J. Wickham, and A. P. Alivisatos, *J. Am. Chem. Soc.* 120, 5343 (1998).
63. V. F. Puentes, K. M. Krishnan, and A. P. Alivisatos, *Science* 291, 2115 (2001).
64. R. A. Ristau, K. Barmak, L. H. Lewis, K. R. Coffey, and J. K. Howard, *J. Appl. Phys.* 86, 4527 (1999).
65. J. B. Michel and J. T. Schwartz, in "Catalyst Preparation Science, IV" (B. Delmon, P. Grange, P. A. Jacobs, and G. Poncelet, Eds.), p. 669. Elsevier Science, New York, 1987.
66. H. Hirai, Y. Nakao, N. Thosima, and K. Adachi, *Chem. Lett.* 905 (1976).
67. M. Boutonnet, J. Kizling, P. Stenius, and G. Maire, *Colloids Surf.* 5, 209 (1982).
68. M. Boutonnet, J. Kizling, R. Touroude, G. Maire, and P. Stenius, *Appl. Catal.* 20, 163 (1986).
69. P. J. F. Harris, "Carbon Nanotubes and Related Structures," p. 16. Cambridge Univ. Press, Cambridge, UK, 1999.
70. A. Cassel, J. Raymakers, J. Kong, and H. Dai, *J. Phys. Chem.* 103, 6484 (1999).
71. J. Kong, H. Soh, A. Cassel, C. Quate, and H. Dai, *Nature* 395, 878 (1998).
72. Y. Zhang, Y. Li, W. Kim, D. Wang, and H. Dai, *Appl. Phys. A* 74, 325 (2002).
73. Z. P. Huang, D. Z. Wand, J. G. Wen, M. Sennett, G. Gibson, and Z. F. Ren, *Appl. Phys. A* 74, 387 (2002).
74. Z. W. Pan, S. S. Xie, B. H. Chang, C. Y. Wang, L. Lu, W. Liu, W. Y. Zhou, W. Z. Li, and L. X. Qian, *Nature* 394, 631 (1998).
75. E. M. Wong, J. E. Bonevich, and P. C. Searson, *J. Phys. Chem. B* 102, 7770 (1998).
76. A. L. Roest, J. J. Kelly, and D. Vanmaekelbergh, *Phys. Rev. Lett.* 89, 36801 (2002).
77. N. Chiodini, A. Paleari, D. DiMartino, and G. Spinolo, *Appl. Phys. Lett.* 81, 1702 (2002).
78. H. Weller, *Adv. Mater.* 5, 88 (1993).
79. K. Uchino, E. Sadanaga, K. Oonishi, T. Morohashi, and H. Yamamura, in "Ceramic Dielectrics: Composition, Processing, and Properties," Ceramic Transactions, Vol. 8. American Ceramic Society, Westerville, OH, 1990.
80. M. H. Frey and D. A. Payne, *Phys. Rev. B* 54, 3158 (1996).
81. T. Maruyama, M. Saitoh, I. Skai, and T. Hidaka, *Appl. Phys. Lett.* 73, 3524 (1998).
82. M. Sternitzke, *J. Eur. Ceram. Soc.* 17, 1061 (1997).
83. Y.-M. Chiang, E. B. Lavik, I. Kosacki, H. L. Tuller, and J. Y. Ying, *J. Electroceram.* 1, 7 (1997).
84. C. J. Brinker and G. W. Scherrer, "Sol-Gel Science." Academic Press, Boston, 1990.
85. J. Y. Ying, Special Issue: Sol-Gel Derived Materials, in *Chem. Mater.* 9, 2247 (1997).
86. C. Sanchez, J. Livage, M. Henry, and F. Babonneau, *J. Non-Cryst. Solids* 100, 65 (1988).
87. V. K. LaMer and R. H. Dinegar, *J. Am. Chem. Soc.* 72, 4847 (1950).
88. W. Stöber, A. Fink, and E. Bohn, *J. Colloid Interface Sci.* 26, 62 (1968).
89. E. A. Barringer and H. K. Bowen, *Langmuir* 1, 414 (1985).
90. M. T. Harris and C. H. Byers, *J. Non. Cryst. Solids* 103, 49 (1988).
91. T. Sato and R. Ruch, in "Stabilization of Colloidal Dispersion by Polymer Adsorption." Dekker, New York, 1980.
92. D. H. Napper, "Polymer Stabilization of Colloidal Dispersion." Academic Press, New York, 1983.
93. T. E. Mates and T. A. Ring, *Colloids Surf.* 24, 299 (1987).
94. J. H. Jean and T. A. Ring, *Langmuir* 2, 251 (1986).
95. J. L. Look and C. F. Zukoski, *J. Am. Ceram. Soc.* 75, 1587 (1992).
96. J. L. Deiss, P. Anizan, S. El Hadigui, and C. Wecker, *Colloids Surf. A* 106, 59 (1996).
97. A. M. Peiró, J. Peral, C. Domingo, X. Domènech, and J. A. Ayllón, *Chem. Mater.* 13, 2567 (2001).
98. R. W. Schwartz, *Chem. Mater.* 9, 2325 (1997).
99. C. Liu, B. Zou, A. J. Rondinone, and Z. J. Zhang, *J. Am. Chem. Soc.* 123, 4344 (2001).
100. S. O'Brien, L. Brus, and C. B. Murray, *J. Am. Chem. Soc.* 123, 12085 (2001).
101. J. J. Urban, W. S. Yun, Q. Gu, and H. Park, *J. Am. Chem. Soc.* 124, 1186 (2002).
102. R. M. Barrer, "Hydrothermal Chemistry of Zeolites." Academic Press, London, 1982.
103. S. Mintova, N. H. Olson, V. Valtchev, and T. Bein, *Science* 283, 958 (1999).
104. C.-C. Wang and J. Y. Ying, *Chem. Mater.* 11, 3113 (1999).
105. J. Ragai and W. Lotfi, *Colloid Surf.* 61, 97 (1991).
106. L. Cao, H. Wan, L. Huo, and S. Xi, *J. Colloid Interface Sci.* 244, 97 (2001).
107. T. Nütz and M. Haase, *J. Phys. Chem. B* 104, 8430 (2000).

108. G. Pang, S. Chen, Y. Koltypin, A. Zaban, S. Feng, and A. Gedanken, *Nano Lett.* 1, 723 (2001).
109. R. S. Hiratsuka, S. H. Pulcinelli, and C. V. Santilli, *J. Non-Cryst. Solids* 121, 76 (1990).
110. C. Goebbert, R. Nonninger, M. A. Aegerter, and H. Schmidt, *Thin Solid Films* 351, 79 (1999).
111. A. P. Rizzato, L. Broussous, C. V. Santilli, S. H. Pulcinelli, and A. F. Craievich, *J. Non-Cryst. Solids* 284, 61 (2001).
112. E. A. Meulenkamp, *J. Phys. Chem. B* 102, 5566 (1998).
113. E. M. Wong, J. E. Bonevich, and P. C. Searson, *J. Phys. Chem. B* 102, 7770 (1998).
114. M. Z. C. Hu, R. D. Hunt, E. A. Payzant, and C. R. Hubbard, *J. Am. Ceram. Soc.* 82, 2313 (1999).
115. G. Pang, S. Chen, Y. Zhu, O. Palchik, Y. Koltypin, A. Zaban, and A. Gedanken, *J. Phys. Chem. B* 105, 4647 (2001).
116. M. D. Fokema, E. Chiu, and J. Y. Ying, *Langmuir* 16, 3154 (2000).
117. E. R. Leite, unpublished work, 2002.
118. D. W. Bahnemann, C. Kormann, and M. R. Hoffmann, *J. Phys. Chem.* 91, 3789 (1987).
119. L. Spanhel and M. A. Anderson, *J. Am. Chem. Soc.* 113, 2826 (1991).
120. N.-L. Wu, S.-Y. Wang, and I. A. Rusakova, *Science* 285, 1375 (1999).
121. A. Vioux, *Chem. Mater.* 9, 2292 (1997).
122. T. J. Trentler, T. E. Denler, J. F. Bertone, A. Agrawal, and V. L. Colvin, *J. Am. Chem. Soc.* 121, 1613 (1999).
123. J. Rockenberger, E. C. Scher, and A. P. Alivisatos, *J. Am. Chem. Soc.* 121, 11595 (1999).
124. E. R. Camargo and M. Kakihana, *Chem. Mater.* 13, 1181 (2001).
125. E. R. Camargo, J. Frantti, and M. Kakihana, *J. Mater. Chem.* 11, 1875 (2001).
126. E. R. Camargo, J. Frantti, and M. Kakihana, *Chem. Mater.* 13, 3943 (2001).
127. E. R. Camargo and M. Kakihana, *J. Am. Ceram. Soc.* 85, 2107 (2002).
128. M. P. Pechini, U. S. Patent 3, 330, 697, 1967.
129. M. Kakihana, *J. Sol-Gel Sci. Technol.* 6, 7 (1996).
130. P. A. Lessing, *Am. Ceram. Soc. Bull.* 168, 1002 (1989).
131. S. G. Cho, P. F. Johnson, and R. A. Condrate, Jr., *J. Mater. Sci.* 25, 4738 (1990).
132. E. R. Leite, C. M. G. Sousa, E. Longo, and J. A. Varela, *Ceram. Int.* 21, 143 (1995).
133. E. R. Leite, C. A. Paskocimas, E. Longo, and J. A. Varela, *Ceram. Int.* 21, 153 (1995).
134. M. Kakihana, T. Okubo, Y. Nakamura, M. Yashima, and M. Yoshimura, *J. Sol-Gel Sci. Technol.* 12, 95 (1996).
135. S. Kumar, G. L. Messing, and W. White, *J. Am. Ceram. Soc.* 76, 617 (1993).
136. M. Kakihana, T. Okubo, M. Arima, O. Uchiyama, M. Yashima, M. Yoshimura, and Y. Nakamura, *Chem. Mater.* 9, 451 (1997).
137. M. Cerqueira, R. S. Nasar, E. Longo, E. R. Leite, and J. A. Varela, *Mater. Lett.* 22, 181 (1995).
138. H. Takahashi, M. Kakihana, Y. Yamashita, K. Yoshida, S. Ikeda, M. Hara, and K. Domen, *J. Alloys Compounds* 285, 77 (1999).
139. M. A. L. Nobre, E. Longo, E. R. Leite, and J. A. Varela, *Mater. Lett.* 28, 215 (1996).
140. E. R. Camargo, E. Longo, and E. R. Leite, *J. Sol-Gel Sci. Technol.* 17, 111 (2000).
141. M. Kakihana and M. Yoshimura, *Bull. Chem. Soc. Jpn.* 72, 1427 (1999).
142. A. L. Quinelato, E. Longo, E. R. Leite, and J. A. Varela, *Appl. Organomet. Chem.* 13, 501 (1999).
143. S. M. Zaneti, E. R. Leite, E. Longo, and J. A. Varela, *Appl. Organomet. Chem.* 13, 373 (1999).
144. S. M. Zaneti, E. R. Leite, E. Longo, and J. A. Varela, *J. Mater. Res.* 13, 2932 (1998).
145. V. Bouquet, M. B. I. Bernardi, S. M. Zaneti, E. R. Leite, E. Longo, J. A. Varela, M. G. Viry, and A. Perrin, *J. Mater. Res.* 15, 2446 (2000).
146. F. M. Pontes, E. R. Leite, E. Longo, J. A. Varela, E. B. Araujo, and J. A. Eiras, *Appl. Phys. Lett.* 76, 2433 (2000).
147. F. M. Pontes, E. R. Leite, E. J. H. Lee, E. Longo, and J. A. Varela, *Thin Solid Films* 385, 260 (2001).
148. F. M. Pontes, J. H. G. Rangel, E. R. Leite, E. Longo, J. A. Varela, E. B. Araujo, and J. A. Eiras, *Thin Solid Films* 366, 232 (2000).
149. E. R. Leite, E. C. Paris, E. Longo, and J. A. Varela, *J. Am. Ceram. Soc.* 83, 1539 (2000).
150. E. R. Leite, E. C. Paris, E. Longo, F. Lanciotti, C. E. M. Campos, P. S. Pizani, V. Mastellaro, C. A. Paskocimas, and J. A. Varela, *J. Am. Ceram. Soc.* 85, 2166 (2002).
151. E. R. Leite, M. A. L. Nobre, M. Cerqueira, E. Longo, and J. A. Varela, *J. Am. Ceram. Soc.* 80, 2649 (1997).
152. C. Greskovich and K. W. Lay, *J. Am. Ceram. Soc.* 55, 142 (1972).
153. E. R. Leite, I. T. Weber, E. Longo, and J. A. Varela, *Adv. Mater.* 12, 965 (2000).
154. E. R. Leite, A. P. Maciel, I. T. Weber, P. N. Lisboa-Filho, E. Longo, C. O. Paiva-Santos, A. V. C. Andrade, C. A. Paskocimas, Y. Maniette, and W. H. Schreiner, *Adv. Mater.* 14, 905 (2002).
155. J. Weissmuller, *J. Mater. Res.* 9, 4 (1994).
156. H. Onaga, M. Nishikawa, and A. Abe, *J. Appl. Phys.* 53, 4448 (1982).
157. I. T. Weber, R. Andrade, E. R. Leite, and E. Longo, *Sensors Actuators B* 72, 180 (2001).
158. N. L. Carreño, A. P. Maciel, E. R. Leite, P. N. Lisboa-Filho, E. Longo, A. Valentini, L. F. D. Probst, C. O. Paiva-Santos, and W. H. Schreiner, *Sensors Actuators B* 86, 185 (2002).
159. D. Aurbach, A. Nimberger, B. Markovsky, E. Levi, E. Sominski, and A. Gedanken, *Chem. Mater.* 14, 4155 (2002).
160. U. Zum Feld, M. Haase, and H. Weller, *J. Phys. Chem. B* 104, 9388 (2000).
161. D. Cummins, G. Boschloo, M. Ryan, D. Corr, S. N. Rao, and D. Fitzmaurice, *J. Phys. Chem. B* 104, 11449 (2000).
162. M. Grätzel, *Nature* 414, 338 (2001).
163. U. Bach, D. Lupo, P. Comte, J. E. Moser, F. Weissörtel, J. Salbeck, H. Spreitzer, and M. Glätzel, *Nature* 395, 583 (1998).
164. M. Boudart and G. Djega-Mariadasson, "Kinetics of Heterogeneous Reaction." Princeton Univ. Press, Princeton, NJ, 1981.
165. I. T. Weber, A. P. Maciel, P. N. Lisboa-Filho, E. Longo, E. R. Leite, C. O. Paiva-Santos, Y. Maniette, and W. H. Schreiner, *Nano Lett.* 9, 969 (2002).
166. R. A. Caruso and M. Antonietti, *Chem. Mater.* 13, 3272 (2001).
167. Y. Lu, Y. Yin, B. T. Mayers, and Y. Xie, *Nano Lett.* 2, 183 (2002).
168. L. M. Liz-Marzán, M. Giersig, and P. Mulvaney, *Langmuir* 12, 4329 (1996).
169. M. A. Correa-Duarte, M. Giersig, and L. M. Liz-Marzán, *Chem. Phys. Lett.* 286, 497 (1998).
170. M. Giersig, T. Ung, L. M. Liz-Marzán, and P. Mulvaney, *Adv. Mater.* 9, 570 (1997).
171. P. Mulvaney, L. M. Liz-Marzán, M. Giersig, and T. Ung, *J. Mater. Chem.* 10, 1259 (2000).
172. G. Oldfield, T. Ung, and P. Mulvaney, *Adv. Mater.* 12, 1519 (2000).
173. I. Bedja and P. V. Kamat, *J. Phys. Chem.* 99, 9182 (1995).
174. C. T. Kresge, M. E. Leonowicz, W. J. Roth, J. C. Vartuli, and J. S. Beck, *Nature* 359, 710 (1992).
175. C. J. Brinker, Y. Lu, A. Sellinger, and H. Fan, *Adv. Mater.* 11, 579 (1999).
176. C. P. Mehnert, D. W. Weaver, and J. Y. Ying, *J. Am. Chem. Soc.* 120, 12289 (1998).
177. T. Hanaoka, H.-P. Kormann, M. Kröll, T. Sawitowski, and G. Schmid, *Eur. J. Inorg. Chem.* 807 (1998).
178. G. Hornyak, M. Kröll, R. Pugin, T. Sawitowski, G. Schmid, J.-O. Bovin, G. Karlsson, H. Hofmeister, and S. Hopfe, *Chem. Eur. J.* 3, 1951 (1997).



179. G. Schmid, *J. Chem. Soc. Dalton Trans.* 1077 (1998).
180. M. L. Anderson, C. A. Morris, R. M. Stroud, C. I. Merzbacher, and D. R. Rolison, *Langmuir* 15, 674 (1999).
181. C. A. Morris, M. L. Anderson, R. M. Stroud, C. I. Merzbacher, and D. R. Rolison, *Science* 284, 622 (1999).
182. M. L. Anderson, R. M. Stroud, and D. R. Rolison, *Nano Lett.* 3, 235 (2002).
183. E. R. Leite, N. L. V. Carreño, E. Longo, A. Valentini, and L. F. D. Probst, *J. Nanosci. Nanotech.* 2, 89 (2002).
184. E. R. Leite, N. L. V. Carreño, E. Longo, F. M. Pontes, A. Barison, A. G. Ferreira, Y. Maniette, and J. A. Varela, *Chem. Mater.* 14, 3722 (2002).
185. N. L. V. Carreno, E. R. Leite, E. Longo, P. N. Lisboa-Filho, A. Valentini, L. F. D. Probst, and W. H. Schreiner, *J. Nanosci. Nanotech.* 5, 491 (2002).
186. F. C. Fonseca, G. F. Goya, R. F. Jardim, R. Muccillo, N. L. V. Carreño, E. Longo, and E. R. Leite, *Phys. Rev. B* 66, 104406 (2002).
187. L. Levy, Y. Sahoo, K.-S. Kim, E. J. Bergey, and P. N. Prasad, *Chem. Mater.* 14, 3715 (2002).
188. S. J. Pennycook and D. E. Jesson, *Ultramicroscopy* 37, 14 (1991); P. D. Nellist and S. J. Pennycook, *Ultramicroscopy* 78, 111 (1999).
189. D. B. Willian, "Transmission Electron Microscopy." Plenum Press, New York, 1996.
190. P. L. Hansen, J. B. Wagner, S. Helveg, J. R. Rostrup-Nielsen, B. S. Clausen, and H. Topsoe, *Science* 295, 2053 (2002).
191. V. Rodrigues, T. Fuhrer, and D. Ugarte, *Phys. Rev. Lett.* 85, 4124 (2000).
192. C. L. Cleveland, U. Landman, T. G. Schaaaff, M. N. Shafigullin, P. W. Stephens, and R. L. Whetten, *Phys. Rev. Lett.* 79, 1873 (1997).
193. R. L. Penn and J. F. Banfield, *Geochim. Cosmochim. Acta* 63, 1549 (1999).
194. J. Weissmüller, "Characterization by Scattering Techniques and EXAFS in Nanomaterials: Synthesis, Properties and Applications" (A. S. Edelstein and R. C. Cammarata, Eds.), p. 219. IOP, Bristol, 1996.
195. C. O. Paiva-Santos, H. Gouveia, W. C. Las, and J. A. Varela, *Mater. Struct.* 2, 111 (1999).
196. R. F. Pettifer, "X-ray absorption studies of glass structure, in Glasses and Glass-Ceramics" (M. H. Lewis, Ed.), p. 41. Chapman and Hall, London, 1989.
197. J. W. Niemantsverdriet, "Spectroscopy in Catalysis, An Introduction," p. 137. VCH, Weinheim, 1993.
198. K. S. Hamad, R. Roth, J. Rockenberger, T. van Buuren, and A. P. Alivisatos, *Phys. Rev. Lett.* 83, 3474 (1999).
199. T. Shido and R. Prins, *J. Phys. Chem. B* 102, 8426 (1998).
200. J. Rockenberger, L. Tröger, A. Kornowski, T. Vossmeier, A. Eychmüller, J. Feldhaus, and H. Weller, *J. Phys. Chem. B* 101, 2691 (1997).
201. C. V. Santilli, S. H. Pulcinelli, G. E. S. Brito, and V. Briois, *J. Phys. Chem. B* 103, 2660 (1999).
202. C. M. Wang, G. S. Cargill, H. M. Chan, and M. P. Harmer, *J. Am. Ceram. Soc.* 85, 2492 (2002).
203. M. Yoshikawa, Y. Mori, H. Obata, M. Maegawa, G. Katagiri, H. Ishida, and A. Ishitani, *Appl. Phys. Lett.* 67, 694 (1995).
204. A. Dieguez, A. Romano-Rodriguez, J. R. Morante, N. Barsan, U. Weimar, and W. Göpel, *Appl. Phys. Lett.* 71, 1957 (1997).
205. A. Dieguez, A. Romano-Rodriguez, A. Vila, and J. R. Morante, *J. Appl. Phys.* 90, 1550 (2001).
206. J.-M. Jehng and I. E. Wachs, *Chem. Mater.* 3, 100 (1991).
207. P. Parayanthal and F. H. Pollak, *Phys. Rev. Lett.* 52, 1822 (1984).
208. I. Kosacki, V. Petrovsky, and H. U. Anderson, *J. Am. Ceram. Soc.* 85, 2646 (2002).

# Nanocrystals from Solutions and Gels

Marc Henry

Université Louis Pasteur, Institut Le Bel, Strasbourg, France

## CONTENTS

1. Introduction
  2. Nucleation
  3. Crystalline Growth
  4. Limited and Secondary Growth
  5. Aggregation
  6. Conclusion
- Glossary  
References

## 1. INTRODUCTION

The interest in nanocrystalline materials comes from the occurrence of a large interface with a surrounding liquid or gaseous medium. A very elementary calculation is helpful here to grasp this importance of size. Any solid matter may be characterized by its molar volume  $M_v$  ( $\text{cm}^3 \text{mol}^{-1}$ ) and its molar surface  $M_s$  ( $\text{cm}^2 \text{mol}^{-1}$ ). For a sphere of radius  $R$ , the number of bulk atoms  $N_v$  should be such that  $N_v \times M_v = N_A (4\pi/3)R^3$ , whereas the number of surface atoms would be given by  $N_s \times M_s = N_A \times 4\pi R^2$  (with  $N_A$  the Avogadro number). Consequently, we may define the atomic surface to volume ratio  $f = N_s/N_v = (3/R) \times (M_v/M_s)$ . As typical values for condensed solid matter would be  $M_v \sim 20 \text{ cm}^3 \text{mol}^{-1}$  and  $M_s \sim 6 \times 10^8 \text{ cm}^2 \text{mol}^{-1}$ , it follows the very simple rule of thumb that  $f \sim 1/R$  (nm). This analysis shows that for  $R = 1$  nm there could exist no core atoms (the nanocrystal is a pure surface as  $f \sim 100\%$ ), while for  $R = 1000$  nm only one atom over 1000 remains accessible. The nanometer range 2–10 nm is thus particularly interesting as in this domain we have enough atoms (at least 50%) into the bulk to insure the existence of some useful mechanical, electrical, optical, magnetic, or chemical property. On the other hand we also have enough atoms (at most 50%) exposed to the outer space, creating an active interface able to deeply modulate the bulk properties. In fact, one may even hope for the appearance of a *new* property. A very nice example is provided by a quite old but very instructive paper

by Gortner concerning the state of water in colloidal and living systems [1]. The author was interested in the difference in mass between a fresh opaque jellyfish (weighting 500 g) and the dried transparent animal (weighting 0.45 g). As the volatile matter at room temperature is water, the conclusion of this simple experience is that the jellyfish was made of 99.9 wt% of water and only 0.1 wt% of solid matter. This solid matter includes all proteins, lipids, carbohydrates, and mineral salts needed to get a living animal. However, just take a glass containing 499.55 g of water and add 0.45 g of a well-dosed amount of organic and inorganic matter. You do not get a living animal, but just an inert more or less stable colloidal solution. Life is here really a *new* property not shared by a glass of water nor by a piece of sugar nor by a drop of oil nor by a chain of amino acids nor by sodium chloride crystals. The key to life apparition in this system is to create a nanosized solid/water interface, where the bulk, the surface, and the solution interact, leading to a system qualitatively different from the sum of its constituents.

This simple example shows that making nanometric sized objects may be quite rewarding. However, in order to remain quite concise we will limit ourselves to the possible mechanisms allowing growing nanocrystalline dispersions and to their stability toward aging and/or aggregation processes. Even if several well-documented reviews already exist covering all these “well-known” aspects, it appears that none take into explicit account the chemical dimension of the problem. This complete absence of chemistry from nucleation, growth, and aggregation equations has the consequence that it is very difficult to establish a causal link between the final equilibrium size of the crystals and the growth conditions. In fact every crystal maker knows that playing with concentration, temperature, pressure, or ionic strength is not enough to fully control crystalline growth. The key to the success of controlled crystal growing lies in the wise use of chemical additives or suitable complexing reagents. It is the aim of this chapter to fully review an often quite old literature and bring to light all the hidden points where chemistry has a role to play. For each important step (nucleation, growth, aging, aggregation) we will put down for the first time a new *analytical* expression, linking the equilibrium final sizes to growth conditions. With these equations in hand crystal

scientists may then understand, on a quantitative basis, why the change in such physical or chemical parameter alters the final equilibrium size.

## 2. NUCLEATION

### 2.1. Physicochemical Parameters

Nanocrystal formation from solutions and gels is ruled by several factors gathered in Figure 1 [2–4]. From the classical nucleation theory (CNT) viewpoint, five parameters are needed to fully characterize the state of the solution. These are the concentration of solute species  $c$  ( $\text{mol l}^{-1}$ ), assumed to bear an electrical charge  $eq$  and moving with diffusion coefficient  $D$ , the dielectric constant of the solvent  $\epsilon$ , and the temperature  $T$ . Recall that for typical molecular solute species we should have a constant value  $D \sim 10^{-5} \text{ cm}^2 \text{ s}^{-1}$ . For the growing solid phase, three parameters may be identified: its solubility  $c_s$  ( $\text{mol l}^{-1}$ ), its density  $\rho$  ( $\text{g cm}^{-3}$ ), or molecular volume  $v = M/\rho N_A$  (with  $M$  molar mass of one structural motif and  $N_A$  the Avogadro number). Notice that another useful way to express the molecular volume is to think to the characteristic molecular size of the structural repeating unit:  $d \sim v^{1/3}$ . For typical binary compounds this value is roughly constant and may be taken approximately equal to  $v \sim d^3 \sim 10^{-28.5} \text{ m}^3$ .

### 2.2. Interfacial Energy

The interfacial energy  $\gamma$  ( $\text{J m}^{-2}$ ) is finally the last critical parameter that remains to be introduced. Its physical meaning is perfectly clear if one refers to the top left diagram of Figure 1. In a growing crystal, two kinds of atoms may be identified. At the bottom, buried inside the core of crystal

are atoms that interact with other similar atoms. The net force acting on these atoms is thus just zero. At the top, exposed to the surface are atoms displaying a clear force unbalance. On one side they are attracted by atoms buried within the bulk of the crystal, but on the other side they are involved in usually much weaker interactions (van der Waals or hydrogen bonds) with solvent molecules. In fact, the highest asymmetric situation is encountered when there is no solvent at all (i.e., crystals are placed under vacuum), leading to a maximum interfacial or surface energy. Consequently, in the presence of a given solvent, this interfacial energy may be strongly reduced. The stronger the interaction with the solvent, the lower the interfacial energy should be. This is just what is expressed by the Gibbs equation:

$$d\gamma = -(\Gamma \times d\mu)_{P,T} \quad (1)$$

Here,  $\Gamma$  stands for the density in adsorption sites (sites  $\text{nm}^{-2}$ ) and  $\mu$  refers to the electrochemical potential of adsorbed species. Table 1 gives some typical values of interfacial energies for aqueous solutions [3, 5–8]. This shows that expected values for this parameter should be in the range  $50 \leq \gamma \leq 400 \text{ mJ m}^{-2}$ . Let us notice that it has been very recently shown that vacuum surface energies may also be derived directly from the knowledge of the crystal structure [9]. In this last study, it was also proved that the surface energy concept remains valid even at a molecular scale.

This last observation is important in a relation with the justified criticism that may be lodged against CNT that assumes constant surface tension for nucleation [10]. The first principles approach in [9] clearly shows that this criticism is not justified. For each crystal, one may define a characteristic vacuum surface energy averaged over a sphere whose value may be fixed (for most simple structures of course) by the relative spatial disposition of less than five atoms!!! Nevertheless, the most serious criticism remains as nucleation is an irreversible process that just cannot be handled by equilibrium thermodynamics. A more correct approach for this review would have then been to use entropy-based nucleation theory [10] instead of CNT. This was, however, not possible as analytical solutions exist only for liquid–vapor interfaces and not for solid–liquid or solid–solid interfaces, the subject of this chapter.

### 2.3. Nucleation Rate $J$

From a macroscopic point of view, the most important quantity governing the final size and number of nanocrystals is the nucleation rate  $J$  (number of nuclei formed per unit volume and per unit time). A detailed analysis of the nucleation phenomenon [6] leads to the following expression for this nucleation rate:

$$J = \frac{D}{v^{5/3}} \times \exp\left(-\frac{\Delta G_N}{kT}\right) \quad (2)$$

In this equation,  $k$  is the Boltzmann constant ( $k \sim 1.38 \times 10^{-23} \text{ JK}^{-1}$ ) and  $\Delta G_N$  is the energetic barrier to nucleation. The value of the pre-exponential factor  $J_0 = J(\Delta G_N = 0) = D/v^{5/3} \sim 10^{32.5} \text{ cm}^{-3} \text{ s}^{-1}$  has a clear physical interpretation. Accordingly, in the absence of any energetic barrier

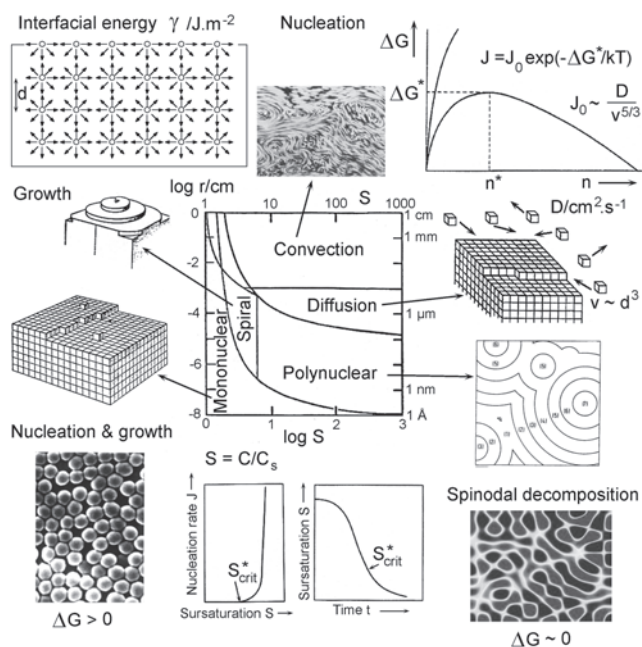


**Figure 1.** A graphical overview of some factors ruling nucleation, growth, and spinodal decomposition processes. See text for details and explanations.

**Table 1.** Interfacial energies for water/solute interfaces derived from nucleation studies in aqueous solutions.

	$\gamma$ (mJ m <sup>-2</sup> )
Halogenes	
KCl	30
KBr	24
KI	17
NH <sub>4</sub> Cl	27
NH <sub>4</sub> Br	19
NH <sub>4</sub> I	8
AgCl	90
AgBr	65
MgF <sub>2</sub>	300
CaF <sub>2</sub>	280
TlCl	92
TlBr	92
TlIO <sub>3</sub>	87
S, Se	
BaSO <sub>4</sub>	135
SrSO <sub>4</sub>	85
CaSO <sub>4</sub> · 2H <sub>2</sub> O	117
PbSO <sub>4</sub>	100
Ag <sub>2</sub> SO <sub>4</sub>	96
Na <sub>2</sub> S <sub>2</sub> O <sub>3</sub> · 5H <sub>2</sub> O	16
BaSeO <sub>4</sub>	88
PbSeO <sub>4</sub>	71
TlSCN	65
Carbon	
BaCO <sub>3</sub>	115
PbCO <sub>3</sub>	125
CH <sub>3</sub> COOAg	113
SrC <sub>2</sub> O <sub>4</sub> · H <sub>2</sub> O	76
PbC <sub>2</sub> O <sub>4</sub>	145
Oxides	
SiO <sub>2</sub>	45
TiO <sub>2</sub>	270
Mg(OH) <sub>2</sub>	123
Ca(OH) <sub>2</sub>	66
Cr, Mo, W	
PbCrO <sub>4</sub>	170
BaCrO <sub>4</sub>	120
Tl <sub>2</sub> CrO <sub>4</sub>	108
Ag <sub>2</sub> CrO <sub>4</sub>	107
SrMoO <sub>4</sub>	100
BaMoO <sub>4</sub>	103
CaMoO <sub>4</sub>	118
SrWO <sub>4</sub>	62
CaWO <sub>4</sub>	151
BaWO <sub>4</sub>	94

for incorporation into a crystalline embryo, the limiting step should be the diffusion of the solute species toward the embryo/solution interface. Consequently, the frequency of incorporation  $\nu_{\text{inc}}$  should scale like  $D/d^2$ . This is because the solute species have just to diffuse over an area of size  $d \times d$  to be immediately incorporated (recall that  $v \sim d^3$  and that  $\Delta G_N \sim 0$ ). As the number of structural repeating units per unit volume is just  $1/v \sim 1/d^3$ , the nucleation rate should scale like  $J_0 \sim \nu_{\text{inc}}/v \sim D/d^5 \sim D/v^{5/3}$ , in good agreement with Eq. (2). Obviously,  $J_0 \sim 10^{32.5} \text{ cm}^{-3} \text{ s}^{-1}$  is an incredibly high value and in most cases  $\Delta G_N > 0$ , leading to a strongly reduced value. In fact, from a practical point of view,

nucleation rates can be experimentally measured only when  $1 \leq J \leq 10^{15} \text{ cm}^{-3} \text{ s}^{-1}$ . Consequently, at room temperature, the nucleation barrier  $\Delta G_N$  should be at least  $80 \text{ kJ mol}^{-1}$  and at most  $170 \text{ kJ mol}^{-1}$ .

## 2.4. Thermodynamic Barrier $\Delta G^*$

Two terms are expected to contribute to the nucleation barrier. The first one  $\Delta G^*$  has a thermodynamic origin. It corresponds to the energetic competition existing between reduction of the supersaturation ratio  $S = c/c_s$  when  $S > 1$  and the necessary increase in area  $A$  of the growing solid phase (energetic cost  $\gamma \times A$ ). Identifying activities  $a$  to concentrations  $c$  ( $\mu = kT \times \text{Ln } a \sim kT \times \text{Ln } c$ ), one may write for the transfer of  $n$  moles of solute species from the solution to the crystal

$$\begin{aligned} \Delta G(n_S \rightarrow n_C) &= n \times (\mu_C - \mu_S) + \gamma \times A \\ &\approx \gamma \times A - nkT \times \ln S \end{aligned} \quad (3)$$

The variation of  $\Delta G$  with  $n$  is visualized at the top right corner of Figure 1. If  $\mu_C \sim \mu_S$  (i.e.,  $c \sim c_s$  or  $S \sim 1$ ), the dominant contribution comes from the positive interfacial term (first monotonic curve in Figure 1). On the other hand, when  $S \gg 1$ , the negative chemical contribution insures that a maximum should be reached for a given number  $n^*$  of solute precursors (second curve in Figure 1). According to this analysis, only embryos such that  $n > n^*$  are able to reach a macroscopic size as  $\Delta G < 0$  for the  $n \rightarrow (n + 1)$  addition (growth). For other embryos such as  $n < n^*$  the  $n \rightarrow (n + 1)$  association is characterized by  $\Delta G > 0$ , meaning that such species should dissolve back into the solution. Embryos such that  $n = n^*$  are called critical nuclei, and the corresponding positive  $\Delta G^*$  value defines the first thermodynamic contribution to the nucleation barrier  $\Delta G_N$ . The magnitude of  $\Delta G^*$  may be readily derived under the assumption that embryos undergo no change in shape (only the mean size is changing among similar bodies) during nucleation. Consequently, the ratio  $K = A/V^{2/3}$  should remain invariant, and if the total volume of a given embryo is  $V \sim n \times v$  then the associated area  $A$  may be written  $A = K \times (n \times v)^{2/3}$ . Inserting this value into Eq. (3) and looking for a maximum by setting  $d(\Delta G)/dn = 0$  leads to the following thermodynamic barrier

$$\begin{aligned} \Delta G^* &= \frac{n^*}{2} \times kT \text{Ln } S & n^* &= 2\beta \frac{\gamma^3 v^2}{(kT \text{Ln } S)^3} \\ \beta &= \frac{(A/3)^3}{(V/2)^2} \end{aligned} \quad (4)$$

Table 2 gives the values of the dimensionless shape factor  $\beta$  for some ideal geometries. As evidenced in Eq. (4) the only way to get  $\Delta G^* = 0$  is to have a vanishing interfacial energy. Such a condition ( $\gamma \sim 0$ ) is easily met in polymer chemistry or in metallic alloys, and in this case phase segregation cannot lead to the sharp boundaries characterizing systems with  $\gamma \gg 0$  (bottom left picture in Figure 1). Instead, for this spinodal decomposition scheme, deeply interconnected patterns

**Table 2.** Dimensionless shape factors, for some common regular 3D geometries.

Shape	Area $A$	Volume $V$	$\beta = 4A^3/27V^2$
Sphere	$4\pi a^2$	$\frac{4}{3}\pi a^3$	$\frac{16\phi}{3} = 16.7552$
Regular icosahedron	$5a^2\sqrt{3}$	$\frac{5a^3\phi^2}{6}$	$\frac{16\sqrt{3}}{\phi^4} = 20.2162$
Regular dodecahedron	$\frac{15a^2\sqrt{\phi^3}}{\sqrt{\sqrt{5}}}$	$\frac{a^3\phi^4\sqrt{5}}{2}$	$\frac{80\sqrt{\phi}\sqrt{5}}{\phi^4} = 22.2012$
Regular octahedron	$2a^2\sqrt{3}$	$a^3\frac{\sqrt{2}}{3}$	$16\sqrt{3} = 27.7128$
Cube	$6a^2$	$a^3$	$8 \times 4 = 32$
Parallelepiped $4a \times 2a \times a$	$28a^2$	$8a^3$	$4 \times \left(\frac{7}{3}\right)^3 = 50.8148$
Regular tetrahedron	$a^2\sqrt{3}$	$a^3\frac{\sqrt{2}}{12}$	$32\sqrt{3} = 55.4256$
Rod $10a \times a \times a$	$42a^2$	$10a^3$	$\frac{14^3}{25} = 109.76$
Plate $10a \times 10a \times a$	$240a^2$	$100a^3$	$\frac{4^3}{5} = 204.8$

Note: Shapes are characterized by one size  $a$  and classified by increasing  $\beta$  value. Here  $\phi$  stands for the golden ratio defined as the positive root of the  $x^2 = x + 1$  equation, viz.  $\phi = (1 + \sqrt{5})/2$ .

with rather diffuse boundaries are typically observed (bottom right picture in Figure 1).

## 2.5. Kinetic Barrier $\Delta G'$

As indicated, the thermodynamic barrier  $\Delta G^*$  is not the only contribution to the nucleation barrier  $\Delta G_N$ . Another kinetic barrier  $\Delta G'$  associated with chemical reactions occurring during jumps across the nucleus–solution interface should also be considered. Obviously, for a solid metallic alloy nucleating from a melt one may expect  $\Delta G' \sim 0$  as the system undergoes only a disorder  $\rightarrow$  order phase transition on going from the liquid to the solid state. During this transition local metallic chemical bonds between atoms are not fundamentally changed, explaining the low kinetic cost  $\Delta G' \sim 0$ . Such would not, however, be the case in other systems.

### 2.5.1. Quartz versus Glass

Consider for instance the growth of quartz crystals from a silica melt. Besides the thermodynamic barrier associated with the quartz/fused silica interface and difference in chemical potentials, one has to take into account the fact that the local structure of both phases is very different. In the quartz crystal,  $\text{SiO}_4$  tetrahedra are strongly engaged into spiral chains, whereas in the melt small oligomeric species (which may be chains, cycles, or cages) are encountered. In order to be able to jump across the nucleus/liquid interface and fit inside the crystalline network, oligomeric species must first be reduced to monomeric  $\text{SiO}_4$  tetrahedra. This means that rather strong Si–O–Si bonds have to be broken, and that a corresponding activation energy  $\Delta G' > 0$  has to be provided before nucleation and growth of quartz crystals can occur.

Let us remark that this activation energy  $\Delta G'$  has absolutely nothing to do with thermodynamics as almost the same Si–O–Si bonds are found before (oligomeric species) and after nucleation (spiral chains). This term is a true kinetic barrier inevitably associated with any kind of reconstructive transformation [11]. Accordingly, glass formation is intimately linked to the existence of a large kinetic barrier  $\Delta G'$  which renders the cost of nucleation quite prohibitive just because  $\Delta G_N = \Delta G^* + \Delta G'$ . If  $\Delta G^*$  were the only contribution to nucleation, glasses would never be formed and should not exist.

### 2.5.2. Sodium Chloride: A Case Study

The same kind of kinetic barrier  $\Delta G'$  is expected when crystallization occurs from solutions or gels. First consider the simplest case: nucleation of a crystalline salt (NaCl for instance) from an aqueous solution. In solution we find ionic species such as  $[\text{Na}(\text{OH}_2)_x]^+$  and  $[\text{Cl}(\text{H}_2\text{O})_x]^-$ . The precise value of the coordination number  $x$  does not matter here as it depends on the molar fraction of sodium chloride. Consequently, variation in  $x$  is well reflected by variation of the chemical potential  $\mu_s$  and should influence only the thermodynamic term  $\Delta G^*$ . Our point of interest is rather how such solute species should be transformed in order to allow them to jump across the NaCl/water interface for further incorporation into the NaCl crystalline network. As this crystal is built from a regular stacking of naked  $\text{Na}^+$  and  $\text{Cl}^-$  ions, it is clear that ion pairing should be the very first step:  $[\text{Na}(\text{OH}_2)_x]^+ + [\text{Cl}(\text{H}_2\text{O})_x]^- \rightarrow [\text{NaCl}(\text{OH}_2)_{2x}]$ . Having formed a neutral species, water removal may then occur:  $[\text{NaCl}(\text{OH}_2)_{2x}] \rightarrow [\text{NaCl}]^0 + 2x \text{H}_2\text{O}$ , and only after that incorporation into the network becomes possible. The origin of the kinetic barrier  $\Delta G'$  lies here in the lability of water molecules around cations and anions.

### 2.5.3. Aquo Cations

For the NaCl case, it is obvious that the lability around  $\text{Na}^+$  or  $\text{Cl}^-$  ions is rather high (Fig. 2), meaning that  $\Delta G' \sim 0$ . But this clearly would not be the case for more charged cations, as it is well known that the kinetics of water splitting,  $[\text{M}(\text{OH}_2)_N]^{z+} \rightarrow [\text{M}(\text{OH}_2)_{N-1}]^{z+} + \text{H}_2\text{O}$ , is considerably slowed down if  $z$  increases or if the ionic radius of the metallic element decreases [12]. Also, for some transition metal elements such as  $\text{Cr}^{3+}$ , crystal field stabilization energies may be so high (leading to  $\Delta G' \gg 0$ ) that nucleation of the corresponding hydroxide  $\text{Cr}(\text{OH})_3$  cannot occur anymore. In such a case, gelation (the equivalent for solutions of glass formation from melts) instead of precipitation is usually observed. Figure 2 shows how the kinetic constant  $k_w$  characterizing the removal of aquo ligand from the metal coordination sphere varies for usual ionic species. It was found that, at room temperature, it lies above  $10^{-6} \text{ s}^{-1}$  ( $\text{V}^{2+}$  or  $\text{Cr}^{3+}$  ions) and below  $10^{10} \text{ s}^{-1}$  ( $\text{Ba}^{2+}$  or  $\text{Cs}^+$  cations) [12, 13].

Now, if  $h$  stands for the Planck constant, the activated complex kinetic theory says that the rate constant may be written  $k_w = (kT/h) \times \exp(-\Delta G_0/kT)$  or for  $T = 300 \text{ K}$  ( $\Delta G_0/\text{kJ mol}^{-1} = 73 - 5.71 \times \log(k_w/\text{s}^{-1})$ ). Consequently, assuming that  $\Delta G' \sim G_0$ , the kinetic barrier for nucleation of a metallic salt or hydroxide should be in the range

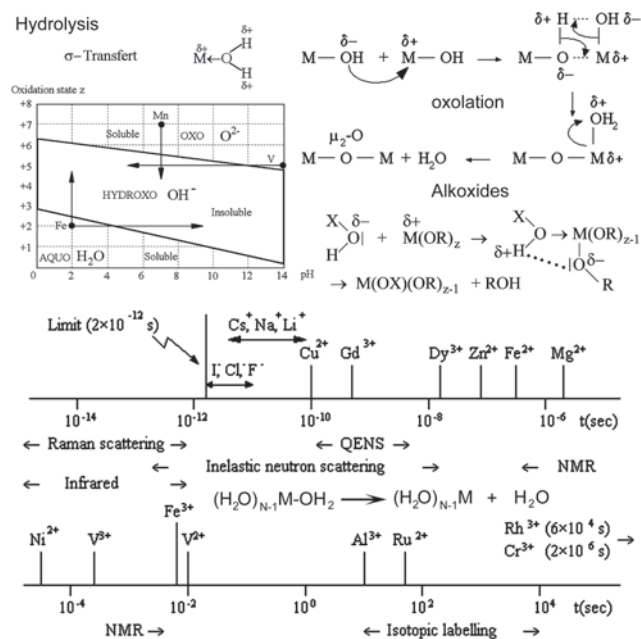


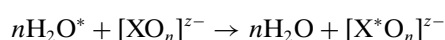
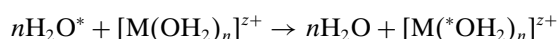
**Figure 2.** Chemical origin of the kinetic barrier  $\Delta G'$  for oxide, hydroxide, or metallic salt nucleation. Top left: type of ligand expected around a metallic cation  $M^{z+}$  in aqueous solutions as a function of pH. Top right: chemical bonds rearrangements expected for oxy ions or metal alkoxides in the case of oxide nucleation. Bottom: techniques used for measuring lability of water molecules around metallic cations  $M^{z+}$  ( $z \leq 3$ , i.e., hydroxide or metallic salt nucleation).

$15 < \Delta G' < 110 \text{ kJ mol}^{-1}$ , depending on the electronic configuration, ionic radius, or total charge of the metallic cation.

### 2.5.4. Oxo Anions

Obviously this picture can be valid only for metallic cations having a low formal oxidation state (typically  $z \leq 3$ ) allowing them to keep the aquo ligand within their coordination sphere. As shown in Figure 2, cations displaying higher formal oxidation states  $z$  are on the contrary extensively hydrolyzed in aqueous solutions. These cations should then lead to oxide rather hydroxide precipitation [14].

Silicon ( $z = +4$ ) is a good example of this behavior, as it is found under low pH conditions under the silanol form  $\text{Si}(\text{OH})_4$ . As this form does not display any aquo ligand in its coordination sphere, a considerable rearrangement of chemical bonds is necessary (Fig. 2) in order to incorporate it in a network based on corner-sharing  $\text{SiO}_4$  tetrahedra (Si–O–Si bridges). However, as a proton transfer is needed in the transition state to form a good leaving group (water), the kinetics of condensation is expected to depend strongly on the solution pH. Accordingly, experiments [15] shows that the kinetic constants for silanol condensation vary from  $10^{1.8} \text{ M}^{-2} \text{ s}^{-1}$  at  $\text{pH} \sim 7$  up to  $10^{3.4} \text{ M}^{-2} \text{ s}^{-1}$  at  $\text{pH} \sim 10$ . Proceeding as before, this corresponds to a kinetic barrier  $50 \text{ kJ mol}^{-1} < \Delta G' < 70 \text{ kJ mol}^{-1}$ . Another possibility of estimating this kinetic barrier  $\Delta G'$  for nucleation from aqua and oxo ions is to use  $^{18}\text{O}$  exchange studies [16]



### 2.5.5. Metal Alkoxides

The same kinetic barrier is encountered when the nanocrystal nucleates after decomposition of metallo-organic complexes in nonaqueous media. Figure 2 shows that, at least in the case of metallic alkoxides precursors, a considerable rearrangement of chemical bonds should also occur. As before, with hydrolysis of the metal alkoxide requiring a proton transfer, the kinetics depends strongly on the amount of acid or base added with the water. As shown in Table 3 for silicon alkoxides [17–22], the height of the kinetic barrier  $\Delta G'$  is at least  $90 \text{ kJ mol}^{-1}$  explaining the difficulty to nucleate quartz directly from the solution at room temperature. Unfortunately, there is a paucity of kinetic data for other metallic cations. To the best of our knowledge, only a global kinetic constant  $k \sim 30 \text{ s}^{-1}$  is available concerning the nucleation of titanium or aluminum oxides from  $\text{Ti}(\text{OEt})_4$  and  $\text{Al}(\text{O}i\text{Bu})_3$  respectively [23]. This would mean that octahedral species may have significantly lower kinetic barriers ( $\Delta G' \sim 65 \text{ kJ mol}^{-1}$ ) relative to tetrahedral silicate species.

## 2.6. Applications

After this rapid outline of the classical nucleation theory, we may take time to see some typical examples, the relative orders of magnitude of the two kinetic barriers  $\Delta G^*$  and  $\Delta G'$ .

### 2.6.1. Ionic Crystals

Consider first the case of a simple crystalline salt such as KCl for instance ( $M = 74.55 \text{ g mol}^{-1}$ ,  $\rho = 1.984 \text{ g cm}^{-3}$ , i.e.,  $v = 10^{-28.2} \text{ m}^3$ ). Referring to Figure 2, the characteristic residence time of water molecules around the potassium cation is  $\tau < 10^{-10} \text{ s}$ . Consequently we may suppose that  $\Delta G' \leq 16 \text{ kJ mol}^{-1}$ . A look at Table 1 shows that for the KCl/ $\text{H}_2\text{O}$  interface we have  $\gamma \sim 30 \text{ mJ m}^{-2}$ . Consequently, at  $T = 300 \text{ K}$  ( $kT = 4.1 \times 10^{-21} \text{ J}$ , or  $RT = 2.48 \text{ kJ mol}^{-1}$ ), we may write

$$n^* = 0.25 \frac{\beta}{(\log S)^3} \quad \text{and} \quad \Delta G^* = 0.714 \frac{\beta}{(\log S)^2} \text{ kJ mol}^{-1} \quad (5)$$

Owing to its cubic structure one may further assume a cube-shaped nucleus ( $\beta = 32$ ); that is,  $n^* = 8/(\log S)^3$  and

**Table 3.** Measured rate constants and associated kinetic barrier  $\Delta G'$  for the chemical reaction  $(\text{RO})_3\text{Si-OX} + \text{HOY} \rightarrow (\text{RO})_3\text{SiOY} + \text{HOX}$ .

$X(R)$	$Y$	Rate constant	pH	$\Delta G'$ ( $\text{kJ mol}^{-1}$ )	Ref.
$\text{CH}_3$	H	$10^{-5.5} \text{ M}^{-1} \text{ s}^{-1}$	5.5	104	[17]
$\text{C}_2\text{H}_5$	H	$10^{-1.3} \text{ M}^{-1} \text{ s}^{-1} [\text{H}^+]^{-1}$	7–2	120–92	[18]
$\text{C}_4\text{H}_9$	H	$10^{-1.7} \text{ M}^{-1} \text{ s}^{-1} [\text{H}^+]^{-1}$	7–2	123–94	[19]
$\text{C}_6\text{H}_{13}$	H	$10^{-2.1} \text{ M}^{-1} \text{ s}^{-1} [\text{H}^+]^{-1}$	7–2	125–96	[19]
H(Me)	Si	$10^{-4} \text{ M}^{-1} \text{ s}^{-1}$		96	[20]
H(Me)	Si	$10^{-2.1} \text{ M}^{-1} \text{ s}^{-1}$	5.5	85	[17]
$\text{CH}_3$	Si	$10^{-4.8} \text{ M}^{-1} \text{ s}^{-1}$		100	[20]
H(Me)	$\text{Si}_2$	$10^{-4.7} \text{ M}^{-1} \text{ s}^{-1}$	2.8	100	[21]
$\text{CH}_3$	$\text{Si}_2$	$10^{-4.9} \text{ M}^{-1} \text{ s}^{-1}$	2.8	101	[21]
$\text{C}_2\text{H}_5$	H	$10^{-4.2} \text{ M}^{-1} \text{ s}^{-1}$	3.1	97	[22]
H(Et)	Si	$10^{-5.3} \text{ M}^{-1} \text{ s}^{-1}$	3.1	103	[22]

Note:  $Y = \text{Si}_2$  refers to the  $(\text{RO})_3\text{SiOSi}(\text{OH})(\text{OR})_2$  dimer.



$\Delta G^* = (22.8 \text{ kJ mol}^{-1})/(\log S)^2$ . Now for  $S = 2$  (two times the solubility of KCl,  $c_s \sim 34.7 \text{ wt}\%$  at  $20^\circ \text{C}$ ), it transpires that about 300 KCl pairs have to meet together, forming a sphere of radius  $r^* \sim (n^*v)^{1/3} \sim 26 \text{ \AA}$ , in order to nucleate the KCl network. The very low probability of such an event is easily understood by looking at the nucleation rate  $J$ . With  $\Delta G^* = 252 \text{ kJ mol}^{-1}$  and making the conservative choice  $\Delta G' = 16 \text{ kJ mol}^{-1}$ , it comes that  $\Delta G_N = 268 \text{ kJ mol}^{-1}$  leading to  $J = 10^{32} \times \exp(-268/2.48) \sim 10^{-15}$  nuclei per  $\text{cm}^3$  and per second. Another statement of this matter of fact is to say that in order to see one such nucleus appear in  $1 \text{ cm}^3$  of solution, one has to wait about 32 Myr!!! Let us now see what would happen by just doubling the supersaturation ratio  $S$ . Now, with  $S = 4$  the same equations tell us that  $n^* = 37$  (critical nucleus with radius  $\sim 13 \text{ \AA}$ ). If the thermodynamic barrier is still dominant, it has nevertheless been reduced down to  $\Delta G^* = 63 \text{ kJ mol}^{-1}$ . The new barrier to nucleation is thus  $\Delta G_N = 79 \text{ kJ mol}^{-1}$  leading to  $J = 10^{32} \times \exp(-79/2.48) \sim 10^{18} \text{ cm}^{-3} \text{ s}^{-1}$ . Consequently, instead of waiting a virtual eternity to see just one nanocrystal, everything is finished (i.e.,  $c \sim c_s$  corresponding to about  $10^{22}$  nanocrystals with radius  $13 \text{ \AA}$ ) in about 8400 s or less than 3 hours.

### 2.6.2. Critical Supersaturation Ratio $S^*$

This example clearly demonstrates that nucleation is basically a critical phenomenon, as a mere doubling of one parameter  $S$  leads to a variation in  $J$  of about 33 orders of magnitude. These considerations are shown graphically at the bottom of Figure 1 (two middle diagrams). Below a critical value  $S^*$ , nothing can happen, while slightly just above this threshold, the nucleation rate displays a very fast divergence (middle left diagram). The main consequence of this burst of nuclei is that the supersaturation is strongly and rapidly reduced and may instantaneously become smaller than  $S^*$  (middle right diagram). This condition is usually met in moderately dilute solutions leading to just one burst of nuclei. Further removal of the remaining supersaturation would only be removed by growth processes (*vide infra*). This is the classical picture for the formation of monodisperse nanocrystals under homogeneous nucleation conditions [24, 25]. On the contrary, for strongly concentrated solutions, the first birth of nuclei is not able to reduce the supersaturation ratio below  $S^*$ , meaning that  $J > 0$  during all the precipitation process. Under such circumstances, a polydispersed system is usually obtained and aggregation phenomena may become competitive for determining the final particle size or shape. From a practical viewpoint, the critical supersaturation ratio  $S^*$  may be defined as the value of  $S$  leading to  $J = 1$  or  $\log J = 0$  [26]

$$\text{Ln } S^* = \sqrt{\frac{\beta\gamma^3 v^2}{(kT)^3 \text{Ln}[(Dv^{-5/3}g_N)/1]}} \quad (6)$$

### 2.6.3. Silica

This example also illustrates the crucial role played by the kinetic barrier  $\Delta G'$ . It is just because the thermodynamic term is dominant and the kinetic one negligible that it is so difficult to keep control over the nucleation

rate. To see that, let us consider the nucleation of silica  $\text{SiO}_2 \cdot 2\text{H}_2\text{O}$  ( $M = 78.08 \text{ g mol}^{-1}$ ,  $\rho = 2.2 \text{ g cm}^{-3}$ , i.e.,  $v = 10^{-28.2} \text{ m}^3$  and  $\gamma \sim 45 \text{ mJ m}^{-2}$ ) [8, 27]. For nuclei displaying spherical shapes, we may write  $n^* = 14/(\log S)^3$  and  $\Delta G^* = (40 \text{ kJ mol}^{-1})/(\log S)^2$ . Now, let us choose  $\Delta G' \sim 100 \text{ kJ mol}^{-1}$  as a typical value characterizing the interfacial oxolation reaction (see Table 3):  $\text{Si-OH} + \text{HO-Si} \rightarrow \text{Si-O-Si} + \text{H}_2\text{O}$ . This choice then leads to  $\Delta G_N \sim 540 \text{ kJ mol}^{-1}$  for  $S = 2$  and  $\Delta G_N \sim 210 \text{ kJ mol}^{-1}$  for  $S = 4$ . Converting these values into nucleation rates according to  $J(\text{cm}^{-3} \text{ s}^{-1}) = 10^{32} \times \exp[-\Delta G_N(\text{kJ mol}^{-1})/2.48]$  leads to  $J \sim 3 \times 10^{-63} \text{ cm}^{-3} \text{ s}^{-1}$  ( $S = 2$ ) and for  $S = 4$ , to only  $J \sim 2 \times 10^{-5} \text{ cm}^{-3} \text{ s}^{-1}$ . Consequently, doubling the supersaturation ratio as before has here no practical consequences, as the nucleation rate remains quite negligible (about 1 nucleus per  $\text{cm}^3$  after one day). Notice that even for  $S = 10$  (10 times the solubility of amorphous silica, or  $c[\text{Si}(\text{OH})_4] \sim 10^{-2} \text{ M}$ ) the nucleation rate is only  $J \sim 3 \times 10^7 \text{ cm}^{-3} \text{ s}^{-1}$ , a perfectly measurable value. The presence of a reasonable kinetic barrier then provides an efficient healing mechanism against the otherwise pathological behavior of the nucleation rate versus supersaturation variation. For oxide or hydroxide precipitation, the kinetic term is provided by the inertness of the metallic cation toward water substitution. It is thus possible to control the nucleation process under dilute conditions through thermal hydrolysis for instance [28].

### 2.6.4. Metallic Salts

For metallic salts (such as carbonates, sulfates, or phosphates for instance) the kinetic barrier should be provided by the slow decomposition of a suitable preformed metallic complex [29]. Only in this case do we get a chance to keep some control over the nucleation process. Among the numerous chemical methods available to control the nucleation stage for sparingly soluble substances, we may cite [29–34]:

- (i) Variation of pH induced by temperature elevation (thermal solvolysis) is a method well suited for acidic media. In order to generate basic conditions a suitable organic reagent able to decompose into ammonia (urea, hexamethylene tetramine) upon heating should be added.
- (ii) Some anions such as  $[\text{CO}_3]^{2-}$ ,  $[\text{C}_2\text{O}_4]^{2-}$ ,  $[\text{SO}_4]^{2-}$ ,  $[\text{PO}_4]^{3-}$  or  $\text{S}^{2-}$  may also be generated *in-situ* after decomposition of various esters or amides.
- (iii) Metallic cations may be masked by formation of a suitable complex that may be carefully destroyed through pH changes or through exchange with another complex.
- (iv) The use of mixed solvents with one volatile component is another useful strategy. Upon aging or heating the volatile species will be evaporated inducing controlled precipitation.
- (v) For transition metals displaying several oxidation states, one may add a reducing reagent for high-valency forms or an oxidizing one for low-valency forms.
- (vi) Finally, if the temperature of the medium cannot be changed, the possibility remains to use a light sensitive molecule that should release one of the

nucleating species upon irradiation with ultraviolet-visible light or even  $\gamma$ -rays.

## 2.7. Heterogeneous Nucleation

It is a well known experimental fact that nucleation from a vapor, melt, or solution is affected considerably by traces of impurities in the system. Indeed, some authors even say that true examples of homogeneous nucleation in the condensed state should be indeed very rare [26]. One may then wonder about the practical utility of this treatment. In fact, it has been shown [35] that if  $R$  is the radius of the foreign nucleating particle and if  $\theta$  stands for the contact angle with the foreign surface, then  $\Delta G^*$  (hetero) =  $\Delta G^*$  (homo)  $\times \Phi(\cos \theta, R/r^*)$  with  $\Phi \sim 1$  when  $R < 10$  nm or when  $\theta = 180^\circ$ . Above 100 nm  $\Phi$  becomes independent of  $R$  (with  $\Phi < 1$ ) leading to [26]

$$R \rightarrow \infty \implies \Delta G_H^* = \Delta G^* \times \left( \frac{2 - 3\cos\theta + \cos^3\theta}{4} \right) \quad (7)$$

$$r^* = \frac{2\gamma v}{kT \ln S} \sin \frac{\theta}{2}$$

The important point is that due to the existence of a kinetic barrier  $\Delta G'$ , homogeneous nucleation is already governed by a sticking probability  $g_N = \exp(-\Delta G'/kT)$

$$J \sim Dv^{-5/3} g_N \times \exp(-\Delta G^*/kT) \quad (8)$$

Now as we know that  $0 \leq \Phi \leq 1$  we may rewrite (7) as  $\Delta G^*$  (hetero) =  $\delta G^*$  (homo) -  $E(\cos \theta, R/r^*)$ , with  $E$  the energetic correction that should be applied and such that  $E = 0$  if  $R = 0$  or  $\theta = 180^\circ$ . As far as the nucleation rate is concerned, we then just have to define a modified sticking probability  $g_H = \exp[(E - \Delta G')/kT]$  showing that only the pre-exponential term is affected. These two terms  $g_N$  and  $g_H$  could then help to understand the considerable spreading of the measured kinetic constant  $J_0 = J(\Delta G^* = 0)$  observed in literature ( $10 \leq J_0 \leq 10^{32} \text{ cm}^{-3} \text{ s}^{-1}$ ) [26]. Obviously, this spreading is no more surprising in view of the earlier analysis but just reflects the importance of the competition between the kinetic barrier  $\Delta G'$  and the heterogeneous activation  $E$ . For this chapter, we will still use (8) as the correct expression for the nucleation rate. However, the  $g_N$  term should be interpreted as a nucleation probability whose value depends on at least three physicochemical parameters:  $\Delta G'$ ,  $\cos \theta$ , and  $R$ . With this new interpretation of the kinetic constant  $J_0$ , the exact nature of the nucleating event (either homogeneous or heterogeneous) becomes immaterial as soon as  $g_N$  reflects the exact physicochemical state of the solution.

## 3. CRYSTALLINE GROWTH

### 3.1. Competitive Growth

Ideally, it is desirable that the nucleation stage should be the whole story of nanocrystal formation from solutions and gels. From a practical point of view, one has then to ensure that other stages such as growth, Ostwald ripening, or aggregation should be avoided. In the following, we will try to understand how this should be possible by studying the

various mechanisms of these competing processes. Kinetically speaking, the dominant process just after nucleation has occurred should be crystal growth. Accordingly, Ostwald ripening is ruled by the Ostwald-Freundlich equation for two spheres with radii ( $a_1, a_2$ ) characterized by their solubility ( $c_1$  and  $c_2$  respectively) [36]

$$kT \times \ln \frac{c_1}{c_2} = 2v\gamma \left( \frac{1}{a_1} - \frac{1}{a_2} \right) \quad (9)$$

It is then expected to become important only when  $a_2 \gg a_1$  in order to have  $c_1 \gg c_2$  (disappearance of small crystals and growth of larger ones). On the other hand, aggregation implies that nuclei have to move through diffusion in order to meet together. According to the Einstein equation  $D = kT/(6\pi\eta a)$ ,  $D$  should be, for a given solution viscosity  $\eta$ , smaller for a nuclei displaying a size  $a$  much larger than that of active solute species for crystal growth. In the following, we consider a solution containing  $N$  nanocrystals per unit volume, all built from incorporation of  $n(t)$  solute species. As  $n$  is changing with time, this means that some characteristic linear size  $r(t)$  increases with time according to a given growth law  $dr(t)/dt = f(c, r)$ . Writing the volume  $V$  of each nanocrystal as  $V = \omega \times r^3$ , where  $\omega$  is a shape factor ( $\omega = 4\pi/3$  for spheres,  $\omega = 8$  for cubes, etc.) means that  $n(t) = \omega \times [r(t)]^3/v$ . According to literature [3, 5], four main mechanisms may be recognized for crystalline growth (see Fig. 1).

### 3.2. Diffusion Controlled Growth

In this first mechanism, each partner is characterized by a linear size [ $r_m$  for solute species and  $r(t)$  for nanocrystals] and a diffusion coefficient ( $D$  for solute species and  $D_r$  for nanocrystals). If the solute species can be incorporated into the crystalline network immediately after sticking to a crystal, the limiting step should be diffusion of solute species toward the solid/liquid interface.

#### 3.2.1. Growth Law

Let  $d\Omega$  be the solid angle spanning the direction in which a sticking event has been observed. The rate for mass increase of the nanocrystals may be written  $d^2n/dt d\Omega = k \times (c - c_s)$  with  $k$  a kinetic constant which may be approximated by  $k \sim (D_r + D)(r + r_m)$ . As  $D_r \ll D$  and  $r \gg r_m$ , it comes  $k \sim D \times r$ , or after integration over all the possible sticking directions:  $dn/dt = 4\pi D(c - c_s)r$ . But as  $n(t) = (\omega \times r^3/v)$ , we should also have  $dn/dt = (3\omega \times r^2/v) \times (dr/dt)$ . The final growth law for pure diffusion may thus be written

$$\frac{dr}{dt} = \left( \frac{4\pi}{3\omega} \right) \frac{Dv(c - c_s)}{r} \iff \frac{dr^2}{dt} = \left( \frac{4\pi}{3\omega} \right) Dv(c - c_s) \quad (10)$$

An interesting point is that irrespective of the original size  $r_0$  at nucleation time ( $t = 0$ ) and provided that  $c \sim c_0$ , then the square of the radius of all particles increases at the same rate [37]. Consequently, calling the absolute width of the distribution  $\Delta r$  for radius  $r$  and  $\Delta r_0$  for radius  $r_0$ , we have  $r \times \Delta r \sim r_0 \times \Delta r_0$ . This means that the absolute width of the distribution becomes narrower with time ( $\Delta r \sim [r_0/r] \times \Delta r_0$ ) while the relative width will decrease even faster ( $\Delta r/r \sim [r_0/r]^2 \times [\Delta r_0/r_0]$ ).

### 3.2.2. Chronomals

From a practical point of view, one way to decide if such a rate law applies is to measure how the concentration in solute species  $c(t)$  changes with time. Knowing  $c(t)$  and the initial concentration  $c_0$ , one may write for spherical shapes ( $\omega = 4\pi/3$ )  $c(t) = c_0 - N \times (4\pi r^3/3v)$  and compute the following quantity

$$x_D = \frac{c_0 - c_t}{c_0 - c_s} \iff r = r_e \sqrt[3]{x_D} \quad (11)$$

Here  $r_e$  is the equilibrium size of the nanocrystals given by  $c_s = c_0 - N \times (4\pi r_e^3/3v)$ . Inserting (11) into (10) then leads to the characteristic  $t = K_D I_D$  law [5] with  $K_D = r_e^2/[3Dv(c_0 - c_s)]$  and

$$I_D = \int_0^{x_D} \frac{dx}{(1-x)\sqrt[3]{x}} = \frac{1}{2} \text{Ln} \frac{1-x_D}{(1-\sqrt[3]{x_D})^3} - \sqrt{3} \tan^{-1} \frac{\sqrt{3}}{2+x_D^{-1/3}} \quad (12)$$

A decisive test (named chronomal analysis) for validating this mechanism would be to observe a straight line for an  $I_D = f(t)$  plot leading to a diffusion coefficient  $D$  (computed from the observed slope  $K_D$ ) close to  $10^{-5} \text{ cm}^2 \text{ s}^{-1}$ . Also notice that for crystals large enough the growth rate through diffusion may be increased by convection according to

$$\frac{dr}{dt} = F \frac{Dv(c - c_s)}{r} \quad (13)$$

Here  $F$  is a complex hydrodynamic factor function of the solution viscosity [3].

### 3.2.3. Characteristic Time

Besides knowing the growth law, one may also be interested in relating the final equilibrium size  $r_e$  to initial concentration in solution  $c_0$ . Let  $t_D$  be the characteristic time below which the condition  $S > S^*$  remains satisfied. In this time domain  $J > 0$  and if the initial concentration is high enough, we are allowed to write  $J(c) \sim J(c_0)$ . When the condition  $S < S^*$  is reached due to solute species consumption during nucleation and growth ( $t > t_D$ ), one should expect that  $J$  drops suddenly from  $J(c_0)$  down to zero. Further matter consumption should then be attributed to crystalline growth only. Now, from the growth law, we know that a nanocrystal nucleated at time  $\tau$  has reached, at time  $t$ , a size

$$r(\tau, t) = \int_{\tau}^t f(c_\theta, r_\theta) \times d\theta \quad (\tau \leq \theta \leq t) \quad (14)$$

Consequently, the concentration in solute species at time  $t$  should be given by

$$c_t = c_0 - \frac{\omega}{v} \int_0^t J(c_\tau) [r(\tau, t)]^3 d\tau \\ \implies v(c_0 - c_t) \approx \omega \int_0^t J(c_0) [r(\tau, t)]^3 d\tau \quad (15)$$

For diffusion growth, the magnitude of  $t_D$  may be evaluated from (10) and (14) by setting  $c_\theta \sim c_0$ , leading to

$$r(\tau, t) = \sqrt{\frac{8\pi Dv c_0}{3\omega}} (t - \tau)^{1/2} \\ \implies v(c_0 - c_t) \approx \left[ \frac{2\omega J(c_0)}{5} \right] \times \left( \frac{8\pi Dv c_0}{3\omega} \right)^{3/2} \times t^{5/2} \quad (16)$$

This shows that concentration of solute species decreases with time according  $c_t = c_0 [1 - (t/t_D)^{5/2}]$  with  $t_D$  given by

$$t_D \approx \left[ \left( \frac{3}{8\pi} \right)^3 \times \left( \frac{5}{2} \right)^2 \right]^{1/5} \left( \frac{\omega}{v c_0} \right)^{1/5} \times \frac{1}{J(c_0)^{2/5} D^{3/5}} \\ \approx \frac{2}{5} \left( \frac{\omega}{v c_0} \right)^{1/5} \times \frac{1}{J_0^{2/5} D^{3/5}} \quad (17)$$

### 3.2.4. Equilibrium Size

The next problem is now to compute the total number of particles  $N \approx \int_0^{t_D} J \times dt$  formed during time  $t_D$ . To do this, one may notice that from (8) and (4) that if  $n^*$  changes slowly with time

$$\frac{\partial \text{Ln } J}{\partial \text{Ln } c} = 2\beta \frac{\gamma^3 v^2}{(kT \text{Ln } S)^3} = n^* \implies J \approx J(c_0) \left( \frac{c}{c_0} \right)^{n^*} \quad (18)$$

Thus, for the particular case of diffusion growth

$$c = c_0 \left[ 1 - \left( \frac{t}{t_D} \right)^{5/2} \right] \implies N \approx J(c_0) t_D f(n^*)$$

$$f(n^*) = \int_0^1 (1 - x^{5/2})^{n^*} dx = \prod_{k=1}^{n^*} \left[ \frac{k}{(k + 2/5)} \right] \quad (19)$$

Then, from the mass conservation law  $N\omega \langle r_e \rangle^3 = (c_0 - c_s)v \sim c_0 v$ , it becomes possible to get an analytical expression linking the average equilibrium size  $\langle r_e \rangle$  of the nanocrystals to the solid phase and solution properties

$$\langle r_e \rangle^3 \approx \frac{v c_0}{\omega N} = \left[ \frac{1}{\omega f(n^*)} \right] \left( \frac{94}{\omega} \right)^{1/5} v^{11/5} c_0^{6/5} g_N^{-3/5} \\ \times \exp \left( \frac{3\beta \gamma^3 v^2}{5(kT)^3 (\text{Ln } S_0)^2} \right) \quad (20)$$

Figure 3 shows the typical variation of  $\langle r_e \rangle$  with concentration in solute species  $c$  for several values of the dimensionless nucleation constant  $\sigma_N = \beta \gamma^3 v^2 / (kT \text{Ln } 10)^3$ . This fundamental curve shows that when  $\sigma_N$  is low,  $\langle r_e \rangle$  remains roughly constant above  $S = 10$ , with typical sizes close to 1 nm. On the other hand, when  $\sigma_N$  is high, nanocrystals with typical sizes close to 10 nm can be formed from concentrated solutions. In all cases, there is a critical concentration domain where average size suddenly drops from the millimetric range down to the nanoscopic one. One may also notice that for given physical conditions (sursaturation ratio  $S$  and nucleation constant  $\sigma_N$  kept constant), chemistry can still play a determinant role on particle size through the sticking probability term (or kinetic barrier)  $g_N$ . As seen in (20), decreasing the sticking probability (i.e., increasing the kinetic barrier) should lead to larger nanocrystals.

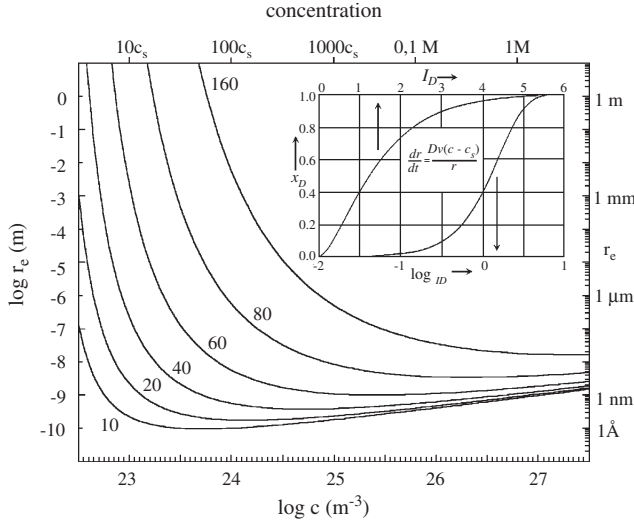


**Figure 3.** Crystalline growth controlled by diffusion. Boxed curve shows the shape of the chronomal function  $I_D$  given by Eq. (9). Other decreasing curves were plotted according to Eq. (20) assuming a spherical shape ( $\omega = 4\pi/3, \beta = 4\omega$ ) with  $\langle f(n^*) \rangle = 1/3$  for six typical values of the nucleation constant  $\sigma_N = \beta\gamma^3 v^2 / (kT \text{Ln } 10)^3$  leading to  $\log r_c = (1/3) \log(18v^{11/5}/4\pi) + (6/15) \log c - (1/5) \log g_N + \sigma_N / [5(\log c/c_s)^2]$ . Other parameters were  $v = 10^{-28.5} \text{ m}^{-3}$ ,  $c_s = 10^{22} \text{ m}^{-3}$ , and  $g = \exp(-\Delta G'/kT) = 10^{-5}$ . The key point is the final nanometer size of the crystal when precipitation occurs in concentrated solutions.

### 3.3. Interface-Limited Growth

One has to remember that (20) applies only when diffusion in solution is the rate limiting step for crystalline growth. Physically, this means that if a sticking probability exists for nucleation ( $g_N \ll 1$ ), the corresponding growth sticking probability  $g_C$  should be close to unity. Obviously, systems satisfying simultaneously these two conditions are not very common, and in most experimental situations if  $g_N \ll 1$ , then  $g_C \ll 1$  too. Consequently, we must look for a possible generalization of (20) in order to be able to cover the widest range of chemical systems.

#### 3.3.1. Surface Nucleation Rate

In this mechanism it is supposed that in order to form a new layer, solute species have to be adsorbed onto the crystal surface and make, through surface diffusion, a critical two-dimensional nucleus. As some chemical reactions must occur to lead to this new 2D nucleus, bulk diffusion in the solution cannot be the rate-determining step. As before, one may define a surface nucleation rate  $J' \sim Dv^{-4/3} \times \exp(-\Delta G_c/kT)$  with  $\Delta G_c = \Delta G'^* + \Delta G''$ . Here, the pre-exponential factor has been written by taking into account that for  $\Delta G_c \sim 0$ , the surface nucleation rate may be approximated by  $J' \sim (1/d^2) \times v_{\text{inc}} = Dv^{-4/3} \sim 10^{25} \text{ cm}^{-2} \text{ s}^{-1}$ . Concerning the thermodynamic barrier  $\Delta G'^*$ , the prime symbol is a reminder for the fact that we are now treating a two-dimensional (2D) problem instead of a 3D one. Similarly, the double prime symbol refers to the kinetic barrier associated with all chemical reactions needed to transfer a structural motif from the surface into the crystalline lattice.

#### 3.3.2. Thermodynamic $\Delta G'^*$ and Kinetic Barrier $\Delta G''$

At first sight, one may think that as the solute species responsible for crystalline growth are the same as those responsible for bulk nucleation, one should have  $\Delta G'' \sim \Delta G'$ . In fact, this cannot be true. For bulk nucleation a crystal/solution interface first has to be created in order to initiate crystalline growth. For interface-limited growth, the solid interface is already there and by its mere presence may catalyze or inhibit the incorporation of the solute species inside the crystalline network. Consequently, in the most general case  $\Delta G'' \neq \Delta G'$ , the equality being realized only in the case of a completely neutral crystalline interface. As before, we should define  $g_C = \exp(-\Delta G''/kT)$  as the growth sticking probability. Concerning the associated thermodynamic barrier to surface nucleation, it should depend on a frontier energy  $\gamma' = (\partial G/\partial L)_{p,T}$  ( $\text{mJ m}^{-1}$ ) similar to the surface energy concept  $\gamma = (\partial G/\partial A)_{p,T}$  ( $\text{mJ m}^{-2}$ ). In order to simplify the problem we will assume that  $\gamma' \sim \gamma d = \gamma v^{1/3}$ . With this simplification the free energy variation for incorporation of  $m$  moles of surface species inside the crystal may be written

$$\begin{aligned} \Delta G_S(m_S \rightarrow m_C) &= m \times (\mu_C - \mu_S) + \gamma' \times L \\ &\approx \gamma' \times L - mkT \times \text{Ln } S \end{aligned} \quad (21)$$

As for 3D nucleation, the magnitude of  $\Delta G'^*$  may be readily derived under the assumption that surface embryos undergo no change in shape (only the mean size is changing among similar bodies) during surface nucleation. Consequently, the ratio  $K' = L/A^{1/2}$  should remain invariant, and if the total area of a given embryo is  $A \sim m \times a$  then its frontier  $L$  may be written  $L = K' \times (m)^{1/2} \times v^{1/3}$ . Inserting this value into Eq. (21) and looking for a maximum by setting  $d(\Delta G_S)/dm = 0$  leads to the following thermodynamic barrier

$$\Delta G'^* = m^* \times kT \text{Ln } S \quad m^* = \beta' \frac{\gamma^2 v^{4/3}}{(kT \text{Ln } S)^2} \quad \beta' = \frac{L^2}{4A} \quad (22)$$

Table 4 gives the values of the dimensionless shape factor  $\beta'$  for some ideal 2D geometries.

**Table 4.** Dimensionless shape factors, for some common regular 2D geometries.

Shape	Length $L$	Area $A$	$\beta' = L^2/4A$
Circle	$2\pi a$	$\pi a^2$	$\pi = 3.1416$
Regular hexagon	$6a$	$\frac{3a^2\sqrt{3}}{2}$	$2\sqrt{3} = 3.4641$
Square	$4a$	$a^2$	4.0000
Rectangle $2a \times a$	$6a$	$2a^2$	$9/2 = 4.5000$
Equilateral triangle	$3a$	$\frac{a^2\sqrt{3}}{4}$	$3\sqrt{3} = 5.1962$
Rectangle $10a \times a$	$22a$	$10a^2$	$121/10 = 12.1000$

Note: Shapes are characterized by one size  $a$  and classified by increasing  $\beta'$  value.

### 3.3.3. Timing Events

Having a suitable expression for the rate of surface nucleation  $J' \sim Dv^{-4/3}g_c \times \exp(-\Delta G^*/kT)$ , two characteristic times have to be considered:

- (i) The time  $\tau_N = (J'A_i)^{-1}$  needed to nucleate a new layer on a perfectly planar interface displaying area  $A_i$ .
- (ii) The time  $\tau_C = a_i/k'$  needed to get a full coverage of the area  $A_i$  just after surface nucleation. Here  $a_i$  stands for the largest linear size found on surface  $A_i$  and  $k' = da/dt$  is the linear growth rate of surface nuclei. This rate should be proportional to the frequency of arrival of solute species at any edge of the surface times a sticking probability ( $v' \sim D \times g_c/d$ ) and should also depend on their average number at the interface [ $n' \sim (c - c_s)v$ ]. Consequently, with  $d \sim v^{1/3}$ , we should have  $k' \sim n' \times v' \sim Dg_c v^{2/3}(c - c_s)$ . Now, depending on the relative values of  $\tau_N$  and  $\tau_C$  two limiting cases may be encountered.

### 3.3.4. Mononuclear Growth Law

For mononuclear crystalline growth, the rate limiting step is the apparition of a new 2D nucleus on the surface ( $\tau_N \gg \tau_C$ ). In this case, the linear growth rate  $dr/dt$  may be written

$$\begin{aligned} \frac{dr}{dt} &= \frac{d}{\tau_N} \sim J'\omega'r^2v^{1/3} \\ &= \omega'Dg_cv^{-1} \exp\left(\frac{\Delta G^*}{kT}\right)r^2 = k_m \times r^2 \end{aligned} \quad (23)$$

Here  $\omega'$  stands for the shape factor of the surface nucleus. It should be obvious that such a mechanism cannot be the whole story as if one starts with a size  $r_0$ , then at time  $t$  one would have  $k_m \int_0^t dt = \int_{r_0}^{r_t} dr/r^2$ ; that is,  $r_t = [r_0/(1 - k_m t r_0)]$ . It thus appears that  $r_t \rightarrow +\infty$  for a finite time  $t \rightarrow 1/(k_m r_0)$ . Such a divergence being unacceptable from a physical standpoint, this means that this mechanism should be valid only for very small sizes.

### 3.3.5. Polynuclear Growth Law

Accordingly, when the exposed surface becomes large enough, the probability to observe several nucleation events on the same area  $A_i$  cannot be neglected and one has to switch to the polynuclear growth. In this alternative mechanism, the rate limiting step is the coverage of a surface by all its surface nuclei ( $\tau_N \ll \tau_C$ ). If the whole area is covered at time  $t = \tau_C$ , then  $dr/dt = d/\tau_C$  for the linear growth rate. In order to find a reasonable value for this time one should consider that at any time  $0 \leq \theta \leq \tau_C$ , a certain amount of surface nuclei  $dn_\theta = (\tau_N)^{-1}d\theta = (J'A_i)d\theta$  have appeared. First assume an independent growth for each germ so that if  $da/dt = k'$  then  $a = \int_0^\theta da = k' \int_0^{\tau_C} dt = k'(\tau - \theta)$ . The total area covered by germs that have appeared at  $t = \theta$  may then be written

$$\begin{aligned} dA_\theta &= \omega'a^2 dn_\theta = \omega'J'A_i k'^2 (\tau - \theta)^2 \\ \implies A_i &= \int_0^{\tau_C} dA_\theta = \frac{\omega'}{3} J'A_i k'^2 \tau_C^3 \end{aligned} \quad (24)$$

Taking into account that in fact germs may overlap during growth we may write  $\tau_C = (\omega'\varphi J'k'^2/3)^{-1/3}$ , where  $\varphi$  is the numerical geometric correction describing the geometric details of the various overlaps. For disk-shaped 2D germs it may be shown that  $\varphi \sim 0.6$  [5]. This gives our final polynuclear growth law

$$\begin{aligned} \frac{dr}{dt} &= \frac{d}{\tau_C} = (\omega'\varphi v/3)^{1/3} Dg_c (c - c_s)^{2/3} \exp\left(-\frac{\Delta G^*}{3kT}\right) \\ &= vk_p c^p \quad p = \frac{m^* + 2}{3} \end{aligned} \quad (25)$$

The expression in the right hand side of (25) comes from an alternative evaluation of  $J'$  based on the observation that from (22):  $\partial(\ln J')/\partial(\ln S) = m^* \Leftrightarrow J' \sim k_c c^{m^*}$ .

It is interesting to compare relations (10) and (25). In both cases, the growth rate depends on the diffusion coefficient  $D$ , and on the difference  $(c - c_s)$ . The differences are that we have a power law for the concentration dependence with a growth rate independent of crystal size in the case of polynuclear growth. According to this last mechanism this means that the absolute width of the size distribution should be constant ( $\Delta r \sim \Delta r_0$ ) at all times and that only the relative width may decrease with time ( $\Delta r/r \sim [r_0/r] \times [\Delta r_0/r_0]$ ).

### 3.3.6. Chronomals and Equilibrium Size

As for the diffusion law, one may introduce a chronomal analysis in order to find the order  $p$  for crystalline growth. Setting  $c = c_0(1 - x_p)$  and  $r = r_e x_p^{1/3}$  then leads to  $t = K_p I_p$ , with

$$K_p = \frac{r_e}{3vc_0^p k_p} \quad \text{and} \quad I_p = \int_0^{x_p} x^{-2/3}(1-x)^{-p} dx \quad (26)$$

Figure 4 shows the variation of  $I_p$  with  $x_p$  for increasing values of  $p$ . Concerning the integrated form of the polynuclear growth law, let  $t_p$  be the characteristic time below which the condition  $S > S^*$  remains satisfied. From (14) and (15) it comes that  $c_t = c_0[1 - (t/t_p)^4]$  with  $t_p$  given by

$$t_p = \left(\frac{12}{\omega\omega'\varphi}\right)^{1/4} J(c_0)^{-1/4} D^{-3/4} g_c^{-3/4} c_0^{-1/4} \exp\left(\frac{\Delta G^*}{4kT}\right) \quad (27)$$

As done, this induction time may be used to evaluate the number of nanocrystals  $N$  formed per unit volume

$$\begin{aligned} c &= c_0 \left[1 - \left(\frac{t}{t_p}\right)^4\right] \implies N \approx J(c_0)t_p F(n^*) \\ F(n^*) &= \int_0^1 (1-x^4)^{n^*} dx = \prod_{k=1}^{n^*} \left[\frac{k}{(k+1/4)}\right] \end{aligned} \quad (28)$$

This in turn leads to an analytical expression linking the average equilibrium size  $\langle r_e \rangle$  of the nanocrystals to the solid phase and solution properties

$$\begin{aligned} \langle r_e \rangle^3 &= \left[\frac{1}{\omega F(n^*)}\right] \left(\frac{\omega\omega'\varphi}{12}\right)^{1/4} v^{9/4} c_0^{5/4} \left(\frac{g_c}{g_N}\right)^{3/4} \\ &\times \exp\left(\frac{3\beta\gamma^3 v^2}{4(kT)^3 (\ln S_0)^2} - \frac{\beta'\gamma^2 v^{4/3}}{4(kT)^2 \ln S_0}\right) \end{aligned} \quad (29)$$

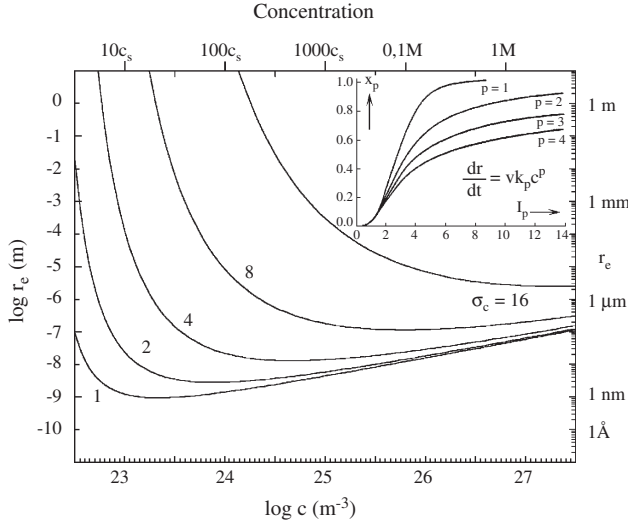


**Figure 4.** Crystalline growth controlled by the interface. Boxed curve shows the shape of the chronomal functions  $I_p$  given by Eq. (24). Other decreasing curves were plotted according to Eq. (29) assuming a spherical shape ( $\omega = 4\pi/3$ ,  $\beta = 4\omega$ ) for 3D nuclei and a disk shape ( $\omega' = \beta' = \pi$ ,  $\varphi = 0.6$ ) with  $\langle F(n^*) \rangle = 3/8$  for five typical values of the growth constant  $\sigma_C = \beta' \gamma^2 v^{4/3} / (kT \text{Ln } 10)^2$ . For these particular shapes we have  $\sigma_N \sim 3(\sigma_C)^{3/2}$  leading to  $\log r_e = (1/3) \log(6v^{9/4}/4\pi) + (5/12) \log c + (1/4) \log(g_C/g_N) + \sigma_C [9\sqrt{\sigma_C} - \log(c/c_s)] / [12(\log c/c_s)^2]$ . Other parameters were  $v = 10^{-28.5} \text{ m}^{-3}$ ,  $c_s = 10^{22} \text{ m}^{-3}$ , and  $g_C/g_N = 10^{-6}$ . As for diffusion controlled growth, nanometer sized nanocrystals are formed when precipitation occurs in concentrated solutions.

Figure 4 shows the typical variation of  $\langle r_e \rangle$  with concentration in solute species  $c$  for several values of the dimensionless growth constant  $\sigma_C = \beta' \gamma^2 v^{4/3} / (kT \text{Ln } 10)^2$ . One may notice that as  $\sigma_N = \beta \gamma^3 v^2 / kT \text{PLn } 10^3$ , the link  $\sigma_N = \beta(\sigma_C/\beta') \sqrt{(\sigma_C/\beta')}$  exists between growth and nucleation constants. As in the case of diffusion, these curves show that when  $\sigma_N$  is low,  $\langle r_e \rangle$  remains roughly constant above  $S = 10$ , with typical sizes close to 100 nm. On the other hand, when  $\sigma_N$  is high, nanocrystals with typical sizes close to 1  $\mu\text{m}$  can be formed from concentrated solutions. Again, in all cases, there is a critical concentration domain where average size suddenly drops from the millimetric range down to the nanoscopic one. One may also see that nucleation and growth terms have antagonist effects on the equilibrium size. Concerning the role of chemistry at the interface larger crystals are expected when  $g' > g$  (i.e., when  $\Delta G'' < \Delta G'$ ).

### 3.4. Dislocation Controlled Growth

When the supersaturation ratio  $S$  is smaller than about 2, the rate of surface nucleation may become so slow that the crystal growth rate becomes practically nil. In fact there are numerous examples in literature where crystalline growth is easily observed even when  $S = 1.01$ . In such cases, it has been shown [2] that growth may be initiated on crystalline defaults (dislocations or stacking faults). Among the possible defaults, it appears that the most efficient ones are screw dislocations leading to the formation of typical Archimedean spirals on the surface [2, 3].

### 3.4.1. Growth Law

In this mechanism, we have to estimate the normal velocity of advancement  $u$  for the leading step of the growing spiral. For a spiral of radius  $R$ , this rate should be proportional to the frequency of arrival of solute species at the leading edge times a sticking probability ( $v' \sim D \times g_C/d$ ) and should also depend on their average number at the interface [ $n' \sim (c - c_R)v$ ]. Consequently, with  $d \sim v^{1/3}$ , we should have  $u \sim n' \times v' \sim Dc g_C v^{2/3} (1 - c_R/c)$ . Now, from (22) with  $\beta' = \pi$ , it is possible to relate the concentration just outside the crystal surface  $c$  to a critical germ radius  $r'^*$  according to  $\pi(r'^*)^2 = m^* \times v^{2/3}$ ; that is,  $r'^* = \gamma v / (kT \text{Ln } S)$ . Moreover, applying (9) with  $r_2 \rightarrow +\infty$  (i.e.,  $c_2 \rightarrow c_s$ ) and  $r_1 = R$  or  $r'^*$  allows one to express the ratio  $c_R/c$  as

$$\frac{c_R}{c} = \exp\left[\frac{\gamma v}{kT} \left(\frac{1}{R} - \frac{1}{r'^*}\right)\right] \approx 1 + \frac{\gamma v}{kT} \left(\frac{1}{R} - \frac{1}{r'^*}\right)$$

$$\Rightarrow \lim_{R \rightarrow +\infty} u = \frac{D\gamma v^{5/3} c}{kT r'^*} g_C \quad (30)$$

Assuming a spiral displaying a stationary shape and rotating with a constant angular velocity  $\omega_S$  (rad  $\text{s}^{-1}$ ), it may be shown that  $\omega_S = u_\infty / (\pi r'^*)$  [38]. Consequently, each spiral turn should deposit a layer of thickness  $d \sim v^{1/3}$  leading to the following linear rate of growth

$$\frac{dr}{dt} \sim \left(\frac{\omega_S}{2\pi}\right) \times v^{1/3} = g_C \frac{DkTc}{2\pi^2 \gamma} (\text{Ln } S)^2 \quad (31)$$

### 3.4.2. Two Limit Cases

Two important limiting cases may be discussed. When  $c \sim c_s$  (i.e.,  $S = 1 + \varepsilon$ ), then  $\text{Ln } S = \text{Ln}(c/c_s) \sim (c - c_s)/c_s$ , and we get a nonvanishing growth rate  $dr/dt = [g_C DkT / (2\pi^2 \gamma c_s)] \times (c - c_s)^2$ . This explains the possibility of growing large single crystals from solutions even when  $S \sim 1$ . On the other hand, when  $c \gg c_s$  the growth rate may become quite large, but very soon the diffusion of solute species toward the spiral leading edge will become rate determining. As both rate laws are known, it is possible to see for which value of  $S$  both processes should contribute equally to the crystalline growth

$$g_C \frac{DkTc}{2\pi^2 \gamma} (\text{Ln } S)^2 \approx \frac{Dv(1 - S^{-1})}{r}$$

$$\Rightarrow \frac{S(\text{Ln } S)^2}{S - 1} \approx \frac{2\pi^2}{g_C} \left(\frac{\gamma v}{kTr}\right) \quad (32)$$

Using  $\gamma \sim 0.1 \text{ J m}^{-2}$ ,  $v \sim 10^{-28.5} \text{ m}^3$ , and  $T = 300 \text{ K}$  as typical values leads to the following condition:  $[g_C r(\text{nm})] \times S(\text{Ln } S)^2 \approx 15.2(S - 1)$ . Setting  $g_C \sim 1$  and  $r = 1 \text{ nm}$  as reasonable limits leads to  $S = 47.338$ . Under these conditions, diffusion should become the rate limiting step as soon as  $S > 50$ . However, if one considers a millimeter-sized single crystal ( $r \sim 10^6 \text{ nm}$ ) with rather low kinetic barrier ( $g_C \sim 1$  for purely ionic crystals such as NaCl or KCl) well developed spirals should be evidenced only if  $S \approx 1 + 15.2/(g_C r) < 1.00001$ . However, if  $g_C \sim 10^{-7}$  (i.e.,  $\Delta G'' \sim 40 \text{ kJ mol}^{-1}$ ), then for the same single crystal size diffusion toward the interface will be rate determining only when  $S \approx \exp[\sqrt{15.2/(g_C r)}] > 10^5$ . A direct consequence of this fact is that nanocrystal formation ( $r \sim 10 \text{ nm}$ ) should never be under diffusion control, unless  $g_C > 0.1$ .



### 3.4.3. Chronomals

Interestingly enough, when spiral growth is the rate limiting step, the chronomal analysis shows that it would be rather difficult to distinguish between the spiral and the polynuclear growth. Proceeding as before by setting  $c = c_0(1 - x_S)$  and  $r = r_e x_S^{1/3}$  leads to  $t = K_S^p I_p$ , where  $I_p$  is the polynuclear chronomal limited to values of  $p = 1$  or  $2$  and  $K_S^p$  stands for two time constants given by

$$K_S^p = \frac{r_e}{3g_C} \times \frac{2\pi^2\gamma}{DkTf_p(c_0)} \quad \text{with}$$

$$I_p = \int_0^{x_S} x^{-2/3}(1-x)^{-p} dx \quad p = 1 \text{ or } 2 \quad (33)$$

The two  $p$ -values correspond to the two previously described limiting cases. When  $c \gg c_s$ , then  $c \sim c - c_s$  and  $\text{Ln } S \sim \text{Ln}(c_0/c_s)$  leading to  $t = K_S^2 I_1$  with  $f_1(c_0) = c_0[\text{Ln}(c_0/c_s)]^2$ . For the other limiting case  $c \sim c_s$ , we have  $t = K_S^2 I_2$  with  $f_2(c_0) = c_s/(c_0 - c_s)^2$ . On the other hand, if diffusion is the rate limiting step, then one should follow the  $I_D$  chronomal given by (12). This analysis shows that observing a crystalline growth law following  $I_D$ ,  $I_1$ , or  $I_2$  chronomals does not rule out the spiral mechanism. In fact the only clear evidence for the occurrence of the polynuclear mechanism would be to follow chronomals  $I_p$  characterized by  $p > 2$ . To the best of our knowledge such a situation has been scarcely reported in literature as most precipitation processes follow either  $I_D$  or  $I_1$  chronomals.

This result may just be a direct consequence of the very high efficiency of the spiral growth for nanocrystals which bypassing the bottleneck of surface nucleation run directly into the one of diffusion toward the interface. If this is true, then all nanocrystals grown using concentrated solutions should in fact be formed from numerous interpenetrating nanospirals and not from overlapping surface nuclei.

### 3.4.4. Equilibrium Sizes

At last, we may consider the integrated form of the spiral growth law, characterized by a time  $t_S$  below which the condition  $S > S^*$  remains satisfied. From (14) and (15) it comes that  $c_t = c_0[1 - (t/t_S)^4]$  with  $t_S$  given by

$$t_S = \left(\frac{4}{\omega}\right)^{1/4} \left[\frac{v}{c_0^2 J(c_0)}\right]^{1/4} \left[\frac{2\pi^2\gamma}{g_C DkT(\text{Ln } S_0)^2}\right]^{3/4} \quad (34)$$

As the power dependence of concentration with time is similar than that observed for polynuclear growth, (28) holds with  $t_p$  replaced by  $t_S$ , leading to

$$\langle r_e \rangle^3 = \left[\frac{1}{\omega F(n^*)}\right] \left(\frac{\omega}{4}\right)^{1/4} v^2 c_0^{3/2} \left(\frac{g_C}{g_N}\right)^{3/4} \left[\frac{kT(\text{Ln } S_0)^2}{2\pi^2\gamma}\right]^{3/4} \\ \times \exp\left(\frac{3\beta\gamma^3 v^2}{4(kT)^3(\text{Ln } S_0)^2}\right) \quad (35)$$

## 3.5. Discussion

At this stage a comparison between Figures 3, 4, and 5 may be useful. All curves display the same characteristic L-shaped aspect, the decreasing left part coming from an exponential term and the increasing right part from a power

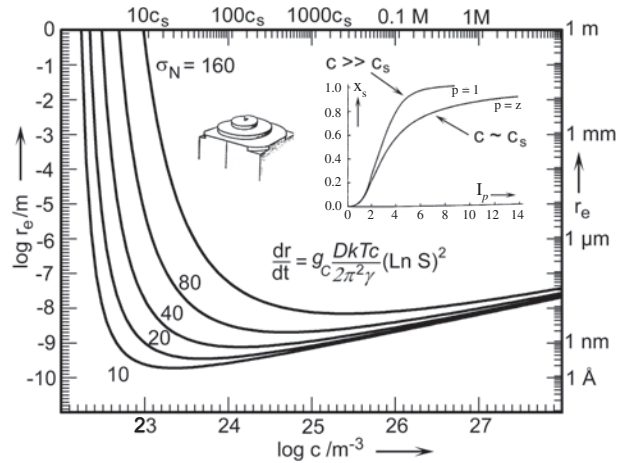


**Figure 5.** Spiral crystal growth controlled by screw dislocations. Boxed curve shows the shape of the two chronomal functions  $I_1$  and  $I_2$  given by Eq. (26). Other decreasing curves were plotted according to Eq. (35) assuming a spherical shape ( $\omega = 4\pi/3, \beta = 4\omega$ ) for 3D nuclei with  $\langle F(n^*) \rangle = 1/2$  for five typical values of the nucleation constant  $\sigma_N = \beta\gamma^3 v^2 / (kT \text{Ln } 10)^3$  leading to  $\log r_e = (1/3) \log(6v^2/4\pi) + (1/2) \log c + (1/4) \log(g_C/g_N) + (1/4) \log[kT(\text{Ln } S_0)^2/2\pi^2\gamma] + \sigma_N/[4(\log c/c_s)^2]$ . Other parameters were  $T = 300$  K,  $v = 10^{-28.5}$  m<sup>3</sup>,  $\gamma = 0.1$  J m<sup>-2</sup>,  $c_s = 10^{22}$  m<sup>-3</sup>, and  $g_C/g_N = 10^5$ . As for other growth mechanisms, nanometer sized nanocrystals are formed when precipitation occurs in concentrated solutions.

of the total concentration  $c_0$ . In these drawings the two sticking probabilities  $g_N$  and  $g_C$  (linked to the occurrence of kinetic barriers  $\Delta G'$  and  $\Delta G''$  for nucleation and growth) have been adjusted in order to have  $r_e > 0.1$  nm in all the investigated concentration range. In the case of diffusion controlled growth, one should have  $g_C \sim 1$  and the size of the nanocrystals will be fixed by the relative values of  $\sigma_N$  and  $g_N$ . This is no more the case for the two other mechanisms, where the two competing terms are  $\sigma_N$  and the  $(g_C/g_N)$  ratio. However, a clear difference exists between polynuclear and spiral growth as one must set  $(g_C/g_N) = 10^{-6}$  for the first mechanism and  $(g_C/g_N) = 10^{+5}$  for the second one in order to get reasonable sizes. The chemical interpretation of this phenomenon is straightforward. Polynuclear (or mononuclear at low  $S$ -values) growth should be suspected as soon as  $g_C < g_N$ , that is, when solute species are more easily incorporated when the nanocrystal has not yet appeared (embryo stage). Chemically speaking, we are in a situation where crystal growth is poisoned by the decomposition products of the solute precursors. In this case, it seems obvious that the highly reactive leading edge of a growing spiral will be much more affected by the poisonous material than a less reactive flat layer. Owing to the presence of the poison, the surface nucleation bottleneck is unavoidable and the polynuclear picture dominates crystalline growth.

In the reverse situation,  $g_C > g_N$ , the decomposition products of solute precursors are expected to show no affinity for the crystal/solution interface. In this case, solute species absorption should occur at the most reactive sites, and one may expect a crossover between polynuclear and spiral growth. It then appears that Eqs. (20), (29), and (35) should cover both qualitatively and quantitatively all the pertinent physical and chemical aspects of nucleation and crystalline growth from solutions.

## 4. LIMITED AND SECONDARY GROWTH

It should be noticed that the previous equations have been reached without any explicit description of the structure of the solution/crystal interface. One should then expect that some other important aspects remain yet hidden, particularly in the interfacial energy  $\gamma$ . In the previous treatment, it was tacitly assumed that the interfacial energy  $\gamma$  was a constant characterizing the solution/crystal interface. In this section, we will consider what should happen to the final equilibrium size of a nanocrystalline dispersion when  $\gamma$  may change owing to variations in pH or ionic strength. To do this we must dispose of a faithful model of the crystal/solution interface. In the following, we will consider mainly oxide/water interfaces that are by far the most commonly encountered experimental cases. Generalizations for nonaqueous or nonoxide interfaces will not be discussed in this chapter.

### 4.1. Solute–Solvent Interface

The best way to understand what the structure of an oxide water interface should be is to start from the molecular scale (Frank and Wen model [39]). Accordingly, X-ray or neutron diffraction studies of aqueous solutions [13, 40] have shown that the molecular environment around a given solute is not a random medium. At less than 0.3 nm, a first shell of frozen solvent molecules is very often found in close contact with the solute species. After this coordination shell, other more or less immobilized shells may be found. The spatial extension of this zone is typically between 0.3 and 0.5 nm. In this critical zone, it may be observed that the local order characterizing the solvent in a pure state may either be broken or strengthened. This comes from the fact that on one side solvent molecules are under the influence of the more or less rigid coordination shell around the solute. On the other side, they are under the influence of the random motions of their congeners that are far from any solute (this holds for sufficiently diluted solutions). When the solute coordination shell is highly structured and rigid, this orderliness tends to be propagated at longer distances. One then speaks of a *structure-forming* solute. Conversely, if the coordination shell is highly labile and disordered, the disorder will also be more or less transmitted to the neighboring shells breaking the original structure of the pure solvent. In this case, one may speak of *structure-breaking* species.

### 4.2. Oxide–Water Interface

This classical picture of the solvent–solute interaction may serve as a faithful basis for a realistic model of the solid/liquid interface. As explained in previous sections, nucleation is an irreversible phenomenon by which several solute precursors meet together in a limited volume (thermodynamic barrier  $\Delta G^*$ ). Within this confined state, they may further expel partly or fully their coordination shell (kinetic barrier  $\Delta G'$ ) in order to build a new solid phase. Chemically speaking, the solid phase may be viewed as the result of a giant polymerization process of solute species. On this basis, one may expect that their respective coordination shells should also merge together defining the solid/liquid

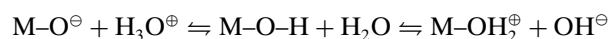
interface. This merging process should, however, also apply to secondary coordination shells leading to a more or less compact layer, tightly bonded to the interface (called hereafter the “Stern” layer). Finally, just outside this more or less immobilized Stern layer a slipping plane for solvent molecules should exist, that may be identified as the “outer Helmholtz plane” (OHP).

Adopting this “natural” model for the solid/liquid interface allows us to zoom more deeply into the crystalline growth process. For instance, the quite vague statement of “diffusion toward the solid/liquid interface” may then acquire an accurate formulation. Accordingly, diffusing solute species may be identified as any kind of fully solvated chemical entity not able to go beyond the OHP. One must realize that the last statement is not an assumption, but a logical consequence of the chosen model. Accordingly, assume that some kind of solute species has been able to jump over the OHP landing inside the Stern layer. The chemical consequence of this hopping should be that some spatial reorganization of the surrounding solvating shell was possible in order to fit the local structure of the Stern layer. If the energetic cost of this reorganization were too expensive, the jumping would have been a very unlikely process. Consequently, the solute species would show no tendency to cross the OHP, preferring to diffuse quietly far away from this unfriendly disturbing spatial zone.

Conversely, it may happen that some otherwise quietly diffusing solute species may experience a very high structural affinity for the Stern layer. Such a species is then expected to cross the OHP ending up right inside the Stern layer. As a result of this jump, a quite new solvating shell more adapted to the local structure of the Stern layer should be adopted, leaving with no regret the older one more adapted to the structure of the bulk solvent. The automatic consequence of fact is the existence of a second kind of molecular plane, named the “inner Helmholtz plane” (IHP). By its very definition this plane lies somewhere outside the solid surface and well below the OHP. From a chemical standpoint, it is formed by the locus of all strongly adsorbed species that are not allowed to diffuse freely into the solution due to their particular affinity for the Stern layer. At last, chemical entities already localized within the Stern layer may exist and could display rather high chemical affinity for the crystalline surface. For such species, full reorganization of their coordination shell needed for a “perfect” sticking to the surface is not a problem. They are thus not expected to stay localized close to the IHP but may undergo a last final jump right inside the crystalline lattice. The immediate result of this ultimate sacrifice is an increase of the spatial extension of the interface by one step, another way of saying that crystalline growth has occurred.

### 4.3. Surface Charge

The next step is now to see how the surface charges may develop. As shown in Figure 6 (top left) metallic cations exposed at the surface are found to be hydroxylated owing to water chemisorption. Consequently, like soluble aquo, hydroxo, or oxo complexes they may acquire or lose protons according to the polarizing power of the metallic cation



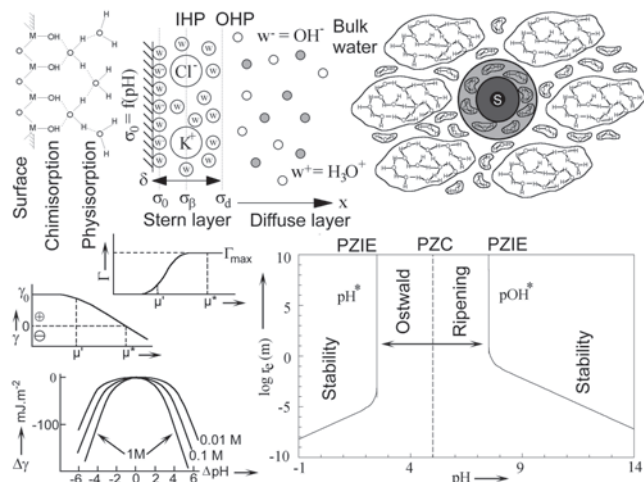


**Figure 6.** A natural model for the oxide/water interface. Top left shows the H-bonded structure of the Stern layer in close contact with the oxide surface. Top right illustrates the Frank and Wen model (scale <math>< 1\text{ nm}</math>) for a solute  $S$  far away from the interface. Black region corresponds to the naked solute. At a distance less than  $0.3\text{ nm}$  from the solute, one finds the coordination shell indicated is dark gray. Between  $0.3$  and  $0.5\text{ nm}$ , one finds more or less perturbed secondary shells (light gray). Above  $0.5\text{ nm}$ , water recovers its characteristic flickering structure. Top middle shows the direct vicinity of the oxide/water interface with the Stern and diffuse layers of counterions (scale <math>< 10\text{ nm}</math>). Bottom left shows the effect of chemisorption at the surface on chemical potentials and interfacial energy. Bottom right is the effect on the equilibrium size of nanocrystals with the domain of thermodynamic instability (Ostwald ripening).

This allows one to define the net surface charge  $\sigma_0 = (F/A)([\text{MOH}_2^{\oplus}] - [\text{MO}^{\ominus}])$ , where  $F$  stands for the Faraday constant ( $F = 96,500\text{ C mol}^{-1}$ ) and  $A$  stands for the exposed surface area ( $\text{m}^2\text{ l}^{-1}$ ). The quantities in brackets are the concentration ( $\text{mol l}^{-1}$ ) in charged surface sites.

#### 4.3.1. Acidity Constants

To a given surface charge distribution, one may associate an electrostatic potential  $\psi_0$  at the interface. Assuming Maxwell-Boltzmann statistics, the surface concentration  $[\text{H}_3^+]$  of protons should be related to the concentration in solution  $[\text{H}^+]$  by  $[\text{H}_3^+] = [\text{H}^+] \times \exp(-F\psi_0/RT)$ . Consequently, these two equilibria may be shifted toward the left or the right by changing the solution pH. To take into account this fact, surface equilibrium constants  $K_0^+$  and  $K_0^-$  may be introduced

$$\begin{aligned} K_0^+ &= \frac{[-\text{MOH}][\text{H}_3^+]}{[-\text{MOH}_2^+]} = K^+ \exp\left(-\frac{F\psi_0}{RT}\right) \\ K_0^- &= \frac{[-\text{MO}^-][\text{H}_3^+]}{[-\text{MOH}]} = K^- \exp\left(-\frac{F\psi_0}{RT}\right) \end{aligned} \quad (36)$$

In this relation,  $K^+$  and  $K^-$  are two affinity ratios characterizing MOH surface group acidity at nil surface potential ( $\psi_0 = 0$ ). These intrinsic constants may change according to the number of bonds (usually one, two, or three) between the hydroxo moiety and the metallic cation. Structural models have been developed in the literature to model this surface acidity as a function of crystallographic structure [41].

#### 4.3.2. Point of Zero Charge

It may be shown that the two constants  $K^+$  and  $K^-$  fully characterize the surface behavior toward pH variations. Accordingly, by looking at their average, one may define the point of zero charge of the interface,  $\text{PZC} = \frac{1}{2}(pK^+ + pK^-) = \frac{1}{2}(pK_0^+ + pK_0^-)$ . Chemically speaking, this corresponds to the pH value at which concentrations of positive  $[\text{MOH}_2^{\oplus}]$  and negative  $[\text{MO}^{\ominus}]$  surface sites are the same, leading to a nil surface charge ( $\sigma_0 = 0$ ). Similarly, their difference,  $\Delta pK = (pK^- - pK^+)$ , helps one to visualize the concentration of charged sites  $N' = [\text{MOH}_2^{\oplus}] = [\text{MO}^{\ominus}]$  at the PZC. This may be easily understood by writing the total number of surface group as  $N = [\text{MOH}_2^{\oplus}] + [\text{MO}^{\ominus}] + [\text{MOH}] = 2N' + [\text{MOH}]$ . Introducing the fraction  $\theta = N'/N$  of charged sites at the PZC, leads to  $\Delta pK = 2 \log[(1 - 2\theta)/\theta]$ . When  $\Delta pK$  is high ( $\Delta pK > 4$ ),  $[\text{MOH}] \gg [\text{MOH}_2^{\oplus}] = [\text{MO}^{\ominus}]$  at the PZC, and the interface may really be viewed as a surface displaying only neutral unionized sites. Conversely, when  $\Delta pK$  is small or even negative, the number of charged groups  $[\text{MOH}_2^{\oplus}]$ ,  $[\text{MO}^{\ominus}]$  is large and the interface behaves like a protein. In this case, its PZC is better interpreted as an isoelectric point in order to reflect a  $\theta \rightarrow \frac{1}{2}$  situation.

#### 4.3.3. Charge-Potential Relationship

One may also be interested in the surface equation of state far from the PZC. Considering a total number of surface groups per unit area  $N_s = ([\text{MOH}_2^{\oplus}] + [\text{MO}^{\ominus}] + [\text{MOH}])/A$ , we may write

$$\sigma_0 = FN_s \frac{[\text{MOH}_2^+]}{[\text{MOH}_2^+] + [\text{MO}^-] + [\text{MOH}]} \quad (37)$$

Using (36) to express  $[\text{MOH}_2^{\oplus}]$  and  $[\text{MO}^{\ominus}]$  as a function of  $[\text{MOH}]$  concentration leads to the relationship linking the net surface charge density  $\sigma_0$  to the surface potential  $\psi_0$ . Concerning the relationship between surface potential and solution pH, one may start from the definition of  $\text{PZC} = \frac{1}{2}(pK_0^+ + pK_0^-)$  and eliminates the  $[-\text{MOH}]$  term using (36) with  $[\text{H}_3^+] = [\text{H}^+] \times \exp(-F\psi_0/RT)$

$$\psi_0 = \frac{RT \text{Ln } 10}{F} (\text{PZC} - \text{pH}) - \frac{RT}{2F} \text{Ln} \frac{[\text{MOH}_2^+]}{[\text{MO}^-]} \quad (38)$$

This shows that interfaces characterized by small or negative  $\Delta pK$  ( $[\text{MOH}_2^{\oplus}] \sim [\text{MO}^{\ominus}]$ ) tend to follow the well-known Nernst law.

#### 4.4. Diffuse Layer

The apparition of a superficial charge at the oxide/water interface also has the consequence of creating at any distance  $x$  from the interface a concentration gradient of ionic solute species  $i$  bearing an electrical charge  $z_i$ . Assuming as before Maxwell-Boltzmann statistics for these ions leads to  $c_i(x) = c_i(\infty) \times \exp[-z_i F\psi(x)/RT]$ , where  $c_i(\infty)$  stands for the concentration of species  $i$  far away from the charged interface. These counterions subjected to both the surface potential and thermal agitation are then distributed in a diffuse layer whose charge  $\sigma_d$  at the OHP compensates for the surface charge  $\sigma_0$ . In the case of specific adsorption

within the Stern layer, this compensation may also include the charge  $\sigma_\beta$  coming from all charges localized at the IHP ( $-\sigma_d = \sigma_0 + \sigma_\beta$ ).

The potential behavior within this diffuse layer may be derived by solving the Poisson equation  $\Delta\psi = -\rho/\varepsilon\varepsilon_0$ , relating density of charges  $\rho$  to potential  $\psi$  through the relative dielectric constant  $\varepsilon$  of the solution and vacuum permittivity  $\varepsilon_0$ . An approximate solution to this problem may be easily found by considering a planar interface (1D problem) submitted to the boundary conditions:  $\psi(x) = \psi_d$  when  $x = d$ , the thickness of the Stern layer, and  $\psi(x) = d\psi(x)/dx = 0$  when  $x \rightarrow \infty$ . For a symmetric  $\pm ze$  electrolyte with solution conditions such that  $zF\psi(x) \ll RT$ , the ionic concentrations at distance  $x$  may be approximated as  $c_\pm(x) \sim c(\infty) \times [1 \mp zF\psi(x)/RT]$ . Consequently, the associated charge density should be  $\rho(x) = zF[c_+(x) - c_-(x)] \sim (-2c_\infty z^2 F/RT)\psi(x)$ . The solution of the Poisson equation should then be  $\psi(x) = \psi_d \times \exp[-\kappa(x - d)]$  and  $\sigma_d = -\varepsilon\varepsilon_0\kappa\psi_d$  with

$$\kappa = \sqrt{\frac{2z^2 F^2 c_\infty}{\varepsilon\varepsilon_0 RT}} = \sqrt{\frac{2000 F^2 I}{\varepsilon\varepsilon_0 RT}} \quad I(\text{mol l}^{-1}) = \frac{1}{2} \sum_{i=1}^n c_i z_i^2 \quad (39)$$

The parameter  $\kappa$  having the dimension of the reciprocal of length, its inverse  $\kappa^{-1}$  is then a measure of the thickness of the diffuse layer. In water at 25 °C ( $\varepsilon = 78.5$ ) it has the value  $\kappa(\text{nm}^{-1}) = 3.29\sqrt{I(\text{mol l}^{-1})}$ , showing its high sensitivity to the concentration and charge of ionic solute species (the diffuse layer is compressed when the ionic strength  $I$  increases). A more correct treatment of the Poisson equation for a symmetric  $z : z$  electrolyte in water at  $T = 25$  °C would have led to [42]:

$$\sigma = \frac{4zFc}{\kappa} \sinh\left(\frac{zF\psi}{2RT}\right) \\ \implies \sigma_d(C \cdot \text{m}^{-2}) = -0.1174\sqrt{c(\text{mol l}^{-1})} \\ \times \sinh[19.46z\psi_d(V)] \quad (40)$$

## 4.5. Thermodynamic Limited Growth

We are now in position to treat the oxide/water interface as a thermodynamic system able to undergo chemical changes occurring through adsorption of charged chemical species. These are not only solvated  $\text{H}^\oplus$  and  $\text{OH}^\ominus$  ions, but also any cationic  $\text{X}^\oplus$  and anionic  $\text{Y}^\ominus$  species coming from a dissolved XY electrolyte.

### 4.5.1. Adsorption Model

As we are dealing with a charged interface, Gibbs relation (1) applies using electrochemical potentials  $\mu = \mu_c + zF\psi$ . Here the  $\mu_c$  component is assumed to carry the concentration dependence (chemical term) while the  $zF\psi$  component takes care of any changes in the total electrical charge (potential term). Let us apply (1) to the oxide/water interface in the presence of an acid HY and an electrolyte XY fixing the ionic strength. Assuming a constant ionic strength

$I$  ( $c_{\text{XY}} \gg c_{\text{HY}}$ ) leads to  $d\mu_{\text{XY}} = 0$ ,  $d\mu_{\text{HY}} = d\mu_{\text{H}} + d\mu_{\text{Y}} \sim d\mu_{\text{H}}$ , and a lowering of the interfacial energy given by [44]

$$d\gamma = -(\Gamma_{[\text{MOH}_2^+]} - \Gamma_{[\text{MO}^-]}) \times d\mu_{\text{HY}} \\ - (\Gamma_{\text{X}^+} - \Gamma_{\text{Y}^-}) \times d\mu_{\text{XY}} \sim -\frac{\sigma}{F} d\mu_{\text{H}} \quad (41)$$

The middle curve at the bottom left part of Figure 6 illustrates Eq. (41). Let us develop the electrochemical potential of the solvated proton as  $d\mu_{\text{H}} = d\mu_{\text{H}}^c + Fd\psi_0$ , where  $\psi_0$  stands for the value of the potential at the charged interface displaying a superficial charge density  $\sigma$ . As we are describing adsorption of a charged species, the Langmuir isotherm (formation of a monolayer) is well suited for describing the  $d\mu_{\text{H}}^c$  chemical contribution, leading to  $d\mu_{\text{H}}^c = RTd[\text{Ln}(\theta/(1-\theta))]$  where  $\theta$  is the fraction of charged sites at the PZC (*vide supra*). Taking into account the fact that the density of adsorption sites is limited by the underlying oxide crystal structure, one may write  $\theta = (\sigma_{\text{max}} + \sigma)/2\sigma_{\text{max}}$  with  $\sigma_{\text{max}} = 2F\Gamma_{\text{max}}$  (top curve at the bottom left part of Fig. 6). This allows us to write the chemical contribution to  $d\gamma$  as

$$d\mu_{\text{H}}^c = RT d \ln \frac{\theta}{1-\theta} = RT d \ln \frac{\sigma_{\text{max}} + \sigma}{\sigma_{\text{max}} - \sigma} = \frac{2RT\sigma_{\text{max}}}{\sigma_{\text{max}}^2 - \sigma^2} d\sigma \quad (42)$$

### 4.5.2. Interfacial Energy Lowering

Now the Gouy–Chapman theory through Eq. (40) with  $z = 1$  (i.e.,  $I = c$ ) allows us to relate the density of charge  $\sigma$  to the potential  $\psi$ , leading by integration of (41) to

$$\Delta\gamma = \int_{\gamma_0}^{\gamma} d\gamma = \gamma - \gamma_0 - \frac{4FI}{\kappa} \int_0^{\psi_0} \sinh\left(\frac{F\psi}{2RT}\right) d\psi \\ - \frac{RT}{F} \sigma_{\text{max}} \int_0^{\sigma_0} \frac{2\sigma d\sigma}{\sigma_{\text{max}}^2 - \sigma^2} \quad (43)$$

Evaluation of the integrals being quite straightforward we may readily evaluate the decrease of the interfacial energy coming from the adsorption of charges at the interface:

$$\gamma = \gamma_0 - \frac{8RTI}{\kappa} \left[ \cosh\left(\frac{F\psi_0}{2RT}\right) - 1 \right] \\ + \frac{RT}{F} \sigma_{\text{max}} \ln\left(1 - \frac{\sigma^2}{\sigma_{\text{max}}^2}\right) \quad (44)$$

Consequently, we note that both the electrical and chemical terms contribute to the lowering of  $\gamma_0$ , the value of the interfacial energy at the PZC (lower diagram at the bottom left of Fig. 6). However, one may notice that if the electrical term remains finite, a divergence of the chemical term is observed when we approach full coverage of available adsorption sites ( $\sigma \rightarrow \pm\sigma_{\text{max}}$ ). As a negative interfacial energy means that surface creation is now a thermodynamically favorable process, more adsorption sites should be created by reducing the equilibrium size  $r_e$  of the crystals. Consequently, if crystalline growth occurs under full saturation of the interface ( $\sigma \sim \pm\sigma_{\text{max}}$ ), then the final equilibrium size will not be fixed by Eqs. (20), (29), and (35), but rather by the concentration in potential determining ions (PDIs) in the solution.

### 4.5.3. Point of Zero Interfacial Energy

In the case of oxide materials PDIs are protons and consequently, there should exist a critical  $\text{pH}^*$  at which full coverage of the interface will occur. This critical point corresponding to a nil interfacial energy [ $\text{pH}^* = \text{point of zero interfacial energy (PZIE)}$ ] may be readily evaluated from (44) if one uses the Gouy–Chapman theory and assumes that the interface obeys the Nernst law given by Eq. (38). Thus, with  $F\psi_0/RT \sim (\ln 10)(\text{PZC} - \text{pH}^*) = (\ln 10)\Delta\text{pH}^*$  and recalling that for large  $x$   $\text{sh}^{-1}(x) = \ln(x + \sqrt{x^2 + 1}) \approx \ln(2x)$ , it comes from the condition  $\sigma \sim \pm\sigma_{\max}$  that

$$\frac{4000FI}{\kappa} \text{sh} \left[ \frac{(\ln 10) \Delta\text{pH}^*}{2} \right] \approx \pm\sigma_{\max}$$

$$\implies |\Delta\text{pH}^*| \approx -\log(2000\varepsilon\varepsilon_0RT) - \log I - 2\log \sigma_{\max} \quad (45)$$

This relation holds for the ionic strength  $I$  expressed in  $\text{mol l}^{-1}$ , the surface charge in  $\text{C m}^{-2}$ , and other constants in SI units. Consequently, for water at  $T = 25^\circ\text{C}$  we may write

$$\text{pH}^* = \text{PZIE} \sim \text{PZC} \pm (\log I - 2\log \sigma_{\max} - 2.5) \quad (46)$$

For instance, an oxide material such that  $\text{PZC} = 5$  and  $\sigma_{\max} = 1 \text{ C m}^{-2}$  placed in a solution containing a one molar 1 : 1 electrolyte would have two PZIE at  $\text{pH}^* = 2.5$  (acid side) and  $\text{pH}^* = 7.5$  (basic side). Consequently, if crystalline growth occurs below  $\text{pH} = 2.5$  or above  $\text{pH} = 7.5$  the interface will be saturated and the final size will be ruled by the exact  $\text{pH}$  value. Under such conditions, the resulting nanocrystal dispersion will be thermodynamically stable with an equilibrium size readily computed from a materials balance [40].

### 4.5.4. Equilibrium Size

Consider a dispersion of  $N$  monodispersed spherical oxide particles (radius  $r$ ) per unit volume formed by precipitation from a solution containing a concentration  $c_0$  of solute precursors. As  $N = 3N_Avc_0/(4\pi r^3)$ , the total area exposed per unit volume is  $A/V = N \times 4\pi r^2 = 3N_Avc_0/r$  and the amount of adsorbed proton per unit volume should be given by  $\sigma A/VF = 3\sigma N_Avc_0/(er)$ . If  $c_H$  is the total acid concentration in solution, we should have  $c_H = \sigma A/VF + c'_H$  where  $c'_H$  is the excess acid concentration not adsorbed by the interface. At the PZIE ( $r = r_e$ ) we know that  $\sigma \sim \sigma_{\max}$  and  $c'_H = c_H^*$ , leading to

$$c_H - c_H^* = \frac{3vc_0}{er_e} \sigma_{\max}$$

$$\iff r_e = \frac{3v\sigma_{\max}}{e} \times \frac{c_0}{c_H - c_H^*} \quad (47)$$

For this example ( $\sigma_{\max} = 1 \text{ C m}^{-2}$ ), with  $\text{PZIE} = 2.5$  ( $c_H^* = 10^{-2.5} \text{ M}$ ), assuming  $v \sim 10^{-28.5} \text{ m}^{-3}$  and  $c_0 = 1 \text{ M}$  would mean that at  $\text{pH} \sim 0$  particles cannot be larger than 0.6 nm. This is a typical size for polycationic species. Consequently, formation of stable polycations before oxide precipitation fits nicely into this treatment. Increasing the  $\text{pH}$  around 1 would allow the formation of a stable 6.2 nm nanocrystalline dispersion, while at  $\text{pH} \sim 2$  the equilibrium size will be much larger with  $r_e \sim 88 \text{ nm}$ . Finally, close to  $\text{pH} \sim 2.5$  (and

above), the thermodynamically allowed equilibrium size is infinite and Eqs. (20), (29), and (35) may be applied. Obviously, owing to the symmetry of our treatment, the same phenomenon may be observed in the presence of a base as shown in the bottom right part of Figure 6. This last diagram thus provides a very nice thermodynamic explanation of the existence of quite stable polyanions and polycations far from the PZC of an insoluble oxide or hydroxide phase. It also explains the possibility of converting an oxide right down to monomeric aquo, hydroxo, or oxo complexes.

## 4.6. Ostwald Ripening

In all the previous treatments we have always considered formation of a monodispersed system in order to relate equilibrium sizes to solution conditions. In fact this should be the case only for thermodynamically, stable dispersions [43].

### 4.6.1. Physical Origin

When crystal growth occurs far from the PZIE (and thus around the PZC), a polydisperse system has to be expected. This may be understood by looking at the top left part of Figure 7 showing the time evolution of the function  $n(r, t)$  giving the number of crystals displaying sizes between  $r$  and  $r + dr$  at time  $t$ . This function may be related to the cumulative  $N(r, t)$  function giving the total number of crystals present at time  $t$  when  $r = 0$ :

$$N(r, t) = \int_r^\infty n(r, t) dr$$

$$\iff -\frac{\partial N(r, t)}{\partial r} = n(r, t)$$

$$\iff -\frac{\partial^2 N(r, t)}{\partial r \partial t} = \frac{\partial n(r, t)}{\partial t} \quad (48)$$

At the beginning of the precipitation, the rate of nucleation will be at its maximum value. Owing to continuous nucleation and growth, the supersaturation ratio declines with time and beyond  $S = S^*$ , its decrease is solely the result of crystal growth. Consequently, the first born nuclei should form the leading edge of the size distribution curve  $n(r, t)$  giving rise to the most numerous and largest crystals. On the other

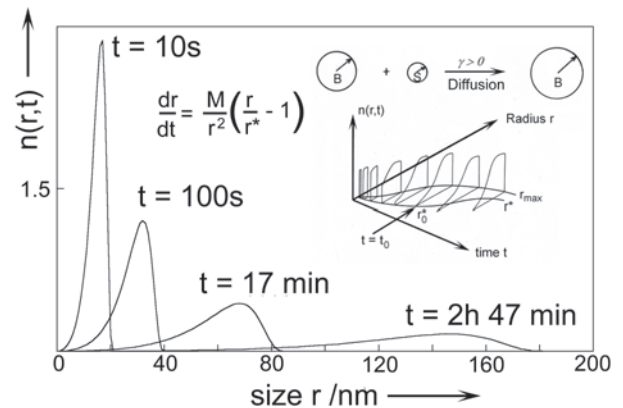


**Figure 7.** Evolution with time through Ostwald ripening of the size distribution  $n(r, t)$  of a nanocrystalline dispersion.



hand, the trailing edge of the distribution gives the number of nuclei born at any time  $t$ . The size of these nuclei is  $r^*$  (the size of the critical nucleus) which should increase with time owing to the decrease in  $S$ . This should easily be understood by applying Eq. (4) to spherical nuclei ( $\beta = 16\pi/3$ ) leading to

$$\frac{4}{3}\pi r(r^*)^3 = n^* \times v \implies r^* = \frac{2\gamma v}{kT \ln S} \quad (49)$$

When the critical supersaturation  $S^*$  is reached, the ordinate of the trailing edge becomes nil (arrow in the diagram) and as  $S$  continues to decline (crystal growth)  $r^*$  continues to increase. The Ostwald ripening may occur as soon as the magnitude of  $r^*$  overtakes the size of the smallest crystals. Consequently, the smallest crystals should redissolve leading to a spreading of the size distribution. Notice that at all times the condition  $r^* < r_{\max}$  (size of the largest crystals) should hold (otherwise the whole precipitate would redissolve). As explained if such a redissolution is thermodynamically allowed, it requires conditions of growth far from the PZC that are not fulfilled here.

#### 4.6.2. General Continuity Equation

The effect of this Ostwald ripening on the size distribution  $n(r, t)$  may be obtained by solving a general continuity equation. This equation may be easily derived by noticing that large crystals will never dissolve. This implies that for large  $r$ , the function  $N(r, t)$  cannot change with time. Accordingly, using the condition  $dN(r, t) = 0$  in conjunction with (48) leads to

$$\begin{aligned} dN(r, t) &= \left[ \frac{\partial N(r, t)}{\partial t} \right] dt + \left[ \frac{\partial N(r, t)}{\partial r} \right] dr = 0 \\ \implies \frac{\partial N(r, t)}{\partial t} - n(r, t) \frac{dr}{dt} &= 0 \end{aligned} \quad (50)$$

Now, taking the partial derivative of (50) relative to size  $r$  leads to the following differential equation for the size distribution  $n(r, t)$ :

$$\frac{\partial n(r, t)}{\partial t} + \frac{\partial}{\partial r} \left[ n(r, t) \frac{dr}{dt} \right] = 0 \quad (51)$$

Integration of (51) is possible analytically only when the system has reached a quasi-steady state after a long time period controlled by diffusion in the solution.

#### 4.6.3. Time Dependence

Let us approximate each crystal by a sphere with radius  $r$  lying in a spherical diffusion field of solute species. The solubility  $c_r$  of the small crystals may be computed from (9) with  $r_2 \rightarrow +\infty$  (i.e.,  $c_2 \rightarrow c_s$ ) and  $r_1 = r$ . A similar relationship also applies to the concentration  $c$  in the bulk that is in metastable equilibrium with the nuclei of size  $r^*$  (now with  $r_1 = r^*$ ). Expanding exponential terms up to second order then leads to the following linear growth rate:

$$\begin{aligned} c &= c_s \exp\left(\frac{2\gamma v}{kTr^*}\right) \quad \text{and} \quad c_r = c_s \exp\left(\frac{2\gamma v}{kTr}\right) \\ \implies \frac{dr}{dt} &= \frac{vD(c - c_r)}{r} \approx \frac{2\gamma v^2 Dc_s}{kTr} \left( \frac{1}{r^*} - \frac{1}{r} \right) \end{aligned} \quad (52)$$

In this diffusion controlled regime all crystals larger than  $r^*$  are growing at the expense of all crystals smaller than  $r^*$ . Consequently, the rate at which the smallest crystals disappear is also the rate at which the total number of crystals  $N(0, t)$  diminishes. Then, using Eqs. (50) and (52) it follows that as  $dN(0, t)/dt$  is always finite and not zero,  $n(r, t)$  should scale like  $r^2$ . Using a dimensionless relative size  $\rho = r/r^*$ , a possible solution may then be written  $n(r, t) = g(t) \times h(\rho) \times \rho^2$ . The differential equation ruling the evolution in time  $g(t)$  may be easily found by applying (48) to  $dN(r \rightarrow 0, t)/dt$  and by insertion of (52) into (50) taking the same limit for the left hand side [44]. Assuming with no loss of generality that  $h(\rho) \rightarrow 1$  when  $r \rightarrow 0$  then leads to

$$\begin{aligned} M &= \frac{2\gamma v^2 Dc_s}{kT} \implies \lim_{r \rightarrow 0} \frac{dr}{dt} = -\frac{M}{(\rho r^*)^2} \\ &\implies \frac{d \ln[g(t)r^*]}{dt} = -\frac{M}{\alpha(r^*)^3} \\ \alpha &= \int_0^\infty \rho^2 h(\rho) d\rho \end{aligned} \quad (53)$$

This may be easily integrated if the total volume of crystalline precipitate  $\phi(t)$  is conserved during the ripening process:

$$\begin{aligned} \phi(t) &= \omega \int_0^\infty n(r, t) r^3 dr \\ \implies g(t)r^* &= \frac{1}{K} \left[ \frac{1}{(r^*)^3} \right] \quad K = \frac{\omega}{\phi} \int_0^\infty \rho^5 h(\rho) d\rho \end{aligned} \quad (54)$$

Accordingly, reporting (54) into (53) and assuming  $dK/dt \sim 0$  leads to  $3(r^*)^2 dr^* = (M/\alpha)dt$ . Then, if Ostwald ripening starts at  $t = t_0$  with a critical size  $r_0^*$ , then at time  $t > t_0$ , one should have

$$\frac{r^*}{r_0^*} = \left[ 1 + \frac{M(t - t_0)}{\alpha(r_0^*)^3} \right]^{1/3} \implies g(t) = g(t_0) \left( \frac{r_0^*}{r^*} \right)^4 \quad (55)$$

#### 4.6.4. Size Distribution

As the time variation of  $r^*$  and  $g(t)$  is known, we may notice that

$$\begin{aligned} \frac{dg(t)}{dt} &= -\frac{4Mg(t)}{3\alpha(r^*)^3} \quad \frac{dr^*}{dt} = \frac{M}{3\alpha(r^*)^2} \\ \implies \left( \frac{\partial \rho}{\partial t} \right)_r &= -\frac{M\rho}{3\alpha(r^*)^3} \end{aligned} \quad (56)$$

In order to get the size dependence  $h(\rho)$  of  $n(r, t)$  one may insert the growth rate given by (52) into (51) leading, after transformation of variable  $r = \rho \times r^*$  and some tedious algebra involving relations (56), to the following differential equation:

$$\begin{aligned} \left[ 6\rho^2 h(\rho) + \rho^3 \frac{dh(\rho)}{d\rho} \right] &= (3\alpha) \left[ (\rho - 1) \frac{dh(\rho)}{d\rho} + h(\rho) \right] \\ \implies \frac{d \ln h(\rho)}{d\rho} &= \frac{3 - (6\rho^2/\alpha)}{\rho^3/\alpha - 3\rho + 3} \end{aligned} \quad (57)$$



At this stage, as from (53)  $\alpha$  is a number depending on the integral of the yet unknown  $h$  function, the solution may seem not obvious. However, we may notice that the denominator in (57) has the simple form  $x^3 = ax + b$  with  $a = -b = 3\alpha$ . A possible solution to this cubic equation is thus  $x = [(b/2) + \Delta^{1/2}]^{1/3} + [(b/2) - \Delta^{1/2}]^{1/3}$ , with  $\Delta = (b/2)^2 - (a/3)^3$  (Cardan formula). Consequently, setting  $\alpha = 9/4$  would lead to  $\Delta = 0$  (i.e., to the most simple root  $x = -3$ ), allowing one to factorize the denominator as  $(\rho + 3)(\rho - 3/2)^2$ . Remembering that with  $h(0) = 1$ , integration of (57) is straightforward:

$$\alpha = \frac{9}{4} \implies h(\rho) = \left(\frac{3}{3+\rho}\right)^{7/3} \left(\frac{3/2}{3/2-\rho}\right)^{11/3} \times \exp\left(-\frac{\rho}{3/2-\rho}\right) \quad (58)$$

Figure 7 illustrates the previous considerations for some typical values of the solid phase and solution parameters, assuming a monodispersed and nanosized dispersion of particles ( $r_0^* = 10$  nm) at the beginning of the Ostwald ripening. It is worth noticing the considerable spreading of the size distribution at long time and its typical asymmetric shape. This characteristic shape emerges from the fact that small particles are disappearing from the solution, allowing the bigger crystals to become still bigger. Concerning the time scale of the ripening, it was mainly ruled by the selection of a diffusion-limited growth mechanism for describing the dissolution–reprecipitation events. Obviously, this should hold only for largely ionic crystals, and for other materials, one may expect an interface-limited ripening. In this case, a numerical solution to the ripening equations (51) and (54) may be the best way of handling the problem [41].

## 5. AGGREGATION

It is now time to remove the assumption that nanocrystals may nucleate and grow independently of each other [i.e., that the  $N(r, t)$  function should be more or less constant during the whole precipitation process].

### 5.1. Position of the Problem

As explained, this assumption was crucial for deriving relations (20), (29), (35), (47), or (54) relating sizes to solution conditions and solid phase properties. Accordingly, even if nanocrystals have their diffusion coefficient 2 or 3 orders of magnitude less than solute species they may nevertheless, from time to time, undergo some collisions between each other. If the sticking probability is high during a collision, aggregates may be formed decreasing by two units the value of  $N(r, t)$ . Obviously, if all possible processes influencing the mean size  $r$  of nanocrystalline dispersions (nucleation, growth, ripening, and aggregation) were occurring with the same rate, the situation would be hopeless. Fortunately, owing to the physics involved in each kind of phenomenon not all these processes are expected to occur simultaneously. For instance, for any kind of reaction to occur, reactants (either complexes or particles) first have to diffuse toward each other. According to the Stokes–Einstein equation

$D = kT/(6\pi\eta a)$ , the diffusion coefficient  $D$  in a solution displaying viscosity  $\eta$  at temperature  $T$  is expected to be the highest for species displaying the lowest size  $a$ . This means that aggregation, like Ostwald ripening, should be important only at long time. However, if ripening is concerned by the behavior of  $N(r, t)$  when  $r \rightarrow 0$  and  $t \rightarrow \infty$ , aggregation focuses on the behavior of this same function when both  $r$  and  $t$  become large.

### 5.2. Fuchs Integral

Consequently, we now assume that after a rather long lapse of time during which the function  $N(r, t)$  has assumed an almost constant value hereafter noted  $N_0$ , this number may change owing to binary collisions between the crystals. Let  $V_T(R)$  be the potential function covering all possible physical or chemical interactions that may occur during the collision. If  $C(R)$  is the concentration of crystals at distance  $R$ , the flux of particles (number of crystals per unit area and per unit time)  $j(t)$  is given by the modified Fick law:

$$j(t) = -D_{\text{rel}} \frac{dC(R)}{dR} - \frac{C(R)}{kT} \times \frac{dV_T}{dR} = -D_{\text{rel}} \exp\left(-\frac{V_T}{kT}\right) \frac{d[C(R) \exp(V_T/kT)]}{dR} \quad (59)$$

In this relationship, the first term arises from the free Brownian motion of the particles. As some external forces  $F_T = -dV_T(R)/dR$  may act on the moving particles, the second term takes care of the additional flux  $C(R) \times v$ , proportional to the speed  $v$  of the particles. As usual, speeds may be related to forces through a friction factor  $f$  ( $v = F_T/f$ ) derived from the Einstein relationship  $D = kT/f$ . Notice that as we are considering a binary collision between two moving particles, the Fick law uses a relative diffusion coefficient  $D_{\text{rel}}$ . The link between  $D_{\text{rel}}$  and  $D_1$  or  $D_2$ , diffusion coefficients of one single particle, may be easily derived by reference to the fundamental law of Brownian motion:  $\langle r_i^2 \rangle = 2D_i t$ . Consequently for a collision between two particles at a relative distance  $(\vec{r}_1 - \vec{r}_2)$  we should have

$$\langle |\vec{r}_1 - \vec{r}_2|^2 \rangle = \langle \vec{r}_1^2 \rangle + \langle \vec{r}_2^2 \rangle - 2\langle \vec{r}_1 \cdot \vec{r}_2 \rangle = 2D_1 t + 2D_2 t = 2D_{\text{rel}} t \implies D_{\text{rel}} = D_1 + D_2 \quad (60)$$

Let us now apply (59) to compute the flux of identical particles across a sphere of radius  $R$ . From (60)  $D_{\text{rel}} = 2D$  and considering the spherical symmetry of the problem, we may write  $J(t) = 4\pi R^2 \times j(t)$  leading after integration to

$$C(R) \exp\left(\frac{V_T}{kT}\right) = -\frac{J}{8\pi D} \int_R^{+\infty} \exp\left(\frac{V_T}{kT}\right) \frac{dR}{R^2} + A \implies J_t \int_{2a}^{+\infty} \exp\left(\frac{V_T}{kT}\right) \frac{dR}{R^2} = 8\pi D C_{\infty} \quad (61)$$

Boundary conditions  $V_T \rightarrow 0$  and  $C(R) \rightarrow C_{\infty} \sim N_0/V$  when  $R \rightarrow +\infty$  and  $C(2a) = 0$  have been applied to get the integration constant  $A$ .

### 5.3. Hard Spheres Model

Let us apply (61) to the most simple case of noninteracting particles characterized by  $V_T \sim 0$  (i.e., by  $J_i^\circ = 16\pi DaC$ ). Now, for a given flux  $J_i$ , half particles are expected to move in a direction allowing a close encounter at  $R = 2a$ , while the other half are moving in the right opposite direction. As all encounters lead to an irreversible sticking of both partners, the rate of disappearance of the crystals through coagulation should be

$$-\frac{dC}{dt} = \frac{1}{2} J_i^\circ C = 8\pi DaC^2$$

$$\Rightarrow C(t) = \frac{C_0}{(1 + 8\pi DaC_0 t)} \quad k_f = 8\pi Da = \frac{4kT}{3\eta} \quad (62)$$

Here  $C_0 = N_0/V$  is the total concentration at time  $t = 0$  that governs the characteristic lifetime  $t_{1/2}$  [such that  $C(t_{1/2}) = C_0/2$ ] of the dispersion. As shown in (62), this time is given by  $t_{1/2} = (k_f C_0)^{-1} = (3\eta/4kTC_0)$ . For water at  $T = 298$  K, we have  $t_{1/2}(s) = 2 \times 10^{11}/C_0(\text{cm}^{-3})$ , showing that the lifetime of dispersions characterized by  $V_T \sim 0$  is quite short (a few milliseconds when  $C_0 \sim 10^{14} \text{ cm}^{-3}$ ).

### 5.4. Attractive Forces

In fact the solution given by (62) is a little bit unrealistic as the situation  $V_T \sim 0$  is never encountered in reality and because the equation applies only to doublets formed by the association of two single particles. For instance, due to the universality of the London dispersion interaction, an attracting potential should always be expected at any distance. Accordingly, quantum mechanical considerations have shown that the potential energy of attraction between two atoms A and B, separated by a distance  $r$ , is given by  $V_A = -L/r^6$  (London force) [45]. The constant  $L$ , characterizing the two interacting atoms, has been roughly estimated by London from the atomic polarizabilities  $\alpha$  and first ionization energies  $I$  as  $L = (3/2) \times [\alpha_A \alpha_B / (4\pi \epsilon_0)^2] \times (I_A^{-1} + I_B^{-1})^{-1}$  [46].

#### 5.4.1. Hamaker Constant $A$

This quantum mechanical expression for the dispersion interaction may readily be used for computing attractive forces between surfaces [42]. For instance, the interaction between an atom and a crown of matter (as always characterized by its molecular volume  $v$ ) of radius  $a$ , width  $da$ , and thickness  $dx$ , is just  $d^2V = -(L/v)(2\pi adadx)r^{-6}$ . If  $R$  is the distance separating the atom from the surface, we may write using Pythagoras's theorem  $r^2 = [(R+x)^2 + a^2]$ , leading after integration (from zero to infinity) against  $x$  and  $a$  to  $V_A = -(\pi L/6v)/R^3$ . Considering that the previous atom belongs in fact to a plate of thickness  $dz$  situated at a distance  $(R+x)$  from the other surface leads to an energy of attraction per unit area  $dv_A = -(\pi L/6v^2)dz/(R+z)^3$ . A last integration against  $z$  from zero to infinity leads to the well-known formula giving the van der Waals interaction between two infinitely large flat plates separated by a distance  $H$ :  $V_A = -A/(12\pi R^2)$ . The parameter  $A = \pi^2(L/v^2)$  characterizing the macroscopic interaction is called the Hamaker constant after the man

who first did this analysis [44]. This is a characteristic value for any condensed substance (whether solid or liquid) as shown in Table 5 [47]. As detailed previously for similar substances one would expect  $L \propto \alpha^2 \times I$  [i.e.,  $A \propto (\alpha^2 \times I)/v^2$ ]. Materials displaying high Hamaker constants are then those with large polarizability  $\alpha$ , high first ionization potential  $I$ , and high atomic density ( $1/v$ ). This explains the extreme position of ice and diamond in Table 5. Obviously, Table 5 should be applicable only for vacuum interactions. When two particles of substance A (Hamaker constant  $A_1$ ) and B (Hamaker constant  $A_2$ ) are immersed in substance C (Hamaker constant  $A_3$ ), one may show [48] that the resulting interaction  $A_{123}$  may be characterized by

$$A_{123} = (\sqrt{A_1} - \sqrt{A_3})(\sqrt{A_2} - \sqrt{A_3})$$

$$= (\sqrt{A_1} - \sqrt{A_3})^2 \quad \text{if } A_1 = A_2 \quad (63)$$

The use of square roots in (63) comes from the fact that  $A \propto (\alpha/v)^2$  while polarizabilities  $\alpha$  are additive quantities. According to this relationship, one may expect for water/oxide interfaces Hamaker constants that are ranging from 0.2 up to 0.5 eV.

As far as nanocrystals are concerned the relationship  $V_A = -A/(12\pi R^2)$  cannot be very useful as it applies to two infinite planar interfaces. Performing the previous integration with spheres displaying radii  $a_1$  and  $a_2$ , with a center to center separation  $S$ , leads to [44]

$$V_A(S) = -\frac{A}{6} \left\{ \frac{2a_1 a_2}{S^2 - (a_1 + a_2)^2} + \frac{2a_1 a_2}{S^2 - (a_1 - a_2)^2} + \ln \frac{S^2 - (a_1 + a_2)^2}{S^2 - (a_1 - a_2)^2} \right\} \quad (64)$$

**Table 5.** Some Hamaker constants  $A$  for condensed matter characterizing the intensity of van der Waals interactions between microscopic objects.

Matter	$A$ (eV)
Hexagonal ice	0.19
Liquid water H <sub>2</sub> O	0.23
Et <sub>2</sub> O, Me <sub>2</sub> CO, MeCOOEt	0.26
MeCOEt	0.29
Benzene, nitrobenzene	0.36
Chloroform, dioxan	0.37
Toluene	0.38
CCl <sub>4</sub> , ethylene glycol	0.39
CS <sub>2</sub>	0.41
Polyethylene oxide	0.42
Glycerol	0.46
Polystyrene	0.49
CaF <sub>2</sub> , polymethylmethacrylate	0.51
Polyvinyl chloride	0.62
SiO <sub>2</sub> quartz	0.92
$\alpha$ -Fe <sub>2</sub> O <sub>3</sub> , haematite	1.02
Silver chloride AgCl	1.07
Silver bromide AgBr	1.14
TiO <sub>2</sub> , anatase	1.28
TiO <sub>2</sub> , rutile	1.41
Diamond	2.81

### 5.4.2. Application

In order to see the effect of such a potential on the rate constant  $k_f$ , we may simplify (64) by writing  $S = R + a_1 + a_2$  and assuming a very small distance  $R \ll (a_1 + a_2)$  between the two spheres. In such a case the first term of (64) is the leading one and  $V_A(R) \sim -(A/6R)[1/a_1 + 1/a_2]^{-1} = -Aa/12R$  for two spheres of equal sizes ( $a_1 = a_2$ ). Replacement of  $V_T$  by  $V_A(R)$  in (61) then leads after integration and expansion of the exponential term up to second order to  $J_i = 16\pi DaC(1 + A/[48kT])$ . As  $A$  is at most a few tens of  $kT$ , the kinetic constant  $k_f$  should be at most multiplied by a factor 2, relative to its value at  $V_T \sim 0$ . Even if this correction appears to be negligible relative to the  $10^{11} \text{ cm}^{-3}$  term, it nevertheless shows that aggregation is accelerated (particularly at low temperature and for materials displaying high Hamaker constant) relative to pure diffusion. Consequently, if the dispersion has to be stabilized against irreversible aggregation, one must play with experimental factors leading to a  $V_T$  curve that must display some maximum positive value  $V_{\max}$  at a given distance  $R > 2a$ . Accordingly, the previous analysis has shown that the additional destabilization factor coming from the region where the potential displays strongly negative values was at most two. Such a modest contribution is then expected to be negligible even in the presence of a small maximum. This observation simplifies integration of Eq. (61) and allows one to write  $J_i = J_i^0/W$ , where  $W$  is the so-called stability ratio  $W \sim \exp(V_{\max}/kT)$ . The higher  $V_{\max}$ , the higher  $W$  and the longer the lifetime of the dispersion as  $k_f \sim 8\pi Da/W$  and  $t_{1/2} = (k_f C_0)^{-1} \propto W$ . For instance, the stabilization for about one year of a dispersion displaying about  $10^{14}$  particles per cubic centimeter would require a stability ratio of about  $10^{10.5}$ . This corresponds to a potential maximum of about  $24 \text{ kT}$  ( $\sim 60 \text{ kJ mol}^{-1}$  or  $0.6 \text{ eV}$  at  $T = 298 \text{ K}$ ).

## 5.5. Repulsive Electrical Forces

The first method widely used to stabilize colloidal dispersion is to work with charged surfaces. For oxide materials, this is done by changing the pH or the ionic strength  $I$ . Owing to the rapid diffusion of protons in aqueous solutions, any pH variation instantaneously affects the surface potential  $\psi_0$  as evidenced by Eq. (38). By playing with the ionic strength, the spatial extensions of the double layers around colloidal particles are deeply affected. Consequently, let us evaluate the time duration  $\tau_B$  of a collision between two charged particles. During this collision, each particle must then diffuse over a length scale of the order of the Debye–Hückel length  $\kappa^{-1}$  given by Eq. (39). If  $D_p$  is the diffusion coefficient of the colliding partners (fixed by radius  $a$  and solution viscosity  $\eta$ ), then  $\tau_B = \kappa^{-2}/2D_p = 3\pi\eta a/(\kappa^2 kT)$ . For water at room temperature ( $T = 298 \text{ K}$ ,  $\eta \sim 10^{-3} \text{ Pas}$ ), we should have  $\tau_B(\text{ns}) = 0.2 \times [a(\text{nm})/I(\text{mol l}^{-1})]$ . For nanosized particles ( $1 \leq a \leq 100 \text{ nm}$ ) with typical ionic strength ( $10^{-3} \leq I \leq 1 \text{ M}$ ), a Brownian collision cannot be shorter than  $100 \text{ ps}$  (small particles or high ionic strength). On the other hand, for larger size or lower ionic strength it cannot be longer than  $0.1 \text{ ms}$ . Due to the geometric changes involved by the collision, several relaxation processes have to occur in order to restore complete equilibrium.

### 5.5.1. Diffuse Layer Relaxation

The first one is the Debye–Hückel relaxation by which counterions located in the diffuse layer move with a diffusion coefficient  $D_i$  in order to adjust the structure of the double layer to the new conditions. The characteristic relaxation time  $\tau_{DH}$  associated with this process is equal to the average time needed for displacement of ions across the double layer:  $\tau_{DH} = \kappa^{-2}/2D_i$ . For aqueous solutions at room temperature  $D_i \sim 10^{-9} \text{ m}^2 \text{ s}^{-1}$  leading to  $\tau_{DH}(\text{ps}) \sim 46/[I(\text{mol l}^{-1})]$ . Consequently, one may safely assume that double layers are always at equilibrium during collision, as even for  $a = 1 \text{ nm}$  we still have  $\tau_B \sim 4\tau_{DH}$ .

### 5.5.2. Stern Layer Relaxation

The second mechanism relies on the adsorption or desorption of all the PDIs involved in the double layer equilibrium. This includes charged species located at the surface as well as those located at the IHP within the Stern layer. Here the rate of charge adjustment is ruled by the value of the exchange current density  $i_0$  between the surface and the Stern layer. For a given charge density ( $\sigma_0 + \sigma_\beta$ ) the characteristic relaxation time may be evaluated as  $\tau_{AD} = (\sigma_0 + \sigma_\beta)/i_0$ . If the exact value of  $i_0$  is highly dependent on the detailed structure of the interface,  $1 \text{ A cm}^{-2}$  is surely a very high value and  $10^{-10} \text{ A cm}^{-2}$  is a very low one [49]. With  $1 \mu\text{C cm}^{-2} \leq (\sigma_0 + \sigma_\beta) \leq 100 \mu\text{C cm}^{-2}$ , it follows that PDI relaxation should take at least  $1 \mu\text{s}$  and may in the worst cases (high surface charge and low mobility of the charges) be as long as several days.

### 5.5.3. Interactions at Constant Charge or Potential

It follows from the last analysis that two limiting cases will be encountered during a Brownian collision between two charged particles:

- (i) For large nanocrystals displaying a low surface charge with high mobility of the PDI and placed under low ionic strength conditions, one may safely assume that  $\tau_B > \tau_{AD}$ . In such a case, the interface, as a whole, is completely relaxed during the collision. This means that at all times the potential remains constant.
- (ii) In all other cases, one may expect that  $\tau_B \ll \tau_{AD}$ , and in this case, only the diffuse part of the double layer is completely relaxed. As  $\sigma = -\epsilon\epsilon_0 d\psi/dx$ , this means that at all times the slope at the surface of the  $\psi = f(x)$  curve cannot change leading to an increase of the surface potential  $\psi_0$ . A consequence of this fact is that the distance of closest approach should not be  $S = 2a$ , but  $S = 2 \times (a + \delta)$ , where  $\delta$  is thickness of the Stern layer holding some of the PDI ions [49]. Obviously, this nonequilibrium situation holds only during a time  $\tau_B$ . If particles remain stuck together after the collision, a discharge current will appear allowing a reduction of the potential toward its equilibrium value. This relaxation allows a still closest approach between the two cores of the particles, until  $S = 2a$  at equilibrium. In this fully relaxed state particles are irreversibly bonded through the van der Waals interaction and cannot be separated anymore.

This constant charge mechanism helps to explain the reptization phenomenon by which a flocculated system may be dispersed again by changing the composition of the medium without stirring [49].

### 5.5.4. Osmotic Pressure and Repulsive Potential

From a physical point of view, the origin of the repulsion between two overlapping double layers comes from the existence of an osmotic pressure  $p_R$ , which develops due to the accumulation of ions between the two surfaces. At sufficiently long distances, the two interacting particles may be viewed as almost planar interfaces. The actual force per unit area exerted on the plates is given by the difference in the osmotic pressure between the solution in the midplane  $\psi_m$  and that in the bulk (concentration  $c_0$ ). With  $c_+$  and  $c_-$  the concentrations at the middle plane, we may write  $p_R = RT(c_+ + c_- - 2c_0)$ . Assuming that  $c_{\pm} = c_0 \exp(\mp zF\psi_m/RT)$  and developing the exponential terms up to second order ( $\frac{1}{2}[e^x + e^{-x}] \sim 1 + x^2/2$  when  $x$  is small) allows one to express this osmotic pressure as  $p_R = \frac{1}{2}\kappa^2\epsilon\epsilon_0\psi_m^2$ . In the case of small overlap between the two plates, potentials are expected to be additive leading to  $\psi_m = 2\psi(x = R/2) \sim 2\psi_d \exp(-\kappa R/2)$ . The resulting repulsion potential is thus obtained after integration over  $R$  leading to

$$\begin{aligned} V_R &= \int_R^\infty p_R dR = \frac{4\kappa^2\epsilon\epsilon_0}{2}\psi_d^2 \int_R^\infty \exp(-\kappa R) dR \\ &= 2\kappa\epsilon\epsilon_0\psi_d^2 \exp(-\kappa R) \end{aligned} \quad (65)$$

Equation (65) is useful as it shows that a high value of  $\psi_d$  is to be associated with a strong repulsive potential. It is, however, not very realistic, as it suggests that high ionic strength (i.e., high  $\kappa$  values) also favors strong repulsion. Keeping the low potential approximation, but considering spheres of radii  $a_1$  and  $a_2$  instead of infinite plates, leads to a more satisfying result when  $|\psi_d| < 60$  mV and  $\kappa a \gg 1$  [50]:

$$\begin{aligned} V_R^\psi &= \frac{\pi\epsilon\epsilon_0 a_1 a_2 (\psi_{d1}^2 + \psi_{d2}^2)}{(a_1 + a_2)} \\ &\times \left[ \frac{2\psi_{d1}\psi_{d2}}{(\psi_{d1}^2 + \psi_{d2}^2)} \ln\left(\frac{1 + \exp[-\kappa R]}{1 - \exp[-\kappa R]}\right) \right. \\ &\quad \left. + \ln(1 + \exp[-2\kappa R]) \right] \end{aligned} \quad (66)$$

When  $a_1 = a_2 = a$  and  $\psi_{d1} = \psi_{d2} = \psi_d$ , (66) reduces to a much simpler expression,  $V_R^\psi = 2\pi\epsilon\epsilon_0 a \psi_d^2 \ln[1 + \exp(-\kappa R)]$ , that does not show the previously noted  $\kappa$  dependence. The  $\psi$  superscript in the previous relationships refers to an overlap between double layers occurring at constant potential. For the other case (constant charge), an additional term has to be subtracted [51]:

$$V_R^\sigma = V_R^\psi - \frac{2\pi\epsilon\epsilon_0 a_1 a_2 (\psi_{d1}^2 + \psi_{d2}^2)}{(a_1 + a_2)} [\ln(1 + \exp[-2\kappa R])] \quad (67)$$

Again, when  $a_1 = a_2 = a$  and  $\psi_{d1} = \psi_{d2} = \psi_d$ , (67) reduces to a much simpler expression,  $V_R^\sigma = -2\pi\epsilon\epsilon_0 a \psi_d^2 \ln[1 - \exp(-\kappa R)]$ . For large distances ( $\kappa R \gg 1$ ) both equations

reduce to an expression similar to (65):  $V_R^\psi = V_R^\sigma = 2\pi\epsilon\epsilon_0 a \psi_d^2 \exp(-\kappa R)$ . Other expressions are available in the literature for situations where the approximations  $|\psi_d| < 60$  mV and  $\kappa a \gg 1$  are not valid [49, 52–55].

### 5.5.5. DLVO Theory

Figure 8 shows the resulting potential curves  $V_T = V_A + V_R^\psi$  obtained when the Hamaker attraction given by (64) is added to the repulsive contribution  $V_R^\psi$  coming from the overlap of double layers given by (66). As shown, four parameters have a deep influence on the occurrence of a maximum. The curve at the top left part of Figure 8 shows the effect of changing the ionic strength for a constant Hamaker constant, size, and surface potential. At high ionic strength or  $\kappa$  there is no maximum and the dispersion should flocculate. This is not true at low ionic strength where the interaction is largely repulsive at all distances  $R > \kappa^{-1}$ . It is a well-known experimental fact (Schulze–Hardy rule) that the critical coagulation concentration (c.c.c.) displays a strong dependence on the valency  $z$  of the coagulating ion (c.c.c.  $\propto 1/z^6$ ). This c.c.c. should correspond to the point at which the maximum in the total potential energy curve just touches the horizontal axis ( $V_T = dV_T/dR = 0$ ). As coagulation implies a low potential and a rather small separation  $R$ , we may use  $V_R^\psi = V_R^\sigma = 2\pi\epsilon\epsilon_0 a \psi_d^2 \exp(-\kappa R)$  and  $V_A(R) = -Aa/12R$  for the repulsive and attractive parts respectively. Applying

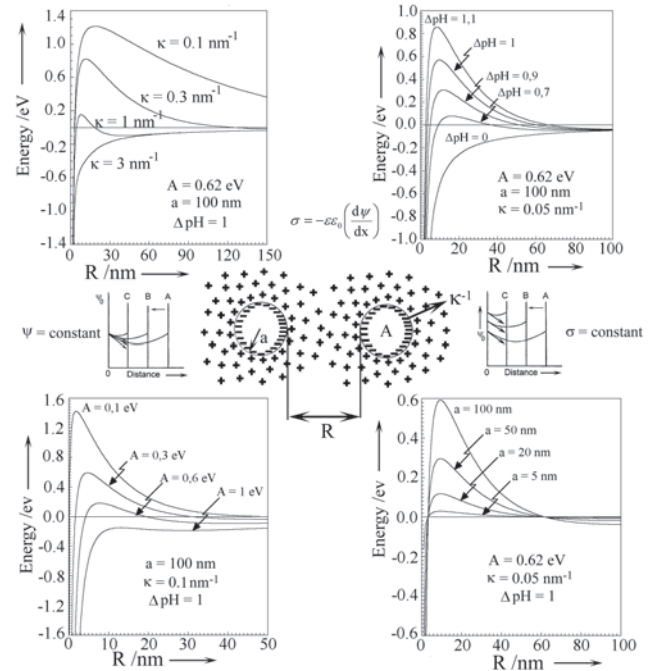


**Figure 8.** DLVO (Deryaguin, Landau, Verwey, and Overbeek) theory for the stabilization of colloidal particles with radius  $a$  against van der Waals attraction (Hamaker constant  $A$ ). The four curves were computed using a potential fixed by the PZC of the particles:  $\psi_0$  (mV) =  $25.7 \times (\text{PZC} - \text{pH}) = 25.7\Delta\text{pH}$ . These curves are the result of adding an attractive contribution,  $V_A(R) = -Aa/12R$ , to a repulsive one,  $V_R$  (eV) =  $0.018 \times a$  (nm)  $\Delta\text{pH}^2 \exp(-\kappa R)$  coming from the osmotic pressure induced by the compression of the diffuse layers characterized by their thickness  $\kappa^{-1}$ .

the conditions  $V_T = V_A(R) + V_R(R) = dV_T/dR = 0$  to this particular form leads to

$$\begin{aligned} \kappa R = 1 &\implies \kappa = \frac{24\pi\epsilon\epsilon_0\psi_d^2}{Ae} = \sqrt{\frac{2z^2 F \text{c.c.c.}}{RT\epsilon\epsilon_0}} \\ &\implies \text{c.c.c.} = \left(\frac{288\pi^2}{e^2 F^2}\right) \left[\frac{RT(\epsilon\epsilon_0)^3}{A^2}\right] \left(\frac{\psi_d^4}{z^2}\right) \quad (68) \end{aligned}$$

This interesting formula shows that the sensibility of a given dispersion to an increase in ionic strength is governed by two main factors. The first factor depends mainly on the physicochemical state of the solvent (temperature, dielectric constant  $\epsilon$ ) and on the chemical nature of the dispersed solid phase (Hamaker constant  $A$ ). Typically a high sensitivity (low c.c.c. value) is expected for materials displaying large polarizability and high density (high Hamaker constant) dispersed in apolar solvents (low dielectric constant) at low temperature. The second factor involves the valency  $z$  of the added ions and the electrokinetic potential  $\zeta \sim \psi_d$ . Here, high sensitivity means low electrokinetic potential and large valency. Recalling that from the Poisson–Boltzmann equation we have  $\sigma_d = -\epsilon\epsilon_0\kappa\psi_d$  with  $\kappa \propto z$ , we may expect that  $\psi_d \propto z^{-1}$ , providing a nice explanation for the empirical Schulze–Hardy rule.

The top right curve in Figure 8 shows the effect of changing the surface potential  $\psi_0 = (RT/F \ln 10)(\text{PZC} - \text{pH})$  at constant Hamaker constant, size, and ionic strength. At the PZC, the attractive term dominates while for  $\Delta\text{pH} \geq 1$  a high maximum always exists. The bottom left curve illustrates the effect of changing the Hamaker constant at constant ionic strength, size, and surface potential. It shows that materials such that  $A > 1$  eV are not good candidates for making stable dispersions. A very high surface charge or low ionic strength is mandatory in this case. At last, the bottom right curve shows the effect of the nanocrystal size at constant ionic strength, surface potential, and Hamaker constant. The interesting point is the absence of maximum for small particles. A direct consequence of this fact is that during a precipitation experiment involving aggregation, the smallest crystals should be selectively removed from the solution, while the largest ones would remain unaffected. This means that starting from a highly polydisperse system, a narrowing of the size distribution is to be expected. This explains the possibility of getting, for any kind of material, dispersions displaying very narrow size distributions as exemplified by the beautiful work of Matijevic [25]. Here, through a fine-tuning of experimental conditions it should be possible to heal by aggregation the inescapable polydispersity generated by nucleation and growth or Ostwald ripening processes.

## 5.6. Entropic Forces

We have so far discussed only enthalpic stabilization. Another possible stabilization mechanism would be to play with entropy instead of enthalpy. In fact, steric stabilization through the adsorption of polymeric species is of widespread use. Accordingly, a polymer can adsorb on the surface of a colloidal particle because of various interactions (charge–charge, dipole–dipole, hydrogen bonding, or van der Waals) acting alone or in combination.

### 5.6.1. Depletion Interaction

When a surface exerts no net attraction on the polymer, a net attractive force may nevertheless exist between the two colloids coming from the unsymmetrical repartition of the osmotic pressure between the overlapping and nonoverlapping zones. Assuming a perfect gas behavior, this osmotic pressure  $\pi = \rho(r)kT$  should be proportional to temperature  $T$  and to the local density  $\rho(r)$  in solute species (here polymers) at distance  $r$  from the surface. Let us further assume that the local density  $\rho(r)$  is close to the bulk density of solute  $\rho_S$ , and that the distance  $d$  is smaller than the sum of the diameters of colloidal  $\sigma_C$  and polymeric species  $\sigma_S$  ( $d < \sigma_C + \sigma_S$ ). Then it is clear that solute species considered as hard spheres should be excluded from the central volume  $V_c$ , leading to a nil osmotic pressure in this central zone. To this depletion phenomenon [56] is associated an attractive potential between the two surfaces given by  $V_{\text{dep}} = -\pi V_c = -kT\rho_S V_c$ . It should be realized that this depletion force is not always attractive. If one looks the interaction at a larger distance ( $\sigma_C + \sigma_S < d < (\sigma_C + 2\sigma_S)$ ), then one finds a repulsive potential. Accordingly, as there is now enough room between the two surfaces, a polymer approaching a surface is pushed against it (negative adsorption) by the osmotic pressure unbalance existing between the surface zone (no polymers) and the bulk solution (density  $\rho_S$ ). Consequently, the local density in polymers in the middle zone should be higher than in the two opposite directions, leading to a neat repulsive force. For a still larger distance ( $(\sigma_C + 2\sigma_S) < d < (\sigma_C + 3\sigma_S)$ ), the potential is again attractive because we have now a system of two coated surfaces displaying again an excluded volume for other polymers in the middle zone. In fact, one may understand that the effective potential for a system of large hard spheres (colloids) in contact with a large amount of smaller hard spheres (polymers) is not a regular one. It always displays a strong attractive component at very small distance (naked surfaces) and displays regular oscillations (period ruled by  $\sigma_S$ ) at longer distances. The higher the volume fraction occupied by the small spheres, the more visible the oscillations and the longer the interaction range.

### 5.6.2. Positive Adsorption

The depletion phenomenon (negative adsorption) will always exist when a polymer solution is near an inert surface. However, if the attractive forces are strong enough, the enthalpy gained overcomes the entropy lost, leading to the model at the bottom of Figure 9 [56]. In this model [57], the links in contact with the surface are called trains. These are adsorbed on the surface, by physical forces invoked above. The loops may be defined as parts of the polymer connecting two trains but displaying no contact with the surface. Finally, the tails are all the nonadsorbed chain ends pointing outside the particle. Using this model, one may define the bound fraction as that fraction of chains forming trains. At very low polymer concentrations, a “pancake” conformation having a relatively large bound fraction may be formed. In this conformation, as there is plenty of room at the surface, the chains in contact with the surface tend to spread out. At higher solution concentrations, severe competition for the available space may occur, leading to shorter

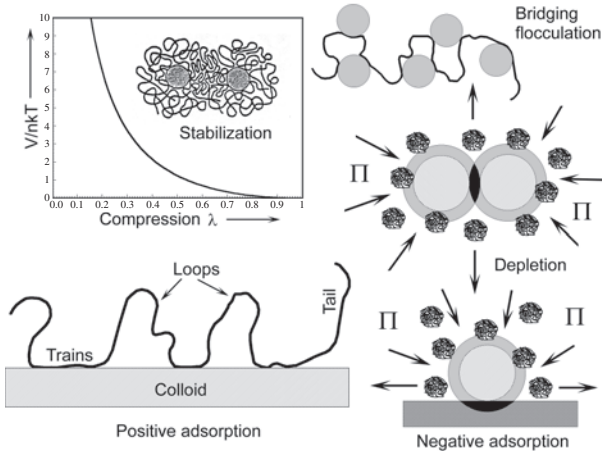


**Figure 9.** Colloidal interactions between solids and polymeric chains. For inert interfaces only depletion and negative adsorption may occur (existence of an excluded volume shown in black leading to osmotic pressure unbalance  $\Pi$ ). Positive adsorption and steric stabilization require some affinity between the surface and the chains. Bridging flocculation is very often observed with small nanocrystals.

trains. In this case, long tails and loops stick out into the solution leading to a “brush” conformation. At last another possibility is that when two particles are brought together it may occur for the loops and tails of one polymer to attach them to bare patches on the other approaching particles (top right drawing in Fig. 9). Obviously, this bridging process is favored if the adsorption density of the polymer is not too high and should be most successful for half-surface coverage and small colloid size.

### 5.6.3. Relaxation Time

Let us now have a closer look at the dynamic aspect of the collision between particles coated with polymeric chains. Relaxation time involved in the adjustment of the conformation of an adsorbed chain or loop has been estimated to be  $2 \times 10^{-4}$  s for polystyrene ( $M = 50,000$ ) in a liquid with viscosity 0.2 Pa s [49]. On the other hand, adjustment of the loop size distribution is a much slower process requiring several minutes. For these systems, the time involved in a Brownian encounter should be defined as the time needed to travel over a distance equal to the thickness of the adsorbed polymeric layer  $\delta$ :  $\tau_B \sim \delta^2/2D_p = 3\pi\eta\delta^2 a/kT$ . For a viscosity  $\eta = 1$  Pa s at  $T = 298$  K,  $\tau_B(\mu\text{s}) = 2.3 \times [a(\text{nm}) \times \delta(\text{nm})^2]$ . With  $1 \leq a \leq 100$  nm and  $1 \leq \delta \leq 10$  nm, we find that the conformation adjustment can follow the collision process. This is not the case for loop size redistribution.

### 5.6.4. Steric Stabilization

With the help of this model, it is easy to track the entropic origin of the steric stabilization. Let  $W$  be the total number of conformations available to the system. Then the corresponding entropy  $S$  should be given by the Boltzmann definition  $S = k \ln(W)$ . Let  $n$  be the number of loops or tails, let  $N_0$  be the number of allowed conformations, and let  $\langle r^2 \rangle$  be the mean square end-to-end distance for each loop or tail.

Provided that a loop or a tail does not approach full extension, the probability that it extends randomly from an arbitrary point  $(x, y, z)$  to another point  $(x + dx, y + dy, z + dz)$  should be given by a simple Gaussian distribution, leading to

$$W = \prod_{i=1}^n W_i$$

$$W_i = N_0 \left( \frac{3}{2\pi\langle r^2 \rangle} \right)^{3/2} \exp\left( -\frac{3}{2} \left[ \frac{\Delta x_i^2 + \Delta y_i^2 + \Delta z_i^2}{\langle r^2 \rangle} \right] \right) \quad (69)$$

In this expression we may replace each  $\Delta x_i^2$ ,  $\Delta y_i^2$ , and  $\Delta z_i^2$  by the mean-square average for the assembly:  $\sum_{i=1}^n \Delta u_i^2 = \langle \Delta u^2 \rangle$  ( $u = x, y, z$ ). The resulting conformation entropy  $S_C$  may then readily be expressed as

$$S_C = k \ln W = nk \ln N_0 \left( \frac{3}{2\pi\langle r^2 \rangle} \right)^{3/2} - \frac{3nk}{2\langle r^2 \rangle} (\langle \Delta x^2 \rangle + \langle \Delta y^2 \rangle + \langle \Delta z^2 \rangle) \quad (70)$$

Let us now consider that the loops are deformed along the  $x$  direction at constant volume. Relation (70) still holds, but the mean-square averages are now  $\Delta x_d = \lambda_x \Delta x$ ,  $\Delta y_d = \lambda_y \Delta y$ ,  $\Delta z_d = \lambda_z \Delta z$ , with  $\lambda_x \lambda_y \lambda_z = 1$ ,  $\lambda_y^2 = \lambda_z^2 = 1/\lambda_x = 1/\lambda$ . For an isotropic medium all directions are equally probable, so that on the average  $\langle \Delta x^2 \rangle = \langle \Delta y^2 \rangle = \langle \Delta z^2 \rangle = \langle r^2 \rangle/3$  leading to

$$S(\lambda) = S_C - \frac{nk}{2} \left( \lambda^2 + \frac{2}{\lambda} - 3 \right) \quad (71)$$

Consequently, any deformation of the loops or tails occurring during a Brownian collision has an unfavorable entropic cost  $V = -2T[S(\lambda) - S(\lambda = 1)] = nkT(\lambda^2 + 2/\lambda - 3)$ . The curve at the top of Figure 9 shows the steep increase in energy provided by the compression of the polymeric chains occurring when the distance between two coated particles is reduced. Obviously, this repulsive potential could play the same role as the repulsive  $V(R)$  term of the DLVO theory. When added to the attractive  $V_A(R)$  term, it should also lead to a maximum at some distance  $R$ . Let us also notice that when the chains belonging to two particles start to overlap, this amounts to a local increase of the concentration. Consequently, besides the repulsive force coming from the volume restriction, another repulsive contribution coming from the apparition of an osmotic pressure is also present (depletion).

## 5.7. Kinetics of Aggregation

We are now in a position to treat the full problem of irreversible aggregation by looking at the time evolution of the aggregate size distribution.

### 5.7.1. Von Smoluchowski Equations

The kinetic equations that must be used had been derived as early as 1916 by Max Von Smoluchowski through the use of aggregation kernels  $K_{ij}$  associated with the following irreversible reaction:  $[i] + [j] \rightarrow [i + j]$ . Here the notation  $[i]$  refers to the ensemble of aggregates containing  $i$  particles



while the  $K_{ij}$  carry all the physical and chemical aspects of the collision. The equations may be written by noticing that  $[k]$  species may appear in solution as a result of the reaction between  $[i]$  and  $[j]$  species such that  $i + j = k$ . But the same  $[k]$  species may also disappear after reaction with any  $[i]$  species. Consequently, if  $c_k$  stands for the number of aggregates of size  $k$  per unit volume, the time evolution of this concentration should be given by

$$\frac{dc_k}{dt} = \frac{1}{2} \sum_{i+j=k} K_{ij} c_i c_j - \sum_i K_{ik} c_i c_k \quad (72)$$

The  $\frac{1}{2}$  factor is there to avoid double counting in the first sum describing the creation of species  $[k]$ . As all the physical and chemical aspects are encapsulated in the  $K_{ij}$  kinetic constants, all the problems lie in getting a meaningful  $i, j$  dependence of these kernels and in the resolution of an infinite system of coupled equations. As for the nucleation and growth steps, it may be useful to consider two limiting cases: diffusion-limited and interface-limited aggregation.

### 5.7.2. Pure Diffusion Kernel

If there is no chemistry involved in the sticking of two aggregates, we may use diffusion equations to get a kernel  $K_{ij}$ . Here, we are interested by the probability  $P_{ij}$  that a cluster with radius  $R_i$  shall be hit in the time interval  $dt$  by another cluster of radius  $R_j$  having the concentration  $c_j$ . This probability should be equal to the diffusion flux  $\varphi_{ij}$  into a sphere of radius  $R_{ij} = (R_i + R_j)$ . From Fick's first ( $j = -D \times \text{grad } c$ ) and second laws ( $dc/dt = D\nabla^2 c$ ) the concentration  $c(\rho, t)$  of species  $[j]$  at a distance  $\rho$  from the center of the sphere of radius  $R_{ij}$  may be written

$$c(\rho, t) = c_j \left\{ 1 - \frac{R_{ij}}{\rho} \left( 1 - \text{erf} \left[ \frac{\rho - R_{ij}}{\sqrt{2Dt}} \right] \right) \right\}$$

$$\Rightarrow \varphi_{ij} = \lim_{t \rightarrow \infty} \left( \frac{dc}{d\rho} \right)_{\rho=R_{ij}} = \frac{c_j}{R_{ij}} \quad (73)$$

As both clusters are undergoing Brownian motion, their relative diffusion coefficient should be  $D_{\text{rel}} = (D_i + D_j)$ . With this diffusion flux of matter, the sticking probability may easily be evaluated as

$$P_{ij} dt = 4\pi R_{ij}^2 D_{\text{rel}} \varphi_{ij} dt \Rightarrow K_{ij} = (D_i + D_j)(R_i + R_j) \quad (74)$$

Now, the Stokes–Einstein equation  $D = kT/6\pi\eta R$  and the fact that for compact objects  $R_k = R_1 \times k^{1/3}$  lead to

$$K_{ij} = \frac{kT}{6\pi\eta} (i^{1/3} + j^{1/3})(i^{-1/3} + j^{-1/3}) \quad (75)$$

### 5.7.3. Getting an Analytical Solution

Consequently, even for the simplest situation, the problem has no analytic solution. However, one may notice that there is no  $i, j$  dependence when  $i = j$  as  $K_{ii} = 4kT/6\pi\eta = K$ . This suggests that one look at what the solution will be if  $K_{ij} = K$  for all clusters (even those for which  $i \neq j$ ). This is obviously a considerable simplification of the problem,

allowing one to find an analytical solution. Inserting  $K_{ij} = K$  into (72) allows one to perform the following factorizations:

$$C = \sum_{k=1}^{\infty} c_k \Rightarrow \frac{dc_k}{dt} = \frac{K}{2} \sum_{i=1}^{k-1} c_i c_{k-i} - Kc_k C$$

$$\Rightarrow \sum_{k=1}^{\infty} \frac{dc_k}{dt} = \frac{dC}{dt} = \frac{KC^2}{2} - KC^2$$

$$= -\frac{KC^2}{2} \quad (76)$$

If we start from an initially monodispersed system (i.e., at  $t = 0$  we have  $c_1 = c_0$  and  $c_k = 0$  for  $k > 1$ ), then the variations with time of the total concentration in clusters  $C(t)$  or in single particles  $c_1(t)$  are obtained after integration of (76):

$$C(t) = \frac{c_0}{[1 + (Kc_0/2)t]} \Rightarrow c_1(t) = \frac{c_0}{[1 + (Kc_0/2)t]^2} \quad (77)$$

$c_1(t), c_2(t)$  may be obtained from (76) by making  $k = 2$  leading to  $dc_2/dt = \alpha[c_0(1 + \alpha t)^{-3} - 2c_2(t)(1 + \alpha t)^{-1}]$  where we have set  $\alpha = (Kc_0/2)$ . A solution to this equation may be easily found by setting  $c_2(t) = g(t)c_0(1 + \alpha t)^{-3}$  with  $g(t)$  satisfying the differential equation  $dg/(1 + g) = \alpha dt/(1 + \alpha t)$  [i.e.,  $g(t) = \alpha t$ ]. These two particular solutions for  $k = 1$  and  $k = 2$  may be put under the following general form:

$$c_k(t) = c_0 \frac{(Kc_0 t/2)^{k-1}}{[1 + (Kc_0 t/2)]^{k+1}}$$

$$\Rightarrow k^2 c_k(t) = \frac{4}{K^2 c_0} \left( \frac{k}{t} \right)^2 \left[ \frac{1}{1 + 2/(Kc_0 t)} \right]^{(k+1)} \quad (78)$$

It is easy to show that (78) is a general solution to (76) leading to

$$\frac{dc_k(t)}{dt} = 0 \Rightarrow t = \frac{(k-1)}{Kc_0}$$

$$\Rightarrow c_k^{\text{max}} = 4c_0 \frac{(k-1)^{(k-1)}}{(k+1)^{(k+1)}} \quad (79)$$

### 5.7.4. Discussion

Consequently, for a given  $k > 1$ ,  $c_k$  goes through a maximum and tends to zero as  $t^{-2}$  for very large times. In this last case (i.e., when  $t \gg 2/Kc_0$ ), the power term in (78) may be developed as

$$\left[ \frac{1}{1 + 2/(Kc_0 t)} \right]^{(k+1)} \approx [1 - 2/(Kc_0 t)]^k$$

$$= \exp(k \ln[1 - 2/(Kc_0 t)])$$

$$\approx \exp\left(-\frac{2k}{Kc_0 t}\right) \quad (80)$$

This shows that for a given time, the size distribution has the shape of a decreasing exponential whose decreasing rate becomes smaller as time increases. It also means that the

size distribution function may be written under an interesting scaling form

$$\langle k \rangle = \frac{\sum_{k=1}^{\infty} k c_k}{\sum_{k=1}^{\infty} c_k} = \frac{c_0}{C(t)} = 1 + \left( \frac{K c_0}{2} \right) t$$

$$\Rightarrow c_k(t \rightarrow \infty) = \langle k \rangle^{-2} \exp\left(-\frac{k}{\langle k \rangle}\right) \quad (81)$$

The important point in this relation is that the  $k$  and  $t$  dependence of  $c_k(t)$  is given through an universal function of a single variable  $k/\langle k(t) \rangle \propto k/t^\gamma$  that does not depend on the initial distribution. For the present case the scaling exponents were  $\tau = 2$  and  $\gamma = 1$ .

## 5.8. Fractal Geometry

Obviously, the case of constant kernel  $K_{ij} = K$  is interesting by its analytical solution but not very realistic and one may seek a more general solution. To do that we may notice that according to (75)  $K_{ij}$  kernels are invariant under any scaling  $\lambda$  as  $K(\lambda i, \lambda j) = K(i, j)$ . In fact it may be shown that it is this very particular scaling relation that is responsible for the asymptotic scaling of the solutions  $c_k \sim \langle k \rangle^{-2} \exp(-k/\langle k \rangle)$ . Let us recall that (74) and (75) were derived under the assumptions of dense aggregates undergoing Brownian motion. A direct observation of these aggregates by transmission electron microscopy has in reality shown that their structures were highly ramified and tortuous exhibiting a scale invariance [59].

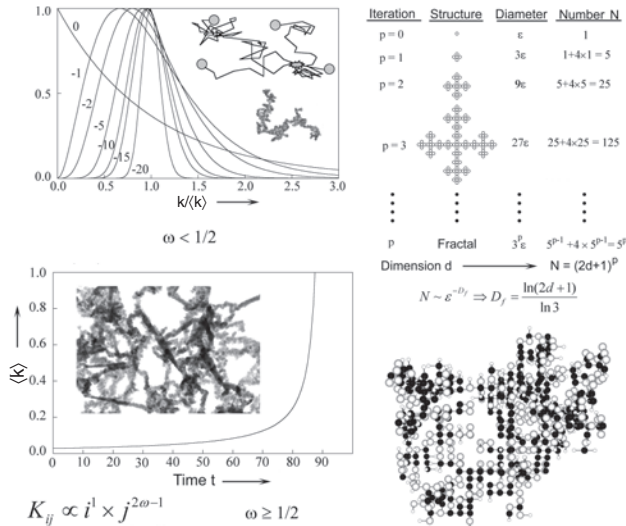


**Figure 10.** Aggregation and fractal aggregates. Top left shows the fractal ( $\omega < 1/2$ ) and limited aggregation ( $\omega < 0$ ) regimes. Bottom left illustrates the case ( $\omega \geq 1/2$ ) leading to a divergence of the mean cluster size (gelation regime). Top right diagram shows how a fractal object may be generated through iteration of simple rules. Bottom right is a 3D-percolation cluster characterized by the fractal exponents  $\delta = 2.53$ ,  $\sigma = 1.84$ ,  $\chi = 1.30$ ,  $\mu = 1.87$ ,  $\beta = 1.143$ ,  $\nu = 3.89$ ,  $\eta = 2.548$  and  $\lambda = 1.374$ . Black spheres correspond to the backbone ( $\mu = 1.87$ ), large gray spheres to the red contacts ( $\beta = 1.143$ ), and small white spheres to dangling ends.

### 5.8.1. Fractal Dimension $\delta$

A direct measure of this scale invariance is provided by the associated fractal dimension  $\delta$  [60]. Figure 10 (top right) shows how a bidimensional ( $d = 2$ ) fractal object may be generated by sticking together identical spherical particles of diameter  $\epsilon$ . First, a seed sphere is centered at the origin. In a second step, four other spheres are added at the left, right, top, and bottom of the seed. In a third step, the ensemble of five spheres is considered a unique object, on which four similar objects may be added using the same rule as before. After a large number of iterations, it is easy to see that the resulting highly ramified object has a diameter  $L = 3^p \epsilon$  and contains  $N = 5^p$  spheres. Now a fractal object characterized by a fractal dimension  $\delta$  may be defined by the property that the minimal number of spheres  $N$  of diameter  $\epsilon$  needed to cover its matter scales like  $N \sim \epsilon^{-\delta}$ . In the present case we have

$$L = 3^p \epsilon \quad N = 5^p$$

$$\Rightarrow p = \frac{\ln(L/\epsilon)}{\ln 3} = \frac{\ln N}{\ln 5}$$

$$\Rightarrow N = \left(\frac{L}{\epsilon}\right)^\delta \quad \delta = \frac{\ln 5}{\ln 3} \approx 1.47 \quad (82)$$

The fact that  $\delta < d = 2$  is here the geometric expression that the object displays holes at any scale.

The same model could be used to derive a fractal dimension when  $d = 3$ . At each step, we have to add two similar objects above and below the plane. For the same diameter, the number of spheres is just  $N = 7^{p-1} + 6 \times 7^{p-1} = 7^p$ , leading to  $\delta = \ln 7 / \ln 3 = 1.77 < d = 3$ . Table 6 gives the fractal dimensions observed for some physical processes leading to highly ramified structure. As can be seen the ideal value of  $\delta = 1.77$  is found to be very close to that found for Brownian cluster-cluster aggregation. This should not be very surprising, as fractal dimensions are universal exponents that do not characterize uniquely the geometry of ramified objects. They just inform us about the kind of growth mechanism that has been used in order to generate the aggregates. Consequently, all objects grown using a hierarchical cluster-cluster mechanism should share the same fractal dimension close to 1.8, even if their local structure may appear quite different.

**Table 6.** Some fractal dimensions  $D_f$  for physical processes leading to ramified structures (compiled from [59]).

Structure	$D_f$
Solvated linear polymer	1.66
Brownian cluster-cluster aggregation	1.77
Ballistic cluster-cluster aggregation	1.91
Ideal linear polymer	2.0
Solvated branched polymer	2.0
Chemical cluster-cluster aggregation	2.04
Ideal branched polymer	2.16
Diffusion limited aggregation	2.50
Percolation cluster	2.49
Ballistic limited aggregation	2.8–3.0
Dense particle	3.0

A direct consequence of this matter of fact is that fractal dimension gives only information on the total mass  $M(R) \sim R^\delta$  found in a sphere of radius  $R$ . In particular, it does not give any details concerning the connectivity properties (the way masses are connected in space). In order to describe these connectivity properties, several other scaling exponents have to be used [59, 60].

### 5.8.2. Bond Dimension $\lambda$

The *bond* dimension  $\lambda$  (or *tortuosity*) gives the minimal distance  $L = R^\lambda$  that must be covered by a walk entirely contained in the object in order to go from two points separated by a Pythagorean distance  $R$ . A high  $\lambda$  value means that very tortuous circumvolutions are present between one point in space to another. However, since the minimum path in the cluster should not be shorter than the Pythagorean distance  $d$  nor longer than a complete random walk, we should have  $1 \leq \lambda \leq 2$ . Usually this exponent is evaluated through the use of numerical simulations. For instance, it has been found that diffusion-limited aggregates ( $\lambda = 1.02$ ) are much less tortuous than cluster–cluster aggregates ( $\lambda = 1.25$ ) [61]. The most tortuous structures are found with 3D-percolation clusters ( $\lambda = 1.374$ ) [62] or branched polymers ( $\lambda = 1.36$ ) [63]. One may notice that both  $\delta$  and  $\lambda$  are *extrinsic* dimensions as they link a fractal property of the object (mass  $M$  or minimal walk  $L$ ) to a Pythagorean distance  $R$  measured in an Euclidian space.

### 5.8.3. Topological Dimension $\sigma$

The *topological* (also *graph* or *chemical*) dimension  $\sigma$  gives the total mass  $M(L) \sim L^\sigma$  visited along a walk of distance  $L$  entirely contained in the object. It may be noticed that this last exponent is not independent of the two others  $\delta$  and  $\sigma$ . Accordingly, as  $L \sim R^\lambda$ ,  $M \sim L^\sigma \sim R^\delta$ , it comes that  $\delta = \lambda\sigma$ . For determinist fractals one usually have either  $\sigma = \delta$  (e.g., the Sierpinski gasket displaying no tortuosity but only lacunarity) or  $\sigma = 1$  (e.g., the Koch curve that has no lacunarity but is tortuous at all length scales). In contrast, with the fractal or bond dimensions,  $\sigma$  is an *intrinsic* dimension as it links two properties (mass  $M$  to the minimal length  $L$ ) of a given fractal object. This fact is also expressed by the relation  $\sigma = \delta/\lambda$  showing that the ratio of two extrinsic dimensions should be another intrinsic one.

### 5.8.4. Spectral Dimension $\chi$

The *spectral* dimension  $\chi$  affects all properties depending not only on space (static dimensions) but also on time (dynamical dimensions). This exponent is linked to the number  $S \sim M \sim t^{\chi/2}$  of distinct sites visited by a random walk (the de Gennes “ant” [64]) after  $t$ -steps, or to the probability  $P_0 \sim t^{-\chi/2}$  that the ant ends up at time  $t$  on its starting point. As  $\chi$  is clearly an intrinsic property independent of the embedding space, it should also be expressed as the ratio of two other extrinsic dimensions. For example a random walk in ordinary homogeneous space is such that the mean square distance varies proportionally to the time  $\langle R^2 \rangle \sim t$ , the proportionality factor  $\langle R^2 \rangle/t$  being the diffusion coefficient. Consequently, for a random walk occurring on a fractal structure one may expect that the mean

square displacement will scale like  $\langle R^2 \rangle \sim t^{2/\nu}$ , the extrinsic exponent  $\nu > 2$  characterizing the fractal walk. Writing that  $M \sim (\langle R^2 \rangle)^{\delta/2} \sim t^{\delta/\nu} \sim t^{\chi/2}$  shows that we have  $\chi = 2\delta/\nu$ . The intrinsic exponent  $\chi$  ratio of two extrinsic dimensions affects all transport properties in a fractal medium. For example, the diffusion coefficient is no more a constant but must depend on the distance  $R$  as  $R^{2-\nu}$ . A similar relation holds for electrical conductivity that becomes size dependent. Concerning the low-energy behavior of the phonon density of states it becomes  $n(E) = E^{\chi/2-1}$ , leading to a density of states per unit frequency  $\rho(\omega) = \omega^{\chi-1}$  (fractons) [65]. A consequence is that the specific heat at low temperature  $T$  scales like  $T^\chi$ .

One of the big advantages of the spectral dimension is that it can be either measured on real objects (mainly through light or neutron scattering) or computed from simulations by at least three independent ways. Strangely enough, very close  $\chi$  values were found from two very different fractal models (percolation cluster with  $\chi = 1.30$  [66] and diffusion-limited aggregates with  $\chi = 1.35$  [61, 67]). This has led to the conjecture that some fundamental link should exist between static and dynamic exponents. For instance, following conjecture  $\nu = 3\delta/2$  (or  $\chi = 4/3 \sim 1.33$ ) [65] may help to explain these data. However, this conjecture does not hold for lattice animals that are characterized by  $\chi = 1.19$  [63] and for screened growth aggregates characterized by  $\chi$  values ranging from 1.10 to 1.22 [68]. However, it may be demonstrated that for any fractal for which loops are irrelevant one should have  $\chi = 2\sigma/(\sigma + 1)$  [68]. This shows that a relation between static and dynamical exponents may occur but only on structures displaying no loops. According to this last relationship, if cluster–cluster aggregation ( $\sigma = 1.42$ ) leads to fractals with no loops, their spectral dimension should be  $\chi = 1.18$ .

### 5.8.5. Backbone Dimension $\mu$

Another exponent has to be introduced for dealing with mechanical properties of fractal aggregates. This is *backbone* dimension  $\mu$  that is always less than the fractal dimension  $\delta$ . It allows one to differentiate between domains connected by at least two contacts and dangling ends that are connected to the backbone only once and hence have no effect on mechanical properties. The backbone dimension is thus the fractal dimension of the object generated by removing all dangling ends to a given fractal. Going one step further one may differentiate between *red* contacts and *blobs*. Red contacts are those parts of the backbone whose removal cuts the object into two independent pieces (particles with coordination number equal to 2). The isolated clusters remaining after this operation and made of all particles having a coordination number of at least 3 are the blobs. The new object made by all the blobs has its own *blob* dimension  $\beta$  that should again be less than the backbone dimension. The backbone and blob dimensions are currently known only from numerical simulation (for a 3D-percolation cluster  $\delta = 2.53 > \mu = 1.87 > \beta = 1.143$ ) [69].

### 5.8.6. Hull Dimension $\eta$

Another important exponent for fractal interfaces is the *hull* dimension  $\eta$  [69]. This exponent relates the external perimeter or surface of the aggregates to the Euclidean distance

between two points. The hull consists of all cluster sites that are connected to infinity through an uninterrupted chain or plane of empty sites. In other words, it is the negative imprint of the aggregates onto the embedding space. Like the backbone and blob dimensions it is currently known only from numerical simulation (for a 3D-percolation cluster  $\eta = 2.548$ ).

## 5.9. General Solution

The previous section has shown that the properties of a fractal object cannot be obtained by rewriting formulae valid on 3D-Euclidean space and simply replacing 3 by  $\delta$ . In fact, one may rigorously define a 3D-Euclidean object by the fact that  $\delta = \sigma = \chi = \mu = \beta = 3$ ,  $\nu = \eta = 2$ , and  $\lambda = 1$ . This degeneracy no longer holds for a fractal such as a 3D-percolation cluster where  $\delta = 2.53$ ,  $\sigma = 1.84$ ,  $\chi = 1.30$ ,  $\mu = 1.87$ ,  $\beta = 1.143$ ,  $\nu = 3.89$ ,  $\eta = 2.548$ , and  $\lambda = 1.374$  [69]. Obviously, it would be hopeless to find an analytical model able to explain all these values from a given set of kernels  $K_{ij}$ . For such situations, numerical simulations are obviously of considerable help. Also, it would have been a very naïve attitude to take the kernel (75) and simply write  $K_{ij} = (kT/6\pi\eta)(i^{1/\delta} + j^{1/\delta})(i^{-1/\delta} + j^{-1/\delta})$  with the hope that everything will run fine. Even if such expression may be found in a large number of papers or textbooks, it is definitely not correct to use the consequence of a growth process (a fractal object characterized by various exponents  $\delta, \sigma, \chi, \mu, \beta, \nu, \eta, \lambda$ ) as the ultimate cause of its appearance. A more correct approach is to guess some general properties for the aggregation kernel  $K_{ij}$  from physical principles. Then one may seek either an analytical or a numerical solution to see if the resulting fractal matches some experimental structure.

### 5.9.1. Realistic and Simple Kernel

The really fundamental point in (75) lies in the scale invariance of the aggregation kernels  $K(\lambda i, \lambda j) = \lambda^0 K(i, j)$ . In this last expression, we have emphasized the null power of the scale parameter  $\lambda$  because one may expect that in the more general case we should have  $K(\lambda i, \lambda j) = \lambda^{2\omega} K(i, j)$ . However, we have to restrict the values of  $\omega$  to the range  $\omega < 1$ , since the averaged active sites in an aggregate cannot grow faster than its size  $i$  or  $j$  [70]. Another physically acceptable assumption is that the largest cluster (say cluster  $[i]$ ) that has the slowest diffusion rate would be explored for a possible reaction among its  $i$  accessible sites by the smallest one  $[j]$  that has the largest diffusion coefficient. As far as seeking the simplest model able to handle the largest number of experimental cases, there is no loss of generality to consider the homogeneous kernel:  $K_{ij} = (kT/6\pi\eta)[i^1 \times j^{2\omega-1}]$ .

The advantage of this quite simple formulation is that all the complex interfacial physics and chemistry are contained in the single  $\omega$ -exponent characterizing the most active aggregate. The restriction comes from the unit power affecting the  $i$ -cluster. This choice reflects the possibility for species  $[j]$  to have full time to explore all exposed sites on cluster  $[i]$ . Consequently, we are limiting ourselves to the case of interface-limited aggregation. The case of diffusion-limited aggregation and derived models will thus not be

covered. However, as it corresponds to an unphysical mechanism for nanocrystal aggregation in solution, we are safe. Another important physical aspect contained in our kernel is the existence of a critical  $\omega$ -value  $\omega^* = \frac{1}{2}$  for which the kernel becomes independent of  $j$ . At this critical point, any  $[j]$  species, whatever its size, is able to stick to any  $i$  site. This is a very clear signal for gelation to occur and one may understand that two qualitatively different regimes may be anticipated.

### 5.9.2. Gelation Regime

Gelling kernels are characterized by  $\omega > \frac{1}{2}$  (Fig. 10). In this regime it may be shown [71] that there exists a finite time  $t_g$  such that

$$t_g = \frac{2\omega - 1}{2\kappa c_0} \implies c_k(t < t_g) = \frac{c_0}{\langle k \rangle^\tau} \psi\left(\frac{k}{\langle k \rangle}\right) \quad \text{with } \langle k \rangle \propto (t_g - t)^{2/(1-2\omega)} \quad (83)$$

In this equation  $\kappa \propto (kT/\eta)$  is a kinetic constant function of temperature and solution viscosity and  $\psi$  is a universal scaling function such that  $\psi(x) \sim Bx^{-\tau}$ . The exponent  $\tau$  should be such that  $\tau = (2\omega + 3)/2 > 2$  ensuring that the mass flux of finite particles (sol) to the infinite cluster (gel) remains bounded for any time  $t > t_g$ . As  $\omega > \frac{1}{2}$  (83) shows that the mean cluster size  $\langle k \rangle$  diverges when  $t \rightarrow t_g$ . In the postgel stage ( $t > t_g$ ) the size distribution is qualitatively different and takes the form  $c_k(t) \sim B(t)k^{-\tau}$  with again  $\tau = (2\omega + 3)/2$ . For this regime,  $\omega > \frac{1}{2}$ , to occur the key point is that we should have a size selectivity mechanism favoring aggregation of large species over smaller ones. This is well evidenced by the power law  $c_k(t) \propto k^{-\tau}$  (with  $\tau > 2$ ) or by the positive contribution in our  $K_{ij}$  kernel of the power of  $[j]$  ( $2\omega - 1 > 0 \Leftrightarrow \omega > \frac{1}{2}$ ). As soon as  $\omega < \frac{1}{2}$ , the power reactivity of  $[j]$  species becomes negative explaining the crossover toward a regime where the size selectivity mechanism favors small clusters over larger ones. Therefore, the probability of finding an infinite cluster occupying the whole solution volume becomes zero in which case only precipitates or size-limited aggregates should be formed (Fig. 10).

### 5.9.3. Fractal Regime

One of the amazing things in this  $\omega < \frac{1}{2}$  regime is that the scaling invariance  $K(\lambda i, \lambda j) = \lambda^{2\omega} K(i, j)$  is sufficient to determine the asymptotic shape  $c_k(t) \sim \langle k \rangle^{-2} \psi(k/\langle k \rangle)$  of the solutions to the Smoluchowski kinetic equations [70, 71]. In this case, the average cluster size  $\langle k \rangle \sim t^\gamma$  carries all the time dependence, whereas the universal function  $\psi$  governs the shape of the size distribution. As this function is universal, it does not depend on the complex details of the aggregation kernels and can be determined by just looking at the most probable configuration coming out of a multinomial distribution [70]

$$\begin{aligned} N_c &= \sum_k n_k & N &= \sum_k k n_k \\ \implies n_k &= \frac{(1-2\omega)^{1-2\omega}}{\Gamma(1-2\omega)} \frac{N_c^2}{N - N_c} \left(\frac{N - N_c}{k N_c}\right)^{2\omega} \\ &\quad \times \left(1 - \frac{k}{N - N_c}\right)^{(1-2\omega)N_c} \end{aligned} \quad (84)$$

In this equation,  $n_k = c_k \times V$ , where  $V$  is the total volume of the solution and  $\Gamma$  is the gamma function. This expression may be further simplified by introducing the reduced variable  $x = k/\langle k \rangle = N_c k/N$  and taking the limit  $N_c \rightarrow 0$  leading to

$$\begin{aligned} n_k &= \frac{N}{\langle k \rangle^2} \psi(x) \\ \implies \psi(x) &= \frac{(1-2\omega)^{1-2\omega}}{\Gamma(1-2\omega)} x^{-2\omega} \exp[-(1-2\omega)x] \\ &\quad \left( \omega < \frac{1}{2} \right) \end{aligned} \quad (85)$$

As explained, the mean cluster size  $\langle k \rangle$  carries all the time dependence that may be expressed as [71]

$$\begin{aligned} \langle k \rangle &= \frac{N}{N_c} \sim [1 + \kappa c_0 (1-2\omega)t]^{1/(2\omega-1)} \sim t^{-\gamma} \\ &\quad \text{with } \gamma = \frac{1}{1-2\omega} \end{aligned} \quad (86)$$

Figure 10 shows the behavior of the normalized size distribution  $\psi(x)$  for several values of the  $\omega$  exponent. It is seen that when  $0 \leq \omega < \frac{1}{2}$ , the size distribution displays a monotonic exponential decreasing behavior. Interestingly enough, when  $\omega = 0$ , we recover exactly the analytical solution of the Von Smoluchowski equation at constant kernel  $K_{ij} = K$ .

#### 5.9.4. Limited Aggregation Regime

When  $\omega < 0$ , another qualitative change of the size distribution occurs. Instead of a monotonic decrease, we have now a bell-shaped curve leading to a narrowing of size distribution as  $\omega$  decreases. This crossover between a highly polydisperse size distribution ( $\omega > 0$ ) and a more monodispersed limited aggregation ( $\omega < 0$ ) is again well modeled by the  $K_{ij} \propto [i^1 \times j^{2\omega-1}]$  kernel. Accordingly, when  $\omega = 0$ , we get the most symmetric kernel  $K_{ij} = i/j$  meaning that no clear distinction exists between the explored cluster and the exploring one. This is no more the case when  $\omega > 0$  modeling a situation where the most probable events are the sticking of the any  $[j]$  species onto the dangling ends of the slowly moving  $[i]$  clusters. One may then understand that the result of this site selectivity (dangling ends more reactive than the backbone) would be a polydisperse collection of objects displaying holes at any scale.

The situation is also unsymmetrical when  $\omega < 0$ . In this regime, we may say that dangling ends are poisoned becoming inactive toward sticking. By consequence, the largest  $[j]$  species, being able to explore only the outer tips of the larger  $[i]$  clusters, cannot participate in the growth process anymore. In this case, the better the poisoning, the lower  $\omega$  and the better the selectivity both in size (only the smallest species are allowed) and in site (backbone free of poison becomes more reactive than dangling ends). This explains the crossover from a fractal regime toward a more compact regime characterized by a bell-shaped size distribution (larger clusters just “eat” the smallest ones without being eaten by their congeners). A high compactness may be expected for large negative values of  $\omega$ , as only very small aggregates are allowed to explore the whole backbone in

order to fill any hole. The larger ones are still there but they are staying quietly outside waiting their turn to fill the holes. Because of this hierarchical mechanism based on a full osmosis between size and site selectivity, one may also expect a strong narrowing of the size distribution as evidenced in Figure 10.

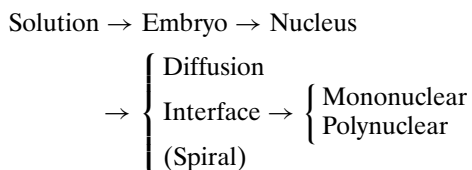
## 6. CONCLUSION

We are now at the very end of the description of all the physical and chemical processes that may cooperate to make nanocrystals appear from initially homogeneous solutions. We have taken care to cover the whole size range, from molecular solute species displaying sizes less 0.5 nm up to macroscopic crystals or gels having size higher than 1 cm. Besides size, one may notice that we have also covered the whole time range starting from nucleation ( $t = 0$ ) and ending with ripened crystals or aggregates ( $t \rightarrow \infty$ ). At each step, analytical expressions have been derived, because this is the only way to be able to fully understand the underlying physics or chemistry involved in experimental or simulation results. At this stage, we want to stress that all the derived equations are in fact very new, even if they share the same analytical shape with already published ones. The novelty comes from the fact that they are all clearly interpreted on a molecular basis, leading to deep conceptual modifications in quite old theories. Moreover, as we have for the first time a full coverage of precipitation from solutions, it is worthwhile to emphasize where fundamental changes have occurred. This will also help us to point to the directions where considerable work remains to be done to get a fully quantitative picture.

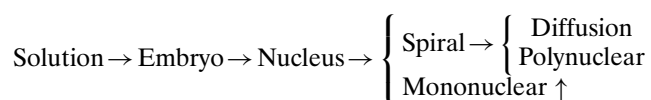
Concerning nucleation theories, the deep change was the explicit introduction of a kinetic barrier  $\Delta G'$  linked to the complex underlying chemistry involved in embryo formation. This chemistry has been reviewed and orders of magnitude have been given. The presence of this additional contribution has led to the appearance of a sticking probability  $g_N = \exp(-\Delta G'/kT)$  in the pre-exponential factor  $J_0$  of the nucleation rate. It was the neglect of this fundamental factor in older theories that explains the differences often observed with experimental measurements [10]. It also allows one to close definitively the controversial discussion relative to homogeneous versus heterogeneous nucleation. Accordingly, for homogeneous nucleation, it was shown that  $g_N$  carries purely chemical structural information. In all the cases where nucleation is really induced by impurities or defaults,  $g_N$  carries additional information about the size of the heterogeneous host and about its chemical nature through a contact angle. In fact, with the introduction of this sticking probability, we have reached the ultimate correct formulation of equilibrium nucleation theory resolving most discrepancies with experiments. Going one step beyond would require one to use nonequilibrium thermodynamics based on entropic fluxes avoiding the use of thermodynamic potentials (Gibbs function) that just cannot be defined for irreversible processes such as nucleation.

By symmetry, the same conceptual change has been introduced in interface-limited crystalline growth, through another kinetic barrier  $\Delta G''$  and through the associated growth sticking probability  $g_C = \exp(-\Delta G''/kT)$ . Another

quite novel aspect was the derivation of Eq. (35) for spiral growth that has never been published before. Here also a deep conceptual change has occurred. In older theories, the accepted paradigm was



This widely accepted view has several conceptual difficulties. First, diffusion should be the rate limiting step only for  $g_C \sim 1$ , a very rare case. Second, the most efficient mechanism (spiral growth) plays a minor role in crystalline growth literature and is usually treated separately from diffusion-limited or interface-limited growth. A much more logical scheme emerges by taking into account the existence of a growth sticking probability:



Here, just after nucleation, the created interface may act either as a catalyst or as an inhibitor for solute species incorporation. In the first case ( $g_C > g_N$ ), we invoke the most efficient mechanism avoiding the bottleneck of surface nucleation. However, owing to its very high efficiency, it very soon ends up either in the bottleneck of diffusion ( $g_C \gg g_N$ ) or switching to the polynuclear mechanism if several spirals compete (high supersaturation ratios) for the same limited crystal volume. The essential point is that as the final morphology is always governed by the slowest growth mechanism, the only chance to see well-developed spirals is to use the supersaturation ratio very close to unity. The second case ( $g_C \ll g_N$ ) means that for some chemical reason, the most reactive growth sites are poisoned. The spiral growth relying on the presence of these active sites is then killed. The only way to proceed is to make somewhere in a flat zone a 2D nucleus that will first grow independently from other nuclei (mononuclear mechanism) and then start to overlap (polynuclear mechanism) at some stage. Future work along these lines would be to reinterpret already published data and design new experimental settings and experiences to validate definitively this simple and logical picture.

Few novelties have been brought in the section devoted to the role of the interface on the growth process. This is because the most important conceptual change (existence of a point of zero interfacial energy or PZIE) has been treated elsewhere [41]. Nevertheless, some new features have been added in order to get a deeper coherence. First, we have pointed to a useful link between the Frank and Wen model of solute–water interface and the double layer model (Stern and diffuse layers) for oxide–water interfaces. Then explicit expressions for the PZIE, Eq. (46), and equilibrium sizes, Eq. (47), have been derived. Finally, a more logical derivation from the Cardan formula of the  $\alpha = 9/4$  value allowing one to solve ripening equations has been proposed. Future work should obviously be oriented toward the elaboration of simple models for nonoxide and nonaqueous solid–liquid

interfaces. New solutions for the ripening equations covering interface-limited growth also have to be derived.

The last section dealing with aggregation processes is surely the most critical one. This is just because, due to their small sizes, individual nanocrystals cannot remain isolated from their congeners. For the same reasons that molecular species may be assembled through weak bonds into supramolecular species, nanocrystals should be used as building blocks for making supracrystalline aggregates. In fact, it may be realized that all major applications involving nanocrystals should handle a more or less ordered array of such objects and not a disordered set. Consequently, if the control of the final size distribution of an assembly of nanocrystals is of the utmost importance, the control of the corresponding mesoscopic or macroscopic texture is yet another scientific challenge. This is the reason we have tried to introduce the very confusing literature devoted to aggregation processes in the most logical and synthetic way. First, we have attempted to make a clear distinction between enthalpy and entropic effects. Furthermore, if we have presented the quite old and criticized DLVO theory, it is just because no other simple theory is yet available. Consequently, if quantum electrodynamics is known to heal some obvious defaults of DLVO theory [72], it is of little practical use, being useful only in some pathological cases. Another highly confusing area concerns the geometric description of fractal objects coming out from aggregation processes. Here most published papers are concerned with the determination or measure of the fractal dimension  $\delta$  of the aggregates. One must realize that reducing such complex objects to a single real number is a considerable loss of valuable information. Moreover, fractal dimension being an extrinsic parameter, it just points to the kind of mechanism that has been used to generate the aggregate in our three-dimensional Euclidian space. In particular, it can say nothing about the internal architecture or detailed topology of the aggregate. To get this kind of crucial information for all practical applications, one has to rely on an intrinsic dimension such as the topological dimension  $\sigma$  or the spectral dimension  $\chi$ . Being the ratio of two extrinsic dimensions (one of them being always the fractal dimension  $\delta$ ), these intrinsic parameters helps us to understand the chemical or physical properties of the associated fractal object. Unfortunately, accurate determination of these very interesting exponents is rather rare and currently limited to ideal mathematical objects coming from numerical simulations. Future work should then be oriented toward the collection of a wealth of experimental data concerning these intrinsic fractal dimensions.

Concerning the kinetics of formation of aggregates, a major conceptual change has been introduced through the  $K_{ij} = (kT/6\pi\eta)[i^1 \times j^{2\omega-1}]$  kernel. The simplicity of this kernel relative to other awkward expressions found in the literature is noteworthy. First, it allows one to understand the existence of three qualitatively different aggregation regimes: gelation (apparition of an infinite cluster if  $\omega \geq \frac{1}{2}$ ), fractal growth (exponential distribution when  $0 \leq \omega < \frac{1}{2}$ ), and limited aggregation (bell-shaped distribution when  $\omega < 0$ ). Second, it avoids the widespread practice of putting at the origin (kernel  $K_{ij}$ ) the result (fractal dimension  $\delta$ ) of the growth process. Obviously, what is still lacking is an analytical link between the exponent  $\omega$  and the molecular



chemistry occurring at the solid–liquid interface. This should be a major challenge for the coming years.

## GLOSSARY

**Aggregate** Large particle formed after irreversible sticking of several small colloidal particles.

**Aggregation** Irreversible sticking of particles undergoing Brownian motion.

**Aggregation kernel** Kinetic constant describing the process by which two aggregates containing  $i$  and  $j$  particles respectively leads to a new aggregate formed of  $(i + j)$  particles.

**Agging** Change of structure, morphology, or porosity with time.

**Aquo cations** Soluble cationic hydrated species  $[M(H_2O)_N]^{z+}$  displaying low electrical charge ( $z < 3$ ) and stable at low pH.

**Backbone dimension** Fractal dimension of an object generated by removing all dangling ends to a given fractal object.

**Blob dimension** Fractal dimension of an object generated by removing all red contacts to a given fractal object.

**Bond dimension** See tortuosity.

**Chemical dimension** See topological dimension.

**Chronomal** Mathematical integral equation  $I(x)$  describing the time evolution  $t = K \times I(x)$  of a phase separation process in terms of a dimensionless reaction coordinate  $x$  and a kinetic constant  $K$ , see Eqs. (12), (26), and (33).

**Classical nucleation theory (CNT)** Theory for nucleation based on equilibrium thermodynamics and mean field approximations.

**Cluster** See aggregate.

**Coagulation** Precipitation of a colloidal solution after addition of an electrolyte.

**Colloidal solution or sol** Dispersion of solid particles (diameter 1–100 nm) in a liquid.

**Critical coagulation concentration (c.c.c.)** Minimal electrolyte concentration allowing spontaneous coagulation of a colloidal dispersion.

**Critical nucleus** Unstable concentration fluctuations that either redissolve or undergo further growth.

**Crystal** Solid matter characterized by a well ordered atomic structure allowing X-ray diffraction.

**Crystal field stabilization energy (CFSE)** Stabilization energy associated to a non-spherical charge distribution of electrons around the atomic nucleus of a transition metal element.

**Debye–Hückel length** Thickness of the double layer function of the solution ionic strength, see Eq. (39).

**Depletion interaction** Net attractive or repulsive force between two colloidal particles induced by the presence of a polymer in the dispersion medium.

**Diffuse layer** Layer of counter-ions around a colloidal particle compensating at the OHP the sum of the surface charges and of the charges located at the IHP. The thickness

of this layer is mainly function of the ionic strength of the solution.

**Diffusion controlled growth** Growth during which the rate-limiting step is the diffusion of solute species towards the solid/liquid interface.

**Diffusion-limited aggregation** Aggregation process during which the rate-limiting step is the diffusion of colloidal particles in the dispersing medium.

**Dislocation controlled growth** Growth initiated on screw dislocations and bypassing the formation of a surface nucleus.

**DLVO theory** Mathematical law giving the interaction energy of two overlapping diffuse layer as a function of their separation derived by first by Derjaguin, Landau, Verwey and Overbeek, see Eqs. (65–67).

**Electrokinetic potential** In a colloidal dispersion, the difference in potential between the immovable layer attached to the surface of the dispersed phase and the dispersion medium (usually approximated by the potential at the OHP).

**Embryos** Unstable concentration fluctuations that are doomed to redissolve at equilibrium.

**Extrinsic dimension** Scaling exponent linking a property of a given fractal object to a Pythagorean distance measured in an Euclidian space.

**Fick's laws** Two mathematical expressions relating through the diffusion coefficient (i) the flux of matter to a gradient concentration and (ii) the variation of concentration with time to its laplacian.

**Fractal** Mathematical object displaying holes at any scale. Corresponding physical objects are porous solids displaying porosity over several order of magnitude of scale length.

**Fractal dimension** Scaling exponent  $\delta$  giving for an aggregate the total mass found in a sphere of radius  $R$ :  $M(R) \sim R^\delta$ .

**Frank and Wen model** Assumption of the existence of at least three structured domains for a solvent around a given solute ( $A$  = solvent in direct contact,  $C$  = bulk solvent and  $B = A/C$  interface).

**Frontier energy** Energy needed for increasing the length of a given surface perimeter by one length unit.

**Fuchs integral** Total flux of particles towards a given colloidal particle corrected for their possible interaction energy.

**Gel** Dispersion of liquid droplets (diameter 1–100 nm) in a solid.

**Gibbs equation** Relationship linking the decrease in interfacial energy to the concentration of adsorbed species (see Eq. (1)).

**Glass** Solid matter displaying no crystalline order showing only X-ray diffusion.

**Gouy–Chapman theory** Mathematical law linking the diffuse layer charge density to its associated potential at the OHP, see Eq. (40).

**Graph dimension** See topological dimension.

**Growth constant** Dimensionless constant incorporating shape factor, frontier energy, molecular volume, temperature, and ruling the change of the growth thermodynamic barrier with the supersaturation.

**Growth rate** Rate of matter addition to an already existing particle and characterized by the rate of change of a characteristic length with time.

**Hamaker constant** Energy parameter measuring attractive forces between surfaces, see Table 5.

**Hull dimension** Scaling exponent relating the external perimeter or surface of a fractal object to the Euclidian distance between two points.

**Inner Helmholtz plane (IHP)** Mean plane defined by all ionic species adsorbed into the Stern layer and not in direct contact with the surface of the colloidal particle.

**Interface limited aggregation** Aggregation process during which the rate-limiting step is the irreversible sticking of two colloidal particles.

**Interface limited growth** Crystalline growth during which the rate-limiting step is the formation of a surface nucleus.

**Interfacial energy or surface energy** Energy needed for increasing the area of a given interface by one surface unit.

**Intrinsic dimension** Scaling exponent linking two properties of a given fractal object.

**Isoelectric point (IEP)** Solution conditions for which there is an equal number of positive and negative adsorbed species.

**Kinetic barrier** Energetic contribution to the nucleation activation energy associated to the crossing of the solid/liquid interface.

**Langmuir isotherm** Mathematical law describing the adsorption at a given interface of a single layer of ions, see Eq. (42).

**Lattice animals** Connected subsets of the square lattice tiling of the plane used for modeling the theta transition displayed by branched polymers in a solvent.

**Loops** Parts of a polymer connecting two trains.

**Metal alkoxides** Organometallic complexes of general formula  $M(OR)_z$  ( $R = C_nH_{2n+1}$ ) leading after hydrolysis and condensation to metallic oxides  $MO_{z/2}$ :  $M(OR)_z + z/2 H_2O \rightarrow MO_{z/2} + z ROH$ .

**Mononuclear growth** Growth process occurring at very low supersaturation and during which a single surface nucleus is able to cover a whole crystalline face.

**Nucleation** Formation of thermodynamically stable particles (solid or liquid) from an initially homogeneous medium (solid, liquid, or gas). It may occur either in the bulk (homogeneous nucleation) or at an interface (heterogeneous nucleation).

**Nucleation constant** Dimensionless constant incorporating shape factor, interfacial energy, molecular volume, temperature, and ruling the change of the nucleation thermodynamic barrier with the supersaturation.

**Nucleation rate** Number of nuclei formed per unit volume and per unit time.

**Nuclei** Stable concentration fluctuations allowed undergoing further growth leading to ultimately to phase separation.

**Ostwald–Freundlich equation** Relationship relating solubility to particle size, see Eq. (9).

**Ostwald ripening** Change upon aging of the size distribution of a collection of particles owing to the occurrence of redissolution/precipitation phenomena.

**Outer Helmholtz plane (OHP)** Slipping plane for solvent molecule defining the thickness of the Stern layer.

**Oxo anions** Soluble anionic species  $[MO_N]^{(2N-z)-}$  displaying high electrical charge ( $z > 4$ ) and stable at high pH.

**Percolation** A simple model in which sites on a lattice are randomly chosen and occupied and where nearest-neighbor particles are then considered to be connected, resulting in clusters of varying sizes and geometries.

**Percolation cluster** Fractal aggregate percolating through an entire lattice network and whose formation is accompanied by the divergence of the mean cluster size and the range of connectivity.

**Point of zero charge (PZC)** Solution conditions for which the surface of a colloidal particle is completely free of ionic species.

**Point of zero interfacial energy (PZIE)** Solution conditions for which full covering of a surface by ionic species occur.

**Poisson–Boltzmann equation** Mathematical law relating the laplacian of the potential to the charge density in volume and to the dielectric constant of the medium.

**Polyanions** Small oligomeric species formed after adding an acid to oxo-anions.

**Polycations** Small oligomeric species formed after adding a base to aquo-cations.

**Polynuclear growth** Growth process during which several surface nuclei compete to cover the same crystalline face.

**Potential determining ions (PDI)** Ions adsorbed on the surface of a colloidal particle or adsorbed into the Stern layer.

**Red contact** Parts of the backbone of a fractal object whose removal cuts this object into two independent pieces.

**Schulze–Hardy rule** Empirical law stating that the c.c.c. of a colloidal dispersion should vary as in the sixth inverse power of the electrolyte valency.

**Screw dislocation** Crystalline defect arising from the occurrence of atomic stacking faults and moving perpendicular to the line joining the two points of an open circuit surrounding the dislocation (Burger's vector).

**Shape factor** Dimensionless quantity linking the volume or the surface of a particle to the cube or the square of its characteristic length (see Tables 2 and 4).

**Sol** See colloidal solution.

**Spectral dimension** Scaling exponent  $\chi$  giving for an aggregate the number of distinct vacant sites  $S$  visited by a random walk involving  $t$ -steps  $S \sim t^{\chi/2}$ .

**Spiral growth** Growth process following a screw dislocation.

**Stability ratio** Dimensionless parameter ruling the life time of a colloidal dispersion.

**Steric stabilization** Stabilization of a colloidal dispersion by entropic forces (usually through polymer adsorption).

**Stern layer** Compact shell of solvent molecules moving with a colloidal particle.

**Sticking probability** Probability of incorporation of solute species according to Maxwell–Boltzmann statistics.

**Stokes–Einstein equation** Relationship linking diffusion coefficient of a particle to its radius and to medium viscosity.

**Surface charge** Density of adsorbed ionic species in direct contact with the surface of the colloidal particle.

**Surface energy** See interfacial energy.

**Sursaturation** Ratio between the concentration in solution at time  $t$  and the concentration at equilibrium (solubility) when  $t \rightarrow +\infty$ .

**Tails** Non-adsorbed chain ends of a polymer pointing towards the solution.

**Thermodynamic barrier** Energetic contribution to the nucleation activation energy associated to concentration fluctuations.

**Topological dimension** Scaling exponent  $\sigma$  giving for an aggregate the total mass  $M$  visited along a walk of distance  $L$  entirely contained in the object:  $M(L) \sim L^\sigma$ .

**Tortuosity** Scaling exponent  $\lambda$  giving for an aggregate the minimal distance  $L$  that must be covered in order to go from two points separated by a pythagorean distance  $R$ :  $L(R) \sim R^\lambda$ .

**Trains** Bonds of a polymer in direct contact with the surface of a colloidal particle.

**Von Smoluchowsky equations** Infinite system of coupled differential equations describing the kinetic of aggregation of a colloidal dispersion.

## REFERENCES

- R. A. Gortner, *Trans. Faraday Soc.* 26, 678 (1930).
- R. L. Fullman, *Sci. Am.* 192, 74 (1955).
- A. E. Nielsen, in "Crystal Growth" (H. S. Peiser, Ed.), p. 419. Pergamon Press, Oxford, 1967.
- K. H. Lieser, *Angew. Chem. Int. Ed.* 8, 188 (1969).
- A. E. Nielsen, "Kinetics of Precipitation." Pergamon Press, Oxford, 1964.
- A. E. Nielsen and O. Söhnel, *J. Crystal Growth* 11, 233 (1971).
- O. Söhnel, *Coll. Czech. Chem. Commun.* 40, 2560 (1974).
- A. Makrides, M. Turner, and J. Slaughter, *J. Colloid Interface Sci.* 73, 345 (1980).
- M. Henry, *Solid State Sciences*, 5, 1201 (2003).
- B. J. Mokross, *J. Non-Cryst. Solids* 284, 91 (2001).
- D. Turnbull and M. H. Cohen, *J. Chem. Phys.* 29, 1049 (1958).
- H. Krüger, *Chem. Soc. Rev.* 11, 227 (1982).
- G. W. Neilson and J. E. Enderby, *Adv. Inorg. Chem.* 34, 195 (1989).
- M. Henry, J. P. Jolivet, and J. Livage, *Struct. Bonding* 77, 153 (1992).
- K. Goto, *J. Phys. Chem.* 60, 1007 (1956).
- H. Gamsjäger and R. K. Murmann, in "Advances in Inorganic and Bioinorganic Mechanisms" (A. G. Sykes, Ed.), Vol. 2, p. 317. Academic Press, London, 1983.
- G. Orcel and L. Hench, *J. Non-Cryst. Solids* 79, 177 (1986).
- R. Aelion, A. Loebel, and F. Eirich, *J. Am. Chem. Soc.* 72, 5705 (1950).
- C. J. Brinker and G. W. Scherer, in "Sol–Gel Science." Academic Press, San Diego, 1990.
- R. A. Assink and B. D. Kay, *J. Non Cryst. Solids* 99, 359 (1988).
- D. H. Doughty, R. A. Assink, and B. D. Kay, *Adv. Chem. Ser.* 224, 241 (1990).
- J. E. Pouxviel and J. P. Boilot, *J. Non-Cryst. Solids* 94, 374 (1987).
- B. J. Ingebrethsen and E. Matijevic, *J. Colloid Interface Sci.* 100, 1 (1984).
- V. K. La Mer and R. H. Dinegar, *J. Am. Chem. Soc.* 72, 4847 (1950).
- E. Matijevic, *Acc. Chem. Res.* 14, 22 (1981).
- T. P. Melia, *J. Appl. Chem.* 15, 345 (1965).
- G. B. Alexander, *J. Phys. Chem.* 61, 1563 (1957).
- E. Matijevic, *Annu. Rev. Mater. Sci.* 15, 483 (1985).
- K. L. Cheng, *Anal. Chem.* 33, 783 (1961).
- R. W. Ramette, *J. Chem. Educ.* 49, 271 (1972).
- L. Gordon and E. D. Salesin, *J. Chem. Educ.* 38, 16 (1961).
- P. F. S. Cartwright, E. J. Newman, and D. W. Wilson, *Analyst* 92, 663 (1967).
- F. H. Firsching, *Talanta* 10, 1169 (1963).
- W. H. Mc Curdy, *Anal. Chem.* 34, 322R (1962).
- N. H. Fletcher, *J. Chem. Phys.* 29, 572 (1958).
- J. Dousma and P. L. De Bruyn, *J. Colloid Interface Sci.* 56, 527 (1976).
- J. Th. G. Overbeek, *Adv. Colloid Interface Sci.* 15, 251 (1982).
- W. K. Burton, N. Cabrera, and F. C. Frank, *Philos. Trans. Roy. Soc. London Ser. A* 243, 299 (1951).
- H. S. Frank and W. Y. Wen, *Discuss. Faraday Soc.* 24, 133 (1957).
- M. Magini, G. Licheri, G. Paschina, and G. Pinna, "X-Ray Diffraction of Ions in Aqueous Solutions." CRC Press, Boca Raton, 1988.
- J. P. Jolivet, M. Henry, and J. Livage, "Metal Oxide Chemistry and Synthesis." Wiley, New York, 2000.
- R. J. Hunter, "Introduction to Modern Colloid Science." Oxford Science, Oxford, 1993.
- R. J. Stol and P. L. DeBruyn, *J. Colloid Interface Sci.* 75, 185 (1980).
- W. J. Dunning, in "Particle Growth in Suspensions" (A. L. Smith, Ed.), p. 3. Academic Press, London, 1973.
- L. Pauling and E. B. Wilson, in "Introduction to Quantum Mechanics," p. 383. McGraw–Hill, New York, 1935.
- F. London, *Z. Phys.* 63, 245 (1930).
- B. Vincent, *J. Colloid Interface Sci.* 58, 408 (1973).
- A. C. Hamaker, *Physica* 4, 1058 (1937).
- J. Th. G. Overbeek, *J. Colloid Interface Sci.* 58, 408 (1977).
- R. Hogg, T. W. Healy, and D. W. Fuerstenau, *Trans. Faraday Soc.* 62, 1638 (1966).
- G. R. Wiese and T. W. Healy, *Trans. Faraday Soc.* 66, 490 (1970).
- L. N. Mc Cartney and S. Levine, *J. Colloid Interface Sci.* 30, 345 (1969).
- A. G. Muddle, J. S. Higgins, P. G. Cummins, E. J. Staples, and I. G. Lyle, *Faraday Discuss. Chem. Soc.* 76, 77 (1983).
- E. Barouch, E. Matijevic, A. Ring, and J. M. Finlan, *J. Colloid Interface Sci.* 67, 1 (1978).
- E. Barouch and S. Kulkarni, *J. Colloid Interface Sci.* 112, 396 (1986).
- E. Jenkel and B. Rumbach, *Z. Elektrochem.* 55, 612 (1951).
- J. F. Joanny, L. Leibler, and P. G. de Gennes, *J. Polym. Sci. Polym. Phys. Ed.* 17, 1073 (1979).
- M. Von Smoluchowski, *Phys. Z.* 17, 585 (1916).
- D. A. Weitz and M. Oliveria, *Phys. Rev. Lett.* 52, 1433 (1984).
- R. Julien and R. Botet, "Aggregation and Fractal Aggregates." World Scientific, Singapore, 1987.
- P. Meakin, I. Majid, S. Havlin, and H. E. Stanley, *J. Phys. A* 17, L975 (1984).
- S. Havlin and R. Nossal, *J. Phys. A* 17, L427 (1984).
- S. Havlin, Z. V. Djordjevic, I. Majid, H. E. Stanley, and G. H. Weiss, *Phys. Rev. Lett.* 53, 178 (1984).
- F. Levyraz and H. E. Stanley, *Phys. Rev. Lett.* 51, 2048 (1983).
- S. Alexander and R. Orbach, *J. Phys. Lett. (Paris)* 43, L625 (1982).
- H. Nakanishi, *Physica A* 196, 33 (1993).
- P. Meakin and H. E. Stanley, *Phys. Rev. Lett.* 51, 1457 (1983).
- P. Meakin, F. Levyraz, and H. E. Stanley, *Phys. Rev. A* 31, 1195 (1985).
- D. Ben-Avraham and S. Havlin, in "Diffusion and Reactions in Fractals and Disordered Systems." Cambridge Univ. Press, Cambridge, UK, 2000.
- R. Botet and R. Julien, *J. Phys. A* 17, 2517 (1984).
- P. G. J. van Dongen and M. H. Ernst, *Phys. Rev. Lett.* 54, 1396 (1985).
- S. Hyde, S. Andersson, K. Larsson, Z. Blum, T. Landh, S. Lidin, and B. W. Ninham, "The Language of Shape." Elsevier, Amsterdam, 1997.

# Nanocrystals in Organic/Inorganic Materials

Peter Reiss, Adam Pron

*CEA Grenoble, Département de Recherche Fondamentale sur la Matière Condensée,  
Laboratoire Physique des Métaux Synthétiques, UMR 5819–SPrAM,  
38054 Grenoble cedex 9, France*

## CONTENTS

1. Introduction
  2. Basic Physical Properties of A(II)B(VI) Semiconductor Nanocrystals
  3. Solution Phase Synthesis of A(II)B(VI) Semiconductor Nanocrystals
  4. Functionalization of Nanocrystals
  5. Conjugated Polymer/Nanocrystal Composite Systems
  6. Hybrid Organic/Inorganic Systems
- Appendix  
References

## 1. INTRODUCTION

Since their discovery about two decades ago, the research devoted to colloidal semiconductor nanocrystals grows exponentially as judged from the increasing number of publications and conferences related to the chemistry, physics, and materials science of these nano-objects. This makes any attempt to provide an exhaustive review of the domain difficult and therefore the selection the data presented in this chapter is purely subjective and reflects the research interests of the authors. Special emphasis is put on the aspects of nanocrystal science which are most closely related to their expected technological and industrial applications. The organization of this chapter is as follows:

The first part of the chapter reviews progress in the synthesis of monodisperse semiconductor nanocrystals and gives a basic introduction to their specific physical properties. In conformity with the literature, the term “monodisperse” is used here to describe colloidal samples in which the standard deviation of the particle diameter does not

exceed 5%. Throughout the text we will restrict ourselves to the description of A(II)B(VI) semiconductor nanocrystals with A being an element of the triad zinc, cadmium, mercury and B an element of the chalcogene group. These systems exhibit optical properties which can be varied in the visible part of the spectrum, near ultraviolet (UV) or near infrared (IR), by changing the nanocrystal size. Monodispersity of the samples is of crucial importance for several reasons. First, size induced tuning of the physical properties of nanocrystals is only possible for their fractions with narrow size dispersions. Second, an appropriate functionalization of monodisperse nanocrystals may lead to well-defined individual objects on the molecular scale with specifically designed properties. Third, assembly of monodisperse nano-objects frequently results in close-packed, highly ordered structures such as “colloidal crystals” and superlattices, opening up routes to novel materials with unusual properties.

At the center of our interest are A(II)B(VI) systems with A = Cd and B = S, Se, or Te, for which the largest number of gram-scale preparation methods have been developed. In spite of the increasing interest in A(III)B(V) semiconductor nanocrystals (A = Ga, In; B = N, P, As), to date the research concerning their synthesis is still less advanced as compared to that carried out on A(II)B(VI) systems.

The second part of the chapter is dedicated to organic/inorganic materials formed by conjugated polymers and nanocrystals. Their use in optoelectronic devices such as light emitting diodes or photovoltaic cells is—besides biological labelling—the most promising application of nanocrystals which has emerged to date.

A number of excellent reviews deal with the synthesis and physical properties of nanocrystals [1–3], whereas less work exists on their organic/inorganic composites [4, 5]. The present chapter gives an overview of the aforementioned research fields with special focus on the latest results and developments including our own work.

## 2. BASIC PHYSICAL PROPERTIES OF A(II)B(VI) SEMICONDUCTOR NANOCRYSTALS

### 2.1. Description

A(II)B(VI) semiconductor nanocrystals are crystalline particles with diameters ranging typically from 1 to 10 nm, comprising some tens to thousands of metal and chalcogene atoms. In the case of colloidal dispersions of nanocrystals the inorganic core consisting of the semiconductor material is capped by a shell of molecules, which provide sufficient repulsion between the crystals to prevent them from agglomeration. In the nanometer size regime many physical properties of the semiconductor particles change with respect to the bulk material. Examples of this behavior are melting points and charging energies of nanocrystals, which are, to first order, proportional to the reciprocal value of their radii. At the origin of the great interest for nanocrystals was yet another observation, namely the possibility to change the semiconductor bandgap—that, is the energy difference between the electron-filled valence band and the empty conduction band—by varying the particle size. In a bulk semiconductor an electron  $e^-$  can be excited from the valence to the conduction band by absorption of a photon with an appropriate energy, leaving a hole  $h^+$  in the valence band. Feeling each other's charge, the electron and hole do not move independently of each other because of Coulomb attraction. The formed  $e^-h^+$  bound pair is called an exciton and has its lowest energy state slightly below the lower edge of the conduction band. At the same time its wave function is extended over a large region (several lattice spacings); that is, the exciton radius is large, since the effective masses of the charge carriers are small and the dielectric constant is high [6]. To give examples, the Bohr exciton radii in bulk CdS and CdSe are approximately 3 and 5 nm. In Table 1 the bandgaps of A(II)B(VI) semiconductors are listed.

Reduction of the particle size to a few nanometers produces the unusual situation that the exciton size can exceed the crystal dimensions. To “fit” into the nanocrystal, the charge carriers have to assume higher kinetic energies leading to an increasing bandgap and quantization of the energy levels to discrete values. This phenomenon is commonly called the “quantum confinement effect” [8], and its theoretical treatment is usually based on the quantum mechanical particle-in-a-box model [9]. With decreasing particle size, the energetic structure of the nanocrystals (often also

referred to as *quantum dots*) changes from a bandlike one to discrete levels. Therefore, in some cases a description by means of molecular orbital theory may be more appropriate, applying the terms highest occupied molecular orbital and lowest unoccupied molecular orbital instead of conduction band and valence band. This ambiguity in terminology reflects the fact that the properties of semiconductor nanocrystals lie between those of the corresponding bulk material and molecular compounds.

Another class of substances characterized by the quantum-confined state is chalcogene bridged transition metal clusters. Here individual, identical molecules in the nanometer or subnanometer range are assembled periodically in single crystals. Although it has not yet been possible for the majority of A(II)B(VI) semiconductors to isolate clusters in the nanometer size range, the impact of cluster science on nanocrystal research is of great importance. Single crystal X-ray diffraction is a powerful tool to obtain crystal structures from clusters and to elucidate their coordination chemistry [10–12]. In view of the lack of a comparable characterization technique for nanocrystals, this information is very worthy for the understanding of their structural properties, since clusters can be considered as model compounds or building blocks for nanocrystals. Furthermore, it has been observed in a large number of examples that, during nanocrystal growth, stable intermediates, often called “magic-sized clusters,” are formed [13, 14]. Quantum chemical calculations on cluster systems can reveal the structures of such thermodynamically stable species as well as their absorption spectra and thus contribute to a more detailed comprehension of the growth process [15, 16]. Finally, established preparation methods for cluster compounds are a helpful guideline for the choice of precursors, solvents, and reaction conditions, especially in the case of organometallic and related synthesis routes for nanocrystals (Sections 3.3 and 3.4).

### 2.2. Optical Properties of A(II)B(VI) Semiconductor Nanocrystals

#### 2.2.1. Absorption

As has already been stated (see Section 2.1), absorption of a photon by the nanocrystal occurs if its energy exceeds the bandgap. Due to quantum confinement, decreasing the particle size results in a hypsochromic (blue)shift of the absorption onset [17, 18]. A relatively sharp absorption feature near the absorption onset corresponds to the excitonic peak, that is, the lowest excited state exhibiting an important oscillator strength (cf. Fig. 1). While its position depends on the bandgap and, consequently, on the particle size, its form and width are strongly influenced by the distribution in size, as well as the form and stoichiometry of the nanocrystals. Therefore polydisperse samples typically exhibit only a shoulder in the absorption spectrum at the position of the excitonic transition. Less pronounced absorption features in the lower wavelength range correspond to excited states of higher energy [19]. As a rule of thumb, it can be asserted that the larger the number of such spectral features and the more distinctly they are resolved in the absorption spectrum, the smaller the size dispersion of

**Table 1.** Energy bandgaps at 300 K of A(II)B(VI) semiconductors [7].

Material	Bandgap (eV)
ZnO	3.4
ZnS	3.8
ZnSe	2.82
ZnTe	2.3
CdS	2.5
CdSe	1.76
CdTe	1.5
HgS	2.1
HgSe	-0.06
HgTe	-0.3 (at 4 K)

the sample. In Figure 1 the absorption and photoluminescence spectra of a series of CdSe nanocrystals differing in size are depicted.

### 2.2.2. Photoluminescence

After absorption of photons by nanocrystals, resulting in the formation of excitons, the system may return to the ground state via radiative electron–hole recombination. The emitted photons have an energy corresponding to the bandgap of the nanocrystals and for this reason the emission color can be tuned by changing the particle size [17, 18]. It should be noted here that efficient room temperature band-edge emission is only observed for nanocrystals with proper surface passivation because otherwise charge carriers are very likely to be trapped in surface states, enhancing nonradiative recombination. Due to spectral diffusion and the size distribution of nanocrystals, the room temperature luminescence linewidths of ensembles lie for the best samples in the range of 20–25 nm [full width at half maximum (FWHM)]. As can be seen in Figure 1, the maxima of the emission peak are redshifted by ca. 10–20 nm as compared to the excitonic peak in the absorption spectra. This phenomenon is usually referred to as *Stokes shift* and has its origin in the particular structure of the exciton energy levels inside the nanocrystal. Models using the effective mass approximation show that in bulk wurtzite CdSe the exciton state ( $1S_{3/2}1S_e$ ) is eightfold degenerate [21]. In CdSe nanocrystals, this degeneracy is partially lifted and the band-edge state is split into five states, due to the influence of the internal crystal field, effects arising from the nonspherical particle shape, and the

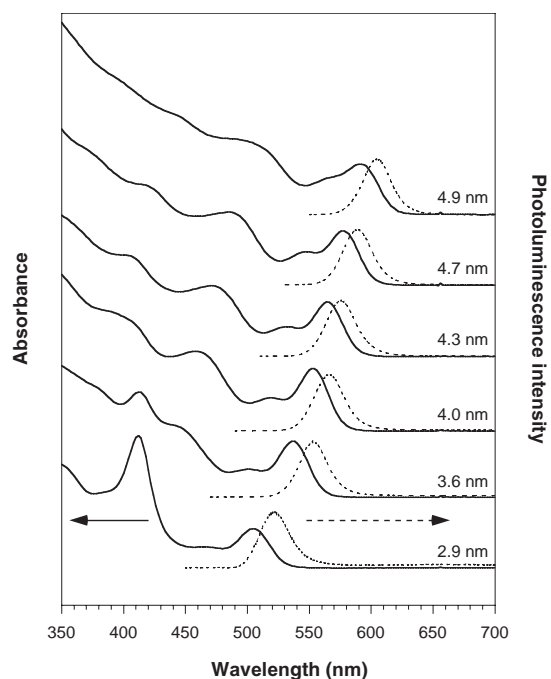


**Figure 1.** Absorption and normalized photoluminescence spectra of CdSe nanocrystals (P. Reiss and J. Bleuse, unpublished data). The diameters have been determined on the basis of data published by Mikulec et al. [20].

electron–hole exchange interaction (see Fig. 2). The latter term is strongly enhanced by quantum confinement [22].

Two states, one singlet state and one doublet state, are optically inactive for symmetry reasons. The energetic order of the three remaining states depends on the size and form of the nanocrystal. In the case of weak excitation of a given state, absorption depends exclusively on its oscillator strength. As the oscillator strength of the second and third excited (“bright”) states is significantly higher than that of the first (“dark”) one, excitation by photon absorption occurs to the bright states. In contrast, photoluminescence depends on the product of oscillator strength and population of the concerned state. Relaxation via acoustic phonon emission from bright states to the dark band-edge state causes strong population of the latter and enables radiative recombination (see Fig. 2). This model is corroborated by the experimental room temperature values of the *Stokes shift*, which are consistent with the energy differences between the related bright and dark states.

### 2.2.3. Emission of Single Nanocrystals, Blinking Phenomenon

Spectroscopic investigation of single semiconductor nanocrystals revealed that their emission under continuous excitation turns on and off intermittently. This blinking is a common feature also for other nanostructured materials, involving porous Si [23] and epitaxially grown InP quantum dots [24], as well as chromophores at the single molecule level such as polymer segments [25], organic dye molecules [26], and green fluorescent protein [27]. However, the origin of the intermittence is completely different for nanocrystals and single dye molecules: in the latter resonant excitation into a single absorbing state takes place. Due to spectral shifting events the excitation is no longer in resonance and a dark period begins. Nanocrystals, on the other hand, are excited nonresonantly into a large density of states above the band edge. While their emission statistics and its modelling are the issue of a large number of publications [28–32], a detailed understanding of the blinking phenomenon has not yet been achieved. As a consequence, experimental efforts to overcome it have not been successful so far. Its resolution would be of great benefit in applications associated with the use of nanocrystals as biological labels, in particular on the single molecule level.

The sequence of “on” and “off” periods resembles a random telegraph signal on a time scale varying over several orders of magnitude up to minutes and follows a temporal statistics described by an inverse power law [30]. Transition from an “on” to an “off” state of the nanocrystal seems to

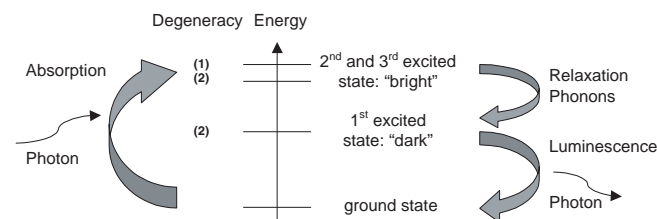


**Figure 2.** Schematic representation of the exciton states of CdSe nanocrystals involved in absorption and emission processes.



occur by photoionization, which implies the trapping of a charge carrier in the surrounding matrix (dangling bonds on the surface, solvent, etc.). A single delocalized electron or hole rests in the nanocrystal core. Upon further excitation this gives rise to fast (nanosecond order) nonradiative relaxation through Auger processes (i.e., energy transfer from the created exciton to the delocalized charge carrier) [33]. Mechanisms for a return to the “on” state are the recapture of the localized charge carrier into the core or the capture of an opposite charge carrier from traps in the proximity. Both pathways can be accompanied by a reorganization of the charge distribution around the nanocrystals. As a consequence the local electric field changes leading to a Stark shift of the photoluminescence peak [31, 32].

#### 2.2.4. Efficiency of the Emission: Fluorescence Quantum Yield

The emission efficiency of an ensemble of nanocrystals is expressed in terms of the fluorescence quantum yield (QY), that is, the ratio between the number of absorbed photons and the number of emitted photons. As a consequence of the blinking phenomenon (vide supra) the theoretical value of 1 is not observed because a certain number of nanocrystals are in “off” states. Furthermore the QY may be additionally reduced as a result of quenching caused by surface trap states. As both of these limiting factors are closely related to the quality of the nanocrystal surface, they can be considerably diminished by its improved passivation. This can be achieved by changing the nature of the organic ligands, capping the nanocrystals after their synthesis. To give an example, after substitution of the trioctylphosphine oxide (TOPO) cap on CdSe nanocrystals by hexadecylamine or allylamine, an increase of the QY from about 10% to values of 40–50% has been reported [34]. In this case better surface passivation probably results from an increased capping density of the sterically less hindered amines as compared to TOPO. On the other hand, in view of further nanocrystal functionalization, it is desirable to provide a surface passivation which is less sensitive to subsequent ligand exchanges. A suitable method consists of the growth of an inorganic shell on the (core) nanocrystals, resulting in core/shell systems as depicted schematically in Figure 3. In order to confine both electrons and holes in the core, a wider bandgap semiconductor with an appropriate band alignment (type I or normal configuration; see Fig. 3) is chosen as the shell material.

Further attention has to be paid to the lattice mismatch parameter between the core and shell lattices. Significant

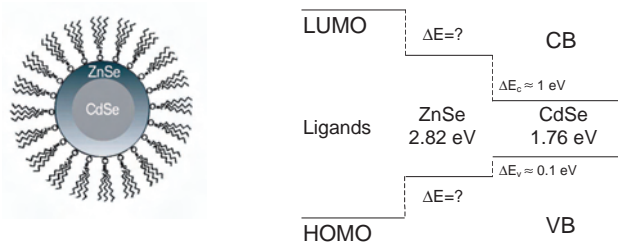


**Figure 3.** Scheme of a CdSe/ZnSe core/shell nanocrystal (left) and of its energy levels (right; CB = conduction band, VB = valence band).

constraints at the core/shell interface lead to the creation of new trapping sites for the charge carriers, which quench the fluorescence. This is clearly visible in the case of the most studied system, CdSe nanocrystals. In terms of bandgap and band alignment ZnS is an excellent candidate as a shell material, which has led to its widespread use. However, due to the large lattice mismatch parameter of 10.6% between CdSe and ZnS, the reported values of QY do not exceed 50–60%. Moreover, only relatively thin shells give rise to an increase of the QY. If a certain shell thickness is exceeded, the QY diminishes, clearly pointing out the formation of structural defects. On the other hand, ZnSe is a shell material which provides less efficient charge carrier confinement with respect to ZnS, due to its lower bandgap. This is especially true for the holes as can be seen from the small conduction band offset in Figure 2 [35]. Nevertheless, as a result of the better crystal lattice matching in CdSe/ZnSe as compared to CdSe/ZnS, higher values for the fluorescence QY are reported in the former case. Table 2 summarizes the properties of different core/shell systems with CdSe as the core material.

### 2.3. Electronic Properties of Nanocrystals

As discussed in Section 2.2, the effects of quantum confinement give rise to a strong size dependence of the optical properties of nanocrystals. However, in such nano-objects essentially all physical properties exhibit size dependence in a more or less pronounced way, including their electronic properties. If one considers a nanocrystal as a spherical capacitor, its capacitance  $C$  is a function of its radius  $r$  [40],

$$C(r) = 4\pi\epsilon_0\epsilon r \quad (1)$$

where  $\epsilon_0$  and  $\epsilon$  are the dielectric constants of the vacuum and of the surrounding medium of the nanocrystal, respectively. Adding a simple charge to the nanocrystal requires the charging energy  $E_c$ ,

$$E_c = e^2/2C(r) \quad (2)$$

At temperatures where  $kT < E_c$ , tunneling of single charges onto nanocrystals can occur, which can be revealed by scanning tunneling microscopy measurements [41–45]. The current–voltage curves obtained in these experiments exhibit a barrier to current flow, arising from  $E_c$ , which is called a Coulomb blockade.

**Table 2.** Shell materials for the overcoating of CdSe nanocrystals: bandgaps (CdSe: 1.76 eV), lattice mismatch parameters  $a$  with respect to CdSe, and reported room temperature QYs of the core/shell systems.

Shell material	Gap (eV)	$a$ (%)	QY (%)	Ref.
CdS	2.5	3.8	$\geq 50$	[36]
ZnS	3.8	10.6	30–50	[37, 38]
ZnSe	2.82	6.3	60–85	[39]

### 3. SOLUTION PHASE SYNTHESIS OF A(II)B(VI) SEMICONDUCTOR NANOCRYSTALS

#### 3.1. Historical Review of the Synthesis Methods

Solution phase (or wet chemical) methods for the synthesis A(II)B(VI) semiconductor nanocrystals can be roughly divided into two general categories:

1. room temperature procedures consisting of nanocrystal precipitation in aqueous media, either in the presence of stabilizers (method 1.1) or within inverse micelles (method 1.2)
2. high temperature reactions in nonaqueous media based on temporal separation of nanocrystal nucleation and growth, applying either organometallic precursors (method 2.1) or inorganic precursors, such as oxides or salts (method 2.2)

Table 3 gives a nonexhaustive overview of reported applications of the aforementioned preparation methods for the fabrication of A(II)B(VI) nanocrystals.

Initially developed procedures comprise nanocrystal formation in homogenous aqueous solutions containing appropriate reagents and surfactant-type or polymer-type stabilizers [53, 61]. The latter bind to the nanocrystal surface and stabilize the particles by steric hindrance and/or electrostatic repulsion in the case of charged stabilizers. In parallel to this monophasic synthesis, a biphasic technique has been developed which is based on the arrested precipitation of nanocrystals within inverse micelles [54, 55, 62, 63]. Here nanometer-sized water droplets (dispersed phase) are stabilized in an oil (continuous phase) by an amphiphilic surfactant. They serve as microreactors for the nanocrystal growth and prevent at the same time particle agglomeration. Both methods provide relatively simple experimental approaches using standard reagents as well as room temperature reactions and were of great importance for the development of nanocrystal synthesis. On the other hand, the samples prepared by these synthetic routes usually exhibit size dispersions exceeding 15% and therefore material consuming

procedures of nanocrystal separation into “sharp” fractions have to be applied in order to obtain monodisperse samples.

The introduction of high temperature preparation methods in 1993 [50] constituted an important step toward the fabrication of CdS, CdSe, and CdTe nanocrystals exhibiting much lower size dispersions as compared to samples prepared in aqueous media. As demonstrated in classical studies by La Mer and Dinegar [64], the synthesis of monodisperse colloids requires a temporal separation of nucleation and growth of the seeds. This can be achieved by rapid injection of the reagents into the hot solvent which raises the precursor concentration in the reaction flask above the nucleation threshold. A nucleation burst takes place which lowers immediately the supersaturation and afterward no new seeds are formed. In an ideal case all crystallization nuclei are created at the same time and undergo identical growth until the precursors (sometimes also called “monomers”) in the solution are consumed. At this stage of the reaction it is possible to carry out subsequent injections of precursors in order to increase the mean particle size without deterioration of the narrow size distribution as long as the concentration of the nucleation threshold is not exceeded. Crystal growth from solution is in many cases followed by a second distinct growth process, which is referred to as Ostwald ripening [65, 66]. It consists of the dissolution of the smallest particles because of their high surface energy and subsequent redeposition of the dissolved matter onto the bigger ones. Thereby the total number of nanocrystals decreases, whereas their mean size increases. If diffusion is assumed to be the rate limiting step, the size dependent growth rate can be expressed by means of the *Gibbs–Thomson equation* [67]:

$$S(r) = S_{\text{bulk}} \exp(2\sigma V_m / rRT) \quad (3)$$

$S(r)$  and  $S_{\text{bulk}}$  are the solubilities of a nanocrystal with radius  $r$  and of the bulk solid, respectively.  $\sigma$  is the specific surface energy,  $V_m$  is the molar volume of the solid,  $R$  is the gas constant, and  $T$  is the temperature. As shown by Reiss [68], Ostwald ripening can lead to smaller size dispersions in the case of micrometer-sized colloids. For nanometer-sized particles, validity of Eq. (3) and focusing of size distributions during the diffusion-controlled nanocrystal growth have been confirmed [69, 70]. Within the framework of the organometallic preparation method, samples with 8–10% standard deviation from the mean size can typically be obtained.

One of the main disadvantages of this preparation method lies in the fact that pyrophoric organometallic precursors such as dimethylcadmium or diethylzinc are applied. Their use requires special experimental precautions and their extremely high reactivity restricts the batches to laboratory scale quantities. As a result, in recent years the development of nanocrystal high temperature synthesis was focused on the replacement of these organometallic precursors by easy to handle standard reagents. To give an example, in the preparation of CdB(VI) nanocrystals, dimethylcadmium can be substituted by cadmium oxide or cadmium salts of weak acids ( $\text{CdAc}_2$ ,  $\text{CdCO}_3$ ) after complexation with long chain phosphonic or carboxylic acids [51, 52]. In the subsequent text this and related procedures will be termed “mixed

**Table 3.** Synthesis methods for A(II)B(VI) nanocrystals.

Method	Material	Ref.
1.1	ZnS	[46]
2.1	ZnSe	[47]
1.2	ZnSe	[48]
2.1	ZnO	[49]
2.1	CdS, CdSe, CdTe	[50]
2.2	CdS, CdSe, CdTe	[51]
2.2	CdSe	[52]
1.1	CdS	[53]
1.2	CdS	[54]
1.2	CdS	[55]
1.2	CdSe	[56]
1.1	CdTe	[57]
1.2	CdTe	[58]
1.1	HgS	[59]
1.1	HgSe, HgTe	[60]

inorganic/organometallic” methods. A further modification of the high temperature methods consists of the appropriate selection of coordinating and noncoordinating solvents, with the goal to determine their influence on the nucleation and growth of the nanocrystals and to reduce their size distributions below 5% [34]. It is very likely that in the near future similar methods for the synthesis of ZnB(VI) and HgB(VI) nanocrystals will be developed.

At the end of this brief historical review, it should be pointed out that essentially all discussed preparation methods have one important point in common: slight variations in the experimental conditions can lead to significant differences in the result. The interested reader who desires to reproduce nanocrystal syntheses in his own laboratory should therefore follow exactly the directions given in the original literature.

## 3.2. Synthesis in Aqueous Media

### 3.2.1. Precipitation in Presence of Stabilizers

Well established preparation methods for CdS and CdTe nanocrystals comprise their precipitation from an aqueous solution containing cadmium ions and appropriate stabilizers such as thioglycerol or thioglycolic acid [71]. If the precipitation is carried out with the use of H<sub>2</sub>S or H<sub>2</sub>Te the pH value is a crucial parameter in the control of the particle size and its dispersion. Alkaline pH values are necessary to shift the equilibrium of the H<sub>2</sub>S (or H<sub>2</sub>Te) dissociation enabling the formation of CdS (or CdTe) seeds:



During the reaction the pH drops to acidic values due to the release of protons and the particles grow either from solution or by Ostwald ripening while no new seeds are formed. The growth can be stopped by increasing the pH to alkaline values once again. An inherent feature of the nanocrystals synthesized by this method is their surface charge, which makes them dispersible in water. Their stabilities as well as their fluorescence efficiencies depend strongly on the nature of the stabilizing agent.

### 3.2.2. Precipitation in Inverse Micelles

Surfactant molecules can be classified into cationic (e.g., amines), anionic (e.g., carboxylic or sulfonic acids), and nonionic (e.g., polyethers) ones. They have an amphiphilic character, which means that they contain both hydrophilic and hydrophobic moieties, and for thermodynamic reasons they self-assemble in aqueous solutions to form aggregates, called micelles. In a biphasic system consisting of water and oil (hydrocarbon), the creation of different shaped micelles is possible such as spherical, cylindrical, or lamellar ones, depending on the relative concentrations of the constituents of the ternary system [72]. A high volume fraction of the oil phase leads to the formation of inverse micelles (i.e., water droplets in oil with the hydrophobic parts of the surfactant molecules sticking out of the droplet). These can be used as compartments for the arrested precipitation of nanocrystals. In this case no stabilizers are necessary to prevent from

particle agglomeration (compare Section 3.2.1), because the individual nanocrystals are shielded by the surfactant and the continuous phase. The most popular system in this context comprises sodium bis(2-ethylhexyl)sulfosuccinate, also known as aerosol OT or Na(AOT), as the surfactant in a water/isooctane or water/heptane mixture [54–56]. In this case the diameter  $d$  of the inverse micelles can be controlled by the water content  $w$  [73]:

$$w = [\text{H}_2\text{O}]/[\text{AOT}] \quad (5)$$

$$d \text{ (nm)} \cong 0.3 w \quad (6)$$

Equation (6) is valid for values of  $w$  superior to 15, whereas it underestimates the micellar size for lower values of this parameter. The synthesis of nanocrystals inside inverse micelles can be carried out in two different ways: either by mixing two micellar solutions, one containing metal ions and the other containing chalcogenide ions in the water droplets, or by bubbling the metal ions containing solution with gaseous hydrogen chalcogenide. In addition to the important size distribution, a drawback of the micellar method is the fact that the maximum size, which can be obtained for semiconductor nanocrystals, is limited to ca. 4 nm [72]. On the other hand, it is very versatile synthesis technique that allows the preparation of a large number of different semiconductor, metal, alloy, and oxide nanoparticles (see [72, 74] and references therein).

## 3.3. Organometallic Synthesis

The organometallic nanocrystal synthesis consists of the reaction between an organometallic metal precursor and an appropriate chalcogene precursor carried out in a coordinating solvent at high temperature. The originally reported preparation method [50] typically yields nanocrystals with size dispersions of 8–10% in the case of CdSe and of 10–15% in the case of CdS and CdTe nanocrystals. The procedure can be divided into three steps:

- (i) Nucleation of the seeds: Nucleation of the seeds is achieved by swift injection of the organometallic precursors into the reaction flask which contains the coordinating solvent vigorously stirred at high temperature (300–350 °C). As mentioned in Section 3.1, such quick addition provokes a transient supersaturation necessary for the nucleation process. Besides, the injection of the cold (ca. 25 °C) precursors results in a significant temperature drop inside the flask.
- (ii) Particle growth: During particle growth, which follows the nucleation step, temperature is maintained between 250 and 300 °C. The growth process can be monitored by the evolution of the absorption spectra of small aliquots taken periodically from the reaction mixture or *in-situ* using a fiber optics probe.
- (iii) Growth termination: When the desired particle size is reached, temperature is dropped below 100 °C to stop crystal growth. Nanocrystals are then isolated by precipitation and purified by washing with adequate solvents in order to remove by-products and excess coordinating solvent.

Although originally developed for the CdB(VI) series, a similar approach has been adapted for the synthesis of ZnB(VI) and HgB(VI) semiconductor nanocrystals (see Table 3). Organometallic metal precursors generally comprise metal alkyls or aryls (dimethylcadmium, diethylzinc, dibenzylmercury) whereas S, Se, or Te sources are mostly chosen from trialkylphosphine chalcogenides ( $R_3PSe$ ,  $R_3PTe$  with  $R = \text{octyl or butyl}$ ) or bistrimethylsilylchalcogenides such as  $(Me_3Si)_2S$ . The trialkylphosphine chalcogenides can easily be prepared by dissolution of the chalcogenide powder in the phosphine. In the case of sulfur, the silylated compound is preferred over the trialkylphosphine sulfide because the latter exhibits too low reactivity in the temperature range used for the synthesis.

The choice of the coordinating solvent is of crucial importance because it influences the reactivity of the precursors as well as the kinetics of the growth process. Furthermore, being the capping agent, it determines the “solubility” of the nanocrystals and the stability of their colloidal dispersions. Usually applied are mixtures of alkylphosphines  $R_3P$ , alkylphosphine oxides  $R_3PO$  [ $R = H(CH_2)_n$  with  $n \geq 4$ ], long-chain alkylamines, etc. Prerequisites for the selection are that the solvent system does not show any decomposition at the high reaction temperatures and that the boiling points of all components are sufficiently high. Further attention has to be paid to the basic strength of the solvent which has to be adapted according to the type of semiconductor nanocrystal to be synthesized. To give an example, the most widely used coordinating solvent for the preparation of CdB(VI) nanocrystals is a mixture of trioctylphosphine oxide/trioctylphosphine or trioctylphosphine oxide/tributylphosphine. For the synthesis of ZnB(VI) analogs of the CdB(VI) family, the previously described solvent mixtures cannot be applied because the interactions between TOPO and the zinc precursor ( $ZnEt_2$ ) are too strong. As a result, the reaction between the metal source and the chalcogenide source is impeded and the nucleation and/or growth process does not occur. This problem can be overcome by the replacement of TOPO with hexadecylamine (HDA) which is a weaker base. The HDA/TOP mixed solvent provides sufficient reactivity between the precursors and enables the growth of ZnB(VI) nanocrystals [47].

A large variety of precursor/coordinating solvent systems, whose mutual interactions can be tuned as to obtain the optimum synthesis conditions for nanocrystals of a given semiconductor, makes the organometallic route a very versatile preparation method. However, the pyrophoric character of organometallic reagents, which implies special experimental precautions, and their high price motivated researchers to develop alternative procedures in recent years. Some of them yield nanocrystals of equal or even superior quality as compared to those prepared by organometallic synthesis (see Section 3.4).

### 3.4. Mixed Inorganic/Organometallic Synthesis

As has been stated, the temporal separation of nucleation and growth is very likely to be of crucial importance for the synthesis of monodisperse nanocrystals. In the framework

of the organometallic preparation route this is achieved by the use of highly reactive metal precursors which decompose readily after their injection into the hot solvent. Nevertheless this reaction type is not limited to organometallic, pyrophoric reagents and a number of inorganic compounds such as oxides or salts can be applied in the same way. The first example reported was the use of cadmium oxide, complexed with alkylphosphonic acids, as a Cd source in the synthesis of CdB(VI) nanocrystals [51]. The resulting cadmium phosphonates are sufficiently reactive toward Se or Te solutions in trioctylphosphine and yield nearly monodisperse CdSe and CdTe nanocrystals in the size range of ca. 2.5–5 nm. In the same manner as in the case of the organometallic synthesis route (Section 3.3) [34], the size distribution can be further lowered to values below 5%, if a mixed solvent of TOPO/HDA is used instead of TOPO alone [39]. Larger sized nanocrystals can be prepared by applying cadmium carboxylates as a Cd source, with the crystal growth rate being inversely proportional to the chain length of the carboxylic acid [52]. By proper choice of the cadmium source and solvent, this method allows the synthesis of CdSe nanocrystals with diameters up to 25 nm, while for the organometallic approach maximum values of ca. 11 nm have been reported [50].

Moreover, this scheme can easily be extended to the synthesis of nanocrystals of shapes different from spherical and in particular to the preparation of “nanorods” (i.e., elongated crystals with a high aspect ratio) [75]. In order to promote and control such a one-dimensional (1D) growth, it is desirable to have less reactive cadmium sources than dialkylcadmium compounds, for example certain cadmium phosphonates. The experimental results show that, as in a number of other examples [10, 13, 14, 76], in the early stages of the reaction a relatively stable, “magic-sized” cluster of ca. 10–20 cadmium atoms is formed. Furthermore the same cluster seems to be at the origin of all different shaped nanocrystals (rod-shaped, rice-shaped, or branched). Thus, for a given temperature, the shape can be controlled by the monomer concentration in the solution, which in all cases of anisotropic growth has to be high compared to the growth of spherical particles.

The latest studies in the framework of the mixed inorganic/organometallic synthesis reveal a further similarity with cluster chemistry. For a long time the use of coordinating solvents such as TOPO or HDA was believed to be indispensable for a controlled nanocrystal growth. Now, like in cluster synthesis, the use of high boiling noncoordinating solvents (e.g., alkanes such as octadecene), in association with a controlled amount of ligands (phosphine oxides, phosphines, amines, carboxylic or phosphonic acids, etc.), provides a much wider approach to nanocrystal synthesis [77]. The latter allows not only the fine-tuning of nanocrystals sizes, size distributions, and shapes but also the transfer of the synthesis scheme to other types of semiconductors, such as InP, InAs [78], or PbSe [79, 80]. The listed advantages make the mixed inorganic/organometallic preparation method a very powerful tool for the design of new materials on the nanometer scale.

### 3.5. Synthesis of Core/Shell Systems

Among all core/shell systems CdSe/ZnS is the most studied case. The large bandgap of ZnS in combination with a favorable band alignment of CdSe and ZnS (see Section 2.2.4) yields core/shell nanocrystals with a significantly improved fluorescence QY with respect to the “bare” core crystals. The procedure for the shell growth is very similar to the organometallic nanocrystal preparation method (Section 3.3), with the use of diethylzinc and bistrimethylsilyl sulfide [37, 38]. Important differences are, however, the slow injection of these precursors in combination with relatively low reaction temperatures (150–210 °C). These measures are necessary in order to promote an epitaxial-type deposition of the shell material on the core crystals and to prevent nucleation of separate ZnS seeds. Furthermore, at higher temperatures Ostwald ripening of the core particles may occur, deteriorating their size distribution.

After the successful introduction of the mixed inorganic/organometallic preparation method to the synthesis of CdB(VI) core nanocrystals, it is a logic step to replace the pyrophoric dialkylzinc precursors, routinely used for the shell preparation, by safer reagents. However, the use of zinc phosphonates, in analogy to the inorganic/organometallic core synthesis, does not result in a successful ZnS shell growth because they exhibit too low reactivity toward the chalcogenide source in the cited temperature range. On the contrary, zinc stearate is an excellent zinc source in this context [39]. This easy to manipulate and commercially available compound reacts readily with both sulfur and selenium precursors to form CdSe/ZnS and CdSe/ZnSe core/shell nanocrystals or CdSe/ZnSe/ZnS core/double shell systems [81].

### 3.6. Size Sorting Procedures

With few exceptions, nanocrystal preparation techniques usually yield samples with a polydispersity significantly exceeding 5% (i.e., the level required for many specific applications of these nano-objects). In such cases postpreparative size-sorting procedures have to be used with the goal to isolate fractions of low polydispersity. The most prominent techniques are based on similar principles as widely applied in polymer technology, size-selective precipitation [50] or size exclusion chromatography [82]. The former method implies the destabilization of the colloidal nanocrystal dispersion by adding a nonsolvent, miscible with the original solvent. Thereby the repulsive force between the nanocrystals due to their capping groups is reduced and the largest ones tend to aggregate because they exhibit the strongest attractive *van der Waals* interactions. They can be separated by centrifugation or filtration from the smaller-size nanocrystals, which do not agglomerate and remain dispersed in the solvent/nonsolvent medium. Subsequent cycles of redispersion in an adapted solvent and partial flocculation of the largest nanocrystals provide quasi-monodisperse samples. The major disadvantage of this technique is its low yield: less than 30% of nanocrystals with a size dispersion of 5% are obtained from an initial sample with a size dispersion of 10% [3].

In the case of size exclusion chromatography (SEC) [82], the nanocrystal dispersion (mobile phase) flows through a column loaded with porous hydrophobic microgels, such as

cross-linked polystyrene (stationary phase). As the smaller crystals penetrate deeper into the pores than the larger ones, their retention time in the column is longer. More precisely, the elution time  $t_e$  of nanocrystals is in direct relationship with their radius  $r$  [83]:

$$t_e = k_1 + k_2 \lg r \quad (7)$$

Additionally, after calibration SEC can be used to determine the mean size and size dispersions of samples containing spherical particles. The technique is limited to nanocrystals, which are well passivated by a cap of nonpolar organic ligands because otherwise they risk being adsorbed permanently inside the column due to strong interactions with the microgel.

On the contrary, gel electrophoresis, another size sorting technique which has been used with the goal to lower the polydispersity of nanocrystals [84], requires charged particles and is well adapted for aqueous solutions. The nanocrystals move through a column filled with a polymer gel such as weakly cross-linked acrylamide, driven by an electrical field between both ends of the column. Particles with a high surface charge and small diameter move most quickly through the gel. After sufficient separation, the gel is cut into thin slices and the nanocrystal fractions in each slice are redissolved while gel residues are filtered off.

## 4. FUNCTIONALIZATION OF NANOCRYSTALS

Nanocrystals possess a very high surface/volume ratio, which increases strongly with decreasing radius. Individual crystals are prevented from agglomeration by means of an organic ligand cap on their surface. At the same time, these ligand molecules complete the coordination sphere of the nanocrystal surface atoms and thus reduce the number of dangling bonds, which cause fluorescence quenching. A large number of potential applications of nanocrystals require nonetheless a modification of this organic ligand cap, with the goal to make the colloids dispersible in various solvents and/or to graft them to other molecules of biological or electronic interest, to solid substrates, etc. By consequence, in recent years different approaches have been developed to perform nanocrystal surface chemistry. A widely applied method consists of the exchange of the organic molecules at the surface by bifunctional ligands X–S–Y [85–87]. Such ligands contain, on the one hand, a functional group X, which provides strong interaction with the metal ions on the nanocrystal surface and on the other hand a second chemical moiety Y, which allows the subsequent binding to molecules or substrates. Typical examples for X are thiol or phosphonic acid groups, whereas carboxyl, amine, or alcohol functions are representative for Y, to name a few. The selection of Y is of crucial importance, not only in view of nanocrystals grafting to given objects, but also for their dispersion in polar solvents and in particular in water, indispensable for biological applications. X and Y are usually separated by a spacer, S, of alkyl or aryl type.

Bifunctional ligands X–S–Y, in which Y is an ionizable group, can also facilitate the formation of a more or less ordered aggregation of nanocrystals with oppositely charged macromolecules via electrostatic interactions. A typical

example is the electrostatic self-assembly of carboxylic acid coated and thus negatively charged nanocrystals and a synthetically engineered, positively charged protein [88]. Since this protein enables the conjugation of biological molecules such as antibodies, highly stable and specific conjugates for immunoassays can be created using this method.

The main problem of the described functionalization methods is the fact that, in the majority of cases, the exchange of the original ligands results in a significant decrease of the fluorescence QY. This problem can be overcome by the use of a so-called “nanocrystal encapsulation method.” Hereby the initial optical properties of the nanocrystals can be essentially maintained, since it does not involve the exchange of the passivating ligands. The procedure will be described here for hydrophobic nanocrystals with TOPO and/or HDA ligands on their surface. The encapsulation is carried out in a three-component system consisting of water, oil, and an appropriate surfactant of amphiphilic nature. The surfactant molecules, being at the interface of the water continuous phase and the droplets of the oil, stabilize the formation of a microemulsion. If hydrophobic nanocrystals are introduced into this microemulsion, micellar-type system, they are placed in the hydrophobic environment (i.e., within the oil microdroplets). After the evaporation of both solvents, alkyl chains of the surfactant molecules “interdigitate” with the alkyl groups of the nanocrystal ligands, encapsulating in such a manner the nanocrystal, while the polar groups of the surfactant are directed on the outside of the encapsulated particle. An example of the successful application of this technique is the nanocrystal encapsulation by phospholipid micelles, enabling *in vivo* imaging experiments [89].

## 5. CONJUGATED POLYMER/NANOCRYSTAL COMPOSITE SYSTEMS

### 5.1. Introduction

Conjugated polymers (i.e., polymers with a spatially extended  $\pi$ -bonding system), although known for many years, did not draw significant research attention because they were intractable and, in many cases, unstable in ambient conditions. However, in the past two decades extensive and systematic research has been devoted to various aspects of the chemistry and physics of this previously underestimated family of macromolecular systems. It resulted in the preparation of stable, processible conjugated polymers offering unique physical properties which cannot be obtained for conventional polymers [90]. Both in their undoped (semiconducting) and doped (conducting) states, conjugated polymers can be used as components of so-called “plastic electronics.” In 2000 A. J. Heeger, A. G. MacDiarmid, and H. Shirakawa—the founders of “conjugated polymer science”—were granted the Nobel Prize in chemistry (Nobel Lectures, [91–93]).

Conjugated polymers in their neutral (undoped) state are materials, which combine electronic properties of intrinsic semiconductors with mechanical properties and solution processibility of macromolecular systems. Moreover they

frequently dissolve in the same solvents as the ones that are used to disperse A(II)B(VI) nanocrystals. Thus conjugated polymer/nanocrystal composite films can relatively easily be prepared by casting from a common solvent. Why are such composite materials of technological interest? First, the electronic properties of the two semiconductor constituents can be tuned individually and adapted to each other. In the case of the nanocrystal component of the composite, this can be done by size control (*vide supra*). The bandgap of the polymeric component can, in turn, controllably be altered by changing the chemical constitution of the conjugated backbone via copolymerization (random or block) and/or by appropriate functionalization with lateral groups exhibiting electron donating or electron withdrawing properties. Second, the interface area between the polymer phase and the nanocrystal one is very large due to the very high surface/volume ratio of the nanocrystals. This enables efficient electronic transport between these two components. Third, the conductivity of the polymeric phase can be varied via oxidative or acid–base doping. For this reason doped conjugated polymers are sometimes used in light emitting diodes as hole or electron transporting layers. They facilitate the charge injection into the emitting layer consisting of an undoped polymer and nanocrystals. Finally, the polymeric phase of the composite assures better mechanical properties of the system as compared to pure inorganic semiconductor materials.

For all aforementioned reasons composites of conjugated polymers and nanocrystals have been used in recent years as components of various electronic, optoelectronic, and sensing devices such as light emitting diodes, photovoltaic cells, electrochemical sensors, to name a few [94, 95].

Although conjugated polymer/nanocrystal composites should exhibit significant advantages over both all-organic materials and inorganic semiconductors, still considerable research efforts have to precede their industrial applications. The main difficulty is caused by the fact that several important properties of the composite, such as charge carrier mobility, electroluminescence, etc., are strongly dependent on even small changes in the polymer supramolecular structure and on the distribution of the nanocrystals within the polymer matrix, which are not easy to control.

In the method outlined previously for the preparation of composite materials, both constituents are synthesized individually and then mixed together using a solvent, which easily dissolves the polymer and disperses the colloidal nanocrystals. Alternatively one can synthesize nanocrystals within an already formed polymer matrix, for example by doping the polymer with nanocrystal precursors. However, the control of the nanocrystal size distribution is, in this case, extremely difficult. Thus, this method is used only for those applications in which monodispersity is not crucial, for example in the preparation of polymer supported heterogeneous catalysts.

### 5.2. Selected Properties of Conjugated Polymer/Nanocrystal Composites

Doped conjugated polymers frequently combine metallic-type conductivity with film forming properties of macromolecular systems. Some of them, like polyaniline



protonated with selected sulfonic acids, are solution processible [96, 97]. Thus doped polymers can provide simple electrical contacts to nanocrystals, which are easy to fabricate in a large variety of configurations.

The same arguments apply to the preparation of composites comprising undoped (semiconducting) conjugated polymers and A(II)B(VI) nanocrystals. It should be, however, noted here that in such composites two semiconductor phases of different properties coexist. At the polymer/nanocrystal interface the former acts as an electron donor and the latter as an electron acceptor due to its higher electron affinity (see Table 4). Thus in a typical conjugated polymer/A(II)B(VI) nanocrystal composite the polymer phase serves as the hole transporting medium and the nanocrystals as the electron transporting one. This property is very important in view of applications of polymer/nanocrystal composites for the fabrication of solar cells (see Section 5.3).

The polymer phase is usually continuous whereas the nanocrystals are dispersed, although some of them may form aggregates of different sizes. Such a picture implies that, if the electron transport is governed by the nanocrystal phase, it must be described in terms of percolation. In the simplest approach the percolation threshold is defined as the lowest volume fraction of the nanocrystal phase which assures an interconnected network of particles and by consequence the transport of the charge carriers on a macroscopic scale. This percolation threshold is strongly dependent on the so-called "aspect ratio" (i.e., the ratio of the longest dimension of the nanoparticle to the dimension perpendicular to it). With an increase of the aspect ratio, the value of the percolation threshold decreases. Thus, it is higher for globular-shaped nanocrystals (aspect ratio = 1) than for rod-shaped nanocrystals (aspect ratio  $\gg 1$ ). Finally, it should be stressed that nanocrystals are incorporated in the polymer matrix not as "bare" objects but together with a layer of (organic) capping ligands on their surface. This ligand layer impedes direct interconnectivity of the nanocrystals and can act as a barrier for the charge carrier transport between adjacent nanocrystals as well as for the charge separation at the polymer/nanocrystal interface. Therefore electrical transport

phenomena in the composite material must involve hopping between individual nanocrystals. In this perspective the chemical nature of the capping ligands is of crucial importance. The exchange of "classical" ligands such as TOPO or HDA, containing aliphatic substituents which act as isolating barriers, for "tailor made" ligands with functional groups facilitating charge transport is a challenging area of nanocrystal and polymer chemistry.

### 5.3. Conjugated Polymer/Nanocrystal Composites as New Materials for the Fabrication of Organic-Inorganic Solar Cells

At the beginning of this section it is instructive to briefly discuss the operation principle of photovoltaic cells and in particular of polymeric solar cells. Photovoltaic cells are devices which transform radiation energy originating from solar light into electricity. A polymeric solar cell, in its simplest version, consists of a layer of a semiconducting conjugated polymer, sandwiched between two electrodes of different work functions. One of them must be transparent and consists usually of ITO (indium tin oxide). Radiation induces the formation of excitons, which then undergo dissociation followed by the migration of the created positive and negative charges to the electrodes. However, in such a simple device the photoinduced charge generation, required for the operation of the cell, is extremely inefficient [101]. Semiconducting conjugated polymers are, in their large majority, good electron donors upon photoexcitation. If an electron-accepting molecule is available in close vicinity, the photoinduced charge generation is facilitated. First electron acceptors used together with conjugated polymers in "plastic" solar cells were fullerene ( $C_{60}$ ) molecules. One can imagine that a fullerene layer is introduced between the anode and the semiconducting polymer layer. This results in an increase of the efficiency of photoinduced charge generation at the polymer layer/fullerene layer interface [102]. Even further improvement of the conversion efficiency is achieved when the previously described bilayered heterostructure is replaced by a single composite layer consisting of  $C_{60}$  dispersed in a conjugated polymer matrix [103]. In this case the large interface area promotes the photoinduced charge generation. The formed charge carriers are then transported to the electrodes via the polymer phase (holes) or the fullerene phase (electrons), which percolates.

The same principle applies to solar cells in which, instead of fullerenes, A(II)B(VI) semiconductor nanocrystals are used as composite components, facilitating the dissociation of excitons [104]. This type of solar cell is schematically depicted in Figure 4.

As in "pure polymeric" solar cells, ITO is used as a transparent cathode, and aluminum, deposited by vacuum evaporation, as the anode. Additionally a hole transporting layer separates the ITO electrode and the polymer/nanocrystals composite with the goal to facilitate the transport of the charge carriers to the cathode. This additional layer consists of a molecular blend of poly(ethylene dioxythiophene) with poly(styrene sulfonic acid) (abbreviated as PEDOT:PSS), the latter serving as the dopant increasing electrical conductivity of PEDOT.

**Table 4.** Electron affinities and energy gaps of selected conjugated polymers and nanocrystals (see Appendix) [98–100].

Material	Electron affinity (eV)	Gap (eV)
Indium tin oxide	−4.7	0.0
CdS (2 nm)	−3.8	3.1
CdS (6 nm)	−4.5	2.6
CdSe (2 nm)	−4.0	2.6
CdSe (5 nm)	−4.7	2.0
MEH-PPV	−3.0	2.4
MDMO-PPV	−3.0	2.3
PANI-EB	−4.0	1.4
PANI-PB	−4.2	2.0
PANI-LEB	−0.5	3.8
PVK	−2.2	3.6
PPV	−2.6	2.5
PTPTB	−3.5	1.8
PEDOT-EHI-ITN	−4.0	0.5
PCBM	−4.1	0.0
Al	−4.3	0.0

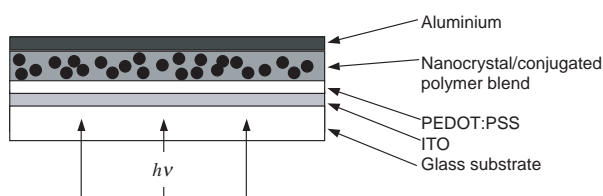


**Figure 4.** Schematic representation of a polymeric/nanocrystal solar cell.

The composite material used in [104] consists of 90 wt% CdSe nanorods (7 nm by 60 nm) in poly(3-hexylthiophene). The authors claim that (1D) nanorods are preferable to spherical (0D) nanocrystals as they exhibit improved electrical transport due to directed particle stacking as a result of the elevated aspect ratio. Very high mass fractions of nanorods in the composite material are necessary to facilitate the transport of electrons, which at low contents of nanorods occurs via inefficient hopping. As shown in earlier studies [98], the capping ligand TOPO, forming a 1.1 nm thick layer at the surface of CdSe nanocrystals, causes a significant decrease in the device efficiency, as it acts as a charge barrier. This problem can be overcome by using a pyridine/chloroform solvent mixture for the preparation of the polymer/nanocrystal composite [104]. Pyridine is known to easily displace TOPO molecules at the nanocrystal surface, acting itself as a weakly bound ligand subsequently.

The extent of photoluminescence quenching in the composite material characterizes the efficiency of the charge separation via exciton dissociation. Many literature examples report a weak remaining photoluminescence of the polymer and/or the nanocrystals, which may originate from a lowering of the polymer/nanocrystal interface area caused by the presence of isolated nanocrystal aggregates and zones significantly enriched in polymer. In this context two types of materials can be distinguished: first, composites in which the conjugated polymer absorbs solar light and excitons can be created in both the nanocrystals and in the polymer matrix; second, composites in which the conjugated polymer does not absorb in the visible spectrum and photoexcitation exclusively takes place in the nanocrystals. In the former, which is the more common case, different photophysical processes are possible [98]:

- (i) absorption and exciton formation in the polymer, followed by electron transfer onto the nanocrystal
- (ii) absorption and exciton formation in the polymer, followed by exciton transfer onto the nanocrystal and subsequent hole transfer onto the polymer
- (iii) absorption and exciton formation in the nanocrystal, followed by hole transfer onto the polymer
- (iv) absorption and exciton formation in the nanocrystal, followed by exciton transfer onto the polymer and subsequent electron transfer onto the nanocrystal

For a given composite material process (ii) excludes process (iv) and vice versa because such *Förster*-type exciton transfer occurs solely from the larger to the lower bandgap component. Further insight into the photophysical properties of a device can be provided by photoconductivity measurements revealing the spectral response of the photocurrent. Hereby the short-circuit current is measured as a function of the

wavelength of the incident light. Obviously the spectral response depends strongly on the absorption spectrum of the composite material. To a first approximation, such a spectrum consists of the sum of the absorption spectra of the conjugated polymer and of the nanocrystals. For the former, the position of the absorption bands depends strongly on the chemical structure, whereas for the latter the absorption threshold depends on size (see Section 2.2.1). Therefore the spectral response can be improved by using CdSe nanocrystals with large diameters, since they absorb the largest part of the visible spectrum. Further improvement toward absorption of solar light in the near infrared region can be achieved by applying either smaller bandgap semiconductor nanocrystals or polymers which absorb in this area. An important parameter is the short-circuit quantum efficiency which represents the numbers of electrons generated per photon. It can be used to determine the optimum content of nanocrystals for a given polymer/nanocrystal couple and solar cell configuration. Although in the majority of cases the charge separation is very efficient, the overall efficiency values may be significantly lower than unity because of problems with charge transport to the electrodes. More precisely, electrons are trapped within the (imperfect) nanocrystal network, in so-called “dead ends,” from which they cannot reach the electrode and recombine instead with holes in the surrounding polymer. This mechanism is consistent with an observed linear dependence of the photocurrent at low intensities. Transmission electron microscopy studies of the composite thin films reveal polymer rich zones separated from nanocrystals [98, 104]. In general, structural and morphological properties of the composites are strongly influenced by the type of the conjugated polymer, nanocrystal form, size, content, type of surface ligands, solvents used, and last but not least the film preparation conditions. As a consequence, it is very difficult to optimize a system and at present the control of the composite morphology is the most important drawback for conjugated polymer/nanocrystal composite devices.

From a technological point of view, conjugated polymer/nanocrystal composite systems offer rather facile processing steps for the fabrication of solar cells, which are in addition not very energy consuming. However, the values of the energy conversion efficiency of these devices are still significantly lower, not only with respect to those reported for crystalline silicon based solar cells, but also in comparison to cells fabricated from amorphous silicon [105]. Given the large number of different parameters which characterize the performance of photovoltaic cells, it is sometimes difficult to compare literature values. To eliminate this problem, all data given in the following represent energy conversion efficiencies under air mass (AM) 1.5 conditions (typical solar spectrum, 100 mW/cm<sup>2</sup>) according to the relationships [4]

$$\text{energy conversion efficiency} \quad \eta = I_{SC} U_{OC} FF / P \quad (8)$$

$$\text{fill factor} \quad FF = I_M U_M / (I_{SC} U_{OC}) \quad (9)$$

where  $I_{SC}$  is the short circuit current and  $U_{OC}$  the open circuit voltage of the cell.  $I_M$ ,  $U_M$  are the current and voltage, which provide maximum power output of the cell and  $P$  stands for the integral radiation power per device surface area.

In Table 5 the energy conversion efficiencies of devices based on conjugated polymer/nanocrystal composites are compared to a number of “all-inorganic” and “all-organic” solar cells. This list is nonexhaustive and serves rather as an illustration of technological trends in solar cell technology. Thermodynamic calculations show that, if one assumes an ideal behavior, there exist a “limit” energy conversion efficiency of ca. 30% and an optimum value for the energy gap of the light absorbing material. The latter accounts for ca. 1.5 eV, a value for which the maximum of energy can be transferred from the incident sunlight to excitons [106]. As can be clearly seen from the data in Table 5, “classical” silicon based devices possess the highest performances approaching the limit value. Furthermore they exhibit an excellent long-term stability versus aging processes such as photocorrosion. The latter parameter is of crucial importance for large-scale terrestrial applications. Nevertheless the high production costs of large-size crystalline silicon devices makes research on substitute materials indispensable.

Recent progress on photovoltaic devices based on conjugated polymer/nanocrystal composites [104] resulted in the fabrication of solar cells with conversion efficiencies reaching the same range as reported for “plastic” solar cells with fullerene admixtures, such as MEH-PPV/C<sub>60</sub> [103].

Taking into account the relatively short time since their discovery and their easy fabrication as compared to crystalline silicon based devices, this research direction seems very promising. Still significant effort must be put into improving their efficiency and long term stability.

#### 5.4. Light Emitting Diodes Made of Conjugated Polymers and Nanocrystals

A light emitting diode (LED) is an electronic device which exploits the phenomenon of electroluminescence. In an elementary manner, electroluminescence can be defined as light generation caused by electrical excitation. In this

**Table 5.** Energy conversion efficiencies reported for photovoltaic devices of various types.

Material	$\eta$ (AM 1.5)	Ref.
Crystalline silicon	24.4% (12–16%)	[107]
Polycrystalline silicon	18% (9–12%)	[108]
Amorphous silicon	13% (4–8%)	[105]
Dye-sensitized mesoporous TiO <sub>2</sub> /redox couple in liquid electrolyte	10–11%	[109]
Dye-sensitized mesoporous TiO <sub>2</sub> /OMeTAD (solid state)	2.6%	[110]
MEH-PPV/C <sub>60</sub>	1.4%	[103]
MDMO-PPV/PCBM	2.5%	[111]
MEH-PPV/CdSe nanocrystals	0.2%	[98]
P3HT/CdSe nanorods	1.7%	[104]

*Note:* In addition to the highest reported value, the numbers in brackets indicate typical values observed for the corresponding device type (see the Appendix).

respect LEDs can be considered as inverse to photovoltaic cells. The simplest version of a LED consists of a single layer of a semiconducting electroluminescent material, sandwiched between two electrodes. Similar to the case of photovoltaic cells, one of the electrodes must be transparent to transmit the light created through electroluminescence. Such a one-layer/two-electrode device is called an electroluminescent diode because it shows  $I$ – $V$  characteristics typical of diodes. This means that up to a given voltage no current flows and, above this onset voltage, the current quickly increases with increasing voltage. If the quantum efficiency for electroluminescence is constant, the luminance–voltage characteristics follow the current–voltage characteristics. The operation of a single-layer device can be described as follows. Opposite charge carriers (holes and electrons) are injected into the semiconductor layer from the anode and cathode, respectively. The injected charges may form either singlet or triplet excitons, while only the former decay radiatively to give out light. In more advanced structures, additional layers, which lower the barriers for hole and electron injection are used, the so-called “hole transporting layer” and “electron transporting layer.” In the past 12 years impressive progress has been achieved in the fabrication of conjugated polymer LEDs, with lifetimes exceeding several thousands of hours and external efficiencies  $\eta_{\text{ext}}$  as high as 20% [112, 113].

An alternative way to fabricate LEDs is the use of an emissive layer made of nanocrystals. However, to date the reported efficiencies of such devices are far below those of presently developed polymeric LEDs, with the highest value being  $\eta_{\text{ext}} = 0.52\%$  [114]. So why is it still interesting to perform research on conjugated polymer/nanocrystal LEDs? The principal reason is that semiconductor nanocrystals of low polydispersity show emissive properties unmatched by any class of polymeric chromophores. Typical electroluminescence linewidths of nanocrystals are as low as ca. 30 nm (FWHM) whereas emissive lines of conjugated polymers are much broader and frequently perturbed by the vibrational structure [113]. One may expect that conjugated polymer/nanocrystal composites may combine the efficiencies of polymeric LEDs with the color purity of semiconductor nanocrystals. In reality this is only possible when an efficient energy transfer from the polymer host to the nanocrystal occurs, resulting in electroluminescence essentially from the nanocrystals. However, the optimization of a LED with an emissive layer consisting of a conjugated polymer/nanocrystal composite is a difficult task. First, an appropriate core/shell system has to be selected, which efficiently shields the created excitons localized in the core from non-radiative relaxation induced by interactions with the polymer host. Simultaneously the energy transfer from the polymer host to the nanocrystals must be possible either through charge transfer or through neutral-excitation energy transfer via Förster or Dexter mechanisms [115]. An advantage of conjugated polymer/nanocrystal LEDs is the precise tunability of their emission color. This can be done throughout the whole visible range of the spectrum in the case of CdSe core nanocrystals. By using a semiconductor with a different bandgap, the flexibility can even be further extended to other spectral regions, for which no appropriate polymeric emitters exist. To give an example, when

InAs/ZnSe core/shell nanocrystals are applied, a conjugated polymer/nanocrystal LED emitting in the near infrared can be realized [116]. Moreover, by mixing polymers with fractions of nanocrystals differing in size one can produce LEDs emitting white light.

Similar to the case of photovoltaic cells [102, 103], two device architectures are possible:

- (i) The nanocrystals and the conjugated polymer form a bilayer structure.
- (ii) The nanocrystals are dispersed in the conjugated polymer.

The latter facilitates energy transfer between the polymer and the nanocrystals; however, it also increases the possibility of different nonradiative relaxation pathways (vide supra).

Composites of semiconductor nanocrystals with conventional polymers, which do not show semiconducting properties, have been used in the fabrication of tuneable “nanocrystal–polymer down-conversion LEDs” [117]. The principle of these devices, based on CdSe/ZnS core/shell nanocrystals, can be outlined as follows. Due to their absorption threshold in the visible part of the spectrum, different sized nanocrystals can be excited simultaneously by a single, shorter wavelength light source. Therefore, if the light of a blue emitting diode passes through a nanocrystal–transparent polymer composite, it is absorbed and re-emitted in a color depending on the size of the nanocrystals (see Fig. 5). By controlling the ratio of different sized nanocrystals one can precisely tune the color of the re-emission.

Of course, the polymer matrix must fulfill several conditions. First, nanocrystals dispersed in the polymer should retain their original emission efficiency to the largest possible extent. Second, the matrix must be amorphous to assure optical transparency. Third, nanocrystals should be homogeneously dispersed in the matrix since their aggregation not only lowers the transparency of the composite but also results in some luminescence quenching. Poly(alkyl methacrylates) with long and branched alkyl substituents, for example poly(lauryl methacrylates), respond to these requirements. The composite can be obtained by radical polymerization of the corresponding monomer (lauryl methacrylate) in the presence of ethyleneglycol dimethacrylate as the cross-linking agent and CdSe/ZnS core/shell nanocrystals [117]. Thereby composites exhibiting good optical quality and low luminescence quenching can be fabricated.

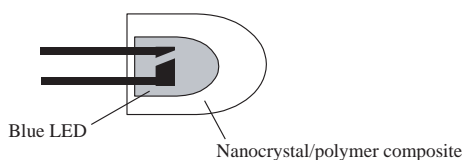


**Figure 5.** Scheme of a nanocrystal/polymer down-conversion LED.

## 6. HYBRID ORGANIC/INORGANIC SYSTEMS

The composite materials described in Section 5 are sometimes referred to as “hybrid systems” in the literature, despite the fact that they are simple physical mixtures of conjugated polymers and nanocrystals of different degrees of dispersion. Thus, from a chemist’s standpoint this is not totally correct since the term “hybrid system” or “hybrid molecule” is reserved to a chemical species consisting of at least two entities of different origin (for example, inorganic and organic), which are linked together by chemical bonds. One can easily imagine several types of true polyconjugated molecules/nanocrystal hybrid systems. This is an emerging area of research and to the best of our knowledge the only true hybrid system reported to date is penta(alkylthiophene) phosphonic acid, grafted on CdSe nanocrystals [118].

The synthesis of this hybrid material, consisting of conjugated oligomer/nanocrystal adducts, is very promising, since phase separation phenomena are less pronounced in this case as compared to the physical mixture of both constituents. Moreover, even relatively short conjugated oligomers usually well mimic the majority of physical properties of their corresponding polymers. If for the grafting reaction linear oligomers with two reactive functional groups were used, a three-dimensional network of nanocrystals linked by conjugated spacers could be created.

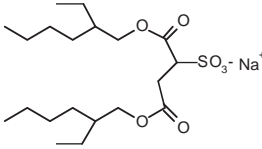
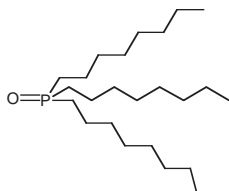
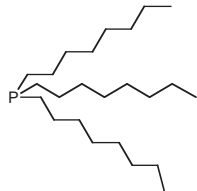
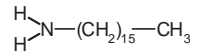
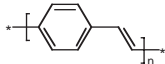
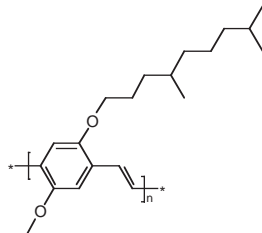
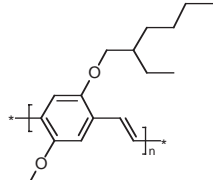
Among other potential approaches leading to conjugated macromolecule/nanocrystal hybrid compounds of different topology, one seems especially interesting. It involves the synthesis of comb-shaped polymers in which the pending groups, attached to the conjugated backbone, bind to nanocrystals. This idea is closely related to the fabrication of so-called “double-cable polymers,” which has recently been developed in connection with the fabrication of polymeric photovoltaic cells of the newest generation [111]. In a double-cable system side groups being good electron acceptors are attached to a conjugated polymer, which is in turn a good electron donor. This can be exemplified by grafting functionalized fullerenes such as PCBM to conjugated polymers [111]. The term “double cable” points out the ability of this true hybrid system to transport simultaneously electrons and holes to the corresponding electrodes. In principle, double-cable polymers containing nanocrystals as pending groups are very promising candidates for the fabrication of photovoltaic cells, especially in view of the fact that even simple physical mixtures of nanocrystals and conjugated polymers yield devices with remarkable efficiencies (see Section 5.3).

Although the research on true conjugated polymer/nanocrystal hybrids is just in the beginning stages, several advantages of these systems with respect to the corresponding composite materials can already be pointed out. First, the separation of charge is facilitated in this case, since both the electron donor and the electron acceptor are inherent parts of the same chemical entity and for this reason no interface, in the classical sense of the term, exists between them. Furthermore, the chemical bonding between the organic and inorganic components eliminates or

at least strongly impedes phase segregation in solid films of hybrid materials. The latter is the principal problem of polymer/nanocrystal composites, showing frequently the coexistence of polymer rich and nanocrystal rich zones. As a result, in true hybrid materials, electron transport to the electrode can occur in a more efficient way, as “dead ends” in the nanocrystal network are suppressed. Generally conjugated polymer/nanocrystal hybrids provide better control of the

material morphology with the possibility to build up really interpenetrating organic/inorganic networks. Finally, from a synthetic point of view, hybrid systems facilitate the preparation of high-quality thin films by casting from solution. This is an advantage over composite materials because for the latter it is sometimes difficult to find a cosolvent, which enables the simultaneous dissolution of the polymer and the colloidal dispersion of the nanocrystals.

## APPENDIX: CHEMICAL STRUCTURES

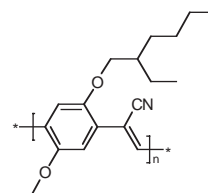
Na(AOT)	Bis(2-ethylhexyl)sulfosuccinate	
TOPO	Trioctylphosphine oxide	
TOP	Trioctylphosphine	
HDA	Hexadecylamine	
PPV	Poly( <i>p</i> -phenylene)vinylene)	
MDMO-PPV	Poly-(2-methoxy-5-(3,7-dimethyloctyloxy)- <i>p</i> -phenylene)vinylene)	
MEH-PPV	Poly-(2-methoxy-5-(2'-ethylhexyloxy)- <i>p</i> -phenylene)vinylene)	

continued

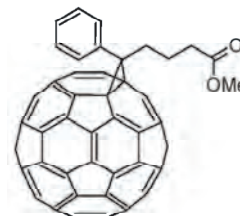
## Appendix. Continued

CN-PPV

Cyano-PPV



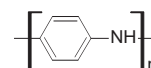
PCBM

{6,6}-Phenyl C<sub>61</sub> butyric acid methyl ester

Polyanilines

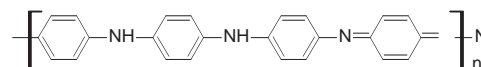
PANI-LEB

Leucoemeraldine base



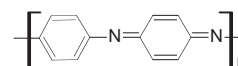
PANI-EB

Emeraldine base



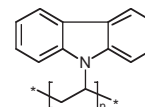
PANI-PB

Pernigraniline base



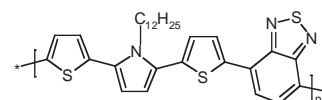
PVK

Poly-N-vinylcarbazole



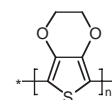
PTPTB

Poly(N-dodecyl-2,5-bis(2'-thienyl)pyrrole-2,1,3-benzothiadiazole)



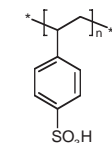
PEDOT

Poly(ethylene dioxythiophene)



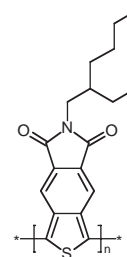
PSS

Polystyrene sulfonic acid



PEDOT-EHI-ITN

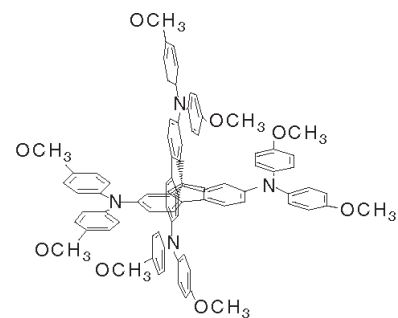
Poly(benzo[c]thiophene-N-2'-ethylhexyl-4,5-dicarboxylic imide)



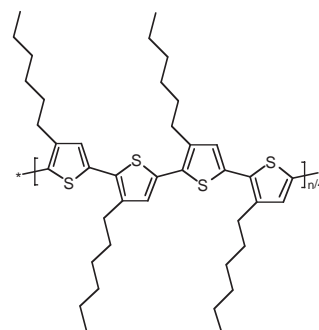
continued



## Appendix. Continued

OMeTAD 2,2',7,7'-Tetrakis(*N,N*-di-*p*-methoxyphenyl-amine)9,9'-spirobifluorene

P3HT Poly(3-hexylthiophene)



## ACKNOWLEDGMENTS

The authors thank Joël Bleuse and Bernard Metz for critical review of the manuscript.

## REFERENCES

- H. Weller, *Angew. Chem. Int. Ed. Engl.* 32, 41 (1993).
- A. P. Alivisatos, *J. Phys. Chem.* 100, 13226 (1996).
- C. B. Murray, C. R. Kagan, and M. G. Bawendi, *Annu. Rev. Mater. Sci.* 30, 545 (2000).
- D. Y. Godovsky, *Adv. Polym. Sci.* 153, 163 (2000).
- A. D. Pomogailo, *Russ. Chem. Rev.* 69, 53 (2000).
- L. E. Brus, *J. Chem. Phys.* 80, 4403 (1984).
- "Physics of II-VI and I-VII Compounds" (O. Madelung, Ed.), Landolt-Börnstein series, Crystal and Solid State Physics, Vol. 17b. Springer-Verlag, Berlin, 1982.
- M. G. Bawendi, M. L. Steigerwald, and L. E. Brus, *Annu. Rev. Phys. Chem.* 41, 477 (1990).
- A. L. Efros, M. Rosen, M. Kuno, M. Nirmal, D. J. Norris, and M. G. Bawendi, *Phys. Rev. B* 54, 4843 (1996).
- V. N. Soloviev, A. Eichhöfer, D. Fenske, and U. Banin, *J. Am. Chem. Soc.* 123, 2354 (2001).
- S. Behrens, M. Bettenhausen, A. C. Deveson, A. Eichhöfer, D. Fenske, A. Lohde, and U. Woggon, *Angew. Chem. Int. Ed. Engl.* 35, 2215 (1996).
- S. Behrens, M. Bettenhausen, A. Eichhöfer, and D. Fenske, *Angew. Chem.* 24, 2797 (1997).
- N. Herron, J. C. Calabress, W. E. Farneth, and Y. Wang, *Science* 259, 1426 (1993).
- T. Vossmeier, G. Reck, B. Schulz, E. T. K. Haupt, and H. Weller, *Science* 267, 1477 (1995).
- K. Eichkorn and R. Ahlrichs, *Chem. Phys. Lett.* 288, 235 (1998).
- P. Deglmann, R. Ahlrichs, and K. Tsereteli, *J. Chem. Phys.* 116, 1585 (2002).
- S. V. Gaponenko, "Optical Properties of Semiconductor Nanocrystals." Cambridge Univ. Press, Cambridge, UK, 1998.
- U. Woggon, "Optical Properties of Semiconductor Quantum Dots." Springer-Verlag, Berlin, 1997.
- D. J. Norris, A. Sacra, C. B. Murray, and M. G. Bawendi, *Phys. Rev. Lett.* 72, 2612 (1994).
- F. V. Mikulec, M. Kuno, M. Bennati, D. A. Hall, R. G. Griffin, and M. G. Bawendi, *J. Am. Chem. Soc.* 122, 2532 (2000).
- A. I. Ekimov, F. Hache, M. C. Schanne-Klein, D. Ricard, A. V. Rodina, I. A. Kudryavtsev, T. V. Yazeva, and A. L. Efros, *J. Opt. Soc. Am. B* 10, 101 (1993).
- M. Nirmal, D. J. Norris, and M. Kuno, *Phys. Rev. Lett.* 75, 3728 (1995).
- M. D. Mason, G. M. Credo, K. D. Weston, and S. K. Buratto, *Phys. Rev. Lett.* 80, 5405 (1998).
- M.-E. Pistol, P. Castrillo, D. Hessman, J. A. Prieto, and L. Samuelson, *Phys. Rev. B* 59, 10725 (1999).
- D. Vanden Bout, W. T. Yip, D. Hu, D. K. Fu, T. M. Swager, and P. F. Barbara, *Science* 277, 1074 (1997).
- X. S. Xie and J. K. Trautman, *Annu. Rev. Phys. Chem.* 49, 441 (1998).
- R. M. Dickson, A. B. Cubitt, R. Y. Tsien, and W. E. Moerner, *Nature* 388, 355 (1997).
- M. Nirmal, B. O. Dabbousi, M. G. Bawendi, J. J. Macklin, J. K. Trautman, T. D. Harris, and L. E. Brus, *Nature* 383, 802 (1996).
- A. L. Efros and M. Rosen, *Phys. Rev. Lett.* 78, 1110 (1997).
- M. Kuno, D. P. Fromm, H. F. Hamann, A. Gallagher, and D. J. Nesbitt, *J. Chem. Phys.* 112, 3117 (2000).
- R. G. Neuhauser, K. T. Shimizu, W. K. Woo, S. A. Empedocles, and M. G. Bawendi, *Phys. Rev. Lett.* 85, 3301 (2000).
- S. Empedocles and M. G. Bawendi, *Acc. Chem. Res.* 32, 389 (1999).
- D. I. Chepic, A. L. Efros, A. I. Ekimov, M. G. Vanov, V. A. Kharchenko, I. A. Kudryavtsev, and T. V. Yazeva, *J. Lumin.* 47, 113 (1990).
- D. Talapin, A. L. Rogach, A. Kornowski, M. Haase, and H. Weller, *Nano Lett.* 1, 207 (2001).

35. S.-H. Wei and A. Zunger, *Appl. Phys. Lett.* 72, 2011 (1998).
36. X. Peng, M. C. Schlamp, A. V. Kadavanich, and A. P. Alivisatos, *J. Am. Chem. Soc.* 119, 7019 (1997).
37. P. Guyot-Sionnest and M. A. Hines, *J. Phys. Chem.* 100, 468 (1996).
38. O. Daboussi, J. Rodriguez-Viejo, F. V. Mikulec, J. R. Heine, H. Mattoussi, R. Ober, K. F. Jensen, and M. G. Bawendi, *J. Phys. Chem.* 101, 9463 (1997).
39. P. Reiss, J. Bleuse, and A. Pron, *Nano Lett.* 2, 781 (2002).
40. M. A. Kastner, *Phys. Today* 46, 24 (1993).
41. R. S. Ingram, M. J. Hostetler, R. W. Murray, T. G. Schaaff, J. Khoury, R. L. Whetten, T. P. Bigioni, D. K. Guthrie, and P. N. First, *J. Am. Chem. Soc.* 119, 9279 (1997).
42. R. P. Andres, T. Bein, M. Dorogi, S. Feng, J. I. Henderson, C. P. Kubiak, W. Mahoney, R. G. Osifchin, and R. Reifengerger, *Science* 272, 1323 (1996).
43. U. Banin, Y. Cao, D. Katz, and O. Millo, *Nature* 400, 542 (1999).
44. O. Millo, D. Katz, Y. Cao, and U. Banin, *Phys. Rev. Lett.* 86, 5751 (2001).
45. E. P. A. M. Bakkers, Z. Hens, A. Zunger, A. Franceschetti, L. P. Kouwenhoven, L. Gurevich, and D. Vanmaekelbergh, *Nano Lett.* 1, 551 (2001).
46. K. Sooklal, B. S. Cullum, S. M. Angel, and C. J. Murphy, *J. Phys. Chem.* 100, 4551 (1996).
47. M. Hines and P. Guyot-Sionnest, *J. Phys. Chem. B* 102, 3655 (1998).
48. F. T. Quinlan, J. Kuther, W. Tremel, W. Knoll, S. Risbud, and P. Stroeve, *Langmuir* 16, 4049 (2000).
49. M. Shim and P. Guyot-Sionnest, *J. Am. Chem. Soc.* 123, 11651 (2001).
50. C. B. Murray, D. J. Norris, and M. G. Bawendi, *J. Am. Chem. Soc.* 115, 8706 (1993).
51. Z. A. Peng and X. Peng, *J. Am. Chem. Soc.* 123, 183 (2001).
52. L. Qu, Z. A. Peng, and X. Peng, *Nano Lett.* 1, 333 (2001).
53. L. Spanhel, M. Haase, H. Weller, and A. Henglein, *J. Am. Chem. Soc.* 109, 5649 (1987).
54. P. Lianos and J. K. Thomas, *Chem. Phys. Lett.* 125, 299 (1986).
55. M. P. Pileni, *J. Phys. Chem.* 97, 6961 (1993).
56. M. L. Steigerwald, A. P. Alivisatos, J. M. Gibson, T. D. Harris, A. R. Kortan, A. J. Muller, A. M. Thayer, T. M. Duncan, D. C. Douglass, and L. E. Brus, *J. Am. Chem. Soc.* 110, 3046 (1988).
57. M. Gao, S. Kirstein, H. Möhwald, A. L. Rogach, A. Kornowski, A. Eychmüller, and H. Weller, *J. Phys. Chem. B* 102, 8360 (1998).
58. D. Ingert, N. Feltin, L. Levy, P. Gouzerh, and M. P. Pileni, *Adv. Mater.* 11, 220 (1999).
59. K. A. Higginson, M. Kuno, J. Bonevich, S. B. Qadri, M. Yousuf, and H. Mattoussi, *J. Phys. Chem. B* 106, 9982 (2002).
60. M. T. Harrison, S. V. Kershaw, M. G. Burt, A. L. Rogach, A. Kornowski, A. Eychmüller, and H. Weller, *Pure Appl. Chem.* 72, 295 (2000).
61. A. Fojtik, H. Weller, U. Koch, and A. Henglein, *Ber. Bunsenges. Phys. Chem.* 88, 969 (1984).
62. A. Henglein, *Ber. Bunsenges. Phys. Chem.* 86, 301 (1982).
63. R. S. Rossetti, S. Nakahara, and L. E. Brus, *J. Chem. Phys.* 79, 1086 (1983).
64. V. K. La Mer and R. H. Dinegar, *J. Am. Chem. Soc.* 72, 4847 (1950).
65. W. Ostwald, *Z. Phys. Chem.* 37, 385 (1901).
66. P. W. Voorhees, *J. Stat. Phys.* 38, 231 (1985).
67. T. Sugimoto, *Adv. Colloid Interfac.* 28, 65 (1987).
68. H. Reiss, *J. Chem. Phys.* 19, 482 (1951).
69. T. Sugimoto and F. Shiba, *J. Phys. Chem.* 103, 3607 (1999).
70. X. Peng, J. Wickham, and A. P. Alivisatos, *J. Am. Chem. Soc.* 120, 5343 (1998).
71. N. Gaponik, D. V. Talapin, A. L. Rogach, K. Hoppe, E. V. Shevchenko, A. Kornowski, A. Eychmüller, and H. Weller, *J. Phys. Chem. B* 106, 7177 (2002).
72. M. P. Pileni, *Langmuir* 13, 3266 (1997).
73. M. P. Pileni, T. Zemb, and C. Petit, *Chem. Phys. Lett.* 118, 414 (1985).
74. B. D. Summ and N. I. Ivanova, *Russ. Chem. Rev.* 69, 911 (2000).
75. Z. A. Peng and X. Peng, *J. Am. Chem. Soc.* 124, 3343 (2002).
76. I. G. Dance, A. Choy, and L. Scudder, *J. Am. Chem. Soc.* 106, 6285 (1984).
77. W. Yu and X. Peng, *Angew. Chem. Int. Ed. Engl.* 41, 2368 (2002).
78. D. Battaglia and X. Peng, *Nano Lett.* 2, 1027 (2002).
79. C. B. Murray, S. H. Sun, and W. Gaschler, *IBM J. Res. Dev.* 45, 47 (2001).
80. B. L. Wehrenberg, C. Wang, and P. Guyot-Sionnest, *J. Phys. Chem. B* 106, 10634 (2002).
81. P. Reiss, S. Carayon, J. Bleuse, and A. Pron, submitted for publication.
82. C. H. Fischer, H. Weller, L. Katsikas, and A. Henglein, *Langmuir* 5, 429 (1989).
83. H. Determann, "Gelchromatographie." Springer-Verlag, Berlin, 1967.
84. A. Eychmüller, L. Katsikas, and H. Weller, *Langmuir* 6, 1605 (1990).
85. H. Mattoussi, J. M. Mauro, E. R. Goldman, R. M. Green, G. P. Anderson, V. C. Sundar, and M. G. Bawendi, *J. Am. Chem. Soc.* 122, 12142 (2000).
86. W. C. W. Chan and S. Nie, *Science* 281, 2016 (1998).
87. S. Pathak, S. K. Choi, N. Arnheim, and M. E. Thompson, *J. Am. Chem. Soc.* 123, 4103 (2001).
88. J. K. Jaiswal, H. Mattoussi, J. M. Mauro, and S. M. Simon, *Nature Biotechnol.* 21, 47 (2002).
89. B. Dubertret, P. Skourides, D. J. Norris, V. Noireaux, A. H. Brivanlou, and A. Libchaber, *Science* 298, 1759 (2002).
90. A. Pron and P. Rannou, *Prog. Polym. Sci.* 27, 135 (2002).
91. H. Shirakawa, *Angew. Chem. Int. Ed. Engl.* 40, 2574 (2001).
92. A. G. MacDiarmid, *Angew. Chem. Int. Ed. Engl.* 40, 2581 (2001).
93. A. J. Heeger, *Angew. Chem. Int. Ed. Engl.* 40, 2591 (2001).
94. L. L. Beecroft and C. K. Ober, *Chem. Mater.* 9, 1302 (1997).
95. A. N. Shipway, E. Katz, and I. Willner, *Chem. Phys. Chem.* 1, 18 (2000).
96. P. N. Adams, P. Devasagayam, S. J. Pomfret, L. Abell, and A. Monkman, *J. Phys. Condens. Matter* 10, 8293 (1998).
97. E. J. Oh, K. S. Jang, and A. G. MacDiarmid, *Synth. Met.* 125, 267 (2002).
98. N. C. Greenham, X. Peng, and A. P. Alivisatos, *Phys. Rev. B* 54, 17628 (1996).
99. J. Libert, J. Cornil, D. A. dos Santos, and J. L. Bredas, *Phys. Rev. B* 56, 8638 (1997).
100. C. J. Brabec, N. S. Sariciftci, and J. C. Hummelen, *Adv. Funct. Mater.* 11, 15 (2001).
101. H. Antoniadis, B. R. Hsieh, M. A. Abkowitz, and S. A. Jenekhe, *Synth. Met.* 62, 265 (1994).
102. N. S. Sariciftci, D. Braun, C. Zhang, V. Srdanov, A. J. Heeger, G. Stucky, and F. Wudl, *Appl. Phys. Lett.* 62, 585 (1993).
103. G. Yu, J. Gao, J. C. Hummelen, F. Wudl, and A. J. Heeger, *Science* 270, 1789 (1995).
104. W. U. Huynh, J. J. Dittmer, and A. P. Alivisatos, *Science* 295, 2425 (2002).
105. J. Yang, A. Banerjee, and S. Cui, *Appl. Phys. Lett.* 70, 2975 (1997).
106. A. Shah, R. Platz, and H. Keppner, *Sol. Energy Mat. Sol. Cells* 38, 45 (1995).
107. J. Zhao, A. Wang, M. A. Green, and F. Ferrazza, *Appl. Phys. Lett.* 73, 1991 (1998).

108. S. Narayanan, S. R. Wenham, and M. A. Green, *Appl. Phys. Lett.* 48, 873 (1986).
109. M. K. Nazeeruddin, P. Pechy, T. Renouard, S. M. Zakeeruddin, R. Humphry-Baker, P. Comte, P. Liska, L. Cevey, E. Costa, V. Shklover, L. Spiccia, G. B. Deacon, C. A. Bignozzi, and M. Grätzel, *J. Am. Chem. Soc.* 123, 1613 (2001).
110. U. Bach, D. Lupo, P. Comte, J. E. Moser, F. Weissörtel, J. Salbeck, H. Spreitzer, and M. Grätzel, *Nature* 395, 583 (1998).
111. S. E. Shaheen, C. J. Brabec, N. S. Sariciftci, F. Padinger, T. Fromherz, and J. C. Hummelen, *Appl. Phys. Lett.* 78, 841 (2001).
112. C. Adachi, M. A. Baldo, M. E. Thompson, and S. R. Forrest, *J. Appl. Phys.* 90, 5048 (2001).
113. A. Kraft, A. C. Grimsdale, and A. B. Holmes, *Angew. Chem. Int. Ed. Engl.* 37, 402 (1998).
114. S. Coe, W. Woo, M. G. Bawendi, and V. Bulovic, *Nature* 420, 800 (2002).
115. M. A. Baldo, M. E. Thompson, and S. R. Forrest, *Nature* 403, 750 (2000).
116. N. Tessler, V. Medvedev, M. Kazes, S. Kann, and U. Banin, *Science* 295, 1506 (2002).
117. J. Lee, V. C. Sundar, J. R. Heine, M. G. Bawendi, and K. F. Jensen, *Adv. Mater.* 12, 1102 (2000).
118. D. J. Milliron, A. P. Alivisatos, C. Pitois, C. Edder, and J. M. Fréchet, *Adv. Mater.* 15, 58 (2003).

# Nanodeposition of Soft Materials

Seunghun Hong, Ling Huang

Florida State University, Tallahassee, Florida, USA

## CONTENTS

1. Introduction
  2. Dip-Pen Nanolithography
  3. Microcontact Printing
  4. Conclusions
- Glossary  
References

## 1. INTRODUCTION

### 1.1. History of Writing

*Direct deposition* is one of the oldest methods to create patterns on solid surfaces. The early Egyptians, Romans, Greeks, and Hebrews utilized *pens* to write on *papyrus and parchment paper*. One of the oldest pieces of writing on papyrus known to us today is the Egyptian “Prisse Papyrus” which dates back to 2000 B.C. The Romans used reed pens to write documents on paper [1]. Then quill pens appeared at about 700 A.D., and it became the main writing tool until 1800 A.D. Quill pens are made of birds’ feathers. When the ink-coated pen is in contact with paper, liquid ink flow is driven onto paper via *capillary flow*. After the development of advanced metallurgy during the industrial revolution, feathers were replaced by metallic nibs. However, the basic strategy of utilizing capillary flow has not changed.

One important event in the history of pens may be the invention of fountain pens. Working fountain pens were first invented by Lewis Edson Waterman in 1884 [2]. Before the invention of fountain pens, one had to dip the pen in the ink well frequently to write long documents. Waterman attached a small ink well as a part of the pen and modified the shape of the nib to achieve stable ink flow. It should be noted that the fountain pen was realized only after proper scientific understanding about liquid flow and technological advances to build small capillary tubes and ink wells.

The development of electronics and mechanics has automated modern *pen writing*. Current ink jet printers, with the help of microelectromechanical system technology, can now

deposit a picoliter volume of liquid ink with  $\sim 20 \mu\text{m}$  spatial resolution. However, modern automated pens still share remarkable similarities with their predecessors: *liquid ink* and *capillary flow*. In all conventional pen writing, *solid ink materials* are first mixed with *solvent* to prepare *liquid ink*, then liquid ink is deposited onto the surface via *capillary flow* or *small driving pressure on it*. After writing, the solvent molecules are vaporized leaving only solid ink patterns on the surface.

Another direct deposition strategy is the *stamping* method in which solid templates with built-in structures are utilized to deposit ink onto the substrate via direct contact. Stamping also has very long history. The “Phaistos disk” found on the island of Crete was produced by pressing relief-carved symbols into the soft clay in 1500 B.C. In 450 A.D., seals were printed with true ink, which was the first instance of actual printing with an incised stamp upon paper. The basic mechanism of the stamping method is quite different from that of pen writing. Unlike pen writing that relies on the *capillary flow* of liquid ink for deposition, the stamping is based on *direct contact between ink and paper*. Since the stamping method patterns the entire surface simultaneously in a parallel manner, it is inherently a faster method than pen writing. However, once the template is made, it is very difficult to change its pattern shape. For these reasons, stamping is suitable for producing multiple copies of identical patterns, while pen writing has been extensively utilized to generate a small amount of arbitrary shape patterns very quickly.

### 1.2. Microfabrication

One of the key technologies that enable modern microelectronics and information technology is the micrometer scale photographic patterning method, *photolithography*. Figure 1 shows the basic steps of the photolithography technique. In this process, solid surfaces are first coated with a polymer resist layer, and then a specific region on the resist layer is exposed to the ultraviolet light through a photographic mask. The exposure of light breaks (or strengthens) the molecular bonding in the polymer resist layer. The exposed (or unexposed) resist layer is specifically removed by immersing the substrate into certain solvents, and the

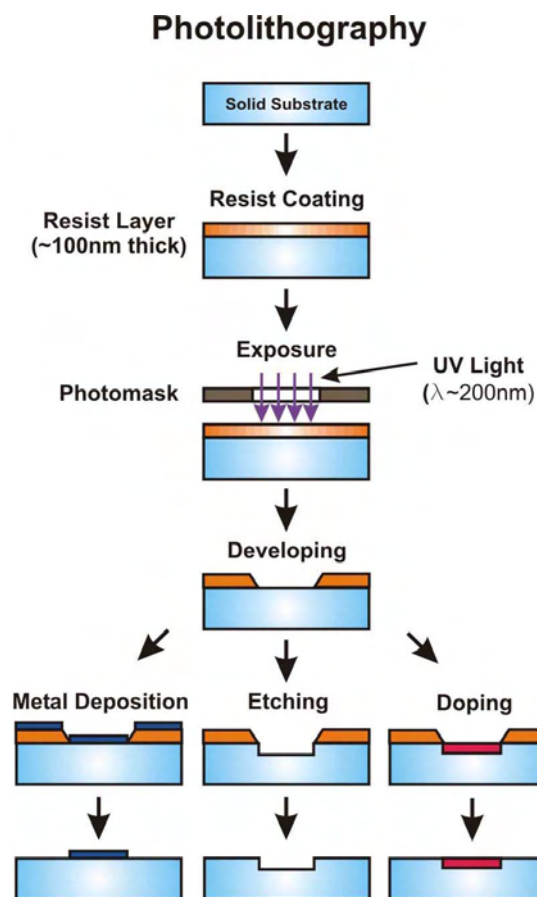


**Figure 1.** Schematic diagram depicting the basic steps of photolithography.

polymer resist patterns were left on the specific area of the substrate. The polymer resist pattern can be used as a resist of subsequent etching or other processing steps. By repeating these processes, many complicated microelectronic components can be created on a single substrate, which enables integrated computer chips and, eventually, modern information technology.

During the last four decades, the semiconductor industry has been extensively working on improving the resolution of photolithography method so that more components can be integrated in a single chip. This size reduction and higher degree of integration are crucial to improve the performance and power efficiency of the integrated circuits, which can effectively reduce the manufacturing cost. Currently, microelectronic chips with feature sizes as small as 90 nm are commercially available.

There are two major parameters determining the ultimate resolution of the photolithography method: (1) wavelength of light and (2) thickness of the resist layer. The resolution of the photolithography method is subject to the limitation set by optical diffraction according to the Rayleigh equation [3],

$$R = k_1 \lambda / NA$$

where  $\lambda$  is the wavelength of the light used,  $NA$  is the numerical aperture of the lens system, and  $k_1$  is a constant

that depends on the photoresist. It is usually believed that resolution of the photolithography is approximately  $\lambda/2$ . Extensive efforts have been given to use shorter wavelength light to improve the resolution. Ultraviolet light with a wavelength of  $\sim 160$  nm has been employed to fabricate  $\sim 90$  nm commercial chips. However, it is increasingly difficult to find a proper optics component for shorter wavelength light.

On the other hand, the minimum feature size is also affected by the thickness of the resist layer. It is due to the unpredictable *slope* at the edge of the photoresist patterns as shown in Figure 1. High-resolution lithography resist layers are usually thinner than 100 nm.

Considering these two parameters, the resolution limit of the photolithography technique is believed to be around  $\sim 100$  nm. Extensive efforts have been given to develop a next generation lithographic technique that can overcome the resolution limit of photolithography and continue to decrease the size of electronic chips. Possible candidates include X-ray lithography, e-beam projectors, scanning probe-based lithography, and soft lithography [4]. These methods demonstrated lithography resolution down to 10 nm. However, it is not yet clear which method will eventually replace the photolithography technique. Modern nanodeposition methods such as dip-pen nanolithography or microcontact printing also have been extensively developed as a possible candidate to replace photolithography. Since the direct deposition strategy does not rely on light, the resolution is not limited by the wavelength of the light.

### 1.3. Hybrid Devices

On the other hand, we can find another important motivation for the development of nanodeposition methods in soft material-patterning applications. Recent dramatic development of nanotechnology and biological science provide us *new nanometer scale building blocks* for functional devices (Fig. 2). By combining these new materials with conventional solid-state devices, one should be able to build

Nanostructures	Diagram	Possible Applications
<b>Protein Motors</b>		Nano-mechanical System
<b>DNA</b>		Information Storage, Highly Selective Molecular Glue
<b>Nanotube</b>		Nanowires, Chemical Sensor
<b>Clusters</b>		Quantum dots
<b>Conjugated Molecules</b>		Nanowires
<b>D-σ-A</b>		Diode

**Figure 2.** New nanostructures and their possible applications.



a generation of new functional devices. These include biological sensors [85–89] to detect harmful viruses and protein motor-based nanomechanical systems [90]. These new generation devices can be termed as *hybrid devices* because they are comprised of *organic materials* as well as *solid-state nanostructures*. These hybrid devices are expected to flourish for the next few decades because there is a huge demand for new functional devices, especially for medical and biological applications.

One significant difference between hybrid devices and conventional solid-state electronics is the mode of fabrication. Since with hybrid devices most of the molecular functional units are first synthesized under *solution* or *vapor* conditions, additional *nanometer scale assembly steps* are required to fabricate such structures. In contrast, the functional components (e.g., transistors, resist) of conventional solid-state devices are directly fabricated by modifying the solid substrate. Conventional microfabrication techniques such as photolithography cannot be used for fabricating molecule-based structures because of the complex chemical reactivity of most of the molecular units.

The nanoscale direct deposition strategy seems to be an ideal method because it can deposit general organic materials directly onto solid surfaces without any complicated processing steps. Nanodeposition methods have been extensively utilized to pattern chemical and biological molecules on solid substrates in a nanometer scale resolution.

#### 1.4. Modern Nanodeposition

As a possible solution to solve the *resolution* problem in the semiconductor industry and the *compatibility* issue in soft materials-based applications, two new direct deposition methods have been drawing attention: (1) dip-pen nanolithography (DPN) and (2) microcontact printing. DPN utilizes an atomic force microscopy (AFM) tip as a nanoscale pen to deposit organic molecular substances onto solid substrates, and its basic idea is similar to that of its macroscale counterpart—the quill pen. The microcontact printing method utilizes micro- and submicrometer scale stamps to print general organic molecules on solid surfaces. Despite their similarities with conventional direct deposition methods, these state-of-the-art nano-deposition methods differentiate themselves from macroscale deposition methods in several aspects: (1) nanoscale resolution and (2) generality in chemical and biological molecular ink.

In the following sections, we will provide a comparative overview of these two nanoscale direct deposition methods. Furthermore, we will try to answer several in-depth questions regarding nanodeposition processes: (1) What are the key scientific aspects which enable the *nanoscale resolution deposition* of general organic molecules? (2) What are the possible future impacts of this new lithographic technology in everyday human life?

## 2. DIP-PEN NANOLITHOGRAPHY

### 2.1. Key Strategy

The DPN process is a new direct deposition technique that was first developed in Mirkin's lab at Northwestern University in 1998 [6–10]. It utilizes an (AFM) tip as a *nanoscale*

*pen*, molecular substances as ink, and solid substrates as *paper*. Figure 3(a) shows the basic mechanism of DPN as well as approximate dimensions of commonly used pen and ink molecules. When the molecule-coated tip is in contact with the substrate, molecules *diffuse* out onto the substrate, *chemically anchor* to the surface, and form well-ordered *self-assembled monolayer* (SAM) patterns. Under ambient conditions, water condenses at the AFM tip/substrate junction and affects the molecular diffusion. Like macroscale quill pens, the molecular ink coating on the tip surface works as an ink reservoir. A number of variables including relative humidity, temperature, and the tip movement speed can be adjusted to control the ink transport rate, feature size, and linewidth.

Figure 3(b) shows an example patterns generated via DPN. With the help of automated lithography software, one can directly print out organic molecular patterns from the PC onto solid substrates like ink-jet printers print graphics on paper.

Even though the DPN technique shares remarkable similarities with ancient quill pens, they also have significant qualitative and quantitative differences.

First of all, the dimensions involved in the DPN process including *the size of the pen* and the *thickness of the generated patterns* are in the nanometer scale regime (Figure 3a), which is crucial in achieving nanoscale patterning resolution. In this case, one can say, “size does matter.” Even with its short history, the DPN method demonstrated unprecedented  $\sim 10$  nm patterning resolution [6]. Considering the resolution of current commercial ink-jet printers,  $\sim 20$   $\mu\text{m}$ ,

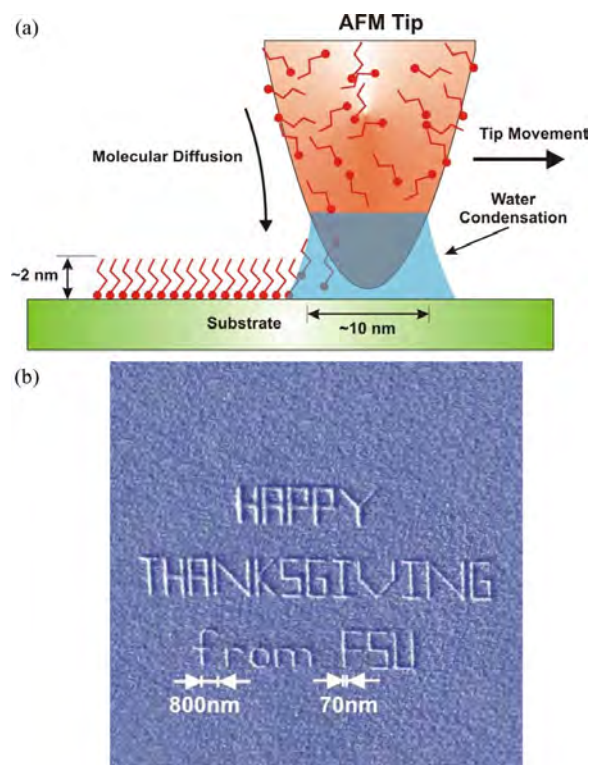


**Figure 3.** (a) Schematic diagram depicting dip-pen nanolithography. (b) Nanoscale “greetings” written via dip-pen nanolithography. The letters are written with 16-mercaptohexadecanoic acid on amorphous Au surface.



the resolution of DPN is revolutionary. This revolutionary resolution can be attributed to several core scientific developments in nanotechnology including the nanofabrication technique for AFM tip preparation, the self-assembled monolayer for a new type of molecular ink, and nanoscale precision control system for nanoscale AFM tip movements.

Second, unlike conventional pens, bulk ink coating on the pen (the AFM tip) usually remains *solid* throughout the DPN process because DPN writing is usually performed below the melting temperature of molecular ink. [However, readers should be cautioned. At this stage, the exact phase *at the tip/substrate junction* is not yet clearly understood. Because of the water meniscus and nanoscale dimension of the junction, the phase of molecules at the junction might be quite different from that on the tip surface (Fig. 3a).] Thus, the behavior of molecular ink in the DPN process can be described by individual *molecular diffusion* rather than *capillary flow* of liquid ink. In case of a macroscale pen that is based on the capillary flow of liquid ink, the ultimate resolution of pen writing is determined by the properties of ink solvent. It is often very difficult to control the liquid flow in nanoscale resolution due to several unpredictable behaviors of liquid such as viscosity change, ink meniscus, etc. However, in most DPN processes, ink molecules behave like a noninteracting two-dimensional gas whose behavior can be described by the Fickian diffusion model [11]. Molecular diffusion based on *random walk* is usually easier to predict and control than the capillary flow of liquid. The nanometer scale precision of DPN can be partly attributed to this different phase of molecular ink and writing mechanism.

It is also worth mentioning several other important characteristics of DPN.

One aspect of practical importance is a *stable ink deposition rate*. When the DPN process is stabilized, the deposition rate of molecules from the tip to the substrate remains almost constant. The stable writing speed can be attributed to the small contact point between the AFM tip and the substrate. As a result, the amount of ink molecules deposited through the contact point is relatively small compared with the amount of molecular ink (ink reservoir) on the AFM tip surface. This is the same reason macroscale quill pens and fountain pens have a stable ink deposition rate.

Second, unlike other scanning probe-based nanolithography methods, DPN is relying on *molecular diffusion* for writing, and it usually does not require *external forces*. With the same environmental conditions, the amount of deposited molecules simply depends on the contact time between the tip and the substrate. However, additional forces such as the electric field can be utilized to achieve better control of the process.

Third, since DPN is based on diffusion of individual molecules, its behavior depends on several environmental conditions including *temperature* and *humidity*. For example, the temperature change can change the *diffusion constant of molecules* on the surface. The change of humidity should alter the amount of water condensation at the tip/substrate junction as well as that on the surface, and it will change the behavior of diffusing molecules. However, it should be noted that DPN is now able to deposit quite a broad range of molecular species with quite different chemical and physical properties [12–20]. Thus, one should be cautious when

understanding this dependence because the results for each molecular ink may be different depending on the properties of individual molecular species such as hydrophobicity and melting temperature.

## 2.2. Experimental Procedure

### 2.2.1. Molecular Ink

Various types of organic molecules have been used for DPN experiments. Most commonly used organic molecules form SAMs on substrates (Fig. 4A). These molecules are comprised of three different parts: (1) a chemisorbing group, (2) an end group, and (3) a spacer (inert part). When these molecules are deposited onto a proper substrate, they chemically anchor to the substrate and form a well-ordered stable crystalline monolayer film with a thickness ranging from 1 to 10 nm. Molecules that form SAMs on various substrates are listed in Table 1. Specific binding groups can be chosen depending on the substrate. By depositing these molecules, one can completely change the chemical properties of the surface to that of end groups. Various end groups can be used for specific applications. For example, one can even use specific sequence DNA or proteins as end groups.

The best characterized systems of SAMs are alkanethiols  $R(\text{CH}_2)_n\text{SH}$  adsorbed on a gold surface (Fig. 4B). Alkanethiols are chemisorbed spontaneously on a gold surface and form alkanethiolates. This process is assumed to occur with the loss of dihydrogen by the cleavage of the S–H bond. Sulfur atoms bonded to the gold surface bring the alkyl chains into close contact: these contacts freeze out configurational entropy and lead to an ordered structure. For alkyl chains of up to approximately 20 carbon atoms, the

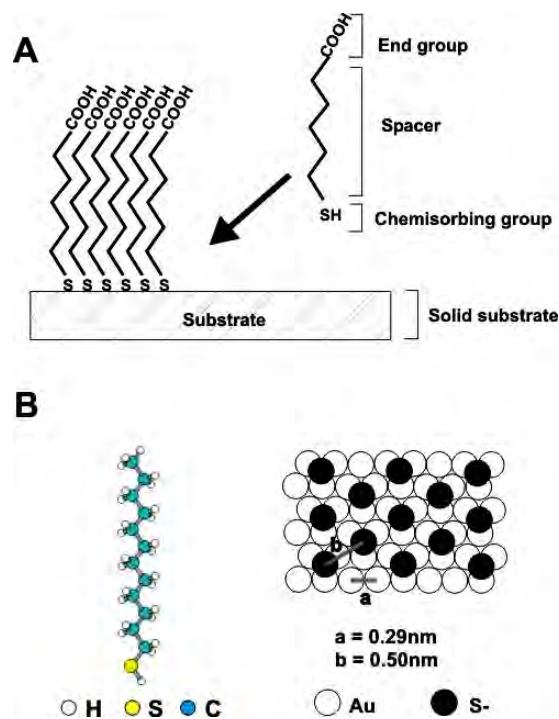


**Figure 4.** (A) Self-assembled monolayer molecules. (B) Alkanethiols on Au(111).

**Table 1.** Self-assembled monolayer molecules on different substrates.

Molecular species	Substrate	Example molecules	Ref.
RSH, ArSH	Au	C <sub>12</sub> H <sub>25</sub> SH, C <sub>6</sub> H <sub>5</sub> SH, 4-PySH	[21–23]
	Ag	C <sub>18</sub> H <sub>37</sub> SH, C <sub>6</sub> H <sub>5</sub> SH	[24, 25]
	Cu	C <sub>6</sub> F <sub>3</sub> SH, C <sub>10</sub> H <sub>21</sub> SH, C <sub>8</sub> H <sub>17</sub> SH	[26–28]
	GaAs	C <sub>18</sub> H <sub>37</sub> SH	[29]
	InP	C <sub>18</sub> H <sub>37</sub> SH, C <sub>6</sub> H <sub>13</sub> SH	[30, 31]
RSSR' (disulfides)	Au	(C <sub>22</sub> H <sub>45</sub> ) <sub>2</sub> S <sub>2</sub> , (C <sub>19</sub> H <sub>39</sub> ) <sub>2</sub> S <sub>2</sub> [CH <sub>3</sub> (CH <sub>2</sub> ) <sub>15</sub> S] <sub>2</sub>	[32, 33]
RSR' (sulfides)	Au	[CH <sub>3</sub> (CH <sub>2</sub> ) <sub>9</sub> ] <sub>2</sub> S CH <sub>3</sub> (CH <sub>2</sub> ) <sub>11</sub> S(CH <sub>2</sub> ) <sub>10</sub> CO <sub>2</sub> H	[34, 35]
RSO <sub>2</sub> H	Au	C <sub>6</sub> H <sub>5</sub> –SO <sub>2</sub> H	[36]
R <sub>3</sub> P	Au	(C <sub>6</sub> H <sub>11</sub> ) <sub>3</sub> P	[37]
RNC	Pt	(C <sub>5</sub> H <sub>6</sub> )Fe(C <sub>5</sub> H <sub>5</sub> )–(CH <sub>2</sub> ) <sub>12</sub> –NC	[38]
RSiCl <sub>3</sub> , RSi(OR') <sub>3</sub>	SiO <sub>2</sub> , glass	C <sub>10</sub> SiCl <sub>3</sub> , C <sub>12</sub> SiCl <sub>3</sub> , C <sub>16</sub> SiCl <sub>3</sub> CH <sub>2</sub> = CHCH <sub>2</sub> SiCl <sub>3</sub> C <sub>12</sub> H <sub>25</sub> SiCl <sub>3</sub>	[39–41]
(RCOO) <sub>2</sub>	Si/Si–H	[CH <sub>3</sub> (CH <sub>2</sub> ) <sub>10</sub> COO] <sub>2</sub> [CH <sub>3</sub> (CH <sub>2</sub> ) <sub>16</sub> COO] <sub>2</sub>	[42]
RCH = CH <sub>2</sub>	Si/Si–H	CH <sub>3</sub> (CH <sub>2</sub> ) <sub>15</sub> CH = CH <sub>2</sub> CH <sub>3</sub> (CH <sub>2</sub> ) <sub>8</sub> CH = CH <sub>2</sub>	[43]
RLi, RMgX	Si/Si–Cl	C <sub>4</sub> H <sub>9</sub> Li, C <sub>18</sub> H <sub>37</sub> Li C <sub>4</sub> H <sub>9</sub> MgX, C <sub>12</sub> H <sub>25</sub> MgX, X = Br, Cl	[44]
RCOOH	metal oxides	C <sub>15</sub> H <sub>31</sub> COOH, H <sub>2</sub> C = CH(CH <sub>2</sub> ) <sub>19</sub> COOH  CH <sub>3</sub> (CH <sub>2</sub> ) <sub>m</sub> OC <sub>10</sub> H <sub>6</sub> COOH, m = 9, [15–19]	[45, 46]
RCONHOH	metal oxides	CH <sub>3</sub> (CH <sub>2</sub> ) <sub>16</sub> CONHOH HO(CH <sub>2</sub> ) <sub>15</sub> CONHOH,	[47]
RPO <sub>3</sub> H <sub>2</sub>	ZrO <sub>2</sub>	Zr(O <sub>3</sub> PCH <sub>2</sub> CH <sub>2</sub> COOH) <sub>2</sub>	[48]
In <sub>2</sub> O <sub>3</sub> /SnO <sub>2</sub> (ITO)	RPO <sub>3</sub> H <sub>2</sub>	(C <sub>5</sub> H <sub>6</sub> )Fe(C <sub>5</sub> H <sub>5</sub> )(CH <sub>2</sub> ) <sub>6</sub> –PO <sub>3</sub> H <sub>2</sub>	[49]

degree of interaction in a SAM increases with the density of molecules on the surface and the length of the alkyl backbones. This assembly is a very quick process that may occur in a couple of seconds. This ability to form ordered structures rapidly might be one of the factors that ultimately determine the success of nanodeposition techniques.

The structures and properties of SAMs of alkanethiolate binding on a gold surface have been extensively investigated using a number of techniques such as contact angle measurement [50], ellipsometry [51], infrared [52], Raman [53], electrochemistry [54], X-ray photoelectron spectroscopy [55], scanning tunneling microscopy (STM) [56], and AFM [57]. As a result, it is generally accepted that sulfur atoms form an overlayer in SAMs. Recent STM studies show that these systems are heterogeneous and structurally complex: The alkyl chains may form a “superlattice” at the surface of the monolayer, that is, a lattice with a symmetry and dimension different from that of the underlying hexagonal lattice formed by sulfur atoms [58].

Significantly, when these molecules are deposited via DPN, they also form high quality crystalline SAMs like those SAMs resulting from bulk solution immersion or vapor deposition methods. For example, when 1-octadecanethiol molecules are deposited onto the atomically flat Au (111) surface via DPN, the molecular patterns show hexagonal crystalline structures (Fig. 5). This implies that DPN is based on a natural molecular diffusion and self-assembly process, and the molecule-coated AFM tip simply directs the formation of the self-assembled monolayers in the desired regions.

Thin self-assembled monolayer formation is an important factor that enables patterning of very large substrate areas via DPN. DPN relies on thin molecular coating on the AFM tip as an ink reservoir. Considering the total size of commercial AFM tips ( $\sim 5 \mu\text{m}$ ), the volume of molecular coating on the AFM tip is  $\sim 1 \mu\text{m}^3$  (Fig. 6), which is very small. However, the thickness of DPN-generated patterns is just a single molecular layer,  $\sim 2 \text{nm}$ , implying that a single molecular coating on the AFM tip is enough to cover a surface area as large as  $500 \mu\text{m}^2$ .

Even though a self-assembled monolayer with chemical surface binding helps reliable DPN writing, the covalent surface binding of molecules to the substrate is not a necessary condition for DPN writing. There are several reports utilizing molecules without covalent binding on the surface. Usually, it is possible to deposit molecules via DPN if the molecules have a *large diffusion constant* and the *affinity to substrate*. Various molecular species that have been utilized in the DPN process are listed in Table 2.

### 2.2.2. Nanoscale Pen

AFM tips with various shapes and chemical surfaces have been utilized as nanopens for the DPN process. Figure 6 shows the scanning electron microscope (SEM) image of a typical AFM tip made of Si<sub>3</sub>N<sub>4</sub>. The shape of the AFM tip is determined by the fabrication step. Most common materials for the AFM tips are Si<sub>3</sub>N<sub>4</sub> and Si. Si<sub>3</sub>N<sub>4</sub> tips usually have a pyramid shape, while Si tips are conical [62]. The heights of usual AFM tips are about 3–10  $\mu\text{m}$ . The diameter of the

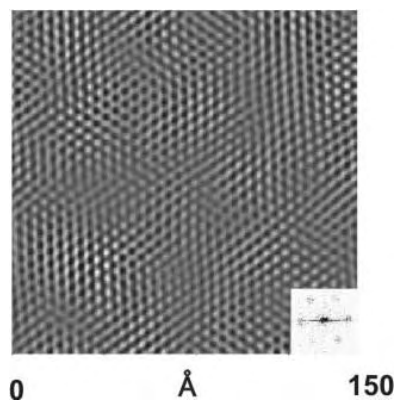


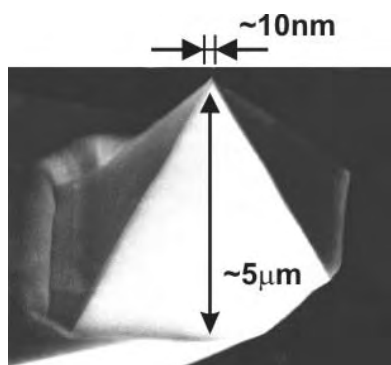
**Figure 5.** Lattice resolved lateral force image of a 1-octadecanethiol self-assembled monolayer deposited onto Au(111) by DPN. The image has been filtered with a fast Fourier filter, and the fast Fourier transform of the raw data is shown in the lower right insert. Adapted with permission from [7], R. D. Piner et al., *Science* 283, 661 (1999). © 1999, American Association for the Advancement of Science.

**Table 2.** Organic molecular ink tested via DPN.

Substrate	Molecules	Binding	Examples	Ref.
Au	alkanethiols	RS–Au	$\text{CH}_3(\text{CH}_2)_{17}\text{SH}$ , $\text{HS}(\text{CH}_2)_{15}\text{COOH}$	[6–10]
Au	thiol modified DNA	RS–Au	5′–HS– $(\text{CH}_2)_6$ –CAC GAC GTT GTA AAA CGA CGG CCA G-3′	[55b]
Au	thiol modified proteins	RS–Au	thiol modified collagen	[20]
$\text{SiO}_2$	DNA	covalent bond	5′–HS– $(\text{CH}_2)_{18}$ –CAC AAA ACG GGG GCG G-3′	[59]
Si, $\text{SiO}_2$	inorganic precursor	Si–O–metal bonding	$\text{SnCl}_4$ and P-23, $\text{AlCl}_3$ and P-123	[19]
Glass	dye molecules	van der Waals	rhodamine 6G (R6G)	[18]
Glass	protein	chemical bond	cysaxonin-1 on silane modified surfaces	[18]
Glass	polymer	hydrogen bond or electrostatic interaction	PAA and PAM PAA, PAH, and SPS	[18]
Si	metal	electric field induced chemical reactions	$\text{H}_2\text{PtCl}_6$	[13]
Mica	water	capillary force	$\text{H}_2\text{O}$	[60]
$\text{SiO}_2$	conducting polymer	electrostatic interaction	DETA	[61]

tip can be as small as  $\sim 10$  nm. The sharpness of the tip is one of the major factors determining the resolution of the DPN process. Utilizing commercial silicon nitride AFM tips, Hong et al. demonstrated patterning of  $\sim 10$  nm size molecular nanostructures via DPN [10]. Further improvement of the resolution can be expected if special tips are utilized. Possible higher resolution tips are carbon nanotube tips [63] and electrodeposited carbon tips [64].

Since DPN relies on molecular ink coating on the tip surface as an ink supply, ink loading on the AFM tip surface is critical for reliable DPN writing. For reliable ink loading, one should consider the surface chemistry of AFM tips. When the AFM tip is coated from the solution of molecular ink, the amount of loaded ink is determined by the adhesion properties of *solvent molecules*. Even though clean  $\text{Si}_3\text{N}_4$  and Si surfaces are *hydrophilic*, the AFM surfaces become *hydrophobic* after a couple of days of air exposure because of carbon contamination. In the case of nonpolar solvent, one can use commercial AFM tips without special treatment. However, many biomolecules can be dissolved only in polar

**Figure 6.** Atomic force microscope tip (nanopen for DPN) made of  $\text{Si}_3\text{N}_4$ .

solvent like water. For stable ink loading of those molecules, surface treatment is required.

One common method for the surface treatment is cleaning AFM tips with the oxygen plasma cleaner. Oxygen plasma treatment creates  $-\text{OH}$  group on the AFM tip surface and makes the surface hydrophilic. However, the effect lasts only for a short time period ranging from a few minutes to a few hours because of the contamination from the air. To achieve the desired functionality on the AFM tip for a relatively long time period, a self-assembled monolayer (e.g.,  $\text{Cl}_3\text{SiR-X}$ ) can be formed on the plasma treated AFM tip surface [65].

An alternative method is thin solid film coating. For example, evaporation of an  $\sim 10$  nm thin titanium coating can make the AFM tip more hydrophilic. However, one should be careful when depositing a metallic film on the AFM tip because solid coating may deform the AFM cantilever significantly. Usually, a solid coating with thickness less than  $\sim 10$  nm can change the surface properties without significant deformation of AFM cantilevers.

One trick that can be utilized for general molecular species is coating the tip surface with the same solid materials as substrates and then coating the tip surface with ink molecules. For example, if one wants to deposit certain thiol molecules on an Au substrate, the AFM tip can be coated with Au followed by the thiol molecules. Thiol molecules can form a monolayer easily on the Au coating on the AFM tip and thus make the tip *compatible* with solvent molecules which will be utilized to prepare molecular solution.

### 2.2.3. Molecular Coating

Molecular coating can be achieved via solution or vapor coating methods. Solution coating is similar to dipping macroscale pens in ink solution. In this method, the solution of a desired molecular species is first prepared utilizing

proper solvents. Then, the AFM tip is dipped into the solution for a short time period (e.g.,  $\sim 30$  sec), and excess molecular ink is *blown dry* by clean nitrogen gas. This process leaves a thin *solid* molecular coating on the AFM tip. In case of 16-mercaptohexadecanoic acid, the AFM tip is usually dipped in the 1 mM solution in acetonitrile for  $\sim 30$  seconds. Reliable coating of organic molecules on the AFM tip is one of the keys for successful DPN writing.

Molecules with a high vapor pressure can be coated via the vapor coating method. In this method, the AFM tip and molecules are placed together in a small closed reaction vessel and the vessel is heated to vaporize the molecular species. When the vessel is cooled down, the vaporized molecules are adsorbed on the AFM tip surface and a thin molecular layer is formed. In case of 1-octadecanethiol (ODT), 200 mg ODT and AFM tips are placed in a small closed tin can ( $\sim 15$  ml) and the tin can is heated up to  $60^\circ\text{C}$  for 20 min. When the tin can is cooled down to room temperature, the vaporized molecules are adsorbed on the AFM tip surface and leave a thin molecular coating. However, the vapor coating method is usually limited for volatile molecular species.

Even though both coating methods leave a *solid* molecular coating on the AFM tip, the properties of the coatings on the AFM tip via two different methods may be quite different. A vapor coated molecular coating is usually pure and contains less impurities. In case of the solution coating method, the molecular coating on an AFM tip contains a significant amount of *solvent molecules* for a time period as long as a couple of hours. During the time period, solvent molecules significantly enhance the diffusion of organic molecules and thus enhance the DPN writing speed. For example, 16-mercaptohexadecanoic acid (MHA) molecules coated from 1 mM acetonitrile solution will contain a significant amount of solvent and will have a fast writing speed for a couple of hours. Also, the residual solvent molecules may alter the behavior of DPN writing under different temperature and humidity conditions.

#### 2.2.4. DPN Writing

Once the tip coating is completed, one can create complicated soft nanostructure patterns on the solid surfaces by putting the AFM tip in direct contact with the substrate. Since DPN writing is driven by natural thermal diffusion of molecules, and it does not rely on the contact force, the contact force does not affect the deposition rate of molecular inks much. In this case, a *smaller contact force* is preferred to avoid any accidental damage on the substrate due to excessive force. In actual DPN writing, the AFM tip is operated in a *contact* mode with a contact force  $\sim 1$  nN and the tip is moved along the substrate to direct the deposition of molecular species onto the desired region.

However, some researchers have demonstrated DPN writing in *tapping* mode. In tapping mode, the AFM tip oscillates and gently taps the substrate. As a result, the AFM tip periodically makes contact with the substrate only in a short time period. In this case, the deposition rate (amount of deposited molecules in a unit time) depends on the AFM set point because the effective contact time changes depending on the set point. The advantage of tapping mode writing is

that the interaction between the AFM tip and the substrate is much weaker than that in contact mode. DPN writing via noncontact mode may be more suitable for extremely soft nanostructures such as weakly bound proteins [66]. The patterned surface can be imaged and tested with the molecule-coated AFM tip. Since the molecular coating on the AFM tip is very thin, one can still image surface patterns with the molecule-coated AFM tip. The most common method for imaging thin organic molecular patterns is *lateral force microscopy* (LFM) in contact mode or *phase imaging* in non-contact mode. Lateral force microscopy measures the tip bending due to the frictional force, while phase imaging measures phase shift of the tip oscillation caused by the attractive force between the AFM tip and the molecular patterns. Since the frictional force also originates from the attractive force, both techniques are, in fact, utilizing the *attractive force map* to characterize the molecular patterns. In the air, the attractive force is usually determined by capillary force due to water meniscus at the tip/substrate junction. The capillary force is larger than any other attractive forces at least by an order of magnitude. Since the magnitude of the capillary force depends on the hydrophobicity of the tip and the surface, LFM or phase images under ambient conditions simply measure the *hydrophobicity* of the molecular patterns.

In the DPN process, complicated patterns can be generated by the combination of two basic patterns: (1) dots and (2) lines. A dot pattern can be generated by holding the molecule-coated AFM tip at a fixed position on the substrate so that molecules diffuse out in a radial direction to form a circular “dot” pattern (Fig. 7A). The size of the dot pattern is determined by the *contact time* between the AFM tip and the substrates. Line patterns can be generated by

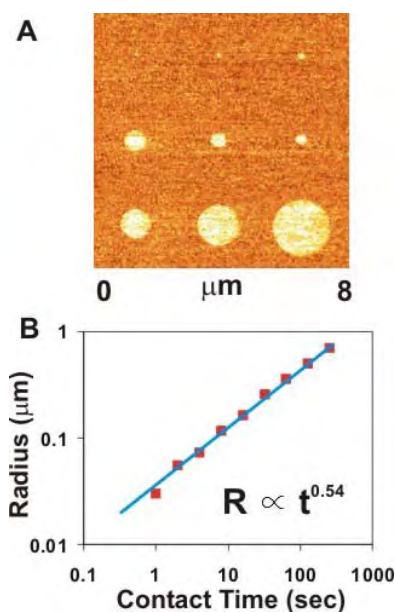


**Figure 7.** (A) Typical DPN-generated “dot” patterns. Each dot is generated by holding the AFM tip coated with 16-mercaptohexadecanoic acid at a fixed point on the Au substrate. If the deposition rate is constant,  $R \sim t^{0.5}$ . (B)  $R$  vs  $t$  graph showing a constant deposition rate of the DPN writing.



moving the AFM tip with a constant speed while in contact with the substrate. Here, the linewidth is determined by the moving *speed* of the AFM tip.

To apply the DPN process for practical lithography applications, one should be able to predict the final shapes of molecular patterns. It is especially crucial to precisely predict the sizes of two basic patterns, “dots” and “lines.” If deposited molecules form SAMs with a uniform density, the *total number of deposited molecules* is proportional to the *area of the molecular patterns*. Utilizing the assumption of “constant deposition rate” which has been experimentally proved in many cases, a simple empirical equation can be utilized to characterize the DPN generated patterns,

$$(\text{Area}) = C \times (\text{Contact time})$$

where  $C$  is the deposition rate. From a practical point of view, this equation implies that if the deposition constant  $C$  is measured once, one can precisely predict the pattern size with known contact time. For example, for *dot* patterns,  $(\text{Area}) = \pi R^2 = Ct$ , which results in the equation for the radius,

$$R = \sqrt{Ct/\pi}$$

For line patterns,  $(\text{Area}) = WL = Ct$  where  $W$  and  $L$  are the width and length of the line, respectively.

$$W = C/(L/t) = C/(\text{speed}).$$

$C$  can be easily measured by a simple test experiment before actual DPN patterning. Once  $C$  is measured, one can generate desired size “dot” and “line” patterns by controlling the *contact time* and *tip sweeping speed*. Eventually, one can get more complicated patterns with a high precision.

In the scanning probe-based lithography processes which rely on a contact force or electric current as a mean of writing, it is very difficult to precisely predict the shape and size of final patterns. However, in the DPN process, once one finds out the diffusion constant  $C$  by a simple test experiment, one can precisely control the pattern size for the rest of the experiments. This *predictability* is one of the most critical advantages of the DPN process as a practical lithographic method.

## 2.3. Lithographic Capability

### 2.3.1. Resolution Limit

Hong et al. demonstrated  $\sim 10$  nm resolution of DPN writing [6]. The ultimate resolution of DPN should depend on various parameters such as the tip diameter, substrate roughness, and the properties of molecules. Figure 8 shows example patterns of MHA on Au (111) and amorphous gold surfaces. On the atomically flat Au (111) surface, molecular dots as small as 25 nm show *isotropic* circular shape (Fig. 8A), while the larger dots on the amorphous Au surface are distorted significantly due to the surface roughness (Fig. 8B). These pictures show a routine resolution which can be easily achieved via DPN under ambient conditions without any special preparation. It should be noted that considering the lattice structures of SAMs, a single 25 nm diameter dot is comprised of only 4500 molecules.

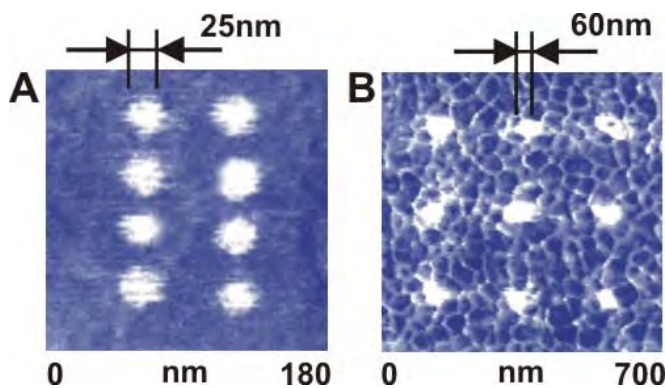


**Figure 8.** (A) Sub-50 nm dot patterns on atomically flat Au (111). Each dot is comprised of 16-mercaptohexadecanoic acid molecules. (B) Molecular dots on an amorphous Au surface showing the effect of surface roughness.

Since DPN relies on direct deposition of molecules utilizing the AFM tip as a pen, its resolution is not limited by the wavelength of light. Sharper tips can be used to achieve better resolution. Current resolution of DPN could be improved if special tips such as carbon nanotube tips are used for DPN writing.

The high resolution of DPN can be attributed partly to the properties of ink molecules. Unlike conventional direct deposition methods, DPN utilizes *solid* ink in most cases, and it relies on molecular diffusion. In case of conventional pens, the ultimate resolution is limited by the ink properties such as capillary size of liquid ink at the pen/surface junction. Since DPN utilizes solid ink, individual molecules diffuse by a random walk, and it is easier to control the molecular flow in the nanometer scale precision. The formation of high quality self-assembled monolayers is another important factor for the high resolution of DPN. It allows one to generate uniform nanoscale patterns reliably via the DPN method.

Moreover, DPN has two major advantages over traditional nanolithographic techniques: *ultrahigh registration* and *multiple-ink patterning* [6]. Because DPN allows one to image nanostructures with the same tool used to form them, one can use DPN to generate and align nanostructures with pre-existing patterns on the substrate with ultrahigh registration (Fig. 9). With the help of the dip-pen nanolithography software, one can generate multicomponent patterns using alignment marks, a strategy analogous to that used to register e-beam lithography patterns. A distinct advantage of this approach over e-beam methods is that it utilizes the scanning probe for generating and locating alignment marks. This is very important because it is less destructive than e-beam methodology for finding alignment marks (i.e., it is compatible with soft materials), and it is an inherently higher resolution imaging technique than optical or electron beam methods.

### 2.3.2. Multiple Pen Writing

DPN writing is based on the thermal diffusion process and does not rely on the *contact force*. As a result, slight variation of the contact force does not affect the deposition rate in the DPN process.

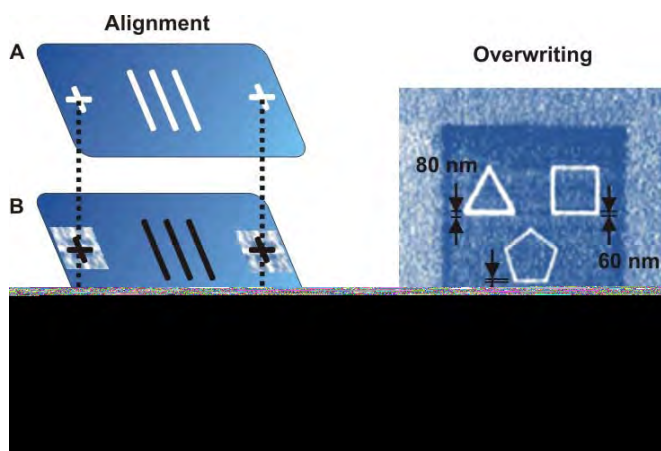


**Figure 9.** Left: Diagram depicting the method for generating aligned soft nanostructures. Right: SAMs in the shapes of polygons drawn by DPN with 16-mercaptohexadecanoic acid on an Au surface. An ODT SAM has been *overwritten* around the polygons. Adapted with permission from [6], S. Hong et al., *Science* 286, 523 (1999). © 1999, American Association for the Advancement of Science.

One major problem in serial writing processes is patterning speed. Since one has to generate complicated patterns with a *single* pen, it usually takes much longer time than parallel patterning methods such as photolithography. One strategy to overcome this limitation is writing with *multiple* pens simultaneously. In most other scanning probe lithography methods, the writing speed depends on the contact force or applied electric field between the AFM tip and substrate. Since these parameters depend on the surface conditions, complicated feedback circuits are required to precisely maintain identical contact forces or electric field on each tip. In this case, to achieve the identical pattern size, one has to build a separate feedback circuit for each AFM tip, which dramatically increases the instrumentation cost.

In the case of DPN with multiple pens, even with different contact forces on each AFM tip, each tip should generate the same patterns. Figure 10 shows a schematic diagram depicting the multiple-pen writing strategy. In this scheme, the laser feedback is applied on the AFM tip with the largest separation from the surface to ensure that all other AFM tips are in contact with the substrate. Although

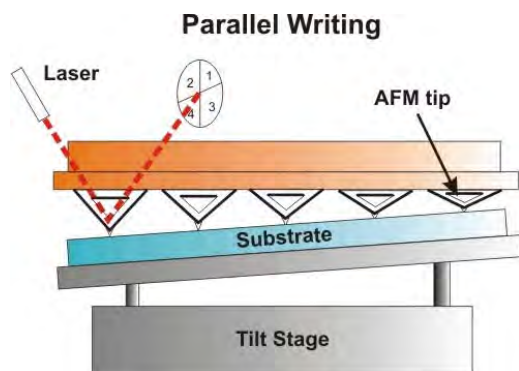


**Figure 10.** Schematic diagram depicting multiple dip-pen writing utilizing a single force feedback system.

the force between the tip and surface may be different, it still results in the same deposition rate. Hong and Mirkin demonstrated that DPN writing with eight pens and a single feedback gives identical nanoscale patterns (Fig. 11) [8]. The possible maximum force variation on the contact point depends on the mechanical strength of SAMs and substrates. Under ambient conditions, there is a report of applying up to 100 nN contact forces on alkanethiol SAMs without significant structural damage [58].

Extensive efforts are currently given to increase the density of tips. Zhang et al. demonstrated high density 32-pen parallel writing (Fig. 12) [67].

## 2.4. Applications

The soft materials patterning capabilities of DPN opens up new possibilities in many practical applications.

### 2.4.1. Etching

Self-assembled monolayer patterns generated via DPN have been utilized to fabricate solid nanostructures (Fig. 13). In this process, the monolayer patterns are used as an *etching resist* layer. Weinberger et al. demonstrated etching of Au utilizing 1-octadecanethiol as an etching resist layer [9]. Then, the etched Au patterns are used as an etching resist for the silicon etching process (Fig. 14).

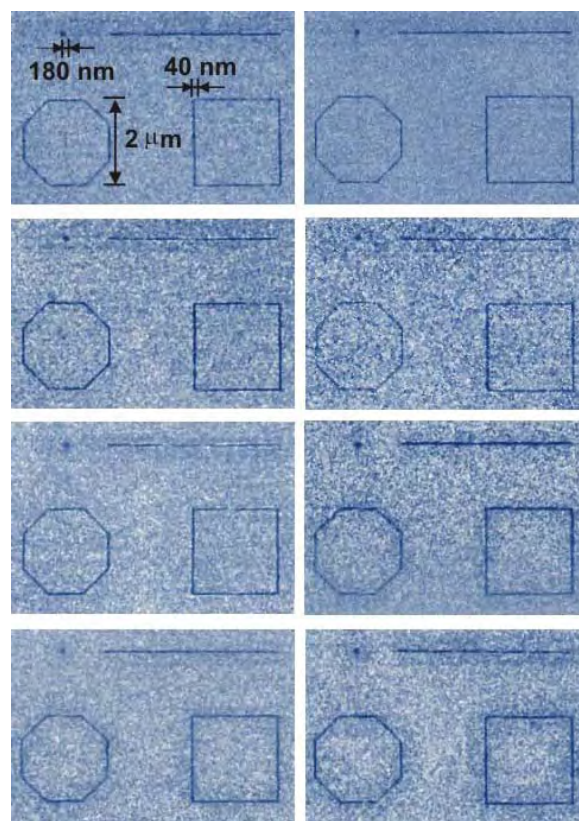


**Figure 11.** Lateral force microscope images of eight identical patterns generated with one imaging tip and eight writing tips coated with 1-octadecanethiol molecules. Adapted with permission [8], S. Hong and C. A. Mirkin, *Science* 288, 1808 (2000). © 2000, American Association for the Advancement of Science.



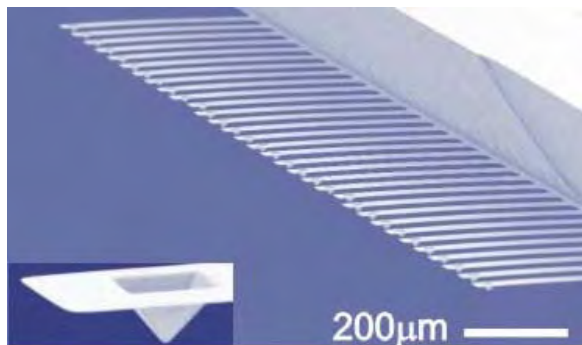


**Figure 12.** SEM micrograph of a 32 DPN probe array. The insert shows an enlarged view of a single tip at the end of a beam. Adapted with permission from [67], M. Zhang et al., *Nanotechnology* 13, 212 (2002). © 2002, Institute of Physics Publishing.

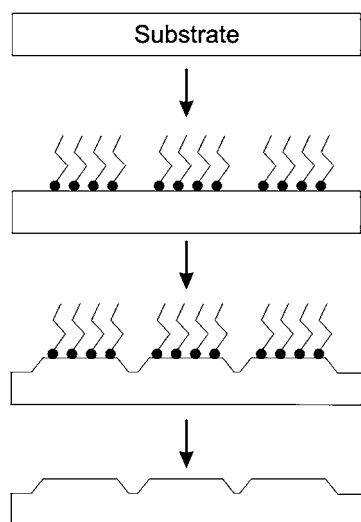


**Figure 13.** Schematic diagram depicting solid nanostructure fabrication via DPN

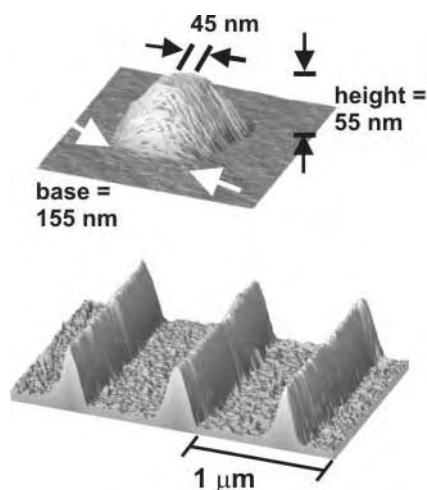


**Figure 14.** Nanoscale silicon structures utilizing DPN-generated SAM patterns as an etching resist layer. Adapted with permission from [9], D. A. Weinberger et al., *Adv. Mater.* 12, 1601 (2000). © 2000, Wiley-VCH.

Significantly, since the thickness of the SAM is  $\sim 2$  nm, it can be an ideal etching resist layer. Also, the resolution of DPN is not limited by optical wavelength. One disadvantage for practical applications might be its speed because DPN is a serial process. Zhang et al. demonstrated fabrication of multiple solid nanostructures via a multiple pen writing strategy [67]. Considering recent active works in multiple pen systems such as Millipede from IBM, further improvement of its speed can be expected. Table 3 shows possible SAM resist layers with corresponding etchants.

#### 2.4.2. Surface-Templated Assembly

Nature uses molecular recognition between complex macromolecules to form sophisticated meso- and macroscopic architectures. Proteins, DNA, and other biomolecular structures all have been programmed to form specific structures based upon relatively simple precursor molecules such as nucleotides or peptides. Recently, significant efforts have been given to construct functional materials utilizing the molecular recognition mechanism.

Specific assembly steps inspired by DPN-generated molecular patterns can be utilized to place nanoscale functional elements at the specific position. In the process as depicted in Figure 15, the desired nanometer scale region on the surface is first functionalized with specific organic molecules via dip-pen nanolithography. The molecules contain specific functional groups which have a strong affinity to desired nanostructures. For example, MHA binds on the Au surface with thiol group and exposes carboxylic acid group on the SAM surface. The  $\text{Fe}_3\text{O}_4$  magnetic nanoparticles have a specific affinity to the carboxylic acid groups. After surface functionalization the remaining surface area should be passivated via the SAM with inert functional groups to avoid nonspecific binding of nanostructures. Methyl ( $-\text{CH}_3$ ) terminated molecules such as 1-octadecanethiol are often used for passivation. Then, the sample is placed in the solution containing desired nanostructures so that nanostructures can assemble onto the desired area via molecular recognition mechanism. Figure 15 shows magnetic nanoparticle patterns assembled onto the SAM surface covered with carboxylic acid groups ( $-\text{COOH}$ ). In this process, nanoscale dot patterns comprised of 16-mercaptohexadecanoic acid are prepared via DPN and the remaining surface is passivated via methyl terminated ODT molecules.

Various interactions can be utilized to specifically assemble nanostructures onto a desired surface area. These include covalent bonding, electrostatic interactions, and

**Table 3.** Possible combination of SAMs and etchants.

SAM	Surface	Etchant	Example molecules	Ref.
Thiol	Au	KCN/ $\text{O}_2$	$\text{HS}(\text{CH}_2)_{15}\text{SH}$ , $\text{HS}(\text{CH}_2)_{18}\text{SH}$	[9, 68–70]
	Ag	KCN/ $\text{O}_2$	$\text{CH}_3(\text{CH}_2)_{15}\text{SH}$	[71, 76]
	Cu	$\text{FeCl}_3/\text{HCl}$	$\text{CH}_3(\text{CH}_2)_{15}\text{SH}$	[69, 72]
	GaAs	$\text{HCl}/\text{HNO}_3$	$\text{CH}_3(\text{CH}_2)_{15}\text{SH}$	[69, 77]
$\text{RPO}_3^-$	Al	$\text{HCl}/\text{HNO}_3$	$\text{C}_{18}\text{PO}(\text{OH})_2$	[74]
$\text{RSiO}_{3/2}$	Si/ $\text{SiO}_2$	$\text{HF}/\text{NH}_4\text{F}$	$\text{HSC}_{15}\text{H}_{30}\text{COOH}$	[78]
$\text{RSiO}_{3/2}$	Glass	$\text{HF}/\text{NH}_4\text{F}$	$\text{HSC}_{15}\text{H}_{30}\text{COOH}$	[78]

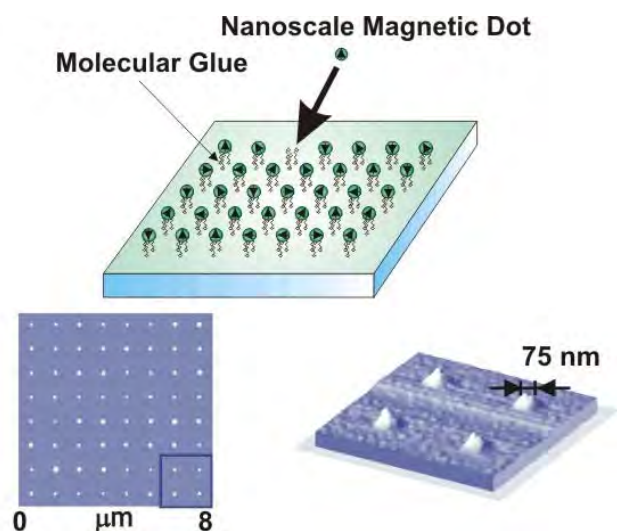


**Figure 15.** Surface-templated assembly process for nanoparticles. An array of iron oxide dots prepared by the surface-templated assembly process. Adapted with permission from [91], X. Liu et al., *Adv. Mater.* 14, 231 (2002). © 2002, Wiley-VCH.

biomolecular interactions. Biomolecular interaction is especially intriguing because of its variety and specificity. Unlike most other molecular recognition mechanisms where possible choices are limited (e.g., thiol to Au, carboxylic acid to aluminum, etc.), biomolecular recognition provides a virtually infinite number of combinations. For example, Demers et al. demonstrated surface functionalization with single strand DNA (ssDNA) molecules [16]. When the functionalized substrate is immersed in the solution of DNA-functionalized nanoparticles, only nanoparticles with a specific *complementary* sequence of ssDNAs can assemble to the desired surface area. Suppose one uses ssDNA with  $n$  base pairs. Since each base pair of ssDNA can have 4 different sequences (A, T, G, or C),  $4^n$  different combinations are possible.

### 2.4.3. Patterning of Biomolecules

Biomolecular patterning via DPN is of huge practical importance. DPN allows one to directly deposit general biological molecules onto solid surfaces with a nanometer scale resolution. This new capability allows one to envision new biomolecular functional devices such as ultrahigh density gene chips or nanoscale biosensors.

Usually, additional consideration is usually required for DPN patterning of biomolecules. First of all, most biomolecules are relatively large compared with other self-assembled monolayer molecules. As a result, the interaction between AFM tip and biomolecules can be very large. Contact mode writing with a small contact force or tapping mode writing is often necessary for stable DPN patterning of large biomolecules [6]. Second, most biomolecules prefer water as solvent. So the AFM tip should be treated to make it hydrophilic. Finally, some biological molecules lose their functionality and are destroyed when dried. Those sensitive molecules could be patterned via a surface-templated assembly process instead of a direct deposition method. In

this method, the surface is first coated with specific functional groups and the assembly of biomolecules is directed via specific assembly.

Wilson et al. demonstrated direct patterning of  $\sim 100$  nm size thiol-modified *collagen* molecules on a Au surface [20]. In this experiment, thiol groups bind to the Au surface and form stable structures. However, they also observed that the contact mode writing is not suitable for patterning large biomolecules because direct contact of the AFM tip to the molecules can destroy the biomolecular structures on the surface. Tapping mode patterning is first applied to generate the organic molecular patterns on the surface. In the tapping mode, the AFM tip gently taps the surface without a direct contact, which can minimize the interaction between AFM tip and the surface nanostructures. It allows one to create stable biomolecular structures with less damage. By this method, Wilson et al. created a collagen patterns with 30 nm linewidth [20].

Demers et al. demonstrated direct deposition of thiol-modified DNA molecules (Fig. 16) [93]. To enhance the ink loading on the AFM tip, the surface of the AFM tip is first modified by 3'-aminopropyltrimethoxysilane, which promotes reliable adhesion of the DNA ink to the tip surface. Demers et al. also demonstrated the direct deposition of DNA onto the SiO<sub>2</sub> surface. Before the DPN writing, the surface of the thermally oxidized Si wafer was activated with 3'-mercaptopropyltrimethoxysilane. Then, DNA molecules with acrylamide groups are deposited via DPN, and they form stable nanostructures on the surface. The final patterns are characterized by nanoparticle assembly and optical methods.

On the other hand, some proteins lose their functionality when dried for DPN experiments. One example might be motor proteins such as actomyosin. In this case, the surface is first patterned via other chemical molecules and the assembly of proteins in the protein buffer solution is directed via electrostatic interaction. This method allows one to pattern sensitive biological molecules while maintaining their functionality. Demers and Mirkin demonstrated patterning of DNA molecules via *indirect surface-templated assembly process* [16].

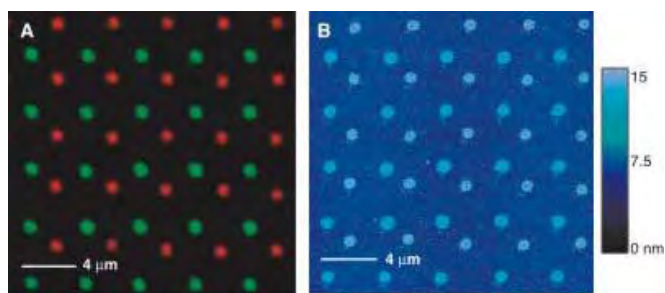


**Figure 16.** Direct patterning of multiple-DNA inks by DPN. (A) Combined red-green epifluorescence image of two different fluorophore-labeled sequences (Oregon Green 488-X and Texas Red-X) simultaneously hybridized to a two-sequence array deposited on a SiO<sub>2</sub> substrate by DPN. (B) Tapping mode AFM image of 5 and 13 nm diameter gold nanoparticles assembled on the same pattern after dehybridization of the fluorophore-labeled DNA. Adapted with permission from [93], L. Demers et al., *Science* 296, 1836 (2002). © 2002, American Association for the Advancement of Science.

## 2.5. DPN Theory

### 2.5.1. Diffusion Model

Jang et al. presented a theoretical model explaining DPN as a three-step process (Fig. 17) [11]: (1) *constant rate molecular deposition*, (2) *lateral diffusion on a monolayer of molecules*, and (3) *termination of diffusion by chemical binding to a substrate*.

In many previous experimental results, DPN writing demonstrated almost *constant deposition rate* (Fig. 7). It is mainly because the amount of deposited molecules is much smaller than the volume of organic molecules on the AFM tip. On the substrate, molecules can diffuse via random walk until they meet the bare Au surface. Whenever the molecules meet the bare substrate, molecules are irreversibly bound onto the surface.

For a tip fixed in a position, the ink diffusion is isotropic, giving (filled) circles on the surfaces. Assuming cylindrical symmetry of diffusion and treating the position of ink molecules as continuous variable, a simple analytical theory for the growth of circles can be derived based on diffusion equations and boundary conditions

$$\frac{\partial C}{\partial t} = \frac{1}{r} \frac{\partial}{\partial r} \left( rD \frac{\partial C}{\partial r} \right)$$

In this picture, molecules cannot move on the bare surface but can diffuse through the region already covered by other molecules. However, the boundary of a circle with radius  $R(t)$  varying in time has been known as a *moving boundary problem*, specifically, for a given boundary,  $R(t)$ , the diffusion equation for the number density within ( $r < R$ ) and outside the boundary with different diffusion constant  $D$  (finite) and  $D' (- > 0)$ , respectively. At the boundary,  $r = R$ , the number density is taken to be the monolayer density  $\rho$ , and the density flux must be continuous,

$$C(R, t) = C'(R, t) = \rho$$

$$D \frac{\partial C}{\partial r} = D' \frac{\partial C'}{\partial r}$$

where  $C(r, t)$  and  $C'(r, t)$  are the densities within and outside the boundary, respectively.

This kind of boundary growth has been solved for various geometries of boundary including spheres, cylinders, and ellipsoids. The derivation of solution is well described in [79].

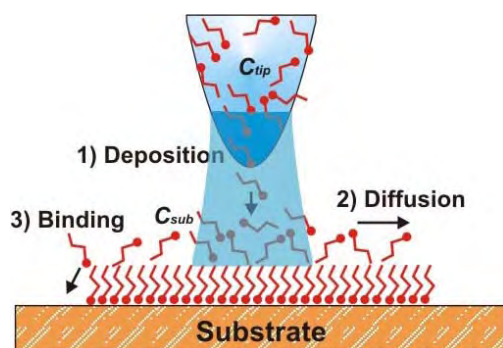


Figure 17. DPN process with strong surface binding.

In order for the first boundary condition to be met for all  $t$ ,  $R(t)$  must take the form

$$R(t)^2 = \lambda^2 4Dt$$

The number densities inside and outside the boundary are given by

$$C(r, t) = \rho - \frac{n}{4\pi D} \left[ Ei\left(\frac{-r^2}{4Dt}\right) - Ei(-\lambda^2) \right]$$

$$C'(r, t) = 0$$

where  $\lambda^2$  satisfies the equation

$$e^{-\lambda^2} = \frac{4D}{(n/\pi\rho)} \lambda^2$$

This analytical result assumed *perfectly circular patterns*. This assumption can be tested via *random walk simulation*. In case of random walk simulation, the results do not have perfect cylindrical symmetry assumed in the analytical theory. Thus the boundary of the circular patterns may fluctuate from a perfect circle. This fuzziness of the circle boundary pertains to the quality of circles generated via DPN and thus is of practical importance. The first step quantifying the noncircular deviation is calculating *circularity*. Moreover, for an  $N$ -side polygon whose peripheral points are uniformly distributed, it has been found that

$$N \cong 1.3869(\mu_R/\sigma_R)^{0.4721}$$

where  $\mu$  and  $\sigma$  are the average and standard deviation of the distance of the peripheral points. The random walk simulation shows that the circularity is independent of the deposition rate and increases as the pattern size increases. This implies that even the very large patterns should have a smooth edge, which is also a very good indication for future DPN patterning applications.

### 2.5.2. Deposition

Jang et al. successfully explained the pattern formation on substrate [11]. However, the theory simply assumed a constant deposition rate and does not provide any explanation about the *deposition* step. Several researchers presented different models.

Sheehan and Whitman adapted a different assumption to describe the DPN process based on the diffusion model [80]. Instead of the constant deposition rate, *the density of molecules below the contact point is assumed to be identical to that on the AFM tip and remains constant through the DPN process*. This assumption provides a solution different from that of Jang et al. The analytical approximation is

$$C(r, t) = C_0 \frac{E_i(r^2/4Dt)}{\ln(4Dt/a^2 e^{2\gamma})}$$

where  $E_i$  is the exponential integral and  $\gamma$  is Euler's gamma ( $\cong 0.577$ ). However, this solution provides only a *decreasing* flux (deposition rate), and it cannot explain the DPN writing cases with a *constant* or *slightly increasing* flux. Considering the complicated geometry of the tip/surface junction

and possible water condensation under ambient conditions, the *constant density* assumption might be too much simplification. This contradiction implies that it is necessary to consider more complicated aspects of tip/substrate junction such as water meniscus to provide the proper description of the DPN process.

Weeks et al. showed a model including the water meniscus at the junction between the AFM tip and substrate [81], where the deposition of organic molecules is explained by *dissolution kinetics* of organic molecules in the water meniscus at the tip/substrate junction. In the model, the total number of molecules  $N$  transferred to the substrate will be given by the integral of the transfer rate  $dN/dt$  over the total tip-surface contact time  $\tau$ . Two terms contribute to  $dN/dt$ : First molecules dissolve from the tip through thermally activated detachment at a rate

$$\left(\frac{dN}{dt}\right)_+ = \frac{A}{\pi a^2} \beta_+ = \frac{A}{\pi a^2} \nu e^{-E_D/kT}$$

where  $A$  is the contact area between the tip and the meniscus,  $\pi a^2$  is the average area per thiol ink molecule,  $E_D$  is the activation energy of ink detachment,  $k$  is Boltzmann's constant,  $T$  is the temperature, and  $\nu$  is an attempt frequency.

Second, molecules return to the tip simply due to improvement and attachment at a rate given by

$$\left(\frac{dN}{dt}\right)_- = A\beta_- C_0 \approx A\left(\frac{kT}{2\pi m}\right)^{1/2} \nu e^{-E_D/kT} C_0$$

where  $m$  is the mass of a thiol,  $E$  is the activation energy for attachment, and  $C_0$  is the concentration of thiols in solution adjacent to the tip. The dot radius is related to  $N$  through  $\pi R^2 = N\pi a^2$ .

Combining these relationships gives

$$R^2 = A\left[\beta_+\tau - \pi a^2\beta_- \int_0^r C_0(r) dt\right]$$

The results show transition to the *diffusive regime* with a slow diffusion rate after a long time. In the model, the density of molecules on the substrate below the AFM tip is assumed to depend on the dissolution kinetics of thiol molecules and surface diffusion.

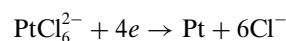
As described in Section 2.5, the DPN process is based on nanoscale molecular diffusion on solid substrates. Since DPN allows one to deposit organic molecules in a nanometer scale resolution and image the result directly without complication, it can be an ideal tool to study the nanoscale surface diffusion process. In addition to practical applications, the development of DPN brought up many scientific questions: What is the phase of diffusion molecules in nanoscale direct deposition processes? What is the effect of environmental conditions? Is there any interaction between diffusing molecules? These are the questions we have to answer in the future.

## 2.6. Variation from Conventional DPN

The conventional DPN process is based on *thermal diffusion* of organic molecules and it usually utilizes self-assembled monolayer molecules which chemically anchor to the substrate. However, one can also apply additional driving forces to provide the better control of the deposition process. Also, it is possible to deposit molecules without covalent bond to the substrate.

### 2.6.1. Electrochemical DPN

Li et al. utilized an electric current to induce electrochemical reactions during the DPN writing process. In the electrochemical DPN, precursor molecules are utilized to create metallic structures on solid surface. For example Li et al. coated the AFM tip surface with  $H_2PtCl_6$  and applied a current inducing chemical reaction [13]



Here, the water meniscus between the AFM tip and surface works as a small reaction vessel. The writing leaves Pt nanostructures on the silicon surface. Li et al. successfully demonstrated the deposition of Au, Ge, Ag, Cu, and Pd via this strategy [13, 82].

These results demonstrate that DPN can be utilized to generate metallic nanostructures on solid surfaces. Metallic nanostructures are of particular interest in the semiconductor industry because they allow one to modify electronic circuits in nanometer scale resolution without any complicated processing steps.

### 2.6.2. Nanodeposition via Electrostatic Interaction

Conducting polymers are of great interest these days due to their possible applications in organic display and flexible electronic circuits. They form well-ordered crystalline structures on insulating surfaces such as on  $SiO_2$ . However, conducting polymers usually do not have strong chemical bindings to the substrate. Since their electronic properties are determined by the crystalline structures, any chemical modification can significantly change their electronic structures. Lim and Mirkin utilized electrostatic interaction between conducting polymers and substrate to create polymer nanostructures on the surface [61].

In the experiment, self-doped sulfonated polyaniline (SPAN) and doped polypyrrole (PPY) conducting polymers dissolved in water are used for writing. SPAN and PPY have negatively or positively charged backbones, respectively. The  $SiO_2$  surface is positively charged by coating the surface with trimethoxysilylpropyldiethylenetriamine (DETA) and negatively by piranha solution. Negatively charged SPAN can be deposited only onto the positively charged DETA coated surface, while positively charged PPY molecules can be assembled onto the piranha solution cleaned surface. This experiment first proves that it is possible to generate stable nanostructures utilizing electrostatic interactions. The *constant deposition rate* is also confirmed in the conducting polymer writing process.



### 2.6.3. Nanografting

In most DPN method, molecules are directly deposited onto bare surface. If molecules are deposited on top of other molecular layers, the *exchange* reaction may occur depending on their binding energies and detailed kinetics. The exchange can be enhanced by a strong contact force during the DPN writing. Xu et al. coated the AFM tip with molecules and wrote patterns on top of other molecular layers [83]. The strong contact force induced the exchange reaction and the molecules from the AFM tip can replace the molecular layer on the surface.

## 3. MICROCONTACT PRINTING

### 3.1. Key Strategy

The microcontact printing method was first developed by Kumar and Whitesides at Harvard University in 1993 [68]. In this method, soft micrometer scale stamps made of poly(dimethylsiloxane) (PDMS) are utilized to deposit organic molecules onto solid substrates via direct contact like macroscale printing techniques (Fig. 18A). Since microcontact stamping is a parallel printing method, it can pattern a large surface area very quickly (Fig. 18B). Stamping methods have demonstrated  $\sim 35$  nm resolution with thiol molecules on a Au surface [69]. However, since the stamps are made of soft polymer materials, the bending of stamps due to swelling of solvent molecules or external pressure is one of the major factors limiting its resolution. In typical applications, the microcontact printing method has been utilized to pattern large surface areas very quickly with a micro- or submicrometer scale resolution.

Dip-pen nanolithography and microcontact printing can be good complimentary methods for general organic materials patterning. Microcontact stamping is a parallel printing

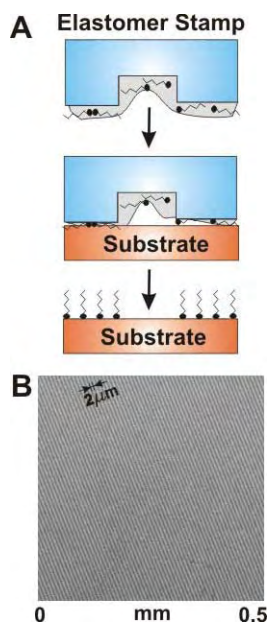


**Figure 18.** (A) Stamping procedure. (B) 1-Octadecanethiol patterns on Au surface generated via microcontact printing.

method which is inherently faster than dip-pen nanolithography utilizing a single pen. However, once stamps are made, it is difficult to modify the design, while DPN allows one to modify and directly print out new patterns from the computer without any intermediate steps. Since the stamping method relies on *direct contact* for molecular deposition, it can be used to deposit quite large molecules or nanostructures such as a few micrometer long carbon nanotubes. The maximum size of molecules that can be deposited via DPN is usually limited by the size of the AFM tips. On the other hand, the DPN process can have additional driving forces for deposition of various materials including metals. By applying electric current at the AFM tip during the DPN process, Li et al. could deposit metallic nanowires onto solid surfaces, while it is extremely difficult, if not impossible, to apply current during the stamping experiment. Overall, microcontact printing is suitable for patterning large surface areas with submicrometer resolution, while DPN is suitable for rapid prototyping of various nanoscale organic structures.

A more comprehensive review about the microcontact printing technique can be found in [4]. Here, we will describe the basic concepts of the microcontact printing method and compare it with the dip-pen nanolithography method.

### 3.2. Procedures to Make Stamp

Figure 19 shows the basic procedure for stamp fabrication. The first step is preparation of a template. The template can be virtually anything with structures. These include TEM grids and photoresist patterns on  $\text{SiO}_2$  surfaces. Then, PDMS elastomer mixed with a curing agent is poured onto the template and is heated up to  $60^\circ\text{C}$  until the PDMS becomes solid. Once the PDMS is cured, it is separated and can be utilized to deposit organic molecules onto substrates.

One key condition to make a good stamp is that the template should not have *undercut* structures. If there are undercut structures as depicted in Figure 19B, it is difficult to separate stamps from the template after the curing process. For example, developed photoresist layer patterns can be a good template because they do not have undercut structures, while etched  $\text{SiO}_2$  substrates are not a good template because wet etching often results in significant undercut structures.

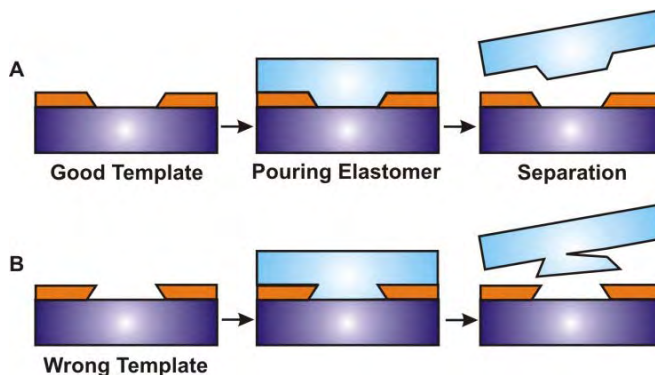


**Figure 19.** Stamp fabrication procedure with (A) a good template and (B) a bad template.

A fabricated stamp surface can be coated with molecules from the solution. For reliable stamping, good adhesion of ink molecules on the surface is very important. In the air, the stamp surface usually remains hydrophobic making it suitable for molecular ink based on nonpolar solvent. Additional treatment is required for stamping of water-based molecular solution. A common method for stamp surface modification is plasma cleaning followed by SAM assembly. Plasma cleaning created hydroxyl ( $-\text{OH}$ ) group on the surface, and desired functionality can be achieved by attaching molecules with silyl chloride group.

Once the good molecular coating is achieved, one can generate submicrometer scale patterns simply by applying the coated stamp to the solid surface (Fig. 18).

### 3.3. Mechanism

The detailed mechanism is well described in [84]. The major deposition mechanism for microcontact printing is direct contact [(a) in Fig. 20]. However, other deposition routes were also observed: (b) diffusion and (c) vaporization.

Direct contact is the major deposition mechanism in the stamping process. The key for successful direct contact is uniform coating of molecules on the stamp surface. In most cases, molecular ink is coated from solution. It is desirable to make the stamp surface favorable to the “solvent.” Another key parameter of stamping is the *fast reaction* of organic molecules with the surface. The reaction speed of self-assembled monolayer varies depending on molecules and environment. For air sensitive molecules, it is required to do the stamping under a controlled environment such as a nitrogen-filled glove box.

Another deposition path is the *diffusion* of molecules on the substrate. Unlike DPN experiments where the diffusion is the major deposition mechanism, the surface diffusion is not a favorable phenomenon in the stamping method because it increases the pattern size and often results in unpredictable pattern shapes. The equation to describe the diffusion results in the stamping method is also quite different from the DPN experiment. For lines with a fixed length  $L$ , the linewidth  $W$  of the stamped patterns is proportional to  $\log t$ , where  $t$  is the contact time. This implies that the deposition rate of molecules in the stamping is proportional to  $1/t$ . In the DPN method, the linewidth is proportional to the total contact time  $t$  since the deposition rate of molecules remains almost constant. This difference comes from different boundary conditions, especially the different shapes of the deposition region in each process. DPN is relying on a *point contact* between the AFM tip and the substrate as a deposition region of molecules. As a result, the amount of deposited molecules is much smaller than the molecules on the AFM tip (ink reservoir) and it does not

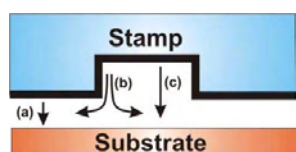


**Figure 20.** Deposition routes of stamps: (a) direct contact, (b) diffusion, and (c) vaporization.

affect the deposition rate in time. However, the deposition region of the stamping method is the *long linear edge* of the stamp and the amount of deposited molecules via the diffusion process is comparable to the total amount of ink in the ink reservoir.

Another deposition path is *vapor deposition*. Some volatile molecules can be vaporized and directly deposited onto the substrate. This is another undesirable phenomenon in both stamping and DPN writing. A small amount of vapor deposited molecules usually forms submonolayer films on substrates. To avoid unwanted vapor deposition, molecular ink with low vapor pressure is preferred in both stamping and DPN methods.

### 3.4. Applications

Since the development of microcontact printing [68], the stamping method has been extensively utilized in many applications. There are three major strategies in stamp-based applications. First of all, various materials have been *directly deposited* on the surface in a parallel manner. These include most of the SAM molecules in Table 1, various biomolecules, and very large nanostructures such as nanoparticles or carbon nanotubes.

Second, the molecular patterns can be utilized as an *etching resist* for semiconductor fabrication. Various devices have been demonstrated via the stamping method including silicon transistors and GaAs devices (Fig. 21). Table 3 shows possible etchants for various SAM molecules.

Third, the patterned surface can be utilized for the surface-templated assembly process to capture additional materials. In this process, the substrates are first patterned with a self-assembled monolayer and then the substrate is

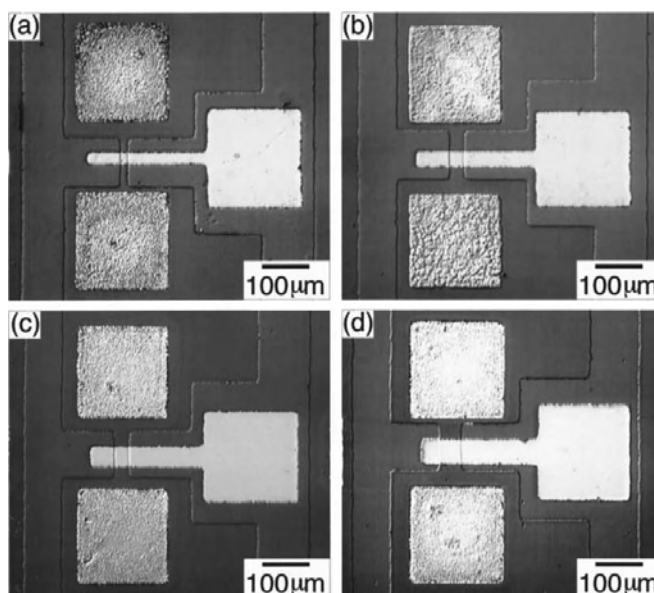


**Figure 21.** Micrographs of FETs with various gate lengths  $L$  and gate widths  $Z$  fabricated by soft lithography. (a)  $L = 26 \mu\text{m}$  and  $Z = 16 \mu\text{m}$ ; (b)  $L = 34 \mu\text{m}$  and  $Z = 30 \mu\text{m}$ ; (c)  $L = 44 \mu\text{m}$  and  $Z = 32 \mu\text{m}$ ; (d)  $L = 52 \mu\text{m}$  and  $Z = 47 \mu\text{m}$ . Adapted with permission from [92], J. Hu et al., *Appl. Phys. Lett.* 71, 2020 (1997). © 1997, American Institute of Physics.



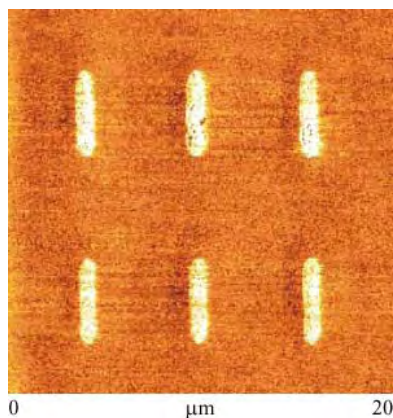


**Figure 22.** Actin proteins assembled onto stamp-generated imidazole SAM patterns.

immersed in the solution which contains desired nanostructures. The desired nanostructures are captured onto the surface via a molecular recognition mechanism. Figure 22 shows actin motor proteins assembled onto stamp-generated imidazole molecular patterns.

#### 4. CONCLUSIONS

DPN and microcontact printing are two complementary methods which allow one to pattern general soft nanostructures on solid substrates. DPN is suitable for nanoscale high resolution patterning with a precision alignment. Since DPN can directly *print out* nanoscale soft material patterns without intermediate processing steps, the time required from pattern design to realization can be extremely short. It is an ideal tool for *rapid prototyping of nanoscale devices*.

On the other hand, the preparation of microcontact stamps takes a long time. However, once stamps are made, they can be utilized to pattern very large surface areas in a parallel fashion quickly. Microcontact printing is an ideal choice to pattern large surface areas with a sub-microscale resolution.

The development of nanodeposition methods can be a historic triggering event that opens up the door to new generation devices. Since one can now combine chemical or biological molecules with conventional solid state devices, it is possible to envision new hybrid devices. These include nanoscale biological sensors which can detect a single biomolecular unit [85–89]. Many researchers are now working on new nanoscale mechanical systems driven by the power of biological motor proteins [90].

As predicted by many pioneering researchers, now is the dawn of the new age when people first begin to understand and manipulate individual molecular functionalities. It is the time when mankind first touches the secret of life at the molecular level. For the next few decades, new functional devices assembled by the newly developed nanodeposition methods could flourish and eventually change the face of everyday human life.

#### GLOSSARY

**Atomic force microscopy (AFM)** One of the most common scanning probe microscopy modes. It operates by measuring attractive or repulsive forces between the tip and the sample and provides information on the topography of the surface. AFM probes the surfaces of the sample with a sharp tip a couple of micrometers long and often less than 100 Å in diameter. Depending on the interaction between the AFM tip and surface, there exist various AFM modes such as contact AFM, noncontact AFM, intermittent contact AFM etc.

**Dip-pen nanolithography (DPN)** A recently developed technique which is very useful in the field of nanofabrication and nanometer sized surface modification. It uses the SPM tip as a pen and the target chemical compound as ink to “write” on the sample surface just like a pen writing on paper. This method can produce nanometer sized patterns, which is critical for the nanofabrication of molecular devices and complicated nanostructures.

**Hybrid nanodevices** A generation of new nanometer sized functional devices that are built by combining soft materials with conventional solid-state devices. These include biological/chemical sensors to detect harmful viruses/environments and protein motor-based nanomechanical systems.

**Microcontact printing** A recently developed high resolution printing method which utilizes micro- or submicrometer scale polymer stamps to “print” general organic molecules onto solid surfaces. It has a principle similar to conventional printing techniques, but unlike conventional printing, it utilizes solid substrates (e.g., gold, silicon, etc.) such as paper and soft materials such as ink. The printed feature size is usually in the micrometer scale, but it can be as small as a few tens of nanometers some considerations.

**Molecular recognition** The ability of molecular components to “recognize” other molecular components based on specific interaction forces (e.g., chemical bond, biomolecular interaction, electrostatic interaction, etc.).

**Nanofabrication** Nanometer-scale precision fabrication technology appeared with the development of nanotechnology. This technique can be used to design and produce nanometer sized devices that have distinct advantages such as ultrasmall size, multifunctionalities, and high sensitivity compared to conventional devices.

**Scanning probe microscopy** A widely used instrument in the field of surface/interface research which can provide atomic scale and real-time/real space topography information of the scanned surface. It works by scanning the nanometer sized tip on the substrate surface (or sample surface scanning under the tip) and measuring various interactions (e.g., attractive or repulsive forces, tunneling current, frictional force, etc.) between the tip and the substrate surface, providing the topographic information of the substrate surface. It includes STM, AFM, magnetic force microscopy, LFM, etc.

**Self-assembled monolayer (SAM)** When certain molecules are in contact with a certain solid surface, the molecules will form a highly packed, naturally uniform monolayer on the solid surface via chemical reactions between the function groups of the molecules and the active atoms of the solid surface. It is now widely used

in the field of corrosion inhibition, surface modification, nanofabrication, etc.

**Soft materials** Materials like classical fluids, liquid crystals, polymers, colloids, and emulsions are representative of what are now identified as “soft” as opposed to “hard” materials. They are materials that flow or distort easily in response to shear and other external forces. When deposited or put on the solid surface, some soft materials can form a chemically stable and highly oriented thin film or even monolayers, which can be used in the fields of nanofabrication and surface modification.

**Surface-templated assembly** A new assembly method based on the interaction force existing between the molecules on the solid surface and the target molecules. In this method, the desired region on the solid substrate is first coated with organic molecules with specific chemical functional groups, and then the substrate is placed in the solution of target molecules (or nanostructures). Due to the specific attractive force between the chemical functional groups on the surface and molecules in the solution, the assembly of molecules (or nanostructures) from the solution is directed only onto the functionalized region of the surface. Especially useful in mass production of some nanometer sized devices.

## ACKNOWLEDGMENTS

We acknowledge the AFOSR for support of our DPN works and the DARPA for supporting our protein motor research. We also thank P. Bryant Chase at Florida State University for supplying protein motors. Pradeep Manandhar is acknowledged for his help in preparing some figures.

## REFERENCES

1. D. Geyer, “Collecting Writing Instruments.” Schiffer, 1990.
2. J. Bourque, “The Waterman Pen.” *Am. Heritage* 43, 30 (1992).
3. S. Okazaki, *J. Vac. Sci. Technol. B* 9, 2829 (1991).
4. Y. Xia and G. M. Whitesides, *Angew. Chem. Int. Ed.* 37, 550 (1998).
5. Y. Cui and C. M. Lieber, *Science* 291, 851 (2001).
6. S. Hong, J. Zhu, and C. A. Mirkin, *Science* 286, 523 (1999).
7. R. Piner, J. Zhu, F. Xu, S. Hong, and C. A. Mirkin, *Science* 283, 661 (1999).
8. S. Hong and C. A. Mirkin, *Science* 288, 1808 (2000).
9. D. A. Weinberger, S. Hong, C. A. Mirkin, B. W. Wessels, and T. B. Higgins, *Adv. Mater.* 12, 1600 (2000).
10. S. Hong, J. Zhu, and C. A. Mirkin, *Langmuir* 10, 7897 (1999).
11. J. Jang, S. Hong, G. C. Schatz, and M. A. Ratner, *J. Chem. Phys.* 115, 2721 (2001).
12. A. Ivanisevic and C. A. Mirkin, *J. Am. Chem. Soc.* 123, 7887 (2001).
13. Y. Li, B. W. Maynor, and J. Liu, *J. Am. Chem. Soc.* 123, 2105 (2001).
14. B. W. Maynor, Y. Li, and J. Liu, *Langmuir* 17, 2575 (2001).
15. L. M. Demers and C. A. Mirkin, *Angew. Chem. Int. Ed.* 40, 3069 (2001).
16. L. M. Demers, S.-J. Park, A. Taton, Z. Li, and C. A. Mirkin, *Angew. Chem. Int. Ed.* 40, 3071 (2001).
17. A. Ivanisevic, J.-H. Kim, K.-B. Lee, S.-J. Park, L. M. Demers, K. J. Watson, and C. A. Mirkin, *J. Am. Chem. Soc.* 123, 12424 (2001).
18. A. Noy, A. E. Miller, J. E. Klare, B. L. Weeks, B. W. Woods, and J. J. DeYoreo, *Nano Letters* 2, 109 (2002).
19. M. Su, X. Liu, S.-Y. Li, V. P. Dravid, and C. A. Mirkin, *J. Am. Chem. Soc.* 124, 1560 (2002).
20. D. L. Wilson, R. Martin, S. Hong, M. Cronin-Golomb, C. A. Mirkin, and D. L. Kaplan, *Proc. Natl. Acad. Sci. USA* 98, 13660 (2001).
21. E. Delamarche, B. Michel, H. Kang, and Ch. Gerber, *Langmuir* 10, 4103 (1994).
22. T. Sawaguchi, S. Yoshimoto, F. Mizutani, and I. Taniguchi, *Electrochim. Acta* 45, 2861 (2000).
23. H. Zhang, H.-X. He, J. Wang, and Z.-F. Liu, *Langmuir* 16, 4554 (2000).
24. P. Fenter, P. Eisenberger, J. Li, N. Camillone, S. Bernasek, G. Scoles, T. A. Ramanarayanan, and K. S. Liang, *Langmuir* 7, 2013 (1991).
25. M. H. Schoenfish and J. E. Pemberton, *J. Am. Chem. Soc.* 120, 4502 (1998).
26. T. Vondrak, C. J. Cramer, and X. Y. Zhu, *J. Phys. Chem. B* 103, 8915 (1999).
27. P. E. Laibinis, G. M. Whitesides, D. L. Allara, Y. T. Tao, A. N. Parikh, and R. G. Nuzzo, *J. Am. Chem. Soc.* 113, 7152 (1991).
28. H. Rieley and G. K. Kendall, *Langmuir* 15, 8867 (1999).
29. J. F. Dorsten, J. E. Maslar, and P. W. Bohn, *Appl. Phys. Lett.* 66, 1755 (1995).
30. Y. Gu, Z. Lin, R. A. Butera, V. S. Smentkowski, and D. H. Waldeck, *Langmuir* 11, 1849 (1995).
31. D. Zerulla, D. Mayer, K. H. Hallmeier, and T. Chassé, *Chem. Phys. Lett.* 311, 8 (1999).
32. H. A. Biebuyck, C. D. Bain, and G. M. Whitesides, *Langmuir* 10, 1825 (1994).
33. R. G. Nuzzo and D. L. Allara, *J. Am. Chem. Soc.* 105, 4481 (1983).
34. E. B. Troughton, C. D. Bain, G. M. Whitesides, R. G. Nuzzo, D. L. Allara, and M. D. Porter, *Langmuir* 4, 365 (1988).
35. E. Katz, N. Itzhak, and I. Willner, *J. Electroanal. Chem.* 336, 357 (1992).
36. J. E. Chadwick, D. C. Myles, and R. L. Garrell, *J. Am. Chem. Soc.* 115, 10364 (1993).
37. K. Uvdal, D. C. Myles, and R. L. Garrell, *Langmuir* 11, 1252 (1995).
38. J. J. Hickman, P. E. Laibinis, D. I. Auerbach, C. Zou, T. J. Gardner, G. M. Whitesides, and M. S. Wrighton, *Langmuir* 8, 357 (1992).
39. J. B. Brzoska, I. B. Azouz, and F. Rondelez, *Langmuir* 10, 4367 (1994).
40. M. J. Wirth, R. W. P. Fairbank, and H. O. Fatunmbi, *Science* 275, 44 (1997).
41. A. N. Parikh, D. L. Allara, I. B. Azouz, and F. Rondelez, *J. Phys. Chem.* 98, 7577 (1994).
42. M. R. Linford and C. E. D. Chidsey, *J. Am. Chem. Soc.* 115, 12631 (1993).
43. M. R. Linford, P. Fenter, P. M. Eisenberger, and C. E. D. Chidsey, *J. Am. Chem. Soc.* 117, 3145 (1995).
44. A. Bansal, X. Li, I. Lauermann, N. S. Lewis, S. I. Yi, and W. H. Weinberg, *J. Am. Chem. Soc.* 118, 7225 (1996).
45. D. L. Allara and R. G. Nuzzo, *Langmuir* 1, 52 (1985).
46. Y. T. Tao, M. T. Lee, and S. C. Chang, *J. Am. Chem. Soc.* 115, 9547 (1993).
47. J. P. Folkers, C. B. Gorman, P. E. Laibinis, S. Buchholz, G. M. Whitesides, and R. G. Nuzzo, *Langmuir* 11, 813 (1995).
48. M. E. Thompson, *Chem. Mater.* 6, 1168 (1994).
49. T. J. Gardner, C. D. Frisbie, and M. S. Wrighton, *J. Am. Chem. Soc.* 117, 6927 (1995).
50. P. E. Laibinis and G. M. Whitesides, *J. Am. Chem. Soc.* 114, 1990 (1992); R. Colorado, Jr., R. J. Villazana and T. R. Lee, *Langmuir* 14, 6337 (1998).
51. S. W. Han, T. H. Ha, C. H. Kim, and K. Kim, *Langmuir* 14, 6113 (1998); C. D. Bain, Y.-T. Tao, J. E. Ewall, G. M. Whitesides, and R. G. Nuzzo, *J. Am. Chem. Soc.* 111, 321 (1989).
52. M. D. Porter, T. B. Bright, D. L. Allara, and C. E. D. Chidsey, *J. Am. Chem. Soc.* 109, 3559 (1987); S. W. Han, C. H. Kim, S. H. Hong, Y. K. Chung, and K. Kim, *Langmuir* 15, 1579 (1999); W. Azzam, B. I. Wehner, R. A. Fischer, A. Terfort, and C. Woll, *Langmuir* 18, 7766 (2002).

53. M. Lewis and M. J. Tarlov, *J. Am. Chem. Soc.* 117, 9574 (1995); S. W. Joo, S. W. Han, and K. Kim, *Langmuir* 16, 5319 (2000).
54. N. K. Chaki, M. Aslam, J. Shama, and K. Vijayamohan, *Proc. Indian Acad. Sci. (Chem. Sci.)* 113, 659 (2001).
55. (a) M. J. Tarlov, D. R. F. Burgess, and G. Fillen, Jr., *J. Am. Chem. Soc.* 115, 5305 (1993). (b) T. M. Herne and M. J. Tarlov, *J. Am. Chem. Soc.* 119, 8916 (1997). (c) H. Takiguchi, K. Sato, T. Ishida, K. Abe, K. Yase, and K. Tamada, *Langmuir* 16, 1703 (2000).
56. T. Sawaguchi, F. Mizutani, and I. Taniguchi, *Langmuir* 14, 3565 (1998); T. Nakamura, H. Kondoh, M. Matsumoto, and H. Nozoye, *Langmuir* 12, 5977 (1996).
57. K. Tamada, M. Hara, H. Sasabe, and W. Knoll, *Langmuir* 13, 1558 (1997).
58. C. B. Gorman, Y. He, and R. L. Carroll, *Langmuir* 17, 5324 (2001).
59. R. Lenigk, M. Carles, N. Y. Ip, and N. J. Sucher, *Langmuir* 17, 2497 (2001).
60. R. Piner and C. A. Mirkin, *Langmuir* 13, 6864 (1997).
61. J.-H. Lim and C. A. Mirkin, *Adv. Mater.*, in press.
62. G. Wurtz, R. Bachelot, and P. Royer, *Rev. Sci. Instrum.* 69, 1735 (1998).
63. S. S. Wong, E. Joselevich, A. T. Woolley, C. L. Cheung, and C. M. Lieber, *Nature* 394, 52 (1998); S. S. Wong, J. D. Harper, P. T. Lansbury, and C. M. Lieber, *J. Am. Chem. Soc.* 120, 603 (1998).
64. C. Bustamante, D. A. Erie, and D. Keller, *Curr. Opin. Struct. Biol.* 4, 750 (1994); C. Bustamante and D. Keller, *Phys. Today* 48, 32 (1998).
65. G. S. Ferguson, M. K. Chaudhury, G. B. Sigal, and G. M. Whitesides, *Science* 253, 1230 (1991).
66. A. A. Baski, in "Advanced Semiconductor and Organic Nanotechniques" (H. Morkoc, Ed.), Part 3, p. 1. Academic Press, San Diego, 2002.
67. M. Zhang, D. Bullen, S.-W. Chung, S. Hong, K. S. Ryu, Z. Fan, C. A. Mirkin, and C. Liu, *Nanotechnology* 13, 212 (2002).
68. A. Kumar and G. M. Whitesides, *Appl. Phys. Lett.* 63, 2002 (1993).
69. J. L. Wilbur, A. Kumar, E. Kim, and G. M. Whitesides, *Adv. Mater.* 6, 600 (1994); A. Kumar, N. L. Abbott, E. Kim, H. A. Biebuyck, and G. M. Whitesides, *Acc. Chem. Res.* 28, 219 (1995); G. M. Whitesides and C. B. Gorman, in "Handbook of Surface Imaging and Visualization" (A. T. Hubbard, Ed.), p. 713. CRC Press, Boca Raton, FL, 1995; J. L. Wilbur, A. Kumar, H. A. Biebuyck, E. Kim, and G. M. Whitesides, *Nanotechnology* 7, 452 (1996); Y. Xia, X.-M. Zhao, and G. M. Whitesides, *Microelectron. Eng.* 32, 255 (1996); H. A. Biebuyck, N. B. Larsen, E. Delamarche, and B. Michel, *IBM J. Res. Dev.* 41, 159 (1997).
70. A. Kumar, H. Biebuyck, and G. M. Whitesides, *Langmuir* 10, 1498 (1994).
71. Y. Xia, E. Kim, and G. M. Whitesides, *J. Electrochem. Soc.* 143, 1070 (1996); X. M. Yang, A. A. Tryk, K. Hasimoto, and A. Fujishima, *Appl. Phys. Lett.* 69, 4020 (1996).
72. T. P. Moffat and H. Yang, *J. Electrochem. Soc.* 142, L220 (1995).
73. Y. Xia, E. Kim, M. Mrksich, and G. M. Whitesides, *Chem. Mater.* 8, 601 (1996).
74. L. B. Goetting, T. Deng, and G. M. Whitesides, *Langmuir* 15, 1182 (1999).
75. Y. Xia, M. Mrksich, E. Kim, and G. M. Whitesides, *J. Am. Chem. Soc.* 117, 9576 (1995); P. M. St. John and H. G. Craighead, *Appl. Phys. Lett.* 68, 1022 (1996); D. Wang, S. G. Thomas, K. L. Wang, Y. Xia, and G. M. Whitesides, *Appl. Phys. Lett.* 70, 1593 (1997).
76. Y. Xia, X.-M. Zhao, E. Kim, and G. M. Whitesides, *Chem. Mater.* 7, 2332 (1995).
77. M. Lercel, R. C. Tiberio, P. F. Chapman, H. G. Craighead, C. W. Sheen, A. N. Parikh, and D. L. Allara, *J. Vac. Sci. Technol. B* 11, 2823 (1993).
78. W. T. Huck, L. Yan, A. Stroock, R. Haag, and G. M. Whitesides, *Langmuir* 15, 6862 (1999).
79. H. S. Carslaw and J. C. Jaeger, "Conduction of Heat in Solids." Oxford Univ. Press, London, 1959.
80. P. E. Sheehan and L. J. Whitman, *Phys. Rev. Lett.* 88, 156104 (2002).
81. B. L. Weeks, A. Noy, A. E. Miller, and J. J. De Yoreo, *Phys. Rev. Lett.* 88, 255505 (2002).
82. B. W. Maynor, Y. Li, and J. Liu, *Langmuir* 17, 2575 (2001).
83. S. Xu and G. Y. Liu, *Langmuir* 13, 127 (1997); K. Wadu-Mesthrige, S. Xu, and G. Y. Liu, *Langmuir* 15, 8580 (1999); N. A. Amro, S. Xu, and G. Y. Liu, *Langmuir* 16, 3006 (2000).
84. E. Delamarche, H. Schmid, A. Bietsch, N. B. Larsen, H. Rothuizen, B. Michel, and H. Beibuyck, *J. Phys. Chem. B* 102, 3324 (1998).
85. T. A. Taton, C. A. Mirkin, and R. L. Letsinger, *Science* 289, 1757 (2000).
86. Y. Cui, Q. Wei, H. Park, and C. M. Lieber, *Science* 293, 1289 (2001).
87. G. S. Wilson and Y. Hu, *Chem. Rev.* 100, 2693 (2000); L. C. Clark, Jr., in "Biosensors: Fundamentals and Applications." Oxford Univ. Press, New York, 1987.
88. M. M. Miller, P. E. Sheehan, R. L. Edelstein, C. R. Tamanaha, L. Zhong, S. Bounnak, L. J. Whitman, and R. J. Colton, *J. Magn. Magn. Mater.* 225, 138 (2001); R. G. Rudnitsky, E. M. Chow, and T. W. Kenny, *Sensors Actuators A* 83, 256 (2000).
89. J. Fritz, M. K. Baller, H. P. Lang, H. Rothuizen, P. Vettiger, E. Meyer, H. J. Güntherodt, Ch. Gerber, and J. K. Gimzewski, *Science* 288, 316 (2000).
90. J. R. Sellers and B. Kachar, *Science* 249, 406 (1990); R. K. Soong, G. D. Bachand, H. P. Neves, A. G. Olkhovets, H. G. Craighead, and C. D. Montemagno, *Science* 290, 1555 (2000).
91. X. Liu, L. Fu, S. Hong, V. P. Dravid, and C. A. Mirkin, *Adv. Mater.* 14, 231 (2002).
92. J. Hu, R. G. Beck, T. Deng, R. M. Westervelt, K. D. Maranowski, A. C. Gossard, and G. M. Whitesides, *Appl. Phys. Lett.* 71, 2020 (1997).
93. L. Demers, D. S. Ginger, S.-J. Park, Z. Li, S.-W. Chung, and C. A. Mirkin, *Science* 296, 1836 (2002).

# Nanodielectrophoresis: Electronic Nanotweezers

P. J. Burke

University of California, Irvine, California, USA

## CONTENTS

1. Introduction
  2. Overview  
of Dielectrophoresis
  3. Electronic versus  
Optical Tweezers
  4. Trapping and Manipulation  
of Micron-Sized Objects
  5. Trapping and Manipulation  
of Nano-Sized Objects
  6. Applications
  7. Unanswered Questions
  8. Conclusions
- Glossary  
References

## 1. INTRODUCTION

At neutral pH, DNA is a charged molecule. As such, it responds directly to an electric field, the phenomenon of *electrophoresis*. In contrast, the phenomenon of *dielectrophoresis* occurs when there is a dc or an ac electric field *gradient*. In that case, the development of nonuniform electric fields causes a force on any polarizable object, charged or neutral. The term dielectrophoresis was coined by Pohl in 1951 [1], and the general principles are outlined in his 1978 book of the same title [2]. Since then, the use of microfabricated electrodes has been employed for separating micron-sized objects such as cells, and this technology is currently being integrated with lab-on-a-chip systems. This review article discusses recent progress at extending the practice of dielectrophoresis to the nanoscale, for applications in nanomanufacturing, nanobiotechnology, and molecular electronics. Compared to the use of dielectrophoresis for the manipulation of cells, the use of electric fields at the nanoscale to assemble nanocircuits is still in its infancy.

## 1.1. Other Reviews

The main reference for the fundamentals of dielectrophoresis is Pohl's 1978 book [2]. The physics of the dielectric properties of biological molecules in solution are covered in a 1979 book by Pethig [3] and a 1978 book by Grant et al. [4]. Pethig [5, 6] has a good review of applications of dielectrophoresis in biotechnology. Another review article covering the manipulation of cells with electric fields is in Führ's 1996 book chapter [7, 8]. The topic of dielectrophoresis is covered in Madou's textbook on microfabrication [9]. A review by Hughes [10] discusses some applications of dielectrophoresis in nanotechnology. This review will also be concerned primarily with the applications of dielectrophoresis in nanotechnology: "nanodielectrophoresis."

## 2. OVERVIEW OF DIELECTROPHORESIS

The discovery of dielectrophoresis (DEP) goes all the way back to at least 600 B.C., when Thales of Miletus in Turkey observed that rubbed amber attracted small particles of fluff [2]. In retrospect the amber, being charged up from the rubbing, generated an electric field which polarized the fluff particles. The induced dipole in the fluff particles was acted on by the (nonuniform) electric fields, attracting it to the charged amber. Today we would call this effect (dc) positive dielectrophoresis.

In Figure 1, the principle is illustrated schematically. If a polarizable object is placed in an electric field, there will be an induced positive charge on one side of the object and an induced negative charge (of the same magnitude as the induced positive charge) on the other side of the object. The positive charge will experience a pulling force; the negative charge will experience a pushing force. In a uniform field, as depicted in Figure 1A, the pulling force will cancel the pushing force, and the net force will be zero. However, in a nonuniform field, as depicted in Figure 1B, the electric field will be stronger on one side of the object and weaker on the other side of the object. Hence, the pulling and pushing

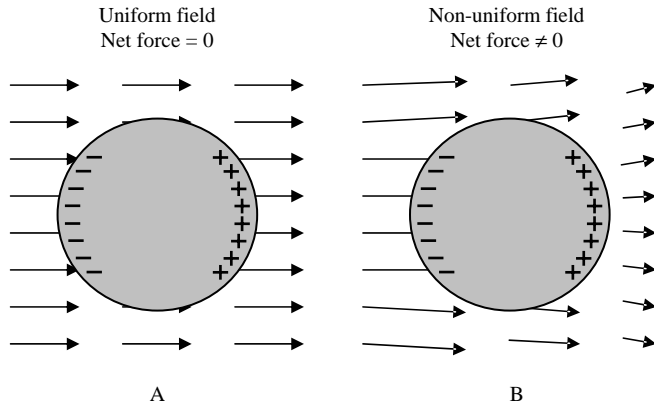


**Figure 1.** Schematic depiction of dielectrophoresis. The direction of the arrows represents the direction of the electric field; the length of the arrows represents the magnitude of the electric field.

forces will not cancel, and there will be a net force on the object.

In this simple overview we have neglected the polarizability of the surrounding medium. If both the medium and the polarizable particle are considered, then one comes to the conclusion that there are two classes of DEP: positive and negative. If the suspended particle has a polarizability higher than that of the surrounding medium, then the DEP force pushes the particle toward the higher electric field region. This is called *positive dielectrophoresis*. If the suspended particle has a polarizability less than the surrounding medium, the particle is pushed toward the region of weaker electric field, and this is called *negative dielectrophoresis*.

## 2.1. Quantitative Force Predictions

In an electric field  $\vec{E}$ , a dielectric particle behaves as an effective dipole with (induced) dipole moment  $\vec{p}$  proportional to the electric field, that is,

$$\vec{p} \propto \vec{E} \quad (1)$$

The constant of proportionality depends in general on the geometry of the dielectric particle. In the presence of an electric field gradient, the force on a dipole is given by

$$\vec{F} = (\vec{p} \cdot \nabla) \vec{E} \quad (2)$$

Combining the two equations, and using known results for the relationship between  $\vec{p}$  and  $\vec{E}$  for a *spherical* particle of radius  $r$  and dielectric constant  $\epsilon_p$ , and taking into account the medium dielectric constant  $\epsilon_m$ , it can be shown that the force acting on a spherical particle (the *dielectrophoresis* force) is given by [2, 11]

$$\vec{F}_{DEP} = 2\pi v \epsilon_m \alpha_r \nabla (\vec{E}_{RMS}^2) \quad (3)$$

where  $v$  is the volume of the particle,  $\vec{E}_{RMS}$  is the RMS value of the electric field (assuming a sinusoidal time dependence), and  $\alpha_r$  is the real part of what is called the *Clausius–Mosotti* factor, which is related to the particle dielectric constant  $\epsilon_p$  and medium dielectric constant  $\epsilon_m$  by

$$\alpha_r \equiv \text{Re} \left( \frac{\epsilon_p^* - \epsilon_m^*}{\epsilon_p^* + 2\epsilon_m^*} \right) \quad (4)$$

Here the star (\*) denotes that the dielectric constant is a complex quantity, and it can be related to the conductivity  $\sigma$  and the angular frequency  $\omega$  through the standard formula

$$\epsilon^* = \epsilon - i \frac{\sigma}{\omega} \quad (5)$$

Equation (5) also takes into account surface conductances [12–14] of the particles.

We must make several comments now about Eq. (3). First of all, the Clausius–Mosotti factor can vary between  $-0.5$  and  $+1.0$ . When it is positive, particles move toward higher electric field regions, and this is termed *positive dielectrophoresis*. When it is negative, the particles move toward smaller electric field regions, and this is termed *negative dielectrophoresis*.

Second, the force grows smaller as the particle volume. This has important implications for the manipulation of nano-sized particles, as we will discuss below. Of course this is a bulk, classical calculation. Surface charges and quantum effects will no doubt be important at the molecular level, and these need to be dealt with. Therefore, the application of Eq. (3) to single molecules may not be quantitatively valid.

Third, the dielectric constants of the medium and particle can be highly frequency dependent. This gives rise to a force that can be different at different frequencies, and this fact can be exploited for practical micro- and nanomanipulations based on dielectrophoresis. For example, at one frequency positive dielectrophoresis may prevail, while at another frequency negative dielectrophoresis may prevail. These effects are all buried in the physics of the dielectric response function  $\epsilon$ .

Fourth, the derivation of Eq. (3) assumes that the electric field does not vary too strongly; this will have implications when we compare to optical tweezers below.

Finally, Eq. (3) is true for both dc *and* ac electric fields. While there are practical advantages to using ac electric fields to be discussed below, the mathematics of the dielectrophoresis force does not differentiate between dc and ac. Furthermore, it should be noted that the *direction* of the electric field does not matter. That is to say, in the dc case, for (e.g.) positive dielectrophoresis, the particle moves from the region of weaker field to the region of stronger field *magnitude*, regardless of the *direction* in which the field is pointing. For an ac field, the particle experiences a time-varying force, but the time-averaged direction of that time-varying force is always the same, even though the direction of the electric field vector is changing in time. In most cases, the ac component of the dielectrophoretic force can be neglected and we need only concern ourselves with the dc (i.e., time-averaged) component, which is the one given by Eq. (3).

## 2.2. Generation of Electric Field Gradients

Historically [2], the use and study of dielectrophoresis was between a sharp pin and a flat surface, because that is the easiest geometry in which one can create a strong field gradient, hence a strong dielectrophoretic force. This has been used to manipulate cells in solution [5, 6], since a cell is polarizable. It has also been used to deflect individual molecules in molecular beams [15]. This application can be considered the first application of nanodielectrophoresis, although the molecular beams were in a high-vacuum system.

Since the advent of optical and then electron-beam lithography, the use of micro- and nanofabricated planar metal electrodes on insulating substrates has achieved much more attention, since it allows many different flexible geometries to be designed, tested, and used. Moreover, by using small gaps between electrodes, large electric field strengths can be achieved, thus further increasing (in general) the achievable dielectrophoretic force.

Although any arbitrary geometry for planar electrodes can be easily designed and fabricated with modern lithography, the three most commonly used geometries are shown in Figure 2. (The DEP force from these and other geometries can be calculated numerically [16, 17].) Part A shows the simplest geometry, a gap between two electrodes. Because the electrodes are planar, there will be fringing fields out of the plane which are very nonuniform. This design is useful for positive dielectrophoresis, in which case particles are attracted to the edges of the electrodes, or negative dielectrophoresis, in which case particles are pushed away from the plane of the electrodes. In order to achieve a higher electric field gradient, geometry B is sometimes used. The castellations can be square (as shown), triangular, or circular. For both geometries A and B, interdigitated fingers are often used. Geometry C is used normally for negative dielectrophoresis. Huang and Pethig showed that particles experiencing negative dielectrophoresis that are in the plane of the electrodes will get trapped in the center of the

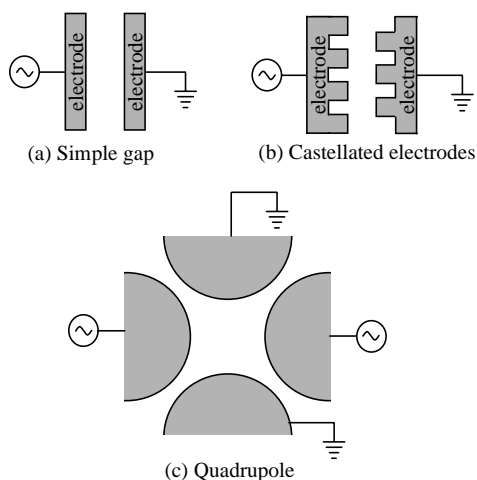


**Figure 2.** The most commonly used geometries for the study of dielectrophoresis. The electrodes are usually thin metal films (1–100 nm) fabricated lithographically on an insulating substrate.

electrode geometry [18]. Another design which has received some attention is a spiral electrode design [19].

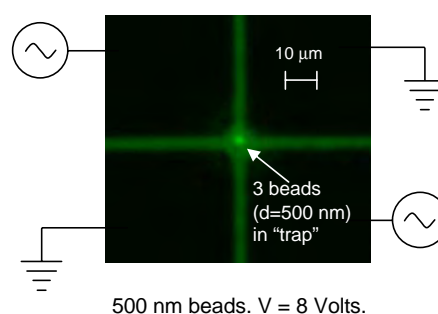
Modern interest in nanodielectrophoresis, in contrast to that applied to molecular beams in high-vacuum environments, is concerned with the manipulation of molecules in solution, especially for applications in nanobiotechnology, where wet environments are necessary for life itself, but also as methods of nanomanufacturing molecular electronic circuits, integrated with micro- and nanofabricated electrodes. After the dielectrophoresis-assisted nanofabrication occurs, the sample can be dried and the remaining molecules that were placed in position while dissolved now can form the basis of some tailor-designed circuit which in principle was fabricated one molecule at a time. This vision is currently under development but in principle there is no reason it cannot be achieved, as we discuss in the remainder of this article.

## 2.3. Traps for Negative Dielectrophoresis

For negative dielectrophoresis, the polarizable objects feel a force pushing them *away* from the high field region. Therefore, for most planar geometries, the particles are pushed away from the substrate where the electrodes reside. In 1991, Huang and Pethig calculated [18] the necessary geometry that electrodes need to have in order to *trap* particles using negative dielectrophoresis at specific locations on the plane of the substrate. The geometry they found which traps a particle at a specific point in the plane of the electrodes is a quadrupole-like geometry. This trap is only in two dimensions, and in the third dimension (perpendicular to the plane of the electrodes), the particle is still not trapped. Gravity or some other force must be exerted to bring the particle close enough to the plane of the electrodes to feel the dielectrophoretic force of the electrodes.

Later, work of Schnelle and co-workers [20] and Fuhr and co-workers [21] considered geometries necessary for trapping of particles in all three dimensions. They name these traps “cages.” The most straightforward geometry realized and tested consisted of two quadrupole traps fabricated on two microscope slides which were mounted facing each other with a small gap (of about 0.1 mm). In that work, they trapped 10- $\mu\text{m}$  latex particles and cells in three dimensions, with applied ac voltages up to 1 GHz in frequency.

We show in Figure 3 an example realization of a quadrupole trap: four gold electrodes surrounding a central



500 nm beads.  $V = 8$  Volts.

**Figure 3.** Electrodes to trap small particles. Three 500-nm beads can be seen fluorescing but not resolved. We have also been able to trap a single 500-nm bead (not shown).



region with 10- $\mu\text{m}$  gaps are used to trap a 500-nm latex bead [22]. The frequency used for these studies was 1 MHz, with a voltage of 8 V. With smaller gaps it should be possible to trap much smaller particles, as we discuss below.

## 2.4. Scaling with Particle and Electrode Size

In order to calculate the force acting on any given polarizable particle, one can use Eq. (3) as long as the electric field intensity and (more importantly) its spatial gradient are known. For arbitrary electrode geometries it is possible to numerically calculate this force. However, some simple electrode geometries can be calculated analytically in order to give some general insight into what can be expected for a more complicated geometry. The case of two concentric spheres in this regard can be very enlightening, as the radius of curvature can be used as a rough estimate for the smallest feature size of a given electrode.

The electric field between two concentric spheres is straightforward to calculate, and based on this one can calculate the gradient of the electric field intensity. One finds [2]

$$\vec{\nabla}(\vec{E}_{RMS}^2) = -\frac{2r_1^2 r_2^2 V^2}{r^5 (r_2 - r_1)^2} \hat{r} \quad (6)$$

where  $\hat{r}$  is a unit vector in the radial direction,  $r_1$  is the radius of the inner electrode,  $r_2$  is the radius of the outer electrode,  $r$  is the distance from the origin, and  $V$  is the applied voltage, as shown in Figure 4. In the case where the inner electrode is very sharp compared to the distance to the outer electrode (i.e.,  $r_1/r_2 \ll 1$ ), this becomes

$$\vec{\nabla}(\vec{E}_{RMS}^2) \approx -\frac{2r_1^2 V^2}{r^5} \hat{r} \quad (7)$$

In this case the force exerted on a particle is given by

$$\vec{F}_{DEP} = -4\pi v \epsilon_m \alpha_r \frac{r_1^2 V^2}{r^5} \hat{r} \quad (8)$$

Now, if the particle were in a vacuum with no other forces acting upon it, then it would respond only to the DEP force. However, in solution, the particle is undergoing Brownian motion, and is continually being bombarded with other molecules of the solution. This thermal motion exerts

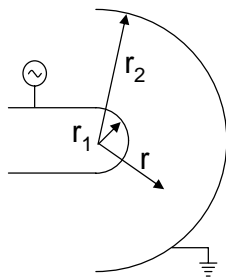


**Figure 4.** Spherical geometry electrodes for analytical calculation of dielectrophoretic force in the text.

an effective random force on the particle, whose maximum value is given roughly by [2]

$$F_{thermal} \approx k_B T / 2r_{particle} \quad (9)$$

where  $k_B$  is the Boltzmann constant,  $T$  is the temperature, and  $r_{particle}$  is the particle radius.

For DEP to be of use, the DEP force must overcome the randomizing thermal motion acting on the particle. In 1978, Pohl used 500  $\mu\text{m}$  for the radius of the inner electrode, 5000 V for the applied voltage, and 1 mm for the particle distance from the electrode, and concluded that particles smaller than 500 nm would not respond very well to the DEP force [2]. These numbers were pessimistic, and it should be possible to trap 1-nm and smaller particles, as we now show.

First, as our experiments [22], as well as other experiments [23–31] show, it is possible to use optical or electron-beam lithography to fabricate electrodes with much smaller radius of curvature than 500  $\mu\text{m}$  (as Pohl originally assumed), and hence to trap submicron particles (see Fig. 3). For example, in our experiments, we trapped 500-nm beads with less than 10 V applied to the electrodes.

Second, it is possible in principle to use carbon nanotubes or other nanowires as the electrodes themselves [22], which would have radius of curvatures of less than 1 nm. In this case, for a 1-nm particle that was a distance 100 nm away from the nanotube electrode, our calculations [32] indicate that the DEP force would exceed the thermal force at an applied voltage of only 50 mV. Experiments to test this scaling prediction with carbon nanotube electrodes are currently underway in the author's lab [22].

## 2.5. Electrorotation

Another effect of an ac electric field on a polarizable object is to *orient* that object with respect to an electric field. Specifically, the induced dipole moment of an object interacts with the electric field to produce a torque given by

$$\vec{T} = \vec{p} \times \vec{E} \quad (10)$$

where  $\vec{p}$  is the induced dipole. This effect can be used to orient DNA and nanotubes in solution, and also nanotubes during growth in gas or vacuum, as we will discuss below. It also can be used to orient cells and other micron-sized objects. The term *electrorotation* is usually applied to a situation where the direction of the electric field is rotating as a function of time. This can be achieved by using four electrodes surrounding a central region, where the ac voltage on each electrode is properly phased. Under the rotating electric field direction, the torque also rotates, and hence the particle rotates. This effect is reviewed in [8, 33].

## 2.6. Traveling Wave Dielectrophoresis

The electrode geometries shown in Figure 2 are useful for trapping particles with either positive or negative dielectrophoresis. However, more sophisticated geometries are possible that allow a particle to be moved. Figure 5 shows schematically a set of electrodes with ac voltages adjusted in such a way as to generate a traveling wave electric field. This traveling wave can act on a polarizable particle and cause

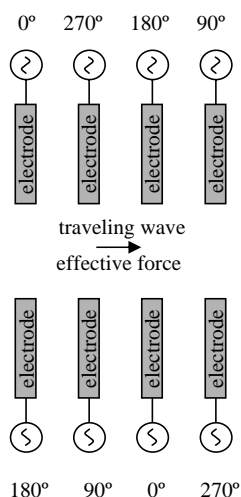


**Figure 5.** Schematic electrode geometry for traveling wave dielectrophoresis.

a net force in the direction of the traveling wave. In [34], Hagedorn et al. analyze geometries optimum for traveling wave dielectrophoresis. Fuhr in 1994 was able to design and demonstrate a particle manipulator that could apply force in two orthogonal directions [35].

## 2.7. Summary

The combined effects of dielectrophoresis, electrorotation, and traveling wave dielectrophoresis (TWD) have all gone under the same name: “pondermotive force,” as they have the same underlying physical origin. The relationship among these effects is explored in more detail in [8, 36–40]. With the combined use of dielectrophoretic traps, traveling wave dielectrophoresis, and electrorotation, it is possible to electronically control (via microfabricated electrodes) the three-dimensional position and orientation of a small micro- or nanoparticle that is suspended in liquid.

## 3. ELECTRONIC VERSUS OPTICAL TWEEZERS

From Eq. (3), we calculate that a typical dielectrophoretic force for a particle of size 100 nm will be roughly 1 fN; the force on a 1- $\mu\text{m}$  particle would be roughly 1 pN. In comparison, the force exerted by optical tweezers [41–46] is also the same order of magnitude. In fact both optical tweezers and dielectrophoresis are the same physical phenomena, only different frequencies. For example, our Eq. (3) is equivalent to Eq. (2) in [44]. (There is a factor of  $4\pi\epsilon_m$  difference due to the units, and an incorrect sign in the denominator of [44].) The equations look a little bit different, because optical engineers like to use the index of refraction, and electrical engineers like to use the dielectric constant; they are of course related through  $n = \sqrt{\epsilon}$ .

A difference between optical tweezers and electronic tweezers is that optical tweezers also affect particles whose size is comparable to the (optical) wavelength, of order  $\mu\text{m}$ , the so-called Mie limit. The analogy with electronic tweezers is more appropriate in the limit where the particle size is

smaller than the optical wavelength  $\lambda$ , the so-called Rayleigh limit. For optical tweezers in the Rayleigh limit (particle size  $\ll \lambda$ ), the force is proportional to the volume of the particle, as in DEP Eq. (3). For optical tweezers in the Mie limit (particle size  $\gg \lambda$ ), the force is independent of the particle size. Furthermore, optical scattering of light in optical tweezers is an important force, whose analog in electronic tweezers is not clear-cut.

One main similarity between optical and electronic tweezers is that, when applied to particles in solution, both must strive to overcome the random forces due to Brownian motion. Hence, it makes sense that the induced forces for both optical and electronic tweezers exert comparable forces. To date, both electronic and optical tweezers have not trapped particles with size below 10 nm. However, with nanowire or nanotube electrodes we predict that electronic tweezers can trap particles down to 1 nm in size, which may be useful for nanoassembly.

An advantage that electronic tweezers have over optical tweezers is *scalability*: millions or even billions of electronic tweezers could be easily, economically integrated onto a silicon chip for low-cost “lab-on-a-chip” systems. Additionally, the electronic trap can in principle hold a particle indefinitely, while the optical tweezers in some cases only last for a few seconds due to laser-induced damage. Third, the use of optical tweezers is not possible in optically opaque systems; in contrast, the use of electronic tweezers is difficult in conducting solutions [47], a severe restriction for *in vivo* operation.

Thus, as with everything, both types of tweezers have their own advantages and disadvantages; the choice of which to use will depend upon the application. In fact, in some applications, both types of tweezers have been used in the same experiment [48].

## 4. TRAPPING AND MANIPULATION OF MICRON-SIZED OBJECTS

### 4.1. Steel Balls

In a pioneering patent [49] granted in 1983, Batchelder proposed the use of lithographically patterned microelectrodes to manipulate and position chemical species, potentially with the ability to manipulate a single molecule, for electronic control of manufacturing. As such, this patent covers the lab-on-a-chip concepts as well as single molecule dielectrophoresis very well, much ahead of its time. Batchelder further described his techniques in a 1983 article [50], where he described one of the first instances of “traveling wave dielectrophoresis.” That was also one of the first instances of photolithographically patterned electrodes for applications in dielectrophoresis. Batchelder’s realization experimental apparatus was capable of manipulating 600- $\mu\text{m}$  steel balls and 1-mm water droplets in heptane.

In 1987, Washizu and co-workers used this effect to manipulate 15- $\mu\text{m}$  solid particles in solution, and also proposed to use it for moving cells [51]. A year later they reported moving blood cells (sheep erythrocytes) using this effect [52]. Those initial experiments were on traditionally machined electrodes.

## 4.2. Cells

Interestingly, in two papers appearing in 1989 and 1990 [53, 54], Masuda and co-workers used photolithography for fabricating microelectrodes in order to use DEP to control the position of living cells. They also developed what they coined “fluidic integrated circuit,” which currently would go by the term “lab-on-a-chip.” They used photolithography and a molding process with silicone to make microfluidic channels capable of handling individual cells, and they made a cell-sorter based on dielectrophoresis: cells entering through one microfabricated inlet could be deflected electronically into one of two microfabricated outlets. We show in Figure 6 an example of using negative dielectrophoresis to trap human breast cancer cells in a planar quadrupole trap [55].

As this review is meant to cover mainly nanodielectrophoresis, we will only briefly highlight some of the applications of dielectrophoresis in cell manipulation. The polarizability of a cell is a complicated function of its membranes and inner workings generally, and generally depends on frequency. By exploiting the difference in the frequency-dependent dielectric properties of different cells, it is possible to separate out many different kinds of cells from one another and from other microorganisms in solution.

The first separation of viable and nonviable (yeast) cells by dielectrophoresis was in 1966 [56]. Chloroplasts were manipulated in 1971 [57]. Cells can undergo both positive and negative dielectrophoresis as was shown in [58, 59]. The separation of viable versus nonviable yeast cells was studied carefully with microfabricated electrodes in [60–62]. Different species of bacteria were separated in [63, 64]. Electrorotation was used to separate leukemia cells from blood in [65]. Electrorotation was used to separate human breast cancer cells from blood in [66]. Concentration of CD34+ from peripheral-stem-cell harvests was achieved in [67].

TWD linear motion of cells was shown in [34, 68]. Viable and nonviable yeast cells were separated with TWD in [69]. TWD was used to separate white blood cells from erythrocytes in [70]. Continuous separation is also possible (viable vs. nonviable yeast cells) [71]. Separation of trophoblast cells from peripheral blood mononuclear cells was achieved in [72]. Separation of breast cancer cells from normal T-lymphocytes (among other things) was achieved using DEP FFF (see next section) in [73]. The manipulation of *E. coli* and other bacteria with photolithography-fabricated electrodes was reported in 1988 in [74]. The *E. coli*

were attracted to the high fringing field regions of interdigitated castellated electrodes. Cervical carcinoma cells were separated from peripheral blood cells in [75]. Living (*Eremosphaera Viridis*) cells were trapped in quadrupole and octopole traps in [20]. An extruded-quadrupole geometry (where the electrodes are metallic posts) was used for cell manipulation in [76]. The effect on cells of the large electric field strengths necessary for DEP (typically  $10^6$  V/m) was investigated by Archer et al. [77], who found a 20–30% increase in the expression of fos protein, as well as up-regulation of unidentified genes. While the large electric fields are not fatal to cells studied, and their long-term effect on cells manipulated with DEP seems to be minimal, at this stage there is insufficient evidence to draw more quantitative conclusions about the effects of exposure to high electric fields.

We note that, once the electrodes are in place for the dielectrophoretic manipulation of cells, it is straightforward and economical to integrate further optical and electronic measurements that are complementary to DEP techniques into the same measurement platform. These can include optical and electronic methods of genetic expression profiling using microarrays, with applications in point-of-care clinical diagnostics, biological warfare detection, and many other applications. For example, Cheng and co-workers separated *E. coli* bacteria from a mixture containing human blood cells and integrated this with cell lysing and DNA hybridization analysis on a single chip [78]. The integration of electrophoresis and dielectrophoresis using the same electrodes for manipulating *E. coli* cells with DEP and antibodies with electrophoresis was developed in [79]. DEP was used to separate certain cell types from complex cell populations, which significantly improved the accuracy of gene expression profiling in [80]. In the spirit of integration mentioned above, an integrated system using DEP, DNA amplification, and electronic DNA hybridization for the detection of *E. coli* and other biological agents was recently developed [81].

## 4.3. Field Flow Fractionation (FFF)

Field flow fractionation (FFF) is a very general chromatographic separation technique in chemistry and biology [82]. The use of dielectrophoresis as the force in field flow fractionation was proposed and analyzed by Davis and Giddings in 1986 [83]. The principle of dielectrophoretic field flow fractionation (DEP FFF) is shown schematically in Figure 7. Part A shows interdigitated finger electrodes, and parts B and C depict the levitation of latex beads when an ac voltage is applied to the electrodes. The levitation height is a function of the dielectric properties of the particle being levitated. If these electrodes are introduced into a laminar flow chamber (typically  $100\ \mu\text{m}$  thick), the flow velocity parallel to the chamber walls is also a function of height, as indicated schematically in part D. Thus, the speed at which a particle is swept through the chamber depends on the height at which it is levitated, which in turn is a function of its dielectric properties. Since different types of particles (or cells) generally have different dielectric properties, each takes a different time to traverse the chamber. This dependence can be used to separate different particles or cells, and is termed dielectrophoretic field flow fractionation (DEP FFF).

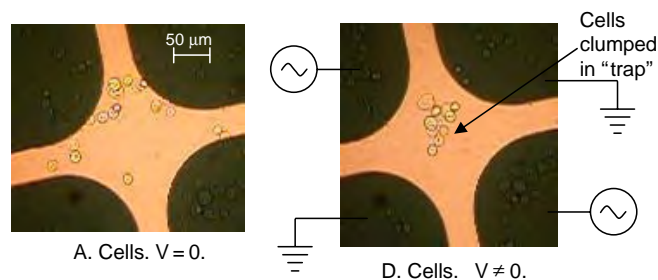


**Figure 6.** Dielectrophoretic trapping of human breast cancer cells (cell line HCC1806 from ATCC).

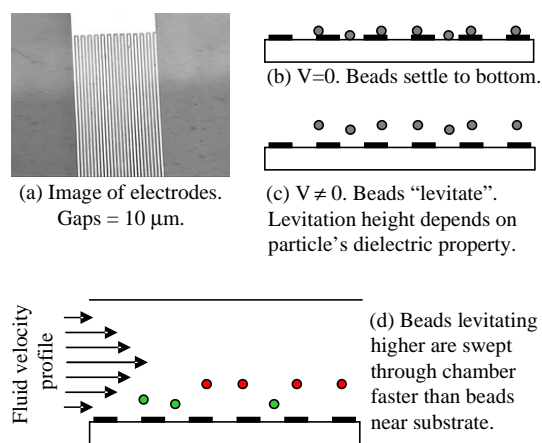


**Figure 7.** Schematic depiction of dielectrophoretic field flow fractionation (DEP FFF).

In 1994, Washizu and co-workers constructed a DEP FFF apparatus and used it to trap DNA of various sizes (9–48 kbp) and the protein avidin [84]. They were able to trap each macromolecule with some efficiency, but separation experiments were not reported. Initial experimental demonstration of DEP FFF separation was reported in 1997, where viable and nonviable yeast cells were separated [85], and human leukemia cells were separated from peripheral blood mononuclear cells [86]. In the same year, demonstration experiments on latex beads were performed [87]. Later experiments have demonstrated the separation of erythrocytes from latex beads [88], separation of mixtures of polystyrene beads [89], and the separation of human breast cancer cells from CD34+ stem cells [73, 90].

Thus, DEP FFF has been successfully demonstrated as a viable technique to separate many micron-sized objects such as cells and latex beads. However, the principles should also be applicable at the nanoscale, and it should in principle be possible to separate objects such as DNA, proteins, viruses, nanoparticles, nanowires, nanotubes, quantum dots, and possibly even small molecules.

## 5. TRAPPING AND MANIPULATION OF NANO-SIZED OBJECTS

In principle, all of the above techniques that have so far proved useful for micron-sized objects such as cells could be useful for nano-sized objects, especially if the nanowires or nanotubes could be used as the electrodes themselves.

### 5.1. Latex Beads

Latex beads have been used extensively in order to test various aspects of dielectrophoresis because they are robust and can be fluorescently labeled, and hence imaged. Furthermore, they are readily available in a variety of sizes from 10  $\mu\text{m}$  to 10 nm.

The Fuhr group in Germany has been able to trap aggregates of 14-nm latex beads, aggregates of viruses of diameter around 100 nm, as well as single latex beads down to 650 nm in size [23, 24]. Subsequently the Morgan group in

England achieved trapping of single 93-nm latex beads in 1998 [25, 26]. Green and Morgan used planar microelectrode arrays to separate a mixture of 93-nm and 216-nm latex beads into their constituent components [27].

In 1999, Hughes and Morgan separated unlabeled and protein-labeled 216-nm latex beads [28]. The dielectrophoretic properties of these beads were carefully modeled in [29, 30]. A detailed study of the DEP response of latex beads as a function of electrolyte composition and conductivity, electric field frequency, and particle size for 93-, 216-, and 282-nm latex beads was presented in [31]. The use of latex beads has been and continues to be a good testbed for the use of DEP in manipulating micro- and nanoparticles.

### 5.2. Molecular Dielectrophoresis

One of the most promising applications of dielectrophoresis in nanotechnology is the possible electronic manipulation of individual molecules. Later in this chapter we discuss the applications such an achievement would enable, such as massively parallel nanomanufacturing of new materials, one molecule at a time, with tailor-designed electronic, optical, magnetic, and mechanical properties. However, to date the clear demonstration of the manipulation by dielectrophoresis of a single molecule has not been achieved for any molecule less than 100 nm in size. A large reason, as discussed in Section 2.4, is that (to date) the thermal Brownian force dominates the dielectrophoretic force for such small objects.

While such an achievement may be possible in the future, it is still true that the nonuniform ac and dc electric fields establish *some* force, which, even though less than the thermal Brownian motion, will still cause a tendency for molecules to move in a certain direction, depending on the geometry of the electrodes. The quantitative study of these effects has been termed “molecular dielectrophoresis” [2].

To date all studies of molecular dielectrophoresis have used positive dielectrophoresis: the DEP force tends to push the molecules toward regions of higher electric fields. The geometry which has been studied almost exclusively is that of two concentric cylinders with the molecules dissolved in a solution in between the cylinders. If the density of the molecules as a function of the radial distance changes, this changes the dielectric constant as a function of the radius, and hence the capacitance from the inner to the outer cylindrical electrode.

In 1954, Debye and co-workers used dc dielectrophoresis of polystyrene (molecular weight 600,000) in cyclohexane [91, 92]. They used a dc non uniform electric field in a cylindrical geometry and monitored the capacitance change by measuring the shift in the resonant frequency of an LC circuit; similar studies were carried out by Prock and McConkey in 1960 [93].

In 1955, Lösche and Hultschig [94] used ac dielectrophoresis to study nitrobenzene in carbon tetrachloride, and poly(vinyl acetate) in nitrobenzene; however, both have permanent (instead of induced) dipoles. In 1973 Eisenstadt and Scheinberg [95, 96] studied dielectrophoresis and measured the diffusion constant of the biopolymers poly- $\gamma$ -benzyl-L-glutamate (PBLG, M.W.  $\approx$  120,000) and poly-n-butyl isocyanate dissolved in ethylene dichloride (EDC);

both have permanent dipoles. By measuring the time dependence of the concentration change of the PBLG concentration due to the dielectrophoretic force, Eisenstadt and Scheinberg were able to determine its diffusion constant.

Thus, while the manipulation of a single nanomolecule is still not yet achieved, the ability to affect the concentration of large numbers of nanoscale molecules in solution with dielectrophoresis has been demonstrated over 30 years ago, giving hope to the use of nanodielectrophoresis at the single molecule level.

### 5.3. Conducting Nanoparticles

#### 5.3.1. DC Dielectrophoretic Trapping

The basic principle of dielectrophoresis applies regardless of whether the field is dc or ac. (For example, the first recorded instance of dielectrophoresis was dc dielectrophoresis in 600 B.C., as discussed in Section 2.) Furthermore, Pohl calculated that metal balls in water would have the largest dielectrophoretic force of many different possible particle/solvent combinations [2]. In 1997, Bezryadin and Dekker combined these two ideas and used (positive) *dc dielectrophoresis* to trap 20-nm Pd nanoparticles between lithographically fabricated electrode gaps of about the same distance, that is, 20 nm [97, 98]. The Pd nanoparticles were dissolved in water. Bezryadin applied 4.5 V dc between the gaps, and then investigated the samples with a scanning electron microscope (SEM) after drying. The SEM images showed clearly the presence of one or a few nanoparticles bridging the gap between the electrodes, and this was confirmed by measuring the electrical resistance between the electrodes.

#### 5.3.2. Pearl Chains

Particles undergoing dielectrophoresis often exhibit mutual attraction. This is due to the fact that dielectrophoresis involves an induced dipole moment in each particle, and dipoles interact and form what are called “pearl chains.” The tendency of a group of particles in a field to form lines has been known for over two hundred years [2, 99]. This is, for example, responsible for the behavior of electrorheological fluids [100]. Pohl also studied this effect extensively in his experiments in cells [2]. In 1999, Bezryadin et al. observed this pearl-chaining phenomenon in conducting graphite nanoparticles ( $d = 30$  nm), and named it self-assembled chains [101]. They used dc dielectrophoresis with the nanoparticles dissolved in toluene, and applied 40 V across a gap of 1  $\mu\text{m}$  between Cr and Pt electrodes. They were able to pass current through this pearl chain of nanoparticles, and furthermore observed Coulomb gap (single electron transistor) behavior at temperatures all the way up to 77 K, because the capacitive charging energy of the nanoparticles was still comparable to the physical temperature even at 77 K.

#### 5.3.3. AC Dielectrophoresis

In 2002, Amlani and co-workers used positive *ac dielectrophoresis* to trap 40- to 100-nm gold nanoparticles between a lithographically fabricated 60-nm gap between two gold electrodes [102]. The gold nanoparticles were dissolved in

water, and a 2.5-V p-p ac voltage between 1 and 10 MHz is found to provide a yield of 100%, much higher than the yield if a dc dielectrophoresis is used. These structures were found to conduct electrically when a single gold nanoparticle was trapped, with a resistance of 3 k $\Omega$ . In a second experiment, prior to the dielectrophoretic trapping, the gold electrodes were coated with a self-assembled monolayer of 1-nitro-2,5-di(phenylethynyl-4\*-thioacetyl)benzene, a compound similar to one previously studied using a nanopore configuration and found to exhibit negative differential resistance [103]. In the dielectrophoresis experiment of Amlani, the current flow was presumably electrode-molecule-nanoparticle-molecule-electrode. Amlani and co-workers also observed negative differential resistance at room temperature, presumably due to the intrinsic electronic properties of the molecules in the self-assembled monolayer.

#### 5.3.4. From Nanoparticles to Nanowires

In 1999, Velev and co-workers developed a biosensor which is chemically selective based on gold nanoparticles and latex micron-sized beads. The latex beads (suitably chemically functionalized) were assembled into a “pearl chain” wire between two electrodes with positive dielectrophoresis. The target molecules would then bind with immunoactive sites on the latex particles, and then a further set of chemically functionalized gold nanoparticles would bind to the target molecules. Then a silver enhancer is introduced to complete the circuit. The net result is a large change in conductance if and only if the target molecule is present above some minimum threshold in the test solution.

Later work by the same group used dielectrophoresis to directly assemble microwires from gold nanoparticles [104]. They found that 10- to 15-nm gold nanoparticles in solution, when subjected to 50- to 200-Hz electric fields by electrodes spaced apart by a few millimeters, grew wires of micron size and conducted electricity. This is analogous to the pearl-chain formation discussed earlier.

### 5.4. DNA

#### 5.4.1. Washizu and Co-Workers

Starting in 1990, Washizu and Kurosawa began studies on DNA which showed that it is indeed possible to use dielectrophoresis to manipulate DNA [105]. They used the electric field produced between two parallel, thin-film aluminum electrodes (thickness 1  $\mu\text{m}$ , spacing 60  $\mu\text{m}$ ) to “stretch” DNA molecules. When large concentrations of DNA molecules are used, they form bands due to the complicated and poorly understood DNA–DNA interactions. When low concentrations of DNA are used, one can see individual DNA molecules through fluorescence, and it is clear that the electric fields “stretch” each individual molecule out. The field strength used is approximately 10<sup>6</sup> V/m, and the frequency is varied from 40 kHz to 2 MHz, with only slight frequency dependence of the effect. Washizu and co-workers studied  $\lambda$  phage DNA (48.5 k base pairs, kbp), so that fully stretched they were about 17  $\mu\text{m}$  long.

It is not clear from that data whether the ac electric field needs to be nonuniform for the stretching. It would be an interesting experiment to determine whether DNA is

stretched in uniform electric fields. Finally, they showed that it is possible to attach DNA to electrodes, which they interpret as being due to positive DEP: Near the edges of the thin electrodes, the electric field gradients are large, hence the DNA is attracted there. Once attached to the Al electrode (in this experiment, only one end is attached), it is bound chemically and remains, even after the electric field is switched off. In Figure 8, the results found by Washizu and co-workers are indicated schematically.

In 1995, Washizu and co-workers described several possible applications of this technique [106]. First, they described an optical/DEP technique to size-sort long DNA (with length greater than 10 kb pairs), which is difficult for conventional gel electrophoresis. This was demonstrated with  $\lambda$  phage DNA (size 48.5 kbp). Second, they measured the activity rate of exonuclease digestion of DNA, by measuring the double strand length as a function of time during digestion. DNA lengths of order 10  $\mu\text{m}$  can be measured because DEP caused the DNA to be stretched out. (They found that single strands of DNA are not stretched by DEP.) A further method was developed to stretch DNA molecules and position them at two different electrodes, using a combination of a floating electrode geometry and also chemically treated (biotin and avidin) electrodes. For unknown reasons, without the floating electrode geometry it was possible to attach one end of a DNA molecule to one electrode, but not the other end to the other electrode. Apparently, the high electric fields near the electrode induced currents away from the electrode, preventing the second end of the DNA molecule from binding, but not the first end.

The DNA so immobilized is shown to still be biochemically active. In 1993, Banata and co-workers used the DEP technique to attach one end of DNA to an aluminum electrode; the other end was free but stretched out with DEP. Just after turning off the electric field, and before the DNA had a chance to re-coil, they imaged single fluorescently labeled RNA polymerase molecules sliding along the DNA [107]. The technique was used to study the DNA-protein interaction with other proteins (*Pseudomonas putida* CamR) in 1999 [108]. Future applications of this technique

may lend insight into DNA-protein interactions in general, and the regulation and control of genetic expression in particular.

In 1999 Ueda and co-workers studied the DEP stretched DNA molecules with AFM, after drying the solvent (water). They concluded that the DEP stretched and trapped molecules do not aggregate but in contrast are trapped individually [109].

In 2000, the Washizu group used dielectrophoresis and floating electrodes to attach both ends of  $\lambda$  phage DNA molecules to aluminum electrodes [48, 110], using the floating electrode technique described above. In this work, they etched the glass slide below the gap between the electrodes so that the DNA was freely suspended. (Although it has gone largely unnoticed by the MEMs community, this technique to assemble freely suspended DNA should have many applications in nanomechanical systems made of DNA.) Since the DNA was freely suspended in solution there is no issue of steric hindrance of biochemical activity. Then, in a further set of experiments [48], they used optical tweezers to manipulate 1- $\mu\text{m}$  latex spheres labeled chemically with the digestive enzymes DNaseI (which has no base pair selectivity) and HindIII (a restriction enzyme which cuts DNA at only specific base sequences). They were able to bring the bead up to the DNA. In the case of DNaseI, the DNA was immediately cut. In the case of HindIII, the bead was moved up and down the DNA until it matched the correct sequence, at which point it was cut.

In 1998, the Washizu group studied the polarization of the fluorescent emission from dielectrophoretically stretched DNA [111]. The polarization of the emitted light was quantitatively measured and correlated with the applied electric field intensity, as well as the pH of the solution. Several interesting results were obtained, indicating that the counterion cloud surrounding the DNA molecules has a large influence on the stretching of DNA by electric fields. The details of this influence are still not fully understood. Many of these results from Washizu and co-workers are reviewed in two book chapters [112, 113].

#### 5.4.2. Asbury and Co-Workers

In 1998, Asbury and van den Engh were able to use dielectrophoresis to trap DNA with a floating electrode geometry: The electric field was applied from external electrodes; floating gold electrodes spaced by 30- $\mu\text{m}$  gaps concentrated the electric field, which served to trap the DNA [114]. They also studied  $\lambda$  phage DNA in de-ionized (D.I.) water, but used gold electrodes (thickness 40 nm), and audio frequency (30 Hz) fields. As in the Washizu experiments, the DNA underwent positive dielectrophoresis: it was attracted to regions of high electric field intensity, which occurs near the edges of the electrodes. Asbury used much lower frequency voltages (typically 30 Hz) than Washizu, and found no stretching of the DNA at these frequencies. Furthermore, Asbury found that the DNA did not become stuck to the gold electrodes, in contrast to Washizu's experiments where the DNA did become stuck to aluminum electrodes.

Regarding the frequency, at dc no more than roughly 1 V can be applied across an electrode/water interface; otherwise electrolysis followed by bubbling can occur. Washizu found

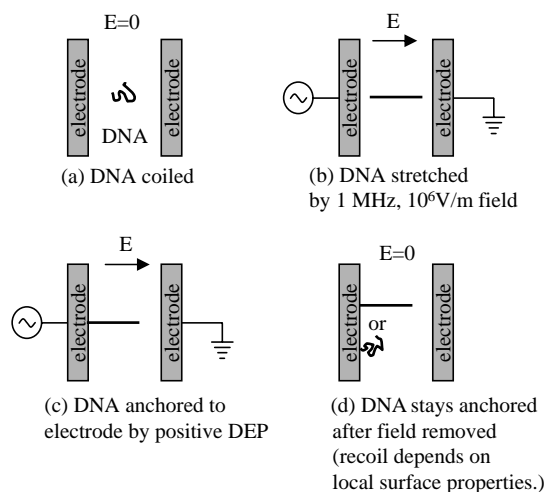


**Figure 8.** Schematic representation of the findings of Washizu and co-workers.



that much larger voltages could be applied as the frequency was increased from 1 kHz to 1 MHz (they did not study frequencies below 1 kHz). In Asbury's experiments, the gold electrodes were floating, but there was still less than 0.5 V between each (floating) electrode pair, so that electrolysis did not occur. Asbury's experiments found that DNA could be trapped in deionized water, but not in isotonic saline. They estimate that the force on the DNA was in the femtonewton range. Since the DNA molecules were not stuck to the gold electrodes, Asbury was able to simultaneously apply a dc field and move the stretched DNA molecules with electrophoresis.

In 2002, Asbury and co-workers continued this work by integrating it with a simple microfluidic device, fabricating a 15- $\mu\text{m}$ -wide PDMS channel on top of gold electrodes which, in contrast to their earlier work, were electrically contacted (not floating) [115]. With the gold electrodes and 30-Hz voltages of roughly 3 V p-p, they were able to trap DNA and then release it using positive dielectrophoresis. Their estimates show that 50% of the DNA introduced into the microfluidic channel was trapped.

Asbury found the trapping "efficiency" to decrease with increasing frequency between 5 Hz and 2 kHz, with an effective time constant of 3 ms. The origin of this frequency dependence is attributed to the distortion of the counterion clouds that surround the DNA molecules in solution, although the details of this effect are currently poorly understood.

#### 5.4.3. Ueda and Co-Workers

In 1997 Ueda et al. used much-lower-frequency ac electric fields, and studied the electronic dielectrophoretic stretching of DNA in polymer laden solutions. They found the polymer (polyacrylamide) assisted the stretching of DNA for applied electric fields in the frequency range of 0.1 to 100 Hz [116]. They found this stretching to occur at field strengths as low as  $10^4$  V/m; no net motion of the DNA was reported.

#### 5.4.4. Chou and Co-Workers

In another work with floating electrodes, Chou and co-workers used *insulating* posts fabricated with micro-machining techniques, and electrodes external to the device [117]. The slightly conductive solution served to enhance the electric field near the gaps between the posts, and DNA was found to be trapped there for voltages on the electrodes of roughly 1000 V and frequencies between 50 Hz and 1 kHz. The corresponding electric field strength was  $10^5$  V/m. In this work, the DNA was apparently not stretched at all, presumably because of the constricted geometry used. In contrast to the work of Asbury, Chou found that the trapping force increased with increasing frequency, and also calculated that the trapping force was roughly 1 fN.

#### 5.4.5. Tsukahara and Co-Workers

In recent work [118], Tsukahara and co-workers studied dielectrophoresis of single DNA molecules using frequencies between 1 kHz and 1 MHz and field strengths around  $10^4$  V/m, using quadrupole electrode patterns similar to those shown in Figure 3. They found that the DNA underwent positive dielectrophoresis (i.e., it was attracted to the

high field regions near the edges of the electrodes) for frequencies between 1 kHz and 500 kHz, and negative dielectrophoresis between 500 kHz and 1 MHz, in contrast with the findings of previous work. This is to date the only reported observation of negative dielectrophoresis of DNA; the discrepancy may be related to the different solvents used, although at this point it is still an open question. Furthermore, Tsukahara and co-workers used electric fields that were roughly a factor of 10 smaller than previous workers, and still were able to observe the dielectrophoretic forces on a single DNA molecule. This may again be due to the solvent used, or the fact that Tsukahara used a quadrupole electrode geometry, which is different than previous works. Additionally, Tsukahara did not observe any stretching of the DNA with the application of an ac electric field.

#### 5.4.6. Porath and Co-Workers

In 2000, Porath and co-workers used positive dc dielectrophoresis to putatively trap 10-nm-long poly(G)-poly(C) double strands of DNA between Pt electrodes with 8-nm spacing [119]. Through a series of control experiments, Porath concluded that the trapped object was indeed DNA, and that its electrical properties were semiconducting. Many other researchers up to and since then have considered the electronic properties of DNA as a molecular wire. The issue is still under investigation [120].

#### 5.4.7. Summary

The detailed mechanisms for the frequency dependence, electric field dependence, concentration dependence, pH and ionic dependence of the dielectrophoretic manipulation of DNA are still not explained in a systematic, quantitative way, and many of these dependences have yet to be quantitatively measured. However, it is clear now that it is possible to use dielectrophoresis to manipulate DNA under a variety of conditions and frequencies. This knowledge could be used in a variety of contexts, including lab-on-a-chip diagnoses and genetic expression profiling, as well as electronic methods of controlling DNA chemistry. This latter possibility has the potential to provide a new nanomanufacturing technology based on both chemical self-assembly techniques and integrated, massively parallel, economical electronic control of the same.

### 5.5. Viruses

#### 5.5.1. Influenza

To date two different research groups have succeeded in trapping at least four different species of virus with dielectrophoresis. The first group to trap viruses was that of Fuhr and co-workers in 1996 [121]. They used quadrupole, three-dimensional traps to trap fluorescently labeled influenza viruses ( $d \approx 100$  nm) using negative dielectrophoresis traps, and 1-MHz electric fields with field strength around  $10^5$  V/m. (The gap between electrodes was approximately 5  $\mu\text{m}$  with 11-V p-p voltage.) They also trapped 14-nm latex beads. In these experiments, the viruses formed aggregates in the centers of the traps. In later work with similar geometries, fields, and frequencies, the same group was also able to trap Sendai viruses into aggregates as well [122].

### 5.5.2. Tobacco Mosaic

In later work, Morgan and co-workers used interdigitated electrode fingers spaced by 4  $\mu\text{m}$  with saw-tooth shapes to manipulate tobacco mosaic viruses [123, 124]. The tobacco virus is rod-shaped, with length of 280 nm, and width of 18 nm. Morgan used field strengths of roughly  $10^6$  V/m, and varied the frequency between 1 kHz and 2 MHz. Although they were not able to observe individual virions, they could see a faint haze as the density increased or decreased in response to the applied electric field. They found both positive and negative dielectrophoresis, depending on the frequency used. Positive dielectrophoresis was observed for frequencies below about 1 MHz, and negative dielectrophoresis for higher frequencies. The crossover frequency was very dependent on medium conductivity, which was varied between  $2 \times 10^{-3}$  and  $10^{-1}$  S/m by varying the potassium phosphate buffer concentration.

### 5.5.3. Herpes

In 1998, Hughes and co-workers used planar quadrupole traps such as the one shown in Figure 3 with 6- $\mu\text{m}$  gaps to trap Herpes simplex viruses, which are spherical with diameter of about 250 nm [125]. They studied dielectrophoresis of the virus with frequencies from 10 kHz to 20 MHz, and observed negative dielectrophoresis for frequencies above about 5 MHz. The field strengths required for the trapping were about  $10^6$  V/m. Later work by the same group found that the crossover frequency between positive and negative dielectrophoresis for the herpes virus was very dependent on the medium conductivity in the range between  $10^{-4}$  and  $10^{-1}$  S/m, and this dependence was strongly affected by the presence or absence of manitol [126, 127].

### 5.5.4. Virus Separation

Using the results from their previous studies, Morgan and co-workers studied both tobacco and herpes virus in the same solution, using quadrupole electrode geometry [124, 128]. At 5 MHz, the herpes virus experiences negative dielectrophoresis and is collected in the center of the quadrupole. In contrast, at 5 MHz the tobacco virus experiences positive dielectrophoresis and is collected at the edges of the quadrupole geometry. Thus, two different virus species were physically separated due to their different frequency response to dielectrophoresis.

## 5.6. Proteins

A protein consists of a long chain of subunits (amino acids) which are folded into very complicated three-dimensional structures; the structure is closely related to the function. Most proteins of biological significance are around 1–10 nm in physical size. All species of life are based on only 20 common amino acids [129]. The modern field of *proteomics* seeks to understand, categorize, and tabulate all proteins useful for life [130].

There have been several studies of the effects of moderate electric fields and strong pulsed fields on the conformational state of proteins such as the helix-coil transition [131]. Reviews of the dielectric properties of biopolymers, dealing predominantly with linear response, low field behavior,

are given in [3, 4, 132–134]. However, given the importance of protein chemistry in modern molecular biology, it is surprising how little work to date has been performed on the interaction between strong electric fields and proteins.

### 5.6.1. Protein Trapping

In 1994, Washizu and co-workers studied the effect of dielectrophoresis on the following proteins: avidin (M.W. 68 kDa), concanavalin A (M.W. 52 kDa), chymotrypsinogen A (M.W. 25 kDa), and ribonuclease A (M.W. 13.7 kDa) [84]. These proteins have diameters ranging from 1 to 5 nm. In this series of experiments, they used aluminum (thickness 1  $\mu\text{m}$ ) electrodes in an interdigitated, castellated geometry with gaps ranging from 4 to 55  $\mu\text{m}$ . The solvent was D.I. water. They used fluorescence to observe the positions of the proteins. They observed excess fluorescence near the electrodes (i.e., near the high field regions), so that they observed positive dielectrophoresis. They knew it was DEP because they found a dependence on the field strength, not the voltage, by using different gaps between the electrodes.

According to rough estimates of the DEP force for their electrodes (a quantitative calculation was not performed), the thermal Brownian motion should overwhelm the DEP force so that nothing should be observed. And yet they observed increased fluorescence in the high field regions. This can be interpreted one of two ways: first, that we do not understand why DEP works so well on proteins; second, that the proteins are accumulating and the agglomerate acts as an effectively large polarizable particle that is less susceptible to Brownian motion and can be trapped.

Washizu argues that the second explanation (agglomeration) is not occurring because when they change the initial concentration by a factor of 10, the time to form the “aggregation” does not vary much, and this is inconsistent with a simple aggregation model of dipole–dipole attraction. Dipole–dipole attraction goes as  $d^{-4}$ , so that the time to form the agglomeration should vary as the density  $n^4$ .

If an optical setup with enough sensitivity to image a single fluorescing protein [135] could be achieved, this issue could be resolved. Washizu was able to demonstrate that trapping of various sized proteins depends on their molecular weight, so that separation of chemical species of various sizes could in principle be observed for applications in nanobiotechnology. Thus a “single molecule fluorescence” experiment, if it could be performed, would be definitive proof the DEP can be used with  $10^6$  V/m to manipulate 1- to 5-nm proteins.

In more recent work, Kawabata and Washizu [136] developed a biosensor for the protein AFP (alpha-fetoprotein, 70 kDa), an important diagnostic protein, which is detected in the serum of a liver-cancer patient. There, they used the DEP properties of proteins (antigens and antibodies) as well as 150-nm latex beads with antibodies immobilized on the surface. This is an example of an important point: even though we have organized this review according to the types of nano-objects that can be manipulated with DEP, the application of DEP to a heterogeneous population of objects could provide even more applications than just manipulating one type of object at a time.

## 5.6.2. Protein Folding

The previous section discussed primarily controlling the location of proteins with dielectrophoresis. However, given that the conformational state of a protein is related to its function, it is natural to consider whether an applied electric field can change a protein's conformational state, and possibly even unfold the entire chain of amino acids into a straight line, as Washizu was able to do with DNA. While the latter is still unproven experimentally, Washizu and co-workers have shown that it is indeed possible to use electric fields to change the conformational state of a certain protein, the flagellum of a bacteria.

The flagellum of certain types of bacteria consists of a single, spiral shaped protein about 20 nm wide and 10  $\mu\text{m}$  long. When it is rotated it acts as a corkscrew, propelling the bacteria forward. However, other conformational states of the amino-acid chain are possible; three in particular are called "straight," "curly," and "coiled." Because the flagellum is a long protein, its conformational state can be directly observed under a microscope, if fluorescently labeled.

Washizu and co-workers found that ac electric fields of roughly  $10^6$  V/m could transform flagella from one conformation state to another [112, 113, 137]. Furthermore, they found this process to be *reproducible and reversible*, observing no permanent damage to the flagella after application of the electric field.

Similar work on the electric field-induced conformation changes in other proteins (e.g., poly-(L-lysine) and poly-(L-glutamic acid)) has been reviewed in [134]. There, the work described involves measurements of optical dichroism as a function of applied electric field pulses. The optical dichroism is also strongly affected by electric field-induced orientation, making it difficult to conclusively demonstrate electric field-induced conformational changes in protein structure.

This relatively unexplored area has great potential for the future. By electronically controlling the conformational state of proteins, it may be possible to electronically control their biological function, or even to engineer new functionality into existing or tailor-designed proteins. This future molecular nanotechnology could have broad applications, which will be discussed toward the end of the review, and could also allow for further scientific studies of the process of protein folding.

## 5.7. Carbon Nanotubes

### 5.7.1. Nanotubes in Solution

Several research groups have successfully used dielectrophoresis to manipulate carbon nanotubes in solution. The general procedure is similar to that of Washizu's manipulation of DNA, with the exception that nanotubes are known to be good conductors. Most experiments demonstrating manipulation of carbon nanotubes in solution are a variation of the general process depicted schematically in Figure 9.

Nanotubes are not known to be soluble in any solvent, but can be dispersed by sonication. Once dispersed, a drop of the solution can be placed onto microfabricated electrodes as shown in Figure 9A. Next, either a dc or an ac voltage is applied. This serves two purposes. First, it induces a dipole moment in the carbon nanotube, and this dipole

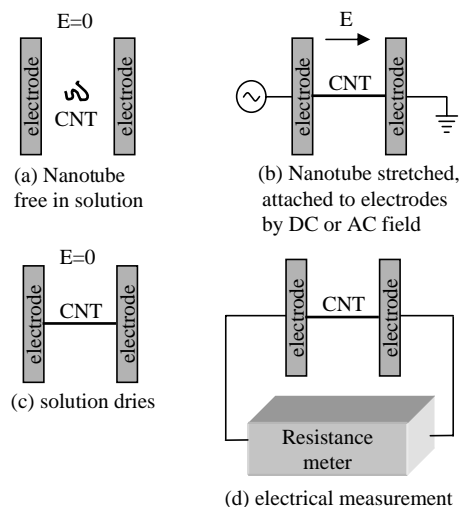


**Figure 9.** Schematic representation of the manipulation of carbon nanotubes in solution.

experiences a torque, given by Eq. (10). This torque tends to align the nanotube with the axis of the electric field. The electric field need not be nonuniform for this alignment, but to date experiments have not tested the dependence of the alignment on the uniformity of the field in any quantitative fashion.

Simultaneously, the induced dipole [138] in the nanotube experiences a force given by Eq. (2). (Equation (3) is not directly applicable as it assumes a spherical particle.) To date all measurements on carbon nanotubes have found that they undergo *positive* dielectrophoresis; that is, they are attracted to regions of high electric field strength. This can be exploited to electrically contact nanotubes: the electrodes which generate the electric field gradient can also be used as electrical contacts to the nanotube. This is indicated schematically in Figure 9D.

When water is used as the solvent (which is desirable for biologically interesting measurements), as discussed above, the applied voltage to the electrodes should be less than 1 V to avoid hydrolysis (and hence bubbling). By using ac voltages, as Washizu et al. found in 1990 [54], the applied voltage (hence electric field strength) required for hydrolysis increases with increasing frequency. If one is willing to use an insulating solvent, then the applied voltage (hence electric field) can be much larger, even at dc. Pohl, for example, used commonly used applied (ac) voltages of thousands of volts with insulating solvents such as organic solvents and  $\text{CCl}_4$  [2].

### 5.7.2. DC Dielectrophoresis and Electrophoresis

The first dielectrophoretic manipulation of nanotube ropes was done using dc dielectrophoresis in 1997 by Bezryadin and Dekker [97]. Bezryadin used cyclohexane as the solvent, and a dc voltage of 4.5 V between AuPd electrodes spaced by 150 nm. He simultaneously measured the dc current flowing between the electrodes, and was able to see an electric current flow as soon as a nanotube rope was trapped.

Bezryadin found that the trapping was effective, but the nanotube ropes were not aligned parallel to the electric field. This is possibly due to the fact that the length of the trapped ropes was much larger than the gap between the electrodes.

When a dc electric field is used, if the object is charged it will respond to the electric field via conventional electrophoresis. A simple way to test whether the nanotubes are charged and experiencing electrophoresis or neutral and experiencing dielectrophoresis is to observe whether they preferentially move toward the cathode or anode or neither. If the nanotubes do not preferentially conglomerate at one polarity, then the effect is dielectrophoresis. Apparently in Bezryadin's experiments, the nanotubes behaved as neutral objects, and underwent dielectrophoresis. However, in two other experiments, multiwalled nanotubes (MWNTs) are found to behave as positively charged, conglomerating at the cathode [139], and negatively charged, conglomerating at the anode [140]. (Chen et al. found that single-walled nanotubes (SWNTs) also conglomerated at the anode under a dc electric field [141].) These discrepancies may indicate that the electrical properties of nanotubes are sensitive to the chemistry of the solvent. This effect, if it can be further characterized and explained, could prove very useful in nanomanipulation of nanotubes with electric fields in solutions.

### 5.7.3. AC Dielectrophoresis of MWNTs

In 1998, Yamamoto and co-workers studied the effects of ac electric fields on MWNTs of lengths between 1 and 5  $\mu\text{m}$ , and diameter 5–20 nm, using Al electrodes with 400- $\mu\text{m}$  gaps and field strength of  $2 \times 10^5$  V/m [142]. The MWNTs were dispersed in isopropyl alcohol. They found that the nanotubes were both *aligned* and attracted to the electrodes (i.e., underwent positive dielectrophoresis) for ac frequencies between 10 Hz and 10 MHz. Yamamoto and co-workers found that the degree of orientation of the nanotubes increased with increasing frequency, and with increasing nanotube length. Furthermore, they found that graphite impurities had a different frequency-dependent response to the ac electric field, which may be important technologically in separating nanotubes from impurities. Yamamoto also found that the alignment was more effective with ac dielectrophoresis than with dc dielectrophoresis [139], consistent with the findings of Bezryadin. A complementary technique of optical polarization measurements showed that ac electric fields could align nanotubes dispersed in ethanol [143].

### 5.7.4. AC Dielectrophoresis of SWNTs

In 2001, Chen and co-workers carried out a similar study of the effects of ac electric fields on SWNTs dispersed in ethanol [141]. They applied fields of  $5 \times 10^6$  V/m in the frequency range from 500 Hz to 5 MHz. They found the SWNTs to be oriented more strongly at higher frequencies, and they found the SWNTs experienced positive DEP for all frequencies studied. They also found no alignment effect from a dc electric field. Thus SWNTs and MWNTs appear to behave similarly under intense ac electric fields.

The first application of ac dielectrophoresis to attach two ends of SWNTs was reported in an e-print in early 2002 [144]. The authors used Ag and Au electrodes spaced

by 100 nm to trap ropes (bundles) of SWNTs dispersed in N,N-dimethylformamide (DMF). They found the nanotubes formed electrical contact with the Ag electrodes, but not the Au electrodes. The trapping was effective for frequencies between 1 kHz and 1 MHz, at applied fields of  $10^7$  V/m. Krupke was also able to simultaneously measure the ac resistance between two electrodes for the 1-kHz trapping experiments, allowing real-time monitoring of the trapping.

Nagahara et al. found similar results [145], trapping SWNT bundles with gold electrodes spaced by either 20–80 nm or 20  $\mu\text{m}$ , and applying 1 MHz and dc electric fields of strength  $10^7$  V/m. They found that the dc fields trapped bundles of SWNTs and graphite impurities, whereas the ac fields trapped only nanotube bundles. They were also able to electrically measure the current through the nanotubes after drying the Triton solvent.

Diehl and co-workers have taken this process one step further, and fabricated cross-bar structures by first aligning and immobilizing SWNT ropes in one direction and then, aligning and immobilizing nanotube ropes in a perpendicular direction [146]. The distance from one rope to the next was not determined by the lithography, but rather the chemical control of the coulombic interactions between the tubes and between the ropes. Diehl's experiments used frequencies between  $10^4$  and  $10^6$  Hz, with very little frequency dependence. The solvent consisted of a mixture of ortho-chlorobenzene and  $\text{CHCl}_3$ . (The field strength was not reported.) This represents an initial step toward one of the ultimate goals of self-assembled systems and nanotechnology in general: nonlithographic, economical, massively parallel manufacturing of electronic circuits on the nanoscale.

While to date there has been no reported trapping of an individual SWNT between two electrodes (as opposed to a bundle), such an achievement does not seem unreasonable to expect in the near future.

### 5.7.5. Controlling Nanotube Growth

Chemical vapor deposition (CVD) of carbon nanotubes is a promising new technique for the growth of high-quality single- and multiwalled carbon nanotubes [147]. The nanotubes grow from catalyst sites that can be lithographically defined on a chip [148]. However, the *direction* of the nanotube growth from these lithographically patterned catalyst sites is generally random, an issue that needs to be solved before massively parallel integrated nanotube circuits can be realized.

One possible technique to control the direction of nanotube growth is to apply an electric field (dc or ac) *during* the growth. The electric field will induce a dipole moment in the (growing) nanotube, which will experience a torque (see Eq. (10)), hence becoming aligned with the electric field. This technique was first applied to the growth of vertically aligned MWNTs in 2001 by Avigal and co-workers [149].

Later work by Zhang and co-workers [150] used both dc and ac (5 MHz) electric fields to direct the growth of SWNTs parallel to the substrate. The field strengths used were  $5 \times 10^5$  V/m, and freely suspended SWNTs up to 40  $\mu\text{m}$  in length were grown. The fields were generated between thin-film electrodes which were electrically contacted during growth. Later work by the same group achieved aligned

nanotube growth where the end result was a SWNT immobilized on the surface of the substrate [151].

### 5.7.6. Nanotubes as the Electrodes

Ultimately, for nano-DEP, one wants the smallest gap possible, and the smallest electrode radius of curvature possible. We would like to suggest that one way to achieve this would be to use nanotubes themselves as the electrodes. Very high electric field gradients should be possible [32].

## 5.8. Nanowires

### 5.8.1. Metallic Nanowires

In 1999, van der Zande and co-workers studied the orientation effects of uniform electric fields on 15-nm-diameter gold rods of lengths 39–259 nm in water using optical polarization techniques [152]. They found that, for an applied field strength of  $10^5$  V/m and an applied frequency of 10 kHz, significant orientation of the gold nanorods could be achieved.

Later work by Smith and co-workers studied gold nanowires down to 35 nm in diameter, although most work was performed in 350-nm-diameter wires of several microns in length [153]. Smith and co-workers used a combination of floating and electrically contacted electrodes, field strengths of up to  $10^7$  V/m, and frequencies from 20 Hz to 20 kHz. They found strong orientation effects and positive dielectrophoretic trapping of the nanowires to the floating electrodes for frequencies above 200 Hz; higher frequencies were most effective. Due to the floating electrode geometry used, the process was self-limiting: as soon as one wire bridged a particular pair of floating electrodes, it would short out the capacitively induced voltage on that pair of floating electrodes, preventing further trapping across that pair. Post manipulation lithographic contact to the floating electrodes showed the nanowires to be in good electrical contact with the trapping electrodes.

### 5.8.2. Semiconducting Nanowires

In 2001, Duan and co-workers used dc dielectrophoresis to align and electrically contact InP nanowires ( $d = 30$  nm) [154]. There, electric field strengths of  $10^7$  V/m were applied from electrodes spaced by 25- $\mu$ m gaps. The solvent used was chlorobenzene, so that electrolysis was not an issue. (DC voltages of 100 V were used.) By selectively energizing different pairs of electrodes, Duan was able to align InP nanowires into a cross-bar topology using layer-by-layer application of dielectrophoresis.

## 6. APPLICATIONS

### 6.1. Molecular Electronics

Recent work of Chen, Reed, and co-workers [103, 155, 156] has investigated the conducting properties of layers of molecules. The investigation of electronic properties of molecular conductors has been termed *molecular electronics*. The use of lithography alone will not allow for the controlled, rational design and fabrication of single molecule conductors.

One possible application of nanodielectrophoresis is the controlled placement of individual molecules for molecular electronics. If nanotubes and nanowires can be used themselves as the electrodes (and then as the interconnects), our calculations [32] show that it should be possible (based on the scaling consideration presented in Section 2.4) to trap individual molecules as small as 1 nm.

In Figure 10, we show one possible application of our proposed nanotube trapping scheme. An electrically contacted nanotube is cut with an AFM, then a large ac voltage is applied. By the method of images, the electric field gradients are the same as a geometry where a nanotube is in close proximity to a large conducting plane; the field gradients of a reasonable voltage (1 V) on the nanoscale should be quite large, allowing us to trap very small objects, possibly even single molecules. Trapping of DNA at the ends of nanotubes does not seem to be out of the question, nor is it impossible to trap any other number of molecules for nanotube-electrode molecular electronics. This electronically assisted chemical self-assembly contains the ingredients for molecular transistors wired up with nanotube interconnects in a possibly massively parallel process for large-scale integrated molecular electronics (“LIME,” if you will).

In Figure 11, we illustrate one possible application of this nano-trapping. 2'-amino-4-ethynylphenyl-4'-ethynylphenyl-5'-nitro-1-benzenethiolate (AEENBT) is used as a model [155]. Note that the hydrogen atom at the end bonded to sulfur can be replaced by other functional groups, for example,  $-\text{COCH}_3$ . Likewise, the protruding hydrogen atom farthest away from the sulfur atom can also be replaced by another group. By chemically selecting and optimizing the bridging molecule, in particular, the end functional groups, can one achieve ideal contact between the bridging molecule and carbon nanotubes?

Using Au as electrical contact, the Reed group [155] has made a molecular random access memory cell [156]. Multiple read write cycles were realized in a self-assembled monolayer film of AEENBT. The bit retention time was found to be of the order of 15 minutes. However, it is very difficult to combine lithography with 2-nm molecules. Nanodielectrophoresis uses the natural nanometer size of carbon nanotubes. With a defined carbon nanotube gap (2 nm) and diameter (1–2 nm), one will have a chance to electrically contact a single AEENBT.

Another potential advantage of trapping molecules with carbon nanotubes is the potentially better contact quality between carbon and other nonmetal atoms. Most molecule-metal junctions are poor circuit elements. The resistance

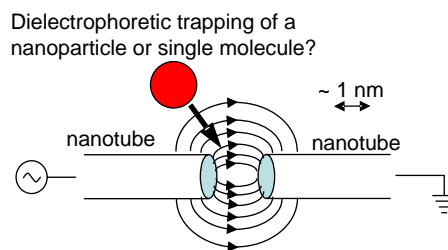


**Figure 10.** Schematic representation of an idea of how to trap 1-nm-sized particles or molecules.

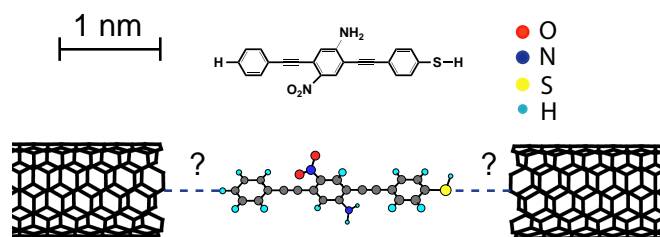


**Figure 11.** An overly simplistic schematic view of potential molecular electronics with carbon nanotubes assembled with nanodielectrophoresis. This technique could allow rapid investigation of many such schemes in a massively parallel fashion.

is usually of the order of 1 M $\Omega$  [157], which is far away from the ideal contact. One of the reasons is the different electronegativity between metals and nonmetals. For example, in a S–Au(Ag) junction, an interfacial dipole leads to a Schottky barrier in that sulfur is more electronegative than gold and silver. Carbon, which is also a nonmetal element, may prove better to contact molecules.<sup>1</sup> One can ultimately investigate more complicated geometries and architectures for integrated molecular electronic devices with nanotube interconnects.

## 6.2. Nanomanufacturing

Future applications of nano-DEP do not need to be limited to the manipulation of individual or small numbers of nanoparticles. Rather, it should be possible to scale up these nanomanipulation methods for massively parallel processing at the single molecule level. Even macroscopic quantities of materials could be fabricated one molecule at a time. New materials with tailor-designed electronic, optical, magnetic, and mechanical properties could go from nano-CAD design to reality in a matter of hours or minutes at very low cost. This integration would be a true synthesis of the top-down and bottom-up approaches to nanotechnology.

## 6.3. Nanomachines

Through rotating electric fields generated by microfabricated electrodes, it has been possible to rotate 5- $\mu\text{m}$  latex beads and also cells in solution [8]. One could call such an apparatus a dielectric micromotor, where the electrodes are the stator and the rotating latex bead the rotor. Hagedorn et al. took this concept one step further and microfabricated a large variety of micro “rotors” out of Al and polyimide, which had dimensions of approximately 100  $\mu\text{m}$  [158]. They were able to demonstrate rotor speeds of up to 3000 RPM.

Recently Hughes has presented a theoretical evaluation of the ultimate limits of rotor performance, using nano-DEP to drive rotors down to 1 nm across [159]. He concluded that a 1- $\mu\text{m}$ -long by 100-nm-wide rotor should be able to generate a torque of  $10^{-15}$  N/m, equivalent to that of a bacterial flagellar motor. Although he does not discuss how one might realize such a rotor, we suggest that using carbon nanotubes as both the rotor and stator is one feasible technique to realize this, since it is known that nanotubes can be contacted

by external electrodes. Such a nanomachine would be a step toward Drexler’s vision of molecular nanotechnology [160], proving Feynman’s statement that “there’s plenty of room at the bottom” [161].

## 6.4. Nanobiotechnology

The applications in nanobiotechnology are practically limitless. For example, Washizu has taken the first step toward DEP FFF of proteins [84], on *one* protein. It is natural to speculate that in the future, DEP FFF may find application in the ability to separate *all* proteins from the human proteome, uniquely based on their dielectric spectral properties. If enough sensitivity could be achieved, one could measure genetic expression of the entire human genome in a single cell. This could have numerous applications in drug screening and discovery.

One does not need to consider only passive, scientific or diagnostic-based measurement of biochemical activity. Nano-DEP has already proved capable of manipulating viruses. This leads one naturally to ask the question: Based in part on nano-DEP, can one design an active, electronically controlled artificial immune system? A nano-liver or a nano-kidney? The answer to this question is not yet known, but would have significant impact on humanity in general if it turns out to be “yes.”

## 6.5. Nanochemistry

The force required to break a single chemical bond is roughly 1 nN [162]. Our calculations show that this can be the same order of magnitude that is generated by DEP on a micro- or nanoparticle, if nanotubes are used as the electrodes [32]. While to date AFM and SPM have been used for studying single molecule chemistry, it is also natural to speculate that nano-DEP experiments can be designed to electronically study and control the breaking of a single chemical bond.

## 7. UNANSWERED QUESTIONS

Although DEPs application in nanotechnology is still in its infancy, it can be considered a proven technique to electronically manipulate micro- and nanosized objects. However, the studies performed to date have left some key questions unanswered:

- What is the effect of Joule heating?
- What is the smallest molecule that can be trapped?
- What field strengths are needed for this?
- Since the forces depend on the field gradient only, is it possible to design different electrode geometries to achieve stronger trapping forces for a given applied voltage?
- Can trapping of individual macromolecules occur in biologically relevant solutions, fraught with conduction ions?
- What is the effect of molecule–molecule interactions on traps that hold more than one molecule?
- What is the role of electrohydrodynamics?

<sup>1</sup> We thank Shengdong Li for pointing this issue out to us.



Joule heating occurs due to current flow through the solution. This is especially a question in solutions of biological significance with ionic concentrations that can also carry current. The heating may cause convective fluidic currents which will overcome the dielectrophoretic forces. The amount of Joule heating is difficult to predict, since the conductive properties of the solution at MHz frequencies may not be known.

Macromolecules may not behave as bulk dielectrics, but have deviations from simple bulk behavior. These issues are difficult to address theoretically and more experiments need to be done to push DEP to the single molecule limit.

At the very high electric fields necessary for DEP to overcome Brownian motion of nanoparticles, the electric field may also interact directly with the fluid itself. The study of the interactions between electric fields and fluids is called electrohydrodynamics. Serious, concerted effort to understand electrohydrodynamics at the nanometer scale has only recently begun [163–169]. Understanding these effects will obviously have important implications for the applications and ultimate limits of nano-DEP.

The importance of these effects was made clear by Washizu et al. [106], who found that, while it was possible to stretch and attach DNA to one electrode, electrohydrodynamical effects prevented attaching the other end of the DNA molecule to a second electrode. Instead, a floating electrode geometry was needed to avoid the electrohydrodynamical effects.

The electrohydrodynamic effects of high electric fields at the nanoscale is a difficult problem to investigate both experimentally and theoretically, and will require considerably more effort to quantify, understand, and eventually control.

## 8. CONCLUSIONS

The use of dielectrophoresis has already found numerous applications in biotechnology, nanotechnology, and nanobiotechnology. Using conducting metal and carbon electrodes fabricated with either optical or electron beam lithography, coupled with modern microfluidic integrated circuits, it has been possible to manipulate, trap, separate, and transport DNA, proteins, viruses, cells of various types from many different species, including both plant and animal, metal nanoparticles, latex beads, carbon nanotubes, semiconducting and metallic nanowires, semiconducting nanoparticles, and quantum dots.

In order to bring this vast body of knowledge to fruition, several steps remain to be taken. First, the power and economy of massively parallel fabrication and manufacturing methods, as well as massively parallel operations on a single chip, have not yet been exploited. While the techniques described here are compatible with the processing techniques of modern semiconductor integrated circuits which achieve routinely millions of transistors on a chip at the cost of only a few dollars, to date most studies and demonstrations of nanodielectrophoresis have only been on a few or at most a dozen operations at a given time, such as the separation of viable and nonviable cells. These processes need to be integrated with each other, with microfluidics, and with

existing silicon microelectronics technology for many (millions) of operations for a true, integrated lab-on-a-chip.

Second, new applications must be found for this massively parallel processing, manipulation, and manufacturing capability. To date the manipulation of nano-sized objects has traditionally been painstaking, expensive, and slow. If massively parallel techniques of nanomanipulation can be manufactured and made readily available, many new opportunities which harness this economy of scale will need to be imagined, designed, and realized, such as new materials and devices with tailor-designed electronic, optical, magnetic, and mechanical properties. By integrating these with biological and chemical functions, artificial cell, immune systems, tissues, and even organs may someday be designed, fabricated, and made readily and cheaply available to every human being on the planet, for medical applications such as point-of-care diagnostics, drug discovery, artificial immune systems, and ultimately the treatment and prevention of disease.

Third, and finally, the next step in size reduction must be taken in order to create a true nanomanufacturing technology. The origins of dielectrophoresis allowed the use of traditionally machined electrodes to manipulate micron-sized objects such as cells. With the advent of photolithography and electron beam lithography, the trapping of objects as small as 10 nm has been enabled. The next step will be to use the electrically contacted nanowires and nanotubes themselves as the electrodes in the next generation of nanodielectrophoresis. These nanoelectrodes, perhaps themselves manipulated and interconnected with microelectrodes, will have even larger electric field gradients and will be able to manipulate 1-nm-sized objects. This is one possible route to molecular electronics. Furthermore, this will provide a new, economical, easy to handle, and direct link to the nanometer world, which could lead to many new discoveries and a truly new technology: nanotechnology.

## GLOSSARY

**Carbon nanotube** A nanometer-scale tube of carbon atoms, which can be either metallic or semiconducting, depending on the chirality.

**DEP field flow fractionation** The separation of objects according to their dielectric properties.

**Dielectrophoresis** The force acting on a polarizable object (neutral or charged) due to an ac or dc electric field gradient.

**Nanobiotechnology** The control of biological processes at the nanometer length scale.

**Nanowires** Narrow-diameter metallic or semiconducting wires whose dimensions (typically less than 10 nm) cannot be realized by lithography alone.

**Traveling wave dielectrophoresis** The transport through space in three dimensions of polarizable objects due to a traveling wave electric field.

## ACKNOWLEDGMENTS

Some of the experimental work presented here was performed by Sunan Liu and Lifeng Zheng. We thank J. Brody and Noo Lee Jeon for experimental assistance with the work, and Marc Madou and Shengdong Li for interesting discussions. This work was supported in part by the Army Research Office and the Office of Naval Research.

## REFERENCES

1. H. A. Pohl, *J. Appl. Phys.* 22, 869 (1951).
2. H. A. Pohl, "Dielectrophoresis." Cambridge University Press, Cambridge, UK, 1978.
3. R. Pethig, "Dielectric and Electronic Properties of Biological Materials." Wiley, Great Britain, 1979.
4. E. H. Grant, R. J. Sheppard, and G. P. South, "Dielectric Behavior of Biological Molecules in Solution." Oxford University Press, Oxford, UK, 1978.
5. R. Pethig and G. H. Markx, *Trends Biotechnol.* 15, 426 (1997).
6. R. Pethig, *Crit. Rev. Biotechnol.* 16, 331 (1996).
7. U. Zimmermann and G. A. Neil, "Electromanipulation of Cells." CRC Press, Boca Raton, FL, 1996.
8. G. Fuhr, U. Zimmermann, and S. G. Shirley, in "Electromanipulations of Cells" (U. Zimmermann and G. A. Neil, Eds.). CRC Press, Boca Raton, FL, 1996.
9. M. J. Madou, "Fundamentals of Microfabrication," 2nd ed. CRC Press, Boca Raton, FL, 2002.
10. M. P. Hughes, *Nanotechnology* 11, 124 (2000).
11. T. B. Jones, "Electromechanics of Particles." Cambridge University Press, Cambridge, UK, 1995.
12. W. M. Arnold, H. P. Schwan, and U. Zimmerman, *J. Phys. Chem.* 91, 5093 (1987).
13. C. Li, D. Holmes, and H. Morgan, *Electrophoresis* 22, 3893 (2001).
14. M. P. Hughes and N. G. Green, *J. Colloid. Interf. Sci.* 250, 266 (2002).
15. N. F. Ramsey, "Molecular Beams." Oxford University Press, London, 1956.
16. X. Wang, X. B. Wang, F. F. Becker, and P. R. C. Gascoyne, *J. Phys. D* 29, 1649 (1996).
17. D. S. Clague and E. K. Wheeler, *Phys. Rev. E* 64, 026605 (2001).
18. Y. Huang and R. Pethig, *Measurement Science and Technology* 2, 1142 (1991).
19. X. B. Wang, Y. Huang, X. Wang, F. F. Becker, and P. R. C. Gascoyne, *Biophys. J.* 72, 1887 (1997).
20. G. Fuhr, W. M. Arnold, R. Hagedorn, T. Müller, W. Benecke, B. Wagner, and U. Zimmermann, *Biochim. Biophys. Acta* 1108, 215 (1992).
21. T. Schnelle, R. Hagedorn, G. Fuhr, S. Fiedler, and T. Müller, *Biochim. Biophys. Acta* 1157, 127 (1993).
22. L. Zheng, P. J. Burke, and J. P. Brody, unpublished.
23. T. Müller, A. M. Gerardino, T. Schnelle, S. G. Shirley, G. Fuhr, G. Degasperis, R. Leoni, and F. Bordoni, *Nuovo Cimento* 17, 425 (1995).
24. T. Müller, A. Gerardino, T. Schnelle, S. G. Shirley, F. Bordoni, G. De Gasperis, R. Leoni, and G. Fuhr, *J. Phys. D* 29, 340 (1996).
25. M. G. Green and H. Morgan, *J. Phys. D* 30, L41 (1997).
26. M. P. Hughes and H. Morgan, *J. Phys. D* 31, 2205 (1998).
27. N. G. Green and H. Morgan, *J. Phys. D* 31, L25 (1998).
28. M. P. Hughes and H. Morgan, *Anal. Chem.* 71, 3441 (1999).
29. M. P. Hughes, H. Morgan, and M. F. Flynn, *J. Colloid. Interf. Sci.* 220, 454 (1999).
30. M. P. Hughes, *J. Colloid. Interf. Sci.* 250, 291 (2002).
31. N. G. Green and H. Morgan, *J. Phys. B* 103, 41 (1999).
32. P. J. Burke, unpublished.
33. W. M. Arnold and U. Zimmermann, *J. Electrostat.* 21, 151 (1988).
34. R. Hagedorn, G. Fuhr, T. Müller, and J. Gimsa, *Electrophoresis* 13, 49 (1992).
35. G. Fuhr, S. Fiedler, T. Müller, T. Schnelle, H. Glasser, T. Lisee, and B. Wagner, *Sensor. Actuator.* 41–42, 230 (1994).
36. X. B. Wang, R. Pethig, and T. B. Jones, *J. Phys. D* 25, 905 (1992).
37. X. B. Wang, Y. Huang, R. Hölzel, J. P. H. Burt, and R. Pethig, *J. Phys. D* 26, 312 (1993).
38. M. P. Hughes, R. Pethig, and X. B. Wang, *J. Phys. D* 28, 474 (1995).
39. X. B. Wang, Y. Huang, F. F. Becker, and P. R. C. Gascoyne, *J. Phys. D* 27, 1571 (1994).
40. X. B. Wang, M. P. Hughes, Y. Huang, F. F. Becker, and P. R. C. Gascoyne, *Biochim. Biophys. Acta* 1243, 185 (1995).
41. A. Ashkin, *Phys. Rev. Lett.* 40, 729 (1978).
42. P. W. Smith, A. Ashkin, and W. J. Tomlinson, *Opt. Lett.* 6, 284 (1981).
43. A. Ashkin, J. M. Dziedzic, and P. M. Smith, *Opt. Lett.* 7, 276 (1982).
44. A. Ashkin, J. M. Dziedzic, J. E. Bjorkholm, and S. Chu, *Opt. Lett.* 11, 288 (1986).
45. A. Ashkin, *Biophys. J.* 61, 569 (1992).
46. K. Svoboda and S. M. Block, *Annu. Rev. Biophys. Biom.* 23, 247 (1994).
47. G. Fuhr, H. Glasser, T. Müller, and T. Schnelle, *Biochim. Biophys. Acta* 1201, 353 (1994).
48. T. Yamamoto, O. Kurosawa, H. Kabata, N. Shimamoto, and M. Washizu, *IEEE Trans. Indust. Appl.* 36, 1010 (2000).
49. J. S. Batchelder, U.S. Patent 4, 390, 403, 1983.
50. J. S. Batchelder, *Rev. Sci. Instrum.* 54, 300 (1983).
51. S. Masuda, M. Washizu, and Iwadare, *IEEE Trans. Indust. Appl.* IA-23, 474 (1987).
52. S. Masuda, M. Washizu, and I. Kawabata, *IEEE Trans. Indust. Appl.* 24, 217 (1988).
53. S. Masuda, M. Washizu, and T. Nanba, *IEEE Trans. Indust. Appl.* 25, 732 (1989).
54. M. Washizu, T. Nanba, and S. Masuda, *IEEE Trans. Indust. Appl.* 26, 352 (1990).
55. S. Liu, P. J. Burke, and J. P. Brody, unpublished.
56. H. A. Pohl and I. Hawk, *Science* 152, 647 (1966).
57. I. P. Ting, K. Jolley, C. A. Beasley, and H. A. Pohl, *Biochim. Biophys. Acta* 234, 324 (1971).
58. P. Marszalek, J. J. Jielinski, and M. Fikus, *Biochemistry and Bioenergetics* 22, 289 (1989).
59. R. Pethig, Y. Huang, X.-B. Wang, and J. P. H. Burt, *J. Phys. D* 25, 881 (1992).
60. Y. Huang, R. Hölzel, R. Pethig, and X. B. Wang, *Phys. Med. Biol.* 37, 1499 (1992).
61. G. H. Markx, M. S. Talary, and R. Pethig, *J. Biotechnol.* 32, 29 (1994).
62. X. B. Wang, Y. Huang, J. P. H. Burt, G. H. Markx, and R. Pethig, *J. Phys. D* 26, 1278 (1993).
63. G. H. Markx, Y. Huang, X. F. Zhou, and R. Pethig, *Microbiology-UK* 140, 585 (1994).
64. G. H. Markx, P. A. Dyda, and R. Pethig, *J. Biotechnol.* 51, 175 (1996).
65. F. F. Becker, X. B. Wang, Y. Huang, R. Pethig, J. Vykoukal, and P. R. C. Gascoyne, *J. Phys. D* 27, 2659 (1994).
66. F. Becker, X. B. Wang, Y. Huang, R. Pethig, J. Vykoukal, and P. R. C. Gascoyne, *Proc. Natl. Acad. Sci.* 92, 860 (1995).
67. M. Stephens, M. S. Talary, R. Pethig, A. K. Burnett, and K. I. Mills, *Bone Marrow Transpl.* 18, 777 (1996).
68. G. Fuhr, R. Hagedorn, T. Müller, W. Benecke, B. Wagner, and J. Gimsa, *Stud. Biophys.* 140, 79 (1991).
69. M. S. Talary, J. P. H. Burt, J. A. Tame, and R. Pethig, *J. Phys. D* 29, 2198 (1996).
70. N. G. Green, M. P. Hughes, W. Monaghan, and H. Morgan, *Microelectron. Eng.* 35, 421 (1997).
71. G. H. Markx and R. Pethig, *Biotech. Bioengineering* 45, 337 (1995).

72. K. L. Chan, H. Morgan, E. Morgan, I. T. Cameron, and M. R. Thomas, *Biochim. Biophys. Acta* 1500, 313 (2000).
73. X. B. Wang, J. Yang, Y. Huang, J. Vykoukal, F. Becker, and P. R. C. Gascoyne, *Anal. Chem.* 72, 832 (2000).
74. J. A. R. Price, J. P. H. Burt, and R. Pethig, *Biochim. Biophys. Acta* 964, 221 (1988).
75. J. Cheng, E. L. Sheldon, L. Wu, M. J. Heller, and J. P. O'Connell, *Anal. Chem.* 70, 2321 (1998).
76. J. Voldman, M. L. Gray, M. Toner, and M. A. Schmidt, *Anal. Chem.* 74, 3984 (2002).
77. S. Archer, T. Li, A. T. Evans, S. T. Britland, and H. Morgan, *Biochem. Biophys. Res. Co.* 257, 687 (1999).
78. J. Cheng, E. L. Sheldon, L. Wu, A. Uribe, L. O. Gerrue, J. Carrino, M. J. Heller, and J. P. O'Connell, *Nat. Biotechnol.* 16, 541 (1998).
79. Y. Huang, K. L. Ewalt, M. Tirado, R. Haigis, A. Foster, D. Ackley, M. J. Heller, J. P. O'Connell, and M. Krihak, *Anal. Chem.* 73, 1549 (2001).
80. Y. Huang, S. Joo, M. Duhon, M. Heller, B. Wallace, and X. Xu, *Anal. Chem.* 74, 3362 (2002).
81. J. M. Yang, J. Bell, Y. Huang, M. Tirado, D. Thomas, A. H. Forster, R. W. Haigis, P. D. Swanson, R. B. Wallace, B. Martinsons, and M. Krihak, *Biosensors and Bioelectronics* 17, 605 (2002).
82. J. C. Giddings, *Sep. Sci. Technol.* 19, 831 (1984).
83. J. M. Davis and J. C. Giddings, *Sep. Sci. Technol.* 21, 969 (1986).
84. M. Washizu, S. Suzuki, O. Kurosawa, T. Nishizaka, and T. Shinohara, *IEEE Trans. Indust. Appl.* 30, 835 (1994).
85. G. H. Markx, J. Rousselet, and R. Pethig, *J. Liq. Chromatogr. R. T.* 20, 2857 (1997).
86. Y. Huang, X. B. Wang, F. F. Becker, and P. C. Gascoyne, *Biophys. J.* 73, 1118 (1997).
87. G. H. Markx, R. Pethig, and J. Rousselet, *J. Phys. D* 30, 2470 (1997).
88. J. Rousselet, G. H. Markx, and R. Pethig, *Colloids and Surfaces A* 140, 209 (1998).
89. X. B. Wang, J. Vykoukal, F. F. Becker, and P. R. C. Gascoyne, *Biophys. J.* 74, 2689 (1998).
90. Y. Huang, J. Yang, X. B. Wang, F. F. Becker, and P. R. C. Gascoyne, *J. Hematol. Stem Cell* 8, 481 (1999).
91. P. Debye, P. P. Debye, and B. H. Eckstein, *Phys. Rev.* 94, 1412 (1954).
92. P. Debye, P. P. Debye, B. H. Eckstein, W. A. Barber, and G. J. Arquette, *J. Chem. Phys.* 22, 152 (1954).
93. A. Prock and G. McConkey, *J. Chem. Phys.* 32, 224 (1960).
94. A. Lösche and H. Hultschig, *Kolloid-Zeitschrift* 141, 177 (1955) (in German).
95. M. Eisenstadt and I. H. Scheinberg, *Science* 176, 1335 (1972).
96. M. Eisenstadt and H. Scheinberg, *Biopolymers* 12, 2491 (1973).
97. A. Bezryadin and C. Dekker, *J. Vac. Sci. Technol. B* 15, 793 (1997).
98. A. Bezryadin, C. Dekker, and G. Schmid, *Appl. Phys. Lett.* 71, 1273 (1997).
99. J. Priestley, "The History and Present State of Electricity with Original Experiments," 2nd ed. London, 1769.
100. T. C. Halsey and W. Toor, *Phys. Rev. Lett.* 65, 2820 (1990).
101. A. Bezryadin, R. M. Westervelt, and M. Tinkham, *Appl. Phys. Lett.* 74, 2699 (1999).
102. I. Amlani, A. M. Rawlett, L. A. Nagahara, and R. K. Tsui, *Appl. Phys. Lett.* 80, 2761 (2002).
103. J. Chen, W. Wang, M. A. Reed, A. M. Rawlett, D. W. Price, and J. M. Tour, *Appl. Phys. Lett.* 77, 1224 (2000).
104. K. D. Hermanson, S. O. Lumsdon, J. P. Williams, E. W. Kaler, and O. D. Velev, *Science* 294, 1082 (2001).
105. M. Washizu and O. Kurosawa, *IEEE Trans. Indust. Appl.* 26, 1165 (1990).
106. M. Washizu, O. Kurosawa, I. Arai, S. Suzuki, and N. Shimamoto, *IEEE Trans. Indust. Appl.* 31, 447 (1995).
107. H. Kabata, O. Kurosawa, I. Arai, M. Washizu, S. Margaron, R. Glass, and N. Shimamoto, *Science* 262, 1561 (1993).
108. N. Shimamoto, *J. Biol. Chem.* 274, 15293 (1999).
109. M. Ueda, H. Iwasaki, O. Kurosawa, and M. Washizu, *Jpn. J. Appl. Phys.* 1 38, 2118 (1999).
110. H. Kabata, W. Okada, and M. Washizu, *Jpn. J. Appl. Phys.* 1 39, 7164 (2000).
111. S. Suzuki, T. Yamanashi, S. Tazawa, O. Kurosawa, and M. Washizu, *IEEE Trans. Indust. Appl.* 34, 75 (1998).
112. M. Washizu, in "Automation in Biotechnology" (I. Karube, Ed.), Elsevier, New York, 1991.
113. M. Washizu, in "Nanofabrication and Biosystems" (H. C. Hoch, L. W. Jelinski, and H. G. Craighead, Eds.), pp. 80–96. Cambridge University Press, Cambridge, UK, 1996.
114. C. L. Asbury and G. van den Engh, *Biophys. J.* 74, 1024 (1998).
115. C. L. Asbury, A. H. Diercks, and G. van den Engh, *Electrophoresis* 23, 2358 (2002).
116. M. Ueda, K. Yoshikawa, and M. Doi, *Polym. J.* 29, 1040 (1997).
117. C.-F. Chou, J. O. Tegenfeldt, O. Bakajin, S. S. Chan, E. C. Cox, N. Darnnton, T. Duke, and R. H. Austin, *Biophys. J.* 83, 2170 (2002).
118. S. Tsukahara, K. Yamanaka, and H. Watarai, *Chem. Lett.* 3, 250 (2001).
119. D. Porath, A. Bezryadin, S. de Vries, and C. Dekker, *Nature* 403, 635 (2000).
120. C. Dekker and M. A. Ratner, *Phys. World* 14, 29 (2001).
121. T. Schnelle, T. Müller, S. Fiedler, S. G. Shirley, K. Ludwig, A. Herrmann, G. Fuhr, B. Wagner, and U. Zimmermann, *Naturwissenschaften* 83, 172 (1996).
122. T. Müller, S. Fiedler, T. Schnelle, K. Ludwig, H. Jung, and G. Fuhr, *Biotechnol. Tech.* 10, 221 (1996).
123. H. Morgan and N. G. Green, *J. Electrostat.* 42, 279 (1997).
124. N. G. Green, H. Morgan, and J. J. Milner, *J. Biochem. Biophys. Meth.* 35, 89 (1997).
125. M. P. Hughes, H. Morgan, F. J. Rixon, J. P. H. Burt, and R. Pethig, *Biochim. Biophys. Acta* 1425, 119 (1998).
126. M. P. Hughes, H. Morgan, and F. J. Rixon, *Eur. Biophys. J.* 30, 268 (2001).
127. M. P. Hughes, H. Morgan, and F. J. Rixon, *Biochim. Biophys. Acta* 1571, 1 (2002).
128. H. Morgan, M. P. Hughes, and N. G. Green, *Biophys. J.* 77, 516 (1999).
129. R. H. Garrett and C. M. Grisham, "Biochemistry." Saunders, Orlando, FL, 1999.
130. A. Pandey and M. Mann, *Nature* 405, 837 (2000).
131. M. Fujimori, K. Kikuchi, K. Yoshioka, and S. Kubota, *Biopolymers* 18, 2005 (1979).
132. R. Pethig and D. B. Kell, *Phys. Med. Biol.* 32, 933 (1987).
133. S. Takashima, "Electrical Properties of Biopolymers and Membranes." Adam Hilger, Bristol, England, 1989.
134. D. Pörschke, *Annu. Rev. Phys. Chem.* 36, 159 (1985).
135. A. M. Kelley, X. Michalet, and S. Weiss, *Science* 262, 1671 (2001).
136. T. Kawabata and M. Washizu, *IEEE Trans. Indust. Appl.* 37, 1625 (2001).
137. M. Washizu, M. Shikida, S. Aizawa, and H. Hotani, *IEEE Trans. Indust. Appl.* 28, 1194 (1992).
138. L. X. Benedict, S. G. Louie, and M. L. Cohen, *Phys. Rev. B* 52, 8541 (1995).
139. K. Yamamoto, S. Akita, and Y. Nakayama, *Jpn. J. Appl. Phys.* 2 31, L34 (1998).
140. F. Wakaya, T. Nagai, and K. Gamo, *Microelectron. Eng.* 63, 27 (2002).
141. X. Q. Chen, T. Saito, H. Yamada, and K. Matsushige, *Appl. Phys. Lett.* 78, 3714 (2001).
142. K. Yamamoto, S. Akita, and Y. Nakayama, *J. Phys. D* 31, L34 (1998).
143. K. Bubke, H. Grewuch, M. Hempstead, J. Hammer, and M. L. H. Green, *Appl. Phys. Lett.* 71, 1906 (1997).

144. R. Krupke, F. Hennrich, H. B. Weber, D. Beckmann, O. Hampe, and S. Malik, Contacting single bundles of carbon nanotubes with alternating electric fields, arXiv:cond-mat/0101574v1, 2002.
145. L. A. Nagahara, I. Amlani, J. Lewenstein, and R. K. Tsui, *Appl. Phys. Lett.* 80, 3826 (2002).
146. M. R. Diehl, S. N. Yaliraki, R. A. Beckman, M. Barahona, and J. R. Heath, *Angew. Chem. Int. Ed.* 41, 353 (2002).
147. H. Dai, in "Carbon Nanotubes Synthesis, Structures, Properties, and Applications" (M. S. Dresselhaus, G. Dresselhaus, and Ph. Avouris, Eds.). Topics in Applied Physics, Vol. 80. Springer, Berlin, 2001.
148. J. Kong, H. T. Soh, A. M. Cassell, C. F. Quate, and H. J. Dai, *Nature* 395, 878 (1998).
149. Y. Avigal and R. Kalish, *Appl. Phys. Lett.* 78, 2291 (2001).
150. Y. Zhang, A. Chang, J. Cao, Q. Wang, W. Kim, Y. Li, N. Morris, E. Yenilmez, J. Kong, and H. Dai, *Appl. Phys. Lett.* 79, 3155 (2001).
151. A. Ural, Y. Li, and H. Dai, *Appl. Phys. Lett.* 81, 3464 (2002).
152. B. M. I. van der Zande, G. J. M. Koper, and H. N. W. Lekkerkerker, *J. Phys. B* 103, 5754 (1999).
153. P. A. Smith, C. D. Nordquist, T. N. Jackson, T. S. Mayer, B. R. Martin, J. Mbindyo, and T. E. Mallouk, *Appl. Phys. Lett.* 77, 1399 (2000).
154. X. Duan, Y. Huand, Y. Cul, J. Wang, and C. M. Lieber, *Nature* 409, 66 (2001).
155. J. Chen, M. A. Reed, A. M. Rawlett, and J. W. Tour, *Science* 286, 1550 (1999).
156. M. A. Reed, J. Chen, A. M. Rawlett, D. W. Price, and J. M. Tour, *Appl. Phys. Lett.* 78, 3735 (2001).
157. M. A. Reed, C. Zhou, C. J. Muller, T. P. Burgin, and J. M. Tour, *Science* 278, 252 (1997).
158. R. Hagedorn, G. Fuhr, T. Müller, T. Schnelle, U. Schnakenberg, and B. Wagner, *J. Electrostat.* 33, 159 (1994).
159. M. P. Hughes, *Nanotechnology* 13, 157 (2002).
160. K. E. Drexler, "Nanosystems: Molecular Machinery, Manufacturing, and Computation." Wiley, New York, 1992.
161. R. Feynman, *Microelectromechanical Systems* 1, 60 (1992), reprinted from 1960 speech at Caltech.
162. M. Grandbois, M. Beyer, M. Rief, H. Clausen-Schaumann, and H. E. Gaub, *Science* 283, 1727 (1999).
163. N. G. Green, A. Ramos, H. Morgan, and A. Castellanos, *Electrostatics 1999, Institute of Physics Conference Series* 163, 89 (1999).
164. B. Ladoux, H. Isambert, J. Leger, and J. Viovy, *Phys. Rev. Lett.* 81, 3793 (1998).
165. A. Ramos, H. Morgan, N. G. Green, and A. Castellanos, *J. Phys. D* 31, 3338 (1998).
166. A. Ramos, H. Morgan, N. G. Green, and A. Castellanos, *J. Electrostat.* 47, 71 (1997).
167. A. Ramos, H. Morgan, N. G. Green, and A. Castellanos, *J. Colloid. Interf. Sci.* 217, 420 (1999).
168. N. G. Green, A. Ramos, and H. Morgan, *J. Phys. D* 33, 632 (2000).
169. N. G. Green, A. Ramos, A. Gonzalez, H. Morgan, and A. Castellanos, *Phys. Rev. E* 61, 4011 (2000).



# Nanoelectromechanical Systems

Josep Samitier, Abdelhamid Errachid, Gabriel Gomila

*University of Barcelona, Barcelona, Spain*

## CONTENTS

1. Introduction: From Micro- to Nanoelectromechanical Systems (NEMS)
  2. NEMS Fabrication Technologies
  3. NEMS Based on Solid-State Suspended Nanostructures
  4. NEMS Based on Nanofluidic Structures
  5. Molecular NEMS: The Ultimate Miniaturization Limit
  6. Concluding Remarks
- Glossary  
References

## 1. INTRODUCTION: FROM MICRO- TO NANO-ELECTROMECHANICAL SYSTEMS (NEMS)

The laws of physics do not forbid the possibility to develop devices and machines at very small scales, even of a few atoms or molecules [1]. Nature is full of examples of such small scale “machines,” which are able to manufacture various substances, to move, and to store information, with everything at very small molecular scale. There are many obvious advantages of making machines and devices as small as possible. Smaller devices are more compact, lighter, faster, and cheaper and they require less power than larger scale devices [2]. Moreover, they offer new capabilities (e.g., access to single molecule properties) not available in larger scale devices.

### 1.1. Microelectromechanical Systems: The First Generation of Small-Scale Mechanical Devices

The first generation of small scale machines and devices appeared in the mid 1980s when the technology of microelectromechanical systems (MEMS) was firmly established [3]. This technology allowed the design and fabrication of electromechanical devices with at least some of their

dimensions in the micrometer range. By “electromechanical” we refer to devices that contain mechanical elements in combination with some electronics that control and read out the mechanical motion or perform some additional functions, as schematically illustrated in Figure 1. In this definition we include microfluidics based MEMS [4–9], which consist of microsystems of channels, pumps, valves, mixers, filters, or separators most often externally controlled by means of electric fields.

MEMS have found many and important commercial applications. Among others we cite arrays of micromechanical mirrors for optical crossbar switches used in the optical communication industry, ink-jet printers using control of fluid jets, accelerometers used as sensors for deploying automobile air bags, microcantilevers for scanning probe microscopes, computer disk read heads, radio switches and filters, and lab-on-a-chip or micro total analytical ( $\mu$ TAS) systems. The latter have found many applications ranging from the life sciences industries for pharmaceuticals and biomedicine (drug design, delivery and detection, diagnostic devices) to industrial applications of combinatorial synthesis (such as chemical analysis and high throughput screening) [6].

Most of the MEMS in practical use today were made with silicon-based technologies [10], because of the well-known methods developed by the microelectronics industry. To this respect, the importance of MEMS technology is not so much the size of the devices, but rather the use of planar processing technologies, related to those used in the fabrication of electronic integrated circuits, that allows simultaneously “machining” of large numbers of relatively simple mechanical devices in an integrated fashion (for a recent example of large-scale integration in microfluidic systems see [11]).

### 1.2. Nanoelectromechanical Systems: The Second Generation of Small Scale Mechanical Devices

With the advent of new nanolithographic techniques (electron and ion beam lithography, nanoimprint lithography, reactive ion etching, etc.), further miniaturization became possible. These techniques allowed scaling down of MEMS into the submicrometer domain thus opening the door to



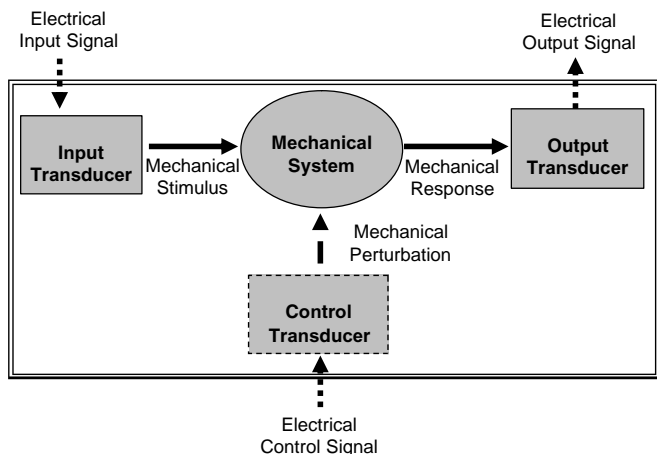


Figure 1. Schematic of an electromechanical device [12].

a new generation of electromechanical devices: nanoelectromechanical systems (NEMS) [12–14]. NEMS can be characterized by critical feature sizes in the range from hundred to a few nanometers, and contrary to the case of MEMS, their small dimensions are relevant for the function of the devices.

In NEMS applications physical properties resulting from the small dimensions may dominate the operation of the devices, and new fabrication approaches may be required, including the use of materials others than Si or the use of fabrication processes with spatial resolution higher than the ones used in the silicon microelectronics industry. In this sense, both top-down (from large to small) and bottom-up (from small to large) fabrication approaches are expected to be necessary in the manufacturing of NEMS.

At present, NEMS are still in a very early stage of development and only elemental devices based on suspended solid-state nanostructures or on nanofluidic systems have been developed. Even though elemental, these developments have shown that NEMS can provide a revolution in applications such as sensors, medical diagnostics, displays, and data storage. In particular, NEMS may enable experiments on the structure and function of individual biomolecules, opening unforeseen biomedical applications. Furthermore, NEMS may offer access to fundamental frequencies in the microwave range, mechanical quality factors in the tens of thousands, active masses in the femtogram range, force sensitivities at the attonewton, mass sensitivity at the level of individual molecules, or heat capacities far below a “yoctocalorie” [12].

### 1.3. Molecular NEMS: The Next Generation

The ultimate limit in the miniaturization of devices and machines will be reached when devices approach molecular or atomistic scales or, more precisely, when the active parts of the devices consist of single molecules or atoms. Fabrication at these scales will generally require a bottom-up approach by using naturally occurring molecules that self-assemble into useful devices or machines. In recent years, the ability to measure and manipulate matter at the level of single molecules has experienced spectacular

advances. Techniques such as scanning probe and tunnelling microscopy or the use of optical tweezers have allowed the characterization of the mechanical and electrical properties of many single molecules, thus making closer to reality the possibility of developing molecular NEMS (i.e., electromechanical devices whose active parts consists of a single molecule or atom). Some preliminary demonstrations based on carbon nanotubes, single proteins, or molecular biomotorson indicate that molecular NEMS can enter into play earlier than expected.

### 1.4. Scope of the Chapter

This chapter will provide an overview of the most relevant advances achieved so far in the emergent field of NEMS. For the purpose of the present chapter we will group NEMS into three main classes: NEMS based on suspended solid-state nanostructures (Section 3), NEMS based on nanofluidic systems (Section 4), and molecular NEMS (Section 5). Fabrication nanotechnologies will be reviewed in Section 1. We end the chapter with some concluding remarks in Section 6.

## 2. NEMS FABRICATION TECHNOLOGIES

The introduction of nonoptical lithography has been announced several times during the last 20 years, but optical methods like projection lithography have always been extended beyond predicted limits. However, a further “simple” downscaling of the optical wavelength beyond 193 nm is not feasible because of the lack of refractive lenses and the problems involved in the fabrication of pure reflective systems with high enough numerical apertures. Hence the need for new lithographic techniques is one of the big challenges for further progress in semiconductor technology. At the moment, several approaches toward sub-100 nm lithography are under discussion that can contribute to nanotechnological development, especially for provision of NEMS. The present section summarizes the principles of operations of some of them.

### 2.1. Electron Beam Nanolithography

Electron beam lithography [15, 16] is at present the essential basis of nanostructure fabrication. Electron beams can be used to write directly onto a substrate using high energy electrons (100 to 200 keV) and a small electron probe size (1 to 10 nm). With electron beams the creation of lines typically 30 nm wide can be satisfactorily produced (widths up to 7 nm have been reported). The resolution limiting factors in electron beam lithography strongly depend on the resist properties. The disadvantages of this technique are the large writing times, causing a low throughput that makes electron beam lithography prohibitively expensive for mass production. However, the approach is certainly useful for making masters for nanoimprinting lithography, which are in turn used multiple times.

## 2.2. Ion Beam Nanolithography

This technique is similar to electron beam nanolithography in terms of application but uses a beam of ions instead of electrons [17]. A fundamental difference is that ions are charged atomic matter that can interact physically and chemically with, and settle into, the exposed material and are many orders of magnitude more massive than electrons. Deep ion beam lithography is a new technique that can be used to produce three-dimensional nanostructures and is particularly good at creating side walls with almost 90-degree angles and slopes.

## 2.3. Nanoimprint Lithography

Nanoimprinting [18, 19] can produce patterns with (sub)micro- and nanometer scales in nanometer thin films in a relatively simple and reliable manner. It makes use of the mechanical deformation of a polymer under pressure and elevated temperature. The master, with its patterned surface, and a sample prepared with a layer of polymer are heated up to the printing temperature, which is above the glass temperature of the polymer to be molded. Then the stamp is pressed against the sample. Stamp and substrate are brought into physical contact and pressure is applied, followed by a down-cooling. After removal from the sample, the resulting polymer relief can be used as a mask for dry etching if the imprinted polymer is resistant enough or as a step in a lift-off process. Figure 2 shows a scheme of this parallel processing technique.

The main advantage of this technique in comparison to electron beam writing is the parallel nature of the process, the high throughput, and the low system costs, because no energetic particle beam generator is needed [20, 21]. In addition, nanoimprinting eliminates a number of adverse effects of conventional lithography techniques [21, 22] like wave diffraction, scattering and interference in the resist, electron backscattering from the substrate, and chemical issues.

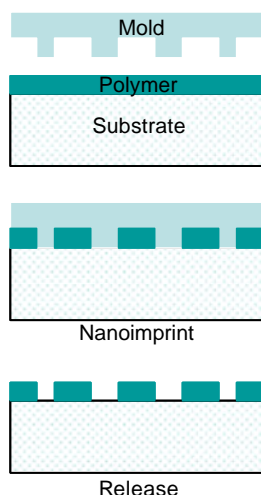


**Figure 2.** Schematic of the nanoimprint lithography process.

## 2.4. Microcontact Printing

The principle of microcontact printing [23, 24] is shown in Figure 3. A stamp consisting of an elastomer is covered by an ink, for example an alkanethiol. Upon contact a self-assembling monolayer is formed within a few seconds which protects the substrate so that a selective wet etch can be performed.

The main advantages of this technique result from the conformal contact to nonflat surfaces, which is due to the elasticity of the stamp. As a consequence flatness of the surface over large areas is not a problem, and even three-dimensional surfaces can be printed.

## 2.5. Scanning Probe

Since their invention, scanning tunnelling microscopy (STM) [25] and atomic force microscopy (AFM) [26] have been promising tools for a wide range of applications: imaging nanostructures, manipulating individual molecules or atoms [27], and more recently for lithography process [28, 29] to build nanostructures. In the technique of STM, a sharp metal tip is brought extremely close to a conducting sample surface. When a bias voltage is placed across the tip-sample junction, electrons tunnel quantum mechanically across the gap between them thus giving rise to measurable tunnelling current (from 10 pA to 10 nA). During image acquisition, the tip is scanned across the sample using  $x$ - $y$  piezoelectric elements, and a feedback circuit typically adjusts the tip height ( $z$  piezo) in order to maintain a constant current. On the contrary, in contact AFM mode, the tip and sample are brought into tip-sample force during scanning, usually by maintaining a constant cantilever deflection. In most commercial AFM, this is achieved by focusing a laser onto the back of the cantilever and measuring its reflected intensity using a photodiode. During scanning, the

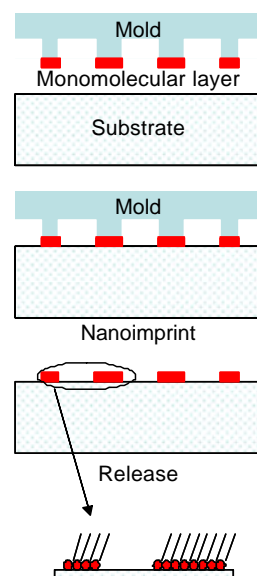


**Figure 3.** Process for the production of a microcontact stamp and the formation of self-assembled monolayers on a substrate.

cantilever motion is then detected via the photodiode signal and a feedback circuit is used to maintain a constant tip-sample force.

In spite of being very young, lithography techniques employing STM/AFM represent a promising way toward the fabrication of new nanodevices for electronic applications with good reproducibility and positioning accuracy. Unfortunately, the serial nature of the writing process makes it time consuming and not economical for commercial applications. One solution to this problem has been the introduction of multiple tip arrays. Techniques such as dip-pen lithography are adaptable to such an array geometry and may eventually yield viable nanodevices applications.

## 2.6. Fabrication Issues for Nanofluidic Applications

Fabrication of nanofluidic structures requires the improvement of two challenges: reduction of size and creation of sealed fluidic channels [8]. The first challenge can be overcome by the use of electron beam, ion beam, or nanoimprint lithographies described previously. Very recently, the fabrication of 10 nm enclosed nanofluidic channels using nanoimprint lithography has been reported [30]. Techniques based on the use of sacrificial materials to create sealed small hollow fluidic structures have gained popularity in recent years [31]. However, steps needed in removing the sacrificial materials such as heating the substrate up to 200–400 °C or wet etching might not be compatible with downstream fabrication process or may limit the use of certain materials.

Concerning sealing techniques, methods such as wafer bonding or elastomeric sealing are suitable for relatively large planar surfaces and provide an effective seal. Wafer bonding consists of creating a bond between a glass slide and a silicon substrate by gentle heating while applying an electric field across the silicon/glass structure to ensure good contact via the associated electrostatic force. Wafer bonding, also called anodic bonding, requires an absolutely defect-free and flat surface. In addition to silicon and glass materials, elastomeric materials have also been considered for the fabrication of micro/nanofluidic structures [32]. These materials provide good sealing properties, fast design times, low cost, the ability to fabricate nanoscale features, and the possibility of deformable shapes.

## 3. NEMS BASED ON SOLID-STATE SUSPENDED NANOSTRUCTURES

A great part of the research developed so far in NEMS has focused on devices consisting of a freestanding or suspended solid-state nanostructure able to freely move in at least one direction and that can be actuated and sensed by means of electromechanical transducers. Nanostructures such as single clamped nanobeams (also known as nanocantilevers) [33–38], doubly clamped nanobeams [39–46], and nanopaddles [47–51] have been fabricated and electromechanically actuated and sensed. A schematic representation of these nanostructures is shown in Figure 4. These nanostructures present at least one dimension in the tens of nanometer range and can be fabricated out of single crystals

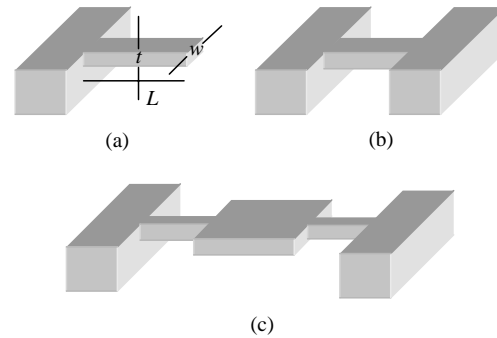


**Figure 4.** Schematic representation of some basic nanostructures for solid-state freestanding NEMS. (a) Single clamped nanobeam, (b) doubly clamped nanobeam, (c) nanopaddle.

or from noncrystalline materials by means of the nanolithographic techniques described in Section 2. Among the materials used in their fabrication we cite Si [39–41], GaAs [47], GaAs/AlGaAs [34, 43, 46], SiC [44], AlN [45], InAs [38], SiN [51], and piezoresistive materials [35]. Very often, the nanostructures are covered with a thin metallic layer for an easier actuation and sensing.

The more relevant physical properties of this class of NEMS, as well as the techniques developed to actuate and sense them, will be described.

### 3.1. Physics of Solid-State Suspended Nanostructures

Solid-state freestanding NEMS are designed basically for two types of applications: very low force measurement and high frequency resonators for communication and sensing applications. For the former application low equivalent elastic spring constants are required. For the latter one, high natural frequencies of oscillation and high quality factors become necessary. The values of these physical properties can vary over a broad range depending on the geometry of the nanostructure, the material used in its fabrication, and the conditions of operation (air, liquid, ultrahigh vacuum). One can estimate these dependencies in the framework of classical elasticity theory [52, 53], which assumes a continuous description of matter, the absence of relevant finite size effects (bulk properties are assumed to hold), and the absence of quantum mechanical effects. Later we will discuss the limitations of this type of description.

#### 3.1.1. Equivalent Elastic Spring Constant

The equivalent elastic spring constant,  $k$ , determines the sensitivity of the nanostructure to external applied forces. It is defined as the force constant a spring would have in order to display an elongation equal to the maximum displacement of the nanostructure in response to a given external force [53]

$$k = \frac{F}{\delta} \quad (1)$$

where  $F$  is the applied force and  $\delta$  is the maximum displacement of the nanostructure. This definition is mainly used for structures of the cantilever type (Fig. 4a). For this type of

nanostructure classical elasticity theory predicts an equivalent elastic spring given by [52]

$$k = \frac{3EI}{L^3} \quad (2)$$

where  $L$  is the length of the beam,  $E$  is the Young elasticity modulus of the material, and  $I$  is the momentum of inertia of the nanobeam cross-section. For the case of a rectangular beam the momentum of inertia is  $I = (1/12)wt^3$ , where  $w$  and  $t$  are the width and thickness of the beam, respectively. The spring constant then reads

$$k = \frac{1}{4} \frac{Et^3w}{L^3} \quad (3)$$

Similar expressions can be obtained for other geometries. The validity of Eq. (3) in the nanorange has been proved for SiC nanorods [54].

By inspection it is clear that structures with large aspect ratios (i.e., large values of the ratio  $L/w$  or  $L/t$ ) will present the smallest spring constants and hence the highest force sensitivity (i.e., they will deform in an appreciable way in response to very small forces). Furthermore, for a given geometry, materials with the lowest values of the Young modulus are expected to give the lowest spring constants. Table 1 presents the values of the equivalent spring constant for different Si nanocantilevers as calculated from Eq. (3).

Suspended solid-state nanostructures are also able to display torsions in response to the action of lateral forces. Torsional phenomena can be described in very much the same way as deflection phenomena. In particular, one can define an equivalent torsional spring constant to characterize the torque sensitivity of the nanostructure as

$$\kappa = \frac{M}{\theta} \quad (4)$$

where  $\theta$  is the maximum angle of twist and  $M$  is the torque producing such a twist. As in the case of deflections, the value of the equivalent spring constant,  $\kappa$ , depends on the properties of the material and on the geometry of the nanostructure. For the simplest case of a single clamped rod classical elasticity theory gives [53]

$$\kappa = \frac{GI_p}{L} = \frac{\pi r^4}{2L} G \quad (5)$$

where  $G$  is the shear modulus of the material,  $I_p$  is the polar momentum of inertia of the rod cross-section, and  $L$  is the length of the nanostructure [in the second equality in Eq. (5) we used that the polar momentum of inertia of a rod is  $I_p = (1/2)\pi r^4$ ]. Similarly, for the case of a single clamped rectangular beam one obtains [52]

$$\kappa = \beta(w/t) \frac{t^3w}{L} G \quad (6)$$

where  $w$  and  $t$  are the width and thickness of the beam, respectively, and  $\beta(w/t)$  is a dimensionless numerical function of the ratio  $w/t$ . Again, in order to reach high torque sensitivity small aspect ratios values are required. The validity of Eq. (6) in the nanorange has been demonstrated with Si nanopaddles [50].

### 3.1.2. Natural Frequencies of Oscillations

The values of the natural frequencies of oscillation of suspended nanostructures determine many of the potential applications of resonant NEMS (e.g., in mass sensors [55–57] or for communication purposes [58, 59]). A very important feature of resonant NEMS is their potential capability to reach the GHz domain (at present, values as high as 380 MHz have been already reported [60]).

The natural frequencies of oscillation of a suspended nanostructure depend basically on the geometry of the nanostructure, on the material used in its fabrication, and on the way the nanostructure is fixed to the supports. Indeed, for the case of transversal oscillations the natural frequencies of oscillation are given by [52]

$$f_n = \frac{C_n^2}{2\pi} \frac{1}{L^2} \sqrt{\frac{EI}{\rho A}} \quad (7)$$

where  $\rho$  is the density of the material,  $A$  is the cross-sectional area, and  $I$  is the momentum of inertia of the cross-sectional area. Moreover,  $C_n$  is a numerical factor that depends on the way the nanostructure is fixed to the supports and on the harmonic considered. For example, for the fundamental mode of oscillation of a rod clamped at one end one has  $C_0 = 1.875$ , while for a rod clamped at both ends one has  $C_0 = 4.730$ . Finally, for a rod clamped at one end and with an external force applied to the free end one has  $C_0 = 1.316$ . For the particular case of a rectangular beam, for which  $I = (1/12)wt^3$ , the natural frequencies of oscillation read

$$f_n = \frac{C_n^2}{2\pi} \sqrt{\frac{E}{12\rho}} \frac{t}{L^2} \quad (8)$$

According to this relationship, the highest frequencies are obtained with nanostructures with the shortest aspect ratios  $L/t$  and the highest  $E/\rho$  ratios. Moreover, doubly clamped structures give frequencies more than one order of magnitude higher than single clamped beams, due to the higher value of the numerical factor  $C_n$ . The validity of Eq. (8) in the nanorange has been tested with SiC [44], AlN [45], and SiN [51] nanobeams. After corrections due to the effects of the thin metallic layer, nonuniform geometries, and tensile stress, good agreement between theory and experiments has been observed.

**Table 1.** Equivalent spring constant for Si nanocantilevers of different geometries as calculated from Eq. (3).

$L \times w \times t$ ( $\mu\text{m} \times \mu\text{m} \times \mu\text{m}$ )	$10 \times 0.2 \times 0.1$	$1 \times 0.2 \times 0.1$	$1 \times 0.05 \times 0.05$
Spring constant, $k$ (N/m)	$9 \times 10^{-3}$	9	0.3

Note: The bulk Si Young modulus is used in the calculations.

Table 2 presents the calculated values of the fundamental frequency of oscillation for Si nanocantilevers of different geometry. We note that high frequencies of oscillation imply in general high force constants. In the MEMS domain this fact has sometimes prevented the possibility of reaching very high frequencies. However, in the NEMS domain very high frequencies seem to be compatible with low force constant [12], as can be seen by comparing Tables 1 and 2.

One of the more relevant applications of resonant solid-state freestanding NEMS is as mass sensors [55–57]. Why these resonators display a so high mass sensitivity can be understood by approximating the nanoresonator by a simple harmonic oscillator. In this case, the fundamental frequency of oscillation is given by

$$f = \frac{1}{2\pi} \sqrt{\frac{k}{m}} \quad (9)$$

where  $k$  is the force constant and  $m$  is the mass. According to this relationship, if a small variation in the mass of a suspended nanostructure,  $\delta m$ , occurs then a frequency shift,  $\delta f$ , on the natural frequency of oscillation,  $f$ , should take place, which is related to the mass increment through the simple relationship

$$\delta m = \frac{k}{4\pi^2} \left( \frac{1}{f^2} - \frac{1}{(f + \delta f)^2} \right) \quad (10)$$

where we have assumed that the value of  $k$  is independent of the mass of the structure. According to Eq. (10), the higher the resonant frequency, the higher the mass sensitivity. With the high frequencies reachable with nanostructures mass variations of the order of single molecules are potentially measurable [55–57].

Suspended nanostructures can also display torsional oscillations. Frequencies up to 18 MHz have been reported for these oscillations [51]. As for the case of transversal oscillations, the values of the frequencies depend on the geometry of the nanostructure and on material properties. A simple method to estimate them is from the relation

$$f = \frac{1}{2\pi} \sqrt{\frac{\kappa}{I_m}} \quad (11)$$

where  $I_m$  is the polar mass momentum of inertia of the system and  $\kappa$  is the torsional spring constant defined previously (this expression is correct except for a numerical factor that can be calculated by using the methods of classical elasticity theory).

It is worth noting that the precise dependence of the torsional frequencies of oscillation on the nanostructure properties is completely different from the one corresponding to transversal oscillations. This fact can be illustrated with a nanopaddle (see Fig. 5), a nanostructure able to display

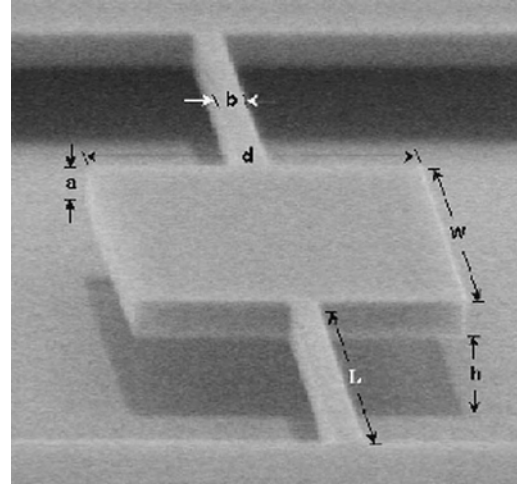


**Figure 5.** Scanning electron micrograph of a nanopaddle. Reprinted with permission from [50], S. Evoy et al., *J. Appl. Phys.* 86, 6072 (1999). © 1999, American Institute of Physics.

both types of oscillations and which has received some attention in the scientific literature [50, 51, 61]. The equivalent torsional spring constant of the two beams subjected to the central rectangular part can be calculated from Eq. (6); that is,

$$\kappa = 2\beta(a/b) \frac{b^3 a}{L} G \quad (12)$$

where the factor 2 affords for the fact that there are two beams subjected to the central structure. Moreover, the mass momentum of inertia of the central part of the paddle (we neglect here the contribution of the beams) is  $I_m = (1/12)md^2$ . Therefore, according to Eq. (12) the fundamental torsional frequency of oscillation of the nanopaddle can be approximated by

$$f = \frac{1}{2\pi} \sqrt{\frac{G}{\rho}} \sqrt{\frac{b^3}{Lwd^3}} \quad (13)$$

On the other hand, by using Eq. (9) the fundamental frequency of transversal oscillations can be taken to be

$$f = \frac{1}{2\pi} \sqrt{\frac{k}{\rho a w d}} \quad (14)$$

with  $k$  being the equivalent spring constant for deflections and which depends only on the properties of the nanobeams but not on the ones of the nanopaddle. As can be seen the frequencies of the torsional and transversal oscillations depend on the width of the nanopaddle as  $d^{-3/2}$  and  $d^{-1/2}$ ,

**Table 2.** Fundamental frequency of oscillation for a single clamped Si nanocantilever for different geometries as calculated from Eq. (8).

$L \times w \times t$ ( $\mu\text{m} \times \mu\text{m} \times \mu\text{m}$ )	$10 \times 0.2 \times 0.1$	$1 \times 0.2 \times 0.1$	$1 \times 0.05 \times 0.05$
Fundamental frequency (MHz)	0.76	75.7	37.8

*Note:* The bulk Si Young modulus is used in the calculations. The frequencies corresponding to double clamped structures can be obtained by simply multiplying by 12.

respectively. These dependencies have been experimentally verified for Si [50] and SiN [51] nanopaddles.

### 3.1.3. Quality Factor

Real resonant structures lose their mechanical energy due to the action of different energy loss mechanisms, generically known as damping mechanisms. This means that in order to keep the nanostructure in motion, energy must be pumped to the resonant structure. The same energy loss mechanisms also induce a broadening of the response of the nanostructure at the resonant frequency, thus reducing considerably the sensitivity for many applications.

The effects of damping on a resonant nanostructure can be understood in a simple way by approximating it by a simple harmonic oscillator subject to friction (proportional to the velocity) and a sinusoidal external driving force with frequency  $f$  and amplitude  $F_0$ . Under these conditions the structure oscillates with frequency equal to the external forcing frequency and with amplitude given by

$$A(\omega) = \frac{\frac{F_0}{m}}{\sqrt{(\omega^2 - \omega_0^2)^2 + \frac{\omega^2 \omega_0^2}{Q^2}}} \quad (15)$$

where  $\omega_0 = 2\pi f_0$  and  $\omega = 2\pi f$ , with  $f_0$  and  $f$  being the natural and forcing frequencies, respectively,  $m$  the mass of the nanostructure, and  $Q$  a dimensionless parameter known as quality factor whose value is determined by the damping mechanisms. In the absence of any damping effects, the quality factor is infinity and the amplitude diverges at the natural frequencies of oscillation. When damping is present the resonant frequency remains almost unchanged (in the usual case that  $Q \gg 1$ ), but the height and width of the resonance are significantly modified, as illustrated in Figure 6. The height and width of the resonance in the presence of damping can be approximated by

$$A_{\max} \sim \frac{F_0 Q}{m \omega_0} \quad \text{and} \quad \Delta f \sim \frac{f_0}{Q} \quad (16)$$

respectively.

A physical interpretation of the quality factor is that  $Q^{-1}$  gives the fraction of energy loss by the resonator in one oscillation or conversely  $Q$  gives the number of oscillations the oscillator performs before losing completely its energy.

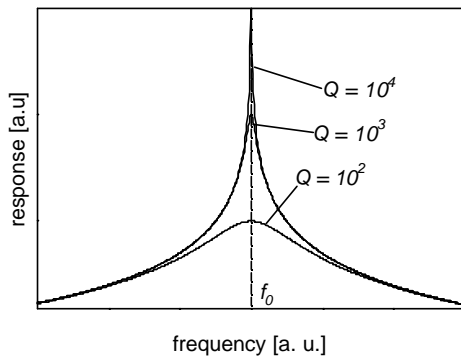


**Figure 6.** Response of a resonator for different levels of damping as a function of frequency.

In resonant nanostructures the values of  $Q$  depend on both intrinsic and extrinsic damping mechanisms [12]. The extrinsic mechanisms include air damping, clamping losses at supports, or coupling losses mediated through the transducers. In particular, viscous damping in ambient conditions is known to be the greatest source of dissipation in MEMS and NEMS structures at atmospheric pressures. Intrinsic damping mechanisms include defects in the bulk or interfaces, fabrication-induced surface damage, adsorbates on the surfaces, or viscoelastic loss mechanisms [62–65] (e.g., thermoelastic damping). Some of these anelastic loss mechanisms can be minimized by a careful choice of the materials, processes, and handling. However, some of them are inherent (e.g., thermoelastic damping), thus imposing an ultimate upper bound to the attainable  $Q$ 's. Intrinsic loss mechanisms related to surface effects have been suggested to play a relevant role in resonant nanostructures due to the high surface to volume ratios [60]. Also the presence of a metallic layer covering the nanostructure has been demonstrated to decrease the quality factor [51, 66].

The relevance of the extrinsic versus intrinsic damping mechanism depends very much on the operation conditions [67]. For pressures in low vacuum extrinsic damping is negligible and only intrinsic damping affects the resonator (internal friction). Experimentally this region happens roughly below 10–100 Pa for microresonators. The highest values of  $Q$  have been obtained under these conditions. For intermediate pressures momentum transfer between the resonator and individual ambient molecules dominates the damping. By neglecting the interaction between the molecules in the ambient the quality factor can be shown to depend inversely on the pressure. This region typically ends around  $10^3$  Pa. Finally for high enough pressures for which the interaction between ambient molecules is relevant, viscous damping dominates. In this regime the quality factor is inversely proportional to the fluid viscosity and takes very low values [68]. In this case, methods of quality factor control can be envisaged to keep functionality of NEMS [68–70].

Experimental results have reported values of  $Q$  in the range from  $10^2$  to  $10^4$  for resonating NEMS [the higher values have been obtained in ultrahigh vacuum (UHV) conditions]. Some of these values greatly exceed those typically available from electrical resonators, although they are orders of magnitude smaller than the values expected from fundamental loss mechanisms. In fact, the maximum attainable value of  $Q$  seems to scale downward with the linear dimension of the resonator when going from the macroscopic to the nanoscale domain [12] (the linear dimension of the resonator is roughly estimated as  $V^{1/3}$ , where  $V$  is the volume of the nanostructure). Currently, there is no clear understanding of the underlying physics determining this unexpected phenomenon.

Damping phenomena always carry with them other phenomena like fluctuations. For instance, a simple harmonic oscillator in the presence of damping experiences random forces whose mean is zero and whose spectral density is given by [12]

$$S_f(f) = \frac{4k_B T \kappa}{2\pi f_0 Q} \quad (17)$$



where  $k$  is the equivalent elastic spring constant of the resonator and  $f_0$  is the fundamental frequency of oscillation. The presence of these fluctuations is unavoidable and limits, among other things, the minimum measurable forces.

Finally, through the quality factor and natural frequencies of oscillation one can estimate the minimum pump energy rate necessary to keep the nanostructure in motion to be [12]

$$P_{\min} \sim \frac{k_B T}{Q} f_0 \quad (18)$$

where  $k_B T$  is the thermal energy and  $f_0/Q$  is the rate at which the resonator exchanges energy. The high  $Q$  values attainable in NEMS imply that a very small amount of power is required to drive the devices, which constitutes one of the big advantages of these systems for communication applications with respect to high frequency microelectronics.

### 3.1.4. Other Factors Determining the Performance of Suspended Solid-State NEMS

In solid-state freestanding NEMS there are other factors, in addition to the ones considered previously, that can alter its performance. These factors should be taken into account when analyzing or designing suspended solid-state NEMS.

**Weight of the Nanostructures** In the estimations performed previously of the equivalent elastic spring constant the effect of the mass of the nanostructure has been neglected. This approximation holds as long as the forces applied to the nanostructure are much larger than the weight of the nanostructure. To give an order of magnitude we note that a  $10 \times 0.2 \times 0.1 \mu\text{m}^3$  Si cantilever weighs  $W = mg = Lwt\rho g = 4.66 \times 10^{-15}$  N while a  $1 \times 0.05 \times 0.05 \mu\text{m}^3$  does  $W = 5.8 \times 10^{-17}$  N (we have taken for the density of Si  $\rho = 2330 \text{ kg/m}^3$ ). Therefore, this effect is not expected to be relevant for most of the applications.

**Phase Noise** The extremely high mass sensitivity of the resonators is predicted to induce a high level of phase noise (i.e., fluctuations in the value of the resonating frequency), the reason being that when operated in air or liquids adsorbates are expected to adsorb and desorb from the surfaces in a random way, thus changing the mass of the resonator and hence the natural resonant frequency. Another source of phase noise can be temperature fluctuations or similar phenomena affecting the resonant frequency [71, 72].

**Nonlinearities** Nonlinear effects are easily observable in suspended solid state nanostructures [42, 44, 60, 73]. The onset of nonlinear effects can occur for small applied forces (and hence lower input power) in large aspect ratio structures. In nanostructures nonlinear effects have been observed for displacements as small as 10–15 nm. A signature of the nonlinear behavior is the presence of an asymmetric resonant response. The nonlinear behavior can be harnessed to create parametric oscillators and possibly could be used to create highly sensitive resonant charge [73], force, and mass sensors [12].

**Strain Effects** In many electromechanical systems bi- or multilayered structures are very often used. In these structures the presence of internal strain or stress is almost unavoidable. Moreover, even for homogeneous mechanical devices (e.g., those patterned from doped semiconductors materials), surface nonidealities may impart significant modifications to the free strain picture. Strain is well known to induce modifications in the values of the equivalent spring constant and resonant frequencies in addition to additional losses. This property has been used to develop state of the art nanomechanical chemical [74] and biological sensors [75]. In the former case use has been made of the fact that analyte molecules chemisorbing or physisorbing on a coated nanocantilever and chemical reactions produce interfacial stress between analyte molecules and the cantilever. In the latter case, the surface strain is induced by a self-assembled monolayer grown on top of one side of a cantilever when it interacts with specific molecules [75]. The induced strain comes from the changes in the configurational entropy and intermolecular energetics of the self-assembled monolayer [76].

**Finite Size Effects** In most of the experiments reported in the literature the values of the Young modulus obtained differ from the value corresponding to bulk materials (usually lower values are observed [37]). It has been suggested that effects due to the finite nature of the structures (finite size effects) could be responsible for such deviations. A theoretical understanding of this phenomenon is still lacking.

**Atomistic Behavior** When going down to smaller scales, one can ask at what scale continuum mechanics breaks down and corrections from atomistic behavior emerge. Molecular dynamics simulations [77] for ideal nanostructures appear to indicate that this becomes manifest only at the truly molecular scale, of the order of tens of lattice constants in cross-section. Hence, for most of the suspended nanostructures the continuum approximation will be adequate.

**Heating Effects** Due to the presence of losses the materials can heat up and as a result the frequency and the spring constant can vary due to changes in dimensions, density, strain, etc. Although it was forecast that these small structures should dissipate heat very efficiently [1], investigations are still on the way to establish the appropriate heat transport laws for nanostructures [47, 78, 79].

**Quantum Effects** The ultimate limit for suspended nanostructures is to operate at, or even beyond, the quantum limit [12, 80]. This regime can be defined by the condition that a mechanical quantum,  $hf_0$ , where  $h$  is the Planck constant and  $f_0$  is the resonant frequency, is of the order of, or greater than, the thermal energy  $k_B T$ . In the quantum regime jumps between discrete quantum mechanical states should be observable. As a rule, very high frequencies and very small temperatures are required (for instance 1 GHz corresponds to 50 mK in temperature). In order to reach the quantum limit a number of challenges have to be overcome, among others, the experimental definition of the resonator discrete quantum states, the development of transducers able to resolve an individual quantum jump, or the cooling of the resonator to very low temperatures in the presence of loss mechanisms [12]. The quantum limit for mechanical

nanoresonators opens fascinating possibilities in the measurement sciences at the molecular level, in the development of new device possibilities for phase coherent measurements and quantum computation or in the control of thermal transport involving the exchange of individual phonons. Furthermore, in this limit the wave nature of matter will become manifest and the division between quantum optics and solid state physics is expected to become increasingly blurred.

### 3.2. Actuating and Sensing Solid State Suspended Nanostructures

Up to now we have focused on the physical properties of suspended solid-state nanostructures for NEMS applications. In addition to the mechanical part, essential components of any NEMS are the transducers in charge of actuating and sensing the mechanical part of the device. For NEMS applications the transducers must be able to detect minute displacements, induce minute forces, detect very high frequencies, or detect very small frequency shifts. Most of these actions are very challenging in the NEMS domain. Below we report the techniques currently available to actuate and sense solid-state suspended nanostructures.

#### 3.2.1. Electrostatic Actuation

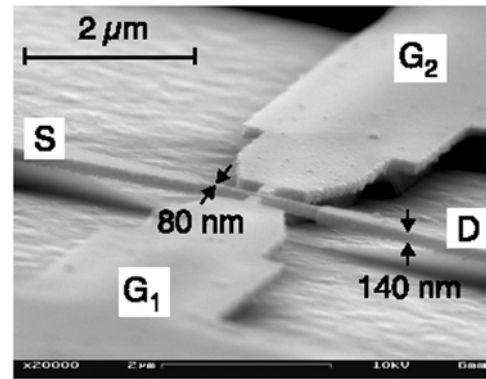
Electrostatic transduction is the method most widely employed in MEMS and can also be applied to NEMS [33, 56, 57]. The principle of actuation of this technique is very simple. It consists of charging electrically the nanostructure and then actuating on it by means of the electrostatic interaction with an external charged element (e.g., a charged substrate), often referred to as the driver. To apply this technique the mechanical element has to be a good conductor or have been recovered by a good conductor. Two examples of driver-free standing nanostructures are shown in Figure 7.

This method of actuation allows both static and dynamic actuation depending on whether a constant or variable potential is applied between the nanostructure and the driver. In the latter case, the system can eventually be driven into resonance.

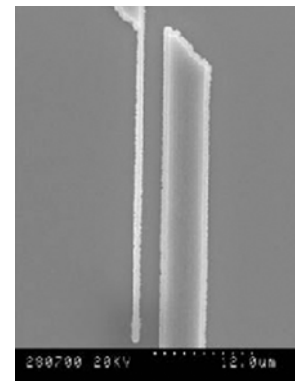
Several factors determine the actual motion induced to the nanostructure by the driver. Among others we cite the geometry of the nanostructure, the geometry of the driver, the coupling between both elements, the environment (air, liquid, UHV), the way the nanostructure is fixed, the damping mechanisms, or even the relevance of the Casimir effect [81, 82].

#### 3.2.2. Magnetomotive Actuation

Magnetomotive actuation [42, 83] makes use of the Lorentz force (i.e., the force exerted by a magnetic field on an electric current). It uses a setup like the one schematically shown in Figure 8, which consists of a closed conducting circuit, which includes the moving mechanical element, located in a strong magnetic field perpendicular to the nanostructure. When a dc current passes through the circuit a force perpendicular to the electric current appears that eventually can bend the suspended nanostructure. For electric current varying with time a dynamic motion can be induced to the nanostructure. This method of actuation also requires electrically conducting nanostructures.



(a)



(b)

**Figure 7.** Scanning electron micrograph of (a) a double clamped nanobeam and (b) a single clamped nanocantilever including the driver for electrostatic actuation. Reprinted with permission from (a) [41], L. Pescini et al., *Nanotechnology* 10, 418 (1999) and (b) [57], G. Abadal et al., *Nanotechnology* 12, 100 (2001). © 1999/2001, Institute of Physics Publishing.

#### 3.2.3. Secondary and Local Actuation

The secondary actuation method consists of using a piezoelectric or another actuator to oscillate the supports where the resonant nanostructure is suspended (Fig. 9a). In scanning probe microscopes this is sometimes the method used to set into resonance the tip. Local actuation [84] consists of using a nanoelement whose dimensions are smaller than the nanostructure (e.g., an STM or AFM tip) to locally induce a motion in the nanostructure (Fig. 9b). This method works better the larger the nanostructure. Both methods

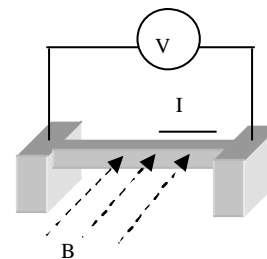


**Figure 8.** Schematic drawing of a freestanding nanostructure magnetomotively actuated.

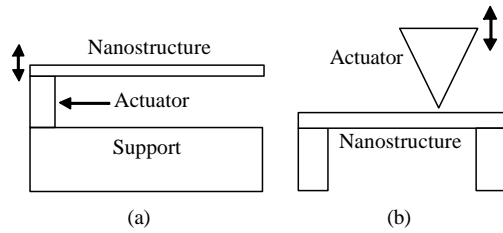


**Figure 9.** Schematic drawing of a nanostructure actuated by (a) secondary actuation and (b) local actuation.

have the advantage of not requiring electrically conducting nanostructures.

### 3.2.4. Actuation by Means of Internal or Superficial Strain

As mentioned before internal or superficial strain can produce the bending of freestanding nanostructures and hence offers a method to actuate them. One way to implement this method has been to use bi- or multilayered structures, with layers having different thermal expansion and light absorption coefficients [85]. When such a nanostructure is irradiated with a continuous wave laser and a standing wave is formed between the freestanding structure and the support, then the more absorbing layer absorbs more energy, and heats up more, than the lower absorbing layer (Fig. 10). Due to the different thermal expansion coefficients of the two layers a strong strain is induced in the nanostructure that eventually can bend it. If the amplitude of the laser light is appropriately modulated a resonant behavior can be induced by this method.

A similar technique can be implemented in a monolayered nanostructure by irradiating only one part of it [86–88]. In this way a temperature gradient can be induced in it that produces the modulation of the elastic constant and hence the bending of the nanostructure.

### 3.2.5. Electrostatic Sensing

Electrostatic sensing of a free suspended nanostructure can be accomplished by measuring the changes in the capacitance of the capacitor formed by the suspended nanostructure and the driver (see Fig. 7). In the case of a resonant structure the equivalent circuit of the system is more complicated than a simple capacitance, but this method can be equally well applied to measure the motion frequencies [56, 57].

Electrostatic sensing, initially developed for MEMS, does not scale well into the domain of NEMS [12]. Very small

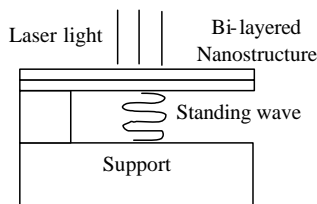


**Figure 10.** Schematic drawing of a nanostructure actuated by means of the induction of internal strain.

electrode capacitances are to be expected for electrodes at the nanoscale, thus making parasitic capacitances dominate the dynamical capacitance of interest. One possible solution would be to eliminate the large embedding and parasitic impedances by locating a subsequent amplification stage directly at the capacitive transducer. This would make the NEMS electrode serve a dual purpose, as both the motion sensor for the NEMS and as the gate electrode of a field effect transistor (FET) readout.

### 3.2.6. Optical Sensing

Very small displacements can be detected by optical methods like simple beam deflection methods or more sophisticated optical and fiber-optic interferometry methods.

In the simple beam deflection scheme [89] a laser beam is focused on top of the nanostructure and its reflection is measured on a photodiode (Fig. 11). This method can be applied to both static deflections as well as dynamic ones. In the latter case a spectrum analyzer is usually used to analyze the frequency components of the electrical signal provided by the photodiode. Scaling down this technique to the NEMS regime can be very challenging since the nanostructure cross-section can become smaller than the size of the focused laser spot.

Interferometry methods [36, 40, 90], on the other hand, use the fact that the motion of the nanostructure modulates the reflected signal as a result of interference phenomena, thus allowing one to detect the amplitude and phase of the nanostructure motion.

For very small size NEMS applications, nonconventional optical methods, like integrated and near-field optical displacement sensors, may become a valid alternative to the above-mentioned methods [12].

### 3.2.7. Magnetomotive Sensing

Magnetomotive sensing is based on Faraday's law (i.e., on the induction of an electromotive force in a closed circuit when the magnetic flux through it changes with time). There are different ways to implement this technique.

One of them consists of using the same setup as the one used for magnetomotive actuation [39] (see Fig. 8). In this case, when the nanostructure is set into motion an electromotive force is induced in the closed circuit, whose measurement provides information on the dynamical response of the device. More elaborate versions of this method, which makes use of a balanced electronic detection [91], have been developed for some especially demanding applications.

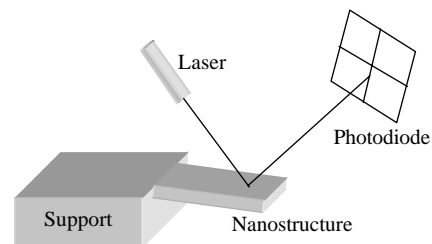


**Figure 11.** Schematic drawing of a nanostructure sensed by a simple beam deflection scheme.

An alternative implementation of this technique could be done in the case that the moving element behaves like a nanomagnet [12]. In this case, a closed conducting loop located close to the nanostructure can be used to induce an electromotive force in it due to the nanostructure motion. This implementation can be used with nonconducting and both single and doubly clamped nanostructures.

### 3.2.8. Piezoelectric Sensing

In the case that the nanomechanical element displays piezoelectric phenomena sensing of the displacements can be achieved by measuring the voltages generated due to the piezoelectric properties. This method has been implemented with nanostructures fabricated with a piezoelectric material [35] and with GaAs/AlGaAs nanostructures [34, 46]. One advantage of piezoelectric sensing with respect to other methods is that it provides a high degree of integration.

### 3.2.9. Sensing by Means of Electron Tunnelling

Electron tunnelling currents between two conducting materials depend exponentially on the separation between them. This property is used in scanning tunnelling microscopes to image material surfaces up to atomic resolution. This same property can be used to sense small displacements in free-standing nanostructures [33], as illustrated in Figure 12. The same restrictions concerning operation conditions and material properties as for STM will apply by using this method.

### 3.2.10. Sensing by *in-situ* SEM or TEM

Finally, one can also use *in-situ* scanning electron microscopy or transmission electron microscopy to sense directly the bending or the motion of the nanostructures [84]. In this case, the usual requirements of these microscopic techniques should be satisfied by the samples.

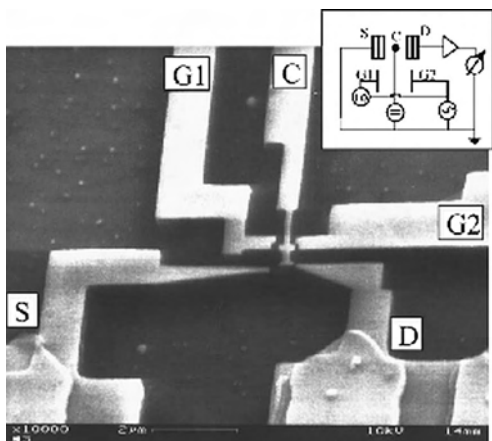


**Figure 12.** Scanning electron micrograph of a nanobell ring sensed by means of electron tunnelling. The inset displays an equivalent circuit representation of the nanoelectromechanical system. Reprinted with permission from [33], A. Erbe et al., *Appl. Phys. Lett.* 73, 3751 (1998). © 1998, American Institute of Physics.

## 3.3. Applications of NEMS Based on Solid-State Suspended Nanostructures

There is no doubt that NEMS based on solid-state suspended nanostructures will find a broad range of applications. A number of NEMS applications are being pursued, which might hold immense technological promise for fields such signal processing in very high frequency, ultrahigh frequency, and microwave bands [58, 59], ultrahigh sensitive magnetic resonance force microscopy [12], noninvasive medical diagnostics devices, BioNEMS for single molecule analysis [12], or ultra-high-density data storage systems. At present, however, most of the research efforts are centered on basic studies of fabrication approaches and on the understanding of the science of nanoscale systems. Functional NEMS devices have been demonstrated only for charge detection [49, 73] and thermal transport studies [47, 78] with relevance for metrology and fundamental science. Moreover, significant advances toward functional NEMS for ultra-precise mass sensors [55, 56] and biomolecular recognition [75, 76] have been recently reported. Based on the present developments, one can anticipate that in a decade or so, one may be seeing a prevalence of solid-state NEMS devices at the level one now finds equivalent MEMS systems [13].

## 4. NEMS BASED ON NANOFUIDIC STRUCTURES

Many potential applications of NEMS, like those involving chemical, biological, and biophysical processes, require the presence of a fluid environment and hence the use of nanofluidic structures. Nanofluidic NEMS may have dimensions in the order of hundreds to a few nanometers, thus displaying characteristic dimensions of the order of the diffusion length of molecules, the molecular sizes, or the electrostatic screening lengths of ionic conducting fluids. At these scales fluids are expected to display qualitatively new behaviors that will allow one to perform techniques and experiments not possible on the microscale. Although transport phenomena in nanoscopic structures are not well understood yet, some relevant advances have been achieved in recent years. In the present section we review the more relevant developments achieved so far in this field.

### 4.1. Physics of Nanofluidic Structures

Fluids confined in nanometric spaces (with at least one dimension in the tens to hundred of nanometers regime) have been observed experimentally and theoretically to exhibit unique structural, dynamical, mechanical, and rheological properties [92]. These properties have been shown to depend on the degree of confinement (e.g., load), operational conditions (e.g., shear rate and temperature), nature of the fluid (e.g., molecular shape, molecular size and molecular complexity), and interactions with the boundaries (e.g., chemical or physical binding) [93, 94]. The understanding of the structure and mechanical properties of fluids at these scales is then of fundamental scientific and practical interest for nanofluidics (as well as for other fields of research such as lubrication, adhesion, or wetting). Experimentally, this problem has been addressed essentially by

the use of three techniques, namely open fluid geometries in which two extremely flat surfaces are immersed to come nearly in contact, optical methods able to probe flow properties near a surface in a macroscopic container, and flow experiments in ultrasmall nanofluidic channels. Extensive molecular dynamic simulations have been developed to complement experimental findings.

In nanofluidic structures whose characteristic dimensions exceed some tens of the molecule fluid diameter, simple fluids behave like a continuum. Otherwise, for smaller structures, the molecular graininess of the fluids becomes important and a discrete molecular description must be adopted.

In the continuum regime the main difference between macro- and nano/microflows (both can be described through the Navier–Stokes equation) comes from the relevance of viscous forces. Viscosity represents the tendency of a fluid to undergo deformation when subject to a shear stress. In the case of a pure liquid consisting of simple molecules, viscosity is an intrinsic property and its value is dependent on the temperature of the fluid alone. For complex fluids, such as solutions of macromolecules, viscosity shows a complex dependence on an additional number of parameters, such as the type of solvent and concentration or molecular weight of the solute. In macroflows, the inertia of fluid mass is usually much larger than the viscous force, while in nano/microflows the opposite condition is found. The relevance of inertial versus viscous forces can be quantified through the Reynolds number, defined as the ratio between these two types of forces

$$\text{Re} = \frac{\rho v l}{\mu} \quad (19)$$

where  $\rho$  is the fluid density,  $v$  is the characteristic velocity of the fluid,  $\mu$  is the fluid viscosity, and  $l$  is a characteristic length. In nano/microfluids the Reynolds number takes low enough values as to allow neglect of the nonlinear terms in the Navier–Stokes equation, thus giving rise to laminar flows (as opposed to turbulent flows present in macrofluidics). For instance, the Reynolds number corresponding to water flow [ $\rho = 1 \text{ g/cm}^3$ ,  $\mu = 0.01 \text{ g/(cm s)}$ ,  $v = 1 \text{ cm/s}$ ] through a micropipe of  $50 \text{ }\mu\text{m}$  in diameter with smooth walls is  $\text{Re} = 0.5$ , largely satisfying the experimental condition  $\text{Re} < 2300$  for laminar flow in a pipe. The linear nature of low Reynolds fluid flows, labeled Stokes flows, can be broken in some cases due to the presence of special boundary conditions, as has been shown recently in a T-shaped microfluidic structure [95]. The laminar nature of the fluid flow in nano/microfluidic applications may have important consequences for mixing, sample concentration, and separation of species [4–9].

Although micro- and nanoflows are both laminar, there is an important difference between both, namely that in nanofluidic flows the condition of zero tangential velocity at the walls (i.e., no-slip boundary condition) does not accurately describe the flow properties. It has been recently shown that in any flow the velocity of the fluid at the walls is nonzero. This effect is characterized by means of a phenomenological slip length,  $\lambda$ , which corresponds to the distance outside the channel at which the liquid velocity extrapolates to zero. The experimental values reported

for this length range in the tens to hundred of nanometers, thus being only relevant for nanofluidic flows. The value of the slip length has been shown to depend strongly on the molecular size of the fluid and on the nature and roughness of the surface. One consequence of the presence of slip at the fluid–solid interface is that flows do not satisfy the standard Poiseuille law. The Poiseuille law describes the pressure driven flow of a fluid through a channel and states that the flow rate,  $Q$ , is proportional to the pressure drop across the channel

$$Q = \frac{\Delta P}{R} \quad (20)$$

where  $R$  is the channel resistance. For a circular geometry one has

$$R = \frac{8\mu L}{\pi r^4} \quad (21)$$

where  $L$  is the channel length,  $\mu$  is the fluid viscosity, and  $r$  is the channel radius. For the case of a rectangular channel whose width,  $w$ , and length,  $L$ , are much greater than the height,  $h$  (an appropriate geometry for nanochannels), one has

$$R = \frac{12\mu L}{h^3 w} \quad (22)$$

Recent experiments have reported significant differences between Eq. (22) and the values measured in fluid flows through nanochannels with heights ranging from  $2.7 \text{ }\mu\text{m}$  to  $40 \text{ nm}$  [96]. The discrepancies between standard theory and experiments have been accounted for by the introduction of slip. The values determined for the slip length are  $\lambda \sim 25\text{--}30 \text{ nm}$  for hexadecane,  $\lambda \sim 14 \text{ nm}$  for decane,  $\lambda \sim 9 \text{ nm}$  for hexane, and  $\lambda \sim 0 \text{ nm}$  for water (note that the larger the molecular size, the larger the slip length). At present, it is not clear how to calculate the magnitude of the slip length from fundamental theoretical principles or how it depends on factors such the molecular size, surface properties, or flow nature [97–104].

Other phenomena related to the physicochemical interaction between fluid molecules and wall molecules include “wall depletion” in dilute polymer solutions [105]. Note that, at these scales, and provided the appropriate boundary conditions are used, the nanofluid can be still treated with the Navier–Stokes flow equations in the framework of low-Reynolds hydrodynamics or “microhydrodynamics” [106].

The presence of slip in nanoflows is not the unique effect due to the confinement of fluids in nanometric structures. For very small structures, of the order of ten times the molecule diameter, effects due to the discrete molecular nature of the fluid start appearing, thus breaking down the continuum description of the fluids. A well known example is the ordering of molecules in layers when the liquid is confined by surfaces [93, 94, 107]. These density variations lead to an oscillatory solvation force which decays exponentially [104] and to a high value of the “apparent” viscosity of the fluid as high as  $10^5$  times the regular viscosity [108]. At these scales, then, the fluid loses its liquidlike behavior and assumes solidlike characteristics [107]. In this regime

the description of the system can be carried out by means of molecular dynamic simulations.

At smaller scales, below one or two molecule fluid diameters one should resort to a quantum-mechanical description, in which the distinction between solids and fluids loses its meaning.

Nanofluidic applications involve in most of the cases the presence of “particles” embedded in the fluid. The term “particles” is used here in a broad sense and includes [7] organic molecules (a few angstroms in size), protein molecules (typical sizes from 2 to 5 nm), large biopolymers such as DNA, and suspended solid particles or cells (typically 100 nm–10 μm). At these scales, due to the large surface to volume ratios, the motion of the “particles” can be largely influenced by surface forces, thus leading to the appearance of finite size effects, not very well understood yet [7]. Moreover, the presence of even small amounts of particles in suspension can modify the rheological properties of the bulk flow resulting in non-Newtonian fluid properties. In some instances, non-Newtonian fluids at low Reynolds number have been shown to display turbulent-like instabilities (elastic turbulence) that could be advantageous for efficient mixing [109].

The special problems involving particles coming into close proximity can be analyzed using the “Stokesian dynamics” approach, where hydrodynamic effects are split into “far field” and “near field” components [110]. A particular case is the analysis of Brownian effects in the so-called “Brownian dynamics.” Stokesian and Brownian dynamics can be regarded as large-scale versions of the molecular dynamics. The interaction of macromolecules with a surrounding fluid phase and, in general, solvent–solute systems at these scales can be simulated by using multispecies molecular dynamics.

Figure 13 summarizes the different transport regimes encountered in nanofluidics. The vertical axis represents the solid fraction of the fluid (the value 0 corresponds to simple fluids and the value 1 to solids). Intermediate values represent solutions with different degrees of solvent). The horizontal axis, ranging from 0.1 nm to 1 μm, represents the scale of the problem or the level of description.

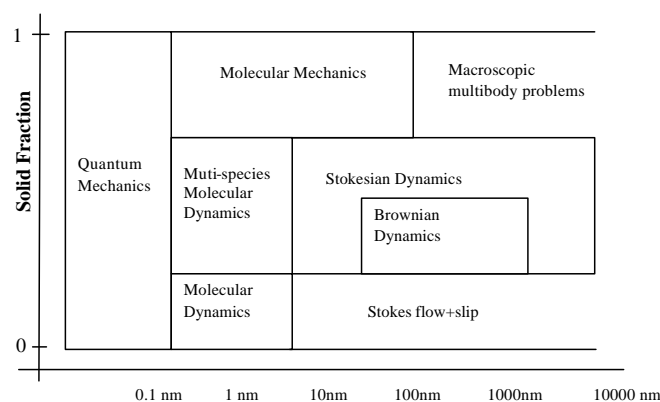


**Figure 13.** Phase diagram of the different transport regimes as a function of the solid fraction and the characteristic spatial scale of the problem [92].

## 4.2. Driving Forces in Nanofluidic Structures

Driving fluids and “particles” through nanofluidic structures constitute an essential issue in the development of nanofluidic applications. We review the properties of the basic forces used for this purpose. For the sake of clarity, we distinguish between forces used to drive fluids and forces used to drive the particles with respect to the fluids.

### 4.2.1. Driving Forces for Fluid Flows

**Hydrodynamic Pressure** Hydrodynamic pressure is the primary force driving fluids in macroflows, but it may be impractical in nanopassages, since the resistance to fluid flow increases with the inverse of the fourth power of the transversal channel dimensions [see Eq. (22)]. This means that in order to reach practical fluid flows very high pressures may be required that in turn may require specific fabrication processes. Furthermore, the sensitivity of the resistance to channel geometry imperfections becomes very high, thus not enabling accurate control of the fluid flow. Finally, actuators inducing the pressures necessary are not easily integrated in lab-on-a-chip systems.

For these reasons, and because they also allow selective driving of the embedded “particles,” electrokinetic forces have been preferred by many researchers in micro/nanofluidics.

**Electroosmosis** Electroosmotic flow [111] is related to the motion of an ionic fluid induced by a dc potential applied along the stream. The electroosmotic flow arises from the fact that the surfaces of a flow channel are generally charged or can be made so with a suitable coating, thus inducing a layer of charged ions next to them. The ionic layer consists of a space charge region composed by a rigid sheet of solvated ions bound to the charged surface (known as Helmholtz layer) followed by a region of mobile ions beyond the Helmholtz layer, with a characteristic dimension given by the Debye screening length (whose value can range from nanometers for high ionic concentrations to μm for deionized water). This charged mobile layer can be made to move by the application of an electric potential, dragging the neutral fluid along with it. The resulting velocity profile is constant across the channel and its value can be estimated from

$$v = \frac{\epsilon E \xi}{\mu} \quad (23)$$

where  $E$  is the tangential electric field,  $\epsilon$  is the permittivity of the medium, and  $\mu$  its viscosity. Moreover,  $\xi$  is the zeta potential (i.e., the potential difference across the mobile part of the double layer). External electrical control of the zeta potential by the application of a transversal electric field has been recently demonstrated [112], thus offering enhanced performance of electroosmotic control of fluid flows. Note that the fact that the velocity profile is flat (as opposed to the parabolic profile of a Poiseuille flow) is advantageous for nanofluidic applications since it introduces less dispersion in the sample. More complicated, nonuniaxial fluid motion can be generated with electroosmotic forces by creating charged patterns along the walls of the channels [113].

Recently, it has been suggested that an ac electric field can induce a more complicated, and sometimes useful, electroosmotic force [114, 115]. The existing theory is nowadays



still far from exactly matching the experimental data for high voltages and medium conductivities, even in its enhanced version [116], and it is still under controversy with other theories developed [117]. Despite all these drawbacks, this theory still seems able to capture the fundamental features of the frequency behavior of low frequency fluid movement experimentally measured in structures with microelectrodes.

**Electrocapillarity** Capillary forces constitute a valid alternative since they can generate large forces in small channels. They require a discontinuity such as an air/liquid interface or immiscible liquids and seem appropriate for filling devices or single-use applications [6]. In recent years, external electrical control of capillary forces (electrocapillarity) has been demonstrated in micro/nanofluidic structures. Electrocapillary fluid motion refers to the motion induced by electrostatic control of the solid/fluid interfacial tension in a micro/nanochannel [118]. The principle of electrocapillarity actuation is based on the fact that the capillary pressure on a fluid/fluid meniscus inside a micro/nanochannel can be controlled by the charge density accumulated at the solid/fluid interface. Based on this phenomenon, and by inserting electrodes inside the walls, control of the fluid motion can be achieved, in some cases in a more efficient way than with electroosmosis [118].

#### 4.2.2. Driving Forces for “Particles” in Fluids

**Viscous Drag** As is well known any particle moving with respect to a fluid experiences a drag force due to viscous forces. In the case of a rigid particle the drag force can be approximated by (we assume a spherical particle of radius  $a$ )

$$F_{\text{drag}} = 6\pi\mu av \quad (24)$$

where  $v$  is the velocity of the particle relative to the fluid and  $\mu$  is the fluid viscosity. For nonrigid particles (e.g., large polymers and macromolecules) the equivalent of the drag force is more complicated to evaluate. The drag force can be approximated by Eq. (24) as long as the size of the “particle” is much larger than the fluid molecule size.

**Electrophoretic Force** The electrophoretic force refers to the electrostatic force acting on a charged particle embedded in a neutral medium in response to an external applied field. The magnitude of the force is easily calculated as

$$\vec{F} = Q\vec{E} \quad (25)$$

where  $Q$  is the charge of the particle and  $\vec{E}$  is the electric field. Moderate voltages applied to short distances, such as the ones characteristic of nanofluidics, give rise to high enough electrophoretic forces to impart significant velocities to the embedded particles. Electrophoretic forces are very often used to separate different species having different sizes. In ionic or polar fluids the presence of other forces can perturb the simple picture presented.

**Dielectrophoretic Force** For neutral particles one has to resort to dielectrophoretic forces to drive the particles with respect to fluids [119]. The origin of this force is found on the electric dipole induced on a neutral particle when an external electric field is applied. The magnitude of the force can be evaluated as follows. Let us represent the electric properties of a dielectric spherical particle of radius  $a$  by means of a complex permittivity of the form

$$\varepsilon_p^* = \varepsilon_p - j\frac{\sigma_p}{\omega} \quad (26)$$

where  $\varepsilon_p$  is the dielectric constant of the particle,  $\sigma_p$  is its conductivity, and  $\omega$  is the frequency of the applied field. Let us suppose that the particle is immersed in a dielectric fluid medium of permittivity

$$\varepsilon_m^* = \varepsilon_m - j\frac{\sigma_m}{\omega} \quad (27)$$

and subjected to an uniform z-directed ac electric field of magnitude  $E_0$  and radian frequency  $\omega$ . Under these conditions the particle presents an effective dipolar momentum given by

$$p_{\text{eff}} = 4\pi\varepsilon_m a^3 \left( \frac{\varepsilon_p^* - \varepsilon_m^*}{\varepsilon_p^* + 2\varepsilon_m^*} \right) E_0 \quad (28)$$

Due to this effective dipolar momentum, a net force, called dielectrophoretic force, acts on the particle [119]

$$\vec{F}_{\text{DEP}}(\omega) = 2\pi\varepsilon_m a^3 \text{Re} \left( \frac{\varepsilon_p^* - \varepsilon_m^*}{\varepsilon_p^* + 2\varepsilon_m^*} \right) \vec{\nabla} |E_{\text{rms}}|^2 \quad (29)$$

where  $E_{\text{rms}}$  is the root mean square value of the electric field. As can be seen this force, due to its dipolar origin, only appears when spatially nonhomogeneous electric fields are present. One of the most interesting features of the dielectrophoretic force is its frequency-dependent behavior. Depending on the electric field frequency and the particle properties, the dielectrophoretic force can attract or repel the particle to the electrical field minima or maxima. When the particle is attracted to the electric field maxima it is said to have a positive dielectrophoretic behavior ( $p$ -DEP). In the opposite case, one refers to a negative dielectrophoretic behavior ( $n$ -DEP). The two behaviors are illustrated in Figure 14 where we display the simulated frequency dependence of the dielectrophoretic force for a 297 nm latex sphere within a medium of conductivity 17  $\mu\text{S}/\text{cm}$  at three different voltages. As can be seen, at low frequencies a  $p$ -DEP region appears due to the greater conductivity of latex particles in front of that of the medium. At higher frequencies an  $n$ -DEP region is observed due to the fact that the medium has a greater permittivity than the particle for these frequencies.

Dielectrophoretic forces have been shown to be able to manipulate or collect tobacco mosaic virus (about  $300 \text{ nm} \times 18 \text{ nm}$ ) [120], macromolecules [121], or bacteria [122, 123] without significant disturbance from Brownian motion.

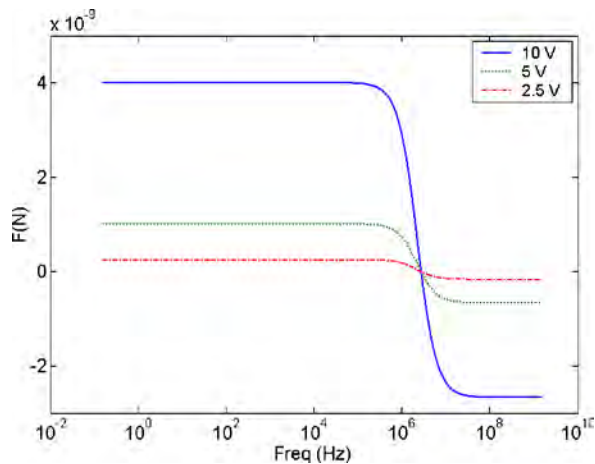


**Figure 14.** Simulated dielectrophoretic force acting on submicrometric latex sphere as a function of the frequency of the applied electric field. Both positive and negative dielectrophoretic behaviors are observed.

**Electrothermal and Other Forces** Other forces exist which are also likely to cause movement in the particles or in the fluid. In addition to gravity (which causes sedimentation) and the van der Waals forces responsible for adhesion, there are electrothermal forces [124], which can cause movement of fluid due to gradients in permittivity and conductivity induced by the temperature gradient in the points where the electrical fields have their strongest nonhomogeneities. Although these forces can become significant at high voltages, it seems not to be relevant compared to the other forces at the typical scales. Nevertheless, as not all the experimental effects are yet fully understood, none of them can be absolutely disregarded in advance. Accordingly, each particular micro/nanoelectrofluidic system must accurately analyzed.

**Brownian Motion** Brownian motion is a stochastic process consisting of the irregular motion of a particle embedded in a fluid due to the random forces imparted by the fluid molecules. On average the forces, and hence the displacement, are zero, but the mean square displacement is not. In a simple one-dimensional picture the mean displacement is given by

$$|\Delta x|^2 = 2Dt \quad (30)$$

where  $t$  is the time variable and  $D$  is the diffusion coefficient of the particle whose value is related to the fluid viscosity. For the case of a spherical particle of radius  $a$  this relation is given by

$$D = \frac{k_B T}{6\pi\mu a} \quad (31)$$

Most often, the Brownian motion is seen as a nuisance that induces dispersion of the particles in a fluid. However, in recent years a positive role to this movement has been identified in nanofluidic applications, as will be discussed.

### 4.3. Applications of NEMS Based on Nanofluidic Structures

Nanofluidic structures provide powerful tools for the field of biotechnology. They have been used for the direct manipulation and analysis of single biomolecules such as stretching genomic DNA in extremely small nanochannels, in scanning for bound transcription factors [125], or to sort DNA molecules [126, 127]. The techniques developed so far make use of the particular properties displayed by long biopolymers in confined fluids, in which the structure dimensions are comparable to the diffusion length or the gyration radius of single biomolecules. Present nanofluidic structures used are still simple and very far from the complexity reached with microfluidics [11]. However, they offer fascinating possibilities not available in microfluidics. We describe the more relevant nanofluidic applications developed so far for biotechnology.

#### 4.3.1. Sorting Biomolecules by Rectification of the Brownian Motion

This technique consists of using the fact that an asymmetric disposition of obstacles in a nanofluidic structure is able to rectify the Brownian motion of molecules in structures with characteristic dimensions of the order of the diffusion length of the molecules. Based on this principle, and due to the relationship between diffusion coefficient and molecular size, a technique to separate macromolecules with different sizes can be developed. This technique has been demonstrated in [126], where a sieve consisting of a two-dimensional lattice of microobstacles disposed in an asymmetric way was used to sort DNA molecules according to size. In the system the DNA molecules were driven through the device by electrophoretic forces [128]. A similar principle has been also used to sort phospholipids in a two-dimensional fluid bilayer [129].

#### 4.3.2. Scanning the Local Structure of Single Macromolecules

The fact that long macromolecules stretch when passing through nanochannels makes it possible to locally probe the structure of the molecules as they move through the device. In order to implement this technique two basic requirements have to be satisfied, namely a good stretching of the macromolecules in the channel (this requires channel dimensions smaller than the persistence length of the macromolecule) and a high local sensing resolution. This technique has been implemented recently for analysis of double stranded DNA molecules [128, 130]. The device consists of a flow geometry in which molecules are driven by an external applied bias through a microchannel with narrow slits on it (see Fig. 15). Based on near-field optical effects the molecule can be probed when passing over the slit regions. Initial resolution was limited to 200 nm. Recent progress in the fabrication of smaller channels (fabrication of arrays of millions of nanochannels (10 nm × 50 nm) over a 100 mm wafer using nanoimprinting lithography to stretch, align, and analyze long genomic DNA in a highly parallel fashion has been recently reported [30, 131]) is expected to increase significantly this initial resolution level [125].

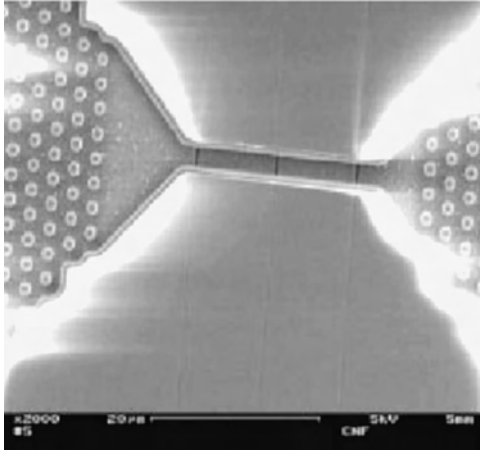


**Figure 15.** Scanning electron micrograph of a nano/microfluidic system to scan the local structure of double stranded DNA. Reprinted with permission from [122], R. H. Austin et al., *IEEE Trans. Nanotech.* 1, 12 2002. © 2002, IEEE.

#### 4.3.3. Sizing Macromolecules

With present fabrication technologies it is possible to build nanofluidic structures small enough as to facilitate single molecule detection and minimize events of simultaneous passage of more than one molecule through the region of measurement. This opens the possibility to develop devices able to determine the distribution and relative proportions of fragments of individual macromolecules, as well as to determine the overall concentration from a single experiment. This technique has been recently implemented for DNA fragment sizing [132]. The device consisted of a T structure in which the smaller regions presented sub-micrometric dimensions. The DNA molecules were passed through the device by means of an external applied field (electrophoretic force) and were detected by means of fluorescence based optical methods. Speeds as high as 5 mm/s were reached corresponding to a few milliseconds of analysis time per molecule.

#### 4.3.4. Separation of Macromolecules by Means of Entropic Traps

Linear polymers tend to form a compact random coil in free solution. For them, it is thermodynamically unfavorable to spontaneously elongate since large free energies to reduce entropy would be required. In confined nanostructures a different behavior has been observed in recent years, and new insights for understanding the confinement-mediated entropic behavior of biopolymers in ultrasmall nanoscale fluidics have started to emerge [127, 133]. In particular, it has been demonstrated that in channels comprising narrow constrictions and wider regions size dependent trapping of DNA molecules occurs at the onset of the constriction. This process determines electrophoretic mobility differences among different macromolecules (surprisingly enough, longer macromolecules move faster than shorter ones) thus enabling efficient separation methods. A demonstration of this method has already been implemented [134] and developed up to a parallel performance [127, 135].

A similar technique has been implemented in the separation of DNA molecules in a device that presented an abrupt interface between regions of vastly different configuration entropy [133, 136]. Based on the same physical principles a separation method based on the motion of macromolecules within a two-dimensional array of interconnected spherical nanocavities has been suggested recently [137].

## 5. MOLECULAR NEMS: THE ULTIMATE MINIATURIZATION LIMIT

As mentioned in Section 1 the ultimate limit in NEMS miniaturization will be reached when the active parts of the devices consist of single molecules or atoms. In this section, and in order to illustrate the great potentialities of molecular NEMS, we review some of the advances performed in this field in recent years. Most of the cases are based on carbon nanotubes but some of them also refer to other molecules and biomolecules, including nanomechanical structures powered by molecular biomotors.

### 5.1. Molecular NEMS Based on Carbon Nanotubes

Carbon nanotubes constitute ideal molecular nanostructures for the fabrication of NEMS devices due to their exceptional mechanical and electrical properties. Carbon nanotubes present a cross-sectional area in the range from a few nanometers up to tens of nanometers and a molecular length in the range from tens of nanometers to micrometers. Furthermore, they display a very high Young modulus (in the TPa regime) and can be both semiconducting and metallic.

The simplest NEMS based on a carbon nanotube consists of a freestanding nanotube, for instance a single clamped nanotube. Due to its exceptionally high Young modulus very high natural frequencies of oscillation are expected for these structures. A rough estimation of these natural frequencies of oscillation can be obtained from the classical expression of a single clamped empty cylinder,

$$f_n = \frac{C_n^2}{8\pi} \frac{1}{L^2} \sqrt{D^2 + D_i^2} \sqrt{\frac{E}{\rho}} \quad (32)$$

where  $D$  and  $D_i$  are the outer and inner diameter,  $E$  is the elastic modulus (which can be identified with the Young modulus of the material if the beam bends by elongation of the outer arc and compression of the inner arc),  $\rho$  is the density,  $C_n$  is a constant for the  $n$  harmonic ( $C_0 = 1.875$  for the first harmonic), and  $L$  is the length of the nanotube. By substituting characteristic values for a nanotube, frequencies in the GHz domain are naturally obtained. Up to now experiments have been performed with long carbon nanotubes and thus lower frequencies (in the MHz domain) have been measured [138, 139].

In addition to its use in freestanding NEMS, carbon nanotubes offers many other possibilities for NEMS applications. One of these applications is in the development of very low friction nanoscale linear bearings [140]. This device uses the retraction force induced by the van der Waals interaction when different shells of a multiwalled carbon nanotube are

pulled apart. The absence of frictional forces (dissipation) in the process opens the possibility to develop high frequency-high  $Q$  resonators [141].

Other applications of carbon nanotubes to NEMS are based on the possibility to actuate electrically these molecules. Among them we find nanotweezers and nanoelectromechanic memories.

The nanotube based nanotweezers [142] consist of two metal arms with a carbon nanotube attached on each of them (see Fig. 16). By applying a bias between the two metallic arms the nanotubes become electrically charged, and then interact with each other. By an appropriate choice of the value of the applied bias the nanotube separation can be adapted at will. The nanotweezers can be used to grasp nanometric objects or to measure the conducting properties of nanoscale objects (by using the nanotubes tweezers as alligator clips).

The nanoelectromechanic memory concept [143] is based on the same principles as the nanotweezers. It consists of a carbon nanotube suspended on top of another nanotube (or a nanowire) in a crossbar configuration (see Fig. 17). By playing with the elastic energy, the van der Waals energy, and the electrostatic energy, one can create a bistable system in which the nanotubes are either in noncontact (OFF state) or in contact (ON state). In order to sense the state of the system the current flowing between the two nanotubes can be used. Indeed, when the applied bias between the nanotubes is small and the system is in the OFF state (not in contact) the electric current between the nanotubes takes place only by tunnelling and is very small. In contrast, when the applied bias reaches a critical value and the system moves to the ON state (in contact) the electric current between the nanotubes increases significantly, thus allowing one to distinguish between the ON and OFF states.

Finally, carbon nanotubes [144] offer great potential for nanofluidic applications [145, 146]. Carbon nanotubes provide cylindrical nanochannels similar to pipes used in macrofluidics, with inner diameters of less than 10 nm and wall thicknesses that may exceed the inner diameter. At present, a lot of effort is devoted to understanding the nanofluidic properties of carbon nanotubes. On the one hand it is believed that the interaction of fluid molecules with the nanotube walls could be conceivably so strong as to prevent through-flow. On the other hand, capillary forces can facilitate filling of thin channels in case of good wettability of the solid wall surface by the fluid [147]. Wetting of nanotubes by liquid metals, salts, oxides, and  $\text{HNO}_3$  has been studied [148] and it has been shown that some liquids could be sucked into nanotubes due to capillary forces [149,



**Figure 16.** Nanotweezers based on carbon nanotubes.

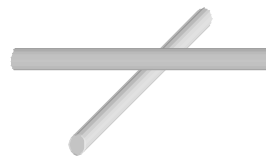


**Figure 17.** Crossbar configuration for a nanomechanical random access memory.

[150]. Studies of the wetting and capillarity of carbon nanotubes demonstrate that only relatively low-surface-tension materials can be drawn inside nanotubes [151]. The reported cutoff value of surface tension of 100–200 mN/m is sufficiently high to allow water and organic solvents to wet and fill the interior of carbon nanotubes. Simple experiments of placing a water droplet (surface tension 73 mN/m) on the surface of a carbon nanotube bundle showed the water to be readily sucked into the capillary channels, eventually leaving a dry surface [152]. The behavior of fluids in nanotubes may differ fundamentally from that in macroscopic pipes or even microcapillaries [153, 154]. The major obstacle to *in-situ* experimental studies of fluid behavior in nanotubes has been the rarity of such systems filled, at least partially, with fluids [155]. A recently suggested hydrothermal method of nanotube synthesis has produced nanotubes with an encapsulated aqueous fluid, which includes segregated liquid and gas, and well-defined interfaces [156].

## 5.2. Molecular NEMS Based on Other Molecules

In principle, any molecule or biomolecule is suitable to be characterized electrically and mechanically. This opens the possibility to develop molecular NEMS based on practically any single molecule or biomolecule. We illustrate this possibility with two examples that have already been realized in practice.

The first example refers to an electromechanical transistor based on a  $\text{C}_{60}$  molecule [157, 158]. It consists of a  $\text{C}_{60}$  molecule adsorbed onto a conducting substrate which is actuated on the other side by a scanning tunnelling microscope tip (Fig. 18). The conductance of the system can be seen to depend on the compression applied to the molecule. Indeed, when compression is applied to the molecule the molecular orbitals change due to the modification of the interatomic distances. As a result, the highest occupied molecular orbital and the lowest unoccupied molecular orbital broaden and shift, thus increasing the weight of the tails of these levels at the electrode's Fermi

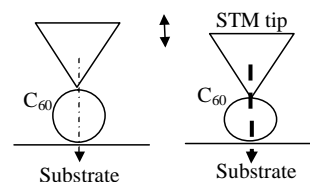


**Figure 18.** Schematic drawing of the operation of a single molecular electromechanical transistor.

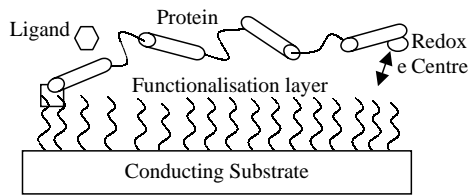


**Figure 19.** Schematic drawing of the operation of a single protein nanobiosensor.

energy, and hence the conductance of the system (in the tunnel regime the conductance depends strongly on the occupancy of the energy band at the Fermi energy). Similar behaviors have been found for other molecules [159].

The second example consists of a single protein based nanobiosensor. This nanobiosensor takes advantage of a structural change occurring at the level of a single protein when it binds a ligand [160]. Essentially, the nanobiosensor consists of some proteins anchored onto a conducting surface (previously functionalized) with one “end” free to move and at which a redox center is inserted (Fig. 19). The redox center can exchange electrons with the conducting substrate, with a rate of exchange depending strongly on the distance of the redox center to the substrate. When the protein binds a ligand it suffers a conformational change that modifies the distance between the redox center and the substrate thus inducing a change in the rate of exchange of electrons that can be detected.

In addition to these examples, it is worth noting that naturally occurring molecular structures, such as lipid membrane pores [161] or lipid nanotubes [162], show promising potential for applications in nanofluidics. In particular, the formation of geometrically complex lipid nanotube-vesicle networks has been reported recently [162].

### 5.3. NEMS Powered by Molecular Biomotors

A fascinating possibility of molecular NEMS is to power them by means of molecular biomotors. Molecular biomotors convert chemical energy into mechanical energy and are able to generate forces compatible with currently available nanostructures (the forces generated by molecular biomotors can range from a few pN to tens of pN [163], thus being large enough to actuate on some engineered nanostructures). Examples of molecular biomotors include step-wise motion of single kinesin molecules along a microtubule track, displacement of an actin filament by single myosin molecule, forces and transcriptional pauses associated with RNA polymerase activity, nonlinear elasticity of single polymers, reversible unfolding of single protein domains by

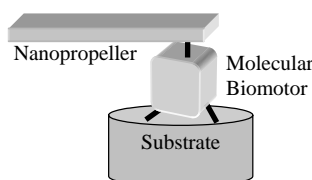
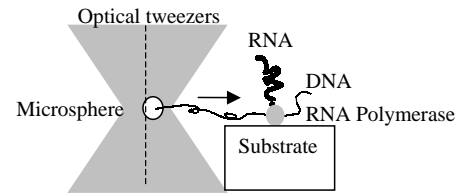


**Figure 20.** Schematic drawing of a nanopropeller powered by a molecular biomotor.



Linear motion of a microsphere powered by RNAP

**Figure 21.** Schematic drawing of the linear motion of a trapped microsphere powered by RNA polymerase [166].

applied force, and discrete rotations of a single  $F_1$  subunit of the  $F_0F_1$ -adenosine triphosphate (ATP) synthase [164]. The properties of these molecular biomotors open the possibility to integrate the power supply in NEMS applications at a molecular level. To illustrate this fact we present below some examples of primitive hybrid nanomechanical systems in which molecular biomotors drive the motion of inorganic nanostructures.

The first example refers to a nanopropeller driven by the  $F_1$ -ATAase biomolecular motor [165]. The device consists basically of three components: an engineered substrate, an  $F_1$ -ATAase biomolecular motor, and a fabricated nanopropeller (Fig. 20). It was demonstrated that rotation of the nanopropeller can be initiated with the addition of adenosine triphosphate to the system and stopped by the addition of sodium azide.

Two other examples refer to RNA polymerase (RNAP). RNAP carries out an essential step of gene expression, the synthesis of an RNA copy out of the template DNA. Each RNA molecule is synthesized in its entirety by a single molecule of RNAP moving progressively along the template. During transcript elongation, RNAP progresses along the DNA at speeds higher than 10 nucleotides per second and generates considerable force, higher than 10 pN. Moreover, rotation at a velocity greater than 100 revolutions per second and torques greater than 5 pN/nm are induced. In the experiments, RNAP was fixed onto a substrate and the forces and torques developed during transcription were used to move [166] and rotate [167] a microsphere trapped in optical tweezers (see Fig. 21) and suspended below a magnet, respectively.

## 6. CONCLUDING REMARKS

Nanoelectromechanical systems offer unique properties for advanced applications in nanoelectronics, biomedicine, and sensor technologies. Among others, NEMS structures may be applied as oscillators for wireless communications, very sensitive mass and magnetic field sensors, devices for single molecule separation, and devices for detection and analysis in lab-on-a-chip systems. The enormous relevance of these applications has made NEMS investigations one of the more active fields of research at present.

NEMS systems exist today at the laboratory level and NEMS production and applications show still many technical obstacles. By comparison with the previous evolution of the MEMS technology, which has taken about 20 years to

become mainstream, the NEMS commercialization opportunities must be considered in a medium term, although in some cases a faster commercial implementation is expected. If NEMS potential is fully realized, there is no doubt that NEMS technology will become a key technology for the 21st century, even surpassing solid-state or biotechnologies.

## GLOSSARY

**Biomotors** Molecular biological motors that convert chemical energy into mechanical energy and are able to generate forces and torques compatible with engineered nanostructures.

**Microelectromechanical system (MEMS)** Device combining mechanical elements with optoelectronic elements, with the mechanical part having at least one dimension in the range from hundred to a few micrometers.

**Nanocantilever** Single clamped freestanding solid-state structure with at least one dimension in the range from a hundred to a few nanometers.

**Nanofluidics** Study of the mechanical and structural properties of fluids confined in structures with at least one dimension in the range from a hundred to a few nanometers.

**Nanoelectromechanical system (NEMS)** Device combining mechanical elements with optoelectronic elements, with the mechanical part having at least one dimension in the range from hundred to a few nanometers.

**Nanoimprint lithography (NIL)** Lithographic technique able to produce patterns with submicro- and nanometer scales based on the mechanical deformation of a polymer under pressure and elevated temperatures.

**Nanoresonator** Electromechanical device whose active part consists of a mechanical nanostructure able to freely oscillate.

## REFERENCES

- R. P. Feynman, There is plenty of room at the bottom, presented at the American Physical Society Meeting, Pasadena, CA, 29 December 1959, originally published in Caltech's Engineering and Science magazine, February 1960; reprint; R. P. Feynman, *J. Microelectromech. Syst.* 1, 60 (1992).
- R. Lifshitz, *Nanotechnol. Forum* 16 (December 2001).
- W. Trimmer, Ed., "Mircomechanics and Mems: Classical and Seminal Papers to 1990," IEEE, New York, 1997.
- G. Whitesides and A. D. Stroock, *Phys. Today* 54, 42 (2001).
- N. A. Polson and M. A. Hayes, *Anal. Chem.* 312A (2001).
- H. A. Stone and S. Kim, *AIChE J.* 47, 1250 (2001).
- C. M. Ho, Tech. Dig. of the 14th IEEE Int. Conf. Microelectromech. Sys., 2001, p. 375.
- N. Giordano and J.-T. Cheng, *J. Phys.: Condens. Matter* 13, R271 (2001).
- D. J. Beebe, G. A. Mensing, and G. M. Walker, *Annu. Rev. Biomed. Eng.* 4, 261 (2002).
- J. Bausells, J. Carrabira, A. Merlos, S. Bota, and J. Samitier, *Sens. Actuators A* 62, 698 (1997).
- T. Thorsen, S. J. Maerkl, and S. R. Quake, *Science* 298, 580 (2002).
- M. L. Roukes, in "Technical Digest of the 2000 Solid-State Sensor and Actuator Workshop," Hilton Head Island, SC, 4–8 June 2000, Transducer Research Foundation, Cleveland, 2000.
- H. G. Craighead, *Science* 290, 1532 (2000).
- M. L. Roukes, *Phys. World* 14, 25 (2001).
- H. Koops and J. Grob, "X-Ray Microscopy," Springer Series in Optical Sciences, Vol. 43. Springer, Berlin, 1984.
- [Http://www.bell-labs.com/projet/SCALPEL/description.html](http://www.bell-labs.com/projet/SCALPEL/description.html), February 1998.
- W. H. Bruenger, H. Bushbeck, E. Cekan, S. Eder, T. H. Fedynshyn, W. G. Hertlein, P. Hudek, I. Kastic, H. Loeschner, I. W. Rangelow, and M. Torkler, *Microelectron. Eng.* 41/42, 237 (1998).
- S. Y. Chou, P. R. Krauss, and P. J. Renstrom, *Appl. Phys. Lett.* 67, 3114 (1995).
- S. Y. Chou, U.S. Patent 5772, 905, 1998.
- A. Leib, Y. Chen, J. Bourneix, F. Carcenac, E. Cambril, L. Couraud, and H. Lounois, *Microelectron. Eng.* 46, 319 (1999).
- S. Y. Chou, P. R. Krauss, and P. J. Renstrom, *J. Vac. Sci. Technol. B* 14, 4129 (1996).
- S. Y. Chou, P. R. Krauss, and P. J. Renstrom, *Science* 272, 85 (1996).
- A. Kumar and G. M. Whitesides, *Appl. Phys. Lett.* 63, 2002 (1993).
- A. Kumar, H. A. Biebuyck, and G. M. Whitesides, *Langmuir* 10, 1498 (1994).
- G. Binnig and H. Rohrer, *Helv. Phys. Acta* 55, 726 (1982).
- G. Binnig, C. F. Quate, and C. Gerber, *Phys. Rev. Lett.* 56, 780 (1986).
- D. M. Eigler and E. K. Schweizer, *Nature* 344, 524 (1990).
- K. Wilder, C. F. Quate, D. Adderton, R. Bernstein, and V. Elings, *Appl. Phys. Lett.* 73, 2527 (1998).
- R. Magno and B. R. Bennett, *Appl. Phys. Lett.* 70, 1855 (1997).
- H. Cao, Z. Yu, J. Wang, J. O. Tegenfeldt, R. H. Austin, E. Chen, W. Wu, and S. Y. Chou, *Appl. Phys. Lett.* 81, 174 (2002).
- L. L. Soares, L. Cescato, N. C. Cruz, and M. B. Moares, *J. Vac. Sci. Technol. B* 18, 713 (2000).
- S. R. Quake and A. Scherer, *Science* 290, 1536 (2000).
- A. Erbe, R. H. Blick, A. Tilke, A. Kriele, and J. P. Kottjaus, *Appl. Phys. Lett.* 73, 3751 (1998).
- R. G. Beck, M. A. Eriksson, M. A. Topinka, R. M. Westervelt, K. D. Maranowski, and A. C. Gossard, *Appl. Phys. Lett.* 73, 1149 (1998).
- J. A. Harley and T. W. Kenny, *Appl. Phys. Lett.* 75, 289 (1999).
- J. Yang, T. Ono, and M. Esashi, *Sens. Actuators A* 82, 102 (2000).
- X. Li, T. Ono, Y. Wang, and M. Esashi, in "Proc. Fifth IEEE Int. Conf. Microelectronic Mechanical Systems," 2002, p. 427.
- H. Yamaguchi and Y. Hirayama, *Appl. Phys. Lett.* 80, 4428 (2002).
- A. N. Cleland and M. L. Roukes, *Appl. Phys. Lett.* 69, 2653 (1996).
- D. W. Carr and H. G. Craighead, *J. Vac. Sci. Technol. B* 15, 2670 (1997).
- L. Pescini, A. Tilke, R. H. Blick, H. Lorenz, J. P. Kottaus, W. Eberhardt, and D. Kern, *Nanotechnology* 10, 418 (1999).
- A. Erbe, H. Kromer, A. Kraus, and R. H. Blick, *Appl. Phys. Lett.* 77, 3102 (2000).
- R. H. Blick, F. G. Monzon, W. Wegscheider, M. Blichler, F. Stern, and M. L. Roukes, *Phys. Rev. B* 62, 17103 (2000).
- Y. T. Yang, K. L. Ekinici, X. M. H. Huang, L. M. Schiavone, M. L. Roukes, C. A. Zoman, and M. Mehregany, *Appl. Phys. Lett.* 78, 162 (2001).
- A. N. Cleland, M. Pophristic, and I. Ferguson, *Appl. Phys. Lett.* 79, 2070 (2001).
- H. X. Tang, M. H. Huang, M. L. Roukes, M. Bichler, and W. Wegscheider, *Appl. Phys. Lett.* 81, 3879 (2002).
- T. S. Tighe, J. M. Worlock, and M. L. Roukes, *Appl. Phys. Lett.* 70, 2687 (1997).
- D. W. Carr, L. Sekaric, and H. G. Craighead, *J. Vac. Sci. Technol. B* 16, 3821 (1998).
- A. N. Cleland and M. L. Roukes, *Nature* 392, 160 (1998).
- S. Evoy, D. W. Carr, L. Sekaric, A. Olkhovets, J. M. Parpia, and H. G. Craighead, *J. Appl. Phys.* 86, 6072 (1999).



51. L. Sekaric, D. W. Carr, S. Evoy, J. M. Parpia, and H. G. Craighead, *Sens. Actuators A* 101, 215 (2002).
52. J. Prescott, "Applied Elasticity." Dover, New York, 1961.
53. E. Volterra and E. C. Zachmanoglou, "Dynamics of Vibrations," p. 57. Merrill, Columbus, 1965.
54. E. W. Wong, P. E. Sheehan, and C. M. Lieber, *Science* 277, 1971 (1997).
55. B. Ilic, D. Czaplewski, H. G. Craighead, P. Neuzil, C. Compagnolo, and C. Batt, *Appl. Phys. Lett.* 77, 450 (2000).
56. Z. J. Davis, G. Abadal, O. Kuhn, O. Hansen, F. Grey, and A. Boisen, *J. Vac. Sci. Technol. B* 18, 612 (2000).
57. G. Abadal, Z. J. Davis, B. Helbo, X. Borrísé, R. Ruiz, A. Boisen, F. Campabadal, J. Esteve, E. Figueres, F. Pérez-Murano, and N. Barniol, *Nanotechnology* 12, 100 (2001).
58. D. Dubuc, K. Greiner, L. Rabbia, A. Tackac, M. Saadoui, P. Pons, P. Caudrillier, O. Pascal, H. Aubert, H. Baudrand, J. Tao, P. Combes, J. Graffeuil, and R. Plana, in "Proc. IEEE Int. Conf. on Microelectronics (MIEL 2002)," 2002, Vol. 1, p. 91.
59. C. T.-C. Nguyen, in "Proc. 60th IEEE Device Research Conference Digest," 2002.
60. D. W. Carr, S. Evoy, L. Sekaric, H. G. Craighead, and J. M. Parpia, *Appl. Phys. Lett.* 75, 920 (1999).
61. H. Dowell and D. Tang, *J. Appl. Phys.* 90, 5060 (2001).
62. S. Evoy, A. Olkhovets, L. Sekaric, J. M. Parpia, H. G. Craighead, and D. W. Carr, *Appl. Phys. Lett.* 77, 2397 (2000).
63. R. Lifshitz and M. L. Roukes, *Phys. Rev. B* 61, 5600 (2000).
64. R. Lifshitz, *Physica B* 316–317, 397 (2002).
65. H. Houston, D. M. Photiadis, M. H. Marcus, J. A. Bucaro, X. Liu, and J. F. Vignola, *Appl. Phys. Lett.* 80, 1300 (2002).
66. A. Olkhovets, S. Evoy, D. W. Carr, J. M. Parpia, and H. G. Craighead, *J. Vac. Sci. Technol. B* 18, 3549 (2000).
67. M. Ho and Y. C. Tai, *Annu. Rev. Fluid Mech.* 30, 579 (1998).
68. L. Sekaric, M. Zalalutdinov, R. B. Bhiladvala, A. T. Zehnder, J. M. Parpia, and H. G. Craighead, *Appl. Phys. Lett.* 81, 2641 (2002).
69. A. N. Cleland and M. L. Roukes, *Sens. Actuators* 72, 256 (1999).
70. K. Schwab, *Appl. Phys. Lett.* 80, 1276 (2002).
71. J. R. Vig and Y. Kim, *IEEE Trans. Ultra. Ferroelec. Freq. Control* 46, 1558 (1999).
72. A. N. Cleland and M. L. Roukes, *J. Appl. Phys.* 92, 2758 (2002).
73. H. Krommer, A. Erbe, A. Tilke, S. Manus, and R. H. Blick, *Europhys. Lett.* 50, 101 (2000).
74. H. P. Lang, M. K. Baller, F. M. Battiston, J. Fritz, R. Berger, J.-P. Ramseyer, P. Fornaro, E. Meyer, H.-J. Guntherodt, J. Brugger, U. Drechsler, H. Rothuizen, M. Despont, P. Vettiger, Ch. Gerber, and J. K. Gimzewski, in "Proc. 12th IEEE Conference on Micro Electromechanical Systems," 1999.
75. J. Fritz, M. K. Baller, H. P. Lang, H. Rothuizen, P. Vettiger, E. Meyer, H. J. Guntherodt, Ch. Gerber, and J. K. Gimzewski, *Science* 288, 316 (2000).
76. G. Wu, H. Ji, K. Hansen, T. Thundat, R. Datar, R. Cote, M. F. Hagan, A. K. Chakrabarty, and A. Majumdar, *Proc. Nat. Acad. Sci.* 98, 1560 (2001).
77. R. E. Rudd and J. Q. Broughton, *Phys. Rev. B* 58, R5893 (1998).
78. K. Schwab, E. A. Henriksen, J. M. Worlock, and M. L. Roukes, *Nature* 404, 974 (2000).
79. W. Fon, K. C. Schwab, J. M. Worlock, and M. L. Roukes, *Phys. Rev. B* 66, 045302 (2002).
80. S. W. Carr, W. E. Lawrence, and M. N. Wybourne, *Phys. Rev. B* 64, 220101 (2001).
81. H. B. Chan, V. A. Aksyuk, R. N. Kleiman, D. J. Bishop, and F. Capasso, *Science* 291, 1941 (2001).
82. E. Buks and M. L. Roukes, *Europhys. Lett.* 54, 220 (2001).
83. A. Kraus, A. Erbe, L. H. Blick, G. Corso, and K. Ritcher, *Appl. Phys. Lett.* 79, 3521 (2001).
84. M. Zalalutdinov, B. Ilic, D. Czaplewski, A. Zehnder, H. G. Craighead, and J. Parpia, *Appl. Phys. Lett.* 77, 3287 (2000).
85. K. Hane and K. Suzuki, *Sens. Actuators A* 51, 179 (1996).
86. M. Zalalutdinov, A. Olkhovets, A. Zehnder, B. Ilic, D. Czaplewski, H. G. Craighead, and J. M. Parpia, *Appl. Phys. Lett.* 78, 3142 (2001).
87. M. Zalalutdinov, A. Zehnder, A. Olkhovets, S. Turner, L. Sekaric, B. Ilic, D. Czaplewski, J. M. Parpia, and H. G. Craighead, *Appl. Phys. Lett.* 79, 695 (2001).
88. L. Sekaric, M. Zalalutdinov, S. W. Turner, A. T. Zehnder, J. M. Parpia, and H. G. Craighead, *Appl. Phys. Lett.* 80, 3617 (2002).
89. S. Sundarajan and B. Bushan, *Sens. Actuators A* 101, 338 (2002).
90. H. Kawakatsu, S. Kawai, D. Saya, M. Nagashio, D. Kobayashi, and H. Toshiyoshi, *Rev. Sci. Instrum.* 73, 2317 (2002).
91. K. L. Ekinci, Y. T. Yang, X. M. Huang, and M. L. Roukes, *Appl. Phys. Lett.* 81, 2553 (2002).
92. M. Ciofalo, M. W. Collins, and T. R. Hennessy, "Nanoscale Fluid Dynamics in Physiological Processes." Wit Press, 1999.
93. B. Bhushan, J. N. Israelachvili, and U. Landman, *Nature* 374, 607 (1995).
94. S. Granick, *Phys. Today* 7, 26 (1999).
95. T. Thorsen, R. W. Roberts, F. H. Arnold, and S. R. Quake, *Phys. Rev. Lett.* 86, 4163 (2001).
96. J.-T. Cheng and N. Giordano, *Phys. Rev. E* 65, 031206 (2002).
97. R. Pit, H. Hervet, and L. Leger, *Phys. Rev. Lett.* 85, 980 (2000).
98. Y. Zhu and S. Granick, *Phys. Rev. Lett.* 87, 096105 (2001).
99. V. S. J. Craig, C. Neto, and D. R. M. Williams, *Phys. Rev. Lett.* 87, 054504 (2001).
100. D. C. Tretheway and C. D. Meinhart, *Phys. Fluids*. 14, L9 (2002).
101. E. Bonaccorso, M. Kappl, and H.-J. Butt, *Phys. Rev. Lett.* 88, 076103 (2002).
102. Y. Zhu and S. Granick, *Phys. Rev. Lett.* 88, 106102 (2002).
103. S. Succi, *Phys. Rev. Lett.* 89, 064502 (2002).
104. G. Sun, E. Buonaccorso, V. Franz, and H.-J. Butt, *J. Chem. Phys.* 117, 10311 (2002).
105. H. A. Barnes, *J. Non Newtonian Fluid Mech.* 56 (1995).
106. S. Kim and S. J. Karrila, "Microhydrodynamics: Principles, and Selected Applications." Butterworth-Heinemann, Boston, 1991.
107. J. N. Israelchavili, "Intermolecular and Surface Forces." Academic Press, San Diego, 1992.
108. M. L. Gee, P. M. Mc Guiggan, J. N. Israelachvili, and A. H. Homola, *J. Chem. Phys.* 93, 1895 (1990).
109. A. Groisman and V. Steinberg, *Nature* 410, 905 (2001).
110. J. F. Brady and G. Bossis, *Annu. Rev. Fluid Mech.* 20, 111 (1988).
111. P. D. Grossman and J. C. Calburn, Eds., "Capillary Electrophoresis." Academic Press, San Diego, 1992.
112. R. B. M. Schasfoort, S. Schlautmann, J. Hendrikse, and A. van den Berg, *Science* 286, 942 (1999).
113. A. D. Stroock, M. Weck, D. T. Chiu, W. T. S. Huck, P. J. A. Kenis, R. F. Ismagilov, and G. M. Whitesides, *Phys. Rev. Lett.* 84, 3314 (2000).
114. A. Ramos, H. Morgan, N. G. Green, and A. Castellanos, *J. Colloid Interface Sci.* 217, 420 (1999).
115. N. G. Green, A. Ramos, A. Gonzalez, A. Castellanos, and H. Morgan, *Phys. Rev. E* 61, 4011 (2000).
116. A. Gonzalez, N. G. Green, A. Ramos, A. Castellanos, and H. Morgan, *Phys. Rev. E* 61, 4019 (2000).
117. M. Scott, R. Paul, and K. V. I. S. J. Kaler, *J. Colloid Interface Sci.* 238, 449 (2001).
118. M. W. J. Prins, W. J. J. Welters, and J. W. Weekamp, *Science* 291, 277 (2001).
119. H. A. Pohl, "Dielectrophoresis." Cambridge Univ. Press, London, 1978.
120. H. Morgan and N. G. Green, *J. Electrostat.* 42, 279 (1997).
121. M. Washizu, S. Suzuki, O. Kurosawa, T. Nishizaka, and T. Shinohara, *IEEE Trans. Industry Appl.* 30, 835 (1994).
122. R. Fernández-Morales, R. Casanella, O. Ruíz, A. Juárez, J. Samitier, A. Errachid, and J. Bausells, in "Proc. Int. Conf. BioMEMS and Biomedical Nanotechnology World," 2000.

123. R. Casanella, J. Samitier, A. Errachid, H. Fernández-Morales, and A. Juárez, in "Proc. 6th Annual European Conf. on Micro- and Nanoscale," 2002.
124. A. Ramos, H. Morgan, N. G. Green, and A. Castellanos, *J. Phys. D* 31, 2338 (1998).
125. R. H. Austin, J. O. Tegenfeldt, H. Cao, S. Y. Chou, and E. C. Cox, *IEEE Trans. Nanotech.* 1, 12 (2002).
126. C. F. Chou, O. Bakjain, S. W. P. Turner, T. A. J. Duke, S. S. Chan, E. C. Cox, H. G. Craighead, and R. H. Austin, *Proc. Nat. Acad. Sci.* 96, 13762 (1999).
127. J. Han and H. G. Craighead, *Science* 288, 1026 (2000).
128. C. F. Chou, R. H. Austin, O. Bakajin, J. O. Tegenfeldt, J. A. Castelino, S. S. Chan, E. C. Cox, H. Craighead, N. Darnton, T. Duke, J. Han, and S. Turner, *Electrophoresis* 21, 81 (2000).
129. A. van Oudebaarden and S. G. Boxer, *Science* 285, 1046 (1999).
130. J. O. Tegenfeldt, O. Bakajin, C. F. Chou, S. C. Chan, R. Austin, W. Fann, L. Liou, E. Chan, T. Duke, and E. C. Cox, *Phys. Rev. Lett.* 86, 1378 (2001).
131. H. Cao, J. O. Tegenfeldt, R. H. Austin, and S. Y. Chou, *Appl. Phys. Lett.* 81, 3058 (2002).
132. M. Foquet, J. Korlach, W. Zipfel, W. W. Webb, and H. G. Craighead, *Anal. Chem.* 74, 1415 (2002).
133. S. W. P. Turner, M. Cabodi, and H. G. Craighead, *Phys. Rev. Lett.* 88, 128103 (2002).
134. J. Han and H. G. Craighead, *J. Vac. Sci. Technol. A* 17, 2142 (1999).
135. J. Han and H. G. Craighead, *Anal. Chem.* 74, 394 (2002).
136. M. Cabodi, S. W. Turner, and H. G. Craighead, *Anal. Chem.* 74, 5169 (2002).
137. D. Nykypanchuk, H. H. Strey, and D. A. Hoagland, *Science* 297, 987 (2002).
138. P. Poncharal, Z. L. Wang, D. Ugarte, and W. A. de Heer, *Science* 283, 1513 (1999).
139. R. Gao, Z. L. Wang, Z. Bai, W. A. de Heer, L. Dai, and M. Gao, *Phys. Rev. Lett.* 85, 622 (2000).
140. J. Cumings and A. Zettl, *Science* 289, 602 (2000).
141. Q. Zheng and Q. Jiang, *Phys. Rev. Lett.* 88, 045503 (2002).
142. P. Kim and C. M. Lieber, *Science* 286, 2148 (1999).
143. T. Rueckes, K. Kim, E. Joselevich, G. Y. Tseng, C. L. Cheung, and C. M. Lieber, *Science* 289, 94 (2000).
144. J. F. Harris, "Carbon Nanotubes and Related Structures." Cambridge Univ. Press, Cambridge, UK, 1999.
145. E. Delamarche, A. Bernard, H. Schmid, B. Michel, and H. Biebuyck, *Science* 276, 779 (1997).
146. M. A. Burns, B. N. Johnson, S. N. Brahma Sandra, K. Handique, J. R. Webster, M. Krishnan, T. S. Sammarco, P. M. Man, D. Jones, D. Hedsinger, C. H. Mastrangelo, and D. T. Burke, *Science* 282, 484 (1998).
147. P. M. Ajayan and S. Iijima, *Nature (London)* 361, 333 (1993).
148. T. W. Ebbesen, "Carbon Nanotubes: Preparation and Properties." CRC Press, Boca Raton, FL, 1997.
149. D. Ugarte, A. Chatelain, and W. A. DeHeer, *Science* 274, 1897 (1996).
150. D. Ugarte, T. Stockli, J.-M. Bonard, A. Chatelain, and W. A. DeHeer, in "The Science and Technology of Carbon Nanotubes" (K. Tanaka, T. Yamabe, and K. Fukui, Eds.), p. 128. Elsevier, Amsterdam, 1999.
151. E. Dujardin, T. W. Ebbesen, H. Hiura, and K. Tanigaki, *Science* 265, 1850 (1994).
152. T. W. Ebbesen, *Annu. Rev. Mater. Sci.* 24, 235 (1994).
153. R. E. Tuzun, D. W. Noid, B. G. Sumpter, and R. C. Merkle, *Nanotechnology* 7, 241 (1996).
154. G. Hummer, J. C. Rasaiah, and J. P. Noworyta, *Nature* 414, 188 (2001).
155. G. E. Gadd, M. Blackford, D. Moricca, N. Webb, P. J. Evans, A. M. Smith, G. Jacobsen, S. Leung, A. Day, and Q. Hua, *Science* 277, 933 (1997).
156. Y. Gogotsi, J. A. Libera, A. Guvenç-Yazicioglu, and C. M. Megaridis, *Appl. Phys. Lett.* 79, 1021 (2001).
157. C. Joachim and J. Gimzewski, *Chem. Phys. Lett.* 265, 353 (1997).
158. C. Joachim and J. K. Gimzewski, *Proc. IEEE* 86, 184 (1998).
159. F. Moresco, G. Meyer, K. H. Rieder, H. Tang, A. Gourdon, and C. Joachim, *Phys. Rev. Lett.* 86, 672 (2001).
160. D. E. Benson, D. W. Conrad, R. M. de Lorimier, S. A. Trammel, and H. W. Hellinga, *Science* 293, 1641 (2001).
161. L. Sun and R. M. Crooks, *J. Am. Chem. Soc.* 122, 12340 (2000).
162. M. Karlsson, K. Sott, M. Davidson, A.-S. Cans, P. Linderholm, and D. Chiu, *Proc. Nat. Acad. Sci.* 99, 11573 (2002).
163. D. E. Smith, S. J. Tans, S. B. Smith, S. Grimes, D. L. Anderson, and C. Bustamante, *Nature* 413, 748 (2001).
164. A. D. Mehta, M. Rief, J. A. Spudich, D. A. Smith, and R. M. Simmons, *Science* 283, 1689 (1999).
165. R. K. Soong, G. D. Bachand, H. P. Neves, A. G. Olkhovets, H. G. Craighead, and C. D. Montemagno, *Science* 290, 1555 (2000).
166. M. D. Wang, M. J. Schnitzer, H. Yin, R. Landick, J. Gelles, and S. M. Block, *Science* 282, 902 (1998).
167. Y. Harada, O. Ohara, A. Takatsuki, H. Itoh, N. Shimamoto, and K. Kinoshita, Jr., *Nature* 409, 113 (2001).



# Nanoelectronics with Single Molecules

Karl Sohlberg

*Drexel University, Philadelphia, Pennsylvania, USA*

Nikita Matsunaga

*Long Island University, Brooklyn, New York, USA*

## CONTENTS

1. Introduction
2. Measurement Techniques
3. Theoretical Techniques
4. Proposed Architectures
5. The Mechanism of Electron Transport
6. Technological Roadblocks
- Glossary
- References

## 1. INTRODUCTION

Over the past 40 years, computer hardware performance has improved with such regularity that predictable advances in computer performance have come to be an expectation of the computer hardware industry. This phenomena is captured in the well known Moore's Law, which holds that typical measures of performance, such as processor speed and memory capacity, double about every 18 months. Mathematically this is written

$$(\text{future performance}) = 2^{\frac{n}{1.5}} \times (\text{current performance}) \quad (1)$$

where  $n$  is time in years. So predictable has been the rate of advance in hardware performance that corporate budgeting decisions actually factor in projected advances. For example, given that computers become unmanageably incompatible when they differ in performance by a factor of ten, it follows that hardware must be replaced at intervals no greater than every five years.

As captured in Figure 1, Moore's Law advances have at their root the fact that the typical feature size in electronic device elements has decreased geometrically with time over the past four decades. There has been a contemporaneous "shrinking" of virtually all consumer electronic equipment.

Also shown in Figure 1 is an extrapolation based on Moore's Law, from which one unavoidable conclusion is that in order to maintain the historical progression, in the near future it will be necessary to fabricate devices with feature sizes on the scale of individual molecules.

Herein we discuss both experimental and theoretical efforts to "do electronics" with single molecules [1]. Some of the questions that will be addressed are as follows:

- How are the electrical properties of an individual molecule measured?
- What theoretical techniques may be used to predict the electrical characteristics of an individual molecule?
- What properties of molecules might be exploited to design a functional electronic device?
- What is the mechanism of electron transport in molecular devices?
- What are the current technological roadblocks to molecular electronics?

Since the term "molecular electronics" is applied to a wide range of phenomena, it is important to delineate some of the closely related areas that are sometimes placed under the umbrella of molecular electronics, but will not be addressed here. The first of these categories is "quantum computing." Quantum computing is a nascent technology whereby one capitalizes on the properties of quantum mechanical systems to carry out computations, a completely different paradigm from the digital computing of today. While it is conceivable that molecular quantum states might form the basis for data representation in a quantum computer, this is at best only tangentially related to doing electronics with individual molecules as circuit components. The interested reader may begin study of this area with Ref. [2]. Second, we will not cover the areas of "conducting polymers" or "organic electronics." These are very real current technologies employing polymeric and organic materials with useful electrical properties in the construction of electronic devices, where their material properties give them

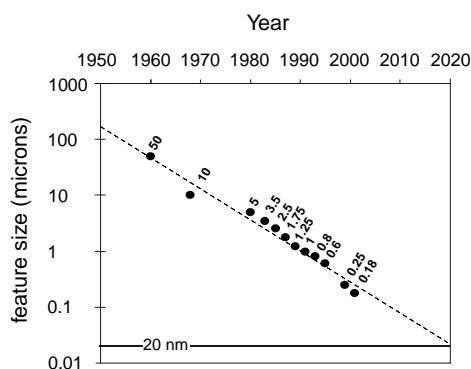


**Figure 1.** Historical progress in microelectronics. Data from [91].

an advantage over traditional metals and semiconductors. While there is considerable effort underway to reduce the physical dimension of electronic device elements that are composed of organic or polymeric materials (as has been true for traditional electronic circuitry over the past half-century), these advances are far from reaching the molecular scale. To begin study of these materials, the reader may wish to start with Ref. [3].

## 2. MEASUREMENT TECHNIQUES

Manipulating a single molecule is a daunting task. While there are millions of known stable molecules, covering an enormous range of sizes, in general the molecular domain is characterized by nanometer and subnanometer length scales. This is nine orders of magnitude smaller than the characteristic dimension of a human (about 2 meters). Manipulating an object smaller in dimension than ourselves by a factor of 10 or 100 is relatively straightforward and requires no special technology. A softball (characteristic length  $\approx 0.1$  m) or a paperclip (characteristic length  $\approx 0.01$  m) can be manipulated manually. At about 1000 times smaller, some sort of technology is required. A poppy seed (characteristic length  $\approx 0.001$  m) is difficult to handle without tweezers. At 10,000 times smaller, objects become essentially invisible to the naked eye. Their manipulation requires technology to aid in their observation as well as manipulation. Imagine attempting to manipulate a leg severed from a flea. Certainly this would require a magnifying device just to see it. In addition, it would be nearly impossible to hold ones hand steadily enough for precise manipulation, assuming it could be grabbed with tiny tweezers.

A flea's leg is only  $10^4$  times smaller than a human. To manipulate a single molecule requires precise control on a length scale  $10^5$  times smaller yet. Said another way, a molecule looks much smaller to a flea than a flea does to a human! It is not even possible to "see" a molecule in the traditional sense. The wavelength of visible light is 400–700 nm, hundreds of times longer than the characteristic length of a molecule. This is but one challenge in use of individual molecules for electronic device elements.

A key challenge of measuring the electrical properties of a molecule involves connecting the single molecule into a closed circuit. Conceptually, one would like to affix a nanometer-scale "alligator clip" onto one end of the

molecule and a second nanometer-scale "alligator clip" onto the other end of the molecule. These alligator clips would be attached to micron-scale wires that would in turn be connected to a macroscopic circuit, including a power source and measuring device as shown schematically in Figure 2. Today's computer chips employ two stages of size reduction. As described previously, a molecular device would require at least three [4]. The problem is discussed in some detail in Ref. [5]. There are no bantam alligator clips, but the concept of capturing a molecule between two classical conductors that are part of a macroscopic circuit has been realized in several ways. We will refer to the generic situation of a molecule in contact with two electrodes as a "molecular junction." A key challenge in measuring the electrical properties of a single molecule is therefore the problem of creating a molecular junction.

One conceptually simple technique is to use a break junction. In this method, a thin wire of some ductile material is immersed in a solution containing the molecular species whose conductivity properties one desires to measure. The wire, while in solution, is then drawn or bent to failure to form opposing tips. The opposing tips then become coated with a self-assembled monolayer (SAM) of the molecular species of interest. The coated tips are then withdrawn from the solution (or more conveniently, the solution is allowed to evaporate). Finally, a potential difference is established between the two tips, and the tips are brought together until current flows [6].

There are several disadvantages to the break junction method. First of all, it is only suitable if the molecular species of interest adheres to form a SAM on the material of the wire. Benzene-1,4-dithiol has proven to be an excellent test species for exactly this reason: the dual thiols serve as alligator clips to attach the ring to the electrodes [7]. It is sometimes necessary to employ protecting groups on the thiolate functions until just prior to the self assembly step, owing to the tendency of thiolates to oligomerize [8]. Thiol linkages have become a *de facto* standard for attaching molecules to metal electrodes. (Selenium (-Se-) linkages have been tried as well but appear to introduce a large potential barrier to electron transport [7].) Second, the break junction technique assumes that a solution can be prepared that contains the species of interest in sufficient concentration. Synthetic chemistry can be employed to address both limitations. Functional groups may be added to the molecule that increase its solubility and/or facilitate

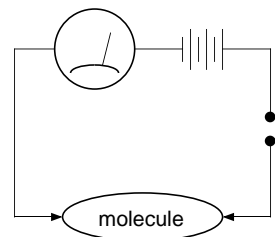


**Figure 2.** Schematic of circuit for measurements on a single molecule. One great difficulty is creating "probes" that are small enough to contact the molecule, but large enough connect into the macroscopic circuit.

its adhesion to the wire material. Nevertheless, these limitations still exist, and functionalization of the molecule almost certainly alters its electrical characteristics. Another disadvantage of the break junction is that it is not possible to guarantee that the tip-molecule-tip geometry is the same upon repeat experiments, or even that a single (and the same) molecule is subjected to measurement. Despite these limitations, replicate measurements of molecular conductance that employ the break junction method have yielded good reproducibility [6], suggesting that the chemistry of the system dictates the formation of similar junctions each time the junction contact is made.

A second, more robust technique involves the construction of a molecular junction within a nanopore by employing a combination of techniques from traditional device manufacture and materials chemistry. This technique starts with a 50 nm thick insulating membrane of  $\text{Si}_3\text{N}_4$ , supported on its edges by silicon. A bowl-shaped 30 nm cavity (nanopore) is made in the nitride membrane with reactive ion etching so that the bottom of the “bowl” just barely breaks through the membrane. The bowl-shaped nanopore is then filled with Au by vapor deposition. This leaves gold exposed in a nanometer-scale window through the nitride membrane. The molecular species of interest is then coated onto this tiny area of exposed Au by a SAM technique. Finally, the SAM side of the device is coated with Au by vapor deposition. A device is thereby created where a SAM of the species of interest is sandwiched between Au contacts in a nanometer-scale region. The junction is then incorporated into a measuring circuit. Exact details of the preparation may be found in [9].

A distinct advantage of the nanopore technique is that it creates a structure that is less fragile than a break junction and therefore more akin to a traditional solid state device. The nanopore technique may be suitable for practical devices, not simply as a measurement technique. The nanopore technique probably results in a molecular junction with several (possibly up to 1000) molecules per junction, although some reduction of scale is conceivable [10].

Another technique that employs some features from conventional semiconductor fabrication and others from synthetic chemistry has been presented by Rinaldi et al. [11]. To form a molecular junction, two triangular shaped metal electrodes are fabricated on a  $\text{SiO}_2$  substrate with electron beam lithography and lift-off processing. The two electrodes are oriented so that they point toward each other, that is, they have adjacent vertices separated by 30–120 nm. A microliter drop of solution containing the molecular species of interest is then deposited between the two electrodes and vacuum evaporated. At sufficiently low evaporation rates, an ordered structure self assembles between the two electrodes.  $I/V$  characteristics are then measured by placing an applied potential across the junction. Such devices have been demonstrated to have good reproducibility over a period of months. As a disadvantage, these measurements have been carried out in a vacuum, and it is not clear whether devices can be fabricated that are useful in atmospheric conditions. As reported [11], these devices are nanoscale, but have not been scaled to the single-molecule level.

Other techniques employ the instruments of ultramicroscopy. It was first demonstrated by Becker et al. [12] that a scanning tunneling microscope (STM) may be used to measure the conductance properties ( $I/V$  curves) of a surface with a spatial resolution on the order of 0.1 nm. This high spatial resolution provides the opportunity to investigate the local electronic structure features of surfaces, such as those associated with point defects [13]. The molecular-scale spatial resolution of the STM has been applied to the problem of measurement of the electrical characteristics of molecules. For example, the electrical properties of single-walled nanotubes [14], self-assembled alkanethiol monolayers [15], and even single  $\text{C}_{60}$  molecules [16] have been measured by capturing them between the tip of a scanning tunneling microscope and a conducting substrate. Denoting the tip-to-substrate distance as  $s$ ,  $I(s)$  measurements (current as a function of tip-to-substrate distance) on  $\text{C}_{60}$  exhibit three distinct regimes. At large  $s$ , the current is very low and shows distance dependence characteristic of a vacuum gap. As the tip is brought closer to the substrate, at a critical separation (corresponding to the inner root of the interaction potential between the tip and the  $\text{C}_{60}$  molecule) there is a shift in the slope of  $I(s)$ , indicating opening of new tunneling channels. Finally, true “electrical contact” is made when the  $\text{C}_{60}$  molecule begins to be deformed or crushed under the force of the tip [16].

An extension of the STM technique allows for its application to a wider class of molecules. To do so, a conducting substrate (typically Au) is coated with a SAM of the molecular species of interest. Nanoparticles of gold are then dispersed onto the SAM. If the tip of an STM is positioned above one of these nanoparticles, the  $I/V$  characteristics of the molecules, caught between the nanoparticle and the conducting surface, may be measured by tracking current flow as a function of the potential difference applied between the tip and conducting surface [17]. Like the nanopore technique, this method incorporates several molecules into the junction. It is estimated that about 60 molecules are active [18]. Scaling to the few-molecule level seems possible.

Another microscopy based measurement technique employs a conducting tip atomic force microscope (AFM) probe [19]. First, a SAM of molecules is formed on a Au (111) surface. A fraction of the molecules is then functionalized with a thiol substituent on the top end (farthest from the surface). This thiol functionality allows for chemical bonding to gold nanoparticles that are subsequently dispersed onto the surface. Contact is made between the AFM tip and one of the gold nanoparticles. The AFM tip and conducting surface are then wired into a circuit containing a power supply and measuring device. This allows for the measurement of the  $I/V$  characteristics of the probed molecules that are bonded to both the Au (111) surface and the gold nanoparticle [20]. This measurement technique has the distinct advantage that  $I/V$  curves are found to be integer multiples of a fundamental  $I/V$  curve, allowing for the identification of *single molecule* junctions.

The final microscopy-based technique that we will discuss here was employed by Frank et al. [21] to demonstrate quantum resistance in carbon nanotubes. Arc-produced carbon nanotubes are sometimes found to be embedded in larger fibers composed of graphitic particles and nanotubes. First,



fibers with a single carbon nanotube protruding from the end are selected. One such fiber is affixed in place of the tip of a scanning probe microscope (SPM). The  $z$ -axis (height) control of the SPM probe is then used to lower the carbon nanotube that protrudes from the fiber tip into a pool of liquid mercury. By connecting an electrical lead to the fiber tip and another to the mercury pool, a single carbon nanotube may be incorporated into a macroscopic circuit.

The carbon-fiber/mercury-pool scheme is very elegant and appears to have the best repeatability of all the measurement schemes reviewed here. The major drawback is that it is specific to nanotubes. It is conceivable that it might be possible to functionalize the nanotube tip by employing some clever chemistry. This would open the application of this scheme to use with any molecular system that can be bonded to a nanotube tip, although this remains a future achievement.

In 1991, Joachim discussed the issues associated with measuring the electrical properties of a molecule [5]. At that time the idea was largely hypothetical (although there had been some successful efforts to create circuits with elements at or near the nanometer scale). As reviewed above, in the ensuing decade, several techniques were developed and successfully employed so that the problem of measuring the electrical properties of a molecule is now effectively solved. This is not to suggest that no problems remain. One of the most important is that the molecule must be affixed in some way to two contacts. This inevitably involves functionalizing the molecule to facilitate chemical bonding to the contacts. Such functionalization alters the electrical characteristics of the molecule. We will return to the issue of the influence of contacts later, when we discuss technical roadblocks to molecular electronics.

### 3. THEORETICAL TECHNIQUES

The theoretical description of electron transport across a molecule is fundamentally a problem in scattering theory. In principle, the entire arsenal of weapons for solving traditional gas-phase scattering problems may be brought to bear on the problem of electron transport in molecular junctions. Theoretical treatments of scattering problems may be divided into two broad categories, time independent approaches (that is, those that solve the time-independent Schrödinger equation) and time dependent ones (those that solve the time-dependent Schrödinger equation). To date, the majority of theoretical treatments of electron transport in molecular junctions have been of the time-independent variety.

#### 3.1. Scattering

In a very primitive picture, the junction molecule presents a potential barrier to electron flow between the source and sink of electrons. (Such a picture is closely related to the contact in a scanning tunneling microscope and many aspects of the theory of STM [22] may be applied.) A schematic molecular junction is shown in Figure 3. (Here we treat the junction molecule as presenting a potential barrier to electron flow, although the shape of the potential varies with the details of the nature of the system.) The quantum

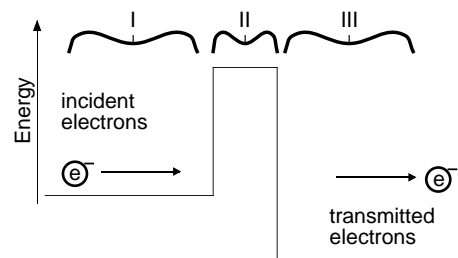


**Figure 3.** Primitive model of electron transport across a molecular junction. The molecule presents a potential barrier along the electron transport coordinate.

mechanical treatment of transmission across a potential barrier (or well) is discussed in many quantum mechanics texts [23]. In the asymptotic regions on either side of the barrier, the potential is constant so we may write down the wavefunction  $\psi(x)$  directly,

$$\psi(x) = A \exp(ikx) + B \exp(-ikx) \quad (\text{I}) \quad (2)$$

$$\psi(x) = C \exp(ikx) + D \exp(-ikx) \quad (\text{III}) \quad (3)$$

where  $A$ ,  $B$ ,  $C$ , and  $D$  are the amplitudes of the left and right propagating waves and  $k = \frac{1}{\hbar}(2m_e E)^{1/2}$ ,  $E$  being the total energy, and  $m_e$  the rest mass of the electron. Based on the form of the wavefunction in the region of the barrier (II), we may find a matrix  $M$  that relates the wave amplitudes in the asymptotic regions.

$$\begin{pmatrix} A \\ B \end{pmatrix} = \begin{pmatrix} M_{1,1} & M_{1,2} \\ M_{2,1} & M_{2,2} \end{pmatrix} \begin{pmatrix} C \\ D \end{pmatrix} \quad (4)$$

The matrix  $M$  is called a *transfer* matrix and is closely related to the scattering matrix  $S$ , which relates the amplitudes of the incoming and outgoing waves,

$$\begin{pmatrix} B \\ C \end{pmatrix} = \begin{pmatrix} S_{1,1} & S_{1,2} \\ S_{2,1} & S_{2,2} \end{pmatrix} \begin{pmatrix} A \\ D \end{pmatrix} \quad (5)$$

The inverse of the transfer matrix  $M^{-1}$  is a transfer matrix as well, relating wave amplitudes in the opposite direction. Independent of the formalism used, the quantity

$$T = \left| \frac{C}{A} \right|^2 \quad (6)$$

is termed the *transmissivity* of the barrier and gives the probability that an electron incident from the left (i.e.,  $D = 0$ ) will pass through the barrier and emerge on the right. It follows that  $T = |S_{1,2}|^2$ . In general,  $T$  has energy dependence. If one knows the incident flux of electrons, the product of this flux with  $T$  yields the current.

The barrier shown in Figure 3 is a constant potential, one for which the transmissivity may be determined exactly, and is given in many quantum mechanics texts [23]. Generalization to nonsquare potential barriers is possible. In such a case, an approximate WKB formula is useful for thick barriers of slowly varying potential. In this case,

$$T \approx \exp\left(2 \int_a^b k(x) dx\right) \quad (7)$$

where  $k = \frac{1}{\hbar}(2m_e(V(x) - E)^{1/2})$ , and  $a$  and  $b$  are the left and right classical turning points of the potential barrier for a particle of energy  $E$  [23].

The above conveys the basic physics of electron transport across a molecular junction, but it is a very primitive model. First of all, it assumes that the electron transport takes place along a hypothetical one-dimensional coordinate. It completely neglects the space-filling three-dimensional nature of a real junction molecule. Second, in a real junction, the incident electrons are unlikely to be monochromatic, so it may be necessary to integrate over a distribution of incident electron energies (typically a Fermi distribution). Perhaps most importantly, the molecule where the scattering takes place interacts with both the source and sink of electrons (electrodes), and the form and strength of these interactions depend on the contacts. The theoretical treatment of electron transport in molecular junctions, therefore, includes several complications that typically do not appear in a traditional gas-phase scattering problem.

### 3.2. The Role of the Fermi Distribution

In a molecular junction, the molecule is typically connected to two metallic electrodes. Within these electrodes, the population of orbitals is dictated by a Fermi distribution. This means that the source of electrons is, generally speaking, not monoenergetic. Given that the transmissivity  $T(E)$  of the molecule is known, the current  $I$  is given by

$$I = \frac{e}{\pi\hbar} \int_{-\infty}^{\infty} T(E)[f(E - \mu_a, \tau) - f(E - \mu_b, \tau)] dE \quad (8)$$

where  $f$  is the Fermi function,  $E$  is energy,  $\tau$  is temperature,  $\hbar$  is the Planck constant divided by  $2\pi$ ,  $e$  is the unit of charge, and  $\mu_a$  and  $\mu_b$  are the electrochemical potentials within the two electrodes so that  $\mu_b - \mu_a = eV$  ( $V$  being the applied voltage). The difference of Fermi functions is interesting. At low  $E$ , both  $f(E - \mu_a)$  and  $f(E - \mu_b)$  are equal to one, so their difference is zero. Similarly, at high  $E$ , both are equal to zero and their difference is also zero. The difference in Fermi functions only has appreciable magnitude when  $E$  falls above the lower of  $\mu_a$  and  $\mu_b$  but below the higher. In this region, the orbitals in the high energy electrode are full, and those in the low energy electrode are empty. This is the only energy region in which there can be appreciable current. Below this region, there are no empty orbitals on the acceptor electrode to accept the transferred electrons. Above this region, there are no full orbitals in the high energy electrode from which the electrons may be transferred.

For very low temperatures and small applied voltages, the function  $f(E - \mu_a, \tau) - f(E - \mu_b, \tau)$  is adequately approximated by a delta function. This “finite-voltage finite-temperature” approximation can be seen quite elegantly in the formalism of Bagwell and Orlando [24]. The difference of Fermi functions is written as a difference of two Heaviside step functions ( $h(\theta)$ ) convoluted with a thermal smearing function

$$\begin{aligned} & f(E - \mu_a, \tau) - f(E - \mu_b, \tau) \\ &= [h(E - \mu_a) - h(E - \mu_b)] \otimes \left( -\frac{\partial f}{\partial E}(E, \tau) \right) \end{aligned} \quad (9)$$

Here  $\otimes$  denotes convolution. From this formalism, it is clear that if the applied potential is small and the temperature broadening is minimal, the expression for current reduces to [25]

$$I = \frac{e^2}{\pi\hbar} TV \quad (10)$$

It follows that

$$R = \frac{\pi\hbar}{e^2 T} \quad (11)$$

which shows that the quantum of conductance [21] is

$$G_0 = \frac{e^2}{\pi\hbar} \quad (12)$$

Eq. (11) assumes that the molecule is in contact with a perfect conductor [25] and is valid for  $T \rightarrow 0$ . More complete analysis [26, 27] yields

$$R = \frac{\pi\hbar}{e^2} \frac{(1 - T)}{T} \quad (13)$$

from which it is clear that  $T \rightarrow 0 \Rightarrow R \rightarrow \infty$  and  $T \rightarrow 1 \Rightarrow R \rightarrow 0$ . Eqs. (11) and (13) agree for  $T \ll 1$ , as in high resistance junctions.

In the WKB approximation, we may write

$$G = G_0 \exp\left(2 \int_a^b k(x) dx\right) \quad (14)$$

For a constant potential,

$$\int_a^b k(x) dx = c_1 L \quad (15)$$

where  $c_1$  is a constant and  $L$  is the width of the barrier. If we describe a molecule of width  $L$  as a one-dimensional tunnel barrier we may then write

$$G = G_0 \exp(2c_1 L) = G_0 \exp(\gamma L) \quad (16)$$

This is the “exponential law,” which is widely used to characterize molecular conductance [28].

The finite-voltage finite-temperature approximation is very common in the theoretical description of electron transport across molecular junctions. As discussed by Bagwell and Orlando [24], this approximation is valid if the applied voltage and thermal broadening are less than any of the features in  $T(E)$ . For the theoretical description of practical devices, where applied voltages are presumably as high as several eV, it is desirable to go beyond this approximation.

### 3.3. Multiple Transmission Channels

At the next level of sophistication, we recognize that there exists a plethora of possible initial states  $|i\rangle$  (chemists may think of these roughly as electrons in orbitals of the electron donor electrode) and a plethora of final states as well  $|f\rangle$  (which chemists may think of as electrons in orbitals of the electron acceptor electrode). The transition matrix  $\mathbf{t}$  has elements  $\langle f|t|i\rangle$  that reflect the coupling of  $|i\rangle$  to  $|f\rangle$  and is related to the scattering matrix by [29]

$$S = \mathbf{I} - i\mathbf{t} \quad (17)$$

The transmission coefficient for a wave incident in  $|i\rangle$  to emerge in  $|f\rangle$  is given by  $|t_{i,f}|^2$ . The structure of the  $\mathbf{t}$  matrix is determined by the electronic structure of the junction molecule and its coupling to the electrodes, and can be found with any of numerous electronic structure techniques. (Several approaches are reviewed next.) The overall energy-dependent transmission coefficient is then given by

$$T(E) = \sum_i \sum_{f \neq i} \frac{v_f}{v_i} |t_{i,f}(E)|^2 \quad (18)$$

where the velocity ratio  $\frac{v_f}{v_i}$  accounts for differences in flux due to differences in velocity. In this formalism, it is easy to see that there are multiple scattering channels and that the overall transmissivity depends on the sum over all channels [30]. The current is then given by [30]

$$I = \frac{2\pi e}{\hbar} \sum_{i,f} f(E_i)[1 - f(E_f + eV)] |t_{fi}|^2 \delta(E_i - E_f) \quad (19)$$

where  $f(E)$  is the Fermi function (for the donor  $i$  and acceptor  $f$  electrodes),  $V$  is the applied potential, and  $\delta(E_i - E_f)$  is a Dirac delta function that ensures contributions only from states in energy resonance. Note in particular that for the donor electrode the Fermi function is employed since the electron must be donated from an occupied state, but for the acceptor electrode  $1 - f(E)$  is used since the electron must be accepted into an empty state.

Eq. (19) is quite general. One common simplification is to assume that  $\mathbf{t}$  is independent of any applied potential. This is a reasonable approximation if one is considering small applied potentials, and may be used effectively in conjunction with the small-voltage low-temperature approximation just described.

### 3.4. Fermi Level Alignment

One important problem in developing a theoretical model of electron transport in a molecular junction is that of ‘‘Fermi level alignment,’’ placing the Fermi level of the electrodes relative to that of the molecular orbitals of the junction molecule [31]. The issue is particularly critical because the electrode/molecule interface directly impacts the electron transport properties of the junction [32].

In the simplest approximation, one might start by relating both the electrode Fermi level and the highest occupied molecular orbital (HOMO) of the junction molecule to some common zero of potential. For example, the

energy cost of removing an electron from a relaxed neutral molecule to infinite separation is simply the ionization energy (IE). Using Koopmans’ theorem, IE is approximated by the negative of the energy of the HOMO of the neutral molecule. Similarly, pulling an electron from a metal electrode out to infinity requires paying the work function  $E_w$ . If one defines the zero of potential as that of an electron removed to infinite separation (as is customary in molecular electronic structure calculations), Fermi level alignment can be achieved by placing the Fermi level at  $-E_w$  and the HOMO at  $-IE$ . There are two problems with this approach. The first is that the HOMO energy is only an approximation to  $-IE$ , and sometimes a poor one. The second is that in a molecular junction, the molecule is in direct contact with the electrode. This close contact both alters the electronic structure of the molecule and obviates the need to remove the electron from the metal to infinity before placing it on the molecule.

It is widely accepted that in the case of zero-applied potential, the Fermi level lies somewhere between the HOMO and the lowest unoccupied molecular orbital (LUMO) of the junction molecule. If the electrode Fermi level were below the HOMO, electron charge would flow from the molecule to the electrodes, completely depleting the HOMO. Likewise, if the Fermi level of the electrodes were to fall above the LUMO of the junction molecule, electron charge would flow onto the molecule to fill the LUMO. With the Fermi level between the HOMO and LUMO, the degree of charge transfer between the molecule and the metallic electrodes depends on the exact position of the Fermi level, and it has been shown that charge transfer can, in some instances, be appreciable [33]. Fermi level alignment and charge transfer are therefore intimately tied together. It is correspondingly unsurprising that the most rigorous approaches to Fermi level alignment require iteration of charge transfer and the molecular energy levels to self-consistency.

Closely related to the issue of Fermi level alignment is describing the distribution of an applied potential across the molecular junction. The most common approach has been to introduce an empirical parameter into the formalism to distribute the applied potential, as described quite elegantly by Datta et al. [34]. Given an applied potential  $V_{ap}$ , in the zero-order approximation one may assume that the potential  $V_{mol}$  is constant within the junction molecule, with the potential drop between the electron-donor and electron-acceptor electrodes partitioned at the interfaces such that the chemical potentials within the left and right electrodes ( $\mu_L$  and  $\mu_R$ ) are given by

$$\mu_L = E_f - eV_{mol} = E_f - \eta eV_{ap} \quad (20)$$

and

$$\mu_R = E_f + eV_{ap} - eV_{mol} = E_f + (1 - \eta)eV_{ap} \quad (21)$$

where

$$\eta = \frac{V_{mol}}{V_{ap}} \quad (22)$$

$E_f$  is the equilibrium Fermi level and  $\eta$  is an empirical parameter, commonly taken to be  $\eta \approx 0.5$  [35]. These expressions show that with zero applied potential, the chemical potentials of the electrodes are set to the equilibrium

Fermi level. This formalism implicitly assumes that in the case of zero applied potential, the zero of potential in the molecule (as defined by whatever molecular electronic structure calculation technique is employed) lines up with the equilibrium Fermi level.

Traditional quantum chemistry techniques may be employed to determine the Fermi level alignment in a non-empirical way, at least in the case of zero applied potential. An *ab initio* molecular electronic structure calculation is carried out on the junction molecule, including part of each electrode into the molecular structure. Effectively one is placing a metal cluster on each end of the molecule. The size of these clusters is then increased and the calculation repeated until a common Fermi level is reached that is not significantly displaced in energy from the Fermi level of the pure metal [31, 36, 37]. This method has been applied to the case of a single  $C_{60}$  molecule bound to two Al electrodes of size similar to the  $C_{60}$  itself [36]. An interesting “natural doping” of the junction molecule is found. Electron charge flow occurs from the Al electrodes to the junction molecule until the LUMO (which is threefold degenerate) is half filled. Qualitatively, this is the most “metallic” distribution of electrons in  $C_{60}$ , presumably leading to enhanced conductance.

As discussed later, an added benefit of including a portion of each electrode into the electronic structure description of the junction is that this allows exact atomistic specification of the electrode/molecule contact geometry, which affords investigation of the influence of variations in contact geometry on electron transport [38].

### 3.5. Examples of Theoretical Studies

We now turn to specific examples of theoretical treatments of electron conduction through molecular junctions and similar systems.

Sautet and Joachim studied the closely related problem of the influence of a single impurity on current flow along an otherwise homogeneous repeating chain [39]. The energy-dependent transmission coefficient is written in terms of the diagonal elements of a transfer matrix, which relates wave amplitudes across the defect as in Eq. (6). The transfer matrix is in turn constructed from the elementary site-to-site propagators through the defect. The construction of these site-to-site propagators requires knowledge of the electronic structure of the system. The electronic structure of the chain polymer is described with a tight-binding Hamiltonian. There are five parameters: 1)  $e$  the coupling of two sites away from the defect, 2)  $h$  the energy of a nondefect basis function, 3)  $\omega$  the energy of the defect site basis function, 4)  $\alpha$  the coupling of the defect site to the site immediately adjacent on the left, and 5)  $\beta$  the coupling of the defect site to the site immediately adjacent on the right. The elementary site-to-site propagators  $\mathbf{P}$  are constructed in terms of these Coulomb and resonance parameters to connect the coefficient vectors across a site

$$\begin{pmatrix} C_{n+1} \\ C_n \end{pmatrix} = (\mathbf{P}) \begin{pmatrix} C_n \\ C_{n-1} \end{pmatrix} \quad (23)$$

In overview, the electronic structure of the system determines the elementary site-to-site propagators  $\mathbf{P}$ . The site-to-site propagators determine the transfer matrix  $\mathbf{t}$ . The

transfer matrix determines the ratio of wave amplitudes across the defect and therefore the transmission function  $T$ .

A multichannel transfer matrix technique for the theoretical description of electron transport in a molecular wire with a lateral (transverse to the direction of conduction) confining potential has been described by Sheng and Xia [40]. For a wire aligned along the  $x$  axis with a confining potential  $U(x, y)$  between  $[0 \leq x \leq L]$ , the wavefunction in the asymptotic regions  $[x < 0]$  and  $[x > L]$  may be written

$$\Psi_L(x, y) = \sum_{n=1}^N (a_n^L e^{ik_n x} + b_n^L e^{-ik_n x}) \Phi_n(y) \quad (24)$$

and

$$\Psi_R(x, y) = \sum_{n=1}^N (a_n^R e^{ik_n x} + b_n^R e^{-ik_n x}) \Phi_n(y) \quad (25)$$

in the regions  $[x < 0]$  and  $[x > L]$ , respectively. Here  $k_n$  may be extracted from

$$\frac{\hbar^2 k_n^2}{2m} = E - E_n \quad (26)$$

where  $E$  is the total energy of the system,  $m$  is the effective electron mass, and  $E_n$  is the energy of the  $n$ th transverse mode. The amplitudes in the left and right asymptotic regions are then related by a transfer matrix  $\mathbf{M}$

$$\begin{pmatrix} \mathbf{a}_L \\ \mathbf{b}_L \end{pmatrix} = (\mathbf{M}) \begin{pmatrix} \mathbf{a}_R \\ \mathbf{b}_R \end{pmatrix} = \begin{pmatrix} \mathbf{M}_1 & \mathbf{M}_3 \\ \mathbf{M}_2 & \mathbf{M}_4 \end{pmatrix} \begin{pmatrix} \mathbf{a}_R \\ \mathbf{b}_R \end{pmatrix} \quad (27)$$

where  $\mathbf{a}_L, \mathbf{a}_R, \mathbf{b}_L, \mathbf{b}_R$  are vectors of incident and reflected wave amplitudes, and  $\mathbf{M}$  is partitioned into submatrices  $\mathbf{M}_1, \mathbf{M}_2, \mathbf{M}_3, \mathbf{M}_4$  for convenience. The transfer matrix is related to the transmission ( $\mathbf{t}$ ) and reflectance ( $\mathbf{r}$ ) matrices in the usual way. Typically, one considers the case where  $\mathbf{b}_R = 0$ , that is, there is no incident flux from the right.

Within the scattering region where the potential is described by  $U(x, y)$ , the wavefunction is expanded as

$$\Psi(x, y) = \sum_{n=1}^N f_n(x) \phi_n(y) \quad (28)$$

where  $\phi_n(y)$  describes the transverse modes and  $f_n(x)$  may be thought of as an  $x$ -dependent expansion coefficient. Substituting Eq. (28) into the Schrödinger equation, multiplying by an arbitrary  $\phi_m(y)$ , and integrating over all  $y$  yields

$$\left[ \frac{-\hbar^2}{2m} \frac{\partial^2}{\partial x^2} + \sum_{n=1}^N U_{mn}(x) f_n(x) + \left( \frac{-\hbar^2}{2m} - E \right) \right] f_m(x) = 0 \quad (29)$$

where  $U_{mn}(x)$  is the matrix element of  $U(x, y)$  between transverse states  $n$  and  $m$ ,  $\langle \phi_n | U(x, y) | \phi_m \rangle$ . Integrating these coupled equations from  $R$  to  $L$  for a linearly independent set of initial conditions and matching the asymptotic boundary conditions for  $f_n(x=0)$  and  $f_n'(x=0)$  yields the transfer matrix. The method is particularly useful for investigating the influence of the lateral confining potential on electron transmission.

Perhaps the most widely used theoretical description of electron conduction across a molecule is that presented by Mujica et al. [30]. The method begins with Eq. (19). The system is partitioned into two metallic reservoirs  $A$  and  $B$  and the molecule  $M$ . The Hamiltonian for the system is then partitioned

$$H = H^0 + V \quad (30)$$

where  $H^0$  is assumed to have orthonormal eigenstates:  $|i\rangle$  corresponding to states of  $A$ ,  $|f\rangle$  corresponding to states of  $B$ , and  $|\alpha\rangle$  corresponding to states of  $M$ .  $V$  is the interaction potential connecting  $M$  to  $A$  and  $B$ . It is assumed that there is no direct coupling of  $A$  and  $B$ . Physically, this corresponds to the approximation that thorough space coupling of the two reservoirs is negligible, quite reasonable for all but the smallest molecules  $M$ , where the separation of the electrodes would be correspondingly small. It is then possible to define a transition matrix  $\mathbf{t}$  connecting the states  $|i\rangle$  of the donor reservoir to the states  $|f\rangle$  of the acceptor reservoir in terms of the coupling matrices  $V_{i,\alpha}$  and  $V_{\alpha,f}$  and the eigenstates of  $H^0$ . The current follows directly from Eq. (19).

In this formalism, the current factors into a contribution from the electronic structure of the wire (coupled to the reservoirs through its end sites) and the density of initial and final states. In the original presentation of Ref. [30], a tight-binding Hamiltonian is used and the matrix  $\mathbf{t}$  is assumed to be independent of any applied potential. The latter assumption limits the valid range to low voltages, but the formal expression of the current is quite general, and these assumptions may in principle be relaxed. The basic scheme of Ref. [30] has been generalized to employ a nonorthogonal basis [41, 42], to include vibrational broadening [35], and to include multiple orbital interactions of the molecule with the electrode [42]. A Floquet theory approach to the case where the wire is driven by a monochromatic radiation field has also been reported [43].

Lang has presented an approach for calculating the current flow across a few-atom wire connecting two metals that is essentially fully first principles [44]. Fermi level alignment and charge transfer are handled in an entirely self-consistent manner. Density-functional theory calculations are employed to produce an initial electronic wavefunction. The electrostatic potential distribution across the junction is computed self-consistently. That is, the charge density distribution resulting from the electronic wavefunction is used in the Poisson equation, which in turn produces the applied electrostatic potential. The electronic structure and applied potential are iterated to self-consistency. Current is calculated from the final self-consistent wavefunction. Electrostatic self-consistency is key to moving beyond the small-voltage low-temperature approximation. The method of Lang and colleagues is therefore one of only a few to be formally applicable to cases of large bias voltage. The technique has been generalized for molecular junctions [32], applied to a hypothetical multiterminal molecular electronic device [45], and used to study temperature effects on electron transport properties of molecules [46].

A different scattering-theory approach has been taken by Emberly and Kirczenow [47, 48]. They start by dividing

the electrode-molecule-electrode system into five conceptual components. The electrodes on the left and right are labeled  $L$  and  $R$ , respectively. Each electrode terminates in a gold cluster, each denoted  $C$ . The molecule  $m$  is trapped between the two clusters so that the overall system may be written symbolically  $LCmCR$ . For the purposes of the theoretical description, three components are identified: the left “lead”  $L$ , the  $CmC$  central supermolecule (shorthand  $M$ ), and the right lead  $R$ . The wavefunction  $|\Psi^\alpha\rangle$  is expanded in a basis of orbitals  $\{|n, j\rangle\}$  where  $n$  denotes the site ( $A$  “site” is a unit cell in  $L$  and  $R$ , and is  $n = 0$  for  $M$ ), and  $j$  denotes the orbital index on the specific site. The overall wavefunction is then a sum over expansions for all three components

$$|\Psi^\alpha\rangle = |\Psi_L^\alpha\rangle + |\Psi_M^\alpha\rangle + |\Psi_R^\alpha\rangle \quad (31)$$

where the superscript  $\alpha$  is a mode index. To find the scattering  $\mathbf{t}$  matrix,  $|\Psi^\alpha\rangle$  is written as a right-propagating wave and a sum over reflected waves whose amplitudes are specified by the reflection matrix  $\mathbf{r}$

$$|\Psi^\alpha\rangle = \sum_{n=-\infty}^{-1} \sum_j \left( c_j^\alpha e^{ink^\alpha} + \sum_{\beta} r_{\beta,\alpha} c_j^\beta e^{ink^\beta} \right) |n, j\rangle \quad (32)$$

Here  $k^q$  is the unitless signed wavenumber for mode  $q$ , and  $c_j^q$  are the expansion coefficients. The index  $j$  sums over molecular orbitals of a unit cell in the lead. The unit cells are indexed  $n$ , ( $n < 0$  for  $L$ ,  $n = 0$  for  $M$ , and  $n > 0$  for  $R$ ).  $|\Psi_M^\alpha\rangle$  is written as a sum over the orbitals in  $M$

$$|\Psi_M^\alpha\rangle = \sum_j a_j^\alpha |0, j\rangle \quad (33)$$

where the site label is denoted 0 for convenience.  $|\Psi_R^\alpha\rangle$  is written as a sum over transmitted waves whose amplitudes are specified by the transmission matrix  $\mathbf{t}$

$$|\Psi_R^\alpha\rangle = \sum_{n=1}^{\infty} \sum_j \sum_{\beta} t_{\alpha,\beta} d_j^\beta e^{ink^\beta} |n, j\rangle \quad (34)$$

Eq. (31), expanded in  $\{|n, j\rangle\}$ , is then substituted into the Schrödinger equation

$$H|\Psi^\alpha\rangle = E|\Psi^\alpha\rangle \quad (35)$$

and closed with the bra  $\langle n, i|$ . This produces a system of equations whose unknowns are the elements of the  $\mathbf{r}$  and  $\mathbf{t}$  matrices

$$\sum_{\beta \in L} r_{\beta,\alpha} \sum_{m,j} A_{n,m}^{i,j} c_j^\beta e^{imk^\beta} + \sum_j A_{n,0}^{i,j} a_j^\alpha + \sum_{\beta \in R} t_{\beta,\alpha} \sum_{m,j} A_{n,m}^{i,j} d_j^\beta e^{imk^\beta} = - \sum_{m,j} A_{n,m}^{i,j} c_j^\alpha e^{imk^\beta} \quad (36)$$

where  $A_{n,m}^{i,j} = \langle n, i|H|m, j\rangle - E\langle n, i|m, j\rangle$  [47]. The current is then related to the  $\mathbf{t}$  matrix in the finite-voltage finite-temperature approximation.

The Hamiltonian  $H$  is expanded as  $H = H^0 + W$ , where  $H^0$  is the Hamiltonian for  $L$ ,  $M$ , and  $R$ , and  $W$  is the coupling of  $L$  to  $M$  and of  $M$  to  $R$ . In the implementation of Emberly and Kirczenow [47],  $H^0$  is based on a tight-binding Hamiltonian. The coupling  $W$  is composed of Hückel (tight binding) matrix elements between the

orbitals of the cluster-molecule-cluster system and the adjacent orbitals in the leads. More sophisticated electronic structure descriptions could in principle be employed within the same formalism. One of the benefits of this method is that the explicit treatment of atoms in the contacts allows for direct investigation of different contact geometries.

A chemically intuitive method of directly relating the electronic structure of a molecule to its resistivity has been discussed by González and Morales [27]. The technique is again based on the inverse relationship between the transmission probability through the molecule and its resistance, Eq. (13). As the transmission nears unit probability, the resistance approaches zero. As the transmission probability approaches zero, the resistance increases without bound. The transmission probability is approximated by the normalized charge-transfer across the molecule from an electron-donor functional group to an electron-acceptor functional group, upon electronic excitation.

A long “wire” molecule is functionalized with a donor substituent on one end ( $D = -\text{CH}_3$ ) and an acceptor substituent on the other ( $A = -\text{CHO}$ ). The charge distribution is analyzed in the molecular ground state and again in the charge-transfer photoexcited state. During photoexcitation, charge is transferred from the Donor  $D$  to the acceptor  $A$ . In the presentation of González and Morales [27], the wire is taken to be  $n$  ethene units ( $-\text{HC}=\text{CH}-$ ) $_n$ . A hypothetical charge transfer for a zero-length molecule  $\Delta Q_0$  may be extrapolated by plotting charge transfer  $\Delta Q_n$  versus  $n$ . The hypothetical zero-length molecule is assumed to have unit transmissivity  $T = 1$ . It follows that for the transmissivity for a wire of  $n$  units one may write,  $T_n \approx \frac{\Delta Q_n}{\Delta Q_0}$ . In principle any molecular wire could be treated within this formalism. The qualitative variation in transmissivity with molecule length predicted by the method of González and Morales [27] is completely consistent with that given by much more sophisticated multichannel scattering calculations [28].

A unique feature of this technique is that it yields information about the resistance *intrinsic* to the molecule, with no contribution from contacts. One shortcoming of this method is that it does not allow the prediction of the  $I(V)$  characteristics of the molecule. Nonlinear effects may be investigated to first order by taking advantage of the fact that the charge transferred differs for different donor and acceptor groups. If calculations are carried out for several pairs of donor and acceptor groups, the resulting molecular resistance  $R$  versus molecule length  $l$  data may be fit to

$$R(l) = \theta_L l + \theta_{NL} l^2 \quad (37)$$

where  $\theta_L$  and  $\theta_{NL}$  are the linear and nonlinear resistance coefficients, respectively.

Other groups have taken the approach of concentrating on the electronic structure of the junction molecule or wire instead of explicit calculation of the current. Molecular orbital studies can provide considerable insight into the electrical behavior.

Seminario et al. [49, 50] have used first principles methods to investigate the influence of torsional distortions on the electronic structure of conjugated oligo(phenylene ethynylene) systems, such as 1,4-(ethynylphenyl)phenylene. (See Fig. 4.) Knowledge of the energy barrier to torsional

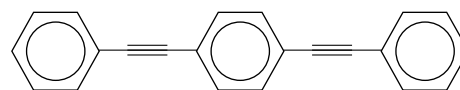


Figure 4. 1,4-(ethynylphenyl)phenylene.

distortion (which is typically quite low, on the order of a few kcal/mole), and of the changes in molecular electronic structure with torsional distortion, allow for a qualitative prediction of the effects of temperature on the electrical transport properties of the system. In an extension of this work, Derosa and Seminario [51] have combined the DFT electronic structure description of the molecule plus a number of Au atoms from each adjacent electrode with a modification of the formalism for transport properties presented by Samanta et al. [41] to describe electron transport through single-molecule junctions.

In related work [52,53], semiempirical methods were employed to investigate the effect of interspersing valence-saturated “spacer” atoms along the otherwise conjugated wire. In particular, the formation of resonances due to changes in the energetic alignment of the molecular orbitals with applied static electric field is discussed.

## 4. PROPOSED ARCHITECTURES

Today, molecules with extended  $\pi$  conjugation are most often identified as candidates for molecular electronic devices [28,54,55]. The property of conjugation allows for effective electron delocalization over great distances, presumably facilitating low resistance electron transport [56,57]. This is most easily visualized with Lewis structure diagrams. Consider a long conjugated chain as depicted in Figure 5. If a charge is introduced at one end (here by removing  $\text{H}^-$  to form a primary carbocation), it is easy to

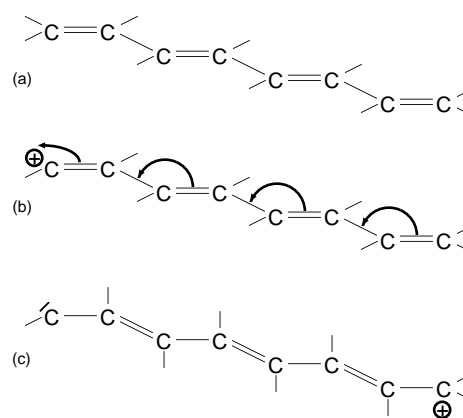


Figure 5. Schematic of electron transfer across linear polyene. (a) A linear polyene. (b)  $\text{H}^-$  is removed from the left-most carbon atom inducing a formal charge of +1. The electrons in the double bonds may then shift as shown by the arrows to transfer the positive charge to the right-most carbon atom. (c) Right-most carbon carries formal charge of +1.



see how the charge can be transported across the molecule by successively shifting the double bonds. In unconjugated systems, such transport can only occur by migration of atoms, or by violating the rules of valence. Since even the lightest atom, hydrogen, is 1836 times heavier than an electron, atom migration is a much less facile method of charge transport. If the system is unconjugated, charge transport by electron transfer requires violating the rules of valence. Such processes are therefore energetically unfavorable.

From the perspective of molecular orbital theory, a conjugated  $\pi$  system can be described through the construction of the molecular  $\pi$  orbitals as linear combinations of atomic  $p$ -orbitals. The atoms forming the conjugated domain must all lie in a plane (or nearly so), here taken to be the  $yz$  plane. To describe the conjugated  $\pi$  system, one may take as a basis a single atomic  $p_x$ -orbital on each atom in this domain. In the construction of molecular orbitals from this basis, there will always be one molecular orbital that consists of a positive contribution from each atomic orbital, that is, a nodeless molecular orbital delocalized over the entire conjugated domain. (See Fig. 6.) Such a structure is widely believed to be favorable for low-resistance electron transport.

Conjugated organic molecules are a particularly attractive choice for molecular electronics, not only because of their electronic structure properties, but also because the chemistry community has more than a century of experience in their synthesis and handling, which should facilitate the fabrication of devices composed of conjugated organic components. The use of individual molecules as device elements has another potentially revolutionary advantage. In a chemical synthesis, a large number of molecules is produced (on the order of Avogadro's number  $6 \times 10^{23}$ ), and they are all absolutely identical (notwithstanding isotopomers, whose chemical properties are essentially indistinguishable). There is the potential, therefore, for the inexpensive fabrication of a staggering number of individual units with near perfect uniformity [54]. Numerous examples may be found in [55].

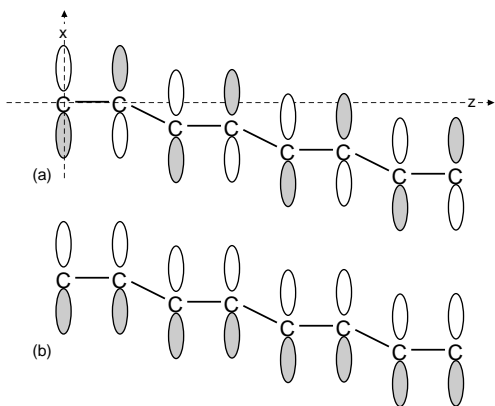


**Figure 6.** A linear polyene with the  $p_x$ ,  $\pi$  orbital structure shown. (a) Highly antibonding linear combination of  $p_x$  orbitals; (b) fully bonding linear combination of  $p_x$  orbitals leads to nodeless  $\pi$  orbital extending across the entire molecule.

## 4.1. Wires

Perhaps the most fundamental component of any circuit is the wire. Molecular electronic circuits will require wires also, and numerous species have been proposed to fill the need. Samanta et al. [41] have proposed molecules consisting of multiple paralinked benzene rings as molecular wires. The generic formula is  $\text{HS}-(\text{C}_6\text{H}_4)_n-\text{SH}$ , where the thiol terminators are the molecular equivalent of alligator clips, which are used to attach the wire to electrodes. Their calculations predict an exponential dependence of resistance on molecular length. This has been observed experimentally for similar molecular species [57,58] and is a consequence of tunneling-dominated electron transport. This feature of molecular wires is qualitatively different from conventional macroscopic wires. Conventional metal wires exhibit a linear dependence of resistance on length. (A wire of length  $l$  and resistance  $R$  when clipped into two halves, produces two wires of length  $l/2$  each with resistance  $R/2$ .) A commonly used descriptor for molecular wires is the  $\beta$  factor. One writes the electron transfer rate constant  $k_{ET}$  as [57]

$$k_{ET} = k_0 \exp(-\beta r_{da}) \quad (38)$$

where  $k_0$  is a kinetic prefactor,  $r_{da}$  is the distance between the electron donor and the electron acceptor (basically the wire length), and  $\beta$  is the characteristic parameter.

Davis et al. [57] have carried out measurements of the electron transfer rate in molecules of the form  $-(\text{C}_6\text{H}_4-\text{CHCH})_n-(\text{C}_6\text{H}_2(\text{OR})_2)-(\text{CHCH}-\text{C}_6\text{H}_4)_n-$ . For these systems, they find  $\beta \approx 0.04 \text{ \AA}^{-1}$ . Sikes et al. [58] have reported similar studies for ferrocene oligophenylenevinylene methyl thiols and report  $\beta \approx 0.06 \text{ \AA}^{-1}$ . This class of molecules is shown in Figure 7. These low  $\beta$  values indicate remarkably weak length dependence in these systems, a desirable characteristic for molecular wires. By contrast, typical  $\beta$  values for unsaturated and saturated electron transfer bridges are  $0.5 \text{ \AA}^{-1}$  and  $1.0 \text{ \AA}^{-1}$ , respectively [58].

As discussed previously, González and Morales [27] have considered polyenic molecules of the form  $\text{D}-(\text{CH}=\text{CH})_n-\text{A}$  as molecular wires. Rather than employing the  $\beta$  parameter, they use Eq. (37) to describe the length dependence of resistance.

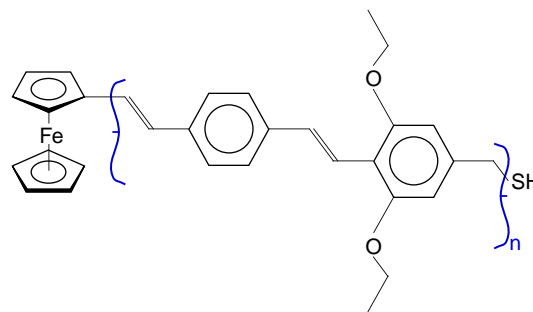


**Figure 7.** Ferrocene oligophenylenevinylene methyl thiols. One possible repeat unit is enclosed in brackets.

## 4.2. Devices

The electronic devices themselves can be broadly classified into two categories: i) those with nonlinear  $I/V$  characteristics, and ii) those whose  $I/V$  characteristics can be influenced by an external stimulus. An example of the first type is a diode. Under positive bias, (forward current flow) the device presents a constant (typically small) resistance to current flow so that the current flow is linearly dependent on the applied potential. Under negative bias, however, the device presents a large resistance to current flow. There is a significant nonlinearity in the  $I/V$  characteristics, near zero applied potential. An example of the second class of devices is a switch. In the closed position, the device presents an essentially infinite (or at least very large) resistance to current flow of either bias, but after the action of some external stimulus (depressing a button for example), a new state is accessed where the device presents little resistance to current flow. Architectures have been proposed for molecular devices of both types.

The idea of creating molecule-sized electronic components has almost certainly been around in science fiction literature for many years. The first serious attempt to identify molecular properties on which one might capitalize to create real molecular devices is widely attributed to Aviram et al. [59].

Much early work focused extensively on the potential use of hydrogen bonds for information storage [60]. In some systems, the hydrogen atom, caught between two highly electronegative atoms in a hydrogen bond, is governed by a double well potential. The system has a local minimum in potential energy when the hydrogen is more closely associated with either one or the other of the two highly electronegative atoms, and these two local minima are separated by a potential barrier. This situation is known as asymmetric hydrogen bonding. Such a situation has two physically distinct states. If the system can be induced to switch from one state to the other by some external stimulus, a binary information storage device has been created. This idea is motivated in part by the observation that DNA accomplishes information storage with hydrogen bonds [59]. While conceptually appealing, experimental studies of 9-hydroxyphenalenones [61] and theoretical and experimental studies of hemiquinones [59] show that in these systems the proton tunneling rate is too high for enduring information storage. This problem might be resolved with massive redundancy or a heavier switching group.

A switching scheme based on enol-keto isomerization in N-salicylidenaniline was studied by Sautet and Joachim [62]. The molecule exhibits qualitatively different transmission properties  $T(E)$  in the enol versus keto tautomers. It is proposed that if this system is embedded into a polyene chain by replacing one of the  $-C=C-$  linkages in the chain with one of the  $C-C$  edges of the  $C_6$  ring in N-salicylidenaniline, then switching between the keto and enol tautomers will change the resistance of the polyene molecular wire. The enol form is shown in Figure 8.

One particularly intriguing idea is to capitalize on the conductivity change that accompanies changes in the relative alignment of phenyl rings along a polyphenyl chain, in a spirit similar to the “conformational switching” concept of

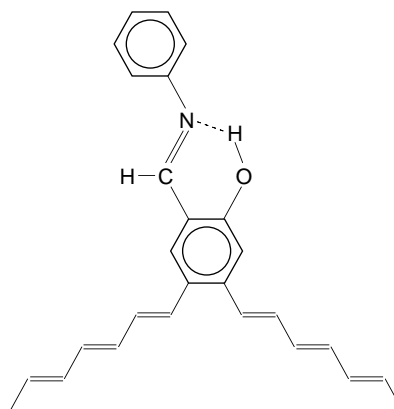


**Figure 8.** N-salicylidenaniline inserted into a polyene chain. The enol tautomer is shown.

Joachim and Launay [63]. Theoretical work has predicted that the conductivity of such a conjugated chain may be varied by  $10^4$  simply by varying the torsional alignment of two adjacent phenyl rings along a polyphenyl chain [41]. More recent studies by Olson et al. [64] have expanded upon this concept, exploring the influence on conduction of molecular vibrations in general along normal mode coordinates. It was reported that for the p-benzene-dithiol molecule, none of the vibrations lead to appreciable changes in current, owing to the rigidity of the molecule. By contrast, DiVentra et al. [46] note that when the molecule is modified with a  $NO_2$  substituent (2-nitro-1,4-benzene-dithiol), twisting of the  $NO_2$  substituent can lead to appreciable changes in the molecular orbital energies and potentially observable changes in the  $I/V$  characteristics. Theoretical studies of atomic-scale aluminum wires have shown that atomic disorder in general alters the electron transport properties, and the effect is stronger for “thin” wires [37, 65]. Clearly there will be some cases where molecular vibrations will have appreciable impact on electron transport. Molecules that exhibit vibronic coupling (coupling of intramolecular vibration to electronic structure) are especially strong candidates. In fact, the Jahn–Teller effect has been implicated as the origin of key features in the tunneling spectroscopy of  $C_{60}$  [66]. If the electron transport properties depend sensitively on a vibrational mode (or modes) with sufficiently low characteristic vibrational frequency, any molecular device incorporating such a component will display temperature-dependent electrical characteristics. Conceivably one might capitalize on such temperature sensitivity to fabricate an extremely sensitive temperature sensor.

When a molecule exhibits changes in its electrical characteristics with vibrational excitation, it results from differences in the electronic structure when vibrationally distorted. Such distorted structures may, in principle, also be sampled mechanically by applying a force to the molecule. This suggests a novel way to control conductivity in a molecular junction, with an applied force. A theoretical formalism to investigate the effect of stretching molecular wires on their electronic properties has been presented by Mikrajuddin et al. [67] and used to demonstrate mechanical/electronic coupling.

A beautiful example of the influence of vibrational motion on electron transport has been demonstrated in  $C_{60}$  transistors [68]. The fabrication of these devices starts with a thin insulating  $SiO_2$  layer on a conducting (doped) Si substrate. A pair of connected nanometer-scale gold electrodes are then fabricated on top of the  $SiO_2$  by electron-beam lithography. A toluene solution of  $C_{60}$  is deposited on the electrodes, and the connection is broken to form a break junction. The conducting Si substrate then serves as the gate and the gold electrodes as the source and drain. The  $I/V$  characteristics between the source and drain are observed to be highly dependent on the gate potential. In addition, the differential conductance of the device exhibits peaks with an energy spacing characteristic of the frequency of the oscillation of the  $C_{60}$  relative to the gold surface, about 1.2 THz. Fabrication of a molecular transistor is, of course, a key step in the advance of molecular electronics. The “transistor effect” in  $C_{60}$  has been the subject to detailed theoretical investigation as well [69, 70].

More recently, a new paradigm for molecular scale electronics capitalizing on changes in the electrostatic potential for information storage and transport has been presented by Tour et al. [54, 71]. The electrostatic potential within a molecule is influenced by the presence of charge. Such changes in the electrostatic potential extend sufficiently far from the molecule that they could, in principle, be used to transfer information to an adjacent molecule. Based on this concept, Tour et al. [54] have proposed architectures for molecular logic gates.

Of the many potential molecular electronics applications, data storage is one of the most advanced, and the first practical implementations of molecular electronics technology quite possibly will evolve in this area. Several actual demonstrations of binary data storage near the single molecule threshold have been reported by a team from the Beijing Laboratory of Vacuum Physics [72–75].

High resistivity polycrystalline thin films of a conjugated organic compound (or binary mixture of compounds) are prepared by vacuum evaporation onto room temperature substrates at a rate  $\leq 5$  nm/min to a thickness of 20 nm on freshly cleaved, highly oriented pyrolytic graphite (HOPG). Local conductance transitions are then induced in the film with a scanning tunneling microscope (STM). A potential pulse (square waveform  $\approx 4$  V  $\times 10$   $\mu$ s) is applied between the STM tip and the conducting graphitic substrate. This pulse induces local changes into the electrical characteristics of the thin film so that an area comparable in size to the crystal unit cell increases conductivity by about  $\times 10^4$ . These tiny regions of high conductivity can be thought of as binary data storage units. Bit densities of  $10^{14}$  cm $^{-2}$  have been reported [72]. The technique has been demonstrated for several materials, including N-(3-nitrobenzylidene)-p-phenylenediamine [73] (NBPDA), 3-phenyl-1-ureidionitrile [72] (PUN), and a 50:50 mixture of 3-nitrobenzal malononitrile (NBMN) and 1,4-phenylenediamine [74, 75] (pDA). (See Fig. 9.) The reverse transition in *individual* marks may be achieved in the latter material by applying a reverse-polarity voltage pulse of  $-4.5$  V for 50  $\mu$ s [76, 77].

Another molecular-scale switching technology has been demonstrated by Collier et al. [78–80]. This technology is based on topologically interesting assemblies of molecules

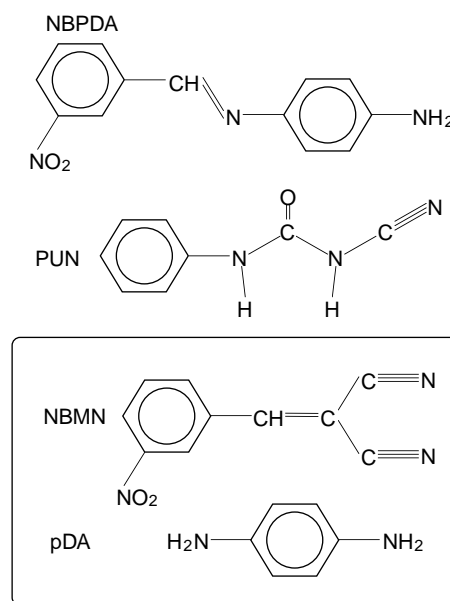


**Figure 9.** Several systems used to form thin polycrystalline films with switchable electrical properties on the nano scale. The boxed pair are used in a 50:50 mixture. N-(3-nitrobenzylidene)-p-phenylenediamine [73] (NBPDA), 3-phenyl-1-ureidionitrile [72] (PUN), 3-nitrobenzal malononitrile (NBMN), and 1,4-phenylenediamine [74, 75] (pDA).

known as catenanes and rotaxanes. These are nanosystems that are composed of two or more molecular components, wherein the components are linked mechanically but not chemically. For example, a  $(CH_2)_n$  ring may be “threaded” with an alkane chain when  $n \geq 18$  [81]. Two such rings, when interlocked, form a catenane. When a single ring is threaded by a linear chain molecule, a rotaxane results. (Note that in a rotaxane, the linear chain component is terminated on each end by a bulky substituent, which prevents the unthreading of the ring. In contrast, a pseudo-rotaxane lacks one or both of these bulky end-groups and thus can be unthreaded.) A catenane, rotaxane, and pseudorotaxane are shown schematically in Figure 10. As shown in Figure 11,

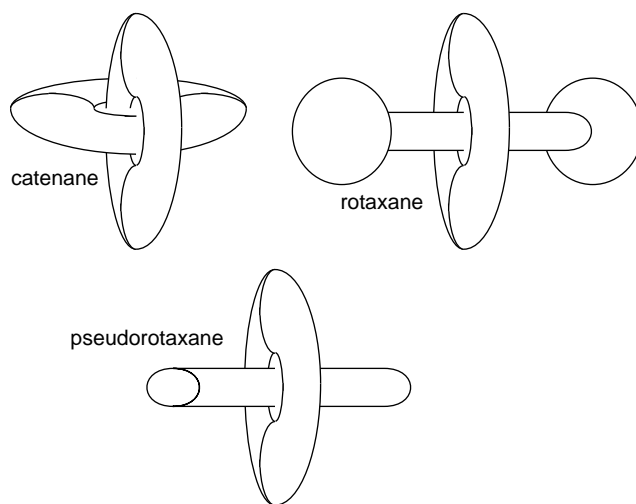


**Figure 10.** Schematic diagrams of a catenane, rotaxane, and pseudo-rotaxane.

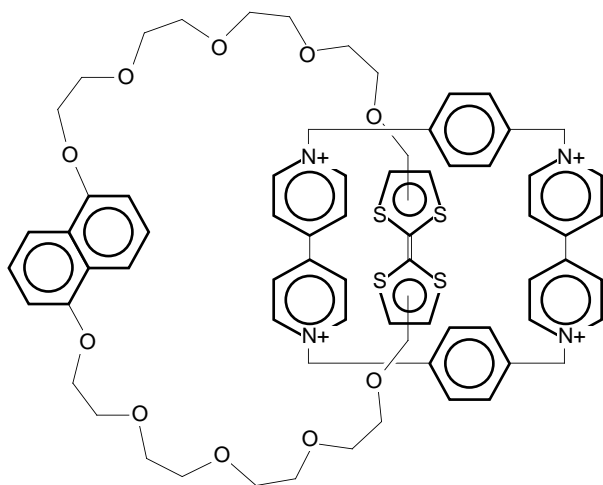


Figure 11. A switchable catenane [80].

Collier et al. [79] have selected a catenane in which one of the rings has charged centers. In this way, the relative orientation of the rings may be influenced by the presence of an applied electric field. The applied bias may then be used to switch the system between two co-conformations. A solid state device is created by sandwiching a monolayer of these catenanes between an *n*-type silicon electrode and a metallic electrode. The device exhibits negligible deterioration after numerous cycles. Collier et al. [78] have employed a similar fabrication to create molecular logic gates. The device is created by sandwiching a monolayer of redox-active rotaxanes between two metal electrodes. By wiring several such devices together, they were able to demonstrate AND and OR logic gates.

A different approach to molecular scale data storage has been presented by Rueckes et al. [82]. The device architecture starts with a conducting substrate topped with a thin layer of SiO<sub>2</sub>. Single-walled carbon nanotubes (SWNT) of diameter *d* are then placed on the surface and aligned in parallel. Separating the nanotubes is an array of insulating organic blocks of thickness *s* arrayed on the surface. This array of blocks is used to support a second set of parallel nanotubes that is perpendicular to the first set. The insulating blocks are sufficiently thick that the upper nanotubes do not contact the lower nanotubes at the crossing points (*s* > *d*), but are still sufficiently close for electrostatic interaction. Each crossing point will therefore have two locally stable minimum energy configurations. In the state described above, elastic forces hold the two nanotubes separated by *s* - *d*. There is also a minimum dictated by van der Waals interactions between the two tubes. By charging two tubes, attractive forces can be generated that will deflect the upper tube down toward the lower tube near the crossing point and bring their separation at the crossing point into this van der Waals minimum. Oppositely charging the tubes can produce repulsive forces to return the junction to the *s* - *d* separation. It has been shown that the resistance between one nanotube and a perpendicular one varies by many orders of magnitude between these two states [82]. Such a device, therefore, represents a rewritable random access memory array on the molecular scale. An array

of  $2N$  nanotubes arranged with  $N$  tubes in the lower layer perpendicular to  $N$  tubes in the upper layer has  $N^2$  addressable junctions. Given the dimensions of carbon nanotubes, data density near  $10^{12}$  bits/cm<sup>2</sup> is possible.

The nanotube-based memory device has two advantages over the thin-film architecture of Ma et al. already described. First, the switching time for the nanotube-based memory is reported to be  $10^{-11}$  s, much faster than  $80 \times 10^{-9}$  s as reported for the thin film case. Secondly, the nanotube-based memory, being based on the intersections of parallel nanotubes, solves the problem of addressing a multitude of spatially separated physical memory locations efficiently. The thin film technology has only been demonstrated with an STM tip for read/write operations and would require some technological innovation to incorporate into a solid-state device with multiple addressable bits.

Carbon nanotubes have also been used to construct logic gates, specifically NOT gates [83]. The construction capitalizes on a fortuitous property of semiconducting SWNTs; they may be made *n*-type (electron carriers) or *p*-type (hole carriers) with proper doping and/or annealing. The logic gates consist of two complementary carbon-nanotube field-effect transistors (CNTFETs). To fabricate the device, gold electrodes are patterned on an oxidized silicon substrate. The unoxidized reverse side of the Si wafer forms the gate. Semiconducting SWNTs are the dispersed onto the surface. One of a pair of SWNTs positioned over Au electrodes is then protected with the common resist material PMMA. Vacuum annealing then converts both SWNT into *n*-CNTFETs. Finally, exposing the system to  $10^{-3}$  Torr of oxygen converts the unprotected *n*-CNTFET to a *p*-type CNTFET, yielding a complementary *n*-type/*p*-type pair. The devices are unstable in air, but air-stable devices can be produced by employing a 10 nm SiO<sub>2</sub> capping layer.

While not strictly single-molecule devices, nanoscale logic storage devices have been fabricated from molecule-gated nanowires [84]. In these devices, nanowires of *p*-type silicon, *n*-type InP, or *n*-type GaN are coated with a layer of cobalt phthalocyanine (CoPc), a redox active species. These nanowires lie on a SiO<sub>2</sub> layer on silicon, the back silicon layer serving as the gate. An applied gate voltage, or source-drain voltage pulse, injects charge into the molecular layer. The nanowire is then switchable between a high and low conductance state, depending on the charge state of the CoPc coating. Assigning each conductance state to a logic "on" or "off" state, yields a logic storage device. Storage times of >20 min have been reported.

## 5. THE MECHANISM OF ELECTRON TRANSPORT

As noted in the preceding section, a considerable array of device architectures has been proposed, and some realized. The mechanism by which electrons are transported in these systems is of great interest, since knowledge of this mechanism would facilitate *a priori* design of molecular electronic devices.

Studies of potential molecular wires have revealed an interesting difference between conventional wires and molecular wires. In a conventional wire, the resistance of the wire to current flow is linearly dependent on its length.

For a given material and cross section, a wire of length  $l$  has twice the resistance (half the conductance) of a wire of length  $\frac{l}{2}$ . Molecular wires, by contrast, exhibit an exponential dependence of current flow on molecular length [27, 56, 57]. If current flow were to take place by a classical transport mechanism, resistance would depend linearly on length, and such current versus length measurements would be expected to show a linear dependence. This is an indication that the actual mechanism of electron transport in molecular wires differs from that in conventional wires, and is probably dominated by tunneling, as supported by the derivation of Eq. (16).

One likely clue to the transport mechanism is the fact that certain molecules, when employed as molecular junctions, exhibit negative differential resistance (NDR) behavior. NDR describes the situation where the current ( $I$ ) passing through a device decreases as the potential difference ( $V$ ) applied across the device is increased. Since  $I/V$  typically has a positive slope, NDR gives rise to peaks in the  $I/V$  curve. The measured  $I/V$  characteristics of these molecular junctions show highly nonlinear characteristics, with current peaking sharply at a critical applied voltage. It has been postulated that as the applied potential ( $V_{ap}$ ) is increased, the junction molecule becomes charged. It is assumed that the uncharged junction molecule is insulating, the singly charged ( $-1$ ) anion is conducting, and the doubly charged ( $-2$ ) anion is again insulating. In the presence of a critical applied potential, the junction molecule would be reduced to its ( $-1$ ) anion and become conducting. Higher applied potentials would further reduce the junction molecule to its ( $-2$ ) anionic state, shutting down the conduction. A simple time-scale analysis, however, suggests that this picture is incomplete. Transit times for transfer of an electron through a molecular junction are estimated at  $10^{-16}$ – $10^{-15}$  s [64, 70]. On the other hand, device currents are typically less than 1 nA. This converts to less than  $10^{10}$  electrons per second, or one electron every  $10^{-10}$  seconds [5]. With five orders of magnitude between the transit time and the time delay between electrons, the electrons are unlikely to interact. In fact, based on theoretical calculations on p-benzene-dithiol as a resonant tunneling transistor, it has been suggested that the electrons do not spend enough time on the junction molecule to charge it [45].

Another proposed mechanism [4] identifies the changes in conductivity that accompany changes in the torsional alignment of adjacent phenyl rings in a conjugated chain as critical to controlling current flow [41]. For example, in 2'-amino-4'-ethynylphenyl-4'-ethynylphenyl-5'-nitro-1-benzenethiolate, (hereafter referred to as AEENB; see Fig. 12) while the system is conjugated, there is little rigidity in the relative alignment of the rings.

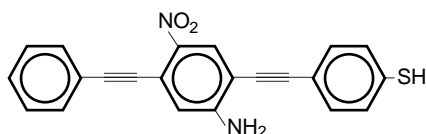


**Figure 12.** 2'-amino-4'-ethynylphenyl-4'-ethynylphenyl-5'-nitro-1-benzenethiolate.

The presence of a large dipole moment due to the amino and nitro substituents affords relatively easy twisting of the central ring through the application of an external electric field [4]. In the natural coplanar arrangement, current flows with relative ease compared to the situation where the rings are in a twisted configuration. This mechanism is consistent with attenuating the conductivity with increasing applied potential. As the applied potential is increased, the torsional misalignment is forced to increase, and conductivity drops. It is more difficult to rationalize, based on this mechanism, why current flow remains negligible up to a critical applied potential, then increases by many orders of magnitude as reported for molecular junctions of AEENB [9].

One intriguing question that remains open is whether charge is carried in molecular junctions by electrons or holes. Both possibilities have been considered by Karzazi et al. [52]. This question is not simply a matter of semantics in the case of conduction in molecular junctions. If the current is carried by electrons, then applied potentials that bring the LUMO of the junction molecule into resonance with the electrode Fermi level may lead to resonance effects, while if the charge is transported by holes, applied potentials that bring the HOMO of the junction molecule into energetic alignment with the electrode Fermi level are key to resonance effects. Since the energy cost to make an ion from a neutral (negative of electron affinity) is generally different than the ionization potential of the molecule, the nature of the charge carrier will play a role in determining the energetics of electron transfer across the junction.

Quantum resonance effects could logically give rise to large increases in conductivity near a critical applied potential as alluded to in [52]. A mechanism based in part on this concept has been given considerable theoretical scrutiny by the present authors [85]. The mechanism is shown schematically in Figure 13.

Consider a molecular junction in the case of no applied potential. Here the two electrodes line up in energy. In the absence of tunneling, for an electron extracted from the left electrode to jump to the molecule forming the junction, it must have sufficient energy to access the ground state of the corresponding molecular anion, at the minimum energy geometry of the neutral molecule. This is the vertical attachment energy  $E_v$  of the junction molecule. Once the anion is formed, it naturally relaxes into its own minimum energy conformation. The difference between this energy and the energy of the relaxed neutral molecule is denoted  $E_a$ , the adiabatic attachment energy of the junction molecule. For the electron to jump from the junction molecule to the right electrode, it must have sufficient energy to reach the ground electronic state of the neutral junction molecule, at the geometry of the relaxed anion. This is denoted  $E_n$ , the vertical detachment energy or vertical reneutralization energy of the anion.

In the case  $\{E_v > E_a \text{ and } E_n > 0\}$ , there is a potential well between the electron-attachment and electron-detachment barriers, which contains resonances. Resonances are solutions of the one-dimensional Schrödinger equation that have a finite lifetime (energy width) owing to the fact that an electron, confined by the two barriers into a resonant state, may escape by tunneling.

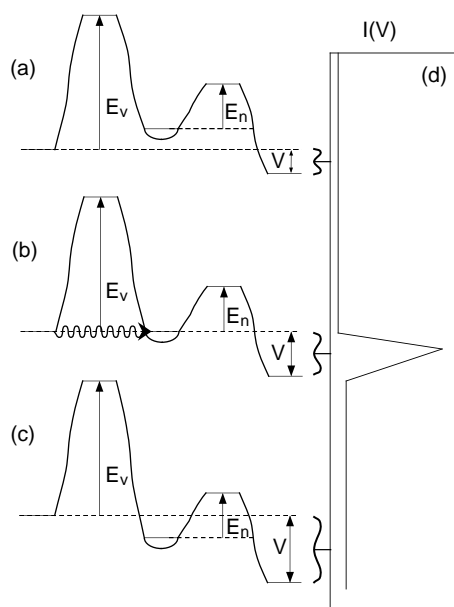


**Figure 13.** Energy variation along the electron transfer coordinate for three representative applied potentials (a)–(c). (d) Schematic  $I/V$  characteristic of a resonant tunneling junction. There will be a dramatic increase in current due to resonant tunneling in the case where the applied potential brings the relaxed anion into resonance with the incident electron energy.

Figure 13 depicts three different cases of an applied potential ( $V$ ). When a potential difference is applied between the two electrodes, the individual electrodes are separated in energy by this difference (shown as  $V$  in Fig. 13). The minimum energy of the potential well between the electron-attachment and electron-detachment barriers will thereby be lowered with respect to the electron-donor (hole acceptor) electrode by some fraction of the applied potential [34]. (Note that since we are considering electron energy, “lowered” here means that the molecule is actually at a higher electrostatic potential.) At some applied potential, a resonant state of the potential well between the barriers will match the incident electron energy. At this point, a large increase in current due to quantum mechanical tunneling through the barrier is expected [86]. This is depicted in Figure 13b. As the applied potential is increased further, the resonant state of the molecular junction will move out of alignment with the incident electron energy and correspondingly, the tunneling current will drop. This is shown in Figure 13c. Clearly, such resonant tunneling will give rise to peaks in the  $I/V$  curve, as shown schematically in Figure 13d. The peak in the  $I/V$  curve will have a finite width due to lifetime broadening.

This mechanism has been tested by computing the values of  $E_v$ ,  $E_a$ , and  $E_n$  for several molecules for which the molecular junctions’ electronic behavior has been reported. In all cases, a highly stable anion, as indicated by a large value of  $E_n$ , correlates with the observation of NDR in the corresponding molecular junction. The origin of this correlation is clear. If the molecular junction molecule exhibits a negative vertical detachment energy, reneutralization is spontaneous and barrier free. In this case, therefore, the junction will not

give rise to a double barrier along the electron transport coordinate, and there is no resonance-enhanced tunneling.

It is interesting to consider the difference between a molecular device and traditional semiconductor band device. To the first approximation, in a molecular device the conducting electron comes from one of the valence atomic orbitals of a gold atom with which the junction molecule is in direct contact. In the case of a thiol-gold contact, for example, the  $S$  atom bonds in an  $fcc$  site [87], giving three adjacent Au atoms. The local density of states for the contact, set by just a few Au atoms, is more molecular in nature than metallic, and therefore sharply peaked. This feature, whereby the density of states is sharply peaked for the species on either side of an interface (electrode and junction molecule here), is key to a molecular device that manifests NDR [88, 89].

Much remains to be developed for this model. First of all, the partitioning of the applied potential drop across the junction molecule and associated contacts is implemented empirically, following Datta et al. [34]. A complete treatment would determine the variations in potential with first-principles theory. Secondly, the model considers a one-dimensional electron transport coordinate. A complete model would incorporate the full three spatial dimensions of the molecular junction. Finally, the model treats only the electronic properties that are *intrinsic* to the junction molecule. Ideally, one would like to include effects due to the molecule/electrode interfaces, which are known to be important [32]. Despite these shortcomings, however, the model gives important insight into the mechanism by which substituents on the junction molecule influence the presence of NDR characteristics in its  $I/V$  performance.

## 6. TECHNOLOGICAL ROADBLOCKS

Just over a decade ago, the principal challenge to molecular electronics appeared to be the problem of manipulation of matter on the nanometer scale. In the ensuing decade, this barrier was breached. This is not to suggest that it is now possible to construct any imaginable molecular device, but several techniques have been demonstrated for measuring and manipulating the electrical properties of individual molecules and molecular-scale domains of bulk material. New techniques and novel modifications of these existing techniques are being reported frequently.

Today, molecular-scale binary data storage appears to be the nearest-term application of molecular electronics technology. Data storage densities well in excess of 10 terabit  $\cdot$   $\text{cm}^{-2}$  have been shown to be possible. Such high data capacities bring a new challenge. How can one read and/or write such enormous amounts of information? Even at the blazing pace of one gigabit per second (1 ns write time), it would take 20 min to write a terabit of information. High-speed massively parallel data I/O technology will be required to take advantage of the data densities possible with molecular electronics technology.

A second major challenge to molecular-scale data storage is data integrity. Molecular-scale data storage techniques have been demonstrated with retention times of a period of days [76, 82]. This duration of data integrity is suitable for random access memory where frequent refreshes may be



employed, but is not suitable for semipermanent storage as with today's hard disk and CD technology.

It seems likely that practical molecular electronic circuits will be realized in the more distant future. The promise of creating circuits by chemical synthesis is great. Even laboratory-scale synthesis produces near-molar quantities ( $\approx 10^{23}$  units) of product. Moreover, all units are identical [4]. This level of reproducibility is unheard of in conventional manufacturing. The technical challenge lies in incorporating each of these units into a practical device. The units must be connected in some predetermined (or at least well known) manner, and the network of interacting units must be connected to a conventional macroscopic system that controls the circuitry and utilizes its interconnectivity. To date, no commercially practical analogue of the three-terminal solid state transistor has been demonstrated at the single-molecule level, although several devices with interesting nonlinear  $I/V$  characteristics have been reported (some of which have been reviewed herein) including some devices with transistor-like functionality.

The development of molecular electronics technology will certainly be guided and accelerated by parallel theoretical work. As reviewed here, the theoretical techniques for describing electron transport in molecular junctions are reasonably mature. Certainly there is great room for further development, but existing techniques are already valuable for yielding physical insight into the nature of electron transport, investigating the influence of different contact geometries on device performance, identifying the effects of changing substituent functional groups on the junction molecule, etc.

Beyond the technical challenges, however, are two other important considerations. First of all, it is possible, likely in fact, that quantum effects will be so important at the molecular level that the laws of conventional electronic circuitry simply will not apply. If Ohm's law, Kirchoff's laws, etc. can not be employed, an entirely new paradigm will be required for molecular electronic circuitry, with new devices, new design equations, etc. Quantum mechanics will serve as the starting point for the development of design equations, of course. Perhaps the computing circuitry will take advantage of the quantum mechanical nature of molecules, but this is in the realm of "quantum computing" and beyond the scope of this chapter. The second consideration is fiscal. Even if molecular scale electronics can be demonstrated, manufacturing costs may dictate the breadth of their applications. When digital computers were first available, they were so costly that they were purchased and used only by governments. Later, the price-to-performance ratio dropped to the point where their acquisition was cost-effective for large corporations, then mid-size institutions, then individuals. Today, digital computers are so inexpensive that they are used even in inexpensive consumer products. It is plausible that computing based on molecular electronics may follow a similar life cycle. A detailed discussion of cost considerations may be found in Ref. [90].

In brief, it is now possible to make a great variety of molecules with interesting electronic properties, and even to measure their electrical characteristics directly, but wiring them together into a circuit, then wiring the circuit to a robust macroscopic system, are outstanding challenges.

Beyond these technical challenges, cost considerations will play a large role in the future of molecular electronics.

## GLOSSARY

**Break junction** A junction formed by breaking a thin conductor, then closing the gap between the two ends until current flows under an applied potential difference.

**Catenane** An assembly of two or more ring molecules that are chemically independent, but mechanically linked, i.e., interlocked rings.

**Chain polymer** Linear molecule with a repeating fundamental unit.

**Conformational switching** A scheme for altering the electrical properties of a molecule by altering its geometric conformation.

**Functional group** A group of atoms that act collectively in forming molecules (Ex:  $-\text{CH}_3$ ,  $-\text{OH}$ ,  $-\text{NO}_2$ ,  $-\text{NH}_2 \dots$ ).

**Molecular junction** A single molecule captured between two metal electrodes.

**Molecular wire** A molecule with physical and electrical properties suitable for charge transport: high aspect ratio and high conductance.

**Moore's Law** A formal statement of the empirical observation that quantitative measures of computer performance (such as processor speed or memory capacity) double every 18–24 months.

**Nanoparticle** A particle of matter with characteristic dimensions in the nanometer range. Nanoparticles are characterized by a high fraction of atoms on the surface, and by electronic properties that are dependent on the size of the particle.

**Nanopore** A cavity in a solid material with characteristic dimensions in the nanometer range.

**Nanotube** Cylindrical arrangement of atoms with a diameter in the nanometer range. Most nanotubes are pure carbon and may be described as sheets of graphite rolled up and joined along opposite edges.

**Negative differential resistance (NDR)** Voltage increase is accompanied by a decrease in current,  $dI/dV < 0$ .

**Pseudorotaxane** A rotaxane that lacks one or both bulky terminal groups and therefore may spontaneously unthread.

**Quantum of conductance** The fundamental unit of conductance,  $G_0 = e^2/(\pi\hbar)$ .

**Rotaxane** An assembly of two or more chemically independent molecules in which a long chain molecule is encircled by one or more rings. The chain component is terminated on both ends with bulky functional groups to prevent unthreading of the ring(s).

**Self-assembled monolayer (SAM)** A single molecular layer that spontaneously forms on a surface, typically in a regular arrangement of molecules.

**Thin film** A thin (typically 1–100 nm) layer of material.

**Thiol** A molecule containing the  $-\text{SH}$  group.

## ACKNOWLEDGMENTS

K. S. acknowledges support from the National Science Foundation Nanoscale Exploratory Research program, Drexel University in the form of generous startup support, and Dupont Corp. for a Dupont Young Professor Award. Computations were partially supported by the National Center for Supercomputing Applications (NCSA) under grant CHE010012N to N.M. and utilized the SGI Origin2000 at NCSA, University of Illinois at Urbana-Champaign.

## REFERENCES

- As this chapter goes to press, a special issue of *Chemical Physics* is appearing with articles from numerous experts on the subject of molecular electronics: *Chem. Phys.*, 281(2,3), 1 August 2002.
- G. J. Milburn, *Computing in Science and Engineering* 6, 87, (2001); N. Gershenfeld and I. L. Chuang, *Sci. Am.* June 1998; R. P. Feynman, *Optics News*, 11, 11 (1985).
- MRS Bulletin*, Theme: Organic and Polymeric Electronic Materials and Devices, Guest Editors: A. J. Epstein and Y. Yang, 22, June (1997); *MRS Bulletin*, Theme: Electroactive Organic Materials, Guest Editors: Z. Bao, V. Bulovic, and A. B. Holmes, 27, June (2002).
- M. A. Reed and J. M. Tour, *Sci. Am.* June (2000), p. 87.
- C. Joachim, *New J. Chem.* 15, 223 (1991).
- M. A. Reed, C. Zhou, C. J. Muller, T. P. Burgin, and J. M. Tour, *Science* 278, 252 (1997).
- W. A. Reinert, L. Jones, T. P. Burgin, C-W. Zhou, C. J. Muller, M. R. Deshpande, M. A. Reed, and J. M. Tour, *Nanotechnology* 9, 246 (1998).
- C. Kergueris, J.-P. Bourgoin, S. Palacin, D. Esteve, C. Urbina, M. Magoga, and C. Joachim, *Phys. Rev. B* 59, 12505 (1999).
- J. Chen, M. A. Reed, A. M. Rawlett, and J. M. Tour, *Science* 286, 1550 (1999).
- M. A. Reed, J. Chen, A. M. Rawlett, D. W. Price, and J. M. Tour, *App. Phys. Lett.* 78, 3735 (2001).
- R. Rinaldi, G. Maruccio, A. Biasco, V. Arima, R. Cingolani, T. Giorgi, S. Masiero, G. P. Spada, and G. Gottarelli, *Nanotechnology* 13, 398 (2002).
- R. S. Becker, J. A. Golovchenko, and B. S. Swartzentruber, *Phys. Rev. Lett.* 55, 2032 (1985).
- J. G. Kushmerick, K. F. Kelly, H.-P. Rust, N. J. Halas, and P. S. Weiss, *J. Phys. Chem. B* 103, 1619 (1999).
- P. G. Collins, H. Bando, and A. Zettl, *Nanotechnology* 9, 153 (1998).
- U. Dürig, O. Züger, B. Michel, L. Häussling, and H. Ringsdorf, *Phys. Rev. B* 48, 1711 (1993).
- C. Joachim, J. K. Gimzewski, R. R. Schlittler, and C. Chavy, *Phys. Rev. Lett.* 74, 2102 (1995).
- M. Dorogi, J. Gomez, R. Osifchin, R. P. Andres, and R. Reifenberger, *Phys. Rev. B* 52, 9071 (1995).
- D. I. Gittins, D. Bethell, D. J. Schiffrin, and R. J. Nichols, *Nature* 408, 67 (2000).
- G. Leatherman, E. N. Durantini, D. Gust, T. A. Moore, A. L. Moore, S. Stone, Z. Zhou, P. Rez, Y. Z. Liu, and S. M. Lindsay, *J. Phys. Chem. B* 103, 4006 (1999).
- X. D. Cui, A. Primak, X. Zarate, J. Tomfohr, O. F. Sankey, A. L. Moore, T. A. Moore, D. Gust, G. Harris, and S. M. Lindsay, *Science* 294, 571 (2001).
- S. Frank, P. Poncharal, Z. L. Wang, and W. A. de Heer, *Science* 280, 1744 (1998).
- G. Doyen, E. Koetter, J. P. Vigneron, and M. Scheffler, *Appl. Phys. A* 51, 281 (1990).
- E. Merzbacher, "Quantum Mechanics," Wiley, New York, 1970.
- P. F. Bagwell and T. P. Orlando, *Phys. Rev. B* 40, 1456 (1989).
- E. N. Economou and C. M. Soukoulis, *Phys. Rev. Lett.* 46, 618 (1981).
- D. S. Fisher and P. A. Lee, *Phys. Rev. B* 23, 6851 (1981).
- C. González and R. G. E. Morales, *Chem. Phys.* 250, 279 (1999).
- M. Magoga and C. Joachim, *Phys. Rev. B* 56, 4722 (1997).
- M. S. Child, "Molecular Collisions Theory," Dover, New York, 1996.
- V. Mujica, M. Kemp, and M. A. Ratner, *J. Chem. Phys.* 101, 6849 (1994).
- J. J. Palacios, A. J. Pérez-Jiménez, E. Louis, and J. A. Vergés, *Phys. Rev. B* 64, (2001), #115411.
- M. DiVentra, S. T. Pantelides, and N. D. Lang, *Phys. Rev. Lett.* 84, 979 (2000).
- Y. Xue, S. Datta, and M. A. Ratner, *J. Chem. Phys.* 115, 4292 (2001).
- S. Datta, W. Tian, S. Hong, R. Reifenberger, J. I. Henderson, and C. P. Kubiak, *Phys. Rev. Lett.* 79, 2530 (1997).
- W. Tian, S. Datta, S. Hong, R. Reifenberger, J. I. Henderson, and C. P. Kubiak, *J. Chem. Phys.* 109, 2874 (1998).
- J. Taylor, H. Gou, and J. Wang, *Phys. Rev. B* 63, (2001), #121104(R).
- G. Taraschi, J.-L. Mozos, C. C. Wan, H. Guo, and J. Wang, *Phys. Rev. B* 58, 13138 (1998).
- J. J. Palacios, E. Louis, A. J. Pérez-Jiménez, E. San Fabián, and J. A. Vergés, *Nanotechnology* 13, 378 (2002).
- P. Sautet and C. Joachim, *Phys. Rev. B* 38, 12238 (1988).
- W.-D. Sheng and J.-B. Xia, *Phys. Lett.* 220, 268 (1996).
- M. P. Samanta, W. Tian, S. Datta, J. I. Henderson, and C. P. Kubiak, *Phys. Rev. B* 53, R7626 (1996).
- S. N. Yaliraki, M. Kemp, and M. A. Ratner, *J. Am. Chem. Soc.* 121, 3428 (1999).
- A. Tikhonov, R. D. Coalson, and Y. Dahnovsky, *J. Chem. Phys.* 116, 10909 (2002).
- N. D. Lang, *Phys. Rev. B* 52, 5335 (1995).
- M. DiVentra, S. T. Pantelides, and N. D. Lang, *Appl. Phys. Lett.* 76, 3448 (2000).
- M. DiVentra, S.-G. Kim, S. T. Pantelides, and N. D. Lang, *Phys. Rev. Lett.* 86, 288 (2001).
- E. G. Emberly and G. Kirczenow, *Phys. Rev. B* 58, 10911 (1998).
- E. G. Emberly and G. Kirczenow, *Nanotechnology* 10, 285 (1999).
- J. M. Seminario, A. G. Zacarias, and J. M. Tour, *J. Am. Chem. Soc.* 122, 3013 (2000).
- J. M. Seminario, A. G. Zacarias, and P. A. Derosa, *J. Phys. Chem. A* 105, 791 (2001).
- P. A. Derosa and J. M. Seminario, *J. Phys. Chem. B* 105, 471 (2001).
- Y. Karzazi, J. Cornil, and J. L. Bredas, *J. Am. Chem. Soc.* 123, 10076 (2001).
- Y. Karzazi, J. Cornil, and J. L. Bredas, *Nanotechnology* 13, 336 (2002).
- J. M. Tour, M. Kozaki, and J. M. Seminario, *J. Am. Chem. Soc.* 120, 8486 (1998).
- J. M. Tour, *Chem. Rev.* 96, 537 (1996).
- C. Joachim and J. F. Vinuesa, *Europhys. Lett.* 33, 635 (1996).
- W. B. Davis, W. A. Svec, M. A. Ratner, and M. R. Wasielewski, *Nature* 396, 60 (1998).
- H. D. Skies, J. F. Smalley, S. P. Dudek, A. R. Cook, M. D. Newton, C. E. D. Chidsey, and S. W. Feldberg, *Science* 291, 1519 (2002).
- A. Aviram, P. E. Seiden, and M. A. Ratner, Ch. I in "Molecular Electronic Devices," F. L. Carter, Ed., Marcel Dekker, New York, 1982.
- F. L. Carter, Ed., "Molecular Electronic Devices," Marcel Dekker, New York, 1982.
- R. C. Haddon and F. E. Stillinger, Ch. II in "Molecular Electronic Devices," F. L. Carter, Ed., Marcel Dekker, New York, 1982.
- P. Sautet and C. Joachim, *Chem. Phys.* 135, 99 (1989).
- C. Joachim and J. P. Launay, *J. Molec. Electron.* 6, 37 (1990).

64. M. Olson, Y. Mao, T. Windus, M. Kemp, M. Ratner, N. Léon, and V. Mujica, *J. Phys. Chem. B* 102, 941 (1998).
65. C. C. Wan, J.-L. Mozos, G. Taraschi, J. Wang, and H. Guo, *Appl. Phys. Lett.* 71, 419 (1997).
66. D. Porath, Y. Levi, M. Tarabiah, and O. Millo, *Phys. Rev. B* 56, 9829 (1997).
67. Mikrajuddin, K. Okuyama, and F. G. Shi, *Phys. Rev. B* 61, 8224 (2000).
68. H. Park, J. Park, A. K. L. Lim, E. H. Anderson, A. P. Alivisatos, and P. L. McEuen, *Nature* 407, 57 (2000).
69. C. Joachim and J. K. Gimzewski, *Chem. Phys. Lett.* 265, 353 (1997).
70. C. Joachim, J. K. Gimzewski, and H. Tang, *Phys. Rev. B* 58, 16407 (1998).
71. J. M. Tour, *Acc. Chem. Res.* 33, 791 (2000).
72. L. P. Ma, W. J. Yang, S. S. Xie, and S. J. Pang, *Appl. Phys. Lett.* 73, 3303 (1998).
73. L. P. Ma, W. J. Yang, Z. Q. Xue, and S. J. Pang, *Appl. Phys. Lett.* 73, 850 (1998).
74. L. P. Ma, Y. L. Song, H. J. Gao, W. B. Zhao, H. Y. Chen, Z. Q. Xue, and S. J. Pang, *Appl. Phys. Lett.* 69, 3752 (1996).
75. H. J. Gao, L. P. Ma, H. X. Zhang, H. Y. Chen, Z. Q. Xue, and S. J. Pang, *J. Vac. Sci. Technol. B* 15, 1581 (1997).
76. H. J. Gao, K. Sohlberg, Z. Q. Xue, H. Y. Chen, S. M. Hou, L. P. Ma, X. W. Fang, S. J. Pang, and S. J. Pennycook, *Phys. Rev. Lett.* 84, 1780 (2000).
77. D. X. Shi, Y. L. Song, H. X. Zhang, P. Jiang, S. T. He, S. S. Xie, S. J. Pang, and H.-J. Gao, *Appl. Phys. Lett.* 77, 3203 (2000).
78. C. P. Collier, E. W. Wong, M. Belohradskjr, F. M. Raymo, J. F. Stoddart, P. Keukes, R. S. Williams, and J. R. Heath, *Science* 285, 5426 (1999).
79. C. P. Collier, G. Mattersteig, E. W. Wong, Y. Lou, K. Beverly, J. Sampaio, F. M. Raymo, J. F. Stoddart, and J. R. Heath, *Science* 289, 1171 (2000).
80. C. P. Collier, J. O. Jeppesen, Y. Luo, J. Perkins, E. W. Wang, J. R. Heath, and J. F. Stoddart, *J. Am. Chem. Soc.* 123, 12632 (2001).
81. T. W. Graham Solomons, "Organic Chemistry," Wiley, New York, 1980.
82. T. Rueckes, K. Kim, E. Joselevich, G. Y. Tseng, C.-L. Cheung, and C. M. Lieber, *Science* 289, 94 (2000).
83. V. Derycke, R. Martel, J. Appenzeller, and Ph. Avouris, *Nano Lett.* 1, 453 (2001).
84. X. Duan, Y. Huang, and C. M. Lieber, *Nano Lett.* 2, 487 (2002).
85. N. Matsunaga and K. Sohlberg, *J. Nanosci. Nanotechnol.* 1, 275 (2001).
86. D. Bohm, "Quantum Theory," Prentice Hall, Englewood Cliffs, NJ, 1951.
87. Y. Yourdshahyan, H. K. Zhang, and A. M. Rappe, *Phys. Rev. B* 63, (2001), (article number 081405R).
88. Y. Xue, S. Datta, S. Hong, R. Reifenberger, J. I. Henderson, and C. P. Kubiak, *Phys. Rev. B* 59, R7852 (1999).
89. N. D. Lang, *Phys. Rev. B* 55, 9364 (1997).
90. C. Joachim, *Nanotechnology* 13, R1 (2002).
91. K. R. Laker, [http://www.seas.upenn.edu:8080/~ee560/EE560\\_MOS\\_Theory\\_P201.pdf](http://www.seas.upenn.edu:8080/~ee560/EE560_MOS_Theory_P201.pdf)

# Nanoembossing Techniques

Yong Chen

*CNRS, Marcoussis, France and Ecole Normale Supérieure, Paris, France*

## CONTENTS

1. Introduction
  2. Mold Fabrication
  3. Nanoembossing at Elevated Temperatures
  4. Nanoimprint Lithography
  5. Nanoembossing of Photocurable Polymers
  6. Applications
  7. Conclusion
- Glossary  
References

## 1. INTRODUCTION

The ability to fabricate well defined large area nanostructures has important implications for both fundamental research and industrial applications [1–3]. In fact, the state of the art microelectronic circuits are made of semiconductor features of a critical dimension close to 100 nm which can only be produced cost-effectively by using high performance optical lithography tools. To extend the current CMOS (complementary metal oxide semiconductor field effect transistor) technology with a critical dimension down to 20 nm, new manufacturing tools will be required because of the diffraction limit of the conventional optical methods. For this reason, the semiconductor industry has developed the so-called next generation lithography by considering new irradiation sources such as extreme ultraviolet (UV) light, X-rays, as well as projection electron or ion beams.

Not only the microelectronic industry but also many research and other industry branches need more and more nanofabrication tools. For example, patterned nanostructures such as photonic crystals are becoming attractive for the development of new optical and optoelectronic devices [4]. Patterned magnetic nanostructures are now studied for ultrahigh density storage and for the fabrication of the emerging spin–electronic devices [5]. In the domain of biology and biomedical research, microarray chips and microfluidic devices are in rapid progress toward a high degree of functionality and integration [6]. In all these areas,

flexible and low-cost manufacturing techniques are required for research, prototyping, and low volume production.

A broad range of conventional and nonconventional nanofabrication methods is under investigation [7]. The challenge is to develop straightforward fabrication tools and processes that allow one to produce patterns with a minimum feature size down to a few nanometers and to integrate various functionalities over large areas. Here, the requirement of the nanometer scale is important for both current research and future development. For example, the fabrication of molecular electronic circuits will be based on molecular self-assembly with high density nanoelectrodes [8].

Nanoembossing is one of the most studied nanofabrication methods during the last few years [9–16]. Unlike conventional lithography methods which use photons or charged particles to expose a resist layer in a way similar to photography [17, 18], nanoembossing relies on pattern replication by physical deformation of a thin polymer layer with a rigid mold. Although the classic embossing techniques have been widely used for many years, only quite recently attention has been paid to the replication ability of ultrasmall features. Compared to the sophisticated optical lithography methods, nanoembossing is more flexible and much less expensive. Compared to electron beam (e-beam) lithography and scanning probe lithography, nanoembossing is well suited for large scale and high throughput production. Due to these advantages, nanoembossing techniques are now considered a new strategy for future nanotechnology development [16].

Nanoembossing technologies include mold fabrication, polymer design, pattern replication, and subsequential pattern transfer. Molds are generally obtained by e-beam lithography which defines pattern in a thin layer of resist and reactive ion etching (RIE) or electroplating for the pattern transfer. Either thermoplastic or thermosetting polymers can be embossed at elevated temperatures but embossing can also be performed at room temperature with photocurable polymers and UV irradiation. In general, the embossed nanostructures can be used directly in plastic device making or as masks for a subsequent pattern transfer. This latter technique, namely nanoimprint lithography, consists of embossing first a thin layer of polymer spin coated on a substrate and then removing the recessed area by reactive

ion etching (Fig. 1). Thus, the resulting resist profiles are comparable to those obtained by optical or e-beam lithography so that a large number of applications can be developed. In this chapter, several nanoembossing techniques are described, including discussions of their fabrication performances and application examples.

## 2. MOLD FABRICATION

All embossing techniques rely on the fabrication of molds which defines the original patterns to be replicated. For nanoscale features, molds are produced by advanced nanofabrication methods. A silicon wafer, with or without a covering of a thin film of dielectric or metal material such as silicon dioxide ( $\text{SiO}_2$ ), silicon nitride ( $\text{Si}_3\text{N}_4$ ), or tungsten (W), can be used as substrate. E-beam lithography is commonly used to expose a resist layer on the substrate [18]. Then, reactive ion etching or electroplating is used for the pattern transfer. Finally, an antisticking film is coated on the mold surface to promote the mold-sample separation.

Commercial e-beam systems working at 50 keV electron energy provide a routine resolution of 50 nm or smaller [19]. Features of higher resolution can be obtained by using the state of the art e-beam systems at high beam energy (100–200 keV) [20, 21]. Under optimal conditions, 10-nm [22] and sub-10-nm features [23–25] can be obtained but particular attention has to be paid to the resist development and the pattern transfer processes. Poly(methylmethacrylate) (PMMA) is commonly used as e-beams resist but the recent development showed that other polymers such as hydrogen silsesquioxane (HSQ) are also suitable for very high resolution patterning [20, 26, 27].

The resist pattern defined by e-beam lithography can then be transferred by reactive ion etching into the underlayer material or by electroplating [28, 29]. If reactive ion etching is used, an etching mask, commonly obtained by a thin metal film deposition and lift-off, is required for high resolution pattern transfer [18]. The quality of the lift-off is mainly affected by the resist profile and the thickness of the deposited metal film is typically three times less than the resist thickness. The reactive ion etching is based on simultaneous exposure of the sample to chemical reaction species and fluxes of energetic particles. The etched materials are then pumped away as volatile gaseous species. For polymers, silicon, silicon-based dielectric materials, and some

metals,  $\text{SF}_6$ ,  $\text{CHF}_3$ , and  $\text{O}_2$  gas mixtures are commonly used to obtain vertically etched sidewalls with an accurate control of the etch depth. If electroplating is used, as a thin layer of metal is first evaporated on the embossed surface, followed by electroplating until a desired thickness is obtained. Then, the electroplated sheet is separated from the resist sample and can then be used as metal mold for embossing. Patterning can also be done with a focused ion beam directly but this method is time consuming and suited only for particular applications.

As mentioned, high resolution patterns can be obtained by high energy e-beam lithography. It is, however, difficult to obtain high density features over large areas. A spatial frequency doubling technique has been tested for the fabrication of gratings of 100-nm period [30]. This technique consists of exposing a grating of 200-nm period by interferometric lithography and then processing a sequence of standard microfabrication steps to double the grating's spatial frequency. Other techniques such as edge defining [31] and photoelectrochemical etching [32] can be used to obtain some specific sub-10-nm features.

To emboss photocurable polymers, transparent molds are generally required which can be obtained by patterning a quartz plate either with or without an indium tin oxide (ITO) thin film coating. More sophisticated mold configurations such as a  $\text{SiO}_2$ /ITO double layer on a substrate have also been tested, showing several advantages in terms of e-beam writing performance (no charging), electron microscope inspection, and pattern transfer because of the high selectivity of dioxide to ITO during a dry etching process [33].

Silicon molds of large etch depth can be obtained by deep RIE [34]. Conventional RIE with SU-8 resist as etch mask has also been used to achieve an etch depth of more than 10  $\mu\text{m}$  and silicon molds containing both shallow and deep features could be obtained using mix and match techniques [12]. Finally, three-dimensional (3D) structures can be obtained by anisotropic wet etching of a silicon substrate [35] or two-step RIE [36, 37]. More complex 3D structures can be obtained by e-beam lithography with a modulated dosage distribution [38]. For example, Ni molds with curved cross-sectional structures could be obtained and tested for the fabrication of diffractive optical elements [39].

Once a master mold has been made, it can be reproduced by nanoimprint lithography, followed by either RIE or electroplating for the hard material pattern transfer. With a well controlled fabrication process, the quality of the copied molds can be comparable to the original ones. Finally, full plastic molds can be obtained by casting-and-molding a thermosetting polymer, which can then be used as conventional molds [40].

In general, a surface treatment of the mold is necessary to avoid the sticking problem. It is known that the sticking or adhesion strength between a mold and a polymer coated sample depends on the physical and chemical properties of the surfaces of the two materials in contact. Physical adhesion is related to the van der Waals force and hydrogen bonds, while chemical adhesion is due to ionic, atomic, or metal bonds between surfaces. The larger the contact area, the stronger the adhesion. An antistick layer deposited on

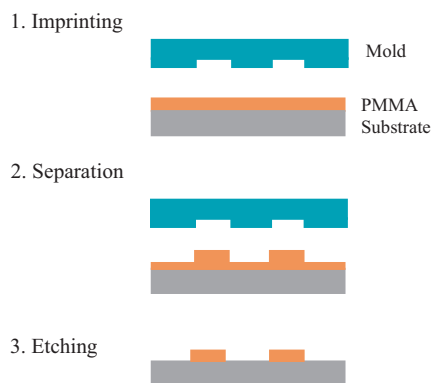


**Figure 1.** Schematic representation of nanoimprint lithography.

the mold is generally necessary to promote the mold separation. A number of layers have been tested including a deposition of metal thin films [41], Teflon-like molecules [42], or fluorinated silanes [43]. Commercial release agents such as manufactured by Dow Corning (DC20) can also be used and a detailed analysis of the antisticking methods can be found in [14]. In practice, the choice of the antisticking treatment depends on the type of the mold and the polymer in use as well as the embossing conditions. For nanoembossing of photocurable polymers for example, specific polymer mixtures and fabrication sequences are required because of the chemical reaction involved during photopolymerization [14].

### 3. NANOEMBOSSING AT ELEVATED TEMPERATURES

Both thermoplastic and thermosetting polymers can be embossed at elevated temperatures. Commercial embossing systems [44, 45] as well as a cheap hydraulic press equipped with a pair of hot plates [46] have been used for nanoembossing with a wide range of working temperatures and pressures. In this section, we focus on “hot embossing” of high resolution polymer features. In the next two sections, we will discuss nanoimprint lithography and nanoembossing of photocurable polymers.

#### 3.1. Nanoembossing of Thermoplastic Polymers

Thermoplastic polymers such as PMMA, polycarbonate (PC), polyvinylchloride, and poly(ethylene terephthalate glycol) can be used for the fabrication of miniaturized plastic pieces [29]. They soften and eventually liquefy when heated and harden when cooled. Nanoembossing of thermoplastic polymers can be performed in different ways: (a) imprinting a commercial plastic plate, (b) imprinting a thin polymer film spin coated on a substrate, and (c) compressing polymer pellets. The first technique is the simplest one. A rigid mold is pressed into a heat-softened polymer plate at temperatures slightly above  $T_g$  under moderate pressure or below  $T_g$  under elevated pressure [47, 48]. The second technique, imprinting a thin polymer film spin coated on a substrate, will be discussed in detail in the next section. The third technique is based on thermal compression of cheap polymer pellets, which takes advantage of both injection molding and imprinting techniques [12, 49] (Fig. 2). Here, polymer pellets are placed on a silicon mold and covered by a flat silicon wafer. They are then inserted between two hot plates of a hydraulic press and the temperature is raised to a value well above the polymer’s  $T_g$ . At the embossing temperature, a pressure is applied and maintained during cooling down. Below  $T_g$ , the pressure is released and the patterned plastic sheet is removed from the mold.

Let us first consider some general properties of thermoplastic polymers. Thermoplastic polymers are formed from monomers via chemical bonding. When an amorphous thermoplastic polymer is heated above its glass transition temperature,  $T_g$ , it behaves like a viscous liquid.  $T_g$  depends on the molecule weight of the polymer [50],

$$T_g(M_w) = T_g(\infty) - \frac{A}{M_w} \quad (1)$$

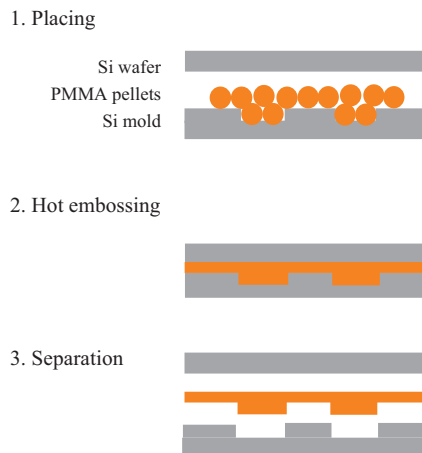


**Figure 2.** Schematic representation of the fabrication method involving hot embossing of thermoplastic polymer pellets.

where  $A$  is a constant and  $T_g(\infty)$  is the value of large molecular weight. For example,  $T_g$  is 113 °C for 50 kg/mol PMMA and 120 °C for 950 kg/mol PMMA.

The deformation rate of a perfect viscous liquid is proportional to the shear stress,

$$\frac{\partial \epsilon}{\partial t} = \frac{1}{\eta} \sigma \quad (2)$$

where  $\eta$  is the viscosity parameter of the liquid which also depends on the molecule weight of the polymer. For small shear,

$$\eta \propto M \quad (M < M_c) \quad (3a)$$

$$\eta \propto M^{3.4} \quad (M > M_c) \quad (3b)$$

where  $M_c$  is the critical value of the molecular weight for the given polymer type. For PMMA,  $M_c = 30$  kg/mol [50].

The viscosity parameter of a polymers decreases rapidly with temperature. For the temperature range well above  $T_g$ , the Arrhénius law can be applied,

$$\eta = \eta_0 \exp\left(\frac{\Delta E}{RT}\right) \quad (4)$$

where  $R$  is the universal gas constant (8.3 J/mol K) and  $\Delta E$  is the activation energy of the viscous flow which is of the order of  $10^4$  J/mol and depends on the specificity of the polymer. Typically, nanoembossing can be done at a temperature of about  $T_g + 60$  °C and the applied pressure must be maintained during cooling so that the embossed articles will retain their sharp sidewall.

We have embossed PMMA pellets (Oroglas V825T,  $T_g = 108$  °C from Atofina) at 180 °C with a pressure of 100 bar for a few minutes. For thick PMMA plates, a metallic frame for lateral confinement is added. Typically, 4 to 5 pellets of roughly  $3 \times 3 \times 3$  mm<sup>3</sup> are needed to produce a  $3 \times 4$  cm<sup>2</sup> PMMA sheet of thickness of several hundred micrometers, while roughly 40 pellets are needed for millimeter-thick plates [12]. The fabricated structures showed well-defined shapes and excellent surface quality, exhibiting a roughness less than 5 nm, as on the mold. Figure 3a displays a scanning



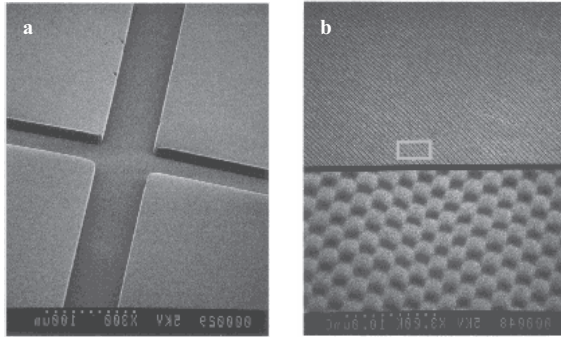


**Figure 3.** Scanning electron micrograph of micro- and nanostructures simultaneously embossed on a PMMA plate: (a) the intersection of two 11- $\mu\text{m}$ -deep and 50- $\mu\text{m}$ -wide microchannels with an excellent surface roughness and (b) a portion of a 300-nm-period triangular array of 150-nm-diameter nanopillars of 200-nm thickness. Reprinted with permission from [12], V. Studer et al., *Appl. Phys. Lett.* 80, 3641 (2002), © 2002, American Institute of Physics.

electron microscopy (SEM) image of the intersection of two 10- $\mu\text{m}$ -deep and 50- $\mu\text{m}$ -wide microfluidic channels. These channels reproduce the high surface quality and vertical sidewalls of the Si master. Figure 3b shows a SEM image of a 300-nm-period triangular array of 150-nm-diameter nanopillars of 200-nm height, created inside a channel of 200-nm depth and 50- $\mu\text{m}$  width, extended over a total length of 7 mm. This structure was initially designed as an artificial gel for DNA molecule separation [51]. The embossed features show extremely good uniformity and can be covered by another PMMA sheet via thermal bonding. Our experiences showed that complex features can be obtained without carefully adjusting process parameters, indicating the simplicity of the process and the ability to produce high resolution plastic devices. Thermoplastic polymers other than PMMA such as cyclo-olefin copolymers have also been used, showing also the ability to replicate nanostructures.

Compared to injection molding which is the common manufacturing technique of plastic articles [52], nanoembossing is more suitable for prototyping and the replication of high aspect ratio features. In practice, all injection machines are designed for high volume production and the fabrication of injection molds requires high accuracy machining and careful mold adaptation. Besides, the large sizes of the injection molding machines are not compatible to the laboratory scale experimentation. Nevertheless, the production rate of injection molding is substantially high which should also enable one to produce nanometer features [53, 54].

### 3.2. Nanoembossing of Thermosetting Polymers

Thermosetting polymers become permanently hard once cured by a chemical reaction at elevated temperatures. Embossing of a thermosetting polymer consists of first filling a mold cavity with a liquid prepolymer (linear polymer with a low molecular weight) and then converting it into hard product with the desired shape. During curing, chemical and structural changes occur by cross-linking which makes the final product dimensionally stable. Compared to

thermoplastic polymers, thermosetting polymers are generally inert and difficult to remove chemically [55]. A number of thermosetting polymers, including epoxies, phenolics, and polyester, can be useful for the embossing experiments [55, 56].

In particular, poly(dimethylsiloxane) (PDMS), which consists of repeated units of  $-\text{OSi}(\text{CH}_3)_2\text{O}-$ , is now widely used for the fabrication of microfluidic devices and stamps for microcontact printing [57–64]. PDMS is attractive because it is mechanically deformable (elastomer), nontoxic, chemically inert, and optically transparent. High resolution PDMS structures can be obtained by casting a liquid prepolymer mixed with a cross-linking catalyzer. After curing at 80 °C for one hour, the solidified PDMS is separated from the mold which can then be used for various applications.

To obtain PDMS thin films, the mold is coated with PDMS prepolymer solution and then covered with a plastic film. After curing under a desired pressure and cooling down, the plastic film is removed. By placing a thicker PDMS carrier on the top of the embossed thin film and thermal bonding, a bilayer PDMS structure is obtained. Repeating this process several times, a multilayer PDMS device can be made [60, 61]. The bilayer PDMS structure can be used for example as a stamp for high resolution microcontact printing [58, 62]. Here, the stamp is first inked with thiol molecules [hexadecanethiol ( $\text{C}_{16}\text{H}_{33}\text{SH}$ ) in ethanol] and then placed on a gold coated substrate for a few seconds. This results in a self-assembled monolayer of the thiol molecules in certain portions which can then be used as a mask for chemical etching. In order to make the microcontact printing fully compatible to other pattern transfer techniques, a resist film can be introduced before depositing the gold layer. After chemical etching of the gold, the pattern can then be transferred into the resist [63, 64]. The advantage of using a bilayer PDMS stamp relies on its enhanced bulk stiffness so that a large area stamp cavity is allowed.

By spin coating PDMS prepolymer liquid on both mold and substrate surfaces and then bonding them together thermally, high quality features can be obtained after removal of the mold [65]. For very thin PDMS structures, the embossed features can be used for pattern transfer via RIE or lift-off [66].

### 3.3. Nanoembossing of Other Types of Materials

Nanoembossing can also be applied to other types of materials. One of the examples is direct embossing of silicon nanostructures with a high power laser irradiation [13]. In the first experience, an excimer laser of 308 nm wavelength and 20 ns pulse duration is used which passes through a quartz mold and melts the silicon surface to a depth of a few hundreds of nanometers. Under pressure, the melt silicon is deformed and then solidified rapidly, resulting in a perfect replication of the mold surface structures. The total processing time including heating, embossing, and cooling is short (250 ns). To illustrate the high resolution ability, replication of a grating of 300-nm period and 110-nm depth has been demonstrated. Under a scanning electron microscope, one can observe a reproduction of 10-nm edge features. The same process has been used to emboss large mesa areas as

well as a polysilicon layer deposited on a silicon wafer separated by a 200-nm silicon dioxide. These results have largely enhanced the interest of nanoembossing techniques because of the direct embossing strategy and fast processing. This technique could be extendable to other materials and fabrication processes [67].

More generally, materials including functional polymers [68–70], photoresists [71], block copolymers [72], liquids [73], metals [74], as well as sol–gels [75] and piezoelectric materials [76] can be directly embossed. In the case of photoresist embossing, for example, a small amount of solvent (<1 mL) is applied to a PDMS mold and then the mold is placed on a layer of photoresist spin coated on a substrate. In this way, the solvent swells the photoresist and forms a gel that conforms to the mold surface relief. After the solvent has diffused into the resist, the mold is removed and a flood illumination can be applied which results in sub-100-nm features [71]. In the case of liquid embossing, isolated features can be obtained by placing a PDMS mold on a sufficiently thin film of liquid (<500 nm). After removing the mold, the liquid remains patterned which enables the rapid patterning of inorganic nanocrystal solution, as capping groups and solvents can volatilize efficiently at the exposed liquid surface [73]. In the case of SiO<sub>2</sub>-TiO<sub>2</sub> sol–gel embossing, a mixture of tetraethoxysilane, titanium tetrabutoxide, catalyst, solvent, and surfactant is first spin-coated onto a silicon wafer and then embossed under high pressure and a ramp of temperature from 17 to 200 °C, followed by a 400 °C annealing for 15 min in air. The embossed structures showed 300 nm gratings without cracking over a few cm<sup>2</sup> [75]. Finally, for embossing piezoelectric materials, a specific process, namely a lost silicon mold process which consists of casting of lead zirconate titanate slurry, drying, and calcinations, followed by a hot isostatic pressing after a glass encapsulation [76], has to be used because of large volume shrinking.

#### 4. NANOIMPRINT LITHOGRAPHY

Nanoimprint lithography was invented in 1995 by Chou et al. [9] and has quickly become a widely applied technique [33, 35, 77–82]. As shown in Figure 1, the main advantage of this technique relies on its simplicity and versatility which is, in particular, fully compatible to most semiconductor fabrication steps. Although the imprinting condition can be optimized experimentally, some simple considerations are helpful for the determination of the important processing parameters.

##### 4.1. General Considerations

The imprint condition changes with the polymer type and the pattern specification. In general, the mold etch depth is in the order of 100 nm and the polymer thickness of the recessed areas after imprinting should be small enough, typically 20 nm, for keeping the imprinted polymer shape during RIE. For a large area pattern replication, polymer flows can take place over a long distance in the mold and sample confined narrow space. A fundamental understanding of how a viscous polymer travels through this narrow space is interesting but a simple schematic of the mold cavity filling is

helpful for the mold design and the determination of first imprinting conditions.

Let us split the imprinting process into three periods, as shown in Figure 4. At the beginning, the imprint speed is high since the mold–sample contact area is small (regime 1). The transient period (regime 2) is characterized by the complete filling of the mold cavity, but no polymer is pushed outside of the mold area. In the end, the total mold area is pressed into the polymer so that a part of the polymer is forced to flow to outside of the mold area (regime 3). Considering a constant polymer volume, we obtain for regime 2

$$h_i = h_c + fh_m \tag{5}$$

where  $h_i$ ,  $h_c$ , and  $h_m$  are respectively the initial thickness of the polymer layer, the final thickness of the recessed area, and the mold etch depth;  $f = A_e/A_t$ ,  $A_e$  and  $A_t$  being the etched area and the total area of the mold, respectively.

If the etched portion of the mold is substantially large ( $A_e \sim A_t$ ), a complete mold filling is obtained when  $h_i \approx h_c + h_m$ . On the contract, if  $A_e \ll A_t$ , a complete filling is difficult and additional etch areas can be introduced to increase the embossing speed.

For periodic structures, the factor  $f$  can be calculated, allowing a close correlation between  $h_i$ ,  $h_c$ , and  $h_m$ . For example, when  $h_m = 150$  nm and  $h_c = 20$  nm, the initial polymer layer thickness should be  $h_i = 95$  nm for a line grating,  $h_i = 140$  nm for a dot array, and  $h_i = 50$  nm for an antidot array of equal line and spacing.

To estimate the imprinting speed, the Navier–Stokes equation reduced for a noncompressive liquid ( $\nabla \cdot \mathbf{v} = 0$ ) and small Reynolds number conditions can be used [83],

$$\eta \Delta \mathbf{v} = \nabla p \tag{6}$$

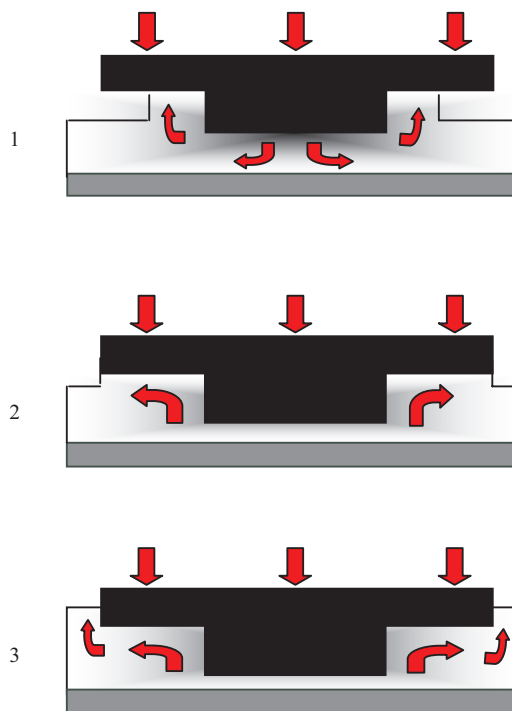


**Figure 4.** Schematic representation of the three regimes describing the mass transport in nanoimprint lithography.

where  $\eta$  is the viscosity of the polymer,  $v$  is the velocity, and  $p$  is the pressure. Assuming a single dot of radius  $a$  located in the center of a disk of radius  $R$ , the pressure under the dot is given by

$$p(r) = p_0 + \frac{3u\eta}{2h^3}(a^2 - r^2) \quad (r < a) \quad (7)$$

where  $h$  is the polymer thickness of the recessing area, and  $u = dh/dt$  is the imprinting speed.  $p_0$  refers to the pressure value outside of the dot area. For a homogenous load, the imprint speed at the beginning (regime 1) and at the end (regime 3) are obtained as

$$u_a = \frac{4h^3}{3\pi\eta a^4}F \quad \text{and} \quad u_R = \frac{4(h + h_m)^3}{3\pi\eta R^4}F \quad (8)$$

where  $F$  is the force applied to the mold. Clearly, at the beginning the load is charged over a small area ( $\pi a^2$ ) and the polymer flow occurs only in the proximity of the dot. In the end, the load is charged over the entire mold area ( $\pi R^2$ ) and the mass transport occurs over a long distance. Obviously, when  $a \ll R$ ,  $u_a \gg u_R$ , suggesting a fast imprinting at the beginning and a very slow deformation in the end.

To estimate the imprint speed, we consider a mold of diameter 10 mm with 100 dots of diameter 100  $\mu\text{m}$  and etch depth 150 nm. When a force of 20 kg is applied to a 100 kg/mol PMMA layer of initial thickness 200 nm heated at 200 °C ( $\eta = 5 \times 10^4$  N s/m<sup>2</sup>), we obtain an imprint speed of 54  $\mu\text{m/s}$  at the beginning ( $h \sim 200$  nm) but only 0.8  $\mu\text{m/s}$  at the end ( $h \sim 150$  nm). When the mold is entirely pressed in the polymer, the imprint speed becomes much slower ( $8 \times 10^{-9}$   $\mu\text{m/s}$ ).

For a more realistic modeling, surface tension, capillary force, as well as size of the polymer molecules have to be taken into account [84, 85]. The later effect is particularly important when the imprinting recessed area is comparable to the molecule size. It is known that polymers are formed of large number of molecular chains; each may bend, coil, and kink. For a linear polymer molecule, the gyration radius  $R_g$  is equal to [53]

$$R_g = \frac{1}{6}l\sqrt{N} \quad (9)$$

where  $l$  is the bond length between chain “atoms” and  $N$  is the total number of bonds in the molecule. For 50 kg/mol (950 kg/mol) PMMA,  $R_g = 20$  nm (100 nm), which are both comparable to the thickness of the imprinting recessed area. It is therefore necessary to solve the Navier–Stokes equation taking into account this effect. Suppose that all contact points between the polymer molecules and the solid surface are fixed; the effective viscosity can be obtained [84] as

$$\eta(z) = \eta_b/W(z) \quad (10)$$

where  $\eta_b$  is the viscosity of the polymer without strain and  $W(z)$  is the probability that a monomer is not in contact with the wall. The solution of the Reynolds problem is then the same as obtained previously [Eqs. (7) and (8)], except that  $\eta$  is replaced by  $\eta_b/\delta$  and

$$\delta = \frac{3}{\pi} \sum_{n=1}^{\infty} \left[ \frac{1}{2n^2} - \frac{4}{\pi^2} \frac{1}{n^2} \right] \exp\left(-\frac{\pi^2 R_g^2 n^2}{h^2}\right) \quad (11)$$

## 4.2. Imprinting Conditions

A number of polymers have been used in nanoimprint lithography. Because of their different characteristics, the imprint conditions must be evaluated for each polymer and each particular pattern [86–88]. For most applications, polymers with a low molecular weight and a low glass transition temperature are preferable because of their low viscosity. For example, the imprinting temperature for the 950 kg/mol PMMA is typically 175 °C while it is only 150 °C for the 50 kg/mol PMMA with the same applied pressure. In general, small and homogenously distributed features can be more easily replicated compared to large features. For example, 1  $\mu\text{m}$  features can be replicated into the 50 kg/mol PMMA at 150 °C but 100  $\mu\text{m}$  features can only be replicated at 175 °C for the same applied pressure. When different types of patterns are presented on the same mold, the imprinting condition has been evaluated for the largest features because it is more difficult to evacuate the polymer from large imprinting areas. Under optimal conditions, features of sizes ranging from 50 nm to 100  $\mu\text{m}$  could be simultaneously replicated over an area of several mm<sup>2</sup> [86].

The RIE resistance of the polymer should be high enough for an easy process control. In addition to PMMA, a number of thermoplastic polymers such as polycarbonate and polystyrene have shown imprinting performances similar to that of PMMA. Commercial resists for both optical and e-beam lithography have also been tested [88, 89]. For example, Shipley resist S1805 which is based on novolac resin allowed the replication of 50-nm features with a better etching resistance to oxygen plasma compared to PMMA and thus a better process control [88].

Several aromatic polymers based on methacrylates (linear polymers) and multifunctional allylestere (crossing polymers) also showed comparable behaviors of the PMMA. In particular, the thermoplastic prepolymer MRT-9000 can be cross-linked during or after embossing to form a patterned polymer layer with a pretty high thermal and chemical stability [90–92].

Hyperbranched polyesteramides (hybranes) were synthesized from di-isopropanolamine and an anhydride of choice; end-capping of the obtained poly-ol with a carboxylic is optional [93]. Depending on the molecules presented in the branched groups, the glass transition temperature of the hybranes varies from 10 to 70 °C [94, 95]. Accordingly, nanoimprinting can be done at relatively low temperatures. Besides, the viscosity of the hybrane polymers decreases more rapidly with temperature compared to PMMA and the etch resistance of hybranes to O<sub>2</sub> plasma is almost twice that of PMMA, allowing a more accurate etch control of the recessed area. Another advantage is that some of the hybrane polymers can be used for low temperature and/or low pressure imprinting. In particular, 75 nm line and space gratings have been successfully replicated at room temperature (RT) with a semicrystalline hybrane (2550).

Generally, semicrystalline polymers are ductile in the temperature range between the glass transition and the melting temperature. For hybrane 2550, the glass transition temperature and the melting temperature are respectively 10 and 40 °C so that at RT nanoimprinting is performed at a solid state. Above the melt temperature ( $\sim 50$  °C), it is a

liquid so that the imprinting can be done under low pressures. Other types of semicrystalline polymers have shown similar behaviors, for example, solid state and melt embossing at 220 and 330 °C for the poly(tetrafluoroethylene-co-hexafluoropropylene) (PEF), 90 and 180 °C and for the polyethylene, and 90 and 300 °C for the polyester, respectively. In particular, submicrometer surface structures have been obtained on a PEF thin film by combining melt (first) and solid state (second) embossing to demonstrate the feasibility of a two level fabrication [96].

Another RT approach is to use a polystyrene (PS) film after a solvent vapor treatment. Since a solvent treated polymer has a decreased glass transition temperature and viscosity, embossing is possible at RT under a high enough pressure. Without solvent treatment, imprinting is still possible due to the plastic flow along with free-volume contraction and plastic deformation of the resist layer. Submicrometer features could be replicated at RT at a pressure between 300 and 1500 bar for 5 to 40 min [97, 98].

Finally, RT imprinting has been demonstrated using a spin on glass (SOG) resist [99]. Here, solution of organosilica [ $\text{Si}(\text{OH})_4 + \text{R}_1\text{COOR}_2$ ] in alcohol was first spin coated on a silicon substrate and then embossed at RT with a typical pressure of 25 bar. Features of 200-nm linewidth could be obtained and transferred into the substrate via lift-off or direct RIE. Because of the presence of silicon, the etch selectivity of SOG is clearly better than that of the PMMA.

Most nanoimprint lithography was performed by imprinting a thin polymer layer on a substrate. Alternatively, one can first spin coat PMMA on both mold and wafer and then transfer the polymer layer of the mold to the wafer substrate. After spin coating, the polymer layers on the mold and the wafer are annealed and the mold and the wafer are pressed against each other at a temperature above  $T_g$  of the polymer. After cooling, the mold is separated from the wafer, leaving a replicated pattern on the surface of the wafer [100]. To promote the adhesion of the polymer film to the substrate, a release agent has to be coated on the mold and an adhesion layer on the wafer. The bonding occurs at pressure and temperatures lower than those of standard nanoimprinting and the problems related to the lateral transport of the polymer disappear in the present configuration. Quite similarly, a reversal imprint lithography has been studied which consists of simply spin coating a polymer layer on a mold and then transferring it onto the substrate by thermal bonding [101]. Either suspended structures over wide gaps or supported patterns on raised features of the substrate could be obtained in this way [102], thus providing a way to form multilayer and three-dimensional polymer structures.

Alignment is required for multilevel applications. So far, most demonstrations have been based on experiences using optical aligners outside the imprint apparatus. For example, multilayer nanoimprint lithography has been performed over 4 in. silicon wafers which showed an alignment accuracy of 1  $\mu\text{m}$  [103]. The mold and the wafer were first aligned with an optical aligner and then fixed with a hold and placed in an imprint machine. An average alignment accuracy of 1  $\mu\text{m}$  with a standard deviation of 0.4  $\mu\text{m}$  in both  $X$  and  $Y$  direction was obtained in 10 consecutive tests. For a higher accuracy, alignment and imprint should be performed with the same machine but no commercial system is

now available. Another problem for high accuracy alignment is the wafer distortion due to different thermal coefficients between mold and an imprint substrate. A method was proposed which consists of comparing directly the mold and wafer alignment marks without intermediate optics [104]. The mold is deliberately deformed with a system of piezoelectric actuators in such a way that the induced distortions precisely match those on the wafer and all of the alignment marks are pulled into registration simultaneously. Experimental demonstration with sophisticated optics and piezoelectric actuators is expected.

Actually, *mix-and-match* processes are more suitable for the fabrication of multilevel devices [105–107]. Whereas nanoimprint lithography is often used for the first level high resolution patterning, UV lithography with alignment can be used to pattern features such as bond pads for electric wiring. In some cases, this order can be inverted but an alignment is generally required before imprinting [106]. Finally, the *mix-and-match* techniques can also be used by combining nanoimprint lithography and other high resolution methods such as X-ray [80], e-beam, focused ion beam, and scanning probe lithography techniques [107].

### 4.3. Pattern Transfer Techniques

The commonly used transfer techniques are lift-off, electroplating, and reactive ion etching. In general, the quality of the transfer depends not only on the imprinted resist profile but also the RIE of the recessed area.

For lift-off, a resist profile of undercut or vertical sidewall is required and the thickness of the deposited metal film should be significantly smaller than the resist thickness. For high quality fabrication, the metal evaporation process has to be optimized to avoid asymmetric deposition, thickness inhomogeneity or crown forms. For gold deposition, an adhesion layer of Ti or Cr is needed. To produce three-dimensional structures such as  $T$  gate and air-bridge structures, sophisticated lift-off techniques can be used [108]. For features of high aspect ratio, a trilayer process is preferable but electroplating can also be used for a number of metals (gold, nickel, cobalt, iron, etc.). Here, the height of the plated metal can be close to or larger than the resist thickness and features of sizes down to 20 nm can be obtained [109, 110]. The third technique of the pattern transfer is RIE by using either resist or metal patterns as etch masks. Polymers containing silicon are studied as etch masks because of their high etch resistivity. Whereas fluorine based gas mixtures are used to etch Si,  $\text{SiO}_2$ ,  $\text{Si}_3\text{N}_4$ ,  $\text{TiO}_2$ , W, and various polymers, chlorine based gas mixtures are commonly used for III–V semiconductors. To etch metallic structures, ion milling is more suitable.

In nanoimprint lithography, high resolution features can only be obtained with a thin resist layer. In order to achieve both high resolution and high aspect ratio, trilayer systems have been developed [64, 88]. A typical trilayer system consists of a thick bottom layer which is thermostable at the imprint temperature PMGI (polymethylglutarimide) [111], a thin intermediate layer (10-nm thick Ge), and a top imaging layer (PMMA) (Fig. 5). After imprinting, the thickness contrast of the top layer is amplified by a sequential etching



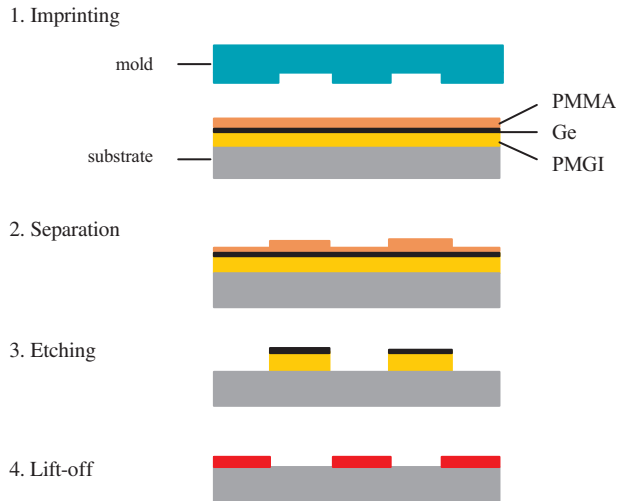


**Figure 5.** Schematic representation of the trilayer nanoimprint process.

of the whole trilayer system with  $O_2$ ,  $SF_6$ , and  $O_2$  plasmas. This trilayer process is particularly useful for systematic studies where different metal thicknesses are required. Moreover, by overetching the bottom polymer layer, structures of different sizes can be obtained with the same mold [88]. Because of the high aspect ratio at the bottom layer, electroplating and direct etching can also be applied for hard material pattern transfer. Besides, trilayer nanoimprint lithography can have large process latitude and good pattern homogeneity over large areas.

Other combinations of multilayer resists have also been tested, including PMMA/Al/novolac resin [85], PS/PMMA, PMMA/novolac resin [112], and P(MMA-MAA)/PMMA systems [113]. For example, the PMMA/Al/novolac resin trilayer system can be etched by a sequential etching with  $O_2$ ,  $BCl_3$ , and  $O_2$  plasma and the patterned structures were studied for metal oxide silicon field effect transistor (MOSFET) fabrication using a silicon on insulator (SOI) substrate with  $0.1 \mu\text{m}$  gate length, showing no degradation of the device performance [85].

## 4.4. Lithography Performances

The performance of nanoimprint lithography depends on a number of factors: the quality of the mold, the characteristics of the polymer, the imprinting parameters, and the details of the etching and lift-off processes [86]. The following assessments outline the state of the art achievements.

### 4.4.1. Resolution

In the earliest reports, Chou et al. have demonstrated a replication of dot arrays with a minimum feature size as small as 6 nm and a pitch size down to 40 nm [10, 77]. More complicated patterns such as Fresnel zone plates with a minimum feature size 75 nm and circuit gratings of 20-nm minimum linewidth were obtained later, by using a silicon mold of etch depth of 100 nm and 70-nm thick and 15 kg/mol PMMA, followed by metal evaporation and lift-off [114]. So far no better result has been reported in terms of the feature size and the pattern complexity. For a routine fabrication, feature sizes down to 50 nm (100-nm pitch) can easily

be achieved with several types of polymers [88]. Figure 6 shows a nickel dot array of 60-nm pitch, obtained by nanoimprint and lift-off. It is believed that within the limit of a few nanometers, the achievable feature size depends mainly on the mold fabrication, (i.e., e-beam lithography patterning). Much effort has to be devoted to ultrahigh resolution patterning over large areas. Other factors such as polymer characteristics (molecule size, viscosity, etching resistance, etc.) and imprint and etching conditions also have to be controlled carefully for sub-50-nm resolution patterning. In general, it is more difficult to replicate large areas and dense lines than dot arrays because of the lift-off difficulty. The minimum linewidth of line and space gratings reported so far is around 100 nm. Replication of 100-nm period grating is currently studied for advanced optical applications [30]. Fine lines can be obtained by overetching the nanoimprint defined structures. Figure 7 shows sub-10-nm silicon lines obtained by trilayer nanoimprint lithography and a sequential RIE of the silicon layer of a SOI substrate.

### 4.4.2. Control of the Critical Dimension

Both the reproducibility and the control accuracy of the critical dimension (CD) depend on the process latitude and the replication environment. The trilayer technique we described provides large process latitude and excellent CD control. In general, polymers with a high etch resistance are preferable for better CD control. With hybrane polymer  $T_g$  of 70 °C for example, the replicated patterns showed a CD control accuracy better than 10 nm; increasing the etch time from 15 to 45 s results in a size increase of 60% for lift-off dots of 100-nm diameter [88] (Fig. 8).

Concerning the reproducibility, no systematic evaluation has been reported so far. With manual loading and down-loading, a mold can be used at least several tens of times without being damaged. Statistic analyses of replication data obtained by several experiments showed that the size variation of 100-nm features is within 10 nm. Since defects can be introduced in molds, substrates, and polymers during manual handling and repeated experimentation, particular attention has to be paid to the free contamination process

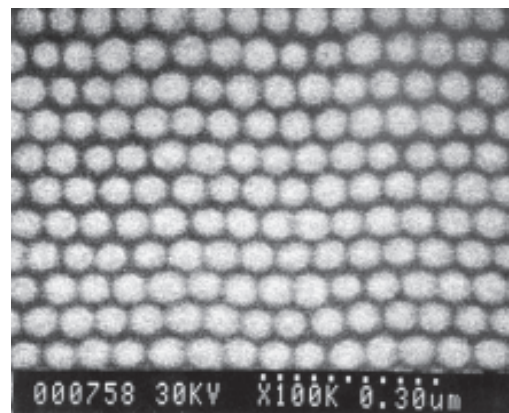


**Figure 6.** SEM image of a 60-nm-period dot array obtained by nanoimprint and lift-off of 20-nm-thick nickel. Reprinted with permission from [167], J. Moritz et al., *J. Appl. Phys.* 91 7314 (2002). © 2002, American Institute of Physics.

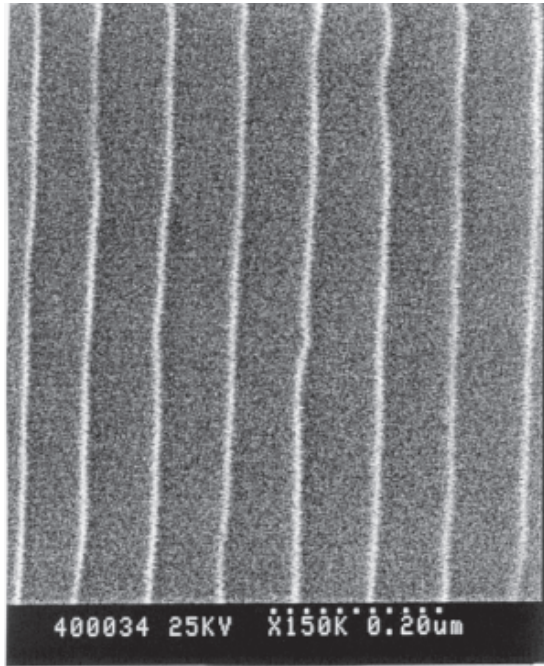


**Figure 7.** SEM image of a silicon line grating of linewidth less than 10 nm obtained by nanoimprint lithography and overetching of silicon layer in a SOI substrate.

but also to the correlation between mold etch depth, polymer layer thickness, and applied press and temperature, as discussed.

#### 4.4.3. Homogeneity and Pattern Placement Accuracy

The homogeneity of nanoimprint lithography depends on the homogeneity of the imprinting pressure, temperature, and feature density over the mold. Under pressure, the mold and the sample should be perfectly parallel. Patterning homogeneity has been studied with 4 [41, 80, 103] and 6-inch [115] wafers. For example, the first experiments on 4-inch wafers performed with a hydraulic press showed no remarkable imprinting inhomogeneity nor pattern distortion

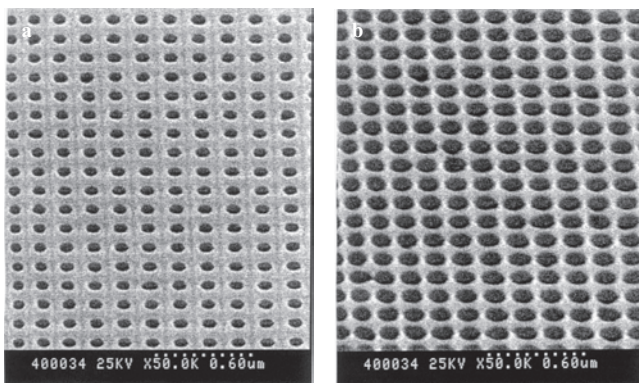


**Figure 8.** SEM images of PMGI resist patterns obtained from trilayer nanoimprinting: (a) hybrane etching time 15 s, and (b) hybrane etching time 45.

for the feature sizes ranging from 100 nm to 100  $\mu\text{m}$ . A commercial wafer bonding system has also been used to evaluate more systematically the imprint performance over large areas [116]. Indeed, mixture features of 400 nm to 100  $\mu\text{m}$  can be homogeneously replicated over the whole wafer area, with a typical temperature of 225  $^{\circ}\text{C}$  and pressure of 55 bar for 5 min.

To investigate the accuracy of the pattern placement, an X-ray stepper has been used to compare a set of alignment marks on of a sample fabricated by nanoimprint lithography to the complementary set on an X-ray mask [80]. The nanoimprint mold and the X-ray mask were first fabricated on 4 inch silicon wafers by e-beam lithography and related pattern transfer techniques. Then, the mold patterns were replicated into a silicon wafer by nanoimprint lithography, followed by a metal film evaporation and lift-off. Afterward, the sample and the fabricated X-ray mask were aligned with the X-ray stepper, showing an alignment accuracy better than 30 nm ( $3\sigma$ ) for a field size of  $30 \times 30 \text{ mm}^2$ . Since both X-ray mask and nanoimprint mold were designed in a similar manner, nanoimprint lithography has not induced notable pattern distortion within the accuracy of the measurements.

#### 4.4.4. Process Latitude

The process latitude refers to the range of acceptable imprinting parameters (pressure, temperature, and etching and lift-off). For conventional lithography methods, the process latitude is limited by the depth of focus (optical lithography) or the range of the dose modulation (e-beam lithography). In nanoimprint, only low pressure and temperature limits are meaningful since within the polymer decomposition limits a higher temperature and pressure are generally more favorable for an easy polymer flow. Depending on the polymer type, pattern density, and distribution, the lowest temperature and/or pressure which can be used to replicate a given pattern can be determined experimentally. For a good pattern transfer, etch parameters need to be controlled accurately but both bilayer and trilayer systems provide larger process latitudes.

#### 4.4.5. Throughput

The production rate of nanoimprint lithography is a function of time required for the wafer loading, alignment, imprinting, separation, and unloading. Without taking into account wafer loading, alignment, and unloading, the imprint step itself needs a few minutes because of the thermal processes. So far, most experiments were performed manually and one can reasonably expect a speed of 10–20 wafers per hour if an automatic wafer loading and unloading system is used. Nevertheless, imprint speed can be significantly higher for the replication of homogeneously distributed features, as discussed in the previous sections. Using low viscosity polymers and trilayer imprint techniques, the imprint speed can also be increased but questions such as the mold lifetime and the total number of imprintings without further antistick mold treatment are still open.

Alternative approaches such as *step-and-flash* (see Section 5) and *step-and-stamp* imprint can be used to considerably increase the throughput. *Step-and-stamp* imprint



lithography has been tested with a commercial flip-chip bonder [117]. A mold is pressed into a polymer layer to create the first imprint and then lifted and moved to the next site to create the second imprint and so forth. Only the mold and the mold pressed polymer area are heated above the glass transition temperature of the resist to assure that the quality of the already imprinted features must not be degraded during the sequential imprinting. As a result, 36 consecutive imprints could be done over a large area, with patterns of 300-nm line and spacing. Obviously, this technique can also be used together with UV lithography for mix-and-match fabrication and large area as well as multilayer imprinting.

Two approaches of roller nanoimprint lithography have been proposed [118]. The first one consists of rolling a cylinder mold on a flat and solid substrate; the second rolls a smooth roller over a flat mold which is placed on a substrate. Both showed sub-100-nm resolution and good imprint uniformity. Because of the reduced pressing area, less force is required and the mold can be continuously used on a large area substrate. The mold fabrication in rolling imprint lithography is one of the main issues in terms of both design and implementation.

## 5. NANOEMBOSSING OF PHOTOCURABLE POLYMERS

The “hot embossing” techniques described in the previous sections are generally performed above the glass transition temperature of a polymer and under high pressure. Because of the heating and cooling processes, the embossing speed as well as the alignment accuracy cannot be very high. Besides, it is difficult to perform step and repeat imprinting with high resolution features. With particular polymers, RT imprinting is possible but high pressure is required. Alternatively, RT nanoembossing can be performed under a moderate pressure with photocurable polymers. In this case, a transparent mask is used to emboss a low viscosity liquid prepolymer, followed by a photocuring with a UV light. Due to the mold release agent, the separation of the sample and the mold is possible and the process can be fast. This technique also makes a fine layer-to-layer alignment possible due to much reduced pressure, low viscosity of the liquid polymer, and the absence of thermal distortion. Despite these advantages, however, only a few groups have been involved in the development of this technique [33, 119–123].

### 5.1. Mold Assisted Photopolymerization

Mold assisted photopolymerization (2P) is performed in the following way. First, a mixture of prepolymer which contains monomers of low molecular weight and photoinitiator is prepared and poured or spin coated on a substrate. Then, a transparent mold is pressed into the prepolymer mixture and the mold is held until the liquid flows into the mold cavities, followed by a 2P process with UV light. By curing, the liquid monomer is solidified which provides a copy of the mold relief. After separation from the mold, the sample is treated by RIE. At this stage, it is important to have the recessed layer as thin as possible, in order to preserve the embossed shape during the dry etching process.

Transparent molds can be obtained by e-beam lithography and RIE of a quartz plate with or without covering of a  $\text{TiO}_2$  layer. Other types of molds including  $\text{SiO}_2/\text{TiO}_2$  double layer on a quartz plate [33], soft molds made of PDMS, and multilayer systems with more specified characteristics are currently under investigation [124]. In all cases, the mold surface has to be treated to prevent sticking of the embossing resist to the mold during detachment.

The prepolymer mixture used for embossing should have a high rate of photopolymerization, low viscosity, good adhesion to the substrate, and low surface energy for the easy separation from the mold. The first experience of the mold assisted 2P of nanoscale features was reported by Haisma et al. in 1996 [119] who used a mixture of pentacythritol-triacrylate and 1,6-hexanediol-diacrylate as photopolymerizable monomers and dimethoxy-phenyl-acetophenone as photoinitiator for UV light. The surface of the mold and the substrate are respectively coated with a release layer and an adhesion primer. A pressure of only 0.1 bar was applied to conform the mold into the liquid because of its low viscosity. Then, the patterned polymer layer was used as dry etching mask for RIE of a quartz plate.

The same method has been used to demonstrate the feasibility of replicating nanocompact disk patterns [120]. Features of 100-nm pitch size could be reproduced by photopolymerization, corresponding to a storage density 100 times of the current compact disks. With the same method, mold assisted 2P has been tested under near-field configurations with an enhanced lithography ability [121].

Contrary to the hot embossing where a large number of polymers have been used, only a few photocurable polymers have been tested. One of the proposed systems is based on a low viscosity organic-anorganic sol-gel which has good adhesion on both silicon and quartz plates. Fluorine-based additives can be used which migrate to the surface during spin-on processes and thus promote the mold-sample separation. It was shown that both polar and dispersive components of the surface energy were significantly reduced by adding 1–2% of fluorine in the sol-gel resist [125, 126]. Consequently, more than 80% of the mold area could be imprinted under a typical pressure of 0.8 bar. Up to 50 times of multiple imprints were tested with one mold, showing no degradation of the mold or the imprint quality. In addition, a self-cleaning effect has been observed due to the involved 2P processes.

In principle, a fine alignment is possible before polymerization due to much reduced pressure and low viscosity of the resist. The mold which is separated from the substrate with a thin film of monomer liquid can be moved laterally with a sub-20-nm accuracy. However, problems arise because of the difficulty to make a perfect contact between the mold and the substrate, keeping the thin layer prepolymer homogeneously distributed. To overcome this technological liability, two strategies are under investigation. The first one, namely step and flash imprint lithography, consists of using a small mold to emboss locally a portion of a large wafer and then repeating the same process many times in different places of the wafer area [122]. The second strategy is based on the use of soft or multilayer molds to achieve a uniform embossing over a large area [124].

## 5.2. Step and Flash UV-Imprint Lithography

Step and flash UV-imprint lithography has been studied for several years [11, 33, 127–129]. A quartz mold of a small size ( $1 \times 1$  inch<sup>2</sup>) is first aligned over a substrate. Then, a drop of a low viscosity liquid is dispensed in the narrow space between the mold and the sample which allows one to fill the mold area by capillary forces. Afterward, the mold is pressed and the prepolymer is irradiated by UV light, resulting in a single field of the mold pattern on the substrate. The whole wafer area can then be filled by step and repeat processing.

Commercial components, including acrylate-based monomer, silylated monomer, dimethyl siloxane derivative, cross-linking agent, and free radical generator, were mixed as prepolymer liquids [127]. Here, the silicon rich organics were introduced to enhance the etch resistance to oxygen plasma. Molds were treated with tridecafluoro-1,1,2,2, tetrahydrooctyl trichlorosilanes [ $\text{CF}_3-(\text{CF}_2)_5-\text{CH}_2-\text{CH}_2\text{SiCl}_3$ ] and a low surface energy, self-assembled monolayer was formed on the mold surface to ensure a selective release of the mold and the polymer. Various aspects have been studied, showing good performance in terms of the nanoscale pattern replication and mold self-cleaning. In addition, the UV imprint lithography has been tested on curved surface [128]. More recently, fabrication of high resolution molds has been demonstrated on an ITO coated quartz plate, and features as small as 20 nm could be replicated by step and flash imprint lithography [33].

To obtain high aspect ratio features, a bilayer system can be used which consists of an underlayer of PMMA and an image layer of the photocurable polymer. With an imprint force of 2 bar, 60-nm features were obtained with 50-nm height in the recessed layer. These features could be then transferred into a 350-nm thick PMMA layer, resulting a mask with an aspect ratio of up to 6:1 [129]. Another advantage of the two-layer technique is its applicability over nonplanar substrates. Finally, an automated stepper is now available allowing for multiple imprints over a 200-mm-diameter wafer and has been employed for defect investigation.

## 5.3. Near-Field Contrast Enhancement

Alternatively, mold assisted photopolymerization can be performed using an improved mold configuration. In this method, the top portions of the mold are coated with a thin layer absorber, which is sufficient to stop the light propagation but allows optical tunneling through small holes. Therefore, a high contrast aerial image can be obtained at the downstream space of the mold. Figure 9 shows a comparison between three different mold configurations. In mold 1, no absorber is coated on the etched quartz plate which will result in a pure thickness contrast as produced in 2P processes. In mode 2, the absorber thickness is too large so that the light intensity downstream of the openings will not be sufficient for a complete polymerization because of the inefficiency of the optical tunneling. On the contrary, in mode 2 no polymerization will take place in the masked areas because of the absorption while the light intensity will remain sufficiently high for the polymerization inside and downstream of the openings. As a result, the residual layer

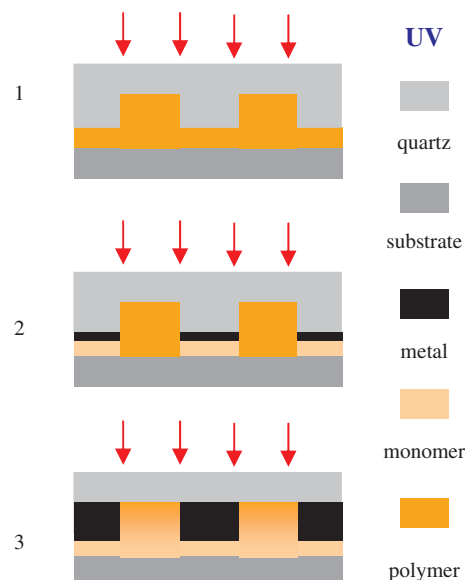


**Figure 9.** Schematic representation of the mold assisted optical lithography with three mold configurations: Whereas type 1 provides a polymer relief and type 3 results in a chemical contrast, type 2 gives rise to both thickness and chemical contrast.

could be easily removed by a solvent dip thus preserving the cured pattern slopes. Both numerical simulation and experimental data showed the feasibility to pattern features of critical dimension as small as 70 nm [121] (Fig. 10).

Other types of masks for near field optical patterning have also been tested under conformal contact printing conditions [130–132]. For example, flexible masks made of a thin membrane or elastomer permits a perfect contact between patterned absorber and the resist layer to be exposed so that the diffraction defined minimum feature size,  $l = 0.5\sqrt{\lambda h}$  ( $h$  being the thickness of the resist layer), can be reached. By using deep UV laser beams and a trilayer resist stack on a substrate, patterns of feature sizes close to 100 nm could be obtainable [133, 134]. Comparable to this technique, nano-embossing of photocurable polymer is more robust which

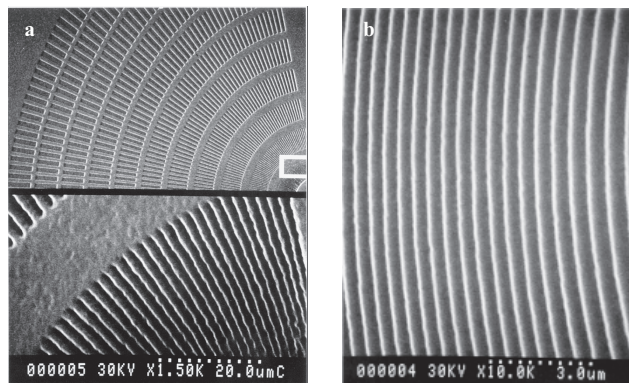


**Figure 10.** SEM images of nanoembossed patterns of 70-nm minimum feature size, obtained by mold assisted near-field photopolymerization. Reprinted with permission from [121], Y. Chen et al., *Microelectron. Eng.* 46, 69 (1999). © 1999, Elsevier.

does not require a sophisticated mask or a deep UV light source for curing.

## 6. APPLICATIONS

Nanoscience and nanotechnology are the most explosive research areas which involve a large number of scientific communities and considerable industrial efforts. As a potential tool for high volume manufacturing, nanoembossing is attractive for many applications. During the past few years, the capability and the feasibility of fabricating nanodevices and nanosystems have been demonstrated in the following areas.

### 6.1. Nanoelectronics

Lithography plays the most critical role for the development of nanoelectronic devices. For the development of ultimate CMOS technology as well as the quantum and molecular electronics, new fabrication tools are required. For this reason, nanoimprint lithography has been used to demonstrate its fabrication ability of MOSFET transistors [77], T-gate transistors [135, 136], quantum contact devices [106], etc. Whereas the advantage of nanoimprint lithography is obvious due to its high speed and low cost, all fabricated electronic devices have shown no evidence of performance degradation compared to those obtained by e-beam lithography.

MOSFET transistors have been obtained by nanoimprint lithography and etching a 110-nm-thick silicon layer of a SOI substrate. A variety of transistor features, including 100-nm wire channels, 250-nm diameter quantum dots, and ring structures with 100-nm ring width [135], were obtained. As expected, the room temperature measurements of the fabricated MOSFET showed common characteristics to those obtained by more conventional fabrication techniques while the quantum dot devices showed oscillations due to the electron Coulomb blockade effect.

High frequency and low noise transistors are commonly fabricated with III–V materials and T-gates which provide a combination of short gate length and low gate resistance. A bilayer resist imprinting procedure has been used to produce 120-nm T-gate transistors for high electron mobility transistors at a temperature and force that are not detrimental to the III–V substrate. Again, the fabricated transistors provided similar characteristics to those obtained on the same materials with gates realized by electron beam lithography [136].

Three-terminal ballistic junctions (TBJ) have also fabricated by nanoimprint lithography. After imprinting, the resist residues were removed in oxygen plasma, followed by wet etching of InP/GaInAs to define the TBJ structures with a high mobility, two-dimensional electron gas with sub-100-nm feature sizes [137]. In agreement with a theoretical prediction, highly nonlinear electrical responses were observed.

The fabrication of split-gate quantum contact point structures has been demonstrated using a mix-and-match technique [106]. The whole process included three optical lithography steps for the Hall bar and ohmic contact definition and one step of nanoimprint lithography for the fabrication of a split-gate pattern over a modulated-doped

GaAs/AlGaAs heterostructure. Before imprinting, the mold and the sample were aligned under backside infrared illumination with an optical aligner and brought into soft contact by slightly pressing the mold into the polymer. Then, the mold-sample assembly was placed onto the imprint machine processing. After imprinting, the split gates in the range between 180 and 400 nm were obtained by metal evaporation and lift-off. Low temperature transport measurements of the fabricated sample showed a well defined conductance quantization as a function of gate voltage, similar to that obtained with split gates defined by e-beam lithography.

More recently, nanoimprint lithography has been used to fabricate short channel polymer organic thin-film transistors. By nanoimprint lithography, interdigitated gold source and drain terminals were produced by lift-off, providing a channel length down to 70 nm. After depositing a layer of SiO<sub>x</sub> to protect the gate oxide and large gold pads for *I*–*V* measurements, a *p*-type semiconducting polymer, poly(3-hexylthiophene), was deposited by spin coating or casting, followed by a capping layer deposition of SiO<sub>x</sub>. The fabricated devices showed the expected increase of drive current density [138].

Finally, nanoimprint lithography holds considerable promise for the fabrication of molecular electronic devices. It is particularly suitable for the fabrication of electrodes for molecular self-assembly. For example, nanoimprint lithography has been used to produce 20-nm wide gold wires on a substrate of silicon dioxide. Applying a pulse of electric current, these nanowire can be broken, resulting in a well defined sub-10-nm gap which should be useful for single molecular electronic device fabrication [36]. Nanoimprint lithography has also been used for the fabrication of electronically addressable crossbar memory circuits. Metal electrodes were first obtained at the sub-50-nm scale. Then, Landmuir–Blodgett molecular thin films with switchable electronic properties were sandwiched between nanoelectrodes, showing a memory density as high as 6.4 Gbit/cm<sup>2</sup> [139].

### 6.2. Nanooptics

Much effort has been devoted to the fabrication of optic and optoelectronic devices such as photodetectors, polarizers, binary diffractive elements, as well as more conventional microoptical components.

Using standard nanoimprint lithography, followed by Cr/Au thin film evaporation and lift-off, GaAs metal-semiconductor-metal photodetectors (MSM PDs) could be realized [140]. The electrode fingers of line and spacing between 200 and 600 nm could be produced by adjusting the etch depth of the imprint mold between 193 and 330 nm. Comparing to the devices obtained by e-beam lithography, these MSM PDs showed no significant difference in the measured dark currents and the *I*–*V* curve under illumination.

A reflective polarizer based on a stacked double layer subwavelength grating has been obtained by imprinting a 200-nm thick PMMA layer and then evaporating in a high vacuum chamber (better than  $5 \times 10^{-6}$  Torr) 5-nm Cr and 70-nm Au thin films [141]. The fabricated gratings of 190-nm period showed a polarization extinction ratio

of over 200 for the normal incidence at 632.8 nm wavelength (54% reflection for transverse magnetic (TM) mode against 0.25% reflection for transverse electric (TE) mode). Similar gratings were realized in the waveguide configuration and showed the expected performance of a broadband waveguide polarizer [142]. In order to develop subwavelength applications, a spatial frequency doubling technique has been used to generate gratings of 100-nm period on a silicon mold [30]. The mold pattern should then be replicated into the PMMA resist layer by nanoimprint lithography for subsequent material processing.

Polymer microring resonators have been fabricated by either direct imprinting of a polymer film (PMMA, PS, PC) or filling the cavity of an imprinted polymer layer, followed by a buffered HF etching to remove partially the supporting SiO<sub>2</sub> layer on a silicon substrate. Optical filtering with a  $Q$  factor of 5800 has been demonstrated [143]. Nanoimprint lithography has also been used to fabricate crossed dipole resonant filters for the infrared frequencies. Using a bilayer system of MMA/PMMA, which is more suitable to obtain undercut for lift-off, filters for 6- $\mu$ m wavelengths were obtained [144].

Photonic crystals are artificial materials in which the dielectric constant is periodically modulated at length scale comparable to optical wavelengths. Various functionalities can be obtained by engineering nanostructures based the concept of photonic crystals, including waveguides, microresonators, etc. Nanoimprinting has been used to test the feasibility of replicating large area photonic structures. For example, a Y-branch defined by a two-dimensional photonic crystal with a hexagonal lattice has been imprinted into polystyrene on oxidized silicon [145] which could be transferable into the substrate.

For the fabrication of binary diffractive elements, nanoimprinting is clearly advantageous because of the requirement of high resolution. Previously, we have replicated binary diffractive elements of various characteristics, followed by lift-off and RIE of a thin TiO<sub>2</sub> layer [146]. Patterned structures with a minimum feature size of 80 nm and an etch depth of 400 nm showed optical properties of the arrays defined by e-beam lithography [147].

Antireflection layers for visible light have been fabricated by embossing high density lines and dots into PC sheets. Nickel molds were first obtained by e-beam lithography and electroplating which include gratings of 200-nm pitch, 200- and 100-nm etch depth, and different duty cycles. The replication has been done by direct embossing of a 1-mm thick PC sheet at 150 °C. The embossed PC gratings showed significantly reduced reflections for both TE and TM polarizations [148].

More conventional diffractive optical elements are widely used and manufactured by injection molding. Although injection molding is a low cost for high volume production, nanoembossing is more convenient for research, prototyping, and the fabrication of nanoscale features. Previously, the ability to replicate diffractive optical elements with curved sectional structures has been demonstrated using a 3D Ni mold [29, 148].

For high density data storage, nanocompact disks have been produced by nanoimprinting with a storage density as high as 400 Gbit/in<sup>2</sup>. Here, a SiO<sub>2</sub> mold of 75-nm etch depth

has been used to imprint a 90-nm thick PMMA layer at 175 °C. The replicated pattern showed a 10-nm feature size and 50-nm track width after a Ti(5 nm)/Au(10 nm) thin film deposition and lift-off [149]. Similarly, read-only disk patterns of 100-nm track pitch have been replicated by using nanoembossing of an acrylate-based 2P process [120].

Nanoembossing has also been used to replicate a diffraction grating of 0.6- $\mu$ m period on a film of bis-benzocyclobutene [150]. Then, a thin film of Alq<sub>3</sub> doped with DCM (4-(dicyanomethylene)-2methyl-6-(*p*-dimethylaminostyryl)-4H-pyran) dye molecules is deposited on the diffraction grating, resulting in an optical pumped laser emission occurring at 655 nm which corresponds to the third order of the grating diffraction. Alternatively, nanoembossing has been used for direct formation of organic light emission structures. PMMA blended with various semiconductor molecules like Alq<sub>3</sub> and DCMI was embossed into 200-nm period and 300-nm height gratings. Embossing was performed in a vacuum of  $\sim$ 1 Torr at a pressure of 54 bar and a temperature of 150 °C. The resulting structures showed no optical degradation of the imprinted films. Moreover, a molecular alignment in the polymer matrix has been observed which may have applications in the field of nonlinear optics and organic optoelectronics [151]. More recently, organic polymer light-emitting pixels have been obtained with feature sizes ranging from 50 down to 2  $\mu$ m. These pixel arrays were first obtained by imprinting a PMMA (insulating) layer spin coated on an ITO glass. Then, a hole transport layer, poly(3,4-ethylenedioxythiophene)-polystyrene sulfonate, and a red emissive polyfluorene derivative polymer layer were consecutively spin coated on the patterned surface, followed by a cathode metal deposition [152].

### 6.3. Nanomagnetism

Patterned magnetic structures can be used for both ultra-high density recording and the fabrication of spin-electronic devices such as randomly accessible memories, spin transistors, resonant tunnel, and nonvolatile programmable logic devices [153–156].

Initially, nanoimprint lithography was proposed by Chou et al. for fabrication of the so-called planar quantum magnetic disks (QMD) which consist of single domain magnetic nanopillars (Ni) uniformly embedded in a disk of nonmagnetic matrix (SiO<sub>2</sub>) [154]. In a QMD, each nanopillar contains two discrete magnetic states with equal but opposite magnetic moments, thus allowing one to store one bit of information. The proposed fabrication sequence is the following: (i) deposition of a thin metal base and then a film of silicon dioxide, (ii) nanoimprint lithography with 200-nm thick PMMA, (iii) shallow evaporation of a chrome layer (on the top of the resist layer but not in the embossed PMMA trenches), (iv) RIE of SiO<sub>2</sub>, (v) removal of the remaining PMMA resist, (vi) electroplating of nickel or cobalt, and finally (vii) chemical mechanical polishing. Now, the concept of planar QMD structures has been proven experimentally [157] and the reported results showed 70-nm diameter and 400-nm height single domain nickel pillars embedded in a SiO<sub>2</sub> matrix, corresponding to a storage density of 18 Gbit/in<sup>2</sup> [157, 158].

Co/Pt and CoNi/Pt multilayers with magnetization perpendicular to the plane have been patterned by nanoimprint lithography and ion milling techniques. We found that the magnetization in these systems depends on the dot size through the spatial distribution of the nucleation centers and that the hysteresis loops become more rounded with a larger coercive field as the diameter decreases [86].

More generally, nanoimprint lithography has been used to study magnetic properties of patterned structures with in-plane magnetization and different geometries (dot, rings, squares, etc.) [159–162]. For example, Co dots of diameter varying in the range 100 to 500 nm and thickness 10 to 100 nm were obtained by trilayer nanoimprint and lift-off techniques, revealing the size and the thickness dependences of the remnant state and the magnetization reversal processes (Fig. 11). Two types of hysteresis loops were found, characterized by the formation of a single domain or a vortex state [159]. Further investigation has been focused on the interdot coupling of densely packed cobalt arrays, showing a number of interesting phenomena due to magnetic dipolar coupling between dots [160, 161].

Magnetic microrings have attracted a particular attention because of the more stable flux close (FC) magnetization states without the formation of the central vortex core. Consequently, undesired interactions between adjacent magnets of the device are minimized because of the absence of the stray field in the FC states. Submicrometer rings were obtained by nanoimprint and lift-off of Co films of thicknesses varying in the range of 10 to 100 nm. Experimental data and simulations all confirmed the formation of stable FC states in microrings. Similar to the case of Co dots, two kinds of magnetization behavior have been observed: one involving the FC state and another near-single domain state (Fig. 11). The observed size and thickness dependencies of the rings are comparable to those obtained with Co rings made by e-beam lithography, from which a phase diagram in ring diameter and thickness could be established [162, 163].

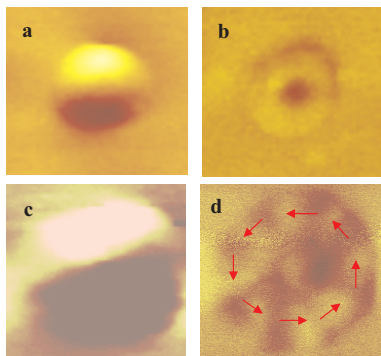


**Figure 11.** MFM images of a cobalt dot of 500-nm diameter and 15-nm thickness showing a single domain (a) and same diameter but 30-nm thickness showing a vortex (b) at remnant states; and a cobalt ring of 400-nm diameter, 200-nm linewidth and 20-nm thickness showing respectively a single domain state under applied field (c) and a vortex state at remnant state (d). The octagonal ring shape was intentionally designed for easy contrast identification. (a) and (b) were reprinted with permission from [159], A. Lebib et al., *J. Appl. Phys.* 89, 3892 (2002). © 2002, American Institute of Physics.

There are other techniques to pattern planar magnetic structures (e.g., ion irradiation induced mixing which can be used to change locally the magnetic properties for ultrathin Co/Pt multilayer thin films) [164, 165]. Here, masks for irradiation can be obtained by lithography methods. The ion irradiation in unmasked areas induces atomic displacements at the Co/Pt interfaces (intermixing), which results in a remarkable change of the magnetic properties in the irradiated zone. Both patterned polymer and dielectric material can be used as masks for ion irradiation. With 450-nm thick SiO<sub>2</sub> layer for example, we obtained a mask feature size as small as 30 nm. Stencil masks can also be used for ion induced mixing [166]. Nanoimprint lithography should be useful for the fabrication of the two types of ion implantation masks.

High quality magnetic nanostructures can also be obtained by depositing magnetic thin films directly on a prepatterned substrate such as silicon, GaAs, etc. The commonly used technique for the substrate patterning is RIE [167] but chemical printing has shown to have a good performance as well [168, 169]. The advantage of using etched substrates is that various deposition techniques such as sputtering and molecular beam epitaxy can be applied, allowing the fabrication of high quality magnetic structures. Embossed polymer structures can also be used as patterned substrates for magnetic thin film deposition. Because of its low cost and flexibility, nanoembossing of full plastic features is well suited for high volume fabrication.

To pattern homogeneously magnetic structures over a very large surface area, a flexible mold which consisted of a 10- $\mu$ m thick polymer mold on an acrylic backing plate obtained by photocuring an acrylate mixture over a SiO<sub>2</sub> master has been used. As a result, 50-nm diameter single domain magnetic islands over 3 cm areas have been demonstrated very recently by the IBM group at Almaden Research Center [170].

In comparison to the study of patterned magnetic structures, much less effort has been devoted to the fabrication of spin devices using nanoimprint lithography. Spin valve structures consisting of a NiFe/Cu/Co multilayer and sizes down to 70 nm  $\times$  1  $\mu$ m have been fabricated by nanoimprint lithography, ion milling, or lift-off [171]. They showed characteristic behaviors in the measured magnetotransport curves and magnetic force microscopy (MFM) images. Both ion milling and lift-off patterning affected the device performance because of the important edge effect and further improvements are expected.

## 6.4. Applications in Biology

During the past decade, a substantial progress has been made in the development of nanotechnology for biological and chemistry applications [172–176]. For example, new methods and tools such as DNA chips and microfluidic devices have been invented for biomedical (gene sequencing, drug discovery, and diagnostics) and medical (minimally invasive therapy, precision surgery, drug delivery, and biosensors) research and applications. While many of them have relied on micro- and nanofabrication technologies, nanoembossing offers some new possibilities. For example,



nanoembossing can be used to produce high density plastic assays as well as functional microfluidic devices. It can also be used to modify the physical or chemical properties of a surface which is useful in a controlled cell culture and neurological studies. Finally, it can be used to fabricate new sensors and biocompatible electronic, microwave, or optical components.

For biological applications, it is often necessary to engineer the properties of the surface at a molecular level. This can be achieved by nanoimprint lithography in a way similar to metal structure fabrication via lift-off. For example, nanoimprint lithography has been used to pattern a 75 kg/mol PMMA layer of thickness 80–120 nm on a silicon dioxide substrate [177]. After imprinting and removal of the recessed area by RIE, a silane layer was deposited and lifted off in acetone. Thus, a patterned silane layer was obtained, showing distinct wetting properties between patterned and unpatterned areas: large water drops were observed mainly in the areas without silanization. Note that silanes are available with various functional groups and they can be deposited by either gas evaporation or solution dip. Therefore, the chemical properties of a surface can be tailored precisely which can then be used for various applications [178, 179]. In addition, once a silane pattern is formed, the unsilanized part can be functionalized with other groups of silanes in such a way that the two regions either promote or resist the adhesion of proteins or cells. Of course, soft lithography is also well suited for the surface modification but nanoembossing can offer a higher resolution and more robust and versatile processes.

Another example is the fabrication of topographic features for cellular engineering. It was found, for example, that cells are guided along micrometer sized grooves but do not adhere to the surface of nanopillars. Nanoembossing of biodegradable polymers showed excellent resolution. It is believed that such patterned topographic features can be used for the fabrication of therapeutic devices such as tendon repair [180].

DNA chips and other types of biochips are now widely used in genetic disease diagnostics, drug design, and biomedical research. The first DNA chips have been manufactured using optical lithography and bioengineering [181]. Different single-stranded DNA sequences are placed selectively on a substrate to form a microarray that allows a later detection of complementary DNA targets by hybridization. Considerable efforts have been made to improve the sensibility of detection and the reliability of data statistics. Further progress is expected based on, for example, a continuous scaling down of the reaction area, which would allow a larger variety of probes and thus increase both hybridization and identification speed. Similarly, proteins and cell chips can be fabricated but they are still challenging because of the increased complicity. In both cases, nanoembossing techniques could be explored for a great diversity of improvements and new functionality implementations.

One of the important applications of the nanoimprint lithography is the fabrication of biosensors, where high resolution patterning techniques are sometimes needed. As one example, biosensors with large area interdigitated nanoelectrodes have been fabricated using a mix-and-match fabrication process [105]. Standard nanoimprint lithography

has been used first to define the interdigitated electrodes of 100-nm linewidth with different spacing over a  $200 \times 200 \mu\text{m}^2$  area, a  $\text{SiO}_2/\text{Si}$  substrate followed by a 20-nm Cr thick evaporation and lift-off. Afterward, UV lithography with alignment was used to pattern the Al contacting areas via lift-off. The fabricated devices showed no creeping current on the surface and a capacitance of about 17 pF was found which did not vary significantly between 1 kHz and 1 MHz.

The most relevant application of nanoembossing in biology areas is perhaps the development of microfluidic devices, also known as lab-on-a chip, bio microelectromechanic systems, and micro total analysis systems. In a microfluidic device, elements such as fluid injectors, filters, pumps, valves, mixers, and detectors are also made on a chip. Previously, several fabrication technologies have been developed, including silicon and glass based micromachining, plastic forming, and soft lithography prototyping [43, 151, 178, 179, 182]. For many applications such as point-of-care clinical diagnostics, disposable assays are needed to avoid cross-contamination. For this reason, biocompatible polymers are the materials of choice and both nanoembossing and soft lithography can be used for the device fabrication.

Compared to laboratory scale experimentation, an on-chip processing of chemical and biological species offers many advantages such as much reduced reagent cost, power consumption, and space occupation. High throughput and high efficiency screening are expected because of the system integration. Moreover, the reaction efficiency can be largely enhanced due significant increases of the surface to volume ratio. For these reasons, a large number of research and industrial laboratories are involved in the development of microfluidic devices, with clear perspectives for a very broad application area, including high throughput screening, clinical diagnostics, environmental analysis, cell analysis, drug discovery to portable devices for minimally invasive therapy, precision surgery, as well as drug delivery [6, 7, 172–175].

All nanoembossing techniques can be used for the development of microfluidic devices. To fabricate all plastic devices for example, nanoembossing can be used in different ways. One of the examples is direct embossing of plastic structures, followed by thermal bonding, as described in [12]. First, a thin plastic plate is first formed by hot embossing which provides microchannels and other desired geometries. Similarly, a thick plastic plate with microfluidic connection sockets can be formed with the help of an additional metallic frame. Then the two plastic plates are thermally bonded, being ready for immediate electrophoresis applications.

Electrophoresis is widely used for the separation of charged molecules (DNA, proteins, etc.) of different sizes according to their different migration velocities [183]. The motion of a charged molecule is also influenced by the electroosmotic flow (EOF) which in turn depends on the surface properties of the microchannel. Basically, EOF is due to the presence of the so-called electric double layer (i.e., an adsorbed layer of cations and a diffuse layer near the microchannel wall). When a voltage drop is applied externally between the two ends of the channel, a force toward the cathode is exerted on the diffuse charge layer, which results in a fluid motion by viscous drag. To improve the



device performance, various surface treatments of the plastic materials have been proposed and a detailed analysis can be found in [43, 179].

Other functionalities can be integrated into the fabricated plastic devices. For example, asymmetric microelectrode arrays can be inserted in the microchannels before thermal bonding [184]. Applying a stationary ac voltage of low amplitude, typically 1 Volt, a net fluid flow could be generated in a microchannel and the pumping velocity reaches a maximum at a frequency of 5 kHz. Within the degradation limit, increasing voltage at a fixed frequency induces a nonlinear rise of the pumping velocity. Other ac effects such as solution mixing and molecule separation and detection are expected. Finally, the demonstrated electrode arrays can be placed in different places on the microchannels, thereby providing an easy method for a high degree of system integration.

Nanoembossing can also be used to fabricate hybrid microfluidic devices such as PDMS placed on a plastic, silicon, or glass substrate. Now, a PDMS top layer is prepared and access holes to the reservoirs are punched by nanoembossing, substrates can be patterned with various functionalities that can be obtained with PDMS. Adhesion of PDMS to low roughness surfaces is excellent and a reversible water-tight seal can be obtained by conformal contact on glass, Si, plastic, as well as PDMS surfaces. For irreversible bonding, oxygen plasma exposure is sufficient. More sophisticated devices which contain valves and pumps were obtained by multilayer PDMS processing.

As one example, nanoimprint lithography has been used to pattern a silicon wafer with high density nanopillars integrated in a functional microchannel [54]. These structures were designed for the long DNA molecule separation. The array of stationary obstacles forces DNA molecules to snake their way through at different velocities according their size and yield improved separation performance. Figure 12 shows a schematic presentation of a microchannel for DNA molecular separation (a) and an area of the fabricated 320-nm period triangular array of 150-nm diameter SiO<sub>2</sub> pillars (b). They were obtained by trilayer nanoimprint lithography, followed by subsequent metal lift-off and RIE of SiO<sub>2</sub> in a CHF<sub>3</sub>/SF<sub>6</sub> gas mixture, allowing one to obtain a homogeneous pattern depth of 500 nm over a large area containing

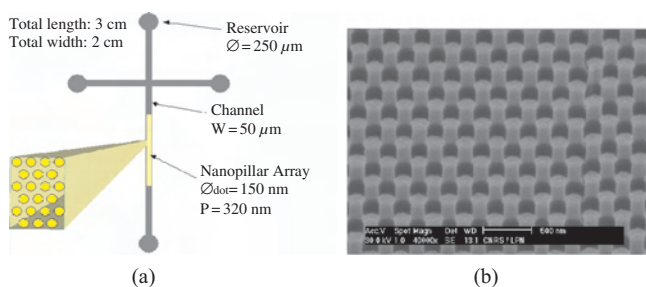


**Figure 12.** Schematic representation of a microchannel for DNA molecular separation (a) and 150-nm dot arrays inserted in the microchannel obtained by nanoimprint lithography and dry etching of 500-nm silicon dioxide (b). Reprinted with permission from [51], A. Pépin et al., *Microelectron. Eng.* 61, 927 (2002). © 2002, Elsevier Science.

both microchannels and nanopillars. Finally, the top PDMS part is fixed on the nanostructured SiO<sub>2</sub>/Si substrate by thermal bonding, after treating the top and bottom parts with oxygen plasma. Similar microfluidic devices could also be obtained based on the all plastic fabrication (Section 3).

More recently, nanoimprint lithography has been used to fabricate nanofluidic channels with a mold of 200-nm period grating obtained by interferometric lithography. After imprinting and etching, 85-nm wide trenches were produced and then sealed by either electron beam evaporation with a tilted sample wafer at various angles or sputtering deposition using a large source target. The channel width down to 10-nm could be achieved by a single step SiO<sub>2</sub> sputtering, thereby providing a way to confine biological molecules into ultrasmall spaces [185].

## 7. CONCLUSION

Nanoembossing is becoming a rapidly growing part of nanofabrication technology because of its ultrahigh resolution, parallel processing, and low cost. In particular, nanoimprint lithography has benefited from the impact of continuous scaling down of feature sizes in microelectronic circuits. In this chapter, we have reviewed several nanoembossing techniques and presented a number of application examples. They illustrated how nonconventional nanofabrication methods are profoundly changing the way of processing and the ability of device manufacturing, although these examples are far from the general interest of the nanoembossing techniques themselves. Much progress is expected on both sides of technological developments and device applications. Finally, nanoembossing is attractive not only for its lithography ability but also for its potentiality of molecular level processing. Nature makes tiny structures and complex patterns by self-organization and template replication. By addressing the molecular level, nanoembossing will be capable of covering much more broad applications areas.

## GLOSSARY

**Critical dimension** The width of a line or space that has been identified as critical to the device being fabricated.

**Glass transition temperature ( $T_g$ )** Amorphous phases such as glasses and plastics are rigid and brittle (like glass) below their glass transition temperature and elastics above it.

**Lift-off** A pattern transfer method used to obtain features on a wafer surface by first depositing a thin film of such as gold over a patterned resist layer and then dissolving the underlying resist, leaving only the portions that are deposited on the wafer surface.

**Lithography** A process to transfer a pattern from one medium to another, for example, transferring a pattern from a mold to a wafer.

**Mold** A plate with a pattern of etched and non-etched areas that can be used to deform mechanically a thin film of polymers on wafers or other materials.

**Photocurable polymers** Pre-polymer mixtures that can be polymerized at a rapid rate by exposure to light.

**Reactive ion etching** A pattern transfer method used to obtain features by both plasma etching and chemical reactions; Under appropriate conditions, reactive ion etch can give highly selectivity and a high degree of anisotropy.

**Resist** A thin film of material coated on wafers that is used to form patterns by lithography and then to mask or protect selected areas of a circuit board from etching, plating or coating processes.

**Resolution** The size of the smallest feature a system can clearly define on a resist layer; in many case the half pitch size of a periodic pattern is used to define the resolution.

**Thermoplastic polymers** They are softened when heated and reharden when cooled; Such a soften-harden sequence can be repeated for many times, subject to possible chemical degradation of the material.

**Thermosetting polymers** They become permanently hard once cured at elevated temperature, because of an irreversible chemical change.

**Tri-layer process** A lithography method used to obtain resist features of an improved profile; One first makes patterns on a top-layer thin film and then performs a pattern transfer by reactive ion etching of intermediate and bottom layers with different gases.

**Viscosity** An internal property of a fluid that describes a resistance to flow; the related shearing stress depends upon the velocity of the flow.

## ACKNOWLEDGMENTS

The author is grateful to E. Cambriel, F. Carcenac, D. Decanini, L. Ferlazzo, A. Lebib, S. P. Li, M. Natali, A. Pépin, D. Payrade, E. Roy, and V. Studer for their valuable contributions. This work was supported in part by the European Commission under the ESPRIT Program #29097 (SPINUP) and the IST Project #2001-37472 (SOUVENIR).

## REFERENCES

- National Technology Roadmap for Semiconductor Industry Association, [http://public.itrs.net/files/1999\\_SIA\\_Roadmap/Home.htm](http://public.itrs.net/files/1999_SIA_Roadmap/Home.htm), 1999.
- European Commission, Technology Roadmap for Nanoelectronics, 2nd ed., (R. Compano, Ed.), 2000.
- National Nanotechnology Initiative: The Initiative and Its Implementation Plan, <http://www.nano.gov/nni2.pdf>, 2001.
- "Confined Electrons and Photons: New Physics and Applications" (E. Burstein and C. Weisbuch, Eds.), NATO ASI Series B, Vol. 340, Plenum Press, New York, 1997.
- D. D. Awschalom and S. von Molnar, in "Handbook of Microlithography, Microfabrication and Microsystems" (P. Rai-Choudhury, Ed.), Vol. 1, p. 438. SPEI Press, Bellingham, WA, 1997.
- See, for example, "Proceedings of Micro Total Analysis Systems ( $\mu$ TAS)." Kluwer Academic, Dordrecht, 1998, 2000, 2002.
- For a recent review, see Y. Chen and A. Pépin, *Electrophoresis* 122, 187 (2001).
- "Nanotechnology" (G. Timp, Ed.). Springer-Verlag, New York, 1998.
- S. Y. Chou, P. R. Krauss, and J. Renstrom, *Appl. Phys. Lett.* 67, 3114 (1995).
- S. Y. Chou, P. R. Krauss, and J. Renstrom, *Science* 85, 272 (1996).
- M. Colburn, A. Grot, M. Amistoso, B. J. Choi, T. Bailey, J. G. Ekerdt, S. V. Sreenivasan, J. Hollenhorst, and C. G. Willson, *Proc. SPIE* 3676, 379 (1999).
- V. Studer, A. Pépin, and Y. Chen, *Appl. Phys. Lett.* 80, 3641 (2002).
- S. Y. Chou, C. Keimel, and J. Gu, *Nature* 417, 835 (2002).
- H. C. Scheer, H. Schulz, T. Hoffmann, and C. M. Sotomayor Torres, Nanoimprint techniques, in "The Handbook of Thin Films" (H. S. Nalwa, Ed.). Academic Press, San Diego, 2001.
- "Alternative Lithography, Book Series on Nanostructure Science and Technology" (C. M. Sotomayor-Torres, Ed.). Kluwer Academic/Plenum, New York, 2002.
- A large number of publications appeared since 1998 in EIPBN (Electron, Ion and Photon Beam Technology and Nanofabrication) and MNE (Micro and Nano Engineering) conferences and more recently in the "Int. Workshop on NanoImprint Lithography" (Lund, 16–17 January 2002) and the "First Int. Conference On Nanoimprint and NanoPrint Technology" (San Francisco, 11–13 December 2002).
- G. L. T. Chiu and J. M. Shaw, *IBM J. Rev. Develop.* 41, 3 (1997).
- M. A. McCord and M. J. Rooks, in "Handbook of Microlithography, Microfabrication and Microsystems" (P. Rai-Choudhury, Ed.), Vol 1, p. 139. SPEI Press, Bellingham, WA, (1997).
- Y. Chen, F. Carcenac, F. Rousseaux, and H. Launois, *Jpn. J. Appl. Phys.* 33, 6923 (1994).
- D. P. Mancini, K. A. Gehoski, E. Ainley, K. J. Nordquist, D. J. Resnick, T. C. Bailey, S. V. Sreenivasan, J. G. Ekerdt, and C. G. Willson, *J. Vac. Sci. Technol. B* 20, 2896 (2002).
- F. Carcenac, C. Vieu, A. Lebib, Y. Chen, and H. Launois, *Microelectron. Eng.* 53, 163 (2000).
- H. G. Craighead, R. E. Howard, L. D. Jackel, and P. M. Mankievich, *Appl. Phys. Lett.* 42, 3841 (1983).
- W. Chen and H. Ahmed, *Appl. Phys. Lett.* 62, 1499 (1993).
- W. Chen and H. Ahmed, *J. Vac. Sci. Technol. B* 11, 2519 (1993).
- Y. Chen, C. Vieu, and H. Launois, *Cond. Mater. Phys.* 6, 22 (1998).
- F. C. M. J. M. Van Delft, J. P. Weterings, A. K. Langen-Suurling, and H. Romin, *J. Vac. Sci. Technol. B* 18, 3419 (2000).
- B. E. Maile, W. Henschel, H. Kurz, B. Reinks, R. Polman, and P. Kaars, *Jpn. J. Appl. Phys., Part 1* 39, 6838 (2000).
- M. Madou, "Fundamentals of Microfabrication." CRC Press, Boca Raton, FL, 1997.
- M. T. Gale, *Microelectron. Eng.* 34, 321 (1997).
- Z. Yu, W. Wu, L. Chen, and S. Y. Chou, *J. Vac. Sci. Technol. B* 19, 2816 (2001).
- D. C. Flanders and A. E. White, *J. Vac. Sci. Technol.* 19, 892 (1981).
- R. Juhasez and J. Linnros, *Appl. Phys. Lett.* 78, 3118 (2001).
- W. J. Dauksher, K. J. Nordquist, D. P. Mancini, D. J. Resnick, J. H. Baker, A. E. Hooper, A. A. Talin, T. C. Bailey, A. M. Lemonds, S. V. Sreenivasan, J. G. Ekerdt, and C. G. Willson, *J. Vac. Sci. Technol. B* 20, 2857 (2002).
- G. T. A. Kovacs, D. I. Maluf, and A. K. E. Petersen, *Proc. IEEE* 86, 1537 (1998).
- H. Schift, C. David, J. Gobrecht, A. D'Amore, D. Simoneta, W. Kaiser, and M. Gabriel, *J. Vac. Sci. Technol. B* 18, 3564 (2000).
- M. Austin and S. Y. Chou, *J. Vac. Sci. Technol. B* 20, 665 (2002).
- D. S. Macintyre, Y. Chen, D. Lim, and S. Thoms, *J. Vac. Sci. Technol. B* 19, 2797 (2002).
- J. M. Sauffer, Y. Oppliger, P. Regnault, L. Baraldi, and M. T. Gale, *J. Vac. Sci. Technol. B* 10, 2526 (1992).
- Y. Hirai, S. Harada, H. Kikuta, Y. Tanaka, M. Okano, S. Isaka, and M. Kobayasi, *J. Vac. Sci. Technol. B* 20, 2867 (2002).
- K. Pfeiffer, M. Fink, G. Ahrens, G. Gructzener, F. Reuther, J. Seekamp, S. Zankovych, C. M. Sotomayor Torres, I. Maximov, M. Beck, M. Graczyk, L. Montelius, H. Schulz, H. C. Scheer, and F. Steingrueber, *Microelectron. Eng.* 53, 411 (2000).
- B. Heidari, I. Maximov, E. L. Sawe, and L. Montelius, *J. Vac. Sci. Technol. B* 17, 1861 (1999).

42. R. W. Jaszewski, H. Schiff, P. Grönig, and G. Margaritondo, *Microelectron. Eng.* 35, 381 (1997).
43. M. Beck, M. Graczyk, I. Maximov, E. L. Sarwe, T. G. I. Ling, and L. Montelius, *Microelectron. Eng.* 61/62, 441 (2001).
44. JenaOptik Mikrotechnik (<http://www.jenaoptik.de>), Obducat (<http://www.obducat.com>), EV Group (<http://www.evgroup.com>), SÜSS MicroTec (<http://www.suss.com>).
45. Nanonex (<http://www.nanonex.com>), Nanoopto (<http://www.nanoopto.com>), Molecular Imprint Inc. (<http://www.molecularimprints.com>).
46. SPECAC (<http://www.specac.com>); see also [65].
47. H. W. Lehmann, R. Widmer, M. Ednoether, A. Wokaun, M. Meier, and S. K. Miller, *J. Vac. Sci. Technol. B* 1, 1207 (1983).
48. H. Becker and L. E. Locascio, *Talanta* 56, 267 (2002).
49. Y. Liu, D. Ganser, A. Schneider, R. Liu, P. Grodzinski, and N. Kroutchinina, *Anal. Chem.* 73, 4196 (2001).
50. D. W. Van Krevelen, "Proprieties of Polymers." Elsevier, Amsterdam, 1990.
51. A. Pépin, P. Youinou, V. Studer, A. Lebib, and Y. Chen, *Microelectron. Eng.* 61/62, 927 (2002).
52. M. Reyne, "Technologie des Plastiques." Hermes, Paris, 1998.
53. M. Macintyre and S. Thoms, *Microelectron. Eng.* 41/41, 211 (1998).
54. H. Schiff, C. David, J. Gobrecht, A. D'Amore, D. Simoneta, W. Kaiser, and M. Gabriel, *Microelectron. Eng.* 53, 171 (2000).
55. J. M. G. Cowie, "Polymers: Chemistry and Physics of Modern Materials." Blackie, New York, 1991.
56. W. P. Callister, Jr., "Materials Science and Engineering." Wiley, New York, 2000.
57. G. M. Whitesides and A. D. Stroock, *Phys. Today* 54, 42 (2001).
58. Y. Xia and G. M. Whitesides, *Angew. Chem. Int. Ed.* 37, 550 (1998).
59. D. Qin, Y. Xia, J. A. Rogers, R. J. Jackman, X. M. Zhao, and G. W. Whitesides in "Microsystem Technology in Chemistry and Life Sciences," (A. Manz and H. Becker, Eds.). Springer-Verlag, Berlin, 1998.
60. M. A. Unger, H. P. Chou, T. Thorsen, A. Scherer, and S. Quake, *Science* 288, 113 (2000).
61. T. Thoeson, S. J. Maerkl, and S. Quake, *Science* 298, 580 (2002).
62. H. Schimid and B. Michel, *Macromolecules* 33, 3042 (2000).
63. Y. Chen, A. Lebib, F. Carcenac, H. Launois, G. Schmidt, M. Tormen, G. Müller, L. W. Molenkamp, M. Liebau, J. Huskens, and S. N. Reinholt, *Microelectron. Eng.* 53, 253 (2000).
64. Y. Chen, A. Lebib, S. Li, D. Peyrade, M. Natali, A. Pépin, and E. Cambriil, *Eur. Phys. J. Appl. Phys.* 12, 223 (2000).
65. M. Tormen, T. Borzenko, G. Schmidt, J. Liu, and L. W. Molenkamp, *Electron. Lett.* 36, 983 (2000).
66. L. Malaquin, F. Carcenac, C. Vieu, and M. Mauzac, *Microelectron. Eng.* 61/62, 379 (2002).
67. Q. Xia, C. Keimel, H. Ge, Z. Yu, W. Wu, and S. Chou, in "First Int. Conf. on Nanoimprint and Nanoprint Technology," San Francisco, 11–13 December 2002.
68. J. Wang, X. Sun, L. Chen, and S. Y. Chou, *Appl. Phys. Lett.* 75, 2767 (1999).
69. M. Behl, J. Seekman, S. Zankovych, C. Sotomayer Torres, R. Zentel, and J. Ahopelto, *Adv. Mater.* 14, 588 (2002).
70. J. R. Lawrence, P. Andrew, W. L. Barnes, M. Beck, G. A. Turnbull, and I. D. W. Samuel, *Appl. Phys. Lett.* 81, 1955 (2002).
71. K. E. Paul, T. L. Breen, J. Aizenberg, and G. M. Whitesides, *Appl. Phys. Lett.* 73, 2893 (1998).
72. G. Fichet, N. Stutzman, B. O. Muir, and W. T. S. Huck, *Adv. Mater.* 14, 47 (2002).
73. C. A. Bulthaupt, E. J. Wilhelm, B. N. Hubert, B. A. Ridley, and J. M. Jacobson, *Appl. Phys. Lett.* 79, 1525 (2001).
74. S. W. Pang, T. Tamamura, M. Nakao, A. Ozawa, and H. Masuda, *J. Vac. Sci. Technol. B* 16, 1145 (1998).
75. M. Li, H. Tan, L. Chen, J. Wang, H. Ge, W. Wu, Z. Yu, and S. Y. Chou, in "First Int. Conf. on Nanoimprint and Nanoprint Technology," San Francisco, 11–13 December 2002.
76. S. Wang, J. F. Li, K. Wakabayashi, M. Esashi, and R. Watanabe, *Adv. Mater.* 11, 873 (1999).
77. S. Y. Chou, P. R. Krauss, W. Zhang, L. Guo, and L. Zhang, *J. Vac. Sci. Technol. B* 15, 2897 (1997).
78. R. W. Jaszewski, H. Schiff, J. Gobrecht, and P. Smith, *Microelectron. Eng.* 41/42, 575 (1998).
79. H.-C. Scheer, H. Schulz, T. Hoffmann, and C. M. Sotomayer Torres, *J. Vac. Sci. Technol. B* 16, 3917 (1998).
80. A. Lebib, Y. Chen, J. Bourneix, F. Carcenac, E. Cambriil, L. Couraud, and H. Launois, *Microelectron. Eng.* 46, 319 (1999).
81. B. G. Casey, W. Monaghain, and C. D. Wilkinson, *Microelectron. Eng.* 35, 393 (1997).
82. I. Nakamura, A. Baba, and T. Asano, *Jpn. J. Appl. Phys. Part 1* 39, 7050 (2000).
83. E. Guyon, J. P. Hulin, and L. Petit, "Hydrodynamique Physique." EDP, Paris, 2002.
84. S. Zaitsev, in "Report on the European ESPRIT project Spinup," unpublished.
85. Y. Hirai, M. Fujiwara, T. Okuno, Y. Tanaka, M. Endo, S. Irie, K. Nakagawa, and M. Sasago, *J. Vac. Sci. Technol. B* 19, 2811 (2001).
86. A. Lebib, Ph.D. Thesis, University of Paris 7, Paris, 2001.
87. C. Gourgon, C. Perret, G. Micouin, F. Lazzarino, J. H. Tortai, and O. Joubert, and J.-P. E. Grolier, *J. Vac. Sci. Technol. B* 21, 1071 (2003).
88. A. Lebib, Y. Chen, F. Carcenac, E. Cambriil, L. Manin, L. Couraud, and H. Launois, *Microelectron. Eng.* 53, 175 (2000).
89. C. Gourgon, C. Perret, and G. Micouin, *Microelectron. Eng.* 61/62, 385 (2002).
90. K. Pfeiffer, G. Bleidiessel, G. Gruetzner, H. Schulz, T. Hoffmann, H. C. Scheer, C. M. Sotomayer Torres, and J. Ahopelto, *Microelectron. Eng.* 46, 431 (1999).
91. K. Pfeiffer, M. Fink, G. Bleidiessel, G. Gruetzner, H. Schulz, H. C. Scheer, T. Hoffmann, C. M. Sotomayer Torres, F. Gaboriau, and Ch. Cardinaud, *Microelectron. Eng.* 53, 411 (2000).
92. H. Schulz, H.-C. Scheer, T. Hoffmann, C. M. Sotomayer Torres, K. Pfeiffer, M. Fink, G. Bleidiessel, G. Gruetzner, Ch. Cardinaud, F. Gaboriau, M. C. Peignon, J. Ahopelto, and B. Heidari, *J. Vac. Sci. Technol. B* 18, 1861 (2000).
93. <http://www.dsm.com/hybrane>.
94. A. Lebib, M. Natali, S. P. Li, E. Cambriil, L. Manin, Y. Chen, H. M. Janssen, R. P. Sijbesma, and E. W. Meijier, *Microelectron. Eng.* 57/58, 411 (2001).
95. A. Lebib, Y. Chen, E. Cambriil, P. Youinou, V. Studer, M. Natali, A. Pépin, H. M. Janssen, and R. P. Sijbesma, *Microelectron. Eng.* 61/62, 371 (2002).
96. N. Stutzmann, T. A. Tervoort, C. W. M. Bastiaansen, K. Feldman, and P. Smith, *Adv. Mater.* 12, 557 (2000).
97. D. Y. Khang and H. H. Lee, *Appl. Phys. Lett.* 76, 870 (2000).
98. D. Y. Khang, H. Yoon, and H. H. Lee, *Adv. Mater.* 13, 749 (2001).
99. S. Matsui, Y. Igaku, H. Ishigaki, J. Fujita, M. Ishida, Y. Ochiai, M. Komura, and H. Hiroshima, *J. Vac. Sci. Technol. B* 19, 2801 (2001).
100. T. Borzenko, M. Tormen, G. Schmidt, and L. W. Molenkamp, *Appl. Phys. Lett.* 79, 2246 (2001).
101. X. D. Huang, L.-R. Bao, X. Cheng, L. J. Guo, S. W. Pang, and A. F. Yee, *J. Vac. Sci. Technol. B* 20, 2872 (2002).
102. L.-R. Bao, X. Cheng, X. D. Huang, L. J. Guo, S. W. Pang, and A. F. Yee, *J. Vac. Sci. Technol. B* 20, 2881 (2002).
103. W. Zhang and S. Y. Chou, *Appl. Phys. Lett.* 79, 845 (2001).
104. D. L. White and O. R. Wood II, *J. Vac. Sci. Technol. B* 18, 3552 (2002).
105. L. Montelius, B. Heidari, M. Graczyk, I. Maximov, E. L. Sarwe, and T. G. Ling, *Microelectron. Eng.* 53, 521 (2000).

106. I. Martini, D. Eisert, D. A. Kamp, and A. Forchel, *Appl. Phys. Lett.* 77, 2237 (2000).
107. H. Schulz, A. S. Körbes, H.-C. Scheer, and L. J. Balk, *Microelectron. Eng.* 53, 221 (2000).
108. M. Li, L. Chen, and S. Y. Chou, *Appl. Phys. Lett.* 78, 3322 (2001).
109. L. J. Heyderman, H. Schiff, C. David, B. Ketterer, M. Auf der Maur, and J. Gobrecht, *Microelectron. Eng.* 57/58, 375 (2000).
110. G. Simon, A. M. Haghiri-Gosnet, J. Bourneix, D. Decanini, Y. Chen, F. Rousseaux, and H. Launois, *J. Vac. Sci. Technol. B* 15, 2489 (1997).
111. M. W. Legenza, D. A. Vidusek, and M. DeGrandpre, *Proc. SPIE* 539, 250 (1985).
112. X. Sun, L. Zhuang, W. Zhang, and S. Y. Chou, *J. Vac. Sci. Technol. B* 16, 3922 (1998).
113. B. Faircloth, H. Rohrs, R. Tiberio, R. Ruoff, and R. R. Krchnavek, *J. Vac. Sci. Technol. B* 18, 1866 (2000).
114. M. Li, J. Wang, L. Zhang, and S. Y. Chou, *Appl. Phys. Lett.* 76, 673 (2000).
115. B. Heidari, I. Maximov, and L. Montelius, *J. Vac. Sci. Technol. B* 18, 3557 (2000).
116. N. Roos, T. Luxbacher, T. Glinsner, K. Pfeiffer, H. Schultz, and H. C. Sheer, paper presented at the "SPIE Symposium of Microlithography," Santa Clara, CA, 27–28 February 2001.
117. T. Haatainen, J. Ahopelto, G. Gruetzner, M. Fink, and K. Pfeiffer, *Proc. SPIE* 3997, 874 (2001).
118. H. Tan, A. Gilbertson, and S. Y. Chou, *J. Vac. Sci. Technol. B* 16, 3926 (1998).
119. J. Haisma, M. Verheijen, K. Van dean Heuvel, and J. van den Berg, *J. Vac. Sci. Technol. B* 14, 4124 (1996).
120. B. D. Terris, H. J. Manin, E. Best, J. A. Logan, D. Ruger, and S. A. Rishton, *Appl. Phys. Lett.* 69, 4262 (1996).
121. Y. Chen, F. Carcenac, C. Ecoffet, D. J. Lounnot, and H. Launois, *Microelectron. Eng.* 46, 69 (1999).
122. P. Ruchhoeft, M. Colburn, B. J. Choi, T. Bailey, S. Damle, M. Stewart, J. G. Ekerdt, J. C. Wofle, and C. G. Willson, *J. Vac. Sci. Technol. B* 17, 2965 (1999).
123. B. Mender, M. Otto, B. Hadam, B. Vratzov, B. Spangenberg, and H. Kurz, *Microelectron. Eng.* 53, 233 (2000).
124. European IST Project "Souvenir," unpublished.
125. M. Otto, M. Bender, B. Hadam, B. Spangenberg, and H. Kurz, *Microelectron. Eng.* 57/58, 361 (2001).
126. M. Bender, M. Otto, B. Hadam, B. Spangenberg, and H. Kurz, *Microelectron. Eng.* 61/62, 407 (2002).
127. T. Bailey, B. J. Choi, M. Colburn, M. Meissl, S. Shaya, J. G. Ekerdt, S. V. Sreenivasan, and C. G. Willson, *J. Vac. Sci. Technol. B* 18, 3572 (2000).
128. T. Bailey, B. Smith, B. J. Choi, M. Colburn, M. Meissl, S. V. Sreenivasan, J. G. Ekerdt, and C. G. Willson, *J. Vac. Sci. Technol. B* 19, 2806 (2001).
129. M. Colburn, A. Grot, B. J. Choi, M. Amistoso, T. Bailey, S. V. Sreenivasan, J. G. Ekerdt, and C. G. Willson, *J. Vac. Sci. Technol. B* 19, 2162 (2001).
130. H. Schmid, H. Biebuyck, B. Michel, O. J. Martin, and N. B. Piller, *J. Vac. Sci. Technol. B* 16, 3422 (1998).
131. H. Schmid, H. Biebuyck, B. Michel, and O. J. Martin, *Appl. Phys. Lett.* 72, 2379 (1998).
132. J. A. Roger, K. E. Paul, R. J. Jackman, and G. M. Whitesides, *Appl. Phys. Lett.* 70, 2658 (1997).
133. J. G. Goodberlet, *Appl. Phys. Lett.* 76, 667 (2000).
134. R. J. Blaikie, M. M. Alkaisi, S. J. McNab, D. R. S. Cumming, R. Cheung, and D. G. Hasko, *Microelectron. Eng.* 46, 85 (1999).
135. L. Guo, P. R. Krauss, and S. Y. Chou, *Appl. Phys. Lett.* 71, 1881 (1988).
136. Y. Chen, D. Macintyre, E. Boyd, D. Moran, I. Thayne, and S. Thoms, *J. Vac. Sci. Technol. B* 20, 2887 (2002).
137. I. Maximov, P. Carlberg, D. Wallin, I. Shorubalko, W. Seifert, H. Q. Xu, L. Montelius, and L. Samuelson, *Nanotechnology* 13, 666 (2002).
138. M. D. Austin and S. Y. Chou, *Appl. Phys. Lett.* 81, 4431 (2002).
139. Y. Chen, in "First Int. Conf. on Nanoimprint and Nanoprint Technology," San Francisco, 11–13 December 2002.
140. Z. Yu, S. J. Schablitsky, and S. Y. Chou, *Appl. Phys. Lett.* 74, 2381 (1999).
141. Z. Yu, P. Deshpande, W. Wu, J. Wang, and S. Y. Chou, *Appl. Phys. Lett.* 77, 927 (2000).
142. J. Wang, S. J. Schablitsky, Z. Yu, W. Wu, and S. Y. Chou, *J. Vac. Sci. Technol. B* 17, 2850 (1999).
143. C. Y. Chao and L. J. Guo, *J. Vac. Sci. Technol. B* 20, 2862 (2002).
144. I. Puscasu, G. Boreman, R. C. Tiberio, D. Spencer, and R. R. Krchnavek, *J. Vac. Sci. Technol. B* 18, 3578 (2000).
145. J. Seekamp, S. Zankovich, T. Maka, R. Slaby, and C. M. Sotomayor, to be published.
146. A. Lebib and Y. Chen, unpublished.
147. M. S. Lee, Ph. Lalanne, J. C. Rodier, P. Chavel, E. Cambril, and Y. Chen, *J. Opt. A* 4, S119 (2002).
148. C. David, P. Häberling, M. Schnieper, J. Söchtig, and C. Zschokke, *Microelectron. Eng.* 61/62, 435 (2002).
149. P. R. Krauss and S. Y. Chou, *Appl. Phys. Lett.* 71, 3174 (1997).
150. M. Berggren, A. Dodabalapur, R. E. Slusher, A. Timko, and O. Nalamasu, *Appl. Phys. Lett.* 72, 410 (1998).
151. J. Wang, X. Sun, L. Zhuang, and S. Y. Chou, *Appl. Phys. Lett.* 77, 166 (2000).
152. X. Cheng, Y. Hong, J. Kanicki, and L. J. Guo, *J. Vac. Sci. Technol. B* 20, 2877 (2002).
153. S. Y. Chou, *Proc. IEEE* 85, 625 (1997).
154. P. R. Krauss and S. Y. Chou, *J. Vac. Sci. Technol. B* 13, 2850 (1995).
155. G. A. Prinz and K. Hathaway, *Phys. Today* 48, 24 (1995); G. A. Prinz, *Science* 282, 1660 (1998).
156. Y. Chen, M. Natali, S. P. Li, and A. Lebib, Application of nanoimprint lithography in magnetism, in "Alternative Lithography, Book Series on Nanostructure Science and Technology" (C. M. Sotomayor-Torres, Ed.). Kluwer Academic/Plenum, New York, 2002.
157. W. Wu, B. Cui, X. Sun, W. Zhang, L. Zhuang, L. Kong, and S. Y. Chou, *J. Vac. Sci. Technol. B* 16, 3825 (1998).
158. B. Cui, W. Wu, L. Kong, X. Sun, and S. Y. Chou, *J. Appl. Phys.* 85, 5534 (1999).
159. A. Lebib, S. P. Li, M. Natali, and Y. Chen, *J. Appl. Phys.* 89, 3892 (2001).
160. M. Natali, A. Lebib, S. P. Li, E. Cambril, and Y. Chen, *J. Vac. Sci. Technol. B* 19, 2779 (2001).
161. M. Natali, A. Lebib, Y. Chen, L. Prejbeanu, U. Ebels, L. Buda, and K. Ounadjela, *Phys. Rev. Lett.* 88, 157203 (2002).
162. Y. Chen, A. Lebib, S. P. Li, M. Natali, D. Peyrade, and E. Cambril, *Microelectron. Eng.* 57/58, 405 (2001).
163. S. P. Li, D. Peyrade, M. Natali, A. Lebib, Y. Chen, U. Ebels, L. D. Buda, and K. Ounadjela, *Phys. Rev. Lett.* 86, 1102 (2001).
164. C. Chappert, H. Bernas, J. Ferré, V. Kottler, J. P. Jamet, Y. Chen, E. Cambril, T. Devolder, F. Rousseaux, V. Mathet, and H. Launois, *Science* 280, 1920 (1998).
165. T. Devolder, Y. Chen, H. Bernas, C. Chappert, J. P. Jamet, and E. Cambril, *Appl. Phys. Lett.* 74, 3383 (1999).
166. B. Terris, L. Folks, D. Weller, J. E. E. Baglin, A. J. Kellock, H. Rothuizen, and P. Vettiger, *Appl. Phys. Lett.* 75, 403 (1999).
167. J. Moritz, S. Landis, J. P. Nozières, A. Lebib, Y. Chen, and B. Dieny, *J. Appl. Phys.* 91, 7314 (2002).
168. S. P. Li, W. S. Lew, J. A. C. Bland, L. Lopez-Diaz, M. Natali, C. A. F. Vaz, and Y. Chen, *Nature* 415, 600 (2002).
169. S. P. Li, W. S. Lew, J. A. C. Bland, L. Lopez-Diaz, C. A. F. Vaz, M. Natali, and Y. Chen, *Phys. Rev. Lett.* 88, 87202 (2002).

170. G. McClelland, M. W. Hart, M. E. Best, C. T. Rettner, K. R. Carter, and B. D. Terris, in "First Int. Conf. on Nanoimprint and Nanoprint Technology, San Francisco, 11–13 December 2002.
171. L. Kong, Q. Pan, B. Cui, M. Li, and S. Y. Chou, *J. Appl. Phys.* 85, 5492 (1999).
172. "Nanofabrication and Biosystems: Integrating Materials Science, Engineering and Biology" (H. C. Hoch, L. W. Jelinski, and H. G. Craighead, Eds.). Cambridge Univ. Press, Cambridge, UK, 1996.
173. "Microsystem Technology in Chemistry and Life Sciences" (A. Manz and H. Becker, Eds.). Springer-Verlag, Berlin, 1998.
174. "MEMS Handbook" (M. Gad-el-Hak, Ed.). CRC Press, Boca Raton FL, 2002.
175. D. R. Meldrum and M. R. Holl, *Science* 297, 1197 (2002) and references therein.
176. M. A. Burns, *Science* 296, 1818 (2002) and references therein.
177. H. Schiff, L. J. Heyderman, C. Padeste, and J. Gobrecht, *Microelectron. Eng.* 61/62, 423 (2002).
178. G. M. Whitesides, E. Ostuni, S. Takayama, X. Jiang, and D. E. Ingber, *Annu. Rev. Biomed. Eng.* 3, 335 (2001).
179. A. Pépin and Y. Chen, Soft lithography and imprint based techniques for microfluidics and biological analysis, in "Alternative Lithography, Book Series on Nanostructure Science and Technology" (C. M. Sotomayor-Torres, Ed.). Kluwer Academic/Plenum, New York, 2002.
180. C. D. W. Wilkinson, A. S. G. Curtis, and J. Crossan, *J. Vac. Sci. Technol. B* 16, 3132 (1998).
181. S. P. Fodor, R. P. Rava, X. C. Hunag, A. C. Pease, C. P. Holmes, and C. L. Admas, *Nature* 364, 555 (1993).
182. H. Becker and U. Heim, *Sensor Actuators* 83, 130 (2000).
183. J. L. Viovy, *Rev. Mod. Phys.* 72, 813 (2000).
184. V. Studer, A. Pépin, Y. Chen, and A. Ajdari, *Microelectron. Eng.* 61/62, 915 (2002).
185. H. Cao and Z. Yu, J. Wang, J. O. Tegenfeldt, R. H. Austin, E. Chen, W. Wu, and S. Y. Chou, *Appl. Phys. Lett.* 81, 174 (2002).

# Nanofabrication by Glancing Angle Deposition

Brian Dick, Michael J. Brett

*University of Alberta, Edmonton, Alberta, Canada*

## CONTENTS

1. Background
  2. Glancing Angle Deposition
  3. Glancing Angle Fundamentals
  4. Fabrication Processes  
for Specialized Applications
  5. Some Properties  
and Applications
  6. Conclusion
- Glossary  
References

## 1. BACKGROUND

### 1.1. History

The art and science of thin film technology have been in existence for several millennia. For most of this period, this technology, in the form of gold beating, was used to create ornaments [1]. For example, leaf samples from Luxor dating to the Eighteenth Dynasty (1567–1320 B.C.) measured 0.3 micrometers in thickness ([2], quoted from Ref. [1]). It is thought that the modern revolution in thin film development and application began in 1857 [3] when Faraday exploded metal wires in an inert atmosphere fabricating the first evaporated thin films. These and subsequent films were found to have properties that either did not exist in, or were significantly enhanced from, the bulk form of the evaporated material. Subsequent studies led to the modern, widespread use of thin films in such fields as antireflection coatings, sensors, packaging, and, most significantly to this work, micro- and nanoelectronics.

### 1.2. Physical and Chemical Vapor Deposition

Thin films deposited in a vacuum environment (first carried out by Nahrwold in 1887 [4]) are widely used in the industry to ensure process quality and control. These vacuum-coating techniques may be broadly defined as chemical vapor deposition (CVD) or physical vapor deposition (PVD) processes. The differences between these two types of processes lie primarily with the pressure of the environment, the number of chemical reactions in the chamber or at the substrate surface, and the source material components. PVD relies on physical mechanisms (i.e., evaporation or collision impact) to bring source atoms into the gas phase and is conducted in a reduced pressure environment to ensure ballistic atom transport. During the time that atoms are ejected from the source material and collide with the substrate, they are collectively referred to as flux. The “physical” portion of PVD is diminished only in reactive PVD, whereby gas (often oxygen) is introduced into the chamber during deposition to react with the flux and change the stoichiometry of the growing film. In contrast, CVD requires gaseous precursors to react chemically at the substrate surface to form a thin film coating.

For the purposes of this chapter, we shall limit our discussion to PVD processes and in particular the deposition techniques of sputtering and evaporation. In sputtering, a working gas (typically argon) is ignited as plasma. Ionized particles are subsequently accelerated onto the target, whereby collisions at the surface dislodge target atoms to form a vapor flux. Typical chamber pressures are on the order of  $10^{-3}$  to  $10^{-2}$  Torr (0.1 to 1.0 Pa).

The flux vapor in evaporation processes is produced by thermal means, either resistive heating of a “boat” containing source material (i.e., thermal evaporation) or electron beam heating of the source material in a crucible (electron beam evaporation). Working pressures for evaporation are less than  $10^{-5}$  Torr ( $10^{-3}$  Pa), and typically on the order of  $10^{-6}$  Torr ( $10^{-4}$  Pa) for refractory metals.



For further information on thin film deposition processes and techniques (including sputtering and evaporation) we refer the interested reader to the numerous review articles and books that have been written on the subject [1, 4–7]. In this chapter, we are concerned with the differences in working pressure for sputtering and evaporation. One of the requirements for the glancing angle technique is near colinear flux (i.e., flux atoms arrive at the substrate following parallel trajectories from the source). Increasing the working gas or background pressure in the deposition chamber decreases the particle's mean free path. Hence, flux is more properly reported as the mean arrival angle of flux plus or minus its angular distribution (i.e.,  $\alpha \pm \Delta\alpha/2$ ). This chapter generally reports films deposited with near colinear flux ( $\Delta\alpha < 2^\circ$ ), and so the angular distribution is usually not stated except in Section 3.3 where its effects on growth are explicitly examined.

### 1.3. Film Nucleation and Growth

Let us first examine physical vapor deposition as it is typically performed. A typical thin film process evaporates or sputters a source material onto the substrate such that the flux arrives at normal incidence ( $\alpha = 0^\circ$ ). Incident atoms efficiently transfer their kinetic energy to the lattice and become loosely bound “adatoms.” These adatoms diffuse over the surface, exchanging energy with the lattice or adsorbed species, until they are either desorbed (through re-evaporation or sputtering) or become trapped at low-energy lattice sites. These incorporated adatoms subsequently readjust their positions within the lattice (referred to as bulk diffusion). Hence, films initiate as small nuclei randomly distributed on the substrate. Further flux deposition, coupled with the natural tendency of the system to minimize its total surface area (or energy), causes the small nuclei to increase in size and agglomerate into islands, eventually forming a continuous, dense, solid film [1, 8, 9].

Films deposited in this fashion exhibit columnar structure. The morphology of these columns is dependent on the conditions under which the structure was formed and is particularly sensitive to the ambient chamber pressure ( $P_c$ ), and the ratio of substrate temperature ( $T$ ) to the melting point of the source material ( $T_m$ ). This sensitivity should not be a surprise as the processes of desorption, surface diffusion, and bulk diffusion identified above are energy related. Each is dependent on characteristic diffusion and sublimation activation energies and hence has a magnitude which scales directly as  $T/T_m$ .

To help understand and describe the resulting film morphology, structure zone models (SZMs) have been built based on  $P_c$  and  $T/T_m$  [10, 11] (see also [1] for a summary). In addition to the energy related processes above, an additional mechanism governing film growth has also been identified: atomic shadowing. Inherently, this mechanism does not depend on the ambient energy but is rather a geometrical effect, determined solely by the surface roughness and the linearity of the incoming flux. Atomic shadowing can be present even when films are deposited at normal incidence, resulting in a typical thin film having a density less than its bulk value.

### 1.4. Deposition at Oblique Flux Incidence

The growth of a thin film becomes more interesting when the substrate is no longer perpendicular to the arriving flux. In this case, the non-normal flux incidence angle ( $\alpha$ ) magnifies the intrinsic shadowing mechanism on the substrate surface. SZMs do not explicitly account for variations in the arriving flux incidence angle, although they do exhibit the effect to a limited degree. Zone 1 morphology is observed to extend into higher  $T/T_m$  ratios at the higher argon pressure present during sputtering [11]. This observation is the direct consequence of the broadening of the angular distribution of vapor flux due to randomizing collisions with the background gas [12]. Obliquely deposited films exhibit considerable changes in their properties, which have orientation dependence. Film stress and density are altered (usually diminished) which introduces anisotropic dependencies into the thermal, electrical, magnetic (commercialized as metal evaporated videotape), and optical properties of the film [13, 14]. Although early researchers did not have access to the necessary tools to directly observe thin film morphologies at suboptical wavelengths, the origins of these anisotropic properties were speculated to be the result of a shadowing mechanism: “the area behind the crystallite is left vacant because it is in the crystallite's shadow” ([15], quoted from [16]). These speculations have now generally been accepted as accurate and are graphically illustrated in the comparison between a normal and obliquely deposited film shown in Figure 1.

At oblique incidence, the columnar morphology of the film is tilted toward the direction of incoming flux. The angle of column growth,  $\beta$ , is a monotonically increasing

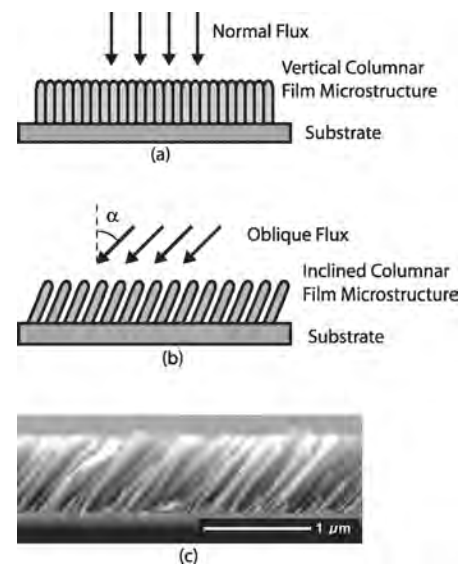


**Figure 1.** In a standard thin film deposition process, vapor flux is incident normal to the substrate, resulting in a dense microstructure (a). If the substrate is tilted relative to the incident flux, the vapor arrives at an oblique angle ( $\alpha$ ) to the substrate normal. Under limited adatom diffusion, adatom shadowing at the substrate surface results in a porous film with columns inclined toward the vapor source (b). A  $\text{SiO}_2$  film deposited at  $\alpha = 85^\circ$  is shown in (c).

function of  $\alpha$ , where  $\beta < \alpha$ . This function depends not only on  $\alpha$  but also on the choice of material, chamber pressure, substrate temperature, and source to substrate separation. The tangent rule, derived empirically by Nieuwenhuizen and Haanstra [17] and shown in Eq. (1), adequately describes the relationship between  $\alpha$  and  $\beta$  for  $\alpha < 60^\circ$  [18, 19]:

$$\tan(\alpha) = 2 \tan(\beta) \quad (1)$$

Some researchers, notably Dirks and Leamy [20], have attempted to explain the tangent rule with varying degrees of success. Generally, however, “it is good to state that this rule does not have any physical meaning, it is merely a description which seems to fit a number of measurements” [16].

## 2. GLANCING ANGLE DEPOSITION

### 2.1. Transition from Oblique to Glancing Incidence

#### 2.1.1. Beginnings

Before 1996, most studies on oblique deposition had taken place at  $\alpha < 60^\circ$ , where the tangent rule is known to be reasonably accurate [16]. Given the tangent rule prediction that  $\beta \rightarrow 90^\circ$  as  $\alpha \rightarrow 90^\circ$ , the amount of film grown at higher flux incidence would be expected to be extremely small [21]. Hence, little interest was taken in the “glancing flux angle” regime. There were a few exceptions to this rule, including an early paper by Holland (1953) [22] investigating the reflectivity of aluminum deposited at a flux incidence of  $\alpha \leq 85^\circ$  and a paper by Cohen (1961) [23] who experimented with the magnetic anisotropy of films deposited at a “grazing angle.” Both these reports seem to show that films deposited at these highly oblique incidence angles did not have columnar angles described by the tangent rule, although a lack of scanning electron microscopy at the time did not allow for direct imaging of the film morphology. Despite this lack of direct imaging, the highly oblique incidence of their depositions leads us to believe that their films were the first to exhibit the highly porous structure characteristic of glancing angle deposition (GLAD) morphology.

Much later, a few studies [18, 24] continued this earlier work by examining the nature of the film morphology at these higher incidence angles. These researchers found that the shadowing mechanism was enhanced, resulting in highly separated columns and a resulting increase in film porosity. Contrary to the tangent rule, however, they found that the columnar angle did not approach  $90^\circ$  with increasing flux incidence but rather reached a maximum somewhat less (typically  $\beta = 60^\circ$ ). Additionally, the effective deposition rate at the substrate did not drop off to zero (as might be expected at extremely high incidence angles) but rather hovered between 0.2 to 0.5x that of a film grown at normal incidence.

#### 2.1.2. Tait's Rule

A simple geometrical approach showed that  $\alpha$  and  $\beta$  could be related for evaporated thin films growth at high incidence angles ( $\alpha > 60^\circ$ ) and limited surface diffusion [18].

This argument was based on observations of ballistic deposition models, which were found to closely resemble real thin film behavior. Hence, it was believed that a discrete particle, shadowing-based expression for columnar angle could be derived [25]. The expression [18], referred to as Tait's rule and shown in Eq. (2), assumed deposition on hemispherically topped columns (the most energetically favorable geometry for low temperature depositions). The center of the column portion receiving flux was then used to determine the direction of growth. A comparison between Tait's rule and the tangent rule is shown in Figure 2a.

$$\beta = \alpha - \sin^{-1}\left(\frac{1 - \cos \alpha}{2}\right) \quad (2)$$

Neither material effects, such as faceting, nor variance in column size (both are observed in real films) are considered. Nevertheless, this equation has been shown to predict  $\beta(\alpha)$  well for Fe and  $\text{MgF}_2$  films and correctly reproduced the general observation that  $\beta$  approaches a value less than  $90^\circ$  as  $\alpha \rightarrow 90^\circ$  [21]. An alternative approach describing  $\beta(\alpha)$  has been adopted by Hodgkinson [24] to correct for a weakness inherent in both Tait's rule and the tangent rule, that is, their being generalized functions of  $\beta(\alpha)$  irrespective of the material being deposited. Hodgkinson replaced the coefficient of  $\frac{1}{2}$  in Eq. (1) with an empirically determined function of  $\alpha$  to take into account the known dependence of column angle on source material. Although this method does allow flexibility for material specific growth, to simplify our treatment of the GLAD technique we will use the generalized case,  $\beta = \beta_{\text{Tait}}$ , as the predicted column angle.

In addition to being inclined relative to the substrate normal, columns grown at oblique incidence also exhibit separation from each other if the flux incidence angle is sufficiently large. A similar geometric model for the derived form of  $\beta(\alpha)$  can be applied to obtaining the normalized column separation,  $a$ , as a function of  $\alpha$ . This function is

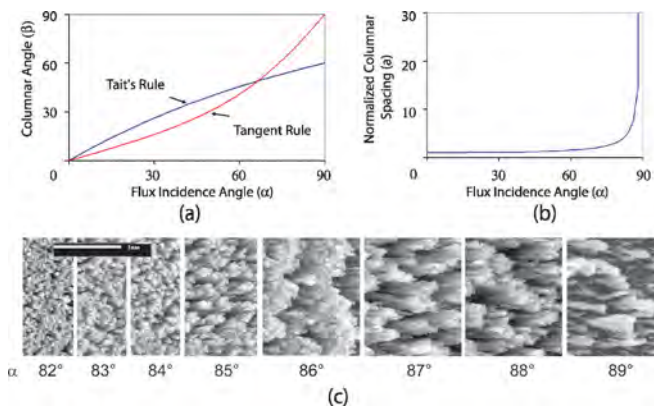


**Figure 2.** The Tait model can be used to predict the effects of deposition angle ( $\alpha$ ) on both (a) the column angle,  $\beta$ , and (b) the normalized columnar spacing,  $a$ . A comparison between Tait's rule and the tangent rule is shown in (a). Note that the  $\beta$  curve describing Tait's rule reaches a value of  $60^\circ$  as  $\alpha \rightarrow 90^\circ$ . In the lower panel, a titanium film deposited at increasingly oblique angles of incidence is used to demonstrate these effects. Figure 2c reprinted with permission from [129], D. Vick et al., *Res. Signpost*, in press. © 2002, Research Signpost.

shown in Eq. (3) and assumes that the incident adatoms are small compared with the column diameter. This assumption results in a relatively small spacing between individual columns.

$$a = \frac{1}{2} \left[ 1 + \frac{1}{\cos \alpha} \right] \quad (3)$$

This expression shows that a dramatic increase in inter-columnar spacing occurs when  $\alpha > 80^\circ$  (i.e., the glancing angle regime). This effect is shown clearly in Figure 2, where both a plot of  $a$  vs  $\alpha$  (Figure 2b) and a titanium film deposited at progressively more oblique angles are illustrated: both  $\alpha$  and the columnar separation,  $a$ , are observed to correspondingly increase significantly for  $\alpha > 80^\circ$ . This property of increased separation of columns can be used to subsequently control the film growth and its resulting microstructure. Films deposited at  $\alpha < 80^\circ$  may be viewed as relatively dense by comparison.

### 2.1.3. Substrate Rotation

In 1959, Young and Kowal observed optical activity and circular Bragg reflection in fluorite films deposited with active rotation of the substrate about an axis normal to its center [26]. This axis will be subsequently referred to as  $\phi$ .

“The possibility of evaporating in vacuum an optically active film of an otherwise isotropic material, by oblique deposition on to a flat glass substrate revolving about its normal as an axis, is confirmed. The helically deposited fluorite films ranged up to about  $18 \mu\text{m}$  thick and turned the plane of polarization of a normally incident beam by as much as  $2.25^\circ$  at  $\lambda = 0.546 \mu\text{m}$ ” ([26], quoted from [27]).

At the time, scanning electron microscopy (SEM) was not available to directly observe the films fabricated by Young and Kowal, although the relatively conservative incidence angle ( $\alpha < 70^\circ$ ) of their deposition indicates that the structures would have been reasonably dense. However, this work represents one of the first attempts to “sculpture” film microstructures to enhance or change the resulting material properties. Unfortunately, their work went relatively unnoticed until recently.

In 1989, Motohiro and Taga [28] deposited columns at an oblique incidence angle of  $\alpha = 70^\circ$  and showed that these films undergo an abrupt transition when the substrate is rotated through  $180^\circ$ . For the initial portion of the film evolution, the column grows at a set angle  $\beta$  toward the flux source. At the point the substrate is rotated by  $180^\circ$ , the column abruptly changes direction so that the column inclination again points toward the incoming flux. Essentially, the column forms a chevron structure (i.e., a “V” lying on its side) where the interface between the two distinct column directions is referred to as the Motohiro–Taga interface [29]. A stacked series of Motohiro–Taga interfaces thus forms a zigzag structure. By significantly increasing the flux incidence angle, these zigzag/chevron structures can be grown isolated from each other as a highly porous medium [30].

Initially, it was assumed that either the tangent rule ( $\alpha < 60^\circ$ ) or Tait’s rule ( $\alpha > 60^\circ$ ) were valid for all types of columnar thin films grown at oblique incidence, including those with chevron microstructure. This assumption incorrectly assumed that errors introduced by differences between the

surface normal and the substrate normal were insignificant for oblique growth. Although for many types of microstructures this assumption is valid, in chevrons the growth plane changes significantly with each subsequent turn in the flux direction: the growth surface is no longer the substrate but the previous chevron “arm.” From the perspective of the new surface normal, flux appears to be arriving at a less oblique angle. A recursive algorithm has been developed to take into account the changes in surface normal with each additional arm grown in the chevron. This algorithm is captured in Eq. (4), which calculates the theoretical  $\beta$  for the  $n$ th arm given  $\beta$  for the previous arm.

$$\beta_n = \tan^{-1} \left[ \frac{\tan(\alpha + \beta_{n-1} - 90^\circ)}{2} \right] - \beta_{n-1} + 90^\circ \quad (4)$$

$\beta_n$  approaches an asymptotic limit as  $n \rightarrow \infty$ , which is typically greater than that described by Tait’s rule [31]. At low incidence angles, the correction factor introduced by Eq. (4) is not significant (i.e., the change in  $\beta$  is not observed in the earlier Motohiro–Taga films), although its effect becomes more apparent as the flux begins to arrive at glancing incidence. For example, if  $\alpha = 85^\circ$ , a swing in  $\beta$  of nearly  $8^\circ$  is observed between the initial arms of the chevron.

Theoretical work by Azzam [32], later expanded on by Lahktakia and Weiglhofer [33], continued the work of Motohiro and Taga by suggesting that a chiral response suitable for unique optical applications may be fabricated by coupling substrate rotation with oblique incidence. After experimental development of highly porous film structures [30] the term “sculptured thin film” (STF) [34] was coined to describe films where the microstructure is actively adjusted during deposition to manipulate its properties. This term is rapidly gaining some acceptance in the literature and is often used to describe relatively dense films fabricated using oblique incidence ( $\alpha < 75^\circ$ ) and substrate rotation [24, 35–37]. Earlier films such as the Young and Kowal experiments mentioned previously are considered to be among the first STFs fabricated.

### 2.1.4. Simple GLAD Structures

Earlier, we showed a figure of an obliquely deposited film to demonstrate the inclination of columns with respect to flux incidence (see Fig. 1). The growth of a structured thin film can be described succinctly by noting that columnar growth occurs in the plane parallel to that defined by the trajectory of the incoming vapor and the substrate normal and is henceforth referred to as the deposition plane. If this plane is moved (either by rotating the substrate and keeping the source fixed, or rotating the source and keeping the substrate fixed) the columnar growth direction can be controlled.

The first porous chiral structures were fabricated by utilizing highly oblique or specifically glancing angle flux incidence to separate the chiral structures and more actively control their resulting porosity and morphology [38]. From Figure 2, it is clear that the difference ( $\Delta = \alpha - \beta$ ) in columnar angle and flux incidence angle increases with increasing  $\alpha$ . More highly separated columns, and the resulting increase in film porosity, are a direct consequence of this

observation. If, for example,  $\alpha = \beta$ , columns would be inclined toward the source, yielding no separation. By choosing a point on the  $\beta$  vs  $\alpha$  plot, the porosity of the film can be easily tailored due to the increasing effect of shadowing on the substrate surface.

This technique, referred to here as glancing angle deposition [39], has since been used to fabricate a range of porous thin film morphologies with isolated microstructures, many of which have been built upon the four simple structures shown in Figure 3 and described below. For these and subsequent examples, the deposition rate,  $r$ , refers to the amount of film deposited at the position of the substrate, but on a plane that is held normal to the arriving flux. This definition is used because it describes the standard geometry for film growth measurements by a crystal thickness monitor.

- *Oblique columns*: Formed when substrate rotation about  $\varphi$  is zero. Porosity is introduced by glancing incidence flux
- *Chevron or zig-zags* [30]: Stacked Motohiro–Taga interfaces deposited at glancing incidence whereby a rotation about  $\varphi$  of  $180^\circ$  occurs for each arm of the chevron.
- *Helices* [38]: Formed when the substrate is rotated slowly and continuously relative to the deposition rate,  $r$ . Typically,  $\delta\varphi/\delta t \sim 0.1$  RPM for  $r \sim 10$  Å/sec. Each complete turn of the substrate results in a single turn of the helical structure. The speed of rotation determines the pitch length (i.e., slow rotation = longer pitch; fast rotation = smaller pitch).
- *Pillars or posts* [40]: A special case of helical growth, though usually treated as its own film morphology. If rotation is sufficiently fast (e.g.,  $\delta\varphi/\delta t > 1$  RPM for  $r = 10$  Å/sec), the pitch of the helix is so small that it

cannot be distinguished. The structure thus appears as a vertical column.

The structural details for all the above film types inherently depend on the source material being used, the substrate, crystallography, and other factors. Low melting point materials, for example, tend to have higher surface diffusion which blurs the distinctiveness of the helical pitch and thus require less rotational speed to form a structure resembling vertical columns. High melting point materials tend to have lower surface diffusion and so take higher rotational speeds to form posts. By utilizing glancing incidence, the user can control both the film porosity and structure, opening up a wide range of applications including, for example, sensing technologies, catalysts, optical devices, and biochip devices.

Some STF papers define the flux incidence and columnar angles relative to the substrate plane, using the symbols  $\chi_v$  for the flux incidence and  $\chi_c$  for the columnar angle. To avoid confusion, in this chapter we will consistently use  $\alpha$  and  $\beta$  defined relative to the substrate normal. This nomenclature is consistent with the majority of GLAD literature (i.e.,  $\alpha \equiv 90^\circ - \chi_v$  and  $\beta \equiv 90^\circ - \chi_c$ ), and the original paper defining the tangent rule [17]. Using these definitions, the flux angles used with the GLAD technique are typically in the regime of  $75^\circ$  or higher: GLAD films can be classified as “dense” for  $75^\circ < \alpha < 80^\circ$ , “porous” for  $80^\circ < \alpha < 85^\circ$ , and “superporous” for  $\alpha > 85^\circ$  [41].

## 2.2. Advanced GLAD Structures

### 2.2.1. Advanced Control System

The power of the GLAD technique does not arise from simply rotating the substrate at oblique incidence, but rather through the dynamic changing of the substrate through  $\alpha$  and/or  $\varphi$  during deposition at glancing incidence [42]. The external control apparatus for growth of GLAD films has evolved considerably since the early “proof-of-concept” experiments. Individual stepper motors, each controlled externally by software running on a single computer, allow the user to adjust both  $\alpha$  and  $\varphi$  independently while the film is being grown. Hence, a variety of microstructure forms can be programmed into the computer and subsequently grown. In addition, the control system can adapt to changing conditions within the deposition chamber through feedback provided by *in-situ* measurement of film growth by a crystal thickness monitor. This growth is reported back to the computer software which adjusts  $\alpha$  and  $\varphi$  accordingly. Figure 4 shows a schematic of the current GLAD setup without the feedback control blocks shown.

### 2.2.2. Pause–Spin Growth

Using this advanced control system, more specialized microstructures can be designed and fabricated in a one-step deposition process. For example, the standard morphological trend suggests that if  $\alpha$  is low, films are dense and the columnar structure is more vertical. If  $\alpha$  is high, films are porous and columns are inclined. The fabrication of separated vertical columns (see Fig. 3c) suggests that while the porosity may be intimately related to the deposition angle, the angle of inclination ( $\beta$ ) may be more dependent on the speed of substrate rotation.

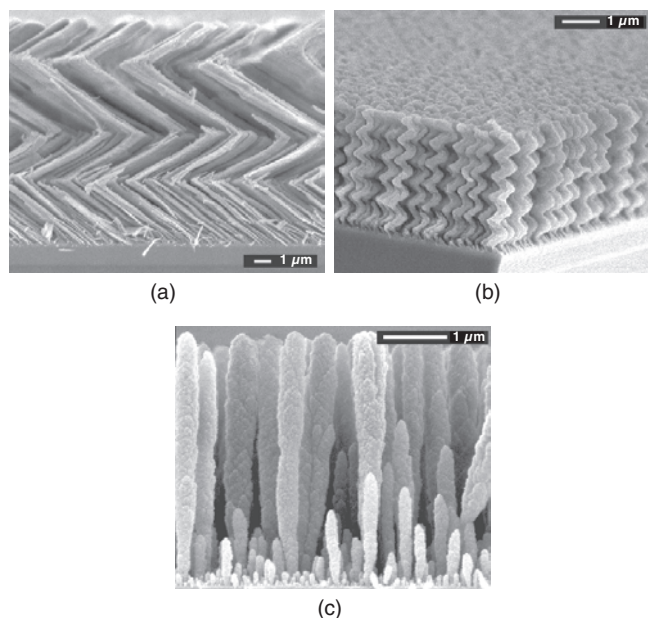


**Figure 3.** Examples of the basic GLAD morphologies: (a) Zigzags or chevron structures fabricated from yttria stabilized zirconia ( $\text{ZrO}_2$ ) at  $\alpha = 85^\circ$ ; (b) helices of  $\text{SiO}$  deposited at  $\alpha = 85^\circ$ , and (c) vertical  $\text{SiO}_2$  posts at  $\alpha = 87^\circ$ .

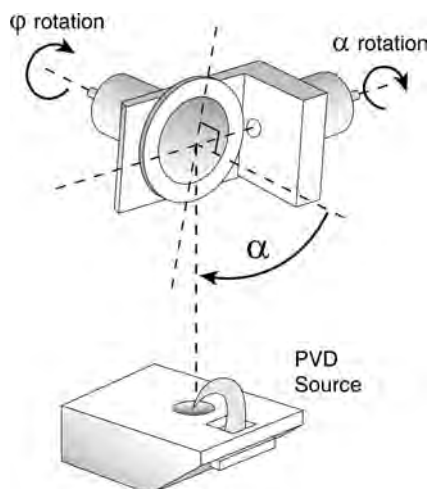


**Figure 4.** The GLAD system schematic. Stepper motors are used to control both the tilt (polar) angle  $\alpha$  and the rotation (azimuthal) angle  $\varphi$  of the substrate holder. Reprinted with permission from [45], S. R. Kennedy et al., *Nanoletters* 2, 59 (2002). © 2002, American Chemical Society.

From the perspective of the film, pillars are grown when flux arrives isotropically from all azimuthal angles. Porosity is imposed by  $\alpha$ , but  $\beta$  is forced to zero because of the high rotational speed. Inclined columns of a desired porosity or separation can be fabricated at any  $\beta$  between zero and  $\beta_{\text{Tait}}$  by using a “spin–pause” approach. In this methodology, pure “paused” growth represents oblique columns (i.e., substrate is stationary), while pure “spin” growth represents vertical columns (i.e., substrate rotates at “infinite” speed). By alternating the phases of spun and paused growth, stacked layers of inclined and vertical columns can be formed. If the stacked layers are made sufficiently small, the individual “pitches” between layers become indistinguishable, and the structure appears as a smooth column. The angle of the resulting column can be set by adjusting the proportion of spun and paused phases of growth, while maintaining a desired porosity set by  $\alpha$ .

Helical growth can also be controlled to some extent. The angle at which a helical arm leaves the substrate is determined by Tait; in other words, it is fixed by  $\alpha$ . Using the pause–spin methodology, the radius and pitch of a helix can be manipulated without adjusting the porosity of the film.

### 2.2.3. Control of Columnar Cross-Sections

The cross-section of columns can also be controlled in a similar fashion. Ideally, posts are formed when the helical pitch ( $p$ ) equals zero; however, in reality this transition typically occurs when the pitch is less than 15 nm. If the column is cut perpendicular to its direction of growth, a circular cross-section occurs because the film sees flux coming from all directions at the same rate. If this rate were to become more anisotropic, the cross-section similarly becomes anisotropic (i.e., more ellipsoidal). Pausing or slowing down the rotation rate at positions along  $\varphi$  can bias the columnar cross-section at points. For example, if the substrate rotation is slowed (or stopped) at  $\varphi = 0$  and  $180^\circ$ , the result is a flattened

cross-section where the column thickness along the axis connecting  $0$  and  $180^\circ$  is significantly greater than that along the axis connecting  $90^\circ$  and  $270^\circ$  [41].

This process can be thought of as adding an artificial anisotropic component to the film growth. Obliquely grown columns also have a natural anisotropic component which can be observed by their tendency to “fan out” perpendicular to the deposition plane [16, 18, 43, 44]. This growth mechanism may be observed from the lower panel in Figure 2 and is probably a manifestation of the shadowing effect. Hence, the observed columnar cross-section is more a measure of whether the deposition rate factor or shadowing factor was dominant during film growth.

### 2.2.4. Other Advanced GLAD Structures

A number of film microstructures can be developed utilizing the advanced GLAD control system, including square spiral staircases (where each arm of the spiral is grown at  $90^\circ$  from the preceding arm) [45], superhelices (where a helical film is modulated by helical growth of higher pitch) [46], twisted ribbons (arguably pillars with a highly ellipsoidal cross section and relatively large pitch) [41], or microstructures with a capping layer [47]. Capping layers provide encapsulation and protection to the porous films beneath them and also allow for multilayer structures [48, 49], while square spirals, particularly when arranged as components in a lattice, have possible application as three-dimensional photonic bandgap filters [50]. Some of these structures will be revisited later in this chapter, while for the others we refer the interested reader to the appropriate references.

### 2.2.5. Periodic Structures

Typically, microstructures fabricated by GLAD are randomly distributed on the substrate. This feature is not detrimental for such applications as sensors, thermal barrier coatings, and catalytic devices. However, some optical (e.g., photonics crystals) [51–53] and magnetic applications [54] require a periodic lattice of structures in order to operate effectively. In addition, some of the fundamental properties of GLAD films are more easily acquired when the exact density of structures per unit area can be calculated [55].

The formation of randomly distributed GLAD structures on the substrate surface is inherently due to the nucleation stage of film growth, when energetically stable clusters of atoms seed randomly on the substrate and subsequently shadow the surrounding area. Recently, it was shown that near identical structures can be formed by enforcing this shadowing effect at the initial stages of film deposition through the use of substrates with a prefabricated seed layer [56]. In this case, the seed structures were created using electron beam lithography, while more recent efforts by other groups have shown that periodic pillars and oblique columns can be grown on plastic embossed substrates [57], and square spirals can be grown on seeds produced using standard photolithography [45]. It is expected that any process that creates small, regular mounds out of an appropriate material may serve as seed layers for a subsequent GLAD deposition to form periodic microstructures.

If the seed morphology is optimized with regard to material parameters (e.g., melting point), substrate temperature,



and the flux incidence angle, growth initially occurs predominantly at the seed sites. The highly oblique incidence of the flux and the subsequent competition effects at the surface force subsequent growth to also occur at these sites. These microstructures grow regularly for some time, the extent of which will be explored later in this chapter.

For most materials deposited by GLAD, surface shadowing is the dominant growth mechanism, allowing the optimal seed separation to be approximated by

$$\delta = t \tan(\alpha) \quad (5)$$

$\delta$  and  $t$  are the seed separation and height, respectively. Figure 5 illustrates the geometry of this expression, while examples of periodic GLAD structures are shown in Figure 6.

The growth of periodic structures, particularly those of helical microstructures, is found to be quite robust. Defects introduced into the lattice in the form of missing seeds or lines of seeds have little effect on the growth of structures surrounding the defect [56]. Defects transfer to the film (the extreme flux incidence angle ensures that there is no flux coverage of the seedless defect area), while the uniformity of the film is preserved outside of the defect area. Structures along the edge of defects tend to increase in density or thicken slightly to take up the flux that would otherwise have gone into the growth of their neighbors. This effect is marginal if the number of missing lattice points is limited to the distance enclosed by one or two seed periods. The demonstration of low defect periodic GLAD arrays is of particular significance, as it may be applied to the introduction of light-guiding structures for use in photonic bandgap devices (see Section 5.5.4).

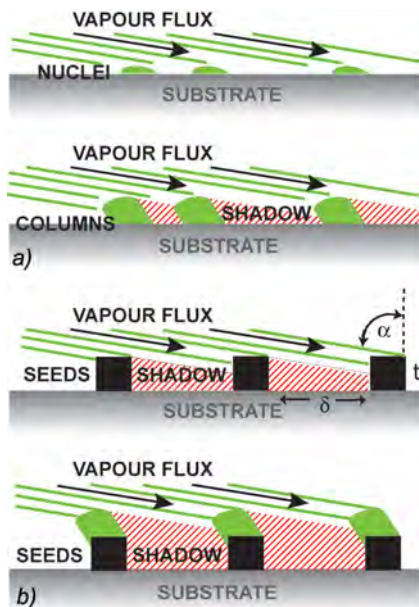


**Figure 5.** The geometry of film growth for a randomly situated film (a) and periodic film (b) are compared. If the seed separation ( $\delta$ ) is optimized relative to the height of the seed ( $t$ ) and the angle of flux incidence ( $\alpha$ ), film growth occurs primarily at the seed sites. This seed separation is loosely based on Eq. (5). If  $\delta \gg \delta_{\text{optimized}}$ , or no seeds are present on the substrate, self-shadowing initializes film growth.

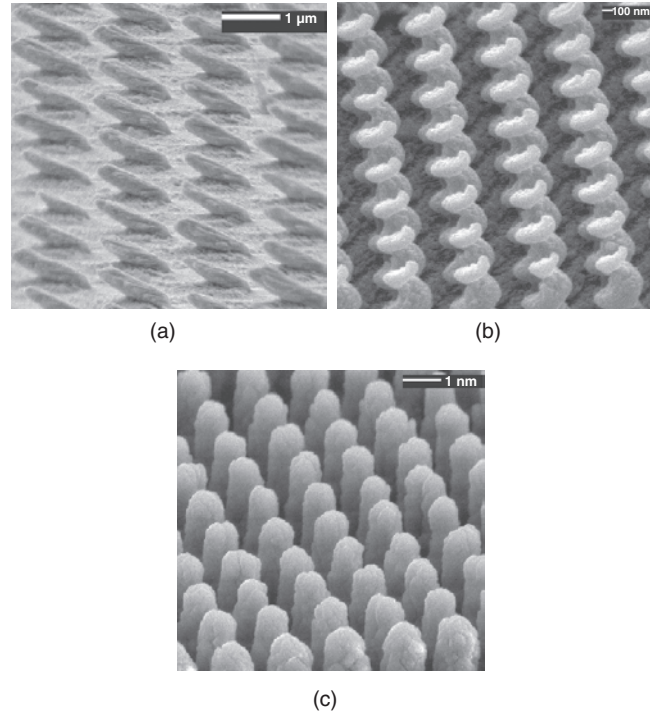


**Figure 6.** Examples of periodic GLAD morphologies grown at  $\alpha = 85^\circ$  are shown above: (a) nickel oblique columns with a lattice period of  $2 \mu\text{m}$ ; (b)  $\text{SiO}_2$  helices with a lattice period of  $600 \text{ nm}$ ; and (c)  $\text{SiO}_2$  posts with a lattice period of  $900 \text{ nm}$ . Figure 6a reprinted with permission from [55], M. Seto et al., *Micromech. Microeng.* 11, 582 (2001). © 2001, Materials Research Society.

For the remaining part of this chapter, we will describe some of the fundamental growth properties of both randomly situated and periodic GLAD films. In addition to the flux incidence angle ( $\alpha$ ) and substrate rotation about  $\varphi$ , which clearly have significant effects on the overall film structure, a number of other parameters affecting growth will be discussed. We will close this chapter with a few application directions and our current understanding of how GLAD films are either demonstrated or expected to function within these fields.

### 3. GLAD FUNDAMENTALS

The isolated structures of GLAD films allow for the study of fundamental thin film growth behavior, particularly in regard to self-shadowing and surface energies. For example, by observing that the diameter of a helix arm gradually increases during deposition, one might assume a number of processes to be at work including [58]:

1. An increase in adatom diffusion length due to an increase in substrate temperature during growth.
2. An increase in the amount of material deposited on a given helix due to the suppression of neighboring structure growth (i.e., columnar competition).
3. Increase in scatter of incident flux between helices.
4. Bifurcation within a helix arm.
5. Preferential growth of fast growing crystal planes.



### 6. Recrystallization and growth of crystallites within a growing helix.

These processes show that not only is the geometry of the deposition system a factor during growth (due to its imposed effect on the shadowing mechanism at the substrate surface), but material properties such as crystallography, vapor pressure, etc. and the deposition technique itself (either sputtering or evaporation) all have strong roles to play in the form of the resulting film microstructure. In the section that follows, we will explore a number of these factors.

### 3.1. Competition, Scaling, and Growth Evolution

In common with solid thin films, GLAD microstructures exhibit self-affine or self-similar behavior [58, 59]. To illustrate this concept and give some insight into how a GLAD film evolves during its deposition, a SiO<sub>2</sub> post film (deposited at  $\alpha = 85^\circ$  with normal pitch set to 10 nm) is shown in Figure 7. The left side of the image shows the complete growth evolution as a side view, while on the right, slices of the film taken at various thickness intervals are displayed.

First we note that the separation of columns occurs early in the growth evolution, as the extreme shadowing at the substrate surface inhibits adatoms from filling in the voids between columns. This behavior is an extreme example of what is classically referred to as Zone 1 behavior: self-shadowing is the dominant growth mechanism, and adatom diffusion is limited [11]. A simple analogy, often referred to as the “grassy lawn” model, is often used to capture the essential concepts of these growth conditions [60]. Blades of grass (representing the columns) grow in proportion to the amount of light they receive (i.e., flux density). This circumstance introduces positive feedback into the growth; if a blade overgrows its neighbor, it receives more light flux and has a higher potential of shadowing its neighbors, thus suppressing their rate of growth. Similarly, adatom diffusion tends to smooth out the surface in the length scale over

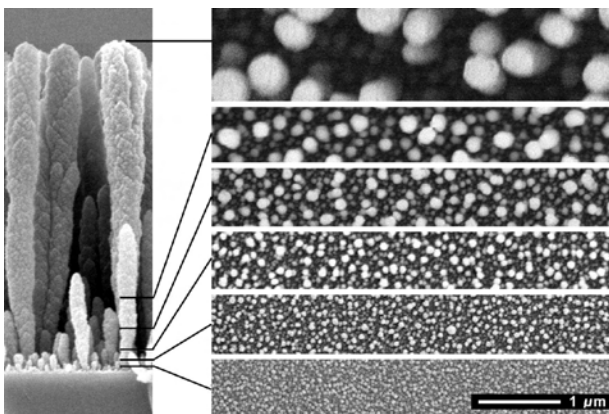


**Figure 7.** The left side of the image shows an edge view of a SiO<sub>2</sub> post film. Plan views of the same film taken at various stages of growth are shown at the right. The representative film thickness of each slice is shown by a line. Reprinted with permission from [129], D. Vick et al., *Res. Signpost*, in press. © 2002, Research Signpost.

which it operates, while shadowing tends to magnify surface roughness [61].

In the SiO<sub>2</sub> film shown here (Fig. 7), column competition, extinction, and broadening can be seen as the film evolves. Transmission electron microscopy (TEM) images have suggested that column broadening correlates on the nanometer scale with bifurcation of the fibers that constitute the columns [62].

The similarity in column morphology suggests that the growth may obey a scaling law. Scanning probe microscopy can be used to quantify the interface width of the tops of films with topography  $h(x, y)$ . This interface width is defined as

$$w = \sqrt{\frac{1}{N} \sum_i^N (h_i - \bar{h})^2} \quad (6)$$

Experiments on fixed and rotated substrates have shown that these films obey a scaling law in the form

$$w(\bar{h}) \sim \bar{h}^\gamma \quad (7)$$

where  $\gamma$  is a growth exponent [63, 64].

### 3.2. Relationship between Flux Incidence and Film Density

The effect of columnar competition and thickening may pose a fundamental limitation on engineering microstructures. In addition, these effects may be detrimental for those applications that require a constant microstructure form throughout the film thickness. Through the use of periodic films and understanding how the film density is affected by flux incidence angle, the onset of competition and columnar thickening effects may be controlled.

Both simulated and experimental studies suggest that the film density ( $\rho$ ) is primarily a function of flux incidence angle [18, 65–68]. Measured densities reported between different laboratories can vary widely due to differences in the respective deposition processes and source materials. In addition, some laboratories report film density as a normalized value (i.e.,  $[\rho_0 - \rho(\alpha = 0^\circ)]/\rho(\alpha = 0^\circ)$ ), while others report densities relative to the bulk density ( $\rho_{\text{bulk}}$ ) of the source material. In the latter case, it is more critical that the system geometry be clearly represented. Generally, film density is observed to fall with increasing flux incidence angle. Decreases of up to 50% are commonly reported in  $\rho_0$  for films deposited between  $\alpha = 50^\circ$  and  $\alpha = 85^\circ$ . From Figure 2b it is clear that film density is most affected by the flux incidence angle when  $\alpha > 75^\circ$  (i.e., in the extremely oblique to glancing angle regime). In this regime, evaporated manganese has shown a reported change in  $\rho_0$  from 0.71 at  $\alpha = 75^\circ$  to 0.40 at  $\alpha = 87^\circ$  [68] while sputtered tungsten has shown a change in  $\rho_0$  of over 40% between a film deposited at  $\alpha = 75^\circ$  and a film deposited at  $\alpha = 85^\circ$  [18, 69].

All these studies, particularly those involving simulation, showed that neither seed period nor, in most cases, substrate rotation rates (see Section 3.4) has an effect on these characteristics.

To maintain a constant density at a given flux incidence angle, increases in the surviving pillar diameter ( $s$ ) are compensated by a corresponding increase in pillar separation

( $p$ ). The ratio of these two parameters is thought to be thickness invariant and dependent on the flux incidence angle ( $\alpha$ ); that is,  $s/p = \eta(\alpha)$  [64]. This property arises through the competitive effects linked to the constancy of flux density striking a given region on the substrate surface.

Films grown on prepatterned substrates may provide an opportunity to minimize columnar competition by optimizing the seed topography to the observed  $s/p$  ratio in randomly situated structures. Although a clearly defined diameter and period do not exist in these latter films, a measure of their values can be obtained. The “average” separation,  $d$ , of randomly situated columns can be determined by scanning probe measurements of GLAD film topography. This separation (governed loosely by Tait’s equation) can be found experimentally by explicitly measuring the distances between surviving columns and averaging the results. These measurements result in values on the order of a few hundred nanometers for film thicknesses of up to a one or two micrometers and with  $\alpha \sim 85^\circ$ . In a similar fashion, the “average” diameter of columns can also be calculated, although the results are not as definitive.

Promising results have indicated that the competitive effects in periodic films can be delayed compared to the randomly situated structures [65]. If periodic pillars deposited under the same deposition conditions and seed geometry are compared based on the spacing of individual seed elements, the following observations can be made:

1. Initial seed separations much larger than  $d$  (i.e., approaching one micrometer), result in larger pillar diameters and a corresponding decrease in intercolumnar competition.
2. Films grown on relatively dense seed arrays (i.e., seed periods less than 100 nm) show highly competitive growth.
3. At a given film thickness, the crossover between increased competitive behavior and increased pillar diameter appears to occur at  $d$ .

Column diameters and separations are based on the interplay of both self-shadowing and the adatom diffusion length of incoming flux. Based on the above observations, it is thought that the averages observed in a randomly growing film represent the optimized geometry for a given set of conditions (i.e.,  $s/d$  is the optimized  $s/p$  for a given  $\alpha$ ).

Let us consider a seed topography consisting of dots with 50 nm diameter, 80 nm height, and 600 nm separation. The flux incidence angle is set to  $85^\circ$ . Initially, a pillar film grown on this substrate will have a low  $s/p$  factor (i.e.,  $s/p = 0.08$ ) compared to a typical value of  $(s/p)_{\text{random}} = 0.4$  to 0.8 for a randomly situated film grown under the same conditions. To compensate for this discrepancy, the pillar diameter increases, effectively delaying the onset of columnar competition within the growth evolution. Competition effects are observed to occur more readily when the pillar diameter reaches a value determined by  $(s/p)_{\text{random}}$  (i.e., in this case  $s \sim 240$  to 480 nm).

It should be noted that competition effects are observed to be significantly diminished in randomly situated and periodic helices, specifically in relation to pillars grown on the same substrate topography. It is believed that this effect may be due to the self-correcting nature of helical growth and its

ability to adjust its pitch arm diameter to counter additional competitive pressures during growth.

### 3.3. Relationship between Flux Angular Distribution and Film Growth

In addition to the flux incidence angle, the angular flux distribution ( $\Delta\alpha$ ) of the incoming flux is also important to GLAD microstructure growth. To control film growth most effectively at glancing incidence, a narrow angular distribution of vapor flux centered at a known oblique incidence angle is required. Indeed, some research has suggested that for incidence angles greater than  $\alpha = 80^\circ$ , small variations in the flux incidence angle result in large changes in film densities [18]. The resulting film density tends to be most greatly influenced by that fraction of flux which is least oblique and, therefore, least subject to the shadowing mechanism.

For most of the applications and films shown in this chapter, electron beam evaporation has been used for film depositions. This process typically yields a flux beam geometry suitable for controlling microstructure growth at glancing angles. Unfortunately, high melting point materials (e.g., tungsten and molybdenum) are not easily deposited in this fashion, and a sputtering process may be required for growing GLAD films from these materials. Standard sputtered PVD generally deposits films with greater flux incidence distribution at the substrate due to the larger target size used and flux scattering off of the working gas. Techniques such as collimated sputtering [70, 71], ionized PVD [72], and low-pressure, long-throw (LPLT) sputtering [73] have been suggested to narrow  $\Delta\alpha$ . Although still not yielding as tight a flux beam geometry as present in typical evaporation processes, the last of these techniques, LPLT, has been used successfully to fabricate randomly situated chevrons [74], and both randomly distributed and periodic structures of helices and pillars [74, 75].

Periodic structures deposited by LPLT sputtering more easily identify the effect of increasing  $\Delta\alpha$  on GLAD film growth. Recent work has shown [75] the following film characteristics:

1. Quasi-helical microstructures are formed when the seed period ( $p$ ) is less than  $d$ .
2. Pillar microstructures are formed when  $p > d$ .

Hence, as the seed period increases, helical structures degenerate into posts. Why does this effect occur? Let us first consider what is meant when incident flux has a given angular flux distribution; for example, if  $\alpha = 85^\circ$  and  $\Delta\alpha = 4^\circ$ , the majority of flux arrives between  $\alpha_{\text{min}} = 83^\circ < x < \alpha_{\text{max}} = 87^\circ$ . Recall that a pillar is simply a helical microstructure within which the pitch is indistinguishable. Hence for large seed separations (i.e., on the order of  $1 \mu\text{m}$ ), although a helical structure may form at  $\alpha = 85^\circ$ , incoming flux arriving at the lower portion of the incidence range tends to “fill in” the helical pitch, smoothing out the resulting microstructure. At lower seed periods, shadowing by neighboring structures diminishes this “filling” effect, albeit at the expense of increased competition. As a result, when the seed period is less than  $d$ , quasi-helices are formed. When  $p > d$ , helices degenerate into posts, while a transitional region between pillars and quasi-helical behavior is observed to exist about  $p = d$ .

### 3.4. Relationship between Substrate Rotation and Film Growth

Substrate rotation is one of the primary means of manipulating the film morphology at glancing angles. As mentioned previously, the film density is not observed to be dependent on the speed of rotation about the  $\varphi$  axis for most materials.

Generally, substrate rotation affects GLAD morphology in the following fashion: Isolated posts are fabricated when flux arrives isotropically from all azimuthal angles (i.e.,  $\delta\varphi/\delta t$  is “infinite”); helices form at various pitch lengths when  $\delta\varphi/\delta t$  is decreased; and, finally, oblique columns are formed when  $\delta\varphi/\delta t = 0$ . This general relation between morphology and  $\delta\varphi/\delta t$  has been presented previously in Section 2.1.4 and is shown in Figure 8.

Recent research suggests that this morphological trend may not be applicable to all materials. Liu et al., studying under the Center for Materials for Information Technology (MINT) at the University of Alabama, found that the growth rate for cobalt increased [76], while iron films display leaflike columnar growth [77] at high rotational speeds ( $\delta\varphi/\delta t \sim 30$  RPM,  $\alpha = 75^\circ$ ). Their results were recently quantified by comparing aluminum, silicon, and silicon dioxide films grown at glancing angles with increasing rotational speeds [78]. This work relied on a gearbox which allowed for simultaneous deposition of six separate films over two orders of magnitude of rotation by stepping up or down the rotation about  $\varphi_n$  relative to the central driving axis,  $\varphi_c$ .

Silicon dioxide and silicon films were found to follow the general trend observed for most materials, while the structure of aluminum was found to be highly dependent on  $\delta\varphi/\delta t$ . The trend for aluminum is shown in Figure 9.

At low rotational speeds, aluminum films have “mushroomlike” growth, whereby with increasing thickness the film

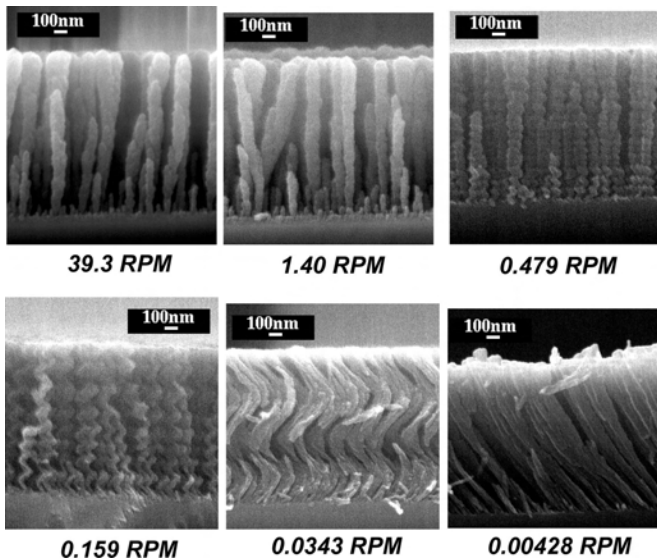


**Figure 8.** Films of  $\text{SiO}_2$  grown with a deposition angle of  $\alpha = 85^\circ$ , and at various rotational speeds (shown below each image). Pillar growth occurs when  $\delta\varphi/\delta t > 1$  RPM (at a deposition rate of  $10 \text{ \AA}/\text{sec}$ ), while helical growth occurs more clearly for  $\delta\varphi/\delta t < 0.1$  RPM.

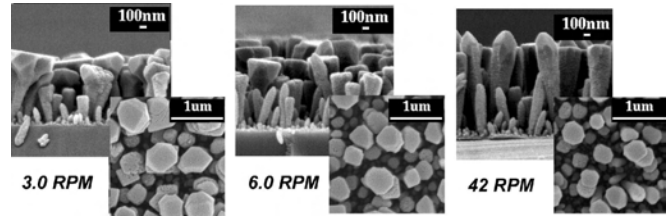


**Figure 9.** Aluminum films deposited at  $\alpha = 85^\circ$  at different  $\delta\varphi/\delta t$ . The films deposited at  $\delta\varphi/\delta t = 3.0$  RPM show a flattened out structure while the film deposited at  $\delta\varphi/\delta t = 42$  RPM shows peaked structures. Faceting is clearly visible in all the films, and TEM analysis that shows the film consists of a simple cubic, monocrystalline structure.

spreads out from a thin base. The tops of these structures are both flat and consistent in height with their neighbors.

As  $\delta\varphi/\delta t$  is increased, the number density of structures with a pyramidal faceted peak increases. Also observed is a corresponding increase in the average thickness of the film. Hence, at  $\delta\varphi/\delta t = 42$  RPM (for most materials, a pillar structure will typically form at 1 RPM, while a helix forms at 0.1 RPM using  $\alpha = 85^\circ$  as a reference), the peaked structures are in the majority, and the film thickness is almost twice that at  $\delta\varphi/\delta t = 3.0$  RPM.

This result, coupled with the previous study by Liu, suggests that the morphological structure is highly dependent on the propensity of the structures to form solid crystals. TEM analysis of the aluminum films showed them to have a simple cubic, monocrystalline structure. A similar analysis of silicon and silicon dioxide films shows both have amorphous structures, consistent with the statement that fiber bundling is thought to contribute to columnar competition in GLAD films [62].

One possible explanation for this behavior is the effective rate of adatom burial at increasing rates of substrate rotation at constant  $\alpha$  [78]. At glancing angles, the effective shadowing mechanism is enhanced. Because all films in a given rotation set were deposited simultaneously, it is not believed that differential temperatures across the individual samples are a factor. The burial rate seems to be dependent on the number of times the flux “visits” a particular spot on the substrate (i.e., at fast rotation, the burial rate increases relative to the slow rotation rate because a particular site is “visited” more often). Hence, different crystal planes are thought to be preferred as the diffusion length of adatoms decreases with  $\delta\varphi/\delta t$ .

Simulations indicate that the diffusion length of adatoms on structures with strongly preferred crystal planes changes with  $\delta\varphi/\delta t$  [78], while experimental results on chromium films deposited at a relatively conservative  $\alpha = 65^\circ$  show a similar result. Figure 10 shows that at high rotational speeds, the film surface shows a number of peaks typical of sputtered chrome surfaces. At low rotation speeds, the surface shows a smaller number of peaks with long channels linking film regions, seemingly indicating a longer effective diffusion length.

It is noted that if this result is confirmed, a similar effect should be apparent on the same materials deposited at lower rotational speeds with an increased deposition rate.

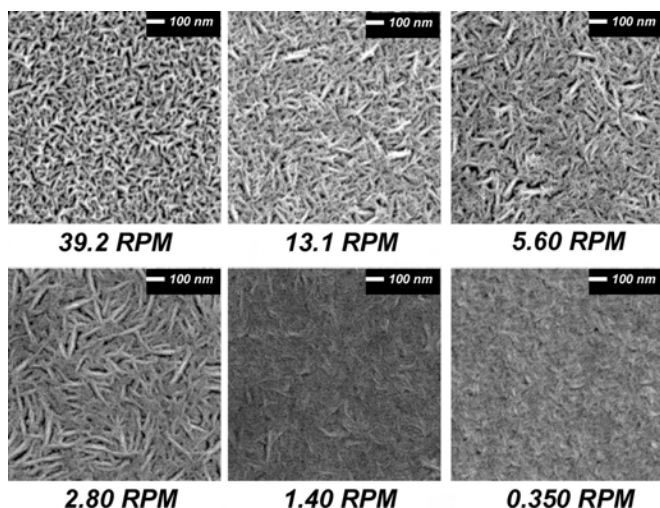


**Figure 10.** The potential effect of substrate rotational speed on adatom diffusion length is apparent from these images of chromium films deposited at  $\alpha = 65^\circ$ . At low rotational speeds, the surface of the film is smooth, while at faster speeds, the surface roughness increases.

### 3.5. Simulation Software

Simulations have been used as tools to describe obliquely deposited films at least since the pioneering work by Dirks and Leamy [20]. Although a number of simulation paradigms exist including continuum models [20], conservation of parallel momentum (primarily supported by a group of Japanese researchers starting with [79] and summarized in [80]), and angular dependent growth [81–83], ballistic deposition simulations have proven the most successful in describing the growth of thin films deposited with limited adatom diffusion and high mean free-path (the typical conditions in a GLAD chamber). In these simulations, particles are serially launched from just above the growing film. Each particle is allowed to follow straight-line trajectories until it strikes the substrate or the film. The subsequent surface diffusion is described by an equilibrium model whereby each particle is allowed to aggregate into the film after diffusing a distance determined by an algorithm which minimizes the surface curvature-dependent chemical potential.

Throughout most of the history of thin film simulation, insufficient computing power has limited software to simple two-dimensional [19, 27] and three-dimensional models [84, 85] which tended to exclude the effects of surface diffusion of adatoms over large scales. This exclusion is important as it is universally accepted that surface diffusion is very important to the growth of obliquely deposited films, as it is for all thin film growth processes. Over the last decade, however, this limitation has been lifted significantly, allowing for the creation of three-dimensional (3D) simulation programs to more properly model both adatom diffusion and the resulting porous thin film structures created at glancing incidence [67, 86]. Typically, for example, even films evaporated obliquely onto *stationary* substrates grow anisotropically, with flakelike morphology and significant growth fanning in the direction perpendicular to the incident flux and parallel to the substrate plane [16, 18, 43, 44].

Although a number of software packages have recently been developed, one simulator that has proven quite successful in the modeling of films deposited at glancing angles is the Monte Carlo ballistic simulator program, 3D-FILMS [67]. This progeny of the two-dimensional simulation package SIMBAD [87] was developed in part to model several aspects of porous thin films. In its simulations, 3D-FILMS models a film as a large number of identical units. Each unit has cubical geometry and represents the statistically averaged behavior of a large number of atoms (typically 1000). Nucleation, self-shadowing, adatom mobility, and a variety of other physical effects are all incorporated into this model, and simulated films can be displayed graphically as three-dimensional images.

Temporal dependence of the incident flux [ $\alpha(t)$ ,  $\varphi(t)$ ] can be introduced to reproduce most of the GLAD film morphologies observed experimentally including simple helices, post, and chevron structures, as well as multilayered and capped structures. Periodic arrays of films can be grown by setting the initial substrate topography to match the desired predefined seed layer geometry. See Figure 11.

A second 3D simulator, the Virtual Film Growth System (VFIGS), has also been recently reported [86]. This simulator, also built around the basic SIMBAD system and following a similar development framework as 3D-FILMS, was primarily created to understand the surface area of STFs (referred to in their work as dynamically obliquely deposited films). By simulating the growth of various film

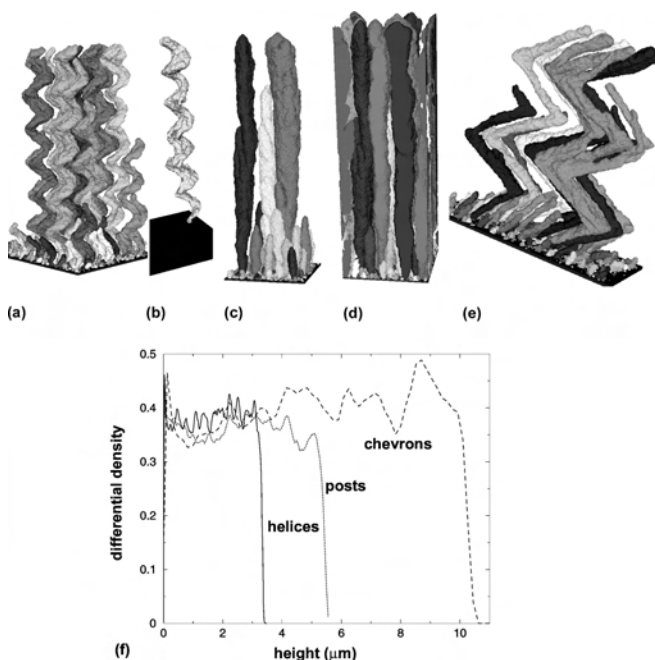


**Figure 11.** 3D-FILMS simulations of different film morphologies deposited at the same flux incidence angle. These morphologies include: (a) helices; (b) a single helix from the simulation of (a); (c), (d) posts; (e) chevrons. A plot of the differential density as a function of height for the simulations at the left is shown in (f). Note that the simulation predicts that the resulting average film density is not dependent on microstructure form. Reprinted with permission from [67], T. Sny et al., *J. Vac. Sci. Technol. A* 18, 2507 (2000). © 2000, AVS—The Science & Technology Society.

morphologies from  $\alpha = 0^\circ$  through  $\alpha = 82^\circ$ , VFIGS found no significant dependency of either packing density or effective surface area on  $\varphi$ . These properties were found to be primarily a function of  $\alpha$ , and, although the packing density diminished in the expected fashion, the effective surface area was observed to increase sharply to a maximum at  $\alpha = 70^\circ$ .

Ballistic simulations of GLAD films have confirmed that only collimated flux and low diffusion length are needed to explain most aspects of these films including column morphology, column extinction and broadening, and bifurcation. In other words, self-shadowing is the primary growth mechanism. See Figure 12.

#### 4. FABRICATION PROCESSES FOR SPECIALIZED APPLICATIONS

One of the strengths of the GLAD process is that it can form a variety of microstructures using a one-step process. However, for some applications (i.e., the periodic films mentioned earlier), either pre- or postprocessing steps are required. In this section we describe a few tools that have been developed for application to GLAD films.

##### 4.1. Perforated Thin Films

There has been a great deal of research into the production of thin films perforated by an organized array of pores. Photoanodic etching has been used to produce  $2\ \mu\text{m}$  diameter pores,  $400\ \mu\text{m}$  deep into a silicon wafer [88], while phosphoric acid can be used to anodically etch high purity aluminum foils to produce regular patterns  $100\ \mu\text{m}$  deep over a limited area [89]. As a final example, Chelnokov used an optical drill to produce triangular lattices of deep pores in photoresist [90].

In all these cases, the perforated films were limited to a regular geometric cross-section (either circular or rectangular) extending perpendicularly into the substrate. GLAD films, however, can be used to provide a template for etching a wider range of geometries into the substrate in a few, simple steps (see Fig. 13) [91]. In the first step, the inverse form of the desired substrate geometry is fabricated using the GLAD process. For the example shown,  $\text{SiO}_2$  helices were deposited at  $\alpha = 85^\circ$  with a pitch of  $300\ \text{nm}$ . The second step requires the filling in of the GLAD template using photoresist, spin-on glass or another similar material to provide not only protection to the underlying substrate but a medium in which the pores can be etched. For our example,

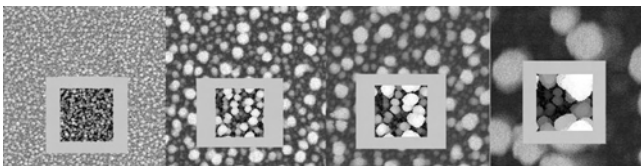


**Figure 12.** Pseudo-SEM images were obtained using a plan perspective of 3D-FILMS simulations. The images are displayed as insets over SEM images of real films. Reprinted with permission from [64], D. Vick et al., *Mater. Res. Soc. Symp. Proc.*, 648, (2001). © 2001, Materials Research Society.

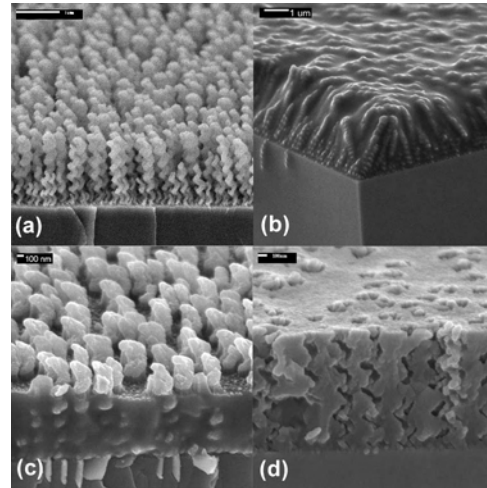


**Figure 13.** The stages involved in the fabrication of a perforated film: (a) template formation; (b) filling; (c) partial etch-back; and, finally, (d) template removal. Reprinted with permission from [91], K. D. Harris et al., *Electrochem. Solid-State Lett.* 4, C39 (2001). © 2001, Electrochemical Society.

HPR504 photoresist was used as the filler medium. To help aid the etching process, in the third step the filler medium is partially removed to reveal the tips of the GLAD structures. Timed immersion in a developer solution was used to remove the photoresist to partially expose the  $\text{SiO}_2$  helices. In the final step, the GLAD film is etched away using a suitable process (here, a 7:1 buffered oxide etch solution was used), to leave behind a mold of the film in the filler medium.

This process has been used successfully to not only create the helical pores shown in Figure 13 but also randomly oriented chevron pores and periodic helical pores.

Subsequent research has taken this process further by showing that it provides a clever means of fabricating GLAD-type microstructures from materials that are not easily deposited using that process. These materials, such as copper, have a low melting point and corresponding high adatom mobility when deposited on uncooled substrates. The high mobility of adatoms smoothes out the microstructure and diminishes the predominance of self-shadowing at the surface. In contrast, finely structured copper helices can be formed by electroplating copper back through a mold prepared by the above process. If the filler material is photoresist, for example, it can be easily etched away by acetone leaving an exact replica of the original template structure in copper [92].

##### 4.2. Raised Topography

In Section 2.2.5 we discussed the fabrication of periodic structures where a single microstructure (i.e., helix, oblique column etc.) made up each element of a larger array. If this seed element is much larger than  $a$ , the columnar separation described by Eq. (4), multiple structures will form on individual seed elements [93]. For most of the envisioned applications mentioned thus far, such multiplicity is an undesirable property, and seed arrays typically are optimized to avoid this circumstance.



However, if the standard GLAD process is applied to seed elements with dimensions several orders of magnitude larger than  $a$ , a wall of dense film is built up at the seed edges [94]. This effect is illustrated in the SEM images shown in Figure 14.

In these images, a helical GLAD film has been deposited on substrates containing arrays of 14  $\mu\text{m}$  tall mesas. Over the majority of the mesa tops, a porous, helical film is grown. At the edge, flux is accumulated as vapor hits at a less oblique angle (more normal). This effect results in a thick solid wall surrounding the porous region, and essentially a deposition in this fashion can be thought to fabricate a highly porous, self-sealing structure. If a complete seal is desired, a capping layer (see [47]) can be easily applied after the required film thickness is deposited. Seto et al. [94] found that walls form naturally around any raised pattern that exhibits sharp edges, and hence a variety of topographies such as T-junctions or via-connected chambers can also be formed. They suggest that such a structure may be suitable for microfluidics chromatography, nano-assay, lab-on-a-chip, biochemical, and other related applications.

### 4.3. Sharpening GLAD Microstructures Using Ion Milling

As a final example of some of the micro- and nanofabrication techniques that can be applied to the GLAD process, we mention the possibility of ion milling microstructures to sharpen their features.

The sputter yield of an ion beam is angularly dependent, with the maximum yield lying typically between  $30^\circ$  and  $60^\circ$ . When columns are milled uniformly across the tip surface

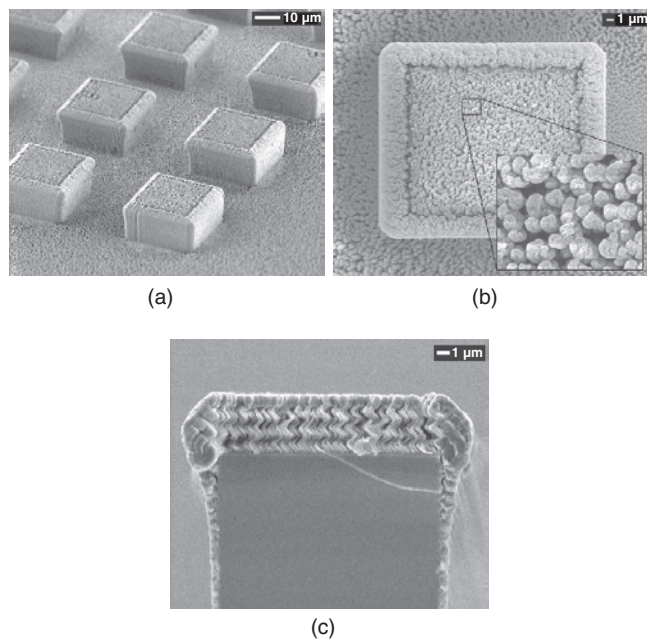


**Figure 14.**  $\text{SiO}_2$  GLAD helices deposited onto etched silicon mesa substrates (a) fabricate a porous helical film with a wall of film built up at the seed edges (b, c). Reprinted with permission from [94], M. Seto et al., *J. Mater. Chem.* 12, 2348 (2002). © 2002, Royal Society of Chemistry.

by a beam incident parallel to the substrate normal, the tips not only become slightly shorter (a perhaps undesirable consequence) but also significantly sharper. A recent article [95] showed that the radii of curvature for vertical columns of silicon and carbon could be decreased to less than 20 nm with a 1 kV (18 mA) ion beam treatment of just 10 minutes in a vacuum. This ion milling treatment produces films that exhibit superior field emission properties when compared to unmilled films.

These structures may be applied as field emitters, which provide electron sources in flat panel displays, plasma generators, analytical instrumentation, and power/high frequency devices. However, these films need not be useful for only field emission, for indeed their potential application could easily be limited by the growing and considerable interest in the possible field emission properties of nanotubes [96, 97]. The sharp features presented by the ends of the columns could find a use as SPM probe tip characterization surfaces, an area of growing importance as these tools become more common in industrial fabrication processes [98]. It has also been suggested that sharpened tips may be suitable for the more esoteric application of providing propulsion for microsattellites.

## 5. SOME PROPERTIES AND APPLICATIONS

### 5.1. Mechanical Properties

Nanoindentation measurements have been done on several films of varying pitch lengths to answer questions on whether GLAD films show resonance properties [55, 99]. Theoretical work indicates that a GLAD film fabricated from a suitable piezoelectric material may form a tunable chiral thin film laser [100], while experimental research has shown that the films undergo elastic deformation when small forces are applied to the surface, corresponding to a stiffness as low as 1/1000th that of a similarly deposited solid film.

Force displacement curves for one, two, and three turn  $\text{SiO}_2$  films have been obtained using a nanoindentation tip as a probe. This probe applied low force indentation measurements on the films over areas much larger than individual columns. To decrease the number of free variables, the thickness was left constant, resulting in pitches of 1900, 850, and 600 nm respectively. Using this technique, displacement at the maximum applied force amounted to less than 15% of the total film thickness. Indentations at the same site showed an overlapping displacement curve, indicating that the deflection is nondestructive or elastic for small deformations. The force–displacement curves for these films are shown in Figure 15.

Somewhat surprisingly, the dependence of film stiffness on spring geometry scales in a manner similar to a bed of macroscopic springs and is on the order of

$$k = \frac{Gs^4}{64R^3n} \left[ 1 - \frac{3s^2}{64R^2} + \frac{3+\nu}{2(1+\nu)} \tan^2(\alpha) \right]^{-1} \quad (8)$$

where  $G$  is the Shear modulus,  $s$  is the column diameter,  $R$  is the coil radius,  $n$  is the number of turns,  $\nu$  is Poisson's ratio, and  $\alpha$  is the rise angle [55]. Although measurements of helical parameters (e.g., coil diameter etc.) could



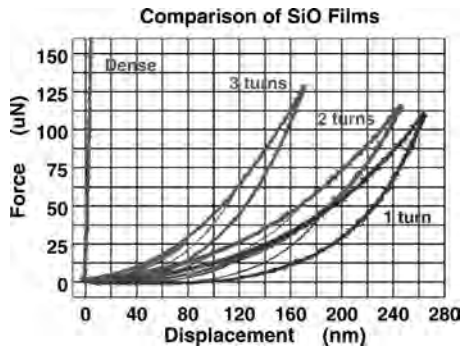


**Figure 15.** Force–displacement curves for single, double, and triple turn helical SiO thin films of comparable thickness. To contrast, an indentation curve for a dense SiO film is also shown. Reprinted with permission from [99], M. Seto et al., *J. Vac. Sci. Technol. B* 17, 2172 (1999). © 1999, Materials Research Society.

not be precisely obtained, the areal stiffnesses of experimental and theoretical films were comparable. These values were on the order of 10 to 18 N/m- $\mu\text{m}^2$  for one to three turn SiO helices, as opposed to the 18,500 N/m- $\mu\text{m}^2$  value for a similarly deposited dense SiO film. From Eq. (8), it is expected that helical films will exhibit a resonant frequency between 10 and 50 MHz and suggests that it may be feasible to engineer beds of microsprints with well-defined stiffness and mechanical response.

Periodic slanted posts can be used to aid in deflection measurements, by diminishing the error inherent within dimension values. These structures resemble cantilevers with rectangular cross-sections, of which an example was shown previously in Figure 6a. The theoretical expression for the displacement of this film is given by

$$\Delta x = \frac{FL^3 \cos^2(\alpha)}{3EI} \quad (9)$$

$F$  is the applied force,  $L$  is the cantilever length,  $\alpha$  is the rise angle,  $E$  is Young's modulus, and  $I$  is the moment of inertia (where for a rectangular cross-section,  $I = wt^3/12$ , where  $w$  is the width and  $t$  is the thickness) [55]. These structures deflected 80 nm under 27  $\mu\text{N}$  of applied force, while Eq. (9) predicted a deflection of 90 nm under the same conditions.

## 5.2. Thermal Properties

Capping and multilayer structures were introduced briefly in Section 2.2.4. It has been suggested that if multilayer GLAD film were constructed out of suitable materials, a thermal barrier coating (TBC) may result. Two types of TBCs are described in the literature:

1. A layer of yttria-stabilized zirconia (YSZ) is applied to a critical surface by plasma spraying, resulting in a highly porous microstructure [101]. Its thermal barrier properties, however, can be significantly reduced by repeated heating cycles that may induce stress, causing cracking due to differing thermal expansion coefficients.
2. Electron beam evaporation is used to deposit the film. The stress-induced deterioration is reduced by the presence of a laterally compliant columnar

microstructure with well-defined boundaries. Unfortunately, these films have less porosity than plasma sprayed coatings and, consequently, have diminished thermal protection.

TBCs deposited by oblique deposition may provide solutions to these problems, and, in particular, it has been suggested that a suitable GLAD structure may provide diminished stress induced deterioration while retaining the film's porosity.

A film was grown with alternating porous and dense layers of YSZ, as shown in Figure 16 [102]. YSZ is used because of its low thermal diffusivity. The inclusion of porosity into the film matrix would be expected to further lower the bulk thermal conductivity.

The thermal properties of these multilayer films were directly measured at the National Institute of Standards and Technology using two techniques. The first, referred to as the  $3\omega$  technique, introduces heat into the coating by an ac current of frequency  $\omega$  flowing through an evaporated resistor [103]. A fit of resistor voltage as a function of frequency yields the thermal conductivity. The second technique is called the Mirage technique. Here, an oscillating temperature was induced immediately above the film using a pulsed laser [104, 105]. A second probe laser aligned parallel to the surface underwent deflection in the boundary layer above the film surface, and the thermal diffusivity was then found by fitting amplitude and phase shift data to the solution of a three-dimensional diffusion equation.

The Mirage method was applied to a dense film of 1  $\mu\text{m}$  thickness, and yielded a room temperature thermal diffusivity of  $0.0053 \pm 0.0007 \text{ cm}^2/\text{s}$ . This value is comparable to those previously reported for YSZ TBCs [106]. Measurements on the GLAD film using both methods led to thermal diffusivity estimates of approximately 9% that of solid YSZ films. It is possible that this result may be improved by further optimizing this YSZ TBC fabrication process.

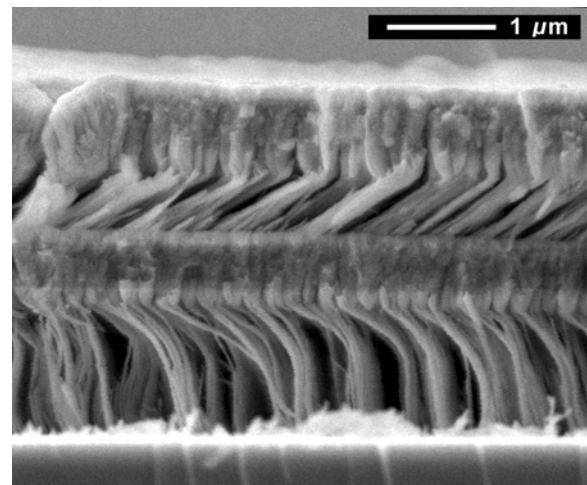


**Figure 16.** YSZ film structures grown from alternating porous and dense layers display a low thermal diffusivity. These films can be grown by dynamic alteration of the deposition angle,  $\alpha$ . Reprinted with permission from [102], K. D. Harris et al., *Surf. Coat. Technol.* 138, 185 (2001). © 2001, Elsevier.

The high thermal resistance of these films offers an alternative use for these film structures. Possibly, the resistance can be exploited as a heating source to increase the operating temperature and/or efficiency of devices created using it as a base.

### 5.3. Enhanced Surface Area Devices

Perhaps the easiest and most directly applicable products for GLAD films are enhanced surface area devices. These films inherently have an extremely high surface area relative to their bulk counterparts [68], which may make them ideal media for a number of applications including humidity sensors, catalysis media, chemical sensors, and lab-on-a-chip devices.

#### 5.3.1. Supercapacitors

High surface area ( $>1000 \text{ m}^2/\text{g}$ ) carbon-based capacitors are commercially available exhibiting specific capacitances of 100–200 F/g. These devices rely on the formation of an electrical double layer between the carbon surface and electrolyte to provide their capacitance [68].

Recently, efforts have been made to develop metal oxides as capacitor materials. These materials utilize a reversible redox reaction as the basis for their pseudo-capacitive behavior. These efforts have primarily focused on rubidium oxides, which have been shown to have specific capacitances of up to 770 F/g [107]. The problem with this material is that rubidium is expensive, leading to the exploration of less expensive alternatives such as  $\text{MnO}_2$ ,  $\text{NiO}$ , and  $\text{Co}_3\text{O}_4$  as faradaic capacitors. Sol-gel [108], colloidal suspensions [109], and electrochemical deposition [110, 111] have all been used to create capacitor media out of one or all of these materials. As examples, Chin et al. [109] observed a specific capacitance of 720 F/g using  $\text{MnO}_2$  via a colloidal solution. Hu et al. used anodic deposition of  $\text{NiO}/\text{CoO}$  mixtures to obtain 720 F/g [110], while a similar process on  $\text{MnO}_2$  resulted in a specific capacitance of 300 F/g [111].

The film microstructures described in this chapter may provide an alternative path for electrochemical capacitor development, based on their high surface area and the notion that vacuum deposition of thin metal films onto flexible substrates is both highly scalable and a well known manufacturing process [68].

Chevron structures have been used for most of the capacitance experiments to date due to its resemblance to the type of structure that would be expected from an obliquely angled multipass coating deposition process. For a 500 nm thick, four-turn chevron structure, the maximum specific capacitance obtained was  $225 \pm 25 \text{ F/g}$  at  $\alpha = 82^\circ$  [68]. Further work may be undertaken to improve the surface area of the films which they believe is the detrimental step in their process.

#### 5.3.2. Humidity and Chemical Sensors

Capacitance measurements on GLAD films are not new, and certainly other applications can arise by applying this property elsewhere. Two of these other applications are relative humidity detection [112, 113] and chemical sensing, where humidity or chemical concentrations are sensed as a

change in capacitance between two parallel plates. A humidity device of this style is typically termed a capacitive relative humidity (RH) sensor.

For these films, the interactions between sensing material, water moisture, and the applied field become strong, making the conventional equivalent circuit model insufficient to explain the observed results [112, 114–117]. Crucial microstructure related parameters are also important, including the diameter of pores and pore size distribution.

Shimizu et al. [115] introduced a computation program demonstrating the importance of these parameters to the sensing characteristics and were subsequently followed by Li [116] who used a similar approach to explain their porous  $\text{Sr}_{1-x}\text{La}_x\text{TiO}_3$  sensors. Khanna and Nahar incorporated the interactions between sensing materials, water moisture, and applied field using Sillars' medium theory [118] to successfully explain the sensing behavior of their porous  $\text{Al}_2\text{O}_3$  sensors fabricated by anodization [117]. Typically, though, these models assume a solid structure within which pores are etched. GLAD films present the opposite approach—essentially, a “void” within which solid structures are grown.

Reasonable capacitive RH characteristics can be obtained by sandwiching a GLAD  $\text{SiO}$  pillar film between two electrodes [113]. A model, based upon a modification of Sillars' medium theory and incorporating the influence of net heat adsorption of water molecules, the change in conductance on the surface of  $\text{SiO}$  film after water adsorption, water condensation in the pores of the sensors due to the capillary effect, changes in conductivity of the condensed water with RH, and the pore size distribution on the sensing characteristics of these devices, was developed and is applicable through an RH range from dry to saturation. This model shows that pore size distribution and porosity have critical effects on the sensing characteristics.

Early RH studies on GLAD films showed that a rapid response time of a few seconds could be obtained, with a capacitive range over five orders of magnitude. This range corresponded to relative humidities of 10% to 90%. Further work on these structures was conducted by Harris et al. at the University of Alberta, who decreased the response time to 25 ms by further optimizing some of the film deposition parameters and measurement techniques [119]. These results are several orders of magnitude quicker than capacitive RH sensors currently on the market. It is thought that the natural pore size in the upper capping layer tends to be near the optimal size for allowing moisture to either adsorb or escape depending on the humidity differential between the film structure and the surrounding air.

Work on humidity sensors opens up the possibility that by modifying the evaporant or using surface treatments, rapid detection of different gases using a similar process design may be obtainable. Engineering a device that incorporates a number of films grown from different materials, it may be possible to differentiate between different gas-borne species.

#### 5.3.3. Catalytic Media

Platinum films have been used as electrodes or catalysts in sensors [120, 121], direct methanol fuel cells [122, 123], and electrochemical deposition systems [124]. The first category

of these applications includes rapid detection of hydrocarbons at low concentrations and is of considerable interest to the automotive industry.

Ford Research Laboratory, in conjunction with the University of Alberta, is studying the catalytic behavior of porous GLAD films for microcalorimetric HC sensors [125]. This method compares the resistance changes between a membrane coated with a catalytic material (in their case platinum, or Pt) and a reference material, when both are subjected to hydrocarbons. Because of the high surface area of GLAD films, a magnification of the detection limit for these particles was expected. It was found, however, that although the performance of the tested films was superior to sputtered Pt films, they were not competitive with commercially available automotive honeycomb monoliths.

Although these results may be improved by optimizing the film thickness, the critical problem remaining is the significant degradation of both the GLAD and sputtered films after repeated use. This problem must be understood and addressed before GLAD films can seriously compete in this particular market.

Titania is a second catalytic material of interest. The columnar morphology in sputtered  $\text{TiO}_2$  has been shown to enhance both photocatalytic and photovoltaic efficiency [126, 127]. The Toyota Central Research and Development Laboratories assessed the photocatalytic activity of obliquely deposited  $\text{TiO}_2$  films on glass substrates [128]. Several film morphologies including chevrons, posts, and helices were fabricated. These films were evaluated by immersing the films in methylene blue solution, irradiating the samples with 350 nm wavelength light, and recording time dependent absorption spectra within the range  $200 < \lambda < 800$  nm.

Several films were tested with angles of incidence between  $0^\circ$  and  $82^\circ$ . All the obliquely deposited films performed slightly better than solid films, although the specific column morphology (i.e., chevron, post, and helical geometry) was not found to be as important as the deposition angle, which had an optimal value at  $\alpha = 70^\circ$ . This optimal value was confirmed by VFIGS simulations, which found  $\alpha = 70^\circ$  to yield a maximum in effective surface area regardless of the specific film morphology [86].

To explain how an optimal value may result from these films, a simplified argument is presented [129]. For many materials, structures of the film separate beyond  $\alpha = 70^\circ$ . If the porous film is treated as an arrangement of identical, isolated cylinders of height  $h$ , radius  $r$ , and occupying an area  $A$ , the resulting number density of columns is given by  $N = 1/A$ . The corresponding surface area of a single column thus scales as  $s \sim r(2h + r)$ , while the fractional density of the film scales as  $\eta \sim r^2/A$ . Hence, the surface area of the film per unit area of substrate scales as  $Ns \sim \eta(2h/r + 1)$ . Thus, for high surface areas, higher densities with long, narrow, isolated columns are preferred. As density is increased (i.e.,  $\alpha$  is decreased), the passages between film columns narrow and eventually close. The characteristic diffusion times for gaseous or liquid-borne species to enter or leave film must therefore increase.

As a result, there is a trade-off between the response time and the surface area for obliquely deposited films. In addition, the role of optical scattering of UV light on photocatalysis in porous films has yet to be assessed.

### 5.3.4. Lab-on-a-Chip

As a final example of enhanced surface area applications, we look at the current research activities taking place in molecular biology, particularly in the separation and identification of genetic materials and proteins. Presently, primarily capillary tubes with inner diameters of  $100 \mu\text{m}$  or more are used for this application [130]. These tubes do not lend themselves well to integration and require equipment which is large, expensive, and monofunctional. Microfluidic structures fabricated by photolithographic processes have been proposed as an alternative means by which genetic materials and proteins can be measured [131]. These structures have demonstrated performance which is similar to capillary tubes but have a compact size, promising increased speed and reduced cost while allowing far greater levels of integration. These areas of research have been termed the “lab-on-a-chip” concept [132].

A common feature to existing and conceived lab-on-a-chip analytical systems is the existence of microchannels. These channels not only provide passageways between different regions on the chip for fluid flow but typically incorporate filtering, separation, or high density reaction sites [133]. It has been shown that a porous  $\text{SiO}_2$  film can be grown in an etched microchannel (see Fig. 17) [134]. Precise alignment of the trench and source is required such that the flux arrives parallel to the trench direction, thus restricting the film morphology to either chevrons or oblique columns. Using this method, a surface area enhancement of two orders of magnitude was obtained.

The limitation in film morphology for this type of device may be removed through the use of raised topography, which was described in the previous section. If the channels are constructed as raised topography, a standard GLAD process can be used to form a variety of microstructure morphologies over the channel surface. This structure would be

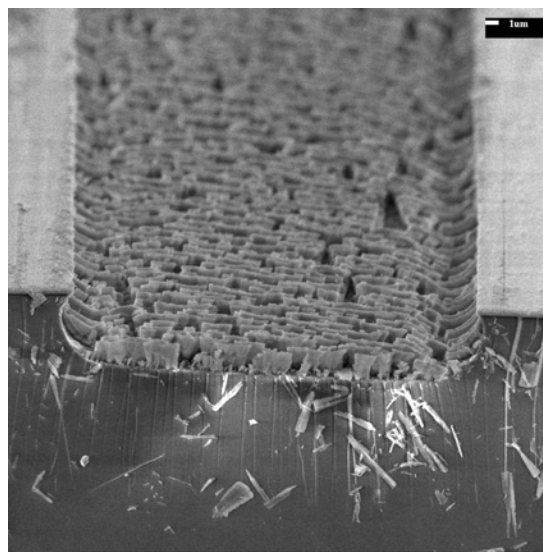


**Figure 17.**  $\text{SiO}_2$  films are shown grown within an etched microchannel. Precise alignment of the flux and channel are required for proper microstructure growth. Reprinted with permission from [134], K. D. Harris et al., *J. Electrochem. Soc.* 147, 2002 (2000). © 2000, Electrochemical Society.

self-sealing at the edges and can be sealed on the top by depositing the appropriate capping layer.

#### 5.4. Magnetic Properties

It would not be unfair to say that the properties of magnetic microstructures are poorly understood. Although in recent years this understanding has grown immensely with the advent of better and faster computer simulations, much research still focuses on film characterization studies. What is well known, however, is that the microstructure of a magnetic thin film significantly affects its magnetic properties [54]. The ability to control the size, shape, orientation, and composition of the magnetic structure on a nanometer (or subdomain) scale offers a greater range in magnetic properties that can be controlled. This level of control can be applied not only to magnetic recording media (i.e., to increase storage densities) but also leads to the ability to test micromagnetic theories/modeling, and the fabrication of more innovative magnetic materials and devices.

Originally, it was thought that periodic GLAD pillars might serve as a suitable medium for high-density storage media. TEM and X-ray diffraction measurements of cobalt pillars grown on a chromium underlayer (to promote epitaxial growth in subsequent layers [135]) show the films to be monocrystalline, hexagonal close-packed structures with a strong crystal axis alignment perpendicular to the substrate. Reasonably defined periodic structures were shown to exhibit the equivalent of approximately 3 Gigabits/in<sup>2</sup>, assuming each particle consisted of a single bit [93]. Subsequent research using a TEM to etch a small sample indicated that nickel films might be grown with periods of less than 10 nm [58]. However, magnetic force microscopy imaging of the domain structure for these and previous films was inconclusive, and subsequent developments in this field (namely demonstrated storage density of over 25.7 Gigabits/in<sup>2</sup> in a commercial device by IBM, and potential research focusing on 1 Terabit/in<sup>2</sup> [136]) rapidly outpaced potential GLAD development.

Certainly, the possibility of growing unique microstructures for magnetic studies remains, and a few researchers have analyzed the hysteresis curves from several GLAD morphologies including columnar structures, helices, and posts [77, 93].

#### 5.5. Optical Properties

Optical properties of films deposited at both oblique and glancing angles have been a study of research for some time. Indeed, the initial experiments into sculptured thin films were borne through the possibility that the optical properties of a thin film could be manipulated by changing its structure [22, 26].

The application of the advanced GLAD technique to a deposition process can give the user considerable latitude in both planning and optimizing the optical properties of a thin film. Two simple examples are used here to introduce these concepts: rugate filters and diffraction gratings [137].

Rugate filters are fabricated when thin films exhibit a spatially modulated index of refraction. The GLAD technique can easily introduce this modulation by introducing

a density gradient across the film thickness (i.e., adjusting the flux incidence angle during deposition). By varying  $\alpha$  between 50° and 80°, filters have been fabricated which exhibit 82% reflection peaks and bandwidths of 50 nm centered at 460 nm [138]. The second example, diffraction gratings, results from the sinusoidal morphology at the cleaved edge of a helical film. This morphology acts like a diffraction grating oriented vertically.

These examples are not particular to the GLAD technique, however, and have been reported for less obliquely deposited films by other researchers (see, for instance, an example of a STF rugate in [139] and a Solč filter in [140]). It is hoped, however, that these references help introduce the reader to the power of simply rotating the substrate at oblique incidence to manipulate the optical properties of a thin film.

##### 5.5.1. Chirality in GLAD Structures

One of the unique properties of some GLAD film structures is their chirality, which is to say that their geometry is nonsymmetric [141]. A necessary and sufficient condition for chirality is that a chiral object cannot be superimposed by rotation and translation onto its mirror image. Some examples of chiral objects include Möbius strips, many types of complex molecules (generally organic substances), and, of course, one's hands. And, just like hands, chiral structures have a both a left- and right-handed version. Helical GLAD films (and their derivatives) are primary examples of chiral structures: their handedness depends on the direction of substrate rotation during deposition (i.e.,  $\varphi$  is clockwise or counterclockwise). An example of a left-handed GLAD helical film is shown in Figure 18.

The chiral nature of these GLAD structures becomes important when we consider the effect on their optical properties. Chiral crystals or molecular structures are known to exhibit optical activity, which is the rotation of the plane

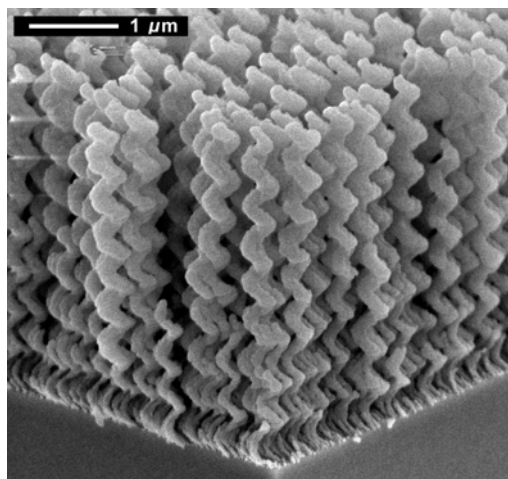


**Figure 18.** An example of a chiral GLAD film. Here, a left-handed SiO<sub>2</sub> helical film with a pitch length of 410 nm and 8.4 turns is shown. Reprinted with permission from [129], D. Vick et al., Glancing angle deposition of thin films, *Res. Signpost*, in press. © 2002, Research Signpost.

of polarization of linearly polarized light [142]. The fundamentals of chiral optical activity were discovered in the mid-19th century, and were mostly studied by chemists who concentrated on natural optical activity (see [141] for a good review). This work led to Louis Pasteur's postulate stating that optical activity may arise due to the chirality of its molecules ([143], from [141]).

The chirality in a GLAD film, however, does not arise through the material but rather through the columnar shape (i.e., a form of artificial chiral media). Research on artificial chiral media initially occurred in the 1920s with experiments on wire spirals and microwave propagation [144, 145]. These results were later confirmed by Tinoco et al. [146, 147] who investigated electromagnetic activity with microwave radiation incident on copper wire helices in a box. The pitch length of these early studies was on the order of 1 centimeter, yielding electromagnetic (EM) activity in the microwave regime. In contrast, thin films (e.g., GLAD helices) can be fabricated with pitch lengths on the order of a few hundred nanometers, yielding EM activity in the visual spectrum ( $\lambda = 400$  to  $700$  nm).

### 5.5.2. Optical Activity

Earlier we mentioned work by Young and Kowal (1959) [26], who investigated optical activity by depositing films at oblique incidence ( $\alpha \sim 70^\circ$ ) onto rotating substrates. These films exhibited rotatory powers of around  $155^\circ/\text{mm}$  (as measured by the amount of angular rotation per thickness of film). In this and all examples that follow, the standard sign convention for optical rotation is used. If we define  $n_A$  as being the index of refraction of the structured material, while  $n_B$  is the index of refraction of the medium surrounding the material, a left-handed film with  $n_A > n_B$  produces a positive (clockwise, looking back at the light source) rotation in the plane of polarization for transmitted light. Its enantiomeric counterpart, a right-handed film produces a negative rotation. In the case where the structure is film material and the surrounding medium is air,  $n_A = n_{\text{film}}$  and  $n_B = n_{\text{air}}$ .

Young and Kowal's results were the first known work where artificial media showed an optical rotatory response. However, although advancement in the production and characterization of nonchiral, obliquely deposited films continued (primarily by groups in New Zealand [148] and Japan [28]), it was not until Robbie et al. [38] fabricated porous helical thin films using the GLAD technique that further spectroscopic measurements of optical activity in a chiral thin film were reported [149–151].

Leading up to Robbie's work, an extensive and growing body of work modeling the interaction of EM waves with chiral media had been reported (see for example, [152–154], and many other works by Lakhtakia). This theoretical modeling indicated that highly porous structures are not suitable for maximizing rotatory power. Experimental results have shown that GLAD films display an average rotatory power ranging from  $0.16^\circ/\mu\text{m}$  for  $\text{MgF}_2$  to  $1.05^\circ/\mu\text{m}$  for  $\text{Al}_2\text{O}_3$  [155], significantly less than that obtainable by denser films which have demonstrated rotation up to  $5^\circ/\mu\text{m}$  for titanium oxide films [156]. Perforated GLAD films, however, being the inverse of the GLAD template (described previously in Section 4.1), show a diminished porosity, while

maintaining the same geometric form. Analysis of optical rotation in right- and left-handed perforated films has found an improvement of up to three times over their GLAD templates. For example, right-handed perforated films had a measured rotation of  $3.93^\circ/\mu\text{m}$  compared to  $-1.53^\circ/\mu\text{m}$  for its template, and the left-handed perforated film had a measured rotation of  $-1.48^\circ/\mu\text{m}$  and  $0.49^\circ/\mu\text{m}$  for its template [92]. The measured power of the perforated film is the reversal of rotation displayed by their respective templates, since the refractive index gradient has been inverted with an air helix ( $n = 1$ ) surrounded by a photoresist matrix ( $n \sim 1.6$ ). The enhanced rotation in the right-handed film is not clear at this time, and both it and the generally stronger optical activity of the perforated films over their GLAD templates bear further study.

### 5.5.3. Liquid Crystal Hybrid Optics

Although the porous nature of GLAD films may not be the most optimal morphology for enhancing the rotatory power of thin films, it does allow for hybrid devices when combined with liquid crystals. These devices are not possible with dense films.

Optimizing the optical properties for liquid crystal (LC) devices requires control over the long-range orientation of the LC molecules. Two techniques serve as common examples of how this orientation is controlled. In the first, thin coatings of polyimides are applied to the substrate surface, which is subsequently rubbed to produce planar alignment of LCs [157]. In the second, obliquely deposited thin films are used as alignment layers to generate a certain "tilt" of LC molecules at the substrate [158, 159].

In both these examples, the influence on LC orientation is felt near the substrate surface only. Controlling the LC orientation in thicker switching cells (particularly with chiral or cholesteric LCs) becomes problematic and can lead to difficulties such as irreversible switching [160].

Techniques that are used to control the orientation of LC molecules through the film media make use of polymer-dispersed liquid crystals or photopolymerization. GLAD helical films can provide an alignment structure or "backbone" for the LC, inducing a chiral nematiclike ordering in nonchiral LC materials. GLAD films filled with birefringent materials such as nematic LCs, for example, show an enhanced transmission difference between left- and right-circularly polarized (LCP and RCP respectively) light [161]. This difference was removed when the films were filled with an isotropic liquid such as water or some polymer materials which had indices of refraction approximately matching the film material.

Switching cells were demonstrated using a  $\text{SiO}_2$  LC/GLAD hybrid [162, 163] fabricated by depositing the GLAD film on glass substrates with an indium tin-oxide (ITO) electrode. A counterelectrode was provided by another ITO coated glass substrate. When brought together, these two pieces form a "sandwich" which can subsequently be filled with LCs (see Fig. 19). Switching can then be accomplished by exploiting the dielectric anisotropy of the LCs. In the unaddressed state (no voltage applied), the LC orientation is controlled by the presence of the GLAD chiral films. Hence, an enhanced transmission is observed. In the

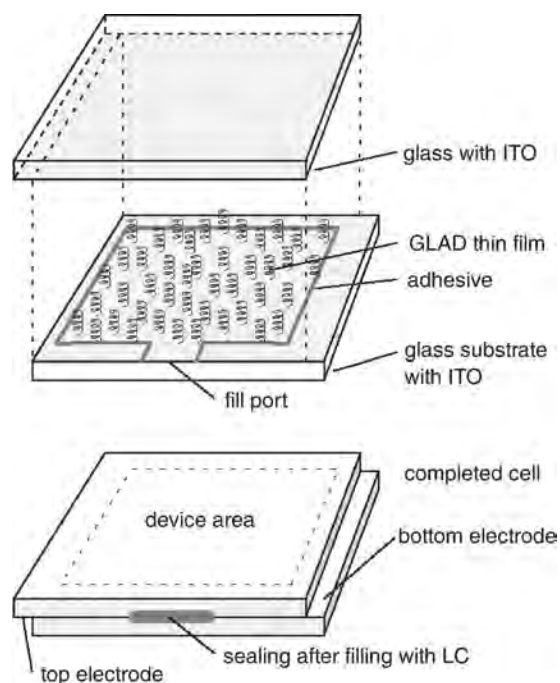


**Figure 19.** Electro-optic switching cells for GLAD/LC composites are constructed from two ITO coated glass substrates containing a LC filled GLAD thin film. The fill port is present to add the LCs after the GLAD film “sandwich” is fabricated. This port is plugged before use. Reprinted with permission from [162], J. C. Sit et al., *Liq. Cryst.* 27, 387 (2000). © 2000, International Society for Optical Engineering (SPIE).

addressed state (a 200 V<sub>pp</sub>, 1 kHz signal applied), the LCs align parallel to the applied field, and no transmission difference between LCP and RCP occurs. In this latter case, light transmitted through the cell along the helical axis (which is now parallel to the LCs) “sees” the ordinary refraction index  $n_0$  of the LC. If the  $n_0$  index matches with the index of refraction of the film, the cell appears to be a homogenous medium ( $n = n_0 = n_{\text{film}}$ ). Thus the chiral optical response vanished in the addressed mode. An illustration of both the addressed and unaddressed states is shown in Figure 20. The lower panel of this diagram shows the transmission difference observed between these two states.

Increasing the porosity of the films allows for a greater degree of LC filling, at the cost of a lower deposition rate (which is dependent on the cosine of  $\alpha$ ). Additionally, when the film microstructures become further separated, the order of LC molecules can become more randomized, resulting in a degradation of the film’s optical properties. These effects must be balanced in an optimal structure. This point has been found to occur at  $\alpha = 85^\circ$  for a similar film to the hybrid example described above [155].

Filling GLAD films with LCs has two beneficial side-effects: The matrix of LCs more closely matches the index of refraction of the film materials, resulting in less light scatter in the film/LC hybrid devices, and the risk of contamination by ambient humidity (which would degrade the effectiveness of the devices) is reduced [164].

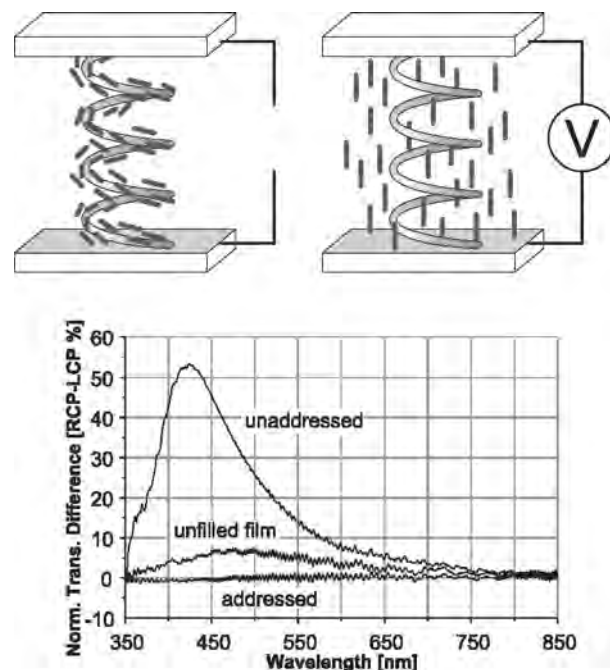


**Figure 20.** Electro-optical switching in GLAD/LC composites consists of two steps: in the unaddressed state (top left), the LC is aligned by the chiral GLAD medium and exhibits a transmission difference between right and left circularly polarized light; when an electric field is applied (top right), the LC molecules align and the transmission difference disappears. Lower panel reprinted with permission from [162], J. C. Sit et al., *Liq. Cryst.* 27, 387 (2000). © 2000, International Society for Optical Engineering (SPIE). Upper panels reprinted with permission from [41], J. C. Sit, *Thin Film/Liquid Crystal Composite Optical Materials and Devices*, Ph.D. Thesis, University of Alberta, Edmonton, 2002.

#### 5.5.4. Photonic Bandgap Optics

A second optical application for GLAD films has been closely investigated. Photonic bandgap (PBG) crystals are artificial, periodic structures which exhibit the characteristics of a bandgap for light. In other words, the propagation of electromagnetic waves within the frequency range of the bandgap is restricted [51, 52, 165]. Hence, a photonic bandgap crystal is the light analogy to the bandgap in a semiconductor material which restricts electron movement based on their energies. This “stop-band” must lie in all directions in the lattice, requiring a three-dimensional structure. Three-dimensional photonic bandgap crystals with a periodicity which exhibit a stop-band falling in or near the visible spectrum are of particular interest.

Recently, it was proposed that a square spiral microstructure should exhibit a large 3D photonic bandgap [50, 166]. This structure consisted of a tetragonal lattice of square spiral posts and was based on the distortion of nonstandard diamond helices. It was suggested that the GLAD process might be ideally adapted to form this morphology.

Soon after this “challenge” was issued, the structures were fabricated using prepatterned substrates and advanced GLAD control [45]. These structures are shown in Figure 21. Here, photolithography was used to design substrate topography with lattice seed diameters of 500 nm and separations of 1  $\mu\text{m}$ . Further optimization of the process



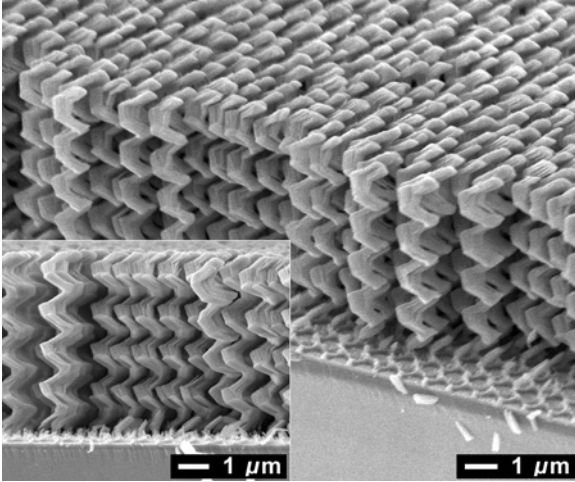


**Figure 21.** A tetragonal square spiral GLAD film which has been suggested as a potential three-dimensional, photonic bandgap material. A side view of this film is shown in the inset. Reprinted with permission from [45], S. Kennedy et al., *Nanoletters* 2, 59 (2002). © 2002, American Chemical Society.

should yield a structure even closer to what the theory originally envisioned.

Photonic bandgap materials manipulate light through the introduction of lattice defects. These defects allow for the confinement and guiding of light, requirements for the application of these media in photonics and integrated optics. As mentioned in Section 2.2.5, these defects can be introduced into a periodic GLAD film without degradation to the microstructure growth [56]. Defects in the seed topography transfer to the film, as the extreme flux incidence angle ensures that there is little or no flux coverage over the non-seeded region. Provided that this defect area is not on the order of the shadowing distance cast by individual seeds, the uniformity of the periodic film is preserved.

A subsequent series of processing steps can be applied to the square spiral films to yield a structure that exhibits an even larger PBG. An inverse square spiral film, which can be fabricated using the perforated film recipe described in Section 4.1, is expected to have a PBG approximately twice the size of the standard structure ( $\sim 24\%$  of the central band frequency, compared with  $\sim 16\%$  [166] of the central band frequency exhibited by the standard structure). At the time of this publication, this structure has not yet been presented.

## 6. CONCLUSION

This review has introduced a promising and versatile tool for materials engineering at the submicrometer scale. GLAD films can be fabricated with relative ease from a variety of materials and are readily incorporated onto lithographically prepared and micromachined surfaces. Examples of such surfaces include interdigitated electrodes, microcantilevers, mesa arrays, and microfluidic channels. In some proposed applications, such as sensors, the films would play an active role in a device. Alternatively, the films may serve as supporting matrix for the active component (e.g., embedded liquid crystals), or as a template in a manufacturing stage

(e.g., porous membranes). The successful demonstration of low defect periodic GLAD arrays is of particular significance and could lead to a method for the manufacture of photonic bandgap devices. It will also be evident from this chapter that much work will be required on both fundamental and applied fronts before this technology fully matures. We may expect a rapid expansion of the field in the coming years as more researchers incorporate GLAD films into their processes and devices.

## LIST OF SYMBOLS

$\alpha$	The angle of incident flux at the substrate measured relative to the substrate normal.
$\Delta\alpha$	A measure of the angular distribution in flux incident at the substrate.
$a$	The normalized column separation as determined by Tait's rule.
$\beta$	Columnar angle measured relative to the substrate normal.
$\chi_c$	Columnar angle measured relative to the substrate plane.
$\chi_v$	The angle of incident flux measured relative to the substrate plane.
$\delta$	The optimized period of seed elements used to grow periodic GLAD structures. At this period, film growth occurs only at the locations of seed elements. In other words, $\delta \equiv p_{\text{optimized}}$ .
$d$	The "average" separation of randomly grown GLAD columns.
$\varphi$	Rotation angle about an axis located at the substrate center, and parallel to its normal.
$p$	The period of seed elements used to grow periodic GLAD structures.
$p_c$	Ambient chamber pressure. For evaporation, $p_c$ is less than $10^{-5}$ Torr ( $10^{-3}$ Pa) and typically on the order of $10^{-6}$ Torr ( $10^{-4}$ Pa) for refractory metals. For sputtering, $p_c$ is on the order of $10^{-3}$ to $10^{-2}$ Torr (0.1 to 1.0 Pa).
$\rho$	Thin film density.
$s$	The diameter of columns grown using the GLAD technique.
$T$	Substrate or film surface temperature.
$t$	The thickness (i.e., height) of individual seed elements used to grow periodic GLAD structures. This parameter, coupled with the flux incidence angle, helps determine the optimal seed period.
$T_m$	Melting temperature of source material.

## GLOSSARY

**3D-films** A 3D, Monte Carlo ballistic simulator, based on the SIMBAD program, which models the creation and dynamic evolution of 3D microstructures in PVD thin films.

**Adatoms** Incident atoms which have transferred their kinetic energy to the substrate lattice and become loosely bound to the surface.

**Ballistic deposition (BD)** Modeling which treats flux as arriving colinearly at the substrate surface. Adatom diffusion and surface shadowing are the primary growth mechanisms.

**Bulk diffusion** Movement of atoms within the film. This process is characteristic of Zone 3 films as described by the Movchan and Demchishin structure zone model.

**Chirality** Material property describing its nonsymmetric geometry. A chiral object cannot be superimposed by rotation and translation onto its mirror image.

**Collimated sputtering** The process by which sputtered atoms outside a desirable incidence angle range are mechanically inhibited from striking the substrate. A honeycomb sheet-metal array is placed perpendicular to and between the target and substrate plane. Although  $\Delta\alpha$  is minimized, the deposition rate at the substrate surface is significantly reduced.

**Column competition** The process by which thin film columns extinguish their neighbors due to shadowing at extremely oblique flux incidence angles. The resulting decrease in column number density is compensated by an increase in individual column diameters, leaving the overall film density constant.

**Columnar growth** The tendency of PVD thin films to grow columnar microstructures. These columns are oriented in the direction of the flux source.

**Chemical vapor deposition (CVD)** A volatile material compound reacts chemically with other gases to produce a nonvolatile solid that deposits onto a substrate as a film.

**Electron beam lithography (EBL)** Technique for creating extremely high resolution patterns. EBL consists of scanning an electron beam across a resist sensitive to electron irradiation, while controlling the beam to create any desired two-dimensional pattern. The technology is capable of creating an infinite number of patterns in a variety of materials at sub-50 nm resolution. However, although very versatile, EBL is more expensive and considerably slower than photolithography.

**Evaporation** The controlled transfer of gaseous atoms from a heated source to a substrate where film forms.

**Porosity** A solidity measurement for a thin film. This parameter is inversely proportional to the density of the thin film compared to its bulk counterpart and is sometimes used as an expression of surface area. Film porosity tends to increase with increasing flux incidence angle and, most significantly, within the glancing incidence regime ( $\alpha > 80^\circ$ ).

**Glancing angle deposition (GLAD)** The use of substrate rotation and flux incidence angle variation to fabricate a range of thin film morphologies with controlled structure and porosity. This technique requires columnar vapor flux to be deposited at extremely oblique incidence angles ( $\alpha > 80^\circ$ ).

**Incident flux** Term used to describe source vapor arriving at the substrate. Usually implies a directional component.

**Lab-on-a-chip** Chemical analyses wherein processing, transport, etc., occur in microchannel structures located on-chip.

**Liquid crystals (LC)** Term used for a type of organic molecule having inherent optical anisotropy. Strongly birefringent media are produced when the molecules are purposefully aligned.

**Low-pressure, long-throw (LPLT) sputtering** Technique by which the sputtering target and substrate are separated by a

relatively large distance (typically greater than 15 cm), and the plasma is ignited under low chamber pressures [ $p_c < 1$  m Torr (0.1 Pa)]. This process attempts to minimize  $\Delta\alpha$  by increasing the mean-free path of particles in the chamber. Flux arrives at the substrate with a linear trajectory, though not necessarily with an origin at the source due to collisions with the working gas atoms.

**Microfluidics** The study of microliter quantities of flowing fluids usually confined to microchannels.

**Movchan and Demchishin SZM** One of the first structure zone models to classify continuous film structure according to substrate temperature during deposition. Three “zones” of film texture are identified: Zone 1, where atomic shadowing effects predominate ( $T/T_m < 0.3$ ); Zone 2, where surface diffusion effects predominate ( $0.3 < T/T_m < 0.5$ ); and Zone 3, where bulk diffusion effects predominate ( $T/T_m > 0.5$ ).

**Motohiro–Taga interface** The transition region occurring when the column angle is abruptly altered through a change of flux incidence angle. The resulting microstructure is similar in form to a chevron, with the apex being the Motohiro–Taga interface.

**Nanoindentation** A process by which a small probe compresses a thin film surface to obtain force versus displacement curves under a variety of loading conditions.

**Normal incidence** A condition for deposition where the substrate is held perpendicular to the incident flux. This substrate configuration typically maximizes the film deposition rate while minimizing surface shadowing effects.

**Oblique deposition** A condition for deposition where the substrate is inclined relative to the incident flux. Columnar growth is inclined toward the flux source.

**Optical activity** Rotation of the plane of polarization for light transmitted through a material.

**Photonic bandgap (PBG) crystals** Artificial, periodic structures.

## ACKNOWLEDGMENTS

The authors thank our colleagues in the Nanotechnology and Microdevices Research Group in Electrical and Computer Engineering at the University of Alberta for their suggestions during the writing of this review. The contributions of Michael Colgan, Martin O. Jensen, Ken Harris, and Douglas Vick are particularly acknowledged for their assistance in editing the final manuscript. We also make special note of George D. Braybrook for his excellent SEM imaging of many of the structures presented in this chapter. This work has been supported in part by the Natural Sciences and Engineering Research Council of Canada (NSERC), Alberta Informatics Circle of Research Excellence (iCORE), and Micalyne, Inc.

## REFERENCES

1. M. Ohring, “The Materials Science of Thin Films,” 2nd ed. Academic Press, Toronto, 2002.
2. E. D. Nicholson, *Gold Bull.* 12, 161 (1979).
3. M. Faraday, *Philos. Trans. Roy. Soc. London* 147, 145 (1857).

4. L. I. Maissel and R. Glang, "Handbook of Thin Film Technology." McGraw-Hill, Toronto, 1970.
5. J. G. Fish, "Deposition Technologies for Films and Coatings." Noyes, Park Ridge, NJ, 1982.
6. H. K. Pulker, "Coatings on Glass." Elsevier, New York, 1984.
7. J. L. Vossen and W. Kern, "Thin Film Processes." Academic Press, San Diego, 1978.
8. R. W. Vook, *Int. Metals Rev.* 27, 209 (1982).
9. D. W. Pashley and M. J. Stowell, *J. Vac. Sci. Technol.* 3, 156 (1966).
10. B. A. Movchan and A. V. Demchishin, *Phys. Met. Metallogr.* 28 (1969).
11. J. A. Thornton, *Annu. Rev. Mater. Sci.* 7, 239 (1977).
12. K. Robbie, Glancing angle deposition, in "Electrical and Computer Engineering." University of Alberta, Edmonton, 1998.
13. T. G. Knorr and R. W. Hoffman, *Phys. Rev.* 113, 1039 (1959).
14. D. O. Smith, *J. Appl. Phys.* 30, 264S (1959).
15. D. O. Smith, M. S. Cohen, and G. P. Weiss, *J. Appl. Phys.* 31, 1755 (1960).
16. L. Abelmann and C. Lodder, *Thin Solid Films* 305, 1 (1997).
17. J. M. Nieuwenhuizen and H. B. Haanstra, *Phil. Tech. Rev.* 27, 87 (1966).
18. R. N. Tait, T. Smy, and M. J. Brett, *Thin Solid Films* 226, 196 (1993).
19. H. J. Leamy, G. H. Gilmer, and A. G. Dirks, The microstructure of vapour deposited thin films, in "Current Topics in Materials Science" (E. Kaldis, Ed.), Vol. 6, p. 309. North-Holland, Amsterdam 1980.
20. A. G. Dirks and H. J. Leamy, *Thin Solid Films* 47, 219 (1977).
21. R. Messier, T. Gehrke, C. Frankel, V. C. Venugopal, W. Otano, and A. Lakhtakia, *J. Vac. Sci. Technol. A* 15, 2148 (1997).
22. L. Holland, *J. Opt. Soc.* 43, 376 (1953).
23. M. S. Cohen, *J. Appl. Phys.* 32, 87S (1961).
24. I. Hodgkinson, Q. H. Wu, and A. McPhun, *J. Vac. Sci. Technol. B* 16, 2811 (1998).
25. R. Fiedler and G. Schirmer, *Thin Solid Films* 167, 281 (1988).
26. N. O. Young and J. Kowal, *Nature* 183, 104 (1959).
27. R. Messier, A. Lakhtakia, V. C. Venugopal, and P. D. Sunal, *Vac. Technol. Coat.* 40 (2001).
28. T. Motohiro and Y. Taga, *Appl. Opt.* 28, 2466 (1989).
29. A. Lakhtakia and R. Messier, *Opt. Eng.* 33, 2529 (1994).
30. K. Robbie, L. J. Friedrich, S. K. Dew, T. Smy, and M. J. Brett, *J. Vac. Sci. Technol. A* 13, 1032 (1995).
31. K. D. Harris, D. Vick, T. Smy, and M. J. Brett, *J. Vac. Sci. Technol. A* 20, in press.
32. R. Azzam, *Appl. Phys. Lett.* 61, 3118 (1992).
33. A. Lakhtakia and W. S. Weighofer, *Proc. Roy. Soc. London Ser. A* 448, 419 (1995).
34. A. Lakhtakia, R. Messier, M. J. Brett, and K. Robbie, *Innov. Mat. Res.* 1, 165 (1996).
35. O. R. Monteiro, A. Vizar, and I. G. Brown, *J. Phys. D* 31, 3188 (1998).
36. G. Y. Slepian and A. S. Maksimenko, *Opt. Eng.* 37, 2843 (1998).
37. A. Lakhtakia and R. Messier, *Opt. Photon. News* 27 (2001).
38. K. Robbie, M. J. Brett, and A. Lakhtakia, *J. Vac. Sci. Technol. A* 13, 2991 (1995).
39. K. Robbie and M. J. Brett, USA, 1999.
40. K. Robbie, C. Shafai, and M. J. Brett, *J. Mater. Res.* 14, 3158 (1999).
41. J. C. Sit, Thin Film/Liquid Crystal Composite Optical Materials and Devices, Ph.D. Thesis, University of Alberta, Edmonton, 2002.
42. K. Robbie, J. C. Sit, and M. J. Brett, *J. Vac. Sci. Technol. B* 16, 1115 (1998).
43. R. N. Tait, T. Smy, and M. J. Brett, *J. Vac. Sci. Technol. A* 10, 1518 (1992).
44. D. Vick, T. Smy, and M. J. Brett, *J. Mater. Res.* 17 (2002).
45. S. Kennedy, M. J. Brett, O. Toader, and S. John, *Nanoletters* 2, 59 (2002).
46. R. Messier, V. C. Venugopal, and P. D. Sunal, *J. Vac. Sci. Technol. A* 18, 1538 (2000).
47. K. Robbie and M. J. Brett, *J. Vac. Sci. Technol. A* 15, 1460 (1997).
48. K. D. Harris, D. Vick, M. J. Brett, and K. Robbie, *Mater. Res. Soc. Symp. Proc.* 555, 97 (1999).
49. M. Suzuki and Y. Taga, *Japan J. Appl. Phys.* 40, L358 (2001).
50. O. Toader and S. John, *Science* 292, 1133 (2001).
51. S. John, *Phys. Rev. Lett.* 58, 2486 (1987).
52. E. Yablonovitch, *Phys. Rev. Lett.* 58, 2059 (1987).
53. S. John, O. Toader, and K. Busch, *Encyclopedia Phys. Sci. Technol.* 12, 133 (2002).
54. S. Y. Chou, *Proc. IEEE* 85, 652 (1997).
55. M. Seto, B. Dick, and M. J. Brett, *J. Micromech. Microeng.* 11, 582 (2001).
56. M. Malac, R. F. Egerton, M. J. Brett, and B. Dick, *J. Vac. Sci. Technol. B* 17, 2671 (1999).
57. B. Dick, J. C. Sit, M. J. Brett, I. M. N. Votte, and C. W. M. Bastiaansen, *Nanoletters* 1, 71 (2001).
58. M. Malac and R. F. Egerton, *Nanotech.* 12, 11 (2001).
59. R. Messier and J. E. Yehoda, *J. Appl. Phys.* 58, 3739 (1985).
60. R. P. U. Karunsiri, R. Bruinsma, and J. Rudnick, *Phys. Rev. Lett.* 62, 788 (1989).
61. M. Malac, R. F. Egerton, and M. J. Brett, *Vac. Technol. Coat.* 48 (2001).
62. M. Malac and R. F. Egerton, *J. Vac. Sci. Technol. A* 19, 158 (2001).
63. D. Le Bellac, G. A. Niklasson, and C. G. Granqvist, *Europhys. Lett.* 32, 155 (1995).
64. D. Vick, T. Smy, B. Dick, S. Kennedy, and M. J. Brett, *Mater. Res. Soc. Symp. Proc.* 648, P3.43.1 (2001).
65. B. Dick, M. J. Brett, and T. Smy, *J. Vac. Sci. Technol. B*, in press.
66. B. A. Orlowski, W. E. Spicer, and A. D. Baer, *Thin Solid Films* 34, 31 (1976).
67. T. Smy, D. Vick, M. J. Brett, S. K. Dew, A. T. Wu, J. C. Sit, and K. D. Harris, *J. Vac. Sci. Technol. A* 18, 2507 (2000).
68. J. N. Broughton and M. J. Brett, *Electrochem. Solid-State Lett.* 5, A279 (2002).
69. R. N. Tait, S. K. Dew, T. Smy, and M. J. Brett, *J. Appl. Phys.* 70, 4295 (1991).
70. R. N. Tait, S. K. Dew, W. Tsai, D. Hodul, T. Smy, and M. J. Brett, *J. Vac. Sci. Technol. B* 14, 679 (1996).
71. S. M. Rossnagel, D. Mikalsen, H. Kinoshita, and J. J. Cuomo, *J. Vac. Sci. Technol. A* 9, 261 (1991).
72. S. M. Rossnagel and J. Hopwood, *Appl. Phys. Lett.* 63, 3285 (1993).
73. J. N. Broughton, M. J. Brett, S. K. Dew, and G. Este, *IEEE Trans. Semicond. Manu.* 9, 122 (1996).
74. J. C. Sit, D. Vick, K. Robbie, and M. J. Brett, *J. Mater. Res.* 14, 1197 (1999).
75. B. Dick, M. J. Brett, T. Smy, M. Belov, and M. R. Freeman, *J. Vac. Sci. Technol. B* 19, 1813 (2001).
76. F. Liu, C. Yu, L. Shen, J. Barnard, and G. J. Mankey, *IEEE Trans. Mag.* 36, 2939 (2000).
77. F. Liu, M. T. Umlor, L. Shen, J. Weston, W. Eads, J. Barnard, and G. J. Mankey, *J. Appl. Phys.* 85, 5486 (1999).
78. B. Dick, M. J. Brett, and T. Smy, submitted for publication.
79. K. Hara, *J. Sci. Hiroshima Univ. Ser. A II*, 139 (1970).
80. K. Hara, M. Kamiya, T. Hashimoto, K. Okamoto, and H. Fujiwara, *J. Magn. Magn. Mater.* 73, 161 (1988).
81. S. Lichter and J. Chen, *Phys. Rev. Lett.* 56, 1396 (1986).
82. J. B. Bindell and T. C. Tisone, *Thin Solid Films* 23, 31 (1974).
83. G. S. Bales and A. Zangwill, *J. Vac. Sci. Technol. A* 9, 145 (1991).
84. P. Meakin, *Phys. Rev. A* 38, 994 (1988).
85. D. Henderson, M. H. Brodsky, and P. Chaudhari, *Appl. Phys. Lett.* 25, 641 (1974).
86. M. Suzuki and Y. Taga, *J. Appl. Phys.* 90, 5599 (2001).
87. M. J. Brett and S. K. Dew, *Thin Films* 22 (1996).

88. J. E. A. M. van den Meerakker, R. J. G. Elfrink, F. Roozeboom, and J. F. C. M. Verhoeven, *J. Electrochem. Soc.* 147, 2757 (2000).
89. A. P. Li, F. Muller, and U. Gosele, *Electrochem. Solid-State Lett.* 3, 131 (2000).
90. A. Chelnokov, S. Rowson, J.-M. Lourtioz, V. Berger, and J.-Y. Coutois, *J. Opt. A: Pure Appl. Opt.* 1, L3 (1999).
91. K. D. Harris, K. Westra, and M. J. Brett, *Electrochem. Solid-State Lett.* 4, C39 (2001).
92. K. D. Harris, J. C. Sit, and M. J. Brett, *IEEE Trans. Nanotech.*, in press.
93. B. Dick, M. J. Brett, T. Smy, M. R. Freeman, M. Malac, and R. F. Egerton, *J. Vac. Sci. Technol. A* 18, 1838 (2000).
94. M. Seto, K. Westra, and M. J. Brett, *J. Mater. Chem.* 12, 2348 (2002).
95. M. J. Colgan, D. Vick, and M. J. Brett, *Mater. Res. Soc. Symp. Proc.* 636, D9.24.1 (2001).
96. W. B. Choi, D. S. Chung, J. H. Kang, H. Y. Kim, Y. W. Jin, I. T. Han, Y. H. Lee, J. E. Jung, N. S. Lee, G. S. Park, and J. M. Kim, *Appl. Phys. Lett.* 75, 3129 (1999).
97. Y.-H. Lee, H. Y. Kim, D.-H. Kim, and B. K. Ju, *J. Electrochem. Soc.* 147, 3564 (2000).
98. D. Vick, M. J. Brett, and K. Westra, *Thin Solid Films* 408, 79 (2002).
99. M. Seto, K. Robbie, D. Vick, M. J. Brett, and L. Kuhn, *J. Vac. Sci. Technol. B* 17, 2172 (1999).
100. F. Wang, A. Lakhtakia, and R. Messier, *Sens. Actuat. A*, in press.
101. S. M. Meier and D. K. Gupta, ASME Paper 92-GT-203, 1992.
102. K. D. Harris, D. Vick, E. J. Gonzalez, T. Smy, K. Robbie, and M. J. Brett, *Surf. Coat. Technol.* 138, 185 (2001).
103. D. G. Cahill and R. O. Pohl, *Phys. Rev. B* 35, 4067, (1986).
104. D. Josell, E. J. Gonzalez, and G. S. White, *J. Mater. Res.* 13, 117 (1998).
105. P. K. Kuo, E. D. Sandler, L. D. Farvo, and R. L. Thomas, *Can. J. Phys.* 64 (1986).
106. R. E. Taylor, *Mater. Sci. E.* A245, 160 (1998).
107. J. P. Zheng and T. R. Row, *J. Electrochem. Soc.* 142, L6 (1995).
108. S. E. Pang, M. A. Anderson, and T. A. Chapman, *J. Electrochem. Soc.* 147, 444 (2000).
109. S. F. Chin, S. C. Pang, and M. A. Anderson, *J. Electrochem. Soc.* 149, A379 (2002).
110. C. C. Hu and C. Y. Cheng, *Electrochem. Solid-State Lett.* 5, H7 (2002).
111. C. C. Hu and C. Y. Cheng, *Electrochem. Comm.* 4, 105 (2002).
112. A. T. Wu, M. Seto, and M. J. Brett, *Sens. Mat.* 11, 493 (1999).
113. A. T. Wu and M. J. Brett, *Sens. Mat.* 13, 399 (2001).
114. R. K. Nahar, V. K. Khanna, and W. S. Khokle, *J. Phys. D: Appl. Phys.* 17, 2087 (1984).
115. Y. Shimizu, H. Arai, and T. Seiyama, *Sens. Actuat.* 7, 11 (1985).
116. G. Q. Li, P. T. Lai, M. Q. Huang, S. H. Zeng, B. Li, and Y. C. Cheng, *J. Appl. Phys.* 87, 8716 (2000).
117. V. K. Khanna and R. K. Nahar, *Sens. Actuat.* 5, 187 (1984).
118. R. W. Sillars, *J. Inst. Elect. Eng.* 8, 378 (1937).
119. K. D. Harris, A. Huizinga, and M. J. Brett, *Electrochem. Solid-State Lett.* 5, H27 (2002).
120. W. Qu, *Sens. Actuat. B* 32, 57 (1996).
121. J. D. Canaday, A. K. Kuriakose, T. A. Wheat, A. Ahmad, J. Gulens, and B. W. Hildebrandt, *Sol. State Ion.* 35, 165 (1989).
122. S. R. Narayanan, T. Valdez, N. Rohatgi, W. Chun, G. Hoover, and G. Halpert, in "Proc. 14th Ann. Battery Conference on Applications and Advances," Long Beach, CA, 1999, p. 73.
123. S. C. Thomas, X. Ren, P. Zelenay, and S. Gottsef, in "Proc. 2nd Int'l Symp. on Proton Conducting Membrane Fuel Cells II," Electrochemical Society, Pennington, NJ, 1999, p. 327.
124. J. M. Elliot, G. S. Attard, P. N. Bartlett, J. R. Owen, N. Ryan, and G. Singh, *J. New Mater. Electrical Syst.* 2, 239 (1999).
125. K. D. Harris, J. R. McBride, K. E. Nietering, and M. J. Brett, *Sens. Mat.* 13, 225 (2001).
126. M. M. Gomez, J. Lu, E. Olsson, A. Hagfeldt, and C. G. Granqvist, *Sol. Ener. Mat. Sol. Cells* 64, 385 (2000).
127. B. R. Weinberger and R. B. Barber, *Appl. Phys. Lett.* 66, 2409 (1995).
128. M. Suzuki, T. Ito, and Y. Taga, *Appl. Phys. Lett.* 78, 3968 (2001).
129. D. Vick, J. C. Sit, and M. J. Brett, *Res. Signpost*, in press.
130. Y. Xiong, S.-R. Park, and H. Swerdlow, *Anal. Chem.* 70, 3605 (1998).
131. C. Backhouse, M. Camaano, F. Oaks, E. Nordman, A. Carillo, B. Johnson, and S. Bay, *Electrophoresis* 21, 150 (2000).
132. K. Fluri, G. Fitzpatrick, N. Chiem, and D. J. Harrison, *Anal. Chem.* 68, 4285 (1996).
133. D. J. Harrison and A. van den Berg, "Micro Total Analysis Systems '98." Kluwer Academic, Dordrecht, 1998.
134. K. D. Harris, M. J. Brett, T. Smy, and C. Backhouse, *J. Electrochem. Soc.* 147, 2002 (2000).
135. J. S. Gau, *J. Magn. Magn. Mater.* 80 (1989).
136. P. Vettiger, G. Cross, M. Despont, U. Drechsler, U. Durig, B. Gotsmann, W. Haberle, M. A. Lantz, H. E. Rothuizen, R. Stutz, and G. K. Binnig, *IEEE Trans. Nanotech.* 1, 39 (2002).
137. A. Y. Elezzabi, J. C. Sit, J. F. Holzman, K. Robbie, and M. J. Brett, *Elect. Lett.* 35, 1 (1999).
138. K. Robbie, A. J. P. Hnatiw, M. J. Brett, R. I. MacDonald, and J. N. McMullin, *Elect. Lett.* 33, 1213 (1997).
139. A. H. McPhun, Q. H. Wu, and K. M. McGrath, *Proc. SPIE* 3790, 184 (1999).
140. A. Lakhtakia, *Opt. Eng.* 37, 1870 (1998).
141. D. L. Jaggard, A. R. Mickelson, and C. H. Papas, *Appl. Phys.* 18, 211 (1979).
142. L. D. Baron, "Molecular Light Scattering and Optical Activity." Cambridge Univ. Press, Cambridge, UK, 1982.
143. L. Pasteur, *Ann. Chim. Phys.* 24, 442 (1848).
144. K. Lindman, *Ann. Phys.* 63, 621 (1920).
145. K. Lindman, *Ann. Phys.* 69, 270 (1922).
146. I. J. Tinoco and M. P. Freeman, *J. Phys. Chem.* 61, 1196 (1957).
147. I. J. Tinoco and R. W. Woody, *J. Chem. Phys.* 32, 461 (1960).
148. I. Hodgkinson and P. W. Wilson, *CRC Crit. Rev. Solid State Mater. Sci.* 15, 27 (1988).
149. K. Robbie, M. J. Brett, and A. Lakhtakia, *Nature* 384, 616 (1996).
150. K. Robbie and M. J. Brett, "Proc. Bianisotropics '97, Glasgow," 1997.
151. P. I. Rovira, R. A. Yarussi, R. W. Collins, V. C. Venugopal, A. Lakhtakia, R. Messier, K. Robbie, and M. J. Brett, *Thin Solid Films* 313-314, 373 (1998).
152. C. Oldano, P. Allia, and L. Trossi, *J. Physique* 46, 573 (1985).
153. A. Lakhtakia, V. K. Varadan, and V. V. Varadan, "Time-Harmonic Electromagnetic Fields in Chiral Media," Lecture Notes in Physics 335. Springer-Verlag, Berlin, 1989.
154. I. V. Lindell, A. H. Sihvola, S. A. Tretyakov, and A. J. Vitanen, "Electromagnetic Waves in Chiral and Bi-Isotropic Media." Artech House, Boston, 1994.
155. S. Kennedy, J. C. Sit, D. J. Broer, and M. J. Brett, *Liq. Cryst.* 28, 1799 (2001).
156. I. Hodgkinson, Q. Wu, A. Lakhtakia, and K. Robbie, *Appl. Opt.* 39, 642 (2000).
157. V. H. Zocher, *Naturwissenschaften* 13, 1015 (1925).
158. J. L. Janning, *Appl. Phys. Lett.* 21, 173 (1972).
159. W. Urbach, M. Boix, and E. Guyon, *Appl. Phys. Lett.* 25, 479 (1974).
160. R. A. M. Hikmet and H. Kemperman, *Nature* 392, 476 (1998).
161. K. Robbie, D. J. Broer, and M. J. Brett, *Nature* 399, 764 (1999).
162. J. C. Sit, D. J. Broer, and M. J. Brett, *Liq. Cryst.* 27, 387 (2000).
163. J. C. Sit, D. J. Broer, and M. J. Brett, *Adv. Mat.* 12, 371 (2000).
164. I. Hodgkinson, Q. C. Wu, and K. M. McGrath, *Proc. SPIE* 3790, 184 (1999).
165. S. John, *Phys. Rev. Lett.* 53, 2169 (1984).
166. O. Toader and S. John, *Phys. Rev. E.* 66, 016610 (2002).



# Nanofibers

Jason Lyons, Frank K. Ko

Drexel University, Philadelphia, Pennsylvania, USA

## CONTENTS

1. Introduction
  2. Formation of Nanofibers
  3. Solution Electrospinning
  4. Melt Electrospinning
  5. Structure and Properties
  6. Modeling of the Electrospinning Process
  7. Applications of Nanofibers
  8. Summary
- Glossary  
References

## 1. INTRODUCTION

Nanofibers are solid-state linear nanomaterials characterized by flexibility and an aspect ratio greater than 1000:1. According to the National Science Foundation (NSF), nanomaterials are matters that have at least one dimension equal to or less than 100 nanometers. Therefore, nanofibers are fibers that have diameter equal to or less than 100 nm. Materials in fiber form are of great practical and fundamental importance. The combination of high specific surface area, flexibility, and superior directional strength makes fiber a preferred material form for many applications ranging from clothing to reinforcements for aerospace structures. Fibrous materials in nanometer scale are the fundamental building blocks of living systems. From the 1.5-nm double helix strand of DNA molecules, including cytoskeleton filaments with diameters around 30 nm, to sensory cells such as hair cells and rod cells of the eyes, nanoscale fibers form the extracellular matrices or the multifunctional structural backbone for tissues and organs. Specific junctions between these cells conduct electrical and chemical signals that result from various kinds of stimulation. The signals direct normal functions of the cells such as energy storage, information storage and retrieval, tissue regeneration, and sensing.

Analogous to nature's design, nanofibers of electronic polymers and their composites can provide fundamental

building blocks for the construction of devices and structures that perform unique new functions that serve the needs of mankind. Other areas expected to be impacted by the nanofiber based technology include drug delivery systems and scaffolds for tissue engineering, wires, capacitors, transistors and diodes for information technology, systems for energy transport, conversion and storage, such as batteries and fuel cells, and structural composites for aerospace structures.

Considering the potential opportunities provided by nanofibers, there is an increasing interest in nanofiber technology. Amongst the technologies including the template method [1, 48], vapor grown [2], phase separation [3], and electrospinning [4–20], electrospinning has attracted the most recent interest. Using the electrospinning process, Reneker and Chun [4] demonstrated the ability to fabricate nanofibers of organic polymers with diameters as small as 3 nm. These molecular bundles, self-assembled by electrospinning, have only six or seven molecules across the diameter of the fiber! Half of the 40 or so parallel molecules in the fiber are on the surface. Collaborative research in MacDiarmid and Ko's laboratory [5] demonstrated that blends of non-conductive polymers with conductive polyaniline polymers and nanofibers of pure conductive polymers can be electrospun. Additionally, *in-situ* methods can be used to deposit 25-nm-thick films of other conducting polymers, such as polypyrrole or polyaniline, on preformed insulating nanofibers. Carbon nanotubes, nanoplatelets, and ceramic nanoparticles may also be dispersed in polymer solutions, which are then electrospun to form composites in the form of continuous nanofibers and nanofibrous assemblies [6]. Specifically, the significance of fiber size effect has been recognized.

### 1.1. Effect of Fiber Size on Surface Area

One of the most significant characteristics of nanofibers is the enormous availability of surface area per unit mass. For fibers having diameters from 5 to 500 nm, as shown in Figure 1, the surface area per unit mass is around 10,000 to 1,000,000 m<sup>2</sup>/kg. In nanofibers that are 3 nm in diameter, and which contain about 40 molecules, about half of the molecules are on the surface. As seen in Figure 1, the high surface area of nanofibers provides a remarkable capacity



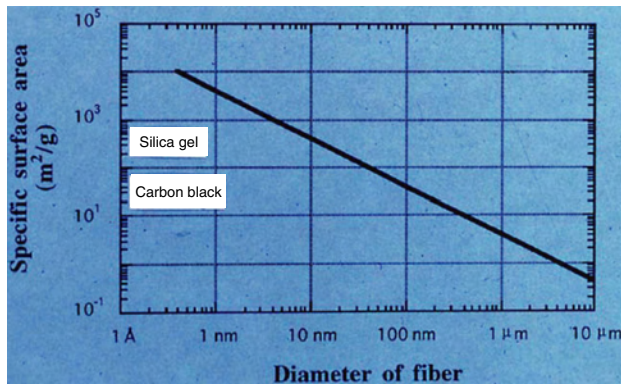


**Figure 1.** Effect of fiber diameter on surface area. Reprinted with permission from D. H. Reneker.

for the attachment or release of functional groups, absorbed molecules, ions, catalytic moieties, and nanometer-scale particles of many kinds.

## 1.2. Effect of Fiber Size on Bioactivity

Considering the importance of surfaces for cell adhesion and migration, experiments were carried out in the Fibrous Materials Laboratory at Drexel University using osteoblasts isolated from neonatal rat calvaria and grown to confluence in Ham's F-12 medium (GIBCO), supplemented with 12% Sigma fetal bovine on PLAGA sintered spheres, 3D braided filament bundles, and nanofibrils [7]. Four matrices were fabricated for the cell culture experiments. These matrices include, (1) 150- to 300- $\mu\text{m}$  PLAGA sintered spheres, (2) unidirectional bundles of 20- $\mu\text{m}$  filaments, (3) 3D braided structure consisting of 20 bundles of 20- $\mu\text{m}$  filaments, (4) nonwoven matrices consisting of nanofibrils. The most proliferate cell growth was observed for the nanofibrils scaffold as shown in the thymidine-time relationship illustrated in Figure 2.

## 1.3. Effect of Fiber Size on Electroactivity

The size of conductive fiber has an important effect on system response time to electronic stimuli and the current carrying capability of the fiber over metal contacts.

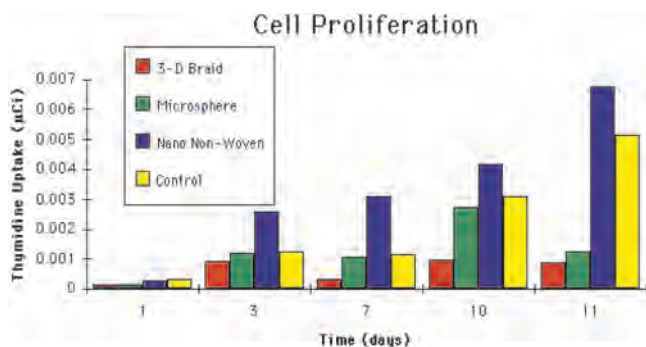


**Figure 2.** Effect of size on cell growth. Reprinted with permission from [47], F. Ko and C. Laurencin, "Society of Biomaterials Proceedings," 1998. © 1998, Society of Biomaterials.

In a doping-de-doping experiment, Norris et al. [8] found that polyaniline/PEO submicron fibrils had response time an order of magnitude faster than that of bulk polyaniline/PEO. There are three types of contact to a nano polymeric wire: ohmic, rectifying, and tunneling. Each is modified due to nano effects. There exist critical diameters for wires below which metal contact produces much higher barrier heights, thus showing much better rectification properties. According to Nabet (unpublished report), by reducing the size of a wire we can expect to simultaneously achieve better rectification properties as well as better transport in a nano wire. In a preliminary study [64], as shown in Figure 3, it was demonstrated, using submicron PEDT conductive fiber mat, that significant increase in conductivity occurs as the fiber diameter decreases. This could be due to intrinsic fiber conductivity effect or the geometric surface and packing density effect or both as a result of the reduction in fiber diameter.

## 1.4. Effect of Fiber Size on Strength

Materials in fiber form are unique in that they are stronger than bulk materials. As fiber diameter decreases, it has been well established in glass fiber science that the strength of the fiber increases exponentially due to the reduction of the probability of including flaws. As the diameter of matter gets even smaller as in the case of nanotubes, the strain energy per atom increases exponentially, contributing to the enormous strength of over 30 GPa for carbon nanotube.

Although the effect of fiber diameter has long been recognized, the practical generation of fibers down to the nanometer scale was not realized until the rediscovery and popularization of the electrospinning technology by Professor Darrell Reneker almost a decade ago [9]. The ability to create nanoscale fibers from a broad range of polymeric materials in a relatively simple manner using the electrospinning process coupled with the rapid growth of nanotechnology in recent years have greatly accelerated the growth of nanofiber technology. Although there are several alternate methods for generating fibers in a nanometer scale, none matches the popularity of the electrospinning technology due largely to the great simplicity of the electrospinning process. Accordingly, our review will be focused

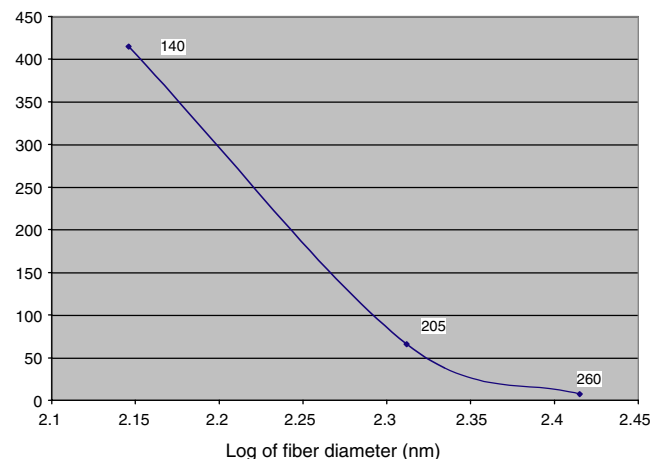


**Figure 3.** Conductivity vs. fiber diameters of a PEDT polymer.

on the electrospinning technology. We will begin with a general overview of the electrospinning technology. The significance of the various processing parameters in solution electrospinning is discussed, followed by a review of the limited work on melt electrospinning. The structure and properties of the fibers produced by the electrospinning process are then examined with particular attention to the mechanical and chemical properties. There is a gradual recognition that the deceptively simple process requires a deeper scientific understanding and engineering development in order to capitalize on the benefits promised by the attainment of nanoscale and to translate the technology from a laboratory curiosity to a robust manufacturing process. Some of the initial efforts in modeling of electrospinning process are reviewed in Section 6. This chapter is closed with a review of the potential applications of nanofibers and a conclusion and projection of the future direction of nanofiber technology.

## 2. FORMATION OF NANOFIBERS

Perhaps the history of this subject begins in 1745 when Bose created an aerosol spray by applying a high potential to a liquid at the end of a glass capillary tube. The ideology behind what is now known as electrospinning was furthered when Lord Rayleigh calculated the maximum amount of charge which a drop of liquid can hold before the electrical force overcomes the surface tension of the drop [10]. On October 2, 1934, Anton Formhals [11] was issued a patent for a process capable of producing monofilament fibers on a micron size scale using the electrostatic forces generated in an electrical field on a variety of solutions. The patent describes how the solutions are passed through an electrical field formed between electrodes in a thin stream or in the form of droplets in order to separate them into groups of filaments. This process, later to become known as a variant of electrospinning, allows the threads, which are repelling each other when placed in the electrical field, to pile up parallel to each other on the filament collector in such a way that they can be unwound continuously in skeins or ropes of any desired length.

In December, 1969, Sir Geoffrey Taylor published a paper titled "Electrically driven jets" describing the shape of the droplet at the end of a tube filled with a viscous fluid when applied to an electrical field. Taylor first introduced the formation of a cone and the resulting jet that forms on the apex known nowadays as the "Taylor cone" [12].

Taylor's contribution was actually the measurement of the potential required to form the Taylor cone for a variety of viscous liquids and then the comparison of these measurements with mathematical calculations. In his paper the derivation began with the expression for the equilibrium state of a droplet at the end of a pressurized tube. The coefficients for the electrostatic potential were then generated by observing the deflection of charged solutions at the end of an inverted capillary:

$$V_c^2 = 4 \frac{H^2}{L^2} \left( \ln \frac{2L}{R} - \frac{3}{2} \right) (0.117\pi\gamma R) \quad (1)$$

where  $V_c$  is the critical voltage,  $H$  is the separation between the capillary and the ground,  $L$  is the length of the capillary,

$R$  is the radius of the capillary, and  $\gamma$  is the surface tension of the liquid.

A similar relationship was developed [13] for the potential required for the electrostatic spraying from hemispherical drop pendant from a capillary tube:

$$V = 300\sqrt{20\pi\gamma r} \quad (2)$$

where  $r$  is radius of the pendant drop. In each case, the conducting drop was assumed to be surrounded by air, and suspended at a stable distance from the capillary tube.

These equations are the appropriate physical models for the formation of a droplet of slightly conducting, monomeric fluids. By examining a small range of fluids, Taylor determined that a 49.3° equilibrium angle balanced the surface tension with the electrostatic forces, and used this value in his derivation. However, it was later shown that the conductivity and the viscosity of the fluid both play vital roles in the electrostatic atomization process and can greatly influence the equilibrium angle as well as other aspects of the process [4]. This dependence on conductivity and viscosity was missing from the previous two equations; however, this relationship between surface tension and applied voltage still serves as a useful guide for slightly conducting, medium-to-low viscosity solutions.

Baumgarten advanced the field by being amongst the first to take the existing atomization techniques and apply them to a polymer solution [14]. He was able to determine the voltage required in order to be capable of electrospinning a PAN/DMF solution, and he also observed a dependence of the fiber diameter on the solution viscosity described through the following equation:

$$d = \eta^{0.5} \quad (3)$$

where  $d$  is fiber diameter, and  $\eta$  is solution viscosity (in poise).

Baumgarten also showed that the diameter of the jet reached a minimum after an initial increase in field strength and then became much larger with increasing fields. This effect was caused by the feed rate of the polymer solution being pulled through the capillary and illustrates one of the many complexities of the electrospinning process. That is, increasing the field does increase the electrostatic stresses, therefore creating smaller diameter fibers, but it also reduces the size of the Taylor cone and draws more material out of the syringe.

Larrondo and Manley observed that the fiber diameter decreased with increasing melt temperature as a result of the decreasing value of the viscosity due to the free movement of the molecular chains. They were able to draw a qualitative correlation between diameter and viscosity [15]. They also determined that doubling the applied electric field decreased the fiber diameters by roughly half. Larrondo and Manley also showed that the strain rate in the spinning jet is an important parameter for orienting the polymer molecules along the fiber axis.

In 1986, another paper was published by Hayati et al. [16] studying the effect of the electric field and the surrounding environment on pendant drops and the factors affecting the formation of stable jets. In this paper it was concluded that

the liquids conductivity is a major factor in the electrostatic disruption of the surface. For example, with conducting liquids such as water, very unstable streams were produced. With insulating liquids such as paraffin oil, no disruption occurred due to lack of sufficient free ions in the bulk liquid. Stable jets having a conical base were only produced with semiconducting liquids (nonpolar liquids with dissolved ionic materials). They also concluded that the cone angle at the base of the jet increased, whereas its length decreased, with an increase in applied voltage. This was in agreement with the experimental results that Baumgarten was observing.

At higher voltages, there have been reports of secondary jets splaying from the primary jet. The number of these splays increases with an increase in the applied field. As the electric field is increased further, the shape of the droplet deforms and in some cases a phase is present in which the droplet simply drips onto the collection plate. Continuing to increase the applied electric field, a potential is reached that is slightly larger than that needed to cause instability of the liquid meniscus. At this critical potential, the liquid ejects either a small droplet or a long filament as was observed by Baumgarten and Lorrondo and Manley.

In case of an insulating liquid, the surface charge is small and hence no appreciable electrostatic force can build up at the interface. The liquid behaves as a dielectric in a nonuniform field which will seek the region of highest field intensity; in this case, the tip of the capillary. In the case of a highly conducting liquid such as water, when the voltage was increased, the pulsating and dripping modes could be observed. However, by further increasing the potential, very unstable streams were produced from the drop which whipped around in different directions. In case of semiconducting liquid such as Isopan M + butanol (conductivity =  $3.3 \times 10^{-7} \text{ S/m}^1$ ), the stable jets could be produced, using an applied voltage of 10–12.5 kV. With an increase in voltage, the conical base of the jet, near the capillary, expands as its cone angle widens, and the cone height becomes shorter.

By measuring the critical voltage for stable jet formation using these capillaries at a constant flow rate [12], it became clear that the small capillaries were most suitable for the formation of stable jets of highly conductive liquids. However, with low conductivity liquids, wide capillaries were needed in order to form a stable jet. For a conductivity in the intermediate range ( $7.14 \times 10^{-9}$  to  $2.22 \times 10^{-6} \Omega^{-1} \text{ m}^{-1}$ ), the effect of capillary diameter, at constant flow rate, altered the velocity of the liquid issuing from the capillary, the velocity being measured as the ratio of the mass flow rate to the cross-sectional area of the tube [16, 17].

The description of electrospinning phenomenon, as seen in Figure 4, was introduced by Smith in 1994 [18]. In his paper he derived the relationship between the capillary radius, capillary plane distance, and the applied voltage:

$$V_0 = A_1 \left[ \frac{2Tr \cos \theta_{0c}}{\epsilon_0} \right]^{0.5} \ln \left( \frac{4h}{r_c} \right) \quad (4)$$

where  $T$  is surface tension,  $\theta_0$  is cone half angle, and  $\epsilon_0$  is permittivity of free space.

Finally he reached the following three conclusions:

1. As capillary radius increases, the onset potential should increase.

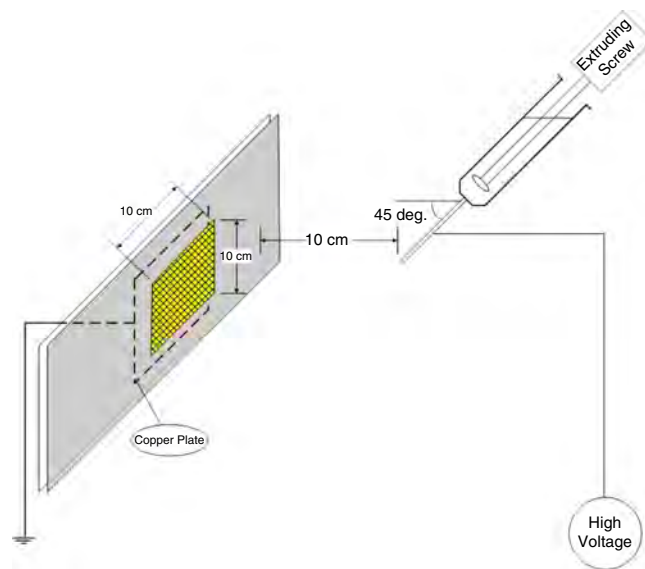


Figure 4. Schematic of an electrospinning station.

2. As the plane distance increases, the onset potential should increase.
3. As the surface tension increases, the onset potential should increase.

In 1995, Doshi and Reneker [9] started using electrospinning as a technique to produce small diameter fibers. In their paper they used poly(p-phenylene terephthalamide) to produce Kevlar fibers with superior physical properties using a dry-jet-wet spinning technique assisted by electrostatic charges. Monofilament Kevlar fibers ranging from 13 to 18  $\mu\text{m}$  were produced with an applied voltage of 12 to 18 kV at a distance of 3 cm in a vertical arrangement.

Doshi and Reneker [9] then shortly described the electrospinning process, processing conditions, fiber morphology, and some of the possible uses of electrospun fibers made from polyethylene oxide (PEO) of (molecular weight)  $M_w = 145,000 \text{ g/mol}$ . They found that for viscosities below 800 centipoise, the polymer solution was too dilute to form a stable jet, and at viscosities higher than 4000 centipoise it was difficult to form fibers due to a lack of sufficient solvent in the solution.

Doshi and Reneker [9] used concentrations varying from 1% to 7%, by weight, and concluded that as the concentration increases, the required voltage to successfully spin is increased. For example, for concentrations of 2.5% and 5%, by weight, the required voltages to electrospin were 9 kV and 12 kV, respectively. This paper also observed that the diameter of the jet increased as the distance between the spinneret and the target decreased due to the shorter time period the stream had to elongate. More than 20 polymers including PEO, nylon, imides, DNA, aramids, and polyaniline have been electrospun by Reneker's group [4].

Buchko et al. [13] proved that polymeric solutions behave differently compared to monomeric liquids during electrostatic atomization in that they persist as elongated jets over a much greater distance. A wide variety of synthetic and natural polymers were electrospun from solution and several polymers including poly(propylene) and poly(ethylene) were

electrospun from the melt. One major difference in the production of fibers from different mediums is the final size. When electrospinning from solution, fibers on the nanometer scale have been successfully produced. On the other hand, melt spun fibers were considerably larger, ranging from tens to hundreds of microns [15].

Nanofibers of aromatic heterocyclic polybenzimidazole (PBI), with a diameter of 300 nm, were later produced by Kim and Reneker [10]. They produced sheets of nonwoven fabric about 8 cm wide and 50 cm long with a compressed thickness of a few microns. The mass per unit area of these sheets was a couple of  $\text{g/m}^2$ . The electro-spun PBI fibers were also found to be birefringent, which indicated that the molecules were to some degree aligned.

Although a vast majority of the research devoted to the production of nanofibers has concentrated on electrospinning, it is important to mention the other experiments that have been and continue to be utilized. It was shown that nanofibers can be made using a radiation polymerization of vinyl monomers trapped in clathrate crystals. This process does not yet allow for the formation of continuous nanofibers but allows for the formation of fibers several microns in length [1]. The architecture of the clathrates is quite similar to that of a tunnel. Multiple tunnels can be placed next to one another and it is possible to have highly oriented nanofibers once the polymerization has occurred.

Other research has mimicked the process to make carbon nanotubes to produce carbon nanofibers using a chemical vapor deposition (CVD) process. In a horizontal tubular reactor, benzene can be used for the carbon source, hydrogen as a carrying gas, and thiophene as the growth promoter. The tube is heated to 1373 K at a speed of 25 °C per minute allowing hydrogen gas to flow into the benzene solution containing thiophene and then into the reaction tube. The ratios of the above can be changed to affect the final diameter of the vapor grown carbon nanofibers [19]. Researchers have been able to successfully produce nanofibers in bulk ranging from 50 to 200 grams per experiment. Using this technology, fibers ranging from 50 nm to several hundred nanometers have been produced [2]. Again, the limiting aspect of this technology is the capability of producing continuous nanofibers.

One final method that has been used to produce nanofibers recently is a method called “islands in the sea” [3]. This method is a combination of two polymers, one implanted inside the other. Islands in the sea uses a special spinneret that allows two polymers to be extruded at once. One polymer acts as the core and another polymer acts as the sheath. Once the fiber(s) has been extruded from the melt, the sheath layer is dissolved using some known solvent, leaving behind several smaller core fibers. It is obvious that the more islands that can be packed into the sea, the smaller the end diameter will be. Hills Inc., in collaboration with North Carolina State University, has produced fibers with up to 3000 islands in the sea, resulting in fibers as small as 500 nm [20]. This may be the best and most efficient way to produce continuous and highly aligned nanofibers, but where this process suffers is the extreme cost that is experienced with such high-tech machinery.

## 3. SOLUTION ELECTROSPINNING

### 3.1. Introduction

Over the years, many papers have been published observing the effects of a single parameter on the electrospinning process. Researchers have developed a relationship between the molecular weight and the concentration to describe the spin-ability of PEO in an aqueous solution [9]. The observation was made that the jet will break up more readily when a lower viscosity solution is being used. Thus, the solution or melt viscosity was shown to affect both the processing window for electrospinning and the diameter of the fibers that were being produced.

Numerous polymers have been electrospun by several groups across the country as shown in Table 1. With solvents of varying pH, polymers with molecular weights ranging from 10,000 to 300,000 and above have been electrospun. An accurate statement can be, “If it has been made, someone has tried to electrospin it.”

### 3.2. Processing Parameters

#### 3.2.1. Voltage

One of the most important and recent studies made by Deitzel et al. [21, 53, 59] on the effect of processing variables on the morphology of electrospun nanofibers concluded that the morphology of the nanofibers produced from PEO is influenced strongly by parameters such as feed rate of the polymer solution, electrospinning voltage, and other properties of the solution such as concentration, viscosity, and surface tension. They also concurred that an increase in the voltage changed the shape of the surface from which the electrospinning jet originated. This shape change was correlated with an increase in the number of beaded defects forming amongst the electrospun fibers as seen in Figure 5.

**Table 1.** List of various polymers that have been electrospun.

Polymer	Solvent	Ref.
Rayon		[11]
Acrylic resin	dimethyl formamide	[14]
PE, PPE	melted	[15]
PEO	water	[4]
PPTA (Kevlar)	98% sulfuric acid	[42]
Polyester	1:1 dichloromethane: trifluoroacetic acid	[49]
DNA	70:30 water:ethanol	[27]
PAN	dimethyl formamide	[5]
Styrene-butadiene- styrene triblock	75:25 tetrahydrofuran/ dimethylformamide	[45]
PVA/nylon 6,6	n/a	[44, 61]
PAN and Pitch	dimethyl formamide	[43, 63]
PANi/PEO	chloroform	[8]
PEO	water	[21]
Silk	HFA-hydrate	[51, 54, 62]
CNT/PAN	DMF	[25]
Polyurethane	DMF	[58]
Nylon-6	95:5 HFIP/DMF	[60]
Poly(ethylene-co-vinyl alcohol)	2-propanol/water	[57]



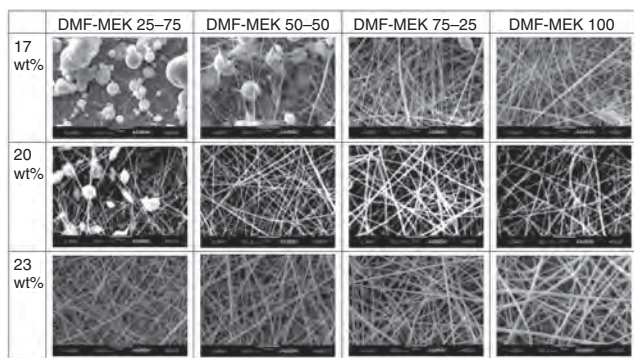


Figure 5. Effect of viscosity on fiber morphology.

### 3.2.2. Concentration/Viscosity

Deitzel [53, 59] also noticed that the diameter of the electrospun PEO fibers increased with solution concentration according to the power law relationship while other noticed, as in Figure 6, that it followed the function of  $x^2$ . This observation was in agreement with others that observed that the polymer's ability to be electrospun was directly dependent on its viscosity. Also, general properties such as surface area of the electrospun fiber mats were evaluated. The textiles were found to have specific surface area in the range of 10–20 m<sup>2</sup>/g. It was also stated that the analysis of the produced fibers by WAXD and DSC showed poor development of any crystalline order.

### 3.2.3. Berry Number

In his study of intrinsic viscosity, Berry developed a number called the Berry Number (Be). Be was used as a measure of molecular conformation [22–24]. This number was the product of the intrinsic viscosity and concentration. Han [50] utilized the work of Berry in an attempt to further understand electrospinning. It has been well documented that the concentration has a major role on the electrospinning process. Han discovered, with PAN, that if the Be was lower than 1, beads would be formed because the viscosity of the solution would not be sufficient to hold together during the electrospinning process. In the other cases (a Be from 1 to 4), the fiber diameters steadily increased as seen in the below chart. Han's study was the first to use Be for electrospinning. It was

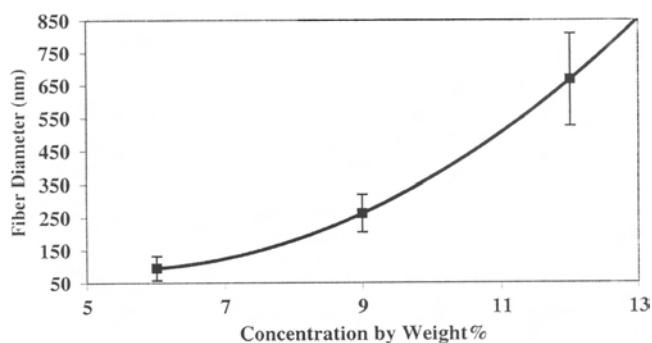


Figure 6. Effect of concentration on fiber diameter.

later shown by Ali that the Be is a function of the polymer being spun and the numbers are not contained between 1 and 4, but this remains an effective way to classify the polymer solution [25].

### 3.2.4. Alternative Fields

In another study, Deitzel et al. [26] tried to control the deposition area of the electrospun PEO fibers by using multiple field electrospinning apparatus that applied a secondary external field of the same polarity as the surface charge on the jet. This mechanism allowed for a greater control over the deposition of the electrospun fiber on a surface and permitted collection of the electrospun fibers in alternative forms to nonwoven mats. After analysis, the yarns produced using this new electrospinning technique indicated the presence of a slight molecular orientation and a poorly developed crystalline microstructure within the fibers.

In addition to what is listed above, there are many factors that can be altered in order to achieve different nanofibrous mats. Deitzel stated that increasing the voltage increased the number of beads that are observed on the created fibers. Other researchers have noted that increasing the voltage will also decrease the fiber size up to a critical value, after which the fiber size will begin to increase as a result of the diminishing Taylor cone.

### 3.2.5. Spinning Distance/Spinning Angle

Two other common parameters that are frequently changed are the spinning distance and the spinning angle. It is commonly noted that the further the increase between the anode and cathode, the finer the fiber diameter will be as a result of having more time and distance to elongate itself. Many angles have been experimented with, 0°, 45°, and 90° being the most common. Although little evidence was seen to affect fiber diameter, fiber uniformity was often increased at 45° because the flow rate was often decreased and gravity was not allowed to form as many beads.

### 3.2.6. Spinneret Diameter

As touched upon earlier, the spinneret diameter has a major effect on the size of the nanofibers produced. The smaller the spinneret, the smaller the fibers tended to be, but the smaller diameter also presented itself to be a problem when higher viscosity fluids were used. It is a constant trade-off between which type of material is being worked with and what size diameter is hoped to be obtained. In addition to the size of the spinneret used, shape has also been recorded to play a major role in electrospun samples. Whether the tip of the spinneret is flat like an extruder or sharp like a syringe, many interesting morphological features were discovered.

### 3.2.7. Annealing

One tactic that is used in the industrial production of fibers that is often overlooked in the realm of electrospinning is annealing. Annealing is a form of post-treatment that heats the polymer while stretched in order to allow the chains to align themselves, giving the fiber far superior mechanical properties. What little work that has been done in this area

has shown promising results, but the problem resides in the capability of isolating single samples to be annealed.

#### 4. MELT ELECTROSPINNING

There has been little work published in the area of melt electrospinning. The first work was published by Lorrondo and Manley in 1981 [15] and nothing has been published since. There are many papers that include solution or melt in their titles, but the work that has been done has concentrated exclusively on solution spun fibers. There are several groups throughout the world trying to break through with new results, including, but not limited to, Drexel University and the University of Akron.

Traditionally melt spun polymers such as polyester [49], polyethylene, and polypropylene have been attempted to be spun by several groups. These polymers have been spun using different temperatures, different voltages, and in different atmospheres. The main reason that there has been nothing published in the last 20 years is that it has been proven to be very difficult to produce fibers in the nano range. In solution spinning, it is believed that one major contributor to the decrease in diameter is the evaporation of the solvent. Solution spun fibers contain as much as 90% solvent and 10% polymer. Simply by understanding that polymer melts contain 0% solvent, an order of magnitude increase in fiber diameter is realized.

In addition to the lack of solvent that helps loosen up the molecular entanglements, melt spinning suffers other drawbacks. One of these hindrances is the effect of the temperature gradient between the polymer and the surrounding temperature. If the surrounding temperature is too cool, the ejected polymer will quench upon exiting the spinneret, preventing any decrease in diameter and orientation of molecular chains leading to improved mechanical properties. If the surrounding temperature is too hot, then the ejected polymer will fuse to itself upon collecting on the target.

Temperature of the melt is another key issue when melt electrospinning polymers. In solution, it has been readily shown that the electrospinning process is highly dependent on viscosity. Polymeric melts are inherently much more viscous than polymer solutions that are being electrospun. Therefore, in order to get the polymer melt to a viscosity that is capable of being electrospun, the melt temperature is often raised well above the melting temperature. If the polymer being used has a degradation temperature that is relatively close to the melting temperature, it will likely not be electrospun.

Analyzing the results that have been seen at conferences around the world, the same processing parameters that apply for solution spun nanofibers apply to melt spun nanofibers. Melt spinning continues to be a hot topic and would be the ideal way to make nanofibers by electrospinning because of the incredibly high yield as compared to solution electrospinning. As referenced before, the islands in the sea method is a form of melt spinning but may not be the most feasible of methods due to the extremely high cost of the machinery.

#### 5. STRUCTURE AND PROPERTIES

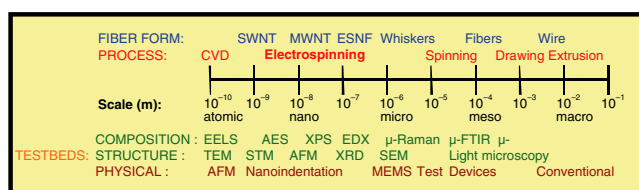
Table 2 represents the spectrum of instruments used to test nanofibers. As shown, instruments are capable of analyzing everything from a few angstroms in diameter to several meters. As more and more machines are used to study the characteristics of electrospun fibers, a better understanding of the process is being developed. In the future, more sophisticated machines will be developed to draw a more accurate portrait of the process, but until that time, researchers will have to be satisfied with what is at hand, such as the following.

The scanning electron microscope (SEM) is one of the most popular and powerful tools that has been used in the literature [4, 9, 15, 27] to measure the diameter of electrospun fibers as well as the general morphology. Kim and Reneker [10] showed that SEM could also be used to examine the fibers' cross section. They stated that the electrospun fibers are mostly circular in cross section but other shapes such as ribbons and coils could be produced. This method is extremely easy to use and more importantly, the sample size required to get useful data is extremely small, less than 1 mm<sup>2</sup>. One drawback of this equipment is that a gold coating is usually needed to enable viewing the fibers and this coating slightly alters the accuracy of the actual diameter. The gold sputtering process typically adds a 0.4-nm layer to the fibers. This can be ignored with larger diameter fibers but with a 4-nm fiber, it becomes more of a concern. Using an environmental scanning electron microscope (ESEM), the gold coating process can be skipped if the micrographs are taken in a low vacuum. However, if the general shape and size of the fibers are needed, SEM and ESEM are fast and easy ways to derive the information that is needed. Another methodology that has been utilized to measure the diameter of smaller diameter samples is transmission electron microscopy (TEM). Fang and Reneker [27] analyzed the electrospun DNA by using TEM and reported diameters as low as 62 nm.

Ko et al. [28] used the TEM to study the morphology and order versus disorder for the electrospun PAN fiber, PAN/CNT, and PAN/GNP nanocomposites. Also, Ye et al. [29] used TEM technique to study the alignment of single-walled carbon nanotubes (SWNT) in two different electrospun polymers (PLA and PAN), as seen in Figure 7, as well as to study the effect of the heat treatment of electrospun PAN/CNT composites on the alignment of the CNT.

Other researchers have utilized equipment such as X-ray diffraction (XRD) and differential scanning calorimetry (DSC) to observe whether there is any degree of crystallinity in the electrospun samples. To this day, the argument persists, with some parties arguing that the samples lack crystallinity while others say that the intense strains to which

**Table 2.** Instrumentation available at various size scales.





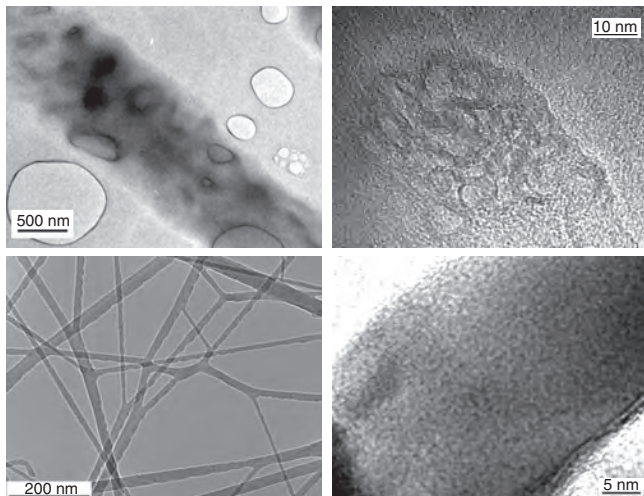


**Figure 7.** Carbon nanotubes inside of PLA (top) and PAN (bottom).

the samples are subjected are sure to produce highly crystalline samples. When spinning from solution, there have been some reports by Deitzel [21] that limited crystallization occurs but not to a high degree using PEO. On the other hand, when spinning from the melt, Lyons [65] demonstrated that a crystallization peak was observed in PET. This peak is consistent in what is seen in quenched polymer systems lacking crystallinity.

An important note to mention is the misnomer that is often associated with fibers on this scale. Researchers will often say that a 500-nm fiber was produced when in reality this is the same as a 0.5- $\mu\text{m}$  fiber. There are several groups that have been doing this with a variety of polymers, yet there are many other polymers that have been unable to break the 100-nm barrier. There have been reports from Reneker of producing fibers as small as 4 nm, yet while dealing with melt electrospinning, many of the fibers are on the micron scale.

Although most of the fibers that are produced through electrospinning are in the form of cylinders, there are occasions when tubes, ribbons, coils, and beaded structures can be produced. Tubes have been discovered by several groups and it was shown by Ali [25] that there was a high likelihood of forming tubes when electrospinning into water. In a similar fashion, ribbons are more than likely the result of collapsed tubes. Polymeric nanotubes elude reproducibility. Today, researchers are focusing on this problem and they are developing more advanced techniques that will allow for continuously produced nanotubes that can be used for drug delivery or hydrogen storage.

The most common way of collecting the nanofibers is in the form of 2D fibrous nonwoven mats. Mats such as these are well suited for filtration and tissue culturing but are not sufficient if single fibers or yarns are desired. It has been shown by Ko [30] that nanofibrous yarns can be directly produced from the electrospinning process under the precise processing parameters with certain polymers.

These yarns tended to be on the micron scale but were composed of numerous fibers that were on the nano scale that were naturally twisted together throughout the process to form the yarn. This was the first step in a positive

direction to one day being capable of producing woven and knitted fabric out of nanofibers.

## 5.1. Mechanical Properties

Measurement of elastic properties of electrospun fibers is very limited in the literature and only a few papers have worked with advanced techniques to determine the elastic properties of the material.

The atomic force microscope (AFM), invented by Binnig, Quate, and Gerber in 1986, was developed to exploit contact and noncontact forces for imaging surface topology and to study new physical phenomena at microscopic dimensions. The heart of the AFM is the cantilever and tip assembly, which is scanned with respect to the surface. For contact imaging the sample is scanned beneath the atomically sharp tip mounted on the cantilever providing a repulsive force. Atomic resolution can be obtained by very light contact and measuring the deflection of the cantilever due to the repulsion of contacting atomic shells of the tip and the sample [29]. Silicon device technology has introduced microfabrication techniques to produce silicon, silicon oxide, or silicon nitride micro-cantilevers of extremely small dimensions, on the scale of  $100\ \mu\text{m} \times 100\ \mu\text{m} \times 1\ \mu\text{m}$  thick. Micro-cantilevers exhibit force constants around 0.1 N/m. In contact imaging, the measurement of cantilever deflection is performed directly (quasi-statically) as the tip is being scanned over the surface [29]. Ko et al. [30] used this AFM technique to measure the elastic modulus of a single fiber produced from an electrospun PAN polymer solution. The atomic force microscope is one of the most powerful and useful techniques that has been used to measure the elastic properties of the electrospun fibers in addition to being able to determine diameter.

Kracke and Damaschke [31] used the AFM to measure the nanoelasticity of thin gold films. Later, Ali [25] showed in Figure 8 similar results obtained using AFM. They based the calculation of the modulus on the following relationships:

$$\frac{dF}{d\delta h} = \left( \frac{2}{\pi^{0.5}} \right) E^* A^{0.5} \quad (5)$$

$$\frac{1}{E^*} = \frac{(1 - \nu_1^2)}{E_1} + \frac{(1 - \nu_2^2)}{E_2} \quad (6)$$

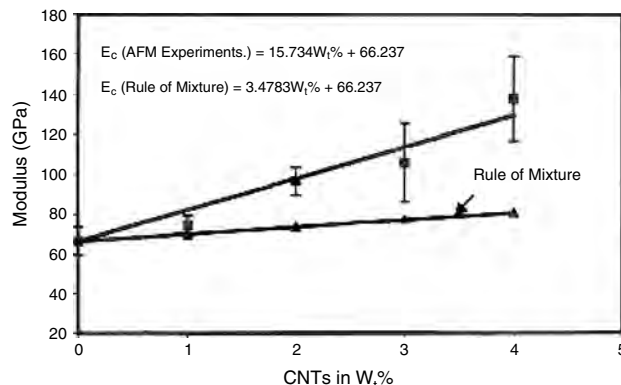


**Figure 8.** Effect of carbon nanotubes in composites.

where  $E_1$ ,  $E_2$ ,  $\nu_1$ , and  $\nu_2$  are the elastic moduli and Poisson numbers of the sample and the tip, respectively,

$$A = \pi r^2 \quad (7)$$

$$F = 2rE^*\delta h \quad (8)$$

where  $r$  is tip radius, and  $\delta h$  is deformation between tip and sample.

Sundrarajan et al. [32] used the AFM technique to evaluate the elastic modulus of nanobeams as well as their bending strength. By using this technique, the measured values were comparable to those measured in bulk. Mechanical properties and the deformation behavior of materials having ultrafine microstructures can also be illustrated by using a nanoindentation machine following the same guidelines. Finally, micro-Raman spectroscopy (MRS) has been used to measure the load transfer in short-fiber, high-modulus/epoxy composites as a function of angle to loading direction [33] as well as to monitor the strain in short fiber composites as a result of fiber to fiber interactions.

## 5.2. Chemical Properties

Raman spectroscopy is one of the more powerful techniques used to detect the presented elements especially on the nano scale. It is also extremely useful in investigating the state of carbon in detail due to its sensitivity to changes in translational symmetry. Duchet et al. [34] used Raman spectroscopy to correlate the molecular structure of the nanoscopic tubules with their conducting properties. Raman spectroscopy has been used for the characterization of carbon nanotubes (CNT) by many researchers [35].

Rao et al. [36] reported that there are two frequencies or bands of the single-walled carbon nanotubes (SWCNT) that can be detected by Raman spectroscopy. One is known as the radial band at  $160 \text{ cm}^{-1}$  and the other is called the tangential band at  $1590 \text{ cm}^{-1}$ . They showed that the first band could be detected at higher Raman shift values ( $10 \text{ cm}^{-1}$  higher) when it was dispersed in a solution.

The ratio ( $I$  (D-band)/ $I$  (G-band)) has been cross-correlated to crystallite size using X-ray diffraction data. This correlation is given by the following equation:

$$L_a = 4.4 \left( \frac{I_D}{I_G} \right)^{-1} \quad (9)$$

where  $L_a$  is the crystallite size in (nm).

Also, Huang and Young [37] showed a linear relationship between the  $I_D/I_G$  band and the  $1/L_a$  for commercialized carbon fibers produced from both PAN and PITCH. In the same paper they showed that there is a variation of the Raman spectra between the skin and core regions. These spectra show that  $I_D/I_G$  decreases from core to skin, which indicates smaller crystallite values in the fiber core more so than on the skin.

Laser Raman spectra have been used by Matsumoto et al. [38] to examine the carbon nanofibers and films produced by hot filament-assisted sputtering and it was found that the films showed three Raman bands at 1581, 1368, and  $179 \text{ cm}^{-1}$ . In this paper they explained the Raman peaks as follows: the first two peaks belong to polycrystalline

graphite and the last peak corresponds to carbene, one of the allotropes of carbon.

## 6. MODELING OF THE ELECTROSPINNING PROCESS

It is crucial that there exists a theoretical understanding of the electrospinning process. With this knowledge, specific parameters can be fine-tuned in order to maximize the efficiency of the process. To date, there have only been a handful of attempts made to theoretically quantify the electrospinning process. In 1971, the first was perhaps Baumgarten who attempted to identify the electric field maps to determine the jet radius. This approach was crude and met only limited success. Ten years later Larrondo and Manley continued to define the velocity gradients and electric fields and also began the first work of molten bead deformation in an electric field.

An analytical modeling of a steady-state jet flow in the electrospinning process made by Spivak et al. [39, 47, 52] showed the applicability of using the power law asymptotic to a wide class of fluid described by the nonlinear Oswald-deWaele law. This group used a one-dimensional differential equation to represent their jet radius and, when compared against experimental results, fared quite well.

In 1999, Reneker et al. [40] submitted the first attempt at a mathematical model that predicted the path of an electrospun fiber from solution. What was unique about this submission is that the group incorporated the instability region and plotted its results in three dimensions. Although capable of predicting the path for the fiber to traverse to a relatively accurate degree, this model was not capable of determining the fiber's diameter upon hitting the target.

Shin et al. [41] continued work on this challenging puzzle by describing the jet behavior in terms of known fluid properties and operating conditions. One of the main differences between this group and the Reneker group is the incorporation of current. Shin et al. described the behavior of two competing instabilities and summarized their results that closely mimic experiment in terms of operating diagrams and delineating regimes of operation in electrospinning.

The evolution of the model has become more and more accurate, but there is still no exact model to predict what the ending fiber diameter will be. All of the models that have attempted to predict the fiber diameter focus on solution spinning; melt spinning has only recently been modeled by Lyons et al. [65]. Many questions, such as what happens to the charge on the fiber while in transit, remain unanswered and a totally accurate model may never be developed.

When a conducting liquid is supplied to a capillary nozzle at a low flow rate and when the interface between air and the liquid is charged to a sufficiently high electrical potential, the liquid meniscus takes the form of a stable cone, whose apex emits a microscopic jet. Farouk et al. (unpublished report) described an axisymmetric formulation of the flow and electric fields of the electrostatically driven meniscus through a capillary nozzle. Based on the governing equations, a numerical model has been developed to calculate the shape of the liquid cone and the resulting jet, the electric fields, and the surface charge density along the liquid surface. The liquid

properties, liquid flow rate, and electrode configuration are needed as input parameters. Two-dimensional axisymmetric equations of continuity, momentum, and Gauss' law are solved numerically.

## 7. APPLICATIONS OF NANOFIBERS

Today's researchers are trying to find as many uses as they can for electrospun fibers. To date, filtration is the primary market for these fibrous mats as researched by Gibson [46, 56]. There is an extremely small pore size that is capable of blocking most particles and hence is quite useful in the filtration industry. Today's society is also directing research toward making protective clothing for military personnel to protect against chemical agents. Nanofibrous mats also have an incredible amount of surface area and industries such as the composite and biomedical industries are taking advantage through usage as wound dressings, tissue scaffolds, and practically any form of reinforcement agent for composites.

Ko and Ali [28] have looked into forming carbon/carbon composites directly from the electrospinning line. PAN was electrospun and carbonized with nanotubes on the inside to form this triple carbon composite. If this fiber, or yarn in Ali's case, is placed in a carbon resin, triple carbon composites can be made and used in ballistic proof plates and helmets of the future.

The ideas are endless as to where an electrospun fiber or mat may be used in the future. The aerospace industry is currently working on developing space antennae, solar sails, light reflectors, and a variety of other devices used in the voids of space. In addition, MacDiarmid and Lec [5] have focused their efforts to the production of electronic systems and many forms of sensors. Biosensors have been an important element of the information revolution of the 20th century, and their role as an enabling factor of the incoming 21st century biotechnology and medical revolution will be essential. Modern biosensors developed with advanced microfabrication and signal processing techniques are becoming inexpensive, accurate, and reliable. Increasing miniaturization of biosensors leads to realization of complex analytical systems such as BioChemLab-on-a-Chip. This rapid progress in miniature devices and instrumentation development will significantly impact the practice of medical care as well as future advances in the chemical, pharmaceutical, and environmental industries.

Important sensor parameters such as sensitivity, selectivity, response time, reproducibility, and aging depend directly on the properties of the sensing film [42, 43]. Sensitivity is of particular interest, because there is a strong need for detection of gases and biological substances and organisms at low concentration. A lower sensor detection limit allows direct measurement of the vapor from explosives and drugs or the presence of a few bacteria and viruses. It is a well-known fact that the sensitivity of a film is proportional to the surface area of the film per unit mass. Therefore new technologies capable of producing thin films with large surface area are of particular interest. In reality, these mats are simply a form of nonwoven fabrics. With that in mind, these electrospun fabrics have the potential to be used in any application that nonwovens are currently being used, such as brake pads, postal envelopes, and insulation, to name a few.

## 8. SUMMARY

Electrospinning is a unique process that produces polymeric fibers having diameters ranging over several orders of magnitude, from the micrometer range typical of conventional fibers down to the nanometer range. Until now, the shape and pattern of produced fibers in all electrospun polymer solutions have taken an in-plane random pattern and are determined by the shape of the collector.

A notable phenomenon has been recognized under certain spinning conditions for PAN solution, which enable the production of continuous yarn containing partially oriented nanofibers. This phenomenon opened the door to achieve many objectives such as the production of carbon-carbon nanocomposites by dispersing CNT's of superior physical properties inside the PAN polymer solution and producing continuous carbon nanotube reinforced PAN based carbon nanocomposite fibrils.

The present study is an attempt to optimize the electrospinning process for truly nanoscale fibers (<100 nm) and understand the electromechanics of electrospinning. In today's labs, reproducibility seems to be a major factor. Many scientists are getting fibers on the nanoscale once or twice but fail to do so repeatedly. Therefore, it is critical that the mechanics behind the process are understood. Efforts from Reneker, Shin, Rutledge, and Lyons [39–41, 47, 55, 64] in the area of modeling will pave the way for future researchers to know what parameters can be altered to accurately develop the exact diameter that is desired.

It seems that the next great barrier to overcome is productivity. Today, the average productivity of nanofibers using a single spinneret is in the range of 0.1 g/hr. This value is incredibly slow, making this process completely unreasonable from an industrial point of view. Researchers have been working on scaling up the process by adding many more spinnerets and have experienced some success, but the productivity is still not as high as commercial nonwoven productivities. A reason for this low productivity is the low yield that is experienced from working with solutions (<10%). If electrospinning from the melt could produce nanofibers consistently, this problem would be overcome, but that has yet to be realized.

One thing that is certain is that the methodologies for producing nanofibers are in their infancy. Perhaps researchers will modify what is known today to form what is desired tomorrow or perhaps a better way to achieve the goal of reaching 100 nm consistently will be discovered. Hybrid processes, such as combining melt blowing and electrospinning may produce the best results to date. Along with new ways to produce the fibers, scientists will also develop better ways to collect and test the nanofibers. While the commercial value of electrospun nanofibers depends on the reproducibility and productivity, the true value of the current electrospinning activities is in their capability to generate nanoscale fibers, thus providing a means to facilitate an assessment of the nanoscale effect for a wide range of materials. Will the day come when people have shirts made from nanofibrous yarns? It is hard to say, but it is assured that researchers will continue to work hard to push this novel field to new limits in hopes of discovering the next big breakthrough.

## GLOSSARY

**Birefringent** The refraction of light in an anisotropic material in two slightly different directions to form two rays.

**Chemical vapor deposition** A chemical reaction which transforms gaseous molecules (precursor) into solid materials in the form of thin films or powders on the surface of a substrate.

**Clathrate crystals** Crystals that crystallize in such a way that cavities exist within their crystal structure.

**Electrospinning** A process in which a polymer solution of melt is exposed to an electric field. At a critical voltage, the electric field will overcome the surface tension of the polymer and a jet will be extruded.

**Electrostatic atomization** The use of an electric charge to form fine droplets from a liquid.

**Nanocomposite** A material that is composed of 2 or more materials that lead to properties that the individual components could not possess by themselves. One of the components must be a nanomaterial.

**Nanomaterials** A material that has at least one dimension that is less than 100 nanometers.

**Nonwoven** A sheet or web structure made by bonding or entangling fibers via mechanical, thermal, or chemical means, and combinations thereof.

**Osteoblasts** A bone forming cell.

**Oswald de-Waele Law** A power law non-newtonian viscosity model.

**Spinneret** A disc, with one or many fine holes, through which a spinning solution or molten polymer is forced to create a continuous fiber or yarn.

**Taylor cone** The structure that forms at the capillary when a liquid medium is exposed to an electric field as the voltage is increased to overcome the surface tension.

## ACKNOWLEDGMENTS

The author would like to acknowledge all of the scientists who are devoting their time to advance the field of electrospinning; in particular, the generous sharing of his knowledge in electrospinning by Professor Darrell Reneker is greatly appreciated. The opportunity provided by the Army Research Office through a MURI program enabled fruitful interaction with Professor Darrell Reneker and with Professor Alan MacDiarmid in the area of electroactive nanofibers. The recent support by NASA, NSF, NTI, and DARPA enables our exploration of the co-electrospinning technology in multifunctional nanofibers and nanocomposites. This support also enables the education of a new generation of students in the area of nanofiber technology.

## REFERENCES

1. H. Allcock and F. Lampe, "Contemporary Polymer Chemistry." Prentice-Hall, Englewood Cliffs, NJ, 1990.
2. Y. Y. Fan, H. M. Cheng, Y. L. Wei, G. Su, and Z. H. Shen, *Carbon* 38, 789 (2000).
3. T. Hongu and G. O. Phillips, *New Fibers* (1997).
4. D. H. Reneker and I. Chun, *Nanotechnology* 7, 216 (1996).

5. A. G. MacDiarmid, W. E. Jones, Jr., I. D. Norris, J. Gao, A. T. Johnson, Jr., N. J. Pinto, J. Hone, B. Han, F. K. Ko, H. Okuzaki, and M. Llaguno, *Synth. Meth.* 119, 27 (2001).
6. F. K. Ko, W. B. Han, A. Rahman, H. Shimoda, and O. Zhou, *Proc. ASC* (2001).
7. D. H. Reneker, Technical Report, University of Akron, 1997.
8. I. D. Norris, M. Shaker, F. K. Ko, and A. G. MacDiarmid, *Synth. Meth.* 114, 109 (2000).
9. J. Doshi and D. H. Reneker, *J. Electron.* 35, 151 (1995).
10. J.-S. Kim and D. H. Reneker, *Polym. Eng. Sci.* 39, 849 (1999).
11. A. Formhals, U.S. Patent 1,975,504, 1934.
12. G. Taylor, *Proc. Roy. Soc. London A* 313, 453 (1969).
13. C. J. Buchko, L. C. Chen, Y. Shen, and D.C. Martin, *Polymer* 40, 7397 (1999).
14. P. K. Baumgarten, *J. Colloid Interface Sci.* 36, 71 (1971).
15. L. Larrondo and R. St. John Manley, *J. Polym. Sci.* 19, 909 (1981).
16. S. Hayati, A. I. Bailey, and T. F. Tadros, *Nature*, 319, 41 (1986).
17. S. Hayati, A. I. Bailey, and T. F. Tadros, *J. Colloid Interface Sci.* 117, 205 (1987).
18. D. F. H. Smith, *IEEE Trans.* 1A-22, 527 (1986).
19. Y. Y. Fan, H. M. Cheng, Y. L. Wei, G. Su, and Z. H. Shen, *Carbon* 38, 921 (2000).
20. Website, <http://www.hillsinc.net/nanofiber.shtml>.
21. J. Deitzel, N. C. B. Tan, J. Kleinmeyer, J. Rehmann, D. Tevaut, D. Reneker, I. Sendjarevic, and A. McHugh, Army Research Lab-TR-1989 (1999).
22. B. L. Hager and G. C. Berry, *J. Polym. Sci.* 20, 911 (1985).
23. G. C. Berry, H. Nakayasu, and T. G. Fox, *Polym. Phys. Edn.* 17, 1825 (1979).
24. G. C. Berry, *J. Chem. Phys.* 46, 4 (1966).
25. A. Ali, Carbon Nanotube Reinforced Carbon Nano Composite Fibrils By Electrospinning, Ph.D. thesis, Drexel University, 2002.
26. J. M. Deitzel, J. Kleinmeyer, J. K. Hirvonen, and N. C. Beck Tan, *Polymer* 42, 8163 (2001).
27. X. Fang and D. H. Reneker, *J. Macromol. Sci. Phys.* B36, 169 (1996).
28. F. K. Ko, S. Khan, A. Ali, Y. Gogotsi, N. Naguib, G. Yang, C. Li, H. Shimoda, O. Zhou, M. J. Bronikowski, R. E. Smalley, and P. A. Willis, "Proceedings of the AIAA Conference," 2002.
29. H. Ye, N. Naguib, S. Khan, A. Ali, Y. Gogotsi, and F. K. Ko, "Texcomp-6 Conference," 2002.
30. F. K. Ko, A. Ali, Y. Gogotsi, G. Yang, C. Li, and P. Willis, "Fiber Society Conference," 2002.
31. B. Kracke and Damaschke, *Appl. Phys. Lett.* 77, 361 (2000).
32. S. Sundararajan, B. Bhushan, T. Namazu, and Y. Isono, *Ultramicroscopy* 91, 111 (2002).
33. M. L. Mehan and L. S. Schadler, *Composite Sci. Technol.* 60, 1013 (2000).
34. J. Duchet, R. Legras, and S. D. Champagne, *Synth. Meth.* 98, 113 (1998).
35. P. Corio, P. S. Santos, V. W. Brar, Ge. G. Samsonidze, S. G. Chou, and M. S. Dresselhaus, *Chem. Phys. Lett.* 370, 675 (2003).
36. A. M. Rao, J. Chen, E. Richter, U. Schlecht, P. C. Eklund, R. C. Haddon, U. D. Venkateswaran, Y. K. Kwon, and D. Tománek, *Phys. Rev. Lett.* 86, 3895 (2001).
37. Y. Huang and R. J. Young, *Carbon* 33, 97 (1995).
38. Y. Matsumoto, M. T. Oo, M. Nakao, K. Kamimura, Y. Onuma, and H. Matsushima, *Mater. Sci. Eng. B.* 74, 218 (2000).
39. A. F. Spivak, Y. A. Dzenis, and D. H. Reneker, NSF Grant DMI-9523022, 1999.
40. D. H. Reneker, A. L. Yavin, H. Fong, and S. Koombhongse, *J. Appl. Phys.* 87, 4531 (2000).
41. Y. M. Shin, M. M. Hohman, M. P. Brenner, and G. C. Rutledge, *Appl. Phys. Lett.* 75, 8 (2001).
42. G. Srinivasan and D. H. Reneker, *Polym. Int.* 36, 195 (1995).
43. I. Chun, D. H. Reneker, H. Fong, X. Fang, J. Deitzel, N. B. Fan, and K. Kearns, *J. Adv. Mater.* 31, 1 (1999).

44. R. Jaeger, M. Bergshoef, C. Martin i Batlle, H. Schonherr, and G. J. Vancso, *Macromol. Symp.* 127, 141 (1998).
45. H. Fong and D. H. Reneker, *J. Polym. Sci. B Polym. Phys.* (1999).
46. P. W. Gibson, H. L. Schreuder-Gibson, and D. Rivin, *AIChE* 45, 190 (1999).
47. A. F. Spivak and Y. A. Dzenis, *Appl. Phys. Lett.* 73, 3067 (1998).
48. H. Dong, V. Nyame, and W. E. Jones Jr., "MRS Proceedings," 1999.
49. J.-S. Kim and D.-S. Lee, *Polym. J.* 32, 616 (2000).
50. B. Han, K. Chandari, F. K. Ko, and A. MacDiarmid, unpublished.
51. A. F. Spivak, Y. A. Dzenis, and D.H. Reneker, *Mech. Res. Comm.* 27, 37 (2000).
52. J. M. Deitzel, J. Kleinmeyer, D. Harris, and N. C. Beck Tan, *Polymer* 42, 261 (2001).
53. J. Yao, H. Masuda, C. Zhao, and T. Asakura, *Macromolecules A* (2001).
54. M. M. Hohman, M. Shin, G. Rutledge, and M. P. Brenner, *Phys. Fluids* 13, 2201 (2001).
55. P. P. Tsai, H. Schreuder-Gibson, and P. Gibson, *J. Electrostat.* 54, 333 (2002).
56. E.-R. Kenawy, G. L. Bowlin, K. Mansfield, J. Layman, D. G. Simpson, E. H. Sanders, and G. E. Wnek, *J. Controlled Release* 1, (2002).
57. M. M. Demir, I. Yilgor, E. Yilgor, and B. Erman, *Polymer* 43, 3302 (2002).
58. J. M. Deitzel, W. Kosik, S. H. McKnight, N. C. B. Tan, J. M. DeSimone, and S. Crette, *Polymer* 43, 1025 (2002).
59. H. Fong, W. Liu, C. S. Wang, and R. Vaia, *Polymer* 43, 775 (2002).
60. B. Ding, H. Y. Kim, S. C. Lee, D. R. Lee, and K. J. Choi, *Fib. Polym.* 3, 73 (2002).
61. K. Ohgo, C. Zhao, M. Kobayashi, and T. Asakura, *Polymer* 44, 841 (2003).
62. H. Yang, S. H. Yoon, Y. Korai, I. Mochida, and O. Katou, *Carbon* 41, 397 (2003).
63. A. El-Aufy, unpublished report.
64. J. Lyons, C. Pastore, and F. Ko, *Polym. Prep.* 44, 122 (2003).

# Nanofluidics

P. Mela, N. R. Tas, A. van den Berg

*University of Twente, Enschede, The Netherlands*

J. E. ten Elshof

*University of Twente, Enschede, The Netherlands*

## CONTENTS

1. Introduction
2. Nanofluidic Manipulation Principles
3. Fluid–Surface Interaction in the Double Layer
4. Technologies for Nanofluidics
5. Realizations and Applications

Glossary

References

## 1. INTRODUCTION

Nanofluidics can be defined as the study, description, and use of fluid flow around and inside nanoscale structures. Knowing and controlling the behavior of fluids in extremely small volumes is of crucial importance for the understanding of a large variety of problems in science, such as biological interactions, fracture propagation, tribology, and adhesion [1]. A good understanding of nanofluidics is essential for the efficient design and operation of new nanoscale devices, and may lead to new concepts that can be used for (bio)chemical synthesis, as well as methods for rapid, sensitive, and selective biochemical analysis. Although nanofluidics looks like a natural extension of the well-established field of microfluidics, the physical dimensions of this new and exciting field are on the order of the relevant length scales in fluidic environments, such as the size of large molecules and the size of the electrical double layer in aqueous solutions, which may lead to a completely different fluid behavior. In addition, the relevant distances are so small that diffusion processes are dominant in mass and heat transfer, and lead to extremely small timescales of (sub)milliseconds. All of these effects lead to new possibilities for manipulating, detecting, and analyzing (single) molecules in fluids.

Furthermore, macroscopic fluid properties such as surface tension, viscosity, and permittivity may take totally different values in nanoscale confinements, where most of the

fluid is close to a (mostly charged) wall. Although the theoretical description of fluid flow through nanochannels has been derived for porous media (in this review, referred to as ensembles of nanochannels), it is only through the recent upcoming of nanotechnologies that the behavior of fluid flow can be studied in individual nanoconfinements. Such nanoconfinements also allow the isolation and localization of single molecules within a very small volume, leading to exciting single-molecule detection principles.

The expectations of nanofluidics are therefore very high. Several scientific and technical breakthroughs are anticipated:

1. new approaches for molecular separation in nanochannels will be developed
2. chemical reactions with extremely small amounts of molecules (even down to single molecules) will be carried out and studied
3. new techniques for the detection and identification of individual molecules will be developed.

These phenomena may lead to breakthroughs in a variety of applications, ranging from high-throughput proteomics to the development of new drugs, and from new molecular filters to new methods for medical diagnostics and screening.

For an overview of the state of the art in, and application of, microfluidics, the reader is referred to several reviews on this topic [2–7]. From these reviews, it is clear that the single most important difference between micro- and macroscopic fluidics is in the magnitude of the Reynolds number ( $Re$ ): usually in microfluidic systems,  $Re < 100$ , therefore the flow is laminar. As such, fluid flows can be described very accurately; it is not surprising that, in microfluidics, the focus has been on constructing more or less complex fluid manifolds capable of carrying out, for example, sample preparation techniques on an extremely small scale, impossible to attain with conventional tools. Contrary to this rather engineering type of work carried out with microfluidic systems, with nanofluidics, the focus is much more on investigating and



understanding the new science involved. In the following sections, we will deal with fluidic manipulation principles with a focus on surface-related effects. This part will be followed by a more in-depth discussion on the fluid–surface interaction in the double layer. In the next section, various technologies for individual nanochannels and ensembles of these will be briefly addressed, whereas the last section deals with nanofluidic devices and applications.

## 2. NANOFUIDIC MANIPULATION PRINCIPLES

### 2.1. Physical Background of Downscaling Effects

Reducing the dimensions of the structures in which fluids are confined results in important effects due to an increased surface/volume ratio. The area will be, in fact, reduced to the power 2 and the volume to the power 3.

The importance of downscaling in fluid behavior can be readily appreciated by considering some of the dimensionless

numbers used in fluid dynamics. Table 1 shows some relevant dimensionless numbers; the dimensional parameters are listed in Table 2 [8]. Particularly interesting are those numbers expressing the relative importance of effects of forces such as inertia, surface tension, gravity, and viscous forces. The Reynolds number represents the ratio between inertia forces and viscous forces. It is used to describe the flow regimes: in microsystems, typical values for the Reynolds number are below 100, meaning that the flow is laminar (in circular macroducts, flow is observed to be laminar up to  $Re = 2100$  [9]). The decreased relevance of inertance in microfluidics is clear in the Weber number (We) as well. This number express the ratio of inertia forces to surface tension forces. With downscaling of dimensions, the Weber number drops, indicating that surface energy becomes a substantial factor in microsystems. The relative importance between viscous and surface tension effects can be determined by dividing the We by the Re number, obtaining what is called the capillary number (Ca). The Bond number (Bo) expresses the ratio between gravitational and surface tension forces, and it decreases with downscaling. Thermal diffusion (conduction) as well as mass diffusion are enhanced by downscaling;

**Table 1.** Overview of dimensionless numbers and their relation to the dimension length (at constant velocity). Reprinted with permission from [8].

Group	Abbreviation	Definition	Interpretation
Biot number	Bi	$\frac{h_T l}{k_T}$	Ratio of internal thermal resistance of a solid to the boundary layer thermal resistance
Mass transfer Biot number	$Bi_m$	$\frac{h_m l}{D_{AB}}$	Ratio of the internal species transfer resistance to the boundary layer species transfer resistance
Bond number	Bo	$\frac{g(\rho_l - \rho_v) l^2}{\sigma}$	Ratio of gravitational and surface tension forces
Euler number	Eu	$\frac{p}{(1/2)\rho v^2}$	Dimensionless pressure drop
Fourier number	Fo	$\frac{\alpha t}{l^2}$	Ratio of the heat conduction rate to the rate of thermal energy storage in a solid; dimensionless time
Mass transfer Fourier number	$Fo_m$	$\frac{D_{AB} t}{l^2}$	Ratio of the species diffusion rate to the rate of species storage
Grashof number	$Gr_L$	$\frac{g\beta\rho^2(T_s - T_\infty)l^3}{\mu^2}$	Ratio of buoyancy to viscous forces
Knudsen number	K	$\frac{l_{\text{free}}}{l}$	Ratio of the mean-free path of a gas and a characteristic length
Lewis number	Le	$\frac{D_{AB}}{\alpha}$	Ratio of the thermal and mass diffusivities
Nusselt number	$Nu_L$	$\frac{h_T l}{k_T}$	Dimensionless temperature gradient at the surface
Peclet number mass transfer	$Pe_D$	$\frac{v l}{D_{AB}}$	Ratio of mass transport by convection and by diffusion
Peclet number heat transfer	$Pe_\alpha$	$\frac{v l}{\alpha}$	Dimensionless independent heat transfer
Prandtl number	Pr	$\frac{c_p \mu}{k_T}$	Ratio of the momentum and thermal diffusivities
Reynolds number	$Re_L$	$\frac{\rho v l}{\mu}$	Ratio of the inertia and viscous forces
Schmidt number	Sc	$\frac{\mu}{\rho D_{AB}}$	Ratio of the momentum and mass diffusivities
Weber number	We	$\frac{\rho v^2 l}{\gamma}$	Ratio of inertia to surface tension forces

**Table 2.** Used dimensional parameters and their units.

Parameter	Description	Units
$\alpha$	thermal diffusivity	$\text{m}^2 \cdot \text{s}^{-1}$
$\beta$	thermal expansion coeff.	$\text{K}^{-1}$
$\varepsilon$	dielectric constant	$\text{C}^2 \cdot \text{N}^{-1} \cdot \text{m}^{-2}$
$\varepsilon_{ij}$	$ij$ oriented strain	—
$\phi$	flow rate	$\text{m}^3 \cdot \text{s}^{-1}$
$\mu$	dynamic viscosity	$\text{Pa} \cdot \text{s}$
$\sigma_{ij}$	$ij$ oriented stress	Pa
$\gamma$	surface tension	$\text{N} \cdot \text{m}^{-1}$
$\rho$	mass density	$\text{kg} \cdot \text{m}^{-3}$
$\tau$	shear stress	Pa
$\theta$	angular coordinate	—
$\zeta$	zeta potential	V
$a, b$	typical dimensions	m
$c_p$	spec. heat at const. pressure	$\text{J} \cdot \text{kg}^{-1} \cdot \text{K}^{-1}$
$D_{AB}$	mass diffusion coefficient	$\text{m}^2 \cdot \text{s}^{-1}$
$e$	electron charge	C
$E$	total applied potential	V
$\dot{E}$	power	$\text{J} \cdot \text{s}^{-1}$
$g$	constant of gravity	$\text{m} \cdot \text{s}^{-2}$
$h_m$	convection mass trans. coeff.	$\text{m} \cdot \text{s}^{-1}$
$h_T$	convection heat trans. coeff.	$\text{W} \cdot \text{m}^{-2} \cdot \text{K}^{-1}$
$K_b$	Boltzmann constant	$\text{J} \cdot \text{K}^{-1}$
$k_e$	specific conductance	$\Omega \cdot \text{m}^{-1}$
$k_T$	thermal conductivity	$\text{W} \cdot \text{m}^{-1} \cdot \text{K}^{-1}$
$l$	(characteristic) length	m
$n_0$	average ion concentration	—
$p$	pressure	Pa
$R_{\text{hyd}}$	hydraulic resistance	$\text{Pa} \cdot \text{s} \cdot \text{m}^{-3}$
$r$	radius	m
$T$	temperature	K
$t$	time	s
$v$	velocity	$\text{m} \cdot \text{s}^{-1}$
$x, y, z$	coordinates	m
$z$	ion valence	—

Source: Reprinted with permission from [8], R. E. Oosterbroek, Ph.D. Dissertation, University of Twente, 1999, The Netherlands.

the dimensionless numbers related to these effects are the thermal and mass Fourier numbers ( $Fo, Fo_m$ ) and the Peclet numbers ( $Pe_\alpha, Pe_D$ ).

Physical effects becoming relevant at the microscale offer new design potentials.

## 2.2. Surface-Related Effects

Principles that use surface effects can be exploited as new fluid-handling mechanisms. Two main principles will be considered in this section: surface energy and double layer.

### 2.2.1. Surface Energy

The surface free energy of a fluid is the energy needed to bring a molecule from the interior to the surface of a fluid. This energy difference is caused by the differences in the interaction forces between a molecule and its neighboring molecules in the bulk of the fluid and at the surface (e.g., van der Waals forces, hydrogen bonds). Liquids tend to adopt shapes that minimize their surface area because molecules in the bulk of the fluid are in a favorable energy configuration. For this reason, droplets are spherical because a sphere is

the geometrical entity with the smallest surface/volume ratio [10]. The Laplace equation

$$P_{\text{in}} = P_{\text{out}} + 2 \frac{\gamma}{r}$$

where  $\gamma$  is the surface tension, shows that the pressure at the concave side of a curved surface is always greater than the pressure at the convex side, the difference decreasing to zero as the radius of curvature becomes infinite. The surface tension of a material is the coefficient between the infinitesimal quantity of work  $dw$  needed to change the area of a surface by an infinitesimal amount  $d\sigma$ :

$$dw = \gamma d\sigma$$

Surface energy can play a role in fluid mechanics when interfaces exist between different phases. The influence of surface energy, causing surface tension effects, is expressed by the Bond and Weber numbers (Table 1).

Surface tension has been indicated as a practical microactuation force in microelectromechanical systems (MEMS): being a unique type of force scaling directly to length (line force), it becomes dominant over pressure (surface force) or mass (body force) when the dimension of interest shrinks down to the micrometer and submicrometer scale. The passive control of surface tension has been demonstrated by chemical modification of surfaces [11, 12], and active control has been proposed for micro- and nanofluidic systems based on electrical [13], thermal [14], optical [15], and electrochemical [16] principles.

### 2.2.2. Double Layer

The double layer in a fluid medium is caused by the surface charge that is naturally present on any surface [17]. The surface charge induces the formation of an electric double layer by attracting oppositely charged ions from the solution. The double layer consists of immobile counterions close to the channel wall within the so-called Stern or Helmholtz layer, and others forming an atmosphere of ions in rapid thermal motion close to the surface, known as the diffuse electric double layer [18]. The plane separating the inner layer of counterions and the outer diffuse layer is called the Stern layer. The potential at this plane is close to the electrokinetic potential or zeta ( $\zeta$ ) potential, which is defined as the potential at the shear surface between the charged surface and the electrolyte solution [19], and is defined with respect to the bulk of the liquid. The shear surface itself is somewhat arbitrary, but characterized as the plane at which the mobile portion of the double layer can “slip” or flow past the charged surface.

In the case of glass or silicon nitride channel walls, charging of the wall can occur due to deprotonation of silanol groups at the surface.

When an electric field is imposed tangentially to the charged surface, two main effects can be distinguished [20]: electrophoresis (EP), which is the transport of ions through the bulk of the liquid, and electroosmosis (EO), also referred to as electroendoosmosis, which is the transport of the fluid due to the drag of the moving charged electric double layer. Another charge-related effect is the

streaming potential, which is the counterpart of electroosmosis, and refers to the charge displacement, and consequently the existence of an electric potential due to fluid transport.

**Double Layer and Double-Layer Overlap in Nanochannels** The surface-charge density  $\sigma_s$  is of critical importance in nanochannels because the enhanced surface-area-to-volume ratio implies that a significant fraction of the total charge is bound to the walls and is immobile. The surface-charge density determines the magnitude of the surface potential and the applicability of the Debye–Hückel [17] approximation for the description of the double-layer length. It also provides an experimental handle to manipulate the molecular processes that influence fluid transport in nanochannels [21]. With respect to the occurrence of double-layer overlap, the relevant parameter to consider is the product of the channel radius  $a$  and the inverse Debye length  $\kappa$ . The Debye length can be roughly approximated by

$$\kappa^{-1} = \sqrt{\frac{\varepsilon_0 \varepsilon_r k_B T}{e^2 \sum_i z_i^2 n_i^0}}$$

where  $\varepsilon_0$  is the permittivity of vacuum,  $\varepsilon_r$  is the relative permittivity of the liquid medium,  $k_B$  is the Boltzmann constant,  $T$  is the temperature,  $n_i^0$  is the number density of the  $i$ th ionic species in the bulk of the electrolyte solution, and  $z_i$  is the charge of the  $i$ th ionic species [17]. Two extreme situations are illustrated in Figure 1. When  $\kappa a < 1$ , the electrical double layer extends across the entire channel. In aqueous systems,  $\kappa^{-1}$  is very large, being limited by the autoprotolysis of water, which means that achieving channels with complete double-layer overlap requires diameters of several hundreds nanometers or less. Under conditions of complete double-layer overlap, the channel becomes virtually impermeable to ions with the same charge as the surface charge, making it a selective barrier for the transport of either cationic or anionic species. Alternatively, under conditions at which  $\kappa a > 1$ , the double layer is confined to a small region near the channel wall, and the center of the channel is electrically uncharged. Under these conditions, both anionic and cationic species can be transported through the nanochannel, although the channel may still retain some permselectivity when the double-layer length is of the same order of magnitude as the channel radius.

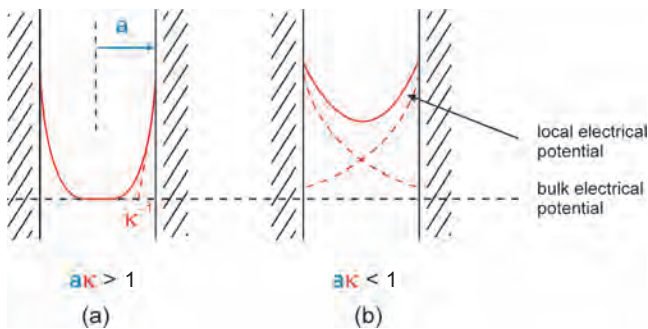


**Figure 1.** Schematic diagram showing (a) absence and (b) presence of double-layer overlap in a nanochannel.

## 2.3. Manipulation Principles

In this paragraph, important fluid manipulation principles, based on surface effects, such as electroosmosis, electrowetting, and bubble pumping, are explained in more detail. These principles have found wide application in microfluidic systems as actuation mechanisms, and are expected to play an important role in nanofluidic systems as well.

### 2.3.1. Electroosmosis

Electroosmosis can occur when the channel wall is charged, inducing the formation of an electric double layer by attracting oppositely charged ions from the solution. When an electric field is imposed tangentially to the surface, the electrical forces acting on the mobile charges in the double layer cause them to migrate toward the oppositely charged electrode. During their migration, these ions transport the surrounding solvent molecules, inducing the overall movement of solution known as electroosmotic flow (EOF). Due to differences in the magnitude of electrical and frictional forces within the double layer, a velocity gradient originates. The flow velocity is zero at the surface, and increases inside the double-layer region (Fig. 2). It reaches a maximum outside the diffuse layer  $v_\infty$ , which is given by the Schmoluchowski equation

$$v_\infty = -\frac{\varepsilon \cdot \zeta}{\eta} \cdot E$$

where  $\varepsilon$  is the permittivity,  $\eta$  is the viscosity of the liquid, and  $E$  is the applied tangential field. In a microchannel, the velocity profile generated by EO is essentially flat across the channel [22, 23]. Figure 3 shows flow profiles in microchannels for pressure-driven [Fig. 3(a)] and EO-driven [Fig. 3(b)] fluids, pointing out the effects of the pumping mechanism on the distortion of a volume of fluid.

The theory of EOF in narrow cylindrical capillary tubes was discussed by Rice and Whitehead [24]. Under the assumption of a small surface potential, they derived an

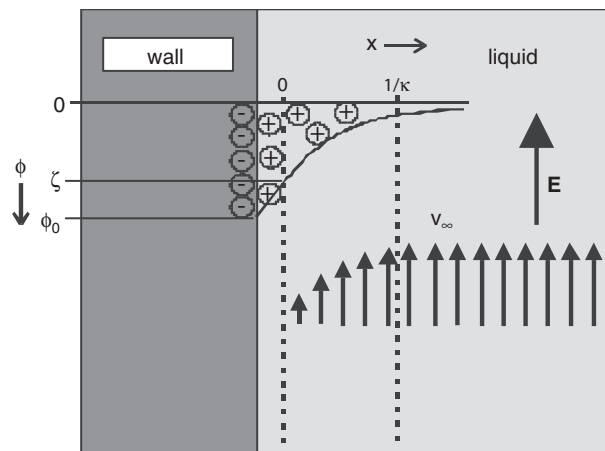


**Figure 2.** Potential and flow velocity distribution  $\phi(x)$  and  $v(x)$  near a negatively charged wall. The velocity profile is the result of the electrical field  $E$  acting on the mobile charges in the double layer.  $1/\kappa$  is a measure for the double-layer thickness.

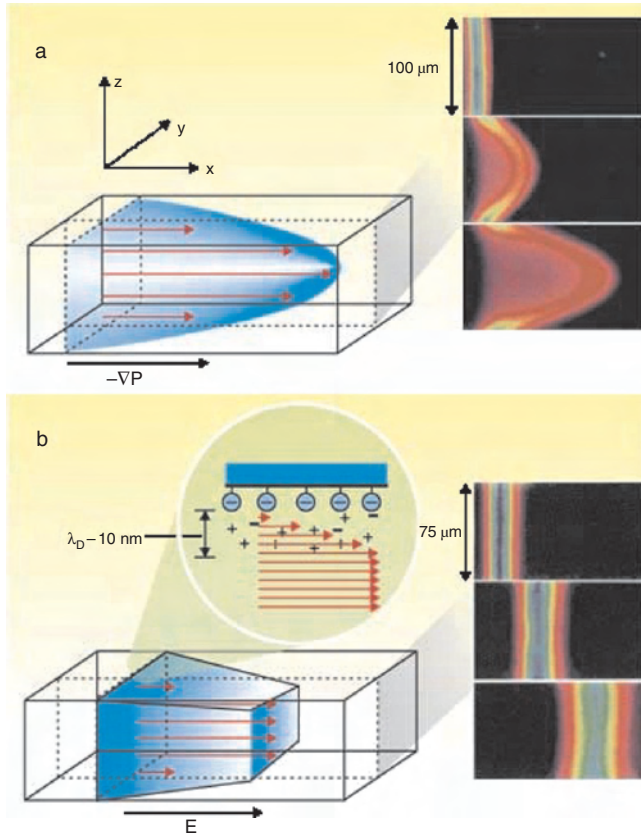


**Figure 3.** Flow profiles in microchannels. (a) A pressure gradient  $-\nabla P$  along a channel generates a parabolic or Poiseuille flow profile in the channel. The velocity of the flow varies across the entire cross-sectional area of the channel. On the right is an experimental measurement of the distortion of a volume of fluid in a Poiseuille flow. The frames show the state of the volume of fluid 0, 66, and 165 ms after the excitation of a fluorescent molecule. (b) In electroosmotic (EO) flow in a channel, motion is induced by an applied electric field  $E$ . The flow speed only varies within the so-called Debye screening layer of thickness  $\lambda_D$ . On the right is an experimental measurement of the distortion of a volume of fluid in an EO flow. The frames show the state of the fluorescent volume of fluid 0, 66, and 165 ms after the excitation of a fluorescent molecule. Reprinted with permission from [23], G. M. Whitesides and A. D. Stroock, *Phys. Today* 54, 42 (2001). © 2001, American Institute of Physics.

expression for the electroosmotic velocity  $u$  in a capillary tube of radius  $a$ , which reads

$$u(r) = -\frac{\varepsilon_0 \varepsilon_r \zeta E}{\eta} \left( 1 - \frac{I_0(\kappa r)}{I_0(\kappa a)} \right)$$

Here,  $\varepsilon_0$  is the permittivity of vacuum,  $\varepsilon_r$  is the relative permittivity of the liquid, and  $r$  represents the distance from the channel center.  $I_0$  indicates the zero-order modified Bessel function of the first kind. Asymptotic expansions show that the functions in brackets approach unity for large values of  $\kappa a$  [25]. The potential  $\zeta$  at the plane of shear between the immobile surface and the mobile part of the double layer of an unconfined solid-liquid interface can be written as

$$\zeta = \frac{2k_B T}{ze} \sinh^{-1} \left( \frac{\sigma_s \kappa^{-1} ze}{2\varepsilon_0 \varepsilon_r k_B T} \right)$$

where  $k_B$  is the Boltzmann constant,  $T$  is the temperature,  $\sigma_s$  is the surface charge density, and  $z$  is the valence of a symmetrical  $z:z$  electrolyte salt such as NaCl ( $z = 1$ ) or  $\text{MgSO}_4$  ( $z = 2$ ) [17]. In small channels, the electroosmotic flow velocity is retarded considerably by double-layer overlap. Even when  $\kappa a = 10$ , the cross-sectional average velocity is already reduced by about 20% in comparison with the EOF velocity in microchannels. At values  $\kappa a$  less than 10, the cross-sectional average velocity decreases rapidly with a further decrease of  $\kappa a$ .

Wei et al. studied the  $I-V$  characteristics of quartz nanopipet electrodes with orifice radii between 20 nm and 20  $\mu\text{m}$  in dilute KCl solutions, and applied potentials between  $-0.4$  and  $+0.4$  V [26]. They observed asymmetrical  $I-V$  behavior under conditions of partial double-layer overlap, while electroosmosis was the main mode of fluid transport through the orifice. The asymmetry was explained by a combination of double-layer overlap and geometrical asymmetry of the electrode orifice. This illustrates the possibility to design nanochannels with rectified electroosmotic flow characteristics.

In microfluidics, EOF is widely used for sample handling in capillary electrophoresis (CE) systems [27].

### 2.3.2. Electrowetting

By electrowetting, a surface can be switched electrically from a hydrophobic state into a hydrophilic state, thus enabling the manipulation of liquid in contact with the surface. Electrowetting is expressed by a change of the contact angle  $\theta$  of a droplet on a surface when an electric field is applied between the droplet and a counterelectrode underneath the droplet.

First reports on this *electrowetting* effect include Minnema et al. [28] from Philips Research Laboratories, who used an insulator between the liquid and the counterelectrode, and Beni et al. [29] from Bell Laboratories who measured the effect with the liquid directly on the metal counterelectrode. For the configuration shown in Figure 4 (liquid on insulator), the electrowetting effect can be explained by an extra term in the free energy of the system due to the electrical energy stored in the insulator [30]. This results in a modification of Young's equation, and can be interpreted as an effective lowering of the surface free energy of the

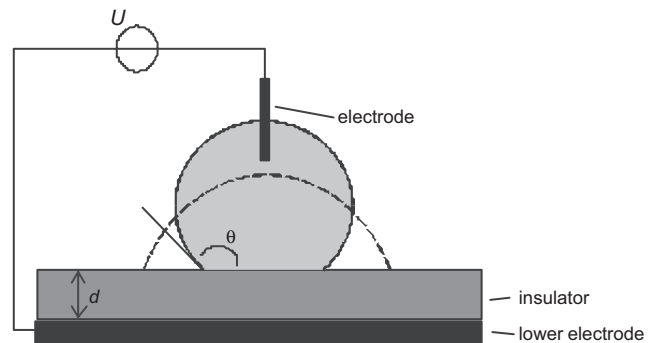


**Figure 4.** Configuration for electrowetting (liquid on insulator). A conducting aqueous droplet is placed on a hydrophobic insulator of thickness  $d$ . Electrowetting is induced by a voltage difference  $U$  between the droplet and an electrode below the insulator. Electrowetting results in a reduction of the contact angle  $\theta$  as indicated by the dashed contour.

solid–liquid interface  $\gamma_{SL}$  by the electrowetting energy term  $\gamma_{EW}$ :

$$\gamma_{LV} \cos \theta = \gamma_{SV} - \gamma_{SL} + \gamma_{EW} \quad (1)$$

Here,  $\gamma_{LV}$  and  $\gamma_{SV}$  are the surface free energy of the liquid–vapor and the solid–vapor interface, respectively. The electrowetting term equals the electrostatic energy stored in the insulator per unit area below the droplet:

$$\gamma_{EW} = \frac{1}{2} \cdot \frac{\epsilon \cdot U^2}{d} \quad (2)$$

where  $\epsilon$  is the permittivity of the insulator. Equations (1) and (2) can be rewritten to obtain a relationship between  $\theta$  and  $U$ :

$$\gamma_{LV} [\cos \theta(U) - \cos \theta_0] = \frac{1}{2} \cdot \frac{\epsilon \cdot U^2}{d}$$

where  $\theta_0$  is the contact angle at 0 V applied.

Verheijen et al. [30] reported a reduction of the contact angle of an aqueous droplet from 119° at 0 V applied down to 60° at  $\pm 240$  V applied. The voltages were applied across a 10  $\mu\text{m}$  thick parylene insulator layer and a thin hydrophobic fluoropolymer top coating impregnated with silicone oil to reduce the contact-angle hysteresis. Prins and colleagues [13] employed electrowetting inside microchannels, and generated pressures up to 800 Pa in arrays of channels with a diameter of about 350  $\mu\text{m}$  by applying voltages up to  $\pm 250$  V across a similar coated insulator system as the one used by Verheijen. Pollack and co-workers [31] managed to move droplets of aqueous KCl solution squeezed between two glass plates containing electrodes which were covered by hydrophobic insulating layers. They reached droplet velocities up to 3 cm/s at 55 V actuation voltage. In a similar configuration, Cho et al. [32] accomplished four fundamental microfluidic operations by electrowetting-on-dielectric: creating, transporting, cutting, and merging of liquid droplets. An actuation voltage of 25 V was required while using a 100 nm silicon dioxide insulator covered by a 20 nm hydrophobic Teflon coating. Washizu [33] could move, sort, and fuse droplets by means of electrostatic actuation. The droplets were placed on top of an array of electrodes covered by a smooth hydrophobic insulator layer, and were actuated by capacitive coupling. Torkkeli et al. [34] improved the speed of electrostatic transport of water droplets by employing superhydrophobic surfaces to reduce the sliding force of the droplets.

**Bubble Pumping** When a gas bubble is introduced in a region of changing diameter, and the bubble is large enough to be confined, surface tension forces will cause it to move to the region of larger diameter, moving the liquid in front and behind it [35]. Recently, this principle was implemented on milliscale in a circular symmetrical configuration [36], and flow rates on the order of 1  $\mu\text{L/s}$  were obtained. Usually, the bubbles are generated inside closed liquid channels by boiling liquid or by electrochemical gas generation [35–39], thereby limiting the nature and composition of liquids to be used. A more generic pumping mechanism is the surface-tension-directed gas injection in a hydrophilic microchannel [40]. The surface-tension control is based on geometrical

variation of the cross section of the hydrophilic channel, and requires no hydrophobic patches inside the channel. The working scheme of the pump is illustrated in Figure 5. Surface-tension forces cause the injected air to go into the taller part of the channel. The liquid volume displaced in a single pump stroke was 40 pL, and can be further reduced by reducing the size of the microchannel between the gas inlet and exhaust [40].

### 3. FLUID–SURFACE INTERACTION IN THE DOUBLE LAYER

The Navier–Stokes and Nernst–Planck equations are generally applicable to model flows of fluids and ions in systems of arbitrary geometry, including nanochannels [41].

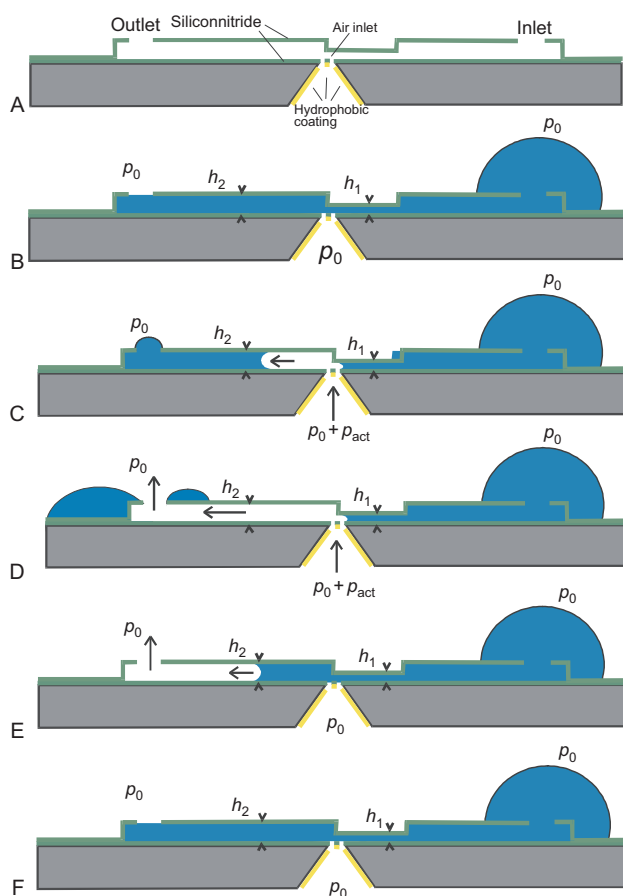


**Figure 5.** Longitudinal cross section of a microchannel explaining the principle of operation, with  $h_1$  and  $h_2$  the channel height in the shallow and deep part of the channel, respectively,  $p_0$  ambient pressure, and  $p_{act}$  actuation overpressure. (A) The microchannel includes a liquid inlet and outlet and a gas injector. The injector is located at the position where the channel height changes. (B) After adding a liquid droplet to the inlet, the empty channel will be filled by capillary forces. (C) Injected gas will move toward the higher channel part because there the capillary counterpressure is lowest. (D) Once the gas reaches the outlet, the liquid is ejected, and a temporary gas flow between the gas injector and outlet is maintained. (E) When the gas pressure drops, the microchannel will refill by capillary forces. (F) The starting situation, (B) is obtained again. Reprinted with permission from [40], N. R. Tas et al., *Anal. Chem.* 74, 2224 (2002). © 2002, American Chemical Society.



However, the predominant feature associated with the latter type of geometry is the occurrence of double layers and double-layer overlap. Sophisticated models like the charge-regulation model [42] incorporate the dynamic interactions between ions from the double layer and bound surface charges on the surface. Since the surface concentration of solute ions is a function of surface potential, the surface charge is related to the surface potential via surface association and dissociation reactions. For example, for an aqueous NaCl solution inside a channel with charged-surface sites  $S^-$ , the following four association–dissociation reactions between mobile ions and surface sites have to be taken into account: (1)  $SH = S^- + H^+$ , (2)  $S^- + Na^+ = S-Na$ , (3)  $SH_2^+ = SH + H^+$ , and (4)  $SH_2^+ + Cl^- = SH_2Cl$ . The equilibrium constant of each possible reaction must be known, and must be incorporated in the description. For the example described above, the surface-charge density can be expressed as  $\sigma_s = e([SH_2^+] - [S^-])$ , where  $e$  is the elementary electron charge and  $[Q]$  denotes the concentration of species  $Q$ . Most ions are known to exhibit some kind of interaction with bound surface charges. Specific interactions between surfaces and solutes are also known [17].

Most existing surface complexation models have been developed for unconfined solid–water interfaces, where overlap of the electrical double layer does not occur. However, a recent experimental study of ion adsorption on mesoporous alumina indicates that nanoscale confinement has a considerable effect on ion adsorption [43]. The effect is most likely explained by the overlap of the electrical double layer. It was found that the surface charge per mass on mesoporous alumina was as much as 45 times higher than on dense alumina particles. These findings show that the development of surface charge in nanochannel geometries may not be predictable *a priori* by the currently existing models for surface–liquid interactions.

While the double layer can be described using the well-known Poisson–Boltzmann equation [17], the simplest descriptions of double layers consider ions as simple point charges. Since the number of ions at the channel wall is higher than in the bulk, an unlimited number of ions could be accommodated in the interfacial region. This is physically impossible, and therefore it becomes necessary to assign a volume to the ions at high electrolyte concentration and/or small channel size. The spatial requirement for an ion is characterized by its hydrated radius, and both undissociated and dissociated hydrated electrolytes can be distinguished [44]. The expression for the distribution of dissociated ions from a binary electrolyte can be written in a modified form of the Boltzmann equation:

$$\frac{n_i}{n_i^b} \left( \frac{v^{-1} - \sum_i n_i^b}{v^{-1} - \sum_i n_i} \right) = \exp \left( -\frac{z_i e \varphi(r)}{k_B T} - \frac{\Delta F_i}{k_B T} \right)$$

where  $n_i$  is the number density of the  $i$ th ionic species near the charged interface,  $v^{-1}$  is the inverse volume of the hydrated ion, and  $\varphi(r)$  is the local electrical potential relative to the potential in the uncharged bulk of the electrolyte solution.  $\Delta F_i$  indicates the hydration-free energy of the  $i$ th ion, a term that is associated with the change of dielectric permittivity of the solvent medium surrounding the ion [44].

It is noted that surface diffusion of sorbed ions is a known phenomenon, but the typical diffusion coefficients associated with this process are typically  $10^4$ – $10^5$  times smaller than the corresponding self-diffusion coefficients in water, so that it does not contribute significantly to the total ionic fluxes, even in very narrow channels with a high surface-area-to-volume ratio [45].

## 4. TECHNOLOGIES FOR NANOFUIDICS

In this review, nanochannels are defined as straight channels with at least one dimension of the cross section in the submicron range (1D nanochannels). We divide nanochannels into nanochannels that can be addressed and used as a unit (“singularly addressable nanochannels”) and channels that exist as an ensemble (“ensembles of nanochannels”), the latter being porous membranes. Among the singularly addressable nanochannels, a further distinction can be made: channels fabricated with Micro System Technology (MST) where dimensions are pushed to the resolution limits (“top down” approach), and channels produced with new synthetic strategies and self-assembly processes (“bottom-up” approach). In this and the following paragraphs, fabrication techniques and the application of nanochannels will be presented according to the above-explained distinctions.

### 4.1. Singularly Addressable Nanochannels

#### 4.1.1. Top-Down Approach

Processes and methods from the semiconductor industry have been successfully applied for the construction of a variety of microsystems. The same top-down approach used in Micro System Technology can be used to fabricate nanosystems. An overview of channel fabrication techniques was recently described by Rasmussen [46]. Technologies for the fabrication of nanochannels are extensively discussed in the chapter by Jansen et al. in this encyclopedia. Here, we will briefly summarize the two main strategies for the fabrication of nanochannels: surface and bulk nanomachining.

**Bulk Machining** In bulk machining, the channel is created in a substrate wafer by way of removing (etching) trenches. Typically, this is done by standard photolithography followed by wet or dry etching of the substrate material. The formed space is closed by bonding another wafer on top of the first one [Fig. 6(a)]. Different bonding methods are found, depending on the bulk material used: polymer bonding for plastic substrates, anodic bonding for alkaline-containing glasses such as Pyrex, eutectic bonding for metallic alloys, fusion bonding for glass, and direct bonding for highly polished substrates such as silicon. In the bonding technique, in general, microvoids should be prevented because they can cause leakage of the fluid from the nanochannel.

With this technique, shallow sub-100 nm trenches are etched in a wafer, and covered by another wafer to form 1D nanochannels. The width of the channel is determined by the resolution of the photolithographic process used. A scanning electron micrograph of channel cross section fabricated using bulk machining is shown in Figure 7.



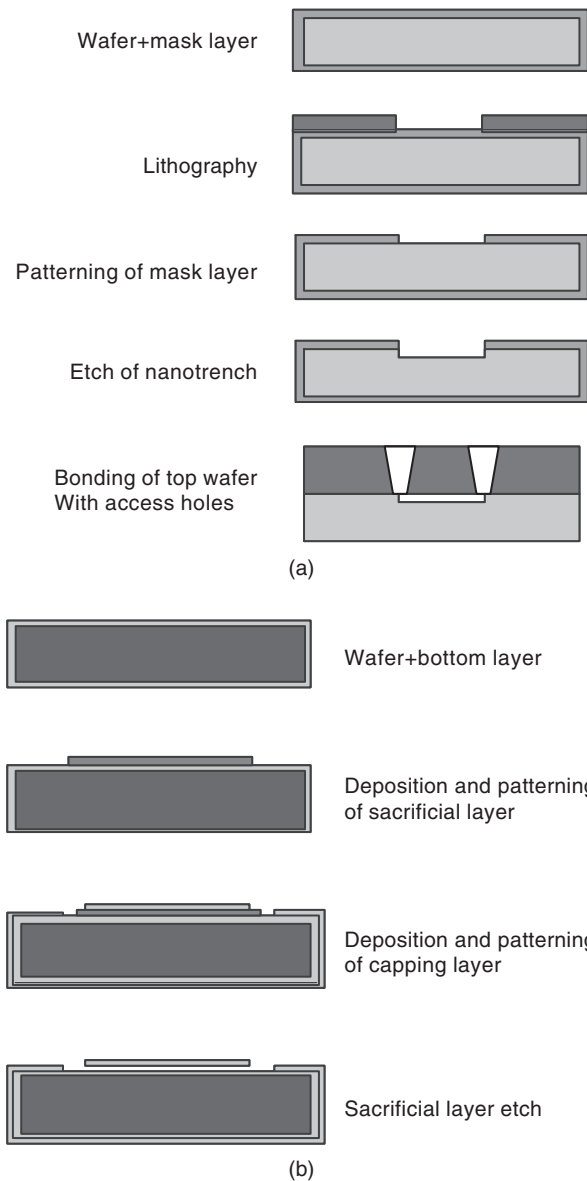


**Figure 6.** Basic fabrication processes for nanochannels. (a) Bulk machining. (b) Surface machining.

**Surface Machining** In surface machining, structures can be obtained on the surface of a wafer by the successive deposition, photopatterning, and etching of a sacrificial layer and a structural layer. In order to fabricate a channel, a patterned and buried sacrificial layer is removed/etched to form the inner part of a channel: a process known as sacrificial layer etching. The essence of this technique is the selective removal of the patterned sacrificial layer to create the inner space of the fluidic channel, leaving the surrounding material to constitute the walls of the channel [Fig. 6(b)]. A variety of sacrificial materials can produce nanochannels, including silicon oxide/nitride [47–49], polysilicon [50, 51], and polymer [52]. Scanning electron micrographs of channel cross sections fabricated using the differential etching are shown in Figure 8. As in the case of bulk machining,

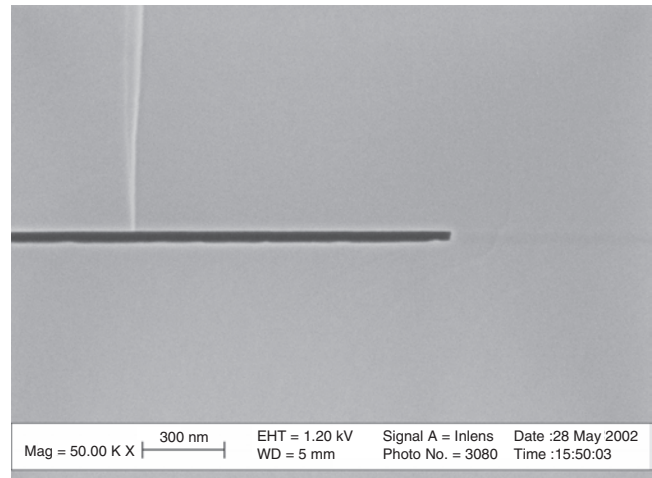


**Figure 7.** Scanning electron micrograph of 50 nm deep channel in  $\langle 110 \rangle$  silicon bonded with silicon cover wafer. Reprinted with permission from [99], J. Haneveld et al., “Proceedings of MME’ 02 Micromechanics Europe,” 2002, pp. 47–50. © 2002,

the width of the channel is determined by the resolution of the photolithographic process used.

However, recently, two new methods have been developed to fabricate nanochannels by conventional micromachining,

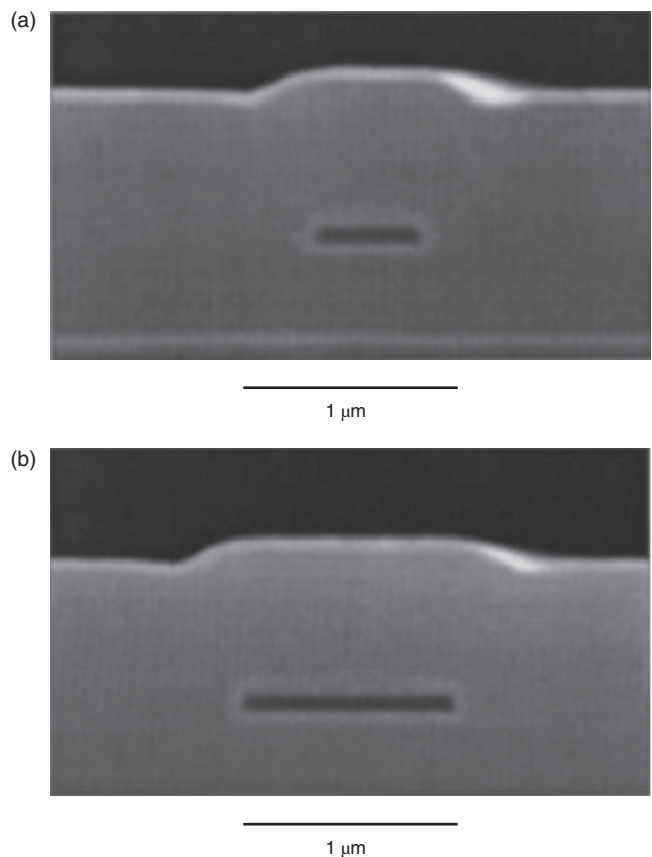


**Figure 8.** Scanning electron micrographs of channel across sections fabricated using the differential etching between Si and  $\text{Si}_3\text{N}_4$  in a TMAH-water solution. (a) 1 μm wide, 100 nm high. (b) 0.5 μm wide, 100 nm high. Reprinted with permission from [51], M. G. Stern et al., *J. Vac. Sci. Technol. B* 15, 2887 (1997). © 1997, American Vacuum Society.

with the width of the channels restricted to the submicrometer scale, while using standard photolithography with a resolution on the order of  $1\ \mu\text{m}$  [53]. Both methods are based on the sacrificial layer etching, as schematically explained in Figure 9(A),(C). Scanning electron microscope (SEM) photographs of the fabricated channels are shown in Figure 9(B),(D).

#### 4.1.2. Bottom-Up Approach

Carbon nanotubes (CNTs) are graphene sheets rolled up into cylinders of only a few nanometers in diameter and an extremely high length-to-width aspect ratio.

They were first observed in 1991 by Sumio Iijima at the NEC Fundamental Research Laboratory in Tsukuba, Japan, while inspecting with a high-resolution transmission electron microscope the soot created in an electrical discharge between two carbon electrodes. These so-called multiwall carbon nanotubes (MWCNTs) consisted of several concentric tubes of carbon nested inside each other. Two years later, in 1993, Iijima's group at NEC and Donald Bethune's group at IBM's Almaden Research Center in California independently observed single-wall carbon nanotubes (SWCNTs) just 1–2 nm in diameter. Nanotubes can be produced by evaporation of solid carbon in arc discharge, laser ablation, catalytic chemical vapor deposition of carbon-containing gases, and catalytic decomposition of fullerenes. A detailed description of manufacturing techniques for CNT falls outside the purpose of this chapter; recently, an extensive review appeared [54].

#### 4.2. Ensembles of Nanochannels

Nanotubular membranes are generally made by template-directed syntheses, with either polycarbonate nuclear track-etched (PCTE) membranes or anodic aluminum oxide films as templates [55, 56]. Commercial  $6\ \mu\text{m}$  thick PCTE membranes with channel densities of  $5\text{--}10 \cdot 10^8\ \text{cm}^{-2}$  and channel diameters down to 10 nm are available. Due to the random nature of the pore production process, the pore direction can deviate from the surface normal up to  $30^\circ$ , while some channels may even intersect somewhere inside the PCTE film. Anodic alumina membranes are also commercially available. They are  $\sim 50\ \mu\text{m}$  thick, and contain cylindrical pores of uniform diameter that are arranged in a hexagonal array. They are prepared by anodization of aluminum metal foils in acidic solutions, and have porosities of 25–40%, which is much higher than in PCTE. The channel diameter can be controlled by the applied voltage during anodization, and is typically between 20 and 200 nm.

### 5. REALIZATIONS AND APPLICATIONS

The recent popularity of nanotechnologies has made possible the development of individual nanoconfinements in which fluid flow can be studied and used in new applications. As this is a relatively new field, there are only few reported applications as yet. More is known on fluid flow through nanochannels in porous media.

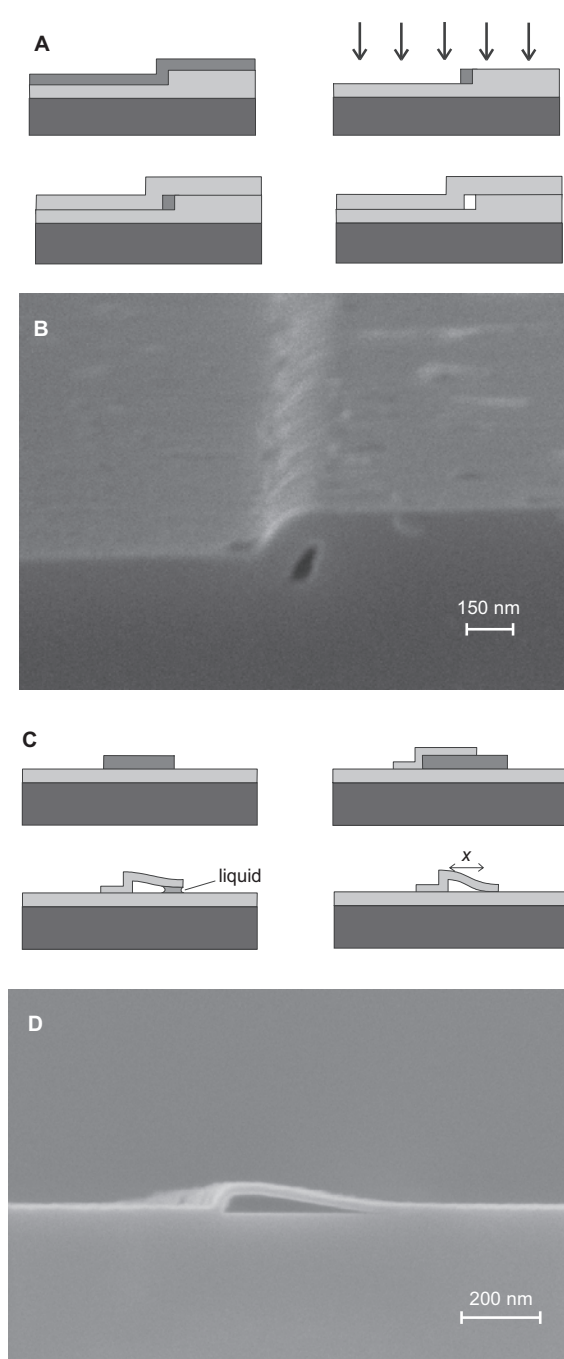


**Figure 9.** Fabrication of 2D confined nanochannels. (A) Method 1 is based on the formation of a nanowire on the side wall of a step. The nanowire is subsequently encapsulated, and finally it is removed by chemical etching to create the nanochannel. (B) SEM photograph of a nanochannel fabricated by method 1. The height and width of the channel are approximately 90 and 40 nm, respectively. (C) Method 2 is based on the etching of a sacrificial strip separating the substrate and the capping layer. During drying of the structure, the capping layer is pulled down by the capillary forces of the remaining liquid, and once brought in contact with the substrate, adheres permanently, forming a nanochannel. (D) SEM photograph of a nanochannel fabricated by method 2. The height and width of the channel are approximately 50 and 400 nm, respectively. Reprinted with permission from [53], N. R. Tas et al., *Nano Lett.* 2, 1031 (2002). © 2002, American Chemical Society.

## 5.1. Singularly Addressable Nanochannels

### 5.1.1. Top-Down Approach

Stern et al. [51] described the design and fabrication of a chemical charge-coupled device (CCD), which is based on the application of electrostatic fields in nanocapillary channels smaller than the Debye length, in order to concentrate ions by stepping them down the channels. Channels down to a height of only 20 nm were fabricated by sacrificial etching of an amorphous silicon layer in a tetramethylammonium hydroxide (TMAH) solution. Turner et al. [57] described the fabrication of a monolithic nanofluidic sieving structure for DNA electrophoresis, by means of the sacrificial layer technique. An array of pillars, 100 nm in diameter and separated by 100 nm spacing, was formed by etching holes in the 400 nm thick sacrificial polysilicon layer, subsequent filling of the holes by the silicon nitride capping layer, and finally sacrificial layer etching of the polysilicon in a TMAH solution. Electron beam lithography was used to define the holes. The pillar array was successfully employed to separate two different DNA chain lengths (43 and 7.2 kbase) by electrophoresis. A similar pillar array was used to study the motion of DNA molecules, caused by confinement-mediated entropic forces [58]. Chou et al. [59] used a nanofluidic sieving structure, consisting of a two-dimensional array of obstacles (Fig. 10) whose asymmetric disposition rectifies the Brownian motion of molecules driven through the devices, causing them to follow paths that depend on their diffusion coefficient. A 6% resolution in molecular length could be achieved in the 15–30 kbp range.

Han et al. [60, 61] presented the mechanism of entropic trapping to induce effective mobility differences between different sized DNA molecules. The trapping occurred in a nanochannel consisting of alternating thick and thin regions when the molecules moved from the thick to the thin region. The nanochannel with variable depths was defined and etched using two-level photolithography. The channel was closed by anodic bonding of a Pyrex coverslip. In the thick regions (0.65–1.6  $\mu\text{m}$  height), the DNA molecules

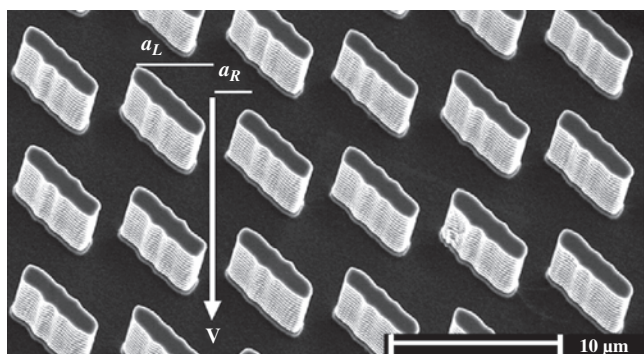


**Figure 10.** Scanning electron micrograph of the array of obstacles. The obstacles are 0.35  $\mu\text{m}$  high and measure  $1.5 \times 6.0 \mu\text{m}$ . The gap between adjacent obstacles is 1.5  $\mu\text{m}$ . An electric field propels the molecules directly through the gaps between the posts with velocity  $v$ . Transverse Brownian motion may cause a molecule to skip one channel to the right if it diffuses through displacement  $a_R$  or, very rarely, one channel to the left if it diffuses through  $a_L$ . Reprinted with permission from [59], C. F. Chou et al., *Proc. Nat. Acad. Sci. USA* 96, 13762 (1999). © 1999,

can relax to their equilibrium spherical shape. As a result, they are entropically hindered from entering the thin region (90 nm height) of the channel. Two different DNA types, T2 (164 kbp) and T7 (37.9 kbp), could successfully be separated by entropic trapping, with a trapping lifetime of T7 to T2 DNA of 1.7–1.9 at the same electric field. In another experiment, the same group managed to separate mixtures with up to eight different types of DNA, in the range of 5–48 kbp [62] (Fig. 11).

Baba and colleagues [63] demonstrated “size exclusion chromatography”-type separation of DNA molecules in a channel with alternating regions with empty space and patterned nanopillar arrays. With such a device, they could separate 5 and 10 kbp DNA molecules. 80  $\mu\text{m}$  wide and 360 nm high channels were made on a silicon wafer by dry etching from a nanopattern of the calixarene resist fabricated by electron beam lithography [64].

Foquet et al. [65] reported the use of nanochannels to confine the electrically driven flow DNA fragments through the optical detection volume of a confocal microscope (Fig. 12). For DNA fragment sizing, channel regions with a height of 270 nm and a width of 1  $\mu\text{m}$  were fabricated

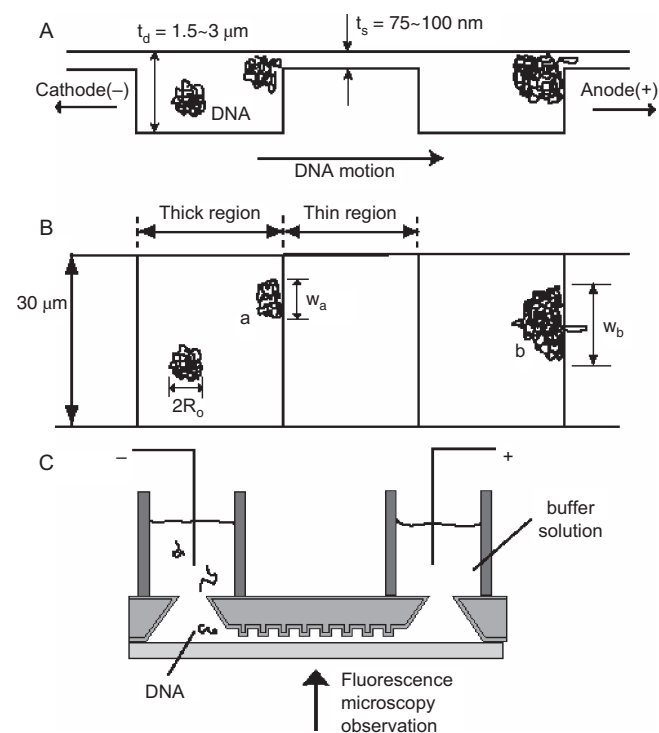


**Figure 11.** Nanofluidic separation device with many entropic traps. (A) Cross-sectional schematic diagram of the device. Electrophoresed DNA molecules are trapped whenever they meet a thin region because their radius of gyration ( $R_g$ ) is much larger than the thin region depth (here,  $t_d$  and  $t_s$  are the thick and thin region depths, respectively). (B) Top view of the device in operation. Trapped DNA molecules eventually escape, with a probability of escape proportional to the length of the slit that the DNA molecule covers ( $w_a$  and  $w_b$ ). Larger molecules have a higher escape probability because they cover wider regions of the slit ( $w_b > w_a$ ). (C) Experimental setup. Reservoirs are made at both ends of the channel, and filled with DNA solution. Reprinted with permission from [62], J. Han and H. G. Craighead, *Science* 288, 1026 (2001). © 2000, American Association for the Advancement of Science.

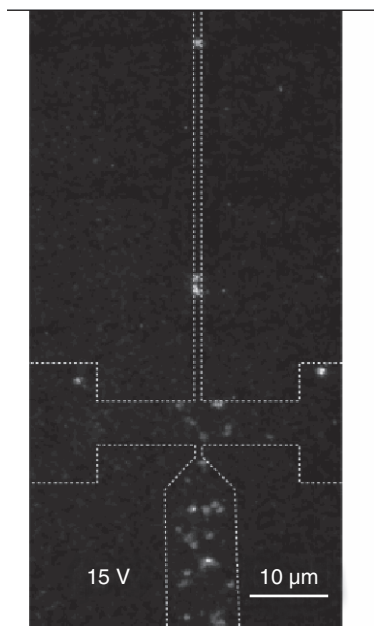


**Figure 12.** The image presents a picture taken with an intensified CCD camera of the single molecule sizing device. The outline of the capillary has been added for clarity. Time series of the motion of single molecules of DNA under the influence of an electric field can be downloaded at <http://www.hgc.cornell.edu/Microfluidics/Movies.html>. Reprinted with permission from [65], M. Foquet et al., *Anal. Chem.* 74, 1415 (2002). © 2002, American Chemical Society.

with the sacrificial layer technology, using material optically transparent and with low fluorescence background. The small channel dimensions facilitate single molecule detection, and minimize events of the simultaneous passage of more than one molecule through the measurement volume. The size of the fluorescent-labeled DNA molecules was determined from the number of photons per photon burst, each burst coinciding with the passage of a single DNA molecule.

Interesting fabrication techniques for the confinement of biological molecules in ultra small spaces were shown by Cao and colleagues [66]. High-density arrays of nanofluidic channels (Fig. 13) were fabricated using nanoimprint lithography (NIL), reactive ion etching, and nonuniform deposition to both reduce the cross section of the nanochannels and, if desired, seal the channels. The resulting sealed channels had a cross section as small as  $10 \text{ nm} \times 50 \text{ nm}$ .

Kameoka et al. [67] presented a refractive index sensor based on photon tunneling in a nanofluidic channel. A nanochannel was etched into a glass wafer, and enclosed by bonding of a second glass wafer to the first. The channel height is less than or comparable to the wavelength of the laser light used, allowing light transmission by photon tunneling if the angle of incidence of the laser light is larger than the critical angle. The photon tunneling probability depends strongly on the refractive index of the material in the nanofluidic channel, and can therefore be used to measure chemical composition changes of the fluid in the test volume.

Nanofluidic pumps and flow sensors can be used in applications where accurate dosing of a chemical substance is required. Wu et al. [49] reported the fabrication and

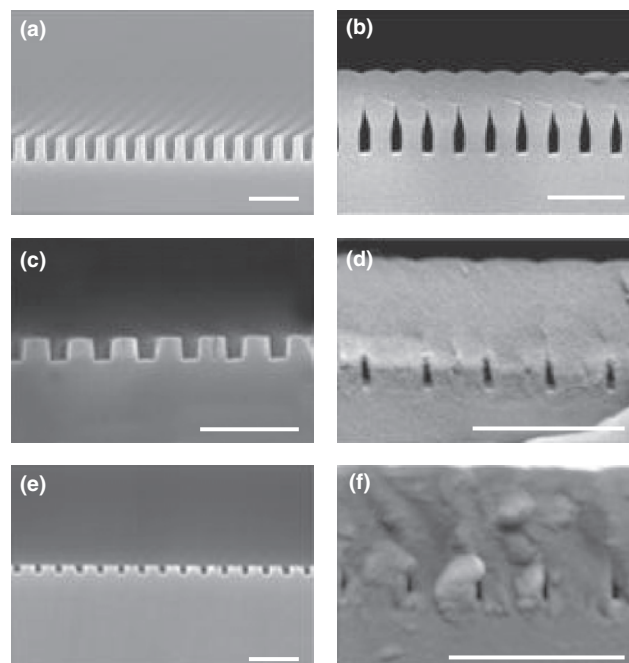


**Figure 13.** (a), (b) Nanofluidic pillar array structures before and after sealing by the sputtering process. (c), (d) Top view images of half-sealed pillar array structures with 200 nm of  $\text{SiO}_2$  deposited and a completely sealed structure after 400 nm of  $\text{SiO}_2$  was deposited. The scale bars are all 500 nm. Reprinted with permission from [66], H. Cao et al., *Appl. Phys. Lett.* 81, 174 (2002). © 2002, American Institute of Physics.

successful testing of a thermal flow sensor fabricated on top of a surface micromachined channel. The sensor uses boron-doped polysilicon thin-film resistors embedded in the silicon nitride wall of a microchannel as the sensing and heating elements. The sensors have demonstrated a flow rate resolution of 0.4 nL/min, as well as the capability to detect microbubbles in the liquid.

Chmela et al. presented an on-chip hydrodynamic chromatography (HDC) system consisting of a shallow, large aspect ratio separation channel ( $1 \mu\text{m}$  deep and  $1000 \mu\text{m}$  wide) fabricated using silicon and glass microtechnology [68]. The basic principle is that, in narrow conduits with a laminar flow, large molecules or particles (size 0.002–0.2 of the conduit size) are transported faster than smaller ones as they cannot fully access slow-flow regions near the conduit walls.

Ramsey and co-workers investigated the electrokinetic (EK) transport of fluids and macromolecules through nanometer-confined channels fabricated using standard photolithography and wet chemical etching techniques [69, 70]. Experimental measurements of electroosmotic mobilities under electrical double-layer overlap conditions showed that the mobilities are reduced, in qualitative agreement with the theory [71]. The authors reported the use of EK transport under double-layer overlap conditions to generate hydraulic pressure, and to separate 100 and 1000 base pair fragments of dsDNA in solution. This could be achieved because of the flow profile in the nanochannel and the hydrodynamic radius of the two sizes of dsDNA molecules (Fig. 14). Unlike the case at microscale, the EK-induced flow profile for the submicron deep channel the authors used



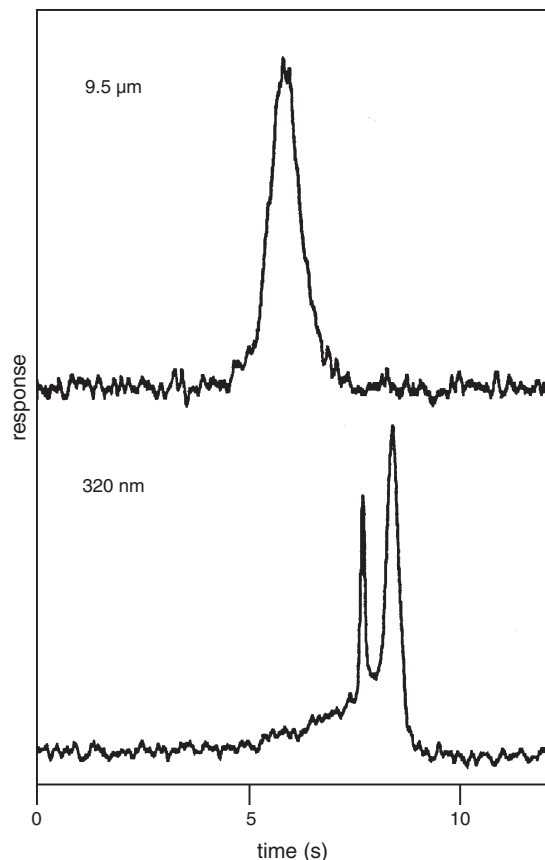


**Figure 14.** Electrokinetic migration of 100 and 1000 base pair dsDNA at two different channel depths (9.5  $\mu\text{m}$  and 320 nm). Reprinted with permission from [70], J. M. Ramsey et al., "Proceedings of Micro Total Analysis Systems 2002," 2002, pp. 314–316. © 2002, Kluwer Academic.

(320 nm) is expected to have a parabolic character. The smaller molecules can, therefore, approach the channel walls more closely, and experience lower flow velocity than the larger molecules.

Kitamori and colleagues [72] studied the behavior of aqueous solutions of rhodamine 6G, sulforhodamine 101, and rhodamine B in nanometer-sized fused silica channels. By using time-resolved spectroscopy, the spectra of the solutions were determined in the nanochannels, and compared to those obtained in microchannels. From the analysis of the fluorescent decays, it was suggested that the solutions had lower dielectric constants and higher viscosities in the nanometer-sized channels. The channels were fabricated on fused silica substrates by a fast atom beam (FAB) etching method and hydrofluoric bonding of cover plates.

### 5.1.2. Bottom-Up Approach

The inner hollow cavity of carbon nanotubes offers the possibility for intriguing nanoscale experiments if it could be filled with other materials in a systematic way [73]. Interesting experiments concerning the capillarity of carbon nanotubes have been carried out. Ajayan et al. [74], Dujardin et al. [73], and Ugarte et al. [75] reported capillarity-induced filling of carbon nanotubes by molten materials (liquid metals, salts, or oxides). Dujardin and colleagues [73] proved that

nanotubes can be wet and filled by substances with low surface tension, the upper limit of the surface tension being less than 200 mN/m. The wetting cutoff value of the surface tension is still sufficiently high to allow wetting by water ( $\gamma \sim 72$  nN/m) and most organic solvents ( $\gamma < 72$  nN/m). Ugarte and co-workers [75] filled open carbon nanotubes with molten silver nitrate by capillary forces. They concluded that there is a size constraint on the capillary filling of nanotubes, the capillarity being reduced for narrow tubes and the wetting depending on the cavity size. They explained this as a result of the increase of the nanotube–salt interface energy with decreasing curvature of the nanotube walls. The authors continued, demonstrating the formation of chains of silver nanobeads separated by high-pressure gas pockets as a result of the silver nitrate decomposition *in-situ* in an electron microscope

Gogotsi et al. and Megaridis et al. [76–78] observed the complex behavior of the gas–liquid interface of aqueous liquid inclusions in carbon nanotubes, upon heating by an electron beam in the transmission electron microscope (TEM). The carbon nanotubes used were produced by hydrothermal synthesis, and had a wall thickness in the 10–25 nm range and an outer diameter of about 100 nm (Fig. 15).

Sun and Crooks employed a 100  $\mu\text{m}$  long single carbon nanochannel with 150 nm diameter embedded in an epoxy matrix as a Coulter counter [79]. Polystyrene particles of  $\sim 60$  nm diameter were used as probes to study the hydrodynamic, electrophoretic, and diffusive transport properties of the nanochannel. The inner surface of the nanotube was found to be essentially charge neutral, so that electroosmotic effects could be neglected. The authors pointed out the advantage of using a single straight nanochannel to obtain information about fundamental modes of transport.

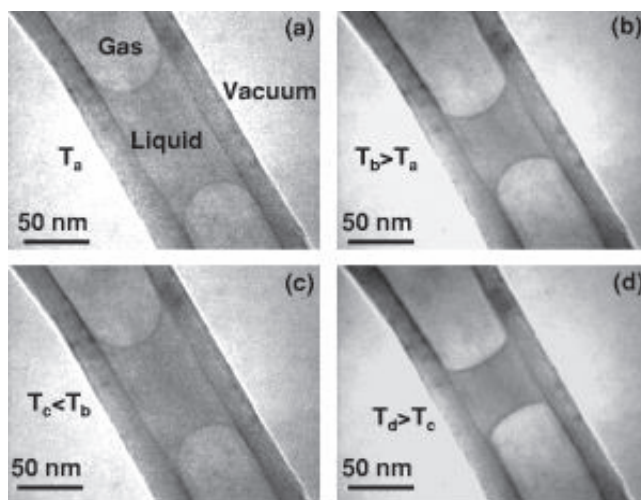


**Figure 15.** TEM micrograph sequence of a typical carbon nanotube portion showing the reversible volume contraction/expansion of a liquid entrapment upon heating/cooling achieved by manipulating the illuminating electron beam. (a) Initial shape of liquid at temperature  $T_a$ . (b) Inclusion gets thinner upon heating at  $T_b > T_a$ . (c) Liquid returns to its initial size upon cooling at  $T_c < T_b$ . (d) Heating is repeated ( $T_d > T_c$ ), resulting in a renewed contraction of the liquid volume. Reprinted with permission from [76], Y. Gogotsi et al., *Appl. Phys. Lett.* 79, 1021 (2001). © 2001, American Institute of Physics.

## 5.2. Ensembles of Nanofluidic Channels as Selective Interconnects

The discussion presented here is limited to ensembles of one-dimensional channels with sub-200 nm radial dimensions.

One of the pioneering works on fluid transport through nanochannels was performed by Martin and co-workers [80, 81]. The internal pore walls of PCTE membranes were coated with a gold layer using the electroless deposition technique, which yielded straight metallic nanotubules with channel diameters of 0.8–10 nm. They placed a membrane between two KF electrolyte solutions of different concentrations, and varied the electrical potential of the membrane relative to the reference potential in the solution with the higher electrolyte concentration. Depending on the sign of the membrane potential relative to the reference electrode, the membrane exhibited complete anion- or cation-permselective behavior. This effect was attributed to double-layer overlap inside the nanotubules, by which means ions of the same sign as the membrane are rejected. The extent of membrane permselectivity can be expressed quantitatively by the transference numbers for cations ( $t_+$ ) and anions ( $t_-$ ). For a 1:1 salt such as KF, the potential  $E_m$  over the membrane is given by

$$E_m = \frac{k_B T}{e} (t_+ - t_-) \ln\left(\frac{a_h}{a_l}\right)$$

where  $a_h$  and  $a_l$  are the activities of the salt at high and low concentration, respectively [82]. The equation indicates that  $E_m$  is positive when the tubules are predominantly cation permselective ( $t_+ > t_-$ ), and negative when they are anion permselective ( $t_+ < t_-$ ). Figure 16 illustrates a series of  $E_m$  values measured at different applied potentials, which proves that Au nanotubules can function as electronically

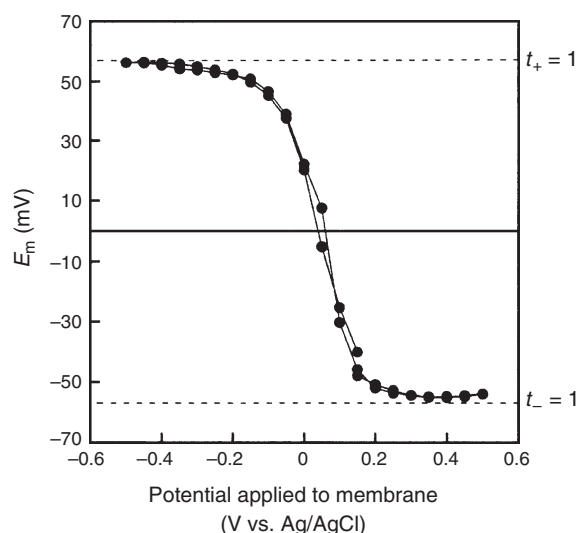


**Figure 16.** Variation of  $E_m$  with potential applied to a gold-nanotubule membrane (1 mM KF on the low concentration side; 10 mM on the high side of the membrane; tubule radius  $\sim 1.1$  nm). The dashed lines indicate the expected  $E_m$  values for ideal cation- and anion-permselective behavior. Reprinted with permission from [80], M. Nishizawa et al., *Science* 268, 700 (1995). © 1995, American Association for the Advancement of Science.

switchable ion-exchange membranes. Studies on the permeabilities of complex cationic and anionic species of  $\sim 1$  nm diameter showed high tunability of the fluxes with variation of potential [83]. Some selected data are listed in Table 3. It was shown that the permeability in 1.5 nm channels was mainly due to electrostatic rather than to steric effects. Another external handle to effect molecular transport in nanosized channels is pH. Bluhm et al. studied the diffusion of mono-, di-, and trivalent cations across anodic alumina membranes with pore diameters of 20 and 100 nm as a function of ionic strength and pH [84, 85]. It was concluded that the cation diffusion coefficients decreased with cation valency, which was attributed to the larger electrostatic interactions between the cations and the positively charged alumina surface at pH below 9. The diffusion rates could be enhanced by increasing the pH of the electrolyte solution from 5 to 8, as this leads to a decrease of the positive surface charge density on the alumina pore walls, and thus to a decreased electrostatic repulsion between cations and the channel wall [84]. Bohn and co-workers also studied the influence of electrolyte strength and pH on the permeability of cationic, anionic, and neutral species in aqueous buffer solution [21, 86]. Further control over the pH dependence of the surface-charge density can be obtained by employing self-assembled monolayers (SAMs) on the pore walls [83, 84]. Stroeve and co-workers modified the surface chemistry of Au-coated 8 nm nanotubular PCTE membranes with a covalently bonded monolayer of acid-functional thiols HS-(CH<sub>2</sub>)<sub>10</sub>-COOH [87]. The diffusion of benzene sulfonate anions was shown to be highly dependent on the external pH of the solution, in contrast to anion diffusion through bare or Au-coated PCTE membranes. This effect is illustrated in Figure 17, and was attributed to the pH-dependent ionization of the surface carboxylic groups in the SAMs and electrostatic interactions between the anions and the surface charge. Cysteine, a thiol-functional amino acid with an isoelectric point around 6.0, was also employed as a surface-modifying agent [83, 88, 89]. Here, the permeating cationic species showed high fluxes at pH 12, where cysteine is negatively charged, and low flux at pH 2, where cysteine is positively charged. The opposite trend with pH was observed for anionic species [88]. The concept of size-based separation was elaborated in a study on size-based protein separation by gold nanotubule membranes [90].

**Table 3.** Flux data of complex ionic species through 1.5 nm gold nanotubular membranes versus potential  $E$  applied to the membrane. Background electrolyte 0.5 mM KF. Concentration of permeation ion 2.5 mM. Ru(bpy)<sub>3</sub><sup>2+</sup> = ruthenium tris-(2,2'-bipyridine) cation; BTA<sup>+</sup> = benzyl tributyl-ammonium cation; NDS<sup>2-</sup> = 2,6-naphthalene disulfonate anion; PTS<sup>-</sup> = p-toluene sulfonate anion.

Permeate ion	Flux ( $10^{-9}$ mol $\cdot$ cm <sup>-2</sup> $\cdot$ s <sup>-1</sup> )		
	$E = -400$ mV	$E = 0$	$E = +400$ mV
Ru(bpy) <sub>3</sub> <sup>2+</sup>	0.30	0.09	0.08
BTA <sup>+</sup>	0.34	0.19	0.11
NDS <sup>2-</sup>	0.002	0.01	0.03
PTS <sup>-</sup>	0.04	0.13	0.20

Source: Data excerpted with permission from [83], M.-S. Kang and C. R. Martin, *Langmuir* 17, 2753 (2001). © 2001, American Chemical Society.



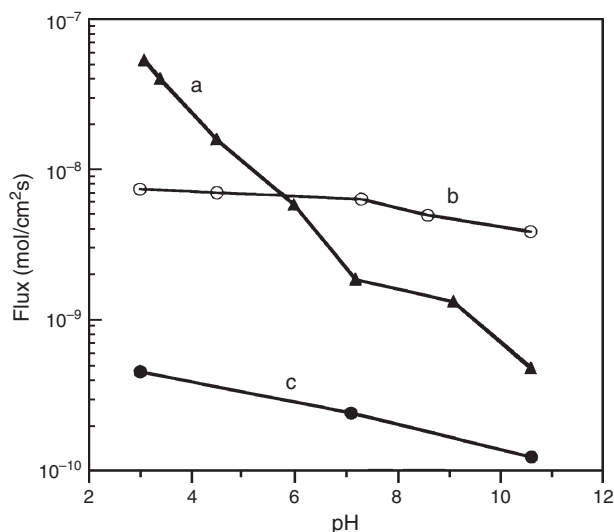


**Figure 17.** Flux of benzene sulfonate anions as a function of external pH obtained with (a) PCTE/Au/HS(CH<sub>2</sub>)<sub>10</sub>COOH, (b) bare PCTE, and (c) PCTE/Au membranes. Tubule radii 8–10 nm. Debye length  $\sim$ 7 nm. Reprinted with permission from [87], Z. Hou et al., *Langmuir* 16, 2401 (2000). © 2000, American Chemical Society.

The Au nanotubule inner diameter was controlled by variation of deposition time of the gold layer inside the PCTE nanochannels. It was shown that the low-molecular-weight protein lysine ( $M_w = 14$  kg/mol) was transported preferentially over high-molecular-weight bovine serum albumin ( $M_w = 67$  kg/mol) through nanochannels of 23 nm diameter. The transport of nonhydrophilic molecules can be enhanced by the covalent attachment of a hydrophobic SAM on the internal channel walls [80, 81, 91, 92]. This allows the preferential separation of *neutral* molecules based on their degree of hydrophobicity/hydrophilicity. Derivatization of gold nanotubules using the hydrophobic thiol HS-C<sub>16</sub>H<sub>33</sub> showed an enhanced transport rate of hydrophobic solvents [91]. Flux and selectivity data for hydrophobic toluene and hydrophilic pyridine through nanotubules modified with hydrophobic and hydrophilic SAMs are listed in Table 4. A similar approach can be utilized to selectively separate *chiral* neutral molecules, as was demonstrated recently [93]. In view of the fact that chiral enantiomers exhibit chemically and physically identical behavior, and are therefore very difficult to separate by simple means, the proposed concept appears very promising. Silica nanotubes were chemically

**Table 4.** Flux and selectivity data for toluene and pyridine through Au nanotubule membranes modified with hydrophobic (–C<sub>16</sub>H<sub>33</sub>) and hydrophilic (–C<sub>2</sub>H<sub>4</sub>OH) SAMs.

Thiol	Channel diameter (nm)	Flux ( $10^{-9}$ mol · cm <sup>-2</sup> · min <sup>-1</sup> )	
		Pyridine	Toluene
HS–C <sub>2</sub> H <sub>4</sub> –OH	3.0	7.0	2.6
HS–C <sub>16</sub> H <sub>33</sub>	3.0	0.46	28
HS–C <sub>2</sub> H <sub>4</sub> –OH	2.0	5.6	0.61
HS–C <sub>16</sub> H <sub>33</sub>	2.0	0.1	20

Source: Data excerpted with permission from [92], S. B. Lee and C. R. Martin, *Chem. Mater.* 13, 3236 (2001). © 2001, American Chemical Society.

synthesized within the 20–35 nm diameter channels of an anodic alumina membrane. An antibody that selectively binds to only one of the enantiomers of a mixture of a clinical drug was chemically bonded to the channel walls of the silica nanotubes, after which the membrane became selectively permeable to the enantiomer that can attach to the antibody. Dynamic control over the channel diameter was demonstrated by Ito et al. [94]. Ionizable thiol-functionalized poly-(L-glutamic) acid polypeptides were covalently bonded to the internal channel walls of a gold-coated PCTE membrane. The polypeptides respond to changes of pH and ionic strength by a conformational change: at low pH, they become positively charged, and fold to form a relatively short ( $\sim$ 1.5 nm)  $\alpha$ -helical coil. Upon deprotonation at high pH, the polypeptide chains form a relatively extended ( $\sim$ 16 nm) random structure. The water permeation rate through the channels can thus be reversibly regulated by pH since the channel diameter can be made larger or smaller. The effect becomes less pronounced at high ionic strength, as illustrated in Figure 18.

The application of carbon nanotubes as nanofluidic channels has been limited so far [79, 95, 96]. Ensembles of straight parallel carbon nanotubes can be formed by the thermal decomposition of ethylene or propylene in an anodic alumina film [97, 98]. EOF studies were performed on  $\sim$ 60  $\mu$ m long carbon nanotubes with an inner diameter of 120–200 nm [95, 96], which is too large for complete double-layer overlap to occur. The direction of the EOF indicated that the as-synthesized tubes have a negative surface charge between pH 3 and 7.2, and the EOF velocity was found to vary linearly with applied current density [95]. An electrochemical derivatization method was used to covalently attach acidic (negative) carboxylate groups to the channel walls, thus increasing the negative surface-charge density and  $\zeta$  potential. In this way, the EOF rate could be increased in comparison with the as-synthesized tubes [96].

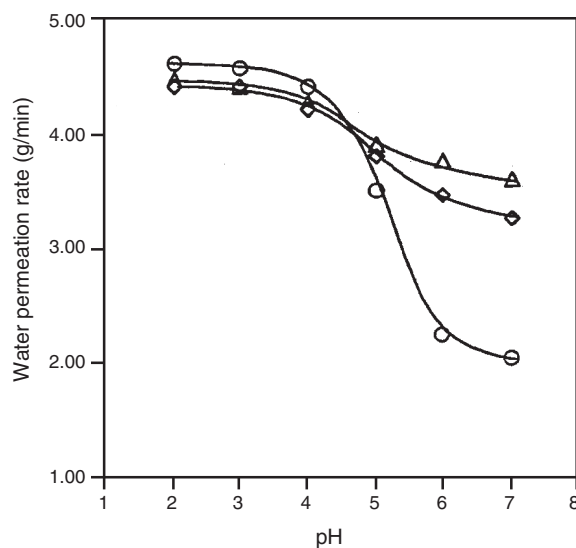


**Figure 18.** pH-dependent permeation of water with different ionic strengths through a PCTE membrane with an internal polypeptide SAM. Ionic strengths were 0 M (circles), 0.1 M (diamonds), and 1.0 M (triangles). Reprinted with permission from [94], Y. Ito et al., *Langmuir* 16, 5376 (2000). © 2000, American Chemical Society.

## GLOSSARY

**Carbon nanotube (CNT)** Carbon nanotubes are graphene sheets rolled-up into cylinders with diameters as small as one nanometer. A single-wall carbon nanotube (SWCNT) is a graphene sheet rolled-over into a cylinder with typical diameter on the order of 1.4 nm. A multi-wall carbon nanotube (MWCNT) consists of concentric cylinders with an interlayer spacing of 3.4 Å and a diameter typically on the order of 10–20 nm. The lengths of the two types of tubes can be up to hundreds of microns or even centimeters. The intriguing electrical and mechanical properties of carbon nanotubes have led to an explosion of research efforts worldwide.

**Double layer, electric double layer (EDL)** The region near a charged surface where counter-ions and co-ions in a polar medium are preferentially distributed, such that the net charge density is not zero. According to the Stern model, a plane (Stern plane) splits the EDL into an inner, compact layer considered to be immobile, and an outer, diffuse layer in which the ions are mobile.

**Electroosmosis (EO)** The movement of ionic conducting fluids through a capillary or a channel under the influence of an applied electric field. An electric field applied along the capillary/channel generates the movement of a thin layer of fluid at the channel walls where a small separation of charges occurs due to the equilibrium adsorption and desorption of ions. As the layer of fluid moves, it drags the fluid bulk resulting in an essentially flat velocity profile across the channel.

**Electrophoresis (EP)** The movement of charged particles suspended in a liquid under the influence of an applied electric field. Particles can be separated by electrophoresis on the basis of their relative electrical charges.

**Microelectromechanical systems (MEMS)** Electromechanical systems fabricated using materials and techniques developed in the integrated circuit (IC) industry. MEMS contain both electronic circuits and mechanical parts with dimensions in the micron range such as transducers, valves, and motors.

**Microsystem technology (MST)** Similar to MEMS with or without the electronic circuitry (e.g. optical, mechanical or fluidic structures).

**Reynolds number (Re)** Dimensionless number that represents the ratio of inertia forces to viscous forces. The Reynolds number of a fluid flow characterizes the regime of the flow as laminar or turbulent.

**Scanning electron microscopy (SEM)** A scanning electron microscope is a type of electron microscope capable of producing high resolution images of a sample. In electron microscopes (EMs) a focused beam of electrons is used to image the specimen and gain information as to its structure and composition. EMs were developed to achieve resolutions higher than those of light microscopes. SEM usually monitors secondary electrons which are emitted from the surface due to excitation by the primary electron beam. The first scanning electron microscope (SEM) was developed in 1942 and it was commercially available around 1965. See also TEM.

**Self-assembled monolayer (SAMs)** SAMs are monomolecular layers of a compound bound to a surface in a highly

organized fashion and with a bond whose strength typically varies between ionic and covalent. The process of self assembly is thermodynamically driven and capable of self repairing: if the layer immersed in the solution of the same compound is damaged, new molecules can replace the empty spaces on the surface. Examples are thiolates, sulfides and dithiols self assembling on gold. The monolayers formed by trialkoxysilanes on glass are erroneously defined as self assembling layers. In fact the coupling to the surface is covalent and not reversible. The concept of monolayer was introduced in 1917 when Langmuir studied film formed by amphiphiles spreading on water. He realized the film had the thickness of one molecule.

**Surface tension** The energy stored at the surface of liquids. The surface tension of a material is the energy needed to increase the surface of a unit area. It arises because of the difference in the intermolecular forces between molecules in the bulk of the liquid and molecules at the surface of the liquid. As the molecules in the bulk of the liquids are in favorable energy configuration, surface tension tries to minimize the surface area, resulting in liquids forming spherical droplets. Surface tension is measured in newtons per meter ( $\text{Nm}^{-1}$ ) which are equivalent to joules per square metre ( $\text{Jm}^{-2}$ ).

**Transmission electron microscopy (TEM)** It is an imaging technique whereby an image of a specimen is produced on a fluorescent screen or layer of photographic film by electrons focused on the specimen and travelling through the specimen. The transmission electron microscope (TEM) was developed by Max Knoll and Ernst Ruska in Germany in 1931. It was the first type of electron microscope to be developed. As its name suggests, the TEM is patterned on the Light Transmission Microscope: the image is produced by detecting electrons that are transmitted through the sample.

**Zeta potential ( $\zeta$ )** The electric potential at the shear plane in the electric double layer. The zeta potential is defined with respect to the potential of the bulk of the solution.

## REFERENCES

1. M. Heuberger, M. Zäch, and N. D. Spencer, *Science* 292, 905 (2001).
2. A. J. Tudos, G. A. J. Besselink, and R. B. M. Schasfoort, *Lab Chip* 1, 83 (2001).
3. E. Verpoorte, *Electrophoresis* 23, 677 (2002).
4. D. R. Reyes, D. Iossifidis, P.-A. Auroux, and A. Manz, *Anal. Chem.* 74, 2623 (2002).
5. P.-A. Auroux, D. Iossifidis, D. R. Reyes, and A. Manz, *Anal. Chem.* 74, 2637 (2002).
6. A. van den Berg and T. S. J. Lammerink, *Top. Curr. Chem.* 194, 21 (1998).
7. D. R. Meldrum and M. R. Holl, *Science* 297, 1197 (2002).
8. R. E. Oosterbroek, Ph.D. Dissertation, University of Twente, Enschede, The Netherlands, 1999.
9. V. L. Streeter, "Handbook of Fluid Dynamics." McGraw-Hill Int., New York, 1961.
10. P. W. Atkins, "Physical Chemistry." Oxford University Press, 1998.
11. B. Zhao, J. S. Moore, and D. J. Beebe, *Science* 291, 1023 (2001).
12. S. Daniel, M. K. Chaudhury, and J. C. Chen, *Science* 291, 633 (2001).

13. M. W. J. Prins, W. J. J. Welters, and J. W. Weekamp, *Science* 291, 277 (2001).
14. T. S. Sammarco and M. A. Burns, *AIChE J.* 45, 350 (1999).
15. K. Ichimura, S. K. Oh, and M. Nakagawa, *Science* 288, 1624 (2000).
16. B. S. Gallardo, V. K. Gupta, F. D. Eagerton, L. I. Jong, V. S. Craig, R. R. Shah, and N. L. Abbott, *Science* 283, 57 (1999).
17. R. J. Hunter, "Introduction to Modern Colloid Science." Oxford University Press, Oxford, 1993.
18. N. Israelachvili, "Intermolecular and Surface Forces." Academic, London, 1992.
19. R. F. Probstein, "Physicochemical Hydrodynamics, An Introduction." Wiley, New York, 1994.
20. A. W. Adamson and A. P. Gast, "Physical Chemistry of Surfaces." Wiley, New York, 1997.
21. T.-C. Kuo, L. A. Sloan, J. V. Sweedler, and P. W. Bohn, *Langmuir* 17, 6298 (2001).
22. P. H. Paul, M. G. Garguilo, and D. J. Rakestraw, *Anal. Chem.* 70, 2459 (1998).
23. G. M. Whitesides and A. D. Stroock, *Phys. Today* 54, 42 (2001).
24. C. L. Rice and R. Whitehead, *J. Phys. Chem.* 69, 4017 (1965).
25. Q.-H. Wan, *Anal. Chem.* 69, 361 (1997).
26. C. Wei, A. J. Bard, and S. W. Feldberg, *Anal. Chem.* 69, 4627 (1997).
27. D. J. Harrison, K. Fluri, K. Seiler, Z. H. Fan, C. S. Effenhauser, and A. Manz, *Science* 261, 895 (1993).
28. L. Minnema, H. A. Barneveld, and P. D. Rinkel, *IEEE Trans. Elec. Insul.* EI-15, 461 (1980).
29. G. Beni and S. Hackwood, *Appl. Phys. Lett.* 38, 207 (1981).
30. H. J. J. Verheijen and M. W. J. Prins, *Langmuir* 15, 6616 (1999).
31. M. G. Pollack, R. B. Fair, and A. D. Shenderov, *Appl. Phys. Lett.* 77, 1725 (2000).
32. S. K. Cho, S.-K. Fan, H. Moon, and C. J. Kim, "Proceedings of IEEE Micro Electro Mechanical Systems Conference," 2002, pp. 32–35.
33. M. Washizu, *IEEE Trans. Ind. Appl.* 34, 732 (1998).
34. A. Torkkeli, J. Saarilahti, A. Häärä, H. Härmä, T. Soukka, and P. Tolonen, "Proceedings of 14th IEEE International Conference on Micro Electro Mechanical Systems," 2001, pp. 475–478.
35. A. P. Papavasiliou, A. P. Pisano, and D. Liepmann, "Proceedings of 11th International Conference on Solid State Sensors and Actuators (Transducers 2001)," 2001, pp. 940–943.
36. X. Geng, H. Yuan, H. N. Oguz, and A. Prosperetti, *J. Micromech. Microeng.* 11, 270 (2001).
37. H. Toshitami, Y. Sato, Y. Takatori, and Y. Shirato, U.S. Patent 4,252,824, 1981.
38. M. Haruta, Y. Yanu, Y. Matsufuji, T. Eida, and T. Ohta, U.S. Patent 4,410,899, 1983.
39. H. Yuan and A. Prosperetti, *J. Micromech. Microeng.* 9, 402 (1999).
40. N. R. Tas, J. W. Berenschot, T. S. J. Lammerink, M. Elwenspoek, and A. van den Berg, *Anal. Chem.* 74, 2224 (2002).
41. S. Basu and M. M. Sharma, *J. Membr. Sci.* 124, 77 (1997).
42. D. E. Yates, S. Levine, and T. W. Healy, *J. Chem. Soc., Faraday Trans. I* 70, 1807 (1974).
43. Y. Wang, C. Bryna, H. Xu, P. Pohl, Y. Yang, and C. J. Brinker, *J. Colloid Interface Sci.* 254, 23 (2002).
44. M. Eigen and E. Wicke, *J. Phys. Chem.* 58, 702 (1954).
45. P. Trivedi and L. Axe, *Environ. Sci. Technol.* 35, 1779 (2001).
46. A. Rasmussen, M. Gaitan, L. E. Locascio, and M. E. Zaghoul, *J. Microelectromech. Syst.* 10, 286 (2001).
47. J. W. Judy, T. Tamagawa, and D. L. Polla, "Proceedings of IEEE Micro Electro Mechanical Systems Workshop," 1991, pp. 182–186.
48. X. Jin, I. Ladabaum, F. L. Degertekin, S. Calmes, and B. T. Khuri-Yakub, *IEEE J. Microelectromech. Syst.* 8, 100 (1999).
49. S. Wu, Q. Lin, Y. Yuen, and Y.-C. Tai, *Sensors Actuators A* 89, 152 (2001).
50. S. Sugiyama, K. Shimaoka, and O. Tabata, "Proceedings of 6th International Conference on Solid-State Sensors and Actuators (Transducers)," 1991, pp. 188–191.
51. M. G. Stern, M. W. Geis, and J. E. Curtin, *J. Vac. Sci. Technol. B* 15, 2887 (1997).
52. C. K. Harnett, G. W. Coates, and H. G. Craighead, *J. Vac. Sci. Technol. B* 19, 2842 (2001).
53. N. R. Tas, J. W. Berenschot, P. Mela, H. V. Jansen, M. Elwenspoek, and A. van den Berg, *Nano Lett.* 2, 1031 (2002).
54. H. Dai, *Surf. Sci.* 500, 218 (2002).
55. J. C. Hultheen and C. R. Martin, *J. Mater. Chem.* 7, 1075 (1997).
56. A. Huczko, *Appl. Phys. A* 70, 365 (2000).
57. S. W. Turner, A. M. Perez, A. Lopez, and H. G. Craighead, *J. Vac. Sci. Technol. B* 16, 3835 (1998).
58. S. W. P. Turner, M. Cabodi, and H. G. Craighead, *Phys. Rev. Lett.* 88, 128103-1 (2002).
59. C. F. Chou, O. Bakajin, S. W. Turner, T. A. Duke, S. S. Chan, E. C. Cox, H. G. Craighead, and R. H. Austin, *Proc. Nat. Acad. Sci. USA* 96, 13762 (1999).
60. J. Han and H. G. Craighead, *J. Vac. Sci. Technol.* 17, 2142 (1999).
61. J. Han, S. W. Turner, and H. G. Craighead, *Phys. Rev. Lett.* 83, 1688 (1999).
62. J. Han and H. G. Craighead, *Science* 288, 1026 (2000).
63. M. Baba, T. Sano, N. Iguchi, K. Iida, T. Sakamoto, and H. Kawaura, "Proceedings of Micro Total Analysis Systems 2002," 2002, pp. 763–765.
64. J. Fujita, Y. Ohnishi, Y. Ochiai, and S. Matsui, *Appl. Phys. Lett.* 68, 1297 (1996).
65. M. Foquet, J. Korlach, W. Zipfel, W. W. Webb, and H. G. Craighead, *Anal. Chem.* 74, 1415 (2002).
66. H. Cao, Z. Yu, J. Wang, J. O. Tegenfeldt, R. H. Austin, E. Chen, W. Wu, and S. Y. Chou, *Appl. Phys. Lett.* 81, 174 (2002).
67. J. Kameoka and H. G. Craighead, *Sensors Actuators B* 77, 632 (2001).
68. E. Chmela, R. Tijssen, M. T. Blom, H. J. Gardeniers, and A. van den Berg, *Anal. Chem.* 74, 3470 (2002).
69. S. C. Jacobson, J. P. Alaire, and J. M. Ramsey, "Proceedings of Micro Total Analysis Systems 2001," 2001, pp. 57–59.
70. J. M. Ramsey, J. P. Alaire, J. S. C., and N. J. Peterson, "Proceedings of Micro Total Analysis Systems 2002," 2002, pp. 314–316.
71. S. Levine, J. R. Marriott, and K. Robinson, *J. Chem. Soc., Faraday Trans. 2* 71, 1 (1975).
72. A. Hibara, T. Saito, H.-B. Kim, M. Tokeshi, T. Ooi, M. Nakao, and T. Kitamori, *Anal. Chem.* 74, 6170 (2002).
73. E. Dujardin, T. W. Ebbesen, H. Hiura, and K. Tanigaki, *Science* 265, 1850 (1994).
74. P. M. Ajayan and S. Iijima, *Nature* 361, 333 (1993).
75. D. Ugarte, A. Chatelain, and W. A. de Heer, *Science* 274, 1897 (1996).
76. Y. Gogotsi, J. A. Libera, A. Güvenc Yazicioglu, and C. M. Megaridis, *Appl. Phys. Lett.* 79, 1021 (2001).
77. Y. Gogotsi, J. A. Libera, A. Güvenc Yazicioglu, and C. M. Megaridis, *Mater. Res. Soc. Symp. Proc.* 633, A7.4.1 (2001).
78. C. M. Megaridis, A. Güvenc Yazicioglu, J. A. Libera, and Y. Gogotsi, *Phys. Fluids* 14, L5 (2002).
79. L. Sun and R. M. Crooks, *J. Am. Chem. Soc.* 122, 12340 (2000).
80. M. Nishizawa, V. P. Menon, and C. R. Martin, *Science* 268, 700 (1995).
81. C. R. Martin, M. Nishizawa, K. Jirage, and M. Kang, *J. Phys. Chem. B* 105, 1925 (2001).
82. N. Lakshminarayanaiah, in "Membrane Electrodes," pp. 50–94. Academic, New York, 1976.
83. M.-S. Kang and C. R. Martin, *Langmuir* 17, 2753 (2001).
84. E. A. Bluhm, E. Bauer, R. M. Chamberlin, K. D. Abney, J. S. Young, and G. D. Jarvinen, *Langmuir* 15, 8668 (1999).

85. E. A. Bluhm, N. C. Schroeder, E. Bauer, J. N. Fife, R. M. Chamberlain, K. D. Abney, J. S. Young, and G. D. Jarvinen, *Langmuir* 16, 7056 (2000).
86. P. J. Kemery, J. K. Steehler, and P. W. Bohn, *Langmuir* 14, 2884 (1998).
87. Z. Hou, N. L. Abbott, and P. Stroeve, *Langmuir* 16, 2401 (2000).
88. S. B. Lee and C. R. Martin, *Anal. Chem.* 73, 768 (2001).
89. C. R. Martin, M. Nishizawa, K. Jirage, M. Kang, and S. B. Lee, *Adv. Mater.* 13, 1351 (2001).
90. S. Yu, S. B. Lee, and C. R. Martin, *Nano Lett.* 1, 495 (2001).
91. K. B. Jirage, J. C. Hulteen, and C. R. Martin, *Anal. Chem.* 17, 4913 (1999).
92. S. B. Lee and C. R. Martin, *Chem. Mater.* 13, 3236 (2001).
93. S. B. Lee, D. T. Mitchell, L. Trofin, T. K. Nevanen, H. H. Söderlund, and C. R. Martin, *Science* 296, 2198 (2002).
94. Y. Ito, Y. S. Park, and Y. Imanishi, *Langmuir* 16, 5376 (2000).
95. S. A. Miller, V. Y. Young, and C. R. Martin, *J. Am. Chem. Soc.* 123, 12335 (2001).
96. S. A. Miller and C. R. Martin, *J. Electroanal. Chem.* 522, 66 (2002).
97. T. Kyotani, L. F. Tsai, and A. Tomita, *Chem. Mater.* 7, 1427 (1995).
98. T. Kyotani, L. F. Tsai, and A. Tomita, *Chem. Mater.* 8, 2109 (1996).
99. J. Haneveld, H. V. Jansen, J. W. Berenschot, N. R. Tas, and M. C. Elwenspoek, "Proceedings of MME' 02 Micromechanics Europe," 2002, pp. 47-50.



# Nanofluids

Stephen U. S. Choi

*Argonne National Laboratory, Argonne, Illinois, USA*

Z. George Zhang

*The Valvoline Company, Lexington, Kentucky, USA*

Pawel Keblinski

*Rensselaer Polytechnic Institute, Troy, New York, USA*

## CONTENTS

1. Introduction
  2. Background of Nanofluids
  3. Making of Nanoparticles
  4. Making of Nanofluids
  5. Measurements in Nanofluids
  6. Models and Mechanisms
  7. Future Directions
  8. Concluding Remarks
- Glossary  
References

## 1. INTRODUCTION

Nanofluids are a new kind of heat transfer fluid containing a very small quantity of nanoparticles that are uniformly and stably suspended in a liquid. The dispersion of a tiny amount, yet tremendous number, of solid nanoparticles in traditional fluids dramatically changes their thermal conductivities. The average size of particles used in nanofluids may vary from 1 to 100 nm. The goal of thermal nanofluids is to achieve the highest possible thermal conductivities at the smallest possible concentrations of the smallest possible nanoparticles (preferably <10 nm). A typical nanofluid may contain very low concentrations (preferably <1% by volume) of solid nanoparticles and no surfactants or other dispersing chemicals. This creative combination of solid nanoparticles and liquid molecules has become an emerging

interdisciplinary field where nanoscience and thermal engineering meet.

Choi coined the term “nanofluids” for this new class of solid/liquid suspensions, developed primarily for heat transfer applications [1]. However, biologists and physicists have used the term nanofluids for different kinds of fluids. For biologists, nanofluids are nanometer-sized bioparticles such as DNA, RNA, and protein molecules in aqueous solutions [2, 3]. For physicists, fluids confined in a nanometer-sized container such as slit nanopores are called nanofluids [4–8].

The primary objectives of current nanofluids R&D are to exploit the unique properties of nanoparticles to develop heat transfer fluids that possess stable particle dispersion and high thermal conductivity, to characterize the transport properties and heat transfer performance of nanofluids, and to develop nanofluid technology for increasing the thermal transport of industrial heat transfer fluids. In this chapter, we address thermal nanofluids, particularly as related to heat transfer applications, and cover the literature on thermal nanofluids published in English since the pioneering work of Choi [1], with focus on the thermal conductivity.

Section 2 provides background on nanofluids, including their emergence in conjunction with a major trend in science and technology, the motivation and concept behind nanofluids, the advantages and new issues on the use of nanoparticles compared to micro- and mesoparticles, and the potential benefits of nanofluids.

Section 3 gives a brief review of the methods used for making nanoparticles to be dispersed in nanofluids and their characterization.

Section 4 presents a brief review of dispersion techniques and reviews the two methods (two-step and single-step) for making nanofluids.



Section 5 reviews the techniques used for measuring the thermal conductivity of nanofluids and the thermal conductivity data obtained with these techniques. This section also treats other transport properties and convection heat transfer of nanofluids.

Section 6 summarizes the conventional models for the thermal conductivity of solid/liquid suspensions and the great discrepancy between measured and predicted thermal conductivity, particularly for copper and nanotube nanofluids. Also covered are potential mechanisms for the enhanced thermal conductivity in nanofluids and molecular dynamics simulations of energy transport in nanoparticles and at the solid/liquid interface.

In Section 7 promising areas for future basic and applied research are identified, potential impacts and applications are suggested, and the interdisciplinary nature of nanotechnology is described.

Finally, in Section 8 we summarize key points of our review.

## 2. BACKGROUND OF NANOFUIDS

In 1959 Nobel prize winner Richard Feynman presented the concept of micromachines at the annual meeting of the American Physical Society held at the California Institute of Technology. Since then, miniaturization has been a clear and major trend in modern science and technology. Almost 40 years later, another Nobel prize winner, H. Rohrer, presented the chances and challenges of the “nanoage” [9]. The steady miniaturization trend has dropped from the millimeter scale of the early 1950s to the present-day atomic scale [10]. As the age of “bigger is better” gives way to the age of “smaller is better,” microelectromechanical systems and nanotechnology are rapidly emerging as the new revolution in miniaturization and as the technology to bring about a second industrial revolution. It is estimated that nanotechnology is at a similar level of development as computer/information technology was in the 1950s [11]. Nanofluids are an outgrowth of these trends in miniaturization and nanotechnology.

With an ever-increasing thermal load caused by the movement toward smaller features for microelectronic devices, more power output for engines, and brighter beams for optical devices, cooling for maintaining the desired performance and reliability of such devices is one of the crucial issues in high-tech industries such as microelectronics and transportation. The conventional method to increase cooling rates is to use extended surfaces such as fins and microchannels [12]. Choi et al. [13] performed an analysis of a silicon microchannel heat exchanger and predicted that power densities of approximately  $2000 \text{ W/cm}^2$  could be readily managed with the use of subcooled liquid nitrogen in microchannel heat exchangers (for a review of microscale heat transfer, see [14]). However, the pressure drop in the microchannels increases significantly as the diameter of the flow passage decreases, and eventually a cryogenic system is needed for liquid nitrogen cooling. Therefore, new and innovative concepts are needed for ultrahigh performance cooling.

Modern fabrication technology provides great opportunities to process and produce materials at the nanoscale.

The thermal, mechanical, optical, magnetic, and electrical properties of nanophase materials are superior to those of conventional materials with coarse grain structures. Consequently, nanophase materials have drawn considerable attention from material scientists and engineers alike. Major advances would be obtained if the coolant flowing in the microchannels were to contain these nanoscale particles to enhance heat transfer. Thus, taking a different tack from extended surface approaches and exploiting the unique properties of nanoparticles, Argonne National Laboratory (ANL) has pioneered ultrahigh thermal conductivity fluids, called nanofluids, by suspending nanoparticles in conventional coolants [1].

Thermal conductivities of traditional heat transfer fluids such as lubricants, engine coolants, and water are inherently low. With increasing global competition, industries have a strong need to develop energy-efficient heat transfer fluids with significantly higher thermal conductivities than are now available. Metals in solid form have orders-of-magnitude higher thermal conductivities than those of fluids. For example, the thermal conductivity of carbon multiwalled nanotubes (MWNTs) at room temperature [15] is about 20,000 times greater than that of engine oil, as shown in Figure 1. Therefore, the thermal conductivities of fluids that contain suspended solid metallic particles could be significantly higher than those of conventional heat transfer fluids.

In fact, numerous theoretical and experimental studies of the effective thermal conductivity of dispersions that contain solid particles have been conducted since Maxwell’s theoretical work was published about 100 years ago [16]. However, the studies on thermal conductivity of suspensions have been confined to millimeter- or micrometer-sized particles. The major problem with suspensions containing millimeter- or micrometer-sized particles is the rapid settling of these particles. If the fluid is circulated to prevent much settling, the microparticles would damage the walls of the pipe, wearing them thin. In contrast, nanoparticles remain in suspension almost indefinitely. Because nanoparticles are so small, they may act very much like molecules in solution, dramatically reducing erosion and clogging. Furthermore, microparticles are too large for microsystems, as mentioned before.

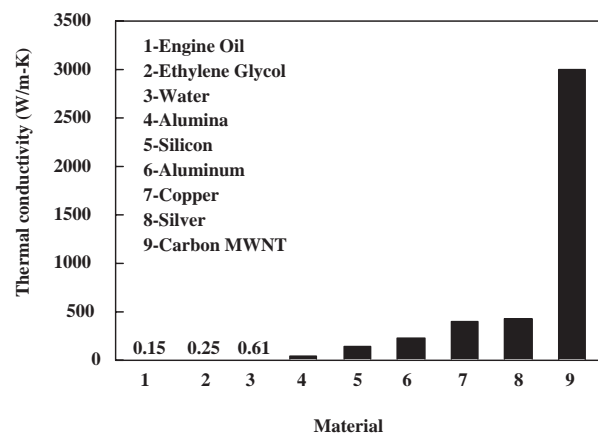


**Figure 1.** Thermal conductivities at 300 K of typical solids, including multiwalled carbon nanotubes and liquids.

A tiny size, along with a large specific surface area, makes nanoparticles attractive for coolant applications. When dispersed into liquids, nanoparticles bring about desirable novel properties such as high stability, high effective thermal conductivities, and less clogging and abrasion. The two novel features of nanofluids are well-suspended particles and thermal conductivities far above those of traditional solid/liquid suspensions. These features make nanofluids strong candidates for the next generation of coolants for improving the design and performance of thermal management systems.

However, as particle size is reduced down to the nanoscale, agglomeration is a new, serious issue, demanding new concepts for making nanofluids. For example, oxide nanoparticles have been dispersed in fluids. However, when dispersants such as alkali or acid were used, some of the original properties of the liquids were diminished or eliminated. Therefore, it is desirable to eliminate the use of chemicals with nanofluids for practical thermal systems. Until recently, the real challenge facing nanoscale thermal engineers was not only to create particles small enough that they would remain suspended for long periods of time but also to disperse them without agglomeration. This challenge was met when copper nanofluids were produced in a single step—an innovative way to make small and nonagglomerating metallic nanoparticles and to directly disperse them into liquids. This accomplishment has demonstrated that stable and highly conductive nanofluids can be produced at one-order-of-magnitude lower concentrations compared with traditional solid/liquid suspensions [17]. Most recently, multiwalled carbon nanotubes have been dispersed in oil and achieved the highest conductivity enhancement ever measured [18]. These developments have helped nanofluids become an emerging and active research area in nanoscale science, engineering, and technology.

Thermal scientists and engineers have been working for decades to develop more efficient heat transfer fluids for a variety of thermal systems. For example, improved engine oils and coolants would make engine cooling systems smaller and lighter, and consequently, lower fuel demands and emissions would do less damage to the environment. The impact of nanofluid technology is expected to be significant, considering that heat transfer performance is vital in numerous multibillion dollar industries. Potential benefits of nanofluids include:

- *Improved heat transfer and stability:* The much larger relative surface areas of nanophase powders, when compared with those of conventional powders, should markedly improve the heat transfer capabilities and stability of the suspensions. Furthermore, microparticles have most of their atoms far beneath their surface and cannot rapidly participate in heat transfer, but nanoparticles finer than 20 nm in diameter have ~20% of their atoms on their surface, allowing them to absorb and transfer heat efficiently.
- *Microchannel cooling:* “Tiny” particles well dispersed into a conventional fluid can significantly improve its ability to transfer heat. Moreover, when “tiny” means no larger than a few nanometers, this opens up the possibility of using nanoparticles in microchannels for many high-heat-load applications. A microchannel heat

exchanger with nanofluids would make a dramatic breakthrough in the development of advanced cooling technology because of a desirable combination of both large heat transfer area and high thermal conductivity [19]. In contrast, conventional meso- and microparticles cannot be used in microchannel flow passages.

- *Minimal clogging:* Micrometer-sized particles cannot be used in practical heat transfer equipment because of severe clogging problems. However, nanoparticles are believed to be ideally suited for applications in which fluids should flow through small passages without clogging, because the nanoparticles are so small that they are expected to behave like molecules of liquid.
- *Miniaturized systems:* Nanofluid technology will support the current industrial trend toward component and system miniaturization by enabling the design of smaller and lighter heat exchanger systems. Miniaturized systems will reduce the inventory of heat transfer fluid.
- *Cost and energy savings:* Successful employment of nanofluids will result in significant energy and cost savings because heat exchange systems can be made smaller and lighter.
- *Dramatically reduced pumping power:* To improve the heat transfer of a conventional fluid by a factor of 2, pumping power must be increased by a factor of about 10. However, if a nanoparticle-based fluid with a thermal conductivity about three times that of a conventional fluid were used in the same heat transfer equipment, the rate of heat transfer would be doubled [1]. Therefore, the potential savings in pumping power is significant with nanofluids.

The next-generation coolants based on nanofluids will likely play an important role in the future cooling applications. We believe that through interdisciplinary research and development, the dreams of designing highly conductive fluids containing very small amounts of nanoparticles, which do not settle in liquids, will come true, and the potential benefits will be realized. Nanofluid technology will thus be an exciting new technology of the 21st century.

### 3. MAKING OF NANOPARTICLES

#### 3.1. Synthesis

Nanoparticles, one of the smallest human-made objects, have unique mechanical, thermal, electronic, magnetic, optical, and chemical (catalytic) properties that are significantly different from those of the same material in bulk. They are the subject of extensive research and development because of their potential applications in many fields, such as nanofluids, electro/magneto/optical devices, catalysts, ceramics, and biological sensors. Various techniques have been developed to synthesize nanoparticles such as mechanical attrition, microemulsion synthesis, inverse micelle techniques, or precipitation techniques (for a review of various synthesis techniques, see [20]); however, most nanoparticles used in nanofluids have been synthesized by physical synthesis techniques, such as the inert-gas-condensation (IGC) process, or chemical synthesis techniques, such as chemical vapor deposition.

Various investigators have produced nanocrystalline  $\text{Al}_2\text{O}_3$  and  $\text{CuO}$  powders using the IGC process [21–26]. Nanoparticles of metals or ceramics in the size range 2–200 nm are generated by the IGC method in which the material is evaporated into a low-density, inert gas [27–30]. Vapors condense and coagulate to form nanoparticles as they diffuse rapidly from the hot source into the surrounding gas, and nanoparticles are transported and deposited by thermophoretic diffusion on a cold finger. After collection, reactant gases such as oxygen can be introduced to produce oxides. Particles are scraped from the cold finger and dispersed into a liquid. However, agglomerated nanoparticles are difficult to disperse in liquids. Because the IGC is a bottom-up approach to nanotechnology, nanoparticle production rates have been very small. The IGC has been a valuable tool for research, but not for production of nanoparticles in large quantities. However, recently the gas condensation technique has been scaled up to produce large quantities of nanoparticles [31]. Nanopowders produced in bulk at low prices can now be used to make nanofluids by the two-step method.

Although the IGC technique works well for oxide nanoparticles, it is not as effective for metal nanoparticles such as copper because agglomeration of individual particles has become a serious problem. Agglomeration of individual particles can be minimized by the direct evaporation–condensation (DEC) method for making and dispersing nanoparticles, as described in Section 4.2. Nanocrystalline  $\text{Cu}$  powders used in various studies [17, 21, 22] were produced by the DEC process.

Also recently,  $\text{SiC}$  nanoparticles were produced by a laser-induced vapor-deposition method using  $\text{SiH}_4$  and  $\text{C}_2\text{H}_4$  as sponsors [32]. The  $\text{SiC}$  nanoparticles were then heated at 650 °C for 30 min, leached with a 5% HF solution, and repeatedly washed with deionized water to eliminate excess carbon on the surface.

One of the best materials produced so far for nanofluids by chemical methods is the MWNTs [18]. Such particles were produced in a chemical vapor deposition reactor, using xylene as the primary carbon source and ferrocene as the iron catalyst [33].

### 3.2. Characterization

Nanoparticle characterization tools, such as transmission electron microscopy (TEM) and scanning electron microscopy (SEM), reveal nanoparticle size and size distribution. TEM was used to characterize nanoparticle sizes and morphologies of agglomerated powders [17, 21–23, 26, 32, 34]. Most nanoparticles used in nanofluids are spherical and their typical size is <40 nm in diameter. One important finding from the TEM studies is that oxide nanoparticles agglomerate to form much larger particles than primary particles.

Choi et al. [18] used high-resolution scanning electron microscopy to show that metallic MWNTs have a mean diameter of ~25 nm and length of ~50  $\mu\text{m}$  (an average aspect ratio ~2000) and contained an average of 30 annular layers. The nanotubes were typically straight in their as-grown form.

Xie et al. [25] used an automated X-ray diffractometer to determine the crystalline phases of alumina nanoparticles and a nitrogen adsorption apparatus to measure the specific surface area of the nanoparticles by the Brunauer–Emmett–Teller method.

Most investigators have used TEM to characterize nanoparticle sizes and morphologies of agglomerated powders. However, dynamic light scattering can be used for the particle size and size distribution measurement of colloidal particles between 3 nm and 5  $\mu\text{m}$  [35, 36]. When fine particles are illuminated by monochromatic light, a fluctuating scattering intensity occurs due to Brownian motion of the particles. The fluctuation is correlated to the diffusion coefficient of the particles. The particle size can be determined because it is inversely proportional to the diffusion coefficient.

## 4. MAKING OF NANOFLUIDS

Techniques for suspending nanoparticles in liquids are crucial to making stable nanofluids. The nanoparticles used in nanofluids come in a wide size range. However, most of them are between 10 and 40 nm. Nanoparticles do away with the old limitation of rapid settling of microparticles. But they pose a new challenge: if nanoparticles become too small, they can easily agglomerate before dispersion, and agglomerates of nanoparticles can settle rapidly just as microparticles do. Therefore, to create a stable nanofluid, the particles should be small enough to be suspended by Brownian motion, or the particles must be protected against aggregation by electric charges, protective coatings, or other means. Because aggregation of particles occurs more easily at high particle concentrations (>20% by volume), low concentration is highly desirable for nanofluids.

Two techniques are used to make nanofluids. First is the traditional two-step method (described in Section 4.1), which first makes nanoparticles as described in the previous section and then disperses them into the base fluid. Second is the new single-step DEC method (described in Section 4.2), which simultaneously makes and disperses the nanoparticles directly into the base fluid. Most researchers have produced oxide nanofluids by the two-step technique. Although the two-step technique works well for oxide nanoparticles, it is not as effective for metal nanoparticles. For nanofluids containing high-conductivity metals, the single-step DEC technique is preferable.

### 4.1. Dispersion of Nanoparticles in Liquids

Before we discuss the various techniques, let us first take a simple colloidal approach and evaluate what are the important factors in making a stable dispersion. Consider a “bare” spherical particle with density  $\rho_p$  and radius  $r_p$ , which is to be dispersed into a fluid with density  $\rho_f$  and viscosity  $\eta_f$ . From Stokes–Einstein theory [37], we can calculate the rate of particle sedimentation or creaming,  $v$ , as

$$v = 2r_p^2|\rho_p - \rho_f|g/9\eta_f \quad (1)$$

This equation indicates that the key to stable particle dispersion is a small  $r_p$ , a small density difference, and a high

fluid viscosity. The latter two are difficult to control or achieve, especially the third item, since higher viscosity is to be avoided in most heat transfer fluids. Careful selection of the nanoparticle and fluid materials may help in minimizing the density difference. A successful dispersion technique should be able to keep the primary particles from agglomerating or aggregating, or to break down large particles into smaller ones. In addition to particle size, density difference, and fluid viscosity, many other factors affect the stability of the dispersions, such as mechanical or sonic energy input, particle surface charge, the presence of surface modifiers (surfactants), and the chemical and rheological properties of the base liquid. A combination of these approaches will be sufficient to suspend nanoparticles in liquids.

The techniques used by researchers to disperse nanoparticles, or any small particles, into liquids can be categorized into two general types: physical and chemical [37, 38].

#### 4.1.1. Physical Methods

In physical processing, two kinds of stabilization methods can be considered: mechanical and ultrasonic dispersion. One means of mechanical dispersion is applying shear force to pull agglomerates apart—high shear mixing. Usually narrow passages and/or relatively high rates of flow are required to generate high shear. For that purpose, a rotor-and-stator construction is used. This includes a high-speed mixer, homogenizer, microfluidizer, Kady mill, and colloid mill. Another means of mechanical dispersion is high-impact mixing, which applies much higher energy to break the tightly bound aggregates apart or to shatter coherent solids into smaller pieces. Usually a grinding material of small particle size is used to exert an impact on the material or particles to be dispersed. Examples include attritor and ball-and-pebble mill.

Ultrasonication is also widely used in making nanofluids. Ultrasonics is a form of mechanical vibratory energy which propagates through a liquid medium as elastic waves. The ultrasonic interactions within a suspension could be mechanical, thermal, or chemical. The activator converts the regular-line frequency to a much higher level (e.g., 20,000 Hz), which is eventually converted into mechanical vibrations in the tips of various shapes (horns). A conventional bath-type sonicator provides less energy density than the tip-type one. The tip of the horn is immersed in a liquid in which the ultrasonic vibrations cause cavitation, which stirs the dispersion or breaks the agglomerates.

#### 4.1.2. Chemical Methods

Chemical methods are always applied as processing aids to the aforementioned physical methods. Long-range, attractive forces resulting from van der Waals interactions between like particles are always attractive and ubiquitous. To overcome van der Waals attraction between particles, an energy barrier is imposed around the primary particles so they cannot aggregate or agglomerate together easily [37]. Thus, if the repulsive barrier is much greater than  $k_b T$ , where  $k_b$  is Boltzmann's constant and  $T$  is temperature, particles repel one another on close approach and are well dispersed.

There are two kinds of stabilization methods: electrostatic and steric dispersion. In electrostatic dispersion, like electrostatic charges of sufficient magnitude are spread on the

surfaces of suspended particles to repel one another and remain in stable suspension, rather than form aggregates. Electrostatic stabilization is based on the famous Deryaguin-Landau-Verwey-Overbeek (DLVO) theory, which predicts the stability of particles suspended in polar liquids where electrolytes or other ionic species (such as detergents) are used [39–41]. However, since the concentration range for stabilization is critical, excessive or insufficient electrolyte may even induce agglomeration, especially where bivalent or trivalent metal ions are involved. Adjusting the pH of an aqueous system can also create electrostatic repulsion. The addition of dispersants such as acid or alkali into a liquid promotes the formation of finely dispersed nanoparticles. However, chemical dispersants have their limits. For example, particles usually settle in a week because of reduced zeta potential. (Zeta potential is defined as the measurement of electrokinetic forces that cause suspended particles to repel each other as a function of increased surface charge density.) For practical thermal systems, it is desirable to eliminate the use of chemicals for electrostatic dispersion. With alkali or acid, some of the original properties of liquids are diminished or eliminated.

Steric stabilization prevents the nanoparticles from getting close enough to coalesce and precipitate by means of dispersants such as surfactants (an acronym for surface active agents), polymers, or polymeric surfactants. All these molecules consist of an anchor moiety and a stabilizing moiety. The anchor moiety “attacks” the particle and adsorbs on the particle surface; the long tail of the molecule creates a steric repulsion for the approaching particles. Commonly used polymeric surfactants for nonaqueous systems may have anchor moieties such as polyarylonitrile, polyoxyethylene, polyethylene, polypropylene, poly(vinyl chloride), poly(methyl methacrylate), and polyacrylamide, and stabilizing moieties such as polystyrene, poly(lauryl methacrylate), poly(12-hydroxystearic acid), polydimethylsiloxane, polyisobutylene, *cis*-1:4-polyisoprene, poly(vinyl acetate), and poly(vinyl methyl ether). Commonly used polymeric surfactants for aqueous systems may have anchor moieties such as polystyrene, poly(vinyl acetate), poly(methyl methacrylate), polydimethylsiloxane, poly(vinyl chloride), and polyethylene, and stabilizing moieties such as polyoxyethylene, poly(vinyl alcohol), poly(acrylic acid), poly(methacrylic acid), polyacrylamide, poly(vinyl pyrrolidone), poly(ethylene imine), and poly(4-vinylpyridine).

Chemical modification on the particle surface is another widely used technology for improved dispersion [42]. This can be done by adding functional groups (hydroxyl, carboxyl, mercapto, etc.) onto the surface of the particles for better anchoring of the surfactants or grafting of a chain (for example, an octadecyl group) onto the particle surface to make a permanent bond. In the latter case, external surfactants may not be necessary due to the presence of the grafted group(s).

Very recently, Tohver et al. reported a new colloid stabilization mechanism, named “nanoparticle halos” [43], which uses highly charged nanoparticles to stabilize negligibly charged colloidal particles. Although this method is intended for stabilizing colloidal particles, further research may lead to its application with nanofluids.

Nearly all the nanofluids reported in the open literature are produced by the two-step method, except copper

nanofluids, which are produced by the one-step DEC process with and without the aid of thioglycolic acid [17]. Excellent suspension properties are also observed, with no significant settling of  $\text{Al}_2\text{O}_3$  and  $\text{CuO}$  nanoparticles occurring in stationary nanofluids over time periods longer than several days.

Various investigators have dispersed commercially available copper and aluminum oxide nanoparticles into base fluids (such as water, ethylene glycol, engine oil, or pump oil) in a mixing container, with or without use of ultrasonic vibration [21–26, 32]. Wang et al. [24] used a number of dispersion techniques, including an ultrasonic bath, to disperse  $\text{Al}_2\text{O}_3$  and  $\text{CuO}$  nanopowders into water, vacuum pump fluid, engine oil, and ethylene glycol and showed that the thermal conductivity of nanofluids depends on the dispersion technique, which might change the morphology of the nanoparticles. They also found that the nanofluids were stable when the volume fraction was  $<5\%$ , but became flocculated when the volume fraction was  $>10\%$ .

Xuan and Li used the two-step process to disperse 100-nm Cu nanoparticles in water or transformer oil [34]. The suspensions were vibrated for 10 hr in an ultrasonic vibrator. Still, they had to use a large amount of dispersants to make stable suspensions. Water-based Cu nanofluids were stable with laurate salt at 9 wt%, and transformer oil-based Cu nanofluids needed oleic acid up to 22 wt% to stabilize the nanoparticles in the mineral oil. Xie et al. [32] prepared nanofluids of SiC of different sizes and shapes in water or ethylene glycol through ultrasonication and magnetic stirring. Lockwood et al. [44] studied soot particles in used diesel engine oils as a model system and compared them with nanofluids made by dispersing carbon black particles into engine oils.

Recently, nanotube-in-oil suspensions were produced by the two-step method [18]: first, MWNTs were generated in a chemical vapor deposition reactor; then the MWNTs were dispersed into a synthetic poly( $\alpha$ -olefin) oil. The metallic MWNTs, which were typically straight in their as-grown form (Fig. 2), had a mean diameter of  $\sim 25$  nm and a length

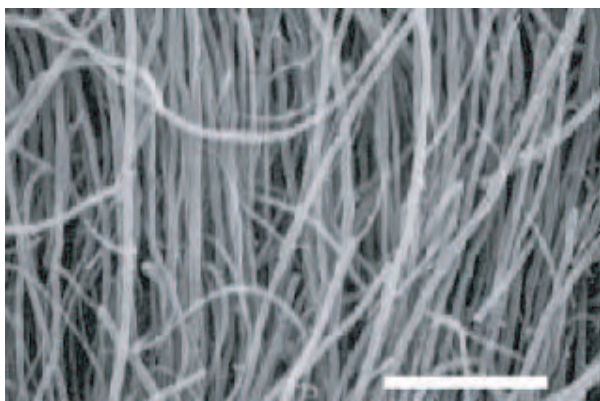


**Figure 2.** Scanning electron photomicrograph of multiwall nanotubes used in MWNT-in-oil nanofluids. A conventional gold sputtering technique was employed to coat sample. Photo taken by a high-resolution HITACHI S-2700 scanning electron microscope. Scale bar is 800 nm. Reprinted with permission from [18], S. U. S. Choi et al., *Appl. Phys. Lett.* 79, 2252 (2001). © 2001, American Institute of Physics.

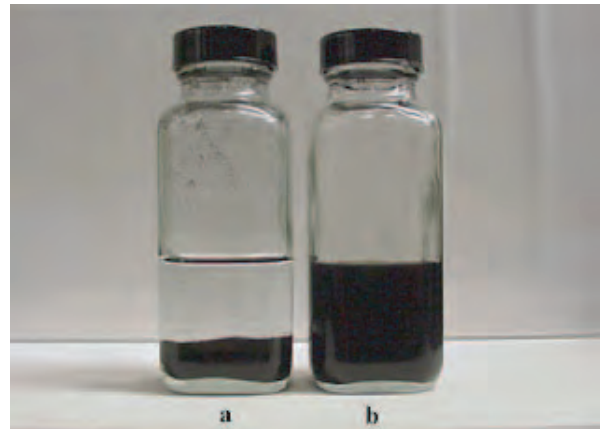


**Figure 3.** Nanotube nanofluids with and without dispersant produced by a two-step method. Because the synthetic polyalphaolefin oil does not wet the nanotubes, two distinctly different products were produced: (a) nanotubes quickly settle without use of a proper dispersant, and (b) nanotubes are well dispersed and suspended in the oil with succinimide dispersant (5 wt%), and the very stable nanotube nanofluid produced by this method is thus suitable for thermal conductivity measurements and future heat transfer applications.

of  $\sim 50$   $\mu\text{m}$  (for an average aspect ratio of  $\sim 2000$ ) and contained an average of 30 annular layers.

Because synthetic oil does not wet the nanotubes well enough (as demonstrated by the clear separation in Fig. 3a), a small amount of dispersant (5 wt%) was added to the oil to wet the nanotubes completely. This resulted in well-dispersed and stable nanotube nanofluids, as seen in Figure 3b. Loadings of up to 1 vol% were produced for thermal conductivity measurements.

#### 4.2. Direct Evaporation–Condensation Method

Conventional dispersion methods, such as electrostatic and steric stabilization of particles, use a dispersing chemical (acid, base, or surfactant) to prevent particle agglomeration and settling. Surfactants used in the steric stabilization of particles will change the physical and chemical properties of nanofluids, but not by much. In contrast, even a small amount of an acid (e.g., HCl) or base (e.g., NaOH) used to control pH in the electrostatic repulsion method may cause serious problems. Although the stability of nanoparticles can be controlled electrostatically for a certain time, typically one week, the particles eventually settle due to the large density difference. Electrostatic repulsion by itself is not enough for stabilizing the nanofluids. Furthermore, stabilizing nanoparticles by adding acids or bases may not be a practical means to produce nanofluids for commercial use. The suspensions with such chemicals are difficult to use in practical thermal systems due to high or low pH values. These pH values can cause corrosion and salt deposition on a heat transfer surface and other problems. Another problem with using acid or base is that they can change other liquid properties. A serious problem with oxide nanoparticles is the high concentrations (approximately 10 times those of metallic nanoparticles) needed to achieve high thermal conductivity enhancement.



Agglomeration of individual particles can be minimized by condensing the vapors from a heated source directly into a flowing low-vapor-pressure fluid. This approach is called “vacuum evaporation onto a running oil substrate” [45], a modification of which was developed recently [46]. The DEC system built at ANL was based on this modified process [17, 21, 22]. For nanofluids containing high conductivity metals, the single-step DEC technique is preferable to gas-condensation processing. Indeed, excellent results were attained when the nanoparticles from pure copper were generated and directly dispersed into a liquid in a single step. As shown in Figure 4, this method resulted in very small (an average diameter of less than 10 nm) particles with little agglomeration. In this one-step process, the materials scientists heated copper to a vapor inside a vacuum chamber. A cooled heat transfer fluid was placed in the chamber, and the copper vapor condensed when it touched the cooled fluid, forming <10 nm nanoparticles in the fluid.

Although nanoparticles produced by the single-step DEC method stay suspended in a liquid significantly longer than those produced by the two-step process, the DEC method is limited to low-vapor-pressure fluids. This is the case even though the liquid is cooled to prevent an undesirable increase in vapor pressure during the evaporation–condensation process due to radiant heating from the resistively heated evaporation source in a crucible. Another problem with metal nanoparticles is their oxidation, which reduces the thermal conductivity of metal nanofluids. Despite these shortcomings, this new approach, unlike previous work dispersing nanoparticles in liquids, uses size control alone to create long-term stable nanofluids and, thus, does not require surfactants or electrostatic control. An ANL nanofluid team was the first to employ size control alone to create nanofluids that are both stable and highly conductive at extremely low particle loadings (<1 vol%). Therefore, the DEC process is promising for producing nanofluids with nonagglomerating nanoparticles that possess the sought-for properties (i.e., stability, with or without acids or bases, and high thermal conductivity at small particle concentrations, while other properties remain unchanged).

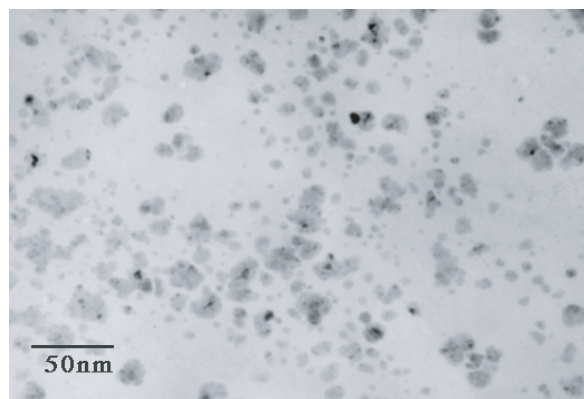


**Figure 4.** Bright-field transmission electron micrograph of Cu nanoparticles produced by direct evaporation into ethylene glycol. Very little agglomeration occurs with this processing method. Reprinted with permission from [17], J. A. Eastman et al., *Appl. Phys. Lett.* 78, 718 (2001). © 2001, American Institute of Physics.

Eastman et al. added a small amount of thioglycolic acid (<1 vol%) to the nanofluids produced by the DEC method, primarily to improve their thermal conductivity [17]. This result shows that establishing good thermal interactions between solid nanoparticles and liquid molecules at the nanometer scale is critical in developing nanofluids. Note that thioglycolic acid ( $\text{HSCH}_2\text{COOH}$ ) is relatively weak compared to HCl or NaOH.

### 4.3. Electrohydrodynamic Spraying System

An electrohydrodynamic spraying system, or electrospray, can generate airborne nanoparticles in the size range of 2–100 nm with a production rate of up to 10 billion particles/s [47, 48]. This system could be used to develop a new method for making nanofluids containing highly charged particles that would not aggregate. These charged nanoparticles can be directly introduced into base fluids. The droplet size and the particle generation rate are functions of the liquid feed rate and the electrical conductivity of the spray solution/suspension. Colloidal suspensions of metal, oxide, and polymer nanoparticles have also been sprayed to form dispersed nanoparticles without aggregation [48]. A dual capillary approach has also been used to provide a sheath liquid of varying conductivity [49]. The sheath liquid can be made with desirable coating materials for producing coated nanoparticles. Recently, a multiple-nozzle approach has been developed to increase the throughput for producing nanoparticles by over 1000 times [50].

## 5. MEASUREMENTS IN NANOFLUIDS

### 5.1. Methods of Measuring Thermal Conductivity

The thermal conductivity of nanofluids has been measured by transient hot-wire (THW), temperature oscillation (TO), and steady-state (SS) methods. The first is the most widely used measurement technique for the thermal conductivity of nanofluids [17, 18, 21–23, 25, 32, 34, 44]. An advantage of THW over SS techniques is the elimination of problems associated with convection since the THW measurement lasts for a period on the order of seconds. The other two methods have been used to measure the thermal conductivity of oxide nanofluids [24, 26].

The THW method is quite accurate in determining thermal conductivities [51, 52]. Briefly, the THW system employs a thin metal line suspended symmetrically in a liquid in a vertical cylindrical container. The wire is used as both heater and thermometer. Platinum is used for the hot wire because its resistance/temperature relationship is well known over a wide temperature range [53]. When used in electrically conducting fluids, the Pt wire is coated with an electrically insulating and thermally conducting epoxy adhesive [52]. Instead of a two-wire compensation system [54], a long hot wire (wire length-to-diameter ratio of  $\sim 3000$ ) can be used as a hot-wire sensor to minimize end conduction loss. The THW method determines the thermal conductivity of nanofluids by measuring the temperature rise of a straight Pt wire in the nanofluid sample in response to a direct current. Because



the thermal conductivity of the liquid is inversely proportional to the slope of the temperature/time response of the wire, conductivity can be calculated by measuring the slope of the straight line [23]. The THW cell requires a very small volume (<60 ml) of nanofluids and is ideal for thermal conductivity measurements of scarce nanofluids samples. Lee et al. [23] performed calibration experiments for ethylene glycol in the temperature range of 290–310 K and at atmospheric pressure and reproduced literature values [55] with an error of <1.5%.

The thermal conductivity of fluids has been measured by the SS method since 1931 [56]. The one-dimensional, parallel-plate SS method was used by Wang et al. [24] to measure the thermal conductivity of oxide nanofluids. A test nanofluid is placed in the liquid cell sandwiched between an upper heater plate and a lower plate, both made of copper. For better control of the temperature surrounding the liquid cell, the liquid cell is housed in a larger cell made of aluminum. The upper heater plate is centered and separated from the inside wall of the aluminum cell by three small glass spacers. Small holes are drilled into the copper plates and the outer aluminum cell. Precalibrated E-type thermocouples are inserted into these holes to measure the temperatures. The thermocouples in the top and lower copper plates are located very close to the lower surface of the upper plate and to the upper surface of the lower plate. Because the thermal conductivity of copper is much higher than that of the liquid, these thermocouples measure temperatures at the surfaces of the plates.

The SS thermal conductivity apparatus has a simple construction, and the thermal conductivity can be determined in a straightforward manner from the one-dimensional heat conduction equation relating the power input to the heater, the temperature difference between the two copper plates, and the geometry of the liquid cell. However, this method is time consuming and requires many corrections for accurate measurements. Yet the experimental error estimated for water and ethylene glycol by comparing the measured thermal conductivity with the published data [57] is  $\pm 3\%$  in the temperature range of 20 to 40 °C [24].

Using the TO method, Das et al. have measured the thermal properties of  $\text{Al}_2\text{O}_3$  and CuO nanofluids as a function of temperature [26]. This purely thermal method measures temperature oscillations at the fluid sample, as outlined in a paper by Czarnetzki and Roetzel [58]. When used with nanofluids, this method has been found to be accurate and to prevent natural convection. More important, room-temperature thermal conductivity data for  $\text{Al}_2\text{O}_3$  and CuO nanofluids agree with the data of Lee et al. [23], even though their THW method differs from the TO technique of Das et al.

## 5.2. Measured Thermal Conductivities

The effective thermal conductivities of nanofluids containing different volume concentrations, materials, and sizes of solid nanoparticles dispersed in various base fluids have been experimentally investigated. The experimental results show that the effective thermal conductivities of all these nanofluids are much improved compared with those of base fluids. Among the tested nanofluids, copper-in-ethylene glycol and

nanotube-in-oil types have the highest thermal conductivity enhancement at the same concentration.

### 5.2.1. Oxide Ceramic Nanofluids

The thermal conductivities of oxide ceramic nanofluids with low particle concentrations (1–5 vol%) were studied experimentally. Lee et al. measured the thermal conductivities of water and ethylene-glycol-based nanofluids containing copper oxide and aluminum oxide nanoparticles and found that these nanofluids have substantially higher thermal conductivities than the same liquids without nanoparticles [23]. The maximum improvement in the thermal conductivity of ethylene glycol (20%) was seen when 4 vol% CuO nanoparticles with average diameter 35 nm were dispersed in this fluid.

Wang et al. [24] measured the effective thermal conductivity of nanofluids with 28 nm  $\text{Al}_2\text{O}_3$  and 23 nm CuO nanoparticles dispersed in distilled water, vacuum pump fluid (TKO-W/7, Kurt J. Lesker Company, Clairton, PA), ethylene glycol, and engine oil (Pennzoil 10W-30). The experimental results show that the effective thermal conductivity of nanofluids increases with decreasing particle size and depends on the dispersion technique.

Most recently, Xie et al. [25] measured the thermal conductivity of nanofluids containing alumina nanoparticles of 12.2–302 nm diameter and found that it depends on the size of the nanoparticle, the pH of the aqueous suspension, and the thermal conductivity of the base fluids.

Using the temperature oscillation technique, Das et al. [26] explored the temperature dependence of the thermal conductivity of water-based nanofluids containing  $\text{Al}_2\text{O}_3$  or CuO nanoparticles. This measurement confirmed the high level of thermal conductivity enhancement at room temperature reported by others [23]. More important was the discovery of a two- to fourfold increase in thermal conductivity enhancement for nanofluids over a small temperature range, 21 to 51 °C. Furthermore, nanofluids containing smaller CuO nanoparticles show more enhancement with temperature. Das et al. suggested that the strong temperature dependence of thermal conductivity is due to the motion of nanoparticles. This discovery, implying that that nanofluids could be smart fluids “sensing” their thermal environment, makes them even more attractive as coolants for devices with high energy density.

### 5.2.2. Nonoxide Ceramic Nanofluids

Xie et al. [32] measured the thermal conductivities of water and ethylene-glycol-based nanofluids containing 26 and 600-nm SiC nanoparticles. The measured data for small-size (26-nm) SiC particle suspensions were  $\sim 20\%$  greater than the value calculated with the Hamilton and Crosser model [59]. However, the model does predict the thermal conductivity of large-size (600-nm) SiC particle suspensions.

### 5.2.3. Metallic Nanofluids

Very stable and highly conductive copper nanofluids were produced by the single-step method [17]. Loadings of up to approximately 0.5 vol% of copper nanoparticles with an average diameter of less than 10 nm were dispersed into ethylene glycol with little agglomeration. For some nanofluids, a small amount of thioglycolic acid (<1 vol%) was added

to further improve the particle dispersion. The thermal conductivity of copper nanofluids was measured at room temperature [17, 22]. Figure 5 shows the measured thermal conductivity of Cu-containing ethylene glycol nanofluids as a function of nanoparticle volume fraction. The effective thermal conductivity of the nanofluid is plotted relative to that of its base fluid ( $k_e$  is the effective thermal conductivity of nanofluids, and  $k_f$  is the thermal conductivity of the base fluid). Figure 5 also shows the thermal conductivity enhancement of ethylene glycol +  $\text{Al}_2\text{O}_3$  and ethylene glycol + CuO [23]. These measurements showed for the first time that metallic nanoparticles increase the effective thermal conductivity by a significant amount over the same volume fraction of oxide nanoparticles. Also, nanofluids containing thioglycolic acid as a stabilizing agent showed dramatically improved behavior compared to nonacid-containing nanofluids. Approximately 0.3 vol% Cu nanoparticles of <10 nm diameter and <1 vol% thioglycolic acid in ethylene glycol improved the effective thermal conductivity by 40%. Interestingly, fresh copper nanofluids exhibited slightly higher conductivities than fluids that were stored up to two months prior to measurement.

Xuan and Li [34] dispersed 100-nm Cu nanoparticles into water and transformer oil by the two-step method with dispersants. Their thermal conductivity data are much lower than those of the nanofluids containing 10-nm Cu nanoparticles dispersed into ethylene glycol by the single-step method [17], possibly due to the different (two vs single step) dispersion techniques.

#### 5.2.4. MWNT Nanofluids

Recently, MWNT-in-oil suspensions with loadings of up to 1 vol% nanotubes were produced by the two-step method, and their thermal conductivity was measured at room temperature [18]. Figure 6 shows the measured thermal conductivity of MWNT-in-oil nanofluids as a function of nanotube volume fraction. Clearly, nanotubes yield an extremely large increase in thermal conductivity (up to a 150% increase in conductivity of oil at approximately 1 vol% nanotubes),

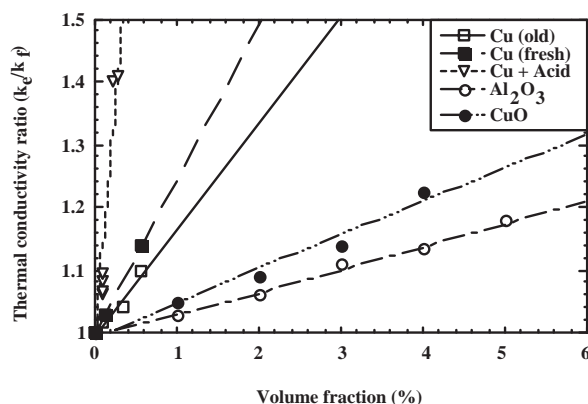


**Figure 5.** Thermal conductivity enhancement of copper, copper oxide, and alumina particles in ethylene glycol. Significantly greater enhancements are seen for nanofluids consisting of <10-nm diameter Cu nanoparticles than for either CuO or  $\text{Al}_2\text{O}_3$  nanoparticles of average diameter 35 nm. Reprinted with permission from [17], J. A. Eastman et al., *Appl. Phys. Lett.* 78, 718 (2001). © 2001, American Institute of Physics.

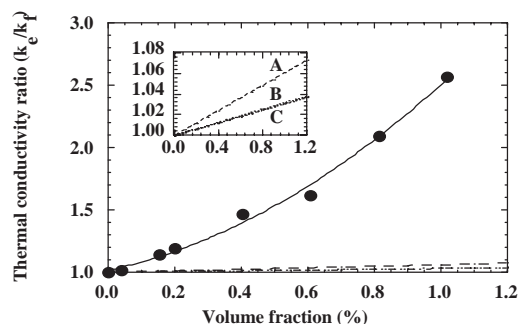


**Figure 6.** Thermal conductivity enhancement of MWNT-in-oil nanofluids. Dispersion of a very small amount of nanotubes produces a remarkable change in effective thermal conductivity of the base fluid, with the thermal conductivity ratio exceeding 2.5 at 1 vol% nanotubes. Comparison of measured data for nanotube suspensions (solid circles) and those predicted by theories (dotted lines) shows that the measured values are one order of magnitude greater than predictions at 1 vol% nanotubes. Because all calculated values are almost identical at the low volume fractions, some of the calculated values are reproduced on an expanded scale in the inset, where line A = Hamilton and Crosser [59]; line B = Bonnecaze and Brady [61, 62]; line C = Maxwell [16]. Reprinted with permission from [18], S. U. S. Choi et al., *Appl. Phys. Lett.* 79, 2252 (2001). © 2001, American Institute of Physics.

which is by far the highest thermal conductivity enhancement ever achieved in a liquid. Similar results have been reported for polymer/nanotube composites [60]. In Figure 6, we see another anomaly. The measured thermal conductivity is nonlinear with nanotube loadings, while all theoretical predictions clearly show a linear relationship [16, 59, 61, 62]. This nonlinear behavior is not expected in conventional fluid suspensions of micrometer-sized particles at such low concentrations. Our experiments imply the existence of nanotube/nanotube interactions, even at extremely low nanotube volume fractions (<1 vol%), possibly because of the astronomical number of nanotubes in the liquid and the extremely high aspect ratio ( $\sim 2000$ ) of the carbon nanotubes.

Several investigators have reported augmentation of the effective thermal conductivities of suspensions with millimeter-sized polystyrene particles under laminar flow [63, 64]. We expect that the effective thermal conductivities of nanofluids under flow conditions might be higher than the experimental results for stationary nanofluids.

#### 5.2.5. Summary

Copper nanoparticles and carbon nanotubes dramatically enhance the thermal conductivity of base fluids. Adding  $\sim 0.3$  vol% of 10-nm copper nanoparticles to ethylene glycol increases its thermal conductivity up to 40%. Nanotubes yield by far the highest thermal conductivity enhancement ever achieved in a liquid: a 150% increase in the conductivity of oil at  $\sim 1$  vol% of 25-nm nanotubes. Oxide nanofluids have the lowest thermal conductivity. Because ceramic oxides are abrasive, they are the least desirable materials for heat transfer applications.

In comparison with oxide nanofluids, the solid concentrations in copper or nanotube nanofluids are one order of magnitude lower for a comparable thermal conductivity enhancement. It should be possible to make the copper or

nanotube nanofluids less viscous than oxide nanofluids of comparable performance. Note that the only nanofluids that can compete in terms of thermal conductivity enhancement with nanotubes are those containing copper and acid produced by Eastman et al. [17]. However, since the degradation of Cu reduces the thermal-conductivity enhancement, nanotubes are, up to now, the best material for use in nanofluids.

Table 1 summarizes the typical nanofluids covered in this chapter, including the materials for nanoparticles and base fluids, dispersion methods, maximum thermal conductivity ratio, and references.

### 5.3. Viscosity

Wang et al. measured the viscosity of water-based nanofluids containing  $\text{Al}_2\text{O}_3$  nanoparticles dispersed by different techniques, that is, mechanical blending (Method I), coating of particles with polymers (Method II), and filtration (Method III) [24]. The solutions dispersed by Methods II and III had lower viscosities, indicating that the particles are better dispersed. The  $\text{Al}_2\text{O}_3$ /water nanofluids achieved a viscosity increase of  $\sim 30\%$  at 3 vol%  $\text{Al}_2\text{O}_3$ , compared to that of water alone. In contrast, the viscosity of  $\text{Al}_2\text{O}_3$ /water used by Pak and Cho [65] was three times higher than that of water. This large discrepancy could occur because Pak and Cho used acid or base in their test fluids and an electrostatic repulsion technique. Compared with the  $\text{Al}_2\text{O}_3$ /water system, the  $\text{Al}_2\text{O}_3$ /ethylene glycol system had a similar viscosity increase, but a higher thermal conductivity increase.

### 5.4. Convection Heat Transfer

Because nanofluids are rather new, relatively few theoretical and experimental studies have been done on their convective

heat transfer coefficients under flow conditions [1, 22, 34, 65, 66].

Assuming that only the thermal conductivity of the nanofluid system varies, and other properties (such as the specific heat, density, and dynamic viscosity) are the same as for the base fluid, Choi [1] estimated the enhancement of heat transfer due to increased thermal conductivity. His theoretical study of the heat transfer enhancement of nanofluids with copper nanoparticles showed that they will dramatically reduce the required heat-exchanger pumping power. For example, to improve the heat transfer of a conventional fluid by a factor of 2, the pumping power should be increased by a factor of about 10. However, if a nanoparticle-based fluid with a thermal conductivity of about three times that of a conventional fluid were used in the same heat transfer equipment, the rate of heat transfer would be doubled.

Xuan and Li [34] and Xuan and Roetzel [66] have proposed two causes of enhanced heat transfer by nanofluids: the enhanced thermal dispersion due to the chaotic movement of nanoparticles and the enhanced thermal conductivity of nanofluids considered by Choi [1].

Pak and Cho [65] dispersed  $\text{Al}_2\text{O}_3$  and  $\text{TiO}_2$  nanoparticles in water and measured the turbulent friction and heat transfer behavior of the dispersed fluids in round-tube flow. They showed that the Nusselt number increased with increasing volume fraction and the Reynolds number. However, the convective heat transfer coefficient of the dispersed fluid at a volume concentration of 3% was 12% smaller than that of pure water when tested under the condition of constant average velocity. This finding may be due to the large difference in the viscosity of the dispersed fluids used by Pak and Cho [65] and by Wang et al. [24], as discussed in Section 5.3.

**Table 1.** Dispersion methods and maximum thermal conductivity ratio for wide range of nanofluids covered in this chapter.

Nanomaterials	Base fluids	Dispersion methods	Maximum $k_e/k_f$ (at loading of vol%)	Ref.
Cu	ethylene glycol	one-step method, thioglycolic acid	1.4 (0.3)	[17]
Multiwalled carbon nanotubes	synthetic base oil, PAO	two-step method, polymer	2.57 (1)	[18]
$\text{Al}_2\text{O}_3$	water	two-step method	1.09 (4)	[23]
CuO	ethylene glycol	two-step method	1.19 (5)	
	water	two-step method	1.12 (3.4)	[23]
	ethylene glycol		1.22 (4)	
$\text{Al}_2\text{O}_3$	ethylene glycol	two-step method with mechanical/ultrasonic mixing	1.4 (8)	[24]
$\text{Al}_2\text{O}_3$	water	two-step method with filtration	1.12 (3)	[24]
CuO	ethylene glycol	two-step method with mechanical/ultrasonic mixing	1.54 (14.7)	[24]
$\text{Al}_2\text{O}_3$	ethylene glycol	two-step method	1.29 (5)	[25]
$\text{Al}_2\text{O}_3$	water	two-step method	1.24 (4)	[26]
CuO	water	two-step method	1.36 (4)	[26]
SiC	DI $\text{H}_2\text{O}$	two-step method	1.23 (4)	[32]
Copper	transformer oil	two-step method oleic acid	1.43 (7.5)	[34]
Copper	water	two-step method laurate salt	1.76 (7.5)	[34]
Soot particles	diesel engine oil	motor oil dispersant	1.14 (1.7)	[44]

Note: Effective thermal conductivity of nanofluids  $k_e$  and thermal conductivity of base fluid  $k_f$ .

Heat transfer tests have been conducted to assess the thermal performance of CuO/water suspensions under flow conditions [22]. At fixed flow rates, the heat transfer coefficient of water containing less than 1 vol% of CuO nanoparticles was improved by >15% compared to that of water without nanoparticles.

Although the convective heat transfer coefficient of oxide nanoparticles/water suspensions has been determined, the heat transfer of the most promising metallic and nanotube nanofluids has not been reported yet.

## 6. MODELS AND MECHANISMS

### 6.1. Effective Thermal Conductivity Models

The problem of predicting the effective properties of two-phase materials has a long history dating back to J. C. Maxwell [16]. Since then, various theories and a large number of models have been developed to predict the thermal conductivity of solid/liquid suspensions [59, 61, 62, 67–70]. While the Maxwell equation only takes the particle volume concentration and the thermal conductivities of particle and liquid into account, other classical models extended the Maxwell model to include the effects of particle shape [59], particle–particle interactions [61, 62, 67–69], and particle distribution [70]. In their numerical simulation, Bonnecaze and Brady considered near- and far-field interactions among two or more particles [61, 62]. For random dispersions of spheres, their simulation results agreed with Jeffrey's equation [67] up to a volume fraction of 20%, while Maxwell's equation [16] gave results within 3% of their calculation for  $\alpha = 10$ , where  $\alpha$  is the ratio of the thermal conductivity of the particle to that of the liquid.

All these mathematical and numerical models predict almost identical enhancements at the low concentrations (<5 vol%) in nanofluids. Therefore, the Maxwell model can be used as representative of all classical models. The calculated results in Figure 7 show that  $k_e/k_f$  depends on the volume fraction of particles and the  $k_p/k_f$  ratio (where  $k_e$  is the effective thermal conductivity of suspensions,  $k_f$  is the

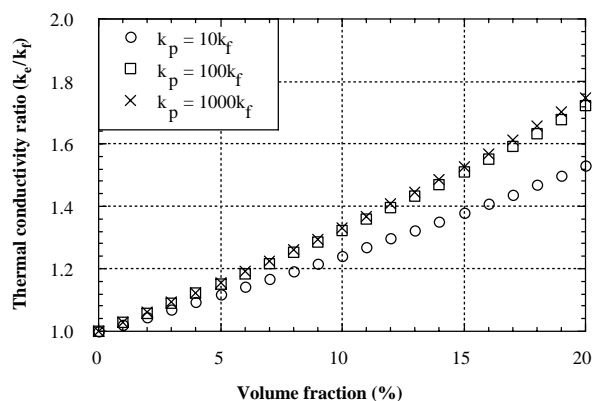


**Figure 7.** Predicted thermal conductivity enhancements for nanofluids with different ratios of particle-to-liquid thermal conductivity. Maxwell's model predicts that the effective thermal conductivity of suspensions increases with the volume fraction of the solid particles and the ratio of particle-to-liquid thermal conductivity.

thermal conductivity of the base fluid, and  $k_p$  is the thermal conductivity of particles). In most nanofluids, the  $k_p/k_f$  ratio exceeds 10. Therefore, the predicted conductivity enhancement from classical models is <5% at 1 vol%, <20% at 5 vol%, and <80% at 20 vol%, as shown in Figure 7. However, the measured thermal conductivity enhancement for the nanofluids is much higher than predicted by existing models.

To compare the measured thermal conductivity data with model predictions, the weight fraction of nanoparticles  $\phi_w$  must be converted to the volume fraction  $\phi_v$  using the conversion formula

$$\phi_v = \frac{\rho_f \phi_w}{\rho_f \phi_w + \rho_p (1 - \phi_w)} \quad (2)$$

where  $\rho_p$  is the particle density, and  $\rho_f$  is the base fluid density.

Figure 8 compares the normalized thermal conductivity data for Cu-in-ethylene glycol (EG), MWNT-in-oil, CuO-in-EG, and  $\text{Al}_2\text{O}_3$ -in-EG samples [17, 18, 23] with estimates based on Maxwell's equation. All calculated values are almost identical for the four nanofluids listed in Figure 8. Also, Cu nanofluids contain a small quantity of thioglycolic acid (<1 vol%) to further improve the particle dispersion behavior and, consequently, to further enhance conductivity. Surprisingly, the observed thermal conductivity enhancement with the copper nanoparticles and nanotubes is an order of magnitude higher than predicted from existing theories, represented by Maxwell's model in Figure 8. In contrast, the agreement between measured and predicted enhancement is good for oxide nanofluids. However, Lee et al. [23] and Wang et al. [24], among others, have shown that the model predictions for oxide nanofluids begin to diverge from the experimental data at low volume fractions.

This large gap between measured and predicted thermal conductivity clearly suggests that conventional heat conduction models for solid/liquid suspensions are inadequate. Several mechanisms that could be responsible for thermal transport in nanofluids have been proposed, as described in the next section.

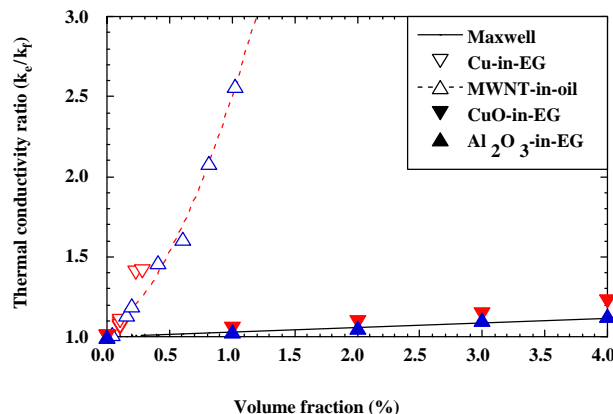


**Figure 8.** Comparison of measured thermal conductivity ratios [17–18, 23] with estimated ratio from Maxwell [16] as function of nanoparticle volume fraction.

## 6.2. Potential Mechanisms for Enhanced Conductivity

Although the classical models for effective thermal conductivity have been successfully verified by experimental data for mixtures with low concentrations [62], the experimental data used in these comparisons included large (mm or  $\mu\text{m}$ ) particles [71, 72]. Therefore, it is not surprising that these theories, which were developed for fluids with particles that are three to six orders of magnitude larger than nanoparticles, cannot accurately predict the thermal conductivity of nanofluids. Only recently have nanoparticles of 50 nm or less become available to investigators. Experiments with nanofluids have shown that existing theories, models, and correlations for thermal conductivity are limited and often contradictory when applied to fluids that contain nanoparticles. Wang et al. [24] and Koblinski et al. [73] have proposed various mechanisms which could enhance thermal transport in nanofluids.

Wang et al. [24] suggested that the microscopic motion of nanoparticles, surface properties, and structural effects may cause enhanced heat transfer in nanofluids. In the classical models, the particles are assumed to be stationary when there is no bulk motion of the fluids. In nanofluids, the microscopic motion of nanoparticles induced by the van der Waals force, the stochastic force (causing the Brownian motion of particles), the electrostatic force, and the hydrodynamic force can be significant. Wang et al. showed that Brownian motion does not contribute significantly to energy transport in nanofluids. However, they indicated that the electric double layer [74] and van der Waals force could have strong electrokinetic effects on the movement of metal oxide nanoparticles dispersed in water. Using transmission electron microscopy, they also found that some particles adhere to form a chain structure and suggested that heat transfer could be enhanced due to this structure.

Koblinski et al. [73] have studied four possible mechanisms for the anomalous increase in nanofluid heat transfer: Brownian motion of the particles, molecular-level layering of the liquid at the liquid/particle interface, the heat transport in the nanoparticles, and the effects of nanoparticle clustering. Like Wang et al. [24], they showed that the effect of Brownian motion on enhanced energy transport in nanofluids is insignificant. However, they showed that the effects of the interface layering of liquid molecules and nanoparticle clustering could provide paths for rapid heat transport. Furthermore, using the molecular dynamics (MD) simulation technique they demonstrated that inside solid particles, heat moves in a ballistic manner, rather than by diffusion. Figure 9 shows a comparison of the autocorrelation functions of the heat flux associated with the solid  $J_{Q_s}$  and liquid  $J_{Q_l}$  parts of the suspension ( $J_Q = J_{Q_s} + J_{Q_l}$ ). The curves indicate monotonic decay of correlations in liquid and oscillatory decay in solid, a signature of ballistic phonons moving back and forth inside the particle. They verified that the period of oscillations corresponds to the time needed for a phonon to travel across the particle, and that it scales with increasing particle size. This new finding is significant when one considers that the central assumption of classical approaches to the prediction of the effective thermal conductivity of a particle-in-liquid suspension is that the

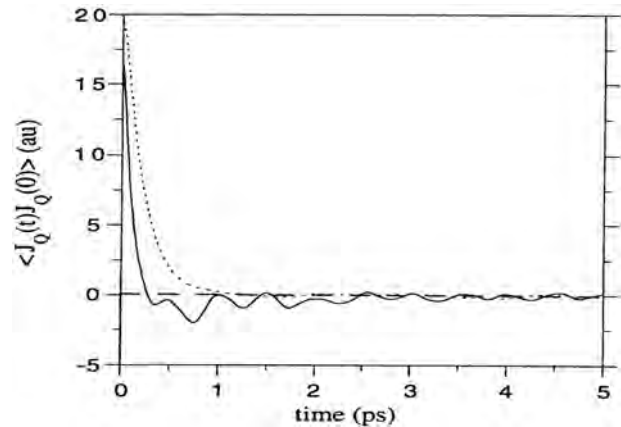


**Figure 9.** Heat current autocorrelation functions for liquid (dashed line) and particle (solid line). Curves indicate monotonic decay of correlations in liquid and oscillatory decay in solid, a signature of ballistic phonons moving back and forth inside the particle. Reprinted with permission from [73], P. Koblinski et al., *Int. J. Heat Mass Trans.* 45, 855 (2002). © 2002, Elsevier Science.

heat transport in each phase is governed by the diffusion equation.

## 6.3. Thermal Transport in Nanocomposite Systems

As discussed previously, the existing understanding of the thermal conductivity of composites and mixtures is derived from *continuum-level* phenomenological formulations which are based on the diffusive heat transport mechanism and typically incorporate only the particle shape and volume fraction with no effects of solid-liquid interfaces or particle mobility taken into account. This approach, while providing a good description of systems with micrometer or larger particles, fails to describe thermal transport of nanofluids.

Modeling and simulations based on the *atomic-level* MD method, where one directly monitors the movement of atoms and associated heat fluxes, can be used to develop a fundamental understanding of the thermal transport properties of nanofluids and nanocomposites. The MD method is particularly appropriate in this context as it avoids assumptions underlying continuum-level formulations, which may be inapplicable for nanometer-sized grains. Furthermore, atomistic simulations allow for “numerical experiments” and detailed characterization, which are experimentally very difficult if not impossible. For example, in a simulation, the interaction energy between the solid particles and fluid can be continuously varied to probe its relative importance systematically.

In view of the fact that macroscopic-based theories have been successful in the description of heat transport, the literature on the atomic-level simulation of heat transport in nanocomposites is rather limited. However, with regard to solid-solid composites, there is a substantial amount of modeling work related to so-called superlattices involving alternating layers of two solid materials. (See, for example, [75].) Here, MD simulations are providing important information,



such as the thermal conductivity dependence on layer spacing and stress [76], scattering of heat-carrying phonons at solid–solid interfaces, and phonon interference effects [77].

For solid–liquid nanocomposites (nanofluids), MD simulations have demonstrated that, inside crystalline solid particles, heat moves in a ballistic manner that involves multiple scattering from the solid/liquid interface [73]. This scattering is associated with the mean free path of the phonon in crystalline solids typically being larger than the typical nanoparticle size. This result suggests that the macroscopic thermal conductivity of the solid might not be a relevant parameter, while the interfacial transmission coefficient might be (i.e., how much heat is able to go through the solid/liquid interface rather than reflect back into the particle), thereby not contributing to macroscopic heat transport.

The solid/liquid interfacial resistance was studied by means of nonequilibrium MD simulations in which a temperature gradient is imposed [78]. These simulations reveal that the strength of the bonding between liquid and solid atoms plays a key role in determining the interfacial thermal resistance. Moreover, it was found that the functional dependence of the thermal resistance on the strength of the liquid–solid interactions exhibits two distinct regimes: exponential dependence for weak bonding (i.e., nonwetting liquid) and power law dependence for strong bonding (i.e., wetting liquid). These findings indicate that nanocomposites or nanofluids characterized by weak atomic bonding at the particle–matrix interfaces will exhibit high thermal resistance. By contrast, for the wetting systems the interfacial resistance will be small and equivalent to a temperature drop in a liquid over several atomic distances ( $\sim 1$  nm) and thus will play a minor role in the case of nanometer-size particles.

Even the limited research on MD simulations of heat transport in nanoscale composites has provided important guidelines for the design of conductive materials. For example, as discussed, MD simulations indicate that the macroscopic thermal conductivity of solid particles might be much less important than the thermal resistance of the solid/liquid interface. We envision that atomic-level modeling and simulations will provide further insights into the origin of the unusual thermal transport properties of nanofluids and other nanocomposites. They will also contribute to the formulation of continuum-level models capable of describing thermal transport in nanoscale composites at larger time and length scales, those accessible to MD simulation.

## 7. FUTURE DIRECTIONS

The anomalous thermal conductivity data for copper and nanotube nanofluids in comparison to predictions by conventional models have raised fundamental questions such as: Why is there such a large gap between data and predictions? What are the mechanisms for increased thermal conductivity? Several mechanisms that could be responsible for thermal transport in nanofluids have been described in the previous section. However, at present, none of them is able to explain adequately the thermal conductivity behavior of nanofluids. Therefore, the mysteries of nanoparticles in fluids remain unsolved, presenting new opportunities and challenges for scientists and engineers. Such research could lead to a major breakthrough in solid/liquid composites for

numerous engineering applications, such as coolant for automobiles, air conditioning, and supercomputers.

According to the models currently used for traditional solid/liquid suspensions, the particle concentration, shape and orientation, distribution, particle–particle interactions, and thermal conductivity of particle and liquid can affect how well solid/liquid suspensions conduct heat. However, the conventional models do not account for particle size, polydispersity index, zeta potential, surface hydrophobicity, particle motion, and nanostructure, which may be key parameters for nanofluids with nanoparticles. As proposed in Figure 10, new models of the thermal conductivity and other properties of nanofluids should include such parameters as nanoparticle motion and nanostructure, as well as particle size and surface characteristics. This clearly demonstrates the interdisciplinary demands of nanofluid science and technology.

One of the greatest challenges for nanofluid research is to develop a tool that will measure the thermal conductance between two nanoparticles that are suspended in liquid less than 50 nm apart. This new tool is needed to better understand the physics responsible for the anomalous increase in conductivity and to validate a new model. Achieving this goal is more challenging than measuring the thermal conductivity of nanotubes [15].

At present, measurements of the heat transfer coefficients of nanofluids are limited to nanofluids containing oxide ceramic nanoparticles. Even greater effects are expected for nanofluids that contain metal nanoparticles and carbon nanotubes. Therefore, there is an urgent need to measure the heat transfer coefficients of these promising nanofluids. Furthermore, nanofluid research has been focused on the thermal characterization of nanofluids without evaporation or condensation. However, nanoparticles in nanofluids can play a vital role in two-phase heat transfer systems. Therefore, there is a great need to characterize nanofluids in boiling and condensation heat transfer.

Applied research on nanofluids is a newly emerging field. Nanoparticles can be added to motor oils, antifreeze

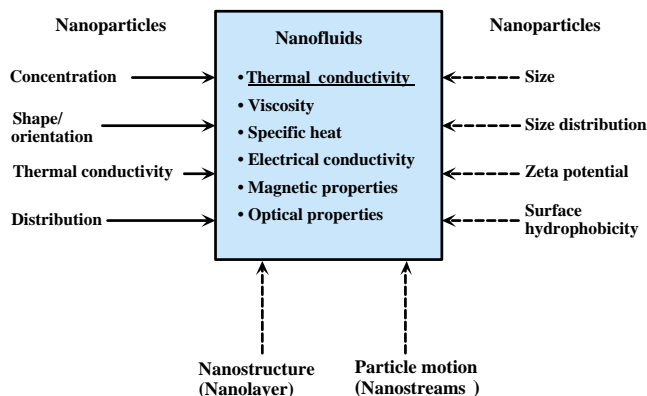


**Figure 10.** Schematic for modeling of nanofluids. Classical models for traditional solid/liquid suspensions account for the particle concentration, shape, orientation, and distribution, as well as particle–particle interactions, and the thermal conductivity of the particle and liquid. In addition to these parameters, new models of the thermal conductivity and other properties of nanofluids should include such parameters as nanoparticle motion, nanostructure, particle size, and surface characteristics.



coolants, automatic transmission fluids, greases, metal-working fluids, and refrigerants. However, technical hurdles such as stability, toxicity, corrosion, particulate formation, emission, fouling, etc. make the applied research challenging. Use of nanoparticle materials for applied research is made even more difficult since the environmental regulations do not favor the introduction of certain metals or metal oxides. Future R&D efforts should focus on the selection of appropriate nanoparticles for the fluid system, the scalable *in-situ* production of nanoparticles in the fluid system, and the adverse thickening effect brought up by nanoparticles.

Since nanoparticles offer several interesting properties which the bulk materials do not possess, such as thermal enhancement, lubrication improvement, chemical activity, and catalytic effect, nanofluids have a spectrum of potential applications. Nanofluids are being developed mainly for applications in automobile engine oils and coolants, but they may also be applicable for cooling electronic devices, laser diode heat sinks, and welding machines. Preliminary tests have shown that nanofluids may solve a number of problems plaguing the heating, ventilation, and air conditioning industry and may change the design of the vehicle radiator completely.

Lee and Choi [19] estimated the performance of microchannel heat exchangers with water, liquid nitrogen, and nanofluids as the working fluids and showed the superiority of the nanofluid-cooled exchanger. As a spin-off of the nanofluid applied research, Lockwood et al. [44] studied the effect of soot loading on the thermal characteristics of diesel engine oils, where the soot-containing diesel engine oil is considered as a practical nanofluid.

Besides the thermal benefits, nanofluids when used in a housing with moving metal parts may provide a lubrication benefit [79]. Hu and Dong [80] report that titanium oxide nanoparticles in oil, unlike conventional particles, reduce the friction coefficient and increase wear resistance.

Nanofluids may find medical applications such as drug delivery and localized cancer treatment [81]. For such medical applications nanoparticles need to be coated with biocompatible materials such as silica, carbon, or  $\text{TiO}_2$ .

At present, copper nanoparticles and carbon nanotubes are very promising for nanofluids. However, copper nanoparticles can only be produced by a very slow single-step process. Also, carbon nanotubes are still expensive to produce, although several firms are looking for production methods that would be viable on a commercial scale. Producing small (1–10 nm) nanoparticles cheaply and dispersing them without agglomeration is the key hurdle to commercialization.

If high-volume, low-cost production methods for nanofluids are developed for industrial applications, nanofluids hold significant potential for revolutionizing industries that are dependent on the performance of fluids that transfer heat faster and consume less power for pumping. Nanofluid technology will thus be an emerging and exciting technology of the 21st century.

## 8. CONCLUDING REMARKS

Traditional heat transfer fluids used in thermal management systems (coolants and oils) are not efficient. Technologies with the potential to improve the fluid's thermal properties

are thus of great interest. Although dispersing solid particles in liquids to enhance the thermal conductivity of liquids has a long history dating back about 100 years, only small effects were observed until recently. Exploiting the unique properties of nanoparticles to develop stable and high-thermal-conductivity fluids, ANL developed nanofluids, a new class of heat transfer fluid prepared by suspending nanometer-size particles in conventional fluids.

Two techniques are used to make nanofluids: the single-step DEC method, which simultaneously makes and disperses the nanoparticles directly into the base fluid, and the two-step method, which first makes nanoparticles and then disperses them into the base fluid. Although the two-step technique works well for oxide nanoparticles, it is not as effective for metal nanoparticles. A unique nanofluid production system has been designed and developed for DEC of metals into low-vapor-pressure liquids. For nanofluids containing high conductivity metals, the single-step DEC technique is preferable to gas-condensation processing.

The thermal conductivity of nanofluids with low particle concentrations (1–5 vol%) was measured by three techniques. The experimental results show that these nanofluids have substantially higher thermal conductivities than the same liquids without nanoparticles.

Overall, copper nanofluids produced by the single-step method and carbon nanotube nanofluids produced by the two-step method are very promising. They could provide a giant leap in cooling power because, compared to oxide nanoparticles which are the traditional materials for solid/liquid suspensions, the volume fraction of copper nanoparticles or carbon nanotubes is reduced by one order of magnitude at comparable conductivity enhancement. Indeed, these two kinds of nanofluids set the distance from oxide nanofluids in that, despite very low volume fractions (<0.01) of nanoparticles, their effect on suspension thermal conductivity is dramatic. Furthermore, the discovery of the strong temperature dependence of the thermal conductivity of nanofluids is exciting because that makes nanofluids even more attractive as coolants for devices with high energy density.

Because the thermal conductivity of copper and nanotube nanofluids is one order of magnitude greater than predicted by existing models, nanofluids offer numerous opportunities for solving interesting, basic scientific questions. Some of the key challenges are to understand the fundamental mechanisms of the enhanced thermal conductivity of nanofluids and to develop new models which can link particle size, polydispersity index, zeta potential, surface hydrophobicity, particle motion, nanostructure, etc. to the properties of nanofluids. Experimentally, we need to develop a tool to measure the thermal conductance between two nanoparticles that are suspended in liquid less than 50 nm apart. This new tool is needed to better understand the physics responsible for the anomalous increase in conductivity and to validate a new model.

While we are focusing on long-term basic research in nanofluids and tools to measure thermal conductivities at the nanoscale, we need to maintain our efforts on short-term goals that are more application specific. As cooling is becoming increasingly important in many applications, the two salient features of nanofluids—well-suspended particles

and thermal conductivities far above those of traditional solid/liquid suspensions—make nanofluids strong candidates for the next generation of coolants. However, we are still in the research stage mainly because, for industrial applications of nanofluids, we need to develop high-volume, low-cost production methods. Producing small (1–10 nm) nanoparticles cheaply and dispersing them without agglomeration will open up new areas of research, including heat transfer in flow, and will facilitate development of commercial products.

Finally, we wish to emphasize that nanofluids are an emerging interdisciplinary field where nanoscience and thermal engineering meet and could prove to be a key for new technology of the 21st century.

## GLOSSARY

**Agglomerate** A collection of primary particles or aggregates joined at their edges or corners, with a specific surface area not markedly different from the sum of the areas of the constituents.

**Aggregate** A group of primary particles joined at their faces, with a specific surface area significantly less than the sum of the area of their constituents.

**Bright field** Use of a brightly lighted background for generating a micrograph.

**Brownian motion** The random motion of micro- or nanoparticles in a fluid owing to thermal agitation.

**Brunauer-Emmett-Teller method** The method used to measure the specific surface areas of nanoparticles as well as other materials.

**Chemical vapor deposition (CVD)** Technique used for making nanoparticles and nanotubes as a result of thermochemical vapor-phase reactions.

**DLVO theory** The Deryaguin-Landau-Verwey-Overbeek (DLVO) theory predicts, based on the concept of long-range attractive and repulsive forces, the stability of particles suspended in polar liquids containing electrolytes or other ionic species (such as detergents).

**Dynamic light scattering (DLS)** A method used to determine the particle size and size distribution of colloidal particles between 3 nm and 5  $\mu\text{m}$ . The scattered light is employed to measure the rate of diffusion of the particles. The data for the particle's motion in a liquid are processed to derive the "Stokes radius" or "hydrodynamic radius" of the particle.

**Effective thermal conductivity** The observed thermal conductivity of a solid-liquid suspension. This apparent property includes the thermal resistance at the solid-liquid interface.

**Electric double layer** A double layer of charge carriers such as electrons or ions formed at a solid-liquid interface. It consists of charge carriers of one charge type fixed to the surface of the solid (the rigid part) and an equal number of mobile charge carriers of the opposite charge, which are distributed in the liquid (the diffuse part).

**Electrostatic force** Force on a charged particle in an electrostatic field.

**Functional group** Functional group such as hydroxyl (-OH), carboxyl (-COOH), and mercapto (-SH) consisting of a group of atoms responsible for the characteristic reactions

of a compound. Functional groups are added onto the surface of nanoparticles for better anchoring of the surfactants or grafting of a chain (for example, an octadecyl group) onto the nanoparticle surface to make a permanent bond.

**Inert-gas condensation (IGC)** A physical synthesis technique for making nanoparticles. In the IGC process, the material is evaporated into a low-density inert gas, and vapors diffuse rapidly from the hot source into the surrounding gas, condense, and coagulate to form nanoparticles. Nanoparticles are transported and deposited by thermophoretic diffusion on a cold finger.

**Mean free path of phonon** The average distance traveled between collisions of phonons in a crystal.

**Miniaturization** Reduction in the size of a device, system, or package.

**Nanofluids** A new kind of heat transfer fluid containing a very small quantity of nanoparticles that are uniformly and stably suspended in a liquid. Also referred to as nanoparticle-dispersed fluids and solid-liquid nanocomposites.

**Nanoparticles** Nanometer-sized particles. Nanoparticles, one of the smallest human-made objects, have unique mechanical, thermal, electronic, magnetic, optical, and chemical properties, which strongly depend on particle size and significantly differ from those of the same material in bulk. Nanoparticles are one of the building blocks of nanotechnology.

**Nanoparticle halos** When highly charged nanoparticles are dispersed into a suspension of negligibly charged colloidal particles, they form "halo"-like structure around the colloidal particles and thus stabilize the whole dispersion.

**Scanning electron microscopy (SEM)** A type of electron microscope in which a beam of primary electrons scans a specimen, and the intensity of secondary electrons generated at the point of impact of the beam on the specimen is measured. This signal is used to modulate a separate electron beam which scans, at the same frequency as the scanning of the specimen, a TV monitor in which a perspective image of the specimen is formed.

**Sputtering** The process by which some of the atoms of the cathode in an evacuated enclosure are ejected as a result of bombardment by heavy positive ions to coat a uniform layer of a metal (such as gold) on an object (such as glass, plastic, metal, or carbon nanotube) in vacuum.

**Surface charge density** The number of electric charges per unit surface area of a nanoparticle.

**Time autocorrelation function** The correlation of the same quantity at various times. For the equilibrium fluctuations of the heat flux  $J_Q(t)$ , the autocorrelation function measures the magnitude of these fluctuations and the lifetime of the correlated heat movement. Macroscopic thermal conductivity is proportional to the time integral of the heat flux autocorrelation function.

**Transmission electron microscope (TEM)** A type of electron microscope in which an electron beam is focused by magnetic lenses and transmitted through a thin specimen. A large image of the small specimen is formed on a fluorescent screen by the scattering of electrons out of the beams.

**van der Waals force** An attractive force between atoms or nonpolar molecules resulting from three factors: dipole-dipole interaction, dipole-induced dipole interaction, and quantum-mechanical electron correlation in atoms and molecules without dipoles.

**X-ray diffractometer** An instrument used to determine the crystal structure of materials such as nanoparticles by passing X-rays through them and measuring the intensities of the diffracted beams at different angles.

**Zeta potential** The electrokinetic potential that exists across the solid-liquid interface. The electrokinetic forces cause suspended particles to repel each other depending on surface charge density. The Zeta potential of particles can be determined by microscopic observation of the migration velocity of suspended particles in the electric field. Knowledge of the Zeta potential is important for determining the stability of suspended particles.

## ACKNOWLEDGMENT

This work was supported by the U.S. Department of Energy, Office of Basic Energy Sciences and Office of Heavy Vehicle Technologies, under contract W-31-109-Eng-38.

## REFERENCES

- U. S. Choi, in "Developments and Applications of Non-Newtonian Flows" (D. A. Siginer and H. P. Wang, Eds.), FED Vol. 231/MD Vol. 66, p. 99. American Society of Mechanical Engineers, New York, 1995.
- S. W. Turner, A. M. Perez, A. Lopez, and H. G. Craighead, *J. Vac. Sci. Technol. B* 6, 3835 (1998).
- J. Han and H. G. Craighead, *J. Vac. Sci. Technol. A* 17, 2142 (1999).
- L. A. Pozhar and K. E. Gubbins, *Phys. Rev. E* 56, 5367 (1997).
- L. A. Pozhar, *Phys. Rev. E* 61, 1432 (2000).
- J. Baugh, A. Kleinhammes, D. X. Han, W. Wang, and Y. Wu, *Science* 294, 1505 (2001).
- J. M. D. MacElroy, L. A. Pozhar, and S. H. Suh, *Colloid Surface A* 187, 493 (2001).
- L. A. Pozhar, E. P. Kontar, and M. Z. C. Hu, *J. Nanosci. Nanotech.* 2, 209 (2002).
- H. Rohrer, *Microelectron. Eng.* 32, 5 (1996).
- L. L. Sohn, *Nature* 394, 131 (1998).
- M. C. Roco, *J. Aerosol Sci.* 29, 749 (1998).
- D. B. Tuckerman and R. F. W. Pease, *IEEE Electron Dev. Lett.* EDL-2, 126 (1981).
- U. S. Choi, C. S. Rogers, and D. M. Mills, in "Micromechanical Systems" (D. Cho, J. P. Peterson, A. P. Pisano, and C. Friedrich, Eds.), DSC Vol. 40, p. 83. American Society of Mechanical Engineers, New York, 1992.
- A. B. Duncan and G. P. Peterson, *Appl. Mech. Rev.* 47, 397 (1994).
- P. Kim, L. Shi, A. Majumdar, and P. L. McEuen, *Phys. Rev. Lett.* 87, 215502 (2001).
- J. C. Maxwell, "A Treatise on Electricity and Magnetism," 2nd ed., pp. 435-441. Oxford Univ. Press, Oxford, 1904.
- J. A. Eastman, S. U. S. Choi, S. Li, W. Yu, and L. J. Thompson, *Appl. Phys. Lett.* 78, 718 (2001).
- S. U. S. Choi, Z. G. Zhang, W. Yu, F. E. Lockwood, and E. A. Grulke, *Appl. Phys. Lett.* 79, 2252 (2001).
- S. P. Lee and U. S. Choi, in "Recent Advances in Solids/Structures and Application of Metallic Materials" (Y. Kwon, D. Davis, and H. Chung, Eds.), PVP Vol. 342/MD Vol. 72, p. 227. American Society of Mechanical Engineers, New York, 1996.
- H. Gleiter, *Progr. Mater. Sci.* 33, 223 (1989).
- J. A. Eastman, U. S. Choi, S. Li, L. J. Thompson, and S. Lee, in "Proceedings of the Symposium on Nanophase and Nanocomposite Materials II," Vol. 457, p. 3. Materials Research Society, Boston, 1997.
- J. A. Eastman, U. S. Choi, S. Li, G. Soye, L. J. Thompson, and R. J. DiMelfi, *J. Metastable Nanocryst. Mater.* 2, 629 (1999).
- S. Lee, U. S. Choi, S. Li, and J. A. Eastman, *ASME J. Heat Transfer* 121, 280 (1999).
- X. Wang, X. Xu, and U. S. Choi, *J. Thermophys. Heat Transfer* 13, 474 (1999).
- H. Xie, J. Wang, T. Xi, Y. Liu, F. Ai, and Q. Wu, *J. Appl. Phys.* 91, 4568 (2002).
- S. K. Das, N. Putra, P. Thiesen, and W. Roetzel, *ASME J. Heat Transfer*, in press.
- A. H. Pfund, *Rev. Sci. Instrum.* 1, 398 (1930).
- K. Kimoto, Y. Kamilaya, M. Nonoyama, and R. Uyeda, *Jpn. J. Appl. Phys.* 2, 702 (1963).
- C. G. Granqvist and R. A. Buhrman, *J. Appl. Phys.* 47, 2200 (1976).
- R. Birringer, *Mater. Sci. Eng. A* 117, 33 (1989).
- Nanophase Technologies Corporation, Burr Ridge, IL.
- H. Xie, J. Wang, T. Xi, and Y. Liu, *Int. J. Thermophys.* 23, 571 (2002).
- R. Andrews, D. Jacques, A. M. Rao, F. Derbyshire, D. Qian, X. Fan, E. C. Dickey, and J. Chen, *Chem. Phys. Lett.* 303, 467 (1999).
- Y. M. Xuan and Q. Li, *Int. J. Heat Fluid Flow* 21, 58 (2000).
- B. Berne and R. Pecora, "Dynamic Light Scattering." Wiley, New York, 1976.
- W. B. Russel, D. A. Saville, and W. R. Schowalter, "Colloidal Dispersions." Cambridge Univ. Press, Cambridge, UK, 1989.
- P. C. Hiemenz and R. Rajagopalan, "Principles of Colloid and Surface Chemistry," 3rd ed. Dekker, New York, 1997.
- S. Ross and I. D. Morrison, "Colloidal Systems and Interfaces." Wiley, New York, 1988.
- B. V. Derjaguin and L. D. Landau, *Acta Physicochim. URSS* 14, 633 (1941).
- E. J. W. Verwey and J. Th. G. Overbeek, "Theory of Stability of Lyophobic Colloids." Elsevier, Amsterdam, 1948.
- H. Reerink and J. Th. G. Overbeek, *Discuss. Faraday Soc.* 18, 74 (1954).
- "Fine Particles: Synthesis, Characterization, and Mechanisms of Growth" (T. Sugimoto, Ed.), Surfactant Science, Vol. 92. Dekker, New York, 2000.
- V. Tohver, J. Smay, A. Braem, P. V. Braun, and J. A. Lewis, *Proc. Nat. Acad. Sci.* 98, 8950 (2001).
- F. E. Lockwood, Z. G. Zhang, S. U. S. Choi, and W. Yu, in "Proc. 2001 Vehicle Thermal Management Systems Conference," p. 205. Society of Automotive Engineers, Inc., Warrendale, PA, 2001.
- H. Akoh, Y. Tsukasaki, S. Yatsuya, and A. Tasaki, *J. Cryst. Growth* 45, 495 (1978).
- M. Wagener, B. S. Murty, and B. Günther, in "Nanocrystalline and Nanocomposite Materials II" (S. Komarnenl, J. C. Parker, and H. J. Wollenberger, Eds.), Vol. 457, p. 149. Materials Research Society, Pittsburgh, 1997.
- D. R. Chen, D. Y. H. Pui, and S. L. Kaufman, *J. Aerosol Sci.* 26, 963 (1995).
- D. R. Chen and D. Y. H. Pui, *Aerosol Sci. Technol.* 27, 367 (1997).
- D. Y. H. Pui and D. R. Chen, U.S. Patent 6, 093, 557, 2000.
- D. Y. H. Pui and D. R. Chen, U.S. Patent Application 2002/0007869 A1, 2002.
- J. J. de Groot, J. Kestin, and H. Sookiazian, *Physica* 75, 454 (1974).
- Y. Nagasaka and A. Nagashima, *J. Phys. E* 14, 1435 (1981).
- J. P. Bentley, *J. Phys. E* 17, 430 (1984).
- H. M. Roder, *J. Res. Nat. Bur. Stand.* 86, 457 (1981).
- "Thermal Properties of Matter" (Y. S. Touloukian and C. Y. Ho, Eds.), TPRC Data Series. Plenum Press, New York, 1970-1977.
- E. Schmidt and W. Sellschopp, *Forsch. Ing. Wes.* 2, 165 (1931).

57. F. P. Incropera and D. P. DeWitt, "Fundamentals of Heat and Mass Transfer," 4th ed. Wiley, New York, 1996.
58. W. Czarnetzki and W. Roetzel, *Int. J. Thermophys.* 16, 413 (1995).
59. R. L. Hamilton and O. K. Crosser, *I&EC Fundamentals* 1, 187 (1962).
60. B. J. Biercuk, M. C. Llaguno, M. Radosavljevic, J. K. Hyun, and A. T. Johnson, *Appl. Phys. Lett.* 80, 2767 (2002).
61. R. T. Bonnecaze and J. F. Brady, *Proc. Roy. Soc. London Ser. A* 430, 285 (1990).
62. R. T. Bonnecaze and J. F. Brady, *Proc. Roy. Soc. London Ser. A* 432, 445 (1991).
63. A. S. Ahuja, *J. Appl. Phys.* 46, 3408 (1975).
64. C. W. Sohn and M. M. Chen, *ASME J. Heat Transfer* 103, 47 (1981).
65. B. C. Pak and Y. I. Cho, *Exp. Heat Transfer* 11, 151 (1998).
66. Y. M. Xuan and W. Roetzel, *Int. J. Heat Mass Transfer* 43, 3701 (2000).
67. D. J. Jeffrey, *Proc. Roy. Soc. London Ser. A* 335, 355 (1973).
68. R. H. Davis, *Int. J. Thermophys.* 7, 609 (1986).
69. S. Lu and H. Lin, *J. Appl. Phys.* 79, 6761 (1996).
70. S. C. Cheng and R. I. Vachon, *Int. J. Heat Mass Transfer* 12, 249 (1969).
71. R. E. Meredith and C. W. Tobias, *J. Electrochem. Soc.* 108, 286 (1961).
72. J. C. R. Turner, *Chem. Eng. Sci.* 31, 487 (1976).
73. P. Keblinski, S. R. Phillpot, S. U. S. Choi, and J. A. Eastman, *Int. J. Heat Mass Transfer* 45, 855 (2002).
74. C. S. Hirtzel and R. Rajagopalan, "Colloidal Phenomena." Noyes, Park Ridge, NJ, 1985.
75. G. Chen, M. Neagu, and T. Borca-Tasciuc, in "Thermoelectric Materials—New Directions and Approaches Symposium" (T. M. M. Tritt, M. G. Kanatzidis, H. B. Lyon, and G. D. Mahan, Eds.), p. 85. Materials Research Society, Pittsburgh, 1997.
76. S. Volz, J. B. Saulnier, G. Chen, and P. Beauchamp, *Microelectron. J.* 31, 815 (2000).
77. P. K. Schelling, S. R. Phillpot, and P. Keblinski, *Appl. Phys. Lett.* 80, 2484 (2002).
78. L. Xue, P. Keblinski, S. R. Phillpot, S. U.-S. Choi, and J. A. Eastman, *J. Chem. Phys.* 118, 337 (2003).
79. M. Chhowalla and G. A. J. Amaratunga, *Nature* 407, 164 (2000).
80. Z. S. Hu and J. X. Dong, *Wear* 216, 92 (1998).
81. L. Levy, Y. Sahoo, K.-S. Kim, E. J. Bergoy, and P. N. Prasad, *Chem. Mater.* 14, 3715 (2002).



# Nanohelical/Spiral Materials

S. Motojima, X. Chen

*Gifu University, Gifu 501-1193, Japan*

## CONTENTS

1. Introduction
  2. Carbon Nanocoils
  3. Ceramic Nanocoils/Nanotubes
  4. Applications
- Glossary  
References

## 1. INTRODUCTION

In cosmos and in nature, maelstrom, spiral, helical, or coil structures, such as a whirled air (typhoons), whirled seawater, vine plants, shellfish, proteins, DNA, etc. are commonly observed. The helical/spiral shapes are also commonly observed in artificial water screws, spiral staircases, retaining screws, bolts/nuts, screw dislocations in solids, etc. Furthermore, electromagnetic waves, spirit or mind, economic cycles, etc. have also a helical/spiral motion pattern. That is, three-dimensional (3D)-helical/spiral structures are the fundamental structure of many natural objects, including science and human livings. The helical morphology of DNA or proteins has essential and critical functional roles in living bodies. Recently, the double helix-shaped DNA, single-helix-shaped proteins, or chiral carbon nanotubes have been attracting attention in biotechnology and nanotechnology [1–3]. Materials with 3D-helical/spiral structures with micrometer to nanometer order dimensions have not been commercially available. Motojima and Chen have prepared regularly coiled carbon fibers (carbon coils) with 3D-helical/spiral structures, which are similar structures to all things in the cosmos, with high coil yield. We named them “cosmomimetic carbon coils” for these carbon coils after “biomimetics” [1]. The helical/spiral materials are expected to have novel functionality and many potential applications such as tunable microdevices/sensors, electromagnetic absorbers, energy changing materials, hydrogen absorbers, chiral catalysts, activators of organisms, etc. In addition to their potential applications, the growth mechanism is very interesting from the scientific point of view.

Although some helical/spiral-formed fibers are referred to in comprehensive reviews on the vapor grown carbon

fibers, by Rodriguez [4] and de Jong and Geus [5], up to now, there has not been any comprehensive review on nanohelical/spiral materials.

In this chapter, we will introduce the preparation processes, morphologies, microstructures, and properties of the helical/spiral-structured substances such as carbon nanocoils and ceramic nanocoils/nanotubes. We also discuss the growth mechanism of the helical/spiral structure and predict the possible applications.

## 2. CARBON NANOCOILS

### 2.1. Introduction

In 1953, Davis and co-workers [6, 7] were the first to report the vapor growth of thin carbon fibers twisted together in the form of a rope. The observation of helical/spiral-coiled carbon nanofibers, with a coil diameter of several micrometers to several nanometers (referred to as “carbon nanocoils” hereafter), from vapor phase using a chemical vapor deposition (CVD) process, were then reported by some carbon filament researchers. Since from the 1970s to the 1980s, Baker and co-workers reported the observation of carbon twisted fibers among the Fe-group metal-catalyzed vapor grown carbon filaments. Furthermore, they extensively studied the effects of H<sub>2</sub>, Cu, Pt, Sn, and other oxides on the growth of carbon filaments and observed the growth of helical carbon filaments. However, before 1990, carbon coils grown by the CVD process were extremely accidental, reproducibility was very poor, and the production was almost excluded as anomalous and unpreferable deposits with helical/spiral forms.

In 1990, Motojima and co-workers [8] first found that regular-coiled carbon fibers (carbon nanocoils) could be obtained with high reproducibility by the catalytic pyrolysis of acetylene containing a small amount of sulfur impurities over transition metal catalysts, and then they extensively examined the preparation conditions, morphology, growth mechanisms, and some properties in detail. Meanwhile, Motojima and co-workers [9–11] also first found that very regularly coiled silicon nitride (Si<sub>3</sub>N<sub>4</sub>) fibers could be obtained by the CVD process. After then, various ceramic coils such as metal carbides, nitrides, and oxides were prepared by the CVD, sol/gel, diffusion, template processes, etc.



Since 2000, carbon coils have attracted interest and carbon coils with diverse morphologies have been reported by many researchers. Among various preparation processes, the CVD process is the process with the most potential for the large-scale preparation of pure carbon coils. So the preparation of carbon coils has been mainly carried out using various CVD reaction systems, mainly using Fe-group metal catalysts and acetylene or ethylene carbon sources.

In this section, we will first summarize some of the earlier literature in which the growth of helical-coiled carbon fibers is referred. Thereafter, we will present recent research progress in the preparation (processes and conditions), morphology, microstructure, and some properties, and we will discuss the growth mechanism. Finally we will predict the potential applications of the carbon nanocoils.

## 2.2. Preparation, Morphology, and Microstructure

In 1953, Davis and co-workers [6, 7] first reported the vapor growth of thin carbon fibers twisted together in the form of a rope (helical threads) by the disproportionation of CO over iron compound catalysts at 450 °C. The obtained helical threads are apparently hollow and are probably formed by coiling of flat ribbons. In 1958, Hillert and Lange [12] reported the growth of a single helical thread and combinations of three helical thread, parallel, or twisted forms from N<sub>2</sub>-heptane source gas mixtures at 1000 °C using Fe catalyst. In 1972, Baker and co-workers [13] reported the growth of twisted carbon fibers with a coil diameter of about 60 nm from a C<sub>2</sub>H<sub>2</sub>/H<sub>2</sub> (or O<sub>2</sub>) gas mixture at 870–1100 K using the Ni catalyst. They introduced H<sub>2</sub> or O<sub>2</sub> to the reaction system preventing Ni particles from being deactivated and found that the catalytic activity of the Ni particles for filament growth ceased after approximately 15 s at 870 K, but it could be regenerated by exposure to H<sub>2</sub> at 1100 K or O<sub>2</sub> at 1000 K. Boehm [14] also obtained carbon braided fibers with herringbone structure by the disproportionation of CO at 650 °C over Fe(CO)<sub>5</sub> or Ni(CO)<sub>4</sub> catalyst. He proposed a growth model for the helical fiber formation, in which he suggested that iron carbide formed on the disorganized carbon, and braided fibers formed on the crystal faces of iron carbide.

In recent years, Park and Baker [15, 16] paid much attention to the growth of carbon filaments by decomposition of ethylene over Fe-group alloy catalysts. During their investigation of the decomposition of a C<sub>2</sub>H<sub>4</sub>/CO/H<sub>2</sub> gas mixture over a series of Fe/Ni catalysts, and detailed analysis of both the gaseous products and the amount of the deposited solid carbons, they revealed that co-adsorption of the two carbon-containing gases produced major modifications in the behavior of the bimetallic catalyst surfaces. It was evident that the addition of CO to a C<sub>2</sub>H<sub>4</sub>/H<sub>2</sub> gas mixture resulted in a substantial increase in the decomposition of the olefin over all the bimetallic catalyst powders with this effect being most pronounced on the Fe-rich systems. The major product from this series of Fe/Ni catalysts was found to be solid carbon in the form of various filamentous structures, including twisted carbon nanocoils with 200 nm diameter produced from the interaction of an Fe catalyst with a C<sub>2</sub>H<sub>4</sub>/CO/H<sub>2</sub>(3:1:1) gas mixture at a 600 °C. A growth tip with bidirectional mode

can be seen, as can the tightly coiled nature of filaments grown with 200 nm diameter from the interaction of an Fe–Ni(2:8) catalyst with a C<sub>2</sub>H<sub>4</sub>/CO/H<sub>2</sub>(3:1:1) gas mixture at 600 °C.

Great attention has been paid to the effect of the impurity on the catalytic effect of Fe-group metals. Baker and co-workers [17] studied the influence of Sn on Fe catalyst and obtained spiral carbon filaments from acetylene at above 800 °C by using the Sn/Fe (Sn coated Fe foils) catalyst. The filaments were nearly all spiraling with a constant coil pitch and commonly branched. Two spiral filaments generally grew from a catalyst particle in opposite directions. Branching of filaments was frequently observed. They found that the addition of Sn into Fe can prevent the catalyst from being poisoned. Baker and Waite [18] also studied the preparation of carbon filaments by the Pt/Fe alloy-catalyzed pyrolysis of C<sub>2</sub>H<sub>2</sub> and found that using this alloy at 690 K, which is a much lower temperature than that using pure Fe, carbon filament grew two orders of magnitude faster than pure Fe. But at a higher temperature, 1175 K, and using ethylene as a carbon source, the growth of very short coils was observed.

In 1984, Galuszka and Back [19] studied the catalytic activity of Fe films formed by thermal decomposition of a solution of ferric nitrate in the presence of mercury vapor. They found that this iron catalyst induced the formation of filamentous carbon during the pyrolysis of methane and that oxidation–reduction of the sputtered iron was shown to lead to fragmentation of the films into particles with a size suitable for the growth of filaments. Among the deposits the springlike single-helix carbon nanofibers were observed.

In 1992, Kim and co-workers [20] used a Cu/Ni (1:1) as the catalyst and acetylene as the carbon source for obtaining the carbon fibers and found that two filaments grew from opposite faces of the catalyst particle at identical rates. Furthermore, during the major part of the growth process, the filaments were relatively smooth and tended to form into large loops. Over a period of time it became clear that many of the filaments were slowly decreasing in width, as a result of catalyst material being dissipated within the structure, and this behavior frequently resulted in the creation of secondary smaller filaments on the parent growth. Furthermore, they also suggested that when the particles reached a size of about a third of the original value, the filaments appeared to undergo a further change in shape and simultaneously started to rotate on an axis perpendicular to the direction of filament growth, causing the filament to acquire a spiral form. When the catalyst is Ni-rich, Cu/Ni (1:1), supported on graphite, 2 Torr, C<sub>2</sub>H<sub>2</sub>, bidirectional filaments with a spiraling mode grew. But when Cu-rich, Cu/Ni (7:3) + C<sub>2</sub>H<sub>4</sub>/H<sub>2</sub>(1:4) at 600 °C, Cu-rich particles tend to grow in a spiral conformation.

Furthermore, in 1997, Krishnankutty and co-workers [21] continued to report the effect of Cu on the structural characteristics of the carbon filaments produced from Fe-catalyzed decomposition of ethylene. Carbon filaments were produced by the decomposition of ethylene over unsupported Fe/Cu catalyst powders in the presence of varying amounts of H<sub>2</sub> at 500–800 °C. Helical coils could be obtained using a Fe/Cu (3:7) catalyst and C<sub>2</sub>H<sub>4</sub>/H<sub>2</sub> (1:4) at 500–600 °C. With catalysts rich in Cu, it was apparent

that although the resulting carbon filaments continued to grow via bidirectional mode, there was a subtle difference in that they acquired a helical conformation. The herringbone arrangement of the graphite platelets is indicated in the catalyst grain present on the fiber tip. Two structures, herringbone (platelets oriented at an angle with respect to the fiber axis with smooth surfaces) and tubular arrangements models, are presented. The effects of Cu in Ni catalysts have been also reported by Bernado and co-workers [22, 23] and Jong and co-workers [24] recently.

Hernadi and co-workers [25] reported the growth of carbon coils in preparation of carbon nanotubes from acetylene at 700 °C over Fe/silica supported catalyst. The carbon coil is a single-helix coil and has a coil diameter of about 80 nm and a coil pitch of about 160 nm as shown in Figure 1. Grobert and co-workers [26] obtained carbon nanocoils by the pyrolysis of solid organic precursor (for example, 2-amino-4, 6-dichloro-*s*-triazine, *s*-triamono-triazine) at 950–1050 °C using laser patterned thin metal (Fe, Co, Ni) as the catalyst and silica substrate. The obtained nanocoils have a coil diameter of 1.2–0.6  $\mu\text{m}$  and a coil pitch of 3–0.3  $\mu\text{m}$  as shown in Figure 2a. Simulated single-walled corkscrew-like carbon nanotubes produced by interspersing five- and seven-membered rings judiciously within the mainly hexagonal network is also depicted in Figure 2b.

Recently, Chesnokov and co-workers [27] reported the growth regularities and mechanism of symmetric twisted carbon filaments formed from butadiene-1, 3 on Ni–Cu/MgO-catalyst at 450 °C. Dissymmetrical spirally twisted carbon filaments have been shown to grow from a single Ni/Cu alloy particle. They suggested that as the filaments grow, a microphase of metastable nickel carbide ( $\text{Ni}_3\text{C}$ ) forms on the particle's frontal side, whereas the crystal particle of Ni/Cu alloy possesses a series of twinning planes (111) that are parallel to the dissymmetry plane of the crystal and separate the blocks of twins from a face-centered structure.

Although it is well known that sulfur acts as a poison for many Ni catalyzed reactions, it is now being recognized that



**Figure 1.** Carbon nanotubes formed in the decomposition of acetylene at 700 °C over Fe/silica (ion-adsorption precipitation using pH = 9 as initial solution, but the pH was close to 7 before filtration) catalyst.

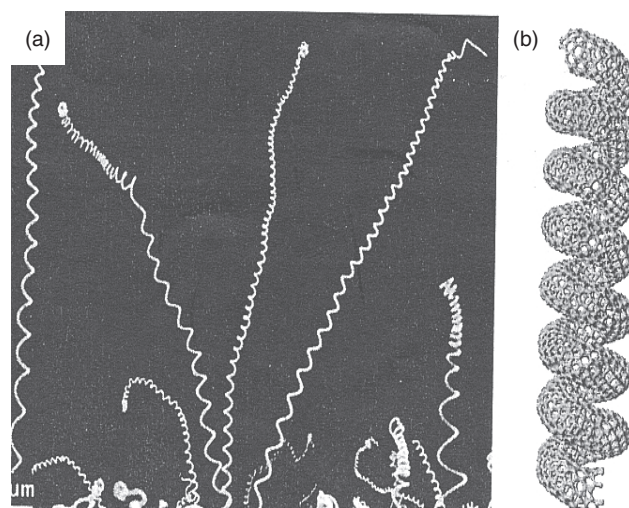


**Figure 2.** (a) Scanning electron microscope image of carbon nanocoils generated by pyrolysis of melamine over Co “aged” catalyst substrate (in air). (b) Simulated single-walled corkscrew-shaped carbon nanotube produced by interspersing five- and seven-membered rings judiciously within the mainly hexagonal network [26].

certain benefits can be derived from following a partial and well controlled sulfidation treatment of the metal. Owens and co-workers [28] reported the effect of sulfur on the interaction of Ni with ethylene. They found the enhancement in carbon filament growth following pretreatment of Ni in low levels of  $\text{H}_2\text{S}$  (4–50 ppm) is related to a reconstruction of the metal surface. The inhibition of catalytic activity resulting from a more severe pretreatment in  $\text{H}_2\text{S}$  is ascribed to the formation of a 2D or 3D bulk sulfide. They considered that re-adsorption of S on Ni induced some major perturbations in the morphological characteristics of the filamentous carbon deposits, which are generated in the form of regularly coiled structures. In contrast, those produced from unadulterated metal particles were found to be relatively straight. This change in growth mode indicates that sulfur is modifying the diffusion characteristics of carbon species through the catalyst particle.

Motojima and co-workers [8] first found that the regularly coiled carbon coils could be obtained with high reproducibility by the catalytic pyrolysis of acetylene, containing a small amount of S impurity, and then extensively examined the relationship between coil yield and preparation conditions, as well as morphology, growth mechanism, and some properties in detail. This process makes it possible to prepare carbon coils in semimass while, to our knowledge, the coil yield of carbon nanocoils is rarely reported by other research group so far. These results are comprehensively presented in the following section.

Figureiredo and co-workers [29] obtained carbon nanocoils by Co-catalyzed pyrolysis of acetylene. The obtained nanocoils are single-helix coils and have very small coil diameters of about 60 nm as can be seen in Figure 3. Rodoriguez and co-workers [30] prepared carbon filaments by pyrolysis of ethane containing a  $\text{H}_2\text{S}$  at 815 to 865 °C using Fe/Ni catalyst. It was observed that a dramatic change occurred in catalyst activity and selectivity when 50 ppm  $\text{H}_2\text{S}$  was added



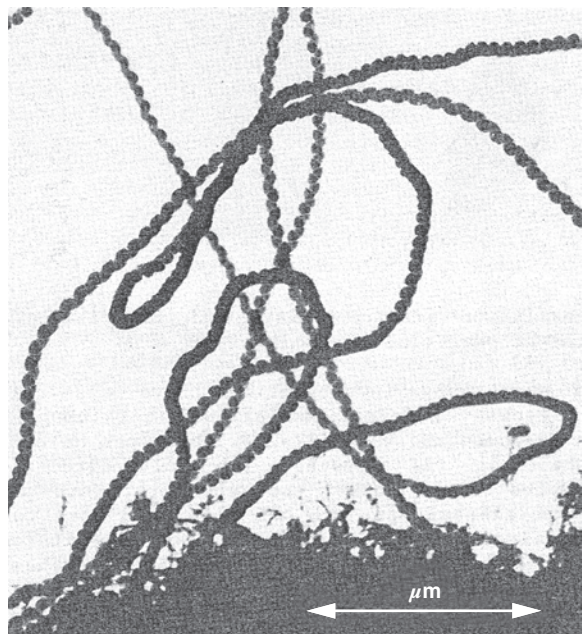


**Figure 3.** Helical filaments formed during the reaction of cobalt with acetylene [29].

to the ethane feed. Graphite shell-like deposits were predominant in the case of the Fe/Ni (5:5) catalyst, while carbon nanofibers in the case of the Fe/Ni (8:2) catalyst were predominant. Carbon nanocoils with a coil diameter of about 700 nm and a coil pitch of about 400 nm were obtained by the pyrolysis of ethane at 815 °C using the Fe/Ni(8:2) catalyst.

Amelinckx and co-workers [31] prepared helix-shaped carbon tubules by the Co-catalyzed pyrolysis of acetylene and examined in detail the morphology and microstructure. The different morphologies and transmission electron microscopy (TEM) images of a tubule are shown in Figures 4 and 5, respectively. Figure 4a shows the helix-shaped tubules having pitches of different magnitudes. Figure 4b shows the complicated interaction between straight and helix-shaped tubules. Figure 4c shows the parallel arrangement of a straight and a helix-shaped tubule, presumably kept together by van der Waals attraction. Figure 4d shows the coiled tubule intercoiling with itself after having made a U-turn. Figure 4e shows the straight tubules making

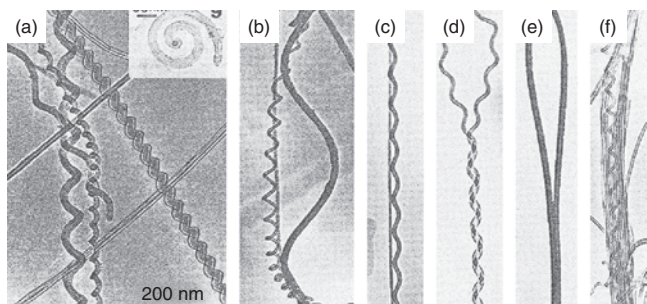


**Figure 4.** Graphite tubules grown by the Co-catalyzed decomposition of acetylene, exhibiting various shapes [31].

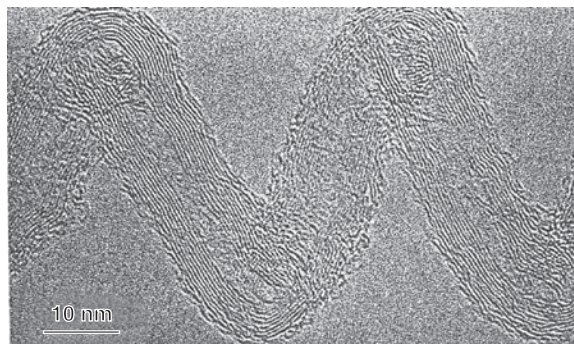


**Figure 5.** High-resolution images of a helix-shaped tubule containing 11 graphene tubules as shown Figure 4a [31].

a closed loop, the straight ends sticking together. Figure 4f shows the bundle of parallel straight tubules and one helix. Figure 4g shows the planar spiral-shaped tubule. It can be seen that these tubules are a multiwalled nanotube. They also introduced the concept of a spatial-velocity hodograph to explain the growth mechanism of the helix-shaped carbon tubules as shown in Section 2.6.

Krishnankutty and co-workers [21] reported the effect of Cu addition on the decomposition of  $C_2H_4$  in  $H_2$  over Fe catalyst at 450–800 °C. The addition of only 2 wt% Cu to Fe caused a 20-fold increase in the amount of carbon filaments formed compared to that produced on pure Fe at 600 °C. They suggested that this behavior is probably caused by inducing electronic perturbations in the Fe atoms, which results in a modification in the chemisorption characteristics of  $C_2H_2$  on such a surface. Carbon coils with a coil diameter of 1.5  $\mu m$  were obtained by the Fe/Cu (3:7)-catalyzed pyrolysis of ethylene at 500–600 °C as shown in Figure 6. The TEM image showed that there are two structures: a herringbone structure in which platelets are oriented at an angle with respect to the fiber axis as shown in Figure 7a and a tubular structure in Figure 7b. These structures are very indicative of the carbon coils as well as carbon nanotubes.

Mao and Xie [32] reported that carbon nanotubes with a coil diameter below 100 nm could be obtained from acetylene (10% in  $N_2$ ) at 650 °C in 150 Torr using a Co-implanted

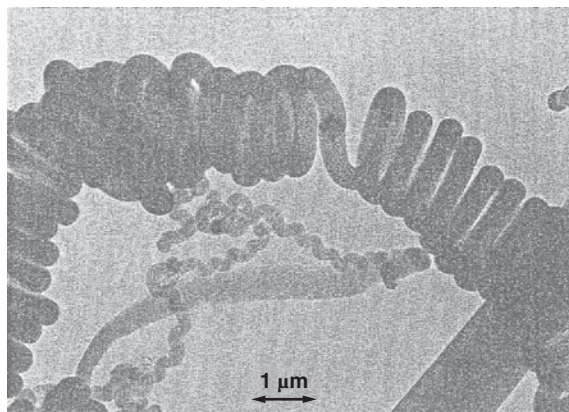


**Figure 6.** Transmission electron micrograph showing the appearance of carbon filaments produced from the Fe/Cu (3:7) catalyzed decomposition of an ethylene/hydrogen (1:4) mixture at 600 °C [21].

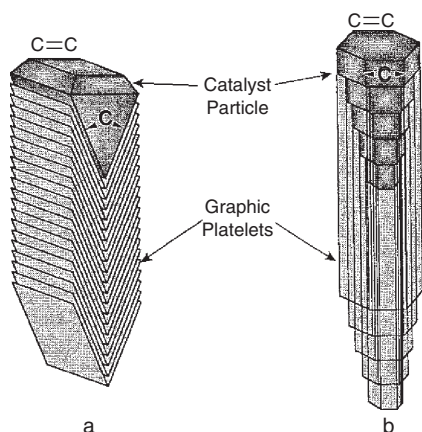


**Figure 7.** Schematic diagram highlighting the essential steps involved in the catalytic growth of carbon filaments from decomposition of a hydrocarbon and the alignment of graphite platelets in the filament structures: (a) herringbone and (b) tubular arrangements [21].

Ge substrate (Co dose:  $1 \times 10^{17} \text{ cm}^{-2}$ ). The formation of these helical nanotubes is considered to be attributed to the different growth velocities of the tubes from different facets of the nanoparticle catalysts as proposed by Amelinckx et al. [31].

Cesar and co-workers [34] reported the synthesis and characterization of twisted carbon filaments with a coil diameter of less than 80 nm by the catalytic pyrolysis of propane using the  $\text{Pd}_3\text{P}$  colloid catalyst at 600 °C. The structure of the filament was amorphous.

Zhang and co-workers [35] prepared carbon tubule nanocoils by the catalytic pyrolysis of propane using Fe-coated indium-tin-oxide (ITO)/glass substrate as the catalyst at 700 °C. The nanocoils usually consist of two or more tubules and each of them grows with its own diameter and pitch. The tubules mostly consist of graphene sheets, and most of the coils have an external diameter range from several tens to several hundred nanometers, most of them are several hundred nanometers. But when using  $\text{Fe}/\text{InO}_x$  or  $\text{Fe}/\text{SnO}_x$  as the catalysts, the coil yield was very low. It is considered that Fe plays an important role in the growth of the carbon tubes, while In, Sn, O, and/or their alloys contribute to the formation of the coils.

Pan and co-workers [36] reported the synthesis of carbon nanocoils by the electroplated Fe/ITO substrate catalyzed pyrolysis of acetylene at 650–800 °C. The fine Fe particles can be effectively mixed with the ITO in this method, which caused the highly efficient growth of small-sized carbon nanocoils with a 100 nm coil diameter. Pan and co-workers [37] also discussed the effects of Fe and indium in the ITO on the growth of carbon tubule nanocoils. It is found that Fe additions lead to the growth of carbon nanotubes, while ITO induces their helical growth. The yield of carbon nanocoils is determined by the elemental ratio of Sn and In, and high yield is obtained at  $\text{Sn}/(\text{Sn} + \text{In}) = 0.1\text{--}0.35$ .

Lee and co-workers [38] reported the growth of carbon nanofibers by the pyrolysis of acetylene using a Ni-deposited sodalime glass as the catalyst at 500 °C. The diameters of carbon nanofibers are uniformly distributed in the range between 50 and 60 nm. Most of the carbon nanofibers are curved or bent in shape, but some are twisted. They

consisted of defective graphitic sheets with a herringbone structure.

Wang and co-workers [39] reported the growth of helical-shaped filaments with a coil diameter of 50–100 nm from a gas mixture of  $\text{C}_6\text{H}_6\text{--H}_2\text{--Ar}$  at below 520 °C using Fe(or Co, Ni)/ $\gamma\text{-Al}_2\text{O}_3$  catalysts by microwave plasma-enhanced CVD. Xie and co-workers [40] also reported the growth of the carbon coils with coil diameters of 5–6  $\mu\text{m}$  by the Ni catalytic pyrolysis of acetylene at 700 °C by the microwave plasma CVD process. Using the plasma CVD process, the addition of sulfur impurity in the reaction atmospheres is not necessary for obtaining carbon coils.

Hernadi and co-workers [41] reported the growth of carbon nanocoils with coil diameters of about 200 nm by the unsupported  $\text{SnO}$ -doped  $\text{Fe}_3\text{C}$  catalytic pyrolysis of acetylene. Figure 8 shows the carbon nanocoil with different morphologies obtained by them.

Bai [42] reported the preferential growth of nanotubes/nanofibers and nanocoils with controlled diameters by the catalytic pyrolysis of acetylene at 650 °C. Catalyst nanoparticles of a Fe, Co, and Ni were dispersed on the anodized Al plate substrate ( $\text{Al}_2\text{O}_3$  thickness deposited on Al plate: a few  $\mu\text{m}$ ), in which a Fe, Co, and Ni sulfate solution was electrochemically impregnated into the nanopores present in an anodized Al plate to deposit fine metal particle. The gas mixture of  $\text{C}_2\text{H}_2$ ,  $\text{N}_2$ , and  $\text{H}_2$  (5%) + Ar(95%) flowed onto a quartz reaction tube at a flow rate of 850 sccm. The concentration of  $\text{C}_2\text{H}_2$  was about 5%. A carbon nanocoil with a coil diameter of 200 nm coil, a coil pitch of 160 nm, and a fiber diameter of about 160 nm was obtained using very fine catalyst particles in the 5–15 nm pores obtained under ac short time electrochemical metal deposition. Carbon coils with a coil diameter of 1.5  $\mu\text{m}$ , a coil pitch of 250 nm, and a fiber diameter of about 200 nm were obtained by longer metal particle deposition times (1 min). Carbon coils with a coil diameter of 16  $\mu\text{m}$ , a coil pitch of 1  $\mu\text{m}$ , and a fiber diameter of about 500 nm were obtained with very thin layers composed of large metal particles under 2 min dc deposition conditions.

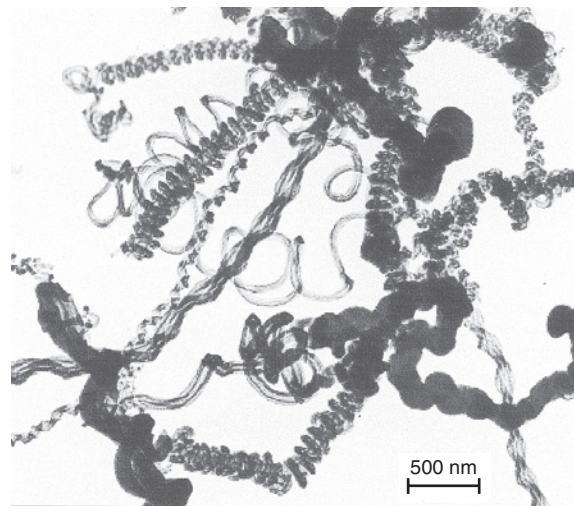


**Figure 8.** EM image of carbon deposit over  $\text{Fe}_3\text{C}(\text{+SnCl}_2)$  [41].



Raman spectroscopy analysis on the carbon coils showed the multiwalled nanotube's nature.

Schliermann and co-workers [43] studied the online-monitoring of gas phase reactions during nanofiber synthesis by fast chromatography. They found that carbon coils grew at the restricted reaction conditions. Hernadi and co-workers [44] prepared the carbon coils with a coil diameter of 100–200 nm and a specific surface area of 44–129 m<sup>2</sup>/g from acetylene using the unsupported SnO-doped Fe<sub>3</sub>C (direct precipitation) catalyst at 600–800 °C. Jong and co-workers [24] prepared the carbon nanotubes from a CH<sub>4</sub>/H<sub>2</sub> gas mixture at ~ 600 °C using the Ni/Cu catalyst by microwave plasma CVD and found that the use of high Cu content catalyst (Cu = 60–80%) results in the growth of helical fibers.

Motojima and co-workers [8, 45–56] examined in detail of the morphology and microstructure of the carbon coils. Figure 9 shows the tip part of the carbon coils obtained using a Ni catalyst [46].

A Ni<sub>3</sub>C catalyst grain is always on the tip part of the carbon coils (arrow), and the catalyst grain is the exclusive growth point. Figures 10 and 11 show the enlarged view of the carbon coils [9]. The carbon coils are generally double coils similar to a DNA, and the coil number right-clockwise and left-clockwise is almost the same. Figures 12 and 13 show the carbon coils with interesting morphologies [57]. The growth of a single coil or multiple coils such as shown in Figure 14 was also sometimes observed. Recently, Motojima and co-workers [58, 59] succeeded in preparing carbon nanocoils with a coil diameter of several hundred to several ten nm in large scale using a magnetic CVD process or various catalysts such as Au, Ni/Au, etc. We also studied on the growth of carbon nanocoils by ceramics supported metal catalyzed methods using various metal catalysts such as Fe, Ni, Co, Cu, and supporters such as Al<sub>2</sub>O<sub>3</sub>, amorphous SiO<sub>2</sub>, and molecular sieves. The carbon nanocoils have generally two coiling forms: twisted forms and springlike helix forms such as shown in Figure 15. Using different catalytic systems, many kinds of carbon nanocoils with different morphologies were obtained. Figure 16 shows the tip part of the carbon nanocoils. Two coils [one is right-clockwise coiled and the other is left-clockwise coiled (twisted)] grew from

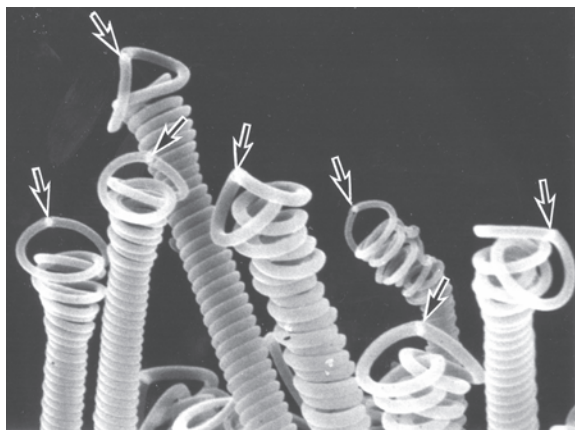


**Figure 9.** Tip part of the carbon coils obtained using Ni catalyst [1, 46]. Arrow indicates a Ni catalyst grain.

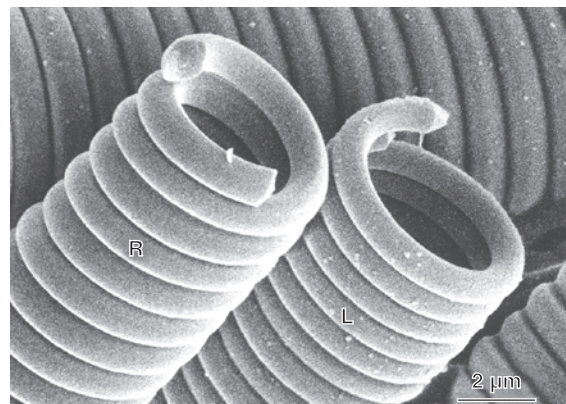


**Figure 10.** (R) Right-clockwise coiled regular double carbon microcoil. (L) Left-clockwise coiled regular double carbon microcoil. Each has a circular or elliptical fiber cross section [1].

a Ni/Al<sub>2</sub>O<sub>3</sub> catalyst grain (arrow). Figure 17 shows the tip part of the carbon coils obtained using the Ni–Fe/molecular sieve catalyst; one coil with fringe on the surface grew from the catalyst grains. The coils in which the chirality and coil axis alternate regularly were prepared by using the Ni–Fe/molecular sieves or WS<sub>2</sub> catalyst by controlled CVD conditions, and the representative coils are shown in Figures 18 and 19. Double twisted carbon nanofibers as well as 2D zigzag nanofibers were also observed in the Ni/Fe catalyzed deposits (Fig. 20).

### 2.3. Large-Scale Preparation of Carbon Nanocoils

In 1990, Motojima and co-workers [8] first found that regularly coiled carbon coils could be obtained with high reproducibility by the catalytic pyrolysis of acetylene containing a small amount of impurities and then extensively examined in detail the preparation conditions, morphology, growth mechanism, and some properties. It was found that the addition of an optimum amount of impurity such as sulfur or phosphorus in the source hydrocarbons is indispensable for obtaining carbon coils with high reproducibility and high coil yield. Between 1993 and 1995, we used phosphorus {PCl<sub>3</sub>,

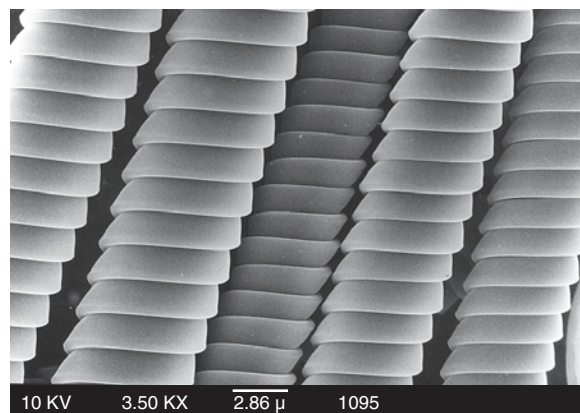


**Figure 11.** Regular-coiled double carbon microcoils which have a flat or rectangular fiber cross section.

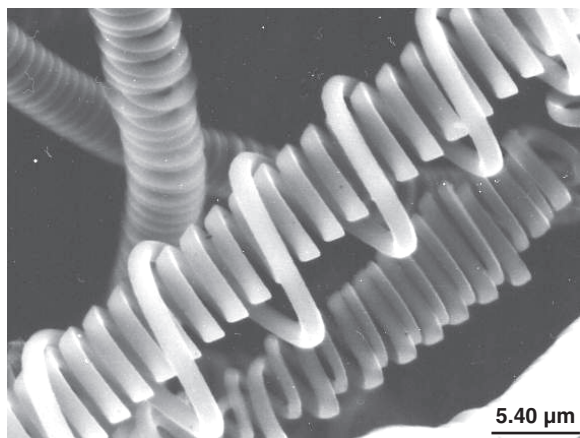


Figure 12. Interesting morphology of the double coils [57].

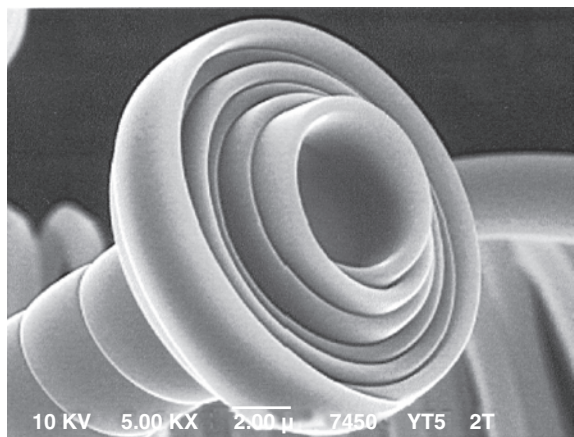


Figure 13. Conically coiled flat carbon coils after growing to the coil axial direction.

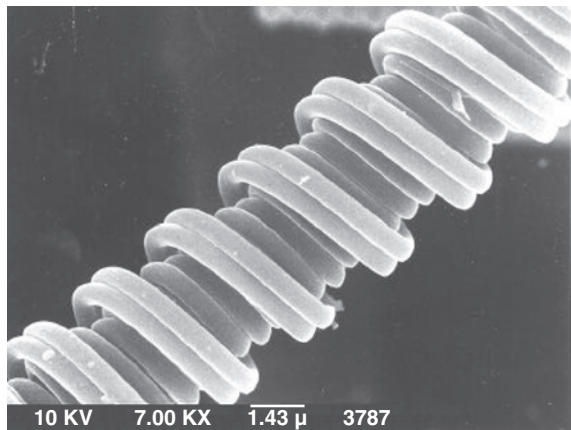


Figure 14. Multiple carbon coils.

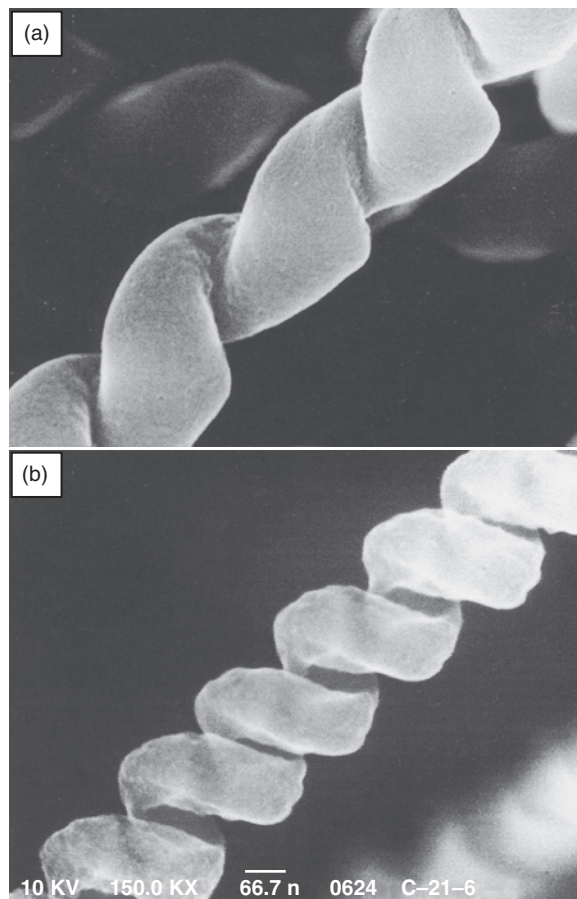


Figure 15. Twisted carbon nanocoils (a) and springlike carbon nanocoils (b).

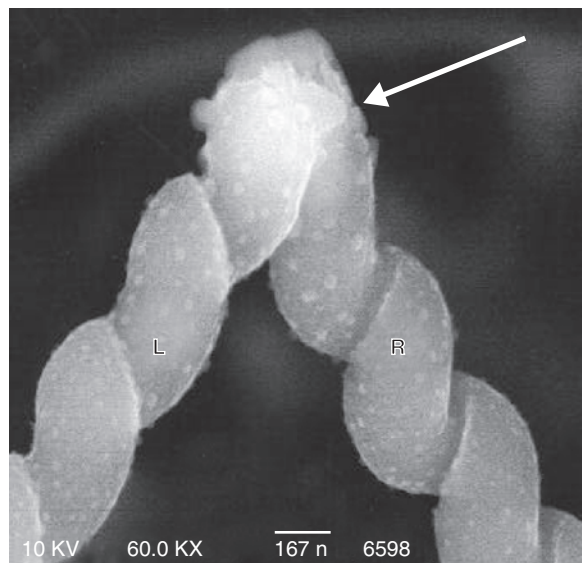
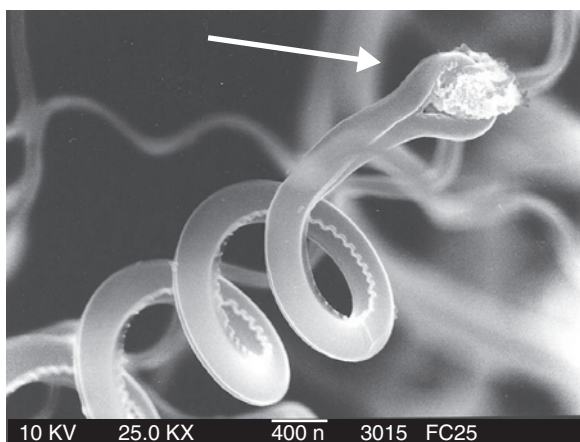
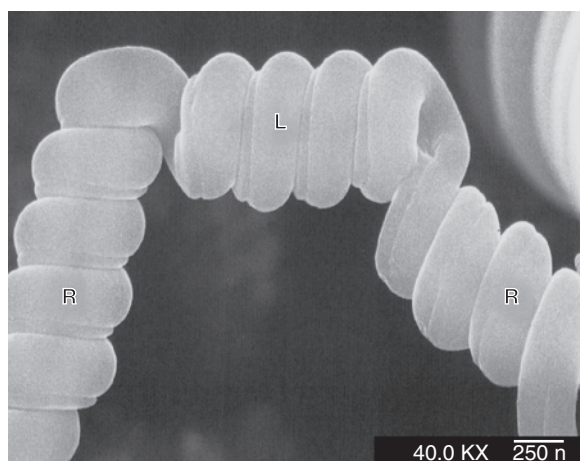


Figure 16. Tip part of the carbon nanocoils. Coiling chirality: (R) Right-clockwise coiling, (L) left-clockwise coiling. Arrow indicates a catalyst grain which is a growing point.





**Figure 17.** Interesting tip morphology of the carbon coils. Arrow indicates a catalyst grain which is a growing point.



**Figure 18.** Carbon coils with changed coiling chirality. (R) Right-clockwise coiling, (L) left-clockwise coiling. Catalyst: stainless steel (SUS 304).

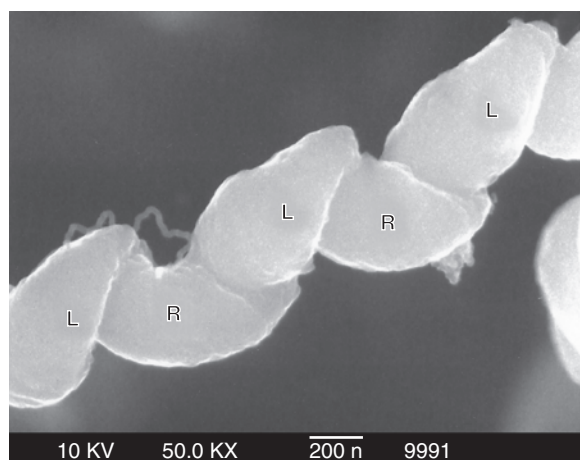


**Figure 19.** Carbon coils with successively changed coiling chirality. (R) Right-clockwise coiling, (L) left-clockwise coiling. Catalyst: stainless steel (SUS 304).

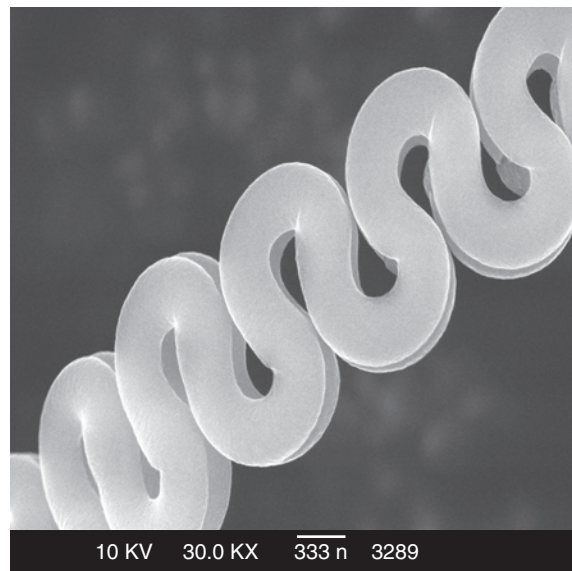


**Figure 20.** Regular zigzag carbon twin fibers.

$\text{PH}_3$ ,  $(\text{C}_2\text{H}_5\text{O})_3\text{P}$  and sulfur compound impurities (thiophene tetrahydrothiophene, diethylsulfide, hydrogen sulfide, and carbon disulfide) to achieve high yield and good reproducibility, and the maximum coil yield was obtained using a thiophene [60–62]. Since 1995 we have tried to prepare carbon microcoils, using various powders or plates of transition metal carbides such as Co, Cr, Fe, Hf, Mn, Mo, Nb, Ta, Ti, V, and W, Ni single crystal plate,  $\text{MoS}_2$ , and  $\text{Ti}_2\text{O}_3$  [62–67]. The results showed that except for Fe, all these metals can be used to obtain carbon coils, but the yield is lower than using a Ni catalyst. Among the carbides used, only TiC powder was effective, but the yield was quite low [63].  $\text{MoS}_2$  and  $\text{Ti}_2\text{O}_3$  were also effective. Since 1996 [63, 67–73], for producing carbon coils efficiently and economically, extensive efforts were made to improve the reaction device and to optimize the reaction conditions (temperature, gas flow pattern, flow rate of acetylene, thiophene,  $\text{N}_2$  and  $\text{H}_2$ ). Multiple gas inlet reactors [72] were developed for the mass-production of the carbon coils. Using this reactor, a coil yield of  $0.2 \text{ kg/m}^2$ -substrate could be obtained.

## 2.4. Preparation Process

The carbon coils are usually prepared by a conventional CVD process. Other preparation processes than the conventional CVD are reported as follows.

### 2.4.1. Laser CVD

Hishikawa and co-workers [74] prepared carbon coils with a coil diameter of  $3 \mu\text{m}$  by the laser CVD process using  $\text{CO}_2$  laser from allene ( $\text{C}_3\text{H}_4$ ) + sulfur hexafluoride ( $\text{SF}_6$ ) gas mixtures using the Fe catalyst.

### 2.4.2. Hot-Filament CVD

Motojima and co-workers [75] prepared carbon fibrillform nanocoils by Zn- or Ni-coated Cu catalyzed pyrolysis of ethylene at  $600 \text{ }^\circ\text{C}$  using the hot-filament CVD process.

### 2.4.3. Microwave-Plasma CVD

Xie and co-workers [40] prepared carbon coils with a coil diameter  $3.5\ \mu\text{m}$  and a fiber diameter of  $200\ \text{nm}$  by the Ni catalyzed pyrolysis of acetylene at  $700\ ^\circ\text{C}$  by the microwave-CVD process. The carbon coils are amorphous and specific surface area is  $62\ \text{m}^2/\text{g}$ .

### 2.4.4. Plasma and Catalyst Technology Process

Motojima and co-workers [61] prepared carbon coils with irregularly coiled form or with very wide coil pitch of  $10\text{--}30\ \mu\text{m}$  by the Ni-catalyzed pyrolysis hydrocarbons at  $770\ ^\circ\text{C}$  using a novel plasma and catalyst technology reactor. It was found that hydrocarbons such as methane, propane, and ethylene were decomposed under plasma and catalyst atmospheres to form acetylene as the main decomposition product, and then this acetylene was further decomposed to form carbon coils.

### 2.4.5. Supersonic CVD

Motojima and co-workers [59, 77] prepared carbon coils under the application of ultrasonic waves in the reaction zone and found that the coil yield and density increased with the application of ultrasonic waves, and that the optimum frequency was  $23\text{--}28\ \text{kHz}$ .

### 2.4.6. Electromagnetic CVD

In the conventional CVD process, an ac electric heater, from which electromagnetic waves (EM) are emitted, is generally used. Furthermore, the carbon coils can significantly absorb EM waves. Accordingly, it can be reasonably expected that the application of EM field as well as bias voltage in the reaction atmosphere may significantly affect the growth of carbon coils. Motojima and co-workers [59, 69, 78–81] first reported on the effect of the EM waves and bias voltage on the growth and properties of the carbon coils. It was found that the coil yield outstandingly increased by applying EM field and bias voltage on the reaction atmosphere.

### 2.4.7. Rotation CVD

Motojima and co-workers [70] reported the preparation of carbon coils using the rotation substrate CVD process.

### 2.4.8. Electroplating Process

Bai [42] obtained carbon nanocoils with a coil diameter of  $35\ \text{nm}$  and a coil pitch of  $30\ \text{nm}$  by the electrolysis of NaCl at  $810\ ^\circ\text{C}$ , showing that the CVD process is not the only way to get coiled carbon fibers.

## 2.5. Microstructure [82–85]

X-ray diffraction (XRD) patterns of the as-grown carbon coils are shown in Figure 21 as well as that of an amorphous pitch-based activated carbon fiber. It can be seen that the carbon coil is almost amorphous. Figure 22 shows the Raman spectra of the as-grown carbon coils obtained by a conventional CVD process and by application of high magnetic field in the reaction atmosphere. It can be seen

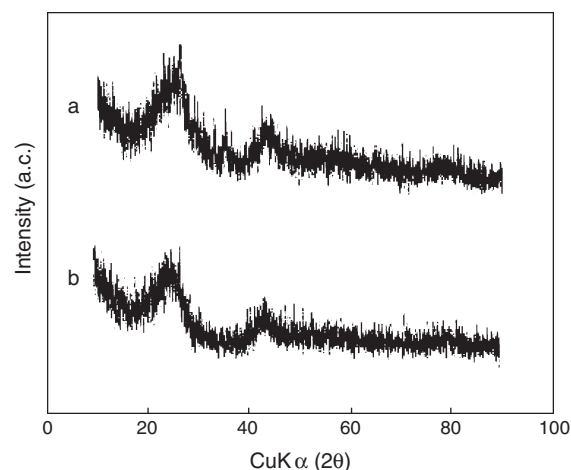


**Figure 21.** XRD patterns. (a) Pitch-based activated carbon, (b) as grown carbon fibers.

that the D-band and G-band intensity is almost the same, indicating an amorphous state, while the strength of the G-band against the D-band increases with increasing applied magnetic strength. Figure 23 shows the TEM image of the as-grown carbon coils. The development of distinct graphite layers cannot be observed while very short-range orderings can be seen. Figure 24 shows the XRD pattern of the heat treated carbon coils in  $\text{N}_2$  or  $\text{Co} + \text{CO}_2$  atmosphere. The amorphous as-grown carbon coils graphitized by the heat treatment without changing coiling morphology, and the graphite coils can be obtained at heat-treatment above  $2500\ ^\circ\text{C}$ . The schematic model of the graphite coils is shown in Figure 25. The graphite coils have distinct graphite layers ( $d = 0.339\ \text{nm}$ ) with an inclination of  $10\text{--}40^\circ$  versus the fiber axis to form a “herringbone” structure.

## 2.6. Growth Mechanism

Why a vapor grown carbon fiber (VGCF) is sometimes successively curled, twisted, or coiled to form “carbon coils” is very interesting from the theoretical and scientific point of view. In an early stage of the research on the VGCF, the

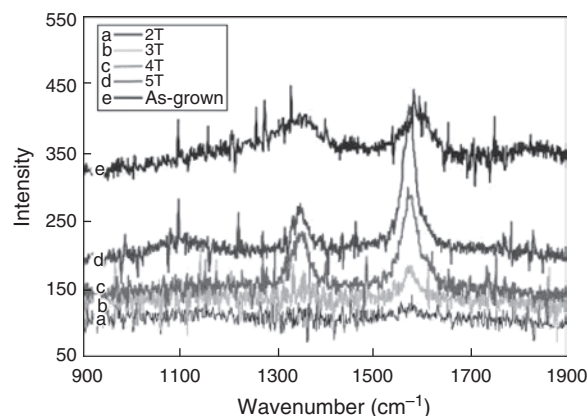


**Figure 22.** Raman spectra of carbon coils. (a–d): Carbon coils prepared with application of high magnetic field of 2–5 Tesla. (e) As-grown carbon coils.

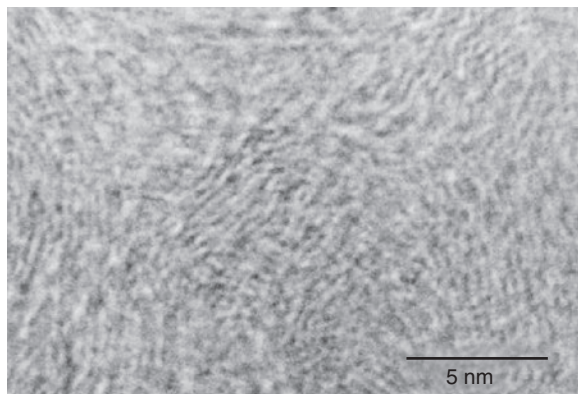


Figure 23. TEM image of the as-grown carbon coils.

growth of the carbon coils with helical, spiral, threadlike, or twisted forms was very rare and extremely accidental, and the reproducibility was very poor. Thus the production was almost excluded as the helical/spiral or twisted form is unusual. Furthermore, the versatile potential applications of the carbon coils were not known and recognized in those days. The reproducibility of the growth of carbon coils from vapor phase was afterward outstandingly improved, and nowadays the carbon coil is semi-mass-produced. The growth mechanism of the VGCF with a straight form has been proposed by many researchers. It may be considered

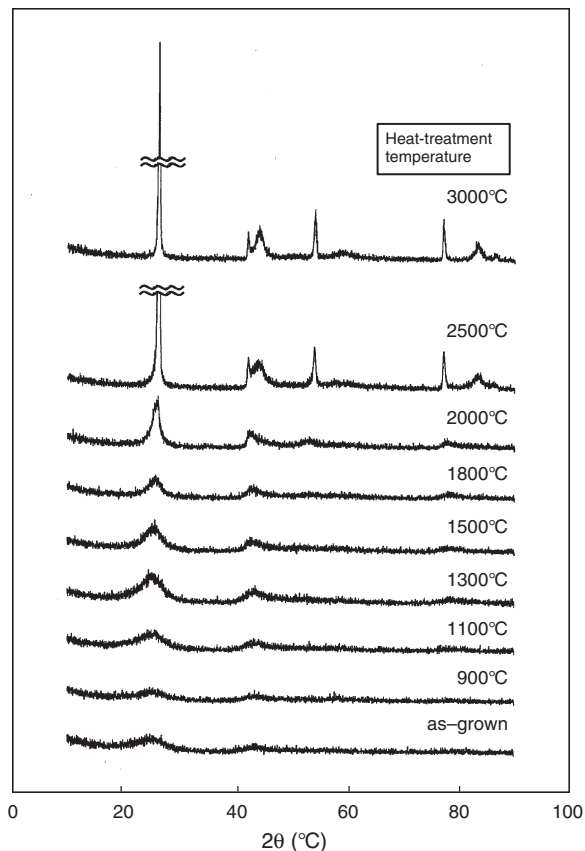


Figure 24. XRD patterns of as-grown and heat-treated carbon coils.

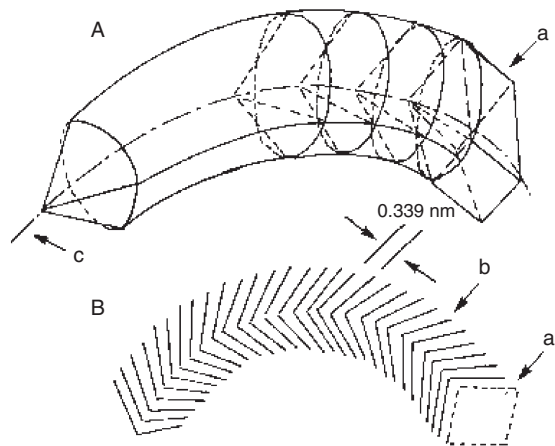


Figure 25. Schematic image of the herringbone structure of the graphite coil: (A) 3D image, (B) 2D image showing graphite layers. (a) Catalyst grain, (b) Graphite layers, (c) Fiber axis [82].

that the growth of carbon coils with various morphologies is the general growth pattern of a VGCF and a straight VGCF is the rather special case. Accordingly, the growth mechanism of the carbon coils has also been proposed by those researchers as well as the establishment of the preparation processes of the carbon coils.

In this section, the growth models or mechanisms of the carbon coils are reviewed.

### 2.6.1. Boehm's Mechanism

Boehm [14] proposed a schematic growth model of filamentary carbon on iron carbide with two active faces at oblique. He considered that if the catalyst particle has an angular shape as shown in Figure 26, a curved carbon fiber would grow from the active crystal faces due to the different diffusion path lengths in the carbide crystals resulting in the growth of helical growth forms if strands grow to any length, and double helices would result if two adjacent crystal faces are active.

### 2.6.2. Baker's Branching Mechanism

Baker and co-workers [17] obtained spiral carbon filaments from acetylene at above 800 °C using the Sn/Fe (Sn coated Fe foils) catalyst. Branching of carbon filaments was common as shown in Figure 27. They suggested the principle means of relieving the stress created by the fact that filaments were often forced against the mass of deposit in two directions, and when this stress became too great the particle was squeezed out from between these two filaments and began to propagate a new pair.

### 2.6.3. Baker's Filament Growth Model

Baker and Chludzinski [81] examined the effect of the various metal oxide additives to the Ni-Fe catalyst on the inhibition of the growth of carbon filaments using  $C_2H_2$  as a source gas. Many filaments formed in the presence of  $TiO_2$  (Ni-Fe/ $TiO_2$  catalyst) were in a spiral conformation, where the catalyst particle was located within the filament, which grew from two faces of the particle in opposite directions.



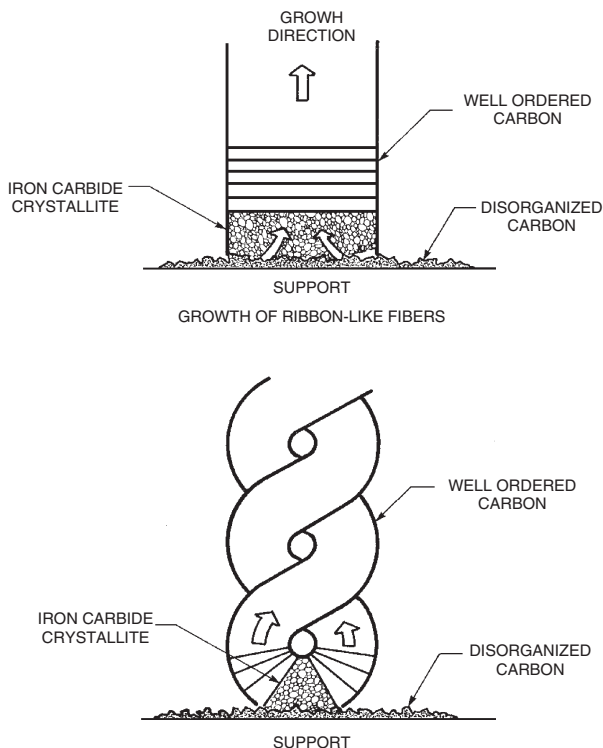


**Figure 26.** Schematics representation of growth mechanism of filamentary carbon on iron carbide (a) on rectangular carbide particle, (b) on carbide particle with two active faces at oblique angle [14, 29].

**2.6.4. Downs–Baker Mechanism**

Downs and Baker [86] obtained various carbon filaments (e.g., branched, spiral, helical, with coil diameter of about 100 nm) using carbon fibers as the substrate as schematically shown in Figure 28. They also proposed the growth mechanism of the coils.

**2.6.5. Kim–Baker Mechanism**

Kim and co-workers [20] reported the growth of coiled carbon fibers using  $C_2H_2$  and Cu/Ni(1:1) at 700 °C. Two filaments grew from opposite faces of the catalyst particles

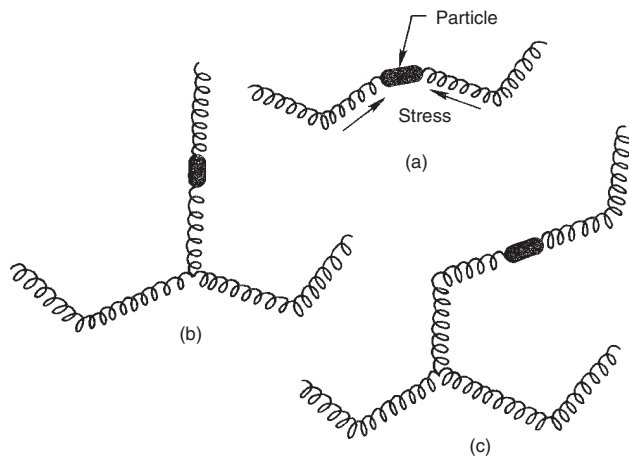


**Figure 27.** Bifilament morphology of coiled carbon fiber observed in the Sn/Fe system. [17, 29].

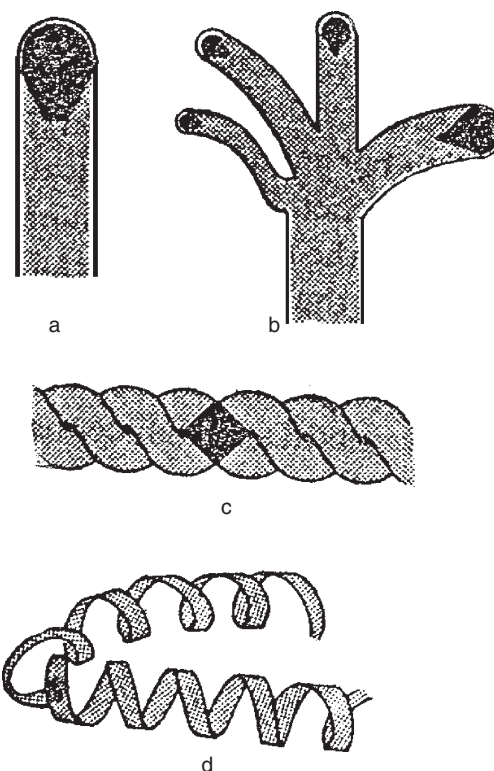


**Figure 28.** Schematic representation of different types of growth morphologies observed in carbon filaments [86]. (a) Whisker-like, (b) branched, (c) spiral, (d) helical.

at identical rates. Furthermore, during the major part of the growth process, the filaments were relatively smooth and tended to form into large loops. The catalyst particles reached a size of about a third of the original value; they appeared to undergo a further change in shape and simultaneously started to rotate on an axis perpendicular to the direction of filament growth, causing the filament to acquire a spiral form. This action normally continued for a relatively short time, being the prelude to catalyst deactivation. This phenomenon was observed at all growth temperatures.

**2.6.6. Amelinckx’s Mechanism**

Amelinckx and co-workers [31] examined in detail the different coiling morphologies of the graphite tubes grown by the Co-catalyzed decomposition of acetylene and proposed a new model based on the concept of the spatial-velocity hodograph to describe quantitatively the extrusion of a carbon tubule from a catalytic particle as shown in Figure 29. The coiled fibers were generally found to be hollow tubes consisting of concentric cylindrical graphene sheets. The tubules can adopt various shapes such as straight, curved, planar-spiral, and helix, often with a remarkably constant coil pitch. It is generally accepted that the tubules grow by the extrusion of carbon, dissolved in a metallic catalyst particle that is supersaturated in carbon at one part of the surface. The most detailed description of this growth process was given by Baker [87].

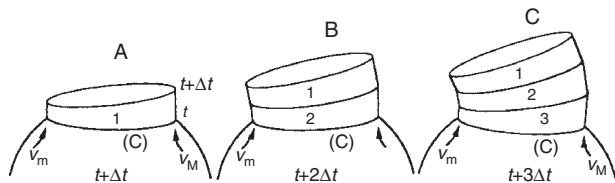


**Figure 29.** Successive stages in the extrusion of carbon according to the hodograph of the extrusion velocities for the case of a uniform bent tubule [31].

### 2.6.7. Owens's Mechanism

Although it is well known that sulfur acts as a poison for many Ni-catalyzed reactions, Owens and co-workers [28] observed that certain benefits of sulfur can be derived from following a partial and well controlled sulfidization treatment of the metal catalyst for the growth of carbon filaments by the nickel catalyzed decomposition of  $C_2H_4/H_2$  mixtures. That is, the pretreatment of Ni in low levels of  $H_2S$  (4–50 ppm) results in a reconstruction of the metal surface and thus induces some major perturbations in the morphological characteristics of the filamentous carbon deposit to regularly form coils. This change in growth mode indicates that sulfur is modifying the diffusion characteristics of carbon species through the catalyst particle.

### 2.6.8. Fonseca–Dunlop Mechanism

Fonseca and co-workers [88, 89] reported a model of perfectly graphitizable coiled carbon nanotubes and discussed the growth mechanism of the coiled carbon nanotubes. The presence of a large amount of curved and coiled nanotubes among the straight tubes produced by the catalytic method stimulated several studies on the theoretical aspect of the coiling mechanism [88, 90–93]. It was proposed that the curving and coiling of the straight tubes can be accomplished by the occurrence of knees (i.e., two straight cylindrical tube sections of the same diameters connecting at an angle). Such knees can be obtained via the insertion in the plane of the knee of diametrically opposed pentagonal and heptagonal carbon rings in the hexagonal networks. The heptagon is on the inner side of the knee and the pentagon is on the outer side. The possibility of such a construction was predicted by Dunlap [94–96]. Theoretical models of curved nanotubes forming toroids of irregular diameters have also been described by Ihara and Itoh [97]. Fonseca suggested a growth mechanism on a catalyst at a molecular level using the heptagon–pentagon construction of Dunlap [95]. Dunlap explained the formation of curved nanotubes, tori, or coils by this concept. Dunlap also observed that the diameter range of the young tube (1 min) is about the same as that of the old ones (80 min). For a long time exposure (5 h) of the tubules to the reaction conditions, only amorphous carbon was deposited on the outer layer and no tubes with higher diameters were observed.

### 2.6.9. Li's Mechanism

Li and co-workers [98] obtained coiled nanotubes by the Fe-catalyzed pyrolysis of acetylene at 973 K and examined the morphology and microstructure in detail. The obtained

coil was a single coil and has a 70 nm coil diameter and a 130 nm coil pitch. It was suggested that the formation of the coiled nanotubes was due to the mismatch between the extrusion velocity by the catalyst particle and the rate of carbon deposition.

### 2.6.10. Motojima's Anisotropy Mechanism

Motojima and co-workers [1, 50, 99] proposed the two- and three-dimensional growth mechanism of the carbon coils based on the anisotropic deposition of carbon on the different catalyst crystal planes. Figure 30 shows the tip part of the carbon coils obtained in an initial growth stage. It can be seen that two carbon fibers grew from a catalyst grain (white part) and curled to form double coils. Figure 31 shows the schematic 2D-growth model. If the catalytic activity of a crystal plane A of a catalyst grain is larger than that of B, the grown fiber will be curled to the right direction to form carbon coils. On the other hand, if there is no difference in catalytic activity between crystal planes A and B, a straight carbon fiber grows. Figure 32 shows the 3D-growth model. Six carbon fibers grew basically from six crystal planes following coalescence to form two fibers. That is, one fiber is formed from fine carbons deposited from three crystal planes, in which three crystal faces may have different catalytic activities. Motojima and co-workers [45, 99] have found that a different crystal face of a Ni single crystal has different catalytic activity for the growth of carbon coil, and the coil yield was 10.2% for Ni(100), 6.7% for Ni(111), and 3.2% for Ni(110). Circular carbon coils with circular fiber cross section are predominantly formed during the initial growth stage and then change to flat coils with increasing reaction time because of the change in the catalyst shape from cubic to slender form. A change in the catalyst form may be effected by the electromagnetic field (force) emitted from the outer electric heater as schematically shown by Chen and co-workers [100]. Yang and Chen [101] reported that for the carbon filament growth using the Ni-catalyzed pyrolysis of methane at 700 °C, the most preferable crystal plane for graphite precipitation was Ni(111) followed by Ni(111) > (311) > (100) > (110). Accordingly, the grown carbon fiber curls such that the fiber plane deposited from higher catalytic plane is outer part of the curled fibers to

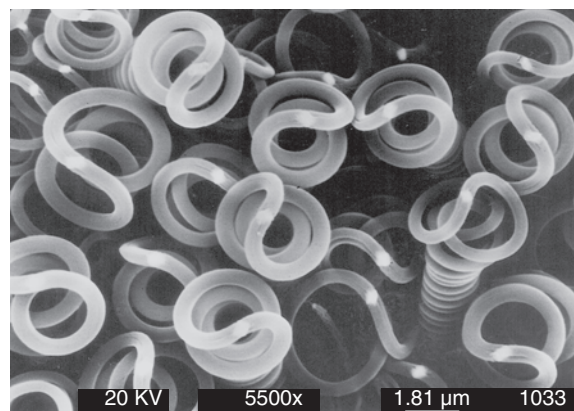


**Figure 30.** Tip of the carbon coils grown on a Ni catalyst in the initial reaction stage [63].

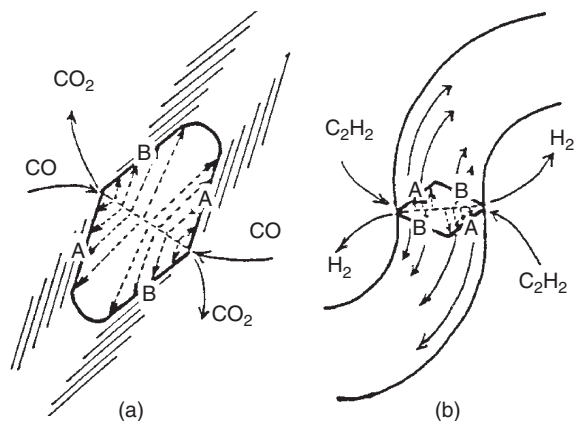


**Figure 31.** 2D-schematic growth model of (a) straight carbon fiber and (b) carbon coil [136].

from carbon coils. The coil diameter is determined by the difference in catalytic activities of A and B, and coil pitch by the difference in B and A or C.

**2.6.11. Chesnokov’s Mechanism**

Chesnokov and co-workers [27] proposed the growth mechanism of the symmetrical helical filamentous carbon fibers obtained by the decomposition of butadiene-1,3 over Ni-Cu/MaO catalyst at 723 K. Figure 33 shows the schematic growth model. In the initial growth stage, butadiene-1, 3 decomposes to form carbon and hydrogen atoms. Carbon atoms diffuse into the Ni/Cu alloy bulk and gradually oversaturate to nucleate and form metastable Ni<sub>3</sub>C on the frontal side of the alloy particle. Planes (111) of Ni/Cu alloy are the most preferable for the graphite nucleation since graphite (002) and alloy (111) planes, which determine the filament growth direction, are similar in symmetry and interatomic distances [27]. Intensive carbon atom diffusion flow toward the crystallization center then occurs, which results

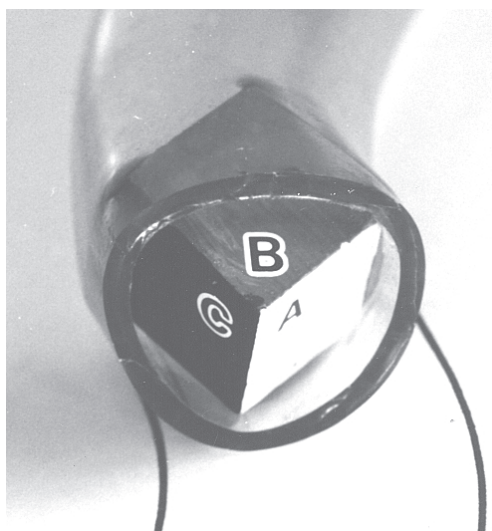


**Figure 32.** 3D-schematic growth model of carbon coils [1]. A, B, and C show the different crystal faces.

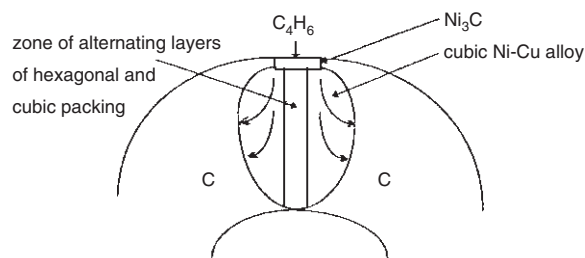


**Figure 33.** Schematic diagram of the growth mechanism of helix filamentous carbon produced from butadiene-1,3 on Ni-Cu crystals [27].

in dislocation of metal atoms and thus distorts the spherical shape of the particle to an elongated form. As can be seen in Figure 23, different carbon atoms pass via unequal diffusion from the places where they enter the alloy particle through the Ni<sub>3</sub>C phase to different surface patches where graphite phase grows. This results in different growth rates and filament twisting [27].

**2.6.12. Chiral Nanotube**

Liu and Cowley [102] reported on the electronic structure of chiral nanotubes. Akagi and co-workers [103] studied general features of the electronic states of helically coiled cages of graphite layers by simple tight-binding models. Ihara and Itoh [97] reviewed the recent status of research of helical and toroidal forms, which contain pentagons, hexagons, and heptagons of carbon atom. Figure 34 shows the schematic model of a helically coiled form of C<sub>360</sub>. The atomic arrangements of the structures of the helically coiled forms of the carbon cage for the single layer, which are found to be thermodynamically stable by molecular-dynamics simulations, are compared to those of the experimentally helically coiled forms of single and multilayers graphite forms that recently have been experimentally observed.

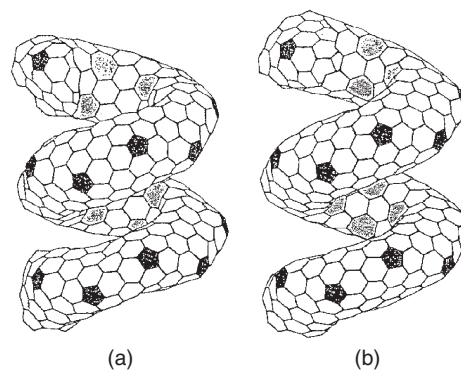


**Figure 34.** Helically coiled form C<sub>360</sub> [97]. One pitch contains a torus C<sub>360</sub>. (a) Coil length = 12.9 Å and (b) coil length = 13.23 Å. The tiling pattern of heptagons in the inner ridge line is changed, though the pattern of pentagons in the outer ridge line remains upon changing the coil length.



## 2.7. Properties

### 2.7.1. Mechanical Properties

The mechanical properties of the carbon coils were evaluated in detail by Motojima and co-workers [46, 104–108]. The circular carbon coils with a circular fiber cross sections and with large coil diameter can be extended elastically up to 4.5–15 times original coil length, while flat coils with flat or rectangular fiber cross sections can only be extended up to 1.5 times the original length. For example, the carbon coil can be extended to nearly straight form as shown in Figure 35 [108]. The carbon coils extend linearly with increasing applied load. The rupture strength of the as-grown carbon coils is 42–114 MPa. The rigidities of the circular and flat as-grown carbon coils are 22–46 GPa and 22–33 GPa, respectively.

### 2.7.2. Electric Properties

The bulk (powder) electrical resistivity of the as-grown carbon coil decreases with increasing the bulk density and is 1–10  $\pi/\text{cm}$  for bulk density 0.3  $\text{g}/\text{cm}^3$  and 0.1–0.2  $\pi/\text{cm}$  for 0.6  $\text{g}/\text{cm}^3$  as shown in Figure 36 [82]. The resistivity of the bulk carbon coils can be decreased steeply with the surface coating by carbon [83], TiC [109], TiN [110], ZrC [104], NbC [111], and TaC [112] but not by graphitizing at high temperature heat treatment [82]. Kaneto and co-workers [113, 114] examined the electrical conductivity of the carbon coils in detail. The electrical conductivity along the helical axis of a piece of carbon coil is 30–100 S/cm. This conductivity is rather small compared with multiwalled carbon nanotubes. Figure 37 shows the current–voltage (*i*-*v*) curve of a piece of carbon coil. The (*i*-*v*) characteristics indicate that the current shows superlinear dependence on the applied voltage at high fields. The fact is explained by heating of the coil by electrical power, because of the higher conductivity at higher temperature, or the high field effect. The temperature dependence of conductivity showed that one of the possible transport mechanisms is the 3D variable range hopping model. Kaneto and co-workers [114] also examined the electrical conductivities of the carbon coils under various gas atmospheres. The conductivity of a single coil increased by 5–20% upon evacuation for several minutes. Furthermore,

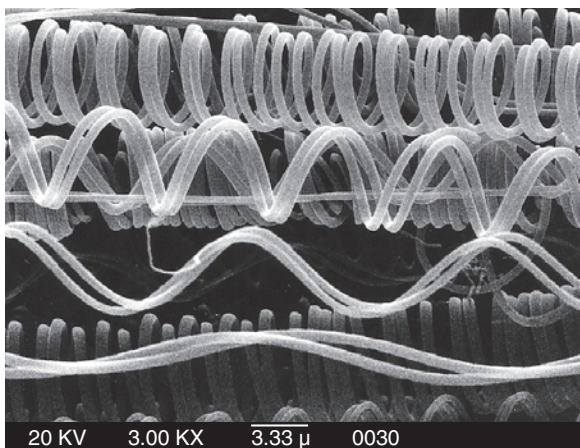


Figure 35. Extended carbon coils [108].

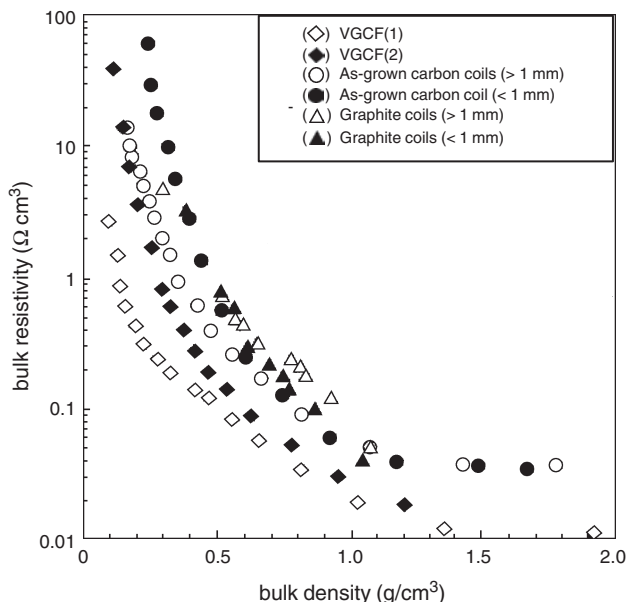


Figure 36. Bulk electrical resistivity obtained at room temperature in air [82].

the conductivity increased by 1–2% upon exposure to iodine (oxidative) gas for several minutes. On the other hand, upon exposure to ammonia (reductive) gas from the vacuum, the conductivity decreased nearly to the same value of the air atmosphere. However, the degree of conductivity was found to be small compared with the case of other  $\pi$  conjugated systems such as conducting polymer.

Fujii and co-workers [115, 116] examined the magnetoresistance of the as-grown and heat-treated carbon coils in the magnetic field in the range from 0 to 12 Tesla at 290 K. The magnetoresistance of the as-grown carbon coil does not change under strong magnetic field up to 12 Tesla. On the other hand, the magnetoresistance is negative for specimens

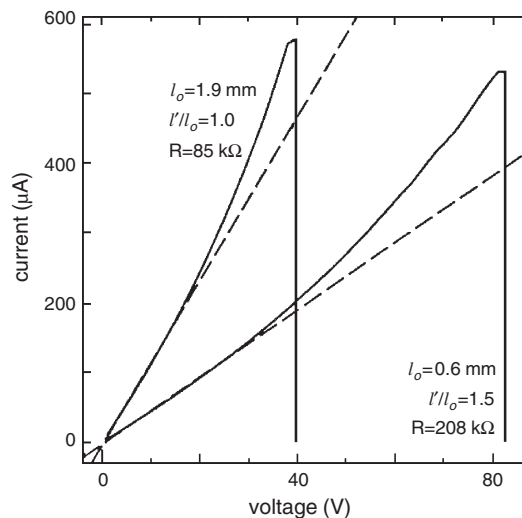


Figure 37. Voltage–current (*i*-*v*) characteristics of a carbon coil [113, 114]:  $l_0$ : coil length before stretch,  $l$ : coil length after stretch,  $R$ : electrical resistivity.

heat-treated at 1500 °C and 2000 °C and positive for specimens heat-treated at 2500 °C and 3000 °C. The absolute value of the magnetoresistance ratio  $\{R(B) - R(0)\}/R(0)$  increased with increasing magnetic field, 40% at parallel magnetic field of 12 T, and 5% at 5 T, and 14% under transverse magnetic field of 12 T as shown in Figure 38.

### 2.7.3. Field Emission Properties

Pan and co-workers [117] reported on the field emission properties of carbon tubule nanocoils. The carbon nanocoils show the low turn-on field of 180 V at a 130  $\mu\text{m}$  gap and high emission current of  $10^{-3}$  A/cm<sup>2</sup> at 300 V as shown in Figure 39 and also shows excellent stability of emission for over 250 hr. These values are sufficient for commercializing the carbon-nanofiber-based field emission displays. Accordingly, the carbon nanocoil is expected to be a novel attractive candidate for the fabrication of flat panel field emission displays.

### 2.7.4. Electromagnetic Properties

It is considered that the carbon coil is a promising candidate as a novel EM wave absorber, especially in the GHz range, because of its microcoiling morphology. That is, the microcoiling morphology is the most effective and ideal one for the generation of inductive current by Faraday's law resulting in absorption of EM waves. Actually, the carbon coils can absorb EM waves in the GHz region without reflection. Motojima and co-workers [47, 83, 118–120] examined the absorption ability (reflection loss) of EM waves, especially in the GHz regions, in detail. The as-grown carbon coils can strongly absorb the EM waves of 13.9 and 16.3 GHz, and the reflection loss is below  $-40$  dB (99.99% absorption). The absorption region can be broadened by addition of other additives. Figure 40 shows the reflection loss of the CMC-containing PMMA (polymethylmetacrylate) beads for 75–105 GHz regions. It can be seen that the reflection loss below  $-30$  dB (99.9% absorption) of EM waves can be obtained by only 1 wt% addition in the PMMA beads.

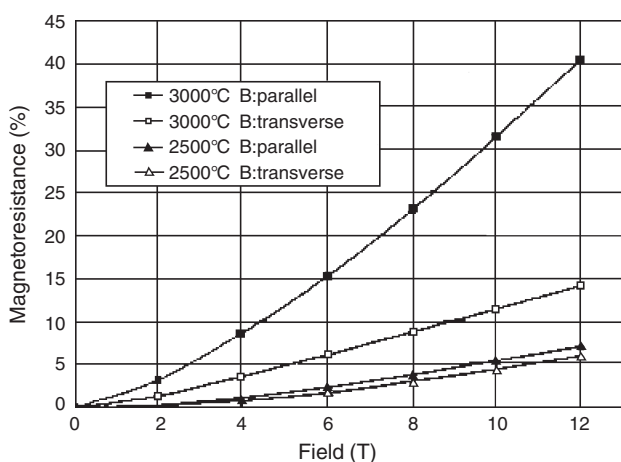


**Figure 38.** Effect of magnetic field on the magnetoresistance of a heat-treated carbon coil (graphite coil): Temperature: heat-treated temperature. Parallel and transverse: the direction of magnetic field is parallel and transverse (vertical) to the coil axis, respectively [116].

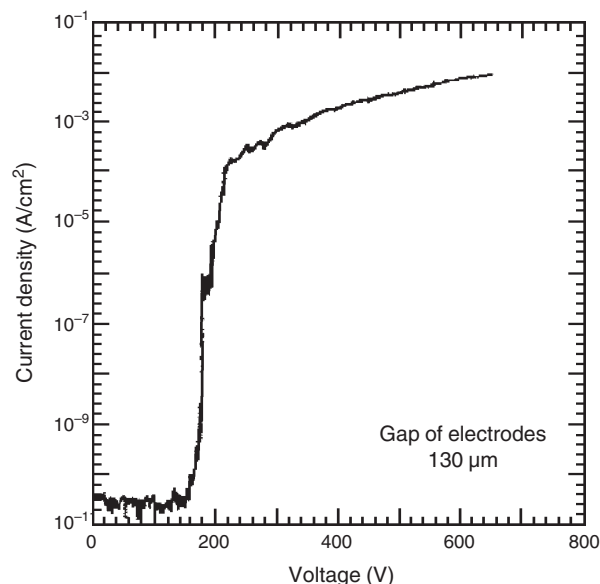


**Figure 39.** Curve of the emission current density vs applied voltage for a typical nanocoil field emitter [117]: The low turn-on voltage and high current density are obtained.

The higher addition above 2 wt% or lower addition below 0.5 wt% results in lower reflection loss. Du and co-workers [121] examined microwave electromagnetic characteristics of a microcoiled carbon fiber/paraffin wax composite in Ku band frequencies (12.4–18 GHz).

### 2.7.5. Chemical Properties

The carbon coil become oxidized at about 450 °C in air, and the weight significantly decreases with increasing temperature and burn out at 700 °C [122]. On the other hand, the graphite coils obtained by the heat treatment of as-grown carbon coils at 3000 °C for 6 hr in CO + CO<sub>2</sub> become oxidized at about 700 °C in air. The oxidation behaviors of the as-grown and heat-treated carbon coils are examined in detail to improve the surface inertness and enhance the

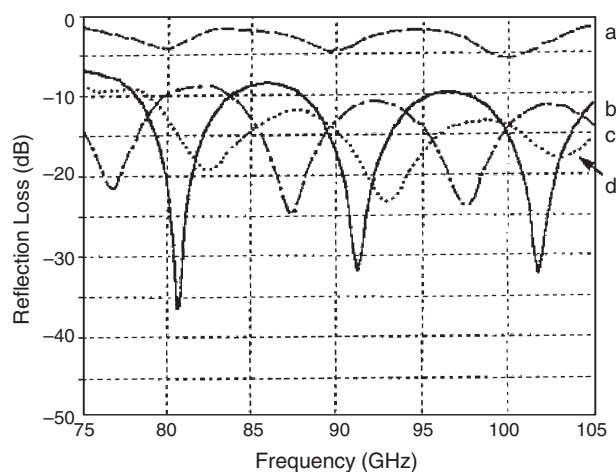


**Figure 40.** Reflection loss of the CMC-impregnated PMMA bead. CMC content: (a) 0 wt%, (b) 1 wt%, (c) 2 wt%, (d) 3 wt%.

chemically active sites [54, 122, 123]. The graphite coil is stable up to about 1200 °C in Ar atmosphere. However, the graphite coil is partially oxidized by the small amount of oxygen impurity included in Ar at the contact part of two graphite layers in which large inner stress may be impressed to form on amorphous state. Shibagaki and Motojima [54, 123] examined in detail the partial oxidation characteristics of the surface of the carbon coils, under low O<sub>2</sub> flow rate at 450–820 °C to improve the surface chemical activities.

### 2.7.6. Thermal Properties [82, 106, 123]

The carbon coils can be heat-treated up to 1000–3000 °C in CO + CO<sub>2</sub>, Ar, or N<sub>2</sub> atmosphere to form graphite coils with full preservation of the coiling patterns of the carbon coils. The elasticity of the as-grown carbon coils is reduced by the heat treatment and became brittle. The ruptured cross section of the fiber which composes the circular graphite coil takes either a trigonal pyramid-like form or a negative pyramidal hollow. On the other hand, the ruptured cross section of the flat graphite coils either has rooflike extrusion or is hollow. These characteristic patterns suggest a growth mechanism of the carbon coils. Many distinct striations, declined at 40–50 deg against fiber axis, can be seen on the surface. The TEM image of the tip part of the ruptured fibers shows that distinct graphite layers ( $d = 0.339$  nm) are developed with an inclination of 35–40 deg versus the fiber axis to form a “herringbone” structure. The lattice parameter is  $a = 0.2464$  nm and  $c = 0.6772$  nm. The “ $c$ ” value is slightly larger than the reported value for graphite of 0.6714 nm while the  $a$  value is the same as that of graphite ( $a = 0.2463$  nm). Raman spectra show that the graphite layers of the graphite coils are not more developed than the 100–200 μm long VGCF. This may be caused by the presence of some disorders in the graphite layers and/or the smaller submicrometer width of the graphite layers in the graphite coils.

## 3. CERAMIC NANOCOILS/NANOTUBES

### 3.1. Introduction

Ceramic materials with a 3D nanocoiled or nanotubed structure (referred to as “ceramic coils” hereafter) are not commercially available. Ceramic coils are very interesting as new functional materials with many potential applications, such as light weight thermal barriers, heat exchangers, gas separation materials, absorbers for electromagnetic waves, microsensors, electrodes materials, catalysts, etc. The growth of various coiled ceramic fibers by CVD process has sometimes been observed with mixing straight fibers so far. These coiled fibers are generally very irregularly coiled, and the growth is extremely accidental and without reproducibility. On the other hand, Motojima and co-workers [9, 10, 124, 125] first found that very regularly coiled silicon nitride (Si<sub>3</sub>N<sub>4</sub>) fibers could be obtained with good reproducibility by the CVD process. After then, they prepared various ceramic coils such as metal carbides, nitrides, and oxides using a carbon coil as a template with high yield. Growth of various ceramic coils by the CVD process, electroplating, or the biomimetic process has also been reported by some researchers.

In this section, preparation, morphology, growth mechanism, and some properties of various ceramic coils/tubes are reviewed.

### 3.2. SiC and Si<sub>3</sub>N<sub>4</sub>

The vapor growth of the helical SiC fibers was first reported by Addamiano [126]. He found that the coiled crystals of 2H-SiC grew in mixing in a mass of straight 2H-SiC whiskers during the hydrogen reduction of methyltrichlorosilane at 1400–1430 °C on graphite substrate. After then, Kang and co-workers [127] reported that irregularly coiled SiC whiskers grew among the straight or irregularly curled SiC fibers during the carbothermal reduction of SiO<sub>2</sub> by carbon at 1500 °C under Ar + CO atmosphere. The springlike SiC whiskers did not grow in the presence of Fe impurity but grew in NaCl impurity. It was suspected that the formation of the springlike whiskers should be closely related to the presence of chlorine impurity.

Motojima and co-workers [68] prepared the SiC coils using a powder mixture of SiO and cooked rice husks at 1400–1450 °C. The SiC coils were triple coils with a 0.5–1 μm coil diameter and a 10–100 μm coil length. Motojima and co-workers [47, 106, 128, 129] also easily prepared the SiC coils by the vapor phase diffusion process using a carbon coil as a template.

Motojima and co-workers [9, 10, 124] first prepared very regularly coiled silicon nitride (Si<sub>3</sub>N<sub>4</sub>) fibers by the Fe-catalyzed CVD process using a Si<sub>2</sub>Cl<sub>6</sub> + NH<sub>3</sub> (or N<sub>2</sub>) + H<sub>2</sub> gas mixture at 1200 °C on a graphite substrate. The Si<sub>3</sub>N<sub>4</sub> coils are single-helix coils and have a coil diameter of 10–15 μm and a coil pitch of 3–5 μm as shown in Figure 41. The coils have a crystalline Si<sub>3</sub>N<sub>4</sub> core surrounded by an amorphous Si<sub>3</sub>N<sub>4</sub> clad [130] and have excellent elastic and mechanical properties [26, 131–133]. Iwanaga and co-workers [134] review the ceramic microcoils including the Si<sub>3</sub>N<sub>4</sub> coils. Vogt and co-workers [135] prepared the microcoiled Si<sub>3</sub>N<sub>4</sub> fibers by the reaction of SiO<sub>2</sub> with NH<sub>3</sub> at 1400 and found that addition of Fe and W impurity in SiO<sub>2</sub> partly promotes the growth of the microcoiled Si<sub>3</sub>N<sub>4</sub> fibers. The Si<sub>3</sub>N<sub>4</sub> coils obtained by them are single-helix coils with a fiber diameter of 2–10 μm and a coil diameter of 5–20 μm.



**Figure 41.** Si<sub>3</sub>N<sub>4</sub> microcoils prepared by a Fe-catalyzed CVD process [9, 10].



### 3.3. TiC, TiN

Motojima and co-workers [136] prepared a TiC microcoil by the CVD process using a source gas mixture of  $\text{TiCl}_4 + \text{H}_2 + \text{PCl}_3$  and a Si + Pd catalyst dispersed on a graphite substrate at 1050 °C. The TiC coils were double-helix coils similar to DNA and have a coil diameter of 1–5  $\mu\text{m}$  and a coil length of 20–150  $\mu\text{m}$ . Motojima and co-workers [47, 109, 128, 129, 137] also obtained TiC coils by a vapor phase diffusion process (titanizing or nitriding) using carbon coils as the template, with full preservation of the coiling morphology of the source carbon coils. The bulk (powder) electrical resistivity of the TiC coils decreased with increasing titanizing ratio and attained 0.01  $\Omega \text{ cm}$  at a bulk density of 1.4  $\text{g/cm}^3$ . Addition of the  $\text{N}_2$  or  $\text{NH}_3$  gases resulted in the formation of TiN microcoils because the nitride phase is thermodynamically more stable than the carbide phase.

### 3.4. ZrC, ZrN

Motojima and co-workers [104, 129] prepared ZrC and ZrN coils by the vapor phase diffusion process using the carbon coils as a template. Depending on the reaction conditions, ZrC/C(carbon coil)/ZrC composite coils to a single phase ZrC coil could be obtained, with full preservation of the coiling morphology of the carbon coil and coil yield 100%. Addition of  $\text{N}_2$  or  $\text{NH}_3$  gases in the reaction atmosphere resulted in the formation of ZrN coils.

### 3.5. NbC, NbN, TaC, TaN, HfC

Motojima and co-workers [47, 106] obtained NbC coils by the vapor phase diffusion process using the carbon coils as the template. Depending on the reaction conditions, NbC/C(carbon coil)/NbC composite coils to single phase NbC coils could be obtained, with full preservation of the coiling morphology of the carbon coil and coil yield 100%. Addition of the  $\text{N}_2$  or  $\text{NH}_3$  gases resulted in the formation of a ZbN/C(carbon coils)/NbN–NbN coils/tubes [138, 139]. The carbides or nitrides of Ta or Hf were also obtained using similar processes [47, 106, 112, 116, 129, 138].

### 3.6. SiO<sub>2</sub>, TiO<sub>2</sub>

Robbie and co-workers [9, 140] found that porous and chiral films of  $\text{SiO}_2$  could be obtained by the GLAD (glancing angle deposition) process using electron-beam evaporation onto the glass substrates coated with an ITO transparent conductor. They showed that using the GLAD process, the microstructure parameters such as helical rise angle, pitch, and handedness could easily be controlled, and structures such as pitch gradients and stacked layers of different pitch and/or handedness were also easily produced. For example, the pitch in a helical GLAD films can be controlled by the ratio of deposition rate to substrate rotation rate, while the handedness can be controlled by the direction of rotation. Figure 42 shows an example of a chiral GLAD  $\text{SiO}_2$  film [141]. This film has left-handed helical columns with 8.4 turns and pitch  $p = 410$ . Robbie and co-workers [140, 142] also obtained chiral liquid crystal films by embedding LC into the porous and chiral  $\text{SiO}_2$  films. Helical/spiral forms are also frequently observed in materials such quartz

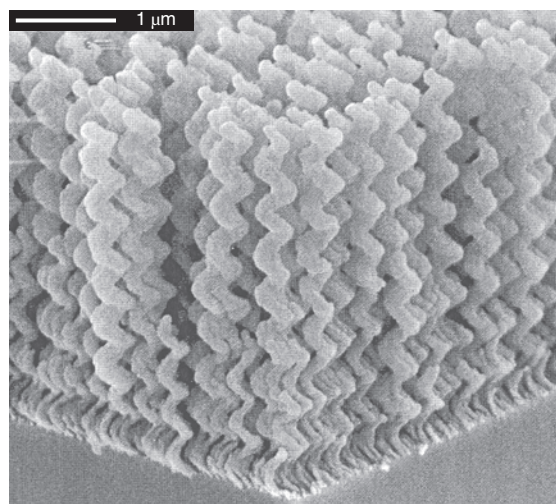


**Figure 42.** Example of a chiral GLAD  $\text{SiO}_2$  film [140]. A left-handed helical film with 8.4 turns of pitch 410 nm is shown. The film pitch is the thickness of one turn of the helix and relates to the wavelength at which peak chiral optical activity is observed.

[143]. Yang and co-workers prepared hollow helicoids made of hexagonal mesoporous silica [144]. Research group of Shinkai studied the preparation of silica fibrils with a novel double stranded helical structure by sol–gel transcription of twisted bilayer ribbons formed by cationic gemini surfactants [145]. Motojima and co-workers [146] prepared  $\text{TiO}_2$  microcoils/tubes by sol–gel and CVD processes using a carbon coils as a template as shown in Figure 43.

### 3.7. Miscellaneous

Gleize and co-workers [147] prepared tubular BN fibers with a helical form by a CVD process using  $\text{B}_2\text{H}_6 + \text{NH}_3$  (or  $\text{N}_2$ ) at 1100 °C using the  $\text{ZrB}_2$  catalyst. The thickness of tubular fiber is 0.1  $\mu\text{m}$ , coil diameter is 0.2  $\mu\text{m}$ , and coil length is 5  $\mu\text{m}$ . Johansson and co-workers [148] proposed a

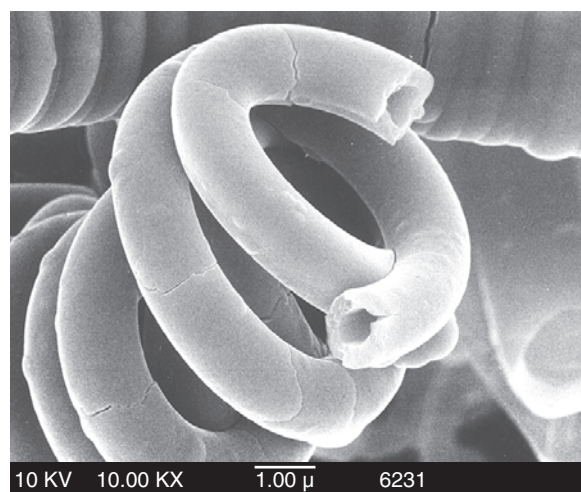


**Figure 43.**  $\text{TiO}_2$  helical coils obtained using a carbon coils as a template.

new method for the preparation of three-dimensional structures in free space, a laser-assisted CVD process with a high-resolution micropositioning system. In this process, a linear three-axis micropositioning system and laser beam which was focused on the tip of the growing point are used. Using this process, they prepared a 3D-boron spring with spring diameter of 350  $\mu\text{m}$  from a gas mixture of  $\text{BCl}_3 + \text{H}_2$  gas mixture. This boron spring has high mechanical properties such as an elastic modulus of 420–450 GPa, fracture strain of 2.7–3.7%, and a fracture stress of 12–17 GPa. Jiang and co-workers prepared AN whiskers with wavy (helical) structure by the SHS (self-propagating high-temperature synthesis) method [149]. The growth of helical fibers of GaP[150], GaAs[151, 152], MnAs[153], ZnS[151], Cu[154], Cu–Zn[154], and  $(\text{SrBa})\text{CO}_3$  [155] from a vapor phase was also reported. Furthermore, the helical calcium carbonates, barium sulfate, and silica were also prepared by the biomimetic process [156–160].

#### 4. APPLICATIONS

Downs and Baker [86] first predicted that the unique structural conformations of helical form which can frequently be found in vapor grown carbon filaments will open up numerous possibilities in the fabrication of new functional materials. Lakeman and co-workers [159] prepared micro-coiled carbon fibers with coil diameters of several hundred micrometer and coil pitches of about 100  $\mu\text{m}$  for the application to the semiconducting infrared detection elements. Pan and co-workers [117] showed that the carbon nanocoils are expected to be novel attractive candidates for the fabrication of a flat panel field emission display. Motojima and Iwanaga [118] showed that the carbon coils have an excellent EM absorption ability, especially in GHz regions. The helical carbon coils will have versatile applications such as EM absorbers, field emitters, hydrogen absorption–desorption materials, energy exchanging materials, tunable microdevices, microsensors, microactuators, micromachines, chiral catalysts, extend–contractable electrodes, reinforcements for soft and/or extendable materials, hydrogen storage materials, activators for organisms, etc.

#### GLOSSARY

**Carbon microcoil** Carbon microcoil (CMC) is a kind of vapor grown carbon fiber obtained by the catalytic pyrolysis of hydrocarbons or disproportionation of CO. The CMC generally has the double-helix coiling morphology similar to DNA, and has a coil diameter of 1–50  $\mu\text{m}$  and a coil length of 0.1–20 mm. The as-grown CMC is almost amorphous and has no pore (tube) in the fiber axis.

**Carbon nanocoil** Carbon nanocoil (CNC) has the generally single-helix morphology with a small coil diameter of 10–500 nm.

**Ceramic microcoil** Ceramic microcoil is generally tuberos ceramic fibers with 3D herical/spiral structure and coil diameter of micrometer order, and can be prepared directly by the chemical vapor deposition (CVD) process, or indirectly by the sol–gel or CVD processes using carbon microcoils/nanocoils or chiral polymers as the templates.

**Coiling-chirality** “Chirality” is generally used in the mean of optical isomerism (enantiomer) with mirror-symmetry of *levo*-rotatory (*l*) and *dextro*-rotatory (*d*). On the other hand three dimensional chiral/coiling morphology has two kind of coiling patterns, right clockwise and left clockwise coiling patterns in mirror symmetry, and they are not superimposed with each other. Accordingly, two kinds of coiling patterns are referred to as a coiling-chirality.

**Cosmomimetic carbon coil** Three dimensional (3D) helical/spiral structures are commonly observed in all objects in cosmos, nature, living bodies, electromagnetic waves, economic cycles, etc. That is, 3D helical/spiral structure is a fundamental structure in all things in the cosmos. Accordingly, the carbon microcoils or nanocoils with 3D helical spiral structure is referred to as “cosmomimetic carbon coil” after the term of “biomimetics”.

**Helix, spiral, coiling** “Helix” is used mainly in the field of living polymers such as DNA or protein, or synthetic polymers, while the terms of “spiral”, “coiling” or “screw” are used in the fields of general substances or materials. The terms of helix, spiral and coiling represent the same means of the three dimensional forms or morphologies such as springs, coils, screws, whirlpools, vortex, etc.

#### REFERENCES

1. S. Motojima and X. Chen, *J. Appl. Phys.* 85, 3919 (1999).
2. J. R. Winker and H. B. Grey, *Acc. Chem. Res.* 31, 698 (1998).
3. B. I. Yokobson and R. E. Smalley, *Am. Sci.* 85, 324 (1997).
4. N. M. Rodriguez, *J. Meter. Res.* 8, 3233 (1993).
5. K. P. de Jong and J. W. Geus, *Catal. Rev. Sci. Eng.* 42, 481 (2000).
6. W. R. Davis, R. J. Slawson, and G. R. Rigby, *Nature* 171, 756 (1953).
7. W. R. Davis, R. J. Slawson, and G. R. Rigby, *Trans. Brit. Ceram. Soc.* 56, 67 (1957).
8. S. Motojima, M. Kawaguchi, K. Nozaki, and H. Iwanaga, *Appl. Phys. Lett.* 56, 321 (1990).
9. S. Motojima, *Nature* 339, 179 (1989).
10. S. Motojima, S. Ueno, T. Hattori, and K. Goto, *Appl. Phys. Lett.* 54, 1001 (1989).
11. S. Motojima, S. Ueno, T. Hattori, and H. Iwanaga, *J. Cryst. Growth* 96, 383 (1989).
12. M. Hillert and N. Lange, *Z. Krist.* 111, 24 (1958).
13. R. T. K. Baker, M. A. Barbber, P. S. Harris, F. S. Feates, and R. J. Waite, *J. Catal.* 26, 51 (1972).
14. H. P. Boehm, *Carbon* 11, 583 (1973).
15. C. Park and R. T. K. Baker, *J. Catal.* 179, 361 (1998).
16. C. Park and R. T. K. Baker, *J. Catal.* 190, 104 (2000).
17. R. T. K. Baker, P. S. Harris, and S. Terry, *Nature* 253, 37 (1975).
18. R. T. K. Baker and R. J. Waite, *J. Catal.* 37, 101 (1975).
19. J. Galuszka and M. H. Back, *Carbon* 22, 141 (1984).
20. M. S. Kim, N. M. Rodriguez, and R. T. K. Baker, *J. Catal.* 134, 253 (1992).
21. N. Krishnankutty, C. Park, N. M. Rodriguez, and R. T. K. Baker, *Catal. Today* 37, 295 (1997).
22. C. A. Bernardo, I. Alstrup, and J. R. Rosytup-Nielsen, *J. Catal.* 96, 517 (1985).
23. M. T. Tavares, C. A. Bernardo, I. Alstrup, and J. R. Rosytup-Nielsen, *J. Catal.* 100, 545 (1986).
24. W. J. Jong, S. H. Lai, K. H. Hong, H. N. Lin, and H. C. Shih, *Diamond Relat. Mater.* 11, 1019 (2002).
25. K. Hernadi, A. Fonseca, J. B. Nagy, D. Bernaerts, and A. A. Lucas, *Carbon* 34, 1249 (1996).

26. N. Grobert, M. Terrones, S. Trasobares, and K. K. Ordatos, *Appl. Phys. A* 70, 175 (2000).
27. V. V. Chesnokov, V. I. Zaikovskii, and R. A. Buyanov, *J. Mol. Catal. A* 158, 267 (2000).
28. W. T. Owens, N. M. Rodriguez, and R. T. K. Baker, *Catal. Today* 21, 3 (1994).
29. J. L. Figueiredo, C. A. Bernardo, R. T. K. Baker, and K. J. Hutter, "Carbon Fiber Filaments and Composites," pp. 1–163, 405–439. Kluwer Academic, Dordrecht, 1990.
30. N. M. Rodoriguez, M. S. Kim, F. Fortin, I. Mochida, and R. T. K. Baker, *Appl. Catal. A* 148, 265 (1997).
31. S. Amelinckx, X. B. Zhang, D. Bernaerts, X. F. Zhang, V. Ivanov, and J. B. Nagy, *Science* 265, 635 (1994).
32. J. M. Mao and S. S. Xie, *J. Mater. Sci. Lett.* 18, 1151 (1999).
33. P. E. Anderson and N. M. Rodriguez, *J. Mater. Res.* 14, 2912 (1999).
34. F. Cesar, J.-O. Bovin, and L. R. Wallenberg, *J. Mater. Res.* 15, 1857 (2000).
35. M. Zhang, Y. Nakayama, and L. Pan, *Jpn. J. Appl. Phys.* 39, 1242 (2000).
36. L. Pan, M. Zhang, A. Harada, Y. Takano, and Y. Nakayama, *Amer. Inst. Phys. Conf. Proc.* 590 (2001).
37. L. Pan, T. Hayashida, A. Harada, and Y. Nakayama, *Physica B* 323, 350 (2002).
38. C. J. Lee, T. J. Lee, and J. Park, *Chem. Phys. Lett.* 340, 413 (2001).
39. X. Wang, Z. Hu, Q. Wu, X. Chen, and Y. Chen, *Thin Solid Films* 390, 130 (2001).
40. J. Xie, P. K. Sharma, V. V. Varadan, V. K. Varadan, B. K. Pradhan, and S. Eser, *Mater. Chem. Phys.* 76, 217 (2002).
41. K. Hernadi, A. Fonseca, J. B. Nagy, Á. Fudala, D. Bernaerts, and I. Kiricsi, *Appl. Catal. A* 228, 103 (2002).
42. J. B. Bai, *Mater. Lett.* 57, 2629 (2003).
43. T. Schliermann, G. Reichenauer, M. Thierley, B. Schmidt, and M. Glora, in "Proc. of Carbon 2002," Beijing, 201.
44. K. Hernadi, A. Fonseca, J. B. Nagy, A. Fudala, D. Bernaerts, and I. Kiricsi, *Appl. Catal. A* 228, 103 (2002).
45. X. Chen, S. Yang, and S. Motojima, *Mater. Lett.*, in press.
46. S. Motojima, M. Hirata, and H. Iwanaga, *J. Chem. Vapor Deposition* 3, 87 (1994).
47. S. Motojima, T. Hamamoto, N. Ueshima, Y. Kojima, and H. Iwanaga, *Electrochem. Soc. Proc.* 97-25, 433 (1997).
48. X. Chen and S. Motojima, *J. Mater. Sci.* 34, 5519 (1999).
49. M. Kawaguchi, K. Nozaki, S. Motojima, and H. Iwanaga, *J. Cryst. Growth* 118, 309 (1992).
50. S. Motojima, X. Chen, W. In-Hwang, T. Kuzuya, K. Kohda, and Y. Hishikawa, *Electrochem. Soc. Proc.* 13, 379 (2000).
51. S. Motojima, X. Chen, W. In Hwang, and Y. Hishikawa, in "Proc. 1st Int. Conf. Carbon," Berlin, 2000, p. 1035.
52. X. Chen, Y. Hishikawa, and S. Motojima, in "Proc. 1st Int. Conf. Carbon," Berlin, 2000, p. 1055.
53. K. Shibagaki, S. Motojima, and M. Hashimoto, *Mater. Technol.* 18, 400 (2001).
54. K. Shibagaki and S. Motojima, *Mater. Technol.* 19, 38 (2001).
55. K. Shibagaki, S. Motojima Y. Umamoto, and Y. Nishitani, *Carbon* 39, 1337 (2001).
56. S. Motojima and H. Iwanaga, *Mater. Technol.* 18, 12 (2000).
57. S. Motojima, Y. Itoh, S. Asakura, and H. Iwanaga, *J. Mater. Sci.* 30, 5049 (1995).
58. C. Kuzuya, Y. Hishikawa, S. Hirako, M. Fujii, H. Iwanaga, and S. Motojima, *Adv. Mater. CVD* 8, 57 (2002).
59. Y. Hishikawa, C. Kuzuya, S. Hirako, W.-I. Hwang, and S. Motojima, *Trans. Mater. Res. Soc. Jpn.* 27, 39 (2002).
60. S. Motojima, M. Kawaguchi, and H. Iwanaga, *TANSO* 151, 41 (1992).
61. S. Motojima, I. Hasegawa, S. Kagiya, S. Asakura, M. Kawaguchi, and H. Iwanaga, *J. Phys. IV* C3, 599 (1993).
62. S. Motojima, I. Hasegawa, S. Kagiya, M. Momiyama, M. Kawaguchi, and H. Iwanaga, *Appl. Phys. Lett.* 62, 2322 (1993).
63. S. Motojima, S. Asakura, M. Hirata, and H. Iwanaga, *Mater. Sci. Eng. B* 34, L9 (1995).
64. S. Motojima, S. Kagiya, and H. Iwanaga, *Mater. Sci. Eng. B* 34, 47 (1995).
65. S. Motojima, Y. Itoh, S. Asakura, and H. Iwanaga, *J. Mater. Sci.* 30, 5049 (1995).
66. S. Motojima, I. Hasegawa, S. Kagiya, K. Ando, and H. Iwanaga, *Carbon* 33, 1167 (1995).
67. S. Motojima, S. Asakura, S. Takeuchi, and H. Iwanaga, *Carbon* 34, 289 (1996).
68. S. Motojima, T. Hamamoto, and H. Iwanaga, *J. Cryst. Growth* 158, 79 (1996).
69. W.-In Hwang, X. Chen, T. Kuzuya, K. Kawabe, and S. Motojima, *Carbon* 38, 565 (2000).
70. W. In-Hwang, H. Yanagida, and S. Motojima, *Mater. Lett.* 43, 11 (2000).
71. X. Chen, S. Motojima, W. In-Hwang, M. Kohda, Y. Hishikawa, and H. Iwanaga, *Trans. Mater. Res. Soc. Jpn.* 25, 565 (2000).
72. X. Chen, W.-I. Hwang, and S. Motojima, *Mater. Technol.* 18, 229 (2000).
73. W.-In Hwang, X. Chen, and S. Motojima, *Mater. Technol.* 18, 263 (2000).
74. Y. Okada and K. Takeuchi, *J. Mater. Sci. Lett.* 11, 1715 (1992).
75. H. Takikawa, M. Yatsuki, R. Miyano, M. Nagayama, T. Sakakibara, et al., *Jpn. J. Appl. Phys.* 39, 5177 (2000).
76. C. Kuzuya, Y. Hayashi, and S. Motojima, *Carbon* 40, 1071 (2002).
77. S. Motojima, C. Kuzuya, Y. Hishikawa, and S. Shimada, *Trans. Mater. Res. Soc. Jpn.* 27, 109 (2002).
78. W. In-Hwang, K. Kawabe, and S. Motojima, *Mater. Sci. Eng. B* 86, 1 (2001).
79. C. Kuzuya, S. Motojima, M. Kohda, and Y. Hishikawa, *Mater. Technol.* 20, 3 (2002).
80. C. Kuzuya, M. Kohda, Y. Hishikawa, and S. Motojima, *Carbon* 40, 1991 (2002).
81. R. T. K. Baker and J. J. Chludzinski Jr., *J. Catal.* 64, 464 (1980).
82. X. Chen, W. In-Hwang, S. Shimada, M. Fujii, H. Iwanaga, and S. Motojima, *J. Mater. Res.* 15, 808 (2000).
83. X. Chen, S. Motojima, and H. Iwanaga, *Carbon* 37, 1825 (1999).
84. W. In-Hwang, T. Kuzuya, H. Iwanaga, and S. Motojima, *J. Mater. Sci.* 36, 971 (2001).
85. T. Hashishin, H. Iwanaga, and S. Motojima, *Mater. Technol.* 19, 293 (2002).
86. W. B. Downs and R. T. K. Baker, *Carbon* 29, 1173 (1991).
87. R. T. K. Baker, *Carbon* 27, 315 (1989).
88. A. Fonseca, K. Hernadi, J. B. Nagy, Ph. Lambin, and A. A. Lucas, *Carbon* 33, 1759 (1995).
89. A. Fonseca, K. Hernadi, J. B. Nagy, P. H. Lambin, and A. A. Lucas, *Synthetic Metals* 77, 235 (1996).
90. D. Bernaerts, X. B. Zhang, X. F. Zhang, G. Van Tendeloo, S. Amelinckx, J. van Landuyt, V. Ivanov, and J. B. Nagy, *Philos. Mag.* 71, 605 (1995).
91. X. B. Zhang, X. F. Zhang, D. Bernaerts, G. Van Tendeloo, S. Amelinckx, J. Van Landuyt, V. Ivanov, J. B. Nagy, Ph. Lambin, and A. A. Lucas, *Europhys. Lett.* 27, 141 (1994).
92. J. H. Weaver, *Science* 265, 511 (1994).
93. Ph. Lambin, A. Fonseca, J.-P. Vigneron, J. B. Nagy, and A. A. Lucas, *Chem. Phys. Lett.* 245, 85 (1995).
94. B. L. Dunlap, *Phys. Rev. B* 46, 1933 (1992).
95. B. L. Dunlap, *Phys. Rev. B* 49, 5643 (1992).
96. B. L. Dunlap, *Phys. Rev. B* 50, 8134 (1992).
97. S. Ihara and S. Itoh, *Carbon* 33, 931 (1995).
98. W. Li, S. Xie, W. Liu, R. Zhao, Y. Zhang, W. Zhou, G. Wang, and L. Qian, *J. Mater. Sci.* 34, 2745 (1999).
99. X. Chen, T. Saito, M. Kusunoki, and S. Motojima, *J. Mater. Res.* 14, 4329 (1999).



100. X. Chen, S. Yang, and S. Motojima, *Mater. Lett.* 3751, 48 (2002).
101. R. T. Yang and J. P. Chen, *J. Catal.* 115, 52 (1989).
102. M. Liu and J. M. Cowley, *Carbon* 32, 393 (1994).
103. K. Akagi, R. Tamura, and M. Tsukada, *Phys. Rev. Lett.* 74, 2307 (1995).
104. S. Motojima, H. Asano, and H. Iwanaga, *J. Euro. Ceram. Soc.* 16, 989 (1996).
105. S. Motojima, S. Ueno, T. Hattori, and H. Iwanaga, *J. Cryst. Growth* 96, 383 (1989).
106. S. Motojima, Y. Kojima, T. Hamamoto, N. Ueshima, and H. Iwanaga, *Electrochem. Soc. Proc.* 97-39, 595 (1997).
107. X. Chen, Y. Hishikawa, W.-I. Hwang, T. Kuzuya and S. Motojima, *Electrochem. Soc. Proc.* 13, 385 (2000).
108. X. Chen, S. Motojima, and H. Iwanaga, *J. Cryst. Growth* 237–239, 1931 (2002).
109. S. Motojima, S. Yang, X. Chen, and H. Iwanaga, *J. Mater. Sci.* 34, 5989 (1999).
110. S. Motojima, W.-I. Hwang, X. Chen, and H. Iwanaga, *J. Electrochem. Soc.* 147, 1228 (2000).
111. S. Motojima, W.-I. Hwang, and X. Chen, *Mater. Res. Bull.* 35, 1517 (2000).
112. S. Motojima, W.-I. Hwang, and H. Iwanaga, *J. Mater. Sci.* 36, 673 (2001).
113. K. Kaneto, M. Makoto, and S. Motojima, *T. IEE Japan* 118, 1425 (1998).
114. K. Kaneto, M. Tsuruta, and S. Motojima, *Synthetic Metals* 103, 2578 (1999).
115. M. Fujii, M. Matsui, S. Motojima, and Y. Hishikawa, *Thin Solid Films* 409, 78 (2002).
116. M. Fujii, S. Matui, S. Motojima, and Y. Hishikawa, *J. Cryst. Growth* 237–239, 1937.
117. L. Pan, T. Hayashida, M. Zhang, and Y. Nakayama, *Jpn. J. Appl. Phys.* 40, 235 (2001).
118. S. Motojima and H. Iwanaga, *Kinou Zairyou* 17, 1 (1997).
119. V. K. Varadan, private communication.
120. S. Motojima, H. Iwanaga, and V. K. Varadan, *Hyomen* 36, 140 (1998); *EMC* 120, 50 (1998).
121. J.-H. Du, C. Sun, S. Bai, G. Su, Z. Ying, and H.-M. Cheng, *J. Mater. Res.* 17, 1232 (2002).
122. S. Motojima, W. In-Hwang, T. Kuzuya, and H. Iwanaga, *J. Mater. Sci.* 36, 71 (2001).
123. K. Shibagaki and S. Motojima, *Carbon* 39, 411 (2001).
124. S. Motojima, S. Ueno, T. Hattori, and H. Iwanaga, *J. Cryst. Growth* 96, 383 (1989).
125. S. Motojima, M. Kawaguchi, K. Nozaki, and H. Iwanaga, in "Proc. 11th Int. Conf. on CVD," Seattle, 1990, p. 573.
126. A. Addamiano, *J. Cryst. Growth* 58, 617 (1982).
127. T.-K. Kang, S.-D. Park, C.-K. Rhee, and I.-H. Kuk, in "Proc. 5th Japan–Korea Ceramic Seminar," Kobe, 1989, p. 249.
128. S. Motojima, S. Kagiya, and H. Iwanaga, *J. Mater. Sci.* 31, 4641 (1996).
129. S. Motojima, I. Hasegawa, and H. Iwanaga, *J. Phys. IV C5*, 1061 (1995).
130. H. Iwanaga, S. Motojima, M. Ichihara, and S. Takeuchi, *J. Cryst. Growth* 100, 271 (1990).
131. H. Iwanaga, T. Iwasaki, S. Motojima, and S. Takeuchi, *J. Mater. Lett.* 9, 731 (1990).
132. H. Iwanaga, T. Iwasaki, and S. Motojima, *J. Sur. Finishing Soc. Jpn.* 41, 578 (1990).
133. S. Motojima, T. Yamana, T. Araki, and H. Iwanaga, *J. Electrochem. Soc.* 142, 3141 (1995).
134. H. Iwanaga, M. Kawaguchi, and S. Motojima, *Jpn. J. Appl. Phys.* 32, 103 (1993).
135. U. Vogt, H. Hoffmann, and V. Kramer, *Key Eng. Mater.* 89, 29 (1994).
136. S. Motojima, S. Kagiya, and H. Iwanaga, *Mater. Sci. Eng. B* 34, 159 (1995).
137. S. Motojima, I. Hasegawa, M. Kawaguchi, K. Nozaki, and H. Iwanaga, *J. Chem. Vapor deposition* 1, 137 (1992).
138. S. Motojima, T. Kuzuya, W.-I. Hwang, X. Chen, M. Fujii, and H. Iwanaga, *J. Phys. IV France* 9, 8 (1999).
139. S. Yang, N. Ueshima, and S. Motojima, *Mater. Sci. Eng. A* 346, 29 (2003).
140. K. Robbie and M. J. Brett, *J. Vac. Sci. Technol. A* 15, 1460 (1997).
141. J. C. Sit, D. J. Borer, and M. J. Brett, *Adv. Mater.* 12, 371 (2000).
142. K. Robbie, D. J. Broer, and M. J. Brett, *Nature* 399, 764 (1999).
143. J. Ballato, R. E. Riman, J. R. Vig, and S. M. Laffey, *J. Mater. Res.* 13, 3144 (1998).
144. S. M. Yang, I. Sokolov, N. Coombs, C. T. Kresge and G. A. Ozin, *Adv. Mater.* 11, 1427 (1999).
145. K. Sugiyasu, S. Tamaru, M. Takeuchi, D. Berthier, I. Huc, R. Oda, S. Shinkai, *Chem. Commun.* 2002, 1212 (2002).
146. S. Motojima et al., in preparation.
147. P. Gleize, M. C. Schouler, P. Gadelle, and M. Caillet, *J. Mater. Sci.* 29, 1597 (1994).
148. S. Johansson, J.-A. Schweitz, H. Westberg, and M. Boman, *J. Appl. Phys.* 72, 5956 (2002).
149. G. Jiang, H. Zhuang, J. Zhang, M. Ruan, W. Li, F. Wu, and B. Zhang *J. Mater. Sci.* 35, 57 (2000).
150. E. Schonherr and E. Winckler, *J. Cryst. Growth* 32, 117 (1976).
151. A. Addamiano, *Nature* 179, 493 (1957).
152. A. Addamiano, *J. Cryst. Growth* 11, 351 (1971).
153. K. Barner and H. Berg, *J. Cryst. Growth* 46, 763 (1979).
154. K. Kishi, *J. Cryst. Growth* 45, 517 (1978).
155. J. M. Garcia-Ruiz and J. L. Amoros, *J. Cryst. Growth* 55, 379 (1981).
156. J. M. Garcia-Ruiz, *J. Cryst. Growth* 73, 251 (1985).
157. S. Mann, *J. Chem. Soc., Dalton Trans.* 21, 3953 (1997).
158. J. D. Hopwood and S. Mann, *Chem. Mater.* 9, 1819 (1997).
159. L. A. Gower and D. A. Tirrell, *J. Cryst. Growth* 191, 153 (1998).
160. Q. Huo, D. Zhao, J. Feng, K. Weston, S. K. Buratto, G. D. Stucky, S. Schacht, and F. Schuth, *Adv. Mater.* 9, 974 (1997).
161. C. D. C. E. Lakeman, G. Pan, N. Muto, M. Miyayama, H. Yanagida, and D. A. Payne, *Mater. Lett.* 13, 330 (1992).
162. S. Motojima, S. Yang, X. Chen, and H. Iwanaga, *Mater. Res. Bull.* 35, 203 (2000).

# Nanoicosahedral Quasicrystal

J. Saida

*Japan Science and Technology Corporation, Sendai, Japan*

A. Inoue

*Tohoku University, Sendai, Japan*

## CONTENTS

1. Introduction
  2. Formation of Nanoicosahedral Phase by Addition of Elements in Zr-Based Glassy Alloys
  3. Formation of Nanoicosahedral Phase by Changing Composition in Zr-Based Glassy Alloys
  4. Nanoicosahedral Phase in Ternary and Binary Alloy Systems
  5. Nanoicosahedral Phase Formation in Glassy Alloys Except Zr-Based Systems
  6. Correlation Between Local Structure in Glassy State and Nanoicosahedral Phase Formation
  7. Origin of Formation of Icosahedral Local Structure
  8. Mechanical Properties of Nanoicosahedral Phase Dispersed Bulk Glassy Alloys
  9. Conclusion
- Glossary  
References

## 1. INTRODUCTION

Since an icosahedral phase was found in a rapidly solidified  $\text{Al}_{84}\text{Mn}_{16}$  alloy [1], a large number of icosahedral alloys have been synthesized in metastable and thermodynamically stable states [2], and the novel structure has been interpreted on the basis of a quasicrystal [3]. It has been reported that the icosahedral quasicrystalline phase is formed in Al- [4–6], Mg- [7], Zn- [8], Ga- [9], Pd- [10], and Ti-based [11]

systems, and so on. It is important to search for a new icosahedral alloy, and to clarify its formation mechanism and fundamental properties because the icosahedral atomic configuration is different from the conventional crystalline structure, leading to a unique property. High hardness, a high Young's modulus, a high elevated temperature strength, low coefficient thermal conductivity, and high resistance against oxidation have been reported in icosahedral quasicrystals originating from the three-dimensional quasiperiodic lattice [12–14]. The structure control, such as volume fraction, grain size, and distribution of icosahedral particles, must be required for the improvement of these properties, and can create new unique properties [15]. It is expected that they can be achieved by the formation of a nanometer-scale icosahedral phase (nanoicosahedral quasicrystal).

The formation of a nanoicosahedral phase is effective by quasicrystallization from the amorphous or glassy structure [16–18] because the homogeneous structure consisting of icosahedral and amorphous or glassy phases can be obtained, and the volume fraction and grain size of the icosahedral particles are easily controlled by changing the annealing condition. The first discovery of icosahedral phase formation from an amorphous state was reported in the  $\text{Pd}_{60}\text{U}_{20}\text{Si}_{20}$  alloy in 1985 [10]. The  $\text{Pd}_{60}\text{U}_{20}\text{Si}_{20}$  amorphous alloy has two exothermic reactions at near 753 and 813 K in the differential scanning calorimetry (DSC) curve [19]. The first one corresponds to the transformation from an amorphous to an icosahedral phase. The precipitated icosahedral particles can grow in the diameter range over 100 nm by annealing. It was found that the icosahedral phase is also obtained from an amorphous state in Al–Si–Mn alloys [5, 20–24]. The  $\text{Al}_{55}\text{Si}_{25}\text{Mn}_{20}$  amorphous alloy, which is a typical icosahedral phase-forming alloy composition, also has a two-stage crystallization process [25]. The icosahedral phase is formed by the first exothermic reaction at approximately 650 K, and grows easily to a diameter of approximately 500 nm. Both of the icosahedral phases in the  $\text{Pd}_{60}\text{U}_{20}\text{Si}_{20}$  and  $\text{Al}_{55}\text{Si}_{25}\text{Mn}_{20}$  alloys decompose to stable crystalline phases through the second exothermic reaction.

Tsai et al. reported the formation of a stable icosahedral phase from the amorphous  $\text{Al}_{75}\text{Cu}_{15}\text{V}_{10}$  alloy [26]. The icosahedral phase is precipitated from the amorphous state through the single exothermic stage, and is melted at about 835 K. The grain size of the icosahedral phase in the alloy is approximately 1  $\mu\text{m}$  in diameter due to its high stability. The above-described icosahedral phases precipitated from the amorphous states have a relatively small nucleation rate and a large growth rate [27, 28]. It is therefore difficult to obtain a unique structure consisting of the nanoicosahedral particles embedded in the amorphous matrix.

It has been thought that the formation of an icosahedral phase from an amorphous state is attributed to the existence of quenched-in nuclei with an icosahedral-like structure [19, 27, 28]. The presumption has also been supported by several experimental and theoretical approaches, where the icosahedral and amorphous phases have a local structural similarity, and the stability of the icosahedral phase is related to the short-range icosahedral order already present in a supercooled liquid [9, 29–32].

The formation of an icosahedral phase in the bulk glass-forming alloy was reported in  $\text{Zr}_{69.5}\text{Al}_{7.5}\text{Ni}_{11}\text{Cu}_{12}$  in 1996 [33]. The  $\text{Zr}_{69.5}\text{Al}_{7.5}\text{Ni}_{11}\text{Cu}_{12}$  glassy alloy has a large supercooled liquid region of 55 K [34], which is defined as the temperature gap between glass transition  $T_g$  and crystallization  $T_x$ . The crystallization proceeds through two-stage reactions, and the first one corresponds to the formation of a quasicrystal. The icosahedral particles are distributed homogeneously in the glassy matrix, and the grain size of the icosahedral phase is approximately 100 nm at a volume fraction of 25%. The maximum nucleation rate for the icosahedral phase formation is about  $5 \times 10^{18} \text{ m}^{-3} \cdot \text{s}^{-1}$ , which is 20 times larger than that in an  $\text{Al}_{75}\text{Cu}_{15}\text{V}_{10}$  amorphous alloy ( $2.4 \times 10^{17} \text{ m}^{-3} \cdot \text{s}^{-1}$ ) and  $10^7$  times larger than that in a  $\text{Pd}_{58.5}\text{U}_{20.6}\text{Si}_{20.6}$  amorphous alloy [35]. However, Zhang et al. reported that the reproducibility of the icosahedral phase formation in the  $\text{Zr}_{69.5}\text{Al}_{7.5}\text{Ni}_{11}\text{Cu}_{12}$  glassy alloy is poor [36]. Subsequently, the enhancement of an icosahedral phase formation by the existence of oxygen impurity was noticed [37–39]. In these studies, the primary phase changes drastically to the icosahedral phase in oxygen contents above 1000 mass ppm in the  $\text{Zr}_{65}\text{Al}_{7.5}\text{Cu}_{27.5}$  glassy alloy and 1600 mass ppm in the  $\text{Zr}_{65}\text{Al}_{7.5}\text{Ni}_{10}\text{Cu}_{17.5}$  glassy alloy. The further reports also indicate that the icosahedral quasicrystal formation is induced by the presence of oxygen contamination in the  $\text{Zr}_{69.5}\text{Al}_{7.5}\text{Ni}_{11}\text{Cu}_{12}$  glassy alloy [40–42].

In 1998, Xing et al. also reported the formation of an icosahedral phase in the  $\text{Zr}_{57}\text{Al}_{10}\text{Ni}_8\text{Cu}_{20}\text{Ti}_5$  glassy alloy with a low oxygen content of approximately 900 mass ppm [43]. They clarified that the transformation of the alloy changes from a single step into two- or three-stage crystallization reactions with decreasing quenching rate. The icosahedral phase formation is significant in a low quenching rate. In particular, the crystalline  $\text{Zr}_2\text{Cu}$  and  $\text{Zr}_2\text{Ni}$  phases are precipitated as main phases in the primary crystallization stage, and a small amount of quasicrystalline phase can be observed in the melt-spun ribbon of 30  $\mu\text{m}$  thickness with a high cooling rate. They supposed that the supercooled  $\text{Zr}_{57}\text{Al}_{10}\text{Ni}_8\text{Cu}_{20}\text{Ti}_5$  melt has a tendency to develop an icosahedral short-range order, which is favored at a low cooling rate. The icosahedral phase was characterized as a nanoscale

quasicrystalline (nanoquasicrystalline) particle in their further studies in 1999 [44]. In the primary crystallization stage, the icosahedral phase has a very fine grain size with a diameter of 2–10 nm in the  $\text{Zr}_{57}\text{Al}_{10}\text{Ni}_8\text{Cu}_{20}\text{Ti}_5$  glassy alloy, and the size increases significantly to 100 nm in diameter with decreasing Ti content in the  $\text{Zr}_{59}\text{Al}_{10}\text{Ni}_8\text{Cu}_{20}\text{Ti}_3$  glassy alloy. The result is recognized as the first finding of the formation of a nanoicosahedral phase; however, strong dependence of the quenching rate indicates the low stability of the icosahedral phase and difficulty of structure control, which leads to a limitation of the shape of materials.

Although these reports have led to the possibility of the nanoicosahedral phase from the glassy phase, the formation condition has not been established due to their poor reproducibility and/or low stability. Based on the systematic approaches for the study of the transformation behavior in glassy alloys, it is expected that the nanoicosahedral phase can be formed by the elimination of impurity and the addition of elements. This chapter describes the formation of a nanoicosahedral phase devitified from the Zr- and Hf-based glassy alloys by the decline of a high glass-forming ability (GFA), which describes the important investigation of the stability of the glassy state, as well as the novel nanoquasicrystal-dispersive bulk glassy alloy with unique mechanical properties.

## 2. FORMATION OF NANOICOSAHEDRAL PHASE BY ADDITION OF ELEMENTS IN Zr-BASED GLASSY ALLOYS

### 2.1. Change in Transformation Behavior

Chen, Inoue, and co-workers found in 1999 [45, 46] the reproducible formation of a nanoicosahedral quasicrystalline phase as a primary precipitation phase in  $\text{Zr}_{65}\text{Al}_{7.5}\text{Ni}_{10}\text{Cu}_{12.5}(\text{Ag}, \text{Pd}, \text{Au}, \text{and Pt})_5$  glassy alloys with an oxygen content less than 700 mass ppm. Figure 1 shows DSC curves of the as-spun  $\text{Zr}_{65}\text{Al}_{7.5}\text{Ni}_{10}\text{Cu}_{12.5}(\text{Ag}, \text{Pd}, \text{Au}, \text{and Pt})_5$  alloys. It is well known that a single-crystallization reaction is observed in the  $\text{Zr}_{65}\text{Al}_{7.5}\text{Ni}_{10}\text{Cu}_{17.5}$  glassy alloy [37, 47]. By noble metal addition, the crystallization process is clearly separated into two or more exothermic reactions, remaining with a significant glass transition. This phenomenon is similar to those in the icosahedral quasicrystal-forming  $\text{Zr}_{69.5}\text{Al}_{7.5}\text{Ni}_{11}\text{Cu}_{12}$  and  $\text{Zr}_{57}\text{Al}_{10}\text{Ni}_8\text{Cu}_{20}\text{Ti}_5$  glassy alloys. The X-ray diffraction (XRD) patterns of the  $\text{Zr}_{65}\text{Al}_{7.5}\text{Ni}_{10}\text{Cu}_{12.5}(\text{Ag}, \text{Pd}, \text{Au}, \text{and Pt})_5$  glassy alloys annealed for 180 s at temperatures just above the first exothermic peak are shown in Figure 2. Sharp diffraction peaks are observed, accompanied by a broad peak originating from the residual glassy phase. All of the diffraction peaks in the patterns are identified as an icosahedral quasicrystalline phase. The bright-field transmission electron microscopy (TEM) images [(a), (c)] and selected-area electron diffraction patterns (SADPs) [(b), (d)] of the alloys containing Pd [(a), (b)] and Pt [(c), (d)] annealed for 120 s at 773 and 753 K, respectively, are shown in Figure 3. Spherical particles with a size of approximately 40 nm for the former and 25 nm for the latter are dispersed homogeneously in the glassy matrices. The SADPs taken from a region

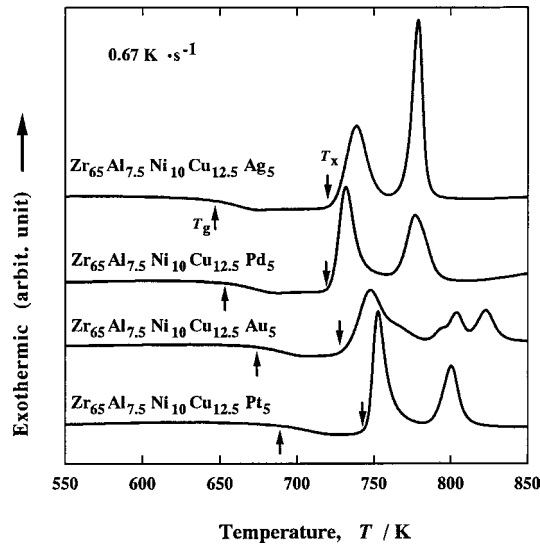


**Figure 1.** DSC curves of the as-spun  $Zr_{65}Al_{7.5}Ni_{10}Cu_{12.5}(Ag, Pd, Au, \text{ and } Pt)_5$  alloys. Reprinted with permission from [46], A. Inoue et al., *Mater. Trans. JIM* 40, 1181 (1999). © 1999, Japan Institute of Metals.

of 1  $\mu\text{m}$  diameter can be identified as a mixture of icosahedral and glassy phases. For further confirmation of the icosahedral phase formation, nanobeam diffraction (NBD) patterns using the beam diameter of 2.4 nm have been performed. The NBD patterns in the alloys containing Pd, Au, and Pt revealing the three kinds of quasiperiodic five-,

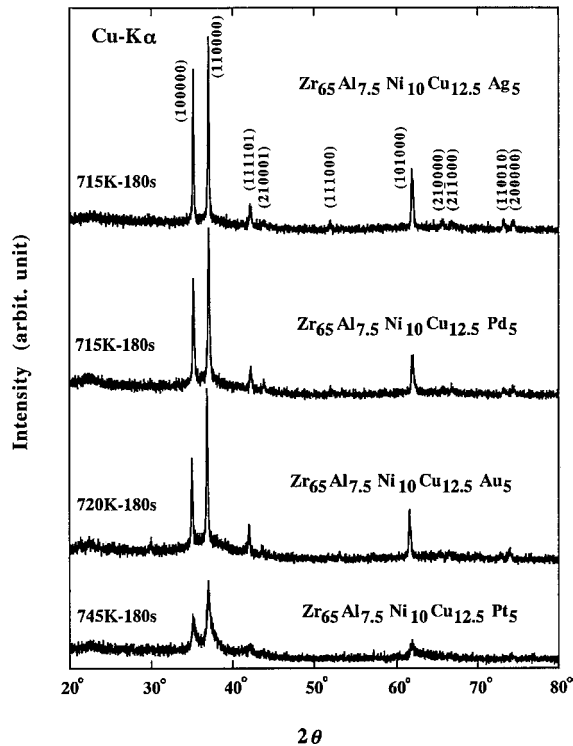
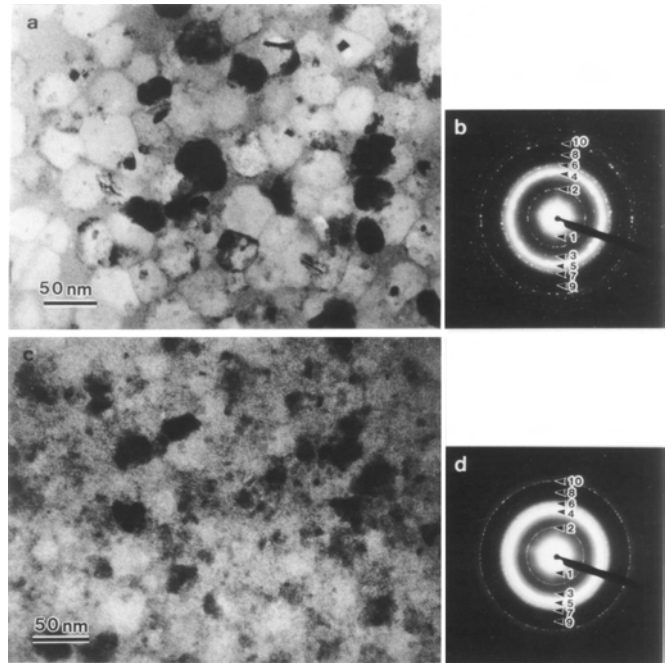


**Figure 2.** XRD patterns of the  $Zr_{65}Al_{7.5}Ni_{10}Cu_{12.5}(Ag, Pd, Au, \text{ and } Pt)_5$  glassy alloys annealed for 180 s at temperatures just above the first exothermic peaks. Reprinted with permission from [46], A. Inoue et al., *Mater. Trans. JIM* 40, 1181 (1999). © 1999, Japan Institute of Metals.



No.	Index	No.	Index
1	(220011)	6	(111101)
2	(111010)	7	(210001)
3	(211001)	8	(111000)
4	(100000)	9	(111100)
5	(110000)	10	(101000)

**Figure 3.** Bright-field TEM images (a), (c) and SADPs (b), (d) of the  $Zr_{65}Al_{7.5}Ni_{10}Cu_{12.5}[Pd \text{ (a), (b) and } Pt \text{ (c), (d)}]_5$  glassy alloys annealed for 120 s at 773 and 753 K, respectively. Reprinted with permission from [46], A. Inoue et al., *Mater. Trans. JIM* 40, 1181 (1999). © 1999, Japan Institute of Metals.

three-, and twofold symmetries are reported [46]. Therefore, it is realized that the nanoicosahedral phase can be formed by the addition of noble metals such as Ag, Pd, Au, or Pt in the  $Zr_{65}Al_{7.5}Ni_{10}Cu_{12.5}$  glassy alloy. A nanoicosahedral phase formation was found in the noble metal (NM) contents of 5–17.5at% in the  $Zr_{65}Al_{7.5}Ni_{10}Cu_{17.5-x}NM_x$  glassy alloys [47–49]. It has also been reported that the nanoicosahedral phase formation has a high stability, and does not depend on the quenching rate for the glassy phase [47, 50]. Lee et al. have clarified that the nanoicosahedral phase transforms into stable crystalline phases of tetragonal  $Zr_2Cu$  and hexagonal  $Zr_6NiAl_2$  through the second exothermic reaction [51, 52].

## 2.2. Formation Factor for Nanoicosahedral Phase

We can expect that the formation factor is clarified by these results, which exhibit the precipitation of the nanoicosahedral phase by the addition of Ti, Ag, Pd, Au, or Pt in Zr–Al–Ni–Cu glassy alloys. Since the noble metals have a strong chemical affinity with Zr, a weak affinity with Ni or Cu, and Ti has no chemical affinity with Zr [53], it is suggested that the addition of elements with a positive or weak mixing enthalpy with one of the constitutional elements in

the Zr–Al–Ni–Cu multicomponent glassy alloy is effective for icosahedral phase formation. In order to examine the formation factor for the icosahedral phase, the transformation of the melt-spun Zr–Al–Ni–Cu–(Nb, Ta, and V) glassy alloys has been investigated [54]. Since the Nb, Ta, and V have a weak or positive chemical affinity with Zr or Cu and a relatively strong affinity with Ni [53], the same effect as those for noble metal addition is expected. DSC curves of the melt-spun  $Zr_{65}Al_{7.5}Ni_{10}Cu_{12.5}X_5$  ( $X = Nb, Ta, \text{ and } V$ ) glassy alloys denote the two or three exothermic reactions after the glass transition for all alloys. The crystallization behavior with a two- or three-stage reaction is similar to those of  $Zr_{65}Al_{7.5}Ni_{10}Cu_{12.5}M_5$  ( $M = Ag, Pd, Au, \text{ and } Pt$ ) glassy alloys [46]. It was clarified that all of the diffraction peaks can be identified as icosahedral phase in the XRD patterns in the Nb, Ta, and V alloys in the annealed state, subject to the transformation due to the first exothermic peak. These icosahedral phases have a very fine grain size in the diameter range less than 50 nm [54]. Very recently, a nanoicosahedral phase formation in a Zr–Al–Ni–Cu–Mo glassy alloy has been found [55], where the mixing enthalpies of Mo with Cu and Ni are +19 and  $-7 \text{ kJ} \cdot \text{mol}^{-1}$ , respectively [53]. The additional elements for the nanoicosahedral phase formation in the Zr–Al–Ni–Cu glassy alloy are summarized in Table 1 [44–46, 54–60]. The table contains the atomic radii and mixing enthalpies with Zr, Al, Ni, and Cu of the additional elements. It is found that all of the additional elements have weak or positive mixing enthalpies, with at least one of the constitutional elements in a Zr–Al–Ni–Cu glassy alloy. Wanderka et al. have reported nanoicosahedral phase formation in a  $Zr_{46.8}Ti_{8.2}Cu_{7.5}Ni_{10}Be_{27.5}$  glassy alloy with a high GFA [61]. This result also satisfies the above criterion.

### 2.3. Effect of Additional Elements on Nucleation and Growth of Nanoicosahedral Phase

Figure 4 shows an Arrhenius plot between the logarithm of the grain growth rate of the primary phase and the reciprocal of the temperature for the  $Zr_{65}Al_{7.5}Ni_{10}Cu_{7.5}Ag_{10}$

and  $Zr_{65}Al_{7.5}Ni_{10}Cu_{17.5}$  glassy alloys [62]. The primary phase is a nanoicosahedral phase in the  $Zr_{65}Al_{7.5}Ni_{10}Cu_{7.5}Ag_{10}$  glassy alloy and a metastable fcc  $Zr_2Ni$  phase in the  $Zr_{65}Al_{7.5}Ni_{10}Cu_{17.5}$  glassy alloy [63]. Their grain growth rates were measured in a time range shorter than the collision among the particles, where the growth rates are found to be constant [64]. Each plot yields a linear relation whose slopes give the activation energy for a grain growth  $Q$  of  $352 \text{ kJ} \cdot \text{mol}^{-1}$  for the  $Zr_{65}Al_{7.5}Ni_{10}Cu_{7.5}Ag_{10}$  glassy alloy and  $382 \text{ kJ} \cdot \text{mol}^{-1}$  for the  $Zr_{65}Al_{7.5}Ni_{10}Cu_{17.5}$  glassy alloy, respectively, by the following equation

$$u = u_0 \exp(-Q/RT) \quad (1)$$

where  $u$  is the grain growth rate,  $u_0$  is a pre-exponential factor, and  $R$  is the gas constant. The activation energy for the growth of the icosahedral phase in the  $Zr_{65}Al_{7.5}Ni_{10}Cu_{7.5}Ag_{10}$  glass is nearly equal to that of the fcc  $Zr_2Ni$  phase in the  $Zr_{65}Al_{7.5}Ni_{10}Cu_{17.5}$  glass, suggesting a similar grain growth mode in both alloys. However, the grain growth rate of the fcc  $Zr_2Ni$  phase is approximately ten times higher than that of the icosahedral phase, which indicates that Ag is effective for the suppression of grain growth.

As shown in Figure 3, the icosahedral particles with a spherical morphology are distributed homogeneously in the Zr–Al–Ni–Cu–NM glassy alloys. Assuming homogeneous nucleation at the initial crystallization stage at temperatures above  $T_g$ , for the phase transformation with isotropic constant growth rate  $u$  and homogeneous nucleation under steady-state conditions, the volume fraction transformed  $y$  during isothermal annealing is given by [65, 66]

$$y = 1 - \exp(-\pi I_v u^3 t_a^4 / 3) \quad (2)$$

where  $t_a$  is the isothermal annealing time and  $I_v$  is the homogeneous nucleation rate. Therefore, we can calculate  $I_v$  from

$$I_v = (-3/\pi u^3 t_a^4) \ln(1 - y) \quad (3)$$

**Table 1.** Additional elements for nanoicosahedral phase formation in Zr–Al–Ni–Cu glassy alloy [44–46, 54–60].

Additional element	Atomic radius ( $\times 10^{-1} \text{ nm}$ )	Mixing enthalpy ( $\text{kJ} \cdot \text{mol}^{-1}$ )				Ref.
		Zr	Al	Ni	Cu	
Ag	1.44	-20	-4	+15	+2	[45]
Pd	1.37	-91	-46	0	-14	[46]
Au	1.44	-74	-22	+7	-9	[46]
Pt	1.39	-100	-44	-5	-12	[46]
Ir	1.35	-76	-30	-2	0	[56]
Re	1.37	-35	-9	+2	+18	[57]
Zn	1.33	-29	+1	-9	+1	[58]
Mo	1.36	-6	-5	-7	+19	[55]
V	1.32	-4	-16	-18	+5	[54]
Nb	1.43	+4	-18	-30	+3	[54]
Ta	1.43	+3	-19	-29	+2	[54]
Cr	1.25	-12	-10	-7	+12	[59]
Sn	1.41	-43	+4	-4	+7	[60]
Y	1.82	+9	-38	-31	-22	[60]
Ti	1.47	0	-30	-35	-9	[44]

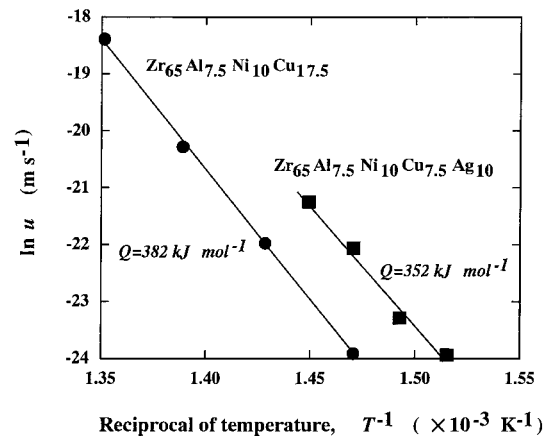


**Figure 4.** Arrhenius plot of the logarithm of grain growth rate of the primary phases and the reciprocal of temperature for the  $Zr_{65}Al_{7.5}Ni_{10}Cu_{7.5}Ag_{10}$  and  $Zr_{65}Al_{7.5}Ni_{10}Cu_{17.5}$  glassy alloys. Reprinted with permission from [62], J. Saida et al., *Philos. Mag. Lett.* 80, 737 (2000). © 2000, Taylor & Francis Ltd.

A  $y$  value of 0.2 is used for the steady state, which is obtained from the DSC thermogram of isothermal annealing, and  $u$  is calculated at various temperatures from the Arrhenius relation shown in Figure 4 from the relation

$$\ln u = -4.23 \times 10^4 T^{-1} + 40.1 \quad (4)$$

for the growth of the icosahedral phase in the  $Zr_{65}Al_{7.5}Ni_{10}Cu_{7.5}Ag_{10}$  glass and

$$\ln u = -4.59 \times 10^4 T^{-1} + 43.7 \quad (5)$$

for the growth of the fcc  $Zr_2Ni$  phase in the  $Zr_{65}Al_{7.5}Ni_{10}Cu_{17.5}$  glass, respectively. The growth rate  $u$  of the fcc  $Zr_2Ni$  phase is  $1.1 \times 10^{-8} \text{ m} \cdot \text{s}^{-1}$ , which is approximately ten times larger than that of the icosahedral phase ( $1.3 \times 10^{-9} \text{ m} \cdot \text{s}^{-1}$ ) at  $T_x$ . The calculated nucleation rate at  $T_x$  of the nanoicosahedral phase ( $3.8 \times 10^{20} \text{ m}^{-3} \cdot \text{s}^{-1}$ ) is approximately  $10^4$  times higher than that of the fcc  $Zr_2Ni$  phase ( $2.6 \times 10^{16} \text{ m}^{-3} \cdot \text{s}^{-1}$ ). The calculated homogeneous nucleation rate is plotted against the reciprocal of annealing temperature in Figure 5. The nucleation rate of the nanoicosahedral phase increases monotonously with increasing annealing temperature up to 695 K in the  $Zr_{65}Al_{7.5}Ni_{10}Cu_{7.5}Ag_{10}$  glassy alloy. It has a maximum value of  $4.4 \times 10^{20} \text{ m}^{-3} \cdot \text{s}^{-1}$  at 695 K, and then decreases slightly with an increase of temperature. This value is approximately  $10^2$  times higher than those of  $Zr_{69.5}Al_{7.5}Ni_{11}Cu_{12}$ ,  $Pd_{58.8}U_{20.6}Si_{20.6}$ , and  $Al_{75}Cu_{15}V_{10}$  alloys, in which an icosahedral phase is transformed from an amorphous state [28, 34, 35]. The nucleation rate of the fcc  $Zr_2Ni$  phase in the  $Zr_{65}Al_{7.5}Ni_{10}Cu_{17.5}$  glassy alloy increases slightly with increasing annealing temperature, whereas the value of the nucleation rate is approximately  $10^{16} \text{ m}^{-3} \cdot \text{s}^{-1}$  over the entire temperature range. Therefore, the nucleation rate increases  $10^4$  times by the addition of 10at% Ag in the Zr–Al–Ni–Cu glassy alloy.

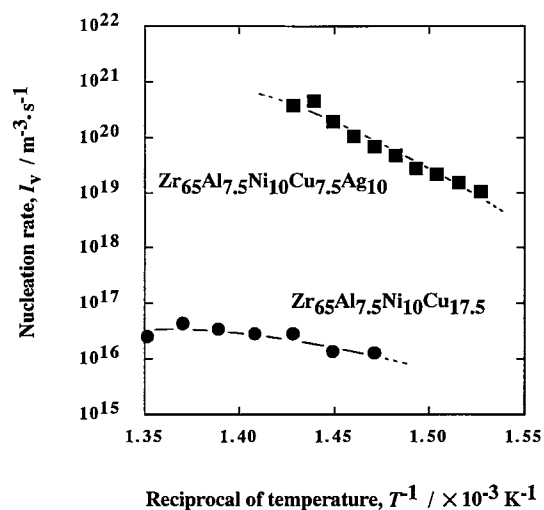


**Figure 5.** Calculated homogeneous nucleation rate against the reciprocal of temperature for the  $Zr_{65}Al_{7.5}Ni_{10}Cu_{7.5}Ag_{10}$  and  $Zr_{65}Al_{7.5}Ni_{10}Cu_{17.5}$  glassy alloys. Reprinted with permission from [62], J. Saida et al., *Philos. Mag. Lett.* 80, 737 (2000). © 2000, Taylor & Francis Ltd.

In order to clarify the influence of the noble metal content in the Zr–Al–Ni–Cu glassy alloys on the nucleation, it was examined in the  $Zr_{65}Al_{7.5}Ni_{10}Cu_{17.5-x}Pd_x$  ( $x = 0, 5, 10,$  and  $17.5$ ) glassy alloys [67]. The calculated homogeneous nucleation rate  $I_v$  of the primary phase at  $T_x$  in the  $Zr_{65}Al_{7.5}Ni_{10}Cu_{17.5-x}Pd_x$  ( $x = 0, 5, 10,$  and  $17.5$ ) glassy alloys is plotted in Figure 6. It is found that the  $I_v$  increases significantly to  $(2.9 \pm 0.3) \times 10^{18} \text{ m}^{-3} \cdot \text{s}^{-1}$  for the precipitation of the nanoicosahedral phase by the addition of only 5at% Pd, and increases almost linearly with increasing Pd content. The  $I_v$  increases to  $(1.1 \pm 0.3) \times 10^{20} \text{ m}^{-3} \cdot \text{s}^{-1}$  for  $x = 10$  and  $(2.9 \pm 0.3) \times 10^{22} \text{ m}^{-3} \cdot \text{s}^{-1}$  for  $x = 17.5$ . The nucleation rate of the nanoicosahedral phase at Pd=5 at% is nearly equal to that of the icosahedral phase in the  $Zr_{69.5}Al_{7.5}Ni_{11}Cu_{12}$  glassy alloy, which contains a large amount of oxygen impurity [34]. The  $I_v$  is  $(2.6 \pm 0.3) \times 10^{16} \text{ m}^{-3} \cdot \text{s}^{-1}$  for the precipitation of the fcc  $Zr_2Ni$  phase at  $x = 0$ . The significant increase of the nucleation rate by the addition of Pd seems to be attributed to the strong chemical affinity between Zr and Pd. The decrease of the grain growth rate of the primary phase with increasing Pd content has also been reported [67].

Thus, we can realize that noble metal addition is effective for the increase in the nucleation rate and the decrease in the grain growth rate. It is concluded that the noble metal plays the role of the enhancement of the precipitation of nanoicosahedral grains by the suppression of the long-range rearrangement of constitutional elements to form the ordinary crystalline phase.

#### 2.4. Precipitation Process of Nanoicosahedral Phase

The precipitation behavior of the nanoicosahedral phase from the glassy state has been investigated. The redistribution behavior of the constituent elements during the precipitation of the nanoicosahedral phase has been clarified by nanobeam energy dispersive X-ray spectroscopy (EDX) analysis in the  $Zr_{65}Al_{7.5}Ni_{10}Cu_{7.5}Pd_{10}$  glassy alloy [68]. It is reported that the Al and Pd contents remain almost

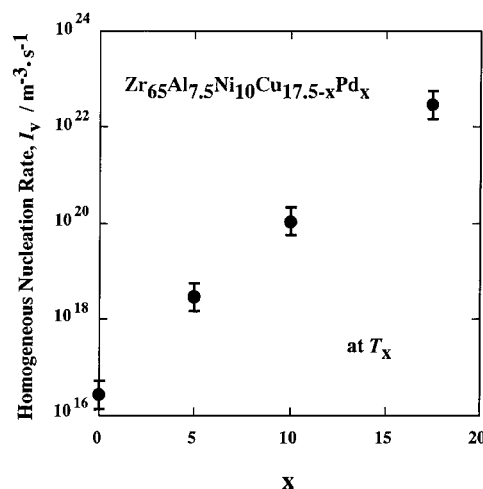


**Figure 6.** Change in homogeneous nucleation rate for the  $Zr_{65}Al_{7.5}Ni_{10}Cu_{17.5}Pd_x$  ( $x = 0, 5, 10,$  and  $17.5$ ) glassy alloys. Reprinted with permission from [67], J. Saida et al., *Mater. Trans. JIM* 41, 1505 (2000). © 2000, Japan Institute of Metals.



unchanged, but the Ni and Cu elements are rejected from the icosahedral phase to the remaining glassy phase, and the Zr element is enriched to the icosahedral phase. The necessity for the redistribution among the constituent elements is expected to cause a low growth rate. The redistribution behavior is consistent with the results that the growth rate of the nanoicosahedral phase decreases significantly with increasing Pd content, and is much lower than that for the crystalline phase [67].

The precipitation kinetics of the nanoicosahedral phase also have been analyzed in the framework of the Johnson–Mehl–Avrami (J–M–A) relation [65, 69]. When the data at the transformation ratios ( $Y$ ) ranging from 0.2 to 0.8 are used, one can see a rather good linearity in the wide temperature range in the relation between  $\ln(-\ln(1 - Y))$  and  $\ln(t_a)$ . The Avrami exponent ( $n$  value) corresponding to the slope of the linear relation is in the range of 2.5–3.6, and can be approximated as 3.0, indicating the diffusion-controlled mode with an increasing nucleation rate [70]. This result is supported by the rearrangement of constitutional elements during nanoquasicrystallization.

### 3. FORMATION OF NANOICOSAHEDRAL PHASE BY CHANGING COMPOSITION IN Zr-BASED GLASSY ALLOYS

As described in Table 1, all of the additional elements for the nanoicosahedral phase formation have positive mixing enthalpies, with at least one of the constitutional elements in a Zr–Al–Ni–Cu glassy alloy. It is interpreted that the icosahedral phase can be formed by deviating from the three component rules for a high GFA, which are described as: (1) multicomponent systems consisting of more than three elements, (2) a significant difference in atomic size ratios above about 12% among the three main constituent elements, and (3) negative heats of mixing among the three main constituent elements [71]. These results also indicate that an icosahedral phase may precipitate by slight deviation from the alloy composition with the highest GFA [72]. In the DSC curves of the melt-spun  $\text{Zr}_{65+x}\text{Al}_{7.5}\text{Ni}_{10}\text{Cu}_{17.5-x}$  ( $x = 0-9$ ) glassy alloys, the crystallization process changes from the single step in the alloys with  $x = 0-4$  into two- or three-stage exothermic reactions in the alloys above  $x = 5$ , accompanied by a significant decrease in the crystallization temperature. It is well known that an fcc  $\text{Zr}_2\text{Ni}$  phase with a large unit cell of  $a = 1.227$  nm is precipitated in the primary phase at the initial crystallization stage in the  $\text{Zr}_{65}\text{Al}_{7.5}\text{Ni}_{10}\text{Cu}_{17.5}$  glassy alloy [63]. It has been clarified that a weak diffraction peak corresponding to an icosahedral phase is observed in addition to the mixture phases of fcc  $\text{Zr}_2\text{Ni}$ ,  $\text{Zr}_2\text{Cu}$ , and  $\text{Zr}_6\text{NiAl}_2$  in the primary crystallization stage of the alloys with  $x = 1$  and 2 annealed for 120 s at  $T_x$ . Subsequently, a single icosahedral phase is formed in the alloys with  $x = 3-6$ . The intensity of the diffraction peaks corresponding to the icosahedral phase decreases significantly, and the bcc Zr phase is precipitated in the alloys with  $x > 7$ . Finally, no icosahedral phase is observed in the alloy with  $x = 9$ .

Figure 7 shows the bright-field TEM image (a) and SADP (b) of the  $\text{Zr}_{70}\text{Al}_{7.5}\text{Ni}_{10}\text{Cu}_{12.5}$  ( $x = 5$ ) alloy annealed for 60 s at 710 K. Dendritic particles with diameters of 500–2000 nm

are observed. The SADP clearly reveals the quasiperiodic five-fold symmetry, indicating the icosahedral structure. A similar result for the formation of the icosahedral phase has been reported in previous studies for the  $\text{Zr}_{69.5}\text{Al}_{7.5}\text{Ni}_{11}\text{Cu}_{12}$  alloy by Köster et al., containing an oxygen impurity over approximately 1000 mass ppm, where the icosahedral phase has a spherical morphology with a diameter of 50–200 nm [33, 34]. The difference in grain size for the icosahedral phase seems to be attributable to a difference in the number of nuclei due to the oxygen impurity [39]. The redistribution of the constituent elements in the alloy during crystallization has been examined by nanobeam EDX. The average compositions of five data points in the residual glassy phase and the icosahedral phase are  $\text{Zr}_{74.6}\text{Al}_{6.9}\text{Ni}_{8.5}\text{Cu}_{10.0}$  and  $\text{Zr}_{78.7}\text{Al}_{6.7}\text{Ni}_{5.1}\text{Cu}_{9.5}$ , respectively. These results indicate that redistribution of the constituent elements is necessary during the quasicrystallization reaction, which is one important factor for the high stability of the supercooled liquid state. However, only the Zr and Cu elements are redistributed for the icosahedral phase formation, which is in contrast to the redistribution of all constituent elements during the precipitation of the fcc  $\text{Zr}_2\text{Ni}$  phase in the  $\text{Zr}_{65}\text{Al}_{7.5}\text{Ni}_{10}\text{Cu}_{17.5}$  glassy alloy [63]. It is presumed that the difference in the redistribution behavior contributes to the difference in the GFA of these alloys.

With a slightly increasing Zr concentration in the  $\text{Zr}_{65+x}\text{Al}_{7.5}\text{Ni}_{10}\text{Cu}_{17.5-x}$  ( $x = 0-9$ ) glassy alloys, the nanoicosahedral phase is precipitated, and a single icosahedral phase is observed as the primary phase in the alloys with  $3 \leq x \leq 6$ . These results indicate that a slight deviation from a high GFA is effective for nanoicosahedral phase formation.

### 4. NANOICOSAHEDRAL PHASE IN TERNARY AND BINARY ALLOY SYSTEMS

#### 4.1. Zr–TM–NM and Zr–NM–NM Ternary Systems

The addition of noble metals in Zr–Al–Ni–Cu glassy alloys is concluded to play an important role in the formation of a nanoicosahedral phase. This is confirmed from the result that

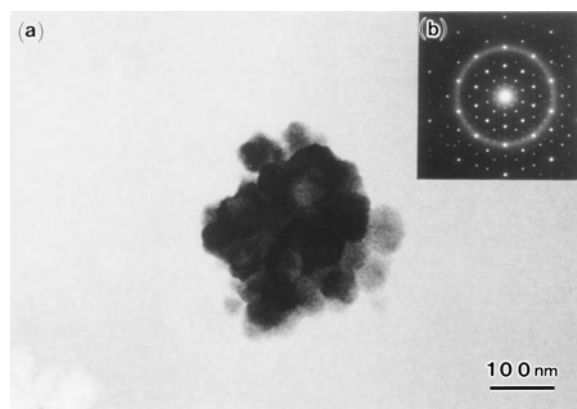


**Figure 7.** Bright-field TEM image (a) and SADP (b) of the  $\text{Zr}_{70}\text{Al}_{7.5}\text{Ni}_{10}\text{Cu}_{12.5}$  glassy alloy annealed for 120 s at 710 K [72].

the icosahedral phase formation is recognized in Zr-based ternary alloys with high noble metal concentrations. The first report about the formation of a nanoicosahedral phase was given in the Zr–Ni–(Pd, Au, or Pt) ternary glassy alloys in 2000 [73]. The crystallization proceeds through two exothermic peaks in the  $Zr_{70}Ni_{10}M_{20}$  ( $M = Pd, Au, \text{ or } Pt$ ) glassy alloys, and the first reaction corresponds to the precipitation of a nanoicosahedral phase from the glassy state. The bright-field TEM image (a) and SADP (b) of the  $Zr_{70}Ni_{10}Pd_{20}$  alloy annealed for 120 s at 700 K are shown in Figure 8. Very fine particles in the diameter range from 5 to 20 nm are seen over the whole area. The precipitates have a nearly spherical morphology, and are homogeneously distributed. The SADP taken from a region of 1  $\mu\text{m}$  in diameter can be identified as an icosahedral single phase. A similar structure consisting of the icosahedral single phase is also obtained for the alloys containing Au, or Pt. The three kinds of NBD patterns revealing quasiperiodic five-, three-, and twofold symmetries are obtained in all of the alloys, which can be identified as the icosahedral structure. Thus, it is clarified that the icosahedral phase is formed in the  $Zr_{70}Ni_{10}(Pd, Au, \text{ or } Pt)_{20}$  alloy systems. Matsushita et al. have reported nanoicosahedral phase formation in the  $Zr_{70}(Fe, Co, \text{ or } Cu)_{10}Pd_{20}$  glassy alloys [74]. These results indicate that a high noble metal content in the Zr–TM (transition metal)-based glassy alloys is effective for the enhancement of nanoquasicrystal-forming ability.

Murty et al. reported the formation of a nanoicosahedral phase in a  $Zr_{70}Cu_{23}Pd_7$  glassy alloy [75], and subsequently, nanoicosahedral phase formation in Zr–Cu-based alloys with low noble metal content has been clarified in the  $Zr_{70}Cu_{20}(Rh \text{ or } Ir)_{10}$  glassy alloys by Li et al. [76, 77]. In their recent study, the  $Zr_{70}Cu_{27.5}Rh_{2.5}$  glassy alloy is found to transform into the nanoicosahedral phase as the primary phase [78]. These reports are interpreted as the significant effect of the noble metals on the nanoicosahedral phase-forming ability in the Zr–Cu glassy alloys. The influence of the addition of noble metals less than 2.5at% on the transformation behavior correlated with the local structure in the Zr-based glassy alloys is discussed later in this chapter. Nanoicosahedral phase formation in the Zr–NM-based ternary alloys has been reported in the  $Zr_{75}Pt_{10}Pd_{15}$  and  $Zr_{70}Au_{10}Pd_{20}$  glassy alloys [79]. It was found that the icosahedral particles in the Zr–NM-based ternary alloys have an

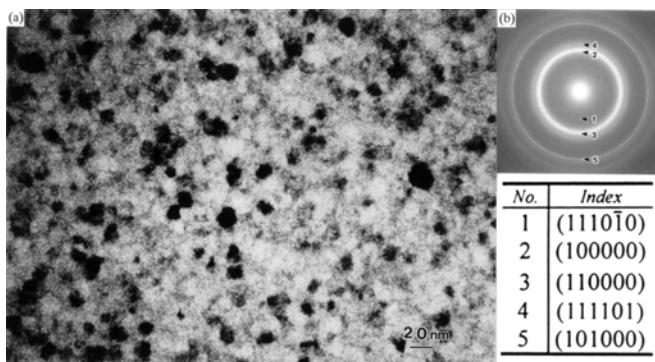


**Figure 8.** Bright-field TEM image (a) and SADP (b) of the  $Zr_{70}Ni_{10}Pd_{20}$  glassy alloy annealed for 120 s at 700 K. Reprinted with permission from [73], J. Saida et al., *Appl. Phys. Lett.* 76, 3558 (2000). © 2000, American Institute of Physics.

extremely fine grain size with a diameter less than 10 nm [80], which indicates the high nucleation rate of the icosahedral phase.

## 4.2. Zr–NM Binary Systems

### 4.2.1. Formation of Nanoicosahedral Phase in $Zr_{70}Pd_{30}$ Glassy and $Zr_{80}Pt_{20}$ Amorphous Alloys

The nanoicosahedral phase in the Zr–NM (NM = Pd, Pt) binary alloy systems has been reported by the authors, Saida et al., and Murty et al. [81–83]. The rapidly quenched  $Zr_{70}Pd_{30}$  and  $Zr_{80}Pt_{20}$  alloys have an amorphous structure at a Cu roll speed of 50  $\text{m} \cdot \text{s}^{-1}$  in the single-roller melt-spinning technique. The crystallization proceeds through two exothermic reactions, followed by the glass transition in the  $Zr_{70}Pd_{30}$  glassy alloy.  $T_x$ , corresponding to the onset temperature of the first exothermic peak, is 723 K. The temperature interval between the two exothermic peaks is approximately 80 K. Although the two-stage crystallization process is also observed in the  $Zr_{80}Pt_{20}$  amorphous alloy, the exothermic peaks are weaker and broader than those in the  $Zr_{70}Pd_{30}$  glassy alloy, and the glass transition disappears. The onset temperature of the first exothermic peak is 717 K, and the peak temperatures of the two exothermic reactions are 757 and 923 K, respectively. The XRD peaks of the  $Zr_{70}Pd_{30}$  and  $Zr_{80}Pt_{20}$  alloys subjected to the annealing treatment corresponding to the first exothermic reaction are identified as the icosahedral structure. Bright-field TEM images, SADPs taken from the region of 1  $\mu\text{m}$  in diameter, and NBD patterns of the  $Zr_{70}Pd_{30}$  alloy annealed for 120 s at 740 K [(a)–(e)] and the  $Zr_{80}Pt_{20}$  alloy annealed for 120 s at 840 K [(f)–(j)] are shown in Figure 9, respectively. Fine particles with diameters less than 20 nm are distributed homogeneously over the whole area in both alloys. The reflection rings in the SADP are characterized as an icosahedral structure. The NBD patterns revealing the five-, three-, and twofold symmetries are also obtained from the precipitated particles, which can be confirmed as an icosahedral structure. Since no diffraction patterns corresponding to other crystalline phases are obtained in both alloys, it is concluded that the first exothermic peak is due to the transformation from an amorphous phase to the nanoicosahedral phase.

For the evaluation of the thermal stability of the nanoicosahedral phase, the structure of the  $Zr_{70}Pd_{30}$  glassy and  $Zr_{80}Pt_{20}$  amorphous alloys subjected to annealing, corresponding to the transformation at the second exothermic peak, was examined [84]. The diffraction peaks of only the  $Zr_2Pd$  phase are recognized in the  $Zr_{70}Pd_{30}$  alloy. In the  $Zr_{80}Pt_{20}$  alloy, mixture phases of Zr, ZrPt,  $Zr_5Pt_3$ , and  $Zr_9Pt_{11}$  are identified. Neither the residual existence of an icosahedral phase nor broad peaks due to an amorphous phase is recognized in both alloys, indicating that the icosahedral phase is a metastable phase. It is therefore concluded that the transformation of the  $Zr_{70}Pd_{30}$  glassy and  $Zr_{80}Pt_{20}$  amorphous alloys can be expressed as follows:

glassy phase  $\rightarrow$  nanoicosahedral phase

$\rightarrow Zr_2Pd$  for the  $Zr_{70}Pd_{30}$  glassy alloy

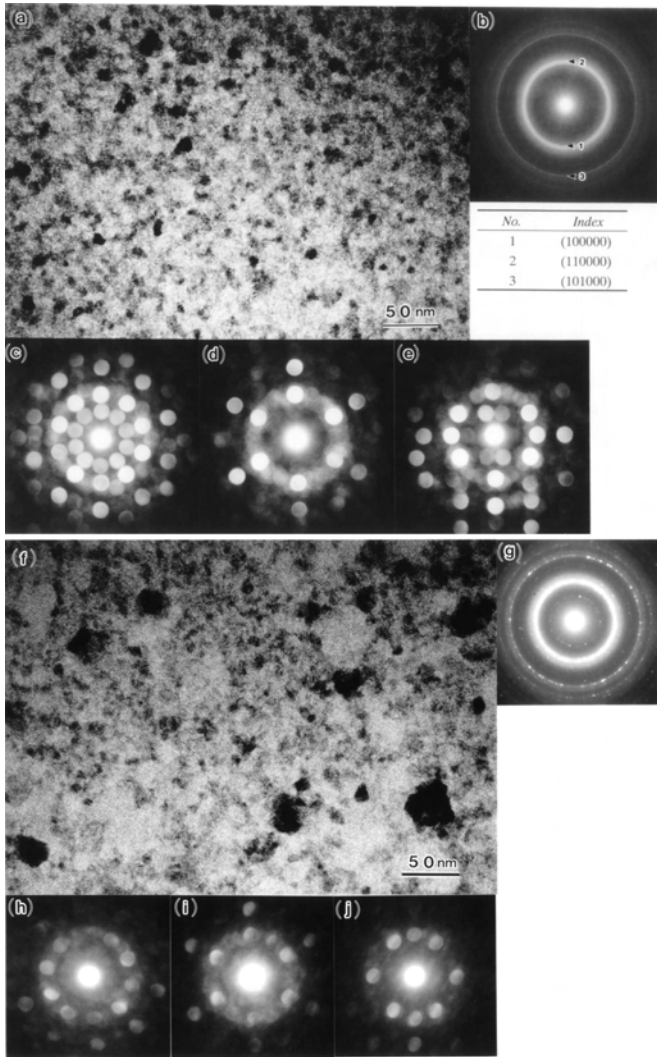


**Figure 9.** Bright-field TEM images, SADPs, and NBD patterns of the  $Zr_{70}Pd_{30}$  glassy alloy annealed for 120 s at 740 K (a)–(e) and the  $Zr_{80}Pt_{20}$  amorphous alloy annealed for 120 s at 840 K (f)–(j) [81]. Reprinted with permission from [84], J. Saida et al., *J. Appl. Phys.* 90, 4717 (2001). © 2001, American Institute of Physics.

and

amorphous phase  $\rightarrow$  nanoicosahedral phase  
 $\rightarrow Zr + ZrPt + Zr_5Pt_3 + Zr_9Pt_{11}$   
 for the  $Zr_{80}Pt_{20}$   
 amorphous alloy [84].

#### 4.2.2. Structural Change with Quenching Rate in $Zr_{80}Pt_{20}$ Alloy

The structure of the melt-spun  $Zr_{80}Pt_{20}$  ribbons prepared by changing the Cu roll speed in the range of 50–10  $m \cdot s^{-1}$  has been reported by the authors [85]. As shown for XRD patterns in Figure 10, no sharp diffraction peaks due to a crystalline phase are contained in the sample prepared at 50  $m \cdot s^{-1}$ , while a mixture of  $ZrPt$ ,  $Zr_5Pt_3$ , and  $Zr_9Pt_{11}$  phases is formed at a roll speed of 20  $m \cdot s^{-1}$ . At a roll

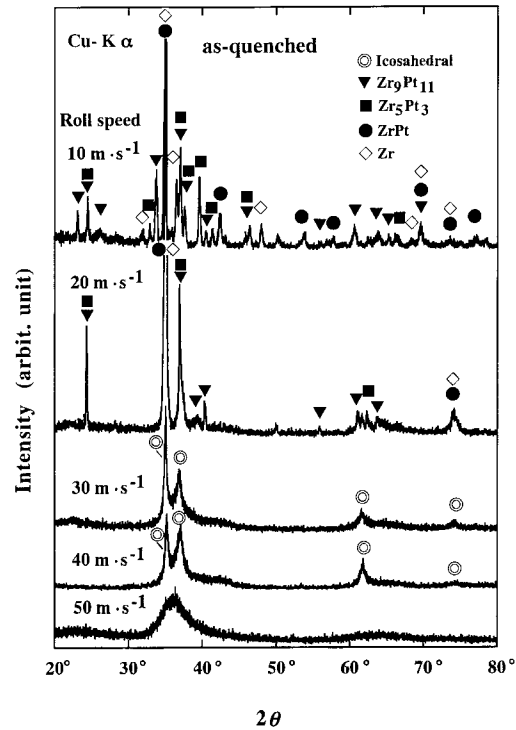


**Figure 10.** XRD patterns of the melt-spun  $Zr_{80}Pt_{20}$  alloy with various roll speeds [82]. Reprinted with permission from [84], J. Saida et al., *J. Appl. Phys.* 90, 4717 (2001). © 2001, American Institute of Physics.

speed of 10  $m \cdot s^{-1}$ , sharp diffraction peaks of the hcp Zr phase appear in addition to the crystalline phases observed at 20  $m \cdot s^{-1}$ . In contrast, we have found that the icosahedral phase is formed at roll speeds of 40 and 30  $m \cdot s^{-1}$ , and no extra peaks corresponding to a crystalline phase are seen. In the bright-field TEM images of the as-spun samples prepared at roll speeds of 40 and 30  $m \cdot s^{-1}$ , very fine particles of diameters less than 10 nm are precipitated over the entire area [82]. The particles have a nearly spherical morphology, and are homogeneously distributed. The NBD patterns revealing the quasiperiodic symmetries reflected from the icosahedral structure are obtained from the precipitates.

#### 4.2.3. Redistribution Behavior During Nanoquasicrystallization in $Zr_{70}Pd_{30}$ Glassy and $Zr_{80}Pt_{20}$ Amorphous Alloys

The compositional changes during the precipitation of a nanoicosahedral phase in  $Zr_{70}Pd_{30}$  and  $Zr_{80}Pt_{20}$  alloys have been examined by nanobeam EDX with a beam diameter of approximately 5 nm [84]. In the  $Zr_{70}Pd_{30}$  alloy, an average composition of five data points in the icosahedral phase is  $Zr_{74.1}Pd_{25.9}$ , which is slightly different from that ( $Zr_{70.9}Pd_{29.1}$ ) in the residual glassy phase. It is clarified that the slight rejection of Pd (approximately 3at%) from the icosahedral phase is necessary for the precipitation and growth of the nanoicosahedral particles. Similar results were obtained by the three-dimensional atom probe (3DAP) technique [86]. In contrast, the same average composition of  $Zr_{79.5}Pt_{20.5}$  is analyzed in the icosahedral and residual amorphous phases in the  $Zr_{80}Pt_{20}$  alloy. These results indicate

the absence of significant redistribution of the constitutional elements during the transformation from an amorphous to a nanoicosahedral phase. We point out that the difference of the rearrangement behaviors during nanoquasicrystallization is correlated with the difference of the exothermic reaction in the DSC curves between the alloys. Heat of the first exothermic reaction in the  $Zr_{70}Pd_{30}$  glassy alloy is calculated to be  $1.66 \text{ kJ} \cdot \text{mol}^{-1}$ , which is considerably larger than that ( $0.99 \text{ kJ} \cdot \text{mol}^{-1}$ ) in the  $Zr_{80}Pt_{20}$  amorphous alloy. The absence of a significant rearrangement seems to be one of the factors for the low heat of quasicrystallization in the  $Zr_{80}Pt_{20}$  amorphous alloy.

#### 4.2.4. Kinetics of Transformation from Glass to Nanoicosahedral Phase in $Zr_{70}Pd_{30}$ Glassy Alloy

The transformation kinetics from the glassy phase to the nanoicosahedral phase have been examined at different temperatures below  $T_x$  of the  $Zr_{70}Pd_{30}$  glassy alloy [87]. The kinetics of the structural transition are analyzed in the framework of the J–M–A equation [65, 69]. The  $n$  value is in the range from 2.9 to 3.2 in the temperature range of 700–715 K, and can be approximated as 3.0 in the J–M–A plots of the  $Zr_{70}Pd_{30}$  glassy alloy. It was reported that the  $n$  value is about 3.0 for the precipitation of the icosahedral phase in the supercooled liquid region of the  $Zr_{65}Al_{7.5}Ni_{10}Cu_{7.5}Pd_{10}$  glassy alloy [68], in agreement with the result in the binary alloy. It is suggested that the transformation proceeds through the diffusion-controlled growth mode with increasing nucleation rate [70]. The compositional change analyzed by nanobeam EDX is consistent with the diffusion-controlled transformation mode. The extremely fine grain size of the icosahedral phase, less than 20 nm in the annealed state, is realized by the increase of the nucleation rate with a continuation of the transformation. However, the J–M–A plots are slightly curved at a late stage of the transformation, indicating a decrease of the Avrami exponent [87]. The change of the Avrami exponent with transformation implies the possibility of the existence of the quenched-in nuclei in the glassy state [19, 28].

The authors have clarified the grain growth kinetics of the nanoicosahedral phase [84]. The icosahedral phase grows almost linearly with increasing annealing time at temperatures between 700 and 715 K. The maximum grain size of the icosahedral phase is approximately 24 nm. With increasing temperature from 700 to 715 K, the growth rate increases from  $1.0 \times 10^{-10}$  to  $2.6 \times 10^{-10} \text{ m} \cdot \text{s}^{-1}$ . The growth rates have nearly the same order as those ( $7.6 \times 10^{-11}$ – $6.7 \times 10^{-10} \text{ m} \cdot \text{s}^{-1}$ ) of the nanoicosahedral phase in the  $Zr_{65}Al_{7.5}Ni_{10}Cu_{7.5}Ag_{10}$  glassy alloy [64]. The change in the growth rate with annealing temperature in the  $Zr_{70}Pd_{30}$  glassy alloy is considerably lower than that in the  $Zr_{65}Al_{7.5}Ni_{10}Cu_{7.5}Ag_{10}$  glassy alloy. These growth rates of nanoicosahedral particles are also approximately ten times smaller than that of the metastable fcc  $Zr_2Ni$  phase in the  $Zr_{65}Al_{7.5}Ni_{10}Cu_{17.5}$  glassy alloy [62]. These results indicate the significant suppression of the grain growth of the nanoicosahedral phase. It is therefore concluded that the formation of the icosahedral phase with nanometer scale is

attributed to a high nucleation rate and a low grain growth rate during the transformation.

The Arrhenius plot of the logarithm of the grain growth rate versus the reciprocal of the annealing temperature yields a linear relationship, whose slope gives an activation energy for the grain growth  $Q$  of  $270 \text{ kJ} \cdot \text{mol}^{-1}$  according to Eq. (1). The activation energy for grain growth is the same as that calculated from the incubation time of quasicrystallization [87], which is in correlation with the initial stage of nucleation. Moreover, it is much smaller than those of the metastable fcc  $Zr_2Ni$  phase in the  $Zr_{65}Al_{7.5}Ni_{10}Cu_{17.5}$  glassy ( $382 \text{ kJ} \cdot \text{mol}^{-1}$ ) and the nanoicosahedral phase in the  $Zr_{65}Al_{7.5}Ni_{10}Cu_{7.5}Ag_{10}$  glassy ( $352 \text{ kJ} \cdot \text{mol}^{-1}$ ) alloys [62], where the differences in the  $Q$  are attributed to the number of components involved in the rearrangements through the grain growth among the alloy systems [33, 88]. Meanwhile, the activation energy of  $270 \text{ kJ} \cdot \text{mol}^{-1}$  is significantly low considering the necessity of rearrangements of Zr and/or Pd [89]. We suggest that the precipitation of the icosahedral phase proceeds without large-scale atomic rearrangements, implying the existence of an icosahedral short- and/or medium-range order in the glassy state [19, 28, 90–93].

## 5. NANOICSAHEDRAL PHASE FORMATION IN GLASSY ALLOYS EXCEPT Zr-BASED SYSTEMS

After the discoveries of the formation of a nanoicosahedral phase in various Zr-based alloys, the quasicrystallization from the glassy state, except for a Zr-based alloy, has been investigated. The first report was presented by Louzguine et al. in the Hf-based glassy alloy in 2000 [94], where the Hf belongs to the same 4A column in the periodic table with Zr. They reported that the nanoicosahedral particles with a diameter of approximately 10 nm are precipitated as a primary phase in the  $Hf_{65}Al_{7.5}Ni_{10}(Pd \text{ or } Au)_{17.5}$  glassy alloy [94, 95]. Li et al. have reported that the nanoicosahedral phase is formed in the  $Hf_{65}Al_{7.5}Ni_{10}Cu_{12.5}(Pd \text{ or } Pt)_5$ ,  $Hf_{59}Al_{10}Ni_8Cu_{20}Ti_3$ ,  $Hf_{60}Ni_{15}Cu_{10}Ti_{15}$ , and  $Hf_{69.5}Al_{7.5}Ni_{11}Cu_{12}$  glassy alloys [96–100]. Recently, nanoicosahedral phase formation has also been reported in Hf–(Cu, Ni)–(Pd, Pt) ternary and Hf–Pd binary glassy alloys by Li et al. [101–107].

It is realized that these discoveries are achieved by the same approach in Zr-based glassy alloys, that is, the nanoicosahedral phase is formed in the Hf-based glassy alloys by the addition of a small amount of an element with a weak or positive chemical affinity with the constituent elements or by the slight deviation from the composition with a high GFA.

In Ti-based alloys, icosahedral phase formation was found in the as-quenched or annealed state in the Ti–Ni, T–Zr–(Ni or Fe), and Ti–Ni–Cu–Si alloys in the period 1985–1996 [11, 108–113]. However, these icosahedral phases have not been recognized as a nanoicosahedral phase due to the comparatively large grain size. Since Kim and Kelton found the formation of a nanoicosahedral phase in an amorphous matrix of the melt-spun  $Ti_{53}Zr_{27}Co_{20}$  alloy in 1996 [114], it has been reported in the multicomponent system in the as-quenched state of a Ti–Zr–(Ni)–Cu alloy [115, 116].

Recently, Wang et al. have also discovered the formation of a nanoicosahedral phase transformed from the amorphous state in the  $\text{Ti}_{60}(\text{Zr or Hf})_{15}\text{Ni}_{15}\text{Cu}_{10}$  alloy [117]. A typical structure of the nanoicosahedral phase with a diameter less than 50 nm in the  $\text{Ti}_{60}\text{Hf}_{15}\text{Ni}_{15}\text{Cu}_{10}$  amorphous alloy is shown in [117]. It is pointed out that the volume fraction of the nanoicosahedral phase can be easily controlled by changing the annealing condition, and it is expected that the nanoicosahedral phase will devitrify from Ti-based glassy alloys with a high GFA in the near future.

## 6. CORRELATION BETWEEN LOCAL STRUCTURE IN GLASSY STATE AND NANOICOSAHEDRAL PHASE FORMATION

### 6.1. Transformation of Glassy Alloys in Low Concentration of Additional Elements

The transformation behavior has been examined for Zr–Al–Ni–Cu glassy alloys with various Pd contents below 4at% to clarify the role of noble metal in the icosahedral phase formation [118]. DSC curves of the melt-spun  $\text{Zr}_{65}\text{Al}_{7.5}\text{Ni}_{10}\text{Cu}_{17.5-x}\text{Pd}_x$  ( $x = 0-4$ ) glassy alloys contain two exothermic peaks for the alloys of Pd contents more than 2at%, and the temperature gap between the two reactions increases with increasing Pd content. In the 1at% Pd alloy, the exothermic reaction has a single peak. However, the peak is broader than that of the non-Pd-containing alloy, indicating the separation of the crystallization reaction. The XRD patterns of the samples annealed for 30 s at  $T_x$ , leading to the precipitation of the primary phase, are shown in Figure 11. For Pd contents above 2at%, all of the diffraction peaks are recognized as a single icosahedral phase. In

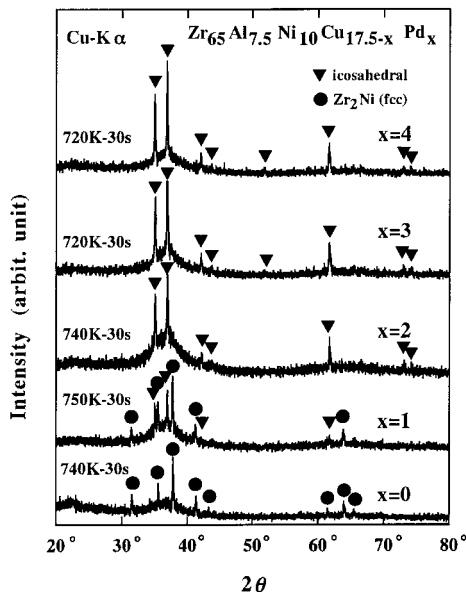


**Figure 11.** XRD patterns of the  $\text{Zr}_{65}\text{Al}_{7.5}\text{Ni}_{10}\text{Cu}_{17.5-x}\text{Pd}_x$  ( $x = 0-4$ ) glassy alloys annealed for 30 s near  $T_x$ . Reprinted with permission from [118], J. Saida et al., *Mater. Trans. JIM* 42, 1497 (2001). © 2001, Japan Institute of Metals.

the  $\text{Zr}_{65}\text{Al}_{7.5}\text{Ni}_{10}\text{Cu}_{16.5}\text{Pd}_1$  glassy alloy, the primary phase is concluded to be a mixture of an icosahedral and fcc  $\text{Zr}_2\text{Ni}$  phases.

For further investigation on the microstructure and composition of the two metastable phases, TEM and nanobeam EDX analyses were performed. The bright-field TEM images [(a) and (c)] and SADP [(b) and (d)] of the  $\text{Zr}_{65}\text{Al}_{7.5}\text{Ni}_{10}\text{Cu}_{16.5}\text{Pd}_1$  glassy alloy annealed for 30 s at 750 K are shown in Figure 12. Two types of particles are observed in Figure 12(a) and (c). The particles in Figure 12(a) have a dendrite structure in the diameter range of 500–1000 nm in the glassy matrix. The SADP taken from the particles clearly denotes twofold icosahedral symmetry, as shown in Figure 12(b). In Figure 12(c), a precipitated particle is also observed in the glassy matrix, whose SADP shown in Figure 12(d) can be identified as the fcc  $\text{Zr}_2\text{Ni}$  phase along the  $[\bar{1}16]$  zone axis. Both precipitates are isolated from each other and homogeneously distributed in the glassy matrix. A similar structure has been obtained in the  $\text{Zr}_{65}\text{Al}_{7.5}\text{Ni}_{10}\text{Cu}_{16.5}(\text{Ag, Au, Pt, or Ta})_1$  glassy alloys [119, 120]. The average compositions of five data points analyzed by nanobeam EDX for the icosahedral, fcc  $\text{Zr}_2\text{Ni}$ , and residual glassy phases are  $\text{Zr}_{72.7}\text{Al}_{7.3}\text{Ni}_{6.9}\text{Cu}_{12.0}\text{Pd}_{1.1}$ ,  $\text{Zr}_{69.3}\text{Al}_{6.9}\text{Ni}_{11.6}\text{Cu}_{11.2}\text{Pd}_{1.0}$ , and  $\text{Zr}_{63.9}\text{Al}_{6.8}\text{Ni}_{10.1}\text{Cu}_{18.5}\text{Pd}_{0.7}$ , respectively. Considering that the icosahedral and fcc  $\text{Zr}_2\text{Ni}$  phases have a similar Pd content and the precipitates consisting of the two metastable phases are isolated from each other at the initial crystallization stage, it is implied that the local structure does not change by the addition of 1at% Pd. Therefore, we can realize that the icosahedral phase is formed without a significant local structural change by the addition of Pd into the Zr–Al–Ni–Cu glassy alloy.

A similar structure is obtained in the alloy whose composition slightly deviates from the  $\text{Zr}_{65}\text{Al}_{7.5}\text{Ni}_{10}\text{Cu}_{17.5}$

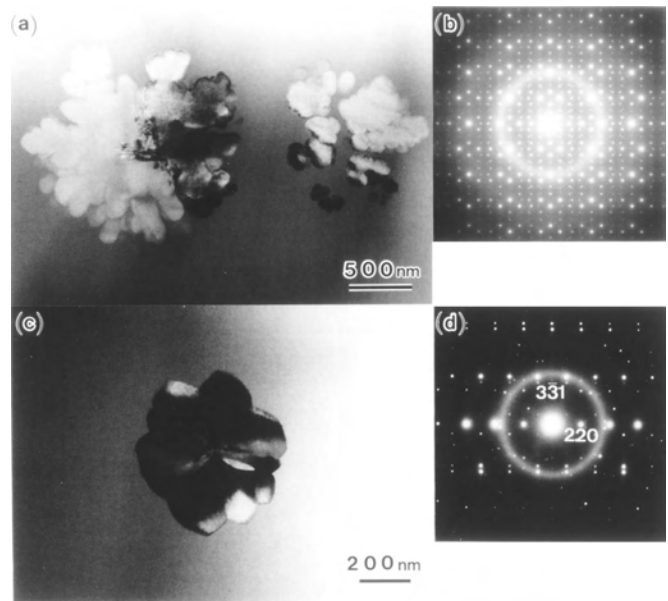


**Figure 12.** Bright-field TEM images (a), (c) and SADPs (b), (d) of the  $\text{Zr}_{65}\text{Al}_{7.5}\text{Ni}_{10}\text{Cu}_{16.5}\text{Pd}_1$  glassy alloy annealed for 30 s at 750 K. Reprinted with permission from [118], J. Saida et al., *Mater. Trans. JIM* 42, 1497 (2001). © 2001, Japan Institute of Metals.

glassy alloy. Figure 13 shows the XRD pattern of the  $Zr_{66}Al_{7.5}Ni_{10}Cu_{16.5}$  glassy alloy annealed for 30 s at 735 K. As the primary phase, two phases of an icosahedral and fcc  $Zr_2Ni$  are confirmed. The bright-field TEM images [(a) and (c)] and SADPs [(b) and (d)] of the  $Zr_{66}Al_{7.5}Ni_{10}Cu_{16.5}$  glassy alloy annealed for 30 s at 735 K are shown in Figure 14. Two types of particles are precipitated in (a) and (c). The SADP taken from the particles in (a) clearly denotes the fivefold icosahedral symmetry as shown in (b), indicating the icosahedral structure. The SADP shown in (d), taken from the particle in (c), can be identified as an fcc  $Zr_2Ni$  phase along the  $[\bar{1}16]$  zone axis. Both precipitates are also isolated from each other, and are homogeneously distributed in the glassy matrix, which is regarded as the same structure as those in the 1at% noble metal-containing Zr–Al–Ni–Cu glassy alloy.

## 6.2. Local Structure in Glassy State for Nanoicosahedral Phase Formation

These results suggest that the fcc  $Zr_2Ni$  and icosahedral phases originate from the same local structure in the glassy state [121]. Figure 15(a) shows a schematic drawing of the unit cell of the fcc  $Zr_2Ni$  structure [122]. This crystalline structure, which is called a *big-cube phase*, has a large lattice parameter of 1.227 nm, and contains 64 Zr and 32 Ni atoms [123, 124]. The structure consists of an icosahedral clusters of Zr and Ni atoms [108, 109]. As an example, two icosahedral clusters around Zr and Ni are extracted from the unit cell in Figure 15(b). Considering that the fcc  $Zr_2Ni$  and icosahedral phases contain an icosahedron in the unit cell, we point out that a local icosahedral order exists in the Zr–Al–Ni–Cu glassy alloys with a small amount of noble metal addition or a slight deviation of the composition from those with a high GFA, and can grow as a nanoicosahedral quasicrystalline phase under high nucleation rates. It is presumed that the slight deviation from the composition with a high GFA is effective for the enhancement of the distortion of the icosahedron in the unit cell of an fcc  $Zr_2Ni$  structure, which is also one of the factors for the precipitation of a nanoicosahedral phase in the Zr–Al–Ni–Cu glassy alloys.

Based on the previously reported experimental data for Zr-based glassy alloys, it has been clarified that the glassy alloys can have: (1) a higher degree of dense randomly

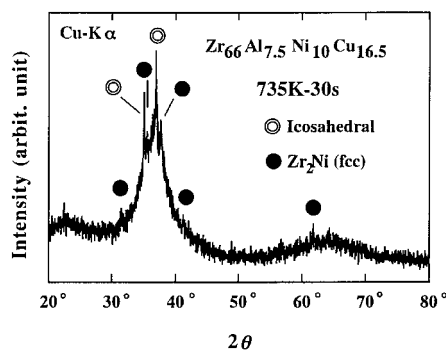


**Figure 13.** XRD pattern of the  $Zr_{66}Al_{7.5}Ni_{10}Cu_{16.5}$  glassy alloy annealed for 30 s at 735 K.

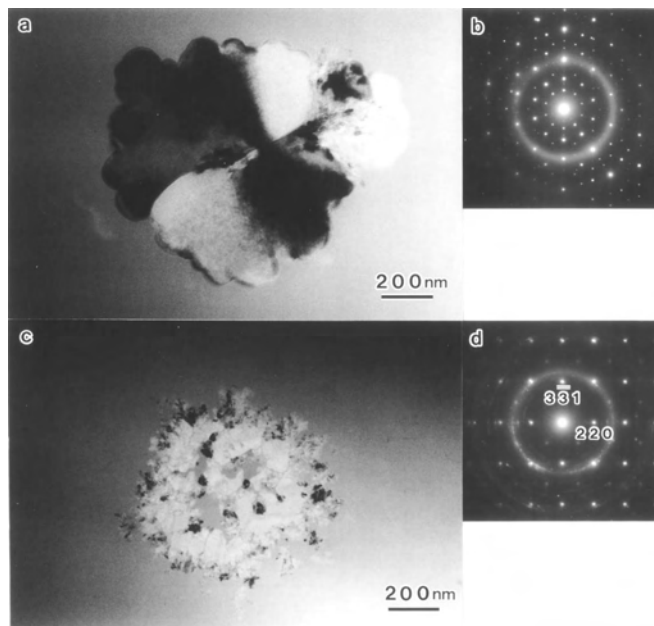
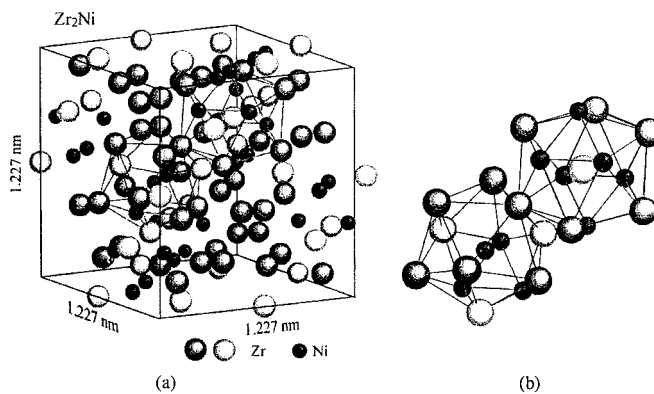


**Figure 14.** Bright-field TEM images (a), (c) and SADPs (b), (d) of the  $Zr_{66}Al_{7.5}Ni_{10}Cu_{16.5}$  glassy alloy annealed for 30 s at 735 K.

packed atomic configurations; (2) new local atomic configurations, which are different from those of the corresponding final crystalline phases; and (3) homogeneous atomic configurations with attractive interaction on a long-range scale [125]. It is noted that the existence of a local icosahedral order satisfies the above-described criteria.

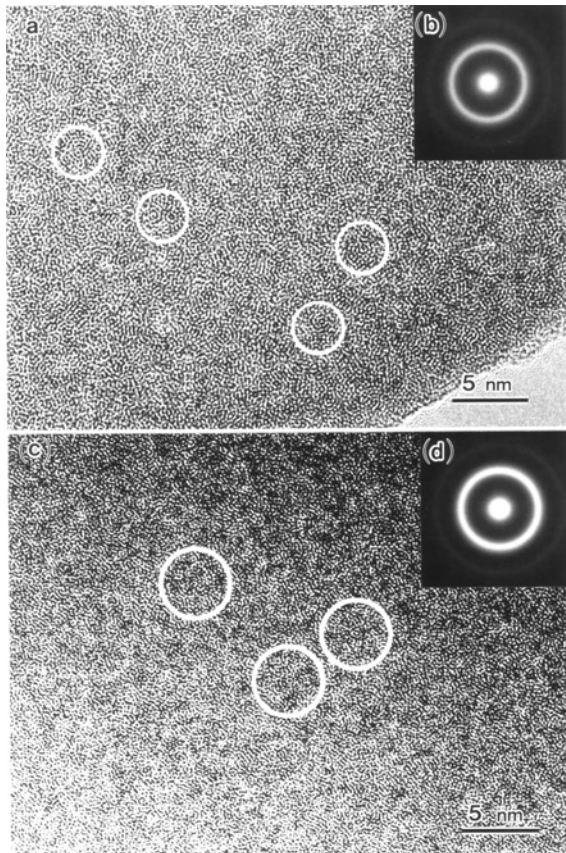
## 6.3. Direct Observation and Structure Analysis of Icosahedral Local Structure by HRTEM Observation

In order to confirm the icosahedral local structure, a high-resolution transmission electron microscopy (HRTEM) observation was performed in the nanoquasicrystal-forming glassy alloys. Figure 16 shows HRTEM images and the SADP of the as-quenched  $Zr_{65}Al_{7.5}Ni_{10}Cu_{7.5}Pd_{10}$  [(a), (b)] and  $Hf_{65}Al_{7.5}Ni_{10}Cu_{12.5}Pd_5$  [(c), (d)] glassy alloys [121]. The SADP consists of only a halo ring, indicating a glassy



**Figure 15.** Schematic illustrations of the fcc  $Zr_2Ni$  phase (a) and icosahedral local atomic configuration in the fcc  $Zr_2Ni$  phase (b) [122].

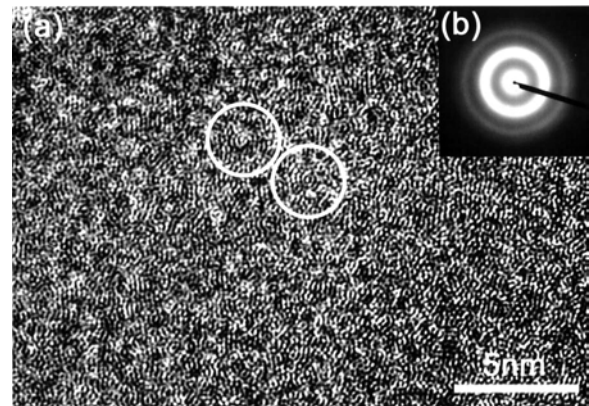




**Figure 16.** HRTEM images and SADPs of the as-quenched  $Zr_{65}Al_{7.5}Ni_{10}Cu_{7.5}Pd_{10}$  (a), (b) and  $Hf_{65}Al_{7.5}Ni_{10}Cu_{12.5}Pd_5$  (c), (d) glassy alloys. Reprinted with permission from [121], J. Saida et al., *J. Mater. Res.* 16, 3389 (2001). © 2001, Materials Research Society.

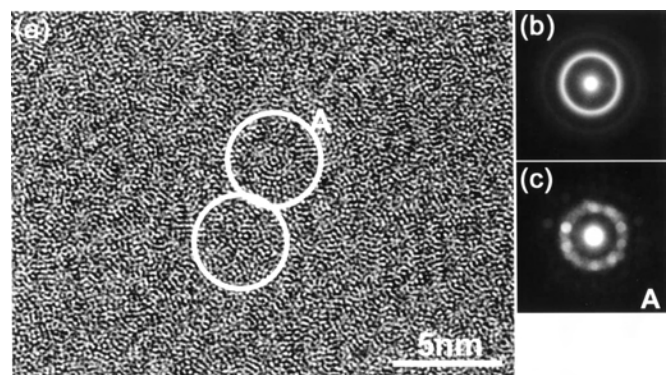
structure. It is found that the HRTEM images have some features of local regions, which are circled in Figure 16(a) and (c). The size of the encircled local regions is below 2 nm. NBD patterns revealing a halo ring are obtained from the encircled local region. The encircled local regions have a similar feature to those in the dense random packed (DRP) structure in the glassy alloy. However, the size of the region is considerably larger than that in the DRP structure, indicating the possibility of the local ordered region. Very recently, Xing et al. have reported a similar HRTEM image in the as-quenched  $Zr_{54.5}Ti_{7.5}Cu_{20}Ni_8Al_{10}$  glassy alloy [92], in which the icosahedral phase is also formed in the annealed state. They suggest that the local region is recognized as an ordered structure, which is indicative of an icosahedral short- and/or medium-range order. Moreover, a similar structure was reported in the simulation results where the icosahedral short-range order is assumed to exist in the glassy state [126]. It may be thought, therefore, that the local regions observed in the as-quenched  $Zr_{65}Al_{7.5}Ni_{10}Cu_{7.5}Pd_{10}$  and  $Hf_{65}Al_{7.5}Ni_{10}Cu_{12.5}Pd_5$  glassy alloys are realized as an icosahedral local structure. For further identification of the local region, HRTEM observation was applied for the simple system of a nanoquasicrystal-forming Zr–Pd binary alloy [127].

Figure 17 shows the HRTEM image (a) and SADP (b) taken from the 1  $\mu\text{m}$  diameter region of the  $Zr_{70}Pd_{30}$  glassy



**Figure 17.** HRTEM image (a) and SADP (b) of the as-quenched  $Zr_{70}Pd_{30}$  glassy alloy. Reprinted with permission from [127], J. Saida et al., *Appl. Phys. Lett.* 79, 412 (2001). © 2001, American Institute of Physics.

alloy. Since the SADP consists of the halo ring, and no diffraction spots can be observed, it is recognized as a glassy structure containing no obvious precipitations in the matrix. In the HRTEM images, features of the local ordered regions, which are circled in the figure, which are the same as those in the multicomponent alloys, are found. The size of the ordered regions is approximately 2 nm in diameter. No NBD patterns, except for a halo ring from the ordered region, can be obtained. The identification of the structure of the ordered regions was carried out by HRTEM observation for the  $Zr_{70}Pd_{30}$  glassy alloy annealed at low temperatures below  $T_x$ . The HRTEM image (a), the SADP taken from the 1  $\mu\text{m}$  region in diameter (b), and the NBD pattern with a beam diameter of 1 nm (c) of the  $Zr_{70}Pd_{30}$  glassy alloy annealed for 120 s at 690 K are shown in Figure 18. The SADP consists of only a halo ring, indicating that the glassy structure remains in the annealing condition. Moreover, no precipitates corresponding to a crystalline or quasicrystalline phase can be seen in the HRTEM image. The same ordered regions as that in the as-quenched sample are confirmed, as marked with a circle in Figure 17(a). The ordered region grows slightly, as is evidenced by the change in diameter



**Figure 18.** HRTEM image (a), SADP (b), and NBD pattern (c) of the  $Zr_{70}Pd_{30}$  glassy alloy annealed for 120 s at 690 K. Reprinted with permission from [127], J. Saida et al., *Appl. Phys. Lett.* 79, 412 (2001). © 2001, American Institute of Physics.

of 3–4 nm. Although the NBD pattern taken from the ordered region (marked with A in the HRTEM image) in Figure 18(c) reveals weak reflection spots due to the small area and fine electron beam, we can identify it as the five-fold symmetry originating from the icosahedral structure. These results are regarded as evidence for the existence of an icosahedral local structure in the  $Zr_{70}Pd_{30}$  glassy alloy. Recently, the icosahedral local structure in the  $Zr_{70}Pd_{30}$  glassy alloy was studied by structural analysis [122, 128, 129]. It is suggested that the icosahedral local structure in the glassy state is attributed to the high stability of the icosahedral atomic configuration during the cooling process from the melt. The stable icosahedral local structure seems to lead to the restraint of the rearrangements of constitutional elements to form a periodic crystalline phase.

The HRTEM image (a) and NBD pattern with a beam diameter of 1 nm (b) for the  $Zr_{70}Pd_{30}$  glassy alloy annealed for 120 s at 710 K are shown in Figure 19 for the investigation of the growth process of an icosahedral medium-range order. The precipitated particle with a diameter of approximately 12 nm is observed in the center of the HRTEM image. The NBD pattern taken from the precipitate clearly indicates the fivefold symmetry, which is identified as an icosahedral quasicrystalline phase. The icosahedral local structure is also detected simultaneously around the interface between the icosahedral particle and the glassy phase, as marked with circles in the image. We suggest that the nanoicosahedral quasicrystalline particle grows from the icosahedral local structure by assimilating the medium-range orders. As discussed in the redistribution behavior through nanoquasicrystallization, the average compositional difference between the icosahedral phase and the residual glassy phase is slight (approximately 3at%) in the  $Zr_{70}Pd_{30}$  glassy alloy [84, 86]. It is therefore realized that the icosahedral local structure grows easily to the icosahedral quasicrystalline phase, which is the dominant factor for the formation of a nanoicosahedral phase.

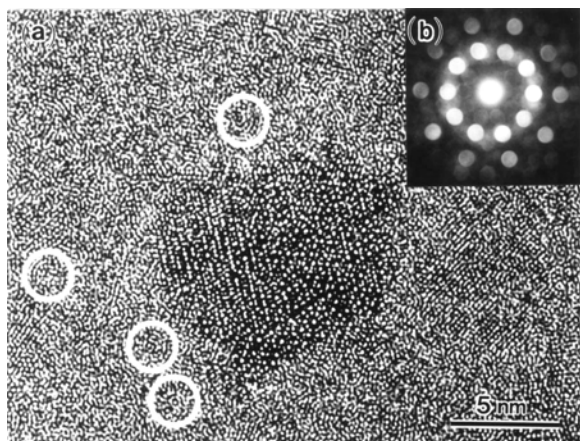


**Figure 19.** HRTEM image (a) and NBD pattern (b) of the  $Zr_{70}Pd_{30}$  glassy alloy annealed for 120 s at 710 K. Reprinted with permission from [127], J. Saida et al., *Appl. Phys. Lett.* 79, 412 (2001). © 2001, American Institute of Physics.

## 7. ORIGIN OF FORMATION OF ICOSAHEDRAL LOCAL STRUCTURE

### 7.1. Nanoicosahedral Phase Formation of Zr–Cu Glassy Alloys by Addition of Small Amount of NMs

In these investigations, it is concluded that the novel local structure with an icosahedral atomic configuration exists in the Zr- and Hf-based glassy alloys. The origin of the icosahedral local structure, which correlates with the stability of the supercooled liquid state, has been studied in the Zr–(Cu, Ni) alloys [130]. For this purpose, the primary precipitated phase in the  $Zr_{70}Cu_{30-x}Pd_x$  ( $x = 0, 0.5, 1,$  and 10at%) melt-spun ribbons has been investigated. A single sharp exothermic reaction is observed after the distinct glass transition in the DSC curve of the  $Zr_{70}Cu_{30}$  alloy. Although we can see no significant change in the crystallization peak by the addition of 0.5at% Pd, the exothermic reaction is clearly separated into two or three peaks by the addition of 1 and 10at% Pd, with the remainder of the glass transition. The separation of the exothermic peak in the 10at% Pd-containing alloy is more distinct than that in the 1at% Pd-containing alloy. XRD patterns of the samples annealed at temperatures near  $T_x$  are given in [130]. Very sharp diffraction peaks are observed, and all of them are identified as a tetragonal  $Zr_2Cu$  ( $a = 0.322$  nm and  $c = 1.118$  nm) phase in the  $Zr_{70}Cu_{30}$  glassy alloy. Meanwhile, it is found that the diffraction peaks, in addition to the halo peak in the  $Zr_{70}Cu_{30-x}Pd_x$  ( $x = 0.5, 1,$  and 10) alloys, are completely different from those in the  $Zr_{70}Cu_{30}$  alloy. All diffraction peaks in the Pd-containing glassy alloys can be identified as an icosahedral phase. Figure 20 shows the bright-field TEM image (a) and NBD pattern with a beam diameter of 2.4 nm (b) of the  $Zr_{70}Cu_{29}Pd_1$  glassy alloy annealed for 120 s at 620 K. Very fine particles in the diameter range less than 50 nm are precipitated in the  $Zr_{70}Cu_{29}Pd_1$  alloy, indicating a high nucleation rate. The particles have a nearly spherical morphology. The NBD pattern taken from the particle shown in (b) clearly indicates fivefold quasiperiodic symmetry, which is identified as the nanoicosahedral phase. Similar TEM images and NBD patterns are obtained in the annealed  $Zr_{70}Cu_{29.5}Pd_{0.5}$  and

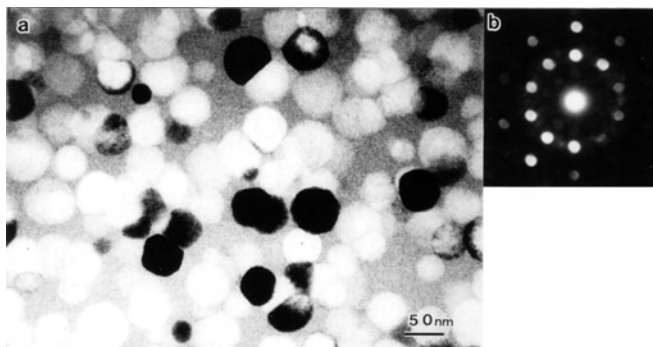


**Figure 20.** Bright-field TEM image and NBD pattern of the  $Zr_{70}Cu_{29}Pd_1$  glassy alloy annealed for 120 s at 620 K. Reprinted with permission from [119], J. Saida et al., *Mater. Trans. JIM* 43, 1937 (2002). © 2002, Japan Institute of Metals.

Zr<sub>70</sub>Cu<sub>20</sub>Pd<sub>10</sub> alloys. The nanoicosahedral phase formation by the addition of 1at% Au or Pt in a Zr<sub>70</sub>Cu<sub>30</sub> alloy has also been reported [119]. These results are in good agreement with those in the Zr<sub>65</sub>Al<sub>7.5</sub>Ni<sub>10</sub>Cu<sub>16.5</sub>(Ag, Pd, Au, or Pt)<sub>1</sub> glassy alloys [119]. Thus, it is concluded that the nanoicosahedral phase is formed as a primary metastable phase by substituting Pd for only 0.5at% Cu in the Zr<sub>70</sub>Cu<sub>30</sub> glassy alloy. However, no icosahedral phase formation is observed in the Zr<sub>70</sub>Ni<sub>30</sub> alloy by the addition of Pd less than 10at% [119, 130].

## 7.2. Local Structure Analysis

In order to examine the local structure of the melt-spun Zr<sub>70</sub>Cu<sub>30</sub> and Zr<sub>70</sub>Ni<sub>30</sub> alloys, an XRD analysis was performed [130]. The interference functions  $Q_i(Q)$  for the melt-spun Zr<sub>70</sub>Cu<sub>30</sub> and Zr<sub>70</sub>Ni<sub>30</sub> alloys exhibit a difference in the higher  $Q$  value, indicating the difference of the local structure in the short and/or medium range. Radial distribution functions (RDFs) for the melt-spun Zr<sub>70</sub>Cu<sub>30</sub> (a) and Zr<sub>70</sub>Ni<sub>30</sub> (b) alloys are shown in Figure 21. It is seen that the RDFs are completely different in the first peaks. The first peak in the RDF of the Zr<sub>70</sub>Ni<sub>30</sub> alloy is clearly separated into two peaks, which correspond to the components of Zr–Zr and Zr–Ni pairs. These results suggest that the Zr–Ni pair in the Zr<sub>70</sub>Ni<sub>30</sub> alloy has a strong chemical affinity as compared with the Zr–Cu pair in the Zr<sub>70</sub>Cu<sub>30</sub> alloy. All of the structural parameters for both samples in the as-quenched state are summarized in Table 2. Data for crystallized phases are also given in the table, calculated from the results in [131]. Atomic distances and coordination numbers in the RDF fitting of the melt-spun Zr<sub>70</sub>Ni<sub>30</sub> alloy are almost the same as those in the calculated results of the tetragonal Zr<sub>2</sub>Ni phase, implying that the local structure in the Zr<sub>70</sub>Ni<sub>30</sub> amorphous alloy is similar to the tetragonal Zr<sub>2</sub>Ni structure. In contrast, the distance and coordination number of the Cu–Cu pair in the melt-spun Zr<sub>70</sub>Cu<sub>30</sub> alloy are 0.256 nm and 2.9, respectively, which are different from those (0.322 nm and 4.0) in the tetragonal Zr<sub>2</sub>Cu phase. These results indicate that the local structure in the Zr<sub>70</sub>Cu<sub>30</sub>

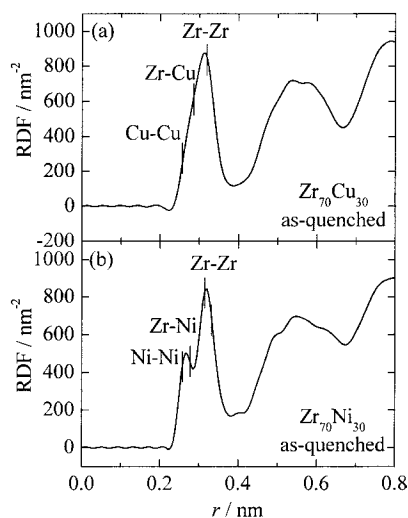


Figure 21. RDFs for the melt-spun Zr<sub>70</sub>Cu<sub>30</sub> (a) and Zr<sub>70</sub>Ni<sub>30</sub> (b) alloys.

glassy alloy differs from the tetragonal Zr<sub>2</sub>Cu structure. Considering that the nanoicosahedral phase is precipitated from the glassy state as a primary phase in the Zr<sub>70</sub>Cu<sub>30</sub> glassy alloy by the addition of only 0.5at% Pd, it is suggested that an icosahedral local atomic configuration exists in the glassy state. Since the coordination number around Zr in the glassy state is approximately 12, the icosahedral local atomic configuration may be formed around the Zr atom.

## 7.3. Correlation Between Stability of Glassy State and Local Structure of Zr–(Cu or Ni) Glassy Alloys

The authors have pointed out that the difference in the local structure of the melt-spun Zr<sub>70</sub>Cu<sub>30</sub> and Zr<sub>70</sub>Ni<sub>30</sub> alloys leads to the difference in the stability of the glassy state. It is well known that a high GFA is attributed to the high stability of the supercooled liquid state [132]. From the distinct glass transition prior to crystallization in the melt-spun Zr<sub>70</sub>Cu<sub>30</sub> alloy, it is suggested that the icosahedral local structure correlates with the high stability of the glassy state, and it retards the rearrangement of the constitutional elements for crystallization. The melt-spun Zr<sub>70</sub>Ni<sub>30</sub> alloy without a distinct glass transition [133] has a tetragonal Zr<sub>2</sub>Ni-like local structure by RDF analysis. However, it was reported that a glass transition is observed in the rapidly quenched Zr–Ni alloys in a wide compositional range by the addition of a small amount of Al [134], implying the introduction of a novel local structure with an icosahedral atomic configuration. Structural study of the Zr<sub>60</sub>Ni<sub>25</sub>Al<sub>15</sub> glassy alloy also reveals the change in the local structure by the addition of Al [135]. The total coordination number around Zr in the as-quenched state is estimated to be 12.5, which is different from those in the crystallized state (13.1), as well as in the melt-spun Zr<sub>70</sub>Ni<sub>30</sub> alloy (10.7). Since the coordination number of 12.5 around Zr in the Zr<sub>60</sub>Ni<sub>25</sub>Al<sub>15</sub> glassy alloy is similar to that (12.4) in the Zr<sub>70</sub>Cu<sub>30</sub> glassy alloy, it suggests the formation of an icosahedral local structure. In order to investigate the local structure and its correlation with the stability of the glassy state, the transformation behavior was examined in the Zr<sub>60</sub>Ni<sub>25-z</sub>Al<sub>15</sub> glassy alloys containing small amounts of Pd [130]. A very wide supercooled liquid region with a temperature interval of approximately 100 K between the glass transition and crystallization temperatures is observed in all of the DSC curves of the melt-spun Zr<sub>60</sub>Ni<sub>25-z</sub>Al<sub>15</sub>Pd<sub>z</sub> ( $z = 0-5$ ) glassy alloys. Although the crystallization proceeds through the single sharp exothermic peak for Pd contents less than 3at%, the peak gets slightly broader and shifts to higher temperatures with increasing Pd content. The crystallization reaction changes drastically to three peaks at Pd = 5at%. For the determination of the primary phase correlated with the local structure in the glassy state, these alloys were annealed for a short time near the crystallization temperature. XRD patterns of the samples annealed for 120 s in the temperature range of 775–795 K are presented in [130]. The hexagonal Zr<sub>6</sub>NiAl<sub>2</sub> phase ( $a = 0.792$  nm and  $c = 0.334$  nm) is formed as the main precipitation phase at the initial crystallization stage in the Zr<sub>60</sub>Ni<sub>25</sub>Al<sub>15</sub> and Zr<sub>60</sub>Ni<sub>24</sub>Al<sub>15</sub>Pd<sub>1</sub> glassy alloys. A small amount of the fcc Zr<sub>2</sub>Ni ( $a = 1.227$  nm) phase is also observed in the alloys [136]. It is found that

**Table 2.** Structural parameters for  $Zr_{70}Cu_{30}$  and  $Zr_{70}Ni_{30}$  alloys in as-quenched state.

Alloys	Pairs	RDF fitting		Total	Crystalline phase	Crystalline phase			
		$r/nm$	$N$			Pairs	$r/nm$	$N$	Total
$Zr_{70}Cu_{30}$	Zr–Zr	0.322	8.7	<b>Zr 12.4</b>	Tetragonal $Zr_2Cu$	Zr–Zr	0.304	4.0	<b>Zr 12.0</b>
	Zr–Cu	0.286	3.7			Zr–Zr	0.322	4.0	
	Cu–Cu	0.256	2.9			Zr–Cu	0.290	4.0	
						Cu–Cu	0.322	4.0	
$Zr_{70}Ni_{30}$	Zr–Zr	0.315	3.0	<b>Zr 10.7</b>	Tetragonal $Zr_2Ni$	Zr–Zr	0.304	1.0	<b>Zr 11.0</b>
	Zr–Zr	0.333	4.1			Zr–Zr	0.307	2.0	
	Zr–Ni	0.279	3.6			Zr–Zr	0.339	4.0	
	Ni–Ni	0.256	2.1			Zr–Ni	0.276	4.0	
						Ni–Ni	0.263	2.0	

Note: Data for crystallized phases are also given, calculated from results in [131].

additional diffraction peaks of the icosahedral phase are obtained in the XRD pattern at a Pd content of 3at%. Finally, all of the XRD peaks of the  $Zr_{60}Ni_{20}Al_{15}Pd_5$  glassy alloy are identified as an icosahedral phase. Figure 22 shows the bright-field TEM image (a) and NBD pattern (b) of the  $Zr_{60}Ni_{20}Al_{15}Pd_5$  glassy alloy annealed for 120 s at 780 K. Fine spherical particles less than 100 nm in diameter are precipitated, where the NBD pattern is characterized as quasiperiodic fivefold symmetry. Thus, it is clarified that a nanoicosahedral phase is formed in the  $Zr_{60}Ni_{25}Al_{15}$  glassy alloy by substituting Pd for Ni. The nanoicosahedral phase is precipitated with the  $Zr_6NiAl_2$  phase of a Pd content of 3at% and as a single phase in the 5at% Pd-containing alloy. Meanwhile, nanoicosahedral phase formation was reported in the  $Zr_{70}Ni_{20}Al_{10}$  glassy alloy by the addition of only 1at% Pd substituted for Al [137]. Since the coordination number around Zr in the  $Zr_6NiAl_2$  crystalline phase is calculated to be approximately 14 [138], which does not coincide with the experimental results (12.5), it is strongly suggested that the local structure in the glassy state takes an icosahedral atomic configuration around Zr in the  $Zr_{60}Ni_{25}Al_{15}$  glassy alloy.

Comparing the transformation behaviors among the Zr–Cu, Zr–Ni, and Zr–Ni–Al alloys, the correlation between the appearance of the supercooled liquid state before crystallization and the nanoicosahedral phase formation as a primary phase is suggested. We conclude that icosahedral local structure exists in the Zr–Cu and Zr–Ni–Al glassy

alloys, and stabilizes the supercooled liquid state by retarding the atomic rearrangements for the formation of stable crystalline phases.

## 8. MECHANICAL PROPERTIES OF NANOICOSAHEDRAL PHASE DISPERSED BULK GLASSY ALLOYS

The formation of a nanoicosahedral phase from the glassy state has also brought us new composite materials consisting of the nanoicosahedral and glassy phases. The improvement of mechanical properties by dispersing the nanoicosahedral particle in the glassy matrix has been studied by Inoue et al. [68, 139]. They prepared cylindrical  $Zr_{65}Al_{7.5}Ni_{10}Cu_{12.5}Ag_5$  rods with diameters of 3, 4, and 5 mm by copper mold casting. It is confirmed that the cast glassy alloy rods exhibit the same two-stage crystallization reaction as that for the melt-spun glassy alloy ribbon. By changing the annealing condition, they controlled the volume fraction of the nanoicosahedral phase in the cast 5at% Ag alloy rod with a diameter of 3 mm. The volume fraction of the nanoicosahedral phase was calculated by the change of the heat of crystallization. Figure 23 shows the Vickers hardness ( $H_v$ ), Young's modulus ( $E$ ), tensile fracture strength ( $\sigma_f$ ), and fracture elongation including elastic elongation ( $\epsilon_f$ ) as a function of volume fraction ( $V_f$ ) of the nanoicosahedral phase for the 5at% Ag alloy rod [140]. The  $\sigma_f$  and  $\epsilon_f$  increase almost linearly with increasing  $V_f$  in the  $V_f$  range up to 45%, and then decrease in the higher  $V_f$  range, although the  $H_v$  and  $E$  values increase monotonously over the whole  $V_f$  range. It is noticed that the dispersion of the nanoicosahedral phase causes a dispersion hardening as well as a dispersion ductilization. Figure 24 shows the fracture surface of the cast 5at% Ag alloy rods in the as-cast glassy single phase [(a) and (b)] and the mixed phases with  $V_f$  of 45% [(c) and (d)] [140]. The fracture of the mixed phase alloy takes place through a maximum shear plane which is declined by about 45° to the direction of tensile load, in agreement with that for the glassy single-phase alloy. However, one can see a difference in the vein pattern on the fracture surface. That is, the mixed phase alloy has considerably smaller spacings among the veins, and a more developed vein pattern subjected to a higher degree of viscous

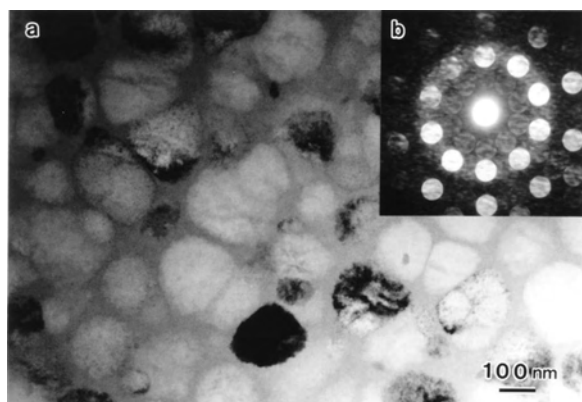


**Figure 22.** Bright-field TEM image (a) and NBD pattern (b) of the  $Zr_{60}Ni_{20}Al_{15}Pd_5$  glassy alloy annealed for 120 s at 780 K.

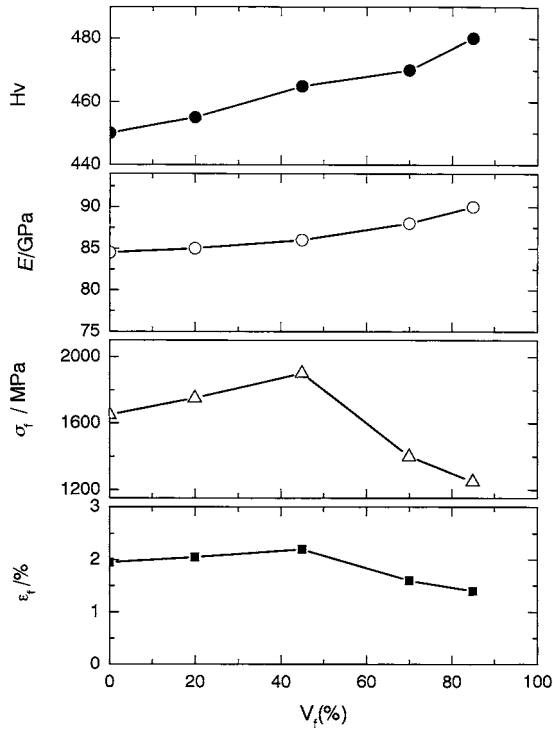


**Figure 23.** Vickers hardness ( $H_v$ ), Young's modulus ( $E$ ), tensile fracture strength ( $\sigma_f$ ), and fracture elongation including elastic elongation ( $\epsilon_f$ ) as a function of volume fraction ( $V_f$ ) of the nanoicosahedral phase for the  $Zr_{65}Al_{7.5}Ni_{10}Cu_{12.5}Ag_5$  alloy rod [140]. Reprinted with permission from [68], A. Inoue et al., *J. Mater. Res.* 15, 2195 (2000). © 2000, Materials Research Society.

flow as compared with the glassy single-phase alloy. Similar improvement of the mechanical properties is also recognized for the  $Zr_{65}Al_{7.5}Ni_{10}Cu_{7.5}Pd_{10}$  alloy. In the compressive stress-strain curves of the  $Zr_{65}Al_{7.5}Ni_{10}Cu_{7.5}Pd_{10}$  alloy in as-cast glassy and annealing-induced nanoicosahedral-based states [46, 139], the Young's modulus, compressive yield strength, compressive fracture strength, and fracture elongation, including elastic elongation, are estimated to be 85 GPa, 1510 MPa, 1640 MPa, and 2.2% for the glassy alloy and 88 GPa, 1780 MPa, 1830 MPa, and 3.1%, respectively, for the nanoicosahedral-based alloy, indicating a distinct increase in strength and ductility by the dispersion of nanoicosahedral particles into the glassy phase. Figure 25 shows the fracture mode and fracture surface of the glassy single-phase [(a) and (b)] and nanoquasicrystalline phase [(c) and (d)] alloys [46, 139]. Although the shear-type fracture mode typical for the glassy single phase remains unchanged, even in the nanoquasicrystalline base alloy, the vein pattern on the fracture surface has smaller distances between the veins and larger vein diameters. Based on the experimental results, it is suggested that deformation followed by adiabatic fracture takes place in the intergranular glassy phase along the maximum shear plane [139]. Table 3 summarizes the reason for the improvement of strength and ductility by the dispersion of nanoicosahedral particles in the glassy phase [68]. In the deformation and fracture mode shown in Figure 25, the intergranular glassy phase must have good ductility. It has been reported that the good ductility of the  $Zr$ - $Al$ - $Ni$ - $Cu$  glassy alloys is independent of the sample preparation method and heat treatment, being an inherent property resulting from the atomic configurations [125]. The high interface strength between the

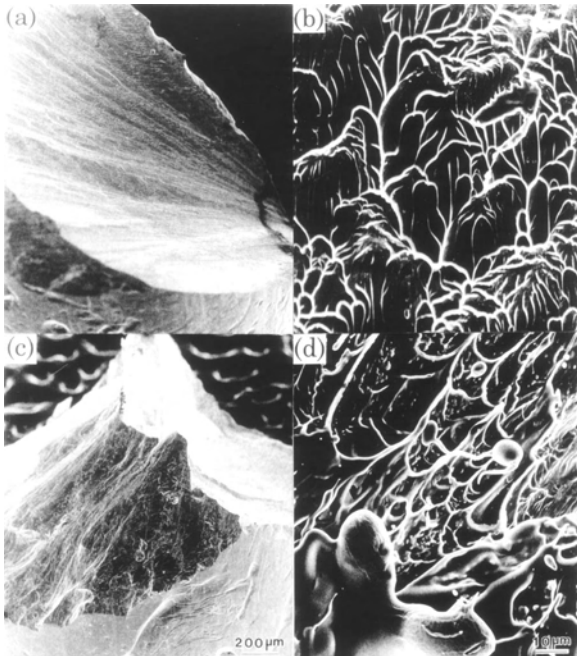


**Figure 24.** Fracture surface of the cast  $Zr_{65}Al_{7.5}Ni_{10}Cu_{12.5}Ag_5$  alloy rods in the as-cast glassy single phase (a), (b) and the mixed phases with  $V_f$  of 45% (c), (d) [140]. Reprinted with permission from [68], A. Inoue et al., *J. Mater. Res.* 15, 2195 (2000). © 2000, Materials Research Society.

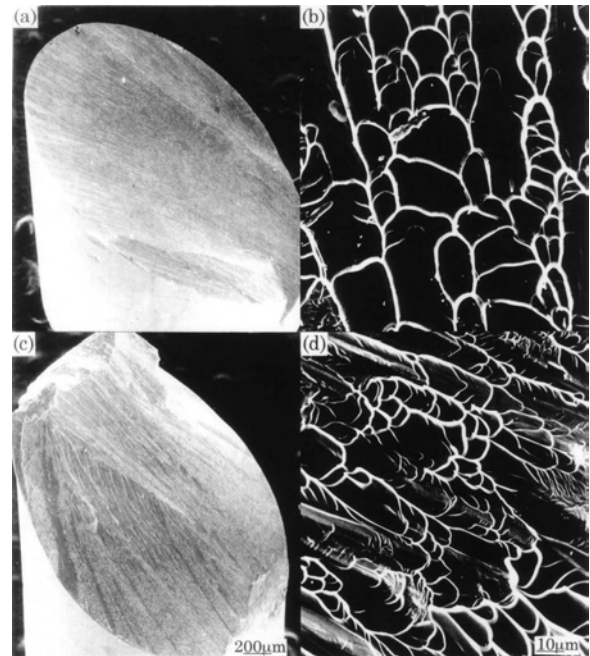


**Figure 25.** Fracture mode and fracture surface of the glassy single phase (a), (b) and nanoquasicrystalline phase ( $V_f = 80\%$ ) (c), (d) alloys [46, 139]. Reprinted with permission from [68], A. Inoue et al., *J. Mater. Res.* 15, 2195 (2000). © 2000, Materials Research Society.

**Table 3.** Reasons for improvement of strength and ductility by dispersion of nanoicosahedral particles in glassy phase [68].

---

Mechanisms for high strength and high ductility of bulk glassy alloys containing nanoscale compound particles

---

1. Nanocrystalline particle effect
    - a. perfect crystal effect (ideal high strength)
    - b. nanoscale effect (suppression of shear deformation in glassy matrix)
    - c. low interfacial energy effect (highly dense packing at the interface)
  2. Metallic glassy phase effect
    - a. insensitivity effect to structural relaxation (large allowance to crystalline phase)
    - b. compressive residual stress effect (difference in thermal expansion coefficient)
    - c. multiaxis stress effect (increase in deformability)
    - d. localized deformation effect (work softening due to an increase in temperature)
- 

glassy matrix and nanoicosahedral particles is obtained by the highly packed interface atomic configuration resulting from the lower glassy/icosahedral interface energy as compared with the solid/solid interface energy. The existence of the high density of nanoicosahedral particles enables us to generate a multiaxis stress state in the remaining glassy phase, leading to an increase in deformability. The water-quenching treatment from the annealing temperature in the supercooled liquid region causes the introduction of a compressive residual stress field in the remaining glassy phase just near the nanoicosahedral particles because of the significant difference in the coefficients of thermal expansion. Furthermore, the localization of deformation into the remaining glassy phase gives rise to an increase in temperature in the remaining glassy phase, leading to an increase in deformability due to the heating-induced softening. The combination of the above-described five factors is presumed to result in improvements of strength and ductility for the nanoicosahedral-based glassy alloys. Similar dispersion strengthening and dispersion ductilization phenomena have also been obtained in Zr-based mixed structure alloys consisting of glass + nanoscale compound phases and glass + ceramic particles [141–154]. It is therefore concluded that the improvement of strength and ductility by the dispersed particles in the Zr-based glassy phase is independent of the structure and component of the particles.

Ishihara and Inoue have studied the superplastic deformation in the nanoicosahedral particles dispersing Zr-based bulk glassy alloys [155]. They reported that the  $Zr_{65}Al_{7.5}Ni_{10}Cu_{12.5}Ag_5$  and  $Zr_{65}Al_{7.5}Ni_{10}Cu_{12.5}Pd_5$  bulk glassy alloys exhibit an elongation of 400–450% at a strain rate of  $1 \times 10^{-3} \text{ s}^{-1}$  near  $T_g$  (673 K), which is considerably larger than that (270–340%) in the  $Zr_{65}Al_{7.5}Ni_{10}Cu_{17.5}$  bulk glassy alloy at strain rates of  $3 \times 10^{-3}$ – $5 \times 10^{-2} \text{ s}^{-1}$  in the supercooled liquid region [156]. These results show that the precipitation of the nanoicosahedral phase is effective for the enhancement of superplasticity. Thus, the application of the mechanisms for dispersion strengthening and ductilization is expected to enable the future fabrication of a new material with improved engineering properties.

## 9. CONCLUSION

The formation and properties of a nanoicosahedral phase from a glassy state are reviewed. The discoveries of the precipitation of the nanoicosahedral particles devitrified from glassy alloys lead to important investigations in the stability of the glassy state. It is clarified that the formation of a nanoicosahedral phase in Zr- and Hf-based glassy alloys is attributed to their novel local structure with an icosahedral atomic configuration. The nanoicosahedral phase precipitates from this novel icosahedral local structure by the enhancement of nucleation due to the slight deviation from the composition with a high GFA. We conclude that the icosahedral local structure originating from the Zr–Cu and Zr–Ni–Al glassy alloys stabilizes the supercooled liquid state by retarding the atomic rearrangements for the formation of stable crystalline phases. It is expected that the stability of the icosahedral local structure will be clarified compared with other local structures in terms of their simulation or energy calculation in the near future. These results will bring us the complete clarification of the factors for a high GFA and nanoicosahedral phase formation. Finally, the improvement of the mechanical strength by the dispersion of nanoicosahedral particles in a glassy matrix is expected to enable the fabrication of a new material with further improved engineering properties.

## GLOSSARY

**Glass-forming ability (GFA)** Ability to form glassy structure during cooling from melt. The empirical conditions for a high GFA have been suggested by one of the authors (Inoue).

**Local structure** Local atomic configuration with short and/or medium range in the metallic glass (glassy alloy). It is not identified as a crystalline or quasicrystalline phase due to the absence of a long-range periodic structure.

**Nanobeam electron diffraction (NBD)** Diffraction method using the electron beam a few nanometers in diameter. This method is useful for structure identification for a nanoscale crystalline or quasicrystalline phase.

**Nanoicosahedral quasicrystal** Nanoscale phase exhibiting a forbidden fivefold symmetry with a long-range order similar to the one of the crystals. The icosahedral quasicrystal was discovered in 1984 by Shechtman et al.

**Supercooled liquid state** Liquid state at the temperature below melting point. A high GFA is equivalent to a high stability of the supercooled liquid state.

## REFERENCES

1. D. Shechtman, I. Blech, D. Gratias, and J. W. Cahn, *Phys. Rev. Lett.* 53, 195 (1984).
2. A. P. Tsai, in “Physical Properties of Quasicrystals” (Z. M. Stadnik, Ed.), p. 5. Springer, Berlin, 1998.
3. D. Levine and P. J. Steinhardt, *Phys. Rev. Lett.* 53, 2477 (1984).
4. P. A. Bancel and P. A. Heiney, *Phys. Rev. B* 33, 7917 (1986).
5. H. S. Chen and C. H. Chen, *Phys. Rev. B* 33, 2814 (1986).
6. A. Inoue, H. M. Kimura, and T. Masumoto, *J. Mater. Sci. Lett.* 22, 1758 (1987).



7. P. Ramachandrarao and G. V. S. Sastry, *Pramana* 25, L225 (1985).
8. W. Phashi and F. Spaepen, *Nature* 330, 555 (1987).
9. H. S. Chen, J. C. Phillips, P. Villars, A. R. Kortan, and A. Inoue, *Phys. Rev. B* 35, 9326 (1987).
10. S. J. Poon, A. J. Drehman, and K. R. Lawless, *Phys. Rev. Lett.* 55, 2324 (1985).
11. V. V. Monokanov and V. N. Chebotnikov, *J. Non-Cryst. Solids* 117, 789 (1990).
12. S. Takeuchi, "Quasicrystals" p. 125. Sangyotosho, Tokyo, 1992.
13. "New Horizons in Quasicrystals" (A. I. Goldman, D. J. Sordelet, P. A. Thiel, and J. M. Dubois, Eds.), p. 1. World Scientific, Singapore, 1997.
14. "Proceedings of the 6th International Conference on Quasicrystals" (S. Takeuchi and T. Fujiwara, Eds.), p. 443. World Scientific, Singapore, 1998.
15. For example, L. Q. Xing, C. Bertrand, J. P. Dallas, and M. Cornet, *Mater. Sci. Eng.* A241, 216 (1998).
16. Y. H. Kim, A. Inoue, and T. Masumoto, *Mater. Trans. JIM* 31, 747 (1990).
17. S. G. Kim, A. Inoue, and T. Masumoto, *Mater. Trans. JIM* 32, 875 (1991).
18. Y. Yoshizawa, S. Oguma, and K. Yamauchi, *J. Appl. Phys.* 64, 6044 (1988).
19. Y. Shen, S. J. Poon, and G. J. Shiflet, *Phys. Rev. B* 34, 3516 (1986).
20. M. Eibschutz, H. S. Chen, and J. J. Hauser, *Phys. Rev. Lett.* 56, 169 (1986).
21. W. W. Warren, Jr., H. S. Chen, and J. J. Hauser, *Phys. Rev. B* 32, 7614 (1985).
22. V. Elser and C. L. Henley, *Phys. Rev. Lett.* 55, 2883 (1985).
23. R. A. Dunlap and K. Dini, *J. Mater. Res.* 1, 415 (1986).
24. H. S. Chen, D. Koskenmaki, and C. H. Chen, *Phys. Rev. B* 35, 3715 (1987).
25. A. Inoue, Y. Bizen, and T. Masumoto, *Metall. Trans. A* 19, 383 (1988).
26. A. P. Tsai, A. Inoue, and T. Masumoto, *Jpn. J. Appl. Phys.* 26, L1994 (1987).
27. A. P. Tsai, A. Inoue, Y. Bizen, and T. Masumoto, *Acta Metall.* 37, 1443 (1989).
28. J. C. Holzer and K. F. Kelton, *Acta Metall.* 39, 1833 (1991).
29. D. Kafolt, S. Nanao, T. Egami, K. M. Wong, and S. J. Poon, *Phys. Rev. Lett.* 57, 114 (1986).
30. E. Matsubara, Y. Waseda, A. P. Tsai, A. Inoue, and T. Masumoto, *Z. Naturforsch A* 43, 505 (1988).
31. E. Matsubara, K. Harada, Y. Waseda, H. S. Chen, A. Inoue, and T. Masumoto, *J. Mater. Sci.* 23, 753 (1988).
32. S. Sachdev and D. R. Nelson, *Phys. Rev. B* 32, 4592 (1985).
33. U. Köster, J. Meinhardt, S. Roos, and H. Liebertz, *Appl. Phys. Lett.* 69, 179 (1996).
34. U. Köster, J. Meinhardt, S. Roos, and R. Busch, *Mater. Sci. Eng.* A226, 995 (1997).
35. A. J. Drehman, A. R. Pelton, and M. A. Noack, *J. Mater. Res.* 1, 741 (1986).
36. T. Zhang, A. Inoue, and T. Masumoto, *Mater. Trans. JIM* 32, 1005 (1991).
37. J. Eckert, N. Mattern, M. Zinkevitch, and M. Seidel, *Mater. Trans. JIM* 39, 623 (1998).
38. B. S. Murty, D. H. Ping, K. Hono, and A. Inoue, *Appl. Phys. Lett.* 76, 55 (2000).
39. B. S. Murty, D. H. Ping, K. Hono, and A. Inoue, *Acta Mater.* 48, 3985 (2000).
40. U. Köster, A. Rüdiger, and J. Meinhardt, "Proceedings of the 6th International Conference on Quasicrystals" (S. Takeuchi and T. Fujiwara, Eds.), p. 317. World Scientific, Singapore, 1998.
41. U. Köster, A. Rüdiger, and J. Meinhardt, *Mater. Sci. Forum* 307, 9 (1999).
42. D. Zander, R. Janlewing, A. Rüdiger, and U. Köster, *Mater. Sci. Forum* 307, 25 (1999).
43. L. Q. Xing, J. Eckert, W. Löser, and L. Schultz, *Appl. Phys. Lett.* 73, 2110 (1998).
44. L. Q. Xing, J. Eckert, W. Löser, and L. Schultz, *Appl. Phys. Lett.* 74, 664 (1999).
45. M. W. Chen, T. Zhang, A. Inoue, A. Sakai, and T. Sakurai, *Appl. Phys. Lett.* 75, 1697 (1999).
46. A. Inoue, T. Zhang, J. Saida, M. Matsushita, M. W. Chen, and T. Sakurai, *Mater. Trans. JIM* 40, 1181 (1999).
47. A. Inoue, T. Zhang, J. Saida, M. Matsushita, M. W. Chen, and T. Sakurai, *Mater. Trans. JIM* 40, 1137 (1999).
48. A. Inoue, J. Saida, M. Matsushita, and T. Sakurai, *Mater. Trans. JIM* 41, 362 (2000).
49. J. Saida, M. Matsushita, and A. Inoue, *Mater. Trans. JIM* 42, 1493 (2001).
50. M. W. Chen, A. Inoue, T. Zhang, A. Sakai, and T. Sakurai, *Philos. Mag. Lett.* 80, 263 (2000).
51. J. K. Lee, G. Choi, D. H. Kim, and W. T. Kim, *Appl. Phys. Lett.* 77, 978 (2000).
52. J. K. Lee, G. Choi, W. T. Kim, and D. H. Kim, *J. Mater. Res.* 16, 1311 (2001).
53. F. R. de Bore, R. Boom, W. C. M. Mattens, A. R. Miedema, and A. K. Niessen, in "Cohesion in Metals," p. 1. North-Holland, Amsterdam, 1988.
54. J. Saida and A. Inoue, *J. Phys.: Condens. Matter* 13, L73 (2001).
55. J. Saida and A. Inoue, *Jpn. J. Appl. Phys.* 40, L769 (2001).
56. C. Li and A. Inoue, *Phys. Rev. B* 63, 172201 (2001).
57. C. Li and A. Inoue, *Mater. Lett.* 50, 318 (2001).
58. C. Li and A. Inoue, *J. Alloys Comp.* 325, 230 (2001).
59. J. Saida and A. Inoue, unpublished work.
60. U. Köster, D. Zander, and R. Janlewing, *Mater. Sci. Forum* 386, 89 (2002).
61. N. Wanderka, M. P. Macht, M. Seidel, S. Mechler, K. Ståhl, and J. Z. Jiang, *Appl. Phys. Lett.* 77, 3935 (2000).
62. J. Saida, M. Matsushita, C. Li, and A. Inoue, *Philos. Mag. Lett.* 80, 737 (2000).
63. J. Saida, M. Matsushita, and A. Inoue, *J. Mater. Res.* 16, 28 (2001).
64. M. Matsushita, J. Saida, T. Zhang, A. Inoue, M. W. Chen, and T. Sakurai, *Philos. Mag. Lett.* 80, 79 (2000).
65. W. A. Johnson and R. F. Mehl, *Trans. Am. Inst. Min. Eng.* 135, 416 (1939).
66. U. Köster, *Key Eng. Mater.* 81, 647 (1993).
67. J. Saida, M. Matsushita, and A. Inoue, *Mater. Trans. JIM* 41, 1505 (2000).
68. A. Inoue, T. Zhang, M. W. Chen, T. Sakurai, J. Saida, and M. Matsushita, *J. Mater. Res.* 15, 2195 (2000).
69. M. Avrami, *J. Chem. Phys.* 7, 1103 (1939).
70. J. W. Christian, in "The Theory of Transformation in Metals and Alloys," p. 542. Pergamon, Oxford, 1975.
71. A. Inoue, *Mater. Trans. JIM* 36, 866 (1995).
72. J. Saida, M. Matsushita, and A. Inoue, *J. Non-Cryst. Solids* 312–314, 617 (2002).
73. J. Saida, M. Matsushita, C. Li, and A. Inoue, *Appl. Phys. Lett.* 76, 3558 (2000).
74. M. Matsushita, J. Saida, C. Li, and A. Inoue, *J. Mater. Res.* 15, 1280 (2000).
75. B. S. Murty, D. H. Ping, K. Hono, and A. Inoue, *Scripta Mater.* 43, 103 (2000).
76. C. Li, L. Wang, and A. Inoue, *J. Phys.: Condens. Matter* 13, L803 (2001).
77. C. Li and A. Inoue, *Mater. Trans. JIM* 42, 1485 (2001).
78. C. Li, L. Wang, and A. Inoue, *Eur. Phys. J. Appl. Phys.* 18, 109 (2002).
79. J. Saida, M. Matsushita, and A. Inoue, *Scripta Mater.* 44, 1245 (2001).
80. J. Saida, M. Matsushita, and A. Inoue, *Mater. Res. Soc. Symp. Proc.* 644, L6.1.1 (2001).

81. J. Saida, M. Matsushita, C. Li, and A. Inoue, *Philos. Mag. Lett.* 81, 39 (2001).
82. J. Saida, M. Matsushita, and A. Inoue, *Appl. Phys. Lett.* 77, 73 (2000).
83. B. S. Murty, D. H. Ping, and K. Hono, *Appl. Phys. Lett.* 77, 1102 (2000).
84. J. Saida, M. Matsushita, and A. Inoue, *J. Appl. Phys.* 90, 4717 (2001).
85. J. Saida, M. Matsushita, and A. Inoue, *Mater. Trans. JIM* 42, 1103 (2001).
86. B. S. Murty, D. H. Ping, M. Ohnuma, and K. Hono, *Acta Mater.* 49, 3453 (2001).
87. J. Saida, M. Matsushita, and A. Inoue, *J. Appl. Phys.* 88, 6081 (2000).
88. G. Ghosh, M. Chandrasekaran, and L. Delaey, *Acta Met. Mater.* 39, 925 (1991).
89. J. Horvath, in "Diffusion in Solid Metals and Alloys," (H. Mehrer, Ed.), p. 437. Springer, Berlin, 1990.
90. E. Matsubara, Y. Waseda, A. P. Tsai, A. Inoue, and T. Masumoto, *J. Mater. Sci.* 25, 2507 (1990).
91. D. Holland-Moritz, D. M. Herlach, and K. Urban, *Phys. Rev. Lett.* 71, 1196 (1993).
92. L. Q. Xing, T. C. Hufnagel, J. Eckert, W. Löser, and L. Schultz, *Appl. Phys. Lett.* 77, 1970 (2000).
93. M. W. Chen, I. Dutta, T. Zhang, A. Inoue, and T. Sakurai, *Appl. Phys. Lett.* 79, 42 (2001).
94. D. V. Louzguine, M. S. Ko, and A. Inoue, *Appl. Phys. Lett.* 76, 3424 (2000).
95. D. V. Louzguine, M. S. Ko, and A. Inoue, *Scripta Mater.* 44, 637 (2001).
96. C. Li, J. Saida, M. Matsushita, and A. Inoue, *Appl. Phys. Lett.* 77, 528 (2000).
97. C. Li and A. Inoue, *Phys. Stat. Sol.* 184, 291 (2001).
98. C. Li, J. Saida, M. Matsushita, and A. Inoue, *Philos. Mag. Lett.* 80, 621 (2000).
99. L. Wang, C. Li, and A. Inoue, *J. Alloys Comp.* 325, L7 (2001).
100. C. Li and A. Inoue, *J. Mater. Res.* 16, 1190 (2001).
101. C. Li and A. Inoue, *J. Non-Cryst. Solids* 289, 163 (2001).
102. C. Li and A. Inoue, *Jpn. J. Appl. Phys.* 39, L1317 (2000).
103. C. Li, S. Ranganathan, and A. Inoue, *Acta Mater.* 49, 1903 (2001).
104. C. Li, L. Wang, and A. Inoue, *J. Mater. Sci. Lett.* 20, 781 (2001).
105. C. Li, L. Wang, and A. Inoue, *Eur. Phys. J. Appl. Phys.* 16, 183 (2001).
106. C. Li, L. Wang, and A. Inoue, *Mater. Lett.* 51, 2038 (2001).
107. C. Li and A. Inoue, *Mater. Trans. JIM* 42, 176 (2001).
108. Z. Zhang and K.H. Kuo, *Philos. Mag. B* 54, L83 (1986).
109. Q. B. Yang, *Philos. Mag. Lett.* 57, 171 (1988).
110. S. P. Alisowa, Y. K. Kovneristyi, J. E. Lasarewa, and P. B. Budberg, *Dokl. Akad. Nauk. SSSR* 315, 116 (1990).
111. K. F. Kelton, W. J. Kim, and R. M. Stroud, *Appl. Phys. Lett.* 70, 3230 (1996).
112. X. Zhang, R. M. Stroud, J. L. Libbert, and K. F. Kelton, *Philos. Mag. B* 70, 927 (1994).
113. W. J. Kim and K. F. Kelton, *Philos. Mag. A* 72, 1397 (1995).
114. W. J. Kim and K. F. Kelton, *Philos. Mag. Lett.* 74, 439 (1996).
115. B. S. Murty, W. T. Kim, D. H. Kim, and K. Hono, *Mater. Trans. JIM* 42, 372 (2001).
116. L. Wang and A. Inoue, *Mater. Trans. JIM* 42, 2637 (2001).
117. L. Wang, C. Li, and A. Inoue, *Mater. Trans. JIM* 42, 528 (2001).
118. J. Saida, M. Matsushita, and A. Inoue, *Mater. Trans. JIM* 42, 1497 (2001).
119. J. Saida, M. Matsushita, and A. Inoue, *Mater. Trans. JIM* 43, 1937 (2002).
120. J. Saida and A. Inoue, *J. Non-Cryst. Solids* 317, 97 (2003).
121. J. Saida, C. Li, M. Matsushita, and A. Inoue, *J. Mater. Res.* 16, 3389 (2001).
122. E. Matsubara, T. Nakamura, M. Sakurai, M. Imafuku, S. Sato, J. Saida, and A. Inoue, *Mater. Res. Soc. Symp. Proc.* 644, L.1.1.1 (2001).
123. Z. Altounian, E. Batalla, J. O. Strom-Olsen, and J. L. Walter, *J. Appl. Phys.* 61, 149 (1987).
124. "Pearson's Handbook of Crystallographic Data for Intermetallic Phases" (P. Villars, and L. D. Calvert, Eds.), Vol. 3, p. 3421. ASM, Materials Park, 1991.
125. A. Inoue, *Acta Mater.* 48, 277 (2000).
126. Y. Hirotsu, K. Anazawa, and T. Okubo, *Mater. Trans. JIM* 31, 573 (1990).
127. J. Saida, M. Matsushita, and A. Inoue, *Appl. Phys. Lett.* 79, 412 (2001).
128. M. Imafuku, J. Saida, and A. Inoue, *J. Mater. Res.* 16, 3046 (2001).
129. T. Takagi, T. Ohkubo, Y. Hirotsu, B. S. Murty, K. Hono, and D. Shindo, *Appl. Phys. Lett.* 79, 485 (2001).
130. J. Saida, M. Kasai, E. Matsubara, and A. Inoue, *Anal. Chimie Sci. Matér.* 27, 77 (2002).
131. "Pearson's Handbook of Crystallographic Data for Intermetallic Phases" (P. Villars, Ed.), Vol. 2, pp. 1604, 2565. ASM, Materials Park, 1997.
132. For example, A. Inoue, in "Bulk Amorphous Alloys—Preparation and Fundamental Characteristics," p. 1. Trans Tech Publications, Zürich, 1998.
133. K. H. J. Buschow and N. M. Beekmans, *Phys. Rev. B* 19, 3843 (1979).
134. A. Inoue, T. Zhang, and T. Masumoto, *J. Non-Cryst. Solids* 156, 473 (1993).
135. E. Matsubara, T. Tamura, Y. Waseda, A. Inoue, T. Zhang, and T. Masumoto, *Mater. Trans. JIM* 33, 873 (1992).
136. U. Köster and J. Meinhardt, *Mater. Sci. Eng.* A178, 271 (1994).
137. J. Saida, M. Matsushita, and A. Inoue, *Intermetallics* 10, 1089 (2002).
138. "Pearson's Handbook of Crystallographic Data for Intermetallic Phases" (P. Villars, Ed.), Vol. 1, p. 454. ASM, Materials Park, 1997.
139. A. Inoue, T. Zhang, M. W. Chen, T. Sakurai, J. Saida, and M. Matsushita, *Appl. Phys. Lett.* 76, 967 (2000).
140. A. Inoue, T. Zhang, M. W. Chen, and T. Sakurai, *Mater. Trans. JIM* 41, 1382 (1999).
141. C. Fan and A. Inoue, *Mater. Trans. JIM* 38, 1040 (1997).
142. A. Inoue, C. Fan, J. Saida, and T. Zhang, *Sci. Tech. Adv. Mater.* 1, 73 (2000).
143. P. S. Frankwicz, S. Ram, and H. J. Fecht, *Appl. Phys. Lett.* 68, 2825 (1996).
144. J. G. Wang, B. W. Choi, T. G. Nieh, and C. T. Liu, *J. Mater. Res.* 15, 798 (2000).
145. C. C. Hays, C. P. Kim, and W. L. Johnson, *Phys. Rev. Lett.* 84, 2901 (2000).
146. H. Choi-Yim and W. L. Johnson, *Appl. Phys. Lett.* 71, 3808 (1997).
147. R. B. Dandliker, R. D. Conner, and W. L. Johnson, *J. Mater. Res.* 13, 2896 (1998).
148. H. Choi-Yim, R. Busch, and W. L. Johnson, *Acta Mater.* 47, 2455 (1999).
149. J. Eckert, A. Reger-Leonhard, B. Weiß, and M. Heilmaier, *Mater. Sci. Eng. A* 301, 1 (2001).
150. U. Kühn, J. Eckert, N. Mattern, and L. Schultz, *Appl. Phys. Lett.* 80, 2478 (2002).
151. H. Kato and A. Inoue, *Mater. Trans. JIM* 38, 793 (1997).
152. B. Bartusch, F. Schurack, and J. Eckert, *Mater. Trans. JIM* 43, 1979 (2002).
153. F. Audebert, F. Prima, M. Galano, M. Tomut, P. J. Warren, I. C. Stone, and B. Cantor, *Mater. Trans. JIM* 43, 2017 (2002).
154. H. S. Kim, S.I. Hong, H. Kato, and A. Inoue, *Mater. Trans. JIM* 43, 2026 (2002).
155. S. Ishihara and A. Inoue, *Mater. Trans. JIM* 42, 1517 (2001).
156. Y. Kawamura, T. Shibata, A. Inoue, and T. Masumoto, *Scripta Mater.* 37, 431 (1997).



# Nanomagnetics for Biomedical Applications

Chong H. Ahn, Jin-Woo Choi, Hyoung J. Cho

*University of Cincinnati, Cincinnati, Ohio, USA*

## CONTENTS

1. Introduction
  2. Superparamagnetism in Nanomagnetics
  3. Magnetic Particles and Magnetic Separation
  4. Nanomagnetic Particles  
in Biomedical Applications
  5. Biosampling in Lab-on-a-Chip Using  
Nanomagnetic Particles
  6. Conclusion
- Glossary  
References

## 1. INTRODUCTION

In recent molecular biology and biotechnology, cell or biomolecule separation is considered as one of the most complex and difficult tasks. New separation technologies capable of treating dilute solutions in both small and large-scale processes, even in the presence of particulate matter, are necessary for the future development of biochemistry and biotechnology at all levels. A magnetic separation technique using nanomagnetic particles, among several available bioseparation techniques, has been considered one of the most promising techniques and could be used in a wide range of applications if the technique is appropriately developed.

Conventional magnetic separation methods have been used for long time as a standard technique in a variety of laboratory and industrial applications, which include the enrichment of low grade iron ore, removal of weakly magnetic colored impurities from kaolin clay, removal of magnetic pollutants from the stack gases from several industrial processes, desulphurization of coal and removal of ferromagnetic impurities from large volumes of boiler water in both conventional and nuclear power plants. Their applications to biochemistry and biotechnology, however, have been restricted and of limited use up to the 1970s. Since then, magnetic separation, labeling, and targeting techniques have

found many useful and interesting applications in various areas of bioscience and biotechnology, which are now being used routinely in molecular biology, cell biology, and microbiology and intensive research is being performed in other areas employing the unique properties of magnetic particles.

The idea of using magnetic separation techniques in cell separation is not new, but it has enjoyed a resurgence of interest over the last decade [1–5]. This has primarily been brought about by the development of new magnetic particles with improved properties for various cell separation procedures such as cancer cell separation. Many researchers have also reported feasibility of magnetic beads for immunomagnetic cell separation [6–10], immunoassay, and drug delivery application [11–14]. The basic concept of magnetic separation technology is described in Figure 1. The most attractive aspect of the magnetic separation technique in biochemistry and biotechnology is ease of manipulation of biomolecules, which are immobilized on magnetic particles. Once target biological cells or molecules are immobilized on magnetic particles, the target biomolecules can be separated from a sample solution, flexibly manipulated in various reagents, and easily transported to a desired location by controlling magnetic fields produced from a permanent magnet or an electromagnet. Another advantage is large surface area of immobilization substrate that results in high population of target biological molecules due to large binding site and high detection signal.

In this chapter, nanomagnetism will be briefly introduced and magnetic separation techniques using nanomagnetic particles will be reviewed including recent developments in lab-on-a-chip applications.

## 2. SUPERPARAMAGNETISM IN NANOMAGNETICS

In recent years, the phenomenon of superparamagnetism in a system of small ferromagnetic particles has attracted much attention due to its relevance both in technological applications as well as in understanding the fundamental physics. Technologically, as the density of magnetic information storage devices increases, the size of the ferromagnetic region

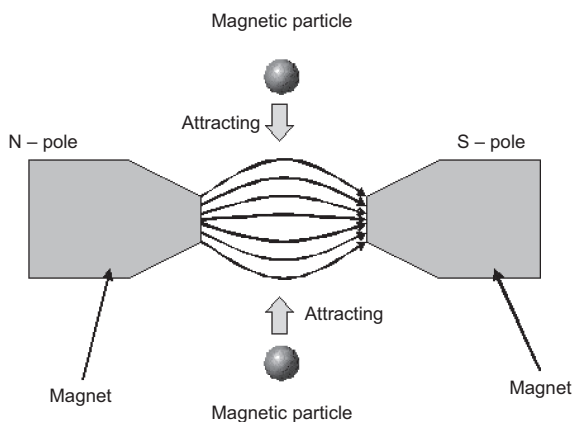


**Figure 1.** Basic concept of magnetic separation technique.

approaches the superparamagnetic limit. From the fundamental point of view, the relaxation and switching behavior of a system of small, single domain ferromagnetic particles is not well understood, partly because of the complicated nature of the interactions among the particles [15–17].

Superparamagnetism is a well-known phenomenon and can be simply described as the lack of hysteresis in the magnetization curve. As the word describes, the superparamagnetic material reveals “super” paramagnetic property.

On the atomic scale, all bodies contain spinning electrons that move around in orbits, and these electrons also produce magnetic fields to make the material paramagnetic or diamagnetic. In most atoms the magnetic moments due to the orbital and spinning motions of the electrons cancel. If the cancellation is not complete, the material is said to be “paramagnetic.” The so-called transition elements, like manganese, are examples of paramagnetic substances. When such a substance is placed in a magnetic field, its atoms are subjected to a torque that tends to align them with the field, but thermal agitation tends to destroy the alignment. In diamagnetic materials, the elementary moments are not permanent but are induced according to the Faraday induction law. All materials are diamagnetic, but orientational polarization may predominate.

Most magnetic devices use ferromagnetic materials, such as iron, in which the magnetization can be orders of magnitude larger than that of either paramagnetic or diamagnetic substances. This large magnetization is attributed to electron spin and is associated with group phenomena in which all the elementary moments in a small region, known as a domain, are aligned. The magnetization of one domain may be oriented at random with respect to that of a neighboring domain. The large magnetizations that are characteristic of ferromagnetic materials are the result of the collective orientation of whole domains.

While paramagnetism and diamagnetism comply linearly as most dielectrics do, ferromagnetic materials are not only highly nonlinear, but their behavior also depends on their previous magnetic history which is also called hysteresis because the aligned magnetic domains may not be restored immediately after removing external magnetic fields.

Extremely fine ferromagnetic particles of single domain or smaller than a domain size, however, do not have such a hysteresis effect because there is no domain to be aligned.

The substance in this region is called a superparamagnetic particle. This concept can be understood by the Néel relaxation or the magnetic relaxation time [18–20]. The Néel time relaxation  $\tau_N$  is correlated with the material properties of the particles by the effective anisotropy constant  $K_{ef}$  and with the mean magnetic volume  $V_m$  of the particles as

$$\tau_N = \tau_0 \exp\left(\frac{K_{ef} V_m}{k_B T}\right) \quad (1)$$

where  $k_B$  is Boltzmann’s constant,  $T$  is the temperature, and  $\tau_0$  is the relaxation time at infinite temperature. For magnetite  $\tau_0$  has the order of magnitude  $10^{-9}$  s. If the volume of particle is small enough then  $\tau_N$  will be almost zero, which means ideally no magnetic hysteresis. For instance, a cobalt (Co) particle of 6.8 nm size has  $10^{-1}$  s of magnetic relaxation time at room temperature but the same particle of 9.0 nm size has  $3.2 \times 10^9$  s, which is about 100 years, of magnetic relaxation time [21].

### 3. MAGNETIC PARTICLES AND MAGNETIC SEPARATION

The basic concept in magnetic separations in biotechnologies including lab-on-a-chip systems is to selectively bind the biomaterial of interest, such as a specific cell, protein, or DNA fragments, to a magnetic particle and then separate it from its surrounding matrix using a magnetic field for manipulation or purification of biological cells/molecules. Magnetic beads of iron oxide ( $\text{Fe}_2\text{O}_3$  or  $\text{Fe}_3\text{O}_4$ ) with diameters ranging from a few nanometers to a few micrometers are typically used for such separations. These magnetic particles are called “superparamagnetic” particles, meaning that they are attracted to a magnetic field but retain no residual magnetism after the field is removed. The material, which is halfway between ferromagnetic and paramagnetic, has superparamagnetism. As the size of magnetic elements scales below the few tens of nanometer range, a superparamagnetic phase emerges in which the room temperature thermal energy overcomes the magnetostatic energy well of the element, resulting in zero hysteresis. In other words, although the element itself is a single-domain ferromagnet, the ability of an individual magnetic domain to store magnetization orientation information is lost when its dimension is below a threshold. Therefore, suspended superparamagnetic particles tagged to the biomaterial of interest can be removed from a matrix using a magnetic field, but they do not agglomerate or stay suspended in the solution after removal of the magnetic field. If the magnetic components (generally iron oxide) are small enough, they will respond to a magnetic field but are incapable of becoming independently magnetic. This is important, as it results in particles that are attracted to a magnetic field yet lose all attraction for each other in the absence of a magnetic field—allowing efficient separation and complete resuspension. Figure 2 illustrates a general structure of magnetic beads that contain superparamagnetic nanoparticles in a polymeric shell and Figure 3 illustrates magnetic separation/resuspension due to superparamagnetism of nanomagnetic particles.

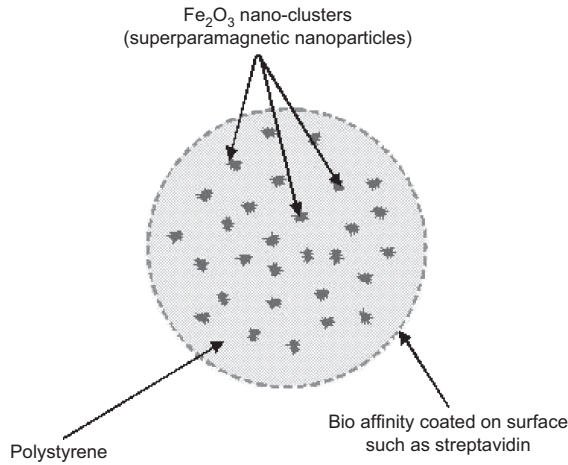


**Figure 2.** General structure of superparamagnetic beads.

With few exceptions, most magnetic particles fall into three broad classes: unmodified (or naked) particles, chemically derivatized particles with general specificity ligands, and chemically derivatized particles with specific recognition groups. General specificity particles are largely produced as substrates to attach a variety of affinity ligands. Magnetic

beads are available with a variety of ligands, such as oligo-(dT), streptavidin, or protein-A, attached. Magnetic beads can also be coated with highly specific recognition groups like antibodies for very specialized applications.

According to electromagnetic field theory, the magnetization density  $\vec{M}$  is introduced to account for the effects of magnetizable materials. The most common constitutive law for  $\vec{M}$  takes the form

$$\vec{M} = \chi_m \vec{H} \quad (2)$$

where  $\chi_m$  is the magnetic susceptibility and  $\vec{H}$  is the magnetic field intensity. Equation (2) is based on the assumption that the material is both isotropic and linear, in other words, that  $\vec{M}$  is proportional to  $\vec{H}$  and in the same direction, which is reasonably true in superparamagnetic materials. Assuming  $N$  as the number of atoms in unit volume and  $\vec{m}$  as the magnetic moment,  $\vec{H}$  can be also expressed as

$$\vec{M} = N \vec{m} \quad (3)$$

The magnetic beads are assumed to be spherical and have a low density in the suspension. Interactions between the particles are not considered. For this case, the magnetic force  $\vec{F}$  has the form

$$\vec{F} = \nabla U = \nabla(\vec{m} \cdot \vec{B}) \quad (4)$$

where  $U$  is the magnetic energy. Applying basic vector calculation, Eq. (4) can be rewritten as

$$\vec{F} = \vec{B} \times (\nabla \times \vec{m}) + \vec{m} \times (\nabla \times \vec{B}) + (\vec{B} \cdot \nabla) \vec{m} + (\vec{m} \cdot \nabla) \vec{B} \quad (5)$$

Based on the assumption that there is no interaction between the particles, the first and the third terms vanish. In addition, absence of the source current at the location of  $\vec{m}$  makes the second term zero. Combining Eqs. (2) and (3) into (5), the magnetic force of attraction from the field on the particle is of the form

$$\vec{F} = (\vec{m} \cdot \nabla) \vec{B} = V \chi_m (\vec{H} \cdot \nabla) \vec{B} \quad (6)$$

where  $V$  is the volume of the particle.

Choosing the  $x$  direction along the channel, the  $x$ -directional force is

$$F_x = V \chi_m \left( H_x \frac{\partial}{\partial x} + H_y \frac{\partial}{\partial y} \right) B_x = V \chi_m \left( H_x \frac{\partial B_x}{\partial x} + H_y \frac{\partial B_x}{\partial y} \right) \quad (7)$$

From the equation, since  $V$  and  $\chi_m$  depend on the selected magnetic beads, the controllable parameters of the separation device are the strength ( $H_x$  and  $H_y$ ) and the gradient ( $\partial B_x / \partial x$  and  $\partial B_x / \partial y$ ) of the magnetic field. The field depends on the performance of the inductive component, which is limited by the allowable size and planar fabrication process. The field strength is, however, usually limited in a microstructure because it is not easy to apply a large current due to its small size, although the field gradient is easier to maximize by choosing an appropriate structure or geometry.

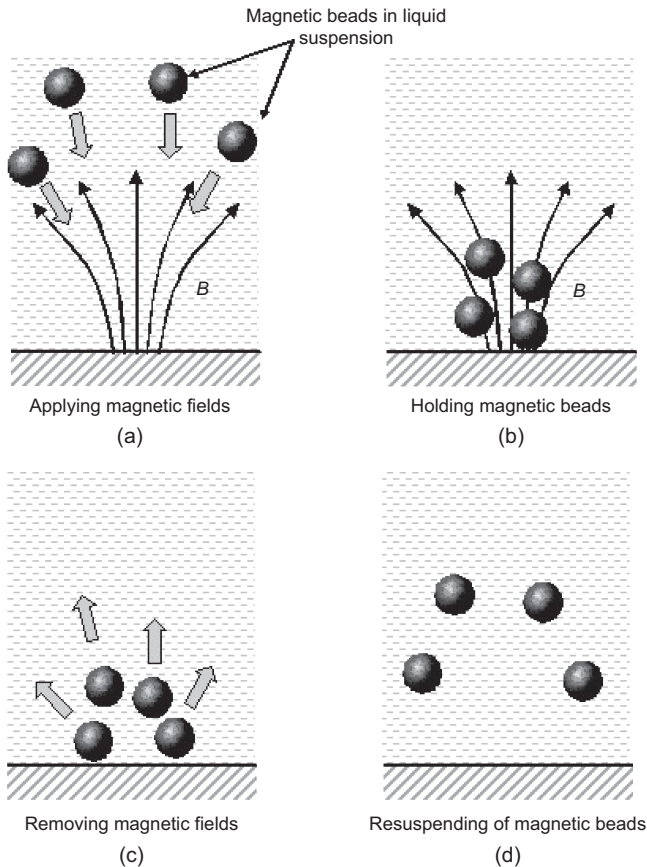


**Figure 3.** Illustration for magnetic separation and resuspension of superparamagnetic beads: (a) magnetic beads are attracted; (b) magnetic beads are held; (c) magnetic beads start to disperse; (d) magnetic beads are resuspended in liquid suspension.



#### 4. NANOMAGNETIC PARTICLES IN BIOMEDICAL APPLICATIONS

Magnetic separations in biology and biotechnology have diversified in recent years, leading to a bewildering array of different particles, affinity mechanisms, and processes. Applications in the nucleic acid realm include products for mRNA isolation from cells or previously purified total RNA preparations, solid-phase cDNA library construction, double-stranded and single-stranded DNA purification, solid phase DNA sequencing, and a variety of hybridization-based methodologies. Magnetic beads also are finding uses in protein purification, immunology, and the isolation of a wide range of specific mammalian cells, bacteria, viruses, sub-cellular organelles, and individual proteins. There are also products that employ nanomagnetic particles for more conventional isolation and purification methods such as affinity and ion exchange and charcoal trapping of small analytes.

A common use of superparamagnetic nanoparticles is for immunospecific cell separations [22–27]. Specific antibody and nanomagnetic particles are mixed together first to immobilize the antibody onto the surface of nanomagnetic particles. The antibody-tagged, nanomagnetic particles are then incubated with a solution containing the cells, proteins, and/or antigens of interest. The nanomagnetic particles bind to the surfaces of the desired cells, and/or proteins, and these biomolecules can then be collected in a magnetic field by collecting the nanomagnetic particles. Methods of this type have been used to isolate or remove numerous cell types, including lymphocytes (cells that control immune response), tumor cells, or specific antigens. In addition to loading microparticles with superparamagnetic nanoparticles, other examples of tagging the desired biomaterial with individual nanoparticles have been reported. An example of immunospecific cell separation is shown in Figure 4.

The other application area is mRNA isolation from cells or previously purified total RNA preparations, solid-phase cDNA library construction, double-stranded and single-stranded DNA purification, solid phase DNA sequencing, and a variety of hybridization-based methodologies [28].

Other uses of nanomagnetic particles in biotechnology include delivery of anticancer drugs to tumors [29]. The idea of drug delivery is that radioactive anticancer materials are immobilized on magnetic particles, which are injected into the body. Then, by placing a magnet to the position of tumor, the anticancer drugs will be collected on a localized area to selectively attack tumor cells as illustrated in Figure 5.

#### 5. BIOSAMPLING IN LAB-ON-A-CHIP USING NANOMAGNETIC PARTICLES

Recent achievements in MEMS (microelectromechanical systems) research make it possible to adopt the magnetic separation technology for biocell separation in microfluidic systems or lab-on-a-chip. There are many advantages using lab-on-a-chip over conventional chemical or biological laboratories. One of the important advantages lies in its low cost. Many reagents and chemicals used in biological and chemical reaction are expensive, so the prospect

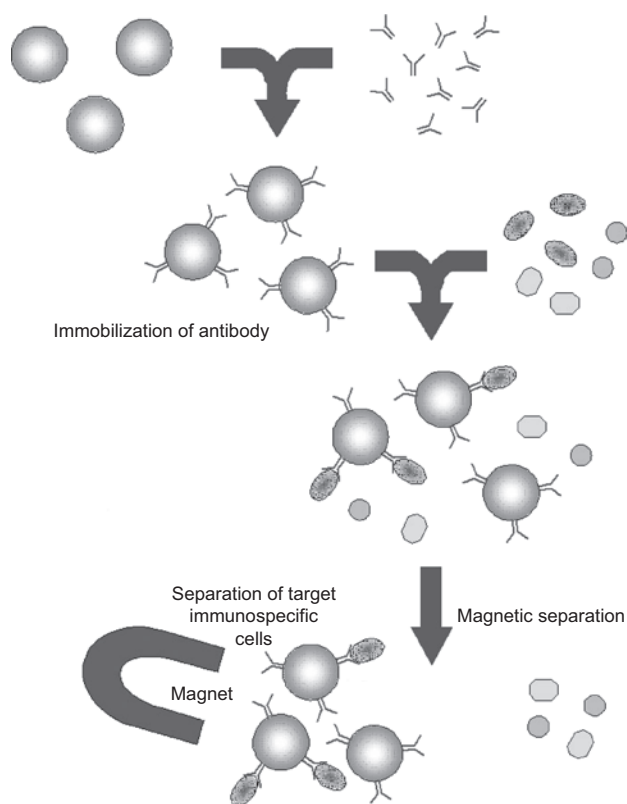


**Figure 4.** An example of immunospecific cell separation.

of using very small amounts (in micro- to nanoliter range) of reagents and chemicals for an application is very appealing. Another advantage is that lab-on-a-chip requires very small amounts of reagents/chemicals, which enables rapid mixing and reaction because biochemical reaction is mainly

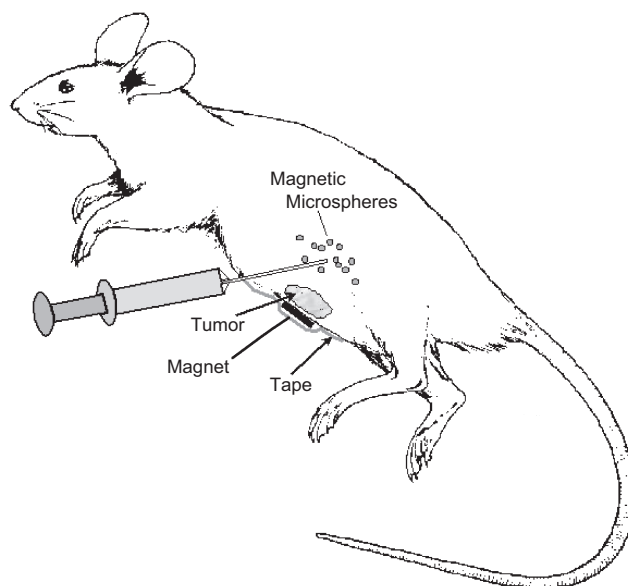


**Figure 5.** Magnetic carriers to deliver anticancer drugs to tumors. Reprinted courtesy of Dr. U. O. Hafeli, The Cleveland Clinic Foundation, USA.

involved in diffusion of two chemical or biological reagents and microscale fluidics reduces diffusion time as reaction probabilities increase. In practical terms, reaction products can be produced in a matter of seconds/minutes compared with laboratory scale taking hours or even days. In addition, lab-on-a-chip systems minimize harmful by-products since their volume is so small.

Complex reactions of many reagents could happen on lab-on-a-chip that has ultimate potential in DNA analysis, biochemical warfare agent detection, biological cell/molecule sorting, blood analysis, drug screening/development, combinatorial chemistry, and protein analysis.

One of the accomplishments was made for biosampling of antigen for on-chip immunoassay systems using nanomagnetic particles [30]. The limited goal was to develop a generic MEMS-based microfluidic system and to apply the fluidic system to detect biomolecules such as specific proteins and/or antigens in liquid samples. Figure 6 illustrates the schematic diagram of a generic microfluidic system for biochemical detection using a magnetic bead approach for both sampling and manipulating the target biomolecules [31]. The analytical concept is based on sandwich immunoassay and electrochemical detection [32] as illustrated in Figure 7.

Nanomagnetic particles are used as the solid phase for the capture of antibodies and as carriers of captured target antigens. A simple concept of magnetic bead-based biosampling with a microfabricated electromagnet for the application of selective biosampling is shown in Figure 8. Antibody coated nanomagnetic particles are introduced to the electromagnet and separated by applying a magnetic field. While holding the antibody-coated beads, antigens are injected into the channel. Only target antigens are immobilized and thus separated onto the magnetic bead surface due to antibody/antigen reaction. Other antigens get washed out with the flow. Since only the target antigens are collected by the magnetic beads, target antigens are also "filtered." Next, enzyme-labeled secondary antibodies are introduced and incubated with the immobilized antigens. The chamber is then rinsed to remove all unbound secondary antibodies. Substrate solution, which will react with enzyme, is injected into the channel and the electrochemical detection is performed. Finally the magnetic beads are released to the waste chamber and the bioseparator is ready for another immunoassay. The lab-on-a-chip system was microfabricated and integrated for nanomagnetic particle-based immunoassay. With the system, full immunoassays were performed following the sequence stated

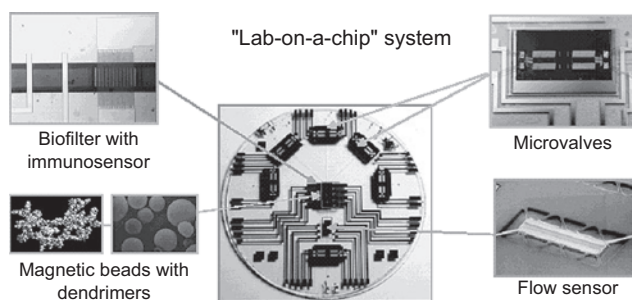


**Figure 6.** A generic microfluidic system for electrochemical immunoassay-based remote biochemical sensors.

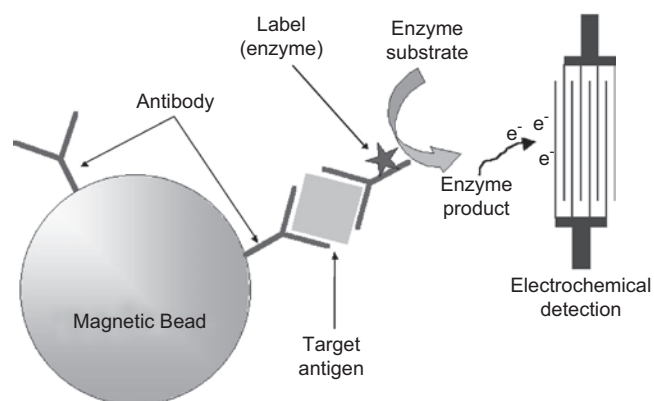


**Figure 7.** Analytical concept based on sandwich immunoassay and electrochemical detection. Reprinted with permission from [30], J.-W. Choi et al., *Lab on a Chip* 2, 27 (2002). © 2002, Royal Society of Chemistry.

for different antigen (mouse IgG) concentrations: 50, 75, 100, 250, and 500 ng/ml. Concentrations of primary antibody (antimouse IgG) coated magnetic beads and conjugated secondary antibody (rat antimouse IgG conjugated alkaline phosphatase) were  $1.02 \times 10^7$  beads/ml and 0.7  $\mu\text{g/ml}$ , respectively. Immunoreactant consumed during one immunoassay was 10  $\mu\text{l}$  and total assay time was less than 20 minutes including all incubation and detection steps.

The methodology and lab-on-a-chip system described has great potential in developing generic biomolecule detection and analysis systems by replacing antibody/antigen with appropriate bioreceptors/reagents such as DNA fragments or oligonucleotides for the application to DNA analysis and/or protein analysis.

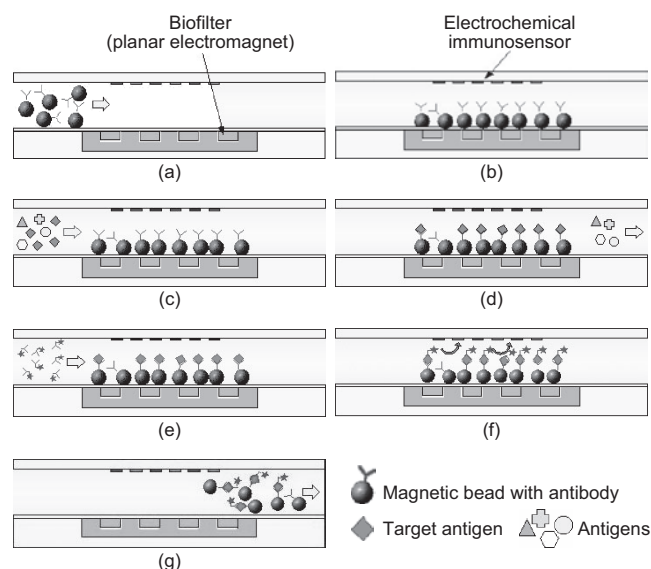


**Figure 8.** Conceptual illustration of biosampling and immunoassay procedure using magnetic bead approach: (a) injection of magnetic beads; (b) separation and holding of beads; (c) flowing samples; (d) immobilization of target antigen; (e) flowing labeled antibody; (f) electrochemical detection; and (g) washing out magnetic beads and ready for another immunoassay. Reprinted with permission from [30], J.-W. Choi et al., *Lab on a Chip* 2, 27 (2002). © 2002, Royal Society of Chemistry.

## 6. CONCLUSION

A brief review on nanomagnetic particles in biomedical applications was given in this chapter. Nanomagnetic particles are advantageous in separation and manipulation of biomolecules such as cells, proteins, and DNA fragments by immobilizing the biomolecules on the surface of magnetic particles. In addition, nanomagnetic particles have large surface area of immobilization substrate that results in high population of target biological molecules due to large binding site. Furthermore, the magnetic separation and manipulation techniques do not cause electrical disturbance during the analysis process, which may result in damage to biomolecules or electrolyzing of sample solutions.

In regards to the nanomagnetic particles in biomedical application, further investigation on behavior of magnetic particles in terms of microfluidics and thermal energy of magnetic particles is needed. One of the main characteristics in nanomagnetic particle separation arising from physical laws is that magnetic forces on superparamagnetic particles are always attractive. That means only one directional control is possible. Although the superparamagnetic particles have relatively large thermal energy due to small size so they have Brownian motion in fluid, quick restoration of the separated magnetic particles to suspension would be required in some applications.

Another challenge will be high throughput two-dimensional magnetic separation. Accurate positioning, in two-dimensional arrays, of magnetic beads with specific biological molecules is strongly required for high throughput DNA and protein analysis. Although the technology using nanomagnetic particles can give several advantages in soaring biotechnology areas such as genomics, proteomics, or drug discovery, as yet very few articles have reported high throughput protein analysis in two-dimensional arrays due to a couple of technical difficulties—there have been heat problems in long operation times with integrated electromagnets as magnetic particle separator or inaccuracies in positioning magnetic particles with conventional rare earth magnets. Ongoing research efforts on separation and purification using nanomagnetic particles in micro- and nanoscale would overcome such difficulties for a better tool for biomedical applications.

Nevertheless, it seems an undoubted trend that magnetic separation using nanomagnetic particles in biomedical applications including lab-on-a-chip systems is becoming one of the revolutionary tools for various applications in biotechnology due to its fascinating aspects over conventional chemical or biological laboratories.

## GLOSSARY

**Complementary DNA (cDNA)** A DNA copy of an mRNA or complex sample of mRNAs, made using reverse transcriptase.

**Deoxyribonucleic acid (DNA)** A naturally occurring polymer composed of deoxy ribonucleotides. Although commonly found as a double-stranded, right-handed helix it can adopt one-, three-, and four-stranded forms having a variety of shapes.

**Diamagnetism** Phenomenon exhibited by materials like copper or bismuth that become magnetized in a magnetic field with a polarity opposite to the magnetic force; unlike iron they are slightly repelled by a magnet.

**Ferromagnetism** Phenomenon exhibited by materials like iron (nickel or cobalt) that become magnetized in a magnetic field and retain their magnetism when the field is removed.

**Immunoassay** A technique for identifying a substance by using antibodies specific to that substance to separate the substance or identify it with a marker.

**Immunomagnetic separation** A biological cell- or molecule-separation technique where magnetic microparticles are first coated with monoclonal antibody, allowed to search and bind to target cells or biomolecules, and are then selectively removed when passed through a magnetic field.

**Lab-on-a-chip** A chip-size device that performs biological and chemical laboratory functions on a microchip platform dealing with smaller amount than a few microliters. Lab-on-a-chip can be used not only to synthesize chemicals efficiently and economically but also to carry out biological and clinical analyses, to perform combinatorial chemistry, and to carry out full-scale analyses from sample introduction to chemical separation and detection, on a single, miniaturized device.

**Messenger RNA (mRNA)** Arises in the process of transcription from the DNA and includes information on the synthesis of a protein.

**Microelectromechanical systems (MEMS)** Refers to technology used to integrate various electro-mechanical functions onto integrated circuits. A typical MEMS device combines a sensor and logic to perform a monitoring function. Examples include sensing devices used to control the deployment of airbags in cars and switching devices used in optical telecommunications cables. MEMS developers will be able to exploit nanotechnologies in fabricating new integrated circuits.

**Microfluidics** The science of designing, manufacturing, and formulating devices and processes that deal with volumes of fluid on the order of nanoliters or picoliters.

**Paramagnetism** Phenomenon exhibited by materials like aluminum or platinum become magnetized in a magnetic field but it disappears when the field is removed. Attraction toward a magnetic field, stronger than diamagnetism, but still weak compared to ferromagnetism.

**Ribonucleic acid (RNA)** A naturally occurring polymer composed of ribonucleotides. Although commonly found in its single-stranded form, it can adopt two-, three-, and fourstranded forms having a variety of shapes.

**Streptavidin** A small bacterial protein that binds with high affinity to the vitamin biotin. This streptavidin-biotin combination can be used to link molecules such as radioisotopes and monoclonal antibodies together. These bound products have the property of being attracted to, and attaching to, cancer cells, rather than normal cells. The radiolabeled products are more easily removed from the body, thus decreasing their toxicity.

**Superparamagnetism** Property of a material that, when placed in a magnetic field, is magnetized to the field to an

extent proportional to the field showing lack of hysteresis in the magnetization curve, particularly for extremely fine ferromagnetic particles of single domain or smaller than a domain size.

## REFERENCES

1. D. Melville, F. Paul, and S. Roath, *IEEE Trans. Mag. MAG-11*, 1701 (1975).
2. G. M. Whitesides, R. Jour. Kazlauskas, and L. Josephson, *Trends Biotechnol.* 1, 144 (1983).
3. S. Roath, A. Smith, and J. H. P. Watson, *J. Mag. Mag. Mater.* 85, 285 (1990).
4. V. Chikov, A. Kuznetsov, A. Shapiro, S. Winoto-Morbach, and W. Mueller-Ruchholtz, *J. Mag. Mag. Mater.* 122, 367 (1993).
5. S. Miltenyi, W. Muller, W. Weichel, and A. Radbruch, *Cytometry* 11, 231 (1990).
6. K. M. Partington, E. J. Jenkinson, and G. Anderson *J. Immunological Methods* 223, 195 (1999).
7. R. Hartig, M. Hausmann, and C. Cremer, *Electrophoresis* 16, 789 (1995).
8. H. Yu, *Anal. Chim. Acta* 376, 77 (1998).
9. A. S. Panphilov and O.-J. L. Bekish, *Immunol. Lett.* 56, 462 (1997).
10. K. M. Partington, E. J. Jenkinson, and G. Anderson, *J. Immunol. Methods* 223, 195 (1999).
11. S. Ghassabian, T. Ehtezazi, S. M. Forutan, and S. A. Mortazavi, *Int. J. Pharm.* 130, 49 (1996).
12. S. Goodwin, C. Peterson, C. Hoh, and C. Bittner, *J. Mag. Mag. Mater.* 194, 132 (1999).
13. S. K. Pulfer, S. L. Ciccotto, and J. M. Gallo, *J. Neuro-Oncol.* 41, 99 (1999).
14. A. S. Lubbe, C. Bergemann, J. Brock, and D. G. McClure, *J. Mag. Mag. Mater.* 194, 149 (1999).
15. J. L. Dormann and D. Fiorani, "Magnetic Properties of Fine Particles." North-Holland, Amsterdam, 1992.
16. E. D. Dahlberg, D. K. Lottis, R. M. White, M. Matson, and E. Engle, *J. Appl. Phys.* 76, 6396 (1994).
17. P. C. Fannin and S. W. Charles, *J. Phys. D* 27, 185 (1994).
18. R. Kotitz, W. Weitschies, L. Trahms, and W. Semmler, *J. Mag. Mag. Mater.* 201, 102 (1999).
19. J. Tejada and X. X. Zhang, *J. Phys. Condens. Matter* 6, 263 (1994).
20. L. Trahms, P. C. Fannin, and R. Kotitz, *J. Mag. Mag. Mater.* 149, 42 (1995).
21. B. D. Cullity, "Introduction to Magnetic Materials." Addison-Wesley, Reading, MA, 1972.
22. M. Q. Deng, K. M. Lam, and D. O. Cliver, *J. Microbiol. Methods* 40, 11 (2000).
23. A. N. Makarovskiy, W. Ackerley III, L. Wojcik, C. K. Halpert, B. S. Stein, M. P. Carreiro, and D. C. Hixson, *J. Clinical Lab. Anal.* 11, 346 (1997).
24. K. C. Cudjoe, T. Hagtvedt, and R. Dainty, *Int. J. Food Microbiol.* 27, 11 (1995).
25. H. Yu, *Anal. Chim. Acta* 376, 77 (1998).
26. K. M. Partington, E. J. Jenkinson, and G. Anderson *J. Immunol. Methods* 223, 195 (1999).
27. A. P. Wright, J. J. Fitzgerald, and R. J. Colello, *J. Neurosci. Methods* 74, 37 (1997).
28. M. Bosnes, A. Dggerdal, A. Rian, L. Korsnes, and F. Larsen, Magnetic Separation in Molecular Biology, in "Scientific and Clinical Applications of Magnetic Carriers" (Hafeli et al., Eds.). Plenum, New York, 1997.
29. U. O. Hafeli, G. J. Pauer, W. K. Roberts, J. L. Humm, and R. M. Macklis, in "Scientific and Clinical Applications of Magnetic Carriers" (Hafeli et al., Eds.). Plenum, New York, 1997.
30. J.-W. Choi, K. W. Oh, J. H. Thomas, W. R. Heineman, H. B. Halsall, J. H. Nevin, A. J. Helmicki, H. T. Henderson, and C. H. Ahn, *Lab on a Chip* 2, 27 (2002).
31. J.-W. Choi, K. W. Oh, A. Han, N. Okulan, C. A. Wijayawardhana, C. Lannes, S. Bhansali, K. T. Schlueter, W. R. Heineman, H. B. Halsall, J. H. Nevin, A. J. Helmicki, H. T. Henderson, and C. H. Ahn, *Biomed. Microdevices* 3, 191 (2001).
32. W. R. Heineman, H. B. Halsall, M. Cousino, C. A. Wijayawardhana, S. Purushothama, S. Kradtap, K. Schlueter, J.-W. Choi, C. H. Ahn, and H. T. Henderson, Electrochemical immunoassay with microfluidic systems, in "PITTCON '99," Orlando, FL, 7-12 March, 1999.



# Nanomagnets for Biomedical Applications

Pedro Tartaj

*Instituto de Ciencia de Materiales de Madrid, Cantoblanco, Madrid, Spain*

## CONTENTS

1. Introduction
  2. Nanoparticles in Biomedicine
  3. Biomedical Applications of Magnetic Nanoparticles
  4. Nanomagnet Production
  5. Surface Modification of Nanomagnets
  6. Summary
- Glossary  
References

## 1. INTRODUCTION

The biotechnology and materials science fields have developed over recent decades to allow the engineering of advanced technical devices and the industrial production of active substances for biomedical applications [1]. This review is mainly focused on emerging approaches to the use of magnetic nanocrystals in biomedicine. This novel and highly interdisciplinary field is closely associated with the interesting properties that materials containing crystallites or particles of nanometer dimensions have shown related to their extremely small size.

Nanostructures are intermediate in size between molecular and microscopic (micrometer-sized) structures. Viewed as molecules, they are so large that they provide access to realms of quantum behavior that are not otherwise accessible; viewed as materials, they are so small that they exhibit characteristics that are not observed in larger (even  $0.1 \mu\text{m}$ ) structures [2]. They combine small size, complex organizational patterns, a potential for very high packing densities and strong lateral interactions, and high ratios of surface area to volume.

For example, when we reduce the physical size of a semiconductor material so that becomes comparable to or smaller than the Bohr radius, the space in which the charge carriers move decreases, and thus additional quantum confinement is imposed on their motion. This leads to an

increase in the bandgap energy, the electron and hole kinetic energy, and the density of the charge carriers within and at the nanoparticle surface [3]. Because of this, as well as the fact that the surface-to-volume ratio greatly increases, new properties not possessed by the macroscopic semiconductor material or by the individual entity that makes the semiconductor are observed [4–9]. In a metal, as we decrease its size and confine its electronic motion, the separation between the valence and the conduction bands becomes comparable to or larger than  $k_{\text{B}}T$ , and the metal becomes a semiconductor. More confinement increases the energy separation further, and the material becomes an insulator. In the size domain at which the metal-to-insulator transition occurs, new properties are expected to be observed that are possessed neither by the metal nor by the molecules or atoms forming the metal [10–14].

Finite-size effects dominate the magnetic behavior of individual nanoparticles, increasing their relevance as the particle size decreases. Surface phenomena also dictate the magnetic behavior of nanomagnets. In general, the magnetic behavior of the particle surface differs from that corresponding to the core because of the different atomic coordination, compositional gradients, and concentration and nature of defects present in both regions. The core usually displays a spin arrangement similar to that of the bulk, whereas the surface presents a much higher magnetic disorder. Finite-sized effects along with surface effects, collective phenomena arising from interparticle interactions and unusual transport properties, cause nanomagnets to exhibit a number of outstanding physical properties such as superparamagnetism, giant magnetoresistance, quantum tunneling of the magnetization, and large coercivities [15–20].

## 2. NANOPARTICLES IN BIOMEDICINE

Nanotechnology is beginning to allow scientists, engineers, and physicians to work at the cellular and molecular levels to produce major benefits to the life sciences and health care. Real applications of nanostructured materials are still rare at the present time. However, the excellent properties of these materials, when compared with those of their bulk counterparts, foreshadow a very promising future for their use in



the field of biomedicine. Logically, we have to assume that when we deal with biomedical applications, unlike what is happening in other fields of nanotechnology, the severe but necessary regulatory laws that rule the use of many biomedical products will generate a long delay until the product is suitable for the market.

Gold nanoparticles that are functionalized with proteins have long been used in the biosciences [21]. For instance, antibody molecules adsorbed on colloidal gold (10–40 nm) are routinely used in histology, thus allowing the biospecific labeling of particular regions of tissue samples and subsequent TEM analysis. More advanced small gold clusters with a diameter of 0.8 or 1.4 nm can be used for the site-specific labeling of biological macromolecules [22–24]. These labels have a number of advantages over colloidal probes, including better resolution, stability, and uniformity. Moreover, their small size improves the penetration and more quantitative labeling of antigenic sites [1].

Gold particles are well-established carriers for the delivery of dsDNA in the so-called gene-gun technology [25]. In this method, plasmid DNA with a typical length of several thousand base pairs is adsorbed to Au or tungsten colloids with a typical size of about 500 nm to several micrometers. The DNA- or RNA-coated particles are loaded into a gun-like device in which a low-pressure helium pulse delivers the particles into virtually any target cell or tissue. An advantage of this technique is that it is not necessary to remove cells from tissue to transform them. The particles penetrate the cells and release the DNA, which is diffused into the nucleus and, for example, incorporated into the chromosomes of the organism.

Chemotherapy with small-sized nanoparticles was performed in tumor-bearing animals. Taxol incorporated into polyvinylpyrrolidone nanospheres with a diameter of 50–60 nm was assayed on a B16F10 murine melanoma transplanted subcutaneously in mice. Mice treated with repeated intravenous injections of taxol-loaded nanospheres showed a significant tumor regression and higher survival rates than mice treated with free taxol [26]. Similarly, the use in a murine tumor model (subcutaneously implanted J774A.1 macrophages) of a dextran-doxorubicin conjugate incorporated into small chitosan nanospheres (100 nm in diameter) was reported to outperform the free conjugate, especially in relation to life expectancy [27]. In both cases, a higher tumor uptake, thanks to the small size and the hydrophilicity of the carrier device, as well as the sustained release of the drug, were supposed to be the key factors in improving the efficacy of the chemotherapy [26, 27].

Nanoparticles can be used for qualitative or quantitative *in vitro* detection of tumor cells. They help the detection process by concentrating and protecting a marker from degradation, to render the analysis more sensitive. For example, streptavidin-coated fluorescent polystyrene nanospheres (Fluospheres (green fluorescence) and Trans-Fluospheres (red fluorescence)) were used in single-color flow cytometry to detect epidermal growth factor receptor (EGFR) on A431 cells (human epidermoid carcinoma cells) [28]. The results showed that the fluorescent nanospheres provided a sensitivity 25 times that of the conjugate streptavidin-fluorescein. The encapsulation of fluorescent markers resulted in objects that were brighter and

more concentrated than when simple conjugates of single dyes were used. Moreover, the fluorescent nanoparticles were used in combination with R-phycoerythrin (R-PE) (reagent for flow cytometry) in multicolor flow cytometry, enabling the concomitant detection of the CD3 and CD4 receptors on Jurkat cells (human acute T-cell leukemia cells) [28].

Another approach was the encapsulation of inorganic biomarkers, rather than fluorescent organic markers. These compounds are more photostable and are not hampered by the intrinsic fluorescence (background signal) emitted by cells and tissues, which makes them more suitable and sensitive for qualitative and, especially, quantitative detection. For example, streptavidin-coated nanoparticles containing lanthanide chelates were used in quantitative immunohistochemistry analysis with time-resolved fluorescence (TRF) imaging [29]. Both the amount of nanoparticles detected and the specific signal measured from a TRF image correlated linearly with the amount of antigen (prostate-specific antigen) used. Quantitative measurement is thus possible.

Cancer researchers have spent years working to starve tumors by blocking blood vessel growth, or angiogenesis, with mixed success [30, 31]. Recently, a study reported in the journal *Science* and led by vascular biologist David Cheresh have used lipid-based nanoparticles that target new blood vessels [32]. The nanoparticle's surface was studded with molecules that bind to  $\alpha v \beta 3$  and embedded with copies of a mutant form of the *Raf-1* gene that disrupts Raf's normal activity. In the mid-1990s, Cheresh and others found signatures specific for different types of blood vessels that they used as target "zip codes." One of these, belonging to a class of membrane proteins called integrins, is apparently always present on angiogenic, or newly growing, blood vessels but rarely on established ones ( $\alpha v \beta 3$ ) [31]. Meanwhile, various teams had become intrigued by cascades of molecular signals that seem critical to new blood vessel growth. One molecule central to several of these cascades is known as Raf. Inhibiting the *Raf-1* gene in mice prevents blood vessels from forming and halts embryonic development [31].

The researchers infused a dose of these particles into the tails of mice that had been injected earlier with malignant cells. A single treatment erased tumors 400 cubic millimeters in size—one-fortieth the size of the mouse, or the equivalent of a 2-kg tumor in an 80-kg person—in about 6 days. Most of the tumors in animals with metastases to the lungs or liver also disappeared. Examining the tumors under a microscope, the researchers saw the expected dead blood vessel cells, which self-destructed after the Raf mutant shuttled inside them.

### 3. BIOMEDICAL APPLICATIONS OF MAGNETIC NANOPARTICLES

By far the most employed material in biomedical applications is magnetite ( $\text{Fe}_3\text{O}_4$ ) or its oxidized form, maghemite ( $\gamma\text{-Fe}_2\text{O}_3$ ). Highly magnetic materials such as cobalt and nickel, toxic and susceptible to oxidation, remain of little interest [33]. Magnetite is a common magnetic iron oxide that has a cubic inverse spinel structure with oxygen forming a fcc closed packing and Fe cations occupying interstitial tetrahedral sites and octahedral sites [34]. Maghemite

(magnetite-hematite) has a structure similar to that of magnetite. It differs from magnetite in that all or most of the Fe is in the trivalent state. Cation vacancies compensate for the oxidation of Fe (II) cations [34]. Maghemite has a cubic unit cell in which each cell contains 32 O ions,  $21\frac{1}{3}$  iron (III) ions, and  $2\frac{1}{3}$  vacancies. The cations are distributed randomly over the 8 tetrahedral and 16 octahedral sites, whereas the vacancies (which are also randomly distributed) are confined to the octahedral sites. Synthetic maghemite often displays superstructure forms, which arise as a result of the cation and the vacancy ordering. The extent of vacancy ordering is related to both the crystallite size of the precursor and the amount of iron (II) in the structure [35]. All of these possible arrangements in the maghemite are partially responsible for the different magnetic behaviors manifested by maghemite nanoparticles prepared by different synthetic routes [36].

Biomedical applications require particles with magnetism that turns “active” upon application of a strong magnetic field and turns “inactive” upon removal of the field. Superparamagnetic particles fulfill this requirement, but superparamagnetism at room temperature only occurs for iron ferrites smaller than about 10–15 nm [36]. Below some critical size, each ferromagnetic nanoparticle can support only a single magnetic domain and so can be viewed as a single large spin with moment of roughly  $10^3$ – $10^5 \mu_B$ . At low temperatures, this moment points along one of the energetically favorable (easy) axes of the particle, giving the particle a nonzero magnetization on laboratory time scales. Above some temperature (the so-called blocking temperature), however, thermal fluctuations can overcome the anisotropy barrier, so the moments can rotate among different easy directions, whereupon the magnetization of each particle vanishes. These materials exhibit superparamagnetic behavior [37].

For most technological applications, magnetic nanoparticles have to be dispersed in liquids, forming the so-called ferrofluids. Ferrofluids, often described as magnetic liquids or stable magnetic colloids, were discovered by Elmore more than 60 years ago [38]. Ferrofluids have several unusual properties that depend on the applied magnetic field gradient, such as apparent density or viscosity. These suspensions have been widely used in, for example, rotary shaft sealing, oscillation damping, and position sensing [39, 40]. The term “ferrofluids” as normally found in bibliographies refers to the use of magnetic nanoparticles for biomedical applications, because on many occasions the particles have been supplied as dispersions in liquid media.

Magnetic nanoparticles useful for biomedical applications can be grouped into two main categories, depending on whether the nanoparticles have to be injected into the body (*in vivo* or *in vitro* applications). *In vivo* applications (Fig. 1) could be further grouped into two different applications: (a) therapeutic applications (mainly hyperthermia and drug targeting); (b) diagnostic applications (mainly NMR imaging). For *in vitro* applications (Fig. 2) the main use of the magnetic nanoparticles is diagnostic (mainly separation and selection, and magnetorelaxometry).

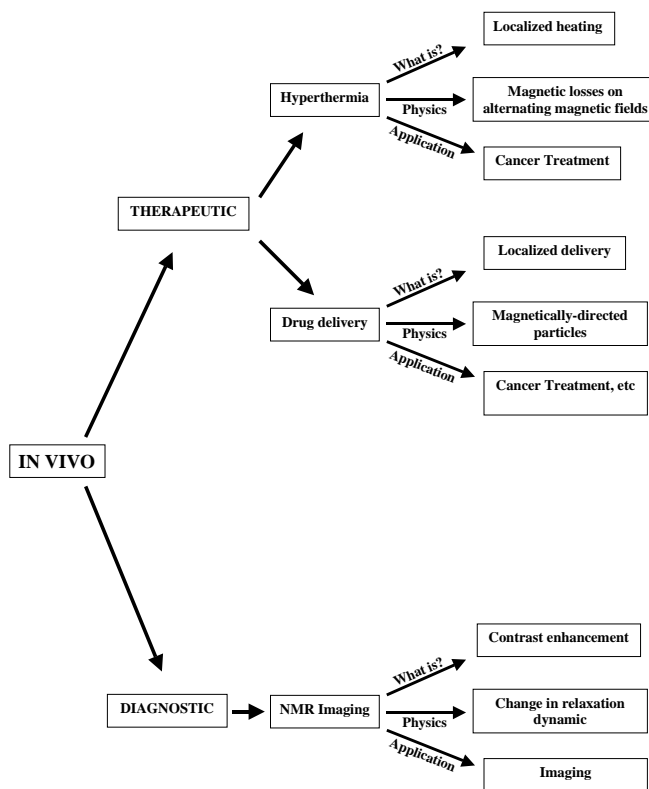


Figure 1. *In vivo* applications of nanomagnets.

### 3.1. *In vivo* Applications

#### 3.1.1. Therapeutic Applications

**Hyperthermia** More than 40 years ago, Gilchrist et al. [41] investigated localized magnetic hyperthermia with the use of fine magnetic particles. Exposed to an alternating magnetic field, these particles might act as localized heat sources at certain target regions inside the human body. The published results raised the hope of realizing a powerful method of cancer treatment within a few years. During the following decades many investigations were carried out, and *in vivo* experiments with animals in particular confirmed the general applicability to human patients. In 1981 Rand et al. [42] considered the method to be “ready for limited clinical application.”

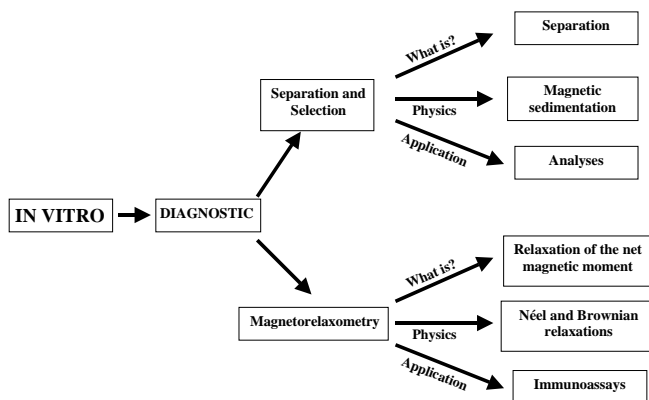


Figure 2. *In vitro* applications of nanomagnets.

Heating of certain organs or tissues to temperatures between 41 °C and 46 °C preferentially for cancer therapy is called hyperthermia [43]. The use of higher temperatures up to 56 °C, which yield widespread necrosis, coagulation, or carbonization (depending on the temperature), is called thermoablation [44, 45]. The two mechanisms act completely differently with respect to biological response and application technique. Classical hyperthermia induces almost reversible damage to cells and tissues, but it enhances radiation injury of tumor cells and chemotherapeutic efficacy. Modern clinical hyperthermia trials focus mainly on the optimization of thermal homogeneity at moderate temperatures (42–43 °C) in the target volume, a problem that requires extensive technical effort and advanced therapy and thermometry systems.

The heating of oxide magnetic materials with low electrical conductivity in an external alternating magnetic field is due to loss processes during the reorientation of the magnetization [46]. If the thermal energy  $k_B T$  is too low to facilitate reorientation, hysteresis losses dominate, which depend on the type of remagnetization process (wall displacement or several types of rotational processes). With decreasing particle size, thermal activation of reorientation processes leads, depending on temperature and measurement frequency, to superparamagnetic behavior of the particle ensemble and the occurrence of the so-called Néel losses [47]. In the case of ferrofluids losses related to the rotational Brownian motion of magnetic particles [48] may also act. Based on the Brown and Néel relaxivity, it was shown that subdomain particles (nanometer in size) absorb much more power at tolerable AC magnetic fields than is obtained by well-known hysteresis heating of multidomain (microns in size) particles [45, 49, 50].

Heating to the target temperatures causes moderate cellular inactivation in a dose-dependent manner. Although thermal dose–response curves look quite similar to radiation or drug dose–response curves, the critical target of thermal inactivation in the cell is not known yet. The most probable reason for this situation is that there is no individual cellular target of hyperthermia, in contrast to the well-known DNA damage after irradiation [51]. Most of the biomolecules, especially regulatory proteins involved in cell growth and differentiation and the expression of certain receptor molecules (involved in signal transduction pathways), are therefore largely influenced by hyperthermia.

Today, many cellular effects are known to be important for thermal inactivation. New insights from molecular biology have shown that a few minutes after hyperthermia, a special class of proteins is expressed in the cell, the so-called heat shock proteins. They protect the cell from further heating or subsequent thermal treatments and lead to an increase of cell survival after preheating, an effect called thermotolerance [52]. Additionally, the activity of certain regulatory proteins, kinases, or cyclins is influenced by hyperthermia, causes alterations in the cell cycle, and can even induce apoptosis, cell death driven by the cell regulatory system itself [53, 54]. Current research is also trying to characterize the interactions of thermal tolerance and multidrug resistance. The combined effect of radiation and hyperthermia takes place at the cellular level and is mainly due to the heat-induced malfunction of repair processes

after radiation-induced DNA damage. They are less effective when heat is given either before or after irradiation, and a well-defined time interval has been described for the two modalities [55]. Further effects were observed on the tissue level, such as changes in microvasculature, blood flow, energy, and oxygen status. Interestingly, heat-treated cancer cells may be better recognized by the host immune system because of alterations of some cell surface receptor molecules, which are then recognized by natural killer cells and inactivate the cancer cells, as has recently been demonstrated *in vitro* [56]. The joint action of all of the molecular mechanisms involved in hyperthermia is still under investigation.

**Magnetic Drug Targeting (Drug Delivery)** Since the pioneering concept proposed by Freeman et al. in 1960 [57] that fine iron particles could be transported through the vascular system and concentrated at a particular point in the body with the aid of magnetic fields, the use of magnetic particles for the delivery of drugs or antibodies to the organs or tissues altered by diseases has become a very attractive field of research [58].

The use of magnetic targeted carriers for drug delivery is intended to target drug to specific sites through the selective application of a magnetic field and to achieve prolonged release of high, localized concentrations of drug by retention of the carriers in the region of interest [59]. The process of drug localization with magnetic delivery systems is based on the competition between forces exerted on the particles by the blood compartment and magnetic forces generated by an applied magnet. When the magnetic forces exceed the linear blood flow rates in arteries ( $10 \text{ cm} \cdot \text{s}^{-1}$ ) or capillaries ( $0.05 \text{ cm} \cdot \text{s}^{-1}$ ), the magnetic particles are retained at the target site and may be internalized by the endothelial cells of the target tissue [58]. Drug delivery, of course, can be significantly improved with the use of drugs with functional groups that are able to specifically recognize the target.

The use of magnetic carriers for drug delivery of chemotherapeutic agents has evolved since the 1970s, when Widder et al. [60] developed albumin microspheres encasing the chemotherapeutic agent adriamycin and used magnetite as the magnetically susceptible component. In their research, Widder and his associates first demonstrated in animals the potential therapeutic benefit of magnetically directing microspheres, containing adsorbed drugs, into the capillary beds of tumors. Further development was not pursued because of the inadequate magnetic susceptibility of microspheres, which restricted the application of the technology to surface tumors. In the mid-1990s, Devineni et al. [61] compared the tissue distribution of methotrexate following intraarterial administration as a solution or as a magnetic microsphere conjugate to the brain. The authors concluded that once the magnetic field is turned off, the microsphere conjugates exit the brain and redistribute to other systemic organs, particularly lung. More recently, Lübke et al. used magnetic nanoparticles combined with epirubicin in preclinical and early clinical work [62].

The treatment of solid tumors with chemotherapy has been limited by systemic toxicity, resulting in suboptimal dosing, and by several other mechanisms (e.g., multiple drug resistance of the tumor cells, tumor architecture limiting

access of the drug to the tumor cells, volume of distribution for the drug), resulting in limited efficacy [59]. Regional therapy achieved through targeted drug delivery could improve efficacy by increasing the drug concentration at the tumor while limiting systemic drug concentrations. Higher drug concentrations at the tumor may be able to overcome the multiple drug-resistant phenotypes by overcoming the P-glycoprotein pump, which functions to pump drug out of cells. Magnetic particles carrying drugs may also achieve wide dispersion throughout the tumor through the action of the magnetic force on the particles. Regional drug delivery, however, will not be effective at treating distant sites of tumor metastases unless the drug is targeted to each known site. If systemic concentrations of drug remain low after regional delivery, it may be possible to systemically administer chemotherapy coincident with regional therapy to optimize efficacy.

The use of magnetic nanoparticles for drug delivery is not limited to cancer therapy. Another application is in the treatment of diseases of hollow organs (heart, stomach, intestine, vesicle, etc.) or joint disease (intraarticular injection in the case of rheumatism or osteoarthritis) [58].

### 3.1.2. Diagnostic Applications

**Nuclear Magnetic Resonance Imaging** The nucleus of an atom is built up of a number of protons and neutrons. Because the atomic particles are grouped in pairs that rotate in different directions, atoms with an even number of protons and neutrons display no external rotation. Nuclei in  $^1\text{H}$ ,  $^{19}\text{F}$ , or  $^{31}\text{P}$  display a weak external rotation or spin. Such nuclei also display a vibration effect or precession. Every object that can be made to vibrate will do so more strongly under the influence of a force applied at the same frequency as the natural resonant frequency of the object. A similar resonance effect occurs when atomic nuclei are subjected to electromagnetic waves at their own vibration frequency.

Among the substances in the human body that are important for nuclear magnetic resonance (NMR) image construction,  $^1\text{H}$ ,  $^{31}\text{P}$ , and  $^{23}\text{Na}$ , the first one ( $^1\text{H}$ ) gives by far the strongest signal, since it is present in almost all tissues and organs. When nuclei of elements with a weak external spin are placed in a strong homogeneous magnetic field, they align themselves with the direction of the field. When a force is applied to spinning atomic nuclei by a radio frequency (RF) at the so-called Larmor frequency, perpendicular to the direction of the magnetic field, the nuclei are tilted away from the aligned equilibrium direction and will perform a precession around the direction of the magnetic field. During this displacement from the equilibrium orientation the nuclei absorb energy. As soon as the RF or excitation is removed, the nuclei will reorient in the direction of the homogeneous field. The time constant describing the return movement of a group of nuclei to the field direction, or longitudinal direction, is known as the longitudinal or spin-lattice relaxation time,  $T_1$ . Since the local magnetic field strength is not homogeneous because of the presence of neighboring atoms, the nuclei precess at slightly different frequencies. As a result, the various nuclei fall out of phase with each other so that, although still rotating, they rapidly adopt different orientations in space; the resonance signals

emitted from the nuclei interfere with each other, resulting in a rapid decay of the received signal. The time constant describing this process is known as the spin-spin relaxation time or transverse relaxation time,  $T_2$ .  $T_1$  and  $T_2$  are dependent on temperature, magnetic field strength, and the chemical compound in which the atom is bound. In liquids, nuclei are relatively free, so that  $T_2$  is almost as long as  $T_1$ . In solids, the interaction between nuclei is much greater, so  $T_2$  is much shorter than  $T_1$ .

NMR imaging is essentially a form of emission tomography; the data required for the production of the image are generated from the electromagnetic signal originating within the body itself. The basis for this signal is, of course, the presence of protons; so the more protons there are in a particular volume, the larger the signal is. However, although proton density is important, it is the variation of signal strength due to the influence of relaxation times ( $T_1$  and  $T_2$ ) that makes proton imaging so flexible and attractive as a diagnostic imaging.

In the last decade the spatially resolved NMR, so-called NMR tomography, has become an important method in the field of biomedical and biophysical research [63]. The development of the NMR imaging technique as a clinical diagnostic modality has prompted the need for a new class of pharmaceuticals (magnetopharmaceuticals). These drugs must be administered to a patient to (1) enhance the image contrast between normal and diseased tissue and/or (2) indicate the status of organ functions or blood flow [64]. A number of different agents have been suggested as potential NMR contrast agents. Most contrast agents used in NMR imaging studies to date have been paramagnetic [65]. Superparamagnetic particles represent an alternative class of NMR contrast agents that are usually referred to as  $T_2$  or  $T_2^*$  contrast agents, as opposed to  $T_1$  agents such as paramagnetic chelates. Because of their large permanent dipole moments these agents are able to relax neighboring nuclei faster than paramagnetic ions. The contrast agents are useful in cases where differences between the  $T_1$  and  $T_2$  values of neighboring tissues are so small that they cannot be distinguished from the variations in these parameters.

The relaxation rate increase produced by magnetic particles is a contribution of several complex mechanisms. The size and the composition of these particles represent the essential parameters. The particles possess very large magnetic moments in the presence of a static magnetic field, and dipolar interactions between the superparamagnetic cores and surrounding solvent protons result in increases in both longitudinal and transverse relaxation rates, especially for small size domain particles (below 10 nm) [66–68].

Superparamagnetic particles have been used as contrast agents in NMR imaging for location and diagnosis of brain and cardiac infarcts, liver lesions, or tumors, where the magnetic nanoparticles tend to accumulate at higher levels because of the differences in tissue composition and/or endocytotic uptake processes [69]. Especially promising results have been detected in the improvement of the sensitivity of detection and delineation of pathological structures, such as primary and metastatic brain tumors, inflammation, and ischemia [70]. One of the potential applications of magnetic nanoparticles is to enhance the sensitivity to image

tissue microcirculation with the goal of direct quantitative measurement of blood flow and blood volume [71].

Lumirem (silica-coated iron oxide particles with a diameter of 300 nm) and Endorem (magnetite nanoparticles 150 nm in diameter, coated with dextran) are commercial names of superparamagnetic iron oxides (SPIOs) available on the market [72]. These nanoparticulate contrast agents are used, respectively, for gastrointestinal tract imaging and for liver and spleen disease detection. In the case of Endorem, the massive uptake of nanoparticles by Kupffer cells has led to an increase in the contrast between healthy and diseased tissue, like tumors or metastases, devoid of Kupffer cells [72].

Sinerem (magnetite nanoparticles 30 nm in diameter, coated with dextran) is an example of USPIO (ultrasmall superparamagnetic iron oxide) on the market [72]. Because of their long-circulating properties, USPIOs can be used for blood pool and tumor imaging (experimental imaging), based upon the detection and characterization of the lesions by their vascular appearance.

Sinerem has been used for lymphography of hyperplastic or metastatic (metastasis of a nickel-induced rhabdomyosarcoma) lymph nodes in rats, after intravenous administration [73]. Another USPIO device consisting of monocrystalline iron oxide nanoparticles (MION-46, a nanoparticulate contrast agent designed specially for lymphography, coated by an extended dextran layer, with a hydrodynamic diameter of 20 nm) was also tested in rats and rabbits to detect lymph node metastases (metastasis of VX2 carcinoma) and tumor-associated lymph node hyperplasia, by different administration routes (subcutaneous, intravenous, and intraarterial). [74] In both assays, hyperplastic lymph nodes showed NMR images consistent with active uptake and clustering of the nanoparticles inside the macrophages of lymphatic sinuses [74, 75]. The differentiation of malignant and normal lymph nodes was sometimes hindered by the following two problems: first, Sinerem nanoparticles showed a slight tumor accumulation, due to diffusive extravasation across the tumoral hyperpermeable vasculature [75]. This effect was so pronounced that in some extreme cases, the tumors could not be differentiated from the healthy lymphatics, as they both take up (even though by different mechanisms) the contrast agent. Second, when the MION-46 formulation was used, there was a lack of contrast agent accumulation in marginal follicles of normal lymph nodes, which, on occasion, rendered them indistinguishable from nodes with micrometastases [74]. Despite these two problems, which should be kept in mind during diagnosis, USPIOs appear to be very efficient tools for NMR imaging.

## 3.2. *In vitro* Applications

### 3.2.1. Diagnostic Applications

**Separation and Selection** Analysis of biologically active compounds or xenobiotics often requires preconcentration of the substance from large volumes of solutions and/or suspensions. This process is often accompanied by partial purification of the substance to be analyzed [76]. Sample preparation is often the most time-consuming step in chemical analysis, accounting on average for 61% of the time

typically required to perform analytical tasks [77]. Sample preparation is also a source of much imprecision and inaccuracy of the overall analysis [78].

At present, considerable attention is being paid to solid-phase extraction (SPE) as a way to isolate and preconcentrate desired components from a sample matrix. SPE offers an excellent alternative to conventional sample preparation methods, such as liquid-liquid extraction (LLE) [78]. The separation and preconcentration of the substance to be analyzed from large volumes of solution can take a lot of time by standard column SPE, and it is in this field that the method using magnetic or magnetizable adsorbents, called magnetic solid-phase extraction (MSPE), gains importance. In this procedure a magnetic adsorbent is added to a solution or suspension containing the target. This is adsorbed to the magnetic adsorbent, and then the adsorbent with the adsorbed target is recovered from the suspension with an appropriate magnetic separator [76].

In protein purification the protein can be precipitated via cross-linked antibodies to a suitable magnetic bead [79, 80] or other particle, which can then be detached from the protein-linked magnetic particle complex by, for instance, changing the pH of the medium [81]. Magnetic nanoparticles coated with dextran are also used for the fractionation of biomolecule (enzyme) systems, for analytical as well as for large-scale purification. These materials increase the kinetics of the process by a factor ranging from 35 to more than 70 [82]. In microbiology, several reports have described the use of magnetic nanocrystals for the separation and accumulation of bacterial and cell suspension of *Mycobacterium tuberculosis* [83], the identification of which in diagnostic specimens (sputum, urine) is the most reliable evidence of the active tuberculosis process.

Effective cell separation is a primary and most important step in many clinical and immunological applications [84, 85]. One of these applications is the separation of red blood cells (RBCs) from whole blood for photopheresis treatment of white cells. In the photopheresis treatment of white blood cells, light is used to activate a compound that binds to the DNA and may cause an increase in immunogeneity and thus stimulate the patient's own immune system [86]. Haik et al. [87] developed a magnetic separation device to isolate the RBCs from whole blood while the photopheresis treatment is administered to the patient's leukocytes.

Most of the tumor diseases and mortality of tumor patients are caused by epithelial tumors. The highest risk for patients is the spread of disseminated tumor cells after resection of the solid tumor [88]. Therefore, it is important to detect these disseminated cells. In the case of a minimal residual tumor disease the determination of the number of circulating tumor cells is of great importance. This and the possibility of characterizing these isolated cells would be an important step in the development of an optimized individual therapy. Conventional histopathological methods are not sensitive enough to detect the small number of circulating tumor cells in peripheral blood [89]. This is a reason why in the last few years cell isolation systems based on magnetic nanocrystals encapsulated in microspheres (e.g., Dynal A.S.) have become increasingly important for research and diagnostics [88].

**Magnetorelaxometry** Recently, magnetorelaxometry was introduced as a method for the evaluation of immunoassays [90]. Magnetorelaxometry measures the magnetic viscosity, that is, the relaxation of the net magnetic moment of a system of magnetic nanoparticles after the removal of a magnetic field [91]. There are two different relaxation mechanisms. First, the internal magnetization vector of a nanoparticle relaxes in the direction of the easy axis inside the core; this is called Néel relaxation [92]. The time constant of this process is

$$\tau_{\text{Néel}} = \tau_0 \exp(KV_{\text{core}}/k_B T)$$

where  $\tau_0$  is usually approximated as  $10^{-9}$  s. The Néel relaxation time depends exponentially on the energy barrier yielded by the product of the core volume  $V_{\text{core}}$  and the magnetic anisotropy constant  $K$ . In real systems of magnetic nanoparticles, the common distribution of the core volume and anisotropy constant leads, by the Néel mechanism, to a modified logarithmic decrease in magnetization as a function of time [93].

Second, particles accomplish rotational diffusion in a carrier liquid, called Brownian relaxation [94]. The corresponding relaxation time is often calculated according to [95]

$$\tau_{\text{Brown}} = 4\pi r^3 \eta / k_B T$$

assuming noninteracting spherical particles with a hydrodynamic radius  $r$ , where  $\eta$  is the dynamic viscosity of the carrier liquid. For an ideal system of monodispersed particles, the time dependence of the Brownian relaxation is a single-exponential decay. For polydisperse nanoparticles with different particle sizes it can be described as a superposition of exponential decays. This relaxation signal still looks like an exponential decay. Therefore, Néel and Brownian relaxation can be distinguished by their different time dependences [96]. Furthermore, Brownian relaxation can take place only in liquids, whereas Néel relaxation does not depend on the state of the nanoparticles.

The fact that magnetorelaxometry depends on the core size, the hydrodynamic size, and the anisotropy allows this technique to distinguish between free and bound conjugates by their different magnetic behaviors and therefore can be used as an analytical tool for the evaluation of immunoassays [91].

## 4. NANOMAGNET PRODUCTION

Biomedical applications impose strict requirements on the particles' physical, chemical, and pharmacological properties, including chemical composition, granulometric uniformity, crystal structure, stability of magnetic properties, surface structure, adsorption properties, solubility, and low own toxicity [97–103]. For example, for magnetic drug targeting to be safe and effective (with the least amount of magnetic particles a maximum of drug should be easily administered and transported to the site of choice), the following parameters of the nanomagnets are critical: (a) particle size (small as possible to improve tissular diffusion, with long sedimentation times and high effective surface areas), (b) surface characteristics (easy encapsulation of the

magnetic nanoparticles protects them from degradation and endows them with biocompatibility), and (c) good magnetic response (possibility of decreasing the nanomagnet concentration in the blood and therefore diminishing the associated side effects). On the other hand, magnetically active particles applicable in separation processes (*in vitro* applications) should be stable units composed of a high concentration of superparamagnetic nanoparticles, with each of the larger entities monodisperse in size and uniform in magnetic particle concentration.

The major difficulty in the synthesis of ultrafine particles is to control the particle size at the nanometric scale. This difficulty arises as a result of the high surface energy in these ultradivided systems. The interfacial tension acts as the driving force for spontaneously reducing the surface area by growth during the initial steps of the precipitation (nucleation and growth) and during aging (Ostwald ripening) [104, 105]. Therefore, the search for facile and flexible synthetic routes able to produce magnetic nanoparticles with the desired size and acceptable size distribution without particle aggregation is of extreme importance to realizing the full potential of these materials in biomedicine.

### 4.1. Synthetic Routes for the Production of Nanomagnets

#### 4.1.1. Coprecipitation

By far the method most employed for the synthesis of magnetic nanoparticles is the Massart method [106, 107]. It essentially consists of the coprecipitation of deaerated aqueous solutions containing iron (II) and iron (III) cations by the addition of a base. Changing the amount or nature of either the iron salt or the base added leads to solids containing magnetic nanoparticles of different sizes and degrees of polydispersity [108].

Modifications of this method are mainly in the direction of the synthesis in the presence of dextran or any other substance that renders the magnetic nanoparticles biocompatible [109]. For example, nanoparticulate magnetic particles are obtained by transferring an acidic iron (II)/iron (III) salt solution into iron (II,III) carbonate by adding equivalent amounts of alkaline carbonate, followed by thermal oxidation to iron (II,III) hydroxide [110]. The size of the particles can be controlled by the thermal reaction velocity and concentration of the iron salts. Thus, small diameters of 20–100 nm can be reached by timely separated building of iron (II,III) carbonate at temperatures of 5–10 °C and subsequent heating. After surplus salts have been removed, the particles can be stabilized with water-soluble polysaccharide or synthetic polymer derivatives. Nanoparticles coated with a starch derivative have a molecular mass of 10 kDa. As a result of the starch matrix, the magnetic particles can retain their dispersion stability in the pH range of 3–12 and in high salt concentrations [111].

#### 4.1.2. Microemulsions

Organized surfactant assemblies such as microemulsions, micelles, hexagonal phases, cubic phases, monolayers, and vesicles are unique reaction media. Indeed, they can solubilize, concentrate, localize, and even organize the reactants. Many naturally occurring biological reactions such as



photosynthesis [112] take place in organized media, and the self-organization obtained with surfactants in solution has opened a systematic exploration of their use to control chemical reactions [113]. Among all of these methods, water-in-oil microemulsions (also called reverse micelles) have recently been shown to be an adequate and simple method of preparing nanosized particles [114–119].

A microemulsion may be defined as a thermodynamically stable isotropic dispersion of two immiscible liquids consisting of nanosized domains of one or both liquids in the other, stabilized by an interfacial film of surface active molecules [115]. Microemulsions may be classified as water-in-oil (w/o) or oil-in-water (o/w), depending on the dispersed and continuous phases. The surfactant-stabilized microcavities (typically in the range of 10 nm) provide a confinement effect that limits particle nucleation, growth, and agglomeration [120].

In w/o microemulsions, the aqueous droplets continuously collide, coalesce, and break apart, resulting in a continuous exchange of solute content [115]. The collision process depends upon the diffusion of the aqueous droplets in the continuous medium (the oil), while the exchange process depends on the attractive interaction between the surfactant tails and the rigidity of the interface, as the aqueous droplets approach each other. The basics of nanoparticle formation can be summarized as follows: if we take two identical w/o microemulsions and dissolve two reactants in each of the respective aqueous phases, upon mixing, because of collision and coalescence of the droplets, the reactants come in contact with each other and form a precipitate. This precipitate is confined to the interior of the microemulsion droplets, and the size and shape of the particle reflect the interior of the droplet.

Magnetite nanoparticles around 4 nm in diameter were prepared by controlled hydrolysis with ammonium hydroxide of  $\text{FeCl}_2$  and  $\text{FeCl}_3$  aqueous solutions within reverse micelle nanocavities generated with the anionic surfactant AOT (sodium bis(2-ethylhexyl)sulfosuccinate) and heptane as the continuous oil phase [121]. Superparamagnetic maghemite nanoparticles have also been prepared by the controlled hydrolysis of  $\text{FeSO}_4$  with tetraethylamine (TEA) within the aqueous pools of the microemulsions [115]. To do this, a microemulsion containing a 0.15 M solution of  $\text{FeSO}_4$  was mixed with a 2 M solution of TEA in octane. Diffusion of TEA through the surfactant monolayer into the aqueous droplets resulted in the hydrolysis of  $\text{Fe}^{2+}$  ions. A second microemulsion, containing sodium nitrite as the dispersed aqueous phase, was added to this suspension, and then the system was kept at 45 °C for 1 h under constant stirring.

Pileni and co-workers prepared nanosized magnetic particles with average sizes from 3.7 to 11.6 nm and a standard deviation ranging from 0.22 to 0.34, also by using microemulsions [122]. A ferrous dodecyl sulfate,  $\text{Fe}(\text{DS})_2$ , micellar solution was used to make nanosized magnetic particles, the size of which is controlled by the surfactant concentration and by temperature. In contrast to what is obtained in a homogeneous solution, iron ferrite particles can be obtained when the synthesis is performed at very low reactant concentrations and room temperature. Furthermore, nanoparticles are obtained when the syntheses are performed with iron (II) as the reactant, whereas in a

homogeneous solution particles in the micrometric range are formed.

The work of Carpenter's group, which prepared metallic iron particles coated by a thin layer of gold by microemulsions [123], deserves special mention. The gold shell protects the iron core against oxidation and provides functionality, making these composites potentially adequate for their use in biomedical applications. The reverse micelle reaction is carried out with cetyltrimethylammonium bromide (CTAB) as the surfactant, octane as the oil phase, and aqueous reactants as the water phase [124]. Varying the water-to-surfactant ratio can cause the formation of micelles ranging in size from 5 to 30 nm, thus leading to careful control over the particle size. A cosurfactant of *n*-butanol is used to help decrease the fraction of the micellar head group that is neutralized and thereby increase the stability of the micelle [125]. Without the addition of the cosurfactant, the amount of free water available to carry on the reactions is greatly reduced, as most of the water is bound in the head group of the CTAB [126].

The metal particles are formed inside the reverse micelle by the reduction of a metal salt with the use of sodium borohydride. The sequential synthesis offered by reverse micelles is utilized to first prepare an iron core by the reduction of ferrous sulfate by sodium borohydride. After the reaction has been allowed to go to completion, the micelles within the reaction mixture are expanded to accommodate the shell, with the use of a larger micelle containing additional sodium borohydride. The shell is formed with the use of an aqueous hydrogen tetrachloroaurate solution. The particles are then washed, collected in a magnetic field, and dried under vacuum.

#### 4.1.3. Bionanoreactors

Nature has developed a variety of protein components that function as carriers or storage devices for metal components. Of these systems, the iron-storage protein ferritin is probably the most intensively studied and best understood [127]. Ferritin consists of a central core of hydrated iron (III) oxide encapsulated by a multisubunit protein shell. During formation, the protein shell self-assembles in the first step to form a hollow cage about 8 nm in diameter. As a consequence, subsequent inorganic mineralization leads to spatially confined nanoparticles of an antiferromagnetic iron oxide similar to the mineral ferrihydrite [128]. Mann and co-workers began to explore the use of ferritin as a nanometer-sized bioreactor for producing metal particles other than the natural ferrihydrite. Horse spleen apoferritin was used as a nanometer-sized reaction vessel to generate manganese oxide and uranyl oxyhydroxide crystals [129]. Later work concerned the production of magnetic proteins by reconstituting apoferritin with the ferrimagnetic minerals magnetite [130] and magnetite/maghemite [131]. As a result of the inner diameter of the nanoreactors, crystalline inorganic particles with a diameter of about 6–7 nm were formed, as determined by transmission electron microscopy. The magnetite/maghemite particles were generated by oxidation of apoferritin with trimethylamino-*N*-oxide, which was loaded with various amounts of iron (II) ions. The magnetic properties were studied by SQUID magnetometry, and

an approximately linear dependence of the superparamagnetic blocking temperature on iron loading was found [130].

#### 4.1.4. Nonhydrolytic Synthetic Methods

Alivisatos and co-workers [132] have demonstrated that injecting solutions of  $\text{FeCup}_3$  (Cup: *N*-nitrosophenylhydroxylamine) in octylamine into long-chain amines at 250–300 °C yields nanocrystals of maghemite. These nanocrystals range from 4 to 10 nm in diameter, are crystalline, and are dispersible in organic solvents. Hyeon and co-workers [133] have also been able to prepare monodisperse maghemite nanoparticles by a nonhydrolytic synthetic method (Fig. 3). For example, to prepare maghemite nanoparticles of 13 nm,  $\text{Fe}(\text{CO})_5$  (0.2 ml, 1.52 mmol) was injected into a solution containing 0.91 g of lauric acid (4.56 mmol), 7 ml of octyl ether, and 0.57 g of  $(\text{CH}_3)_3\text{NO}$  (7.60 mmol) at 100 °C in an argon atmosphere, with vigorous stirring. As soon as  $\text{Fe}(\text{CO})_5$  was injected into the mixture, the temperature rose to 120 °C and the solution became dark red, which indicated the successful oxidation of  $\text{Fe}(\text{CO})_5$ . The reaction mixture was then stirred for 1 h at 120 °C, and the solution was slowly heated to reflux. The solution color gradually became black, indicating that nanoparticles were being formed. After refluxing for 1 h, the solution was cooled to room temperature, and a black precipitate was obtained with the addition of excess ethanol and centrifuging. The precipitate can easily be redispersed in octane or toluene.

Very recently, Shen and Zeng [134] have been able to prepare monodisperse magnetite nanoparticles with sizes from 3 to 20 nm by the high-temperature (265 °C) reaction of iron (III) acetylacetonate in phenyl ether in the presence of alcohol, oleic acid, and oleylamine. In particular, magnetite nanoparticles of about 3 nm were obtained by the thermal

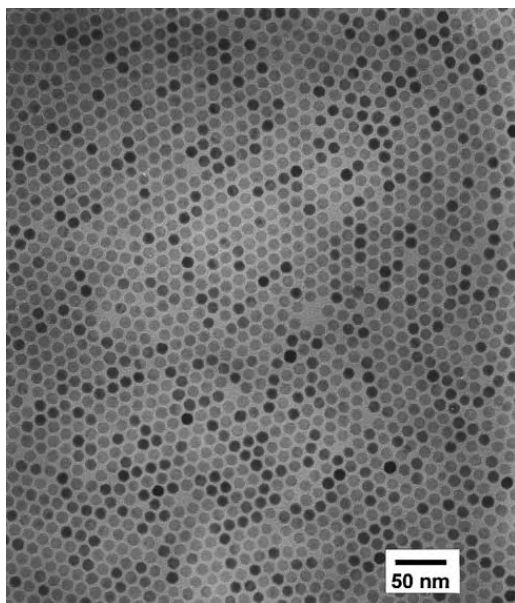


**Figure 3.** TEM image of monodisperse 11-nm  $\gamma\text{-Fe}_2\text{O}_3$  nanocrystallites prepared by thermal decomposition of  $\text{Fe}(\text{CO})_5$ . Reprinted with permission from [133], T. Hyeon et al., *J. Am. Chem. Soc.* 123, 12798 (2001). © 2001, American Chemical Society.

decomposition of the iron precursor, but to obtain diameters up to 20 nm a seed-mediated growth method using 4-nm-diameter magnetite particles was needed.

#### 4.1.5. Other Synthetic Routes

Dendritic macromolecules, or dendrimers, are synthetic three-dimensional macromolecules that are prepared in a stepwise fashion from simple branched monomer units, the nature and functionality of which can be easily controlled and varied. Their unique architecture and monodisperse structure have been shown to result in numerous previously unknown or significantly improved physical and chemical properties when compared with traditional linear polymers. As a consequence, dendrimers are now considered to be one of the prime nanometer-scale building blocks for the construction of nanoscale objects, molecular devices and molecular “machines,” advanced drug-delivery systems, etc [135–139].

Recently, iron ferrite nanoparticles have been prepared with dendrimers as templating hosts [140]. Carboxylated poly(amidoamine) PAMAM dendrimers (generation 4.5) were utilized for the synthesis and stabilization of ferrimagnetic iron oxide nanoparticles. Oxidation of Fe(II) at slightly elevated pH and temperature resulted in the formation of highly soluble nanocomposites of iron oxides and dendrimer, which are stable under a wide range of temperatures and pH. Size exclusion chromatography indicated aggregates in the nanometer size regime, consistent with the oligomeric nature of the composite material. Transmission electron microscopy revealed small assemblies of mineral cores with electron diffraction and high-resolution transmission electron microscopy data indicative of the mineral maghemite. SQUID magnetometry demonstrated that this crystalline composition exhibited superparamagnetism at room temperature. NMR relaxation studies of solvent (water) protons revealed unusually high  $T_1$  and  $T_2$  relaxivities, which make these materials excellent candidates as contrast agents for NMR imaging.

Rajamathi et al. [141] have reported very recently the synthesis of magnetic nanoparticles by the reaction of  $\text{FeCl}_3$  in propylene glycol under reflux. Maghemite nanoparticles were prepared under reflux in 50 cm<sup>3</sup> of 1,2-propanediol, starting with 4.0 g (0.015 moles) of  $\text{FeCl}_3 \cdot 6\text{H}_2\text{O}$ , 3.7 g (0.045 mol) of sodium acetate as the hydrolyzing agent, 3 cm<sup>3</sup> of water, and 5.5 cm<sup>3</sup> of the capping agent *n*-octylamine. Reflux was carried out in a 250 cm<sup>3</sup> round-bottomed flask that was fitted with a water condenser held at 283 K. After refluxing for 5 h, the material was precipitated with the help of a permanent magnet and the addition of a large volume (approximately threefold excess) of 2-propanol. The material was washed with ether to remove excess amine and glycol and then dried in air at 50 °C to obtain the crude product.

Electrochemical methods have also been used for the production of maghemite nanoparticles [142]. The electrochemical synthesis of nanoparticles of  $\gamma\text{-Fe}_2\text{O}_3$  was performed in an organic medium. The size was directly controlled by the imposed current density, and the resulting particles were stabilized as a colloidal suspension with the use of cationic surfactants. The size distributions of the particles were narrow, with the average sizes varying from 3 to 8 nm. <sup>57</sup>Fe

Mössbauer spectroscopy and magnetization measurements indicated that the dry powders exhibit superparamagnetic behavior at room temperature.

A number of other techniques have been developed to synthesize magnetic nanoparticles. Some of these are inert gas condensation [143], mechanical attrition [144], solvated-metal-atom dispersion [145], laser pyrolysis [146], and aerosol pyrolysis [147].

#### 4.1.6. Size Selection Methods

Biomedical applications like magnetic resonance imaging, magnetic cell separation, or magnetorelaxometry utilize magnetic properties of the nanoparticles in magnetic fluids such as their magnetic moment. Furthermore, these applications also depend on the hydrodynamic size. All of the parameters mentioned exhibit a broad distribution in common magnetic fluids. Therefore, in many cases only a small portion of particles contribute to the desired effect. The relative amount of the particles with the desired properties can be increased by the fractionation of magnetic fluids [91, 148].

Common methods currently used for the fractionation of magnetic fluids are centrifugation [149] and size-exclusion chromatography [150, 151]. Centrifugation separates on the basis of the particle size and density difference between the liquid and solid phases. Sedimentation of material in a centrifugal field may be described by

$$v = d^2(\rho_s - \rho_l)\omega^2 r F_s / 18\eta\theta$$

where  $v$  is the rate of sedimentation,  $d$  is the particle diameter,  $\rho_s$  is the particle density,  $\rho_l$  is the solution density,  $\omega$  is the angular velocity in radians  $s^{-1}$ ,  $r$  is the radius of rotation,  $\eta$  is the kinematic viscosity,  $F_s$  is a correction factor for particle interaction during hindered settling, and  $\theta$  is a shape factor ( $=1$  for spherical particles).  $F_s$  depends on the volume fraction of the solids present, approximately equaling 1, 0.5, 0.1, and 0.05 for 1%, 3%, 12%, and 20% solid volume fraction, respectively.

Size-exclusion chromatography (SEC), also called gel-filtration or gel-permeation chromatography (GPC), uses porous particles to separate molecules or particles of different sizes. It is generally used to separate biological molecules and to determine molecular weights and molecular weight distributions of polymers. Molecules that are smaller than the pore size can enter the particles and therefore have a longer path and longer transit time than larger molecules that cannot enter the particles. Nunes and Yu [150] were able to prepare seven different magnetic fractions (sizes between 7 and 17 nm), starting from a commercial ferrofluid EMG805 from Ferrofluids Corporation, by using size-exclusion chromatography. To do this, the authors placed 1  $cm^3$  of this fluid at the top of a 50-cm Sepharose Cl-4B200 column eluted with distilled water to which a small Dowdite-1 (*O*-phenylphenol) had been added to retard spilage. The elution rate was approximately 0.5  $ml \cdot min^{-1}$ . All of these methods separate in accordance with nonmagnetic properties like density or size.

Massart and co-workers have proposed an original size-sorting procedure based on the thermodynamic properties of aqueous dispersions of nanoparticles [152]. The

positive charges of the maghemite surface allow their dispersion in aqueous acidic solutions and make it possible to obtain dispersions stabilized through electrostatic repulsions. With increasing acid concentration (in the range of 0.1 to 0.5  $mol \cdot liter^{-1}$ ), the interparticle repulsions are screened and phase transitions are induced. Using this phenomenon, these authors describe a two-step size-sorting process, to get significant amounts of nanometric monosized particles (with typical diameters monitored between 6 and 13 nm). As the surface of the latter is not modified by the size-sorting process, common procedures are used to disperse them in several aqueous or oily media.

Preference should be given, however, to partitions based on the properties of interest, in this case the magnetic properties. So far, magnetic methods have been used only for the separation of magnetic fluids, for example, to remove aggregates (magnetic filtration) [153], weakly magnetic or nonmagnetic materials like synthesis by-products [154], or unlabeled material on the basis of magnetic labeling [155]. Recently, the fractionation of magnetic nanoparticles by flow field-flow fractionation was reported [156]. Field-flow fractionation is a family of analytical separation techniques [157]. The separation is carried out in a flow with a parabolic profile running through a thin channel. An external field is applied at a right angle to force the particles toward the so-called accumulation wall. In flow field-flow fractionation the external field is generated by a secondary transverse flow, the so-called cross-flow [148].

## 4.2. Synthetic Routes for the Production of Superparamagnetic Composites

The main problem when dealing with magnetic fluids is the presence of anisotropic magnetic dipolar attraction [158], which renders the suspensions unstable, even in the absence of an external magnetic field. Strategies for preventing this attraction are mainly based on the coating of magnetic particles in such a way that, in a zero magnetic field, magnetic fluids behave as an isotropic magnetic dispersion, whereas in the presence of an external magnetic field the particles reversibly form anisotropic structures [159].

For separation processes (*in vitro* applications) the size restrictions are not as severe (particles below the micrometer size can be used) as in *in vivo* applications (as mentioned above, the smaller the size the better the tissular diffusion). Therefore the microstructure for *in vitro* applications could consist of superparamagnetic nanocrystals dispersed in sub-micrometer diamagnetic particles that are expected to have long sedimentation times in the absence of a magnetic field (screening of the anisotropic magnetic dipolar attraction). Moreover, by the adequate selection of the diamagnetic matrixes, the superparamagnetic composite could be provided with functionality and biocompatibility. For example, superparamagnetic polysaccharide nanoparticles with a size range below 300 nm have some advantages over synthetic magnetic microparticles for applications in biomedicine, diagnostics, and molecular biology. They are biocompatible and nontoxic and have higher effective surface areas and lower sedimentation rates. The hydrophilic surface of polysaccharide particles decreases nonspecific adsorption processes for proteins and antibodies [160].

### 4.2.1. Deposition of Nanomagnets on Colloidal Templates

One of the most promising techniques for the production of superparamagnetic composites is the layer-by-layer (LBL) self-assembly method. This method was first developed for the construction of ultrathin films [161, 162]. It consists of the stepwise adsorption of charged polymers or nanocolloids and oppositely charged polyelectrolytes to flat surfaces, exploiting primarily electrostatic interactions for layer buildup. Notably, it allows the controlled formation of multilayers of various materials (and combinations thereof) on selected substrates in a straightforward and versatile manner and uniquely permits nanoscale control over the multilayer thickness.

Caruso, Möhwald, and co-workers have used the LBL method for the controlled synthesis of novel nanocomposite core-shell materials and hollow capsules [163, 164]. The significant modification is that they use colloidal templates instead of flat surfaces (Fig. 4). With this strategy, colloidal particles have been coated with alternating layers of polyelectrolytes [165, 166], nanoparticles [163, 167–169], and proteins [170]. Furthermore, the same authors have demonstrated that submicrometer-sized hollow silica spheres [163] or polymer capsules [166] could be obtained after removal of the template from solid-core multilayered-shell particles either by calcination or by chemical extraction.

Using this approach, these authors have been able to produce monodisperse magnetic dense and hollow spheres [171, 172] that in principle could be used in biomedical applications. For the preparation of superparamagnetic dense polystyrene spherical particles, magnetite nanoparticles with an average diameter of 10–15 nm were alternately deposited with either poly(diallyldimethylammonium chloride) (PDADMAC) or poly(allylamine hydrochloride) (PAH) on 640-nm diameter PS lattices. Multilayer shells of  $\text{Fe}_3\text{O}_4$  and polyelectrolyte (PDADMAC or PAH) were prepared on PS lattices precoated with a precursor three-layer polyelectrolyte film: the outermost layer was PDADMAC or PAH, therefore providing a positively charged surface for  $\text{Fe}_3\text{O}_4$  deposition. Alternate depositions of  $\text{Fe}_3\text{O}_4$  and PAH or PDADMAC on precoated PS lattices, under conditions where the nanoparticles and polyelectrolyte are oppositely charged (pH  $\sim$  5–6), produce magnetic nanoparticle/polyelectrolyte multilayer shells. Qualitative proof of multilayer magnetic shell buildup was obtained from electrophoretic mobility measurements: the zeta potential of the coated particles alternates in magnitude from +25 mV when the polycation is the outermost layer to +5 mV when  $\text{Fe}_3\text{O}_4$  is the outer layer. Formation of the magnetite shell

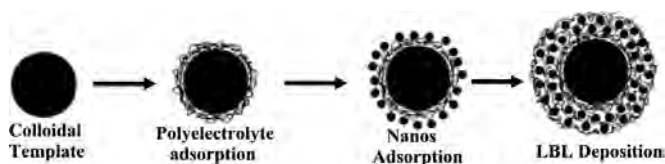


**Figure 4.** Schematic illustration of the layer-by-layer electrostatic assembly of nanoparticles on spherical colloidal templates (nanoparticles are adsorbed to the polyelectrolyte because of their opposite charge density).

covering the PS core can be directly visualized by transmission electron microscopy (TEM). A similar methodology was used for the production of hollow spheres, though in this case once the deposition process was finished, the polystyrene template was removed by heating at 500 °C. It is interesting that the researchers prepared hollow spheres with the inner and outermost layers composed of silica, which render these particles particularly useful for separation applications.

Inorganic and hybrid coating (or shells) on colloidal templates have also been commonly prepared by precipitation and surface reactions [173–178]. By the adequate selection of experimental conditions (mainly the nature of the precursors, temperature, and pH) this method can be used to create uniform and smooth coatings and therefore monodisperse spherical composites. With this technique sub-micrometer-sized anionic polystyrene lattices have been coated with uniform layers of iron compounds by aging, at elevated temperature, dispersions of the polymer colloid in the presence of aqueous solutions of ferric chloride, urea, hydrochloric acid, and polyvinylpyrrolidone (Fig. 5). The thickness of the deposited layers could be altered by suitable adjustment of the reactant concentrations, and they could also be increased by further aging of the coated particles in the presence of aqueous solutions of ferric chloride. Hollow colloidal spheres of iron compounds were obtained by calcinations of the polystyrene matrix at elevated temperature in air. Different chemical compositions of hollow colloidal spheres were obtained by heating them in hydrogen [179–180].

### 4.2.2. Polymer Encapsulation of Nanomagnets

Encapsulation of inorganic pigments in organic polymers endows pigments with important properties that bare pigments lack. Polymer coatings on pigments enhance

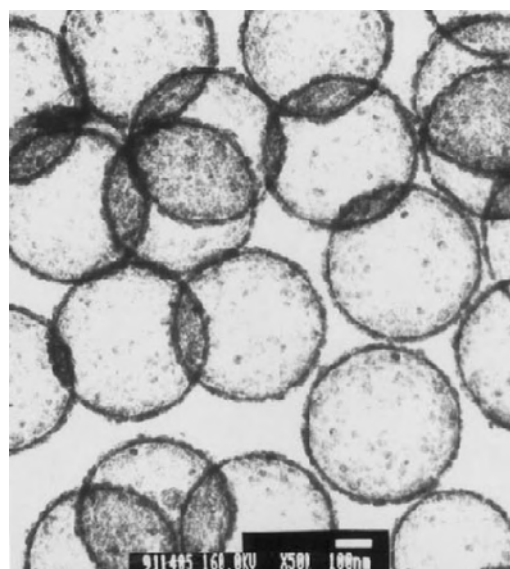


**Figure 5.** TEM micrographs of hollow iron oxide particles. Adapted with permission from [180], H. Shiho and K. Kawahashi, *J. Colloid Interface Sci.* 226, 91 (2000). © 2000, Academic Press.

compatibility with organic ingredients, reduce susceptibility to leaching, and protect pigment surfaces from oxidation. Consequently, encapsulation improves dispersibility, improves chemical stability, and reduces toxicity. Therefore it is not surprising that there is great interest in polymer-coated pigments for the preparation of paint, ink, pharmaceutical, and cosmetic formulations [181]. Rather than depositing magnetic particles on the surface of latex particles, uniformly dispersing the magnetic nanoparticles throughout the entire ensemble of latex particles should theoretically allow higher concentrations of nanoparticles per latex particle.

Polymer-coated magnetite nanoparticles were synthesized by seed precipitation polymerization of methacrylic acid and hydroxyethyl methacrylate in the presence of magnetite nanoparticles [182]. Cross-linking of polymers has also been reported to be an adequate method for the encapsulation of magnetic nanoparticles. To prepare composites by this method, mechanical energy must first be supplied to create a dispersion of magnetite in the presence of aqueous albumin [183], chitosan [184], or polyvinylalcohol [185] polymers. More energy creates an emulsion of the magnetic particle sol in cottonseed [183], mineral [184], or vegetable oil [185]. Depending upon the composition and reaction conditions, the addition of a cross-linker and heat results in magnetic latex, 0.3 to 30 micrometers in average diameter, polydisperse in size, with up to 24 wt% magnetite content [183]. Superparamagnetic, monodisperse (~135 nm), and charged polystyrene spheres (17.1 wt% iron oxide content) have also been synthesized by emulsion polymerization of styrene, methyl methacrylate, and sodium styrene sulfonate in the presence of iron oxide nanoparticles with a surface modified with oleic acid [186]. The reaction temperature was set to 70 °C, and ammonium persulfate was added to initiate the polymerization.

Recently the preparation of superparamagnetic latex via inverse emulsion polymerization has been reported [33]. The structure-directing nature of block copolymers, combined with the “mini-emulsion” polymerization process, facilitate the synthesis of superparamagnetic latex loaded with nanometric magnetic iron oxide. A “double-hydrophilic” diblock copolymer (polyethylene oxide block-co-polymethacrylic acid), present during the precipitation of magnetic iron oxide, directs nucleation, controls growth, and sterically stabilizes the resulting 5 nm of superparamagnetic iron oxide. After drying, the coated particles spontaneously reprecipitate into a mixture of hydroxyethylmethacrylate and methacrylic acid monomers, creating a ferrofluid-like dispersion. Inverse emulsification of the ferrofluid (magnetic particles plus monomer) into decane, aided by small amounts of diblock copolymer emulsifier along with ultrasonication, creates minidroplets (180 nm) filled with magnetic particles and monomer. Subsequent polymerization generates magnetic latex.

A novel approach to preparing magnetic polymeric nanoparticles by synthesis of the magnetite core and polymeric shell in a single inverse microemulsion was reported by Chu and co-workers [187]. Stable colloid dispersions of magnetic nanoparticles with a narrow size distribution were thus produced. The microemulsion seed copolymerization of methacrylic acid, hydroxyethyl methacrylate,

and cross-linker resulted in a stable hydrophilic polymeric shell of nanoparticles. The preparation of the nanoparticles was also carried out by the two-stage microemulsion process and seed precipitation polymerization. The particle size was varied in the range of 80–320 nm by changing the monomer concentration and water/surfactant ratio. The magnetic properties and the size distribution of the nanoparticles synthesized by these three methods were compared. The polymeric nanoparticles synthesized in a single microemulsion have superparamagnetic properties and the narrowest size distribution.

#### 4.2.3. Inorganic Encapsulation of Nanomagnets

An appropriate tuning of the magnetic properties is essential for the potential use of the superparamagnetic composites. In this way, the use of inorganic matrixes and, in particular of silica, as dispersion media of superparamagnetic nanocrystals has been reported to be an effective way to modulate magnetic properties by a simple heating process [188–190].

Another advantage of having a surface enriched in silica that is especially appropriate for separation applications is the presence of surface silanol groups that can easily react with alcohols and silane coupling agents [191], not only to produce dispersions that are stable in nonaqueous solvents, but also to provide the ideal anchorage for the covalent binding of specific ligands. The strong binding makes desorption of these ligands a difficult task. In addition, the silica surface confers high stability on suspensions of particles at high volume fractions, during changes in pH, or at high electrolyte concentration [192].

For separation applications a high loading of magnetic material is essential to generate the response of the material to a magnetic field gradient, precluding the use of some methods described earlier [193]. By combining the Lorentz equation for the force on a magnetic particle of radius  $R$  with the Stokes law for viscous drag for spheres, the sedimentation velocity,  $V$ , of a ferrofluid particle in a magnetic field gradient  $\nabla H$  is given by [194]

$$V = 2\mu_0 M_S R^2 \nabla H / 9\eta$$

where  $\mu_0$ ,  $M_S$ , and  $\eta$  are the permeability of vacuum, magnetic saturation, and viscosity, respectively. From the equation we can infer that the highest  $M_S$  (i.e., the highest the amount of magnetic material) generates the fastest sedimentation velocity,  $V$ .

Very recently, our group has been successful in preparing submicronic silica-coated magnetic hollow and dense spheres [195–196] by aerosol pyrolysis. The thermal decomposition of liquid aerosols (aerosol pyrolysis) represents a convenient procedure for obtaining finely dispersed particles of predictable shape, size, and variable composition. The resulting powders generally consist of spherical particles, the final diameter of which can be predetermined from that of the original droplets. The method offers certain advantages over other, more commonly used techniques (such as precipitation from homogeneous solution), as it is simple, rapid, and continuous [197].

Silica-coated  $\gamma$ -Fe<sub>2</sub>O<sub>3</sub> hollow spherical particles with an average size of 150 nm (Fig. 6) were prepared by the aerosol pyrolysis of methanol solutions containing iron ammonium citrate and tetraethoxysilane (TEOS) at a total salt concentration of 0.25 M [195]. An illustration of the possible formation mechanism of the silica-coated magnetic hollow spheres is shown in Figure 7. During the first stage the rapid evaporation of the methanol solvent favors the surface precipitation (i.e., formation of hollow spheres) of components [197]. The low solubility of the iron ammonium citrate in methanol when compared with that of TEOS promotes the initial precipitation of the iron salt solid shell. During the second stage the probable continuous shrinkage of this iron salt solid shell facilitates the enrichment at the surface of the silicon oxide precursor (TEOS). In the third stage, the thermal decomposition of precursors produces the silica-coated  $\gamma$ -Fe<sub>2</sub>O<sub>3</sub> hollow spheres. The formation of the  $\gamma$ -Fe<sub>2</sub>O<sub>3</sub> is associated with the presence of carbonaceous species coming from the methanol solvent and from the iron ammonium citrate and TEOS.

On the other hand, the aerosol pyrolysis of iron nitrate and TEOS at a total salt concentration of 1 M produced silica-coated dense  $\gamma$ -Fe<sub>2</sub>O<sub>3</sub> spherical particles of an average size of 250 nm (Fig. 8). The increase in salt concentration to a value of 1 M favored the formation of dense spherical particles instead of hollow ones.

A water-in-oil microemulsion method has also been applied for the preparation of silica-coated iron oxide nanoparticles [198]. Three different nonionic surfactants (Triton X-100, Igepal CO-520, and Brij-97) have been used for the preparation of microemulsions, and their effects on particle size, crystallinity, and magnetic properties have been studied. The iron oxide nanoparticles are formed by a coprecipitation reaction of ferrous and ferric salts with inorganic bases. A strong base, NaOH, and a comparatively mild base, NH<sub>4</sub>OH, have been used in each surfactant to observe whether the basicity has some influence on the crystallization process during particle formation. Transmission electron microscopy, X-ray electron diffraction, and superconducting quantum interference device magnetometry have been employed to study both uncoated and silica-coated iron oxide nanoparticles. All of these particles show magnetic behavior close to that of superparamagnetic materials. With this method, magnetic nanoparticles as small as 1–2 nm and of very uniform size (percentage standard deviation is less than 10%) have been synthesized. A uniform silica coating as thin as 1 nm encapsulating the bare nanoparticles is

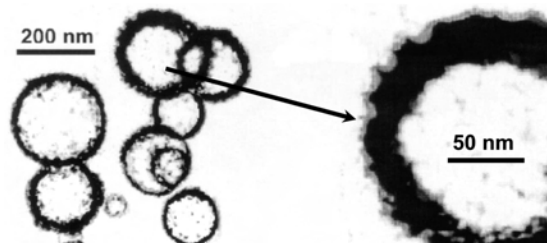


**Figure 6.** TEM picture of the silica/iron oxide composites prepared by aerosol pyrolysis of a mixture of iron ammonium citrate and TEOS. Details of a hollow spherical particle showing an outer particle layer mainly constituted (according to TEM microanalyses) by SiO<sub>2</sub>.

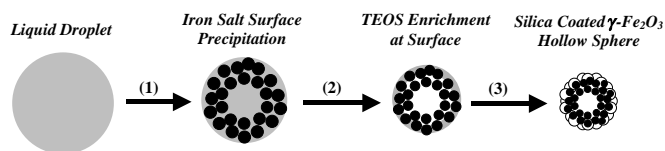


**Figure 7.** Illustration of the formation mechanism of the silica coated magnetite hollow particles.

formed by base-catalyzed hydrolysis and the polymerization reaction of TEOS in microemulsion.

## 5. SURFACE MODIFICATION OF NANOMAGNETS

### 5.1. Biocompatibility

The biocompatibility of biomaterials in direct contact with the blood depends closely on the ability of these materials not to be recognized by the coagulation, the complement, and the platelet systems [199]. This is true for massive biomaterials like endovascular prosthesis, but also for nanosized suspensions injected intravenously, like superparamagnetic iron oxide nanoparticles [200]. For *in vivo* applications, the internalization of nanoparticles into specific cells is the critical step and is severely limited by three

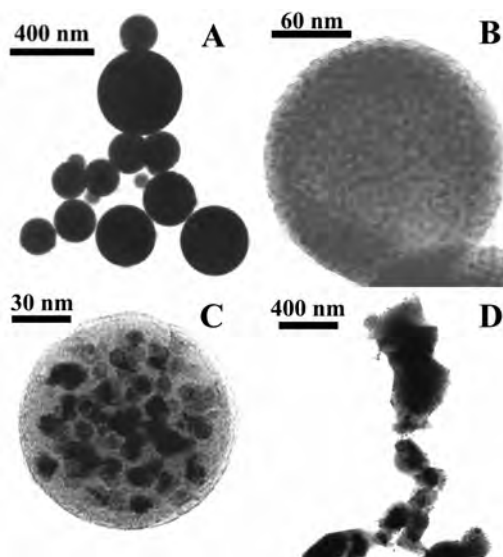


**Figure 8.** TEM micrographs of silica/iron oxide composites prepared by aerosol pyrolysis of a mixture of iron nitrate (20 mol%) and TEOS (A) and further heated in a conventional furnace for 2 h at 900 (B), 1050 (C), and 1200 °C (D). Note in the sample heated at 1050 °C the presence of  $\gamma$ -Fe<sub>2</sub>O<sub>3</sub> (dark regions) nanoparticles smaller than 20 nm dispersed in a microspherical silica particle (lighter regions). At this temperature, the enrichment of silica on particle outerlayers is clearly observed. It is important to note that microstructures similar to that displayed in micrographs (B) and (C) were observed for smaller and bigger particles. Note also the high stability of the spherical magnetic composites (the particles lost their spherical shape only at a temperature of 1200 °C as a consequence of sintering). Reprinted with permission from [196], P. Tartaj et al., *Langmuir* 18, 4556 (2002). © 2002, American Chemical Society.



factors: (a) a short blood half-life of the particles, (b) non-specific targeting, and (c) low efficiency of internalization to endocytosed ligands grafted to the nanoparticles [201].

The rapid elimination of nanoparticles from the bloodstream after their injection is due to their recognition by macrophages of the mononuclear phagocyte system [202]. Nanoparticles have a large surface area/volume ratio and tend to agglomerate and absorb plasma proteins. When the nanoparticles agglomerate, or are covered with adsorbed plasma proteins, they are quickly cleared by macrophages before they can reach target cells. Two types of coating yielding “stealth” particles have been successfully developed: high-density layered polymeric brushes (e.g., PEG, polysaccharides as dextran, poloxamines, and poloxamers) [203–205] and ganglioside-containing liposomes [206]. In the first case, the low proteic adsorption and complement activation seem to be linked to the entropic repulsion of free proteins by mobile polymeric chains [203, 207, 208]; in the second case, the polar head group of neuraminic acid inhibits the autocatalytic activation of the complement system [206], allowing the adsorption of only one proteic layer.

As mentioned above, one possible approach to increasing the circulation time of nanoparticles in the bloodstream is to modify the particles with poly(ethylene glycol) (PEG) films to disperse them and minimize or eliminate protein adsorption. Surfaces covered with PEG are biocompatible (i.e., nonimmunogenic, nonantigenic, and protein-resistant) [209]. This is due to the fact that PEG has uncharged hydrophilic residues and very high surface mobility, leading to high steric exclusion [210, 211]. Therefore, covalently immobilizing PEG on the surfaces of superparamagnetic magnetite nanoparticles is expected to effectively improve the biocompatibility of the nanoparticles. In addition, it has been demonstrated that particles with PEG-modified surfaces cross cell membranes, in nonspecific cellular uptake [212]. The possible mechanism for this uptake is that PEG can dissolve in both polar and nonpolar solvents and have high solubility in cell membranes [213, 214]. For the past decades, significant effort has been devoted to surface modification of various polymer drug carriers with PEG to improve their biocompatibility, to resist protein adsorption, and to increase their circulation time and internalization efficiency [215]. Little work has been done on the surface modification of magnetic nanoparticles for the same purpose. Zhang et al. [216] have shown that the surface modification of nanoparticles with PEG could be used to resist the protein adsorption and thus avoid the particle recognition by macrophage cells, and to facilitate the nanoparticle uptake to specific cancer cells for cancer therapy and diagnosis.

Once the magnetic nanoparticles are modified to provide them with biocompatibility, the effective hydrodynamic radius of the plasma-located nanoparticles grows well above their core radius [199, 217]. Therefore, another limiting factor is that the overall dimensions of the antibodies and their inherent immunogenicity cause nanoparticles to diffuse poorly through biological barriers [218]. The development of thin coating layers would thus allow major impacts in the particulate targeting of tissular recognition sites. Low-molecular-weight targeting agents such as folic acid have been demonstrated to preferentially target cancer cells, because the folate receptor is frequently overexpressed on

the surface of cancer cells [219]. The folate receptor is not only a tumor marker, but also has been shown to efficiently internalize molecules coupled to folate [220, 221]. Furthermore, folic acid itself is stable and generally poorly immunogenic. Despite the well-known ability of folate receptor to facilitate the internalization of polymeric particles [221, 222], little effort has been expended on the delivery of magnetic nanoparticles modified with PEG and folic acid into cells. Zhang et al. [210] have shown that the surface modification of nanoparticles with folic acid could be used to resist protein adsorption and thus avoid particle recognition by macrophage cells, and to facilitate nanoparticle uptake to specific cancer cells for cancer therapy and diagnosis.

Denizot and co-workers checked different organic biocompatible molecules that in principle could generate thin coatings on the surface of magnetic nanoparticles and therefore reduce the hydrodynamic size [199, 217, 223]. These authors first tried with phosphorylcholine-derived polymers that are known to protect prostheses against protein contamination [224, 225]. But pure phosphorylcholine coatings do not allowed colloidal stability at physiological pH [199]. Because of this relative failure, they tried to improve adsorption stability by systematic modifications of the fixation site on the iron oxides with functions such as phosphonates, phosphates, sulfonates, and carboxylic acids, all known for their adsorption properties on metallic surfaces. Coating with bisphosphonates, the more interesting fixation moiety, leads to small (less than 15 nm) and stable objects in a wide range of pH, including neutrality. From stability data, the coating density was evaluated at around 1.6 molecules per nm<sup>2</sup>. Including a quaternary ammonium salt in the coating molecule lowers the electrophoretic mobility. Moreover, this type of coating protects steel plates against contamination without significant desorption. All of these properties allow further developments of these nanoparticles for biomedical applications [217].

## 5.2. Specificity

*In vitro* applications such as separation, purification, and immunoassay methods rely on coating of magnetic particles with proteins or monoclonal antibodies, which endow the particles with the ability to bind the specific cancer cell, DNA fragment, or enzyme of interest and remove that entity from the fluid upon the application of a magnetic field [226–228]. For example, albumin-based magnetic particles have been used for the magnetic separation of red blood cells [229]. The same authors also checked the efficiency of polystyrene magnetic microspheres and showed that albumin-based magnetic particles have a higher coupling efficiency [230].

Koneracká et al. [231] have shown that enzymes such as chymotrypsin and streptokinase can be immobilized as fine magnetic particles. One of the important applications the authors are considering and exploring is in the treatment of coronary thrombosis and in peripheral arterial occlusions. In coronary arterial occlusions during a heart attack, plasminogen tissue is an ideal drug for lysing a clot because of its specific targeting capacity.

Safarikova and Safarik [76] immobilized copper phthalocyanine dye on fine silanized magnetite particles. This

reactive was used as a specific adsorbent for the preconcentration of organic compounds with planar molecular structures (polyaromatic hydrocarbons and their derivatives [232–234] and triphenylmethane dyes [76]). Magnetic particles are often sensitized with streptavidin to take advantage of its extremely high-affinity interaction with biotin. Because biotin can be easily conjugated with many different diagnostic reagents, a variety of assays for different analytes in several formats can be developed [235, 236].

## 6. SUMMARY

Drug and gene delivery will continue to have a significant impact on the practice of biomedicine. Magnetic drug-targeting will undoubtedly dramatically improve the therapeutic potential of many water-insoluble and unstable drugs. The new development of drugs able to target selected cells or organs within the body will also deeply improve the benefits of some of the *in vivo* biomedical applications of nanomagnets.

One of the topics of importance is the controlled release of therapeutic agents. For example, cells that make up tumors are a nonsynchronous population. Since chemotherapeutic drugs are active during specific phases of the cell cycle (e.g., DNA synthesis), a short burst of drug may not kill a substantial portion of tumor cells [59]. Retention of magnetic carriers within the tumor may act as a drug reservoir. As drug desorbs from the particles over time, effective concentrations of drug may be maintained as more tumor cells cycle through the S phase.

The main applications of magnetic carriers have been derived from the fact that specific ligands (e.g., streptavidin, antibodies) can be covalently bound to the polymer matrix, permitting binding to diverse target substances/organs such as cells, proteins, or nucleic acids. The strong binding makes the desorption of these ligands a difficult task. In contrast, ionically bound ligands can easily be eluted from the matrix simply by a change in either ionic strength or the pH. Bergemann and co-workers [111] have succeeded in developing novel nano- and microsized magnetic particles and beads to which ion-exchange groups were attached, thereby enabling simple and reversible binding of ligands. The remarkable feature of pharmaceutical drugs ionically bound to the surface of particulate drug delivery systems is that the active low-molecular-weight substances can desorb from the carriers after a defined time span and hence can diffuse from the vascular wall into the tissue.

Application of magnetic liposomes (lipid vesicles, containing submicron-sized magnetic nanoparticles in their structure, either in the lipid bilayer or in the aqueous compartment) as “vehicles” for targeted drug delivery appears to be a promising technique [237]. Liposomes can be used for encapsulation of many biologically active substances and can prolong their therapeutic action by gradual release of the drug [238–240]. Magnetic components of the liposomes allow concentration of the liposomes in the desired area of the patient’s organs by magnetic forces, often augmented by magnetic agglomeration. Special mention deserves the work of Bulte and co-workers [241]. These authors have developed magnetic liposomes derivatized with the hydrophilic

polymer polyethylene glycol (PEG) that may escape rapid uptake by cells of the reticuloendothelial system.

Similar promising methods rely on the preparation of micro- and nanocapsules as containers of magnetic carriers by a layer-by-layer approach. In particular, the preparation of polyelectrolyte (PEM) capsules is of significant interest [242]. One of the advantages of PEM capsules is their versatility of physical and chemical properties, created by variation of composition and fabrication as well as application conditions. Several dozen natural and synthetic polyelectrolytes or other charged substances are suitable as layer components, including chitosan, chitosansulfate, poly(L-lysine), poly(acrylic acid), poly(diallyldimethylammonium chloride), dextran sulfate, and proteins. Many of them can be functionalized to provide special surface structures of biological or technical relevance. They are applied as containers for inorganic and organic matter, such as drugs or macromolecules [243].

Magnetically directed microspheres containing radionuclides have been used for internal radiotherapy [58]. However, little work has been done on the use of magnetic nanoparticles in radiotherapy. One strategy under active investigation to improve dose localization is that of administration of drugs, metabolites, and so forth that have been labeled with radioactive isotopes in a quantity sufficient to inactivate tumor cells [244]. In this way, the use of surface-activated magnetic nanoparticles could have a tremendous impact on improving the efficiency of the cancer treatments.

Extensive application of hyperthermic cancer treatment presents serious problems that have not been sufficiently cleared up [44]. In particular, the temperature distribution inside as well as outside the target region must be known as a function of the exposure time to provide a level of therapeutic temperature and, on the other hand, to avoid overheating of and damage to the surrounding normal tissue. Several theoretical studies are being carried out to check the possibility of determining the spatial temperature distribution by means of mathematical simulation on the basis of known physical parameters [44, 245–247].

Efficient drug targeting is vital for the medical treatment of various diseases, among them cardiovascular episodes, like stenosis and thrombosis. Ferrofluids, magnetoliposomes, and magnetic micro- and nanospheres are promising candidates for delivering drugs to specific locations within the body, with high accuracy and little or no surgical intervention, and at maximum concentration. However, the hydrodynamics of these materials after injection in blood remains little known. The ternary phase structure of blood (white cells, red cells, and plasma), as well as the plethora of particles that are present in the blood flow, makes hemodynamics an exceedingly complex research field. Moreover, the response of blood to magnetic fields is not yet completely known, though there are some indications of the diamagnetic, paramagnetic, or ferromagnetic character of its various constituents [248–251]. In this way, the theoretical studies carried out by Voltairas et al. [252] could help to increase the understanding of the physics of magnetic drug targeting. In particular, these authors have developed a general theory for treating magnetic drug targeting. With minor corrections, the theory can also be applied when the carrier

is not a typical ferrofluid, but rather a lipid vessel (magnetoliposome). All necessary physical parameters, like the strength and the orientation of the magnetic field, the magnetic composition of the drug, the blood composition and velocity, are introduced in a model case.

Another important goal to achieve in the future is to better understand the magnetic behavior of nanocrystals. This topic is extremely important if magnetic nanoparticles are to be widely used in biomedical applications. Magnetic behavior can vary widely, depending on the size and distribution of the nanocrystalline particles. For example, an enhancement of the effective magnetic anisotropy with respect to the bulk material coming fundamentally from surface anisotropy has been reported [147, 190, 253, 254]. Furthermore, for nanoparticles a reduction in  $M_s$  values associated with spin canting at the surface and/or the interior of the particles is normally observed [36]. In addition to the particle size, the magnetic behavior also depends on the volume fraction and on the interaction of the nanomagnets with the matrix [255–257]. Interparticle interactions (usually of a dipolar nature) will affect the effective anisotropy energy and change the temperature at which a particle becomes superparamagnetic [18, 258].

Another important field under continuous development is the search for new synthetic routes or the improvement of established ones to produce reliable magnetic nanoparticles with adequate characteristics (improved tissular diffusion, colloidal stability, biocompatibility, and specificity) [217]. If we can gain sufficient understanding and control of biological reactions with magnetic nanoparticles, we may be able to control the rejection of nanomagnets. Ultimately, better materials and understanding of their interaction with the body may lead to biocompatible nanomagnets.

We can even envisage a future in which nanomagnets could be used for the repair of the human body with prosthetics or artificial replacement parts. In this field special mention must be made of the pioneering work of Dailey et al., who have reported the synthesis of silicon magnetic fluid for use in eye surgery [259]. Retinal detachment is a major cause of vision loss in adults. It occurs when the retina separates from the choroid, resulting in the eventual death of the retina and a subsequent loss of vision. As a normal part of aging, the vitreous gel normally undergoes liquefaction, collapse, and separation from the retina. The goal of surgery is to close the holes in the retina, preventing further fluid flow into the subretinal space, allowing for reattachment of the retina.

Present techniques for treating retinal detachment consist of a silicon band sewn to the outside of the eye to compress the wall of the eye inward to close the holes in the retina. Other methods employ halogenated gas ( $\text{SF}_6$ ,  $\text{C}_3\text{F}_8$ ) or silicon oil as internal tamponades. These materials can be placed inside the vitreous cavity and block the hole from within. Currently used internal tamponades ( $\text{SF}_6$ ,  $\text{C}_3\text{F}_8$ , or silicon fluid) float upward, leaving the inferior retina unprotected. Other materials sink (fluorosilicon), leaving the superior retina unprotected. Moreover, current tamponades fill the vitreous cavity, decreasing vision, and contact anterior chamber structures, causing cataracts and glaucoma. Dailey et al. [259] have developed an internal tamponade from modified silicon fluid containing sterically stabilized

4–10-nm metal particles, which will be held in place with an external magnetized scleral buckle. Magnetization procedures for the solid silicon band currently used for the scleral buckle were well preceded. With an appropriate magnetic fluid inside the vitreous cavity, they can produce a stable, 360° internal tamponade. The encircling magnetized scleral buckle and magnetic fluid would produce a ring of silicon oil in apposition to the retinal periphery. The central vitreous cavity would be free of the magnetic fluid, and there would be no contact between the magnetic fluid and the lens, anterior chamber structures, or macula, thus avoiding the complications of currently available treatment modalities.

## GLOSSARY

**Apoferitin** Empty ferritin. Ferritin in which the iron hydroxide central core has been extracted.

**Bohr radius** In semiconductors, excitation involves the separation of electrons and holes (the charge carriers) by distances that encompass a number of the molecules or ions making up the lattice. Such a distance, known as the Bohr radius, is on the nanometer length scale.

**Deoxyribonucleic acid (DNA)** It is the primary chemical component of chromosomes and the material of which genes are made. Each strand of DNA, is a chemically linked chain of nucleotides, which each consists of a deoxyribose sugar, a phosphate, and one of four varieties of “aromatic” bases. Because DNA strands are composed of these nucleotide subunits, they are polymers.

**Diamagnetism** A weak repulsion in a magnetic field generated by the current of the orbiting electron. All materials are naturally diamagnetic, although paramagnetism is stronger in materials with unpaired electrons.

**Ferromagnetism** The development of extremely strong magnetic properties in certain materials which occurs when magnetic domains become aligned in the absence of an applied field, below a temperature known as the Curie temperature. Ferromagnetism is believed to be caused by magnetic fields generated by the electrons' spins in combination with a mechanism known as exchange coupling, which aligns all the spins in each magnetic domain.

**Fluorescence** The emission of visible light from a substance under the stimulation of radiation of a shorter wavelength.

**Gene** The word “gene” is shared by many disciplines, including whole organism-based or “classical” genetics, molecular genetics, evolutionary biology and population genetics. It has multiple uses within each of these contexts. But in the primary sense “genes” are material things that parents pass to offspring during reproduction and through which they propagate their biological traits or characteristics. This sense, which is common to all of the above disciplines, is also the original historical meaning of “gene.”

**$H_c$  Coercivity** The magnetic field needed to reverse a given magnetization.

**$k_B$  Boltzmann constant** The product  $k_B T$  is the thermal energy. In magnetic materials the thermal energy acts to randomize magnetic moments. In particular, when this term is similar to the magnetic anisotropy energy (defined as the

product of the magnetic anisotropy constant and the volume of particles), magnetic materials become superparamagnetic. Superparamagnetism, thus, occurs when the material is composed of very small crystallites (1–10 nm). In this case even though the temperature is below the Curie or Neel temperature and the thermal energy is not sufficient to overcome the coupling forces between neighboring atoms, the thermal energy is sufficient to change the direction of magnetization of the entire crystallite. The resulting fluctuations in the direction of magnetization cause the magnetic field to average to zero. The material behaves in a manner similar to paramagnetism, except that instead of each individual atom being independently influenced by an external magnetic field, the magnetic moment of the entire crystallite tends to align with the magnetic field.

**Magnetic anisotropy** The dependence of magnetic properties on a preferred direction is called magnetic anisotropy. There are several different types of anisotropy such as magnetocrystalline anisotropy, shape anisotropy or surface anisotropy.

**Magnetic dipolar energy** Interaction energy between two magnetic moments.

**$M_s$  saturation magnetization** The magnetization attained when all magnetic moments in the sample are aligned (maximum magnetization).

**Ribonucleic acid (RNA)** It is structurally distinguished from DNA by the presence of an additional hydroxyl group attached to each pentose ring and functionally distinguished by its role in the transmission of genetic information from DNA (by transcription) and into protein (by translation).

**Superconducting quantum interference device (SQUID)** Experimental technique used to determine the magnetic behavior of a material.

## ACKNOWLEDGMENTS

The author thanks Dr. T. González-Carreño, Dr. M. P. Morales, and O. Bomati-Miguel for stimulating discussions. Financial support from the Spanish Ministry of Science and Technology (Ministerio de Ciencia y Tecnología) is gratefully acknowledged.

## REFERENCES

1. C. M. Niemeyer, *Angew. Chem. Int. Ed.* 40, 4128 (2001).
2. G. Whitesides and P. Alivisatos, in "Nanotechnology Research Directions" (P. Alivisatos, M. C. Roco, and R. S. Williams, Eds.), IWGN Workshop Report, 1999.
3. M. A. El-Sayed, *Acc. Chem. Res.* 34, 257 (2001).
4. M. L. Steigerwald and L. E. Brus, *Acc. Chem. Res.* 23, 183 (1990).
5. M. Haase, H. Weller, and A. Henglein, *J. Phys. Chem.* 92, 4706 (1988).
6. A. P. Alivisatos, A. L. Harris, N. J. Levinos, M. L. Steigerwald, and L. E. Brus, *J. Chem. Phys.* 89, 4001 (1988).
7. J. R. Heath, *Science* 270, 1315 (1995).
8. C. B. Murray, C. R. Kagan, and M. G. Bawendi, *Science* 270, 1335 (1995).
9. J. Z. Zhang, *Acc. Chem. Res.* 30, 423 (1997).
10. U. Kreibig and M. Vollmer, "Optical Properties of Metal Clusters." Springer-Verlag, Berlin, 1995.
11. J. M. Thomas, *Pure Appl. Chem.* 60, 1517 (1988).
12. S. Link, C. Burda, C., Z. L. Wang, and M. A. El-Sayed, *J. Chem. Phys.* 111, 1255 (1999).
13. N. Del Fatti, F. Vallee, C. Flytzanis, Y. Hamanaka, and A. Nakamura, *Chem. Phys.* 251, 215 (2000).
14. J. Y. Bigot, V. Halte, J. C. Merle, and A. Daunois, *Chem. Phys.* 251, 181 (2000).
15. E. Gu, E. Ahmad, S. J. Gray, C. Daboo, J. A. Bland, L. M. Brown, and J. C. Chapman, *Phys. Rev. Lett.* 78, 1158 (1997).
16. M. Mehn, K. Punadjela, J. Bucher, F. Rousseaux, D. Decanini, B. Bartenlian, and C. Chappert, *Science* 272, 1782 (1996).
17. B. Martínez, X. Obradors, L. I. Balcells, A. Rovinet, and C. Monty, *Phys. Rev. Lett.* 80, 181 (1998).
18. S. Mørup, F. Bødker, P. V. Hendriksen, and S. Linderoth, *Phys. Rev. B* 52, 287 (1995).
19. R. H. Kodama, *J. Magn. Magn. Mater.* 200, 359 (1999).
20. X. Battle and A. Labarta, *J. Phys. D: Appl. Phys.* 35, R15 (2002).
21. J. Kreuter, "Microcapsules and Nanoparticles in Medicine and Pharmacy." CRC Press, Boca Raton, FL, 1992.
22. D. E. Safer, L. Bolinger, and J. S. Leigh, *J. Inorg. Biochem.* 26, 77 (1986).
23. D. E. Safer, J. Hainfeld, J. S. Wall, and J. E. Reardon, *Science* 218, 290 (1982).
24. J. F. Hainfeld and F. R. Furuya, *J. Histochem. Cytochem.* 40, 177 (1992).
25. V. B. Vassilev, L. H. Gil, and R. O. Donis, *Vaccine* 19, 2012 (2001).
26. D. Sharma, T. P. Chelvi, J. Kaur, K. Chakravorty, T. K. De, A. Maitra, and R. Ralhan, *Oncol. Res.* 8, 281 (1996).
27. S. Mitra, U. Gaur, P. C. Gosh, and A. N. Maitra, *J. Controlled Release* 74, 317 (2001).
28. M. K. Bhalgat, R. P. Haugland, J. S. Pollack, S. Swan, and R. P. Haugland, *J. Immunol. Methods* 219, 57 (1998).
29. V. Väisänen, H. Härmä, H. Lilja, and A. Bjartell, *Luminescence* 15, 389 (2000).
30. E. Marshall, *Science* 295, 2198 (2002).
31. J. Couzin, *Science* 296, 2314 (2002).
32. J. D. Hood, M. Bednarski, R. Frausto, S. Guccione, R. A. Reisfeld, R. Xiang, and D. A. Cheresch, *Science* 296, 2404 (2002).
33. K. Wormuth, *J. Colloid Interface Sci.* 241, 366 (2001).
34. R. M. Cornell and U. Schwertmann, "The Iron Oxides. Structure, Properties, Reactions, Occurrence and Uses." VCH, Weinheim, 1996.
35. K. Haneda and A. H. Morrish, *Solid State Commun.* 22, 779 (1977).
36. M. P. Morales, S. Veintemillas-Verdaguer, M. I. Montero, C. J. Serna, A. Roig, Ll. Casas, B. Martinez, and F. Sandiumenge, *Chem. Mater.* 11, 3058 (1999).
37. G. A. Held, G. Grinstein, H. Doyle, S. Sun, and C. B. Murray, *Phys. Rev. B* 64, 012408 (2001).
38. W. C. Elmore, *Phys. Rev.* 54, 1092 (1938).
39. K. Raj and B. Moskowicz, *J. Magn. Magn. Mater.* 85, 233 (1990).
40. K. Raj, B. Moskowicz, and R. Casciari, *J. Magn. Magn. Mater.* 149, 174 (1995).
41. R. K. Gilchrist, R. Medal, W. D. Shorey, R. C. Hanselman, J. C. Parrott, and C. B. Taylor, *Ann. Surg.* 146, 596 (1957).
42. R. W. Rand, H. D. Snow, D. G. Elliott, and M. Snyder, *Appl. Biochem. Biotechnol.* 6, 265 (1981).
43. P. Wust, B. Hildebrandt, G. Sreenivasa, B. Rau, J. Gellermann, H. Riess, R. Felix, and P. M. Schlag, *Lancet Oncol.* 3, 487 (2002).
44. W. Andrä, C. G. d'Ambly, R. Hergt, I. Hilger, and W. A. Kaiser, *J. Magn. Magn. Mater.* 194, 197 (1999).
45. A. Jordan, R. Scholz, P. Wust, H. Föhling, and Roland Felix, *J. Magn. Magn. Mater.* 201, 413 (1999).
46. R. Hiergeist, W. Andrä, N. Buske, R. Hergt, I. Hilger, U. Richter, and W. Kaiser, *J. Magn. Magn. Mater.* 201, 420 (1999).
47. L. Néel, *C.R. Acad. Sci.* 228, 664 (1949).
48. M. I. Shliomis, *Sov. Phys. Usp.* 17, 153 (1963).

49. A. Jordan, P. Wust, and H. Fähling, *Int. J. Hyperthermia* 9, 51 (1993).
50. D. C. F. Chan, D. B. Kirpotin, and P. A. Bunn, *J. Magn. Magn. Mater.* 122, 374 (1993).
51. C. Streffer and D. van Beuningen, "Hyperthermia and the Therapy of Malignant Tumors." Springer-Verlag, Berlin, 1987.
52. P. Burgman, A. Nussenzweig, and G. C. Li, in "Thermoradiotherapy and Thermochemotherapy," Vol. 1: "Biology, Physiology, Physics." Springer-Verlag, Berlin, 1995.
53. Y. S. Takano, B. V. Harmon, and J. F. R. Kerr, *J. Pathol.* 163, 329 (1991).
54. K. S. Sellins and J. J. Cohen, *Radiat. Res.* 126, 88 (1991).
55. A. W. T. Konings, in "Thermoradiotherapy and Thermochemotherapy," Vol. 1: "Biology, Physiology, Physics." Springer-Verlag, Berlin, 1995.
56. G. Multhoff, C. Botzler, and M. Wiesnet, *Int. J. Cancer* 61, 272 (1995).
57. M. W. Freeman, A. Arrot, and H. H. L. Watson, *J. Appl. Phys.* 31, 404 (1960).
58. J. C. Joubert, *An. Quim. Int. Ed.* 93, S70 (1997).
59. S. Goodwin, C. Peterson, C. Hoh, and Craig Bittner, *J. Magn. Magn. Mater.* 194, 132 (1999).
60. K. J. Widder, R. M. Morris, and G. Poore, *Proc. Natl. Acad. Sci. USA* 78, 579 (1981).
61. D. Devineni, A. Klein-Szanto, and J. Gallo, *J. Neuro-Oncology* 24, 143 (1995).
62. A. S. Lübke, C. Bergemann, and H. Riess, *Cancer Res.* 56, 4686 (1996).
63. K. H. Hausser and H. K. Kalbitzer, "NMR in Medicine and Biology." Springer-Verlag, Berlin, 1991.
64. I. Coroiu, *J. Magn. Magn. Mater.* 201, 449 (1999).
65. S. H. Koenig and R. D. Brown, III, "Magnetic Resonance Annual 1987." Raven, New York, 1987.
66. Y. Ayant, E. Belorizky, J. Alizon, and J. Gallice, *J. Phys. A* 36, 991 (1975).
67. J. H. Freed, *J. Chem. Phys.* 68, 4034 (1978).
68. R. N. Muller, P. Gillis, F. Moyny, and A. Roch, *Magn. Reson. Med.* 22, 178 (1991).
69. D. K. Kim, Y. Zhang, J. Kher, T. Klason, B. Bjelke, and M. Muhammed, *J. Magn. Magn. Mater.* 225, 256 (2001).
70. P. L. Roberts, N. Chuang, and H. C. Roberts, *Eur. J. Rad.* 34, 166 (2000).
71. A. Zavaljevski, S. K. Holland, and A. P. Dhawan, *IEEE Trans.* 48, 711 (1999).
72. B. Bonnemain, *J. Drug. Target* 6, 167 (1998).
73. C. J. Chen, Y. Haik, and V. M. Pai, U.S. Patent 6036857, 2000.
74. R. Weissleder, J. F. Heautot, B. K. Schaffer, N. Nossiff, M. I. Papisov, A. Bogdanov, and T. J. Brady, *Radiology* 191, 225 (1994).
75. O. Clément, R. Guimaraes, E. de Kerviler, and G. Fria, *Invest. Radiol.* 29, S226 (1994).
76. M. Safarikova and I. Safarik, *J. Magn. Magn. Mater.* 194, 108 (1999).
77. J. S. Fritz, P. J. Dumont, and L. W. Schmidt, *J. Chromatogr. A* 691, 133 (1995).
78. L. A. Berrueta, B. Gallo, and F. Vicente, *Chromatographia* 40, 474 (1995).
79. I. Giaver, U.S. Patent 3970518, 1977.
80. I. Giaver, U.S. Patent 4115535, 1978.
81. J. Lenfeld, *Angew. Makromol. Chem.* 212, 147 (1993).
82. P. Wikström, S. Flygare, S. Gröndalen, and P. O. Larsson, *Anal. Biochem.* 167, 331 (1987).
83. M. A. Vladimirov, A. A. Kuznetsov, and V. I. Philippov, *J. Magn. Magn. Mater.* 122, 371 (1993).
84. A. Rembaum and S. Margel, *Br. Polym. J.* 10, 275 (1978).
85. A. Rembaum and W. J. Dreyer, *Science* 208, 364 (1980).
86. R. Edelson, *Sci. Am.* 259, 68 (1988).
87. Y. Haik, V. M. Pai, and C. J. Chen, *J. Magn. Magn. Mater.* 194, 254 (1999).
88. S. Sieben, C. Bergemann, A. Lübke, B. Brockmann, and D. Rescheleit, *J. Magn. Magn. Mater.* 225, 175 (2001).
89. B. Wörmann, G. G. Griesinger, and H. Hiddemann, *Internist* 38, 1083 (1997).
90. W. Weitschies, R. Kötz, T. Bunte, and L. Trahms, *Pharm. Pharmacol. Lett.* 7, 5 (1997).
91. T. Rheinländer, R. Kötz, W. Weitschies, and W. Semmler, *J. Magn. Magn. Mater.* 219, 219 (2000).
92. L. Néel, *Ann. Geophys.* 5, 99 (1949).
93. R. Street and J. C. Woolley, *Proc. Phys. Soc. A* 62, 562 (1949).
94. P. Debye, "Polar Molecules." Chemical Catalog Company, New York, 1929.
95. J. Popplewell and L. Sakhnini, *J. Magn. Magn. Mater.* 149, 72 (1995).
96. R. Kötz, W. Weitschies, L. Trahms, W. Brewer, and W. Semmler, *J. Magn. Magn. Mater.* 194, 62 (1999).
97. N. A. Brusentsov, M. V. Lukashevich, and V. V. Gogosov, *Magn. Hydrodyn.* 2, 215 (1994).
98. A. A. Novakova, T. S. Gendler, and N. A. Brusentsov, *Hyperfine Interact.* 71, 1315 (1992).
99. M. I. Papisov, A. Bogdanov, Jr., B. Schafer, N. Nossiff, T. Shen, R. Weissleder, and T. J. Brady, *J. Magn. Magn. Mater.* 122, 383 (1993).
100. D. C. Chan, D. B. Kirpotin, P. A. Bunn, "Scientific and Clinical Applications of Magnetic Carriers." Plenum Press, New York, 1996.
101. M. A. Lunina and A. Novozhilov, *Colloid J.* 31, 467 (1969).
102. A. A. Khachatryan and M. A. Lunina, *J. Magn. Magn. Mater.* 85, 17 (1990).
103. O. A. Kuznetsov, N. A. Brusentsov, A. A. Kuznetsov, N. Y. Yurchenko, N. E. Osipov, and F. S. Bayburtskiy, *J. Magn. Magn. Mater.* 194, 83 (1999).
104. A. E. Nielsen, "Kinetics of Precipitation," p. 108. Pergamon Press, Oxford, 1964.
105. T. Sugimoto, *Adv. Colloid Interface Sci.* 28, 65 (1987).
106. R. Massart, *IEEE Trans. Magn. Mater.* 17, 131 (1981).
107. R. Massart and V. Cabuil, *J. Chem. Phys.* 84, 967 (1987).
108. J. P. Jolivet, P. Belleville, E. Tronc, and J. Livage, *Clays Clay Miner.* 40, 531 (1992).
109. S. Palmacci and L. Josephson, U.S. Patent 5262176, 1993.
110. C. Bergemann, German Patent DE 19624426 A1, 1996.
111. C. Bergemann, D. Müller-Schulte, J. Oster, L. Brassard, and A. S. Lübke, *J. Magn. Magn. Mater.* 194, 45 (1999).
112. J. H. Fendler, *Chem. Educ.* 60, 872 (1983).
113. J. H. Fendler, "Membrane Mimetic Chemistry: Characterization and Applications of Micelles, Microemulsion, Monolayers, Bilayers, Vesicles, Host-Guest Systems and Polyions." Wiley, New York, 1975.
114. I. Lisiecki and M. P. Pileni, *J. Am. Chem. Soc.* 7, 115 (1993).
115. V. Pillai, P. Kumar, M. J. Hou, P. Ayyub, and D. O. Shah, *Adv. Colloid Interface Sci.* 55, 241 (1995).
116. K. Zhang, C. H. Chew, G. Q. Xu, J. Wang, and L. M. Gan, *Langmuir* 15, 3056 (1999).
117. A. J. Zarur and J. Y. Ying, *Nature* 403, 65 (2000).
118. P. Tartaj and L. C. De Jonghe, *J. Mater. Chem.* 10, 2786 (2000).
119. P. Tartaj and J. Tartaj, *Chem. Mater.* 14, 536 (2002).
120. M. P. Pileni, *J. Phys. Chem.* 97, 6961 (1993).
121. M. A. López-Quintela and J. Rivas, *J. Colloid Interface Sci.* 158, 446 (1993).
122. N. Feltin and M. P. Pileni, *Langmuir* 13, 3927 (1997).
123. E. E. Carpenter, *J. Magn. Magn. Mater.* 225, 17 (2001).
124. M. Boutonnet, J. Kizling, and P. Stenius, *Colloids Surf., A* 5, 209 (1982).
125. M. Valiente and E. J. Rodenas, *Colloids Interface Sci.* 127, 522 (1989).

126. M. Valiente and E. J. Rodenas, *J. Am. Chem. Soc.* 95, 3368 (1991).
127. N. D. Chasteen and P. M. Harrison, *J. Struct. Biol.* 126, 182 (1999).
128. S. Mann, J. V. Bannister, and R. J. P. Williams, *J. Mol. Biol.* 188, 225 (1986).
129. F. C. Meldrum, V. J. Wade, D. L. Nimmo, B. R. Heywood, and S. Mann, *Nature* 349, 684 (1991).
130. F. C. Meldrum, B. R. Heywood, and S. Mann, *Science* 257, 522 (1992).
131. K. K. W. Wong, T. Douglas, S. Gider, D. D. Awschalom, and S. Mann, *Chem. Mater.* 10, 279 (1998).
132. J. Rockenberger, E. C. Scher, and A. P. Alivisatos, *J. Am. Chem. Soc.* 121, 11595 (1999).
133. T. Hyeon, S. S. Lee, J. Park, Y. Chung, and H. B. Na, *J. Am. Chem. Soc.* 123, 12798 (2001).
134. S. Shen and H. Zeng, *J. Am. Chem. Soc.* 124, 8204 (2002).
135. D. A. Tomalia and P. R. Dvornic, *Nature* 372, 617 (1994).
136. J. F. G. A. Jansen, E. M. M. de Brabander-van den Berg, and E. W. Meijer, *Science* 1226, 266 (1994).
137. R. F. Service, *Science* 267, 458 (1995).
138. D. L. Jiang and T. Aido, *J. Chem. Soc., Chem. Commun.* 1523 (1996).
139. R. M. Crooks, M. Zhao, L. Sun, V. Chechik, and L. K. Yeung, *Acc. Chem. Res.* 34, 181 (2001).
140. E. Strable, J. W. M. Bulte, B. Moskowitz, K. Vivekanandan, M. Allen, and T. Douglas, *Chem. Mater.* 13, 2201 (2001).
141. M. Rajamathi, M. Ghosh, and R. Seshadri, *Chem. Commun.* 1152 (2002).
142. C. Pascal, J. L. Pascal, F. Favier, M. L. Elidrissi-Moubtassim, and C. Payen, *Chem. Mater.* 11, 141 (1999).
143. H. Gleiter, *Prog. Mater. Sci.* 33, 223 (1989).
144. C. C. Koch, *Nanostruct. Mater.* 9, 13 (1997).
145. D. Zhang, G. Glavee, K. J. Klabunde, G. C. Hadjipanayis, and C. M. Sorensen, *High Temp. Mater. Sci.* 36, 93 (1996).
146. S. Veintemillas-Verdaguer, M. P. Morales, and C. J. Serna, *Mater. Lett.* 35, 227 (1998).
147. B. Martinez, A. Roig, E. Molins, T. González-Carreño and C. J. Serna, *J. Appl. Phys.* 83, 3256 (1998).
148. T. Rheinländer, D. Roessner, W. Weitschies, and W. Semmler, *J. Magn. Magn. Mater.* 214, 269 (2000).
149. C. E. Sjögren, C. Johansson, A. Naevestad, P. C. Sontum, K. Briley-Saebo, and A. K. Fahlvik, *Magn. Res. Imag.* 15, 55 (1997).
150. A. C. Nunes and Z. C. Yu, *J. Magn. Mater.* 65, 265 (1987).
151. R. Weissleder, G. Elizondo, J. Wittenberg, C. A. Rabito, H. H. Bengel, and L. Josephson, *Radiology* 175, 489 (1990).
152. S. Lefebure, E. Dubois, V. Cabuil, S. Neveu, and R. Massart, *J. Mater. Res.* 13, 2975 (1998).
153. K. O'Grady, H. R. Stewardson, R. W. Chantrell, D. Fletcher, D. Unwin, and M. R. Parker, *IEEE Trans. Magn. Magn.* 22, 1134 (1986).
154. D. Kirpotin, D. C. F. Chan, and P. A. Bunn, U.S. Patent 5411730, 1993.
155. S. Miltenyi, W. Müller, W. Weichel, and A. Radbruch, *Cytometry* 11, 231 (1990).
156. S. K. R. Williams, H. Lee, and M. M. Turner, *J. Magn. Magn. Mater.* 194, 248 (1999).
157. J. C. Giddings, *Science* 260, 1456 (1993).
158. J. B. Hayter and R. Pynn, *Phys. Rev. Lett.* 4, 1103 (1982).
159. A. P. Philipse, M. P. B. van Bruggen, and C. Pathmamanoharan, *Langmuir* 10, 3500 (1994).
160. C. Grüttner and J. Teller, *J. Magn. Magn. Mater.* 194, 8 (1999).
161. J. H. Fendler, "Nanoparticles and Nanostructured Films: Preparation, Characterization and Application." Wiley-VCH, Weinheim, 1998.
162. A. Ulman, "An Introduction to Ultrathin Organic Films: From Langmuir-Blodgett to Self-Assembly." Academic Press, Boston, 1991.
163. F. Caruso, R. A. Caruso, and H. Möhwald, *Science* 282, 1111 (1998).
164. F. Caruso, *Adv. Mater.* 13, 11 (2001).
165. F. Caruso, E. Donath, and H. Möhwald, *J. Phys. Chem. B* 102, 2011 (1998).
166. E. Donath, G. B. Sukborukov, F. Caruso, S. A. Davies, and H. Möhwald, *Angew. Chem. Int. Ed.* 37, 2201 (1998).
167. F. Caruso, H. Lichtenfeld, H. Möhwald, and M. Giersig, *J. Am. Chem. Soc.* 120, 8523 (1998).
168. F. Caruso and H. Möhwald, *Langmuir* 15, 8276 (1999).
169. F. Caruso, R. A. Caruso, and H. Möhwald, *Chem. Mater.* 120, 8523 (1999).
170. F. Caruso and H. Möhwald, *J. Am. Chem. Soc.* 121, 6039 (1999).
171. F. Caruso, A. S. Susha, M. Giersig, and H. Möhwald, *Adv. Mater.* 11, 950 (1999).
172. F. Caruso, M. Spasova, A. Susha, M. Giersig, and R. A. Caruso, *Chem. Mater.* 13, 109 (2001).
173. A. Garg and E. Matijević, *Langmuir* 4, 38 (1988).
174. B. Aiken and E. Matijević, *J. Colloid Interface Sci.* 126, 645 (1988).
175. B. Aiken, W. P. Hsu, and E. Matijević, *J. Mater. Sci.* 25, 1886 (1990).
176. M. Ocaña, W. P. Hsu, and E. Matijević, *Langmuir* 7, 2911 (1991).
177. V. V. Handicar and E. Matijević, *J. Colloid Interface Sci.* 221, 133 (2000).
178. L. C. Varanda, P. Tartaj, T. González-Carreño, M. P. Morales, T. Muñoz, K. O'Grady, M. Jafelicci, Jr., and C. J. Serna, *J. Appl. Phys.* 92, 2079 (2002).
179. H. Shiho, Y. Manabe, and N. Kawahashi, *J. Mater. Chem.* 10, 333 (2000).
180. H. Shiho and N. Kawahashi, *J. Colloid Interface Sci.* 226, 91 (2000).
181. E. Bourgeat-Lami and J. J. Lang, *J. Colloid Interface Sci.* 197, 293 (1998).
182. V. S. Zaitsev, D. S. Filimonov, I. A. Presnyakov, R. J. Gambino, and B. Chu, *J. Colloid Interface Sci.* 212, 49 (1999).
183. P. K. Gupta, T. C. Hung, F. C. Lam, and D. G. Perrier, *Int. J. Pharm.* 43, 167 (1988).
184. E. E. Hassan, R. C. Parish, and J. M. Gallo, *Pharm. Res.* 9, 390 (1992).
185. D. Müller-Schulte and D. Brunner, *J. Chromatogr. A* 711, 53 (1995).
186. X. Xu, G. Friedman, K. D. Humfeld, S. A. Majetich, and S. A. Asher, *Adv. Mater.* 13, 1681 (2001).
187. P. A. Dresco, V. S. Zaitsev, R. J. Gambino, and B. Chu, *Langmuir* 15, 1945 (1999).
188. G. Ennas, A. Musinu, G. Piccaluga, D. Zadda, D. Gatteschi, C. Sangregorio, J. L. Stanger, G. Concas, and G. Spano, *Chem. Mater.* 10, 495 (1998).
189. F. del Monte, M. P. Morales, D. Levy, A. Fernandez, M. Ocaña, A. Roig, E. Molins, K. O'Grady, and C. J. Serna, *Langmuir* 13, 3627 (1997).
190. P. Tartaj and C. J. Serna, *Chem. Mater.*, 14, 4396 (2002).
191. A. Ulman, *Chem. Rev.* 96, 1533 (1996).
192. P. Mulvaney, L. M. Liz-Marzán, M. Giersig, and T. Ung, *J. Mater. Chem.* 10, 1259 (2000).
193. A. P. Philipse, M. P. van Bruggen, and C. Pathmamanoharan, *Langmuir* 10, 92 (1994).
194. D. Fletcher, *IEEE Trans. Magn.* 27, 3655 (1991).
195. P. Tartaj, T. Gonzalez-Carreño, and C. J. Serna, *Adv. Mater.* 13, 1620 (2001).
196. P. Tartaj, T. Gonzalez-Carreño, and C. J. Serna, *Langmuir* 18, 4556 (2002).
197. G. L. Messing, S. Zhang, and G. V. Jayanthi, *J. Am. Ceram. Soc.* 76, 2707 (1993).
198. S. Santra, R. Tapeç, N. Theodoropoulou, J. Dobson, A. Hebard, and W. Tan, *Langmuir* 17, 6000 (2001).
199. B. Denizot, G. Tanguy, F. Hindre, E. Rump, J. J. Le Jeune, and P. Jallet, *J. Colloid Interface Sci.* 209, 66 (1999).



200. C. Chouly, D. Pouliquen, I. Lucet, J. J. Le Jeune, and P. Jallet, *J. Microencapsulation* 13, 245 (1996).
201. B. Stella, S. Arpicco, M. T. Peracchia, D. Desmaele, J. Hoebeke, M. Renoir, J. D'Angelo, L. Cattel, and P. Couvreur, *J. Pharm. Sci.* 89, 1452 (2000).
202. E. Allemann, R. Gurny, and E. Doelker, *Eur. J. Pharm. Biopharm.* 39, 173 (1993).
203. V. P. Torchilin, M. I. Papisov, A. A. Bogdanov, V. S. Trubetskoy, and V. G. Omelyanenko, in "Stealth Liposomes," p. 51. CRC Press, London, 1995.
204. T. M. Allen, *Adv. Drug Delivery Rev.* 13, 285 (1994).
205. I. Brigger, C. Dubernet, and P. Couvreur, *Adv. Drug Delivery Rev.* 54, 631 (2002).
206. P. C. Ghosh and B. K. Bachhawat, in "Stealth Liposomes," p. 13. CRC Press, London, 1995.
207. S. I. Jeon, J. H. Lee, J. D. Andrade, and P. G. de Gennes, *J. Colloid Interface Sci.* 142, 149 (1991).
208. S. I. Jeon and J. D. Andrade, *J. Colloid Interface Sci.* 142, 159 (1991).
209. C. G. Gölander, J. N. Herron, K. Lim, P. Claesson, P. Stenius, and J. D. Andrade, "Poly(ethylene Glycol) Chemistry, Biotechnical and Biomedical Applications," pp. 221–245. Plenum Press, New York 1992.
210. M. Zhang, T. Desai, and M. Ferrari, *Biomaterials* 19, 953 (1998).
211. M. Zhang and M. Ferrari, *Biomed. Microdevices* 1, 81 (1998).
212. P. Caliceti, O. Schiavon, A. Mocali, and F. M. Veronese, *Farmaco* 44, 711 (1989).
213. M. Yamazaki and T. Ito, *Biochemistry* 29, 1309 (1990).
214. L. T. Boni, J. S. Hah, S. W. Hui, R. Mukherjee, J. T. Ho, and C. Y. Jung, *Biochim. Biophys. Acta* 775, 409 (1984).
215. G. Storm, S. O. Belliot, T. Daemen, and D. D. Lasic, *Adv. Drug Delivery Rev.* 17, 31 (1995).
216. Y. Zhang, N. Kohler, and M. Zhang, *Biomaterials* 23, 1553 (2002).
217. D. Portet, B. Denizot, G. Tanguy, E. Rump, J. J. Le Jeune, and P. Jallet, *J. Colloid Interface Sci.* 238, 37 (2001).
218. E. Tomlinson, *Adv. Drug Delivery Rev.* 1, 87 (1987).
219. S. D. Weitman, R. H. Lark, L. R. Coney, D. W. Fort, V. Frasca, V. R. Zurawski, and B. A. Kamen, *Cancer Res.* 52, 3396 (1992).
220. L. R. Coney, A. Tomassetti, L. Carayannopoulos, V. Frasca, B. A. Kamen, M. I. Colnaghi, and W. R. Zurawski, *Cancer Res.* 51, 6125 (1991).
221. A. C. Antony, *Blood* 79, 2807 (1992).
222. S. Wang, R. J. Lee, C. J. Mathias, M. A. Green, and P. S. Low, *Bioconjugate Chem.* 7, 56 (1996).
223. L. Babes, B. Denizot, G. Tanguy, J. J. Le Jeune, and P. Jallet, *J. Colloid Interface Sci.* 212, 474 (1999).
224. T. Oishi, T. Fukuda, H. Uchiyama, F. Kondou, H. Ohe, and H. Tsutsumi, *Polymer* 38, 3109 (1997).
225. A. A. Durrani, J. A. Hayward, and D. Chapman, *Biomaterials* 7, 121 (1986).
226. P. L. Lim, *J. Immunol. Methods* 135, 257 (1990).
227. J. Roger, J. N. Pons, R. Massart, A. Halbreich, and J. C. Bacri, *Eur. Phys. J. Appl. Phys.* 5, 321 (1999).
228. R. Tyagi and M. N. Gupta, *Biocatal. Biotrans.* 12, 293 (1995).
229. J. Chatterjee, Y. Haik, and C. J. Chen, *Colloid Polym. Sci.* 279, 1073 (2001).
230. J. Chatterjee, Y. Haik, and C. J. Chen, *J. Magn. Magn. Mater.* 225, 21 (2001).
231. M. Koneracká, P. Kopcansky, M. Antalík, M. Timko, C. N. Ramchand, D. Lobo, R. V. Mehta, and R. V. Upadhyay, *J. Magn. Magn. Mater.* 201, 427 (1999).
232. I. Safarik, *Water Res.* 60, 34 (1995).
233. H. Hayatsu, *J. Chromatogr.* 597, 37 (1992).
234. A. C. Povey and I. K. O'Neil, *Carcinogenesis* 11, 1989 (1990).
235. E. P. Diamandis and T. K. Christopoulos, *Clin. Chem.* 37, 625 (1991).
236. L. Dorgan, R. Magnotti, J. Hou, T. Engle, K. Ruley, and B. Shull, *J. Magn. Magn. Mater.* 194, 69 (1999).
237. A. A. Kuznetsov, V. I. Filippov, R. N. Alyautdin, N. L. Torshina, and O. A. Kuznetsov, *J. Magn. Magn. Mater.* 225, 95 (2001).
238. L. B. Margolis, V. A. Namiot, and L. M. Kljukin, *Biochim. Biophys. Acta* 735, 193 (1983).
239. A. A. Bogdanov, C. Martin, R. Weissleder, and T. J. Brady, *Biochim. Biophys. Acta* 1193, 212 (1994).
240. H. Chen and R. Langer, *Pharm. Res.* 14, 537 (1997).
241. J. W. M. Bulte, M. de Cuyper, D. Despres, and J. A. Frank, *J. Magn. Magn. Mater.* 194, 204 (1999).
242. A. Voigt, N. Buske, G. B. Sukhorukov, A. A. Antipov, S. Leporatti, H. Lichtenfeld, H. Bäuml, E. Donath, and H. Möhwald, *J. Magn. Magn. Mater.* 225, 59 (2001).
243. F. Caruso, D. Trau, H. Möhwald, and R. Renneberg, *Langmuir* 16, 1485 (2000).
244. H. Suit, *Int. J. Radiat. Oncol., Biol., Phys.* 53, 798 (2002).
245. X. Q. Lu, E. C. Burdette, B. A. Bornstein, J. L. Hansen, and G. K. Svensson, *Int. J. Hypertherm.* 12, 375 (1996).
246. N. Tsuda, K. Kuroda, and Y. Suzuki, *IEEE Trans. Biomed. Eng.* 43, 1029 (1996).
247. Z. P. Chen, R. B. Roemer, and T. C. Cetas, *Med. Phys.* 19, 989 (1992).
248. M. Iwasaka, S. Ueno, and H. Tsuda, *J. Appl. Phys.* 75, 7162 (1994).
249. M. Iwasaka, S. Ueno, and H. Tsuda, *IEEE Trans. Magn.* 30, 4695 (1994).
250. T. Higashi, N. Ashida, and T. Takeuchi, *Physica B* 237, 616 (1997).
251. Y. Haik, V. Pai, and C. J. Chen, *J. Magn. Magn. Mater.* 225, 180 (2001).
252. P. A. Voltairas, D. I. Fotiadisa, and L. K. Michalisb, *J. Biomech.* 35, 813 (2002).
253. F. Bødker, S. Mørup, and S. Linderorth, *Phys. Rev. Lett.* 72, 282 (1994).
254. J. F. Hochepped, P. Bonville, and M. P. Pileni, *J. Phys. Chem. B* 104, 905 (2000).
255. C. Liu and Z. J. Zhang, *Chem. Mater.* 13, 2092 (2001).
256. P. Katiyar, D. Kumar, T. K. Nath, A. V. Kvit, J. Narayan, S. Shatopadhyay, W. M. Gilmore, S. Coleman, C. B. Lee, J. Sankar, and R. K. Singh, *Appl. Phys. Lett.* 79, 1327 (2001).
257. J. L. Dormann, D. Fiorani, and E. Tronc, *Adv. Chem. Phys.* 98, 283 (1997).
258. M. El-Hilo, K. O'Grady, and R. W. Chantrell, *J. Magn. Magn. Mater.* 114, 295 (1992).
259. J. P. Dailey, J. P. Phillips, C. Li, and J. S. Riffle, *J. Magn. Magn. Mater.* 194, 140 (1999) and references therein.

# Nanomaterials by Severe Plastic Deformation

Yuntian T. Zhu

*Los Alamos National Laboratory, Los Alamos, New Mexico, USA*

Darryl P. Butt

*University of Florida, Gainesville, Florida, USA*

## CONTENTS

1. Introduction
  2. Severe Plastic Deformation Techniques
  3. Nanostructures
  4. Properties
  5. Applications
  6. Concluding Remarks
- Glossary  
References

## 1. INTRODUCTION

Bulk nanostructured materials can be defined as solids with nanoscale (typically 1–100 nm) substructures in at least one dimension [1–4]. Siegel [3] has classified nanostructured materials into four categories according to their dimensionality: 0D—nanoclusters (particles); 1D—multilayers; 2D—nanograined layers; and 3D—equiaxed bulk solids. In short, he has described the 3D nanostructured materials as “. . . three-dimensionally modulated, synthetic materials with average grain, phase, or other structural domain sizes below 100 nm.” In this review, we are primarily concerned with 3D nanostructured materials.

Two complementary approaches have been developed to synthesize nanostructured materials. The first one is a “bottom-up” approach, in which bulk nanostructured materials are assembled from individual atoms or nanoscale building blocks such as nanoparticles [5]. Gleiter’s pioneering work [6] is a typical example of a “bottom-up” approach. Various chemical and physical methods have been developed to synthesize nanopowders for small-scale laboratory

investigations as well as for large-scale commercial use. Such methods include inert gas condensation (IGC) [6], high-energy ball milling [7], spray conversion processing [8], sputtering [9], physical vapor deposition [10], chemical vapor deposition [11], sol-gel processing [12], sliding wear [13], and spray forming [14]. The bottom-up approach has a number of applications such as films, coatings, electronic devices, drug deliveries, cosmetics, paints, lubricants, rocket fuels, catalysts, and reinforcements for nanocomposites.

Most bottom-up approaches produce nanopowders. For structural applications, the nanopowders need to be consolidated into bulk nanomaterials. However, consolidation of nanopowders has been a challenge. Gleiter [6] and Nieman et al. [15] cold-compacted IGC-produced nanopowders *in-situ* in ultrahigh vacuum and obtained nanostructured discs typically a few hundred micrometers in thickness and less than 10 mm in diameter. Their as-produced samples contained many flaws that masked the intrinsic mechanical properties [16]. Flaws included gas filled pores, cracks, poorly bonded grains, etc. These flaws render the material brittle, especially under tension. More recently, Sanders et al. [17] used warm compaction to reduce the density and size of such flaws and found improvement in the mechanical properties. However, flaws such as porosity and trapped gas still exist in the consolidated nanomaterials. A series of other conventional and new techniques, such as hot pressing, hot isostatic pressing (HIP) [18], rapid hot forging [19, 20], and plasma activated sintering [21], have been used to consolidate nanopowders. Most of these techniques involve the applications of heat and pressure. Grain growth usually occurs during consolidation, although nanopowder oxidation and contaminants may help impede grain growth. However, it should be noted that the existence of some degree of porosity is not always undesirable. For instance, the existence of small amounts of porosity may be responsible, in part, for the increase of short-range diffusional deformation

in certain ceramics. This, in turn, renders them more strain rate sensitive and more ductile [3], which could be useful in their forming and applications.

The second approach for producing nanostructured materials is a “top-down” approach, in which existing coarse-grained materials are refined into nanostructured materials. The most successful “top-down” approach has been via severe plastic deformation (SPD) techniques, among which the most developed are equal channel angular pressing (ECAP) and high-pressure torsion (HPT) [22]. The latter has also been referred to as severe plastic torsion straining (SPTS) [23], but was redefined as HPT for a more accurate description of the process at a NATO workshop on SPD in 1999 [24]. The ECAP technique was first invented by Segal in 1972 [25], and was later used to produce nanostructured materials [26]. Recently, new SPD techniques have been developed, such as accumulative roll bonding [27], multipass coin-forging (MCF) [28], and repetitive corrugation and straightening (RCS) [29, 30]. SPD-produced materials such as Cu, Fe, and Ti typically have an average grain size of 60–200 nm [23], somewhat above 100 nm, the upper bound often used to define the nanostructured materials. However, subgrains with low misorientation angles, dislocation cell structures [29], and the coherent crystallite domains as measured by X-ray analysis are usually smaller than 100 nm. It was agreed at the NATO workshop that the materials produced by SPD can be indeed classified as nanostructured materials.

Nanostructured materials produced by SPD techniques are free of porosity and contaminants, and can be used to study their intrinsic deformation mechanisms. These materials have unique micro- and nanostructures such as high dislocation density, nonequilibrium grain (subgrain) boundaries, and dislocation cells [23]. Recently, it was discovered that SPD-processed Cu and Ti have an extraordinary combination of both high strength and high ductility [31]. In addition, both strength and ductility were observed to increase with increasing SPD strain, which is contrary to the usual behavior of materials processed by conventional forming methods such as rolling and drawing, where plastic deformation increases the strength but usually decreases the ductility. SPD is also at present the only approach that can produce large, bulk nanostructured materials for structural applications, such as medical implants and aerospace components.

This review first describes recent developments in severe plastic deformation (SPD) techniques, followed by the unique structures and properties of nanostructured materials processed by SPD and the potential applications of these materials.

## 2. SEVERE PLASTIC DEFORMATION TECHNIQUES

The practice of shaping and forming metals and alloys through plastic deformation is several thousand years old. It was a primary method that blacksmiths used to make metal objects such as swords and horse shoes. Modern shaping and forming technologies include rolling, extrusion, drawing,

etc. Although these industrial practices can refine grains and improve mechanical properties of metals and alloys, they usually cannot produce nanostructured materials. They usually produce dislocation cell structures instead of grains with high angle grain boundaries [23]. Very high plastic strains are required to produce nanostructures in metals and alloys. The industrial shaping and forming technologies mentioned above reduce the cross section of a work piece that is deformed. As a result, the work piece is usually reduced to a geometry of thin foil or wire before nanostructures are formed inside it, which makes further plastic deformation difficult and the work piece unsuitable for most structural applications.

A common feature of SPD techniques for producing nanostructured materials is their capability of imparting large plastic deformation into a work piece without significantly changing its geometry. This makes it possible to repeatedly deform the work piece so that severe plastic strains can be introduced into it to create nanostructures.

Bridgman [32] first studied aspects of SPD processing of materials in the 1940s and 1950s, and established basic knowledge of material responses to severe deformation [33]. However, it was the work of Segal et al. [34] on equal channel angular extrusion (ECAE) in 1981 that gave birth to SPD processing of nanostructured materials. As discussed later, ECAE is also referred to as ECAP. Segal demonstrated the concept of subjecting a work piece to simple shear in order to modify its microstructure and enhance its properties. The work of Valiev et al. [35–37] significantly advanced the ECAE technique and created a momentum in the research and development of various aspects of the ECAE process and ECAE-processed materials. Recently, several new SPD techniques have been developed for processing nanostructured metals and alloys. This chapter focuses on SPD research and developments since Segal published his first work in international archival literature in 1981.

### 2.1. Principle of Grain Refinement through Plastic Deformation

It is not clear how the nanostructures are formed during the SPD processes. To make the matter more complex, each SPD technique generates a unique deformation mode, which refines grains in its own unique way. Hansen and co-workers [38] have done extensive work on the grain refinement mechanism during rolling. Their work primarily focuses on the early microstructural evolution at low to medium strains, for example, less than 100%. Although their work focuses on the microstructural evolution during rolling, we found that the general concept also applies to other deformation modes [39]. However, the detailed microstructural evolution may vary with deformation mode. In this section, we will discuss the microstructural evolution at low to medium strains, following the work of Hansen et al. Grain refinement processes at higher strains has not been well studied, and will only be discussed briefly.

Plastic deformation refines grains by a combination of several mechanisms, including dislocation glide, accumulation, interaction, tangling, and spatial rearrangement. Several polycrystalline deformation models have been helpful in

understanding the grain refinement process, including Sach's zero constraint model [40], Taylor's full constraint model [41], and the relaxed constraint model [42]. For equiaxed grains, it is generally agreed that Taylor's model is most appropriate [42, 43]. According to Taylor's model, slip is uniform within each grain and strain compatibility is achieved by simultaneous operation of at least five slip systems. However, it was found that the deformation within each grain is often not uniform in real materials. Consequently, the Taylor model has been modified.

It has been observed that in coarse-grained fcc materials, such as copper, each grain is divided into many volume elements during plastic deformation [44–60] and there are differences in the number and selection of active slip systems among neighboring volume elements [48, 49]. Each volume element deforms under a reduced number (less than 5) of slip systems, but a group of adjacent volumes act collectively to fulfill the Taylor criterion. Each volume element is usually subdivided into cells with dislocations forming cell boundaries. For this reason, the volume elements are referred to as cell blocks (CBs). Dislocations from neighboring CBs meet at their boundaries and interact to form CB boundaries. This type of boundaries is called geometrically necessary boundaries (GNB) since they are needed to accommodate the misorientation in neighboring CBs. The dislocation cell boundaries are called incidental boundaries since they are generated by statistical mutual trapping of glide dislocations [48], often supplemented by “forest” dislocations [61].

The misorientations are very small across cell boundaries but are much larger across cell-block boundaries. With increasing strain, the misorientations across cell and CB boundaries increase, and the sizes of cell blocks become smaller due to further division. At a certain strain, the misorientation between neighboring cells becomes so high that additional slip system may be triggered in the cells, which converts incidental boundaries into GNBs and makes the dislocation cells act like CBs. Domains surrounded by GNBs, such as CBs and CB-like dislocation cells, are called subgrain structures, and the GNBs are also called subgrain boundaries [48]. With further strain, large subgrains may further divide into smaller subgrains, and the misorientation between subgrains may increase to form low-angle GBs and high-angle ( $>15^\circ$ ) GBs. The above theory reasonably explains rolling-induced microstructures in metals with a medium to high stacking fault energy such as Cu and Al [45–47, 54], although the formation of subgrain structure from dislocation cells has not been experimentally observed.

Once the grains and subgrains reach a minimum size, they cannot be further divided into smaller grains/subgrains under a certain set of deformation parameters such as strain rate and temperature. We believe that when sufficiently small, each grain/subgrain can only sustain one set of slip systems, and therefore will deform uniformly. However, each grain may not have five active slip systems as hypothesized in Taylor's model. Instead, these small grains may deform in a coordinated way. Also, when the grains are very small, grain boundary sliding and grain rotation may also play a role in the deformation, assisting the coordinated deformation. Further experimental and theoretical studies are needed to clarify these issues.

## 2.2. Severe Plastic Deformation Techniques

### 2.2.1. Equal Channel Angular Pressing

ECAP is the most developed among all SPD techniques. It is also referred to as ECAE and equal channel angular (ECA) processing. We use the term ECAP in this review because it most precisely describes the physical process.

As shown in Figure 1, an ECAP die contains two channels, which are equal in cross section and intersect each other at an angle of  $\Phi$ . An outer arc, with an angle,  $\Psi$ , connects the two channels [62]. As a work piece is pushed through the channel, the shear strain imposed on the work piece from each ECAP pass is [63]

$$\gamma = 2 \cot\left(\frac{\Phi}{2} + \frac{\Psi}{2}\right) + \Psi \operatorname{cosec}\left(\frac{\Phi}{2} + \frac{\Psi}{2}\right) \quad (1)$$

When the outer arc angle  $\Psi = 0$ , the shear strain becomes

$$\gamma = 2 \cot\left(\frac{\Phi}{2}\right) \quad (2)$$

The most widely used ECAP geometry is a channel intersection angle of  $90^\circ$  and an outer arc angle of  $0^\circ$ , that is,  $\Phi = 90^\circ$  and  $\Psi = 0^\circ$ , which results in a shear strain of 2.

To compare the strains introduced by different deformation mode, we need to use von Mises equivalent strain, which is defined as

$$\varepsilon = \sqrt{\frac{2}{3} \left( \varepsilon_x^2 + \varepsilon_y^2 + \varepsilon_z^2 + \frac{\gamma_{xy}^2 + \gamma_{yz}^2 + \gamma_{zx}^2}{2} \right)} \quad (3)$$

The von Mises equivalent strain after one ECAP pass is

$$\varepsilon = \left[ \frac{2 \cot\left(\frac{\Phi}{2} + \frac{\Psi}{2}\right) + \Psi \operatorname{cosec}\left(\frac{\Phi}{2} + \frac{\Psi}{2}\right)}{\sqrt{3}} \right] \quad (4)$$

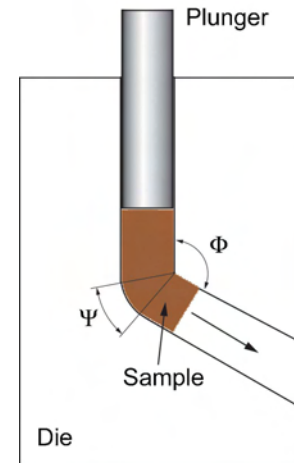


**Figure 1.** An ECAP die with a channel intersection angle  $\Phi$  and an outer arc angle  $\Psi$ .

For the special case of  $\Phi = 90^\circ$  and  $\Psi = 0^\circ$  (see Fig. 2), the equivalent strain is 1.15. Because of its simplicity, this is the die geometry most researchers have used to study fundamental issues in ECAP processing [22, 64–89]. As shown, a work piece is subjected to a simple shear at the shear plane.

Since the ECAP process does not change the sample cross section after each pass, it is possible to process a work piece for many passes, provided that the work piece does not fracture during the ECAP process. The multiple ECAP passes make it possible to rotate the billet around its longitudinal axis between adjacent passes, creating different ECAP routes [68, 71, 73, 90–94]. Four rotation routes have been used to study the microstructural development during the ECAP [68, 71, 73, 90–94]. They are defined by the rotation scheme of the billet around its axis (see Fig. 3) between two consecutive passes: route A: the billet is not rotated; route B<sub>C</sub>: the billet is rotated 90° clockwise; route B<sub>A</sub>: the billet is rotated 90° clockwise and counterclockwise alternately; route C: the billet is rotated 180°. Although both round and square channel cross sections have been reported, the square cross-section channel is preferred for fundamental studies because it allows accurate rotation of the work piece in different ECAP routes.

It has been found that the efficiency in refining grains and forming nanostructures varies with ECAP route [65, 67–69, 71, 77, 92, 94, 95]. For a  $\Phi = 90^\circ$  die, route B<sub>C</sub> has been found most effective in refining grains [67–69, 71, 77]. For a  $\Phi = 120^\circ$  die, route A is found most effective [92]. The effectiveness in grain refinement by different ECAP routes may be related to the unique shear strain plane/path of each ECAP route [77] (Fig. 4). We shall only discuss the special case of  $\Phi = 90^\circ$  in this review. Readers are referred to [77, 92] for more details for the  $\Phi = 120^\circ$  case.

As shown in Figure 4, in route A the odd-numbered passes shear along a plane that is perpendicular to the shear plane of even-numbered passes. In route B<sub>C</sub>, the odd-numbered passes shear along a plane that is 60° to the shear plane of even-numbered passes. In route B<sub>A</sub>, the shear plane orientations are a mixture of those in routes A and B<sub>C</sub>. In route C, the shear plane does not change, but the shear direction in odd-numbered passes is opposite to those in even-numbered passes. Therefore, the shear strain produced in even-numbered passes reverses the strain in odd-numbered passes.

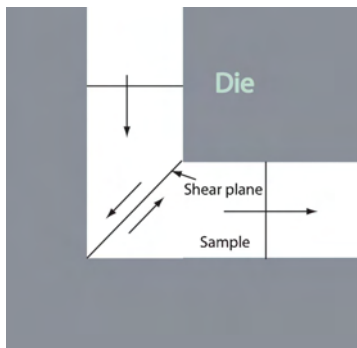


**Figure 2.** Schematics of an ECAP die with  $\Phi = 90^\circ$  and  $\Psi = 0^\circ$ . The sample is subjected to a shear strain of 2 at the shear plane.

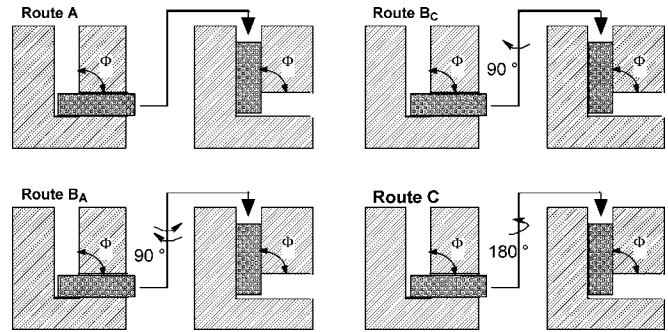


**Figure 3.** Rotation schemes of four ECAP routes. Reprinted with permission from [77], Y. T. Zhu and T. C. Lowe, *Mater. Sci. Eng. A291*, 46 (2000). © 2000, Elsevier Science.

Not surprisingly, the unique shear planes (or paths) of an ECAP route affect how the work piece is deformed during the ECAP. Assuming a cubic element is pressed through an ECAP die, it will be sheared into different shapes by different ECAP routes [62]. After the first ECAP pass, the cubic element is elongated (see Fig. 5). Obviously, the first pass is the same for all ECAP routes. The second ECAP pass by route A elongates the element further (see Fig. 6). The element will be continuously elongated with more ECAP passes by route A [62].

The second ECAP pass in route B<sub>A</sub> and route B<sub>C</sub> deform the element in the same way (see Fig. 7). In route B<sub>C</sub>, the element will be restored to cubic shape after the fourth pass, and every 4 $n$ th pass thereafter, where  $n$  is an integer. Route B<sub>A</sub> will continue to elongate the element into filamentary shapes. The second ECAP pass in route C restores the element to the cubic geometry (see Fig. 8). Route C restores the element to the cubic shape at every even-numbered pass. Readers are referred to [62, 69] for more details.

The grains in a sample are deformed in a way similar to the way a cubic element is, at least in the first few ECAP passes. For example, after the second ECAP pass in route C, the grains were found restored to the initial equiaxed shape [68], as a cubic element would. However, subgrain structures

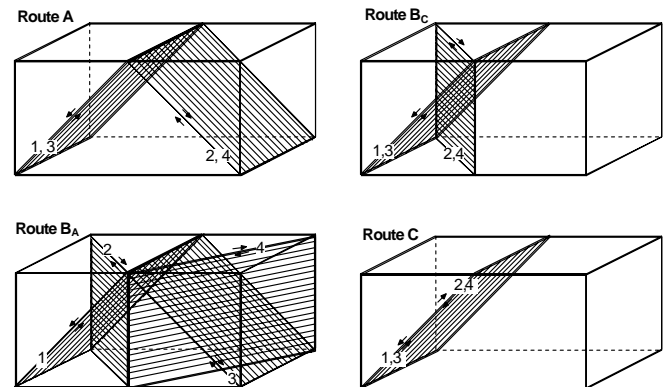


**Figure 4.** Shear-strain planes for each ECAP route for a die with  $\Phi = 90^\circ$ . The number on the shear plane indicates the sequence of an ECAP pass. Reprinted with permission from [77], Y. T. Zhu and T. C. Lowe, *Mater. Sci. Eng. A291*, 46 (2000). © 2000, Elsevier Science.

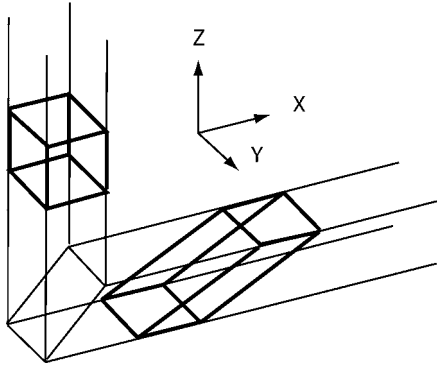


**Figure 5.** The deformation of a cubic element through the first ECAP pass.

were developed within initial coarse grains, although the shapes of initial coarse grains were not changed. For an ECAP die with  $\Phi = 90^\circ$ , substantial grain refinement is obtained after only one pass and the grain size usually reaches a minimum value after four passes. However, the fraction of high-angle grain boundaries continues to increase with further ECAP passes. It has also been found that ECAP route  $B_C$  is most effective in increasing the grain boundary angles [78] and produces most equiaxed grains, indicating that ECAP route affects the efficiency of grain refinement as well as nanostructural evolution.

ECAP has been used to process various metals and alloys, including Cu and Cu alloy [73, 96, 97], Al and Al alloys [65, 68, 71, 73, 91–94], Ni [90, 98], iron and steel [99–102], Ti and Ti alloy [74, 78], and W [103]. It has also been combined with other deformation techniques to obtain the best mechanical properties [104–106].

**2.2.2. High Pressure Torsion**

High-pressure torsion (HPT) is perhaps the most effective technique in grain refinement. It subjects a work piece to shear strain under high pressure. Two types of HPT processes have been reported [107]. One is unconstrained HPT (see Fig. 9), in which the sample is not contained on the side. This allows the sample to flow sideways during the HPT

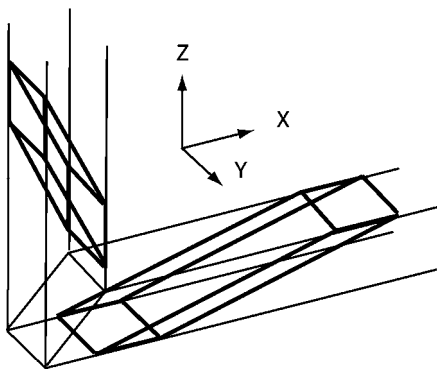


**Figure 6.** The element is further elongated after the second ECAP pass by route A.

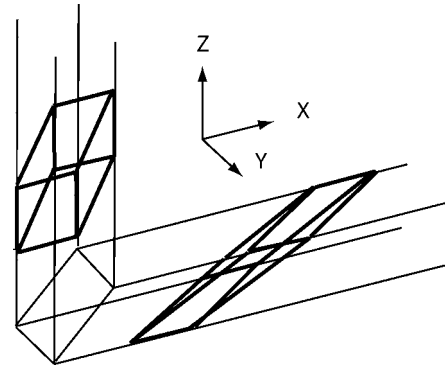


**Figure 7.** The deformation of an initially cubic element after the second ECAP pass in routes  $B_A$  and  $B_C$ .

processing. As a result, the sample thickness after HPT is not uniform, with the center of the sample thicker than the edge [108]. The nonuniform sample thickness also results in nonuniform pressure, with the highest pressure at the center of the sample.

Another type of HPT is constrained HPT, as shown in Figure 10 [31]. In constrained HPT, the sample is completely contained and a uniform sample thickness and pressure is maintained during the HPT process. Obviously, the constrained HPT is an improvement over the unconstrained HPT.

One major feature of the HPT process is the nonuniform deformation from the center of a sample to its edge [108]. The shear strain in an HPT-processed sample can be calculated as

$$\gamma = \frac{2\pi rn}{t} \tag{5}$$

where  $t$  is the sample thickness,  $r$  is the distance from the center of a sample disk, and  $n$  is the number of rotations in turns. Equation (5) can be easily applied to the constrained HPT (Fig. 10) because the thickness  $t$  remains constant. However, there could be slippage between the sample surface and the plunger and the lower die surface, making it difficult to know the real shear strain in the sample.

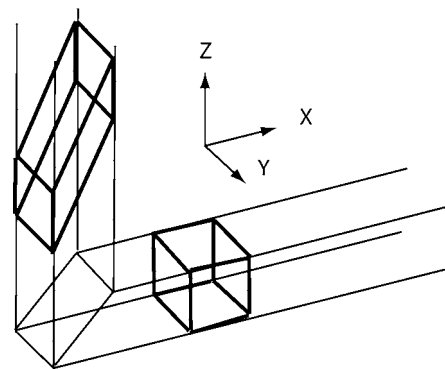


**Figure 8.** The second pass in route C restores the element to cubic geometry.



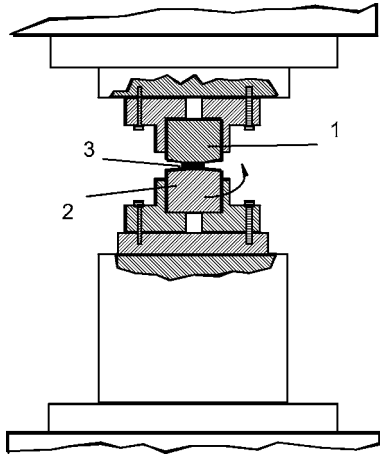


**Figure 9.** The schematics of an unconstrained HPT. Sample 3 is processed between heads 1 and 2.

As discussed earlier, for unconstrained HPT, due to the lack of side constraint, the sample flows in the radius direction during the process, resulting in a reduction of thickness. Moreover, the samples do not have a uniform thickness along the radius. The center of the sample is thicker than the edge. There may also be slippage between the sample and die surfaces (parts 1 and 5 in Fig. 9). These factors make it impossible to rigorously apply Eq. (5) to calculate the shear strain.

The microstructural evolution in Cu processed by unconstrained HPT has been studied by Jiang et al. [108]. Although Eq. (5) predicts a zero shear strain at the center of the sample disc, it is found that the grains are nevertheless refined and the microhardness increased at the center (see Fig. 11). Not surprisingly, the microstructure and hardness are not uniform from the center of the sample disc to its edge. Figure 11 shows the radial distributions of microhardness in copper discs processed by unconstrained HPT for varying turns. One can easily observe three salient features: (i) for all samples, the microhardness in the center is lower than that in the outer region, (ii) the microhardness increases with increasing number of HPT turns (strain), and (iii) near the outer edge, the microhardness does not

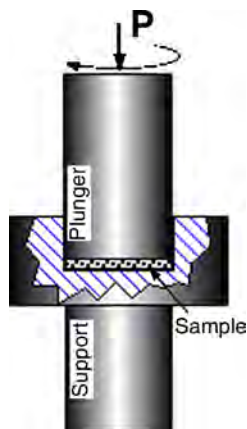


**Figure 10.** The schematics of a constrained HPT.

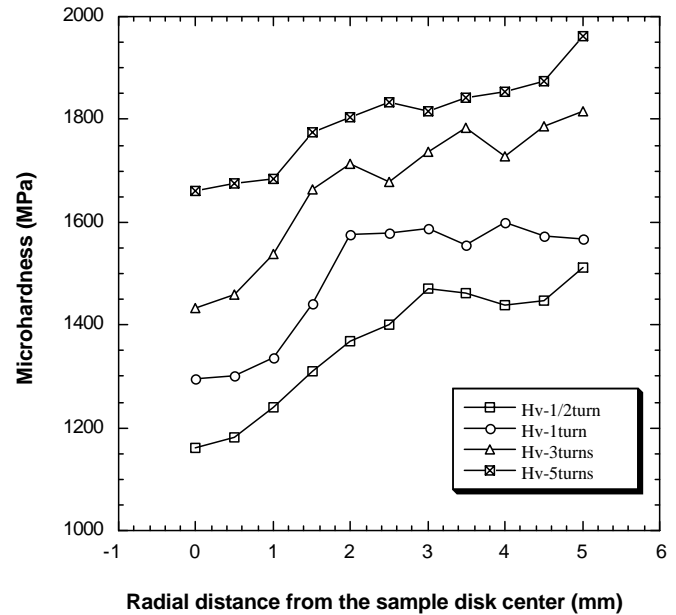


**Figure 11.** Radial distribution of the microhardness in Cu discs processed by HPT for varying turns.

change significantly with radial distance from the center. The microhardness saturation near the sample disc edge is attributed to the lower axial pressure and slippage, because the sample edge was thinner than the center.

No systematic studies on constrained HPT have been reported in the literature. It would be interesting to compare the evolution of microstructures and microhardness in materials processed by constrained HPT with that by unconstrained HPT.

In addition to being used for processing solid metals and alloys, HPT has also been used to consolidate powders and simultaneously produce nanostructures [23, 107, 109]. HPT generally can produce smaller nanograins than ECAP because of its high pressure as well as high strain.

### 2.2.3. Accumulative Roll Bonding

Accumulative roll bonding was developed in Japan in 1998 [27, 110–113]. Its principle is shown in Figure 12. As discussed before, the key to obtaining nanostructures through deformation is to keep the cross section of a work piece nearing constant. However, although rolling is one of the most efficient deformation techniques, it reduces the thickness of the work piece. The ARB technique solves this problem by stacking two sample sheets together. As shown in Figure 12, the process starts with cleaning the surface of metal sheets, stacking two sheets together, rolling the stacked sheets into the thickness of one sheet to bond them together, cutting the rolled sheet, and repeating the above cycle. This process cycle can be repeated many times until nanostructures are obtained. A critical step of the ARB process is the surface cleaning, which ensures that the two sheets bond well.

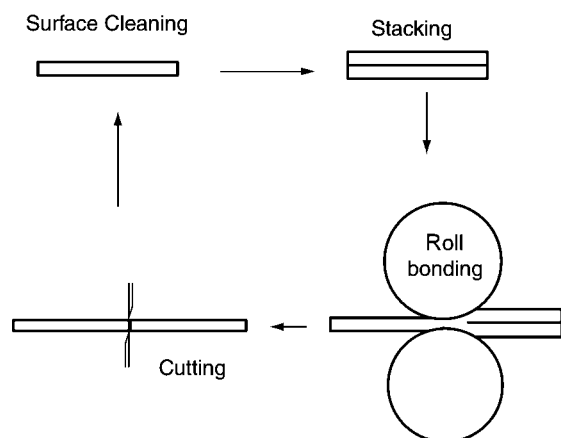


Figure 12. The principle of the ARB process.

### 2.2.4. Multipass Coin-Forging

Multipass coin-forging (MCF) is a new technique developed for producing nanostructured metals [28]. In the MCF process, a sample plate is deformed between two die platens with sine-wave-shaped grooves. The grooves indent the surface of the sample, producing a wavy surface, similar to coin-forging. The workpiece is then rotated and pressed again. The process can be repeated many times, thus the term multipass coin-forging.

MCF is a surface deformation technique, since the shallow grooves only deform the surface layer of a workpiece. However, as the surface layer is work hardened with increasing MCF passes, the workpiece is deformed progressively toward its center. Correspondingly, the grain refinement starts at the surface layer and progressively moves to the center of a work piece with increasing MCF passes.

### 2.2.5. Repetitive Corrugation and Straightening

Repetitive corrugation and straightening (RCS) was recently invented by Zhu et al. [29, 114]. Its principle is illustrated in Figure 13. One RCS processing cycle consists of two steps. The first step is carried out by deforming the work piece to a corrugated shape (Fig. 13), and the second step is accomplished by straightening the corrugated work piece between two flat platens. The processing cycle can be repeated many times. RCS has been used to process Cu, and effectively produced nanostructures in a Cu sample with an initial average grain size of  $760 \mu\text{m}$  [29, 39].

The RCS setup was initially designed to provide only bending deformation to the work piece. However, the setup in Figure 13 subjects the work piece to both bending and shear strain, which turns out to promote the grain refinement. Our recent results show that bending alone is not effective in refining grains because the bending strain is limited during each RCS cycle [115]. Recently, Shin et al. [116, 117] used a setup similar to Figure 13 to refine the grains of Al, and also found that the grains can be refined effectively.

The advantage of RCS is that it can be adapted easily to current industrial rolling facilities. It is not difficult to machine corrugating teeth onto the rollers of a conventional

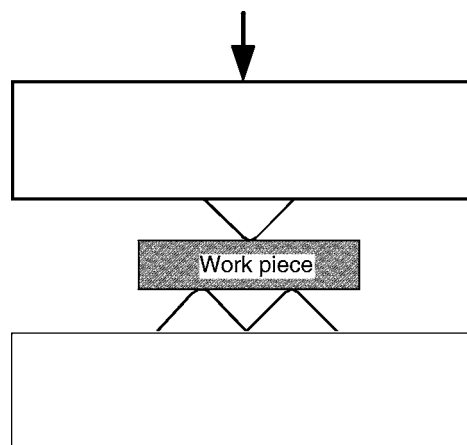


Figure 13. Die and work-piece setup for discontinuous RCS process.

rolling machine, which creates a continuous RCS process. Such a process has the potential to produce nanostructured materials in a continuous, economic way. The RCS technique is currently in its infancy and further R&D is needed to develop it into a mature SPD technique for producing nanostructured materials.

## 3. NANOSTRUCTURES

Nanomaterials synthesized by SPD techniques have unique nanostructures. The grain size distribution usually follows a lognormal statistical function [23]. ECAP, especially route  $B_C$ , in which the work piece is rotated  $90^\circ$  clockwise between adjacent passes, can produce equiaxed grains (see Fig. 14) [31]. In small grains, very few lattice dislocations are observed; in grains of intermediate size, a high density of lattice dislocations exists; and in large grains, subgrains are observed [22]. The nanostructures of metals and alloys processed by ECAP and HPT techniques have been reported by many research groups [22, 65, 73, 118]. In the following section, the nanostructures in a copper sample processed by RCS is presented. Although nanostructures generated by different SPD techniques are expected to be different,

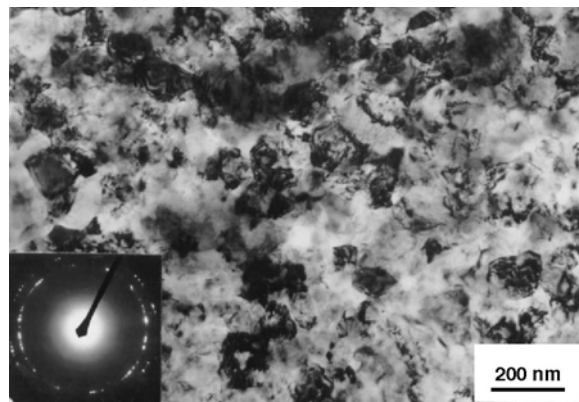


Figure 14. TEM micrographs of Cu after ECAP for 16 passes. Reprinted with permission from [31], R. Z. Valiev et al., *J. Mater. Res.* 17, 7 (2002). © 2002, Materials Research Society.

they are all produced by plastic deformation and therefore have some common features. We believe that most of the nanostructures discussed below are general structural features generated by SPD.

A pure Cu bar was processed by discontinuous RCS (see the setup shown in Fig. 13) [29]. The average grain size of the copper before RCS processing is  $760\ \mu\text{m}$ . The copper bar was immersed in liquid nitrogen for 3 minutes before each RCS cycle. The RCS cycle was repeated 14 times with  $90^\circ$  rotations between consecutive cycles along the longitudinal axis of the Cu bar.

The nanostructure of the RCS-processed copper observed under TEM is shown in Figure 15. It is seen that the grain size ranges from twenty to a few hundred nanometers. Most of the crystallites are separated by low-angle grain boundaries that consist of dislocation arrays, as pointed out by the black arrowheads. Boundaries separating grains with a misorientation less than  $15^\circ$  are defined as low-angle grain boundaries. High-angle grain boundaries also exist in many places, as marked by the long white arrows. Figure 15 also shows high dislocation densities in most of the new grains. In some of the larger grains, the distribution of dislocations is fairly homogeneous in the grain interior (see the grain marked H), while in other large grains dislocations form cell walls (see the grain marked C).

Subgrains exist in RCS-processed nanostructured copper [39]. As shown in Figure 16a, dense dislocation walls (DDWs) [44], which are almost parallel to the two sets of  $\{111\}$  planes, delineate a subgrain with a size of about  $250\ \text{nm}$ . High-density dislocations exist inside the subgrain and are forming cell structures. Figure 16b is a high-resolution TEM (HRTEM) image of the DDW subgrain boundary at the point marked by an arrowhead in Figure 16a. The dislocation density is estimated as  $3 \times 10^{17}\ \text{m}^{-2}$  at

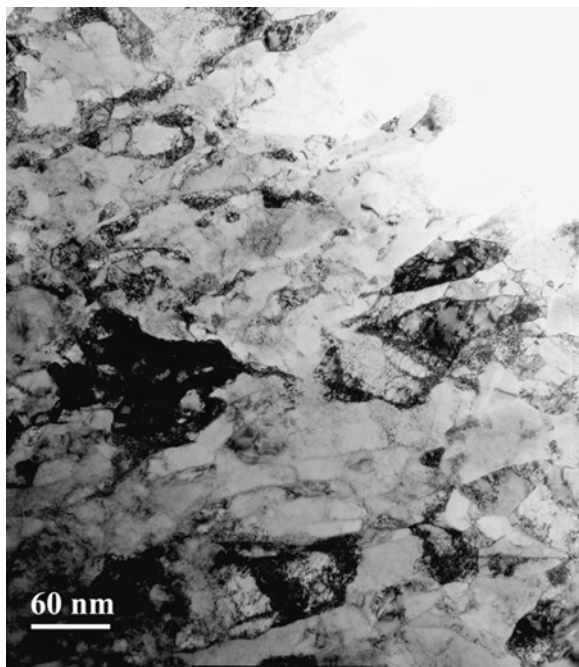


**Figure 15.** TEM micrograph shows nanostructures in copper processed by RCS.

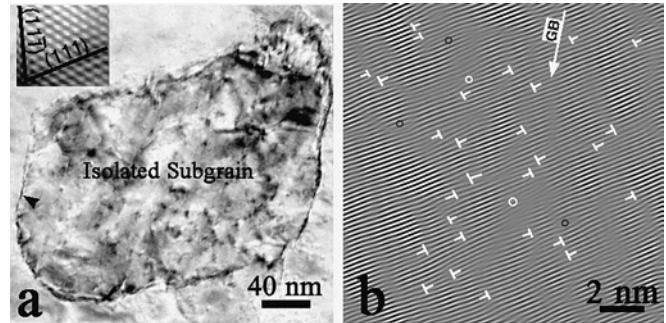


**Figure 16.** (a) A TEM micrograph of a subgrain; (b) an HRTEM image from the DDW as pointed out by an arrowhead in (a). The dislocations are glissile type. The longer arrow points out the grain boundary orientation. The black and white circles mark interstitial and vacancy loops, respectively. Reprinted with permission from [39], J. Huang et al., *Acta Mater.* 49, 1497 (2001). © 2001, Elsevier Science.

the DDW. Interstitial loops (marked by black circles) and vacancy loops (marked by white circles) also exist. The dislocations are mostly glissile type. In addition, the lattice planes near the cell walls are heavily distorted. The misorientation across the subgrain boundary is measured as about  $5^\circ$ . There are significantly more dislocations than required to accommodate the misorientation. Thus, this subgrain boundary is in a nonequilibrium state.

Both equilibrium and nonequilibrium grain boundaries (GBs) exist in nanostructured materials synthesized by SPD. Shown in Figure 17a is a low-angle GB with a misorientation of  $9^\circ$  in RCS-processed Cu [39]. HRTEM images from the upper-left frame are shown in Figure 17b. Figure 17c is a structural model for the low-angle GB in Figure 17b. It is seen from Figure 17c that two types of dislocations, marked with T and  $\bar{T}$  respectively, are needed to accommodate the geometrical misorientation. In other words, these are geometrically necessary, or intrinsic, dislocations [22]. Figure 17b clearly shows three more T-type dislocations than Figure 17c does, which indicates that three extrinsic (or non-geometrically necessary) dislocations exist at the GB shown in Figure 17b. Therefore, this segment of low-angle GB is in a high-energy configuration and should be called nonequilibrium GB. On the other hand, Figure 17d shows that the GB in the lower-right frame is in an equilibrium state with no extrinsic dislocations.

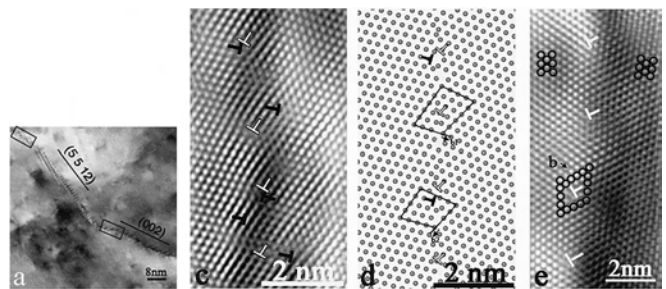


**Figure 17.** (a) A TEM micrograph of a low-angle GB; (b) and (c) an HRTEM image and a structural model of the GB in the upper-left frame in (a); (d) an HRTEM image of the GB in the lower-right frame. Reprinted with permission from [39], J. Huang et al., *Acta Mater.* 49, 1497 (2001). © 2001, Elsevier Science.

Figure 18 shows a TEM micrograph of a grain with a diameter of about 500 nm in RCS-processed Cu [39]. A number of fine structures were observed in the interior of the grain. As pointed out by two arrowheads, an array of dislocations piled up along the (111) plane. Consequently, two subgrains (denoted by 1 and 2) with a misorientation of about  $1^\circ$  were produced. A low-angle GB was also found in this grain, as marked by four stars. The low-angle GB was formed by the accumulation of a number of glissile dislocations. It is not edge-on but overlapped, as revealed by the periodic Moiré fringes. The misorientation of the two grains as measured from an HREM image is about  $5^\circ$ .

Dislocation cell structure was also observed in subgrain 3 in Figure 18. These cells may form individual subgrains upon further plastic straining. Dislocation tangling was frequently observed in the interior of grains, as marked by a white circle, where the grain is heavily strained. Such a region was referred to as dislocation-tangle zone (DTZ). In the area marked by a white square, dislocation cells are forming from tangled dislocations.

## 4. PROPERTIES

### 4.1. Mechanical Properties

It is well known that plastic deformation induced by conventional forming methods such as rolling, drawing, or extrusion can significantly increase the strength of metals [119, 120]. However, this increase is usually accompanied by a loss of ductility. For example, as shown in Figure 19, with increasing

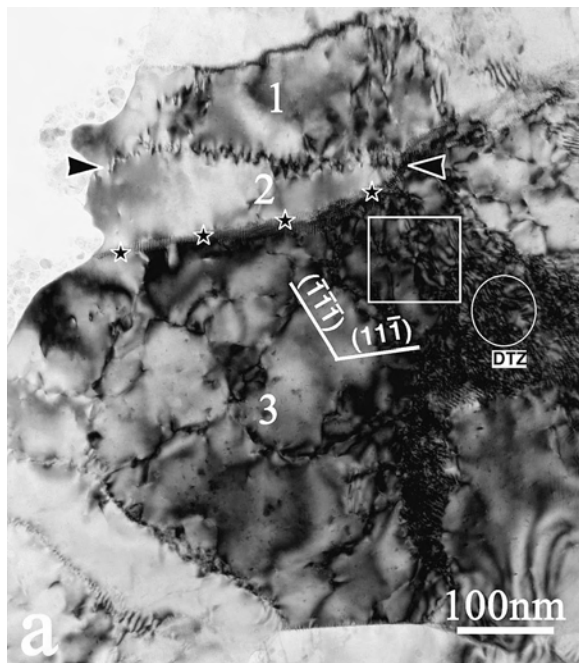


**Figure 18.** A TEM micrograph showing fine deformation structures in a grain. The numbers 1, 2, and 3 denote three subgrains; the two arrowheads point out an array of dislocations; the four stars mark a low-angle GB; the white circle marks a dislocation tangle zone (DTZ); the white square marks a transition from DTZ to dislocation cells. Reprinted with permission from [39], J. Huang et al., *Acta Mater.* 49, 1497 (2001). © 2001, Elsevier Science.

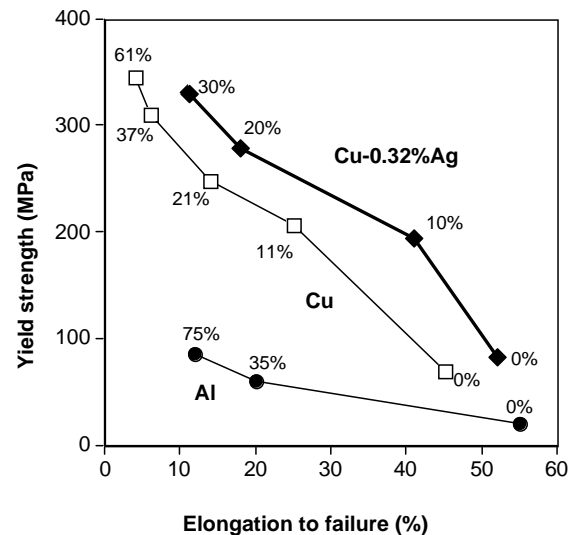


**Figure 19.** With increasing rolling strain, the yield strengths of Al, Cu, and a Cu alloy increase but their ductilities decrease.

rolling strain, the yield strengths of Al, Cu, and Cu-0.32Ag alloy monotonically increase, accompanied by a monotonic decrease in ductility (elongation to failure). The same trend is also true for other metals and alloys. Note that for heavily rolled metals, the ductility could slightly increase with increasing rolling strain. However, this increase is very limited and the overall ductility is usually very low. For example, elongation to failure of pure Ni and Al increased from 1.2% to 4% and from 6% to 8%, respectively, when the rolling strain increased from 4 to 6 for Ni and 2 to 4 for Al [121].

In contrast, nanostructured metals and alloys processed by SPD techniques such as ECAP and HPT have demonstrated high strength, while retaining high ductility. Horita et al. [122] compared the strength and ductility of 3004 aluminum alloy processed by ECAP and cold rolling. As shown in Figure 20, for both cold-rolled and ECAPed 3004 alloy, the yield strength increased monotonically with increasing equivalent strain imparted into the alloy by cold rolling or ECAP. However, the ductility of the alloy demonstrated different trends for the two different processing methods. Note that in Figure 20, each ECAP pass imparts an equivalent strain of 1. After one ECAP pass (a strain of 1), the elongation to failure (ductility) of the 3004 alloy decreased from 32% to about 14%. Further ECAP passes (or larger ECAP strains) did not decrease the ductility further. In contrast, the cold rolling decreased the ductility of the 3004 alloy in a similar magnitude initially, but further decreases the ductility with increasing rolling strain, although at a slower rate. This demonstrates that the deformation mode (or strain path) has a significant effect on the ductility of the metals. Cold rolling introduces plastic strain into the work piece with one deformation mode (strain path), while ECAP changes the strain path by rotating the work piece  $90^\circ$  clockwise between two adjacent passes (ECAP route B<sub>C</sub>) [77, 122]. Consequently, the ECAP processing resulted in equiaxed grains, in contrast to the elongated grains typically produced by cold rolling. The different microstructure as well as texture rendered remarkably different ductilities.

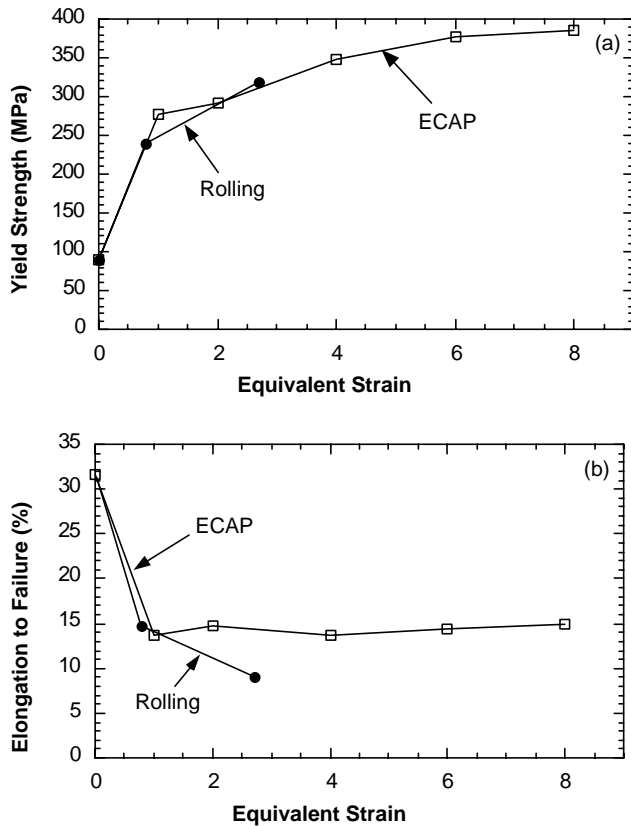


**Figure 20.** Comparison of yield strength and ductility of the 3004 Al alloy processed by cold rolling and ECAP [122].

The high ductility of the ECAP-processed metals is highly desired for structural applications.

Recently, even higher ductility was found in copper and titanium processed by ECAP and HPT to a higher strain [31]. Pure Cu (99.996%) was processed using ECAP with 90° clockwise rotations along the billet axis between consecutive passes, while pure Ti (99.98%) was processed using HPT. All processes were performed at room temperature. Strength and ductility were measured by uniaxial tensile tests performed using samples with gauge dimensions of  $5 \times 2 \times 1$  mm. Resulting engineering stress-strain curves are shown in Figure 21. Results for Cu tested at room temperature in its initial and three processed states are shown in Figure 21a. The initial coarse-grained Cu, with a grain size of about  $30 \mu\text{m}$ , has a low yield stress but exhibits significant strain hardening and a large elongation to failure. This behavior is typical of coarse-grained metals. The elongation to failure is a quantitative measure of ductility, and is taken as the engineering strain at which the sample broke. Cold rolling of the copper to a thickness reduction of 60% significantly increased the strength (curve 2 in Fig. 21a), but dramatically decreased the elongation to failure. This is consistent with the classical mechanical behaviour of metals that are deformed plastically [123, 124]. This tendency is also true for Cu subjected to two passes of ECAP (curve 3 in Fig. 21a). However, further deforming the Cu to 16 ECAP passes simultaneously increased both the strength and the ductility (curve 4 in Fig. 21a). Furthermore, the increase in ductility is much more significant than the increase in

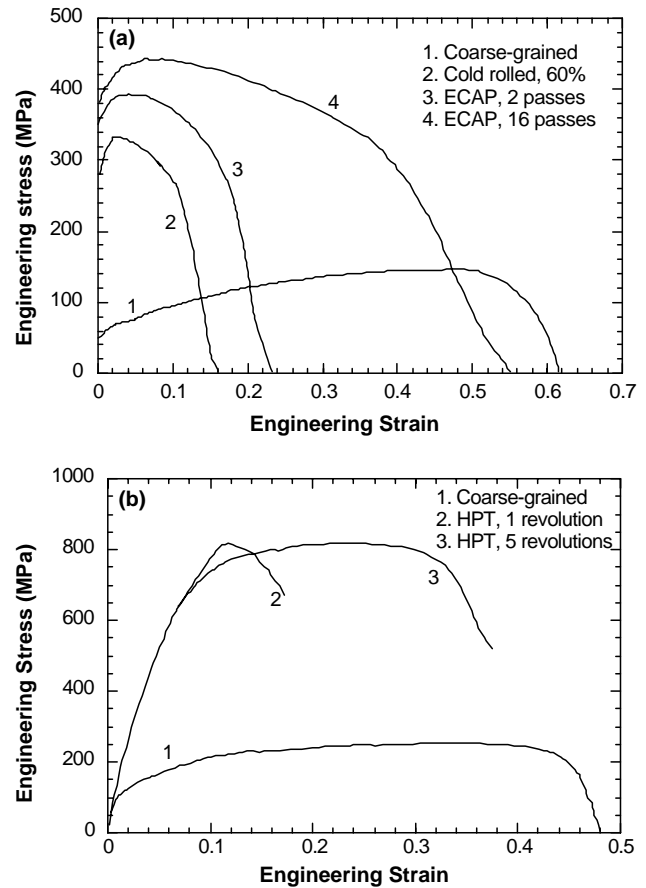


**Figure 21.** Tensile engineering stress-strain curves of (a) Cu tested at 22 °C and (b) Ti tested at 250 °C. Both were tested at a strain rate of  $10^{-3} \text{ s}^{-1}$ . The processing conditions for each curve are listed on the figure. Reprinted with permission from [31], R. Z. Valiev et al., *J. Mater. Res.* 17, 7 (2002). © 2002, Materials Research Society.

strength. Such results have never been observed before and challenge our current understanding of mechanical properties of metals processed by plastic deformation.

Similar results were also observed in Ti samples subjected to HPT, which were tested in tension at 250 °C. The coarse-grained Ti with a grain size of  $20 \mu\text{m}$  exhibits a low strength and a large elongation to failure (curve 1 in Fig. 21b). After being processed by HPT for 1 revolution, the Ti material had a very high strength but significantly decreased ductility. Further HPT processing to 5 revolutions dramatically increased the ductility and slightly increased the strength (curve 3 in Fig. 21b).

Figure 21 shows that small SPD strains (2 ECAP passes or 1 HPT revolution) significantly increase the strength at the expense of the ductility, which is consistent with the results shown in Figure 20, while very large SPD strains (16 ECAP passes or 5 HPT revolutions) dramatically increase the ductility and at the same time further increase the strength. This is contrary to our classical understanding of the mechanical behavior of metals that were deformed plastically. Greater plastic deformation by conventional techniques such as rolling, drawing, or extrusion introduces greater strain hardening, which in turn increases the strength, but decreases the ductility of the metal. The extraordinary mechanical

behavior in metals processed by SPD at high strains suggests a fundamental change in deformation mechanisms. It also suggests the possibility of tailoring the microstructures through SPD to obtain superior mechanical properties.

It is not clear what nanostructures are responsible for the excellent ductility shown in Figure 21. In most SPD-processed nanomaterials, good ductility is maintained with high strength. The mechanical behavior of nanostructured Ti processed through warm ECAP + cold rolling was studied by Jia et al. [125]. It has a high yield strength of  $\sim 900$  MPa and a good ductility of about 9% (much higher than that for typical cold-rolled Ti). There was no strain hardening in the compressive stress-strain curve except at the beginning when the strain is less than 0.05. Early necking was observed in the tensile stress-strain curve. The strain rate sensitivity was found to be lower than that of coarse-grained Ti. The good ductility was observed despite the lack of strain hardening and low strain rate sensitivity. Significant post-necking strain was observed, indicating excellent resistance to fracture during the necking process. SEM micrographs of fracture surfaces show that the nanostructured Ti formed much finer voids than the coarse-grained Ti, which explains the high fracture resistance of nanostructured Ti [126].

## 4.2. Superplasticity

Superplasticity is a material behavior in which a material sustains a tensile strain of hundreds to thousands percent without failure. Such behavior is usually observed in materials with micrometer-sized grains at a relatively high temperature ( $0.5\text{--}0.6 T_m$ ) and low strain rate ( $10^{-3}$  to  $10^{-4}$ ), where  $T_m$  is the melting temperature of the material [22]. Due to their fine grain size, nanostructured materials processed by SPD exhibit superior superplasticity at higher strain rate and lower temperature [22, 67, 72, 97, 127–132].

Pure nanostructured metals have low thermal stability, and therefore are not suitable for superplastic deformation [22]. It is critical to maintain a stable grain structure during the superplastic deformation, which will be destroyed by excess grain growth. McFadden et al. observed superplasticity in nanostructured Ni, intermetallic  $\text{Ni}_3\text{Al}$ , and Al alloys processed by SPD at low temperatures [131]. They also observed moderate grain growth during the superplastic deformation of nanostructured materials, due to the unstable nature of nanostructures in these materials.

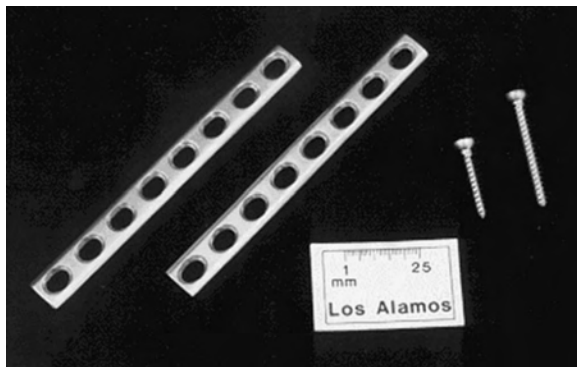


**Figure 22.** Plate-implants for bone osteosynthesis made of nanostructured Ti.

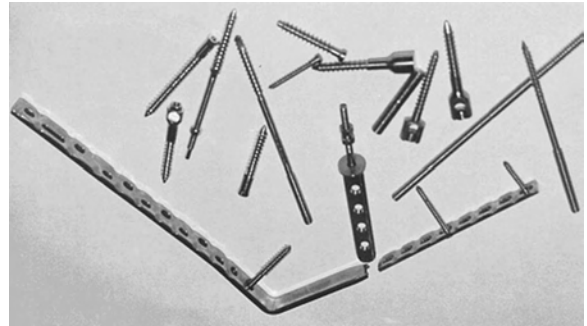


**Figure 23.** Various medical implants and devices made of nanostructured Ti.

Horita et al. [127] observed superplasticity with a maximum elongation of 2280% in an Al-3%Mg-0.2%Sc at  $400^\circ\text{C}$  and a high strain rate of  $3.3 \times 10^{-2} \text{ S}^{-1}$ . An Al-3%Mg-0.2%Sc-0.12%Zr alloy processed by ECAP exhibited excellent thermal stability at  $500^\circ\text{C}$  and was superplastically deformed to an elongation of 1680% at  $500^\circ\text{C}$  and a strain rate of  $\times 10^{-2} \text{ S}^{-1}$  [128]. Nanostructured Cu-based alloys processed by ECAP also showed superplasticity [133].

## 5. APPLICATIONS

SPD can produce nanostructured materials in bulk form large enough for structural applications. With their superior mechanical properties, nanostructured materials produced by SPD are very attractive in applications such as medical devices and implants such as stents, prosthetics, bone screws and dental implants, sport goods such as golf clubs and bicycle frames, as well as aerospace structures. Due to their high production costs, the realistic applications of SPD-processed nanostructured materials will be in the high-valued medical market in the near term. ECAP is so far the most developed SPD technique and produces relatively large bulk nanostructured materials (see Fig. 24).

As more economical SPD techniques are developed, such as continuous ECAP and RCS, nanostructured materials will be cost competitive in other lower-valued markets. Pilot medical implants and devices have already been developed in a joint project between Los Alamos National Laboratory



**Figure 24.** An ECAP processed Ti rod, which is about 50 mm in diameter and 170 mm in length.



and Russian institutes (see Figs. 22 and 23) [134]. These medical implants, made of nanostructured Ti, are already on medical trials in Russia.

## 6. CONCLUDING REMARKS

Severe plastic deformation has great commercial potential for producing nanostructured materials for structural applications. Among all the SPD techniques, ECAP is the most developed and can so far produce the largest bulk nanostructured materials. However, ECAP is a discontinuous technique, which makes it a labor-intensive and relatively expensive process. Continuous ECAP and other continuous SPD techniques such as RCS are currently being developed, which may pave the way for large-scale applications of nanostructured materials.

Nanostructured materials show a combination of high strength and good ductility. However, the relationship between nanostructures and the mechanical properties is not well understood. It is possible to obtain both high strength and high ductility in nanostructured materials processed by SPD by tailoring their nanostructures. However, better understanding of structural-property relationship is needed before it is possible to optimize the nanostructures for optimum mechanical properties.

## GLOSSARY

**Accumulative roll bonding (ARB)** An SPD technique with each process cycle consisting of roll-bonding metal sheets and then restacking them for the next roll bonding.

**Bottom-up approach** An approach that builds bulk nanostructured materials from individual atoms or nanoscale building blocks.

**Constrained HPT** An HPT technique with the work piece fully constrained on all sides.

**Equal channel angular pressing (ECAP)** An SPD technique in which a work piece is pressed through two channels that are equal in cross section and intersect each other at an angle. It is also referred to as equal channel angular extrusion (ECAE).

**ECAP route A** A route that does not rotate the work-piece billet between adjacent ECAP passes.

**ECAP route B<sub>A</sub>** A route that rotates the work-piece billet 90° clockwise and counterclockwise alternately.

**ECAP route B<sub>C</sub>** A route that rotates the work-piece billet 90° clockwise.

**ECAP route C** A route that rotates the work-piece billet 180°.

**Equilibrium grain boundary** A grain boundary that contains only crystalline defects, such as dislocations, that are necessary for accommodating the grain misorientation across the boundary.

**Extrinsic dislocations** Dislocations that are at or near a grain boundary but are not needed for accommodating the grain misorientation across the boundary.

**Geometrically necessary boundary (GNB)** A boundary that separates two subgrains with two different sets of active slip systems.

**High-angle grain boundary** A boundary with the two grains across it having a misorientation higher than 15°.

**High-pressure torsion (HPT)** An SPD technique that refines metal and alloys into nanostructured materials by torsion under high pressure.

**Intrinsic dislocations** Dislocations that are required for forming a grain boundary.

**Multipass coin-forging (MCF)** An SPD technique that repetitively deforms the surface layer of a work piece so that grains are refined progressively from the surface of a work piece to its center.

**Nanostructured materials** Solids with nanoscale (1–100 nm) structural domains in at least one dimension.

**Nonequilibrium grain boundary** A grain boundary that has higher energy than minimum energy required by the grain misorientation across it.

**Repetitive corrugation and straightening (RCS)** An SPD technique that refines the grains of metals and alloys by repetitively corrugating and straightening them.

**Severe plastic deformation (SPD)** Techniques that refine coarse-grained metals and alloys into nanostructured materials by imparting extremely large plastic deformation into them.

**Subgrains** Volumes formed inside a grain by plastic deformation, with each volume (subgrain) containing one set of active slip systems. Subgrain boundaries are geometrically necessary boundaries.

**Top-down approach** An approach that refines existing coarse-grained materials into nanostructured materials.

**Unconstrained HPT** An HPT technique with the side of the work piece unconstrained.

## ACKNOWLEDGMENT

The author acknowledges the support of US Department of Energy Initiative for Proliferation Prevention (IPP) program.

## REFERENCES

1. H. Gleiter, *Acta Mater.* 48, 1 (2000).
2. C. Koch, Nanostructure Science and Technology, A Worldwide Study, Final Report, WTEC Panel, 1999, p. 93.
3. R. W. Siegel, in "Fundamental Properties of Nanostructured Materials" (D. Fiorani and G. Sberveglieri, Eds.), pp. 3–19. World Scientific, Singapore, 1993.
4. C. Suryanarayana, *Int. Mater. Rev.* 40, 41 (1995).
5. E. L. Hu and D. T. Shaw, Nanostructure Science and Technology, A Worldwide Study, Final Report, WTEC Panel, 1999, p. 15.
6. H. Gleiter, in "Deformation of Polycrystals: Mechanisms and Microstructures" (Hansen et al., Eds.), p. 15. Risø National Laboratory Roskilde, Denmark, 1981.
7. C. Koch, *Nanostr. Mater.* 2, 109 (1993).
8. B. H. Kear and L. E. McCandish, *Nanostr. Mater.* 3, 19 (1993).
9. H. Chang, C. J. Altstetter, and R. S. Averback, *J. Mater. Res.* 7, 2962 (1992).
10. R. Bickerdike, D. Clark, J. N. Easterbrook, G. Hughes, W. N. Mair, P. G. Partridge, and H. C. Ranson, *Int. J. Rapid Solidif.* 1, 305 (1985).
11. W. Chang, G. Skandan, S. C. Danforth, M. Rose, A. G. Balogh, H. Hahn, and B. Kear, *Nanostr. Mater.* 6, 321 (1995).

12. R. A. Roy and R. Roy, *Mater. Res. Bull.* 19, 169 (1984).
13. D. A. Rigney, *Ann. Rev. Mater. Sci.* 18, 141 (1988).
14. B. Li and E. J. Lavernia, in "Non-Equilibrium Processing of Materials" (C. Suryanarayana, Ed.), pp. 153–189. Pergamon, New York, 1999.
15. G. W. Nieman, J. R. Weertman, and R. W. Siegel, *Scripta Metall.* 23, 2013 (1989).
16. S. R. Agnew, B. R. Elliott, C. J. Yongdahl, K. J. Hemker, and J. R. Weertman, *Mater. Sci. Eng.* A285, 391 (2000).
17. P. G. Sanders, G. E. Fougere, L. J. Thompson, J. A. Eastman, and J. R. Weertman, *Nanostr. Mater.* 8, 243 (1997).
18. J. Rawers, G. Slavens, D. Govier, C. Dogan, and R. Doan, *Metall. Mater. Trans. A* 27, 3126 (1996).
19. L. He and E. Ma, *J. Mater. Res.* 11, 72 (1996).
20. G. R. Shaik and W. W. Milligan, *Metall. Mater. Trans. A* 28, 895 (1997).
21. R. S. Mishra, J. A. Schneider, J. F. Shackelford, and A. K. Mukherjee, *Nanostr. Mater.* 5, 525 (1995).
22. R. Z. Valiev, R. K. Islamgaliev, and I. V. Alexandrov, *Progress in Materials Science* 45, 103 (2000).
23. I. V. Alexandrov, Y. T. Zhu, T. C. Lowe, R. K. Islamgaliev, and R. Z. Valiev, *Metall. Mater. Trans. A* 29, 2253 (1998).
24. T. C. Lowe and R. Z. Valiev, in "Investigations and Applications of Severe Plastic Deformation" (T. C. Lowe and R. Z. Valiev, Eds.), p. xiii. Kluwer Academic, Dordrecht, 2000.
25. V. M. Segal, *Mater. Sci. Eng.* A271, 322 (1999).
26. R. Z. Valiev, O. A. Kaibyshev, R. I. Kuznetsov, R. Sh. Musalimov, and N. K. Tsenev, *Doklady Akademii nauk SSSR* 301, 864 (1988).
27. N. Tsuji, Y. Ito, Y. Koizumi, Y. Minamino, and Y. Saito, in "Ultrafine Grained Materials II" (Y. T. Zhu, T. G. Langdon, R. S. Mishra, S. L. Semiatin, M. J. Saran, and T. C. Lowe, Eds.), p. 389. The Minerals, Metals & Materials Society, 2002.
28. A. K. Ghosh and W. Huang, in "Investigations and Applications of Severe Plastic Deformation" (T. C. Lowe and R. Z. Valiev, Eds.), p. 29. Kluwer Academic, Dordrecht, 2000.
29. Y. T. Zhu, H. Jiang, J. Huang, and T. C. Lowe, *Metall. Mater. Trans.* 32A, 1559 (2001).
30. Y. T. Zhu, T. C. Lowe, R. Z. Valiev, V. V. Stolyarov, V. V. Latysh, and G. I. Raab, U.S. Patent 6, 399, 215.
31. R. Z. Valiev, I. V. Alexandrov, Y. T. Zhu, and T. C. Lowe, *J. Mater. Res.* 17, 7 (2002).
32. P. W. Bridgman, "Studies in Large Plastic Flow and Fracture." McGraw-Hill, New York, 1952.
33. T. C. Lowe, Y. T. Zhu, S. L. Semiatin, and D. R. Berg, in "Investigations and Applications of Severe Plastic Deformation" (T. C. Lowe and R. Z. Valiev, Eds.), p. 347. Kluwer Academic, Dordrecht, 2000.
34. V. M. Segal, V. I. Reznikov, A. E. Drobyshvskiy, and V. I. Kopylov, *Russ. Metall.* 1, 99 (1981).
35. R. Z. Valiev, O. A. Kaibyshev, R. I. Kuznetsov, R. Sh. Musalimov, and N. K. Tsenev, *DAN SSSR* 301, 864 (1988).
36. R. Z. Valiev, N. A. Krasilnikov, and N. K. Tsenev, *Mater. Sci. Eng. A* 168, 141 (1993).
37. R. Z. Valiev, A. V. Korznikov, and R. R. Mulyukov, *Mater. Sci. Eng. A* 168, 141 (1993).
38. B. Bay, N. Hansen, D. A. Hughes, and D. Kuhlmann-Wilsdorf, *Acta Mater.* 40, 205 (1992).
39. J. Huang, Y. T. Zhu, H. Jiang, and T. C. Lowe, *Acta Mater.* 49, 1497 (2001).
40. G. Sachs, *Z. Ver. Dtsch. Ing.* 72, 734 (1928).
41. G. I. Taylor, *J. Inst. Met.* 62, 307 (1938).
42. U. F. Kocks, in "Texture and Anisotropy" (U. F. Kocks, C. N. Tomé, and H.-R. Wenk, Eds.), p. 391. Cambridge University Press, Cambridge, UK, 1998.
43. M. G. Stout and J. A. O'Rourke, *Metal. Trans.* 20A, 125 (1989).
44. N. Hansen, *Mater. Sci. Tch.* 6, 1039 (1990).
45. B. Bay, N. Hansen, D. A. Hughes, and D. Kuhlmann-Wilsdorf, *Acta Mater.* 40, 205 (1992).
46. D. A. Hughes and N. Hansen, *Acta Mater.* 45, 3871 (1997).
47. B. Bay, N. Hansen, and D. Kuhlmann-Wilsdorf, *Mater. Sci. Eng.* A113, 385 (1989).
48. D. Kuhlmann-Wilsdorf and N. Hansen, *Scripta Metall. Mater.* 25, 1557 (1991).
49. N. Hansen, *Scripta Metall. Mater.* 27, 1447 (1992).
50. Q. Liu and N. Hansen, *Scripta Metall. Mater.* 32, 1289 (1995).
51. V. S. Ananthan, T. Leffers, and N. Hansen, *Scripta Metall. Mater.* 25, 137 (1991).
52. N. Hansen and X. Huang, *Acta Mater.* 46, 1827 (1998).
53. N. Hansen and D. A. Hughes, *Phys. Stat. Sol. (b)* 149, 155 (1995).
54. N. Hansen and D. Juul Jensen, *Phil. Trans. R. Soc. Lond. A* 357, 1447 (1999).
55. Q. Liu, D. Juul Jensen, and N. Hansen, *Acta Mater.* 46, 5819 (1998).
56. C. Rey, *Rev. Phys. Appl.* 23, 491 (1988).
57. C. S. Barret and L. H. Lewenson, *Trans. Met. Soc., AIME* 137, 113 (1940).
58. C. S. Barret, *Trans. Am. Inst. Min. Met. Eng.* 161, 15 (1945).
59. W. A. Wood and W. A. Rachinger, *J. Inst. Met.* 76, 237 (1950).
60. W. A. Wood and R. F. Scrutton, *J. Inst. Met.* 77, 423 (1950).
61. D. Kuhlmann-Wilsdorf, *Mater. Sci. Eng.* A113, 1 (1989).
62. M. Furukawa, Z. Horita, M. Nemoto, and T. G. Langdon, *J. Mater. Sci.* 36, 2835 (2001).
63. Y. Iwahashi, J. Wang, Z. Horita, M. Nemoto, and T. G. Langdon, *Scripta Mater.* 35, 143 (1996).
64. S. Komura, Z. Horita, M. Nemoto, and T. G. Langdon, *J. Mater. Res.* 14, 4044 (1999).
65. Y. Iwahashi, M. Furukawa, Z. Horita, M. Nemoto, and T. G. Langdon, *Metall. Mater. Trans.* 29A, 2245 (1998).
66. P. B. Berbon, M. Furukawa, Z. Horita, M. Nemoto, and T. G. Langdon, *Metall. Mater. Trans.* 30A, 1989 (1999).
67. M. Nemoto, Z. Horita, M. Furukawa, and T. G. Langdon, *Mater. Sci. Forum* 304–306, 59 (1999).
68. Y. Iwahashi, Z. Horita, M. Nemoto, and T. G. Langdon, *Acta Mater.* 46, 3317 (1998).
69. M. Furukawa, Y. Iwahashi, Z. Horita, M. Nemoto, and T. G. Langdon, *Mater. Sci. Eng.* A257, 328 (1998).
70. K. Nakashima, Z. Horita, M. Nemoto, and T. G. Langdon, *Mater. Sci. Eng.* A281, 82 (2000).
71. K. Oh-Ishi, Z. Horita, M. Furukawa, M. Nemoto, and T. G. Langdon, *Metall. Mater. Trans.* 29A, 2011 (1998).
72. M. Furukawa, Z. Horita, M. Nemoto, and T. G. Langdon, *Mater. Sci. Eng.* A324, 82 (2002).
73. S. Ferrasse, V. M. Segal, K. T. Hartwig, and R. E. Goforth, *Metall. Mater. Trans.* 28A, 1047 (1997).
74. S. L. Semiatin, V. M. Segal, R. E. Goforth, N. D. Frey, and D. P. Delo, *Metall. Mater. Trans.* 30A, 1425 (1999).
75. D. P. Delo and S. L. Semiatin, *Metall. Mater. Trans.* 30A, 2473 (1999).
76. D. P. Delo and S. L. Semiatin, *Metall. Mater. Trans.* 30A, 1391 (1999).
77. Y. T. Zhu and T. C. Lowe, *Mater. Sci. Eng.* A291, 46 (2000).
78. V. V. Stolyarov, Y. T. Zhu, I. V. Alexandrov, T. C. Lowe, and R. Z. Valiev, *Mater. Sci. Eng. A* 299, 59 (2001).
79. T. R. McNelley, D. L. Swisher, Z. Horita, and T. G. Langdon, in "Ultrafine Grained Materials II" (Y. T. Zhu, T. G. Langdon, R. S. Mishra, S. L. Semiatin, M. J. Saran, and T. C. Lowe, Eds.), p. 15. The Minerals, Metals & Materials Society, 2002.
80. P. L. Sun, P. W. Kao, and C. P. Chang, in "Ultrafine Grained Materials II" (Y. T. Zhu, T. G. Langdon, R. S. Mishra, S. L. Semiatin, M. J. Saran, and T. C. Lowe, Eds.), p. 35. The Minerals, Metals & Materials Society, 2002.
81. C. Xu and T. G. Langdon, in "Ultrafine Grained Materials II" (Y. T. Zhu, T. G. Langdon, R. S. Mishra, S. L. Semiatin,

- M. J. Saran, and T. C. Lowe, Eds.), p. 163. The Minerals, Metals & Materials Society, 2002.
82. R. Z. Valiev, in "Ultrafine Grained Materials II" (Y. T. Zhu, T. G. Langdon, R. S. Mishra, S. L. Semiatin, M. J. Saran, and T. C. Lowe, Eds.), p. 313. The Minerals, Metals & Materials Society, 2002.
  83. Z. Horita, K. Neishi, and T. G. Langdon, in "Ultrafine Grained Materials II" (Y. T. Zhu, T. G. Langdon, R. S. Mishra, S. L. Semiatin, M. J. Saran, and T. C. Lowe, Eds.), p. 449. The Minerals, Metals & Materials Society, 2002.
  84. D. P. DeLo and S. L. Semiatin, in "Ultrafine Grained Materials II" (Y. T. Zhu, T. G. Langdon, R. S. Mishra, S. L. Semiatin, M. J. Saran, and T. C. Lowe, Eds.), p. 539. The Minerals, Metals & Materials Society, 2002.
  85. R. Ye. Lapovok and R. E. Cottam, in "Ultrafine Grained Materials II" (Y. T. Zhu, T. G. Langdon, R. S. Mishra, S. L. Semiatin, M. J. Saran, and T. C. Lowe, Eds.), p. 547. The Minerals, Metals & Materials Society, 2002.
  86. N. Q. Chinh, G. Voros, Z. Horita, and T. G. Langdon, in "Ultrafine Grained Materials II" (Y. T. Zhu, T. G. Langdon, R. S. Mishra, S. L. Semiatin, M. J. Saran, and T. C. Lowe, Eds.), p. 567. The Minerals, Metals & Materials Society, 2002.
  87. K. Xia and J. Wang, in "Ultrafine Grained Materials II" (Y. T. Zhu, T. G. Langdon, R. S. Mishra, S. L. Semiatin, M. J. Saran, and T. C. Lowe, Eds.), p. 575. The Minerals, Metals & Materials Society, 2002.
  88. I. J. Beyerlein, R. A. Lebensohn and C. N. Tome, in "Ultrafine Grained Materials II" (Y. T. Zhu, T. G. Langdon, R. S. Mishra, S. L. Semiatin, M. J. Saran, and T. C. Lowe, Eds.), p. 585. The Minerals, Metals & Materials Society, 2002.
  89. S. R. Agnew, G. M. Stoica, L. J. Chen, T. M. Lillo, J. Macheret, and P. K. Liaw, in "Ultrafine Grained Materials II" (Y. T. Zhu, T. G. Langdon, R. S. Mishra, S. L. Semiatin, M. J. Saran, and T. C. Lowe, Eds.), p. 643. The Minerals, Metals & Materials Society, 2002.
  90. V. M. Segal, *Mater. Sci. Eng.* A197, 157 (1995).
  91. S. Ferrasse, V. M. Segal, K. T. Hartwig, and R. E. Goforth, *J. Mater. Res.* 12, 1253 (1997).
  92. P. B. Prangnell, A. Gholinia, and V. M. Markushev, in "Investigations and Applications of Severe Plastic Deformation" (T. C. Lowe and R. Z. Valiev, Eds.), p. 65. Kluwer Academic, Dordrecht, 2000.
  93. K. Nakashima, Z. Horita, M. Nemoto, and T. G. Langdon, *Acta Mater.* 46, 1589 (1998).
  94. Y. Iwahashi, Z. Horita, M. Nemoto, and T. G. Langdon, *Acta Mater.* 45, 4733 (1997).
  95. T. G. Langdon, M. Furukawa, M. Nemoto, and Z. Horita, *JOM* 52, 30 (2000).
  96. S. R. Agnew, U. F. Kocks, K. T. Hartwig, and J. R. Weertman, in "Proceedings of 19<sup>th</sup> Risø International Symposium on Materials Science: Modeling of Structure and Mechanics from Microscale to Product" (J. V. Carstensen, T. Leffers, T. Lorentzen, O. B. Pedersen, B. F. Sørensen and G. Winther, Eds.), pp. 201–206. Roskilde, Denmark, 1998.
  97. K. Neishi, T. Uchida, A. Yamauchi, K. Nakamura, Z. Horita, and T. G. Langdon, *Mater. Sci. Eng.* A307, 23 (2001).
  98. K. Neishi, Z. Horita, and T. G. Langdon, *Mater. Sci. Eng.* A325, 54 (2002).
  99. M. A. Gibbs, K. T. Hartwig, L. R. Cornwell, R. E. Goforth, and E. A. Payzant, *Scripta Mater.* 39, 1699 (1998).
  100. D. H. Shin, W. J. Kim, and W. Y. Choo, *Scripta Mater.* 41, 259 (1999).
  101. D. H. Shin, C. W. Seo, J. Kim, K. T. Park, and W. Y. Choo, *Scripta Mater.* 42, 695 (2000).
  102. Y. Fukuda, K. Oh-ishi, Z. Horita, and T. G. Langdon, *Acta Mater.* 50, 1359 (2002).
  103. R. Z. Valiev, private communication, 2002.
  104. V. V. Stolyarov, Y. T. Zhu, T. C. Lowe, and R. Z. Valiev, *Nano-Structured Materials* 11, 947 (1999).
  105. V. V. Stolyarov, Y. T. Zhu, T. C. Lowe, and R. Z. Valiev, *Mater. Sci. Eng.* A303, 82 (2001).
  106. V. V. Stolyarov, Y. T. Zhu, T. C. Lowe, and R. Z. Valiev, *J. Nanoscience Nanotechnology* 1, 237 (2001).
  107. I. V. Alexandrov, Y. T. Zhu, T. C. Lowe, and R. Z. Valiev, *Powder Metallurgy* 41, 11 (1998).
  108. H. Jiang, Y. T. Zhu, D. P. Butt, I. V. Alexandrov, and T. C. Lowe, *Mater. Sci. Eng.* A290, 128 (2000).
  109. I. V. Alexandrov, Y. T. Zhu, T. C. Lowe, R. K. Islamgaliev, and R. Z. Valiev, *NanoStructured Materials* 10, 45 (1998).
  110. Y. Saito, H. Utsunomiya, N. Tsuji, and T. Sakai, "Proceedings of the 6<sup>th</sup> International Conference on Aluminum Alloys (ICAA-6)," 1998, p. 2003.
  111. Y. Saito, N. Tsuji, H. Utsunomiya, T. Sakai, and R. G. Hong, *Scripta Mater.* 39, 1221 (1998).
  112. N. Tsuji, Y. Saito, H. Utsunomiya, and S. Tanigawa, *Scripta Mater.* 40, 795 (1999).
  113. S. B. Kang, H. W. Kim, C. Y. Lim, and Z. P. Xing, in "Ultrafine Grained Materials II" (Y. T. Zhu, T. G. Langdon, R. S. Mishra, S. L. Semiatin, M. J. Saran, and T. C. Lowe, Eds.), p. 661. The Minerals, Metals & Materials Society, 2002.
  114. Y. T. Zhu, H. Jiang, J. Huang, and T. C. Lowe, U.S. Patent 6, 197, 129 B1, 2001.
  115. Y. T. Zhu and H. Jiang, unpublished result, 2002.
  116. J. J. Park and D. H. Shin, in "Ultrafine Grained Materials II" (Y. T. Zhu, T. G. Langdon, R. S. Mishra, S. L. Semiatin, M. J. Saran, and T. C. Lowe, Eds.), p. 253. The Minerals, Metals & Materials Society, 2002.
  117. D. H. Shin, J. J. Park, Y. S. Kim, and K. T. Park, *Mater. Sci. Eng.* A298, 98 (2002).
  118. D. H. Shin, B. C. Kim, K. T. Park, and W. Y. Choo, *Acta Mater.* 48, 3245 (2000).
  119. P. W. Bridgman, "Studies in Large Plastic Flow and Fracture." McGraw-Hill, New York, 1952.
  120. E. Schmid and W. Boas, "Plasticity of Crystals, with Special Reference to Metals." Chapman and Hall, London, 1968.
  121. S. S. Hecker and M. G. Stout, in "Deformation, Processing and Structure" (G. Krauss, Ed.). ASM, Materials Park, OH, 1984.
  122. Z. Horita, T. Fujinami, M. Nemoto, and T. G. Langdon, *Metall. Mater. Trans.* 31A, 691 (2000).
  123. E. A. Brandes and G. B. Brook, "Smithells Metals Reference Book," 7<sup>th</sup> ed., Ch. 22. Butterworth-Heinemann Ltd., Oxford, 1992.
  124. E. R. Parker, "Materials Data Book for Engineers and Scientists." McGraw-Hill, New York, 1967.
  125. D. Jia, Y. M. Wang, K. T. Ramesh, E. Ma, Y. T. Zhu, and R. Z. Valiev, *Appl. Phys. Lett.* 79, 611 (2001).
  126. Y. T. Zhu, J. Y. Huang, J. Gubicza, T. Ungár, E. Ma, and R. Z. Valiev, submitted to *J. Mater. Res.*
  127. Z. Horita, M. Furukawa, N. Nemoto, A. J. Barnes, and T. G. Langdon, *Acta Mater.* 48, 3633 (2000).
  128. S. Lee, A. Utsunomia, H. Akamatsu, K. Neishi, M. Furukawa, Z. Horita, and T. G. Langdon, *Acta Mater.* 48, 3633 (2002).
  129. R. S. Mishra, R. Z. Valiev, S. X. McFadden, and A. K. Mukherjee, *Mater. Sci. Eng.* A252, 174 (1998).
  130. R. Z. Valiev, R. K. Islamgaliev, V. V. Stolyarov, and R. S. Mishra, *Mater. Sci. Forum* 269–272, 969 (1998).
  131. S. X. McFadden, R. S. Mishra, R. Z. Valiev, A. P. Zhilyaev, and A. K. Mukherjee, *Nature* 398, 684 (1999).
  132. M. Furukawa, Z. Horita, and T. G. Langdon, in "Ultrafine Grained Materials II" (Y. T. Zhu, T. G. Langdon, R. S. Mishra, S. L. Semiatin, M. J. Saran, and T. C. Lowe, Eds.), p. 449. The Minerals, Metals & Materials Society, 2002.
  133. Z. Horita, K. Neishi, and T. G. Langdon, in "Ultrafine Grained Materials II" (Y. T. Zhu, T. G. Langdon, R. S. Mishra, S. L. Semiatin, M. J. Saran, and T. C. Lowe, Eds.), p. 459. The Minerals, Metals & Materials Society, 2002.
  134. R. Z. Valiev and Y. T. Zhu, unpublished, 2001.

# Nanomaterials for Cell Engineering

Xiaoyue Zhu, Tommaso F. Bersano-Begey, Shuichi Takayama

University of Michigan, Ann Arbor, Michigan, USA

## CONTENTS

1. Introduction
  2. Nanoscale Biological Recognition and the Cellular Nanoenvironments
  3. Materials with Controlled Nanogeometry
  4. Materials with Controlled Nanochemistry
  5. Materials with Controlled Nanomechanics
  6. Conclusion and Future Prospects
- Glossary  
References

## 1. INTRODUCTION

If we were to look from a sufficient distance, we would not be able to distinguish between a plain gray surface and the blurring of black texts and white background on a page of a book. However, it is exactly these minute features (the letters and their precise arrangement into words and sentences) that give meaning to a book. The same is true for cells and the materials they secrete or interact with. Any attempt to engineer cells for tissue reconstruction, biomedical research, and applications has to start from recognizing the role played by the nanoscale elements around the cells, because the cells “read” and interact with surrounding surfaces, materials, and other cells at this scale.

Nowhere else is nanotechnology more at work than in living organisms. The genetic information of living organisms is encoded on a 2 nm wide nucleic acid “tape” called deoxyribonucleic acid (DNA) [1]. This information is translated into machineries called proteins, which have average dimensions ranging from 3 to 150 nm [2]. Proteins can function individually as chemical factories (enzymes) [3], molecular motors (kinesins) [4], and docking modules (receptors and adaptor molecules) [3]. Multiple proteins, nucleic acids, and other molecules can assemble into larger complexes (tens to hundreds of nanometers in size) to fulfill more complicated functions such as supporting cell structure and movement, functioning as railroad tracks to transport cellular cargos (microtubules) [5], serving as pipes and valves (ion channels) [6], generating power or pumping ions (adenosine

triphosphatases) [7], acting as sources and sensors for light (rhodopsins) [8], heat transient receptor potential cation channel, subfamily M, member 8 (TRPM8s) [9], electricity [10], tension [11], and chemicals [3], and translating messenger RNA information into amino acid sequences to produce proteins (ribosomes) [12]. Electron tomography, which allows visualization of intact cell organelles and the dynamic reorganization of cell architecture in three dimensions [13], reveals that the 80 S ribosomes are ~27 nm in size and 26 S proteasomes are ~45 nm in length in *Dictyostelium* cells [14].

Many cellular activities require nanoscale machineries. For example, the cell membrane has nanometer scale channels that only allow ions and molecules of a certain size, charge, and polarity to pass through [15, 16]. The channels can achieve such selectivity because their pore sizes are on the same order as those of the molecules that pass through them [17]. The selectivity helps to maintain a steady intracellular environment in terms of pH and concentrations of ions and molecules. The concentration gradients of potassium, sodium, and calcium ions maintain a constant electric potential across the membrane that regulate many cellular phenomena including the function of neuronal cells [18]. In another example, molecular motors and cytoskeletal movements minimize energy requirements by taking advantage of Brownian motion. These molecular devices are nanoscale ratchets—structures that only allow movement in one direction. The molecular ratchets use random molecular vibration of Brownian motion to generate directed movement of cellular machineries with minimal energy cost [19].

The extracellular environment is highly controlled and is as dependent on nanoscale features and structures as the internal cellular components are. With the exception of single cell organisms such as bacteria, cells are “designed” to live in an ordered architecture to form tissues, in which cells interact with each other and communicate with the extracellular environment. Cells maintain their structures and perform coherent functions inside tissues under the guidance of nanoscale materials outside the cells, which are collectively termed the extracellular matrix (ECM) [20]. The ECM is a matrix composed of a variety of proteins and carbohydrates that have nanoscale structures and organizations that can be recognized by cells [2]. The ECM directs complex,

cooperative events such as embryogenesis [21] and organogenesis [22]. Cells respond to cues presented by topographical features [23], chemical patterns [24], and mechanical characteristics [25] of the ECM [26].

Cells constantly monitor their environments to decide their behavior [3, 27]. A large majority of cells are adherent and cell-ECM interactions are crucial in determining cell functions such as growth [28], development [29], and wound healing [30]. Abnormal cell-ECM interactions can cause diseases such as cancer and other functional defects [31]. Because the basic features of cells and the ECM lie in their nanoscale composition, it is necessary to understand, match, and manipulate these nanoscale features to control and induce certain desired cell behaviors. The development of nanoscale materials is crucial for engineering cells in applications such as tissue engineering, cell-based assays for drug delivery, and studies of basic cell biology and mechanisms of disease [24, 32–34].

This chapter describes recent work in developing nanoscale materials for engineering cells and is organized as follows. Section 2 gives an overview of the cellular nanoenvironment and the cell-ECM interactions in more detail. Sections 3, 4, and 5 address efforts to synthesize materials with nanoscale topography, nanoscale chemical patterns, and nanoscale mechanical properties that mimic the natural ECM. Section 6 discusses future prospects for nanomaterials in engineering cellular functions.

## 2. NANOSCALE BIOLOGICAL RECOGNITION AND THE CELLULAR NANOENVIRONMENTS

The majority of the cells in our body need to attach to appropriate substrates, such as the ECM, to survive and function properly [20, 35]. The ECM surrounds anchorage-dependent cells, connects them into tissue structures [36], and influences tissue development [2], cell migration [37], proliferation [35, 38, 39], and morphology [40]. Figure 1 shows some of the important nanoscale interactions between cells and the ECM.

Reflecting its complex regulatory function, the ECM has a correspondingly diverse composition [41] and a three-dimensional (3D) structural organization [26, 42, 43]. *In vivo* (that is, within a living organism), the ECM is made and oriented mainly by fibroblasts or other cells that produce ECM precursor molecules. The precursor molecules are chemically processed (enzymatically cleaved, sulfated, oxidized, and cross-linked) as they assemble with other components of the ECM [41]. After initial assembly, cells further rearrange the ECM molecules through physical interactions. For example, even *in vitro* (that is, in an artificial environment outside the living organism), fibroblasts mixed with a meshwork of randomly oriented collagen fibrils will tug on the collagen and cause the fibers to align into nanolines [44–47] (Fig. 1E). The assembly of this matrix is thus a highly regulated and dynamic process that results in distinct structures at the molecular, nanometer, and micrometer length scales. The relative amounts of the different matrix components and the ways they are organized into the extracellular matrix

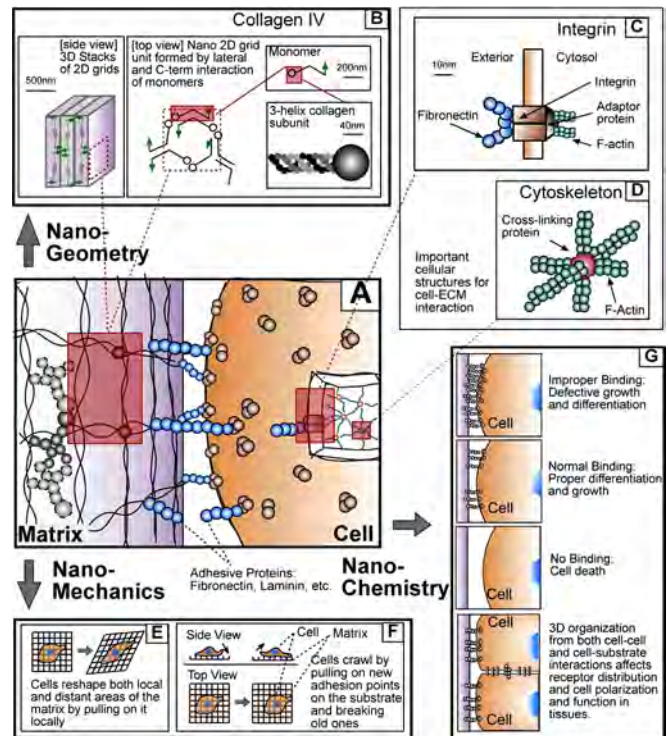


**Figure 1.** Interactions between cell and substrate. The large image in the center (A) shows a conceptual view of the interaction interface between a cell and the extracellular matrix. Both surfaces have unique nanogeometry, nanochemistry, and nanomechanics and are patterned with proteins. The matrix of basal lamina is composed of type IV collagen proteins shown in (B), assembled together through lateral (lines) and C-term (circles) interactions to form a rigid 2D network similar to a grid. (Other matrix configurations found in the skin, tendon, bone, and other tissues use fibrillar collagen forms instead, which is not shown). Once a 2D grid plane is assembled, the N-term domain (arrows) from each monomer induces the formation of multiple 2D grid layers. The nanoscale mesh formed by collagen and other matrix proteins is essential for many of the nanomechanical and nanochemical mechanisms exhibited by cells. The relative rigidity of the grid-like nanostructures, for example, allows cells to migrate or crawl by forming and releasing new bonds with the matrix and pulling on them (F). In addition, since the junctions of the grid can be more easily pivoted than stretched, cells can also remodel the matrix by pulling on parts of it so that these distortions propagate through it (E). Migration is involved in many important cellular processes such as wound healing and organ formation. The density and arrangement of receptor binding between cells and matrix or between cells themselves (G) can also act as signals for apoptosis (programmed cell death), contact inhibition of growth, differentiation into different cell types, and cell polarization, in which cells form different structures on different sides of the cell, as determined by their arrangement with respect to substrates such as basal lamina and other surrounding cells. The connection between matrix proteins such as collagen and the cell interior is formed by cell surface receptor proteins such as integrin (C). Integrins connect through adaptor proteins to a complex 3D mesh inside the cell, called the cytoskeleton (D). The cytoskeleton is essential for maintaining cell shape and anchoring cell surface receptors such as integrins on the membrane surface. The cell can rearrange its cytoskeleton by inducing polymerization or depolymerization of the filamentous actin (F-actin) to lengthen or shorten them. The resulting changes in the cytoskeleton can be used to push or pull on the integrins and on the matrix and substrate connected to it and thus allow the cell to crawl or rearrange the substrate.



give rise to an amazing diversity of forms, each adapted to the functional requirements of particular tissues [41].

Cells “read” these ECM cues through cell surface receptors. One of the critical adhesion receptors is integrin (Fig. 1C). It is named based on its function as an integrator of the ECM and the cytoskeleton (“cell bones,” Fig. 1D) [47, 48]. Integrins are a family of heterodimeric receptors. They extend across the cell membrane and mediate communication between the cells and the ECM by translating features of extracellular materials into intracellular signals [47–49]. There are three levels of integrin signaling: (i) molecular recognition of specific ligands at the single integrin level [50], (ii) nanometer scale recognition of clusters of ligands that leads to aggregation of integrins [51], and (iii) mechanical signaling where clusters of integrins separated by micrometers serve to transmit forces through the cell [49].

The ECM must display appropriate ligands for receptors such as integrins to bind to them [52]. Having the right ligand available, however, does not guarantee desired responses from cells. Even with the same total number of ligands, the response of a cell can be totally different depending on the nanometer scale organization of the ligands (Fig. 3). For example, Griffith et al. [53] studied cell proliferation and migration on dendrimers with different numbers of ligands per dendrimer. Compared with solitary integrins, the integrin clusters that assembled around dendrimers presenting multiple RGD (Arg-Gly-Asp peptides) ligands differed in their ability to recruit adaptor proteins and cytoskeleton components to the intracellular portion of integrins. In another study, RGD ligand density at a substrate surface was shown to be critical for inducing C2C12 skeletal myoblast (muscle precursor cell) differentiation (Fig. 1G) [51, 54–56]. The ECM also regulates cells through mechanical signaling. Ingber et al. [57–59] performed a number of elegant studies that correlated cell growth, death, and differentiation with mechanical signaling on artificially engineered substrates, focusing particularly on cell shape. Results showed that micropatterns of cell-adhesive proteins on a material can regulate cell growth, apoptosis, and differentiation through control of cell shape and cytoskeleton tension.

In humans and other animals, abnormal ECM can influence embryonic development, cell polarity, migration, differentiation, growth, tissue organization, and wound regeneration [28–30, 60]. Invasiveness of tumor cells also depends critically on the nature of the ECM material surrounding the cells. The loss of ECM binding in epithelial cells is often a sign of tumor aggression [61–63].

The importance of understanding nanoscale environments and the corresponding cellular behaviors has led to the development of man-made materials that mimic certain aspects of the ECM. These materials allow controlled, systematic perturbation and analysis of the crucial environmental cues to elicit specific cellular responses. Such efforts can be divided into three categories; study of nanometer-sized (i) structural features, (ii) chemical and molecular patterns, and (iii) mechanical properties. There are major challenges in engineering such materials due to the small size scale and high spatial resolution that are prerequisites for mimicking the ECM. In contrast to the highly regulated and

complex nanoscale organization of the ECM *in vivo*, conventional biomaterials commonly present unorganized micro- and nanoenvironments to cells.

The following three sections and Table 1 summarize the current knowledge on man-made nanomaterials used for cell engineering. The sections focus on the nanoscale geometrical structures, chemical patterns, and mechanical properties of the materials. They also summarize the techniques used to fabricate the nanomaterials.

### 3. MATERIALS WITH CONTROLLED NANOGOMETRY

One of the steps necessary to mimic physiological cellular environments is to study the nanogeometry of the ECM. Topographical features of the ECM have been explored with scanning electron microscopy, transmission electron microscopy, and atomic force microscopy. These studies have revealed that the ECM is a mesh of various fibrils that create topographical features such as pores, ridges, and grooves at nanometer scale [64] (Fig. 2). For example, in the porcine carotid artery, the surface topography of the ECM has feature heights of approximately  $1\ \mu\text{m}$  [65] whereas the ECM of the primate corneal epithelia has average feature

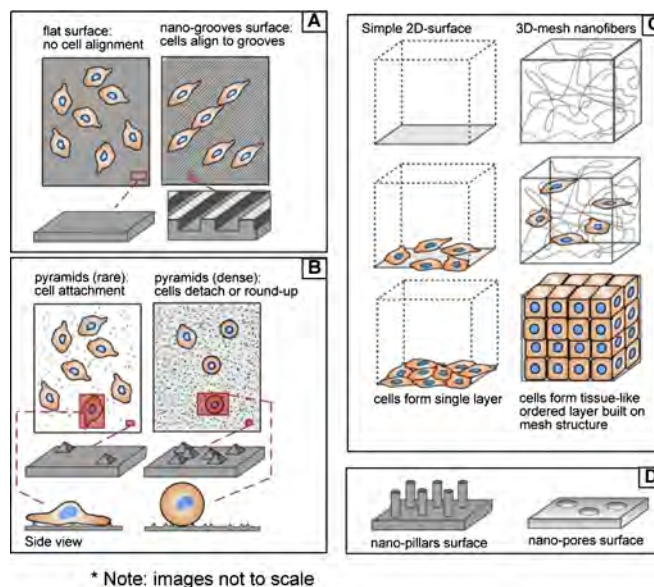


**Figure 2.** Nanofabricated synthetic features can affect cells by mimicking topography present on biological surfaces. Structures with different geometries affect cellular processes such as attachment and focal adhesion generation, cell alignment, and tissue formation. For example, a surface with embedded nanogrooves (A) causes cells to align and grow in the direction of the grooves similar to how certain cells align based on structural cues in biological tissues. (Nanowaves have a similar effect on cells even though they only possess rounded corners unlike the sharp corners on grooves). Pyramids (B) can interfere with focal adhesion formation and if present in sufficient density can cause cells to detach. (Rough surfaces and nanopillars (D) can have similar effects by presenting a surface that does not have sufficient contiguous space for cells to make functional focal adhesion point.) Three-dimensional meshes of ECM or polymer-based fibers (C) can act as scaffolds and allow cells to form tissue-like 3D constructs.



heights of 147–191 nm [66, 67]. In general, the average diameters of ECM fibers range from 3 to 500 nm in different species and tissues [2].

The bulk of nanomaterials research that is aimed at engineering cell function has been focused on controlling nanogeometry. These efforts are aided in large part by fabrication technology developed in the semiconductor industry. Commonly used techniques include photolithography, laser holography, chemical vapor deposition, various etching procedures [8, 68], and soft lithography [69]. In addition, isolation techniques (extracting ECM from tissues) allow incorporation of natural ECM components into artificial materials [66, 67].

A range of different nanoscale geometries have been engineered to mimic those of the ECM [70–72]. These surfaces include features such as fibers, groove/ridges, cliffs, pores, pillars, and pits. Some features, such as pillars, are seldom observed in physiological environments [73, 74]. Nonetheless, such artificial features are still useful in studying and engineering cellular behavior and in inducing or preventing cell attachment [75].

Collagen, one of the most abundant ECM components, plays a major role in determining the nanogeometrical features of ECM. Collagen forms fibrils and bundles of fibrils, which are three to hundreds of nanometers in diameter [41]. A variety of 3D architectures of collagen fibers are seen in different tissues, such as parallel bundles (in muscle, tendons, and ligaments), basket-weaves (in skins and bones), and orthogonal lattices (in corneas) [41, 76] [Fig. 1B shows an example of how collagen IV monomers assemble into stacked two-dimensional (2D) grids in basal laminae]. Fibrils of collagen are known to cause myoblasts, endothelial cells, and other types of cells to align [77]. Other components that comprise the ECM are proteins such as fibronectin and laminin and heavily glycosylated macromolecules such as glycosaminoglycans and peptidoglycans. Different features resulting from diverse combinations of these components give rise to specific cellular responses such as adhesion, orientation, proliferation, and differentiation.

The following paragraphs describe studies in which engineered nanogeometrical features were used to elicit specific responses from cells. Our definition of nanogeometry is material features that have at least one dimension that is equal to or less than 1  $\mu\text{m}$  (1000 nm). There are many studies that use larger, microscale structures to control cell behavior, but these are not included in this chapter because of space limitations and also because they have been reviewed extensively elsewhere [8, 64, 78].

### 3.1. Effect of Nanogeometry on Cells

#### 3.1.1. Nanofibers

One of the most direct ways to mimic the ECM architecture is to construct nanofibrous materials (Table 1). The cellular response to a number of nanofibers features has been investigated. For example, a meshwork of poly(lactic-co-glycolic acid) (PLGA) fibers guides cell spreading and motility as 3D tissue engineering scaffolds [72]. Osteoblasts increase proliferation with the decreasing diameters of the carbon fibers [32]. Further correlation between cellular responses

and reconstructed ECM-like nanofiber features are under investigation by multiple groups.

#### 3.1.2. Nanogrooves

Grooves are another type of engineered surface features that are commonly used to study the effect of surface topography on cell behavior (Fig. 2A). Many cell types elongate and orient in the direction of the grooves, whereas some align perpendicular to the grooves and others do not align at all (Table 1). Cellular response to nanoscale grooves can be used to study the mechanism of tissue formation. Clark et al. used groove features to investigate myogenesis (formation of muscle). It was discovered that myoblasts had a strong tendency to orient and elongate themselves along ultrafine grooved surfaces. Although such topographical features restrict the movement of myoblasts in one direction and inhibit lateral contact between cells, the linear aggregation of myoblasts still occurred and led to the fusion of mononucleated myoblasts into myotubes. Combined with results from a different experiment in which myoblasts were observed to form myotubes of constant diameter independent of the degree of lateral contact with other cells [167], studies using ultrafine grooves suggested that end-to-end interaction between myoblasts is the critical aspect for myotube formation [101]. Nanoscale grooved features have also been used for investigating the alignment of other cell types such as fibroblasts and adhesion and phagocytic activity of macrophages [75].

#### 3.1.3. Rough Surfaces

Surface roughness is another type of surface geometry. Rough surface features include waves, hills with round edges, and other features that are less well defined with respect to shape and uniformity (in comparison to fibers and grooves). The features are often created by molding or by less-controlled fabrication methods such as grinding, polishing, or etching (Table 1).

Roughness may sometimes be unintentionally produced during fabrication due to the techniques used. Even “smooth” surfaces used for control experiments are likely to have some topographical roughness on the order of a few nanometers, if they are not “derived by cleaving a perfect crystal or obtained by cooling a melt under vibration-free conditions” [168]. Although some cells are indifferent to such imperfections [112], many show significant differences in behavioral response to nanoscale roughness [65]. For example, human gingival osteoblasts change their morphology based on the amount and type of roughness they were exposed to [124]. Endothelial cells spread and proliferate more rapidly on substrates that replicate the topographical roughness of the natural ECM.

#### 3.1.4. Pores, Pillars, Pyramids, and Pits

The geometry of a substrate can be composed of numerous discontinuous and more pronounced structures such as pores, pillars, pyramids, and pits of various sizes and densities (Fig. 2B, and D). A variety of such features affect the behavior of single and even multicellular epithelial tissue sheets. For example, surfaces with 0.1–0.8  $\mu\text{m}$  pores

**Table 1.** Materials with engineered geometrical, chemical, and mechanical cues and their effect on cells.<sup>a</sup>

Features	Materials	Feature sizes	Cell or biomolecule types	Effect on cells	Fabrication technique	Ref.
<i>Materials with Controlled Nanogeometry</i>						
Fibers	PLGA	500–800 nm	BALB/c C7 and hMSC	Cells spread, maintained phenotype, and grew into 3D multicellular network along nanofibers	Ejection of polymer solution by electrostatic force between a syringe needle and a collecting plate	[72]
	Carbon with or without pyrolytic outer layer	60–200 nm	HOB	Osteoblast proliferation increased with decreasing fiber diameters; more alkaline phosphatase synthesis and extracellular calcium deposition on small diameter fibers	Chemical vapor deposition	[32]
Grooves	PDMS	0.5 $\mu\text{m}$ depth, 2.0–10.0 $\mu\text{m}$ wide ridge/groove	RDF	Orientation of intercellular and extracellular proteins on grooves	PDMS was cast against the silicon oxide mold fabricated by photolithography	[79]
		1.0–10.0 $\mu\text{m}$ wide ridge/groove with 0.45–1.0 $\mu\text{m}$ depth	RDF	Cells highly oriented on ridge <4.0 $\mu\text{m}$ ; ridge width instead of groove width and depth affects cell size, shape or orientation		[80]
		2.0–10.0 $\mu\text{m}$ ridge/groove with 0.5 $\mu\text{m}$ depth	Fibroblasts, erythrocytes, lymphocytes, macrophages	Lower number of inflammatory cells and higher number of blood vessels formed on grooved implants		[81]
		2.0–10.0 $\mu\text{m}$ ridge/groove with 0.5 $\mu\text{m}$ depth	RDF	Cell proliferation not affected by the presence of grooves; RDF oriented and elongated on 2.0 and 5.0 $\mu\text{m}$ grooves; Cells able to span the grooves		[82]
	PDMS (with or without precoated fibronectin)	0.5 $\mu\text{m}$ deep, 2, 5, 10 $\mu\text{m}$ wide	Human skin fibroblasts and HUVEC cells	Texture affects fibronectin deposition and focal contact assembly, attachment	PDMS was cast against a silicon oxide mold fabricated by photolithography	[83]
	PS	1 $\mu\text{m}$ deep, 1–10 $\mu\text{m}$ ridge/groove	RDF	Focal adhesion and cytoskeleton were oriented; position of the cell depended on the width of the groove	Mold against photoetched silicon wafer	[84]
		0.5–5.4 $\mu\text{m}$ deep, 1–20 $\mu\text{m}$ wide ridge/groove	RDF	Cell orientation increased with increasing depth, but narrowest and deepest grooves have less cell proliferation because cells bridge over the groove without attaching to the bottom to form focal adhesions	Mold against photoetched silicon wafer	[85]
		0.5 $\mu\text{m}$ deep, 1–10 $\mu\text{m}$ wide ridge/groove	RDF	F-actin in lamellipodia determines orientation; F-actin in the cell body not the reason but the result of orientation	Mold against photoetched silicon wafer	[86]

continued

Table 1. Continued

Features	Materials	Feature sizes	Cell or biomolecule types	Effect on cells	Fabrication technique	Ref.
	PS, Ti-coated Si, PLA	1–10 $\mu\text{m}$ wide ridge/groove with 0.5 $\mu\text{m}$ depth	RDF	Same topography but different chemistry affects cell contact guidance, morphology, orientation, proliferation	Mold against photoetched silicon wafer	[87]
	Titanium	1.0–10.0 $\mu\text{m}$ ridge/groove	RDF	Cells and stress fibers oriented along the 1.0 and 2.0 $\mu\text{m}$ wide groove; cell and FAP localization depends on the width of groove	Titanium wafer etched by plasma chemistry with photolithographically defined mask	[88]
	Glass covered by collagen and poly-L-lysine, or a layer of fixed aligned HSF	0.1–2 $\mu\text{m}$ depth and diameter	Neurons from CEB and DRG	Growth cone aligned along scratches and along the long axes of fibroblasts; crowded cultures of neurons ignore the guidance cues	Single scratch on coverslips	[89]
	Nitinol	1, 3, 15, 22 $\mu\text{m}$ ridge/groove	Endothelial cells	Alignment, elongation, increased migration, and proliferation on grooved surfaces		[90]
	PLA and PS	1–10 $\mu\text{m}$ ridge/groove, 0.5–1.5 $\mu\text{m}$ groove depth	RBM	No effect on cell proliferation; actin filaments and focal adhesion points aligned with the groove, but pattern different on different surfaces	Cast polymer against photolithographically produced silicon mold, followed by radiofrequent glow-discharge treatment	[91]
		1–10 $\mu\text{m}$ gratings, 0.5–1.5 $\mu\text{m}$ groove depth		On PLA surface, cell and matrix aligned to the groove; More mineralized ECM on 1 and 2 $\mu\text{m}$ wide, 1 $\mu\text{m}$ deep groove; increased alkaline phosphatase activity on grooved PLA surfaces		[92]
	Silica	30–282 nm depth	P338D1 cells and normal rat peritoneal macrophages	Increased adhesion, spreading, number of membrane protrusions, F-actin, and phagocytotic activity; F-actin and vinculin were colocalized along the edges of the steps and grooves, accompanied by phosphorylation of tyrosine	Reactive ion etching the silica sample through patterned photoresist mask	[75]
		5, 10, 25 $\mu\text{m}$ wide and 0.5, 1, 2, 5 $\mu\text{m}$ depth	Baby hamster kidney fibroblasts	Actin aggregation at the discontinuity (edge of ridge/groove) is prerequisite for cell orientation		[93]
	Silicon and PS	0.03–2.0 $\mu\text{m}$ depth, 0.5–100 $\mu\text{m}$ ridge	<i>Uromyces appendiculatus</i>	The fungus differentiated on ridge of 0.5–6.7 $\mu\text{m}$ , a step size that mimics topographical features on leaves of plants the fungus naturally grow on	Electron beam lithography	[68]

Silicon coated with titanium	125° interior corner V shape grooves: 3 $\mu\text{m}$ deep, 30 $\mu\text{m}$ pitch, 15 $\mu\text{m}$ wide; 3 $\mu\text{m}$ deep, 6–9 $\mu\text{m}$ pitch; 0.5 $\mu\text{m}$ deep, 1 $\mu\text{m}$ pitch	HGF	Microscale grooves align cells with either intact micro-tubule or actin filament; nanoscale grooves fail to align microtubule-deficient cells, but able to align actin-deficient cells	Photolithography and etching	[23]
6FDA-6FAP	100–150 nm wide, 4–5 nm unevenness	HeLa cells	HeLa cells aligned strongly on the rubbed surfaces	Rubbing the surface with a cylinder wrapped with cotton velour cloth	[94]
		Rat fibroblasts, platelets	Rubbed surfaces affect IgG absorption, platelets adhesion, fibroblasts adhesion proliferation, aggregation and collagen production		[95]
Quartz	260 nm ridge/groove of various depths (100, 210, and 400 nm)	BHK cells, MDCK cells, and chick embryo cerebral neurons	Alignment of BHK cells and elongation of MDCK cells depends on depth; chick embryo neurons do not respond.	Laser holography and micro-electronic fabrication	[96]
Quartz with or without pre-coated poly-L-lysine and laminin	1–8 $\mu\text{m}$ gratings, 0.08–0.8 $\mu\text{m}$ depth grooves and steps	Various CNS neuroblasts	Neuroblasts either align perpendicular or parallel to the grooves; Perpendicular alignment was observed on grooves with 0.3–0.8 $\mu\text{m}$ depth, 1 $\mu\text{m}$ width	Laser holography and photolithography	[97]
Quartz	14–1100 nm depth, 1–4 $\mu\text{m}$ wide	<i>Xenopus</i> spinal cord neurons and rat hippocampal neurons	Neuron extended and aligned parallel or perpendicular to the grooves, depending on cell age and type	Electron beam lithography and etching	[98]
	14–1100 nm depth, 1–4 $\mu\text{m}$ wide	<i>Xenopus</i> spinal cord neurons and rat hippocampal neurons	Topography affected filopodia and microtubule patterning; $\text{Ca}^{2+}$ channel and protein kinase C were involved in perpendicular contact guidance; Filopodia and cytoskeleton were not required for orientation		[99]
Quartz coated with poly-D-lysine	0.13–1.0 $\mu\text{m}$ wide ridge/groove, 0.10–1.17 $\mu\text{m}$ depth	Various neurons	Content of actin and cell alignment depends on cell type and topography; glial cells most sensitive to topographical guidance	Etching and laser holography	[100]
Quartz pre-coated with poly-L-lysine and laminin	130 nm wide groove/ridge, 210 nm depth	Myoblasts	Myotube formation was in end-to-end manner	Laser holography	[101]
PMMA	Groove 0.5–1.0 $\mu\text{m}$ wide, 1 $\mu\text{m}$ deep	WI38 cells	Oriented along the groove	Electron beam lithography	[102]

continued

Table 1. Continued

Features	Materials	Feature sizes	Cell or biomolecule types	Effect on cells	Fabrication technique	Ref.
Smooth groove and rough surfaces	Titanium coated with TiO <sub>2</sub> and carbonaceous layer	1–10 μm ridge/groove	Leukocytes	Leukocytes on rough surfaces had higher numbers of normal receptors; topography had larger impact than oxide thickness	Annealing commercially available titanium to generate oxide	[103]
Waves	PDMS precoated with fibronectin	0.1–10 μm wavelength, 0.01–1 μm depth	BCE cells	Cell alignment in the direction of grooves; Sharp edge of the groove is not necessary for contact guidance	Relaxing oxidized PDMS from stretching position creates continuous wavy features	[104]
Rough surfaces	PS	Feature size not mentioned	P338D1, WI38, VA13, VA13, L929, H615, and ts3T3 cells	Attachment depends on cell type	Untreated, sulfuric acid- and palladium-treated PS	[105]
	PET	R <sub>a</sub> of sinuous hills of treated surface is 19.04 nm, untreated surface 3.46 nm	3T3-L1, JEG-3, and MCF-7 cells	Cytoskeletal proteins, cell morphology, and proliferation not affected by the roughness; differentiation and apoptosis are more on plasma-treated surfaces, although the effects are moderate	Plasma treatment	[106]
	Biomer (polyurethane)	Typical height difference 1 μm; many features on the order of 100 nm	BAEC	Cells maintain physiological phenotype, spread rapidly, and become confluent	Replica molding of natural ECM	[65]
	Ti <sub>6</sub> Al <sub>4</sub> V	Various surface average roughness 160, 300, 430, 610 nm, 2.19 and 3.4 μm. R <sub>a</sub> = 0.32–0.874 μm	MC3T3-E1 cells and human osteoblastic cells Human bone marrow stromal cells	Negative correlation between roughness and cell proliferation and adhesion; for all surfaces, human osteoblast adhesion increase with time Cell attachment and proliferation increase with surface roughness; human serum albumin preferentially adsorb onto smooth surface; rough surface binds higher total protein and fibronectin	Polishing mechanically or manually to generate parallel orientation of residual grooves Polishing Ti alloy disks with SiC metallographic paper	[107, 108] [109]
	Ti <sub>6</sub> Al <sub>4</sub> V and titanium	R <sub>a</sub> = 0.22–4.2 μm	MG63 cells	Cell proliferation, differentiation, protein synthesis and local factor production depend on roughness and composition	Polishing or grinding	[110]
	Cp-titanium, Ti <sub>6</sub> Al <sub>4</sub> V and Ti <sub>30</sub> Ta	R <sub>a</sub> = 0.04–1.36 μm	HGF	Cell orientation increases with increasing roughness; round shape cells on Ti <sub>6</sub> Al <sub>4</sub> V due to release of vanadium	Grinding or polishing	[111]

Ti <sub>6</sub> Al <sub>4</sub> V, pure titanium	$R_a = 0.07\text{--}3.5 \mu\text{m}$	HOB	EE surface favors cell proliferation and adhesion; when substrate topography is comparable with cell size, cells prefer rough surfaces; when below cell size (nanoscale), cells prefer smooth surfaces	Machine-tooling, EE, polishing	[112]
NiTi alloy and titanium	Nano to microscale roughness	HGF	Highest orientation and lowest proliferation on the highest surface roughness	Polishing	[113]
Porous Si, polycrystalline Si, bulk Si wafers	Porous Si: 40 nm core size; polycrystalline Si: 10 nm; nanocrystallite size	B50 cells	Viability greatest on porous Si, much less on PECVD Si and bulk Si	Etch with HF for porous Si, PECVD for polycrystalline Si	[114]
Porous Si and Ge, crystalline Si and Ge, amorphous Si		CHO cells	Calcium phosphate deposited on nanoporous surfaces; cells attached to all porous substrates and were confluent; cell number greatest on low-porous Si	Electrochemically etched or chemically etched	[115]
Porous Si, polycrystalline Si, bulk Si wafers and glass	Feature size not mentioned in detail	CHO and B50 cells	CHO cells prefer polycrystalline Si and B50 cells prefer porous Si	Porous Si fabricated by stimulated plasma etching; polycrystalline Si fabricated by plasma-enhanced chemical vapor deposition	[116]
Bulk, porous, and polycrystalline Si	$\sim 10$ nm pore size for the porous Si	CHO, B50, and A431 cells	CHO cells grow best on polycrystalline silicon surface; B50 and A431 cells grow best on porous silicon	HF etching	[117]
Si	$R_a = 20\text{--}70$ nm	Substantia nigra cells	Surface roughness affects cell viability and attachment; cells form networks of neuron, with evidence of pathfinding by the axon	Etching	[118]
Oxidized crystalline Si and porous Si precoated with FBS and collagen	70% porosity with average pore size 2–5 nm	Primary rat hepatocytes	Cell increase adhesion on FBS and collagen precoated substrate	Etching	[119]
Alumina and titania	23 nm grain size alumina and 32 nm grain size titania	Osteoblasts	In the presence of 10% FBS, osteoblast adhesion on nanophase alumina and titania significantly greater than on borosilicate glass; the critical grain size for osteoblast adhesion is between 49 and 67 nm for alumina and 32 and 56 nm for titania	Mold/compact nanophase grains into disks	[120]

continued



Table 1. Continued

Features	Materials	Feature sizes	Cell or biomolecule types	Effect on cells	Fabrication technique	Ref.
	Alumina and HA	Grain size less than 100 nm	Rat bone marrow cells	Cells increased synthesis of TRAP and formation of resorption pits on nanophase alumina and HA	Compacting alumina powders in a die then sintering; HA was fabricated via wet chemistry	[121]
	Titanium	$R_a = 0.3\text{--}0.9 \mu\text{m}$	Saos-2 cells	Cells spread in the presence of serum, fibronectin, or vitronectin, increase roughness increase cell proliferation	Titanium discs were acid etched or sand blasted	[122]
	Epoxy resin coated with titanium coating	$R_a = 0.54$ and $4.92 \mu\text{m}$ $R_a = 0.58\text{--}5.55 \mu\text{m}$	MG63 cells HGF	Protein kinase A and phospholipase A <sub>2</sub> mediate cell adhesion Cell morphology and thickness are different, but volume remains the same when cells attach to different surfaces	Commercially available	[123]
	HAPEX	$R_a = 0.03 \pm 0.01$ for polished samples; $0.25 \pm 0.05$ for machined samples	HOB	Faster and larger numbers of cells attach to the rough surfaces and cells maintain more developed cytoskeleton than on micromachined surfaces	Titanium coating was generated on top of replicas that were molded against surfaces of different roughness HAPEX was created by incorporating 40% HA into PE via extrusion and compression molding; discs of HAPEX were machined or polished followed by sonication roughening with alumina particles	[124]
Pores	Polycarbonate and polyester coated with various polymer films	$0.1 \mu\text{m}$ pore size, $4 \times 10^8$ pores/cm <sup>2</sup> , $0.3 \mu\text{m}$ pore size, $2 \times 10^6$ pores/cm <sup>2</sup>	Cornea epithelial tissues	Migration on nonporous surface increased with surface contact angle and hydrophilicity, decreased with surface mobile chemistry; combination of $0.1 \mu\text{m}$ pore and hydrophilicity resulted in maximum migration speed	Track-etched	[126]
	Polycarbonate	$0.1, 0.4, 0.8, 1.0, 2.0$ , or $3.0 \mu\text{m}$ diameter pores	Cornea epithelial cells/tissues	Surfaces with $0.1\text{--}0.8 \mu\text{m}$ pores support assembly and maintenance of tissue stratification and protein deposition	Track-etched	[127]
		$0.1, 0.4$ , and $0.8 \mu\text{m}$ diameter pores	Cornea epithelial cells and tissues	Surfaces with $0.1$ or $0.4 \mu\text{m}$ pores stimulated epithelial tissue sheet and individual epithelial cell migration	Track-etched	[128]
		$0.1\text{--}3.0 \mu\text{m}$ pore diameter	Cornea epithelial tissues	Basement membrane and hemidesmosomal plaque deposition is related to the pore size of the substrates; tissue attachment affected by pore size and polymer surface	Commercially available, track-etched	[129]

Polycarbonate and cellulose acetate/nitrate coated with collagen or fibronectin	0.1–3 $\mu\text{m}$ columnar pores on polycarbonate membrane; 0.22–3 $\mu\text{m}$ tortuous pores on cellulose acetate/nitrate membrane	Cornea epithelial cells/tissues	Tissue migration was inhibited with increasing pore size and completely halted on 0.9 $\mu\text{m}$ pore membrane; coatings facilitated tissue outgrowth; cells reduce migration with pore sizes larger than 0.9 $\mu\text{m}$ , resume at 2.3 $\mu\text{m}$ pore membrane; single cell migration more sensitive to porous surface than that of tissues	Commercial cellulose acetate/nitrate membrane. Track-etched polycarbonate membrane either pretreated with PVP or PVP-free.	[130]
PIPAAm grafted porous membrane	Surface roughness 4.40 nm, pore size 0.45 $\mu\text{m}$	BAEC single cells and confluent cell sheet	Quicker detachment from porous surface than nonporous surface	Electron beam irradiation grafts PIPAAm onto porous membrane (Cell Culture Insert) or tissue culture polystyrene dish	[131]
Cellulose acetate and polyethersulfone	0.1–0.2 $\mu\text{m}$ and 0.8 $\mu\text{m}$ in diameter	Platelets and leukocytes	Higher platelet adhesion and leukocyte viability on 0.8 $\mu\text{m}$ pore size membrane	Commercially available	[132]
PLGA	Foam pore size: 150–300, 300–500, 710 $\mu\text{m}$	Stromal osteoblasts	The foams support proliferation, alkaline phosphatase activities, and bone formation	Solvent-casting particulate-leaching technique	[133]
Pillars and grooves	PS 5 $\mu\text{m}$ blazed ridge/groove, 850 nm ridge/groove, and 60 nm diameter pillars with 300 nm center to center spacing 80 nm base, 300 nm center-to-center spacing	Epitenon cells Rat tendon cells	Much fewer cells on pillar surfaces than on planar ones No attachment on nanopillars	Embossing into PS with an electron beam patterned perspex die	[73]
Pillars or pits or cliffs	Polycaprolactone Pillars or pits were 50 nm in diameter with center-to-center spacing of 75, 150, or 300 nm; cliffs were 200 nm high and 10 $\mu\text{m}$ apart Pillar: 0.5–2.0 $\mu\text{m}$ width, 0.5–5.0 $\mu\text{m}$ gap, 1.0 $\mu\text{m}$ height; well: 1.0 $\mu\text{m}$ deep, 0.5 $\mu\text{m}$ diameter, 0.5–2.0 $\mu\text{m}$ gap	HGTFN cells and rat epitenon fibroblasts LRM55 cells	Cell adhesion enhanced at cliff edge (asymmetric features); symmetrical arrays of pits or pillars inhibit adhesion 70% of cells prefer attachment to pillars and 40% prefer wells (compared with smooth surfaces); polarized distribution of actin and vinculin on pillars	Replica molding of electron beam defined patterns Replica molding of patterned surfaces generated by electron beam lithography and etching	[74, 134] [135]
Pillars and wells	Silicon	LRM55 cells	70% of cells prefer attachment to pillars and 40% prefer wells (compared with smooth surfaces); polarized distribution of actin and vinculin on pillars	Photolithography and etching	[136]

continued

Table 1. Continued

Features	Materials	Feature sizes	Cell or biomolecule types	Effect on cells	Fabrication technique	Ref.
		Randomly distributed pillars with average diameter 57 nm, 230 nm heights; wells 100–250 nm in width, $\leq 115$ nm in roughness	LRM55 cells and primary cortical astrocytes	LRM55 cells prefer to attach to wells; primary astrocytes prefer to attach to pillars	Photolithography and wet etching	[137]
Particles	Titania and alumina	430 and 620 nm	Human osteoblasts and chondrocytes	Cells increase proliferation in the presence of nanophaser particles but not with micrometer size particles	Aggregation	[33]
Pyramids	Germanium islands on silicon	15 nm high, 60 nm $\times$ 60 nm base	U937 cells	Pyramid density strongly affects cell viability and protein release	Chemical vapor deposition	[138]
Islands	PS and poly(4-bromostyrene)	Microscale wide, 13, 35 and 95 nm height islands	HGTFN cells	Cells spread and contain more developed cytoskeleton on topographical substrates than on flat ones; responses were related to the heights of the islands	Dimixing PS and poly(4-bromostyrene) to produce nanometer height islands	[139]
Fibers	PLLA, PLGA, PDLLA/THF PLLA/THF	Nanoscale fibrous matrix			Cross-linking	[71]
		Nanofibrillar matrices with particulate macropores $R_p = 0.3\text{--}4.9$ nm			Cross-linking	[70]
Rough Surfaces	Cuprophane, AN69, PS, and glass surfaces		Fibronectin, fibrinogen, and albumin	Membrane topography affects protein adsorption	Commercially available	[140]
	Silicon surface coated with Ti and Au	Nanodots 15 nm high and 60 nm in diameter separated by a distance of 50–150 nm	Collagen adsorption	Collagen forms layers, aggregates and no aggregates on smooth hydrophilic, smooth hydrophobic, and rough hydrophobic surfaces	Rough surface made by colloidal lithography, then coated with Ti and Au, followed by SAM to add functional chemical groups	[141]
	Titanium	Lines of 1–2 nm and 3–4 nm depths; Full width at half maximum 40 nm.	F-actin	Low adsorption and random orientation on 4 nm height structures; High adsorption and orientation on 1–2 nm height structures	Local anodic oxidation with AFM	[142]
	Titanium	$R_p = 8$ to 1200 nm	Human plasma fibrinogen	Different surface result in different protein adsorption	Mechanical polishing, grinding, sand blasting, and etching	[143]

		<i>Materials with Controlled Nanochemistry</i>		
Dots	Clusters of RGD on PMMA surfaces	Clusters separated by 1, 2, and 5 $\mu\text{m}$	WTNR6 fibroblasts	Increasing cell attachment and spreading with increased RGD cluster density [144]
	RGD peptide on protein-resistant PMMA-PEO substrate	Clusters at nanoscale with 32 nm spacing	WTNR6 fibroblasts	Tethered RGD to P(MMA- $\gamma$ -POEM) comb polymers [55]
	RGD clusters on PLA		WTNR6 fibroblasts	Surface segregation of the P(MMA- $\gamma$ -POEM) comb polymers blended in PLA [56]
	RGD peptide on protein-resistant PMMA-PEO substrate	Average cluster spacing varying from 6–300 nm	WTNR6 fibroblasts	Tethered RGD to P(MMA- $\gamma$ -POEM) comb polymers [53]
	RGD	32 nm clusters, separated by 14–25 nm	WTNR6 fibroblasts	Tethered RGD to P(MMA- $\gamma$ -POEM) comb thin films [37]
Lines	Varying RGD density and alginate type		C2C12 cells	Different alginate monomeric ratio [54]
	Fibronectin	0.7–5 $\mu\text{m}$	Myoblasts	Urea crystals were washed away after drying with fibronectin [145]
	SAM coated with HS(CH <sub>2</sub> ) <sub>5</sub> CO <sub>2</sub> H	1 $\mu\text{m}$	P19 cells	Gold surface was coated with EG <sub>6</sub> OH-terminated SAM; the groove was scalpel blade scratched and coated with HS(CH <sub>2</sub> ) <sub>5</sub> CO <sub>2</sub> H [146]
Other patterns	IgG, lysozyme, retromectin protein patterns PDDA(PAA/TiO <sub>2</sub> ) <sub>5</sub>	100–350 nm	3T3 Swiss fibroblasts	Dip-pen nanolithography [24]
	Thiolated ssDNA on alkanethiol SAM surfaces	External diameter 10–30 nm; wall thickness 3–5 nm 10–25 nm wide lines, nanoscale squares	PCI2 cells Enzyme	Assemble Ag/TiO <sub>2</sub> nanoparticles with PAA [147]
Dots				AFM nanografting [148]

continued

Table 1. Continued

Features	Materials	Feature sizes	Cell or biomolecule types	Effect on cells	Fabrication technique	Ref.
	Single or multiple types of oligonucleotides on gold or silicon oxide surfaces	Many microns to less than 100 nm	Sequence-specific DNA	Sequence-specific DNA could bind to the patterned DNA	DPN	[149]
	Streptavidin-coated glass and positively charged glass	Micrometer scale	Biotinylated DNA, protein G		Nanopipette delivering	[150]
	Au with SAM monolayer	Resolution down to individual molecules	LYZ, BSA, IgG		Nanografting and SAM	[151, 152]
	Au coated with glycol monolayer	Nanometric scale	Rabbit IgG antigen patterns; goat anti-rabbit IgG Fab'-SH fragment patterns		SPL	[153]
Lines	<i>Sporosarcina ureae</i> S-layer	1.9 nm diameter	Platinum		Reduce $K_2PtCl_4$ to Pt and deposit it onto the S-layer	[154]
	Glass	3–4 nm high, 300 nm wide stripes	IgG		Microcontact printing with PDMS stamps	[155]
	Single or multiple layers of patterns	30–50 nm wide	Collagen fibers and collagen-like peptide		Using AFM tip to write directly	[156]
	Si with oxide layer	Various nanometric scale	Thiol and protein patterns		Nanografting and NPRW	[157]
Other patterns		600 nm × 250 nm (ridge × groove), 5–10 nm thick	S-layer of <i>Bacillus sphaericus</i> CCM 2177		Deep UV radiation	[158]
	Au	3.0 nm height, 289 nm periodicity	Cyclic peptides, porphyrin thiols, silane coupling reagents		Templating-assisted protein nanopatterning	[159]
3D matrices	Collagen		BSA		Particle nanolithography	[160]
	ECM and fibrinogen		Mouse and human fibroblasts	Local and long-distance matrix movements induced by fibroblasts	Polymerizing collagen	[47]
			Fibroblasts	Adhesion on 3D substrates different from 2D in the content of integrin, paxillin, cytoskeletal components, and FAK; mechanical stress and chemical composition of the substrate also affect cell adhesion	Isolating tissue-derived 3D matrix, cell-derived 2D matrix, 3D fibrinogen	[26]

Collagen	Human dermal fibroblasts	TGF- $\beta$ 1 and $\beta$ 3 function as mechanoregulatory GFs; alteration of cell stress stimulated integrin expression	Mixing collagen with DMEM	[161]
Collagen-chitosan	K562 cells	Cell proliferation decreased, cytokine release increased with increasing ratio of chitosan	Mixing at different ratios	[162]
Agarose	E9 chick DRG neurites	Increasing gel concentrations decreased elongation rate	Dissolving agarose powder in saline	[25]
Agarose and type I collagen gels	Rat cortical neurons	Collagen gel supported cell viability, normal neuronal polarity and extension of neurites; low-density agarose gels resulted in cell apoptosis	Cross-linking/gelation	[163]
Agarose-alginate coupled gel	E9 chick DRG neurites	Sensory ganglia extension of neurites depends on 3D gels, pore size, and charge of the polymer	Mixing	[164]
Corneal epithelium basement membrane cross-linked ECM fibers	Different pore size and charge 149 $\pm$ 60, 191 $\pm$ 72, 147 $\pm$ 73 nm, mean fiber diameter 77 $\pm$ 44 nm and pore diameter 72 $\pm$ 40 nm		EDTA soaking then remove epithelium or endothelium	[66, 67]
Clusters	32 nm clusters, separated by 14–25 nm	RGD cluster density and clustering affect cell response; mechanical stimuli enhance cell response for higher ligand densities; Fibronectin-coated surfaces do not affect adhesion reinforcement	Tethered RGD to P(MMA- $\gamma$ -POEM) comb thin films	[37]
Pillars	0.8 $\times$ 0.8 $\times$ 0.3, 0.4 $\times$ 0.4 $\times$ 0.3 $\mu$ m pillar with 2–30 $\mu$ m spacing	Focal adhesion is force dependent; local forces related to the orientation and area of focal adhesions	Soft-lithography	[165]
Modify adhesiveness	Varying cell surface receptor and substrate material	Cell aggregation is equilibrium of force between cell–cell cohesivity and cell–substrate adhesiveness	Cell transfection	[166]

<sup>a</sup> Some of the nanofeatured materials are promising but have not yet been utilized for cell engineering. Such kinds of nanomaterials are listed at the end of each category.  
 Note: 2D, 2-dimensional; 3D, 3-dimensional; **6FDA-6FAP**, fluorinated polyimide; **AFM**, atomic force microscopy; **BAEC**, bovine aortic endothelial cells; **BCE**, bovine capillary endothelial; **BHK**, baby hamster kidney; **BSA**, bovine serum albumin; **CEB**, chick embryo brains; **CHO**, Chinese hamster ovary; **CNS**, central nervous system; **DMEM**, Dulbeccos modified Eagle's medium; **DPN**, dip-pen nanolithography; **DRG**, dorsal root ganglions; **ECM**, extracellular matrix; **EDTA**, ethylenediamine tetraacetic acid; **EE**, electroerosion; **F-actin**, actin filament; **FBS**, fetal bovine serum; **GF**, growth factor; **HA**, hydroxyapatite, i.e., Ca<sub>5</sub>(PO<sub>4</sub>)<sub>3</sub>(OH); **HGF**, human gingival fibroblasts; **HGTEN**, human granulosoma tendon **hMSC**, human bone-marrow-derived mesenchymal stem cells; **HOB**, human osteoblasts; **HSF**, human skin fibroblasts; **HUVEC**, human umbilical vein endothelial cells; **IgG**, immunoglobulin G; **LYZ**, lysozyme; **MDCK**, Madin-Darby canine kidney; **NPRW**, nanopen reader and writer; **PAA**, poly(acrylic acid); **PDDA**, poly(dimethyl diallyl ammonium chloride); **PDLLA**, poly(DL-lactic acid); **PDMS**, polydimethylsiloxane; **PE**, polyethylene; **PECVD**, physically etched chemical vapour deposited; **PEO**, poly(ethylene oxide); **PET**, polyethylene terephthalate; **PtPAAm**, poly(*N*-isopropylacrylamide); **PLA**, poly-L-lactic acid; **PLGA**, poly(DL-lactide-co-glycolide); **PLLA**, poly(L-lactic acid); **PMMA**, poly(methyl methacrylate); **POEM**, poly(oxethylene); **PS**, polystyrene; **PVP**, poly(vinylpyrrolidone); **R<sub>g</sub>**, average roughness; **RBM**, rabbit bone marrow; **RDF**, rat dermal fibroblasts; **RGD**, Arg-Gly-Asp peptides; **SAM**, self-assembled monolayers; **Si**, silicon; **S-layer**, surface layer; **ssDNA**, single-stranded DNA; **TGF**, transforming growth factor; **THF**, tetrahydrofuran; **TRAP**, tartrate-resistant acid phosphatase; **UV**, ultraviolet.



stimulate epithelial tissue sheet migration [127–129]. The migration of this stratified tissue decreases with increasing pore sizes and halts completely for pore sizes larger than  $0.9\ \mu\text{m}$  [130]. Lymphocytes, leukocytes, and platelets display increased adhesion and viability on  $0.8\ \mu\text{m}$  pore substrates [132].

Cellular behavior depends on the cell type and can be significantly affected by the size of surface elements found on the substrate that the cell is adhered to. Epitendon, tendon, and fibroblast cells are unable to attach to surfaces with nanopillar arrays of 50-nm diameter [73, 74, 135], whereas primary astrocytes show preferential attachment to similar sized pillars [136, 137]. It is hypothesized that pillars that are only tens of nanometers in diameter are not large enough for many cell types to form focal contacts on [74]. In contrast, pillars with diameters of 500 nm and larger are able to support attachment of a larger variety of cell types [136]. When pillar diameters are of sufficient size to support cell attachment, the height of the pillars also becomes an important factor. For example, endothelial cell response differs greatly, depending on pillar height [125, 139]. Studies of U937 cells on nanoscale pyramid structures show a negative correlation between pyramid densities and cell viability and protein production. The cells showed decreased production of inflammatory cytokines such as interleukin- $1\beta$  and tumor necrosis factor, and less proliferation on substrates with higher pyramid densities [138] (Fig. 2B).

### 3.1.5. Three-Dimensional Architectures

Most artificial nanostructures are created on flat surfaces, mainly because of limitations in nanomanufacturing methods. The physiological cellular environment, however, is 3D in that cells contact materials on multiple planes, not just on the horizontal ones. It is well known that 3D environments are crucial for the tissue formation and function of a variety of cell types including endothelial cells [26], neurons [169], and fibroblasts [72]. The current technology for providing cells with a 3D environment is to use scaffolds made of polymer foams or gels that contain microscale pores and ill-defined nanogeometries (Fig. 2C). The development of new 3D nanofabrication technologies and their application in cell studies are areas of great potential for further research. The effect of 3D substrates on cell behavior is closely associated with the mechanical stress that is induced by the substrate on cells (see also Section 5).

## 3.2. Mechanism of Cellular Response to Nanogeometries

Although the exact mechanism is still unclear, certain cellular components have been shown to be crucial for cellular response to nanogeometries. The morphological response of cells, such as alignment to geometrical features, requires proper spatial arrangement of cytoskeletal components such as actin filaments and microtubules. Thin actin filaments in the cell periphery support membrane extension, whereas the large, axial bundles of actin stress fibers in the main cell body enable contractile movements. Cells cultured on grooved substrates will often show orientation of the actin

cytoskeleton in the direction of the grooves [75, 91]. Microtubules are another cytoskeletal component involved in cellular response to geometrical features. The intracellular alignment of both actin filaments and microtubules in the direction of the grooves is critical in determining overall alignment of the whole cell [23].

It is important to understand that cellular response to surfaces can be completely different depending on the type of cell and even the state of that cell, even when the nanogeometry of the substrate is the same. Cell type, cell density, and cell age are three main parameters that affect cellular response to nanogeometrical features. Endothelial cells [90], myoblasts, and fibroblasts align parallel to groove features [79–82, 85–88, 102, 170]. Neuronal cells, however, align either parallel [89] or perpendicular to nanofeatures [97–99], depending on the width of the groove and density of the cells. The orientation and spatial distribution of neurons also depends on their age and origin [98–100]. Cellular response to nanoscale geometry is not limited to mammalian cells. The *Uromyces appendiculatus* fungus responds strongly to engineered nanoscale steps that mimic the features of their host plant in nature by orienting their direction of growth and differentiation along the step features [68]. These fungi are amazingly selective in what size step features they respond to. Germ tubes of the fungus are highly oriented by ridges of 500–600 nm that mimic the host environment but not by features with sizes larger than  $1\ \mu\text{m}$  or less than 250 nm. It is also proposed that cell–cell contact sometimes has a higher priority than cell–substratum contact [96, 171]. Evidence can be seen from the experiment of Fitton et al. [130]: the migration of dissociated single cells is more sensitive to polymer topography than that of tissue.

The mechanism by which nanogeometrical features affect cell behaviors can be indirect. For example, Denis et al. [141] found that collagen deposited onto smooth/hydrophilic substrates formed 6 nm thick protein layers, whereas deposition onto smooth/hydrophobic substrates resulted in 20 nm thick protein layers that contained elongated protein aggregates. Deposition of collagen onto a rough/hydrophobic substrate resulted in a 20 nm thick layer that contained no aggregates. In this case, the response of cells to different nanogeometries could be due not to the direct effect of surface topography but rather to the indirect effect of differences in the proteins adsorbed onto it. Adsorption of fibrinogen (an abundant blood protein that can be proteolytically activated to form fibrin clots that stop bleeding) can be affected by nanostructured titanium with different roughnesses [143]. Bovine serum albumin, fibronectin, and vitronectin orient along grooves on silicon surfaces [79, 88]. Serum albumin prefers to attach to smooth substrates whereas fibronectin and total proteins adsorb more on rough surfaces [109]. Nanometer topographical features can render a material more biocompatible by changing adsorption of proteins and attachment of cells [118, 138].

The material composition and mechanical properties of the substrate also have a large influence on cell behaviors. Materials used for fabrication of nanogeometrical features include metals (titanium, silicon, and germanium) [68, 122, 138], alloys (Nitinol and  $\text{Ti}_6\text{Al}_4\text{V}$ ) [90, 107], inorganic materials (quartz, glass, carbon, silica, and hydroxyapatite (HA)) [32, 75, 89, 96, 121], polymers [polystyrene, poly(ethylene

terephthalate)(PET), polyurethane, polycarbonate, poly(*N*-isopropylacrylamide)(PIPAAm), polyethersulfone, agarose, polycaprolacton, poly(dimethylsiloxane)(PDMS), PLGA, poly(lactic acid) (PLA), fluorinated polyimide (6FDA-6FAP), hydroxyapatite reinforced polyethylene composite (HAPEX), poly(methylmethacrylate), and poly(L-lactic acid)] [65, 71, 72, 79, 84, 87, 92, 94, 101, 106, 125, 129, 131, 132], and other biologically derived materials (cellulose acetate/nitrate, corneal epithelium basement membrane, and collagen–chitosan matrices) [66, 67, 130, 162]. An individual cell will exhibit different behaviors on different materials, even in the presence of the same nanogeometries. For example, rat dermal fibroblasts cultured on very similar groove features showed differences in contact guidance, morphology, orientation, and proliferation on porous silicon, PLA, silicon, and titanium substrates [85, 87]. Materials can be altered during processing. Roughening of  $Ti_6Al_4V$  surfaces, for example, not only changes the material geometry but also increases aluminum oxides presented on the surface compared with untreated controls. Both the geometry and the materials properties contribute to the differences in protein adsorption between smooth and rough surfaces [102].

#### 4. MATERIALS WITH CONTROLLED NANO-CHEMISTRY

To enable materials to elicit specific and desired cellular response, it is necessary to generate chemical patterns that mimic those in the ECM. The cell membrane is covered with numerous nanoscale sensors such as receptors and structural microdomains such as lipid rafts, which probe the environment and send signals to cytoskeletal structures and organelles within the cell [3, 172] (Fig. 1A). The spatial distribution of receptors on the cell surface as well as their degree of clustering depends critically on what type of ligands are present as well as on the nanoscale arrangement of those ligands on the ECM (Fig. 3). The clustering of receptors generates a cascade of signals inside the cell to regulate cell function and behavior.

The basic molecular components of the natural ECM are collagens, laminins, fibronectins, proteoglycans, and hyaluronic acids, with collagens being the most abundant [3, 64]. Each of these molecules presents unique binding sites with distinct binding specificities to various cell surface receptors [173]. The complexity of cell–ECM interactions lies not only in these variations in molecular specificities of binding, but also in the diversity of spatial arrangements of the binding sites. Different types of collagens polymerize differently and form an assortment of fibrous structures. For example, type IV collagen forms intricate meshes of collagen fibers (Fig. 1B) whereas type I collagen forms long fibers. Further mechanical and chemical processing of collagen by cells defines its nanoscale spatial organization (Fig. 1E). Other proteins and carbohydrate molecules bind to specific regions of the collagen to create distinct ECM architectures. Cross-shaped laminin molecules and type IV collagen, for example, form a thin sheet-like ECM called the basal lamina, which is approximately 60–100 nm in thickness [3] (Fig. 1A, and B). Fibronectin is another common multiadhesive protein that facilitates cell attachment and migration.

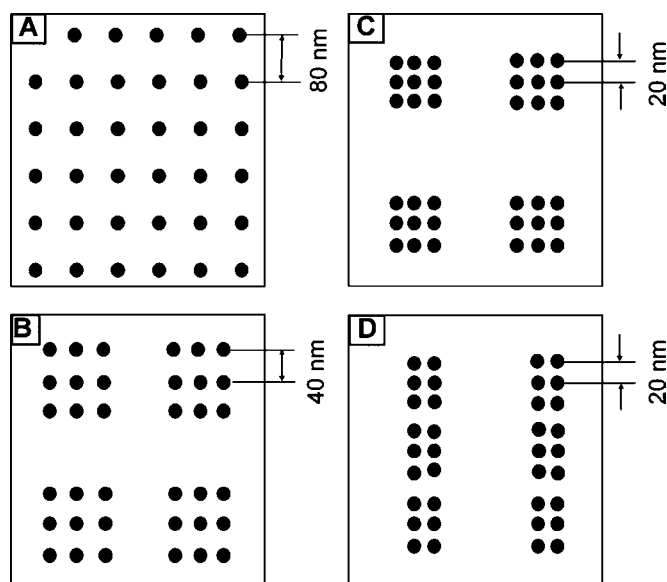


**Figure 3.** Examples of different nanochemistries—that is, how the same number of adhesion ligands can be organized into different nanoscale patterns on a materials surface. Each black dot represents a chemical entity, such as an RGD motif, that binds to receptors. The dots can be grouped into clusters containing different numbers of ligands separated by different distances (local ligand density, A–C). The clusters can be arranged to have different intercluster distances and positions (intercluster arrangement, B–D). In the examples shown, the local ligand density and the intercluster arrangements are different, but the total number of ligands per surface area (bulk ligand density) is constant. The intercluster arrangements can be such that the clusters are evenly distributed (A–C) or arranged in lines or other geometries (D). Appropriate local ligand densities produce synergistic binding through multivalent interactions. In multivalent interactions the total binding strength is more than the sum of the individual bonds. Intercluster arrangements are also important as they determines the spatial organization of subcellular components and overall cell shape. For example, the shape of cell–material adhesion complexes observed inside the body (3D matrix adhesions) are often longer and thinner compared with adhesions formed on man-made materials (focal adhesions).

The spatial arrangement of the adhesive ligands presented on a substrate will determine the extent of receptor clustering, binding strength, organization of adaptor proteins and cytoskeleton, and shape of the attached cell (Fig. 1C and G). These changes will ultimately affect gene expression within the cell and determine its fate.

Although chemical patterning at the microscale is well established and commonly used to engineer cell function, methods for manufacturing nanoscale chemical patterns are rare. The use of man-made chemical nanopatterns to engineer cells is even rarer.

Two major categories of chemical nanopatterning technologies are microcontact printing and surface probe microscope mediated methods. Microcontact printing ( $\mu$ CP) transfers molecular inks, such as alkane thiols or biologically active proteins, from a stamp to a substrate [155, 174].  $\mu$ CP has the advantage of being able to pattern delicate molecules, such as proteins, because it does not require the use of harsh conditions such as the acids or bases that are necessary in photolithographic patterning [175]. Furthermore,  $\mu$ CP can be used for patterning large areas and

is also simple, quick, and inexpensive. By using small and well-defined features on the stamp, proteins are patterned onto substrates with high resolution and contrast. Images of nanopatterns created by microcontact printing have been taken with scanning probe microscopy techniques [24, 149, 151, 176]. The feature sizes are generally larger than 100 nm.

Scanning probe microscopy can be used to both image and generate features on a surface. There are two major methods of generating chemical patterns using the probe tips. One method, represented by dip-pen nanolithography (DPN), uses the probe tips of atomic force microscopes in a manner similar to that of a fountain pen where ink is transferred from the probe tip to the substrate. For example, DPN has been used to write collagen lines with widths of 30–50 nm [156]. The other method, known as nanografting, uses the probe tips to generate scratches on self-assembled monolayers (SAMs) after which the scratches are backfilled or grafted with desired biomolecules [153]. Another related method is the use of nanopipettes. This technique has been used to print biotinylated DNA onto streptavidin-coated glass substrate with submicrometer resolution [150].

Other techniques used to generate biochemical nanopatterns include particle lithography [160] and the use of ligand-bearing nanoparticles. Griffith et al. [37, 55, 56, 177, 178] used star polymers and branched polymers with different densities of RGD peptides to create biochemical nanoclusters. The RGD peptides, which are amino acid sequences that are integrin specific, mediate cell adhesion and are vital for cell survival, differentiation, and motility. Different spatial distributions of RGD peptides strongly influence integrin signaling. Rowley and Mooney [54] also observed that myogenesis depends critically on densities of RGD ligands in the ECM and showed that higher densities of ligands promote differentiation. Turner et al. [145] generated 0.7–5  $\mu\text{m}$  wide, parallel fibronectin lines via evaporation of a protein solution and used the resulting substrate to assay myoblast adhesion, migration, and contact guidance. Myoblasts plated onto these patterned substrates were found to orient and fuse into long, aligned myotubes. The features observed on the fibronectin nanolines were distinct from those of the circular clones seen in most conventional cultures.

The impact of protein patterning in the field of biomaterials is not limited to engineering cells. Microarrays of proteins as well as DNAs can be used as diagnostic tools and sensors to rapidly analyze large numbers of proteins and genes [152, 160]. In comparison to nanogeometry, nanochemistry is not as well developed. There is a lack of efficient methods to generate desired protein nanopatterns on biomaterials. It is an area that presents many challenges and opportunities for future nanoscale research.

## 5. MATERIALS WITH CONTROLLED NANOMECHANICS

In addition to topographical and chemical cues, mechanical stimuli, such as stretching and compression, also play a significant role in modulating cell behaviors. Mechanical interactions between the ECM and cells affect signal transduction, gene expression and protein synthesis [49].

As a result, mechanical stimuli can alter cell viability [49], development, motility [179], and morphology [180]. Mechanotransduction is also involved in biological functions such as touch sensation, hearing, maintenance of cardiovascular tone, and sensing gravity [181–183]. Researchers have identified a number of mechanotransducers on the cell membrane (such as stress-sensitive ion channels [184, 185]), which mediate the conversion of extracellular mechanical stimuli into intercellular chemical signals. For example, in bacteria such as *Escherichia coli*, there are ion channels of small conductance that are activated by stretching and is involved in sensing osmotic changes [11]. In eukaryotes such as mammals and yeast, stretch-activated channels regulate the influx of extracellular calcium. Calcium regulates production of actomyosin-based contractile forces [186–189], the structure and dynamics of the actin cytoskeleton [186, 190, 191], and the formation and disassembly of cell–substratum adhesions [192, 193]. Calcium also serves as a second messenger in many biochemical signal transduction pathways [157].

Other cellular components crucial for mechanotransduction include integrins and the cytoskeleton [35, 49, 194, 195]. Integrins link the internal actin cytoskeleton to the ECM through a group of adaptor proteins (Fig. 1C). They also form focal adhesions where integrins, adaptor proteins, growth factor receptors, ion channels, and various signaling enzymes are clustered together within a small region of the cell. When forces are applied to integrins or to cytoskeletal elements, the mechanical signals are converted to biochemical signals, in large part through the various molecular machineries localized to focal adhesions.

A challenge in the study of mechanotransduction lies in designing biomaterials with well-defined mechanical properties at the nanometer length scale. Biodegradable PLGA has been used widely as scaffolding material for bone regeneration because of its tensile properties, which are comparable to those of human cartilage and skin [72]. Collagen or agarose gels have also been used to investigate the effect of mechanotransduction on cells. Because gel stiffness varies with chemical composition, researchers have used different mixing ratios to investigate the relationship between the mechanical properties of the substrate and cell behavior [25]. Tan et al. [162] found that when the chitosan to collagen ratio in the gel was greater than three, cell proliferation decreased with increased chitosan concentration in the gel.

An example of how cellular responses can differ depending on presence or lack of tension even with the same geometry and chemistry has been demonstrated using collagen gels [196]. Gels attached to the surface of the container in which they were polymerized develop an intrinsic tension whereas gels detached from the surface releases any such tension within the gel. Myoblasts proliferated when plated on “stressed” gels but were quiescent when plated in gels that were relaxed.

An important component of cellular nanomechanics research is the measurement of mechanical forces generated by single cells or parts of cells. Forces exerted by cells on flexible substrates micropatterned with varying sizes of adhesive spots have been reported [165, 197]. Sheetz et al. [198, 199] used microcantilevers to measure traction forces generated by cells during migration. Taylor et al. [200] measured forces generated by single cells during cell division by

observing wrinkles formed on flexible silicone substrates by the cell tugging, and centrifugal detachment has been used to quantify the adhesive strengths of cells attached to substrates presenting similar overall ligand densities but with different size RGD ligand nanoclusters [37].

## 6. CONCLUSION AND FUTURE PROSPECTS

Biological nanomaterials research, which is at the crossroads between biology and nanotechnology, presents an exciting area with many challenges and opportunities. This chapter has focused on nanogeometry, nanochemistry, and nanomechanics to categorize biomaterials and their ability to engineer cell behavior. A number of intriguing examples show how nanoscale material properties can be used to elicit certain behaviors from cells. These results are promising for improvements and developments in tissue engineering, cell-based therapy and diagnosis, drug discovery, cell-based biosensors, and machine–cell hybrids.

To truly optimize cellular behavior using biomaterials, however, simultaneous control of multiple materials properties—preferably in real time—is necessary. Currently, the majority of research on the effect of different nanoproperties on cell behavior is opportunistic and nonsystematic, and often the mechanism for how the material properties are translated into cellular response is unclear. One of the most significant challenges at hand is the development of nanofabrication techniques that are able to pattern nanoscale features over large areas on three-dimensional biomaterials via inexpensive, quick, and reliable methods.

Although much work lies ahead before we can freely “write” nanoscale information to elicit specific desired functions from cells, we are well on our way in learning the basic “abc’s” necessary to develop biological nanomaterials that can guide cellular responses. The rapid progression of nanotechnology ensures that our nanoscale “vocabulary” for developing materials that can control cellular functions will continue to increase rapidly.

## GLOSSARY

**Cellular microenvironment/nanoenvironment** The local environment that surrounds and exerts influences on cells by set of microscale or nanoscale structures, molecules, and interactions.

**Clustering** The process of aggregation or grouping of molecules. For example, receptors diffusing freely in a cell membrane may bind to closely grouped ligand molecules on a surface to form closely grouped clusters of receptors. Receptor clustering is important for cell signaling.

**Cytoskeleton** The internal three-dimensional mesh-like network of proteins (including actin filaments, microtubules, and intermediate filaments) that gives shape and structural support to eucaryotic cells and also supports functions such as cell movement and transport of materials within the cell.

**Extracellular matrix (ECM)** Network of proteins (such as collagen) and carbohydrates that are secreted by cells to form a matrix with nanoscale structures and organization.

The ECM is recognized by cells and used for functions such as structural support in tissue formation and cell migration.

**Integrin** Heterodimeric receptors that extend across the cell membrane and mediate communication between the cells and the extracellular matrix by translating extracellular materials features into intracellular signals.

**Mechanotransduction** The conversion of extracellular mechanical stimuli into intracellular chemical signals.

**Micro-contact printing ( $\mu$ CP)** A micro- and nanopatterning fabrication technology that transfers molecular inks, such as alkane thiols or biologically active proteins, from a stamp to a substrate.

**Nanochemistry** The nanoscale spatial arrangement of chemicals such as ligands on a surface. For example, the same number of ligands (same bulk density) can be arranged into (separate/more distant) groups of two or more nearby ligands to more effectively match complex receptors structure and arrangement on cells (see Fig. 3).

**Nanogeometry** The nanoscale topographical features, shape, and patterns of a material (such as the pyramids, pores, grooves, or pillars of Fig. 2 or the collagen mesh of Fig. 1).

**Nanomechanics** Mechanical interactions and forces induced by nanoscale features of a material.

**Signal transduction** The process used by cells to transfer an extracellular signal or environmental stimulus to the cell or cell nucleus, usually through a relay of proteins and ligands.

**Soft lithography** A collection of microfabrication and micropatterning techniques that generates features and patterns by using soft, elastomeric polymers.

## ACKNOWLEDGMENTS

We thank the Whitaker Foundation, the National Science Foundation, and the National Institutes of Health for financial support. We thank Joong Hwan Bahng, Eva C. Lee, and Nandita Phadke for their critical reviewing of this article.

## REFERENCES

1. J. D. Watson and F. H. C. Crick, *Nature* 171, 737 (1953).
2. E. D. Hay, in “Cell Biology of Extracellular Matrix,” 2nd ed. (E. D. Hay, Ed.). Plenum, 1991.
3. H. Lodish, A. Berk, S. L. Zipursky, P. Matsudaria, D. Baltimore, and J. E. Darnell, “Molecular Cell Biology,” 4th ed. Freeman, San Francisco, 2000.
4. C. E. Walczak and T. J. Mitchison, *Cell* 85, 943 (1996).
5. X. F. Wu and J. A. Hammer, *Pigment Cell Res.* 13, 241 (2000).
6. C. M. Armstrong and B. Hille, *Neuron* 20, 371 (1998).
7. T. Elston, H. Y. Wang, and G. Oster, *Nature* 391, 510 (1998).
8. D. R. Jung, R. Kapur, T. Adams, K. A. Giuliano, M. Mrksich, H. G. Craighead, and D. L. Taylor, *Crit. Rev. Biotechnol.* 21, 111 (2001).
9. A. M. Peier, A. Moqrich, A. C. Hergarden, A. J. Reeve, D. A. Andersson, G. M. Story, T. J. Earley, I. Dragoni, P. McIntyre, S. Bevan, and A. Patapoutian, *Cell* 108, 705 (2002).
10. M. L. Struik, H. G. Steenbergen, A. S. Koster, F. Bretschneider, and R. C. Peters, *Comp. Biochem. Physiol.*, A 130, 607 (2001).
11. R. B. Bass, P. Strop, M. Barclay, and D. Rees, *Science* 298, 1582 (2002).

12. T. Subkhankulova, S. A. Mitchell, and A. E. Willis, *Biochem. J.* 359, 183 (2001).
13. E. Goldman, *Science* 298, 1155 (2002).
14. O. Medalia, I. Weber, A. S. Frangakis, D. Nicastro, G. Gerisch, and W. Baumeister, *Science* 298, 1209 (2002).
15. O. Beckstein, P. C. Biggin, and M. S. P. Sansom, *J. Phys. Chem. B* 105, 12902 (2001).
16. C. E. Capener and M. S. P. Sansom, *J. Phys. Chem. B* 106, 4543 (2002).
17. R. MacKinnon, *Nature* 416, 261 (2002).
18. C. M. Colbert and E. H. Pan, *Nat. Neurosci.* 5, 533 (2002).
19. Y. Ishii, S. Esaki, and T. Yanagida, *Appl. Phys. A* 75, 325 (2002).
20. F. M. Watt, *Trends Biochem. Sci.* 11, 482 (1986).
21. M. D. Martin-Bermudo, *Development* 127, 2607 (2000).
22. R. Perris and D. Perissinotto, *Mech. Dev.* 95, 3 (2000).
23. C. Oakley, N. A. F. Jaeger, and D. M. Brunette, *Exp. Cell Res.* 234, 413 (1997).
24. K. B. Lee, S. J. Park, C. A. Mirkin, J. C. Smith, and M. Mrksich, *Science* 295, 1702 (2002).
25. A. P. Balgude, X. Yu, A. Szymanski, and R. V. Bellamkonda, *Biomaterials* 22, 1077 (2001).
26. E. Cukierman, R. Pankov, D. R. Stevens, and K. M. Yamada, *Science* 294, 1708 (2001).
27. K. Nakamura, E. Bossy-Wetzler, K. Burns, M. P. Fadel, M. Lozyk, I. S. Goping, M. Opas, R. C. Bleackley, D. R. Green, and M. Michalak, *J. Cell Biol.* 150, 731 (2000).
28. P. J. Simpson-Haidaris and B. Rybarczyk, *Fibrinogen* 936, 406 (2001).
29. D. J. Schroen and H. T. Cheung, *Cell. Immunol.* 167, 141 (1996).
30. H. Cook, P. Stephens, K. G. Harding, and D. W. Thomas, *J. Dent. Res.* 79, 1176 (2000).
31. A. A. Hakim, *Cancer Gene Ther.* 6, PD23 (1999).
32. K. L. Elias, R. L. Price, and T. J. Webster, *Biomaterials* 23, 3279 (2002).
33. L. G. Gutwein and T. J. Webster, *J. Nanopart. Res.* 4, 231 (2002).
34. A. Musso, M. Rizetto, A. Levine, J. Hensold, and C. Fiocchi, *Gastroenterology* 116, G3384 (1999).
35. M. A. Schwartz and M. H. Ginsberg, *Nat. Cell Biol.* 4, E65 (2002).
36. B. E. Vogel and E. M. Hedgecock, *Development* 128, 883 (2001).
37. L. Y. Koo, D. J. Irvine, A. M. Mayes, D. A. Lauffenburger, and L. G. Griffith, *J. Cell Sci.* 115, 1423 (2002).
38. C. K. Miranti and J. S. Brugge, *Nat. Cell Biol.* 4, E83 (2002).
39. F. Podesta, T. Roth, F. Ferrara, E. Cagliero, and M. Lorenzi, *Diabetologia* 40, 879 (1997).
40. J. J. Tomasek and E. D. Hay, *Anat. Rec.* 199, A257 (1981).
41. U. K. Zatterstrom, U. Felbor, N. Fukai, and B. R. Olsen, *Cell Struct. Funct.* 25, 97 (2000).
42. P. Friedl and E. B. Brocker, *Cell. Mol. Life Sci.* 57, 41 (2000).
43. E. Cukierman, R. Pankov, and K. M. Yamada, *Curr. Opin. Cell Biol.* 14, 633 (2002).
44. D. Stopak and A. K. Harris, *J. Cell Biol.* 95, A137 (1982).
45. D. Stopak, N. K. Wessells, and A. K. Harris, *Proc. Nat. Acad. Sci. U.S.A.* 82, 2804 (1985).
46. A. K. Harris, D. Stopak, and P. Wild, *Nature* 290, 249 (1981).
47. R. K. Sawhney and J. Howard, *J. Cell Biol.* 157, 1083 (2002).
48. J. Takagi, B. M. Petre, T. Walz, and T. A. Springer, *Cell* 110, 599 (2002).
49. F. J. Alenghat and D. E. Ingber, *Science's STKE* 119, 6 (2002).
50. Q. Yuan, K. F. Austen, D. S. Friend, M. Heidtman, and J. A. Boyce, *J. Exp. Med.* 186, 313 (1997).
51. F. G. Giancotti and E. Ruoslahti, *Science* 285, 1028 (1999).
52. K. Maung, D. J. Easty, S. P. Hill, and D. C. Bennett, *Oncogene* 18, 6824 (1999).
53. G. Maheshwari, G. Brown, D. A. Lauffenburger, A. Wells, and L. G. Griffith, *J. Cell Sci.* 113, 1677 (2000).
54. J. A. Rowley and D. J. Mooney, *J. Biomed. Mater. Res.* 60, 217 (2002).
55. D. J. Irvine, A. M. Mayes, and L. G. Griffith, *Biomacromolecules* 2, 85 (2001).
56. D. J. Irvine, A. V. G. Ruzette, A. M. Mayes, and L. G. Griffith, *Biomacromolecules* 2, 545 (2001).
57. C. S. Chen, M. Mrksich, S. Huang, G. M. Whitesides, and D. E. Ingber, *Science* 276, 1425 (1997).
58. L. E. Dike, C. S. Chen, M. Mrksich, J. Tien, G. M. Whitesides, and D. E. Ingber, *In Vitro Cell. Dev. Biol. Anim.* 35, 441 (1999).
59. S. Huang and D. E. Ingber, *Nat. Cell Biol.* 1, E131 (1999).
60. C. H. Damsky and D. Ilic, *Curr. Opin. Cell Biol.* 14, 594 (2002).
61. D. H. Yang, E. R. Smith, C. Cohen, H. Wu, C. Patriotis, A. K. Godwin, T. C. Hamilton, and X. X. Xu, *Cancer* 94, 2380 (2002).
62. J. H. McKerrow, V. Bhargava, E. Hansell, S. Huling, T. Kuwahara, M. Matley, L. Coussens, and R. Warren, *Mol. Med.* 6, 450 (2000).
63. J. Ashkenas, C. A. Myers, C. Schmidhauser, Z. Werb, and M. Bissell, *Mol. Biol. Cell* 6, 2228 (1995).
64. R. G. Flemming, C. J. Murphy, G. A. Abrams, S. L. Goodman, and P. F. Nealey, *Biomaterials* 20, 573 (1999).
65. S. L. Goodman, P. A. Sims, and R. M. Albrecht, *Biomaterials* 17, 2087 (1996).
66. G. A. Abrams, S. L. Goodman, P. F. Nealey, M. Franco, and C. J. Murphy, *Cell Tissue Res.* 299, 39 (2000).
67. G. A. Abrams, S. S. Schaus, S. L. Goodman, P. F. Nealey, and C. J. Murphy, *Cornea* 19, 57 (2000).
68. H. C. Hoch, R. C. Staples, B. Whitehead, J. Comeau, and E. D. Wolf, *Science* 235, 1659 (1987).
69. G. M. Whitesides, E. Ostuni, S. Takayama, X. Y. Jiang, and D. E. Ingber, *Annu. Rev. Biomed. Eng.* 3, 335 (2001).
70. R. Y. Zhang and P. X. Ma, *J. Biomed. Mater. Res.* 52, 430 (2000).
71. P. X. Ma and R. Y. Zhang, *J. Biomed. Mater. Res.* 46, 60 (1999).
72. W. J. Li, C. T. Laurencin, E. J. Caterson, R. S. Tuan, and F. K. Ko, *J. Biomed. Mater. Res.* 60, 613 (2002).
73. B. G. Casey, D. R. S. Cumming, I. I. Khandaker, A. S. G. Curtis, and C. D. W. Wilkinson, *Microelectron. Eng.* 46, 125 (1999).
74. C. D. W. Wilkinson, M. Riehle, M. Wood, J. Gallagher, and A. S. G. Curtis, *Mater. Sci. Eng., C* 19, 263 (2002).
75. B. Wojciak-Stothard, A. Curtis, W. Monaghan, K. Macdonald, and C. Wilkinson, *Exp. Cell Res.* 223, 426 (1996).
76. M. Jacob, B. Christ, and H. J. Jacob, *Anat. Embryol.* 157, 291 (1979).
77. M. L. Burgess, J. C. McCrea, and H. L. Hedrick, *Mech. Ageing Dev.* 122, 1739 (2001).
78. H. G. Craighead, C. D. James, and A. M. P. Turner, *Curr. Opin. Solid State Mater. Sci.* 5, 177 (2001).
79. E. T. den Braber, J. E. de Ruijter, L. A. Ginsel, A. F. von Recum, and J. A. Jansen, *J. Biomed. Mater. Res.* 40, 291 (1998).
80. E. T. den Braber, J. E. de Ruijter, L. A. Ginsel, A. F. von Recum, and J. A. Jansen, *Biomaterials* 17, 2037 (1996).
81. E. T. den Braber, J. E. de Ruijter, and J. A. Jansen, *J. Biomed. Mater. Res.* 37, 539 (1997).
82. E. T. den Braber, J. E. de Ruijter, H. T. J. Smits, L. A. Ginsel, A. F. von Recum, and J. A. Jansen, *Biomaterials* 17, 1093 (1996).
83. T. G. van Kooten and A. F. von Recum, *Tissue Eng.* 5, 223 (1999).
84. X. F. Walboomers, H. J. E. Croes, L. A. Ginsel, and J. A. Jansen, *Biomaterials* 19, 1861 (1998).
85. X. F. Walboomers, W. Monaghan, A. S. G. Curtis, and J. A. Jansen, *J. Biomed. Mater. Res.* 46, 212 (1999).
86. X. F. Walboomers, L. A. Ginsel, and J. A. Jansen, *J. Biomed. Mater. Res.* 51, 529 (2000).
87. X. F. Walboomers, H. J. E. Croes, L. A. Ginsel, and J. A. Jansen, *J. Biomed. Mater. Res.* 47, 204 (1999).
88. E. T. den Braber, H. V. Jansen, M. J. de Boer, H. J. E. Croes, M. Elwenspoek, L. A. Ginsel, and J. A. Jansen, *J. Biomed. Mater. Res.* 40, 425 (1998).
89. E. Stepien, J. Staniszc, and W. Korohoda, *Cell Biol. Int.* 23, 105 (1999).

90. J. C. Palmaz, A. Benson, and E. A. Sprague, *J. Vasc. Intervent. Radiol.* 10, 439 (1999).
91. K. Matsuzaka, F. Walboomers, A. de Ruijter, and J. A. Jansen, *Clini. Oral Implants Res.* 11, 325 (2000).
92. K. Matsuzaka, X. F. Walboomers, J. E. de Ruijter, and J. A. Jansen, *Biomaterials* 20, 1293 (1999).
93. B. Wojciakstothard, A. S. G. Curtis, W. Monaghan, M. McGrath, I. Sommer, and C. D. W. Wilkinson, *Cell Motil. Cytoskeleton* 31, 147 (1995).
94. S. Nagaoka, K. Ashiba, and H. Kawakami, *Artific. Organs* 26, 670 (2002).
95. S. Nagaoka, K. Ashiba, and H. Kawakami, *Mater. Sci. Eng., C* 20, 181 (2002).
96. P. Clark, P. Connolly, A. S. G. Curtis, J. A. T. Dow, and C. D. W. Wilkinson, *J. Cell Sci.* 99, 73 (1991).
97. I. Nagata, A. Kawana, and N. Nakatsuji, *Development* 117, 401 (1993).
98. A. M. Rajnicek, S. Britland, and C. D. McCaig, *J. Cell Sci.* 110, 2905 (1997).
99. A. M. Rajnicek and C. D. McCaig, *J. Cell Sci.* 110, 2915 (1997).
100. A. Webb, P. Clark, J. Skepper, A. Compston, and A. Wood, *J. Cell Sci.* 108, 2747 (1995).
101. P. Clark, G. A. Dunn, A. Knibbs, and M. Peckham, *Int. J. Biochem. Cell Biol* 34, 816 (2002).
102. J. A. Alaerts, V. M. De Cupere, S. Moser, P. V. B. de Aguilar, and P. G. Rouxhet, *Biomaterials* 22, 1635 (2001).
103. C. Eriksson, J. Lausmaa, and H. Nygren, *Biomaterials* 22, 1987 (2001).
104. X. Y. Jiang, S. Takayama, X. P. Qian, E. Ostuni, H. K. Wu, N. Bowden, P. LeDuc, D. E. Ingber, and G. M. Whitesides, *Langmuir* 18, 3273 (2002).
105. A. Rich and A. K. Harris, *J. Cell Sci.* 50, 1 (1981).
106. Y. B. Xie, T. Sproule, Y. Li, H. Powell, J. J. Lannutti, and D. A. Kniss, *J. Biomed. Mater. Res.* 61, 234 (2002).
107. K. Anselme, P. Linez, M. Bigerelle, D. Le Maguer, A. Le Maguer, P. Hardouin, H. F. Hildebrand, A. Iost, and J. M. Leroy, *Biomaterials* 21, 1567 (2000).
108. K. Anselme, M. Bigerelle, B. Noel, A. Iost, and P. Hardouin, *J. Biomed. Mater. Res.* 60, 529 (2002).
109. D. D. Deligianni, N. Katsala, S. Ladas, D. Sotiropoulou, J. Amedee, and Y. F. Missirlis, *Biomaterials* 22, 1241 (2001).
110. J. Lincks, B. D. Boyan, C. R. Blanchard, C. H. Lohmann, Y. Liu, D. L. Cochran, D. D. Dean, and Z. Schwartz, *Biomaterials* 19, 2219 (1998).
111. E. Eisenbarth, J. Meyle, W. Nachtigall, and J. Breme, *Biomaterials* 17, 1399 (1996).
112. M. Bigerelle, K. Anselme, B. Noel, I. Ruderman, P. Hardouin, and A. Iost, *Biomaterials* 23, 1563 (2002).
113. L. Ponsonnet, V. Comte, A. Othmane, C. Lagneau, M. Charbonnier, M. Lissac, and N. Jaffrezic, *Mater. Sci. Eng., C* 21, 157 (2002).
114. S. C. Bayliss, L. D. Buckberry, I. Fletcher, and M. J. Tobin, *Sens. Actuators, A* 74, 139 (1999).
115. S. C. Bayliss, P. J. Harris, L. D. Buckberry, and C. Rousseau, *J. Mater. Sci. Lett.* 16, 737 (1997).
116. S. C. Bayliss, R. Heald, D. I. Fletcher, and L. D. Buckberry, *Adv. Mater.* 11, 318 (1999).
117. S. C. Bayliss, L. D. Buckberry, P. J. Harris, and M. Tobin, *J. Porous Mater.* 7, 191 (2000).
118. Y. W. Fan, F. Z. Cui, L. N. Chen, Y. Zhai, Q. Y. Xu, and I. S. Lee, *Appl. Surf. Sci.* 187, 313 (2002).
119. V. Chin, B. E. Collins, M. J. Sailor, and S. N. Bhatia, *Adv. Mater.* 13, 1877 (2001).
120. T. J. Webster, R. W. Siegel, and R. Bizios, *Biomaterials* 20, 1221 (1999).
121. T. J. Webster, C. Ergun, R. H. Doremus, R. W. Siegel, and R. Bizios, *Biomaterials* 23, 1327 (2001).
122. I. Degasne, M. F. Basle, V. Demais, G. Hure, M. Lesourd, B. Grolleau, L. Mercier, and D. Chappard, *Calcif. Tissue Int.* 64, 499 (1999).
123. B. D. Boyan, V. L. Sylvia, Y. H. Liu, R. Sagun, D. L. Cochran, C. H. Lohmann, D. D. Dean, and Z. Schwartz, *Biomaterials* 20, 2305 (1999).
124. M. Wieland, B. Chehroudi, M. Textor, and D. M. Brunette, *J. Biomed. Mater. Res.* 60, 434 (2002).
125. M. J. Dalby, M. V. Kayser, W. Bonfield, and L. Di Silvio, *Biomaterials* 23, 681 (2002).
126. J. G. Steele, G. Johnson, K. M. McLean, G. J. Beumer, and H. J. Griesser, *J. Biomed. Mater. Res.* 50, 475 (2000).
127. B. A. Dalton, M. D. M. Evans, G. A. McFarland, and J. G. Steele, *J. Biomed. Mater. Res.* 45, 384 (1999).
128. B. A. Dalton, G. A. McFarland, and J. G. Steele, *J. Biomed. Mater. Res.* 56, 83 (2001).
129. M. D. M. Evans, B. A. Dalton, and J. G. Steele, *J. Biomed. Mater. Res.* 46, 485 (1999).
130. J. H. Fitton, B. A. Dalton, G. Beumer, G. Johnson, H. J. Griesser, and J. G. Steele, *J. Biomed. Mater. Res.* 42, 245 (1998).
131. O. H. Kwon, A. Kikuchi, M. Yamato, Y. Sakurai, and T. Okano, *J. Biomed. Mater. Res.* 50, 82 (2000).
132. P. Malmberg and H. Nygren, *Biomaterials* 23, 247 (2002).
133. S. L. Ishaug, G. M. Crane, M. J. Miller, A. W. Yasko, M. J. Yaszemski, and A. G. Mikos, *J. Biomed. Mater. Res.* 36, 17 (1997).
134. C. D. W. Wilkinson, A. S. G. Curtis, and J. Crossan, *J. Vac. Sci. Technol., B* 16, 3132 (1998).
135. A. S. G. Curtis, B. Casey, J. O. Gallagher, D. Pasqui, M. A. Wood, and C. D. W. Wilkinson, *Biophys. Chem.* 94, 275 (2001).
136. A. M. P. Turner, N. Dowell, S. W. P. Turner, L. Kam, M. Isaacson, J. N. Turner, H. G. Craighead, and W. Shain, *J. Biomed. Mater. Res.* 51, 430 (2000).
137. S. Turner, L. Kam, M. Isaacson, H. G. Craighead, W. Shain, and J. Turner, *J. Vac. Sci. Technol., B* 15, 2848 (1997).
138. M. Riedel, B. Muller, and E. Wintermantel, *Biomaterials* 22, 2307 (2001).
139. M. J. Dalby, M. O. Riehle, H. Johnstone, S. Affrossman, and A. S. G. Curtis, *Biomaterials* 23, 2945 (2002).
140. M. Conti, G. Donati, G. Cianciolo, S. Stefoni, and B. Samori, *J. Biomed. Mater. Res.* 61, 370 (2002).
141. F. A. Denis, P. Hanarp, D. S. Sutherland, J. Gold, C. Mustin, P. G. Rouxhet, and Y. F. Dufrene, *Langmuir* 18, 819 (2002).
142. C. Galli, M. C. Coen, R. Hauert, V. L. Katanaev, M. P. Wymann, P. Groning, and L. Schlapbach, *Surf. Sci.* 474, L180 (2001).
143. P. Cacciafesta, K. R. Hallam, A. C. Watkinson, G. C. Allen, M. J. Miles, and K. D. Jandt, *Surf. Sci.* 491, 405 (2001).
144. P. Banerjee, D. J. Irvine, A. M. Mayes, and L. G. Griffith, *J. Biomed. Mater. Res.* 50, 331 (2000).
145. D. C. Turner, J. Lawton, P. Dollenmeier, R. Ehrismann, and M. Chiquet, *Dev. Biol.* 95, 497 (1983).
146. G. P. Lopez, M. W. Albers, S. L. Schreiber, R. Carroll, E. Peralta, and G. M. Whitesides, *J. Am. Chem. Soc.* 115, 5877 (1993).
147. D. S. Koktysh, X. R. Liang, B. G. Yun, I. Pastoriza-Santos, R. L. Matts, M. Giersig, C. Serra-Rodriguez, L. M. Liz-Marzan, and N. A. Kotov, *Adv. Func. Mater.* 12, 255 (2002).
148. M. Z. Liu, N. A. Amro, C. S. Chow, and G. Y. Liu, *Nano Lett.* 2, 863 (2002).
149. L. M. Demers, D. S. Ginger, S. J. Park, Z. Li, S. W. Chung, and C. A. Mirkin, *Science* 296, 1836 (2002).
150. A. Bruckbauer, L. Ying, M. Rothery, D. Zhou, A. I. Shevchuk, C. Abell, Y. E. Korchev, and D. Klenerman, *J. Am. Chem. Soc.* 124, 8810 (2002).
151. K. Wadu-Mesthrige, S. Xu, N. A. Amro, and G. Y. Liu, *Langmuir* 15, 8580 (1999).
152. K. Wadu-Mesthrige, N. A. Amro, J. C. Garno, S. Xu, and G. Y. Liu, *Biophys. J.* 80, 1891 (2001).



153. J. R. Kenseth, J. A. Harnisch, V. W. Jones, and M. D. Porter, *Langmuir* 17, 4105 (2001).
154. M. Mertig, R. Kirsch, W. Pompe, and H. Engelhardt, *Eur. Phys. J. D* 9, 45 (1999).
155. A. Bernard, E. Delamarche, H. Schmid, B. Michel, H. R. Bosshard, and H. Biebuyck, *Langmuir* 14, 2225 (1998).
156. D. L. Wilson, R. Martin, S. Hong, M. Cronin-Golomb, C. A. Mirkin, and D. L. Kaplan, *Proc. Natl. Acad. Sci. U.S.A.* 98, 13660 (2001).
157. G. Y. Liu and N. A. Amro, *Proc. Natl. Acad. Sci. U.S.A.* 99, 5165 (2002).
158. D. Pum, G. Stangl, C. Sponer, K. Riedling, P. Hudek, W. Fallmann, and U. B. Sleytr, *Microelectron. Eng.* 35, 297 (1997).
159. M. S. Boeckl, T. Baas, A. Fujita, K. O. Hwang, A. L. Bramblett, B. D. Ratner, J. W. Rogers, and T. Sasaki, *Biopolymers* 47, 185 (1998).
160. J. C. Garno, N. A. Amro, K. Wadu-Mesthrige, and G.-Y. Liu, *Langmuir* 18, 8186 (2002).
161. R. A. Brown, K. K. Sethi, I. Gwanmesia, D. Raemdonck, M. Eastwood, and V. Mudera, *Exp. Cell Res.* 274, 310 (2002).
162. W. Tan, R. Krishnaraj, and T. A. Desai, *Tissue Eng.* 7, 203 (2001).
163. S. M. O'Connor, D. A. Stenger, K. M. Shaffer, and W. Ma, *Neurosci. Lett.* 304, 189 (2001).
164. G. P. Dillon, X. J. Yu, A. Sridharan, J. P. Ranieri, and R. V. Bellamkonda, *J. Biomater. Sci. Polym. Ed.* 9, 1049 (1998).
165. N. Q. Balaban, U. S. Schwarz, D. Riveline, P. Goichberg, G. Tzur, I. Sabanay, D. Mahalu, S. Safran, A. Bershadsky, L. Addadi, and B. Geiger, *Nat. Cell Biol.* 3, 466 (2001).
166. P. L. Ryan, R. A. Foty, J. Kohn, and M. S. Steinberg, *Proc. Natl. Acad. Sci. U.S.A.* 98, 4323 (2001).
167. P. Clark, D. Coles, and M. Peckham, *Exp. Cell Res.* 230, 275 (1997).
168. A. Curtis and C. Wilkinson, *Biomaterials* 18, 1573 (1997).
169. R. Bellamkonda, J. P. Ranieri, N. Bouche, and P. Aebischer, *J. Biomed. Mater. Res.* 29, 663 (1995).
170. X. F. Walboomers, W. Monaghan, A. S. G. Curtis, and J. A. Jansen, *J. Biomed. Mater. Res.* 55, 669 (2001).
171. P. Clark, P. Connolly, A. S. G. Curtis, J. A. T. Dow, and C. D. W. Wilkinson, *Development* 108, 635 (1990).
172. P. Draber and L. Draberova, *Mol. Immunol.* 38, 1247 (2002).
173. R. L. Juliano, *Annu. Rev. Pharmacol. Toxicol.* 42, 283 (2002).
174. B. Michel, A. Bernard, A. Bietsch, E. Delamarche, M. Geissler, D. Juncker, H. Kind, J. P. Renault, H. Rothuizen, H. Schmid, P. Schmidt-Winkel, R. Stutz, and H. Wolf, *IBM J. Res. Dev.* 45, 697 (2001).
175. C. D. James, R. C. Davis, L. Kam, H. G. Craighead, M. Isaacson, J. N. Turner, and W. Shain, *Langmuir* 14, 741 (1998).
176. R. D. Piner, J. Zhu, F. Xu, S. H. Hong, and C. A. Mirkin, *Science* 283, 661 (1999).
177. D. J. Irvine, K. A. Hue, A. M. Mayes, and L. G. Griffith, *Biophys. J.* 82, 120 (2002).
178. D. J. Irvine, A. M. Mayes, and L. G. Griffith, "Abstracts of Papers of the American Chemical Society" 1998, Vol. 216, 464-PHYS.
179. K. K. Parker, A. L. Brock, C. Brangwynne, R. J. Mannix, N. Wang, E. Ostuni, N. A. Geisse, J. C. Adams, G. M. Whitesides, and D. E. Ingber, *FASEB J.* 16, 1195 (2002).
180. J. Garcia-Anoveros and D. P. Corey, *Ann. Rev. Neurosci.* 20, 567 (1997).
181. M. Kanzaki, M. Nagasawa, I. Kojima, C. Sato, K. Naruse, M. Sokabe, and H. Iida, *Science* 285, 882 (1999).
182. H. Sackin, *Annu. Rev. Physiol.* 57, 333 (1995).
183. A. S. French, *Annu. Rev. Physiol.* 54, 135 (1992).
184. S. I. Sukharev, P. Blount, B. Martinac, and C. Kung, *Annu. Rev. Physiol.* 59, 633 (1997).
185. J. E. Gale, W. Marcotti, H. J. Kennedy, C. J. Kros, and G. P. Richardson, *J. Neurosci.* 21, 7013 (2001).
186. J. Lee, A. Ishihara, G. Oxford, B. Johnson, and K. Jacobson, *Nature* 400, 382 (1999).
187. D. A. Rees, J. Charlton, P. Ataliotis, A. Woods, A. J. Stones, and S. A. Bayley, *Cell Motil. Cytoskeleton* 13, 112 (1989).
188. S. Citi and J. Kendrickjones, *Bioessays* 7, 155 (1987).
189. R. Strohmeier and J. Bereiterhahn, *Exp. Cell Res.* 154, 412 (1984).
190. J. Condeelis, *Annu. Rev. Cell Biol.* 9, 411 (1993).
191. J. H. Hartwig and H. L. Yin, *Cell Motil. Cytoskeleton* 10, 117 (1988).
192. M. D. Sjaastad and W. J. Nelson, *Bioessays* 19, 47 (1997).
193. E. Crowley and A. F. Horwitz, *J. Cell Biol.* 131, 525 (1995).
194. B. M. Chen and A. D. Grinnell, *J. Neurosci.* 17, 904 (1997).
195. W. M. Kuebler, X. Y. Ying, and J. Bhattacharya, *Am. J. Physiol. Lung Cell. Mol. Physiol.* 282, L917 (2002).
196. F. Grinnell, *Trends Cell Biol.* 10, 362 (2000).
197. N. Wang, E. Ostuni, G. M. Whitesides, and D. E. Ingber, *Cell Motil. Cytoskeleton* 52, 97 (2002).
198. C. G. Galbraith and M. P. Sheetz, *Proc. Natl. Acad. Sci. U.S.A.* 94, 9114 (1997).
199. C. G. Galbraith and M. P. Sheetz, *J. Cell Biol.* 147, 1313 (1999).
200. K. Burton and D. L. Taylor, *Nature* 385, 450 (1997).

# Nanomaterials from Discotic Liquid Crystals

Gregory P. Crawford, Robert H. Hurt

*Brown University, Providence, Rhode Island, USA*

## CONTENTS

1. Introduction
2. Liquid Crystalline Phases
3. Reactive Mesogens
4. Anchoring and Confinement
5. Applications of Synthetic Discotics
6. Applications of Mesophase-Derived Carbons
7. New Carbon Nanomaterials

Glossary

References

## 1. INTRODUCTION

Disk-shaped organic molecules form the basis for an exciting variety of new and emerging materials, including molecular wires, polarizing filters, compensation films, and advanced carbon materials such as fibers, foams, and microbeads. Of special interest are those discotics that form liquid crystals—orientationally ordered liquid phases [1]. The high molecular mobility and long-range order in liquid crystalline phases allow material structures to be created through equilibrium self-assembly processes driven by soft intermolecular interactions. Most of the current discotic applications are best classified as “nanostructured” materials since they have supramicron overall dimensions but derive their unique properties from the self-organized structures involving their constituent molecular disks of diameter 1–5 nm. In addition, however, there is an emerging class of true nanomaterials, formed by confining discotic liquid crystals within nanometric templates.

Interestingly, most discotics are not used in the dynamic liquid crystalline (LC) state, which typically exists only above room temperature. Rather the liquid crystalline phases serve as intermediates in the synthesis of ordered materials that perform their desired function in the solid state. In this respect they differ from calamitic, or rodlike liquid crystals as used in display technology and other photonic devices.

For discotics, the order developed in the liquid crystalline state is preserved either by quenching or by polymerization of reactive mesogens. The largest class of discotic-based solids is carbon materials, in which high-temperature polymerization is used to convert the discotic supramolecular assemblies into an arrangement of “graphene” (graphite-like) layers which preserve the liquid-phase orientational order.

This chapter gives an overview of discotic molecules (Section 1), their liquid crystalline behavior (Sections 2 and 3), and their applications as nanostructured materials (Sections 4 and 5) and emerging carbon nanomaterials (Section 6). The chapter covers both the science and technology aspects of discotics, but emphasizes practical synthesis routes for new material structures and their potential technological uses.

### 1.1. Discotic Molecular Structures

Carbon in  $sp^2$ -hybridization forms a set of three equivalent bonds lying in a single plane separated by  $120^\circ$ . Six-membered rings of  $sp^2$ -hybridized carbon are particularly common due to their enhanced stability arising from structural resonance. These aromatic and polyaromatic (multiple ring) compounds are nature’s intrinsically planar organic building blocks (see Fig. 1). Organic molecules containing a preponderance of  $sp^2$ -hybridized bonds begin to fill two-dimensional space as their molecular weights increase to form extended planar structures that can be plate- or disklike (see Fig. 1C, D).

Discotic structures can also include  $sp$ -hybridized carbon (with carbon/carbon triple bonds) that form linear segments bridging the  $sp^2$ -hybridized carbon as shown by the unique ring discotic molecule in Figure 2, or can include other bonding types in flexible groups that decorate a rigid ring (Fig. 2) or a rigid core (Fig. 3), which is most typically a polyaromatic rigid core (Fig. 4). Other discotic structures include synthetic dendrimers [2] and natural porphyrins [3].

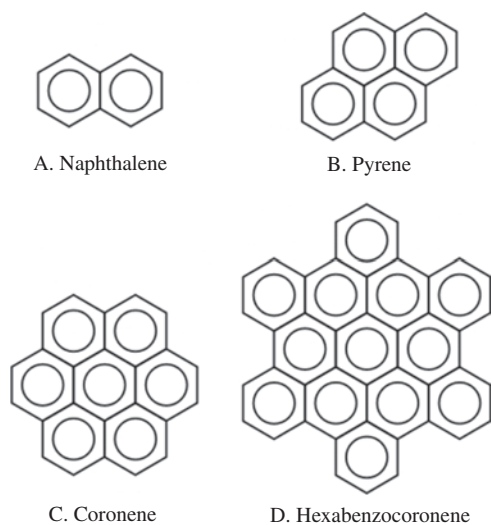


**Figure 1.** Common planar polyaromatic compounds of increasing molecular weight. (A) Naphthalene; (B) pyrene; (C) coronene; (D) hexabenzocoronene.

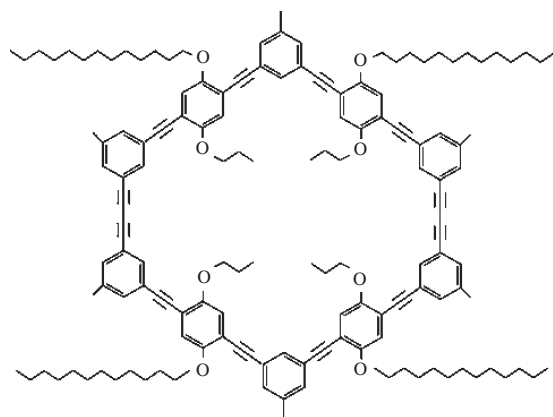


**Figure 2.** Unusual discotic molecule with rigid ring and flexible core from [45]. Most discotic molecules are polyaromatics (Fig. 1) or contain a polyaromatic core with one or more peripheral side chains.

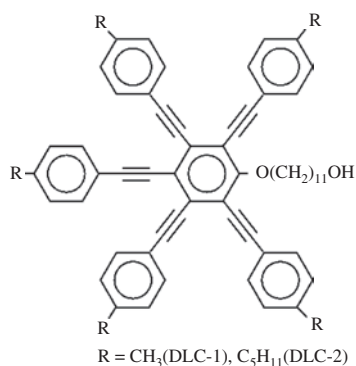


**Figure 3.** Discotic liquid crystalline compound with a rigid aromatic core and flexible aliphatic side chains.

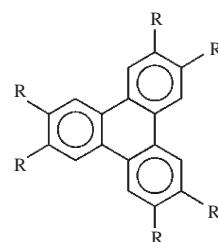


**Figure 4.** The first reported synthetic discotic liquid crystalline compound [13], and basic model for most discotic liquid crystals today. It consists of polyaromatic core (here based on triphenylene) with multiple flexible aliphatic side chains.

### 1.1.1. Polycyclic Aromatic Hydrocarbons

The polycyclic aromatic hydrocarbons (PAHs) that are the basis for most discotics are common products of high-temperature organic reactions, as they lie along the minimum free energy pathway in C/H space between organic matter and the atmospheric-pressure thermodynamic end-state, graphite. The sp<sup>2</sup>-hybridized bonding leads to intrinsically planar molecules, in which each carbon is covalently bonded to three other carbons or two carbons and a hydrogen at the periphery. Curvature can be introduced with five-membered rings, or through steric hindrances in oligomers of smaller polyaromatic clusters connected by aryl linkages (C-C single bonds) or other cross-linking groups.

PAHs are ubiquitous in nature where they are of special interest as pollutants in the atmosphere and soil [4, 5], as biologically active compounds that form carcinogen-DNA adducts [6, 7] and exert complex effects on the immune system [8], as components in the interstellar medium [9], and as components in petroleum that cause harmful deposits in processing equipment [10]. In technology PAHs find use as liquid crystalline cores [11–14]; as optoelectronic devices including diodes and organic molecular thin films [15–19]; as organic superconductors; as feedstocks for advanced carbon material [20, 21]; and as enabling elements of nanotechnology used for molecular recognition [22], as molecular wires [18], or as coupling agents for sidewall functionalization of nanotubes [23].

The largest commercially available PAH is coronene (see Fig. 1), which melts at 440 °C into an isotropic liquid phase. The even larger PAH, hexabenzocoronene with six-fold rotational symmetry (see Fig. 1), can be readily synthesized [18, 24–26], and has been used as a sublimation source to form epitaxial molecular thin films [18]. Larger PAHs are seldom the subject of liquid-phase studies in pure form, as they typically decompose before melting. An even larger planar C<sub>60</sub> has been reported [27].

## 1.2. Discotic Liquid Crystals

Most discotic liquid crystals are based on polyaromatic compounds, but require some modification to avoid the very high melting crystalline solid phases. The following sections describe the two major classes of discotic liquid crystals: polyaromatic hydrocarbon *mixtures* (“pitches”) and synthetic polyaromatics with substituent side chains to promote liquid crystallinity (“synthetic discotic mesogens”).

### 1.2.1. Pitches

Among the naturally occurring polyaromatics are those of high molecular weight (300–2000 Daltons), which can be disklike or platelike (see Fig. 5). Most very large PAHs (>700 Daltons) are available only as complex mixtures referred to as “pitches,” and this has limited our fundamental understanding of their behavior. Interestingly, it is the multicomponent nature of pitches that is responsible for liquid crystalline behavior [28], since large, regular, unsubstituted polyaromatics are insoluble [27, 28], nonvolatile [10], and form high-melting solid phases that prevent discotic liquid crystalline formation [28].

Pitches are derived from heat soaking and/or extraction of petroleum fractions [29], coal tar, or from the polymerization of smaller organic compounds (see Fig. 5) [20, 30, 31]. Pitches are technologically important precursors for advanced carbon materials and the only source of liquid crystalline PAH. Synthetic pitches from catalytic polymerization of naphthalene were developed by Mochida and co-workers [20, 30] and are now commercially available through Mitsubishi Gas Chemical under the trade name of AR resins. They are brittle solids at room temperature, but soften near 280 °C to form a 100% anisotropic discotic liquid (bulk mesophase). The ready availability of homogeneous bulk mesophases should greatly accelerate the development of mesophase-based materials and nanomaterials in the coming years.

Pitches are complex materials, regardless of whether they are of natural origin (fossil-fuel derived) or synthetic, and a large literature has accumulated on the characterization [25, 26, 32–35] formation chemistry and kinetics [25, 36–38] of pitches, as well as on processing methods including solvent interactions [25, 29, 39], rheological aspects [40], blending [41], and air blowing [25] to improve or optimize pitch properties.

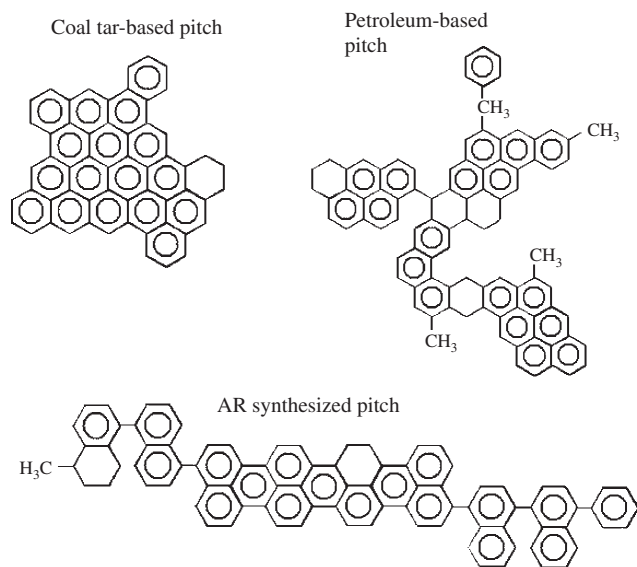


**Figure 5.** Examples of large, irregular PAHs found in pitches of different origin.

### 1.2.2. Synthetic Discotic Mesogens

Synthetic, single-component discotic liquid crystals are commonly based on polyaromatics, but require the addition of substituent groups to the core which disrupt packing in the solid phase (see Fig. 4). The ordered liquid phase is typically observed only when the length of the side chains falls within a certain range; for example, the nematic phase in hexa-*N*-alkoxybenzoates of triphenylene occurs only in the presence of substituent chains on the benzoate side groups of formula  $R = C_nH_{2n+1}O$ , with  $n$  from 8 to 12. It is currently believed that the side chains of an appropriate number and length are critical to the achievement of discotic mesophases. The importance of the length of the side chains suggests that the stability of columnar phases requires some kind of amphiphilic interaction [42] (in which the cores and side chains have different interaction potentials leading to preferential core/core attraction and chain/chain attraction). The cores and chains tend to segregate, producing a columnar structure in which the chains also provide lubrication between the columns to promote liquid-like behavior.

The first synthetic discotic was reported 12 years after the discovery of the carbonaceous discotic phase by Brooks and Taylor in 1965 [1]. Since then a wide variety of discotic liquid crystals have been synthesized and new discotic liquid crystals continue to be announced each year [43–46].

## 2. LIQUID CRYSTALLINE PHASES

### 2.1. Introduction

The term liquid crystal describes a state of matter that is intermediate between an isotropic liquid and a crystalline solid. Since their discovery in the late nineteenth century by Renitzer [47] and Lehmann [48], there have been thousands of compounds identified to exhibit a liquid crystalline phase. The essential prerequisite for liquid crystallinity is that the molecule must exhibit a high degree of shape anisotropy (e.g., rodlike or disklike). Depending on the nature of the molecular structure, a compound may pass through one or many different liquid crystal phases, characterized by order and symmetry, before transforming into a truly isotropic liquid. There are two generic classes of liquid crystals, those whose transitions are driven by thermal processes, known as thermotropic, and those strongly influenced by solvents, known as lyotropics. Liquid crystals are cataloged as either rodlike (calamitic) or disklike (discotic). In this section we briefly review their structure and ordering properties.

### 2.2. Calamitic Liquid Crystals

The majority of thermotropic liquid crystals are composed of rodlike molecules, which can be broadly classified as nematic, cholesteric, and smectic. Figure 6 illustrates a particular phase sequence as the temperature is increased: crystal, smectic A, nematic, and isotropic liquid. The conventional crystal structure possesses both positional and orientational order. The smectic A phase (the simplest smectic phase) possesses orientational order and a density modulation due to the arrangement of molecules in “bookshelf-type” layers. The orientational order is characterized by the nematic director,  $\mathbf{n}$ , which defines the average direction of

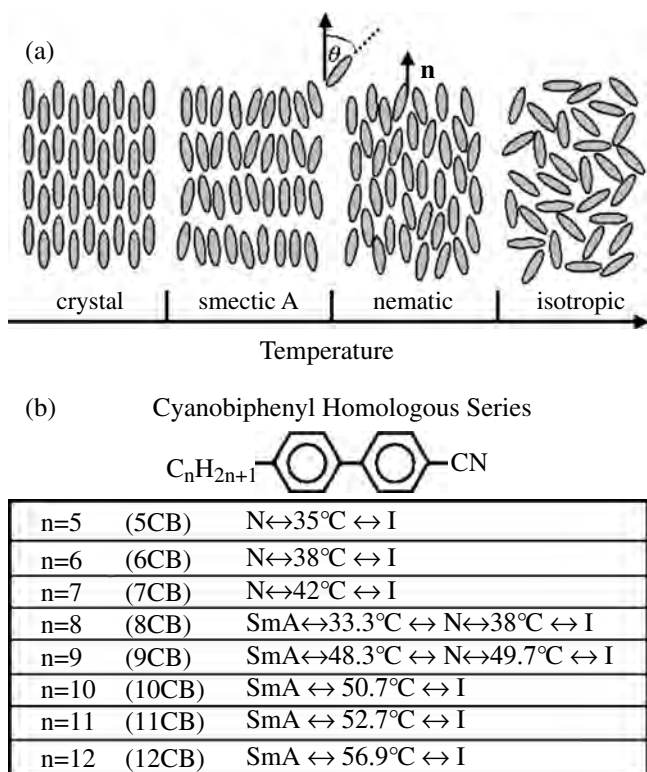


**Figure 6.** A typical phase sequence of a thermotropic liquid crystal (a) and transition temperatures of a typical cyanobiphenyl homologous series known as nCB (b).

an ensemble of molecules. The molecules within the smectic planes do not exhibit any correlation between their centers of mass (i.e., fluidity within layers). The nematic phase also possesses long-range orientational order, but no positional order. The nematic phase, the simplest of all the liquid crystal phases, differs from a truly isotropic liquid in that the molecules are approximately oriented with their long axis parallel to one another much like the smectic A phase with the absence of layers. The preferred direction of molecules in the nematic phase usually varies from point to point; however, an aligned specimen is optically uniaxial and birefringent.

An example of a family of rodlike liquid crystal compounds is shown in Figure 6b; these compounds are known as cyanobiphenyls. This particular family can have a rich variety of phase behavior depending on the length of the aliphatic chain. For example, the phase sequence of 5CB is crystal-nematic-isotropic, 8CB is crystal-smectic A-nematic-isotropic, and 12CB is crystal-smectic A-isotropic. There are also an intriguing variety of other smectic phases which are classified by order and symmetry but are not pertinent to this review [49]. In addition, the nematic phase can exhibit chirality and the molecules can exhibit a helical structure [50].

The Maier-Saupe theory has been phenomenally successful at quantifying the degree of orientational order in liquid crystals. Based on a mean-field approximation (i.e., each molecule is subject to an average internal field which is independent of any local variations or short-range ordering), the

temperature dependence of an orientational order parameter,  $S$ , can be determined [51]. The order parameter is defined as

$$Q = P_2 \langle (\cos \theta) \rangle = \frac{1}{2} (3 \langle \cos^2 \theta \rangle - 1) \quad (1)$$

where  $\theta$  is the angle which the long molecular axis makes with the nematic director,  $\mathbf{n}$ , and denotes an ensemble average. For perfect crystalline order,  $\langle \cos^2 \theta \rangle = 1$  and  $Q = 1$ . For complete disorder in the isotropic phase,  $\langle \cos^2 \theta \rangle = \frac{1}{3}$  and  $Q = 0$ . For the nematic phase,  $Q \sim 0.3-0.4$  near the nematic-isotropic transition and  $Q \sim 0.7-0.8$  deep in the nematic phase.

McMillan [52] extended the Maier-Saupe theory (based on Kirkwood-Monroe melting) [53] to describe the one-dimensional [translational periodically] at the layered smectic A phase. The orientational order parameter,  $S$ , is identical to the Maier-Saupe theory (Eq. (1)). A new parameter,  $\sigma$ , expressed as

$$\sigma = \left\langle \cos \left( \frac{2\pi z}{d} \right) \left( \frac{3 \cos^2 \theta - 1}{2} \right) \right\rangle \quad (2)$$

is a measure of the amplitude of the density modulation characteristic of the layer structure and defines the degree of smectic ordering. In the smectic A phase,  $\sigma \neq 0$  and  $S \neq 0$ ; in the nematic phase,  $\sigma = 0$  and  $S \neq 0$ ; and in the isotropic phase,  $\sigma = 0$  and  $S = 0$ .

We have briefly described the basic principles of calamitic (rodlike) liquid crystals. There is a vast amount of literature in this area, because of the rich fundamental physical phenomenon and application in optical devices (e.g., liquid crystal displays) [54]. The shape anisotropy of calamitic liquid crystals manifests itself in two often very important properties: (1) birefringence and (2) dielectric constant. Because of the anisotropy in the dielectric constant, the molecules can align parallel or perpendicular to applied fields depending on the sign of their dielectric anisotropy. The most common are compounds that exhibit a positive dielectric anisotropy ( $\Delta\epsilon > 0$ ) that align parallel to applied electric fields. The ability to align liquid crystals to a new orientation with an applied electric field enables one to manipulate the index of refraction, which is the basis for most liquid crystal-based optical technology.

### 2.3. Discotic Liquid Crystals

The general thought that a material must be composed of rodlike molecules in order for liquid crystallinity or mesomorphism to occur was defeated when it was demonstrated that compounds with disklike constituents also exhibit mesophases. They were first discovered in carbon precursor materials with a transient existence by Brooks and Taylor [1] in stable low molecular weight systems [55]. Discotic liquid crystals are generally classified into various categories depending on the nature of their ordering. The simplest configuration is the columnar phase (often denoted by D) consisting of stacks of disklike molecules forming columns as shown in Figure 7. The columns can organize in a variety of ways, such as hexagonal  $D_h$ , rectangular  $D_r$ , and even

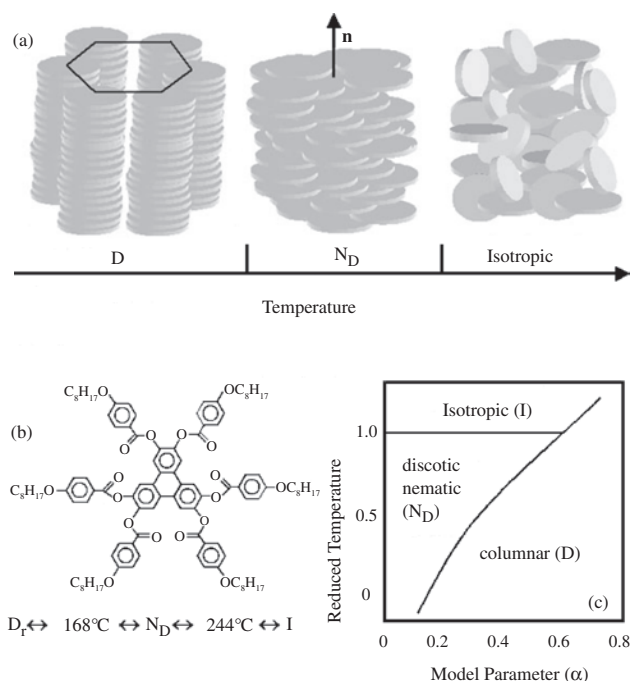


**Figure 7.** A typical phase sequence of a thermotropic discotic liquid crystal phase (a). A discotic liquid crystal molecule that possesses a columnar rectangular phase, discotic nematic phase, and isotropic phase (b). A phase diagram based on an extended McMillan framework where  $\alpha$  is a parameter that is proportional to the chain length on the discotic molecule.

tilted. A hexagonal phase is shown in Figure 7a. The discotic nematic phase (often denoted as  $N_D$ ) is also shown in Figure 7a where the disks order along the nematic director  $\mathbf{n}$  (orthogonal to plane of molecule) but they do not organize into columns.

Transitions between the columnar and the discotic nematic phases occur in certain compounds. An example compound is shown in Figure 7b, known as 2,3,6,7,10,11-(triphenylene hexaocetylloxy benzoate), exhibits a rectangular hexatic phase and discotic nematic [56]. Like low molecular weight rodlike molecules, transitions can occur between  $N_D$  and the isotropic or between D and the isotropic phase as well, depending on the molecular configuration. To develop a quantitative description of the D- $N_D$ -isotropic transitions, an extended McMillan mean-field model can be employed; such a model is analogous to smectic A phase model where the density wave is now periodic in two dimensions [57–59].

The D phase can be described by a superposition of three density waves with wavevectors:

$$\begin{aligned} \mathbf{A} &= \frac{4\pi}{\sqrt{3}d} \mathbf{j} \\ \mathbf{B} &= \frac{4\pi}{\sqrt{3}d} \left( \frac{\sqrt{3}}{2} \mathbf{i} - \frac{1}{2} \mathbf{j} \right) \\ \mathbf{C} &= \mathbf{A} + \mathbf{B} \end{aligned} \quad (3)$$

where  $\mathbf{i}$  and  $\mathbf{j}$  are conventional unit vectors and  $d$  is the lattice constant. The orientational order parameter is identical to that of a rodlike nematic  $Q = \langle P_2(\cos \theta) \rangle$  and the

order parameter coupling the orientational and the transitional order is given by

$$\sigma = \frac{1}{3} \langle [\cos(\mathbf{A} \cdot \mathbf{r}) + \cos(\mathbf{B} \cdot \mathbf{r}) + \cos(\mathbf{i} \cdot \mathbf{r})] P_2(\cos \theta) \rangle$$

In the development of this model, the form of the potential ensures that the energy of the molecule is minimum when the disk is centered in the column with its plane normal to the z-axis. There are three possible minimum solutions to the energy, where  $Q = 0$  and  $\sigma = 0$  in the isotropic phase,  $Q \neq 0$  and  $\sigma = 0$  in the  $N_D$  phase, and  $Q \neq 0$  and  $\sigma \neq 0$  in the D phase. The phase diagram is shown in Figure 7c as a function of  $\alpha$ , which is a measure of the chain length in the McMillan model.

Discotic mesogens can also be of high molecular weight when attached to a backbone or as side groups as shown in Figure 8. When rod-shaped molecules form repeating units, conventional mesophases are observed as in low molecular weight compounds. Disk shape moieties can also repeat to form a side chain and main chain polymers as shown in Figure 8a and b, respectively. A polyester with disk-shaped triphenylene as the repeating unit in the main chain separated by flexible spacers forms a hexagonal column structure with intercolumn binding and intracolumn backfolding as shown in Figure 8c [60]. Rigid aromatic polyamides and polyesters with discotic units in the main chain exhibit a new type of mesophase known as sanidic (i.e., boardlike). In the sanidic nematic phase, the boards organize parallel to one another as shown in Figure 8d [61]. The incorporation of an electron acceptor molecule to discotic polymer certain non-mesogenic materials have been shown to induce mesophases—called the column nematic.

### 3. REACTIVE MESOGENS

These materials form liquid crystal phases whose order can be captured indefinitely by polymerization, often photocentrized. For completeness, we have also included the work on calamitic materials since there is significant synergy with mesophase-derived carbons in Sections 6 and 7.

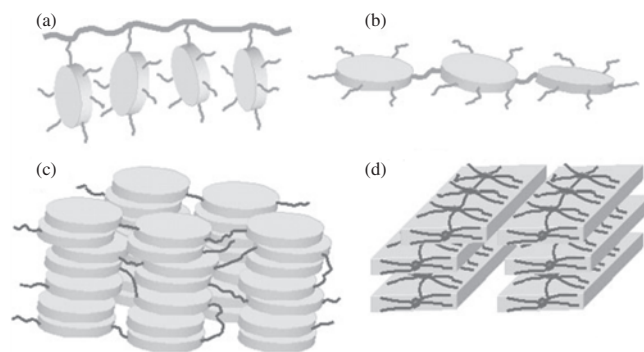


**Figure 8.** Examples of polymeric discotic liquid crystals where liquid crystalline moieties are attached to the backbone as side chains (a) and main chain (b). A diagram illustrating intercolumnar binding and intracolumnar backfolding of the main chain (c) and the sanidic nematic phase composed of boards stacked parallel to one another (d).



### 3.1. Synthetic

Tailoring the molecular ordering profile of polymers in three dimensions is a highly desired property with many practical implications. The methods used in creating these ordering arrangements are limited in number and no generic algorithm exists, which enables complete and unrestricted control over the orientation of molecules in all directions. A method that approaches this ambitious goal focuses on photopolymerization of reactive monomers, which possess an intrinsic liquid crystal phase (these materials are often referred to as reactive mesogens). The well-known techniques to establish monolithic order in low molecular weight liquid crystals, based on their susceptibility to external fields and sensitivity to surface interactions, can be used to capture sophisticated ordered molecular architectures in thin polymer films. Tailored planar films created from reactive mesogens have recently become an inconspicuous passive optical element in liquid crystal displays to resolve their long-standing viewing angle problem (example given in Section 5.2). When reactive mesogens are polymerized in nonreactive liquid crystals, many other exciting applications are possible including bistable displays and switchable mirrors.

In addition to planar films, novel microstructures can also be created from reactive mesogen compounds. A typical reactive mesogen calamitic liquid crystal is shown in Figure 9 (known as RM257, available from EM Industries).

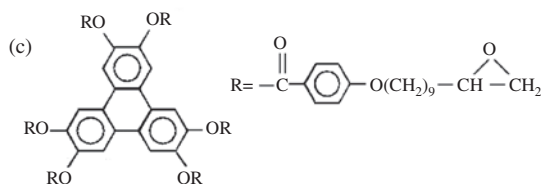
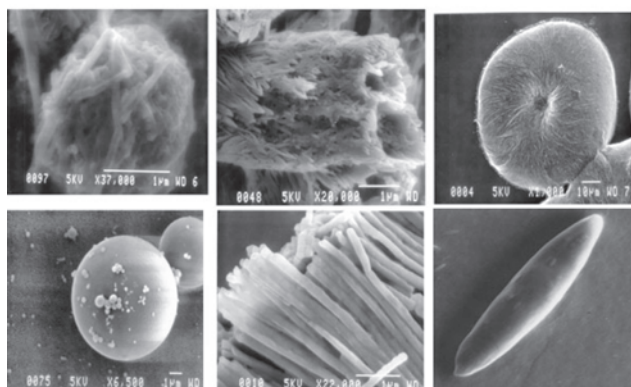
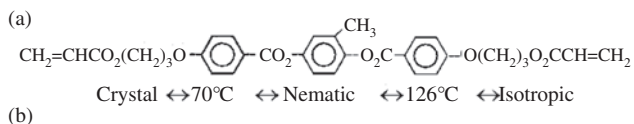


**Figure 9.** A reactive liquid crystal (mesogen) with a stable nematic liquid crystal phase. This material is known as RM257 and is commercially available from EM Industries (a). Scanning electron microscope photographs of microstructures created from reactive mesogens (b): yarn-ball, tube, and toroid (top) and sphere, rod, and ellipsoid particles (bottom). An example of a reactive discotic, epoxy-based discotic liquid crystal (c).

It is a diacrylate monomer with a stable nematic liquid crystal phase between 70 °C and 126 °C, and can be photopolymerized with UV light. Figure 9b shows scanning electron microscope photographs of a variety of novel microstructures, such as yarn-balls, hollow tubes, toroids, solid spherical balls, solid cylindrical rods, and ellipsoid-shaped particles.

The yarn-balls, tubes, and toroids are actually created through a self-assembly process. The reactive mesogen material (e.g., RM257) is dissolved in solvent and capillary filled into the channels (0.2  $\mu\text{m}$  in diameter) of Anopore membranes. Anopore membranes are porous alumina matrix ( $\text{Al}_2\text{O}_3$ ). The solvent is evaporated after the fill, and the sample is then subjected to UV light to polymerize the reactive mesogen while the material is held at constant temperature to stabilize the liquid crystal phase. It is believed that the reactive mesogen is ordered on the surface of the channels after evaporation, forming a thin ordered layer. The Anopore membrane is then etched away with a NaOH solution, leaving behind the polymerized reactive mesogen. Depending on the concentration of reactive mesogen in the solvent and the boundary conditions induced by the channel walls, various self-assembled microstructures have been reported: yarn-balls, hollow tubes, and toroids. It is also interesting to note that these microstructures (e.g., yarn-balls) will transition into a planar structure when subjected to an applied external field.

In order to create ordered solid microstructures using reactive mesogens, the material is filled into templates, heated to a temperature where the nematic phase is stable, and then photopolymerized with UV light. Figure 9b shows solid spherical balls created in a glycerin binder, solid rods created in an Anopore template, and ellipsoidal particles created in a stretched polyvinyl alcohol (PVA) binder. The spherical balls have also been shown to rotate with the application of electric fields since they have a captured dielectric anisotropy.

Up to this point we have discussed calamitic reactive mesogens, but there also exist reactive mesogens with stable discotic phases as shown in Figure 9c. These have tremendous application in flat panel displays as will be discussed in Section 5.2. Many of the process steps described in this section have also been applied to carbonaceous materials to form intriguing nanoforms.

### 3.2. Carbonaceous Mesophase

The class of reactive discotic mesogens includes carbonaceous mesophase, the naturally occurring discotic liquid crystal mixture that forms spontaneously during high-temperature treatment (>300 °C) of certain organic starting materials [28]. It is arguably the most important of all discotics, reactive or stable, due to its many technological uses, and a number of review articles have been dedicated to carbonian mesophase [23, 62–68]. It is classified here as a reactive mesogen since its main use is not in the liquid state or as a quenched mesophasic glassy solid, but as a precursor for ordered carbon materials, in which the order is established in the liquid phase and then “captured” by heating at temperatures in excess of 500 °C. This heating process captures order through loss of the lower molecular weight components that give mobility to the liquid crystalline phase as

well as through chemical coalescence of polyaromatic compounds accompanied by hydrogen evolution.

Remarkably, the discovery of carbonaceous mesophase predates the discovery of synthetic discotics in the late 1970s. Prior to the discovery of fullerenes, the discovery of carbonaceous mesophase in 1965 was the most celebrated advance in carbon science [28]. Despite its early discovery, carbonaceous mesophase is not as well understood as most other liquid crystalline systems. Its complex composition and chemical instability have discouraged systematic investigation of its key fundamental properties. Because of its importance in carbon materials, however, there has been a great deal of work over the last several decades to overcome these challenges and develop a deeper understanding of this unique liquid crystal and the practical carbons and nanocarbons derived from it.

### 3.2.1. Synthesis and Forms

Carbonaceous mesophase is formed by heating lower molecular weight organic material, typically in the absence of oxygen at temperatures from 300–500 °C. Chemical pathways in this thermal process have been reviewed by Lewis [69]. Carbonaceous mesophase first forms by precipitation of an ordered second liquid phase from the original isotropic liquid, and in some applications grows during further heating to eventually form a homogeneous, single-phase liquid crystal. As discussed in the introduction, it is often formed *in-situ* as an intermediate in the conversion of isotropic organic matter into carbon, but increasingly is manufactured as a bulk liquid crystal phase and marketed as “mesophase pitch” for further processing or applications.

### 3.2.2. Phase Behavior

Although carbonaceous mesophase shares many features with conventional (synthetic) liquid crystal systems, there are some notable differences. First, carbonaceous mesophase typically forms upon *heating*, in contrast to most liquid crystal systems which adopt ordered configurations upon cooling. Heating induces chemical reactions, a form of two-dimensional polymerization that increases the mean size and aspect ratio of the disk-like molecules and thus increases their liquid crystal forming tendency. Second, heating causes vaporization of smaller molecules in the mixture (which have weak LC-forming tendencies) and thus increases the concentration and mutual interaction of the larger molecules (mesogens), favoring order development as in lyotropic liquid crystals.

Further, the formation of carbonaceous mesophase is typically irreversible. At high temperature, mesogen cross-linking and evaporative loss of lower molecular weight fractions typically trap the liquid crystalline order in a permanent solid phase. Only when chemical growth and vaporization are limited, such as in the experiments of Lewis [70] on pitches of high chemical stability, is it possible to observe a reversible phase transition upon temperature cycling. In this particular case, temperature cycling between 650 and 770 K led to mesophase appearance on cooling and the appearance of an isotropic liquid phase (a “clearing” event) upon heating. This demonstrates the thermotropic nature of

the phase transition and implies the importance of attractive forces in the formation of liquid crystal order. Overall, it appears that carbonaceous mesophase has a dual thermotropic and lyotropic nature [28]. Liquid crystal formation is caused by a combination of intermolecular attractive forces between disks (thermotropic nature) and the loss of low molecular weight non-mesogenic material upon heating (lyotropic nature).

The quantitative treatment of phase equilibrium in mesophase-containing pitches is a major challenge due to the complex chemical makeup of pitch materials and their chemical reactivity. To date there have been only three attempts to quantitatively describe the liquid crystal phase behavior of pitches: one by Shishido et al. [71] and a series of two more recent papers [72, 73]. Shishido et al. [71] applied a statistical theory of liquid crystalline mixtures developed by Luckhurst and co-worker [74] to an experimental phase diagram reported previously by Mochida and Korai [75]. In the original experiments, Mochida and Korai separated a petroleum pitch into benzene soluble (BS) and benzene insoluble (BI) fractions and recombined them in various weight ratios and at various temperatures to obtain the partial phase diagram reproduced in the top panel of Figure 1. Shishido et al. [71] treated both fractions (BS, BI) as pseudo single components (rather than mixtures), thus reducing the complex phase equilibrium problem to a tractable binary problem. They further assumed the benzene soluble fraction to be non-mesogenic, that is, to have no liquid crystal forming tendency. This pioneering attempt at the quantitative treatment of mesophase formation involved no adjustable parameters and gave an impressive, if imperfect, description of the observed phase behavior.

Hurt and Hu [72] subsequently proposed a simple multicomponent model based on virtual clearing temperatures for pseudo-components of differing molecular weight. Both of the early modeling attempts are based on ideal solution behavior, that is, on the assumption that orientational molecular order is the main variable governing free energy. In fact, there is evidence that the various molecular weight fractions in pitches are chemically different, and the corresponding differences in intermolecular interactions, even in the absence of molecular order, strongly influence phase behavior. The most recent treatment of phase behavior combines statistical theories of the liquid crystalline state with nonideal mixing submodels based on the solubility parameter approach coupled with combinatorial contributions to the excess mixing entropy [73]. This model has been applied to several literature data sets, including the phase diagram of Mochida and Korai [75], the detailed fractionation data of Greinke and Singer [76], and the visual observations of phase behavior in naphthalene pitch from the hot stage microscope experiments of Lewis [70].

Sensitivity studies with the model indicate the importance of two distinct driving forces for mesophase formation: (a) poor solubility of high molecular weight aromatic molecules in the lower molecular weight fractions (the nonideal mixing effect), and (b) reduction in the system free energy by molecular orientation of the larger, disklike molecules (orientational ordering effect), the latter being enhanced by expulsion of some of the smaller, less oriented

molecules to a separate isotropic phase. For the cases examined in that study [72], both contributions are significant and must be considered.

### 3.2.3. Other Ordering Mechanisms

In common with other liquid crystals, carbonaceous mesophase can be aligned using fields [77–79], flows [21, 80], and surfaces [81, 82]. Surface and confinement effects are of particular importance and are treated in the following section.

## 4. ANCHORING AND CONFINEMENT

Liquid crystals constrained to confining geometries are currently a subject of intense research stimulated by fundamental interest and potential in electro-optic devices. Confined liquid crystals exhibit a rich variety of different structures, which strongly depend on the delicate balance between elastic, surface, and external field forces. Varying the temperature, field, surface conditions, and geometry can induce transitions among these structures. The focus of our article is on carbon materials processed through an intermediate discotic liquid crystal phase. There is a tremendous wealth of work on low molar mass liquid crystals confined to various geometrical shapes that can be leveraged to predict and better understand new carbon forms. We believe that this background is important for the future of carbon materials formed from discotic liquid crystal intermediates. Here we are interested in phenomena which occur on distances much longer than the nematic correlation length so that Frank elastic theory [83] can be employed.

### 4.1. Phenomenology of Nematic Ordering

We briefly review the phenomenology of bulk nematic liquid crystals and then focus our attention on the influence of the confinement. Although we will deal with elastic theory based on the director field description of nematic liquid crystals, we will try to see its limitations by first examining a more general tensorial description. Such a phenomenological approach, known as Landau–de Gennes theory, is based on the tensor order parameter  $\underline{Q}$  with components  $Q_{ij}$ . In the eigenframe defined by the nematic director,  $\mathbf{n}$ , the corresponding degrees of order are measured by eigenvalues  $Q$  (nematic order parameter) and  $P$  (biaxial order parameter), respectively. In this approach the free energy is expanded in terms of symmetry allowed powers of the order parameter and its derivatives. In zero external field, the expansion of the free energy density  $f_n$  must have second-, third-, and fourth-order terms in  $\underline{Q}$  to describe the nematic-isotropic transition, and terms quadratic in the first derivatives of  $\underline{Q}$  and linear in the second derivative to describe the weakly nonuniform states [84, 85]:

$$\begin{aligned} f_n = & f_0(T) + a(T - T^*)Q_{kj}Q_{kj}/2 - bQ_{ki}Q_{ij}Q_{jk}/3 \\ & + c_1(Q_{kj}Q_{kj})^2/4 + c_2Q_{jk}Q_{ki}Q_{ij}Q_{jk}/4 + L_1^{(1)}Q_{ij,ij} \\ & + L_1^{(2)}Q_{jk,i}Q_{jk,i} + L_2^{(2)}Q_{ij,i}Q_{kj,k} + L_3^{(2)}Q_{jk,i}Q_{ik,j} \\ & + L_1^{(2)}e_{ijk}Q_{il}Q_{jl,k} + L_5^{(2)}Q_{ik,ij}Q_{jk} + L_6^{(2)}Q_{jk,ii}Q_{jk} \end{aligned}$$

$$\begin{aligned} & + L_1^{(3)}Q_{ij}Q_{ij,k}Q_{kl,l} + L_2^{(3)}Q_{ij}Q_{ij,k}Q_{jk,l} \\ & + L_3^{(3)}Q_{ij}Q_{jk,k}Q_{jl,l} + L_4^{(3)}Q_{i,j}Q_{ik,l}Q_{jk,l} \\ & + L_5^{(3)}Q_{ij}Q_{ik,l}Q_{jl,k} + L_6^{(3)}Q_{ij}Q_{jk,l}Q_{kl,j} + \dots \end{aligned} \quad (4)$$

Here  $a(T - T^*)$ ,  $b$ ,  $c_1$ , and  $c_2$  are expansion coefficients of the homogeneous nematic phase and we use the  $L_i^{(j)}$  coefficients of the expansion in the non-uniformly ordered phase. We choose the standard notation where two equal indices indicate summation and the indices preceding the comma represent the derivatives.

The application of an external magnetic (or similarly electric) field  $\mathbf{H}$  adds to the free energy density in the following anisotropic contribution [86]:

$$f_f = 1/2\mu_0\Delta\chi_0\mathbf{H}\underline{Q}\mathbf{H} \quad (5)$$

where  $\Delta\chi_0$  is the difference between the principal values of the susceptibility tensor in a completely ordered nematic phase. The addition of this term “smooths” the first-order nature of the nematic-isotropic phase transition and may possibly result in its disappearance with increasing external field [87].

The combined free energy density  $f = f_n + f_f$  can qualitatively describe all features of a bulk nematic liquid crystal system. Taking into account the basic thermodynamic principle that the free energy of a system approaching equilibrium state at constant temperature and volume tends towards its minimum value, one can develop a formal procedure for the determination of the stable structures. Comparison of the theoretical predictions with experimental data for the order parameter, susceptibility, and specific heat, yields the values of expansion coefficients [20]. It is noted that fluctuations are neglected, and therefore the formalism cannot describe all details of the critical behavior.

### 4.2. Frank Elastic Theory

The free energy function (Eq. (4)) indicates that variations of the eigenvalues  $\underline{Q}$  and the director  $\mathbf{n}$  contribute in different ways. Spatial variations in the eigenvalues  $Q$  or  $P$  are characterized by the nematic correlation length [86]  $\xi = \xi_0|T/T^* - 1|^{-1/2}$  with  $\xi_0 = [(L_1^{(2)})/(aT^*)]^{1/2}$ , which does not exceed a few molecular lengths even close to the  $T_{NI}$ . Variations in  $\mathbf{n}$  tend to spread over the entire available space to reduce the contribution to the free energy of the deformation of the orientation field [86]. Therefore, on scales large compared to  $\xi$ , the degree of order ( $Q$ ) is nearly constant and the director slowly varies through the space. For a uniaxial nematic phase, such a constant order parameter approximation leads to the following:

$$Q_{ij}(r) = \frac{1}{2}Q[3n_i(r)n_j(r) - \delta_{ij}] \quad (6)$$

and consequently the nematic structure can only be described by the director field  $\mathbf{n}(\mathbf{r})$  with the  $\mathbf{n} = -\mathbf{n}$  symmetry [86].

The field contributing to the free energy density transforms into the following:

$$f_f = \frac{1}{2} \mu_0 \Delta \chi (nH)^2 \quad (7)$$

with  $\Delta \chi = \mathbf{Q} \Delta \chi_0$ , where  $\chi_0$  is the magnetic susceptibility of the perfectly ordered nematic phase. To measure the relative strength of the external field  $\mathbf{H}$ , the inverse magnetic coherence length  $\xi_M^{-1} = (\Delta \chi \mu_0 / K)^{1/2} H$  is employed, where  $K$  represents a specific elastic constant or an appropriate combination. Similarly for the electric field case, the inverse electric correlation length is  $\xi_E^{-1} = (\Delta \varepsilon \varepsilon_0 / K)^{1/2} E$ , where  $\Delta \varepsilon$  is the dielectric susceptibility.

The nematic free energy thus reduces to the Frank elastic free energy [88–90]:

$$f_d = \frac{1}{2} \{ K_{11} (\nabla \cdot \mathbf{n})^2 + K_{22} (\mathbf{n} \cdot \nabla \times \mathbf{n})^2 + K_{33} (\mathbf{n} \times \nabla \times \mathbf{n})^2 \} - \frac{1}{2} \{ K_{24} \nabla \cdot (\mathbf{n} \times \nabla \times \mathbf{n} + \mathbf{n} \nabla \cdot \mathbf{n}) + K_{13} \nabla \cdot (\mathbf{n} \nabla \cdot \mathbf{n}) \} \quad (8)$$

where the Frank elastic constants are related in the following way to the  $L_{ij}$  constants [22]:

$$\begin{aligned} K_{11} &= 9Q^2 \frac{(2L_1^{(2)} + L_2^{(2)} + L_3^{(2)} - L_5^{(2)} - 2L_6^{(2)})}{2} \\ &\quad + 9Q^3 \frac{(-L_2^{(3)} + 2L_3^{(3)} + L_4^{(3)} + 2L_5^{(3)} - L_6^{(3)})}{4} \\ K_{22} &= 9Q^2 (L_1^{(2)} - L_6^{(2)}) + \frac{9Q^3}{4L_4^{(3)}} \\ K_{33} &= 9Q^3 \frac{(2L_1^{(2)} + L_2^{(2)} + L_3^{(2)} - L_5^{(2)} - 2L_6^{(2)})}{2} \\ &\quad + 9Q^3 \frac{(2L_2^{(3)} - L_3^{(3)} + L_4^{(3)} - L_5^{(3)} + 2L_6^{(3)})}{4} \\ K_{24} &= 3QL_1^{(1)} + \frac{9Q^{(2)}}{2(2L_1^{(2)} + L_3^{(2)} - L_5^{(2)} - 2L_6^{(2)})} \\ &\quad + 9Q^{(3)} (L_4^{(3)} + 2L_5^{(3)} - L_6^{(3)}) \\ K_{13} &= 3QL_1^{(1)} + 3Q^{(2)} \frac{L_5^{(2)}}{4} \end{aligned} \quad (9)$$

The constants  $K_{11}$ ,  $K_{22}$ , and  $K_{33}$  correspond to splay, twist, and bend elastic deformations, respectively. Further,  $K_{24}$  and  $K_{13}$  are the saddle-splay and mixed splay-bend elastic constants [86–90]. The volume integral of terms describing the corresponding deformations in Eq. (8) can be readily reduced to a surface integral because of the divergence in the volume integral. Therefore, they are often called surface elastic constants, a misleading term because they have nothing to do with surface properties of the material. Recently the name divergence elastic constants was introduced by Lavrentovich and Pergamenschik.

### 4.2.1. Deformed States

In a bulk nematic system, which does not exhibit a spontaneous deformation, a nonuniform director field is unstable or metastable. One can distinguish between the following situations:

1. Weak inhomogeneities caused by thermal fluctuations.
2. Large-scale inhomogeneities that can relax to the stable by a continuous transformation of the director field.
3. Large inhomogeneities/singularities (defects) which cannot relax by a continuous transformation of the director field.

In real systems, deformations with or without singularities can be stabilized by external constraints (surface or fields). Here we will briefly review some aspects of the defects in the director field.

The points or lines in space where the director field is singular or not defined are called disclinations. Although they have been known since the observations of Lehman [91] and Fridel [92] many years ago, the attempt of a qualitative description was performed by Frank [17] much later. Disclinations are usually categorized by their defect strength  $s = \Phi / (2\pi)$ . The rotation angle of the director  $\Phi$  caused by encircling the defect is usually determined by polarization microscopy. Possible defects that occur in uniaxial nematic phases are shown in Figure 10a. For more details consult the literature [86, 93–95].

The phenomenology of point and line defects is well explained with a topological theory using homotopic groups [96–98] and supplemented by a free energy analysis.

Defects are in the same homeotropy class if their director field can be continuously deformed into another. This simply explains the transformation of a singular  $s = 1$  disclination line in a uniaxial nematic phase into a structure with a nonsingular director field with an escape into the third dimension [99–102]. One can find comprehensive reviews in this field [103], analogies with helium [104], and even arguments on how they are related to cosmological systems [105]. Since the elastic energy density in the defects cannot exceed the difference between the free energy of the nematic and isotropic phase, the order there is partially depressed (partial melting of the nematic phase) or it becomes biaxial. “Pushing” beyond the constant order parameter description and solving equations for either scalar or tensorial order parameters, one finds that solutions for  $Q$  or eigenvalues of the tensor  $\mathbf{Q}$  change continuously. The size of the area where they substantially deviate from bulk values, usually referred to as the defect core, is comparable to the nematic correlation length  $\xi$ . Order parameter variations close to an  $s = 1$  point defect are shown in Figure 10b.

### 4.2.2. Confining Surfaces

Perturbation of the orientational direction caused by the structure and interactions with the confining surface usually propagates through the entire confined liquid crystal sample. This enables the assessability of interesting phenomena not available in simple solids or liquids.

The coupling between surface and liquid crystal molecules depends on their structure. Excluding chemical bonding, the

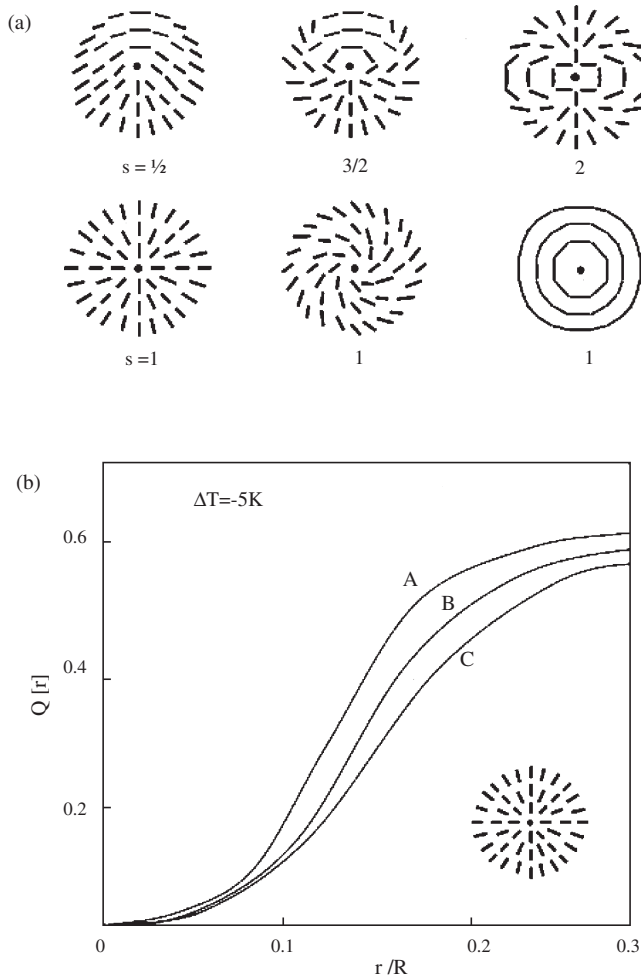


**Figure 10.** Director fields of six different types of defects with their corresponding strengths (a). Variation of the order parameter  $Q$  in the vicinity of an  $s = 1$  point defect (b). The material parameters  $a$ ,  $T^*$ ,  $b$ ,  $c_1$ ,  $c_2$ , and  $L_1^{(2)}$  are particular to 5CB. Curve A corresponds to  $L_2^{(2)} = -L_1^{(2)}$ , curve B to  $L_2^{(2)} = 0$ , and curve C to  $L_2^{(2)} = L_1^{(2)}$ . The value of  $R$  is chosen to be 100 nm.

main contributions to the ordering “field” in the interfacial region are sterical repulsion, van der Waals interactions, and dipolar coupling. The non-polar coupling induced nematic ordering can also persist far away from the surface. The dipolar part is relevant for establishing polar order in the surface layer when molecules are amphiphilic and the surface is either polar or aliphatic [106]. The description of surface effects using the microscopic approach is limited to simple models describing the effective aligning interactions [107–109].

A direct prediction of nematic ordering has been performed using the Monte Carlo method; but this approach is limited to very small droplets [110]. The main value of these microscopic approaches is that they enable a prediction of the coefficients of the phenomenological Landau–de Gennes description of surface phenomena [111]. In recent years, Zumer and co-workers have significantly pushed Monte Carlo simulations to new levels to better understand confined liquid crystals.

It is instructive to examine possible symmetry breaking of the orientational ordering caused by surfaces:

**Translational symmetry** is directly broken by the presence of boundaries and indirectly by the nonuniform positional and orientational ordering caused by confinement. This can lead to layering.

**Oriental symmetry** is broken on surfaces because of restricted molecular orientations. This results in preferred anchoring direction.

**Rotational symmetry** (around the axis along the director) is lost on the surface and in the rest of the volume where the liquid crystalline ordering is distorted. This leads to biaxial ordering and flexoelectric polarization [20].

**Inversion symmetry** (rotation around the short molecular axis) can be lost in the surface layer if the molecular interaction is such that the head, tail, or other parts, of the liquid crystal molecule have a preferred position relative to the surface. This usually manifests in nonzero surface polarization.

Macroscopic description of surface effects is based on the contribution to the free energy given by an integral of the surface free energy density (fs)–surface tension–over the entire confining surface. For a review of this field see the paper by Jerome [112].

If the surface is not planar, it is convenient to distinguish a supramolecular scale (comparable to the nematic correlation length  $\xi$ ) where the surface is characterized by its roughness, and the macroscopic scale (distances  $\gg \xi$ ) where shape of the surface is characterized by its radii of curvature.

#### 4.2.3. Anchoring Energy

The term anchoring energy was introduced to describe the part of surface tension associated with the deviation of the nematic ordering direction at the surface from its preferred value at the surface, caused by elastic torques in the constrained liquid crystal. The omission of the variation of the degree of orientational order can be justified on similar grounds as in the case of the Frank elastic theory. For many systems, orientational anchoring can be broadly classified as homeotropic, tilted, or planar anchoring depending on whether the preferred direction is perpendicular, tilted, or parallel to the surface. Additionally, the last two cases can be monostable, bistable, multistable, or degenerate depending on the nature of the surface.

In our discussion we are going to deal with homeotropic and monostable (usually called homogeneous) planar anchoring when the lowest order terms in the surface free energy density expansion are retained. This well-known Rapini–Paupolar form of the anchoring free energy is given by

$$f_s = f_{s0} + \frac{1}{2} W_\theta \sin^2 \theta \quad (10)$$

for homeotropic anchoring and has a similar form [60]

$$f_s = f_{s0} + \frac{1}{2} (W_\theta \cos^2 \phi + W_\theta \sin^2 \phi) \sin^2 \theta \quad (11)$$



for monostable planar anchoring. Here  $\theta$  is the angle between the director  $\mathbf{n}_s$  and preferred anchoring direction  $\mathbf{m}_s$  and  $\Phi$  is the angle measuring the azimuthal direction of  $\mathbf{n}_s$ , as presented in Figure 11. The parameter  $W_\theta$  represents the polar anchoring strength associated with any variation of the angle  $\theta$  in the homeotropic case and with out-of-plane variations in the planar case, while  $W_\phi$  represents the azimuthal anchoring strength associated with in-plane director deviations in the planar case. Anchoring transitions, sometimes called alignment transitions, can be driven by the temperature [113], the concentration of adsorbed aligning molecules at the surface [114], or the chain length of the surface aligning molecules. Discrete [110, 114] and continuous changes in the tilt angle [115, 116] have been observed. Theoretical considerations based on a microscopic model [46] and Landau–de Gennes theory [117, 118] are in agreement with observations.

#### 4.2.4. Total Free Energy

Within the limitations of the director field approach, which combines bulk and surface contributions of the free energy, it is possible to predict all stable and even metastable structures of a confined nematic liquid crystal. For instructive purposes, let us choose a relatively large spherical cavity where the director field does not deviate much from the case of infinitely strong anchoring and make an order of magnitude estimate of both contributions. It is instructive to compare the elastic deformation in the bulk and surface anchoring contributions. The surface contribution to the free energy (Eq. (10)) is thus  $W_\theta(\Delta\Theta)^2R^2$ , where  $\Delta\Theta$  is the average deviation of the director angle from the preferred surface anchoring angle. The bulk contribution estimated from Eq. (8) is  $\sim KR$  and the reduction from this value is  $\sim K\Delta\Theta R$  because the anchoring angle is not perfect. The minimization of total free energy indicates that  $\Delta\Theta \sim K/(W_\theta R)$ . A similar estimate can be made also for cylindrical cavities. The parameter  $K/(W_\theta R)$  will be further used to distinguish between (1) weak anchoring regime  $K/(W_\theta R)I$ , usually realized in cavities of micrometer size; (2) strong anchoring regime  $K/(W_\theta R) \gg I$ , usually realized in supramicrometer-size cavities.

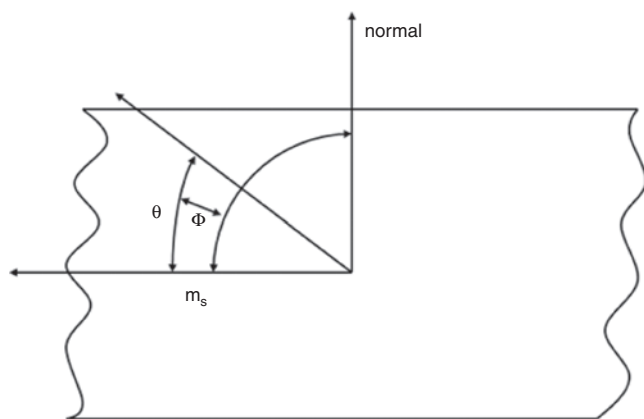


**Figure 11.** Schematic presentation of the anchoring geometry with the symbols used in the text.

### 4.3. Calamitic Nematic Structures and Structural Transitions in Confined Liquid Crystals

We will briefly review some simple systems reported in the literature for low molar mass systems. We focus on spherical and cylindrical systems. For simplicity we limit our discussion to surfaces, which support either homeotropic or planar anchoring and materials.

#### 4.3.1. Calamitic Nematic Microdroplets

Let us first consider a transition in micrometer-size droplets which can be studied with optical polarizing microforms and reasonably well described by Frank elastic energy, but is still small enough to be in a relatively weak anchoring regime. The first, more quantitative study of transitions in nematic liquid droplets, as shown in Figure 12, dispersed in a polyurethane matrix, was performed by Erdmann and co-workers [119]. The first-order transition from a radial to an axial director field (see Fig. 12d) in droplets with homeotropic anchoring was induced by either temperature (Fig. 10a) or applied electric fields. The inset in Figure 12d shows the applied external electric field data. A single elastic constant  $K_{11} = K_{22} = K_{33} = K$  free energy without surface elastic terms supplemented by Rapini–Papoular surface coupling (Eq. (10)) was used. The dimensionless variables  $R/d$ ,

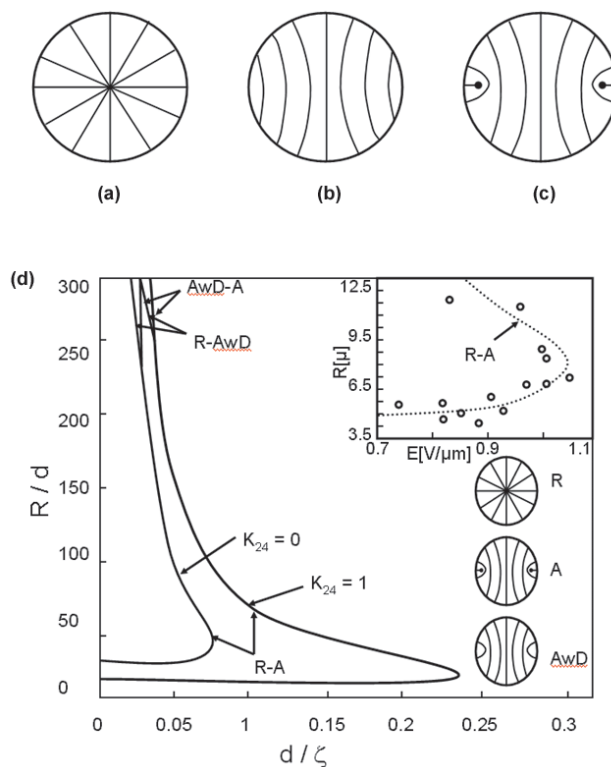


**Figure 12.** Stable nematic director fields in spherical geometries: (a) radial, (b) axial in the weak anchoring regime, and (c) axial in the strong anchoring regime, with an equatorial line disclination. The calculated stability diagram of droplets with homeotropic anchoring in the external field for two values of  $K_{24}$  constant (d). The experimental phase diagram is shown as an inset.



where  $d$  is the extrapolation length [86] and  $d/\xi_E$ , where  $\xi_E^{-1}$  is the inverse electric coherence length, are employed. The comparison with experiments was used to determine anchoring energy  $W_\theta$  as a function of temperature and to estimate the effective internal electric field whose small values (five to seven times smaller than applied field) were attributed to the dielectric properties of liquid crystal and polymer. A more detailed calculation taking into account  $K_{24} \neq 0$  shows that besides the axial structures without a defect (see Fig. 12b), there is in the strong anchoring regime ( $W_\theta R/K \gg 1$ ) a stable region where an axial structure with a  $s = \frac{1}{2}$  ring defect in the diametrical plane (Fig. 12c) is stable. The stability area of this structure terminates in a triple point (see Fig. 12d). One must be aware that in this strong anchoring limit the transitions exhibit a large hysteresis because of the high energy barrier between the two structures [120]. The lines of coexistence have two other interesting points: the zero transition point  $(0(R/d)_0)$  and the inversion point  $((d/\xi_E)_i, (R/d)_i)$  corresponding to the largest  $d/\xi_E$  (field) where radial structure is still stable. The nonzero  $K_{24}$  value broadens the stability range of the radial structure (see Fig. 12d), which is the basis of the two methods for simultaneous determination of  $K_{24}$  and  $W_\theta$ .

### 4.3.2. Calamitic Nematic Liquid Crystals in Cylindrical Cavities With Homeotropic Anchoring

The structures considered in this section are stable in case of homeotropic surface anchoring conditions. The four structures to be reviewed are schematically presented in Figure 13.

**Planar-Radial Structure** The planar-radial (PR) configuration has been treated in detail by Dzyaloshinskii [121], Cladis and Kleman [100], Meyer [101], and Saupe [89], and is illustrated in Figure 13. Since  $\mathbf{n}$  is normal to surface,

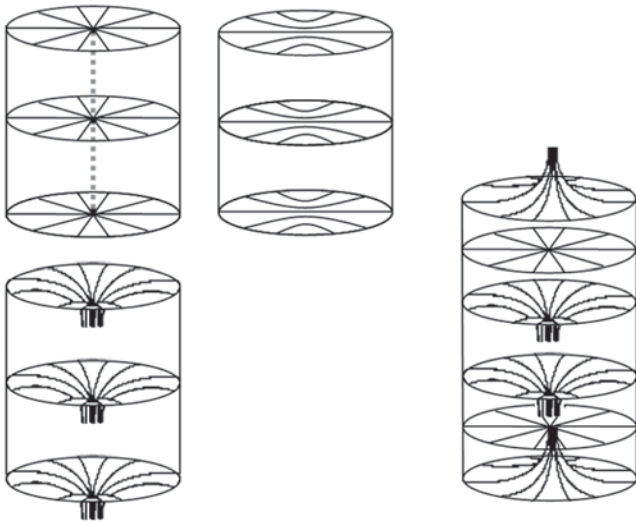


**Figure 13.** Stable nematic direction fields in cylindrical geometries when homeotropic anchoring is enforced at the cylindrical walls.

the free energy per unit length of the cylinder (pure splay energy) is expressed by

$$F_{PR} = \pi K_{11} \ln(R/\rho) \quad (12)$$

where  $\rho$  is the radius of the line disclination which is of the order of molecular dimensions where elastic theory breaks down. This configuration is independent of the surface anchoring energy since  $\mathbf{n} \parallel \mathbf{r}$ .

**Planar-Polar Structure** The planar-polar structure (PP) can be specified by  $\mathbf{n} = \cos \psi(r, \theta) \mathbf{i}_r + \sin \psi(r, \theta) \mathbf{i}_\theta$ , where  $\psi$  is the angle between the local nematic director and the direction of the symmetry axis as illustrated in Figure 13 [122]. The exact solution to the director field in the  $K_{11} = K_{33} = K$  approximation is given by

$$\psi(r, \theta) = \frac{\pi}{2} = \tan^{-1}\{(R^2 + \gamma r^2) \tan \theta / (R^2 - \gamma r^2)\} \quad (13)$$

where  $\gamma = (\varsigma^2 + 1)^{1/2} - \varsigma$  and  $\varsigma = 2K/RW_\theta$ . The PP director field is therefore a strong function of the effective anchoring strength  $RW_\theta/K$  and independent of  $K_{24}$ . The free energy per unit length is given by

$$F_{PP} = \pi K \{1 \ln(2\gamma\varsigma) + (1 - \gamma)/\varsigma\} \quad (14)$$

The calculation for the PP structure becomes more involved for  $K_{11} \neq K_{33}$  since no analytical solution exists and one must resort to numerical methods.

**Escaped-Radial Structure** The escaped-radial (ER) structure, illustrated in Figure 13, was studied in the strong anchoring limit by Cladis and Kleman [100], Meyer [101], and Saupe [89], and later researchers [122], included  $K_{24}$  and  $W_\theta$ . The nematic director field can be completely specified by  $\mathbf{n} = \cos \Omega(r) \mathbf{i}_r + \sin \Omega(r) \mathbf{i}_z$ , where  $\Omega$  is the angle between  $\mathbf{n}$  and the cylinder axis  $\mathbf{i}_z$ , and only depends on the radial coordinate  $\mathbf{n}$ . Employing the one-constant approximation  $K_{11} = K_{33} = K$ , the nematic director field has the following analytical form:

$$\Omega(r) = 2 \tan^{-1}\{r \tan(\alpha/2)/R\} \quad (15)$$

where the molecular anchoring angle is  $\alpha = \Omega(r = R) = \cos^{-1}(1/\sigma)$  and  $\sigma = RW_\theta/K + K_{24}/K - 1$  is the dimensionless surface parameter. Equation (13) is valid for  $\sigma > 1$ . If the physical constants are such that  $\sigma < 1$ , then the director field is aligned along the cylinder axis ( $\Omega = 0$ ). The free energy per unit length in the one-constant approximation is

$$F_{ER} = \pi K (3 - K_{24}/K - 1/\sigma) \quad (16)$$

where  $\sigma = RW_\theta/K + K_{24}/K - 1$  is the dimensionless surface parameter. Equation (14) is valid for  $\sigma > 1$ , and for  $\sigma < 1$  the free energy becomes  $\pi K (RW_\theta/K)$ . There also exists an analytical form for the situation when  $K_{11} \neq K_{33}$  [84]. It should be emphasized that the  $K_{11}$  contribution, because of the cylindrical symmetry, only renormalizes the anchoring strength.

**Escaped-Radial Structure with Point Defects** In practice, the ER structure is seldom realized. Fluctuations that are intrinsic near the nematic-isotropic transitions and irregularities of the cavity walls often lead to an ER structure with alternating radial and hyperbolic defects along the cylinder axis. This director field is called the escaped-radial structure with point defects (ERPD) and is schematically shown in Figure 13. In cylindrical cavities of finite length, it is stabilized by the boundary conditions on both ends [123]. The structure has the lowest free energy when it is periodic in the  $z$  direction. The period  $2L$  is the distance between two defects of the same type.

The ERPD structure does not have an analytical solution even in the one-constant approximation. There have been two methods employed to treat this structure [124]. The simpler is to construct a trial function that satisfies all necessary boundary conditions, the case where defects are equally spaced. Restricting our interest to the region  $L/R > 2$  and  $0 \rightarrow 1$ , an appropriate trial function is given by

$$\Omega(r, z) = \tan^{-1} \left\{ \frac{\sigma r}{z(1 - z/L)[\sigma - (\sigma - 1)r/R]} \right\} \quad (17)$$

for  $r < R$  and  $0 < z < L$ . Points in the region  $-L < z < 0$ , which make up the half of the unit cell, have angle  $\Omega$  that is the supplement of angle  $\Omega$  at the corresponding point in the region  $0 < z < L$  ( $\Omega(-z) = \pi - \Omega(z)$ ). Periodic repetition of this cell produces a lattice of alternating radial and hyperbolic defects of spacing  $L$  that is consistent with observations. The trial function (Eq. (17)) of the director field for the ERPD structure satisfies the director field near the radial point defect at  $r = z = 0$ , given by  $\Omega(r, z) = \tan^{-1}(r/z)$ , and the director near the hyperbolic defect given by  $\Omega(r, z) = \tan^{-1}(r/[1 - zL])$ , and simplifies to  $\mathbf{n} = \mathbf{i}_r$  at the surface in the strong anchoring limit; therefore, it is a reasonable approximation of the true director field. The resulting free energy per unit length for the ERPD trial function is given by

$$F_{\text{ERPD}} = \pi K \{ -4 \ln(L/R)/3 + 3 - K_{24}/K + 8/9 + (3\sigma)^{-1} + (6\sigma^2)^{-1} + \pi L(\sigma - 1)/5\sigma R \dots \} \quad (18)$$

A more precise way to model the ERPD director field is to pursue numerical solutions of the Euler–Lagrange equations for this case as was performed by Vilfan et al. [125]. In these numerical studies they discovered that in the case of very weak anchoring, the radial defect can be substituted by an aligned defectless structure similar to the axial structure in droplets illustrated in Figure 12b.

### 4.3.3. Calamitic Nematic Liquid Crystals in Cylindrical Cavities With Parallel Anchoring

The structures considered in this section are stable for parallel surface anchoring conditions. The four structures are schematically presented in Figure 14.

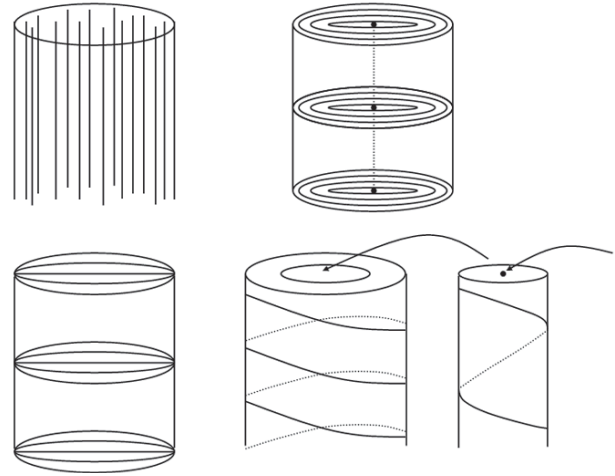


**Figure 14.** Stable nematic director fields in cylindrical geometries when parallel anchoring is enforced.

**Planar-Concentric Structure** The planar-concentric (PC) structure is a planar director field with a pure deformation and a line disclination along the cylinder axis as illustrated in Figure 14. This structure was first predicted by Dzyaloshinskii [121] and Cladis and Kleman [100]. The free energy per unit length is given by

$$F_{\text{PC}} = \pi K_{33} \ln(R/4\rho) \quad (19)$$

where  $\rho$  is the radius of the line disclination.

**Planar-Bipolar Structure** The planar-bipolar (PB) structure is a splay-bend director field with two surface disclinations running parallel to the symmetry axis of the cylinder connecting the poles of the planar director field (see Fig. 14) [126]. It is completely specified by  $n = \cos \psi(r, \varphi) \mathbf{i}_r - \sin \psi(r, \varphi) \mathbf{i}_\phi$ , where  $\Phi$  is the angle between the radial vector and the symmetry axis of the structure. The nematic director field has an analytic solution given by the expression

$$\psi(r/\varphi) = \tan^{-1} \{ \cot \phi (R^2 + \gamma r^2)/(R^2 - \gamma r^2) \} \quad (20)$$

where  $\gamma = (s^2 + 1)^{1/2} - s$  and  $s = 2K/RW_\theta$ . It depends only on the polar anchoring strength  $W_\theta$ . The finite anchoring conditions prohibit the presence of both surface disclination lines of the structure. The free energy per unit length of the PC structure is given by the expression

$$F_{\text{PC}} = \pi K \{ -\ln(2\gamma s) + (1 - \gamma)/s \} \quad (21)$$

There is no analytical solution for the  $K_{11} \neq K_{33}$  structure.

**Escaped-Twisted Structure** The escaped-twisted (ET) structure is a defectless director field illustrated in Figure 14 where the director is everywhere parallel to the surface and stabilized by the presence of the azimuthal anchoring  $W$  [126]. We consider the case where the preferred parallel anchoring direction on the surface is everywhere perpendicular to the cylinder axis. The bend-twist deformation of such a structure is specified by the cylindrical coordinates  $n = \sin \alpha(r) \mathbf{i}_r + \cos \alpha(r) \mathbf{i}_z$ , where  $\alpha$  is the angle between

the local nematic director and the cylinder axis. The equilibrium configuration for  $k = K_{33}/K_{11} > 1$  is given by the expression [61]

$$\left[ \frac{[1 + (k-1)\sin^2\alpha]^{1/2} - \cos\alpha}{[1 + (k-1)\sin^2\alpha]^{1/2} + \cos\alpha} \left( \frac{\sigma+1}{\sigma-1} \right) \right]^{1/2} \quad (22)$$

where  $\sigma = RW_\theta/K + K_{24}/K - 1$  is the dimensionless surface parameter. The free energy per unit length in the one-constant approximation is given by

$$F_{ET} = \pi K(3 - K_{24}/K - 1/\sigma) \quad (23)$$

The ET structure has no analytical solutions for the situation when  $K_{11} \neq K_{33}$  [126].

**Parallel Axial Structure** The parallel axial (PA) structure has a director field everywhere parallel to the cylinder axis ( $\alpha = 0$ ). The free energy per unit length is given by  $\pi K(RW_\theta/K)$  [126].

#### 4.3.4. Confined Discotic Liquid Crystals

The tracing and modeling in this section has focused on studies performed on low molar mass calamitic liquid crystal systems. However, it is equally applicable to discotic liquid crystals. Figure 15 illustrates possible director configurations for discotic liquid crystals with face-on and edge-on anchoring. Since the director of a discotic liquid crystal is orthogonal to the molecule, the director profile and molecular ordering are orthogonal. For calamitic liquid crystals, the director field is parallel to the long axis of the liquid crystal.

**Experimental Studies of Discotic Anchoring and Confinement** For discotics and calamitics, surface anchoring states are determined by a complex interplay of the molecular structure of the liquid crystal molecules, the substrate chemistry, the substrate topology, and possible surface texture induced by directional rubbing [127–131].

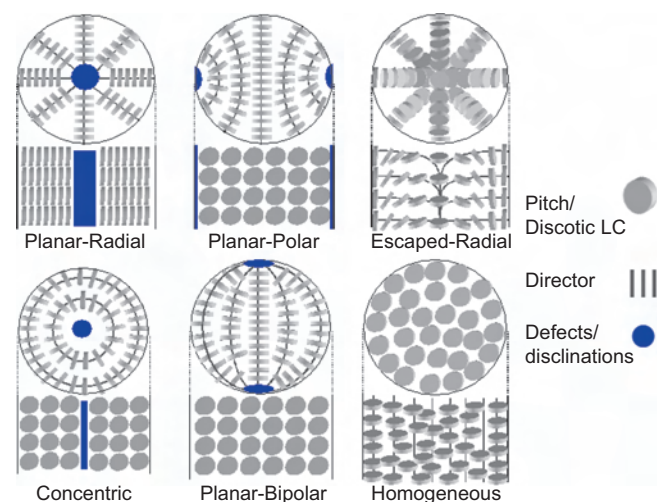


**Figure 15.** Possible direction-field configurations of discotic liquid crystals in cylindrical geometries for homeotropic or face-on anchoring (top) and planar and edge-on anchoring (bottom). Reprinted with permission from [141], K. Jian et al., *Adv. Mater.* (2003). © 2003, Wiley-VCH.

Because of this complexity, anchoring behavior and confinement effects must be investigated experimentally for the liquid crystal/substrate pair of interest. To our knowledge there have been two studies of confined discotics [132, 133]. The phase transitions of hexa-n-octanoate of rufigallol were probed within the fibrous pores of a millipore filter [132] and calorimetry showed the phase transitions to be modified relative to the bulk liquid crystal. The study did not report specific anchoring states or detailed director fields in confinement. In the second study, a columnar discotic phase has been dispersed in a solid polymer matrix, which is reported to modify its phase behavior, optical properties, and electron transport properties [133].

There have been only a few systematic studies of discotic surface anchoring [12, 14, 129]. Vauchier et al. [129] report planar (edge-on) orientation on a lamellar silicate and on muscovite mica. In addition, Furumi et al. [134] demonstrate the alignment of spin-coated discotic thin films on silica using oblique illumination of nonpolarized 436-nm light, and the exploitation of this effect to achieve micropatterning. Anchoring of the discotic HPT has been observed to be planar (edge-on) heterogeneous on Si, and  $\text{CaF}_2$ , and planar homogeneous on ZnSe, and ZnS [12], with a transition occurring to homeotropic (face-on) with time and temperature under some conditions. Anchoring is partly determined by the competition between intermolecular and molecular/substrate forces, and it can be expected that planar (edge-on) anchoring would be the most common state [12], as it preserves the favorable intermolecular face-to-face interaction between discs. The lack of order in the anchoring plane (heterogeneous cases) is an indicator of weak interaction with the substrate. Nylon coating of the same substrates favored homeotropic (face-on) anchoring, which has been attributed to favorable interactions of the side chains with the nylon polymer chains achievable for face-on disks [14]. Generally, research on surface anchoring and alignment techniques for discotics lags behind that for rodlike liquid crystals due to their intrinsic high viscosity and high mesophase temperatures [134]. These are in turn a consequence of strong intermolecular forces as cited previously.

#### Experimental Studies of Anchoring in Mesophase Pitch

Recent anchoring studies have targeted the carbonaceous mesophase, the discotic nematic mixture, due to its importance as a carbon materials precursor. Anchoring at the free surface is reported to be planar heterogeneous (edge-on) for the naphthalene-derived AR mesophase [81, 135], as apparent from the strong anisotropy of these surfaces in polarized reflected light (Fig. 16). Planar free surface anchoring was reported earlier for a petroleum-derived mesophase by White and co-workers [136]. Edge-on anchoring at the free surface is believed to be favored because it preserves internal  $\pi$ - $\pi$  bonds, which require face-to-face interactions among the polyaromatics [3]. Indeed  $\pi$ - $\pi$  bonding, a geometrically favored van der Waals interaction, is strong enough in these planar molecules to cause their early aggregation into short columnar segments (2–4 layers) even in disordered aromatic-rich liquids.

Anchoring on solids is found to be edge-on or face-on depending on the choice of substrate. Table 1 provides the



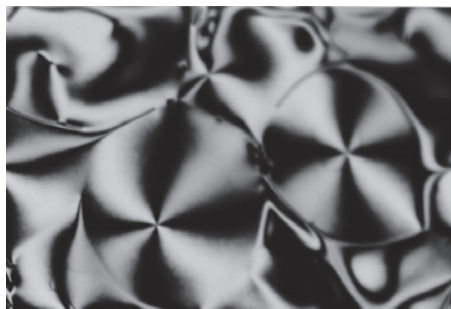


**Figure 16.** Polarized light micrograph of unpolished free surface of mesophase pitch: crossed polars. Edge-on anchoring makes these free surfaces highly anisotropic. Note that mesophase pitch is opaque to visible light, so the standard analytical technique uses polarized reflection microscopy. Here we see concentric circular features ( $s = 1$  defects) in the nematic disclination pattern.

anchoring data on 20 solid substrates, all obtained by this technique. Most surfaces are edge-on, but important exceptions are carbons (especially sphere-based surfaces [66, 77, 81]), mica, and the metals, silver, platinum, and nickel.

There have been only two measurements of elastic constants for carbonaceous mesophase: a value of  $10^{-5}$  dynes

**Table 1.** Anchoring states on various substrates determined by direct microscopic observation of the interfacial plane [135].

Pitch	Substrate	Observed anchoring <sup>a</sup>
AR-HP	Gas phase	edge-on
AR-HP	PTFE	edge-on
AR-HP	PTFE rubbed with nylon cloth	edge-on
AR-HP	Bisque alumina	edge-on
AR-HP	Borosilicate glass	edge-on
AR-HP	Quartz	edge-on
AR-HP	Sapphire	edge-on
AR-HP	Indium tin oxide (film on glass)	edge-on
AR-HP	Stainless steel	edge-on
AR-HP	Aluminum (foil)	edge-on
AR-HP	Brass	edge-on
AR-HP	Copper (TEM grid)	edge-on
AR-HP	Cobalt (99.95%, 1 mm foil)	edge-on <sup>b</sup>
AR-HP	Zinc (99.9985%, 1 mm foil)	edge-on
AR-HP	Nickel (99.5%, 6.35 mm plate)	face-on <sup>b</sup>
AR-HP	Mica (natural muscovite sheet)	face-on <sup>b</sup>
AR-HP	Silver (99.998%, 0.025 mm foil)	face-on
AR-HP	Platinum (99.99%, 0.025 mm foil)	face-on
AR-HP	Graphite basal plane	
AR-HP	—HOPG	face-on
AR-HP	—flexible graphite sheet	face-on
AR-HP	Glassy carbon	face-on
Pet. Mes.	Gas phase	edge-on
Pet. Mes.	Borosilicate glass	edge-on
Pet. Mes.	PTFE	edge-on
Pet. Mes.	Stainless steel	edge-on
Pet. Mes.	HOPG	face-on

<sup>a</sup> All face-on cases were strictly optically isotropic upon direct examination of the interfacial plane. This anchoring state is referred to as “homeotropic” in liquid crystal nomenclature. All edge-on states were optically active with random in-plane orientations, referred to as “planar heterogeneous” in liquid crystal nomenclature.

<sup>b</sup> In these samples, examples of both anchoring states were found in different regions of the substrate. The state listed was the more prevalent of the two.

for the bend-splay elastic constant [77] and  $3 \times 10^{-5}$  dynes for the bend elastic constant  $K_{33}$  [137].

Zimmer and Weitz [77] determined this bend-splay elastic constant from optical measurement of the magnetic coherence length ( $7 \mu\text{m}$ , for a field strength of 5500 G) in the vicinity of carbon fiber acting as cracking surfaces, together with a repeated value for the diamagnetic anisotropy of  $-0.69 \times 10^{-6}$  emu/g [138] for carbon mesophase. The face-on anchoring on carbon fibers in that study was strong enough to resist the 5500 G field which favored the opposite alignment [77].

A complete quantitative theory of anchoring state selection is not yet available for these materials, but the data do show a number of trends. The preferred anchoring state is the one that minimizes the interfacial energy,  $\gamma$ , composed of both entropic and energetic terms. Entropic effects are believed to favor face-on anchoring, since this state reduces the excluded volume at the interface [130]. The magnitude of this entropic contribution on flat surfaces is significant, but is expected to decrease with increasing surface roughness.

Attractive forces, however, also play a role in anchoring, and indeed many aspects of molecular orientation are discussed in terms of a balance between intermolecular forces *within* the film and *between* the film and substrate [127]. A theory has been proposed [135], that pitch interacts primarily through dispersive forces (rather than polar interactions), and that the liquid/substrate dispersion was inhibited by a geometric mismatch between the large planar mesogens and most surfaces. Only surfaces of lamellar materials that are atomically flat (graphene layers, mica) are capable of dispersive interactions with large pitch mesogens that are sufficiently strong to overcome internal  $\pi$ - $\pi$  bonds and produce face-on anchoring. To achieve the face-on state, the pitch mesogens must give up one set of internal  $\pi$ - $\pi$  bonds in order to form a  $\pi$ -surface bond, and therefore this is the less common state, as it requires strong interaction and/or very good geometric accommodation between the planar mesogens and the substrate. For this reason, there is a strong (but imperfect) correlation between wetting behavior and anchoring, with face-on orientation often associated with a small contact angle [135].

These basic considerations can be used to interpret the larger anchoring data set in Table 1. First, the anchoring is edge-on on the very low energy surfaces (gas phase, PTFE) as expected, as these surfaces offer little or no energetic interaction to overcome internal  $\pi$ - $\pi$  bonds. Edge-on anchoring is also seen for all glasses/oxides with the exception of mica. The oxides can be expected to offer modest dispersive interactions, and these are inhibited by the non-atomically-planar nature of these surfaces. The polar contribution that raises the total surface energy of the oxides does not interact with the pitch to promote either wetting or face-on anchoring [135]. The natural lamellar materials graphite and mica have a high entropic contribution for face-on anchoring coupled with good geometric accommodation to the flat polyaromatic molecules which increases the effective dispersion interaction.

The metals provide an interesting data subset with both edge-on and face-on cases. No complete theory has been offered, but a correlation has been noted with oxidation

potential (well-developed surface oxide films favoring edge-on anchoring [135]) and with the ability of metal surfaces to form  $\pi$ -d or other electron transfer complexes with aromatic rings [135, 139, 140], which requires face-on orientation.

There have been very few studies of carbonaceous mesophase in confinement [77, 141], and these viscous materials often exhibit persistent disclinations (defects) in all but the smallest spaces. The disclination structures in carbonaceous mesophase have been reviewed by Zimmer and White [142].

**Behavior of Single-Component Polyaromatic Compounds** Single-component polyaromatics do not form liquid crystals, but the interfacial behavior of these disklike compounds is nevertheless of great interest in nanotechnology. Reports from the molecular thin-film literature indicate face-on configuration for single pentacene molecules on silicon(001), but edge-on orientation for multimolecular islands, suggesting the greater importance of intermolecular interactions among pentacene molecules relative to pentacene/substrate interactions [15]. Face-on orientation on HOPG has been reported for coronene [17] and hexa-peri-benzocoronene [16], at least for monolayer and submonolayer coverage.

The largest PAH studied, hexa-peri-hexabenzocoronene, adsorbs face-on on two atomically flat layered materials (HOPG,  $\text{MoS}_2$ ), and edge-on on the atomically rough oxidized silicon(001) and polycrystalline gold, similar to the trends reported here [18]. The film structure of hexa-peri-hexabenzocoronene on HOPG was not stable during annealing at 425 K, however, and converted to edge-on needle-like domains, which has been attributed to intermolecular interactions that favor tilted herringbone structures, which are mismatched to the atomically flat HOPG surface [18].

In general, surface molecular orientation in pitch anchoring, pure discotic anchoring, and PAH epitaxial deposition are all governed by a balance of soft interactions—a competition between intrafilm intermolecular forces and substrate/overlayer forces, the same considerations that apply to molecular thin films [19]. As a result, the effect of substrate on surface orientation is similar in the three types of interfacial systems, but exhibits some differences. Most notable is the tendency of the regular PAH in thin-film studies to pack in edge-on herringbone patterns in multilayer films where the molecules do not lie in any single plane and are thus poorly compatible with face-on orientation on lamellar substrates.

## 5. APPLICATIONS OF SYNTHETIC DISCOTICS

The flat panel display industry has been engaged in nanoscience and nanotechnology for years. There are several application examples of discotic liquid crystals used in or being considered for flat panel displays: (1) thin-film polarizers, (2) compensation films, (3) electroluminescent discotics, (4) photovoltaics, and (5) molecular wires [143]. In this section we will focus on a few potential applications for discotic liquid crystals.

### 5.1. Thin-Film Polarizers

Molecular engineering of discotic textile dyes has produced unique materials that can be used to manufacture thermally stable thin-film polarizers. One of the most intriguing applications is thin-film polarizers for flat panel displays. These compositions of organic dye material possess a lyotropic liquid crystal phase when dissolved in water. The dye molecules are flat and therefore form liquid crystalline phases (molecules stack on top of each other). Several dyes that have been investigated for thin-film polarizer applications are shown in Figure 17a [144–146]. They are very attractive for liquid crystal display applications because of low light leakage at oblique viewing angles [147] and an overall improvement of the viewing angle for certain applications [148–150].

Water-soluble dyes of flat molecular architecture are oriented in two steps as shown in Figure 17b. The first step is the formation of a lyotropic liquid crystal and the second step is the crystallization of pre-aligned complexes on the surfaces by evaporating off the water. Using a Meyer bar, the lyotropic liquid crystal molecular complexes are ordered along the direction that the Meyer rod is rolled as shown in Figure 17b.

The polarizers that are created by this process are e-type and therefore transmit the polarization component with the e-vector parallel to the direction of alignment and absorb if

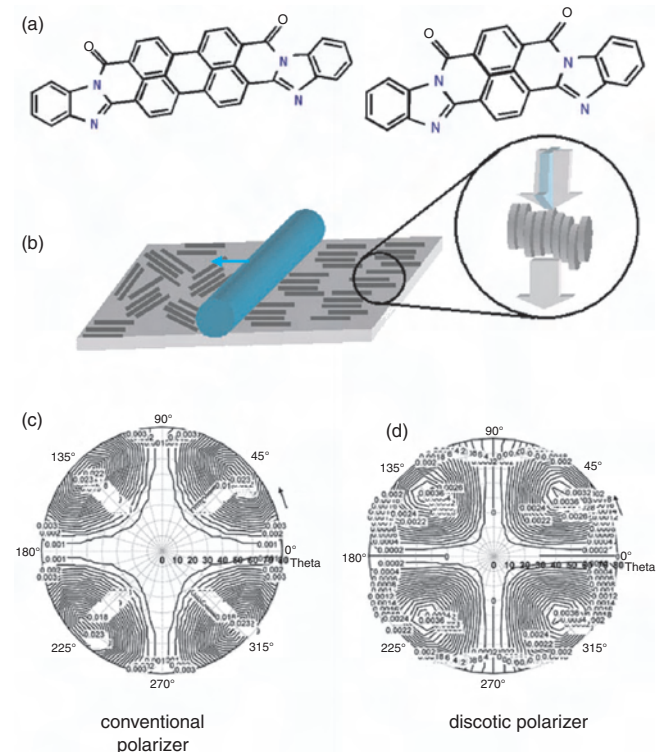


**Figure 17.** Examples of textile ink molecules that when dissolved in water form lyotropic liquid crystal phases (a). When these materials are distributed over a substrate surface with a Meyer Bar, a thin-film e-type polarizer is created (b). Isotransmittance curves comparing the performance of conventional polarizers (o-type) (c) to the discotic e-type polarizer (d). Isotransmittance curves courtesy of Dr. Michael Paukshto of Optiva.

it is perpendicular, as shown in the inset of Figure 17b. The iso-transmittance curves of a conventional polarizer (known as o-type) are compared to an e-type polarizer formed with the discotic-like materials. There has been a great deal of work on the applied front with these materials because of their potential as polarizers in displays. There have been a few more basic studies on these lyotropic liquid discotic materials to better understand their structure [151, 152] and rheological properties [153]. Optiva is currently pursuing commercialization of these materials.

## 5.2. Compensation Films

Liquid crystal displays are known to have an inferior viewing angle due to the anisotropic nature of the liquid crystal alignment. This effect is most noticeable when gray scale images are displayed. The poor viewing angle can be compensated by a passive film created out of reactive discotic liquid crystals. Sample reactive discotic compounds are shown in Figure 18a. They are low molecular weight and therefore can be ordered with surfaces of external fields. This ordered configuration is then captured indefinitely with photopolymerization [154].

The concept of optical compensation is shown in Figure 18b. The viewing angle problem in liquid crystal displays is due to the optical retardation of the liquid crystal, which in most cases is positive uniaxial. This results in light

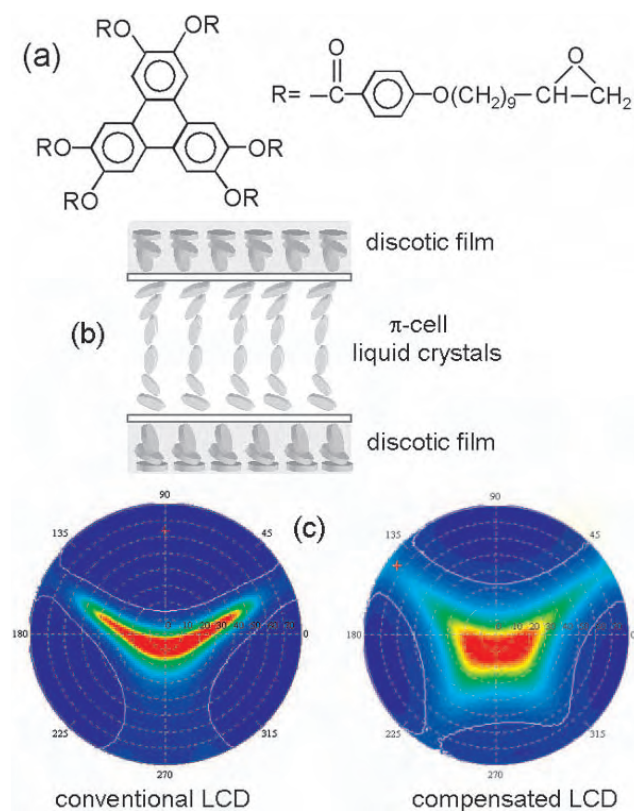


**Figure 18.** An example of reactive discotic material that can be photopolymerized (a) and the configuration of a photoreactive discotic film used to compensate a p-cell liquid crystal display (b). Isotransmittance curves demonstrating how the viewing angle of a liquid crystal display can be broadened using discotic liquid crystal compensation films (c). Viewing angle curves courtesy of Ichiro Amimori of Fuji Film.

leakage through crossed polarizers at wide angles since the display is typically optimized for normal incidence. By suppressing the amount of light leakage at oblique angles in the optically dark state, the viewing angle of the display can be compensated to achieve better performance (i.e., better optical contrast at all incident angles). The underlying concept of viewing angle compensation using a reactive discotic liquid crystal film is as follows. The viewing angle dependence of the positive birefringence of the liquid crystal can be compensated by a negative birefringence whose optic axis is parallel to that of the positive birefringence.

Compensation films based on reactive discotic mesogens can be used in many types of liquid crystal display configurations [155–157]. One example is shown in Figure 18b where the discotic film is used to compensate a  $\pi$ -cell liquid crystal display. A  $\pi$ -cell is a homogeneous liquid crystal display configuration with opposing pretilt angles of the liquid crystal molecule at the surfaces as shown in Figure 18b. To achieve a dark state, an electric field is applied to align the liquid crystal molecules. To compensate such a complicated structure, the compensation film must have a mirror image of the director configuration so that each liquid crystal pairs up with a corresponding discotic molecule with a negative birefringence. When the liquid crystal is sandwiched between two compensating films as shown in Figure 5c and viewed between cross polarizers, the viewing angle becomes broader and more symmetric. These materials are now being commercialized by Fuji Film Corporation and are utilized by many display manufacturers.

## 5.3. Electrofluorescent Columnar Liquid Crystals

Discotic liquid crystals offer unique properties which can be exploited in organic light-emitting diode (O-LED) applications [158–162]. Characteristic features of light-emitting liquid crystals are the anisotropy of the electric properties, a strong coupling to external fields, and a tendency to form spontaneously monodomain films. It is well known that discotic columnar liquid crystals have great potential as hole transporting layers. In the columnar phase, the charge carrying mobility is  $\mu = 10^{-1} \text{ cm}^2 \text{ V}^{-1} \text{ s}^{-1}$  (this is greater than values for amorphous organic materials and slightly smaller than values for molecular single crystals) [163]. One very attractive feature of columnar liquid crystals is their ability to expel defects upon the annealing process.

Benning and co-workers [162] studied the homologous series of 3,4,9,10-tetra-(n-alkoxycarbonyl) perylenes  $\text{C}_{20}\text{H}_8(\text{CO}_2(\text{CH}_2)_{n-2}\text{CH}_3)_4$  [164]. They demonstrated red shift in dilute solutions of the compounds and the columnar phase of pure compounds. Additionally, they demonstrated long fluorescent lifetimes. This intriguing behavior was explained by the formation of excimers in the liquid crystal phase. These materials may have potential in LED applications.

## 5.4. Photovoltaic Discotic Liquid Crystals

The self-organization feature of discotic liquid crystals and crystalline-conjugated materials has been used to create thin-film photovoltaic devices. Schmidt-Mende and co-workers [165] demonstrated that the discotic liquid



crystal hexa-perihexabenzocoronene could be implemented with perylene dye to produce thin films with vertically segmented perylene and hexabenzocoronene. By implementing these materials into a diode configuration, the device has a photovoltaic response with quantum efficiencies of >24% at 490 nm. The mechanism of these efficiencies is photoinduced charge transfer between hexabenzocoronene  $\pi$  systems. These systems, along with their simple processing cast from solution, have the potential to create low-cost, high-performance thin-film photovoltaic technology.

### 5.5. Electron Transport in Discotic Liquid Crystals

One-dimensional molecular electronic conductors are of interest because of their potential as molecular wires. Most conducting and semiconducting organic materials that have been reported in the literature, such as charge-transfer complexes [166], metallo-organic complexes [167], and doper polymers, tend to exhibit anisotropic (or quasi-1D) electrical conductivity. There has been a considerable amount of interest in discotic liquid crystals as an alternative class of conducting one-dimensional materials.

Conductivity has been investigated in a broad class of discotics, such as metalomesogens [168, 169] and polynuclear aromatic mesogens, and by modifying organic charge-transfer complex [168, 169]. For example, peripherally substituted metallophthalocyanines display stable columnar mesophases over an extended temperature range [170]. Another example is copper octa-*n*-octyloxyphthalocyanine, which in its columnar mesophase state has a conductivity of  $\sigma = 3 \times 10^{-3} \text{ S m}^{-1}$ . Charge-transfer salts of highly oriented fibers of crystalline 2,3,4,6,7,10,11-hexapentyloxytriphenylene have been processed by drawing strands from the columnar phase followed by oxidation with bromine [171]. The conductivity of these samples is more than three orders of magnitude greater ( $\sigma \sim 10^{-2} \text{ S m}^{-1}$ ) than powdered samples ( $\sigma \sim 10^{-5} \text{ S m}^{-1}$ ).

Boden and Lowerkens [172] have shown a new class of quasi-one-dimensional p-type semiconducting materials, formed by doping the hydrocarbon chain matrix of discotic liquid crystals. They studied the discotic liquid crystal material 2,3,4,7,10,11-hexahexyloxytriphenylene (HAT6) doped with the Lewis acid  $\text{AlCl}_3$ , and discovered many new phenomena: (1) HAT6 when doped with  $\text{AlCl}_3$  is converted from an insulated to a quasi-one-dimensional semiconductor, with conduction along the column being three orders of magnitude greater than perpendicular to it; (2) the frequency dependence of the conductivity along the column axis can be modeled as a single charge-transfer process in which charge carriers hop between localized sites, which [suggest charge transport ones macroscopic distances] (100 nm); and (3) charge transport proceeds stochastically by phonon-assisted tunneling between neighboring states.

## 6. APPLICATIONS OF MESOPHASE-DERIVED CARBONS

This section deals with discotic-based nanostructured carbon materials, some of which are rather advanced in their development and are already incorporated in commercial

products. Nanomaterials based on discotics (nanofibers, nanotubes, nanophase particulate) are an emerging materials class and are covered in the subsequent section.

The almost exclusive use of carbonaceous mesophase is as an intermediate in the synthesis of carbons, especially highly crystalline graphitic forms that are formed upon heat treatment near 3000 °C. The spontaneous formation of long-range (>1  $\mu\text{m}$ ) molecular order in mesophase establishes the basic layer structure early, so that the high-temperature annealing process must only “flatten” the meandering structure and remove local defects. If long-range orientational order is not established in a low-temperature carbon, it cannot typically be produced after the fact by high-temperature annealing, even at 3000 °C. Traditionally, mesophase was formed *in-situ* during carbonization of nonmesogenic precursors, but increasingly, a single-phase liquid crystalline pitch is selected as the starting material. Pitches derived from petroleum, coal-tar, or the polymerization of small PAH all find use as precursors for different carbon products. The recent commercial availability of AR-mesophase, a naphthalene homopolymer manufactured by Mitsubishi Gas Chemical, provides a homogeneous liquid crystalline mixture in a consistent formulation for research on advanced materials. The advantages of mesophase pitch as a carbon precursor include:

1. Spontaneous development of long-range order (>1  $\mu\text{m}$  and often much larger) in the liquid phase, which is used to impart similar long-range crystallographic order in carbons.
2. High solids yield upon carbonization. For an organic liquid it has a low H/C ratio and low volatile content, and thus produces a large increase in density in a single infiltration step when used as a matrix material in composites.
3. Ability to obtain very-long-range anisotropy in material properties through flow ordering of the discotic molecules (extrusion, fiber spinning) or through surface anchoring phenomena (e.g., in interfiber spaces in C/C composites).

To understand the significance of mesophase in carbon synthesis, some background on carbon materials and their structure/property relations is necessary. Carbons are a diverse class of materials ranging from the high-temperature structural materials used in rocket nozzles and aerospace applications (C/C composites) to disordered porous materials used as environmental sorbents (activated carbon). Most are crystallographically related to graphite, but consist of finite snippets of the graphite lattice of “graphene layers” that adopt a variety of spatial configurations. The graphite lattice is highly anisotropic in its bonding and properties, with strength, modulus, electrical conductivity, and thermal conductivity are much higher within the covalently bonded planes than across them. For example, the elastic constants of single-crystal graphite are 1060 GPa within the covalently bonded planes and only 36 GPa between planes. The opposite trend is observed for the coefficient of thermal expansion, which is about  $30 \times 10^{-6} \text{ K}^{-1}$  across the primary planes, but less than  $1 \times 10^{-6} \text{ K}^{-1}$  within the planes. As a result of the anisotropy in the graphite lattice, the arrangement of the

graphite snippets in real carbon materials, that is, the carbon nanostructure, strongly influences the bulk properties of practical materials and their directional dependencies. For example, the stiffness of carbon fibers may be 30 GPa if the graphene layers are oriented randomly, but can reach 800 GPa if the layers have a high degree of alignment along the fiber axis [28]. Nanostructure also determines the space filling properties of the solid phase and thus the ultrafine pore structure that governs the accessibility of internal surface sites by small probe molecules. This accessibility is key to the high adsorptivity of activated carbons, which have total internal surface areas as high as 1500 m<sup>2</sup>/gm.

A key to designing carbon materials, therefore, is the ability to create desired configurations of graphene layers. For example, ordered configurations are desired where high stiffness, strength, or conductivity along a specified axis is desired, such as is the case for carbon nanotubes, or high modulus carbon fibers. The ability to manipulate the discotic molecules in the mobile yet ordered mesophase becomes a critical advantage. With this background, some of the most important mesophase-derived carbon products are summarized in the following.

### 6.1. High Modulus Carbon Fibers

Mesophase pitch can be used to manufacture carbon fibers with superior stiffness, relatively high strength, and electrical and thermal conductivities along the fiber axis. The favorable properties arise from the preferential ordering of the graphene layer planes parallel to the fiber axis, which in turn arises from molecular flow ordering in the fiber spinning process [21, 79, 173]. Fibers are typically melt spun above the softening point, then quenched and stabilized by low-temperature oxidation, which cross-links and thermosets the structure to preserve the flow-induced discotic molecular order. Fibers are then carbonized ( $T \sim 1000$  °C) or graphitized ( $T \sim 3000$  °C) as required by the particular application.

Discotic liquid crystalline flow is a complex process most often described by the Leslie–Erickson continuum theory [21]. The theory makes a simple prediction that the extensional flow accompanying fluid acceleration into the narrow spinning nozzle orients the discotic molecules with their planes parallel (directors perpendicular) to the extensional flow axis [174], in agreement with observation. The perpendicular director field is not a unique structure, however, and there are a variety of possible director configurations in the plane perpendicular to the fiber axis—so-called transverse textures, that provide a challenge for prediction [174, 175]. There is a significant literature on fiber transverse textures, including experimental studies [21] and theoretical treatments motivated by a desire to understand the origin of carbon fiber textures and develop methods of tailoring them for specific fiber applications [21, 174, 176]. Experiments have observed radial, concentric, and “zig-zag” structure in the transverse sections [174]. A significant barrier to the decisive application of theory is the lack of liquid crystal material constants for mesophase pitch, including as a minimum set, the elastic constants for bend, splay, and twist, and the directional or Miesowicz viscosities. Theoretical treatments have often been restricted to solution forms

and trends, but have nevertheless provided insight into real fiber textures.

Recent R&D efforts on advanced pitch-based carbon fibers have focused on the new pitch formulation, on the spinning of elongated fibers or “tapes” with radial or laminar transverse textures that depend on flow conditions [177], on the origin and theoretical prediction of transverse textures [21, 174, 176, 178], mesoscale structures [179, 180], and of course fiber properties and applications [21, 181, 182].

### 6.2. C/C Composites

Mesophase pitches find use as binder phases in carbon fiber composites to make all-carbon (C/C) materials of special use in very-high-temperature applications. The discotic molecules enter the interfiber spaces driven by pressure or capillary forces and are converted to carbon matrices by further heating. Fibers act as anchoring surfaces for the discotic mesogens and the 1- to 10- $\mu$ m interfiber spaces provide the confined geometry that leads to distinct liquid crystal patterns as described in Section 4. Most or all studies report face-on (homeotropic) anchoring on the fiber surfaces, which causes the graphene layers to align parallel to the fiber axis and enhances the tensile strength and stiffness of the composite [77]. The interfiber spaces are small enough to produce primarily homogeneous (defect-free) liquid crystal domains, and the influence of the surface is sufficient to resist the reorienting effects of a Gauss magnetic field [77]. In the absence of the confining surfaces, this or similar magnetic fields have been shown to successfully orient carbonaceous mesophase.

### 6.3. Mesocarbon Microbeads

The anisotropic spherical droplets that led to the original discovery of carbonaceous mesophase in 1965 are now produced commercially under the name “mesocarbon microbeads.” The microbeads are formed by slow heat soaking of aromatic-rich hydrocarbon phases and are typically separated from the surrounding material by solvent extraction, and then used/marketted in green form, or in carbonized form after heat treatment above 700 °C. A variety of laboratories synthesize and characterize mesocarbon microbeads [183, 184], while an important commercial source is Osaka Gas Chemicals Co., LTD. A number of studies have been carried out focused on formation, structure, and applications.

#### 6.3.1. Structure and Formation Mechanism

Mesocarbon microbeads are most commonly found to have the bipolar (Brooks–Taylor) structure shown [184–186], but a variety of other liquid crystal structures have also been reported (see Fig. 19). The carbon literature contains a variety of casual terms for these structures that differ from the terms used for nematic droplets in the generic liquid crystal literature. In this chapter, structures are named from the symmetry of their director configuration. For example, the bipolar configuration in discotics is a result of edge-on anchoring, as compared to the bipolar structure in low molar mass compounds, which has planar anchoring. Independent of the anchoring regimes, the director profile is analogous. The origins of the different molecular configurations are

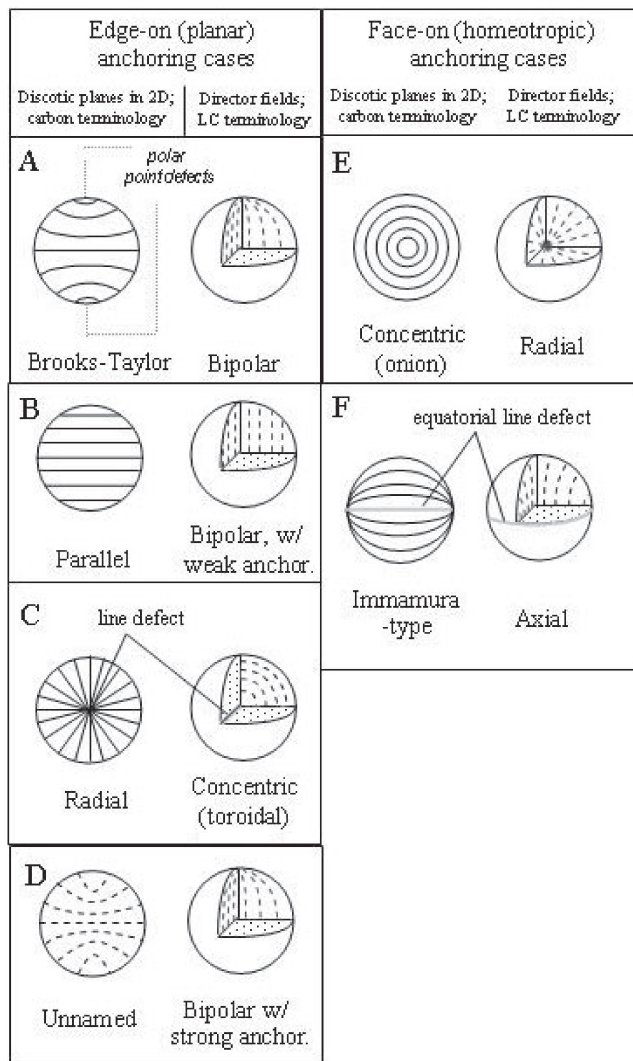


**Figure 19.** Molecular configurations in carbonaceous mesophase droplets; all but (C) have been experimentally observed. The 2D spheres on the left show the orientations of the discotic planes, as is the convention in the mesophase and carbon literature, and give the corresponding names in that literature if any. The 3D spheres at the right show the director fields, as is the convention in the liquid crystal literature, and the structure name common in that literature. Note the directors run perpendicular to the discotic molecular planes. Structures are as follows: (A) Brooks–Taylor (bipolar) [1, 66, 184, 185]; (B) Parallel (bipolar with very weak anchoring) [119, 184, 192]; (C) Radial (concentric or toroidal); (D) Unnamed variant of a report under very low temperature formation conditions (bipolar with strong anchoring) [78]; (E) Concentric (radial) [184]; (F) Bipolar with planar anchoring (axial) in presence of carbon black [78]; and in presence of isotropic coke (carbon) particles [184]. Note that (F) is not bipolar, but rather has a circumferential line defect at the equator. Other types reported include an asymmetrical version of the concentric structure (E) and a version of the bipolar homeotropic structure (F) but containing defects when made in the presence of anisotropic coke [184].

poorly understood, but generally believed to arise from the interplay of anchoring at the mesophase/isotropic interface and elastic director strain, and thus to be governed by the science of confined liquid crystals as discussed in general terms in Section 4.

Studies of discotic surface anchoring find edge-on anchoring to be the most common form and especially prevalent at the pitch/gas interface and on low-energy surfaces. Since organic liquid surfaces have lower energies than most solid surfaces, the preference for edge-on anchoring in these forms (A–D in Fig. 19) is expected. A likely explanation for at least some of the observed homeotropic cases (E, F in Fig. 19) is the presence of impurities that can serve as nucleation centers or accumulate at the surfaces of the mesophase droplets where they may affect anchoring. Especially common are carbon solids as impurities in pitches (“quinoline insolubles”) or additives such as coke or carbon black used in some studies [184]. Since anchoring is face-on (homeotropic) on carbon, mesophase spheres assembled under these conditions are likely to exhibit structures E or F in Figure 19, as generally borne out by experiment. Structure E is reported to be a stable form in the presence of face-on (homeotropic) anchoring [187], while F occurs in the presence of fields or if anchoring is weaker [188]. The asymmetrical form of E [184] has also been seen in other liquid crystals, when an external field shifts the point defect from the center toward the surface [189].

Considering the more common edge-on (planar anchoring) cases, A–D in Figure 19, the bipolar or Brooks–Taylor structure is predicted by Zumer and co-workers [188] to be the most stable when elastic constants,  $K_{11}$ ,  $K_{22}$ ,  $K_{33}$ , are similar. Indeed, it was the first structure found and is the most commonly reported for carbonaceous mesophase. Only for very low bend/splay ratio ( $K_{33}/K_{11}$ ) is the radial (toroidal) structure, C, predicted to have the lowest free energy [190, 191] propose that  $K_{33} > K_{11}$  for the high molecular weight carbonaceous mesophases, which would make the radial (toroidal) structure unlikely, and indeed this structure has not to our knowledge been reported in mesocarbon microbeads.

Structure B in Figure 19 apparently represents weak anchoring, although it is easy to imagine this simple structure arising in the early stages of growth to bipolar spheres, perhaps as a metastable intermediate. One of the reports of the laminar structure is for very small ( $<1 \mu\text{m}$ ) droplets [192], and indeed there are theoretical reasons to expect a transition to weak anchoring as size decreases, as is the case in low molecular weight liquid crystal systems [99]. The overall free energy is composed of an anchoring contribution (of order  $W_0$  in  $\text{mJ}/\text{m}^2$ ) and an elastic contribution of order  $K/L$ , where  $K$  is an elastic constant and  $L$  is the length scale of curvature. As droplet size decreases ( $L \rightarrow 0$ ), the elastic term increases in importance and the molecules deviate from the preferred anchoring state to minimize the dominant elastic strain contribution. A similar argument has been put forth by Yang [193] to explain the homogeneously ordered liquid crystal domains of approximately 100 nm in a mesophase-derived porous carbon (see Section 6). This weak anchoring condition may be common in carbonaceous mesophase droplets or grains of submicron size.

In general, more work is needed to fully understand the origin of all the sphere types in Figure 19. Some structures may represent metastable, nonequilibrium states, a distinct possibility for these viscous materials with high cohesive energy density and high rotational barriers. Nevertheless,

the major trends in Figure 19 are those expected from liquid crystal theory and from the anchoring rules derived from simple experiments on planar substrates.

### 6.3.2. Microbead Applications

Mesocarbon microbeads are of interest primarily as precursors for advanced carbon materials, including anodes for Li-ion batteries [184, 194]. An advantage of mesocarbon microbeads is their active surface populated preferentially by graphene edge sites. Compared to carbon black particles with concentric structure, mesophase spherules have been shown to be more amenable to electroless metal plating following surface oxidation by nitric acid. The nitric acid treatment introduced 3.5 mmol/g of acid sites to the mesophase spherules (material M6G) compared to 0.76 mmol/g for carbon black, despite a total physical surface area of the carbon black over 150 times as great. Mesocarbon microbeads are also self-sintering [195]—an advantage for binderless applications.

The properties/performance of the different sphere types have not been systematically compared for most applications. In one exception [184], Chang et al. report on the suitability of various mesocarbon microbeads as anodes for Li-ion batteries. The discharge capacity and cyclability show a modest variation with structure. The lamellar and BT forms show generally highest initial capacities, consistent with the expected higher mobility for Li ions into the interlayer spaces. Differences become less pronounced upon cycling, possibly indicating structural rearrangements in the less “open” forms to accommodate Li exchange [184]. All types show increase in capacity with increases in heat treatment temperature from 2400 to 3000 °C.

### 6.4. Other Applications

Mesophase pitches are used in the production of graphite foams for lightweight thermal management applications [196, 197]. Vapor bubbles produced by volatilization of the lower molecular weight fractions cause volume expansion of the liquid and following high-temperature heat treatment lead to low-density, high-conductivity foams. The biaxial extensional flow caused by bubble growth leads to parallel alignment in the bulk of the stretched bubble cavity membranes, so that the dominant alignment of the graphene layers is parallel to the bubble surfaces. The overall result is a foam with desirable *isotropic* thermal conductivity, reflecting the distribution of orientational vectors around the spheres. Pitch has been at least evaluated as a precursor for other carbon products, including gas membranes [198], conducting additives in electronic cells [199], and activated carbons [200].

## 7. NEW CARBON NANOMATERIALS

There is tremendous excitement surrounding new structural forms of carbon, both as components in emerging nanotechnologies and as subjects of scientific inquiry. This section begins with a brief review of carbon nanoforms, then proceeds to demonstrate a new, flexible concept for nanocarbon synthesis based on discotic liquid crystals.

### 7.1. Brief Overview of Carbon Nanoforms

In recent years the classical picture of  $sp^2$ -hybridized carbon as flat sheets has given way to a host of structural possibilities based on closed spheres (fullerenes [201], onions generated in electron beams [202] and in immersed arcs [203]), multi- and single-walled nanotubes [204], nanotubes that are Y-shaped [205], bent or helical [206], graphite fibrils with scroll-like structure [207], and single-atomic-width monolayer graphite films on metal surfaces [208].

A variety of synthetic routes have been demonstrated including arc evaporation of carbon, catalytic decomposition of hydrocarbons on metal particles [209–211], and templating methods using nanochannel membranes [212–214]. Most of these new carbon forms are assembled at high temperature from vapor-phase precursors, including nanotubes by arc evaporation, CVD, PECVD, or thermal deposition on templates; fullerenes from flames or arcs; and graphite whiskers grown by catalytic decomposition of hydrocarbon gases [210, 215, 216]. These catalytic, “vapor-grown” carbon nanofibers exhibit a variety of sphere layer structures that depend on the crystal facets of the catalyst particle. Forms include concentric, “platelet,” “herringbone,” and cup-shaped nanofibers [166, 177, 217–219].

Some condensed-phase routes to nanocarbons have also been demonstrated. These include the impregnation of nanochannel alumina membranes with polyacrylonitrile [220] or furfuryl alcohol [221], the latter giving tubes with internal cell structures similar to natural bamboo. Templated nanocarbons include layered forms made by carbonizing furfuryl alcohol in clay templates [222], the thermal carbonization of polymer thin films, and nanostructured porous carbons made using templates in the form of silica nanoparticles [223], mesoporous silica materials [224], zeolites [225], silica gel or porous glass [226, 227], or from etching nanocomposites made by sol-gel processing [228]. These studies include double templating methods, in which the interior of the carbon nanotubes provides the geometric constraints for growth of second phases, such as nanorods, plates, or particles of Pt, Ag, Fe, or NiO [229–231]. Further nanostructured porous carbon forms have been produced from sucrose pyrolysis within mesoporous silica molecular sieves as templates [232], or from pyrolysis of recorcinol/formaldehyde in the presence of a silica solution [233]. Zakhidov et al. [234] have produced “inverse opal” carbons using partially fused silica sphere templates with three-dimensional periodicity. By filling the 3D sphere arrays with phenolic resin followed by carbonization, or by chemical vapor deposition with propylene, a porous templated carbon material is formed that is capable of Bragg reflection of visible light [234]. For the plasma-enhanced CVD variant of this procedure, the graphene layer orientations were probed by high-resolution TEM and found to lie parallel to the former sphere surfaces, producing onion-like structures [235]. Templated nanocarbons show promise in a variety of application fields, where they may serve as conductive catalyst supports for fuel cell electrodes, anodes for lithium ion batteries, components in nanocomposites [236], ultracapacitors, and chemical filters, with many of the applications requiring ordered arrays [237].

As with other carbon materials, these new nanoforms possess the basic  $sp^2$ -hybridized bonding of graphite, but

differ in the spatial arrangement of their graphene layer. As discussed earlier in the chapter, graphene layers, like the graphite lattice itself, are highly anisotropic in their electrical, thermal, and chemical properties [28], and thus their orientational patterns are key to most carbon and nanocarbon properties. Most of the reported nanocarbon forms are assembled at high temperature under reactive conditions, where thermodynamic driving forces attempt to minimize the number of high-energy edge sites having unsatisfied valencies. The result is an edge-to-edge assembly process that produces closed structures (tubes, spheres, shells, parallel films), in which the exposed surfaces consist primarily of graphene basal planes. For example, multi-wall nanotubes are concentric structures in which the curved graphene planes lie parallel to the tube axis and face outward at the tube periphery; as a result, they have high axial conductivities, stiffness, and strength but are inert to many chemical processes, leading to weak bonding in assemblies and difficulties with sidewall functionalization [21]. The templated nanotubes of Kyotani et al. [214] and Martin and co-workers [238] formed by vapor-phase deposition also show preferential alignment of the graphene layers parallel to the channel walls, and thus have basal-plane-rich surfaces, similar to other pyrolytic carbon films. The next section describes alternative carbon nanoforms with edge-rich surfaces produced by a new route based on discotic mesogenic precursors.

## 7.2. Templated Carbon Forms from Discotic Precursors

The phenomenon of discotic surface anchoring discussed earlier in this chapter opens new possibilities for the molecular design of carbon and nanocarbon materials, including the synthesis of nanocarbons with active edge-rich surfaces. Table 1 can be used as a guideline for selecting templates to produce films of orientationally ordered discotics that can be converted to carbon materials by polymerization about 400 °C.

### 7.2.1. Patterned Surfaces

This concept of surface anchoring templates was first exploited to make periodic microarrays of edge-on and face-on surfaces in solidified discotic mesophase using a Cu/HOPG two-component anchoring template [135]. Figure 20 shows an example micropatterned surface in quenched AR-mesophase. When these ordered polyaromatic thin films are thin ( $<50 \mu\text{m}$ ), oxidative stabilization at around 200 °C followed by heat treatment above 700 °C can convert them to carbon surfaces possessing the same spatial pattern of graphene edge and basal sites [135].

### 7.2.2. Orthogonal Carbon Nanofibers

Using anchoring templates, the surface-induced order typically propagates only micrometer or submicrometer distances into the bulk discotic phase, after which it gives way to flow-induced domains in the interior of these viscous materials [193]. Therefore, for macroscopic carbon bodies, anchoring templates can determine *surface* orientational patterns, but not bulk structure. If, however, the

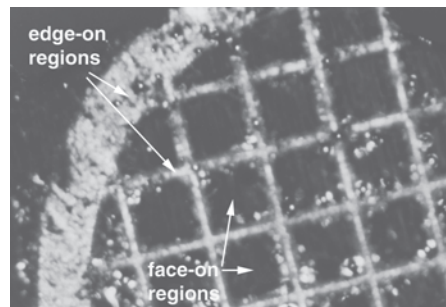


**Figure 20.** Optical micrograph (crossed polars) showing polyaromatic solid surface with microscale molecular orientational pattern established with a two-component surface anchoring template. The template was a Cu TEM grid (imparting edge-on anchoring) on a cleaved HOPG graphite basal surface (imparting face-on anchoring). After physical removal of the template, the grid pattern is clearly evident as bright anisotropic (edge-on) regions at former Cu interface and dark isotropic (face-on) regions at the former graphite interface. It is anticipated that a variety of new carbon forms with programmed graphene layer orientations can be synthesized by this principle. Reprinted with permission from [81], R. H. Hurt et al., *Chem. Mater.* 14, 4558 (2002). © 2002, American Chemical Society.

idea is extended to three-dimensional templating in confined nanospaces, the surface-induced order can propagate fully across the nanoform to produce wholly new carbon forms. A first example of this approach was carbon nanofibers (see Fig. 21) produced by capillary impregnation of mesophase pitch (AR) into nanochannel alumina templates [193]. Except for the liquid crystalline precursor, this method is similar to previous templating methods used to create conducting polymers [213, 239, 240], mesogenic polymers [241, 242], metals [243], and semiconductors [244].

The remarkable feature of these nanofibers is the “orthogonal” arrangement of the graphene layers. The high-resolution TEM fringe image in Figure 21 shows the layers to lie perpendicular to the fiber axis with a statistical meandering about the mean orientational vector, which is characteristic of a solidified discotic nematic phase. Digital processing of image using the technique of Shim et al. [245] yields an estimated two-dimensional order parameter of 0.88, which translates to a three-dimensional order parameter of about 0.45 for a HRTEM Bragg tolerance of 10° using the projection mapping function derived in the same study [245]. The very edge of the nanofiber appears to show an atomic-scale parallel film of one or two layers, which is an adsorbed contaminant (commonly seen on surface at atomic resolution) or the result of layer rearrangement or deposition during carbonization or etching. The orthogonal arrangement is significant as it is the opposite of normal flow-induced order. Both elongational flow (into the channels) and shear stress (across the diameter) during in-channel flow align the discotic molecular planes parallel to the channel long axis [246], which is the same essential phenomenon that gives rise to axial alignment in conventional (supermicron) mesophase-pitch-based fibers.

The origin of the observed orthogonal structure likely lies in static equilibrium states for confined liquid crystals. Figure 15 previously illustrated the possible configurations for discotics, which depend on the delicate interplay of



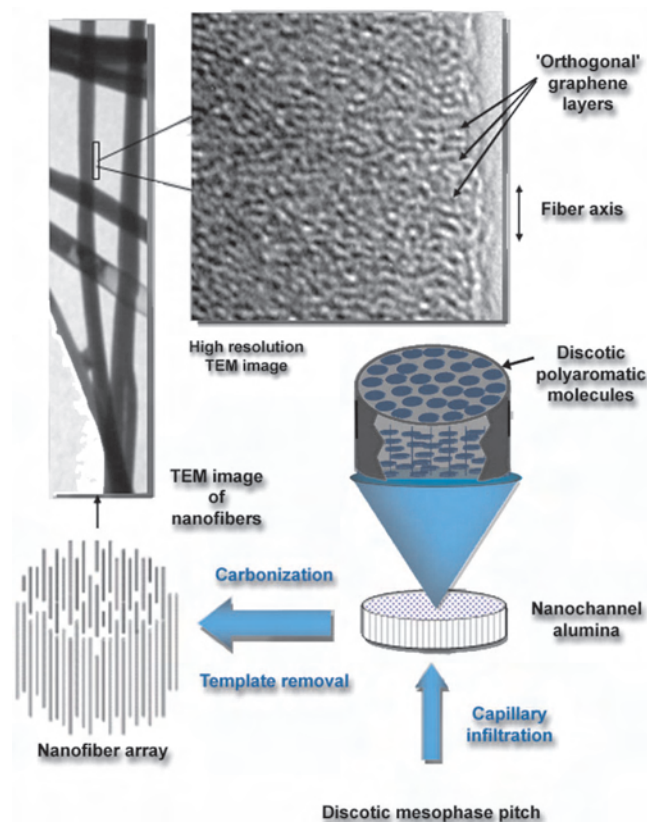


**Figure 21.** Example of nanomaterial synthesis using confined liquid crystals. Here is the synthesis route for “orthogonal” carbon nanofibers from mesophase pitch confined in commercial nanochannel alumina templates. Reprinted with permission from [141], K. Jian et al., *Adv. Mater.* (2003). © 2003, Wiley-VCH.

surface anchoring and energies and the various modes of elastic strain energy (splay, bend, twist). For edge-on anchoring (the known favored state on alumina), the concentric configuration exhibits a line disclination along the cylindrical axis; planar-bipolar exhibits two line defects, and the homogeneous configuration is defect free. There also exists a twisted-concentric structure [247], which is improbable in discotic systems. The observed orthogonal structure corresponds to the “homogeneous” configuration in Figure 15, which is the lowest free energy state available, since it is the only configuration that preserves the favored edge-on anchoring and has no elastic strain or defects.

The homogeneous “orthogonal” configuration of our nanofibers distinguishes itself from the graphene layer configuration in classical nanotubes (concentric), in vapor-deposited alumina templated nanotubes (concentric with imperfect order [214]), and in conventional isotropic carbon fibers (random orientation) or conventional high-modulus fibers based on pitch or PAN (axial alignment with a variety of transverse textures [21, 80]). The most similar documented structures are the herringbone and platelet fibers produced by catalytic decomposition of vapor-phase hydrocarbons under certain conditions [210], but these forms do not exhibit mesophasic order, that is, small graphene layers with meandering, long-range orientational order. It is also noteworthy that continuous, dense fibers can

be produced here without the usual bubble formation and foaming, which would cause expulsion of a majority of the liquid from the channels. Most mesophase-derived materials require an extra synthesis step: low-temperature ( $\sim 200^\circ\text{C}$ ) oxidative stabilization to thermoset their molecular structure and physical form prior to carbonization to prevent resoftening and swelling. The fact that the current nanofibers can be produced by a one-step process (omitting oxidative stabilization) is likely due to the suppression of bubble nucleation by nanoconfinement or to early formation of carbonized caps that prevent swelling.

There are a variety of potential applications for such nanofibers as electrodes, catalyst supports, sorbents, thermal protection materials, and chemical sensor components, driven by their high density of surface active sites, easy access to interlayer spaces, and low axial conductivities. Further, they can be produced from a low-cost precursor (mesophase pitch rather than synthetic discotics), using simple one-step processing, and in the form of dispersed fibers, large arrays, or alumina-matrix composites. As yet these application possibilities remain unexplored.

### 7.2.3. Nanophase Mesocarbon

A similar carbon nanomaterial with all-edge surfaces can be produced using porous inorganic templates [193]. Figure 22 shows a porous carbon material with nanometric grains ( $\sim 100\text{ nm}$ ) created by capillary infiltration of AR mesophase pitch into controlled pore glass. After carbonization at  $700^\circ\text{C}$  and template removal with NaOH, the resulting carbon has a high concentration of edge-sites on the internal surfaces that were originally in contact with the glass

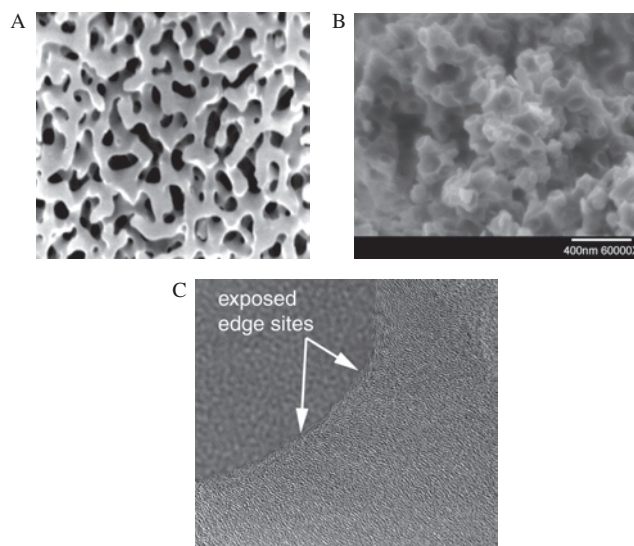


**Figure 22.** “Nanophase mesocarbon,” a monolithic porous carbon with nanometric internal grains having a high concentration of active graphitic edge sites. Material produced by capillary infiltration of mesophase pitch into nanoporous glass templates followed by heating and NaOH etching. (A) glass template, SEM; (B) nanophase mesocarbon, SEM; (C) nanophase mesocarbon, high-resolution TEM showing internal crystal structure, in which most graphene layers lie perpendicular to the concave inner surfaces that mark the original glass/pitch interface.



template (see high-resolution TEM in Fig. 22). This crystal structure is expected based on the known edge-on (planar) anchoring on glass (Table 1). This configuration of graphene layers is in contrast to that produced by plasma-enhanced CVD of carbon on silica opal templates [248] and most other known carbon forms, which are dominated by “closed” structures in which the accessible surfaces are rich in graphene basal planes.

This new nanostructured carbon form can be made as coarse particles similar in size to the original porous glass template particles (0.3  $\mu\text{m}$ ), or as a type of nanophase particulate carbon after grinding to liberate the 100-nm grains [193]. The classical carbon nanoparticulate is carbon black or soot, a high-temperature form that consists of partially fused 10–100 nm diameter primary particles that consist of spherically concentric graphene layers (onion structure). The new material with edge-rich outer surfaces has a similar graphene layer arrangement to mesocarbon microbeads (see Section 6) but has overall nanometric dimensions. For this reason the material might be referred to as “nanophase mesocarbon,” or to pursue the analogy with classical carbon particulate, “inverse soot.”

#### 7.2.4. Nanocarbons from Isotropic Phases

Additional materials can be made by varying the discotic precursor and/or introducing solvents. Infiltrating a dilute solution of polyaromatics into nanochannels yields tubes whose inner hollow space is created by the volume loss associated with solvent evaporation. As an example, Figure 23 shows carbon nanotubes made by capillary uptake of a pyridine extract of AR-mesophase pitch into nanochannel alumina, followed by carbonization and template removal. The heating and etching procedures are the same as for orthogonal nanofibers.

In summary, the infiltration of discotic precursors into nanometric templates is a new and powerful synthesis route for a variety of novel carbon materials. In the case of liquid crystalline discotics, the graphene layer arrangements can be systematically engineered by intelligent template selection using anchoring rules derived from simple experiments on planar substrates. Table 1 in this chapter can serve as a guide for selecting templates to achieve the desired anchoring state. Discotic nanocarbon materials have just been introduced, and this topic is fertile ground for research and development in the coming years.

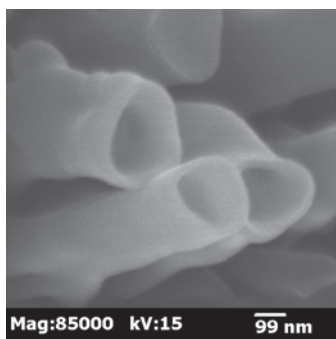


**Figure 23.** Carbon nanotubes made by capillary infiltration of solvated discotic mesophase pitch into nanochannel alumina.

## GLOSSARY

**Discotic** Disklike molecules, as opposed to the more common rodlike or “calamitic” liquid crystalline systems.

**Graphene layers** Carbon sheets of single-atom thickness that are the building block of many carbon and nanocarbon materials.

**Liquid crystal** A fluid phase with one or more degrees of orientational molecular order.

**Lyotropic** A liquid crystal that undergoes order/disorder phase transitions with change in concentration in solution.

**Mesophase** A liquid crystalline phase (“meso-” signifying intermediate between the liquid and solid phases).

**$\pi$  bonding** Molecular interactions involving  $\pi$  electron orbitals such as those found in planar aromatic organic molecules.

**Pitch** Multicomponent mixtures of high molecular weight organic compounds formed by thermal or catalytic polymerization of low molecular weight precursors. Pitches are solid at ambient temperature and soften upon heating to viscous liquid or liquid crystalline phases.

**Surface anchoring** The phenomenon in liquid crystalline phases of preferred molecular orientation at a foreign surface or phase boundary.

**Thermotropic** A liquid crystal that undergoes order/disorder phase transitions with change in temperature.

## REFERENCES

1. J. D. Brooks and G. H. Taylor, *Nature* 206, 697 (1965).
2. S. Zimmerman, F. Zeng, D. Reichert, and S. Kolotuchin, *Science* 271, 1095 (1996).
3. C. Hunter, M. Meah, and J. Sanders, *Am. Chem. Soc.* 112, 5773 (1990).
4. M. Dimashki, L. H. Lim, R. M. Harrison, and S. Harrad, *Environ. Sci. Tech.* 35, 2264 (2001).
5. K. M. Arzayus, R. M. Dickhut, and E. A. Canuel, *Environ. Sci. Tech.* 35, 2178 (2001).
6. R. A. Perlow and S. Brooyde, *J. Molec. Biol.* 309, 519 (2001).
7. C. H. Lin, X. W. Huang, A. Kolbanovskii, B. E. Hingerty, S. Amin, S. Brooyde, N. E. Gecintov, and D. J. Patel, *J. Molec. Biol.* 306, 1059 (2001).
8. S. W. Burchiel and M. I. Luster, *Clin. Immunol.* 98, 2 (2001).
9. F. Salama, *J. Molec. Struct.* 563, 19 (2001).
10. K. Qian, K. E. Edwards, and M. Siskin, *Energy and Fuels* 15, 949 (2001).
11. S. P. Brown, I. Schnell, B. Didrich, K. Müllen, and H. W. Spiess, *J. Am. Chem. Soc.* 121, 6712 (1999).
12. T. S. Perova, J. K. Vij, and A. Kocot, *Europhys. Lett.* 44, 198 (1998).
13. N. H. Tinh, C. Destrade, and H. Gasparoux, *Phys. Lett.* 72A, 251 (1979).
14. B. Orgasinska, T. S. Perova, K. Merkel, A. Kocot, and J. K. Vij, *Mater. Sci. Eng.* C8-9, 283 (1999).
15. F. J. Meyer zu Heringdorf, M. C. Reuter, and R. M. Tromp, *Nature* 412, 517 (2001).
16. A. Schmitz-Hübsch, F. Sellam, R. Staub, M. Rörker, T. Fritz, C. Kübel, K. Müllen, and K. Leo, *Surf. Sci.* 445, 358 (2000).
17. C. D. England, G. E. Collins, T. J. Schuerlein, and N. R. Armstrong, *Langmuir* 10, 2748 (1994).
18. M. Keil, P. Samoir, D. A. dos Santos, T. Kugler, S. Stafström, J. D. Brand, K. Müllen, J. L. Bredas, J. P. Rabe, and W. R. Salaneck, *J. Phys. Chem. B.* 104, 3967 (2000).
19. D. E. Hooks, T. Fritz, and M. D. Ward, *Adv. Mater.* 13, 227 (2001).

20. I. Mochida, K. Shimizu, Y. Korai, H. Otsuka, Y. Sakai, and S. Fujiyama, *Carbon* 28, 311 (1990).
21. J. J. McHugh and D. D. Edie, *Carbon* 34, 1315 (1996).
22. C. A. Hunter and J. K. M. Sanders, *J. Am. Chem. Soc.* 112, 5525 (1990).
23. R. J. Chen, Y. Zhang, D. Wang, and H. Dai, *J. Am. Chem. Soc.* 123, 3838 (2001).
24. M. Müller, C. Kübel, and K. Müllen, *Chem.-Eur. J.* 4, 2099 (1998).
25. S. Brown, I. Schnell, and J. D. Brand, K. Müllen, and H. W. Spiess, *J. Am. Chem. Soc.* 121, 6712 (1999).
26. W. Boenigk, M. Haenel, and M. Zander, *Fuel* 74, 305 (1995).
27. V. Iyer, K. Yoshimura, and V. Enkelmann, *Angew. Chem. Int. Ed.* 37, 2696 (1998).
28. R. H. Hurt and Z.-Y. Chen, *Phys. Today* 39, March (2000).
29. F. M. Dauche, G. Bolanos, A. Blasig, and M. C. Thies, *Carbon* 36, 953 (1998).
30. I. Mochida, Y. Korai, C. H. Ku, F. Watanabe, and Y. Sakai, *Carbon* 38, 305 (2000).
31. M. Dumont, G. Chollon, M. A. Dourges, R. Pailler, X. Bourrat, R. Naslain, J. L. Bruneel, and M. Couzi, *Carbon* 40, 1475 (2002).
32. K. Murakami, M. Okomura, and Y. Masaharu, *Carbon* 34, 187 (1996).
33. M. Zander, *Recent advantages in pitch characterization*, April (1987).
34. R. Greinke and L. Singer, *Carbon* 26, 665 (1988).
35. K. Lafdi, S. Bonnamy, and A. Oberlin, *Carbon* 29, 831 (1991).
36. K. Azami and S. Yamamoto, *Carbon* 32, 947 (1994).
37. M. Bates and G. Luckhurst, *J. Chem. Phys.* 104, 6696 (1996).
38. I. Lewis, *Carbon* 18, 191 (1980).
39. J. Venner and R. Diefendorf, *Am. Chem. Soc.* 260, 13 (1984).
40. B. Rand, *Fuel* 66, 1491 (1987).
41. H. Tushima, I. Mochida, Y. Korai, and T. Hino, *Carbon* 30, 773 (1992).
42. P.-G. de Gennes and J. Prost, "The Physics of Liquid Crystals." Clarendon, Oxford, UK, 1993.
43. H. Finkelmann, *Liquid Cryst.* 29, 559 (2002).
44. A. Attias, C. Cavalli, B. Donnio, D. Guillon, P. Hapiot, and J. Malthete, *Chem. Mater.* 14, 375 (2002).
45. S. Höger, V. Enkelmann, K. Bonrad, and C. Tschierske, *Ang. Chem. Int. Ed.* 39, 2268 (2000).
46. S. Chandrasekov, B. Schdushira, and K. Suresh, *Pramana* 9, 471 (1977).
47. F. Renitzer, *Monat. Chem.* 9, 421 (1888).
48. O. Lehmann, *Z. Phys. Chem.* 4, 462 (1889).
49. S. Chandrasekhar, "Liquid Crystals," Chap. 6. Cambridge University Press, 1992.
50. H. S. Kitzerow, "Chirality in Liquid Crystals."
51. W. Maier and A. Saupe, *Z. Naturforsch.* 15, 287 (1960).
52. W. L. McMillan, *Phys. Rev. A* 4, 1238 (1971).
53. J. G. Kirkwood and E. Monroe, *J. Chem. Phys.* 9, 514 (1941).
54. M. E. Escuti and G. P. Crawford, in "Encyclopedia of Imaging Science and Technology" (J. P. Hornak, Ed.) Volume 2, pp. 995-969. Wiley-Interscience, New York, 2002.
55. S. Chandrasekhar, B. K. Sadashiva, and K. A. Suresh, *Pramana* 9, 471 (1977).
56. N. H. Tinh, H. Gasparoux, and C. Destrade, *Mol. Cryst. Liq. Cryst.* 68, 101 (1981).
57. E. I. Kats, *Sov. Phys. JETP* 48, 916 (1978).
58. G. E. Feldkamp, M. A. Handschy, and N. A. Clark, *Phys. Lett. A* 359 (1981).
59. S. Chandrasekhar, K. L. Sarithramina, and N. V. Madhusudana, *ACS Symposium on Ordufluids* 4 (1982).
60. O. Herrmann-Schoenherr, J. H. Wendorf, and H. Ringsdorf, *Makromol. Chem. Rapid Commun.* 7, 97 (1986).
61. O. Herrmann-Schoenherr, J. H. Wendorf, H. Ringsdorf, and P. Tschirner, *Makromol. Chem. Rapid Commun.* 791 (1986).
62. M. Dekker, *Chem. Phys. Carbon* 15, 230.
63. H. Honda, *Carbon* 26, 139 (1988).
64. J. White, *Progr. Solid State Chem.* 9, 59 (1974).
65. R. Diefendorf, *Am. Chem. Soc.* 12, 210 (1984).
66. J. Brooks and G. Taylor, *Chem. Phys. Carbon* 4 (1968).
67. S. Otani, *Mol. Cryst. Liq. Cryst.* 63, 249 (1981).
68. J. Dubois, C. Agache, and J. Hite, *Metallography* 3, 337 (1970).
69. I. C. Lewis, *Carbon* 20, 519 (1982).
70. I. C. Lewis, *Carbon* 18, 191 (1980).
71. M. Shishido, H. Inomata, K. Arai, and S. Saito, *Carbon*, 35, 797 (1997).
72. R. H. Hurt and Y. Hu, *Carbon* 37, 281 (1991).
73. Y. Hu and R. H. Hurt, *Carbon* 39, 887 (2001).
74. R. L. Humphries and G. R. Luckhurst, *Proc. R. Soc. Lond. A* 352, 41 (1976).
75. I. Mochida and Y. Korai, *J. Fuel Soc. Jpn.* 64, 796 (1965).
76. R. A. Greinke and L. S. Singer, *Carbon* 26, 665 (1988).
77. J. E. Zimmer and R. L. Weitz, *Carbon* 26, 579 (1988).
78. T. Imamura, M. Nakamizo, and H. Honda, *Carbon* 16, 487 (1978).
79. D. D. Edie, *Carbon* 36, 345 (1998).
80. L. Wang and A. D. Rey, *Liq. Cryst.* 23, 93 (1997).
81. R. H. Hurt, G. Krammer, G. P. Crawford, K. Jian, and C. Rulison, *Chem. Mater.* 14, 4558 (2002).
82. R. T. Lewis and R. Bacon, "19th Conference on Carbon," 1989.
83. F. C. Frank, *Discuss. Faraday Soc.* 25, 19 (1958).
84. G. Vertogen and W. H. de Jeu, "Thermotropic Liquid Crystals, Fundamentals." Springer, Berlin, 1988.
85. S. Kralj and S. Zumer, *Phys. Rev. A* 45, 2461 (1992).
86. P. G. de Gennes and J. Prost, "The Physics of Liquid Crystals." Oxford Scientific, Oxford, UK, 1993.
87. I. Lelidis and G. Durand, *Phys. Rev. E* 48, 3822 (1993).
88. S. Kralj and S. Zumer, *Phys. Rev. A* 45, 2461 (1992).
89. A. Saupe, *J. Chem. Phys.* 75, 5118 (1981).
90. J. Nehring and A. Saupe, *J. Chem. Phys.* 54, 337 (1991).
91. O. Lehmann, "Flussige Kristalle." Leipzig, 1904.
92. G. Fridel, *Ann. Phys.* 18, 273 (1992).
93. S. Chandrasekhar, "Liquid Crystals." Cambridge Univ. Press, Cambridge, 1977.
94. M. Kleman, "Points, Lines, and Walls: In Liquid Crystals, Magnetic Systems, Various Ordered Media." Wiley, New York, 1983.
95. S. Chandrasekhar and G. S. Ranganath, *Adv. Phys.* 35, 507 (1986).
96. G. Toulouse and M. Kleman, *J. Phys. Lett. (Paris)* 37, L149 (1976).
97. G. E. Volovik and V. P. Mineyev, *Zh. Exp. Phys. Teor. Fiz.* 72, 2256 (1977).
98. N. D. Mermin, *Rev. Mod. Phys.* 51C, 591 (1979).
99. C. E. Williams, P. I. Pieranski, and P. E. Cladis, *Phys. Rev. Lett.* 29, 90 (1972); C. E. Williams, P. E. Cladis, and M. Kleman, *Mol. Cryst. Liq. Cryst.* 21, 355 (1973).
100. P. E. Cladis and M. Kleman, *J. Phys. (Paris)* 33, 591 (1972).
101. R. B. Meyer, *Philos. Mag.* 27, 405 (1973).
102. A. Saupe, *Mol. Cryst. Liq. Cryst.* 21, 211 (1973).
103. M. Kleman, *Rep. Prog. Phys.* 52, 555 (1989).
104. N. D. Mermin and T. T. Ho, *Phys. Rev. Lett.* 36, 594 (1976).
105. A. Pargellis, N. Turok, and B. Yurke, *Phys. Rev. Lett.* 67, 1570 (1991).
106. M. B. Feller, W. Chen, and Y. R. Shen, *Phys. Rev. A* 43, 6778 (1991).
107. T. J. Sluckin and A. Pioniewierski, *Phys. Rev. Lett.* 55, 2907 (1985).
108. B. Tjijto-Margo and D. E. Sullivan, *J. Chem. Phys.* 88, 6620 (1988).
109. P. I. Teixeira and M. M. Telo da Gamma, *J. Phys. Condens. Matter* 3, 111 (1991).
110. C. Chiccoli, P. Pasini, F. Semeria, and C. Zannoni, *Phys. Lett. A* 150, 311 (1990); 176, 428 (1993).
111. P. I. C. Teixeira and T. J. Sluckin, *J. Chem. Phys.* 97, 1510 (1992).
112. B. Jerome, *Rep. Prog. Phys.* 54, 391 (1991).
113. K. Flatischler, L. Komitov, S. T. Lagerwall, B. Stebler, and A. Strigazzi, *Mol. Cryst. Liq. Cryst.* 198, 119 (1991).

114. J. Bechhoefer, J. L. Duvail, L. Masson, B. Jerome, R. M. Hornreich, and P. Pieranski, *Phys. Rev. Lett.* 64, 1911 (1990).
115. G. Porte, *J. Phys. (Paris)* 37, 1245 (1976).
116. J. S. Patel and H. Yokoyama, *Nature* 362, 525 (1993).
117. G. Barbero, Z. Gabbasova, and M. A. Osipov, *J. Phys. II* 1, 691 (1991).
118. P. I. C. Teixeira, T. J. Sluckin, and D. E. Sullivan, *Liq. Cryst.* 14, 1243 (1993).
119. J. H. Erdmann, S. Zumer, and J. W. Doane, *Phys. Rev. Lett.* 64, 1907 (1990).
120. V. G. Bondar, O. D. Lavrentovich, and V. M. Pergamenschik, *Sov. Phys. JETP* 74, 60 (1992).
121. E. Dzyaloshinskii, *Zh. Eksp. Teor. Fiz.* 31, 773 (1970).
122. G. P. Crawford, D. W. Allender, and J. W. Doane, *Phys. Rev. A* 45, 8693 (1992); S. Kralj and S. Zurner, *Phys. Rev. E* 51, 366 (1995).
123. B. J. Liang and S. H. Chen, *Jpn. J. Appl. Phys.* 30, L1955 (1991).
124. G. P. Crawford, D. W. Allender, J. W. Doane, M. Vilfan, and I. Vilfan, *Phys. Rev. A* 44, 2570 (1991).
125. I. Vilfan, M. Vilfan, and S. Zumer, *Phys. Rev. A* 43, 6875 (1991).
126. R. J. Ondris-Crawford, G. P. Crawford, S. Zumer, and J. W. Doane, *Phys. Rev. Lett.* 70, 194 (1993).
127. L. T. Creagh and A. R. Kmetz, *Mol. Cryst. Liq. Cryst.* 24, 59 (1973).
128. A. A. Sonin, "The Surface Physics of Liquid Crystals." Gordon and Breach, Luxembourg, 1995.
129. C. Vauchier, A. Zann, P. L. Barny, J. C. Dubois, and J. Billard, *Mol. Cryst. Liq. Cryst.* 66, 103 (1981).
130. T. Uchida and H. Seki, in "Liquid Crystals Applications and Uses" (B. Bahadur, Ed.), Vol. 3. World Scientific, Singapore, 1992.
131. P. Hubert and Y. Galerne, *Appl. Phys. Lett.* 71, 1050 (1997).
132. L. Corvazier and Y. Zhao, *Liq. Cryst.* 27, 137 (2000).
133. A. Bayer, J. Kopitzke, F. Noll, A. Seifert, and J. Wendorff, *Macromolecules* 34, 3600 (2001).
134. S. Furumi, D. Janietz, M. Kidowaki, M. Nakagawa, S. Morino, J. Stumpe, and K. Ichimura, *Chem. Mater.* 13, 1434 (2001).
135. K. Jian, H.-S. Shim, D. Tuhus-Dubrov, C. Woodward, S. Bernstein, M. Pfeffer, D. Steingart, S. Sachsmann, T. Gournay, G. P. Crawford, and R. H. Hurt, submitted to *Carbon*.
136. J. L. White, M. Buecheler, and C. B. Ng, *Carbon* 20, 536 (1982).
137. L. Singer, *Chem. Soc.* 79, 176 (1985).
138. P. Delhaes, J. Rouillon, G. Fug, and L. Singer, *Carbon* 17, 435 (1979).
139. J. E. Demuth and D. E. Eastman, *Phys. Rev. Lett.* 32, 1123 (1974).
140. J. B. Benziger, *Successful Design of Catalysis* 81 (1988).
141. K. Jian, H.-S. Shim, A. Shwartzmann, G. P. Crawford, and R. H. Hurt, *Adv. Mater.* 15, 164 (2003).
142. J. Zimmer and J. White, *Adv. Liq. Cryst.* 5, 157 (1982).
143. H. Ringsdorf, R. Wuestefeld, E. Zesta, M. Ebert, and J. H. Wendorff, *Angew. Chem. Int. Ed. Engl.* 28, A14 (1989).
144. L. Ignatov, P. Lazarev, and N. Ovchinnikova, *Proc. Soc. Inform. Display* 30, 834 (2000).
145. C. Cobb, L. Ignatov, P. Lazarev, V. Nazarov, and M. Paukshto, *Proc. Asia Soc. Inform. Displays* 2000, 475 (2000).
146. P. Yeh and M. Paukshto, *Molec. Mater.* 14, 1 (2000).
147. P. Lazarev and M. Paukshto, *J. Soc. Inform. Displays* 9, 101 (2001).
148. Y. Bobrov, C. Cobb, P. Lazarev, P. Bos, D. Bryant, and H. Wondaly, *Proc. Soc. Inform. Displays* 31, 1102 (2000).
149. M. Paukshto and L. Silverstein, *Proc. Soc. Inform. Displays* 32, 902 (2001).
150. M. Paukshto and L. Silverstein, *Proc. Soc. Inform. Displays* 33, 722 (2002).
151. P. Lazarev, K. Lokshin, and V. Nazarov, *Molec. Mater.* 14, 303 (2001).
152. T. Fiske, L. Ignatov, P. Lazarev, V. Nazarov, and M. Paukshto, *Proc. Soc. Inform. Displays* 33, 8666 (2002).
153. S. Remizov, A. Krivoshchepov, V. Nazarov, and A. Grodsky, *Molec. Mater.* 14, 179 (2002).
154. T. Sergan, M. Sonpatki, J. Kelly, and L. C. Chien, *Proc. Soc. Inform. Displays* 31, 1091 (2000).
155. H. Mori, Y. Itoh, Y. Nishiura, T. Nakamura, and Y. Shinagawa, *Jpn. J. Appl. Phys.* 36, 143 (1997).
156. T. Higano, T. Ishinabe, T. Miyashita, and T. Uchida, *Proc. Asia Soc. Inform. Displays* 7, 171 (2000).
157. H. Mori and P. J. Bos, *Jpn. J. Appl. Phys.* 38, 2837 (1999).
158. T. Christ, B. Glusen, A. Greiner, A. Kettner, R. Sander, V. Stumpflen, V. Tskruk, and J. H. Wendorff, *Adv. Mater.* 9, 48 (1987).
159. I. Stapff, V. Stumpflen, J. H. Wendorff, D. A. Spohn, and D. Mobius, *Liq. Cryst.* 23, 613 (1997).
160. G. Lusser and J. H. Wendorff, *Polym. Adv. Technol.* 9, 443 (1998).
161. A. Bacher, I. Bleyl, C. H. Erdelen, D. Harper, W. Paulus, and H. W. Schimdt, *Adv. Mater.* 9, 1031 (1997).
162. S. Benning, H. S. Kilzerw, H. Bock, and M. F. Archard, *Liq. Cryst.* 27, 901 (2000).
163. D. Adam, P. Schuhmacher, J. Simmer, L. Haussling, K. Siemensmeyer, K. H. Eitzbach, H. Ringsdorf, and P. Haaren, *Nature* 371, 141 (1994).
164. R. Stolarski and K. J. Fiksinski, *Dyes Pigments* 24, 295 (1994).
165. L. Schmidt-Mende, X. Fechtenkötter, K. Müller, E. Moons, R. H. Friend, and J. D. Mackenzie, *Science* 293, 1119 (2001).
166. I. A. Howard, "Semiconductors and Semimetals" (E. Conwell, Ed.), Vol. 27. Academic Press, London, 1988.
167. H. Schultz, H. Lehmann, M. Rein, and M. Hanack, *Structure and Bonding* 74, 41 (1991); T. J. Marks, *Angew. Chem. Int. Ed. Engl.* 29, 857 (1990); A. M. Giroudgodquin and P. M. Mailtli, *ibid.* 30, 375 (1991).
168. J. Simon and C. Sirlin, *Pure Appl. Chem.* 61, 1625 (1989); C. Piechocki, J. Simon, A. Skoulios, D. Guillon, and P. Weeder, *J. Am. Chem. Soc.* 104, 5245 (1982).
169. D. A. Gregg, M. A. Fox, and A. J. Bard, *J. Am. Chem. Soc.* 111, 3024 (1989); P. G. Schouten, J. M. Warman, M. P. de Haas, M. A. Fox, and H.-L. Pan, *Nature* 353, 736 (1991); S. Gaspard, P. Maillard, and J. Dillard, *Mol. Cryst. Liq. Cryst.* 123, 369 (1985).
170. J. F. VanDer Pol, E. Neelman, J. W. Zwiker, R. J. M. Nolte, E. W. Drenth, J. Aerts, R. Visser, and S. J. Picken, *Liq. Cryst.* 6, 577 (1989).
171. L. Y. Chiang, J. P. Stokes, C. R. Safinya, and A. N. Dloch, *Mol. Cryst. Liq. Crystals* 125, 279 (1985).
172. N. Boden, R. J. Rushby, and J. Clements, *J. Mater. Sci.* 5, 83 (1994).
173. B. Rand, in "Handbook of Composites" (Watt and Perov, Eds.), Vol. 1, p. 495. North-Holland, Amsterdam, 1985.
174. L. Wang and A. Rey, *Liq. Cryst.* 23, 93 (1997).
175. A. Rey, *Phys. Rev. A* 51, 6278 (1995).
176. A. S. K. Ho and A. D. Rey, *Rheol. Acta* 30, 77 (1991).
177. B. Rand, C. Blanco, S. Lu, H. Daniels, and R. Brydson, Structure and Properties of Highly Oriented Mesophase Graphite Tapes of High Conductivity, Univ. of Leeds.
178. S.-H. Hong, Y. Korai, and I. Mochida, *Carbon* 38, 805 (2000).
179. S.-H. Hong, Y. Korai, and I. Mochida, *Carbon* 36, 79 (1998).
180. S.-H. Hong, Y. Korai, I. Mochida, K. Yokogawa, S. Fukuyama, and M. Yoshimura, *Carbon* 34, 83 (1996).
181. A. Barnes, F. Dauche, N. Gallego, C. Fain, and M. Thies, *Carbon* 36, 855 (1998).
182. D. Edie, K. Robinson, S. Jones, and C. Fain, *Carbon* 32, 1045 (1994).
183. J. Li, C. Papadopoulos, and J. M. Xu, *Nature* 402, 253 (1999).
184. Y. Chang, H. Sohn, C. Ku, Y. Wang, Y. Korai, and I. Mochida, *Carbon* 37, 1285 (1999).
185. D. Auguie, M. Oberlin, A. Oberlin, and P. Hyvernats, *Carbon* 18, 337 (1980).
186. D. Auguie, M. Oberlin, and A. Oberlin, *Carbon* 18, 337 (1980).
187. A. K. Myers and J. B. Benziger, *Langmuir* 3, 414 (1987); E. Dubois-Violette and O. Parodi, *J. Phys. C* 4, 57 (1969).

188. S. Kralj, S. Zumer, and D. W. Allender, *Phys. Rev. A* 43, 2943 (1991).
189. S. Kralj, S. Zumer, and J. W. Doane, *Phys. Rev.* 34, 3373 (1986).
190. S. Zumer and P. Drzaic, *Mol. Cryst. Liq. Cryst.* 154, 289 (1988).
191. L. Wang and A. D. Rey, *Model. Simul. Mater. Sci. Eng.* 5, 67 (1997).
192. A. Oberlin, S. Bonnamy, and P. G. Rouxhet, in "Chemistry and Physics of Carbon" (P. Thrower and L. R. Radovic, Eds.), Vol. 26. Marcel Dekker, New York, 1999.
193. N. Yang, K. Jian, G. Crawford, and R. Hurt, *J. Nanoscience Nanotechnology*, in press.
194. K. Kinoshita and K. Zaghbi, *J. Power Sources* 110, 416 (2002).
195. M. Martinez-Escandell, P. Carreira, and M. Rodriguez-Valero, *Carbon* 37, 1662 (1999).
196. D. Gaies and K. Faber, *Carbon* 40, 1137 (2002).
197. J. Klett, R. Hardy, and E. Romine, *Carbon* 38, 953 (2000).
198. C. Liang, G. Sha, and S. Guo, *Carbon* 37, 1391 (1999).
199. W. Lu and D. Chung, *Carbon* 40, 447 (2002).
200. E. Daguerre, A. Guillot, and X. Py, *Carbon* 38, 59 (2000).
201. H. W. Kroto, J. R. Heath, S. C. O'Brian, R. F. Curl, and R. E. Smalley, *Nature* 318, 162 (1985).
202. D. Ugarte, *Nature* 359, 707 (1992).
203. N. Sano, H. Wang, M. Chhowalla, I. Alexandrou, and G. A. J. Amaratunga, *Nature* 414, 506 (2001).
204. D. S. Bethune, C. H. Kiang, M. S. de Vries, G. Gormn, R. Savoy, J. Vasquex, and R. Beyers, *Nature* 363, 605 (1993).
205. C. Papadopoulos, A. Rikitin, J. Li, A. S. Vedenev, and J. M. Xu, *Phys. Rev. Lett.* 85, 3476 (2000).
206. D. Bernaerts, X. B. Zhang, X. F. Zhang, S. Amelinckx, G. Van Tendeloo, J. Van Landuyt, V. Ivanov, and J. B. Nagy, *Philos. Mag. A* 71, 605 (1995).
207. R. Bacon, *J. Appl. Phys.* 31, 283 (1960).
208. N. R. Gall, E. V. Rutkov, and A. Y. Tontegode, *Int. J. Mod. Phys. B* 11, 1865 (1997).
209. J. Li, C. Papadopoulos and J. M. Xu, *Appl. Phys. Lett.* 75, 367 (1999).
210. N. M. Rodriguez, *J. Mater. Res.* 8, 3233 (1993).
211. N. M. Rodriguez, A. Chambers, and R. T. K. Baker, *Langmuir* 11, 3862 (1995).
212. C. R. Martin, *Science* 266, 1961 (1994).
213. J. C. Hulthen, H. X. Chen, C. K. Chambliss, and C. R. Martin, *Nanostruct. Mater.* 9, 133 (1997).
214. T. Kyotani, L. Tsai, and A. Tomita, *Chem. Mater.* 8, 2109 (1996).
215. C. H. Kiang, M. S. Dresselhaus, R. Beyers, and D. S. Bethune, *Chem. Phys. Lett.* 259, 41 (1996).
216. A. Chambers, C. Park, R. T. K. Baker, and N. M. Rodriguez, *Phys. Chem. B* 102, 4253 (1998).
217. M. Endo, *Carbon* September (2002).
218. P. Pinheiro, M. Schouler, P. Gadelle, M. Mermoux, and E. Dooryhees, *Carbon* 38, 1469 (2000).
219. J. Librea and Y. Gogotsi, *Carbon* 39, 1307 (2001).
220. R. V. Parthasarathy, K. L. N. Phani, and C. R. Martin, *Adv. Mater.* 7, 869 (1995).
221. T. Kyotani, B. K. Pradhan, and A. Tomita, *Bull. Chem. Soc. Jpn.* 72, 1957 (1999).
222. T. Kyotani, T. Mori, and A. Tomita, *Chem. Mater.* 6, 2138 (1994).
223. S. Han, K. Sohn, and T. Hyeon, *Chem. Mater.* 12, 2227 (2000).
224. J. Lee, S. Yoon, T. Hyeon, S. M. Oh, and K. B. Kim, *Chem. Commun.* 2177 (1999).
225. T. Kyotani, T. Nagai, S. Inoue, and A. Tomita, *Chem. Mater.* 9, 609 (1997).
226. Gilbert, J. H. Knox, and B. Kaur, *Chromatographia* 16, 138 (1982).
227. J. H. Knox, B. Kaur, and G. R. Millward, *J. Chromatogr.* 3, 352 (1986).
228. D. Kawashima, T. Aihara, Y. Kobayashi, T. Kyotani, and A. Tomita, *Chem. Mater.* 12, 3397 (2000).
229. T. Kyotani, L. Tsai, and A. Tomita, *Chem. Commun.* 701 (1997).
230. T. Kyotani, B. K. Pradhan, and A. Tomita, *Bull. Chem. Soc. Jpn.* 72, 1957 (1999).
231. B. K. Pradhan, T. Toba, T. Kyotani, and A. Tomita, *Chem. Mater.* 10, 2510 (1998).
232. R. Ryoo, S. H. Joo, and S. Jun, *Phys. Chem. B.* 103, 37 (1999).
233. S. Han and T. Hyeon, *Carbon* 37, 1645 (1999).
234. A. A. Zakhidov, R. H. Baughman, Z. Iqbal, C. Cui, I. Khayrullin, S. O. Dantas, J. Marti, and V. G. Ralchenko, *Science* 282, 897 (1998).
235. A. A. Zakhidov, R. H. Baughman, Z. Iqbal, C. Cui, I. Khayrullin, S. O. Dantas, J. Marti, and V. G. Ralchenko, *Science* 282, 897 (1998).
236. K. Lau and D. Hui, *Carbon* 40, 1597 (2002).
237. G. Che, B. B. Lakshmi, E. R. Fisher, and C. R. Martin, *Nature* 393, 366 (1998).
238. G. Che, B. B. Lakshmi, C. R. Martin, E. R. Fisher, and R. S. Ruoff, *Chem. Mater.* 10, 260 (1998).
239. C. G. Wu and T. Bein, *Science* 266, 1013 (1994).
240. M. Lu, X.-H. Li, and H.-L. Li, *Mater. Sci. Eng.* A334, 291 (2002).
241. D. R. Cairns, N. S. Eichenlaub, and G. P. Crawford, *Mol. Cryst. Liq. Cryst.* 352, 275 (2000).
242. P. A. Kossyrev and G. P. Crawford, *Appl. Phys. Lett.* 77, 3752 (2000).
243. C. J. Brumlik and C. R. Martin, *J. Am. Chem. Soc.* 113, 3174 (1991).
244. J. D. Klein, R. D. Herrick, D. Palmer, M. J. Sailor, C. J. Brumlik, and C. R. Martin, *Chem. Mater.* 5, 902 (1993).
245. H. S. Shim, R. H. Hurt, and N. Y. C. Yang, *Carbon* 38, 29 (2000).
246. J. Yan and A. D. Rey, *Phys. Rev. E* 65, 1713 (2002).
247. R. Ondris-Crawford, G. P. Crawford, S. Zummer, and J. W. Doane, *Phys. Rev. Lett.* 70, 194 (1993).
248. A. A. Zakhidov, R. H. Baughman, Z. Iqbal, C. Cui, I. Khayrullin, S. O. Dantas, J. Marti, and V. G. Ralchenko, *Science* 282, 897 (1998).

